



**FAA CENTER OF EXCELLENCE FOR
ALTERNATIVE JET FUELS & ENVIRONMENT**

Annual Technical Report

2023

For the period

October 1, 2022 – September 30, 2023

Boston University
Georgia Institute of Technology
Massachusetts Institute of Technology
Missouri University of Science and Technology
Oregon State University
Pennsylvania State University
Purdue University
Stanford University
University of Dayton
University of Hawaii
University of Illinois
University of North Carolina
University of Pennsylvania
University of Tennessee
University of Washington
Washington State University



This work was funded by the US Federal Aviation Administration (FAA) Office of Environment and Energy as a part of ASCENT Project AJFE under FAA Award Number 13-C. Any opinions, findings, and conclusions or recommendations expressed in this material are those of the authors and do not necessarily reflect the views of the FAA or other ASCENT Sponsors.



Table of Contents

Overview Michael Wolcott and R. John Hansman, Center Directors	1
Project 001(A) Alternative Jet Fuel Supply Chain Analysis Lead Investigators: Michael Wolcott, Christina Sanders, Manuel Garcia-Perez, Xiao Zhang, Ji Yun Lee	7
Project 001(B) Alternative Jet Fuel Supply Chain Analysis Lead Investigator: Scott Q. Turn	24
Project 001(C) Alternative Jet Fuel Supply Chain Analysis Lead Investigator: Farzad Taheripour	43
Project 001(D) Alternative Jet Fuel Supply Chain Analysis Lead Investigator: Lara Fowler	50
Project 001(E) Alternative Jet Fuel Supply Chain Analysis Lead Investigators: Timothy Rials, T. Edward Yu	65
Project 001(F) Alternative Jet Fuel Supply Chain Analysis Lead Investigators: Steven R. H. Barrett, Raymond L. Speth, Florian Allroggen	81
Project 002 Understanding Changes in Aviation Emissions Due to SAF with New Combustor Technology Lead Investigator: Philip D. Whitefield	99
Project 003 Cardiovascular Disease and Aircraft Noise Exposure Lead Investigator: Junenette L. Peters	102
Project 009 Geospatially Driven Noise -estimation Module Lead Investigators: Dimitri N. Mavris, Holger Pfaender	116
Project 010 Aircraft Technology Modeling and Assessment Lead Investigators: Dimitri N. Mavris, William Crossley, Jimmy Tai, Daniel A. DeLaurentis	161
Project 018 Community Measurements of Aviation Emission Contributions to Ambient Air Quality Lead Investigator: Kevin J. Lane, Jonathan I. Levy	202
Project 019 Development of Aviation Air Quality Tools for Airshed-Specific Impact Assessment: Air Quality Modeling Lead Investigator: Saravanan Arunachalam	240
Project 022 Evaluation of FAA Climate Tools: Aviation Portfolio Management Tool (APMT) Lead Investigator: Donald Wuebbles	276
Project 023 Analytical Approach for Quantifying Noise from Advanced Operational Procedures Lead Investigator: R. John Hansman	279



Project 025 National Jet Fuels Combustion Program – Area #1: Chemical Kinetics Combustion Experiments Lead Investigator: Ronald K. Hanson	283
Project 031(A) Alternative Jet Fuels Test and Evaluation Lead Investigator: Steven Zabarnick	289
Project 033 Alternative Fuels Test Database Library Lead Investigator: Tonghun Lee	299
Project 037 CLEEN II System-level Assessment Lead Investigator: Dimitri N. Mavris, Jimmy Tai	310
Project 038 Rotorcraft Noise Abatement Procedures Development Lead Investigator: Kenneth S. Brentner	325
Project 044 Aircraft Noise Abatement Procedure Modeling and Validation Lead Investigators: R. John Hansman, Jacqueline Huynh	335
Project 046 Surface Analysis to Support AEDT Aircraft Performance Model (APM) Development Lead Investigator: Hamsa Balakrishnan, Thomas G. Reynolds	344
Project 047 Clean-Sheet Supersonic Aircraft Engine Design and Performance Lead Investigator: Steven R. H. Barrett	349
Project 049 Urban Air Mobility Noise Reduction Modeling Lead Investigator: Kenneth S. Brentner	355
Project 050 Over-Wing Engine Placement Evaluation Lead Investigators: Dimitri N. Mavris, Chung Lee	374
Project 051 Combustion Concepts for Next-Generation Aircraft Engines Lead Investigator: Steven R. H. Barrett	421
Project 052 Comparative Assessment of Electrification Strategies for Aviation Lead Investigators: Steven R. H. Barrett, Florian Allroggen, Raymond Speth	425
Project 053 Validation of Low-Exposure Noise Modeling by Open Source Data Management and Visualization Systems Integrated with AEDT Lead Investigator: Juan J. Alonso	433
Project 054 AEDT Evaluation and Development Support Lead Investigators: Dimitri N. Mavris, Michelle Kirby	463
Project 055 Noise Generation and Propagation from Advanced Combustors Lead Investigator: Timothy Lieuwen	497
Project 056 Turbine Cooling Through Additive Manufacturing Lead Investigator: Karen A. Thole, Stephen Lynch	562



Project 057 Support for Supersonic Aircraft En-route Noise Efforts in ICAO CAEP Lead Investigator: Victor W. Sparrow	581
Project 058 Improving Policy Analysis Tools to Evaluate Higher-Altitude Aircraft Operations Lead Investigators: Steven R. H. Barrett, Sebastian D. Eastham	599
Project 059(B) Jet Noise Modeling and Measurements to Support Reduced LTO Noise of Supersonic Aircraft Technology Development Lead Investigator: Krishan K. Ahuja	628
Project 059(C) Modeling Supersonic Jet Noise Reduction with Global Resolvent Modes Lead Investigator: Daniel J. Bodony	663
Project 059(D) Physics-Based Analyses and Modeling for Supersonic Aircraft Exhaust Noise Lead Investigator: Sanjiva K. Lele	674
Project 059(E) Moderate-Fidelity Simulations for Efficient Modeling of Supersonic Aircraft Noise Lead Investigators: Philip J. Morris	691
Project 060 Analytical Methods for Expanding the AEDT Aircraft Fleet Database Lead Investigators: Dimitri N. Mavris, Yongchang Li	703
Project 061 Noise Certification Streamlining Lead Investigators: Dimitri N. Mavris, Michael Balchanos	716
Project 062 Noise Model Validation for AEDT Lead Investigators: Dimitri N. Mavris, Victor W. Sparrow	761
Project 064 Alternative Design Configurations to Meet Future Demand Lead Investigators: Dimitri N. Mavris, Michelle R. Kirby	793
Project 065(A) Fuel Testing Approaches for Rapid Jet Fuel Prescreening Lead Investigator: Joshua Heyne	807
Project 065(B) Fuel Testing Approaches for Rapid Jet Fuel Prescreening Lead Investigator: Tonghun Lee	818
Project 066 Evaluation of High Thermal Stability Fuels Lead Investigator: Joshua Heyne	830
Project 067 Impact of Fuel Heating on Combustion and Emissions Lead Investigator: Robert P. Lucht, Carson D. Slabaugh	843
Project 068 Combustor Wall Cooling with Dirt Mitigation Lead Investigator: Karen A. Thole	861
Project 069 Transitioning a Research nvPM Mass Calibration Procedure to Operations Lead Investigator: Philip D. Whitefield	878



Project 070 Reduction of nvPM Emissions from Aero-Engine Fuel Injectors Lead Investigator: Wenting Sun	886
Project 071 Predictive Simulation of nvPM Emissions in Aircraft Combustors Lead Investigator: Suresh Menon	899
Project 072 Aircraft Noise Exposure and Market Outcomes in the United States Lead Investigators: R. John Hansman, Christopher R. Knittel, Steven R.H. Barrett, Jing Li, Florian Allroggen	926
Project 073 Fuel Composition Impact on Combustor Durability Lead Investigator: Scott Stouffer	932
Project 074 Low Emissions Pre-Mixed Combustion Technology for Supersonic Civil Transport Lead Investigator: Adam Steinberg	942
Project 075 Improved Engine Fan Broadband Noise Prediction Capabilities Lead Investigator: Sheryl Grace	966
Project 076 Improved Open Rotor Noise Prediction Capabilities Lead Investigators: Dimitri N. Mavris, Jimmy Tai	979
Project 077 Measurements to Support Noise Certification for UAS and UAM Vehicles and Identify Noise Reduction Lead Investigator: Eric Greenwood	1005
Project 078 Contrail Avoidance Decision Support and Evaluation Lead Investigator: Steven R. H. Barrett	1031
Project 079 Novel Noise Liner Development Enabled by Advanced Manufacturing Lead Investigator: Timothy W. Simpson	1053
Project 080 Hydrogen and Power-to-Liquid Concepts for Sustainable Aviation Fuel Production Lead Investigator: Manuel Garcia-Perez, Michael P. Wolcott, Steven R. H. Barrett, Florian Allroggen	1069
Project 082(A) Modeling of the Committee on Aviation Environmental Protection Stringency Analysis Lead Investigator: Dimitri N. Mavris, Michelle R. Kirby	1084
Project 082(B) Integrated Noise and CO ₂ Standard Setting Analysis Lead Investigator: Raymond Speth	1103
Project 083 NO _x Cruise/Climb Metric System Development Lead Investigator: Raymond Speth	1107
Project 084 Noise Modeling of Advanced Air Mobility Flight Vehicles Lead Investigator: R. John Hansman	1112



Project 086 Study on the Use of Broadband Sounds to Mitigate Sleep Disruption Due to Aircraft Noise Lead Investigator: Mathias Basner	1121
Project 088 A Method for Rapidly Assessing Jet Fuel Compatibility with non-Metallic Materials Lead Investigator: John Graham	1126
Project 089 Characterization of Compositional Effects on Dielectric Constant Lead Investigator: Steven Zabarnick	1138
Project 090 World Fuel Survey Lead Investigator: Zachary West	1150
Project 091(A) Environmental Impacts of High-Altitude and Space Vehicle Emissions Lead Investigator: Raymond Speth, Steven R.H. Barrett	1154
Project 091(B) Environmental Impacts of High Altitude and Space Vehicle Emissions Lead Investigator: Donald Wuebbles	1167
Project 092 Advanced Two-Stage Turbine Rig Development Lead Investigator: Karen A. Thole	1171
Project 093(A) Collaborative Research Network for Global SAF Supply Chain Development Lead Investigator: Raymond Speth, Florian Allroggen	1181
Project 093(B) Collaborative Research Network for Global SAF Supply Chain Development: South East Asia Lead Investigator: Scott Turn	1195
Project 093(C) Collaborative Research Network for Global SAF Supply Chain Development: Latin America and Caribbean (LAC) Lead Investigator: Manuel Garcia-Perez, Michael P. Wolcott	1201
Project 094 Probabilistic Unmanned Aircraft Systems (UAS) Trajectory and Noise Estimation Tool Lead Investigator: Dimitri N. Mavris, Holger Pfaender	1208
Publications Index	1231
Funding Tables	1245



Overview

This report covers the period October 1, 2022, through September 30, 2023. The Center was established by the authority of FAA solicitation 13-C-AJFE-Solicitation. During that time the ASCENT team launched a new website, which can be viewed at ascent.aero. The next meeting(s) will be held during the months of April and May 2024.

Over the last year, the ASCENT team has made great strides in research, outreach, and education. The team's success includes the following:

- **72 active research projects***.

The projects are divided into five main categories: tools, operations, noise, emissions, and alternative fuels, with cross-cutting research in aircraft technology innovation and supersonics. See the project category descriptions for more detail on each category and a summary of the projects. Funding for these projects comes from the FAA in partnership with Transport Canada.

*Note that projects 001, 059, 065, 082 and 093 include several separately funded projects within a single project number. An individual report section is provided for each of these funded "sub-projects" and are titled Projects 001A-001E, 059A-059E, 065A-B, 082A-B and 093A-C.

- **203 publications, reports, and presentations by the ASCENT team.**

Each project report includes a list of publications, reports, and presentations. A comprehensive list of the publications, reports, and presentations for all projects is available in the publications index.

- **243 students participated in aviation research with the ASCENT team.**

ASCENT research projects were supported by 209 graduate students and 34 undergraduate students. Each project report includes the names and roles of the graduate and undergraduate students in the investigator's research. Students are selected by the investigators to participate in this research.

- **75 active industry partners involved in ASCENT.**

ASCENT's industry partners play an important role in the Center. Industry partners may contribute matching funds, participate on the Advisory Board, or both. Four new industry partners joined the Advisory Board in 2023. Advisory Board members provide insight into the view of stakeholders, advice on the activities and priorities of the Center's co-directors and ensure research will have practical application. The committee does not influence FAA policy. Industry partners also play a direct role in some of the research projects, providing matching funds, resources, and expertise to the project investigators.

Leadership

Dr. Michael Wolcott
Center Director and Technical Lead for Alternative Jet Fuels Research
Washington State University
(509) 335-6392, wolcott@wsu.edu

Dr. R. John Hansman
Center Co-Director and Technical Lead for Environmental Research
Massachusetts Institute of Technology
(617) 253-2271, rjhans@mit.edu

Dr. Jonathan Male
Assistant Vice Chancellor for Research and Director of National Laboratory Partnerships
Washington State University
jonathan.male@wsu.edu

Anna Oldani
Chief Scientific and Technical Advisor for Environment and Energy, Office of Environment and Energy
Federal Aviation Administration
anna.oldani@faa.gov





Research Topics

Research projects within ASCENT are divided into five categories: alternative fuels, emissions, noise, operations, tools, aircraft technology innovation and supersonics. The list below includes all ASCENT funded research projects. This report includes research on active projects only. Reports for projects marked as COMPLETE are available on the ASCENT website at: <https://ascent.aero/project/>.

Alternative Fuels

The development of alternative jet fuels (AJFs) -- or sustainable aviation fuels (SAF) -- is of great interest to an array of aviation stakeholders, including aircraft and engine manufacturers and airlines. Alternative fuels that are produced from non-fossil feedstocks provide sustainable jet fuel alternatives that not only help alleviate environmental impacts from aviation emissions but can also create jobs in rural areas and lessen our reliance on foreign petroleum supplies.

Effective research and development, co-funded by the federal government and industry, enables SAF development by reducing the costs of producing renewable fuel. ASCENT research provides the scientific expertise and data to evaluate the environmental benefits associated with these sustainable fuels. ASCENT's collaborative R&D activities focuses on evaluating promising sustainable aviation fuel pathways to ensure environmental and social benefits, reduce technical uncertainties, inform aviation emission policies, and promote private sector investment in production.

Projects include:

- 001A-F - Alternative Jet Fuel Supply Chain Analysis
- 025 - National Jet Fuels Combustion Program - Area #1: Chemical Kinetics Combustion Experiments
- 026 - (COMPLETE) - National Jet Fuels Combustion Program - Area #2: Chemical Kinetics Model Development and Evaluation
- 027 - (COMPLETE) National Jet Fuels Combustion Program - Area #3: Advanced Combustion Tests
- 028 - (COMPLETE) National Jet Fuels Combustion Program - Area #4: Combustion Model Development and Evaluation
- 029A - (COMPLETE) National Jet Fuels Combustion Program - Area #5: Atomization Tests and Models
- 030 - (COMPLETE) National Jet Fuels Combustion Program - Area #6: Referee Swirl-Stabilized Combustor Evaluation/Support
- 031 - Alternative Jet Fuels Test and Evaluation
- 032 - (COMPLETE) - Worldwide LCA of GHG Emissions from Petroleum Jet
- 033 - Alternative Fuels Test Database Library
- 034 - (COMPLETE) National Jet Fuels Combustion Program - Area #7: Overall Program Integration and Analysis
- 052 - Comparative Assessment of Electrification Strategies for Aviation
- 065 - Fuel Testing Approaches for Rapid Jet Fuel Prescreening
- 066 - Evaluation of High Thermal Stability Fuels
- 067 - Impact of Fuel Heating on Combustion and Emissions
- 073 - Combustor Durability with Alternative Fuel Use
- 080 - Hydrogen and Power-to-Liquid (PtL) Concepts for SAF Production
- 088 - A Method for Rapidly Assessing Jet Fuel Compatibility with non-Metallic Materials
- 089 - Characterization of Compositional Effects on Dielectric Constant
- 090 - World Fuel Survey
- 093 A-C - Collaborative Research Network for Global SAF Supply Chain Development

Emissions

The demand for passenger and cargo air transportation has grown rapidly over the last several decades. According to the U.S. Bureau of Transportation Statistics (BTS), in 2023 there were 946 million domestic air travelers. The 2024 FAA Aerospace Forecast calls for U.S. carrier domestic passenger growth over the next 20 years to average 2.5 percent per year. This staggering growth is accompanied by airport expansions and increases in emissions from aircraft, ground services equipment, and vehicle traffic on and near airports. The increases in these activity-based emissions impact the air quality around airports, cumulatively contribute to global climate change, and can negatively affect human health.

ASCENT researchers are analyzing data and improving predictive models to understand the effects of aircraft and ground vehicle emissions, create and refine emission-based analytical techniques at both airport-specific and global scales, and assess how policy changes affect emissions and its impacts.



Projects include:

- 002 - (COMPLETE) Ambient Conditions Corrections for Non-Volatile PM Emissions Measurements
- 013 - (COMPLETE) - Micro-Physical Modeling & Analysis of ACCESS 2 Aviation Exhaust Observations
- 014 - (COMPLETE) - Analysis to Support the Development of an Aircraft CO₂ Standard
- 018 - Community Measurement of Aviation Emission Contribution of Ambient Air Quality
- 019 - Development of Improved Aviation Emissions Dispersion Capabilities for AEDT
- 020 - (COMPLETE) - Development of NAS wide and Global Rapid Aviation Air Quality
- 021 - (COMPLETE) - Improving Climate Policy Analysis Tools
- 022 - Evaluation of FAA Climate Tools
- 024 - (COMPLETE) - Emissions Data Analysis for CLEEN, ACCESS, and Other Recent Tests
- 039 - (COMPLETE) - Naphthalene Removal Assessment
- 047 - Clean Sheet Supersonic Aircraft Engine Design and Performance
- 048 - (COMPLETE) Analysis to Support the Development of an Engine nvPM Emissions Standard
- 051 - Combustion Concepts for Next-Generation Aircraft Engines
- 052 - Comparative Assessment of Electrification Strategies for Aviation
- 058 - Improving Policy Analysis Tools to Evaluate Higher-Altitude Aircraft Operations
- 064 - Alternative Design Configurations to Meet Future Demand
- 067 - Impact of Fuel Heating on Combustion and Emissions
- 068 - Combustor Wall Cooling Concepts for Dirt Mitigation
- 069 - Transitioning a Research nvPM Mass Calibration Procedure to Operations
- 070 - Reduction of nvPM emissions via innovation in aero-engine fuel injector design
- 071 - Predictive Simulation of nvPM Emissions in Aircraft Combustors
- 074 - Low Emissions Pre-Mixed Combustion Technology for Supersonic Civil Transport
- 078 - Contrail Avoidance Decision Support and Evaluation
- 081 - Measurement and Prediction of Non-Volatile Particulate Matter (nvPM) Size and Number Emissions from SAF and Conventional Aviation Fuels
- 082 A-B - Integrated Noise and Emissions CO₂ Standard Setting Analysis
- 083 - NO_x Cruise/Climb Metric System Development
- 091 A-B - Environmental Impacts of High Altitude and Space Vehicle Emissions

Noise

ASCENT researchers are working to fully understand community noise impacts of aviation including how aircraft noise affects human health and wellbeing and how elements such as motion and atmospheric parameters affect noise. They are also creating tools for analyzing aircraft noise, informing policies related to noise, and conducting outreach and education about aircraft noise reduction efforts.

Projects include:

- 003 - Cardiovascular Disease and Aircraft Noise Exposure
- 004 - (COMPLETE) - Estimate of Noise Level Reduction
- 005 - (COMPLETE) - Noise Emission and Propagation Modeling
- 007 - (COMPLETE) - Civil, Supersonic Over Flight, Sonic Boom (Noise) Standards Development
- 008 - (COMPLETE) - Noise Outreach
- 009 - Geospatially Driven Noise Estimation Module
- 017 - (COMPLETE) -Pilot Study on Aircraft Noise and Sleep Disturbance
- 038 - Rotorcraft Noise Abatement Procedures Development
- 040 - (COMPLETE)Quantifying Uncertainties in Predicting Aircraft Noise in Real-world Situations
- 041 - (COMPLETE) Identification of Noise Acceptance Onset for Noise Certification Standards of Supersonic Airplane
- 042 - (COMPLETE) Acoustical Mode of Mach Cut-off
- 043 - (COMPLETE) Noise Power Distance Re-Evaluation
- 044 - Aircraft Noise Abatement Procedure Modeling and Validation
- 049 - Urban Air Mobility Noise Reduction Modeling
- 050 - Over-Wing Engine Placement Evaluation
- 053 - Validation of Low Exposure Noise Modeling by Open Source Data Management and Visualization Systems Integrated with AEDT
- 055 - Noise Generation and Propagation from Advanced Combustors



- 057 - Support for Supersonic Aircraft En-route Noise Efforts in ICAO CAEP
- 059A-E - Modeling and Measurements of Supersonic Civil Transport Jet Noise
- 061 - Noise Certification Streamlining
- 062 - Noise Model Validation for AEDT
- 063 - Parametric Noise Modeling for Boundary Layer Ingesting Propulsors
- 072 - Aircraft noise exposure and market outcomes in the US
- 075 - Improved Engine Fan Broadband Noise Prediction Capabilities
- 076 - Improved Open Rotor Noise Prediction Capabilities
- 079 - Novel Noise Liner Development Enabled by Advanced Manufacturing
- 082A-B - Integrated Noise and Emissions CO₂ Standard Setting Analysis
- 084 - Noise Modeling of Advanced Air Mobility Flight Vehicles
- 086 - Study on the use of broadband sounds to mitigate sleep disruption due to aircraft noise

Operations

Aviation operations result in fuel burn, emissions, and noise impacts. The nature and scale of these effects depends on a number of related factors, including:

- Aircraft flight paths and profiles,
- Schedule and frequency of operations, and
- Aircraft fleet mix.

ASCENT research focuses on identifying and accelerating the implementation of operational concepts that will reduce aviation environmental impacts and/or improve energy efficiency while maintaining the efficiency of the National Airspace System. The research spans multiple phases of flights and targets all environmental impact areas.

Projects include:

- 006 - (COMPLETE) - Rotorcraft Noise Abatement Operating Conditions Modeling
- 015 - (COMPLETE) - Cruise Altitude and Speed Optimization
- 016 - (COMPLETE) - Airport Surface Movement Optimization
- 023 - Analytical Approach for Quantifying Noise from Advanced Operational Procedures
- 038 - Rotorcraft Noise Abatement Procedures Development
- 044 - Aircraft Noise Abatement Procedure Modeling and Validation
- 053 - Validation of Low Exposure Noise Modeling by Open Source Data Management and Visualization Systems Integrated with AEDT
- 077 - Measurements to Support Noise Certification for UAS/UAM Vehicles and Identify Noise Reduction Opportunities

Tools

The aviation system operation involves complex interactions between many different components when aircraft are on the ground, taking off, in the air, and when landing. Aviation system operations also require the understanding of how to optimize aviation activities, which is best done by implementing advanced modeling tools.

The Federal Aviation Administration's suite of modeling tools have been developed to characterize and quantify the interdependences of aviation-related noise and emissions, impacts on human health and welfare, and the costs and market impacts to industry and consumers under varying policies, technologies, operations, and market scenarios.

The ASCENT researchers are further developing and expanding the capabilities of these modeling tools in a variety of ways, from improving the way basic physical properties are represented and effectively modeled to how new technologies will enter the aircraft fleet and identifying the benefits of such technologies.

Projects include:

- 009 - Geospatially Driven Noise Estimation Module
- 010 - Aircraft Technology Modeling and Assessment
- 011 - (COMPLETE) - Rapid Fleet-wide Environmental Assessment Capability
- 012 - (COMPLETE) - Aircraft Design and Performance Assessment Tool Enhancement



- 035 - (COMPLETE) - Airline Flight Data Examination to Improve flight Performance Modeling
- 036 - (COMPLETE) - Parametric Uncertainty Assessment for AEDT2b
- 037 - CLEEN II Technology Modeling and Assessment
- 040 - (COMPLETE) - Quantifying Uncertainties in Predicting Aircraft Noise in Real-world Situations
- 043 - (COMPLETE) Noise Power Distance Re-Evaluation (NPD+C) to Include Airframe Noise in AEDT
- 045 - (COMPLETE) Takeoff/Climb Analysis to Support AEDT APM Development
- 046 - (COMPLETE) Surface Analysis to Support AEDT APM Development
- 049 - Urban Air Mobility Noise Reduction Modeling
- 053 - Validation of Low Exposure Noise Modeling by Open Source Data Management and Visualization Systems Integrated with AEDT
- 054 - AEDT Evaluation and Development Support
- 058 - Improving Policy Analysis Tools to Evaluate Higher-Altitude Aircraft Operations
- 060 - Analytical Methods for Expanding the AEDT Aircraft Fleet Database
- 062 - Noise Model Validation for AEDT
- 064 - Alternative Design Configurations to meet Future Demand

Aircraft Technology Innovation

The evolution of airframes and engines has resulted in modern designs that significantly reduce aviation fuel use, emissions and noise on a per-flight basis. ASCENT researchers conduct the analyses, modeling and testing required to demonstrate the viability of innovative airframe, engine and flight management technologies that reduce noise, emissions, and fuel burn. Future innovations will drive further improvements and the ASCENT research helps accelerate technology development.

Projects include:

- 010- Aircraft Technology Modeling and Assessment
- 037 - CLEEN II System Level Assessment
- 047 - Clean Sheet Supersonic Aircraft Engine Design and Performance
- 050 - Over-Wing Engine Placement Evaluation
- 051 - Combustion Concepts for Next-Generation Aircraft Engines
- 052 - Comparative Assessment of Electrification Strategies for Aviation
- 055 - Noise Generation and Propagation from Advanced Combustors
- 056 - Turbine Cooling through Additive Manufacturing
- 059 - Modeling and Measurements of Supersonic Civil Transport Jet Noise
- 063 - Parametric Noise Modeling for Boundary Layer Ingesting Propulsors
- 064 - Alternative Design Configurations to Meet Future Demand
- 066 - Evaluation of High Thermal Stability Fuels
- 067 - Impact of Fuel Heating on Combustion and Emissions
- 068 - Combustor Wall Cooling with Dirt Mitigation
- 070 - Reduction of nvPM emissions via innovation in aero-engine fuel injector design
- 071 - Predictive Simulation of Soot Emission in Aircraft combustors
- 074 - Low Emissions Pre-Mixed Combustion Technology for Supersonic Civil Transport
- 075 - Improved Engine Fan Broadband Noise Prediction Capabilities
- 076 - Improved Open Rotor Noise Prediction Capabilities
- 077 - Measurements to Support Noise Certification for UAS/UAM Vehicles and Identify Noise Reduction Opportunities
- 094 - Probabilistic Unmanned Aircraft Systems (UAS) Trajectory and Noise Estimation Tool

Supersonics

ASCENT supersonics research supports implementation of new technologies by advancing the understanding of the perception of sonic boom noise over a range of sonic boom levels, assessing Mach cut-off levels that will allow supersonic flight over land and furthering development of supersonic aircraft noise certification standards.

Projects include:

- 007 (COMPLETE) - Civil, Supersonic Over Flight, Sonic Boom (Noise) Standards Development
- 010- Aircraft Technology Modeling and Assessment
- 022 - Evaluation of FAA Climate Tools



- 041 - (COMPLETE) Identification of Noise Acceptance Onset for Noise Certification Standards of Supersonic Airplanes
- 042 - (COMPLETE) Acoustical Model of Mach Cut-off
- 047 - Clean Sheet Supersonic Aircraft Engine Design and Performance
- 057 - Support for Supersonic Aircraft Noise Efforts in ICAO CAEP
- 058 - Improving Policy Analysis Tools to Evaluate Aircraft Operations in the Stratosphere
- 059 - Jet Noise Modeling to Support Low Noise Supersonic Aircraft Technology Development
- 074 - Low Emissions Pre-Mixed Combustion Technology for Supersonic Civil Transport



Project 001(A) Alternative Jet Fuel Supply Chain Analysis

Washington State University

Project Lead Investigator

Michael P. Wolcott
Regents Professor
Department of Civil & Environmental Engineering
Washington State University
PO Box 642910
Pullman, WA 99164-2910
509-335-6392
wolcott@wsu.edu

University Participants

Washington State University (WSU)

- P.I.s: Michael P. Wolcott, Regents Professor; Christina Sanders, Acting Director, Division of Governmental Studies and Services; Manuel Garcia-Perez, Professor; Xiao Zhang, Professor; and Ji Yun Lee, Assistant Professor
- FAA Award Number: 13-C-AJFE-WaSU-023, 026
- Period of Performance: October 1, 2022 to September 30, 2023
- Tasks:
 1. Prepare and assess design cases
 2. Evaluate the most promising biorefinery concepts for alternative jet fuel (AJF) production
 3. Supplement and maintain the current inventory of biorefinery infrastructures that are useful for AJF production, as identified in the conversion design cases
 4. Perform a community social asset assessment
 5. Refine and deploy facility siting tools to determine regional demand and potential conversion sites to be used in regional analyses
 6. Perform a refinery-to-wing stakeholder assessment.
 7. Conduct a supply chain analysis
 8. Provide analytical support for regional Commercial Aviation Alternative Fuels Initiative (CAAFI) and U.S. Department of Agriculture (USDA) jet fuel projects

Project Funding Level

This project has received \$3,941,805 in FAA funding over its lifetime, \$3,666,922 in matching funds, and state-committed graduate school contributions for four PhD students. Faculty time for Michael Wolcott, Manuel Garcia-Perez, and Xiao Zhang contributes to the cost share.

Investigation Team

Washington State University

Prof. Michael Wolcott (P.I.), Tasks 3, 5, 7, and 8
Christina Sanders (co-P.I.)
Season Hoard (co-P.I.)
Prof. Manuel Garcia-Perez (co-P.I.), Tasks 1, 2, and 7
Xiao Zhang (co-P.I.), Tasks 1 and 2
Assist. Prof. Ji Yun Lee (co-P.I.)
Michael Gaffney (faculty), Tasks 4, 6
Kristin Brandt (adjoint faculty)
Dane Camenzind (staff engineer)
Lina Pilar Martinez Valencia (postdoctoral research associate)



Chenxi Wang (assistant research professor)
Kelly Nguyen (graduate student)
Fangjiao Ma (graduate student)
Claudia Marcela Valderrama (graduate student)

Collaborating Researchers

University of Tennessee

Burton English
Edward Yu

University of Hawaii

Scott Turn

Massachusetts Institute of Technology

Florian Allroggen

U.S. Department of Transportation Volpe Center

Kristin C. Lewis

Project Overview

As part of an effort to realize an “aviation system in which air traffic will move safely, swiftly, efficiently, and seamlessly around the globe,” the FAA set a series of goals and supporting outcomes, strategies, and performance metrics (Hileman et al., 2013). The goal entitled “Sustaining our Future” outlines several strategies collectively aimed at reducing the environmental and energy impacts of the aviation system. To achieve this goal, the FAA set an aspirational goal for the aviation industry to utilize one billion gallons of AJF by the year 2018. This goal was created according to economic, emission, and overall feasibility perspectives (Richard, 2010; Staples et al., 2014). Over the past year, the goals for U.S. AJF use have been updated with the Sustainable Aviation Fuel (SAF) Grand Challenge that the United States will produce and use three billion gallons of SAF by 2030, with an increase to 35 billion gallons in 2050 and a minimum reduction of 50% in lifecycle greenhouse gases (White House, 2021).

Most approaches to supply chain analyses for AJF optimize feedstock-to-refinery and refinery-to-wing transportation logistics (Bond et al., 2014). One of the greatest barriers to large-scale AJF production is the high capital of greenfield facilities, which translates to risk in the investment community (Huber et al., 2007). The cost of cellulosic ethanol plants ranges from \$10 to \$13 per gallon capacity (Hileman & Stratton, 2014); moreover, the additional processing steps required to convert the intermediate to a drop-in AJF could increase this cost to more than \$25 per gallon capacity (Hileman, 2014).

Motivated by the realities of converting these initial commercialization efforts into second-generation AJF, researchers have considered alternative conversion scenarios, including the transitioning of existing facilities (Brown, 2013). The conversion of existing refineries to produce renewable diesel and AJF is underway at both the Martinez and Rodeo refineries in California (Marathon, 2022; Phillips 66, 2022). Research on approaches for achieving the SAF Grand Challenge goals for AJF consumption has relied on “switching” scenarios, in which existing and planned capacities are used to produce drop-in fuel (Malina, 2012). These approaches require the identification of existing industrial assets, similar to refinery conversions, that can be targeted for future AJF production. Thus, siting becomes not only an exercise for optimizing feedstock transportation but also a necessary task for aligning this critical factor with the existing infrastructure, markets within regions, and the appropriate social capital for developing this new industry (Henrich et al., 2007; Seber et al., 2014).

To date, all published AJF supply chain analyses have been limited to stand-alone jet fuel production technologies that do not generate bioproducts. Hence, future studies must consider the potential techno-economic and environmental benefits of using the existing industrial infrastructure and the production of co-products with respect to the development of jet fuel production scenarios.

Design cases of stand-alone AJF production facilities will be used in supply chain evaluations. Social asset modeling is not well developed, and efforts are likely to be hampered by difficulties in quantifying social assets when compared with improved environmental performance or reductions in AJF costs, which may be better observed by optimizing economic and environmental constraints. However, the community characteristics of a potential site must be considered when



determining preferred locations for a new biorefinery. Community resistance or enthusiasm for the AJF industry can strongly influence the success or failure of a facility (Martinkus et al., 2014; Rijkhoff et al., 2017). Thus, community social asset modeling efforts conducted within this project, such as those based on the Community Asset and Attribute Model (CAAM), will inform disciplinary applications and advances. Clearly, social factors can have substantial effects, either positive or negative, on project adoption and implementation, particularly in high-technology or energy-related projects (Lewis et al., 2012; Martinkus et al., 2012; Mueller et al., 2020). The consideration of social factors in site selection and implementation decisions can maximize positive social support and minimize opposition and social negatives, thereby substantially promoting the success of a project. In this regard, the CAAM originally piloted in the Northwest Advanced Renewables Alliance project was designed to provide a quantitative rating of select social factors at the county level (Martinkus et al., 2014).

Focusing on regional supply chains, this research aims to identify the key barriers that must be overcome to meet AJF targets. We will address this overall goal by developing tools to support the AJF supply chain assessment performed at the Volpe Center. Our efforts will provide facility siting analyses that assess conversion design cases combined with regional supply chain assets and social capacity assessments for communities to act collectively toward development goals. Finally, a refinery-to-wing stakeholder assessment will support modeling and accounting of AJF distribution for downstream fuel logistics.

References

- Bond, J. Q., Upadhye, A. A., Olcay, H., Tompsett, G. A., Jae, J., Xing, R., Alonso, D. M., Wang, D., Zhang, T., Kumar, R., Foster, A., Sen, S. M., Maravelias, C. T., Malina, R., Barrett, S. R. H., Lobo, R., Wyman, C. E., Dumesic, J. A., & Huber, G. W. (2014). Production of renewable jet fuel range alkanes and commodity chemicals from integrated catalytic processing of biomass. *Energy Environ. Sci.*, 7(4), 1500–1523. <https://doi.org/10.1039/C3EE43846E>
- Brown, N. (2013). *FAA Alternative Jet Fuel Activities*. Overview. Presented to: CLEEN Consortium.
- Henrich, E. (2007). *The status of FZK concept of biomass gasification*. 2nd European Summer School on Renewable Motor Fuels. Warsaw, Poland.
- Hileman, J. I., De la Rosa Blanco, E., Bonnefoy, P. A., & Carter, N. A. (2013). The carbon dioxide challenge facing aviation. *Progress in Aerospace Sciences*, 63, 84–95. Doi: [10.1016/j.paerosci.2013.07.003](https://doi.org/10.1016/j.paerosci.2013.07.003)
- Hileman, J. I., & Stratton, R. W. (2014). Alternative jet fuel feasibility. *Transport Policy*, 34, 52–62. Doi: [10.1016/j.tranpol.2014.02.018](https://doi.org/10.1016/j.tranpol.2014.02.018)
- Hileman, J. (2013). *Overview of FAA alternative jet fuel activities*. Presentation to the Biomass R&D Technical Advisory Committee, Washington DC.
- Huber, G. W., & Corma, A. (2007). Synergies between bio- and oil refineries for the production of fuels from biomass. *Angewandte Chemie International Edition*, 46(38), 7184–7201. Doi: [10.1002/anie.200604504](https://doi.org/10.1002/anie.200604504)
- Lewis, K., Mitra, S., Xu, S., Tripp, L., Lau, M., Epstein, A., Fleming, G., & Roof, C. (2012). Alternative jet fuel scenario analysis report. Publication No. DOT/FAA/AEE/2011-05. (<http://ntl.bts.gov/lib/46000/46500/46597/DOT-VNTSC-FAA-12-01.pdf>) (Retrieved on 2014-07)
- Malina, R. (2012). *HEFA and F-T jet fuel cost analyses*. Laboratory for Aviation and the Environment. MIT.
- Marathon (2022). *Martinez Renewable Fuels*. <https://www.marathonmartinezrenewables.com/>
- Martinkus, N., Kulkarni, A., Lovrich, N., Smith, P., Shi, W., Pierce, J., & Brown, S. (2012). *An Innovative Approach to Identify Regional Bioenergy Infrastructure Sites*. Proceedings of the 55th International Convention of Society of Wood Science and Technology, Beijing, China.
- Martinkus, N., Shi, W., Lovrich, N., Pierce, J., Smith, P., & Wolcott, M. (2014). Integrating biogeophysical and social assets into biomass-to-alternative jet fuel supply chain siting decisions. *Biomass and Bioenergy*, 66, 410-418.
- Mueller, D., Hoard, S., Roemer, K., Sanders, C., & Rijkhoff, S. (2020). *Quantifying the Community Capitals Framework: Strategic Application of the Community Assets and Attributes Model*. Community Development.
- Phillips 66 (2022). *San Francisco Refinery: The Evolution of Rodeo Renewed*. <https://www.phillips66.com/refining/san-francisco-refinery/>
- Rijkhoff, S. A. M., Hoard, S. A., Gaffney, M. J., & Smith, P. M. (2017). Communities ready for takeoff Integrating social assets for biofuel site-selection modeling. *Politics and the Life Sciences: The Journal of the Association for Politics and the Life Sciences*, 36(1), 14–26. PMID: 28884650
- Richard, T.L. (2010). Challenges in scaling up alternative jet fuels infrastructure. *Science*, 329:793.
- Seber, G., Malina, R., Pearlson, M. N., Olcay, H., Hileman, J. I., & Barrett, S. R. H. (2014). Environmental and economic assessment of producing hydroprocessed jet and diesel fuel from waste oils and tallow. *Biomass and Bioenergy*, 67, 108–118. Doi: [10.1016/j.biombioe.2014.04.024](https://doi.org/10.1016/j.biombioe.2014.04.024)

Staples, M. D., Malina, R., Olcay, H., Pearlson, M. N., Hileman, J. I., Boies, A., & Barrett, S. R. H. (2014). Lifecycle greenhouse gas footprint and minimum selling price of renewable diesel and jet fuel from fermentation and advanced fermentation production technologies. *Energy Environ. Sci.*, 7(5), 1545–1554. Doi: [10.1039/C3EE43655A](https://doi.org/10.1039/C3EE43655A)

White House (2021). FACT SHEET: Biden Administration Advances the Future of Sustainable Fuels in American Aviation. <https://www.whitehouse.gov/briefing-room/statements-releases/2021/09/09/fact-sheet-biden-administration-advances-the-future-of-sustainable-fuels-in-american-aviation/>

Task 1 – Prepare and Assess Design Cases

Washington State University

Objectives

In previous years, our team has worked toward completing reviews and final reports of design cases for six stand-alone AJF technologies (Table 1) and four relevant industries (sugarcane, pulp and paper, corn ethanol, and petroleum refineries). The status of each stand-alone AJF techno-economic analysis (TEA) and report is shown in Table 1. Results on pyrolysis and alcohol-to-jet (ATJ) pathways have been published in the referenced peer-reviewed journals. The work conducted from October 1, 2021 to September 30, 2022 focused on the following tasks:

1. Complete a detailed analysis of a “catalytic hydrothermolysis pathway for jet fuel production,” including two publications.
2. Conduct a detailed analysis of a new AJF pathway for hydrothermal liquefaction (HTL) processing.
3. Conduct TEA on the integration of lignin co-product technologies in the ATJ pathway to determine the potential for reducing fuel costs.
4. Develop a new case report focusing on a technology review, an evaluation of lipid conversion processes (hydroprocessed esters and fatty acids [HEFA], catalytic hydrothermolysis [CH], SBI, Forge, Tyton, and decarboxylation), and new technologies for the production of alternative lipids (HTL and sugar-to-lipid).
5. Prepare manuscripts for publication.

Table 1. Evaluated stand-alone alternative jet fuel technologies.

	Literature review and design report date	Publications	Techno-economic analysis (TEA) model
Pyrolysis	Literature review based on a design report, 138 pages (2017)	<i>Energy Fuel</i> 33, 4683, 2019; <i>Fuel Process Technology</i> 195, 106140, 2019	A standardized TEA is complete and available for use by university partners.
Alcohol-to-jet (ATJ)	Literature review based on a design report, 28 pages (2015)	<i>ChemSusChem</i> 11, 3728, 2018	A standardized TEA is complete and available for use by partners.
Synthetic kerosene and synthetic aromatic kerosene (SK-SKA)	Literature review based on a design report, 36 pages (2015)	Manuscript based on the case design report in preparation	This work was based on a Sasol process, for which we have not found any significant development since 2016. Because of a lack of adequate process information/data on SK-SKA production from renewable feedstock, we are not able to build a reliable TEA.
Direct sugar-to-hydrocarbon	Literature review based on a design report, 88 pages (2017)	<i>Biomass and Bioenergy</i> 145:105942, 2021	A standardized TEA is complete and available for use by partners.
Virent BioForming process	Literature review based on a design report, 46 pages (2015)	<i>Biomass and Bioenergy</i> 145:105942, 2021	A standardized TEA is complete and available for use by partners.
Catalytic hydrothermolysis (CH)	Literature review based on a design report, 35 pages (2018)	<i>Renewable and Sustainable Energy Reviews</i> 115:111516, 2021; <i>Data in Brief</i> 39:107514, 2021	A standardized TEA is complete and has been posted on the Washington State University repository.
Gasification Fischer Tropsch (GFT)	No literature review conducted	<i>Biomass and Bioenergy</i> 145:105942, 2021	A standardized TEA is complete and available for use by partners.



Microchannel GFT (microGFT)	No exhaustive literature review written; capital costs found in the open literature for microchannel FT deemed unreliable	Capital cost results deemed unreliable	A standardized microGFT TEA was completed; however, the cost information is considered unreliable.
Hydroprocessed esters and fatty acids (HEFA)	No literature review conducted	<i>Biomass and Bioenergy</i> 145:105942, 2021	A standardized TEA is complete and available for use by partners.

Research Approach

Background

We have conducted a detailed literature review and prepared design case reports on six AJF pathways, including pyrolysis, ATJ, synthetic kerosene, direct sugar-to-hydrocarbon, Virent BioForming, and CH. We have also collected data from the literature to conduct TEAs for these pathways. The results from these design cases were applied in the development of supply chains and the identification of synergies that may eventually lead to the construction of integrated AJF production systems that take advantage of the infrastructure in a given region. An analysis of the locations of existing infrastructure demonstrated that the United States can be divided into regions according to the dominant biomass. Thus, we believe that the generation of advanced biorefinery concepts focused on petroleum refineries, pulp and paper mills, sugarcane mills, and corn ethanol mills is a viable approach for evaluating the synergy among AJF pathways, existing infrastructure, and co-products. We can then compare the biorefinery concepts developed for each technology to identify the most promising approach, which can subsequently be used in supply chain analyses.

Stand-alone design case reports were generated by reviewing relevant research in the academic literature and public information provided by commercial entities developing the corresponding technology. The published manuscripts were subjected to an industrial expert review. The reports provide details regarding the processes involved in each conversion pathway and outline the technology readiness and particular barriers to implementation. Publicly available information regarding the commercial processes and research literature will provide a foundation of information to be used in modeling efforts. In cases lacking detailed process engineering information, new models will be built to estimate the parameters needed to complete assessments such as techno-economic modeling and supply chain modeling. Aspen Plus primarily generates process models and details, including mass balances, energy balances, energy requirements, and equipment size and cost. These results will also provide the basis for a comparative analysis of design cases, which will identify the key advantages and markets for each technology.

Each design case has the following components:

- Feedstock requirements
- Companies developing/commercializing the technology
- Current locations of units in the United States and worldwide
- Block and flow diagram of the technology
- Unit operations and process conditions (reactor type, separation unit type, catalysts, product yield, and jet fuel yield)
- Properties of the produced jet fuel
- Identification of potential intermediates
- Current and potential uses of wastes and effluents
- Developed co-products
- Potential methods for coprocessing intermediates, wastes, and co-products by using existing infrastructure (e.g., petroleum refineries or pulp and paper mills)
- Preliminary TEA
- Technological challenges and gaps

We have submitted technical reports and supplementary Microsoft Excel files with mass and energy balances and TEAs for the pathways listed below. Furthermore, we have conducted a strategic analysis to identify the overall weaknesses of the technologies under study. All files are available on shared drives for the Project 001 team members.



- Pyrolysis-bio-oil hydro-treatment concept (hydro-treated depolymerized cellulosic jet): The TEA is complete.
- ATJ: A manuscript with information on the mass and energy balances and the TEA has been published.
- Fischer Tropsch (FT): Two design cases have been prepared for biomass gasification. The first case focuses on microreactors, and the second design case is applicable to technology based on larger standard reactors (reviews on the TEAs for gasification FT (GFT) and microchannel GFT have been completed). However, the limited reliability of the microreactor capital costs hinders the value of the practical impact of our microreactor TEA study. The TEAs are available for use by partners. In addition to gasification, the harmonized TEA was updated to include power-to-liquids with assistance from collaborators at the Massachusetts Institute of Technology.
- HEFA: A stochastic TEA was created in MATLAB and was confirmed to match the completed, deterministic TEA when the assumptions and costs match (deterministic TEA review completed). The TEA is now available for use.
- CH: The TEA is complete.

Major progress has been made on the analysis of corn ethanol, sugarcane, and petroleum refinery infrastructure that could support jet fuel production. A manuscript on the conversion of corn ethanol mills was published in *Biomass and Bioenergy*. Two additional manuscripts on repurposing either sugarcane mills or petroleum refineries to reduce AJF production costs were also published.

We have worked with the Pacific Northwest National Laboratory and completed a case design report on HTL for AJF conversion.

A summary manuscript reviewing several lipid conversion pathways, including SBI, Forge, Tyton, decarboxylation, and coprocessing, entitled “Lipid and Bio-processing Technologies: An Insight into Bioconversion Potential of Process Intensification and Continuous Flow-Through Reaction (PICFTR), Lipid to Hydrocarbon (LTH) and TYTON Bioenergy” has been prepared.

Milestones

A Microsoft Excel file with TEAs for all AJF technologies has been completed, and design cases for the corn ethanol and sugarcane industries have been completed. A detailed analysis entitled “Catalytic Hydrothermolysis Pathway for Jet Fuel Production” has been completed, and a manuscript entitled “Jet Fuel Design Case: Hydrothermal Liquefaction Case Design Report” has been published. A summary report entitled “Lipid and Bio-processing Technologies: Process Intensification and Continuous Flow-Through Reaction (PICFTR), Lipid-to-Hydrocarbon (LTH), Tyton, Decarboxylation and Coprocessing” has been produced, and corresponding manuscripts have been prepared for publication.

The five SAF technology TEAs were updated to include policies defined in the 2022 Inflation Reduction Act. Users can now model a variety of policy time horizons, values, and company structure scenarios. Specifically, both a blender tax credit and a production tax credit can be included with starting and ending at user-defined timelines.

Major Accomplishments

A manuscript entitled “Economic Analysis of Catalytic Hydrothermolysis Pathway for Jet Fuel Production” has been published in *Renewable and Sustainable Energy Reviews*, and a TEA dataset on the CH pathway for jet fuel production was published in *Data in Brief* in 2021. A manuscript reporting on a preliminary TEA of biorefinery lignin for fine chemical production was published in *Green Chemistry* in 2021. We have also updated two draft manuscripts: “Hydrothermal Liquefaction Case Design Report” and “Lipid and Bio-processing Technologies: An Insight into Bioconversion Potential of Process Intensification and Continuous Flow-Through Reaction (PICFTR), Lipid to Hydrocarbon (LTH) and TYTON Bioenergy.” A manuscript entitled “Comparison of Techno-economic and Environmental Performance of Alternative Jet Fuel Production Technologies” has been prepared, reviewed, and updated in preparation for FAA review. We intend to submit these manuscripts to the FAA for review within the next four months. We are working on the construction of a TEA for lignin extraction and utilization in a biorefinery process (NREL, 2018).

We have assisted the International Civil Aviation Organization (ICAO), Committee on Aviation Environmental Protection (CAEP) through participation in the Fuel Task Group and the Long-Term Aspirational Goal Task Group. An Excel spreadsheet of publicly announced global AJF producers has been updated, and work with ICAO for integrating the historical portion of these data with their database is ongoing. In addition, a separate U.S. database that does not include ICAO-specific assumptions and data is being maintained to assist in tracking progress toward meeting the SAF Grand Challenge goals.

Six Excel spreadsheet-based TEAs have been published on the WSU repository site to make these tools publicly available for analyses. These TEAs include HEFA, ATJ, FT with both solid and gaseous feedstocks, FT feedstock preparation, pyrolysis, and CH. The TEAs are being used by other ASCENT member universities and interested industry and government parties.

Data generated from the design cases have been made available to 001A partners to assist with supply chain analysis and techno-economic modeling by improving the conversion and cost figure database values. Evaluations of the effects of process variations in the chemical properties of the generated products are being used to provide insight into the challenges that will be faced when AJFs are blended into commercial jet fuel.

Publications

None.

Outreach Efforts

During the preparation of design case reports, we have closely interacted with industrial companies, including Gevo, LanzaTech, Sky Energies, and Agrisoma (now NuSeed). These companies have also helped us review reports and draft manuscripts. Our results have been presented to the FAA, Office of the Chief Economist (OCE), Department of Energy, ICAO, and CAAFI. Six harmonized TEAs have been posted on the WSU Research Repository for public use. We have also made several presentations to graduate and undergraduate students.

Awards

None.

Student Involvement

Several graduate students (Sudha Eswaran, Kelly Nguyen, Abid Hossain Tanzil, Anamaria Paiva, and Lina Pilar Martinez Valencia) and one undergraduate student (Kitana Kaiphanliam) participated in the creation, editing, and updating of design cases for stand-alone AJF technologies, relevant existing infrastructure, and lignin co-products.

Plans for Next Period

We will focus on the following areas and plan to submit three to five manuscripts on lignin co-product analyses and AJF technology analyses. The following are the proposed manuscripts to be completed this project year:

1. Lipid and Bio-processing Technologies: Process Intensification and Continuous Flow-Through Reaction (PICFTR), Lipid-to-Hydrocarbon (LTH), Tyton, Decarboxylation, and Coprocessing
2. The Opportunity for Lignin Co-Products to Improve the Economics of Sustainable Aviation Fuel Production

We will continue to support ICAO work through participation in the CAEP Fuel Task Group.

References

National Renewable Energy Laboratory. (2018). *Process Design and Economics for the Conversion of Lignocellulosic Biomass to Hydrocarbon Fuels and Coproducts: 2018 Biochemical Design Case Update* (Publication No. NREL/TP-5100-71949). <https://www.nrel.gov/docs/fy19osti/71949.pdf>

Task 2 – Evaluate the Most Promising Biorefinery Concepts for AJF Production

Washington State University

Objectives

Continuation from previous years

We have completed our evaluation of biorefinery scenarios for AJF production using corn ethanol, sugarcane, and pulp and paper mills and petroleum refineries.

We will conduct detailed TEAs on the integration of lignin co-product technologies and the ATJ pathway to determine the potential for reducing fuel costs.

Research Approach

Background

In this task, we used design cases for existing infrastructure, AJF production technology, and identified co-products to generate new biorefinery concepts for petroleum refineries, pulp and paper mills, sugarcane mills, and corn ethanol mills. The results from this effort will allow us to identify and select the most commercially feasible biorefinery concepts. Major technical gaps or barriers to the commercialization of each biorefinery concept will also be determined from the results of this study.

The integration of process technologies will be assessed via an approach similar to that for the stand-alone design cases. The integration concepts will be developed by pairing stand-alone cases with these concepts to evaluate the economic and environmental advantages of the integration approaches. Over this period, we have conducted detailed analyses of ATJ conversion and integration with pulp mill operations. We have also investigated the potential contribution of lignin co-products to the overall process economy.

A dry-grind corn ethanol mill with a capacity of 80 million gallons of ethanol per year was studied to evaluate potential biorefinery scenarios for AJF production. Similarly, we used a sugarcane mill with a sugarcane processing capacity of 12,444 million tons per day that produces raw sugar, molasses, surplus bagasse, and surplus electricity. The petroleum refinery used as the base case processes 120,000 barrels of crude oil per day. Five AJF technologies were studied: Virent’s BioForming, ATJ, direct sugar-to-hydrocarbon, fast pyrolysis, and GFT. A standardized methodology was adopted to compare the biorefinery concepts for a dry-grind corn ethanol mill, sugarcane mill, and petroleum refinery in several integration scenarios with six jet fuel production scenarios. For all cases, we estimated the fuel minimum selling price (MSP) and greenhouse gas emissions.

A manuscript on the integration of ATJ technologies with pulp mill infrastructure was published. Three additional manuscripts were published with results for corn ethanol mills, sugarcane mills, and petroleum refineries.

The next step in our analysis is to use a p-graph to generate and rank biorefinery concepts utilizing a database of SAF technological pathways built from a database of unitary operations created by our team. A PhD student (Claudia Marcela Valderrama) has been hired to work on the integration and construction of the database and the use of p-graphs to create new unit operations.

This year, we have started to investigate methanol-to-SAF conversion technology. We have established an Aspen Plus process model based on current technical processes for aviation fuel production in conventional refineries as well as the integration of methanol into an existing ATJ fuel process (Figure 1). There are three major unit operations in methanol for SAF processing: olefination of methanol, hydrogenation of oligomers, and fractionation of aviation fuel base stock. The UOP/Hydro process for the olefination of methanol was referenced to generate C2 and C3 olefins as input feedstocks for the oligomerization reaction. The oligomerized products are then hydro-treated to be used as the precursors for SAF. We plan to publish a review paper on methanol-to-SAF process development.

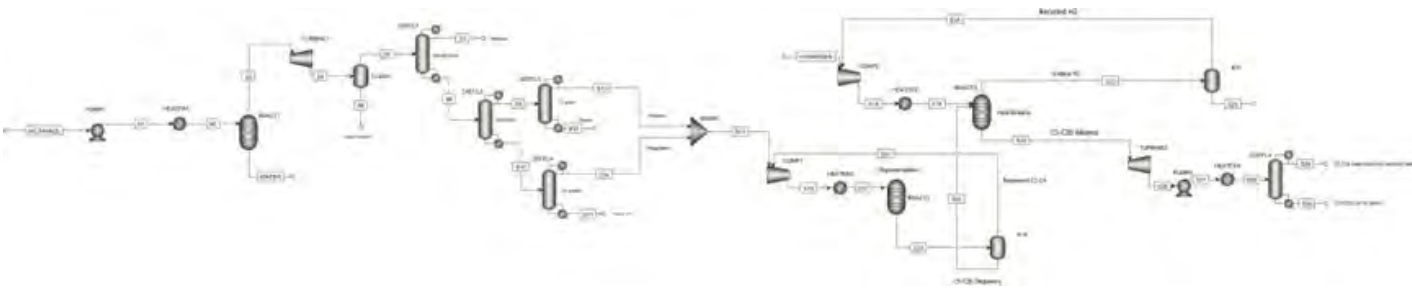


Figure 1. Aspen Plus flow sheet for methanol-to-aviation-fuel base stocks.

Major Accomplishments

None.

Publications

None.

Outreach Efforts

None.

Awards

None.

Student Involvement

Graduate students (Senthil Subramaniam, Kelly Nguyen, Abid Hossain Tanzil, Lina Martinez Valencia, and Anamaria Paiva) have received training in this project. An undergraduate student, Kitana Kaiphanliam, funded under a National Science Foundation Research Experience for Undergraduates grant, assisted in building techno-economic models for co-product production scenarios.

Senthil Subramaniam, who has been supported by this project, graduated with a PhD degree from WSU (December 2020).

Kelly Nguyen, who has been supported by this grant, graduated with a Master's degree from WSU (May 2020).

Abid Hossain Tanzil submitted and defended a PhD dissertation during the fall 2020 semester.

Plans for Next Period

In the next period, Dr. Zhang's team will complete a preliminary TEA analysis of methanol-to-SAF conversion and prepare a draft review paper for FAA internal review. Dr. Garcia-Perez's team will work to generate new biorefinery systems using p-graphs.

Task 3 – Supplement and Maintain the Current Inventory of Biorefinery Infrastructures That Are Useful for AJF Production, as Identified in the Conversion Design Cases

Washington State University

Objective

This task requires periodic evaluation of the databases to add new facilities or update the status of closed facilities in each category to ensure that the geospatially specific assets are current.

Research Approach

The use of existing infrastructure assets is a key component of retrofit approaches for advances in this industry. To differentiate between the relative values of various options, the specific assets must be valued with respect to their potential use within a conversion pathway. Regional databases of industrial assets that might be utilized by a developing AJF industry have been assessed on the national level. These baseline databases have been compiled from a variety of sources, including industry associations, universities, and news outlets. These databases will be expanded, refined, and validated as the conversion design cases indicate additional needs for regional analyses.

Milestones

National databases have been compiled, geolocated, validated, and shared for biodiesel, corn ethanol, energy pellet, pulp and paper, and sugar mill production. We have evaluated the databases as necessary to add new facilities or to change the status of closed facilities in each category, to ensure that the geospatially specific assets are current.

The geospatial infrastructure data were converted for use in supply chain resiliency models. Tools were updated for transportation cost modeling, which should lead to future improvements.

Major Accomplishments

National databases have been compiled, validated, and shared with the 001A teams. All metadata are available for use in regional analyses.

Publications

None.

Outreach Efforts

None.

Awards

None.

Student Involvement

None.

Plans for Next Period

None.

Task 4 – Update CAAM Measures

Washington State University

Objective

The objective of this task is to update the CAAM with the latest available data.

Research Approach

Based on a community capitals framework, we created the CAAM, which provides quantitative indicators of four social assets: social, cultural, human, and political capital. The CAAM provides quantitative proxy measures of qualitative concepts for initial site-selection assessments. Variations of the model have been applied to the Pacific Northwest, Idaho, Montana, Colorado, and Wyoming. Manuscripts on applications of the CAAM have been published in *Community Development, Politics and Life Sciences, Biomass & Bioenergy*, and *Frontiers in Energy Research*. The CAAM is currently being updated with the latest available data, with plans to make the CAAM more publicly accessible for use. As the social capital data have not been updated for several years, the research team is working on updating the data or creating our own measures to be validated in future use.

Milestones

Political capital and human capital data have been updated, and alternative social capital data sources have been investigated. The new U.S. Census resilience measure has also been reviewed to determine if/how this measure should be incorporated into the CAAM.

Major Accomplishments

None.

Publications

None.

Outreach Efforts

None.

Awards

None.

Student Involvement

Nana Bamea Kyei-Boadu (School of Economic Sciences, WSU) worked on reviewing the Census resilience measure and collected data for the capitals.

Plans for Next Period

We will finalize our update of the CAAM and work to make the CAAM more useable for the public.

Task 5 – Refine and Deploy Facility Siting Tools to Determine Regional Demand and Potential Conversion Sites to be Used in Regional Analyses

Washington State University

Objective

This task's objective is to develop tools for siting potential conversion facilities. Two primary tools are needed for this task: a generalized tool to site initial locations that meet the needs of a specific conversion facility type and a second tool to select optimal conversion facility sites from the initial set of locations.

Research Approach

We began developing a geospatial siting pre-selection (GSP) tool in early 2019. This tool is a Python-based script that automates ArcGIS to produce points representing locations that suit the needs of a conversion facility. The GSP tool uses a combination of buffer and cost datasets. Buffer datasets ensure that a candidate is sited in proximity to the necessary infrastructure, such as roads, rails, and natural gas pipelines. Because the candidate set generated by using only buffers will be very large, cost datasets have been added to distinguish candidates from each other. Cost datasets represent geospatially variable costs, including electricity, natural gas, and transportation. In early 2020, a graphic user interface was added to the GSP tool to make it more user-friendly. An additional script was developed in 2022 to model the transportation cost inputs for the GSP tool based on the local density of feedstock, the maximum feasible travel distance from the facility for feedstock collection, and regional road characteristics. This script also includes a rudimentary user interface. In 2023, we performed a retrospective analysis of corn ethanol plants using the GSP, with the objective of performing a pseudo-validation. This study showed that the facility locations of the mature ethanol supply chain were located in areas that the GSP would have prioritized for siting, indicating that the tool is likely a good fit for other similar supply chains, such as SAF supply chains. We also performed an extensive study in 2023 to show how the number of candidates and locations of candidates affect the optimization model solution time. The results of this study showed that a small number of candidates generated by the GSP performed significantly better than the same number of points laid out in a square grid.

The Many-Step Transshipment Solver (MASTRS) is a Python-based script that models large supply chains across multiple levels by building and solving mixed-integer linear programming problems. The model starts with feedstock spread across many locations and then models the distribution and conversion of feedstock into biofuels and other co-products through multiple levels of intermediate facilities that may include temporary storage, pre-treatment, and fuel production, before new products are sent to their destinations. Intermediate facilities may include existing facilities or new candidate facilities that are generated by the GSP tool. The MASTRS output shows the flow of materials throughout the supply chain and the most cost-efficient capacities and locations for new facilities.

The modeling combination of GSP and MASTRS scripts has been implemented for several regional supply chains. MASTRS was first implemented for the Pacific Northwest oilseed-to-jet-fuel supply chain in 2018. Since 2019, the GSP and MASTRS scripts have been used together for two supply chain models for both the production of jet fuel from forest residuals and lumber production byproducts in the Pacific Northwest. The first supply chain model uses single-stage conversion at integrated biorefineries, and the second supply chain model is a multi-stage model with distributed preprocessing facilities.

Milestones

The GSP and MASTRS tools have undergone continual development to become more practical. Along with the expansion of tool capabilities, substantial improvements have been made regarding tool accessibility for new potential users.

Major Accomplishments

None.

Publications

None.

Outreach Efforts

None.

Awards

None.

Student Involvement

None.

Plans for Next Period

We plan to begin the process for publishing manuscripts that define the GSP and MASTRS tools. We will continue implementing the GSP and MASTRS tools in regional supply chain analyses and will complete a supply chain analysis for the Bioenergy Alliance Network of the Rockies (BANR).

Task 6 – Perform a Refinery-to-Wing Stakeholder Assessment

Washington State University

The full report for this task is provided in the report for Award No. 13-C-AJFE-PSU-002.

Objective

We will extend the stakeholder assessment to a limited sample of informed stakeholders in the remaining sections of the country to provide insight into market and industry dynamics, with the aim of optimizing successful outcomes.

Research Approach

A national survey of airport management, fixed-base operators, aviation fuel handlers, and relevant airlines was completed in 2019 to assess opinions on factors impacting the adoption and diffusion of AJF. Unfortunately, low response rates impacted data collection and analysis.

Milestones

None.

Major Accomplishments

None.

Publications

None.

Outreach Efforts

None.

Awards

None.

Student Involvement

None.

Plans for Next Period

We plan to complete an updated publication based on national results.

Task 7 – Conduct a Supply Chain Analysis

Washington State University and U.S. Department of Transportation Volpe Center

Objective

WSU and Volpe have each developed modeling tools that apply transshipment optimization to model the geospatial layout of developing supply chains. A comparison of these tools would be useful to identify the strengths and weaknesses of each tool.

The objective of Task 7 is to develop a simulation framework for assessing supply chain risk, aimed at providing a quantitative basis for risk-informed decisions on supply chain design and management. To achieve this objective, WSU has developed various models and tools that simulate natural hazards, their interactions with supply chain components, and potential effects on supply chain system performance.

Research Approach

Focusing on the use of woody-biomass-to-jet-fuel conversion via fast pyrolysis and the upgrading of a supply chain centered in the northern Rockies, a series of comparison studies was conducted by using optimization tools from Volpe and WSU. Each modeling approach was required to determine sites for new pyrolysis depots and upgrading refineries. Forest production data were provided by the land use and resource allocation (LURA) model from the University of Idaho. Pyrolysis depot locations were selected by candidate generation tools included in each approach, and existing petroleum refineries were used as candidates for upgrading refineries. Cities, ports, and airport hubs throughout the U.S. West Coast and Rocky Mountain regions were used as markets for road transportation fuel, bunker fuel, and jet fuel.

Probabilistic wildfire risk assessment

The development of a wildfire risk assessment platform for supply chains requires highly complex tasks that integrate sequential modules, including wildfire simulation, vulnerability assessment, and supply chain analysis, as illustrated in Figure 2. In the wildfire simulation module, we have developed a set of machine-learning models to estimate wildfire likelihood and to model fire growth and suppression. In the vulnerability assessment module, a retrospective approach has been taken to establish a statistical link between potential explanatory variables and supply chain component failures. Finally, the last module has incorporated the impacts of fires on components into supply chain analysis to assess network-wide risks. The outputs from this platform can be used to support risk-informed decisions on cost-effective, wildfire-resilient supply chain layout and operation.

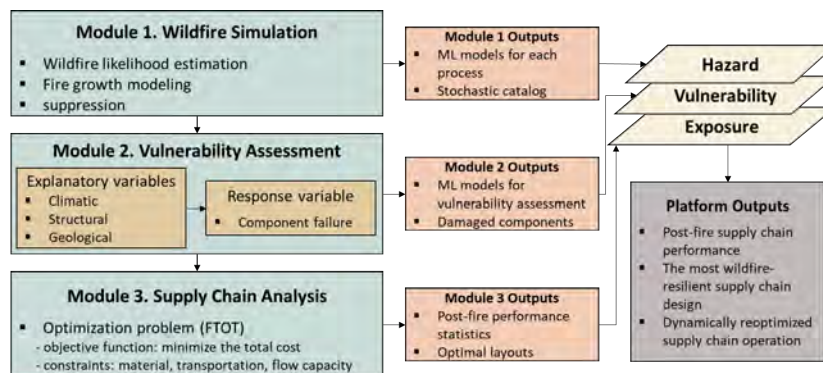


Figure 2. Procedure for the wildfire risk assessment platform for supply chains. FTOT: Freight and Fuel Transportation Optimization Tool; ML: machine learning.

Milestones

None.

Major Accomplishments

The WSU MASTRS and Volpe Freight and Fuel Transportation Optimization Tool were compared for siting analyses in the BANR region. Similar and differing modeling assumptions were identified, and the appropriate model for a given objective was determined.

We published a review on the selection and cost estimation of commercially available equipment involved in the collection and adequation of feedstock. The publication includes aggregated information regarding equipment cost, energy consumption, efficiency, feedstock storage, and transportation systems. Five feedstock types for producing AJF were studied: (1) agricultural residues and grasses, (2) forest residues, (3) urban wood waste, (4) oilseeds, and (5) fats, oils, and greases.

A paper entitled “Multi-component resilience assessment framework for a supply chain system” was published in April 2023 in *Sustainability*.

Publications

Zhao, J., Lee, J.Y., Camenzind, D., Wolcott, M.P., Lewis, K.C., & Gillham, O. (2023). Multi-component resilience assessment framework for a supply chain system. *Sustainability*, 15(7), 6197.

Outreach Efforts

None.

Awards

None.

Student Involvement

Dane Camenzind, MS in Environmental Engineering, WSU, graduated in September 2019 and is currently employed by WSU as an operations research engineer.

Fangjiao Ma, PhD candidate in Civil Engineering, WSU, graduated in December 2023. In October 2023, he started his new position as a postdoctoral research fellow at the National Oceanic and Atmospheric Administration Cooperative Institute for Severe and High-Impact Weather Research and Operations at the University of Oklahoma.

Plans for Next Period

We will utilize regional supply chain tools to assess forest residuals for SAF using pyrolysis methods, as described below for Task 8.

Task 8 – Provide Analytical Support for Regional CAAFI and USDA Jet Fuel Projects

Washington State University

Objectives

We will develop a readiness-level tool to assess the status of regional SAF production projects and will use supply chain and stand-alone design cases to support the USDA BANR project in TEA and supply chain analysis. This regional community agricultural project focuses on the use of softwood forest salvage feedstock for fuels via a catalyzed pyrolysis conversion pathway.

We will assess the regional feedstock, conversion pathways, and MSP for SAF manufactured in the northwest United States. The aim of this work, requested by the Port of Seattle, is to determine whether the Seattle-Tacoma International Airport can attain its 10% SAF goal by using SAF manufactured in the region from regional feedstock.

Research Approach

We will develop a readiness-level tool for regional projects to assess the status of developing fuel projects and to identify critical missing components. This tool will be similar in form to the CAAFI Feedstock and Fuel Readiness Levels tools and will be used to assist CAAFI in understanding the development stage of projects of interest and to assess critical gaps. In addition, we will assist the regional USDA BANR team in deploying TEA and supply chain analysis for their project. This effort will focus on the use of softwood forest salvage feedstock in a thermochemical conversion process to produce fuels and co-products.

The facility siting tools discussed in Task 5, i.e., GSP and MASTRS, have been implemented for the BANR supply chain and Port of Seattle project. The most recent model runs included feedstock and markets in an 11-state region including the West Coast and Intermountain regions. Feedstocks include forest residue from logging operations, mill residues from lumber production, and beetle-killed timber. The model results generated by MASTRS will help determine the relationships between facility location, fuel MSP, and conversion facility revenue.

The Port of Seattle project required a detailed feedstock survey for forest residuals, municipal solid waste, and lipids. Forest residuals were quantified with the LURA model for Oregon, Washington, Idaho, and Montana. Regional landfills were identified and located, scales were determined, and the remaining lifetimes were assessed to determine the most viable biorefinery location. The composition of municipal solid waste in the region was determined, as well as a method and related costs for sorting the material to match the SAF conversion pathway. Lipids were separated into two major categories: (1) waste fats, oils, and greases and (2) vegetable oil. Each feedstock was quantified and then paired with a compatible SAF conversion pathway to determine the SAF MSP by using ASCENT-developed TEAs.

U.S. federal (Renewable Fuel Standard, Inflation Reduction Act) and state (CA, OR, WA, IL) policies that incentivize the production of AJF, its co-products, or feedstock (green H₂, CO₂ capture and utilization) were mapped in a series of flow charts. An initial decision support tool was programmed using Python and converted to an Excel spreadsheet to facilitate its sharing among stakeholders. This tool enables a user to identify applicable policies for specific scenarios and returns generalized values per volume of fuel or mass of feedstock. Values can be selected for different time ranges, confidence interval values, and multiple summary statistics. The decision tool is under internal ASCENT review. Feedback and validation of the information have been requested through presentations to key groups. The output from this tool is a direct input into the harmonized TEAs to more accurately determine the economic viability of an AJF production pathway in the United States.

Information about facilities and infrastructure has been supplemented with information about the current consumption of feedstocks. Using information from the Census Bureau, Energy Information Administration, California Air Resources Board, and annual company reports, we have compiled data that show how lipid feedstocks have been consumed for fuels in the United States since HEFA fuels were first produced in the United States in 2014.

A financial model that uses a system dynamics approach was conceptualized and developed. This model analyzes the effects of federal and state policies on the financial performance of projects to produce SAF. This model can perform both deterministic and stochastic analyses. Three conversion technologies (HEFA, ATJ, FT) and nine feedstocks (fats, oils, and greases; vegetable oil; municipal solid waste; forest and agricultural residues; first- and second-generation ethanol; direct air capture; and flue gas) have been analyzed. We will assess the influence of green hydrogen, renewable electricity and gas, and carbon capture utilization and storage on the financial metrics. A draft manuscript of this work is in progress.

Technical support to the CAEP Fuel Task Group was provided. This support included (a) information compilation, analysis, development of communication material, and presentation of SAF accounting and reporting systems, (b) continuous participation in the International Air Transport Association/Airlines for America Book and Claim Collaborative Workshops, (c) identification of a possible metric option for clean energy for international aviation and parameters for fuel accounting, (d) maintenance of the global database of SAF fuel production announcements, and (e) an update to the SAF “Rules of Thumb” with the addition of two technologies: power-to-liquid and pyrolysis. For power-to-liquid technology, additional information was included to demonstrate the impact of uncertain prices of both green hydrogen and carbon dioxide. Carbon dioxide abatement costs were calculated for new and existing technology and feedstock combinations. This work was presented to Technology Production and Policy subgroup as well as the full the Fuels Task Group and was published on the ICAO website, replacing the previous version.



An assessment of the practical pathway to meet the SAF Grand Challenge was compiled and presented to various industry, academic, and government groups. A more in-depth version of this work, updated with the U.S. production database and related summary statistics, is planned for a joint paper with the National Renewable Energy Laboratory. A draft of this paper has been started. WSU will be responsible for the short-term (2030) goal, and the National Renewable Energy Laboratory will use a Bioenergy Scenario Model to complete the long-term (2050) analysis. Both institutions are working to harmonize assumptions and methodologies to provide a cohesive overall analysis. In addition, the SAF Grand Challenge support work includes participation in a working group that is compiling existing feedstock and supply chain models and identifying gaps that need to be filled. We also completed a maximum feedstock price analysis for the OCE for SAF manufactured using HEFA. The maximum price of each analyzed feedstock was determined for a variety of policy scenarios. This work is ongoing and will be presented to ASCENT researchers and a wider OCE audience in 2024.

Milestones

We are making progress in the use of supply chain and stand-alone design cases to support the USDA BANR project in TEA and supply chain analysis. Additionally, we have supported the BANR team in creating TEAs for the technologies under consideration.

The Port of Seattle analysis and report have been completed, submitted, and presented.

A review entitled “Supply chain configuration of sustainable aviation fuel: review, challenges, and pathways for including environmental and social benefits” was published in *Renewable and Sustainable Energy Reviews*. A companion manuscript that analyzes the effect of policies that incentivize CO₂e reductions on the financial performance of AJF using municipal solid waste as feedstock and GFT was published in the *Journal of Cleaner Production*.

Major Accomplishments

We have collaborated with the USDA BANR project team and attended their annual meeting to coordinate analyses. We currently await their completion of dead wood estimates to complete the supply chain analysis. Moreover, analyses with previous forest-residue data have been successfully modeled.

The Port of Seattle feedstock and SAF assessment was completed, presented to the Port of Seattle, and released to the public.

Publications

Martinez-Valencia, L., Garcia-Perez, M., & Wolcott, M. P. (2021). Supply chain configuration of sustainable aviation fuel: Review, challenges, and pathways for including environmental and social benefits. *Renewable and Sustainable Energy Reviews*, 152, 111680. doi: [10.1016/j.rser.2021.111680](https://doi.org/10.1016/j.rser.2021.111680)

Martinez-Valencia, L., Peterson, S., Brandt, K., King, A. B., Garcia-Perez, M., & Wolcott, M. (2023). Impact of services on the supply chain configuration of sustainable aviation fuel: The case of CO₂e emission reductions in the US. *Journal of Cleaner Production*, 404, 136934.

Outreach Efforts

- Martinez-Valencia, Lina; Wolcott, Michael. 2023. SAF accounting and reporting systems. International Air Transport Association workshop. Brussels, Belgium, March 14.
- Brandt, Kristin; Wolcott, Michael; Martinez, Lina; Camenzind, Dane. 2023. Introduction to Techno-Economic Analyses. ASCENT Spring Meeting. Seattle, WA, April 25.
- Wolcott, Michael; Brandt, Kristin; Martinez, Lina. 2023. ASCENT Project 001(A): Alternate Jet Fuel Supply Chain Analysis. ASCENT Spring Meeting. Seattle, WA, April 26.
- Martinez-Valencia, Lina; Wolcott, Michael. 2023. SAF accounting and reporting systems. ICAO Assistance, Capacity-building and Training for Sustainable Aviation Fuels series. October 12.
- Fowler, Lara; Brandt, Kristin; Martinez-Valencia, Lina; Wolcott, Michael. 2023. Policy support for SAF/ASCENT Fall Meeting. Alexandria, VA, October 24.
- Turn, Scott; Camenzind, Dane; Yu, Edward. Supply Chain Introduction for Students. ASCENT Spring Meeting. Seattle, WA, April 25.
- Brandt, Kristin; Wolcott, Michael. 2023. Policy Support of Sustainable Aviation Fuel Summary of Existing U.S. Legislation. Washington Sustainable Aviation Fuel Working Group Meeting. Seattle, WA, September 28.



- Brandt, Kristin; Wolcott, Michael. 2023. ASCENT Project 001(A): Alternate Jet Fuel Supply Chain Analysis. ASCENT Spring Meeting. Seattle, WA, April 26.
- Brandt, Kristin; Wolcott, Michael. 2023. SAF Grand Challenge: A Path to 3-Billion Gallons by 2030. Biomass R&D Operations Committee Meeting. April 13.
- Brandt, Kristin; Wolcott, Michael. 2023. SAF Grand Challenge: A Path to 3-Billion Gallons by 2030. U.S. Department of Energy. April 13.
- Brandt, Kristin; Wolcott, Michael; Martínez-Valencia, Lina; Camenzind, Dane. 2023. Introduction to Techno-Economic Analyses. Bio D virtual with Columbia. April 4.
- Brandt, Kristin; Wolcott, Michael. 2023. SAF Grand Challenge: A Path to 3-Billion Gallons by 2030. U.S. OCE. March 27.
- Brandt, Kristin; Wolcott, Michael; Malina, Robert. 2023. Updated SAF “Rules of Thumb” FTG/03-WP 07. 2023. ICAO Fuel Task Group. March 9.
- Brandt, Kristin; Wolcott, Michael. 2022. SAF Grand Challenge: A Path to 3-Billion Gallons by 2030. Bio-In meeting. December 6.
- Brandt, Kristin; Wolcott, Michael. 2023. SAF Grand Challenge: A Path to 3-Billion Gallons by 2030. U.S. Federal Aviation Administration & U.S. Office of the Secretary for the U.S. Department of Transportation. June 13.

Awards

None.

Student Involvement

Dane Camenzind, MS in Environmental Engineering, WSU, graduated in September 2019 and is currently employed by WSU as an operations research engineer.

Lina Martinez, PhD in Agricultural and Biological Engineering, WSU, graduated in April 2022 and now works for WSU as a postdoctoral research associate.

Plans for Next Period

- Analysis of the BANR region is underway and will be completed in 2022.
- The Port of Seattle report will be adapted for peer-reviewed publication.



Project 001(B) Alternative Jet Fuel Supply Chain Analysis

University of Hawai'i

Project Lead Investigator

Scott Q. Turn
Researcher
Hawai'i Natural Energy Institute
University of Hawai'i
1680 East-West Rd., POST 109
Honolulu, HI 96822
808-956-2346
sturn@hawaii.edu

University Participants

University of Hawai'i (UH)

- P.I.: Scott Q. Turn, Researcher
- FAA Award Number: 13-C-AJFE-UH, Amendment 005
- Period of Performance: October 1, 2015 to August 4, 2021
- Tasks:
 - 1.1 Inform regional supply chains
 - 1.2 Identify supply chain barriers in the Hawaiian Islands
- FAA Award Number: 13-C-AJFE-UH, Amendment 007
- Period of Performance: October 1, 2016 to August 4, 2021
- Tasks:
 - 2.1 Inform regional supply chains
 - 2.2 Support Indonesian alternative jet fuel (AJF) supply initiatives
- FAA Award Number: 13-C-AJFE-UH, Amendment 008
- Period of Performance: August 1, 2017 to August 4, 2021
- Tasks:
 - 3.1 National lipid supply availability analysis
 - 3.2 Hawai'i regional project
- FAA Award Number: 13-C-AJFE-UH, Amendment 011
- Period of Performance: May 31, 2019 to August 4, 2021
- Task:
 - 4. Hawai'i regional project
- FAA Award Number: 13-C-AJFE-UH, Amendment 013
- Period of Performance: June 5, 2020 to August 4, 2021
- Task:
 - 5. Hawai'i regional project
- FAA Award Number: 13-C-AJFE-UH, Amendment 017
- Period of Performance: October 1, 2021 to September 30, 2022
- Task:
 - 6. Hawai'i regional project



- FAA Award Number: 13-C-AJFE-UH, Amendment 019
- Period of Performance: December 22, 2022 to December 31, 2023
- Task:
 7. Hawai'i regional project

Project Funding Level

Under **FAA Award Number 13-C-AJFE-UH, Amendment 005**, the Alternative Jet Fuel Supply Chain Analysis–Tropical Region Analysis project received \$75,000 in funding from the FAA and cost-share funding of \$75,000 from the State of Hawai'i.

Under **FAA Award Number 13-C-AJFE-UH, Amendment 007**, the Alternative Jet Fuel Supply Chain Analysis–Tropical Region Analysis project received \$100,000 in funding from the FAA, cost-share funding of \$75,000 from the State of Hawai'i, and \$25,000 of in-kind cost match in the form of salary support for Scott Turn from UH.

Under **FAA Award Number 13-C-AJFE-UH, Amendment 008**, the Alternative Jet Fuel Supply Chain Analysis–Tropical Region Analysis project received \$125,000 in funding from the FAA and cost-share funding of \$125,000 from the State of Hawai'i.

Under **FAA Award Number 13-C-AJFE-UH, Amendment 011**, the Alternative Jet Fuel Supply Chain Analysis–Tropical Region Analysis project received \$200,000 in funding from the FAA and cost-share funding of \$200,000 from the State of Hawai'i.

Under **FAA Award Number 13-C-AJFE-UH, Amendment 013**, the Alternative Jet Fuel Supply Chain Analysis–Tropical Region Analysis project received \$200,000 in funding from the FAA and cost-share funding of \$200,000 from the State of Hawai'i.

Under **FAA Award Number 13-C-AJFE-UH, Amendment 017**, the Alternative Jet Fuel Supply Chain Analysis–Tropical Region Analysis project received \$100,000 in funding from the FAA and cost-share funding of \$100,000 from the State of Hawai'i.

Under **FAA Award Number 13-C-AJFE-UH, Amendment 019**, the Alternative Jet Fuel Supply Chain Analysis–Tropical Region Analysis project received \$150,000 in funding from the FAA and cost-share funding of \$150,000 from the State of Hawai'i.

Investigation Team

University of Hawai'i

- Dr. Scott Turn (P.I.; Hawai'i Natural Energy Institute), All Tasks
- Dr. Trevor Morgan (assistant researcher; Hawai'i Natural Energy Institute), Tasks 1–3
- Dr. Richard Ogoshi (assistant researcher; Department of Tropical Plant and Soil Sciences), Tasks 1 and 2
- Dr. Adel H. Youkhana (junior researcher; Department of Tropical Plant and Soil Sciences), Tasks 1 and 2
- Dr. Curtis Daehler (professor; Department of Botany), Task 1
- Ms. Sharon Chan (junior researcher; Hawai'i Natural Energy Institute), Tasks 2, 5, and 7
- Mr. Gabriel Allen (undergraduate student; Department of Biochemistry, Task 2
- Dr. Jinxia Fu (assistant researcher; Hawai'i Natural Energy Institute), Task 3
- Dr. Quang Vu Bach (postdoctoral fellow; Hawai'i Natural Energy Institute), Tasks 3,4, 6, and 7
- Ms. Sabrina Summers (undergraduate student; Department of Bioengineering), Task 3
- Ms. Sarah Weber (undergraduate student; Department of Molecular Biosciences and Biotechnology), Task 3
- Mr. Taha Elwir (undergraduate student; Department of Chemistry), Task 3

Other Lead Personnel

University of Tennessee

- Prof. Tim Rials (co-P.I.)
- Prof. Burt English (co-P.I.)



Washington State University (WSU)

Prof. Michael Wolcott (P.I.)
Prof. Manuel Garcia-Perez (co-P.I.)

Volpe National Transportation Systems Center

Kristin Lewis (principal technical advisor and P.I.)

The Pennsylvania State University

Prof. Lara Fowler (P.I.)

Project Overview

The research effort under **Task 1** has two objectives. The first objective is to develop information on regional supply chains for use in creating scenarios of future AJF production in tropical regions. Outputs from this project may be used as inputs to regional supply chain analyses being developed by the FAA and Volpe Center. The second objective is to identify key barriers in regional supply chains that must be overcome to produce substantial quantities of sustainable aviation fuel (SAF) in the Hawaiian Islands and similar tropical regions.

The project goals of **Task 1** are as follows:

- Review and summarize the following:
 - The available literature on biomass feedstocks for the tropics
 - The available literature on pretreatment and conversion technologies for tropical biomass feedstocks
 - The available literature on geographic information system (GIS) datasets available for assessing AJF production systems in the tropics
- Identify AJF supply chain barriers in the Hawaiian Islands.

The research effort under **Task 2** has two objectives. The first objective is to develop information on regional supply chains for use in creating scenarios of future SAF production in tropical regions. Outputs from this project may be used as inputs to regional supply chain analyses being developed by the FAA and Volpe Center. This objective includes the development of fundamental property data for tropical biomass resources to support supply chain analysis. The second objective is to support the memorandum of understanding between the FAA and the Indonesian Directorate General of Civil Aviation to promote the development and use of sustainable alternative aviation fuels.

The project goals of **Task 2** are as follows:

- Support the Volpe Center and Commercial Aviation Alternative Fuels Initiative (CAAFI) Farm to Fly 2.0 supply chain analysis
- Use GIS-based estimates of fiber crop production potential to develop preliminary technical production estimates of jet fuel in Hawai'i
- Develop fundamental property data for tropical biomass resources
- Transmit data and analysis results to other ASCENT Project 001 researchers to support the improvement of existing tools and best practices
- Support Indonesian SAF supply initiatives

The research effort under **Task 3** has two objectives. The first objective is to support a national lipid supply availability analysis that will inform industry development and guide policy. The second objective is to conduct a targeted supply chain analysis for a SAF production facility based on the Hawai'i regional project.

The project goals of **Task 3** are as follows:

- Support ASCENT partners conducting the national lipid supply availability analysis by contributing information on tropical oilseed availability
- Evaluate supply chains for targeted waste streams and purpose-grown crops in Hawai'i to a location in the principal industrial park on the island of O'ahu

For the research effort under **Task 4**, the main objective is to conduct bench-scale testing of tropical feedstocks for use in targeted supply chain analysis for a SAF production facility based on the Hawai'i regional project initiated under Amendment 008.

The project goals of **Task 4** are as follows:

- Survey bench-scale systems available for relevant SAF conversion technology options
- Down-select from the available bench-scale systems to no more than two systems capable of conducting feedstock testing and quantifying product yields and contaminant concentrations
- Conduct bench-scale feedstock tests and quantify product yields, quality, and contaminant concentrations

The project goals of **Task 5** are as follows:

- Conduct tropical oil-to-SAF supply chain analyses
- Develop management strategies for elements present in construction and demolition (C&D) waste that affect use in thermochemical-conversion-based SAF production pathways

The project goals of **Task 6** are as follows:

- Explore the impacts of HB2386 on waste management in Hawai'i and potential for waste-based SAF production systems

The project goals of **Task 7** are as follows:

- Evaluate greenhouse gas (GHG) implications of tropical oil-to-SAF supply chains in Hawai'i based on life cycle methods

Task 1.1 – Inform Regional Supply Chains

University of Hawai'i

Objectives

This task included two activities: (1) reviewing the archival literature on existing tropical crops and potential new crops that could provide feedstocks for SAF production and (2) reviewing relevant pretreatment and conversion technology options and experiences with the feedstocks identified in (1).

Research Approach

Activity 1

The archival literature was reviewed to construct an updated database of relevant citations for tropical crops; new potential energy crops were identified and added to the database. Available information on agronomic practices, crop rotation, and harvesting techniques was included. The database was shared to serve as a resource for the ASCENT Project 001 team and Volpe Center analyses of regional supply chains.

Activity 2

A database of relevant pretreatment and conversion technology options, as well as experiences with potential tropical feedstock materials, was assembled from the archival literature and from existing Project 001 team shared resources. Of particular interest were inventories of material and energy flows associated with the pretreatment and conversion unit operations fundamental to the design of sustainable systems and underlying analyses. Pairings of pretreatment and conversion technology options provided a starting point for the evaluation of tropical biorefineries that can be integrated into ASCENT Project 001 team and Volpe Center activities.

Milestones

Activity 1

- Identified a target list of databases to search for relevant literature
- Provided an interim report summarizing progress in the literature search

Activity 2

- Identified a target list of databases to search for relevant literature
- Provided an interim report summarizing progress in the literature search

Major Accomplishments

This work has been completed. A report was produced for each of the two activities, and the two reports were combined into a manuscript published in the journal *Energy & Fuels*.

Publications

Peer-reviewed journal publication

Morgan, T. J., Youkhana, A., Ogoshi, R., Turn, S. Q., & Garcia-Perez, M. (2019). Review of biomass resources and conversion technologies for alternative jet fuel production in Hawai'i and tropical regions. *Energy & Fuels*, 33(4), 2699–2762. doi: 10.1021/acs.energyfuels.8b03001

Outreach Efforts

On February 21, 2018, the P.I. participated in a ThinkTech Hawai'i broadcast focused on SAFs, with collaborators from WSU and CAAFI (<https://www.youtube.com/watch?v=Ci4oWITPRKQ&feature=youtu.be>).

Awards

None.

Student Involvement

None.

Plans for Next Period

None.

Task 1.2 – Identify Supply Chain Barriers in the Hawaiian Islands

University of Hawai'i

Objective

The objective of this task was to identify key barriers in regional supply chains that must be overcome to produce substantial quantities of SAF in the Hawaiian Islands and similar tropical regions.

Research Approach

UH developed the Hawai'i Bioenergy Master Plan for the State of Hawai'i (<http://www.hnei.hawaii.edu/wp-content/uploads/Hawaii-Bioenergy-Master-Plan.pdf>), which was completed in 2009. In that plan, UH was tasked with determining whether Hawai'i had the capability to produce 20% of land transportation fuels and 20% of electricity from bio-based resources. To this end, the plan included assessments of (a) land and water resources that can support biomass feedstock production, (b) potential biomass resources and their availability, (c) technology requirements, (d) infrastructure requirements to support logistics, (e) economic impacts, (f) environmental impacts, (g) availability of human capital, (h) permitting requirements, and (i) limitations to developing complete value chains for biomass-based energy systems. In keeping with the stakeholder-driven development of the Hawai'i Bioenergy Master Plan, barriers to the development of regional supply chains for ASCENT were identified through interactions with key stakeholder groups. Green Initiative for Fuels Transition Pacific (GIFTPAC) meetings are held quarterly and attended by biofuel development interests in Hawai'i, including representatives of large landowners, producers of first-generation biofuels, petroleum refineries, electric utilities, the State Energy Office, U.S. Pacific Command, biofuel entrepreneurs, county government officials, and UH. Additional stakeholders are invited as necessary to fill gaps in information and the value chain. These meetings serve as excellent opportunities to receive stakeholder input, identify barriers to supply chain development, and organize data collection efforts that span supply chain participants.

Milestones

- Introduced activities at the next regularly scheduled GIFTPAC meeting after contract execution
- Prepared an interim report outlining two tropical supply chain scenarios developed in consultation with the Project 001 team, with input from GIFTPAC participants



Major Accomplishments

This task has been completed. A stakeholder meeting was held and documented in a report submitted to the FAA. The stakeholders identified barriers to SAF production in Hawai'i and ranked the barriers in order of importance as follows:

- Economic constraints (e.g., high costs of entry for production factors such as land) throughout the entire production chain
- Issues associated with access to capital, including high initial risks and uncertain returns on investment
- Insufficient government support in the form of incentives and favorable policies to encourage long-term private investment
- Cost, availability, and competition for water
- SAF production technologies (emerging but not yet demonstrated to have full commercial viability)
- Insufficient or inadequate infrastructure (e.g., harbors, roads, fuel distribution infrastructure, irrigation systems) to support the entire production chain

Several of these barriers also arise at locations in the continental United States; however, those related to water and infrastructure are unique characteristics of an island state.

Publications

None.

Outreach Efforts

This activity engaged stakeholders to identify barriers to SAF production in Hawai'i. Preparation included reviewing stakeholder lists from previous activities. Facilitators appropriate to the stakeholder group were retained. The stakeholder meeting included a presentation of the scope and goals of the larger ASCENT program and other aspects of the UH ASCENT project.

Awards

None.

Student Involvement

None.

Plans for Next Period

This task is complete, but stakeholder outreach activities will continue under other tasks, as outlined below.

References

hnei.hawaii.edu

Task 2.1 – Inform Regional Supply Chains

University of Hawai'i

Objectives

Building on activities from fiscal year 2016, additional supporting analyses will be conducted for proposed supply chains in Hawai'i, including the following:

Activity 2.1.1

Support Volpe Center and CAAFI Farm to Fly 2.0 supply chain analysis

Activity 2.1.2

Use GIS-based estimates of fiber crop production potential to develop preliminary technical production estimates of jet fuel in Hawai'i

Activity 2.1.3

Develop fundamental property data for tropical biomass resources

Activity 2.1.4

Transmit data and analysis results to support the improvement of existing tools (e.g., POLYSYS; <https://bioenergykdf.net/content/polysys>)

Research Approach

Activity 2.1.2 has been conducted by using GIS data to identify areas suitable for purpose-grown crop production of feedstocks for SAF production in Hawai'i. The approach has used GIS layers for land capability class (LCC), slope, and zoning as preliminary screens for suitability. Lands are classified by the Natural Resources Conservation Service with ratings from 1 to 6. LCCs 1-3 are generally suitable for agricultural production, LCC 4 can be productive with proper management, and LCCs 5 or 6 can support less intensive production and may be suitable for forestry. The slopes of terrains affect aspects of production, including mechanization and erodibility. An elevation GIS layer was used to derive a slope layer. Zoning layers were acquired from state and county GIS offices. Only agricultural zoning was deemed suitable for this analysis.

The EcoCrop model was used to develop yield models for the crops selected in Task 1, according to annual rainfall and mean minimum monthly temperature data. EcoCrop includes model parameters on sugarcane, bana grass, five species of eucalyptus, *Gliricidia*, *Leucaena*, *Pongamia*, *Jatropha*, and sorghum. The parameters for sugarcane have been used to provide a base case assessment for comparison with historical sugarcane acreage and yield. Through sensitivity analysis, the model can be tuned to account for differences between parameters developed from global sugar production and a century of production experience in Hawai'i that has been refined through plant breeding to adapt sugarcane varieties to a wide variety of agro-ecosystems. The analysis has purposely avoided land-use conflict with food production by limiting suitability to areas capable of sustaining AJF feedstocks under rain-fed conditions. Areas suitable for SAF production that do not conflict with current agricultural land use (i.e., fallow land) have also been identified.

Pongamia (*Millettia pinnata*) was the initial focus of Activity 2.1.3. *Pongamia* is an oilseed-bearing leguminous tree with production potential in Hawai'i and Florida. The tree produces pods containing oil-bearing seeds. Pods, oilseed cake, and oil were evaluated from trees growing on the island of O'ahu. Fundamental measurements of chemical composition were conducted and reported. Torrefaction of pods as a coproduct in oil production has been conducted. An investigation of pretreatment methods to improve pod feedstock properties for thermochemical conversion applications has been completed.

Milestones

- Identified target opportunities to augment POLYSYS, the Alternative Fuel Transportation Optimization Tool (<https://trid.trb.org/view/1376122>), and conversion modules
- Reviewed previously developed GIS information layers for tropical fiber crops and identified updating requirements
- Conducted preliminary estimates of SAF technical potential in Hawai'i, according to previously developed GIS information layers

Major Accomplishments

The GIS-based analysis of SAF production potential is ongoing. The assessment of potential lands meeting the requirements for LCC, slope, and land-use zoning has been completed. The EcoCrop model was implemented to predict yield as a function of minimum mean monthly temperature and annual rainfall. This process identified potential SAF feedstock crops for land areas capable of supporting their production under both rain-fed and irrigated conditions. This analysis provided information necessary for determining cropping patterns and assessing costs for transport to processing facility locations. The EcoCrop model's prediction of sugarcane potential was determined, and the results were compared with historical sugarcane acreage, both rain-fed and irrigated. EcoCrop's upper and lower values for temperature and rainfall that support optimal sugarcane production were varied to calibrate the prediction against historical acreage. The difference between the EcoCrop values and those representative of conditions in Hawai'i is attributable to improvements due to plant breeding and unique combinations of environmental conditions, e.g., the relatively young volcanic soils present in high-rainfall areas on the island of Hawai'i that enable high drainage rates and accommodate sugar production.

Calibration of the EcoCrop model using historical sugarcane planted acreages was completed in 2018. This effort used a confusion matrix approach for validation (resulting in a kappa value >0.4) and demonstrated that the mean annual temperature was a better indicator of environmental capability than the minimum mean monthly temperature

recommended by the EcoCrop developers. This effort highlights the need to adapt models to local conditions. Model predictions for suitable cropping are being compared with current land uses to provide another indicator of agreement.

The GIS analysis of SAF feedstock production potential has been completed. Statewide working maps for each of the species have been summarized in a draft report currently undergoing internal review. This report will serve as the basis for a journal article publication.

Dr. Curtis Daehler (UH, Department of Botany) has completed a report assessing the invasiveness of *Pongamia*. Retrospective analyses have shown that predictive weed risk assessment systems correctly identify many major pest plants, but their predictions are not 100% accurate. The purpose of this study was to collect field observations of *Pongamia* planted around O'ahu to identify direct evidence of *Pongamia* escaping from plantings and becoming an invasive weed. Seven field sites were visited in various environments across O'ahu. Although some *Pongamia* seedlings were found in the vicinity of some *Pongamia* plantings, particularly in wetter, partly shaded environments, almost all observed seedlings were restricted to areas directly beneath the canopies of mother trees. This finding suggests a lack of effective seed dispersal away from *Pongamia* plantings. According to its current behavior in the field, *Pongamia* is not invasive or established outside of cultivation on O'ahu. Because of its limited seed dispersal and low rates of seedling establishment beyond the canopy, the risk of *Pongamia* becoming invasive can be mitigated through monitoring and targeted control of any rare escapes in the vicinity of plantings. Because seeds and seed pods are dispersed by water, future risks of *Pongamia* escape and unwanted spread can be minimized by avoiding planting at sites near flowing water, near areas exposed to tides, or on or near steep slopes. Although vegetative spread by root suckers was not observed around plantings on O'ahu, monitoring for vegetative spread around plantations is recommended; unwanted vegetative spread might become a concern in the future that could be addressed with localized mechanical or chemical control.

Pods, oilseed cake, and oil have been evaluated from a number of trees growing on the island of O'ahu. TerViva, a company pursuing *Pongamia* commercialization, provided material from orchards on O'ahu. Fundamental measurements of chemical composition were made for seeds, pods, extracted oil, and post-extraction seed material. Measured values included C, H, N, and S elemental composition; energy content; volatile matter, fixed carbon, and ash content; and trace element composition. Oils were characterized for peroxide value, iodine value, fatty acid profile, free fatty acid content, flash point, density, viscosity, and phase transition temperatures. The chemical composition and fuel properties of the oilseed cake and the pod material were characterized. A manuscript summarizing the results of this effort has been published in the journal *ACS Omega*.

Coproduct evaluation of *Pongamia* pod feedstock for thermochemical conversion has been conducted. Evaluation included both untreated pods and pods pretreated by a torrefaction process to improve their properties. Torrefaction produces a material with improved grindability and storage stability and diminished oxygen content and microbial availability. The effects of process conditions on feedstock properties relevant to thermochemical conversion technologies, proximate and ultimate composition, heating value, and Hardgrove grindability index were measured. The chemical structure, reactivity, and changes in elemental composition of the torrefied materials were also investigated. A manuscript summarizing the results of this effort has been published in the journal *Fuel*.

Pongamia seedpods are recognized as a potential feedstock for SAF production because of the relatively high oil content of the seeds. *Pongamia* pods are byproduct residues available after seed separation. Pods have high chlorine and potassium content that may be problematic in thermochemical energy conversion systems. Leaching experiments were performed to remove inorganic constituents of the pods and thereby decrease the potential for fouling, slagging, and agglomeration. A manuscript summarizing the results of this effort has been published in the journal *Fuel*.

The state tree of Hawai'i, *Aleurites moluccanus* (commonly known as kukui and candlenut), is an oil-nut-bearing tree frequently found in the tropics. Nuts from a number of trees growing on the island of O'ahu were collected, and the nut shell, oilseed cake, and oil components were fractionated and analyzed for common properties necessary for designing SAF production systems. A manuscript has been submitted to the journal *Biomass & Bioenergy*. Revisions are in process.

Publications

Peer-reviewed journal publications

Fu, J., Allen, G., Weber, S., Turn, S. Q., & Kusch, W. (2021). Water leaching for improving fuel properties of pongamia pod: Informing process design. *Fuel*, 305, 121480. doi:10.1016/j.fuel.2021.121480

Fu, J., Summers, S., Turn, S. Q., & Kusch, W. (2021). Upgraded pongamia pod via torrefaction for the production of



bioenergy. *Fuel*, 291, 120260. doi:10.1016/j.fuel.2021.120260

Fu, J., Summers, S., Morgan, T. J., Turn, S. Q., & Kusch, W. (2021). Fuel properties of pongamia (*Milletia pinnata*) seeds and pods grown in Hawai'i. *ACS Omega*, 6, 9222–9233. doi:10.1021/acsomega.1c00635

Written reports

Chan, S., Ogoshi, R. & Turn, S. Feedstocks for sustainable jet fuel production: An assessment of land suitability in Hawai'i. A draft report has been prepared and a draft manuscript is under preparation for publication.

Outreach Efforts

Outreach in this task has focused on interactions with TerViva, a startup company that has identified *Pongamia* germplasm production and marketing as the central focus of its business plan.

Chan, S., Ogoshi, R. & Turn, S. (2020, July 6-9). *Feedstocks for Sustainable Jet Fuel Production: An Assessment of Land Suitability in Hawai'i* [Poster presentation]. European Biomass Conference and Exhibition. Virtual.

Fu, J., Summers, S. & Turn, S. "Upgraded *Milletia Pinnata* Pod via Torrefaction for the Production of Bioenergy in Hawai'i" was presented orally at the 2020 Thermal & Catalytic Sciences Virtual Symposium.

Turn, S. (2019, December 3). *Regional Supply Chain Analysis for Alternative Jet Fuel Production in the Tropics* [Poster presentation]. Hawai'i Aviation and Climate Action Summit, Honolulu, HI, United States.

Fu, J., Allen, G., Weber, S., Turn, S. Q., & Kusch, W. (2021, August 22-26). *Water Leaching for Improving Fuel Properties of Pongamia Pods* [Oral and virtual presentation]. 2021 Fall National Meeting of the American Chemical Society, Atlanta, GA, United States.

Fu, J., Summers, S. & Turn, S. "Upgraded *Milletia Pinnata* Pod via Torrefaction for the Production of Bioenergy in Hawai'i" was presented virtually and orally at the 2021 Spring National Meeting of the American Chemical Society, April 5-16, 2021.

Fu, J., Weber, S. & Turn, S. "Comprehensive Characterization of Kukui Nuts for Bioenergy Production in Hawai'i" was presented orally at the 2022 Fall American Chemical Society National Meeting & Exposition, Chicago, IL, August 21-25, 2022

Awards

A poster entitled "Feedstocks for Sustainable Jet Fuel Production: An Assessment of Land Suitability in Hawai'i" was presented at the European Biomass Conference and Exhibition held virtually July 6-9, 2020 and received the Best Visual Presentation Award.

Student Involvement

Gabriel Allen, Seren Weber, and Sabrina Summers, three undergraduate students, are involved in the project; their primary responsibility is processing and analyzing samples of biomass materials selected for evaluation as potential SAF feedstocks. The *Pongamia* torrefaction work was the focus of an Undergraduate Research Opportunity Program project for Sabrina Summers, a bioengineering and chemistry double major. The results of her work were presented at the Fall 2019 American Chemical Society meeting in San Diego, California. The *Pongamia* pod leaching work was the focus of an Undergraduate Research Opportunity Program project for Gabriel Allen, a biochemistry major.

Plans for Next Period

A report summarizing the GIS analysis of SAF feedstock production potential and a companion manuscript will be completed. Apart from this report and manuscript, this task is complete.

Task 2.2 – Support Indonesian AJF Supply Initiatives

University of Hawai'i

Objectives

This task supports the memorandum of understanding between the FAA and the Indonesian DGCA to promote the development and use of sustainable alternative aviation fuels. Under the coordination of the FAA, efforts to establish points of contact and coordinate with Indonesian counterparts are ongoing.

Research Approach

To begin this process, the team will work with the FAA to establish points of contact to coordinate efforts with Indonesian counterparts. Members of the Indonesian Aviation Biofuels and Renewable Energy Task Force include Universitas Indonesia, Institut Teknologi Bandung, and Universitas Padjadjaran. A prioritized list of tasks will be developed in consultation with Indonesian counterparts, and data required to inform sustainability and supply analyses and potential sources of information will be identified. The information collected may include Indonesian jet fuel use and resources for SAF production, airport locations, and annual and monthly jet fuel consumption patterns. Characterization of sustainable biomass resources with potential for use in producing SAF supplies may include developing preliminary GIS mapping information of their locations and distributions and preliminary estimates of their technical potential.

Milestones

- Identify points of contact at Indonesian universities participating in the Aviation Biofuels and Renewable Energy Task Force
- Identify research needs and develop a project plan
- Develop data for potential projects

Major Accomplishments

The P.I. traveled to Jakarta in the first week of August 2017 and met with the following individuals:

- Cesar Velarde Catolfi-Salvoni (International Civil Aviation Organization)
- Dr. Wendy Aritenang (International Civil Aviation Organization)
- Dr. Ridwan Rachmat (Head of Research Collaboration, Indonesian Agency for Agricultural Research and Development)
- Sylvia Ayu Bethari (Head of Aviation Fuel Physical and Chemical Laboratory, Research and Development Centre for Oil and Gas Technology)
- Dr. Ina Winarni (Forest Product Research and Development Center, Ministry of Environment and Forestry)
- Dr. SD Sumbogo Murti (Center of Technology Energy Resources and Chemical Industry, Agency for the Assessment and Application of Technology)

The activities of the tropical supply chain analysis effort were presented to the group, and a general discussion followed. From this introductory meeting, it was concluded that the Indonesian counterparts would seek agreement on how to move forward with future cooperation.

The P.I. traveled to Jakarta and met with Dr. Wendy Aritenang of the International Civil Aviation Organization's Jakarta office. The same trip included meetings with renewable energy researchers at Universitas Indonesia. After the meeting, Dr. Aritenang suggested several points of contact for future engagement: Frisda Panjaitan from the Palm Oil Research Institute and Tatang Soerawidjaja, Tirta Prakoso Brodjonegoro, and Imam Reksowardojo from the Bandung Institute of Technology.

In October 2022, the P.I. traveled to Jakarta and met with Dr. Wendy Aritenang in Jakarta. The following day, the P.I. and Dr. Aritenang traveled to Bandung to visit the Bandung Institute of Technology and met with faculty members Professor Adiwan Aritenang (Department Head of Regional Planning) and Professors Tatang Soerawidjaja, Tirta Prakoso Brodjonegoro, and Iman Reksowardojo from the Faculty of Industrial Technology. Ongoing UH ASCENT activities were presented, and the Bandung Institute of Technology researchers discussed their SAF-related research efforts.

Publications

None.

Outreach Efforts

Outreach efforts by the P.I. are described in the Major Accomplishments section above. In addition, the P.I. participated in the Asia Pacific Economic Cooperation event "Energy Transition toward Carbon Neutrality, APEC BCG Economy Thailand 2022: Tech to Biz" in Bangkok and gave a presentation entitled "US Initiatives on Sustainable Aviation Fuel."

Awards

None.

Student Involvement

None.

Plans for Next Period

This activity will be continued under ASCENT Project 093B.

Task 3.1 – National Lipid Supply Availability Analysis

University of Hawai'i

Objective

In this task, the team will support ASCENT partners working on a national lipid supply availability analysis by sharing data on tropical oilseed availability developed under previous years' activities.

Research Approach

This support will include estimates of *Pongamia* production capability in the state, in addition to assessments of waste cooking oil and tallow.

Milestones

Milestones will coincide with the schedule of the lead institution (WSU) for the national lipid supply analysis.

Major Accomplishments

Additional seeds and pods were collected from the *Pongamia* tree on the UH campus, Foster Botanical Garden, and Ke'ehi Lagoon Beach Park. Large quantities (tens of kilograms) of material were acquired from TerViva's plantings on O'ahu's north shore for use in oil evaluation. Two oilseed presses were acquired, and safety documents were developed. Pods, oilseed cake, and oil were evaluated from a number of trees growing on the island of O'ahu. Fundamental measurements of chemical composition were made for seeds, pods, extracted oil, and post-extraction seed material. Measured values included C, H, N, and S elemental composition; energy content; volatile matter, fixed carbon, and ash content; and trace element composition. Oils were characterized for peroxide value, iodine value, fatty acid profile, free fatty acid content, flash point, density, viscosity, and phase transition temperatures. The development of coproducts from pods and oilseed cake was explored.

Areas in Hawai'i with agricultural zoning suitable for rain-fed production of *Pongamia* have been identified. Conflicts with current agricultural land use have been identified.

Waste oil resources in Hawai'i are estimated to be on the order of 2-3 million gallons per year, according to the de facto population, and are directed to biodiesel production.

Publications

Fu, J., Summers, S., Morgan, T. J., Turn, S. Q., & Kusch, W. (2021). Fuel properties of pongamia (*Milletia pinnata*) seeds and pods grown in Hawai'i. *ACS Omega*, 6(13), 9222–9233. doi:10.1021/acsomega.1c00635

Outreach Efforts

Data were presented at the April 2019 ASCENT review meeting in Atlanta, Georgia.

Awards

None.

Student Involvement

Three undergraduate students (Sabrina Summers, Sarah Weber, and Taha Elwir) are involved in the project. Their primary responsibility is processing and analyzing samples of biomass materials selected for evaluation as potential SAF feedstocks.

Plans for Next Period

This task is complete. Results will underpin future tasks.

Task 3.2 – Hawai‘i Regional Project

University of Hawai‘i

Objectives

A supply chain based on fiber feedstocks transported to a conversion facility located at Campbell Industrial Park (CIP) on O‘ahu will be evaluated (Figure 1). CIP is the current site of two oil refineries. C&D wood waste from the PVT Land Company’s landfill could provide a primary source of feedstock. Other sources will be evaluated from elsewhere on O‘ahu and outer islands, including municipal solid waste streams from outer islands and mining of current waste-in-place stocks. Waste streams and purpose-grown crops form the basis of a hub-and-spoke supply system, with the hub located on O‘ahu. Pipelines for jet fuel transport are in place from CIP to Daniel K. Inouye International Airport and the adjacent Joint Base Pearl Harbor/Hickam. Other coproduct offtakers for alternative diesel fuel include the Hawaiian Electric Company and several military bases, including Schofield Barracks (~50-MW alternative fuel-capable power plant under development) and Kaneohe Marine Corps Base. Hawai‘i Gas (a local gas utility) is also seeking alternative sources of methane if methane or feedstock suitable for methane production is available as a coproduct. Hawai‘i Gas currently offtakes feedstock (naphtha) from the refinery.

Research Approach

Task 3.2.G1. Analyze feedstock-conversion-pathway efficiency, product slate (including coproducts), and maturation

Building on activities from previous years, additional supporting analyses will be conducted for proposed supply chains in Hawai‘i, as follows:

- 3.2.G1.1 Assess feedstock suitability for conversion processes (e.g., characterization, conversion efficiencies, and contaminants) (UH and WSU [Manuel Garcia-Perez])
- 3.2.G1.2 Acquire data on feedstock size reduction, particle size of materials, and bulk densities (UH, WSU [Manuel Garcia-Perez])
- 3.2.G1.3 Evaluate coproducts at every step of the supply chain (ASCENT Project 001 team)

Task 3.2.G2. Assess the scope of techno-economic analysis (TEA) issues

This task will determine the current TEA status of targeted SAF production technologies that use fiber feedstocks as production inputs (UH, WSU [Manuel Garcia-Perez], Purdue University [Wally Tyner]).

Task 3.2.G3. Conduct a screening-level GHG life-cycle assessment (LCA)

This task will conduct screening-level GHG LCA on the proposed target supply chains and SAF conversion technologies.

Subtasks:

- 3.2.G3.1 Assess Massachusetts Institute of Technology (MIT) waste-based GHG LCA tools in the context of application to Hawai‘i (MIT [Mark Staples])
- 3.2.G3.2 Assess requirements to link previously completed eucalyptus energy and GHG analysis to the edge of the plantation with available GHG LCA information for conversion technology options (MIT [Mark Staples], UH)
- 3.2.G3.3 Identify and fill information/data gaps

Task 3.2.G4. Identify supply chain participants/partners

Subtasks:

- 3.2.G4.1 Define C&D landfill case
- 3.2.G4.2 Identify eucalyptus in existing plantations, landowners, leaseholders/feedstock producers, harvesting contractors, truckers, etc. (UH)
- 3.2.G4.3 Define other feedstock systems as identified (ASCENT Project 001 Team)



Possible Locations of Value Chain Participants



PVT Land Company



Figure 1. Possible locations of value chain participants for a fiber-based alternative jet fuel production facility located at Campbell Industrial Park (CIP), O’ahu.

Task 3.2.G5. Develop an appropriate stakeholder engagement plan

Subtasks:

- 3.2.G5.1 Review stakeholder engagement methods and plans from past work to establish baseline methods (UH, WSU [Season Hoard])
- 3.2.G5.2 Identify and update engagement strategies according to the updated Community Social Asset Modeling/Outreach support tool (UH, WSU [Season Hoard])

Task 3.2.G6. Identify and engage stakeholders

Subtasks:

- 3.2.G6.1 Identify stakeholders along the value chain and create a database based on value chain location (UH)
- 3.2.G6.2 Conduct a stakeholder meeting by using the instruments developed in Task 3.2.G5 (UH, WSU [Season Hoard])
- 3.2.G6.3 Analyze stakeholder response and feedback to the process (UH, WSU [Season Hoard])

Task 3.2.G7. Acquire transportation-network and other regional data needed for the Freight and Fuel Transportation Optimization Tool and other modeling efforts

Subtasks:

- 3.2.G7.1 Acquire necessary data to evaluate harbor capacities and current usage (UH, Volpe [Kristin Lewis], WSU [Michael Wolcott])
- 3.2.G7.2 Acquire data on inter-island transport practices (UH, Volpe [Kristin Lewis], WSU [Michael Wolcott])

Task 3.2.G8. Evaluate infrastructure availability

Subtasks:

- 3.2.G8.1 Evaluate inter-island shipping options and applicable regulation (UH, Volpe [Kristin Lewis], WSU [Michael Wolcott])
- 3.2.G8.2 Evaluate transport or conveyance options from conversion location to end users and applicable regulation (UH, Volpe [Kristin Lewis], WSU [Michael Wolcott])

Task 3.2.G9. Evaluate feedstock availability

Subtasks:

- 3.2.G9.1 Refine and ground-truth prior evaluations of options for purpose-grown feedstock supply (UH)
- 3.2.G9.2 Conduct projections of future C&D waste supply and mining of waste-in-place on O’ahu, municipal solid waste, and mining of waste-in-place on other islands (UH)

Task 3.2.G10. Develop a regional proposal

This task will use the information collected in Tasks 3.2.G1–3.2.G9 to develop a regional project proposal.

Milestone

One milestone is associated with each of the subtask activities identified in the Research Approach section above.

Major Accomplishments

Characteristics of the feedstock generated at the landfill have been determined and summarized in a publication.

The elemental compositions of feedstock materials have been used as the basis for equilibrium analysis of gasification systems using oxygen, steam, and steam-oxygen mixtures to inform process design.

Material flows relevant to the screening-level GHG analysis of C&D waste as SAF feedstock have been assembled. Preliminary discussions of GHG analysis of C&D-based SAF systems with landfill operators have been initiated.

Plans for solid waste management from all counties in Hawai’i have been used to provide a broader picture of the waste stream composition, diversion, recycling practices, and planned uses.

Publications

Peer-reviewed journal publications

Bach, Q. V., Fu, J., & Turn, S. (2021). Construction and demolition waste-derived feedstock: fuel characterization of a potential resource for sustainable aviation fuels production. *Frontiers in Energy Research*, 9, 711808. doi: 10.3389/fenrg.2021.711808

Bach, Q. V. & Turn, S. Fate of arsenic and other inorganic elements during gasification of construction and demolition wastes – thermochemical equilibrium calculations. Draft manuscript in process.

Outreach Efforts

Results of the fuel sampling, fuel analyses, and gasification equilibrium analyses were presented at the October 2019 ThermoChemical Biomass 2019 Conference in Chicago, Illinois.

Information from this task was included in the talk “Regional Supply Chain Analysis for Alternative Jet Fuel Production in the Tropics” presented at the Hawai’i Aviation and Climate Action Summit, December 3, 2019, at the Hawai’i State Capitol.

Data acquired under this task were presented to the management of PVT Land Company and their consultants from Simonpietri Enterprises and T. R. Miles Technical Consultants, Inc.

A poster entitled “Construction and Demolition Waste as an Alternative Energy Source: Fuel Characterization and Ash Fusion Properties” was presented at the 2020 Thermal & Catalytic Sciences Virtual Symposium.

Discussion with Dr. Kristin Lewis and Volpe Center staff on the addition of Hawai‘i transportation infrastructure to the Freight and Fuel Transportation Optimization Tool was initiated and deferred until a clearer definition of the system emerges.

As suggested by FAA management, UH worked with the Servicios y Estudios para la Navegación Aérea y la Seguridad Aeronáutica (SENASA) to identify a counterpart university in the Canary Islands, Spain. Universidad de la Laguna (ULL) was selected, and a memorandum of understanding was signed between UH and ULL. A nondisclosure agreement was subsequently signed among SENASA, ULL, UH, and the Spanish company Abengoa Energía, S.A. Regularly scheduled meetings have been held biannually with Professor Dr. Ricardo Guerrero Lemus from ULL to discuss common research themes and were continued in 2023.

Awards

None.

Student Involvement

Three undergraduate students (Sabrina Summers, Sarah Weber, and Taha Elwir) have been involved in sample preparation and in operating the laboratory analytical equipment used for sample analysis.

Plans for Next Period

Manuscripts covering the prediction of gasification product streams including contaminant concentrations will be completed and submitted. Comparative data from bench-scale gasification tests (see Task 4) at ThermoChem Recovery International facilities were received in October 2023. These data will be supplemented with the results of C&D waste sample analyses using a differential thermal analyzer paired with an inductively coupled plasma mass spectrometer (DTA-ICPMS) to provide information on the release of inorganic elements as a function of temperature. Contracting for DTA-ICPMS analytical services at the University of California, Davis Interdisciplinary Center for Plasma Mass Spectrometry is underway. With these experimental data, the manuscripts will be completed.

Task 4 – Hawai‘i Regional Project

University of Hawai‘i

Objective

This task builds upon results from the previous years’ work under the Hawai‘i regional project, with a focus on the data and analysis necessary to plan a project that uses C&D waste as feedstock for SAF production. The Task 4 objective is to use C&D feedstock characterization data and thermochemical equilibrium analysis from the previous years to conduct bench-scale gasification tests and to quantify the product gas yield, composition, and contaminant concentrations. These results will be compared with equilibrium prediction used to identify contaminants that must be addressed before end use and will provide the basis for designing contaminant control systems.

Research Approach

Bench-scale gasification tests will be conducted on samples of C&D wastes characterized in the earlier tasks, to measure product yields, identify contaminants, and investigate element partitioning between product phases.

Information gained from the tests will be used to identify opportunities to improve TEA, identify coproducts, inform supply chain participants and stakeholders, and identify necessary infrastructure improvements.

Milestones

- Identify and evaluate capabilities of experimental bench-scale facilities for gasifier tests
- Specify system performance parameters to be measured
- Specify techniques to sample and analyze contaminants
- Select and engage an experimental bench-scale facility for testing

- Prepare and ship feedstock from Hawai'i to the experimental test facility
- Conduct tests, reduce data, and prepare a summary report of the results

Major Accomplishments

Operational measurements to be conducted as part of the bench-scale tests were summarized, and a test plan was developed; these were used as the basis for entertaining proposals for test services.

Through a competitively structured proposal process, ThermoChem Recovery International, Inc. was engaged to provide bench-scale test services for C&D waste feedstock and other opportunity fuels of relevance to Hawai'i and the tropics.

A synthetic C&D waste recipe was developed according to the results published in *Frontiers in Energy Research* (Bach et al., 2021). Component fractions in the recipe were determined by a least-squares approach to matching critical fuel characteristics, including volatile matter, fixed carbon, and ash content; higher heating value; and concentrations of the elements Na, Mg, Al, Si, P, S, Cl, K, Ca, Ti, Cr, Mn, Fe, Cu, Zn, As, Ru, and Pb. This recipe will enable a reproducible C&D waste fuel lot to be assembled and will aid in decreasing test-to-test variability.

In November and December 2021, tests were conducted in the bench-scale facility at the ThermoChem Recovery International facility in Durham, NC. After shakedown testing was completed, two subsequent tests were conducted: one test using *Leucaena leucocephala* stemwood and a second test using synthetic C&D waste. Test reports for the two bench-scale gasification tests at ThermoChem Recovery International facilities were finalized in October 2023.

Publications

Peer-reviewed journal publications

Bach, Q. V., Fu, J., & Turn, S. (2021). Construction and demolition waste-derived feedstock: fuel characterization of a potential resource for sustainable aviation fuels production. *Frontiers in Energy Research*, 9, 711808. doi: 10.3389/fenrg.2021.711808

Outreach Efforts

None.

Awards

None.

Student Involvement

None.

Plans for Next Period

Planning for additional bench-scale tests at the Gas Technology Institute began in 2023. Moving the mini bench-scale gasifier unit between facilities at the Gas Technology Institute delayed the tests. Tests are now planned for early 2024.

Test results will be shared with stakeholder communities.

Task 5 – Hawai'i Regional Project

University of Hawai'i

Objective

Subtask 5.1: Tropical oil-to-SAF supply chain analysis

The goal of Subtask 5.1 is to develop a model for tropical oil supply chains for SAF and associated coproducts. Hawai'i will be the initial focus, but the modeling tools will be developed for wider use in island settings.

Subtask 5.2: Contaminants in the gasification of C&D waste

The goal of Subtask 5.2 is to develop management strategies for elements present in C&D waste that affect its use as a feedstock for thermochemical conversion.



Research Approach

Subtask 5.1

Prior ASCENT EcoCrop GIS modeling activities identified growing locations for *Pongamia*, kamani, croton, and *Jatropha*, according to suitable environmental conditions, geography, and zoning. If unavailable, primary data on the chemical and physical characteristics of these tropical oils and their coproducts (e.g., pods/shell and oilseed cake) were acquired. The project will use these earlier results as the basis for developing supply chain models for AJF production. Model results will identify feedstock production areas as well as locations and scales of primary processing sites for shell and pod separation, oil extraction from seeds, and oil conversion to SAF. Potential sources of hydrogen from oilseed coproducts, other renewable resources, and fossil sources will be analyzed and included in the model. Options for points of production, SAF production technologies (e.g., ARA, SBI, or Forge), transportation strategies, and blend ratios at airports (or for specific end users, e.g., the military) across Hawai'i will affect model outcomes and will be evaluated. Options for coproducts such as animal feeds and high-value materials will be evaluated and incorporated into the model decision-making process. Criteria used to drive the model solution might include minimizing SAF production costs while meeting a minimum total production benchmark or a minimum blending rate for annual state jet fuel consumption. Other criteria, such as system resiliency to extreme weather events and climate change, provision of environmental services, and stakeholder acceptability, will also be of importance and will be used to evaluate model solutions.

Subtask 5.2

Thermochemical gasification of biorenewable resources is the initial conversion process for two entry points to AJF production: (1) synthesis gas used in the direct production of Fischer-Tropsch liquids and/or (2) green/renewable hydrogen used in biorefineries for hydrotreating lipids or in existing petroleum-refining activities for the production of hybrid jet fuel. Urban wood waste from C&D activities provides a reliable source of biorenewable material and requires a tipping fee for disposal, characteristics that enhance its attractiveness as feedstock. Negative aspects of C&D feedstock are its physical and chemical inhomogeneity. In the latter case, inorganic elements present in the feedstock can negatively influence the gasification process (e.g., corrosion of, or accumulation on, reactor working surfaces, bed material agglomeration, catalyst deactivation, or pollutant emissions). Using data generated from previous ASCENT Project 001 tasks, this project will assess methods for managing contaminants in C&D feedstocks. This project will be based on gasification systems proposed for the production of synthesis gas/Fischer-Tropsch liquids and green hydrogen. Technology options for contaminant removal or conversion to benign forms will be assessed at each step in the conversion process, including presorting at the waste generation site, sorting/diversion at the C&D waste intake facility, removal by physical/chemical/other methods before gasification, in situ reactor control methods, and gas cleanup. Technology options based on existing process industries and the scientific literature will be considered. Laboratory-scale testing of removal techniques will be conducted to provide a preliminary assessment of selected promising technology options. Integrated gasification process options and contaminant control options will be evaluated as complete systems to guide system design and to enable system comparisons. Risks associated with technology options will also be assessed to guide implementation and risk mitigation of the system as a whole. Impacts of processing scale (e.g., Mg waste/day) on the selection of technology options will also be assessed.

Milestones

Subtask 5.1: Established a model framework for an oilseed-based SAF supply chain in an island setting, using the scenario of Hawai'i

Subtask 5.2: Completed a review of options for managing contaminants along the supply chain; conducted bench-scale tests to confirm the efficacy of options

Major Accomplishments

On the basis of the *Pongamia* production areas identified by GIS analysis in Task 3 (described above), sites for processing *Pongamia* (pod and seed separation, oil extraction from seed) have been evaluated on each island. Candidate processing sites in the analysis included (a) brownfield sites with industrial zoning and (b) greenfield sites identified as lands with a slope of less than 5%, a contiguous area of 50 hectares, and agricultural zoning. The ArcGIS "minimized impedance" and "origin-destination" analysis tools were used to determine transportation cost index values for all potential processing facility locations, using the *Pongamia* production estimates and the road network distances from production sites to candidate processing sites. Analyses were performed for each island and included four *Pongamia* production scenarios.

Publications

None.

Outreach Efforts

Results of the analyses were shared with personnel from Par Hawai'i, the refinery located on the island of O'ahu, and with Pono Pacific, a land management company engaged in sustainable agricultural development. Par Hawai'i has announced plans to produce SAF in partnership with Hawaiian Airlines. Pono Pacific is pursuing oilseed production to supply Par Hawai'i with lipids for SAF production via the production pathway for hydroprocessed esters and fatty acids.

Awards

None.

Student Involvement

None.

Plans for Next Period

Subtask 5.1: Costs for *Pongamia* delivered to the processing site gate will be used with TEA spreadsheets (oilseed crushing, hydroprocessed esters and fatty acids, etc.) developed by WSU collaborators to provide estimates of SAF production costs according to supply chain scenario assumptions.

Subtask 5.2: A review of options for managing contaminants along the supply chain will be conducted. Results of the review and contaminant measurements from the bench-scale gasification tests in Task 4 will be used to target bench-scale contaminant control tests.

Task 6 – Hawai'i Regional Project

University of Hawai'i

Objective

Task activities in Year 6 will explore the impacts of Hawai'i State Legislative Bill HB2386 on waste management and the potential for waste-based SAF production systems. HB2386 requires 0.5-mile buffer zones around waste and disposal facilities (including landfills) and restricts facilities from land with conservation-district zoning.

Research Approach

The goal of this task is to assess and evaluate the impacts of HB2386 on waste management strategies in Hawai'i. HB2386 was disruptive to disposal practices for C&D waste on the island of O'ahu, and its impacts are currently not fully understood. The aims of Task 6 are to collect updated waste generation data, elucidate how HB2386 will affect current management strategies, and develop scenarios for waste-based SAF production under the new regulatory environment. The impacts of HB2386 on the capacity to perform landfill mining will also be considered. A preliminary assessment of restricted and unrestricted sites for waste and disposal facilities will be reviewed and refined as necessary. Preliminary impacts on GHGs and SAF technology choices will be explored.

Milestone

The impacts of removing or diminishing the role of an active C&D landfill as a supply chain participant will be evaluated.

Major Accomplishments

None.

Publications

None.

Outreach Efforts

None.

Awards

None.

Student Involvement

None.

Plans for Next Period

A postdoctoral fellow will be recruited to work on this task, and analysis will begin.

Task 7 – Hawai‘i Regional Project

University of Hawai‘i

Objective

Activities proposed for Task 7 will continue to develop the information needed for the Hawai‘i regional projects begun in previous years. These activities will support efforts by the State of Hawai‘i and Hawai‘i energy service providers to reduce GHG emissions. Task activities will explore the GHG intensity of *Pongamia* as a feedstock producer in Hawai‘i regional pathways.

Research Approach

The goal of this task is to assess and evaluate the GHG implications of a *Pongamia*-based feedstock supply chain for SAF production. Based on analyses from previous years, life cycle inventories (LCIs) for *Pongamia* production, oil extraction, and oil conversion to SAF will be completed. The LCIs will be used to conduct GHG assessments of *Pongamia*-based SAF production systems. Different *Pongamia* land use scenarios, extraction options, and conversion technologies can be considered and compared.

Milestone

We will produce a complete set of LCIs for the *Pongamia* production system.

Major Accomplishments

None.

Publications

None.

Outreach Efforts

None.

Awards

None.

Student Involvement

None.

Plans for Next Period

A postdoctoral fellow will be recruited to work on this task, and analysis will begin.



Project 001(C) Alternative Jet Fuel Supply Chain Analysis

Purdue University

Project Lead Investigator

Farzad Taheripour
Research Professor
Department of Agricultural Economics
Purdue University
403 West State Street
West Lafayette, IN 47907-2056
765-494-4612
tfarzad@purdue.edu

University Participants

Purdue University

- P.I.: Farzad Taheripour, Research Professor
- FAA Award Number: 13-C-AJFE-PU, Amendments 25, 29, 34, 36, 41, 48, 51
- Part One: Period of Performance: October 1, 2022 to September 30, 2023
- Part Two: Period of Performance: December 22, 2022 to December 31, 2023
- Tasks:
 1. Provide required analyses on induced land use change (ILUC) and direct land use change (DLUC) emissions and other analyses related to land use emissions at the global, regional, and country levels. This task will provide required support to calculate a portion of the carbon intensity (CI) of alternative sustainable aviation fuel (SAF) pathways that are related to land use changes (LUCs).
 2. Develop economic models, collect data, and conduct analyses to support the Fuels Task Group (FTG) subgroups, such as the Core Life Cycle Analysis (LCA), Technology Production Policy (TPP), Emission Reductions Accounting (ERA), and Sustainability subgroups, to achieve the goals and tasks defined for 2023.
 3. Help the Carbon Offsetting and Reduction Scheme for International Aviation (CORSA)/FTG to better assess the CI of SAF pathways due to LUCs, including the following subtasks:
 - 3.1. Provide a critical review of the existing tier-1 data sources that have been commonly used in determining land use emission factors in assessing ILUC emission values for biofuels, including SAFs. Determine the advantages and disadvantages and validate the credibility of each data source.
 - 3.2. Generate a new emission factor dataset at a grid cell level for the entire world that represents the carbon content of each type of land cover item for use in ILUC and DLUC calculations. The new dataset will provide up-to-date data on soil organic carbon (SOC), above and underground carbon in vegetation, and other land carbon sources.
 - 3.3. Provide a dataset to assess changes in SOC due to the cultivation of feedstock for SAF production at the farm level.
 - 3.4. Generate a new carbon accounting software to facilitate ILUC calculations for each selected emission factor dataset.
 - 3.5. Develop a methodology for assessing DLUC at the farm level based on experimental observations at the farm level and enhance the accuracy of ILUC values based on these experiments.
 - 3.6. Augment the Global Trade Analysis Project model for Biofuels (GTAP-BIO) to calculate ILUC emissions for pathways that use significant amounts of solar electricity.



Project Funding Level

- Amendment 3: \$250,000
- Amendment 6: \$110,000
- Amendment 10: \$230,000
- Amendment 15: \$373,750
- Amendment 19: \$400,000
- Amendment 29: \$400,000
- Amendment 36, 41: \$523,000
- Amendment 48, 51: \$350,000, \$394,844

Current cost sharing for this project year was provided by Melissa Sabatine from Neste US, Inc.

Investigation Team

Prof. Farzad Taheripour (P.I.), All Tasks
Prof. Dominique van der Mensbrugghe (co-P.I.), Tasks 3.2 and 3.4
Prof. Qianlai Zhuang (co-P.I.), Tasks 3.1, 3.2, and 3.3
Maksym Chepeliev, (co-P.I.; research economist), Tasks 1, 2, and 3.5
Erwin Corong (co-P.I.; research economist), Task 1 and 2
Angel Aguiar (research economist), Tasks 1 and 2
EhsanReza Sajedinia (PhD student), All Tasks
Omid Karami (postdoctoral fellow; left Purdue in August 2023), All Tasks
Shuo Chen (PhD student), Tasks 3.1, 3.2, and 3.3
Xiangyu Liu (PhD student), Tasks 3.1, 3.2, and 3.3
Ye Yuan (PhD student), Tasks 3.1, 3.2, and 3.3
Lauren Benavidez (PhD student), All Tasks

Project Overview

In this project, our team has worked on the three main tasks listed above and made significant progress on each task in this performance time period. The first task is focused on providing required analyses on ILUC and DLUC assessments and advancing methodologies for ILUC and DLUC calculations. The second task aims at supporting the FTG subgroups, including the Core LCA, TPP, ERA, Sustainability, and other FTG groups, to accomplish their tasks and achieve their goals. This task includes developing a techno-economic analysis (TEA) for determining the profitability and feasibility of SAF pathways under alternative economic conditions and policy environments. The third main task and its subtasks are focused on various activities including assessing the existing data and approaches that provide land use emission factors; developing and improving carbon calculation models that have been used in assessing ILUC values; studying and proposing a methodology to measure, check, and verify changes in the soil carbon content of cropland including SOC at the farm level due to SAF production; and creating a new GTAP-BIO model to evaluate ILUC values for SAF pathways that use significant amounts of sustainable electricity for production.

Task 1 – Provide Required Analyses on ILUC and DLUC Emissions and Other Analyses Related to Land Use Emissions at the Global, Regional, and Country Levels

Purdue University

Objectives

This task concentrates on calculating ILUC and DLUC values for new SFA pathways, improving ILUC modeling approaches, collecting required data to more accurately estimate ILUC, updating the GTAP-BIO database to represent the global economy in recent years, and providing analyses that help to better elucidate LUCs across the world.



Research Approach

We collected the required data and developed the required analyses for both TEA and LCA to determine the cost structure of each new SAF pathway to be included in the GTAP-BIO model to support ILUC calculations. We then used the modified model to assess the LUCs associated with new SAF pathways.

To update the GTAP-BIO database to represent the global economy in 2014, we collected a wide range of data items at the global scale by country for 2014. The most important collected data items were crop outputs and harvested areas, crop prices, changes in land cover items (cropland, pasture land, and forest land), supplies and uses of vegetable oils and meals, and production and consumption of all types of conventional road biofuels. These data items were used to modify the 2014 standard GTAP database, which does not represent these data items. Several computer programs (e.g., Split.Com and GTAP-Adjust) were used to revise the standard GTAP database and create the new GTAP-BIO database for 2014.

Milestones

Over this period, new ILUC values were calculated upon request by the FTG. The new GTAP-BIO database, which represents the global economy in 2014, is ready to be implemented by the FTG. Several SAF pathways have been added to this new database. Upon approval from the FTG, we can begin to use this new database for ILUC assessment. The new database has been used to establish ILUC values for conventional biofuels (ethanol and biodiesel) upon request by the U.S. Environmental Protection Agency (EPA). These ILUC assessments have been used by the EPA in revising the U.S. Renewable Fuel Standard.

Major Accomplishments

Accomplishments in Task 1 include providing various assessments for SAF produced in Brazil using corn alcohol-to-jet technology; participating in a model comparison exercise conducted by the U.S. EPA regarding ILUC calculations for U.S. biofuel pathways; assessing the applicability of low-LUC risk practices on second corn in Brazil; and determining potential definitions for marginal land to represent ILUC assessments for SAF pathways that use cellulosic crops as feedstock.

Publications

Written reports

Taheripour participated in developing the following report related to ILUC calculations for U.S. biofuel pathways:

- Environmental Protection Agency (2023). "Model Comparison Exercise: Technical Document." Transportation and Climate Division Office of Transportation and Air Quality, U.S. Environmental Protection Agency, EPA-420-R-23-017.

Conference papers

- CAEP/13-FTG/02-WP/08 – "Pathway definition", October 31 to November 4, 2022, Montréal, Canada.
- CAEP/13-FTG/02-WP/09 – "Brazilian second corn ATJ", October 31 to November 4, 2022, Montréal, Canada.
- CAEP/13-FTG/03-WP/13 – "ILUC assessment for Brazilian second corn ATJ", March 6 to 9, 2023, Virtual Meeting.
- CAEP/13-FTG/03-WP/14 – "Applicability of the Low Land Use Change (LUC) risk practices on 2nd Crop in Brazil", March 6 to 9, 2023, Virtual meeting.
- CAEP/13-FTG/03-WP/14 – "Definition of marginal land", March 6 to 9, 2023, Virtual meeting.
- CAEP/13-FTG/03-IP/06 – "ILUC and DLUC updates on Soil Organic Carbon (SOC), ILUC calculations for pathways with significant amounts of electricity, and potential data base and modelling updates", March 6 to 9, 2023, Virtual meeting.
- CAEP/13-FTG/04-WP/07 – "Modeling Brazil corn ATJ pathway", July 24-28, 2023, Turin, Italy.
- CAEP/13-FTG/04-WP/08 – "Updates Low LUC Risk Practice", July 24-28, 2023, Turin, Italy.
- CAEP/13-FTG/04-WP/09 – "Definition of Marginal Land", July 24-28, 2023, Turin, Italy.
- CAEP/13-FTG/05-WP/05 – "Definitions of land and specifications for negative ILUC pathways", September 5-7, 2023, virtual.

Outreach Efforts

- Taheripour participated in ASCENT Advisory Group meetings in Fall 2022 and Spring 2023 and shared the findings of this research with the ASCENT community.
- Taheripour has reviewed many academic papers for various journals that provide publications in research areas associated with Task 1.

Awards

None.

Student and Postdoctoral Fellow Involvement

- EhsanReza Sajedinia, current PhD student, Purdue University, full-time assistantship (50%) for data collection and running simulations
- Lauren Benavidez, current PhD student, Purdue University, full-time assistantship (50%) for data collection and working with land use emission data and models
- Omid Karami, postdoctoral fellow, Purdue University, full-time until the end of July 2023, providing summations and data analyses

Plans for Next Period

Upon approval from the FTG, we will reassess ILUC values for the approved SAF pathways using the new 2014 GTAP-BIO database. We will also work on a new GTAP-BIO database that represents the global economy in 2017. We will continue to work on TEAs to support calculations of LUC emissions associated with new SAF pathways.

Task 2 – Develop Economic Models, Collect Data, and Conduct Analyses to Support the FTG Subgroups to Achieve the Goals and Tasks Defined for 2023

Purdue University

Objectives

- Provide required data and analyses to support the FTG subgroup in accomplishing tasks related to land use and land use emission subjects
- Coordinate with the FTG subgroups to avoid conflicts between the ILUC subgroup activities and activities performed by other subgroups

Research Approach

This task incorporates many varied assignments and components. We followed standard approaches to support FTG subgroups, including the Core LCA, TPP, ERA, and Sustainability subgroups. Using the GTAP-BIO model, we collected data and provided appropriate analyses to accomplish this task. Taheripour is the co-lead of the FTG ILUC group. Taheripour collaborates with the LCA, TPP, ERA, and Sustainability subgroups of the International Civil Aviation Organization (ICAO) Committee on Aviation Environmental Protection (CAEP) FTG.

Milestones

Taheripour participated in the CAEP13/FTG02, CAEP13/FTG03, CAEP13/FTG04, and CAEP13/FTG05 meetings and was involved in many of the tasks and document preparation activities for these meetings. He also responded to other subgroup requests for help and collaboration. He has led efforts in ILUC modeling and ILUC-related tasks associated with other subgroups. He continued to examine ILUC values for SAF pathways.

Major Accomplishments

In addition to participating in meetings with FTG subgroups and reviewing their working and information papers, Taheripour collaborated with the FTG secretary and FTG co-rapporteurs to develop reports for ICAO Steering Group meetings. Examples are presented in the publications (written reports) section.

Publications

Written reports

- CAEP/13-FTG/05-WP/03 – “Cutoff dates for Low LUC Risk Practices”, September 5-7, 2023, virtual.
- CAEP/13-FTG/05-WP/04 – “Amendments to the ICAO document “CORSIA methodology for Calculating Actual Life Cycle Emission Values””, September 5-7, 2023, virtual.
- CAEP/13-FTG/05-WP/05 – “Amendments to the ICAO document “CORSIA Default Life Cycle Emission Values for CORSIA Eligible Fuels””, September 5-7, 2023, virtual.

- CAEP/13-FTG/05-WP/06 – “Amendments to the ICAO document “CORSA Eligibility Framework and Requirements for Sustainability Certification Schemes””, September 5-7, 2023, virtual.

Conference papers

Lewis K., Obnamia J., Allroggen F., Taheripour F., Malina R. (2023) “*Sustainability Challenges and Opportunities of Power-to-Liquid Fuels*,” 26th Annual Conference on Global Economic Analysis, June 14-16, Bordeaux, France.

Outreach Efforts

See outreach efforts under Task 1.

Taheripour has reviewed many academic papers for various journals that provide publications in research areas associated with Task 2. Taheripour has also collaborated with various journals that publish papers associated with Task 2.

Taheripour attended the ASCENT Advisory Group meetings in Fall 2022 and Spring 2023 and discussed the findings of this task with members of this community.

Awards

None.

Student Involvement

- EhsanReza Sajedinia, current PhD student, Purdue University, full-time assistantship (50%) for data collection and running simulations
- Omid Karami, postdoctoral fellow, Purdue University, full-time until the end of July 2023, providing summations and data analyses

Plans for Next Period

We will collaborate with the Core LCA subgroup to develop a methodology to check and verify changes in soil carbon content at the farm level. We will continue to support FTG subgroups, including the Core LCA, TPP, and ERA subgroups, in accomplishing the required LCAs for new SAF pathways. In addition, we will continue to develop the required TEAs to include the cost structure of new SAF pathways in the GTAP-BIO database.

Task 3 – Help the CORSIA/FTG to Better Assess the CI of SAF Pathways due to LUCs

Purdue University

Objectives

This major task includes the following subtasks: (a) review the existing data sources that have been commonly used in determining land use emission factors for assessing ILUC emissions for biofuels and determine the advantages and disadvantages of each data source, (b) generate a new emission factor dataset at a grid cell level for the entire world that represents the carbon content of each type of land cover item for use in ILUC calculations, (c) assess changes in SOC due to the cultivation of feedstock for SAF production at the farm level, (d) develop a new carbon accounting software to facilitate ILUC calculations for each selected emission factor dataset, (e) define a methodology for assessing DLUC at the farm level based on experimental observations at the farm level and enhance the accuracy of ILUC values based on these experiments, and (f) provide a new version of the GTAP-BIO model to calculate ILUC emissions for wind and solar electricity.

Research Approach

To accomplish the goals of this task, we have identified the existing data sources on land use emission factors and reviewed the corresponding literature. Data sources that represent historical LUCs at the global scale have been identified and evaluated. Biophysical models (e.g., Terrestrial Ecosystem Model (TEM), Daycent, and other similar models) that can be used in assessing land emission factors have been identified. The Intergovernmental Panel on Climate Change (IPCC) guidelines (published in 2006 and 2019) for assessing land use emission factors have been reviewed. The emission

accounting models used in the United States have been identified and reviewed. Datasets that are needed to estimate the production of solar electricity at the global scale have been collected and processed.

Milestones

- The advantages and disadvantages of the existing data sources on land use emission factors have been identified.
- Using a grided dataset, we have determined historical LUCs and transition matrices at the global scale for 2000–2020 by country.
- A primary test using TEM has been conducted to evaluate land carbon content at the global scale.
- The agro-ecological zone emission factor (AEZ-EF) carbon calculator model has been revised to follow the IPCC guidelines for LUCs.
- Regional and global ILUC values for CORSIA-approved SAF pathways have been re-assessed and presented to the FTG.
- A program has been developed to convert AEZ-EF and Carbon Calculator for Land Use and Land Management Change from Biofuels Production (CCLUB) emission models from Excel to GAMS to make these models more user-friendly and transparent.
- A new GTAP-BIO model has been developed to assess ILUC values for SAF pathways that use a significant amount of solar electricity. This model has been tested for several regions, and results have been reported to the FTG.

Major Accomplishments

- 1) Existing data sources of land use emission factors have been validated.
- 2) We have assessed LUCs for 2000–2020 at the global scale.
- 3) The AEZ-EF model has been revised to follow the IPCC 2019 guidelines.
- 4) New codes have been developed for the AEZ-EF and CCLUB models to operate in GAMS.
- 5) We have augmented the GTAP-BIO model to calculate ILUC for SAF pathways that use solar electricity.

Publications

Peer-reviewed journal publications

Taheripour F., Mueller S., Emery I, Karami O., Sajedinia E., Zhuang Q., Wang M (2023) “Biofuels induced land use change emissions: The role of implemented emission factors in assessing terrestrial carbon fluxes,” *Sustainability*: Under Review.

Conference papers

Taheripour F., Sajedinia E., Chepeliev M., Karami O. (2023) “Land use change implications of Power-to-Liquid Fuels”, 26th Annual Conference on Global Economic Analysis, June 14-16, Bordeaux, France.

Written reports

Several working papers and information papers have been produced based on our work for this task. Working and information papers presented at FTG meetings include the following:

- CAEP/13-FTG/04-WP/06 – “Soil organic carbon including a case study”, July 24-28, 2023, Turin, Italy.
- CAEP/13-FTG/04-WP/10 – “Updating the AEZ-EF model according to 2019 IPCC guideline and ILUC revisions”, July 24-28, 2023, Turin, Italy.
- CAEP/13-FTG/04-WP/09 – “Assessing ILUC for a representative power to liquid SAF pathway”, July 24-28, 2023, Turin, Italy.

Outreach Efforts

Taheripour attended several meetings to present research outcomes on this task, including the following:

- GTAP 26th Annual Conference on Global Economic Analysis, June 14-16, Bordeaux, France.
- ASCENT Advisory Group meetings in Fall 2023 and Spring 2023, where Taheripour discussed the findings of this task with members of this community.

Taheripour has reviewed many academic papers for various journals that produce publications in research areas associated with Task 3.

EhsanReza Sajedinia attended several meetings to present research outcomes on this task, including the following:

- 2023 Agricultural & Applied Economics Association Annual Meeting, Washington DC, July 23–25.



- ASCENT Advisory Group meeting in Spring 2023, where EhsanReza discussed the findings of this task with students participating in this meeting.

Awards

None.

Student Involvement

- EhsanReza Sajedinia, current PhD student, Purdue University, full-time assistantship (50%) for data collection and running simulations
- Shuo Chen, current PhD student, Purdue University, full-time assistantship (50%) for data collection and data processing
- Xiangyu Liu, current PhD student, Purdue University, full-time assistantship (50%) for data collection and data processing
- Ye Yuan, current PhD student, Purdue University, full-time assistantship (50%) for data collection and data processing
- Lauren Benavidez, current PhD student, Purdue University, full-time assistantship (50%) for data collection and data processing

Plans for Next Period

We will continue working to serve the FTG during the CAEP13 cycle to accomplish the following tasks:

- We will re-assess ILUC values for CORSIA-approved SAF pathways with the 2014 GTAP-BIO database or 2017 GTAP-BIO database upon approval from the FTG.
- We will continue to carry out computations of ILUC emissions associated with SAF production for requested world regions, for use in CORSIA.
- We will review the approach to ILUC in light of emerging scientific evidence and data.
- A report will be developed on the quality of existing data sources on land use emission factors.
- The land use database for 2000–2020 generated by this research will be used to establish a benchmark dataset to evaluate the soil carbon content using the Moderate Resolution Imaging Spectroradiometer (MODIS) land cover data for 2020 based on TEM and satellite data.
- A benchmark dataset will be produced to represent soil carbon content by land type at a global scale by country.
- A methodology will be defined to measure, check, and verify changes in SOC at the farm level due to changes in agricultural practices.
- We will continue to improve the AEZ-EF model.
- We will investigate potential gains in soil carbon content due to agricultural practices. Particular attention will be given to improvements in soil carbon content due to new technologies that improve crop plant root systems to deposit more carbon in the soil.



Project 001(D) Alternative Jet Fuel Supply Chain Analysis

The Pennsylvania State University

Project Lead Investigator

Lara Fowler
Chief Sustainability Officer, The Pennsylvania State University
Director, Penn State Sustainability Institute
Professor of Teaching, Penn State Law
Affiliate Faculty, Penn State School of International Affairs
The Pennsylvania State University
103 Land & Water Research Building
University Park, PA 16802
814-865-4806
Lbf10@psu.edu

University Participants

The Pennsylvania State University (Penn State)

- P.I.s: Lara Fowler, Director, Penn State Sustainability Institute; Professor of Teaching, Penn State Law; Anne Menefee, Assistant Professor of Energy and Mineral Engineering (from Period B); Armen Kemanian, Professor of Production Systems and Modeling (from Period B); Seth Blumsack, Professor of Energy Policy and Economics and International Affairs
- FAA Award Number: 13-C-AJFE-PSU, RISK-INFORMED ALTERNATIVE JET FUEL (AJF)
- Periods of Performance: **Period A:** August 1, 2017 to January 31, 2022; **Period B:** June 14, 2022 to November 13, 2023; **Period C:** October 1, 2022 to September 30, 2023.
- Tasks:
 - Period A (August 1, 2017 to January 31, 2022)**
 1. 1.3.1: Risk-reward profit-sharing modeling for first facilities
 - 1.3.2: Additional quantification of risk and uncertainties in supply chains (foundational part of Task 1.3.1)
 - 1.3.3: Supply chain risk analysis tools for farmer adoption
 - 1.4.1: National survey of current and proposed state and federal programs that monetize ecosystem services
 - 1.4.3: Support of stakeholder engagement efforts
 - Period B (June 14, 2022 to November 13, 2023)**
 - 1.1: Research on existing federal law and policy drivers
 - 1.2: Research on existing state and regional law, and policy drivers
 - 1.3: Research on proposed legislation (federal and state)
 - 1.4: Research on other law/policy issues, as identified by the ASCENT 001 team
 - 2. 2.1: Work with ASCENT 001 to identify stakeholder engagement opportunities
 - 2.2: Development of a list of potential stakeholders critical to discussion
 - 2.3: Development of agenda/materials for critical discussions; meeting facilitation as needed
 - 3. 3.1: Work with ASCENT 001 team members to identify critical questions, and refine the scope of work related to carbon capture and sequestration (CCS)
 - 3.2: Conduct literature review regarding CCS and its potential use in conjunction with alternative jet fuels (AJFs)
 - 3.3: Draft a review manuscript examining opportunities to integrate CCS and AJF
 - 4. 4.1: Work with ASCENT 01 team members to identify critical questions, and refine the scope of work related to soil organic carbon (SOC)
 - 4.2: Conduct literature review regarding SOC and its potential relation to AJF
 - 4.3: Draft review manuscript examining opportunities for SOC and AJF



Period C (October 1, 2022 to September 30, 2023)

1. 1.1: Research on existing and proposed federal law and policy drivers
- 1.2: Research on existing and proposed state and regional law and policy drivers
- 1.3: Research on other law/policy issues, as identified by the ASCENT 001 team
2. 2.1: Work with ASCENT 001 to identify stakeholder engagement opportunities
3. 3.1: Research on integration of CCS
- 3.2: Work with ASCENT 01 team to refine the scope of work and current needs
- 3.3: Research and review manuscript on geologic carbon storage potential, with emphasis on permanence and risks (both technical and legal)
4. 4.1: Refine global modeling systems by using level 3 Global Administrative Areas (GADM Level 3), soils from the International Soil Reference and Information Center (ISRIC), and weather data from the North American Land Data Assimilation System (NLDAS)
- 4.2: Use machine learning to generate SOC profiles for Business as Usual (BAU) conditions, or machine learning and combination of Cycles for automated soil organic carbon (SOC) stock calculations; initial geographic target is the continental United States CONUS
- 4.3: Apply Cycles-A to the task of fitting sustainable aviation fuel (SAF) crops in the current agricultural matrix of the United States, focusing on oil crops as an example
- 4.4: Complete a SOC modeling manuscript, with the goal of standardizing methods for SOC (and nitrous oxide) calculations in relation to the carbon intensity (CI) under BAU and SAF production scenarios

Washington State University (WSU)

- Michael Wolcott, Regents Professor (for funding period from June 14, 2022 to November 13, 2023)
- Kristin Brandt, Staff Engineer (through funding period ending January 31, 2022)

Project Funding Level

FAA funding: \$100,000 (for period C, October 1, 2022 to September 30, 2023)

Matching from Penn State: \$100,000

Total funding: \$200,000

Investigation Team

In addition to the PIs listed above, the investigation team has included or includes the following:

- Researcher: Saurabh Bansal, Prof. of Supply Chain Management, Penn State Smeal College of Business, Task 1 (Period A).
- Researcher: Burt English, Professor, Ag and Economics, University of Tennessee, Task 1 (Period A)
- Researcher: Michael Helbing, Staff Attorney, Penn State Center for Energy Law and Policy, Tasks 1, 2, 3
- Researcher: Ekrem Korkut, Legal Research Postdoctoral Associate, Tasks 1, 2
- Researcher: Yuning Shi, Associate Research Professor, Penn State College of Ag Sciences, Task 4

Period A (August 1, 2017 to January 31, 2022)

Task 1.3.1 (Bansal; supported by Brandt and English): Risk-reward profit-sharing modeling for first facilities

Task 1.3.2 (Bansal; supported by Brandt and English): Additional quantification of risk and uncertainties in supply chains (foundational part of Task 1.3.1)

Task 1.3.3 (Bansal; supported by Brandt and English): Supply chain risk analysis tools for farmer adoption

Task 1.4.1 (Fowler; supported by Korkut): National survey of current and proposed state and federal programs that monetize ecosystem services

Task 1.4.3 (Fowler; supported by Korkut): Support of stakeholder engagement efforts

Period B (June 14, 2022 to November 13, 2023)

Task 1.1 (Fowler, supported by Korkut): Research on existing federal law and policy drivers

Task 1.2 (Fowler, supported by Korkut): Research on existing state and regional law, and policy drivers

Task 1.3 (Fowler, supported by Korkut): Research on proposed legislation (federal and state)

Task 1.4 (Fowler, supported by Korkut): Research on other law/policy issues, as identified by ASCENT 001 team

Task 2.1 (Fowler, supported by Korkut): Work with ASCENT 001 to identify stakeholder engagement opportunities
 Task 2.2 (Fowler, supported by Korkut): Development of a list of potential stakeholders critical to discussion
 Task 2.3 (Fowler, supported by Korkut): Development of agenda/materials for critical discussions; meeting facilitation as needed

Task 3.1 (Menefee): Work with ASCENT 001 team members to identify critical questions, and refine the scope of work related to CCS

Task 3.2 (Menefee): Conduct literature review regarding CCS and its potential use in conjunction with AJFs

Task 3.3 (Menefee): Draft a review manuscript examining opportunities to integrate CCS and AJF

Task 4.1 (to be determined, supported by Wolcott): Work with ASCENT 01 team members to identify critical questions, and refine the scope of work related to SOC

Task 4.2 (to be determined, supported by Wolcott): Conduct literature review regarding SOC and its potential relation to AJF

Task 4.3 (to be determined, supported by Wolcott): Draft review manuscript examining opportunities for organic soil carbon and AJF

Period C (October 1, 2022, to September 30, 2023)

Task 1.1 (Fowler, supported by Helbing and Korkut): Research on existing and proposed federal law and policy drivers

Task 1.2 (Fowler, supported by Helbing and Korkut): Research on existing and proposed state and regional law and policy drivers

Task 1.3 (Fowler, supported by Helbing and Korkut): Research on other law/policy issues, as identified by the ASCENT 001 team

Task 2.1: Work with ASCENT 001 to identify stakeholder engagement opportunities

Task 3.1 (Menefee and Helbing): Research on integration of CCS

Task 4.1 (Kemanian): Accounting for SOC and nitrous oxide emissions by using agroecosystem models

Project Overview

For the first period of performance (period A), this project focused on developing a qualitative and quantitative understanding of factors to help establish biofuel supply chains for AJFs. Although efforts to establish these supply chains are underway, many challenges exist because of a lack of clarity regarding the incentives that stakeholders would require to engage in these supply chains and to devote their resources to investing in the facilities required for these supply chains. To this end, this project has two goals:

1. Develop pro forma cash flows that represent the financial status of various participants in biofuel supply chains for AJFs, to inform a transparent risk-sharing tool
2. Understand the policy landscape in various parts of the United States, to encourage AJF supply chains and identify additional policy initiatives that may be necessary

During the second period of performance (period B), this project continues to focus on understanding the law and policy drivers associated with AJF, while also expanding focus to include two new areas—CCS and organic soil carbon—and their potential linkages to AJF.

During the third period of performance (period C), this project continues to stay up to date on the law and policy changes associated with AJF, and has also started to focus on important opportunities and knowledge gaps surrounding CCS and SOC. Two new P.I.s were on-boarded to focus on these emerging areas and provide relevant expertise across the ASCENT 01 team.

Period A, Task 1.3.1 – Risk–Reward Profit-sharing Modeling for First Facilities

The Pennsylvania State University

Objective

Develop a transparent risk-sharing tool to provide all partners with an understanding of the cash flows and risks faced by all supply chain partners

Research Approach

We first collected many risk-sharing tools that have been proposed in the supply chain literature. Subsequently, we narrowed this list to 9–12 mechanisms. We created an Excel-based framework in which the cash flows of all supply chain partners are modeled on the basis of data from the techno-economic analyses developed by WSU. This framework incorporates the risk-sharing mechanisms.

Milestone

We developed Excel models for four realistic configurations by using data from techno-economic analysis models developed by WSU.

Major Accomplishments

We developed an Excel-based framework showing the cash flows of four key stakeholders in AJF supply chains: farmers, preprocessors, refineries, and airlines. The framework shows various risk-sharing contracts that each of the stakeholders could extend to others, as well as the financial burdens or opportunities associated with these mechanisms. The framework also shows the government’s financial burden of supporting these mechanisms. The framework was developed for four levels of refinery capacity. Overall, this framework can be used as a decision support tool by various stakeholders to determine whether to engage in alternative jet biofuel supply chains and negotiate with one another.

Publications

We have provided the tool to the sponsor and will provide training on its use to the project sponsor upon request.

Outreach Efforts

Our tool has been presented and discussed at three ASCENT advisory committee meetings.

Awards

None.

Student Involvement

None.

Period A, Task 1.3.2 – Additional Quantification of Risk and Uncertainties in Supply Chains (Foundational Part of Task 1.3.1)

The Pennsylvania State University

Objective

Develop methods to rely on expert judgments to quantify uncertainties associated with biofuel supply chains

Research Approach

We developed a new econometric approach to quantify the probability distributions of uncertain quantities, such as yield or demand, when an expert panel provides judgments regarding the most likely values. This approach exploits the well-known theory of generalized least squares in statistics for the context in which historical data are available to calibrate expert judgments or when these data are not available.



Milestones

We have described this method in two manuscripts. In the first manuscript, "[Using Subjective Probability Distributions to Support Supply Chain Decisions for Innovative Agribusiness Products](#)," we developed a two-stage procedure to calibrate expert judgments regarding the distribution of biofuel uncertainties, such as the uncertain yields of new varieties of oilseeds, demand, or selling price. In the first step of the procedure, we calibrated the expert judgments by using historical data. Specifically, we used prior judgments provided by experts, and compared them with actual realizations (such as predicted yield versus actual yield) to determine the frequency at which each expert over- or underestimated the uncertainty (e.g., expert 1 underestimated the yield 60% of the time, whereas expert 2 underestimated the yield 90% of the time). In the second manuscript, "[Optimal Aggregation of Individual Judgmental Forecasts to Support Decision Making in a R&D Program](#)," we used this information to determine the optimal approach for aggregating the experts' judgments to determine the mean and standard deviation of the probability distributions. In this manuscript, we developed a new optimization protocol for determining the optimal acreage for growing specific crops by considering the estimated mean and standard deviation, as well as incorporating the variability in these estimates. This manuscript won two awards at a professional conference (INFORMS 2021) in November 2021 and in October 2022.

Major Accomplishments

Theoretical development and a numerical study have demonstrated the promise of this approach.

Publications

Peer-reviewed journal publications

Bansal, S., & Gutierrez, G. J. (2020). Estimating uncertainties using judgmental forecasts with expert heterogeneity. *Operations Research*, 68(2), 363-380. doi: 10.1287/opre.2019.1938

Written reports

Bansal, S., & Wang, T. (2019). Using subjective probability distributions to support supply chain decisions for innovative agribusiness products. Report for the *Federal Aviation Administration*.

<https://s3.wp.wsu.edu/uploads/sites/2479/2021/05/ASCENT-Project-001D-attachment-1.pdf>

Bansal, S., & Gutierrez, G. J. (2021). Optimal aggregation of individual judgmental forecasts to support decision making in a R&D program. Submitted to *Operations Research*.

<https://s3.wp.wsu.edu/uploads/sites/2479/2021/05/ASCENT-Project-001D-attachment-2.pdf>

Outreach Efforts

None.

Awards

2021 Decision Analysis Practice Award, INFORMS, November 2021

2022 Decision Analysis Best Publication Award, INFORMS

Student Involvement

None.

Plans for Next Period

This work has been completed. No plans exist for the next period.

Period A, Task 1.3.3 – Supply Chain Risk Analysis Tools for Farmer Adoption

The Pennsylvania State University

Objectives

Understand farmers' risk preferences over a long duration, and how these preferences affect decisions to grow crops that can support AJF supply chains

Research Approach

We surveyed farmers to understand their risk preferences over extended durations. Specifically, we presented farmers with sample yield ranges over extended periods, then asked them to estimate the lowest equivalent guaranteed yield that they would be willing to accept, given the uncertain yields. We used these responses to perform statistical analyses.

Milestone

We have completed the survey and have written a manuscript based on the survey.

Major Accomplishments

We compiled data from 43 farmers in central Pennsylvania regarding their preferences, given uncertain yields from their land. The results quantify the loss of value that farmers attribute to uncertain yield. Results have been reported for both 1-year and 10-year horizons. For the 10-year horizon, we have also reported results for an initial yield build-up, as often arises with most biofuel crops. The key findings from this study are as follows: (a) farmer valuations of a new crop decrease acutely as the uncertainty in yield increases, and (b) the initial build-up period of low yields can be a major deterrent that inhibits farmers from adopting new crops for the purpose of supporting biofuels.

Publications

A manuscript detailing this work has been written and provided to the sponsor.

Outreach Efforts

None.

Awards

None.

Student Involvement

None.

Plans for Next Period

This work has been completed. No plans exist for the next period.

Period A, Task 1.4.1 – National Survey of Current and Proposed State and Federal Programs that Monetize Ecosystem Services

The Pennsylvania State University

Objectives

Conduct a survey, and summarize current and proposed state and federal programs to monetize ecosystem services

Research Approach

This Task builds on and continues the work performed under ASCENT Project 001, Task 8.1, which focused on the biomass and water-quality benefits to the Chesapeake Bay watershed. In previous years, we examined the biofuel law and policy landscapes of the Pacific Northwest and Southeast regions, as well as the state of Hawaii. During this most recent reporting time period (October 1, 2021 to September 30, 2022), we focused on federal biofuel law and policy, and how both have been affected by international drivers.

Milestones

Our research was previously circulated in three region-specific white papers. In addition, we developed a federal-level white paper in the list of Tasks, which was subsequently published (see below).

Copies of these documents are available online:

- Western U.S. policy manuscript (with a focus on Washington state, last updated in 2019): [Western US Bioenergy Law & Policy - Draft 5.docx](#)



- Southeast policy manuscript (with a focus on Tennessee): [Southeast Bioenergy Law & PolicyDraft3.docx](#)
- Hawaii policy manuscript: [Hawaiian Biofuel Law & Policy_v5.docx](#)
- Federal-level white paper: [2021_01_08_SAF paper draft_circulated for review_KCL_NB \(1\).docx](#)

Major Accomplishments

In addition to developing the white papers described above, we adapted the federal-level white paper for publication (see below). We also provided a briefing and presented a poster during the ASCENT fall meeting (October 2021). Additionally, P.I. Lara Fowler is involved in another project, funded by the USDA National Institute of Food and Agriculture, entitled "Consortium for Cultivating Human and Naturally Regenerative Enterprises" (USDA-NIFA Sustainable Agricultural Systems Award 2020-68012-31824), dubbed the "C-CHANGE" project. She has built upon her work in this ASCENT project to link to the regenerative agriculture work being pursued in C-CHANGE, including providing a briefing on second-generation biofuel law and policy.

Publications

Peer-reviewed journal publications

Korkut, E. & Fowler, L. B. (Nov. 2021). Regulatory and policy analysis of production, development and use of sustainable aviation fuels in the United States." *Frontiers in Energy Research*, 9, 750514. doi:10.3389/fenrg.2021.750514.

Outreach Efforts

Presentations

- Fowler, L. B., & Lewis, K. (October 2021). Sustainable aviation fuel development: Law, policy and the blender's tax credit. Manuscript presented at the ASCENT Annual Meeting.

Awards

None.

Student Involvement

Ekrem Korkut graduated from the Penn State School of International Affairs in May 2021 and transitioned to working as a postdoctoral associate on this project (50% of his time; the other 50% is funded by another project).

Plans for Next Period

As noted above, we will continue adapting the existing white papers for publication. The next step will again focus on regional efforts. As needed, we will provide support to working groups under the SAF Grand Challenge. Of note, work on this Task was delayed by the lack of a contract in the 4.5 months from February 1, 2022 to June 14, 2022.

Period A, Task 1.4.3 – Help Support Stakeholder Engagement Efforts

The Pennsylvania State University

Objective

Facilitate dialogue among producers, industry, government, and other affected stakeholders

Research Approach

Our work under this objective has focused on stakeholder engagement and facilitation of effective dialogue to help bridge gaps among producers, industry, government, and other affected stakeholders. This role supports the needs of other team members.

Milestone

These efforts have supported stakeholder engagement efforts led by other teams, including but not limited to the regional partners identified in ASCENT Project 01, Tasks 3.1, 3.2, and 3.3.

Major Accomplishments

This set of Tasks has been relatively limited, and no major accomplishments have been made to date. We have continued to participate in discussions and calls related to potential stakeholder engagement needs.

Publications

None.

Outreach Efforts

None.

Awards

None.

Student Involvement

None.

Plans for Next Period

Future work under this objective will include presenting to the project partners on facilitation skills and tactics. Additional support for regional projects will be offered as needed for facilitation and stakeholder engagement sessions as the regional projects move to the deployment stage. We will provide support to working groups under the SAF Grand Challenge as necessary.

Of note, although the proposed contract period was intended to start on February 1, 2022, no contract was in place from February 1, 2022 to June 13, 2022, thus leaving a gap of approximately 4.5 months without funding.

Period B, Task 1 – Law and Policy Research

The Pennsylvania State University

Objectives

Understand existing federal law and policy drivers related to SAF at the national level, including participation by the United States in international discussions and agreements (Task 1.1); research existing state law and policy drivers (Task 1.2); research potential law and policy drivers as needed (Task 1.3); and explore other issues identified by the ASCENT 001 team, as needed (Task 1.4).

Research Approach

Following up on the publication of the *Frontiers in Energy* review of law and policy, we began research on the recently adopted Blender's Tax Credit and the potential Sustainable Skies Act. In addition, we updated our legal and policy research on various states' activities regarding SAF (California, Oregon, Washington, and others).

Milestone

We engaged in team meetings and provided updates on legal research topics.

Major Accomplishments

We provided real-time analysis of pending federal legislation (the Inflation Reduction Act), at the request of Project Manager Nate Brown. In addition, we researched and shared information related to pending Securities and Exchange Commission rulemaking on greenhouse gas emissions accounting.

Publications

We are exploring possibilities for another formal publication.

Outreach Efforts

Our research has been discussed in several presentations:



- Fowler, L. B., & Korkut, E. (December 2022). ASCENT 001 Team Briefing on pending Securities and Exchange Commission Greenhouse Gas Emission rules.
- Fowler, L. B. (October 2022). Briefing to Volvo Corporation on Opportunities Related to the Renewable Fuel Standard and SAF.
- Fowler, L. B., & Korkut, E. (July 2022). Update on State Legal and Regulatory Opportunities for SAF. ASCENT 001 Project Meeting.
- Fowler, L. B. (June 2022). Legal and Regulatory Drivers of Sustainable Aviation Fuel. Global Council for Science and the Environment.

Awards

None.

Student Involvement

None.

Plans for Next Period

We will continue to work with the ASCENT 001 team to identify potential law and policy concerns and opportunities. We are additionally exploring how SAF and renewable natural gas might be developed in synergistic ways.

Period B, Task 2 – Support Stakeholder Engagement Efforts

The Pennsylvania State University

Objective

Facilitate dialogue among producers, industry, government, and other affected stakeholders

Research Approach

Our work under this objective has focused on stakeholder engagement and facilitation of effective dialogue to help bridge gaps among producers, industry, government, and other affected stakeholders. This role supports the needs of other team members.

Milestone

These efforts have supported stakeholder engagement efforts led by other teams, including but not limited to the regional partners identified in ASCENT Project 001.

Major Accomplishments

This set of Tasks has been relatively limited, and no major accomplishments have been made to date. We have continued to participate in discussions and calls related to potential stakeholder engagement needs.

Publications

None.

Outreach Efforts

None.

Awards

None.

Student Involvement

None.

Plans for Next Period

Future work under this objective will include presenting to the project partners on facilitation skills and tactics. Additional support for regional projects will be offered as needed for facilitation and stakeholder engagement sessions as the regional projects move to the deployment stage. As needed, we will provide support to working groups under the SAF Grand Challenge.

Period B, Task 3 – Carbon Capture and Sequestration

The Pennsylvania State University

Objective

Understand how CCS could be integrated with sustainable aviation fuel development

Research Approach

The new area of research involves a technical focus on integration of CCS with liquid fuel production and examination of SOC. For this Task, Anne Menefee will focus on the technical viability and sustainability of integrating liquid fuel production with CCS. Her research is broadly focused on decarbonization of the energy sector; she has extensive experience specifically in carbon sequestration. Across scales, her research includes exploring fundamental geochemical-geomechanical feedback in stress-fracture systems that are targeted by subsurface sequestration operations, and evaluating the system-level environmental impacts of emerging technologies that can both curb net emissions and be self-sustaining in the market. Most relevantly, she has worked on life-cycle and techno-economic assessments of subsurface technologies for carbon sequestration and waste management in the energy sector.

Milestone

This work has recently started.

Major Accomplishments

None.

Publications

None.

Outreach Efforts

None.

Awards

None.

Student Involvement

None.

Plans for Next Period

Because approval for this work was delayed, the work has only just started. Additional consultation with the ASCENT 001 team is needed regarding the proposed and potential next steps. This technical work should support implementation of the SAF Grand Challenge, the International Civil Aviation Organization Committee on Aviation Environmental Protection, and/or both.

Period B, Task 4 – Soil Organic Carbon

The Pennsylvania State University

Objective

Understand how organic soil carbon might be integrated with sustainable aviation fuel development

Research Approach

This effort is another new area of research identified by the ASCENT 001 team. As part of the request on this topic, we identified Armen R. Kemanian to join the ASCENT 001 team. The research approach for this Task will involve identifying critical questions and refining the scope of work (Task 4.1); conducting a literature review (Task 4.2); and drafting a review manuscript analyzing the opportunities to link organic soil carbon and SAF (Task 4.3).

Milestone

This work has recently started. Dr. Kemanian provided an initial presentation of ideas to consider during the August 25, 2022 ASCENT 001 team meeting.

Major Accomplishments

None.

Publications

None.

Outreach Efforts

Presentation, ASCENT 001 team (August 2022): "Agroecosystem Productivity and Carbon Intensity when Producing Aviation Fuel: Amplifying Opportunities and Taming Trade-offs."

Awards

None.

Student Involvement

None.

Plans for Next Period

Because approval for this work was delayed, the work has only just started. Additional consultation with the ASCENT 001 team is needed regarding the proposed and potential next steps. As with the technical work associated with CCS, this technical work should support implementation of the SAF Grand Challenge, the International Civil Aviation Organization Committee on Aviation Environmental Protection, and/or both.

Period C, Task 1 – Law and Policy Research

The Pennsylvania State University

Objectives

Stay up to date with existing and proposed federal law and policy drivers affecting SAF, including participation by the United States in international discussions and agreements (Task 1.1); research existing and proposed state law and policy drivers (Task 1.2); and explore other issues identified by the ASCENT 001 team, as needed (Task 1.3)

Research Approach

Following up on publication of the *Frontiers in Energy* review of law and policy, we began research on the recently adopted Inflation Reduction Act provisions related to SAF, including the Producer's Tax Credit (IRC § 45Z), Clean Hydrogen Tax credit (IRC § 45V), and CCSC (IRC § 45Z). In addition, we updated our legal and policy research on various states' activities regarding SAF (California, Oregon, Washington, Illinois, and others).

Milestone

At biweekly team meetings and semi-annual conferences, we provided updates on legal research topics.

Major Accomplishments

We presented "SAF Development: Law, Policy and the Blender's Tax Credit" and "Sustainable Aviation Fuel Law & Policy 101" at the ASCENT Advisory Committee Meeting in April 2023. In addition, we researched and shared information related to

pending Securities and Exchange Commission rulemaking, and California public disclosure rules on greenhouse gas emissions accounting.

Publications

We are exploring possibilities for another formal publication.

Outreach Efforts

Our research has been discussed in several presentations:

- Fowler, L. B., Korkut, E., & Helbing, M. (April 2023). ASCENT 001 Advisory Meeting “SAF Development: Law, Policy and the Blender’s Tax Credit.”
- Fowler, L.B. (April 2023). ASCENT 001 Advisory Meeting “Sustainable Aviation Fuel Law & Policy 101.”
- Fowler, L. B., & Korkut, E. (December 2022). ASCENT 001 Team Briefing on pending Securities and Exchange Commission Greenhouse Gas Emission rules.
- Fowler, L. B. (October 2022). Briefing to Volvo Corporation on Opportunities Related to the Renewable Fuel Standard and SAF.

Awards

None.

Student Involvement

None.

Plans for Next Period

We will continue to work with the ASCENT 001 team to identify potential law and policy concerns and opportunities. We are additionally exploring how SAF and renewable natural gas might be developed in synergistic ways.

Period C, Task 2 – Support Stakeholder Engagement Efforts

The Pennsylvania State University

Objective

Facilitate dialogue among producers, industry, government, and other affected stakeholders

Research Approach

Our work under this objective has focused on stakeholder engagement and facilitation of effective dialogue to help bridge gaps among producers, industry, government, and other affected stakeholders. This role supports the needs of other team members.

Milestone

These efforts have supported stakeholder engagement efforts led by other teams, including but not limited to the regional partners identified in ASCENT Project 001.

Major Accomplishments

This set of Tasks has been relatively limited, and no major accomplishments have been made to date. We have continued to participate in discussions and calls related to potential stakeholder engagement needs.

Publications

None.

Outreach Efforts

None.

Awards

None.

Student Involvement

None.

Plans for Next Period

Future work under this objective will include presenting to the project partners on facilitation skills and tactics. Additional support for regional projects will be offered as needed for facilitation and stakeholder engagement sessions as the regional projects move to the deployment stage. As needed, we will provide support to working groups under the SAF Grand Challenge.

Period C, Task 3 – Carbon Capture and Sequestration

The Pennsylvania State University

Objectives

Work with ASCENT 01 team to identify critical questions and needs surrounding the potential for CCS in SAF/AJF supply chains, and support other Tasks aimed at integrating aspects of CCS, e.g., carbon footprint, techno-economic, and feasibility analyses; conduct a literature review to understand the potential opportunities, challenges, research needs, etc.

Research Approach

The initial stages of the CCS Task involve an in-depth literature review to understand knowledge gaps and existing pathways for integrating CCS into AJF supply chains. As described below, we have refined our approach and objectives through discussions with the ASCENT 01 team, to focus more on policy and risk related to CCS, and to identify hurdles that must be addressed to (a) enable integration into AJF/SAF supply chains and (b) achieve real and quantifiable emission reductions.

Milestone

P.I. Menefee along with researcher Helbing were onboarded to the ASCENT 01 team during this project period. Through sub-meetings with ASCENT 01 team members, they have refined the scope of work to focus more on providing information and recommendations related to geologic carbon storage (GCS) policy and permanence, e.g., GCS paths that would enable or preclude actual and measurable CO₂ emission reductions. Menefee mentored an undergraduate student (funded through a department program) to conduct a literature review specifically on the integration of CCS with AJF/SAF production for various feedstocks and production pathways, and is currently working with an undergraduate student funded by this project to complete the white paper related to these issues raised by the ASCENT 01 team in support of other Tasks.

Major Accomplishments

We are compiling a draft literature review and recommendations to accommodate key questions and needs surrounding the permanence of GCS and most viable and tenable CCS pathways for aviation.

Publications

None.

Outreach Efforts

None.

Awards

None.

Student Involvement

P.I. Menefee is currently mentoring one undergraduate student on this Task, who will continue to work with her on the project in the Fall 2023 and Spring 2024 semesters. She mentored an undergraduate student in Summer 2023 to help conduct the initial literature review (who was funded through a different program in her department).

Plans for Next Period

The near-term goal for the next award period is to complete a white paper addressing the questions and needs related to CCS and SAFs that P.I. Menefee has solicited from ASCENT 01 team members during this award period. P.I. Menefee will focus on technical risks/opportunities, and Helbing will focus on policy hurdles, primarily those surrounding geologic storage that would enable AJF/SAF emission reductions through CCS. As needed, we will provide support and expertise to other Tasks.

Period C, Task 4 – Organic Soil Carbon

The Pennsylvania State University

Objective

Incorporate Penn State expertise on soil carbon and nitrogen cycling in the context of the calculation of the carbon intensity of SAF.

This process will include incorporating carbon-cycling modeling and uncertainty bounds, and methods for standardizing calculations that encompass baseline (or reference) scenarios and SAF production scenarios. These methods must be applicable worldwide, but the initial focus is CONUS. In addition, we anticipate similar work accounting for the nitrogen cycle, including the carbon footprint associated with the use of fertilizers and accounting for the emissions of nitrous oxide, whose equivalent carbon footprint can surpass that of SOC as a positive or negative climate forcing.

Research Approach

Develop a standard method to account for land use and SAF production by using Earth State and level 3 Global Administrative Areas (GADM) to report calculations on a field basis as well as on political units of relevance that are standardized worldwide. Overlay the North American Land Data Assimilation System (NLDAS) reanalysis climate databases and SoilGrids soils, so that the model Cycles (developed in P.I. Kemanian's laboratory) can be operated through the cropland domain. Use machine learning combined with a standardized initialization procedure to estimate steady-state soil carbon stocks under BAU and alternative SAF production scenarios. Researcher Yuning Shi involved with this work.

Milestone

Establish a stable database of land use, weather data, and soils, along with automated methods to run simulations with Cycles. Download and curate the USDA-NRCS pedon database for machine learning analysis.

Major Accomplishments

The modeling system has been established and tested. Cycles can be run to test scenarios globally. Realistic simulations of BAU and alternative scenarios can be run in CONUS. System tests have indicated that cropland areas are simulated with accuracy when the subsoil does not present a water table that interacts with the root zone, whereas those with a water table and artificial tile drainage (large areas of Iowa, Illinois, Minnesota, and other states in the Midwest) require further work. Under those conditions, simulating nitrous oxide emissions can be challenging, particularly when the areas of interest are amended with animal manure from confined animal feeding operations (almost 30% of the cropland area in Iowa). Machine learning work continues to progress. Developing a standardized system to initialize soil organic carbon will be a critical step to enable the use of methods compatible with other SAF carbon intensity accounting systems.

Publications

None.

Outreach Efforts

None.



Awards

None.

Student Involvement

The project has not included students to date. However, P.I. Kemanian is recruiting a graduate student to work on this project for Fall 2024.

Plans for Next Period

First (Task 1), develop a machine-learning-based algorithm to feed Cycles with automatic generation of SOC profiles for BAU. Test whether the algorithm provides outputs that improve upon the existing ISRIC database and the use of Cycles to establish BAU. Second (Task 2), use Cycles-A, an algorithm to automate crop sequence generation, to seek the inclusion of SAF crops in the current production matrix. This effort will be the first large-scale application of Cycles-A. Initial targets are specific watersheds in the United States that can accommodate oil crops. Third, consider the use of corn stover for ethanol-SAF production with return of high lignin residue to the soil (this pathway is unaccounted for and requires development). Tasks 1 and 2 will yield manuscripts for publication. In addition, a team led by Dr. Kemanian will prepare a summary of existing models and their use for carbon intensity accounting, building toward a standard method for handling of land use effects on the carbon intensity of SAF.



Project 001(E) Alternative Jet Fuel Supply Chain Analysis

University of Tennessee

Project Lead Investigator

Timothy Rials
Professor and Director
Center for Renewable Carbon
University of Tennessee
2506 Jacob Dr., Knoxville, TN 37996
865-946-1130
trials@utk.edu

University Participants

University of Tennessee (UT)

- P.I.: T. Edward Yu, Professor
- FAA Award Number: 13-C-AJFE-UTenn, Amendments 09, 11, 13, 15, 17
- Period of Performance: October 1, 2022 to September 30, 2023
- Tasks:
 1. Assess and inventory regional forest and agricultural biomass feedstock
 2. Develop national lipid availability analysis as feedstock for sustainable aviation fuel (SAF)
 3. Lay the groundwork for developing regional SAF economy in Tennessee and the southeastern United States
 4. Conduct soil organic carbon (SOC) analysis in the United States

Project Funding Level

Total estimated project funding: \$1,375,000 (total six-year funding)

Total federal and non-federal funds: \$1,375,000 (total six-year funding)

The UT Institute of Agriculture, in support of the project, provided faculty salary. Additional non-federal support was derived from contributions from the stakeholder group.

Investigation Team

Timothy Rials (project director (P.D.)/P.I.), Task 3
T. Edward Yu (co-P.D./P.I.), Tasks 1-4
Joshua Fu (co-P.I.), Task 4
Burton English (faculty), Tasks 1 and 2
Jim Larson (faculty), Task 2
Carlos Trejo-Pech (faculty), Task 1
David Hughes (faculty), Task 3
Hannah Rubin (PhD student), Task 4
Kumar Bolakhe (master's student), Tasks 1 and 2
Tongtong Li (master's student), Task 2

Project Overview

UT leads the feedstock production component of the project. This component targets the need to assess and inventory regional forest and agricultural biomass feedstock options and delineate the sustainability impacts associated with various feedstock choices, including land-use effects. UT also leads the national lipid supply availability analysis, using POLYSYS to develop information on the potential impacts and feasibility of using lipids to supply aviation fuel. The team at UT facilitates regional deployment/production of SAF by laying the groundwork and developing a regional deployment plan.

Additionally, UT collaborates with Purdue University and Pennsylvania State University (PSU) to estimate SOC in the United States in Task 4 to assist the agency in better understanding the related influence of SAF feedstock production.

Major goals include the following:

1. Develop a rotation-based oilseed crop scenario and evaluate potential with POLYSYS.
2. Reevaluate the production potential of biomass feedstocks and evaluate potential with POLYSYS and a supply chain optimization model.
3. Continue webinars with Central Appalachia stakeholders.
4. Develop an SOC benchmark/baseline in the United States.

Task 1 - Assess and Inventory Regional Forest and Agricultural Biomass Feedstock

University of Tennessee

Objectives

1. Complete the economic viability analysis for switchgrass, short-rotation woody crops, crop residues, forest residues, and cover crops.
2. Assist in risk-reward profit-sharing modeling by providing information from past work on cellulosic supply chains to PSU.
3. Develop new supply curves for both lignocellulosic and oilseed feedstock for SAF. Because the markets for lignocellulosic biomass (LCB) feedstock (i.e., grasses, short-rotation woody crops, and agricultural residues) are currently not well established, evaluation of the feasibility of supplying those LCB feedstocks is important. The production, harvesting, and storage costs of the feedstocks are included in the assessment. A variety of potential crop and biomass sources will be considered in the feedstock path, including the following:
 - Oilseed crops:** potentially including pennycress (*Thlaspi arvense*), camelina (*Camelina sativa*), and carinata (*Brassica carinata*) as “cover crops”
 - Perennial grasses:** switchgrass (*Panicum virgatum*), miscanthus (*Miscanthus sinensis*), and energy cane (*Saccharum complex*)
 - Short-rotation woody crops:** poplar (*Populus* species), willow (*Salix* species), loblolly pine (*Pinus taeda*), and sweetgum (*Liquidambar styraciflua*)
 - Agricultural residues:** wheat straw, corn stover, and other agricultural residues
 - Forest residues:** forest residue
4. Evaluate the potential economic impacts of a mature SAF industry on regional, state, and national economies.

Research Approach

County-level estimates of all-live total woody biomass, as well as average annual growth, removals, and mortality, were obtained from the Forest Inventory and Analysis (FIA) database. Mill residue data were not incorporated because most of that material already has a market. Forest residue encompasses removal of logging residues, thinnings, and unmerchantable trees. Forest residue excludes any logs from areas defined as supplying sawtimber but does include the logging residues that occur from sawtimber harvest.

We used the FIA sample database to estimate the logging residues at a fine resolution in a given area. Four layers of timber were categorized: hardwood sawtimber, hardwood pulpwood, softwood sawtimber, and softwood pulpwood based on the trees' diameters. We first interpolated the FIA sample data to generate the forest inventory level for the entire study area using the Kriging method and further downscaled it into higher-resolution levels for each of the four layers. Next, wood demand for sawmills was approximated by the capacity of sawmills, which was categorized from size 1 to size 6. A deep learning method was used to interpolate the demand for 263 newly opened sawmills after 2009. The demand was adjusted by a factor to ensure that the sum of mill demand in each state matches the data in the Timber Products Output (TPO) database maintained by the U.S. Forest Service. Finally, the ratio of logging residue over wood harvested was calculated using the TPO data at the county level. The available logging residue data layer was then derived by multiplying the simulated wood harvests based on sawmill capacity with the ratio of logging residues over wood harvests for the feedstock quantity and location analysis at the first stage of modeling.

Figure 1 illustrates the design of a two-stage logging residues-based SAF supply chain network that extends from forest harvesting to SAF delivery to airports. In the first stage, we determined the location and quantity of logging residues based on forest inventory and sawmill location and capacity by maximizing the forest harvest density. In the second stage, we identified the logging residues supply chain from field to airport, including the location of depots, biorefineries, and the airports to be served.

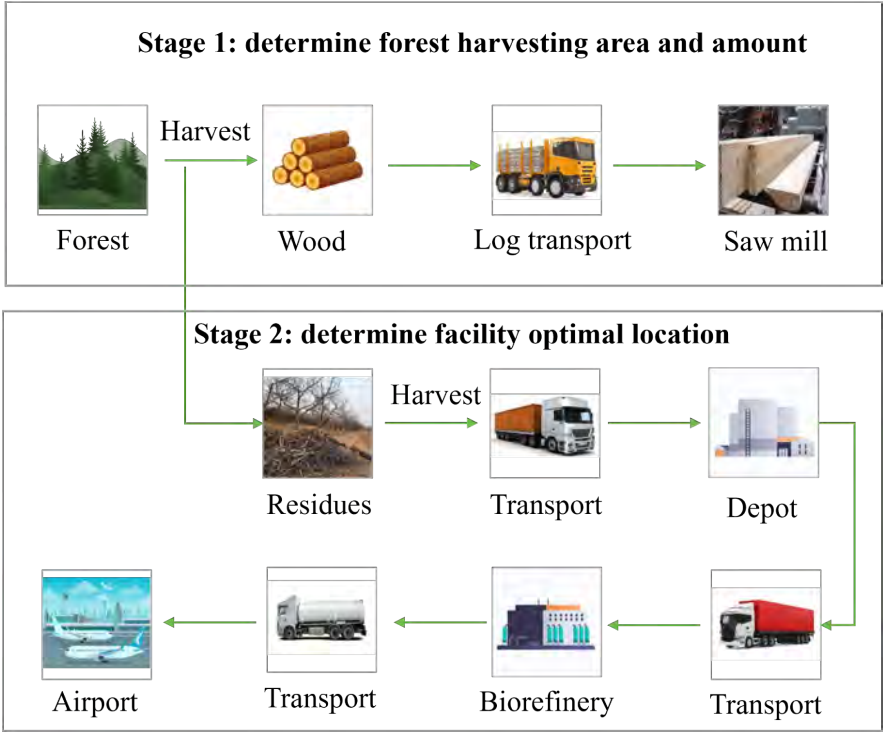


Figure 1. The network of sustainable aviation fuel produced from forest residues.

We evaluated and compared the SAF cost and volume from two conversion pathways and two preprocessing systems. The two conventional pathways were Fischer-Tropsch gasification and pyrolysis. The two preprocessing technologies were hammermill and rotary shear. In addition, we considered three preprocessing and depot systems:

- Hammermill at depots attached to biorefinery (HDA)
- Hammermill at depots unattached to biorefinery (HDU)
- Hammermill/rotary shear at depots unattached to biorefinery (HRDU)

Several assumptions are imposed. We followed the techno-economic analysis (TEA) of conversion pathways provided by the Washington State University ASCENT team. TEA of size-reduction techniques were based on another U. S. Department of Agriculture project. Willingness to harvest forest residues and a cap of logging residue harvests (70%) was implemented for the environmental consideration. The distance between forest harvesting, depots, biorefineries, and airports was assumed to be 50, 50, and 75 miles, respectively.

Milestones

- Generated data have been passed on to the ASCENT 1 database for hardwood and softwood forest residues in the southeastern United States.
- The potential SAF production from different preprocessing and conversion systems in the southeastern United States has been evaluated.



Major Accomplishments

The results of the maximum SAF that can be produced are presented in Figure 2. Applying the Fischer-Tropsch process with different size-reduction technologies to forest residues in the Southeast could produce up to 550 million gallons of SAF per year, meeting up to 19% of the SAF Grand Challenge target in 2030. The pyrolysis process could generate up to 650 million gallons of SAF and satisfy up to 22% of the target. The rotary shear technology outperforms the hammermill regarding SAF production because of a higher system mass-flow. Detaching hammermill from biorefinery can reach more forest residues in distance for SAF production.

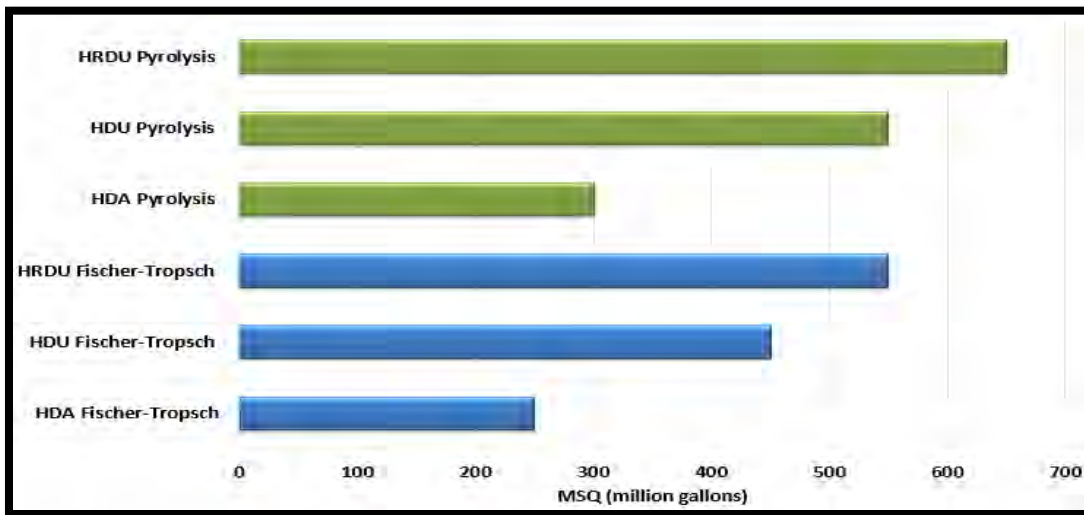


Figure 2. The maximum sustainable aviation fuel that could be produced from logging residues in the southeastern United States. HDA, hammermill at depots attached to biorefinery; HDU, hammermill at depots unattached to biorefinery; HRDU, hammermill/rotary shear at depots unattached to biorefinery. MSQ: maximum supply quantity

The breakeven cost (BEC) in Figure 3 shows that the pyrolysis pathway had an economic advantage over the Fischer-Tropsch process because of its lower capital and operation cost. Detaching the hammermill from biorefinery led to a higher cost due to additional capital investment but more SAF could be made. Adopting the rotary shear technology could lower the BEC from the hammermill system due to the difference in throughput and resulting lower feedstock need.

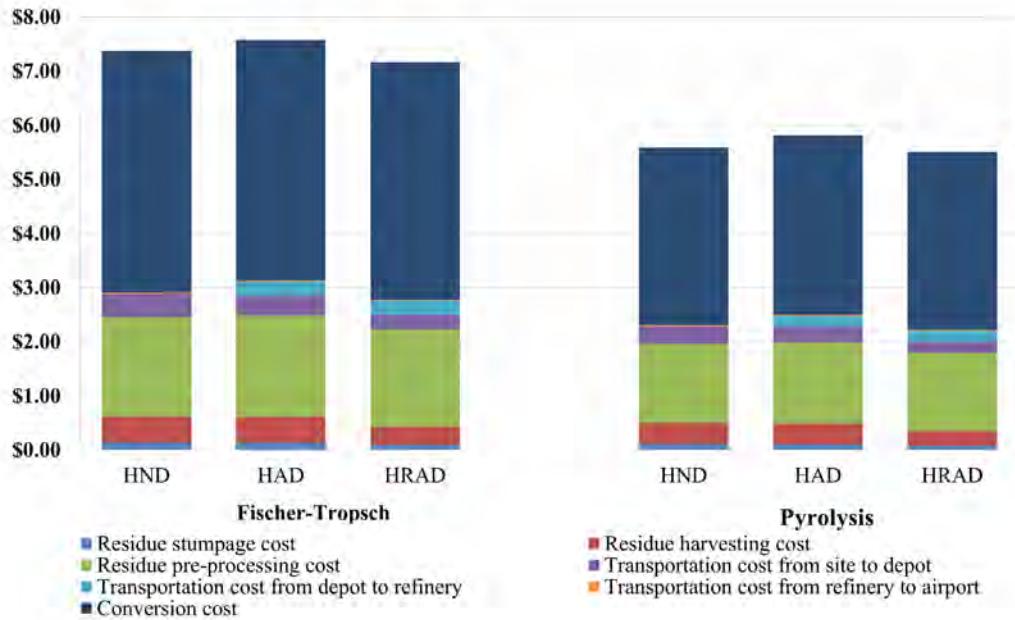


Figure 3. Breakeven cost of the maximum sustainable aviation fuel from different supply chain systems. HDA, hammermill at depots attached to biorefinery; HDU, hammermill at depots unattached to biorefinery; HRDU, hammermill/rotary shear at depots unattached to biorefinery.

The distribution of the hardwood and softwood species in the southeastern United States varies considerably. Softwood residues are more common in the southeast, whereas hardwood residues are more prevalent in the northern areas. Thus, the SAF supply chain displacement would be very different also when utilizing the two types of wood as feedstock separately. Applying the most efficient system (pyrolysis conversion + rotary shear preprocessing + independent depots) to hardwood and softwood residues represents different placement of supply chains. The SAF maximum volume from softwood forest residues could reach 250 million gallons, whereas hardwood residues could supply up to 400 million gallons of SAF. The BEC is slightly higher in the softwood supply chain as the relatively lower inventory of softwood residues results in a lower biorefinery utilization rate compared with using hardwood residues.

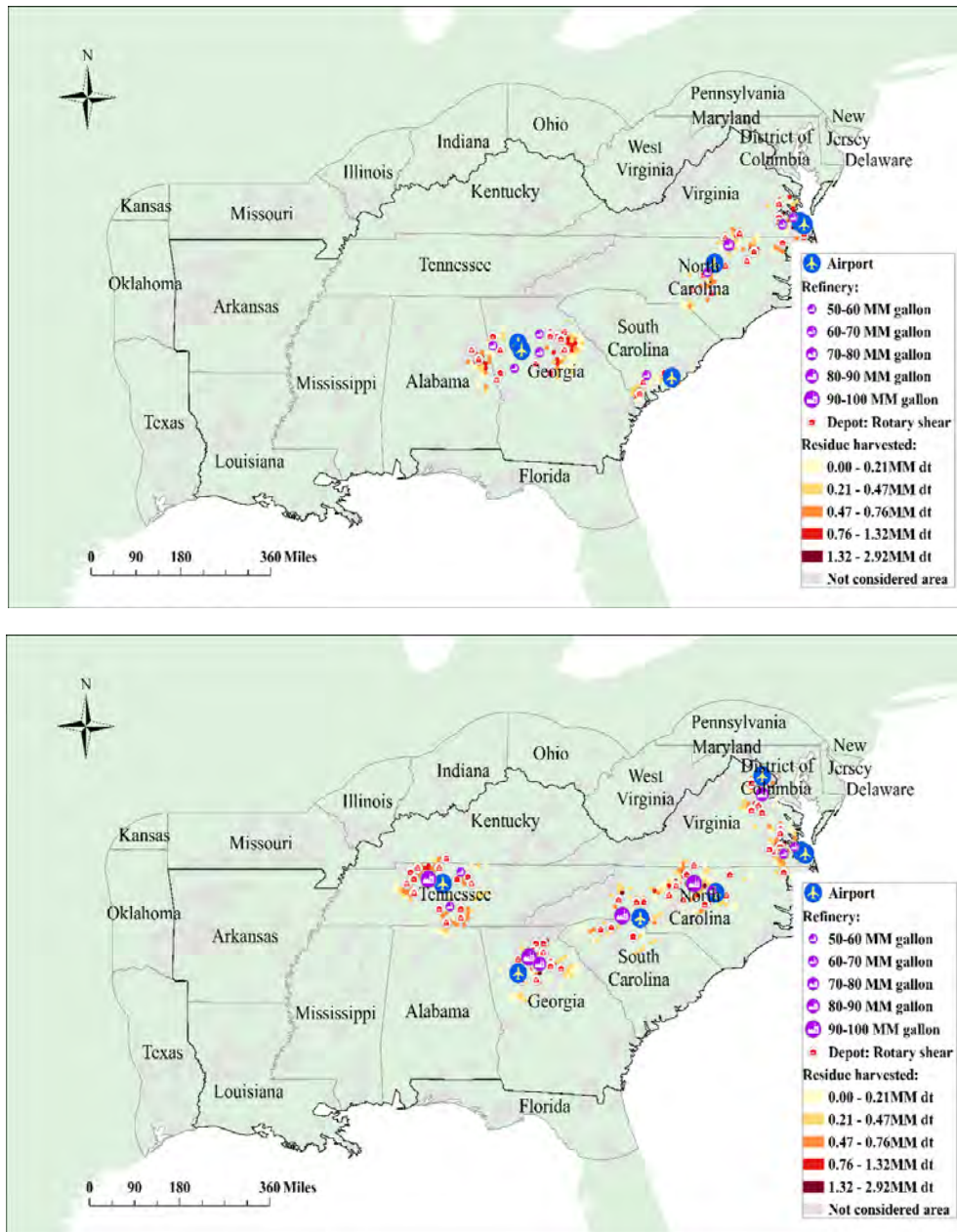


Figure 4. Softwood residues (top) and hardwood residues (bottom) supply chain for sustainable aviation fuel production.

Publications

Li, P., T.E. Yu, C. Trejo-Pech, J.A. Larson, B.C. English, and D. Lanning. "Assessing the Impact of Preprocessing and Conversion Technologies on the Sustainable Aviation Fuel Supply from Forest Residues in the Southeast U.S." accepted for 2024 TRB Annual Meeting presentation and publication on *Transportation Research Record*.

Yu, T.E. "Local Sustainable Aviation Fuel Supply Chain Analysis", Texas Aviation Conference, Galveston, TX, April 12-14, 2023

Bista, B., C.O. Trejo-Pech, J.A. Larson, and T.E. Yu. "Risk Assessment of Publicly Traded Biofuel Firms." Selected presentation. SAEA annual meeting. Oklahoma City, OK. February 4-8, 2023.

Fontanilla-Diaz, C., T.E., Yu, C. Trejo-Pech, J.A. Larson, B.C. English, and B. Wilson. "Economic Analysis of the Sustainable Aviation Fuel Supply Chain from Hybrid Poplar in the US Southeast Considering Alternative Preprocessing Technologies." TRB annual meeting online, 23-3566, Washington, D.C. January 8-12, 2023.

Outreach Efforts

The UT Institute of Agriculture and the Commercial Aviation Alternative Fuels Initiative have partnered to identify sites with optimal woody biomass and essential supply chain infrastructure, because these factors present challenges for processors with limited resources to conduct site assessments with sufficient detail to attract investment capital. The initial attempt will highlight the availability of woody biomass in the region and thereby extend its potential utilization. Analysis has been initiated for DRAX Group and USA BioEnergy.

Awards

None.

Student Involvement

Master's graduate student Kumar Bolakhe developed the woody biomass supply chain optimization model.

Plans for Next Period

- Complete several manuscripts
- Continue our work on the forest sector feedstock supply
- Continue our work on the stochastic analysis focusing on pennycress feasibility in the southeastern United States
- Continue to work on the Memphis airport region analysis using winter canola as feedstock
- Work on feedstock sustainability issues
- Continue working with stakeholders

Task 2 - Develop National Lipid Supply Availability Analysis

University of Tennessee

Objective

The UT team continues the national lipid supply availability analysis by using POLYSYS to develop information on the potential impacts and feasibility of using lipids for SAF production.

Research Approach

POLYSYS has been used to estimate and assess the supply and availability of these feedstock options at the regional and national levels. This U.S. agricultural sector model forecasts changes in commodity prices and net farm income over time. Analysis requires consistency among crops. Budgets have been reevaluated for pennycress, camelina, and carinata for consistent assumptions, where possible. These budgets have been uploaded into the PSU BOX platform and sent to Washington State University, and are available at <https://arec.tennessee.edu/>. Yields have been compared with literature sources (also available at <https://arec.tennessee.edu/>).

Milestones

1. The pennycress budget incorporating yield variation risk into the analysis was completed and is under review.
2. We made a risk analysis of a short-rotation woody crop (hybrid poplar), perennial grass (switchgrass), and winter oilseeds (pennycress).

Major Accomplishments

We assessed the financial risks of producing biomass feedstock, including hybrid poplar, switchgrass, and pennycress, considering uncertainty in feedstock yield, diesel prices, and fertilizer costs in Tennessee. We define the soybean-corn rotation as the baseline farming strategy and included three scenarios: (1) soybeans-pennycress (as a cover crop)-corn rotation (C-P-S), (2) adopting hybrid poplar (as a short-rotation woody crop), and (3) adopting switchgrass (as an

herbaceous grass). By engaging Monte Carlo simulations in the stochastic budgeting models, the BEC of all scenarios and associated probabilities are illustrated in Figure 5. Hybrid poplar has the highest average BEC of all the crops, with an average BEC of \$633.69/acre. The average BEC distribution for the C-P-S rotation, with an average of about \$612.83/acre, is the second highest. The average BEC for corn-soybean rotation (baseline) is around \$546.46/acre. The average BEC for switchgrass is the lowest among all feedstocks, at \$318.72/acre. Adding pennycress to a corn-soybean rotation will increase farmers' income.

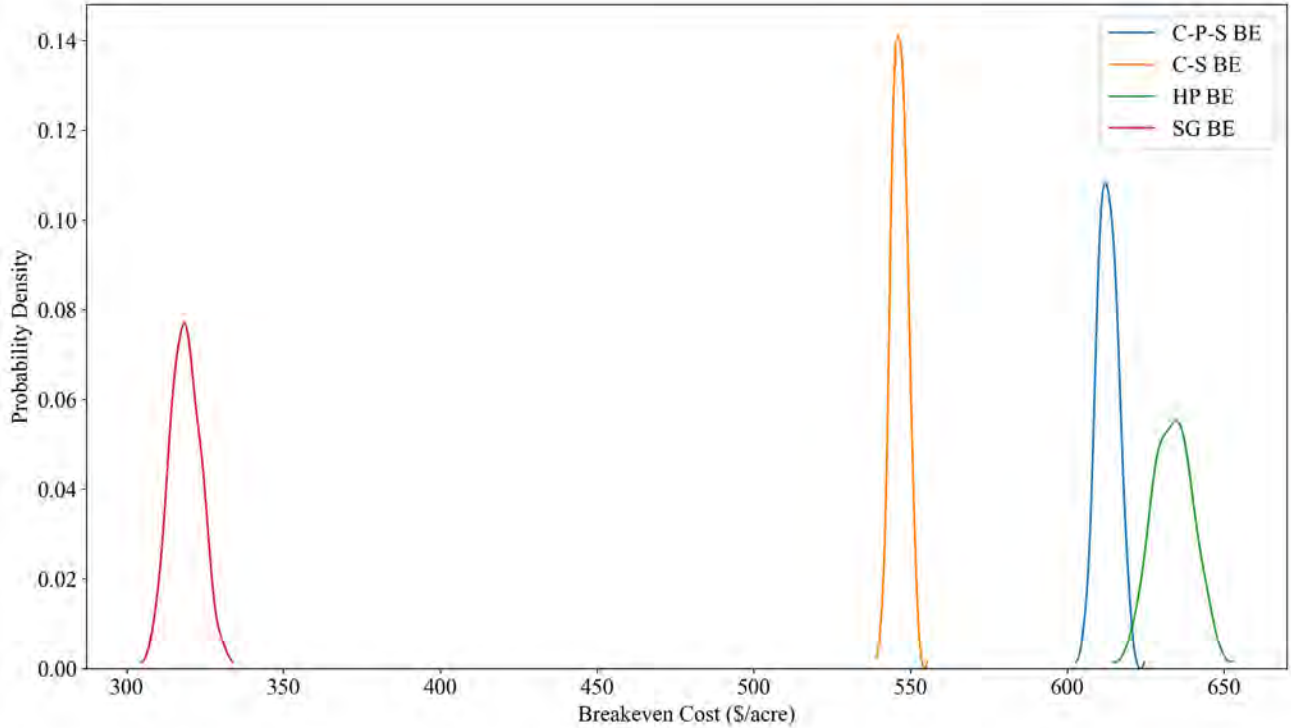


Figure 5. Probability density of breakeven (BE) cost. C-P-S, corn-pennycress-soybean rotation; C-S, corn-soybean rotation; HP, hybrid poplar; SG, switchgrass.

Results from the stochastic efficiency with respect to function in Figure 6 suggest that switchgrass has the highest risk efficiency compared with other biomass feedstock under different risk-averse farmer attitudes at the same market price. Given the risk aversion assumption, farmers have little incentive to replace the corn-soybean rotation with hybrid poplar.

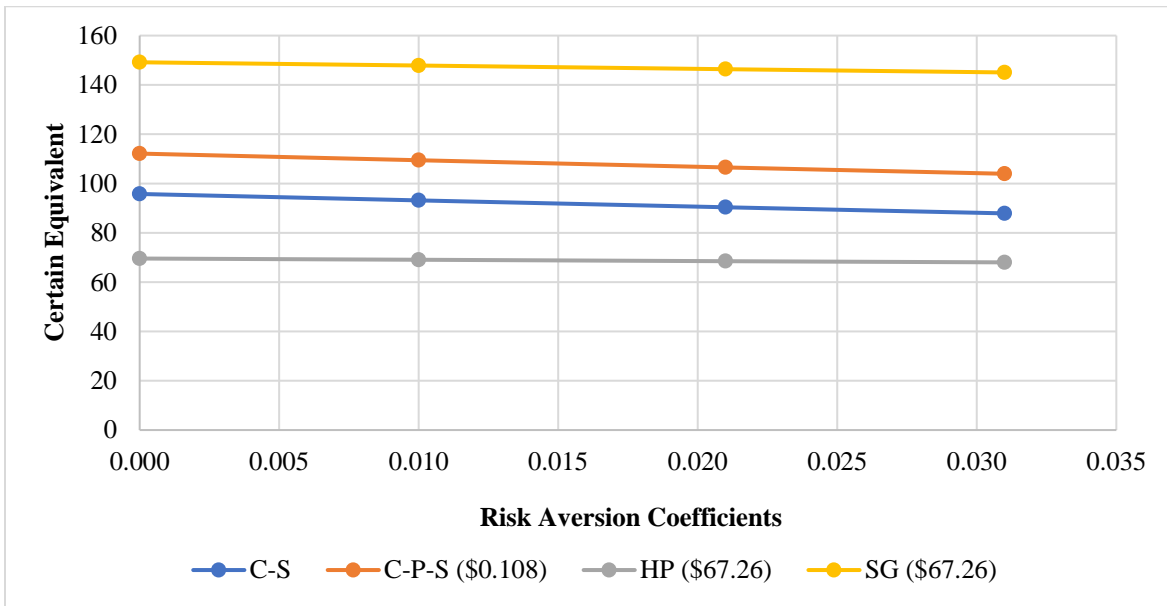


Figure 6. Certainty equivalents of all evaluated biomass feedstock versus the baseline. C-S, corn-soybean rotation; C-P-S, corn-pennycress-soybean rotation; HP, hybrid poplar; SG, switchgrass.

Publications

Li, T. "Evaluating the Potential Risks of Producing First- and Second-Generation Bioenergy Crops in Tennessee," MS Thesis, summer 2023.

Outreach Efforts

None.

Awards

None.

Student Involvement

Master’s graduate student Tongtong Li developed the stochastic budget model for pennycress. Master’s graduate student Kumar Bolakhe developed the stochastic optimization model for SAF supply chain from winter oilseeds.

Plans for Next Period

We will develop a stochastic optimization analysis for regional SAF supply chain produced from winter oilseed crops and illustrate the analysis in a case study.

Task 3 - Laying the Groundwork for Developing Regional SAF Economy in Central Appalachia and Tennessee

University of Tennessee

Objectives

The team at UT will facilitate regional deployment/production of SAF by completing the groundwork phase of the regional feedstock-to-biofuel pathway and developing a proposal for regional deployment in Central Appalachia.

Research Approach

- The approach is as in Task 1 and focused on small areas such as Central Appalachia, Memphis, and Nashville.
- A workforce analysis based on the available labor supply and the demand for the biofuel industry is utilized.
- We conducted a series of webinars for potential stakeholders of the SAF supply chain.

Major Accomplishments

- The Nashville modeling work using cover crop oilseeds has been completed. The next step will be to develop a regional deployment plan after risk and uncertainty are evaluated.
- The Central Appalachia project has regular stakeholder webinars to discuss state and national incentives for SAF development in the region.

Central Appalachia

The team updated the previous workforce analysis for Central Appalachia. The goal is to assess the nature of the demand for workers (quantity and quality) that a wood-based biofuel processing facility would have on a regional economy, and the ability and willingness of workers in the area to meet this demand, by using Bureau of Economic Analysis (BEA) region 46 as an example. To assess the former, the level of employment required by the biofuel firm (IMPLAN sector 163) is translated into a set of demands for specific workers by occupation. Occupations are then translated into a set of skill sets via IMPLAN’s analysis of O*NET skills by occupation analysis. To assess the latter, we estimate changes in the local workforce to determine candidates likely to seek employment. Major changes in employment by economic sector are translated into occupational changes and then skill changes by using the IMPLAN-O*NET analysis. A weighted average is then used to provide a supply of workers by skill set; the skill sets in turn are compared with those likely to be sought in prospective workers at the biofuel firm.

As shown in Table 1, in terms of the skill characteristic ability, workers assumed to be regional job seekers do not necessarily have the skills sought by the biofuel processing firm. Attributes that show a “good” match in terms of worker demand (IMPLAN sector 163) and supply (job seekers) include problem sensitivity, oral comprehension, near vision, deductive reasoning, and information ordering. However, attributes such as oral expression, speech clarity, and perceptual speed are relatively important to the biofuel firm, but job seekers are less likely to have these attributes in the region. Across all 52 ability attributes that we examined, a Wilcoxon test statistic (663) indicated a significant difference in rank (alpha = 0.01 level), indicating a possible mismatch between the skills desired by the firm and the ability of the available regional workforce to supply such skills.

Table 1. Ability as worker characteristic for biofuel firms (Section 163) versus regional job seekers’ rank of attribute importance (over 52 attributes).

Ability category	IMPLAN sector 163	Job seekers
<u>Problem Sensitivity</u>	<u>1</u>	<u>2</u>
Oral Expression	2	12
<u>Oral Comprehension</u>	<u>3</u>	<u>7</u>
<u>Near Vision</u>	<u>4</u>	<u>1</u>
Written Comprehension	5	14
<u>Deductive Reasoning</u>	<u>6</u>	<u>6</u>
Speech Recognition	7	16
Speech Clarity	8	19
<u>Information Ordering</u>	<u>9</u>	<u>8</u>
Perceptual Speed	10	22

Note: Underlining indicates a close match and bold denotes a possible mismatch between the demand for worker skills and the ability of local workers to provide such skills.

Two stakeholder webinars to facilitate regional deployment of SAF were held in this project year: one on August 2 (see Figure 7) and another on September 27 (see Figure 8). A total of 53 and 62 people registered for the two webinars, respectively. We received positive feedback from the attendees, who appreciated the information included in the webinars.

On August 2, we invited Dr. Prem Lobo from FAA to give an update on the SAF Grand Challenge Roadmap and talked about the potential funding program of FAST-SAF. Dr. Dave Hughes at the University of Tennessee then presented a preliminary workforce analysis for the SAF industry using BEA region 46 as a case study. We then opened to questions and updates from the attendees. The Virginia Department of Forestry is very interested in collaborating and learning more about current and future projects. Rick and Todd Campbell at ATIP Foundation gave an update on the work they are doing specifically in Virginia. Kentucky and West Virginia also gave updates.



CENTRAL APPALACHIA SAF

• • • • •

MEETING

Presentation from FAA - with updates on Sustainable Aviation Fuel Grand Challenge, Inflation Reduction Act and more opportunities

Feedstock Supply Chain Discussion

SAF - Updates in and around Central Appalachia

**VIRTUAL - WEDNESDAY, AUGUST 2
10:00 A.M. EST**

REGISTER







Figure 7. Announcement of sustainable aviation fuel stakeholder webinar on August 2, 2023.

In the webinar on September 27, we invited the leadership of two regional airports in the Central Appalachia region to present “How Airports Can Lead in Bio-Based Economic Development.” The presenters were Chad Willis, director of planning and sustainability for the Allegheny County Airport Authority, and Seth Cutter, VP of public affairs for Cincinnati/Northern Kentucky International Airport (CVG). Chad shared their potential of serving SAF at Pittsburgh International Airport (PIT), given its fuel storage capacity, local transportation network, regional ethanol production, and technology adoption. PIT has a desire to deliver SAF to aircraft and the east coast. The CVG airport participates in the Kentucky Sustainable Aviation Fuel Coalition, including Airlines for American, Airport Council International, Amazon Air, American Airlines, Atlas Air Worldwide, ATSG, Boeing, Bluegrass Airport, Cargo Airline Association, Delta, DHL, General Electric, Kalitta Air, Louisville Muhammad Ali International Airport, Marathon Petroleum, Sunflower Fuels, and UPS. The Coalition is an industry partnership focused on developing a SAF ecosystem in the mid-South and Midwest. Seth indicated that Kentucky is in a good position to develop a regional SAF ecosystem, given the commercial airline activity, air cargo prowess, presence of original equipment manufacturers (OEMs) and aviation industry, R&D strength and potential, and agricultural and feedstock availability.

HOW AIRPORTS CAN LEAD IN BIO-BASED ECONOMIC DEVELOPMENT

Airport leaders in the wider Appalachian region will discuss efforts to build a SAF ecosystem for local production, regional consumption, and broader export potential.



Seth Cutter,
VP Public Affairs





Chad A. Willis
A.A.E. ENV SP







Sept., 27, 2023
Virtual



10:00 am - 11:00 am
EST



REGISTER NOW

Figure 8. Announcement of sustainable aviation fuel stakeholder webinar on September 27, 2023.

Publications

None.

Outreach Efforts

See above webinar descriptions.

Awards

None.

Student Involvement

None.

Plans for Next Period (Year)

- Complete the Central Appalachian Regional Deployment Plan

Task 4 - Conduct Soil Organic Carbon (SOC) Analysis in the United States

University of Tennessee

Objective

Provide an estimate of SOC related to SAF feedstock production.

Research Approach

To estimate the SOC change from SAF feedstock production, we propose to improve SOC estimates and investigate long-term trends in the United States using in-situ measurements from soil carbon networks and previous studies and incorporating satellite imagery from the Landsat archive for more complete spatial coverage. We will also compare several machine learning techniques to generate a finer resolution map and better understand SOC dynamics.

Milestones

- Compiled nearly 29,980 soil profiles corresponding to available SOC observations
- Applied machine learning techniques to estimate annual SOC stocks in the most areas from 1984 to 2022

Major Accomplishments

Georeferenced SOC measurements in the United States were taken from the International Soil Carbon Network from 1952 to 2014. Each SOC measurement is also associated with a long-term average temperature and precipitation amount from WorldClim and an elevation from a United States Geological Survey (USGS) 10-m digital elevation model. For each of the 29,979 30-cm soil profile observations in the continental United States (CONUS), we extracted the previous 5 years of annual Normalized Difference Vegetation Index (NDVI) (median, 5th percentile, and 95th percentile), maximum temperature, minimum temperature, precipitation, and land cover, in addition to the elevation, aspect, slope, geology, and clay content. We found that of the 8 machine learning models, the random forest algorithm performed best when predicting SOC, according to root mean square error (RMSE), mean absolute error (MAE), and coefficient of determination (R^2) values. We then applied the random forest model to annual NDVI pixels across the CONUS for 2022 to map SOC for the year. We also mapped change in SOC over time from 1992 to 2022. We continue to refine the model and apply it to all NDVI pixels from all years with available satellite records for the previous 5 years (1990–2022). We randomly split our data into training (80%) and validation (20%). Figure 10 presents the georeferenced SOC dataset for machine learning.

We assessed model performance (Table 2) with RMSE, MAE, R^2 , and the slope of the predicted versus observed line. We then exported the “greenest” Landsat pixels for the CONUS for 2022 and applied the best-performing model (i.e., the model with the lowest out-of-bag error) to predict SOC for the year across the spatially continuous 30 m × 30 m pixels (Figure 9). The “greenest” pixels are defined as having the highest NDVI of the year for each Landsat overpass location. This is the maximum boundary value of SOC for each location for 2022.

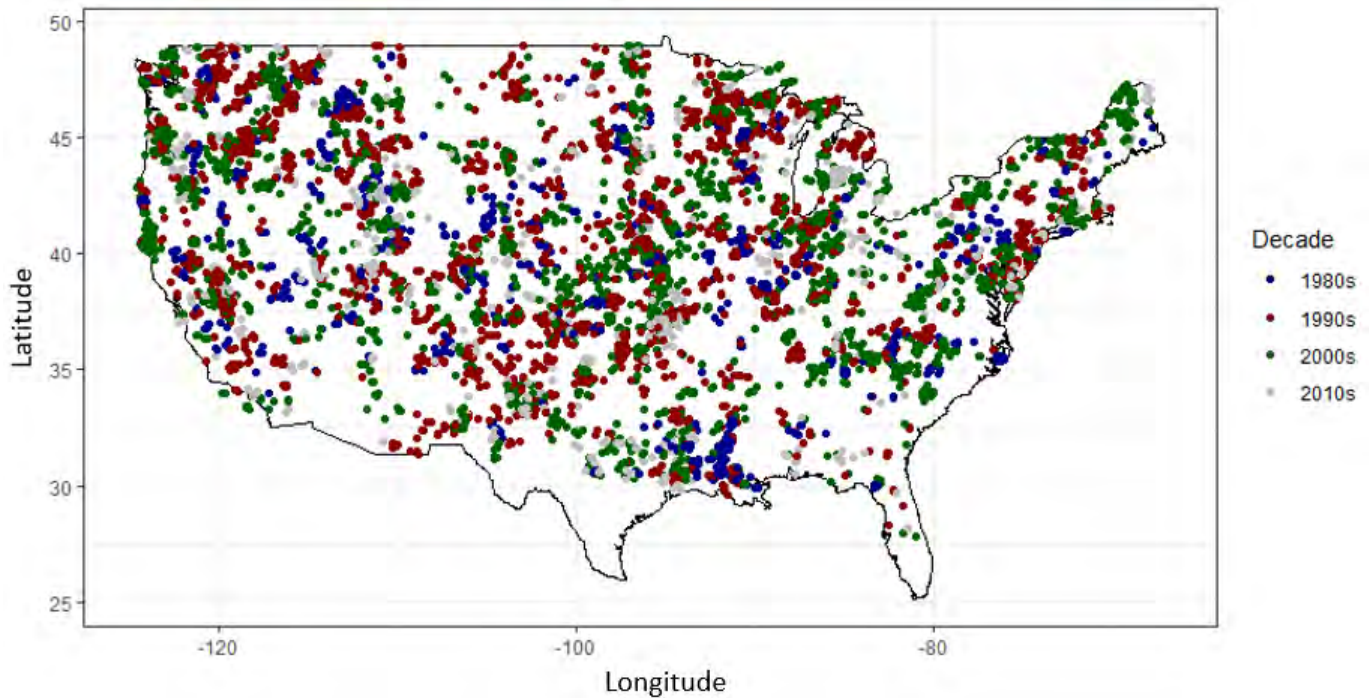


Figure 9. Georeferenced soil organic carbon (SOC) dataset.

Table 2. Model performance on training (80%) and validation (20%) datasets. Mean absolute error (MAE) and root mean square error (RMSE) are in g/cm². “Slope” means the slope of the line of the plot of predictions versus observations.

Model	Training				Validation			
	MAE	RMSE	Slope	R ²	MAE	RMSE	Slope	R ²
Linear regression	0.38978	0.62722	0.09	0.08627	0.39435	0.63622	0.07	0.0536
Random forest	0.01066	0.03647	0.99	0.99688	0.01115	0.03378	0.99	0.9973
Gradient boosting (GBM)	0.35583	0.52623	0.23	0.52906	0.35706	0.53159	0.21	0.5322
Gradient boosting (XGBoost)	0.00918	0.01654	0.99	0.99939	0.01026	0.01893	0.99	0.9992
Support vector machine	0.33723	0.65764	0.08	0.06647	0.33605	0.66528	0.06	0.0395

Below are the maps of annual SOC stocks from 1984 to 2022 and rate of change over time in different locations. Satellite-based NDVI (a measure of greenness) and annual meteorological variables allow us to compare trends in both climate and land use that help explain patterns in SOC. The values in the map present the difference between modeled values and observations. Figure 10 depicts SOC estimates (modeled values, not observations) in California in 2022 from a random forest model; R² is 0.84 for training and 0.59 for validation. Figure 11 shows the change in SOC in the southeastern United States over the same period, predicted from a random forest model. Blue indicates an increase and red indicates a decrease from 1992 to 2022; R² is 0.77 for the southeast region.

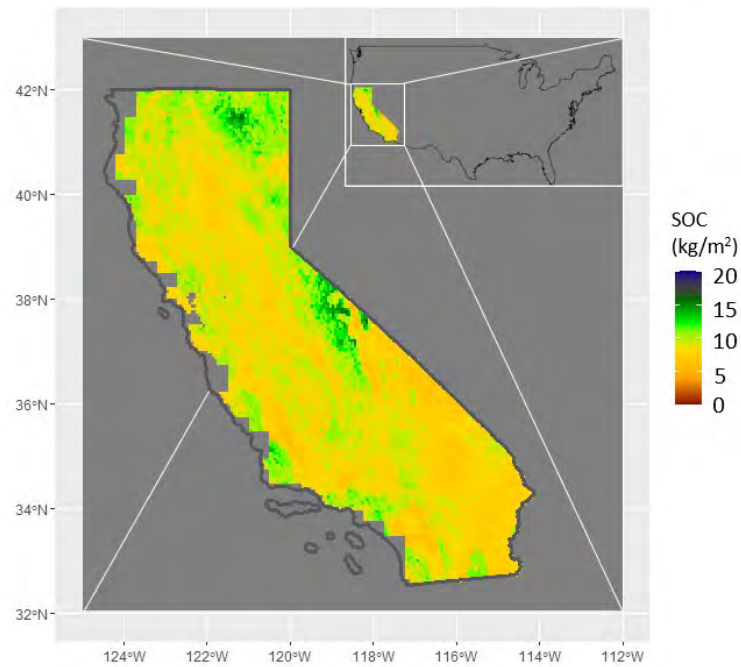


Figure 10. Average soil organic carbon (SOC) predicted from a random forest model in California in 2022.

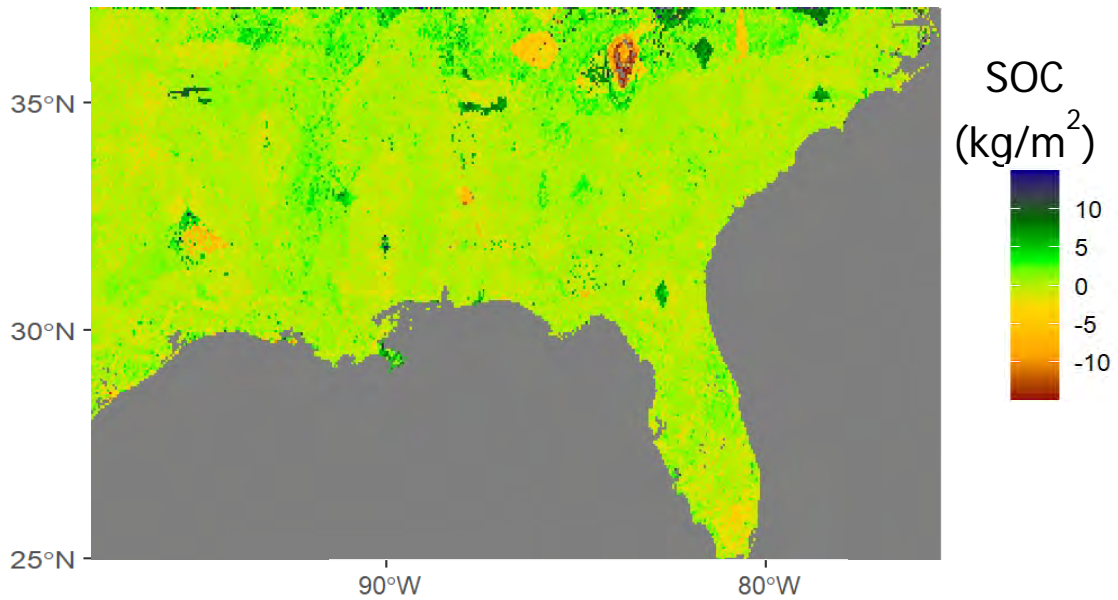


Figure 12. Estimated soil organic carbon (SOC) changes from a random forest model in the southeastern United States, 1992 to 2022.

Publications

None.



Outreach Efforts

None.

Awards

None.

Student Involvement

Hannah Rubin conducted the SOC analysis.

Plans for Next Period

- Complete the SOC benchmark/baseline in the United States
- Validate the performance of machine learning with field experiment data



Project 001(F) Alternative Jet Fuel Supply Chain Analysis

Massachusetts Institute of Technology Hasselt University

Project Lead Investigators

Steven R. H. Barrett
Professor of Aeronautics and Astronautics
Director, Laboratory for Aviation and the Environment
Massachusetts Institute of Technology
77 Massachusetts Ave, Building 33-207, Cambridge, MA 02139
617-253-2727
sbarrett@mit.edu

Dr. Raymond L. Speth
Principal Research Scientist
Laboratory for Aviation and the Environment
Massachusetts Institute of Technology
77 Massachusetts Ave, Building 33-322, Cambridge, MA 02139
617-253-1516
speth@mit.edu

Dr. Florian Allroggen
Executive Director Aerospace Climate & Sustainability; Research Scientist
Laboratory for Aviation and the Environment
Massachusetts Institute of Technology
77 Massachusetts Ave, Building 33-115A, Cambridge, MA 02139
617-715-4472
fallrogg@mit.edu

University Participants

Massachusetts Institute of Technology (MIT)

- P.I.: Professor Steven R. H. Barrett;
- co-P.I.s: Dr. Florian Allroggen, Dr. Raymond Speth
- FAA Award Number: 13-C-AJFE-MIT, Amendment Nos. 003, 012, 016, 028, 033, 040, 048, 055, 058, 067, 082, 088, 096, and 115 (no-cost extension to September 30, 2024)
- Period of Performance: August 1, 2014 to September 30, 2024
- Tasks (for reporting period October 1, 2022 to September 30, 2023):
 1. Support and provide leadership for U.S. participation in the International Civil Aviation Organization (ICAO) Committee on Aviation Environmental Protection (CAEP) to enable appropriate crediting of the use of sustainable aviation fuels (SAFs) under the Carbon Offsetting and Reduction Scheme for International Aviation (CORSIA)
 2. Support U.S. participation in the ICAO CAEP by performing core life-cycle analysis (CLCA) to establish default values for use under CORSIA
 3. *(omitted, led by Hasselt University)*
 4. Develop methods for probabilistic life-cycle analyses (LCAs) and techno-economic analyses in the context of assessing U.S.-based SAF production
 5. Support knowledge sharing and coordination across all ASCENT Project 01 (A01) universities working on SAF supply chain analyses.



Hasselt University (UHasselt, through subaward from MIT)

- P.I.: Professor Robert Malina
- Period of Performance: September 1, 2016 to August 31, 2024 (via no-cost extension)
- Tasks (for reporting period October 1, 2022 to September 30, 2023):
 1. Support and provide leadership for U.S. participation in ICAO CAEP to enable appropriate crediting of the use of SAFs under CORSIA
 2. Support U.S. participation in ICAO CAEP by performing CLCA to establish default values for use under CORSIA
 3. Contribute to the development of fuel production assessment for CORSIA-eligible fuels (CEFs)
 4. *(omitted, led by MIT)*
 5. *(omitted, led by MIT)*

Project Funding Level

\$4,035,000 FAA funding and \$4,035,000 matching funds. Sources of matching are approximately \$632,000 from MIT, plus third-party in-kind contributions of \$809,000 from Byogy Renewables, Inc., \$1,038,000 from Oliver Wyman Group, \$1,155,000 from NuFuels LLC, and \$401,000 from Savion Aerospace Corp.

Investigation Team

Massachusetts Institute of Technology

Prof. Steven Barrett (P.I.), All MIT Tasks
Dr. Florian Allroggen (co-P.I.), All MIT tasks
Dr. Raymond Speth (co-P.I.), MIT Task 4
Matthew Pearlson (research specialist), MIT Tasks 2 and 4
Dr. Niamh Keogh (postdoctoral associate), MIT Task 1
Tae Joong Park (graduate research assistant), MIT Tasks 1 and 2
Sarah Demsky (graduate research assistant), MIT Task 4

Hasselt University

Prof. Robert Malina (P.I.), All UHasselt Tasks
Dr. Freddy Navarro Pineda (postdoctoral associate), All UHasselt Tasks
Dr. Gonca Seber (postdoctoral associate), UHasselt Task 2
Dr. Anne Nobel (postdoctoral associate), UHasselt Task 3
Francis Mwangi (graduate research assistant), UHasselt Task 3
Pieter Fonteyn (graduate research assistant), UHasselt Task 2

Project Overview

The overall objectives of A01 are to (a) derive information on regional supply chains to explore scenarios for future SAF production and (b) identify supply-chain-related obstacles to commercial-scale production in the near term and to larger-scale adoption in the longer term. For the reporting period, the MIT/UHasselt team contributed to these goals by (a) providing leadership in the ICAO CAEP CLCA Task Group of the Fuels Task Group (FTG), which has been tasked with calculating life-cycle greenhouse gas (GHG) emissions associated with the use of SAF, (b) performing core life-cycle GHG emission analyses to enable the inclusion of additional SAF pathways under CORSIA or to verify CLCA values calculated by other institutions, (c) contributing to SAF availability assessments, (d) analyzing the potential of U.S.-produced SAFs and their life-cycle emissions and costs, and (e) contributing to knowledge transfer among the A01 team.

Task 1 – Support and Provide Leadership for U.S. Participation in ICAO CAEP to Enable Appropriate Crediting of the Use of SAFs under CORSIA

Massachusetts Institute of Technology and Hasselt University

Objectives

The overall objective of this task is to provide leadership and support for the FAA in its engagement with the ICAO CAEP FTG during the CAEP/13 cycle. The specific focus of the work during this reporting period was to (a) review emission scope

definitions, especially regarding process fuels, (b) develop an actual value method for including carbon capture and storage (CCS) in the CORSIA framework, and (c) provide guidance on the inclusion of power-to-liquid (PtL) fuels in CORSIA.

Research Approach

To achieve the goals outlined above, the team continued to co-lead the CLCA subgroup of the FTG. Prof. Malina acted as a co-lead. This role ensures that Prof. Malina remains a focal point of CLCA research, such that specific research tasks can be guided efficiently and effectively. The following research has been conducted in support of the leadership role:

Review of emission scope definitions

All default CLCA values in CORSIA assume that heat and electricity needs that cannot be satisfied internally in the process are met by the electricity grid or by natural gas (in the case of heat). For actual values, fuel producers can bring forward emission inventories based on electricity and heat produced from biomass. However, this biomass might be associated with (positive or negative) emissions from induced land-use changes (ILUCs) that are outside of the system boundary of the actual (and default) LCA methodology.

The UHasselt team explored the significance of ILUC emissions from such biomass-derived process fuels. For this purpose, the team augmented existing emission inventories from the CORSIA GREET (greenhouse gases, regulated emissions, and energy use in transportation) model to consider electricity and/or heat requirements to be satisfied by biomass-derived process fuels. The team then parametrically included a range of ILUC values bounded by established ILUC values within CORSIA. The results are shown in Table 1 and Figure 1. The impact of the inclusion of ILUC for biomass-derived process fuels for a given ILUC value is found to be sensitive to the magnitude of external energy needs. In cases of high external energy needs (e.g., for the corn ethanol or corn isobutanol pathway) and under the assumption of ILUC emissions similar to extreme values under CORSIA, the total emissions change by more than 10 g CO₂e per MJ of SAF.

Table 1. Change in life-cycle greenhouse gas emissions per feedstock-to-fuel pathway for a set of different induced land-use change (ILUC) values for biomass-based energy generation (heat and electricity). Data are given in g CO₂e/MJ of sustainable aviation fuel. ATJ: alcohol-to-jet; FTJ: fermentation-to-jet; HEFA: hydroprocessed esters and fatty acids; MSW: municipal solid waste; SIP: synthesized isoparaffins.

Pathway	Feedstock	ILUC values for the biomass-based energy generation (gCO ₂ e/MJ _{biomass})												
		-26.00	-20.80	-15.60	-10.40	-5.20	-2.60	0.00	2.60	5.20	10.40	15.60	20.80	26.00
HEFA	Brassica carinata	3.83	3.06	2.30	1.53	0.77	0.38	0.00	-0.38	-0.77	-1.53	-2.30	-3.06	-3.83
	Corn oil	2.62	2.10	1.57	1.05	0.52	0.26	0.00	-0.26	-0.52	-1.05	-1.57	-2.10	-2.62
	Palm fatty acid distillate	2.40	1.92	1.44	0.96	0.48	0.24	0.00	-0.24	-0.48	-0.96	-1.44	-1.92	-2.40
	Palm oil	2.57	2.06	1.54	1.03	0.51	0.26	0.00	-0.26	-0.51	-1.03	-1.54	-2.06	-2.57
	Rapeseed/canola	4.05	3.24	2.43	1.62	0.81	0.40	0.00	-0.40	-0.81	-1.62	-2.43	-3.24	-4.05
	Soybean	4.12	3.30	2.47	1.65	0.82	0.41	0.00	-0.41	-0.82	-1.65	-2.47	-3.30	-4.12
	Tallow	3.47	2.78	2.08	1.39	0.69	0.35	0.00	-0.35	-0.69	-1.39	-2.08	-2.78	-3.47
	Used cooking oil (UCO)	3.47	2.78	2.08	1.39	0.69	0.35	0.00	-0.35	-0.69	-1.39	-2.08	-2.78	-3.47
Ethanol ATJ	Agricultural residues	10.32	8.26	6.19	4.13	2.06	1.03	0.00	-1.03	-2.06	-4.13	-6.19	-8.26	-10.32
	Corn grain	14.49	11.59	8.70	5.80	2.90	1.45	0.00	-1.45	-2.90	-5.80	-8.70	-11.59	-14.49
	Forest residues	7.75	6.20	4.65	3.10	1.55	0.77	0.00	-0.77	-1.55	-3.10	-4.65	-6.20	-7.75
	Miscanthus	6.60	5.28	3.96	2.64	1.32	0.66	0.00	-0.66	-1.32	-2.64	-3.96	-5.28	-6.60
	Switchgrass	6.60	5.28	3.96	2.64	1.32	0.66	0.00	-0.66	-1.32	-2.64	-3.96	-5.28	-6.60
Isobutanol ATJ	Sugarcane	0.00	0.00	0.00	0.00	0.00	0.00	0.00	0.00	0.00	0.00	0.00	0.00	0.00
	Agricultural residues	2.64	2.11	1.58	1.05	0.53	0.26	0.00	-0.26	-0.53	-1.05	-1.58	-2.11	-2.64
	Corn grain	12.73	10.18	7.64	5.09	2.55	1.27	0.00	-1.27	-2.55	-5.09	-7.64	-10.18	-12.73
	Forest residues	1.36	1.09	0.82	0.54	0.27	0.14	0.00	-0.14	-0.27	-0.54	-0.82	-1.09	-1.36
	Miscanthus	4.75	3.80	2.85	1.90	0.95	0.48	0.00	-0.48	-0.95	-1.90	-2.85	-3.80	-4.75
FTJ	Sugarcane	0.60	0.48	0.36	0.24	0.12	0.06	0.00	-0.06	-0.12	-0.24	-0.36	-0.48	-0.60
	Switchgrass	4.18	3.35	2.51	1.67	0.84	0.42	0.00	-0.42	-0.84	-1.67	-2.51	-3.35	-4.18
	Corn Stover	0.00	0.00	0.00	0.00	0.00	0.00	0.00	0.00	0.00	0.00	0.00	0.00	0.00
	Forest residues	0.00	0.00	0.00	0.00	0.00	0.00	0.00	0.00	0.00	0.00	0.00	0.00	0.00
	Miscanthus	0.00	0.00	0.00	0.00	0.00	0.00	0.00	0.00	0.00	0.00	0.00	0.00	0.00
SIP	MSW	0.00	0.00	0.00	0.00	0.00	0.00	0.00	0.00	0.00	0.00	0.00	0.00	0.00
	Switchgrass	0.00	0.00	0.00	0.00	0.00	0.00	0.00	0.00	0.00	0.00	0.00	0.00	0.00
	Wheat Straw	0.00	0.00	0.00	0.00	0.00	0.00	0.00	0.00	0.00	0.00	0.00	0.00	0.00
SIP	Sugarcane	0.00	0.00	0.00	0.00	0.00	0.00	0.00	0.00	0.00	0.00	0.00	0.00	0.00
	Sugarbeet	0.00	0.00	0.00	0.00	0.00	0.00	0.00	0.00	0.00	0.00	0.00	0.00	0.00

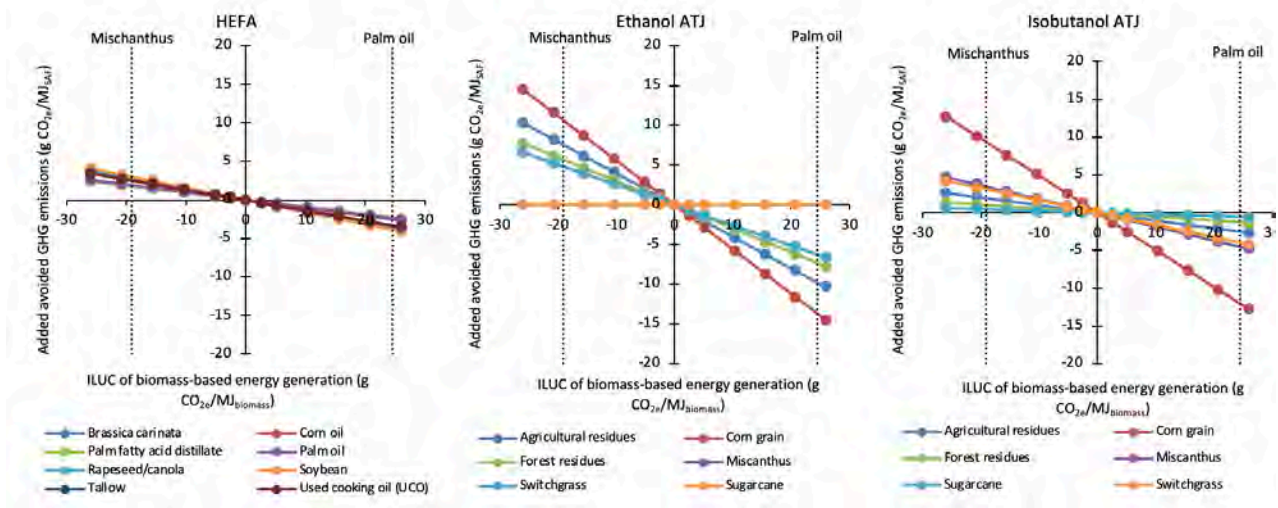


Figure 1. Change in life-cycle greenhouse gas (GHG) emissions per feedstock-to-fuel pathway as a function of induced land-use change (ILUC) values for biomass-based energy generation (heat and electricity). Data are presented in g CO_{2e}/MJ of sustainable aviation fuel. ATJ: alcohol-to-jet; HEFA: hydroprocessed esters and fatty acids.

Actual value method for CCS

The potential for mitigating GHG emissions by integrating CCS in the production of SAF was explored. In line with the general system boundary considered for CEF production, the capture of carbon dioxide emitted during the SAF production process, its transportation, injection into a storage reservoir, and long-term storage are reasonably considered to be within the system boundary (see Figure 2).

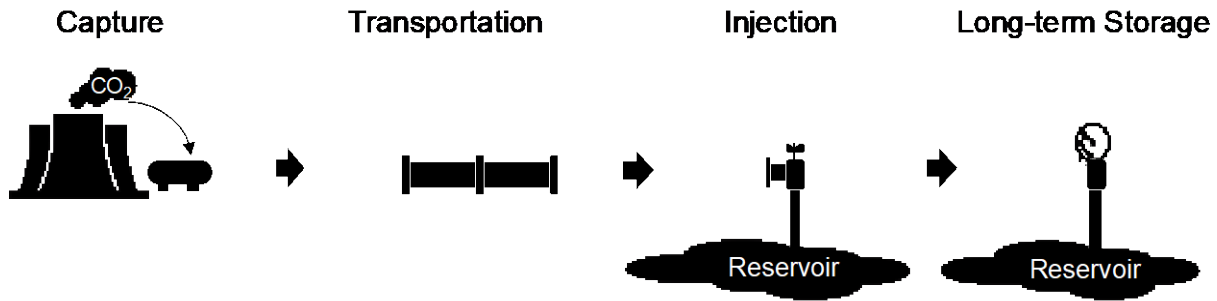


Figure 2. System boundary for assessing the life-cycle greenhouse gas emissions achieved by integrating carbon capture and sequestration into the process of sustainable aviation fuel production.

To calculate the net sequestration from CCS activities in line with the above system boundary, the GHG emissions associated with each of these processes must be considered in line with existing CORSIA methods. Most importantly, the GHG emissions associated with the heat, electricity, and material inputs for operating the capture unit (including purification and compression of CO₂) and the potential leakage of captured CO₂ are to be included. At the transport stage, the GHG emissions associated with the energy and material inputs and the potential leakage of each transportation mode (e.g., pipelines, trucks) and transfer station are considered. For the injection of captured carbon into the reservoir, GHG emissions associated with the material and energy inputs needed and potential leakage during the injection process are evaluated.

The GHG emissions from long-term storage include emissions related to the leakage of captured carbon; the energy and material inputs associated with the maintenance reservoir, including expected leakage mitigation measures; and, in the case of enhanced oil recovery, intentional removal of CO₂ from the reservoir. A review of the literature showed that the

percentage of CO₂ expected to remain in the reservoir can vary by reservoir type and storage handling practice. Thus, it was determined that the GHG emissions associated with this step can only be determined through site-specific analysis, modeling, and risk assessment of the geological reservoir.

Guidance on including fuels produced with significant electricity inputs

The team followed the general approach outlined during the previous reporting period and considered three focus areas for developing a framework to calculate the CLCA values of fuels that are produced with significant electricity input.

Embodied emissions of electricity and threshold development

Currently, CORSIA’s life-cycle emission assessment methods do not include embodied emissions (ICAO, 2022A, 2022B). For biomass-based SAF, such an assumption can generally be justified, as the level of embodied emissions associated with the production facilities is small. However, for fuels produced with significant electricity input, this assumption may not hold. Wind and solar electricity are associated with embodied emissions from raw materials, processing, and transportation required to build and ship the turbines and panels. Sample emission factors for different sources of electricity, inclusive of embodied emissions, are shown in Table 2. For a Fischer-Tropsch fuel with CO₂ sourced from direct air capture, hydrogen (H₂) from electrolysis, and all electrified processes (e.g., heating) (with a high estimate of 4 MJ of electricity input to produce 1 MJ of fuel), an electricity source with high embodied emissions such as solar power would result in 4 MJ electricity/1 MJ fuel x 1 kWh/3.6 MJ x 40 g CO₂e/kWh solar electricity = 44 g CO₂e/MJ SAF. Without accounting for embodied emissions, the CLCA value could reach zero, thereby neglecting substantial emissions.

Table 2. Electricity emission factors in North America, given in g CO₂e/kWh (source: Argonne National Laboratory, 2022). BWR: boiling water reactor; CCS: carbon capture and storage; CI: carbon intensity; EGS: enhanced geothermal system.

Source	Embodied CI	Non-Embodied CI	Total CI
Hydro	7.6	0	7.6
Wind	10.4	0	10.4
Solar	40	0	40
Geothermal (binary)	21.7	0	21.7
Geothermal (EGS)	21.8	0	21.8
Geothermal (flash)	4.9	95.7	4.9
Nuclear (BWR)	0.3	6.6	6.9
Oil	0.7	1,109.1	1,109.8
Natural gas (NG)	0.5	960.8	961.3
NG combined cycle + CCS	0.4	46.7	47.1
Coal	0.8	1,049.7	1,050.5
Coal + CCS	0.8	154.6	155.4
Biomass	0.9	20.5	21.4
U.S. grid	3.0	464.8	467.8
U.S. grid mix estimate	2.0	608.3	610.3

Such levels remain small for existing SAF production pathways, as represented by today’s default CLCA values. An analysis of existing SAF production pathways found that the ethanol-to-jet corn grain pathway, as currently represented by default values, has the highest share of electricity input among the currently considered pathways, at 3.3% of electricity over the total energy input. When multiplied by the U.S. grid embodied emission value of 2 g CO₂e/kWh (Table 2), this leads to a CLCA contribution of 0.03 g CO₂e/MJ jet from embodied emissions of electricity. However, as the level of electrification of SAF production pathways increases and electricity with lower carbon intensity is employed, the contribution of embodied carbon emissions to the LCA values of a SAF could increase, as shown in Table 3 for a range of pathways and electrification scenarios.



Table 3. Life-cycle analysis (LCA) impact of increased electrification for select CORSIA pathways, given in g CO₂e/MJ of jet fuel. CORSIA: Carbon Offsetting and Reduction Scheme for International Aviation; CORSIA LCA: baseline full default values; Embod.: embodied; ETJ: ethanol-to-jet; F-T: Fischer-Tropsch; GHG: greenhouse gas; HEFA: hydroprocessed esters and fatty acids; iBuOHtj: isobutanol-to-jet; N/A: not applicable; PV: photovoltaic; SIP: synthesized isoparaffins; UCO: used cooking oil; w/: with; w/o: without; WGS: water gas shift.

Process	Feedstock	CORSIA LCA	Baseline			Electrolytic H ₂			Elec. H ₂ +Elec. Heat			Elec. H ₂ +Heat+Farming		
			Grid Elec. GHGs	PV Elec. w/ Embod. GHGs	PV Elec. w/o Embod. GHGs	Grid Elec. GHGs	PV Elec. w/ Embod. GHGs	PV Elec. w/o Embod. GHGs	Grid Elec. GHGs	PV Elec. w/ Embod. GHGs	PV Elec. w/o Embod. GHGs	Grid Elec. GHGs	PV Elec. w/ Embod. GHGs	PV Elec. w/o Embod. GHGs
HEFA	Rapeseed	47.4	1.6	0.1	0	17.2	1.5	0	32.9	2.8	0	34.5	2.9	0
	UCO	13.9	1.5	0.1	0	17.4	1.5	0	35.6	3.0	0	N/A for waste feedstock		
ETJ	Corn grain	65.7	7.3	0.6	0	15.2	1.3	0	65.4	5.6	0	66.9	5.7	0
iBuOHtj		55.8	6.7	0.6	0	14.3	1.2	0	57.6	4.9	0	59.0	5.0	0
SIP	Sugarbeet	32.4	0 (Net elec. export)			16.3	1.4	0	No heat requirement			17.8	1.5	0
	Sugarcane	32.8	0 (Net elec. export)			0 (from internal elec. gen.)			No heat requirement			0 (from internal elec. gen.)		
F-T	Corn stover	7.2	N/A – Heat & elec. from internal gen.			N/A – H ₂ from bio-syngas+WGS			N/A – Heat from internal gen.			2.2	0.2	0

These results show that continued omissions of embodied emissions, especially for fuels produced with significant electricity input, may be a source of concern for the integrity of CLCA calculations. At the same time, the team currently does not see indications that past decisions to exclude embodied emissions for biomass-, waste-, or residue-based SAF production processes need to be revisited. Thus, to maintain consistency with the default and actual value calculation methods and to avoid issues of burdening actual value calculations with the inclusion of negligible embodied emissions of electricity, the possibility of a threshold approach was explored. Such an approach considers embodied emissions when a certain level of electricity use is surpassed and/or a certain level of embodied emissions is found in the electricity mix. To facilitate these additional calculations, the team further presented a table of potential standard embodied emission values as well as a method for SAF producers to manually calculate embodied emissions for their electricity source.

Carbon sourcing

When considering fuels produced with significant electricity input, additional carbon sources beyond biomass can be used for SAF production, including the following:

- CO₂ captured from the atmosphere through direct air capture
- CO₂ from waste gases

The team worked to provide guidance on how SAF production using such carbon sources can be properly considered under CORSIA’s actual value method.

Electricity sourcing

For CEFs produced with significant electricity input, three questions associated with electricity sourcing arise:

1. Physical connectedness: Does there need to be a physical connection between the power generation and electricity consumed for CEF production?
2. Temporal matching: In the case of a power purchase agreement, does the electricity demand from CEF production have to match the electricity supply on a defined time scale (hourly, annually)?
3. Choice of power generation source: Can CEF producers leverage existing renewable resources? Or should CEF producers rely upon “new” power generation to avoid displacing renewable capacity that was to be used for other purposes? How is “new” power generation defined?

To address these questions, the MIT team analyzed the carbon intensity of CEFs produced with significant electricity inputs from two perspectives:

1. Producer perspective: The goal of this analysis is to understand concerns around temporal matching. The goal was to analyze how a SAF producer would use grid electricity as back-up power (in lieu of storage) during times when renewable electricity sources are not available. The study leveraged results obtained under ASCENT Project 52. The results showed that if grid back-up power can be utilized, a producer may not utilize any energy storage for renewable electricity sources if the grid power is relatively cheap. Such temporary use of grid back-up power (with



potentially high carbon intensity) may be associated with high GHG emissions, which may not be considered in the CEF CLCA value with less stringent (annual) matching of electricity demand to supply.

2. Grid perspective: The A01 team is exploring the impacts of adding renewable power generation and additional electricity demand for CEF production to the grid. Using detailed energy system models (see Cybulsky et al. (2023) for details), the team is assessing the impacts of different matching requirements and analyzing grid-wide emission impacts. This study has been started and will continue into the next reporting period.

Milestones

UHasselt and MIT have brought forward analyses to support progress in the areas outlined above. The results have been presented to the FTG during FTG meetings and numerous CLCA subgroup and expert meetings. Most importantly, UHasselt and MIT experts participated in and contributed to numerous FTG meetings, including CAEP13_FTG/01 (May 2022), CAEP13_FTG/02 (November 2022), CAEP13_FTG/03 (March 2023), CAEP13_FTG/04 (July 2023), and CAEP13_FTG/05 (September 2023).

Major Accomplishments

The MIT and UHasselt team accomplished the following under this task:

1. As co-lead of the FTG CLCA Task Group, Prof. Malina drafted CLCA progress reports for FTG meetings, where CLCA topics were discussed. In addition, Prof. Malina co-led several task group meetings.
2. The team brought forward a detailed assessment of the ILUC implications of biomass-derived process fuel use.
3. The team developed a framework for capturing CCS in CEF production processes under the CORSIA actual value method.
4. The team provided data and guidance for capturing fuels produced with significant electricity input under CORSIA. This effort included potential thresholds for capturing embodied emissions of electricity, different carbon sources, and assessments of electricity sourcing requirements from a producer and grid perspective.

Publications

- CAEP/13-FTG/03-IP/05: Actual Value Method of CORSIA Eligible Fuels (CEF) Using Significant Electricity Input: Modeling Update
- CAEP/13-FTG/03-WP/10: Summary of the progress of the core LCA subgroup
- CAEP/13-FTG/04-WP/12: Summary of the progress of the core LCA subgroup
- CAEP/13-FTG/04-WP/17: Actual Value Method for fuels with high electricity input
- CAEP/13-FTG/04-WP/19: Carbon Capture and Storage (CCS) Technology in CEF Production

Outreach Efforts

Progress on these tasks was communicated during weekly briefing calls with the FAA and other U.S. delegation members to the FTG, as well as during numerous FTG teleconferences between meetings. In addition, UHasselt and MIT experts participated in and contributed to FTG meetings, including CAEP13_FTG/02 (November 2022, Montréal), CAEP13_FTG/03 (March 2023, virtual), CAEP13_FTG/04 (July 2023, Turin), and CAEP13_FTG/05 (September 2023, virtual).

Student Involvement

During this reporting period, Tae Joong Park (graduate student, MIT) was involved in this task.

Plans for Next Period

In the coming year, the MIT/UHasselt ASCENT Project 01 team will continue its work with the FTG. Default CLCA values will be calculated and proposed for additional pathways. Prof. Malina will continue to lead the CLCA Task Group. A particular focus will be finalizing the actual value method improvement for calculating LCA values for fuels requiring substantial electricity inputs and CCS.

References

- Argonne National Laboratory. (2022A). *Greet: The greenhouse gases, regulated emissions, and energy use in Transportation Model*. Energy.gov. (n.d.-a). <https://www.energy.gov/eere/bioenergy/articles/greet-greenhouse-gases-regulated-emissions-and-energy-use-transportation>
- Argonne National Laboratory. (2022B). *Energy Systems and Infrastructure Analysis – GREET Aviation Module*. https://greet.es.anl.gov/greet_aviation

Cybulsky, A., Giovaniello, M., Schittekatte, T., Mallapragada, D., 2023. Producing hydrogen from electricity: How modeling additionality drives the emissions impact of time-matching requirements. <https://energy.mit.edu/wp-content/uploads/2023/04/MITEI-WP-2023-02.pdf>

ICAO., (2022A). *CORSIA Eligible Fuels – Life Cycle Assessment Methodology (CORSIA Supporting Document)*. ICAO, Montreal, Canada. https://www.icao.int/environmental-protection/CORSIA/Documents/CORSIA_Eligible_Fuels/CORSIA_Supporting_Document_CORSIA%20Eligible%20Fuels_LCA_Methodology_V5.pdf

ICAO., (2022B). *CORSIA Methodology for Calculating Actual Life Cycle Emission Values*. ICAO, Montreal, Canada. https://www.icao.int/environmental-protection/CORSIA/Documents/CORSIA_Eligible_Fuels/ICAO%20document%2007%20-%20Methodology%20for%20Actual%20Life%20Cycle%20Emissions%20-%20June%202022.pdf

Task 2 – Support U.S. Participation in ICAO CAEP by Performing CLCA to Establish Default Values for Use Under CORSIA

Massachusetts Institute of Technology and Hasselt University

Objectives

During the CAEP/11 and CAEP/12 cycle, the MIT ASCENT Project 01 team took leadership in applying the agreed-upon CLCA method to establish default CLCA values for CEFs. However, the list of pathways is not exhaustive, and further CLCA analysis is required to enable the inclusion of SAF technologies nearing commercialization. During the current reporting period, the team supported (a) a review of mixed animal fat hydroprocessed ester and fatty acid (HEFA) fuels and (b) a sensitivity analysis of CLCA values to investigate the sensitivity of the CLCA default values to changes in input parameters.

Research Approach

CLCA of HEFA fuels from poultry fat, beef tallow, swine lard, and mixed animal fats

During the current reporting period, the team estimated the life-cycle GHG emissions of HEFA from poultry fat, beef tallow, swine lard, and mixed animal fats. The system boundaries of calculations as well as the U.S.-specific data sources used for the calculation are summarized in Table 4. Compared with the existing analysis for tallow HEFA in CORSIA, step 1 was added because the transportation step from the slaughterhouse to the rendering facility should be part of the fuel life cycle.

More specifically, we note the following:

1. The feedstocks involved in this pathway include slaughterhouse outputs from beef, poultry, and pig slaughtering. These feedstocks are assumed to have zero GHG emissions, as they are considered a by-product derived from the slaughterhouses.

Table 4. General assumptions for estimating the core life-cycle analysis emissions of hydroprocessed ester and fatty acid fuels from mixed animal fats. CORSIA: Carbon Offsetting and Reduction Scheme for International Aviation; GREET: greenhouse gases, regulated emissions, and energy use in transportation; JRC: Joint Research Center; USDA: U.S. Department of Agriculture.

Stage	Assumptions
Transportation of feedstock to the rendering facility	The default transportation distance from the GREET model was used (805 km). Following JRC data, feedstock was assumed to be transported by truck only (25 tons).
Rendering	Energy requirements are estimated as a function of moisture content, considering the correlation curve from Lopez (2010) and rendering product ratios for lard from Hicks et al. (2016).
Transportation of rendered product to the fuel production facility	According to default data from the GREET model, 20% of the feedstock was assumed to be transported 644 km by rail, and the remaining fraction was transported 161 km by truck (25 tons).
Fuel production	Hydrogen requirements for tallow, poultry fat, and lard were adjusted compared with those for soybean hydrogen consumption based on the molar stoichiometry of the hydroprocessing reactions. Other energy and utility inputs are equivalent to those in the last calculation from CORSIA.
Fuel transportation	According to default data from the GREET model, 63%, 8%, and 29% of the fuel were assumed to be transported 80 km by truck, 837 km by barge, and 1288 km by rail, respectively.
Mixed animal fats	According to data from the USDA, tallow, poultry fat, and lard comprise 56%, 23%, and 21% of animal fat production in the United States, respectively.

2. The rendering stage refers to the heat treatment of fat, bone, offal, and related material derived from carcasses of livestock. The slaughterhouse outputs are crushed and subsequently heated inside a cooking chamber by means of indirect steam, which yields rendered lipids, meat and bone meal, and water. Table 5 summarizes the inputs and outputs of the rendering process. We assume that the energy requirements for the rendering depend on moisture content. Lopez et al. (2010) provided a correlation curve of rendered products versus energy use corresponding to the amount of water removed from cattle and chicken by-products. Using the correlation curve from Lopez et al. (2010) and rendering product ratios for lard from Hicks et al. (2016), we estimated rendering inputs for lard.
3. Washington State University provided inputs to the process by assessing the amount of animal fat production worldwide. More importantly, they produced conversion coefficients for the amount of animal fat production per animal in the United States. These conversion coefficients were applied to worldwide meat production data from the Organisation for Economic Co-operation and Development and the Food and Agricultural Organization to find the fat production worldwide. The production share was calculated for each type of animal fat.



Table 5. Inputs and outputs of the rendering of animal by-products. Data are expressed per kg of rendered product (i.e., unrefined fat). MBM: meat and bone meal. UH: Hasselt University.

Parameter	Unit	Beef	Poultry	Lard
		UH	UH	UH
Inputs				
Slaughterhouse waste	kg	3.6	4.8	3.4
Light fuel oil for steam generation	MJ	2.22	3.45	2.39
Diesel	MJ	0.02	0.02	0.02
Heat, from natural gas	MJ	3.47	5.36	3.75
Electricity, low voltage	MJ	1.04	1.1	0.85
Animal fat	MJ	1.82	2.81	1.97
Outputs				
Rendered product (as unrefined fat)	kg	1.00	1.00	1.00
MBM	kg	0.82	0.91	0.49
Water	kg	1.75	2.88	1.93
Other				
Total energy input	MJ	8.56	12.7	8.98
Moisture content	—	49%	60%	57%
Lower heating value of animal fat	MJ/kg	40.1	39.5	40.1
Lower heating value of MBM	MJ/kg	17.0	17.0	17.0
Allocation to fat (energy criteria)	—	74%	72%	83%
Production share (over total animal fat production)	—	56%	23%	21%

- The fuel production stage refers to the transformation of rendered product into SAF, which requires upgrading of the feedstock and subsequent hydrotreatment and isomerization. Table 6 summarizes the inputs and outputs of the transformation of animal fats into HEFA fuels. We assume that hydrogen consumption of tallow during upgrading to HEFA fuel might differ from that for poultry fat and lard, as these materials have different fatty acid compositions. Inputs for the upgrading of tallow to HEFA fuel in CORSIA were taken from Seber et al. (2014). Here, data from Pearlson (2011) on soybean HEFA were used, and hydrogen consumption for tallow has not been adjusted. We used 27 kg of hydrogen per MT of soybean oil, with the same assumption for tallow. In an attempt to update the hydrogen consumption for tallow and provide inputs for poultry fat and lard, we utilized the molar stoichiometry of the hydroprocessing reactions. For this, the reaction molar stoichiometry in the reactor (from a combination of reactions from unsaturated to saturated triglycerides, propane loss, and decarboxylation) was calculated for soybean oil, tallow, poultry fat, and lard. Then, using the hydrogen input for soybean oil from CORSIA Supporting Information (Table 61 in the Supporting Information), we adjusted the amount of hydrogen for tallow, poultry fat, and lard. Natural gas and electricity as utility inputs were kept the same as in Table 61 from CORSIA.

Table 7 summarizes the estimated GHG emissions from animal-fat-based SAF production.

Table 6. Inputs and outputs of the transformation of unrefined animal fats into hydroprocessed ester and fatty acid fuels. Data are expressed per kg of jet fuel.

Parameter	Unit	Beef	Poultry	Lard
		UH	UH	UH
Inputs				
Unrefined animal fat	kg	1.27	1.27	1.27
Phosphoric acid	g	0	0	0
Sodium hydroxide	g	0	0	0
Natural gas	MJ	3.60	3.60	3.60
Electricity, low voltage	MJ	0.20	0.20	0.20
Hydrogen	MJ	2.74	3.29	3.09
Outputs				
Jet fuel	kg	1.00	1.00	1.00
Co-product	MJ	0.10	0.10	0.10
Propane fuel mix	kg	0.074	0.074	0.074
Naphtha	kg	0.023	0.023	0.023
Other				
Total energy input	MJ	6.54	7.09	8

Table 7. Estimated greenhouse gas emissions from the production of animal-fat-based sustainable aviation fuel (SAF). Data are given in g CO₂e/MJ_{SAF}. HEFA: hydroprocessed esters and fatty acids. UH: Hasselt University.

Stage	Beef tallow HEFA	Poultry fat HEFA	Lard fat HEFA	Mixed animal fat HEFA
	UH	UH	UH	UH
Production share	56%	23%	21%	—
Transport to the rendering facility	5.80	7.50	6.13	6.26
Rendering	10.60	14.80	12.20	11.90
Transport to the SAF facility	0.35	0.35	0.35	0.35
SAF production	10.50	11.50	10.90	10.81
SAF distribution	0.40	0.40	0.40	0.40
Total	27.65	34.55	29.98	29.73

Sensitivity analysis of CLCA values

The team analyzed the sensitivity of the default CLCA value with regard to key parameters. Because the default CLCA value for a SAF pathway is defined as the mid-point value in the estimates produced by different modeling teams, it is not possible to conduct a sensitivity analysis for these mid-point values. Instead, we assessed the sensitivity around the LCA values in ICAO-GREET, the CORSIA calculation tool based on the GREET model v.2.8 (2019).

The analysis was conducted for six conversion pathways and a set of different feedstocks:

- Fischer-Tropsch jet fuel from switchgrass, miscanthus, corn stover, wheat straw, forest residues, and municipal solid waste
- HEFA from tallow, used cooking oil, palm fatty acid distillate, corn oil, soybean oil, rapeseed/canola oil, palm oil, brassica carinata
- Synthetic isoparaffinic jet fuel from sugarcane and sugarbeet
- Isobutanol-to-jet fuel from sugarcane, agricultural residues, corn grain, sugarcane, forest residues, miscanthus, and switchgrass
- Ethanol-to-jet fuel from sugarcane, agricultural residues, corn grain, sugarcane, forest residues, miscanthus, and switchgrass (stand-alone plant configurations)
- Lipid co-processing from soybean, tallow, and used cooking oil



A set of parameter values was varied in the sensitivity analysis:

- Conversion efficiency: Biomass input requirements for the SAF production in its conversion stage were changed by -10% and +10%.
- Heat requirements: Many SAF production pathways require external heat sources during the production process. Those requirements are assumed to be satisfied by natural gas, and we vary these requirements by -10% and +10%.
- Heat source: The default values are modelled with the assumption that external heat requirements are satisfied by natural gas. In the sensitivity analysis, we quantify the effect of using a fully decarbonized heat source and the effect of using coal.
- Electricity requirements: Electricity requirements during SAF production are varied by -10% and +10%.
- Electricity mix: External electricity requirements are assumed to be satisfied by national grid mixes in the default value calculations, often the U.S. and/or European Union mix. We examine the effect of electricity coming from a fully decarbonized grid or a grid fully based on coal, as well as for an electricity mix equivalent to those of countries with grids of relatively high GHG-emission intensity (China and India).
- Hydrogen source: Hydrogen is an important input in many SAF pathways. In the default values, it was assumed that hydrogen is produced from natural gas by means of steam methane reformation. In the sensitivity analysis, we quantify the emission effect of hydrogen from a zero-carbon source and hydrogen from coal.
- Sulfuric acid and ammonia requirements: Ethanol- and isobutanol-based SAF production requires sulfuric acid and ammonia to pretreat lignocellulosic feedstocks. Sulfuric acid and ammonia requirements for SAF production in the conversion stage were changed by -10% and +10%.

Table 8 provides a summary of the results. Green-shaded cells indicate an emission reduction whereas red-shaded cells indicate an emission increase, with the level of color shading denoting the magnitude of the effect. Darker colors represent stronger effects. With regard to conversion efficiency, electricity requirements, heat requirements, and sulfuric acid and ammonia requirements, the impact of a 10% change in each parameter is less than 3 g CO_{2e}/MJ SAF for all pathways. With regard to the hydrogen source, when coal is used for hydrogen production, emissions increase by more than 5 g CO_{2e}/MJ SAF for the HEFA and synthesized isoparaffin pathways. When the heat source is changed to coal, emissions for the HEFA pathways and most isobutanol and ethanol pathways increase by more than 4 g, with a maximum value of 17 g CO_{2e}/MJ SAF for the corn grain ethanol pathway. Turning to the electricity source, satisfying all external electricity needs by means of coal would increase emissions in the corn grain ethanol and isobutanol pathways by more than 8 g CO_{2e}/MJ SAF, whereas this increase is less than 4 g for all other pathways. However, when a realistic change in grid electricity emissions is introduced by assuming the China or India grid electricity mix instead of the baseline mix used in the default value calculations, emissions change by less than 4 g (Figure 3).



Table 8. Sensitivity analysis results. Data are given in g CO₂e/MJ of sustainable aviation fuel. ATJ: alcohol-to-jet; FTJ: fermentation-to-jet; HEFA: hydroprocessed esters and fatty acids; MSW: municipal solid waste; SIP: synthesized isoparaffins.

Pathway	Feedstock	Feedstock conversion efficiency		Heat requirements		Sulfuric acid requirements		Ammonia requirements		Electricity requirements		Source of hydrogen production		Source of heat		Source of electricity		
		-10%	10%	-10%	10%	-10%	10%	-10%	10%	-10%	10%	Decarbonized source	Coal	Decarbonized source	Coal	Decarbonized source	Coal	
FTJ	Switchgrass	-0.93	1.34	0.00	0.00	0.00	0.00	0.00	0.00	0.00	0.00	0.00	0.00	0.00	0.00	0.00	0.00	0.00
	Miscanthus	-0.83	1.01	0.00	0.00	0.00	0.00	0.00	0.00	0.00	0.00	0.00	0.00	0.00	0.00	0.00	0.00	0.00
	Corn Stover	-0.56	0.68	0.00	0.00	0.00	0.00	0.00	0.00	0.00	0.00	0.00	0.00	0.00	0.00	0.00	0.00	0.00
	Wheat Straw	-0.49	0.60	0.00	0.00	0.00	0.00	0.00	0.00	0.00	0.00	0.00	0.00	0.00	0.00	0.00	0.00	0.00
	Forest Residue	-0.30	0.36	0.00	0.00	0.00	0.00	0.00	0.00	0.00	0.00	0.00	0.00	0.00	0.00	0.00	0.00	0.00
	MSW	-1.75	2.14	0.00	0.00	0.00	0.00	0.00	0.00	0.00	0.00	0.00	0.00	0.00	0.00	0.00	0.00	0.00
HEFA	Tallow	-1.02	1.02	-0.76	0.76	0.00	0.00	0.00	0.00	-0.07	0.07	-6.63	5.65	-7.62	4.91	-0.67	0.80	
	Used cooking oil (UCO)	-0.03	0.03	-0.76	0.76	0.00	0.00	0.00	0.00	-0.07	0.07	-6.63	5.65	-7.62	4.91	-0.67	0.80	
	Palm fatty acid distillate	-0.63	0.63	-0.60	0.60	0.00	0.00	0.00	0.00	-0.11	0.11	-7.81	6.66	-6.00	1.56	-0.67	0.80	
	Corn oil	-1.73	1.73	-0.51	0.51	0.00	0.00	0.00	0.00	-0.06	0.06	-6.63	5.65	-5.10	3.34	-0.57	0.80	
	Soybean	-0.63	0.77	-0.84	0.84	0.00	0.00	0.00	0.00	-0.17	0.17	-6.68	5.70	-10.73	4.75	-1.68	1.83	
	Rapeseed/Canola	-1.21	1.10	-0.83	0.83	0.00	0.00	0.00	0.00	-0.16	0.16	-6.67	5.69	-8.23	4.70	-1.60	1.73	
SIP	Palm oil	-1.48	1.48	-0.51	0.51	0.00	0.00	0.00	0.00	-0.10	0.10	-6.68	5.70	-7.20	2.83	-0.97	1.08	
	Brassica carinata	-1.56	1.56	-0.78	0.78	0.00	0.00	0.00	0.00	-0.15	0.15	-6.71	5.72	-7.77	4.44	-1.55	1.68	
Isobutanol (ATJ)	Sugarcane	-2.16	2.16	0.00	0.00	0.00	0.00	0.00	0.00	0.00	0.00	-8.50	7.43	0.00	0.00	0.00	0.00	
	Sugarsweet	0.00	0.00	0.00	0.00	0.00	0.00	0.00	0.00	0.00	0.00	-8.28	7.24	0.00	0.00	0.00	0.00	
	Sugarcane	-1.52	1.52	-0.15	0.15	0.00	0.00	0.00	0.00	0.00	0.00	-0.06	0.05	-1.43	0.98	0.00	0.00	
	Agricultural residues	-0.79	0.79	-0.64	0.64	-0.02	0.02	-0.69	0.69	0.00	0.00	-1.84	1.61	-6.35	4.34	-0.01	-0.01	
	Forest residues	-0.49	0.49	-0.33	0.33	-0.68	0.68	-0.66	0.66	0.00	0.00	-1.81	1.59	-3.27	2.14	-0.01	-0.01	
	Corn grain	-1.88	1.88	-2.28	2.28	-0.04	0.04	-0.04	0.04	-0.69	0.69	-3.15	2.75	-12.78	14.65	-6.86	8.20	
Ethanol (ATJ)	Switchgrass	-1.56	1.57	-1.02	1.02	-0.70	0.70	-0.68	0.68	0.00	0.00	-3.16	2.76	-10.12	6.53	-0.02	-0.02	
	Miscanthus	-1.41	1.41	-1.08	1.08	-0.67	0.67	-0.65	0.65	-0.06	0.06	-3.16	2.76	-10.84	6.85	-0.64	0.74	
	Sugarcane	-1.57	1.57	0.00	0.00	0.00	0.00	0.00	0.00	0.00	0.00	-3.34	2.92	-0.04	0.04	0.00	0.00	
	Corn grain	-1.89	1.89	-2.63	2.63	0.00	0.00	-0.04	0.04	-0.75	0.75	-3.33	2.91	-16.23	16.89	-7.53	9.01	
	Agricultural residues	-0.65	0.65	-2.12	2.12	-0.02	0.02	-0.13	0.13	-0.33	0.33	-3.37	2.95	-11.14	13.56	-3.29	3.92	
	Forest residue	-0.40	0.41	-2.39	2.39	-0.02	0.02	-0.13	0.13	-0.33	0.33	-3.35	2.93	-15.39	9.95	-2.86	3.40	
Lipid co-processing	Miscanthus	-1.01	1.01	-2.12	2.12	-0.02	0.02	-0.13	0.13	-0.33	0.33	-3.33	2.91	-12.61	8.16	-2.86	3.40	
	Switchgrass	-1.08	1.08	-2.12	2.12	-0.02	0.02	-0.13	0.13	-0.33	0.33	-3.33	2.92	-12.61	8.16	-2.86	3.40	
	Soybean oil	-1.37	1.37	-0.03	0.03	0.00	0.00	0.00	0.00	-0.02	0.02	-0.30	0.29	-0.98	0.16	-0.27	0.37	
	Tallow	-1.05	1.05	-0.03	0.03	0.00	0.00	0.00	0.00	-0.02	0.02	-0.30	0.29	-0.98	0.16	-0.27	0.37	
	Used cooking oil (UCO)	-0.41	0.41	-0.03	0.03	0.00	0.00	0.00	0.00	-0.02	0.02	-0.30	0.29	-0.98	0.16	-0.27	0.37	

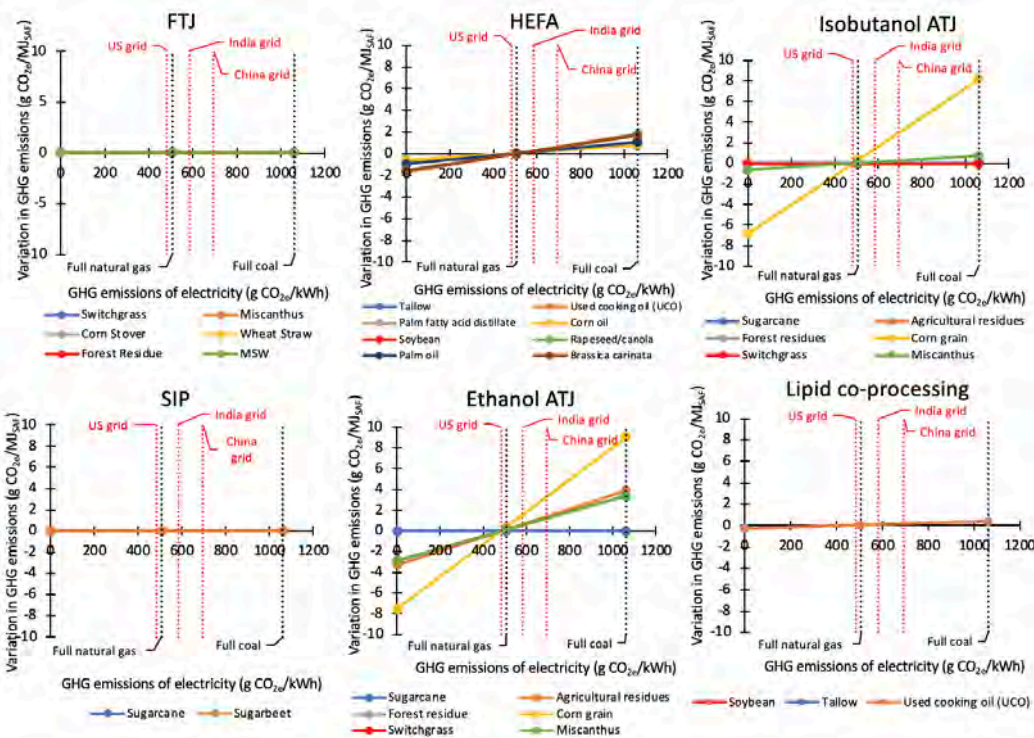


Figure 3. Effect of the source of electricity generation on the core life-cycle analysis value. ATJ: alcohol-to-jet; FTJ: fermentation-to-jet; GHG: greenhouse gas; HEFA: hydroprocessed esters and fatty acids; MSW: municipal solid waste; SAF: sustainable aviation fuel; SIP: synthesized isoparaffins.

Milestones

The work described above has been documented in working papers and information papers submitted to the FTG. Furthermore, the team discussed the work outlined above with various technical experts. UHasselt and MIT experts participated in and contributed to the FTG meetings held during the reporting period, including CAEP13_FTG/01 (May 2022), CAEP13_FTG/03 (March 2023), CAEP13_FTG/04 (July 2023), and CAEP13_FTG/05 (September 2023).

Major Accomplishments

The MIT and UHasselt team accomplished the following under this task:

1. Sensitivity analysis of the default CLCA values in CORSIA for a broad set of pathways
2. Inclusion of mixed animal fats, lard, and poultry fat HEFA pathways in CORSIA, with contributions to updating the tallow HEFA default value

Publications

Written reports

- CAEP/13-FTG/04-WP12: Progress of the core LCA subgroup, July 2023.
- CAEP13/FTG04/IP03: Sensitivity analysis for the core LCA values, July 2023.
- CAEP13/FTG03/IP04: Sensitivity analysis for the core LCA values (preliminary), March 2023.
- CAEP/13/FTG03/WP10: Summary of the progress of the core LCA subgroup, March 2023.

Student Involvement

Pieter Fonteyn (graduate student, UHasselt) was involved in this task.

Outreach Efforts

Progress on these tasks was communicated during weekly briefing calls with the FAA and other U.S. delegation members to the FTG, as well as during numerous FTG teleconferences between meetings. In addition, UHasselt and MIT experts participated in and contributed to FTG meetings, specifically CAEP13_FTG/01 (May 2022), CAEP13_FTG/02 (November 2022), CAEP13_FTG/03 (March 2023), CAEP13_FTG/04 (July 2023), and CAEP13_FTG/05 (September 2023).

Plans for Next Period

The team will continue to perform attributional CLCA to establish default values for use under CORSIA. More specifically, the team will be involved in a review of the alcohol-to-jet pathways within CORSIA and additional pathways as needed.

References

- Lopez et al. 2010. Energy Life Cycle Assessment for the Production of Biodiesel from Rendered Lipids in the United States. *Ind. Eng. Chem Res.* 49, 2419-2432.
- Hicks, T. et al. 2016. Meat Industry Protein By-Products: Sources and Characteristics in "Protein By-products: Transformation from Environmental Burden into Value-Added Products. In: *Protein Byproducts. Transformation from Environmental Burden Into Value-Added Products.*
- Pearlson, M. 2011. A Techno-Economic and Environmental Assessment of Hydroprocessed Renewable Distillate Fuels. MIT S.M. Thesis.
- Seber, G., et al. 2014. Environmental and economic assessment of producing hydroprocessed jet and diesel fuel from waste oils and tallow. *Biomass and Bioenergy* 67, 108-118.

Task 3 – Contribute to the Development of the Fuel Production Assessment for CEFs

Hasselt University

Objective

The team aimed to contribute to the development of the fuel production assessment for CEFs to the year 2030 and beyond, on the basis of detailed information gathered in a fuel production database. During the reporting period, the team worked jointly with researchers from Washington State University to provide updated estimates in support of the Conference on Aviation and Alternative Fuels (CAAF/3) meeting.

Research Approach

A scenario-based approach was chosen, in which a set of four production scenarios was developed. These scenarios differ regarding the type of companies included, the maturity of the production plans, product slate assumptions, and assumptions about the success rate of announced production plans. The scenarios are representative of more optimistic or pessimistic developments of the SAF market in the short term. Scenario definitions have been agreed upon within the ICAO CAEP FTG.

The scenarios were applied to available information on SAF production and production announcements out to 2030. A forecasting approach was used to estimate the potential SAF production for years 2028, 2029, and 2030 because of the scarcity of additional announcements for those years.

Milestone

Both the SAF production scenarios and the fuel production scenarios for fuels produced from waste CO₂ and atmospheric CO₂ provide a scientific basis for fuel availability assessments under the related long-term aspirational goal (LTAG).

Major Accomplishments

The team developed comprehensive scenarios of the future availability of SAFs and provided the data as input to LTAG. The results were included in the LTAG report. The update of the short-term projections has been used to inform the CAAF/3 conference.

Publications

CAEP13/FTG03/WP08: SAF production scenarios out to 2030.

Student involvement:

Francis Mwangi (graduate student, UHasselt) was involved in this task.

Outreach Efforts

Progress on these tasks was communicated during weekly briefing calls with the FAA and other U.S. delegation members to the FTG, as well as during numerous FTG and LTAG teleconferences. Results have been included in the LTAG report and are regularly presented as part of the results.

Plans for Next Period

The team will continue to update scenarios and projections as needed.

Task 4 – Develop Methods for Probabilistic LCAs and Techno-economic Analyses in the Context of Assessing U.S.-based SAF Production

Massachusetts Institute of Technology

Objectives

Work conducted under this task in previous reporting periods has shown that the availability of biomass may limit biomass-based SAF production in the United States. Furthermore, work under this task has explored how additional SAF could be produced as existing biomass production is re-routed to SAF production (e.g., as electric cars are scaled up, which reduces the ethanol demand for road fuels) and how SAF production could be decoupled from the bioenergy supply through PtL pathways. During the current reporting period, the team expanded upon prior work to explore how agricultural practices could increase bioenergy production. Specifically, the team analyzed the potential of double-cropping for increasing the supply of biomass for SAF production in the United States.

Research Approach

Double-cropping is a type of multi-cropping in which two crops are sequentially grown on the same land in one year. This practice has been discussed as a method for expanding crop production through intensified land use. According to the U.S. Department of Agriculture, during 1999–2012, only 2% of all cropland in the United States was double-cropped.

To assess the potential of producing SAF via double-cropping, we consider double-cropping with seven plants that were chosen based on their suitability for cultivation in the United States and the availability of mature SAF production pathways: corn, sorghum, wheat, sunflowers, soybeans, canola, and camelina. For crop pairings, wheat, canola, and camelina were designated as winter crops because of their resistance to cold, whereas corn, sorghum, sunflowers, and soybeans were designated as primary crops. In total, twelve different crop pair combinations were analyzed.

Using data with high geographical resolution, the potential for SAF production from double-cropping was quantified under current and future conditions. The underlying method involves (a) suitability analysis for each crop or crop pairing, which was determined by considering local temperature and rainfall data, (b) yield analysis, which was conducted on the basis of the fundamental production potential of a crop under local climatic and soil conditions in combination with historical yield analysis to capture potential technology advancements, (c) land availability to exclude urban areas, forests, savannas, and wetlands, and (d) representation of feedstock conversion pathways for SAF production. In addition, the life-cycle GHG emission savings of the resulting energy products (including SAF) were calculated. This method is summarized in Figure 4.

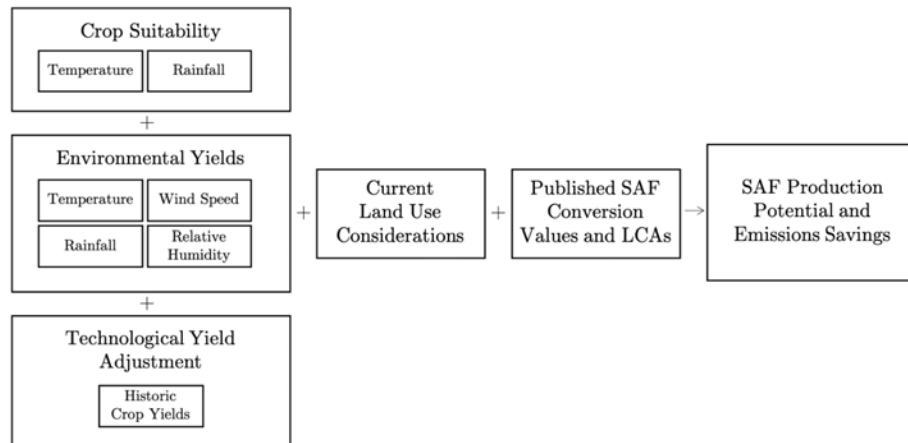


Figure 4. Overview of method for assessing double-cropping potential in the United States. LCA: life-cycle analysis; SAF: sustainable aviation fuel.

Milestones

A full analysis of biomass availability, including double-cropping, was presented to the A01 team in Summer 2023. This work has been documented in a Master’s thesis, and a manuscript is in preparation for future publication.

Major Accomplishments

The results of this study have shown that double-cropping can intensify agricultural production. The resulting production potential is sufficient for meeting SAF demand at U.S. airports; this scenario does not require re-allocation of land currently used for agricultural production or the use of any waste or residues. The suitability for double-cropping and associated production can be expected to grow at a pace that is sufficient to meet future SAF demand at U.S. airports. In fact, depending on the land turnover time, U.S.-based SAF production from energy crops using double-cropping could be up to 30% higher than SAF demand at U.S. airports in 2050. Such scenarios largely rely on corn or soybean as primary crops. Furthermore, demand would be almost entirely met by existing cropland, therefore curbing the need for land-use changes and associated emissions.

Publications

Demsky, S., 2023. Analysis of Double Cropping to Expand Sustainable Aviation Fuel Production in the United State. MIT Master’s thesis. <https://hdl.handle.net/1721.1/151600>.

Outreach Efforts

The MIT team presented the work under this task at the A01 team meeting in September 2023.

Student Involvement

Sarah Demsky (graduate student, MIT) was involved in this task.

Plans for Next Period

This task is complete. The MIT team will pursue publication of results.



Task 5 – Support Knowledge Sharing and Coordination Across All A01 Universities Working on SAF Supply Chain Analyses

Massachusetts Institute of Technology

Objective

The objective of this task is to provide support for coordination of work by all A01 universities on SAF supply chain analysis. The sharing of methods and results decreases the replication of work on similar topics among A01 universities.

Research Approach

The MIT A01 team performed several functions to accomplish this task. Specifically, the team participated in bi-weekly A01 coordination teleconferences, which served as a venue to discuss progress in various grant tasks and learn about the activities of other ASCENT universities.

Milestone

The MIT A01 team presented current research to other ASCENT universities.

Major Accomplishments

The major accomplishments associated with this task include participation in bi-weekly A01 coordination teleconferences and presentation of current research to other ASCENT universities.

Publications

None.

Outreach Efforts

See above.

Awards

None.

Student Involvement

See above for briefings.

Plans for Next Period

The MIT A01 team will continue to engage in bi-weekly teleconferences and other events to disseminate MIT's A01 work.



Project 002 Understanding Changes in Aviation Emissions Due to SAF with New Combustor Technology

Missouri University of Science and Technology, Aerodyne Research Inc., and The Boeing Company

Project Lead Investigator

Philip D. Whitefield
 Professor Emeritus of Chemistry
 Department of Chemistry
 Missouri University of Science and Technology
 400 W 11th Street, Rolla, MO 65409
 573-465-7876
pwhite@mst.edu

University Participants

Missouri University of Science and Technology (MS&T)

- P.I.: Prof. Philip D. Whitefield
- FAA Award Number: 13-C-AJFE-MST, Amendments 002, 003, 005, 008, 010, 012, 019, and 030
- Period of Performance: September 18, 2014 to March 3, 2025

Project Funding Level

Project	Funding	Matching	Source
13-C-AJFE-MST-002	\$1,288,836.34	\$1,288,836.34	EMPA letter
	\$284,613.66	\$284,613.66	Transport Canada
13-C-AJFE-MST-003	\$500,000.00	\$500,000.00	EMPA letter
13-C-AJFE-MST 005	\$500,000.00	\$500,000.00	EMPA letter
13-C-AJFE-MST-008	\$579,234.00	\$579,234.00	EMPA letter
13-C-AJFE-MST-010	\$725,500.00	\$725,500.00	EMPA letter
13-C-AJFE-MST-012	\$1,217,221.00	\$1,217,221.00	EMPA letter
13-C-AJFE-MST-019	\$521,246.00	\$521,246.00	GE letter
13-C-AJFE-MST-030	\$3,050,812.00	\$3,050,812.00	Boeing letter

Investigation Team

MS&T

Prof. Philip Whitefield, (P.I.)
 Prof. Klaus Woelk, (co-P.I.)
 Steven Achterberg, (research technician)
 Max Trueblood (research technician)

Aerodyne Research, Inc.

Dr. Richard Miake-Lye, (subcontractor)

The Boeing Co.

Dr. Steven Baughum, (subcontractor)
 Dr. William Griffin, (subcontractor)

Project Overview Objectives

In the last quarter of 2022, a decision was made to re-target ASCENT Project 02 to focus on emissions impacts measurements resulting from the adoption of sustainable aviation fuels (SAFs) by current and future anticipated global commercial fleets. Funds were de-obligated and re-obligated to underwrite the cost of these new emissions measurements. The ASCENT MS&T team, with the guidance of emissions specialists at Boeing, General Electric, and Gulfstream, proposed to make three high-priority ground-based field measurement campaigns of nonvolatile particulate matter (nvPM) and combustion gas emissions from engines on a commercial widebody transport, a business jet aircraft, and a new technology combustor burning both conventional fuels and candidate SAF. These measurements were scheduled to occur in three 21-day test campaigns in the fourth quarter of 2023 (Boeing/ecoDemonstrator; see link below) and, at times currently in negotiation, in the third and fourth quarter of 2024 (GE and Gulfstream). The analysis and reporting of the data arising from these studies is expected throughout 2024. Each campaign will be preceded by test design, planning, and preparation, beginning in the second quarter of 2023. The cost to ASCENT has been, and will be, to (a) support the MS&T team’s participation in and management of the three ground-based emission studies and (b) defray some of the costs incurred for the fuels (SAFs and conventional jet fuels) that will be burned to conduct both ground-based and in-flight emissions testing. During this reporting period, the preparations for the ecoDemonstrator subproject were on schedule for the testing window of the measurement campaign, i.e., the month of October 2023.

Link - [Boeing 737-10 EcoDemonstrator Tackles SAF Contrail Study | Aviation Week Network](#)

Work Schedule

- Tasks 1–3 describe the work required to successfully perform the ground testing associated with an in-flight emissions study on a wide-body airframe (potentially the Boeing-sponsored ecoDemonstrator study), a business jet (potentially the Gulfstream study), and a new technology combustor (potentially the GE study).
- Task 1 – 3.1 plans the test matrices for up to a 3-week deployment to a ground testing venue to be provided by the sponsoring original equipment manufacturer (OEM; anticipated to be Boeing, Seattle, WA; Gulfstream, Savannah, GA; and GE, Cincinnati, OH). This planning exercise was or is being undertaken in coordination with NASA (which is anticipated to be a test participant) and focuses on sampling fuel-specific emissions from a wide-body commercial aircraft, a business jet, and a new technology combustor/engine combination.
- Task 1 – 3.2: Prepare the MS&T and Aerodyne instrument packages housed in mobile laboratories, including calibration of the individual PM mass number and compositional systems.
- Task 1 – 3.3: Transport and set up the MS&T and Aerodyne instrument packages (mobile laboratories). This task includes deployment of test personnel to the test site and the interconnection of the instrument packages to the communal sampling probe assembly. During this setup activity, sampling system loss analyses will be performed.
- Task 1 – 3.4: Execute the test matrices defined in Task 1.1.
- Task 1 – 3.5: Tear-down transport the mobile laboratories and test personnel to their home locations.
- Task 1 – 3.6: Conduct post-test data reduction and analysis including participation in post-test workshops whose locations are yet to be defined.
- Task 1 – 3.7: Prepare and deliver interim and final reports.
- Task 1 – 3.8: The OEMs with the assistance of the FAA, through this effort, have or will coordinate the procurement, fuel properties analysis, delivery, handling, and loading logistics for various fuels in support of the 2023–2024 emissions testing, including the fuel volume required to support testing of the source and chase aircraft. In the case of the ecoDemonstrator subproject (Task 1), the fuels burned are as follows:
 - Fuel 1: low-sulfur Jet A, per ASTM D1655, total percentage by mass maximum objective of 0.0001 (maximum total sulfur target of 1 ppm)
 - Fuel 2: 100% HEFA-SPK, per ASTM D7566, Tables 1, A2.1, and A2.2
 - Fuel 3: approved SAF blend (e.g., 30% HEFA-SPK), per ASTM D7566, Table 1

The fuel provider delivered the following fuel quantities to Boeing for Task 1 at a base of operations in the Puget Sound region. The test fuel description quantities (in U.S. gallons) were as follows:



- Fuel 1: low-sulfur Jet A 21,4 00 gal
- Fuel 2: 100% HEFA-SPK 27, 600 gal
- Fuel 3: commercial SAF blend, 127,300 gal

Milestones

- Task 1 – 3.1: Test matrices were planned for up to a 3-week deployment to a ground testing venue to be provided by the sponsoring OEM, anticipated to be Boeing, Seattle, WA (COMPLETED); Gulfstream, Savannah, GA (under discussion during reporting period); and GE, Cincinnati OH (under discussion during the reporting period).
- Task 1.2: MS&T and Aerodyne instrument packages were housed in mobile laboratories, including calibration of the individual PM mass number and compositional systems (COMPLETED).
- Task 1.3: MS&T and Aerodyne instrument packages (mobile laboratories) were transported to, and set up at, the test site, including deployment of test personnel to the test site and interconnection of the instrument packages to the communal sampling probe assembly. During this setup activity, sampling system loss analyses will be performed (prepared for; actual deployment started October 4, 2023).

Major Accomplishments

- Reconfigured ASCENT 02 project objectives;
- Restructured ASCENT 03 funding;
- Negotiated subcontracts with Aerodyne and Boeing; and
- Completed Tasks 1.1, 1.2, and 1.3 on schedule.

Publications

None.

Outreach Efforts

Restructuring of ASCENT 02 reported at the combined ASCENT Advisory Board and Emissions Roadmap Meeting, May 2023.

Awards

None.

Student Involvement

No graduate students were employed in this task; however, four undergraduate research assistants (Dominic Torre, Zachary Alton, Aleck Barchenski, and Zachary Achterberg) were employed in pretest activities, including individual component testing and calibration, and data reduction and interpretation.

Plans for Next Period

- Task 1 – 3.4: Execute the test matrices defined in Tasks 1–3.
- Task 1 – 3.5: Tear-down transport the mobile laboratories and test personnel to their home locations.
- Task 1 – 3.6: Conduct post-test data reduction and analysis, including participation in post-test workshops whose locations are to be defined.
- Task 1 – 3.7: Prepare and deliver an interim and a final report.
- Task 1 – 3.8: The OEMs, with the assistance of the FAA, through this proposed effort will coordinate the procurement, fuel property analysis, delivery, handling, and loading logistics for various fuels in support of the 2024 emissions testing, including the fuel volume required to support testing of the source and chase aircraft.



Project 003 Cardiovascular Disease and Aircraft Noise Exposure

Boston University

Project Lead Investigator

Junenette L. Peters
Associate Professor
Department of Environmental Health
Boston University School of Public Health
715 Albany St., T4W, Boston, MA 02118
617-358-2552
petersj@bu.edu

University Participants

Boston University

- P.I.s: Prof. Jonathan Levy (university P.I.), Prof. Junenette Peters (project P.I.)
- FAA Award Number: 13-C-AJFE-BU-032
- Period of Performance: October 1, 2022 to September 30, 2023

Massachusetts Institute of Technology

- Sub-P.I. and co-P.I.: Prof. R. John Hansman (sub-P.I.), Dr. Florian Allroggen (sub-co-P.I.)

- **Tasks** (performance period)

Boston University

1. Write up and publish final results on sleep quantity and quality and aircraft noise exposure.
2. Write up and publish final results on cardiovascular disease (CVD) and aircraft noise exposure.
3. Write up and publish final results on supporting analyses of trends in aircraft noise exposure.
4. Present preliminary results of analyses and generate final results on night-time noise and hypertension.
5. Generate final results of analyses on aircraft noise and the intermediary risk factor of adiposity.
6. Develop an analysis plan for analyses of an intermediary risk factor (diabetes) and aircraft noise.
7. Gain approval for human subject noise research for new cohorts.

Massachusetts Institute of Technology

8. Assess the relationship between a perceived increase in aircraft noise and increases in aircraft visibility.

Boston University and Massachusetts Institute of Technology

9. Prepare a second draft of the report on study results related to 2018 FAA Reauthorization, Section 189 for policymakers.

Project Funding Level

Total funding (3-year funding): \$1,999,608

Matching funds: \$1,999,608

Sources of matching funds: Nonfederal donors to the Nurses' Health Study (NHS) and Women's Health Initiative (WHI) cohorts

Investigation Team

Boston University

Prof. Junenette Peters (P.I.)
Prof. Jonathan Levy (P.I.)



Dr. Levy participates in noise exposure assessment and provides expertise in the areas of predictive modeling and air pollution. Dr. Peters is responsible for directing all aspects of the proposed study, including study coordination, design and analysis plans, and co-investigator meetings.

Harvard University/Brigham and Women's Hospital

Prof. Francine Laden
Prof. Jaime Hart
Dr. Tianyi Huang
Dr. Susan Redline

Dr. Laden and Dr. Hart are our NHS sponsors for this ancillary study. Dr. Hart assigns aircraft noise exposures to the geocoded address history coordinates of each cohort member. Dr. Laden and Dr. Hart also assist in documenting data from the NHS, on the basis of their previous experience in research on air pollution and chronic disease outcomes in these cohorts, and in performing appropriate analyses of hypertension and cardiovascular outcomes. Dr. Redline and Dr. Tianyi Huang guide efforts related to noise and sleep disturbance in the NHS and WHI.

University of North Carolina

Dr. Eric Whitsel
James Stewart

Dr. Whitsel is our WHI, National Longitudinal Study of Adolescent to Adult Health (Add Health), and Hispanic Community Health Study/Study of Latinos (HCHS/SOL) sponsor for the ancillary studies. Along with James Stewart, Dr. Whitsel assigns aircraft noise exposure to the geocoded addresses of cohort members. Dr. Whitsel also assists in documenting data from these cohorts based on multiple years of combined leadership and service on WHI and Add Health morbidity and mortality classification, outcomes adjudication, and ancillary study committees.

Massachusetts Institute of Technology

Prof. R. John Hansman (sub-P.I.)
Dr. Florian Allroggen (sub-co-P.I.)

Dr. Hansman and Dr. Allroggen are responsible for the economic impact analysis (reported in a previous report) and visibility analysis and participate in drafting the report for policymakers.

Project Overview

Exposure to aircraft noise has been associated with physiological responses and psychological reactions (Bluhm and Eriksson, 2011; Hatfield et al., 2001), including sleep disturbances, sleep-disordered breathing, nervousness, and annoyance (Hatfield et al., 2001; Rosenlund et al., 2001). However, the extent to which aircraft noise exposure increases the risk of adverse health outcomes is still not well understood. The literature, formerly primarily European studies, provided early evidence of a relationship between aircraft noise and self-reported hypertension (Rosenlund et al., 2001), increased blood pressure (Haralabidis et al., 2008; Jarup et al., 2008; Haralabidis et al., 2011; Evrard et al., 2008), antihypertensive medication use (Bluhm and Eriksson, 2011; Greiser et al., 2007; Franssen et al., 2004; Floud et al., 2011), and incidence of hypertension (Eriksson et al., 2010; Dimakopoulou et al., 2017). One study found that aircraft noise exposure was associated with incident diabetes (Eze et al., 2017). Other studies found a stronger but marginal association between aircraft noise and incident diabetes in women as well as an association with waist circumference (Eriksson et al., 2014; Zare Sakhvidi et al., 2018). Experimental, "everyday," and traffic noise exposures have been related to heart rate variability (El Aarbaoui et al., 2020; El Aarbaoui et al., 2017; Sim et al., 2015; Walker et al., 2016; Kraus et al., 2013), but no study, to date, has reported on heart rate variability relative to aircraft noise. Findings of a cardiovascular relationship were supported by a report by the World Health Organization European Centre for Environmental Health, which evaluated the association between residential exposure to environmental noise and CVD and found substantial evidence for biological plausibility and positive associations between environmental noise and hypertension, myocardial infarction, and ischemic heart disease (Babisch and Kim, 2011; WHO, 2018).

The goal of this ongoing project is to continue to examine the potential health impacts attributable to noise exposure resulting from aircraft flights. This project also leverages ongoing work within ASCENT and is responsive to Section 189 of the FAA Reauthorization Act of 2018 (Pub. L. 115-254), which called for a study on the potential health and economic impacts attributable to aircraft overflight noise and an assessment of the relationship between a perceived increase in aircraft noise and increases in aircraft visibility. To date, our work has leveraged existing collaborations with well-recognized and respected studies that have followed over 250,000 participants through the course of their lives to understand factors that affect health. These studies include the NHS and NHSII as well as the Health Professionals Follow-Up Study. Furthermore, this work has aligned with a concluded effort funded by the National Institutes of Health to examine these associations in the WHI. The research team continues to leverage aircraft noise data for 90 U.S. airports from 1995 to 2015 and has linked these data to demographic, lifestyle, and health data for the participants of long-term health studies. These studies have provided considerable geographic coverage of the United States, including all of the geographic areas specified in Section 189. Furthermore, our work to date has also included a first-of-its-kind empirical assessment of the economic impacts on businesses located beneath flight paths at selected U.S. airports responsive to the requirements set forth in Section 189.

We recently added to the literature by reporting on U.S. studies evaluating the degree to which aircraft noise affects health. We found a suggestive positive association between aircraft noise exposure and the risk of hypertension (Kim et al., 2022). However, there are fewer studies on the potential effect of noise on mental health (Seidler et al., 2017; Wright et al., 2018). Updated guidelines from the World Health Organization reported a lack of high-quality evidence for aircraft noise and mental health and highlighted the need for additional high-quality studies (WHO, 2018; Clark et al., 2020). Potential biological mechanisms of action of noise on health include induced release of stress hormones (Ising and Kruppa, 2004; Spreng, 2000; Selander et al., 2009; Lefevre et al., 2017) and markers of inflammation and oxidative stress, effects on vascular function (Munzel et al., 2017), and indirect effects on sympathetic activity, which is associated with adverse metabolic outcomes (Selander et al., 2009; Grassi, 2006; Mancia et al., 2006; Mancia et al., 2007). To better understand these potential relationships, we have increased the diversity of participants in our studies with a focus on vulnerable populations by adding the HCHS/SOL and Add Health cohorts. Furthermore, we are evaluating potential impacts of aircraft noise on additional health outcomes beyond those previously explored, including cardiovascular intermediaries and mental health outcomes in NHS, NHSII, WHI, HCHS/SOL, and Add Health.

The overall aims for this multi-year project as it relates to our continuing efforts are as follows:

Tasks under Amendment No. 32:

1. Assign aircraft noise exposures over time to geocoded participant addresses for HCHS/SOL and Add Health.
 - a. Intersect geocoded addresses with day-night average sound level (DNL) and equivalent sound levels for night (L_{night}) and day (L_{day}) aircraft noise exposure levels currently available from 2005 to 2015.
 - b. Estimate the percent of participants across noise exposure categories and assess overall trends in participant noise exposure levels over time, including an evaluation of sociodemographic and other predictors of aircraft noise exposure to facilitate the design and interpretation of epidemiological analyses.
2. Estimate the potential association between cardiovascular intermediaries and aircraft noise exposure.
 - a. Develop analysis plans and manuscript proposals to gain approval to investigate potential relationships between aircraft noise exposure and health intermediaries or cardiometabolic markers such as adiposity and heart rate variability in the NHS, WHI, HCHS/SOL, and Add Health cohorts.
 - b. Perform statistical analyses, undergo manuscript reviews, and present and publish results.
3. Investigate the potential impact of aircraft noise exposure on mental health.
 - a. Conduct an in-depth literature search to identify relevant mental health outcomes.
 - b. Determine the applicable assessments of these outcomes (i.e., depression and anxiety) within the various cohort studies.
 - c. For each cohort, develop an analysis plan and gain approval of manuscript proposals on the potential relationships between aircraft noise exposure and mental health outcomes.
 - d. Perform statistical analyses, undergo manuscript reviews, and present and publish results.
4. Explore the addition of noise-related survey questions to NHS3.

Tasks under Amendment No. 16 as it relates to Section 189 are as follows:



1. Finalize analyses assessing the relationship between a perceived increase in aircraft noise and increases in aircraft visibility.
2. Prepare a final draft of the study report related to Section 189 of the FAA Reauthorization Act of 2018 (Pub. L. 115-254) for policymakers.

Task 1 - Write Up and Publish Final Results on Sleep Quantity and Quality and Aircraft Noise Exposure

Boston University

Objective

The aim of this task is to write up and publish the final results of our analyses on aircraft noise (DNL and L_{night}) and identified sleep outcomes.

Research Approach

We intersected modeled night-time noise exposure surfaces for 1995, 2000, 2005, 2010, and 2015 based on geocoded addresses of the participants over the follow-up period (in NHS). We selected a relevant set of variables a priori to be examined as confounders and/or effect modifiers. We used generalized estimating equations to estimate the odds from repeated measures of sleep insufficiency over multiple survey years and used conditional logistic regression models of sleep quality to estimate the odds for one survey year.

Milestones

- Publish analyses on aircraft noise and sleep quantity and quality.

Major Accomplishments

- Responded to journal reviewer comments and revised our manuscript based on comments.
- Published paper ‘Associations between Aircraft Noise Exposure and Self-Reported Sleep Duration and Quality in the United States-Based Prospective Nurses’ Health Study’ in *Environmental Health Perspectives*.

Table 1. Odds ratios of the relationships between $L_{\text{night}} \geq 45$ vs. < 45 dB and repeated measures of sleep insufficiency and a one-time measure of poor sleep quality in the Nurses’ Health Study.

Model	Sleep insufficiency	Poor sleep quality
$L_{\text{night}} \geq 45$ vs. < 45 dB	OR (95% CI)	OR (95% CI)
Model 1: Age-adjusted	1.34 (1.17, 1.53)	0.93 (0.72, 1.20)
Model 2: Model 1 + other demographics	1.27 (1.11, 1.45)	0.94 (0.71, 1.21)
Model 3: Model 2 + behaviors & comorbidities	1.26 (1.10, 1.44)	0.92 (0.71, 1.20)
Model 4: Model 3 + other environmental factors	1.23 (1.07, 1.40)	0.91 (0.70, 1.19)

OR, odds ratio; CI, confidence interval.

Age-adjusted (age, age²) models were sequentially further adjusted as indicated with other demographics, behaviors and comorbidities, and other environmental factors. Other demographics: U.S. region of residence, race, living alone, spouse’s education. Behaviors: alcohol consumption, smoking status. Comorbidities: diabetes, hypertension. Environmental: greenness (normalized difference vegetation index), light at night.

Interpretation using $L_{\text{night}} \geq 45$ dB as an example

In Model 4, exposure to levels of $L_{\text{night}} \geq 45$ was associated with higher odds of short self-reported sleep duration (< 7 h/24-h day) compared with levels of $L_{\text{night}} < 45$. Participants in NHS exposed to $L_{\text{night}} \geq 45$ had 23% greater odds of short sleep duration than participants exposed to $L_{\text{night}} < 45$, with a 95% confidence interval (CI) of 7%–40%. In Model 4, no relationship was observed between noise and self-reported sleep quality (frequent trouble falling/staying asleep). Participants exposed to $L_{\text{night}} \geq 45$ had 9% lower odds of poor sleep quality than participants exposed to $L_{\text{night}} < 45$, with a 95% CI of –30% to 19%.

Task 2 - Write Up and Publish Final Results on CVD and Aircraft Noise

Boston University

Objective

The aim of this task is to perform a final analysis of the potential relationship between CVD and aircraft noise.

Research Approach

We designed a statistical analysis and selected a large set of a priori variables to be examined as confounders and/or effect modifiers in NHS and NHSII. We compiled appropriate data sets and conducted descriptive statistics analysis. We used time-varying Cox proportional hazards models to estimate the CVD risk associated with time-varying aircraft noise exposure.

Milestones

- Publish analyses on aircraft noise and CVD.

Major Accomplishments

- Responded to journal reviewer comments and revised our manuscript accordingly.
- Published ‘Associations between long-term aircraft noise exposure, cardiovascular disease, and mortality in US cohorts of female nurses’ in *Environmental Epidemiology*.

Table 2. Hazard ratios (95% confidence intervals) for associations between aircraft noise exposure (day-night average sound level) and cardiovascular disease in Nurses’ Health Study I and II, meta-analyzed.

DNL (dB)	Cases	Person-time	Basic	Parsimonious	Fully adjusted
≥50	317	122,642	1.01 (0.90, 1.13)	1.00 (0.89, 1.12)	0.97 (0.87, 1.09)
<50	4,212	1,583,635	Ref.	Ref.	Ref.
Continuous, per 10 dB	4,529	1,706,278	0.99 (0.84, 1.18)	0.98 (0.83, 1.16)	0.97 (0.82, 1.15)

Basic model: adjusted for age and calendar year.
 Parsimonious model: basic model + race/ethnicity, marital status, spouse’s educational attainment, neighborhood socioeconomic status score, region of residence, fine particulate matter (PM_{2.5}), and population density.
 Fully adjusted model: parsimonious model + physical activity, smoking status, alcohol use, diet, menopausal status, and family history of cardiovascular disease.

Interpretation using DNL ≥50 dB as an example

In the basic models comparing exposure to DNL ≥50 dB, participants in NHS/NHSII exposed to DNL ≥50 dB had a 1% greater risk of CVD than participants exposed to DNL <50 dB, with a 95% CI of –10% to 13%. In the fully adjusted model, participants exposed to DNL ≥50 dB had a 3% lower risk of CVD than participants exposed to DNL <50 dB, with a 95% CI of –13% to 9%.

Task 3 - Write up and Publish Final Results on Supporting Analyses of Trends in Aircraft Noise Exposure

Boston University

Objective

The aim of this task is to understand changes in aircraft noise exposure that will facilitate the interpretation of time-varying exposure measures in noise-health analyses and to understand the sociodemographic patterning of noise exposure that may confound or modify potential associations between noise and health.

Research Approach

We overlaid noise contours for 2000, 2005, 2010, and 2015 with census block data from the U.S. Census Bureau and American Community Surveys for 2000, 2010, and 2015 in a geographic information system to estimate population

changes within noise levels. We used group-based trajectory modeling to statistically identify fairly homogeneous clusters of airports that follow similar changes in outcomes over time. We used linear fixed-effects models to estimate changes in the sizes of exposure areas according to airport clusters for DNL values ≥ 65 dB and ≥ 45 dB and L_{night} values ≥ 45 dB.

Milestones

- Publish supporting analyses characterizing aircraft noise trends and sociodemographic patterns of exposure to aviation noise.

Major Accomplishments

- We responded to journal reviewer comments and revised our manuscript based on comments.
- Published ‘Characterizing temporal trends in populations exposed to aircraft noise around U.S. airports: 1995–2015’ in the *Journal of Exposure & Environmental Epidemiology*.
- We evaluated geographic and airport characteristics as predictors of patterns of exposed area over time. Among our sample of 90 U.S. airports, we found that non-monotonic trends in noise contour areas over time by airport characteristics peaked in 2000, then generally decreased until 2010, and subsequently increased from 2010 to 2015. Using group-based trajectory modeling at three cut points—DNL 45 dB and 65 dB and L_{night} 45 dB—we identified four distinct trajectory groups of airports that shared underlying airport characteristics (Figure 1 for 45 dB for (a) DNL and (b) L_{night}). We also found that populations who identified as White or non-Hispanic/Latino had the highest counts of exposure, yet underrepresented groups (e.g., Hispanic, Black/African American, Asian, etc.) carried a disproportionate burden of exposure among their respective sub-populations.

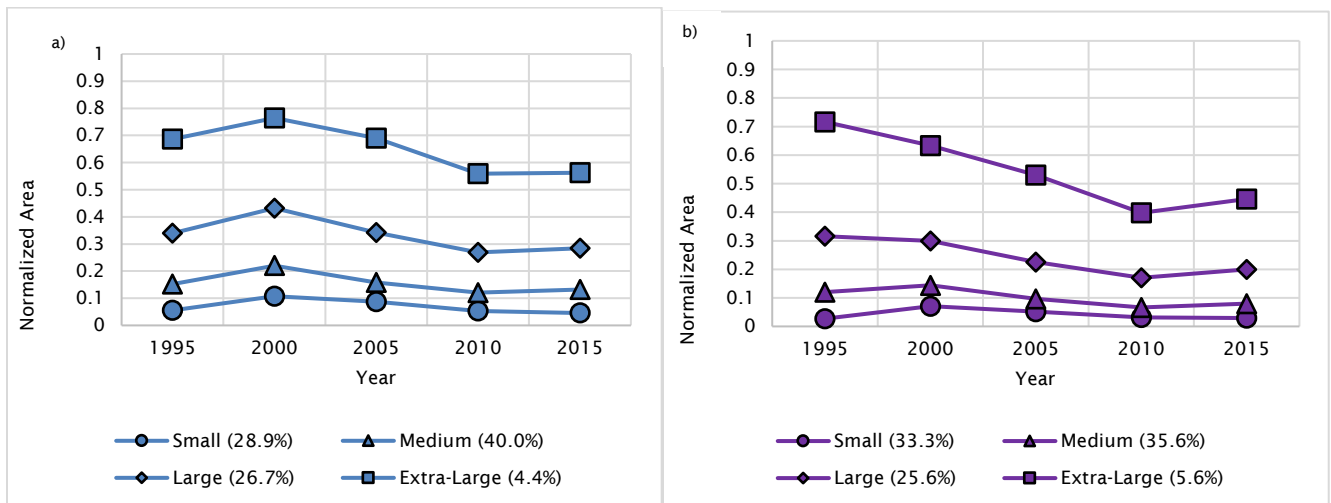


Figure 1. Trends in noise contour areas by clustering of airport types using group-based trajectories for (a) DNL ≥ 45 dB(A) and (b) $L_{\text{night}} \geq 45$ dB(A).

Task 4 - Present Preliminary Results of Analyses and Generate Final Results on Night-time Noise and Hypertension

Boston University, Harvard University

Objective

The aim of this task is to present preliminary results of analyses and generate final results on analyses of aircraft noise (L_{night}) and hypertension.

Research Approach

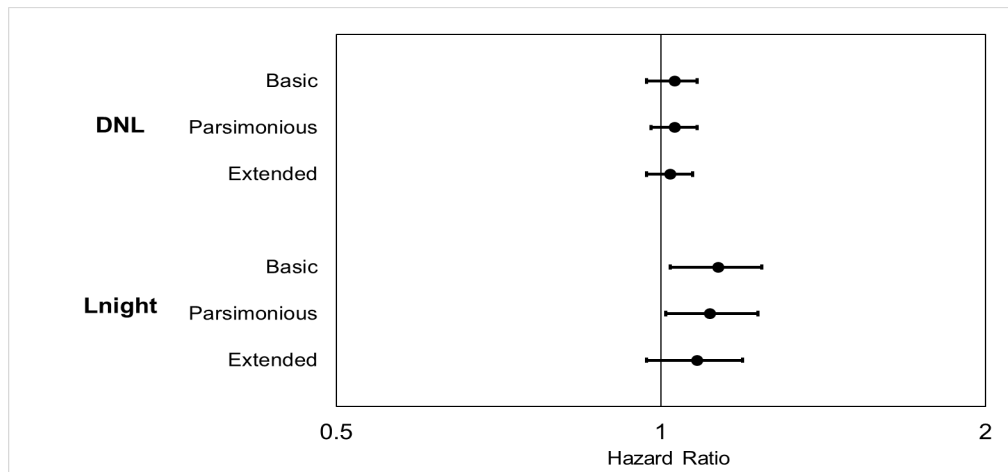
We intersected modeled noise exposure surfaces for 1995, 2000, 2005, 2010, and 2015 based on geocoded addresses of the participants over the follow-up period in NHS and NHSII. We selected a large set of a priori variables to be examined as confounders and/or effect modifiers and used time-varying Cox proportional hazards models to estimate the hypertension risk associated with time-varying night-time aircraft noise exposure, while adjusting for both fixed and time-varying covariates. We also performed sensitivity analyses to address potential biases.

Milestones

- Present findings at the 14th International Commission on Biological Effects of Noise (ICBEN) Congress June 2023
- Generate final results on aircraft noise (L_{night}) and hypertension.

Major Accomplishments

- Generated figures comparing results from our study on aircraft noise (DNL) and hypertension with results for L_{night} and hypertension (Figure 2).
- Generated final results on L_{night} and hypertension.
- Drafted a manuscript reporting results on analyses of L_{night} noise and hypertension.
- Presented research on aircraft noise (L_{night}) and hypertension at the ICBEN Congress.



Basic model adjustment: age and calendar year.

Parsimonious model adjustment: basic model + race, physical activity, smoking status, alcohol use, Dietary Approaches to Stop Hypertension, spouse’s education attainment, neighborhood socioeconomic status, region of residence, nitrogen dioxide, and fine particulate matter ($PM_{2.5}$).

Extended model adjustment: parsimonious model + body mass index, menopausal status, medications, and family history of hypertension.

Figure 2. Hazard ratios (95% confidence intervals) of the association between aircraft noise at 45 dB and hypertension, comparing previous findings of day-night level (DNL) (Kim et al., 2021) and night-time noise (L_{night}) in the Nurses’ Health Study (NHS) and NHSII.

Interpretation of night-time noise and hypertension results using the L_{night} 45-dB cut point

In the combined parsimonious model, participants in NHS and NHSII exposed to L_{night} levels ≥ 45 dB had an 11% greater risk of hypertension than participants exposed to L_{night} levels < 45 dB, with a 95% CI of 1%–23%. In the combined fully adjusted model, participants exposed to $L_{night} \geq 45$ dB had an 8% greater risk (95% CI: –3%, 19%) than unexposed individuals. The hazard ratios were relatively stable across the sensitivity analyses, even after controlling for air pollution and shiftwork.

Task 5 - Generate Final Results of Analyses on Aircraft Noise and the Intermediary Risk Factor of Adiposity

Boston University, Harvard University

Objective

The aim of this task is to develop an analysis plan and generate preliminary results of analyses on aircraft noise and an intermediary risk marker (adiposity, a measure of cardiometabolic disease).

Research Approach

We developed an analysis plan for studying adiposity and aircraft noise and obtained approval from the NHS oversight committee. We designed a statistical analysis and selected a large set of a priori variables to be examined as confounders and/or effect modifiers. We compiled appropriate data sets and performed descriptive statistics analysis. We are using generalized estimating equations to estimate the relationship between aircraft noise and longitudinal, repeated measures of adiposity (body mass index [BMI]).

Milestones

- Produce final results of analyses on aircraft noise and adiposity.

Major Accomplishments

- Performed a final analysis of noise in relation to adiposity (results for three ordinal BMI categories of 18.5–24 [reference], 25–29, and ≥ 30 kg/m²; see Figure 3).
- Drafted a manuscript reporting the results of analyses on aircraft noise and adiposity.

Table 3. Odds ratio of increasing body mass index (BMI) groups (reference: 18.5–24 kg/m²) for exposure day-night average sound level ≥ 55 vs. < 55 dB.

Model	BMI Group (kg/m ²)		
	18.5–24.9	25.0–29.9	≥ 30.0
Model 0: Age	Ref.	1.10 (1.07, 1.14)	1.23 (1.13, 1.33)
Model 1: 0 + demographics & lifestyle	Ref.	1.05 (1.01, 1.08)	1.14 (1.05, 1.23)
Model 2: 1 + environmental	Ref.	1.04 (1.00, 1.07)	1.10 (1.02, 1.20)

Model 0: age; Model 1: 0 + demographics: region, race, individual socioeconomic status, parity, menopausal status, hormone therapy, smoking status, alcohol use, diet quality, physical activity; Model 2: 1 + neighborhood socioeconomic status, greenness, environmental noise, light at night.

Interpretation using DNL ≥ 55 dB as an example

From Model 2, there was 14% higher odds (95% CI: 4%, 24%) of being in the 25.0–29.9 BMI category and 12% higher odds (95% CI: 0%, 25%) of being in the ≥ 30.0 BMI category versus being in the 18.5–24.9 BMI category among those exposed to aircraft noise (DNL) ≥ 55 dB compared with those exposed to < 55 dB.

Task 6 - Develop an Analysis Plan for Analyses of an Intermediary Risk Factor (Diabetes) and Aircraft Noise

Boston University, Harvard University

Objective

The aim of this task is to develop an analysis plan for assessing aircraft noise and diabetes.

Research Approach

We developed an analysis plan for studying diabetes and aircraft noise and obtained approval from the NHS oversight committee. We designed a statistical analysis and selected a large set of a priori variables to be examined as confounders and/or effect modifiers. We compiled appropriate data sets to perform descriptive statistics analysis.

Milestones

- Develop an analysis plan and produce descriptive statistics to investigate aircraft noise and the risk of diabetes.

Major Accomplishments

- Developed an analysis plan
- Obtained approval from the NHS oversight committee
- Produced descriptive statistics of incident diabetes and numbers of participants exposed for DNL categories in NHS and NHSII
- Determined relevant confounders and effect modifiers

Table 4. Number of participants in the Nurses’ Health Study (NHS, NHSII) at risk for diabetes (did not have diabetes at the time of the first noise measure) and those who developed diabetes during the study period according to day-night average sound level (DNL) categories.

Model	NHS		NHSII	
DNL	At Risk	Cases	At Risk	Cases
<45	90,946	7,076	100,968	6,391
45-49	4,340	313	5,281	276
50-54	2,018	165	2,419	137
55-59	751	60	954	56
60-64	179	17	238	20
≥65	39	3	55	7
Total	98,273	7,634	109,915	6,887

Task 7 – Gain Approval for Human Subject Noise Research for New Cohorts

Boston University, University of North Carolina

Objective

The aim of this task is to gain approval for human research on noise and health in the new cohorts.

Research Approach

We submitted an application to the University of North Carolina’s institutional review board (IRB) to link aircraft noise data and to perform noise- and health-related human subject research at the geocoded addresses of the new cohort participants (HCHS/SOL and Add Health).

Milestones

- Gain IRB approval to link aircraft noise data and perform noise- and health-related research for the HCHS/SOL and Add Health cohorts.

Major Accomplishments

- Developed and submitted an IRB application



Task 8 – Assess the Relationship Between a Perceived Increase in Aircraft Noise and Increases in Aircraft Visibility

Massachusetts Institute of Technology

Objective

The aim of this task is to understand how changes in flight paths may alter aircraft visibility.

Research Approach

During the current reporting period, the team applied a first-principles-based method to count the number of visible aircraft flying below 10,000 ft above ground level and above a 45° angle to the horizon (method outlined in previous report). Recorded flight trajectories were used to model the number of aircraft overflights that were visible from the surface at locations around the airport under idealized conditions, i.e., without additional obstruction at viewing angles such as buildings or weather conditions that reduce visibility. In addition, several noise metrics were calculated for the same locations, including DNL and the number of flights associated with a maximum noise level (L_{max}) above 60 dB (denoted N60). The analysis was conducted for peak days of operation in 2010 and 2017 for Boston Logan International Airport (KBOS). We note that the analysis focused on arrivals from runway 4R and departures from runway 33L.

Milestones

- Finalize the visibility analysis for Boston Logan International Airport.

Major Accomplishments

- Performed an analysis that included the number of visible aircraft flying <10,000 ft above ground level and above a 45° angle to the horizon

The results show a correlation between the number of flights visible from the surface (N_{vis}) and the number of flights that are audible at $L_{max} > 60$ dB (N60) (see Figure 3). This finding implies that noise change analyses based on the N60 metric are largely representative of changes in aircraft visibility. It is important to note that at locations closer to the airport, the visibility contours will be smaller than the noise contours because the aircraft are at lower altitudes, which attenuates the size of noise contours but reduces visibility in the first-principles-based model.

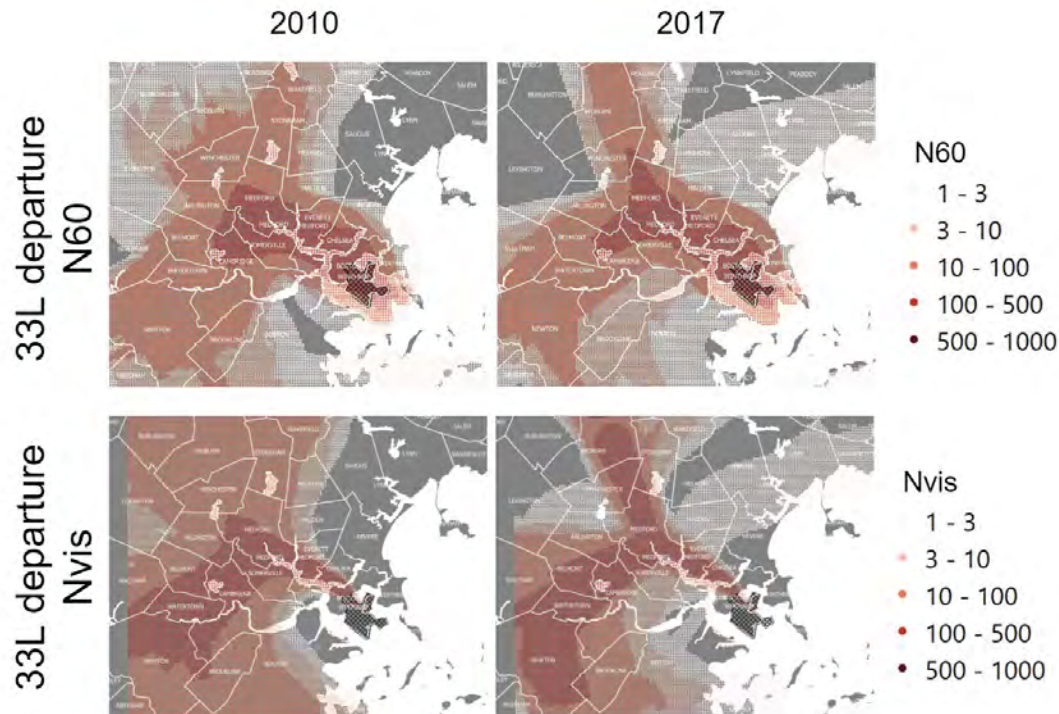


Figure 3. Number of visible aircraft (Nvis) and number of overflights with $L_{max} > 60$ dB (N60) in 2010 and 2017.

Task 9 – Prepare a Second Draft of the Report on Study Results Related to 2018 FAA Reauthorization, Section 189 for Policymakers

Boston University, Massachusetts Institute of Technology

Objective

The aim of this task is to develop a report of overall study results in response to 2018 FAA Reauthorization, Section 189 for policymakers.

Milestone

- Generate a second draft of the report on overall study results in response to Section 189 for policymakers.

Major Accomplishments

- Provided a revised second draft report summarizing the overall study results in relation to Section 189

Publications

- Nguyen D.D., Levy J.I., Kim C., Lane K.J., Simon M.C., Hart J.E., Whitsel E.A., VoPham T., Malwitz A., Peters J.L. (2023). Characterizing temporal trends in populations exposed to aircraft noise around U.S. airports: 1995–2015. *Journal of Exposure Science and Environmental Epidemiology*. <https://doi.org/10.1038/s41370-023-00575-5>
- Grady S.T., Hart J.E., Laden F., Roscoe C., Nguyen D.D., Nelson E.J., Bozigar M., VoPham T., Manson J.E., Weuve J., Adar S.D., Forman J.P., Rexrode K., Levy J.I., Peters J.L. (2023). Associations between long-term aircraft noise exposure, cardiovascular disease, and mortality in US cohorts of female nurses. *Environmental Epidemiology*, 7(4): e259. doi: 10.1097/EE9.0000000000000259
- Bozigar M., Huang T., Redline S., Hart J.E., Grady S.T., Nguyen D.D., James P., Nicholas B., Levy J.I., Laden F., Peters J.L. (2023). Associations between aircraft noise exposure and self-reported sleep duration and quality in the United



States-Based prospective Nurses' Health Study cohort. *Environmental Health Perspectives*, 131(4):47010. doi: 10.1289/EHP10959

Nguyen D.D., Whitsel E.A., Wellenius G.A., Levy J.I., Leibler J.H., Grady S.T., Stewart J.D., Fox M.P., Collins J.M., Eliot M.N., Malwitz A., Manson J.E., Peters J.L. (2023). Long-term aircraft noise exposure and risk of hypertension in postmenopausal women. *Environmental Research*, 218:115037. doi: 10.1016/j.envres.2022.115037.

Outreach Efforts

Oral presentation on current progress during the ASCENT Fall Meeting (October 25–27, 2022) and ASCENT Spring Meeting (April 19–20, 2023)

Oral presentation on “Long-term Nighttime Noise Exposure and Incident Hypertension in a National U.S. Cohort of Female Nurses” at the 14th ICBEN Congress (June 18–22, 2023).

Oral presentation on “Associations between Environmental Noise and Biomarkers of Neurodegeneration in the Chicago Health and Aging Project” at ICBEN Congress (June 18–22, 2023).

Awards

None.

Student Involvement

The dissertation of Daniel Nguyen (doctoral graduate, BU) included a characterization of the temporal trends in aviation noise surrounding U.S. airports. Daniel Nguyen graduated in the spring of 2022 and is currently working for the Centers for Disease Control and Prevention.

The dissertation of Stephanie Grady (doctoral candidate, BU) includes developing and performing statistical analyses on noise and hypertension risk, cardiovascular event risk, and biomarkers of neurodegeneration.

The thesis of Zhishen Wang (master's student, MIT) includes the visibility analysis.

Plans for Next Period

(October 1, 2023 to September 30, 2024)

- Complete analyses to estimate the risk of hypertension associated with night-time aircraft noise exposure.
- Complete analyses to evaluate the relationship between aircraft noise and a measure of adiposity (BMI).
- Continue analyses to evaluate the risk of diabetes associated with aircraft noise exposure.
- Complete our report on visual analysis.
- Verify, document, and publish results.
- Continue processes related to adding noise to additional cohorts and exploring other health outcomes (e.g., mental health).
- Document results for policymakers in iterative drafts and a final report.

References

- Babisch, W., & Kim, R. (2011). Environmental noise and cardiovascular disease. *WHO European Centre for Environmental Health, ed. Burden of disease from environmental noise: Quantification of healthy life years lost in Europe. World Health Organization*, 15-44.
- Bluhm, G., & Eriksson, C. (2011). Cardiovascular effects of environmental noise: research in Sweden. *Noise and Health*, 13(52), 212-216.
- Clark, C., Crumpler, C., & Notley, H. (2020). Evidence for environmental noise effects on health for the United Kingdom policy context: a systematic review of the effects of environmental noise on mental health, wellbeing, quality of life, cancer, dementia, birth, reproductive outcomes, and cognition. *International journal of environmental research and public health*, 17(2), 393.
- Dimakopoulou, K., Koutentakis, K., Papageorgiou, I., Kasdagli, M. I., Haralabidis, A. S., Sourtzi, P., ... & Katsouyanni, K. (2017). Is aircraft noise exposure associated with cardiovascular disease and hypertension? Results from a cohort study in Athens, Greece. *Occupational and environmental medicine*, 74(11), 830-837.



- El Aarbaoui, T., & Chaix, B. (2020). The short-term association between exposure to noise and heart rate variability in daily locations and mobility contexts. *Journal of Exposure Science & Environmental Epidemiology*, 30(2), 383-393.
- El Aarbaoui, T., Méline, J., Brondeel, R., & Chaix, B. (2017). Short-term association between personal exposure to noise and heart rate variability: The RECORD MultiSensor Study. *Environmental Pollution*, 231, 703-711.
- Evrard, A. S., Lefèvre, M., Champelovier, P., Lambert, J., & Laumon, B. (2017). Does aircraft noise exposure increase the risk of hypertension in the population living near airports in France?. *Occupational and environmental medicine*, 74(2), 123-129.
- Eriksson, C., Bluhm, G., Hilding, A., Östenson, C. G., & Pershagen, G. (2010). Aircraft noise and incidence of hypertension—gender specific effects. *Environmental research*, 110(8), 764-772.
- Eriksson, C., Hilding, A., Pyko, A., Bluhm, G., Pershagen, G., & Östenson, C. G. (2014). Long-term aircraft noise exposure and body mass index, waist circumference, and type 2 diabetes: a prospective study. *Environmental health perspectives*, 122(7), 687-694.
- Eze, I. C., Foraster, M., Schaffner, E., Vienneau, D., Héritier, H., Rudzik, F., ... & Probst-Hensch, N. (2017). Long-term exposure to transportation noise and air pollution in relation to incident diabetes in the SAPALDIA study. *International journal of epidemiology*, 46(4), 1115-1125.
- Floud, S., Vigna-Taglianti, F., Hansell, A., Blangiardo, M., Houthuijs, D., Breugelmans, O., ... & Jarup, L. (2011). Medication use in relation to noise from aircraft and road traffic in six European countries: results of the HYENA study. *Occupational and environmental medicine*, 68(7), 518-524.
- Franssen, E. A. M., Van Wiechen, C. M. A. G., Nagelkerke, N. J. D., & Lebrecht, E. (2004). Aircraft noise around a large international airport and its impact on general health and medication use. *Occupational and environmental medicine*, 61(5), 405-413.
- Grassi, G. (2006). Sympathetic overdrive and cardiovascular risk in the metabolic syndrome. *Hypertension Research*, 29(11), 839-847.
- Greiser, E., Janhsen, K., & Greiser, C. (2007). Air traffic noise increases prescriptions of cardiovascular drugs in the vicinity of a major airport. *Epidemiology*, 18(5), S33.
- Haralabidis, A. S., Dimakopoulou, K., Velonaki, V., Barbaglia, G., Mussin, M., Giampaolo, M., ... & HYENA Consortium. (2011). Can exposure to noise affect the 24 h blood pressure profile? Results from the HYENA study. *Journal of Epidemiology & Community Health*, 65(6), 535-541.
- Haralabidis, A. S., Dimakopoulou, K., Vigna-Taglianti, F., Giampaolo, M., Borgini, A., Dudley, M. L., ... & Jarup, L. (2008). Acute effects of night-time noise exposure on blood pressure in populations living near airports. *European heart journal*, 29(5), 658-664.
- Hatfield, J., Job, R. F. S., Carter, N. L., Peploe, P., Taylor, R., & Morrell, S. (2001). The influence of psychological factors on self-reported physiological effects of noise. *Noise and health*, 3(10), 1-13.
- Ising, H., & Kruppa, B. (2004). Health effects caused by noise: evidence in the literature from the past 25 years. *Noise and Health* 6 (22): 5-13.
- Jarup, L., Babisch, W., Houthuijs, D., Pershagen, G., Katsouyanni, K., Cadum, E., ... & Vigna-Taglianti, F. (2008). Hypertension and exposure to noise near airports: the HYENA study. *Environmental health perspectives*, 116(3), 329-333.
- Kim, C. S., Grady, S. T., Hart, J. E., Laden, F., VoPham, T., Nguyen, D. D., ... & Peters, J. L. (2022). Long-term aircraft noise exposure and risk of hypertension in the Nurses' Health Studies. *Environmental research*, 207, 112195.
- Kraus, U., Schneider, A., Breitner, S., Hampel, R., Rückerl, R., Pitz, M., ... & Peters, A. (2013). Individual daytime noise exposure during routine activities and heart rate variability in adults: a repeated measures study. *Environmental health perspectives*, 121(5), 607-612.
- Lefèvre, M., Carlier, M. C., Champelovier, P., Lambert, J., Laumon, B., & Evrard, A. S. (2017). Effects of aircraft noise exposure on saliva cortisol near airports in France. *Occupational and environmental medicine*, 74(8), 612-618.
- Mancia, G., Bousquet, P., Elghozi, J. L., Esler, M., Grassi, G., Julius, S., ... & Van Zwieten, P. A. (2007). The sympathetic nervous system and the metabolic syndrome. *Journal of hypertension*, 25(5), 909-920.
- Mancia, G., Dell'Oro, R., Quarti-Trevano, F., Scopelliti, F., & Grassi, G. (2006). Angiotensin-sympathetic system interactions in cardiovascular and metabolic disease. *Journal of Hypertension*, 24, S51-S56.
- Matsui, T. (2004). The Okinawa study: effects of chronic aircraft noise on blood pressure and some other physiological indices. *J Sound Vib*, 277, 469-470.
- Münzel, T., Daiber, A., Steven, S., Tran, L. P., Ullmann, E., Kossmann, S., ... & Kröller-Schön, S. (2017). Effects of noise on vascular function, oxidative stress, and inflammation: mechanistic insight from studies in mice. *European heart journal*, 38(37), 2838-2849.
- Rosenlund, M., Berglind, N., Pershagen, G., Järup, L., & Bluhm, G. (2001). Increased prevalence of hypertension in a population exposed to aircraft noise. *Occupational and environmental medicine*, 58(12), 769-773.



- Sakhvidi, M. J. Z., Sakhvidi, F. Z., Mehrparvar, A. H., Foraster, M., & Davvand, P. (2018). Association between noise exposure and diabetes: a systematic review and meta-analysis. *Environmental research*, 166, 647-657.
- Seidler, A., Hegewald, J., Seidler, A. L., Schubert, M., Wagner, M., Dröge, P., ... & Zeeb, H. (2017). Association between aircraft, road and railway traffic noise and depression in a large case-control study based on secondary data. *Environmental research*, 152, 263-271.
- Selander, J., Bluhm, G., Theorell, T., Pershagen, G., Babisch, W., Seiffert, I., ... & Järup, L. (2009). Saliva cortisol and exposure to aircraft noise in six European countries. *Environmental health perspectives*, 117(11), 1713-1717.
- Sim, C. S., Sung, J. H., Cheon, S. H., Lee, J. M., Lee, J. W., & Lee, J. (2015). The effects of different noise types on heart rate variability in men. *Yonsei medical journal*, 56(1), 235-243.
- Spreng, M. (2000). Possible health effects of noise induced cortisol increase. *Noise and health*, 2(7), 59-63.
- Walker, E. D., Brammer, A., Cherniack, M. G., Laden, F., & Cavallari, J. M. (2016). Cardiovascular and stress responses to short-term noise exposures—A panel study in healthy males. *Environmental research*, 150, 391-397.
- World Health Organization. (2018). *Environmental noise guidelines for the European region*. World Health Organization. Regional Office for Europe.
- Wright, D. M., Newell, K., Maguire, A., & O'Reilly, D. (2018). Aircraft noise and self-assessed mental health around a regional urban airport: a population based record linkage study. *Environmental Health*, 17(1), 1-10.



Project 009 Geospatially Driven Noise-estimation Module

Georgia Institute of Technology

Project Lead Investigators

Prof. Dimitri N. Mavris
Director, Aerospace Systems Design Laboratory
School of Aerospace Engineering
Georgia Institute of Technology
Phone: 404-894-1557
Fax: 404-894-6596
dimitri.mavris@ae.gatech.edu

Dr. Holger Pfaender
Aerospace Systems Design Laboratory
School of Aerospace Engineering
Georgia Institute of Technology
Phone: 404-385-2779
Fax: 404-894-6596
holger.pfaender@ae.gatech.edu

University Participants

Georgia Institute of Technology

- P.I.s: Prof. Dimitri Mavris, Dr. Holger Pfaender
- FAA Award Number: 13-C-AJFE-GIT-059
- Period of Performance: June 5, 2020 to September 30, 2023
- Tasks:
 1. Literature review and evaluation of geographic information systems (GIS) software
 2. Investigation of emerging computational technologies
 3. Collaboration with the unmanned aircraft system (UAS) computation module development team
 4. Noise computation engine integration

Project Funding Level

The Georgia Institute of Technology has received \$499,999 in funding for this project. The Georgia Institute of Technology has agreed to a total of \$250,000 in matching funds. This total includes salaries for the project director, research engineers, and graduate research assistants as well as for computing, financial, and administrative support, including meeting arrangements. The institute has also agreed to provide tuition remission for students whose tuition is paid via state funds.

Investigation Team

Georgia Institute of Technology

Prof. Dimitri Mavris (P.I.)
Dr. Holger Pfaender (co-P.I.)
Research Faculty: Raphael Gautier
Graduate Students: Joaquin Matticoli, Deepika Singla, Xi Wang, Hugues Chardin, Aroua Gharbi, Martin Delage

Project Overview

Context and Motivation

The UAS market is expected to grow rapidly in coming years, with projections estimating the civil UAS market at \$121 billion in the next decade (Teal Group, 2022). Multiple operators are currently developing and testing various concepts of operations that fall under the umbrella of urban air mobility (UAM), with the two main use cases being drone delivery and e-taxi operations. Similar to traditional aircraft operations, these novel concepts are expected to influence the environment in which they operate, particularly regarding noise. In the same way that noise assessments of terminal operations are carried out today for commercial aviation, noise assessments of UAM operations are expected to be necessary in the future.

Problem Definition

UAM operations bring unique requirements. First, UAM operations are expected to be denser than current general or commercial aviation operations, possibly by orders of magnitude. Thus, noise-assessment methods should be able to handle such large vehicle densities. Second, the vehicles are expected to be smaller and therefore quieter; for example, small drones for deliveries or helicopter-sized vehicles for e-taxi applications, but these vehicles are also expected to benefit from novel electric-propulsion systems. As a result, the noise footprint of such vehicles is expected to be more localized. Therefore, noise exposure levels should be estimated with sufficient resolution. Third, instead of primarily following fixed trajectories dictated by approach and departure routes around airports, UAM vehicles are expected to operate point-to-point within populated areas. Departure and arrival locations are expected to vary from day to day; delivery drones may depart from warehouses or mobile staging locations and deliver goods to different customers each day, and e-taxis may pick up and drop off customers throughout an urban area. Thus, noise-assessment methods should be sufficiently flexible to accommodate changing flight paths, and the resulting noise assessments should account for corresponding variability.

Research Objectives

In view of these requirements, the methods used to perform noise assessments in terminal areas, such as the Aviation Environmental Design Tool (AEDT), are not fully suitable for UAM assessments; these methods are usually limited to studies of relatively low-density operations around airports, with vehicles following predefined ground tracks. Thus, there is a need to develop new noise-assessment capabilities tailored to UAM operations, which is the focus of this project.

Research Approach

Research efforts supporting the development of a UAS noise-assessment tool have been broken down into four tasks.

First, GIS capabilities are expected to play a major part in the development of this tool, as the scenarios under consideration and the resulting noise metrics are to be visualized and overlaid on the geographical area of study. Therefore, Task 1 focuses on a literature review and evaluation of GIS software.

Second, the complexity of assessing noise in the context of UAM-use cases, as discussed in the previous section, calls for an investigation of emerging technologies in multiple computational domains. The size of these problems and the flexibility needed to analyze a wide variety of operational scenarios require the introduction of recent innovations to address the challenges discussed previously. This is the focus of Task 2.

This research was conducted in collaboration with other entities, starting with Mississippi State University (MSU), and followed by subsequent collaborations, which are presented under the umbrella of Task 3.

Finally, Task 4 focuses on the integration of all components investigated or provided by other tasks into the actual UAS noise-assessment engine. Technical details pertaining to the implementation, as well as preliminary results on benchmark test cases, are presented in this section.



Task 1 - Literature Review and Evaluation of GIS Software

Georgia Institute of Technology

Task 1 Contents

- 1.1 Objectives
- 1.2 Research Approach
- 1.3 GIS Libraries
- 1.4 GIS Applications

1.1 Objective

This task aims to identify the leading open-source GIS software using preset evaluation criteria.

1.2 Research Approach

This review focused on open-source options. For an adequate evaluation of the options, six criteria were set forth:

1. Data import: ability to read shape files with different formats of input geometrical data as well as rasterized (gridded) data
2. Data storage: capability to store geospatial data in either shape/vector formats or as rasterized data
3. Geometric calculations: ability to convert to and from a Cartesian coordinate system and other Earth model coordinates and ability to compute polygon areas and lengths as well as unions and subtractions
4. Geospatial calculations: ability to perform calculations on given vector or raster data and to draw contour plots
5. Display: ability to print raw or processed geospatial data as various map displays and to enable standard desktop and web applications
6. Map data: capability to display results with relation to landmasses, political boundaries such as states and counties, and roads and buildings

In addition to evaluating software, we also investigated GIS applications to examine the option of creating a stand-alone, customized library or component.

1.3 GIS Libraries

1.3.1 QGIS

QGIS is a user-friendly, open-source GIS written in C++. The latest version is 3.24 (released in February 2022). QGIS runs on Linux, Unix, Mac OSX, Windows, and Android and supports numerous vector, raster, and database formats and functionalities. As well as its intrinsic, built-in functionalities, QGIS allows users to install and create their own plug-ins. New applications can also be created in QGIS through C++ and Python languages. Screenshots of QGIS are shown in Figure 1.



Figure 1. QGIS screenshots.

Evaluation Criteria

1. Data import: imports shape files such as GPX, GPS, DXF, DWG, and OpenStreetMap, as well as raster files
2. Data storage: stores geospatial data in vector and raster formats



3. Geometric calculations: supports Cartesian (x, y), polar (length, angle), and projected (x-north, y-east) calculations; calculates length or area of geometrical features; and provides overlay, union, and difference between areas
4. Geospatial calculations: creates a vector contour map from an elevation raster and carries out raster-to-vector conversion
5. Display: can provide web mapping with QGIS2Web; can publish data on the internet using a webserver with the University of Minnesota MapServer or GeoServer installed
6. Map data: displays geospatial data such as countries, states, and counties as well as roads

1.3.2 OpenJUMP

OpenJUMP is a Java-based, open-source GIS (latest version: 2.0, released in March 2022). OpenJUMP works on Windows, Linux, and Mac platforms with Java 1.7 or later. OpenJUMP's features include reading and writing vector formats, displaying geospatial data, and executing geometric calculations. Additional plug-ins for more capabilities are also available. OpenJUMP is distributed under the GNU General Public License version 2. Screenshots of OpenJUMP are shown in Figure 2.

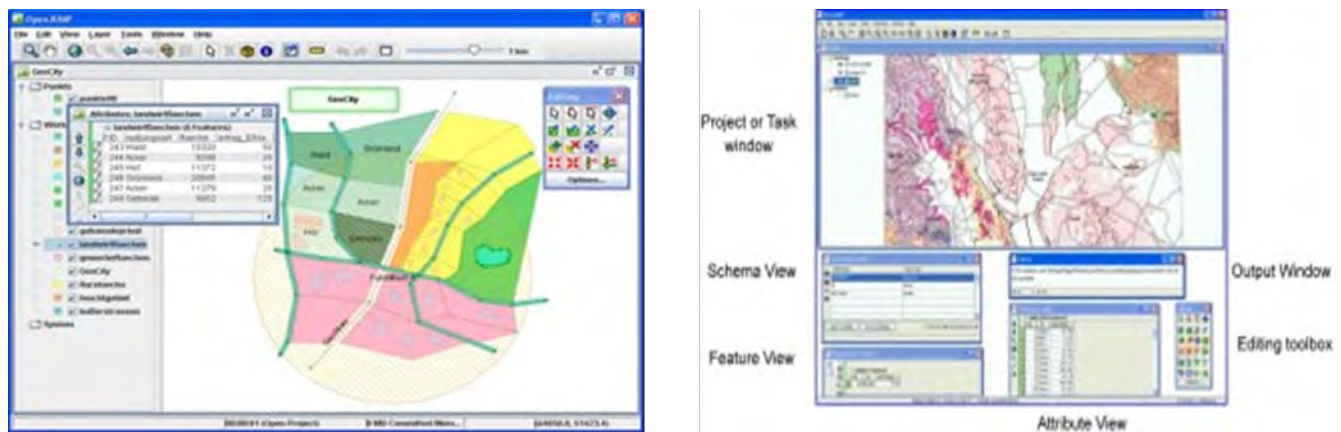


Figure 2. OpenJUMP screenshots.

Evaluation Criteria

1. Data import: imports shape and raster files
2. Data storage: stores geospatial data in vector and raster formats
3. Geometric calculations: supports coordinate reference system (CRS) (Cartesian [x, y, z], geographic [longitude, latitude, height], and projected [x-north, y-east]) conversions; provides a CRS transformation tool (PROJ4); calculates length or area of geometrical features; provides overlay, union, and subtraction
4. Geospatial calculations: provides conversion between desired file formats (raster-to-vector conversion); does NOT provide contour plots
5. Display: does NOT provide a web application
6. Map data: displays geospatial data such as countries, states, and counties as well as roads

1.3.3 System for Automated Geoscientific Analyses (SAGA)

The System for Automated Geoscientific Analyses (SAGA) is an open-source, cross-platform GIS software written in C++ (latest version: 2.0, released in June 2007). SAGA can be run on Windows, Linux, FreeBSD, and Mac (OS X). SAGA provides multiple libraries for GIS calculations: digital terrain analysis, image segmentation, fire spreading analysis and simulation, etc. In addition to these libraries, SAGA allows the scripting of custom models through the command line interface (CLI) and Python interface. Screenshots showing the SAGA environment are shown in Figure 3.

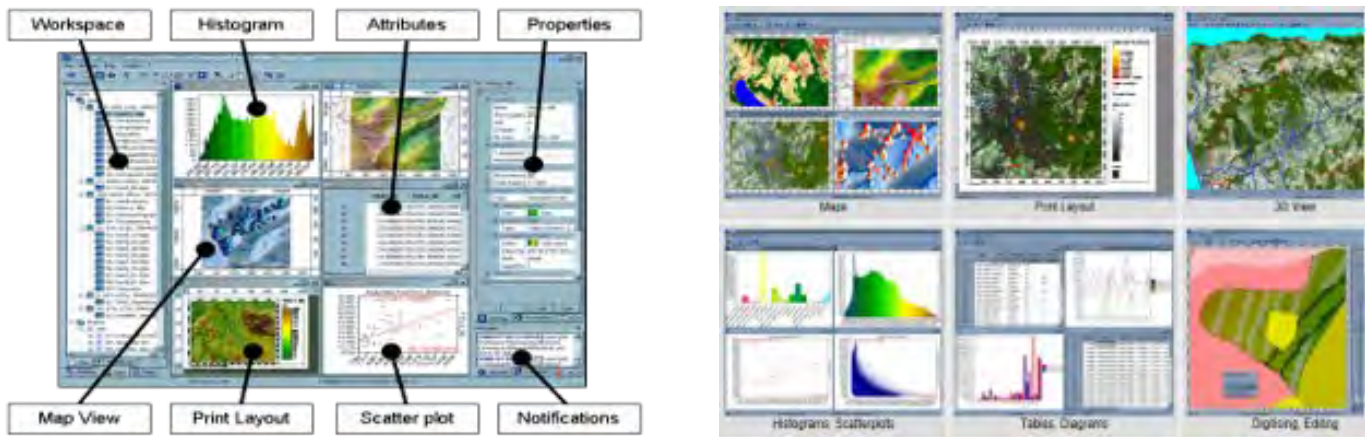


Figure 3. Screenshots showing the SAGA environment.

Evaluation Criteria

1. Data import: imports shape and raster files
2. Data storage: stores geospatial data in vector and raster formats
3. Geometric calculations: supports geographic coordinate system (latitude, longitude) and Universal Transverse Mercator (UTM) calculations; computes polygon areas or lengths
4. Geospatial calculations: performs raster-to-vector conversions and can create contour lines
5. Display: displays data as histograms and scatter plots
6. Map data: enables visualization of spatial data as cartographic maps; can also import maps from Web Map Service and OpenStreetMap

1.3.4 Deck.gl

Deck.gl is a WebGL visualization framework for large datasets (latest version: 8.7.3, released in March 2022). Deck.gl allows users to map data (JavaScript Object Notation [JSON] objects, comma-separated values [CSVs]) into a stack of layers. These layers can be imported directly from a catalog or built by the user.

Evaluation Criteria

1. Data import: reads shape files and CSV/GeoJSON files
2. Data storage: can store geospatial data as vector or shape files
3. Geometric calculations: supports geographic coordinate system (latitude, longitude) using Web Mercator; does NOT calculate polygon areas or lengths
4. Geospatial calculations: does not convert raster data to vector data; can create contour lines for a given threshold and cell size
5. Display: offers an architecture for packaging advanced WebGL-based visualizations; enables users to rapid obtain impressive visual results with limited effort
6. Map data: easily displays geospatial data with relation to roads and buildings

1.3.5 Kepler.gl

Kepler.gl is an open-source geospatial analysis tool for large-scale datasets (version 2.5.5). The most recent update was made in September 2021. A user interface was created to facilitate the process of saving a map to back-end storage, and a graphics processing unit (GPU) data filter was added, with the ability to create polygon filters in the user interface.



Evaluation Criteria

1. Data import: ability to read CSV/GeoJSON files and Kepler.gl's sample datasets; must convert shape files to a GeoJSON file to be consumable by Kepler.gl
2. Data storage: cannot store geospatial data as vector or shape files
3. Geometric calculations: supports geographic coordinate system (latitude, longitude) using Web Mercator; does NOT calculate polygon areas or lengths
4. Geospatial calculations: does not convert raster data to vector data; can create contour lines
5. Display: offers an architecture for packaging advanced WebGL-based visualizations and can easily handle sample data to visualize
6. Map data: easily displays geospatial data with relation to roads and buildings

1.3.6 Geographic Resources Analysis Support System GIS

Geographic Resources Analysis Support System (GRASS) is an open-source, Java-based software for vector and raster geospatial data management, geoprocessing, spatial modeling, and visualization. GRASS has compatibilities with QGIS, meaning that QGIS can run some features of GRASS GIS as a plug-in. Already developed add-ons are available, along with the capability to develop additional add-ons. The latest version (8.0, released in March 2022) has an improved graphical user interface (GUI) and Python scripting. GRASS provides rapid linking of external raster files and spatiotemporal data analysis with an improved internal data structure. A vector attribute update was also found with Python syntax. A typical screenshot from GRASS GIS is shown in Figure 4.



Figure 4. Typical screenshot from the Geographic Resources Analysis Support System (GRASS).

Evaluation Criteria

1. Data import: imports vector and raster files
2. Data storage: stores geospatial data in vector and raster formats
3. Geometric calculations: supports coordinate reference system (CRS) (Cartesian [x, y, z] and geographic [longitude, latitude, height]) conversions; provides a CRS transformation tool (PROJ4); calculates length or area of geometrical features; provides overlay, union, and subtraction
4. Geospatial calculations: provides conversion between desired file formats (raster-to-vector conversion); creates contour lines
5. Display: provides a Web Mapping Service and graphics display monitor that can be controlled from the command line; can display frames on the user's graphic monitor
6. Map data: displays geospatial data such as countries and states by using Inkspace

1.3.7 gvSIG

gvSIG is an open-source GIS written in 2021 that runs on Windows, Linux, and Mac platforms. Screenshots from gvSIG are shown in Figure 5.

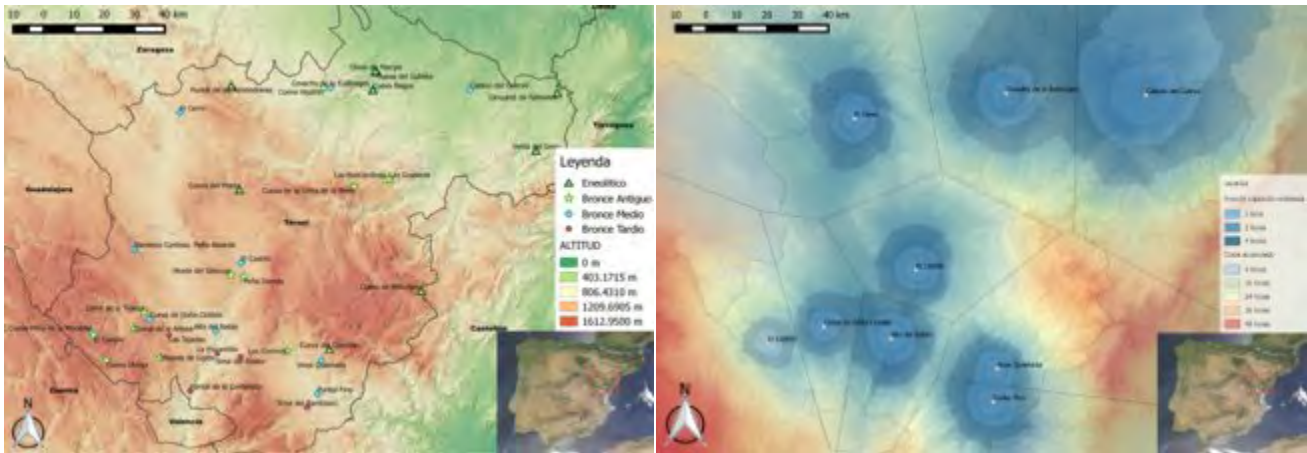


Figure 5. Screenshots from gvSIG.

Evaluation Criteria

1. Data import: can import shape and raster files
2. Data storage: can store geospatial data in vector and raster formats
3. Geometric calculations: supports geographic coordinate system (latitude, longitude) using Web Mercator; does NOT calculate polygon areas or lengths; supports CRS (Cartesian [x, y, z] and geographic [longitude, latitude, height]) coordinates; provides a CRS transformation tool (PROJ4); calculates length or area of geometrical features; provides overlay, union, and subtraction
4. Geospatial calculations: can convert other file types to the desired file format; does NOT produce contour plots
5. Display: does NOT provide a web application
6. Map data: displays geospatial data such as countries and states by using Inkspace

1.3.8 MapWindow GIS

MapWindow GIS is an open-source GIS written in C++ using optimal features from the .NET framework v4/4.5. MapWindow runs on Windows (latest version: 5.3.0, released in 2019), as shown in Figure 6. This version was compiled using VS2017. The new version supports tiles from a local file system and provides extendable snapping events. MapWindow was licensed under the Mozilla Public License.

Evaluation Criteria

1. Data import: can import shape and raster files
2. Data storage: can store geospatial data in vector and raster formats
3. Geometric calculations: supports geographic coordinate system (latitude, longitude) and UTM calculations; can calculate length or area of geometrical features
4. Geospatial calculations: can convert other file types to the desired file format; does NOT produce contour plots
5. Display: allows multi-threaded HTTP tile loading
6. Map data: displays geospatial data such as countries and states by using Inkspace

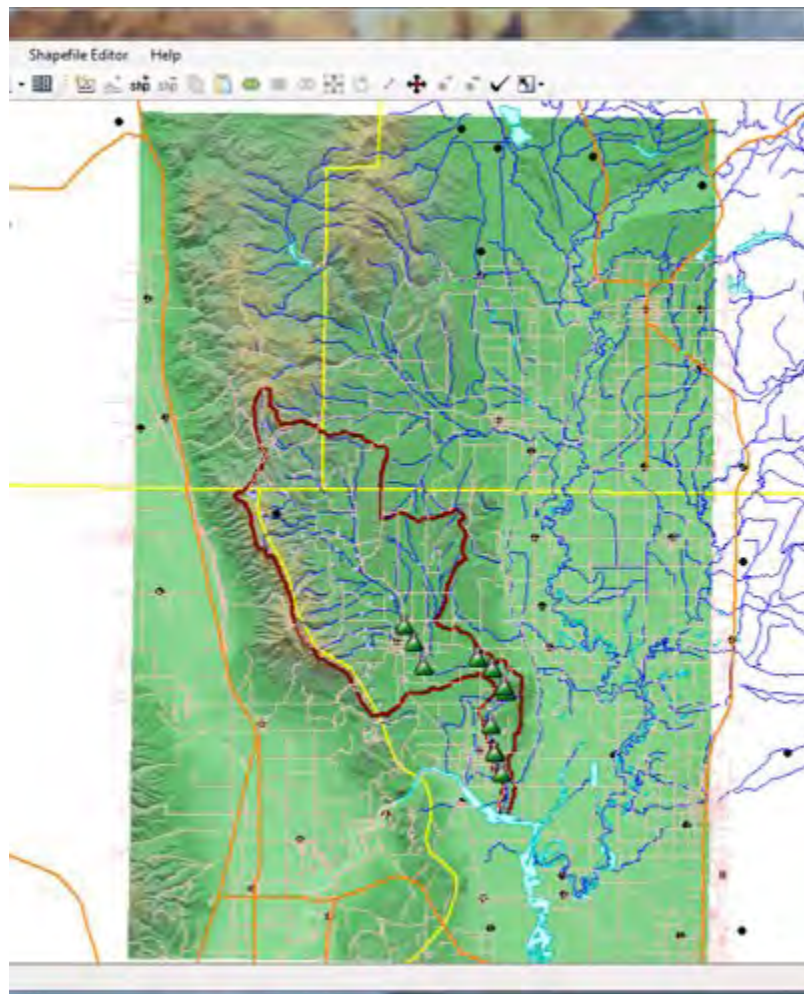


Figure 6. Screenshot from the MapWindow geographic information system.

1.3.9 GeoPandas

GeoPandas is an open-source project developed in Python to provide a useful library for working with geospatial data, as shown in Figure 7. GeoPandas can run on distributions of Linux and Windows. This software primarily uses the Python packages pandas (as a base for its data storage), shapely (to manipulate the shapes stored in the advanced database), Fiona (for file access), and Descartes and matplotlib (for data visualization). GeoPandas is most adept at displaying discrete sections of data in a geospatial visualization. It is limited in its ability to display graphics outside of the Python environment and does not support conversion to the desired raster/vector formats. The last update was made in 2021, which improved the software from v0.5.0 to v0.10.2 and corrected the regression in the overlay and plotting.

Evaluation Criteria

1. Data import: reads almost any vector-based spatial data format
2. Data storage: stores geospatial data in vector and raster formats
3. Geometric calculations: supports CRS calculations; cannot calculate the length or area of geometrical features; has overlay functions, such as intersections between two or more areas, union (merges the areas of one layer to one single area), difference (A-B areas), and polygons
4. Geospatial calculations: does not convert to any desired file formats (no raster-to-vector formats); does not provide a contour plot function



5. Map data: uses various map projections using the Python library Cartopy
6. Display: does not provide a web application; provides a good representation in three-dimensional (3D) color space using matplotlib

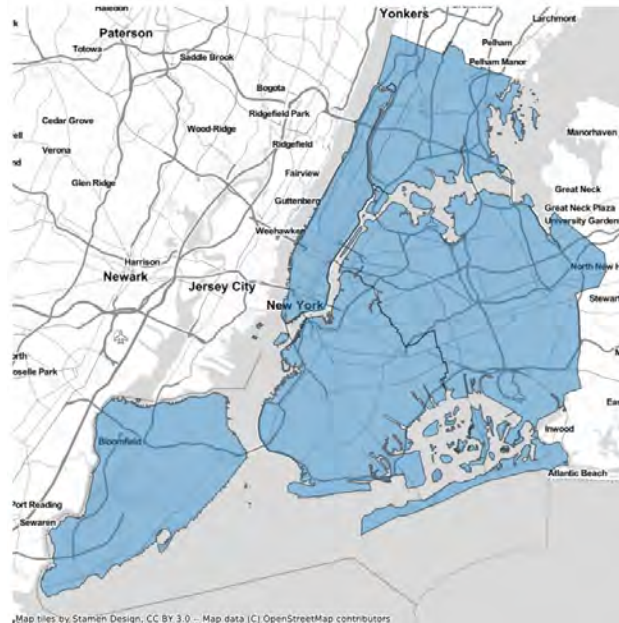


Figure 7. An example of how GeoPandas can overlay processed geospatial data over existing maps.

1.3.10 WorldWind

WorldWind is an open-source, virtual 3D globe-visualization application programming interface (API) developed by NASA in partnership with the European Space Agency. WorldWind is written in both Java (for desktop and Android devices) and JavaScript (for web applications). After its development was suspended in 2019, it was restarted in August 2020. WorldWind can import a variety of input files with geospatial data, stores the data in both raster and vector formats, provides sufficient geometric and geospatial calculations, and produces good visualizations with comprehensive map data. WorldWind finds its application in unmanned aerial vehicle imagery, where such vehicles can provide continuous monitoring of an active fire, with higher resolution and more frequent updates. WorldWind was licensed under NASA Open-Source Agreement Version 1.3. Screenshots of WorldWind are shown in Figure 8.

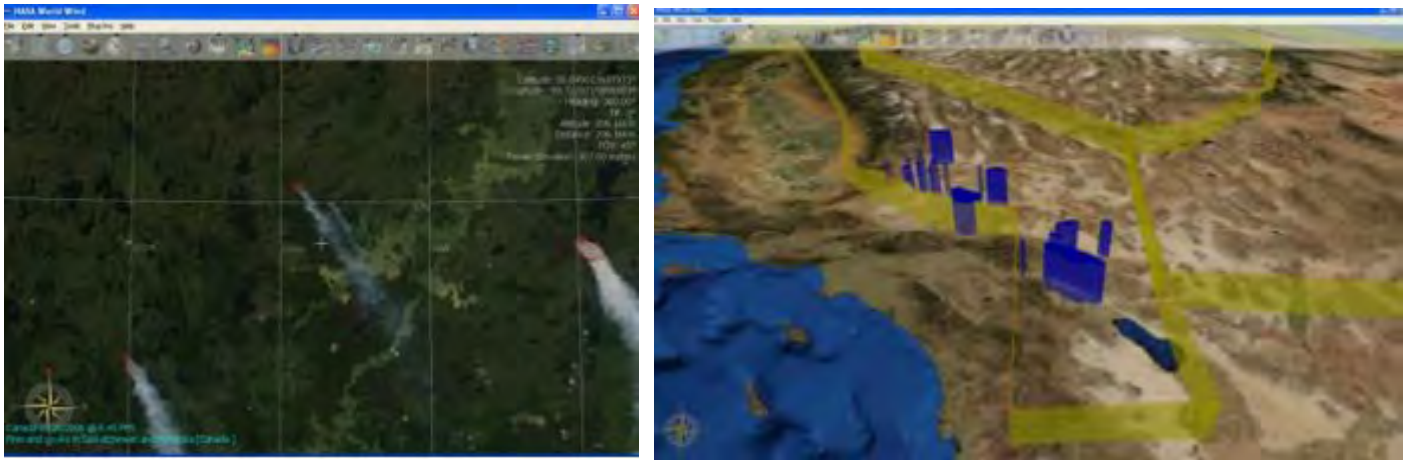


Figure 8. Screenshots from WorldWind.

Evaluation Criteria

1. Data import: imports shape files, KML, VPF, GML, GeoJSON, GeoRSS, GPX, NMEA, etc.
2. Data storage: stores geospatial data in vector and raster formats
3. Geometric calculations: supports geographic coordinate system (latitude, longitude), UTM, and Military Grid Reference System calculations; can draw and measure distance and area across a terrain
4. Geospatial calculations: displays contour lines on surface terrain at a specified elevation
5. Map data: provides visual representations of scalar values, such as noise, over a grid of geographic positions; can visualize the results on web and Android platforms
6. Display: displays geospatial data divided into country, state, and city

1.3.11 Overall Evaluation

An overall evaluation of all of the investigated libraries is provided in Table 1. QGIS seems to surpass the other libraries with respect to our defined metrics.

Table 1. Comparison of different libraries.

	Intuitive GUI	Compatibility	Statistical Analyses	Data Import	Data Storage	Geometrical Calculations	Geospatial Calculations	Map Data	Display	Total
QGIS	3	5	3	5	5	5	5	5	4	40
OpenJUMP	3	4	1	5	5	5	3	5	2	33
SAGA	3	3	4	5	5	4	5	5	4	38
Deck.gl	4	3	1	5	5	3	3	5	5	34
Kepler.gl	4	5	1	1	1	3	3	5	5	28
GRASS	4	3	1	5	5	4	5	5	4	36
gvSIG	3	4	1	5	5	4	3	5	2	32
MapWindow	3	4	1	5	5	3	3	4	2	30
GeoPandas	2	4	1	5	5	4	1	2	2	26
WorldWind	5	5	1	5	5	4	4	5	5	39



1.4 GIS Applications

GIS applications can be broadly classified in two categories: desktop and web-based applications.

WebGIS applications use web technologies to display and communicate geospatial information to an end user. Every WebGIS application has five common elements:

1. A web application: the interface used by the client, which has tools for visualizing, analyzing, and interacting with geographic information and can be run on a web browser or a GPS-enabled device
2. Digital base maps: the geographical context for the application (e.g., transportation, topography, imagery)
3. Operational layers: the layers used in order for the results of an operation to be displayed (e.g., observations, sensor feeds, query results, analytic results)
4. Tasks and tools: tools to perform operations beyond mapping
5. Geodatabase(s): container of geographical data, which can consist of geodatabases, shape files, tabular databases, computer-aided design files, and so on

WebGIS applications come with multiple advantages and limitations. Table 2 presents a inexhaustive list of these advantages and limitations.

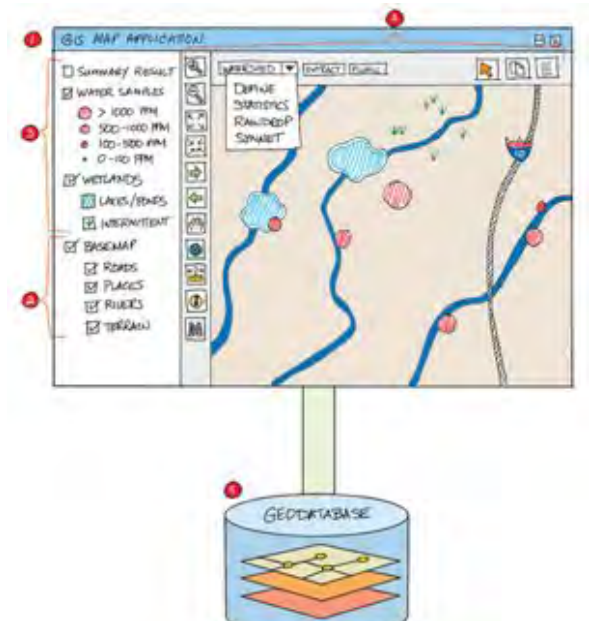


Figure 9. Schematic of a web geographic information system (WebGIS) application.

Table 2. Advantages and disadvantages of web geographic information systems (WebGISs).

Advantages of WebGIS	Disadvantages of WebGIS
<ul style="list-style-type: none"> Provides a broader reach for customers compared with a traditional desktop application Better cross-platform capability with the different web browsers that can be used Easy to use for customers with different levels of geographic information systems (GIS) expertise Extendable to cloud services, hence allowing manipulation and use of big GIS data Lower cost to entry (most libraries and tools are open-source with good community support) Allows real-time analysis 	<ul style="list-style-type: none"> Harder to build (developers need to have a good knowledge of multiple scripting languages to build the app [Python, JavaScript, html, etc.]) Data security may depend on a third party Application may need to be hosted outside of the organization

Our team has started a dialogue with the AEDT development team regarding which GIS functionalities will be required to be able to integrate the UAS noise engine with the AEDT in the future.

Task 2 - Investigation of Emerging Computational Technologies

Georgia Institute of Technology

Task 2 Contents

- 2.1 Task 2 Overview
- 2.2 GIS-visualization Technologies
- 2.3 Parallel-computing Technologies
- 2.4 Data-processing Technologies
- 2.5 Support for GPU-backed Computations and Scaling Study
- 2.6 Cloud-based Computations on Amazon Web Services (AWSs)

2.1 Task 2 Overview

2.1.1 Context and Motivation

As explained in the project overview, assessing noise exposure for UASs brings unique requirements that existing frameworks do not meet. Three primary abilities are needed: (a) the ability to analyze scenarios involving large volumes of flights; (b) the ability to cover large areas with small resolution; and (c) the ability to account for sources of uncertainty related to the evolving UAS concepts of operation. Thus, there is a need for the development of a new analysis capability that can fulfill these requirements.

2.1.2 Problem Definition

Although the actual estimation of noise exposure levels plays a central role in noise-assessment tools, many other peripheral functions are also needed: inputs must be read and preprocessed, computations must be implemented in such a way that they meet the requirements listed in the previous section, and a visualization of the operational scenario and noise assessment results must be provided in a manner that is intuitive to the user. Each of these functionalities requires a substantial development effort and can leverage specific computational technologies.

2.1.3 Research Objectives

In this task, we aim to investigate the emerging technologies that could be used to implement the variety of functions to be performed by the noise-assessment tool. In particular, we are seeking technologies that are compatible with the stringent requirements related to UAS operations.

2.1.4 Research Approach

For this task, the following areas of emerging technologies were identified and investigated. Figure 10 presents a partial depiction of these areas and the associated technologies.

First, GIS visualization techniques were investigated. Within the noise-assessment tool, these techniques are used to visualize the defined operational scenarios, such as the flights included in the scenario, as well as the analysis results, in the form of noise levels mapped over a predefined geographical area.

Second, parallel computation approaches were investigated to address the problem of performing noise computations with large problem sizes encountered due to (a) the large flight volumes in UAM scenarios; (b) the low resolution and large areas needed to effectively cover populated areas; and (c) the temporal discretization needed to properly assess noise exposure.

Third, data pre- and postprocessing approaches were investigated, because working with geographical data usually requires many transformations, such as clipping to the analysis area or converting from one CRS to another.

Fourth, motivated by the need to speed up noise computations to enable faster uncertainty quantification, we investigated running the noise engine on a GPU.

Finally, we developed the capability to run the noise engine on cloud-based platforms, specifically AWS, since this approach allows us to scale noise computations for a large number of workers and large amounts of total memory, enabling the analysis of problems the size of which would be prohibitively large for execution on a single machine.

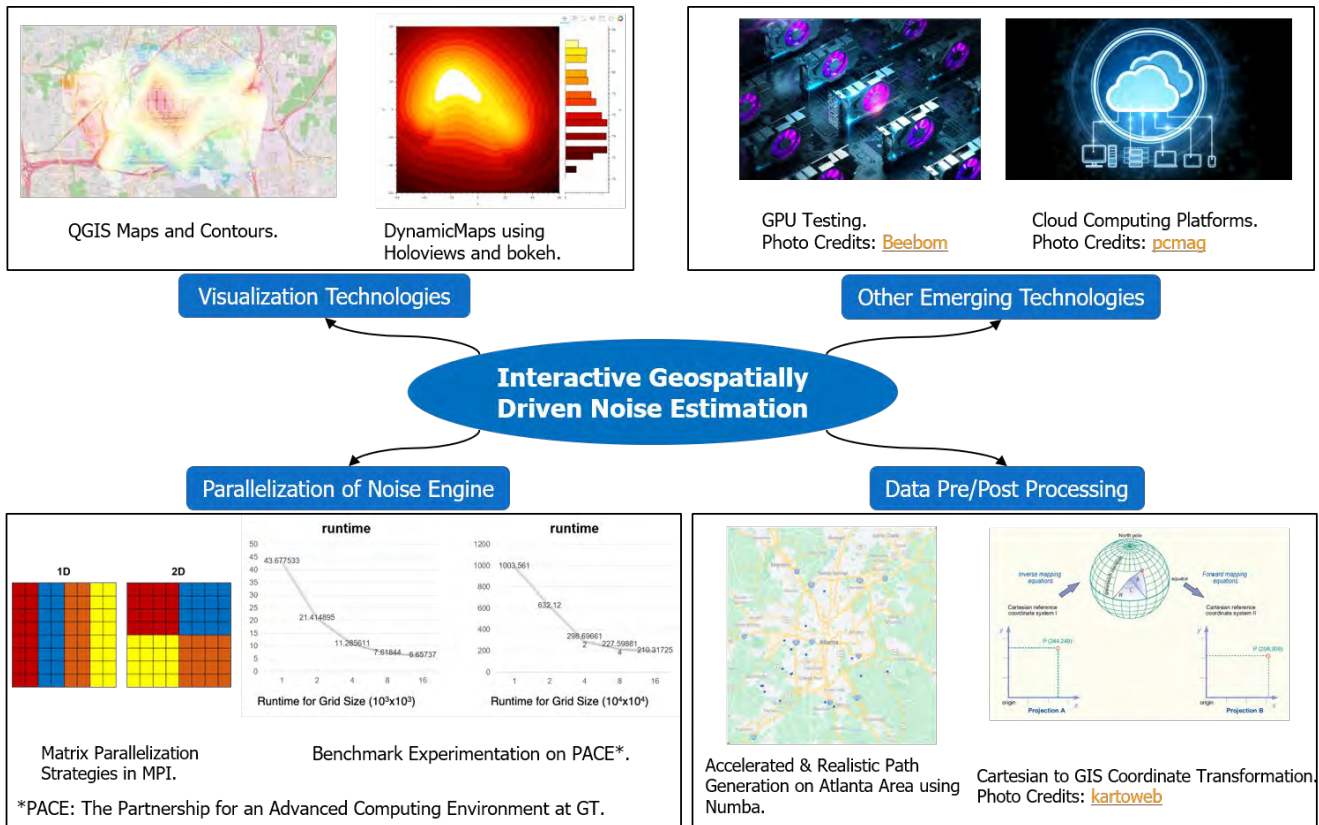


Figure 10. Visual summary of the emerging technologies under investigation. GIS: geographic information system; GPU: graphics processing unit; GT: Georgia Institute of Technology; MPI: message passing interface.

2.2 GIS-visualization Technologies

The team focused on technologies that provide interactive visualizations of large data on maps, which narrowed the choices to QGIS and interfaces based on Python or JavaScript. Working with large datasets on QGIS requires the use of a structured query language (SQL) plug-in as a conduit for data communication. Furthermore, the GUI aspect of QGIS limits the interactive capabilities that can be achieved.

Therefore, the focus was directed to JavaScript and Python libraries and interfaces, including the D3 library for JavaScript and Bokeh for Python. Bokeh emerged as the preferred choice as it builds on JavaScript visualizations without the need to explicitly use JavaScript. Furthermore, with this library, it is possible to code both the front-end and back-end of a web application using Python.

2.3 Parallel-computing Technologies

Parallel computing technologies are critical for calculations that involve large grids. These grids can be expressed as matrices and hence take advantage of their regular structures for the partition of computation tasks.

The team initiated their analysis by exploring the standards for parallel programming via the message passing interface (MPI) implemented on different libraries, such as OpenMPI, MPICH, and MVAPICH. As the noise computation engine is built from common mathematical and computational operations, OpenMPI was selected for its portability and its ability to support most existing platforms.

Parallel algorithms for matrix computations have been well documented in the literature. Typically, the data are partitioned either along one axis of the matrix or both, as shown in Figure 11. These algorithms are usually designed with considerations of the communication overhead and the computation cost for individual processors.

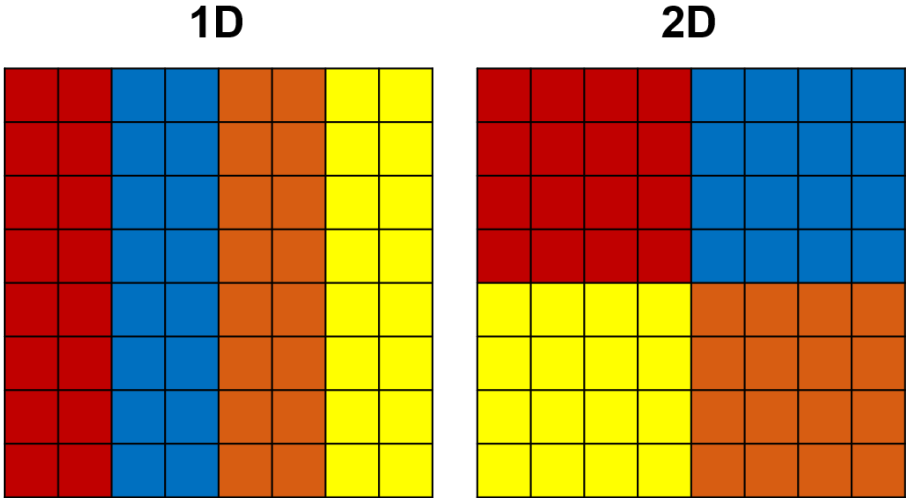


Figure 11. Common partition strategies for matrix computations.

The noise engine can be viewed as a large, dense matrix problem in which the calculations for each element do not depend on its neighbors. Instead, these calculations depend on the path of the noise source, which can be modeled as a vector. Hence, the partition strategies shown are theoretically the same, where the main challenge is to manage the data communicated. In addition to communicating the path data to each partition, the engine needs to collect the results and send them to the visualization tool.

These considerations prompted us to examine the input/output (IO) operations in parallel, as shown in Figure 12. There are three main approaches for parallel IO operations, as briefly defined below:

- Nonparallel: A central unit is uniquely responsible for the IO operations.
- Independent parallel: Each process writes to a separate file.
- Cooperative parallel: All processors collaboratively write in one file.

The main advantages and disadvantages for each approach are summarized in Table 3. Although the cooperative parallel approach has the potential to achieve the best performance, it is limited in terms of the file types that can be used, and it may result in performance that is worse than that of the sequential algorithm. Therefore, we did not select a cooperative parallel IO approach. Instead, the choice will depend on other characteristics of the overall noise module.

Table 3. Parallel input/output (IO) operations.

Parallel IO Approach	Advantages	Disadvantages
Nonparallel	<ul style="list-style-type: none"> • Easy to code 	<ul style="list-style-type: none"> • Poor performance (worse than sequential)
Independent Parallel	<ul style="list-style-type: none"> • Easy to parallelize • No interprocess communication 	<ul style="list-style-type: none"> • Generates many small files to manage
Cooperative Parallel	<ul style="list-style-type: none"> • Performance can be great • Only one file is needed 	<ul style="list-style-type: none"> • More complex to code • Depends on implementations of concurrent updates in file types, which are rare

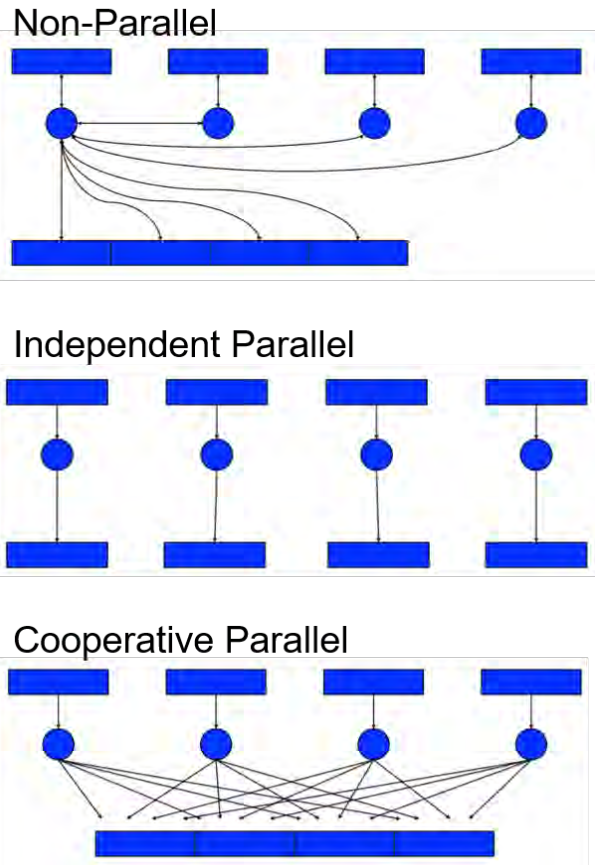


Figure 12. Schematic illustrating the input/output operations in a message passing interface.
Source: William Gropp, Introduction to MPI I/O

The analysis of parallel IO approaches led to the need to examine the file formats used in parallel as well. Three major categories of file formats are listed in Table 4, along with their major advantages and disadvantages.

Table 4. Benefits and drawbacks of file formats.

File Format	Advantages	Disadvantages
ASCII	<ul style="list-style-type: none"> • Human-readable • Portable 	<ul style="list-style-type: none"> • Requires a larger amount of storage • Costlier for read/write operations
Binary	<ul style="list-style-type: none"> • Efficient storage • Less costly for read/write operations 	<ul style="list-style-type: none"> • Needs formatting to read
Standard scientific libraries (HDF5, NetCDF, etc.)	<ul style="list-style-type: none"> • Allows data portability across platforms • Data stored in binary form • Includes data description 	<ul style="list-style-type: none"> • Has a risk of corruption

This analysis was conducted with a gridded data format in mind. Instances of these files that are encoded in binary format are relatively straightforward to create and manage in parallel because the MPI writes to binary format by default. Instances that use ASCII characters are more difficult to use, however, because a binary-ASCII conversion is needed for formatting.

To showcase the runtime difference between ASCII files and binary files, a test case was run with a fixed problem size and a variable number of processors. The test used the independent parallel approach to eliminate the need for a central unit that collects the results. Figure 13 illustrates the runtimes of text file problems and binary problems for 2 to 16 processors. The “runtime no IO” scenario was included in Figure 13 as a baseline to showcase the cost of communication due to the IO operations. As expected, for a fixed problem, the runtime decreased as the number of processors increased; however, the difference between runtimes with respect to the file formats is quite apparent.

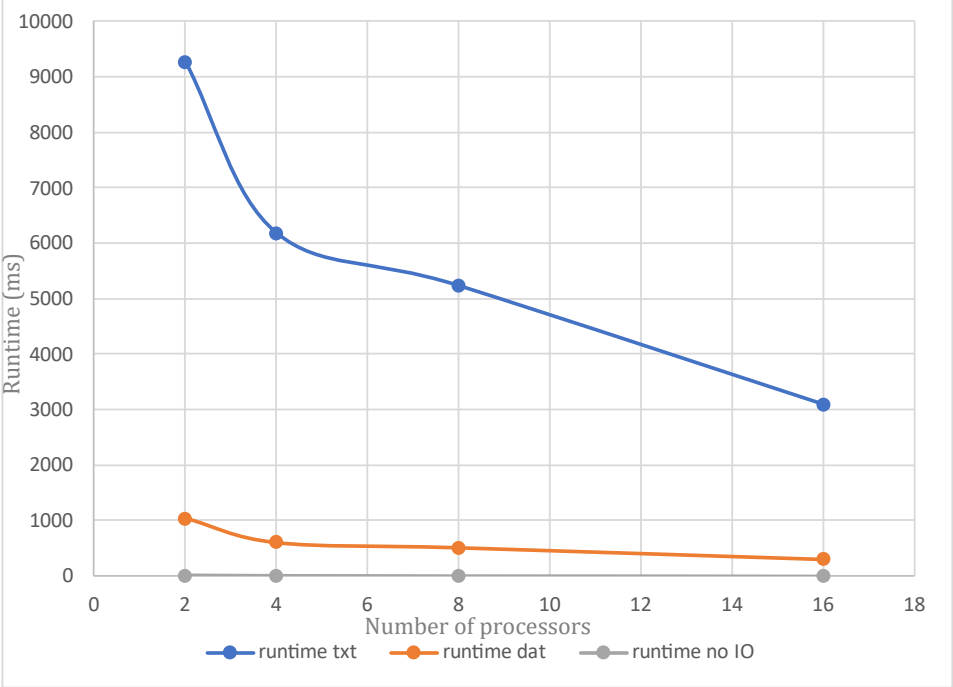


Figure 13. Runtime vs. number of processors for different input/output (IO) formats.

Furthermore, for any format used, storage space will be needed to contain the data, as shown in Figure 14, which reveals an exponential growth in size as the grid becomes finer. This test case demonstrates that the available memory of the hardware used will play an important role in the calculation of large grids.

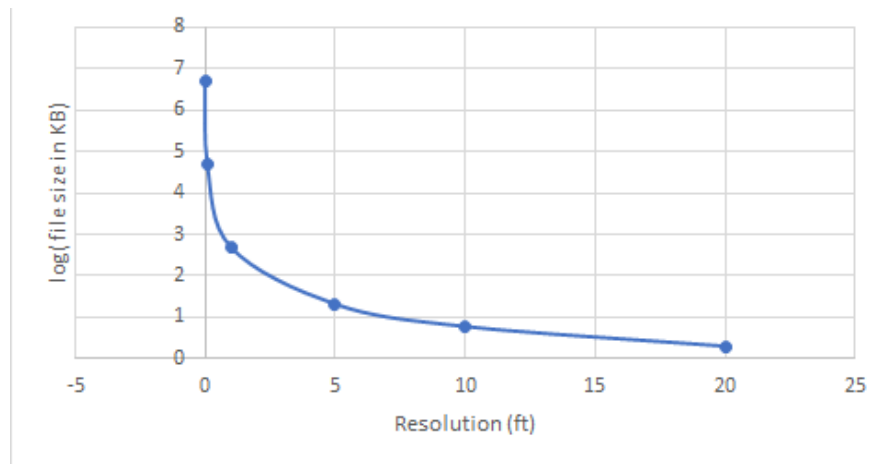


Figure 14. Log(file size in kB) vs. resolution (ft).

The choice of programming language is another important aspect to consider in this investigation. Programming languages such as C and C++ combined with MPI libraries are the primary choice of many high-performance computing (HPC) practitioners, as they have some access to low-level machine language, which results in good performance for parallel computations. However, the main challenge in using these languages is the integration with interactive GIS visualization tools. Higher-level languages such as MATLAB and Python provide these libraries with much less scripting and easier integration, but this comes at the expense of speed in running parallel code. In particular, MATLAB requires the setup of a virtual network computing session prior to launching any calculations. Python, despite being slower than C/C++, emerged as an adequate choice for the noise module, as it is better equipped to facilitate large interactive GIS visualizations without greatly sacrificing speed for this particular application while still being able to act as a wrapper for rapid C/C++ implementations of the computational code.

2.4 Data-processing Technologies

The team investigated libraries for processing GIS data. As the investigation of visualization techniques favored the use of Python to code the application, libraries such as GeoPandas and GeoTIFF were explored to assess their compatibility with the goals of this project.

The GeoPandas library brings the powerful functionalities of pandas to geospatial operations. The GeoTIFF format allows the embedding of geospatial data into images. GeoPandas is more suited to work with vector data, whereas GeoTIFF supports both raster and vector formats. Each of these libraries has its own merits and utilizations and can be used in the noise calculation engine. The final choice will depend on the data pipeline from the computation to the visualization and the data conversions needed in this process.

2.5 Support for GPU-backed Computations and Scaling Study

2.5.1 Context and Motivation

The ability to account for variability in operations, as well as other sources of uncertainty emanating from currently unknown parameters, is one of the main requirements for the UAS noise-assessment tool. Indeed, the need for this ability is one of the reasons why existing tools are not adapted for UAS use cases and why the development of a new capability is needed.

Once sources of uncertainty have been characterized and quantified, Monte Carlo simulations are, a priori, the preferred option for propagating the impact of those uncertainty sources to system-level responses of interest. Monte Carlo simulations are preferred because, among the multiple options available to propagate uncertainty, running full Monte Carlo simulations (a) usually does not require any additional assumptions regarding the nature of the uncertainty sources or the system model, and (b) gives access to full probability distributions for system-level responses, which can be used to estimate any statistical quantity related to these responses. In contrast, approximate uncertainty propagation methods (a) may require uncertainty sources and the system model to behave a certain way to produce valid results, and (b) may only approximate a few statistics, such as the mean of the responses.

In the case of UAM operations, the nature of uncertainty sources (e.g., vehicles may depart and arrive in different locations, the number of flights may vary), as well as the nature of the system model, does not immediately appear to be prone to an approximation method; therefore, a full Monte Carlo simulation will be conducted. Applying approximate uncertainty quantification on this problem will be the topic of future research.

2.5.2 Problem Definition

An initial Monte Carlo study was conducted using the initial Dask implementation of the noise-assessment tool running on a central processing unit (CPU). The setup and results of this study are discussed under Task 4. One of the main observations was the long runtime required to conduct the study: It took several weeks to complete the study, despite the use of Georgia Tech's HPC environment. This motivated the exploration of methods to speed up the execution of the noise engine.

Multiple options are available for speeding up the execution of the computer code: Applying surrogate modeling and running the code on GPUs were considered as options. In the context of uncertainty propagation, a surrogate would need to take the uncertain parameters as inputs, then output the system-level quantities of interest. Because of the nature of the problem and the sources of uncertainty, building such a surrogate is not immediately possible: it requires multiple steps, which were beyond the scope of this project. Instead, this will be the topic of future research.

In contrast, attempting to run the code on a GPU falls within the scope of this project (under the exploration of emerging computational technologies) and does not require a fundamental change in the computational setup. Moreover, the ability to execute the noise computations on a GPU is fully compatible with other ways of speeding up execution, such as surrogate models, as this would allow training data to be produced more rapidly.

2.5.3 Research Objective

The research objective of this subtask was to measure the benefits of running noise computations on a GPU instead of a CPU. This subtask first required that the noise computations be implemented in such a way that they can run on a GPU. Then, two studies were conducted. First, the CPU and GPU runtimes were compared to confirm the benefits brought by the GPU in terms of runtime; because the runtime on a CPU is high, this first study was conducted on relatively small problems. Second, to estimate the ability of GPU-backed computations to handle larger problems, a scaling study was performed, in which the evolution of GPU runtime was estimated as a function of the problem size. Along with runtime, memory requirements also become a challenge for large problems; thus, the memory requirements were estimated.

2.5.4 Technical Approach

Dask is a framework for executing parallel processing across many machines, while presenting the user with simple and familiar storage and computational approaches. Internally, Dask includes optimization routines that optimize the flow of code and data across machines. Because Dask's GPU capabilities presented limitations, Google's JAX, another computational framework, was selected to run the noise engine on a GPU. JAX is a cutting-edge computational framework developed at Google that combines XLA, the computational back-end behind TensorFlow, with other tools such as autodiff for automatic differentiation, all while keeping the same simple API as numpy, Python's de facto standard library for numerical computations. JAX allows reuse of the exact same code to run on a GPU instead of a CPU when available.

As discussed previously, runtime and memory use are the two metrics on which we focus to (a) compare CPU and GPU implementation, and (b) study GPU scaling. In our case, runtime is simply measured using wall-clock time: the time instants before and after the computations are recorded, and their difference yields the elapsed wall-clock time. Care was taken to ensure that computations were actually carried out within the measured time interval: Dask, among others, implements the concept of "lazy evaluation," in which expressions may not be actually evaluated until the result is accessed.

Measuring memory use is more challenging, as it depends on the back-end (CPU or GPU). For the CPU, we could not find a way to directly measure the amount of memory used by specific processes. This step is more difficult with Dask because multiple processes may be spawned to manage computations. As a work-around, the total memory use is recorded before computations are started and then continuously updated at regular intervals while the computations are running, and only the maximum system memory use is retained. Memory use is estimated by the difference between maximum memory use during computations and the precomputation system memory use. This estimation assumes that the difference in memory usage can be solely attributed to the noise assessment computations and that other mechanisms, such as memory swapping to disk, do not occur. To avoid swapping, the problem dimensions considered when performing the computations on the CPU were kept relatively small.

Measuring GPU usage was not possible via JAX’s built-in functions, as a mismatch was observed between actual GPU memory usage and the value returned by JAX’s helper functions. As a consequence, we applied the same approach used for the CPU, except that CUDA-specific commands were issued when polling the GPU memory usage.

As explained previously, the first step of this study was to compare CPU and GPU runtimes. For completeness, the original Dask back-end was also considered in the comparison, both with and without atmospheric absorption improvements (as briefly discussed under Task 4). We varied the problem size by varying the resolution of the square analysis grid. CPU runs were executed locally on a PC equipped with an Intel Core (i7-9700 CPU and 16 GB of RAM). GPU runs were executed on nodes of Georgia Tech’s PACE (Partnership for an Advanced Computing Environment) cluster equipped with a Tesla V100 (32 GB) GPU.

In the second step, we focused on GPU runs only. Multiple dimensions of the problem were varied to obtain a wide range of problem size. We varied the resolution, as in the first part of the study, and the number and maximum length of the trajectories. In the current implementation, trajectories are handled sequentially, while for a given trajectory, the complete grid as well as all of the trajectory’s time steps are simultaneously computed. Thus, we expect all of those dimensions to influence runtime, while memory use should not be affected by the number of trajectories, since they are treated sequentially.

To increase the maximum allowable GPU memory use, and therefore the maximum size of the problems under consideration, a dual-GPU implementation was developed. This dual-GPU implementation took advantage of the fact that Georgia Tech’s PACE cluster offers some nodes with two GPUs, totaling 64 GB of GPU memory. In the current implementation, the analysis grid on which noise exposure levels are computed is split into two regions: the first half is processed on one GPU while the second half is processed on the second GPU. Because all analysis points are independent, this approach does not introduce communication overhead.

2.5.5 Results

Figure 15 depicts the evolution of the runtime duration in seconds as a function of the analysis grid resolution for four cases: the original Dask implementation with and without atmospheric absorption, JAX (CPU), and JAX running on a GPU. Here, a log scale is used for the duration on the y-axis. We observe that JAX on a GPU is faster than CPU-based computations by approximately two orders of magnitude: running the same code on a GPU instead of a CPU allows a 100-fold speed-up. This gain is significant, especially when considering the many cases that need to be run as part of an uncertain propagation study using Monte Carlo simulations.

The differences between the different CPU implementations can be justified as follows: First, neglecting atmospheric absorption consistently reduces runtime across the considered grid resolutions compared with the Dask version of the noise engine that accounts for atmospheric absorption. We found that the CPU JAX version of the code initially runs faster than its Dask counterpart for small resolutions, but appears to match the Dask implementation for higher resolutions. We hypothesize that this result is due to the overhead introduced by Dask when setting up its scheduler and workers: while this overhead is significant for low-resolution grids that can be rapidly analyzed, it becomes negligible compared with the actual cost of computations once the resolution increases sufficiently.

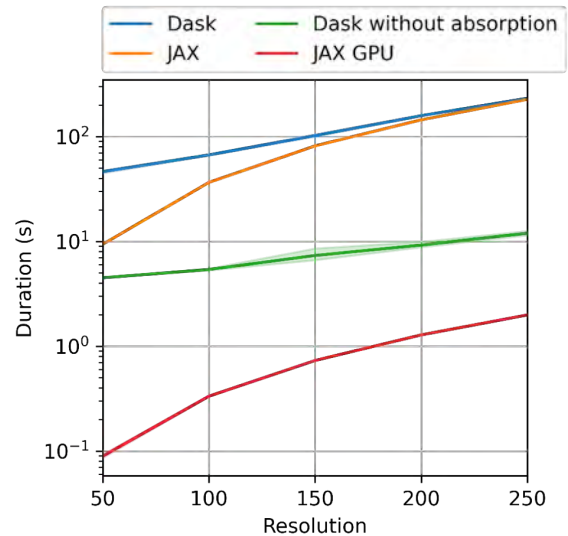


Figure 15. Runtime comparison between different implementations of the noise model. GPU: graphics processing unit.

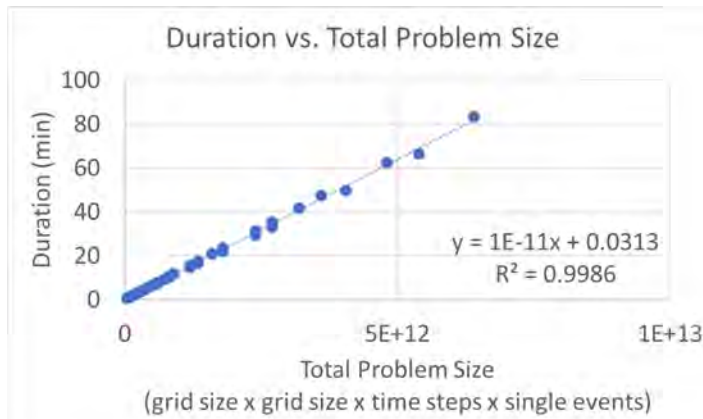


Figure 16. Runtime scaling of the graphics processing unit (GPU) implementation.

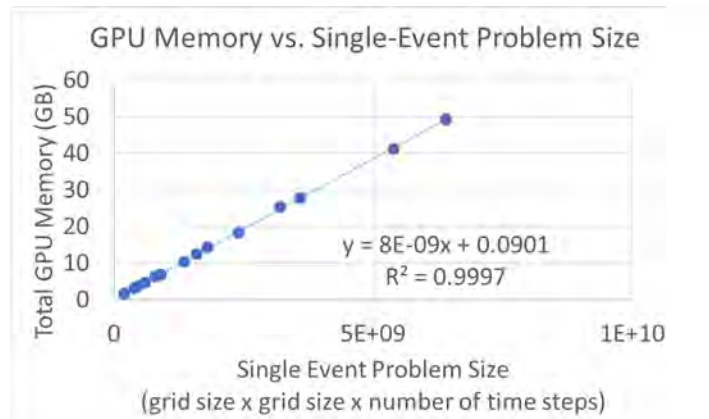


Figure 17. Memory-use scaling of the graphics processing unit (GPU) implementation.

Figures 16 and 17 depict (a) the evolution of the runtime duration as a function of the total problem size, and (b) GPU memory as a function of the single-event problem size, respectively. As discussed previously, while the total problem size encompasses all dimensions of the problem, including the number of trajectories (referred to as single events here), the single-event problem size corresponds to the problem size for a given trajectory. As expected, the duration depends on the total problem size, whereas the total GPU memory depends on the single-event problem size because trajectories are processed sequentially by the current implementation. In both cases, linear regression confirms a linear dependence.

These graphs can be used to estimate the runtime and GPU memory use when running a new case: the total and single-event problem sizes can be computed from the individual problem dimensions, and the linear formulas provided here can be used to obtain a runtime and memory use estimate. In practical applications, this information can be used to estimate the total duration of, for example, a Monte Carlo simulation, or to ensure that the memory use will not exceed the available GPU memory.

2.5.6 Conclusions

The two studies conducted in this section confirm the benefits brought by GPU computation. Thanks to the JAX framework, the same code can be used on a CPU for local development and testing and then on a GPU when additional speed is needed. These benefits are substantial: a 100-fold increase in speed was observed when the code was run on a GPU compared with that run on a CPU. In the Task 4 Section, we will see that this enables us to run a Monte Carlo simulation in a couple of hours, when it would have taken weeks if run on a CPU.

2.6 Cloud-based Computations on AWS

2.6.1 Context and Motivation

Among emerging technologies suitable for use in the development of the UAS noise-assessment tool, cloud-based options were retained because they enable a flexible selection of the amount of computational resources allocated to solving a problem. For example, when using Dask paired with AWS Elastic Compute Cloud (EC2), the user can choose the number and characteristics of workers across which computations are distributed: each worker will be executed within a dynamically spawned AWS instance with its own resources, and individual instance resources can be selected based on AWS's offerings. This flexibility allows us to tackle a wide spectrum of problem sizes, from the small problems encountered, for example, when developing and debugging the noise engine to the larger problems encountered when running a full-fledged noise assessment on a large urban area.

2.6.2 Problem Definition and Research Objective

While executing the noise engine on AWS EC2 is made easier by using Dask as a computational framework, the level of maturity of these frameworks still does not allow for a plug-and-play experience. Multiple hurdles had to be overcome in order to successfully run noise computations in the cloud. In this section, we document the required steps to ease the process for future users and developers of the tool.

Because ASDL does not have specific resources allocated to AWS EC2, this development effort was conducted using Amazon's free-tier instances, which have limited computational power and system memory (a single virtual CPU and 1 GB of RAM). Therefore, it was not possible to demonstrate the ability to run large problems in the cloud; instead, the objective was to develop a proof-of-concept end-to-end workflow using a simplistic scenario (small grid and very few flights). Scaling to larger problems should not raise additional technical hurdles, but should simply require the allocation of additional resources, which can be easily done by the user via simple configuration parameters.

2.6.3 Technical Details

The content of this section is very detailed; at the time of implementation, such details are needed in order to benefit from the advantages of cloud-based computations.

Initial Setup Steps

The following steps can be followed to set up AWS. Depending on the organizational setup, some steps may be skipped or require different actions. For example, instead of creating a root account and using it to create a lower-privilege account, a lower-privilege account may need to be directly requested from the administrators of the organizational AWS EC2 account.

1. If not already available, create an AWS root account.
2. Create a lower-privilege account. For the security policy, allow programmatic access to EC2 only, "AmazonEC2FullAccess." More details on how to create a user [can be found in AWS' documentation](#).
3. Install and configure AWS CLI on the client machine. Use "pip install awscli" to install the CLI tool, followed by "aws configure" to proceed with the initial configuration. This step requires the user's AWS access key ID as well as their secret access key.
4. Install the dask_cloudprovider library for AWS using "pip install dask_cloudprovider[aws]."
5. The cryptography package is also needed and can be installed via "pip install cryptography."

More details are [available in Dask's documentation](#).

Disable TLS Certificates

Dask automatically provisions AWS EC2 instances by sending a script via the AWS API. The size of this script is limited to 16 kB. However, Dask's configuration often exceeds 16 kB, mainly due to the transmission of self-signed TLS certificates used to secure cluster communications. This is a known Dask limitation discussed in the project's issue tracker:

- <https://github.com/dask/dask-cloudprovider/issues/249>
- <https://github.com/dask/distributed/pull/4465>

The proposed solution is to not use TLS certificates. This is achieved by instantiating the Dask cluster by setting the security keyword argument to False:

```
cluster = EC2Cluster(env_vars=credentials, security=False)
```

As a result, for example, the Dask dashboard is not available through https, only http. Additional steps can be taken to properly secure the dashboard if served from a publicly accessible server.

More details on the user-provided setup scripts for creating AWS EC2 instances can be found in AWS EC2's documentation:

- <https://docs.aws.amazon.com/AWSEC2/latest/UserGuide/ec2-instance-metadata.html>
- <https://docs.aws.amazon.com/AWSEC2/latest/UserGuide/instancedata-add-user-data.html>

Python and Package Versions

Other errors may arise when using Python 3.9/3.10, and the solution is to use Python version 3.8 or earlier. The relevant tracked issue is located at <https://github.com/dask/dask-cloudprovider/issues/359>.

We must ensure that package versions match between client and EC2 instances that are automatically set up by Dask. Dask issues a warning when versions mismatch. This is important, because class instances created on EC2 using one version are serialized and sent back to the client, which may not be able to deserialize them.



Debugging the AWS EC2 Workers

Debugging is difficult due to the fact that the workers are ephemeral EC2 instances. Workers are automatically terminated by Dask when an error is encountered. The only output that can be easily accessed after EC2 instances are terminated is the system log. Dask can be configured to log to the system log. The steps to achieve this are documented in the Dask and Python logging library documentations:

- <https://docs.dask.org/en/stable/how-to/debug.html?highlight=logging#logs>
- <https://docs.python.org/3/library/logging.handlers.html>

Manually Copying Scripts to Workers and Manually Configuring Workers' Python Environments

All of the additional scripts called from the main script used to launch the Dask instance (such as library files not installed through pip) need to be manually copied to the workers (EC2 instances) using `client.upload_file()`. Likewise, Python environments local to the workers also need to be manually set up, using Dask's `PipInstall` "worker plug-in."

2.6.4 Conclusions

A proof of concept was developed to illustrate how the noise-assessment tool can run in the cloud. Because of the limited resources available to the team, a problem of very limited size was considered. This effort allowed us to gauge the ease of using Dask's cloud functionalities. Although the capability to run a computation with minimal changes to the initial Dask implementation exists, the experience is not yet seamless. Hopefully, the documentation provided here will help streamline the use of Dask in the cloud.

Task 3 - Collaboration with the UAS Computation Module Development Team

Georgia Institute of Technology

Task 3 Contents

- 3.1 MSU Collaboration
- 3.2 Volpe Collaboration
- 3.3 PACE Collaboration
- 3.4 Improvements to MSU's Trajectory Generation Code

3.1 MSU Collaboration

3.1.1 Objective

In this task, we collaborated with the UAS computation module development team at MSU to explore ways in which the teams can effectively exchange data and ideas.

3.1.2 Research Approach

The ASCENT9 team met with the team working on the eCommerce project at MSU on a biweekly basis. Led by Dr. Adrian Sescu, this team provided demand data and a data generator to create random UAS paths. The teams discussed the simulation of noise footprints from a notional UAS delivery network in the Memphis area. The ASCENT9 team shared an early version of the noise engine calculation with the MSU team.

The eCommerce project revolved around emerging UAS networks and their implications in national airspace system integration. The project's case study is an analysis of an Amazon UAS delivery network using ground support. The MSU team collected data for warehouses in the greater Memphis area along with the residential addresses served by these warehouses. Trucks were placed in the area to reduce the flight time of the UASs and to help with last-mile delivery. These warehouses are shown in Figure 18. Multiple scenarios were considered in this study:

- 8 drones per warehouse and 4 drones per truck (1,132 drones)
- 12 drones per warehouse and 6 drones per truck (1,698 drones)
- 16 drones per warehouse and 8 drones per truck (2,264 drones)
- 24 drones per warehouse and 12 drones per truck (3,396 drones)
- 32 drones per warehouse and 16 drones per truck (4,528 drones)
- 55 drones per warehouse and 50 drones per truck (12,305 drones)

The ASCENT9 team shared an early version of the noise engine developed under Task 4 with the MSU team, who verified that they were able to run the noise engine on their systems.

The ASCENT9 team used the first scenario to test the noise engine with variable grid precision. These trajectories are shown in Figures 18 and 19. The trajectories span an area of approximately 40 miles, with each trajectory’s length varying between 3,000 and 8,000 ft.

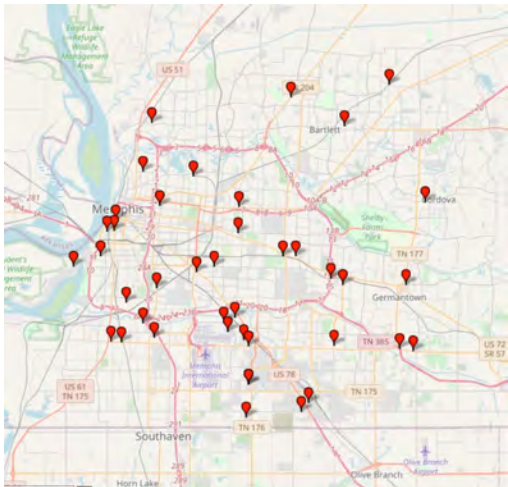


Figure 18. Warehouses in the Memphis, TN area.

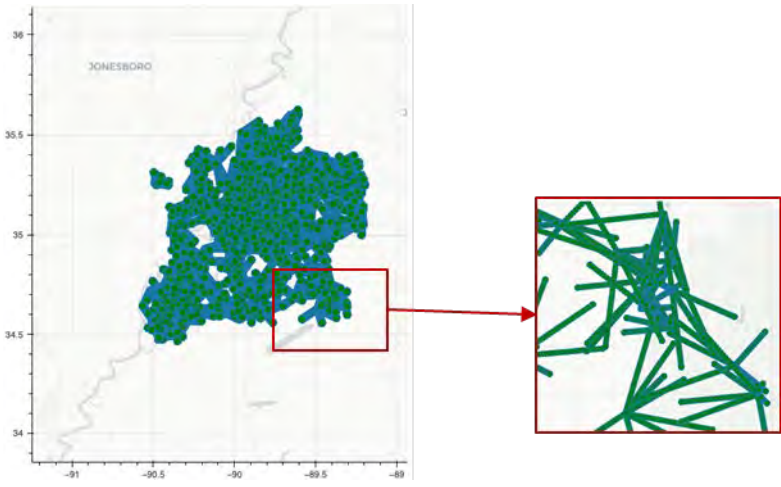


Figure 19. Random trajectories provided by Mississippi State University.

3.2 Volpe Collaboration

In addition to collaborating with MSU, the ASCENT9 team collaborated with the Volpe Research Center to acquire national transportation noise data. These data consist of combined gridded road, aviation, and railroad noise for the entire United States provided in A-weighted 24-hr exposure levels. These data are used as background noise that is added to the noise calculated by the engine module. A cropped overview of these data for the greater Memphis area is shown in Figure 20.

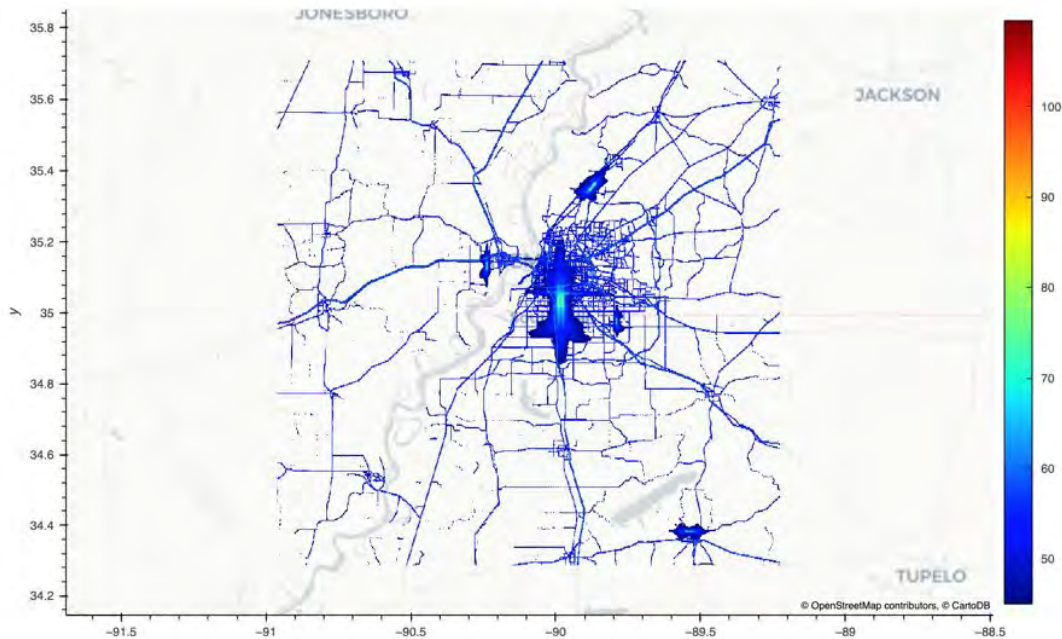


Figure 20. National transportation noise data for the greater Memphis area.

3.3 PACE Collaboration

In addition to these external collaborations, this research was also supported in part through research cyber-infrastructure resources and services provided by PACE at the Georgia Institute of Technology. This computing environment consists of a large computing cluster that was used to develop and test the noise engine under Task 4. This cluster was also used to conduct experiments and help tune various parameters and aspects of how the noise engine is executed in parallel. For example, parameters range from the number of computing nodes to the amount of memory per node and the number of parallel processes per node.

3.4 Improvements to MSU’s Trajectory-generation Code

After the MSU collaboration ended, the initial trajectory-generation code was reworked. In addition to introducing a more efficient implementation and increased flexibility, the code was broken down into multiple logical steps that relate to different phases of the workflow, as presented in the Task 4 Section.

Prior to the proper noise computations, the first step consists of creating tuples of staging locations, delivery locations, and vehicles. In general, these locations are the start and end points of a flight. For example, if different use cases are considered, such as for an e-taxi, these locations would map to pick-up and drop-off locations. The generation of these so-called pairings is dictated by the concept of operations, and these pairings are then used as input for the actual noise assessment. Currently, the implementation of this step is simple because only straight trajectories are considered, with either hover, cruise climb, or cruise flight segments. This logic could be made more complex in the future to accommodate new concepts of operations. Here, this logic is separated because it is independent from the noise computations and can therefore be developed in parallel, as long as the data interface between these two steps of the workflow is properly maintained.

In the second step, the definitions of the flights, or flight segments, are discretized in time. We have included this step as part of the preliminary analysis because the need for time discretization is purely an artifact of the current analysis method. If another analysis method were to directly take in flight segments as inputs instead of vehicle locations, then the flight segments would not need to be discretized.

This split also has the advantage of allowing for a more compact representation of a scenario; that is, a set of daily flights.

Among other improvements, the vehicle attributes are now provided externally and stored in a CSV file instead of being hard-coded.

Task 4 - Noise-computation Engine Integration

Georgia Institute of Technology

Task 4 Contents

- 4.1 Task Overview
- 4.2 Initial Noise Computation Engine Implementation
- 4.3 Initial Benchmark Demonstration
- 4.4 Initial Monte Carlo Study
- 4.5 Implementation of the SAE5534 Atmospheric Absorption Model
- 4.6 Workflow Definition and Code Refactor
- 4.7 Study of Interactions Between Trajectories
- 4.8 Uncertainty Propagation Leveraging GPU

4.1 Task Overview

The motivation for developing a noise-assessment tool specific to UASs was presented in the previous sections, and the previous tasks aimed at investigating the building blocks for this tool. Once promising technologies have been identified for the application components, they must be integrated within a coherent and easy-to-use tool, and this is the purpose of Task 4.

The following sections are organized chronologically: An initial implementation was developed and used to conduct an initial benchmark study and an initial Monte Carlo study. Then, a consequent refactor of the code was undertaken to improve both the internal code structure and the user interface. The refactor was intended to make it easier to work with and extend the codebase. This latest iteration was used to study the effect of interactions between trajectories. Finally, a new uncertainty propagation study is discussed, in which we took advantage of the speed-up brought by the GPU implementation discussed and studied in Task 2.

4.2 Initial Noise Computation Engine Implementation

The investigation conducted in Task 2 led to the identification of adequate tools to build a high-performance, interactive, GIS-based noise module for UASs. A Python web application was set to be built with the ability to run either locally or in a distributed setting provided by the HPC infrastructure of Georgia Tech PACE. As Python was already determined to be the programming language for this module, different libraries enabling parallel matrix computation and large interactive visualization were explored. The selection process resulted in four libraries, as shown in Figure 21.







	<ul style="list-style-type: none"> • Python library for interactive visualizations on web browsers • Developers use bokeh to create dashboards with graphs and interaction for the users
	<ul style="list-style-type: none"> • Python library for parallel computing • Enables the use of computer clusters to handle heavy computation
	<ul style="list-style-type: none"> • Accurate rendering of large datasets • Allows users to easily represent and analyze large datasets
	<ul style="list-style-type: none"> • Efficient handling of multi-dimensional arrays (including raster and GeoTiff files) • Implements operations on labeled arrays (e.g., array of longitude and latitude coordinates) for clearer and faster manipulation of datasets

Figure 21. Enabling capabilities for the unmanned aircraft system (UAS) noise engine prototype.

Before showcasing the architecture of the web application, we discuss the structure of the Python object for the grid. Noise metrics are built on the distances between the grid and the path of the noise source. In other words, for each point in the path, its distance to every point in the grid must be calculated. This information can be stored as a 3D matrix, where the third dimension matches the number of points in the path. A notional sketch of this structure is shown in Figure 22. This choice benefits from the highly optimized methods of numpy, a Python library for multi-dimensional arrays.

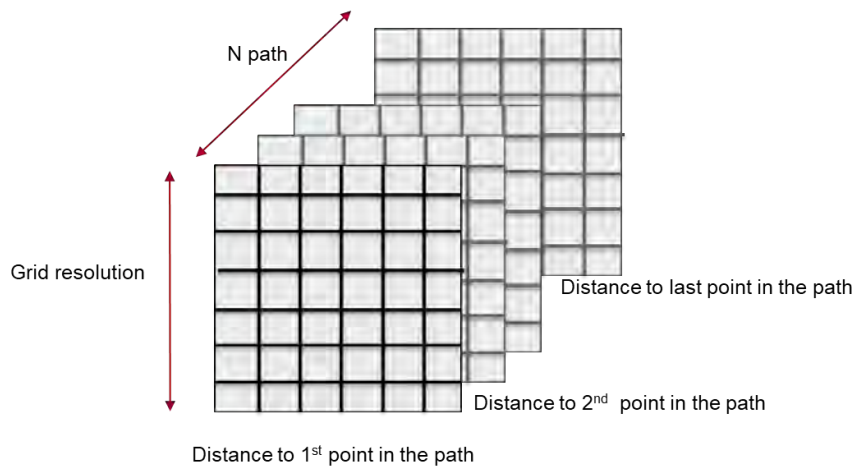


Figure 22. Notional structure of the noise module object.

The UAS prototype must demonstrate the calculation and visualization of two types of noise metrics: peak metrics and exposure metrics. The individual steps to calculate each metric are presented in Figure 23.

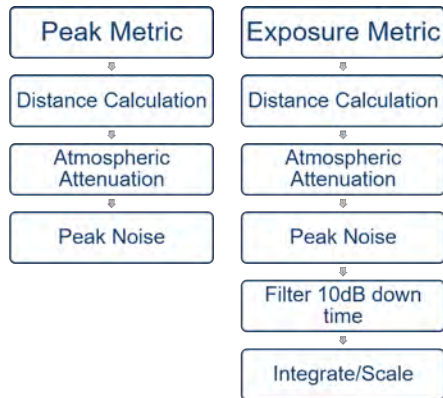


Figure 23. Steps for calculating peak and exposure noise metrics.

The parallel execution of the noise engine is conducted using the Dask library, with the following implementation steps:

1. Define computational steps as operations on generic datasets
2. Prepare datasets
3. Define computational resources
4. Launch the dynamic scheduler and map/apply operations on the datasets
5. Collect results

The computational resources are defined by the hardware available for parallel computation, which is characterized by the number of cores or workers and the available memory per core. In addition to allowing parallel computations on single machines, Dask supports cluster schedulers such as PBS and Slurm and is supported by AWS.

The dynamic scheduler is one of the most powerful features of Dask as it handles data partitioning and calculations without much user interference. This scheduler creates an optimized directed acyclic task graph to transfer data and apply computations using the given resources. An example of such a task graph is shown in Figure 24. This graph corresponds to a peak metric event calculation using 10 workers.

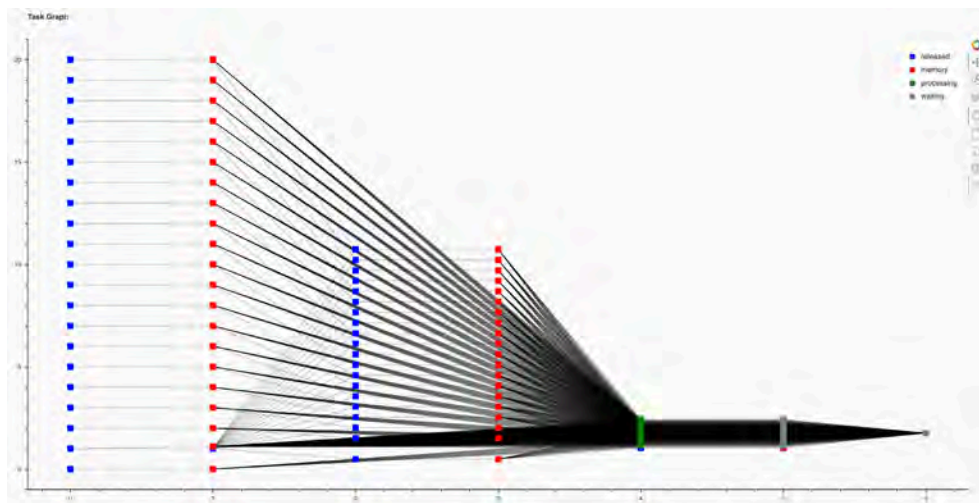


Figure 24. Task graph generated by Dask’s dynamic scheduler.

The generic implementation steps on Dask are illustrated in Figure 25, where the client refers to the web browser used to visualize the noise contours.

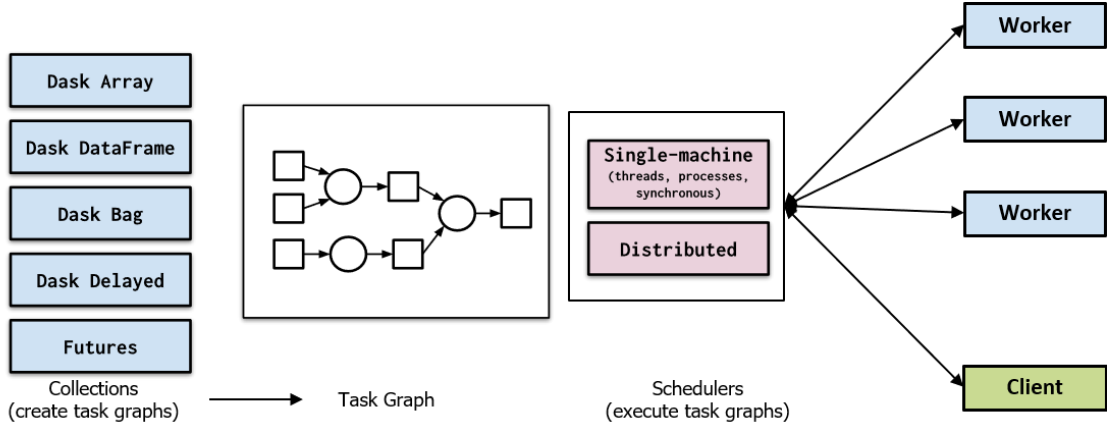


Figure 25. Implementation steps in Dask.

To visualize these contours on the browser, the Dask data objects need to undergo packaging operations using xarray and datashader. There is a limitation on the number of points a browser can support; therefore, datashader is used to allow the data to be sampled and visualized in a meaningful way. Datashader objects are integrated in Bokeh, but they do not support Dask arrays. Xarray was used to wrap the Dask objects for use within datashader. This data pipeline is illustrated in Figure 26.

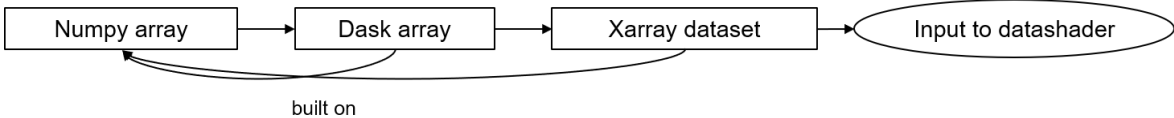
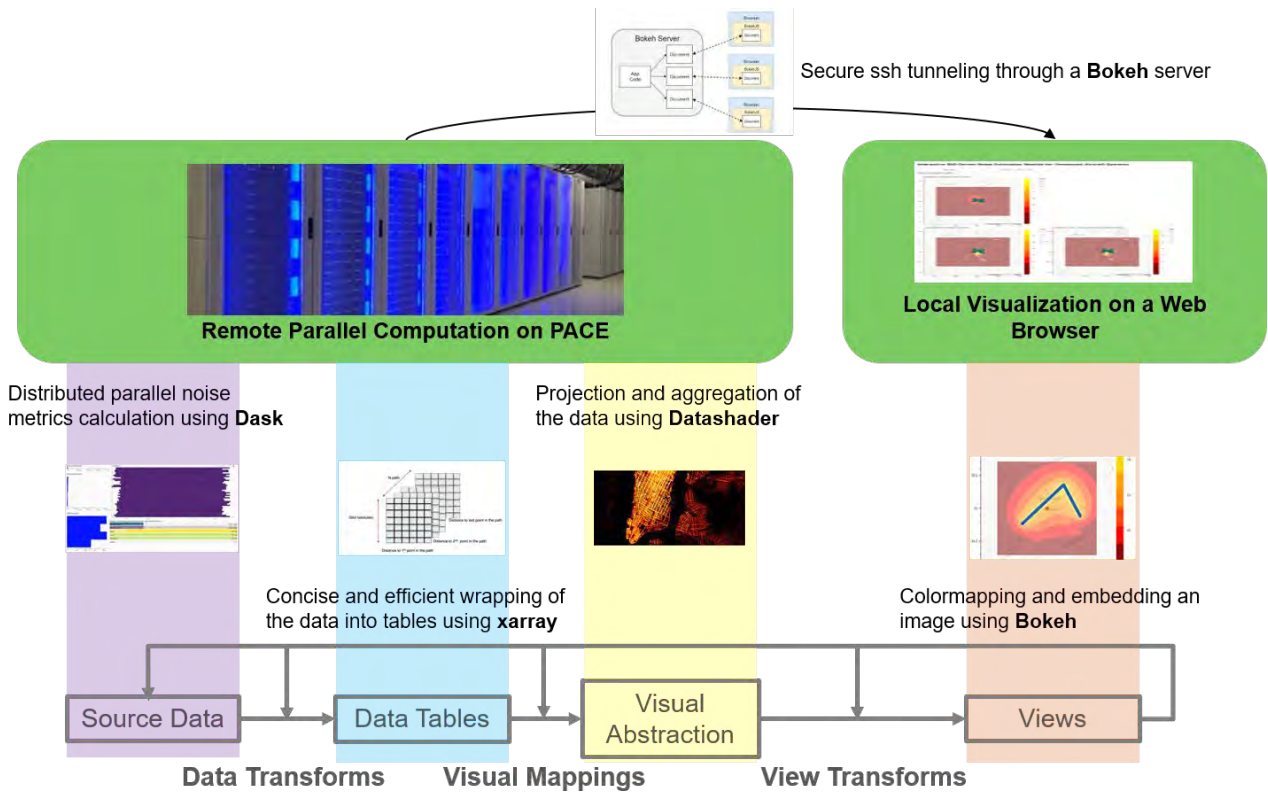


Figure 26. The data pipeline from Dask to Bokeh.

The overall architecture of the UAS noise calculation prototype is displayed in Figure 27. The noise contours are calculated and stored on the PACE distributed cluster. For visualization, Bokeh requests a portion of the data that is aggregated and projected using datashader. This step requires continuous communication between the Dask scheduler and the workers writing the data that have been bypassed to files. Alternatively, a central file could be created to collect the results. However, this comes with a high communication cost that must be considered. The data are accessible from the Bokeh server through secure ssh tunneling to the PACE interface. This is a major advantage of web applications over desktop applications, as it provides broader cross-platform access for clients.



THE INFORMATION VISUALIZATION REFERENCE MODEL

Source: Joseph A. Cottam, Andrew Lumsdaine, Peter Wang, "Abstract rendering: out-of-core rendering for information visualization"

Figure 27. Overview of the noise module. PACE: Partnership for an Advanced Computing Environment.

4.3 Initial Benchmark Demonstration

This benchmark study aimed to simulate the noise footprint from a notional UAS delivery network in the greater Memphis area. In this study, 40 warehouses serving approximately 30,000 residential addresses were considered. Trucks that serve as UAS staging platforms are positioned near some neighborhoods, which reduces UAS range requirements and delivery times. For this study, eight UASs per warehouse were considered, with four UASs per truck and a total of 1,132 total flights. The paths for these flights are shown in Figure 28.

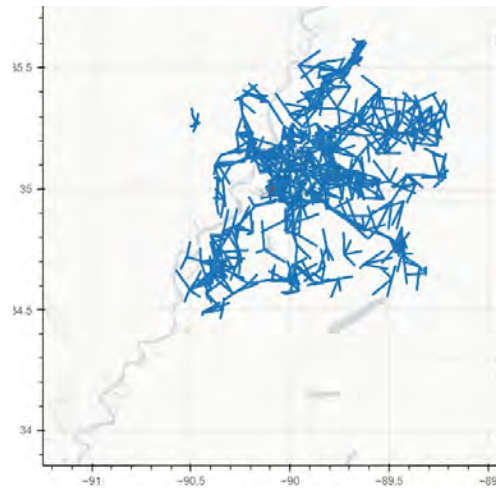


Figure 28. Flight paths used in the benchmark study.

The national transportation noise map was used as background to supplement the engine’s computations. The contours of this background noise are shown in Figure 29. The cumulative L_{Aeq} noise contours generated uniquely from UAS activities are displayed in Figures 30 and 31. The effect of UAS activity on the existing noise in the greater Memphis area is shown in Figure 32.

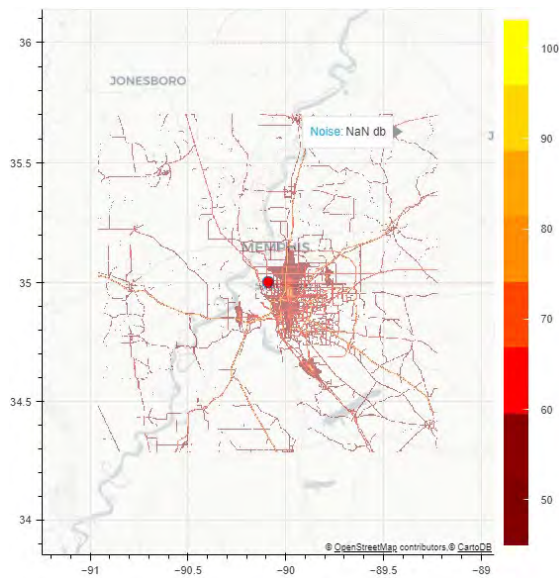


Figure 29. National transportation noise map of the greater Memphis area.

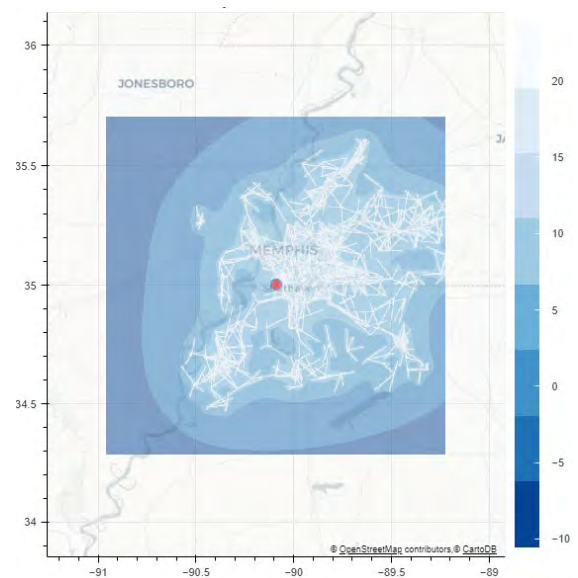


Figure 30. Computed unmanned aircraft system (UAS) noise ($L_{Aeq,24hr}$).

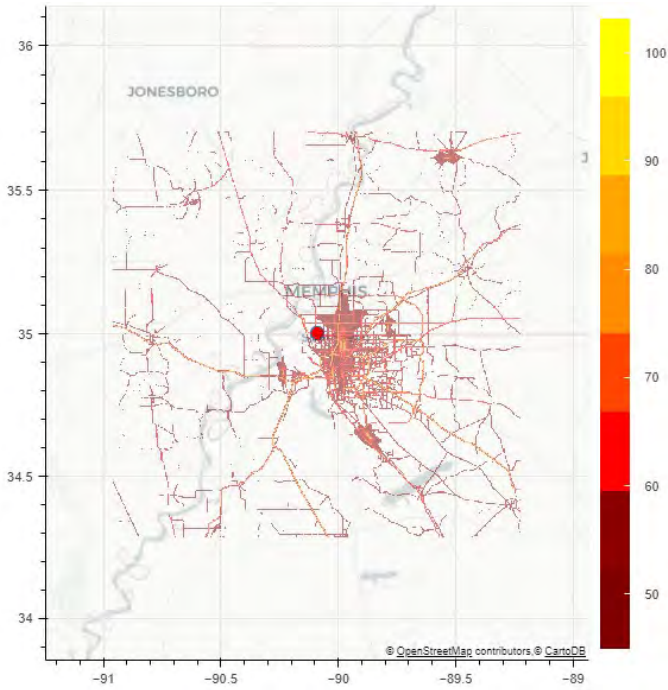


Figure 31. Combined noise ($L_{Aeq,24hr}$).

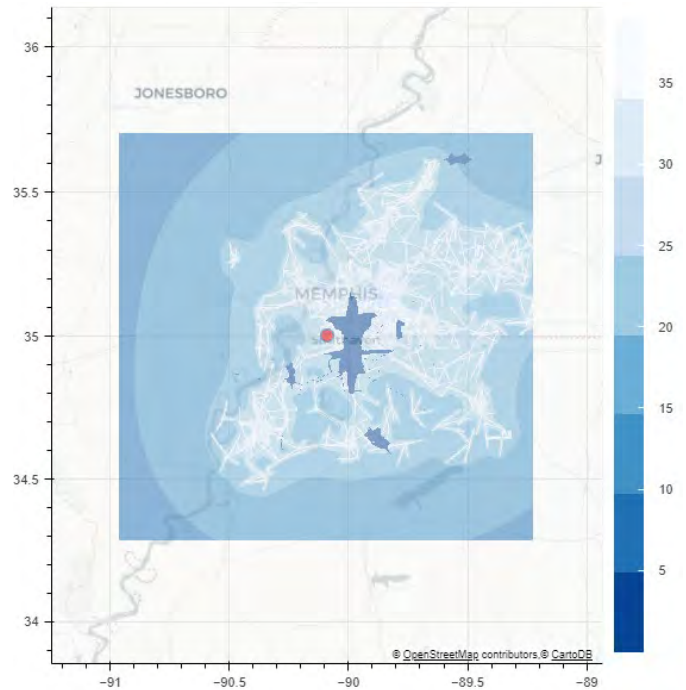


Figure 32. Change in $L_{Aeq,24hr}$.

The $L_{A,max}$ value for UAS noise with the interactive demo is illustrated in Figures 33 and 34. This figure indicates the potential difference in noise impacts across areas with high noise exposure levels compared with areas that currently have limited noise-exposure levels. A large difference is found between exposure and peak metrics. The interaction can be better understood by including the background noise.

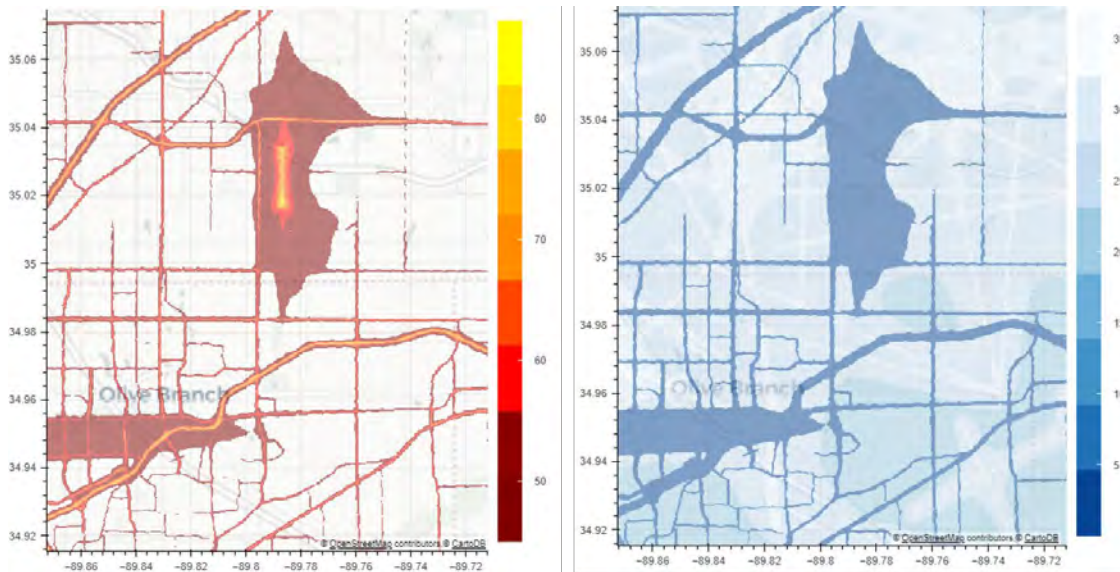


Figure 33. Combined noise $L_{Aeq,24h}$ (left) and change in $L_{Aeq,24h}$ (right).

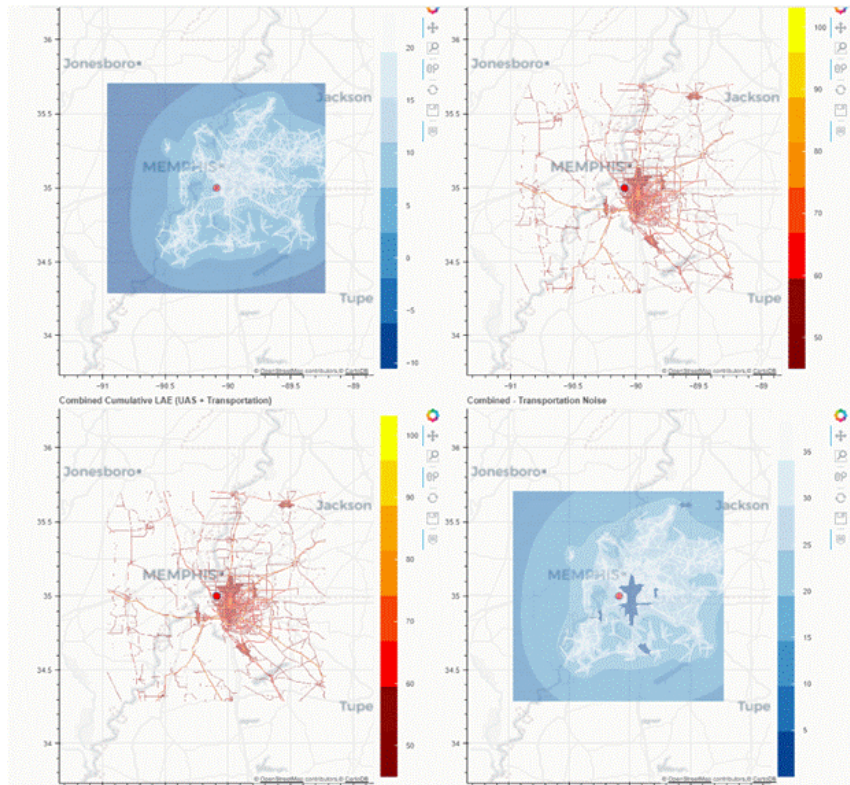


Figure 34. Interactive demo.

4.4 Initial Monte Carlo Study

Because UAS operations are stochastic in nature, individual flight trajectories for each day depend on daily orders and demand, as shown in Figure 35. In some cases, staging locations can also vary. The operator strategy applied to the trajectory planning can also include noise dispersion and altitude constraints to minimize the noise. The annual average day metrics are not capable of capturing daily changes.

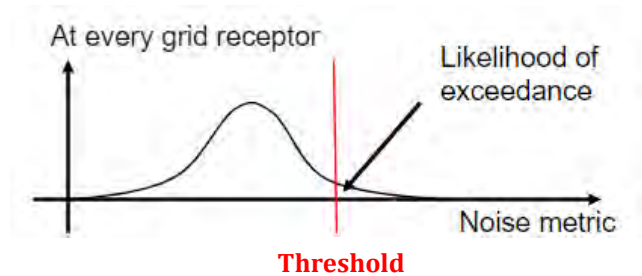
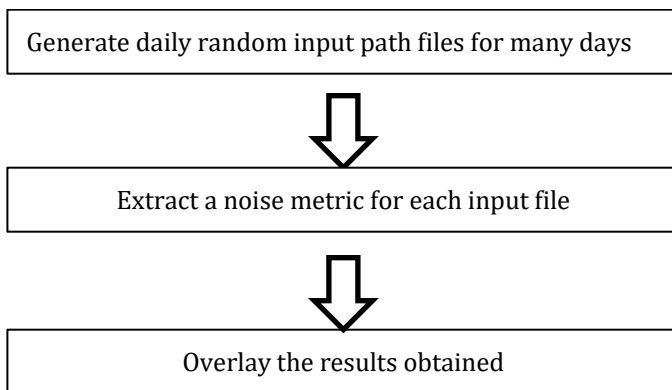


Figure 35. Notional workflow for a probabilistic approach to noise assessment.

A question arises: What is the likelihood of exceeding some threshold on any given day and how many locations will exceed this threshold? We first attempted to answer this question using a Monte Carlo simulation. However, this process is

computationally expensive. The goal of this probabilistic assessment is to obtain the likelihood of exceedance contour. The first attempt included 100 daily deliveries for 3,800 days on a coarse grid (250k points). The CPU time included 10,000 simulated days and resulted in collecting multiple noise metrics at the same time. To a first-order approximation, the delivery noise distribution was based on the address/population distribution.

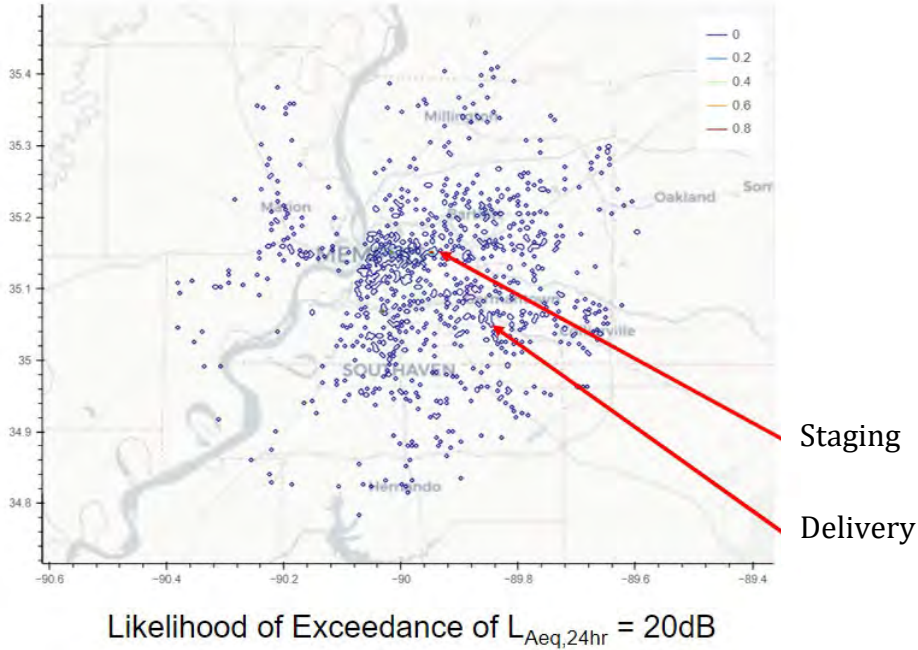


Figure 36. Likelihood of exceedance for $L_{Aeq,24hr} = 20$ dB.

The choice of metric and threshold has a significant impact on the observed results, as demonstrated in Figure 37, which shows the likelihood of exceedance when L_{Amax} is increased from 20 to 50 dB.

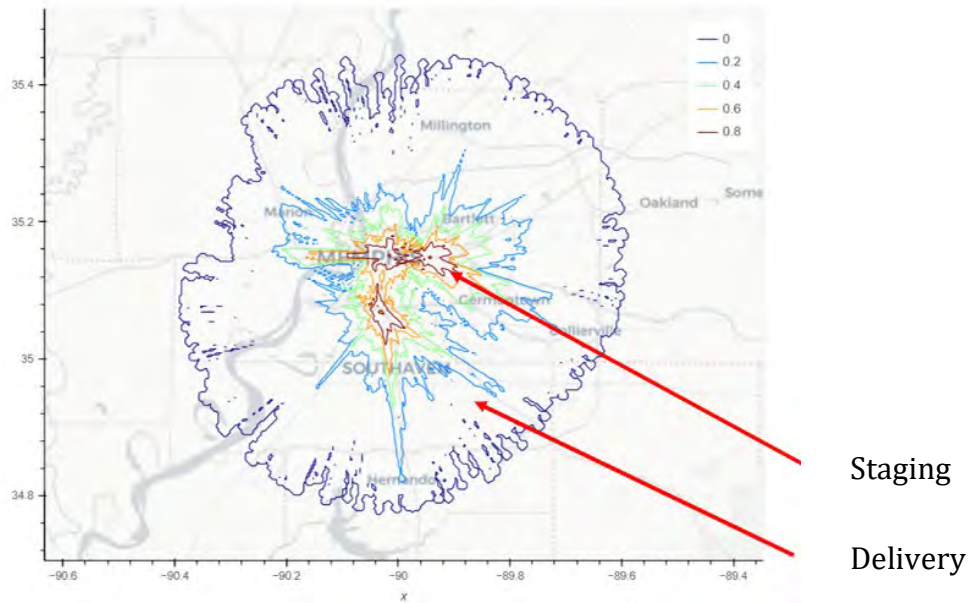


Figure 37. Likelihood of exceedance for $L_{Amax} = 50$ dB.

4.5 Implementation of the SAE5534 Atmospheric Absorption Model

The team implemented the atmospheric absorption losses defined in SAE ARP5543. This implementation provides a more realistic method of atmospheric sound absorption than the very simplified method used at the beginning of this project. This approach also builds on earlier standards, such as ARP866A, and allows the modeling of noise absorption to be sensitive to humidity and temperature, as expected. The current implementation works as a function that replaces the simplistic distance scaling. This function is also included in the Dask implementation as a function that utilizes parallel execution. The JAX implementation serves as the basis of a GPU shader function. While there is some penalty in the execution speed in both cases, the current implementation appears to work reasonably well. The team also worked to ensure accuracy in the implementation by comparing the implementation's output to the reference data supplied in ARP5543. In addition, the team compared the current implementation with AEDT's implementation. Both comparisons yielded only minor differences attributable to floating point precision and rounding differences.



4.6 Workflow Definition and Code Refactor

4.6.1 Workflow Definition

The analysis workflow was formalized in order to drive the development of the new GUI. The resulting workflow is depicted in Figure 38. In the first step, all of the inputs to the analysis are specified and/or loaded. This step includes defining the analysis area, generating or retrieving trajectories, and loading the background transportation noise. In the second step, analysis settings are provided by the user, and the proper noise assessment is executed. Finally, the results are visualized.

4.6.2 Code Refactor

A code refactor was undertaken to make the codebase more modular. By modular, we mean, for example, logically splitting the code between the GUI-related parts and the analysis-related parts. Within the part of the code devoted to the GUI, modularity means defining clear interfaces between components. For example, the map displayed in the main noise-assessment tool can now easily be reused within Jupyter notebooks in the context of a stand-alone study.

Many new features were developed, including the ability to display more operational scenario details (staging and delivery locations, flights, etc.), the inclusion of multiple input panels allowing the user to specify analysis inputs (instead of hard-coded values), and an integrated display of all output metrics on a single map.

As mentioned in the Task 2 section, the trajectory generation was also enhanced, with more flexibility in defining new vehicles and their noise characteristics.

4.6.3 Upgraded GUI

The upgraded GUI is shown in Figure 39. Similar to most GIS software, the map occupies most of the screen. On the left-hand side, a tab-divided panel contains all of the controls necessary to follow the workflow defined in the previous section.

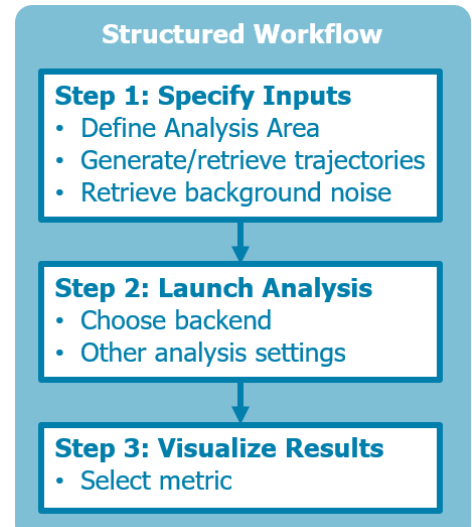


Figure 38. New structured workflow.

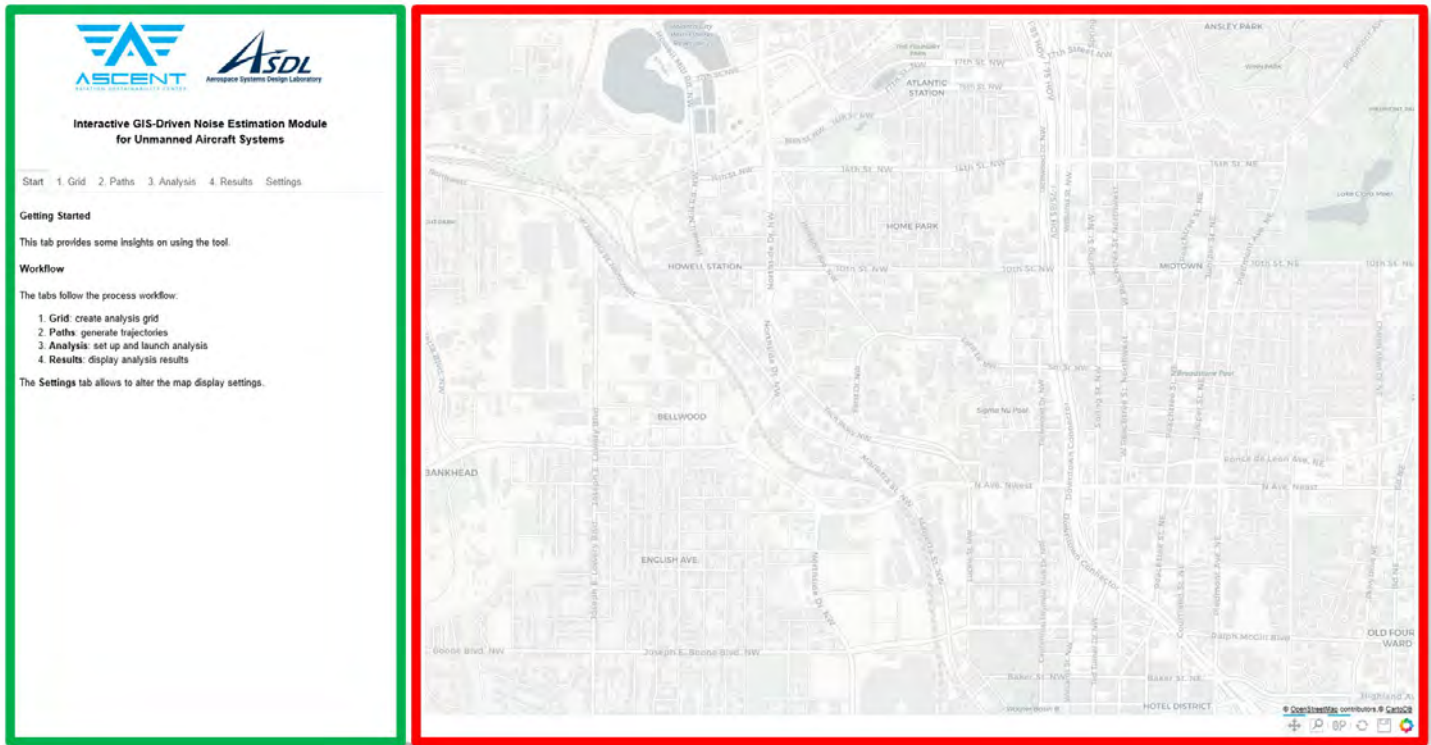


Figure 39a. Annotated screenshot of the new graphic user interface. The left-hand side (shown in a green box for emphasis) displays the control panel, featuring tab-based navigation. The visualization map occupies the remaining space on the right-hand side (shown in a red box for emphasis).

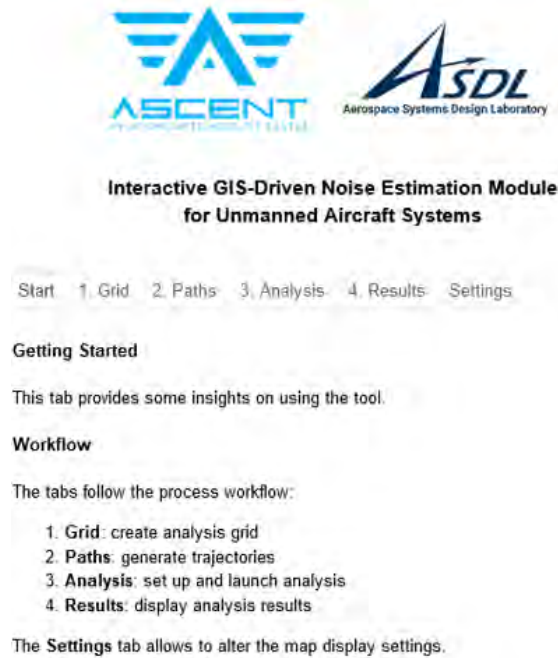


Figure 39b. Screenshot of the control panel of the new graphic user interface.



4.7 Study of Interactions Between Trajectories

4.7.1 Motivation and Objective

In the current implementation of the noise engine, trajectories are processed separately. Therefore, the combined impact of two flights at the same geographical location (i.e., the same virtual microphone) is not considered. To assess the validity of this simplification in the context of the operational scenarios under consideration, we conducted a study to quantify the discrepancy introduced by this approach.

Instead of using a full operational scenario to characterize the discrepancy, we focused on a smaller test case and proceeded in two steps. First, using two vehicles, we illustrated the error that results when the two vehicles are considered independently. We then generalized this error to a larger number of vehicles; because of the simple noise model being used, the error could be computed analytically as a function of the vehicle number. This first part of the study allowed us to identify the types of situations in which the error was significant; namely, when multiple vehicles were simultaneously close to a microphone location. Then, in a second step, we sought to determine the frequency at which such situations occurred in the considered operational scenarios.

More specifically, we aimed to assess the impact of computing the $L_{A,max}$ metric by considering all vehicles independently, rather than summing the individual sound intensities of nearby vehicles at every microphone location. We focused on the $L_{A,max}$ metric because this is the only metric of interest that is affected by an independent treatment of trajectories. The other metrics result from a time integration, making the concurrency of events irrelevant to their final computed value.

The following simplifications were made compared with the usual noise assessment setup:

- The analysis grid consists of a single microphone;
- All vehicles had the same noise level at 100 ft (65 dBA);
- All vehicles flew at the same altitude/z-coordinate (100 ft); and
- Each vehicle was located at a set distance from the microphone in the horizontal x-y plane.

4.7.2 Two Vehicles with Varying Distance from the Microphone

We considered two vehicles and varied their respective distances, d_1 and d_2 , to the microphone in the x-y plane (same altitude, same source noise level). As shown in Figure 40, the difference in the two metrics approaches zero when the vehicles are far from each other (one has a significantly higher contribution than the other; therefore, taking the maximum of the two noise levels becomes a good approximation). When the two vehicles are located the same distance from the microphone, the intensity is underestimated by 1/2 when the maximum is used instead of the sum of intensities, and accordingly, the difference between the two noise level metrics is $10 \log(2) = 3.01$.

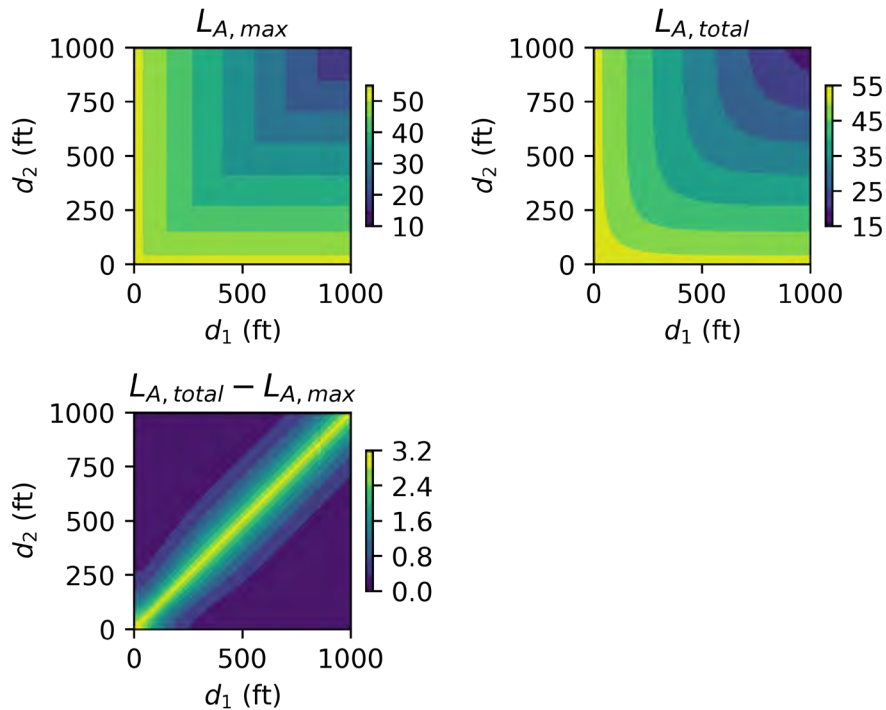


Figure 40. Evolution of $L_{A,max}$ (upper left), $L_{A,total}$ (upper right), and the difference between these two quantities (lower left).

4.7.3 Varying the Number of Vehicles

We varied the number of vehicles from 2 to 100. All vehicles were assumed to be at an altitude of 100 ft and a distance of 1,000 ft from the microphone. These assumptions correspond to the diagonal of the previously shown plots; that is, the situation in which the difference between the two metrics is the largest.

In the previous section, the noise level was underestimated by $10 \log(2)$ because we were considering two vehicles. Here, we expect the difference to be $10 \log(N_{vehicles})$, which is confirmed in Figure 41.

4.7.4 Assessing Situations in which Multiple Vehicles are Simultaneously Close to a Geographical Location

In the previous sections, we assessed situations in which multiple vehicles are simultaneously located within a relatively close distance to a given geographic location. We sought to verify whether such a situation would arise in a drone delivery scenario. In the following, we applied a fixed time window for the simulation (e.g., 1 hr).

Within this time window, a fixed number of vehicles depart and proceed to deliver packages. The departure times were chosen so as to be uniformly distributed within the time window. Delivery trips that would exceed the time window were truncated.

We plotted the duration during which more than a certain threshold number of vehicles are within a certain threshold distance (measured in feet) of the grid point. Here, we set the threshold number of vehicles to two or five and the threshold distance to 100, 500, or 1,000 ft. The total number of vehicles in the simulation was set to 100, 500, or 1,000 vehicles.

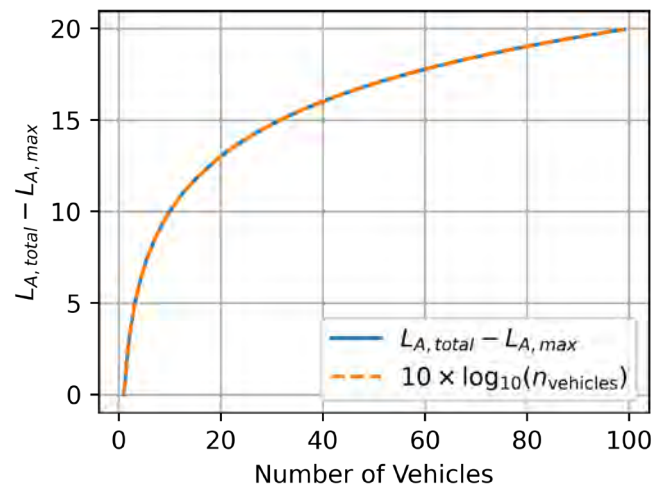


Figure 41. Evolution of the approximation error.

These results correspond to situations in which the value of $L_{A,max}$ may significantly differ based on the method of computation.

Creating the Flight Schedule

We created a flight schedule and stored it in a 3D array whose dimensions are (a) the number of time steps, (b) the total number of vehicles in the simulations, and (c) four data values. The last dimension, which has a size of 4, contains the (x, y, z) coordinates of the vehicle and the noise level at 100 ft. In the present study, the vehicle's noise level is not used because we only focus on distances. Here, we keep the number of 1-s-long time steps fixed to 3,600 (1 hr), but we vary the total number of vehicles departing within that flight window.

Counting the Number of Nearby Flights

To obtain a quantity that can be easily represented on a map, for each location on the grid, we counted the number of time steps in which the threshold number of vehicles was exceeded within the threshold distance. Both the threshold distance and the threshold number of vehicles were varied.

Results

We used Texas data as an example, where the locations and vehicle noise values are loosely based on the Noise Assessment for Wing Aviation [8], with two warehouses used as staging locations for the drones. Results are shown for the different threshold values in Figures 42–44.

Observations and Conclusions

From Figures 42–44, we observe the following:

- As we increase the distance threshold, the number of time steps for which the condition is met increases; there are more situations in which vehicles are within a 500-ft radius of a grid point than situations in which they are located within 100 ft.
- As we increase the threshold number of vehicles, the number of time steps in which the condition is met decreases; there are fewer situations in which five vehicles are within a given distance of a grid point than situations in which only two vehicles are within this distance.
- As the total number of vehicles simulated within the 1-hr time window increases, the number of time steps in which multiple vehicles can be found within a given distance of a grid point increases. As the vehicle concentration increases, it becomes easier to find situations in which multiple vehicles are simultaneously within a given distance of a grid point.
- There are two main grid points for which many vehicles may be found simultaneously, corresponding to the two warehouses from which vehicles depart.

These observations match our expectations; the zones of high traffic correspond to the neighborhoods of the staging locations. When the total number of vehicles remains relatively low, there are few situations in which two or more vehicles are found simultaneously near a grid point, and these situations occur only when the radius is set to 500 or 1,000 ft. These correspond to situations in which the sound levels would be relatively low because of the relatively high distance, and the noise would need to be summed for fewer than five vehicles.

As the number of vehicles increases, such situations become more common, and more than five or more vehicles may be found within the threshold distances used in this study. However, such occurrences are relatively rare and are concentrated at locations from which the vehicles depart. For 1,000 vehicles departing within a 1-hr time window, we begin to observe ray-shaped zones, for which multiple vehicles may be present within a given distance. However, this level of traffic most likely exceeds realistic levels (a rate of 1,000 departures per hour corresponds to a departure every 3.6 s). Moreover, if such a high density of traffic were needed, more staging locations would most likely be used, therefore reducing the noise impact at each of the staging locations.

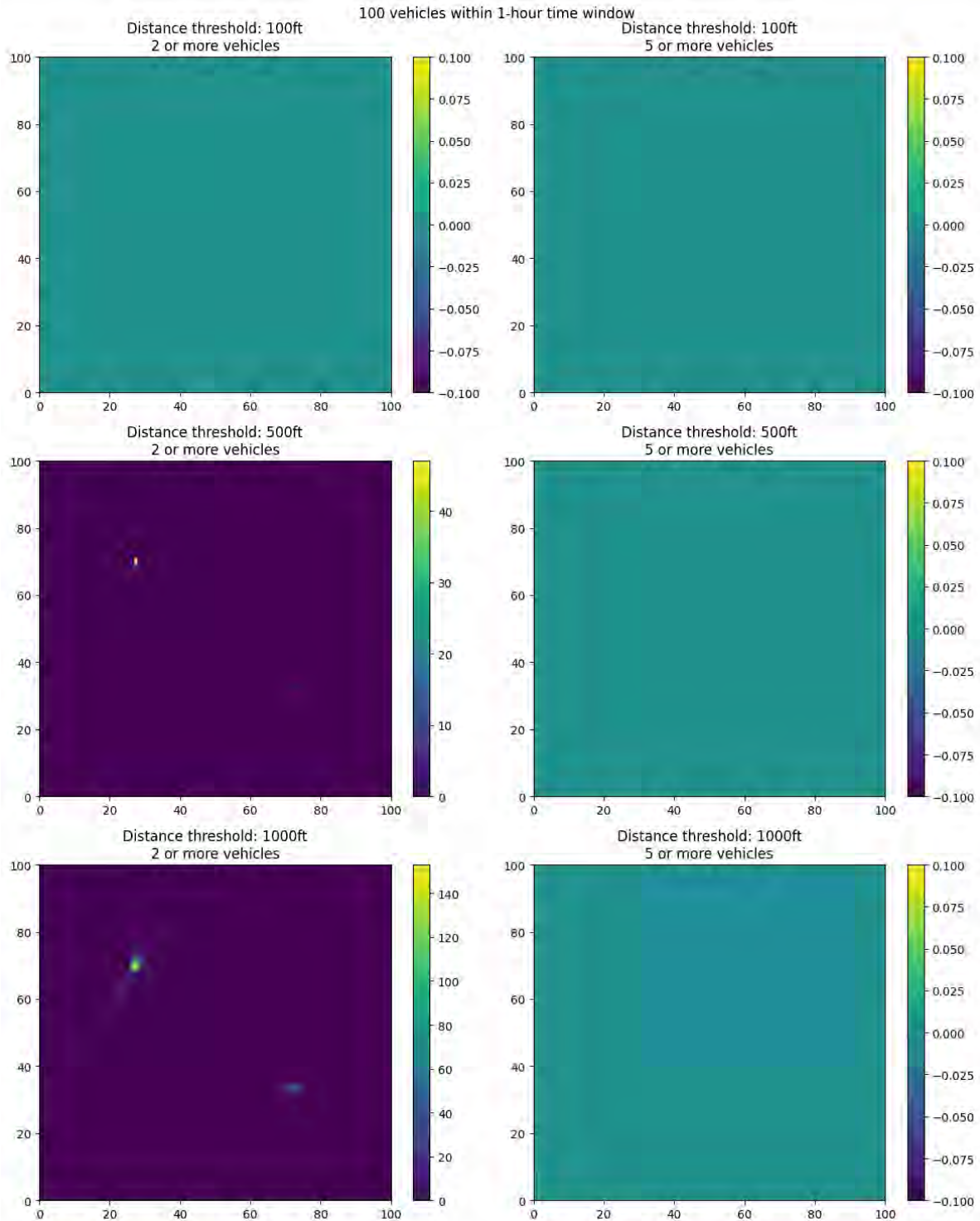


Figure 42. Number of occurrences in which the number of vehicles simultaneously flying within a certain threshold distance of a location in the study area exceeds a threshold number of vehicles. Results are shown for the least dense scenario: 100 vehicles within a 1-hr time window.

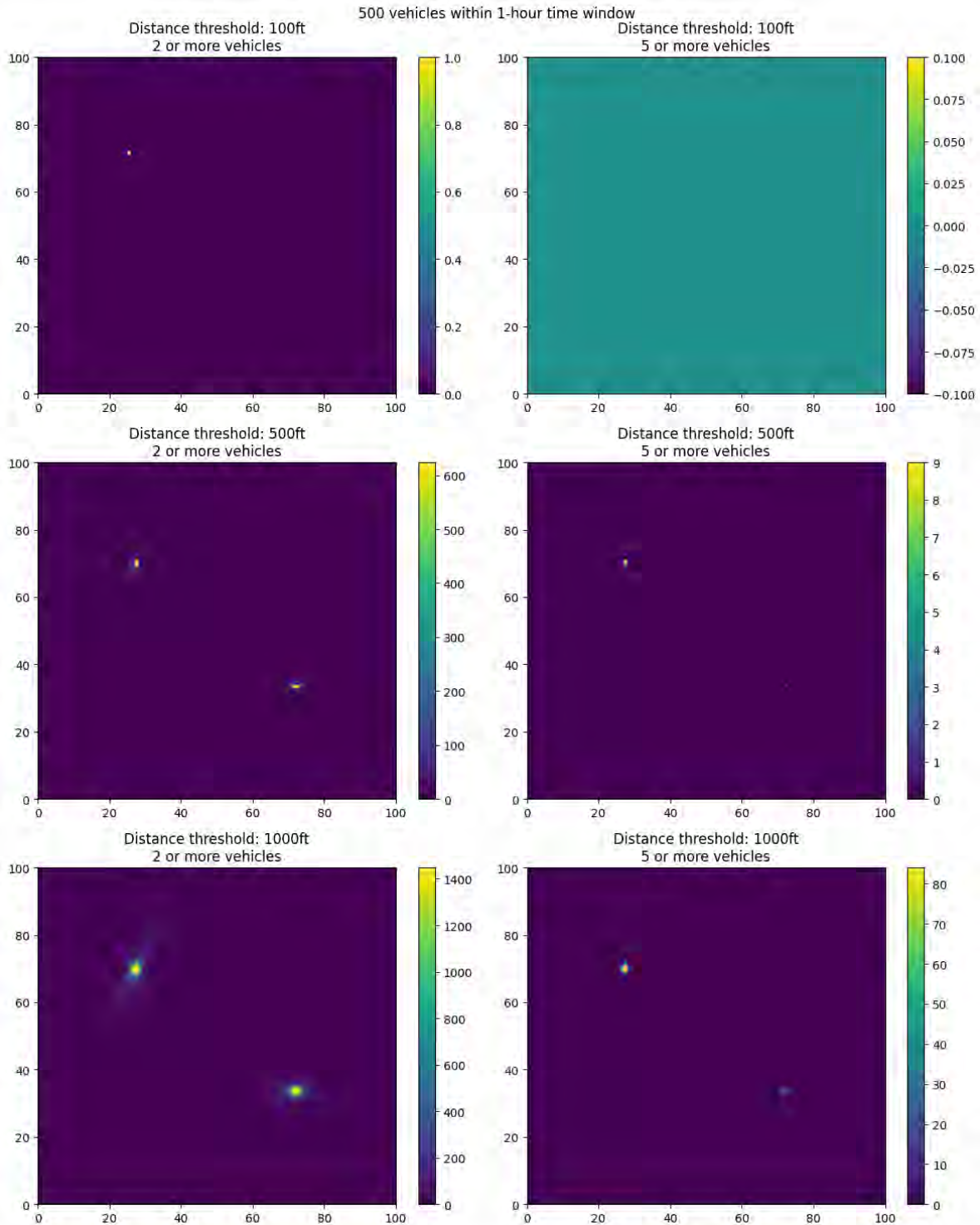


Figure 43. Number of occurrences in which the number of vehicles simultaneously flying within a certain threshold distance of a location in the study area exceeds a threshold number of vehicles. Results are shown for the least dense scenario: 500 vehicles within a 1-hr time window.

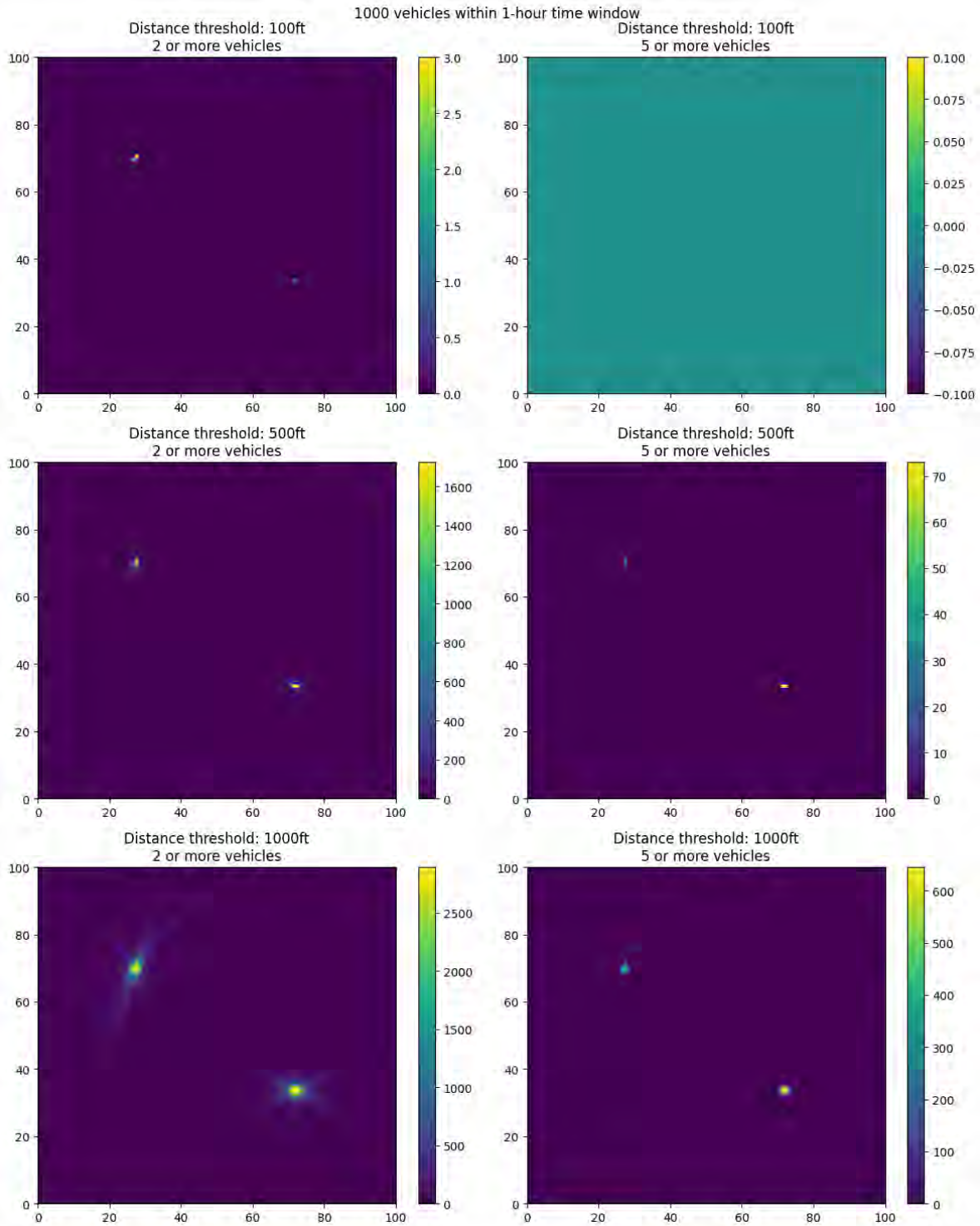


Figure 44. Number of occurrences in which the number of vehicles simultaneously flying within a certain threshold distance of a location in the study area exceeds a threshold number of vehicles. Results are shown for the least dense scenario: 1,000 vehicles within a 1-hr time window.

4.8 Uncertainty Propagation Leveraging GPU

4.8.1 Motivation and Objective

UAS operations are subject to multiple sources of variability, including the following:

- Daily individual flight trajectories are dependent on orders/demand;
- Staging locations may change day to day (e.g., when trucks are used for staging drones); and
- Operator strategies for trajectory planning may include noise dispersion and altitude constraints to minimize noise.

Thus, UAS operations should be modeled as a stochastic process, as annual average day metrics do not capture daily changes. Instead of seeking deterministic measures of noise exposure, we aim to estimate the likelihood of exceedance for some threshold on any given day across the study area. In mathematical terms, we consider $P(L_{A,max} \geq X \text{ dBA})$ the probability that $L_{A,max}$ will exceed $X \text{ dBA}$. Results are depicted as contours on a map of the study area, with the level X being varied, therefore leading to different contour plots for each value of X . This study is the second attempt at a Monte Carlo simulation, which takes advantage of the GPU speed-up.

4.8.2 Setup

The study area covers the urban region of Memphis, TN, representing a 60-mile \times 60-mile square. Delivery drones may depart from one of 41 warehouses, and delivery locations are uniformly sampled from residential locations within the study area. The resolution of the analysis grid is 1,056 cells in each direction. As a result, the sides of the square cells measure approximately 300 ft. In the considered operational scenario, 500 deliveries are performed per day, and the simulation is repeated for 10,000 days. The only source of variability considered in this study is the day-to-day variability of the flights.

Compared with the first Monte Carlo study, the grid is approximately 4-times larger, and there are approximately 5-times more flights per day, resulting in an overall 20-fold-larger problem size.

4.8.3 Results and Conclusions

The results of this study are shown in Figure 45. As discussed previously, each plot corresponds to a different noise exposure level threshold: 10, 20, 30, or 40 dBA. Warehouses are shown as red dots. We observe that the high-probability area shrinks as the threshold increases, consistent with expectations. The geographical areas with a high probability of exceeding 40 dBA are concentrated near the staging locations.

The full Monte Carlo simulation was completed in approximately 7 hr by using 50 GPUs from Georgia Tech’s PACE cluster. Each run takes approximately 2 min to complete. This runtime is orders of magnitude shorter than the first Monte Carlo attempt that was run on a CPU

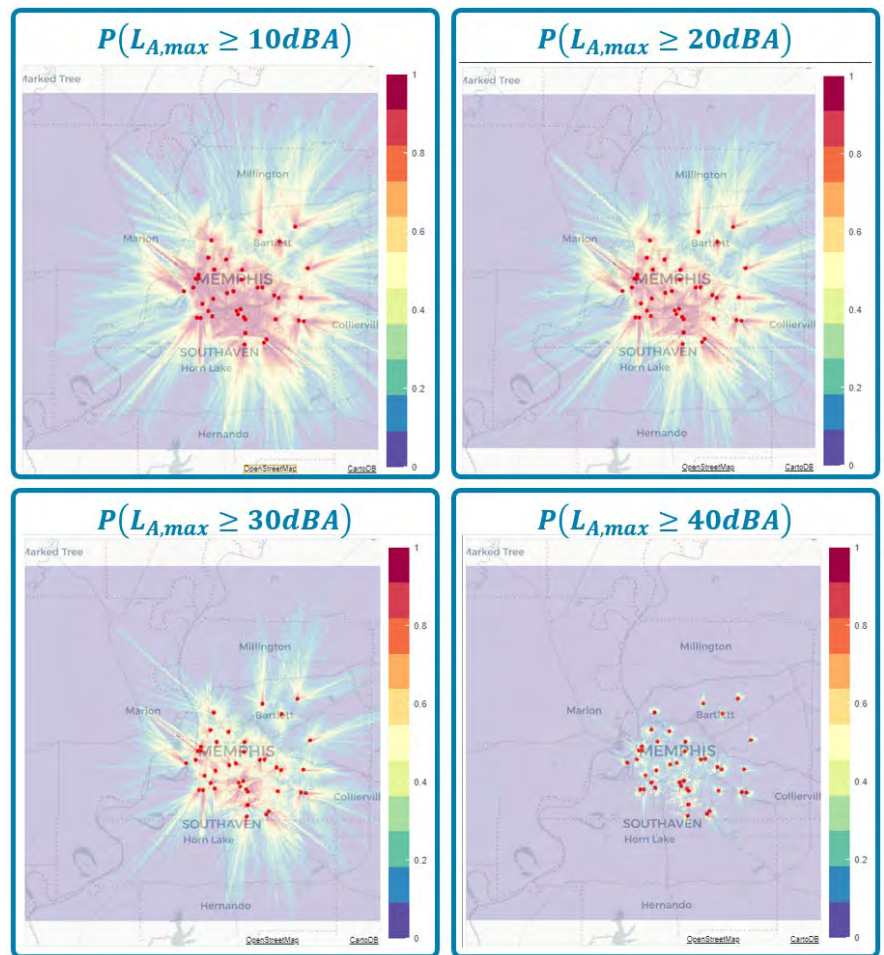


Figure 45. Results of the graphics processing unit (GPU) Monte Carlo simulation. Contour plots denote the probability that $L_{A,max}$ exceeds a threshold level. Threshold levels were varied at 10, 20, 30, and 40 dBA.

(hours instead of weeks), thus confirming the benefits achieved when running the noise engine on GPUs.

4.9 Packaging of the Noise-assessment Tool

Although Python offers access to a variety of quality off-the-shelf packages that fulfill many computational and analysis needs, it requires setting up a suite of software on the client machine on which the Python tool needs to be executed, including Python itself, as well as third-party packages the software depends on. This complexity compounds with the configuration management problem: Python version and third-party packages must not only be installed; they also need to be compatible versions. To address these shortcomings and remove the setup burden from the user of the noise-assessment tool, the goal of this effort was to package the tool in such a way that the setup on a new client machine required minimal effort.

Among the several options available in the Python ecosystem, PyInstaller stood out as the most mature and promising solution. This is not, however, a plug-and-play solution; although PyInstaller automates most of the process of packaging the Python tool and its dependencies in a stand-alone folder or executable, certain libraries require additional work to be integrated to this executable. A version of the noise-assessment tool relying only on CPU was successfully packaged and tested on Windows. The packaging of the GPU version of the noise-assessment tool was initiated but could not be thoroughly tested due to the lack of access to a machine featuring a GPU.

Milestone

The team delivered a recommendation for an updated GIS system to the FAA and members of the AEDT development team.

Major Accomplishments

The team presented an initial prototype of the UAS noise engine with an interactive display while running on a parallel computing cluster to the FAA.

Publications

None.

Outreach Efforts

The team engaged in outreach and coordination with the ASSURE Center of Excellence team and their work at MSU. The team also collaborated with the Volpe Center and participated in the NASA UAM Noise Technical Working Groups.

Awards

None.

Student Involvement

The Georgia Institute of Technology student team consists of three graduate research assistants. At the beginning of the project, all graduate research assistants engaged in the GIS background research. The team is now divided to tackle the different aspects and implementation of the noise engine, novel computational technology testing, and the creation of benchmark studies that serve as a test bed for testing the computational scaling of different approaches.

Plans for Next Period

This is the final report for Project 9. Continuation of this work is taking place as part of Project 94, which builds on the capabilities developed in the context of Project 9, extends the modeling to more diverse concepts of operations, and introduces probabilistic aspects to the noise assessment.

References

- Aftomis, M. J., Berger, M. J. & Alonso, J. J. (2006). *Applications of a Cartesian mesh boundary-layer approach for complex configurations* [Meeting presentation]. 44th AIAA Aerospace Sciences Meeting, Reno NV, United States.
- Gropp, W. (n.d.). Introduction to MPI I/O [CS 598, Lecture Notes]. University of Illinois, Urbana-Champaign, IL, United States.
- The Office of Spatial Analysis and Visualization at the Bureau of Transportation Statistics, U.S. Department of Transportation
- Bokeh Development Team. (2018). *Bokeh: Python library for interactive visualization*. <http://www.Bokeh.pydata.org>



- Dask Development Team. (2016). *Dask: Library for dynamic task scheduling*. <https://dask.org>
- Cottam, J. A, Lumsdaine, A., & Wang, P. (2014). Abstract rendering: Out-of-core rendering for information visualization. *Proc. SPIE 9017, Visualization and Data Analysis 90170K*. <https://doi.org/10.1117/12.2041200>
- Teal Group (2022). *2021/2022 Civil UAS Market Forecast*.
- HMMH (2021). *Noise assessment for wing aviation proposed package delivery operations in Frisco and Little Elm, Texas*. (HMMH Report No. 309990.003-2.)



Project 010 Aircraft Technology Modeling and Assessment

Georgia Institute of Technology Purdue University

Project Lead Investigators

Dimitri Mavris (P.I.)
Regents Professor
School of Aerospace Engineering
Georgia Institute of Technology
Mail Stop 0150
Atlanta, GA 30332-0150
404-894-1557
dimitri.mavris@ae.gatech.edu

William Crossley (P.I.)
Professor
School of Aeronautics and Astronautics
Purdue University
701 W. Stadium Ave
West Lafayette, IN 47907-2045
765-496-2872
crossley@purdue.edu

Jimmy Tai (co-P.I.)
Senior Research Engineer
School of Aerospace Engineering
Georgia Institute of Technology
Mail Stop 0150
Atlanta, GA 30332-0150
404-894-0197
jimmy.tai@ae.gatech.edu

Daniel DeLaurentis (co-P.I.)
Professor
School of Aeronautics and Astronautics
Purdue University
701 W. Stadium Ave
West Lafayette, IN 47907-2045
765-494-0694
ddelaure@purdue.edu

University Participants

Georgia Institute of Technology (Georgia Tech)

- P.I.s: Dr. Dimitri Mavris (P.I.), Dr. Jimmy Tai (co-P.I.)
- FAA Award Numbers: 13-C-AJFE-GIT-006, 13-C-AJFE-GIT-012, 13-C-AJFE-GIT-022, 13-C-AJFE-GIT-031, 13-C-AJFE-GIT-37, 13-C-AJFE-GIT-041, 13-C-AJFE-GIT-50, 13-C-AJFE-GIT-52, 13-C-AJFE-GIT-56, 13-C-AJFE-GIT-76, and 13-C-AJFE-GIT-94





- Period of Performance: September 1, 2022 to August 31, 2023
- Tasks:
 1. SST Aerodynamic Modeling
 2. SST Propulsion System Modeling
 3. Mission Analysis
 4. LTO Trajectory and Noise Modeling
 5. Engine Cycle and Takeoff Trajectory Space Exploration

Purdue University

- P.I.s: Dr. William A. Crossley (P.I.), Dr. Daniel DeLaurentis (co-P.I.)
- FAA Award Numbers: 13-C-AJFE-PU-004, 13-C-AJFE-PU-008, 13-C-AJFE-PU-013, 13-C-AJFE-PU-018, 13-C-AJFE-PU-026, 13-C-AJFE-PU-032, 13-C-AJFE-PU-035, 13-C-AJFE-PU-044, and 13-C-AJFE-PU-047
- Period of Performance: September 1, 2022 to August 31, 2023
- Tasks:
 6. Purdue Fleet Analysis

Project Funding Level

The project is funded by the FAA at the following levels: Georgia Tech: \$200,000; Purdue University: continuing on a no-cost extension. Cost-sharing details are below:

Georgia Tech has agreed to a total of \$200,000 in matching funds. This total includes in-kind cost-sharing from Boom Supersonics; salaries for the project director, research engineers, and graduate research assistants; and funding for computing, financial, and administrative support, including meeting arrangements. The institute has also agreed to provide tuition remission for the students, paid by state funds.

The most recent FAA funding to Purdue University for this project provided a total of \$225,000. Purdue provides matching support through salary support for the faculty P.I.s, as well as salary support, and tuition and fee waivers for one graduate research assistant working on this project. OAG Aviation Worldwide Limited also provided in-kind cost-sharing to the Purdue team. The total of these matching funds is \$225,000.

Investigation Team

Georgia Institute of Technology

Dimitri Mavris (P.I.), All Tasks
Jimmy Tai (co-P.I.), Tasks 1, 2, 3, 4 and 5
Jai Ahuja (research faculty; vehicle modeling technical lead), Task 1
Christian Perron (research faculty; vehicle modeling technical lead), Task 1
Chung Lee (research faculty; vehicle modeling technical lead), Task 1
Brennan Stewart (research faculty; vehicle modeling technical lead), Task 1, 4, and 5
James D. Kenny (research faculty; vehicle modeling technical lead), Task 2
Holger Pfaender (research faculty, fleet modeling technical lead), Task 3
Edan Baltman (graduate student), Task 2 and 5
Joao De Azevedo (graduate student), Task 4 and 5
Barbara Sampaio (graduate student), Task 1
Jiajie (Terry) Wen (graduate student), Task 3
Ted Vlady (graduate student), Task 2
Nikhil Iyengar (graduate student), Task 1
Zayne Roohi (graduate student), Task 2
Srikanth Tindivanam Varadharajan (graduate student), Task 2
Carter J. Tegen (graduate student), Task 2
Divya K. Kalaria (graduate student), Task 1
Madeleine E. Graham Macy (Undergrad student), Task 1

Purdue University

William Crossley (P.I.), Task 6
Daniel DeLaurentis (co-P.I.), Task 6



Muharrem Mane (research faculty), Task 6
Tien-Yueh Fung (graduate student), Task 6
Krinal Doma (Undergrad student), Task 6

Project Overview

Georgia Tech and Purdue University teams have partnered to investigate the future demand for supersonic air travel and the environmental impacts of supersonic transports (SSTs). In the context of this research, the environmental impacts include direct carbon dioxide (CO₂) emissions, noise, and fuel consumption. The research is conducted as a collaborative effort to leverage the capabilities and knowledge of the multiple entities that make up the ASCENT university partners and advisory committee. The primary objective of this research project is to support the FAA in modeling and assessing the potential future evolution of the next-generation supersonic aircraft fleet. The research in this project consists of five integrated focus areas: (a) establishing fleet assumptions and performing demand assessment (completed in 2021); (b) performing preliminary SST environmental impact prediction (ongoing); (c) developing approaches to model SSTs within the FAA Aviation Environmental Design Tool (completed in 2022); (d) performing vehicle and fleet assessments of potential future supersonic aircraft (ongoing); and (e) performing physics-based modeling of SSTs and conceptual design by using the Framework for Advanced Supersonic Transport (FASST) (ongoing).

To better understand the potential demand for supersonic air travel, the team has developed a parametric airline operating-cost model to explore the sensitivities of key vehicle, operational, and cost parameters on the required yield that an airline would need to target for ticket prices on potential new supersonic aircraft. However, the current model assumes fixed parameters for key vehicle metrics, which can be changed but do not include sensitivities to key vehicle design choices, such as vehicle size, design cruise Mach number, and maximum range. The fleet analysis work examines the implications of the physical and technical dependencies on airline operational cost. Through the vehicle performance sensitivities, such as passenger capacity and design cruise Mach number, the combined “sweet spot,” i.e., the most profitable vehicle for an airline to operate, can be determined. To accomplish this goal, the existing vehicle models created in the prior year are used and supplemented with the additional vehicles proposed in this period of performance. These vehicles together serve as the foundation to create credible sensitivities regarding parameters such as vehicle size and design cruise Mach number. These sensitivities are then embedded in the airline operating-cost estimation model and used to explore the combined vehicle and airline operational space to identify the most economically feasible type of supersonic vehicle.

In an independent complementary approach, to consider the demand and routes for supersonic aircraft, the Purdue team has developed a ticket pricing model for possible future supersonic aircraft. The model relies on the “as-offered” fares before the novel coronavirus (COVID-19) pandemic, for business-class and first-class tickets on routes expected to have passenger demand for supersonic aircraft. Through considering the number of passengers potentially demanding fares at business class or above on a city-pair route, the distance of that city-pair route, an adjustment to increase the over-water distance of the route where the aircraft can fly supersonically to allow for the shortest trip time, and the range capability of a low-fidelity modeled medium SST (55 passenger [pax]) to fly that route with the shortest trip time, the Purdue team has identified a network among 257 airports that could potentially allow for supersonic aircraft service in a network of routes with at least one end (i.e., origin or destination) in the United States.

One major accomplishment of the project during the performance period is the provision of preliminary results for the design of a 65-pax SST designed for a mission of 4,250 nmi. Two versions of this vehicle have been designed, on the basis of the assumption of cruise occurring at Mach 1.4 or at Mach 1.7. An 8-pax business jet has also been designed, which would cruise at Mach 1.4 for a design range of 4,000 nmi. The preliminary results were arrived at through computational fluid dynamics (CFD)-based vehicle shape optimization, engine cycle modeling with Numerical Propulsion System Simulation (NPSS), and noise modeling with NASA’s Aircraft Noise Prediction Program (ANOPP), and mission analysis and detailed landing and takeoff (LTO) analysis incorporating a variable noise-reduction system (VNRS) by using the Flight Optimization System (FLOPS). These modeling approaches and programs were integrated into FASST, thus allowing the Georgia Tech team to generate interdependency results between fuel burn (or maximum takeoff weight) and certification cumulative noise levels (in effective perceived noise in decibels [EPNdB]). The other major accomplishment is the Georgia Tech team’s support of an environmental assessment study of Greensboro airport to enable a potential supersonic airframe manufacturer to perform flight tests. The environmental assessment study required the Georgia Tech team to model a generic transport SST representative of the potential supersonic airframer’s concept, except with marginal noise characteristics (small cumulative noise margin). The rationale was to account for noise at the current limiting, highest-

noise case (bounded within the existing subsonic stage 5 noise certification limits of compliance), so that developmental SST configurations operated at or below this upper maximum takeoff weight can be built, tested, and refined according to these noise goals.

The Georgia Tech team has also performed a study of variable takeoff climb-speed requirements ($V_2 + x$) on a Mach-1.7, 65-pax SST. Although subsonic aircraft takeoff climb speeds for certification are restricted to between $V_2 + 10$ and $V_2 + 20$, whether this constraint is appropriate for supersonic vehicles is unclear. This study's objective was to determine how block fuel and certification noise might be affected by a variety of $V_2 + x$ studies. One trade was conducted by fixing the block fuel and instead trading noise performance as the optimal vehicle trajectory was determined for a sweep of takeoff climb-speed values. A second trade was conducted by setting a target noise value and trading vehicle block fuel as the optimal trajectory was determined for a sweep of takeoff climb-speed values.

The Purdue team has pursued three subtasks as part of the fleet analysis task. During this year, the team has created and used the performance and cost coefficient of six additional SST concepts of combinations of passenger capacity and Mach number, implemented a sustainable aviation fuel (SAF) price evolution model, and estimated the effects of SAF utilization in subsonic-only and subsonic and supersonic scenarios. With modifications to FLEET to accommodate these changes, the team has estimated the impacts on future environmental emissions when different types of SST concepts are introduced into the fleet and when SAFs are used to reduce the impact of the SST.

Milestones

The Georgia Tech team had four milestones for this year of performance:

1. Completing aerodynamic design and drag polar generation for two configurations
2. Generating interdependency results showing trades between fuel burn and cumulative noise levels
3. Conducting a study on the effects of $V_2 + x$ on cumulative noise levels and fuel burn
4. Provision of FASST SST descriptions and characteristics in Microsoft PowerPoint format

The Purdue team had three milestones for this year of performance:

1. Generating aircraft cost coefficients for alternative SST aircraft concepts
2. Generating a SAF model for evolution of SAF prices
3. Analyzing future operations of all SST aircraft concepts and SAF utilization

To expand the analytical capability of FLEET and assess the potential environmental emission of alternative SST concepts, the additional aircraft SST models provided by the Georgia Tech team have been used to generate performance coefficients for all routes in the network. This process has led to creation of a database of seven SST concepts and their respective performance coefficients.

Because of the anticipated high emissions of SST aircraft, the team has considered and assessed the impacts of using SAFs. To do so, the team has created a model for the evolution of SAF prices, implemented in FLEET, thus enabling FLEET to capture the effects of changes in ticket prices and demand due to the introduction and use of SAFs.

Finally, the team has analyzed multiple scenarios in which airlines use various SST concepts and also use SAF. The results capture the changes in travel demand and the potential reduction in overall emissions when SAF is used.

Major Accomplishments

Major accomplishments of the project during the period of performance include the generation of preliminary results for the design of two 65-pax SSTs cruising at Mach 1.4 or Mach 1.7 for a 4,250-nmi design mission. These results have been obtained through CFD-based aerodynamic shape optimization of the aircraft geometry, NPSS engine modeling, noise modeling in ANOPP, and mission analysis coupled with detailed LTO analysis incorporating VNRS through FLOPS. In addition, the Georgia Tech team has used the 65-pax, Mach-1.7 design to conduct two $V_2 + x$ studies focusing on the interdependencies between certification takeoff climb speed and block fuel/takeoff noise, to examine whether the current subsonic requirements might be appropriate for supersonic vehicles.

One major accomplishment of the Purdue team during this year's effort has been the successful implementation of the SAF model in FLEET and the estimation of the impacts of SAF on future operations including supersonic service; these efforts

have increased the analytical capability of FLEET and enabled more comprehensive assessment of the environmental impacts of supersonic transportation.

Task 1 – SST Aerodynamic Modeling

Georgia Institute of Technology

Objectives

The two primary objectives were as follows:

- Aerodynamic shape optimization of the SST outer mold line for a given cruise Mach number (for a fixed planform area and wing capture area)
- Generation of parametric drag polars for the optimized vehicle that capture aerodynamic performance across the entire flight envelope, as a function of wing planform area and inlet capture area

Research Approach

Analysis workflow

A general analysis process was developed to determine the aerodynamic performance of multiple aircraft designs. This process was then automated with Python and implemented by using Georgia Tech's high-performance computing facilities. Because the analysis workflow was automated and easily parallelizable, many designs were able to be analyzed at once. The ability to complete hundreds of aerodynamic analyses in a matter of hours enabled rapid evaluation of designs and generation of drag polars.

Starting from a set of design variables, the first step was to generate a computer-aided design (CAD) representation of the aircraft geometry. This process used the Engineering Sketch Pad, a lightweight, open-source CAD tool developed by the Massachusetts Institute of Technology (Haimes & Dannenoffer, 2013), which allows users to easily script the generation of complex geometries and expose design parameters. Therefore, changing global parameters, such as the sweep angle or taper ratio, automatically and seamlessly scaled and repositioned the different sections of the wing. After a new geometry was defined, it was then saved to a generic CAD file (in EGADS format in the current workflow) and tessellated for later use in CFD analysis.

The outer mold line was tailored to maximize the lift/drag (L/D) ratio at the design cruise Mach number as a surrogate to minimize mission fuel burn. The optimization was divided into three stages: two initial phases focusing on the fuselage and vertical tail (VT) design, and one main stage focusing on the wing planform optimization. Both inviscid (Euler) and Reynolds-averaged Navier–Stokes (RANS) CFD analyses were used in a multi-fidelity optimization approach to decrease design time and cost. NASA's Cart3D (NASA Advanced Supercomputing Division, n.d.) was used as the inviscid solver, and Siemens' STAR-CCM+ (Siemens, n.d.) was used as the RANS solver. The following sections detail each airframe design phase.

Fuselage design

With the number of passengers set according to the requirements, the fuselage design, in terms of minimum cabin length and width requirements, is constrained by the cabin layout. Whereas slender fuselages are preferable for supersonic cruise performance, care must be taken to avoid an excessively long body, because takeoff rotation constraints necessitate longer and thus heavier landing gear. After the cabin layout is frozen (cabin layout assumed for the 65-pax aircraft shown in Figure 1), additional refinements are conducted on the fuselage nose and tail cone sections, in terms of length and cross-sectional radius, to optimize for cruise L/D . During this fuselage design process, the wing planform is frozen. A design of experiments (DoE) is developed, with the length of the nose, length of the tail, and cross-sectional radii for various stations of the fuselage as independent variables. CART3D with a single-pass viscous correction is used for the aerodynamic analysis. The results from this DoE are used to train a neural-network surrogate, which in turn is used to optimize the vehicle for cruise L/D . The resulting fuselage design is then frozen and used in the wing optimization stage.

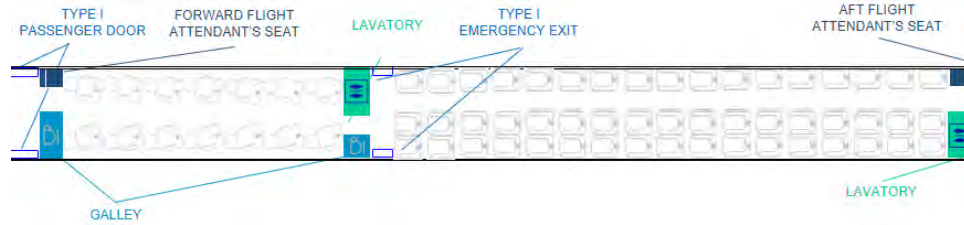


Figure 1. Cabin layout for a 65-pax aircraft.

VT design

The VT design is based primarily on two critical Federal Aviation Regulations (FAR): §25.147 for directional control under two-engine inoperative conditions and §25.237 for cross-wind requirements. Directional stability is analyzed with first-order principles and semi-empirical relations, rather than CFD. The design variables considered are wing planform area, aspect ratio, taper ratio, leading edge sweep, and thickness to chord. The goal is to find the smallest VT planform area satisfying the requirements for the furthest feasible VT location relative to the wing. A symmetric biconvex airfoil is used, with a thickness-to-chord ratio (t/c) fixed to a value that ensures an adequate cross-sectional thickness for the rudder actuators but is sufficiently small to avoid penalizing supersonic cruise performance. The rudder chord length to mean aerodynamic chord fraction is set to 0.35.

Wing planform design

Because the aerodynamic performance of the vehicle is strongly dependent on the wing planform, most of the optimization effort is focused on this component. As such, RANS CFD is used to analyze the performance of each design perturbation. The wing is defined by two sections, inboard and outboard, and five airfoil profiles. Global variables such as the taper ratio, aspect ratio, sweep, and dihedral apply to the entire wing, whereas the delta variables control the difference between the inboard and outboard sections. The wing break location variable determines the spanwise extent of the inboard section relative to the outboard, for a fixed total span. Biconvex airfoils are used to define the wing, with twist and camber being part of the design space. The maximum camber is limited to half the specified t/c ratio.

Given the dimensionality of the problem and the cost of each function call, this optimization exercise must be performed strategically. As such, a gradient-free active subspace approach is first used to reduce the dimensionality of the design space by using the less expensive inviscid CFD. Subsequently, adaptive sampling is performed in this reduced design space with RANS simulations to improve the L/D . A high-level overview of this process is shown in Figure 2. The goal of the active subspace method (Constantine et al., 2014) is to reduce the high-dimensional input space of some function to a lower-dimensional subspace, the so-called active subspace. For instance, given a function $f(x)$, where $x \in \mathbb{R}^d$ is a high-dimensional input vector, the following approximation is made:

$$f(x) \approx g(z) = g(\mathbf{W}^T x) \quad (1)$$

where $g(z)$ is an approximate predictor of $f(x)$, and $\mathbf{W} \in \mathbb{R}^{d \times k}$ is a projection matrix that maps the inputs x to a low-dimensional representation $z \in \mathbb{R}^k$, which are referred to as the active variables with $k < d$. That is, the active subspace method aggregates potentially many design variables into several modes that best capture the variability of the output. Consequently, the efficiency of optimization with respect to the active variables increases, because the size of the design space is exponentially reduced. Fitting a surrogate to predict the output of interest is also made easier, because the active subspace alleviates the infamous “curse of dimensionality.” The main difficulty of the active subspace method is in finding the matrix \mathbf{W} that best approximates the variability of $f(x)$. Although most dimensionality reduction methods are unsupervised, the active subspace is a supervised approach. Thus, the reduction of the input spaces is not based on the similarity between design vectors but instead is informed by the functional dependence between the input and the output spaces.

The classical active subspace approach for dimensionality reduction proposed by Constantine relies on the gradient information of the objective function, which can be challenging to obtain. Although gradient-free approaches have been proposed in the literature (Tripathy et al., 2016; Seshadri et al., 2019; Gautier et al., 2021), these methods require extensive sampling of the objective function, which can be costly in scenarios in which the objective is being evaluated by high-fidelity codes, such as RANS solvers. To counter this drawback, Mufti et al. (2022) have proposed a gradient-free

multi-fidelity approach in which a lower-fidelity and relatively less expensive code, in this case Cart3D, is used to extract an approximation of the RANS active subspace. The requirement for this approach is an initial DoE that samples the design space. Each case in this DoE is evaluated in Cart3D, and the L/D is recorded. The proposed multi-fidelity approach is then applied to obtain a reduced representation of the design variables, on the basis of the lower-fidelity results. Although the inviscid L/D results from Cart3D are not as accurate as those obtained with RANS, both tend to have similar behaviors. Therefore, an active subspace computed by using inviscid results can reasonably be assumed to be a good representation of the corresponding subspace that would be obtained with RANS results. Mufti et al. have demonstrated that this assumption holds for the design of transonic airfoils and wings. Although using lower-fidelity results to compute the active subspace has drawbacks and does reduce the accuracy of the method, it also significantly decreases the cost of computing the active subspace. For the purposes of this work, this trade-off between accuracy and computational cost is considered acceptable.

After the reduced representation of the design variables is determined, the RANS optimization process begins. The objective function is maximized through an adaptive sampling approach using the efficient global optimization (EGO) method (Jones et al., 1998). To start the process, a warm-start DoE is run to train a Kriging surrogate model. The Kriging model not only provides a prediction of the objective function at non-sampled points but also provides an estimate for the model’s prediction uncertainty between two sampled points. These two components are used in the EGO method to balance “exploration” versus “exploitation” of the design space. In the current context, “exploration” refers to sampling in regions where model uncertainty is high, and “exploitation” denotes sampling in regions close to the optimum. After the initial warm-start DoE and model training, a small number of candidate points are selected that maximize the “expected improvement” criterion of the objective function. These samples are then evaluated in RANS, the Kriging model is retrained, the expected improvement is recomputed, and the process repeats until a user-defined stopping condition is met. In this fashion, the aerodynamic performance of the vehicle is improved iteratively. The sample size of the warm-start DoE and the number of additional samples required depend on the dimension of the design space; consequently, the active subspace dimensionality reduction in the previous step is critical for minimizing the overall design time and cost.

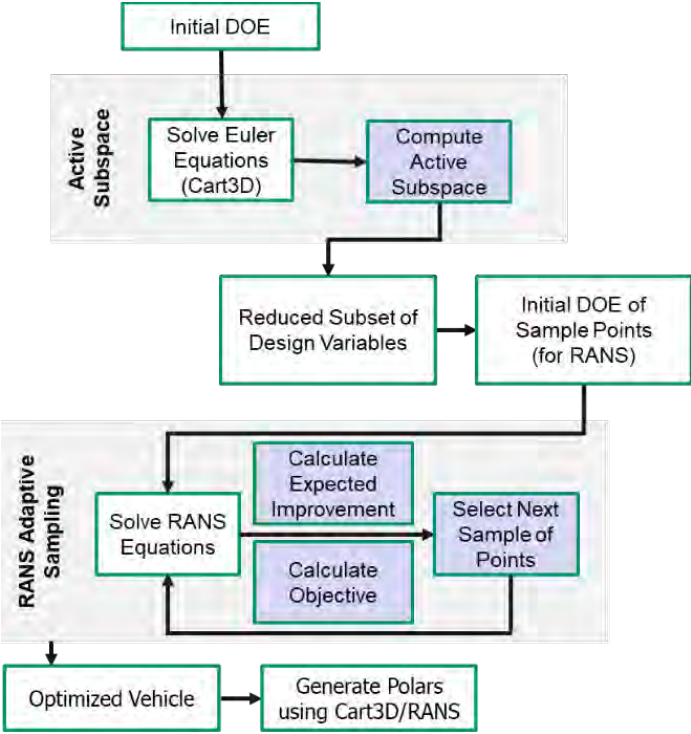


Figure 2. Aerodynamic optimization process (DOE, design of experiments; RANS, Reynolds-Averaged Navier–Stokes).

Of note, for some vehicles, the optimization process would converge on a wing design with an excessive sweep and aspect ratio. The resultant vehicle would then have a large wing weight during the system analysis, which would severely hinder mission performance, because the wing planform design is purely aerodynamic and lacks any structural consideration. To circumvent this issue, an upper limit on wing weight has been added to the adaptive sampling approach. Consequently, the EGO algorithm searches for new samples that maximize the expected improvement of the objective while having a high probability of meeting the wing weight constraint according to the process described previously (Forrester & Keane, 2009). For this purpose, the wing weight is estimated from a given planform by using the FLOPS weight equations (Wells et al., 2017). From these weight estimates, an additional Kriging model is trained, which is then used to predict the likelihood of a new design to satisfy the weight constraint. Figure 3 shows an example of a design optimized with or without the wing weight constraint.

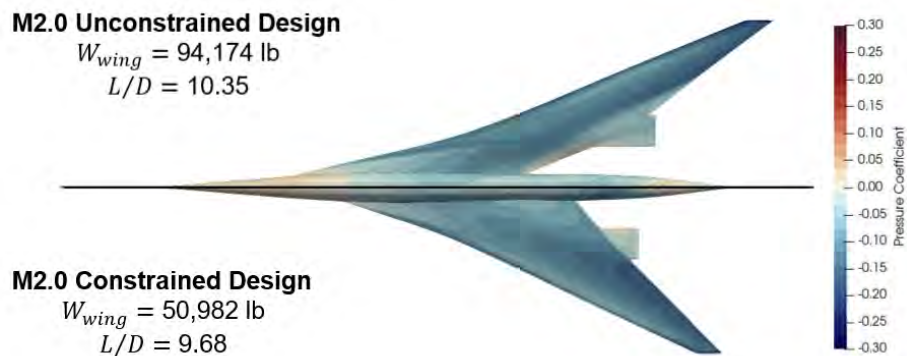


Figure 3. Comparison between an unconstrained and a wing-weight-constrained optimum (W_{wing} , wing weight; L/D , lift-to-drag ratio).

Drag polar generation for an optimized vehicle

After the vehicle with the highest cruise L/D is obtained, to enable mission analysis, drag polars for every point in the operating envelope are generated in the form of a table with Mach, altitude, lift coefficient (C_L), and drag coefficient (C_D) as the columns. Generating a drag polar that covers the entire envelope is quite costly to perform solely with RANS CFD. Therefore, a hybrid approach is used, as shown in Figure 4. First, the less expensive Cart3D is used to generate a set of "baseline polars" for all Mach-number and angle-of-attack combinations. Because Cart3D is an inviscid solver, altitude is not an input, because it affects only viscous forces. RANS CFD is then used to sample a subset of the low-fidelity flight conditions. In this case, 15 RANS samples are considered. The flight conditions for these RANS cases are chosen strategically to minimize the root-mean-square error of the surrogate model and the number of high-fidelity cases required to achieve such minimization. Because altitude is not a consideration for the low-fidelity CFD, values are assigned to each RANS sample to spread them out uniformly in the expected Reynolds-number range. These viscous results are then used to calibrate the inviscid polars to account for viscous effects. Hierarchical Kriging (Han & Görtz, 2012), a type of multi-fidelity surrogate model, is used. In this situation, the low-fidelity data are the numerous Cart3D results, and the high-fidelity samples are the few RANS CFD solutions.

Parametric drag polars capturing the effects of changing wing planform area and inlet capture area

Aerodynamic optimization is conducted for a fixed-wing planform area and inlet capture area. However, as part of vehicle sizing and mission analysis, both the engine size and wing planform area are allowed to scale. To account for the effects of these changes on the aerodynamic performance of the vehicle, having a set of drag polars that are a function of these design variables is desirable. This objective is efficiently achieved through a proper orthogonal decomposition (POD) reduced-order model (ROM).

A parametric ROM approximates the prediction of a function by mapping an m -dimensional input vector to a d -dimensional output vector. In contrast to a conventional surrogate model, the quantity being predicted is a high-dimensional vector. The development of parametric drag polars at a high level is illustrated in Figure 5 and largely follows previously described work (Lee et al., 2011) using a similar approach for a parametric engine deck. The main steps are as follows. First, a DoE is created to sample the design space spanned by the wing planform area and inlet capture area. Ten samples are defined

with unique combinations of the two design variables. The nacelle length is correlated with the inlet capture area and is thus a fallout. A multi-fidelity mission drag polar is generated for each of sample in the DoE through the process outlined in the preceding section. These drag polars are then used as observations to train the ROM. After the modes and coefficients for the POD model are obtained, a radial basis function is used as the interpolating mechanism for the POD coefficients, such that drag polars can be predicted at previously unseen values of the design variables.

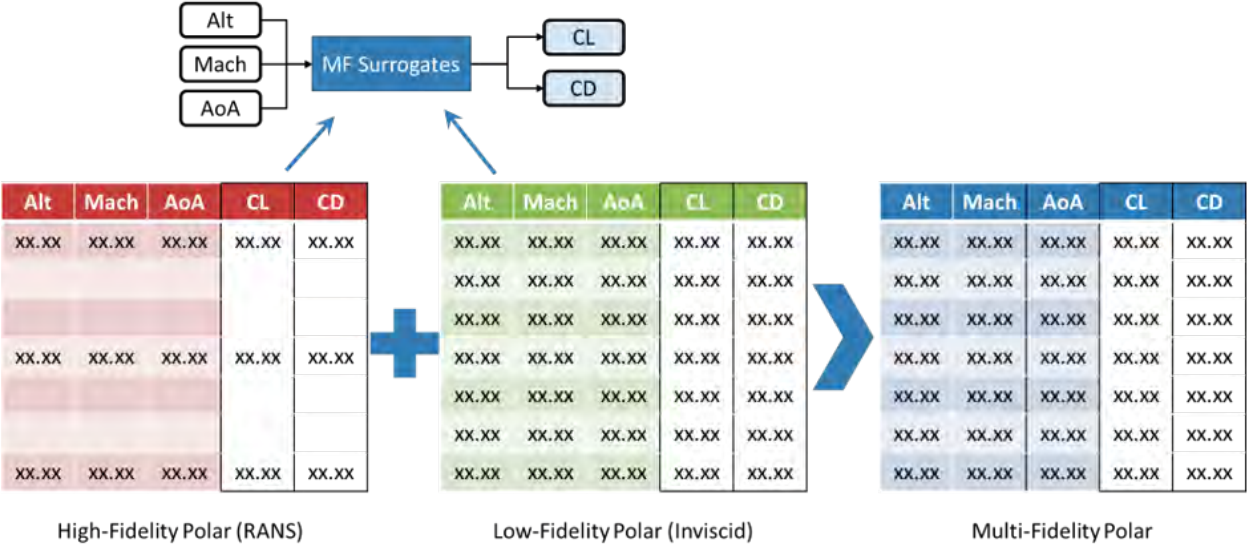


Figure 4. Schematic of the multi-fidelity drag polar generation process (Alt, altitude; AoA, angle of attack; MF, multi-fidelity; C_L , lift coefficient; C_D , drag coefficient).

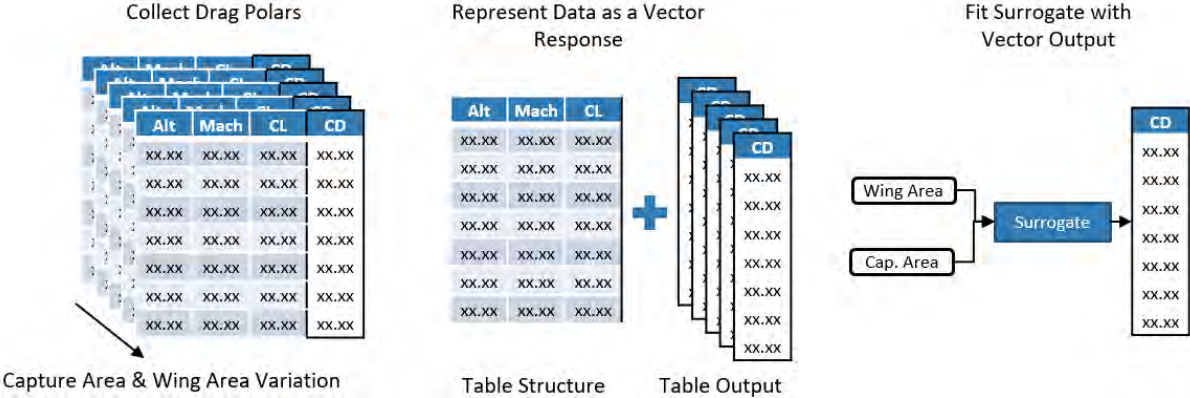


Figure 5. Schematic of the construction of the parametric drag polars (Alt, altitude; C_L , lift coefficient; C_D , drag coefficient).

Results

The aerodynamic process discussed above was applied to all supersonic transport designed within the past 2 years of this project. The intent for 2023 was to generate parametric drag polars for the 65-pax SST for Mach 1.4, 1.7, and 2.0, to investigate the effects of design Mach number on the fuel burn versus cumulative noise Pareto front. If time permits, the design Mach study was planned to be conducted for the 8-pax class SST for Mach 1.4, 1.6, and 1.8. The 65-pax, Mach-1.7 aerodynamic design was completed in 2022, and the Mach-2.0 design was completed in 2022. Results for the 65-pax, Mach-1.4 design are presented herein. In addition, this report describes the beginning of the 8-pax, Mach-1.4 aerodynamic design. Unfortunately, the design Mach study could not be completed in 2023, because of redirection to conduct a $V_2 + x$ study for the current Committee on Aviation Environmental Projection cycle.



65-pax, Mach-1.4 SST design

The fuselage and VT used for this aircraft remained fixed during the design process. The present aircraft shared the same fuselage and VT used by the 65-pax vehicles described in the 2022 report. The vehicle wing design was performed to obtain the optimum geometry for this cruise Mach number. The wing design is described below.

In this study, the planform area of the wing is fixed at 5,125 ft². In total, 18 geometric variables are considered (Table 1), and angle of attack is a 19th variable in CFD simulations. One hundred warm-start cases are initially executed to sample the design space, and are followed by an additional 90 adaptive samples. The adaptive sampling is stopped when the expected improvement in *L/D* is on the order of 0.01. Figure 6 shows the distribution of *L/D* over the warm-start and adaptive samples. Some adaptive samples with lower *L/D* (between 5 and 9) correspond to early points in the adaptive sampling, i.e., during the “exploration phase” of the optimization.

Table 1. Wing design variables and bounds.

Parameter	Lower bound	Upper bound	Parameter	Lower bound	Upper bound
Overall taper	0.1	0.3	Delta c/4 sweep break (degrees)	-20	0
Overall Aspect Ratio (AR)	2.25	4	Section 1 (twist, maximum camber)	[0, 0%]	[1.5, 0.5(<i>t/c</i>)]
Overall c/4 sweep (degrees)	40	62	Section 2 (twist, maximum camber)	[-5, 0%]	[5, 0.5(<i>t/c</i>)]
Overall dihedral (degrees)	-5	5	Section 3 (twist, maximum camber)	[-5, 0%]	[5, 0.5(<i>t/c</i>)]
Delta taper break	0	0.3	Section 4 (twist, maximum camber)	[-5, 0%]	[5, 0.5(<i>t/c</i>)]
Delta dihedral break (degrees)	-5	5	Section 5 (twist, maximum camber)	[-5, 0%]	[5, 0.5(<i>t/c</i>)]
Wing break location	0.15	0.6			

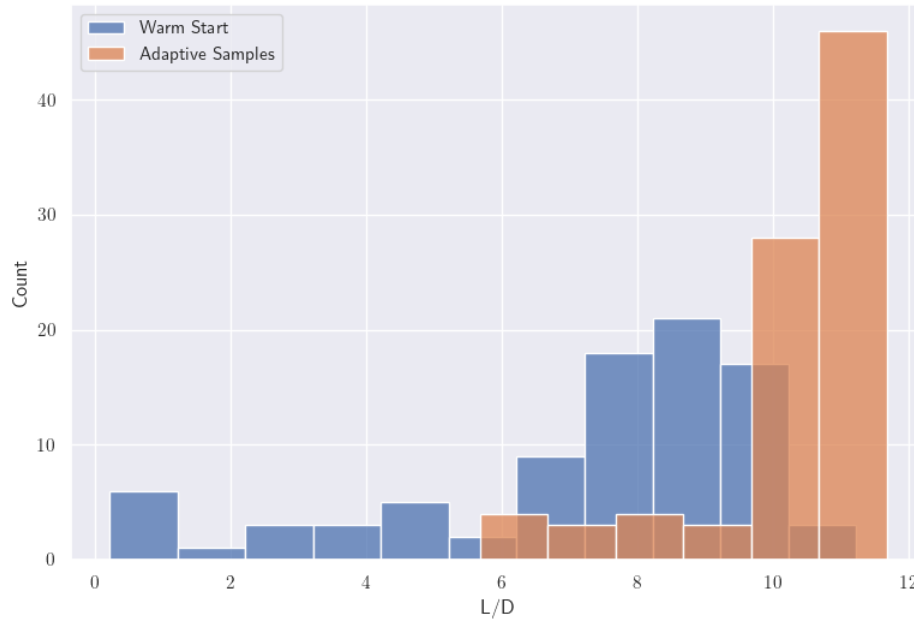


Figure 6. Distribution of lift to drag (L/D) over warm-start and adaptive sampling.

Figure 7 shows the optimized wing planform with the design variable values defined in Table 2. The major differences in the optimized vehicle relative to the baseline are a larger sweep, an inboard shift in the wing break location, and a change in the twist distribution and camber of the wing. The highest L/D for this vehicle at cruise is 11.23 for a C_L of 0.183.

Table 2. Comparison of baseline and optimized wing design variables.

Parameter	Baseline	Optimized	Parameter	Baseline	Optimized
Overall taper	0.1	0.117	Delta dihedral break (degrees)	0	0.087
Overall Aspect Ratio (AR)	2.5	2.837	Section 1 (twist, maximum camber)	[0, 0%]	[0.77, 0.88%]
Overall c/4 sweep (degrees)	52.5	60.49	Section 2 (twist, maximum camber)	[0, 0%]	[0.56, 0.27%]
Overall dihedral (degrees)	0	-2.31	Section 3 (twist, maximum camber)	[0, 0%]	[1.93, 0.55%]
Delta taper break	0.2	0.086	Section 4 (twist, maximum camber)	[0, 0%]	[-1.40, 0.8%]
Delta c/4 sweep break (degrees)	-10	-14.36	Section 5 (twist, maximum camber)	[0, 0%]	[-1.55, 0.49%]
Wing break location	0.45	0.178			

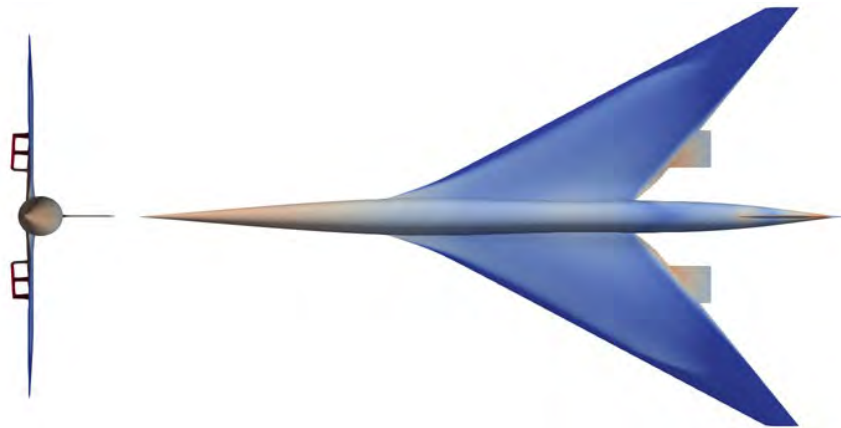


Figure 7. Optimized wing planform of a 65-pax, Mach-1.4 SST.

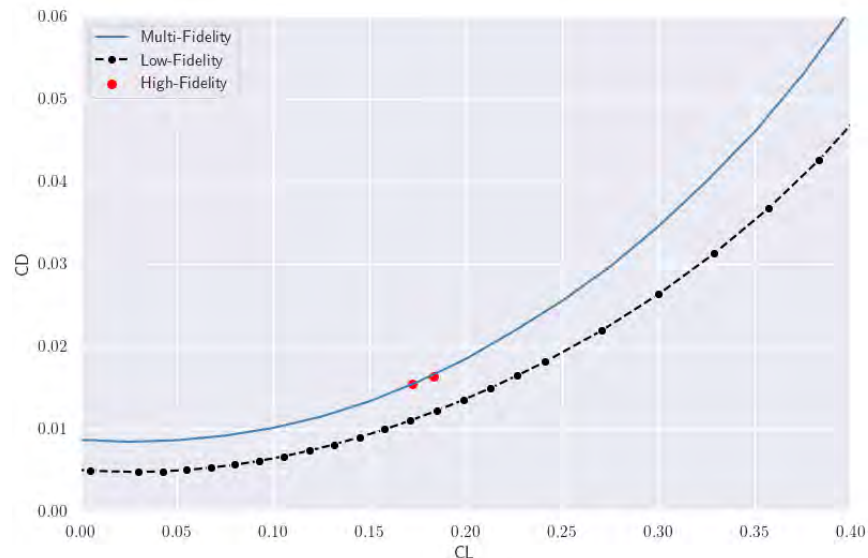


Figure 8. Multi-fidelity drag polar at cruise conditions (C_L , lift coefficient; C_D , drag coefficient).

Figure 8 shows the multi-fidelity drag polar at cruise conditions for the optimized vehicle. The red points represent the RANS samples at this flight condition. The black points are the inviscid data from Cart3D, and the black low-fidelity curve represents the drag polar obtained from the low-fidelity data only. The blue multi-fidelity curve thus depicts the final drag polar for this vehicle, generated by the multi-fidelity surrogate by using both inviscid and RANS data. The effect of the multi-fidelity surrogate can be summarized by an upward shift of the inviscid drag polar, which can be attributed to the effect of friction drag.

Eight-pax, Mach-1.4 SST design

The fuselage and VT used for this aircraft remained fixed during the design process. The present aircraft shared the same fuselage as the NASA STCA. The vehicle wing design was performed to obtain the optimum geometry for this cruise Mach number. The wing design is described below.

The design of the 8-pax vehicle closely follows the approach described previously for the 65-pax vehicle. For this study, the planform area of the wing is fixed at 1,638 ft². In total, 18 geometric variables (Table 3) are considered, and angle of

attack is the 19th design variable. The same variables listed in Table 3, are used, with initial generation of 100 warm-start cases. One hundred additional cases are adaptively generated until the expected improvement is below a given threshold.

Figure 9 shows the distribution of L/D over the warm-start and adaptive samples. Some adaptive samples with lower L/D (between 5 and 9) correspond to early points in the adaptive sampling, i.e., during the “exploration phase” of the optimization.

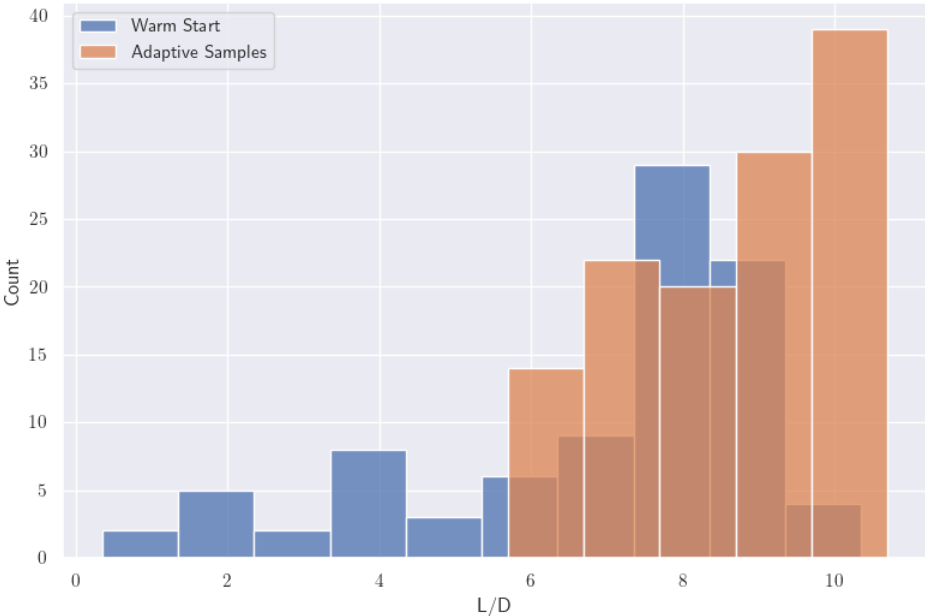


Figure 9. Distribution of lift to drag (L/D) over warm-start and adaptive sampling.

The table below lists the optimized design parameters of the 8-pax, Mach-1.4 SST aircraft, and Figure 10 shows the optimized vehicle geometry.

Table 3. Comparison of baseline and optimized wing design variables (8-pax, Mach-1.4 SST).

Parameter	Baseline	Optimized	Parameter	Baseline	Optimized
Overall taper	0.1	0.114	Delta dihedral break (degrees)	0	1.038
Overall Aspect Ratio (AR)	2.5	2.816	Section 1 (twist, maximum camber)	[0, 0%]	[0.09, 0.99%]
Overall c/4 sweep (degrees)	52.5	55.74	Section 2 (twist, maximum camber)	[0, 0%]	[-1.08, 0.36%]
Overall dihedral (degrees)	0	-0.56	Section 3 (twist, maximum camber)	[0, 0%]	[-0.03, 0.27%]
Delta taper break	0.2	0.28	Section 4 (twist, maximum camber)	[0, 0%]	[-2.44, 0.88%]
Delta c/4 sweep break (degrees)	-10	-5.36	Section 5 (twist, maximum camber)	[0, 0%]	[-1.21, 0.37%]
Wing break location	0.45	0.20			

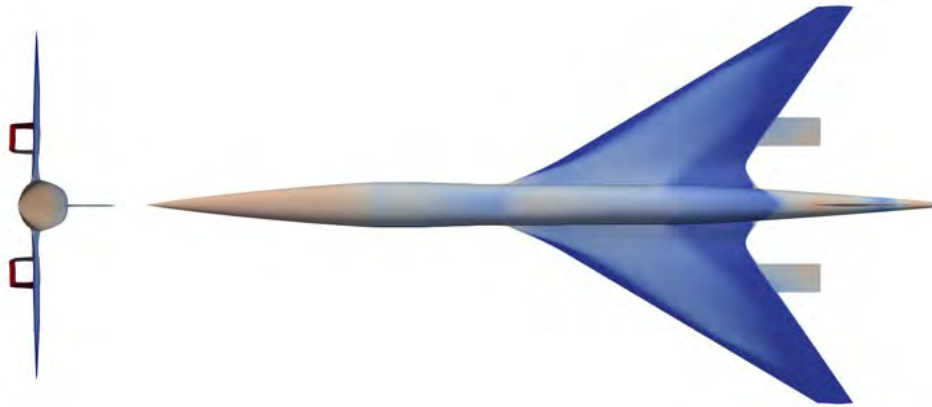


Figure 10. Optimized wing planform for an 8 pax, Mach-1.4 SST.

References

- Constantine, P. G., Dow, E., & Wang, Q. (2014). Active subspace methods in theory and practice: applications to kriging surfaces. *SIAM Journal on Scientific Computing*, 36(4), A1500-A1524.
- Forrester, A. I. J., & Keane, A. J. (2009). Recent advances in surrogate-based optimization. *Progress in Aerospace Sciences*, 45(1-3), 50-79. <https://doi.org/10.1016/j.paerosci.2008.11.001>
- Haimes, R., & Dannenhoffer, J. (2013). The engineering sketch pad: A solid-modeling, feature-based, web-enabled system for building parametric geometry. In *21st AIAA Computational Fluid Dynamics Conference* (p. 3073).
- Gautier, R., Pandita, P., Ghosh, S., & Mavris, D. (2021). A fully Bayesian gradient-free supervised dimension reduction method using Gaussian processes. *International Journal for Uncertainty Quantification*, 12(2), 1-32.
- Han, Z.-H., & Görtz, S. (2012). Hierarchical Kriging model for variable-fidelity surrogate modeling. *AIAA Journal*, 50, 1885-1896. <https://doi.org/10.2514/1.J051354>
- Jones, D. R., Schonlau, M., & Welch, W. J. (1998). Efficient global optimization of expensive black-box functions. *Journal of Global Optimization*, 13(4), 455-492. <https://doi.org/10.1023/A:1008306431147>
- Lee, K., Nam, T., Perullo, C., & Mavris, D. N. (2011). Reduced-order modeling of a high-fidelity propulsion system simulation. *AIAA Journal*, 49(8). <https://doi.org/10.2514/1.J050887>
- Mulfti, B., Chen, M., Perron, C., & Mavris, D. N. (2022). A multi-fidelity approximation of the active subspace method for surrogate models with high-dimensional inputs [Conference presentation]. AIAA Aviation Forum, Chicago, IL. <https://doi.org/10.2514/6.2022-3488>
- NASA Advanced Supercomputing Division (n.d.) *Cart3D Documentation* <https://www.nas.nasa.gov/publications/software/docs/cart3d/>
- Seshadri, P., Yuchi, S., & Parks, G. T. (2019). Dimension reduction via gaussian ridge functions. *SIAM/ASA Journal on Uncertainty Quantification*, 7(4), 1301-1322.
- Siemens (n.d.) *Simcenter STAR-CCM+*. <https://www.plm.automation.siemens.com/global/en/products/simcenter/STAR-CCM.html>
- Tripathy, R., Bilonis, I., & Gonzalez, M. (2016). Gaussian processes with built-in dimensionality reduction: Applications to high-dimensional uncertainty propagation. *Journal of Computational Physics*, 321, 191-223.
- Wells, D. P., Horvath, B. L., & McCullers, L. A. (2017). *The flight optimization system weights estimation method*. NASA/TM-2017-219627

Task 2 – SST Propulsion System Modeling

Georgia Institute of Technology

Objectives

The propulsion system plays an important role in performance metrics, such as fuel burn, gross weight, and takeoff field length, as well as in environmental metrics, such as noise and emissions. As such, the objective of the propulsion system modeling was to develop the capability to analyze and predict the necessary data to model those metrics of interest. The

developed model needed to provide thrust and fuel flow as a function of Mach number, altitude, and throttle setting. Engine dimensions needed to be predicted and provided to aerodynamic analysis to assess aircraft drag. The engine weight needed to be predicted as part of the overall aircraft empty weight. Additionally, the propulsion analysis needed to provide the necessary information to model the noise produced by the engine.

Research Approach

Many details for the propulsion model have been described in prior reports (Mavris et al., 2019). In brief, the propulsion system models a mixed-flow turbofan engine cycle. The engine cycle performance is modeled with NPSS, and the dimensions, flow path, and weight are modeled with Weight Analysis of Turbine Engines (WATE++) (Tong & Naylor, 2008). This report focuses on changes applied to the propulsion model over the past year. Further details on the propulsion model can be found in the report from previous years and an American Institute of Aeronautics and Astronautics article (Baltman et al., 2022).

Results

The following provides a summary of updates made to the propulsion system modeling during the current reporting period. Details on past propulsion developments can be found in reports from previous years. The turbine model was updated from an older nickel alloy to CMSX-4 along with a Larson–Miller parameter creep-life model (Scholz et al., 2009). The creep-life model was used to set a reasonable metal temperature, which in turn was used by the cooling flow prediction. The cooling flow prediction was updated from an advanced impingement and film cooling technology to a more conservative model for full coverage film cooling based on Gauntner (1980). Table 4 and Table 5 show the propulsion-specific performance characteristics, geometry, and weight for the vehicle discussed in Task 5. Further details on the vehicle design and selection can be found in Task 5. The results presented below are engine specific.

Table 4. Engine performance for the current selected design.

Engine metric	Aerodynamic design point Mach 1.2/39 kft/ISA	Top-of-climb Mach 1.7/55 kft/ISA	Takeoff Mach 0.3/SL/ISA + 18F	Sea-level static uninstalled Mach 0.0/SL/ISA
Fan pressure ratio	1.99	1.92	1.99	1.99
Bypass ratio	3.16	3.25	3.16	3.16
Overall pressure ratio	22.73	21.39	22.65	22.70
Compressor exit temperature (T3; R)	1,316	1,563	1,417	1,350
Burner exit temperature (T4; R)	2,994	3,534	3,170	3,012
Turbine inlet temperature (T41; R)	2,876	3,400	3,048	2,897
Corrected airflow at the fan face (lbm/s)	950.9	923.6	962.0	962.5
Percentage of design corrected fan speed	100.0	98.4	100.0	100.0
Thrust (lbf)	9,446	7,746	30,000	38,742
Thrust-specific fuel consumption ($\frac{lbm}{lbf \cdot h}$)	0.877	1.029	0.644	0.469
Nozzle pressure ratio	4.20	7.83	1.83	1.79
Jet velocity (ft/s)	1,909	2,425	1,359	1,301

Table 5. Engine geometry and weight for the current selected design.

Engine geometry variable	Value
Fan diameter (in)	69.3
Inlet capture area (in ²)	3,742
Engine pod length (in)	414.6
Engine pod weight (lb)	12,535

References

- Baltman, E., Tai, J. C., Ahuja, J., Stewart, B., Perron, C., De Azevedo, J., ... & Mavis, D. N. (2022). A methodology for determining the interdependence of fuel burn and LTO noise of a commercial supersonic transport. In *AIAA AVIATION 2022 Forum* (p. 4110).
- Gauntner, J. W. (1980). *Algorithm for Calculating Turbine Cooling Flow and Resulting Decrease in Turbine Efficiency*. <https://ntrs.nasa.gov/search.jsp?R=19800011581>
- Mavis, D., Crossley, W., Tai, J., & Delaurentis, D. (2019). *Project 010 aircraft technology modeling and assessment*. <https://s3.wp.wsu.edu/uploads/sites/2479/2020/05/ASCENT-Project-010-2019-Annual-Report.pdf>
- Scholz, A., Wang, Y., Linn, S., Berger, C., & Znajda, R. (2009). Modeling of mechanical properties of alloy CMSX-4. *Materials Science and Engineering: A*, 510–511(C), 278–283. <https://doi.org/10.1016/j.msea.2008.04.103>
- Tong, M. T., & Naylor, B. A. (2008). An object-oriented computer code for aircraft engine weight estimation. *Proceedings of the ASME Turbo Expo*, 1(December), 1–7. <https://doi.org/10.1115/GT2008-50062>

Task 3 – Mission Analysis

Georgia Institute of Technology

Objectives

The objective of mission analysis was to synthesize the results from the aerodynamics, propulsion, and weight analyses to enable the simulation of the aircraft dynamics and performance (e.g., fuel burn) over a specific mission. Because the vehicles under consideration are not based on existing vehicles, an additional objective was to size the gross weight, wing, and engine sizes for the specified design range. The top-level requirement for sizing the current SST was to cruise at Mach 1.7, carrying 65 pax for 4,250 nmi.

Research Approach

As in previous work, Georgia Tech researchers leveraged the FASST modeling and simulation environment to model the supersonic vehicles for this task. This framework was based on the Environmental Design Space (EDS). EDS and FASST have the same goal of providing a modeling and simulation environment that enables trade-offs and interdependencies among aircraft system-level metrics. The difference between them is that EDS was designed for subsonic aircraft; therefore, modifications were implemented to enable the modeling and simulation of supersonic aircraft. In the case of FASST, the system-level metrics of greatest interest are the vehicle weight, design mission fuel burn, and LTO certification noise. The flow diagram for the FASST environment (Figure 11) shows the inputs, outputs, and interconnections among each discipline’s analysis module in the modeling and simulation environment.

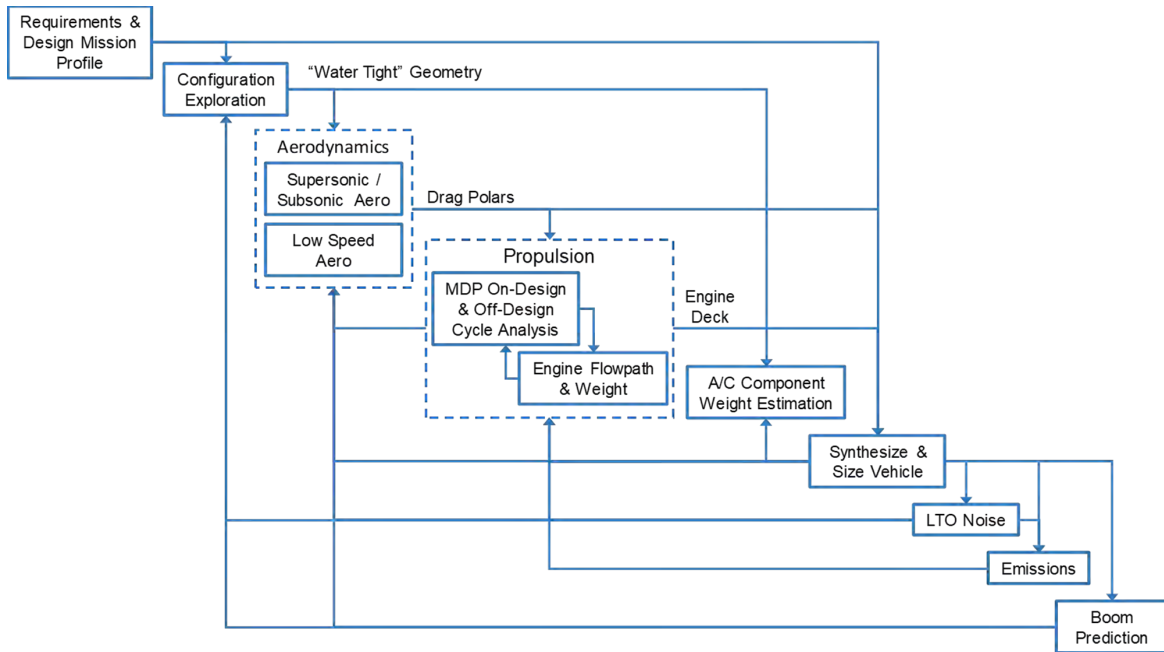


Figure 11. Framework for Advanced Supersonic Transport (FASST) flow diagram.

The requirements and design mission, as specified by the research team, are outlined in the following sections. The high-level requirements in the case of the Mach-1.7, 65-pax SST are the number of passengers (65), the design Mach number (1.7), and the design mission range (4,250 nmi). The configuration exploration and aerodynamics drag polar generation are performed in a local setting outside FASST and are described in Task 1. The resulting drag polars are fed into the mission analysis and vehicle sizing module. The engine cycle modeling is performed in NPSS, and flow path and weight estimation is conducted with WATE++. The engine architecture is a mixed-flow turbofan. The propulsion system modeling, discussed in Task 2, provides an engine deck, engine weight, and engine dimensions to the mission analysis and vehicle sizing module. For the vehicle empty weight, mission analysis and sizing, the NASA code FLOPS is used (McCullers, 1984) **Error! Bookmark not defined.** FLOPS uses the inputs of engine deck, drag polar, and other vehicle configuration parameters to estimate the overall empty weight of the aircraft. FLOPS then iterates on the vehicle gross weight to complete the mission prescribed by the designer. FLOPS also scales the engine thrust and wing area to produce the designer specified wing loading and thrust loading. If the engine is scaled in FLOPS, it is subsequently rescaled in the engine analysis to obtain an updated engine performance and weight. This iteration continues until the engine no longer requires scaling. After sizing, the vehicle is analyzed through a series of off-design missions.

A paper by NASA provides further descriptions of the mission segments within FLOPS: climb, cruise, refueling, payload releases, accelerations, turns, hold, and descent (McCullers, 1984). Many of these mission segments were developed for modeling military aircraft. The mission segments used for this study are climb, cruise, loiter, and descent; the performance of each segment is determined with a step integration method to compute fuel burn, elapsed time, distance covered, and changes in speed and altitude. The mission consists of a 9-min taxi-out time at ground power setting, a 1-min takeoff at takeoff power, a minimum fuel climb and acceleration to supersonic cruise, a supersonic cruise-climb, a descent at maximum L/D ratio, and a taxi-in time of 5 min at ground power. A reserve mission is also flown, which consists of a missed approach, a 200-nmi reserve mission to an alternative airport, and a 30-min hold at Mach 0.38 and 6,000 ft. The reserve mission to an alternative airport consists of a minimum fuel climb to an optimal subsonic cruise altitude below 30,000 ft and Mach 0.95, a cruise at optimum Mach and altitude, and a descent at maximum L/D . The reserve fuel has an additional safety margin of 5% of total trip fuel. The mission is constrained by a maximum altitude of 60,000 ft, a maximum Mach number of 1.7, and a maximum dynamic pressure limit of 600 psf. Additionally, the aircraft is not allowed to fly faster than 250 KCAS when below 10,000 ft. Although not part of the synthesis and sizing process, the detailed LTO module of FLOPS is used to provide detailed information on the LTO trajectories for both 14 CFR Part 25 performance and 14 CFR Part 36 LTO noise analysis. The LTO noise prediction is discussed in the next task (Task 4, LTO Noise Modeling).



Results

The block mission results for the Mach-1.7 SST carrying 65 pax for 4,250 nmi (excluding the reserve mission) are listed below and depicted in Figure 12. The aircraft begins by accelerating and climbing to 250 KCAS and 10,000 ft, in accordance with Federal Regulation 14 (CFR Part 91.117(a)). The aircraft then accelerates at nearly constant altitude until it encounters the dynamic pressure limit. The aircraft then primarily climbs and accelerates at constant dynamic pressure, deviating from the dynamic pressure limit for only short periods of time. After reaching Mach 1.7, the aircraft continues the climb at constant Mach number until reaching the cruise altitude, where the aircraft has 300 fpm of excess power. The aircraft performs a cruise-climb from 49,907 ft to 56,929 ft. The aircraft then descends at maximum *L/D*. In doing so, the aircraft initially decelerates at constant altitude until approximately Mach 1.3, then both descends and decelerates beyond that point. The reserve-mission cruise is conducted at Mach 0.88 and at 30,000 ft. A weight breakdown of the vehicle is provided in Table 6.

Table 6. Vehicle weight breakdown.

Weight Item	Weight (lb)	Weight Item (continued)	Weight (lb)
Wing	83,800	Crew and baggage (two flight, two cabin)	760
Vertical tail	2,306	Unusable fuel	1,251
Fuselage	31,115	Engine oil	318
Landing gear	19,392	Passenger service	2,245
Structure total	136,613	Cargo containers	604
Engines	50,123	Operating weight	236,712
Thrust reversers	4,963	Passengers and baggage (65)	13,650
Miscellaneous systems	215	Zero fuel weight	250,362
Fuel system	3,071	Taxi-out fuel	1,357
Propulsion total	58,372	Takeoff fuel	1,098
Surface controls	6,872	Climb fuel	26,685
Auxiliary power	888	Cruise fuel	126,197
Instruments	1,091	Descent and landing fuel	4,039
Hydraulics	3,201	Missed-approach fuel	2,196
Electrical	3,804	Reserve-mission fuel	16,987
Avionics	1,852	Hold fuel	10,194
Furnishings and equipment	15,023	Mission fuel	188,753
Air conditioning	3,512	Ramp weight	439,115
Anti-icing	306		
Systems and equipment total	36,548		
Weight, empty	231,534		

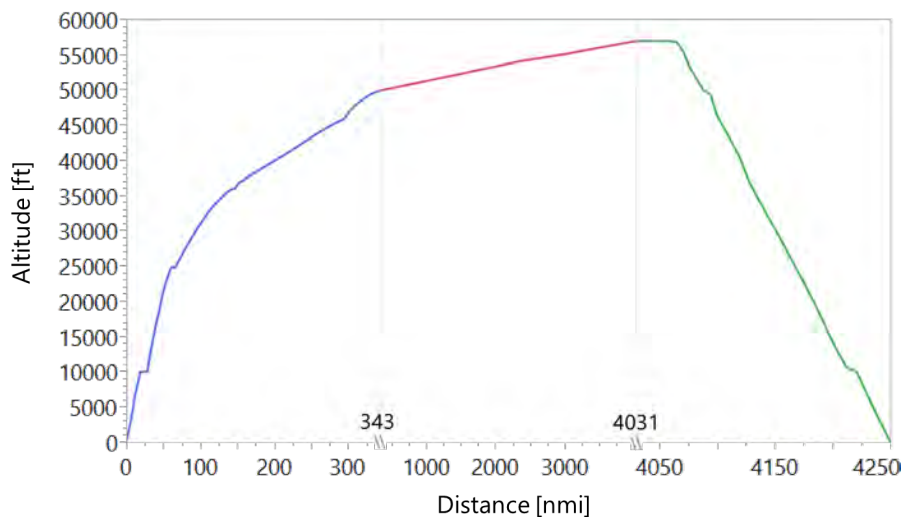


Figure 12. Mission profile for medium supersonic transport



References

General Operating and Flight Rules, 14 C.F.R. Part 91

McCullers, L. A. (1984). Aircraft configuration optimization including optimized flight profiles. *NASA. Langley Research Center Recent Experiences in Multidisciplinary Analysis and Optimization, Part 1.*

McCullers, A. (1984). *Recent experiences in multidisciplinary analysis and optimization, Part 1*, NASA-CP-2327-PT-1, 395-412.

Task 4 – LTO Trajectory and Noise Modeling

Georgia Institute of Technology

Objective

The objective of this task was to simulate an aircraft’s LTO trajectory by using a VNRS to study the effects of different takeoff procedures on LTO noise.

Research Approach

LTO trajectory analysis is performed in FASST after the mission analysis sized the vehicle for the design mission. The LTO trajectory analysis uses the detailed LTO module from the NASA code FLOPS. The aircraft is flown with a VNRS procedure consisting of a series of pilot-initiated and automatic (i.e., no pilot control) changes to engine and airframe configurations during a takeoff run to help reduce noise.

For the detailed takeoff analysis, FLOPS numerically integrates the equations of motion, reproduced as Equations (2)–(6), on the basis of the assumption that the aircraft is a point mass with a free-body diagram similar to that in Figure 13.

$$\frac{ds}{dt} = V_{\infty} \cos \gamma \quad (2)$$

$$\frac{dh}{dt} = V_{\infty} \sin \gamma \quad (3)$$

$$m \frac{dV_{\infty}}{dt} = T(V_{\infty}, h, \theta) \cos \alpha - D(V_{\infty}, h, \alpha) - W \sin \gamma \quad (4)$$

$$m \frac{dV_{\infty}^2}{dr_v} = mV_{\infty} \frac{d\gamma}{dt} = L(V_{\infty}, h, \alpha) + T(V_{\infty}, h, \theta) \sin \alpha - D(V_{\infty}, h, \alpha) - W \cos \gamma \quad (5)$$

$$\frac{dW}{dt} = -\frac{dW_f}{dt} = -T(V_{\infty}, h, \theta) TSFC(V_{\infty}, h, \theta) \quad (6)$$

The VNRS takeoff procedure is parameterized by several characteristics. The first characteristic is the initial power reserve (identified by the FLOPS variable VARTH). The next element is the programmed high-lift device (PHLD) schedule. The PHLD consists of a flap deflection schedule optimized for the aerodynamic efficiency for the required lift at each point in the takeoff trajectory, which is controlled by the flight management system. The programmed thrust lapse rate (identified by the FLOPS variable programmed lapse rate [PLR]) is an additional thrust reduction that is automatically controlled by Full Authority Digital Engine Control (FADEC). In the framework of VNRS, both the PHLD and the PLR are implemented immediately after the aircraft clears the obstacle during takeoff. The final few parameters pertain primarily to the trajectory taken after clearing the obstacle; these parameters are the flight-path angle post obstacle (γ_2), the constant speed transition altitude (h_3), and the cutback altitude (h_4). The main idea is to allow the aircraft to accelerate post obstacle before transitioning to a faster climb before the pilot-initiated cutback. A schematic of this procedure is depicted in Figure 14.

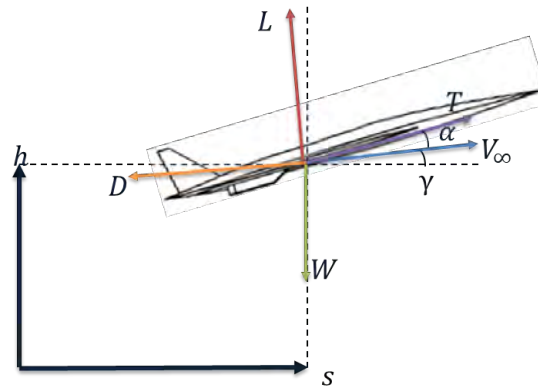


Figure 13. Free-body diagram.

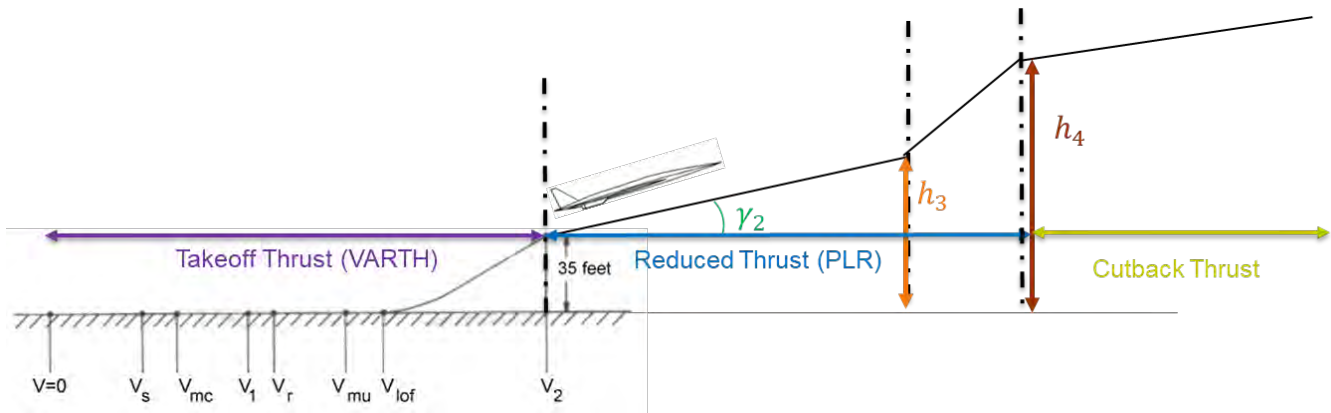
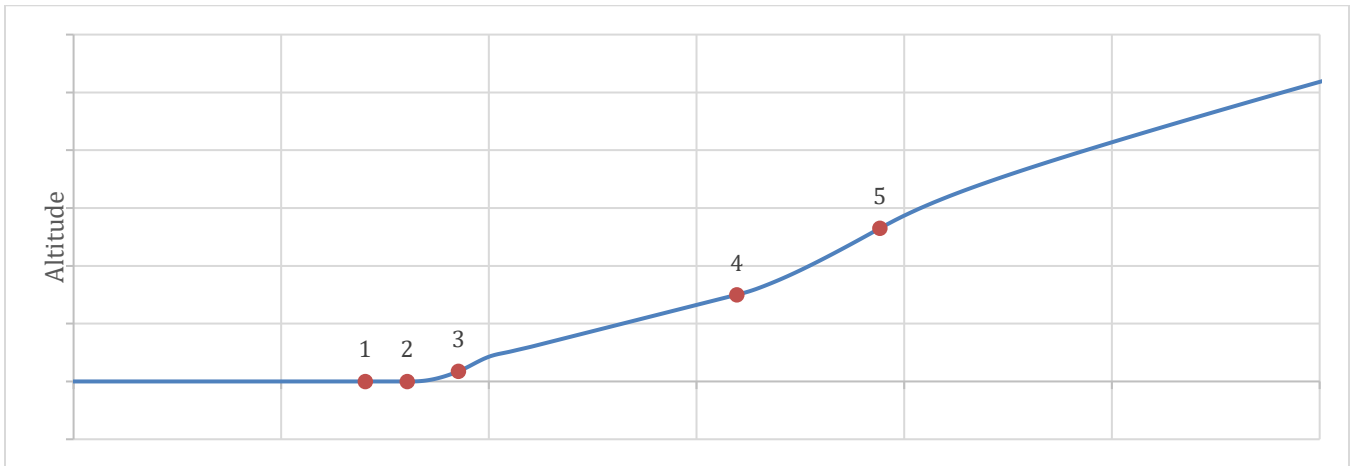


Figure 14. VNRS takeoff procedure.

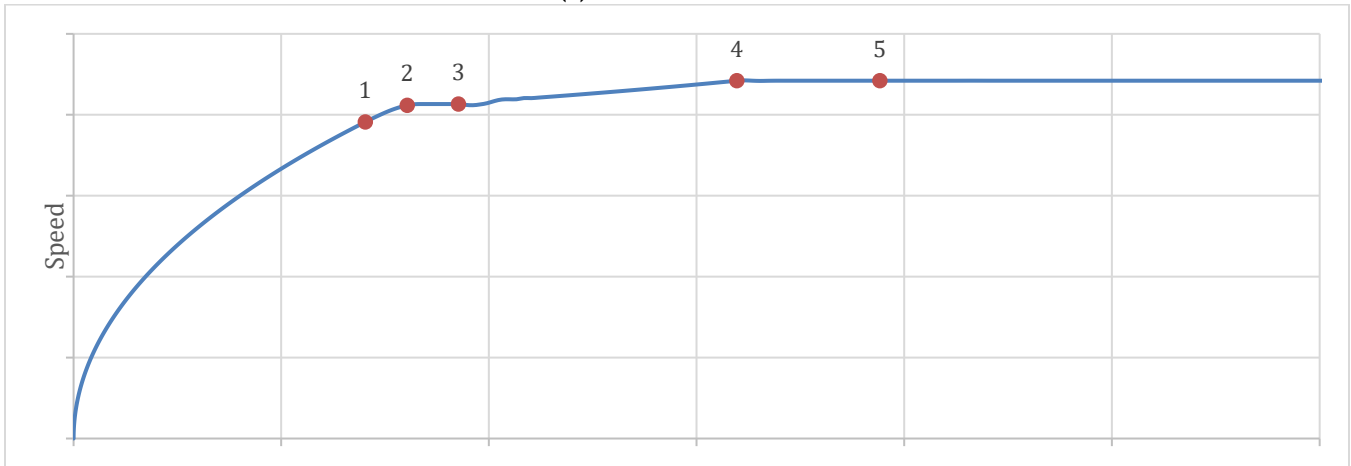
The takeoff trajectory is simulated as follows:

0. From a resting position, the aircraft releases its brakes and accelerates forward with a specified power reserve.
1. After reaching the minimum unstick velocity (within a safety margin), the aircraft starts to increase the angle of attack.
2. After the lift force produced exceeds the weight of the aircraft, the aircraft lifts off from the runway. The aircraft then starts flying at a constant speed until it reaches the obstacle altitude of 35 ft.
3. After clearing the obstacle, the aircraft engages the PHLD schedule, reduces power to the specified lapse rate, and switches to a constant thrust flight at a prescribed flight-path angle.
4. After reaching a prescribed altitude, the aircraft switches to a constant thrust flight at the speed obtained in the previous segment, to allow the aircraft to climb.
5. Finally, at a second prescribed altitude, the aircraft performs the pilot-initiated cutback and then maintains the current settings until it flies off the aerodrome (50,000 ft distance from break release). The cutback thrust is calculated internally, such that the thrust is sufficient to maintain a 2.29° (i.e., 4% gradient) flight-path angle with all engines operating and to maintain level flight with one engine inoperative.

NASA's FLOPS detailed LTO module is used to predict the vehicles LTO trajectory according to the prescribed VNRS procedure parameters. A notional visualization of this simulation is shown in the plots in Figure 15. Each plot also highlights points 1–5 itemized above, to help clarify the procedure.



(a) Altitude vs. distance



(b) Speed vs. distance



(c) Throttle vs. distance

Figure 15. Notional VNRS takeoff.

Federal regulation Part 25.107(c) indicates the requirements for V_2 are as follows: “ V_2 , in terms of calibrated airspeed, must be selected by the applicant to provide at least the gradient of climb required by § 25.121(b) but may not be less than— (1) V_{2min} ; (2) VR plus the speed increment attained (in accordance with Part 25.111(c)(2)) before reaching a height of 35 feet above the takeoff surface; and (3) A speed that provides the maneuvering capability specified in § 25.143(h)”. V_{2min} is defined according to stall speed and is calculated internally in FLOPS, whereas VR plus the speed increment attained before reaching a height at 35 ft is taken as the speed at which the vehicle clears the obstacle.

The Georgia Tech team does not examine maneuvering capabilities beyond those internally calculated by FLOPS. Georgia Tech measure the V_2 value as the speed at which the vehicle transitions into a constant speed climb. At this point in Georgia Tech analysis, $V_2 + \Delta V$ margin was defined as the delta between the V_2 value and the greater of V_{2min} and obstacle speed. Georgia Tech enforced an optimization constraint such that the value of ΔV should not be less than 10 KEAS, and $V_2 + \Delta V$ must respect the 250-KEAS terminal area speed limit below 10,000 ft MSL, according to federal regulation Part 91.117(a). In addition, in accordance with Appendix B to 14 CFR Part 36, specifically section B36.7(b)(1)(ii)(A), a lower-bound constraint is enforced to accept only designs in which the pilot-initiated cutback altitude (identified as h_4 in Figure 14) is greater than 689 ft.

Finally, the noise assessment for each aircraft configuration is performed with NASA’s program ANOPP. The resulting trajectory and aircraft state along the trajectory (thrust, angle of attack, altitude, distance, speed, etc.) is passed from the FLOPS analysis to ANOPP. In performing these assessments, several assumptions are made in selecting and using different ANOPP modules. Table 7 presents a breakdown of the ANOPP input file structure and the rationale applicable to each module or section.

Table 7. Modules used in aeroacoustics analysis.

Component	ANOPP module	Acronym	Rationale
Trajectory	Source Flyover Module	SFO	Separate trajectories (prescribed by FLOPS) were considered for the sideline and the cutback/approach noises assessments. The difference was that the sideline trajectory did not include a cutback section after the second-segment acceleration; both cases used a VNRS takeoff trajectory.
Airframe	Fink’s Airframe Noise Module	FNKAFM	This module was used to predict the broadband noise from the dominant components of the airframe, on the basis of a method developed by Fink for the FAA.
Jet	Single Stream Circular Jet Noise Module	SGLJET	The single-stream jet mixing noise was calculated with a method based on SAE ARP 876, which is known to be the best representation of the current nozzle type.
Fan	Heidmann Fan Noise Module	HDNFAN	The fan inlet and discharge noises were assessed separately for their tone and broadband contributions, with a method based on correlations to model and full-scale test data.
Treatment	Fan Noise Treatment Module	TREAT	Given that the chosen fan module is based on the assumption that the inlet and discharge ducts have no acoustic treatment internal to HDNFAN, the attenuation spectra were applied to separate predictions of the inlet and aft radiated source noise produced by the source noise module, and a total attenuated fan noise prediction was produced.
Combustor	Combustion Noise Module	GECOR	The combustor noise was predicted with a method developed by General Electric and later adopted by the SAE A-21 Committee.
Shielding	Wing Module	WING	This module was used to compute the geometric effects of wing shielding or reflection on the propagation of engine noise (depending on the engine placement/configuration).

Results

The key metric of merit for the LTO analysis for design/cycle selection is certification effective perceived noise level. The results of the analyses provide a procedure, trajectory, aircraft state, and effective perceived noise level for the three noise-certification observers (sideline/takeoff, cutback/flyover, and approach), the noise margin relative to Chapter 14 for each observer, and the cumulative sum. These results are used in Task 5, Engine Cycle and Takeoff Trajectory Space

Exploration, to understand how different trajectories affect LTO noise and to quantify a Pareto front between fuel burn and LTO noise.

References

General Operating and Flight Rules, 14 C.F.R. Part 91
 Airworthiness Standards: Transport Category Airplanes, 14 C.F.R. Part 25
 Noise Standards: Aircraft Type and Airworthiness Certification, 14 C.F.R. Part 36

Task 5 – Engine Cycle and Takeoff Trajectory Space Exploration

Georgia Institute of Technology

Objective

The objective of this task was to explore a design space consisting of engine cycle, vehicle sizing, and LTO operational parameters to answer various questions regarding how changes to these variables affect different response metrics of interest. One particular question of interest pertained to the interdependency between fuel burn and LTO noise. In answering this question, the goal was to find a Pareto front (i.e., set of non-dominated designs, such that any other potential design is worse in at least one objective) between the objectives of design block fuel burn and cumulative LTO noise margin. Another question currently of interest is how changes to the reference speed $V_2 + x$ (typically $V_2 + 10$ kts) affect the noise. Through engine cycle and takeoff trajectory space exploration, these questions can be answered to allow policymakers to understand the implications of setting regulatory limits and enable designers to better understand how to design vehicles to meet various potential regulatory thresholds.

Research Approach

All modeling elements described previously make up the modeling and simulation environment called FASST. FASST is used as the analysis tool to predict objectives (e.g., block fuel and LTO noise margin) and constraints (e.g., $V_2 + x$, takeoff field length, approach speed, span, etc.) as a function of the design variables. The design space exploration and multi-objective optimization described in the following paragraphs use a design space consisting of engine cycle, vehicle sizing, and LTO operational variables. Airframe design variables are not considered in this task, because the airframe geometry design was optimized separately, as described in Task 1. However, because the aircraft is sized in FLOPS for a thrust loading and wing loading over a design mission range of 4,250 nmi, the wing size and engine size change. The effects of changes in the size of the wing and engines on aerodynamics are captured by the parametric drag polar described in Section 1. The effects of wing weight changes are handled by the FLOPS weight equations, and changes in engine weight are handled by WATE++ (Wells et al., 2017; Tong & Naylor, 2008). The engine cycle variables consist of the fan pressure ratio, overall pressure ratio, extraction ratio, top-of-climb corrected fan speed, and maximum turbine rotor inlet temperature. The fan pressure ratio and overall pressure ratio are typical parameters for a turbofan. The extraction ratio, the total pressure ratio at the mixer entrance between the bypass and the core, is used to determine the bypass ratio, because keeping the extraction ratio in the vicinity of 1 is generally desirable. The maximum turbine rotor inlet temperature is generally an operational limit but should be set to balance cooling air penalties with the performance benefits of the higher gas temperature. Because the maximum turbine rotor inlet temperature is treated as a design variable rather than a constant, the top-of-climb percentage corrected fan speed, rather than the throttle ratio, is used as the parameter determining the design point turbine rotor inlet temperature. The use of a top-of-climb fan speed target is similar to procedures used during the High-Speed Research (HSR) program, wherein a top-of-climb mass flow lapse was used as a design parameter (Pratt and Whitney and General Electric Aircraft Engines, 2005). Standard vehicle sizing parameters of thrust loading and wing loading are also treated as design variables. The thrust loading is defined as the ratio of the 100%-corrected fan speed thrust at sea-level static to the takeoff gross weight of the aircraft. The wing loading is the ratio of the takeoff gross weight of the aircraft to the wing area. LTO operational parameters consist of the PLR, second-segment flight-path angle, fixed-speed transition altitude, and pilot-initiated cutback altitude. Tasks 2, 3, and 4 provide further details on the definitions of these variables and the analyses. Altogether, 11 parameters are considered (summarized in Table 8).

The first phase involved constructing a Latin-hypercube DoE to generate a large set of 20,000 design alternatives. Each of the 20,000 designs was simulated with FASST. To accelerate the simulation time, HTCondor was used to distribute the simulations across ~1,700 cores (HTCondor, n.d.). The results were analyzed and plotted in JMP v16 (SAS Institute Inc., n.d.). Design variable ranges were refined, and additional data were generated as necessary. These data points were used

to generate neural-network surrogate models, by using JMP, to represent both objectives (e.g., block fuel and LTO noise) and important constraints. The objectives and constraints considered herein are summarized in Table 9. The two objectives considered are the block fuel of the design mission, which is the fuel from the beginning of taxi-out at departure to the end of taxi-in at destination, but does not include the reserve mission. The mission analysis section provides more details on calculation of the design block fuel. The cumulative noise is the sum of the three LTO observers (takeoff/sideline, flyover/cutback, and approach). The cumulative LTO noise margin is the difference between the allowable cumulative LTO noise for stage 5/chapter 14 and the actual cumulative LTO noise. More details on how the noise was calculated are provided in Task 4. The takeoff field length is the FAR takeoff field length or balanced field length; this is the distance from brake release to reaching 35 ft altitude if an engine is lost at the decision speed V_1 and is also equal to the distance to stop if the takeoff is aborted after engine failure at V_1 . The landing field length is the FAR landing field length, which is determined by dividing the calculated landing field length by 0.6 to account for variations in landing conditions. The approach speed is the aircraft’s airspeed for a 3° glide slope in the landing configuration and at landing weight. The approach speed is constrained for a category D aircraft according to the United States Standard for Terminal Instrument Procedures. The aircraft wingspan is constrained to fit in category III gates, as defined in FAA Advisory Circular 150/5300-13. The second-segment thrust is the excess thrust available for a 3% climb gradient with gear up at V_2 ; this is constrained to be greater than zero to ensure sufficient thrust. The speed below 10,000 ft is constrained to less than 250 KCAS. The distance at which cutback occurs is constrained to occur before the position of the cutback observer. The post-obstacle acceleration is constrained to ensure that the aircraft climbs at a speed of at least $V_2 + 10$ kts.

The surrogate models are then used to conduct a multi-objective optimization by using the SMS-EMOA evolutionary algorithm from the Python multi-objective optimization framework called Pymoo (Pymoo, n.d.) to determine the Pareto front between the design mission block fuel and cumulative LTO noise margin. Because this Pareto front is based on surrogate models, which are approximations of the FASST analysis, the surrogate predicted Pareto front is used to select additional designs to be simulated in FASST. However, rather than using a space-filling DoE, such as a Latin-hypercube design as in the original set of FASST runs, this second run targets designs near the approximated Pareto front. This process is accomplished by sampling points from a normal distribution around each point on the predicted Pareto front, where the mean is the value of design variables at each point on the predicted Pareto front, and the coefficient of variation is used to control the standard deviation (typically set to 0.01). The final set of data, containing more than 60,000 designs, is filtered for all constraints. The set of non-dominated solutions is determined to establish the Pareto front between block fuel burn and the cumulative LTO noise margin subject to the constraints.

Table 8. Design variables.

Engine cycle variables	Vehicle sizing variables	LTO operational variables
1. Fan pressure ratio	6. Thrust loading	8. Programmed lapse rate
2. Overall pressure ratio	7. Wing loading	9. Second-segment flight-path angle
3. Extraction ratio (i.e., bypass ratio)		10. Fixed-speed transition altitude
4. Maximum turbine inlet temperature		11. Cutback altitude
5. Top-of-climb corrected fan speed (i.e., throttle ratio or design turbine inlet temperature)		

Table 9. Objectives and constraints.

Metric	Type	Rule
Design block fuel	Objective	Minimize
Cumulative LTO noise margin	Objective	Maximize
Takeoff field length	Constraint	$\leq 11,000$ ft
Landing field length	Constraint	$\leq 11,000$ ft
Approach speed	Constraint	≤ 165 kts
Cutback altitude limit	Constraint	≥ 689 ft
Span	Constraint	≤ 118 ft
Second-segment net thrust	Constraint	≥ 0 lb
Speed below 10,000 ft	Constraint	≤ 250 kts
Cutback distance	Constraint	$\leq 21,325$ ft
Post-obstacle speed increment (i.e., x in $V_2 + x$)	Constraint	≥ 10 kts



In examining various operational constraints such as reference speed ($V_2 + x$) and cutback altitude, the first step was to examine how these changed the Pareto front between fuel burn and LTO noise margin. Georgia Tech reformulated the multi-objective optimization problem to change the inequality constraint for the post-obstacle speed increment for different threshold values. The optimization was then run for values of $V_2 + 0$, $V_2 + 10$, $V_2 + 20$, and $V_2 + 40$. From the resulting Pareto fronts, comparisons were made on fuel burn and gross weight change to obtain a noise margin of 5 EPNdB. Another comparison was made on noise margin when compared at a constant fuel burn of 160,000 lb.

Results

The results in this section pertain to a 65-pax aircraft designed for Mach-1.7 cruise and a range of 4,250 nmi. More than 60,000 designs were simulated in FASST, and surrogate models were created to map design variables to responses. Pymoo was used to generate a Pareto front of designs subject to various post-obstacle speed increments (i.e., x in $V_2 + x$). Constraints considered were $x = 0, 10, 20$, and 40 . Table 10 and Table 11 show eight configurations selected from those Pareto fronts in attempts to select the vehicle closest to 5 EPNdB and selecting a configuration predicting a block fuel of ~160,000 lbs. This exercise demonstrated a trade-off between $V_2 + \Delta V$ and fuel burn/noise margin. To achieve the same cumulative noise margin with increasing the ΔV requirement, the fuel burn increases. To achieve the same fuel burn with increasing ΔV requirement, the cumulative noise margin decreases. With increasing the ΔV requirement, the PLR for VNRS approaches 1 (i.e., no programable lapse rate). With increasing the ΔV requirement, the constant-speed transition altitude (h_3) increases. With increasing ΔV requirement, the engine cycle and vehicle sizing, Thrust to Weight Ratio and Wing Loading, (T/W and W/S), variables change in addition to the operational variables. Of note, these results remain preliminary. For final results Georgia Tech plan to perform this exercise through FASST results instead of surrogate-model predictions, to eliminate surrogate prediction error as a confounding factor in this study.

Table 10. Comparison of different takeoff ΔV constraints at constant fuel burn of 160,000 lbs.

	$\Delta V > 0$	$\Delta V > 10$	$\Delta V > 20$	$\Delta V > 40$
Block fuel (lb)	160,060	160,100	160,045	159,552
Takeoff Gross Weight (lb)	449,578	449,468	449,253	443,340
Cumulative noise margin (EPNdB)	6.12	5.42	4.29	2.35
Approach Flyover Lateral margin (EPNdB)	6.8 5.4 6.5	6.7 5.2 6.1	6.5 5.4 5.5	6.8 6.5 2.4
Fan Pressure Ratio Overall Pressure Ratio	1.88 22.6	1.90 23.2	1.93 23.2	2.04 23.1
$T41_{max}$ (R)	3,146	3,120	3,100	3,200
Bypass ratio	3.28	3.20	3.12	3.08
T/W W/S (psf)	0.304 81.8	0.309 82.1	0.316 82.1	0.304 80.2
Power reserve	0.90	0.91	0.93	1.0
Programmable lapse rate	0.81	0.81	0.83	0.97
Flight-path angle (°)	2.76	3.14	2.83	3.22
Transition altitude (ft)	143	296	376	532
$V_2 + \Delta V$ (kts)	205.2 + 4.3	203.4 + 10.2	202.1 + 20.1	202.3 + 40.2
Cutback altitude (ft)	689	689	689	689


Table 11. Comparison of different takeoff ΔV constraints at a constant noise margin of 5 EPNdB.

	$\Delta V > 0$	$\Delta V > 10$	$\Delta V > 20$	$\Delta V > 40$
Block fuel (lb)	158,541	159,719	161,428	159,552
Takeoff Gross Weight (lb)	446,382	449,468	453,800	443,340
Cumulative noise margin (EPNdB)	5.12	5.14	5.05	2.35
Approach Flyover Lateral margin (EPNdB)	6.3 5.1 6.4	6.3 5.1 6.2	6.8 5.7 5.6	6.8 6.5 2.4
Fan Pressure Ratio Overall Pressure Ratio	1.88 22.5	1.90 23.0	1.92 23.3	2.04 23.1
T41 _{max} (R)	3129	3125	3116	3,200
Bypass ratio	3.25	3.26	3.25	3.08
T/W W/S (psf)	0.304 81.1	0.310 81.8	0.316 83.0	0.304 80.2
Power reserve	0.90	0.90	0.93	1.0
Programmable lapse rate	0.81	0.81	0.83	0.97
Flight-path angle (°)	2.74	3.14	2.87	3.22
Transition altitude (ft)	141	296	377	532
V ₂ + ΔV (kts)	204.5 4.3	202.9 + 10.8	203.2 + 20.0	202.3 + 40.2
Cutback altitude (ft)	689	689	689	689

References

- HTCondor (n.d.). Computing with HTCondor. <https://research.cs.wisc.edu/htcondor/>
- Pratt and Whitney and General Electric Aircraft Engines (2005) *Critical Propulsion Components Volume 1: Summary, Introduction, and Propulsion Systems Studies*.
- Pymoo (n.d.). <https://pymoo.org/algorithms/moo/sms.html>
- SAS Institute Inc. (n.d.). JMP®, Version 16. https://www.jmp.com/en_us/events/mastering/topics/new-in-jmp16-and-jmp-pro16.html
- Tong, M. T., & Naylor, B. A. (2008). An object-oriented computer code for aircraft engine weight estimation. Proceedings of the ASME Turbo Expo, 1(December), 1–7. <https://doi.org/10.1115/GT2008-50062>
- Wells, D. P., Horvath, B. L., & McCullers, L. A. (2017). *The flight optimization system weights estimation method*. NASA/TM-2017-219627

Task 6 – Purdue Fleet Analysis

Purdue University

Objectives

The Purdue team pursued three subtasks as part of the fleet analysis task. During this year, the team created and used the performance and cost coefficient of six additional SST concepts of combinations of passenger capacity and Mach number, implemented a SAF price evolution model, and estimated the effect of SAF utilization in subsonic-only and subsonic and supersonic scenarios. With modifications to FLEET to accommodate these changes, the team estimated the impacts on future environmental emissions when different types of SST concepts were introduced in the fleet and when SAFs were used to reduce the impact of the SST.

Subtask 1: Analysis of alternative SST concepts

Simple SST sizing approach (Placeholder 2.0)

In previous work, the authors used a 55-seat “placeholder” commercial supersonic aircraft model to identify potential supersonic routes in a U.S.-touching route network; the placeholder model was based on Boom’s Overture concept with an over-water supersonic cruise speed of Mach 2.2 and an over-land subsonic cruise speed of Mach 0.95. The “placeholder” notation is applied because these aircraft models were used only for identifying potential supersonic routes and have been replaced in FLEET simulations by higher-fidelity supersonic aircraft models developed by colleagues at Georgia Tech. The maximum range of the placeholder aircraft was designated to be 4,500 nmi. The *L/D* ratio and the specific fuel consumption value for sizing the placeholder supersonic aircraft were based on several improvements over the Concorde’s values. For performance calculations, the over-land segment was assumed to be equally split at each end of the over-water segment. In reality, the over-land segment is dependent on the airport pair and route (e.g., for one airport pair, the origin might be close to the ocean and the destination further inland; the return flight on this pair would have the opposite); consequently, a higher-resolution representation of the routes for aircraft performance calculations would lead to different fuel burn characteristics for each direction on each route.

In this work, the authors develop an updated version of the placeholder commercial supersonic aircraft model, dubbed the “placeholder v2.0” aircraft model. The *L/D* ratio and specific fuel consumption value for the placeholder v2.0 model are based on the higher-fidelity supersonic aircraft models developed by our colleagues at Georgia Tech. Additionally, the placeholder v2.0 model takes into account the higher-resolution representation of the routes for aircraft performance calculations, thereby reflecting the difference in fuel burn (and the aircraft range capability) for each direction on each route.

This work includes different size and speed supersonic aircraft in the FLEET simulations. The set includes 55-seat, 75-seat, and 100-seat supersonic aircraft operating at multiple supersonic cruise speeds.

Table 12. Alternative supersonic transport concepts (developed by the Georgia Tech team).

Vehicle seating capacity	Supersonic cruise Mach Number		
55 pax	1.8	2.0	2.2
75 pax	2.2	2.2	2.2
100 pax	1.6	1.8	2.0

Each combination of seat capacity and cruise speed leads to a different aircraft configuration, with the higher-fidelity models provided by our colleagues at Georgia Tech. A total of seven aircraft are available for implementation in FLEET. The authors adapt the placeholder v2.0 aircraft model to depict all seven aircraft and identify potential supersonic routes for each aircraft type.

Supersonic flight path calculations

Previous work relied on a simplistic method of flight-path calculation, wherein the distance flown was calculated from the great-circle path distance. The over-land and over-water distances were calculated by dividing the total distance by given fixed over-water percentages. The work presented herein uses a polygon approach to calculate accurate over-water distances, and the intersection between the flight path and the coastline separates over-land and over-water segments. The block time is then simply calculated by dividing segment distance by the over-land or over-water airspeed. This approach also accounts for the differences in fuel burn when flying in different directions on the same route, i.e., when flying from A to B and B to A.

The block time for each origin destination pair is calculated as follows:

1. Calculate the great-circle path between the origin airport and the destination airport of a route.
2. Deviate the midpoint by $\pm 7^\circ$ with 1° intervals along the direction perpendicular to the heading at the midpoint.
3. Separate each route by land-water intersections into *k* segments.
4. Calculate the distances of each segment and record the sum of over-water distances.
5. Calculate the block time of each route option.
6. Find the minimum block time path for both forward and return directions.

The calculation of block time follows the equation below, where k is the total number of segments within the route, d_k is the distance of segment k , and V_k is the airspeed at that segment. Because all supersonic operations are restricted to over-water, aircraft fly at $V_{supersonic}$ on over-water segments and at $V_{subsonic}$ on over-land segments.

$$\text{Block time} = \sum_{k=1}^N \frac{d_k}{V_k}$$

$$V_k = V_{supersonic} \text{ (} k \text{ \textasciitilde{} over-water segment)}$$

$$V_k = V_{subsonic} \text{ (} k \text{ \textasciitilde{} over-land segment)}$$

All available nonstop routes are found by filtering all routes by range. To extend flight range, a search algorithm finds all available fuel stops along the path for each origin-destination pair. The routes with fuel stops are again filtered on the basis of the design range of “placeholder v2.0” aircraft.

Identification of SST-eligible routes: nonstop routes

Nonstop supersonic routes—for example, Los Angeles, California (LAX)–Taipei, Taiwan (TPE), shown in Figure 16—are shorter than 4,500 nmi and do not require a fuel stop (in the figure, midpoints are deviated by $\pm 7^\circ$ with 1° increments). The green lines represent the deviated routes, and the red triangles represent the midpoints of each route. As shown in the figure, the top route path has more overlap with land, which would increase block time. In this case, the bottom route path has the least block time and is the best route for the example under consideration.

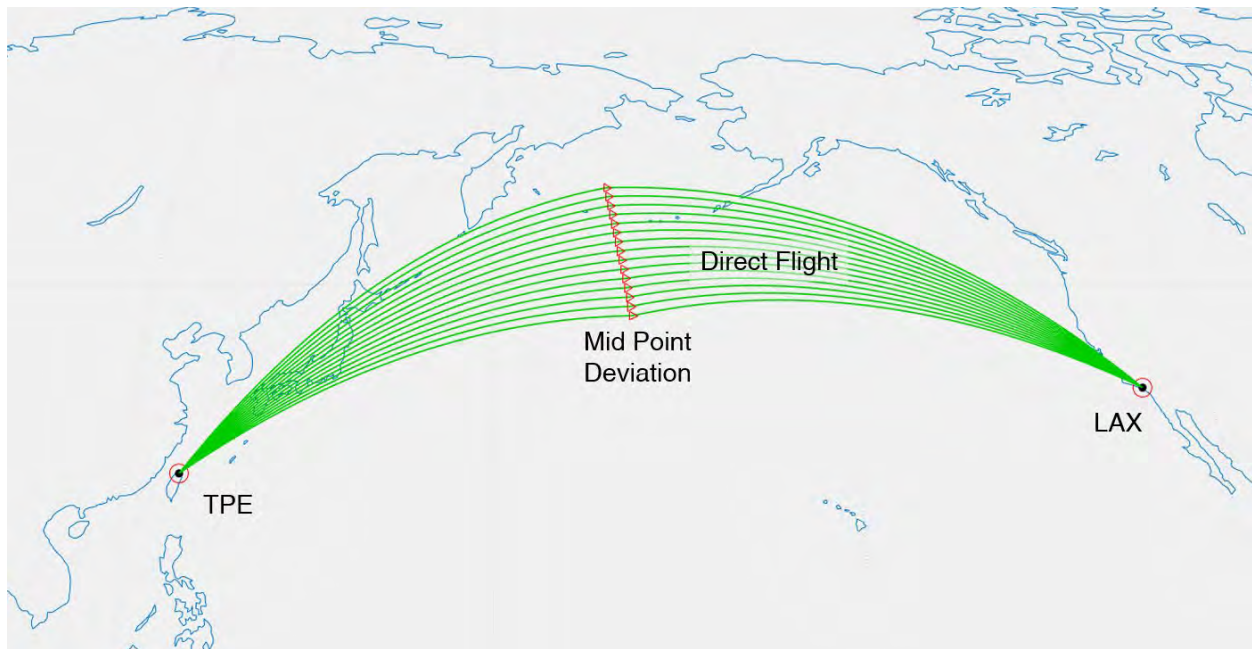


Figure 16. Example supersonic route (LAX-TPE) that does not require a fuel stop.

Identification of SST-eligible routes: routes with fuel stops

Earlier, the fuel-stop options for routes longer than 4,500 nmi included only Honolulu, Hawaii (HNL) and Anchorage, Alaska (ANC) for cross-Pacific routes, and Shannon, Ireland (SNN); Keflavik, Iceland (KEF); Oslo, Norway (OSL); and San Juan, Puerto Rico (SJU) for cross-Atlantic routes. This approach was valid only for the U.S.-touching route network and required manual inputs to select the appropriate fuel stop. To capture fuel stops for all global routes, an automated area-search method is developed and implemented. For each origin-destination pair, a search area is placed on the great-circle path between them. All airports within the area would be captured as potential fuel stops. To avoid the case in which the supersonic aircraft lands for a fuel stop immediately after takeoff, a circular search area is placed at the route’s midpoint (Figure 17) to ensure that airports in the vicinity of the origin or the destination are not captured. The diameter of the search area is

set to a 35° spherical arc to include the maximum possible fuel-stop options; the arc size was determined through trial and error.

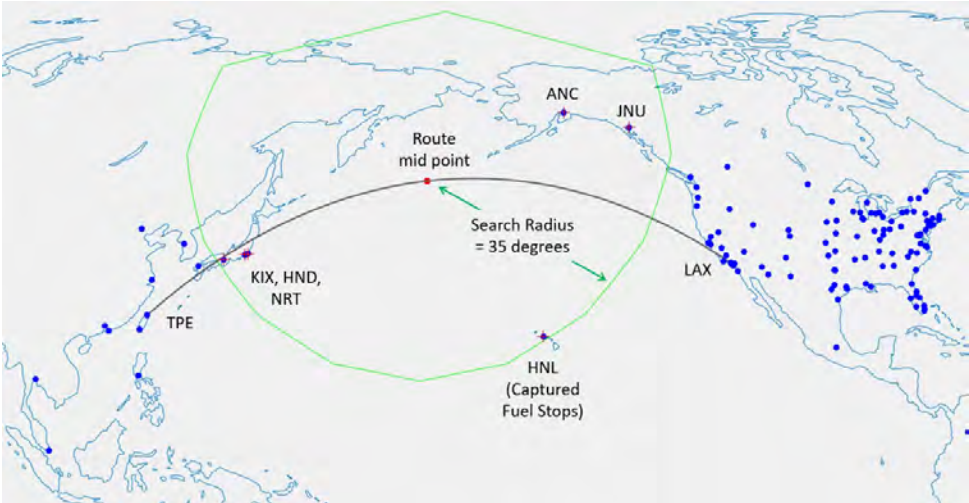


Figure 17. Example supersonic fuel-stop search process for supersonic route (LAX-TPE).

With each fuel stop, a deviation process similar to that in nonstop supersonic routes is implemented for both segments and both directions to find the minimum block time path of each path. In the case shown in Figure 18, HNL and ANC are selected as fuel-stop options for the LAX-TPE route. The gray routes depict the deviated routes with fuel stops, whereas the red triangles depict the midpoints for each deviated route; the red route path represents the path with minimum block time.

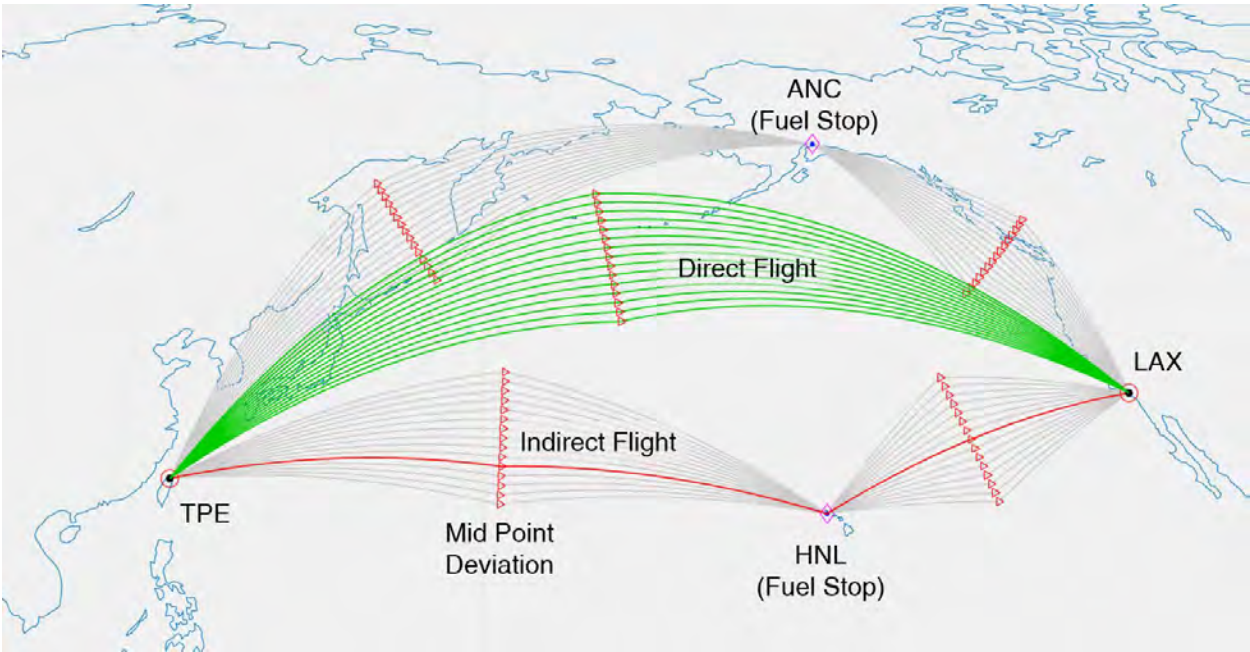


Figure 18. Example supersonic route requiring a fuel stop.

The fuel required to fly any such route is calculated by modeling both segments of the route, accounting for the departure and arrival of each segment. The block time accounts for the extra time required to land and take off at the fuel-stop airport. The fuel-stop approach almost doubles the range of supersonic routes and allows for an 18%–28% increase in eligible routes. For example, a 55-pax, Mach-2.2 aircraft has 895 direct flight routes. With fuel stops, an additional 252 routes become available (28% increase) and extend the range from 4,911 nmi to 8,350 nmi.

Supersonic aircraft over-water percentage study

In our exploration of various potential supersonic routes, the question of how far the supersonic aircraft can travel at various supersonic segment percentages arose. Our hypothesis was that an aircraft optimally designed to operate under supersonic conditions would show a decrease in performance, namely in terms of range, if the subsonic segments were to increase. Because the supersonic segment, by regulation, must occur above water, Georgia Tech termed this study the “over-water percentage to range trade-off study,”

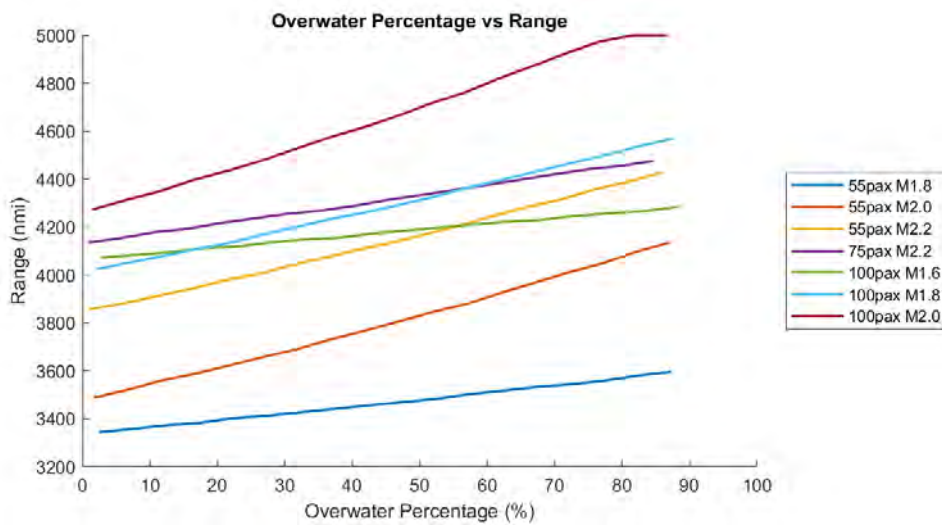


Figure 19. Supersonic aircraft over-water percentage vs. range.

To understand the trade-offs between a maximum possible range at a given over-water flight percentage, Georgia Tech used the FLOPS version 9.0 executable as a core for this study. Given that FLOPS takes the aircraft design range and defined mission profile as input, and fuel consumption as output, the FLOPS file was wrapped by an external optimization program (MatLab fminbnd) that maximizes fuel usage until only reserve fuel remains (keeping 5%). The over-water (supersonic) segments are centered at the mission profile cruise segment.

The results for each aircraft configuration (Figure 19) show that the relationship between the over-water percentage and range is quite linear. The waviness results from the optimization program not fully reducing the fuel residuals. Overall, the results align with the expectation in which each aircraft has the maximum range at close to full supersonic flights and has poor range when flying subsonic.

Table 13 shows the results culminating from Figure 19. The smaller the aircraft, the less fuel it carries, and subsequently the less range it can reach. Notably, the original aircraft design mission profile produced an approximately 86% over-water percentage, below the maximum of 90%–94%.

Higher-resolution supersonic aircraft modeling and routing

The computational models of the 55-seat, 75-seat, and 100-seat supersonic aircraft for this study were developed by colleagues at Georgia Tech. These models provide mission performance characteristics, including fuel consumption and block time, for the supersonic aircraft to operate on routes in the FLEET network. Because the supersonic aircraft can operate at supersonic speed only over water, the ground path of the flight to optimize a combination of fuel consumption

and block time can significantly deviate from typical subsonic aircraft routes. For consistency in the ASCENT project, the studies presented herein also use flight-path ground tracks generated by teammates at Georgia Tech.

Table 13. Over-water percentage results for each aircraft configuration.

Aircraft configuration	Maximum fuel capacity (lbs)	Range (nmi)	Maximum over-water percentage (%)
55 pax, Mach 1.8	123,538.9	3,737.6	92.34
55 pax, Mach 2.0	149,773.7	4,280.1	93.03
55 pax, Mach 2.2	174,831.6	4,480.9	92.12
75 pax, Mach 2.2	199,183.4	4,506.9	90.38
100 pax, Mach 1.6	187,829.5	4,583.8	94.10
100 pax, Mach 1.8	201,961.3	4,618.9	93.38
100 pax, Mach 2.0	228,262.8	4,999.9	90.69

The Purdue team consider two generations of supersonic aircraft with entry-into-service dates of 2025 (generation 1) and 2038 (generation 2). The generation 2 supersonic aircraft show a 10% improvement in fuel burn with no change in aircraft noise or sonic boom characteristics.

The detailed supersonic routing developed by the Georgia Tech team identifies the optimum supersonic route path by solving an optimization problem to minimize a weighted sum “cost to the goal” objective function. The goal is to minimize a combination of block time and block fuel values for flying supersonic aircraft on a supersonic route. This approach essentially finds a supersonic route path that is a trade-off between the time-optimal-only route and fuel-optimal-only supersonic route path. A simplistic representation of this approach is as follows:

$$\text{weightedsum}_{\text{objective}} = \alpha \times \frac{\text{BlockFuel}}{\text{BlockFuel}_{\text{min}}} + (1 - \alpha) \times \frac{\text{BlockTime}}{\text{BlockTime}_{\text{min}}}$$

This work uses $\alpha = 0.4$ as the recommended value for the weighted-sum supersonic routing (on the basis of various supersonic routing tests conducted by our partners at Georgia Tech). The authors use FLOPSv9 to “fly” the detailed supersonic aircraft models on the weighted sum routes, conducting separate FLOPS runs for each direction of a supersonic route; different block fuel values (and in some cases, block times) are observed when flying the detailed notional supersonic aircraft in different directions on a supersonic route.

Subtask 2: Modeling SAFs

The aviation industry is responsible for approximately 2.5% of global carbon emissions (Ritchie & Roser, 2023). Although this figure is relatively low, with continued increases in passenger air travel and the potential introduction of supersonic transport, the aviation industry faces pressure to adopt advanced solutions for decreasing its share of CO₂ emissions. One near-term potential solution to mitigate this global emissions situation is to operate existing aircraft with SAF. This solution requires almost no modification to current aircraft and therefore is the “quickest” approach to reducing aviation carbon emissions, although the actual impact will be determined by the degree to which airlines adopt and use SAF, the ticket-price impact of SAF, the future growth of travel demand, and the impact of supersonic transport. The research team used FLEET to assess the aggregated impacts of these factors for a subsonic-only future fleet of aircraft and for a combination of subsonic and supersonic aircraft serving passenger travel demand.

SAF price and penetration levels

SAF is a mixture of biofuels and conventional jet fuel (CJF) and has different properties depending on the type of biofuel. The SAFs from different production pathways and feedstocks have different production costs and life-cycle carbon emission intensities. According to the American Society for Testing and Materials International Specification D7566 (Sissine, 2010), SAF is a mixture of biomass-derived synthesized paraffinic kerosene (SPK) and CJF. SPK usually includes biofuels based on biomass feedstocks. The common feedstocks for biofuel production are camelina, algae, and used cooking oil. Although camelina is not the primary oilseed grown in the United States, commercial airlines have used biofuel developed from this feedstock (Hileman et al., 2009).

Although aircraft emit similar amounts of carbon when using CJF or SAFs (Stratton et al., 2010), the biomass feedstocks from SPK production pathways can capture carbon dioxide from the atmosphere. Hence, SAFs have lower carbon emission intensity than CJF when the life cycle of both types of fuels is considered, including the net carbon emissions from “well to wake” in CJF and “seed to wake” in SAF. Hydro-processed esters and fatty acids (HEFA) biofuels have a reported emission intensity of 2.312 lb CO₂-equivalent per lb consumed fuel, in contrast to the 3.775 lb CO₂-equivalent of conventional fossil fuels (Doliente et al., 2020). The research team used these emission intensity factors when comparing the CO₂ emissions of SAF and conventional fossil fuels.

Two important factors in considering the utilization of biofuels in aviation are price and penetration level across the fleet (biomix). Sissine (2010) revealed that among the various SAF alternatives, HEFA fuels have the lowest production cost (\$0.6879/lb), in contrast to the \$0.2642/lb for CJF. In its 2020 report on renewables (International Energy Agency, 2020), the International Energy Agency has reported that market prices for HEFA aviation biofuels ranged between 2.9 and 5.2 times that of CJF in 2020. Before 2020 and the COVID-19 pandemic, the median cost of biofuels was approximately twice that of jet kerosene fuel.

Scaling up SAF output would be likely to realize economies of scale in production and supply, and decrease the production costs and ultimately price. Despite uncertainty regarding the possible cost reduction and the trajectory that this reduction would have, for the purposes of this study, the research team assumed three possible biofuel price evolution models: SAF price equivalent to twice the price of fossil fuel, SAF price beginning at twice the price of fossil fuel and decreasing along an S-curve until reaching the same price as fossil fuel by 2045, and SAF price beginning at six times the price of fossil fuel and decreasing along an S-curve until reaching the same price as fossil fuel by 2045. These models cover the reported variations in biofuel prices while making assumptions regarding how those prices may evolve. Figure 20 presents these models in terms of SAF fuel price multipliers.

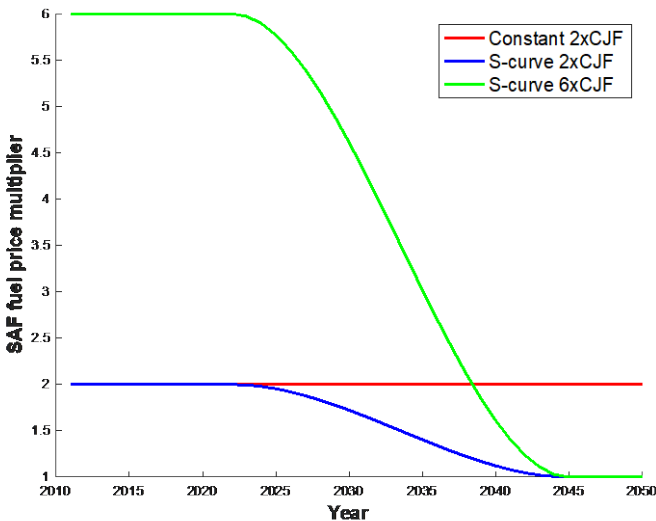


Figure 20. SAF price evolution models considered in the study.

The HEFA fuel market penetration level affects the SAF price and the carbon emission intensities of the biofuel mix. Because

the biofuel industry is in its infancy, the high risk and high production costs depress the initial penetration level (Chao et al., 2019). In 2017, the Renewables for Aviation Technology Brief from the International Renewable Energy Agency (2017) reported that the operational capacity of the world’s current (as of 2017) HEFA facilities would meet less than 1.5% of the world’s jet fuel consumption. Additionally, according to the American Society for Testing and Materials regulations, SAFs are currently approved in blends of 10%–50% (U.S. Department of Energy, Office of Energy Efficiency and Renewable Energy, 2020). For the purposes of this study, the research team use the biomix evolution presented in Figure 21, which assumes utilization of biofuels in 2022 and increasing penetration levels until 2050.

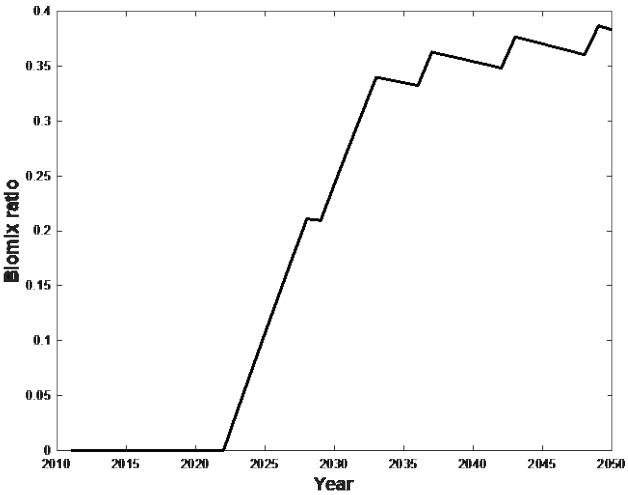


Figure 21. Penetration level of SAF (biomix).

Combining the SAF pricing model with the penetration levels yields the projected fuel prices presented in Figure 22. The red line represents the case in which the SAF price is twice that fossil fuels; the blue line represents SAF prices with an S-curve price evolution with a maximum of twice (2x) the cost of fossil fuel; and the green line represents SAF prices with an S-curve price evolution with a maximum of six times (6x) the cost of fossil fuel.

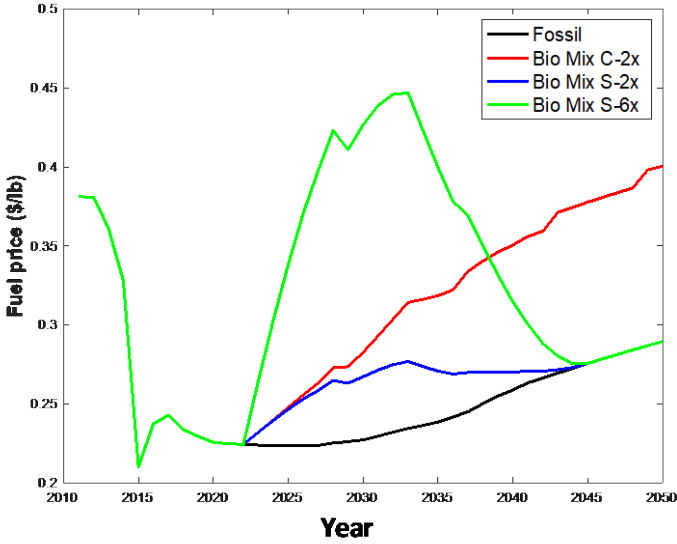


Figure 22. Fuel price evolution combining estimated SAF prices and penetration levels.

These estimated trends in fuel price evolution will affect the direct operating cost of the aircraft and the expected passenger demand, via the demand-price elasticity. The research team has implemented these projections in FLEET and analyzed airline operations when subsonic aircraft were the only type of aircraft in the fleet. Figure 23 presents evolution of ticket prices and passenger demand for these three cases and the baseline case of no SAF utilization.

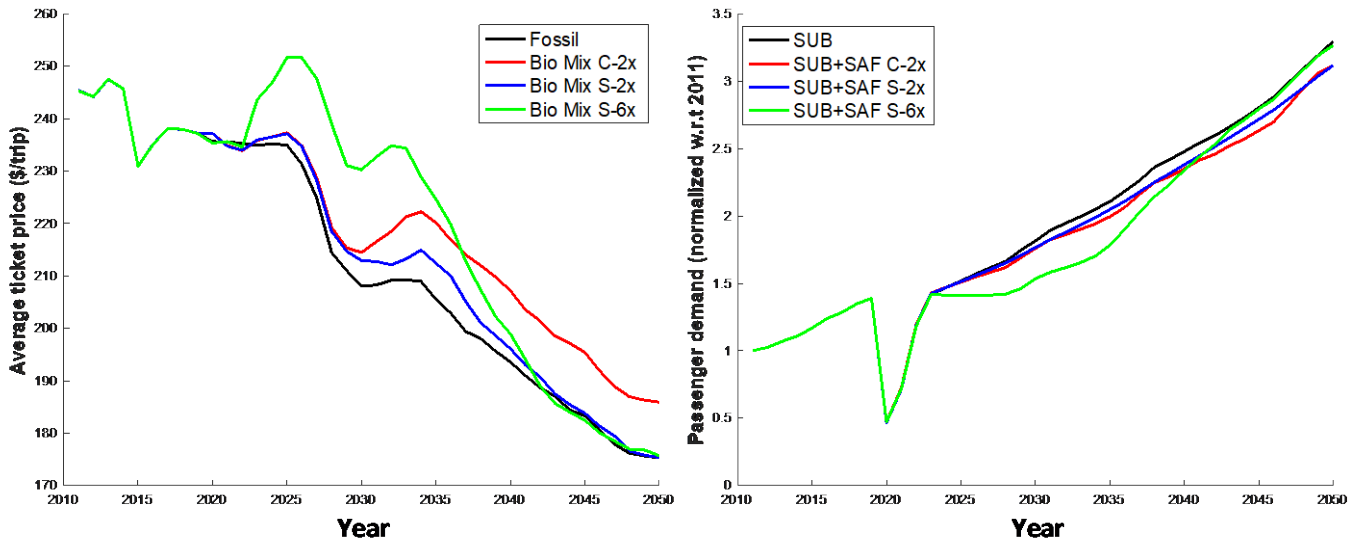


Figure 23. Average ticket price and passenger demand evolution.

The results shown are the output from the FLEET analysis, and therefore include not only the impact of fuel prices but also the impact of the evolution of the fleet of aircraft on the average ticket prices and passenger demand. Hence, the overall reduction in average ticket prices is a function of the utilization of more fuel efficient and lower-cost new-technology aircraft. Comparison of the differences among the different scenarios shows that the scenario with the highest fuel price, which assumes SAF prices starting six times that of fossil fuels (Bio Mix S-6x), has the highest ticket price and also the lowest level of passenger demand, because of the effect of demand-price elasticity. Because the fuel prices of the S-curve SAF price scenarios eventually reach the price of fossil fuels, the ticket prices in both these cases also converge to the ticket price of the scenario in which no SAF is used by the fleet of aircraft. Of note, however, given that demand-price elasticity operates on changes in ticket prices, the passenger demand of the S-2x scenario does not reach the fossil-fuel-only levels by 2050, because the change in ticket price remains insufficient to cause more passengers to choose air travel as their mode of transportation.

Subtask 3: Scenario analyses and results

Effects of different SST concepts on CO₂ emissions

To assess the impacts of the introduction of a supersonic transport into future operations, the research team considered seven configurations of SST. Higher-fidelity models were developed by colleagues at Georgia Tech, who collaborate with the authors on an FAA ASCENT project¹. These models reflect differences in fuel burn and range capability for both directions on each route. Table 14 lists the seven supersonic aircraft included in this study, each of which has a corresponding individual set of potential routes.

¹U.S. Federal Aviation Administrative (FAA) Office of Environment and Energy Award Number: 13-C-AJFE-GIT-056



Table 14. SST concepts analyzed in the study.

Seat capacity	Supersonic speed	Subsonic speed	Maximum range
55 pax	Mach 1.8, Mach 2.0, Mach 2.2	Mach 0.95	4,500 nmi
75 pax	Mach 2.2	Mach 0.95	4,500 nmi
100 pax	Mach 1.6, Mach 1.8, Mach 2.0	Mach 0.95	4,500 nmi

Potential supersonic routes consist of nonstop routes, and routes with fuel stops with minimum block time. Potential supersonic routes are required to save at least 1 hr in flight time with respect to a subsonic flight. Each of the seven supersonic configurations has a unique set of potential routes, because of the differences in fuel capacity and block time. In addition, a set of routes exists that is not supersonically feasible, because of the routing requirements necessary for over-water flight. Consider, for example, the ground track for the Lisbon, Portugal (LIS)–Oslo, Norway (OSL) route shown in Figure 24 (right). In this route, the aircraft must navigate between the English Channel, where it would be required to slow to subsonic speed (in the vicinity of populated areas) for 46 nmi and immediately climb and accelerate to supersonic speed in 9 nmi. The horizontal distance is simply not sufficient to climb to supersonic altitude with the given engine thrust. Therefore, this route is determined not to be feasible for supersonic flights.

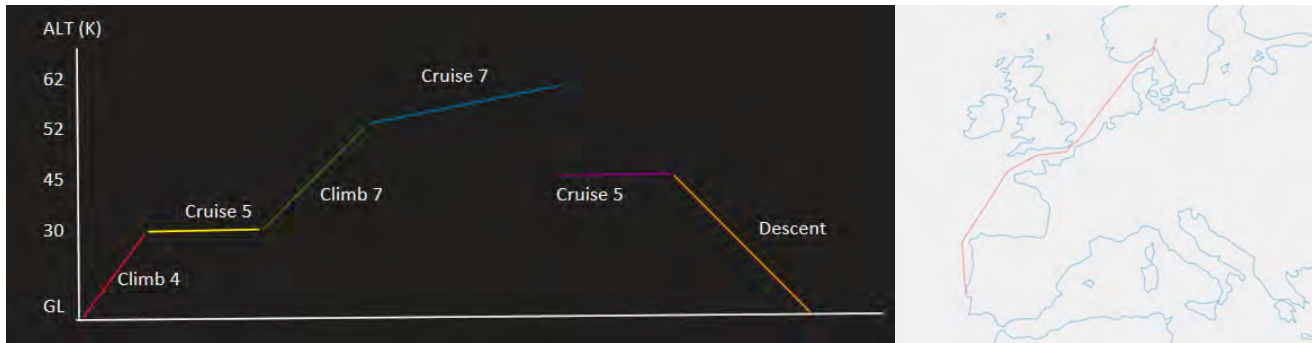


Figure 24. Mission profile of SST concepts (left) and the ground track for the LIS-OSL route (right).

The size of the route networks for each aircraft concept, divided into direct routes and routes that require a fuel stop, is shown in Table 15. The resource allocation problem determines which of these routes have sufficient demand to generate positive profit.

Table 15. Potential supersonic routes in the worldwide network.

Seat capacity	Cruise speed	Direct routes	Routes with fuel stops	Total routes
55 pax (original)	Mach 1.8	271	37	308
55 pax (modified)	Mach 1.8	686	252	938
55 pax	Mach 2.0	840	252	1,092
55 pax	Mach 2.2	776	317	1,028
75 pax	Mach 2.2	767	228	995
100 pax	Mach 1.6	929	178	1,107
100 pax	Mach 1.8	889	163	1,052
100 pax	Mach 2.0	881	163	1,044

Of note, the 55-pax, Mach-1.8 aircraft has fewer potential routes than the other SST concepts. This difference arises from the capability of this aircraft. The FLOPS model of the 55-pax, Mach-1.8 aircraft provided by the Georgia Tech team is designed for a 4,500-nmi mission and includes an engine deck that enables it to complete this mission. However, in economic missions, a routing path that maximizes over-water cruise and still achieves block time savings must be considered. For this particular aircraft, the lengths of the over-water cruise segments imposed by geography are such that a considerable number of economic missions would either not provide sufficient time savings or not have a sufficiently long cruise segment to reach the supersonic cruise altitude, given the engine performance (as discussed earlier). To retain this SST concept in the study, the team have modified the engine deck and essentially created a new SST concept that uses a scaled-down version of the engine deck used by the 55-pax, Mach-2.0 aircraft. A comparison of the modified aircraft is presented in Table 16. The implications of the smaller number of potential supersonic routes for the 55-pax, Mach-1.8 aircraft will be observed when the CO₂ emissions are estimated.

Table 16. Comparison of a modified 55-pax, Mach-1.8 SST concept.

	55 pax, Mach 1.8 (original)	55 pax, Mach 1.8 (modified)
Engine thrust (lbs)	24,313	24,313
Operating empty weight (lbs)	96,453	94,317
Maximum fuel weight (lbs)	123,539	126,746
Takeoff gross weight (lbs)	231,542	232,614

To estimate the environmental emissions and the impact of introducing a supersonic aircraft in the fleet, the research team introduces each SST configuration in the existing fleet of aircraft independently. In each simulation year, FLEET estimates the inherent airline passenger demand growth and adopts the price-demand elasticity to show how ticket-price changes can influence demand in subsequent years. FLEET assumes that supersonic demand makes up 5% of the total overall demand, and allocates the fleet of subsonic and supersonic aircraft to maximize profit. The allocation of the supersonic and subsonic aircraft demand is performed simultaneously, with the goal of maximizing airline profit. Passenger demand on supersonic routes that do not generate sufficient revenue to be profitable is served by subsonic aircraft, thus resulting in seven possible scenarios for airline operations between 2011 and 2050. Figure 25 presents the estimated growth in CO₂ emissions for all SST concepts.

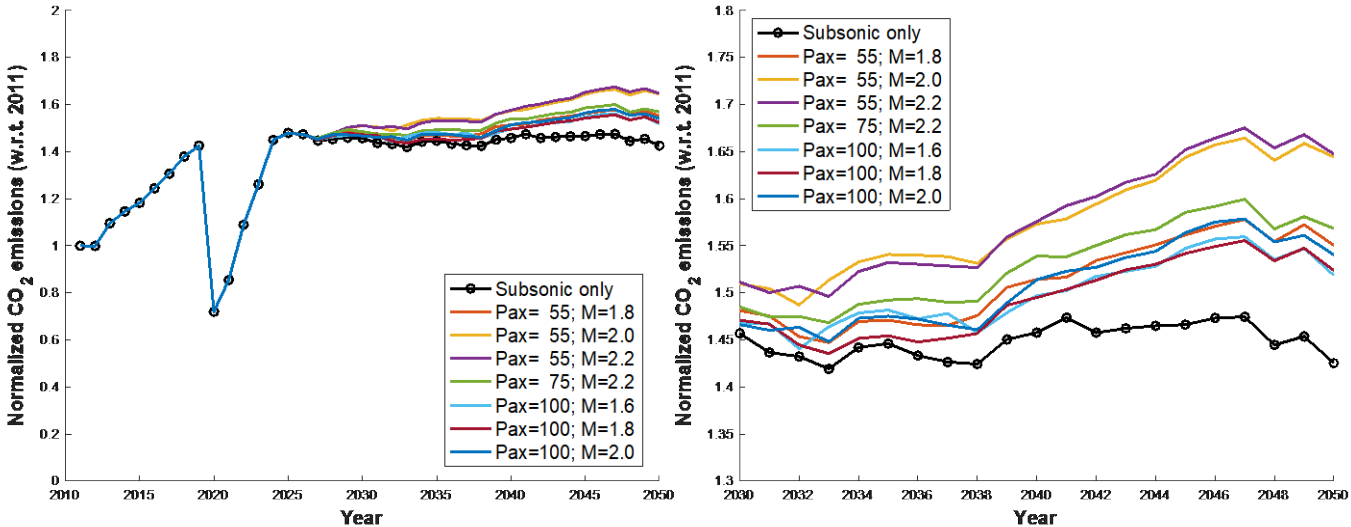


Figure 25. Estimated growth in CO₂ emissions for all SST concepts.

With respect to the baseline case (no SST), the estimated CO₂ emissions continue to be higher when the SST is part of the fleet, regardless of its size and speed, although higher passenger-capacity SST concepts lead to lower emissions. Moreover, even though higher-passenger-capacity aircraft have lower emissions per seat-nautical mile, the trends observed are also affected by the level of service in each scenario. Figure 28 shows the evolution of the number of routes serviced by SST concepts. After SST entry in service, the number of routes continues to increase as demand grows. However, the smaller-capacity SST concepts can serve more routes, in agreement with the assumption regarding available supersonic demand and the ability of the SST concept to achieve a profitable load factor. However, this finding is not the case for the 55-pax, Mach-1.8 aircraft, which serves fewer supersonic routes because of its inability to provide time savings, given the over-water routing requirement.

As shown in Figure 26 (right), the number of passengers per trip necessary to result in profitable operations is lower for the lower-passenger-capacity SST concepts. Fifty passengers per trip are needed for the 55-pax, Mach-2.2 aircraft to be profitable on 180 routes, whereas 88 pax per trip are needed for the 100-pax, Mach-2.0 aircraft to be profitable on 180 routes. Although these results depend on operating-cost assumptions, the overall trend is consistent with the relationship between aircraft gross weight (and therefore passenger capacity) and acquisition and operating costs. If demand were unchanged but the market supported a higher ticket price for supersonic travel, more routes could be served.

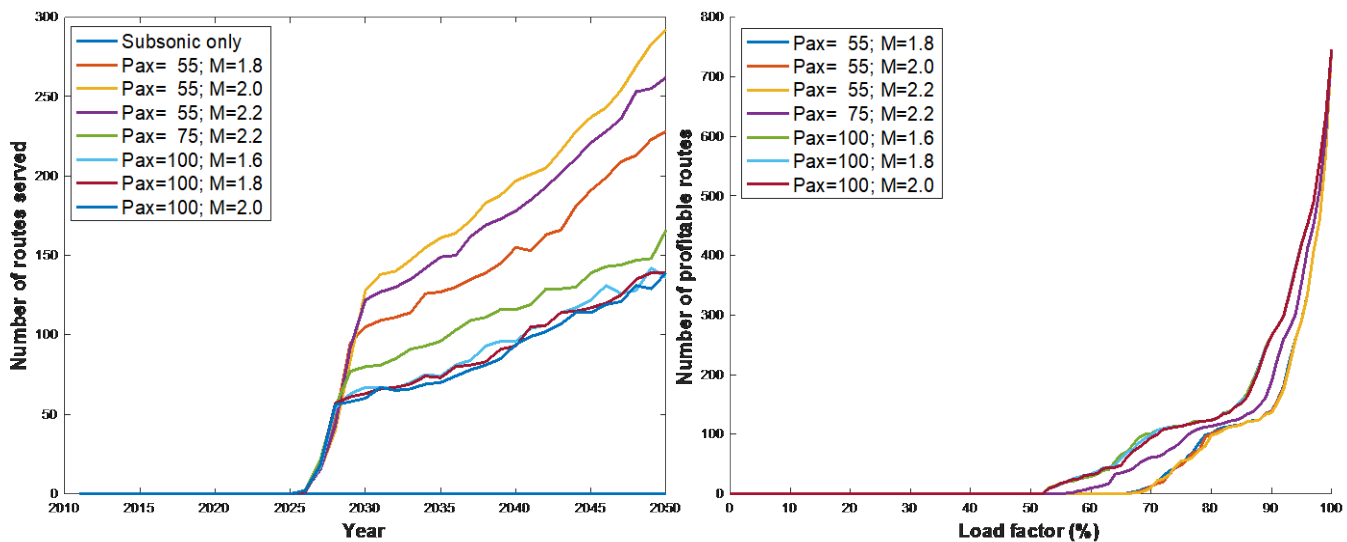


Figure 26. Routes served and profitable routes for each SST concept.

Successful and economically sustainable SST operations require a sufficiently large travel market to be profitable. The current assumption that supersonic and business-class fares are similar may be realistic, but the estimated cost to own and operate supersonic aircraft does leave little room for profits. Hence, an important question regarding SST operations is what ticket pricing can be supported by the market. Given the current assumptions regarding cost and ticket price, lower-capacity SST concepts would be able to provide more profitable operations. However, higher-fidelity market analysis including market size and price point would be important future areas of study. The level of supersonic service and environmental emissions depend on the profitability of operations. The assumption that the supersonic ticket price is based on the price of business-class travel means that operating cost is an important factor for both the profitability and environmental impacts of the SST. Travel demand is the largest driver of environmental emissions, and if future demand follows growth trends in gross domestic product, the fuel efficiency of future SST concepts must greatly improve if environmental emissions are to be curtailed. This aspect is particularly important if the removal of the overland bans results in increased demand for supersonic travel. The increased environmental impacts of supersonic aircraft present a challenge to the viability of commercial supersonic operations.

Impacts of SAF Use

To assess the impact of SAF utilization on future CO₂ emissions, the research team used the SAF models described earlier in this report, then applied FLEET to capture the changes in passenger demand due to the different fuel prices and estimated the resulting CO₂ emissions. The combined effects of changes in passenger demand and utilization of SAF on a fleet comprising only subsonic aircraft is shown in Figure 27.

Figure 27 (left) presents the estimated fuel burn for the baseline scenario in which no SAF is used, as well as the three SAF price scenarios discussed earlier (constant SAF price twice that of fossil fuel, decreasing SAF price with an initial price twice that of fossil fuel, and decreasing SAF price with an initial price six times that of fossil fuel). Because the utilization of SAF does not affect fuel burn, the differences among scenarios are due to the level of passenger demand resulting from the changes in ticket prices. As expected, passenger demand is a key driver in fuel burn and environmental emissions, and economic factors that affect passenger demand are always expected to significantly influence environmental emissions. Figure 29 (right) presents the direct impact on CO₂ emissions of the demand levels of each scenario as well as the carbon intensity of SAF. All scenarios that use SAF are expected to decrease CO₂ emissions, and the differences among them are due to the level of demand in each scenario.

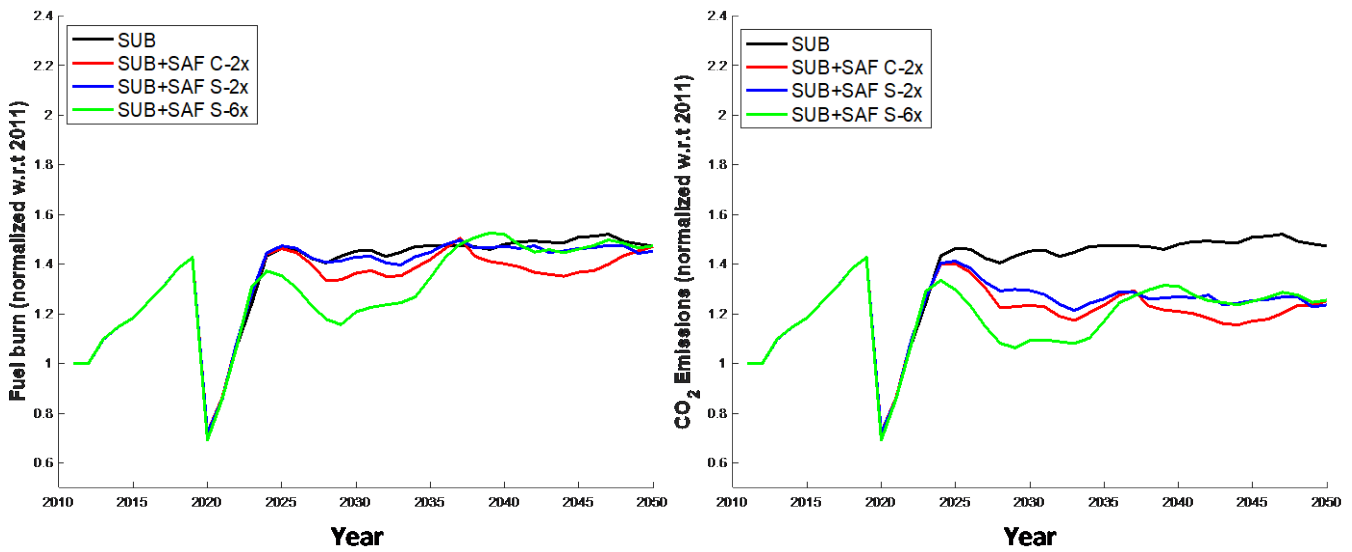


Figure 27. Estimated fuel burn and CO₂ emissions for a subsonic-only fleet of aircraft.

Impacts of SAF on supersonic operations

As shown in Figure 25, the introduction of supersonic aircraft is expected to result in relatively large increases in CO₂ emissions, although the amount of passenger demand served by supersonic aircraft is relatively low. The introduction and utilization of SAF have the potential to decrease the environmental impact of supersonic aircraft. The research team estimated this impact by considering SAF fuel prices beginning at six times the cost of fossil fuel and continuing to decrease to fossil fuel price levels by 2045. The estimated CO₂ emissions of all seven SST concepts are presented in Figure 28, in which the emissions with no SAF are presented on the left, and emissions with SAF are presented on the right.

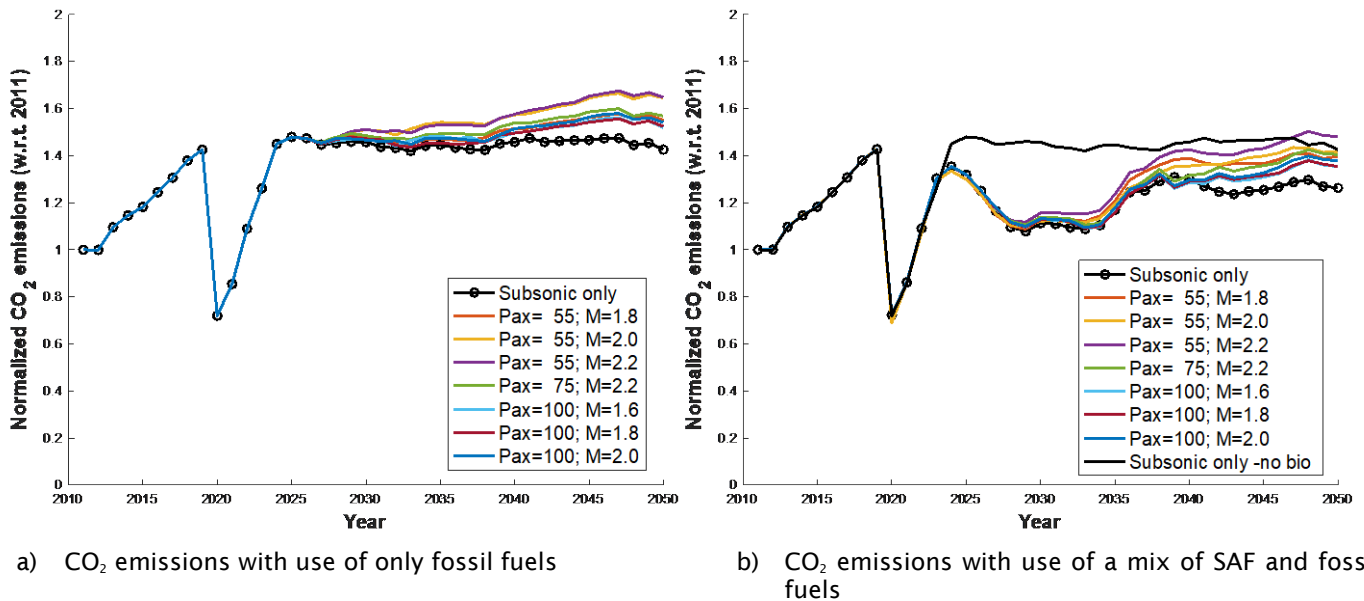


Figure 28. Estimated CO₂ emissions for a mix of subsonic and supersonic aircraft in the fleet.

As discussed previously, the introduction and utilization of SAF affects life-cycle CO₂ emissions as well as the level of passenger demand, because of the effect of demand-price elasticity. As shown in Figure 29, when SAF is used in the fleet, the initially higher fuel prices decrease passenger demand.

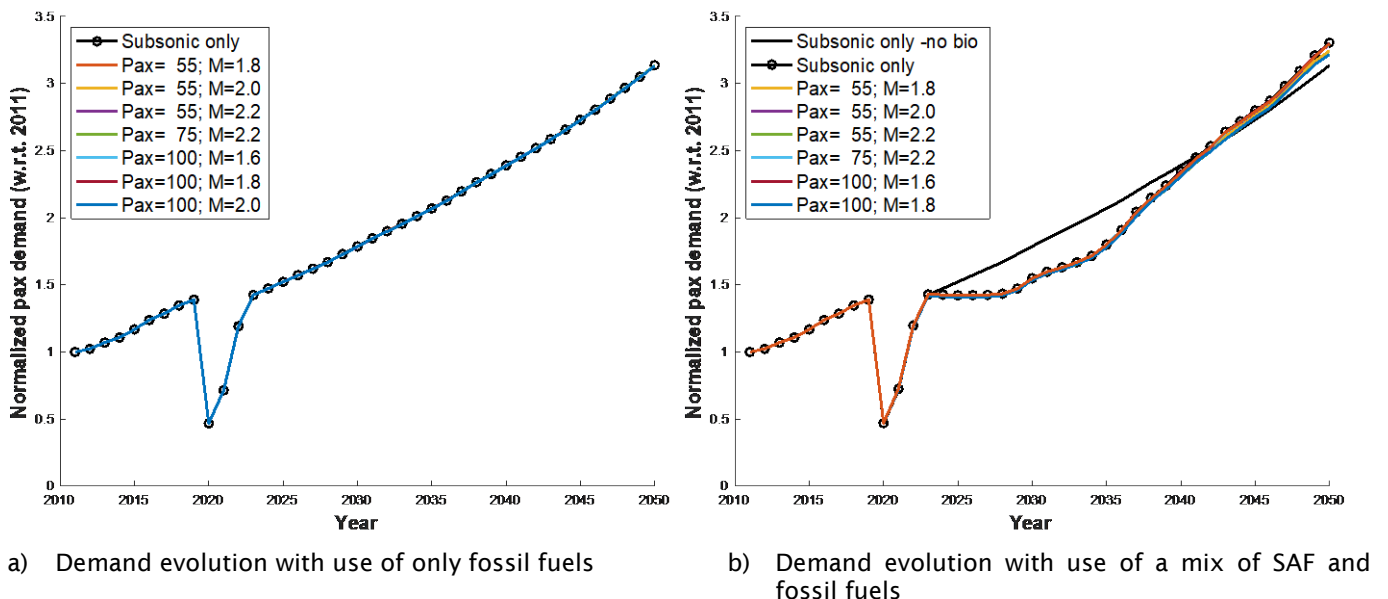


Figure 29. Demand evolution.

As the fuel price of the biomix reaches the same price as that of fossil fuel (by 2045), demand increases again. Of note, because of demand-price elasticity, which reflects the change in passenger demand as a function of the change in ticket

price, the level of increase in passenger demand is larger, thus resulting in higher demand by 2050. The higher fuel prices contribute to lower passenger demand and therefore lower emissions. However, as the price of fuel decreases, and the level of supersonic travel increases, emissions continue to increase and reach higher levels than those in scenarios in which only subsonic aircraft are used to meet passenger demand.

Future Work

Further work on this task will entail improving the fidelity of the subsonic and supersonic aircraft models to generate a better approximation of ownership and operating costs. Refinement of the operational model of the various types of business jet operators is another area of improvement that will increase the fidelity of the analysis. Identifying meaningful assumptions regarding the daily operating hours of each operator will enable the model to more accurately estimate the number of aircraft required to satisfy demand. Although the estimation of fuel burn, environmental emissions, and the number of operations at a given airport would not be affected, the ability to estimate the degree of penetration of supersonic aircraft in the fleet mix, and the evolution of new aircraft and associated aircraft technologies, will require more accurate information.

Publications

During this period of performance, the Georgia Tech team published the following:

Baltman, E., Tai, J. C., Ahuja, J., Stewart, B., Perron, C., De Azevedo, J., Vlady, T. R., & Mavris, D. N. (2022). A Methodology for Determining the Interdependence of Fuel Burn and LTO Noise of a Commercial Supersonic Transport. AIAA AVIATION 2022 Forum, 1-16. <https://doi.org/10.2514/6.2022-4110>

During this period of research, the Purdue team published the following:

Boning Yang, Mane Muharrem, Crossley William, "An Approach to Evaluate Fleet Level CO2 Impact of Introducing Liquid-Hydrogen Aircraft to a World-Wide Network," AIAA Aviation Forum 2022, <https://doi.org/10.2514/6.2022-3313>

Samarth Jain, Hsun Chao, Muharrem Mane, William A. Crossley and Daniel A. DeLaurentis "Estimating the Reduction in Future Fleet-Level CO2 Emissions From Sustainable Aviation Fuel," Frontiers in Energy Research, Nov 2021, doi: 10.3389/fenrg.2021.771705

Outreach Efforts

None.

Awards

None.

Student Involvement

The Purdue team included one graduate student and one undergraduate student during this year's effort, who have been conducting tasks in support of the project. Fung Tien-Yueh continued his PhD work, and Krinal Doma continued his undergraduate studies.

The Georgia Tech team also included the following graduate students during this year's effort:

Edan Baltman, Joao De Azevedo, Barbara Sampaio, Jiajie (Terry) Wen, Ted Vlady, Nikhil Iyengar, Zayne Roohi, Srikanth Tindivanam Varadharajan, Carter J. Tegen, and Divya K. Kalaria.

The Georgia Tech team also trained one undergraduate student, Madeleine Graham, in matters related to CFD and optimization, using the 65-pax, Mach-1.7 baseline configuration as a starting point.

Plans for Next Period

Although this project is not being continued in the next period, one more update will be provided for research performed between October 1 and December 31, 2023. This final update will focus on the final $V_2 + x$ study and will serve as the final report for the A10 project.



References

- Chao, H., Agusdinata, D. B., & DeLaurentis, D. A. (2019). The potential impacts of Emissions Trading Scheme and biofuel options to carbon emissions of US airlines. *Energy Policy*, 134, 110993.
- Doliente, S. S., Narayan, A., Tapia, J. F. D., Samsatli, N. J., Zhao, Y., & Samsatli, S. (2020). Bio-aviation fuel: a comprehensive review and analysis of the supply chain components. *Frontiers in energy research*, 8, 110.
- Hileman, J. I., Ortiz, D. S., Bartis, J. T., Wong, H. M., Donohoo, P. E., Weiss, M. A., & Waitz, I. A. (2009). *Near-term feasibility of alternative jet fuels* (No. PARTNER-COE-2009-001). Rand Corporation.
- International Energy Agency (2020) Renewables. Available at: https://iea.blob.core.windows.net/assets/1a24f1fe-c971-4c25-964a-57d0f31eb97b/Renewables_2020-PDF.pdf, accessed Aug 2023.
- International Renewable Energy Agency (2017). Biofuels for Aviation: Technology Brief. Available at: https://www.irena.org/-/media/Files/IRENA/Agency/Publication/2017/IRENA_Biofuels_for_Aviation_2017.pdf
- Ritchie, H., & Roser, M. (2023). Climate change and flying: what share of global CO2 emissions come from aviation?. *Our World in Data*.
- Sissine, F. (2010). Renewable Fuel Standard Program (RFS2) Regulatory Impact Analysis. *Assessment and Standards Division, Office of Transportation and Air Quality*.
- Stratton, R., Wong, H. M., & Hileman, J. (2010). *Life cycle greenhouse gas emissions from alternative jet fuels* (No. PARTNER-COE-2010-001). Partnership for Air Transportation Noise and Emissions Reduction.
- U.S. Department of Energy, Office of Energy Efficiency and Renewable Energy (2020). Sustainable Aviation Fuel: Review of Technical Pathways. Available at: <https://www.energy.gov/sites/default/files/2020/09/f78/beto-sust-aviation-fuel-sep-2020.pdf>



Project 018 Community Measurements of Aviation Emission Contributions to Ambient Air Quality

Boston University School of Public Health

Project Lead Investigator

Kevin J. Lane
Assistant Professor
Department of Environmental Health
Boston University School of Public Health
715 Albany St. T4W
Boston, MA 02118
617-414-8457
klane@bu.edu

University Participants

Boston University School of Public Health (BUSPH)

- P.I.s: Kevin J. Lane, Assistant Professor; Jonathan I. Levy, Professor and Chair
- FAA Award Number: 13-C-AJFE-BU, Amendment 7
- Period of Performance: August 30, 2022 to September 30, 2023
- Tasks:
 1. Construct regression models using monitoring data, flight activity, and meteorological covariates collected through August 31, 2022 to determine the contributions of aviation sources to particle number concentrations (PNCs) at varying distances from Boston Logan International Airport (KBOS)
 2. Conduct descriptive analyses of air pollution concentrations collected during 2020-2022 to inform aviation source-attribution modeling efforts being conducted by ASCENT Project 19
 3. Continue targeted mobile and stationary monitoring in communities near KBOS to allow for future analyses of changing aviation source contributions through atypical (reduced flight activity during pandemic years) and typical periods
 4. Utilize insights from monitoring and modeling efforts to date to provide recommendations on the ideal attributes of future monitoring campaigns at other airports (i.e., ideal airport and community attributes, design of site network, frequency, duration, etc.)
 5. Provide regression model outputs for comparisons between atmospheric dispersion models developed by ASCENT Project 19 and aviation-attributable concentrations determined from our regression models

Project Funding Level

FAA provided \$599,000 in funding. Matching funds were provided by a non-federal donor to the Women's Health Initiative cohort studies as cost-sharing support to Boston University through Project 3.

Investigation Team

Boston University School of Public Health (aka BUSPH)

Prof. Jonathan I. Levy, ScD (ASCENT BUSPH Director and Project 18 Co-Investigator Professor of Environmental Health, Chair of the Department of Environmental Health) is the Boston University P.I. for ASCENT. He initiated ASCENT Project 18 and serves as the director of BUSPH ASCENT research.

Prof. Kevin J. Lane, PhD (ASCENT Project 18 P.I.: Assistant Professor of Environmental Health, Department of Environmental Health) joined the Project 18 team in July 2017. Dr. Lane has expertise in the assessment of ultrafine particle (UFP) exposure, geographic information systems, statistical modeling of large datasets, and cardiovascular health outcomes associated with air pollution exposure. He has contributed to study design and



data analysis strategies and, as of October 1, 2017, has taken over the primary responsibility for project execution. Dr. Lane also contributes to the manuscripts and reports produced.

Dr. Prasad Patil (Assistant Professor) is a machine-learning and regression modeling expert who is assisting Dr. Lane with modeling of the 2017–2019 UFP data.

Sean Mueller (doctoral student) has been analyzing aviation-related PNC results obtained during COVID-19. Daniel Kojis is a doctoral student examining model generalizability and transferability between sites.

Breanna van Loenen and Maria Bermudez (research assistants) are supporting the analysis of mobile monitoring and stationary monitoring data.

Tufts University

Dr. John Durant, PhD (Associate Professor) oversees the Tufts Air Pollution Monitoring Laboratory (TAPL) team, leads the development of field study design, and contributes to scientific manuscript preparation.

Dr. Neelakshi Hudda, PhD (Research Professor) joined the Project 18 team in September 2020 and is managing the TAPL team as well as mobility data analysis, field study design and implementation, and scientific manuscript preparation.

Camille Gimilaro, Olivia Moore, Isabelle Woollacott, and Lily Sandholm (undergraduate students) are working on the mobile monitoring platform and helping to clean the air pollution data.

Project Overview

The primary goal of ASCENT Project 18 for the 2022–2023 time period was to conduct an air pollution monitoring campaign beneath flight paths to and from Boston Logan International Airport, using a protocol specifically designed to determine the magnitude and spatial distribution of UFPs in the vicinity of arrival flight paths. Data were collected to assess whether aircraft emissions, particularly arrival emissions, significantly contribute to UFP concentrations at appreciable distances from the airport. Task 1 aims to further investigate the contributions of variation sources to PNCs at stationary sites using regression and machine-learning models. Tasks 2 and 3 leverage the infrastructure previously developed for our field campaign and enable measurements that address a broader set of research questions than those evaluated in the previous monitoring year, with additional data collection for UFP size distributions and nitrogen dioxide (NO₂). Task 4 utilizes the investigation team's insight on monitoring and modeling efforts to provide best-practices recommendations for future monitoring campaigns at other airports and to create a publicly available best-practices report. Finally, Task 5 utilizes the atmospheric dispersion models developed by ASCENT Project 19 for comparison with aviation-attributable pollutant concentrations from our regression models to further investigate the ability of statistical analyses of real-time concentration measurements to capture aircraft source contributions.

We have continued our monitoring campaign to collect and analyze community air pollution measurements to determine the contributions of in-flight arrival and departure aircraft to ground-based concentrations. We have used state-of-the-art air pollution monitoring technology that can measure different air pollutants every 1–5 s. Stationary sites have been established at varying distances from flight paths for Boston Logan International Airport, with measurements collected across multiple seasons. We have also employed a mobile monitoring system (electric vehicle) outfitted with the same monitoring equipment to drive throughout these communities to better characterize geographic variations in air pollution. Statistical analyses will compare the stationary and mobile measurements with flight activity data from the U.S. FAA and meteorology to determine aircraft contributions to ground measurements. We will compare these source attribution estimates with comparable outputs from atmospheric dispersion models.

A summary of all project methods and data collection is included below to describe the continued application of Project 18 data and 2022–2023 study tasks.

Task 1 – Construct Regression Models Using Monitoring Data, Flight Activity, and Meteorological Covariates Collected through August 31, 2022 to Determine the Contributions of Aviation Sources to PNCs at Varying Distances from KBOS

Boston University School of Public Health

Objectives

The mobile and fixed-site monitoring data collected from 2020–2022 under ASCENT Project 18 were further analyzed to investigate the spatiotemporal patterns of aviation-related contributions to UFP, as well as the relative influence of flight arrivals and departures in different locations and underneath different runways. Broadly, this effort builds on the methodological foundation developed under ASCENT Project 18 and within earlier PARTNER projects, in which we developed and applied statistical techniques to model short-term pollution measurements with high variability and high autocorrelation. The fact that these data were collected during the pandemic across time periods in which flight activity changed substantially while traffic followed slightly different patterns provides a “natural experiment” that will enhance our ability to conduct source attribution.

Research Approach

We have used two statistical approaches to quantify aviation contributions to community ambient air quality. First, we used multivariable generalized linear models to examine the association between air pollutant concentrations and real-time flight activity, accounting for aircraft locations in space relative to the monitor and including terms for wind speed/direction, temperature, mixing height, and other relevant meteorological covariates. Second, we applied machine-learning regression models such as random forest modeling and gradient boosts to improve model performance, while applying Shapley analysis to provide source attribution quantification. Each study site was modeled individually to assess the location-specific impact of aircraft arrivals and departures along with meteorological and other local environmental conditions, and in future work, combined models will be explored. Because of the complexity of interactions among predictors (i.e., flight activity will be influenced by wind speed and direction, which will also affect plume dispersion and resulting concentrations at individual monitors), we explored advanced statistical techniques for covariate selection and model ensembling, including random forest regression and other machine-learning regression techniques. Preliminary findings from an application of machine-learning techniques to our UFP measurements indicate that machine-learning methods are able to explain more variability than generalized linear models or related techniques. These predictions will subsequently be shared with Project 19, where investigators are developing comparable estimates of aviation-attributable concentrations near Logan Airport, and we will conduct analyses to compare predictions from dispersion models and regression models.

Mobile monitoring data were used to (a) generate summary statistics characterizing the spatial and spatiotemporal variability of measured pollutants in the study area, (b) aid in source attribution, and (c) build and evaluate spatially explicit predictive models of pollutant concentrations in the East Boston, Chelsea, Revere, and Winthrop communities. Exploratory spatial data analyses were performed to identify areas of clustering for spatial autocorrelation of PNC within the mobile monitoring routes, which may warrant further analysis or special treatment in subsequent modeling efforts. Source apportionment of measured pollutants and drivers of variability in the mobile monitoring data were examined via geographically weighted regression and/or cluster analysis.

With each of the regression models, we are able to estimate the amount of measured air pollution attributable to flight on a short-term and long-term basis. In other words, by zeroing out the flight activity terms and determining the predicted concentrations, we can ascertain the portion of measured concentrations attributable to aircraft arrivals and departures.

Broadly, these analyses make multiple important contributions not available elsewhere. We worked with a unique dataset of stationary and mobile measurements collected over the first two years of the COVID-19 pandemic in a variety of locations near a major airport, and we applied advanced statistical techniques to better ascertain source contributions. This work builds upon the aviation air pollution exposure literature and yields novel insights.

Major Accomplishments

We successfully developed a random forest machine-learning model to predict PNCs based on changing meteorology and flight activity variables. PNC data were collected by TSI water-based condensation particle counters (CPCs) at 1-s resolution and then aggregated to 15-min and hourly averages. The model was developed based on 2017 data collected from six stationary air monitoring sites along 4R/4L, which is the most frequently used arrival pathway into Logan airport. Figure 1 presents corresponding pollution roses, which indicate that the PNC is elevated when the sites are downwind from the airport. PNC data were collected by CPC devices at 1-s resolution and then merged into hourly averages as a proxy for the total UFP. An initial descriptive analysis of these data is illustrated in Figure 2, which shows the hourly PNC distribution across the six included study sites along with the frequency of data collection per hour at each location.

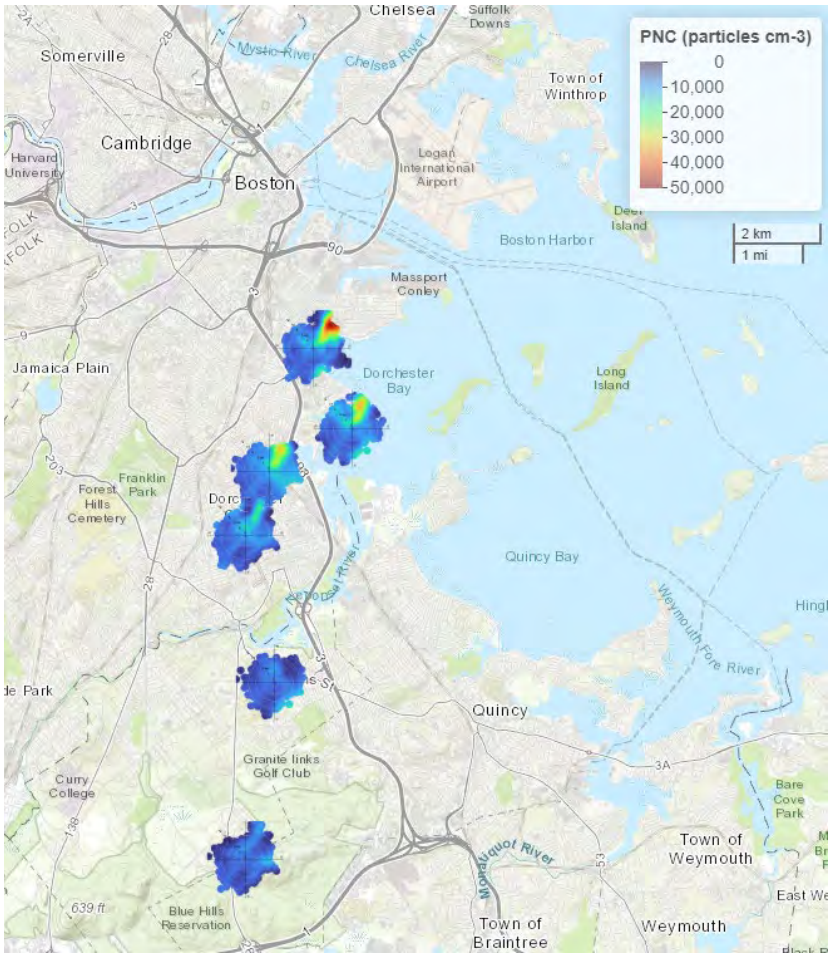


Figure 1. Map of six monitoring sites downwind of Logan Airport that were active in 2017. PNC: particle number concentration.

The random forest model predicted UFP concentrations based on changing meteorology and flight activity variables. The model was developed based on 2017 data collected from the six stationary air monitoring sites (N1, N2, I1, I2, F1, F2)¹ that were active between April and September. The hourly average PNC for each site is colored-coded in Figure 2 to show

when overlapping periods of two or more monitoring sites had coincidental data collected across the study sites.

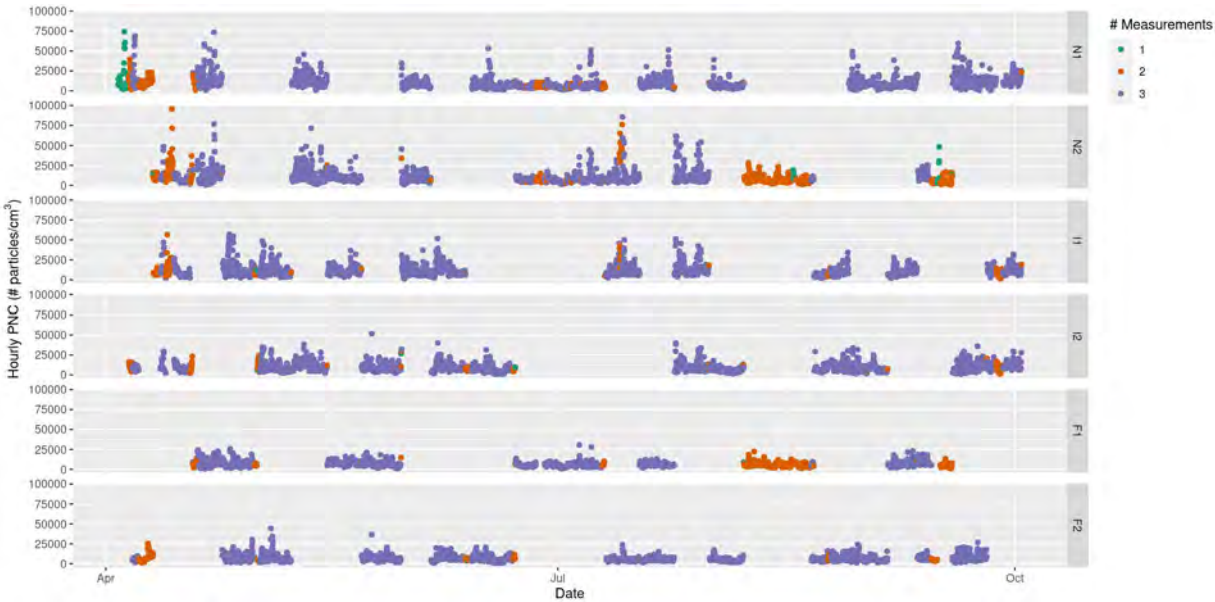


Figure 2. Distribution of hourly particle number concentration (PNC) measurements across sites. Colors indicate how many overlapping observations were made across sites for a given hour.

The data in Figures 1 and 2 were used to develop random forest models for each site. Model performance was evaluated using R^2 and the root mean squared error (RMSE). Prediction variables included in the analysis were meteorological parameters, specifically wind direction, wind speed, temperature, precipitation, humidity, air pressure, and cloud coverage, as well as flight activity variables including total airport arrivals, total departures, and total combined hourly flights. The analysis outlines the associations between these variables and the observed PNC, which were used to train each random forest model to predict PNC under various conditions. The overall model performance for each individual site measured as R^2 was 0.65–0.73 (Table 1), indicating that our approach has a strong ability to explain the observed variation in PNC at each site.



Table 1. Combined and site-specific random forest model performance measured as R², root mean squared error (RMSE), and model accuracy/sensitivity/specificity when the observed particle number concentration (PNC) and predicted PNC are broken into quintiles.

Model	R ²	RMSE	Accuracy	Sensitivity and Specificity				
				0-19	20-39	40-59	60-79	80-100
Overall	0.753	0.319	0.58	0.75, 0.94	0.50, 0.87	0.45, 0.86	0.49, 0.87	0.73, 0.93
N1	0.7	0.369	0.55	0.70, 0.93	0.46, 0.86	0.43, 0.86	0.44, 0.86	0.73, 0.93
N2	0.697	0.381	0.55	0.76, 0.94	0.47, 0.87	0.39, 0.86	0.44, 0.86	0.70, 0.92
I1	0.723	0.306	0.53	0.73, 0.93	0.46, 0.87	0.40, 0.85	0.39, 0.85	0.68, 0.92
I2	0.702	0.330	0.54	0.77, 0.94	0.46, 0.86	0.40, 0.85	0.41, 0.85	0.66, 0.91
F1	0.669	0.314	0.53	0.75, 0.94	0.46, 0.86	0.39, 0.85	0.42, 0.86	0.64, 0.91
F2	0.654	0.325	0.53	0.72, 0.93	0.44, 0.86	0.39, 0.85	0.40, 0.85	0.68, 0.92

When sites were combined into a single model, the performance improved overall. Whereas our group is the first to apply machine-learning models to PNC prediction in aviation-exposed environments, our model performance is similar to that of roadway PNC models. The outputs of the combined random forest modeling of PNC are shown in Figure 3. We observe a high R² and low RMSE, similar to road traffic UFP machine-learning efforts.

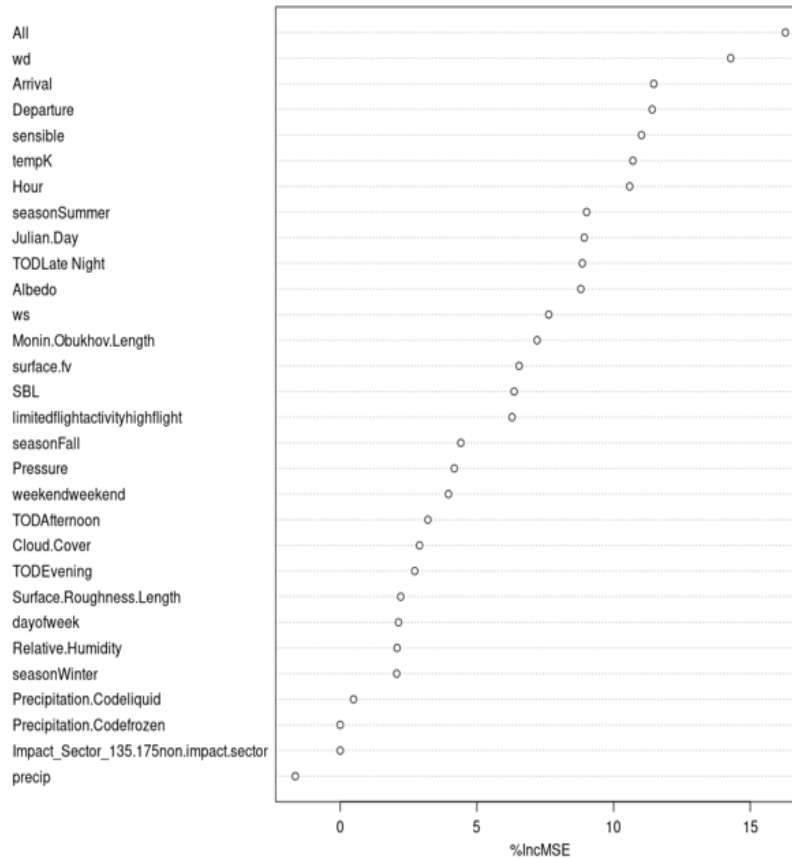


Figure 3. Outputs of the random forest particle number concentration model.

However, when we examined the relative contribution of each variable to the PNC prediction by individual sites, there was significant variation in the importance of arrival and departure flights between community sites located closer to the airport versus further away. Variable importance was defined as the percent improvement in mean square error when a given variable was included in the random forest model compared with when it was excluded from the model. Table 2 provides a ranking from 1 (most) to 16 (least) with regards to variable performance. The most important variable in predicting UFP concentrations across all six sites was wind direction, whereas variables such as cloud coverage and precipitation had low significance at all site locations.

Table 2. Relative variable importance by stationary monitoring site, including variance by site. The variables are ranked in relative importance from 1 (most) to 16 (least) important. WD: wind direction; WS: wind speed.

Variable	Overall model	N1	N2	I1	I2	F1	F2
WD (cos)	1	1	1	2	1	3	3
WS	2	3	3	3	2	2	2
Rel. Hum.	3	5	2	8	3	1	1
Temp (K)	4	4	4	6	4	5	4
WD (sin)	5	2	5	1	6	7	5
Total Arrivals	6	6	6	5	5	10	8
Pressure	7	8	7	7	9	6	7
Day	8	9	9	10	7	4	6
A_4L4R	9	7	13	4	8	14	11
Total Dep.	11	10	11	9	10	12	12
Month	10	12	8	11	11	8	10
Hour (cos)	12	13	10	12	12	9	9
Hour (sin)	13	11	12	13	14	11	13
Cloud Cover	14	14	14	14	13	13	14
D_4L4R	15	15	15	15	15	15	15
Precip	16	16	16	16	16	16	16
N	12042	2274	2094	1851	2125	1809	2147
R ²	73.61	69.97	69.52	72.38	70.22	66.85	65.19

Meteorological parameters such as wind direction, wind speed, and temperature are important, as they show strong contributions in the model. We also observe that arriving flights have a stronger contribution than departing aircrafts at the monitoring sites closest to the airport.

Building on the modeling of data collected prior to the COVID-19 pandemic, we developed additional machine-learning models to assess the contribution of aviation-related activity to the community PNC using SHAP waterfall plots. This approach allows us to quantify the increase or decrease above the hourly average PNC due to all model variables for each hour of the model. Using a gradient boost model, we found the average prediction of our model to be a PNC of approximately 15,000 #/cm³ per hour for the study area. SHAP takes each record of data in the model and quantifies each predictor’s contribution to increase or decrease the hourly average PNC to explain the difference between the study area mean across all hours and a single observed hourly average. Figure 4 provides an example of 1 hr of data in the model for which the PNC was 50,000 #/cm³. The SHAP plot provides a quantification of each covariate’s contribution to the difference between the prediction (50,000 #/cm³) and mean (15,000 #/cm³) across all model parameters.

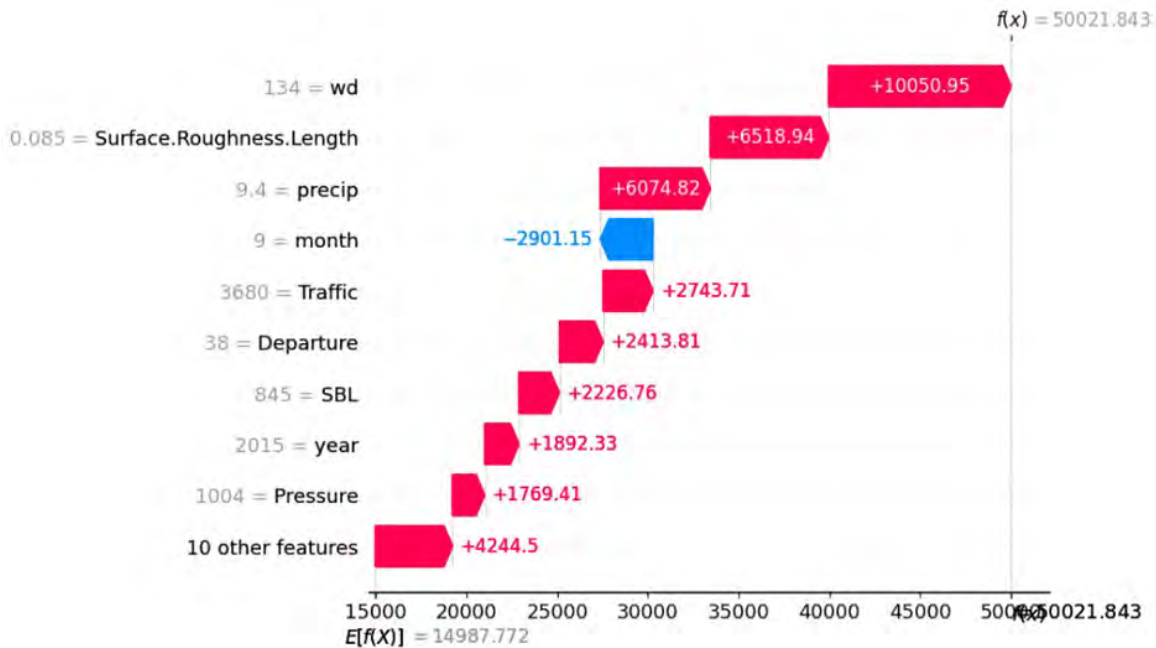


Figure 4. SHAP waterfall plot showing the contributions of different features to the hourly average particle number concentration prediction in the gradient boost model. WD: wind direction.

We see that given the set of feature values shown in Figure 5, the contribution of wind direction (“wd”) when aligned with being downwind from the airport contributed approximately 10,000 #/cm³ in this hour of the model, corresponding to the largest contribution in the model. In contrast, traffic, with 3,680 vehicles, contributed 2,700 #/cm³ PNC. There were 38 departures at the airport during this hour, which contributed 2,400 #/cm³ PNC. Overall, we observe that high flight activity with increased traffic and the wind being downwind in the impact sector resulted in approximately 3-fold higher PNC compared with the average (50,000 #/cm³ versus 15,000 #/cm³ = ~3-fold increase).

By using aggregated predicted SHAP values across all hours of the dataset from 2018–2022 for our Chelsea monitoring site, we have obtained a robust dataset capable of quantifying source contributions with higher accuracy. Figure 5 shows how the top features in the dataset impact the model’s prediction, ranked from top to bottom by their mean absolute SHAP values across all hours of data. Each hourly prediction is represented by a single dot on each feature row, with the x position of the dot determined by the SHAP-predicted increase or decrease in PNC from the total model hourly average of 15,000 #/cm³. Temperature, year, and wind speed are the most significant features, on average (Figure 5). The PNC was the highest when the wind was from the south-southeast (SSE), providing a face validity comparison, as this result would be anticipated from a physical model as well as traditional regression approaches. When the wind is from the SSE direction, the site is downwind from the airport. Holding all other variables constant, we can see this feature contributes 5,000 #/cm³ to 35,000 #/cm³ above the mean predicted PNC of 15,000 #/cm³. Furthermore, we can see that, on average, traffic contributed more to the predicted PNC than flight activity, and departure flights had a higher average effect magnitude than arrival flights.

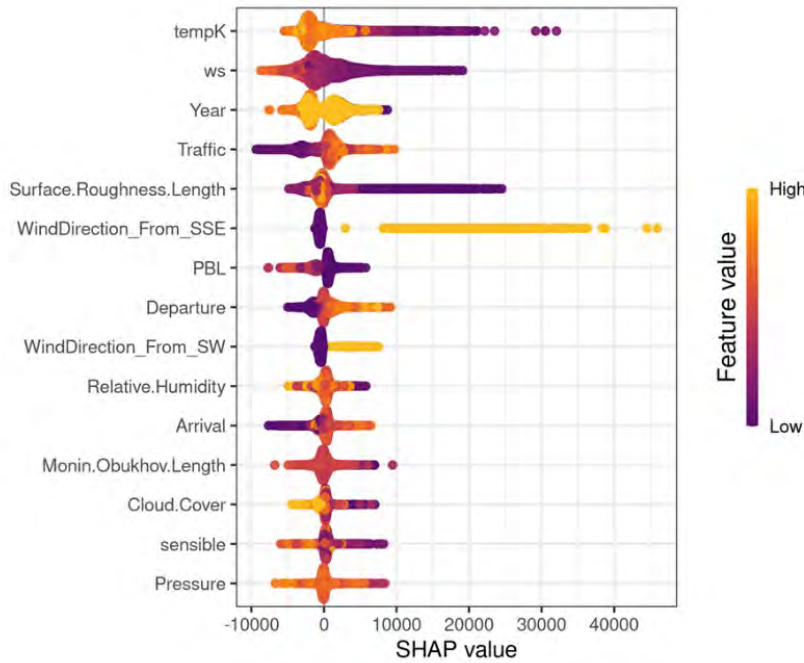


Figure 5. Plot of predicted contributions from gradient boost model features to increasing/decreasing the hourly average particle number concentration (measured in $\#/cm^3$, referred to here as the SHAP value). Each hour is represented by a single dot on each feature row, with the position of the dot determined by the SHAP value. SSE: south-southeast; SW: southwest; WS: wind speed.

Our model is able to address covariate interactions as well as linear and non-linear predictions of PNC, which allowed us to further explore the relationship between departures, traffic, and wind direction in PNC using SHAP dependence plots (Figure 6). SHAP dependence plots enable a quantification of possible feature interactions in the machine-learning model for PNC prediction. The dependence plot of the feature “road traffic per hour” (Figure 6A) shows that, overall, the predicted PNC increases as traffic increases. We see a steeper rate of increase from 0–4,000 automobiles per hour compared with a traffic level of $>4,000$ automobiles per hour. The dependence plot of the interaction between wind direction and departures per hour (Figure 6B) shows a non-linear effect of flight departures on PNC. We see that when there are fewer than 30 departure flights per hour, there is a negligible increase in the predicted PNC above the mean prediction. However, when there are more than 30 departure flights per hour, we see a non-linear increase in contribution to the PNC, indicating an interaction between flight activity and being downwind from the airport. Although increased departure flight activity results in increased PNC from all wind directions, the rate of increase is higher when the wind is from the SSE ($3,750 \#/cm^3$) versus any other wind direction ($1,250 \#/cm^3$). This difference of approximately $2,500 \#/cm^3$ results from the interaction between wind direction and flight activity when flight activity is 30–50 flights per hour. The plot of wind speed dependence (Figure 6C) shows that, in general, as the wind speed increases, the predicted PNC decreases. Overall, when hourly average wind speeds are low ($<2.5 \text{ m/s}$), this feature contributes an increase of $5,000\text{--}8,000 \#/cm^3$ to the predicted PNC above the mean PNC. By examining all points (non-stratified), we see an exponential decrease in PNC as the wind speed increases. However, when the wind is from the SSE and the wind speed is $5\text{--}10 \text{ m/s}$, the wind speed contributes to an increase of $2,500 \#/cm^3$ above the mean prediction, whereas for all other directions, the wind speed contributes an average decrease of $2,500 \#/cm^3$ below the mean prediction. This difference of approximately $5,000 \#/cm^3$ indicates an interaction between wind speed and wind direction when the wind speed is $5\text{--}10 \text{ m/s}$.

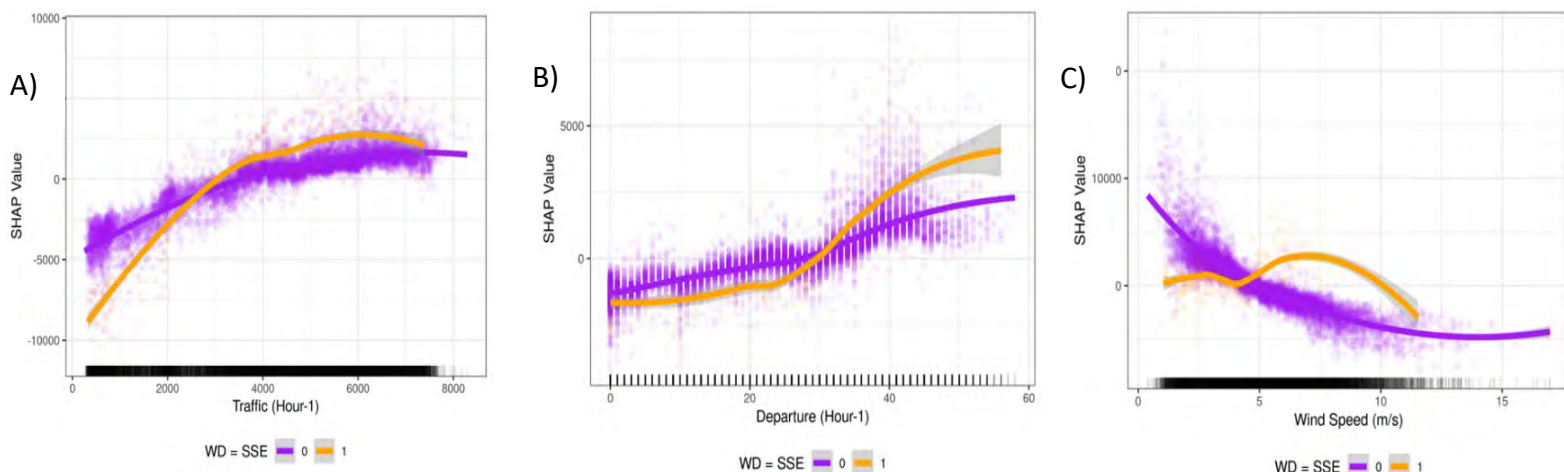


Figure 6. SHAP dependence plots. The y-axis represents the SHAP value (the feature’s contribution to the difference between the actual prediction and mean prediction), and the x-axis represents the (A) road traffic per hour, (B) number of departures for all runways per hour, and (C) wind speed averaged over 1 hr. The points are colored by wind direction (WD), with yellow indicating that the wind originates from the south-southeast (SSE) and purple indicating that the wind originated from another direction.

Milestones

In addition to our major accomplishments, we have also reached the following milestones:

- Completed significant advancements in mobile monitor spatiotemporal data analysis to elucidate the limitations of stationary monitoring alone in determining accurate UFP exposure across geographic locations in communities around Logan Airport
- Finalized two upcoming manuscripts, one on machine-learning models to predict UFP exposure and one on the particle size distribution of UFPs at the Winthrop and University of Massachusetts (UMASS) monitoring sites
- Presented preliminary machine-learning models at the International Society for Environmental Epidemiology
- Presented at the Aviation Emissions Characterization meeting and ASCENT Fall 2022 and Spring 2023 meetings (Kevin Lane)

Publications and Presentations

- Chung CS, Lane KJ, Black-Ingersoll F, Kolaczyk E, Schollaert C, Li S, Simon MC, Levy JI. Assessing the impact of aircraft arrival on ambient ultrafine particle number concentrations in near-airport communities in Boston, Massachusetts. *Environ Res.* 2023 May 15; 225:115584. View Related Profiles. PMID: 36868447; PMCID: PMC10079358; DOI: 10.1016/j.envres.2023.115584;
- Mueller SC, Hudda N, Levy JI, Durant JL, Patil P, Lee NF, Weiss I, Tatro T, Duhl T, Lane K. Changes in Ultrafine Particle Concentrations near a Major Airport Following Reduced Transportation Activity during the COVID-19 Pandemic. *Environmental Science & Technology Letters.* 2022; 9(15):706-711.
- Mueller S, Patil P, Levy JI, Hudda N, Durant JL, Gause E, Loenen BV, Lane KJ. Examining Impacts of Cross-Validation Approaches on Machine Learning Model Performance for Ultrafine Particle Exposure Assessment. *International Society for Exposure Science. Annual Conference, Chicago, Illinois, USA.* 2022 (Oral).
- Lane KJ and Durant J. ASCENT Project 18 Air Pollution monitoring and Modeling. ASCENT Fall meeting 2022, Washington DC. (Oral).
- Lane KJ and Durant J. Airport Air Quality Monitoring and Source Apportionment. FAA Aviation Emissions Characterization Meeting, Washington DC. May 2023 (Oral).

Outreach Efforts

None.

Awards

None.

Student Involvement

Sean Mueller, PhD student in the Department of Environmental Health, Boston University
Daniel Kojis, PhD student in the Department of Biostatistics, Boston University

Plans for Next Period

We plan to submit our two machine-learning manuscripts for publication. We are also developing a combined stationary and mobile monitoring machine-learning model using data from 2020–2023.

Task 2 – Conduct Descriptive Analyses of Air Pollution Concentrations Collected During 2020–2022 to Inform Aviation Source-Attribution Modeling Efforts Being Conducted by ASCENT Project 19

Objectives

Utilizing NO₂ air pollution data collected during the 2021–2022 campaign, we built on the methods and insights from our descriptive analyses of stationary site UFP data collected during our previous monitoring campaigns. We analyzed concentrations as a function of wind conditions and flight activity to help inform the structure and form of subsequent regression models. The contributions of aircraft to ambient NO₂ concentrations will be preliminarily examined by comparing measurements during periods of high versus low aviation activity and by considering concentration patterns as a function of meteorological conditions and other key predictors across sites and pollutants. We examined concentrations across sites as a function of wind speed and direction under varying flight activity conditions, as our analyses to date have shown elevated UFP concentrations at sites close to arrival flight paths only when the sites are downwind from those flight paths. Results from these and other descriptive analyses will inform the development of a regression model in future years, which is beyond the scope of our efforts in the proposed project year.

Research Approach

We have continued working directly with ASCENT Project 19, with the long-term objective of improving both dispersion and regression modeling approaches to quantify arrival and takeoff aircraft contributions to NO₂ concentrations in communities near KBOS. In collaboration with Project 19, we are sharing data to provide monitored data and to coordinate the collection of flight activity data to be used in both projects. The use of accurate and high-resolution flight activity data from the FAA (e.g., aircraft type, number of engines, engine type, latitude, longitude, elevation, tail number) is essential for both Projects 18 and 19 for the development of an aviation attribution regression model and emission inventory for dispersion modeling, respectively. We included the location of each flight as well as basic aircraft characteristics, which could be linked with the Aviation Environmental Design Tool to determine aircraft-specific attributes that may be predictive of emissions and corresponding concentrations.

These efforts allow us to (a) compare air pollution monitoring data collected under Project 18 against dispersion model outputs developed under ASCENT Project 19, (b) identify key predictors in both dispersion and regression modeling of aviation-related air pollution, (c) use the same flight activity data and covariates to develop a regression model (Project 18) and to support dispersion modeling tasks (Project 19) for aviation-attributable NO₂, and (d) compare regression model contributions with dispersion model outputs in the future. Comparisons of both project models will guide future efforts toward the development of a robust model to predict fine-scale concentrations of aviation-attributable air pollution.

Major Accomplishments

We continued to monitor NO, NO₂, and NO_x in 2022 at stationary sites (Chelsea and Winthrop) while also collecting data via our mobile monitoring platform. The aim was to continue data collection and to conduct descriptive statistical analyses during 2022 to inform aviation source attribution modeling efforts conducted by ASCENT Project 19. Direct absorption measurements of NO₂ were obtained via cavity-attenuated phase shift spectroscopy (model CAPS NO₂, Aerodyne Research, Inc., Billerica, MA). A total of 1,831,356 NO, NO₂, and NO_x data points were collected in 2022 (Table 3) with a mean

concentration of 10.6 ppb. The hourly average NO, NO₂, and NO_x dataset had a total of only 4,032 data points, as shown in Table 4.

Table 3. Monitoring data for NO, NO₂, and NO_x at the Winthrop site for 2022. SD: standard deviation.

	NO (N=610452)	NO2 (N=610452)	NOx (N=610452)
ppb			
Mean (SD)	3.14 (6.62)	12.7 (7.15)	15.8 (12.2)
Median [Min, Max]	1.60 [0, 302]	10.3 [0, 160]	12.1 [0, 462]

Table 4. Hourly average monitoring data for NO, NO₂, and NO_x at the Winthrop site for 2022. SD: standard deviation.

	NO (N=1344)	NO2 (N=1344)	NOx (N=1344)
mean_ppb_hr			
Mean (SD)	2.73 (4.65)	12.9 (6.11)	15.6 (9.60)
Median [Min, Max]	1.69 [0, 75.6]	11.0 [0, 44.6]	12.9 [0, 117]

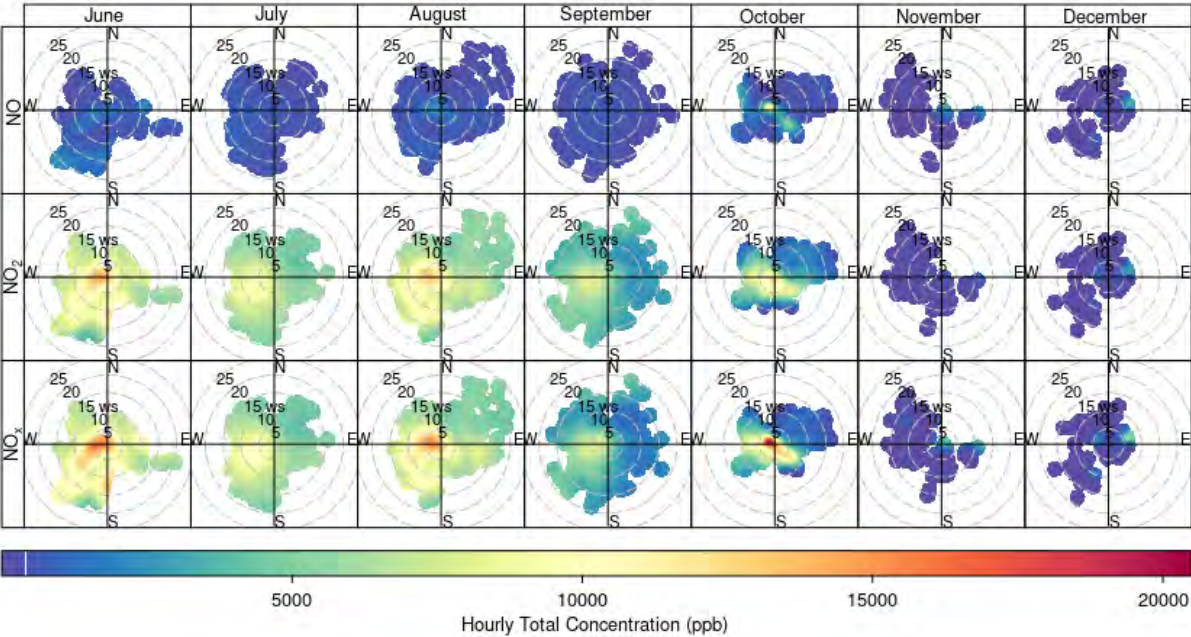


Figure 7. Hourly average NO, NO₂, and NO_x pollution rose plots for the Winthrop stationary site during 2022.

Milestones

In addition to our major accomplishments, we have also reached our core milestone of incorporating descriptive analyses of these data and sharing these data with ASCENT Project 19.

Publications

None.

Outreach Efforts

None.

Awards

None.

Student Involvement

None.

Plans for Next Period

We plan to continue monitoring NO₂ at our Boston sites and to include our Dulles monitoring campaign setup as well.

Task 3 – Continue Targeted Mobile and Stationary Monitoring in Communities Near KBOS to Allow for Future Analyses of Changing Aviation Source Contributions Through Atypical (Reduced Flight Activity During Pandemic Years) and Typical Periods

Objectives

We are currently conducting air pollution monitoring at four stationary sites at varying distances from the airport and the arrival flight path to runways in communities around KBOS, and we have collected substantial mobile monitoring data. While maintaining a comparable data collection effort is beyond the scope of the project during the upcoming year, given our heavy emphasis on data analysis and deriving insights regarding future field efforts (see Task 4), we will continue to collect measurements at core sites to ensure that we have a long-term concentration dataset for future analyses. Precisely which sites to maintain will depend on multiple factors, including field logistics, preliminary insights from statistical analyses, and key questions that appear unresolved in either regression model development or in planning for future investigations of aviation source contributions as input for Task 4. We will prioritize sites for which we have previously established relationships with individuals or businesses, to simplify the process of monitor deployment. We will also incorporate additional monitoring equipment to enhance our air pollution analysis to include UFP size distribution and NO/NO₂.

Research Approach

Stationary field monitoring

We have collected air pollution data at a single site in Chelsea since April 2020, allowing us to capture nearly the entire COVID-19 time period with a full mobile and stationary monitoring launch that began September 2020. UFP data have also been collected from three other long-term monitoring sites in Revere (starting September 2020), South Boston (starting May 2021), and Winthrop (starting January 2021), allowing for a comparison of PNC results within our monitored communities. Each monitoring site is located more than 200 m from major roadways and intersections and is near the arrival and takeoff locations on runways 4/22 or 9. The map in Figure 8 indicates the locations of the stationary monitoring sites in relation to the airport.

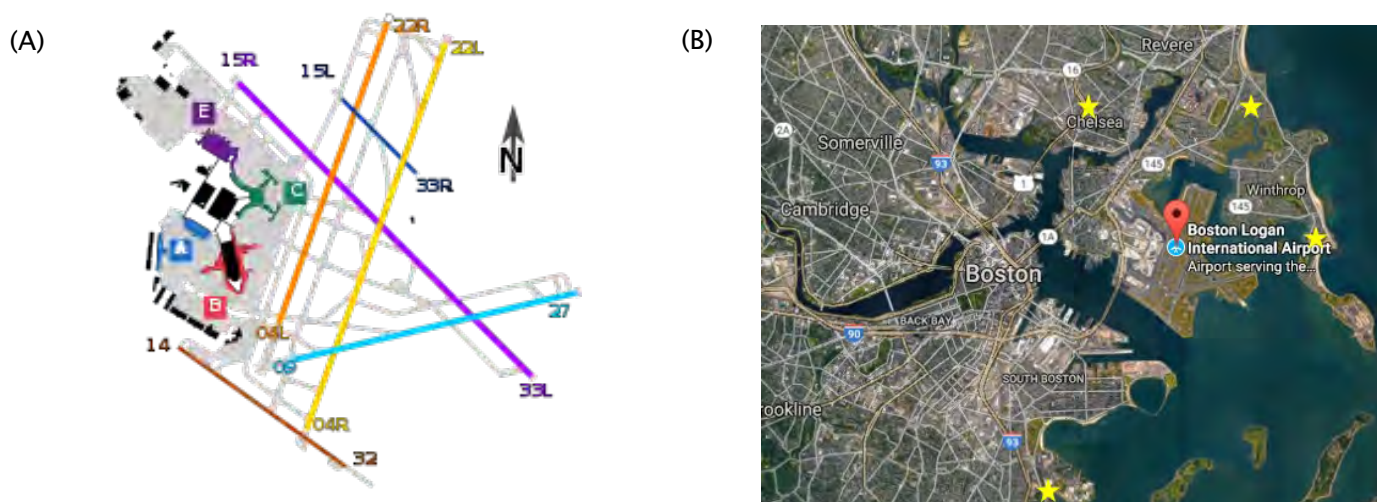


Figure 8. (A) Boston Logan International Airport runway configuration. (B) ASCENT Project 18 monitoring sites.

Each stationary site is outfitted with a climate-controlled enclosure that allows for year-round sampling. Monitoring sites have a combination of UFP (TSI CPC or TSI fast mobility particle sizer [FMPS]), NO/NO₂/NO_x (2BTechnology), and black carbon (Magee Scientific AE22) monitors. An example of the box setup with climate control is shown in Figure 9.

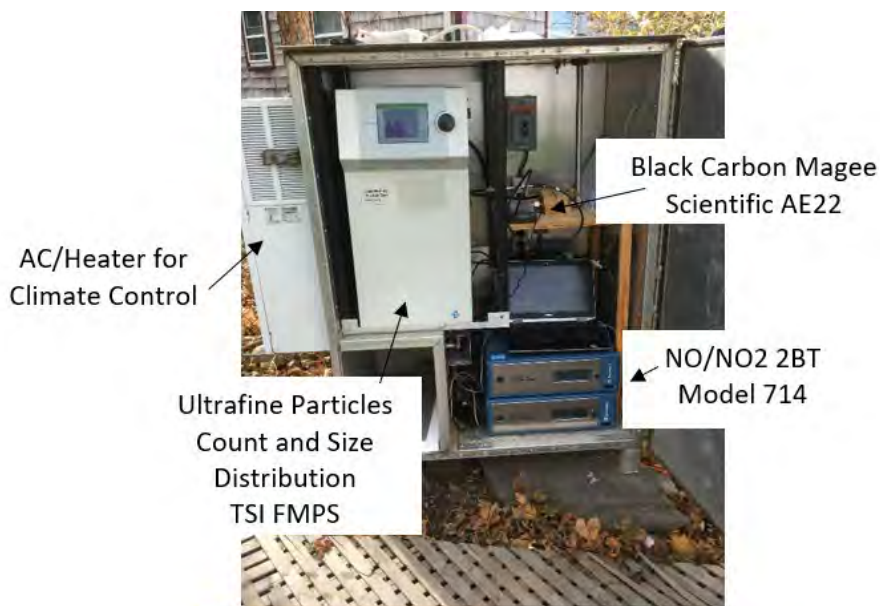


Figure 9. Long-term air pollution monitoring box at Winthrop, MA. AC: air conditioner; FMPS: fast mobility particle sizer.

Mobile monitoring

TAPL instruments Real-time measurements of air pollutants are also being acquired with the TAPL, a mobile platform equipped with fast-response instruments for monitoring gas- and particle-phase pollutants that facilitates the collection of reliable and robust data (Figure 10). The TAPL is an electric vehicle (2017 Chevrolet Bolt) equipped with instruments powered by six 12-V marine deep cycle batteries, which are connected in series to a 2-kW inverter/charger (Xantrex 2000). Individual measurements are matched to location by 1-s-interval global positioning system (GPS) readings. The TAPL monitoring setup is currently outfitted with a combination of air pollution monitors, including a CPC to measure UFP

(model 3775, TSI; 4–1,000 nm), an aethalometer to measure black carbon (model AE-33, Magee Scientific), and a CO₂/water vapor analyzer (model LI-840A, LI-COR Environmental, Lincoln, NE). Direct absorption measurements of NO₂ are obtained via cavity-attenuated phase shift spectroscopy (model CAPS NO₂, Aerodyne Research, Inc., Billerica, MA).

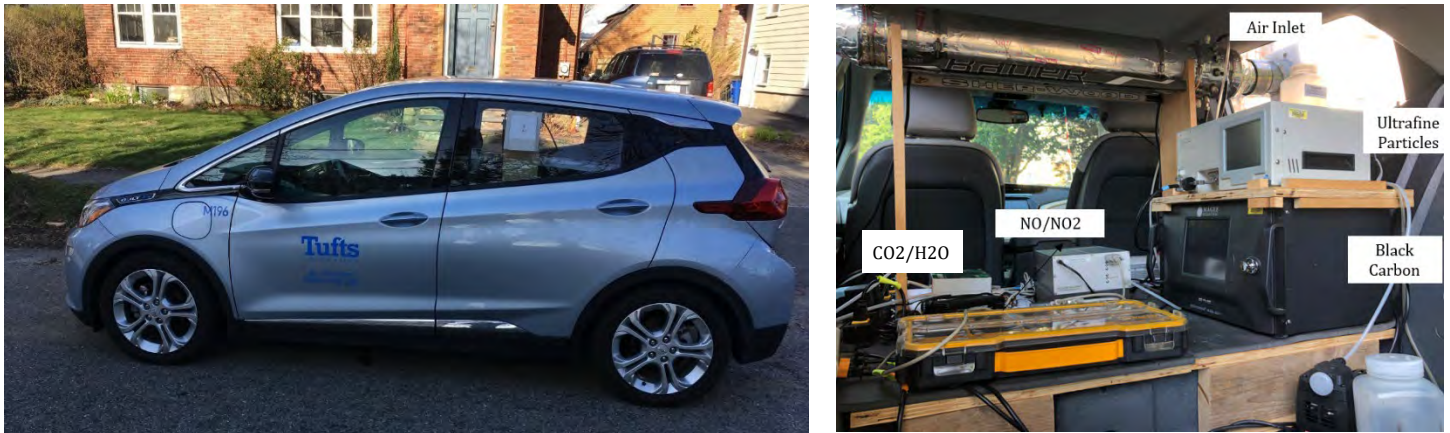


Figure 10. Exterior and interior images of the Tufts Air Pollution Monitoring Laboratory.

Data acquisition and data processing Data from the instruments are recorded in real time on a laptop in the TAPL. After each monitoring day, the data files are screened and collated in a master database. Air pollution measurements are matched to location by 1-s-interval GPS readings. The database then undergoes a quality assurance and quality check process, where the data are screened for errors flagged by instruments and quality criteria developed by the research team. Both the raw data and quality-assurance-processed database are stored on a secure server.

Monitoring routes Two monitoring routes that encompass the communities impacted by the most commonly used runways at Logan were developed: (1) a route to the north (north route) that includes all or parts of the communities of Winthrop, Revere, Chelsea, East Boston, and Lynn located 1–4 miles from the airport and (2) a route to the south (south route) that includes all or parts of the communities of South Boston, Dorchester, and Quincy located 1–6 miles from the airport. The routes are shown in Figure 11. Criteria applied in determining the routes included (a) coverage of communities in proximity to the airport, (b) coverage under main flight paths, (c) spacing of transects underneath flight paths such that spatial gradients of air pollutants can be assessed over a large area, (d) ability to perform measurements on multiple transects in an area within a relatively short period of time (1–2 hr) to capture both spatial and temporal changes in aviation impacts within the study area, and (e) ability to cover the entire route within the period associated with peak and off-peak flight activity periods (3–4 hr).

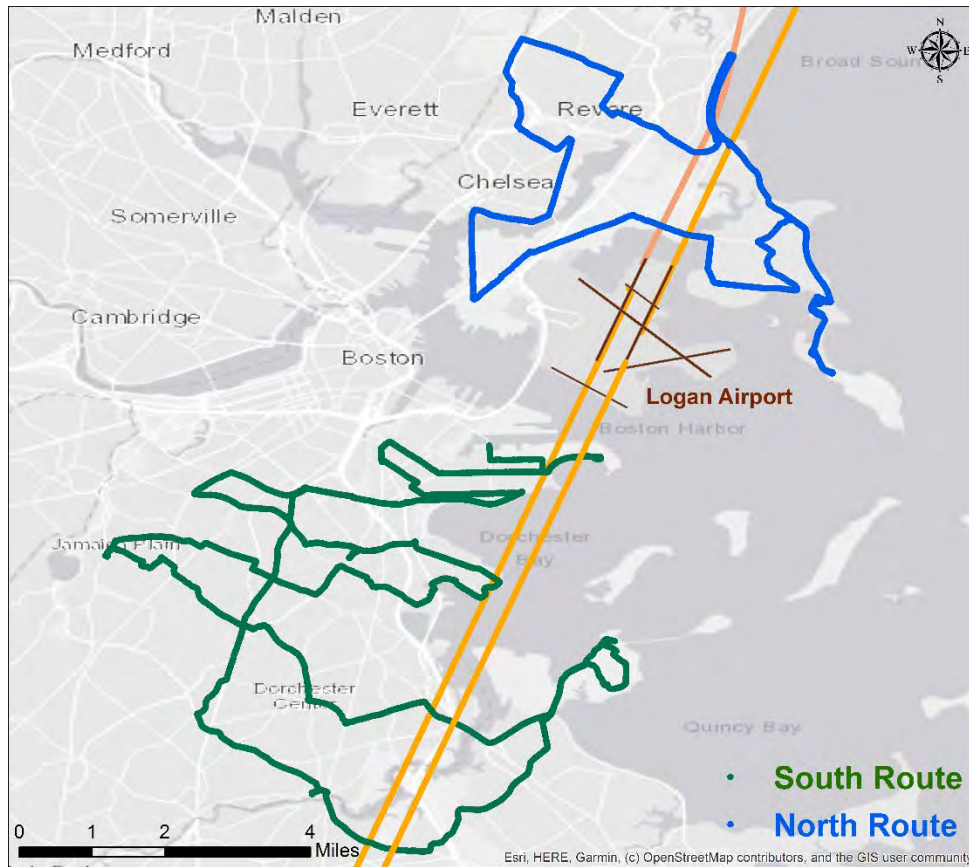


Figure 11. Map showing the north and south monitoring routes, the airport, and typical flight trajectories for arrivals on multiple runways at Logan Airport.

Beginning in May 2022, “adaptive” sampling routes were developed to complement the north and south routes. The spatial coverage of the adaptive routes is determined on a day-to-day basis according to observed and predicted wind direction and runway usage. In contrast to the routine routes, the adaptive routes cover a smaller geographic area but have a higher spatial resolution (Figure 12). The adaptive routes are selected based on the regions within the study domain expected to lie downwind of the airport on a given sampling day and are monitored to delineate and characterize impacts from landing/takeoff (LTO) activities within neighborhoods downwind of Logan Airport.



Figure 12. Map showing an example of an adaptively selected route, the airport, and the prevailing wind direction observed during sampling.

Monitoring schedule and protocol Measurements are collected under a variety of meteorological and airport-activity conditions. We have adopted a purposeful, flexible monitoring approach rather than a rigid, repetitive schedule. The advantage of this approach is that it allows us to capture a much wider range of meteorological and airport-activity conditions and to thereby more fully characterize the main factors that influence aviation-related pollutant concentrations in the two study areas. The following criteria are used to guide the monitoring schedule:

1. Maximal coverage of the periods of the day associated with peak and off-peak flight activity,
2. Coverage of the periods of the day associated with predictable diurnal variations in air pollution due to changes in meteorological factors (e.g., temperature, mixing height, on-shore and off-shore winds),
3. Coverage of seasonal wind patterns (we are aiming to reasonably mimic the natural distribution [2/3 westerly flow vs. 1/3 easterly flow] that is prevalent in the research area and are scheduling the monitoring runs to cover different wind speed/direction combinations),
4. Coverage of various temperature regimes (e.g., seasonal and diurnal), and
5. Coverage of various active runway configurations.

The standard operating procedure for preparation of a mobile monitoring route (see Figure 13) begins with (a) checking weather conditions including wind direction and speed, as reported by Massport, (b) checking a real-time flight tracker to identify flight paths and which communities are being flown over, (3) preparing monitoring equipment and driving to the starting point of the route, and (4) driving the route and subsequently downloading data.

Mobile Monitoring Setup & Processing

(1) Check weather and record wind, temperature, and other conditions

(2) Check Flight Tracker to predict where planes will be landing

FlightAware <https://flightaware.com/>
 Weather data <https://forecast.weather.gov/MapClick.php?lat=42.39&lon=-71.08&lg=english&FcstType=digital>

Monitoring Date	Route	Time (24 hr)	Temp (F)	Winds	Wind Speed (m)	Sky Cover (%)	Precipitation (%)	Landing On (Runway)
8/10/2020	Winthrop		90-92	SW (5-7 mph)				
8/12/2020	Winthrop		90-84	W (6-9 mph)				
8/14/2020	Dorchester	13	81	NE		40		4's
8/14/2020	Dorchester	14	82	E		40		4's
8/14/2020	Dorchester	15	82	E		40		4's
8/14/2020	Dorchester	16	82	E		40		4's
8/14/2020	Dorchester	17	81	E		41		4's
08/18/2020	Winthrop	12	83	WSW	9			22
08/18/2020	Winthrop	13	82	W	14			22
08/18/2020	Winthrop	14	84	W	14			22
08/21/2020	Winthrop							



(3) Start machinery and wait for warmup period (30 minutes)

- CPC 3007/3783 (UFP)
- LI-840A (CO2 and H2O)
- AE33 (Black Carbon)
- Nitrogen dioxide

Commuter time to routes:
 South route: 40 mins round trip
 North route: 40 mins round trip
 South Route: 3 hrs/loop
 North Route: 1.25 hrs/loop

(4) Post monitoring data processing in MapSource, Aerosol Instrument Manager, Excel, and ArcMap (1.5 hrs)

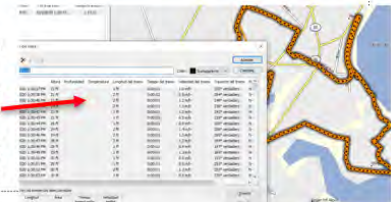


Figure 13. Standard operating procedure for mobile monitoring route preparation. CPC: condensation particle counter; UFP: ultrafine particle.

Major Accomplishments

Stationary monitoring of pollutants continued at the four sites, which include Chelsea (since April 2020), Revere (since July 2020), Winthrop (since August 2020), and UMASS (since February 2021). Each site collected 31-100 million records of 1-s PNC data. The pollution plots in Figure 14 show UFP concentration versus wind speed and wind direction at four stationary monitoring sites from January 2021 to December 2022.



Figure 14. Polar plots of ultrafine particle number concentration (PNC) versus wind speed and direction at four sites near Logan Airport based on measurements from January 2021 to December 2022.

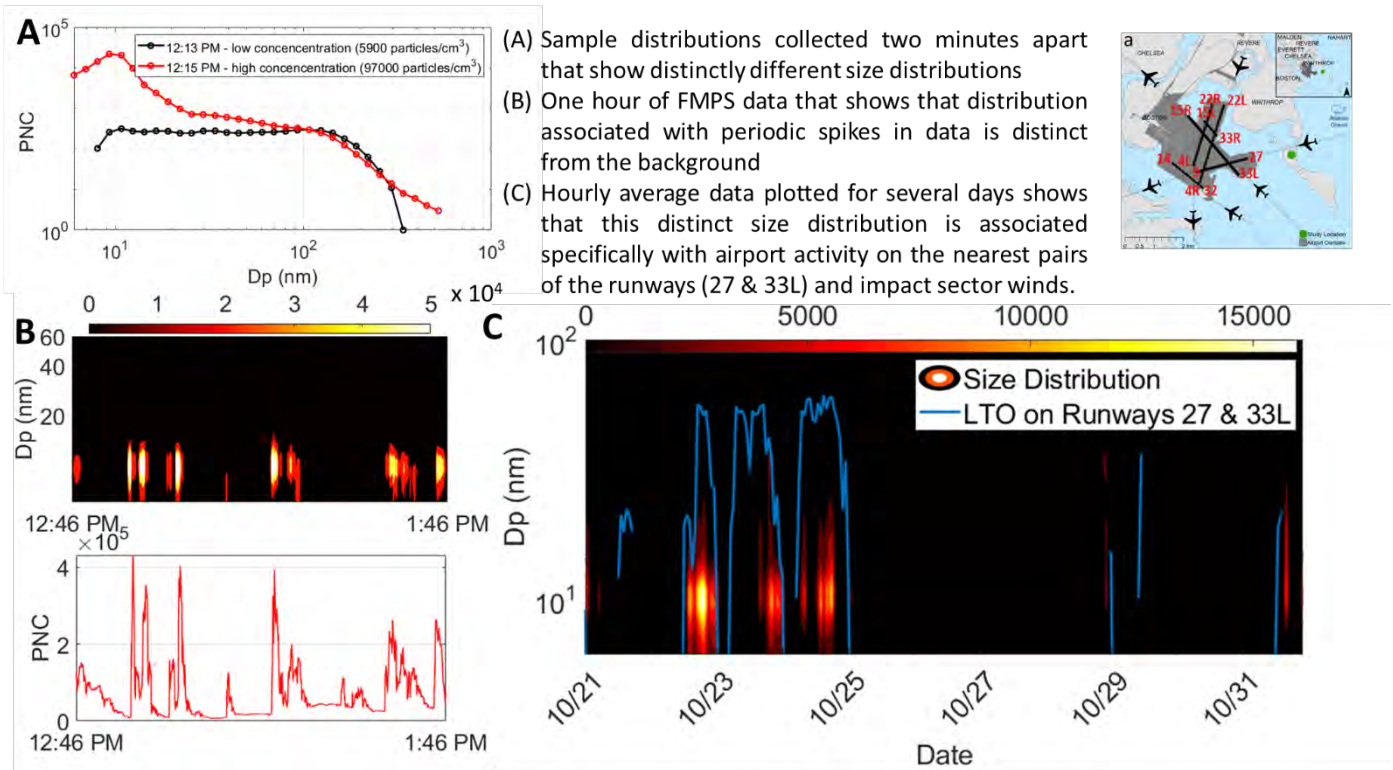


Figure 15. Size distribution measurements near Logan International Airport. (A) Sample size distributions collected 2 min apart. (B) One hour of fast mobility particle sizer (FMPS) data distribution associated with periodic spikes in data. (C) Hourly average data plotted for several days showing that a distinct size distribution is specifically associated with airport activity on the nearest pairs of runways (27 & 33L) and impact sector winds. LTO: landing/takeoff; PNC: particle number concentration.

Figure 16 provides polar plots showing hourly PNC by particle size distribution (6–25 nm) measurements at the UMASS stationary site in South Boston. We observe meaningful variation in the hourly PNC size distribution, with higher PNC levels corresponding to particle sizes of 8–19 nm when the dominant wind direction is downwind from the airport.

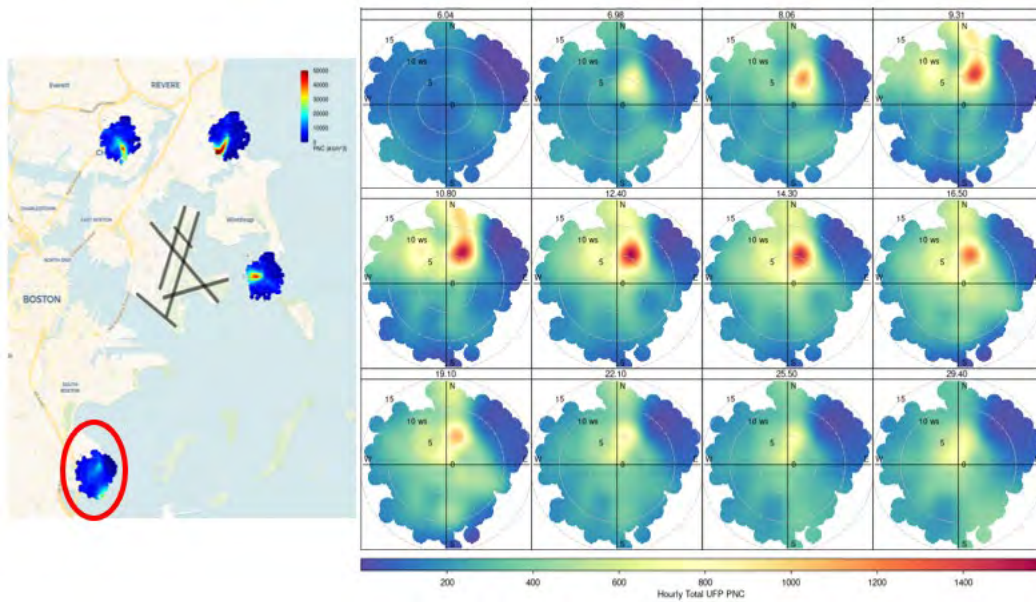


Figure 16. Pollution rose plots showing particle size distribution measurements at the University of Massachusetts stationary site (size: 6–40 nm).

Figure 17 presents polar plots of the hourly PNC by particle size distribution measurements (>40 nm) at the UMASS stationary site in South Boston. We observe unexpected high PNC levels corresponding to particle sizes of 80.6–143.30 nm in the southeast when the dominant wind direction is upwind from the airport.

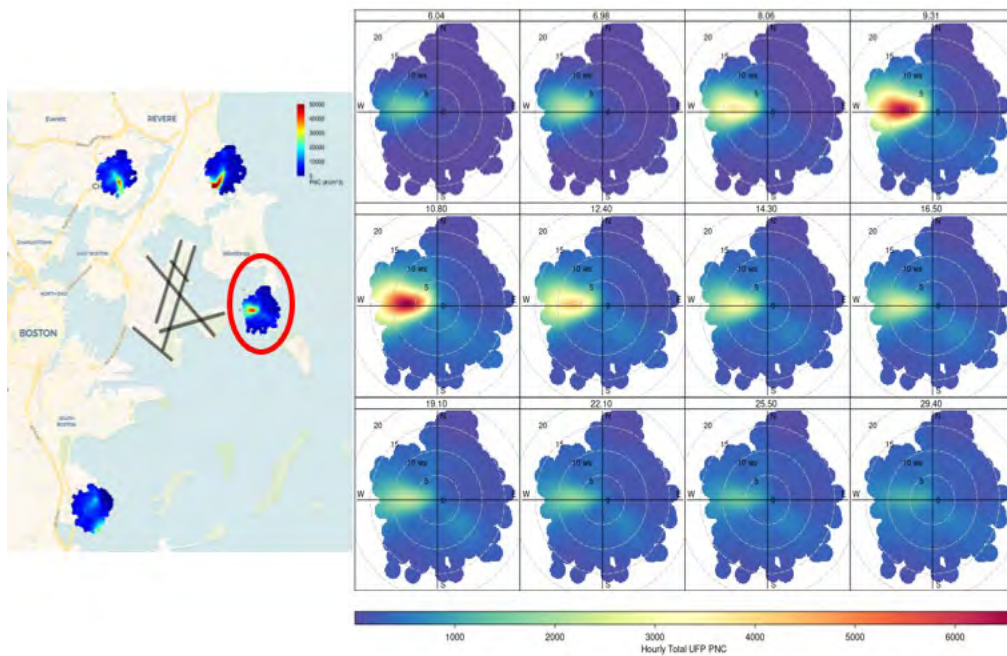


Figure 17. Pollution rose plots showing particle size distribution measurements at the Winthrop stationary site (size: 6–40 nm).

Mobile monitoring data analysis We successfully completed preliminary analyses on the mobile monitoring PNC data for North Boston, which includes all or parts of the communities of Winthrop, Revere, Chelsea, East Boston, and Lynn located 1-4 miles from the airport. Mobile monitoring PNC maps were created for various days to examine PNC levels across the route and within the impact sector (area downwind from the airport).

The first mobile monitoring PNC map (Figure 18) shows one day of mobile monitoring (July 5, 2022). Approximately 28 days of mobile monitoring (42% of 2021 monitoring runs) had conditions and impact sectors similar to those for the monitoring on July 5, 2022. Higher PNC levels are observed in segments that fall within the impact sector. The second mobile monitoring PNC map (Figure 19) shows a different day of mobile monitoring (March 14, 2022). Approximately 16 days of mobile monitoring (57% of 2022 monitoring runs) had conditions and impact sectors similar to those for the monitoring on March 14, 2022. Higher PNC levels are observed in segments that fall within the impact sector.

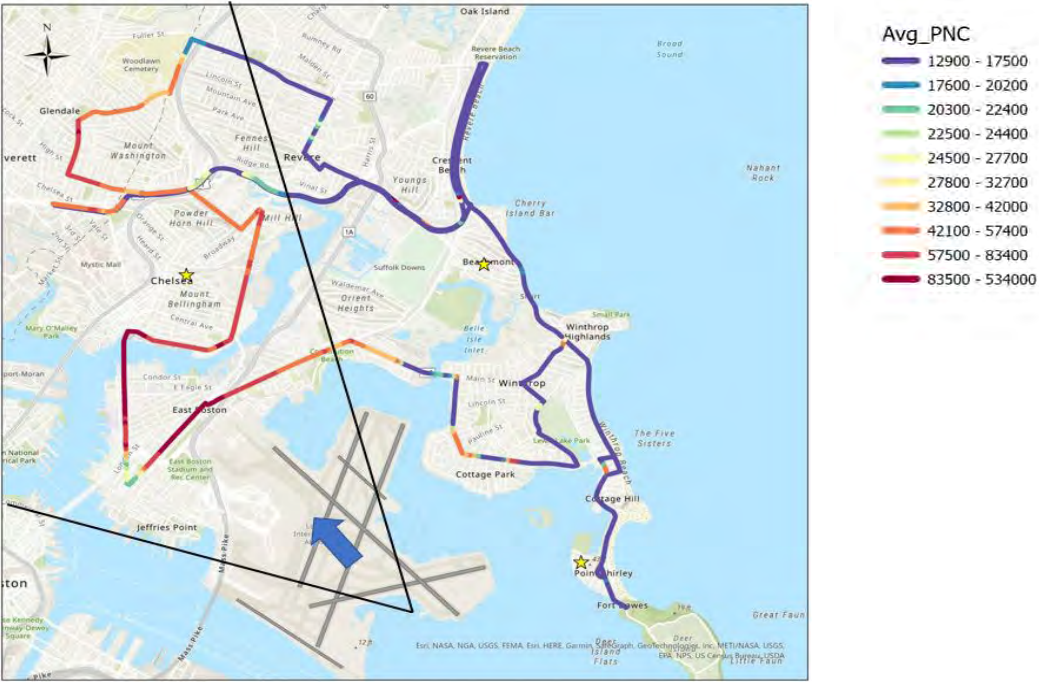


Figure 18. Mobile monitoring particle number concentration (PNC) map showing the monitoring route on July 5, 2022 in the northern portion of the study area, with stationary sites marked in yellow and the impact sector marked in black.

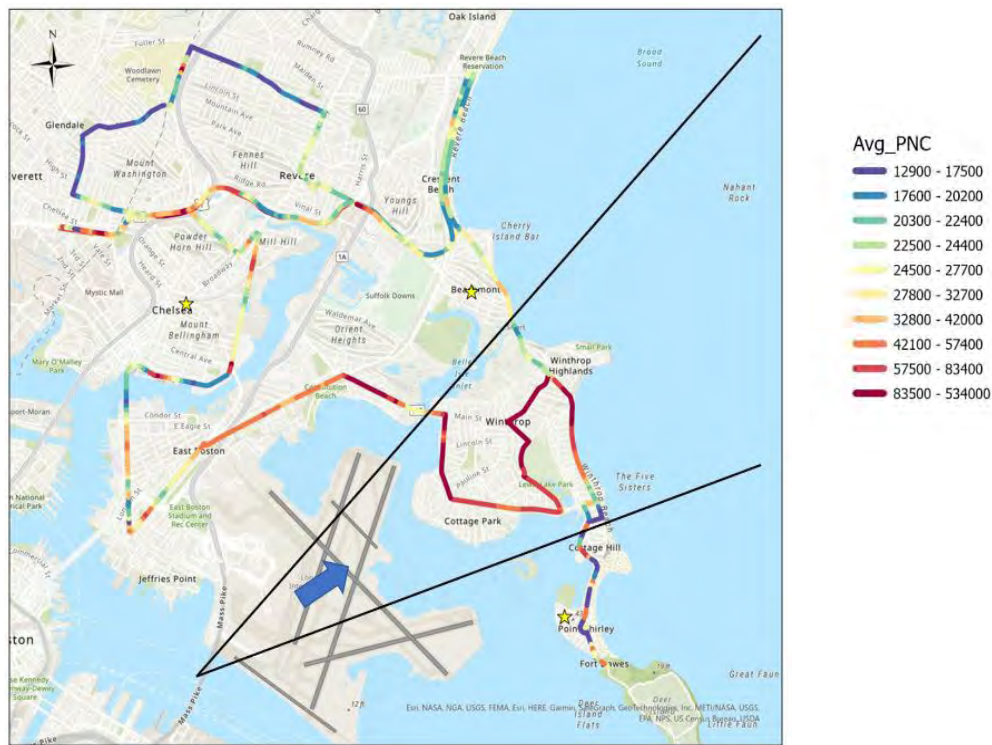


Figure 19. Mobile monitoring particle number concentration (PNC) map showing the monitoring route on March 14, 2022 in the northern portion of the study area, with stationary sites marked in yellow and the impact sector marked in black.

Mobile monitoring PNC data for 2021 and 2022 were further evaluated by visualizing the average PNC by segment (#/cm³) in the impact sector versus the non-impact sector (Figure 20 and Figure 21). The average PNC by segment was higher within the impact sector compared with the non-impact sector for both the 2021 and 2022 monitoring campaigns. A preliminary analysis of the mobile monitoring data facilitated a further understanding of PNC levels near airport communities as well as the agreement between stationary and mobile PNC measurements.

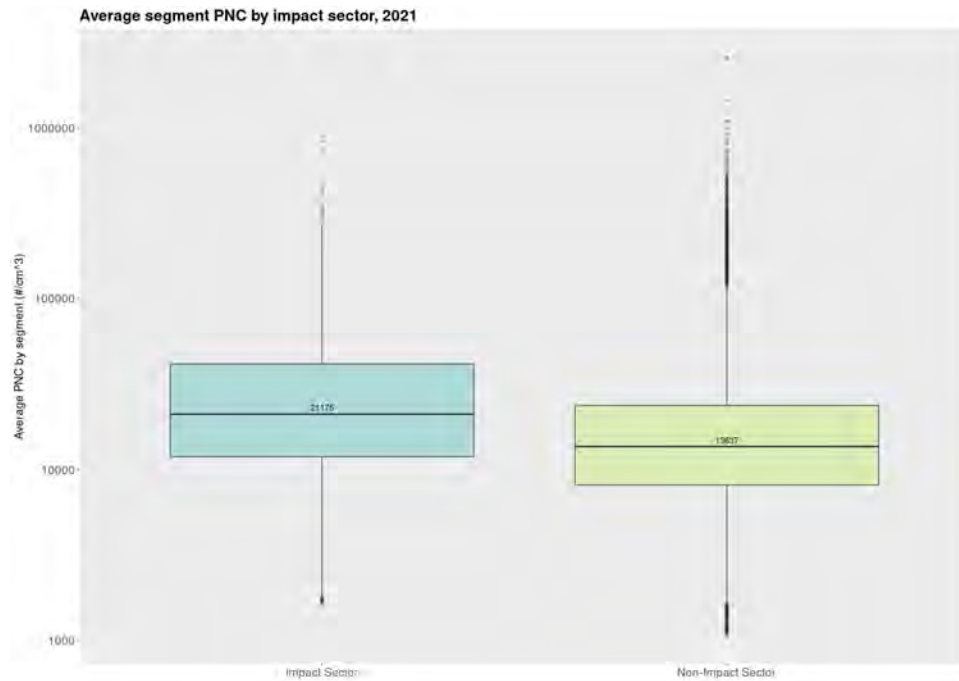


Figure 20. Average segment particle number concentration (PNC) by segment for mobile monitoring in North Boston in 2021.

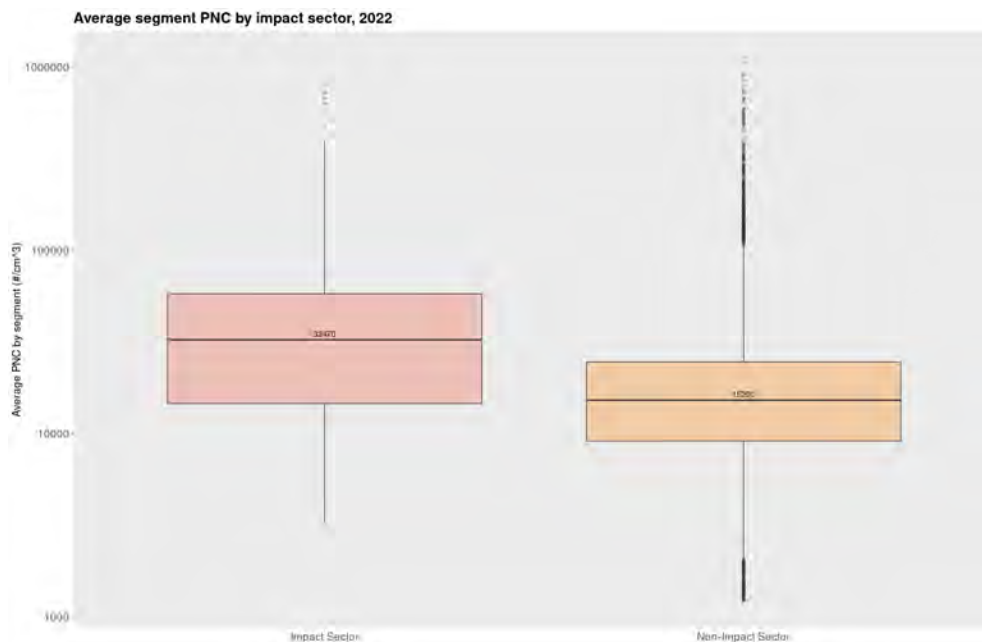


Figure 21. Average segment particle number concentration (PNC) by segment for mobile monitoring in North Boston in 2022.

Furthermore, we have made great progress in processing mobile monitoring data for the South Boston route. We have processed the road segments of the continuous and adaptive routes for South Boston and are finalizing the data-processing step for the pollutant mobile monitoring data.

We followed the same segment analysis methods used for the north mobile monitoring route, as this approach was determined to be the ideal method for examining these data. Thus, the typical south driving route was separated into approximately 982 segments of approximately 50 m in length via ArcGIS Pro (version 3.0.2). UFP concentrations were collected as the PNC along this route 80 times during 2020–2022 via a CPC at a semi-regular frequency (about two times per month). To preserve comparability, we selected only the data that fell within a 35-m buffer around the typical north driving route; consequentially, approximately 26% of the data points (~200,000) were removed from the analysis, accounting for approximately 3,340 min of driving time.

Each road segment and monitoring data point were assigned a unique identifier. These identifiers were used to match each data point to the nearest road segment. Once data points were assigned to a segment, the average PNC along that segment was calculated for each day. Approximately eight data points were assigned to each segment on average, with wide variation based on traffic patterns (minimum = 1, maximum = 4,474). To account for time variations, if a segment was driven over multiple times on the same day, multiple averages were calculated for the single segment based on 10-min and hourly thresholds. Figure 22 shows a time series plot of the average PNC across the study period (2020–2022), where each dot represents a segment average taken on the day indicated.

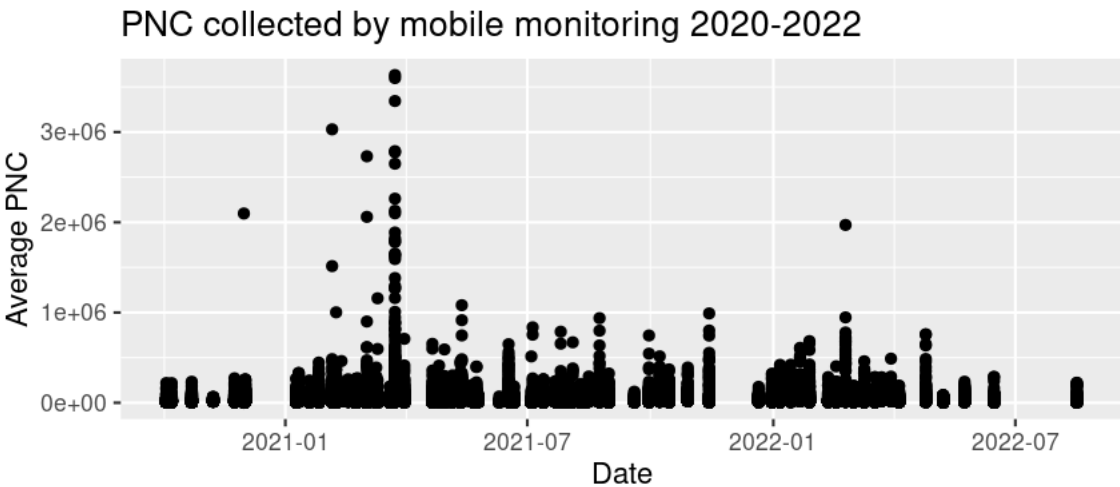


Figure 22. Time series plot showing the average particle number concentration (PNC) per road segment per day across the study period (2020–2022) along the South Boston mobile monitoring route.

We completed a preliminary map of the average PNC by segment for 2020–2022 along the South Boston mobile monitoring route (Figure 23), where red indicates a higher average PNC and purple indicates a lower average PNC. Next steps include merging the segment averages with hourly meteorology data and flight data as well as calculating PNC averages by impact sector versus non-impact sector.

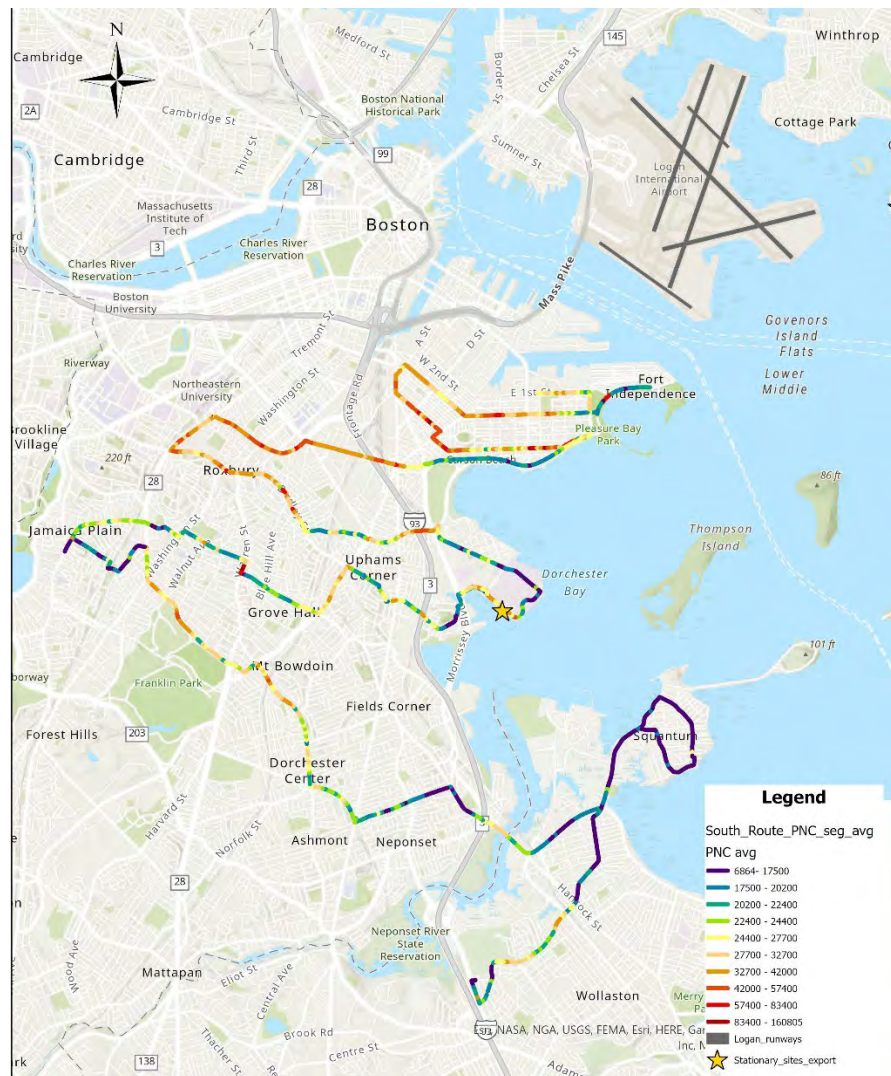


Figure 23. Average particle number concentration (PNC) by segment along the monitoring route (2020–2022) in the southern portion of the study area, with stationary sites marked in yellow.

Milestones

In addition to our major accomplishments, we have also reached the following milestones:

- Obtained permission to continue monitoring at each stationary site as well as a new monitoring site at Evan’s Field in South Boston
- Completed annual manufacturer cleaning and calibration of the CPCs and FMPS and performed a side-by-side PNC calibration
- Designed a protocol for mobile monitoring data processing and analysis to integrate mobile monitoring for community measurements of aviation-related UFPs, including adaptively selected routes for a more detailed characterization of aviation impacts on downwind communities
- Characterized differences in typical UFP concentrations in downwind and non-downwind locations within the study area as a function of observed variations in drivers of UFP variability (temperature, wind speed, time of day, etc.)

Publications

- Chloe S. Chung, Kevin J. Lane, Flannery Black-Ingersoll, Eric Kolaczyk, Claire Schollaert, Sijia Li, Matthew C. Simon, Jonathan I. Levy. (2023). Assessing the impact of aircraft arrival on ambient ultrafine particle number concentrations in near-airport communities in Boston, Massachusetts, Environmental Research. Volume 225, 115584, ISSN 0013-9351, <https://doi.org/10.1016/j.envres.2023.115584>.

Outreach Efforts

None.

Awards

None.

Student Involvement

Data analyst Breanna van Loenen is leading the mobile monitoring data processing and analysis efforts.

PhD student Camille Gimilaro as well as Olivia Moore, Isabelle Woollacott, and Lily Sandholm, undergraduate students at Tufts University, have been assisting with the collection and processing of stationary site monitoring data.

Plans for Next Period

We will continue to monitor for and analyze the source attribution of aviation contributions to ambient air quality while integrating geographically weighted regression and universal kriging of the mobile monitoring data.

Task 4 – Utilize Insights from Monitoring and Modeling Efforts to Date to Provide Recommendations on the Ideal Attributes of Future Monitoring Campaigns at Other Airports (i.e., Ideal Airport and Community Attributes, Design of Site Network, Frequency, Duration, etc.)

Objectives

We have conducted substantial monitoring at KBOS and have previously worked at other selected airports (e.g., PVD, LAX). Our experiences have shown that while many conclusions derived from an individual airport monitoring campaign are generalizable, others are site-specific. Thus, it may be important to conduct new monitoring studies in other airport settings, but only after we identify the airport and community attributes that should be considered as well as the field study design that would yield maximal insight with efficient field data collection.

Research Approach

We evaluated the data obtained during the ongoing monitoring campaign to determine both the strengths and challenges associated with the available data. We assessed potential future analyses that could not only provide insight about source attribution or dispersion model performance but could also help evaluate the implications of key changes in airport activities via a “natural experiment” design.

To select candidate airports, we developed inclusion/exclusion criteria and recommendations for campaign design. For example, we retain the exclusion criterion of proximity to a major roadway or other major local source of air pollution, to help isolate the effects of aircraft within future statistical analyses for validation of dispersion models. We also map key flight paths to determine geographic areas that meet our selection criteria. We prioritize sites for which we have previously established relationships with individuals, businesses, government agencies, or academic institutions to simplify the process of monitor deployment for an airport not geographically proximate to BUSPH. We coordinated with ASCENT Project 19 and FAA to identify key criteria to improve the validation of statistical and dispersion modeling efforts. Finally, we derived insights from statistical analyses about the importance of various meteorological conditions and ideal site locations, to evaluate whether a campaign at a given airport would be informative. These various factors will be used to create a list of ideal candidate airports for answering key FAA questions regarding community exposures to aviation-related ambient air pollution as well as for developing a best-practices report for campaign design with public availability.

The best-practices report will outline a series of questions and suggestions that may help decision-makers evaluate the monitoring campaign design.

Major Accomplishments

In addition to selecting a new monitoring campaign site at Dulles International Airport, the ASCENT 18 research team drafted a report outlining suggestions and best practices for pollutant monitoring in airports titled “Recommended Practices for Using Monitoring and Statistical Analysis to Estimate Aircraft Contributions to Air Quality in Nearby Communities.” The report is meant to record practices used for monitoring aircraft contributions to air quality for researchers, communities, and other stakeholders to consider methods for monitoring campaign design and management.

We draw on the findings of ASCENT Project 18 monitoring campaigns at Boston Logan International Airport, the research team’s experience at several other U.S. airports, and the most current literature. We propose a series of questions that may help decision-makers evaluate the utility of such an undertaking at a specific airport. Because of the unique attributes of each individual airport (e.g., runway configuration, meteorological conditions, surrounding land use patterns, population distributions) as well as the range of questions that can be answered by a monitoring campaign, there is not a one-size-fits-all solution. Yet, adoption of the best practices recommended in this document will lead to a robust understanding of air quality impacts because the recommendations presented here are grounded in general principles of good study design, first principles about pollutant dispersion, and years of experience at a wide variety of airports.

Three broad types of air quality monitoring strategies have been employed at airports: stationary monitoring, mobile monitoring, and a hybrid of the two. Our experiences indicate that a hybrid monitoring strategy is generally the most resource-effective, although this decision is conditional on the specific study questions of interest. Once the monitoring strategy is determined, there are specific considerations for the number and location of monitoring sites, size of area monitored, and frequency and duration of monitoring. Recommendations underscore the importance of adapting the study design to local meteorology, which is a crucial influential factor in determining air quality impacts from aviation sources as well as other local sources. We also discuss the importance of fast-response and high-temporal-resolution capacity in instruments that are fit for the purpose of monitoring aircraft impacts. Because of the large volume of data involved, practices for assuring data quality during monitoring and timely and accurate data management are key, and we describe best practices for this aspect. Lastly, because the monitoring data alone cannot provide insights regarding aviation source contributions given the presence of other nearby sources, we discuss best practices for data analysis and interpretation.

We propose to pursue the following questions in monitoring campaign strategies:

1. *What new information is needed or what knowledge gap needs to be filled by the study?* For example, is the airport located at a unique latitude/longitude or altitude or in particularly complex terrain that leads to poorly understood downwind exposure conditions? Are there plans for a terminal or runway expansion, change in fuel composition, or change in runway configuration that may significantly alter the air quality impacts? Is there capacity to accurately characterize air quality impacts with dispersion modeling?
2. *Is the study responsive to a need for knowledge or data expressed by a stakeholder?* A range of questions can be addressed by a monitoring campaign and associated statistical analysis, some of which may not be readily ascertained by a dispersion modeling approach. A study should ideally be responsive to a specific data need articulated by a local stakeholder (e.g., policymakers, airport operators, community members, government, researchers, etc.).
3. *Is a robust study feasible and cost-effective?* Many airports are situated at the convergence of land uses (e.g., commercial, residential, and transportation); thus, distinguishing the unique contributions of aviation sources from contributions of other local sources may not always be cost-effective or even feasible. For example, the complexity and cost of conducting a characterization study at an airport such as Newark Liberty International Airport (Newark, NJ), which is located near industrial plants, oil refineries, a major seaport, and multiple highways, should be weighed against the benefits of conducting a characterization study at another airport in the region with similar meteorology but less complex surroundings and then scaling the findings to Newark based on aviation activity. The uncertainty in scaling could be weighed against the uncertainties in working in a complex urban environment with superimposed (confounding) impacts from multiple sources.
4. *How long would the study findings be valid? Conversely, is there a unique opportunity with a short-term window to characterize an impact?* Before undertaking a monitoring study at an airport, any plans for major flight path changes, capacity expansion, or fleet-type/fuel-type changes should be considered to assess the duration for which results will be valid if a study is undertaken before the major changes are implemented. However, major or even minor changes in operations (such as a several-month runway shutdown for improvements or expansion)

often offer a unique opportunity to characterize impacts by leveraging the contrast offered by the change, and a monitoring study can often provide insight that may not be available through a dispersion modeling approach.

In our report, we explore these various questions as well as considerations for monitoring instruments, stationary monitoring, mobile monitoring, hybrid monitoring, and data management and analysis.

Stationary site monitoring: Considerations for the number and location of stationary sites, spatial extent of the monitoring area, and frequency and duration of monitoring

Stationary site monitoring is valuable for measuring temporal variations in air quality, for providing an analytical dataset for source attribution in which spatial variation does not need to be explicitly addressed, and for providing valuable insight about how the magnitudes of aviation contributions differ spatially. The number of stationary monitoring sites and the spatial extent of monitoring near an airport will depend on several factors, including wind direction variability, which can be quite significant (see contrasting wind roses in Figure 24 for the Houston Intercontinental Airport for June versus September), runway orientation, operation patterns such as the dispersion of flight paths and volume of operations, topography of the surrounding area, and the presence of other major emission sources nearby. These parameters will also depend on the precise study questions of interest (e.g., quantifying all parts of the LTO cycle vs. separating arrivals from departures, characterizing LTO contributions vs. all airport sources).

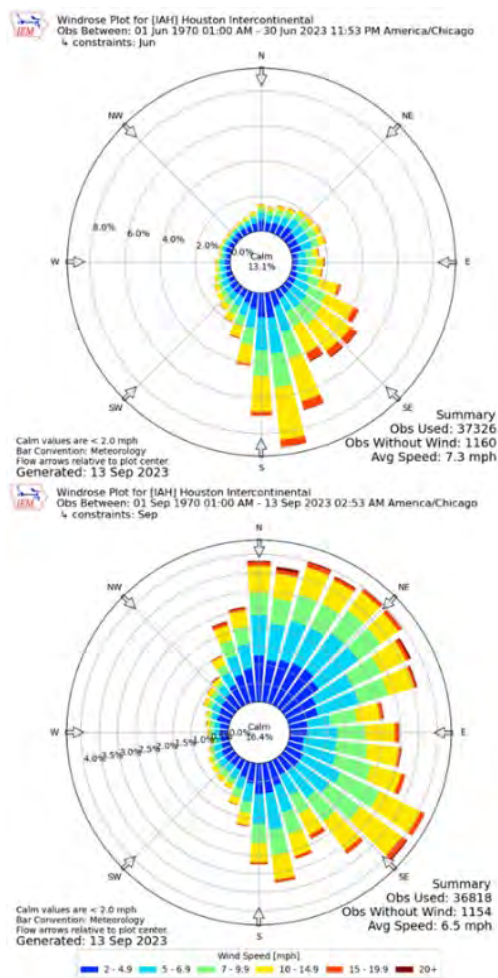


Figure 24. Wind rose plot for Houston Intercontinental Airport, showing significantly different prevalent winds and a different spread in June versus September.



Although each airport is unique in terms of airport operations (e.g., number of flights, mix of plane types), dominant wind patterns, and proximity and distribution of nearby populations, the following general guidelines can be used to assist with study design:

- Stationary sites should be aligned upwind (≥ 1 site) and downwind (≥ 2 sites) along the major runways and should be operated simultaneously to measure pollutant gradients.
- Long-term stationary sites maintained for at least 1 year can provide seasonal and inter-annual variation, which can be significant. For this reason, it is highly recommended that characterization studies maintain sites for at least 1 year or, ideally, multiple years. If stationary sites are maintained for a shorter duration because of logistical or resource challenges, monitoring should be optimized to cover the two most contrasting seasons in terms of meteorological and airport operation differences (e.g., winter and summer). Short-term monitoring capturing days or weeks within a season is only recommended for informing hypothesis development or for capturing novel scenarios, not for the characterization of long-term impacts. For example, a community located under the flight path of a specific runway could be interested in evaluating the impacts from aircraft activity on the runway, and the runway is expected to be temporarily closed for improvements or maintenance. This would be a scenario in which a short-duration study taking advantage of the natural experiment (before the runway shuts down, during the shutdown, and after the runway reopens, all within the same season) may yield useful insights, but it would not inform long-term source attribution.
- If more than two downwind stationary sites are deployed, they should be spaced such that more sites are located in regions where pollutant gradients are steepest and variations in concentration are greatest.
- Monitoring locations should be selected with a consideration of the proximity to other emission sources and with a consideration of whether the locations adequately represent the surrounding area in terms of land use, building types, vegetation, and topography. Topographical features such as valleys and the lees of buildings should be avoided. Additionally, given the large contribution of major roadways to traffic-related air pollutants, it is recommended that stationary monitoring locations be located at >200 m from major roadways to minimize confounding effects.
- Stationary site networks can be used to measure the lateral dispersion of plumes, but the network should adequately cover all areas that are downwind based on the spread/variation in wind direction along the path of prevalent winds. Note that these paths can vary significantly with season at the same airport (see Figure 24). In areas of large lateral spreading, the use of stationary site networks is not a cost-effective strategy.

Mobile monitoring: Considerations for establishing the spatial extent of the mobile monitoring area and the frequency and duration of monitoring

Mobile monitoring using a vehicle (e.g., car, bicycle, boat, or drone) equipped with rapid-response monitors is valuable for measuring the spatial distribution of pollutant concentrations and can serve as a useful complement to stationary site monitoring. Alternatively, because mobile campaigns generally have a shorter duration (compared with stationary monitoring campaigns) and involve measurements taken at a limited number of time points at any given location, mobile monitoring is sufficient to stand alone in scenarios where information on spatial variation is desired but not long-term trends. The following general guidelines can be used to assist in designing a mobile monitoring campaign.

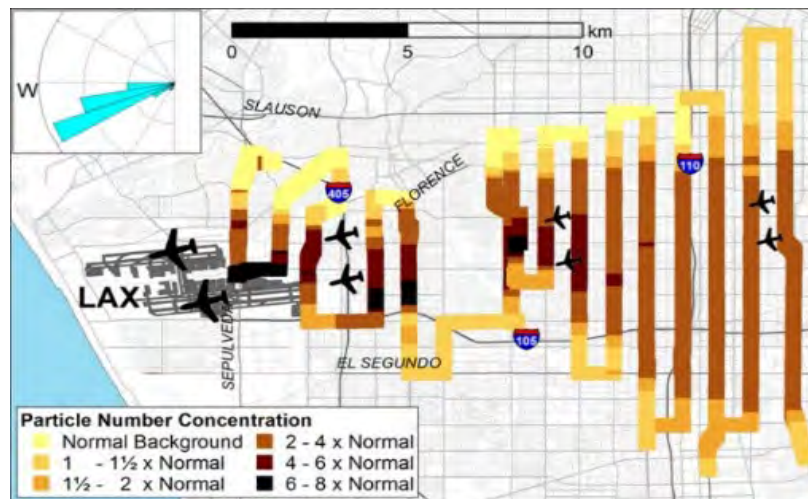


Figure 25. Spatial pattern of ultrafine particle number concentrations (colored by deciles) downwind from Los Angeles International Airport (LAX), showing a large zone of impact.

- Mobile monitoring routes should be designed such that they can be completed under current meteorological conditions and flight activity levels. In other words, the route should not be so long that rapidly changing meteorological conditions and consequent changes in active runway usage would push the emission plumes into a different impact zone far from the monitoring route.
- Mobile monitoring routes should encompass the full lateral and downwind expanse of the impacted areas. Because the impacted area can often only be determined by mobile monitoring, some preliminary data collection to establish the final mobile monitoring routes would be warranted. In addition, the monitoring route should be designed to include upwind areas as well as cross-validation stops at stationary sites.
- Using mobile monitoring is more cost-effective than using a stationary site network if the study goal is to cover the lateral expanse of downwind areas and to characterize the spatial heterogeneity within that lateral expanse. See the example of work around Los Angeles International Airport in Figure 25, which shows a large lateral spread that was efficiently covered by mobile monitoring.
- The frequency of mobile monitoring (frequency per week, season, or meteorological condition) should be weighed to capture the expected temporal variation in concentrations. Emphasis should be placed on capturing the temporal variation in emissions at the airport rather than following a fixed schedule (such as once/week or thrice/month on the same day and at the same time, etc.).
- Campaigns should be planned to capture a strong temporal contrast in airport activity, as well as other influential factors (meteorology, ground transportation). Peak or high flight traffic days such as holidays compared with unexpected shutdowns due to inclement weather or runway maintenance can offer a contrast in data that increases the confidence of findings.
- Spot mobile monitoring (parking at a spot and making measurements), if employed, should be conducted for a long enough duration to capture a contrasting change related to aviation so that the data can be robustly interpreted. Results should be verified by repeating measurements at the same spot.

Combined stationary and mobile monitoring

Stationary and mobile monitoring approaches each have strengths and limitations. For example, stationary monitoring is essential for capturing fine-scale temporal variations in air quality, but it has the inherent limitation of capturing only a handful of locations in space, which is acceptable for temporally focused analyses but will not give insight into the spatial extent of impact or the concentration gradient across key neighborhoods. Similarly, mobile monitoring is useful for characterizing pollutant concentration variations across a study area, but it has the inherent challenge related to distinguishing between temporal and spatial variability, given that routes are monitored briefly (e.g., 5–10 hr/week) and often only a limited number of times. Alternatively, protocols that use both mobile monitoring to capture high-resolution spatial patterns and stationary monitoring to capture long-term temporal trends and impacts at key sites are often optimal. A hybrid monitoring approach could be the optimal strategy for many airports, as it can address the key limitations in a

cost-effective manner.

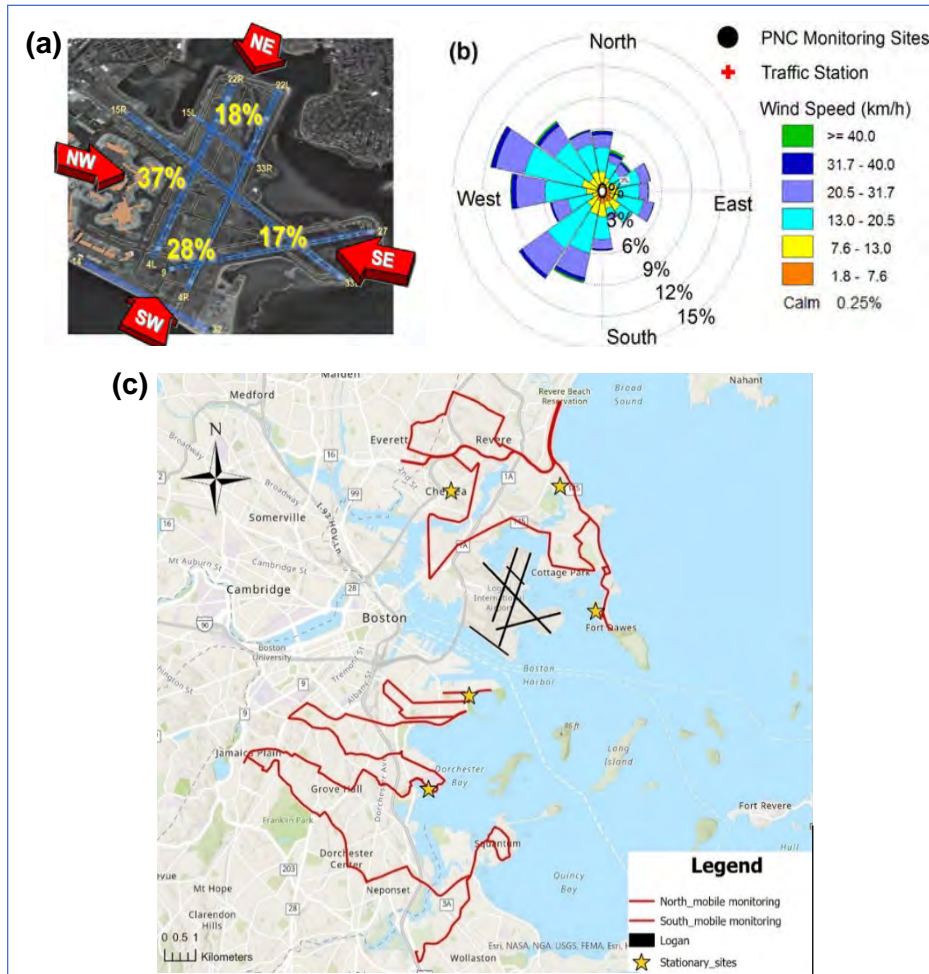


Figure 26. (a) Runway configuration and percent flight activity at Boston Logan International Airport. (b) Wind rose plot of annual ultrafine particle number concentration (PNC) at Boston stationary sites. (c) Map of five stationary sites and two mobile monitoring routes near Logan International Airport.

Because of its runway configurations and runway operation patterns as well as the meteorology (particularly the rapidly shifting winds [Figure 26]), Boston Logan International Airport is a good example of an airport that presents significant challenges to characterization using only stationary monitoring or only mobile monitoring. In a wide downwind sector to the east and northeast of the airport, there is relatively little land, and to the south and west, the airport is surrounded by water and highway infrastructure. Further, the street layout in Boston and vicinal communities does not allow for designing mobile monitoring routes with rectilinear traverses at regular distances (see Figure 25) to capture the extent of impacts and pollutant concentration gradients. Instead, as part of our investigation of Logan Airport, the ASCENT Project 18 team adopted a monitoring approach that combined the strengths of stationary and mobile monitoring into a hybrid strategy.

Our monitoring approach for Logan includes five stationary sites located in the near-airport communities of Chelsea, East Boston, Revere, South Boston, and Winthrop (Figure 26c). The sites are aligned with the major runways and runway usage as well as the more frequently prevalent winds (which are northwesterly in winters and southwesterly in summers; Figure



26b). We also designed two mobile monitoring routes north and south of the airport that cover wide swaths in downwind communities (Figure 26c). Mobile monitoring was conducted along these fixed routes in a variety of conditions, including when routes were upwind of the airport to characterize background air quality. We also modified the routes in real-time when plume touchdown was observed downwind of the airport to capture finer-scale temporal variations. Many statistical analysis approaches can leverage data from both stationary and mobile monitoring sites to provide optimal spatiotemporal insights.

Considerations for selecting pollutants and instruments

There are several factors to consider when deciding which pollutants and instruments to use for a particular study. First, pollutant concentration spikes near airports can vary in duration from several seconds to several minutes and often occur at the same frequency as flight activity. As a result, the signal from an emission event may or may not have time to decay to background before the next spike is recorded. Moreover, individual spikes can become superimposed and the distinction between events can be lost if measurements do not have adequate temporal resolution. This issue is further complicated by the lag between when the pollutant is emitted and when the plume reaches the monitor, which will vary by distance, source type, and meteorological conditions. Second, spikes from in-flight aircraft can mix with emissions from taxiing aircraft and ground-based support equipment. Therefore, understanding contributions from various airport-related activities and sources requires careful investigation at fine temporal resolution. Away from the airfield, the challenges associated with distinguishing airport-related from non-airport-related contributions become increasingly important.

In general, the signal from ground-based activity manifests as a gradual change in concentration associated with winds from the direction of the airport. Over and above that signal, emissions from in-flight aircraft may be superimposed but are only present intermittently with a narrow spread in communities near the airport but a wider spatial spread as distance from the airport increases and plumes disperse over larger areas. Away from the airfield, it is critical to make measurements for a long enough period of time to capture attenuated, dispersed concentration spikes.

Based on these factors, we offer the following guidance to inform choices regarding monitoring instruments and pollutants.

- We recommend monitoring UFPs and particle size distribution, which are both excellent indicators of jet emissions, as well as nitrogen dioxide, sulfur dioxide, and black carbon, which will all demonstrate spatial heterogeneity in near-airport communities with varying contributions from different sources.
- Fine particulate matter ($PM_{2.5}$) and inhalable particulate matter (PM_{10}) are generally not recommended as the focus of near-airport studies, because of the large contribution of long-range transport and the modest signal from local aviation or other local sources. That said, there is often a health-based or regulatory rationale for including particulate matter mass in monitoring studies. If particulate matter is monitored, this should be done at a 1-hr resolution, which is the finest possible temporal resolution that can be reliably derived from FEM monitors. The use of handheld optical counters calibrated to Arizona dust or low-cost sensors is not recommended because the noise will likely exceed the signal. The use of time-integrated sampling methodologies that allow for analysis of the chemical composition of particulate matter is an approach that merits consideration in some contexts.
- For mobile monitoring, it is essential to use fast-response instruments that can respond quickly to rapidly changing pollutant concentrations. Instruments that can measure at a rate of 1 Hz (1/s) are recommended.
- Near the airfield, stationary site monitoring should also be conducted at 1-Hz resolution. Monitoring instruments for making 1-Hz measurements are commercially available for many aviation-related pollutants, including UFPs, particle size distribution (measured simultaneously across all channels), nitrogen oxides, and black carbon. Farther from the airfield, where dispersion and mixing are greater, the need for 1-Hz measurements may be less critical, and the use of 1/60-Hz (1/min) resolution would suffice.
- Adherence to a quality assurance and project plan is strongly recommended. Instruments should be regularly factory-calibrated and/or cross-validated with reference instruments (e.g., at regulatory sites). A strict protocol of checks should be established and maintained to ensure comparability of data collected at various locations.
- The use of low-cost sensors is generally not recommended. However, if deployed by an experienced and qualified team using a quality assurance and project plan with regular cross-validation with reference instruments and periodic calibration, low-cost sensors can be useful for developing a better understanding of broad spatial and temporal gradients in ground-level air quality.

Considerations for data management planning and analysis

Monitoring campaigns require detailed data management of the various sources of data, including monitoring data from multiple instruments, GPS coordinates, flight activity data, and meteorological data (Figure 27). These various data sources are essential for charactering aircraft contributions to air pollutant exposures. Flight activity data used in analyses can include runway-specific arriving and departing flight counts (generally at hourly and 15-min resolution), flight tracks, and 15-min taxi times near runways for arriving and departing flights. Where available, information related to aircraft type that correlates with emission rates would also be warranted. Meteorological data significant to source attribution analysis include 1-min and 5-min measurements of wind speed and wind direction, as well as hourly upper atmosphere data.

An analysis that combines regression and machine-learning approaches allows for a better prediction of aviation-specific contributions from other sources of air pollutants, given the complex interactions among multiple predictors. Multivariable generalized linear models can be used to examine the association between air pollutant concentrations and real-time flight activity. Variables that might be of interest for the regression model include meteorological covariates such as wind speed, wind direction, temperature, etc. For analyses of mobile monitoring data, covariates reflecting proximity to the airport grounds, flight paths, and other key sources would also be warranted. Because of the complex interactions among predictors (i.e., flight activity will be influenced by wind speed and direction, which will also affect plume dispersion and resulting concentrations at individual monitors), it is important to explore advanced statistical techniques for covariate selection and model ensembling. Furthermore, for stationary site data, each study site must be modeled individually to examine the location-specific impact of aircraft arrivals and departures on air pollutant concentrations due to variations in meteorological covariates at each location.

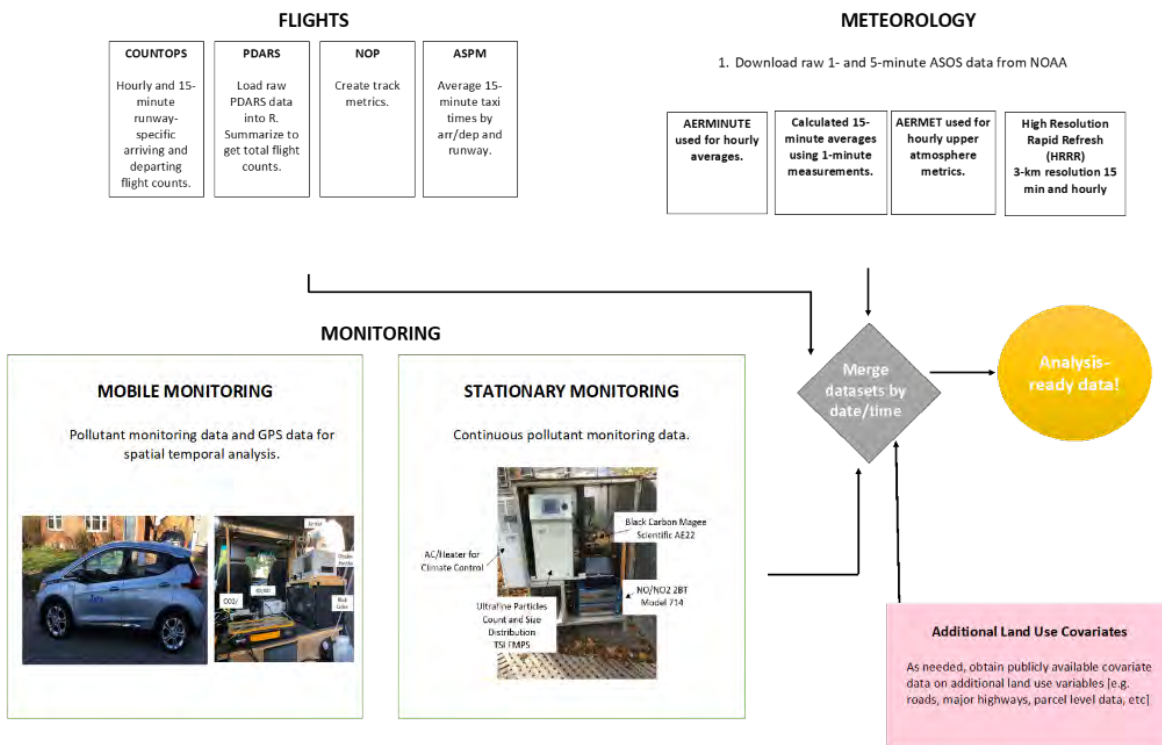


Figure 27. Data management and plan. FMPS: fast mobility particle sizer; GPS: global positioning system; NOAA: National Oceanic and Atmospheric Administration.



Considerations for monitoring data interpretation and publicity of findings

- Comparisons to regulatory standards should be made with caution and only when the collected data are consistent with the structure of the federal standards (e.g., 98th percentile of 1-hr daily maximum concentrations averaged over 3 years, annual mean, etc.).
- Quantitative comparisons with other studies are predicated on comparable monitoring methodology (including instruments used and other protocol details) and comparable statistical methods. For example, UFPs can be measured using various instruments that differ in their lower cut-points, ranging from as low as 3 nm to 15 or 20 nm. The higher end of this range overlaps with the part of the size distribution where large quantities of aviation-origin particles are present; thus, the PNCs will differ depending on which instrument is used. Similarly, because of the high temporal variation in aviation impacts, the time period for data aggregation is a key factor to note when comparing study results. In summary, a difference in concentrations between studies (such as two studies conducted at two different airports comparing impacts from airport-origin emission, where one of the studies includes other large sources near the airport) should not be interpreted as a difference in impact unless instrument and methodological comparability has been established.
- Relatedly, findings from an airport study should not be generalized or scaled to another airport without a careful consideration of local conditions at each airport. It is critical to not underestimate the role of local meteorology and flight operation patterns. For example, Los Angeles has a large downwind spatial extent for ultrafine particulate matter, which is partially due to its consistent wind fields; in contrast, another airport with even more operations may have a smaller impact. We are not stating that it is necessary to monitor every airport to understand associated impacts. Yet, it is important to recognize that there is a wide variation in factors that influence ground-level air quality impacts near airports, and caution is warranted when generalizing results from the relatively few airports that have been monitored.
- Implementing the aforementioned recommendations in their entirety requires substantial expertise and labor, and there may be circumstances in which community groups or local researchers may wish to conduct monitoring, but do not have the resources to follow best practices for monitoring or analysis. This is not an automatic invalidation of data or findings. Instead, it is recommended that decision-makers or evaluators seek to understand the fidelity of the data collected, assess whether the data are consistent with the broad study objectives, and be open to multiple study types that may generate potentially useful information.

Milestones

We presented a best-practices report to the Aviation Emissions Characterization meeting in the fall of 2023. We also submitted a draft report to the FAA.

Publications

- Lane KJ and Durant J. Best Practices for Airport Air Quality Monitoring and Source Apportionment of Ultrafine Particles. FAA Aviation Emissions Characterization Road Map Meeting, online. October 2023 (Oral).

Outreach Efforts

None.

Awards

None.

Student Involvement

Camille Gimilaro, doctoral student in Civil and Environmental Engineering, Tufts University

Plans for Next Period

We will apply the best-practices report in establishing our new monitoring site locations and in identifying a mobile monitoring route for the Dulles Airport.

Task 5 – Provide Regression Model Outputs for Comparisons Between Atmospheric Dispersion Models Developed by ASCENT Project 19 and Aviation-attributable Concentrations Determined From our Regression Models

Objectives

We analyzed UFP and NO/NO₂/NO_x data from our 2020–2021 stationary site and mobile monitoring campaign to provide insight regarding the ability of statistical analyses of real-time concentration measurements to capture aircraft source contributions. Our analyses indicate that we can explain significant variability in UFPs across multiple monitoring sites, with statistically significant terms for aviation flight activity as well as meteorology and other site attributes. We have also implemented quantile regression forests to better model the entire conditional distribution of UFP concentration and to extract and compare the relative importance of explanatory flight activity and meteorology at different concentration quantiles. We continued to develop these modeling approaches, applying them to the complete 2020–2021 UFP dataset as well as NO/NO₂/NO_x concentrations from this campaign. Our estimates of aviation-attributable UFP and NO/NO₂/NO_x concentrations will be directly shared with Project 19 for comparison with dispersion model estimates. More generally, by determining the optimal statistical approach for source attribution in this context, we rapidly analyzed the NO₂ and SO₂ concentration data from the 2021–2022 campaign and will provide timely aviation-attributable concentration estimates to Project 19 in future years. While we have constructed numerous regression models for source attribution within Project 18, the richness of these datasets (including multiple pollutants, both fixed-site and mobile measurements over a lengthy period, and the potential for synthesizing multiple fixed-site and mobile measurements for the same period) will allow for key refinements that will improve estimation and directly inform dispersion model validation.

Research Approach

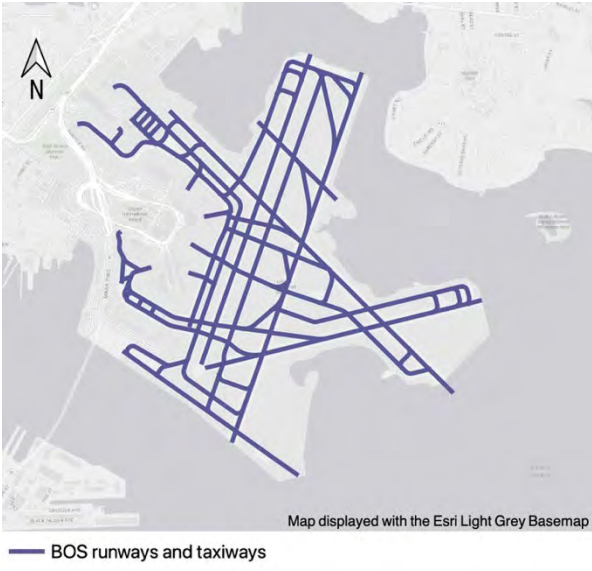


Figure 28. Map of the connectivity of Boston Logan International Airport runways and taxiways.

Team members from ASCENT Project 18 and ASCENT Project 19 have met several times to discuss how we can best support each other’s continued progress. ASCENT Project 18 staff have prepared analysis-ready datasets that combine all of our stationary UFP monitoring data from the 2017 monitoring campaign merged with relevant and timely meteorology data as well as runway-specific flight activity data at Boston Logan International Airport and have shared these datasets with ASCENT Project 19 for use in their dispersion models. Project 18 staff have also curated and made available estimates of taxiing time at Boston Logan International Airport, geographic information system files of the Logan runway configuration, and a topological analysis of Logan runway and taxiway connectivity to identify potential taxi paths (Figure 28). This sharing of resources across projects allows both teams to avoid duplicating efforts, thus accelerating research



progress. Sharing data also ensures that the results of our individual modeling approaches will ultimately be comparable, thus providing helpful context in interpreting the varied approaches. To facilitate this data sharing between project groups, ASCENT Project 18 has granted access to their internal data storage and analysis server cluster environment to members of ASCENT Project 19.

Major Accomplishments

All analysis-ready data from the 2017 monitoring period have been shared by the ASCENT Project 18 team with the ASCENT Project 19 team.

Milestones

In addition to our other major accomplishments, we have reached the following milestones:

- The ASCENT Project 18 team has similar analysis-ready data prepared for the current and ongoing stationary and mobile monitoring campaigns around Boston Logan International Airport that are ready to be shared when needed.
- ASCENT Project 18 staff have created a data-processing pipeline to ensure timely updates by periodically cleaning and preparing continuously collected datasets during the current monitoring campaign.

Publications

None.

Outreach Efforts

None.

Awards

None.

Student Involvement

None.

Plans for Next Period

We will continue to provide ASCENT Project 19 with additional raw air pollution data as well as modeled PNC and NO₂ contributions.



Project 019 Development of Aviation Air Quality Tools for Airshed-specific Impact Assessment: Air Quality Modeling

University of North Carolina at Chapel Hill

Project Lead Investigator

Saravanan Arunachalam, PhD
Research Professor
Institute for the Environment
University of North Carolina at Chapel Hill
123 W. Franklin St., Suite 330B
Chapel Hill, NC 27516
919-966-2126
sarav@email.unc.edu

University Participants

University of North Carolina at Chapel Hill

- P.I.: Saravanan Arunachalam, Research Professor and Deputy Director
- FAA Award Number: 13-C-AJFE-UNC Amendments 1-21
- Period of Performance: October 1, 2022 to September 30, 2023
- Tasks:
 1. Develop and evaluate a new dispersion model for aircraft sources.
 2. Develop and evaluate a multiscale Weather Research and Forecasting (WRF)-Sparse Matrix Operator Kernel Emissions (SMOKE)-Community Multiscale Air Quality (CMAQ) model application for Boston Logan International Airport (KBOS) focused on ultrafine particles (UFPs).
 3. Implement volatile particulate matter (voIPM) plume-scale modeling into a CMAQ application.

Project Funding Level

FAA provided \$650,000 in funding. The Barr Foundation provided matching cost-share via Harvard C-CHANGE.

Investigation Team

Prof. Saravanan Arunachalam (P.I.), All Tasks
Gavendra Pandey (postdoctoral fellow), dispersion modeling
Christos Efstathiou (postdoctoral fellow), emissions modeling
Praful Dodda (graduate student)
Hyeongseok "Darby" Kim (graduate student)
Farzaneh Taksibi (graduate student)
Brian Naess (geographic information systems specialist)
Huy Tran (air quality modeler)
Dr. Akula Venkatram (consultant, University of California at Riverside)

Project Overview

Aviation is predicted to grow steadily in upcoming years (Boeing, 2010); thus, a variety of aviation environmental policies will be required to meet emission reduction goals in aviation-related air quality and health impacts. Tools are needed to rapidly assess the implications of alternative policies for an evolving population and atmosphere. In the context of the International Civil Aviation Organization's Committee on Aviation Environmental Protection, additional approaches are required to determine the implications of global aviation emissions.



The overall objective of this project is to develop a new aircraft-specific dispersion model and continue the development and implementation of tools, both domestically and internationally, to allow for an assessment of year-to-year changes in significant health outcomes. These tools must be acceptable to the FAA (in the context of Destination 2025) and/or other decision makers. More importantly, this new model must have the capability to address the 1-hr form of the NO₂ National Ambient Air Quality Standard (NAAQS) in the United States, as well as to support National Environmental Policy Act and/or NAAQS analyses that may be needed by airports. The developed methods must also rapidly provide output to support a variety of “what if” analyses and other investigations. While the tools for use within and outside the United States need not be identical, several goals are desirable for both cases:

- Enable the assessment of premature mortality and morbidity risks due to aviation-attributable particulate matter (PM) having a diameter up to 2.5 μm (PM_{2.5}), ozone, and other pollutants known to exert significant health impacts;
- Capture airport-specific health impacts at regional and local scales;
- Account for the impact of landing/take-off (LTO) versus non-LTO emissions, including a separation of effects;
- Allow for an assessment of a wide range of aircraft emission scenarios, including differential growth rates and emission indices;
- Account for changes in non-aviation emissions;
- Allow for assessments of sensitivity to meteorology;
- Provide domestic and global results;
- Include quantified uncertainties and differences with respect to Environmental Protection Agency (EPA) practices, which are to be minimized when scientifically appropriate; and
- Be computationally efficient such that tools can be used in time-sensitive rapid turnaround contexts and for uncertainty quantification.

During this period of performance, the team at the University of North Carolina at Chapel Hill (aka UNC) Institute for the Environment performed work on the three tasks below.

Task 1 - Develop and Evaluate a New Dispersion Model for Aircraft Sources

University of North Carolina at Chapel Hill

Objectives

The FAA’s Aviation Environmental Design Tool (AEDT) is currently coupled with the American Meteorological Society/EPA Regulatory Model (AERMOD) dispersion model for modeling aircraft sources and is the required regulatory model in the United States for modeling airport-level aircraft operations during LTO cycles.

Recent studies have shown several limitations in the use of AERMOD for modeling aircraft sources. The Airport Modeling Advisory Committee developed a series of recommendations in 2011 to improve jet exhaust modeling. Since then, Airport Cooperative Research Program (ACRP) project 02-08 developed guidance for airport operators on conducting measurements and modeling of air quality at airports, published in ACRP Report 70 (Kim et al., 2012), with a measurement and modeling study conducted at Washington Dulles International Airport. Subsequently, ACRP project 02-58 developed the final ACRP Report 171 (Arunachalam et al., 2017) providing dispersion modeling guidance for airport operators for local air quality and health. This study applied four different models—AERMOD, CALPUFF, Second Order Closure Integrated Puff Model with Chemistry (SCICHEM), and the United Kingdom’s Atmospheric Dispersion Modeling System for Airports (ADMS-Airport)—for the Los Angeles International Airport (LAX) and compared model predictions with high-resolution measurements taken during the LAX Air Quality Source Apportionment Study (AQAS). Each of these reports identified several limitations with AERMOD and developed a series of recommendations for improving dispersion modeling of aircraft emissions for airport-level air quality.

In 2017, UNC developed the C-AIRPORT dispersion model for application to LAX (Arunachalam et al., 2017). Initially, C-AIRPORT was designed to be part of the C-TOOLS series of community-scale, web-based modeling systems. The objective of C-TOOLS was to create a web-based interface for modeling multiple source types for short-term or long-term pollutant concentration averages and for analyzing various “what if” scenarios to assess changes in air quality at local scales due to changes in inputs. C-AIRPORT used a line source-based approach to model aircraft sources, based upon the C-LINE modeling system (Barzyk et al., 2015), and a preliminary evaluation of the algorithms against LAX AQAS was conducted.



Under the previous year's funding, UNC completed development of a modeling framework that addresses known limitations from the above tasks and proposed a viable and suitable approach for modeling pollutants from aircraft sources. The primary objective of this plan was to demonstrate that a robust, improved pollutant dispersion model for aircraft can be developed for U.S. regulatory compliance purposes. The proposed new model will disperse pollutants from aircraft sources in a more technically and scientifically advanced manner (compared with current AERMOD capabilities), with the ultimate goal of becoming a potential U.S. regulatory compliance tool, based on future discussions with the FAA and EPA. This plan will include an itemized list of known limitations along with a corresponding proposed developmental approach and recommendations for addressing the limitations.

As part of the proposed ASCENT research under this task, we will continue to implement the plan with a specific focus on four broad areas, over a period of 2 years. We give a very high-level summary here, because the actual specifics of this implementation have been described in previous documents and reports that were independently developed earlier.

Our approach is to ensure that the new model will be "robust" and based on the state of science on physical and chemical processes and associated algorithms.

1) Source characterization

Existing approaches in AEDT/AERMOD treat aircraft sources as an area source segment. In ongoing work, we are moving away from this conventional approach to treat aircraft sources as line segments, as described by Arunachalam et al. (2019). During the previous year, we adapted new high-resolution aircraft movement dataset from a research version of AEDT for an airport for use in the new dispersion model. We will finalize the approach with a streamlined tool for data processing in the dispersion model, and this tool will be tested and verified for implementation in AEDT.

2) Physical processes

We will go beyond the initial implementation developed during the previous year, with a new focus on the following:

- i. Treatment of dispersion under low wind conditions and assessment of effects of atmospheric stability
- ii. Treatment of dry and wet deposition
- iii. Exploration of additional options for aircraft exhaust plume rise such as the fluid mechanical entrainment fluid-mechanical entrainment model (FEM) described in ACRP Report 179, where four new options can be implemented and evaluated, as well as other options:
 - a. An empirical model for plume rise and initial dispersion based on light detection and ranging (LIDAR) measurements at LAX (Wayson et al., 2004);
 - b. An FEM based on the average ground roll speed along the runway;
 - c. An FEM as a function of the ground roll speed or distance down the runway (i.e., a different plume rise for each AERMOD area source, which is a function of runway distance); and
 - d. An FEM based on both distance and time as independent variables describing the plume.
- iv. Incorporation of aircraft downwash effects
- v. Treatment of complex terrain and building downwash

3) Chemical processes

- We will go beyond the initial implementation of the previous year, with a new focus on the following:
 - i. The 1-hr form of the NO₂ NAAQS
 - The 1-hr form of the NO₂ NAAQS is a critical issue for air quality around U.S. airports, with several modeling studies showing overestimates compared with observations. It is important that the new model performs adequately to capture this short-term form of the NO₂ NAAQS.
 - ii. A new detailed chemical mechanism for NO₂ including the generic reaction set (Valencia et al., 2018; Venkatram et al., 1994) or other components
 - iii. Condensed version of the aerosol treatment as included in the CMAQ and SCICHEM and described by Chowdhury et al. (2015)

4) Model evaluation

- Ongoing model evaluation has involved evaluating model predictions using only measurements from the LAX AQSAS for winter 2012. We will now consider developing and testing the model for other case studies, including the following:
 - i. LAX AQSAS for summer 2012



- ii. One of three airports (Copenhagen, Madrid, and Zurich) with measurements being undertaken as part of the EU-AVIATOR project, a new measurement-modeling study called AVIATOR undertaken in Europe through funding from the European Union (see <https://aviatorproject.eu/>)
 - We will rely on the AVIATOR team to provide emission inventories for the chosen airport. If emission inventories are not directly available for use, we will obtain airport operations data for the campaign period and develop an inventory using AEDT.
 - iii. New measurements from ASCENT 18 investigators at KBOS and Washington Dulles International Airport
 - *This is a new collaboration that will help focus on both designing the monitoring campaign to assist in obtaining valuable data for characterizing the impact of aircraft emissions on air quality and developing the aircraft dispersion model (ADM), as well as in source attribution of the measured fields to the aircraft or other source types.*
- Model evaluation will focus on the model's ability to capture the behavior of the plume related to aircraft sources during LTO cycles at an airport, while comparing with available observations and identifying strengths and weaknesses compared with another existing model.
 - In collaborating with Boston University (BU), we will rely on BU to perform appropriate clean-up and quality assurance/control of observation data before using these data in our model evaluation routines. We will also work closely with BU to ensure appropriate and careful interpretation of the data. UNC and BU have collaborated extensively on similar projects in the past, and we expect to obtain a robust model measurement and modeling assessment from the KBOS study.

Research Approach

In this research, we describe progress made on the three subtasks.

Subtask 1: Develop and Evaluate a New Dispersion Model for Aircraft Sources

1. Source characterization

1.1 Aircraft source characterization in AERMOD

Airports are small cities with several dynamic mobile sources, especially during the LTO cycle. These sources influence air quality in and around the airport, and depending on the number of aircraft operations, the effect can be potentially significant. Modeling these airport/aircraft-related sources is very challenging. AERMOD incorporates a variety of conventional source types (i.e., point, area, and volume sources) that can be utilized to characterize the intended emission source, leaving the question of which conventional source types best characterize aircraft activities across the four modes of the LTO cycle, namely approach, take-off, climb out, and taxi/idle, unanswered. As of now, the publicly released version of FAA's AEDT (v3e) models aircraft emissions as a series of area source segments. In this version, there is a hidden feature behind a hash key (not publicly available) that allows users to model aircraft sources—both fixed-wing and rotorcraft—as a series of volume sources in AERMOD, but there is still a lack of incorporation of plume rise treatment for jet exhaust. Here, we describe an evaluation of AERMOD predictions when aircraft sources are modeled during LTO cycles as area vs. volume sources along with a detailed comparison of spatiotemporal patterns in emissions and input parameters. The case study for this evaluation is the LAX airport, with observations during the summer campaign (July 18 to August 28, 2012) from the LAX AQSAS (Arunachalam et al., 2017; Tetra Tech, 2013). We summarized various comparisons that were performed to quantify emission estimates when using area- and volume-based treatments and then the AERMOD-based concentration predictions of SO₂ for these two contrasting approaches.

1.1.1 Source number and emission comparisons

We compared the number of sources in AEDT-generated AERMOD-ready input files for area and volume treatments and found that the volume source treatment had many sources in both the surface and airborne categories. For the volume treatment, the number of taxi sources increased almost 14-fold (approximately 1,239%) as compared with the area source (Table 1). The higher number of volume taxi sources arises because each taxi link is assigned as a single area source (as a rectangle) for area sources, but each taxi link is divided into 20 × 20 m squares with a fixed aspect ratio of 1:1 for volume sources. However, the number of runway and airborne sources increased by 38% and 45%, respectively, for the volume treatment compared with the area treatment (Table 1). This increment is related to the aircraft category; in the volume treatment, each aircraft type is defined as a separate source for each cuboid. Despite increasing the number of sources and changing the source characterization of each source group, the SO₂ emissions were identical for this study period in

both treatments. However, the hourly averaged total emissions in the 42 days of the study period were also identical in both treatments (Figure 1). Thus, we confirmed that the emission magnitudes are identical in both treatments despite large differences in the source number.

Table 1. Quantitative comparison of source numbers for area and volume treatments.

Source group		Number of sources in each treatment		
		Area	Volume	Increase (%)
Airborne	AIRG300M	19,013	26,296	38.31
	AIRL300M	4,729	7,142	51.03
Surface	Runway	2,593	3,569	37.64
	Taxi	248	3,320	1,238.71
	Gate	21	21	0
Total		26,604	40,348	51.66

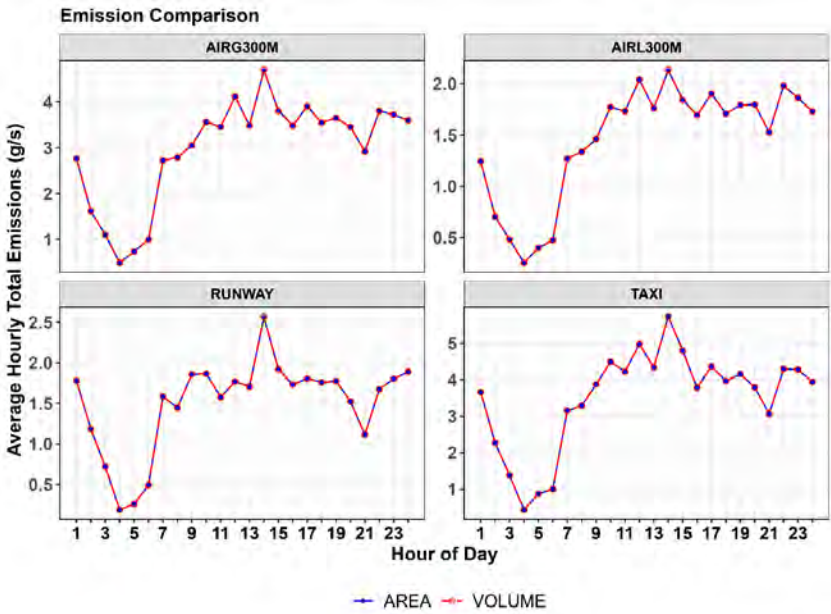


Figure 1. Average hourly total emissions at each hour for the 42-day summer study period in (a) area and (b) volume source treatments for each of the four source groups.

1.1.2 Dispersion comparisons from both AERMOD treatments (v21112)

We compared the AERMOD predictions using both treatments (AEDT-generated AERMOD-ready input files) only and plotted the volume source predictions with respect to area source predictions in the form of scatter plots for the overall concentration distribution of all four core sites in both stable and unstable conditions for three different source groups, including runway, taxi (emissions at the surface [12 m in height]), and airborne (all emissions above a 12-m height); we denoted this analysis as the base case (Figure 2). We have not included the gate sources here because the number of sources, as well as the source characterization, in both treatments is the same as that of the area-polygon treatment. As shown in Figure 2 (a, b) for the base case, runway volume sources increased by approximately 38%, taxi volume sources increased by 1,239%, and airborne volume sources increased by 45% from the area source treatment. In Figure 2 (a, b), we have added a one-to-one line to indicate the over- and underpredictions of the concentrations. In addition, in Figure 2 (a), we added a linear regression line (solid line) between both treatments to observe how much and in what direction the volume predictions vary when the area predictions change. We also added a regression equation for each source group for

both stable and unstable conditions (using different colors). The regression lines for stable and unstable conditions in Figure 2 (a) show good agreement between the two source treatments. Figure 2 (b) is similar to Figure 2 (a), except that a logarithmic scale is applied in Figure 2 (b) to enhance the visualization of the lower-concentration predictions. From Figure 2, we can clearly see that the mid- to high-range concentrations decrease in the runway and taxi source groups when the volume source treatment is used (Figure 2 (a)), whereas low-range concentrations increased significantly with volume source treatment in all three source groups (Figure 2 (b)). In the airborne source group, the concentration predictions are much lower than the surface predictions from both source treatments, and mid- to high-range concentrations increased significantly for most of the time in stable conditions in the volume source treatment (Figure 2 (a)). However, the area source treatment had several zero predictions because the AERMOD area source treatment calculation is based on the Romberg numerical integration method and numerical integration was not performed for portions of the area source that were closer than 1.0 m upwind of the receptor (U.S. EPA, 2022).

Additionally, we compared the overall AERMOD model’s computational runtimes for each source treatment in minutes and seconds. We ran AERMOD on a Linux AMD EPYC 7702 64 - Core processor with 32 GB RAM. We found that the base area treatment took 25 min and 32 s for the 42-day period whereas the base volume treatment took 34 min and 56 s, a 37% increase.

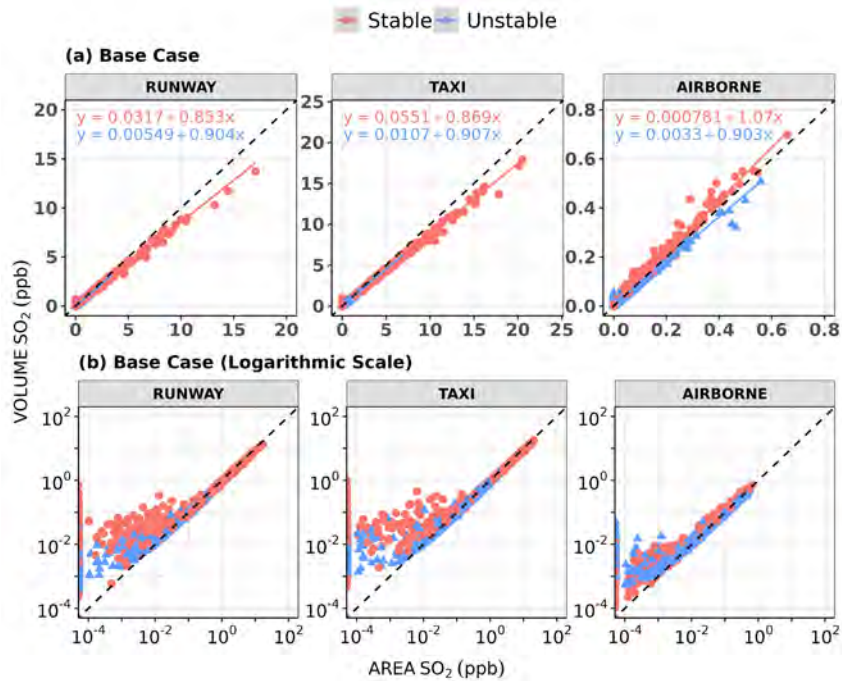


Figure 2. Scatter plots of concentrations predicted by the American Meteorological Society/EPA Regulatory Model for area and volume source treatments by source category. The different colors represent stability conditions. ppb: parts per billion.

Overall, we found under- and overprediction by volume source treatment for the high and low concentrations, respectively, compared with the area source concentrations. However, this trend raises several questions:

- 1) Was this result due to an increase in the initial vertical dispersion parameter (σ_{z_0}) from 4.1 m to 14 m in the area versus volume source treatment?
- 2) Was this result due to the difference in the source characterization and the use of a meander component in the volume source treatment?
- 3) Was this result due to the 51% increase in source number in the volume source treatment as compared with the area source treatment?

To address these questions, we performed additional sensitivity analyses for each individual question, as discussed in the next section.

1.1.3 Sensitivity analysis

We performed sensitivity simulations based on the initial vertical dispersion parameter (σ_{z_0}), source number, and meander component in the volume source treatment. We provide further description and analysis details in Table 2. We used the same type of scatter/logarithmic-scatter plots (Figures 3 and 4) and regression analysis employed in Figure 2 for all cases defined in Table 2. We also included the AERMOD runtime for each individual case on the same processor in minutes and seconds, as described above.

Table 2. Sensitivity analysis description for each question and the runtime for each case.

Question	Case ID	Description	Analysis Source Type (Source Number)		Runtime (mm:ss)	
			Area	Volume	Area	Volume
	Base Case	Standard AEDT-generated files for area and volume sources, denoted as base	Base (26,604)	Base (40,348)	25:32	34:56
1	Case 1	Change σ_{z_0} from 14 m to 4.1 m in base volume files	Base (26,604)	Modified (40,348)	25:32	34:42
2 & 3	Case 2	Convert all base volume sources into area sources, fix σ_{z_0} as 14 m, and modify the meander component to zero (FRAN = 0) in AERMOD source code for base volume source treatment	Modified (40,348)	Base with FRAN zero (40,348)	40:27	34:44

1.1.3.1 Case 1

To assess the differences between the predictions and to answer the first question, we changed the initial vertical dispersion parameter (σ_{z_0}) to 4.1 m from 14 m in the originally AEDT-generated AERMOD-ready volume source file (base volume) and compared our findings with the base area results (originally AEDT-generated AERMOD-ready area source file); we denoted this analysis as Case 1. As shown in Figure 3 (a), the mid- to high-range predictions decreased with an increase in σ_{z_0} in the volume sources and approached the one-to-one line, especially under stable conditions (base case to case 1). This change can also be seen from the regression equation and the regression line for the runway and taxi source groups (Figure 3 (a)). In contrast, this change is almost negligible under unstable conditions, as the regression equations from the base case and case 1 are identical for the runway and taxi source groups as well as for the airborne source group (Figure 3 (a)). During stable conditions for the airborne source group, mid- to high-range concentrations decreased with a reduction in σ_{z_0} (Figure 3 (a)). This result was consistent with the fact that ground-level concentrations associated with elevated releases decrease as the plume spread decreases. However, the change in lower concentrations was not as evident as that related to higher concentrations (Figures 3 (a) and 4 (a)) for all source groups.

1.1.3.2 Case 2

In this case, we examined the effect of source number as well as the role of the meander component, which was included in the volume source treatment but not in the area source treatment. The meander component accounts for the meandering of the mean wind during low wind speeds accompanied by comparable values of the standard deviation of horizontal velocity fluctuations. Under these conditions, the horizontal concentration distribution was taken to be a combination of the usual Gaussian distribution and a uniform distribution over 360°; the uniform distribution represented the limit of zero mean wind associated with wind meandering over 360°. The factor that weighs the two distributions depends on the magnitude of the horizontal velocity fluctuations relative to the mean wind. We first suppressed the inbuilt meander component (FRAN) of the volume source treatment (U.S. EPA, 2022) in the AERMOD source code and ran the model.

We converted/modified the standard AEDT-generated AERMOD volume (base volume) source-ready input files into the same number of area source files. The σ_{z_0} value (14 m) was taken to be the same as that of the volume sources. As shown

in Figures 3 (b) and 4 (b), for the surface source groups (runway and taxi groups), the low- to high-concentration predictions (0.01–20 parts per billion [ppb]) from both source treatments were very similar and lied mostly on the one-to-one line.

in contrast, for the airborne source group, the concentration behavior was unusual in both stability regimes for all concentrations from the low to high (0–0.62 ppb) range (Figures 3 (b) and 4 (b)).

From all of the above observations, we can summarize that both the source number and the meander component play a key role in the AERMOD volume source treatment. In the next section, we will compare AERMOD predictions with SO₂ observations measured at four core LAX AQSAS sites (AQ, CN, CS, and CE).

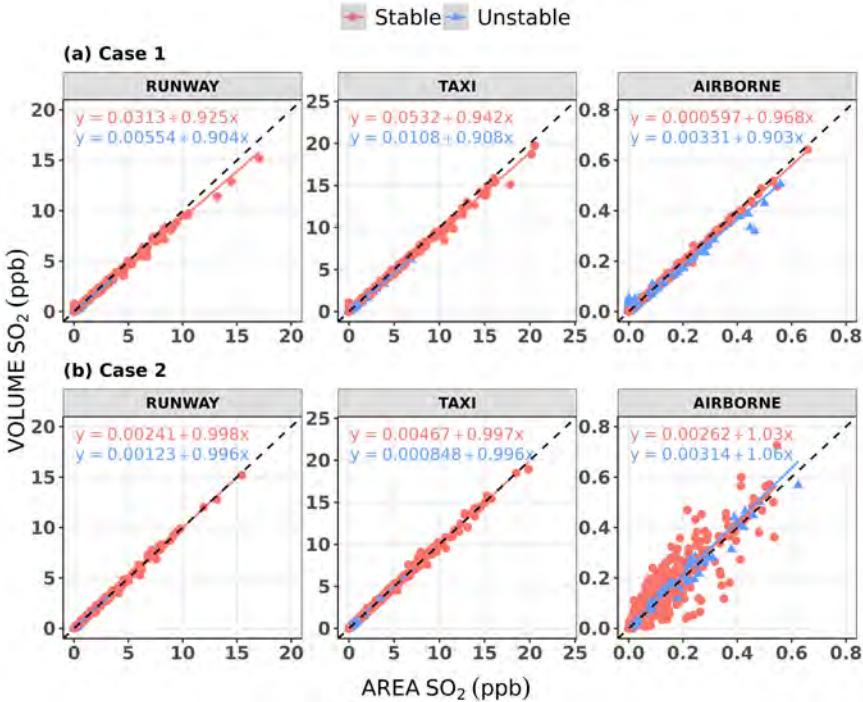


Figure 3. This plot is the same as Figure 2 (a), except that results are presented for each sensitivity case. ppb: parts per billion.

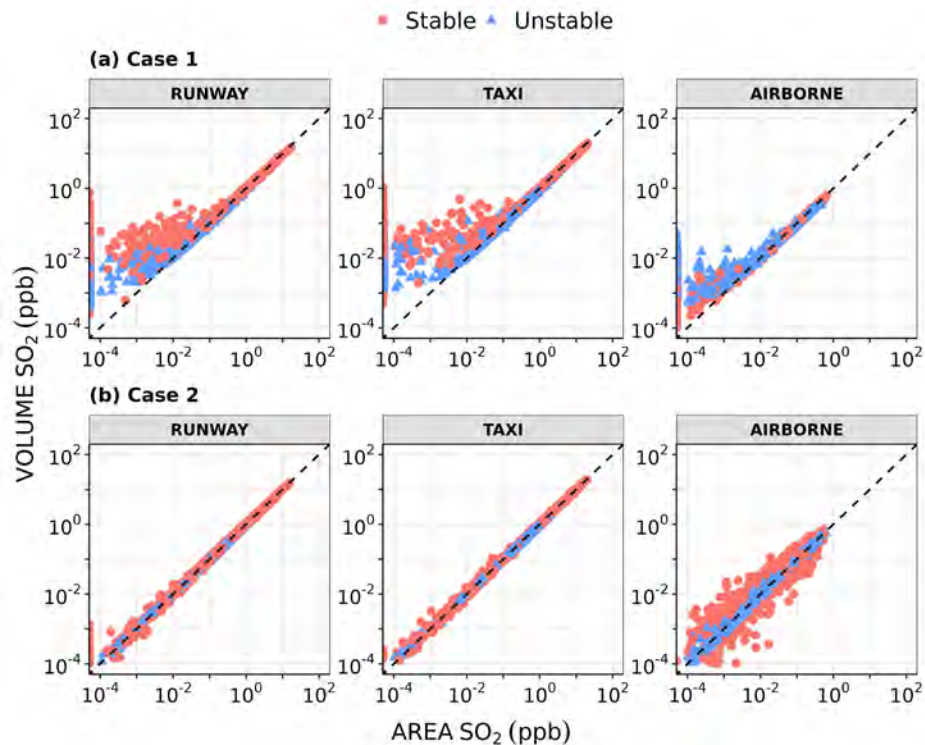


Figure 4. This plot is the same as Figure 2 (b), except that results are presented for each sensitivity case. ppb: parts per billion.

1.1.4 Comparison with observation

We compared the SO₂ model predictions from both treatments (with the same source number and initial vertical dispersion parameters) with the combined SO₂ observations at all four core sites – Air Quality, Community North, Community South and Community East (labeled AQ, CN, CS, and CE) in the summer season of the LAX AQSAS (Phase III) with the help of quantile-quantile (Q-Q) plots.

Figure 5 shows a comparison of the results for AERMOD area (AA), volume (AV), and volume with no meander (AVNM) (with FRAN=0) treatments with the observed SO₂ concentrations under stable and unstable conditions. We found that standard AV source treatment was better in its ability to predict low-range concentrations in both conditions when compared with AA and AVNM; these two treatments were similar to each other, as the concentrations overlapped each other for all ranges (Figure 5).

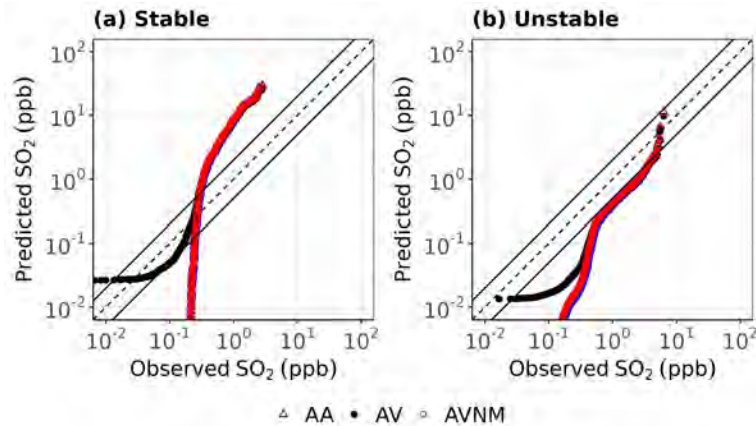


Figure 5. Quantile-quantile plots showing the effect of each source characterization, such as area and volume treatment, in the American Meteorological Society/EPA Regulatory Model (AERMOD) for different stability regimes. AA: AERMOD area; AV: AERMOD volume; AVNM: AERMOD volume with no meander; ppb: parts per billion.

We also calculated statistical measures such as the ratio of the top 26 robust highest concentrations (RHCs) and factor of two (FAC2) for the observations (Cox & Tikvart, 1990). We found that AA and AVNM had similar RHC ratios whereas AV had a 10% lower RHC ratio compared with AA and AVNM under both stable and unstable conditions (Table 3). The FAC2 value increased under stable conditions for AV, whereas it remained nearly constant under unstable conditions (Table 3).

Table 3. Comparison of model performance statistics from the American Meteorological Society/EPA Regulatory Model using area (AA), volume (AV), and volume with no meander (AVNM) treatments in different stability regimes. FAC2: factor of two; RHC: robust highest concentration.

Statistics	Site/Stability	Stable			Unstable		
		AA	AV	AVNM	AA	AV	AVNM
RHC ratio	All	9.49	8.64	9.39	0.97	0.86	0.98
FAC2 (%)	All	7	43	6	1	1	1

Based upon these statistical measures of model performance, we can state that the meander component is important; however, we needed to further assess model predictions in low- and high-wind-speed categories, because the meander component is important during low- and variable-wind conditions. For this, we divided the modeled and observed concentrations into two categories, low wind ($0 < U \leq 2 \text{ m/s}$) and moderate to high wind ($U > 2 \text{ m/s}$), and plotted the modeled concentrations with respect to observations in the form of Q-Q plots (Figure 6).

We found that in both wind categories, the predictions for AA and AVNM were similar (Figure 6). In contrast, better concentration predictions were obtained for AV at the low to intermediate range (0.65–0.02 ppb) in the low-wind category and at the low range (0.02–0.003 ppb) for the moderate- to high-wind category (Figure 6). Quantitatively, the RHC ratios were higher for the AA and AVNM models in both categories when compared with the AV results (Table 4). The FAC2 value was higher for the AV case in the low-wind category, whereas the results were similar across the three cases for moderate to high winds (Table 4).

However, we note that we modeled only aircraft sources at LAX, while other on-airport and off-airport sources had a smaller contribution (approximately 2% and 73%, respectively), with the exception of a refinery situated south of the south runway near the CS site (52% of total off-airport emissions) that could have contributed 30%–40% more at the CS site only as well as marine sources situated in the ocean far from the study domain (42% of total off-airport emissions). The contributions from these sources were almost negligible (Tetra Tech, 2013). While excluding some emission sources may not be ideal for assessing model performance against observations, our objective here was to understand and identify the best approach for characterizing aircraft sources within the AERMOD dispersion model and to assess the model’s behavior under different configurations in comparison with observations.

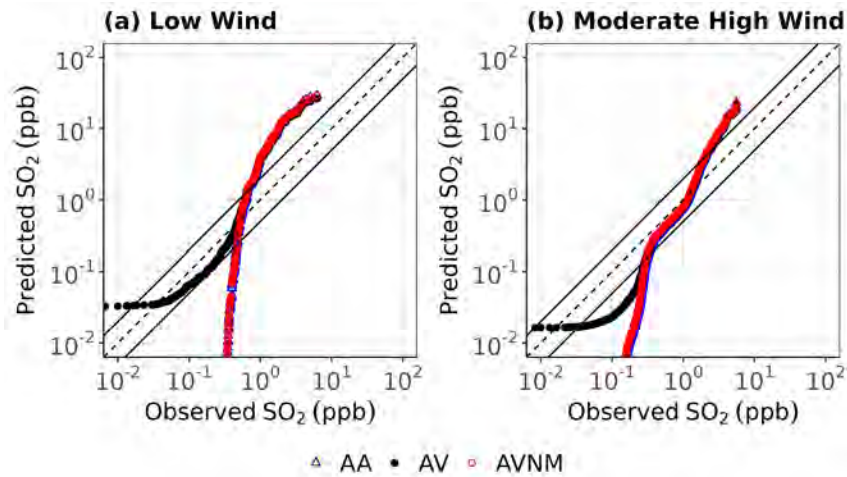


Figure 6. Quantile-quantile plots showing the effect of area and volume characterization in the American Meteorological Society/EPA Regulatory Model (AERMOD) for different wind categories. AA: AERMOD area; AV: AERMOD volume; AVNM: AERMOD volume with no meander; ppb: parts per billion.

Table 4. Comparison of model performance statistics from the American Meteorological Society/EPA Regulatory Model using area (AA), volume (AV), and volume with no meander (AVNM) treatments for different wind categories. FAC2: factor of two; RHC: robust highest concentration.

Statistics	Site/Wind Regime	Low Wind			Moderate High Wind		
		AA	AV	AVNM	AA	AV	AVNM
RHC Ratio	All	5.31	5.01	5.39	4.08	3.86	4.10
FAC2 (%)	All	8	64	8	43	37	41

1.1.5 Summary

We performed a detailed comparison of area and volume source treatments in AERMOD to potentially improve AERMOD’s model performance when modeling aircraft sources. For this, we performed a detailed sensitivity analysis based on the initial vertical dispersion parameter (σ_{z_0}), source number, and meander component in the volume source treatment. We found that the volume source treatment showed better performance in the context of intermediate- to high-level (up to 12% fewer overpredictions) and low-level concentrations (approximately 80% fewer underpredictions) compared with the standard AERMOD area source treatment. In addition, we found that the volume source treatment without the meander component was similar to the standard AERMOD area source treatment. The AERMOD area treatment adds approximately 21% more runtime compared with the volume source treatment for the same LAX study because of differences in the concentration calculation methodology. Here, we modeled only aircraft sources at LAX, whereas non-aircraft sources were not modeled. From the above analysis, it is clear that the meander component is important in the context of modeling air pollution dispersion, as it reduces the overpredictions and enhances the model predictions for low-level concentrations. Hence, it is recommended that the meander algorithm be used within the AERMOD area source treatment, as the area and volume source treatments without meander are similar except for the higher runtime for the area treatment. However, there are still additional key physical processes for aircraft sources that must be included, such as plume rise and wake turbulence caused by wing tip vortices; these processes should be included in AERMOD for both area and volume source treatments as aircraft sources are highly buoyant, specifically during LTO operations.

2. Physical Processes

2.1 Development and implementation of an aircraft plume rise algorithm in AERMOD

Aircraft emissions have horizontal momentum corresponding to the forward thrust of the aircraft. In addition, aircraft emissions have buoyancy corresponding to the heat rejected from the aircraft engine. These plume dynamics are not included in the latest version (v22112) of the area/volume source algorithm in AERMOD. The effects of the plume on



ground-level concentrations are accounted for through an initial plume height and width based on LIDAR observations at the end of the runway. Ground-level concentrations determined via this approach are likely to lead to overestimates of ground-level concentrations because they do not account for the increase in plume height with distance from the source. Here, we propose a plume rise formulation for aircraft emissions modeled with AERMOD. Plume rise is modeled using the weighted average of the characteristics of the aircraft that pass through the area/volume source in 1 hr, the average time used in AERMOD.

Before describing the details of the proposed plume rise formulation, we first review the different types of aircraft engines and their characteristics that are relevant to plume rise. Aircraft engines can be grouped into two categories. The first category is turbine-based: turbojet and turbofan engines (Figure 7). The exhaust from these engines has both buoyancy and horizontal momentum. The second category includes shaft-based engines: turboprop, turboshaft, and piston engines (Figure 7), in which the exhaust might not possess horizontal momentum.

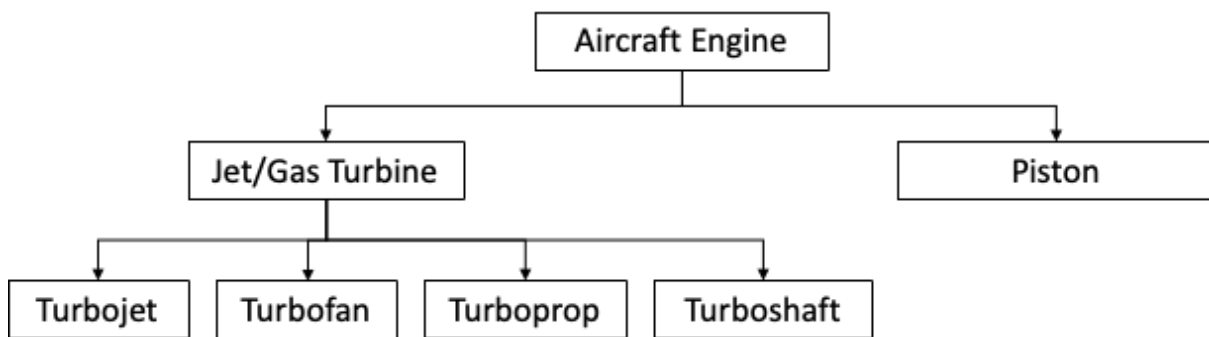


Figure 7. Types of aircraft engines.

When an aircraft travels in the airport, it lays down a plume along its path (Figure 8). It is useful to conceptualize a line thermal (Arunachalam et al., 2017) as a cylinder that contains the energy rejected by the engines. If t is the time spent by an aircraft in an area source, the length of the air cylinder affected by emissions of the aircraft traveling at an average speed, v_a , into a head wind, U_{eff} , is $(v_a + U_{eff})t$. If Q_e is the heat rejected per unit time by the aircraft, the heat content per unit length of the thermal is $Q_e/(v_a + U_{eff})$. We realize that the ambient U_{eff} is not always in the direction opposite to v_a . However, because the area source treatment of emissions does not trace the path of every aircraft in a source area, we add the velocities to ensure that we recover the expression for the plume rise when v_a is close to zero or is large compared with U_{eff} .

We incorporate this expression for the energy content per unit length of the line thermal into the familiar buoyancy parameter, F_b , used to compute a plume rise from a point source (Briggs, 1965):

$$F_b = \frac{g}{T_a} v_e r_0^2 (T_e - T_a) \tag{1}$$

where v_e and T_e are the velocity and temperature of the exhaust plume, T_a is the ambient temperature, g is the acceleration due to gravity, and r_0 is the effective radius of the point source. Equation (1) can be re-written as

$$F_b = \frac{g}{T_a} \frac{Q_e}{\pi \rho_e C_p} \tag{2}$$

where Q_e is the heat rejected by the aircraft engine, ρ_e is the density, and C_p is the specific heat of the exhaust gases.

Once an aircraft creates a line thermal in its path in an area source, the line thermal becomes detached from the aircraft and its behavior is governed by the energy and momentum that it contains. The buoyancy associated with a unit length of the line thermal is $F_b/(v_a + U_{eff})$, and the plume rise, h_{pb} , of the elements of the line thermal associated with a representative aircraft in the area source is as follows (Venkatram & Schulte, 2018):



$$h_{pb} = \left(\left(\frac{r_0}{\beta} \right)^3 + \frac{3}{2\beta^2} \frac{F_b}{(v_a + U_{eff})} \left(\frac{x}{U_{eff}} \right)^2 \right)^{1/3} - \left(\frac{r_0}{\beta} \right) \quad (3)$$

where $\beta = 0.6$ is an entrainment constant, x is the effective distance between the source and receptor, U_{eff} is the effective velocity that governs the transport of the elements of the line thermal, and r_0 is the initial radius of the line thermal. The travel time from the source to the receptor is x/U_{eff} , where the effective distance, x , is measured from the center of mass of the area source. Note that Equation (3) reduces to the plume rise equation for stationary sources if the speed of the aircraft, v_a , is zero.

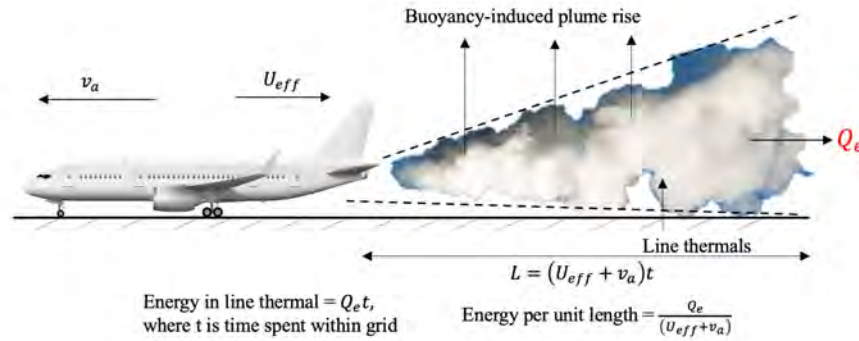


Figure 8. Schematic of a line thermal behind an airplane at the surface.

In addition to buoyancy, a plume rise is also governed by the horizontal momentum of the exhaust gases, which in turn depends on the thrust generated by the engine.

2.1.1 Accounting for jet momentum

We assume that the horizontal momentum is conserved as the radius of the horizontal plume grows with distance from an aircraft within the area source.

For a top-hat profile of velocity within the plume, the momentum balance can be written as

$$\rho_p U_p (U_p - U_a) \pi r^2 = T \quad (4)$$

where ρ_p is the plume density. U_p is the velocity inside the plume, and U_a is the ambient velocity at the level of the plume; these velocities are measured relative to the moving aircraft so that $U_a = v_a + U_{eff}$. The initial momentum flow inside the plume is equivalent to the thrust, T , exerted by the engine on the air. A version of this equation is derived in Appendix A1 of Arunachalam et al. (2017).

Following Barrett et al. (2013), we assume that the radius of the jet exhaust grows linearly with distance from a point within the area source:

$$r = \alpha x + r_0 \quad (5)$$

where $\alpha = 0.1$ is an entrainment constant and r_0 is the radius of the engine exhaust. This estimate of the plume radius allows us to calculate the velocity of air, U_p , inside the plume from Equation (4):

$$U_p = (v_a + U_{eff}) \left[0.5 + 0.5 \left(1 + \frac{4T}{\pi r^2 \rho (U_{eff} + v_a)^2} \right)^{1/2} \right] \quad (6)$$

The radius of the momentum-induced plume is assumed to grow until the difference between the plume and ambient velocities is comparable to the standard deviation of the ambient horizontal velocity fluctuations, $\sigma_u = 2.0u_*$, where u_* is the surface friction velocity. Then, the maximum plume radius is given by the following relationship:

$$T = \pi \rho_a r_m^2 ((v_a + U_{eff}) + \sigma_u) \sigma_u, \quad (7)$$

where ρ_a is the ambient density. Then, r_m is given by



$$r_m = \left(\frac{T}{\pi \rho_a ((v_a + U_{eff}) + \sigma_u) \sigma_u} \right)^{1/2} \quad (8)$$

The plume rise associated with momentum, h_{pm} , is taken to be the radius of the plume:

$$h_{pm} = \begin{cases} r_o + \alpha x, & x \leq x_m \\ r_m, & x > x_m \end{cases} \quad (9)$$

where x_m is the distance at which the radius reaches its maximum value:

$$x_m = \frac{(r_m - r_o)}{\alpha} \quad (10)$$

The effect of buoyancy is treated by assuming that the buoyancy acts independently on the expanding jet plume. However, the buoyancy is allowed to interact with the horizontal momentum through the initial radius, R_0 , which is taken to be the average value of the radius of the momentum-induced plume between 0 and x :

$$R_0 = \frac{1}{x} \int_0^x r(x) dx \quad (11)$$

which yields

$$R_0 = \begin{cases} r_o + \alpha x/2, & x \leq x_m \\ \frac{x_m}{x} \left(r_o + \frac{\alpha x_m}{2} \right) + r_m \left(1 - \frac{x_m}{x} \right), & x > x_m \end{cases} \quad (12)$$

Equation (12) must be solved iteratively because the wind speed at the plume height is not known a priori.

The total plume rise is then

$$h_p = h_{pb} + h_{pm} \quad (13)$$

where the second term on the right-hand side is the plume rise associated with the momentum, which is negligible for turboshaft or piston engines.

2.1.2 Maximum plume rise calculation

The rise of the plume associated with buoyancy is limited to the height at which the standard deviation of the vertical velocity fluctuations, σ_w , is equal to the rate of rise of the plume, dh_{pb}/dt . The travel time, t_{max} , associated with the maximum plume rise is then given by the solution of a nonlinear algebraic equation (Venkatram & Schulte, 2018):

$$\begin{aligned} \frac{dh_{pb}}{dt} &= \frac{d}{dt} \left[\left(\left(\frac{R_0}{\beta} \right)^3 + \frac{3}{2\beta^2} \frac{F_b}{(v_a + U_{eff})} t^2 \right)^{1/3} - \frac{R_0}{\beta} \right] = \sigma_w \\ &\text{or} \\ \left(\left(\frac{R_0}{\beta} \right)^3 + \frac{3}{2\beta^2} \frac{F_b}{(v_a + U_{eff})} t^2 \right)^{-\frac{2}{3}} F_b / (v_a + U_{eff}) t &= \sigma_w \beta^2 \end{aligned} \quad (14)$$

Equation (14) is solved by using a bi-section approach to yield t_{max} . Note that the solution of Equation (14) accounts for the plume spread induced by momentum, R_0 . The maximum plume rise is then given by Equation (3) with $t = t_{max}$.

When the boundary layer is stable, the plume rise is limited by the final rise in a stable atmosphere with a potential temperature gradient:

$$h_{max} = 2.66 \left(\frac{F_b}{(v_a + U_{eff}) N^2} \right)^{1/3} \quad (15)$$

where N is the Brunt-Vaisala frequency:

$$N = \left(\frac{g}{T_a} \frac{d\theta}{dz} \right)^{1/2} \quad (16)$$

The total plume rise is also limited by the height of the mixed layer.



2.2 Computing buoyancy parameters from engine characteristics

2.2.1 Turbine-based engines

Figure 9 shows the operation of a modern turbofan engine.

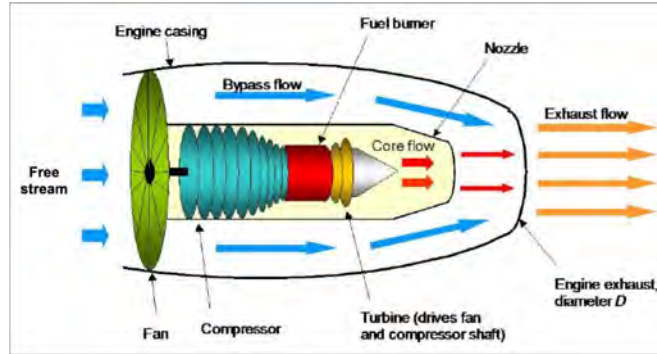


Figure 9. Schematic of a turbofan jet engine (source: ADMS-Airport Manual (CERC, 2020)).

The exhaust temperature and rejected heat required in Equation (2) to compute the buoyancy parameter are not available for jet/gas turbine engines. Thus, these variables must be estimated by using the available engine characteristics: the thrust, T , aircraft velocity, v_a , fuel burn rate, \dot{m}_f , air-fuel ratio, AF , and bypass ratio, $bypr$.

We can derive an expression for Q_e by writing the energy balance:

$$\dot{m}_f H_f \eta_c = \frac{\dot{m}}{2} (v_e^2 - v_a^2) + Q_e \quad (17)$$

where \dot{m}_f is the fuel consumption rate and H_f is the heating value of the fuel. The combustion efficiency, η_c , is close to unity. The air mass flow rate, \dot{m} , is related to the fuel burn rate, \dot{m}_f , through

$$\dot{m} = \dot{m}_f AF(1 + bypr) \quad (18)$$

where AF is the air-fuel ratio and $bypr$ is the engine bypass ratio.

According to Equation (17), the power supplied by the fuel (left-hand side) is the sum of the increase in kinetic power and thermal power added to the air passing through the engine.

The average exhaust velocity, v_e , of the gases from the engine follows from the expression for thrust:

$$T = \dot{m}(v_e - v_a) \quad (19)$$

where v_a is the aircraft velocity, so that

$$v_e = v_a + \frac{T}{\dot{m}} \quad (20)$$

Equations (18) and (20) provide \dot{m}_f and v_e , which are required to compute Q_e , from Equation (17).

The preceding equations allow us to compute the buoyancy parameter, F_b , from

$$F_b = \frac{g}{T_a} \frac{Q_e}{\pi C_p \rho_e} \quad (21)$$

where the exit density, ρ_e , is computed from the energy conservation equation and the equation of state:

$$\rho_e = \frac{p_a}{R_a T_e} \quad (22)$$



$$T_e = \frac{Q_e}{\dot{m}c_p} + T_a \quad (23)$$

where p_a is the ambient pressure and R_a is the gas constant of air. We see that the inputs required to compute F_b are the thrust, T , aircraft velocity, v_a , fuel burn rate, \dot{m}_f , air-fuel ratio, AF , and engine bypass ratio, $bypr$.

2.2.2 Shaft-based engines

The turboshaft engine is another common type of jet/gas turbine engine. A turboshaft engine delivers power to a shaft that drives something other than a propeller. The greatest difference between a turbojet and turboshaft engine is that in a turboshaft engine, most of the energy produced by the expanding gases is used to drive a turbine rather than to produce thrust. Many helicopters use a turboshaft gas turbine engine. In addition, turboshaft engines are widely used as auxiliary power units on large aircraft (Aeronautics-Guide, 2022).

In a turboshaft engine, the propeller is driven by a gas turbine. The air passing through the propeller is not heated. Thus, the hot exhaust from the turbine constitutes the primary source of buoyancy. The heat ejected by the turbine can be estimated if the compression ratio of the compressor in the turbine, CR , is specified. The compression ratio is the ratio of the stagnation pressures at the outlet and inlet of the compressor.

For an ideal turbine, CR determines the thermal efficiency of the turbine, which is given by

$$\eta_t = 1 - \frac{1}{\alpha_1} \quad (24)$$

$$\alpha_1 = CR^{\frac{k-1}{k}}, \quad (25)$$

where $k = \frac{c_p}{c_v} = 1.4$ is the ratio of the specific heats of air at constant pressure and volume.

An alternate expression for determining the thermal efficiency of the turbine is as follows:

$$\eta_t = \frac{p_s P_r}{\dot{m}_f H_f}, \quad (26)$$

where p_s is the power setting and P_r is the rated power.

Then, the power transferred to the propeller is $W = \dot{m}_f H_f \eta_t$, and the rejected heat is

$$Q_e = \dot{m}_f H_f (1 - \eta_t) = \frac{\dot{m}_f H_f}{\alpha_1}, \quad (27)$$

where H_f is the heating value of the fuel and \dot{m}_f is the fuel rate.

The temperature of the exhaust is

$$T_e = T_a + \frac{(1 - \eta_t) H_f}{C_p AF}, \quad (28)$$

where AF is the air-fuel ratio.

This temperature is used to compute the density, assuming that the pressure is ambient, p_a :

$$\rho_e = \frac{p_a}{R_a T_e}. \quad (29)$$

This density is used in the formula for the buoyancy parameter (Equation (21)).

2.3 Impact of plume dynamics on ground-level concentrations

We first provided estimates of plume rise associated with aircraft emissions as a function of aircraft speed and ambient velocity. We then estimated the impact of the plume rise formulation on ground-level concentrations of SO_2 using data from LAX AQSAS Phase III.

The final plume rise in an unstable boundary layer is proportional to $F_b / ((U_{eff} + v_a) \sigma_w^2)$ and the distance to the final rise is proportional to $\left(\frac{F_b}{\sigma_w^3}\right) \left(\frac{U_{eff}}{U_{eff} + v_a}\right)$ if we neglect the initial radius R_0 in Equation (14). These results reflect the impact of the



aircraft speed, v_a , in determining the plume rise through its role in governing the energy imparted to a unit length of the line thermal laid down by a moving aircraft.

Figure 10 shows the magnitudes of total plume rise corresponding to engine characteristics of a typical aircraft operating at LAX during take-off and taxiing. The buoyancy parameter during take-off is $1,864 \text{ m}^4/\text{s}^3$, reflecting full power, and is approximately 38-fold greater than the taxiing value of $49 \text{ m}^4/\text{s}^3$. The take-off thrust of 88,242 N is approximately 15 times that during taxiing. These differences in engine parameters are reflected in the variations of plume rise with effective wind speed and aircraft speed, as shown in Figures 10 and 11. The meteorological variables correspond to daytime when the planetary boundary layer height is 960 m and the standard deviation of vertical velocity fluctuations, σ_w , is 0.71 m/s.

Figure 10 (a) shows that the final plume rise and the distance to the final rise are sensitive to aircraft speed when the effective wind speed is 2 m/s. The final plume rise increases from approximately 150 m to 350 m when the aircraft speed decreases from 60 m/s to 20 m/s. The final plume rise decreases as the wind speed increases, as shown in Figure 10 (b), and the distance at which the plume reaches its final height increases with wind speed, as expected. This effect is clearly shown in Figure 10 (c) as the wind speed increases to 8 m/s.

Figure 11 shows similar effects of aircraft speed and effective wind speed on plume rise during taxiing. The smaller buoyancy of $49 \text{ m}^4/\text{s}^3$ is reflected in the much smaller buoyancy-induced plume rise of less than 20 m, which is compensated to some extent by a decrease in aircraft speed, resulting in a net decrease by a factor of approximately 10 even though the buoyancy decreases by a factor of 30. We see that the momentum-induced plume rise is much more important during taxiing and can exceed that induced by buoyancy, as shown in Figure 11 (a). Recall that the maximum momentum-induced plume rise is proportional to $\left(\frac{T}{U_{eff} + v_a}\right)^{1/2}$. Thus, the decrease in thrust accompanied by an aircraft speed factor from take-off to taxiing translates into a reduction by half in the momentum-induced plume rise when the effective wind speed is 2 m/s, shown as a comparison in Figures 10 (a) and 11 (a).

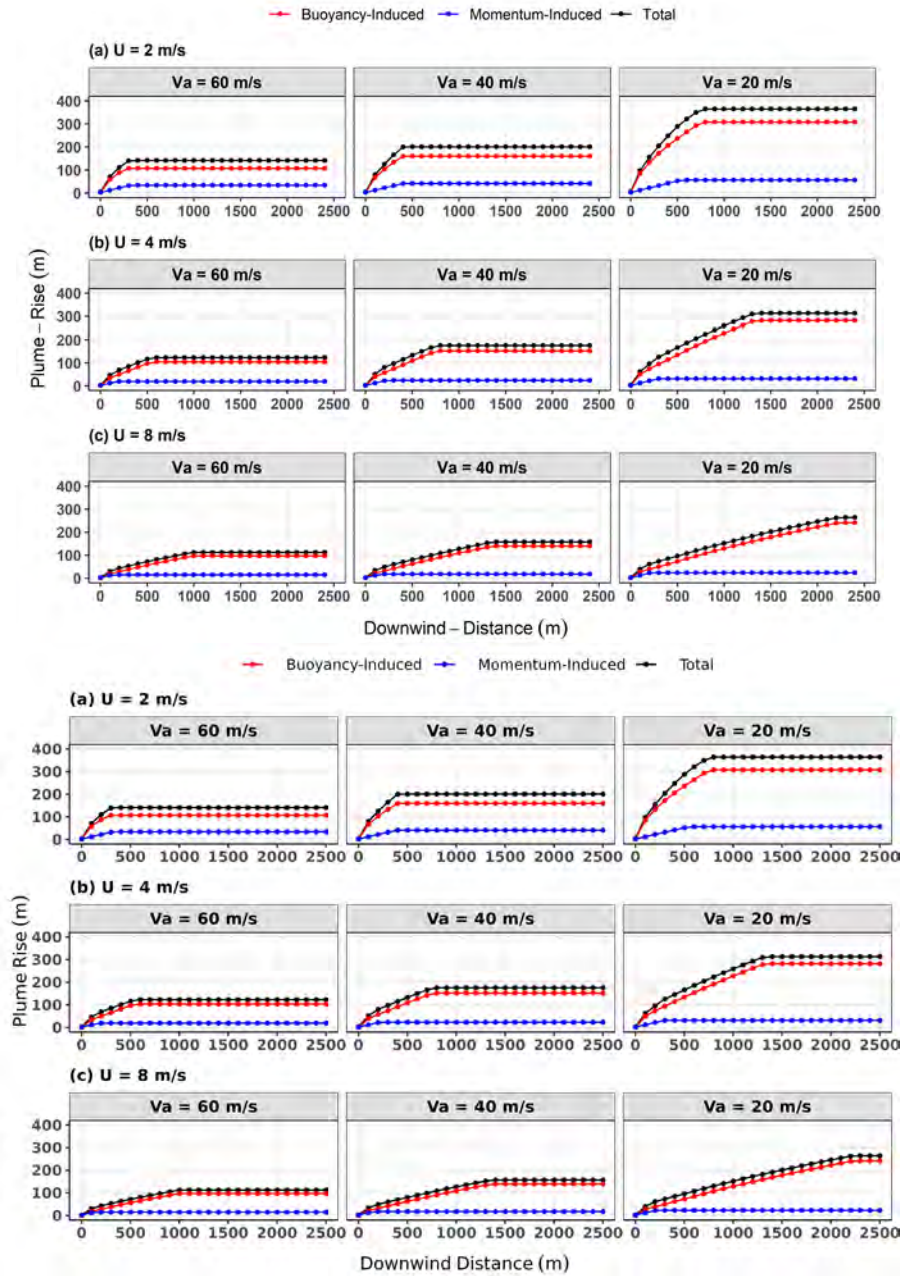


Figure 10. Variation in momentum- and buoyancy-induced plume rise with aircraft and ambient velocities for a typical aircraft during take-off. Thrust = 88,242 N; buoyancy parameter = 1,863 m⁴/s³.

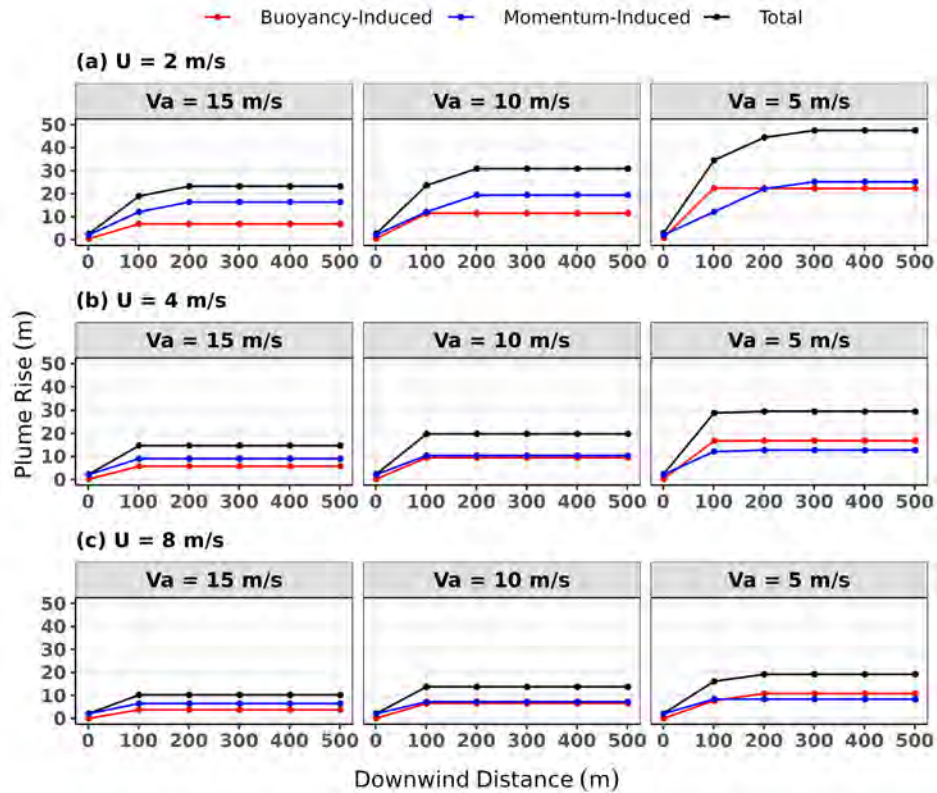


Figure 11. Variation in momentum- and buoyancy-induced plume rise with aircraft and ambient velocities for a typical aircraft during taxiing. Thrust = 5,741 N; buoyancy parameter = $49 \text{ m}^4/\text{s}^3$.

We see that an increase in wind speed and aircraft velocity decreases the plume rise at a fixed distance from a stationary point in the area source used to model emissions from an aircraft moving within an area. The concentration at a receptor decreases with transporting wind speed but increases as the plume rise decreases with increasing wind speed. Thus, the concentration at a receptor should be relatively insensitive to wind speed if these two effects compensate for each other. To observe this effect on modeled concentrations, we implemented this plume rise approach in AERMOD (v22112).

The above methodology has been presented with some initial results in *Atmospheric Environment* (Pandey et al., 2023).

2.4 Model results

We compared measurements with the AERMOD results obtained when airport sources were modeled as area sources, with and without the new plume rise algorithm, in describing the dispersion of jet plumes. The performance of the approach with the plume rise addition (AERMOD_PR) and with meteorological modifications (AERMOD_PR(MM)) was evaluated against SO_2 observations taken at four core sites (AQ, CN, CS, and CE) as a part of the LAX AQAS during the summer of 2012 (July 18 to August 28). Meteorological modifications were taken from Pandey et al. (2022), and the AERMOD model was evaluated at the four core sites using (i) diurnal variations in concentrations averaged over the season and (ii) overall concentration distribution analysis (Q-Q distribution).

To examine the effect of aircraft-related activity at the four monitors (AQ, CN, CS, and CE), we examined the wind speed and wind direction data generated using AERMET, the meteorological preprocessor of AERMOD. During the summer, the winds blew from the west approximately 90% of the time. The winds were relatively calm during the period of 01:00 to 08:00.

To focus on the impact of aircraft-related emissions on the four core sites, the concentrations were filtered using winds that brought emissions from aircraft operations to the monitors. We selected concentrations corresponding to 90° – 270° for AQ, 180° – 315° for CN, 270° – 90° for CS, and 225° – 315° for CE.



2.4.1 Diurnal variation in concentrations averaged over the season

For SO₂ pollutant, at site AQ, there was one observed peak around 1 ppb in the early morning that the AERMOD model overestimated; however, the AERMOD modeled with the plume rise and modified meteorology better captured this peak (Figure 12).

As shown in Figure 12, modeled concentrations above 0.8 ppb were higher than observed values at CN; in particular, the model had a large peak in the late evening when the AERMOD model was employed without any modifications. With the addition of the plume rise and the modification of model inputs based on wind flow, the model predictions were improved and better matched the observed diurnal behavior, especially in the early morning and late night hours; however, during the daytime, the model still underestimated the diurnal concentrations. This underestimation could be due to the substantial effect of background/off-airport sources. The CS site was largely impacted by emissions when the wind was directed from the northeast. The observed diurnal concentration had a single peak in the morning whereas the AERMOD model without any modifications showed two large peaks, one in the morning and one in the late evening. After the aircraft-specific plume rise and modified meteorology were applied, the model-predicted concentrations showed a better match to the observed diurnal concentrations; the model captured the observed morning peak but provided slight overpredictions in the late evening. We can state that the AERMOD model predictions showed a better match to observations at CS when the modifications were included. At CE, the model predictions were close to observations during daytime for both the modification and updates, whereas the AERMOD model with the plume rise and modified meteorology captured the observed diurnal features during early morning and late night hours.

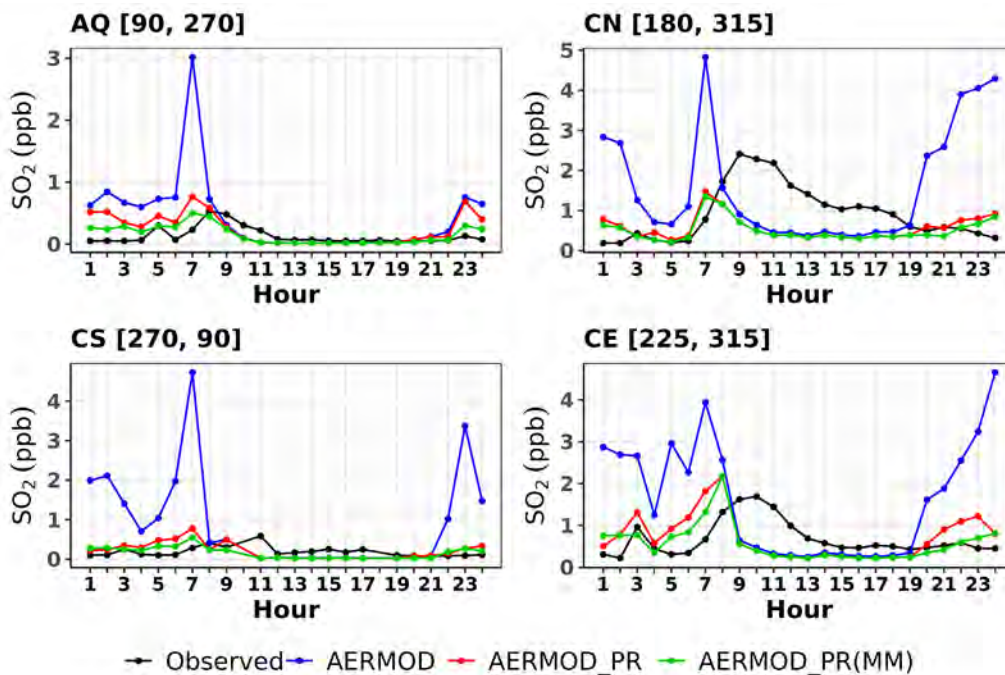


Figure 12. Diurnal variation of SO₂ concentrations averaged over each hour of the summer season for each site. AERMOD: American Meteorological Society/EPA Regulatory Model; MM: modified meteorology; ppb: parts per billion; PR: plume rise.

2.4.2 Overall concentration distribution analysis based on Q-Q plots

As shown in Figure 13, the highest concentrations at AQ were overpredicted by the model without the plume rise and modified meteorology, whereas the concentrations from the middle to lower range were within the FAC2 lines. For the model with the aircraft plume rise and modified meteorology, the higher concentrations showed a better match to the one-to-one line, which is very important for air quality assessment. At CN, the model with the aircraft plume rise and modified meteorology provided predictions very close to the one-to-one line at higher concentrations, whereas the model with both modifications gives slight underpredictions at the lower concentrations. At CS, the model without the plume rise or modified meteorology substantially overpredicted the concentrations. Figure 13 shows that the predictions improved

greatly upon the addition of the plume rise and modified meteorological parameters. The overall concentration showed a better match to the one-to-one line with these updates. At CE, slight changes were seen after the plume rise and modified meteorological parameters were implemented. However, at higher concentrations, the predictions obtained with the plume rise and modified meteorology were closer to the one-to-one line.

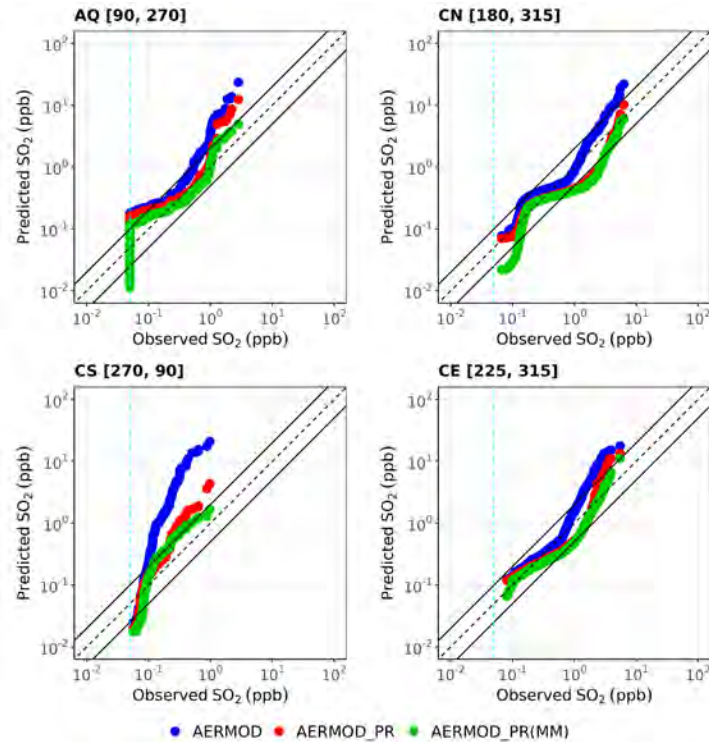


Figure 13. Quantile-quantile plots showing the effect of aircraft-specific plume rise and modified meteorological inputs for summer SO₂ concentrations at each site. AERMOD: American Meteorological Society/EPA Regulatory Model; MM: modified meteorology; ppb: parts per billion; PR: plume rise.

These results suggest the importance of incorporating the plume rise in AERMOD when estimating the impact of aircraft emissions on air quality in areas downwind of airports. More detailed evaluations with measurements of plume rise at a large airport are needed to further improve the formulation described above. We plan to apply and evaluate the algorithm with additional airport air quality studies in an extension of this study at multiple airports, both within and outside the United States.

3. Chemical processes

UNC began to implement the seven-reaction Generic Reaction Set Mechanism (GRSM) based on Venkatram et al. (1994) within the AERMOD source code. We are evaluating these updates by comparing them against existing chemical mechanisms.

4. Preparing AEDT emission inventories

UNC was involved in all AEDT updates to generate the AERMOD-ready inputs for aircraft plume rise. For this, UNC developed a plume rise algorithm for both types of aircraft engines (turbofan/jet and shaft-based engines). During this development, we found several bugs in the AEDT that were fixed by the Volpe National Transportation Systems Center (Volpe). Based on the file exchange of plume rise parameters and analyses of those files, UNC performed numerous statistical analyses for the algorithm and files. From this work, Volpe updated the AEDT model to generate AERMOD-ready input files as well as files for AEDT2ADM, the module that UNC developed to convert AEDT outputs for ADM.



Milestones

Completed implementation of plume rise algorithm in AERMOD in v22321 and v23132 and submitted to the EPA for inclusion in the Federal Register and EPA Rulemaking.

Major Accomplishments

- EPA released the new version of AERMOD (v23132) with aircraft-specific plume rise as an ALPHA option (developed by UNC/FAA).

Publications

- Pandey, G., Venkatram, A., & Arunachalam, S. (2022). Evaluating AERMOD with measurements from a major U.S. airport located on a shoreline. *Atmospheric environment*, 119506.
- Pandey, G., Venkatram, A., & Arunachalam, S. (2023). Accounting for plume rise of aircraft emissions in AERMOD. *Atmospheric environment*, 120106.
- Pandey, G. Venkatram, A., and Arunachalam, S. (2024). Modeling the Air Quality Impact of Aircraft Emissions: Is Area or Volume the Appropriate Source Characterization in AERMOD? *Air Quality, Atmosphere & Health, Under Revisions.*

Outreach Efforts

We presented the ADM work in multiple arenas, including the 2022 Community Modeling and Analysis System (CMAS) conference held in Chapel Hill, NC (October 2022), the Aviation Emissions Characterization Roadmap meeting held in Washington, DC (May 2023), the International Technical Meeting conference held in Chapel Hill, NC (May 2023), and the George Mason University conference held in Virginia (June 2023).

Awards

None.

Student Involvement

Praful Dodda, is a PhD student involved in developing ADM chemistry.

Plans for Next Period

- Finalize manuscript that shows detailed evaluation of plume rise in AERMOD using data from LAX AQSAS.
- Revisit ADM development with focus on improved model performance and incorporating other physical processes.
- Finalize NO₂ chemistry implementation in ADM.

References

- Aeronautics-Guide. (2022). Aircraft Gas Turbine Engines Types and Construction. Retrieved December 21, 2022, from <https://www.aircraftsystemstech.com/p/gas-turbine-engines-types-and.html?m=1>
- Chowdhury, B., Karamchandani, P. K., Sykes, R. I., Henn, D. S., & Knipping, E. (2015). Reactive puff model SCICHEM: Model enhancements and performance studies. *Atmospheric environment*, 117, 242-258.
- Cox, W. M., & Tikvart, J. A. (1990). A statistical procedure for determining the best performing air quality simulation model. *Atmospheric Environment. Part A. General Topics*, 24(9), 2387-2395.
- Kim, B., Rachami, J., Robinson, D., Robinette, B., Wyle, K. N., Arunachalam, S., Davis, N., et al. (2012). *Guidance for quantifying the contribution of airport emissions to local air quality*. Washington, D.C.: Transportation Research Board.
- Tetra Tech, Inc. (2013). *LAX Air Quality and Source Apportionment Study*. Los Angeles World Airports. Available at: <http://www.lawa.org/airQualityStudy.aspx?id=7716>. Retrieved July 30, 2022, from <http://www.lawa.org/airQualityStudy.aspx?id=7716>
- U.S. EPA. (2022). *User's Guide for the AMS/EPA Regulatory Model (AERMOD)*.

Task 2 - Develop and Evaluate a Multiscale WRF-SMOKE-CMAQ Model Application for KBOS Focused on UFPs

University of North Carolina at Chapel Hill

Objectives

In this project, we partnered with ASCENT 18 investigators from BU, focusing specifically on modeling KBOS across various spatial scales. The primary objective was to conduct a thorough intercomparison of measurements and models, with a special emphasis on ultrafine PM, mass, and number concentrations resulting from aircraft emissions.

To achieve this goal, we delved into the utilization of two distinct modeling approaches: the CMAQ and SCICHEM models. The SCICHEM model stands out for its integration of comprehensive gas-, aqueous-, and aerosol-phase chemistry within the advanced Gaussian puff model SCIPUFF (Second-order Closure Integrated Puff; Chowdhury et al., 2015). Noteworthy is its capacity to characterize aircraft impacts with high precision in the immediate vicinity of the airport, thereby offering a significant advancement in the estimation of aircraft-attributable PM compared with previous assessments.

It is crucial to highlight that while both CMAQ and SCICHEM share a common aerosol treatment, SCICHEM excels in capturing fine-scale details around the airport. A key outcome of this project is the enhancement of predictions related to aircraft-attributable PM compared with previous estimates. It is worth noting that the use of SCICHEM, which focuses solely on PM mass concentrations, necessitated the development of postprocessing routines. These routines were designed to convert PM mass into a UFP number concentration (UFPNC) using a methodology consistent with CMAQ. Additionally, it is important to mention that, until now, SCICHEM has not been employed to predict UFPNC. This effort introduces a novel avenue of research in our project, showcasing our commitment to pushing the boundaries of knowledge in this domain.

In 2017, ASCENT 18 investigators made multiple measurements of UFPs at seven locations south and west of KBOS. We collaborated with BU to obtain these measurements to perform an intercomparison against model outputs.

1) CMAQ application for KBOS

- For this assignment, we developed a nested application of the WRF-SMOKE-CMAQ modeling system. The initial and boundary conditions for the outermost grid, set at 12-km resolution, are derived through downscaling from CMAQ applied to the northern hemisphere at a higher resolution of 108 km. This process ensures that the larger-scale atmospheric conditions are appropriately captured for the outermost grid. Following standard practices in modeling, the subsequent 4-km and 1-km grids are nested down accordingly from the immediate outer grid. This nested approach enables a seamless transition and refinement of atmospheric conditions, allowing for a more detailed and accurate representation of the dynamics as the spatial resolution increases. This configuration was applied across two distinct seasons, namely summer and winter, for contribution analysis.
- For this application, the emission inventories pertaining to non-aviation sectors draw upon data provided by the EPA's National Emissions Inventory (NEI) for the year 2017, which are projected from NEI 2016. This source is instrumental for capturing a comprehensive picture of emissions from various non-aviation activities during the specified year. To complement this dataset, the meteorological fields essential for the modeling process are downscaled from NASA's Modern-Era Retrospective Analysis for Research and Applications (MERRA) version 2 (v2), as documented by Rienecker et al. (2011). The utilization of MERRA v2 ensures that the atmospheric conditions incorporated into the model are derived from a reliable and widely accepted dataset, enhancing the accuracy and reliability of the simulation results.

The base CMAQ model application is configured as follows:

- a) Aircraft emissions for KBOS 2017 from AEDT processed through AEDT Proc;
- b) Background emissions from NEI processed through SMOKE v3.6;
- c) Meteorology from MERRA downscaled with WRF v3.8;
- d) Lightning NO_x;
- e) Inline photolysis; and
- f) Latest version of CMAQ (v5.32) enhanced with the new aircraft-specific emissions module as described by Huang et al. (2017).



2) Contribution of KBOS emissions

- To enhance our modeling study, we aim to procure KBOS-specific airport-level emission inventories for the year 2017 directly from AEDT through collaboration with Massport, the public authority responsible for managing KBOS. If these specific inventories are not readily accessible during the proposed period of performance, we plan to leverage existing AEDT-based full-flight aircraft inventories. We anticipate obtaining these from one of the global-scale 2015 inventories available through FAA/Volpe (AEDT-Volpe). Our strategy involves extracting Boston operations during the LTO phases to effectively support the assessment and goals of our study. This approach ensures that we have comprehensive and relevant data to contribute to the accuracy and reliability of our modeling efforts. Thus far, our approach has involved the utilization of NEI emission data and AEDT-Volpe (2015) in our modeling and analysis processes.

Two emission scenarios are considered (SMOKE):

- i. KBOS emissions in NEI 2017 (based on AEDT) during LTO cycles; and
- ii. KBOS emissions exported by AEDT-Volpe 2015 during LTO cycles.

3) Aircraft-specific aerosol size distribution in CMAQ

- We conducted multiple sensitivity simulations using both the CMAQ v5.3 base model and an enhanced version incorporating the new Detailed Emission Scaling, Isolation, and Diagnostic (DESID) module, as outlined by Murphy et al. (2021). This innovative module introduces a third mode alongside the traditionally used Aitken and accumulation modes in all prior CMAQ applications.
- A significant modification was made to the default aerosol size distribution (ASD) parameters within the CMAQ model. Historically, the geometric mean diameter (GMD) was set at 60 nm with a geometric standard deviation (GSD) of 1.7 nm. However, for this study, we tailored these parameters to accommodate aircraft-specific ASD (AASD) characteristics. In this updated scenario, the GMD is adjusted to 23.2 nm, accompanied by a corresponding GSD of 1.56 nm. This refined set of parameters, referred to as the geometric mean diameter and standard deviation (GMDS) scenario for the model, aligns with the specifics outlined by Moore et al. (2017).

Four emission scenarios are considered:

- i. Background + KBOS emissions during LTO cycles with default ASD;
- ii. Background + KBOS emissions during LTO cycles with GMD;
- iii. Background + KBOS emissions during LTO cycles with GSD; and
- iv. Background + KBOS emissions during LTO cycles with GMDS.

4) Assessment of UFPs through field observations

- Once the model application has been developed and assessed, UNC will undertake an evaluation of 2017 field observations conducted by the ASCENT 18 team at BU. This evaluation involves comparing the model predictions with actual measurements, specifically focusing on UFPs from aircraft emissions at KBOS. BU collected measurements at seven fixed-site locations along the arrival path of aircraft at KBOS in 2017.
- In this task, the collaboration between UNC and BU will include a comparative analysis of regression and dispersion model-based assessments of UFPs originating from KBOS. This collaborative effort with the ASCENT 18 investigators will necessitate a continuous exchange of information and sharing of results throughout the entire period of performance. The ongoing collaboration will result in an integrated assessment that combines measurements and modeling, providing a comprehensive understanding of UFPs attributed to aircraft emissions at KBOS. The synergy between measurement data and model predictions will contribute to a more robust and reliable assessment of the impact of aircraft emissions on UFPs in the Boston area.

5) Development of AEDT-UNC (2017) emission inventories for KBOS

- We will utilize the Aircraft Designer tool within AEDT-3e to generate approach and departure tracks specifically tailored for KBOS. We will then systematically construct an exhaustive study database for KBOS Performance Data Analysis and Reporting System (PDARS) operations by populating essential tables through SQL. This involves the assignment of default values to variables that were previously undefined, following the guidelines outlined in the user manual. Our initial implementation involved successfully running AEDT-3e for a 1-day PDARS operational scenario. At present, our primary objective is to expand the scope of this simulation to cover an entire month, specifically July 2017. To facilitate this undertaking, we plan to acquire aircraft operations data from the FAA. We will then employ the latest publicly available version of AEDT to formulate a KBOS-specific airport-level emission inventory, aligning with the timeframe of the measurement campaign.

This comprehensive approach ensures a robust and accurate representation of the emission landscape during the specified period.

1. CMAQ application for KBOS

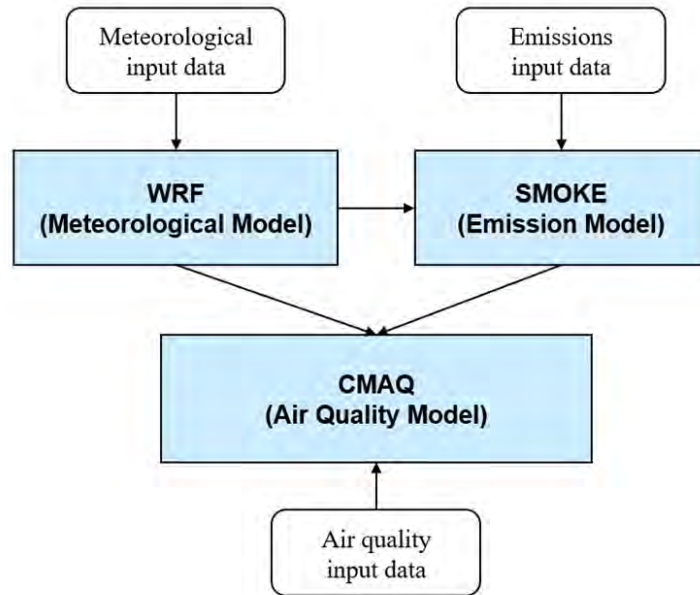


Figure 14. Weather Research and Forecasting–Sparse Matrix Operator Kernel Emissions–Community Multiscale Air Quality Model (WRF-SMOKE-CMAQ) modeling system.

1.1 WRF

The WRF model was collaboratively developed by the National Center for Atmospheric Research and the National Center for Environmental Prediction within the National Oceanic and Atmospheric Administration. This meteorological model employs fully compressible non-integer equations, with its horizontal grid adopting the Arakawa-C grid system. Additionally, WRF utilizes vertical coordinates of hydrostatic barometric pressure based on topography. The WRF modeling software consists of a dynamic processing module, specifically the Advanced Research WRF solver. This module includes preprocessing functionalities, bidirectional and unidirectional nesting capabilities, and a variety of postprocessing programs. The comprehensive suite of tools within the WRF model enables dynamic and accurate simulations of atmospheric conditions, making it a valuable resource for meteorological research and forecasting.

1.2 CMAQ model

The CMAQ system is widely employed across diverse fields by researchers worldwide. CMAQ's preprocessing components include an initial conditions processor, which is responsible for generating initial conditions, the boundary conditions processor, which generates boundary conditions, and the meteorology–chemistry interface processor, which is utilized for preprocessing meteorological data. Additionally, the chemical transport module, consisting of a chemical transport model, plays a crucial role in the CMAQ system. Utilizing results obtained from the preprocessing module as input data, the chemical transport model numerically calculates the three-dimensional advection–diffusion equation to determine pollutant concentrations in space on an hourly basis. Throughout this process, various factors such as horizontal and vertical advection, horizontal and vertical diffusion, deposition, and gaseous chemical reactions are considered. These calculations adhere to the principles of mass conservation in the advection process, providing a comprehensive and accurate representation of pollutant dynamics in the atmosphere. CMAQ was used to evaluate the impact of airport emissions with the configuration described in Table 5 for the winter (January) and summer (July) of 2017.

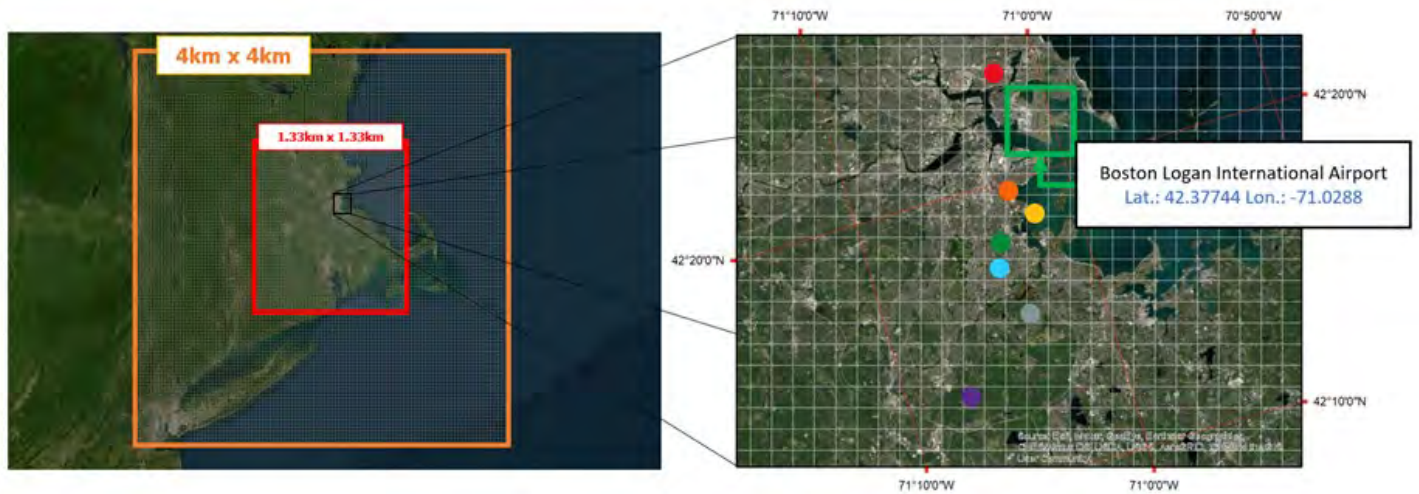


Figure 15. Boston Logan International Airport domain with the location of seven monitoring stations.

Table 5. Community Multiscale Air Quality (CMAQ) v5.3.3 model configuration. SMOKE: Sparse Matrix Operator Kernel Emissions. [AERO6: Aerosol module 6; POA: Primary Organic Aerosol]

	Domain 1	Domain 2	Domain 3
Horizontal Grid	459 × 299 (12US2)	102 × 108	126 × 141
Resolution (km)	12 km × 12 km	4 km × 4 km	1.33 km × 1.33 km
Vertical Grid	35 Layers		
CMAQ Chemical Option	<ul style="list-style-type: none"> · Carbon Bond 6 r3 · AERO6 non-volatile POA (sixth-generation CMAQ aerosol module) 		
SMOKE Input Data	· Emission from 2017 National Emissions Inventories		
Modeling Period	January 1–31, 2017		July 1–31, 2017
	2-week spin-up in December 2016		2-week spin-up in June 2017

2. Contribution of KBOS emissions

AEDT-based flight segment data provided by FAA/Volpe from the year 2015 were processed for KBOS, as depicted in Figure 16. It is noteworthy that although flight patterns might exhibit similarities between 2015 and 2017 (Mueller, 2022), certain changes have been identified. A comparative analysis of NEI-KBOS emissions for 2017 and AEDT-Volpe emissions for 2015 was conducted. Aggregating emissions for July revealed discrepancies in certain pollutants. Notably, carbon monoxide (CO) and fine PM (PM FINE) were underestimated by AEDT-Volpe, while nitrogen oxides (NO_x) were overestimated. The overestimation of NO_x can be attributed to the larger portion of NO₂ in AEDT-Volpe compared with NEI-KBOS. These findings emphasize the importance of carefully considering and validating emission data to ensure accurate representation in modeling and analysis, especially when transitioning between different datasets and years.

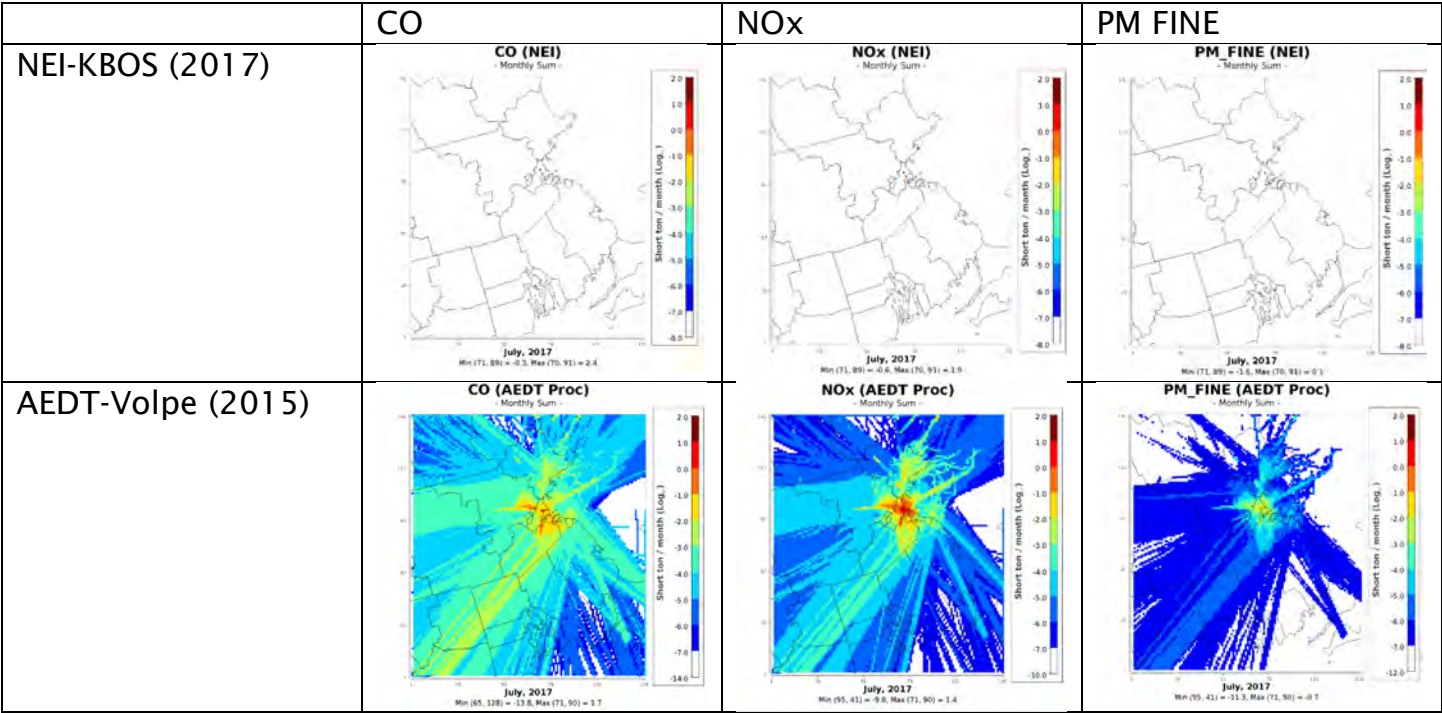


Figure 16. Spatial monthly sum of emission from the National Emissions Inventory (NEI) for Boston Logan International Airport (KBOS) (2017) and emissions based on Aviation Environmental Design Tool Volpe (AEDT Proc) (2015) for July 2017. PM: particulate matter.

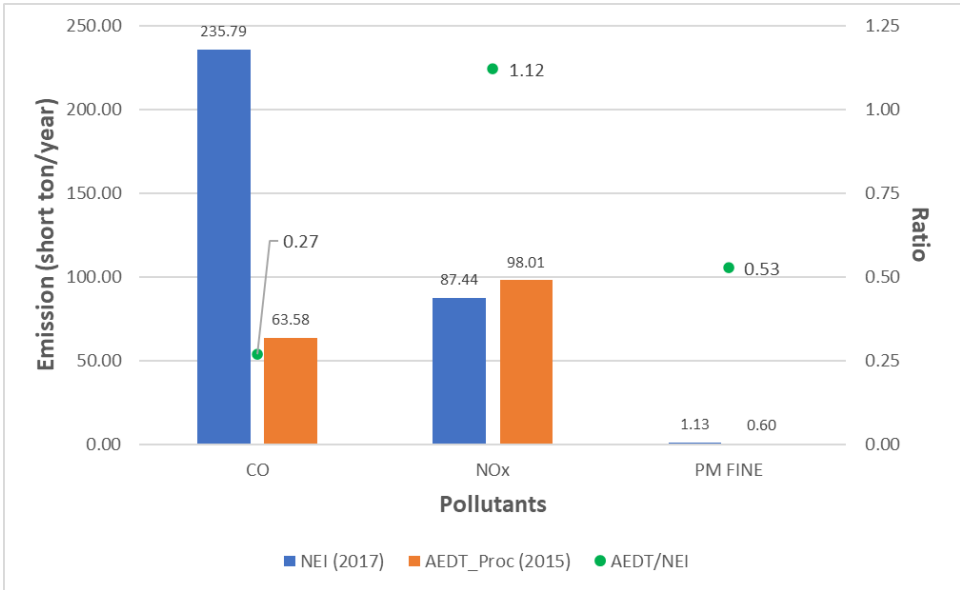


Figure 17. Total of emission from the National Emissions Inventory (NEI) for Boston Logan International Airport (2017) and emissions based on Aviation Environmental Design Tool Volpe (AEDT Proc) (2015) during July 2017. PM: particulate matter.

3. AASD in CMAQ

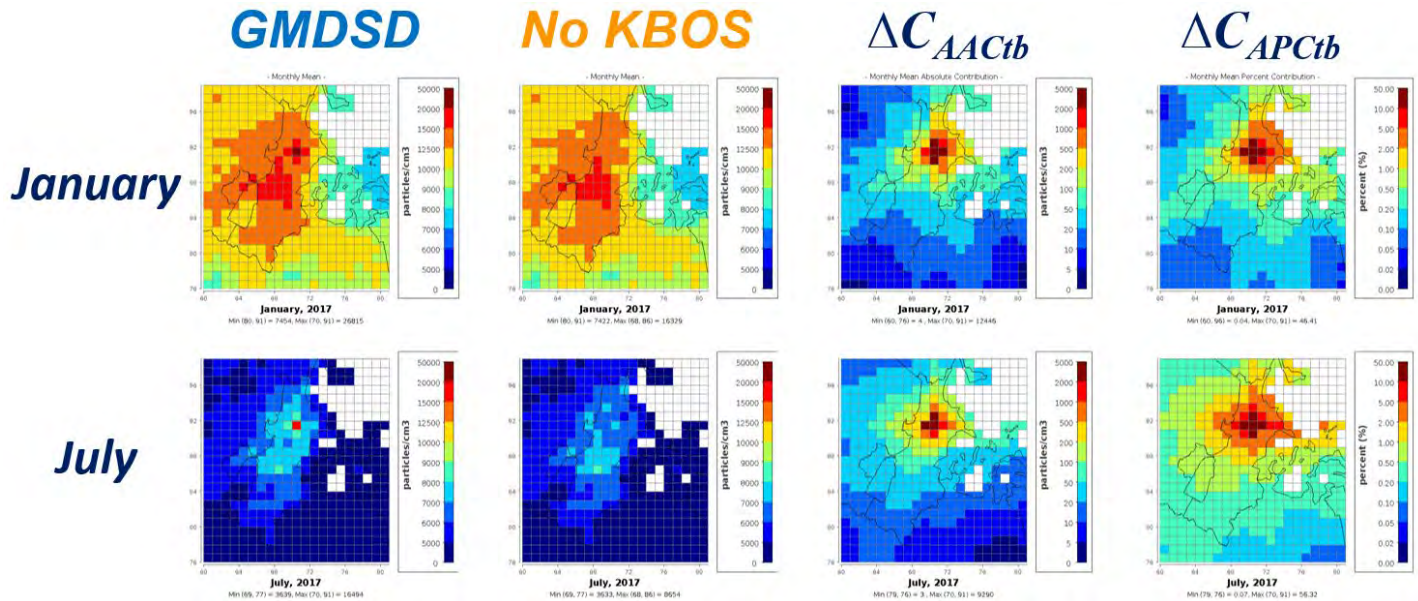


Figure 18. Monthly average ultrafine particle number concentration and contribution of the airport with two scenarios during January (top) and July (bottom) of 2017. GMDSD: geometric mean diameter and standard deviation; KBOS: Boston Logan International Airport.

CMAQ simulations focused on KBOS were executed, with the DESID module applied for the ASD. The default ASD parameters in CMAQ, characterized by a GMD of 60 nm and a GSD of 1.7 nm, were altered to accommodate an AASD configuration (GMD: 23.2 nm; GSD: 1.56 nm). This adjustment, referred to as the GMDSD scenario, was applied exclusively to KBOS.

The impact of KBOS on UFPNC increased significantly following the application of an AASD. In January, KBOS contributed a relatively small percentage (8.0%) to the UFPNC, equivalent to 1,242 particles/cm³. However, with the implementation of the aircraft-specific GMDSD scenario, the contribution of KBOS surged to 46.4%, resulting in a UFPNC of 12,446 particles/cm³. This increased pattern of KBOS contribution to UFPNC in July mirrored that observed in January. Although the July concentration (12,446 particles/cm³) was larger than the January contribution (9,290 particles/cm³), the percentage contribution of KBOS to the UFPNC, denoted by CAPCtb, rose from 46.4% in January to 56.3% in July. These findings underscore the notable influence of the GMDSD scenario on KBOS emissions and the subsequent impact on the UFPNC, emphasizing the need for a detailed consideration of aerosol size parameters in modeling efforts.

4. Assessment of UFPs through field observations

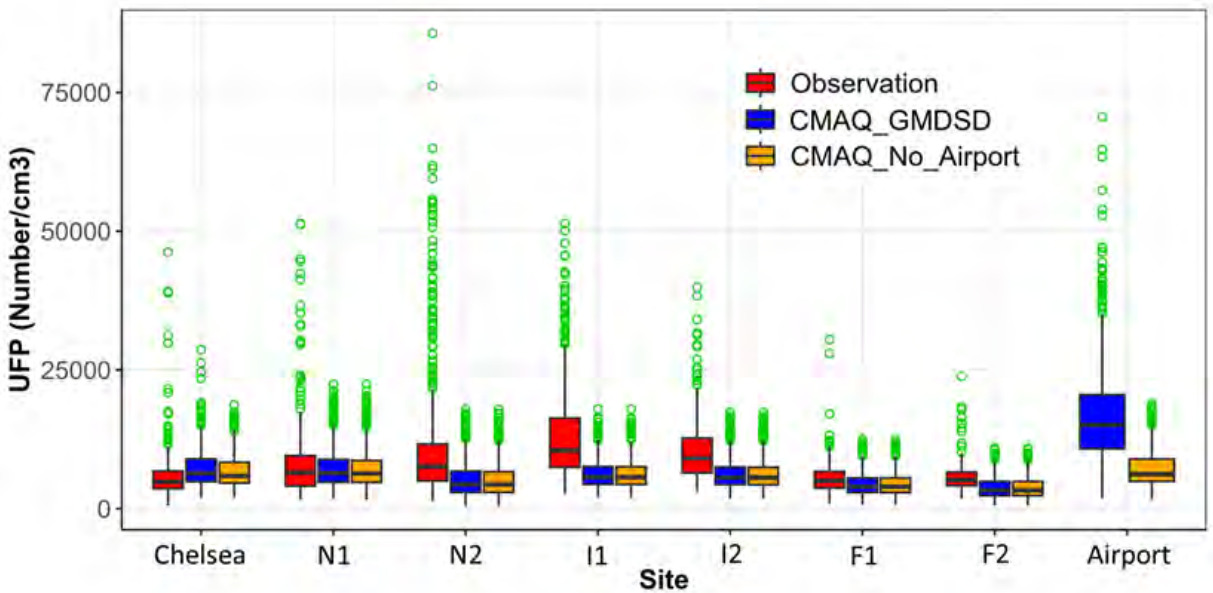


Figure 19. Boxplot of observed and modeled (GMDSD and No KBOS) ultrafine particle (UFP) number concentration at seven monitoring sites and airport grid-cells (July). CMAQ: Community Multiscale Air Quality; GMDSD: geometric mean diameter and standard deviation; KBOS: Boston Logan International Airport.

Observations indicated that the UFPNC changed with distance from KBOS, the aircraft pathway (runway), and other emission sources such as on-road traffic. In contrast, CMAQ results indicated that the UFPNC was primarily influenced by the distance from KBOS. CMAQ struggled to capture observed extreme events because emissions were assigned to single grid-cells based on NEI estimates. To address this limitation, ongoing efforts involve using AEDT-3e to distribute single-point aircraft emissions across a three-dimensional grid-cell structure, potentially enhancing the model's ability to capture extreme events in line with observations.

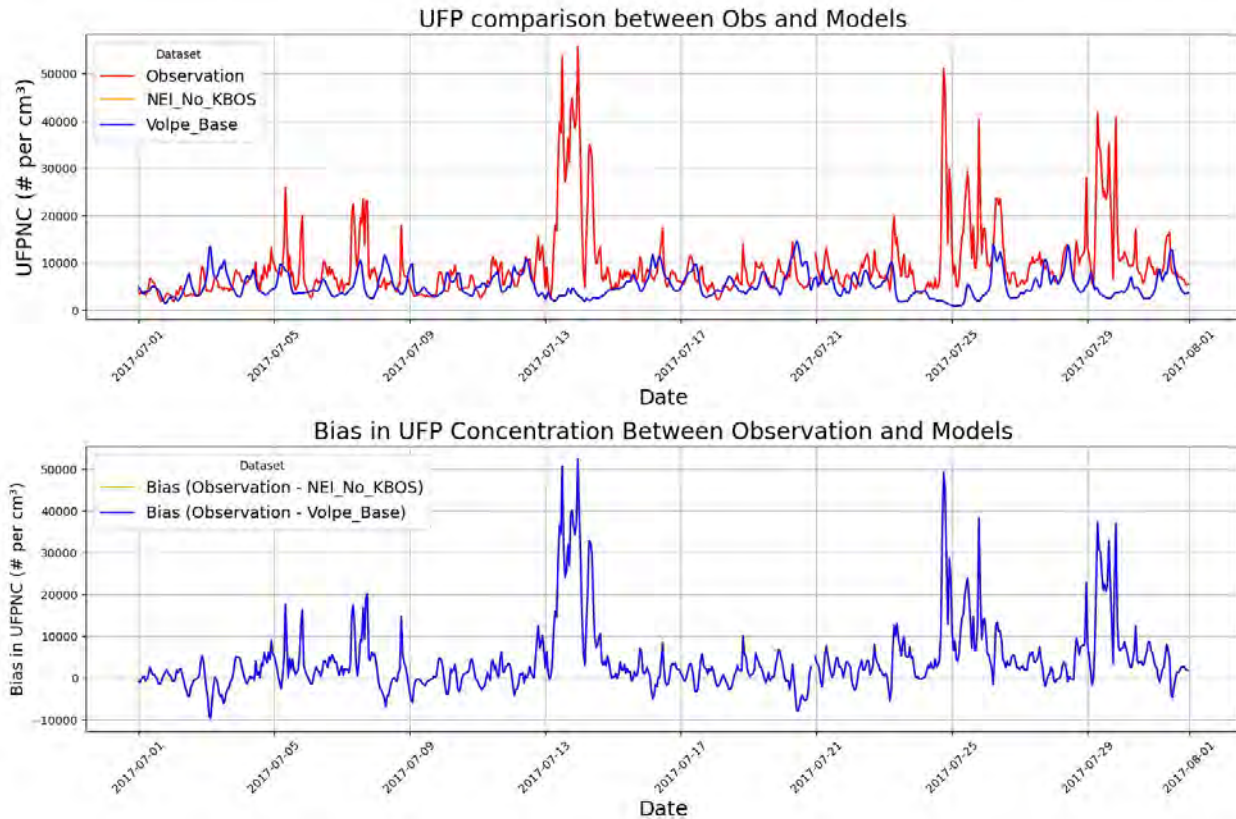


Figure 20. Comparison of ultrafine particle (UFP) number concentrations from observations (Red) (average of seven Boston University [BU] sites) and two model scenarios (Blue: Volpe_Base; blue: NEI_No_KBOS). Top: concentrations; bottom: differences between observations and model. Volpe_Base: Emissions created by Volpe; KBOS: Boston Logan International Airport.

The comparison between observations and the CMAQ model involved two scenarios, namely Volpe_Base (2015) and NEI_No_KBOS, for July 2017 (refer to Figure 20). CMAQ demonstrated accurate UFPNC predictions when UFPNC values were below 15,000 particles/cm³. However, notable underestimations were observed, reaching up to 53,500 particles/cm³, particularly in grid-cells corresponding to the seven monitoring sites, when the UFPNC exceeded 20,000 particles/cm³.

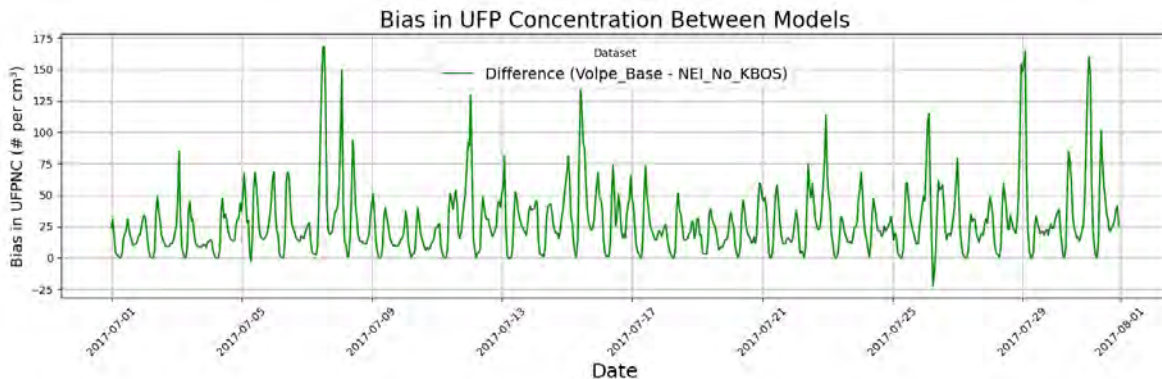


Figure 21. Bias in ultrafine particle (UFP) number concentration between two models (Volpe_Base - NEI_No_KBOS).

A secondary comparison, focusing on model-to-model assessments for July 2017 (Figure 21), was conducted to discern whether CMAQ could capture peaks attributed to KBOS. Although Figure 21 does not distinctly highlight differences in UFPNC, despite small quantities (-20 to 175 particles/cm³), the bias between the two scenarios revealed clear distinctions in UFPNC values originating from KBOS when concentrations exceeded 20,000 particles/cm³. In essence, the peaks identified in both the observation data and model-to-model bias exhibited similar patterns throughout July (on days 5, 7, 11-14, 16, 22, 24-27, and 29-30). These findings underscore the importance of considering KBOS emissions in the modeling process, especially during periods of elevated UFPNC values. The similarities in patterns enhance our confidence in the model's ability to capture the influence of KBOS on UFP levels.

The comparison between observation and the CMAQ model involved two scenarios, namely Volpe_GMDSD_X10 (2015) and NEI_No_KBOS, for July 2017, as shown in Figure 22. In this analysis, the performance of CMAQ in predicting the GMDS scenario aligned well with UFPNC values below 15,000 particles/cm³, similar to the results modeled in the Volpe_Base scenario. Volpe_GMDSD_X10 and Volpe_Base differ in their implementation of AASD and a 10-fold increase in KBOS emissions. This adjustment resulted in a notable mitigation of the underestimation in CMAQ regarding UFPNC, and the model successfully captured the peak occurrence on July 28, 2017. The maximum quantity difference exhibited a significant increase, surging from 180 particles/cm³ in Volpe_Base to 12,000 particles/cm³ in Volpe_GMDSD_X10. This observation emphasizes the impact of implementing AASD and increasing KBOS emissions on the model's ability to predict UFPNCs, showcasing improvements in capturing peak events and reducing underestimations.

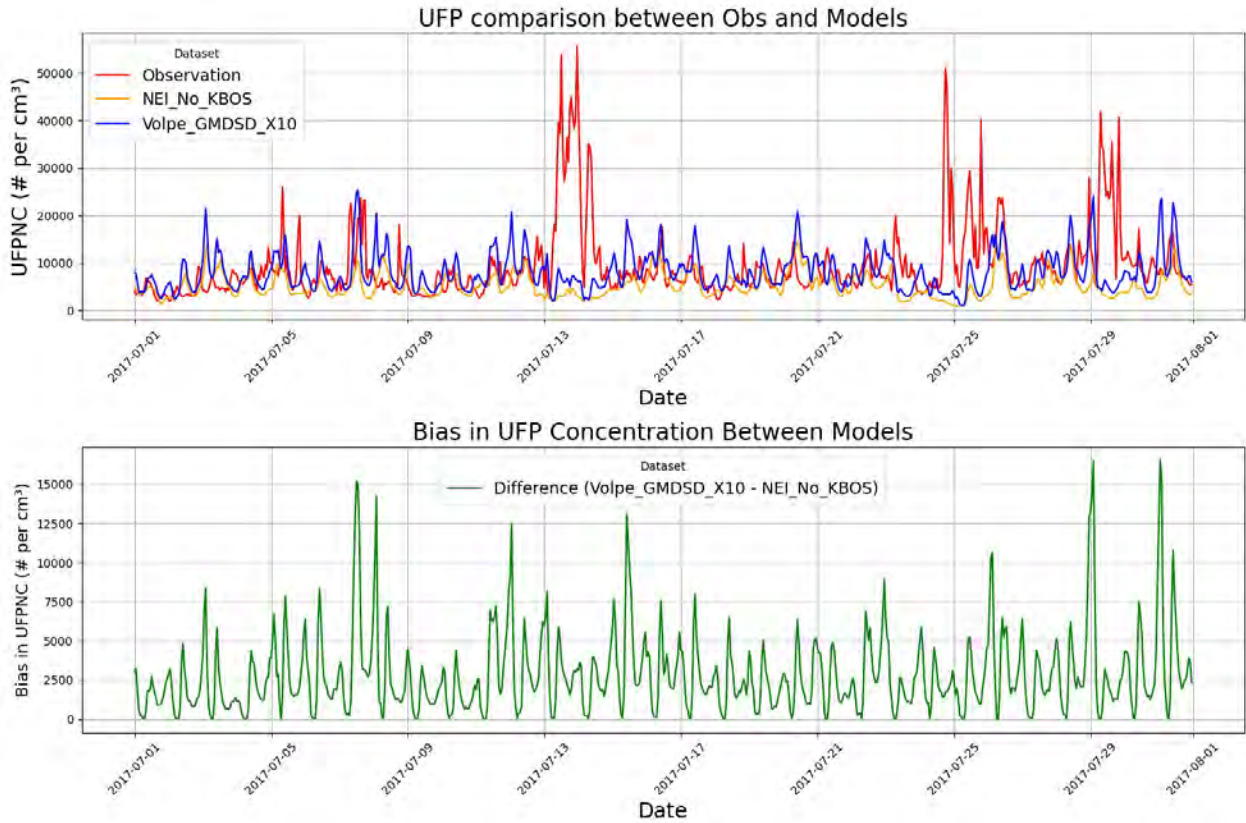


Figure 22. Comparison of ultrafine particle (UFP) number concentrations from observations (red) (average of seven Boston University [BU] sites) and two model scenarios (blue: Volpe_GMDSD_X10; orange: NEI_No_KBOS). Top: concentrations; bottom: differences in UFPNC between two models (Volpe_GMDSD_X10 - NEI_No_KBOS). GMDSD: geometric mean diameter and standard deviation; KBOS: Boston Logan International Airport.



In Table 6, a comparison was conducted among the Base_NEI, Volpe_Base, and Volpe_GMDSD X10 scenarios to assess model performance. UFPNC differences between the Base_NEI and Volpe_Base scenarios were minimal, with variations of less than 2 particles/cm³, except at Chelsea. The introduction of the GMDSD scenario, involving a 10-fold increase in emissions, led to noticeable changes in the bias between the model and observation, resulting in improvements of up to 20%.

The observed bias could potentially be attributed to several factors, including CMAQ reproducibility in both vertical and horizontal dimensions, emission distribution characteristics, or potential underestimations in the modeling process. Further investigations and sensitivity analyses may be necessary to pinpoint the specific contributors to the observed bias and to enhance the accuracy of the model's predictions.

Table 6. Monthly average bias of ultrafine particles with observations at seven monitoring sites. Volpe: Emissions created by Volpe; GMDSD: geometric mean diameter and standard deviation; NEI: National Emissions Inventory.

Site	Base_NEI	Volpe_Base	Volpe_GMDSD X10
CHE	761.4	725.6	1,180.3
N1	-956.1	-957.9	-697.0
N2	-6,452.4	-6,451.3	-5,998.9
I1	-7,322.1	-7,322.4	-7,041.3
I2	-4,691.4	-4,691.1	-4,343.9
F1	-978.3	-977.9	-921.3
F2	-1,803.0	-1,803.0	-1,798.6

5. Development of AEDT-UNC (2017) emissions inventory for KBOS

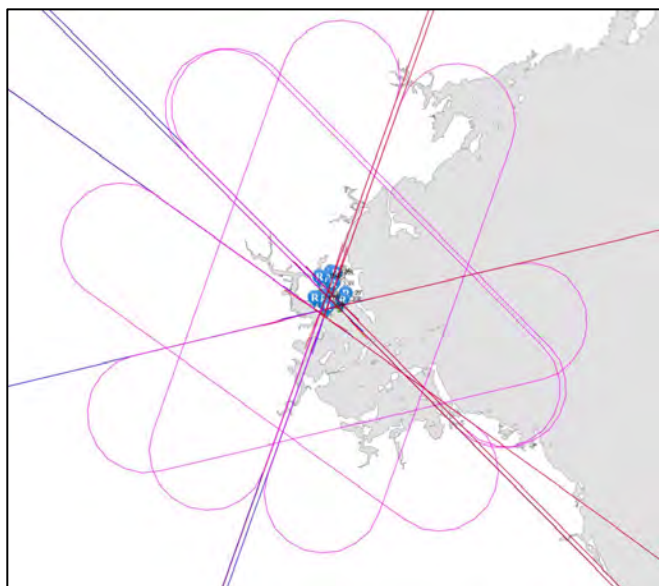


Figure 23. Layout of the Boston Logan International Airport for August 2017.



We are utilizing track locations extracted from shapefiles to generate tracks and gather additional information required for AEDT. Approach and departure tracks for KBOS were developed using the Aircraft Designer tool in AEDT-3e, as shown in Figure 23.

Table 7. AEDT-UNC (2017) from the Performance Data Analysis and Reporting System at Boston Logan International Airport for August 1, 2017. AEDT: Aviation Environmental Design Tool; AFE: above field elevation; PM: particulate matter; UNC: University of North Carolina at Chapel Hill; VOC: volatile organic compounds.

Operation Group	Mode	Duration	CO (ST)	VOC	NOx	PM 2.5	PM 10
Aug_01_2017	Taxi Out	00:00.0	0.00E+00	0.00E+00	0.00E+00	0.00E+00	0.00E+00
Aug_01_2017	Climb Ground	24:04.5	2.96E+01	8.50E-01	2.09E+02	9.88E-01	9.88E-01
Aug_01_2017	Climb Below 1,000 ft AFE	34:16.8	7.68E+01	1.62E+00	3.25E+02	1.56E+00	1.56E+00
Aug_01_2017	Climb Below Mixing Height	31:20.6	2.04E+02	3.67E+00	6.15E+02	3.09E+00	3.09E+00
Aug_01_2017	Climb Below 10,000 ft AFE	10734:47:20.380	7.04E+02	1.01E+01	1.17E+03	6.45E+00	6.45E+00
Aug_01_2017	Above 10,000 ft AFE	04:58.7	7.37E-03	2.64E-04	1.89E-01	1.15E-03	1.15E-03
Aug_01_2017	Descend Below 10,000 ft AFE	26042:14:53.810	1.49E+03	6.69E+01	2.77E+02	6.48E+00	6.48E+00
Aug_01_2017	Descend Below Mixing Height	17024:32:41.510	8.98E+02	5.12E+01	2.47E+02	5.90E+00	5.90E+00
Aug_01_2017	Descend Below 1,000 ft AFE	16:29.2	2.74E+02	7.13E+00	6.26E+01	1.19E+00	1.19E+00
Aug_01_2017	Descend Ground	03:28.1	5.11E+01	3.22E+00	2.70E+01	6.48E-01	6.48E-01
Aug_01_2017	Taxi In	00:00.0	0.00E+00	0.00E+00	0.00E+00	0.00E+00	0.00E+00
Aug_01_2017	Full Flight	36779:07:12.870	2.20E+03	7.70E+01	1.45E+03	1.29E+01	1.29E+01

We established a comprehensive study database for KBOS PDARS operations by populating essential tables through SQL, including the assignment of default values to unknown variables as outlined in the user manual. A successful 1-day run (August 1, 2017) of AEDT-3e for PDARS operations at KBOS has been completed, and our ongoing efforts are dedicated to expanding this simulation to cover an entire month.

Milestones

Completed a successful 1-day run of AEDT-3 for KBOS.

Major Accomplishments

- Gained substantial knowledge in running AEDT for creating airport-level emissions inventory.

Publications

None.



Outreach Efforts

None.

Awards

None.

Student Involvement

Hyeongsook (Darby) Kim, is a PhD student involved in this task, performing CMAQ simulations and AEDT modeling.

Plans for Next Period

- Complete development of KBOS inventories using AEDT for July 2017 and repeat CMAQ simulations.
- Demonstrate model performance and perform UFP source attribution.

References

- Huang, J., Vennam, P., Binkowski, F. S., Murphy, B., & Arunachalam, S. (2017). *A Nationwide Assessment of Particle Number Concentrations from Commercial Aircraft Emissions in the U.S.* Presented at the 36th Annual Conference of the American Association for Aerosol Research.
- Murphy, B. N., Nolte, C. G., Sidi, F., Bash, J. O., Appel, K. W., Jang, C., Kang, D., Kelly, J., Mathur, R., Napelenok, S., Pouliot, G., & Pye, H. O. T. (2021). The Detailed Emissions Scaling, Isolation, and Diagnostic (DESID) module in the Community Multiscale Air Quality (CMAQ) modeling system version 5.3.2. *Geoscientific Model Development*, 14(6), 3407–3420.
- Woody, M., H.-W. Wong, J.J. West, S. Arunachalam (2016), Multiscale predictions of aviation-attributable PM_{2.5} for U.S. airports modeled using CMAQ with plume-in-grid and an aircraft-specific 1-D emission model, *Atmos. Environ.*, 147, 384 – 394. <http://dx.doi.org/10.1016/j.atmosenv.2016.10.016>.

Task 3 - Implement volPM Plume-scale Modeling into a CMAQ Application

University of North Carolina at Chapel Hill

Objectives

Under previous research funded by PARTNER/ASCENT, UNC implemented a plume-scale model into CMAQ. In CMAQ advanced plume treatment (APT) simulations, a plume-scale treatment was applied to aircraft emissions from 99 major U.S. airports over the contiguous United States in 2005 (see Woody et al. (2016) for details). In addition to the plume-scale treatment, we accounted for the formation of non-traditional secondary organic aerosols from the oxidation of semi-volatile and intermediate-volatility organic compounds emitted from aircraft and utilized alternative emission estimates from the Aerosol Dynamics Simulation Code (ADSC). The ADSC is a one-dimensional plume-scale model that estimates engine-specific PM emissions and the emission of semi-volatile and intermediate-volatility organic compounds under ambient conditions, accounting for relative humidity and temperature. We estimated monthly and contiguous U.S. average aviation-attributable PM_{2.5} values to be 2.7 ng/m³ in January and 2.6 ng/m³ in July using CMAQ with the Advanced Plume Treatment (CMAQ-APT) with ADSC emissions. These values represent increases of 40% and 12% in January and July, respectively, over impacts obtained via traditional modeling approaches (traditional emissions without APT). The maximum fine-scale (subgrid-scale) hourly impacts at a major airport were 133.6 mg/m³ in January and 165.4 mg/m³ in July, considerably higher than the maximum grid-based impacts measured at the airport of 4.3 mg/m³ in January and 0.5 mg/m³ in July. To extend this work, a new volatile PM (volPM) plume-scale model has been developed by Aerodyne. This model uses the volPM modeling tool developed under NASA and Department of Defense (Strategic Environmental Research and Development Program) support to provide an additional physical perspective on volPM properties and evolution for quantities that are difficult to measure directly or continuously.

The parametric set of volPM modeling studies usually spans the range of experimental conditions that have been measured or may be measured in the foreseeable future. These studies also enable an assessment of impacts on volPM properties such as size and composition due to changes in fuel sulfur and on fuel hydrocarbon (HC) levels and composition. The interactions between these changes in condensable species and existing soot particles are tracked as a function of fuel sulfur content (5 bins), HC concentrations (3 bins), HC profiles (3), and concentrations modeled at 250 m and 1000 m downstream. We propose to take advantage of this parameterization and extend previous work by Woody et al. (2016) to



obtain a volPM plume model in CMAQ-APT, making this a complete plume-to-grid-scale model that considers both non-volatile PM and volPM components for an airport-level air quality study. We hypothesize that this capability will enable accurate characterization of PM_{2.5} formation (similar to the findings of Woody et al. (2016) related to volPM) at local scales in the immediate vicinity of the airport and enhance air quality health impact studies. Resources permitting, we will develop this application for a single airport or the contiguous United States, similar to the study of Woody et al. (2016) or Vennam et al. (2017), with a more recent emission inventory.

We started work on this project to review previous modeling efforts and explore the optimal CMAQ configuration to be used given recent advances in CMAQ since the work of Wood et al. (2016). We also established contact with Aerodyne to obtain the latest version of the ADSC with volPM treatment. We obtained the ADSC and ran a series of tests to ensure that we can benchmark the model. After obtaining initial benchmarking results, we ran the model for multiple combinations of engines and atmospheric conditions to create a lookup table for use in CMAQ. We have worked closely with Aerodyne to document model issues as they come up for future reference and updates.

Milestones

None.

Major Accomplishments

We obtained the ADSC with volPM treatment from Aerodyne and installed and ran the model to create a new lookup table.

Publications

None

Outreach Efforts

None.

Awards

None.

Student Involvement

Farzaneh Taksibi is a PhD student involved in the ADSC-CMAQ coupling study.

Plans for Next Period

- Finalize a detailed evaluation of the aircraft plume rise with AERMOD and finalize a manuscript for submission.
- Finalize AEDT data for the Boston case study and repeat CMAQ modeling using AEDT data for Boston.
- Finalize ADM development and evaluate both ADM and AERMOD with LAX AQSAS data.
- Finalize ADSC runs and begin configuring the CMAQ model application.

References

- Aeronautics-Guide. (2022). Aircraft Gas Turbine Engines Types and Construction. Retrieved December 21, 2022, from <https://www.aircraftsystemstech.com/p/gas-turbine-engines-types-and.html?m=1>
- Arunachalam, S., Isakov, V., Barzyk, T., Venkatram, A., Weil, J., Naess, B., Valencia, A., et al. (2017). C-AIRPORT: A New Web-based Air Quality Model for Community-Scale Assessments around Airports. Presented at the 18th International Conference on Harmonization within Atmospheric Dispersion Modeling for Regulatory Purposes, Bologna, Italy, October.
- Arunachalam, S., Valencia, A., Woody, M. C., Snyder, M. G., Huang, J., Weil, J., Soucacos, P., et al. (2017). *Dispersion modeling guidance for airports addressing local air quality health concerns*. ACRP Report, 179. Washington, D.C.: Transportation Research Board.
- Barrett, S. R. H., Britter, R. E., & Waitz, I. A. (2013). Impact of aircraft plume dynamics on airport local air quality. *Atmospheric environment*, 74, 247–258.
- Barzyk, T. M., Isakov, V., Arunachalam, S., Venkatram, A., Cook, R., & Naess, B. (2015). A near-road modeling system for community-scale assessments of traffic-related air pollution in the United States. *Environmental Modelling & Software*, 66, 46–56.



- Boeing Commercial Airplane Market Analysis, 2010.
- Briggs, G. A. (1965). A Plume Rise Model Compared with Observations. *Journal of the Air Pollution Control Association*, 15(9), 433-438.
- CERC. (2020). *ADMS - Airport (Version 5.0) Technical Specification*. Cambridge Environmental Research Consultants.
- Chowdhury, B., Karamchandani, P. K., Sykes, R. I., Henn, D. S., & Knipping, E. (2015). Reactive puff model SCICHEM: Model enhancements and performance studies. *Atmospheric environment*, 117, 242-258.
- Cox, W. M., & Tikvart, J. A. (1990). A statistical procedure for determining the best performing air quality simulation model. *Atmospheric Environment. Part A. General Topics*, 24(9), 2387-2395.
- Huang, J., Vennam, P., Binkowski, F. S., Murphy, B., & Arunachalam, S. (2017). *A Nationwide Assessment of Particle Number Concentrations from Commercial Aircraft Emissions in the U.S.* Presented at the 36th Annual Conference of the American Association for Aerosol Research.
- Kim, B., Rachami, J., Robinson, D., Robinette, B., Wyle, K. N., Arunachalam, S., Davis, N., et al. (2012). *Guidance for quantifying the contribution of airport emissions to local air quality*. Washington, D.C.: Transportation Research Board.
- Moore, R. H., Shook, M. A., Ziemba, L. D., DiGangi, J. P., Winstead, E. L., Rauch, B., Jurkat, T., Thornhill, K. L., Crosbie, E. C., Robinson, C., Shingler, T. J., & Anderson, B. E. (2017). Take-off engine particle emission indices for in-service aircraft at Los Angeles International Airport. *Scientific Data*, 4, 170198.
- Murphy, B. N., Nolte, C. G., Sidi, F., Bash, J. O., Appel, K. W., Jang, C., Kang, D., Kelly, J., Mathur, R., Napelenok, S., Pouliot, G., & Pye, H. O. T. (2021). The Detailed Emissions Scaling, Isolation, and Diagnostic (DESID) module in the Community Multiscale Air Quality (CMAQ) modeling system version 5.3.2. *Geoscientific Model Development*, 14(6), 3407-3420.
- Pandey, G., Venkatram, A., & Arunachalam, S. (2022). Evaluating AERMOD with measurements from a major U.S. airport located on a shoreline. *Atmospheric environment*, 119506.
- Pandey, G., Venkatram, A., & Arunachalam, S. (2023). Accounting for plume rise of aircraft emissions in AERMOD. *Atmospheric environment*, 120106.
- Rienecker, M. M., Suarez, M. J., Gelaro, R., Todling, R., Bacmeister, J., Liu, E., Bosilovich, M. G., et al. (2011). MERRA: NASA's Modern-Era Retrospective Analysis for Research and Applications. *Journal of climate*, 24(14), 3624-3648.
- Tetra Tech, Inc. (2013). *LAX Air Quality and Source Apportionment Study*. Los Angeles World Airports. Available at: <http://www.lawa.org/airQualityStudy.aspx?id=7716>. Retrieved July 30, 2022, from <http://www.lawa.org/airQualityStudy.aspx?id=7716>
- U.S. EPA. (2022). *User's Guide for the AMS/EPA Regulatory Model (AERMOD)*. .
- Valencia, A., Venkatram, A., Heist, D., Carruthers, D., & Arunachalam, S. (2018). Development and Evaluation of the R-LINE Model Algorithms to Account for Chemical Transformation in the Near-road Environment. *Transportation research. Part D, Transport and environment*, 59, 464-477.
- Venkatram, A., Karamchandani, P., Pai, P., & Goldstein, R. (1994). The development and application of a simplified ozone modeling system (SOMS). *Atmospheric environment*, 28(22), 3665-3678.
- Venkatram, A., & Schulte, N. (2018). *Urban transportation and air pollution*. Elsevier.
- Vennam, L.P.*, W. Vizueté, K. Talgo, M. Omary, F.S. Binkowski, J. Xing, R. Mathur, S. Arunachalam (2017). Modeled Full Flight Aircraft Emissions on Air Quality, and their Sensitivity to Grid Resolution, *J. Geophys. Res.*, 122. <https://doi.org/10.1002/2017JD026598>
- Wayson, R. L., Fleming, G. G., Kim, B., Eberhard, W. L., & Brewer, W. A. (2004). *Final report: the use of LIDAR to characterize aircraft initial plume characteristics* (No. FAA-AEE-04-01;DTS-34-FA34T-LR3;). FAA. Retrieved October 30, 2022, from <https://rosap.ntl.bts.gov/view/dot/9916>
- Woody, M., H.-W. Wong, J.J. West, S. Arunachalam (2016), Multiscale predictions of aviation-attributable PM2.5 for U.S. airports modeled using CMAQ with plume-in-grid and an aircraft-specific 1-D emission model, *Atmos. Environ.*, 147, 384 - 394. <http://dx.doi.org/10.1016/j.atmosenv.2016.10.016>.



Project 022 Evaluation of FAA Climate Tools: Aviation Portfolio Management Tool (APMT)

University of Illinois at Urbana-Champaign

Project Lead Investigator

Dr. Donald Wuebbles
Department of Atmospheric Sciences
University of Illinois
105 S. Gregory Street
Urbana, IL 61801
Tel: (217) 244-1568
Fax: (217) 244-4393
Email: wuebbles@illinois.edu

University Participants

University of Illinois at Urbana-Champaign

PI: Dr. Donald Wuebbles

- FAA Award Number: 13-C-AJFE-UI-029
- Period of Performance: October 1, 2022 to September 30, 2023 (project started February 5, 2020)
- Tasks:
 1. Examine effects of fleets of supersonic aircraft on ozone and climate using the state-of-the-art Whole Atmosphere Community Climate Model (WACCM), a global climate-chemistry model.
 2. Analyze emissions provided to us for fleets of proposed supersonic aircraft designs.

Project Funding Level

Support from the FAA over this time period was about \$200,000, with an additional \$200,000 in matching in-kind support from the DLR, Germany.

Investigation Team

Dr. Donald Wuebbles (PI), All Tasks

Swarnali Sanyal and Dharmendra Singh (postdocs), responsible for conducting studies and performing analyses using the Community Earth System Model (CESM) WACCM, a 3-dimensional (3D) atmospheric climate-chemistry model

Task 1 - Revisiting High-speed Civil Transports and Their Potential Effects on Ozone and Climate

University of Illinois at Urbana-Champaign

Major Goals

This project utilizes state-of-the-art modeling and technical knowledge to analyze the potential global environmental effects of aircraft and to perform analyses that underpin the development of analytical tools that can assess the costs and benefits to inform decision-making on technology development. The studies rely on state-of-the-art models of the earth system that can provide useful scientific input for considerations by decision-makers. The analyses in the project will aid decision-making by translating complex models into simpler tools for use in cost-benefit analyses.



Objectives

To quantify the costs and benefits of using advanced aircraft and engine technologies, FAA uses tools that are underpinned by state-of-the-art technical knowledge. These tools are used to inform decision-making by providing the benefits and costs of various options that could enable technology development. The overall objective of this project is to enhance our understanding of the relationships between subsonic and proposed supersonic aircraft and the atmospheric state, and the development and evaluation of the capabilities, limitations, and uncertainties of metrics and simple models (e.g., APMT) to assist decision-makers. This project will use state-of-the-art geophysical models of the earth system that fully represent tropospheric and stratospheric processes to evaluate the costs and benefits of technologies that could advance subsonic aviation and enable supersonic aviation. Specific project goals include the following: (1) science-based evaluation of analytical tools used by the FAA; (2) development of ideas and concepts for the next-generation treatment of aviation's effects on the earth system; (3) updated evaluation and analyses of the science of aviation effects on atmospheric composition; and (4) evaluation of potential environmental effects from assumed fleets of supersonic commercial and business jet aircraft to compare with their benefits in terms of decreased time for air travel.

Research Approach

The study will use the WACCM of the CESM, developed by the National Center for Atmospheric Research (NCAR). This model has 66 layers from the ground to the middle of the mesosphere and provides a comprehensive treatment of tropospheric and stratospheric chemical processes. WACCM is one of the most advanced models worldwide for studying atmospheric processes and one of the few with a complete representation of stratospheric and mesospheric processes and higher; for example, it is one of very few models to represent the quasi-biennial oscillation that is important to stratospheric ozone. This makes it ideal for the study of the environmental impacts from supersonic and subsonic aircraft.

Results and discussion

In 2022, we completed analyses for a journal paper that was submitted to the journal *Earth's Future*. This study examined a high-altitude emissions scenario for a supersonic commercial aircraft designed and evaluated for emissions of a mature fleet of these aircraft by Georgia Tech University under project A10. Our analyses used the latest version of the climate-chemistry WACCM model. Evaluated effects were developed for changes in atmospheric composition (e.g., ozone, water vapor, particles) and for the radiative forcing on climate. This paper was published in spring 2023.

Various companies and academic institutions have been actively considering the designs of such supersonic aircraft. As these new designs are developed, the environmental impact on ozone and climate of these realistic fleets needs to be explored. This study examines one such proposed supersonic fleet that is projected to fly at Mach 2.2, corresponding to cruise altitudes of 17–20 km, and that would burn 122.32 Tg of fuel each year and emit 1.78 Tg of NO_x. Our analyses indicate that this proposed fleet would cause a 0.74% reduction in global column ozone (~2 Dobson Units), which is mainly attributed to the large amounts of nitrogen oxides released in the atmosphere from the supersonic aircraft. The maximum ozone loss occurs at the tropics in the fall season, with a reduction of 1.4% in the total column ozone regionally. The stratospheric-adjusted radiative forcing on climate from this fleet was derived based on changes in atmospheric concentrations of ozone (59.5 mW/m²), water vapor (10.1 mW/m²), black carbon (-3.9 mW/m²), and sulfate aerosols (-20.3 mW/m²), resulting in a net non-CO₂, non-contrail forcing of 45.4 mW/m², indicating an overall warming effect.

In summer 2023, we received emissions for two different supersonic commercial aircraft designs and associated mature fleets from the Massachusetts Institute of Technology (aka MIT). Model runs for these emissions are now complete, and the analysis of findings is almost completed. However, the comparison of MIT's results with our results was delayed because the student involved in the study was on an internship. We are currently interacting closely with MIT to compare our analyses. Initial findings show some differences that we are still trying to explain.

A review of current modeling capabilities in treating the climate effects of contrails has been completed, and the resulting paper has been submitted for journal publication (Singh et al., 2023).

Milestones

- Journal paper published this year by the journal *Earth's Future*. This paper, Zhang et al. (2023), examines the potential impacts on ozone and climate for a projected fleet of supersonic aircraft based on an aircraft design made by Georgia Tech University.



- New studies are completed and being evaluated for comparison with similar modeling studies made by MIT for the potential impacts on ozone and climate of several fleets of supersonic aircraft based on aircraft designs made by MIT.
- These studies provide important context for the studies of actual projected fleets that we will be examining next in our studies.

Publications

Zhang, J., D. Wuebbles, D. Kinnison, J. Holger Pfaender, S. Tilmes, and N. Davis, 2023: Potential Impacts on Ozone and Climate from a Proposed Fleet of Supersonic Aircraft. *Earth's Future*, 11, <https://doi.org/10.1029/2022EF003409>.

Singh, D. K., S. Sanyal, and D. J. Wuebbles, 2023: Understanding the role of contrails and contrail cirrus in climate change: A global perspective. *Atmospheric Chemistry and Physics*, submitted.

Outreach Efforts

- Presentations at ASCENT Meetings in May 2023 and October 2023.
- Presentation made at FAA AEC Roadmap meeting in May 2023.
- Presentation made at the FAA REDAC meeting in March 2023, based on slides we sent to the FAA.
- Biweekly meeting with project manager.
- ICAO Impacts and Science Group (ISG) meetings (monthly) for Dr. Wuebbles.

Awards

None.

Student Involvement

Two postdocs, Swarnali Sanyal and Dharmendra Singh, were responsible for the analyses and modeling studies within the project and leading the initial preparation of the project reports. A prior graduate student, Jun Zhang, did most of the research for the Georgia Tech University supersonic aircraft analyses.

Plans for Next Period

- Complete and publish studies based on the emission inventories developed by ASCENT Project 10 to consider specific designs of supersonic transports (SSTs) from MIT and compare those results to model analyses done by MIT for the same scenario plus their similar analyses of the Georgia Tech SST fleet.
- Use the results from this study to inform the development of Aviation Portfolio Management Tool - Impacts Climate (APMT-IC) for supersonic impacts (ASCENT Project 58).
- Perform additional sensitivity analyses of potential supersonic aircraft fleets to enhance understanding of the envelop of potential impacts on ozone and climate from such aircraft.

References

Zhang, J., D. Wuebbles, D. Kinnison, J. Holger Pfaender, S. Tilmes, and N. Davis, 2023: Potential Impacts on Ozone and Climate from a Proposed Fleet of Supersonic Aircraft. *Earth's Future*, 11, <https://doi.org/10.1029/2022EF003409>.

Singh, D. K., S. Sanyal, and D. J. Wuebbles, 2023: Understanding the role of contrails and contrail cirrus in climate change: A global perspective. *Atmospheric Chemistry and Physics*, submitted.



Project 023 Analytical Approach for Quantifying Noise from Advanced Operational Procedures

Massachusetts Institute of Technology

Project Lead Investigator

R. John Hansman
T. Wilson Professor of Aeronautics & Astronautics
Department of Aeronautics & Astronautics
Massachusetts Institute of Technology
Room 33-303
77 Massachusetts Avenue, Cambridge, MA 02139
617-253-2271
rjhans@mit.edu

University Participants

Massachusetts Institute of Technology

- P.I.: R. John Hansman
- FAA Award Number: 13-C-AJFE-MIT, Amendment Nos. 008, 015, 022, 031, 046, and 051
- Period of Performance: October 1, 2022 to September 30, 2023
- Tasks:
 1. Evaluate factors limiting the ability to develop and utilize low-environmental-impact flight procedures.
 2. Review current and proposed air traffic management (ATM) modernization plans for potential environmental impact benefits.
 3. Identify potential opportunities for incorporating operational environmental optimization.
 4. Propose a path forward for high-potential opportunities.

Project Funding Level

The FAA provided \$860,000 in funding, and matching funds totaling \$860,000 were provided by the Massachusetts Institute of Technology (MIT) (approximately \$80,000) and the Massachusetts Port Authority (Massport) (approximately \$780,000).

Investigation Team

Prof. R. John Hansman (P.I.), All Tasks
Sandro Salgueiro (graduate student), All Tasks
Clement Li (graduate student), All Tasks
Zhishen Wang (graduate student), All Tasks
Mina Cezairli (graduate student), All Tasks

Project Overview

In this project, the team is evaluating the noise reduction potential of advanced operational procedures in the terminal (arrival and departure) phases of flight. The noise impact of these procedures is not well understood or modeled in current environmental analysis tools, presenting an opportunity for further research to facilitate ATM system modernization. This project leverages a noise analysis framework previously developed at MIT under ASCENT Project 23 to evaluate a variety of sample procedures. In conjunction, this project contributes to the memorandum of understanding between the FAA and Massport to identify, analyze, and recommend procedure modifications at Boston Logan International Airport (hereafter, Boston Logan Airport).

Task 1 - Evaluate Factors Limiting the Ability to Develop and Utilize Low-environmental-impact Flight Procedures

Massachusetts Institute of Technology

Objectives

This task involves the identification of factors driving operational stakeholder acceptance constraints, which limit when low-environmental-impact procedures may be utilized and, consequently, also impact the feasibility of their implementation. Interviews with stakeholders may be conducted to better understand the operational requirements that different stakeholders have in the context of procedure acceptance.

Research Approach

- Review relevant literature, including prior human-in-the-loop studies, to identify the effects of novel performance-based navigation (PBN) flight procedure concepts on air traffic control (ATC) and pilot tasks.
- Identify the relationship between operational stakeholder concerns and safety, in the context of the implementation of advanced low-noise flight procedure concepts.

Major Accomplishments

- Identified a preliminary set of operational stakeholder concerns related to pilot and ATC tasks during the operation of low-noise flight procedures
- Held discussions with both pilot and ATC stakeholders to understand potential mitigations for stakeholder concerns related to the implementation of certain low-noise procedures at Boston Logan Airport
- Identified potential mechanisms to mitigate stakeholder concerns, including new merging and spacing tools and collision mitigation capabilities
- At Boston Logan Airport, identified the use of overlay RNAV GPS approach procedures as a way to mitigate merging and spacing concerns related to RNP AR approaches, due to the much higher aircraft equipage for RNAV.

Task 2 - Review Current and Proposed ATM Modernization Plans for Potential Environmental Impact Benefits

Massachusetts Institute of Technology

Objectives

This task involves the review of historical, current, and proposed ATM capabilities that influence how operational stakeholders perceive the acceptance of new flight procedure concepts. Examples of capabilities to be analyzed include ATC decision support tools (including merging and spacing tools), trajectory-based operations (TBO), and aircraft navigation capabilities. Both U.S. and international capabilities are to be reviewed.

Research Approach

- Review relevant literature on both existing and proposed ATM modernization plans, including ATC and pilot decision support tools.
- Analyze noise monitor data from Boston Logan Airport to evaluate noise benefits achieved with the implementation of new low-noise procedures that were developed as part of prior work.

Major Accomplishments

- Identified a legacy set of ATC decision support tools used for merging and spacing of aircraft on final approach
- Identified current efforts towards deployment of new merging and spacing tools, including the Terminal Sequencing and Spacing (TSAS) tool in the United States and Point Merge in Europe
- Obtained a large set of noise monitor and aircraft trajectory data for a full year of operations at Boston Logan Airport, enabling new quantitative analyses on the noise effects of procedure changes
- Analyzed noise monitor data for a new overwater required-navigation-performance (RNP AR) approach implemented at Boston Logan Airport (runway 33L)



- Preliminary results show a significant noise reduction associated with the new procedure, matching prior modeling results

Task 3 - Identify Potential Opportunities for Incorporating Operational Environmental Optimization

Massachusetts Institute of Technology

Objectives

This task will consider the potential of the ATM modernization capabilities identified in Task 2 to address the limitations identified in Task 1 or to enable environmentally desirable trajectories. Potential enhancements or additional capabilities will be identified.

Research Approach

- Review potential effects of ATC and pilot support tools identified in Task 2 towards mitigating the operational stakeholder concerns identified in Task 1.

Major Accomplishments

- Conducted a study of factors affecting the required separation between flight procedures in terminal airspace, which appears as a significant constraint in the design of low-noise procedures
- Developed a framework for capturing how improvements in communication, navigation, and surveillance capabilities propagate to the performance of collision mitigation capabilities and ultimately to the separation required between flight procedures
 - This framework may contribute to the identification of opportunities to re-evaluate the required separation between procedures based on the development of new collision mitigation capabilities.

Task 4 - Propose a Path Forward for High-potential Opportunities

Massachusetts Institute of Technology

Objectives

This task will synthesize findings from Tasks 1, 2, and 3 to identify key capability development paths that could enable concepts of low-environmental-impact flight procedures. Areas of investigation will include requirements for each capability, functions served by it, and what changes it may drive in the roles and training of operational stakeholders (controllers and pilots).

Research Approach

- Synthesize findings from Tasks 1, 2, and 3 and identify development paths for future low-noise capabilities.

Major Accomplishments

- N/A, pending conclusion of Tasks 1, 2, and 3

Publications

- Hansman, R. J., Jensen, L., Huynh, J., O'Neill, G., Yu, A. (2017). *Block 1 procedure recommendations for Logan Airport community noise reduction*. <http://hdl.handle.net/1721.1/114038>
- Thomas, J., & Hansman, J. (2019). Framework for analyzing aircraft community noise impacts of advanced operational flight procedures. *Journal of Aircraft*, 6(4). <https://doi.org/10.2514/1.C035100>
- Thomas, J., Yu, A., Li, C., Toscano, P., & Hansman, R. J. (2019, June 17-21). *Advanced operational procedure design concepts for noise abatement*. [Seminar presentation.] Thirteenth USA/Europe Air Traffic Management Research and Development Seminar, Vienna, Austria.
- Yu, A., & Hansman, R.J. (2019, January 7-11). *Approach for representing the aircraft noise impacts of concentrated flight tracks*. [Conference presentation.] AIAA Aviation Forum, Dallas Texas, United States.



- Salgueiro, S., Thomas, J., Li, C., & Hansman, R. J. (2021, January 11-21). *Operational noise abatement through control of climb profile on departure*. [Conference presentation.] AIAA SciTech Forum
- Hansman, R. J., Salgueiro, S., Huynh, J., Li, C., Jansson, M., Mahseredjian, A., Zimmer, K. (2021). *Block 2 procedure recommendations for Logan Airport community noise reduction*. <https://hdl.handle.net/1721.1/131242>
- Salgueiro, S., Hansman, R. J. (2023). *Identifying, Visualizing, and Communicating Constraints in PBN Flight Procedure Design*. [Conference presentation.] AIAA Aviation Forum, San Diego, CA, United States. <https://doi.org/10.2514/6.2023-3968>

Outreach Efforts

- September 27, 2017: Poster to the ASCENT Advisory Board
- December 5, 2017: Call with Boeing to discuss procedure noise impact validity
- March 16, 2018: Discussion with Minneapolis-St. Paul Airport about metrics
- April 4, 2018: Poster to the ASCENT Advisory Board
- May 7, 2018: Presentation to the FAA 7100.41 PBN Working Group
- June 24, 2018: Discussion with air traffic controllers about dispersion concepts
- July 23, 2018: Briefing at the FAA Joint University Program research update meeting
- October 9, 2018: Poster to the ASCENT Advisory Board
- November 8, 2018: Presentation to the Airline Industry Consortium
- March 3, 2019: Presentation at the Aviation Noise and Emissions Symposium
- October 15, 2019: Presentation to the ASCENT Advisory Board
- November 12, 2019: Presentation to the Airline Industry Consortium
- May 21, 2020: Meeting with operational stakeholders from the FAA 7100.41 process to discuss Block 2 concepts
- September 23, 2021: Public hearing to present Block 2 procedure recommendations for Boston Logan Airport
- Numerous community meetings
- Numerous briefings to politicians representing eastern Massachusetts (local, state, and federal)
- Briefing to the FAA Management Advisory Council
- In-person outreach and collaboration with Massport, an operator at Boston Logan Airport, and an ASCENT Advisory Board member
- April 1, 2022: Presentation of a summary of lessons learned from the Boston project to an audience of FAA, Massport, and HMMH stakeholders
- August 16, 2022: Presentation of work on flight procedure constraints at the FAA Technical Center in Atlantic City, NJ as part of the Joint University Program
- September 20-21, 2022: 7100.41 Working Group meeting at the Boston terminal radar approach control facilities (A90); presentation to air traffic and airline stakeholders on flight procedures proposed for Boston Logan Airport as part of Block 2; approval received for all presented procedures for further implementation work

Awards

- 2018 Department of Transportation/FAA Centers of Excellence Outstanding Student of the Year Award to Jacqueline Thomas
- 2021 Massachusetts Port Authority Logan Stars Award to the MIT International Center for Air Transportation research group
- 2023 American Institute of Aeronautics and Astronautics Orville and Wilbur Wright Graduate Award to Sandro Salgueiro

Student Involvement

Graduate students have been involved in all aspects of this research in terms of analysis, documentation, and presentation.

Plans for Next Period

The next phase of this project will focus on the continuation of all tasks, with a particular focus on the analysis of ATM modernization plans and the identification of potential noise benefits enabled by future capabilities. Current efforts include the analysis of noise monitor data from Boston Logan Airport, which will be used to quantify the change in noise impacts due to the implementation of Block 1 and Block 2 procedures.



Project 025 Shock Tube Studies of the Kinetics of Jet Fuels

Stanford University

Project Lead Investigator

Ronald K. Hanson
Woodard Professor
Mechanical Engineering Department
Stanford University
452 Escondido Mall
650-723-6850
rkhanon@stanford.edu

University Participants

Stanford University

- P.I.: Prof. Ronald K. Hanson
- FAA Award Number: 13-C-AJFE-SU-027
- Period of Performance: October 1, 2022 to September 30, 2023
- Task:
 1. Chemical kinetics combustion experiments

Project Funding Level

2022-2023: \$200,000 from the FAA, with 1:1 matching funds of \$200,000 from Stanford University

Investigation Team

Prof. Ronald K. Hanson (P.I.)
Jesse W. Streicher (research scientist)
Vivek Boddapati (graduate student)

Project Overview

The ninth year of this program has focused on developing and refining strategies for the accurate prediction of jet fuel properties (chemical and physical) and composition. To achieve this goal, the research has focused on two areas: correlation of the physical and combustion properties of hydrocarbon fuels with their infrared (IR) spectral features using nonlinear regression models, and evaluation of these nonlinear models and previously developed linear models on new candidate sustainable aviation fuel (SAF) samples and against standardized property test methods. The results of the IR spectral analysis work will be used to establish the strong sensitivity of the physical and chemical properties of jet fuels to their molecular structure, with the ultimate goal of developing a rapid prescreening approach, requiring minimal fuel volume, to streamline the testing and certification process of alternative jet fuels.

Task 1 - Chemical Kinetics Combustion Experiments

Stanford University

Objectives

This work is aimed at developing fuel prescreening tools based on the IR absorption cross-section measurements of jet fuels and their constituent molecules. Specific fuel analysis objectives include developing effective strategies for correlating (a) chemical, physical, and combustion properties and (b) functional group and molecular species composition of jet fuels with their IR spectra.

Research Approach

An important goal of the current research is to characterize jet fuel composition and properties based on the fuel's mid-IR absorption spectrum, measured using a Fourier transform IR (FTIR) spectrometer. Over the past four years, a database of spectroscopic measurements and property data for a variety of jet fuels and jet fuel components has been acquired. Using this database, we have developed correlations between the spectroscopic properties of jet fuels with fuel composition and with important physical/chemical properties such as density, derived cetane number (DCN), net heat of combustion (NHC), and flash point. Here, we present an overview of the two research areas (development of nonlinear models for predicting fuel properties and evaluation of model performance), along with key results obtained over the past year.

Development of nonlinear models for predicting fuel properties

Over the past four years of this program, four strategies (Strategies 1–4) were developed for estimating physical and chemical properties, functional group fractions, and molecular species constituents of fuels directly from mid-IR spectra. In the previous year, Strategy 1 elastic-net-regularized linear models were trained for different properties through the use of an expanded training dataset. While these linear models achieved good prediction accuracy for most properties, certain properties such as the DCN and flash point, which have a nonlinear dependence on fuel composition, showed scope for further improvement. In the current year, nonlinear Strategy 3 models (principal component [PC] analysis + support vector regression [SVR]) were developed for different properties, and their performance was compared with that of the linear Strategy 1 models. The methodology of Strategy 3 is discussed below, along with some results.

Strategy 3 models were developed for nine key physical and chemical properties: molecular weight (MW), hydrogen-to-carbon (H/C) ratio, density, NHC, DCN, threshold sooting index (TSI), initial boiling point (IBP), flash point, and kinematic viscosity (KV). The training dataset included the 2- to 15- μm FTIR spectra of 228 fuels, spanning neat hydrocarbons, blends of neat hydrocarbons, and conventional and alternative jet fuels.

To build Strategy 3 models, the FTIR spectra are first preprocessed by performing PC analysis, which linearly transforms the spectra into a set of orthogonal PCs, in decreasing order of variance captured. This step enables the selection of a subset of PCs as predictors for training regression models, greatly reducing the dimensionality without a significant loss of information. An SVR model is then trained on the transformed features to obtain the best-fit hyperplane for predicting the property of interest. The number of PCs, N_{PC} , and the optimal values of the other model parameters C and σ are chosen via a 10-fold cross-validated grid search. By experimenting with different values of these three parameters, the model selects the combination that results in the minimum cross-validation error (CVE) for each property. This process is demonstrated for the property DCN in Fig. 1. Using the cross-validation approach, only the first 10 PCs are chosen to build the SVR model for DCN. As shown in the left panel of Fig. 1, the first 10 PCs can cumulatively capture close to 99% of the total variance in the FTIR dataset. Thus, discarding the subsequent PCs causes virtually no loss of spectral information. The right panel of Fig. 1 demonstrates the model tuning process over a grid of C and σ values, with N_{PC} fixed at its optimal value of 10. The dashed white lines correspond to the combination of C and σ with the lowest CVE. Therefore, the optimal parameters describing the Strategy 3 model for DCN are $N_{PC} = 10$, $C = 38.05$, and $\sigma = 0.088$.

The performance of the optimized Strategy 3 model was evaluated on the training dataset based on three performance metrics: CVE (an estimate of future prediction error), coefficient of determination (R^2 , a measure of goodness of fit), and root-mean-squared error (RMSE) of prediction. The results from the Strategy 3 model were also compared with those of the Strategy 1 model to highlight the improvement in predictive performance due to the use of nonlinear regression. Figure 2 shows the performance of the Strategy 1 and Strategy 3 models on the training dataset for DCN. Figures 2a and 2b show the predicted versus actual DCN and the corresponding residuals obtained using the Strategy 1 model, whereas Figs. 2c and 2d show the predicted versus actual DCN and residuals obtained using the Strategy 3 model. The CVE, R^2 , and RMSE for these models are listed in the figure headings. The Strategy 3 model for DCN shows distinctively improved predictive

performance compared with the Strategy 1 model, as evidenced by a reduced CVE and RMSE and increased R^2 . Although the CVE of the Strategy 3 model is only 5% lower than that of the linear model, the RMSE is reduced by a factor of 2. Additionally, the higher R^2 value for the Strategy 3 model indicates a stronger correlation between the FTIR spectra and DCN. Similarly improved predictive performance was observed for the Strategy 3 models trained on most of the other properties.

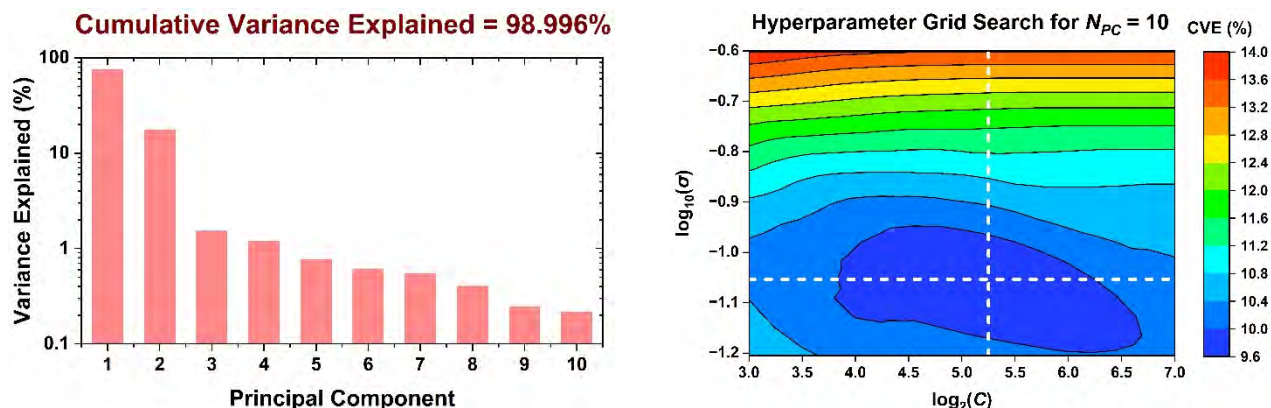


Figure 1. Left: Percentage of variance explained by each of the first 10 principal components. Right: Cross-validated grid search for selecting optimal values of the model parameters C and σ (indicated by dashed white lines). CVE: cross-validation error.

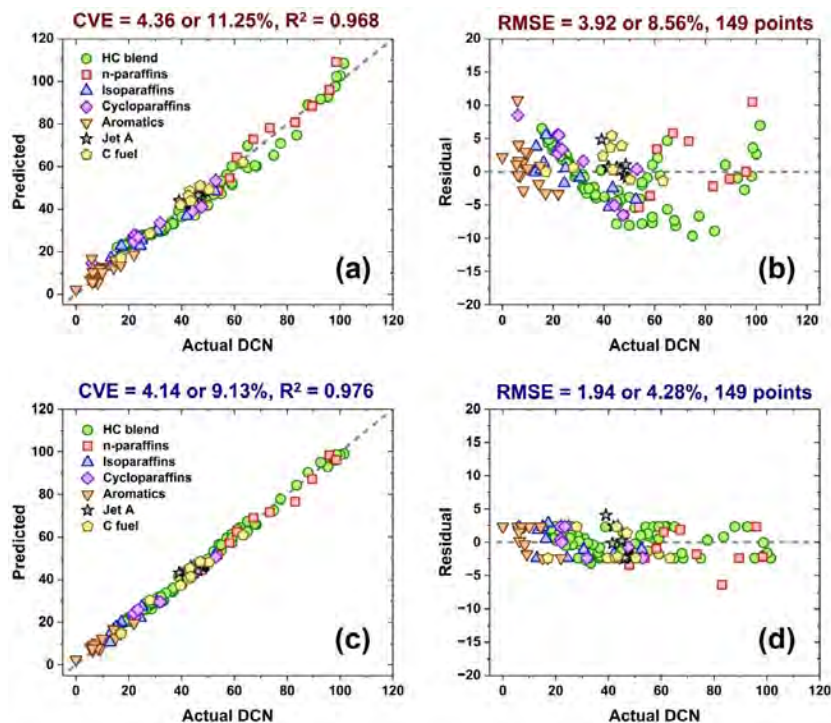


Figure 2. Performance of derived cetane number (DCN) model on training data. (a) Predicted DCN and (b) residuals obtained using the Strategy 1 linear model; (c) predicted DCN and (d) residuals obtained using the Strategy 3 nonlinear model. CVE: cross-validation error; HC: hydrocarbon; RMSE: root-mean-squared error.

Evaluation of model performance

Comparing the prediction accuracy of the IR analysis strategies with standard property test methods is a crucial step in evaluating model performance. To enable such a comparison, the reproducibility RMSE values associated with standard test methods for all properties were calculated via correlations obtained from the literature, as shown in Table 1. The exception is MW, which is typically estimated using two-dimensional gas chromatography (GCxGC), as no standard reproducibility errors have been reported in the literature for MW estimation using this method. Also included in Table 1 are the prediction RMSE values of both the Strategy 1 and Strategy 3 models for these properties. As shown in this table, the Strategy 3 models for density, NHC, DCN, and flash point have lower RMSE values than the corresponding Strategy 1 models. In particular, the use of nonlinear regression greatly improves the prediction accuracy for the DCN and flash point. Whereas Strategy 1 has a lower prediction error than the reproducibility error of the ASTM method for three of the properties (H/C ratio, NHC, and TSI), Strategy 3 achieves a lower RMSE than the ASTM reproducibility error for five properties (H/C ratio, NHC, DCN, TSI, and flash point). This result suggests that the uncertainty associated with these experimental property values in the training dataset is expected to impact the uncertainty in the predicted property values to a greater extent than the modeling approach itself. In contrast, the ASTM reproducibility errors associated with density, IBP, and KV are smaller than their respective Strategy 3 prediction errors. Hence, the contribution of the modeling approach to the uncertainty in these property estimations is comparable to, if not slightly greater than, that of the measurement uncertainty in the training data.

Table 1. Comparison of the predictive performance of Strategy 1 and Strategy 3 models for eight physical and chemical properties with the reproducibility errors of the corresponding standard test methods from ASTM.

Property	Standard ASTM method	ASTM reproducibility error (%)	RMSE (%) of Strategy 1	RMSE (%) of Strategy 3
H/C ratio	D5291	5.80	1.69	1.86
Density	D4052	0.28	1.41	1.02
NHC	D4809	0.747	0.213	0.154
DCN	D6890	4.70	8.56	4.28
TSI	D1322	22.63	2.93	3.81
IBP	D86	3.11	3.54	5.09
Flash pt.	D93	10.94	15.22	6.29
KV	D445	0.50	3.43	4.18

DCN: derived cetane number; H/C: hydrogen to carbon; IBP: initial boiling point; KV: kinematic viscosity; NHC: net heat of combustion; RMSE: root-mean-squared error; TSI: threshold sooting index.

Table 2. Molecular class distributions of the five new sustainable aviation fuel samples, according to gas chromatography (GCxGC) analysis.

Molecular class	Weight % (GCxGC)				
	14080 (Swedish Biofuels)	14113 (Global Bioenergies)	14314 (Swedish Biofuels)	13350 (Virent)	14197 (CSIR)
n-paraffins	1.40	0.03	1.16	0.03	18.68
isoparaffins	83.13	99.34	56.95	0.19	63.00
cycloparaffins	8.68	0.22	28.22	2.04	12.05
aromatics	6.78	<0.01	13.66	97.73	6.32

CSIR: Council of Scientific and Industrial Research.

Another key step in assessing model performance involves making predictions on unseen test data that were not included in the training dataset. To that end, five candidate SAF samples were acquired in the previous year from other ASCENT members (Steve Zabarnick). These fuels showed considerable differences in their molecular class distribution, as detailed in Table 2. A brief description of these five SAFs is provided below:

- POSF 14080: synthetic jet fuel processed from biomass; manufactured by Swedish Biofuels
- POSF 14314: synthetic jet fuel processed from biomass; manufactured by Swedish Biofuels
- POSF 14113: bio-sourced isoparaffinic jet fuel; manufactured by Global Bioenergies
- POSF 13350: synthesized aromatic kerosene; manufactured by Virent
- POSF 14197: biojet fuel; manufactured by the Council of Scientific and Industrial Research-Indian Institute of Petroleum (CSIR-IIP)

The Strategy 1 and Strategy 3 models were employed to predict the properties of these five SAF candidates based on their measured 2- to 15- μm FTIR spectra. The predictions of both the Strategy 1 and Strategy 3 models are shown in Table 3, along with the reference property values for one of these samples, POSF 14197. The Strategy 1 and Strategy 3 model predictions match closely with the reference values of all properties for this fuel. However, the nonlinear Strategy 3 models outperform the linear Strategy 1 models for five properties: MW, H/C ratio, density, KV, and flash point. Similar performance improvements were observed in the case of the remaining four SAF samples, with Strategy 3 performing better than Strategy 1 for most properties considered. The reduced prediction error of the Strategy 3 models compared with the Strategy 1 models further highlights the impact of the nonlinear regression technique on predictive performance.

Table 3. Strategy 1 and Strategy 3 property predictions for the POSF 14197 sustainable aviation fuel sample (from the Council of Scientific and Industrial Research-Indian Institute of Petroleum).

Property	Strategy 1 model		Strategy 3 model		Reference values
	Predicted	Error (%)	Predicted	Error (%)	
MW (g/mol)	159	0.62	160	0	160
H/C ratio	2.08	-1.23	2.12	0.66	2.106
NHC (MJ/kg)	43.8	0.23	43.5	-0.46	43.7
Density @ 20°C (g/cm ³)	0.762	0.21	0.760	-0.05	0.7604
IBP (°C)	161	1.90	162	2.53	158
KV (mm ² /s)	3.81	-2.05	3.86	-1.02	3.9
Flash Pt. (°C)	47.5	3.26	44.8	-2.61	46

H/C: hydrogen to carbon; IBP: initial boiling point; KV: kinematic viscosity; MW: molecular weight; NHC: net heat of combustion.

Overall, the IR analysis results obtained over the past year for the nonlinear regression models showed improved predictive performance relative to the spectral analysis strategies developed in the previous years of this work and were found to achieve high prediction accuracy on candidate SAF samples. These strategies provide the capability to accurately predict the physical and chemical properties of alternative jet fuels directly based on their IR spectra.

Milestones

Major milestones included regularly reporting experimental results and analyses at the Fall and Spring ASCENT meetings (October 2022 and April 2023) and presenting results at the 13th U.S. National Combustion Meeting (March 2023, College Station, TX) and the 29th International Colloquium on the Dynamics of Explosions and Reactive Systems (July 2023, Seoul National University Siheung, Korea).



Major Accomplishments

During the ninth year of this program, major advances were made in several areas:

- With the use of an expanded, extended-wavelength-range training dataset, Strategy 3 models were trained for nine physical and chemical properties: MW, H/C ratio, density, NHC, DCN, TSI, IBP, flash point, and KV. The model parameters were chosen based on a 10-fold cross-validated grid search to achieve optimal predictive performance for each property;
- The nonlinear Strategy 3 models showed an improvement in prediction accuracy compared with the previously developed linear Strategy 1 models for most of the properties in terms of three performance metrics: CVE, R^2 , and RMSE;
- The prediction RMSE values of both the Strategy 1 and Strategy 3 models were compared with the reproducibility errors of standard ASTM property test methods. The Strategy 3 models achieved lower prediction errors than the ASTM methods for five properties: H/C ratio, NHC, DCN, TSI, and flash point; and
- The Strategy 1 and Strategy 3 models were used to predict properties of five candidate SAF samples. While both strategies were able to predict the SAF properties to a high degree of accuracy, the Strategy 3 models generally performed better than the Strategy 1 models on these fuel samples.

Publications

Peer-reviewed journal publications

Boddapati, V., Ferris, A. M., & Hanson, R. K. (2024). Predicting the physical and chemical properties of sustainable aviation fuels using elastic-net-regularized linear models based on extended-wavelength FTIR spectra. *Fuel*, 356, pp. 129557.

<https://doi.org/10.1016/j.fuel.2023.129557>

Outreach Efforts

Our IR fuel analysis work was presented at the Fall ASCENT Advisory Committee Meeting (October 25–27, 2022) and the Spring ASCENT SAF Meeting (April 25–27, 2023). Research was also presented at the 13th U.S. National Combustion Meeting (March 19–22, 2023) in College Station, TX, and the 29th International Colloquium on the Dynamics of Explosions and Reactive Systems (July 23–28, 2023) at Seoul National University Siheung, Korea. An abstract titled “Towards the development of an IR spectra-based approach for characterizing fuel properties and combustion behavior” was accepted for presentation at the Joint Army Navy NASA Air Force Interagency Propulsion Committee meeting (December 2023).

Awards

None.

Student Involvement

Graduate students are actively involved in the acquisition and analysis of all experimental data and model development. Vivek Boddapati (current graduate student) performed the IR spectral analysis/fuel prescreening. Jesse Streicher (current research scientist) has also contributed to the project through research management.

Plans for Next Period

In the next period, we plan to

- review other fuel property prediction methods (e.g., GCxGC, near-IR methods, Raman spectroscopy, etc.) reported in the literature and compare their prediction accuracies with those attainable via our FTIR method;
- continue expanding the training dataset by measuring the 2- to 15- μm spectra of relevant neat hydrocarbons, conventional jet fuels, and SAFs and investigate the value of further extending the wavelength range beyond the 2- to 15- μm region, particularly to access strong, isolated spectral features corresponding to molecular classes such as cycloparaffins and olefins;
- explore batch distillation of multicomponent fuels as a potential way to isolate molecular classes with weaker spectral features (e.g., cycloparaffins, aromatics, etc.) and possibly identify strategies to make more accurate property predictions based on the FTIR spectra of individual distillate fractions; and
- explore the potential for predicting additional thermochemical properties of fuels based on FTIR spectra (e.g., gas-phase specific heat capacity, enthalpy, and entropy).

Project 31 Alternative Jet Fuel Test and Evaluation

University of Dayton Research Institute

Project Lead Investigator

Steven Zabarnick, PhD
 Division Head, Fuels and Combustion
 University of Dayton Research Institute
 300 College Park
 Dayton, OH 45469-0043
 937-266-7231
Steven.Zabarnick@udri.udayton.edu

University Participants

University of Dayton Research Institute (UDRI)

- P.I.: Steven Zabarnick, Division Head
- FAA Award Number: 13-C-AJFE-UD
- Overall Period of Performance: April 8, 2015 to September 30, 2022
- Tasks:
 - Period of Performance: April 8, 2015 to March 14, 2016; Amendment No. 006
 1. Evaluate the performance of candidate alternative fuels via the ASTM) D4054 approval process
 - Period of Performance: August 13, 2015 to August 31, 2016; Amendment No. 007
 2. Evaluate the performance of candidate alternative fuels via the ASTM D4054 approval process
 - Period of Performance: August 5, 2016 to August 31, 2017; Amendment No. 012
 3. Manage the evaluation and testing of candidate alternative fuels
 - Period of Performance: July 31, 2017 to August 31, 2019; Amendment No. 016
 4. Manage the evaluation and testing of candidate alternative fuels
 - Period of Performance: August 30, 2018 to August 31, 2019; Amendment No. 021
 5. Manage the evaluation and testing of candidate alternative fuels
 - Period of Performance: Extended period of performance end from September 10, 2019 to September 9, 2020; Amendment No. 023
 - Period of Performance: February 5, 2020 to February 4, 2021; Amendment No. 025
 6. Manage the evaluation and testing of candidate alternative fuels
 - Period of Performance: Extended period of performance end from September 9, 2019 to September 9, 2021; Amendment No. 028
 - Period of Performance: February 4, 2021 to February 5, 2022; Amendment No. 032
 7. Manage the evaluation and testing of candidate alternative fuels
 - Period of Performance: August 10, 2021 to February 10, 2022; Amendment No. 033
 - No-cost extension (Amendment No. 033 is not task-specific)
 - Period of Performance: October 1, 2021 to September 30, 2022; Amendment No. 038
 - Period of Performance: October 1, 2022 to September 30, 2023; Amendment No. 043
 - Period of Performance: October 1, 2023 to September 30, 2024; Amendment No. 049

Project Funding Level

Amendment No. 006	\$309,885
Amendment No. 007	\$99,739
Amendment No. 012	\$693,928
Amendment No. 016	\$999,512
Amendment No. 021	\$199,966

Amendment No. 025	\$1,926,434
Amendment No. 032	\$1,049,700
Amendment No. 038	\$499,784
Amendment No. 043	\$1,499,940
Total	\$7,278,888

In-kind cost sharing has been obtained from the following organizations:

Organization	Amount	Year
LanzaTech	\$55,801	2015
LanzaTech	\$381,451	2016
UDRI	\$43,672	2016
Neste	\$327,000	2017
Boeing	\$2,365,338	2017
Shell	\$280,000	2019
IHI	\$1,150,328	2019
Shell	\$325,000	2020
Global Bioenergies	\$6,875,900	2021
Global Bioenergies	\$290,000	2021
Total	\$12,094,490	

Investigation Team

Steven Zabarnick, (P.I.), new candidate-fuel qualification and certification
 Linda Shafer, (researcher), fuel chemical analysis and composition
 John Graham, (researcher), fuel seal swell and material compatibility
 Zachary West, (researcher), fuel property evaluation
 Rhonda Cook, (technician), fuel property testing
 Sam Tanner, (technician), fuel sampling and shipping
 Carlie Anderson, (researcher), fuel chemical analysis
 Shane Kosir, (researcher), fuel analysis and property testing
 Amanda Arts, (researcher), fuel analysis
 April Landsaw, (technician), fuel analysis and property testing
 Willie Steinecker, (researcher), fuel analysis

Project Overview

Alternative jet fuels offer the potential benefits of reduced global environmental impacts, greater national energy security, and stabilized fuel costs for the aviation industry. The FAA is committed to the advancement of “drop-in” alternative fuels. The successful adoption of alternative fuels requires approval for use by the aviation community, followed by large-scale production of fuel that is cost-competitive and meets the safety standards for conventional jet fuel. Alternative jet fuels must undergo rigorous testing to become qualified for use and to be incorporated into ASTM International specifications.

Cost-effective, coordinated performance testing capability (in accordance with ASTM D4054) is needed to support the evaluation of promising alternative jet fuels. The objective of this project is to provide the necessary capability to support fuel testing and evaluation of novel alternative jet fuels.

The proposed program should provide the following capabilities:

- Identify alternative jet fuels, including blends with conventional jet fuel, with the potential to be economically viable and to support FAA’s NextGen environmental goals for testing
- Perform engine, component, rig, or laboratory tests, or any combination thereof, to evaluate the performance of alternative jet fuels in accordance with ASTM International standard practice D4054
- Identify and conduct unique testing, beyond that defined in ASTM International standard practice D4054, to support the evaluation of alternative jet fuels for inclusion in ASTM International jet fuel specifications



- Obtain baseline and alternative jet fuel data to assess the effects of alternative jet fuels on aircraft performance, maintenance requirements, and reliability
- Coordinate efforts with activities sponsored by the Department of Defense and/or other governmental parties that may be supporting relevant work
- Report relevant performance data for the alternative fuels tested, including quantified effects of the alternative fuel on aircraft and/or engine performance and air-quality emissions relative to conventional jet fuel; share reported data with the FAA National Jet Fuel Combustion Program, the broader community (e.g., ASTM International), and the ASCENT Center of Excellence Program 33 “Alternative Fuels Test Database Library.”

Tasks 1 and 2 - Evaluate the Performance of Candidate Alternative Fuels via the ASTM D4054 Approval Process and Manage the Evaluation and Testing of Candidate Alternative Fuels

University of Dayton Research Institute

Objective

Cost-effective, coordinated performance testing capability (in accordance with ASTM D4054) is needed to support the evaluation of promising alternative jet fuels. The objective of this project is to provide the capability necessary to support either (a) the evaluation of to-be-determined alternative fuels selected in coordination with the FAA or (b) a fuel testing and evaluation project with specific alternative fuels in mind.

Research Approach

The intent of this program is to provide the capability needed to perform specification and fit-for-purpose evaluations of candidate alternative fuels, with the aim of providing a path through the ASTM D4054 approval process. The UDRI team can perform many of these evaluations and is prepared to work with other organizations, such as the Southwest Research Institute (SwRI) and engine original equipment manufacturers (OEMs), with unique test capabilities, as needed. These assessments include additional engine, auxiliary power unit, component, and rig evaluations. The UDRI testing capabilities include efforts at the laboratories of the Fuels Branch of the Air Force Research Laboratory and at our campus laboratory facilities.

The following lists provide examples of the evaluations that can be provided by UDRI:

Tier 1

1. Thermal stability (quartz crystal microbalance)
2. Freeze point (ASTM D5972)
3. Distillation (ASTM D86)
4. Hydrocarbon range (ASTM D6379 and D2425)
5. Heat of combustion (ASTM D4809)
6. Density, American Petroleum Institute gravity (ASTM D4052)
7. Flash point (ASTM D93)
8. Aromatics (ASTM D1319)

Tier 2

1. Saybolt color (ASTM D156 or D6045)
2. Total acid number (ASTM D3242)
3. Aromatics (ASTM D1319 and D6379)
4. Sulfur (ASTM D2622)
5. Sulfur mercaptan (ASTM D3227)
6. Distillation temperature (ASTM D86)
7. Flash point (ASTM D56, D93, or D3828)
8. Density (ASTM D1298 or D4052)
9. Freezing point (ASTM D2386, D5972, D7153, or D7154)
10. Viscosity at $-20\text{ }^{\circ}\text{C}$ (ASTM D445)
11. Net heat of combustion (ASTM D4809)



12. Hydrogen content (ASTM D3343 or D3701)
13. Smoke point (ASTM D1322)
14. Naphthalenes (ASTM D1840)
15. Calculated cetane index (ASTM D976 or D4737)
16. Copper strip corrosion (ASTM D130)
17. Existent gum (ASTM D381)
18. Particulate matter (ASTM D2276 or D5452)
19. Filtration time (MIL-DTL-83133F Appendix B)
20. Water reaction interface rating (ASTM D1094)
21. Electrical conductivity (ASTM D624)
22. Thermal oxidation stability (ASTM D3241)

Extended physical and chemical characterization

1. Lubricity evaluation: ball-on-cylinder lubricity evaluator test (ASTM D5001)
2. Evaluation of low-temperature properties: scanning Brookfield viscosity
3. Detection, quantification, and/or identification of polar species, as necessary
4. Detection, quantification, and/or identification of dissolved metals, as necessary
5. Initial material compatibility evaluation: optical dilatometry and partition coefficient measurements to determine the fuel-affected swell and fuel solvency in three O-ring materials (nitrile, fluorosilicone, and fluorocarbon) and up to two additional fuel system materials
6. Experimental thermal stability evaluation: quartz crystal microbalance to measure thermal deposition tendencies and oxidation profiles at elevated temperatures
7. Evaluation of viscosity versus temperature: ASTM D445 to determine the fuel viscosity at 40 °C and –40 °C, to assess the viscosity variation with temperature

In addition to the above physical and chemical fuel evaluation capabilities, UDRI has extensive experience in evaluating microbial growth in petroleum-derived and alternative fuels. These evaluations include standard laboratory culturing and colony counting methods, as well as advanced techniques, such as quantitative polymerase chain reaction and metagenomic sequencing. These methods enable quantitative measurements of microbial growth rates in candidate alternative fuels for comparison with petroleum fuels.

UDRI also has extensive experience in the evaluation of elastomer degradation upon exposure to candidate alternative fuels. Various methods are used to evaluate seal swell and O-ring fixture leakage, including optical dilatometry, sealing pressure measurements, fuel partitioning into the elastomer, and the use of a pressurized temperature-controlled O-ring test device.

Moreover, UDRI can perform fuel-material compatibility testing by using the D4054 procedures for fuel soak testing, postexposure nonmetallic and metallic material testing, and surface and microstructural evaluation. The 68 “short-list” materials and the 255 materials on the complete list can be tested.

Milestones

The schedule for this project is dependent on the receipt of alternative fuel candidates for testing. As candidate fuels are received, a testing schedule will be established via coordination with the FAA and collaborators. Our existing relationships with these organizations will help expedite this process.

Major Accomplishments

Shell IH² Testing

Most recently (December 2023), we learned that Shell is actively seeking a commercialization partner for this technology. As a result, they are putting fuel production on hold. We are awaiting larger volumes of fuels, as additional Tier 3 testing was recommended by the OEM committee because of the high cycloparaffin level of this fuel.

Global Bioenergies

With testing completed, this fuel was balloted in the spring of 2023. The feedstock is wood residue, and jet fuel is produced via isobutylene oligomerization. The ballot has passed at ASTM, and the new ASTM D7566-23b version includes this new pathway via modifications to Annex A5 (ATJ).

Swedish Biofuels

With testing completed, this fuel was also balloted in the spring of 2023. The feedstock consists of a variety of mixtures of alcohols. The ballot has passed at ASTM, and the new ASTM D7566-23b version includes this new pathway via the new Annex A8 (ATJ-SKA).

Council of Scientific and Industrial Research-Indian Institute of Petroleum

The Council of Scientific and Industrial Research-Indian Institute of Petroleum (CSIR-IIP) has developed a single-step process to convert lipids (plant-derived oil and animal-derived fats) into hydrocarbons containing aromatic compounds. Three fuel samples have been received, and Tier 1 and 2 testing has been completed. The OEM committee has recommended that this fuel proceed along the full approval pathway (rather than the Fast Track process).

Revo

The Revo fuel is a hydroprocessed ester and fatty acid (HEFA)-type fuel containing a higher level of cycloparaffins. Three fuel samples have been received, and Tier 1 and 2 testing has been completed. This fuel is likely to be balloted during 2024.

Virent Synthesized Aromatic Kerosene

Virent's synthesized aromatic kerosene (SAK) is an aromatics-only stream produced from a sugar feedstock. The OEM committee has recommended that this candidate be re-evaluated as a blend with petroleum jet fuel. Testing was completed, but additional work on materials compatibility at lower aromatics levels was recommended by the OEM committee.

OMV

The OMV ReOil candidate is produced from waste plastics via pyrolysis. The OEM committee has approved this fuel for entry to the Fast Track process after reviewing initial fuel property and composition data. Testing is complete on two fuel samples.

Methanol to Jet

A number of samples were received from ExxonMobil, Honeywell-UOP, and Topsoe. The Tier 1 and 2 results are nearly complete. The ExxonMobil and UOP samples are primarily isoparaffinic, while the Topsoe sample is primarily cycloparaffinic with aromatics. Discussions are underway regarding how to proceed with approval of these fuels of varying composition.

Co-processing of Hydroprocessed HEFA

A new co-processing pathway was balloted, approved by ASTM, and included in a new version of ASTM D1655-23. This pathway allows the co-processing of up to 24% previously hydroprocessed esters, fatty acids, and triglycerides. Up to 10% of the product will be allowed in finished jet fuels.

Publications

Written reports

ASTM International. (2019). *Modification of ASTM D1655: Co-processing of Fischer-Tropsch feedstocks with petroleum hydrocarbons for jet production using hydrotreating and hydrocracking*. (Modification of Report No. ASTM D1655).

(2019). *Evaluation of synthesized paraffinic kerosene from algal oil extracted from botryococcus braunii (IHI Bb-SPK)*. (Report No. D4054).

ASTM International. (2020). *Standard specification for aviation turbine fuels*. Report No. ASTM D1655-20. <https://astm.org/d1655-20.html>

(2022). *Evaluation of Global Bioenergies' isobutene derived synthetic paraffinic kerosene (IBN-SPK)*. (Research Report D02 - WK71952).

(2022). *Evaluation of alcohol-to-jet synthetic kerosene with aromatics (ATJ-SKA) fuels and blends*. (Research Report).

Outreach Efforts

Presentations on Project 31 activities were given at the April 2023 and October 2023 ASCENT meetings. Meetings were held with the OEM team, FAA, fuel producers, and others at numerous virtual FAA/OEM meetings (generally two meetings per month).

Awards

None.

Student Involvement

None.

Plans for Next Period

We will continue discussions with new fuel producers, and we expect new candidates to enter the process in the coming months.

Tasks 3 and 4 - Manage the Evaluation and Testing of Candidate Alternative Fuels

University of Dayton Research Institute

Objective

The objective of this work is to manage the evaluation and testing of candidate alternative jet fuels in accordance with ASTM International standard practice D4054 (Figure 1).

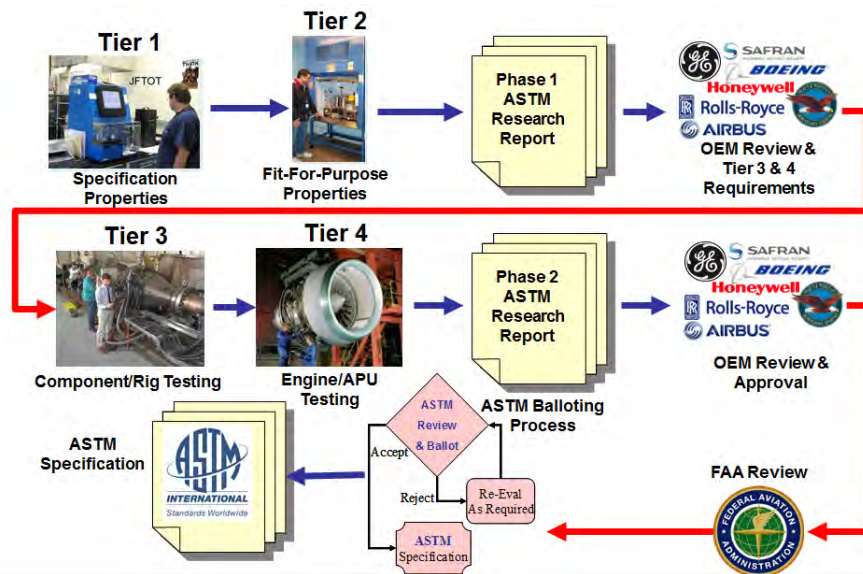


Figure 1. ASTM D4054 qualification process. APU: auxiliary power unit; ASTM: American Society for Testing and Materials International; JFTOT: jet fuel thermal oxidation tester; OEM: original equipment manufacturer.

Research Approach

UDRI will subcontract with other research organizations, testing laboratories, and/or OEMs to conduct the following tasks in support of the evaluation and ASTM specification development for alternative jet fuels. The purpose of this project is to manage and coordinate the D4054 evaluation process to facilitate the transition of alternative fuels to commercial use.

Subtask 1: General support

- Develop and make available a D4054 process guide describing logistical procedures for the handling of test fuels, documentation requirements, test report issuance and delivery, and contact information, to provide clear instructions for candidate-fuel producers entering the ASTM D4054 process



Subtask 2: Phase 1 support

- Coordinate the handling of Phase 1 candidate test fuel samples for Tier 1 and 2 testing
- Review process descriptions provided by the fuel producer to determine the acceptability for incorporation into the Phase 1 research report
- Review test data from Tier 1 and 2 testing to determine acceptability for incorporation into the Phase 1 research report
- Issue and deliver a Phase 1 research report to OEMs
- In conjunction with the fuel producer, review and respond to comments regarding the Phase 1 research report, as submitted by the OEMs
- Conduct additional Tier 1 or 2 testing in response to OEM comments, as required
- Review and consolidate OEM requirements for D4054 Tier 3 and 4 testing, as submitted by the OEMs
- Deliver consolidated D4054 Tier 3 and 4 testing requirements to the fuel producer

Subtask 3: Phase 2 support

- Coordinate the funding and scheduling of D4054 Tier 3 and 4 testing with OEMs and other test facilities
- Coordinate the handling of Phase 2 candidate test fuel samples for Tier 3 and 4 testing
- Review test data from Tier 3 and 4 testing to determine acceptability for incorporation into the Phase 2 research report
- Issue and deliver the Phase 2 research report to OEMs
- In conjunction with the fuel producer, review and respond to comments submitted by OEMs regarding the Phase 2 research report
- Conduct additional Tier 3 or 4 testing in response to OEM comments, as required
- Issue and deliver Phase 2 research report addenda reporting the additional Tier 3 or 4 test results, as required

Subtask 4: OEM review meetings

- Schedule periodic OEM meetings to review the testing status and research report evaluations
- Identify suitable meeting venues and support equipment
- Develop agendas and coordinate with attendees for participation in these meetings
- Record meeting minutes, including agreements, commitments, and other action items
- Issue and distribute meeting minutes to all attendees

Subtask 5: Single-laboratory two-dimensional gas chromatography method documentation

- Document UDRI two-dimensional gas chromatography (GCxGC) methods for hydrocarbon type analysis
- Develop reference materials for the creation of GCxGC hydrocarbon type templates
- Measure single-laboratory precision of GCxGC methods

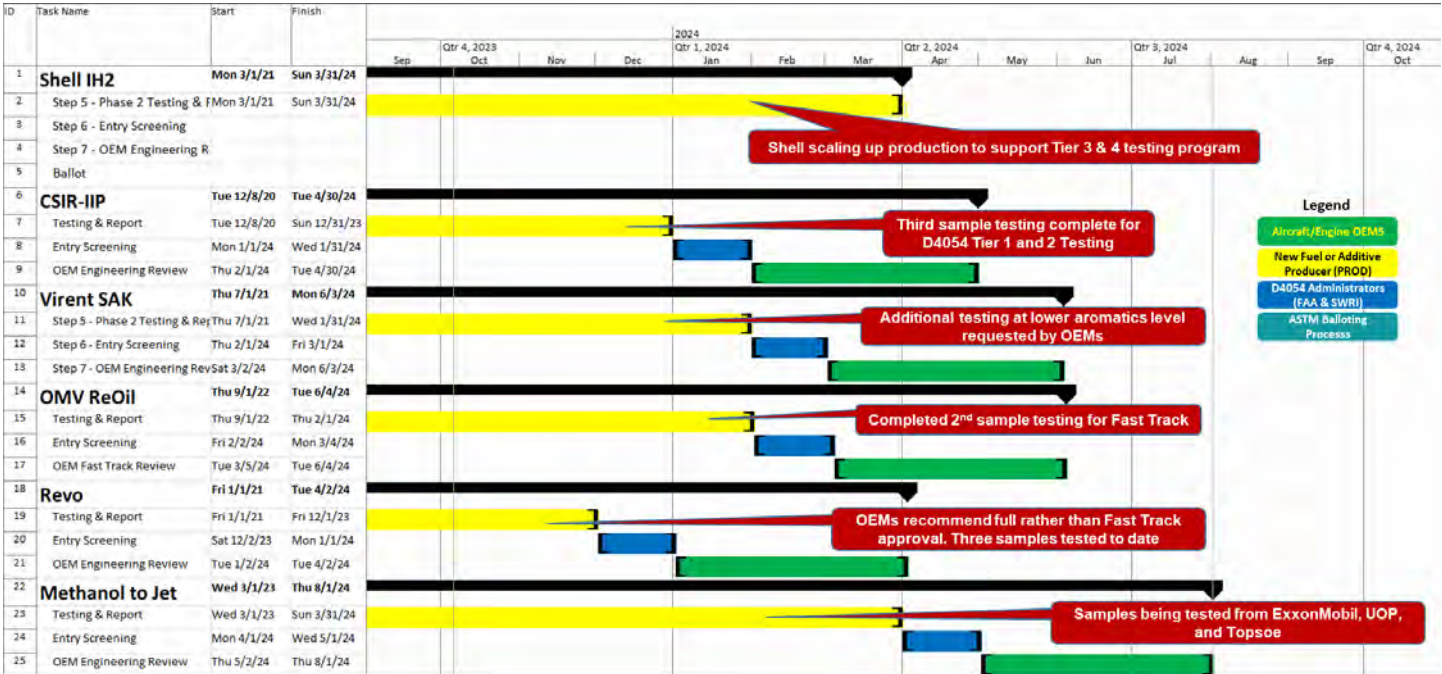
Subtask 6: Multi-laboratory GCxGC method documentation

- Validate the precision of GCxGC methods across multiple laboratories
- Identify alternative GCxGC methods, including column selection and order and modulation techniques
- Perform a correlation study to determine the agreement among laboratories, methods, and hardware choices

Milestones

The schedule for this project is dependent on the receipt of alternative fuel candidates for testing. As candidate fuels are received, a testing schedule will be established via coordination with the FAA and collaborators. Our existing relationships with these organizations will help expedite this process. Figure 2 shows a Gantt chart schedule for the testing and approval of candidate fuels that are either currently under evaluation or will soon enter the evaluation process.

D4054 Clearinghouse Forecasted Fuel Evaluation Schedule



Oct 6, 2023

Figure 2. Schedule for fuel evaluations.

Major Accomplishments

GCxGC precision: Intra- and interlaboratory comparisons

To investigate the precision of GCxGC hydrocarbon type analyses, we assessed a single fuel over several years with a single instrument (intralaboratory comparison). We also compared two different GCxGC systems: flow modulation with a nonpolar initial column and a polar secondary column versus thermal modulation with a polar initial column and a nonpolar secondary column. We also compared measurements between two laboratories (UDRI/Air Force Research Laboratory versus NASA Glenn) for multiple fuels with the same instrument type and column configuration. In addition, we have recently compared measurements among multiple laboratories using several different GCxGC systems and methods.

A report describing these results has been drafted and submitted to the FAA for comments (UDR-TR-2021-159). This report details the following:

- 2.0 Phase 1 results: Single-laboratory GCxGC method documentation
 - 2.1 Methods and documents describing UDRI methods
 - 2.2 Development of reference materials
 - 2.3 Single-laboratory precision
- 3.0 Phase 2 results: Multi-laboratory GCxGC method documentation
 - 3.1 Precision validation of normal phase GCxGC, flow modulation with an outside laboratory (reproducibility)
 - 3.2 Identification of alternative methods
 - 3.3 Correlation study

Most recently, the GCxGC precision results were reported at the September 2022 meeting of the International Association for Stability, Handling, and Use of Liquid Fuels, Inc., in Dresden, Germany. A proceedings manuscript is being prepared.

Civil Aviation Administration of China

The Chinese government has approached the FAA/OEM committee with a request to evaluate two jet fuel additives for approval for use. These additives include a static dissipator additive and a corrosion inhibitor/lubricity improver additive. These additives have been received, and testing has been completed on both additives. Based on an initial review of the results, the OEM committee recommended additional testing, which has also been completed. The OEM committee has commenced communications with representatives of the Civil Aviation Administration of China to find a pathway forward.

Inductively coupled plasma mass spectrometry

Recent observations of inconsistent results for dissolved metal concentrations in fuel evaluated in the D4054 Clearinghouse have prompted an evaluation of these analyses. In particular, the phosphorus results have presented an issue in ongoing evaluations. UDRI acquired an inductively coupled plasma mass spectrometry system and has developed new methods for measuring phosphorous and silicon via standard addition, as these atoms have interferences that preclude the use of an external calibration curve.

OEM committee coordination

Ongoing efforts in ASTM OEM committee coordination continued during this period. These efforts involve coordinating engine and airframer OEM meetings, which have typically occurred in concert with the biannual ASTM Committee D02 sessions and at the annual U.K. Ministry of Defense Aviation Fuels Committee meeting in London. During travel restrictions due to the COVID-19 pandemic, these meetings have been occurring virtually and more frequently, once or twice per month. SwRI continues to receive funding to aid in coordinating the OEM meetings and in communicating with the OEMs for discussions and research report reviews of new candidate alternative jet fuels. In addition, a Gantt schedule is updated monthly; this schedule shows a queue of candidate fuels and the completed and expected schedules as these fuels move through the ASTM D4054 process of testing, review, balloting, and approval. A recent version of this schedule is shown in Figure 3. In support of the ongoing OEM committee coordination, subcontracts with Boeing, GE Aviation, Honeywell, Rolls Royce, Pratt & Whitney, and SwRI have been extended to our ASCENT grant end date of September 30, 2024.

With the departure of Mark Rumizen from the FAA, we have instituted an OEM Committee Steering Group to help plan and focus the OEM meeting discussions. This steering group currently consists of representatives from UDRI, FAA, SwRI, ASTM J6 Chair, U.K. Clearinghouse, E.U. Clearinghouse, and E.U. Aviation Safety Agency. We will be making adjustments to this group membership as needed. In addition, we are committed to working closely with the nascent U.K. and E.U. Clearinghouses to assure that fuel composition and property data are aligned between the laboratories.

Boeing EcoDemonstrator fuel testing support

During the latter part of the year, we supported the Boeing EcoDemonstrator program with fuel property and composition measurements. There was particular interest in monitoring the fuel composition and properties as the fuel moved from storage tanks, to refuelers, and finally to aircraft fuel tanks. A total of 21 fuel samples were studied for the following properties: mono-aromatics, di-aromatics, total aromatics, smoke point, naphthalenes, hydrogen content, gross heat of combustion, net heat of combustion, total sulfur, total nitrogen, flashpoint, "density at 15 °C," "viscosity at -20 °C," and GCxGC (total aromatics, di-aromatics, and hydrogen content).

Publications

Written reports

- (2018). *UDRI Method FC-M-101: Flow modulation GCxGC for hydrocarbon type analysis of conventional and alternative aviation fuels.* (Report No. UDR-TR-2018-40).
- (2018). *UDRI Method FC-M-102: Identification and quantification of polar species in conventional and alternative aviation fuel using SPE-GCxGC.* (Report No. UDR-TR-2018-41).
- (2020). *Evaluation of integrated hydrolysis and hydroconversion (IH²) cycloparaffinic kerosene (CPK-0).* (Report No. D4054).
- (2019). *Evaluation of synthesized paraffinic kerosene from algal oil extracted from Botryococcus braunii (IHI Bb-SPK).* (Fast Track Research Report).
- (2021). *Alternative jet fuel evaluation and specification development support: GCxGC methods draft report.* (Report No. UDR-TR-2021-159).
- (2022). *Evaluation of Global Bioenergies' isobutene derived synthetic paraffinic kerosene (IBN-SPK).* (Research Report D02 - WK71952).
- (2022). *Evaluation of alcohol-to-jet synthetic kerosene with aromatics (ATJ-SKA) fuels and blends.* (Research Report).



Outreach Efforts

Presentations on Project 31 activities were given at the April 2023 and October 2023 ASCENT meetings. Meetings were held with the OEM team, FAA, fuel producers, and other attendees at numerous virtual FAA/OEM meetings (generally two per month). We have also met with multiple candidate-fuel producers, including Global Bioenergies, OMV, CSIR-IIP, Revo, Par Hawaii Refining, BioWright, Greenfield Global, ExxonMobil, Uzbekistan GTL, Vertimass, Green Lizard, Virent, Swedish Biofuels, Deutsche Energie-Agentur, Zero Petroleum, Licella, and Varo Energy.

Awards

None.

Student Involvement

None.

Plans for Next Period

We plan to continue coordinating the OEM committee reviews. We will continue to hold both in-person and virtual OEM committee meetings.



Project 033 Alternative Jet Fuels Test Database (AJFTD) Library

University of Illinois Urbana-Champaign

Project Lead Investigator

Tonghun Lee
Professor
Mechanical Science & Engineering
University of Illinois at Urbana-Champaign
1206 W. Green St.
Urbana, IL 61801
517-290-8005
tonghun@illinois.edu

University Participants

University of Illinois at Urbana-Champaign

- P.I.: Tonghun Lee, Professor
- FAA Award Number: 13-C-AJFE-UI-038
- Period of Performance: October 1, 2022 to September 30, 2023
- Tasks:
 1. Online database development: Domestic airport network and international program connection
 2. Analysis of chemical kinetic mechanisms

Project Funding Level

FAA funding level: \$150,000

Cost-sharing: Software license support from Reaction Design (ANSYS)

Investigation Team

- Tonghun Lee (P.I.), All Tasks
- Alex Solecki (graduate student), Task 1
- Ji Hun Oh (graduate student), Task 2
- Audrey Godsell (graduate student), Tasks 1 and 2

Project Overview

This study seeks to develop a comprehensive and foundational database of current and emerging alternative jet fuels by integrating relevant pre-existing jet fuel data into a common archive that can support scientific research, enhance operational safety, and provide guidelines for the design and certification of new jet fuels. In light of the September 2021 White House statement on advancing the future of sustainable aviation fuels (SAFs) in the United States, the database now has even greater potential for serving the national agenda. In previous years of this project, efforts focused on the integration and analysis of pre-existing jet fuel data from various government agencies and individual research groups. In 2020, we converted all of the compiled data to a new nonstructured query language (NoSQL) format by using a JavaScript object notation (JSON) schema, thus allowing the data to be analyzed in a flexible manner via various programming languages. To this end, we have launched the second generation of our online database, the National Alternative Jet Fuels Test Database (AJFTD), which uses the new nonrelational database structure. This version is equipped with interactive analysis functions for users and flexible methods for plotting and downloading data. In 2022, we extended this effort to incorporate advanced machine-learning algorithms into the analysis process. Additionally, we integrated our database with the database assembled by the European JETSCREEN program. Over the past year, efforts have involved engaging domestic airports in establishing a new data pipeline. Successful efforts have led to an initial mutual relationship between domestic

airport fuel consortia and our database. In the future, expanded data acquisition from domestic and international airports will aid in further development of the database and will support its use as a repository for all SAF-related property and test data.



Figure 1. Alternative Jet Fuels Test Database webpage (<https://altjetfuels.illinois.edu/>).

We hope that the database will, one day, serve not only as a comprehensive and centralized knowledge base used by the jet fuel research community, but also as a resource to enhance global operation efficiency and safety. Future efforts will include linking real-time fuel usage and certification data from domestic and international airports. Connecting our database with ongoing European projects, such as ALIGHT and NewJET, will help create avenues for future database development in this area. Given the prolific diversification of new alternative jet fuels expected in the near future, the ability to track critical fuel properties and test data from both research and operation perspectives will be highly valuable for the future of commercial aviation. Furthermore, increasing the breadth of data categories available on the database, from fuel data to global usage trends, will make the database relevant to a greater audience. We hope that ongoing website development and an improved user interface will also allow the general public to engage with high-level information regarding SAFs, thereby increasing the general public’s knowledge and awareness of SAFs and further supporting the national visibility of sustainable aviation.

Task 1 – Online Database Development: Domestic Airport Network and International Program Connection

University of Illinois at Urbana-Champaign

Objectives

The main objective of this task is to upgrade and debug the generation II online AJFTD functions and link the database to domestic airport fuel test data. The generation II database was designed by using a new architecture based on a NoSQL data format that allows for flexible analysis and scaling. This format can accommodate various data types that can be easily accessed by any common programming language, and basic analysis functions have been built directly into the web interface. Additionally, substantial effort has been made over the past year to improve the data organization and retrieval process for both website administrators and standard users. Ensuring that all users can efficiently locate and collect all relevant data samples for their purposes is the main objective for future website adjustments and improvements. The main Task 1 objectives are as follows:

- Establish methods for acquiring real-time airport fuel data from domestic U.S. airports, beginning with Seattle-Tacoma International Airport.

- Detail data type, frequency, and sharing methods with the ALIGHT program led by Copenhagen Airport and the NewJET program led by the University of Birmingham.

Research Approach

Generation II database debugging and upgrade

The current generation II version of the AJFTD web interface maintains most of the functional features present in the originally developed database. Much like generation I, generation II is an HTML-oriented program built on a layer of metadata that supports search functions for users. The tree structure applied to organize the data folders in the first database has been retained in the second version, thereby allowing users to access the data in a similar manner. The main difference is that an additional inner core houses the JSON files, where the test data reside. Currently, the database has grown to house more than 25,000 separate fuel records.

The catalog of data currently available in the database is primarily assembled from four separate sources. Fuels with POSF (Air Force Research Laboratory fuel database code) number designations were added from the internal database maintained by the Air Force Research Laboratory at the Wright Patterson Air Force Base. The second dataset was obtained from Petroleum Quality Information System reports of the Naval Air Systems Command and corresponds to a compilation of fuel data primarily geared for government use. The third set was provided by Metron Aviation, consisting of fuel properties from samples collected at airports through a previous ASCENT project. The dataset resulting from this study has proven valuable by showing the landscape of fuels currently used in commercial aviation and will guide our future efforts focused on capturing this type of data in real time. The final dataset was obtained from the National Jet Fuel Combustion Program within ASCENT.

Over the past year, changes have been made to the generation II database to fix bugs and upgrade various aspects of the database. Two of the key changes to the database are summarized below.

- Users of the generation II database are able to export a text file containing the properties and composition of a fuel of their choice from the website. This is done by navigating to the “Search Fuels” page under the “Fuels” tab. Users can search for fuels of interest and select one or more fuels. Selecting the “Export” button then guides users to a page where various properties and composition parameters can be selected to include in the exported text file. Selecting “Export Data” produces a single text file containing rows of data with each of the chosen parameters for each selected fuel. Previously, no fuel metadata were included in this export. New changes have been added to include metadata for each exported fuel at the end of the text file. The metadata include information such as a fuel’s origin, class, sampling date, and more.
- The website contains almost 600 documents relevant to fuel composition and certification. Many of these documents have been included on the database for years. Efforts are ongoing to update and reclassify these documents as well as to add newer research papers related to SAF combustion. The University of Illinois at Urbana–Champaign conducts shock tube and rapid compression machine experiments using SAFs, blends of SAFs, and conventional jet fuels. In the future, some of these results will be incorporated into the documents in the database. Minor bugs were discovered within the database administrative document editing feature and were resolved prior to beginning this effort.

Integration of the database with domestic airports

The AJFTD will continue to acquire new data through connection with domestic airports. Initially, the project targeted Chicago O’Hare International Airport (ORD) as a key stepping stone for data collection because of its proximity to the University of Illinois at Urbana–Champaign. Contact with fuel personnel at ORD was established, and a productive meeting was held; however, a reliable data pipeline is still in progress. Our focus shifted to other airports of interest, including New York LaGuardia Airport (LGA) and Los Angeles International Airport (LAX), indicated on the map in Figure 2. With help from the FAA, we established a relationship with Seattle–Tacoma International Airport (SEA), located in the state of Washington. We have received two dozen certificates of analysis (CoAs) from SEA in 2023: three for each month starting in January and ending in August, with the expectation to continue receiving CoAs until the end of the year and for the foreseeable future. In the coming months, we plan to expand our network to other airports in the region, starting with San Francisco International Airport (SFO).

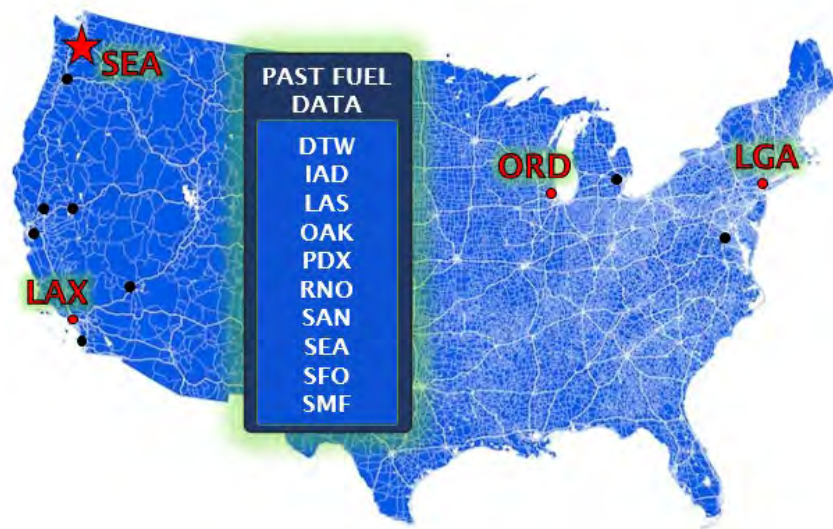


Figure 2. Domestic airports of interest for data collection (in red) and historic database data suppliers (listed and indicated by black markers).

Among the target airports outlined, SEA provides unique opportunities as a launching point for new fuel data collection efforts because the AJFTD already houses old SEA data from 2015 and 2016. Part of the value of the database lies in the ability to view trends in fuel composition and properties over time as airlines source and blend fuels differently. With the addition of new SEA data, we were able to compare past SEA Jet A measurements with recent SEA Jet A tests. Figure 3 shows new Jet A data in orange and existing AJFTD data in blue. The left plot depicts aromatics content in the fuel, and the right plot depicts mercaptan sulfur content. These data visualizations can provide insights into testing practices and documentation over time, as well as into seasonal variations in fuel properties. These results have also inspired a new opportunity for the AJFTD. In exchange for receiving fuel data to upload for public and scientific perusal, we can provide data analysis for airlines and airport fuel consortia. Sharing our AJFTD-driven data analysis with suppliers could help shape SAF implementation in the coming decade.

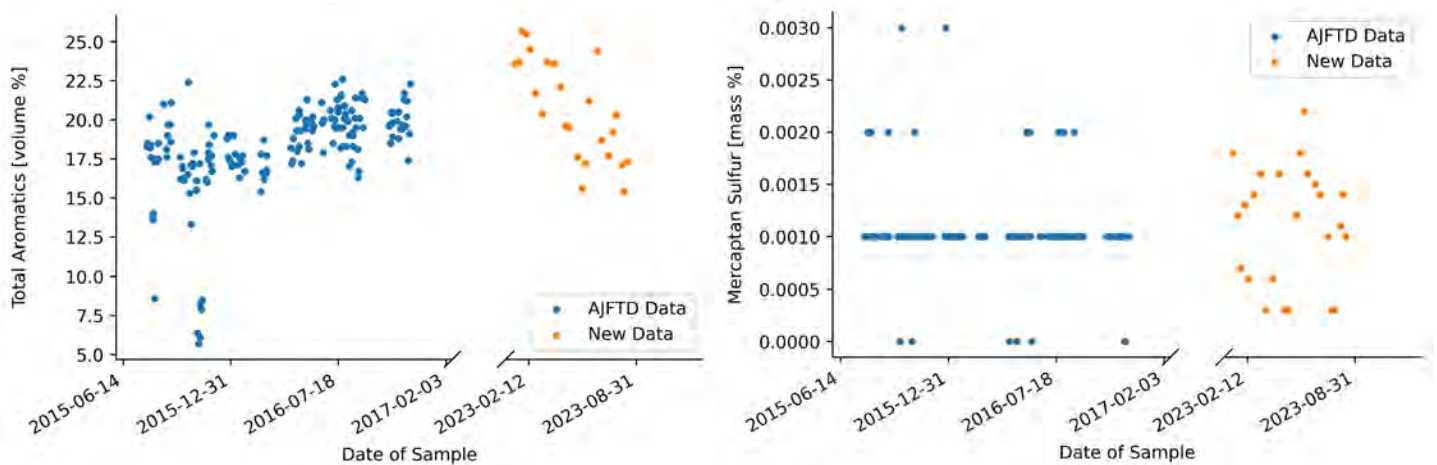


Figure 3. Comparison of aromatics and mercaptan sulfur content between historic Alternative Jet Fuels Test Database (AJFTD) data and new certificate of analysis reports for SEA.

One of the challenges of incorporating airport data into the database is data formatting. The CoAs received this year containing Jet A data were in portable document format (PDF). The database, however, relies on a flexible JSON format to allow for a variety of programming languages to parse and analyze fuel data. To store new data within the database, the PDFs must first be converted to a JSON format. We expect to continue receiving CoAs in PDF format, necessitating a method for converting data from PDF to JSON. As our network of fuel data grows, we anticipate receiving larger volumes of CoA PDFs. Copying fuel data for each CoA by hand into a JSON format is tedious and leaves room for human error; thus, we have begun developing a script that can automatically populate a new JSON file for each new CoA PDF received.

Writing such a script entails a number of challenges. First, CoA PDFs may be organized differently depending on their origin. The CoA PDFs received this year already have two distinct styles, even though they were obtained from the same source. The script must be robust enough to handle differently organized PDFs regardless of the organization or verbiage used. In the PDFs received thus far, most property and composition data are contained within a table at the core of the CoA. Data outside of the table are often metadata, such as the date and time of fuel sampling and testing, the fuel name, the location of testing, etc. The script must be able to extract data from both outside and inside the table in the PDF.

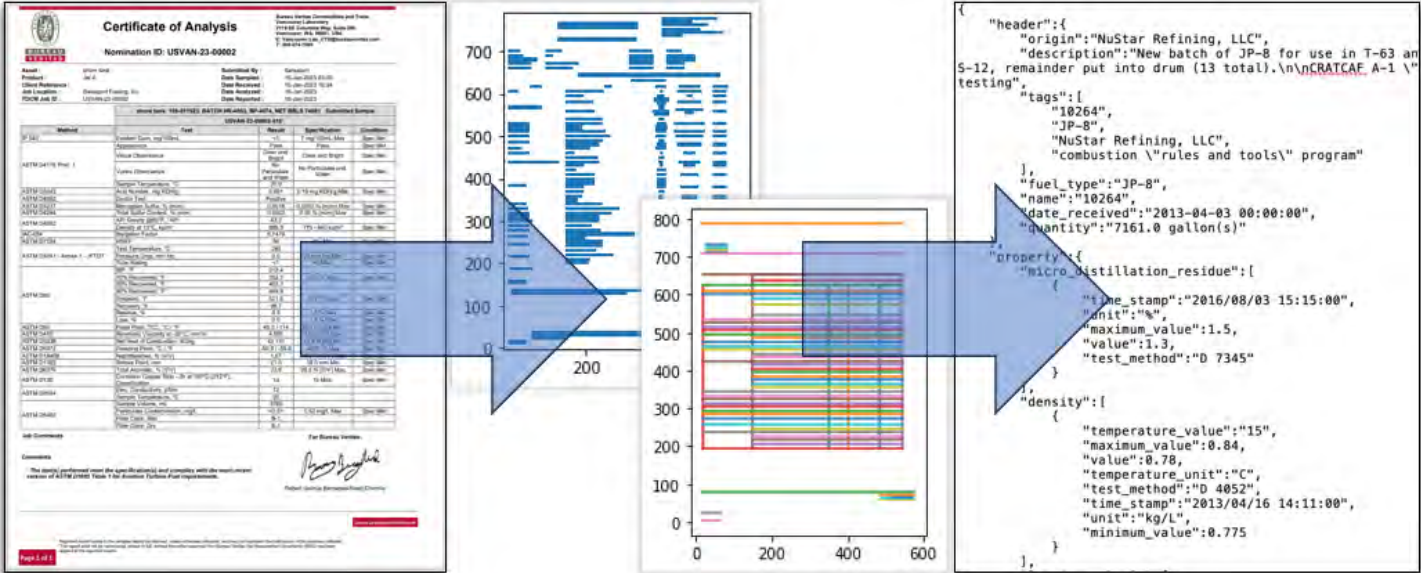


Figure 4. Pipeline from the airport certificate of analysis to database JSON format.

At present, the script is capable of identifying tabulated regions within the PDFs and extracting tabulated data, as shown in the left and center panels of Figure 4. The next challenge for the script, which will be addressed heavily over the next year, is to convert the extracted table data into the desired JSON format. However, unexpected complexities arise in this stage of the conversion process. Rarely will differently formatted PDFs refer to the same property with the exact same string of characters. For example, one PDF may list "Net Heat of Combustion, MJ/kg" while another merely states "Net Heat of Combustion." The script must be able to match these two different phrases to the same property, regardless of the wording used or whether units or other information are included in the phrase. This problem is compounded by the fact that many properties are denoted by similar words or units. This problem is expected to be resolved in the upcoming year.

Integration of the database with international airports and programs

Past efforts with the database have included integration with the JETSCREEN program, a milestone in which we established a foundation for international data incorporation with the AJFTD. Other programs of interest for linking with the AJFTD are ALIGHT and NewJET. The ultimate goal of international database integration is to help monitor and evaluate fuels used in the international airspace and to paint an accurate picture of how fuel composition and usage trends are changing over time. As new fuels are integrated into the global supply chain, a means for tracking these properties will become critical. Such an interconnected database will provide the most representative information needed for research and certification of new SAFs.



Future efforts to broaden data sources for fuel data available on the website will include connecting our database with other ASCENT projects, including the World Fuel Survey, which will largely replicate the global data collection process for the 2006 Coordinating Research Council's World Fuel Survey, and the Washington SAF repository. These connections will provide a substantial source for developing a dataset of physical and chemical properties of recent, regionally representative conventional jet fuels and SAFs.

Milestones

3 months

- Debugging and optimization of the data structure in the generation II database
- Following up with United Airlines at ORD

6 months

- New data export functionality for users
- Bug fixes in document editing section and document editing underway
- Reaching out to ORD and SEA about fuel data

9 months

- Successful contact with SEA and pipeline for continual receipt of CoAs established
- Draft plan created for a script to convert PDF CoAs to database JSON format

12 months

- PDF to JSON conversion script foundation programmed
- Initial work on improving administrative functionality on the AJFTD website

Major Accomplishments

Securing domestic and international airport connections

Correspondence with relevant contacts for data collection at SEA and ORD has been initiated, and plans to proceed in establishing a mutually beneficial exchange of data are in place. The team has met with personnel relevant to the aforementioned international programs to discuss shared objectives. These connections will serve as new sources for acquiring greater amounts of fuel data and will enable the expansion of data categories available on the database to categories such as usage and emission data. Continued international collaboration will increase the long-term potential for support and data sharing with other international programs as they form. Connections with domestic airports will also support the long-term reliability of in-country data acquisition, if consistent avenues for data sharing are built and maintained, thus providing the database with the most up-to-date and relevant information available.

Publications

None.

Outreach Efforts

The database has been made accessible through <https://altjetfuels.illinois.edu/>.

Awards

None.

Student Involvement

This project was primarily conducted by two graduate students (Alex Solecki and Audrey Godsell).

Plans for Next Period

In the next period, the team will focus on ramping up data collection from domestic airports and expanding data sources beyond SEA. Extensive analyses of new data will be performed and shared with new fuel contacts as requested. In addition, the next World Fuel Survey and SAF repositories will yield data in the coming years that will also be integrated into the database. Collaboration with all involved parties will ensure that the data are properly treated and represented online and that all proprietary information is protected on both ends of the data sharing pipeline.

Additional efforts anticipated to improve the functional and aesthetic features of the database are summarized below.

- User interface and online analysis tools: Moving forward, administrative functionality will be increased, allowing for better management of the website and data within. Documentation will continue to be updated and supplemented with newer resources for users to reference. A series of features allowing further first-level data analysis will be completed. These features include, for example, a mass-compare function capable of quickly building graphs and charts for comparing the composition or properties of a single or group of fuel samples with all other samples in a relevant category, such as all samples of fuel type Jet A or all samples of fuel class SAF. These features will encourage use of the website and will enable meaningful interactions with the database for a wider audience.
- Domestic and international data collection: The focus of this next period will be to increase the volume of fuel data received from SEA and to expand fuel collection efforts to other airports within the United States. In addition, further steps will be taken for the integration of data from the ALIGHT and NewJET projects. Connections will be established with the World Fuel Survey and Washington SAF repository ASCENT projects in order to build toward a future of cooperation and shared fuel data.

Task 2 – Analysis of Chemical Kinetic Mechanisms

University of Illinois at Urbana-Champaign

Objectives

The main objective of this task was to investigate the rapid development of chemical kinetic mechanisms for aviation fuels for potential future integration into the AJFTD. Chemical kinetic mechanisms are critical to practical simulations involving combustion processes and play a fundamental role in certification efforts for new fuels. As new SAFs appear in the aviation industry worldwide, mechanisms will need to be developed to help with numerical simulations in terms of computational fluid dynamics or to support certification. However, creating and reducing detailed chemical kinetic mechanisms requires a substantial amount of computing power and time, often more than is practical for a new SAF that may or may not turn out to be a valuable investment. Thus, methods for rapidly developing reliable and efficient chemical kinetic mechanisms for SAFs are a key ingredient to greater SAF implementation across the globe. This effort aims to explore methods for rapidly constraining mechanisms to this end. Specifically, the major goals are as follows:

- Identify data-driven optimization methods
- Devise a chemistry-based approach for applying these methods
- Perform an example mechanism optimization using the selected approach
- Quantify uncertainties and effectiveness of the constraining approach

Research Approach

Data-driven optimization strategy

The fuel chosen for this investigation was commercial Jet A aviation fuel blended to have a cetane number (CN) of 30 while maintaining physical parameters related to atomization and vaporization. We refer to this blend as either Jet A-CN30 or CN30. First, a data-driven method based on hybrid chemistry was used to create a baseline chemical kinetic mechanism for this fuel. Essentially, this involves using an evolutionary algorithm to optimize reaction rate parameters. Reaction rate parameters are tied to a set of chemical reactions that govern the chemical species involved in the breakdown and combustion of Jet A-CN30. The algorithm takes up to one day or more of computational time to narrow in on a set of rate parameters for these equations to describe a chemical kinetic mechanism for the fuel. The reaction rate parameters are optimized based on an input of ignition delay times (IDTs). For this particular simulation, the experimentally obtained IDTs for Jet A-CN30 are shown as yellow triangles in Figure 5. However, running the optimization with all of these experimental points is extremely costly in terms of computing resources and time; therefore, a simple spline fit of the experimental data was applied. The blue circular markers in Figure 5 are points chosen to be representative of the trend of the experimental data because of their closeness to the spline. These eight points for each curve were input into the optimization software to create the final chemical kinetic mechanism.

Using the mechanism creation tool described above is quite costly. A machine-learning-based response surface method was conceived, with the objective of creating a less costly surrogate model to replace the old mechanism tool. Ideally, the surrogate model would produce mechanism results with minimized error from the experimental data shown in Figure 5.

The output of the surrogate model is an IDT estimation for a fixed set of temperature and equivalence ratio conditions, with a variable set of input reaction rate coefficients. This approach is different from the traditional model, in which a set of reaction rate coefficients is fixed to produce actual ignition delays for any given set of temperature and equivalence ratio conditions. The traditional method involves solving ordinary differential equations, which the surrogate model can circumvent, resulting in a computational time that is shorter by several orders of magnitude.

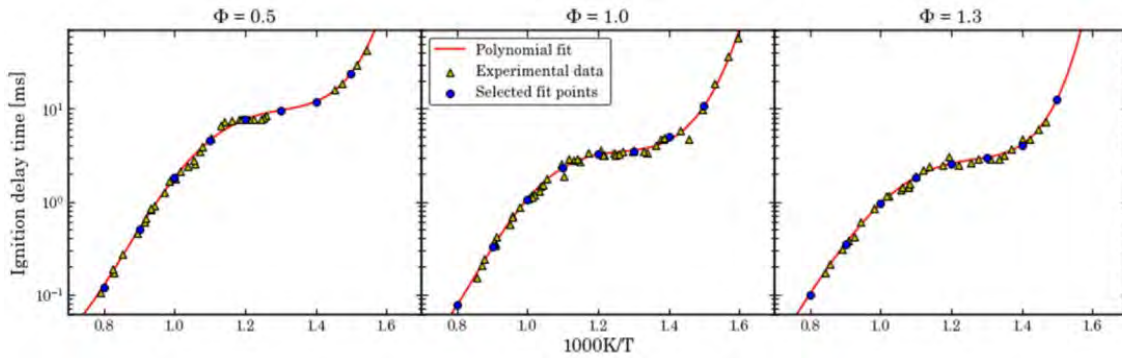


Figure 5. Ignition delay time measurements, fitted polynomials, and extracted target datapoints for Jet A-CN30.

Results from the surrogate modeling approach were analyzed by using an inverse uncertainty quantification (UQ). This involved performing an inverse problem in which the target IDTs were used to constrain the uncertainty of the reaction rates used to generate the IDTs. This step helps to show the level of confidence we can apply to the surrogate modeling method.

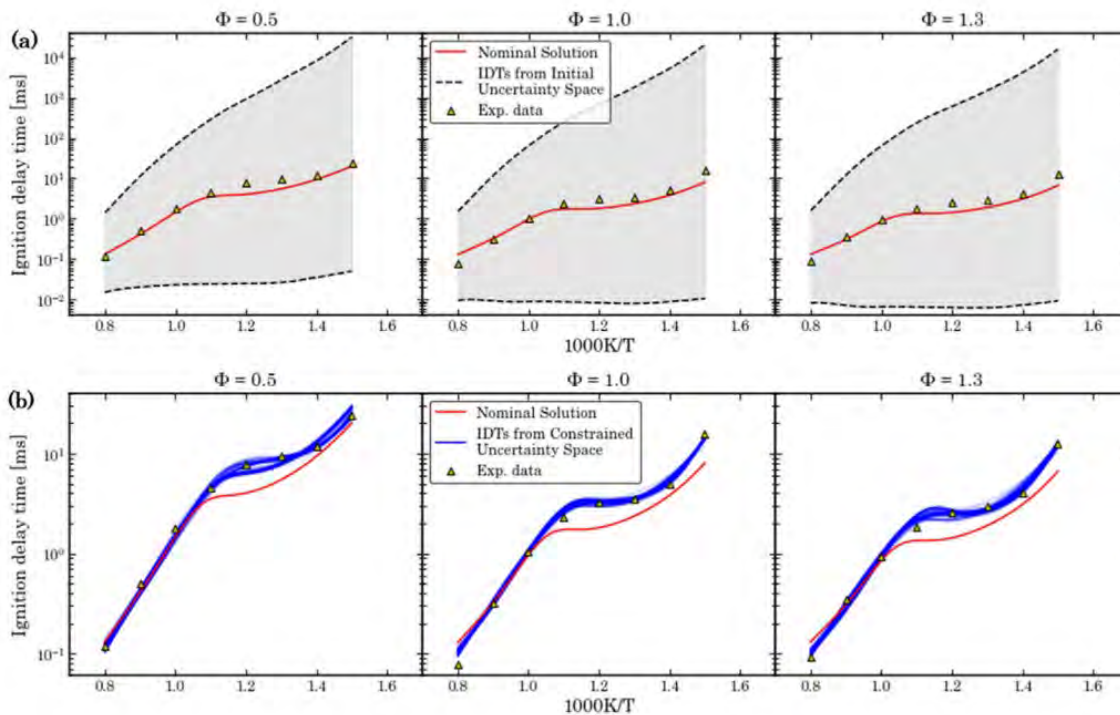


Figure 6. Simulated target ignition delay times (IDTs) before (a) and after (b) inverse uncertainty quantification, plotted against the nominal solution.



Initially, the outputs of the model resembled the graphs in Figure 6(a). The red line at the center is the mechanism derived from the original method. The shaded regions surrounding the line represent areas for which the surrogate model produced solutions, termed the “uncertainty space.” This region was constrained by using inverse UQ to produce the plots in Figure 6(b). The blue lines show the IDTs simulated by the surrogate modeling approach and constrained to closely resemble the experimental data.

Figure 6 presents results for a pressure condition of 2 MPa. The model was extrapolated to a pressure condition of 5 MPa to test the effectiveness of the model. These results, displayed in Figure 7, show good agreement between the simulated IDTs and the nominal mechanism solution, demonstrating the ability of this model to create solutions comparable to those obtained by solving the exhaustive ordinary differential equations traditionally used to develop these mechanisms.

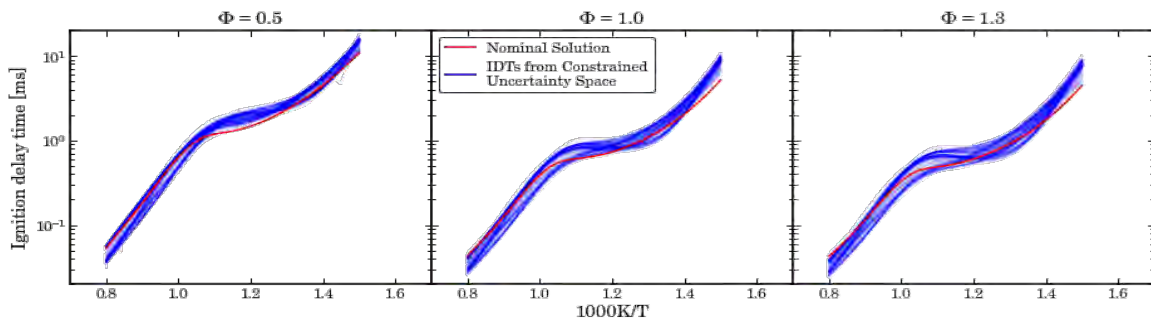


Figure 7. Simulated ignition delay times (IDTs) extrapolated to a non-target pressure condition of 5 MPa.

Each simulated mechanism is associated with a time history of species concentrations throughout a combustion event, such as those shown in Figure 8. Each species shows two or three distinct modes in concentration over time. This result arises as the model is optimized based on a limited amount of data, which cannot be avoided. Ideally, the simulated mechanisms would converge to create a single path for each species over time. The visualization of species shown in Figure 8 is unique and represents the first such visualization performed thus far, made possible only by using the response surface approach to accelerate the calculation. It would have taken over one month on a high-performance supercomputer to map a similar space via the traditional approach. Future work will focus on assessing which species measurements can be input to the simulation to reduce the possible paths of species over time during the combustion event.

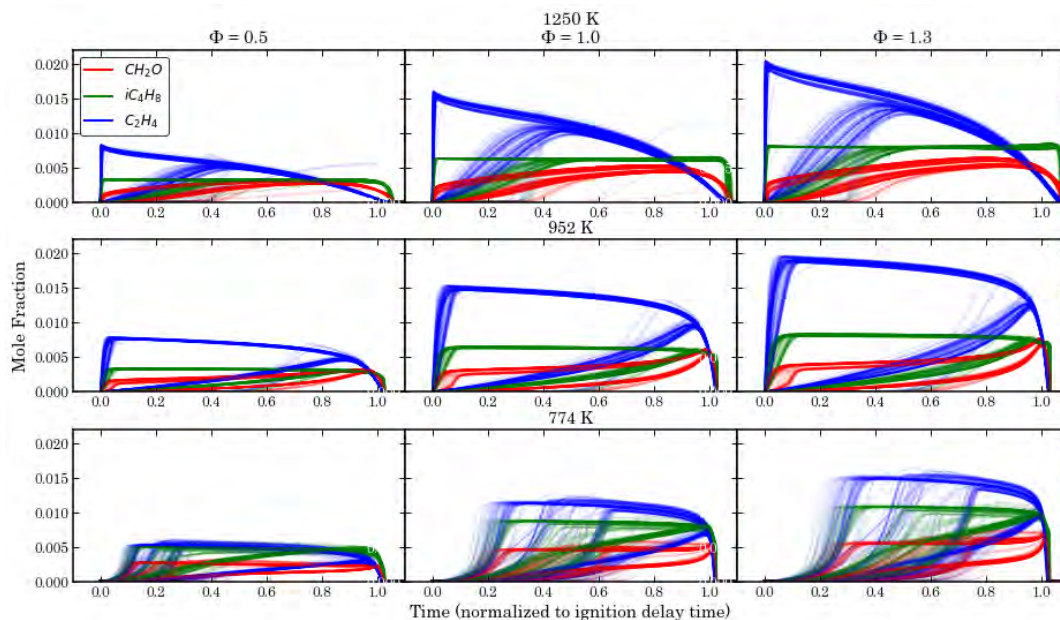


Figure 8. Simulated time histories of three species for three different equivalence ratios and temperatures.

Milestones

3 months

- Formalization of the mechanism optimization plan

6 months

- Establishment of scripts and algorithms for implementation of mechanism constraining
- Organization of data from experimental tests at the University of Illinois at Urbana-Champaign for use in mechanism constraining

9 months

- Implementation of scripts

12 months

- Adaptation of scripts for optimization

Major Accomplishments

Over the past year, two peer-reviewed publications have been derived from this work. Robust response surface models have been created for Jet A-CN30 and a similar fuel, CN40. We have examined the uncertainty of these models and constrained them to experimental data, creating an output set of simulated mechanisms able to produce species concentrations over time for different temperatures and equivalence ratios. A repeatable and significant method has been established to generate and reduce the uncertainty of the mechanisms, allowing this work to expand to different fuels and different combustion processes.

Publications

Peer-reviewed journal publications

- J. Oh, P. Wiersema, K. Kim, E. Mayhew, J. Temme, C. Kweon, T. Lee, Fast Uncertainty Reduction of Chemical Kinetic Models with Complex Spaces using Hybrid Response-Surface Networks, *Combustion and Flame*, 253, 112772 (2023)
- J. Oh, A. Oldani, A. Solecki, T. Lee, Learning to predict sustainable aviation fuel properties: A deep uncertainty quantification viewpoint, *Fuel*, 356, 15, 129508 (2023)



Outreach Efforts

The database has been made accessible through <https://altjetfuels.illinois.edu/>.

Awards

None.

Student Involvement

This project was primarily conducted by two graduate students (Ji Hun Oh and Audrey Godsell).

Plans for Next Period

Moving forward, our focus will fall on further constraining the resulting mechanisms to reduce the number of possible species pathways in time histories. This effort involves an in-depth qualitative and quantitative analysis of each possible parameter's effect on the overall model. In the long term, we aim to link this effort with AJFTD data, someday allowing database users to select fuels and rapidly create accurate simulated mechanisms for these fuels based on the set of experimental data stored in the database.



Project 037 CLEEN II System-level Assessment

Georgia Institute of Technology

Project Lead Investigator

Dimitri Mavris
Regents Professor
School of Aerospace Engineering
Georgia Institute of Technology
Mail Stop 0150
Atlanta, GA 30332-0150
(404) 894-1557
dimitri.mavris@ae.gatech.edu

University Participants

Georgia Institute of Technology

- P.I.s: Prof. Dimitri Mavris, Dr. Jimmy Tai, Dr. Joshua Brooks
- FAA Award Number: 13-C-AJFE-GIT-055
- Period of Performance: October 1, 2022 to September 30, 2023

Project Funding Level

FAA provided \$250,000 in funding to Georgia Institute of Technology (GT). GT has agreed to a total of \$250,000 in matching funds. This total includes salaries for the project director and research engineers, as well as funding for computing, financial, and administrative support, including meeting arrangements. The institute has also agreed to provide tuition remission for students, paid from state funds.

Investigation Team

Prof. Dimitri Mavris, (P.I.)
Dr. Jimmy Tai, (co-P.I.)
Dr. Joshua Brooks, (co-P.I.), program management
Holger Pfaender, (technical lead), fleet modeling
Brennan Stewart, (technical lead), noise modeling
Students: Joao De Azevedo, Madelyn Focaracci, Sebastian Seubert, Krutik Desai, Mitchell Mu, Martina Tehubijuluw, Justin Purser, Todd Goehmann, Tabitha D'Amato, Dante Cyrus, George Blackwell, James Tsangarides, Kayley Lewis, and Ballard Huey

Project Overview

The objective of this research project is to support the FAA by independently modeling and assessing the technologies that are being developed under the Continuous Lower Energy, Emissions, and Noise (CLEEN) II and CLEEN III programs. This will involve direct coordination and data sharing with CLEEN-funded companies in order to accurately model the environmental benefits of these technologies at the vehicle and fleet levels.

GT was previously selected to perform all system-level assessments for the CLEEN program under Partnership for Air Transportation Noise and Emission Reduction (PARTNER) Project 36 and ASCENT Project 10. As a result, GT is in a unique position from both the technical and programmatic standpoints to continue the system-level assessments for CLEEN II. From a technical perspective, GT has significantly enhanced the Environmental Design Space (EDS) over the past 5 years to incorporate advanced, adaptive, and operational technologies targeting fuel burn, noise, and emissions. EDS has been successfully applied to all CLEEN I contractor technologies including the following: GE open rotor, twin annular premixing swirler (TAPS) II combustor, Flight Management System (FMS)-Engine, and FMS-Airframe; Pratt & Whitney geared fan; Boeing

adaptive trailing edge and ceramic matrix composite (CMC) nozzle; Honeywell hot section cooling and materials; and Rolls-Royce turbine cooling technologies. GT has also gained extensive experience in communicating system-level modeling requirements to industry engineers and translating the impacts to fleet-level fuel burn, noise, and emissions assessments. This broad technical knowledge base covering detailed aircraft and engine design, as well as high-level benefits assessments, places GT in a unique position to assess CLEEN II technologies.

Because the ultimate goal of this work is to conduct fleet-level assessments for aircraft representative of future “in-service” systems, GT will need to create system-level EDS models using a combination of both CLEEN II and other public domain N+1 and N+2 technologies. The outcomes of the technology and fleet assumptions-setting workshops conducted under ASCENT Project 10 are used for this effort. Non-CLEEN II technologies for consideration, along with potential future fleet scenarios, will help to bound the impact of CLEEN II on future fleet fuel burn, emissions, and noise.

The FAA will be performing a portion of the EDS technology modeling work. Therefore, periodic (i.e. weekly) EDS training sessions were provided to the FAA during the period of performance. This training provided the requisite skill set for using EDS. In the prior year of this project, GT continued modeling activities with the CLEEN II contractors. This modeling process included validation of underlying EDS models, information and data exchange necessary to model the individual technologies, and related EDS modeling activities. In addition, GT has assisted the FAA with in-house EDS modeling. This process has increased the number of FAA personnel performing EDS system-level assessment modeling.

Work conducted during this period of performance focused on completing vehicle- and fleet-level assessments for CLEEN II. Final technology modeling details for each of the CLEEN II industry contractors have been delivered, with the exception of the final acoustic technologies. Final vehicle-level fuel burn and emissions assessments and preliminary noise assessments have been generated and compared to current best-in-class values. Final fleet-level estimates of fuel burn and emissions have been constructed and delivered to the FAA. The final fleet-level estimates of noise, including community noise impact estimates for a standard representative airport, are awaiting the completion of the final technology modeling effort underway with the contractors for the remaining acoustic technologies. Quantifying this impact will provide an understanding of the increased number of operations per day that CLEEN II technologies enable without worsening the surrounding community’s noise exposure. Although airports in the United States are not generally noise constrained, some European airports have limited capacity to meet noise constraints. Understanding the impact of technologies on the future U.S. fleet will be critical to quantifying the interaction between economic growth (i.e., increased flight operations at a given airport) and community noise impacts. In order to preserve contractor confidentiality, individual technology impacts to the vehicle airframe and engine will not be reported.

Next year’s work will focus on closing the outstanding noise technology modeling and fleet-benefit assessment work of CLEEN II, continuing technology modeling within CLEEN III, and initializing the CLEEN III fleet-benefit assessment. During this period of performance, the GT team and FAA agreed on a collection of updated fleet-benefit assessment conditions for incorporation into the preliminary assessments of the CLEEN III program. These updates include an upgrading of the analysis environment, baseline vehicles, and analysis scope to include 2018 to 2050. Replacement matrices will be upgraded to align with near-term and mid-term entry-into-service dates for future vehicles and technologies, and the demand forecast will be updated to the 2018 Common Operations Database (COD). Finally, the technologies included in the analysis will be audited in terms of their appropriateness for inclusion, timeline of entry, and magnitude of impact, and a new technology integration scenario will be introduced to account for the impacts of the CLEEN III program technologies directly. Each of these changes will be introduced into the preliminary fleet-benefit assessment of the CLEEN III program in the next performance period. In addition, conversations and modeling activities with contractors will continue toward modeling each of the CLEEN III technologies. The table in the next section shows the current status of the technology modeling. Where work remains, a brief description is provided after the table.

Milestones

The major milestones and their planned due dates are listed below:

Task No.	Milestone	Planned Due Date
1	Update CLEEN III Fleet-Benefit Assessment Assumptions	August 31, 2023
2	Initialization of CLEEN III Modeling of Technologies and Advanced Configs	August 31, 2023
3	Finalize CLEEN II Analysis	August 31, 2023

Major Accomplishments

- The modeling for Pratt & Whitney’s compressor and turbine aero-efficiency technologies is complete.
- The modeling for Honeywell’s blade outer air seal system is complete.
- The modeling effort for Honeywell’s advanced HPC system, a late-addition CLEEN II+ technology, is complete.
- Final fleet fuel burn assessment is complete.
- Final fleet landing and take-off (LTO) nitrogen oxides (NOx) assessment is complete.
- Preliminary fleet noise assessment is currently complete.

Task 1 - Update CLEEN III Fleet-benefit Assessment Assumptions

Georgia Institute of Technology

Objectives

During this period of performance, the GT team and FAA agreed on a collection of updated fleet-benefit assessment conditions for incorporation in the preliminary assessments of the CLEEN III program. The following overarching changes will be incorporated into the fleet-benefit assessment of the CLEEN III program:

Vehicle analysis environment upgrade to EDS v7.0

When transitioning from the first phase of the CLEEN program to the second, the vehicle analysis environment was upgraded from EDS v5.0 to EDS v5.4, to best align with GT’s latest EDS version. Similarly, the CLEEN III assessments will be performed using GT’s latest EDS version, v7.0.

The demand forecast will be updated to the 2018 COD

For updating the demand forecast, the 2018 COD, the VOLPE/FAA inventory, ADS-B Aggregators, and the Official Airline Guide were considered. Of these, GT and FAA felt that the 2018 COD provided the greatest opportunity for informing this study inside of the framework traditionally used by GT to perform similar studies in the past.

Analysis scope will be updated to include 2018-2050

This change aligns with the selected demand forecast: 2018 COD

Baseline vehicles to be upgraded to 2018 best-in-class

The baseline vehicles, along with the classes of included vehicles, will be updated to represent a 2018 best-in-class selection. These vehicles compared to the CLEEN II baseline vehicles are shown in Table 1.

Table 1. CLEEN III baseline vehicle updates.

Vehicle Class***	CLEEN I & II (2010 baseline)	CLEEN III (2018 baseline)
RJ (50 - 100 pax)	CRJ-900/CF34-8C5	-
SSA (101 - 150 pax)	-	E190-E2/PW1922G * + LEAP1B-28 **
LSA (151 - 235 pax)	B737-800/CFM56-7B27	B737-8/LEAP1B-28 * + PW1127 **
STA (236 - 300 pax)	B767-300ER/CF6-80C2B5F	B787-8/GEEnX-1B70/P2 *
LTA (301 - 400 pax)	B777-200ER/GE90-94B	B787-10/GEEnX-1B76/P2 *
VLA (400+ pax)	B747-400ER/CF6-80C2B5F	B747-8/GEEnX-2B67 * (New vehicles updated to B777x in 2025)

* EIS Dates: E190-E2 (2018), B737-8 (2017), B787-8 (2011), B787-10 (2018), B747-8 (2012)

** Notional system with alternative engine architecture

*** RJ – Regional Jet, SSA – Small Single Aisle, LSA – Large Single Aisle, STA – Small Twin Aisle, LTA – Large Twin Aisle, VLA – Very Large Aircraft

Replacement matrices to align with near-term + mid-term technology introduction

The replacement matrices will be updated to align with near-term and mid-term entry-into-service dates of 2027 and 2037, respectively. Engine architectures will be split across each of the vehicles between advanced direct drive, (ADD), engines and geared turbofan, (GTF), engines. A geared fan engine for wide-body aircraft will be introduced in the mid-term timeframe. Table 2 shows the new replacement matrix.

Table 2. Tentative CLEEN III replacement matrix.

Vehicle	Engine	Timeframe	2018	2019	2020	2021	2022	2023	2024	2025	2026	2027	2028	2029	2030	2031	2032	2033	2034	2035	2036	2037	2038	2039	2040	2041	2042	2043	2044	2045	2046	2047	2048	2049	2050		
SSA	ADD	Nearterm	0	0	0	0	0	0	0	0	0	12.5	25	37.5	50	50	50	50	50	50	50	37.5	25	12.5	0	0	0	0	0	0	0	0	0	0	0	0	
		Midterm	0	0	0	0	0	0	0	0	0	0	12.5	25	37.5	50	50	50	50	50	50	37.5	25	12.5	0	0	0	0	0	0	0	0	0	0	0	0	
	GTF	Nearterm	0	0	0	0	0	0	0	0	0	0	0	0	0	0	0	0	0	0	0	0	12.5	25	37.5	50	50	50	50	50	50	50	50	50	50	50	50
		Midterm	0	0	0	0	0	0	0	0	0	0	0	0	0	0	0	0	0	0	0	0	12.5	25	37.5	50	50	50	50	50	50	50	50	50	50	50	50
LSA	ADD	Nearterm	0	0	0	0	0	0	0	0	0	12.5	25	37.5	50	50	50	50	50	50	50	37.5	25	12.5	0	0	0	0	0	0	0	0	0	0	0	0	0
		Midterm	0	0	0	0	0	0	0	0	0	0	12.5	25	37.5	50	50	50	50	50	50	37.5	25	12.5	0	0	0	0	0	0	0	0	0	0	0	0	0
	GTF	Nearterm	0	0	0	0	0	0	0	0	0	0	0	0	0	0	0	0	0	0	0	0	12.5	25	37.5	50	50	50	50	50	50	50	50	50	50	50	50
		Midterm	0	0	0	0	0	0	0	0	0	0	0	0	0	0	0	0	0	0	0	0	12.5	25	37.5	50	50	50	50	50	50	50	50	50	50	50	50
STA	ADD	Nearterm	0	0	0	0	0	0	0	0	0	25	50	75	100	100	100	100	100	100	100	75	50	25	0	0	0	0	0	0	0	0	0	0	0	0	0
		Midterm	0	0	0	0	0	0	0	0	0	0	0	0	0	0	0	0	0	0	0	0	12.5	25	37.5	50	50	50	50	50	50	50	50	50	50	50	50
	GTF	Nearterm	0	0	0	0	0	0	0	0	0	0	0	0	0	0	0	0	0	0	0	0	12.5	25	37.5	50	50	50	50	50	50	50	50	50	50	50	50
		Midterm	0	0	0	0	0	0	0	0	0	0	0	0	0	0	0	0	0	0	0	0	12.5	25	37.5	50	50	50	50	50	50	50	50	50	50	50	50
LTA	ADD	Nearterm	0	0	0	0	0	0	0	0	0	25	50	75	100	100	100	100	100	100	100	75	50	25	0	0	0	0	0	0	0	0	0	0	0	0	0
		Midterm	0	0	0	0	0	0	0	0	0	0	0	0	0	0	0	0	0	0	0	0	12.5	25	37.5	50	50	50	50	50	50	50	50	50	50	50	50
	GTF	Nearterm	0	0	0	0	0	0	0	0	0	0	0	0	0	0	0	0	0	0	0	0	12.5	25	37.5	50	50	50	50	50	50	50	50	50	50	50	50
		Midterm	0	0	0	0	0	0	0	0	0	0	0	0	0	0	0	0	0	0	0	0	12.5	25	37.5	50	50	50	50	50	50	50	50	50	50	50	50
VLA	ADD	Nearterm	0	0	0	0	0	0	0	0	0	25	50	75	100	100	100	100	100	100	100	75	50	25	0	0	0	0	0	0	0	0	0	0	0	0	0
		Midterm	0	0	0	0	0	0	0	0	0	0	0	0	0	0	0	0	0	0	0	0	12.5	25	37.5	50	50	50	50	50	50	50	50	50	50	50	50
	GTF	Nearterm	0	0	0	0	0	0	0	0	0	0	0	0	0	0	0	0	0	0	0	0	12.5	25	37.5	50	50	50	50	50	50	50	50	50	50	50	50
		Midterm	0	0	0	0	0	0	0	0	0	0	0	0	0	0	0	0	0	0	0	0	12.5	25	37.5	50	50	50	50	50	50	50	50	50	50	50	50

Technology integration scenarios expanded to include “CLEEN III Aggressive” case

A new technology integration scenario will be included to isolate the impacts of the CLEEN III technologies. Additional attention will be applied to appropriately consider the impacts of the CLEEN I technologies as many of these, or equivalent technologies, have made their way into service.

Public technology set to be updated

The public technology set employed through CLEEN phase II will be audited for its appropriateness within the near-term to mid-term timelines considered in this study. In addition, the technologies will be reassessed against their expected entry-into-service dates, level of development effort, and evolutionary or aggressive scenario inclusion. Finally, the actual magnitudes of the impacts considered for each technology will be updated to reflect their most realistic values against the updated CLEEN III baseline vehicles.

These updates will be incorporated into a preliminary CLEEN III fleet-benefit assessment in the coming period of performance.

Task 2 - Modeling of Aircraft Technologies and Advanced Configurations

Georgia Institute of Technology

Objectives

In order to estimate the impact of CLEEN relevant technologies at the vehicle system level, each of these technologies must be modeled regarding their impacts on aircraft fuel burn, noise, and emissions using EDS.

Research Approach

GT was previously selected to perform all system-level assessments for the CLEEN program under ASCENT Project 10. Because the ultimate goal of this work is to conduct fleet-level assessments for aircraft representative of future “in-service” systems, GT will need to create system-level EDS models using a combination of both CLEEN (phases I, II, and III) and other public domain near-term and mid-term entry-into-service (EIS) technologies. Vehicle system-level modeling for all relevant CLEEN technologies will be performed using EDS. Table 3 presents an update on the vehicle system-level modeling effort regarding each of the CLEEN relevant technologies.



Table 3. Update on CLEEN technology modeling.

Modeling Planned: 08/01/23 – 07/31/24					
Modeling Planned: 08/01/22 – 07/31/24					
Contractor	Technology/Model Impact Area	Fuel Burn	NOx	Noise	Percentage Complete
Boeing	Quiet Landing Gear			X	5%
	Quiet High-Lift System			X	5%
	Advanced Inlet	X		X	0%
	Intelligent Operations	X		X	5%
Collins	Large Cell Novel Core Exhaust			X	0%
Delta/MDS/America’s Phenix	Fan Leading Edge Protective Coating	X			10%
GE	MESTANG III	X			5%
	Open Fan	X		X	5%
	Advanced Thermal Management	X			5%
	Hybrid Electric Integrated Generation	X			5%
	Combustor Technology	X	X		5%
	Advanced Acoustics			X	5%
Honeywell	Efficient High Pressure Green Core	X	X		0%
	High Efficiency Fan Module	X		X	0%
	High Work / High Lift Low Pressure Turbine	X		X	0%
	CLEEN II Acoustic Technologies			X	50%
Pratt and Whitney	Fan Noise Technologies			X	5%
	Fan Performance Technologies	X			5%
	Combustor – Swirlers			X	0%
	Combustor – Cooling Technologies	X			0%
	Combustor- Low Pattern Factor	X			0%
	Combustor – NOx Reduction		X		0%
Rolls-Royce	Centrifugal Compressor	X			0%
Safran	Short Inlet			X	0%

Remaining modeling work (scheduled for the next performance period)

- CLEEN II - Remaining Acoustic Technologies
 - Preliminary modeling is underway. Additional modeling results were delivered in October 2023 that will enable modeling of these technologies to be completed.
- CLEEN III - Boeing Quiet High-lift System and Quiet Landing Gear System
 - GT has attended the preliminary design review for this system.
 - System-level modeling effort was kicked off with the contractor in late 2023.
- CLEEN III - Delta/MDS/America’s Phenix fan blade leading edge coating



- System-level modeling effort was kicked off with the contractor in early 2023.
- Preliminary modeling is underway.
- CLEEN III - GE MESTANG III, Advanced Brayton Cycle, and Hybrid Electric Integrated Generation
 - System-level modeling effort was kicked off with the contractor in late 2023.
- CLEEN III - Honeywell Core technologies
 - System-level modeling effort was kicked off with the contractor in late 2023.
- CLEEN III - Pratt and Whitney Fan Module performance and acoustic technologies
 - System-level modeling effort was kicked off with the contractor in mid-2023.
 - Preliminary modeling is underway.

Task 3 - Finalize CLEEN II Analysis

Georgia Institute of Technology

Objective

To evaluate the impact of CLEEN relevant technologies as propagated forward into the U.S. civil fleet of domestic and international departing aircraft. Specifically, the impact of CLEEN technologies on fleet-level noise, fuel burn, and NOx emissions.

Research Approach

Vehicle system-level modeling for all relevant CLEEN II technologies will be performed using EDS. Fleet-benefit assessments for aircraft fleet fuel burn, NOx, and noise through the year 2050 will be performed using the information delivered by the vehicle system-level modeling effort alongside fleet replacement matrices, technology integration scenarios, and projected aviation demand schedules.

CLEEN II Fleet Assumptions

For the fleet-level analysis, the reference year used was the FAA 2015 Inventory, but with local flights (flights to/from the same airport) removed. The domestic flights are then processed through the Fratar algorithm, which serves to differentially scale each airport's flights to the activity levels prescribed in the Terminal Area Forecast (TAF). The flights departing from the United States in the international regions are scaled by the implied increase in flight activity. The sum of the computed fuel for domestic flights plus international departures serves as a comparison anchor point to the total jet fuel sales inside the United States. This includes major airlines, regional carriers, and reporting international carriers.

Final Fuel Burn Assessment

GT and FAA have finalized the fleet-level fuel burn assessment. This update includes the results of an audit of the previously presented study, with the objective of ensuring the traceability of all relevant technology impacts and the repeatability of the fleet-benefit assessment. Technologies included in the fleet-benefit assessments are shown in Table 4. Technology scenarios defined in Table 4, includes both public set and CLEEN technologies. Technology scenarios included in CLEEN are: the Fixed Technology Introduction scenario, (FTI), which does not included any public set or CLEEN technologies, the Evolutionary scenario, (EV), which only includes public set technologies with an EIS plan, the Aggressive with CLEEN II or just the CLEEN I + II scenario, (AG), which includes both CLEEN I and II technologies and public set technologies with and without EIS plans, the Aggressive with CLEEN I or just the CLEEN I scenario, (CI), which includes only CLEEN I technologies and public set technologies with and without EIS plans, the Aggressive without CLEEN scenario, (AG-C), which includes only public set technologies with and without EIS plans and specifically excluded all CLEEN technologies. Technology scenarios are divided into N+1 and N+2 generations, technologies scenarios introduced in the N+2 generation are designated with a 2. For example, EV2 is the N+2 generation of the Evolutionary technology set. Some CLEEN technologies are included in the EV scenario because there is a comparable public set technology to a CLEEN technology, however, without additional CLEEN funding the EV equivalent might be delayed compared to the CLEEN scenario. The fuel burn assessment only includes domestic U.S. flights and U.S. departures, which may represent lower growth rates than a more global analysis. The applied fleet analysis definition and underlying assumptions have remained consistent throughout the CLEEN program. To validate the fleet-level analysis, GT compared the predicted 2015 fuel burn for the baseline case, which was predicted to be 19.91 billion gallons, to the total jet fuel and aviation gasoline fuel consumption reported by the FAA for both passenger and cargo carriers in 2015, which was reported to be 19.37 billion gallons (FAA, 2023). There is a ~2.8% difference between GT's 2015 predicted value and the FAA's 2015 reported value.



Table 4. Technology package definition.

	CLEEN I Funded Technology		Packages							
	CLEEN II Funded Technology		EV	EV2	AG	AG2	CI	C12	AG-C	AG2-C
1 Boeing CMC Exhaust Core Nozzle				EV2	AG	AG2	CI	C12		
2 Boeing Adaptive Trailing Edge				EV2	AG	AG2	CI	C12		
3 Honeywell Cooling				EV2	AG	AG2	CI	C12		
4 Rolls-Royce Cooling				EV2	AG	AG2	CI	C12		
5 TAPS II			EV	EV2			CI	C12		AG2-C
6 Advanced GF Cycle			EV	EV2	AG	AG2	CI	C12	AG-C	AG2-C
7 GE FMS-Engine										
8 GE FMS Air Traffic Management										
9 Open Rotor										
10 Aurora Double Bubble						AG2				
11 Boeing SEW					AG	AG2				
12 Boeing Compact Nacelle				EV2	AG	AG2				
13 Boeing Compact Nacelle Acoustic Treatment				EV2	AG	AG2				
14 Delta/MDS/America's Phenix Leading Edge Protective Coating			EV	EV2	AG	AG2				
15 TAPS III Low NOx Combustor				EV2	AG	AG2				
16 GE MESTANG					AG	AG2				
17 GE FMS					AG	AG2				
18 Honeywell Compact Combustor					AG	AG2				
19 Honeywell Turbine Blade Outer Air Seal					AG	AG2				
20 Pratt & Whitney Compressor and Turbine Aero-Efficiency Technologies					AG	AG2				
21 Collins Slim Nacelle					AG	AG2				
22 Collins Noise Liner Technologies					AG	AG2				
23 Rolls-Royce Advanced ROL Low NOx Combustor					AG	AG2				
24 Aft Cowl Liners			EV	EV2	AG	AG2	CI	C12	AG-C	AG2-C
25 Integrally Bladed Disk (Blisk)			EV	EV2	AG	AG2	CI	C12	AG-C	AG2-C
26 Combustor Noise Plug Liner			EV	EV2	AG	AG2	CI	C12	AG-C	AG2-C
27 Composite Technologies (2010 Baseline)			EV	EV2	AG	AG2	CI	C12	AG-C	AG2-C
28 Excrescence Reduction			EV	EV2	AG	AG2	CI	C12	AG-C	AG2-C
29 Fixed Geometry Core Chevrons			EV	EV2	AG	AG2	CI	C12	AG-C	AG2-C
30 Polymer Matrix Composites (PMC) - Fan Blade with Metal Leading Edge			EV	EV2	AG	AG2	CI	C12	AG-C	AG2-C
31 Polymer Matrix Composites (PMC) - Bypass Duct			EV	EV2	AG	AG2	CI	C12	AG-C	AG2-C
32 Polymer Matrix Composites (PMC) - Fan Case			EV	EV2	AG	AG2	CI	C12	AG-C	AG2-C
33 Polymer Matrix Composites (PMC) - Fan Stator			EV	EV2	AG	AG2	CI	C12	AG-C	AG2-C
34 Polymer Matrix Composites (PMC) - Nacelles			EV	EV2	AG	AG2	CI	C12	AG-C	AG2-C
35 Ti-Al - LPT Aft Blades			EV	EV2	AG	AG2	CI	C12	AG-C	AG2-C
36 Ti-Al - LPT Vane			EV							
37 Ti-Al - LPT Forward Blades				EV2	AG				AG-C	
38 Variable Area Nozzle			EV	EV2	AG	AG2	CI	C12	AG-C	AG2-C
39 Zero Splice Inlet			EV	EV2	AG	AG2	CI	C12	AG-C	AG2-C
40 Winglet			EV	EV2	AG	AG2	CI	C12	AG-C	AG2-C
41 Advanced TBC Coatings - HPT Vane			EV							
42 Advanced TBC Coatings - LPT Vane			EV							
43 Advanced TBC Coatings - HPT Blade				EV2	AG		CI		AG-C	
44 Advanced TBC Coatings - LPT Blade				EV2	AG		CI		AG-C	
45 Low Interference Nacelle			EV	EV2	AG	AG2	CI	C12	AG-C	AG2-C
46 Natural Laminar Flow - Nacelle			EV	EV2	AG	AG2	CI	C12	AG-C	AG2-C
47 Advanced Powder Metallurgy Disk - HPC Last Stage Disc				EV2	AG	AG2	CI	C12	AG-C	AG2-C
48 Advanced Turbine Superalloys - HPT						AG2		C12		AG2-C
49 Advanced Turbine Superalloys - LPT						AG2		C12		AG2-C
50 Active Flow Control For Aircraft Tail				EV2	AG	AG2	CI	C12	AG-C	AG2-C
51 Continuous Moldline Link for Flaps				EV2	AG	AG2	CI	C12	AG-C	AG2-C
52 Damage Arresting stitched composites- Fuselage				EV2	AG	AG2	CI	C12	AG-C	AG2-C
53 Damage Arresting stitched composites- Wing				EV2	AG	AG2	CI	C12	AG-C	AG2-C
54 Landing Gear Integration - Main				EV2	AG	AG2	CI	C12	AG-C	AG2-C
55 Landing Gear Integration - Nose				EV2	AG	AG2	CI	C12	AG-C	AG2-C
56 CMC Combustor Liner				EV2	AG	AG2	CI	C12	AG-C	AG2-C
57 CMC HPT Vane + Hi Temp Erosion Coating				EV2		AG2		C12		AG2-C
58 CMC LPT Vane + Hi Temp Erosion Coating				EV2	AG	AG2	CI	C12	AG-C	AG2-C
59 Soft Vane				EV2	AG		CI		AG-C	
60 Short Nacelle Lip Liner				EV2	AG	AG2	CI	C12	AG-C	AG2-C
61 Highly Loaded Compressor						AG1		C12		AG2-C
62 Over the Rotor Acoustic Treatment						AG2		C12		AG2-C
63 DRE for HLFC - Wing						AG2		C12		AG2-C
64 Compound Rotor Sweep for UHB Fan						AG2		C12		AG2-C
65 Riblets Structures - Fuselage						AG2		C12		AG2-C
66 Riblets Structures - Wing						AG2		C12		AG2-C
67 Active Turbine Clearance Control						AG2		C12		AG2-C
68 Active Turbine Flow Control						AG2		C12		AG2-C
69 Cooled Cooling - Turbine						AG2		C12		AG2-C
70 Out-of-Autoclave Composite Fabrication - Fuselage						AG2		C12		AG2-C
71 Out-of-Autoclave Composite Fabrication - Wing						AG2		C12		AG2-C
72 Thrust Reversers - Nacelles						AG2		C12		AG2-C
73 Active Compressor Clearance Control						AG2		C12		AG2-C
74 Improved Primary Structure Joining Methodologies - Fuselage						AG2		C12		AG2-C
75 Improved Primary Structure Joining Methodologies - Wing						AG2		C12		AG2-C
76 Active Film Cooling						AG2		C12		AG2-C
77 Highly Loaded HP Turbine						AG2		C12		AG2-C
78 Slat Inner Surface Acoustic Liner						AG2		C12		AG2-C
79 Noise Cancelling Stator (GTF)						AG2		C12		AG2-C
80 Gust Load Alleviation						AG2		C12		AG2-C

The final fleet fuel burn result for the estimated annual cost savings attributed to CLEEN I and CLEEN II, relative to the evolutionary scenario, is shown in Figure 1. Here, it can be seen that CLEEN I and CLEEN II contribute a potential annual savings of \$1.10 billion and \$4.21 billion in 2050, with a combined potential impact of \$5.31 billion. This assumes a cost of fuel at \$2/gallon and includes all carriers (domestic and foreign flag) flying domestic routes within the United States and international departures from the United States. Results for the estimated cumulative fuel burn savings attributed to CLEEN I and CLEEN II, relative to the evolutionary scenario, are shown in Figure 2. It can be seen that CLEEN I and CLEEN II contribute potential cumulative savings of 11.5 and 39.6 billion gallons by 2050, with a combined potential impact of 51.1 billion gallons. This combined cumulative potential impact of 51.1 billion equates to approximately 500 Mt less CO₂ emitted over the same period, which is equivalent to removing about 3.6 million cars from the road. Figures 3 and 4 shows these same benefits when only domestic carriers flying domestic routes within the United States and international departures from the United States are considered. Here, it can be seen that CLEEN I and CLEEN II contribute a potential annual savings of \$0.90 and \$3.56 billion in 2050, with a combined potential impact of \$4.46 billion for domestic carriers. Additionally, it is shown that CLEEN I and CLEEN II contribute potential cumulative savings of 9.7 and 33.3 billion gallons by 2050, with a combined potential impact of 43.0 billion gallons for domestic carriers. This combined cumulative potential impact of 43.0 billion equates to approximately 421 Mt less CO₂ emitted over the same period, which is equivalent to removing about 3.0 million cars from the road.

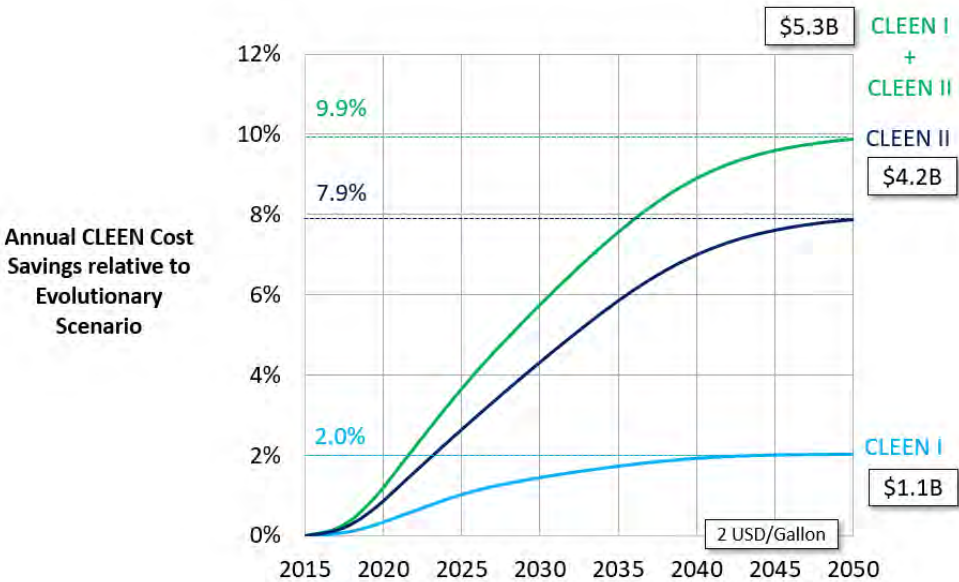


Figure 1. CLEEN technology annual cost savings from U.S. commercial and foreign flag carriers.

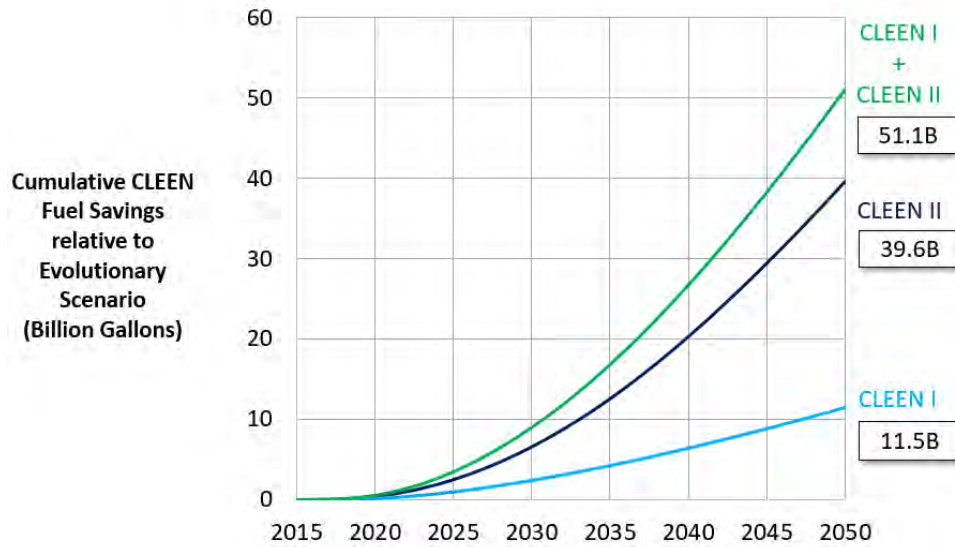


Figure 2. CLEEN technology cumulative fuel savings from U.S. commercial and foreign flag carriers.

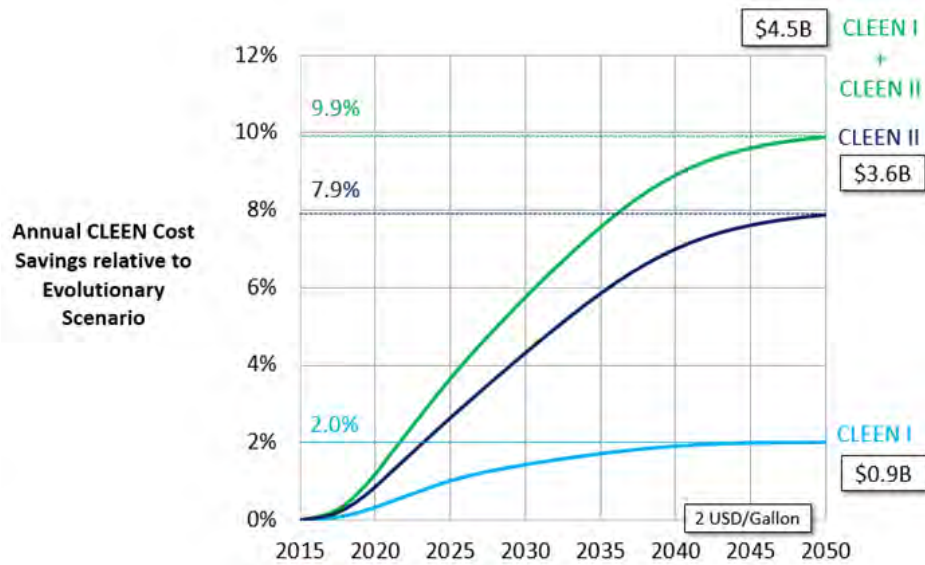


Figure 3. CLEEN technology annual cost savings from U.S. carriers only.

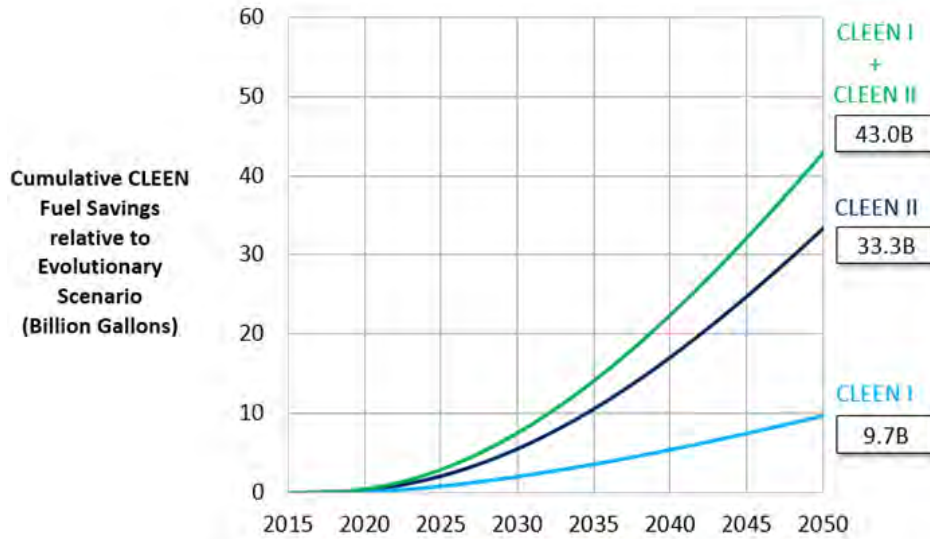


Figure 4. CLEEN technology cumulative fuel savings from U.S. carriers only.

Final fleet NOx emissions assessment

Fleet-level NOx emissions results were generated using Global and Regional Environmental Aviation Tradeoff, (GREAT), in combination with the technology assumptions shown in Table 4, with the same replacement assumptions applied in the fuel burn assessment. The baseline combustors used in this work are the GE SAC combustor used in the CFM56-7B engine and the TAPS I combustor. AG-C includes advanced combustors in the N+2 cases as an advanced combustor would need to be developed to meet projected emissions regulations.

Table 5. Combustor technology package definition.

GE TAPS I
GE TAPS II
GE TAPS III
GE SAC for CFM56-7B
Honeywell Compact Combustor
Rolls-Royce RQL Combustor

	RJ	SA	STA	LTA	VLA
EV - ADD	TAPS II	TAPS II	TAPS I	TAPS I	TAPS I
EV - GTF	TAPS II	TAPS II	TAPS I	TAPS I	TAPS I
EV2 - ADD	TAPS II	TAPS II	TAPS III	TAPS III	TAPS III
EV2 - GTF	TAPS II	TAPS II	TAPS III	TAPS III	TAPS III
AG-ADD	HW	HW	TAPS III	TAPS III	TAPS III
AG-GTF	RR	RR	TAPS III	TAPS III	TAPS III
AG2-ADD	HW	HW	TAPS III	TAPS III	TAPS III
AG2-GTF	RR	RR	TAPS III	TAPS III	TAPS III
AG2-C-ADD	TAPS II	TAPS II	TAPS I	TAPS I	TAPS I
AG2-C-GTF	TAPS II	TAPS II	TAPS I	TAPS I	TAPS I
AG-C-ADD	SAC	SAC	TAPS I	TAPS I	TAPS I
AG-C-GTF	SAC	SAC	TAPS I	TAPS I	TAPS I
CI-AG-ADD	TAPS II	TAPS II	TAPS I	TAPS I	TAPS I
CI-AG-GTF	TAPS II	TAPS II	TAPS I	TAPS I	TAPS I
CI-AG2-ADD	TAPS II	TAPS II	TAPS I	TAPS I	TAPS I
CI-AG2-GTF	TAPS II	TAPS II	TAPS I	TAPS I	TAPS I

Each of the combustors in Table 5 includes a P3T3 correlation, either constructed from public data or provided directly from its contractor, which relates the emission index of nitrous oxide (EI NO_x) (g/kg fuel) to the thermodynamic state of the air entering the burner. During a single vehicle analysis, the total NO_x emissions in the LTO cycle are calculated using Equation 1, where \dot{m}_{fuel} is the fuel flow rate (lbm/min), and $t_{segment}$ is the segment duration (min).

$$m_{NOx} = \sum_{LTO\ segments} EI\ NOx * \dot{m}_{fuel} * t_{segment} \quad (1)$$

Equation 1 considers NO_x production across all four segments of the LTO cycle. The segment names, durations, and percent maximum engine thrust setting for the LTO cycle are included in Table 6.

Table 6. Landing and take-off cycle definition.

Segment	Time (min)	Thrust (% Max)
Take-off	0.7	100
Climb	2.2	85
Approach	4	30
Taxi	26	7

The total NO_x is articulated as Dp/F_{oo} (g/kN) using Equation 2, where F_{oo} is the sea-level static uninstalled thrust.

$$Dp/F_{oo} = \frac{m_{NOx}}{F_{oo}} \quad (2)$$

Finally, the vehicle LTO NO_x emissions is found using Equation 3, where $n_{engines}$ is the number of engines on the vehicle. All vehicles use two engines with the exception of the “very large aircraft” (VLA), which uses four engines.

$$m_{NOxLTO} = \left(Dp/F_{oo} \right) * F_{oo} * n_{engines} \quad (3)$$

The amount of LTO NO_x emitted does not vary with the mission distance of the vehicle as the cycle is tied to specific uninstalled engine operation performance. Therefore, LTO NO_x emissions are considered by GREAT as a function of the number of operations, not the specific operating distances accomplished by each vehicle. The NO_x fleet assessment maintained the same set of assumptions as the fuel burn analysis, including identical fleet replacement matrices, demand forecast, technology integration scenarios, and scope (U.S. domestic + international departures) and includes all carriers, (domestic and foreign flag). Again, the impact of CLEEN I + II technologies was evaluated by examining the difference between the AG scenario and the AG-C scenario. This result for the estimated annual LTO NO_x savings attributed to CLEEN I and II, relative to the evolutionary scenario, is shown in Figure 5. Here, it can be seen that CLEEN I and CLEEN II potentially contribute an annual impact of 71.1 thousand metric tonnes (kt) and 91.5 kt of LTO NO_x potential savings in the year 2050, respectively, with a combined potential impact of 162.6 kt of LTO NO_x savings. The result for the estimated cumulative LTO NO_x savings attributed to CLEEN I and CLEEN II, relative to the evolutionary scenario, is shown in Figure 6. CLEEN I and CLEEN II potentially contribute cumulative savings of 1.29 and 1.50 million metric tonnes (Mt) of LTO NO_x emissions in the year 2050, respectively. The potential cumulative impact of both phases of the CLEEN program technologies is estimated at 2.79 Mt of LTO NO_x by 2050, compared to the evolutionary scenario.

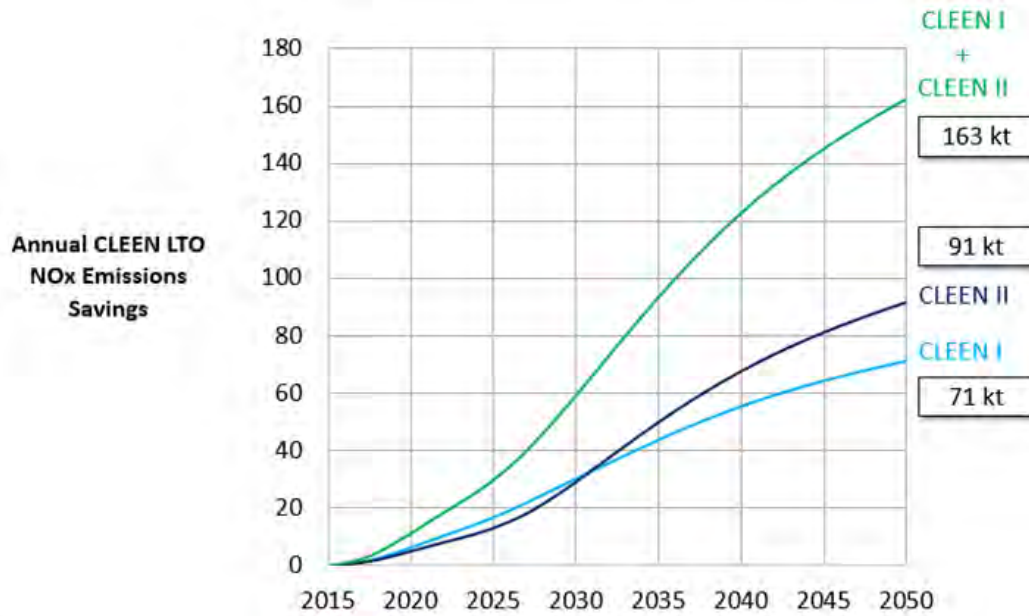


Figure 5. CLEEN technology annual NOx savings.

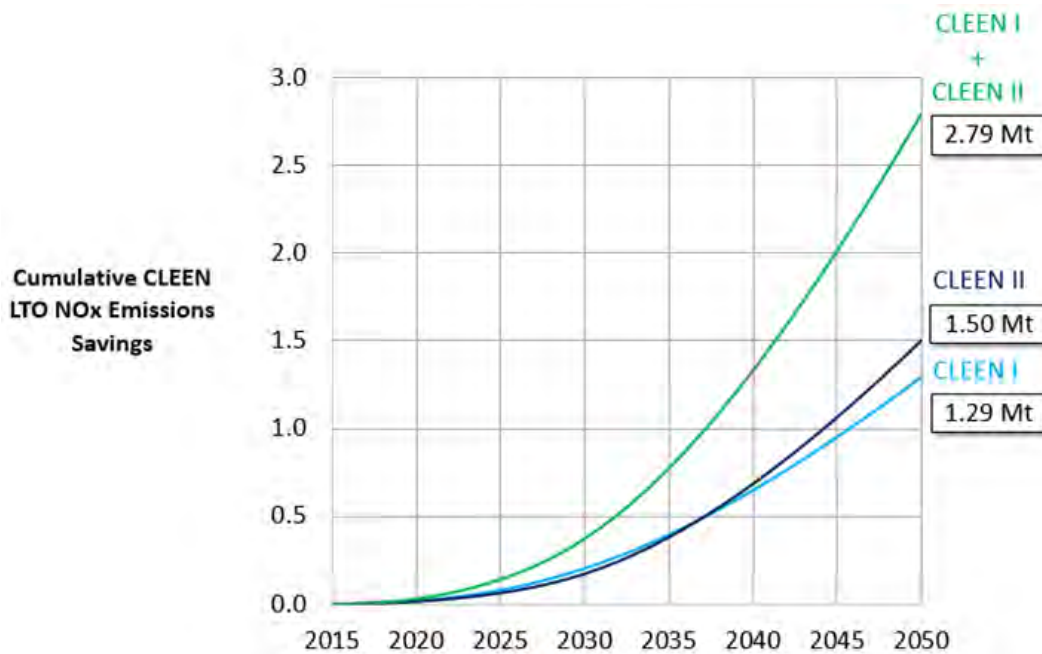


Figure 6. CLEEN technology cumulative landing and take-off (LTO) NOx savings.

Preliminary fleet-noise assessment

Fleet-level noise emissions results were generated using GREAT in combination with the technology liner assumptions shown in Table 7, the remaining acoustic technology assumptions shown in Table 4, and with the replacement assumptions defined in the fleet fuel burn and emissions studies. The Fan Noise Treatment Module (TREAT) liners serve as

baseline technology cases and are evaluated as stock production liners using the Aircraft Noise Prediction Program's (ANOPP's) uncorrected TREAT module.

Table 7. Noise liner technology package definition.

Boeing Compact Nacelle Acoustics
Collins Advanced Acoustics
Honeywell Advanced Acoustics
TREAT - ANOPP Stock Liner

	RJ	SA	STA	LTA	VLA
EV - ADD	TREAT	TREAT	TREAT	TREAT	TREAT
EV - GTF	TREAT	TREAT	TREAT	TREAT	TREAT
EV2 - ADD	TREAT	Boeing	Boeing	Boeing	Boeing
EV2 - GTF	TREAT	Boeing	Boeing	Boeing	Boeing
AG-ADD	HW	Boeing	Boeing	Boeing	Boeing
AG-GTF	Collins	Boeing	Boeing	Boeing	Boeing
AG2-ADD	HW	Boeing	Boeing	Boeing	Boeing
AG2-GTF	Collins	Boeing	Boeing	Boeing	Boeing
AG2-C-ADD	TREAT	TREAT	TREAT	TREAT	TREAT
AG2-C-GTF	TREAT	TREAT	TREAT	TREAT	TREAT
AG-C-ADD	TREAT	TREAT	TREAT	TREAT	TREAT
AG-C-GTF	TREAT	TREAT	TREAT	TREAT	TREAT
CI-AG-ADD	TREAT	TREAT	TREAT	TREAT	TREAT
CI-AG-GTF	TREAT	TREAT	TREAT	TREAT	TREAT
CI-AG2-ADD	TREAT	TREAT	TREAT	TREAT	TREAT
CI-AG2-GTF	TREAT	TREAT	TREAT	TREAT	TREAT

During the vehicle analysis, generic noise contours were generated for each vehicle class and technology integration scenario. In each case, the average 65 DNL (day night level) exposure area was calculated for each analysis year. Output noise results were generated for analysis years set at every 5 years between 2020 and 2050. The noise fleet assessment maintained the same set of assumptions as the fuel burn analysis, including identical fleet replacement matrices, demand forecast, technology integration scenarios, and scope: U.S. domestic + international departures and all carriers: domestic and foreign flag. An example resultant noise contour is shown in Figure 7. This notional contour shows how the 65 DNL exposure area changes across each of the technology integration scenarios across vehicles.

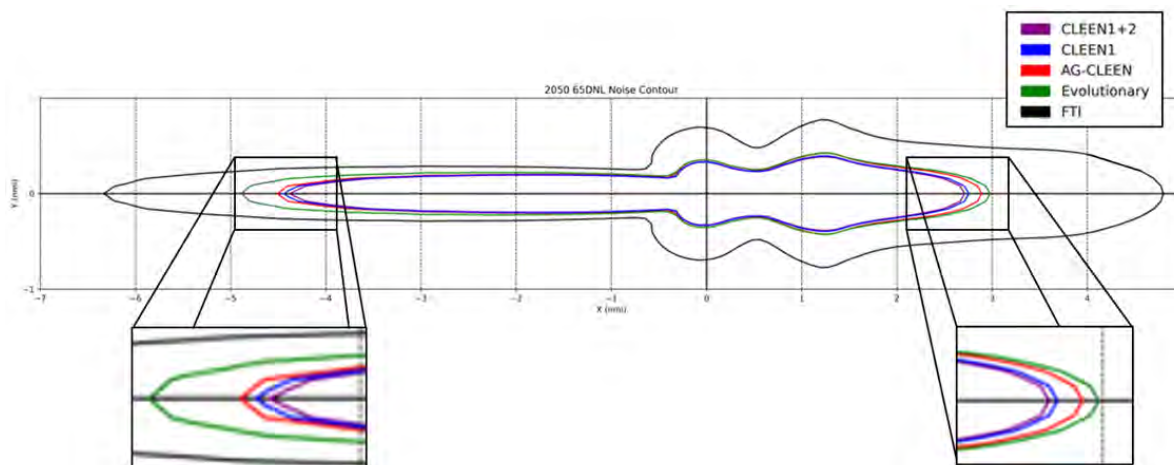
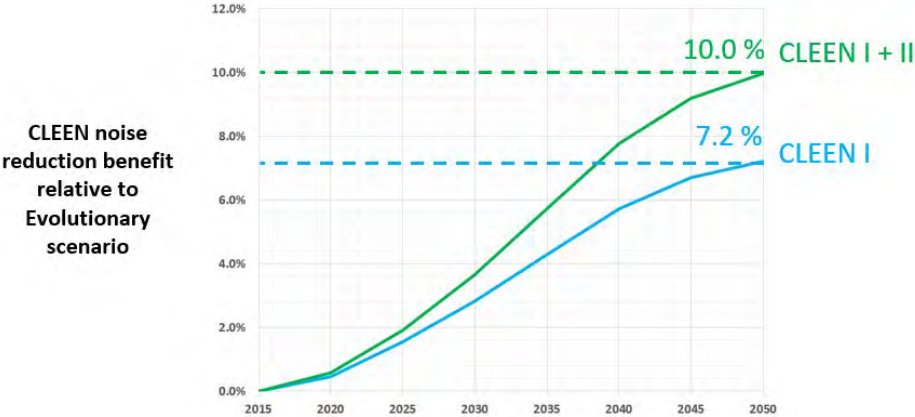


Figure 7. Notional airport 2050 65 day night level (DNL) noise contour.

In order to isolate the impact of CLEEN I and CLEEN I + II technology sets, the difference between the AG-C (red) line and the CLEEN I (blue) line and CLEEN I + II scenario (purple) line, respectively, may be calculated. Further, the impact of CLEEN II may be estimated by subtracting the impact of CLEEN I from the impact of CLEEN I + II. The fleet noise assessment computes 65 DNL noise exposure areas across 95 U.S. airports and averages these to articulate fleet benefits. The result for the estimated average annual 65 DNL exposure area reduction attributed to CLEEN I and CLEEN II, relative to the evolutionary scenario, is shown in Figure 8. Here, CLEEN I and the cumulative impact of CLEEN I + II potentially contribute an annual noise reduction benefit of 7.2% and 10% in 2050, respectively, compared to the evolutionary scenario. This suggests that CLEEN I + II technologies enable increased operations of 10%, with minimal impact to the noise exposure that would be expected in the evolutionary scenario in 2050.

PRELIMINARY



Note: Not all technologies are modeled/included at this time.

Figure 8. CLEEN technology annual 65 day night level (DNL) exposure area reduction relative to the evolutionary case.

The final fleet-level noise benefit assessment of CLEEN phase II is underway. Detailed test data for the remaining acoustic technologies were delivered to GT in October 2023. Results are expected to be complete by early 2024.

Publications

None.

Outreach Efforts

The Georgia Tech attended the spring and fall CLEEN consortium in 2023. A day of each spring consortium was dedicated to university outreach, which included the opportunity for students to present their contributions to the ascent program. Additionally in the spring 2023 consortium, Dr. Brooks participated in an academia/industry panel discussing the impact of the CLEEN program to a combined academia and industry audience.

Awards

None.

Student Involvement

Twelve graduate students received funding from this effort in 2023. Two of the graduate students are PhD track students, Joao De Azevedo and Kayley Lewis, and the other ten, Madelyn Focaracci, Sebastian Seubert, Krutik Desai, Mitchell Mu, Martina Tehubijuluw, Justin Purser, Todd Goehmann, Tabitha D’Amato, Dante Cyrus, George Blackwell, James Tsangarides, and Ballard Huey, are Masters degree track students



Plans for Next Period

Future work will focus on completing technology modeling and the fleet noise assessment with the remaining technologies. Data for the last remaining CLEEN II acoustic technologies were received in October 2023. GT plans to close out CLEEN II by the first quarter of 2024. The next period will include the continued transition of efforts toward the incoming CLEEN III initiative.

This transition includes the implementation of the updated fleet assessment assumptions regarding the exercised demand forecast, replacement matrix, technology integration scenarios, and baseline vehicles. GT plans to complete calibration of updated baseline vehicles by December 2023. For each baseline vehicle, GT is calibrating an engine model, the vehicle airframe, and the vehicle's acoustics. In parallel, the GT team will be working with contractors to kick off our technology modeling process. These kickoffs entail meeting with each contractor to present to them the GT fleet-level modeling and how we incorporate their technologies into it while protecting their proprietary data. In these meetings, GT will work to further our understanding of contractor technologies and will clarify the technologies' impacts and implementation. GT will make a request to each contractor regarding the data required to model the technologies. These kickoffs assist in allowing a quicker technology modeling timeline once data are available.

This work will also support attendance at CLEEN consortium meetings and contractor preliminary and detailed design reviews to identify any updates required to the technology models developed in prior years.

References

DuBois, D., & Paynter, G. (2006). "Fuel Flow Method2" for Estimating Aircraft Emissions. *SAE Technical Papers*. 10.4271/2006-01-1987.

Federal Aviation Administration. 2023 U.S. Commercial & Foreign Flag Carriers (Table 23). <https://www.faa.gov/dataresearch/aviation/us-commercial-foreign-flag-carriers-tables-5-2-3>

ICAO. ICAO Aircraft Emissions Databank. [2021-07-01]. <https://www.easa.europa.eu/en/domains/environment/icao-aircraft-engine-emissions-databank>



Project 038 Rotorcraft Noise Abatement Procedure Development

**The Pennsylvania State University
Continuum Dynamics, Inc.**

Project Lead Investigator

Kenneth S. Brentner
Professor of Aerospace Engineering
Department of Aerospace Engineering
The Pennsylvania State University
233 Hammond Building
University Park, PA
814-865-6433
ksbrentner@psu.edu

University Participants

The Pennsylvania State University (Penn State)

- P.I.: Kenneth S. Brentner, Professor of Aerospace Engineering
- FAA Award Number: 13-C_AJFE-PSU-038, Amendment No. 95
- Period of Performance: October 1, 2022 to September 30, 2023
- Tasks (during this period):
 1. Study and resolve deficiencies in noise prediction of 2017 and 2019 flight test data
 2. Development of shrouded rotor noise modeling
 3. Update flight simulator (to PSUDEPSim) and enhance coupling
 4. Refine analysis of helicopter noise abatement flight procedures
 5. Demonstrate the PSU noise prediction system (PSU-NPS) at Volpe and FAA Technical Center

Project Funding Level

This project received FAA funding of \$150,000; Continuum Dynamics, Inc. (point of contact: Dan Wachspres) will provide \$150,000 of cost sharing in the form of a 1-year license for the Comprehensive Hierarchical Aeromechanics Rotorcraft Model (CHARM) rotorcraft comprehensive analysis software to Penn State and the FAA or their designee. Penn State will provide \$20,000 in academic year salary for the principal investigator.

Investigation Team

The Pennsylvania State University

Kenneth S. Brentner (P.I.; acoustic prediction lead), All Tasks
Joseph F. Horn (co-P.I.; flight simulation lead), All Tasks
Sagar Peddanarappagari (graduate research assistant), developing new CHARM models, performing acoustic predictions, DEPSim models, and documentation for existing noise prediction system

Continuum Dynamics, Inc. (CDI)

Daniel A. Wachspres (co-P.I.), rotor loads, wake integration, and CHARM coupling
Mrunali Botre (co-P.I.), support for rotor loads, wake integration, and CHARM coupling

Project Overview

Rotorcraft noise consists of several components, including rotor noise, engine noise, and gearbox and transmission noise. Rotor noise is typically the dominant component of rotorcraft noise to which the community is exposed upon takeoff and



landing and along the flight path of the helicopter. Rotor noise arises from multiple noise sources, including thickness noise and loading noise (the combination of these is known as rotational noise), blade-vortex-interaction noise, high-speed-impulsive noise, and broadband noise. Each noise source has its own unique directivity pattern around the helicopter. Furthermore, aerodynamic interactions among rotors, interactions between the airframe wake and a rotor, and unsteady time-dependent loading generated during maneuvers typically substantially increase loading noise. The combination of all potential rotor noise sources makes the prediction of rotorcraft noise highly complex, although not all noise sources are present at any given time in the flight (e.g., blade-vortex-interaction noise usually occurs during descent, and high-speed-impulsive noise occurs only during high-speed forward flight).

In ASCENT Project 6, “Rotorcraft Noise Abatement Operating Conditions Modeling,” the project team coupled a MATLAB-based flight simulation code with CHARM and PSU-WOPWOP to perform rotorcraft noise prediction. The PSU-NPS was used to develop noise abatement procedures through computational and analytical modeling. Although the PSU-NPS cannot predict engine noise or high-speed-impulsive noise, it was thoroughly validated via a comparison between predicted noise levels for a Bell 430 aircraft and flight test data (Snider et al., AHS Forum, 2013) for several observer positions and operating conditions.

In previous work for ASCENT Project 38, representative helicopters were recommended for noise abatement procedure development. These helicopters were selected to enable determination of whether noise abatement procedures could be developed for various categories of helicopters (two-blade light, four-blade light, two-blade medium, etc.) or whether aircraft-specific design considerations would be required. Aircraft models were established for the following aircraft: Bell 430, Sikorsky S-76C+ and S-76D, Bell 407 and 206L, Airbus EC130 and AS350, and Robinson R66 and R44. Predictions were made before the 2017 FAA/NASA noise abatement flight test to provide guidance for the flight test. After the flight test, a comparison of A-weighted sound pressure level time histories and sound exposure level contour plots revealed a problem in the broadband noise prediction, which was subsequently corrected. Initial validation comparisons demonstrated that the simulations were within several A-weighted decibels (dBA) of the flight test data; however, some discrepancies in the simulations (simplifications) remained, thus requiring a detailed examination. Work was also performed on the PSU-NPS, including modifying PSU-WOPWOP to output plots of the maximum dBA, as plotted in the flight test. Further work was conducted to enhance the postprocessing of noise data to enable a direct comparison with flight test data. Detailed analysis of the noise components and noise sources was performed for several helicopters in the 2017 FAA/NASA flight test. Further enhancements were added to compute moving averages and devise strategies for window overlapping in the post processing of predicted noise data. In the cases studied, de-Dopplerization (used in flight test data processing) and moving observers (used in noise predictions to eliminate Doppler effects) were demonstrated to be effectively equivalent (typically within 0.5 dB or less). Next, a comparison of the effectiveness of noise abatement procedures by helicopter class was performed by using the 2017 and 2019 flight test data. In particular, the Bell 205, 206, and 407 aircraft were compared for various flight conditions in the flight tests. In the predictions, the Pegg broadband noise prediction did not work as well for some aircraft, and a simple scaling of the broadband noise was considered as a potential correction. Unfortunately, no clear relationship for scaling among aircraft was observed. In addition, an analysis of the 2019 FAA/NASA flight test was performed by comparison of prediction and experimental data for 3° and 4.5° descents and left and right turns at different bank angles (25° and 45°, respectively) for two aircraft (Bell 205 and Sikorsky S-76D). Preliminary coupling between the PSU-NPS and Volpe’s Advanced Acoustics Model (AAM) software was implemented.

The objective of this continuing project is to reduce the need for flight testing of each rotorcraft of interest for continued development of low-noise operating procedures. Current guidelines provided to pilots and operators in the Fly Neighborly guide are based on recommendations from manufacturers, but this guidance is not required and often not provided. Other methods for developing noise abatement procedures at the FAA and NASA are empirical, based on previous flight measurements of specific aircraft. The tasks described below will enable analyses of new flight procedures and noise analysis strategies through computations alone. This year’s efforts included further analyses and investigation of the 2017 and 2019 FAA/NASA noise abatement flight tests, development of shrouded rotor noise modeling, updates to the flight simulator and enhancing couplings, and preparation of documentation and training materials to enable the FAA and their partners to use the PSU-NPS.

Task 1 - Study and Resolve Deficiencies in Noise Prediction of 2017 and 2019 Flight Test Data

The Pennsylvania State University

Objective

The objective of this task (Task 8.1 in the 2022–2023 proposal) is to study the areas where the PSU-NPS has not predicted the noise well during validation with the FAA/NASA flight test data. These situations include overprediction of noise as the aircraft approaches, underprediction of peak noise as the aircraft is overhead, and overprediction again as the aircraft is downrange. This study is expected to lead to better noise abatement procedures and perhaps even procedures tailored to helicopter models.

Research Approach

The research approach is to review and update current aircraft models for the PSU-NPS, duplicate previous noise predictions for flight test conditions in the 2017 and 2019 FAA/NASA flight tests and confirm the deficiencies in the new predictions. The source of the deficiencies will be studied and modeling enhancements proposed to address the deficiencies.

Milestones

The milestones for this task include (a) updating and correcting the helicopter models for aircraft from the 2017 and 2019 flight tests; (b) studying flight test noise measurements for similar flight conditions for the same aircraft, and for nominally the same flight conditions for different aircraft; and (c) using the PSU-NPS to identify the primary sources of noise during flight maneuvers.

Major Accomplishments

The PSU-NPS developed in ASCENT Projects 6 and 38 was used, helicopter models were updated to correct some issues that were found with their setup, and flight test prediction cases were rerun. The EC-130 main and tail rotor were modeled in the CHARM standalone code for noise prediction. In this case, the lack of shroud around the tail rotor (i.e., a Fenestron for the EC-130) is a significant source of error, which is addressed in Task 2 this year. The other deficiencies were verified; that is, overprediction of the noise as the aircraft approaches and as it travels downrange (by 2 dB or more), and that broadband noise does not agree throughout the higher frequency range, but only blade self-noise is currently modeled (errors of more than ± 2 dB were observed). Turbulence ingestion noise from either the atmosphere, airframe, or rotor-rotor interaction is postulated as a possible source of the broadband noise prediction error. The acoustic scattering of the broadband noise and its time-dependent nature may also contribute, but this was not studied at this time. (Acoustic scattering of higher frequency noise sources, such as tail rotor and broadband noise, is likely more important than the lower frequency content of a main rotor.) New models to address these problems are being considered in Task 2, ASCENT Project 49, and other non-FAA PSU projects. Furthermore, it was decided that upgrading the flight simulation component of the PSU-NPS (in Task 3) should be done before additional modeling efforts to correct deficiencies are undertaken, so that part of this task was delayed.

Publications

None.

Outreach Efforts

None.

Awards

None.

Student Involvement

Sagar Peddanarappagari, a graduate assistant at Penn State working on his MS degree, updated the helicopter models and performed predictions.

Plans for Next Period

During the next period, several tasks are planned to address the deficiencies observed, including modeling shrouded rotor noise, enhancing broadband noise prediction, and further aircraft model updates and conversion from PSUHeloSim to PSUDEPSim.

Task 2 - Development of Shrouded Rotor Noise Modeling

The Pennsylvania State University

Objective

The objective of this task (Task 8.2 in the 2022–2023 proposal) is to develop a simplified method to calculate the shrouded rotor noise so that the noise can be properly included in aircraft procedure assessment and noise abatement procedure development.

Research Approach

Basic information on how to model the shrouded rotor noise has been developed, but these models will be explored, further developed, and implemented in the PSU-NPS. The primary approach is based on work that CDI has done for rotor-structure interactions (rods and cones) (Botre et al., 2022) and older work modeling the shroud using a panel method. Unsteady pressure is on the shroud due to the passing rotor blades and is then given to PSU-WOWOP to predict the noise generated by the unsteady aerodynamic excitation on the shroud. The Airbus EC130 (2017 FAA/NASA noise abatement flight test) and, to a lesser extent, the Airbus Dauphin (2019 FAA/NASA noise abatement flight test) can be used to evaluate modeling approaches and validate the final model of shrouded rotor noise. Other experiments of isolated shrouded rotors, in anechoic or wind tunnel environments, will also be used to validate the model.

Milestones

Three milestones for this task have been met during the past year: (a) evaluating the approach of Botre et al. (2022) and other modeling methods; (b) predicting the noise from model shrouded rotors and/or the Airbus EC-130 aircraft flown in the 2017 FAA/NASA flight test; and (c) evaluating the prediction approach(es) by comparing with test data.

Major Accomplishments

Two modeling approaches were considered for shrouded rotor noise. First, a low-fidelity shrouded rotor model was developed that used acoustic pressure incident on shroud surface as unsteady loading for acoustic predictions. The goal with this method was to approximately capture the acoustic scattering effect created by the shroud. To assess the accuracy of the approximate acoustic scattering method, the acoustic predictions were compared with experimental data from the Zawodny & Boyd (2017) rotor-airframe interaction noise paper. The experiment consisted of a rotor and a rod placed below the rotor. During the experimental campaign, the rod was stationed at three different distances below the rotor. The comparison in the plot below (Figure 1) shows that the approximate acoustic scattering model's prediction matches experimental data well when the spacing is large, but overpredicts significantly when the rod is 0.1 rotor radii below the rotor – its nearest location.

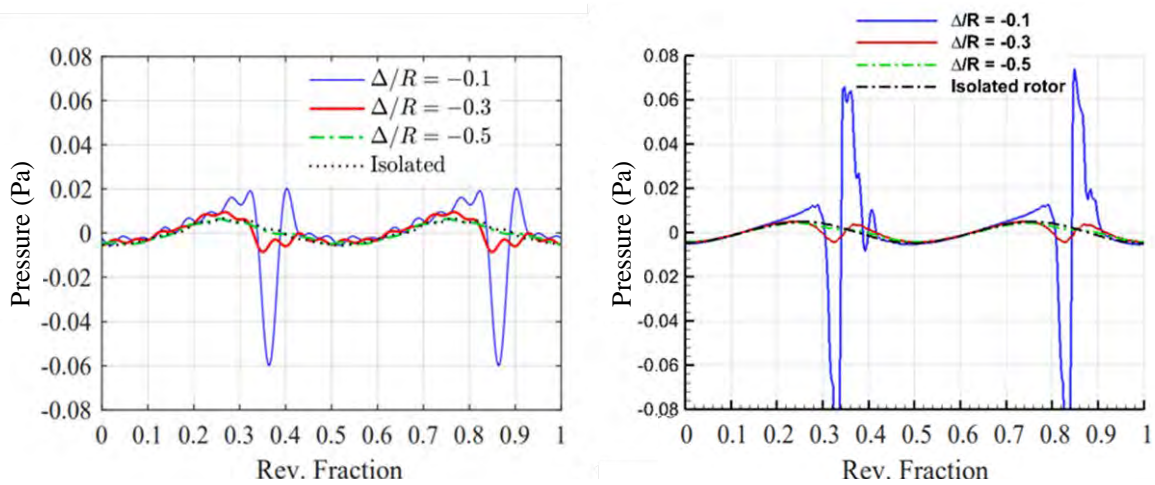


Figure 1. Experimental measurements (left) (Zawodny & Boyd, 2017) and approximate acoustic scattering predictions (right) compared. Δ/R is the nondimensional distance the rod was placed below the rotor.

To understand this model better, the focus of analysis was switched to a simpler scattering problem: acoustic scattering of an omni-directional source by a spherical surface. The results from the approximate acoustic scattering prediction were compared with NASA Fast Scattering Code (FSC) predictions presented by Lee et al. (2009). The comparison between NASA FSC predictions and approximate acoustic scattering predictions agree better on the side of the sphere where the acoustic source is located, and not as well behind the spherical scattering body (see Figure 2).

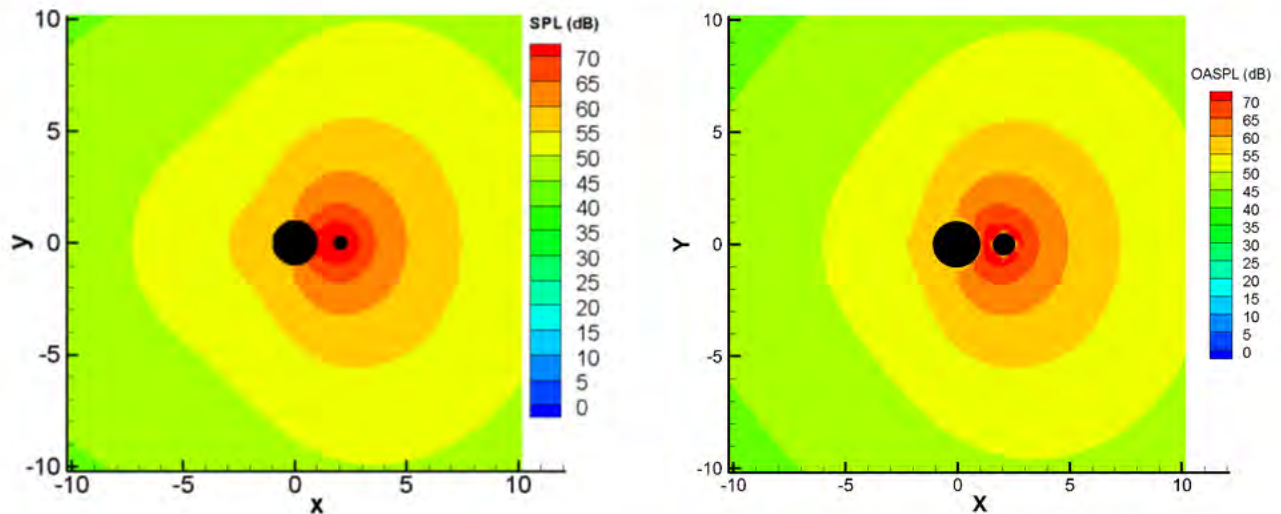


Figure 2. Time-domain acoustic scattering predictions for $ka = 1$ (left) compared with approximate acoustic scattering predictions (right). SPL and OASPL are sound pressure level and overall sound pressure level, respectively. In this single frequency case, they are equivalent.

The second modeling approach was to compute the unsteady aerodynamic pressures on the rotor and the duct with CHARM. The rotor was modeled as a lifting line and the duct was modeled with a panel method to capture the time-dependent, distributed pressures on the surface. Then the noise prediction code PSU-WOPWOP used the unsteady surface

pressures on the duct to compute the noise radiated by the duct and the lifting line loading to compute the noise generated directly by the rotor blades. The noise from the duct and the rotor could be determined separately or together. The noise of the rotor, duct, and acoustic scattering were all compared at several observer locations, with one of the positions shown in Figure 3. In Figure 3, the impact of the duct is dominant over both that of the rotor and the approximate acoustic scattering. The approximate scattering is nearly negligible except for spikes added to the positive peaks in the signal. These spikes are thought to be non-physical errors like the when the rod was in the nearest position in Figure 1. For this reason, and the fact that the approximate acoustic scattering was not robust, we decided to not continue developing that approach at this time.

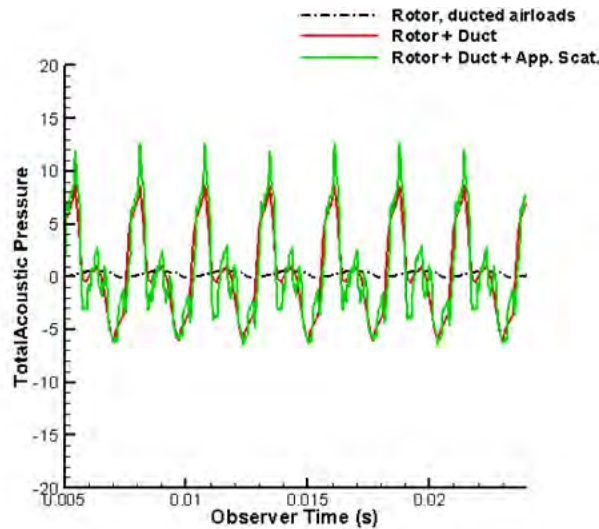


Figure 3. Acoustic pressure predictions for rotor, rotor + duct, and rotor + duct + approximate acoustic scattering for an observer 9.22R from the rotor hub and 2.83° forward of the rotor plane.

The second modeling approach — modeling the duct with the panel method in CHARM and predicting the acoustic pressure generated by the duct and the rotor — was evaluated further for validation with an experiment by Cuppoletti and Riley (2022). In the test, the noise from a 3-bladed rotor mounted in a short duct was measured at multiple locations inside an anechoic chamber. The rotor and duct were stationary in the test, simulating a shrouded rotor in hover (in flight test measurements, it is difficult to achieve steady hover flow in this experiment due to main rotor and atmospheric turbulence). The measured acoustic spectrum of both the unducted rotor and the rotor with the duct are shown in Figure 4. For this example, the unducted rotor prediction (blue line with square symbols on the left plot, Figure 4) underpredicts the measurement (black line) by approximately 4 dB at the first blade passage frequency (BPF) and by 6 dB at the second BPF. Subsequent BPFs are observed to have even larger differences. The higher levels of the blade harmonic noise (i.e., the peaks), especially at frequencies >1 kHz, are thought to be due to recirculation in the anechoic chamber in the test. The ducted rotor predictions are closer (see left panel in Figure 4), and the noise levels are not as impacted by recirculation due to the presence of the duct. The ducted rotor prediction (green line with diamond symbols) for the first BPF overpredicts the measurement (red line) by approximately 1 dB, and the second BPF is underpredicted by about 2 dB. Several of the following BPF predictions are also close to the measurement but some are not. Note that the first few harmonics of the BPF are higher in the ducted rotor case than for the unducted rotor at this microphone location. This is thought to be due to the extra noise generated by the fluctuating airloads on the duct. Even though higher noise levels for the ducted rotor are contrary to what might be expected, it has been observed in flight tests and is measured and predicted here. This is why the ducted rotors in this work have been also called “shrouded” rotors, because the duct is not long enough and does not have enough treatment for noise reduction benefits.

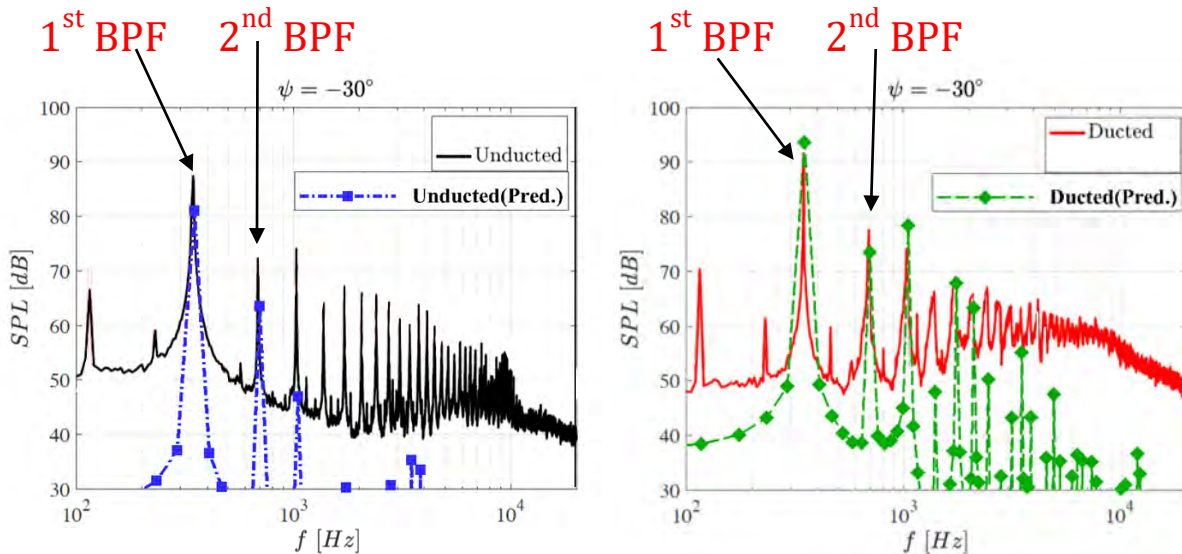


Figure 4. Acoustic spectrum for isolated rotor and ducted rotor (red and black) measurements and predictions are shown. On the left, the unducted rotor experiment (black) and prediction (blue) are compared; on the right is the same comparison for the ducted rotor prediction (experiment: red, prediction: green). BPF, blade passage frequency; SPL, sound pressure level; f , frequency.

Publications

None.

Outreach Efforts

None.

Awards

None.

Student Involvement

Sagar Peddanarappagari, a graduate assistant at Penn State working on his MS degree, set up the cases, performed the acoustic predictions, and analyzed the simulations.

Plans for Next Period

The noise of the Airbus EC130 and the Airbus Dauphin will be studied because these aircraft are equipped with shrouded rotor antitorque devices (Fenestron). These aircraft need to be modeled in the PSUDEPSim flight simulator because there have been some issues with properly modeling the Fenestron and achieving robust trim solutions for these aircraft in PSUHeloSim. The approach developed by CDI (Botre et al., 2022) and used this year should be sufficient when the flow in the duct is attached. An investigation into how compressibility effects (propagation delay) can be included by using the propagation times computed in PSU-WOPWOP is planned. In particular, the goal is to match the main noise directivity trends that are unique to a shrouded rotor.

References

- Botre, M., Wachspress, D., Brentner, K., & Gan, Z. F. T. (2022). Aeroacoustic Prediction and Validation of Variable RPM Rotors and Rotor-Airframe Interactions for Advanced Air Mobility Applications,” Paper presented at 78th Vertical Flight Society Annual Forum and Technology Display, FORUM 2022, Fort Worth, Texas, United States.
- Cuppoletti, D. R., and Riley, T. (2022), “Time-Resolved Flow Field and Acoustic Measurements of a Ducted and Unducted Rotor,” Presented at the 28th AIAA/CEAS Aeroacoustics 2022 Conference, June 14-17, Southampton, UK, <https://doi.org/10.2514/6.2022-2947>.

Lee, S., "Prediction of acoustic scattering in the time domain and its applications to rotorcraft noise," Ph.D. dissertation, The Pennsylvania State University, May 2009.
Zawodny, N. S., and Boyd Jr, D. D. (2017), "Investigation of Rotor-Airframe Interaction Noise Associated with Small-Scale Rotary-Wing Unmanned Aircraft Systems," Presented at the AHS International 73rd Annual Forum, May 9-11.

Task 3 - Update Flight Simulator to PSUDEPSim and Enhance Coupling

The Pennsylvania State University

Objective

The objective of this task (Task 8.3 in the 2022-2023 proposal) is to update the current PSUHeloSim/CHARM/PSU-WOPWOP system to use the newly developed PSUDEPSim flight simulator in place of PSUHeloSim. This integration will help integrate the new modeling advances made in ASCENT 49 and take advantage of the integration with the newer versions of CHARM rotor module (e.g., CHARM rotor module v7).

Research Approach

In this task, PSUDEPSim will be integrated into the PSU-NPS with new work focused on modifying the PSUDEPSim integration for helicopter applications (e.g., engine model instead of electric motor model). Moving forward, there will be a single tool chain for both ASCENT 38 and 49, which will also make it easier for users to learn the PSU-NPS. Coupling between the codes will also be enhanced as needed to streamline and speed up predictions. CDI will perform extensions to the current PSUDEPSim/CHARM couplings to enable helicopter predictions, and Penn State will develop and test couplings for the flight simulation and noise predictions.

Major Accomplishments

DEPSim has been modified at PSU by Dr. Horn's group for use in helicopter simulations (engine model added). CDI has developed and assessed the new coupling for the DEPSim flight simulator and CHARM, but PSU has not been able to implement these changes yet and test with PSU-WOPWOP. An AS350 helicopter model was set up in DEPSim for use in the updated PSU-NPS. Work is underway to create models of other aircraft as well. Models will be validated with flight test data and current (PSUHeloSim based) PSU-NPS simulation results.

Publications

None.

Outreach Efforts

None.

Awards

None.

Student Involvement

Sagar Peddanarappagari, a graduate assistant at Penn State working on his MS degree, learned to use the DEPSim simulator and created a new AS350 aircraft model in the new simulator.

Plans for Next Period

Penn State will work with CDI to evaluate recent updates made to DEPSim/CHARM coupling to validate the acoustic prediction capability. New DEPSim aircraft models will be created from existing HeloSim models and validated with results from old simulations and FAA/NASA flight test data.

Task 4 - Refine Analysis of Helicopter Noise Abatement Flight Procedures

The Pennsylvania State University

Objective

The objective of this task (Task 8.4 in the 2022–2023 proposal) is to evaluate and demonstrate the updated features and enhancements in the PSU-NPS (Tasks 1-3) on the helicopter noise abatement procedures that have been performed previously in the project. This testing will determine the impact of these improvements on previous predictions.

Research Approach

The updated NPS will duplicate the noise predictions from FAA/NASA flight test validations for select aircraft (e.g., Airbus AS350) and flight conditions. Then, the previous predictions along with flight test data will be used to assess the expected improvements that result from the system updates.

Major Accomplishments

Progress was made in setting up the cases to be used in this task, but the work in Tasks 1-3 did not reach the point where the new noise prediction updates were ready to evaluate.

Publications

None.

Outreach Efforts

None.

Awards

None.

Student Involvement

Sagar Peddanarappagari, a graduate assistant at Penn State working on his MS degree, set up the cases in preparation for the new computations.

Plans for Next Period

The updated features and enhancements in the PSU-NPS will be evaluated and demonstrated. The decelerating approach and descending turning cases will be considered for the AS350 and EC130 helicopters and other helicopters if time permits. Assessment of new prediction capabilities for understanding of noise abatement procedures will be performed.

Task 5 - Demonstrate PSU-NPS at Volpe and FAA Technical Center

The Pennsylvania State University

Objective

The objective of this task (Task 8.5 in the 2022–2023 proposal) is to develop documentation and training materials for the PSU-NPS. The PSU-NPS will be demonstrated and transferred to Volpe and the FAA Technical Center.

Research Approach

The PSU-NPS was developed to predict noise for various helicopters performing many different maneuvers through previous work in ASCENT Project 6 and ASCENT Project 38. The system has been validated with 2017 and 2019 FAA/NASA flight test data, but the cases have not been packaged with significant documentation to be easily used for training. In this effort, the cases, including the data files necessary to perform actual runs of the NPS with all the components and correct results files from all the codes, are organized and documented so that new users can learn to run the system and check their results. Individual components of the system have their own documentation, and a document will be drafted to describe how to install the PSUHeloSim/CHARM/PSU-WOPWOP software. Documentation of how to run the system will be developed, along with training materials for independent learning or to serve as reference material for a training course.



Milestones

The key milestones for this period were to (a) complete the first revision of the documentation for the PSU-NPS, including a revision of the documentation for the individual software components; (b) develop sample cases from the cases that have previously been used for validation of the noise prediction system; and (c) develop and deliver the training and training materials.

Major Accomplishments

The existing documentation has been improved and changes to the software have been made to simplify operation of the system. Work has progressed on preparing the sample cases for use in training. These cases will be documented and explained for new users. The result will be compared with flight test data as was done in previous work, but now with current best practices and recommended input parameter values. These results will be the “correct” cases in which individuals learning the tools can compare their own results. A presentation on December 5, 2023, was given to researchers at Volpe and FAA personnel. That presentation highlighted the composition of the PSU-NPS and how well it performed in validation cases in previous ASCENT 38 research.

Publications

None.

Outreach Efforts

None.

Awards

None.

Student Involvement

Sagar Peddanarappagari, a graduate assistant at Penn State working on his MS degree, worked on the documentation and example case creation.

Plans for Next Period

Training documentation and sample case development will be completed and delivered to Volpe, FAA users, and other interested parties. Collaboration is desired to provide feedback for improving the documentation, training materials, and example cases. The task will also help transfer this technology to both the FAA and industrial partners. Documentation will be updated for use with the new PSUDEPSim-based noise prediction system.



Project 044 Aircraft Noise Abatement Procedure Modeling and Validation

Massachusetts Institute of Technology

Project Lead Investigator

R. John Hansman
T. Wilson Professor of Aeronautics & Astronautics
Department of Aeronautics & Astronautics
Massachusetts Institute of Technology
Room 33-303
77 Massachusetts Avenue
Cambridge, MA 02139
617-253-2271
rjhans@mit.edu

University Participants

Massachusetts Institute of Technology (MIT)

- P.I.: Prof. R. John Hansman
- FAA Award Number: 13-C-AJFE-MIT, Amendment Nos. 050, 057, 073, 084, 105, 109, and 115 (to September 30, 2024)
- Period of Performance: September 1, 2018 to September 30, 2024
- Tasks:
 1. Evaluate general approaches to aircraft noise validation
 2. Develop validation approach options
 3. Develop flight test plans
 4. Perform initial experimental runs on targets of opportunity
 5. Evaluate experimental results and implications for advanced operational flight procedure noise modeling and low-noise procedures

University of California, Irvine (UCI; subaward from MIT)

- P.I.: Prof. Jacqueline Huynh
- Award Number: MIT Subaward Purchase Order No. S5171-PO 523807
- Period of Performance: September 1, 2020 to December 31, 2023 (to September 30, 2024 anticipated)
- Tasks:
 1. Evaluate general approaches to aircraft noise validation
 2. Develop validation approach options
 3. Develop flight test plans
 4. Perform initial experimental runs on targets of opportunity
 5. Evaluate experimental results and implications for advanced operational flight procedure noise modeling and low-noise procedures

Project Funding Level

\$845,000 FAA funding and \$845,000 matching funds. Sources of matching funds are approximately \$176,000 from MIT and \$669,000 from Massachusetts Port Authority (Massport).

Investigation Team

Massachusetts Institute of Technology

- Prof. R. John Hansman, (P.I.), Tasks 1-5



- Ayaka Miyamoto, (graduate student), Tasks 1-5
- Sandro Salgueiro, (graduate student), Tasks 1-5
- Ara Mahseredjian, (graduate student), Tasks 1-5
- Clement Li, (graduate student), Tasks 1-5
- Phillip Hood, (undergraduate student), Tasks 1-5

University of California, Irvine

- Prof. Jacqueline Huynh, (co-P.I.), Tasks 1-5
- Trinity Lee, (graduate student), Tasks 1-5
- Melissa Lepe, (graduate student), Tasks 1-5

Project Overview

This project uses empirical noise data to develop validation methods from noise and flight surveillance datasets and to improve existing noise models. Field measurements of aircraft noise on approach and departure have historically shown significant variation (on the order of 10 dB), which has traditionally been attributed to factors such as varied power settings, aircraft configuration differences, and propagation effects. Recent analyses in this and other ASCENT projects have attempted to account for these factors but have been constrained by limited detailed flight data. This project explores approaches to combine emerging sources of flight data from flight data recorders (FDRs) and other sources such as Automatic Dependent Surveillance-Broadcast (ADS-B) with current and emerging networks of ground noise monitors, to validate or improve aircraft noise models and to validate proposed noise abatement procedures. The rise of data-mining techniques has substantially enabled new insights and modeling capabilities based on the use of large datasets without requiring full a priori knowledge of all relevant physics. The development of advanced data-mining approaches applied to noise modeling is expected to provide insight into aircraft noise prediction for refining or validating noise models and for developing strategies for noise mitigation, through either new aircraft technologies or operational changes. Furthermore, improved noise modeling capabilities are expected to enable more informed decision-making for stakeholders considering the options and consequences of operational or technological changes, thus facilitating the minimization of noise impacts on communities. Because noise is becoming an increasingly important factor in operational decisions regarding airports in the National Airspace System, an accurate understanding of noise impacts is necessary to minimize unnecessary disruptions to, or inefficiencies in, National Airspace System operations.

Task 1— Evaluate General Approaches to Aircraft Noise Validation

Massachusetts Institute of Technology
University of California, Irvine

Objectives

The goal of this task is to evaluate the different options for validation of the Aircraft Noise Prediction Program (ANOPP) source component models and to confirm noise reductions from proposed low-noise procedures. Approaches to experimental design were considered, including dedicated engineering flight trials involving parametric sweeps of velocity and aircraft configuration under various power conditions. This process involves collaborating with airline operators, who must be willing to fly trials of procedures, and air traffic control, which must approve the procedures. A ground measurement system must be in place under the departure tracks.

Potential monitoring approaches will also be considered, including distributed microphone arrays or single-microphone installations, as well as potential phased-array microphone configurations. In addition, alternative flight data sources will be obtained, through either airline sources or available surveillance data. Sources of noise data from existing and emerging noise monitoring systems will be identified. Seattle-Tacoma International Airport (SEA) has agreed to provide data, and additional airports will be approached to participate in the effort. Emerging open-source and community noise monitoring systems, such as those being developed under ASCENT Project 53, will also be investigated. Opportunities for collaboration will be explored, with a focus on providing correlated flight data and noise datasets.

This task will use a systems approach and will explore options with potential collaborators regarding experimental opportunities to validate research concepts.

Research Approach

- Evaluate different options for validation of the ANOPP source component models and confirm any noise reductions from proposed procedures
- Identify potential existing data sources for noise validation
- Model aircraft flight profiles by using existing surveillance (e.g., ADS-B or Airport Surface Detection Equipment, Model-X) data to generate noise estimates (readily available surveillance data are easier and less expensive to acquire than FDR data and data from dedicated flight tests)
- Evaluate flight profiles to understand why some procedures are quieter than others

Milestones

- Identified SEA and Boston Logan International Airport (BOS) noise monitor networks as potential sources of noise data for validation
- Identified the OpenSky and Threaded Track surveillance database as a source of flight procedure data for noise validation

Major Accomplishments

- Approach and departure ADS-B and noise monitoring data were collected for 1 year at SEA.
- A framework was developed to generate flight profiles by using raw ADS-B and atmospheric data. Noise monitor recordings were correlated with ADS-B data.
- Flight profiles were generated from raw ADS-B data for various departures and arrivals at SEA. Flight profiles were used to identify factors potentially making a significant contribution to noise measurement variation.
- Quieter flyover cases were analyzed, and trends in aircraft altitude, airspeed, and lateral position were identified.
- Sources of weather data as a function of altitude were identified to make atmospheric absorption corrections for noise modeling validation.

Publications

Published conference proceedings

- Jensen, L., Thomas, J., Brooks, C., Brenner, M., & Hansman, R. J. (2017). *Analytical approach for quantifying noise from advanced operational procedures* [Presentation]. European Air Traffic Management Research and Development Seminar. Seattle, Washington.
- Reynolds, T., Sandberg, M., Thomas, J., & Hansman, R. J. (2016). *Delayed deceleration approach noise assessment* [Presentation]. 16th AIAA Aviation Technology, Integration, and Operations Conference, Washington, DC.
- Salgueiro, S., Thomas, J., Li, C. & Hansman, R. J. (2021). *Operational noise abatement through control of climb profile on departure* [Presentation]. AIAA Scitech 2021 Forum, Washington, DC. <https://doi.org/10.2514/6.2021-0007>.
- Salgueiro, S., Huynh, J., Li, C. & Hansman, R. J. (2022). *Aircraft Takeoff and Landing Weight Estimation from Surveillance Data* [Presentation]. AIAA Scitech 2022 Forum, San Diego, CA. doi: 10.2514/6.2022-1307.
- Thomas, J., Jensen, L., Brooks, C., Brenner, M., & Hansman, R. J. (2017). *Investigation of aircraft approach and departure velocity profiles on community noise* [Presentation]. AIAA Aviation 2017 Forum, Grapevine, TX.
- Thomas, J., Yu, A., Li, C., Maddens Toscano, P., & Hansman, R. J. (2019). *Advanced operational procedure design concepts for noise abatement* [Presentation]. 13th USA/Europe Air Traffic Management Research and Development Seminar, Vienna, Austria.
- Thomas, J., Yu, A., Li, C., Toscano, P., & Hansman, R. J. (2019). *Advanced operational procedure design concepts for noise abatement* [Presentation]. 13th USA/Europe Air Traffic Management Research and Development Seminar, Vienna, Austria.
- Thomas, J., & Hansman, R. J. (2020). *Modeling and assessment of delayed deceleration approaches for community noise reduction* [Presentation]. AIAA Aviation Forum, Dallas, TX.
- Yu, A., & Hansman, R. J. (2019). *Approach for representing the aircraft noise impacts of concentrated flight tracks* [Presentation]. AIAA Aviation Forum 2019, Dallas, TX. doi: [10.2514/6.2019-3186](https://doi.org/10.2514/6.2019-3186)

Written reports

- Jensen, L. & Hansman, R. J. (2018). *Data-driven flight procedure simulation and noise analysis in a large-scale air transportation system* (Report No. ICAT-2018-02). Massachusetts Institute of Technology, Cambridge, MA.
- Jensen, L., O'Neill, G., Thomas, J., Yu, A., & Hansman, R. J. (2018). *Block 1 procedure recommendations for Logan Airport community noise reduction* (Report No. ICAT-2017-08). Massachusetts Institute of Technology, Cambridge, MA.



- Thomas, J., & Hansman, R. J. (2017). *Modeling performance and noise of advanced operational procedures for current and future aircraft* [S. M. thesis, Massachusetts Institute of Technology]. DSpace@MIT. <https://dspace.mit.edu/handle/1721.1/108937>
- Thomas, J., & Hansman, R. J. (2020). *Systems Analysis of Community Noise Impacts of Advanced Flight Procedures for Conventional and Hybrid Electric Aircraft* [Ph.D. thesis, Massachusetts Institute of Technology]. DSpace@MIT. <https://dspace.mit.edu/handle/1721.1/125995>
- Thomas, J., & Hansman, R. J. (2020). *Evaluation of the impact of transport jet aircraft approach and departure speed on community noise* (Report No. ICAT-2020-03). Massachusetts Institute of Technology, Cambridge, MA.
- Yu, A., & Hansman, R. J. (2019). *Aircraft noise modeling of dispersed flight tracks and metrics for assessing impacts* [S. M. thesis, Massachusetts Institute of Technology]. DSpace@MIT. <https://hdl.handle.net/1721.1/122382>
- Mahseredjian, A., Huynh, J., & Hansman, R. J. (2022). *A Data-Driven Approach to Departure and Arrival Noise Abatement Flight Procedure Development* [S. M. thesis, Massachusetts Institute of Technology]. DSpace@MIT. <https://hdl.handle.net/1721.1/144311>

Outreach Efforts

- September 28, 2021: presentation to Stanford
- Collaboration with Port of Seattle to obtain noise data for arrivals and departures over 1 year
- Weekly teleconferences and meetings with FAA Technical Monitors
- Outreach and collaboration with Massport, an operator at BOS, and ASCENT Advisory Board members
- Presentations at the biannual ASCENT Advisory Board meetings

Awards

None

Student Involvement

Graduate and undergraduate students have been involved in all aspects of this research in terms of analysis, documentation, and presentation.

Plans for Next Period

The next phase of this project will continue outreach to other projects using noise monitor data in airport noise validation research.

Task 2 — Develop Validation Approach Options

Massachusetts Institute of Technology
University of California, Irvine

Objectives

Based on the results of Task 1 and discussions with collaborators (measurement experts, model developers, manufacturers, operators, and test locations), one or more validation options will be identified. Targets of opportunity will be explored in which noise measurements may supplement other planned flight trials. For each option, the potential advantages and disadvantages will be identified, and preliminary flight test plans will be developed in coordination with the identified collaborators and in consultation with subject-matter experts such as NASA. Potential advantages include the willingness of operators or collaborators to participate and provide test resources, including aircraft and measurement systems. Other factors include measurement system resolution and the discrimination of noise sources. Timing and location may also be considered. On the basis of this analysis, recommendations for next steps will be made.

Research Approach

- Identify methods to correct variations in modeled noise due to flap setting, aircraft weight, and ambient atmospheric conditions; apply these methods to approaches at BOS and SEA
- Acquire ADS-B data from the OpenSky Network and atmospheric data from the National Oceanic and Atmospheric Administration's High-Resolution Rapid Refresh; use these data to estimate weight from true airspeed and atmospheric attenuation from relative humidity and temperature
- Model noise at various flap configurations to identify the noise impact of high-lift devices



Milestones

- Noise was modeled under various flap configuration settings for several approach procedures.
- A method was developed to relate OpenSky and Threaded Track surveillance operational data to atmospheric data and noise monitor data at particular time stamps.

Major Accomplishments

- Demonstrated the impacts of aircraft configuration and weather on modeled and measured noise over noise monitors of interest at SEA
- Developed a data-driven approach for assessing departure noise as a function of various operational, weather, and carrier factors
- Presented data driven-approach results at the 2022 and 2023 InterNoise conference and in a 2022 Journal of Aircraft manuscript
- Demonstrated the noise benefit of delayed-deceleration approaches using empirical data; analyzed flyovers of various monitors at BOS and SEA; demonstrated a correlation between the fastest flyovers, flying at indicated airspeeds consistent with clean or almost-clean flap configurations, and the quietest noise monitor recordings

Publications

Peer-reviewed journal publications

Thomas, J., & Hansman, R. J. (2019). Framework for analyzing aircraft community noise impacts of advanced operational flight procedures. *Journal of Aircraft*, 6(4), 1407-1417. doi: 10.2514/1.C035100

Huynh, J., Mahseredjian, A., & Hansman, R. J. (2022). Delayed Deceleration Approach Noise Impact and Modeling Validation. *Journal of Aircraft*, 59(4), 992-1004. doi:[10.2514/1.C036631](https://doi.org/10.2514/1.C036631)

Published conference proceedings

Mahseredjian, A., Thomas, J., & Hansman, R. J. (2021). *Advanced procedure noise model validation using airport noise monitor networks* [Presentation]. Inter-Noise 2021, Washington, DC. doi: 10.3397/IN-2021-2842.

Mahseredjian, A., Huynh, J., & Hansman, R. J. (2022). *Analysis of community departure noise exposure variation using airport noise monitor networks and operational ADS-B data* [Presentation]. Inter-Noise 2022, Glasgow, Scotland.

Jacqueline Huynh, Melissa Lepe, Trinity Lee, Philip Hood, and R. J. Hansman. "Comparison of data-based and modeled-based analysis of aircraft departure noise using noise monitor network recordings", Internoise 2023, Tokyo, Japan.

Outreach Efforts

- Weekly teleconferences and meetings with FAA Technical Monitors
- Outreach and collaboration with Massport, an operator at BOS, and ASCENT Advisory Board members
- Presentations at the biannual ASCENT Advisory Board meetings

Awards

None

Student Involvement

Graduate and undergraduate students have been involved in all aspects of this research in terms of analysis, documentation, and presentation.

Plans for Next Period

The next phase will involve determining additional methods and data for evaluating aircraft noise variation, such as procedure type (area navigation versus instrument landing system, for example).



Task 3 — Develop Flight Test Plans

Massachusetts Institute of Technology
University of California, Irvine

Objectives

For the recommended validation options identified in Task 2, detailed flight test plans will be developed. Flight test plans for dedicated engineering flights involve detailed planning of the speed, configuration, and thrust of each trial. Test plans for flight trials in collaboration with airline operators will focus on documenting the flown profiles to analyze the associated data measurements. Opportunity exists in both types of trials to validate not only the expected effects of aircraft speed versus noise in the analysis models but also the expected noise impacts of procedures, including delayed deceleration approaches, steeper approaches, and continuous approaches.

Research Approach

- Develop flight test plans, where appropriate, for the validation of low-noise procedures
- Collaborate with airline operators and industry to determine appropriate data collection for trial flight tests

Milestones

- Sought partnerships with operators for FDR data (MIT was unable to obtain FDR data because of operator restrictions on the sharing of flight data)

Major Accomplishments

- Determined that validation for low-noise flight procedures, such as the delayed deceleration approach, can be performed by using available surveillance and noise monitoring data, if reasonable assumptions regarding the weight, flap and slat configuration, and atmospheric attenuation are made
- Examined additional lower-noise departure procedures for 1 year of noise monitoring data from SEA
- Identified contributing noise factors for departure and arrival procedures of various aircraft at SEA from a full year of noise monitor recordings for Boeing 737-800, Airbus A320, and Boeing 777 flights

Publications

None

Outreach Efforts

- Weekly teleconferences and meetings with FAA Technical Monitors
- Outreach and collaboration with Massport, an operator at BOS, and ASCENT Advisory Board members
- Presentations at the biannual ASCENT Advisory Board meetings

Awards

None

Student Involvement

Graduate and undergraduate students have been involved in all aspects of this research in terms of analysis, documentation, and presentation.

Plans for Next Period

Preliminary identified contributing noise factors will be revised based on findings from the data-mining and machine-learning techniques identified.



Task 4 — Initial Experimental Runs on Targets of Opportunity

Massachusetts Institute of Technology
University of California, Irvine

Objective

If targets of opportunity are identified in Task 2 that would occur within the period of performance of this proposed research, initial experimental runs will be conducted after consultation with the FAA Office of Environment and Energy and other relevant parties.

Research Approach

- Document procedural recommendations to enable flight trials
- Meet with airline technical pilots and representatives from aircraft manufacturers to discuss operational constraints and test opportunities
- Develop test plans and protocols for potential flight trials
- Develop test plans and protocols for potential noise measurement campaigns
 - Specific flight test locations
 - Operational field measurements

Milestones

- Conventional and delayed deceleration approach procedures were observed in surveillance data at BOS and SEA and were identified as sufficient for noise analysis instead of dedicated flight test plans.
- A supervised learning approach using XGBOOST's decision-tree and gradient-boosting prediction algorithm was identified.

Major Accomplishments

- Instead of using dedicated flight test plans, approach flights from the surveillance data were grouped by altitude and analyzed for varying speed, configuration, and thrust. The noise monitor readings from these flights were then compared. For departures, measured noise levels versus weight, thrust, speed, altitude, weather factors, and airline were examined through a multivariate approach.
- For approach procedures, flights for which the speeds were more likely to have been in the clean configuration when the aircraft flew over the monitors were shown to correlate with lower recorded noise levels than flights that were more likely to have been in a dirty configuration when the aircraft flew over the monitors.
- For departure procedures, aircraft that achieved higher altitudes early in the flight profiles were found to correlate with lower measured noise levels.

Publications

Peer-reviewed journal publications

Thomas, J., & Hansman, R. J. (2021). Modeling of delayed deceleration approaches for community noise reduction. *Journal of Air Transportation*, 29(3), 127-136. doi: 10.2514/1.D0237

Outreach Efforts

- Weekly teleconferences and meetings with FAA Technical Monitors
- Outreach and collaboration with Massport, an operator at BOS, and ASCENT Advisory Board members
- Presentations at the biannual ASCENT Advisory Board meetings

Awards

- 2021, 2020 AIAA Air Transportation Systems Best Student Paper Award "Modeling, Assessment, and Flight Demonstration of Delayed Deceleration Approaches for Community Noise Reduction" (AIAA-2020-2874) by Jacqueline L. Thomas and R. John Hansman

Student Involvement

Graduate and undergraduate students have been involved in all aspects of this research in terms of analysis, documentation, and presentation.



Plans for Next Period

The main goal of the upcoming work is to understand the causes of variation in both measured departure and arrival noise. The approach to understanding noise level variation uses a data-driven analysis framework for examining the impacts of various operational, weather, and airline factors on noise levels. Flight profiles and noise models will be generated for cases of interest. Different data-mining approaches such as multivariate correlations, clustering, and machine learning will be applied to the data to examine trends in variables affecting aircraft noise, including those due to aircraft weight, thrust, distance to the monitor, airspeed, ambient atmospheric conditions, and compounding factors.

Task 5 — Evaluate Experimental Results and Implications for Advanced Operational Flight Procedure Noise Modeling and Low-Noise Procedures

Massachusetts Institute of Technology
University of California, Irvine

Objectives

Contingent on the availability of data from Task 4 or other data identified as part of the experimental approach and discussions with collaborators, this task, in coordination with NASA, will involve the following:

- Evaluating Advanced Operational Flight Procedure Noise Modeling relative to experimental results;
- Identifying discrepancies requiring correction; and
- Determining whether the results and data are sufficient to improve discrepancies or whether continued validation and testing are required.

The implications for Advanced Operational Flight Procedure Noise Modeling from the data will be evaluated.

Validation of procedures, such as delayed deceleration approaches, will also create opportunities for the development of further low-noise procedures.

Research Approach

- Treat noise monitoring data from SEA and BOS as experimental data, which could serve as a benchmark for comparison against ANOPP component-based noise models.
- Model departure noise for various departures from SEA and identify the characteristics of the quietest departures; determine whether learning can be applied to future departure noise abatement procedure designs.

Milestones

- Noise monitor recordings versus modeled results were determined to be acceptable approaches for comparing measured noise data to noise models when weather factors and operational factors were taken into account.

Major Accomplishments

- Noise models demonstrated similar trends to monitor recordings for approach procedures when proper assumptions regarding flap configuration were made. Both speed and configuration were shown to influence the noise model results.
- Aircraft weight and thrust levels were shown to influence the noise modeling results for approach procedures.
- Aircraft altitude and thrust levels were found to have the strongest correlations with measured noise for the procedures examined.
- Weather factors such as relative humidity, temperature, and wind magnitude and direction were found to have some correlations, albeit weaker, with the measured noise levels on departure.

Publications

Published conference proceedings

Thomas, J., Mahseredjian, A., & Hansman, R. J. (2021). *Delayed deceleration approach procedure noise modeling validation using noise measurements and radar data* [Paper presentation]. AIAA Aviation 2021 Forum, Virtual Meeting. doi: 10.2514/6.2021-2135.



Outreach Efforts

- Weekly teleconferences and meetings with FAA Technical Monitors
- Outreach and collaboration with Massport, an operator at BOS, and ASCENT Advisory Board members
- Presentations at the biannual ASCENT Advisory Board meetings

Awards

- 2018 Department of Transportation/FAA Center of Excellence Outstanding Student of the Year Award to Jacqueline Thomas

Student Involvement

Graduate and undergraduate students have been involved in all aspects of this research in terms of analysis, documentation, and presentation.

Plans for Next Period

The next phase of this project will evaluate how different variables identified in the previous tasks influence aircraft noise and will inform the design of future advanced flight procedures intended to reduce aircraft noise.



Project 046 Surface Analysis to Support AEDT Aircraft Performance Model (APM) Development

Massachusetts Institute of Technology and Massachusetts Institute of Technology Lincoln Laboratory

Project Lead Investigator

Hamsa Balakrishnan
William E. Leonhard (1940) Professor of Aeronautics and Astronautics
Massachusetts Institute of Technology
77 Massachusetts Ave., 33-328
Cambridge, MA 02139
617-253-6101
hamsa@mit.edu

University Participants

Massachusetts Institute of Technology (MIT)

- P.I.: Prof. Hamsa Balakrishnan
- FAA Award Number: 13-C-AJFE-MIT, Amendment Nos. 021, 035, 044, 047, 063, 068, 077, and 092
- Period of Performance: July 7, 2016 to February 13, 2023
- Task:
 1. AIR: Fuel Flow Rates for Jet-Powered Commercial Aircraft Taxi Operations

MIT Lincoln Laboratory (via internal university allocation from MIT Main Campus)

- P.I.: Dr. Thomas G. Reynolds
- Award Number: Cost Object No. 1276191
- Period of Performance: Sept 1, 2019 to February 13, 2023
- Task:
 1. Develop SAE International Aerospace Information Report (AIR) "Fuel Flow Rates for Jet-Powered Commercial Aircraft Taxi Operations" to document recommendations from ASCENT46 project.

Project Funding Level

This project received \$700,000 in FAA funding and \$700,000 in matching funds from MIT.

Investigation Team

- Prof. Hamsa Balakrishnan, co-P.I. - MIT (Task 1)
- Dr. Tom Reynolds, co-P.I. - MIT Lincoln Laboratory (Task 1)

Project Overview

The AIR document summarizes prior empirical findings to recommend a modified baseline fuel flow rate model for jet-powered commercial aircraft during taxi operations on the airport surface that better reflects operational values (Chati, 2018; Clemons et al., 2018). Existing standard modeling approaches have been found to significantly overestimate the taxi fuel flow rate; therefore, application of a modified multiplicative factor to these existing approaches is recommended to make them more accurate. Results from the analysis of operational flight data have been reported, which form the basis for the modeling enhancements being recommended.

Task 1 – Develop AIR document “Fuel Flow Rates for Jet-Powered Commercial Aircraft Taxi Operations”

Massachusetts Institute of Technology
Massachusetts Institute of Technology Lincoln Laboratory

Objectives

The objective of this research project is to identify and evaluate methods for improving airport taxi performance modeling in the Aviation Environmental Design Tool (AEDT) to better reflect actual operations (Clemons et al., 2018). This objective is being met through the analysis of relevant data sources, including surface surveillance (Airport Surface Detection Equipment, ASDE-X), Aviation System Performance Metrics taxi time, Flight Data Recorder (FDR), and air quality monitoring datasets. Prior phases of the ASCENT46 project have identified first-order enhancements to the AEDT Aircraft Performance Model for surface operations. Specific improvement areas include enhanced baseline taxi fuel flow models; improved taxi times at different airports; and estimation of pre-taxi engine and auxiliary power unit fuel burn, and a detailed assessment of surface operations and associated air quality impacts at Los Angeles International Airport, because of the extensive data availability at that location. These enhancements were described in prior reports. Recently, we have documented our work on enhanced taxi fuel flow models in an SAE Aerospace Information Report (AIR), in preparation to release it for a vote by the SAE A-21 Committee. The remainder of this report consists of the proposed AIR.

Research Approach

Introduction

Models of aircraft taxi operations on the airport surface and associated fuel flow and emissions are used for several purposes, such as assessing the impacts of changes to operational procedures, airport infrastructure and fleet mixes, and conducting environmental studies. A standard method of modeling jet aircraft taxi fuel flow, for example, in the FAA’s AEDT (FAA, 2022), is to assume a constant engine-specific thrust level (and resulting fuel flow rate) determined by applying a correction factor for installation effects to engine manufacturer certification data (ICAO, n.d.). However, the resulting estimate of the fuel flow rate can significantly differ from the actual characteristics during operational conditions for a given aircraft (Nikoleris et al., 2011). This difference can be due to a variety of factors, such as engine age (as the engine ages, the amount of fuel that it burns changes) and pilot techniques (such as “riding the brakes” instead of throttling down the engines when coming to a stop). The AIR analyzes operational data to develop more realistic fuel flow models for taxi operations to improve the accuracy of airport surface fuel and emissions calculations.

Current Taxi Fuel Flow Modeling

Figure 1 shows a typical fuel flow rate profile (post-pushback and engine start) during taxi operations. This profile is from a common narrow-body twin engine commercial aircraft. Although the fuel flow magnitudes vary with aircraft type, the shape is representative of most jet-powered commercial aircraft. The fuel flow rate profile can be divided into two distinct types of regions: baseline regions (two of which are identified by dashed-line ovals) and fuel flow spike regions (one of which is identified with a dotted-line oval). The baseline fuel flow regions are characterized by a nearly constant (low variation) fuel flow rate over extended time intervals under normal moving taxi conditions, and the fuel flow spike regions correspond to the periods of increased thrust needed to re-start movement after a period of being stopped.

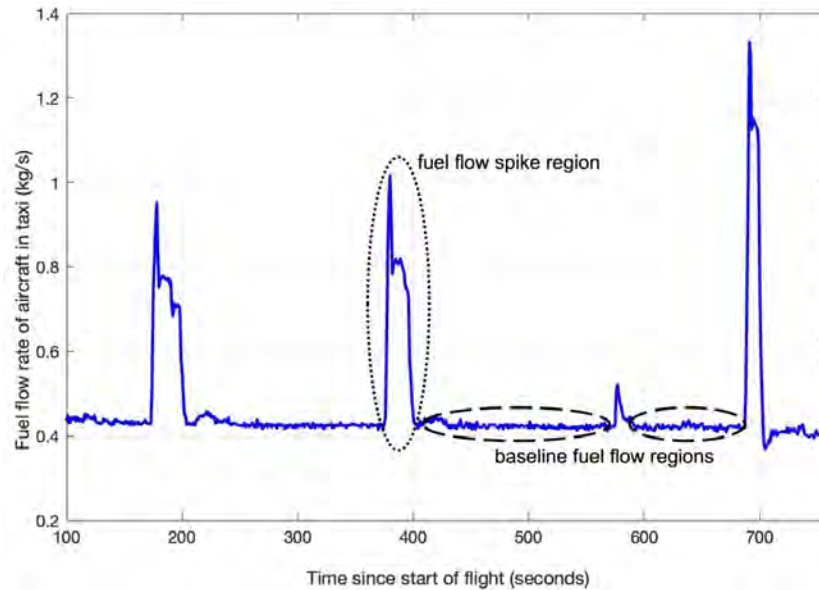


Figure 1. Typical fuel flow rate profile during taxi operations for twin-engine narrow-body commercial aircraft.

Although the spikes correspond to periods of higher thrust and higher fuel flow rates, more than 90% of the total taxi fuel consumption occurs during periods when the fuel flow rate is close to the baseline (flat) value (Chati, 2018). Therefore, the recommendations in this technical manuscript relate to the baseline taxi fuel flow rate. The spikes in fuel flow rate are important for emissions and noise calculations, and contribute to the variability in fuel burn between flights. Future studies could investigate these time periods further.

Standard fuel flow modeling approaches such as those documented in SAE AIR6183 (SAE, 2022), which have been extended for use in taxi operations in AEDT (FAA, 2022), use the Boeing Fuel Flow Method (BFFM2). The form of BFFM2 used in FAA (2022) for the taxi phase is given by:

$$\dot{m}_f = B_m \dot{m}_{f_{ICAO}} \delta \theta^{-3.8} e^{-0.2M^2} \quad (1)$$

where \dot{m}_f is the fuel flow rate in kg/s at non-reference conditions, B_m is a dimensionless adjustment factor, $\dot{m}_{f_{ICAO}}$ is the fuel flow rate in reference (certification 7% idle power setting) conditions, as contained in the ICAO Aircraft Engine Emissions Databank (ICAO, n.d.), δ is the static pressure ratio (ambient to sea level), θ is the static temperature ratio (ambient to sea level), and M is the Mach number. In DuBois & Paynter (2006) and FAA (2022), an adjustment factor of 1.1 is used in the taxi mode to account for engine installation effects. As in BFFM2, this equation is normally used to correct at-altitude fuel flow to sea-level conditions and vice versa. Of note, in the taxi phase, the Mach number is close to 0, and the temperature and pressure ratios for most operations are close to 1. That is, the taxi phase fuel flow rate approximates to:

$$\dot{m}_{f_{Taxi}} \approx 1.1 \dot{m}_{f_{ICAO \text{ 7\% Setting}}} \quad (2)$$

Enhanced Taxi Fuel Flow Modeling

To compare this current model to the fuel flow rates during actual operations, Chati (2018) and Clemons et al. (2018) conducted ordinary least squares (OLS) regression of baseline fuel flow rates per engine during taxi for different aircraft and engine types, to obtain a model that is consistent with BFFM2 (Equation 1). For this purpose, FDR data containing operations from a major European carrier and a major Middle Eastern carrier from 2016 were obtained (full details in Chati, 2018). Consequently, the narrow-body aircraft flights in this dataset were to or from airports primarily in Europe and the Middle East, whereas the wide-body aircraft included many flights to or from major international airports in the United States. The FDR dataset reported key aircraft and engine parameters (including fuel flow rates) as time-series data at a 1-Hz sampling rate.

The flights in the FDR data set were split into two disjoint sets, one used to build the model and the other used as the test data set. The resulting proposed enhanced models for the (anonymized) aircraft/engine types available in the dataset are shown in Table 1. The right side of Table 1 shows the resulting errors for the proposed OLS-based model compared with the estimates based on the original model (Equation 1 with $B_m = 1.1$) for the test data set. The mean percentage and absolute errors are substantially reduced with the OLS-based model. The original model is seen to be a significant overestimate relative to the values observed in operational data. Furthermore, the median value of the multiplicative constant estimated from FDR data across the aircraft/engine types is calculated to be 0.80. Of note, this proposed value represents both engine installation effects and (most importantly for this application) the actual operational power settings of aircraft during airport taxiing and idling conditions. In the SAE AIR, we also presented a validation of these findings using different data sources.

Table 1. Proposed models for mean taxi fuel flow rate built from operational FDR data and error performance relative to the existing model in AEDT (Clemons et al., 2018).

Aircraft/engine type (number of flights available for training)	Proposed model (θ & δ terms were close to unity and are omitted)	Mean error (%): estimated - actual		Mean absolute error	
		Proposed model	Original model	Proposed model	Original model
Narrow-body twin engine 1 (103)	0.81 \dot{m}_f	1.0	36.3	13.3	39.4
Narrow-body twin engine 2 (46)	0.80 \dot{m}_f	3.8	47.1	14.9	50.1
Wide-body twin engine 1 (117)	0.78 \dot{m}_f	-3.0	36.4	5.8	39.1
Wide-body twin engine 2 (81)	0.75 \dot{m}_f	-2.2	42.3	3.1	43.1
Wide-body four engine 1 (37)	1.02 \dot{m}_f	-0.7	7.8	9.1	12.5
Twin engine regional jet 1 (95)	0.97 \dot{m}_f	0.1	17.7	5.5	19.3

Summary and Recommendations

The analyses presented in this report indicate that the current commonly used baseline taxi fuel flow rate model (FAA, 2022), namely:

$$\dot{m}_{f_{Taxi}} = B_m \dot{m}_{f_{ICAO\ 7\% \ Setting}} \quad (3)$$

where $B_m = 1.1$ for the taxi mode, to represent installation effects, results in a significant overestimation of the baseline taxi fuel flow rates relative to operationally observed values. Considering the findings of the analyses of the operational datasets, the median value of the estimated multiplicative factor across all aircraft types considered was found to be 0.80, including both installation and operational factors. Therefore, standard aircraft taxi fuel flow models are recommended to be modified to use an additional taxi fuel flow rate adjustment factor $B_f = 0.80/1.1 = 0.73$, thus yielding a new taxi fuel flow rate model:

$$\dot{m}_{f_{Taxi}} = B_m B_f \dot{m}_{f_{ICAO\ 7\% \ Setting}} \quad (4)$$

where $B_m = 1.1$ accounts for installation effects as in the existing model, and the new multiplicative factor $B_f = 0.73$ accounts for operational effects, such that the product $B_m B_f = 0.80$, in agreement with the recommendations from this analysis.

Milestones

We have primarily worked on the SAE A-21 report and are providing support in the implementation of a new queuing model within AEDT. We are also preparing for the final report.

Major Accomplishments

The AIR document described in this report was recently approved by SAE Committee A21 for adoption as a new SAE standard (SAE AIR-8035). Furthermore, AEDT 3f updates the fuel flow rates for taxi emissions as per SAE AIR-8035.

Publications

None.

Outreach Efforts

None.



Awards

None.

Student Involvement

None.

Plans for Next Period

This task of Project 46 is complete as of Feb 13, 2023.

References

- Clemons, E., Reynolds, T., Badrinath, S., Chati, Y., & Balakrishnan, H. (2018, June 25). Enhancing aircraft fuel burn modeling on the airport surface. *2018 Aviation Technology, Integration, and Operations Conference*. 2018 Aviation Technology, Integration, and Operations Conference, Atlanta, Georgia. Doi: 10.2514/6.2018-3991
- Chati, Y.S. (2018). *Statistical Modeling of Aircraft Engine Fuel Burn* [Ph.D. Thesis, Department of Aeronautics and Astronautics, Massachusetts Institute of Technology] <https://dspace.mit.edu/handle/1721.1/115658>.
- FAA. (2022). *Aviation Environmental Design Tool (AEDT), Version 3e, Technical Manual*. https://aedt.faa.gov/Documents/AEDT3e_TechManual.pdf.
- ICAO. (2023). *Aircraft Engine Emissions Databank*. <https://www.easa.europa.eu/domains/environment/icao-aircraft-engine-emissions-databank>.
- Nikoleris, T., Gupta, G., & Kistler, M. (2011). Detailed estimation of fuel consumption and emissions during aircraft taxi operations at Dallas/Fort Worth International Airport. *Transportation Research Part D: Transport and Environment*, 16(4), 302–308. Doi: 10.1016/j.trd.2011.01.007
- SAE. (2022). *Procedures for the Calculation of Airplane Fuel Consumption* (Publication No. AIR6183). <https://www.sae.org/standards/content/air6183/>.
- DuBois, D., & Paynter, G. C. (2006). "Fuel flow method2" for estimating aircraft emissions. 2006-01-1987. Doi: 10.4271/2006-01-1987



Project 47 Clean-sheet Supersonic Aircraft Engine Design and Performance

Massachusetts Institute of Technology

Project Lead Investigator

Steven R. H. Barrett
Professor of Aeronautics and Astronautics
Department of Aeronautics and Astronautics
Massachusetts Institute of Technology
77 Massachusetts Avenue
Cambridge, MA 02139
617-452-2550
sbarrett@mit.edu

University Participants

Massachusetts Institute of Technology (MIT)

- P.I.: Prof. Steven R. H. Barrett
- FAA Award Number: 13-C-AJFE-MIT, Amendment Nos. 052, 059, 074, 076, 090, 106, 110, and 115 (NCE to September 30, 2024)
- Period of Performance: March 29, 2019 to September 30, 2024 (with the exception of funding and cost-share information, this report covers the period from October 1, 2022 to September 30, 2023)
- Tasks:
 1. Evaluate the effects of fan diameter and unconventional architectures on the environmental impacts of clean-sheet engines

Project Funding Level

\$1,650,000 FAA funding and \$1,650,000 matching funds. Sources of match are approximately \$340,000 from MIT, plus third-party in-kind contributions of \$177,000 from Byogy Renewables, Inc.; \$982,000 from NuFuels, LLC; and \$151,000 from Savion Aerospace Corporation.

Investigation Team

Prof. Steven Barrett, (P.I.), Task 1
Dr. Raymond Speth, (co-P.I.), Task 1
Dr. Choon Tan (co-P.I.), Task 1
Dr. Jayant Sabnis, (co-investigator), Task 1
Dr. Prakash Prashanth, (postdoctoral associate), Task 1
Mr. Wyatt Giroux, (graduate student), Task 1

Project Overview

Engines for supersonic aircraft, compared with those for subsonic aircraft, present unique challenges in terms of fuel consumption, noise, and emissions impacts, because of their unique operating conditions. The propulsion systems currently proposed by the industry are derivative engines (Figure 1) designed around the unmodified core (high-pressure compressor, combustor, and high-pressure turbine) of existing subsonic engines, with modifications to the low-pressure spool (fan and low-pressure turbine).

This project is aimed at evaluating the design space of “clean-sheet” engines designed specifically for use on civil supersonic aircraft, and to determine the resulting environmental performance of such engines. Unlike previous

commercial supersonic engines, which were adapted from military aircraft, or planned propulsion systems derived from current commercial engines, a clean-sheet engine takes advantage of recent advances in propulsion system technology to substantially improve performance and reduce emissions and noise footprints. This project will quantify these benefits for a range of engine designs relevant to currently proposed civil supersonic aircraft. Conventional clean-sheet engines have been examined by the Project 47 team. To further characterize the clean-sheet design space, more unconventional engine architectures, namely hybrid-electric systems, are investigated. Specifically, we aim to assess the relative performance of hybrid-electric clean-sheet and conventional clean-sheet engines.

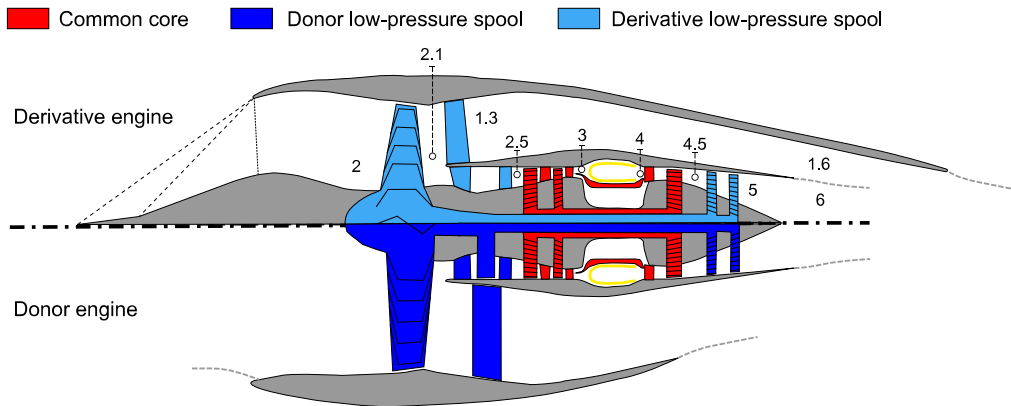


Figure 1. Engine architecture schematic. The lower half shows the subsonic donor engine. The high-pressure spool (red) core is used in the derivative engine (top half) along with modifications to the inlet, fan, and nozzle, as shown in the top half.

Task 1 – Evaluate the Effects of Fan Diameter and Unconventional Architectures on the Environmental Impacts of Clean-Sheet Engines

Massachusetts Institute of Technology

Objective

The objective of this task is to quantify the effects of fan diameter constraints and use of unconventional engine architectures on the emissions of clean-sheet engines. In particular, we examine the combined impact of the following cases:

- Effect of fan diameter on supersonic drag sources, and subsequent impacts on thrust requirements and engine performance
- Use of hybrid-electric systems powered primarily with conventional fuel alongside a battery-based supplement used during landing and takeoff (LTO) flight

The work presented is done for the airframe and mission of the Supersonic Transport Concept Aircraft (STCA) developed by NASA (Berton et al., 2020).

Research Approach

Numerical Propulsion System Simulation (NPSS) software (Claus et al., 1991) was chosen for analysis of engine performance and emissions. Because it is an industry-standard tool, it facilitates future collaboration with the broad user base. The clean-sheet engine cycle deck from Prashanth et al. (2023) is used to obtain a baseline design.

Supersonic drag sources

Supersonic drag forces on an engine fall primarily into three categories: bypass drag, spillage drag, and wave drag. Bypass and spillage drag represent losses due to off-design operation of a supersonic inlet. In this work, engine inlets are assumed to be operated on-design or to contain variable-geometry components to maintain well-matched operation across

the mission. Therefore, we assume that the contributions of spillage and bypass drag are negligible. The effects of such systems (weight, complexity, etc.) are not considered here.

The Fraenkel model for external cowl drag on open-nosed bodies of revolution (as presented by Seddon and Goldsmith (1999)) is used to model the remaining supersonic drag source, wave drag. The aspect ratio of the inlet cross-section (radius/length) is taken to be constant and equal to the value for the existing STCA engine. Fan diameter is used as a proxy for maximum inlet radius and is allowed to vary. A conical profile is conservatively used to minimize drag.

Although the exact value of the wave drag due to the engine inlet cowls on the baseline aircraft is unknown, it can be estimated with the above model. Consequently, the difference in wave drag can be estimated for a clean-sheet engine with a specified fan diameter relative to the baseline design. This difference is then used alongside steady flight assumptions to obtain the difference in thrust requirement relative to the baseline mission presented in Berton et al. (2020).

Previous hybrid-electric assessments

Before implementing a full hybrid-electric NPSS engine model, we first qualitatively assess the potential benefits of hybrid electrification. We assume an architecture wherein electric systems are used only during the LTO phase of flight, when the greatest demand is placed on the engine. Consequently, the gas turbine component of the engine can be sized more closely to cruise requirements. Similar analyses in subsonic systems (Kang et al., 2022; Lammen & Vankan, 2020; Lents et al., 2016; Seitz et al., 2018) suggest specific fuel consumption benefits on the order of 5%, alongside minor improvements to nitrogen oxide (NO_x) emissions. These benefits are hypothesized to manifest through three primary mechanisms:

- Lower peak gas turbine corrected fan speed requirement: This aspect could allow the gas turbine to operate closer to the design condition (100% corrected speed) during cruise, improving component efficiency.
- Lower peak engine turbine-entry-temperature (TET): If the maximum TET point occurs during LTO, electric systems could be used to reduce the TET required by the gas turbine, thereby potentially improving NO_x emissions and propulsive efficiency.
- Lower thrust requirements at pinch points: Electric systems could be used to reduce the thrust requirements of the gas turbine at the pinch points of the mission, thereby allowing the engine to be sized more closely to cruise thrust requirements.

The final mechanism, thrust requirement, was implemented indirectly to maintain the known mission profile. The time in the mission at which a given constraint is placed was varied, and the altitude, Mach number, and thrust requirement could then be calculated at that new time. As an example, the thrust pinch point occurs at 27 kft at a Mach number of 0.85. In a hybrid-electric engine, the gas turbine would not be able to produce sufficient thrust at that point alone and would require assistance by the electric systems. To model this scenario while maintaining the STCA mission profile, the engine is sized for thrust at a slightly later (positive time deviation) or slightly earlier (negative time deviation) mission point. An engine sized for thrust at either of these points will not produce sufficient thrust at the actual thrust pinch point but may be sized more optimally for cruise. This procedure of varying the time at which a thrust constraint is applied is repeated for other key points in the mission.

To test these mechanisms, NPSS is used to examine the sensitivity of emissions metrics to the corrected fan speed, turbine inlet temperature, and thrust requirement (with time as a proxy) at several points in the STCA LTO profile. These points are the thrust pinch point (27 kft., Mach 0.85), the thermal pinch point (42 kft., Mach 1.4), and the aerodynamic design point (ADP; 41 kft., Mach 1.4). Emissions are then evaluated at the beginning of cruise point (44 kft., Mach 1.4) as an estimate of overall cruise emissions.

Major Accomplishments

Supersonic drag implementation

The wave drag was first estimated for several supersonic regime Mach numbers for the original STCA engine design. The fan diameter (D_f) was then allowed to vary. The percentage deviation in drag area ($C_d A$) is shown in Figure 2 as a function of Mach number. The drag area of an engine cowl monotonically increases with a local sensitivity of $\partial C_d A / \partial D_f = 3.5$. The drag area relative to the baseline STCA was found to have minimal variation due to the Mach number. At a fixed fan diameter, the change in drag area was between 1.6% at -10% fan diameter and 3.3% at $+10\%$ fan diameter. Notably, the effect of Mach number grows with increasing fan diameter, thus indicating that this effect would need to be accounted for at high fan diameters.

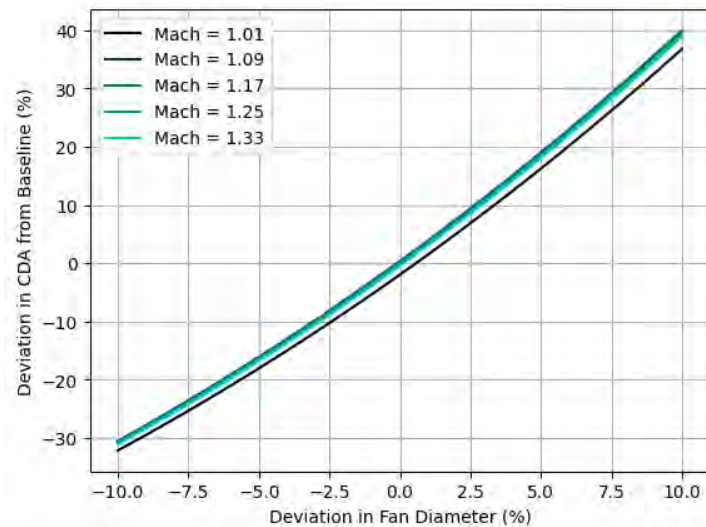


Figure 2. Effect of fan diameter variation on engine external cowl drag area (CDA), as a function of Mach number.

Sensitivities

The supersonic drag model described above was implemented into the NPSS clean-sheet cycle deck, and sensitivities of specific air range (SAR), thrust specific fuel consumption (SFC), and fan diameter were calculated due to variation in TET, corrected fan speed, and thrust (with time as a proxy). The resulting sensitivities are generally non-linear (Figure 3). Variations in emissions metrics and fan diameter due to turbine inlet temperature have negligible dependence on the point at which the temperature was prescribed, thus suggesting strong correlations between temperature changes at one point with resulting changes at the other two points. We see improved SAR and SFC for increasing turbine inlet temperature, to maxima on the order of 0.5%. SFC was minimized with a corrected fan speed deviation of -5% for all three points of interest. While SAR exhibits a maximum, the value of that maximum is decreased, because of the resultant increase in fan diameter and thus drag.

The emissions and fan diameter sensitivities due to sizing time variation are not smooth, because variations in time equate to variations in altitude, Mach number, and thrust, in accordance with the prescribed LTO mission profile. As such, when an inflection point of the mission (e.g., end of climb) is reached, the behavior of the mission parameters with respect to time changes suddenly. From the time sensitivities, we see SAR and SFC benefits resulting from a positive deviation of time at the thrust pinch point. This finding indicates that sizing the engine thrust to a later point in the mission and producing insufficient thrust at the actual pinch point do improve cruise emissions.

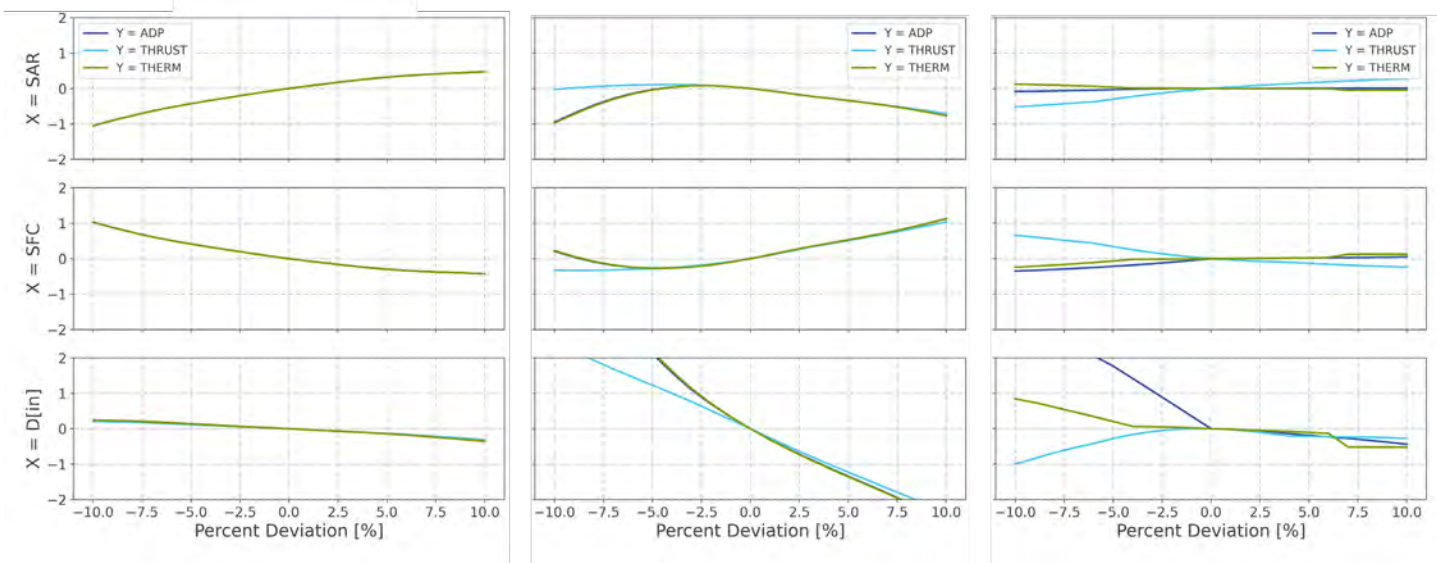


Figure 3. Sensitivity of metric X at the beginning of cruise to turbine inlet temperature (left), corrected fan speed (middle), and time (right) at point Y.

Publications

None

Outreach Efforts

Results were presented to the FAA Project Manager during regular teleconferences.

Awards

None

Student Involvement

This work was performed primarily by graduate research assistant Wyatt Giroux, working under the supervision of Dr. Prakash Prashanth, Dr. Jayant Sabnis, Dr. Raymond Speth, and Dr. Choon Tan.

Plans for Next Period

In the next period, we will create a dedicated hybrid electric NPSS engine model including the effects on thrust requirement due to battery weight, nacelle weight, and nacelle drag. This model, alongside the sensitivities above, will be used to determine optimal hybrid-electric engine designs for several fan diameters and electric system sizes. These results will then be compared with the results obtained by Prashanth et al. (2023) for conventional clean-sheet designs, to determine the effects of hybrid electrification on SST emissions.

References

- Berton, J. J., Huff, D. L., Geiselhart, K., & Seidel, J. (2020). Supersonic Technology Concept Aeroplanes for Environmental Studies. In *AIAA Scitech 2020 Forum*. American Institute of Aeronautics and Astronautics. <https://doi.org/10.2514/6.2020-0263>
- Claus, R. W., Evans, A. L., Lylte, J. K., & Nichols, L. D. (1991). Numerical Propulsion System Simulation. *Computing Systems in Engineering*, 2(4), 357-364. [https://doi.org/10.1016/0956-0521\(91\)90003-N](https://doi.org/10.1016/0956-0521(91)90003-N)
- Kang, S., Roumeliotis, I., Zhang, J., Broca, O., & Pachidis, V. (2022). Assessment of Engine Operability and Overall Performance for Parallel Hybrid Electric Propulsion Systems for a Single-Aisle Aircraft. *Journal of Engineering for Gas Turbines and Power*, 144(041002). <https://doi.org/10.1115/1.4052880>
- Lammen, W., & Vankan, J. (2020). Energy Optimization of Single Aisle Aircraft with Hybrid Electric Propulsion. In *AIAA Scitech 2020 Forum*. American Institute of Aeronautics and Astronautics. <https://doi.org/10.2514/6.2020-0505>



- Lents, C. E., Hardin, L. W., Rheaume, J., & Kohlman, L. (2016). Parallel Hybrid Gas-Electric Geared Turbofan Engine Conceptual Design and Benefits Analysis. In *52nd AIAA/SAE/ASEE Joint Propulsion Conference*. American Institute of Aeronautics and Astronautics. <https://doi.org/10.2514/6.2016-4610>
- Prashanth, P., Voet, L. J. A., Speth, R. L., Sabnis, J. S., Tan, C. S., & Barrett, S. R. H. (2023). Impact of Design Constraints on Noise and Emissions of Derivative Supersonic Engines. *Journal of Propulsion and Power*, 39(3), 1-10. <https://doi.org/10.2514/1.B38918>
- Seddon, J., & Goldsmith, E. L. (1999). *Intake Aerodynamics*. American Institute of Aeronautics and Astronautics.
- Seitz, A., Nickl, M., Stroh, A., & Vratny, P. C. (2018). Conceptual study of a mechanically integrated parallel hybrid electric turbofan. *Proceedings of the Institution of Mechanical Engineers, Part G: Journal of Aerospace Engineering*, 232(14), 2688-2712. <https://doi.org/10.1177/0954410018790141>



Project 049 Urban Air Mobility Noise Reduction Modeling

**The Pennsylvania State University
Continuum Dynamics, Inc.**

Project Lead Investigator

Kenneth S. Brentner
Professor of Aerospace Engineering
Department of Aerospace Engineering
The Pennsylvania State University
233 Hammond Building
University Park, PA
814-865-6433
ksbrentner@psu.edu

University Participants

The Pennsylvania State University (Penn State)

- P.I.: Kenneth S. Brentner, Professor of Aerospace Engineering
- FAA Award Number: 13-C-AJFE-PSU-049, Amendment No. 96
- Period of Performance: October 1, 2022 to September 30, 2023
- Tasks:
 1. Develop acoustically aware flight control strategies
 2. Validate electric vertical take-off and landing (eVTOL) noise prediction system with uncrewed aerial system (UAS) or helicopter flight tests
 3. Complete the implementation of time-varying noise modeling
 4. Study aerodynamic interaction effects on eVTOL noise
 5. Document the use of the eVTOL noise prediction system

Project Funding Level

The FAA provided \$280,000 in funding. Continuum Dynamics, Inc. (point of contact: Dan Wachspress) will provide \$75,000 of cost sharing in the form of a 1-year license for the CHARM rotorcraft comprehensive analysis software to the FAA for its designee. Penn State will provide \$50,000 in equipment cost sharing, and \$155,000 in academic year salary for the P.I., corresponding to a total of \$280,000 in cost sharing.

Investigation Team

The Pennsylvania State University

Kenneth S. Brentner (P.I.; acoustic prediction lead), Tasks 1-5
Eric Greenwood (co-P.I.; acoustics prediction/analysis), Tasks 1-5
Joseph F. Horn (co-P.I.; flight simulation lead), Tasks 1,2, and 5
Ze Feng (Ted) Gan (graduate research assistant; developing PSU-WOPWOP noise prediction software and performing acoustic predictions), Tasks 2, 3, and 5
Bhaskar Mukherjee (graduate research assistant; software coupling, establishing new aircraft models, developing simulations for new aircraft types, performing acoustic predictions, and developing flight abatement procedures), Tasks 1-5

Continuum Dynamics, Inc.

Daniel A. Wachspress (co-P.I.; rotor loads, wake integration, and CHARM coupling), Tasks 1, 2, 4, and 5

Project Overview

A wide variety of unconventional configurations for urban air mobility (UAM) and eVTOL aircraft, most with many electrically driven propellers and lifting rotors, have been proposed and are currently under development by companies worldwide. These novel configurations comprise a new category of aircraft that will need to be certified, particularly for acceptable noise levels, given their urban operations. Furthermore, the noise of UAM and eVTOL vehicles is expected to be one of the considerations of passengers and communities. Therefore, first-principles noise predictions of these aircraft will be important for providing the FAA with information independent from that provided by manufacturers and before manufacturer flight test or certification noise data are available. For clarification, UAS (also known as drones), UAM, and eVTOL vehicles all share electric motors as the source of power to drive the rotors; therefore, UAS noise characteristics can also shed light on UAM/eVTOL noise. In most cases, UAM vehicles are likely to use batteries, but the electrical power could come from fuel cells, gas generators, or other sources. Furthermore, although most UAS and UAM vehicles are likely to have VTOL capabilities, such capabilities are not a requirement. In this report, the terms UAM and eVTOL are used synonymously, whereas UASs are eVTOL drones.

In ASCENT Project 38, the helicopter noise prediction system initially developed in ASCENT Project 6 was successful in accurately predicting the noise of helicopters (usually within sound exposure levels of 1–3 dBA), when the predictions were compared with results from an FAA/NASA rotorcraft noise abatement flight test performed in August and October 2017. Sound exposure level contours from the flight test were compared with predictions for several flight procedures. The noise prediction system developed in Project 38 consisted of the PSUHeloSim flight dynamics simulation code coupled to the CHARM aeromechanics modeling software and the PSU-WOPWOP noise prediction code. This coupling with the flight simulation code was demonstrated to be important for noise prediction, which markedly improved when the simulation was modified to track the time-dependent aircraft position, velocity, and attitude flown in an individual run, rather than the nominal flight path.

To build upon the success of ASCENT Project 38, ASCENT Project 49 employs an analogous approach of coupling a flight simulation code with CHARM and PSU-WOPWOP. The PSUHeloSim flight simulation component of the noise prediction system used in Project 38 was replaced with DEPSim, a flight simulation code designed for many electrically driven rotors with unique control strategies to fly such vehicles effectively. Coupling of DEPSim with CHARM was performed in work outside ASCENT, whereas DEPSim–CHARM coupling with PSU-WOPWOP was performed in this project.

The goal of this project is to develop a noise prediction system with the initial capability to analyze the noise from UAM and eVTOL vehicles with unique configurations under any flight conditions. This project should enable the FAA, manufacturers, and related entities to investigate how this new class of vehicles—and their noise—might be integrated into the national airspace. Emphasis is placed on modeling the unique features of UAM and eVTOL configurations not commonly seen in conventional rotorcraft, such as rotors with variable rotation speed, and complex unsteady aerodynamic interactions between the many rotors and the airframe. Because UAM vehicles will probably have lower tip speeds to achieve acceptable noise levels, broadband noise is expected to become the dominant rotor noise source; accordingly, rapid physics-based modeling of rotor broadband noise is a goal of this project. Another goal is to use the noise prediction system developed in this project to provide guidance on how to fly these vehicles in a quiet manner through flight operations. Because the analysis and computations are based on fundamental physics, noise abatement procedures for novel vehicles can be developed.

Task 1 – Develop Acoustically Aware Flight Control Strategies

The Pennsylvania State University

Objective

The goal of this task is to develop flight control strategies balancing aircraft noise, controllability, and performance. The current task explores new flight control strategies based on lessons learned in previous tasks (14, 16 in the 2022 annual report). The exploration was also expanded to include different trajectories that the aircraft can utilize to transition from rotorcraft mode to full forward flight at an altitude that makes the aircraft quieter on the ground.

Research Approach

Task 14 (2022 annual report) explored two flight control strategies for a notional lift-plus-cruise eVTOL aircraft: (1) variable rotor revolutions per minute (RPM) with fixed pitch and (2) variable rotor pitch with constant RPM. A constant

setpoint is used to refer to either a fixed pitch or constant RPM, depending on the context; in this work, the setpoint schemes were used for the lifting rotors. The variable RPM scheme was found to be sub-optimal for aircraft controllability and handling qualities because of limitations in electric motor torque generation. Both control strategies were also found to result in poorer performance for the entire transition flight envelope and higher noise due to blade stall. This behavior was attributed to the usage of either constant pitch or constant RPM, regardless of the flight conditions. Thus, a new control strategy was developed in which the rotor pitch was varied by the flight controller to stabilize the aircraft while the rotor speed was varied to mitigate stall and, in turn, to reduce stall noise. Various notional flight trajectories were simulated via the noise prediction system, and their corresponding impacts on performance and acoustics were investigated.

Milestones

- Development of a new notional lift-plus-cruise aircraft (PSU Reference Aircraft 2)
- Development of a strategy for building a rotor setpoint schedule based on flight conditions
- Investigation of the correlation between aerodynamic interactions and flight controller design
- Simulation of transition maneuver trajectories and their impact on performance and noise

Major Accomplishments

A new notional lift-plus-cruise aircraft (PSU Reference Aircraft 2) was developed based on publicly available information on the commercial Alia-250 aircraft developed by Beta Technologies. This design is considered to be more representative of real aircraft than PSU Reference Aircraft 1. As shown in Figure 1(a), the aircraft has four lift rotors and one cruise rotor/propeller, which is the same as Reference Aircraft 1. The difference is that the lift rotors are canted in the lateral and longitudinal directions (Figure 1(b)). The lateral cant ($\gamma = 3^\circ$) aids in yaw control authority, and the longitudinal cant ($\chi = 6^\circ$) aids in the transition to forward flight. The transition maneuver for PSU Reference Aircraft 2 occurs when the aircraft begins to hover and eventually gains enough airspeed to allow the wing to generate enough lift to balance the weight of the aircraft while the lift rotors are phased off. The lift rotors in PSU Reference Aircraft 2 begin to phase off at an airspeed of 70 knots, and the transition is completed at 110 knots.

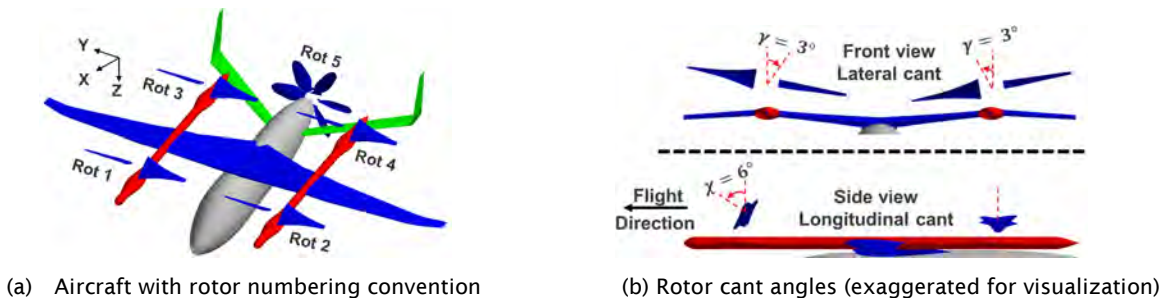


Figure 1. The Pennsylvania State University Reference Aircraft 2 (Mukherjee et al., 2023).



Figure 2. Strategy for building the rotor setpoint schedule (Mukherjee et al., 2023).

For an acceptable transition maneuver, it is important that the aircraft be quiet, consume a low amount of energy, and be safe with a high motor power margin. As discussed in the “Research Approach” section above, the thrust of the lift rotor will be controlled by varying the collective pitch. However, the rotor speed will still be varied based on a predetermined schedule derived from the characteristics of the maneuver. Although the potential operating space of the rotor RPM is large, it can be constrained based on the goals of efficient low-noise operation. The acoustic impact of the rotor is minimized by lowering the rotor tip Mach number, while the performance is optimized by discarding rotor speeds with significant stall. These constraints were combined into a new strategy for development of the rotor setpoint schedule in Mukherjee et al. (2023).

The schedule was developed for airspeeds of 10–70 knots in intervals of 10 knots. For each airspeed, a parameter sweep of an isolated rotor was conducted (Figure 3). This sweep consists of aerodynamic simulations in CHARM for an isolated lift rotor, where the tip Mach number and collective pitch are varied for different airspeeds. Stall conditions were discarded, as indicated by the empty regions in Figure 3. The rotor RPM was selected to obtain the lowest possible rotor speed with a sufficient power margin for safe operation of the electric motor.

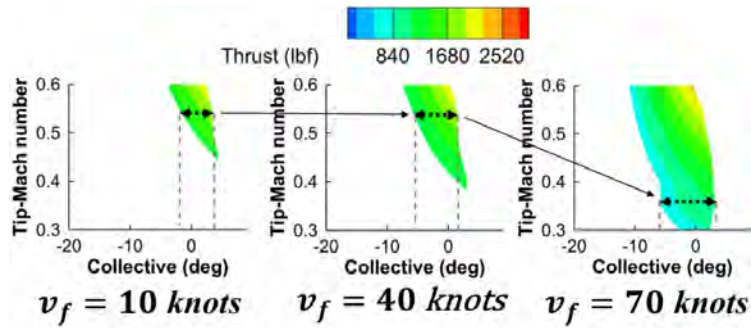
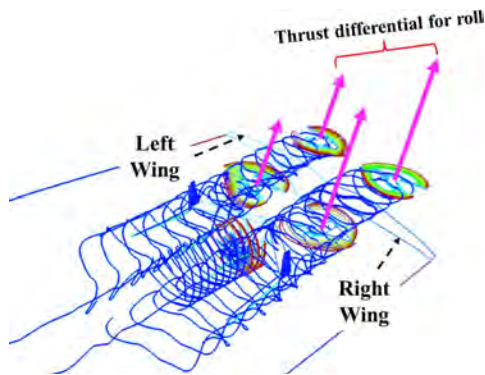
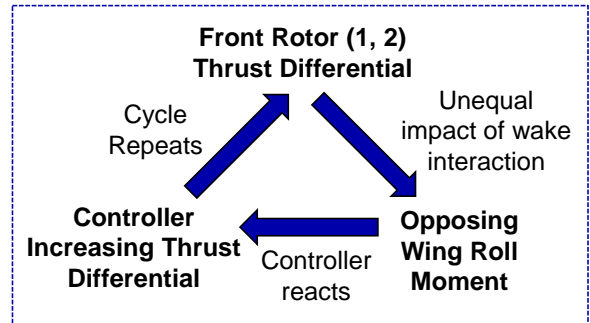


Figure 3. Building the rotor tip Mach number schedule based on a parameter sweep (Mukherjee et al., 2023).

Once the parameter sweep provided an initial guess for the rotor RPM for various airspeeds, the schedule was verified with steady flight simulations in DEPSim. These flight simulations revealed the significant role of aerodynamic interactions between the lift rotors in the front and the wing (Figure 4(a)), especially at airspeeds higher than 30 knots.



(a) Steady flight simulation at 70 knots: CHARM wake visualization



(b) Adverse roll moment mechanism due to the original design of the control mixer

Figure 4. Aerodynamic interactions between the lift rotors and the wing resulting in an adverse roll moment (Mukherjee et al., 2023).

A deeper connection between the design of the flight controller and the impact of aerodynamic interactions was also investigated. It was found that the design of the control mixer plays a significant role. As shown in Figure 4(b), the “original mixer” for the aircraft used the thrust differential between the front rotors to counteract any roll moment destabilizing the aircraft. During forward flight (after 30 knots), the wake from the front rotors would be the source of an opposing roll moment as their circulation strengths would be unequal. The “original mixer” design would aggravate the problem by increasing the thrust differential even more, thus creating a cycle broken only by saturation of ailerons. This behavior is represented in Figure 5(a). The spike in opposing roll moments due to wake interactions can be seen to drastically increase in magnitude compared with moments generated in the absence of interactions before settling at a steady value. Modifying the controller design, where the commands for counteracting the aircraft roll are decoupled from the thrust differential of the front rotors, results in a drastic reduction in the peak magnitude of roll moments due to aerodynamic interactions (as shown in Figure 5(b)). This design is denoted as the “New Mixer” and was used for simulating transition maneuvers.

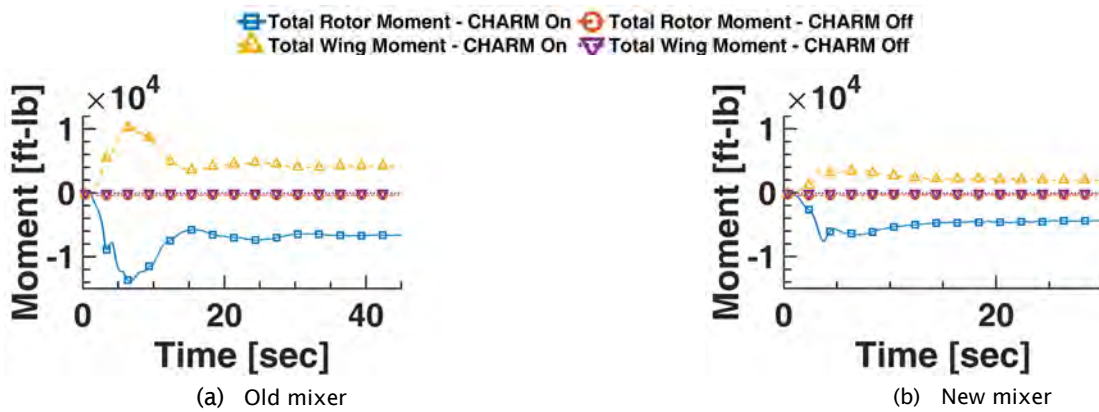


Figure 5. Steady flight simulation at 70 knots: breakdown of the roll moment between two different mixers (Mukherjee et al., 2023).

The transition maneuver was previously defined as an aircraft starting at low airspeed and ending at a speed of 110 knots with the lift rotors fully turned off. However, there are several different ways that an aircraft could transition. Three maneuvers were simulated in Mukherjee et al. (2023) with different strategies (shown in Figure 6). To make the noise from different transition maneuvers comparable, all of the maneuvers start at a hover at an altitude of 50 ft and end with the aircraft at an airspeed of 110 knots and an altitude of 1,000 ft (Figure 6(a)). In maneuver 1, the aircraft accelerates at a low altitude until it reaches 110 knots and then starts climbing to 1,000 ft. In maneuver 2, the aircraft accelerates vertically upwards until it reaches 1,000 ft and then accelerates to an airspeed of 110 knots. Maneuver 3 is a combination of maneuvers 1 and 2, where the aircraft is climbing and accelerating at the same time and at the same rates. The horizontal

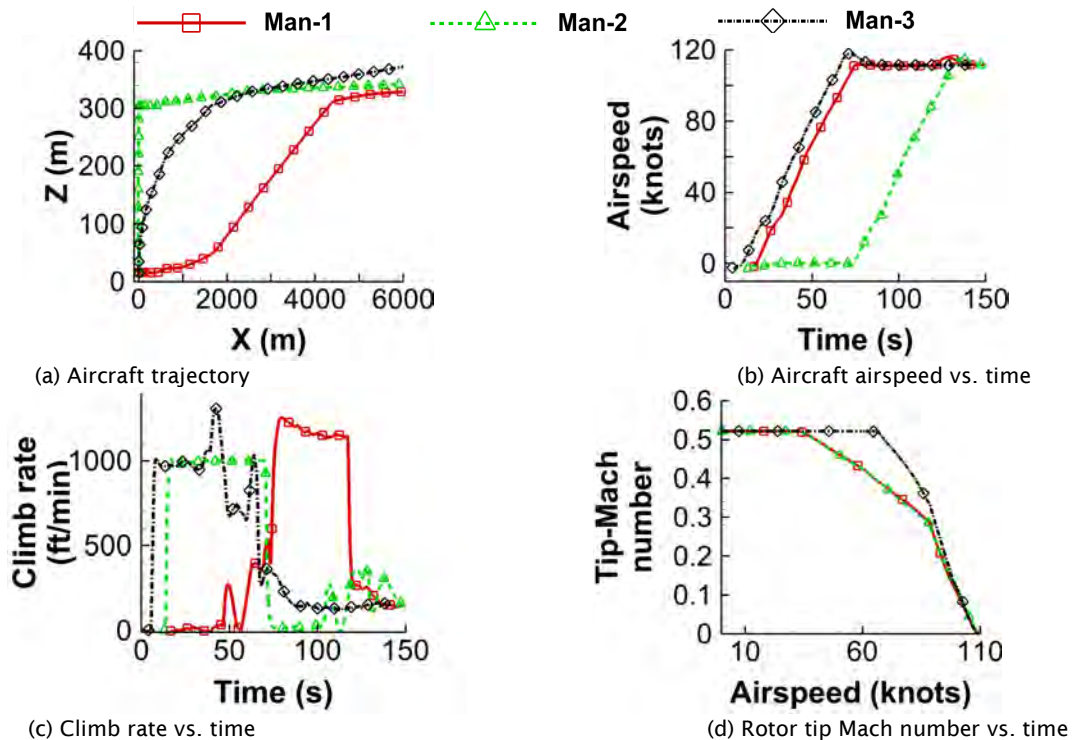


Figure 6. Aircraft trajectory and states throughout maneuvers 1-3 (Mukherjee et al., 2023).

and vertical accelerations are 0.1g for all maneuvers. Figure 6(d) shows that all maneuvers follow the same rotor speed schedule, except for maneuver 3, as the rotors need to generate more thrust to maintain the horizontal and vertical accelerations.

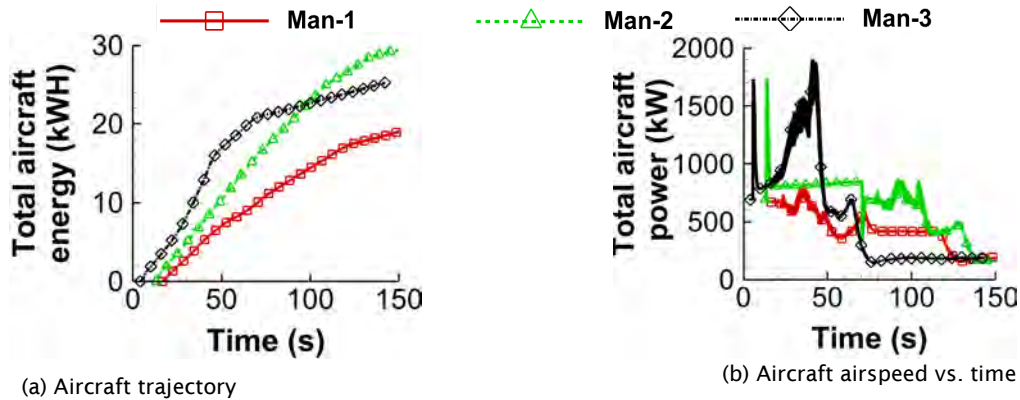


Figure 7. Comparison of aircraft energy and power for transition maneuvers (Mukherjee et al., 2023).

A review of aircraft energy and power consumptions (Figure 7) shows that maneuver 2 consumes the most energy, whereas maneuver 3 has the highest peak power requirement, indicating that the aircraft utilizing the wing for the longest possible time has the more efficient operation, as in maneuver 1. This benefit in efficiency is also reflected in the noise levels. The sound exposure level for the whole maneuver was calculated on a measurement plane, as shown in Figures 8-10.

Maneuver 1 was observed to have the lowest acoustic impact of the three maneuvers (Figure 8); however, this low-climb rate may be difficult to use from vertiports in urban areas. The efficacy of the rotor RPM schedule determined previously can be observed by comparing the total aircraft noise with and without the component of stall. The differences between contours in Figures 8(a) and (b) are small, indicating the success of the rotor RPM schedule in mitigating stall noise. This trend can be seen by comparing the lateral extent of the 60 dBA contour for the case with stall (see Figure 8(a)), which extends slightly more than $\pm 1,500$ m, whereas the lateral extent is slightly less than $\pm 1,500$ m for the case without stall (see Figure 8(b)). Similar observations can be made in Figure 9, where the rotor speed schedule is successful in mitigating stall noise. However, Figure 10 shows that stall noise is not mitigated for maneuver 3 with the current rotor RPM schedule.

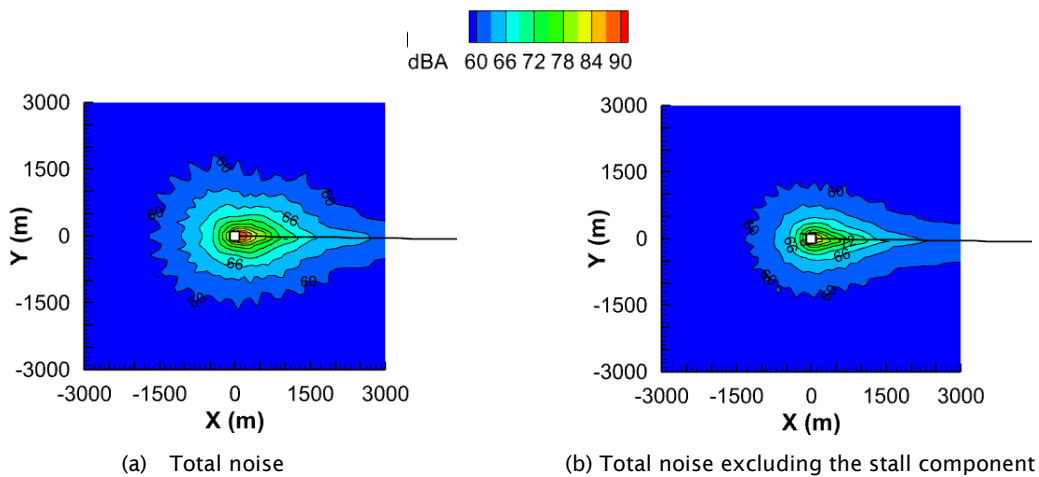


Figure 8. Sound exposure levels for a level-acceleration maneuver (maneuver 1) (Mukherjee et al., 2023).

This result can be attributed to the fact that the setpoint schedule was developed for a rotor operating in level flight, whereas the rotor operating in maneuver 3 is continuously climbing. Comparing Figures 9(b) and 10(b) reveals that maneuver 3 could have a lower acoustic impact than maneuver 2 if the stall is mitigated well.

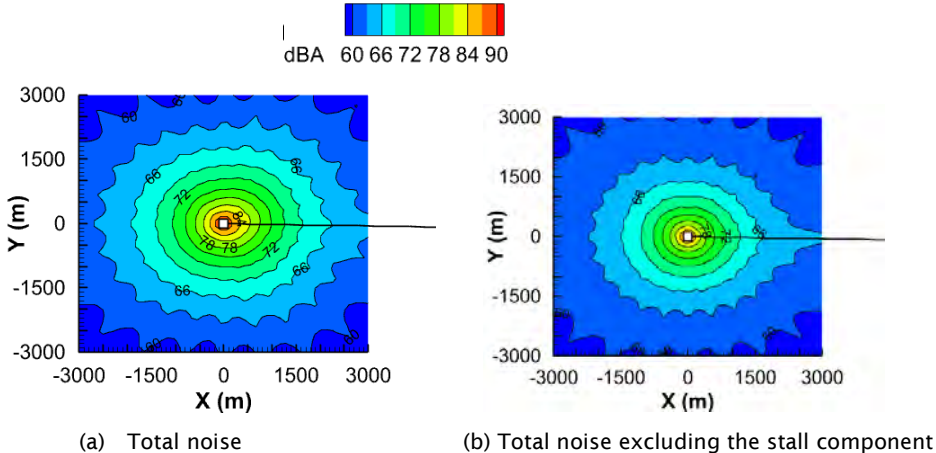


Figure 9. Sound exposure levels for an axial-climb maneuver (maneuver 2) (Ref. 17.1).

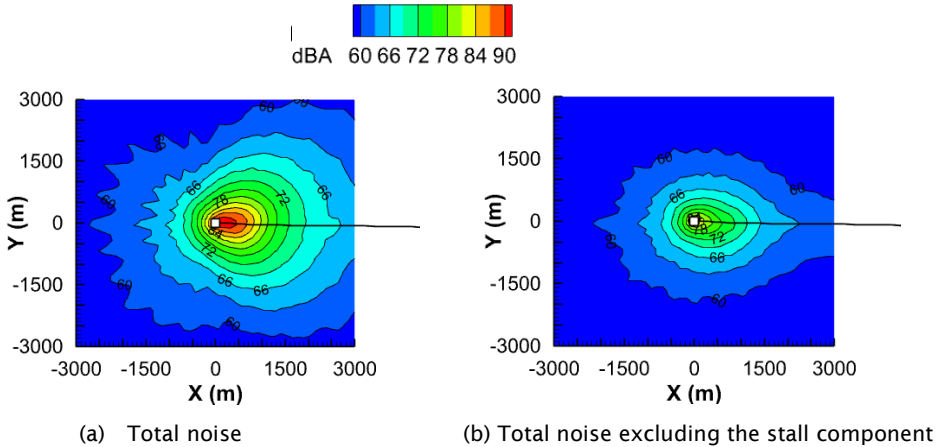


Figure 10. Sound exposure levels for a continuous-climb maneuver (maneuver 3) (Mukherjee et al., 2023).

Publications

Mukherjee, B., Jue, A., Theron, J. P., Brentner, K. S., Greenwood, E., & Horn, J. F. (2023). Investigation of departure transition noise for lift-plus-cruise eVTOL aircraft. In *79th Vertical Flight Society Annual Forum and Technology Display, FORUM 2023*. Vertical Flight Society.

Outreach Efforts

None.

Awards

None.

Student Involvement

Bhaskar Mukherjee, a graduate assistant pursuing his PhD at Penn State, is working on flight control and piloting strategies for low-noise operations of eVTOL aircraft.

Plans for Next Period

The acoustic analysis conducted in this task did not include potentially important sources of noise such as blade vortex interactions, blade wake interactions (BWIs), or the wing as a source of loading noise. Future work aims to extend current analyses and to revisit the conclusions drawn in Mukherjee et al. (2023).

Reference

Mukherjee, B., Jue, A., Theron, J. P., Brentner, K. S., Greenwood, E., & Horn, J. F. (2023). Investigation of departure transition noise for lift-plus-cruise eVTOL aircraft. In *79th Vertical Flight Society Annual Forum and Technology Display, FORUM 2023*. Vertical Flight Society.

Task 2 – Validate eVTOL Noise Prediction System with UAS or Helicopter Flight Tests

The Pennsylvania State University

Objective

One objective of this task is to validate predictions of time-varying multirotor broadband noise using experimental data. This effort includes determining and quantifying causes of broadband noise modulation that is aperiodic with the blade passage frequency (BPF) observed in experimental data.

Research Approach

Multirotor noise measurements were analyzed to study how azimuthal phasing between rotors affects broadband noise modulation. The dataset studied was collected for ASCENT Project 77, consisting of three rotors of a small UAS in fixed hover in an anechoic chamber.

To study the causes of broadband noise modulation that is aperiodic with the BPF observed in experiments, the aperiodicity caused by random sample realizations of stochastic noise (caused by random turbulent fluctuations) was predicted. This step helps to quantify how much of the observed aperiodic broadband noise modulation is caused by stochastic realizations versus physical sources of aperiodicity (e.g., aerodynamic interactions, state variable fluctuations).

Milestones

The milestones reached for this task include demonstrating the importance of time-varying multirotor broadband noise, which involved determining that the modulation amplitudes are significant (i.e., the broadband noise modulations of individual rotors do not sum to be constant with time) even when rotor rotation speeds fluctuate. Furthermore, the relative azimuthal phasing between rotors was shown to significantly affect the amplitude of the total broadband noise modulation.

Another milestone reached was the development of a data processing framework for predicting broadband noise that is aperiodic with the BPF caused by realizations of random samples of stochastic broadband noise, which is then compared with the total aperiodic broadband noise modulation. This framework was validated by using synthetic bandpass noise.

Major Accomplishments

Our results showed that multirotor broadband noise modulation is significant and varies greatly depending on the azimuthal phasing between rotors. Noise was measured for three rotors of a small UAS in fixed hover in an anechoic chamber for ASCENT Project 77. All rotors were operated at the same nominal rotation rate, controlled to be as constant as possible, but small fluctuations are always present in experiments because the rotors were not mechanically connected. The azimuthal phasing between rotors was varied in the following cases:

- Incoherent phase offset: No effort is made to synchronize the azimuthal phase between rotors, which is characteristic of typical flight.
- Zero phase offset: All rotors always have the same azimuthal phase, which is characteristic of typical predictions.

- “Optimal” and “pessimal” phase offsets: All rotors are controlled to attempt to maintain the same azimuthal phase *offset* throughout operation. The values for the “optimal” and “pessimal” phase offsets were determined by attempting to minimize (“optimal”) and maximize (“pessimal”) the time-averaged overall sound pressure level (OASPL) measured for a few observers. Broadband noise modulation was NOT optimized, hence the quotes around “optimal” and “pessimal.”

The modulation depths at the BPF for each of these cases, as well as that of a single rotor for reference, are summarized in Table 1. Modulation depth is defined as the difference between the maximum and minimum sound pressure levels (SPLs) in decibels (dB) during the time variation. For Table 1, the broadband SPL (BBSPL) was calculated as follows:

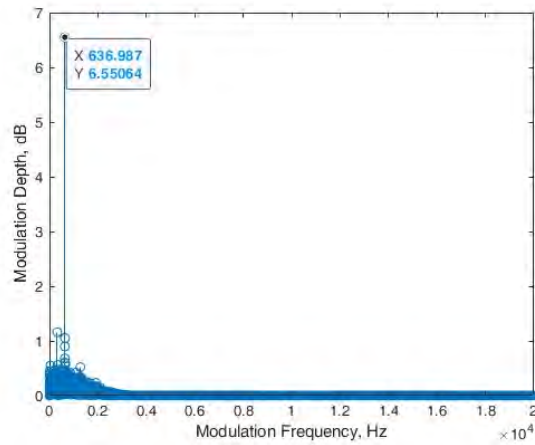
1. The spectrogram is computed by using a time window smaller than the blade passage period.
2. Each spectrogram window is integrated within the broadband noise frequency range, chosen to be above discrete frequency tones. For the data in Table 1, the broadband noise frequency range was chosen as 5–20 kHz, which gives a time history of the BBSPL.
3. The power spectral density of the BBSPL time history is determined. The power spectral density gives the modulation amplitude of the BBSPL as a function of modulation frequency, which is not to be confused with noise frequency.
4. The modulation amplitude is added and subtracted at each modulation frequency about the time-averaged broadband noise (i.e., BBSPL at zero modulation frequency). This step gives the modulation depth at each modulation frequency.

Table 1. Multirotor broadband noise modulation as a function of azimuthal phasing. All microphones are located in the far field at -27° elevation. BPF: blade passage frequency.

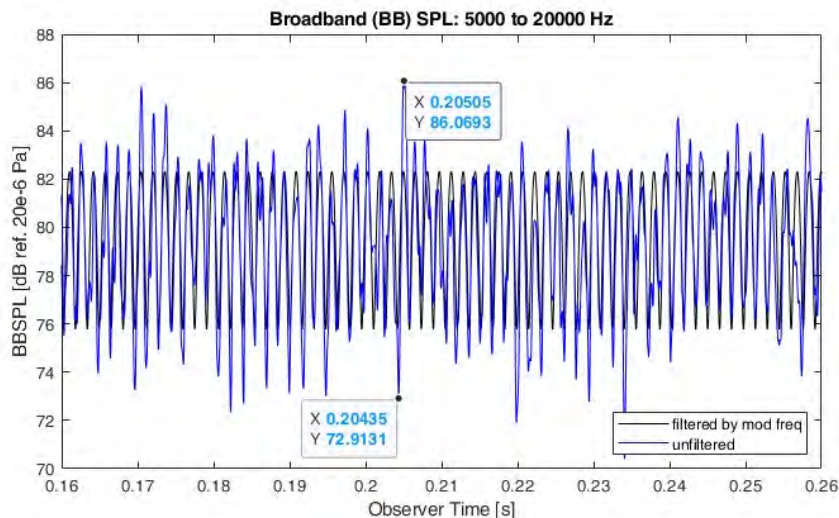
Case	Time-averaged broadband noise, dB	Modulation depth at BPF, dB
Single rotor	59.6	8.1
Three rotors: incoherent phase	66.6	3.5
Three rotors: zero-phase offset	66.4	6.5
Three rotors: “optimal” phase offset	66.6	2.6
Three rotors: “pessimal” phase offset	66.7	8.5

For all cases in Table 1, the broadband noise varies significantly over time. This is contrary to predictions in the literature, which predict broadband noise to be fairly constant with time for many rotors, with the modulation depth decreasing as the number of rotors increases (Li & Lee, 2022). In fact, the modulation depth of a single rotor is not necessarily always larger than that of multiple rotors summed together. Such a result is seen for the “pessimal” case in Table 1, which has a greater modulation depth than the single-rotor cases. However, note that the single rotor has lower time-averaged broadband noise than the multirotor cases and that decibels are nonlinear units. Table 1 also demonstrates the importance of azimuthal phasing between rotors in multirotor broadband noise modulation, despite fluctuations in rotor rotation rates causing variations in the phase offsets between rotors. For example, there is a 6-dB difference in modulation depth between the “optimal” and “pessimal” cases. This result not only demonstrates opportunities for phase control to reduce broadband noise modulation, but also emphasizes the need to predict this uncertainty in multirotor broadband modulation caused by phase variations.

The results shown in Table 1 consider only the broadband modulation at the BPF, which is dominant. Figure 11(a) shows the modulation depth as a function of modulation frequency, calculated using the procedure described above. In Figure 11(a), modulation frequencies aside from the BPF of 637 Hz seem to contribute much smaller modulation depths individually; however, note that the modulation depths with different modulation frequencies cannot be linearly added using decibel units. Although Figure 11(a) suggests that modulation frequencies aside from the BPF are not significant, the other modulation frequencies cause significant aperiodic modulation about the BPF, as demonstrated in Figure 11(b), where the modulation at the BPF alone (black line) is compared with the total modulation (blue line). Although the BPF well represents the average modulation, occasional instances show modulation depths that are more than 6 dB greater than the BPF modulation, for example, as indicated by the data markers in Figure 11(b).



(a) Power spectral density of the modulation depth of the BBSPL time history as a function of modulation frequency, for a three-rotor case with zero phase offset.



(b) BBSPL time history for the three-rotor case with zero phase offset: raw/unfiltered (blue) and filtered to only include modulation with the blade passage frequency (black).

Figure 11. Broadband sound pressure level (BBSPL) modulation for the three-rotor case with zero phase offset.

The results in Figure 11 motivate further analysis of this broadband noise modulation that is aperiodic with the BPF. To quantify how much of the observed aperiodicity is caused by stochastic realizations versus physical sources of aperiodicity (e.g., aerodynamic interactions, state variable fluctuations), the aperiodicity caused by stochastic realizations was predicted and compared with the total aperiodicity.

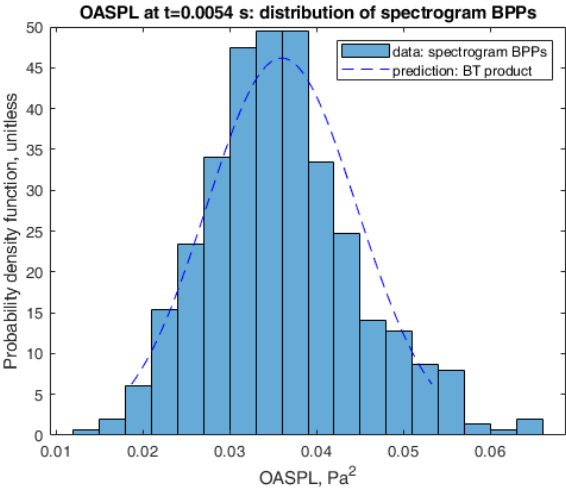
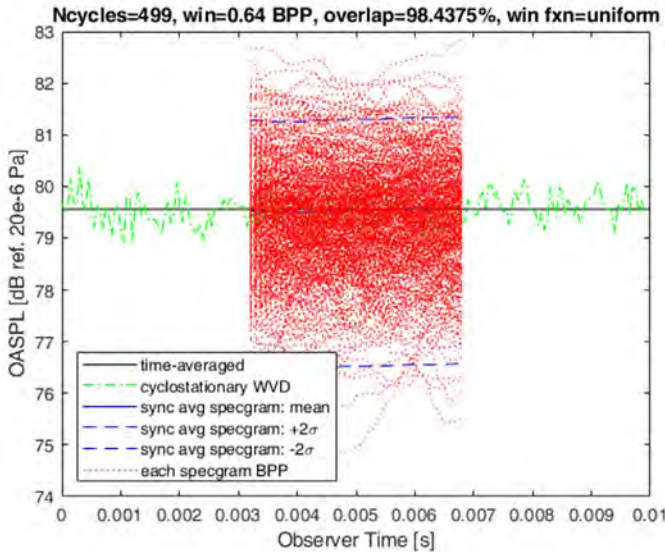
The total aperiodicity was computed by dividing the acoustic pressure time history into individual blade passages and then computing the time variation of the BBSPL (as described previously in this section) for each blade passage. At each timestep/phase in the blade passage period, the variance in BBSPL across all blade passages represents the total aperiodicity in broadband noise modulation between blade passages.

Next, the aperiodicity in broadband noise modulation caused by realizations of stochastic noise alone was predicted by using the bandwidth-time (BT) product. The statistical bandwidth B (Bendat & Piersol, 2011) is predicted at each

timestep/phase within the blade passage period by synchronously averaging (at each time) the spectrogram of all blade passages. The time duration T is the time window length used to compute the spectrogram and BBSPL. The BT product predicts the variance (and standard deviation) of the BBSPL at each timestep/phase in the blade passage period caused by stochastic realizations alone. This method predicts the BBSPL to have a Gaussian distribution at each timestep, such that the 95% confidence interval is ± 2 standard deviations σ away from the mean BBSPL, which is obtained by synchronously averaging the BBSPL across all blade passages.

To demonstrate and validate these methods of quantifying aperiodic broadband noise modulation, the methods were applied to synthetic bandpass noise. Figure 12(a) shows the time variation in OASPL over a chosen “blade passage period” of 0.01 s, which is representative of rotorcraft (e.g., helicopter tail rotor, UAS, or UAM). Each of the red lines in Figure 12(a) represents the OASPL time variation of individual blade passages, which demonstrate significant aperiodic deviations from the mean time-averaged OASPL (solid black line). This aperiodicity must be caused by stochastic realizations alone, as this is a synthetic case. In particular, the short time window T , which must be less than a blade passage period, causes substantial variation in the OASPL level between blade passages. The blue dashed lines in Figure 12(a) show the 95% confidence interval predicted using the BT product, which does indeed appear to include 95% of the individual blade passages (red lines).

The distribution of OASPL across all blade passages is better represented at a single timestep in Figure 12(b), where the bars of the histogram represent the total aperiodicity of all blade passages, and the dashed line represents the aperiodicity predicted using the BT product. The aperiodicities computed by these two independent methods show good agreement, demonstrating that the total aperiodic broadband noise modulation is caused solely by realizations of stochastic noise, as expected for this synthetic case. Therefore, the data processing framework developed to quantify causes of broadband noise modulation that is aperiodic with the BPF has been successfully validated.



(a) Time variation of the OASPL of bandpass noise over the BPP: time-averaged noise (solid black), individual blade passages (dashed red), and 95% confidence interval predicted using the BT product (long dashed blue).

(b) Distribution of the OASPL among blade passages at a single timestep: from individual blade passages (bars) and predicted by the BT product (dashed line).

Figure 12. Data processing framework for quantifying broadband noise modulation that is aperiodic with the blade passage frequency. BPP: blade passage period; BT: bandwidth–time; OASPL: overall sound pressure level; WVD: Wigner–Ville decomposition.

Publications

None.

Outreach Efforts

None.

Awards

None.

Student Involvement

Ze Feng (Ted) Gan, a graduate research assistant currently working toward his PhD degree at Penn State, analyzed time-varying (multirotor and aperiodic) broadband noise for this task.

Plans for Next Period

The multirotor broadband noise modulation results described in the Major Accomplishments section motivate a study of how the broadband noise modulations of individual rotors sum together, including the impact of phase. This aspect will be explored by comparing noise measurements of individual and simultaneously operating rotors, as well as predictions. Predictions will be enhanced to estimate the broadband noise modulation that is aperiodic with the BPF caused by stochastic realizations.

The data processing framework developed to quantify causes of broadband noise modulation that is aperiodic with the BPF, which was described and validated in the Major Accomplishments section above, will be applied to experimental data. If the total aperiodicity cannot be predicted from stochastic realizations alone, this would imply that the excess aperiodic broadband noise modulation must be caused by physical sources of aperiodicity.

References

Bendat, J. S., & Piersol, A. G. (2011). *Random data: analysis and measurement procedures*. John Wiley & Sons.
Kevin Li, S., & Lee, S. (2022). Acoustic analysis and sound quality assessment of a quiet helicopter for air taxi operations. *Journal of the American Helicopter Society*, 67(3), 1-15.

Task 3 – Complete the Implementation of Time-varying Noise Modeling

The Pennsylvania State University

Objective

The objective of this task is to implement time-varying broadband noise predictions in the PSU-WOPWOP noise prediction code for external release. This framework enables computation of the time variation of the broadband noise spectrum within a rotor or blade passage period, caused by edgewise flight and/or aerodynamic interactions. Time-varying broadband noise has been shown to be important for helicopters, but the full ramifications are not understood for helicopters, let alone UAM aircraft.

In contrast, aircraft noise literature typically analyzes only time-averaged spectra, neglecting time variation within a blade passage period. Previous time-varying broadband noise results, e.g., those published in Gan et al. (2021) and Gan et al. (2023), were generated using a prototype code not available for external release.

Research Approach

The Brooks, Pope, and Marcolini model for airfoil self-noise was implemented as a time-varying broadband noise model. Self-noise refers to the broadband noise generated by turbulence that develops over the airfoil. This airfoil broadband noise model was implemented using a blade element approach by incoherently summing the noise from blade sections under a quasi-steady assumption. The quasi-steady assumption assumes that the noise generated by an airfoil in an unsteady flow is equivalent to the noise generated by an airfoil in the same steady flow conditions.

Milestone

The milestone reached for this task was full implementation of time-varying broadband noise predictions in PSU-WOPWOP for external release, including capabilities for observer parallelization and postprocessing. See Task 21 for documentation of the added PSU-WOPWOP capabilities.



Major Accomplishments

Time-varying broadband noise prediction capabilities were successfully added to PSU-WOPWOP for external release. Features of this improved prediction code include observer parallelization, enabling the noise to be computed for many observers in parallel, thus reducing the run-time. Postprocessing options include atmospheric attenuation and A-weighting. Adding these capabilities required fixing a pre-existing bug that prevented postprocessing of overlapping time segments.

Time-varying noise result files conveniently include all timesteps in one file, for both single observers (Tecplot file format) and multiple observers (Plot3D file format) and both discrete-frequency and broadband noise. Previously, time-varying discrete-frequency noise results in PSU-WOPWOP were output in one file per time segment, but this would generate a prohibitively large (hundreds to thousands) number of files for time-varying broadband noise, which analyzes many time segments within a single rotor revolution. The standard output file formats allow the time-varying noise results to be used in a variety of plots (e.g., spectrograms, animated contour plots, and hemispheres) in various commonly used data visualization software.

Publications

None.

Outreach Efforts

None.

Awards

None.

Student Involvement

Ze Feng (Ted) Gan, a graduate research assistant currently working toward his PhD degree at Penn State, implemented the time-varying broadband noise prediction code for this task.

Plans for Next Period

The completed code will be used to study time-varying broadband noise of a variety of aircraft under various flight conditions.

References

- Gan, Z. F. T., Brentner, K. S., & Greenwood, E. (2021, January). Time variation of rotor broadband noise. In *Vertical Flight Society 9th Biennial Autonomous VTOL Technical Meeting, Virtual* (pp. 26-28).
- Gan, Z. F. T., Brentner, K. S., & Greenwood, E. (2022). Time variation of helicopter rotor broadband noise. In *28th AIAA/CEAS Aeroacoustics 2022 Conference* (p. 2914).

Task 4 – Study Aerodynamic Interaction Effects on eVTOL Noise

The Pennsylvania State University

Objective

Aerodynamic interaction effects are expected to be an important contributor to eVTOL noise. Task 16 (2022 annual report) indicated the need to include turbulent ingestion noise (TIN) and other aerodynamic interactions when calculating broadband noise from eVTOL aircraft. The goal of this task is to integrate fundamental physics governing TIN into aerodynamic and acoustic calculations.

Research Approach

To better fit with the time-domain tools used in the Penn State eVTOL noise prediction system, a new tool, PSU-MULTINoise, was developed. This tool is the time-domain implementation of Amiet's broadband noise theory (Amiet, 1975). PSU-MULTINoise is responsible for generating unsteady airloads, which in turn generate broadband noise scattered from the leading and trailing edges of an airfoil.



Milestones

The milestones reached for this task include the following:

- Validation of the PSU-MultINoise code with data reported by Paterson and Amiet (Amiet, 1975)
- Expansion of the PSU-MultINoise code to calculate BWI airloads and preliminary validation with data from the HART-II rotor test campaign (Burley & Brooks, 2004)

Major Accomplishments

This code is fundamentally based on Amiet’s leading edge scattering theory (Amiet, 1975). Amiet successfully derived a formulation describing pressure loads developed by a flat-plate airfoil in a turbulent stream. It should be noted that the turbulent stream can be non-isotropic; however, for simplicity, Amiet started with an isotropic turbulent gust formulation. When this gust impinges on the airfoil, a surface dipole distribution is induced to satisfy the condition of no flow through the airfoil surface and the Kutta condition at the trailing edge. This surface dipole distribution causes a pressure jump Δp across the airfoil given by the following:

$$\Delta p(y_1, y_2, t) = 2\pi\rho_0 U \int_{-\infty}^{\infty} \tilde{w}(k_1, k_2) g(y_1, k_1, k_2) e^{i(k_1 U t - k_2 y_2)} dk_1 dk_2, \quad (1)$$

where y_1, y_2 are the coordinates along the chord and span of a flat-plate airfoil, U and ρ_0 are the freestream velocity and density, respectively, $\tilde{w}(k_1, k_2)$ is the wavenumber spectrum of an unsteady gust $w(y_1, y_2, t)$ with amplitude w_0 , and $g(y_1, k_1, k_2)$ is the dual wavenumber transfer function. Amiet derived an expression for the transfer function for a flat-plate airfoil. Casper and Farassat (2002) used the real component of the complex-valued unsteady pressure jump provided by Equation 1 to derive a time-domain formulation of surface pressure that can be used for predicting the desired broadband noise. The infinite wavenumber domain was integrally discretized and truncated to the largest wavenumber $k_{1,N}$, representing an “upper cutoff” wavenumber beyond which the spectral density amplitude (represented by $w(k_1, k_2)$) is considered negligible. An important input here is in the description of $w(k_1, k_2)$. Various analytical expressions such as the von Kármán interpolation (von Kármán, 1948) describe turbulent fields in terms of velocity gust components. Equation 1 provides the unsteady airloads on a flat-plate airfoil that can be fed into PSU-WOPWOP, where the noise can be propagated to an observer using Farassat’s Formulation 1A.

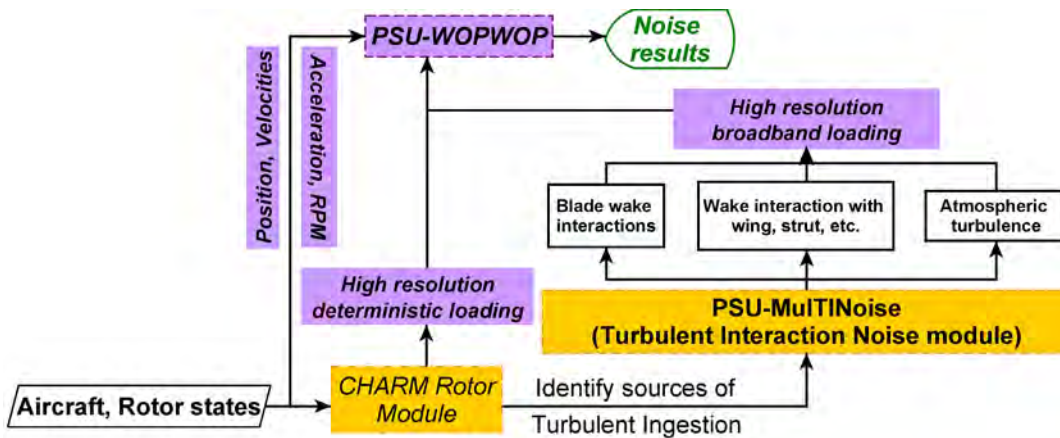


Figure 13. CHARM-PSUMultINoise-PSUWOPWOP system. RPM: revolutions per minute.



This implementation with PSUMultINoise was validated by comparing the results with experimental data measured by Paterson and Amiet (Paterson & Amiet, 1977). In their experiment, a NACA-0012 wing section was placed in a wind tunnel with turbulence generated by a mesh upstream impinging on the wing section. Experimental measurements provided the required inputs to represent this turbulence as a von Kármán spectrum that is used to describe the various components of outburst as an input to Equation 1. Note that the acoustic spectrum from PSU-WOPWOP has been filtered to the same bandwidth as the experiment (55.7 Hz) and shear-layer corrections have also been included as described by the experimental data processing methodology (Paterson & Amiet, 1977). Figure 14 shows excellent agreement between the predictions of PSU-WOPWOP (using loads from PSU-MULTINoise) and experimentally measured data.

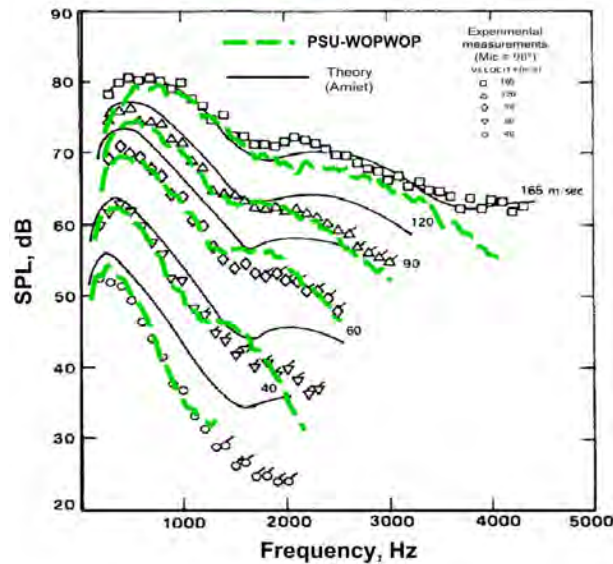


Figure 14. Comparison between spectra predicted by PSU-MULTINoise and measured experimentally (Paterson & Amiet, 1977). SPL: sound pressure level.

To calculate the loading due to BWI in PSU-MULTINoise, an output file from CHARM is used, which contains information on various wake interactions as well as interaction angles and miss distances between the vortex cores and interacting blades. This information is processed to identify locations of potential BWI. A semi-empirical model by Glegg et al. (1999) is implemented to calculate the required gust velocities ($w(y_1, y_2, t)$) as an input to Equation 1. This model is a modified von Kármán spectrum (Figure 15). PSU-MULTINoise then calculates the unsteady pressure loads along the chord of the blade section undergoing BWI as an input to PSU-WOPWOP.



To validate the implementation of this model, a case was created using information provided by Burley & Brooks (2004) for the HART-II rotor (four-bladed rotor). For the test case, the blades have a rectangular planform with a chord length of 0.121 m and NACA 23012 airfoil sections. The rotor is rotating at 1,040 rpm and operating at an airspeed of 32.9 m/s. The flight angle of attack is 5.3° (in ascent). Data files for the geometry, loading, and Brooks, Pope, and Marcolini model are obtained from CHARM. Figure 16 shows a comparison between the PSU-WOPWOP prediction for various broadband noise components and the prediction obtained by Brooks and Burley at observer locations of (2.0, 1.6, -2.3) m and (-0.5, 2.2, -2.3) m. Note that the “jaggedness” in the spectrum is a result of the time-domain calculations and is physical. Filtering techniques can be used to smooth the spectrum. However, the predictions qualitatively capture the trends, including the slope of the spectrum. The BWI peak is underpredicted.

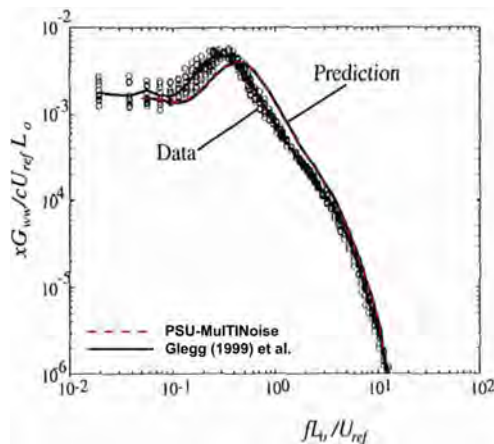


Figure 15. Comparison of wake spectral density (G_{ww}) between the Glegg et al. (1999) model and PSU-MultiNoise.

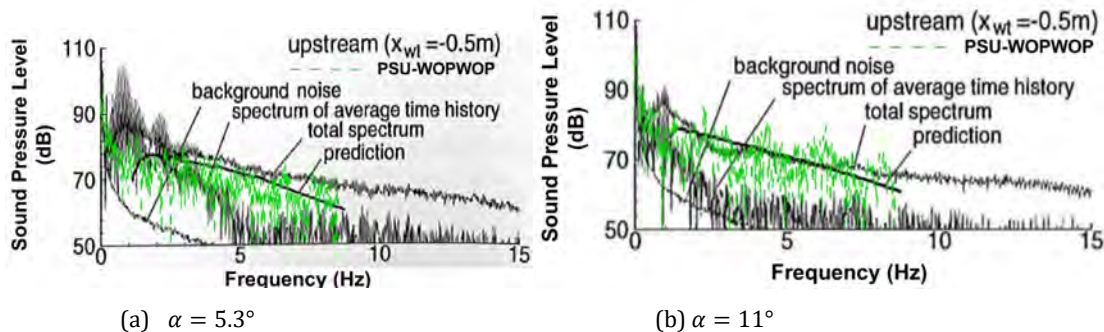


Figure 16. Comparison between blade wake interactions predicted by PSU-WOPWOP and those predicted in Figures 28–29 of Burley & Brooks (2004) for observer location (-0.5 m, 1.6 m, -2.3 m).

Publications

None.

Outreach Efforts

None.

Awards

None.

Student Involvement

Bhaskar Mukherjee, a graduate assistant working on his PhD at Penn State, is creating PSU-MULTINoise to predict airloads responsible for generating broadband noise due to interaction with turbulence.

Plans for Next Period

- The BWI implementation will be validated with helicopter flight test data, previously investigated in ASCENT Project 38.
- PSU-MULTINoise will be updated to include other rotor wake interaction mechanisms. The time-domain approach will be implemented for multiple rotors.

References

- Amiet, R. K. (1975). Acoustic radiation from an airfoil in a turbulent stream. *Journal of Sound and vibration*, 41(4), 407-420. DOI: [https://doi.org/10.1016/S0022-460X\(75\)80105-2](https://doi.org/10.1016/S0022-460X(75)80105-2).
- Burley, C. L., & Brooks, T. F. (2004). Rotor broadband noise prediction with comparison to model data. *Journal of the American Helicopter Society*, 49(1), 28-42. DOI: <https://doi.org/10.2514/6.2001-2210>.
- Casper, J., & Farassat, F. (2002). A new time domain formulation for broadband noise predictions. *International Journal of Aeroacoustics*, 1(3), 207-240. DOI: <https://doi.org/10.1260/147547202320962574>.
- Glegg, S. A., Devenport, W. J., Wittmer, K. S., & Pope, D. S. (1999). Broadband helicopter noise generated by blade wake interactions. *Journal of the American Helicopter Society*, 44(4), 293-301. DOI: <https://doi.org/10.4050/JAHS.44.293>.
- Paterson, R. W., & Amiet, R. K. (1977). Noise and surface pressure response of an airfoil to incident turbulence. *Journal of Aircraft*, 14(8), 729-736. DOI: <https://doi.org/10.2514/3.58845>.
- von Kármán, T., "Progress in the Statistical Theory of Turbulence", Proceedings of the National Academy of Sciences of the United States of America, Vol. 34, No. 11, 1948, pp. 530-539.

Task 5 – Document the Use of the eVTOL Noise Prediction System

The Pennsylvania State University

Objective

The objective of this task is to document the eVTOL noise prediction system and its components, including example cases, such that new users can easily learn to use this tool.

Research Approach

In addition to documentation describing how to use the noise prediction system, example cases are provided to highlight new prediction capabilities and file formats. These example cases also serve as validation cases to ensure that the system is operating as expected. Example cases are automatically validated according to a regression testing procedure (checksuite).

Milestones

The milestones reached for this task include documenting new prediction capabilities for time-varying broadband noise, as summarized in Task 19 above. The existing PSU-WOPWOP user manual was updated to include instructions on how to predict time-varying broadband noise. Example cases are provided, and the checksuite was updated to automatically validate the file formats of these new time-varying noise results.

Major Accomplishments

Instructions describing the user input options for predicting time-varying broadband noise were documented in an updated version of the PSU-WOPWOP user manual. The user manual was also updated to describe the new time-varying result file formats, for both single observers (Tecplot file format) and multiple observers (Plot3D file format). Example cases based on the ideally twisted rotor of NASA (Pettingill et al., 2021)) are provided for cases with single and multiple observers. The checksuite was updated to automatically validate time-varying noise result files for multiple observers (Plot3D format). The checksuite was also updated to enable automatic validation of result files located in nested directories.



Publications

None.

Outreach Efforts

None.

Awards

None.

Student Involvement

Ze Feng (Ted) Gan, a graduate research assistant currently working toward his PhD degree at Penn State, documented time-varying broadband noise prediction capabilities for this task.

Plans for Next Period

Although the checksuite was updated to automatically validate time-varying noise result files for multiple observers (Plot3D format), the checksuite must also be updated to automatically validate time-varying noise result files for single observers (Tecplot file format). For now, single-observer time-varying noise result files are validated by visual inspection of the results.

The PSU-WOPWOP user manual will be updated to make the tools more accessible to users, including sample cases, which will be described in detail. The user manual revision will also provide more in-depth theory of time-varying broadband noise predictions, including the underlying assumptions. This information has already been outlined in past conference papers published on the work of this project (Gan et al., 2021; Gan et al., 2023).

Example files (e.g., Tecplot layout files) will be provided to illustrate common visualizations, such as spectrograms, contour plots, and hemispheres for a single timestep and contour plot and hemisphere animations between timesteps.

References

- Gan, Z. F. T., Brentner, K. S., & Greenwood, E. (2021, January). Time variation of rotor broadband noise. In *Vertical Flight Society 9th Biennial Autonomous VTOL Technical Meeting, Virtual* (pp. 26-28).
- Gan, Z. F. T., Brentner, K. S., & Greenwood, E. (2022). Time variation of helicopter rotor broadband noise. In *28th AIAA/CEAS Aeroacoustics 2022 Conference* (p. 2914).
- Pettingill, N. A., Zawodny, N. S., Thurman, C., & Lopes, L. V. (2021). Acoustic and performance characteristics of an ideally twisted rotor in hover. In *AIAA Scitech 2021 Forum* (p. 1928).



Project 050 Over-Wing Engine Placement Evaluation

Final Report

Georgia Institute of Technology

Project Lead Investigators

Principal Investigator:

Professor Dimitri N. Mavris

Director, Aerospace Systems Design Laboratory

School of Aerospace Engineering

Georgia Institute of Technology

Phone: (404) 894-1557

Fax: (404) 894-6596

Email: dimitri.mavris@ae.gatech.edu

Co-Principal Investigator:

Dr. Chung Lee

Research Engineer

Aerospace Systems Design Laboratory

School of Aerospace Engineering

Georgia Institute of Technology

Phone (c/o): (404) 894-0197

Fax: (404) 894-6596

Email (c/o): jimmy.tai@ae.gatech.edu

University Participants

Georgia Institute of Technology

- P.I.: Dr. Dimitri Mavris and Co-P.I. Dr. Chung Lee
- FAA Award Number: 13-C-AJFE-GIT-057
- Period of Performance: February 5, 2020 through February 29, 2024
- Tasks relevant for this period:
 1. Creation of single aisle aircraft mission model and a baseline high bypass turbofan propulsion cycle model
 2. Parametric geometry generation
 3. Formulation of MDAO problem
 4. Generation of CFD templates and automation scripts
 5. Stage 1 design: nacelle and wing optimization (forward mounted OWN)
 6. Create ANOPP noise models
 7. Stage 2 design: engine re-design and airframe re-optimization (forward mounted OWN)
 8. Stage 3 design: nacelle and wing optimization (aft mounted OWN)
 9. Trajectory optimization and mission analysis
 10. Takeoff/high lift physics study

Project Funding Level

Georgia Institute of Technology (Georgia Tech) was initially funded at \$590,000 for a two-year project. Georgia Tech agreed to a total of \$590,000 in matching funds. Georgia Tech was then funded an additional at \$300,000 for a one-year project extension. Georgia Tech agreed to a total of \$300,000 in matching funds. This total includes salaries for the project director, research engineers, and graduate research assistants, as well as computing, financial, and administrative support, including meeting arrangements. The institute has also agreed to provide tuition remission for the students, paid for by state funds.



Investigation Team

PI: Dimitri Mavris

Co-Investigator: Chung Lee

2020

Propulsion and Systems Lead: Jonathan Gladin

Aerodynamics and CAD Geometry: Srujal Patel

Graduate Students: Salah Tarazi, Kenneth Decker, Stephanie Zhu, Christopher Eggert, Andrew Burrell, Christian Perron, and Jai Ahuja

2021-2022

Aerodynamics and Parametric Geometry: Jai Ahuja, Srujal Patel, and Kenneth Decker

MDAO Methods: Christian Perron

Mission and Systems Integration: Evan Harrison

Graduate Students: Mengzhen Chen, Sam Crawford, Marc Koerschner, Bilal Mufti, James Van der Linden, Anish Vegesna, Andrew Burrell, Savri Gandhi, Richard D'Cruz, and Samuel Moore

2023-2024

Aerodynamics and Parametric Geometry: Jai Ahuja and Srujal Patel

Propulsion Lead: Jai Ahuja

MDAO Methods: Christian Perron

Mission and Systems Integration: Evan Harrison

Graduate Students: Samuel Moore, Richard D'Cruz, Savri Gandhi, Bilal Mufti, and Kavya Navaneetha Krishnan

Project Overview

The over-wing nacelle (OWN) aircraft concept has promising environmental benefits due to the engine noise shielding provided by the wings and the potential to reduce landing gear height and therefore gear noise. However, if not optimized, this engine placement may cause penalties in fuel burn due to aerodynamic interactions between the wing and propulsor. In this work, the team aims to develop an MDAO method for OWN aircraft. This task builds on past efforts by including noise shielding effects and optimizing the airframe geometry to minimize cruise fuel burn, and then optimizing the mission flight profile to minimize trip fuel burn. One major challenge is the computational expense of analyses such as computational fluid dynamics (CFD). Thus, the approach relies on multidisciplinary design analysis and optimization (MDAO) and efficient adaptive sampling techniques to use high-fidelity analyses where they are most needed for system analysis.

The optimization of an OWN aircraft configuration over a mission with noise constraints would enable accurate trade-offs between noise benefits and fuel burn. As a secondary benefit, the MDAO method sought to demonstrate efficient sampling methods for coupled, computationally intensive simulations in system analysis. These methods are useful to the FAA because many current applications require high-fidelity simulations to accurately assess physics phenomena such as noise and emissions. Both the OWN results and the MDAO techniques will enable more physics-informed decisions about the environment.

Work in 2020 focused on preliminary tasks to prepare a software tool chain and workflow for optimization, whereas efforts in 2021 focused on the execution of a full-scale MDAO process using supercomputing resources. Thus, the efforts in 2021 focused on a two-stage design process: nacelle location selection and preliminary shape optimization of the wing and nacelle. In 2022, we completed a second-stage shape optimization. We deliberately assumed the same basic engine cycle and aircraft size while optimizing both over-wing and under-wing configurations. We found a 4% higher fuel flow at cruise for the OWN design. However, this preliminary result did not account for higher bypass ratio engines that are possible due to engine clearance above the wing or for other mission segments such as climb. Higher bypass ratio engines were therefore a major focus of 2023 work.

In 2023, we designed a new engine cycle to reflect recent technology levels, and the larger bypass engine was used in both OWN and UWN optimization. In this effort, we also found that the OWN had substantially higher fuel burn than the UWN. However, this year, we also linked the aero-propulsion analyses to mission flight path (trajectory) optimization rather than simply computing fuel flow at a particular Mach and altitude scenario during cruise. The result is that an optimized OWN has approximately 7% higher fuel burn than a similarly optimized UWN over a reference mission. This prediction is based on

governing force-and-motion equations implemented for this effort to facilitate accounting for the intercoupled aero-propulsive effects influential in an OWN design and obtained by an optimal-control trajectory optimization with identical constraints between the two configurations. The researchers feel the results do not provide evidence that the OWN configuration considered here would be more fuel-efficient than its UWN counterpart.

2023 work differs from previous years by emphasizing two subsidiary goals in addition to the comparison of optimized OWN and UWN vehicles. First, we mentioned earlier that a trajectory optimization was conducted in each case to yield not only cruise fuel flow rate but also fuel burn over an entire mission. We used NASA’s Dymos optimal controls software and integrated coupled CFD-propulsion surrogates to optimize trajectories to minimize fuel burn. This development allowed a mission-level comparison of fuel burn. Finally, at request of FAA stakeholders, we also conducted a physics study of low speed/high lift configurations of OWN and UWN. The placement of the OWN nacelle allows the jet exhaust plume to blow over the wing, potentially increasing circulation and improving lift (and drag) characteristics. We did not optimize the geometries for takeoff, but simply used the 2022 final geometries that were optimized for cruise and analyzed high lift and takeoff characteristics. We found that even without optimizing for takeoff, the OWN placement provided significant improvements in aerodynamic characteristics. However, when we optimized takeoff trajectories using the OWN and UWN high lift aerodynamic polars, we found that the OWN had a relatively modest improvement in takeoff field length, using methods as in an example code. Our current view is that the OWN vs. UWN takeoff performance may be within the uncertainty of other physics assumptions that we had to make due to the small scope of our study.

Finally, in the last two months of this project’s period of performance, we repeated a similar exercise as we did in 2022, but for an aft mounted OWN configuration. Although the baseline aft-mounted design showed substantially lower fuel burn compared to the baseline forward mounted OWN configuration, which initially motivated study into this location, the gains from optimization were much smaller and as such, the resulting design had a 5% higher fuel burn at cruise compared to the UWN.

We emphasized two major themes in research methodology: (a) posing a more controlled comparison of OWN vs. UWN aircraft and (b) carefully accounting for numerical uncertainty. These are repeated here for emphasis.

A more controlled comparison of OWN and UWN aircraft is needed

Physics code uncertainty dominated the MDAO and research strategies. There can be significant discrepancies between un-calibrated CFD predictions and the flight performance of actual vehicles. Therefore, in the absence of validation data, it would be uninformative or misleading to compare the CFD-based performance of an optimized OWN with that of actual UWN vehicles. In addition to the physics discrepancy, there is an inconsistency in the MDAO problem for an OWN study with a two-year scope compared with the UWN configuration, which has been refined by the aircraft industry for around 70 years.

It is not practical for the present OWN study to include more design physics such as flight mechanics, static and dynamic structural constraints, nacelle geometry constraints due to acoustical liners and de-icing components, or pylon aero-thermo-structural mechanics. However, this can result in OWN performance that is overly optimistic due to an under-constrained problem formulation. This approach can lead to unrealistic conclusions about OWN compared with traditional UWN designs.

The goal is to provide FAA stakeholders with evidence to gauge the intrinsic aero-propulsive (dis)advantages of OWN vs. UWN designs. It is impossible to pose a perfectly controlled experiment; however, we adopted a dual-parallel approach of optimizing OWN and UWN under the same MDAO formulation. This is an important decision in study methodology as it leads to a more controlled comparison and more credible conclusions.

Careful attention to valid OWN vs. UWN comparisons and numerical uncertainty thus informed much of the detailed work in our tasks, in hopes that such a research strategy would not lead to a simplistic performance comparison between the two configurations, but rather more credible and complex conclusions to inform FAA stakeholders about potential environmental impacts of each configuration.

Notation and Abbreviations

- 2-DoF: two-degree-of-freedom
- α : angle of attack
- ANN: artificial neural network
- ANOPP: Aircraft Noise Prediction Program
- C_D : drag coefficient



C_L : lift coefficient
CFD: computational fluid dynamics
CST: class function / shape function transformation
EDS: Environmental Design Space
FLOPS: Flight Optimization System
 L/D : lift-to-drag ratio
MDAO: multidisciplinary design analysis and optimization
NPSS: Numerical Propulsion System Solver
 $O(\cdot)$: order of magnitude
OEI: one engine inoperative
OWN: over-wing nacelle
pax: passenger [capacity]
UWN: under-wing nacelle

Task 1 - Creation of Single Aisle Aircraft Mission Model and a High Bypass Turbofan Propulsion Cycle Model

Objective(s)

The study focuses on the impact of an OWN installation on a 150 passenger (“pax”) single-aisle aircraft. An aircraft mission model is needed to compute fuel burn and other responses for a typical mission. A cycle analysis is also required for this aircraft mission model to provide thrust, fuel burn, and other key quantities, as well as to solve a coupled problem with aerodynamics (CFD) through the exchange of boundary conditions. The aircraft mission model uses propulsion cycle analysis and some aerodynamic drag data from CFD to yield fuel burn.

Research Approach

This model is developed in the Environmental Design Space (EDS) framework (Kirby and Mavris 2008, Nunez, Tai and Mavris 2021) which integrates the engine cycle analysis code NPSS, an engine weight prediction tool WATE++, and the aircraft performance and mission analysis code FLOPS. The main ingredients for an aircraft model are as follows:

1. Development of an engine architecture model in NPSS
2. Selection of engine cycle design variables
3. Development of an airframe model in FLOPS
4. Specification of requirements such as a mission profile, desired range, cruise Mach number and altitude, etc.

The baseline engine selected for this vehicle is based off a notional Pratt and Whitney geared turbofan, specifically, the PW1100 series GTF. A general model of the mechanical design, geometry, and thermodynamics of the engine is created in NPSS using publicly available information. This model is then ‘calibrated’ to ICAO databank values of sea level static thrust and fuel flow, assuming that the calibration factors applied for that flight condition are valid throughout the operating envelope. The engine however is rubberized (Mattingly, Heiser and Pratt 2002), which means that the engine can be scaled up or down in thrust based on the results of the mission analysis, for a fixed thrust to weight ratio (T/W). The baseline T/W selected for this vehicle is 0.31, based on public information for the A320neo commercial transport airliner by AIRBUS Group, which is in the same passenger class considered for this study.

The preliminary mission analysis used FLOPS (Flight Optimization System), which is a NASA code. This model discretizes a mission into segments and enforces some conservation laws for a point-mass representation of the aircraft. Even though the conservation laws are applied on a point mass, the aircraft has attributes such as drag and engine performance data from internal models and external data tables that are based on physics/geometry inputs such as wing area, aspect ratio, etc. However, its formulation does not generalize well to more complex configurations with coupled lift and drag, as was found later.

The airframe model in FLOPS is built around the CFD geometry of the vehicle. The detailed geometry used for CFD is substantially based on the NASA Common Research Model (CRM). For example, the baseline airfoil stack is adopted from the CRM. However, conceptual-level sizing parameters were adopted from the A320neo because this aircraft model has been used previously in FAA-sponsored mission analyses.

Key variables like fuselage length, width, depth, wing planform area, aspect ratio, taper ratio, quarter chord sweep, and dihedral for example are matched between the CFD geometry and the FLOPS representation of this geometry. These variables impact the weight and aerodynamic performance predictions in FLOPS. The FLOPS aircraft model is sized for 150 passengers, at an assumed weight of 225 pounds per passenger (baggage + pax weight). The design range is specified to be 3415 nmi, with a cruise Mach number of 0.8 at 39,000 ft. A reserve mission for a 200 nmi trip to an alternate airport was also initially considered part of the requirements, though this reserve phase was excluded from the trajectory optimization results (presented in a later section) due to implementation challenges.

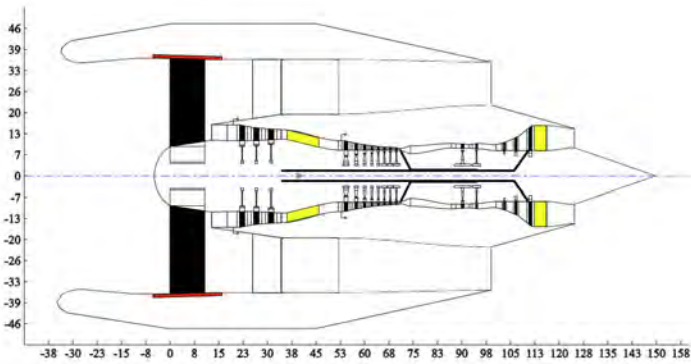
The mission analysis is initially conducted with FLOPS internal predictions for aerodynamics. The resulting engine dimensions and engine deck are then used to update the CFD model of the engine (both geometry and boundary conditions). RANS simulations of the airframe and engine (under-wing) are performed at cruise for an angle of attack sweep to generate a drag polar. A typical cruise part power condition is assumed to obtain the engine boundary conditions for this polar run. The resulting polar is then used to ‘tune’ the FLOPS internal aerodynamic predictions by adjusting FLOPS scaling factors on

parasitic drag and induced drag such that the cruise polar predicted by FLOPS matches the CFD generated polar. Following this tuning, EDS is re-run for the same inputs as before to determine a new engine size that meets the mission requirements. It is this new engine that is used for all subsequent CFD analyses on both OWN and UWN configurations.

It is important to emphasize that while EDS and CFD should theoretically be evaluated in a coupled manner till there is consistency between the engine used in the mission analysis and that used to generate the polars that feeds into the mission analysis, this iterative procedure is quite costly. As such, only a one pass update is used for establishing the vehicle model and the engine model in CFD. The main focus of this effort is to solve the aero-propulsive coupling problem within the CFD domain. *So, for a fixed engine size*, the goal is to match the engine operating conditions and inputs assumed by the NPSS model to those in the CFD domain through an iterative exchange of boundary conditions between the two disciplines. The engine size convergence between the NPSS model and that assumed in CFD is not closed. Table 1 and Figure 1 below summarize some key characteristics of the airframe and engine model.

Table 1. Summary of 150-pax aircraft model.

Name	Value
Fuselage Length (ft)	128.7
Fuselage Max Width (ft)	12.2
Fuselage Max Depth	12.2
Wing Planform Area (ft ²)	1642
Wing Aspect Ratio	8.4
Wing Quarter Chord Sweep (°)	33.76
Wing Taper Ratio	0.2
Wing Dihedral (°)	7.95
Design Payload (lb)	33,750
SLS Thrust/Engine (lb)	26,580
Thrust to Weight Ratio	0.31
Design Fan Pressure Ratio	1.525
Overall Pressure Ratio	47.91
Bypass Ratio	11.06
Design Range (nmi)	3451
Cruise Mach	0.8
Cruise Altitude (ft)	39,000



Weights		Dimensions	
Bare Engine Weight	4928.5	Engine Length	124.7
Accessories Weight	731.2	Engine Pod C.G.	39.5
Engine Weight	5659.7	Engine Max Diameter	72.6
Inlet/Nacelle Weight	89.4	Nacelle Max Diameter	0.0
Total Engine Pod Weight	5749.1	Total Engine Pod Length	124.7

Figure 1. WATE++ Outputs for the Final Engine Model Used in CFD (all dimensions are in inches and weights in pounds).

Milestone(s)

System level modeling to compute fuel burn and develop an engine model is complete.

Major Accomplishments

Baseline aircraft and engine models allow the propagation of aero-propulsion analysis to mission fuel burn and other system-level responses. An engine model was defined in terms of geometry and boundary conditions has been developed for use in CFD analysis of both the OWN and UWN configurations.

Publications

Ahuja, J., Lee, C, H., Perron, C., and Mavris, D. N., "Comparison of Overwing and Underwing Nacelle Aero-Propulsion Optimization for Subsonic Transport Aircraft," *Journal of Aircraft, Articles in Advance*, 2023, pp. 1-16
<https://doi.org/10.2514/1.C037508>

Outreach Efforts

None

Awards

None

Student Involvement

Jai Ahuja and Andrew Burrell contributed to the development of the baseline aircraft model.

Task 2 - Parametric Geometry Generation

Objective(s)

The solution to the MDAO problem involves the reduction of physics disciplines to functions such as $f(\mathbf{X})$ where \mathbf{X} is an array of design variables. An important and time-consuming preparatory step is to select candidate design parameters and create scripts through CAD or CAD-like software to generate water-tight geometry suitable for mesh generation. In the performance period, this parametric geometry effort focused on the outer mold line (OML) geometries of the fuselage, wing, and nacelles.

Research Approach

The selection of baseline aircraft mainly relied on two criteria: 1) applicability of the geometry to our current study of a single-aisle commercial airliner; 2) existing wind-tunnel/CFD data for such geometry in the public domain. By these two criteria, the NASA Common Research Model (CRM) (Vassberg, et al. 2008) was deemed as the most appropriate geometry available in the public domain. Since the CRM geometry was derived from a twin-aisle 300-passenger Boeing 777 design, it was determined that for the OWN problem, the baseline vehicle shall be a scaled-down version to match the overall dimensions of 150-passenger-class single-aisle Airbus A320neo aircraft.

To generate the fully parametric CAD model, the section data for the CRM fuselage, wing, horizontal tail, etc. were extracted from the original STEP file. Then the data was post-processed using Python-based scripts to make it import-ready for CAD model generation, which required the class function/shape function transformation (CST) parametrization (explained in later paragraphs) and data re-organization for generating closed profile sketches. Figure 2 shows the sections extracted from the STEP file.

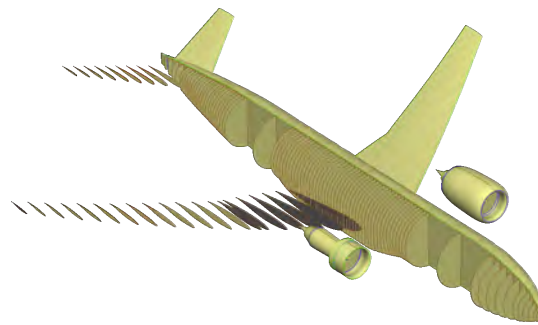


Figure 2. Cross-sections extracted from NASA CRM model for parametric model creation.

Implementation in Engineering Sketch Pad (ESP)

Two parametric geometry modeling tools were evaluated for this study: OpenVSP and Engineering Sketch Pad (ESP). Engineering Sketch Pad was chosen as the tool for this study mainly due to two advantages over OpenVSP: a) ESP’s ability to design complex shapes and apply additional features to those shapes (e.g., blends and fillets) that are crucial in aerodynamic optimization studies based on CFD b) OpenVSP initially did not have interface to an adjoint feature in the inviscid CFD tool CART3D, which was the major drawback for its use in this study.

The ESP tool allows for a script-based bottom-up modeling approach to build complex CAD models using Constructive Solid Geometry concepts (Haimes and Dannenhoffer 2013). The tool generates complex geometries using feature trees and parameters commonly used in CAD software, allows for the creation of wire-bodies and sheet-bodies, is compatible with multiple operating systems, and uses a browser-based user interface. In the following subsections, we will discuss how various OWN baseline aircraft components were modeled in ESP.

Wing Design

The wing was modeled using airfoil sections extracted from the original CRM wing geometry and then lofting a surface through those sections, as shown in Figure 3. The airfoil geometry was specified using Engineering Sketch Pad’s in-built Kulfan function which uses the class function / shape function transformation (CST) parametrization method (Kulfan 2008).

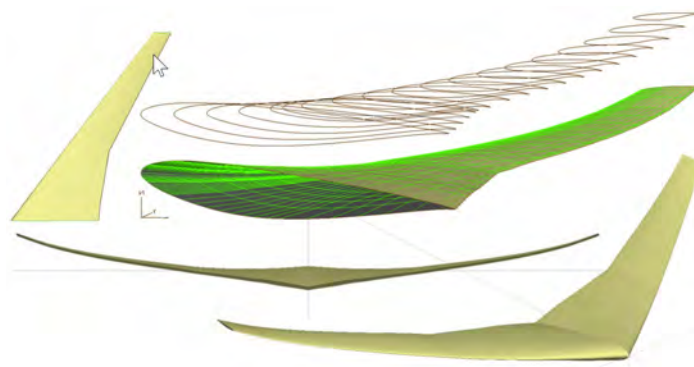


Figure 3. Example ESP output for wing.

The CST method allows for defining airfoil shapes using a simple analytic and well-behaved "shape function" that describes the geometry. The "shape function" provides the ability to directly control key geometry parameters that affect the airfoil drag, such as leading-edge radius, trailing edge boat-tail angle, and closure to a specified aft thickness. The shape function is mathematically represented by simple Bernstein polynomials, the coefficients of which become the parameters for controlling the airfoil shape (Tejero, et al. 2019). Therefore, the CST method requires relatively few variables to represent a large enough design space to contain optimum aerodynamic shapes for a variety of design conditions and constraints.

Initially, the wing was parameterized with one twist and eight CST coefficients (four each for the top and bottom of airfoils) at 21 spanwise stations. However, it was found that this parameterization allowed for physically unreasonable designs such as the exaggerated view in Figure 4.

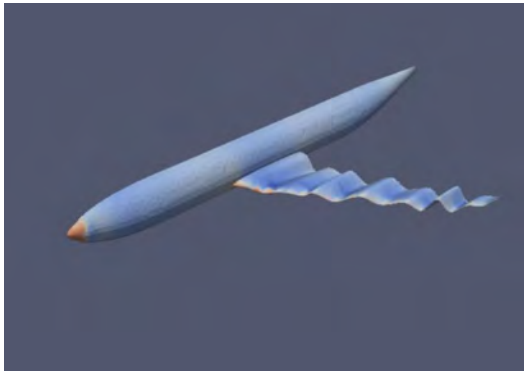


Figure 4. Example; parameterization method tries to limit such physically unreasonable cases in design domain.

In particular, this parameterization did not account for spatial correlation or dependence of design variables. For example, the twist in one spanwise station is highly correlated to its adjacent, neighboring stations. Therefore, the twist and airfoil CST coefficients were modified such that each parameter type across 21 stations is governed by a spline with control points. In later tasks, such as design variable screening and reduction, this spline parameterization was found to be much more efficient in terms of the fraction of feasible designs produced in sample domains.

Engine/Nacelle Design

The engine geometry was derived from approximating the overall dimensions of the Pratt and Whitney PW1000G engine family, which consists of high-bypass geared turbofan engines commonly seen on today’s aircraft such as the Airbus A220, the Mitsubishi SpaceJet, the Embraer’s second generation E-Jets, and as an option on the Irkut MC-21 and Airbus A320neo.

For CFD solver stability reasons, the engine bypass and core flows were modeled as annuli in CFD. The powered engine boundary conditions were implemented on surface patches in the end walls of the annuli and the flow was allowed to expand through channels. These channels are non-physical (i.e. not a realistic representation of actual engines) but are used to represent the exhaust flow. The main reason for this strategy is the numerical stability and robustness of the CFD solver setup across a wide range of nacelle designs and boundary conditions.

Particular geometry requirements arose because of this CFD strategy. The propulsion cycle analysis predicts properties, such as mass flows, which are linked to exit areas of the bypass and core streams using 1D governing physics equations. However, it is difficult to define a corresponding area in 3D or 2D axisymmetric CFD. The geometry was parameterized using Bézier curves such that there is a constriction near the exit from the bypass and core channels. This constriction was created such that the flow would choke (Mach = 1) close to the exit planes of the channels. This allows for the estimation of an exit area that corresponds to the nozzle exit area in propulsion cycle analysis.

These geometry modeling decisions are not without drawbacks. In particular, there are difficulties in defining design domains *a priori* that would produce physically reasonable geometries. For example, if the tail cone angle is steeper (narrowing to a point sooner), then the outer wall of the bypass annulus (underside of the outer nacelle “airfoil”) must be correspondingly deflected inward to avoid large regions of separated flow. Yet, this requires accompanying changes near the trailing edge of the outer “airfoil” for geometric compatibility. This can cause failed geometries or at least highly unfavorable aerodynamic designs. The nacelle parameterization was thus a compromise between the robustness of the CFD, ease of propulsion-aerodynamics integration, and the desire to yield feasible/reasonable geometries for much of the design space. Figure 5 shows the finished engine geometry ready for CFD simulation.

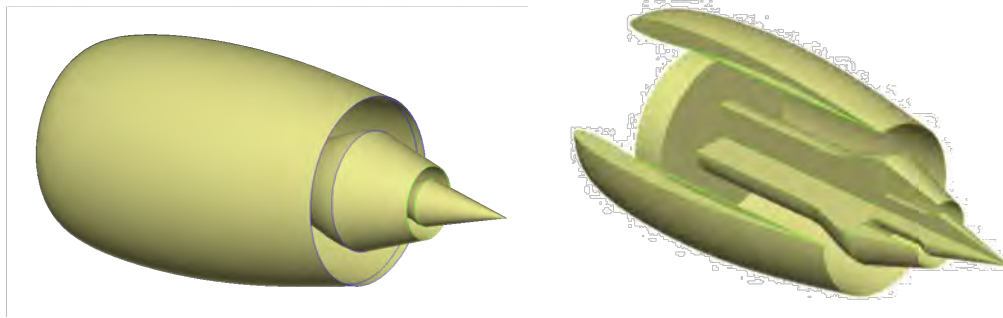


Figure 5. Fully Parametric OWN Engine Geometry generated in ESP.

Fuselage/Horizontal Tail Design

A process similar to the wing design process was used to model the horizontal tail and the fuselage of the aircraft, i.e., by generating sketches from extracted section data and then lofting a surface through those sketches to generate the final geometry. As described earlier, the OWN aircraft geometry is a scaled-down version of the original CRM geometry. Figure 6 depicts the complete CRM aircraft before and after the scale-down process. The horizontal tail was eventually not used in the CFD models and instead an extra drag term was added to the CFD predicted drag to account for the empennage.



Figure 6. Side-by-side comparison of the Original NASA CRM aircraft and scaled-down version of the OWN baseline aircraft (modeled in ESP). Top view (Left) and front view (Right). The scale factor is 60.2% for the fuselage, 60.9% for the wing, and 62.25% for the horizontal tail (scaled with respect to longest dimension).

High Lift Surfaces Design

High lift geometry variant of the parametric wing geometry was produced by first extracting the data from the NASA CRM High Lift Prediction Workshop 5 (HLPW5) clean geometry. This geometry, pictured in Figure 7, has slightly different airfoil sections at the leading edge as compared to the original NASA CRM geometry, as well as a lack of wing bending effects to allow for ease in manufacturing wind tunnel models for high lift surfaces (Lacy and Sclafani 2016). Once the clean geometry was generated, the high lift surfaces were extracted based on the geometric variables as outlined in the reference paper (Lacy and Clark 2020). In particular, slat and flap kinematics were modeled by running a MATLAB-based optimizer script that satisfies the constraints for the input variables gap, height and deflection for slat and gap, overlap and deflection for inboard and outboard flaps. In particular, linkages and fairings were not modeled to avoid incurring additional computational costs during mesh generation and CFD execution. The final geometry matches the complexity of High Lift Prediction Workshop 3 (HLPW3) geometry, with four main elements: main wing, one slat, and two flaps, as seen in Figure 7.

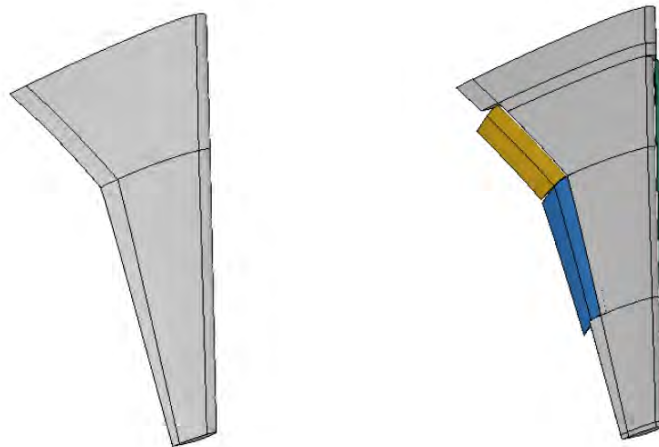


Figure 7. Fully Parametric High Lift Wing Geometry generated in ESP. The clean geometry (left) was first generated by replicating NASA HLPW5 model. Using this model as the baseline, high lift surfaces are extracted (right) based on the high lift design parameters.

Milestone(s)

The reference airframe and the engine geometry were parametrically modeled and are ready for CFD simulations.

Major Accomplishments

A baseline aircraft design was successfully created based on reduction of the NASA Common Research Model. Aircraft wing and nacelle design variables were parameterized and implemented in Engineering Sketch Pad scripts.

Publications

None

Outreach Efforts

None

Awards

None

Student Involvement

Salah Tarazi (PhD student at the time) played a major role in adapting the NASA CRM and implementing the baseline vehicle geometry in Engineering Sketch Pad. Stephanie Zhu (PhD student at the time) was involved in wing parameterization in Engineering Sketch Pad and its linkage to CFD software.

Task 3 - Formulate MDAO problem

Objective(s)

The overall goal was to state a multidisciplinary analysis and optimization (MDAO) (Martins and Lambe 2013) problem to assess a single aisle OWN transport aircraft. The MDAO process was originally intended to use CFD, noise analysis codes such as ANOPP, as well as weights, engine cycle, and mission analysis. The formulation evolved during the project in light of the results. The original statement of the problem:

- **Minimize:** fuel burn
- **Subject to:** design requirements including aircraft range, and detailed side constraints such as wing/tail ground strike and tip-over requirements
- **With respect to:** design variables including engine nacelle position (focusing on forward placement), nacelle and wing geometry, engine cycle and operating condition
- **Given:** baseline single-aisle aircraft model and mission profile

In discussions with FAA technical advisors, more emphasis was placed on optimizing aerodynamic performance rather than noise, which is necessarily of lower fidelity. The single objective function of steady-state fuel burn in cruise was to be minimized with respect to geometry and propulsion variables, with total mission fuel burn computed as a secondary response using a newly developed mission analysis capability, though noise was evaluated as a response at certain design points.

Given this general MDAO problem, a large portion of the task focused on providing more detailed definition to the aero-propulsion aspect of the MDAO formulation.

Research Approach

One of the most computationally intensive aspects of the MDAO is the aero-propulsion coupling problem. The aerodynamics discipline uses results from the propulsion cycle analysis (the NPSS code) as boundary conditions, and vice versa. A valid MDA solution is found only when these coupling variables, which are shared between disciplines, converge to a consistent value. There are different MDA methods to achieve such interdisciplinary closure, and they have different costs in the number of function calls. Therefore, this effort focused on the most important aero-propulsion aspects of MDAO, which drive the overall architecture of the problem. Noise and detailed side constraints mentioned above are important, as they allow solutions to capture realistically important physics trade-offs such as the noise reduction due to shorter landing gears enabled by over-wing engines. However, those constraints were never incorporated into the final MDAO formulation.

In research such as this, each CFD simulation could cost at least O(1000) core-hours, so it was important to minimize the number of iterative function calls to converge a single MDA. The overall MDAO design problem had constraints related to physical equilibrium. These were restated as equality constraints for interdisciplinary consistency:

- Core flow consistency: $h_1 = |W_7^{NPSS} - W_7^{CFD}| \leq \epsilon_1$
- Bypass flow consistency: $h_2 = |W_{17}^{NPSS} - W_{17}^{CFD}| \leq \epsilon_2$
- Inlet pressure recovery consistency: $h_3 = |\eta_{PR}^{NPSS} - \eta_{PR}^{CFD}| \leq \epsilon_3$
- Streamwise force balance: $h_4 = |\sum F_x^{CFD} + F_x^{FLOPS}| \leq \epsilon_4$
- Stream-normal or lift force balance: $h_5 = |C_L^{CFD} - C_L^{Target}| \leq \epsilon_5$

Here, W is the weight (or mass) flow, with subscripts 7 and 17 indicating engine stations equivalent to the CFD boundary condition for exhaust flow. F_x^{FLOPS} is the streamwise force contribution from empirical drag models for components other than the wing-body-nacelle modeled in CFD. All of these constraints h_i were set to small tolerances ϵ_i .

Several MDA methods were tested with different levels of geometric complexity before selecting a final MDA method. Initial research focused on a relatively simple, 2-D axisymmetric, isolated nacelle to test MDA strategies using a subset of the above constraints h_i . For example, a simple, looping method (Gauss-Seidel) was used in Figure 8.

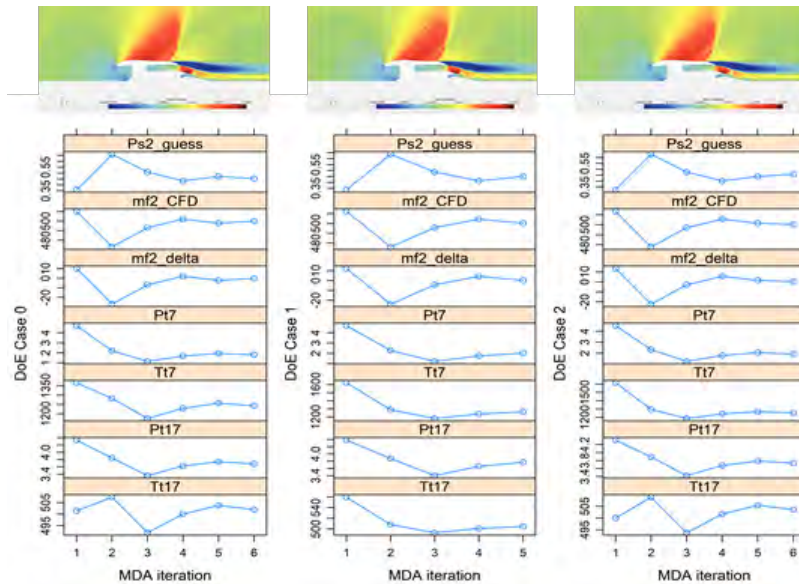


Figure 8. Example convergence history of aero-propulsion coupling variables for three design cases of a 2-D/axisymmetric nacelle.

During the course of this research, we realized an important potential discrepancy between NPSS propulsion cycle assumptions and CFD boundary conditions. The “0-D” NPSS code does not spatially discretize flow equations but rather connects analytic/empirically tuned flow equations for different turbomachinery elements at different stations in the engine. For example, at a nozzle station, 1D isentropic nozzle flow equations (with any tuning factors) can be used along with entry/exit areas to yield a solution coupled with all other cycle elements.

This nozzle element is of interest. In typical propulsion cycle analysis, it is assumed that the nozzle exhausts a flow to external flow conditions, typically free-stream conditions. However, the nozzle exit flow may not actually reach free-stream conditions at the nominal outlet location and area. In Figure 9, it can be seen in an example CFD case that the bypass and core exhaust streams may not reach free-stream pressure at their respective, nominal “ A_8 ” and “ A_{18} ” exit areas.

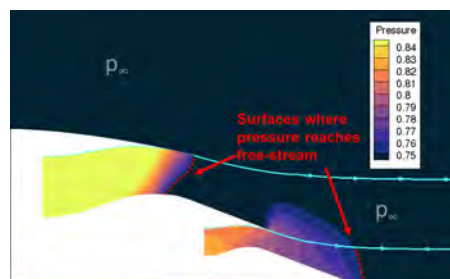


Figure 9. Areas at which exhaust streams reach free stream pressure can be significantly different from nominal bypass and core exit areas.

This led to a physics inconsistency between cycle analysis and CFD which was considered as essentially internal and external aero-thermal analyses which must pass consistent information over boundary conditions. The situation was furthered complicated in forward-mounted OVN applications because the presence of a wing aft of the engine strongly affects the exhaust flow compared to the isolated engine assumed in NPSS.



Figure 10. Mach contour plot shows influence of wing on exhaust streams of engine.

A major development was to adjust the aero-propulsion MDA problem to enforce the consistency constraints shown earlier by manipulating fictitious “exit areas” A_8 and A_{18} in the propulsion cycle. This is tantamount to an iterative CFD-based calibration of NPSS model to account for complex OWN aero-propulsive interactions.

We tested several different MDA and MDAO architectures to find a method that efficiently enforces the above MDA equality constraints, h_1, h_2, \dots, h_5 . For example, Figure 11 shows a snapshot of a Bayesian adaptive sampling approach based on (Lee and Mavris 2012) that progressively learns the settings for coupling variables that most likely satisfy the constraints.

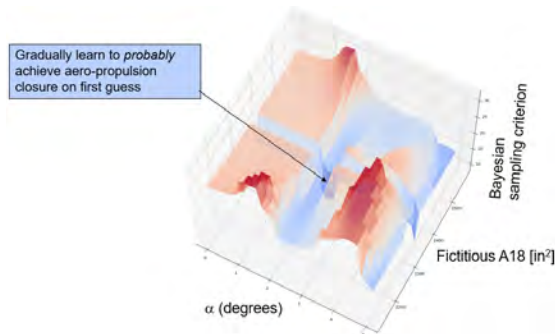


Figure 11. Bayesian method showing coupling variable domain regions with high probability of MDA closure.

We finally selected a simple method based on the commercial STAR-CCM+ CFD code’s macro scripts. This was an intrusive alteration of the CFD solution process to enforce the MDA constraints. Surrogate models of NPSS were created and included inside the CFD solver script. While the CFD code iteratively solves its governing equations with respect to the flowfield state variables, it also manipulates coupling variables by querying the NPSS surrogates until MDA closure is achieved.

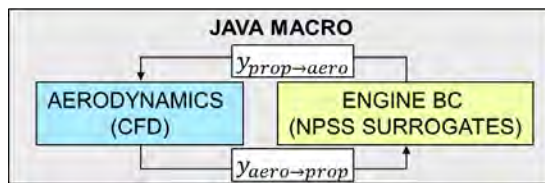


Figure 12. Final aero-propulsion coupling method: solver macros intrusively enforce MDA consistency within the CFD code.

Reducing Dimensionality of the Problem

The external shape of aerodynamic bodies, such as wings and nacelles, is characterized by complex and detailed surfaces. In turn, the definition of these surfaces necessitates many design parameters. This design problem contained a total of 44 variables which are listed in Table 1. This large number of design variables hinders the design exploration of the aircraft design due to a phenomenon referred to as the *curse of dimensionality* in machine learning literature. Therefore, to effectively tailor the airframe for a given engine location, some steps must be taken to bring down the dimension of the design space to a more reasonable value.

Table 2. List of original design variables before reduction.

Group	Variable Name	Dimension
Nacelle	Highlight lip radius	1
	Cowl maximum radius	1
	Cowl maximum radius location	1
	Cowl trailing edge angle	1
	Cowl trailing edge curvature	1
	Inlet throat location	1
	Nacelle X location	1
	Nacelle Z location	1
Wing	Wing CST coefficients (upper surface)	16
	Wing CST coefficients (lower surface)	16
	Wing twist distribution	4
Total		44

For the current problem, the dimension of the design space is reduced using the active subspace method as described in (Constantine 2015), which is a type of supervised dimensionality reduction technique. Assuming a generic function that depends on many inputs, this method identifies a linear subspace of the input spaces which is responsible for most of the variability of the function. The active subspace is defined using an orthogonal basis whose vectors represent a linear combination of the original design variables. Designs in the original space can then be projected into the active subspace, and the resulting coordinates are called active variables. Note that the transformation from the active variable to the original design variables is also straightforward as it only requires the transpose of the computed orthogonal basis. Conceptually, one can also consider the active subspace as a rotated set of axes in the design space for which the function variation is best captured as shown in Figure 13.

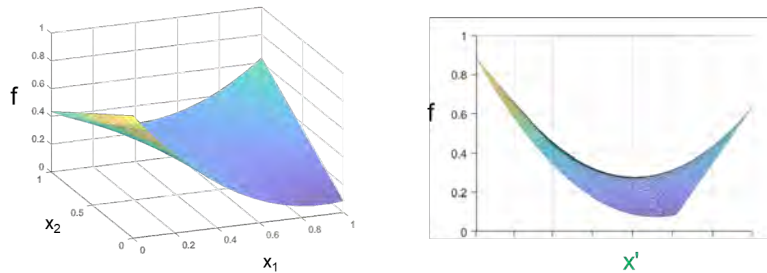


Figure 13. Notional view of active subspace for two original design variables (left). The rotated view (right) shows that a single new variable x^1 captures important features of function f .

The classical active subspace method requires the computation of the gradient of the function of interest. However, in the last few years, some authors have proposed alternative methods that can extract the subspace in a gradient-free manner. One of these methods is the manifold optimized active subspace (MOAS) which was initially proposed by (Tripathy, Billionis and Gonzalez 2016) and improved by (Rajaram, et al. 2020). Specifically, the MOAS method uses a Gaussian process (GP) to link the function inputs and outputs, and the active subspace is obtained by maximizing the likelihood of the GP via a manifold optimization algorithm. While the analysis tools used in this work can provide gradient information, the airframe uses the gradient-free MOAS approach. This decision was motivated by the additional computation cost of computing the gradient and initial testing that showed noise in the gradient results which negatively impacted the accuracy of the active subspace. Note that the MOAS results are computed using the framework developed by (Gautier, et al. 2022), which is openly available¹.

¹ Source code available at <https://gitlab.com/raphaelgautier/bayesian-supervised-dimension-reduction>

Additionally, while the active subspace method can facilitate the exploration of a high-dimensional design space, a substantial amount of training data must still be generated initially. This can be quite costly when used in combination with high-fidelity RANS simulations. As such, to further reduce the computational cost of the design exploration, the active subspace in this work is computed using inviscid results obtained with Cart3D CFD software. The computed subspace is then used directly for the generation of RANS results. While the inviscid active subspace is likely different than the RANS one, the difference between the two is assumed to be relatively small since the aerodynamic performance of the aircraft is expected to depend strongly on inviscid effects such as shock waves and induced drag. The potentially lower accuracy is also compensated for by the inexpensive generation of inviscid data.

Scope of Design Variables

The parameterization of geometric design variables is covered separately, but the MDAO formulation effort provided bounds for the scope of optimization. In consultation with FAA technical advisors, the NASA Common Research Model (CRM) was chosen as a baseline geometry (Vassberg, et al. 2008). Many parts of the aircraft geometry were deemed to be out of scope for the present research. Other than scaling from 300 to 150-passenger size, the fuselage is fixed. The justification for these decisions is an emphasis on credibility and reproducibility in the main research goal: a comparison between under-wing and over-wing nacelle configurations. In actual practice, an aircraft outer mold line (OML) geometry may involve thousands of detailed design variables, many more physics disciplines, flight scenarios, and constraints. For example, one consequence of simply scaling the fuselage shape is that the cockpit windows are much smaller. It is unlikely that pilot visibility requirements simply scale linearly with a fuselage length scale. Yet, this simple scaling of the CRM geometry is easily understood and replicable by the wider aeronautics research and industry communities. It avoids arbitrary detailed design decisions by the researchers.

Because of this concern with credible and replicable comparison, several other parts of the aircraft geometry are not included in the MDAO study. The empennage requires flight mechanics and detailed mass estimation (ex: trimming the horizontal tail plane requires knowledge of the center of gravity). Therefore, it is not included in high-fidelity simulation, although mission analysis included friction drag of the empennage via the detailed aero-propulsion surrogates. The landing gear pod region is not modified. The wing airfoils design space is constrained to a relatively small domain such that the structural thickness is not radically altered. The wing planform is also fixed.

The current approach is to not design a pylon joining the wing and nacelle, even though it undoubtedly plays an important role in interference drag for an over-wing nacelle. Because the present effort includes no structural or thermal analysis, the pylon geometry would involve many potentially unrealistic guesses. To give decision-makers a fair assessment of the potential benefits of OWN installation, we argue that a comparison of OWN and UWN should be made with no pylons or with thin placeholder/default pylons based on similar geometry rules for the two cases.

Finally, one of the most important variable scoping decisions is to limit the study to the forward placement of nacelles. This decision was made in discussions with the FAA and was driven by interest in the noise shielding effect from the wing. A nacelle aero-propulsive optimization was initiated for rearward placement after the main period of performance ended, but not incorporated into the mission analysis.

Adaptive Sampling Optimization

The main optimization was performed with a Bayesian adaptive sampling technique. It sequentially fit a Gaussian Process or Kriging model and added new sample points according to an acquisition function or infill criterion. In our case, we used the expected improvement (EI) infill criterion. EI has been described in literature such as (Jones, Schonlau and Welch 1998) and is shown notionally in Figure 14 below. This procedure was carried out until the EI was of a similar order of magnitude as the numerical uncertainty due to the CFD grid (described in a later section).

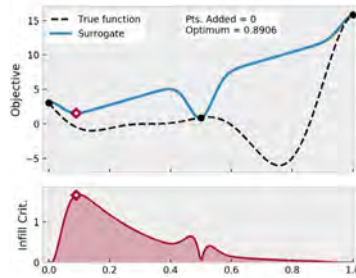


Figure 14. Snapshot of an adaptive sampling process. The infill criterion is maximized to identify the most favorable location for evaluating a sample point.

Milestones

- Various methods tested for aero-propulsion coupling:
- Direct multi-disciplinary feasible (MDF) method tested on 2D axisymmetric, isolated nacelles
- Direct multi-disciplinary feasible (MDF) method tested on full aircraft
- Rejection sampling method tested using 3D nacelle and wing (no fuselage)
- Bayesian adaptive sampling method tested for 3D nacelle and wing
- Fully coupled, intrusive method tested with full aircraft wing-body-nacelle.
- Active subspace methods compared and selected

Major Accomplishments

- Draft of a Design Structure Matrix (Lambe and Martins 2012) and variable breakdown for geometry-integrated MDAO.
- Formulation of MDAO problem in terms of disciplinary analyses available and under development, scoped down according to sponsor interest and feasibility of implementation.
- Aero-propulsion MDAO method selected and implemented: fully coupled method implemented to incorporate propulsion cycle surrogate models within CFD macro solver scripts
- Active subspace variables used successfully in design study

Outreach Efforts

None

Awards

None

Student Involvement

Kenneth Decker and Bilal Mufti were PhD students at the time who contributed by testing different MDAO formulations on reduced order or inviscid test cases. Bilal Mufti and Mengzhen Chen tested different MDA architectures using CFD and NPSS propulsion cycle analysis.

Publications

Ahuja, J., Lee, C, H., Perron, C., and Mavris, D. N., "Comparison of Overwing and Underwing Nacelle Aero-Propulsion Optimization for Subsonic Transport Aircraft," *Journal of Aircraft, Article in Advance*, 2023, pp. 1-16
<https://doi.org/10.2514/1.C037508>

Outreach Efforts

None

Awards

None

Task 4 - Generation of CFD Templates and Automation Scripts

Objective(s)

In order to solve an MDAO problem, the workflow between the geometry generation to the CFD solution and post-processing must be reduced to a robust function call. CFD meshing in particular is difficult to automate as a “fire-and-forget” process without human inspection or intervention. Yet, a high degree of automation is needed to allow modern design techniques such as active subspace, adaptive sampling, and multi-fidelity methods. This detailed development work may be of less interest to the stakeholder or decision-maker, but it is identified as a separate task because it accounts for a large share of actual effort and calendar time. The goal of this task is also to generate CFD grids of different resolutions and compare the solution for accuracy. Also, the impact of the accuracy on the fuel burn calculations was quantified. The results were used to guide MDAO convergence criteria such that the optimization is not continued beyond the uncertainty “floor” of the physics analysis.

Research Approach

In the example below in Figure 15, an off-line design of experiments (DoE), or sample specification, is used as a placeholder for an MDAO driver or optimizer.

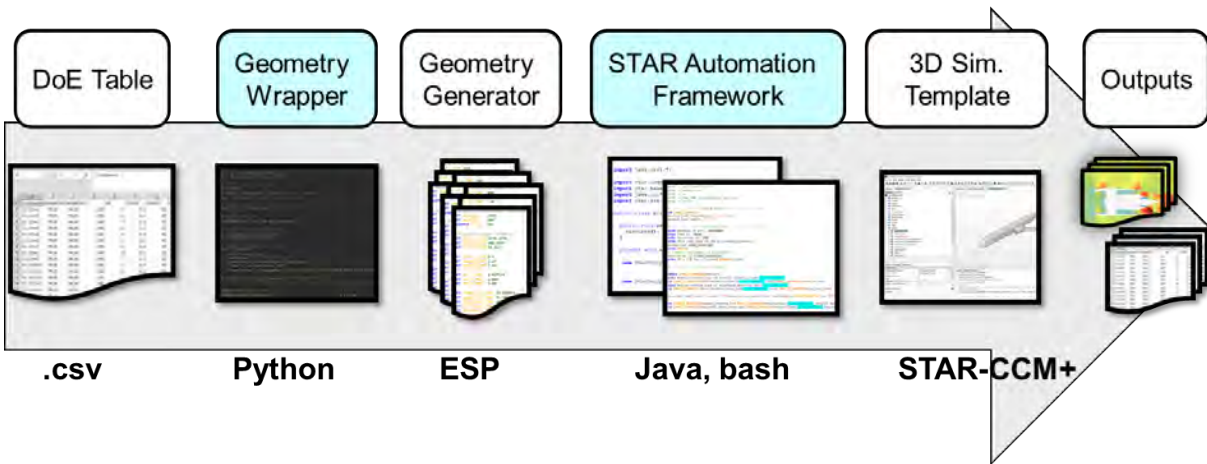


Figure 15. Automated workflow for example design activity (design of experiments, or DoE).

STARCCM+ Reynolds Averaged Navier Stokes CFD solver was used for this optimization study. STARCCM+ in-built unstructured grid generator was used to generate hybrid volume mesh containing orthogonal prismatic cells, also known as prism cells, near the surface to resolve the boundary layer and polyhedral cells for the remaining volume mesh. Through the literature survey, it was found that previous OWN configuration optimization studies have meshes ranging from 0.8M to 30M cells (Fujino and Kawamura 2003, Hill, Kandil and Hahn 2009, Renganathan, et al. 2018). Therefore, for the current study, a detailed grid sensitivity analysis was performed before finalizing the grid to establish a reference uncertainty floor. The six grids (see Table 3) that were used ranged from the coarsest size of 19.5M cells to the finest size of 475M cells, with the latter being used as the reference case to compare the accuracy. The net L/D calculation error for all cases compared to the reference case was within 2% for the coarsest grid. Based on the findings, the 76M grid was chosen for the optimization study.

Table 3. Grid Convergence Study Results.

	CFD Mesh Cell Count					
	19.5M	33M	76M	161M	303M	475M (Reference)
% L/D Error	1.955	1.495	0.476	-0.329	0.179	0

The CFD error in drag computations associated with different grid sizes was propagated to mission fuel burn change (Figure 16) in a rapid estimate. The study was carried out using a modified version of FLOPS which allows user-specified data tables for the aerodynamic model of the aircraft. Results are in Table 4. As before, the change in drag coefficient (ΔC_D) for only the cruise condition was obtained for all cases by keeping the drag value obtained for the 475 million cells grid as the baseline. For a rough estimate of the uncertainty impact of CFD mesh-related error, the ΔC_D was applied to the empirically-based aerodynamics models of FLOPS. The drag polar for the complete aircraft at different flight conditions was computed using empirical drag estimation techniques (EDET). This baseline drag polar was perturbed by adding ΔC_D using a blending function such that the change in drag is maximum at flight conditions at which ΔC_D was computed and decreases linearly as the Mach number is changed.

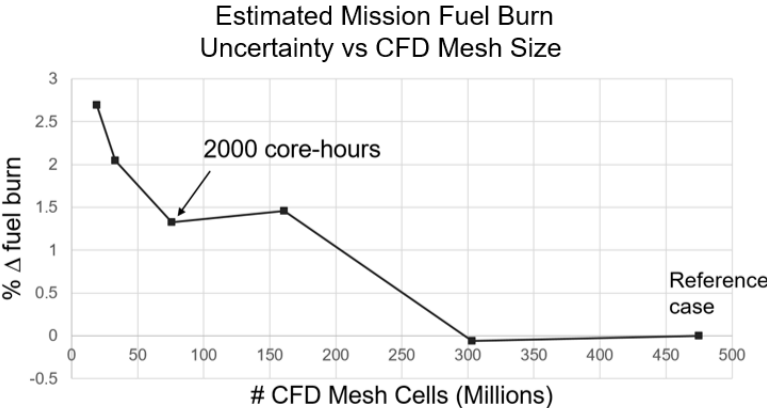


Figure 16. Mission fuel burn change associated with CFD data generated on meshes of various sizes.

Table 4. CFD error propagation to Mission Fuel Burn Calculations.

Grid Size (Millions)	ΔC_D	Estimated % Discrepancy in Mission Fuel Burn
19.5	6.78E-4	2.69
33	5.19E-4	2.05
76	3.37E-4	1.32
161	3.72E-4	1.46
303	-0.154E-4	-0.06
475 (Reference)	0	0

When examining the CFD solutions, there are often only subtle physical differences in flowfields. For example, there is over a 2% discrepancy in estimated mission fuel burn for the two mesh settings below in Figure 17. However, note that much of the recently published OWN literature may be qualitatively similar to the coarser of these two extremes.

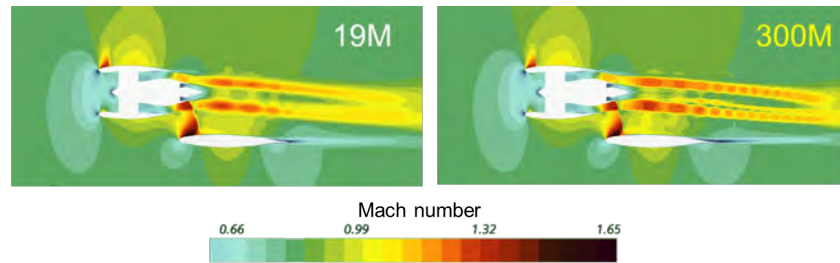


Figure 17. Subtle differences in flowfields of different mesh cell counts associated with mission fuel burn discrepancies.

Milestone(s)

A mesh sensitivity study was completed.

Major Accomplishments

Initial automation of 2D axisymmetric CFD nacelles contributes to development of screening/variable reduction methods and MDAO techniques in later tasks. Uncertainty impact of CFD mesh propagated to uncertainty in system-level metric — fuel burn.

Publications

Ahuja, J., Lee, C. H., Perron, C., and Mavris, D. N., “Comparison of Overwing and Underwing Nacelle Aero-Propulsion Optimization for Subsonic Transport Aircraft,” *Journal of Aircraft*, *Article in Advance*, 2023, pp. 1-16
<https://doi.org/10.2514/1.C037508>

Outreach Efforts

None

Awards

None

Student Involvement

Salah Tarazi played a major role in adapting the NASA CRM and implementing the baseline vehicle geometry in Engineering Sketch Pad. Stephanie Zhu was involved in wing parameterization in Engineering Sketch Pad and its linkage to CFD software. PhD student Bilal Mufti propagated the CFD numerical uncertainty through the mission analysis to estimate fuel burn impact.

Task 5 - Stage 1 Design: Nacelle and Wing Optimization (Forward Mounted OWN)

Objective(s)

As discussed previously, the overall goal was multidisciplinary analysis and optimization (MDO) of an OWN aircraft. This was scoped down over the course of the project to exclude noise from the MDO problem, and the focus narrowed to coupled aero-propulsion CFD and cycle analysis to inform a mission analysis (further described in a later section). The working MDO problem statement may be expressed as:

- **Minimize:** fuel burn for a baseline mission
- **Subject to:** range and detailed side constraints
- **With respect to:** design variables including engine nacelle position (focusing on forward placement), nacelle and wing geometry, engine operating condition
- **Given:** baseline single-aisle aircraft model and mission profile
- **Returning:** fuel burn

In discussion with FAA technical advisors, more emphasis is placed on aerodynamic performance optimization rather than noise, which is necessarily of lower fidelity. So, the single objective function of fuel burn is minimized, though noise was evaluated for specific settings of design variables (see section on noise studies). To control the “curse of dimensionality,” the stage 1 optimization process was broken into two steps. The first step focused on the commitment of nacelle location before more detailed shape optimization in step 2.

Research Approach

We focused first on the nacelle location relative to the wing-body in the X-Z plane, at a fixed span-wise Y location. Figure 18 below shows examples of how the nacelle location was varied. The black dots show positions of a reference point on the nacelle. The 3x5 grid of black dots were sampled with the results shown in Figure 19. The blue nacelles are closest to the wing, and the grey nacelles are farthest. We selected the orange cases as final locations for second-stage, detailed optimization.

We note that the selection of these orange cases was highly subjective, especially for the OWN case, but were made in consultation with FAA advisors. We emphasize that this was an arbitrary, human decision. But this is not a result of ignorance of rigorous optimization methods; rather, it is an unavoidable consequence to focusing on an aero-propulsion physics scope. The results showed that fuel efficiency at cruise improves as the nacelle moves farther away from the wing. This is a consequence of the reduced MDO problem statement that does not include a structures/weights discipline. In a larger scale, more realistic problem, the structural weight and drag of pylon as well as wing structure would penalize nacelle placements far from the wing.

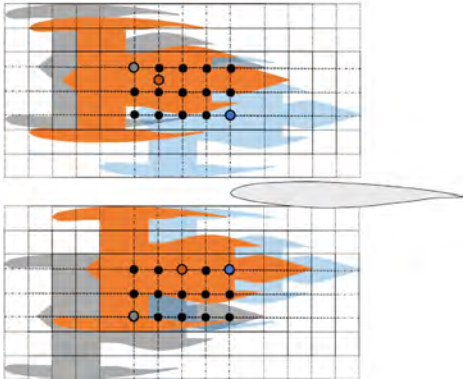


Figure 18. Orange locations are final selections for OWN and UWN.

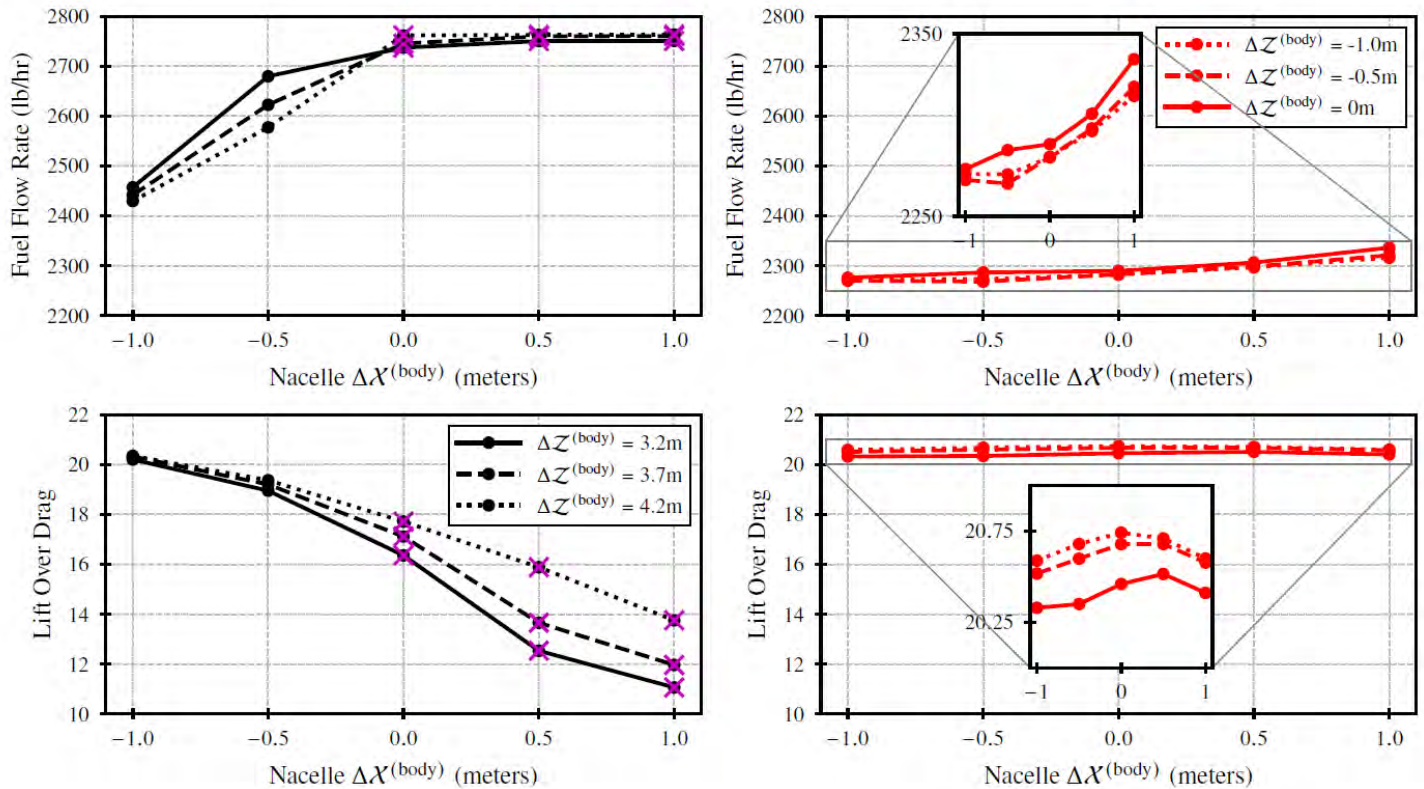


Figure 19. Results of the Nacelle Perturbation Study.

There are few publicly available empirical pylon weight values, so we referred to physics models used in MDAO studies for order-of-magnitude estimates. For example, Gazaix and colleagues report an optimized pylon mass of roughly 700 kg for a similar class of aircraft (Gazaix, et al. 2019). Perturbing weight values in our baseline FLOPS mission analysis (not the mission analysis used for final optimized trajectories as discussed later) showed order-of-magnitude sensitivities of O(1%) change in mission fuel burn due to O(1000 lbf) aircraft weight perturbation. It is difficult to guess precisely how the pylon mass increases with nacelle distance from the wing attachment points, but it is reasonable to assume the weight increases at least proportionally (Or even higher) with increases in this distance. Therefore, we roughly estimated that doubling the pylon length has O(1%) mission fuel burn impact. With this in mind, we selected arbitrary intermediate nacelle locations for further refinement.

After down-selecting a nacelle location, we then focused on more detailed shape optimization of the nacelle and wing. We used a gradient-free active subspace technique to reduce 44 wing and nacelle shape variables to 7 active modes or hybrid design variables that captured the major features of the original variables, as discussed in a previous section. We show theoretical details of this technique for aerodynamic examples in a conference paper (Mufti, et al. 2022). For optimization of the active variables, we used a kriging or Gaussian process-based adaptive sampling method to minimize fuel flow rate at cruise (Mach 0.8, 39,000 ft). The procedure is a variant of a common expect improvement or “efficient global optimization” (EGO) method described by (Jones, Schonlau and Welch 1998).

Note that this is a reduced/approximate version of the overall problem statement of minimizing fuel burn over an entire mission. The adaptive sampling continued until the expected improvement in fuel flow fell within the uncertainty in the coupled aero-propulsion analysis.

Results of analyses of the propulsion and aerodynamics optimized designs are shown below in Table 5.

Table 5. Stage 2 optimization results.

Parameter	Baseline OWN	Optimized OWN	Baseline UWN	Optimized UWN
Fuel flow rate (lb/h) at cruise	2600	2330	2290	2240
L/D	19.3	21.5	20.5	21.3
Power code (throttle)	48.3	45.4	44.9	44.4
Pressure recovery	0.9965	0.9975	0.9975	0.9976

Surface pressure contours for baselines and optima for the two cases are shown below in Figure 20. In both cases, there are significant shocks between the nacelle and fuselage. The shocks are slightly weakened but the differences are visually difficult to discern in the color maps. For OWN, the shock over the nacelle weakens substantially and moves aft. This is related to an increased maximum radius near the highlight for the optimized OWN.

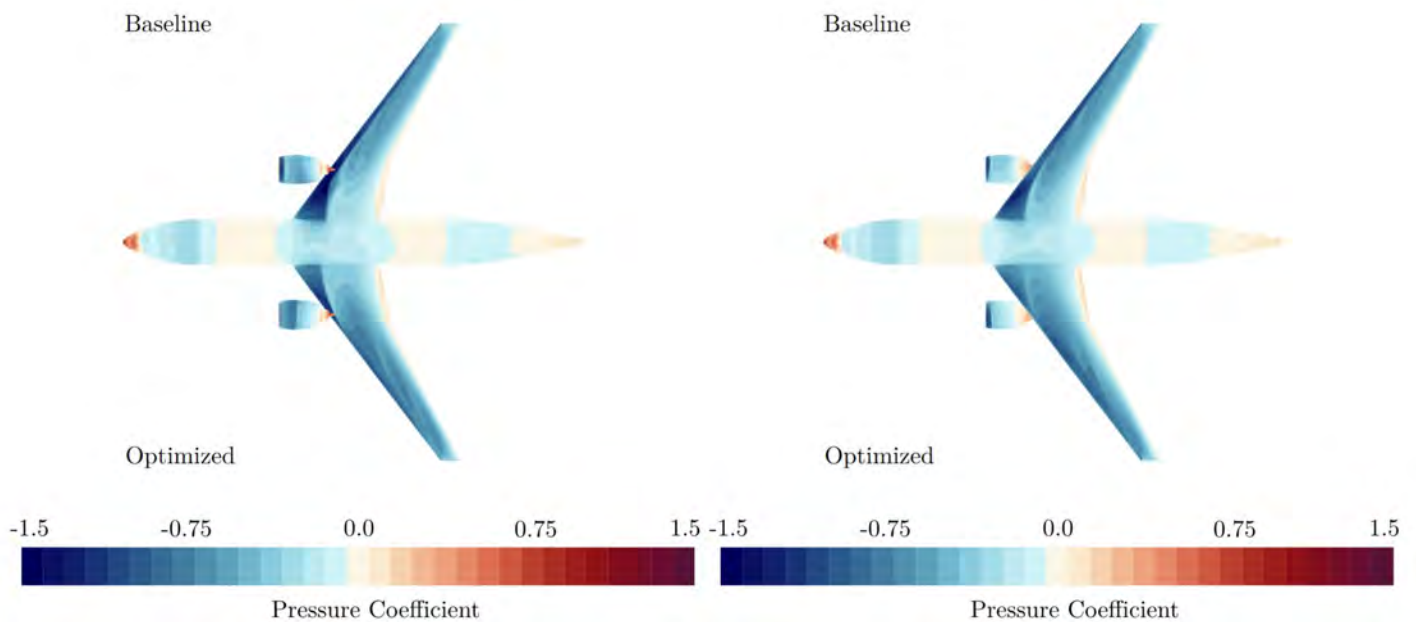


Figure 20. Pressure contours shown for OWN baseline and optimum (left) and UWN (right).

The analysis shown here corresponds to an OWN design with a 4% higher fuel flow rate than UWN, but we avoid broad conclusions or generalizations from this result. This study deliberately aimed to control many factors to first compare the effect of moving an engine of fixed size between the two configurations.

Major Accomplishments

Estimates were provided of realizable performance for a grid of nacelle positions. Baseline nacelle locations for OWN and UWN were selected in discussion with FAA technical advisors. Optimization and comparison of OWN and UWN at cruise conditions was completed for a fixed engine cycle and size. Final configurations were used to produce aero-propulsion data for training surrogate models used later in mission analysis.

Publications

- Bilal Mufti, Mengzhen Chen, Christian Perron and Dimitri N. Mavris. "A Multi-Fidelity Approximation of the Active Subspace Method for Surrogate Models with High-Dimensional Inputs," AIAA 2022-3488. AIAA AVIATION 2022 Forum. June 2022.

- Ahuja, J., Lee, C. H., Perron, C., and Mavris, D. N., “Comparison of Overwing and Underwing Nacelle Aero-Propulsion Optimization for Subsonic Transport Aircraft,” *Journal of Aircraft*, *Article in Advance*, 2023, pp. 1-16 <https://doi.org/10.2514/1.C037508>

Outreach Efforts

Researchers collaborated with NASA over-wing nacelle expert during regular telecons.

Awards

None

Student Involvement

Mengzhen and Bilal Mufti were PhD students at the time who contributed by testing different MDAO formulations using coupled propulsion cycle and CFD analyses.

Task 6 - Create ANOPP Noise Models

Objective(s)

One of the main anticipated benefits of the OWN configuration is noise shielding from the wing. Despite the importance of modeling noise, high fidelity physics modeling is out of scope for this present project due to the complexity and computational cost of analysis. Rather than a direct objective function in optimization, a lower order analysis is used to model noise (originally considered as a constraint but later simply evaluated as a response) while optimization focuses on aero-propulsion responses. The goal of this task was to use a noise analysis code, such as the Aircraft Noise Prediction Program (ANOPP), to generate approach, cutback, sideline, and cumulative noise data via a design of experiments, thereby allowing surrogate models to be fit to the data set to predict changes in aircraft noise due to nacelle location.

Research Approach

Acoustics are modeled using a lower fidelity mode of ANOPP software. The NASA Aircraft Noise Prediction Program (ANOPP) code (Zorumski, ANOPP Theoretical Manual, Pt. 1 1982, Zorumski, ANOPP Theoretical Manual, Pt. 2 1982) is used to model engine noise as a single source. Because of the relatively coarse spatial representation of noise, it is assumed that the dependence of noise responses with respect to nacelle geometry placement are crude at best. ANOPP is selected as a suitable noise analysis code based on the required level of detail and tools available to the researchers.

Nonetheless, keeping the above caveats in mind, initial configuration studies addressed the following questions:

- Does the aft engine noise dominate the conversation moving forward?
- How much benefit does shielding provide for the forward mounted configuration?

A preliminary study was conducted by decomposing forward-radiated vs. aft-radiated engine noise. The engine was simply moved above and below the wing by up to +/- 1.38 nacelle diameters for a baseline engine geometry. Comparisons were made for different technology assumptions (corresponding to years 2017, 2027, 2037) for sideline and cutback noise. An example result is shown in Figure 21.

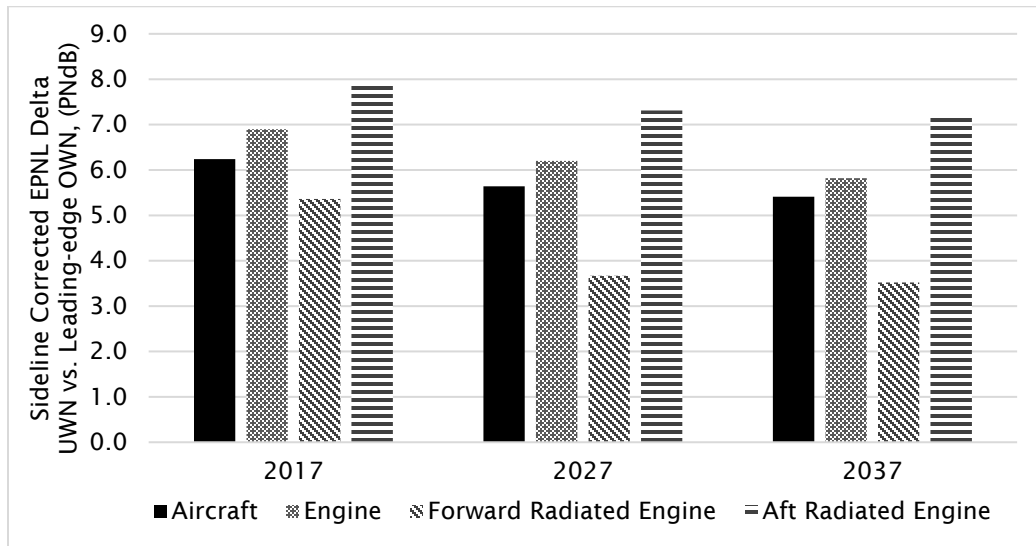


Figure 21. Preliminary (pre-optimization) sideline noise comparison of UWN and leading-edge-mounted OWN configurations under different technology assumptions.

Five-level full factorial and 100-case Latin-hypercube designs of experiments are combined into a single design of experiments to thoroughly sample the nacelle location design space within ANOPP. The ANOPP noise responses are fit to the nacelle location parameters using a single layer artificial neural network (ANN) with hyperbolic tangent nodes (see surrogate profiler plots in Figure 22), resulting in a root mean square EPNdB error of less than 0.105.

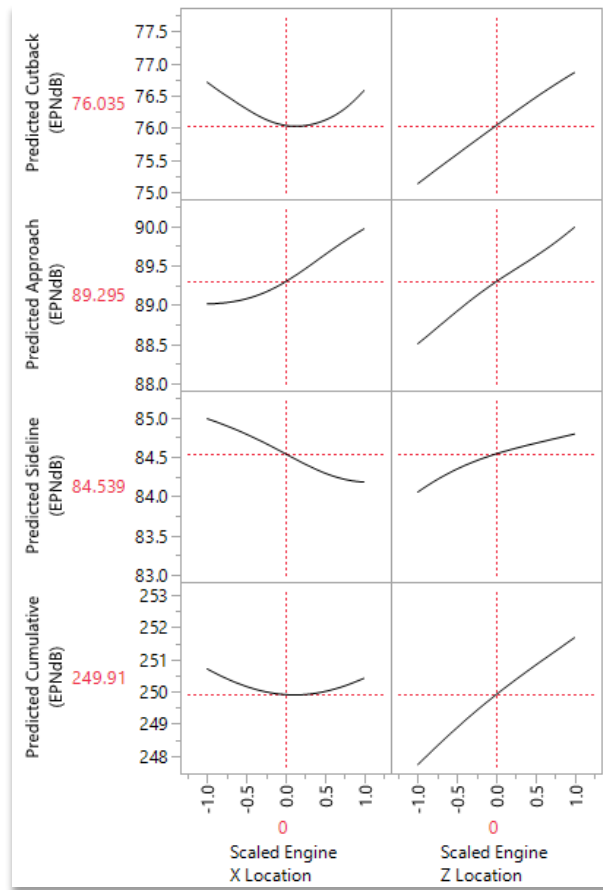


Figure 22. Example view of ANOPP surrogate model.

Milestone(s)

Initial ANOPP noise analysis was performed.

Major Accomplishments

ANNs were fit to the approach, cutback, sideline, and cumulative forward mounted OWN and UWN noise responses as a function of the nacelle location parameters. This directly supported generating data to select nacelle location in Task 5.

Publications

None

Outreach Efforts

None

Awards

None

Student Involvement

Andrew Burrell (Ph.D. student at the time) ran ANOPP and fit surrogate models to the noise responses.

Task 7 – Stage 2 Design: Engine Re-design and Airframe Re-optimization (Forward Mounted OWN)

Objectives

The following working MDAO problem statement was adopted:

- **Minimize:** fuel burn for a baseline mission
- **Subject to:** range and detailed side constraints
- **With respect to:** design variables including engine nacelle position (focusing on forward placement), nacelle and wing geometry, engine cycle, and operating condition
- **Given:** baseline single-aisle aircraft model and mission profile
- **Returning:** fuel burn

This task continues previous work with a higher bypass/larger diameter engine to potentially exploit the additional clearance above the wings.

Research Approach

The stage 2 optimization approach is identical to the stage 1 approach and will not be repeated here. We describe details of the process in (Ahuja, et al. 2023). However, we made new assumptions and redesigned the engine cycle. These assumptions are described here.

The bypass ratio can potentially improve the propulsive efficiency of an engine. This can be achieved by re-designing both the core and the fan, although the former is a significantly more expensive endeavor than the latter. Engine manufacturers typically do not design new cores for a single aircraft unless there is a significant market demand and financial incentive to do so. As such, assuming the OWN configuration were to come out within the next 10 years, the most viable option is to use a commercial off-the-shelf (COTS) engine that has the necessary thrust for the vehicle. The OWN configuration we investigate is similar in size to the A320neo and as far as current commercial off-the-shelf engines are concerned, the PW1100 Geared Turbofan engines are likely candidates for this vehicle.

However, one of the biggest advantages of the OWN configuration is the ability to integrate higher bypass ratio engines above the wing as ground clearance constraints for the nacelle are not a factor. However, if the PW1100 GTF series engines represents the best state of the art engine for this class of airframe and a new engine development program is not financially feasible, a middle ground could be a re-fan of the engine, which would be substantially cheaper than designing a new engine from scratch.

In this process, the engine core is fixed, but the components on the low-speed spool i.e. the low-pressure compressor and the fan are allowed to change. Thus, an increase in bypass ratio is achieved by decreasing the fan pressure ratio (allowing the low-pressure compressor pressure ratio to change accordingly), which results in a larger fan diameter. Thus, more airflow passes through the fan/bypass duct rather than the core, which increases bypass ratio and thus propulsive efficiency. The power produced by the fixed core, however, limits how much the fan can grow and thus there is a limit to the bypass ratio that can be achieved with this approach. Other limitations come from the aerodynamic performance of a larger nacelle and its detrimental impact on drag. At some point, the drag penalty from a larger nacelle overcomes the fuel benefit from a higher bypass ratio engine, limiting the feasible growth of the fan. Whether the core mechanical power constraint or the aerodynamic penalty constraint is hit first depends on the engine core design and the aerodynamic characteristics of the airframe, so it is problem dependent.

The baseline engine selected for this project is a notional PW1133 geared turbofan currently found on the A321neo models. A derated version of this engine is also found on the A320neo, a 150-pax class vehicle which the OWN and UWN configurations studied here were scaled to. This notional model of the engine was developed in EDS using publicly available data such as from the ICAO Emissions Databank and the EASA Type Certificate Data Sheet.

FLOPS-NPSS-WATE++ models of the OWN and UWN configurations were developed to get initial estimates of the block fuel burn for each case. Then, the fan pressure ratio was decreased from the baseline value of 1.52, keeping a fixed core, and the block fuel burn for each configuration was tracked. Note, that the weight impacts of a larger fan were tracked through WATE++, and FLOPS empirical wetted area/form factor estimates for nacelle drag were used to monitor the drag penalty of

the larger nacelle. The plots below show the block fuel vs FPR trend for OWN and UWN as well as the fan diameter variation with FPR.

From the monotonic trends in block fuel burn in Figure 23 (ignoring the FPR 1.5 case as a likely numerical convergence anomaly), it is apparent that the improved propulsive efficiency from a larger fan is the driving force behind the fuel burn reductions, given our modeling assumptions. It should be noted that NPSS consistently failed to converge for any FPR lower than 1.4, suggesting that this notional PW1133 core cannot power a larger fan.

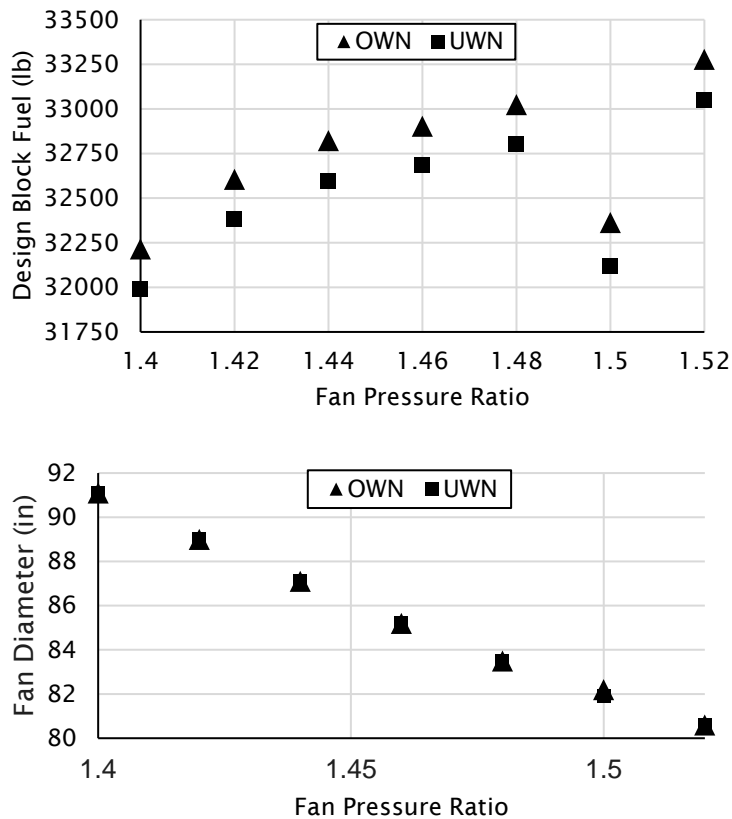


Figure 23. Design block fuel depends on fan pressure ratio, which in turn depends on fan diameter.

The results above show that a FPR of 1.4 will produce the lowest block fuel burn for both OWN and UWN, however, only the OWN can accommodate the larger fan. The UWN concept has ground clearance constraints that limit how much the fan can grow. To determine the smallest allowable FPR for the UWN that does not violate ground clearance constraints, we first looked at the airport planning manual for the A320neo aircraft featuring the derated PW1133 engine. The minimum ground clearance for this configuration is 18 inches. When comparing the A320neo to the A320-200 (older) variant, it is apparent that Airbus was able to fit a new engine on the same airframe with minimal changes but required a 4-inch reduction in minimum ground clearance. The 737-8 on the other hand makes more significant changes to the 737-800 airframe to accommodate the larger engines and takes a 1-2-inch reduction in minimum ground clearance.

Assuming we cannot reduce minimum ground clearance below 17 inches, to mount a larger fan for the UWN, we would need some combination of the following options:

- Mount the nacelle closer to the wing like The Boeing Company did with the 737-8, which would have aerodynamics implications,
- Incorporate a longer landing gear, but that would have weight penalties,
- Change the wing dihedral, which would have stability constraints, or



- Use thinner nacelles.

To avoid major airframe re-design, a fan diameter increase of 3 inches for UWN could be accommodated by mounting the engine further up with a thinner nacelle without going below 17-inch minimum clearance. This corresponds to an FPR of 1.48. For OWN, to maintain the same clearance between the wing and nacelle as in 2022 work, we moved the nacelle farther above the wing by about 9 inches.

We repeated the optimization procedure of stage 1 for with these assumptions. There was a surprising result: when the optimized shapes from stage 1 were simply adjusted for different engine diameters and nacelle position, these adapted stage 1 optimum shapes performed better than the stage 2 optimized results. The OWN had a fuel flow rate of 2362 lb/h at 40,000 ft, Mach 0.8, while the UWN had 2241 lb/h; the OWN fuel flow rate is 5.4% higher. There are many possible explanations, including a less effective geometry parameterization through an active subspace dimensionality reduction technique (Mufti, et al. 2022).

Milestone(s)

Optimization of OWN and UWN with larger engines was completed.

Major Accomplishments

Optimization and comparison of OWN and UWN designs was completed under cruise conditions for engines with larger bypass ratios.

Publications

None.

Outreach Efforts

None.

Awards

None.

Student Involvement

None.

Task 8 – Stage 3 Design: Nacelle and Wing Optimization (Aft Mounted OWN)

Objectives

The following working MDAO problem statement was adopted:

- Minimize: fuel burn for a baseline mission
- Subject to: range and detailed side constraints
- With respect to: design variables including engine nacelle position (focusing on aft placement), nacelle and wing geometry, engine cycle, and operating condition
- Given: baseline single-aisle aircraft model and mission profile
- Returning: fuel burn

This task continues stage 1 work using the same engine and airframe models, except aft-mounted engine locations are considered rather than forward-mounted locations.

Research Approach

The stage 3 optimization approach is identical to the stage 1 approach, described in (Ahuja, et al. 2023). The engine and airframe models are also identical to those used in Stage 1. The only difference between stage 1 and 3 is the location of the nacelle.

Like in stage 1, we first conducted a nacelle placement study and picked a baseline location for optimization semi-arbitrarily as shown in Figure 24. The results from this study showed that like for the forward mounted OWN configuration, moving the nacelle farther away from the wing is better for performance, as seen in Figure 25. As such, we picked a baseline TE location that was roughly as far away from the wing as the OWN LE case in Stage 1.

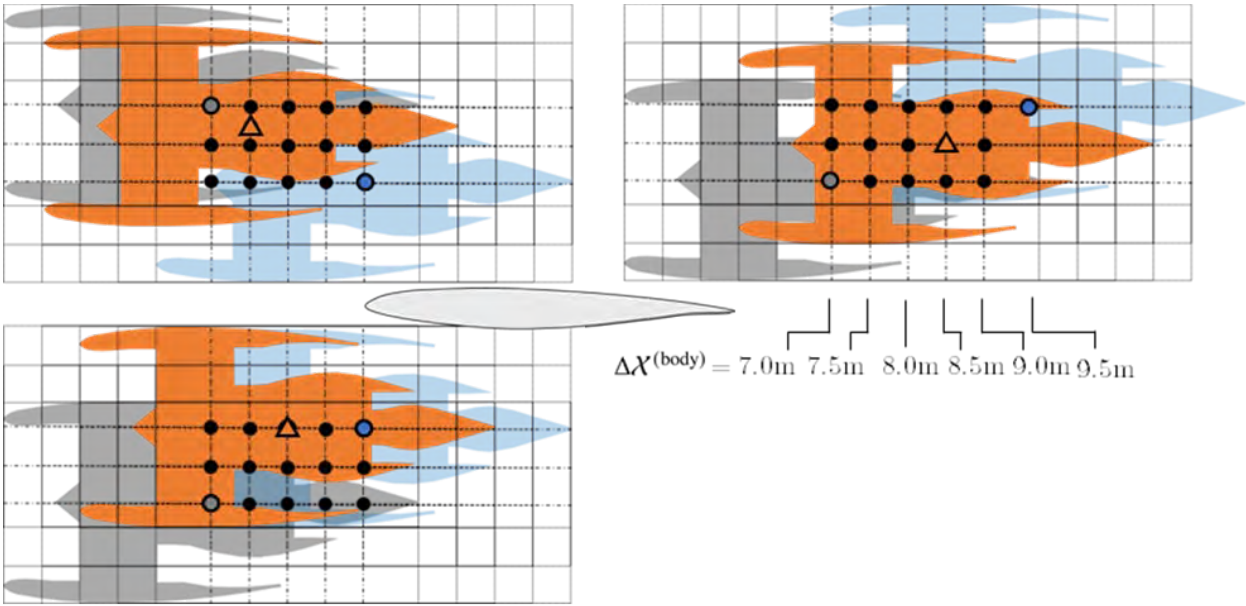


Figure 24. Orange locations are final selections for OWN and UWN.

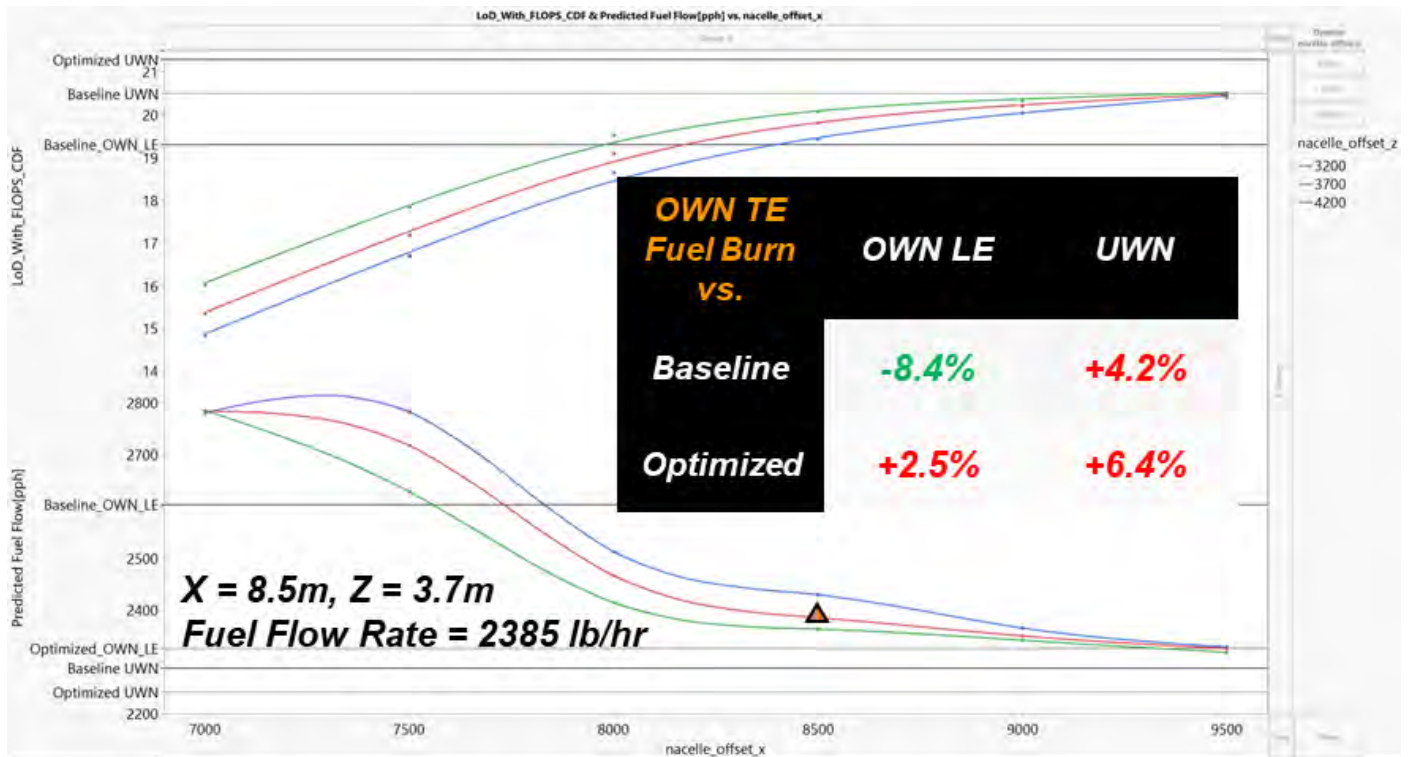


Figure 25. L/D and fuel flow trends with aft nacelle location with the chosen location's baseline performance highlighted

We repeated the optimization procedure of stage 1 for with these assumptions. The results of the optimized configuration are compared to the UWN and OWN LE configurations in Figure 26. We see that even though the baseline OWN TE configuration outperforms the baseline OWN LE case, the improvement in performance is much smaller. Thus, the optimized OWN TE case has a roughly 5% higher cruise fuel flow rate than the optimized UWN as opposed to 4% for the OWN LE case.

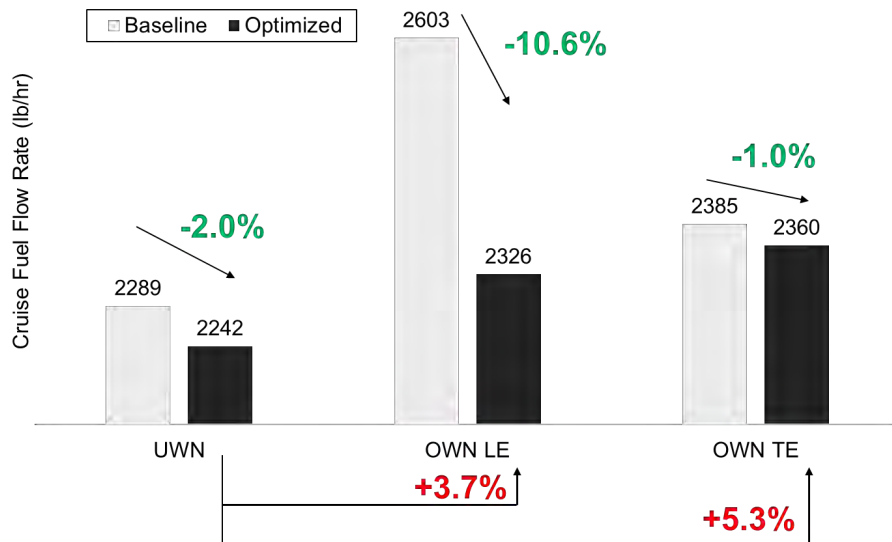


Figure 26. Comparison of the optimized OWN TE configuration cruise fuel flow rate to the OWN LE and UWN configurations.

Milestone(s)

OWN TE configuration optimization was completed.

Major Accomplishments

Completed optimization and comparison of OWN and UWN designs under cruise conditions for forward and aft mounted locations.

Publications

None.

Outreach Efforts

None.

Awards

None.

Student Involvement

None.

Task 9 - Mission Analysis and Trajectory Optimization Setup

Objectives

In a separate task, we performed CFD-based aero-propulsion optimization for cruise conditions. We then aimed to evaluate fuel burn for OWN and UWN configurations over a mission including other mission phases such as climb and descent. Since 2022 (see ASCENT A50 2022 annual report), we reoriented our objective to delve into a more fundamental reformulation of aero-propulsion-mission analysis.

Research Approach

The mission analysis task has diverged substantially from what we envisioned at the beginning of this research in 2020. Georgia Tech had previously relied heavily on its Environmental Design Space suite of mission sizing and synthesis tools built around NASA’s FLOPS mission analysis and the propulsion cycle analysis based on NASA’s Numerical Propulsion System Simulation (NPSS). During our research, we learned that our aero-propulsion integration physics required fundamental changes to mission analysis assumptions. This problem arose because almost all existing conceptual mission analysis codes assume relative independence between airframe aerodynamic drag polars and propulsion cycle (see ASCENT A50 2022 annual report for more information). Such assumptions may be highly inaccurate if there is tight coupling of aero-propulsion physics in novel concepts such as those for OWN or boundary layer ingesting aircraft. Our preliminary tests suggested that fuel burn errors due to traditional mission analysis tools may be comparable or even larger than the difference between OWN and UWN results. At about the same time in 2022, we had very fruitful discussions with NASA experts who were working in a similar area. In consultation with our FAA project manager, we directed our effort toward developing novel mission analysis methods and code. In 2023, we completed mission analysis to allow comparison of OWN and UWN optimum configurations in Task 1.

The mission analysis method which produced the results presented here is based on a what is broadly known as *trajectory optimization* (Kelly 2017), which is a process for finding the state values (e.g., position, velocity) across the trajectory (e.g., time history) which are somehow dependent on a set of control variables and produce a value in some objective function, which is a function of the entire trajectory, in general. The optimizer seeks to optimize the objective function with respect to these control variables and the system’s resulting states, subject to the governing equations of the problem (referred to in this context as “equations of motion” or as the system’s “dynamics model”).

We used a two degree-of-freedom (2-DoF) dynamics model (Equation 1) based on Newton's Second Law (Chakraborty and Mishra 2021) ignoring the earth’s curvature and rotation (Anderson 1999) avoiding an energy-based climb and descent optimization used in FLOPS and similar codes (Capristan and Welstead 2018). The details of the model are given in the 2022 Annual Report. We built the trajectory optimization with NASA’s Dymos optimal control library (Falck, et al. 2021) for NASA’s OpenMDAO framework (Gray, et al. 2019).

$$\dot{V} = \frac{F_{w,z}}{m} - g \sin(\gamma)$$

$$\dot{\gamma} = \frac{1}{V} \left[\frac{F_{w,x}}{m} + g \cos(\gamma) \right]$$

- V Tangential velocity magnitude
- \dot{V} Time rate of change of velocity magnitude (tangential acceleration)
- $F_{w,x}$ Force applied (not due to gravity) in wind axis system parallel to velocity
- $F_{w,z}$ Force applied (not due to gravity) in wind axis system perpendicular to velocity in vertical plane
- γ Flight path angle between velocity vector and horizontal datum (flat earth assumed)
- $\dot{\gamma}$ Time rate of change of flight path angle
- m Mass of vehicle
- g gravitational acceleration (assumed constant)

Equation 1. Equations of motion governing 2-DoF mission analysis

During the first half of 2023, we began a series of developmental experiments to compare mission fuel burn under different physics modeling assumptions. While originally it was planned to develop at least three distinct iterations of the mission analysis, not all three were implemented fully within the span of the project.

The first of the three iterations of the mission analysis, as noted above, used direct reading or surrogate modeling of FLOPS disciplinary analyses results, but ran the trajectory optimization in a different program, the Dymos optimal control library in the OpenMDAO framework from NASA. In one test, we used identical aerodynamics polars, engine model (“engine deck”), and the weights model from FLOPS results while using the newer equations of motion formulation (Equation 1). In this test, we found on the order of 1% fuel burn discrepancy is attributable to the equations of motion alone. Other discrepancies on the order of 1% are attributable to different assumptions about regulatory requirements in descent, for example, with mission phase constraints representative of real operational constraints (e.g., maximum speed of 250 kn below 10,000 ft altitude, as required by FAR-91.117 (United States Department of Transportation, Federal Aviation Administration 2024).

The second of these iterations was intended to replace the imported FLOPS results with custom in-the-loop implementations of FLOPS disciplinary (e.g. weights, aerodynamics, propulsion) methods within the analysis code (termed “Olympus” by the development team) to attempt to reproduce these results with only the input data used by FLOPS. Some routines were implemented by referring to published literature (Wells, Horvath and McCullers 2017). Others were implemented by referring directly to the FLOPS 8 source code and FLOPS 8 and FLOPS 9 documentation. As an aside, the Aviary analysis code by NASA (Aretskin-Hariton, et al. 2024, Gratz, Jasa and Kirk 2023), released in December 2023, implements these methods as well. This intermediate, second iteration was run in a semi-complete form, but the mission analysis of the OWN aircraft never converged in this iteration. Due to time constraints, and a focus on testing, this was prematurely put on hold to pursue final mission analysis results integrating the high-fidelity aero-propulsive surrogates from CFD analysis. Attempts to replace direct execution of the EDET methods with surrogate models of the EDET results were unsuccessful, due to unresolved errors in the partial derivatives (Jacobian) computation.

The third and final iteration of mission analysis development for this project incorporated artificial neural network aero-propulsive surrogates based on the OWN and UWN forward-mounted optimized nacelle and airframe geometries from earlier stages of the project. These were used in the mission analysis, replacing the propulsion and aerodynamics methods and results previously read from FLOPS output. The “final” results reported for this project were produced in this iteration, which is deemed the most accurate iteration of the mission analysis development as it accounts for the coupled aero-propulsion interactions inherent in the OWN configuration, not captured by the FLOPS analysis.

By running the third iteration mission trajectory optimization codes for the UWN and OWN 150-pax configurations, state timeseries (Figure 29) were produced for the OWN and UWN vehicles. These trajectories include only the central, in-flight portion, beginning with climb, of the specified design mission (Figure 27-Figure 31). Reserve mission trajectories were developed earlier in the design process but are not presented here in the results.

The results for these trajectories are consistent with the prediction of higher fuel burn with OWN than UWN, as indicated by the lower final gross weight for OWN compared to UWN shown in Figure 27 and Figure 31. A reference case was run in the FLOPS tool with the same sizing parameters as used in the 2-DoF analysis, and that data is plotted in these figures as well. The problem formulation and optimization methods are slightly different between these tools. FLOPS may minimize the fuel burned or time elapsed during only the climb segment, or maximize the L/D ratio for the descent (Capristan and Welstead 2018), while the 2-DoF approach presented here wholistically optimizes the fuel burn *over the entire mission*, and no distinction is made in the objective for different phases.

The free variables the optimizer adjusts to optimize the mission fuel burn are the normalized tangential control mapped to an engine control and the normalized vertical control parameter which is mapped to angle of attack α in this process. These are inputs, along with the altitude and Mach number, to the aero-propulsion surrogates used to predict the coupled aerodynamic force coefficients and the engine fuel burn rate.

The states which the optimizer adjusts in pursuit of physical consistency with the controls throughout the mission are the altitude, distance traveled over the ground, speed (assuming no wind), flight path angle, and the gross weight of the aircraft. All but the latter define the position and velocity of the point-mass aircraft model in the mission, and the latter is related to the thrust via the fuel burn rate of the propulsion system, assuming that fuel burn is the sole source of change in weight. These are plotted, directly or indirectly (in the case of flight path angle, the speed and flight path angle are used to find the climb rate) in Figure 28 in terms of distance and in Figure 29 in terms of time (which may be considered another state, but

one which is independent of all others). A typical presentation of an aircraft’s operating envelope may use a “sky map” such as the one plotted in Figure 30 for the trajectory of each configuration. In this figure, most of the flight is spent at or near the upper right corner where the aircraft cruises at a relatively high Mach number and altitude. To highlight the difference in the final converged trajectory based on the 2-DoF equations of motion and the mission-level objective function versus the legacy FLOPS mission analysis optimization routines, the climb and descent phases are highlighted in Figure 31. Note that the 2-DoF Olympus program attempts something resembling a “step climb” (Figure 28, Figure 29, and Figure 31) where it begins to plateau in altitude and velocity partway between 20,000 and 30,000 ft altitude, finding an apparently more optimal path than what FLOPS follows.

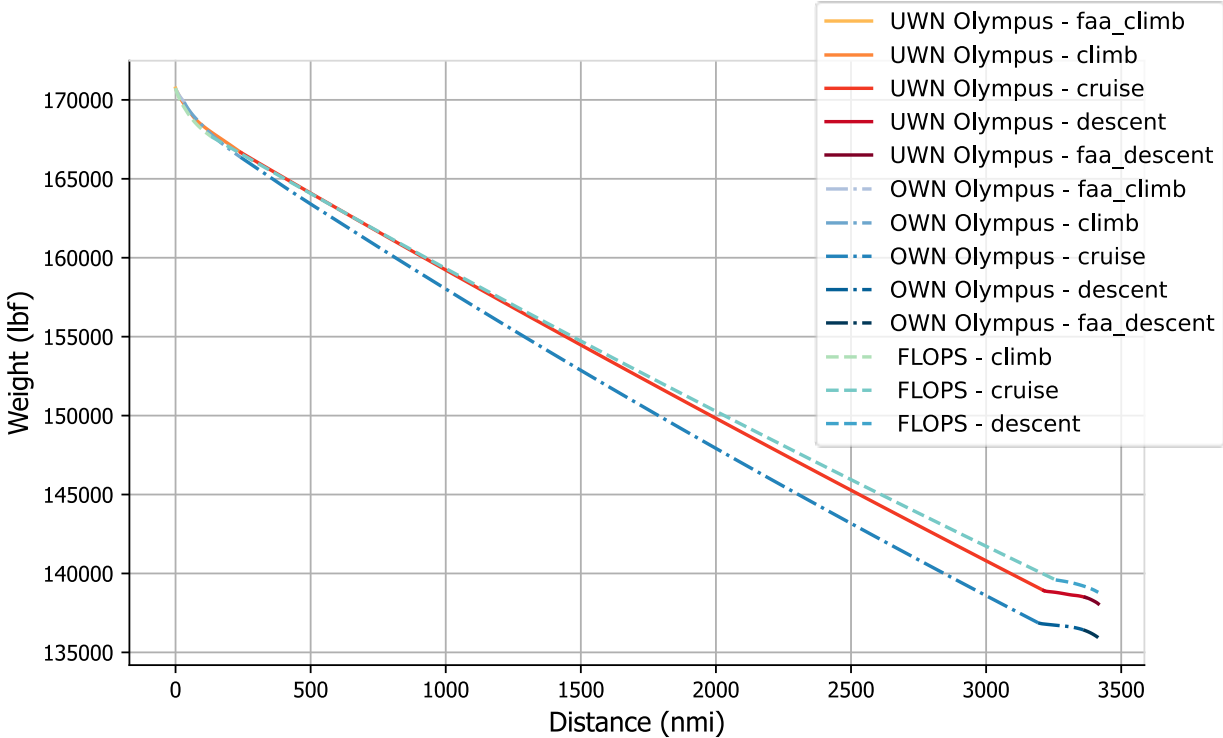


Figure 27. Gross weight versus distance for different configurations’ mission analyses.

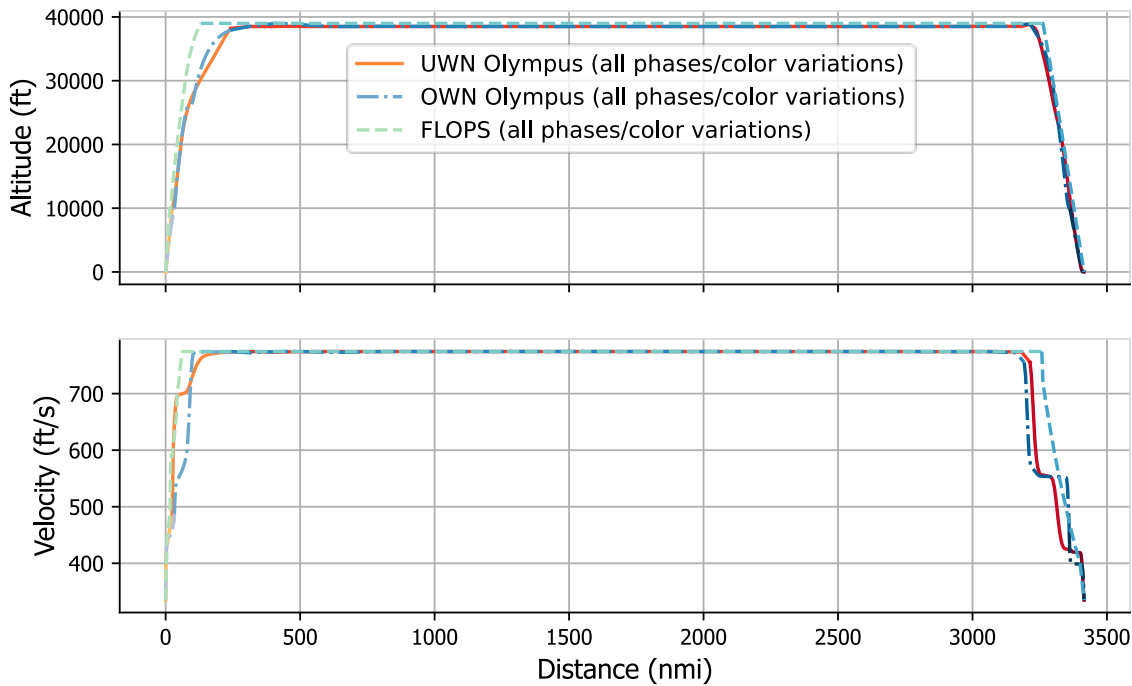


Figure 28. Flight conditions vs distance over the ground for different configurations' optimized trajectories, lighter colors appearing earlier in the mission than darker colors.

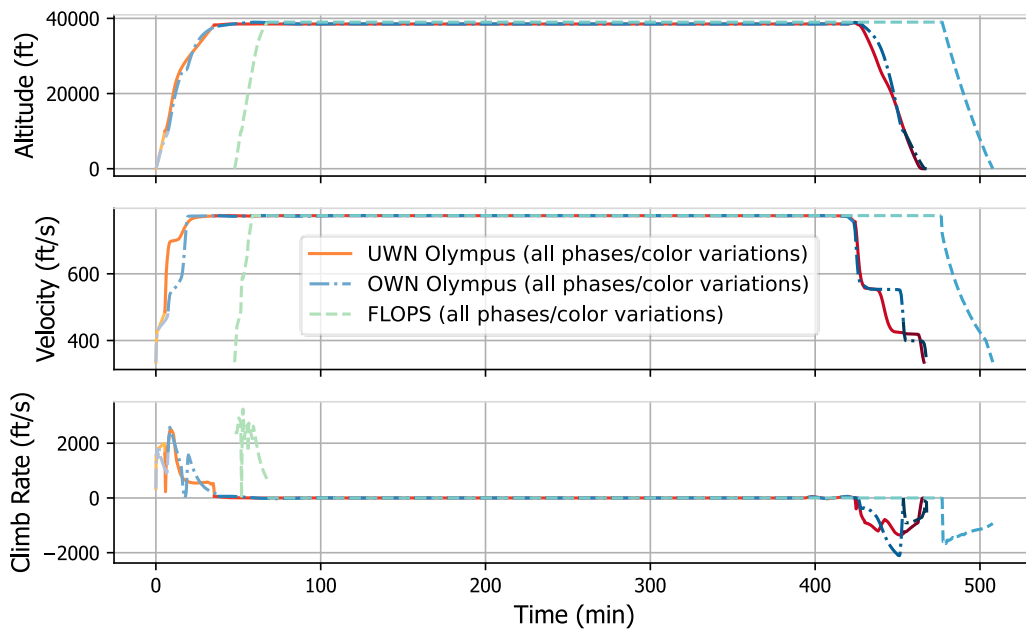


Figure 29. Design mission timeseries optimized (for minimum fuel burn via maximum final weight) for OWN and UWN configurations using 2-DoF ("Olympus") mission analysis code, with FLOPS' discontinuity (bottom plot) in climb rate at transition from climb to steady cruise.

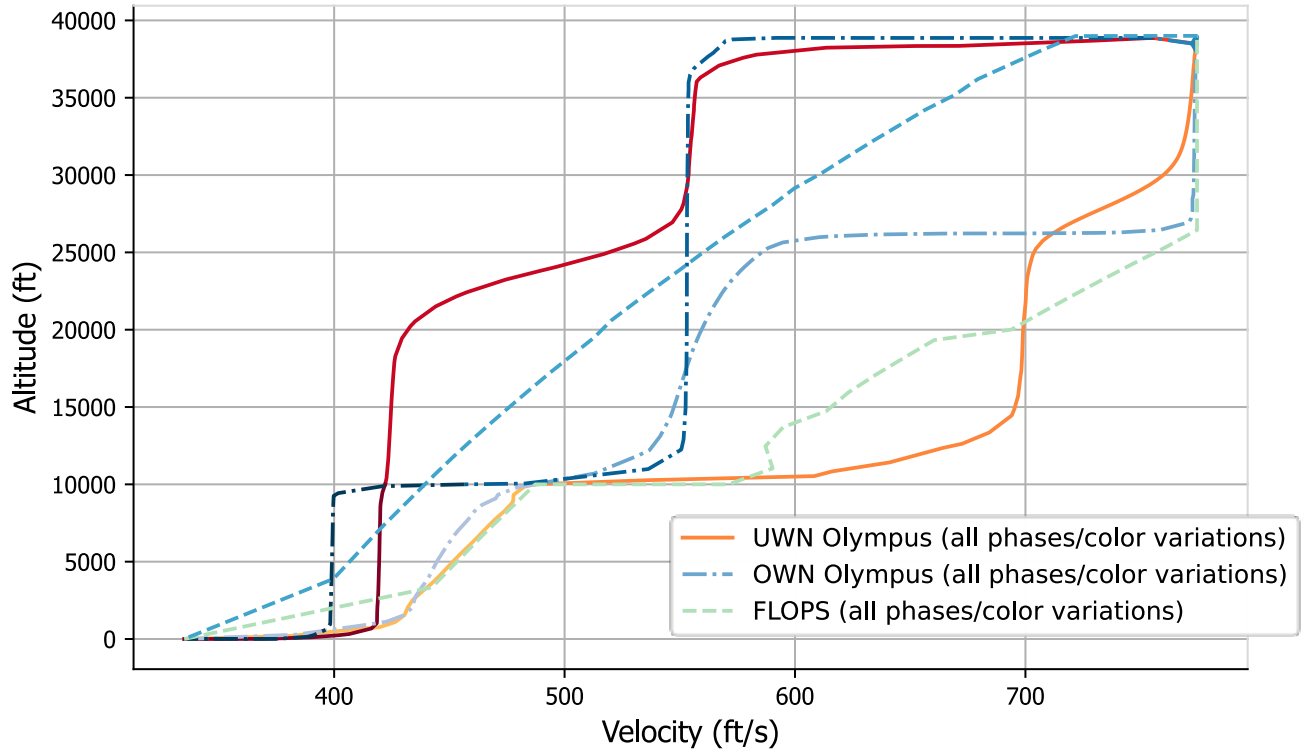


Figure 30. "Sky map" of flight condition history for each vehicle's optimized flight trajectory.

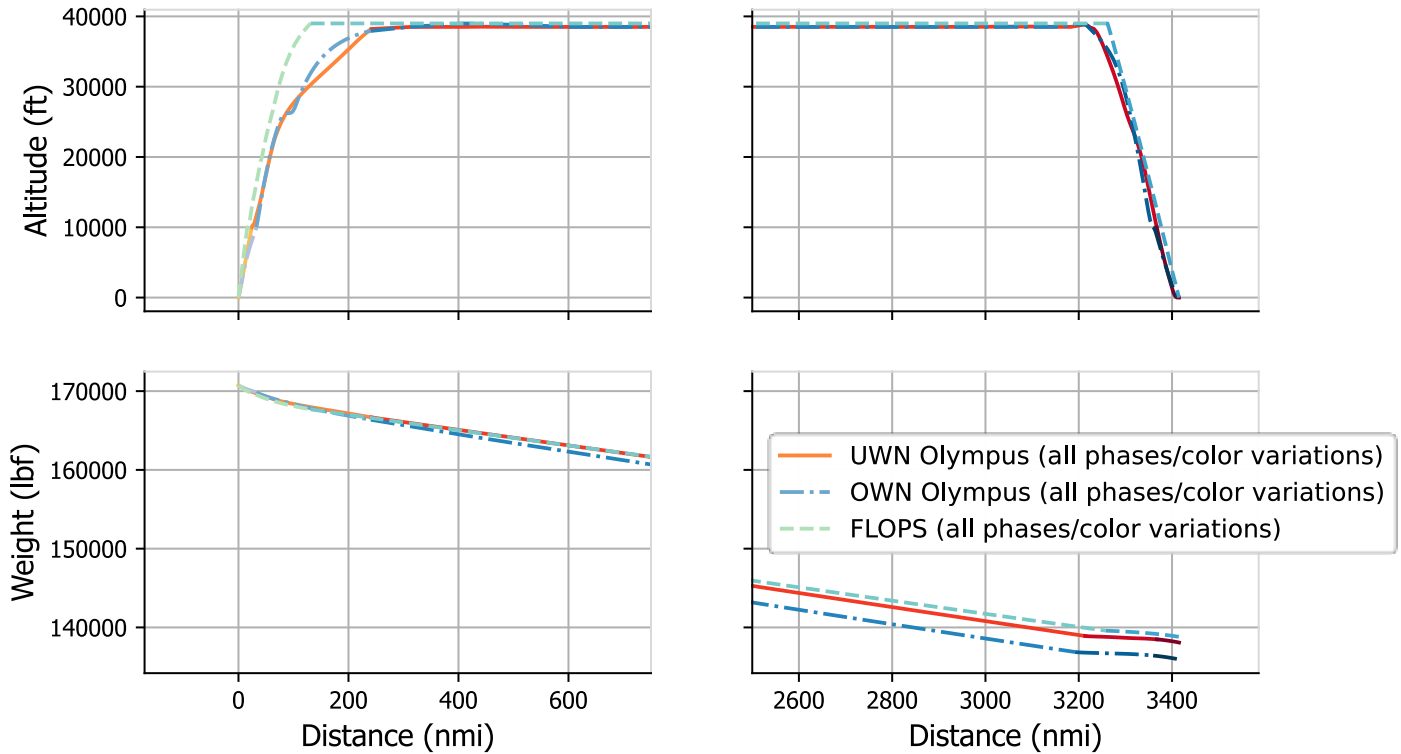


Figure 31. Close-up of mission end phases — climb and descent — for each trajectory

Convergence of the trajectories were non-trivial to achieve, once the models were built and the aero-propulsion surrogates integrated, requiring extensive adjustment optimizer settings and trial-and-error. The “final” results presented here likely depend on those optimizer settings, among other variables. The settings used for the IPOPT optimizer which converged the final trajectories shown here are given in Table 6.



Table 6. Optimizer settings used for final trajectory optimization (OWN and UWN)

Setting	Value
acceptable_tol	1e-06
alpha_for_y	safer-min-dual-infeas
compl_inf_tol	1e-05
constr_viol_tol	1e-05
file_print_level	5
hessian_approximation	limited-memory
linear_solver	mumps
max_iter	1500
mu_init	0.1
mu_strategy	adaptive
nlp_scaling_method	gradient-based
print_level	0
print_user_options	yes
sb	yes
tol	1

The mission-level fuel burn and comparison between the results for each configuration are shown in Table 7. First, the endpoint total (gross) weights (starting at climb, ending at the end of descent) are shown for each of the vehicle missions modeled using the 2-DoF analysis code written for this study. It shows the difference in these as the fuel burn (the only accounted change in weight), and the percent changes between the configurations relative to the configuration named in the column header (first relative to the FLOPS analysis, then relative to the UWN 2-DoF analysis). It can be seen from this that the final difference between the UWN and OWN configurations (according to the 2-DoF analysis) was a 7% higher fuel burn for the UWN configuration compared to the OWN configuration.

Table 7. Summary results for mission optimization for fuel burn for OWN, UWN, and FLOPS.

	Start [lbf]	Final [lbf]	Fuel Weight [lbf]	% Diff (OWN FLOPS)	% Diff (UWN Oly)
OWN FLOPS	170740	138805	31935	0%	-2%
UWN Olympus	170740	138079	32661	2%	0%
OWN Olympus	170740	135934	34806	9%	7%

No “simulation” (time-stepping numerical integration) based on the equations of motion in any of the development iterations was successful. The researchers conjectured it might be due to the handling of discrete variables (number of engines, for example) in the OpenMDAO framework, which seems to have limited support for discrete variables in gradient-based optimization problems (The OpenMDAO Development Team 2022). The implication of this is that the final, converged, “optimal” trajectory may very well be physically inaccurate in terms of the precise states and state rates it predicts at points in time along the mission. A simple example of this phenomenon is shown in the documentation example for a simple, canonical mass-spring-damper problem (The Dymos Development Team 2022).

Milestone(s)

A comparison was conducted of 2-DoF vs. FLOPS mission fuel burn, controlling for aerodynamics, weights, and propulsion disciplines. Trajectory optimization was completed after OWN and UWN configurations were optimized in Task 7.

Major Accomplishments

A more general drag-free, thrust-free mission and trajectory analysis method was developed. An initial implementation was done in OpenMDAO and Dymos software.

Publications

None.

Outreach Efforts

Researchers met and collaborated with the NASA GASPy (predecessor of Aviary) and OpenMDAO development team.

Awards

None.

Student Involvement

Mengzhen Chen re-implemented some EDET aerodynamic methods from FLOPS for second-iteration Olympus development. Samuel Crawford implemented propulsion “engine deck” modeling/lookup functionality replicating FLOPS propulsion module’s capability for first and second-iteration mission analysis and developed early mission analysis mimicking FLOPS mission analysis methods (replaced later by implementation in OpenMDAO framework). Samuel Moore and Savri Gandhi were PhD students at the time who contributed to the comparison of FLOPS with results from the framework implementing 2-DoF simulation, or development of scaffolding for debugging the mission analysis.

Task 10 – High Lift Physics Study

Objectives

By request from FAA stakeholders in 2022, we investigated a variety of physics phenomena and their potential impacts on high lift vehicle performance during takeoff. We focused on the aerodynamics of blowing or increased circulation. We optimized takeoff trajectories (for takeoff length) for both OWN and UWN configurations and investigated the effects of ground effect and an inoperative engine.

Research Approach

The high lift investigation was intended to be an opportunistic investigation of smaller scope than the other tasks. There was no shape optimization, and we used fixed designs for both OWN and UWN. To parallelize work alongside the previous tasks, we used the optimized designs from 2022 as starting points, as described in the 2022 Annual Report as well as our publication (Ahuja, et al. 2023). Those designs were optimized for cruise fuel burn and did not include flaps or slats. In this shorter effort, we did not optimize the flaps and slats but rather scaled and adapted geometries from the NASA High Lift Common Research Model (CRM-HL) as described in (Lacy and Clark 2020). Note that the present OWN vehicle is a 150-pax aircraft while the CRM is a larger 300-pax as shown in Figure 32.

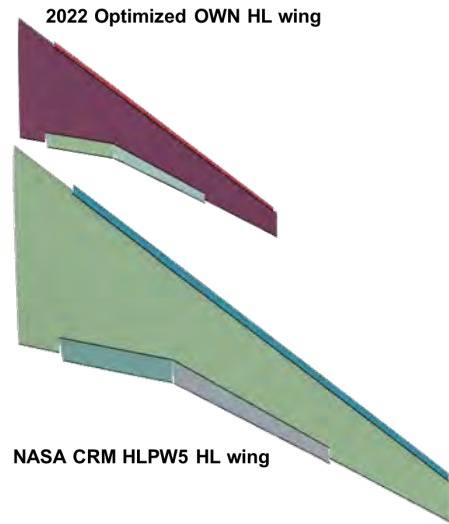


Figure 32. The slats and flaps configuration used in this study are based on the larger NASA CRM-HL.

For this effort, we did not design internal linkages or include detailed kinematic rules for the slats and flaps, though some flap geometry scripts were developed using Bezier curves. For another example of work on this area, see (Marfatia and Bergeson 2021). Rather, using the CRM-HL as a basis, we assumed two settings (“low” and “high”) for high lift surface deflections. The low flap deflection is 10°, and the high deflection is 25° as shown in Figure 33. The slat settings are tied to the flap deflection, and the slats are in a sealed position for the low deflection setting. We emphasize that these settings are not optimized.

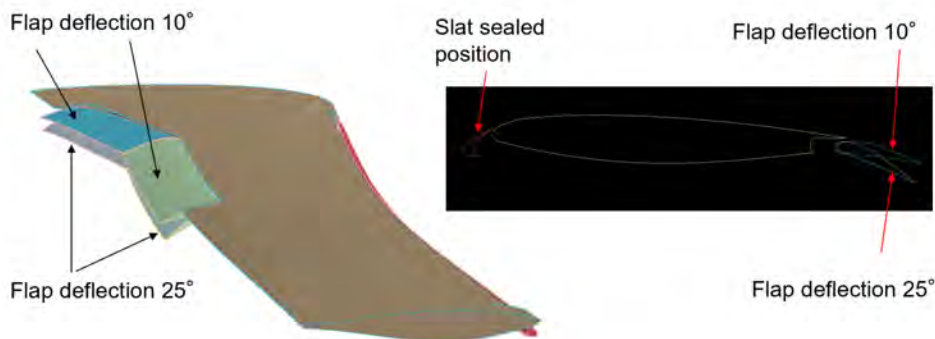


Figure 33. Two combinations of flap and slat settings are used in this study.

Example flowfields are shown for Mach = 0.2 and angle of attack $\alpha = 16^\circ$ for both OWN and UWN with the two flap/slat settings. All cases use the same engine cycle model and power code of 50 (full throttle).

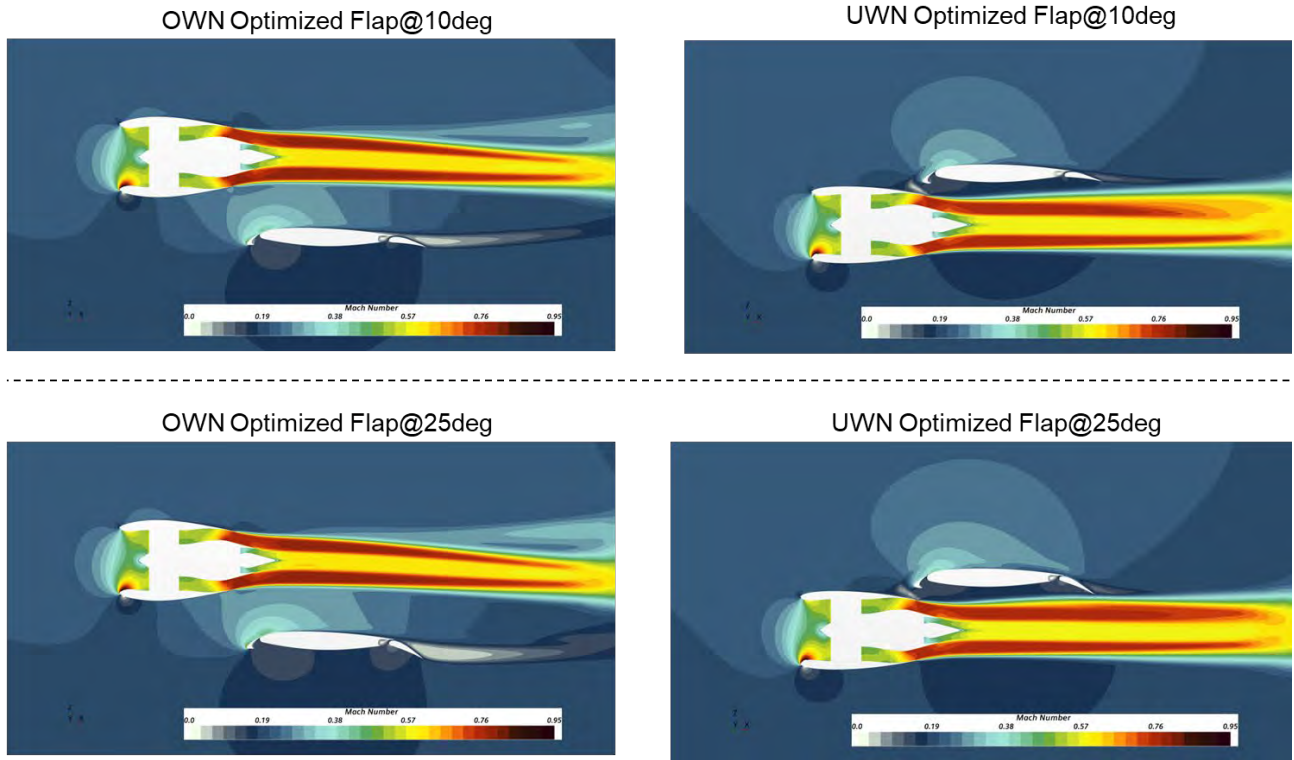


Figure 34. Example flowfields shown for OWN and UWN with two deflection settings at vehicle $\alpha = 16^\circ$.

Example lift and drag polars are shown below in Figure 35. There appears to be a significant aerodynamic advantage for both lift and drag in this case.

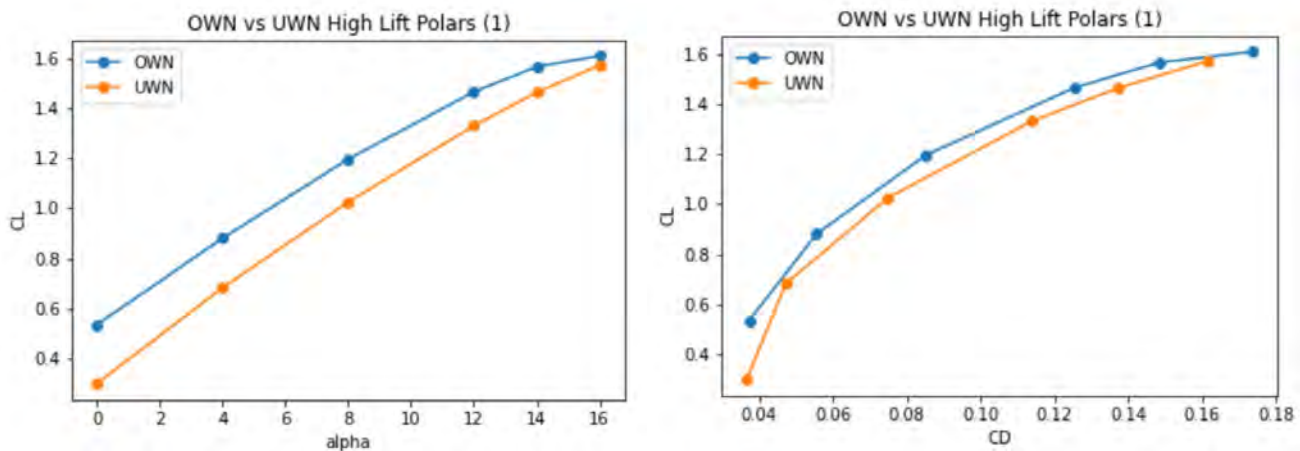


Figure 35. Example lift and drag polars with "low" settings for flaps and slats, Mach = 0.2, PC = 50.

We next accounted for ground effect during the takeoff ground roll and rotation. Figure 36 below shows an example flowfield with the ground modeled as an inviscid slip wall boundary condition. We assumed the location of rear landing gears and pivoted the aircraft about this location when performing a sweep over angle of attack.

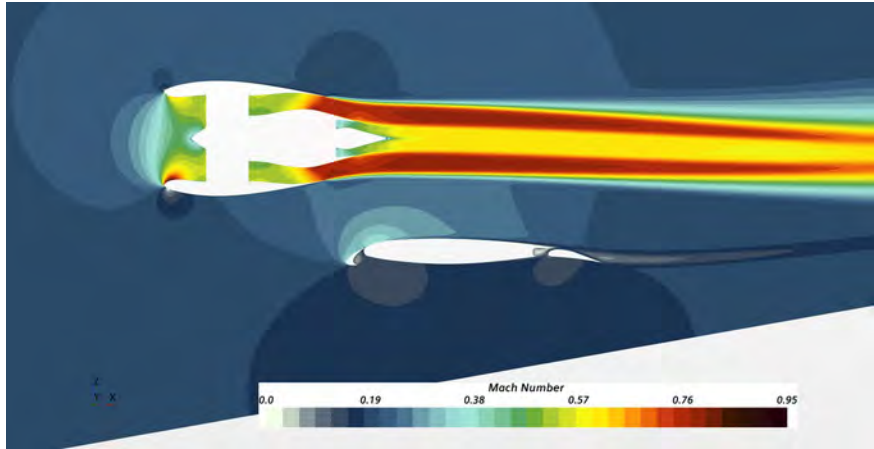


Figure 36. Ground effect modeled with an inviscid slip wall.

Figure 37 shows the pressure coefficients on the aircraft surface as well as the ground. Figure 38 shows a comparison of example lift polars for OWN and UWN with ground effect – there is again an aerodynamic advantage for OWN.

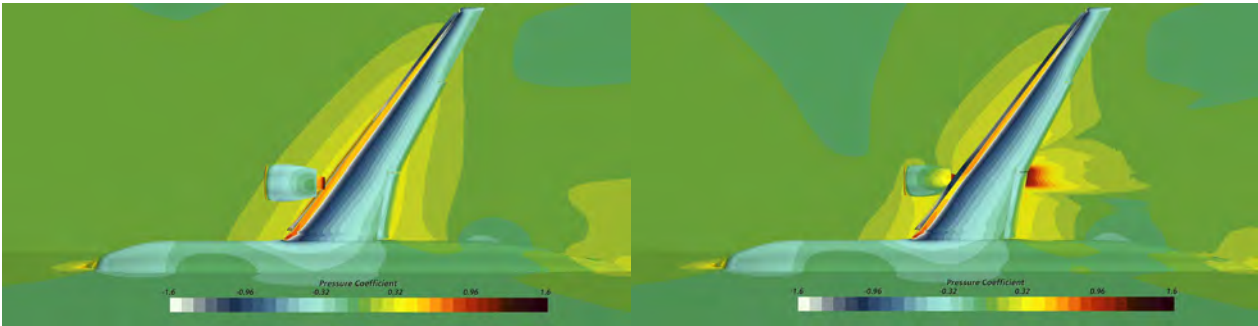


Figure 37. Pressure coefficients shown for aircraft and ground for OWN (left) and UWN (right).

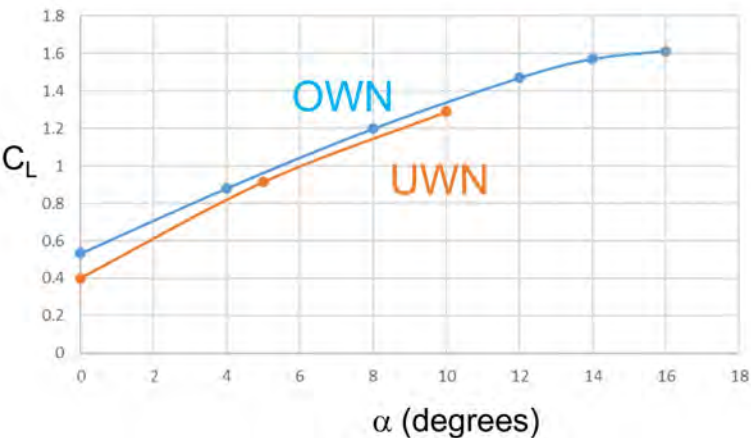
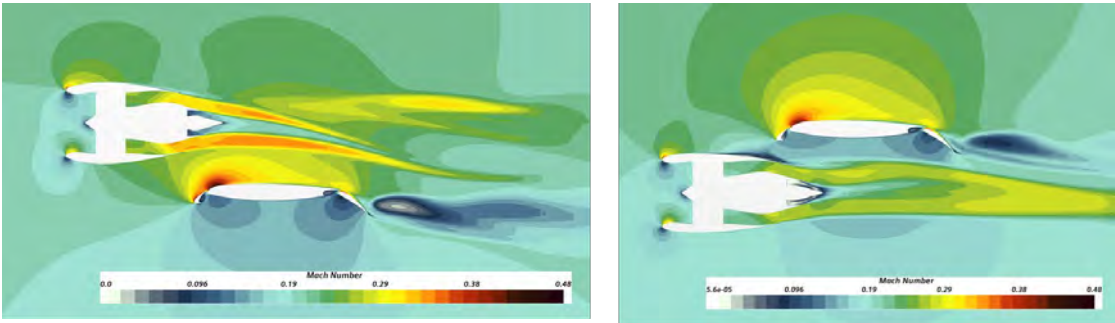


Figure 38. Example lift polars with ground effect showing potential OWN lift benefit (shown for “low” flap/slat settings).

Finally, we also studied the “one engine inoperative” (OEI) condition. FAR-25 requirements for OEI performance affect the calculation of balanced field length. However, there is no clear mapping to CFD boundary conditions. For example, we might implement impermeable wall boundary conditions for the nacelle such that the inoperative engine is essentially a bluff body. However, we judged this to be unrealistic because a malfunctioning engine is unlikely to instantly freeze or to completely stop mass flow. For a qualitative analysis, we used idle power settings of PC=21. In our preliminary analyses, we found that the aerodynamic performance was not significantly affected by this setting. We judged that the simplifying assumptions of our OEI CFD analysis were too crude such that they are likely within the uncertainty of other physical simplifications. For example, we did not account for yaw, sideslip, and control surface deflections accompanying the loss of one engine. In subsequent takeoff trajectory analyses, we simply treated the OEI condition as a loss of half of the available thrust.



Mach = 0.2 , Altitude = 0 ft, alpha = 12°

Figure 39. Example flowfields shown for OEI condition.

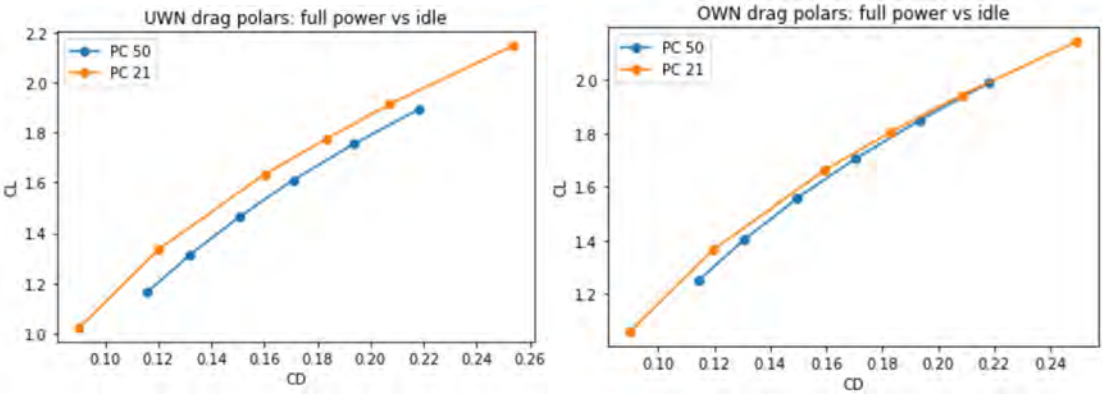


Figure 40. OEI modeled as idle power (PC=21). Note the lower aerodynamic penalty for OVN.

Finally, the above physics effects and aerodynamic polars were used to compare optimized takeoff field lengths for OVN and UWN vehicles. We used as a template an example OpenMDAO Dymos tutorial case for “Aircraft Balanced Field Length Calculation” (The Dymos Development Team 2022). We modified that aerodynamic polars to use quadratic response surface equations for the lift and drag polars and drag polars described previously. Preliminary findings for low flap/slat settings show an approximately 400 ft shorter takeoff field length for the OVN aircraft. Figure 41 shows an example result for balanced field length for the OVN. There is a bifurcation in the trajectory because the balanced field length (The Dymos Development Team 2022) must meet requirements for two scenarios: aborted takeoff and braking to a stop on the runway and takeoff with one engine inoperative and clearing an obstacle at the end of the runway. The OVN configuration has a balanced field length of about 5800 ft and the UWN requires 6200 ft.

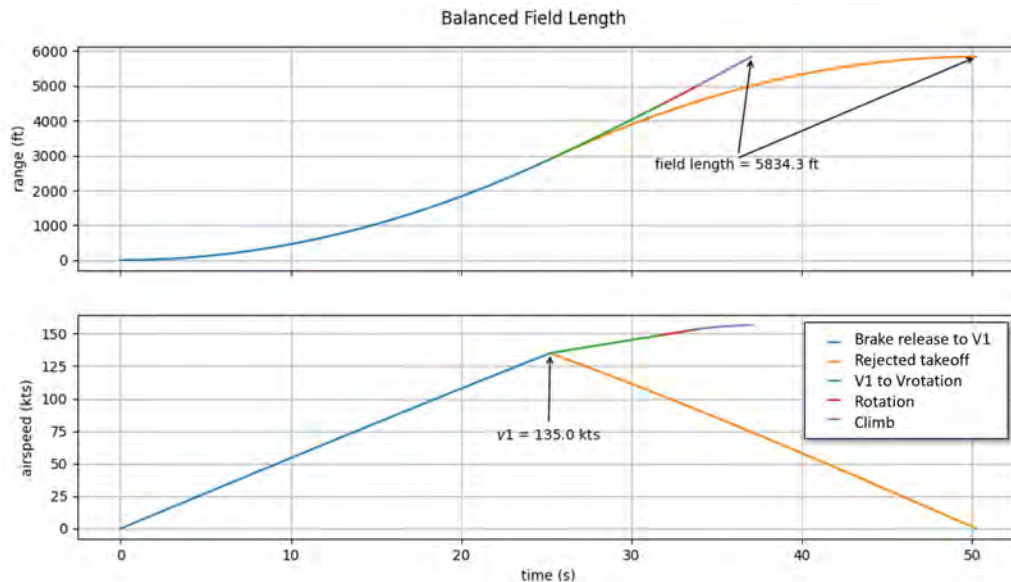


Figure 41. Example balanced field length calculation for OWN.

However, we presently judge that the 400 ft shorter field length for OWN is not significant enough to claim any major advantage. A complete redesign around the OWN configuration would potentially include different landing gear lengths/weights, different operations such as rotation angles, and different fuselage geometry to allow different rotation angles. Despite the apparent advantages in aerodynamic coefficients and takeoff field lengths in our simplified calculation, we can only make modest conclusions: there are no immediately obvious, qualitative “showstoppers” in OWN takeoff performance.

Milestone(s)

Automation scripts were created for high lift configurations. CFD polars were computed with ground effect as well as an OEI condition.

Major Accomplishments

Trajectory optimization for minimum takeoff length was completed using CFD polars in Dymos optimal controls software.

Publications

None.

Outreach Efforts

None.

Awards

None.

Student Involvement

Kavya Krishnan (PhD student at the time) contributed to high lift geometry preparation. Savri Ghandi (PhD student at the time) also supported this effort for some time.



References

- Ahuja, Jai, Chung H. Lee, Christian Perron, and Dimitri N. Mavris. "Comparison of Overwing and Underwing Nacelle Aeropropulsion Optimization for Subsonic Transport Aircraft." *Journal of Aircraft* (American Institute of Aeronautics and Astronautics, Inc.), September 2023: 1-16.
- Anderson, John D. *Aircraft Performance and Design*. McGraw-Hill Companies, Inc., 1999.
- Aretskin-Hariton, Eliot, et al. "Multidisciplinary Optimization of a Transonic Truss-Braced Wing Aircraft using the Aviary Framework." *AIAA SCITECH 2024 Forum*. American Institute of Aeronautics and Astronautics, Inc., 2024.
- Capristan, Francisco M., and Jason R. Welstead. "An Energy-Based Low-Order Approach for Mission Analysis of Air Vehicles in LEAPS." *AIAA Science and Technology Forum and Exposition*. Kissimmee: American Institute of Aeronautics and Astronautics, Inc., 2018.
- Chakraborty, Imon, and Aashutosh Aman Mishra. "Generalized Energy-Based Flight Vehicle Sizing and Performance Analysis." *Journal of Aircraft* 58, no. 4 (2021): 762-780.
- Constantine, Paul G. *Active Subspaces: Emerging Ideas for Dimension Reduction in Parameter Studies*. Philadelphia: SIAM, 2015.
- Falck, Robert, Justin S. Gray, Kaushik Ponnappalli, and Ted Wright. "dymos: A Python package for optimal control of multidisciplinary systems." *Journal of Open Source Software* 6, no. 59 (2021): 2809.
- Fujino, Michimasa, and Yuichi Kawamura. "Wave-Drag Characteristics of an Over-the-Wing Nacelle Business-Jet Configuration." *Journal of Aircraft* (American Institute of Aeronautics and Astronautics Inc.) 40, no. 6 (November 2003): 1177-1184.
- Gautier, Raphaël, Piyush Pandita, Sayan Ghosh, and Dimitri Mavris. "A Fully Bayesian Gradient-Free Supervised Dimension Reduction Method Using Gaussian Processes." Edited by Habib N. Najm. *International Journal for Uncertainty Quantification* (Begell House, Inc.) 12, no. 2 (2022): 19-51.
- Gazaix, A., et al. "Industrial Application of an Advanced Bi-level MDO Formulation to an Aircraft Engine Pylon Optimization." *AIAA Aviation Forum*. Dallas: American Institute of Aeronautics and Astronautics, Inc., 2019.
- Gratz, Jennifer, John Jasa, and Jason Kirk. "Mission Analysis Demonstration for ONERA and University of Michigan." *Technical Exchange between NASA, ONERA, and University of Michigan*. Virtual: National Aeronautics and Space Administration, Scientific and Technical Information program, May 10, 2023.
- Gray, Justin S., John T. Hwang, Joaquim R. R. A. Martins, Kenneth T. Moore, and Bret A. Naylor. "OpenMDAO: an open-source framework for multidisciplinary design, analysis, and optimization." *Structural and Multidisciplinary Optimization* 59, no. 4 (April 2019): 1075-1104.
- Haimes, Robert, and John Dannenhoffer. "The Engineering Sketch Pad: A Solid-Modeling, Feature-Based, Web-Enabled System for Building Parametric Geometry." *21st AIAA Computational Fluid Dynamics Conference*. San Diego: American Institute of Aeronautics and Astronautics, Inc., 2013.
- Hill, Geoffrey A., Osama A. Kandil, and Andrew S. Hahn. "Aerodynamic Investigations of an Advanced Over-the-Wing Nacelle Transport Aircraft Configuration." *Journal of Aircraft* 46, no. 1 (January 2009): 25-35.
- Jones, D. R., M. Schonlau, and W. J. Welch. "Efficient Global Optimization of Expensive Black-Box Functions." *Journal Global Optimization* 13 (1998): 455-492.
- Kelly, Matthew. "An Introduction to Trajectory Optimization: How to Do Your Own Direct Collocation." *SIAM Review* 59, no. 4 (2017): 849-904.
- Kirby, Michelle R., and Dimitri N. Mavris. "The Environmental Design Space." *26th International Congress of the Aeronautical Sciences*. Anchorage: International Council of the Aeronautical Sciences, 2008.
- Kulfan, Brenda M. "Universal Parametric Geometry Representation Method." *Journal of Aircraft* (American Institute of Aeronautics and Astronautics, Inc.) 45, no. 1 (2008): 141-158.
- Lacy, Doug S., and Adam M. Clark. "Definition of Initial Landing and Takeoff Reference Configurations the High Lift Common Research Model (CRM-HL)." *AIAA AVIATION 2020 Forum*. Virtual: AIAA, 2020.
- Lacy, Doug S., and Anthony J. Sclafani. "Development of the High Lift Common Research Model (HL-CRM): A Representative High Lift Configuration for Transonic Transports." *54th AIAA Aerospace Sciences Meeting*. San Diego: American Institute of Aeronautics and Astronautics, Inc, 2016.
- Lambe, Andrew B., and Joaquim R. R. A. Martins. "Extensions to the Design Structure Matrix for the Description of Multidisciplinary Design, Analysis, and Optimization Processes." *Structural and Multidisciplinary Optimization* 46 (2012): 273-284.
- Lee, Chung, and Dimitri Mavris. "Bayesian Collaborative Sampling for Aero-Propulsion Design of an Engine and Nacelle." *48th AIAA/ASME/SAE/ASEE Joint Propulsion Conference & Exhibit*. Atlanta: American Institute of Aeronautics and Astronautics, Inc., 2012.
- Marfatia, Kiran J., and Jennifer D. Bergeson. *Aircraft Flaps Modeling in OpenMDAO*. White Paper, NASA Glenn Research



- Center, Cleveland: National Aeronautics and Space Administration, Scientific and Technical Information Branch, 2021.
- Martins, Joaquim R. R. A., and Andrew B. Lambe. "Multidisciplinary Design Optimization: a Survey of Architectures." *AIAA Journal* (American Institute of Aeronautics and Astronautics, Inc.) 51, no. 9 (2013): 2049–2075.
- "Engine Selection: Parametric Cycle Analysis." In *Aircraft Engine Design*, by Jack D. Mattingly, William H. Heiser, & David T. Pratt, 95–137. Reston: American Institute of Aeronautics and Astronautics, 2002.
- Mufti, Bilal, Mengzhen Chen, Christian Perron, and Dimitri N. Mavris. "A Multi-Fidelity Approximation of the Active Subspace Method for Surrogate Models with High-Dimensional Inputs." *AIAA AVIATION 2022 Forum*. Chicago and virtual, 2022.
- Nunez, Luis Salas, Jimmy Tai, and Dimitri N. Mavris. "The Environmental Design Space: Modeling and Performance Updates." *AIAA SciTech 2021 Forum*. Virtual: American Institute of Aeronautics and Astronautics, Inc., 2021.
- Rajaram, Dushhyanth, Raphael H. Gautier, Christian Perron, Olivia J. Pinon-Fischer, and Dimitri Mavris. "Non-Intrusive Parametric Reduced Order Models with High-Dimensional Inputs via Gradient-Free Active Subspace." *AIAA AVIATION 2020 FORUM*. Virtual: American Institute of Aeronautics and Astronautics, Inc., 2020.
- Renganathan, Ashwin, et al. "Sensitivity Analysis of Aero-Propulsive Coupling for Over-Wing-Nacelle Concepts." *2018 AIAA Aerospace Sciences Meeting*. Kissimmee: American Institute of Aeronautics and Astronautics, Inc., 2018.
- Tejero, Fernando, Matthew Robinson, David G. MacManus, and Christopher Sheaf. "Multi-objective Optimisation of Short Nacelles for High Bypass Ratio Engines." *Aerospace Science and Technology* (Elsevier Masson SAS) 91 (August 2019): 410–421.
- The Dymos Development Team. *Aircraft Balanced Field Length Calculation*. NASA. 2022.
https://openmdao.github.io/dymos/examples/balanced_field/balanced_field.html (accessed February 28, 2024).
- . *Modeling Dynamic Systems with Dymos*. 2022.
https://openmdao.github.io/dymos/getting_started/intro_to_dymos/intro_ivp.html (accessed February 28, 2024).
- The OpenMDAO Development Team. *Discrete Variables*. National Aeronautics and Space Administration. 2022.
https://openmdao.org/newdocs/versions/latest/features/core_features/working_with_components/discrete_variables.html?highlight=discrete#discrete-variable-considerations (accessed February 29, 2024).
- Tripathy, Rohit, Ilias Bilonis, and Marcial Gonzalez. "Gaussian Processes with Built-In Dimensionality Reduction: Applications to High-Dimensional Uncertainty Propagation." *Journal of Computational Physics* 321 (September 2016): 191–223.
- United States Department of Transportation, Federal Aviation Administration. "Title 14 — Aeronautics and Space, Chapter I, Subchapter F, Part 91, Subpart B — Flight Rules." *eCFR*. Online. Washington, District of Columbia: United States Archives Records Administration, February 16, 2024.
- Vassberg, J., M. Dehaan, M. Rivers, and R. Wahls. "Development of a Common Research Model for Applied CFD Validation Studies." *26th AIAA Applied Aerodynamics Conference*. Honolulu: American Institute of Aeronautics and Astronautics, Inc., 2008.
- Wells, Douglas P., Bryce L. Horvath, and Linwood A. McCullers. *The Flight Optimization System Weights Estimation Method*. Technical Memorandum, NASA Langley Research Center, Hampton: National Aeronautics and Space Administration, Scientific and Technical Information program, 2017.
- Zorumski, William E. *Aircraft Noise Prediction Program Theoretical Manual, Part 1*. Technical Memorandum, NASA Langley Research Center, Hampton: National Aeronautics and Space Administration, Scientific and Technical Information Branch, 1982.
- Zorumski, William E. *Aircraft Noise Prediction Program Theoretical Manual, Part 2*. Technical Memorandum, NASA Langley Research Center, Hampton: National Aeronautics and Space Administration, Scientific and Technical Information Branch, 1982.



Project 051 Combustion Concepts for Next-generation Aircraft Engines

Massachusetts Institute of Technology

Project Lead Investigator

Steven R. H. Barrett
Professor of Aeronautics and Astronautics
Director, Laboratory for Aviation and the Environment
Massachusetts Institute of Technology
77 Massachusetts Ave, Building 33-322, Cambridge, MA 02139
(617) 253-2727
sbarrett@mit.edu

University Participants

Massachusetts Institute of Technology (MIT)

- P.I.: Prof. Steven R. H. Barrett
- FAA Award Number: 13-C-AJFE-MIT, Amendment Nos. 061, 071, 079, 097, and 115 (NCE to September 30, 2024)
- Period of Performance: February 5, 2020 to September 30, 2024 (reporting here with the exception of funding level and cost sharing only for the period October 1, 2022 to September 30, 2023)
- Tasks:
 1. Evaluate effects of alcohol-Jet A dual-fuel injection on NO_x emissions
 2. Use computational fluid dynamics (CFD) simulations to inform improvements to reactor network combustor models

Project Funding Level

This project received \$900,000 in FAA funding and \$900,000 in matching funds. Sources of match are approximately \$226,000 from MIT, plus third-party in-kind contributions of \$674,000 from NuFuels LLC.

Investigation Team

Prof. Steven Barrett, (P.I.), Tasks 1 and 2
Dr. Raymond Speth, (co-P.I.), Tasks 1 and 2
Dr. Jayant Sabnis, (co-investigator), Tasks 1 and 2
Yang Chen, (graduate student), Tasks 1 and 2

Project Overview

The objective of this project is to evaluate the impacts of novel combustion concepts on aircraft engine performance. Specifically, the performance characteristics of interest are engine efficiency and emissions. With advances in material technology in the past 50 years, aircraft engines with higher pressure and temperature ratios have been designed to improve the engine's total efficiency and reduce fuel consumption. However, the increase in combustor temperatures tends to produce higher nitrogen oxide (NO_x) emissions, which account for a substantial portion of aviation's environmental impact. Different combustor techniques have been developed to both reduce emissions and maintain high efficiencies. The novel combustion concept currently being investigated in this project is an alcohol-Jet A dual-fuel injection scheme in axially staged combustors. These concepts are being studied using aircraft mission simulation tools (Transport Air System Optimization, TASOPT), engine modeling tools (Numerical Propulsion System Simulation, NPSS), and combustor emissions simulation (Pycaso).



Task 1 - Evaluate Effects of Alcohol-Jet A Dual-fuel Injection on NO_x Emissions

Massachusetts Institute of Technology

Objectives

Compared with traditional Jet A combustion, combustion of alcohols has been shown to potentially reduce NO_x, unburnt-hydrocarbons (UHC), and soot emissions owing to the hydroxyl group (O-H) within their chemical structures. The oxygen atom from the hydroxyl group acts as a diluent to lower combustion temperature and NO_x emissions. The oxygen, once freed through pyrolysis, also accelerates oxidation of UHCs and reduces their emission. At the other end of the hydroxyl group, the strong C-O bonding prevents one carbon from forming a C-C structure and reduces soot emissions.

Despite the emissions reduction benefit from alcohol combustion, they have not been widely utilized in aviation fuel due to their reduced specific energy compared with Jet A, which would require airplanes to carry a larger quantity of alcohol fuel compared with Jet A to fly the same distance. To realize the emissions benefits of using alcohol in airplane engines, it is possible that combining alcohol combustion with an axially staged combustor design could alleviate the fuel burn penalty from alcohol weight while leveraging the NO_x emissions reduction benefit from alcohol combustion.

An axially staged combustor has fuel injection through two axially arranged locations. The first/pilot flame zone ensures combustion stability, whereas the second/main zone reduces NO_x emissions through lean-burn combustion. As the flow through the pilot zone also passes through the main zone, the effective residence time of pilot zone flow is higher and tends to result in more NO_x emissions. Thus, NO_x reduction techniques applied to the pilot zone are theorized to have larger impacts than those applied to the main zone. Specifically, we aim to evaluate whether using alcohol in the pilot zone might effectively reduce NO_x emissions more than using alcohol in the main zone. If traditional Jet A is used in the main zone, less alcohol will need to be carried on board and thus the fuel burn penalty will be lower.

In contrast to the abundance of research done separately in the fields of alcohol combustion, axially staged combustion, and alcohol-diesel internal combustion engine dual-fuel injection, alcohol-Jet A dual-fuel injection for the gas turbine engine combustor has not been thoroughly investigated. In this task, chemical reactor networks are used to numerically study the emissions performance of a generic gas turbine axially staged combustor. For the two stages of the combustor, the emissions levels for Jet A-Jet A, alcohol-alcohol, Jet A-alcohol, and alcohol-Jet A injection will be compared, along with the performance from different Jet A-alcohol blend-fuel injections.

Research Approach

- Calibrate the chemical reactor network structure by matching the predicted NO_x and CO emissions levels from the pilot-stage-only operation with experimentally measured emissions from a CFM-56 engine running on an RQL (Rich-Quench-Lean) combustor.
- Adjust the main-stage fuel injection to represent different fuel-air and jet-in-crossflow unmixedness in the main stage of an axially staged combustor.
- Take the determined combustor internal fuel distribution and replace either first- or second-stage jet fuel with alcohol while matching the same combustor outlet temperature.
- Compare emissions from different injection schemes to evaluate the emissions reduction benefit from dual-fuel injection.
- Compare the total fuel flow rate from different injection schemes to evaluate the weight penalties resulting from dual-fuel injection.

Major Accomplishments

- During cruise operations, ethanol-Jet A dual-fuel injection offers nearly the same NO_x reduction benefit (63%) as pure ethanol injection because main-stage combustion during the thrust level produces very little NO_x.
- Ethanol-Jet A dual-fuel injection reduces the fuel burn penalty of using an alcohol fuel by 28% compared to pure ethanol injection and by 23% compared to the corresponding blend-fuel injection.
- NO_x emissions reductions diminish as thrust increases and main zone NO_x emissions start to dominate.

Publications

None.

Outreach Efforts

Results were presented to the FAA Project Manager during regular teleconferences.

Awards

None.

Student Involvement

This task was conducted by Yang Chen, working under the supervision of Dr. Jayant Sabnis and Dr. Raymond Speth.

Plans for Next Period

We plan to further investigate the impacts of main-stage fuel-air unmixedness on the NO_x reduction benefits of dual-fuel injection.

Task 2 – Use CFD Simulations to Inform Improvements to Reactor Network Combustor Models

Massachusetts Institute of Technology

Objective

When modeling fuel-air unmixedness in the pilot zone of an axially staged combustor, a set of parallel well-stirred reactors with a normally distributed fuel-air equivalence ratio has been used. This modeling method successfully captures NO_x and CO emissions from both the stoichiometric burning flame surface and rich and lean heat diffusion zones. However, the mixing environment is more complex in the main zone of the axially staged combustor, where fuel, air, and pilot exhaust all mix. Two primary levels of unmixedness have been shown to impact NO_x emissions by previous studies: fuel-air unmixedness and jet-in-crossflow unmixedness. Most previous work utilizing chemical reactor network (CRN) models either studied each source of unmixedness independently or assumed premixed fuel-air combustion in the main zone, which does not capture the true physics in the main zone. To more accurately model the mixing physics in the main zone, CRN models deduced from CFD simulated flow field are investigated.

Many previous studies have used CFD simulations in deriving CRN structures to capture combustion emissions. Thermal, chemical, and flow criteria, such as temperature, mixture fraction, and turbulent kinetic energy, have been used to divide the flow field domain into multiple semi-homogeneous parcels, each of which is modeled as a well-stirred reactor or a plug flow reactor. In this task, these techniques are used to create a CRN structure representing the main zone of an axially staged combustor. To facilitate the computational speed, a flamelet model is used instead of the species transport model to roughly capture the flame position in the combustor.

Research Approach

- Use the OpenFOAM flamelet simulation to create a simplified jet-in-crossflow injection simulation for gaseous fuel and air.
- Employ flame zone identification criteria to dissect the flow domain into a CRN structure.
- Perform reacting flow CFD simulation for the simplified case to create validation data for NO_x and CO emissions.
- Simulate emissions from the deduced CRN structure and compare against the reacting flow's simulated emissions for validation.
- Extract a generic parametric CRN structure to represent the main zone flow field of an axially staged combustor.

Major Accomplishments

- A simplified flamelet CFD simulation has been generated.
- Initial approaches to flow domain dissection using mixture fractions and fluid age have been investigated.



Publications

None.

Outreach Efforts

Preliminary results were presented to the FAA Project Manager during regular teleconferences.

Awards

None.

Student Involvement

This task was conducted by Yang Chen, working under the supervision of Dr. Jayant Sabnis and Dr. Raymond Speth.

Plans for Next Period

Tuning of the criteria for domain dissection is required to optimize for the minimum number of reactors required to represent the flow field.



Project 052 Comparative Assessment of Electrification Strategies for Aviation

Massachusetts Institute of Technology

Project Lead Investigators

Steven R. H. Barrett
Professor of Aeronautics and Astronautics
Director, Laboratory for Aviation and the Environment
Massachusetts Institute of Technology
77 Massachusetts Ave, Building 33-207
Cambridge, MA 02139
617-452-2550
sbarrett@mit.edu

Florian Allroggen
Executive Director, Aerospace Climate and Sustainability & Research Scientist
Laboratory for Aviation and the Environment
Department of Aeronautics and Astronautics
Massachusetts Institute of Technology
77 Massachusetts Ave, Building 33-115A
Cambridge, MA 02139
617-715-4472
fallrogg@mit.edu

Raymond Speth
Principal Research Scientist
Laboratory for Aviation and the Environment
Department of Aeronautics and Astronautics
Massachusetts Institute of Technology
77 Massachusetts Ave, Building 33-322
Cambridge, MA 02139
617-253-1516
speth@mit.edu

University Participants

Massachusetts Institute of Technology (MIT)

- P.I.: Prof. Steven R. H. Barrett
- FAA Award Number: 13-C-AJFE-MIT, Amendment Nos. 062, 072, 080, 093, 098, and 115 (NCE to September 30, 2024)
- Period of Performance: February 5, 2020 to September 30, 2024
- Tasks (reported for the period October 1, 2022 to September 30, 2023):
 1. Develop a suite of roadmaps for aircraft electrification (covered in previous reporting periods; not reported for this period)
 2. Develop a system-level engineering model of power conversion processes and aircraft energy requirements (covered in previous reporting periods; not reported for this period)
 3. Develop a model for analyzing the economics and emissions of electrification strategies (covered in previous periods; not reported during the current reporting period)
 4. Analyze the system-level costs and benefits of the electrification strategies, specifically comparing liquid hydrogen (LH₂) and Power-to-Liquid (PtL) pathways
 5. Analyze the benefits of energy storage for PtL fuel production



Project Funding Level

\$1,060,000 FAA funding and \$1,060,000 matching funds. Sources of match are approximately \$276,000 from MIT, plus third-party in-kind contributions of \$460,000 from NuFuels, LLC; \$110,000 from Savion Aerospace Corporation; and \$214,000 from Google, LLC.

Investigation Team

Prof. Steven Barrett, (P.I.), Tasks 1–4
Dr. Florian Allroggen, (co-P.I.), Tasks 1–4
Dr. Raymond Speth, (co-P.I.), Tasks 1, 2, and 4
Dr. Sebastian Eastham, (co-investigator), Task 4
Nicolas Gomez-Vega, (postdoctoral associate), Task 4
Arthur Brown, (postdoctoral associate), Task 4
James Abel, (graduate researcher), Tasks 3 and 4
Dun Tan, (graduate researcher), Tasks 2 and 4
Bjarni Kristinsson, (graduate researcher), Task 4

Project Overview

The long-term goal of this project is to quantify the costs, emissions, and environmental impacts (i.e., climate and air-quality impacts) of various electrification approaches for commercial aviation. The electrification pathways include battery-electric (“all-electric”) aircraft, as well as aircraft using drop-in sustainable aviation fuels (SAFs) made with substantial electricity input (“PtL”) and LH₂-powered aircraft. The project helps identify the best approach for using one unit of electric energy to power aviation. For this purpose, we develop both system-level engineering and system-level economic models, to assess electricity generation, fuel production, fuel transportation and storage, aircraft energy requirements, and aircraft operations. The models analyze different electrification pathways by using what can be described as a “power station to wake” approach. They quantify differences in costs and emissions associated with each electrification approach and compare them to a set of baseline aircraft powered by petroleum-derived fuels or drop-in SAFs made from biomass or waste streams. The outputs are used in a cost-benefit analysis, which provides insights into the net benefits associated with each technology, while also considering each technology’s environmental impacts.

Task 4 – Analyze the System-level Costs and Benefits of the Electrification Strategies

Massachusetts Institute of Technology

Objective

The goal of this task is to develop system-level analyses for comparing various electrification strategies while integrating the engineering and assessment models developed previously. During the current reporting period, we analyzed the societal cost of PtL- or LH₂-powered aviation systems, specifically including climate externalities and fuel costs. The goal of this effort is to better understand when a PtL- or LH₂-powered aviation system is more beneficial. The analysis encompasses societal costs in an effort to capture trade-offs between fuel costs and environmental benefits.

Research Approach

The system model builds on previous work under this project (see reports for previous reporting periods) and is summarized in Figure 1. It consists of three main models: a techno-economic model, which estimates the fuel production cost; a climate model, which calculates the emissions (life cycle and flight) per unit fuel use and quantifies the climate impact; and an aircraft fuel burn model, which computes the societal (fuel and climate) costs, normalized by available seat kilometer (ASK).

The fuel production model is divided into three steps: renewable power generation, fuel production, and fuel distribution. The models are identical for PtL and LH₂ fuels until the hydrogen production step, then subsequently diverge to reflect the different production and distribution processes.

The climate impact model consists of two stages: a reduced-order model for the warming potential and associated cost per unit emission (computed via the FAA’s Aviation environmental Portfolio Management Tool - Impacts Climate, or APMT-IC), and a model for the emission intensity per unit fuel burn.

The aircraft fuel burn model uses an aircraft design tool (Transport Aircraft System OPTimization, or TASOPT) to assess the potential fuel burn penalties of an LH₂ aircraft due to fuel storage in the fuselage and the corresponding increase in empty weight. The model also quantifies leakage of LH₂ from storage onboard the aircraft. The sensitivity of the societal fuel cost to input parameters with uncertainty is computed with a Monte Carlo study.

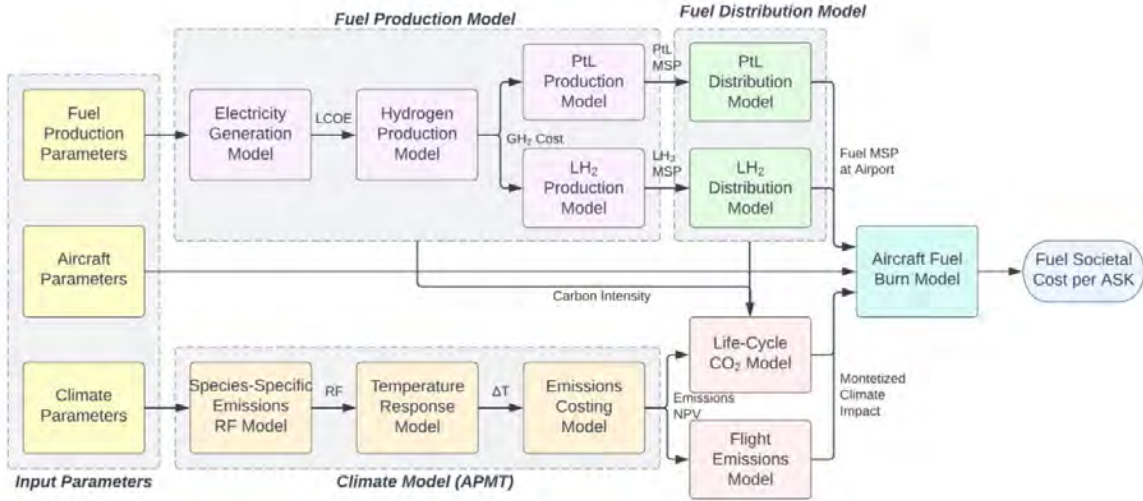


Figure 1. Block diagram showing overall modeling architecture.

Milestones

The model has been completed, and the results have been summarized in a thesis and manuscript.

Major Accomplishments

We compared an aviation system using either PtL, SAF, or LH₂ as a fuel, wherein the LH₂ aircraft relies on hydrogen combustion. With baseline input parameters, the total societal cost of a flight with LH₂ and PtL was found to be \$1.71 and \$1.83 per liter Jet A equivalent, respectively (for comparison, the December 2023 Jet A price was approximately \$0.70 per liter). However, these values do not consider the potentially higher energy demand of flight with an LH₂ aircraft. When potential fuel penalties are accounted for, the baseline societal cost becomes \$3.07 and \$2.63 per 100 ASK for LH₂ and PtL, respectively. This finding highlights the importance of comparing fuels’ ability to power a flight. For reference, the total societal cost of fossil Jet A is \$2.17 per liter Jet A or \$3.12 per 100 ASK, as computed with the average Jet A price in 2022 of \$0.88/L and a life-cycle carbon intensity of 89 gCO₂e/MJ, following Carbon Offsetting and Reduction Scheme for International Aviation (CORSIA) values. The results indicated that direct air capture (DAC), both capital and power demand, and power generation costs are the main drivers of the societal cost of PtL fuel. Similarly, the main contributors to the societal cost of LH₂ flight are power generation, fuel transport, contrail formation, and the capital cost of liquefaction.

The sensitivity of flight with PtL and LH₂ to the parameters with the greatest impact is shown in Figure 2. The bars represent how the difference in total cost between these fuels changes as each parameter is varied between its minimum (blue) and maximum (red) possible value, while all other parameters are held constant. Values on the right indicate that PtL has a lower total societal cost for a given set of inputs, whereas values on the left indicate that the total societal cost is lower for LH₂. The hatched bars show how the difference in cost changes if each parameter is varied by ±10% from its baseline value. The main parameter affecting the cost competitiveness of PtL is the capital cost of DAC: if this cost remains high, the high production cost of PtL may justify investment in LH₂ aviation infrastructure. For LH₂, the parameters with the greatest sensitivity are the intensity and warming potential of contrails, the aircraft fuel penalties, and the fuel distribution costs. Specifically, we note the high uncertainty regarding the contrail impacts of an LH₂-powered aircraft.

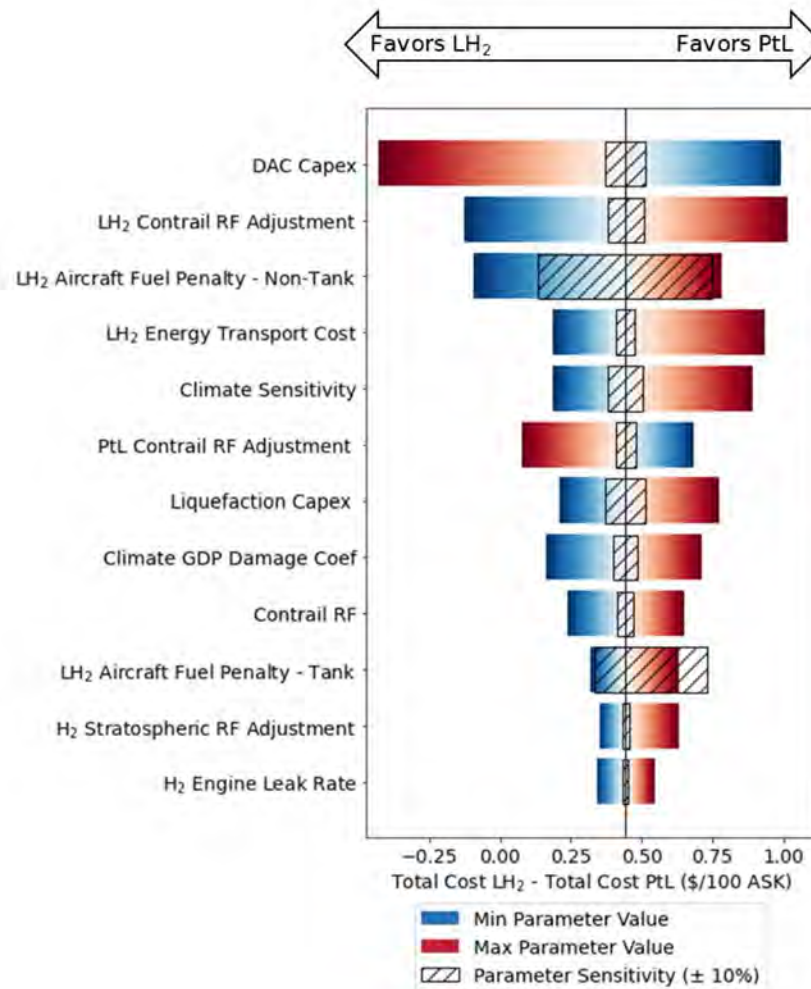


Figure 2. Sensitivity of the difference in societal cost between a unit of flight powered by LH₂ or PtL. Red values indicate increasing the underlying parameters, whereas blue values increased decreased cost.

Publications

Abel, J.M., 2023. Comparative Assessment of the Societal Cost of PtL and LH₂ as Aviation Fuels. Master’s Thesis, Massachusetts Institute of Technology. To be published via MIT DSpace.

Abel, J., Allroggen, F. 2023. Global costs and infrastructure requirements for LH₂ Airport Refueling. AIAA Aviation 2023-3406.

Outreach Efforts

- Presentations to numerous industry stakeholders and governmental agencies
- Previous work on airport infrastructure requirements for an LH₂-powered aviation system, presented during the AIAA Aviation 2023 conference
- Previous work on global LH₂ and PtL supply chains, presented during the Global Trade Analysis Project 2023 conference in Bordeaux



Student Involvement

During the reporting period, the MIT graduate students involved in this task were James Abel and Bjarni Kristinsson.

Plans for Next Period

Over the coming reporting period, the team will continue with efforts to assess various non-drop-in fuels from a system-level perspective.

Task 5 – Analyze the Benefits of Energy Storage for PtL Fuel Production

Massachusetts Institute of Technology

Objective

This task focused on how PtL production can be optimized considering an intermittent energy source. This question is particularly important for PtL production, because capital-intensive DAC and conversion facilities would benefit from continuous operations, whereas electricity from renewable sources such as wind and solar energy follow variable load profiles.

Research Approach

The PtL production model developed for this task is shown in Figure 3 and requires three types of modeling contributions: (a) techno-economic assumptions and technology development scenarios, (b) modeling of renewable electricity availability, and (c) production system optimization.

- The inputs into the techno-economic analysis model are the capital expenditure, operational cost, conversion efficiencies, greenhouse gas life-cycle emissions, and other operational assumptions regarding the production system. Two technology development scenarios are considered: an advanced technology development scenario (2050) and a moderate technology development scenario (2030). The technology assumptions have been documented in reports for previous reporting periods.
- Solar photovoltaic (PV) and wind electricity are considered. Hourly solar and wind data are obtained from Modern-Era Retrospective Analysis for Research and Applications (MERRA) and MERRA-2 global meteorological data for the year 2019. The dataset captures the diurnal and seasonal characteristics of the intermittent energy sources. The weather data are processed with the renewables.ninja PV and wind simulation methods to generate hourly electricity profiles. The input power and gases are assumed to be produced onsite; hence, no transmission and transportation losses are included.
- A linear optimization model is used to formulate an optimal PtL plant. The optimization routine tailors the production capacity and storage of the key feedstocks and products: (a) electricity, (b) hydrogen, (c) carbon dioxide, (d) heat, and (f) liquid fuel. The objective function is to minimize the annual system cost while constraining the system to minimum seasonal fuel production and physical plant constraints (see publications for details).

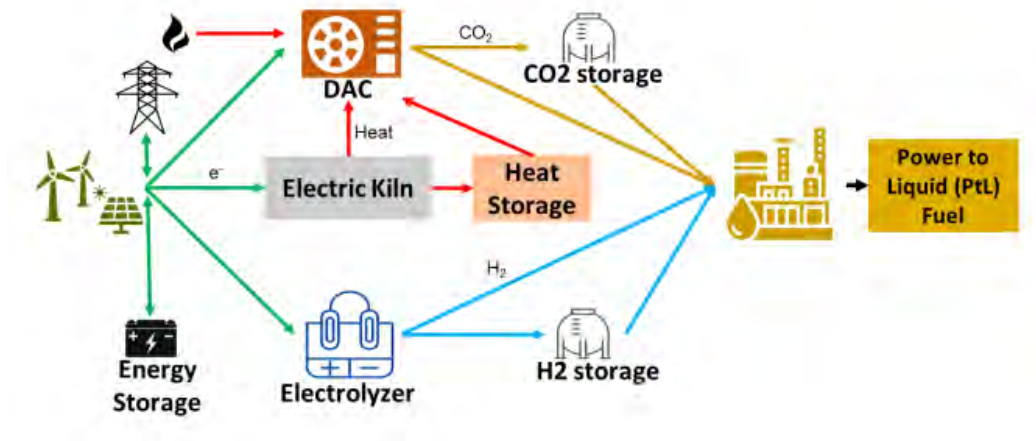


Figure 3. Process diagram of a PtL fuel system model.

Milestone

The model has been completed, and the results have been summarized in a thesis and manuscript draft.

Major Accomplishments

First, optimal sizing of storage buffers (i.e., gas storage of CO₂ or batteries for energy storage) can decrease PtL production costs by 20%–40%, by allowing capital-intensive components such as the DACs to operate continuously, thereby decreasing their size (Figure 4). The lowest life-cycle emissions can be obtained by a wind-powered PtL system. However, the addition of gas storage, and then energy storage can decrease the life-cycle emissions for all power generation options. Storage solutions offer the largest life-cycle emissions from PV systems, as much as 20%. The effect is on the order of ~5% for a hybrid power generation system.

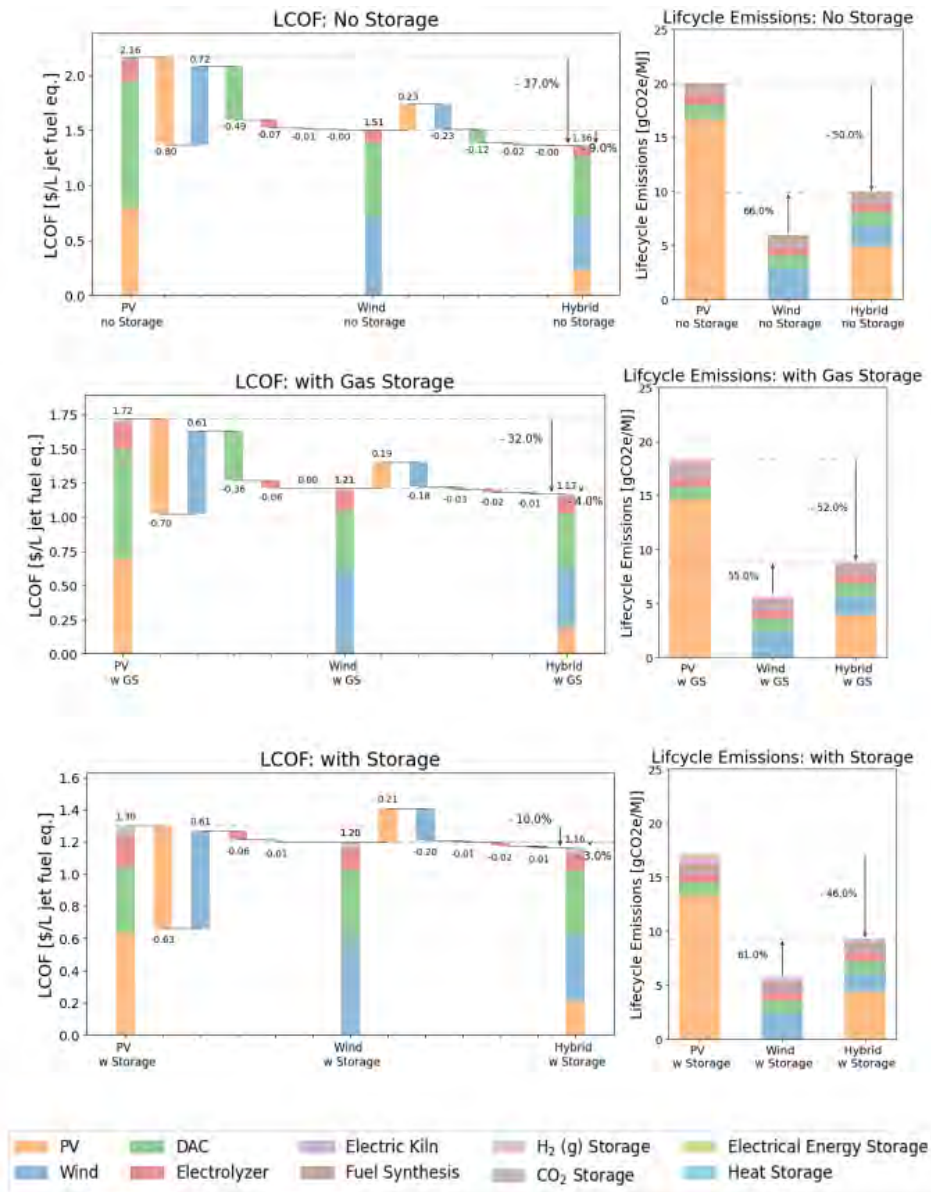


Figure 4. Levelized cost of fuel (left) and life-cycle emissions (right) for a hybrid wind-PV-based PtL system. From left to right: PV, wind, hybrid. Top: case with no gaseous and energy storage. Middle: case with gaseous storage only. Bottom: case with gaseous storage and energy storage.

Second, a hybrid wind-PV system can yield cost reductions in the range of 2%–8% less than the cost of a standalone PV or wind system, because of shorter downtime due to insufficient power generation from a combination of wind and solar energy sources. For the United States, the greatest benefit in a hybrid power generation setup is located along the coasts of the Northern Pacific and the Atlantic.

Using grid electricity to supplement the intermittency of renewable electricity can be advantageous in lowering the cost of PtL fuel but can substantially increase the life-cycle emissions of the fuel, to levels even exceeding the emissions of conventional jet fuel. A carbon price of \$50–100/tCO₂ would be sufficient to ensure low emissions of PtL fuel in most locations of the United States in 2050.



Publications

Tan, D.Y., 2023. Implications of Intermittency of Renewable Energy on Power-to-Liquid SAF Production. Master's Thesis, Massachusetts Institute of Technology. To be published via MIT DSpace.

Outreach Efforts

- Presentation during the Spring 2023 ASCENT meeting
- Presentations to numerous industry stakeholders and governmental agencies
- Presentation of results from the analysis during the Global Trade Analysis Project 2023 conference in Bordeaux

Student Involvement

During the reporting period, the MIT graduate student involved in this task was Dun Tan.

Plans for Next Period

This task has been completed. The MIT team will seek to publish the results.



Project 053 Validation of Low Exposure Noise Modeling by Open-Source Data Management and Visualization Systems Integrated with AEDT

Stanford University

Project Lead Investigator

Juan J. Alonso
Vance D. and Arlene C. Coffman Professor
James and Anna Marie Spilker Chair of Aeronautics & Astronautics
Department of Aeronautics & Astronautics
Stanford University
Stanford, CA 94305
Phone: (650) 723-9954
E-mail: jjalonso@stanford.edu

University Participants

Stanford University

- P.I.(s): Prof. Juan J. Alonso
- FAA Award Number: 13-C-AJFE-SU-022
- Period of Performance: October 1, 2022 to September 30, 2023
- Task(s):
 1. Complete prototype of MONA, including AEDT integration. Completed.
 2. Validation and verification of AEDT noise predictions in DNL 55-65 dB areas. Results presented in this report are only for arrival operations and preliminary.
 3. Data science formats and scientific computing for large-scale airspace analyses. Completed.
 4. Viable alternative approach routes into the SF Bay Area metroplex. Pending/de-scoped.

Project Funding Level

Additional funding in the amount of \$250,000 was used this past year (2023) to complete Task 1, the entire set of work related to arrivals (and some development for departures) for Task 2, and the finalization of data formats for Task 3 of ASCENT Project 53. Cost sharing in excess of this amount has been identified from various sources. Mr. Thomas Rindfleisch is contributing all of his time, uncompensated, and Mr. Donald Jackson is also contributing a significant part of his time (approximately 65% FTE), uncompensated, to the project. In addition, contractor costs for the continued development of the MONA project website, the cost of undergraduate student support and summer interns, and some equipment purchases (and installation costs) are also being used to generate cost share for this project. During the first 48 months of this project, a total of more than \$1.7M of cost share has already been accounted for.

Investigation Team

The investigation team is made up of the faculty, graduate and undergraduate students, and collaborators listed below with their respective areas of expertise / areas of contribution:

1. Juan J. Alonso (PI, Stanford Aeronautics & Astronautics): overall responsibility for the project and its technical and administrative elements.
2. Nick Bowman (Former graduate Student, Stanford Computer Science, now a research scientist at NASA JPL): MONA project cloud infrastructure, cloud-based execution of AEDT analyses, Apache Kafka-based data collection. Incidental bug fixes and minor contributions, Oct 1, 2022-Sept 30, 2023.



3. Brian Munguía (Graduate Student, Stanford Aeronautics & Astronautics): AEDT, cloud-based AEDT study execution, AEDT debugging; departures study development and initial debugging. Oct 1, 2022-Sept 30, 2023.
4. Donald Jackson (Collaborator, software developer): overall MONA project infrastructure (servers, databases, hardware / software monitoring), GIS, web-based visualization deployment, technical guidance. Oct 1, 2022-Sept 30, 2023.
5. Thomas Rindfleisch (Collaborator, Sr. Research Scientist, Emeritus, Stanford University): noise monitoring and filtering, aircraft trajectory collection / processing, visualization, data analysis. Oct 1, 2021-Sept 30, 2023.
6. Aditeya Shukla (Undergraduate Student, Stanford Aeronautics & Astronautics, now a PhD student at MIT Aero & Astro): AI/ML classification of aircraft trajectories, real-time Sound-Level Monitoring (SLM) software, AI/ML noise modeling. Oct 1, 2022-June 30, 2023.

Project Overview

The MONA project (Metroplex Overflight Noise Analysis) was started to provide real-time and objective data, analyses, and reports to key stakeholders and policy makers to mitigate the noise impacts of the deployment of new NextGen procedures. This system (a) collects and archives air traffic data using a network of antennae and ADS-B receivers, (b) analyzes noise impacts using a variety of metrics, (c) visualizes resulting large-scale datasets, and (d) uses a network of sound-level monitors (SLMs) to validate and enhance the quality of noise predictions. The focus of this ASCENT project is to improve upon the noise predictions of MONA through tighter integration with AEDT. In particular, our work is focused on the following three tasks: (1) integrate and automate AEDT's noise analysis capabilities, (2) Validate and Verify (V&V) AEDT's noise predictions in DNL 55-65 dB areas, and (3) propose software engineering/architectural choices for future AEDT development to enhance usability in multiple workflows including API (Application Programming Interface) formulation, visualization interfaces, resilient data acquisition and storage, and cloud computing.

The expected benefits of this project mirror the tasks mentioned above, including (a) ability to automate complex noise analyses in metroplexes so they are available in near-real time after the preceding 24-hr period, (b) a better understanding of the accuracy of AEDT's current noise models in high- (DNL >65 dB) and low-noise (DNL 55-65 dB) areas and the reasons for the discrepancies (if any) in existing predictions, and (c) recommendations to software developers on flexible architectures and APIs for AEDT so that the tool is more versatile and generally applicable. AEDT predictions are built around the policy context of an average annual day. The majority of the V&V results produced and shared by the MONA team had focused on a cumulative daily basis for which flight track data is directly collected but, as a major accomplishment of this period of performance, we have continued to automate the cloud-based analysis (using many parallel instances of AEDT) of *every flight into SFO for a period of an entire year (July 1, 2021-June 30, 2022)* and therefore some of our results also include DNL levels for an actual entire year of flight operations. The focus of the work reported here is on arrivals into SFO with main attention paid to arrivals into runway 28L/R. The vast majority of the effort this past year has been in ensuring (a) that the noise analysis of flight trajectories resulting from AEDT (including both the standard version and one in which altitude and speed controls are included, and both with ANP/BADA 3 and BADA 4 models of the aircraft involved) is as accurate as the performance and noise models in AEDT are capable of, (b) that the results from the comparisons between experimental data and AEDT predictions has been vetted for peer-review publication, and (c) that a similar capability for departures (together with noise monitoring station data from SFO) can be used to complete, this coming year, a full analysis of AEDT noise predictions for *all operations in and out of SFO*. This report presents a summary of what has been submitted as a journal publication relating all of our results to date. In addition, and although not an original part of this proposal and not reported here, we have used the vast amounts of data collected by the MONA system and predicted by AEDT to begin the development of machine-learning (ML) models of noise that could, one day, be used to improve the current noise predictions in the AEDT model.

Background and Previous Accomplishments

The MONA project started approximately 5 years ago with the main objective of providing real-time and objective data, analyses, and reports to key stakeholders and policy makers to help in mitigating the noise impacts of the deployment of new NextGen procedures. Since then, we have put together and deployed a system that (a) collects, archives, and makes available air traffic data using a series of networked antennae and ADS-B receivers 24/7, (b) analyzes noise impacts using a variety of metrics (based on both a MONA-developed noise prediction tool and the noise prediction tools within AEDT), (c) visualizes resulting large-scale datasets in a simple, user-friendly fashion using both a bespoke website and Uber's kepler.gl and deck.gl large-scale data visualization toolboxes, and (d) has deployed a small network of low-cost, Stanford-owned, sound-level monitors scattered across the South Bay part of the Bay Area and has included the data from the noise

monitors deployed by SFO to cross-calibrate measurements by MONA and SFO monitors, collect noise measurements more widely geographically, and enhance noise predictions so they describe exactly the actual noise levels experienced.

The longer-term objectives of the MONA project are to (a) ensure the validation and verification of all noise predictions provided (by AEDT or other tools) in both areas near the airport and in other areas further away from the airport, (b) achieve full automation of complex noise analyses in regions around airports in the US, including AEDT-based noise predictions, (c) make all results web-accessible for in-depth interpretations of historical and proposed changes, (d) eventually study potential alternative traffic patterns in complex airspace to mitigate aviation environmental impacts, and (e) export the proven/validated MONA technology to other airport regions via open-source software/hardware.

The current status of the MONA system has matured considerably over the past few years to the point that a full-system prototype has now been operational for multiple years. In fact, for all arrival operations into SFO, we consider the system to be fully operational. To recall the main elements of the system, the MONA team has deployed a small network of ADS-B / MLAT antennae and has completed the software necessary to merge the data streams from all of these antennae including de-duplication of sightings, identification of aircraft equipment and routes flown, physical interpolation of data missing from the joint observations, and archiving (in appropriate database formats) of the information collected for successive analysis. Moreover, for arrival operations, we have spent considerable time and effort understanding the best ways to utilize AEDT (by understanding the ways to most accurately model aircraft trajectories, aircraft equipment, and aircraft noise) so that any comparisons between experimental data and the results obtained from AEDT may be affected as little as possible by confounding variables. In fact, we have spent time in using AEDT in multiple ways including the standard version of AEDT that is approved for regulatory use in the U.S. and an improved version that leverages higher-fidelity aircraft performance models (BADA 4) and detailed descriptions of individual aircraft trajectories (using the so-called altitude and speed controls that result from the ADS-B data and its post-processing).

The MONA system has achieved a level of integration with FAA's AEDT software that enables fully-automatic processing of noise exposure at arbitrary receptor locations for arrival and departure routes into the San Francisco Bay Area airports. This year's report includes our most accurate and comprehensive assessment of the comparison between AEDT predictions and noise-monitoring stations created to date, with an entire year of flights observed at multiple locations. In total, more than 200,000 datapoints give statistical significance to the results that we have obtained, that are presented here, and that we submitted for peer-reviewed publication.

Finally, and although not an explicit task of ASCENT 53, we have continued our efforts to interface the above-described MONA software modules with the kepler.gl open-source visualization framework to be able to visualize and animate aircraft positions and paths, noise predictions, various routes and procedures, etc., to better communicate the results of our work (see the image below for our use of the kepler.gl and deck.gl data and graphics systems for a visualization of traffic patterns in the San Francisco Bay Area including a 24-hr view of aircraft traffic patterns. The display can be set to show shorter intervals).

As a result of our efforts during the performance period covered by this yearly report, we now have a full understanding of the accuracy of the noise predictions, in arrival routes to SFO and at locations of either low (DNL 55-65 dB) or high (DNL > 65 dB) noise, including all types or aircraft equipment, in all types of weather situations, and over an entire period of 12 months. The rest of this report focuses on our methodology, the detailed results we have obtained, and the main conclusions of our work thus far. Note that, the majority of the effort this past year centered around "Task 2. Validation and verification of AEDT noise predictions in DNL 55-65 dB areas" which, for arrivals, and including DNL > 65 dB areas, is now complete. The departures part of this task is intended to be completed during the coming year. Task 1 - Complete prototype of MONA, including AEDT integration; is now deemed to be complete and has been reported on in previous yearly reports and project publications. Task 3 - Data science formats and scientific computing for large-scale airspace analyses, is also deemed to be completed, since the functional MONA prototype is using all of these formats, databases, and processing architectures on a daily basis. This work has also been reported on. Task 4 in our original proposal, Viable alternative approach routes into the SF Bay Area metroplex, is one we are going to de-scope because it is expected that the V&V process of departure flights will take the majority of our efforts during Year 3 of the project. With that said, we still plan on including suggestions that could be used for further development of approach routes in our project final closing report next year. Through the involvement of undergraduate research assistants at Stanford, we have been able to do a preliminary investigation, which resulted in a publication at the AIAA SciTech 2023 conference, of the use of all the data accumulated by the MONA system and collected from our AEDT analyses for the development of machine-learning-based

models of the noise emitted by some of the most common aircraft classes that arrive in SFO (single-aisle and regional-jet categories). These results are not reported here but show promise.

Task 2 - AEDT Noise Prediction Assessment in DNL 55-65 and DNL > 65 dB Areas

Stanford University

Our main accomplishments over the past 12 months focus on the statistically-significant characterization of the discrepancies between the measured noise at 2 different noise-monitoring stations and the predictions using AEDT in various ways with increasing levels of modeling fidelity. By *statistically significant* we mean that the observations and conclusions are based on large amounts of data that are deemed to have converged probability distributions and statistical moments (e.g. expected value / mean and standard deviations). In other words, we do not attempt to draw conclusions about the predictive qualities of AEDT noise models based on 5-10 flights (as has been common in the literature) but that, rather, we focus on large-enough numbers of observations: at least 10,000 flights / data points for the main aircraft types and over 200,000 flights, over a 12-month period, for our entire study. Moreover, the actual data we draw conclusions from is highly curated to eliminate any noise events that are even slightly unlikely to be the result of aircraft overflights alone, as well as other situations where multiple aircraft may pass over a noise-monitoring station nearly simultaneously. This is to say that we feel confident that the data presented is of the highest quality possible.

In previous yearly reports we have presented preliminary results. The results presented here represent a very large number of validations, modeling enhancements, filtering of suspect data, and the use of best practices for modeling with AEDT.

Study Design and Methodology

AEDT Noise Metric Predictions

AEDT comprises an enhanced aircraft performance modeling system that relies on different performance models based on the available data, the phase of the flight, and the purpose for which the model will be used. To predict noise in the terminal area, AEDT primarily uses the performance modeling approach provided in the International Civil Aviation Organization (ICAO) Doc 9911 manual^{1,2,3}. A newer EUROCONTROL BADA 4 model can be used throughout the flight profile when the appropriate data are available for the aircraft being modeled. Outside of the terminal area, the older BADA 3 performance model,⁴ initially developed by EUROCONTROL in the 1990s, is used when BADA 4 data are not available, but only to provide enroute performance modeling beyond the Doc 9911 intended range (i.e., above 10,000 ft MSL). The use of the BADA models for the enroute regions is needed because the Doc 9911 performance model was developed only for modeling the terminal area performance (i.e., below 10,000 ft MSL). The noise modeling parameters needed for computing noise in all cases are obtained from the ICAO *Aircraft Noise and Performance database* (ANP)⁵ and are provided by the aircraft manufacturers.

For routine regulatory use to assess flight impacts in airport environments, the FAA prescribes the use of the Doc 9911, ANP, and BADA 3 performance models, which rely on procedural profiles, or in some cases fixed-point profiles, in conjunction with the aircraft ground tracks (i.e., only latitude and longitude data for track points) defined by the user.⁶

BADA 4, announced in 2010, addresses BADA 3 limitations by using both higher fidelity performance models and data (i.e., latitude and longitude data plus altitude and airspeed data for track points) for existing cruise flight regions and new data and methods for operations in the terminal area. These expansions of the model allow BADA 4 to be used for all flight

¹ Society of Automotive Engineers, Committee A-21, Aircraft Noise, Procedure for the Computation of Airplane Noise in the Vicinity of Airports, Aerospace Information Report No. 1845, Warrendale, PA: Society of Automotive Engineers, Inc., March 1986.

² ICAO Doc 9911, "Recommended Method for Computing Noise Contours around Airports", Second edition, 2018.

³ B Silva, D Rhodes, and ER Boeker, Recommended Method for Computing Noise Contours Around Airports – Recent Updates to ICAO Doc 9911, EnvironmentalReports 2019, Chapter 2, pp 62-65.

⁴ Eurocontrol Experimental Center (EEC). User Manual for the Base of Aircraft Data (BADA), Revision 3.9. EEC Note No. 11/06/15-25. June 2011.

⁵ ICAO ANP Database v2.1, <http://www.aircraftnoise.model.org/>, 2016.

⁶ FAA Aviation Environmental Design Tool Release Notes for AEDT 3e, p 37. May 9, 2022.

phases.⁷ BADA 4 capabilities were introduced in release AEDT 3b in September 2019. However, no BADA 4 aircraft models are currently approved for FAA regulatory use.⁸⁶

To model an aircraft flight arrival with AEDT, we create a study file specifying:

- Aircraft type/model (ANP_ID and EQUIP_ID),
- Arrival airport and runway,
- The aircraft ground track, a sequence of [longitude, latitude] pairs (optionally augmented with altitude and/or airspeed controls), typically based on *Automatic Dependent Surveillance-Broadcast* (ADS-B) data.⁹ We estimate calibrated airspeed using the ADS-B reported groundspeed in conjunction with NOAA High-Resolution Rapid Refresh (HRRR) atmospheric data,¹⁰ and
- BADA 4 model usage (true/false): if false, ANP/BADA 3 modelling is employed.

An ANP/BADA 3 ground track may optionally include an altitude control at each [lon, lat] position, and a BADA 4 ground track may optionally include an airspeed and/or an altitude control(s) at each [lon, lat] position.

In our work for Task 2 we compared AEDT’s noise predictions using two different modeling approaches:

- **AEDT-R:** ANP/BADA 3, with no altitude or airspeed controls specified. This is the modeling approach required by FAA for regulatory purposes.
- **AEDT-AE:** BADA 4, with both altitude and airspeed controls specified for each ground-track position to enhance the predictive capabilities of AEDT and to provide the predictions with the highest-fidelity physics available to us via AEDT.

To be clear, we attempted the full set of combinations including (a) BADA 3 vs BADA 4 and (b) altitude and airspeed controls vs standard profiles for both altitude and airspeed, and, based on the results, we focused on the two alternatives described above because the other two alternatives did not show significant value and, are not reported here. In this work, we have attempted to use AEDT to the best of its predictive abilities. For example, we have based our assessments, wherever possible, on the latest AEDT modeling features and we have consulted with FAA and Volpe Center experts to optimize the preparation of flight-profile data to fit AEDT modeling constraints (e.g., smoothing flight profile parameters and limiting profile altitude or speed changes).

It should be noted that we are validating AEDT’s “out of the box” capabilities, i.e., using its existing flight trajectory-based track controls and flight modeling tools. We have not tried to develop user-defined flight modeling profiles, although such efforts might result in a closer match between AEDT predictions and sound-level monitor (SLM) measurements.

Sound Measurements

We have developed a sound level analysis system that matches and associates noise peaks with aircraft overflights (via ADS-B trajectory data) to identify the flight that gives rise to each peak detected by the monitor. We adaptively measure the background sound-level within each matched noise peak and subtract it from the raw peak to obtain the aircraft contribution alone. We then measure the aircraft peak L_{Amax} and compute the SEL.

In published noise studies, the sound-monitor measurements have generally been considered a “gold standard,” but the real world is more complex. In our experience:

- Random variations in sound propagation and attenuation between aircraft and sound monitors can arise due to atmospheric conditions, turbulence, cell structure, stratification, and reflections,
- Local ambient noise sources of all sorts can interfere with and distort recorded noise peaks,

⁷ Poles, D et al., *Advanced aircraft performance model for ATM - analysis of BADA model capabilities*, October 2010, [https://www.eurocontrol.int/sites/default/files/2019-07/advanced-aircraft-performance-model-for-atm-BADA 2010.pdf](https://www.eurocontrol.int/sites/default/files/2019-07/advanced-aircraft-performance-model-for-atm-BADA%2010.pdf).

⁸ Aviation Environmental Design Tool Release Notes for AEDT 3e (Federal Aviation Administration, Washington, DC), p. 37.

⁹ ICAO (2012). ICAO Doc 9871, Technical Provisions for Mode S and Extended Squitter (2 ed.). International Civil Aviation Organization. ISBN 978-92-9249-042-3.

¹⁰ Alexander, C. et al., Rapid Refresh (RAP) and High-Resolution Rapid Refresh (HRRR) Model Development, American Meteorological Society, 100th Annual Meeting, 12-16 January 2020, Boston, MA.

- In busy metroplexes it is not uncommon for two aircraft to pass close to an SLM nearly simultaneously, so that one cannot distinguish contributions from any single aircraft of interest (without resorting to complex phased monitor arrays).

These effects are independent of aircraft noise per se. We have tried to account for uncertainties in the noise measurements as carefully as possible by excluding “contaminated” data. We eliminate peaks that have contributions from multiple aircraft. We also use a goodness-of-fit (GoF) metric to evaluate each sound peak against an idealized sound model to decide whether to include it in our study data. Our use of very large, statistically-meaningful data sets allows us to derive more stable statistical validation assessments of AEDT, and to break the data down into finer subsets to reveal aircraft-type or ANP-profile-dependent cohorts that more clearly elucidate the strengths and weaknesses of AEDT.

For a more detailed mathematical discussion of how this processing is done, we refer the reader to Appendix A of this report.

Aircraft Cohort Selection

As shown in Figure 1 and Figure 2, the number of airports in the Bay Area, the extensive fleet mix of aircraft, and the traffic volume produce a complex air traffic pattern. To explore AEDT performance for a wide variety of aircraft types with a solid statistical base, we have focused our validation studies on routes that force all aircraft to fly similar flight profiles. We have selected flights on three route segments: final approach toward each of the two main parallel SFO arrival runways, 28L and 28R, and approach traffic from a highly-concentrated, high-volume arrival procedure, SERFR, that is used by traffic from the south and southwest US, Central America, and South America (see Figure 3). Runway 28L is used primarily by aircraft arriving from established procedures BDEGA-West, PIRAT, and SERFR. Runway 28R is used primarily by aircraft arriving from procedure DYAMD and BDEGA-East.



Figure 1. The SF metroplex includes three international airports (labeled KOAK, KSFO, and KSJC), five regional airports, and two medical centers.



Figure 2. Typical daylong crowded traffic pattern in the SF metroplex (June 29, 2022). The flight path color codes indicate altitude range.

We have data from a large number of SLMs scattered around the Bay Area (approximately 35) but in this report, we focus on two SLMs that collect data from flights on these three route segments: SFO NMT-12 and SIDBY, as indicated by the circled blue dots in Figure 3.

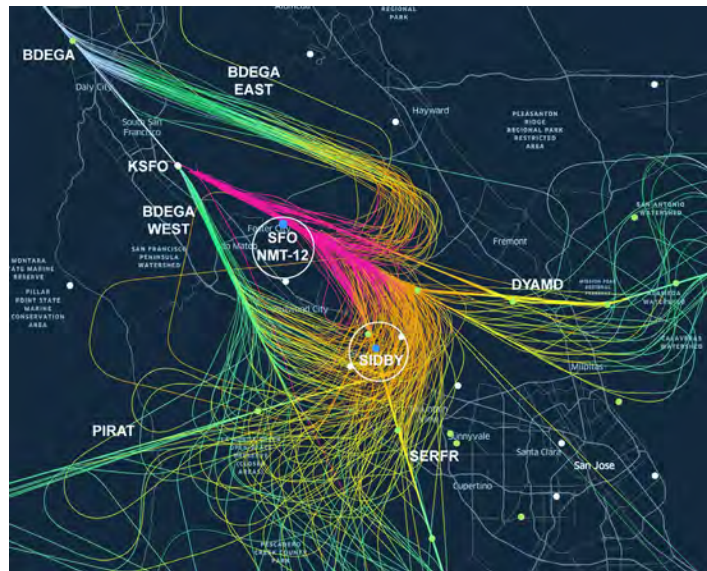


Figure 3. SFO arrival traffic along the four main routes: BDEGA, PIRAT, SERFR, and DYAMD on June 29, 2022. The color indicates the aircraft altitude along the trajectory.

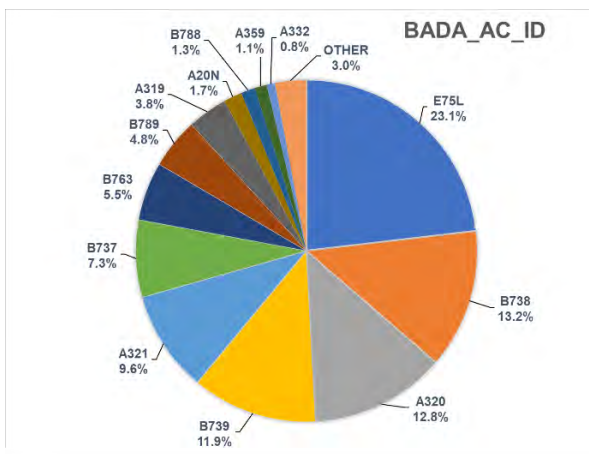


Figure 4. Relative aircraft mix observed for SFO 28L/R approach by BADA aircraft code.

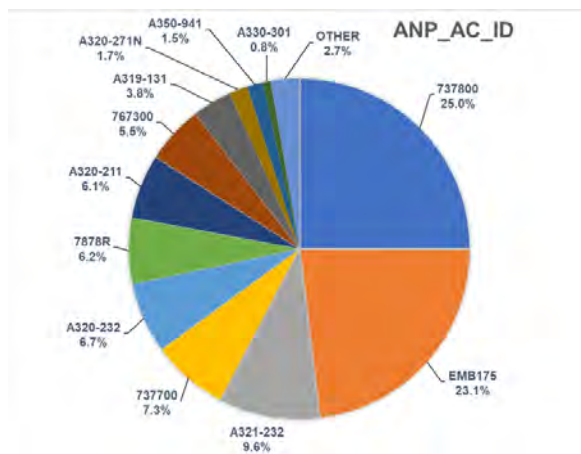


Figure 5. Relative aircraft mix observed for SFO 28L/R approach by ANP performance model code.

The overall fleet mix of aircraft arriving at SFO over the 1-year study period is shown from two perspectives in Figure 4 and Figure 5. The first Figure shows relative percentages of aircraft types by BADA aircraft identification codes and the second shows the percentages of aircraft by ANP performance model types. The majority of aircraft are grouped in approximately 15 models, by count, dominated by regional jets and single-aisle aircraft. A smaller number of large twin-aisle aircraft (also called “heavies”) are also represented.

In some early/preliminary results, the identification of individual aircraft had comingled some CL600 aircraft types and some variants of CRJs into a single aircraft category. This issue was identified during the debugging and validation and verification stages and, when reported in this document, CL600 aircraft contain *only CL600-class aircraft*. We continue to improve on our ability to identify individual CRJ variants, which are not reported on in this document. They will be included in future reports and publications, that will also include assessments of departure operations from SFO. Also to be noted is

that the ANP database contains Doc 9911 performance and noise data for only a subset of actual aircraft, so many of the aircraft/engine combinations in the flying fleet have to be mapped to ‘substitute’ aircraft in the ANP database. These substitute aircraft have similar characteristics but are not identical in performance and noise emissions to the actual aircraft. In the AEDT FLEET database there are 3,580 distinct Airframe-Engine combinations, including military aircraft, which are mapped to 298 ANP fixed-wing aircraft types; of these, 1,041 were in service in 2023 and corresponded to 152 ANP aircraft types.

Infrastructure

We have developed a modern hardware/software infrastructure that collects continuous real-time data about the aircraft traffic and ground noise generated by flight patterns in a complex metroplex environment and deployed it initially in the San Francisco Bay Area.¹¹ This has been mainly the result of our efforts in Tasks 1 and 3 of this proposed work and that, as mentioned above, are now considered complete. We have been collecting metroplex-wide annotated ADS-B flight profile data from seven receivers in the Bay Area mid-peninsula area since late 2018. We also have access to 24-hour sound data from more than 30 strategically located SLMs¹² that measure sound levels continuously at 1-second intervals. We currently collect *daily* data for over 2,500 different aircraft, flying over 5,000 flight segments, and with over 1.5 million annotated ADS-B sightings.

The MONA AEDT study preparation subsystem automatically preprocesses the ADS-B flight profile data to detect and smooth out ADS-B errors and selects a compact set of GPS, altitude, and calibrated airspeed control points to feed to AEDT via its Microsoft SQL Server database. These profiles include relevant parameters to estimate noise metrics (L_{Amax} and SEL) for all the sound monitor receptors in our geographic study domain. Individual AEDT-R and AEDT-AE study runs are farmed out in parallel to clusters of virtual machines in a commercial cloud to run thousands of studies per day over year-long periods.

Validation Process

To validate the noise predictions of AEDT, we compare and analyze the differences between AEDT-estimated noise metrics and ground SLM measurements. For flights along each of the three chosen route segments, we compare the L_{Amax} and SEL metrics predicted by AEDT using “trajectory-driven flight performance”¹³ and SLM measurements, both in terms of their absolute values and their differences (AEDT – SLM). The AEDT-R results incorporate those aircraft types in our fleet mix that have ANP/BADA 3 models, whereas AEDT-AE results are limited to the aircraft types in our fleet mix that have BADA 4 models.¹⁴

Table 1. Summary of data volume statistics for ADS-B and SLM data pairs on three SFO approach paths between July 1, 2021 and June 30, 2022.

Data volume statistics:	SFO Runway 28L	SFO Runway 28R	SIDBY SERFR-DIRECT
Number of input AEDT/SLM pairs	226,876	226,876	113,113
Number of pairs skipped as GA	4,927	4,927	2,145
Number of pairs skipped for low GoF	55,861	55,861	70,130
Number of pairs skipped for multiple PCAs	9,756	9,756	525
Number of pairs skipped for trajectory criteria	58,282	105,988	14,020
Number of post-filter pairs	98,050	50,344	26,293
Number ANP/BADA 3	55,793	30,214	14,112
Number BADA 4	42,257	20,130	12,181

¹¹ Jackson DC, Rindfleisch TC, Alonso JJ. A System for Measurement and Analysis of Aircraft Noise Impacts. Engineering Proceedings. 2021; 13(1):6. <https://doi.org/10.3390/engproc2021013006>

¹² In addition to our MONA SLMs, we are fortunate to have access to noise data from a network of SLMs deployed by the San Francisco International airport around the entire Bay Area. These data are provided to us monthly and are processed, curated, and added to our database just as the noise data from MONA ground stations is prepared.

¹³ FAA AEDT Version 3d Technical Manual, March 2021, Section 3.9, p 145.

¹⁴ FAA AEDT Version 3d Technical Manual, March 2021, Section 3.2, p 57.

The noise predictions for flights on final approach to runways 28L and 28R are compared with recordings from the SFO monitor NMT-12 in Foster City, CA ~0.4 miles line-of-sight distance from the flight paths. Predictions for approaches along the SERFR-DIRECT route are compared with recordings from the MONA monitor in Palo Alto, CA, ~0.9 miles line-of-sight distance from the flight path, at the SIDBY waypoint. All general aviation aircraft are excluded. In following sections, we present a breakdown of these results into various aircraft subtype cohorts defined by their ANP performance models. The table below summarizes the total number of flights successfully studied for each modeling approach and how various subsets of flights were discarded for failing quality and relevance criteria.

The rows in the table describe the results of our data screening. The *input AEDT/SLM pairs* represent all flight profiles for which a successful AEDT study was run with ANP/BADA 3 and/or BADA 4 modeling, and which were detected at the SLM associated with the column heading. These counts exclude flights intended to be modeled as BADA 4 but which AEDT downgraded to ANP/BADA 3 modeling for any reason. The *Number of Pairs skipped as GA* row is the count of those discarded as general aviation flights. The *pairs skipped for low GoF* is the count of pairs for which the SLM peak shape was suspect because it was distorted relative to an analytic model peak using our goodness-of-fit metric. Those pairs skipped due to low GoF have values of GoF < 0.7, which, as shown in Appendix A, isolates noise events that are very well correlated with aircraft peaks. In fact, studies not reported here assessed the sensitivity of the outcomes to the actual threshold value of GoF selected and saw that, below GoF = 0.7, the changes in the results were negligible. The *pairs skipped for multiple PCAs* is the count of pairs for which the SLM peak was suspect because the arrival time of the sound maximum at the SLM could be attributed to more than one aircraft. The *pairs skipped for trajectory criteria* is the count of pairs that do not conform geometrically to the arrival flight path criteria (i.e., distance, elevation, altitude, speed, heading, etc.)

Several things stand out in Table 1. First, the count of AEDT/SLM pairs for the SIDBY waypoint is lower than for the SFO approach routes because SIDBY only sees flights coming from SERFR-DIRECT. These flights are also counted in the Runway 28L/R numbers because they ultimately land there. Second, the number of flight profiles skipped because of GoF criteria is high for all route segments but is especially high for flights along the SERFR route. This indicates that there are many factors that affect sound peak quality in general, but they are exacerbated for SERFR because the line-of-sight distance between the SLM and the aircraft at the point of closest approach is significantly longer than for the SLM near the 28L/R runways, resulting in more atmospheric interference with the sound transmission. Also, in SIDBY’s residential environment, the background noise level is higher relative to the sound-peak maxima. Third, the number of flight profiles skipped because of multiple PCAs is higher for the 28L/R runway final approaches because the two runways are about 750 ft apart and the traffic into SFO is heavy during much of the day. This means more times when the SLM detects sounds from two or more aircraft during a nearly simultaneous approach.

AEDT-R Results

SFO 28L AEDT-R (ANP/BADA 3) Metric Value and Difference Assessment

In an earlier section we mentioned in passing the FAA “regulatory” mode of AEDT analysis (AEDT-R) that must use ANP/BADA 3 modeling with “standard AEDT flight profiles,” i.e., without experimentally-observed altitude and speed trajectory control point constraints.^{14, 15, 16} The use of standard profiles essentially imposes fixed flight paths (using predefined altitude and speed profiles) on all aircraft within a given ANP performance model. This results in essentially constant values for predicted L_{Amax} and SEL metrics for a given aircraft type at a given SLM location, independent of the actual flight profile. Slight variations in the predictions are attributable to weather variations (at SFO) that are used by AEDT-R’s noise prediction models, but the distributions are nearly delta-function like. This procedure ignores the actual physical dynamics of individual flights that BADA 4 modeling seeks to include and that we will describe in the AEDT-AE section.

A scatter plot of AEDT-R SEL values versus SLM SEL values from SFO runway 28L traffic is shown in Figure 6. The purple dots are located at coordinates given by matched pairs of SLM SEL measurements (abscissa) and AEDT-R SEL predictions (ordinate). There are 57,004 such data points in the plot. The diagonal turquoise line is the ideal plot that would result if the SLM measurements and AEDT predictions were in perfect agreement.

¹⁵ FAA AEDT Version 3d Technical Manual, March 2021, Section 3.6, p 72.

¹⁶ International Civil Aviation Organization (ICAO), Recommended Method for Computing Noise Contours around Airports, Doc 9911, Second Edition, 2018.

As is evident in the figure, for each labeled ANP performance model, there is a horizontal band of nearly constant AEDT-R SEL values, independent of the much broader range of SLM SEL values measured for the actual flight profiles flown. The red dots mark the centroids of the SLM SEL value distributions for each aircraft type and the vertical distance from each dot to the diagonal line indicates how much each AEDT-R SEL prediction would have to change (generally increase) to match the average SLM value. Note that, as mentioned earlier in this document, the CL600 category which represents the most significant underprediction, only contains CL600 aircraft. While we understand that such significant underprediction skews the average metrics presented later in Figure 10 and Table 2, they are reported here so the reader has access to all the data computed.

To better understand what is going on for individual performance models, Figure 7 shows histograms of the separate marginal distributions of the scatter plot in Figure 6.¹⁷ The solid blue curve is the AEDT-R SEL distribution projected along the ordinate. The dotted blue curve is the aggregate SLM SEL distribution for *all* performance models projected along the abscissa. The fact that the AEDT-R SEL histogram peaks are largely separated is a result of the simplistic way in which AEDT-R forces each aircraft performance model type to fly its prescribed model flight profile. The peaks with multiple types assigned means they are not fully resolved with the 0.2 dB histogram bins shown. The aggregate SLM distribution on the other hand shows no resolution of subprofiles by aircraft type in this Figure.

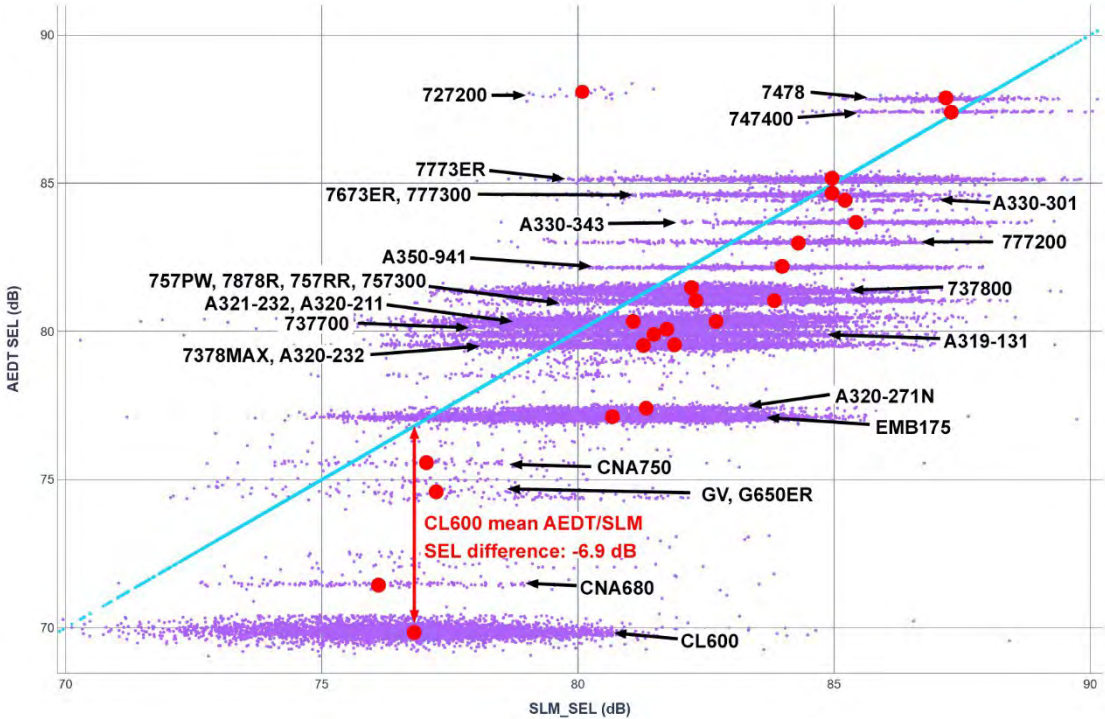


Figure 6. Scatter plot of predicted ANP AEDT-R SEL values versus measured SLM SEL values for the SFO runway 28L approach as observed at SLM NMT-12. The diagonal turquoise line represents perfect agreement between AEDT-R prediction and SLM measurement. Only ANP models that have at least 150 examples in our study year are shown.

¹⁷ The histogram profiles are produced by counting the frequency distributions of the raw data exactly in the 0.2 dB bins. The profile is then smoothed with a cubic spline routine (Prelipin, E, Cubic Spline Approximation (Smoothing) – CSAPS, May 30, 2022) to make overplotting and interpretation easier. No important histogram shape information is lost.

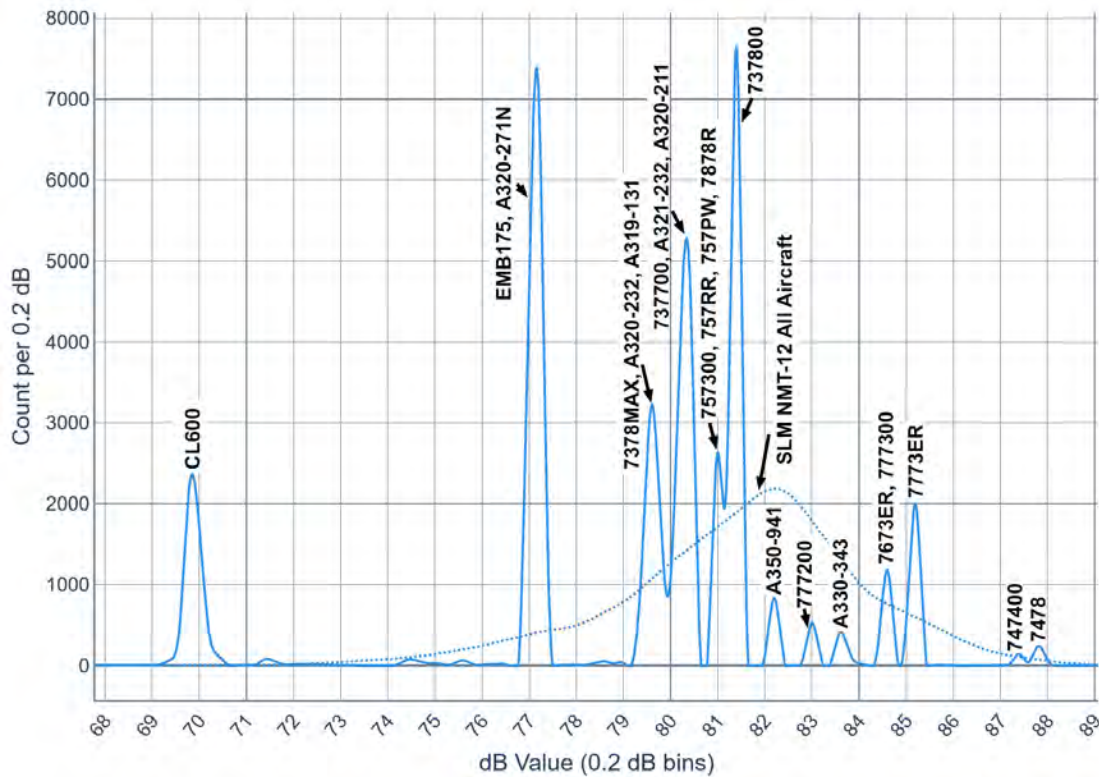


Figure 7. The AEDT-R SEL marginal distribution for SFO NMT-12 runway 28L is shown by the solid blue curve. The various subpeaks are annotated with the ANP performance models used. The dotted curve represents the much broader SLM SEL marginal distribution aggregated from all aircraft types.

Still, there is an SLM SEL subdistribution for each model type that can be derived from the data set by selecting the SLM SEL values from the cohort of AEDT/SLM pairs corresponding to flights with a given aircraft model type. AEDT/SLM paired histogram examples for five major peaks are illustrated in Figure 8.

Each example model pair is annotated with the ANP performance model AEDT-R used for predicting SEL values (solid lines). The corresponding SLM measurement distribution is shown with a similarly annotated dotted line. The average AEDT-R subpeak standard deviation width is *very* narrow, 0.31 dB, indicating that ANP uses a very simple fixed flight profile description for each model type and certain assumptions about aircraft weight. The average SLM subpeak standard deviation width is much broader, 1.55 dB, indicating significant variations in SLM SEL measurements for real-world flight profiles for a given aircraft type. The actual distributions of AEDT - SLM differences for the illustrative ANP models are shown in Figure 9.

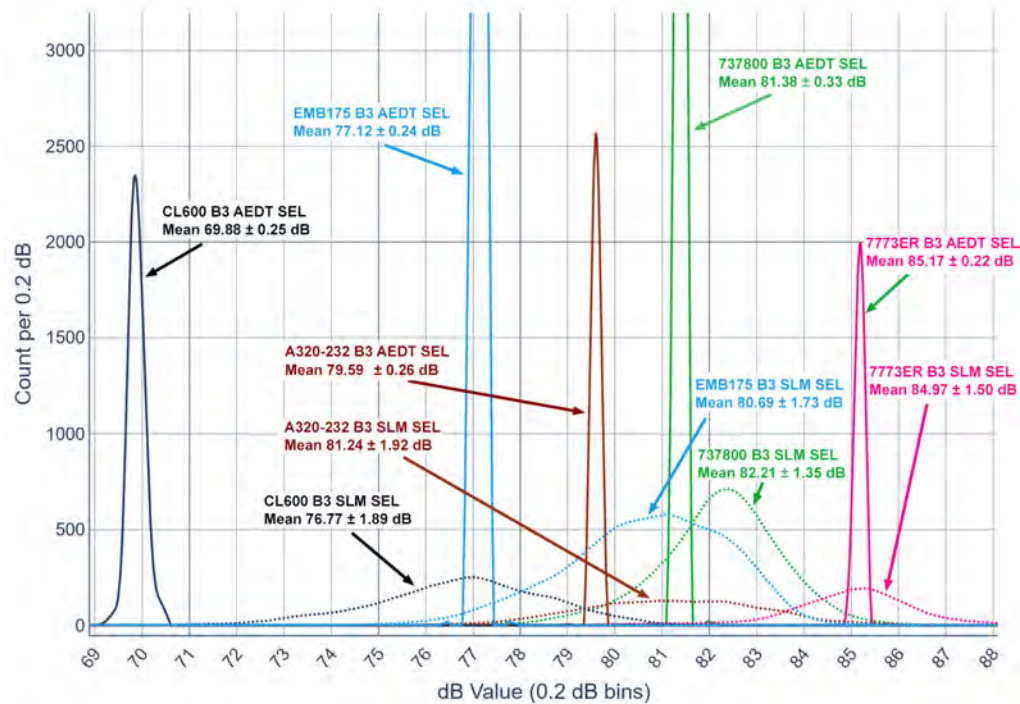


Figure 8. Examples of SEL ANP performance model pair distributions for AEDT-R predictions (solid lines) and corresponding SLM measurement distributions (dashed lines) for major model types from SFO 28L flights observed at the NMT-12 SLM.

As can be seen in Figure 9, the mean per-model differences range from 0.15 dB to -6.89 dB, with other model differences scattered in between. The average standard deviation for the SLM/model difference distributions is 1.60 dB, a figure dominated by the SLM distribution widths.¹⁸ The results of the analyses for all of the ANP models seen in the AEDT-R SEL predictions for the SFO arrival fleet mix, are detailed in Figure 10 (ordered by absolute difference value) and Table 2 (ordered alphabetically by performance model type).

An analysis of the L_{Amax} metric is done in an exactly analogous way, working with the ensemble of AEDT-R/SLM pairs and separating the pairs according to their ANP performance model. The ANP L_{Amax} difference data by ANP model are also summarized in Figure 10 and Table 2. The average (AEDT - SLM) SEL difference for the entire cohort is -2.31 ± 2.53 dB. The average (AEDT - SLM) L_{Amax} difference is -3.58 ± 2.31 dB. The average model L_{Amax} errors are larger than those for the SEL metric by ~1.3 dB, as might be expected for a point-based metric (maximum peak value at the PCA) as opposed to an integrated metric. Still the large relative uncertainty in the average error is about the same, 2.5 dB versus 2.3 dB.

¹⁸ If the AEDT and SLM distributions were Gaussian, the standard deviation of the difference distribution would be given by $\sigma_{diff} = \sqrt{\sigma_{AEDT}^2 + \sigma_{SLM}^2}$.

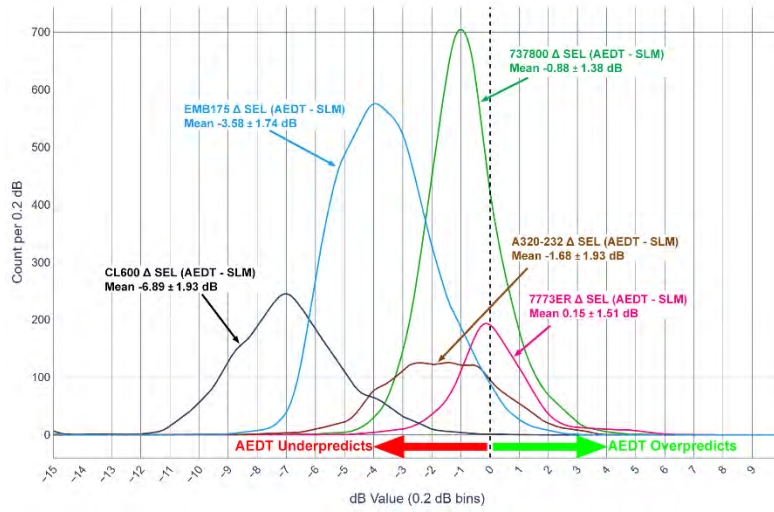


Figure 9. Histograms of SEL difference (AEDT – SLM) distributions for AEDT-R predictions by ANP performance model for the example types shown in Figure 8. The data are drawn from SFO 28L flights observed at the SFO NMT-12 SLM.

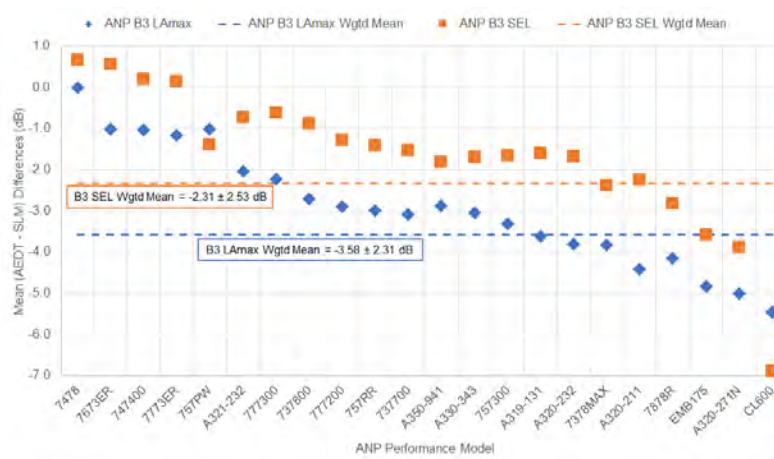


Figure 10. ANP (AEDT – SLM) mean SEL differences for SFO NMT-12 runway 28L by ANP performance model.

Table 2. ANP (AEDT - SLM) mean L_{Amax} and SEL differences with standard deviations for SFO NMT-12 runway 28L by ANP performance model used.

ANP ID	BADA AC ID (#B3 / #B4)	B3 Count	AEDT - SLM L _{Amax} Difference	AEDT - SLM SEL Difference
ALL-ACS	All BADA 3 AC Types	57004	-3.58 ± 2.31	-2.31 ± 2.53
737700	[B737 (3381 / 2681)]	3381	-3.08 ± 1.87	-1.52 ± 1.50
737800	[B738 (5954 / 5523), B739 (4270 / 4267)]	10224	-2.71 ± 1.65	-0.88 ± 1.38
7378MAX	[B38M (532 / 0), B39M (1075 / 0)]	1620	-3.82 ± 1.72	-2.38 ± 1.51
747400	[B744 (178 / 177)]	178	-1.04 ± 1.60	0.20 ± 1.36
7478	[B748 (302 / 302)]	302	0.00 ± 1.03	0.65 ± 0.88
757300	[B753 (509 / 0)]	509	-3.31 ± 1.88	-1.65 ± 1.76
757PW	[B752 (209 / 0)]	209	-1.02 ± 2.16	-1.39 ± 1.84
757RR	[B752 (393 / 0)]	393	-2.98 ± 1.83	-1.41 ± 1.65
7673ER	[B763 (1214 / 1212)]	1214	-1.01 ± 1.81	0.57 ± 1.58
777200	[B772 (552 / 0)]	552	-2.90 ± 2.08	-1.27 ± 1.79
777300	[B77L (194 / 0)]	194	-2.23 ± 1.49	-0.62 ± 1.23
7773ER	[B77W (2686 / 0)]	2686	-1.16 ± 1.74	0.15 ± 1.51
7878R	[B788 (531 / 530), B789 (1879 / 1878)]	2487	-4.14 ± 1.81	-2.81 ± 1.63
A319-131	[A319 (2262 / 2250)]	2262	-3.62 ± 2.20	-1.60 ± 1.94
A320-211	[A320 (2076 / 2072)]	2076	-4.41 ± 1.81	-2.24 ± 1.57
A320-232	[A320 (3260 / 3196)]	3260	-3.81 ± 2.22	-1.68 ± 1.93
A320-271N	[A20N (662 / 661)]	662	-5.01 ± 1.69	-3.89 ± 1.48
A321-232	[A321 (4261 / 4249)]	4261	-2.04 ± 1.97	-0.73 ± 1.67
A330-343	[A332 (420 / 417)]	577	-3.04 ± 1.97	-1.69 ± 1.55
A350-941	[A359 (775 / 773), A35K (197 / 197)]	972	-2.88 ± 2.14	-1.81 ± 1.77
CL600	[CL30 (251 / 0), CL60 (4955 / 0)]	5208	-5.46 ± 1.92	-6.89 ± 1.93
EMB175	[E75L (12661 / 12627)]	12661	-4.83 ± 1.89	-3.58 ± 1.74

Discussion of AEDT-R Results

The validation results for the other two route segments lead to similar observations, so we are not including the details here. The conclusion drawn from these analyses, using a statistically-significant sample, is that the AEDT-R (ANP/BADA 3) metric predictions are essentially constant for a given ANP performance model and do not reflect the actual flight conditions. The predictions for a given model would approximate actual SLM measurements only if the mean of the AEDT ANP/BADA 3 predictions for that model matched the mean of the SLM measurements. This is almost the case for “heavies” such as ANP models for 747400, 7478, 7673ER, and 7773ER types. For other (more frequent) models though, the AEDT-R predictions fall more randomly short of the measured SLM values. If these means do not match up model by model, AEDT-R will produce unreliable metric estimates that will depend on the fleet mix specifics. The often-discussed possibility that averaging over very large numbers of flights and aircraft types makes the results of AEDT-R predictions more accurate is mathematically implausible under the observed circumstances.

Using AEDT-R, we observe prediction differences on approach trajectories that average -2.31 dB for the entire aircraft cohort (weighted average by ANP type frequency) using the SEL metric, and -3.58 dB using the L_{Amax} metric. Given the reliance of AEDT-R on standard profiles and the inherent uncertainties on aircraft weight, aircraft state, weather conditions these observations are not entirely surprising. It must also be mentioned that the majority of these flight trajectories in the neighborhood of the SLM are over often rough San Francisco bay water, whereas the noise models in AEDT only model soft ground.

Our pre-analysis expectation was that, using the as-flown trajectories and BADA4 modeling (using AEDT-AE, see next section) these results would improve. AEDT-AE results are reported at the end of the next section.

AEDT-AE Results

As a reminder, in this section we discuss results using the AEDT-AE model for predictions of aircraft noise. Unlike AEDT-R, AEDT-AE uses BADA 4 for the modeling of the aircraft performance and includes both altitude and airspeed controls specified for each ground-track position. AEDT-AE uses the exact same noise propagation model but, because of the better modeling of the trajectory, the aircraft airspeed, and the presumably more accurate thrust-level predictions, it is deemed to potentially quantify the noise at the source better and therefore would be expected to result in better noise predictions. We re-iterate that AEDT-AE is simply used here as part of a research study to quantify differences between predicted and measured noise. The noise predictions based on the BADA 4 performance model are still based on the noise data from the ANP database.

SFO 28L AEDT-AE (BADA 4) Metric Value and Difference Analysis

We begin the statistical analysis of the pair-by-pair relations between AEDT-AE L_{Amax} estimates and the corresponding SLM measurements by showing a series of histogram plots like we displayed earlier for the AEDT-R runs. Using BADA 4 performance data from final approaches to SFO runway 28L (43,349 pairs including 14 ANP aircraft types), Figure 11 shows histograms of the AEDT-AE L_{Amax} estimates (solid line) and of the SLM L_{Amax} measurements (dotted line). As the histogram labels indicate, the average AEDT-AE L_{Amax} level is 68.59 ± 1.51 dB and that measured by the SLM is 71.27 ± 2.16 dB — on average AEDT underestimates the L_{Amax} value by 2.68 dB. Also note that the profile of the predicted AEDT values has significant internal structure, indicated by the subpeaks, including one sidelobe at 70.95 dB, and inflection points in the non-Gaussian shape. No discrete subpeaks are present however, as were prominent in the AEDT ANP/BADA 3 predictions. This reflects the more sophisticated physics modeled in AEDT BADA 4 aircraft performance and the spread in the trajectories actually flown that are considered in this analysis.

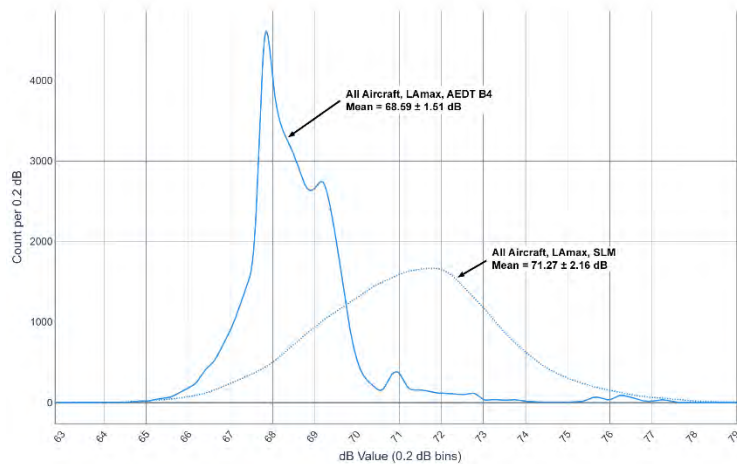


Figure 11. Histograms of L_{Amax} values predicted by AEDT-AE (solid blue line) and measured by SLM SFO NMT-12 (dashed blue line) for all collected BADA 4 flight profiles on final approach to SFO runway 28L.

This structure can be elaborated by overplotting histograms for various aircraft subcohorts modeled with particular ANP noise data as shown in Figure 12. To simplify the plot, only three major aircraft types are shown. One can see that the AEDT-AE calculations produce histogram profiles with quite varied shapes and that the differences in mean L_{Amax} values between the AEDT predictions and the SLM measurements differ significantly (see the green profile for ANP model 737800 in particular).

It is evident from this plot (and by extension for the entire cohort of BADA 4 aircraft types and ANP noise data) that there are important model-based differences between the estimates AEDT-AE makes and what the SLM measures. These are important in that for the most part the AEDT predictions fall short of the SLM measurements — a result analogous to that seen for the AEDT-R BADA 3 analysis above.

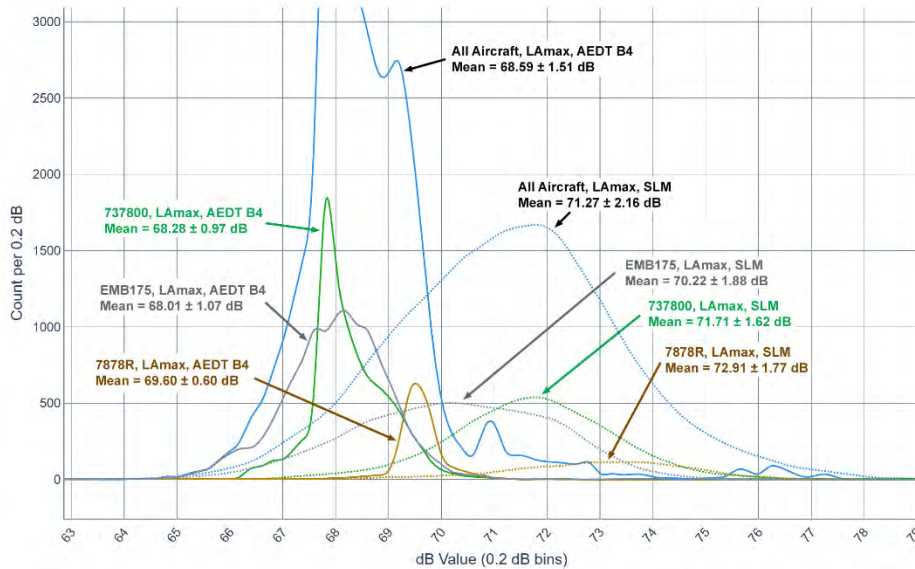


Figure 12. Histograms of LAmox values predicted by AEDT-AE and measured by SLM SFO NMT-12 for selected frequent ANP aircraft types with flight profiles on final approach to SFO runway 28L. The vertical scale has been expanded over that in Figure 11 to show the subcohort data more clearly.

We can illustrate the AEDT – SLM differences and their distributions by ANP aircraft type by computing the metric difference directly for each AEDT/SLM pair and then plotting the histogram of those differences. This comparison is illustrated in the histograms in Figure 13, both for the overall cohort and for a subset of individual ANP aircraft types for the most frequent types. These differences range from -1.64 dB for the A321-232 performance model to -3.44 dB for the 737800 model, all with standard deviations ~2 dB (which result from the relatively broad SLM measurement distributions).

Based on the analyses illustrated in Figure 11 through Figure 13, we compute the difference error statistics for all 14 ANP aircraft types found in the aircraft cohort on final approach to runway 28L between July 2021 and June 2022.¹⁹ Figure 14 shows an ordered plot of the error values and Table 3 shows the detailed sample flight counts, difference values, and standard deviations.

The SEL metric data we have collected from AEDT-AE study runs and SLM measurements are analyzed with exactly the same approach we used for LAmox. The presentation of SEL summary results for the SFO 28L approach are also shown in Figure 14 and Table 3.

¹⁹ We ignore those types that have fewer than 150 flight profile examples and hence less reliable statistics.

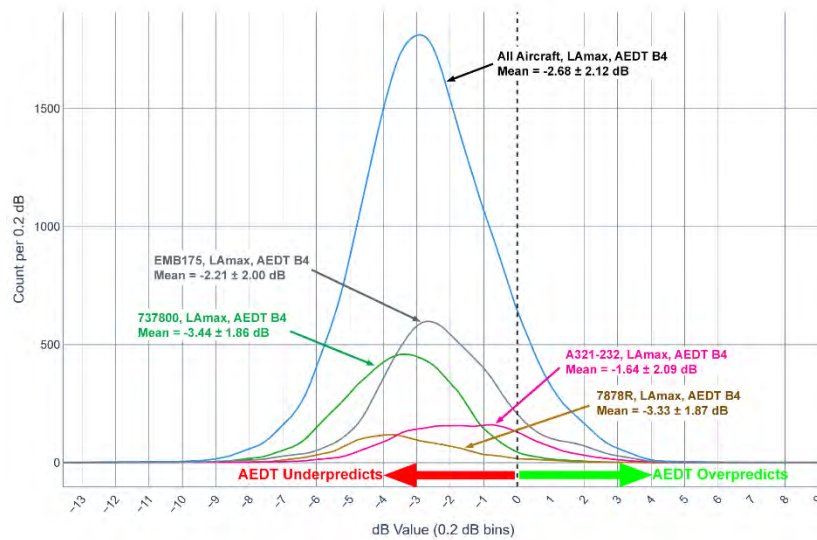


Figure 13. Histograms of LAmix difference distributions (AEDT - SLM) measured at SFO NMT-12 for selected frequent ANP aircraft types with flight profiles on final approach to SFO runway 28L.

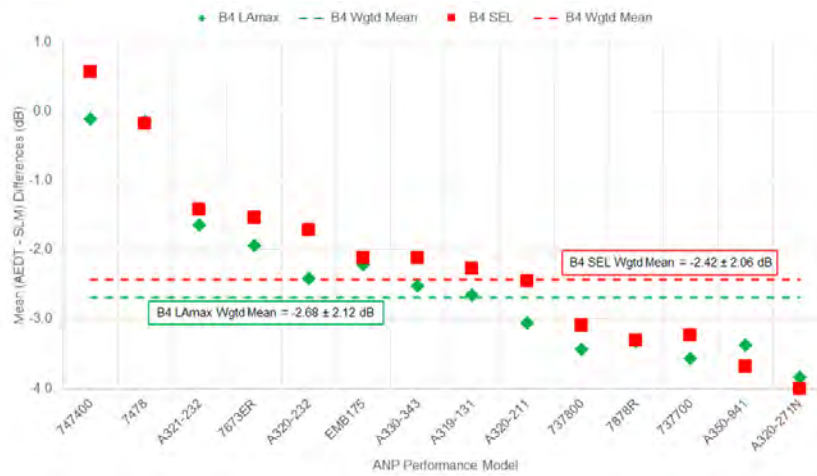


Figure 14. Plot of mean LAmix and SEL differences (AEDT - SLM) for the major ANP aircraft types found in final approaches to SFO runway 28L. The average standard deviation for each estimate is somewhat greater than 2 dB. Note the green diamond for 7478 LAmix is hidden behind the red SEL square.

Table 3. Table of ANP aircraft types, BADA aircraft types, flight counts, mean AEDT – SLM L_{Amax} and SEL differences, and standard deviations.

ANP ID	BADA AC ID (#B3 / #B4)	B4 Count	AEDT - SLM L _{Amax} Difference	AEDT - SLM SEL Difference
ALL-ACS	All BADA 4 AC Types	43,349	-2.68 ± 2.12	-2.42 ± 2.06
737700	[B737 (3281 / 2626)]	2,681	-3.57 ± 1.78	-3.23 ± 1.66
737800	[B738 (5760 / 5391), B739 (4112 / 4151)]	9,790	-3.44 ± 1.86	-3.09 ± 1.72
747400	[B744 (175 / 175)]	177	-0.11 ± 1.65	0.57 ± 1.55
7478	[B748 (296 / 300)]	302	-0.15 ± 1.35	-0.18 ± 1.29
7673ER	[B763 (1206 / 1205)]	1,212	-1.94 ± 2.06	-1.54 ± 1.96
7878R	[B788 (571 / 573), B789 (1831 / 1843)]	2,408	-3.33 ± 1.87	-3.31 ± 1.77
A319-131	[A319 (2109 / 2130)]	2,250	-2.65 ± 2.22	-2.27 ± 2.12
A320-211	[A320 (1997 / 2002)]	2,072	-3.06 ± 1.83	-2.45 ± 1.76
A320-232	[A320 (3054 / 3019)]	3,196	-2.41 ± 2.19	-1.71 ± 2.05
A320-271N	[A20N (650 / 653)]	661	-3.84 ± 1.96	-4.00 ± 1.85
A321-232	[A321 (4119 / 4129)]	4,249	-1.64 ± 2.09	-1.42 ± 1.91
A330-343	[A332 (413 / 411), A333 (86 / 85)]	505	-2.52 ± 1.98	-2.12 ± 1.79
A350-941	[A359 (762 / 772), A35K (195 / 196)]	970	-3.37 ± 2.43	-3.68 ± 2.36
EMB175	[E75L (12150 / 12223)]	12,627	-2.21 ± 2.00	-2.12 ± 2.08

As is evident in Figure 14 there are major differences in the accuracy of the AEDT-AE L_{Amax} predictions. For example, the differences for “heavy” aircraft (ANP models 747400 and 7478) are relatively small, indicating that the corresponding models seem to be fairly accurate. For the other aircraft though, the accuracy of the AEDT-AE modeling appears to produce systematically low estimates, ranging from ~ -1.5 dB to -3.9 dB. The overall L_{Amax} error weighted by frequency counts is -2.68 dB.

The overall difference between AEDT SEL predictions and SLM measurements for SFO 28L is slightly less — -2.42 dB versus -2.68 dB for L_{Amax}. On the other hand, the same basic observations about their variable nature and the inability of AEDT-AE to model sound metrics accurately for different ANP aircraft types apply.

In the next two sections we present brief statistical summaries of the comparisons between AEDT-AE predictions and SLM measurements of L_{Amax} and SEL values for the other two route segments we considered — final approach to SFO runway 28R and the SERFER-DIRECT approach over the SIDBY waypoint. The analysis is done in exactly the same way as for the final approach to SFO runway 28L.

SFO 28R AEDT-AE (BADA 4) Metric Value and Difference Analysis — Brief Summary

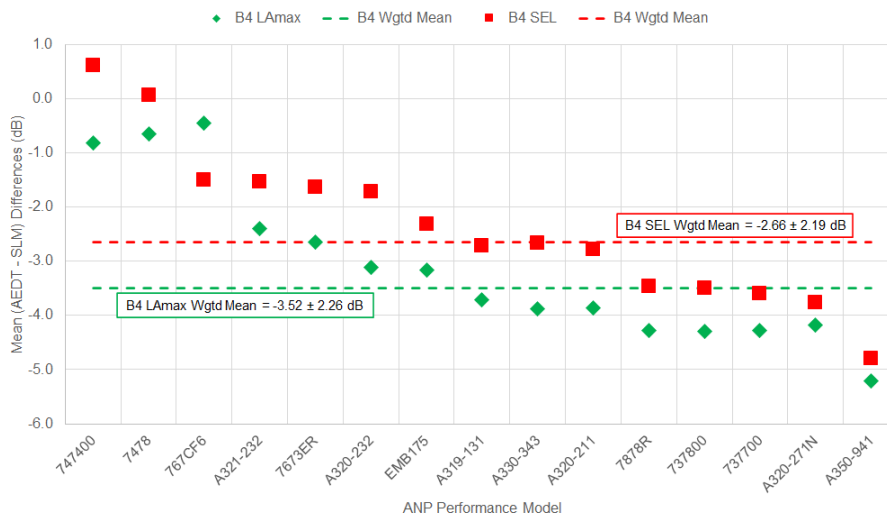


Figure 15. Plot of mean L_{Amax} and SEL differences (AEDT – SLM) for the ANP aircraft types found in final approaches to SFO runway 28R. The average standard deviation for each individual type estimate is > ~2 dB.

Table 4. Table of ANP aircraft types, BADA aircraft types, flight counts, mean AEDT – SLM L_{Amax} and SEL differences, and standard deviations.

ANP ID	BADA AC ID (#B3 / #B4)	B4 Count	AEDT - SLM L _{Amax} Difference	AEDT - SLM SEL Difference
ALL-ACS	All BADA 4 AC Types	20,351	-3.52 ± 2.26	-2.66 ± 2.19
737700	[B737 (1118 / 862)]	862	-4.28 ± 1.69	-3.59 ± 1.62
737800	[B738 (2675 / 2502), B739 (2531 / 2527)]	5,029	-4.29 ± 1.79	-3.50 ± 1.73
747400	[B744 (267 / 267)]	267	-0.82 ± 1.96	0.61 ± 1.62
7478	[B748 (290 / 290)]	290	-0.65 ± 1.60	0.06 ± 1.54
7673ER	[B763 (1498 / 1498)]	1,498	-2.65 ± 2.33	-1.64 ± 2.13
767CF6	[B762 (188 / 188)]	188	-0.45 ± 2.25	-1.50 ± 2.13
7878R	[B788 (375 / 373), B789 (1508 / 1510)]	1,883	-4.28 ± 2.10	-3.47 ± 2.04
A319-131	[A319 (859 / 854)]	854	-3.72 ± 2.37	-2.71 ± 2.26
A320-211	[A320 (1056 / 1055)]	1,055	-3.87 ± 1.75	-2.79 ± 1.68
A320-232	[A320 (1027 / 1013)]	1,013	-3.11 ± 2.19	-1.72 ± 2.13
A320-271N	[A20N (288 / 288)]	288	-4.18 ± 2.27	-3.76 ± 2.01
A321-232	[A321 (2577 / 2572)]	2,572	-2.40 ± 1.99	-1.54 ± 1.80
A330-343	[A332 (199 / 197)]	247	-3.88 ± 1.76	-2.67 ± 1.70
A350-941	[A359 (383 / 383), A35K (119 / 119)]	502	-5.21 ± 2.31	-4.79 ± 2.19
EMB175	[E75L (3561 / 3522)]	3,522	-3.17 ± 2.17	-2.32 ± 2.10

SIDBY SERFR-DIRECT AEDT-AE (BADA 4) Metric Value and Difference Analysis — Brief Summary

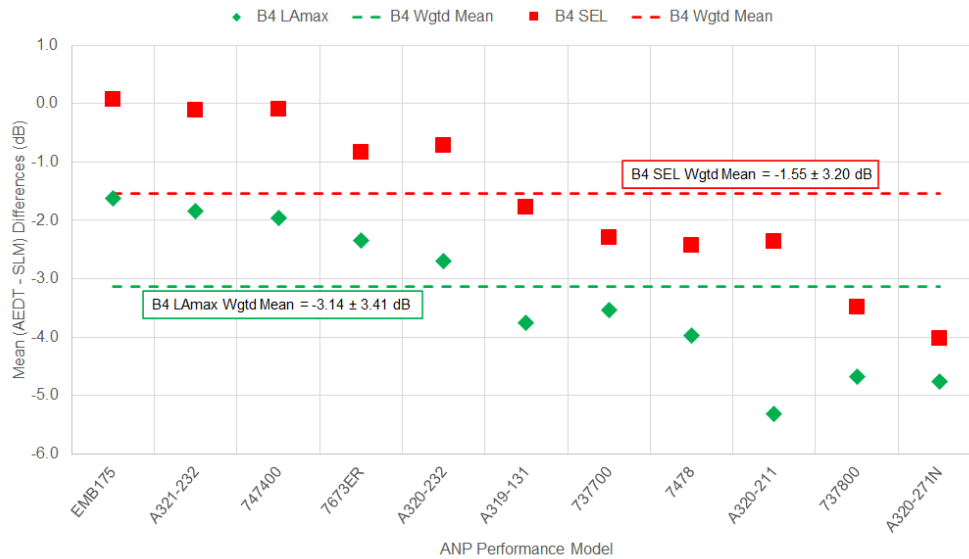


Figure 16. Plot of mean L_{Amax} and SEL differences (AEDT – SLM) for the ANP aircraft types found in SFO approaches along the SERFR-DIRECT route. The average standard deviation for each type estimate is > ~3 dB.

Table 5. Table of ANP aircraft types, BADA aircraft types, flight counts, mean AEDT – SLM L_{Amax} and SEL differences, and standard deviations.

ANP ID	BADA AC ID (#B3 / #B4)	B4 Count	AEDT - SLM L _{Amax} Difference	AEDT - SLM SEL Difference
ALL-ACS	All BADA 4 AC Types	35,424	-3.14 ± 3.41	-1.55 ± 3.20
737700	[B737 (4602 / 4488)]	4,488	-3.54 ± 3.24	-2.30 ± 2.94
737800	[B738 (5709 / 5379), B739 (3036 / 3036)]	8,415	-4.67 ± 2.98	-3.49 ± 2.71
747400	[B744 (849 / 849)]	849	-1.96 ± 2.37	-0.10 ± 2.10
7478	[B748 (732 / 732)]	732	-3.98 ± 2.40	-2.43 ± 2.05
7673ER	[B763 (894 / 894)]	894	-2.34 ± 3.15	-0.84 ± 2.90
A319-131	[A319 (1662 / 1656)]	1,656	-3.76 ± 3.64	-1.77 ± 3.15
A320-211	[A320 (1596 / 1590)]	1,590	-5.32 ± 2.64	-2.37 ± 2.39
A320-232	[A320 (3996 / 3915)]	3,915	-2.69 ± 3.28	-0.71 ± 2.91
A320-271N	[A20N (675 / 675)]	675	-4.76 ± 2.38	-4.03 ± 2.29
A321-232	[A321 (1602 / 1602)]	1,602	-1.84 ± 3.52	-0.11 ± 3.26
EMB175	[E75L (10437 / 10410)]	10,410	-1.62 ± 3.26	0.07 ± 2.95

Calibrated Air Speed Effects on Modeled Metric Values

We noted an interesting anomaly between AEDT-AE predicted and SLM measured L_{Amax} and SEL pairs that can be seen in a pair-wise scatter plot against Calibrated Air Speed (CAS). Figure 17 shows data for two single-aisle aircraft types (ANP aircraft types 737700 and 737800) on final approach to runway 28L, as observed at SFO NMT-12. It is clear that AEDT underestimates both L_{Amax} and SEL as noted in the analyses presented above. However, there is another clearly visible effect.

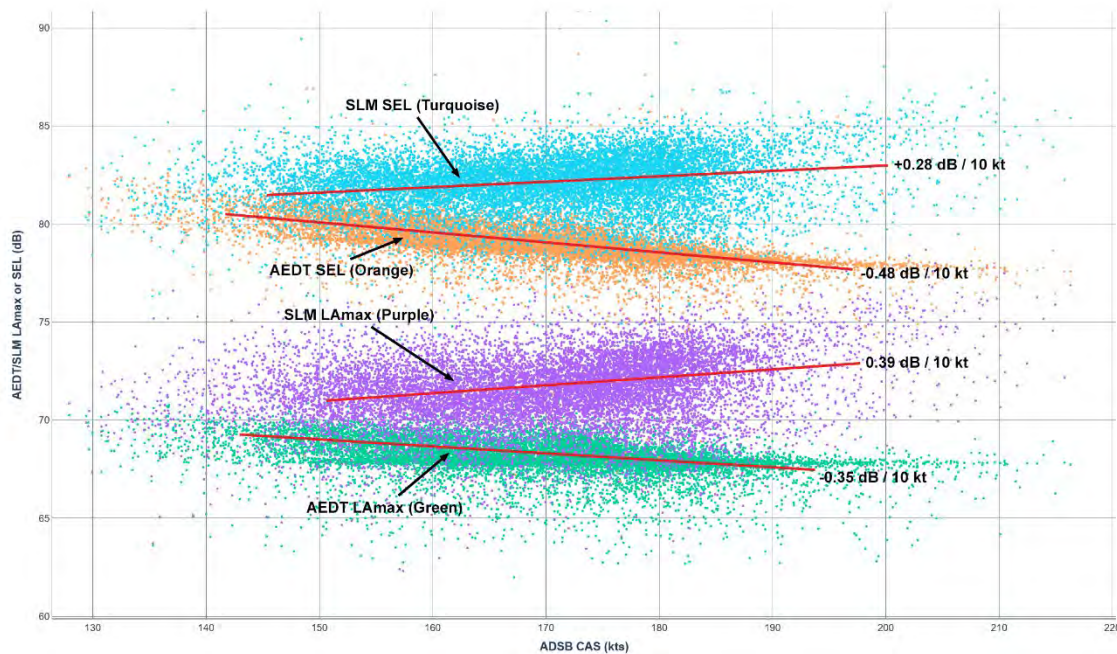


Figure 17. Comparison of AEDT-AE L_{Amax} and SEL predictions plotted against CAS with SLM measurements for final approaches to SFO runway 28L. The discrepancy appears as a decrease in noise metric levels for AEDT predictions as opposed to an increase in noise metric levels for SLM measurements.

With increasing CAS and all other factors remaining constant, physics tells us that sound metrics should increase primarily because of the dependence of airframe noise on airspeed (from flaps, slats, and/or landing gear deployed). This effect is

indeed observed in the SLM measurements, but AEDT-AE predicts a lessening of noise metrics. The plot shows linear trend lines to illustrate and quantify the rate of metric change, but we note that the effect is more complicated than a linear one. We tentatively attribute this observation to the fact that AEDT-AE modeling is based primarily on engine noise estimates, which may in fact decrease as aircraft near touchdown, whereas airframe noise sources from auxiliary lift equipment and landing gear deployment will increase and eventually overpower engine noise, particularly on approach trajectories.²⁰ As discussed in our conclusions, it appears that a more complex and accurate modeling of the physics, particularly of airframe noise, will be needed to make AEDT-AE better conform to ground truth in aircraft arrival situations. Similar results are found for the other route segments (final approach to SFO runway 28R and SERFR-DIRECT over the SIDBY waypoint).²¹

This observation indeed highlights the limitations of noise prediction models that rely on NPD (Noise-Power-Distance) data. In both the EU and in the US (through ASCENT Project 43, for example) there have been attempts to develop improvements for NPD-based approaches that account for the aircraft configuration and its airspeed, but those efforts will eventually have to rely on data provided by the manufacturers, which is not available at this time. Alternative noise modeling approaches that focus on the understanding of the source noise from various aircraft components (such as NASA's ANOPP2 tool) represent other important approaches that have the potential to result in closer predictions of noise.

Discussion of AEDT-AE Results

For all three route segments, our analyses showed similar AEDT/SLM variation by ANP aircraft type, regardless of the line-of-sight distance and ambient noise level for each location. AEDT-AE consistently predicts L_{Amax} and SEL values below the levels measured by the SLMs.

It is difficult to properly attribute to root causes the underpredictions we observe, but we believe that the differences are most likely attributable to (a) shortcomings in the SAE-AIR-1845/Doc 9911 model (particularly on arrivals and for areas further away from the airport, where the airframe noise contribution is substantial and potentially dominant over engine noise contributions; on departures operations and especially close to the airport boundary, the predictive quality of the SAE-AIR-1845 model is expected to be significantly better), to (b) the lack of exact knowledge of the both the aircraft weight, aircraft state and the atmospheric conditions, and to (c) the noise model in AEDT only being capable of considering soft-ground boundary conditions.

There are lots of complicating effects with the SLM measurements such as atmospheric turbulence, interfering ambient sounds, and uncertainties in sound level variations because of differing individual aircraft weights or flight details. There are also differences in the ground characteristics on which SLM instruments are mounted that can affect sound absorption and reflection coefficients. For these reasons, we have eliminated badly distorted sound peaks, such as multiple aircraft fly over and unusual noise events around noise meters by means of our goodness-of-fit metric. Since we are concerned with real noise effects in urban and residential areas and how that is perceived, and since there is real variability in the perceived noise that depends on ground absorption and reflection, our choice of the threshold value of the goodness-of-fit metric is such that it allows this kind of variability to be reflected in the comparisons between measured and predicted noise levels.

On the AEDT side, there are also additional areas of unknown accuracy such as the extension of the use of Noise Power Distance (NPD) curves (supplied by the manufacturers) to the modeled conditions, and the fact that the physical noise model was specifically designed to represent certain classes of aircraft with relatively-low bypass ratio engines and in high-noise-level areas. To clarify, we understand that NPD curves are validated to be within 1 dB of experimental measurements under reference conditions and at the standard microphone locations, but we are measuring noise at locations that are farther away. For example, the approach microphone (for certification purposes) is located 2,000 m upstream of the start of the take-off roll and the closest SLM location we have considered in this study, the SFO-NMT-12 microphone, is located about 10,000 m from the same location. Without *Flight Operations Quality Assurance* (FOQA) data, we do not know details of an aircraft's weight, the exact value of the thrust employed along the flight profile, when auxiliary lift equipment is deployed, etc. Most often FOQA data are confidential and tightly held by airlines. Even the NPD modeling data per aircraft are confidential (and encrypted within the AEDT data structures) in order to preserve proprietary interests of aircraft

²⁰ Lopes LV and Burley CL, Design of the Next Generation Aircraft Noise Prediction Program: ANOPP2, 17th AIAA/CEAS Aeroacoustics Conference (32nd AIAA Aeroacoustics Conference), June 2011, Portland, Oregon, <https://doi.org/10.2514/6.2011-2854>

manufacturers. Weather and atmospheric conditions are similarly hard to control for and would limit the strength of a validation study based on just a handful of flights.

As before with AEDT-R (ANP/BADA 3), one cannot expect or rely on the “law of averages” for error cancellation across the fleet mix so that AEDT might be able to produce a more accurate *average* value. In addition, existing AEDT-AE models seem to violate the expected physics of approach airframe noise generation by not adequately accounting for increased noise levels with increased calibrated airspeed from auxiliary high-lift equipment and landing gear deployment.

Task 2 - Study Conclusions – Arrival Operations Only

In the work we have completed for Task 2, we have collected and analyzed a very large dataset of over 200,000 observations of pairs of AEDT noise predictions matched with carefully curated SLM measurements of the noise observed on the ground. We have focused on SFO arrivals along three high-density route segments (final approaches to each of the parallel runways 28L and 28R, and the SERFR-DIRECT approach) using two SLM locations (SFO NMT-12 in Foster City, CA next to the arrival runways and the MONA SLM near the SIDBY waypoint in Palo Alto, CA). Our data covers an entire year of observations from July 1, 2021 through June 30, 2022, so seasonal traffic and weather variations are accounted for. We have included analyses for all individual aircraft types in the SFO fleet mix that have ANP/BADA 3 (AEDT-R) and BADA 4 (AEDT-AE) performance models and that have at least 150 observation pairs per ANP model during the year. We have thousands of pairs for most individual performance models. We have analyzed both individual-flight and aggregate metrics.

Analyses using the FAA AEDT regulatory mode (AEDT-R) based on ANP aircraft models with standard profiles and without altitude and speed control data are summarized in Table 6. The resulting statistical data indicate that this type of modeling differs, based on mean values, anywhere between -3.58 dB and -1.82 dB (for L_{Amax}) and between -2.31 dB and -1.29 dB (for SEL) with ground SLM measurements. As mentioned earlier, AEDT-R is the FAA-prescribed regulatory mode for AEDT use.

Table 6. Summary of AEDT-R (ANP/BADA 3) L_{Amax} and SEL predictions as compared with SLM measurements for the three SFO route segments studied across all ANP performance models present in the data set.

Route Segment	B3 Pair Count	Mean AEDT - SLM L _{Amax} Differences	Mean AEDT - SLM SEL Differences
SFO 28L	57004	-3.58 ± 2.31	-2.31 ± 2.53
SFO 28R	30455	-3.51 ± 2.62	-1.73 ± 2.77
SERFR-DIRECT	41037	-1.82 ± 4.11	-1.29 ± 3.63

Analyses of our data set points to a systematic underestimation by AEDT-AE in its predictions for L_{Amax} and SEL metrics by significant but highly-varied amounts depending on aircraft type and performance model. We summarize the results for the three route segments we studied in Table 7.

Table 7. Summary of AEDT-AE (BADA 4) L_{Amax} and SEL predictions as compared with SLM measurements for the three SFO route segments studied across all ANP aircraft models present in the data set.

Route Segment	B4 Pair Count	Mean AEDT - SLM L _{Amax} Differences	Mean AEDT - SLM SEL Differences
SFO 28L	43349	-2.68 ± 2.12	-2.42 ± 2.06
SFO 28R	20351	-3.52 ± 2.26	-2.66 ± 2.19
SERFR-DIRECT	35424	-3.14 ± 3.41	-1.55 ± 3.20

Current AEDT-AE aircraft modeling results in little to no improvement in noise predictions over the AEDT-R modeling, and it predicts metrics that differ from SLM measurements anywhere between -3.14 dB and -2.68 dB (for L_{Amax}) and between -1.55 dB and -2.42 dB (for SEL). These again vary by aircraft type and ANP aircraft model and suggest that AEDT-AE

modeling can be improved by adjusting the internal representation of the applicable physics, e.g., the NPD curves and modeling of engine and airframe noise at various stages of flight.

We showed that AEDT-AE modeling does not appear to include some key aircraft characteristics that affect noise on approach. In some instances, the predictions indicate a decrease in sound metrics (L_{Amax} and SEL) with increasing calibrated airspeed. The expectation, supported by SLM measurements (see Figure 17) is that both L_{Amax} and SEL metrics will increase with increasing calibrated airspeed. Increased calibrated airspeed correlates directly with increases in both airframe and engine noise and thus producing higher levels of L_{Amax}. Even if increased CAS results in a shorter time of integration for the SEL metric, noise levels being higher, the total value of SEL also increases with CAS, as shown in the measurements. The current noise model in AEDT was not designed for these situations and the data suggest that AEDT-AE does not adequately account for airframe noise sources. In order to more accurately model individual overflights, it would be ideal to have access to FOQA data, but that is often considered confidential. It may be possible to guess factors (weight, auxiliary lift configuration, etc.) affecting airframe noise generation on average in order to use more advanced physical models such as the *Aircraft Noise Prediction Program* (ANOPP2) to better estimate airframe noise.²² Another approach is to use machine learning methods to characterize the modeling error in terms of ADS-B, SLM data, and other flight parameters so they can be applied to improve the accuracy of airframe noise component prediction. **Error! Bookmark not defined.**²³ We have pursued this effort using the same datasets described in this report. The details can be found in the publication referenced above (AIAA SciTech 2023).

Major Accomplishments

- Fully operational MONA system including data collection (ADS-B and sound data), data curation, AEDT-R and AEDT-AE analysis automation, and formats / databases for storage of information related to aircraft trajectories, noise measurements, and all associated metadata.
- Largest and most statistically-significant study of the discrepancies between measured noise data and predicted noise data (using both AEDT-R and AEDT-AE) at two different locations with vastly different DNL levels. In comparisons with previous studies, which at best use tens of flights to draw conclusions, our study is the first ever to look at hundreds of thousands of flights to draw conclusions. The data observations include a full 12-month period, all relevant aircraft types, and all weather conditions. This study is the first of a kind and we hope that additional studies can match the low level of error in our statistics.
- We have presented conclusions from the comparisons between AEDT-R and AEDT-AE predictions and SLM measurements at two locations (SIDBY and SFO-NMT-12) under the arrival routes to SFO. These conclusions point to a systematic underestimation of the L_{Amax} and SEL noise metrics by the predictive tools.
- An investigation into the trends of AEDT-AE noise prediction methods with CAS has been concluded and our results have been reported.

Publications

Jackson, D.C., Rindfleisch, T.C., & Alonso, J.J. (2021). A System for Measurement and Analysis of Aircraft Noise Impacts. *Eng. Proc.*, 13, 6. <https://doi.org/10.3390/engproc2021013006>

Alonso, J. J., Shukla, A., Jackson, D. C., & Rindfleisch, T. C. (2023). Improving Noise Predictions of the Aviation Environmental Design Tool (AEDT) Using Deep Neural Networks and Sound-level Monitor Data, AIAA 2023-0735. *AIAA SCITECH 2023 Forum*. January. <https://arc.aiaa.org/doi/10.2514/6.2023-0735>

Rindfleisch, T. C., Alonso, J. J., Jackson, D. C., Munguia, B. C., & Bowman, N. W. (2024). A Large-Scale Validation Study of AEDT Noise Modeling for Aircraft Arrivals, *J. Acoust. Soc. Am.* 155 (3), March. <https://doi.org/10.1121/10.0025276>

Outreach Efforts

Over the past year, we nurtured our relationship with San Francisco International Airport (SFO) and the technical leads at EnviroSuite, which deploys, monitors, and makes available the noise data at around 40 locations around the Bay Area. We have hosted technical interactions with both groups on various topics including the non-aircraft-noise filtering techniques

²² Geissbuhler, M, Behere, A, et al., Improving airport-level noise modeling by accounting for aircraft configuration-related noise at arrival, AIAA SciTech Forum, January 2022, San Diego, CA.

²³ Alonso, JJ, Shukla, A., Jackson, DC, and Rindfleisch, TC, Improving Approach Noise Predictions for Aircraft Environmental Impact Models Using Deep Neural Networks and Sound-level Monitor Data, AIAA SciTech Forum, January 2023, National Harbor, MD.

that we have developed in ASCENT 53. These outreach efforts have resulted in the sharing of noise data at a large number of locations including both historical data sets and a commitment to continue to share the data as it is acquired in the future.

Awards

None.

Student Involvement

A number of undergraduate and graduate students are / have been part of our team during this past year. Their names and areas of responsibility are listed at the beginning of this document. Several of the students have graduated during the current period of performance but we have managed to enlist new students to continue our work. Their contributions are acknowledged here as the project would not be as far along without them.

Plans for Next Period

The focus of the last year of ASCENT 53 will be on the completion of the full study, including arrivals (presented here) and departures (under investigation) to paint a complete picture of the areas where AEDT-R and AEDT-AE can and cannot provide the required accuracy in the noise predictions and to more effectively pinpoint areas of potential noise modeling improvements that may be undertaken by AEDT developers to continuously improve the quality of the predictions and, therefore, the quality of proposed new routes accounting for noise impacts on the ground. A second journal paper is expected this coming year detailing the entire set of results, but focusing on the departure routes. We expect the predictions for departure routes, which are dominated by engine noise, to produce better results than those that we have achieved for arrivals.

Appendix A: Sound-Level Monitor Data Processing

This appendix summarizes the process by which we isolate sound monitor peaks and identify the aircraft that cause them, as well as how we create metrics to curate the sound peaks for quality prior to inclusion in our AEDT metric prediction analyses.

Figure 18 shows a 25-minute portion of a typical sound profile that was recorded on May 9, 2022, by the SFO NMT-12 SLM located close to the final approach paths to runways 28L/R. The sound profile consists of ambient background sounds and the sounds contributed by overflying aircraft that are identified with green labels in the Figure. Our processing isolates aircraft peaks from the background and matches each peak with the aircraft that produced it. We use non-linear time-series filters to estimate the background sound level as a function of time (forward and backward recursive filters) and to locate those peaks above a background-derived threshold in the sound profile that may have been caused by aircraft overflights (cubic spline shape filters). These peaks are then precisely time matched with ADS-B closest approach data for all flights observed in the neighborhood of a given SLM to identify the aircraft giving rise to each sound peak. The net profiles of isolated peaks above the background are analyzed to extract desired noise metrics for each identified overflight event (LAm_{ax} and SEL). Each isolated peak is then compared to an ideal peak model to determine a goodness-of-fit metric and to identify the possible contributions of simultaneous overflights with similar times and distances of closest approach.

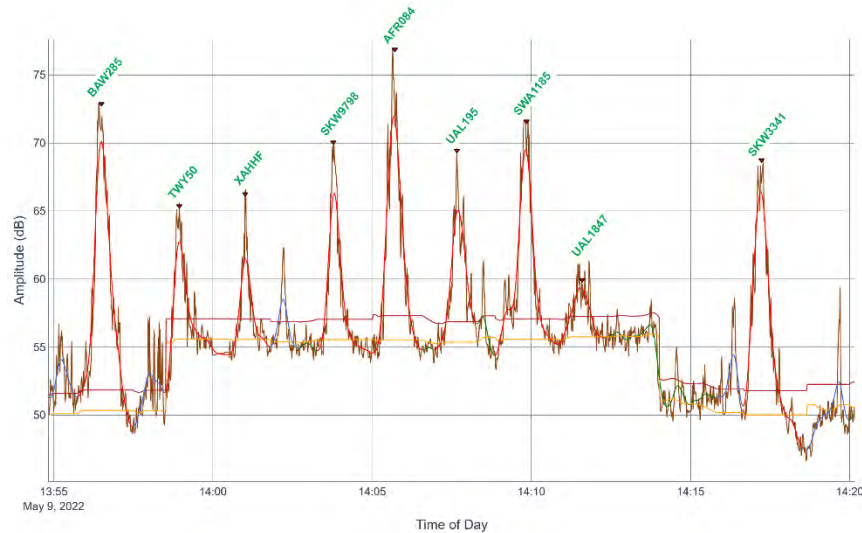


Figure 18. Portion of a typical sound profile measured by an SLM, consisting of a series of peaks of various sizes and shapes, plus varying background noise. The peaks caused by aircraft overflight events are outlined in red and are labeled with the specific flights that caused them. Peaks that were not linked to aircraft have a blue outline, e.g., ~13:55, ~13:58, ~14:02, ~14:16, and ~14:20. The more slowly varying background is indicated by the gold trace. A peak-detection threshold trace, derived from variations of the sound levels about the background trace is shown in dark red. Note that the level of background noise increases suddenly just before 14:00, and then drops back to its earlier level 15 minutes later.

Raw Sound Monitor Profile Filtering

Aircraft overflight sounds are confounded by additive background noise, the perturbations of aircraft sound signals by non-linear atmospheric propagation interference, the under-sampling of the aircraft sounds with the prescribed 1-second monitor sampling rate, and the time-varying nature of both background and signal statistics. To extract the aircraft profile morphology, we use a heuristic, non-linear methodology to filter and detect aircraft signals from the background soundscape. Specifically, we use a cubic-spline smoothing filter, CSAPS^{24, 25} that balances the exact reproduction of the profile envelope against a reduction of an overall roughness/curvature measure. The smoothing spline, f , minimizes the cubic-spline error metric, E_{CS} , defined in Equation 1.

$$E_{CS} = p \sum_{j=1}^n w_j |y_j - f(x_j)|^2 + (1 - p) \int \lambda(t) |D^2 f(t)|^2 dt$$

Equation 1. Cubic-spline error metric for smoothing sound data.

Here p is the smoothing parameter in the range $[0, 1]$. For $p = 0$, the smoothing spline is the least-squares straight-line fit to the data (zero curvature). For $p = 1$, the smoothing spline is the natural cubic-spline interpolant of the raw data. Within the full range $[0, 1]$, p controls the trade-off between the smoothness of f and the accuracy of its fit to each data point. The first term is the squared error measure between the data values $\{x_j, y_j\}$ and f . The error weights w_j are equal to 1 by default but can be adjusted along the range of x to allow variable fit emphasis. The second term is the roughness measure where $D^2 f$ denotes the second derivative of the function f . The weighting function λ is equal to 1 by default, but again can be used to emphasize smoothness at different parts of the data series. We choose the value of p experimentally based on the typical duration of aircraft sound peaks, currently $p = 0.001$.

²⁴ Prelipin, E, Cubic Spline Approximation (Smoothing) – CSAPS, May 30, 2022 (a web version of the documentation is at <https://csaps.readthedocs.io/en/latest/formulation.html>, or a pdf file at <https://csaps.readthedocs.io/downloads/en/latest/pdf/> last accessed 9/12/2022).

²⁵ de Boor, C, A Practical Guide to Splines, Springer-Verlag, 1978

Identifying Points of Closest Approach (PCAs)

From the ADS-B data collected from the metroplex, we know when and where individual aircraft pass overhead close to any given sound monitor. To match a particular flight trajectory to a particular sound peak, we must identify the point of closest approach along that trajectory with the minimum line-of-sight distance to the monitor. At the PCA, the aircraft emits the sound level that will be the maximum recorded by a monitor on the ground, after considering the delay caused by the time of transit for the sound to travel from the aircraft to the monitor. If we measure the half-widths of potential aircraft peaks, we can create relevant time interval windows in which to compare the times when sounds from various aircraft arrive at a monitor. Arrival times that fall within a given peak window allow us to establish which aircraft gave rise to the peak (and which did not). This also lets us associate each confirmed aircraft peak with identifying information about the aircraft that caused the peak.

Figure 19 shows the idealized geometry of an aircraft that passes close to an observer or a receptor (sound monitor) on the ground. The profile of the resulting sound peak is illustrated by the red trace next to the monitor/observer. In this figure, d is the minimum ground distance from the monitor to the ground track of the aircraft, h is the aircraft's altitude, and v is its ground speed. The time, t , marks the progress of the aircraft along its flight path and $r(t)$ is the three-dimensional distance of the aircraft from the monitor as a function of time. The minimum line-of-sight distance from the monitor to the aircraft occurs at $t = t_o$ and is labeled r_{min} . For simplicity, we assume that near the point of closest approach the flight path is a straight line with constant altitude and ground speed.

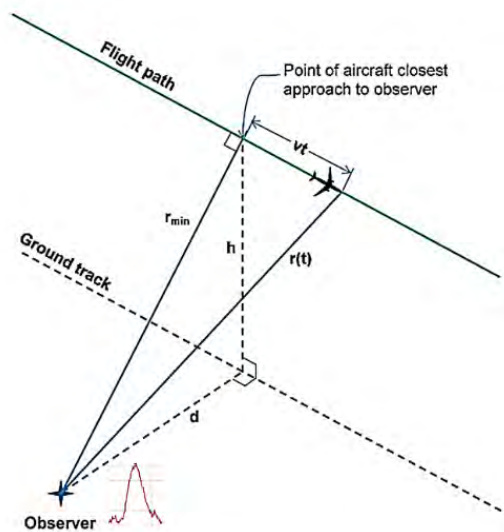


Figure 19. Idealized overflight path relative to a ground receptor or sound-level monitor.

From the ADS-B data for each the aircraft trajectory, we obtain a set of parametric equations for the flight path: latitude, $lat(t)$, longitude, $lon(t)$, altitude, $alt(t)$, and ground speed, $sp(t)$. ADS-B data are subject to random errors, generally caused by transmission problems such as occur when the aircraft is distant from the receiver or is at a low altitude. We use two filters to smooth out these errors: (1) a spike-noise filter that detects individual data-point deviations greater than the average deviation of a Gaussian-filtered profile, and (2) the same cubic-spline smoothing filter that we use for smoothing sound data, again with $p = 0.001$. Also, the ADS-B sighting data are collected at uneven intervals, depending on when the aircraft transmits and when a receiver gets a clean message. We interpolate the parametric equations, using the CSAPS formalism to accurately locate the PCA to within ± 0.25 seconds. The calculations that follow use the smoothed data. At the PCA, h is $alt(t_o)$ and v is $sp(t_o)$. We can calculate d from $lat(t_o)$, $lon(t_o)$, and the known coordinates of the sound monitor. We can calculate the rest of the geometry as shown in Equation 2.

$$\begin{aligned} \text{a) } r(t) &= \sqrt{d^2 + h^2 + [v * (t - t_0)]^2} \\ \text{b) } r_{min} &= r(t_0) = \sqrt{d^2 + h^2} \end{aligned}$$

Equation 2. Analytic geometry representation of the overflight geometry from Figure 19.

Once we know r_{min} , we can use the speed of sound, c , to compute the time, t_{stm} , when the aircraft sound emitted at the time of closest approach arrives at the sound monitor, as shown in Equation 3.

$$t_{stm} = t_0 + \frac{r(t_0)}{c}$$

Equation 3. Time at which the sound monitor records the maximum aircraft sound.

In this way, we examine the trajectory of every aircraft that passes overhead close to a given monitor and try to associate the monitor's potential aircraft peaks with any aircraft that might have caused or contributed to it within the half-width window of tolerance. A peak may be the combined result of more than one nearly simultaneous overflight events, such as occur when aircraft approach or depart large airports with multiple parallel runways, or around multiple airports with air traffic layered by altitude.

Data Quality Assessment, Goodness of Fit

To facilitate screening sound peaks in terms of their "quality", we have evaluated the shapes of confirmed aircraft peaks that we identified in monitor sound profiles. We developed an analytic model for the ideal aircraft overflight peak shape for the trajectory configuration illustrated in Figure 19. We use this idealized sound model to calculate the goodness-of-fit metric, GoF , in order to determine how closely a given sound peak matches the model.

Based on the assumptions of our idealized model, the aircraft-generated sound energy per second (power) recorded by an SLM over time, $E(t_{ac})$, has the form of a Cauchy or Lorentzian distribution,²⁶ as shown in Equation 4. There, E_{max} is the maximum peak amplitude in linear energy space, α is the effective atmospheric attenuation coefficient, $r(t_{ac} - t_0)$ is the line-of-sight distance between the aircraft and the monitor at aircraft time t_{ac} , v is the aircraft ground speed (assumed constant), t_0 is the time at the aircraft when the sound emitted will result in the SLM peak maximum, and r_{min} is the line-of-sight distance of closest approach.

$$E(t_{ac}) = \frac{E_{max} e^{-\alpha * r(t_{ac}-t_0)}}{1 + \left(\frac{v * (t_{ac} - t_0)}{r_{min}}\right)^2}$$

Equation 4. Sound energy per second (power) received at an SLM as a function of aircraft time for a simple point-source emitter.

In addition, the energy distribution in the peak as recorded by the SLM is delayed by the transit time from aircraft to SLM and altered by the Doppler effect. As the aircraft approaches the observer, the sounds have a higher frequency (more energy per second) than at the point of closest approach. As the aircraft recedes, the sounds have lower frequency (less energy per second). The total energy arriving at the monitor during the peak is the same as it would be without the Doppler effect, but the leading edge of the peak is steeper, and the trailing edge is less steep.

The Doppler effect is governed by Equation 3, which defines the time at which a sound emitted by the aircraft will reach the monitor, namely delayed by the line-of-sight distance between the aircraft and the monitor divided by the speed of sound, c .²⁷

²⁶ See, for example, https://en.wikipedia.org/wiki/Cauchy_distribution.

²⁷ Note that Equation 4, as written, applies to the delay at the time of closest approach. The general form for any time along the aircraft flight profile is $t_{stm} = t_{ac} + \frac{r(t_{ac}-t_0)}{c}$

Equation 5 shows the relationship between a time interval at the aircraft, dt_{ac} , during which the aircraft emits sound energy that is received at the monitor during its sampling interval, dt_{stm} (nominally one second in our case) as a function of time along its trajectory.

$$dt_{ac} = \frac{dt_{stm}}{1 + \frac{v^2 * (t_{ac} - t_0)}{c \sqrt{r_{min}^2 + [v * (t_{ac} - t_0)]^2}}}$$

Equation 5. Interval at the aircraft during which it emits sound that will be received during a sound monitor’s sample interval.

One can see from Equation 5 that when the aircraft is approaching the monitor ($t_{ac} < t_0$), the interval of aircraft sound emission is greater than monitor’s sampling interval ($dt_{ac} > dt_{stm}$). That is, more energy is collected during the monitor sampling interval, so the sound peak rises more quickly than without the Doppler effect. When the aircraft is receding from the monitor ($t_{ac} > t_0$), the opposite occurs, so $dt_{ac} < dt_{stm}$.

There are only two free parameters in this simple analytical model — the sound peak maximum power, E_{max} , and the time of peak maximum, t_0 . The other model parameters, α , v , and r_{min} , are determined by ADS-B measurements and weather data. Even so, the model fits the real-world data quite well. Figure 20 shows a typical example of the model fit to actual flight data, in this case flight ASA766, a B738 from SEA overflying monitor SFO NMT-12 on 7/16/2021 at 7:52:36. This peak is quite well-formed in that, while there are evident effects on the peak envelope from atmospheric turbulence and under-sampling, the overall peak shape is not badly distorted. On the other hand, at 7:49:33 as detected by the same SLM, a peak for flight SKW5531, an E75L, was more strongly affected by a background disturbance as shown in Figure 21. The background level below the distorted peak was ~56 dBA and the peak envelope had higher amplitude fluctuations, whereas the level below the clean peak was ~46 dBA and few ambient fluctuations.

This ability of the theoretical model to fit real peak profiles has led us to define a goodness-of-fit metric that allows us to distinguish well-formed peaks from peaks that are distorted by atmospheric turbulence, multiple contributing aircraft, and/or ambient background noise. If we use the least-squares method to fit the theoretical model to a given aircraft peak, we can define the goodness-of-fit in a way similar to the definition of the R^2 metric for linear-regression fits. Such a metric provides a measure of how well observed peaks are approximated by the model, based on the proportion of total variation of measurements explained by the model.²⁸

²⁸ See, for example, Coefficient of determination, https://en.wikipedia.org/wiki/Coefficient_of_determination (last accessed 9/18/2022).



Figure 20. Example of the theoretical aircraft-peak model fit to a clean, raw sound peak recorded by the SFO sound monitor at NMT-12.

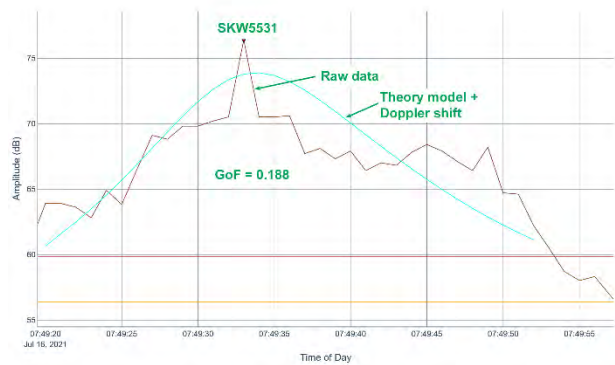


Figure 21. Example of the theoretical aircraft-peak model fit to a distorted, raw sound peak recorded by the SFO sound monitor at NMT-12.

Equation 6 defines *GoF*, the goodness of fit (coefficient of determination) of a model $f_i = f(x_i)$ to a data set $\{x_i, y_i\}$, where \bar{y} is the mean of y_i . Our goodness-of-fit metric generally ranges between 0 and 1 but may go negative for particularly poor fits (large numerator).

$$GoF = 1 - \frac{\sum_i (y_i - f_i)^2}{\sum_i (y_i - \bar{y})^2}$$

Equation 6. Goodness-of-fit of a model to a data set.

Using this definition, we obtain a *GoF* of 0.905 for the well-formed peak in Figure 20 and 0.188 for the distorted peak in Figure 21. We computed *GoF* values for each confirmed aircraft peak over many days and, by experiment, find that a *GoF* value of at least 0.7 constitutes an acceptable quality peak. By “acceptable,” we mean that the peak is clean enough to use its maximum aircraft sound level (L_{Amax}) and integrated aircraft sound exposure level (SEL) as a basis for validating noise-prediction software.

Returning to the sound peak profile example we used earlier, Figure 22 shows the theoretical model fit (in light green) overlaid on the confirmed aircraft peaks from Figure 18. The four peaks outlined with dark green boxes have *GoF* values above 0.7. The *GoF* values for the other five confirmed aircraft peaks fell below this standard primarily because of envelope distortion caused by atmospheric turbulence and background ambient noise.

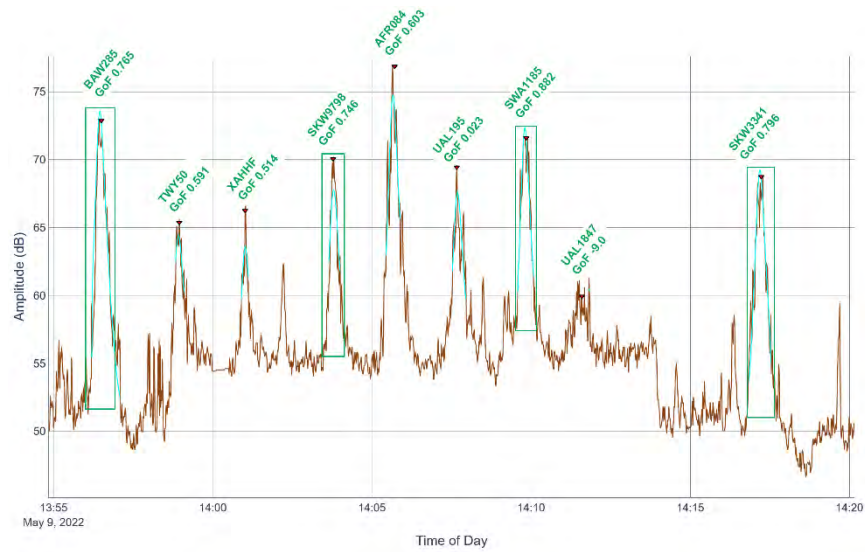


Figure 22. Confirmed aircraft peaks from Figure 18 overlaid in light green with theoretical model fit to their raw sound data in brown. *GoF* values are shown above each confirmed peak and the four peaks in dark green boxes have acceptable *GoF* values (greater than 0.7).



Project 054 AEDT Evaluation and Development Support

Georgia Institute of Technology

Project Lead Investigator

Prof. Dimitri N. Mavris
Director, Aerospace Systems Design Laboratory
School of Aerospace Engineering
Georgia Institute of Technology
275 Ferst Drive NW, Atlanta, GA 30332
(404) 894-1557
dimitri.mavris@ae.gatech.edu

Dr. Michelle Kirby
Chief, Civil Aviation Division
Aerospace Systems Design Laboratory
School of Aerospace Engineering
Georgia Institute of Technology
275 Ferst Drive NW, Atlanta, GA 30332
(404) 385-2780
michelle.kirby@ae.gatech.edu

University Participants

Georgia Institute of Technology (Georgia Tech)

- P.I.s: Dr. Dimitri Mavris, Dr. Michelle Kirby
- FAA Award Numbers: 13-C-AJFE-GIT-098, 114, and 122
- Period of Performance: September 24, 2021 to September 20, 2023
- Tasks:
 1. Improved departure modeling
 2. Arrival profile modeling
 3. Full flight modeling
 4. System testing and evaluation of the FAA's Aviation Environmental Design Tool (AEDT)
 5. Supersonic transport aircraft (SST) modeling in AEDT (former ASCENT 10)

Project Funding Level

Georgia Tech has received \$900,000 in funding for this project. In terms of cost-share details, Georgia Tech has agreed to a total of \$900,000 in matching funds. This total includes salaries for the project director, research engineers, and graduate research assistants, as well as computing, financial, and administrative support, including meeting arrangements. Georgia Tech has also agreed to provide tuition remission for the students, paid for by state funds.

Investigation Team

Prof. Dimitri Mavris, (P.I.), Tasks 1-5
Dr. Michelle Kirby, (co-Investigator), Tasks 1-5
Dr. Ameya Behere, (research faculty), Tasks 1-5
Mr. Jirat Bhanpato, (research faculty), Tasks 1-5
Dr. Raphael Gautier, (research faculty), Tasks 1-5
Dr. Dushhyanth Rajaram, (research faculty), Tasks 1-5
Mr. David Anvid, (research faculty), Tasks 1-5
Tanmay Daga, (graduate student), Task 1
Ranya Almarzooqi, (graduate student), Task 1



- Howard Peng, (graduate student), Task 1
- Anushka Moharir, (graduate student), Task 2
- Hansen Lian, (graduate student), Task 2
- Nitya Maruthuvakudi Venkatram, (graduate student), Tasks 2 and 5
- Hyungu Choi, (graduate student), Task 3
- Yash Vinod, (graduate student), Task 3
- Bogdan Dorca, (graduate student), Task 4
- Santusht Sairam, (graduate student), Task 4
- Baptiste Cramette, (graduate student), Task 5

Project Overview

This project provides data and methods to continue to improve modeling of aircraft weight, takeoff thrust, and departure and arrival procedures within the FAA’s AEDT, as well as the AEDT’s full flight modeling capabilities. Some of the modeling assumptions in AEDT are considered excessively conservative and could be improved through use of industry and airport flight operation data. Funding for this project will continue to support the implementation of these methods and data in AEDT4. To facilitate these efforts, the Georgia Tech team will use real-world flight data and noise monitoring data to improve departure, full flight, and arrival modeling.

Task 1 – Improved Departure Modeling

Georgia Institute of Technology

Objective

In previous reporting periods, noise abatement departure procedures (NADPs) were explored to give users additional departure modeling options. Two NADP profiles were recommended to be implemented in AEDT in addition to the pre-existing standard modeling option. In this reporting period, the objective was to determine the validity of the recommended NADP profiles with comparisons to real-world Threaded Track data (TTD) and Flight Operations Quality Assurance (FOQA) data.

Research Approach

Methods

Two real-world datasets, Threaded Track data for 2021 operations and FOQA data for 2019 operations, were used in this task. The TTD are an extensive collection of all aviation operations occurring at major U.S. airports. Georgia Tech has obtained TTD from the FAA for the 30 busiest U.S. airports for all airline operations. A key drawback of the TTD is that information regarding flight parameters immediately after liftoff is absent; instead, the information starts at an altitude of about 1,000 ft above field elevation (AFE) from the airport.

The FOQA dataset is used to help mitigate this issue, because it contains data below 1,000 ft altitude and is far more comprehensive, including information such as thrust setting, wind direction, flap setting, and landing position. This dataset is also used to validate the departure procedures obtained from the TTD.

The operations covered in the TTD are not limited to commercial aviation but also consist of instances from helicopters, business, and regional jets. For this project, filtering out such flights was necessary to better represent commercial departure operations relevant to the scope of this task. According to the definitions from AEDT SQL tables, Threaded Track flights were filtered on the basis of the parameters in Table 1.

Table 1. Threaded Track filtering parameters.

Parameter	Value
DESIGNATION	C (civil)
SIZE_CODE	L (large)/H (heavy)
USAGE_CODE	P (passenger)/C (cargo/transport)
ACFT_TYPE	C (commercial)

On the basis of the results from the filtering, the five U.S. airports with the most commercial operations were shortlisted for the departure profile analysis. The airports included in this study, along with the number of operations before and after filtering, are described in Table 2. Most airports had only a small percentage of flights removed, with the notable exception of Las Vegas airport, because of its relatively larger proportion of helicopter and business aviation operations.

Table 2. Departure operations at the five busiest U.S. airports.

Airport	Number of departure operations	Number of departure operations after filtering	Percentage of flights removed
Atlanta, KATL	350,538	342,392	2.32%
Chicago O’Hare, KORD	335,919	322,864	3.89%
Denver, KDEN	291,004	274,596	5.64%
Los Angeles, KLAX	253,784	232,000	8.58%
Las Vegas, KLAS	230,621	149,539	35.16%

Analysis of the altitude v/s ground track distance trajectory plots for the filtered operations, as shown in Figure 1, indicated two concerns requiring cleaning and refinement of the raw TTD. First, the data contained some erroneous trajectories, which were traced to faulty metadata or faulty time series data. Second, a large offset in takeoff start location of approximately 0.5–0.7 nautical miles (nmi) was observed, which required correction. This offset was attributed to the assumption that all flights begin their takeoff from the runway threshold, which is not always the case. Because the TTD do not contain any information about the flight trajectories below 1,000 ft, the exact starting location of the takeoff ground roll could not be identified.

To address these concerns, we first removed the anomalous flights from the dataset, by comparing their altitudes at distances farther from the airports and removing the flights that did not show the expected behavior. The next step was incorporating corrections to the takeoff start location. Instead of using runway thresholds, we performed comprehensive analyses using FOQA data for each airframe at different airports, and the average distance from the runway threshold from the takeoff operation was adjusted to the distance calculations, as shown in Figure 2.

$$\text{Updated cumulative distance (nmi)} = \text{cumulative distance from threshold} - \text{takeoff offset distance (FOQA)}$$

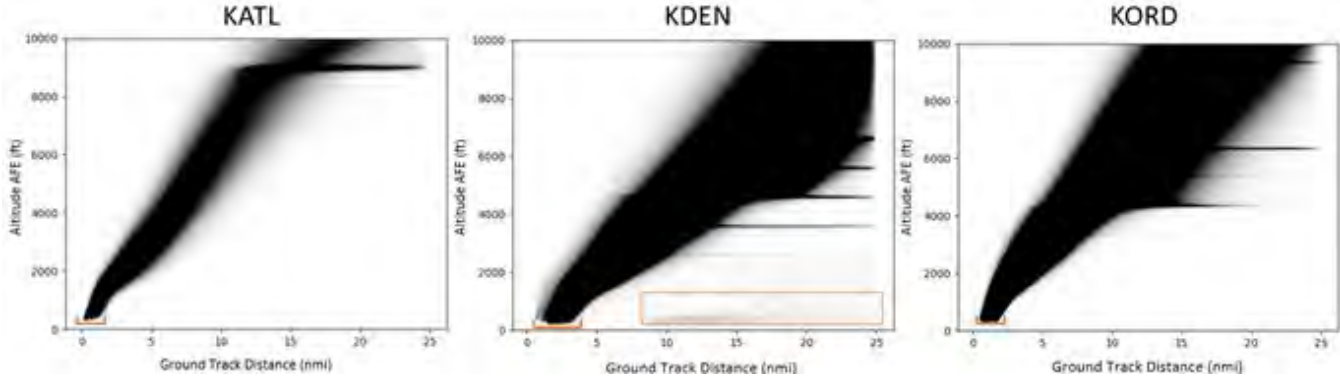


Figure 1. Erroneous flights and lift-off point variation visualized at KATL, KDEN, and KORD.

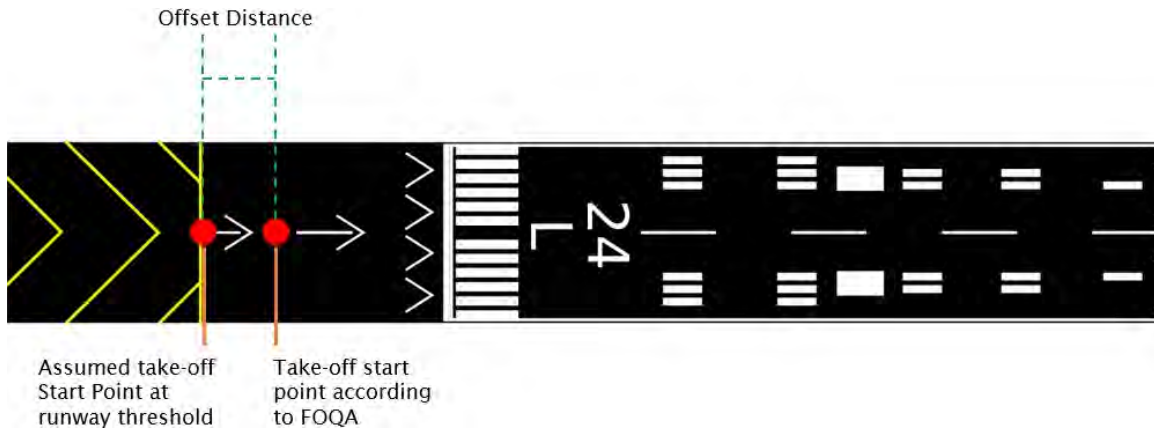


Figure 2. Visualization of average takeoff distance variation between the runway threshold and FOQA.

Profile comparison

The TTD were first compared against the FOQA data, which served as a supplementary layer of flight data to validate the accuracy and reliability of TTD before the comparisons were made against the existing NADP profiles. As shown in Figure 3, the comparison indicated that FOQA departure procedures resembled the average behavior of TTD profiles; consequently, we proceeded with further analysis.

To facilitate the comparisons against NADP profiles, we further broke the two datasets down according to the stage lengths, measured on the basis of the great circle distance between the departure and arrival airports. An increase in stage length directly correlates to greater takeoff weight of the aircraft, thus affecting climb performance during the takeoff phase.

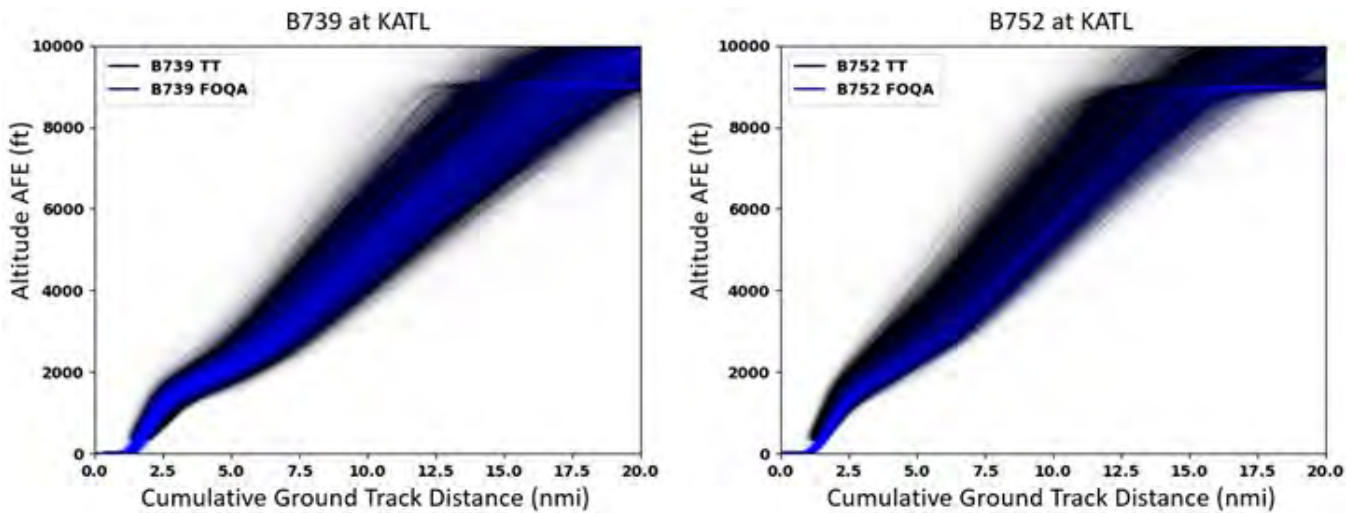


Figure 3. Threaded Track comparison against FOQA for B739 and B752 at KATL.

Using a set of Python scripts, we interpolated the real-world datasets at a set of equal intervals and averaged at those points to obtain a single profile referencing the average behavior of the datasets. This process also aided in clearer comparison between NADP profiles and real-world data.

The datasets were first iteratively compared against STANDARD and reduced thrust profiles, with a thrust reduction of 5% at each iteration and a maximum 15% reduction. The profiles were then compared with the MODIFIED_AW profiles, which

are meant to account for the higher takeoff weights and load factors observed in modern operations, as compared with AEDT standard definitions. Finally, the NADP profiles were introduced with both STANDARD and MODIFIED_AW configurations for the comparison.

The observations demonstrated that the slope of climb was lower for real world data than the full thrust and legacy stage-length weight version of NADPs. With the inclusion of alternate weight and the reduced thrust settings, the results improved; the modified alternate weight and 15% reduced thrust departure profiles showed the greatest resemblance to the real-world data. However, substantial offset remained between profiles (Figure 4). Therefore, we performed further investigations to understand how the thrust and weight settings differ between the existing NADPs for AEDT and the real-world data; this work is currently ongoing.

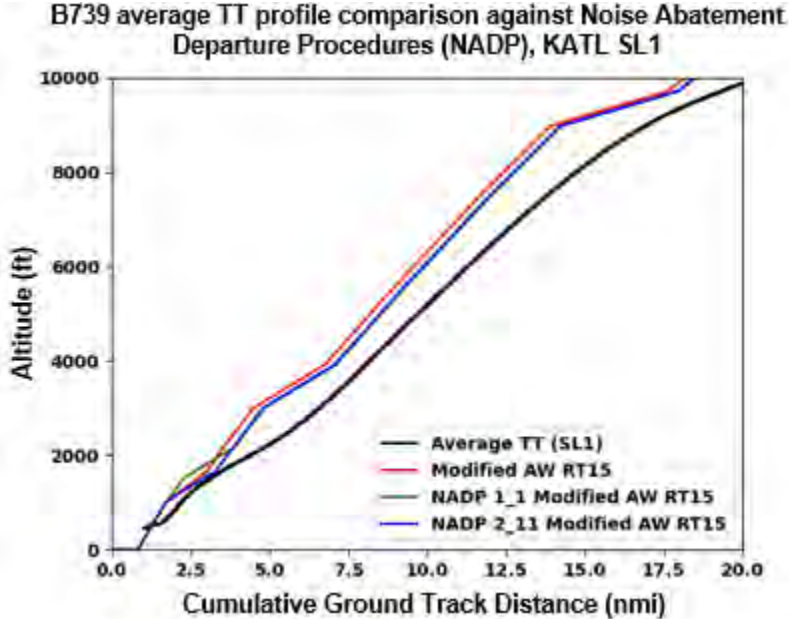


Figure 4. Average threaded track profile compared against MODIFIED_AW NADPs.

Milestones

None.

Major Accomplishments

- Established a workflow and supporting programming scripts for the new 2021 Threaded Track dataset for departure modeling efforts.
- Compared real-world data to AEDT modeling options to further improve AEDT departure modeling capabilities.

Publications

None.

Outreach Efforts

- Biweekly calls
- Biannual ASCENT meetings

Awards

None.



Student Involvement

Graduate research assistants Tanmay Daga, Ranya Almarzooqi, and Howard Peng participated in this research.

Plans for Next Period

1. Analyze the differences in real-world flight trajectories compared with AEDT
2. Develop a heuristic to exclude real-world flights which may carry tankered fuel

Task 2 – Arrival Profile Modeling

Georgia Institute of Technology

Objective

The current model in AEDT models arrival profiles by using specified fixed-point trajectories or manufacturer-provided procedures. The primary objective of Task 2 is to compare data from real-world flights against the AEDT models to make recommendations for enabling AEDT to better capture aircraft behavior during arrival.

This year, the specific focuses of this task were to: (a) continue with the previous year’s task of modeling arrival profiles in AEDT, derived from the cluster analysis, to understand the impacts of different level-off parameters on the environmental metrics and (b) perform a comprehensive analysis of the newly obtained real-world FOQA and TTD, to delve deeper into procedural profile definitions in AEDT. The end goal of this project is to provide recommendations regarding which AEDT arrival profiles should be integrated into the system and what information those profiles should include.

Research Approach

Investigation 1: AEDT Modeling of Clustering Results

Methods

The dataset used previously for Task 2 comprised aircraft approach data from 95 airports with 2,786,015 flights provided as part of the 2019 Threaded Track dataset. These flights were clustered into 10 groups with similar level-off arrival operations. Clustering was performed to reduce the number of arrivals to be analyzed by finding logical groupings. After testing of various algorithms, the *K*-means and BIRCH algorithms were found to have the best results. Each level-off arrival operation was characterized by three key parameters: level-off height, level-off distance, and level-off speed change.

To capture the range of behaviors displayed by the parameters, we focused on modeling five percentile values of the parameters in addition to the median, as shown in Figure 5. This process represented a change from previous work in which randomly selected parameter values within a cluster were modeled instead.

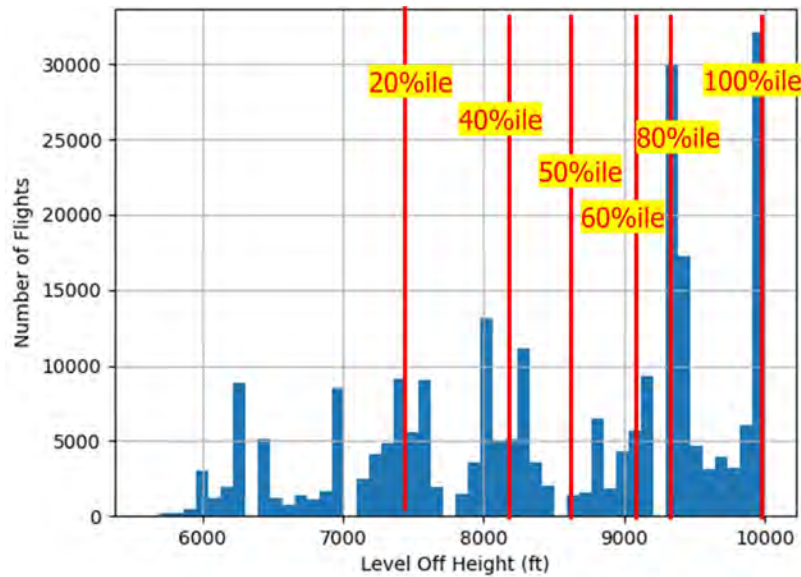


Figure 5. Histogram of level-off height for cluster 1 with percentile distribution.

Results and discussion

Cluster 1 consisted of 248,575 flights and was characterized by flights with higher level-off heights. Modeling was performed at the ORD airport with the Boeing 737-800, because this airport had the most flights (51,926) in cluster 1. Tableau was used as a data visualization platform for visualizing the environmental metrics obtained after modeling of the five percentile values of a flight in AEDT. As depicted in Figure 6, to understand the impacts of level-off parameters on environmental metrics, we held the level-off heights constant during modeling of level-off length profiles, and vice versa. For comparison, the AEDT STANDARD profile is also included in the plot.

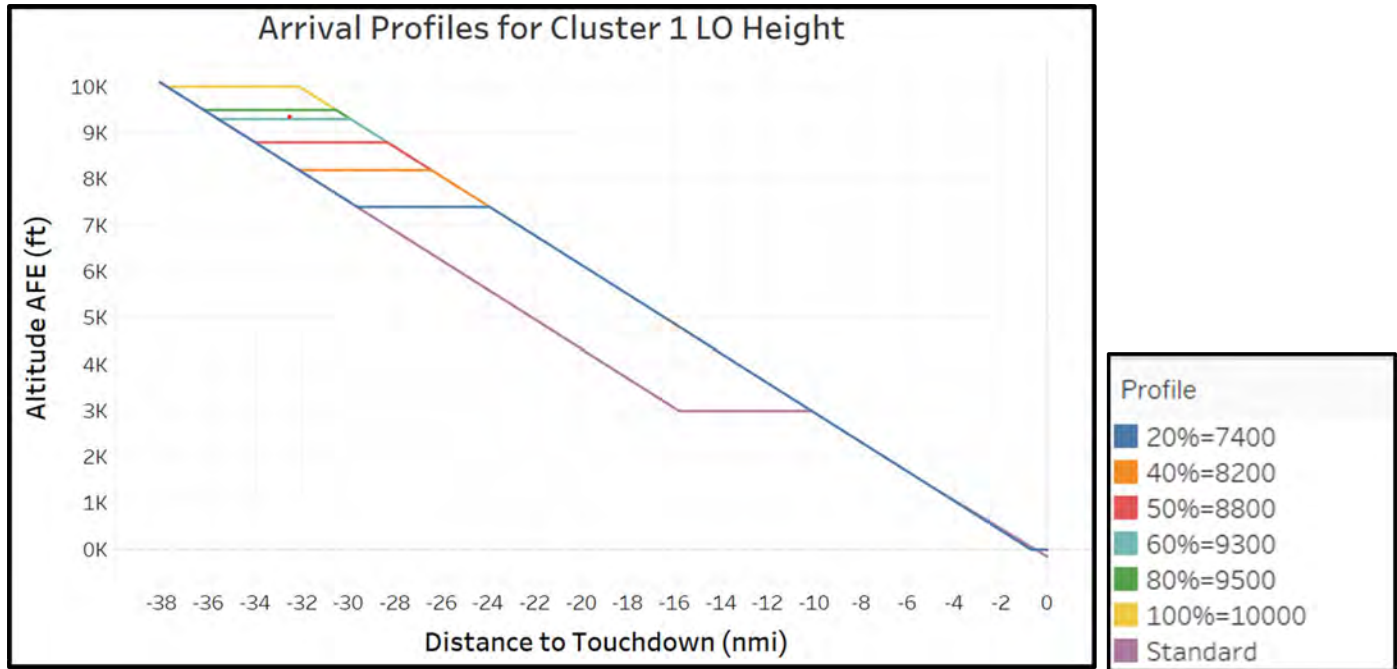


Figure 6. Arrival profile for cluster 1 level-off height.

The thrust per engine, plotted against the distance to touchdown, is depicted in Figure 7. Minor differences in thrust variation were observed, and the location of the change in thrust varied across profiles.

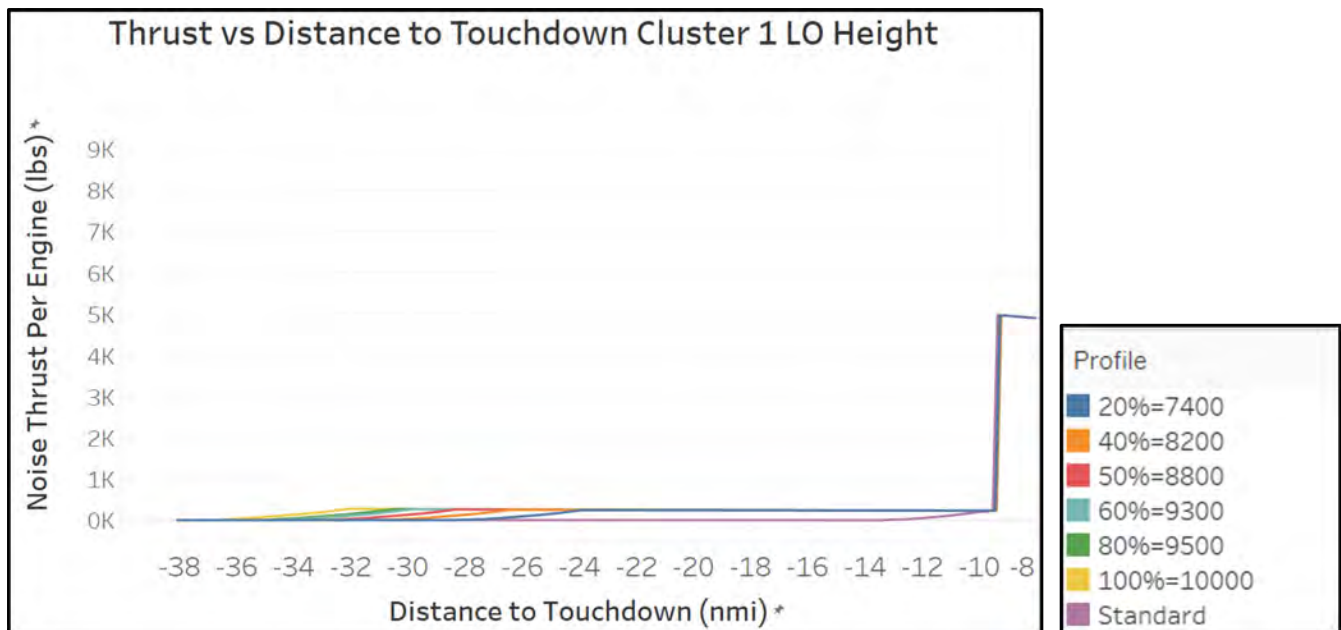


Figure 7. Thrust vs. distance to touchdown for cluster 1 level-off height.

Figure 8 illustrates the percentage change with respect to the STANDARD profile in terms of fuel burn and nitrogen oxide (NO_x) emissions. For cluster 1, level-off heights exerted greater effects on fuel burn and NO_x emissions than the STANDARD AEDT profile, with emissions increasing by 2%–4% from the 20th percentile level-off height profile.

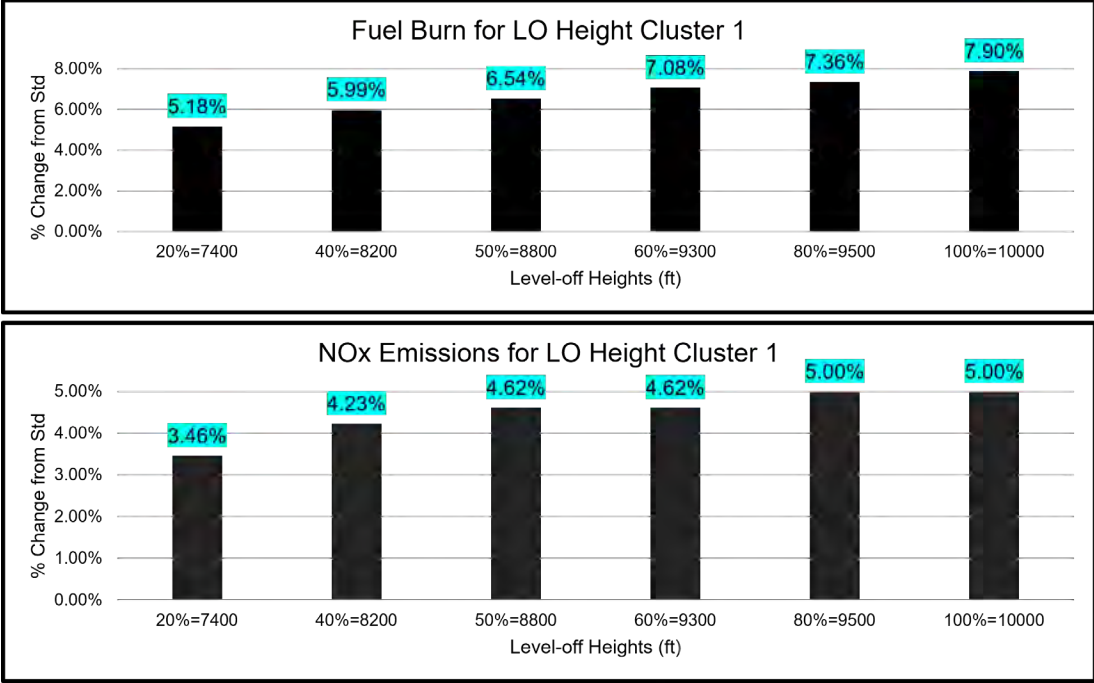


Figure 8. Fuel burn and NO_x emissions for cluster 1 level-off height.

Investigation 2: Analysis of Real-world Flight Data

Methods

After the most recent FOQA and Threaded Track datasets for the 2019 calendar year were obtained, we realigned our efforts to perform a comparative study focusing on the arrival profiles. Atlanta airport was chosen for this analysis, because of its status as one of the busiest airports and the availability of FOQA flight data. Furthermore, the analysis was scoped down to the 737-900 aircraft type, which had the most operations (4,827) in the FOQA data for this airport. During this analysis, as shown in Figure 9, the TTD terminated midair at ~500–600 ft AFE. Additionally, on the basis of the glideslope angles, high variability in the perceived touchdown point was observed.

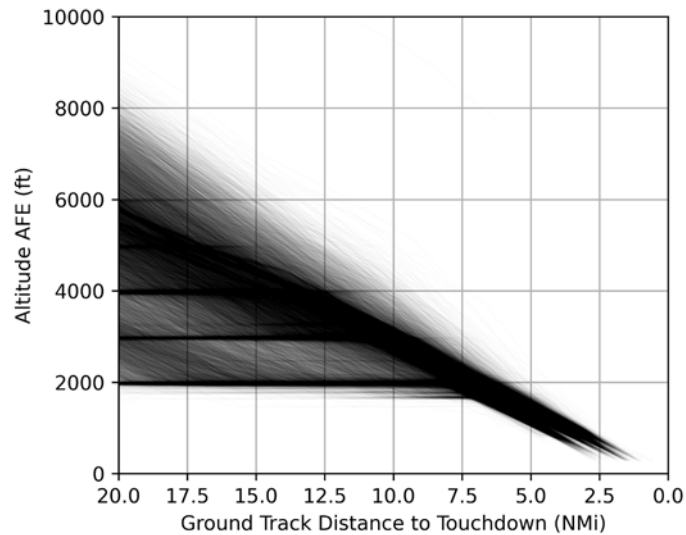


Figure 9. Variability in arrival profiles for 737-900 flights on final approach at KATL.

The extent of the variability observed could not be attributed entirely to real-world effects. To reduce the variability, the reference point for distance to touchdown and altitude AFE calculations was changed from an airport reference to the landing runway end. This process resulted in the convergence of arrival profiles, as shown in Figure 10.

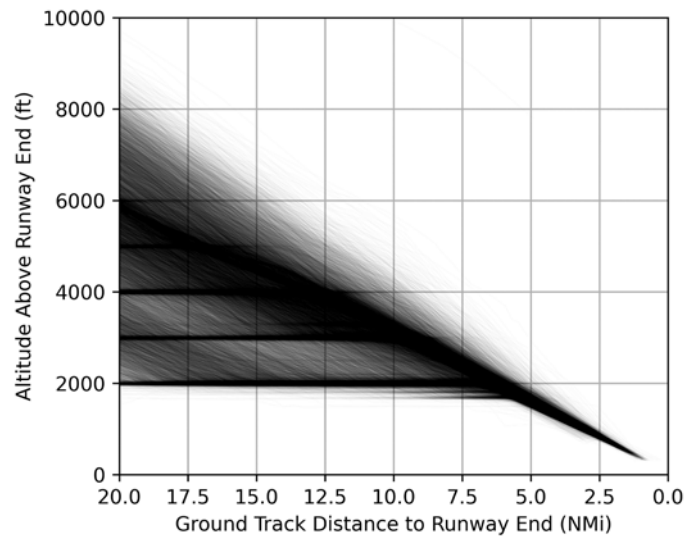


Figure 10. Stabilized arrival profiles for 737-900 flights with the runway end as the reference point at KATL.

To anchor the Threaded Track flights to touchdown, a new method, illustrated in Figure 11, was developed. This approach was based on the threshold crossing height and glideslope angle information for each runway end. The information available at the beginning of the descent phases included the following:

1. The landing runway from the Threaded Track metadata
2. Altitude mean sea level (MSL) and ground track distance from the Threaded Track trajectory final point
3. Threshold crossing height, threshold offset, runway end coordinates, and glideslope angle information from the AEDT database

First, the altitude was converted from MSL to AFE, on the basis of runway end elevation. Displaced threshold coordinates were calculated if the threshold was displaced for any runway. A threshold crossing point was created above the threshold,

at an altitude equal to the threshold crossing height. From that point, a line was projected down to the runway end with the glideslope angle and the intersection point on the runway giving the estimated touchdown point. Another projection was made from the threshold crossing point upward to the threaded track final point's altitude AFE. This process resulted in a gap between the actual flight trajectory and the projected flight, because of differences in ground track distance. This gap was closed by addition of the offset to the ground track distance. This process ensured that all flights were anchored to the estimated touchdown point, and the variability observed during touchdown was transferred upstream when the flights were still airborne.

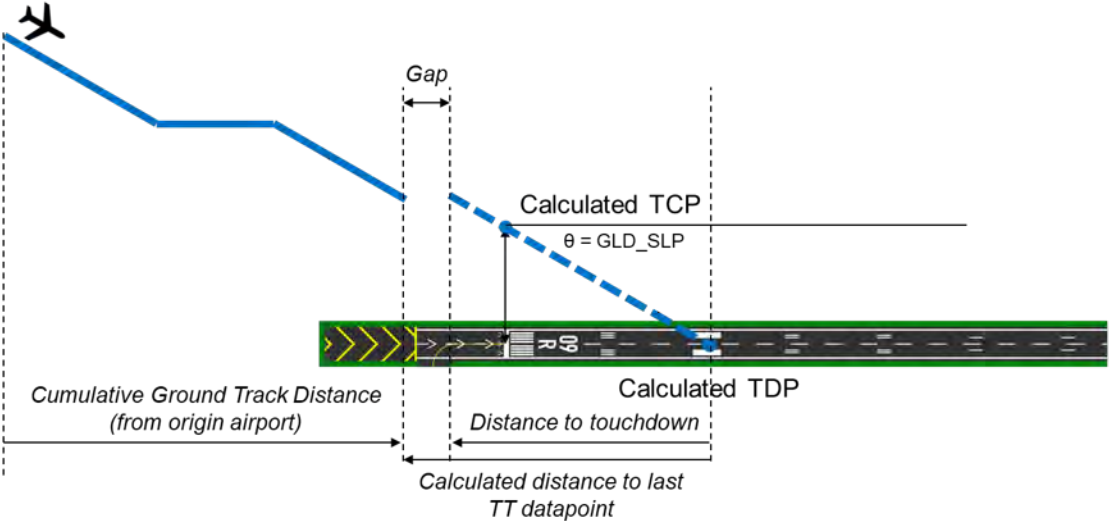


Figure 11. Method to anchor Threaded Track flights to the touchdown point on the runway.

Results and discussion

After application of the method to anchor Threaded Track flights, the flight trajectories converged at a single runway point, as shown in the right plot of Figure 12. Similarly, trajectories of 737-900 flights arriving at Atlanta airport, derived from FOQA data, are depicted in the left plot of Figure 12. A comparison of both plots revealed similar trends in level-offs.

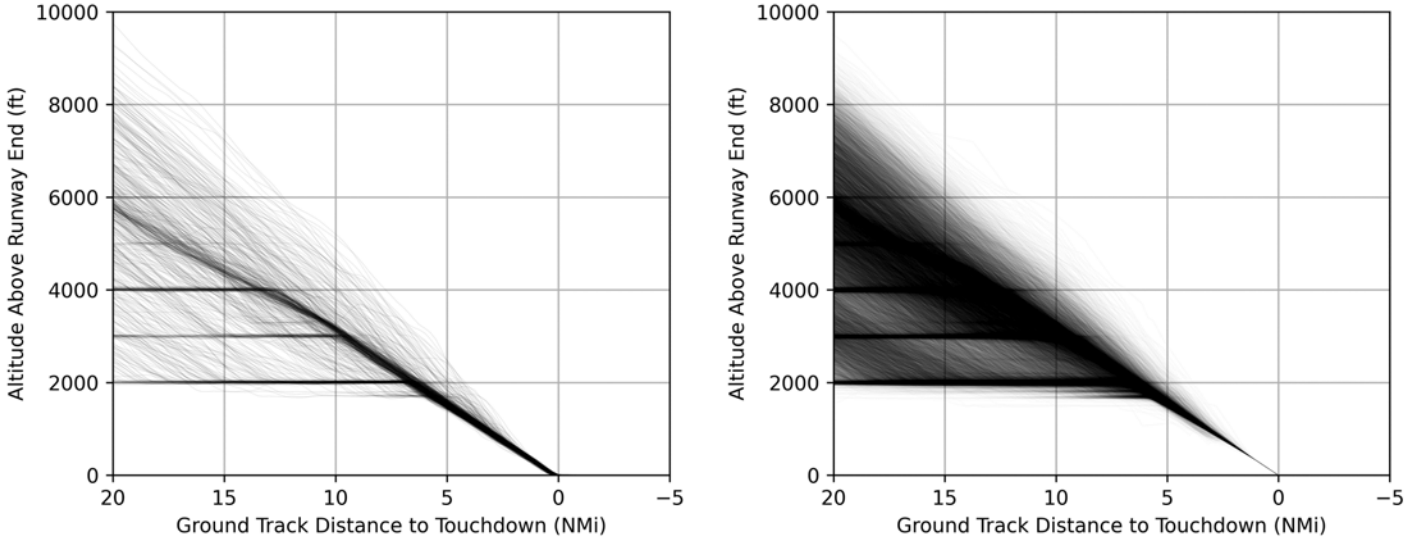


Figure 12. Arrival profiles using FOQA and Threaded Track datasets for 737-900 flights arriving in KATL.



Investigation 3: Updated Noise-Power-Distance Curves

In the past performance period, our team worked to develop a regression that corrects aircraft noise-power-distance (NPD) values as a function of airspeed and flap deflection. Our initial attempt to develop these data led to a much greater magnitude of correction than observed in flight test data captured by Boeing, because of varying velocity. Examination of this response in collaboration with Boeing revealed a need to recalibrate the noise sources within Aircraft Noise Prediction Program (ANOPP) to better reflect the engine-airframe noise contribution split of the modeled aircraft. The team has applied an updated calibration method to correct the acoustic model of the aircraft used as the baseline data. This method relies on calibrating the aircraft acoustic model to the NPD data collected in the Aircraft Noise and Performance database created by the European Union Aviation Safety Agency.

Through our collaboration with Boeing in this process, Boeing provided an estimate for the engine-airframe noise contributions for the approach conditions, which we used as an additional constraint. Initially, miscommunication occurred regarding the exact thrust level and altitude at which the engine-airframe split should be measured for this constraint; therefore, recalibration was necessary after the correct conditions were known. Additionally, examination of the initial regression creation attempt revealed that the corrections did not vary with the flap deflection angle, because of an error in our ANOPP script relating to the implementation of the Boeing Airframe Noise Module. Recent releases of ANOPP have changed the implementation of flap models for the Boeing Airframe Module within ANOPP, and our NPD generation script had not been properly updated to reflect that change. To avoid complete rewriting of our NPD generation script, which would have required considerable effort, we decided that we would update the Module within ANOPP used for modeling flap noise from the Boeing Airframe Module to the Fink Airframe Module. Our team has completed revisions of the ANOPP NPD generation script and is continuing with work to recalibrate the baseline aircraft model.

Milestones

None.

Major Accomplishments

- Modeled representative flights from clustering analysis, and compared flight performance, trajectories, and environmental impacts.
- Established a workflow and supporting programming scripts for the new 2021 Threaded Track dataset for departure modeling efforts.

Publications

None.

Outreach Efforts

- Biweekly calls
- Biannual ASCENT meetings

Awards

None.

Student Involvement

Graduate research assistants Anushka Moharir, Hansen Lian, and Nitya Maruthuvakudi Venkatram participated in this research.

Plans for Next Period

1. Continue with analysis of the newly obtained real-world data for other airports.
2. Detect CDA vs. level-offs for both Threaded Track and FOQA datasets.
3. Recalibrate the baseline aircraft model within ANOPP for NPD+C development.

Task 3 – Full-flight Modeling

Georgia Institute of Technology

Objective

The aim of this task is to improve the full-flight modeling capabilities within AEDT by developing an alternative modeling workflow that can complement the often complicated and time-consuming process of using the default sensor path functionality in AEDT. In recent years, this task has undergone a verification process in which sensor path model outputs were compared and validated against the real/historical flight data provided by FOQA datasets. The insights gained in the previous year led to an understanding of how AEDT can support simple statistical modeling for the analysis of cumulative fuel burn and emissions for full flights. This year's research used TTD to identify flight patterns in flight behavior and derive statistically significant data from real-world flight data, building on prior analyses of en route flight distances and average wind conditions by using FOQA data.

The tasks for this year are divided into two main sub-sections, each comprising methods, findings, and a discussion:

- Analysis of wind-reporting anomalies in full-flight modeling.
- Evaluation of en-route flight distances using TTD.

Research Approach

Investigation 1: Analysis of Wind-reporting Anomalies in Full-flight Modeling

Methods

Last year, we evaluated AEDT sensor path model performance by comparing its outputs, derived from both Base of Aircraft Data (BADA) 3 and BADA4 workflows, against real-world historical flight data from the FOQA dataset. This evaluation was enhanced by incorporation of Modern-Era Retrospective Analysis for Research and Applications (MERRA)-2 instantaneous weather data, thus providing a more precise assessment than using airport average weather data. Findings from this comparison indicated that the AEDT outputs, when the BADA4 models were used, showed substantial fuel flow discontinuities (high fuel flow rates over a short time). These discontinuities resulted in a discrete step to the integrated fuel burn - a phenomenon not observed in outputs using the BADA3 model with MERRA-2 instantaneous weather data. Further investigation of these BADA4 discontinuities revealed errors in the wind data reporting.

Two specific input files are required to import flight trajectory data into the AEDT study database using the Sensor Path Importing tool: an input trajectory file representing the flight path and an input operation file detailing a single operation for each flight. After these files were imported into the AEDT database, a fuel consumption study was implemented by using MERRA-2 weather data and AEDT 3e public release version 174.0.15710.1. To address potential inconsistencies in weather data reporting in the comparative analysis between the FOQA dataset and AEDT outputs, we used flight trajectory input files in two formats: Coordinated Universal Time (UTC) and the local time corresponding to the departure airport of each flight.

Results and discussion

In the study to examine the anomalies referred to as BADA4 discontinuities, FOQA data were compared with the outputs from AEDT performance reports after a fuel consumption study was run in AEDT. To facilitate this comparative analysis, we created plots focusing not only on parameters related to fuel consumption but also weather conditions. A significant discrepancy emerged in wind speed in the comparison of FOQA inputs and AEDT outputs. Figure 13 presents a case study of a flight from Seattle (KSEA) to Atlanta (KATL). The plot illustrates the relationship between flight time and wind speed, with flight time plotted on the x axis and wind speed plotted on the y axis. FOQA wind speeds are shown in blue, BADA3 is shown in yellow, and BADA4 is shown in green. The plot indicates that wind speeds estimated by BADA3 are more consistent with the actual wind speeds recorded by FOQA, thus demonstrating the better accuracy of the BADA3 model in this regard.

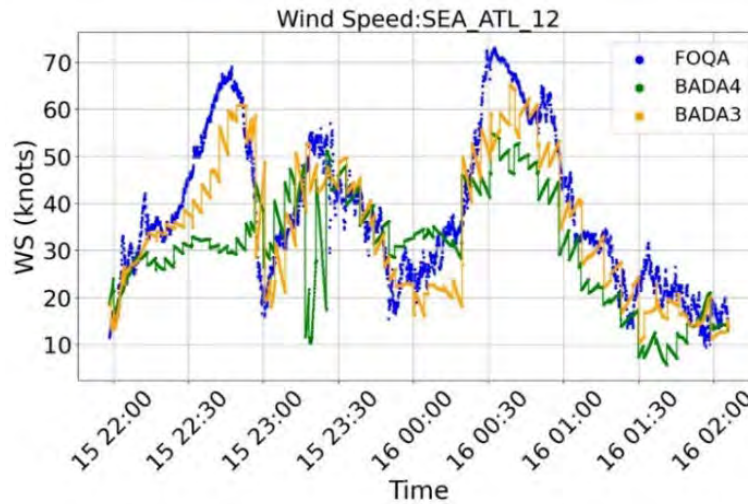


Figure 13. Comparative analysis of wind speeds: FOQA vs. AEDT models (before).

The Georgia Tech team reported the observed inconsistencies in wind speed to the AEDT development team. An investigation indicated that the issue was due to the AEDT system's inconsistent use of time references between the BADA3 and BADA4 models. Unlike BADA3, which relies on the actual segment time to retrieve weather data, BADA4 applies the UTC offset to the segment time for the same purpose, thus leading to the observed mismatches in wind speed. The discrepancy in wind speed data between models arose from how weather data are queried in UTC versus local time. This discrepancy also influenced the accuracy of fuel predictions, by creating differences in the flight's calculated airspeeds and thrust.

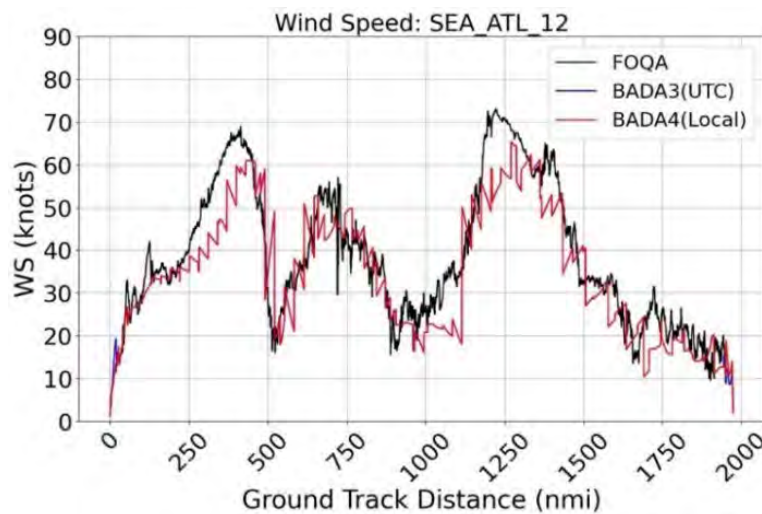


Figure 14. Comparative analysis of wind speeds: FOQA vs. AEDT models (after).

Figure 14 illustrates the synchronized wind speed comparisons between FOQA data and AEDT model outputs, with BADA3 times in UTC (marked in blue) and BADA4 times in local time (marked in red). The wind speed difference observed in the earlier plot is resolved in the updated plot. The AEDT development team has worked on addressing this issue through software changes in the next release.

Investigation 2: Evaluation of En-route Flight Distances Using TTD

Methods

This section investigates real-world airline flight data to determine the patterns of full flight routes. First, 16 origin-destination (OD) pairs from the FOQA dataset were chosen according to flight frequency, stage length, and aircraft diversity. An initial statistical analysis of en-route flight distances and average wind conditions was conducted to better understand flight pattern trends.

Building on this foundation, we expanded the research to include TTD, which offers a broader dataset and the opportunity to gain more detailed insights into the flight patterns of many additional OD pairs. This year's work has focused on additional city pairs and on analyzing seasonal flight concentration biases, thereby ensuring a more balanced analysis. Table 3 details the flight frequencies for each OD pair. The TTD involve approximately 38,000 flights and provided a substantial dataset for our comprehensive study.

Table 3. Sixteen OD pairs with flight frequencies for each route.

* Number of total flights: approximately 38,000 flights

City Pair	Num. of flights	City Pair	Num. of flights	City Pair	Num. of flights	City Pair	Num. of flights
LAS - SLC	1889	SLC - LAS	2051	ATL - DCA	4379	DCA - ATL	4314
ATL - JFK	1664	JFK - ATL	1563	ATL - LGA	3411	LGA - ATL	3323
MSP - ATL	2682	ATL - MSP	2811	SLC - ATL	878	ATL - SLC	1551
LAS - ATL	1532	ATL - LAS	1396	SEA - ATL	2464	ATL - SEA	2244

The TTD and FOQA datasets record key flight metrics such as latitude, longitude, altitude, and speed. However, the TTD lacks fuel-related parameters, weather information, and thrust data, which are readily available in FOQA. To address the missing direct distance information in the TTD, we used the Haversine formula to calculate the aircraft's flight distance between two trajectory points for each flight record. Figure 15 illustrates the method used to extract the necessary distance information for analyzing en route flight distances and average wind.

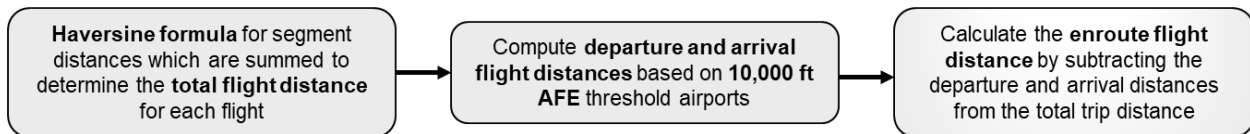


Figure 15. Method for computing flight distance.

Aircraft typically follow predetermined flight plans that guide them from departure to arrival airports. However, these routes may change because of unforeseen circumstances, such as adverse weather conditions or Air Traffic Control rerouting instructions, which can alter the actual distance flown, thus making the flight longer or shorter than initially planned. In this study, an analysis of en route flight distances was conducted to explicitly examine the factors that influence these variations. This analysis deliberately excluded direct considerations of weather and Air Traffic Control management data. The identified contributing factors are detailed below:

- Takeoff and landing direction combinations
 - Overall flight heading direction and its difference from the takeoff and landing runways
- Season (spring, summer, fall, or winter)
- Flight local departure time

Results and discussion

In this section, en-route flight distances using data from 16 OD pairs are analyzed. The analysis focused on factors such as the combinations of takeoff and landing directions, the effects of seasonal changes, and the local departure time of the aircraft. Specifically, the KATL-KDCA OD pair was selected as a case study to examine how these factors influenced

changes in flight distance. This study discusses the impacts of both the combination of takeoff and landing directions and the effects of seasonal changes.

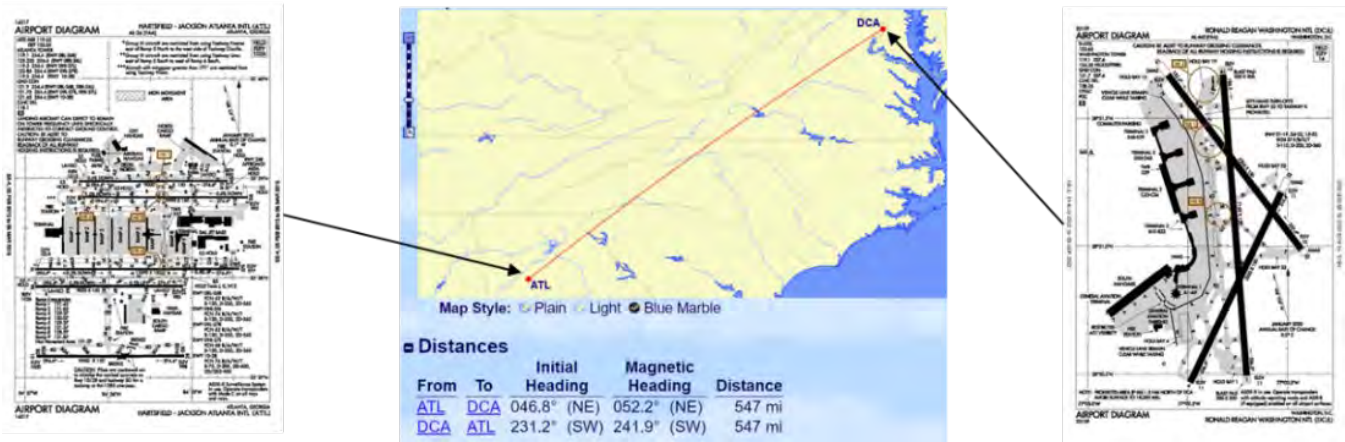


Figure 16. Great circle route and runway orientation for the ATL-DCA pair.

The first influential factor identified was the combination of takeoff and landing directions. Figure 16 illustrates the great circle route along with the runway orientations for KATL-KDCA. Aircraft at KATL take off and land in east-west orientations, whereas at KDCA, operations are predominantly in north-south directions. Flights were categorized into four groups according to the combinations of the two takeoff directions at KATL and the two landing directions at KDCA. This categorization enabled analysis of the impacts of these directional combinations on flight distances.

Table 4. Analysis of en-route flight distances across groups.

Group	Takeoff dir.	Landing dir.	Num. of flights	Mean. trip dist. (nmi)	Med. trip dist. (nmi)
1	East	North	1013	445.5	443.6
2	East	South	744	462.7	461.5
3	West	North	1688	471.1	469.2
4	West	South	934	488.3	486.8

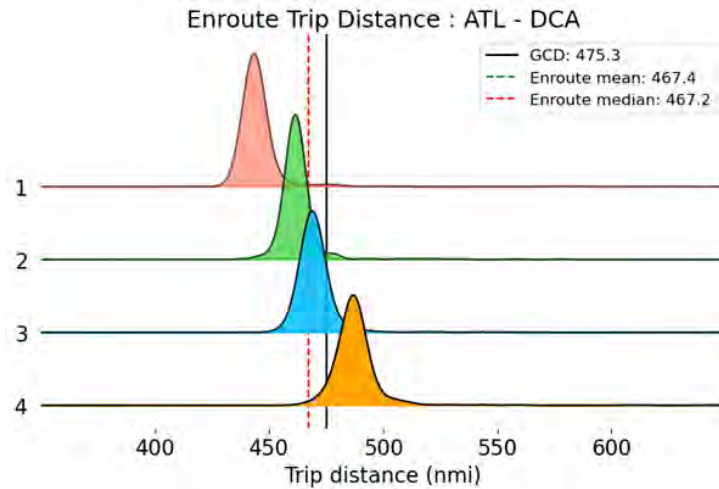


Figure 17. En-route flight distance distribution across groups.

Different combinations of takeoff and landing directions at KATL and KDCA significantly affected the en route distance of the KATL–KDCA route. As illustrated in Table 4, eastward departures from KATL and northward arrivals at KDCA averaged shorter distances, at approximately 446 nmi, because of more direct routes. In contrast, westward departures from KATL and southward arrivals at KDCA resulted in the longest distances, averaging approximately 487 nmi. Figure 17 further highlights these variations, demonstrating the substantial influence of route design on flight route length, particularly in OD pairs with shorter stage lengths.

Table 5 and Figure 18 present the results of a seasonal analysis of flight distances on the KDCA–KATL route. The table displays the mean and median path distances, separated by season, and the figure illustrates the seasonally varied trajectories. Minimal variation was observed in the median path distance across seasons for this OD pair. However, as indicated in Figure 18, the fluctuations in trajectories were more pronounced during spring and summer.

Table 5. Analysis of en-route flight distances across seasons.

Season	No. of flights	% of the Total	Mean trip dist. (nmi)	Med. Trip dist. (nmi)
Spring	1012	23.1	468.1	468.4
Summer	1139	26.0	471.0	467.0
Fall	1289	29.4	464.8	466.3
Winter	939	21.4	465.9	467.3

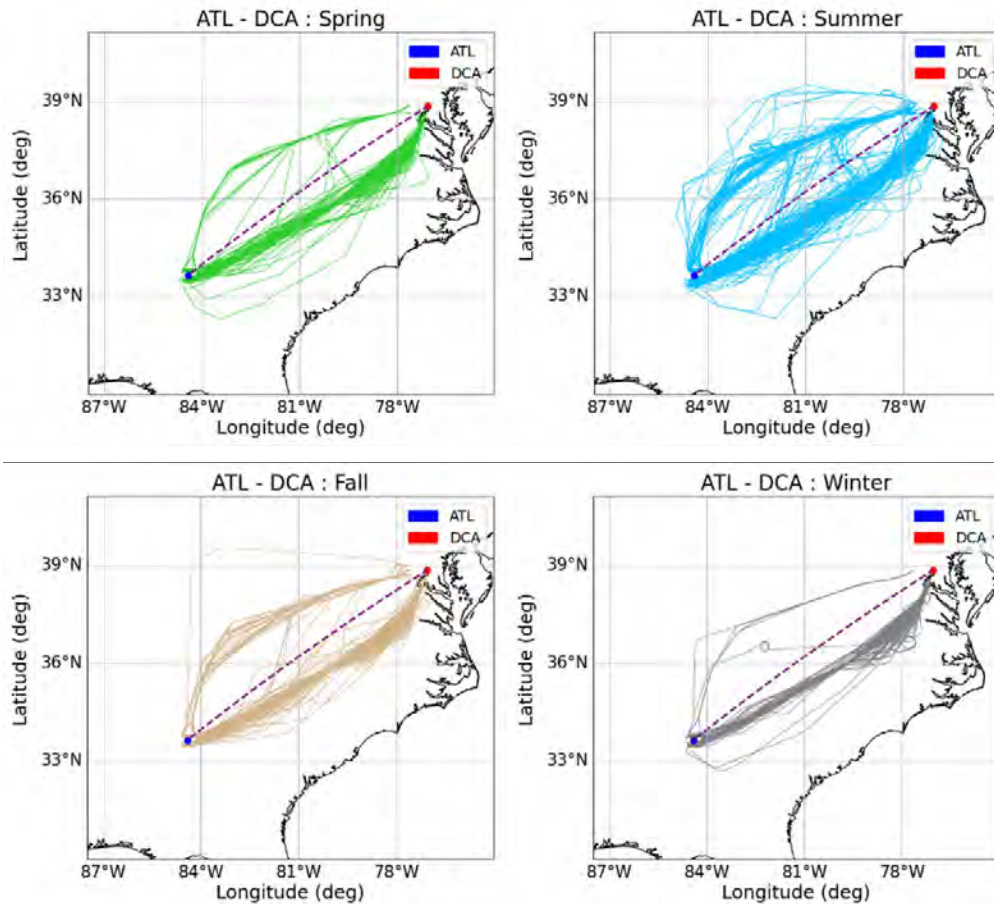


Figure 18. En-route flight distance distribution across seasons.

Milestones

None.

Major Accomplishments

- Detected anomalies in wind data reporting within the AEDT performance model and coordinated with the AEDT development team for resolution.
- Conducted an analysis of en-route flight distances and time by using TTD, taking into account factors such as the combination of takeoff and landing directions, seasonal variations, and local time of flight departure.

Publications

None.

Outreach Efforts

- Biweekly calls
- Biannual ASCENT meetings

Awards

None.

Student Involvement

Graduate research assistants Hyungu Choi and Yash Vinod participated in this research.

Plans for Next Period

1. Continue analyzing en-route flight distances and time using 2019 and CY21 FOQA.
2. Develop a simplified model based on real-world flight data to predict fuel consumption.

Task 4 – System Testing and Evaluation of AEDT

Georgia Institute of Technology

Objective

To provide the best possible environmental impact modeling capabilities in AEDT, the FAA Office of Environment and Energy continues to develop AEDT by improving existing modeling methods and data, and adding new functionalities. The FAA Office of Environment and Energy seeks an independent effort in system testing to evaluate the accuracy, functionality, and capabilities of AEDT, and support future model development. The objective of this task is to provide the FAA with high-quality systematic testing and evaluation of the capabilities of AEDT, and to identify gaps in the tools' functionality and areas for further development.

Research Approach

Within this task area, the Georgia Tech research team has been coordinating with the FAA and Volpe National Transportation Systems Center on upcoming AEDT features, and testing and evaluating newly incorporated capabilities. For each AEDT release, depending on the update type, key features and functionalities are identified for capability demonstration to ensure that the implemented features are working properly. The scope and test cases for the system testing and evaluation effort are either directly provided or must be defined by the Georgia Tech team. These cases are typically defined according to the key changes to the AEDT version from the previous releases. Because of the dynamic nature of the AEDT development process, the team remains flexible in the choice of the testing and evaluation approach and the scope of work. The best available methods and data are used to ensure accuracy in the functionalities of newly released AEDT versions. When required, uncertainty quantification analysis is conducted to understand the sensitivity of output responses to variation in input variables and to quantify the major contributors to output uncertainty.

In the following subsections, the various features and functionalities tested between October 2022 and September 2023 are described. In addition, various bugs were identified, reported, and retested to support the AEDT development process.

Touch-and-go/circuit profile development

This task focused on the development of touch-and-go and circuit profiles for two new aircraft in AEDT 3e, EMB190E2 and EMB195E2, by using the existing approach and departure procedures as the baseline. This development was performed for both Aircraft Noise & Performance database fixed-wing civil aircraft with defined procedural profiles. The developed profiles were provided to the AEDT development team for integration into the Fleet Level Environmental Evaluation Tool database.

Profiles were created by use of programming scripts to copy appropriate steps from the relevant departure or arrival profile. All created profiles were tested for accuracy by modeling of noise metric results over a noise grid.

Harmonization of noise and emissions inventory from engine runups

AEDT 3f allows users to generate noise reports and emissions inventories for engine runups by using the same inputs via the graphical user interface (GUI). This feature was tested through the creation of new aircraft operations for the Boeing 737-800 and Airbus A320-211, and subsequent generation of performance and noise reports through the user interface. The same tests were performed on edited versions of existing operations to test GUI robustness, thus resulting in the resolution of minor visual discrepancies. Finally, the accompanying GUI was examined to ensure the presence of proper constraints on input values for latitude, longitude, heading, thrust, and duration through an intentional consideration of exaggerated or impossible values.

The results indicated successful implementation of the feature and the ability for concurrent output of reports for engine runup segments sharing identical input conditions.

Support for emissions dispersion modeling of engine runups

AEDT 3f broadens the scope of emissions dispersion modeling through the introduction of metric generation throughout engine runup. The testing process indicated issues with runups exceeding 24 hours in length, which were subsequently remedied through the imposition of run-time constraints in the GUI. Follow-up studies validated the proper application of constraints and successfully generated dispersion metrics for operations in AEDT’s default study, DULLES.

Additional source groups added for dispersion modeling

AEDT 3f further expands options for emissions dispersion modeling through the introduction of new source groups and detailed emissions source breakdown during modeling. The successful implementation of this feature was examined through a test of the “processing options” feature under the dispersion window in the GUI. AEDT’s default study, DULLES, was rerun with altered dispersion protocols leveraging the new processing options to confirm both GUI and model functionality.

Updates to support AERMOD/AERMET version 22112

AEDT 3f has been upgraded to generate files compatible with American Meteorological Society/Environmental Protection Agency regulatory model (AERMOD)/AERMET version 22112. Given the largely internal nature of this process with minimal user input, this feature was tested through the creation of a new study by using the most recent version of AERMOD (.mod) files and generating emissions results. The successful creation of metric results validated the compatibility with AERMOD/AERMET version 22112. As of December 2023, AEDT implements AERMOD/AERMET version 23132.

Additional AERMOD modeling options

AEDT 3f provides options for the customization of NO₂ modeling and the inclusion of two new methods to account for low wind parameters within AERMOD. The implementation of these modeling options was first examined via the GUI, to ensure the presence of, and adequate constraints on, low-wind parameters and NO₂ calculation methods. This preliminary analysis indicated successful incorporation of wind parameter constraints and higher-fidelity weather file (incorporating ozone) requirements for the Travel Time Reaction Method–2 NO₂ model.

Full feature functionality was tested through altering wind parameters via the GUI and subsequent comparison of default and altered NO₂ emissions. Figure 19 shows the results of one such analysis and validates the correct implementation of the feature.

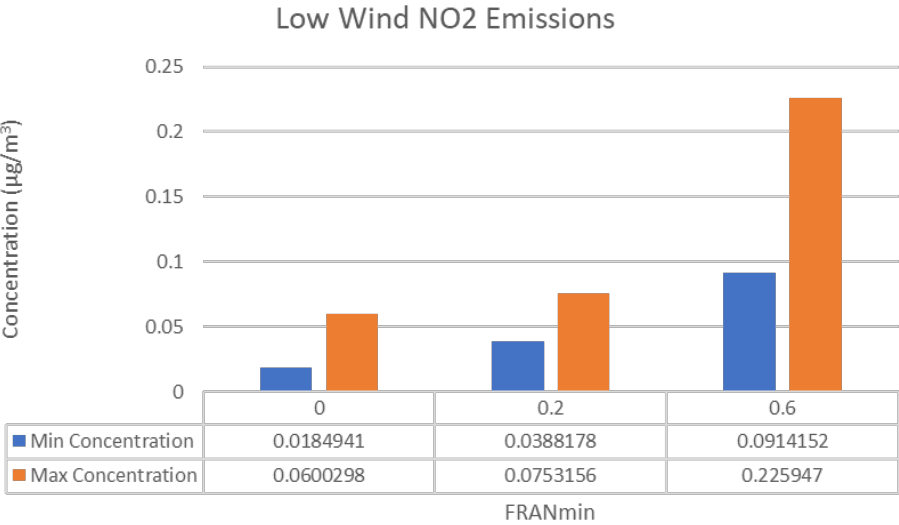


Figure 19. Comparison of default and altered NO₂ emissions.

Engine Emissions Databank QA/QC

This feature is aimed at automating the process of incorporating new and/or updated European Union Aviation Safety Agency emissions values into the AEDT database through the creation of a pipeline capable of comparing newly published engine emissions databanks (EEDBs) to existing SQL counterparts.

A script was created to generate and compare delimited versions of EEDB and SQL data, highlight points of divergence across versions, and automatically update AEDT's delimited data, where possible. Functionality was subsequently extended to facilitate internal comparisons across separate EEDB and SQL versions.

Code accuracy was tested through a comparison of new EEDB values with outdated emissions tables from AEDT 3e, and further comparisons of separate EEDB tables and AEDT versions. The test results indicated full code functionality and the capability for automatic generation of new emissions text files in line with existing conventions.

AERMOD Performance Updates

AEDT's AERMOD module performs modeling of pollutant dispersion within short distances of industrial sources, and its integration into the software enables higher-fidelity emission analyses. This task was aimed at discerning the extent to which AERMOD taxes computer memory in its calculations and to identify specific computational bottlenecks in these processes.

Testing was conducted through the creation of a large-scale study featuring more than 1.5 million arrival and departure operations split across auxiliary power units (APUs) and ground support equipment (GSE). AERMOD's involvement in emission calculations was monitored with software designed to track memory usage at important computational junctures and was compared with results from both prior tests and varying study settings.

The results demonstrated a 15% improvement in overall AERMOD efficiency relative to prior AEDT releases, but these outcomes were localized only to cases involving emission dispersion calculations (rather than inventory tabulations).

CSV Import of APU Duration of Aircraft Operations

In AEDT 3f, users can now specify separate default APU durations for arrival and departure operations by using the CSV import feature. To test this new feature, we created a study with a single airport layout with all desired elements (e.g., runways, gates, and tracks).

The following types of files were imported for testing purposes:

- Aircraft operation CSV input file
- Aircraft tracks CSV input file
- APU landing and take-off (LTO) input file
- Ground support equipment LTO operation input file

Testing was performed by attempting to import a series of both properly and improperly formatted aircraft CSV files. The default input files from STUDY_DULLES were all imported successfully. A minor bug was identified in which the APU LTO Input file was not imported while open in Excel. To inform users about this issue, the AEDT Development team opted to display a warning message inside the GUI. The same warning message was already present inside AEDT for the other three input file types.

In an attempt to break this feature, we used very high positive and negative APU durations. Both the negative and the very high APU durations produced APU emissions results.

Support for SQL Server 2022 and Migration Tool

The public release of AEDT 3f will support both SQL Server 2017 and SQL Server 2022. New AEDT3f studies were created in SQL Server 2022 and ran without issues. Old studies from previous features were upgraded from SQL Server 2017 to SQL Server 2022. Again, no issues were identified, and the upgrades were completed successfully.



ESRI contour generation

The objective for this feature was to compare contour differences between the existing ESRI in AEDT 3f_build_18606 and the new ESRI.NET in a zipped version of AEDT. The following test plan was proposed (accounting for different aircraft, airports, receptor grid spacing, weather, noise metrics, and flight profiles):

Table 6. ESRI contour testing test plan.

Test cases	Aircraft type	Airport	Weather	Metric	Receptor grid spacing, nmi	Profile
1	737-800	KATL	Default	SEL	0.06	STANDARD Arrival
2	737-800	KATL	Low temperature	DNL	0.06	STANDARD Arrival
3	737-800	KATL	High temperature	LAMAX	0.06	STANDARD Departure SL 1
4	737-800	KATL	Low humidity	EPNL	0.08	STANDARD Departure SL 1
5	777-200	KATL	High humidity	SEL	0.08	STANDARD Arrival
6	777-200	KATL	Default	DNL	0.08	STANDARD Arrival
7	777-200	KDEN	Default	LAMAX	0.1	STANDARD Departure SL 1
8	777-200	KDEN	Default	EPNL	0.1	STANDARD Departure SL 1
9	CRJ-9ER	KDEN	Default	SEL	0.1	STANDARD Arrival
10	CRJ-9ER	KDEN	Default	DNL	0.12	STANDARD Arrival
11	CRJ-9ER	KDEN	Default	LAMAX	0.12	STANDARD Departure SL 1
12	CRJ-9ER	KDEN	Default	EPNL	0.12	STANDARD Departure SL 1
13	737-800	KATL (curved track)	Default	SEL	0.1	STANDARD Departure SL 1
14	737-800	KATL (curved track)	Default	PNLTM	0.1	STANDARD Departure SL 1
15	Multiple (study INM)	KSFO	Default	DNL	0.16	Multiple

The log files from both AEDT versions were first compared to ensure that different ESRI versions were used. Contours were compared across a wide variety of testing scenarios including different aircraft, airports, weather, noise metrics, and receptor spacings. No differences in contour overlays were visually observed. Comparison of contour areas revealed small differences, of the order of $10^{-7}\%$ to $10^{-9}\%$. The maximum absolute difference in contour area during the testing was found to be 14 m^2 . This difference was found for test case 8, a Boeing 777-200 aircraft departing from KDEN, by using the EPNL noise metric (comparison shown in Figure 20).

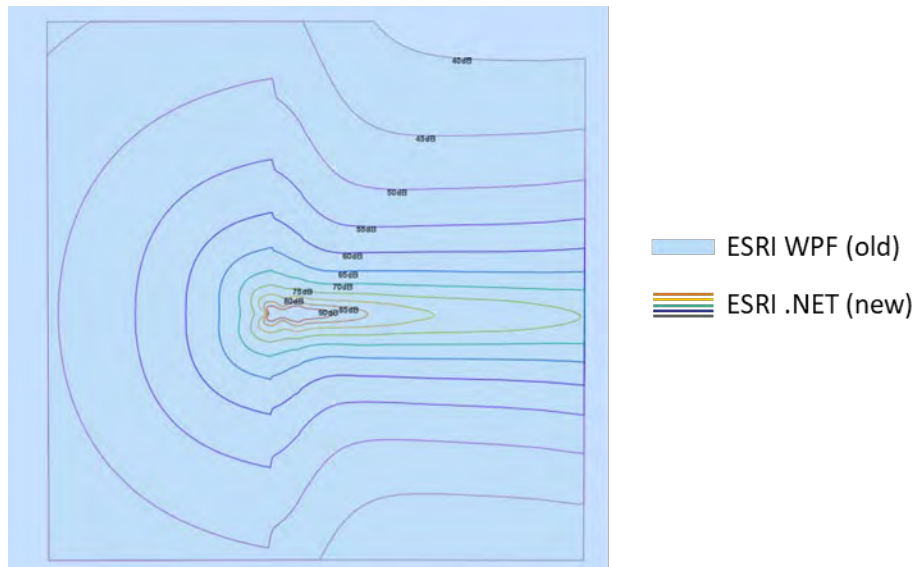


Figure 20. 777-200 departure KDEN (EPNL) ESRI comparison.

We concluded that computations with the new ESRI.NET version cause numerically insignificant, visually imperceptible changes in noise contours.

Non-volatile particulate matter five-point interpolation

This feature encapsulates AEDT 3f's updated non-volatile particulate matter (nvPM) calculation methods, which use newer equations and an interpolative process (via the addition of a new point of consideration in-flight) to generate nvPM and emissions index values above mixing height. Code from the preceding quality assurance/quality control feature was leveraged to convert outdated emissions indices into updated values for aircraft in the AEDT database containing the necessary information for such an overhaul. The functionality of this code was tested via a comparison with manually calculated indices and nvPM numbers for the candidate aircraft and was shown to be successful in the conversion process.

Additional testing was performed with respect to the underlying equations themselves, and their proper implementation as a prerequisite for the aforementioned code pipeline. The process used to determine indices and nvPM conditions in AEDT was validated by hand, with results from the aircraft with updated interpolation values, and was shown to match the expected results. This parity between manual calculations and AEDT results indicated successful ability to generate new nvPM and emissions indices values above mixing height.

MERRA-2 weather bug fix

Diagnostic results in AEDT 3f indicated that weather was being retrieved for the local time rather than the UTC time in many cases, because of a bug in .NET (UTC time reverted back to local time). To verify whether this issue was resolved, we took weather-related parameters (e.g., pressure and humidity) from the RSLT_EMISSIONS_SEGMENT table and compared them between BADA3 and BADA4 in AEDT 3f.

Because BADA3 and BADA4 results have different numbers of segments, we used cumulative ground track distance as a basis for comparison. A numerical method was necessary to reduce the number of comparisons by using the following methods:

1. Interpolate results onto a common basis
2. Calculate differences at each common basis point
3. Find the maximum difference magnitude
4. Find the flight with the highest maximum difference for each parameter



5. Visually compare these identified flights

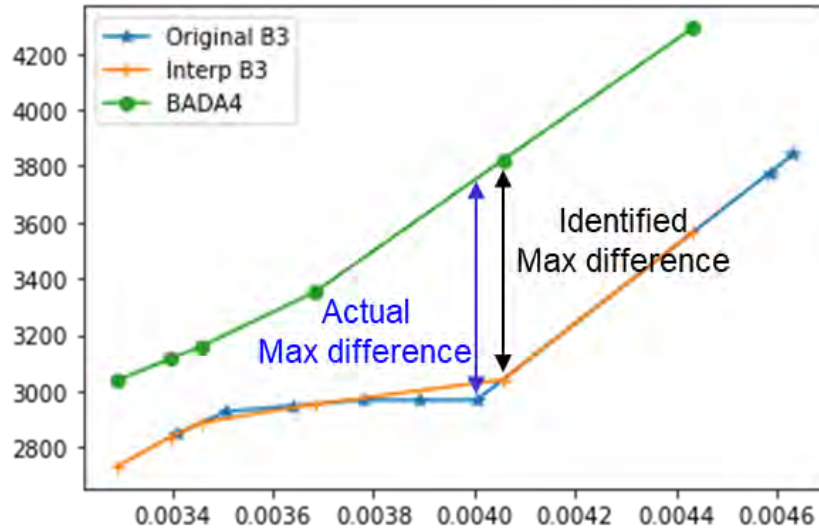


Figure 21. MERRA-2 comparison format.

An example of one of the worst offenders in the form of wind speed is shown in Figure 22. Other metrics showing noticeable discrepancies were dew point, humidity, thrust, and sea level pressure and metric. Metrics showing minor discrepancies were altitude, pressure, speed, and temperature. The discrepancies were deemed to be acceptable, because BADA3 uses the weather at the endpoint of each segment, whereas BADA4 uses the weather at the midpoint of each segment, thus resulting in discrepancies.

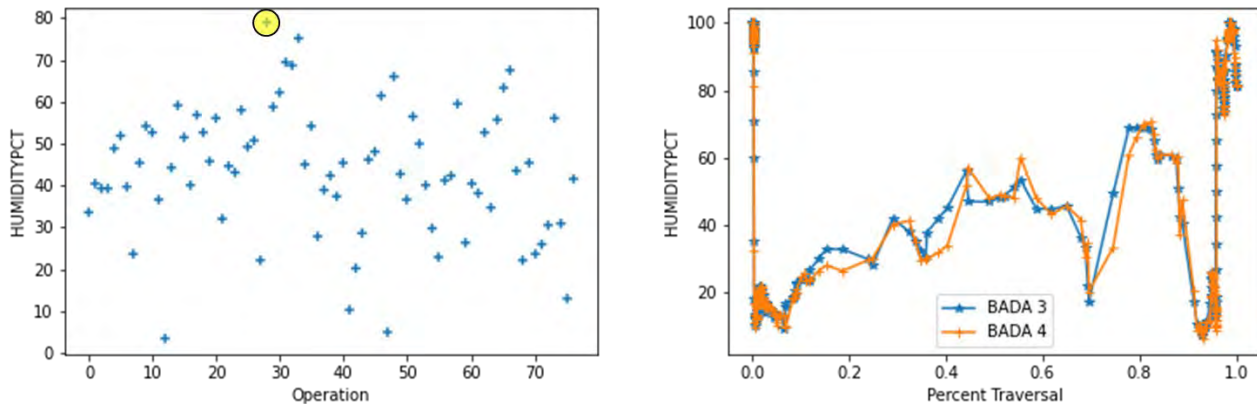


Figure 22. MERRA-2 wind speed comparison (worst offender).

Finally, testing also indicated zeroes in the descent ground values for some sensor path operations. An investigation revealed that the departure airport was being used to calculate the altitude AFE for the arrival operation's segments. After the fixes were implemented by the development team, the MERRA2 study emissions report was verified, and no further issues were found in this case.

Milestones

None.

Major Accomplishments

- Conducted several detailed investigations and testing efforts for system testing of new AEDT features.
- Completed the first draft of a comprehensive uncertainty quantification report, which is currently being reviewed by the FAA.

Publications

None.

Outreach Efforts

- Biweekly calls
- Attendance at biannual ASCENT meetings

Awards

None.

Student Involvement

Graduate research assistants Bogdan Dorca and Santusht Sairam participated in this research.

Plans for Next Period

1. Continue system testing efforts to support ongoing AEDT development.
2. Revise the uncertainty quantification report draft according to FAA feedback, and finalize the draft for publication.

Task 5 – SST Modeling in AEDT

Georgia Institute of Technology

Objectives

The SST modeling task has two primary objectives:

- Develop a predictive model for the propulsion system, encompassing thrust, fuel flow, engine dimensions, weight, and noise generation, and additionally accounting for variations in Mach number, altitude, and throttle setting, to enable comprehensive analysis of performance metrics such as fuel burn, gross weight, takeoff field length, and environmental factors including noise and emission.
- Generate parametric drag polar models for the optimized vehicle that capture aerodynamic performance across the entire flight envelope as a function of Mach number, altitude, and lift coefficient.

Research Approach

Leveraging its suite of sophisticated high-fidelity SST-modeling tools and datasets, our team has undertaken the development of a lower-fidelity surrogate model named ASCENT SST. This regression-based specification serves as a comprehensive framework for modeling both propulsion and aerodynamics in SST.

Propulsion modeling specifications

The propulsion modeling outlines distinct sub-domains based on specified ranges of Mach number, altitude, and power code (PC) for a given aircraft. The number and extent of these propulsion sub-domains vary depending on the aircraft. Crucially, these sub-domains, although defined within a three-dimensional operational parameter space, cannot overlap. However, they are allowed to share boundaries or portions.

For an aircraft operating within the confines of a propulsion sub-domain, the net thrust and fuel flow can be expressed as a function of various parameters, including the Mach number (M), PC, static pressure ratio (δ_s), and total temperature ratio (θ_t). The coefficients (a_n) in the function are specific to both the propulsion sub-domain and the response quantity, which can be either net thrust per engine (in pounds-force) or fuel flow rate per engine (in pounds per hour).

$$R = a_0 + a_1M + a_2M^2 + a_3M^3 + a_4M^4 + a_5M^5 + a_6PC + a_7PC^2 + a_8PC^3 + a_9PC^4 + a_{10}PC^5 + a_{11}\delta_s + a_{12}\delta_s^2 + a_{13}\delta_s^3 + a_{14}\delta_s^4 + a_{15}\delta_s^5 + a_{16}\theta_t + a_{17}\theta_t^2 + a_{18}\theta_t^3 + a_{19}\theta_t^4 + a_{20}\theta_t^5$$



$$+a_{21}MPC + a_{22}M\delta_s + a_{23}M\theta_t + a_{24}PC\delta_s + a_{25}PC\theta_t + a_{26}\delta_s\theta_t \\ +a_{27}MPC\delta_s + a_{28}MPC\theta_t + a_{29}M\delta_s\theta_t + a_{30}PC\delta_s\theta_t + a_{31}MPC\delta_s\theta_t$$

where

- R is the response quantity, which is either net thrust per engine (lbf) or fuel flow rate per engine (lbm/hr)
- $PC = 30 \times \frac{F}{F_{max}} + 20$

where

- F is the net thrust generated by the engine (lbf)
 - F_{max} is the net thrust available from the engine (lbf)
 - $\theta_t = \frac{T_t}{T_0} = \frac{T}{T_0} \times (1 + 0.5 \times (\gamma - 1) \times M^2)$
- where
- γ is the ratio of specific heats for a calorically perfect gas = 1.4
 - M is the Mach number
 - T is the static temperature at a given altitude (K)
 - T_t is the total temperature (K)
 - T_0 is International Standard Atmosphere sea-level temperature (K)

- For altitudes below 11 km:

$$\delta_s = \frac{P}{P_0} = (1 - 2.25577 \times 10^{-5} \times h)^{5.25588}$$

where

- P_0 is the normal pressure at sea level (standard day) = 101325 Pa
- For altitudes above 11 km:

$$\delta_s = \frac{P}{P_0} = 1 + \frac{L_b}{T_0} \cdot (h - h_b) \cdot \frac{g_0 M}{R L_b}$$

where

- P_0 is the normal pressure at sea level (standard day) = 101,325 Pa
- T_0 is the standard temperature at sea level (K)
- L_b is the standard temperature lapse rate = -0.0065 (K/m)
- h is the height above sea level (m)
- h_b is the height at the bottom of the atmospheric layer (m)
- R is the universal gas constant = 8.31432 (N · m/mol · K)
- g_0 is the gravitational acceleration constant = 9.80665 (m/s²)
- M is the molar mass of the Earth's air = 0.0289644 (kg/mol)

To derive coefficients for net thrust and fuel consumption in the context of SST, we subjected the engine deck data specific to a fifth-order least squares linear regression in JMP statistical regression software. This regression involves key parameters of the static pressure ratio (δ_s), total temperature ratio (θ_t), Mach number (M), and power code (PC), thus serving as inputs for both net thrust and fuel flow. Consequently, two regression equations, one for net thrust and another for fuel flow, are established, each comprising 31 coefficients (unknowns) plus an intercept.

Given the challenge of achieving an optimal fit for all operating conditions within a single regression equation, distinct boxes are defined. These boxes represent combinations of Mach number, altitude, and power code intervals. The union of these boxes encapsulates both the design mission and other hypothetical missions specific to the SST concept under consideration. The design mission involves sizing the aircraft and engine to meet payload and range requirements, determining the maximum takeoff mass, and influencing overall aircraft performance. After the sizing process, the vehicle can be operated at different payload and range combinations, referred to as "off-design" missions.

The engine deck data are then filtered on the basis of these designated boxes, and the aforementioned regression process is repeated for each box. This iterative approach yields two regression equations, one for net thrust and another for fuel flow, for every designated box, thereby providing a comprehensive understanding of the propulsion system's behavior across various mission scenarios.

Table 7 shows the box definitions for the propulsion regressions. Currently, the boxes are defined from 10,000 ft, allowing the fixed-point profiles (FPPs) to cover the takeoff and landing segments below 10,000 ft.



Table 7. Propulsion box definitions.

Box	Altitude (ft)	Mach	PC
1 (ascent)	10,000–45,000	0.6–0.85	32–50
2 (ascent)	29,000–53,000	0.8501–1.2	38–50
3 (ascent)	30,000–60,000	1.2001–1.5	38–50
4 (ascent)	30,000–60,000	1.5001–1.75	38–50
5 (ascent)	30,000–60,000	1.7501–2.2	38–50
6 (descent)	35,000–60,000	1.7501–2.2	21–22
7 (descent)	35,000–60,000	1.4501–1.75	21–22
8 (descent)	35,000–60,000	1.3001–1.45	21–22
9 (descent)	35,000–60,000	1.0001–1.3	21–22
10 (descent)	15,000–58,000	0.8001–1.0	21–22
11 (descent)	10,000–40,000	0.6–1.0	21–22

Assessing the accuracy of the fits within each designated box involves comparing the predicted values for net thrust and fuel flow, derived from the regression equations, with the corresponding values from the engine deck of the conceptualized SST (Table 8).

Table 8. Accessing the accuracy of propulsion regressions.

Box	Points/Box	Training dataset				Validation dataset			
		Net thrust		Fuel flow		Net thrust		Fuel flow	
		Mean (%)	Standard deviation	Mean (%)	Standard deviation	Mean (%)	Standard deviation	Mean (%)	Standard deviation
1	2696	0.00407	0.4912	-0.0029	0.6803	-0.0031	0.4977	0.0072	0.671
2	4451	0.00415	1.2268	-0.0064	1.147	-0.0235	1.209	-0.0048	1.073
3	2395	-0.001	0.8933	-0.0034	0.796	0.0237	0.8854	0.0036	0.7778
4	1981	0.00162	0.4096	-0.0071	0.9176	-0.0275	0.4058	-0.0169	0.9322
5	1973	1.01E-05	0.2361	-0.0045	1.3425	0.0095	0.2436	-0.0206	1.5255
6	424	0.00039	0.239	-0.0003	0.1869	-0.006	0.2578	-0.006	0.2059
7	544	0.00423	0.7763	-0.0005	0.2074	0.1034	0.738	0.0222	0.2133
8	248	-0.0024	0.6272	-0.0002	0.2035	-0.0647	0.782	0.0031	0.2074
9	501	-0.0002	0.2226	4.99E-05	0.3472	0.0076	0.241	0.006	0.3705
10	545	-0.0005	0.306	-0.0003	0.1583	-0.0174	0.3678	-0.0128	0.1691
11	495	0.00052	0.3238	-0.0005	0.2634	0.019	0.2902	0.034	0.2646

Aerodynamic modeling specifications

For a given aircraft, the aerodynamic modeling component of the specification establishes two sets of key values: a group of four distinct cardinal lift coefficients (C_L) denoted C_{L_i} , and a set of seven distinct cardinal Mach numbers denoted M_i (Figure 23).

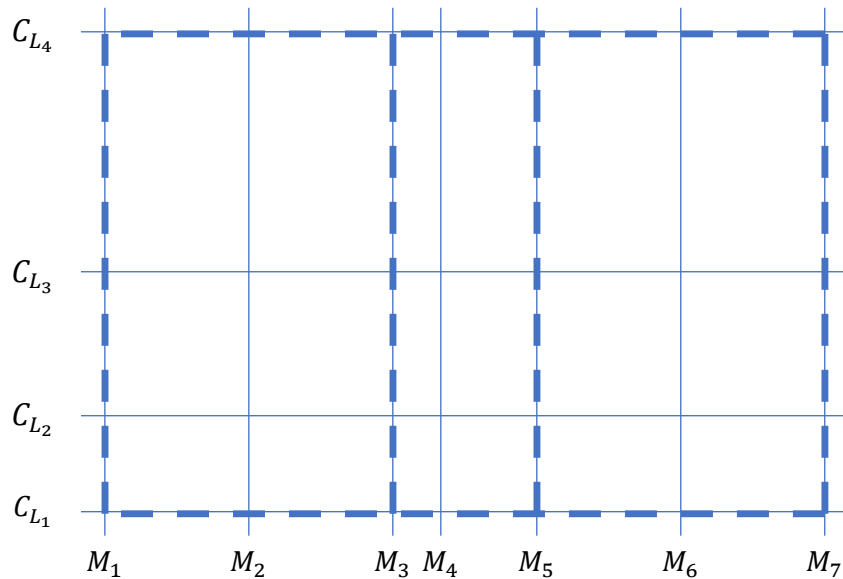


Figure 23. Aerodynamic regressions: boxes.

The Mach cardinals M_1 and M_7 , along with the lift coefficient cardinals C_{L_1} and C_{L_4} , define the operational state envelope for the aircraft. Specifically, the modeling specification is applicable for $\{M, C_L\}$ coordinates, where $M_1 \leq M \leq M_7$ and $C_{L_1} \leq C_L \leq C_{L_4}$.

Within the Mach- C_L envelope, Mach cardinals divide the range into three regimes: the "subsonic" regime ($M_1 \leq M \leq M_3$), the "transonic" regime ($M_3 \leq M \leq M_5$), and the "supersonic" regime ($M_5 \leq M \leq M_7$). Each regime corresponds to a structured irregular grid of cardinal values (3 by 4) and has a specific altitude range.

When modeling an aircraft within an aerodynamic sub-domain or along unshared bounds, the drag coefficient C_D at any cardinal grid point $\{M_i, C_{L_j}\}$ is modeled as a function of altitude (h).

$$C_{D_{i,j}} = a_1 + a_2h + a_3h^2 + b_{1,i} + b_{2,i}h + c_{1,j} + d_{1,i,j}$$

where

- h is the altitude
- All coefficients are specific to the aircraft and aerodynamic sub-domain
- Coefficients $b_{1,i}$ and $b_{2,i}$ are further specific to the cardinal Mach value M_i
- Coefficient $c_{1,j}$ is further specific to the cardinal value C_{L_j}
- Coefficient $d_{1,i,j}$ is further specific to the combination of cardinal values $\{M_i, C_{L_j}\}$

For any supported combination of Mach and lift coefficient $\{M, C_L\}$, the drag coefficient is modeled through bi-quadratic interpolation between $C_{D_{i,j}}$ values at cardinal grid points within the relevant Mach regime.

To derive coefficients for the regression of drag coefficients in each SST concept, the design team uses raw aerodynamic data containing the essential Mach number, C_L , altitude values, and their corresponding C_D . The approach involves initially regressing the drag coefficient on these cardinal values through a stepwise fit, followed by quadratic interpolation.

The team used JMP for the stepwise regression, considering Mach number, altitude, and C_L . Given the distinct behavior of the drag coefficient in subsonic, transonic, and supersonic phases, three separate boxes are typically created and subjected to regression (Table 9). The chosen set of cardinal values was required to encompass the design mission to prevent extrapolation.

Table 9. Aerodynamic regressions: box definitions.

Box	Mach	Altitude (ft)	CL
Subsonic	0.6, 0.7, 0.8	10,000–70,000	0, 0.1, 0.25, 0.5
Transonic	0.8, 0.88, 1.05		
Supersonic	1.05, 1.8, 2		

Similarly to the process for propulsion regressions, the validation of aerodynamic regressions involves comparing the predicted drag coefficient values from the regression against the actual C_D values derived from the aerodynamic data (Table 10).

Table 10. Assessment of the accuracy of the aerodynamic regressions.

Mode	Points/box	Training dataset		Validation dataset	
		Mean (%)	Standard deviation	Mean (%)	Standard deviation
Subsonic	116/40	0.012985%	0.446911	-0.038757%	0.412414
Transonic	123/33	0.0176288%	0.895849	-0.121732%	0.898749
Supersonic	120/36	-0.068553%	1.064485	0.144743%	0.912550

Validation of propulsion and aerodynamic regressions against Flight Optimization System (FLOPS) data

The validation process involves using the developed propulsion and aerodynamic regressions to derive values for thrust, fuel flow, and drag coefficient based on Flight Optimization System (FLOPS)-generated data for both the SST concept's design mission and off-design missions. The next step is to compare these predicted values with the actual values obtained from the data by computing the percentage error. Probability density function distributions are then constructed to visualize the results. To streamline and expedite this validation exercise, we crafted a Python script that takes the propulsion and aerodynamic regression equations, along with the FLOPS mission data, as inputs. The script calculates the percentage error between the predicted regression outputs and the actual FLOPS outputs for net thrust and fuel flow. Figure 24 shows a flowchart outlining the validation process and the development of the Python script.

The chosen off-design missions flown by the SST concept were as follows:

- Dubai (OMDB)–Bangkok (VTBS)
- Alaska (PANC)–South Korea (RKSI)
- Los Angeles (KLAX)–Hawaii (PHNL)
- Shanghai (ZSPD)–Singapore (WSSS)
- Rio de Janeiro (SBGL)–Lisbon (LPPT)
- New York (KJFK)–Heathrow (EGLL)

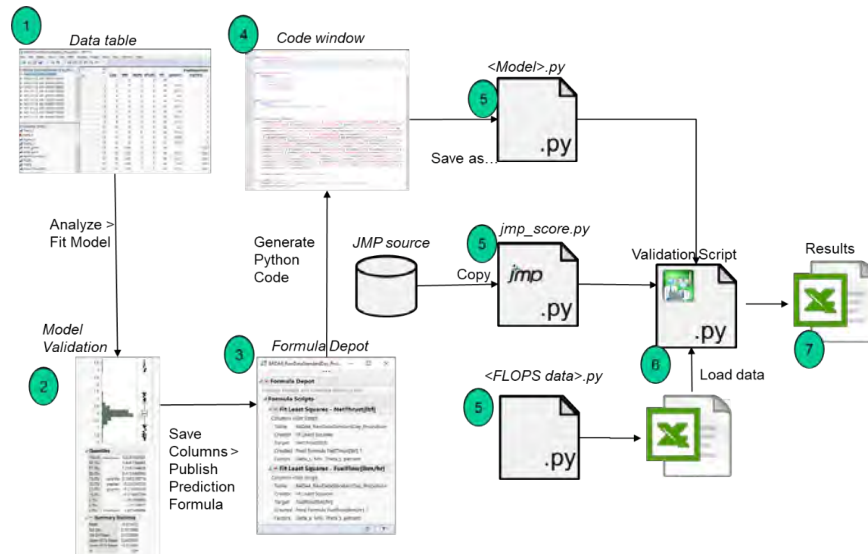


Figure 24. Validation procession for the developed regressions against FLOPS.

The off-design mission process involves two key steps:

1. **Ground track:** In this step, the optimal ground track and associated speed targets for each OD pair are identified. Our in-house developed Python code, SSTRT, handles this ground tracking exercise. The optimization parameter, Alpha, plays a crucial role and has values between 0 and 1. A value of 0 emphasizes time-based optimization, whereas a value of 1 prioritizes fuel-based optimization. The results of this exercise, captured in speed_changes.csv and track_changes.csv files for each route, outline the target Mach numbers and track details, indicating whether each segment is over water.
2. **Route writing:** The route writing script uses the outputs from ground tracking, combined with engine deck data. It runs FLOPS, providing the mission profile for each OD pair. The speed and track changes, along with the engine deck data, serve as inputs to this script. The FLOPS outputs are compiled into CSV format and exported to JMP. Subsequently, the aerodynamic and propulsion regressions are compared against the FLOPS outputs, and adjustments are made accordingly.

Figure 25 illustrates a flowchart detailing the entire process. This comprehensive approach ensures the determination of an optimized ground track and associated speed targets, followed by the execution of FLOPS for mission profile generation.

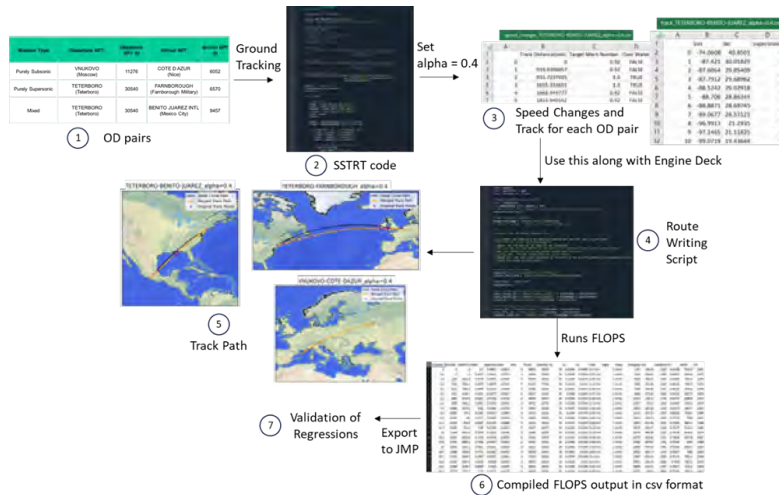


Figure 25. Off-design mission process.

The results of validation of the propulsion and aerodynamic regressions using the off-design missions (FLOPS data) are shown in Figure 26.

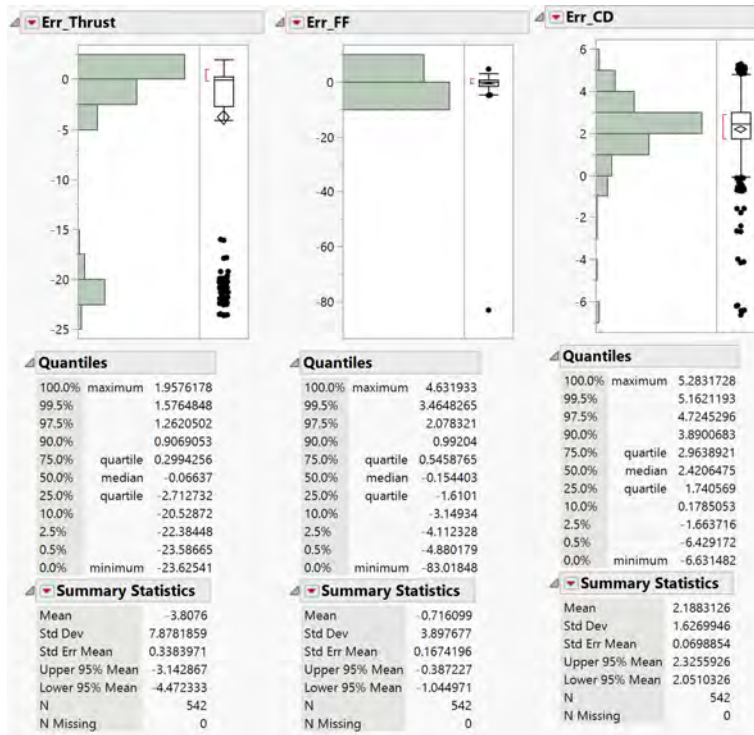


Figure 26. Propulsion (left) and aerodynamic (right) regression validation.

In the propulsion regressions, the percentage error in thrust and fuel flow is notably high for specific points, primarily because the ranges for the Mach number do not fully encompass the boundaries at certain altitudes, thus resulting in extrapolation of regressions and consequently higher errors. To address this issue, adjustments will be made to the

updated engine deck. We plan to redo the fits and validation to ensure improved accuracy and reliability in the modeling outcomes. In contrast, the aerodynamic regressions have been very well validated for the off-design mission, as reflected by the low errors (<5%) in the drag coefficients.

Terminal area: fixed-point profiles

Currently, propulsion and aerodynamic regressions are focused on capturing the mission parameters exclusively above 10,000 ft. To account for detailed takeoff and landing performance, fixed point profiles are used up to the altitude threshold of 10,000 ft. In this case, smooth connectivity must be ensured between the fixed-point profiles and the rest of the mission.

Detailed Takeoff Segment (one of the off-design missions: (OMDB-VTBS))

Figure 27 depicts the plots of altitude (AFE) and true air speed (knots) against distance (nmi) for the detailed takeoff segment merging into the rest of the mission. The FPP for takeoff transitions smoothly to the remaining mission from FLOPS.

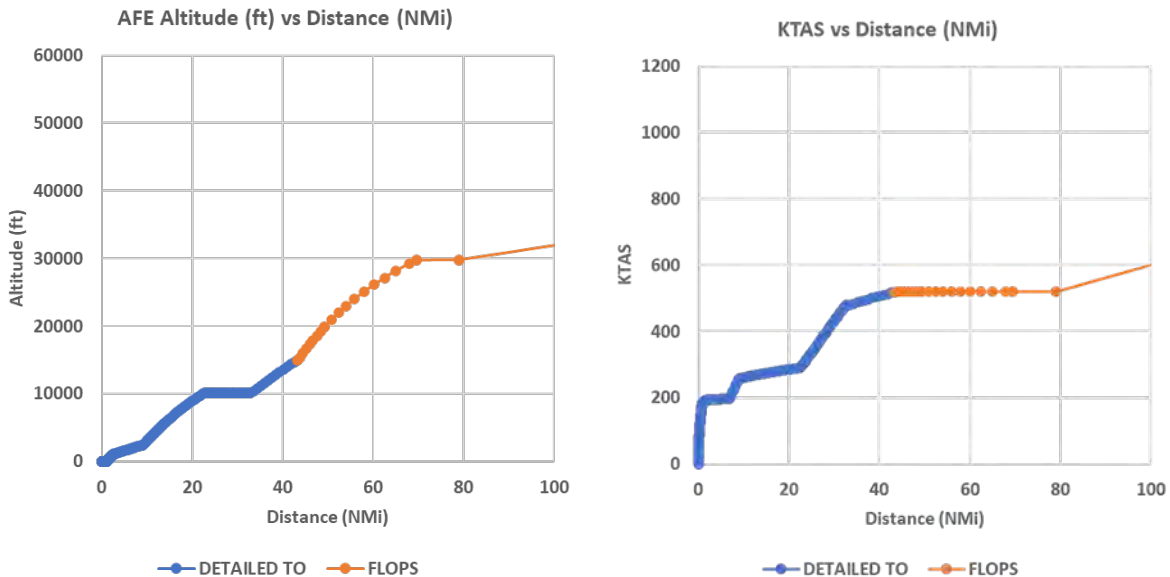


Figure 27. Altitude vs. distance (left) and true airspeed vs. distance (right), OMDB-VTBS, fixed-point profile takeoff.

Detailed landing (arrival) segment (one of the off-design missions: (OMDB-VTBS))

After the transition from the mission to the detailed landing modeling, the FLOPS descent mission enforces a 250-kts limit below 10,000 ft, as observed as a slight deviation from the standard 3° glide slope in the plot of altitude vs. distance (Figure 28). Furthermore, FLOPS also assumes full flaps and gear deployment from the specified altitude of descent, in this case, 15,000 ft. However, realistically, full flaps and gear deployment begin at a much lower altitude, thus causing discontinuities in the plots of true airspeed vs. distance (Figure 29).

To mitigate these discrepancies and ensure a smooth and consistent transition into arrival, we decided to begin the descent mission from a lower altitude and extend the propulsion and aerodynamic regressions to this altitude to cover the gap.

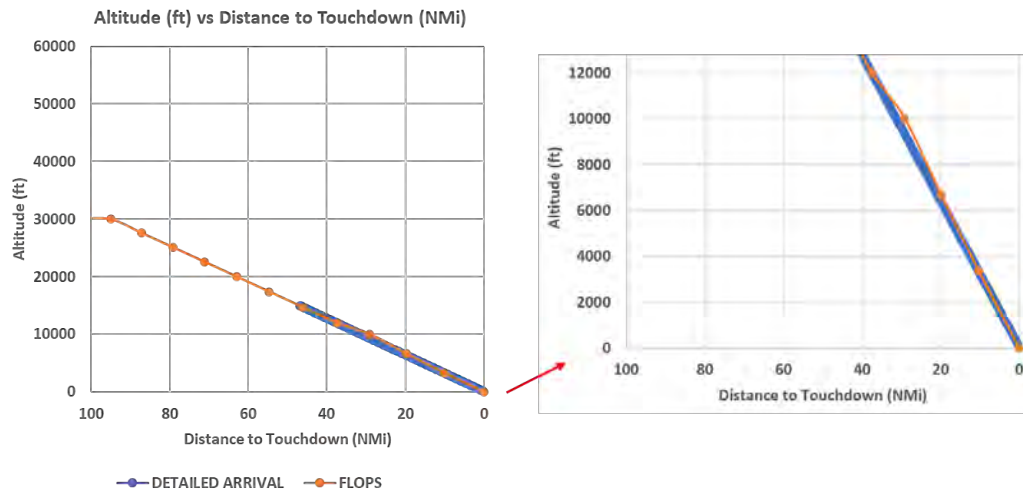


Figure 28. Altitude vs. distance: OMDB-VTBS-FPP arrival.

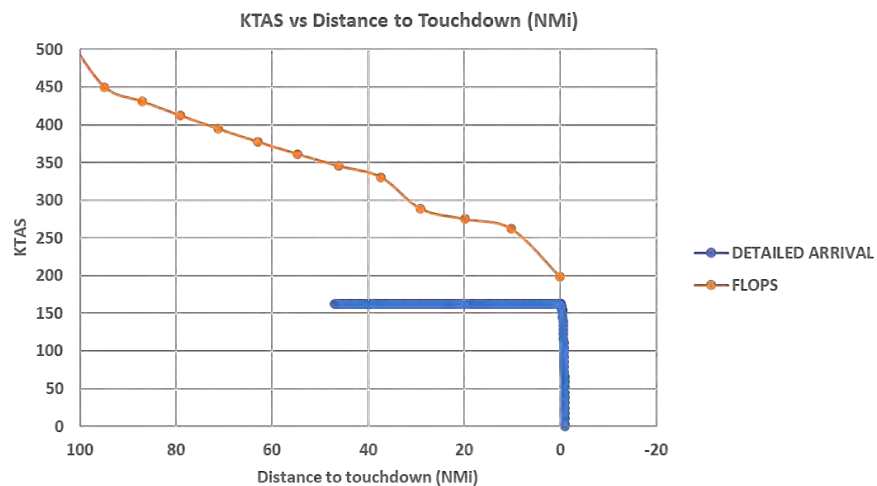


Figure 29. True airspeed vs. distance: OMDB-VTBS-FPP arrival.

Milestones

None.

Major Accomplishments

None.

Publications

None.

Outreach Efforts

- Biweekly calls
- Attendance at biannual ASCENT meetings



Awards

None.

Student Involvement

Graduate research assistants Nitya Maruthuvakudi Venkatram and Baptiste Cramette participated in this research.

Plans for Next Period

1. Perform propulsion and aerodynamic regressions with the updated engine deck.
2. Update the bounds of the regressions to 6,000-ft altitude (AFE) to allow for smooth transition into landing.
3. Develop FPP for all other chosen off-design mission routes.



Project 055 Noise Generation and Propagation from Advanced Combustors

**Georgia Institute of Technology
Raytheon Technologies Research Center**

Project Lead Investigator

Timothy Lieuwen
Professor
Daniel Guggenheim School of Aerospace Engineering
Georgia Institute of Technology
270 Ferst Drive (M/C 0150)
Atlanta, GA 30332-0150
404-894-3041
tim.lieuwen@aerospace.gatech.edu

University Participants

Georgia Institute of Technology (GT)

- P.I.s: Prof. Timothy Lieuwen, Prof. Suresh Menon, Prof. Adam Steinberg, Dr. Vishal Acharya, Benjamin Emerson, David Wu
- FAA Award Number: 13-C-AJFE-GIT-058
- Period of Performance: February 5, 2020 to September 30, 2024
- Tasks:
 - 1. Facility development at GT**

This task addresses the design of experiments that will be performed at GT. The task involves coordination between the teams to develop and define the aerodynamic design of a rich-quench-lean (RQL), quick quench, lean burn combustor for this study. This task is led by Tim Lieuwen and Adam Steinberg, with support from Ben Emerson and David Wu.
 - 2. Simulations of the GT experiment**

This task includes simulating the GT experiment, with a focus on the pre-combustion flow dynamics, flame dynamics, and post-combustion dynamics of pressure and entropy disturbances. This task is led by Suresh Menon.
 - 3. Reduced-order modeling**

This task consists of creating a reduced-order model (ROM) framework for the unsteady response of the flame and the generation of entropy disturbances due to unsteady heat release. This task is led by Vishal Acharya.

Raytheon Technologies Research Corporation (RTRC)

- P.I.s: Dr. Jeffrey Mendoza, Dr. Duane McCormick, Dr. Julian Winkler, Dr. Lance Smith
- FAA Award Number: 13-C-AJFE-GIT-058 (subaward through GT)
- Period of Performance: February 5, 2020 to September 30, 2024
- Tasks:
 - 4. Facility development at RTRC**

This task addresses the design of experiments that will be performed at RTRC. The task involves coordination between the teams to develop and define the aerodynamic design of an RQL combustor for this study. This task is led by Jeffrey Mendoza, Lance Smith, and Duane McCormick.
 - 5. Post-combustion modeling**

This task consists of both post-processing and simulation efforts. First, the post-combustion simulation data from the simulation of the GT experiment are mined to investigate the dynamics of entropy



fluctuations and their transport. Next, simulations are used to model noise propagation in the post-combustion architecture of the engine. The simulations are split across the different sections: nozzle, turbine, and far-field. This task is led by Jeffrey Mendoza and Julian Winkler.

Project Funding Level

FAA funding: \$4,500,000 (GT: \$2,500,000; RTRC: \$2,000,000)

Cost-sharing: \$4,273,000 (GT: \$2,273,000 from AE school; RTRC: \$2,000,000 from company funds)

Total funding: \$8,773,000

Investigation Team

Georgia Institute of Technology

Prof. Tim Lieuwen, (P.I.), lead P.I. responsible for overseeing all tasks; specifically, he leads the GT experiments and design in Tasks 1 and 2, along with Professor Steinberg. In addition, he co-leads the modeling tasks in Task 1 for pre-combustion, flame response, and post-combustion modeling, along with Dr. Acharya.

Prof. Adam Steinberg, (co-P.I.), responsible for design of experiment diagnostics and measurements.

Prof. Suresh Menon, (co-P.I.), responsible for simulations of the GT experiment.

Dr. Vishal Acharya, (co-P.I.; principal research engineer), responsible for all modeling tasks for the pre-combustion, combustion, and post-combustion physics, along with Professor Lieuwen. In addition, as administrative coordinator, he is responsible for general project management, such as project deliverables, group meetings, and interfacing with the FAA project manager.

Dr. Benjamin Emerson, (co-P.I.; principal research engineer), responsible for designing and maintaining experimental facilities, as well as experimental operations and management, and graduate students' safety.

David Wu, (co-P.I.; research engineer-II), responsible for designing and maintaining experimental facilities, as well as experimental operations and management, and graduate students' safety.

Dr. Achyut Panchal, (research engineer), simulation of the GT experiment.

Shivam Patel, (graduate student), maintenance, construction, and operation of the experiment at GT.

Sungyoung Ha, (graduate student), lead experimentalist on the GT rig.

Jananee, (graduate student), responsible for optical diagnostics on the GT rig.

Parth Patki, (graduate student), the hydrodynamics modeling subtask (pre-combustion disturbances).

Raytheon Technologies Research Corporation

Dr. Jeffrey Mendoza, (P.I.; technical fellow acoustics), leads the RTRC team and oversees its contributions to the project. He leads the subtasks related to modeling, measurements, and simulation for post-combustion disturbances, nozzle interactions, turbine interactions, and far-field sound propagation.

Dr. Lance Smith, (co-P.I.; technical fellow combustion), design and measurements of the RTRC experiment. He works closely with the GT team to ensure similarities between both experiment setups.

Dr. Duane McCormick, (co-P.I.; principal research engineer), design and measurements of the RTRC experiment as well as finite-element calculations in the design process.

Dr. Julian Winkler, (co-P.I.), responsible for the simulation tasks at RTRC and focuses on post-combustion disturbances, nozzle interactions, turbine interactions, and far-field sound propagation.

Dr. Jordan Snyder, design, measurements, and data processing using tunable diode laser absorption spectroscopy and chemiluminescence in the RTRC combustor rig.

Dr. Kenji Homma, far-field sound propagation simulations.

Dr. Aaron Reimann, ROM and high-fidelity (HiFi) modeling of the propagation of direct and indirect noise sources through the turbine nozzle and supports the far-field sound propagation simulations.

Dr. Sudarshan Koushik, post-processing the GT large eddy simulation (LES) data to model post-combustion disturbances.

Project Overview

The objective of this project is to develop and validate physics-based design tools that can predict noise production mechanisms and their relative dominance, and ultimately reduce the noise output of future engines. The motivation for this project stems from recent and future advances in aircraft engine technology. High-bypass engine technology has significantly reduced the traditionally dominant engine noise sources, namely fan and jet exhaust noise. Noise generated in the combustor has become a dominant source of engine noise for future advanced aircraft designs. In addition, as

combustors evolve to increase efficiency and decrease pollutant emissions, methods for predicting and mitigating combustion noise have severely lagged, and legacy methods are insufficient to predict noise from next-generation combustors. This drawback has motivated the objective of this project, which addresses the critical need for physics-based design tools. The resultant understanding of noise generation and propagation, along with validated noise prediction tools, will enable more rapid and cost-effective designs of low-noise engines for future aircraft.

The project objectives will be achieved through a program of cooperative experiments, high-fidelity simulations, and physics-based ROM. The physical processes involved are tightly coupled and directly determine the project tasks, as shown in Figure 1.

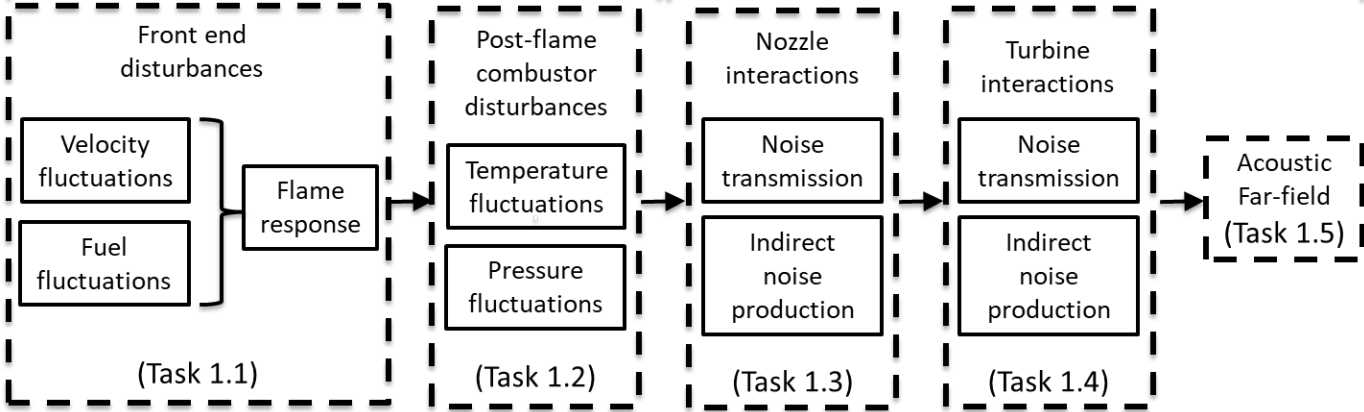


Figure 1. Physical processes and project tasks for noise generation.

The physics of noise generation begins with source disturbances upstream of the combustion zone, which involve unsteady dynamics in the flow and incoming fuel (spray), followed by the response of the combustion zone (flame) to these upstream disturbances. The fluctuations in the unsteady heat release led to the generation of pressure and entropy fluctuations. These fluctuations propagate further downstream in the combustor, interact with the nozzle and turbine, and eventually lead to far-field sound generation. Given the complex interplay of unsteady physics in the different parts of the engine, developing a ROM is challenging.

An important goal of this project is to generate high-quality reference data from both measurements and validated high-fidelity simulations, including measurements of the flow, spray, and flame unsteadiness in the head end of the combustor. Subsequently, the secondary combustion zone is characterized. The generation of entropy and pressure disturbances is then characterized through measurements of temperature and pressure fluctuations, followed by measurements of noise reflection and transmission through the turbine and nozzle section, and sound measurements in the far field. The measurements are accompanied by LES and finite-element simulations that are validated against the measurements. Collectively, these data are generated across a range of operating parameters and provide a source database for the modeling task.

The main goal of this project is to develop a robust design tool that can predict noise at operating points for which prior measurements or data are unavailable. To achieve this goal, two major tasks are necessary. First, ROM and frameworks must be developed for different aspects of the engine architecture: flow/spray models, flame response models, entropy generation models, entropy propagation models, nozzle interaction models, turbine interaction models, and far-field noise generation models. The ROM for each of these aspects involves simplifications and assumptions that are validated against the source database. The validation study and iterative improvement of model predictions serve as the second task to achieve this goal.

In this report, we summarize the efforts of both teams from October 2022 to September 2023. The efforts primarily include improvements to the GT rig to achieve a better match with RTRC experiments as well as RTRC rig campaigns with the Continuous Lower Energy, Emissions, and Noise (CLEEN) rig. In addition, ROM frameworks and simulations have been further advanced. A workflow has been established to transfer simulation data to ROM tasks, and multiple subtask

benchmarking targets have been identified. Finally, task input-output relationships among the various transfer functions have been identified, in the first step toward building the toolchain implemented in the design tool.

Task 1 – Facility Development at GT

Georgia Institute of Technology

Objective

The objective of this task was to make improvements and additional measurements with the RQL combustor designed in the previous year. The first portion of this year was dedicated to the manufacturing and assembly of new components. After the combustor was installed at the GT facility, diagnostic tools were installed to measure the flame and pressure dynamics. A test matrix was developed and used to enable comparison and validation of the GT and RTRC data, particularly at the overlapping points of the approach condition.

Research Approach

In the previous years, we conducted an iterative cycle of tests, data analysis, and rig improvements. Last year, the rig was updated with a stronger liner frame, improved windows, and a more reliable igniter. This year, the rig was used to conduct another data campaign. Measurements focused on acoustics data, with companion high-speed chemiluminescence imaging. Test conditions focused on the baseline approach point that was established by Raytheon. A test matrix was established around this point, and was set up with perturbations to investigate different heat release ratios and flow rates for the head end vs. the quench zone. These perturbations were detailed to additionally match (or nearly match) some of the perturbations in the Raytheon test matrix. The test matrix also included an extra combustor inlet temperature perturbation with acoustics data only, to understand the sensitivity of tonal noise that can confound the interpretation of broadband noise. The RTRC test points have been redacted from this report, and only GT parameters are presented herein. Figure 2 shows the test matrix design.

Chemiluminescence Data?	Notes	Test Factor	Total Airflow	Swirl / (Sw + Q)	Fuel %	P3 [psi] (upstream of swirler)	T3 [F]	Swirler Phi	Global phi	Quench/Main Split	Main Air [lb/s]	Quench Air [lb/s]	Window Air [lb/s]	Total Air [lb/s]	Primary Fuel [lb/hr]	Secondary Fuel [lb/hr]	Total Fuel [lb/hr]	FAR4	Total Air	FAR4 Eng
Yes	Z0. Shakedown (Approach point)	Z0		29%	100%	118	752	1.487	0.37	2.50	0.207	0.517	0.103	0.827	22.6	52.7	75.2	0.025	1.034	0.020221
Yes	1. Low swirler flow, match global phi	1	100%	26%	100%	118	752	1.662	0.37	2.91	0.185	0.539	0.103	0.827	22.6	52.7	75.2	0.025	1.034	0.020221
Yes	2. High swirler flow, match global phi	2	100%	32%	100%	118	752	1.346	0.37	2.17	0.228	0.495	0.103	0.827	22.6	52.7	75.2	0.025	1.034	0.020221
Yes	3. Low swirler flow, match swirler phi	3	100%	26%	89%	118	752	1.487	0.33	2.91	0.185	0.539	0.103	0.827	20.2	47.1	67.8	0.023	1.034	0.018093
Yes	4. High swirler flow, match swirler phi	4	100%	32%	110%	118	752	1.487	0.41	2.17	0.228	0.495	0.103	0.827	24.9	58.2	83.1	0.028	1.034	0.022342
Yes	5. High FAR4. Drop airflow a little to maintain P	5	92%	29%	115%	118	752	1.830	0.46	2.45	0.193	0.473	0.103	0.769	26.0	60.6	86.5	0.031	0.961	0.025004
No	6. Low T3. Raise airflow a little to maintain P	6	104%	29%	100%	118	552	1.415	0.36	2.45	0.217	0.532	0.103	0.852	22.6	52.7	75.2	0.025	1.065	0.01962

Figure 2. Test matrix design for the 2023 test campaign.

	Case numbers	Core air (g/s)	Quench air (g/s)	Fuel (g/s)	T3 (K) (± 5K)	P upstream of swirler (psi)	Notes
Match (Z0)	001, 002	94	235	9.5	655	124	
Low swirler flow, match global phi (Z1)	003, 004	84	245	9.55	655	122	
High swirler flow, match global phi (Z2)	007, 008	104	225	9.37	655	114	
Low swirler flow, match swirler phi (Z3)	009, 010	84	245	8.52	655	119	
High swirler flow, match swirler phi (Z4)	005, 006	104	225	9.72	655	120	
High FAR (Z5)	011, 012	88	215	11	655	117	
Near lean blowoff 1	013, 014	94	235	9.28	655	114	
Near lean blowoff 2	015, 016	94	235	9.96*	655	115	Fuel flow rate measurement seems off a bit
Rich	017, 018	94	235	12.65	655	127	

Figure 3. Achieved test conditions.

A series of test campaigns was conducted to work through the test matrix. The actual test points achieved are shown in Figure 3. Repeat tests were conducted for all cases, to assess repeatability. We first review the repeatability of the measurements. Figures 4-9 compare proper orthogonal decomposition through principal orthogonal dynamics (POD) analyses of the chemiluminescence data, showing the first six modes. The figures compare the mode shapes and temporal spectra, as well as the modal energies. The RTRC test points have been redacted from this report, and only GT parameters are presented herein. In general, these comparisons showed excellent repeatability when each test point was revisited.



Figure 4. GT combustor repeatability study, baseline (Z0) approach condition.

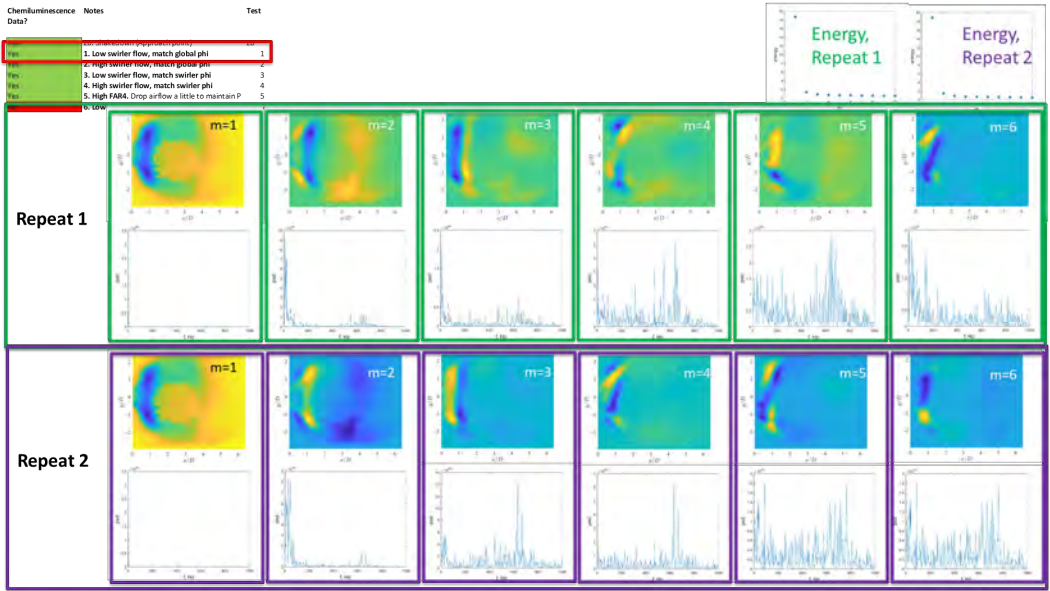


Figure 5. GT combustor repeatability study, condition 1.

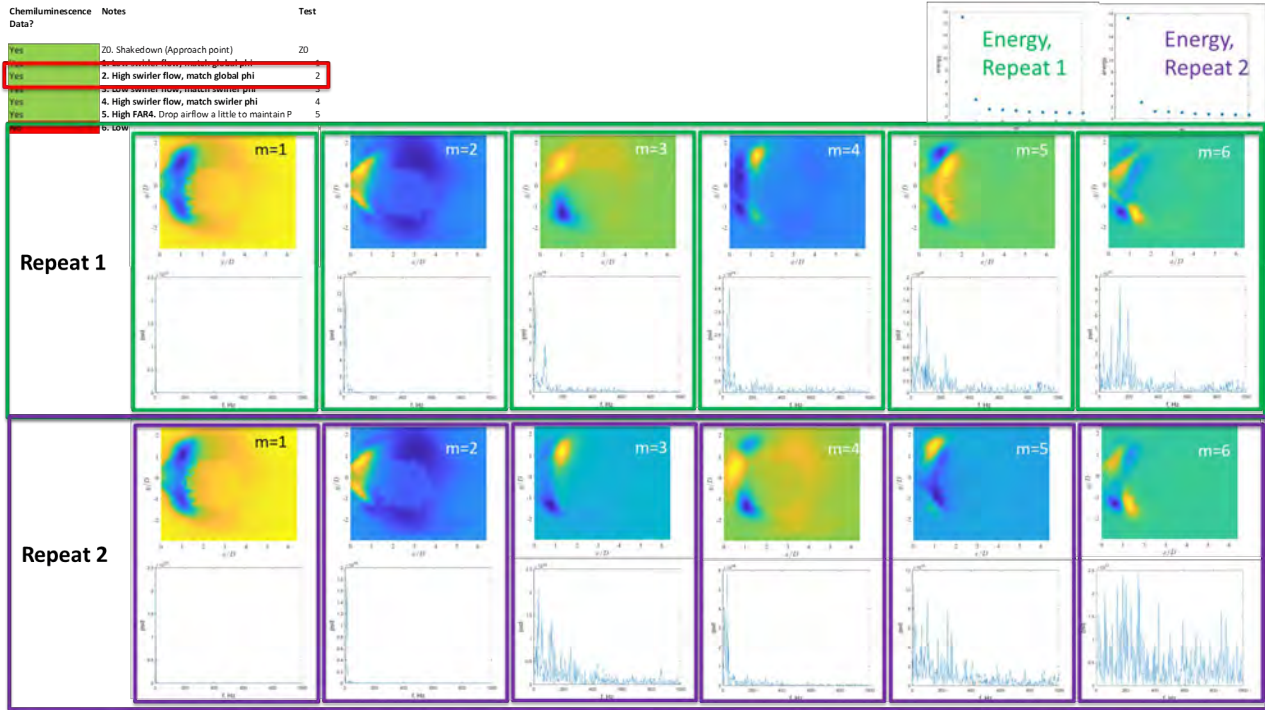


Figure 6. GT combustor repeatability study, condition 2.

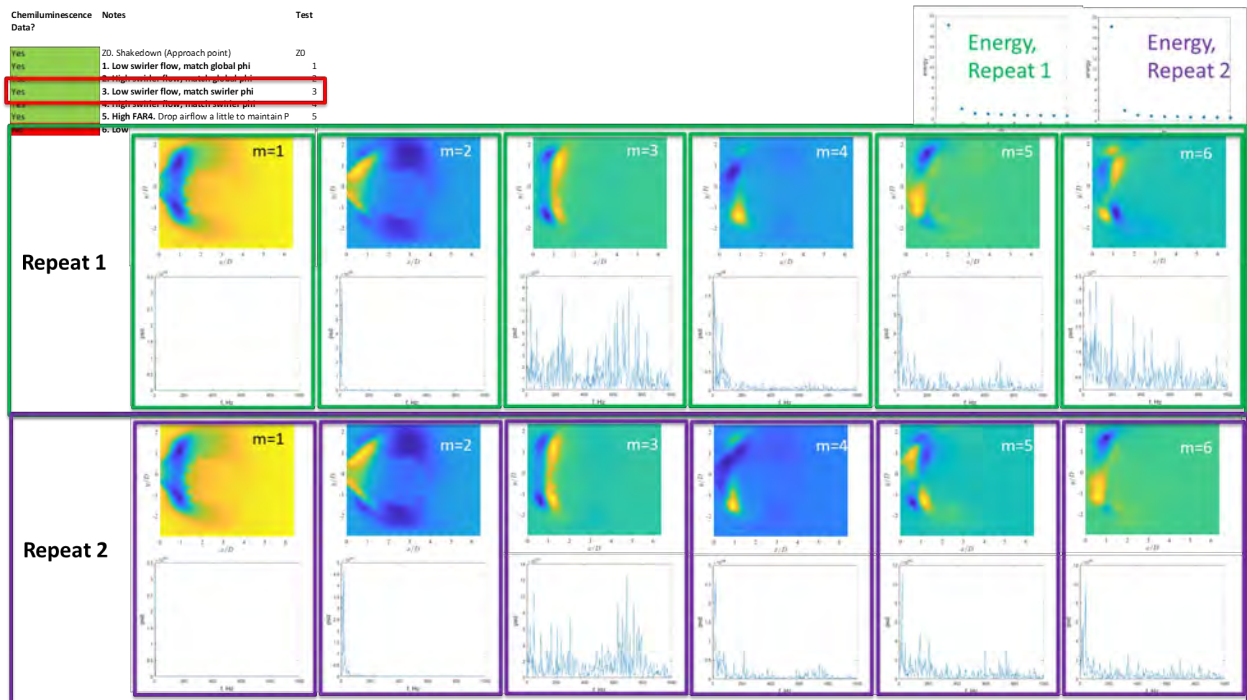


Figure 7. GT combustor repeatability study, condition 3.

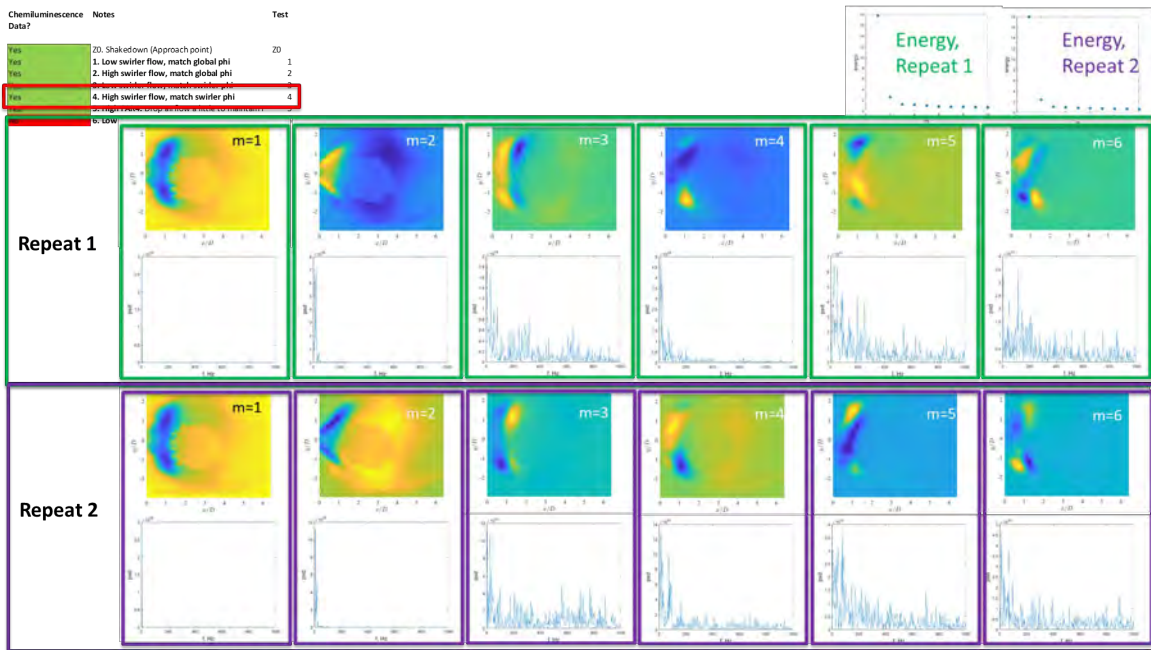


Figure 8. GT combustor repeatability study, condition 4.

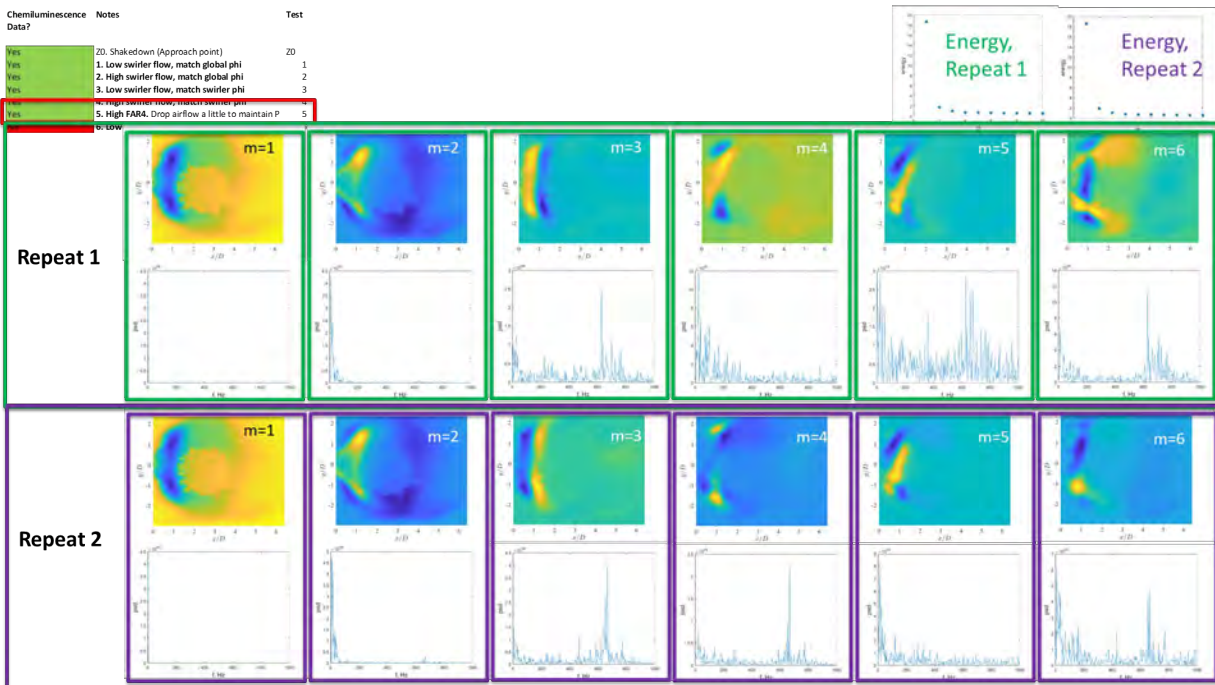


Figure 9. GT combustor repeatability study, condition 5.

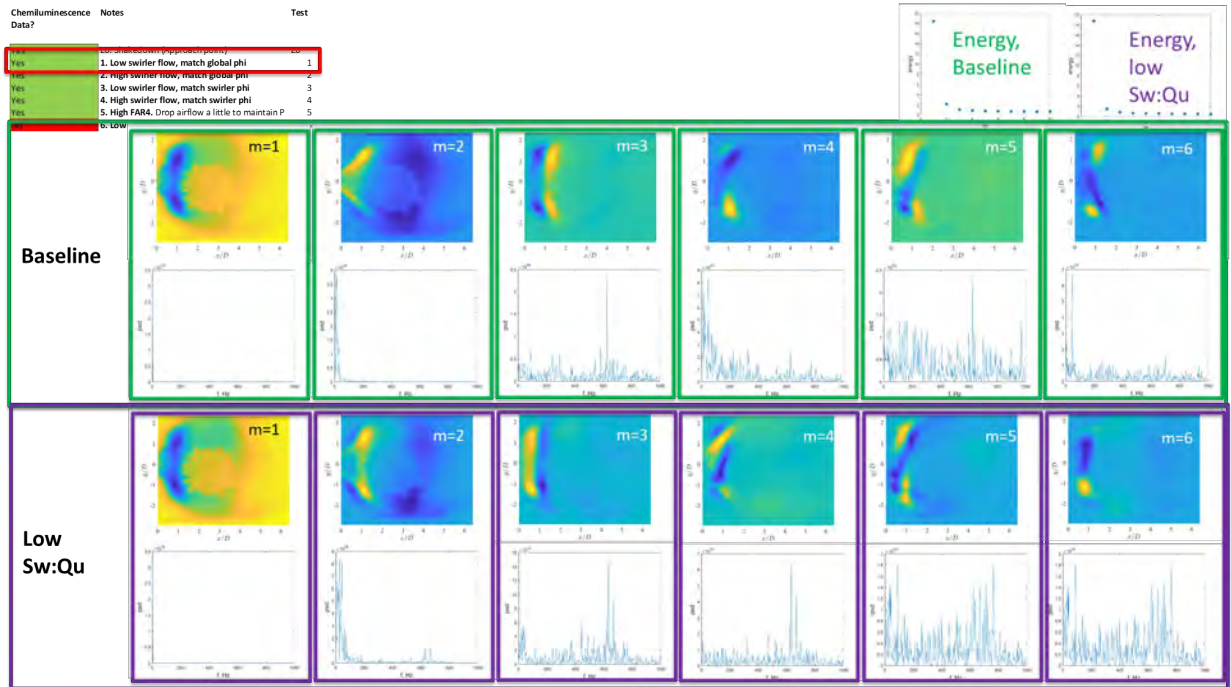


Figure 10. GT combustor study, first six chemiluminescence POD modes; comparison of condition 1 to the baseline (Z0) approach condition. Effect of reduced swirler-to-quench flow.

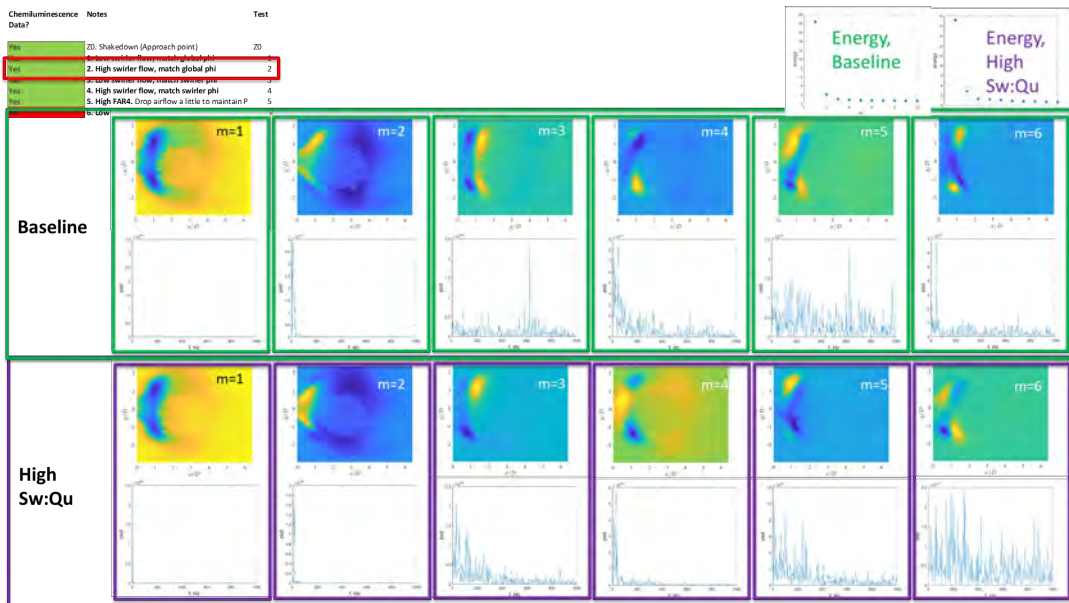


Figure 11. GT combustor study, first six chemiluminescence POD modes; comparison of condition 2 to the baseline (Z0) approach condition. Effect of increased swirler-to-quench flow.

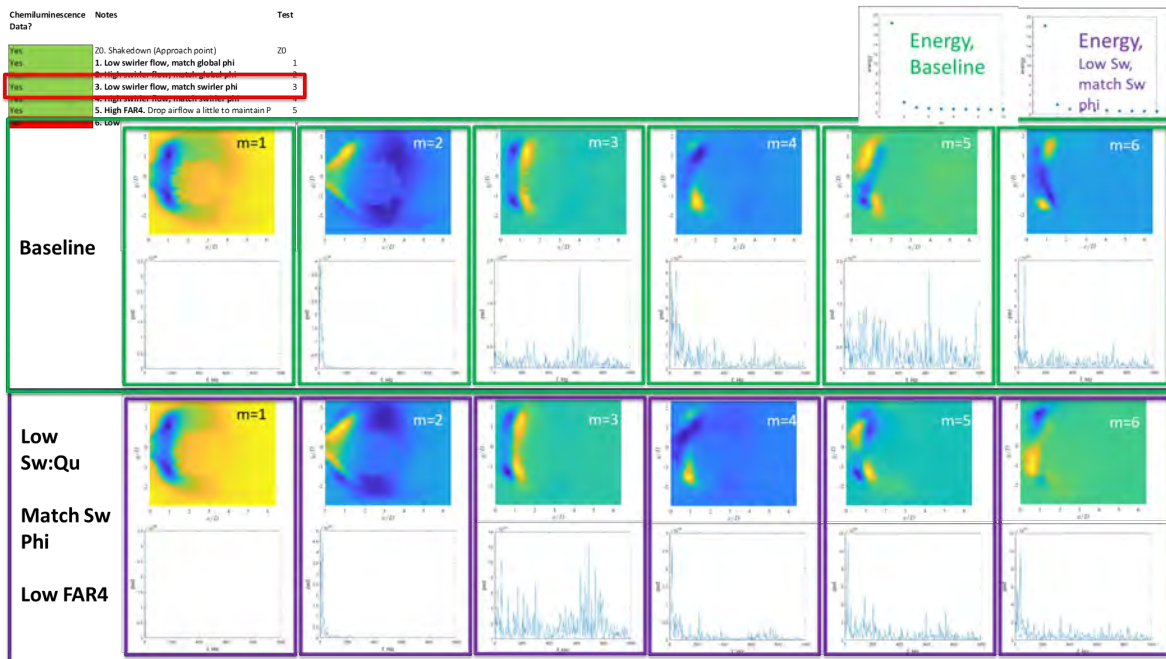


Figure 12. GT combustor study, first six chemiluminescence POD modes; comparison of condition 3 to the baseline (Z0) approach condition. Effect of reduced quench equivalence ratio (reduced quench zone heat release) relative to head-end heat release.

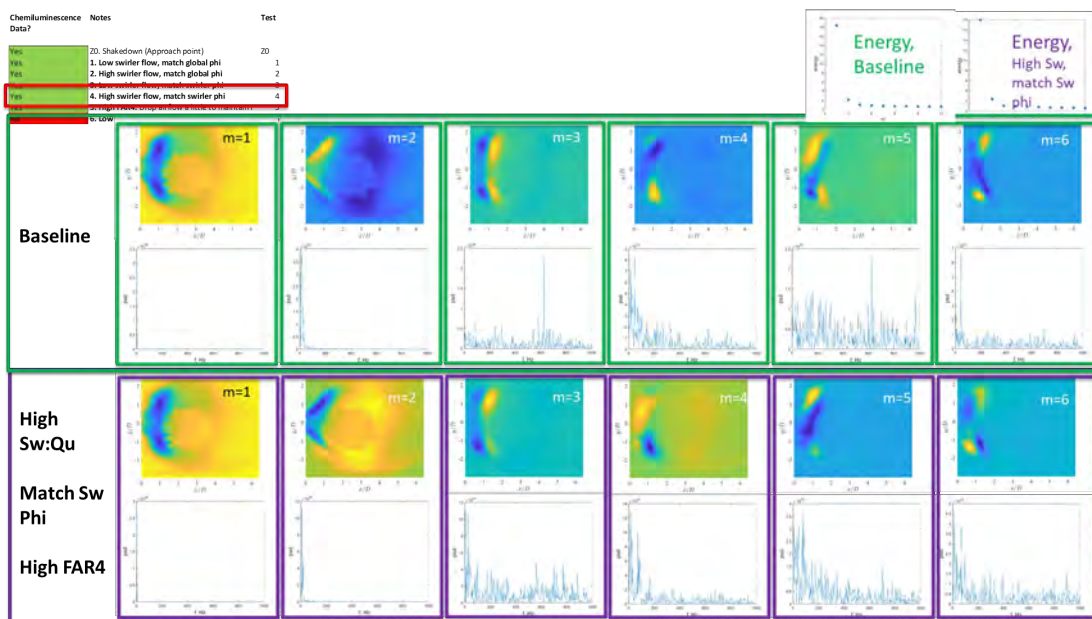


Figure 13. GT combustor study, first six chemiluminescence POD modes; comparison of condition 4 to the baseline (Z0) approach condition. Effect of increased quench equivalence ratio (increased quench zone heat release) relative to head-end heat release.

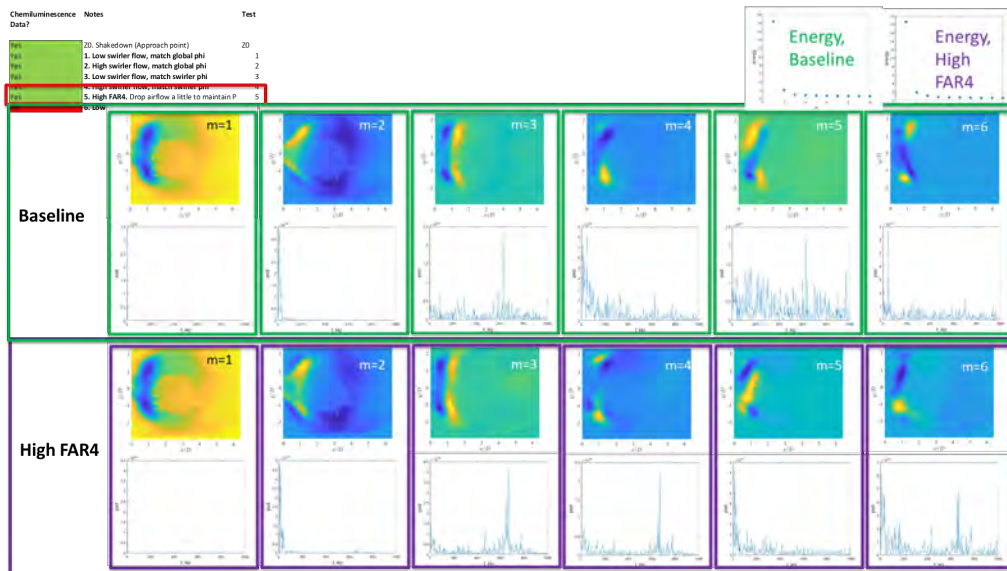


Figure 14. GT combustor study, first six chemiluminescence POD modes; comparison of condition 5 to the baseline (Z0) approach condition. Effect of increased overall heat release (increased FAR4, increased turbine inlet temperature).

Next, we review comparisons of the acoustic data from each case to the baseline (Z0) approach case. The most notable result is the sensitivity of tonal noise (~600 Hz) to these perturbations. Interestingly, these perturbations substantially manipulate the quench zone, and the chemiluminescence images of the head end are insensitive to these operating-condition perturbations. These observations suggest that this mid-range frequency (~600 Hz) noise is produced in the quench zone.

Chemluminescence Data?	Notes	Test
1	1. Low swirler flow, match global phi	1
2	2. High swirler flow, match global phi	2
3	3. Low swirler flow, match swirler phi	3
4	4. High swirler flow, match swirler phi	4
5	5. High FAR4, Drop airflow a little to maintain P	5
6	6. Low T3, Raise airflow a little to maintain P	6

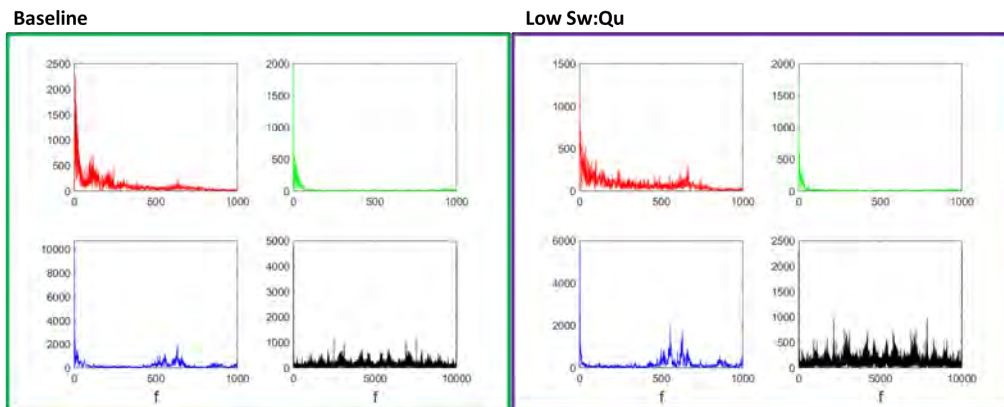


Figure 15. GT combustor study, acoustic spectra from the four ramp acoustic ports; comparison of condition 1 to the baseline (Z0) approach condition. Effect of reduced swirler-to-quench flow.

Chemluminescence Data?	Notes	Test
Yes	Z0. Shakedown (Approach point)	Z0
Yes	1. Low swirler flow, match global phi	1
Yes	2. High swirler flow, match global phi	2
Yes	3. Low swirler flow, match swirler phi	3
Yes	4. High swirler flow, match swirler phi	4
Yes	5. High FAR4. Drop airflow a little to maintain P	5
Yes	6. Low T3. Raise airflow a little to maintain P	6

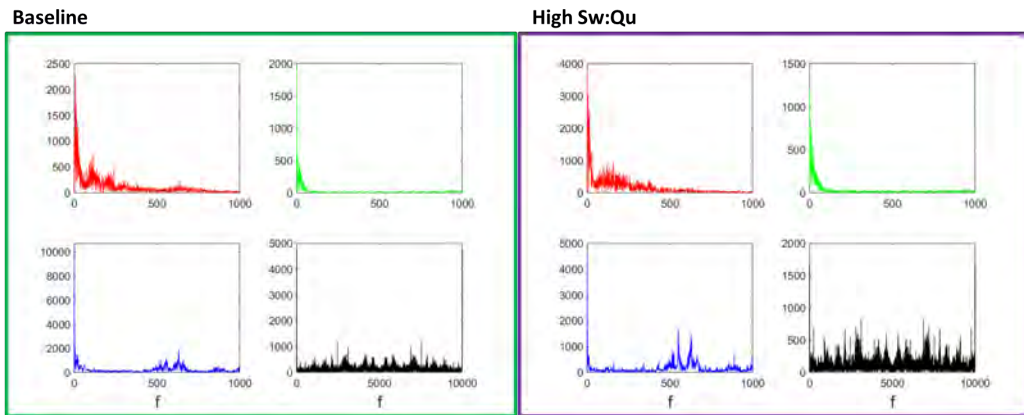


Figure 16. GT combustor study, acoustic spectra from the four ramp acoustic ports; comparison of condition 2 to the baseline (Z0) approach condition. Effect of increased swirler-to-quench flow.

Chemluminescence Data?	Notes	Test
Yes	Z0. Shakedown (Approach point)	Z0
Yes	1. Low swirler flow, match global phi	1
Yes	2. High swirler flow, match global phi	2
Yes	3. Low swirler flow, match swirler phi	3
Yes	4. High swirler flow, match swirler phi	4
Yes	5. High FAR4. Drop airflow a little to maintain P	5
Yes	6. Low T3. Raise airflow a little to maintain P	6

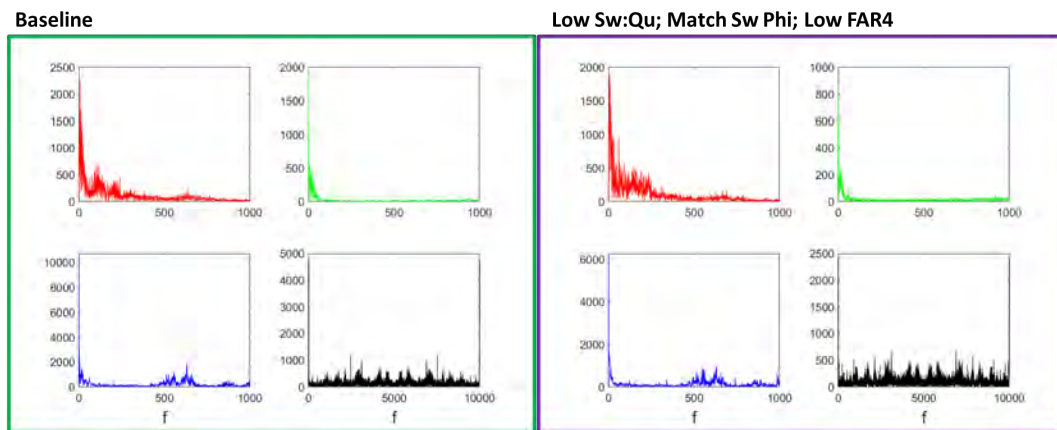


Figure 17. GT combustor study, acoustic spectra from the four ramp acoustic ports; comparison of condition 3 to the baseline (Z0) approach condition. Effect of reduced quench equivalence ratio (reduced quench zone heat release) relative to head-end heat release.

Chemluminescence Data?	Notes	Test
20	Shakedown (Approach point)	20
1	1. Low swirler flow, match global phi	1
2	2. High swirler flow, match global phi	2
3	3. Low swirler flow, match swirler phi	3
4	4. High swirler flow, match swirler phi	4
5	5. High FAR4. Drop air flow a little to maintain P	5
6	6. Low T3. Raise air flow a little to maintain P	6

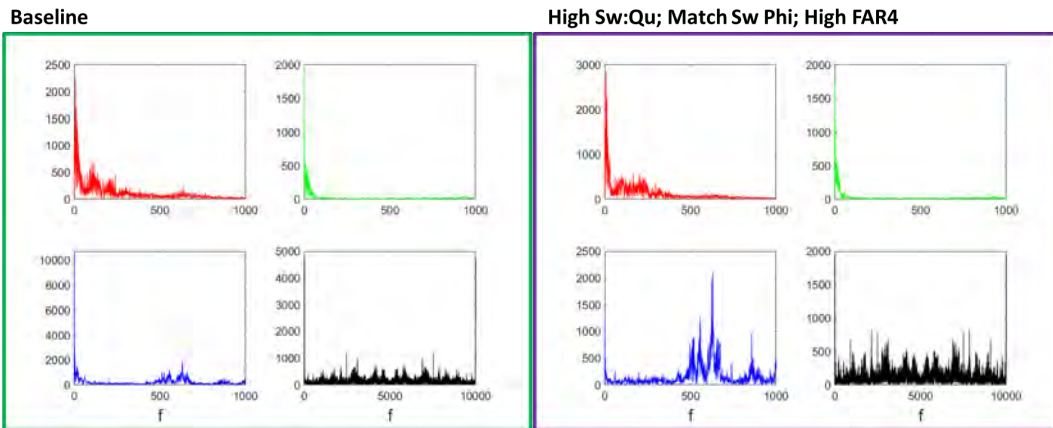


Figure 18. GT combustor study, acoustic spectra from the four ramp acoustic ports; comparison of condition 4 to the baseline (Z0) approach condition. Effect of increased quench equivalence ratio (increased quench zone heat release) relative to head-end heat release.

Chemluminescence Data?	Notes	Test
20	Shakedown (Approach point)	20
1	1. Low swirler flow, match global phi	1
2	2. High swirler flow, match global phi	2
3	3. Low swirler flow, match swirler phi	3
4	4. High swirler flow, match swirler phi	4
5	5. High FAR4. Drop air flow a little to maintain P	5
6	6. Low T3. Raise air flow a little to maintain P	6

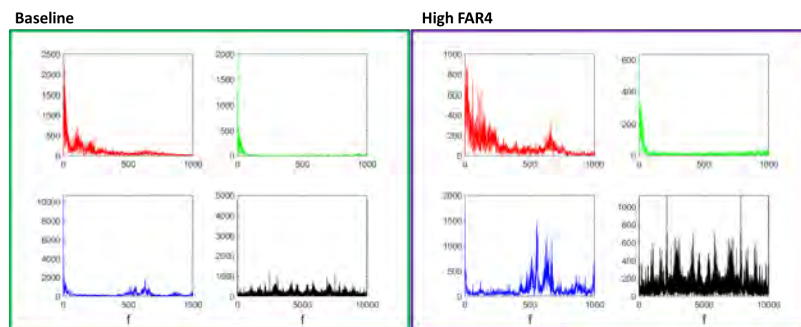


Figure 19. GT combustor study, acoustic spectra from the four ramp acoustic ports; comparison of condition 5 to the baseline (Z0) approach condition. Effect of increased overall heat release (increased FAR4, increased turbine inlet temperature).

We attempted to correlate the acoustic pressure signals with the heat release rate (HRR) data from the high-speed chemiluminescence. Correlations with the spectra of the HRR from the head-end zone with the acoustic data were poor, thereby suggesting coupled physics in the quench zone. During this analysis, the GT team realized that the analysis of HRR vs. acoustics coherence is a nuanced and requires further development for the differentiation of direct noise, indirect noise, narrowband sound, and background noise. A major pivot in this task has been the development of these methods and dissemination to the combustion community. These developments are further detailed in this report.



Milestones

- The GT team has completely re-designed the combustor and its structural support/plumbing layout.
- The GT team has completed a test cell cleanout and procurement, manufacturing, and assembly of a new combustor.
- The GT team has shaken down the combustor, overcome all hurdles uncovered in the shakedown, and begun testing the new combustor.

Major Accomplishments

The designed RQL combustor was manufactured and installed at the GT facility. The rig has been re-designed and rebuilt to enable higher-quality data, better durability, and improved matching to the RTRC rig.

Publications

None.

Outreach Efforts

None.

Awards

None

Student Involvement

- **Amalique Acuna (GT):** Graduate Student. Mr. Acuna works on and operates the experiment at GT. Mr. Acuna has graduated.
- **Shivam Patel (GT):** Graduate Student. Mr. Patel is funded on a NASA ULI contract, but he actively contributes to the maintenance, construction, and operation of the experiment at GT.
- **Sungyoung Ha (GT):** Graduate Student. Mr. Ha is the lead experimentalist on the GT rig.
- **Jananee (GT):** Graduate student. Jananee is responsible for the optical diagnostics on the GT rig.
- **Archit Bapat (GT):** Graduate student. Mr. Bapat is funded as a teaching assistant. He is assisting with the optical diagnostics on the GT rig.

Plans for Next Period

The GT rig team plans to continue the measurement campaign during the next period, with the inclusion of additional diagnostic methods throughout the process.

Task 2 – Simulations of the GT Experiment

Georgia Institute of Technology

Objectives

The first objective of this task is to validate and justify the compressible reactive LES approach for modeling the GT experimental rig at match point. In addition to the match point, the second objective is to evaluate the LES's ability to capture trends across different conditions. The last objective is to collect time-dependent three-dimensional (3D) snapshots of conservative variables from the LES for GT experimental conditions and transfer those findings to the RTRC and GT modeling teams. Sample post-processing scripts for computing additional variables from the 3D snapshots will also be provided.

Research Approach

Solver details

A fully compressible Eulerian finite-volume formulation for the gas phase and a Lagrangian formulation for the liquid phase are used in this study. An eddy-viscosity approach with a one-equation subgrid kinetic energy (k_{sgs}) model is used for the closure of gas-phase subgrid-scale fluxes. Because regions in which turbulence is not well established may exist in the plenum or outflow duct, the k_{sgs} -equation coefficients are set to constant values rather than being dynamically computed. Subgrid dispersion for spray particles is modeled with a stochastic separated flow model. Modeling of dense spray,

corresponding compressible volume blockage effects, and breakup are also available, as we have previously shown, but these conditions are not considered herein; instead, a dilute injection of spray is considered. A well-established secondary breakup model based on Kelvin–Helmholtz instability is used, and its effect is evaluated in this study.

The combustion is modeled via a finite-rate kinetics approach, by using a two-step, six-species mechanism for kerosene. Subgrid closure for turbulent combustion is provided by a simplified partially stirred reactor model, wherein the mixing time (τ_m) is computed locally by using k_{sgs} , and the chemical time (τ_c) is precomputed for the operating conditions from laminar premixed flame solutions under stoichiometric conditions. Further details about our modeling approach can be found in our recent works and are not repeated herein, for brevity.

The equations are solved at GT with the in-house solver LESLIE. LESLIE is a well-established multi-block, structured, fully compressible finite-volume solver. A hybrid second-order central and third-order upwind method is used for the gas-phase evolution. A fourth-order Runge–Kutta solver is used for solving the Lagrangian equations. For computational efficiency, instead of tracking individual Lagrangian particles, the particles are grouped together in “parcels,” which are tracked in a Lagrangian manner. A particle-per-parcel value of 8 is used in this work, which has been shown to provide a good balance between accuracy and efficiency for gas-turbine combustor LES.

The current version of the GT compressible solver contains three parts: CFDPrecProc, LESLIE, and CFDPstProc. CFDPrecProc is a pre-processor that can perform functions such as creating a grid and setting boundary conditions. LESLIE is a core compressible solver that conducts multi-phase reactive LES. The latest LESLIE code (improved during the Year 2 efforts) outputs 3D snapshots of conservative variables that are directly solved for in our compressible framework, including the density, momentum, total energy, and partial densities. Primitive variables remain required for the computation of noise-related quantities; therefore, CFDPstProc CFD post-processing software is used to read the conservative variable-based 3D snapshots and compute additional primitive quantities. This code is provided to the RTRC and GT ROM teams along with the 3D snapshots. The conservative variables form an exclusive and exhaustive set of variables; therefore, all other quantities can be computed from this set.

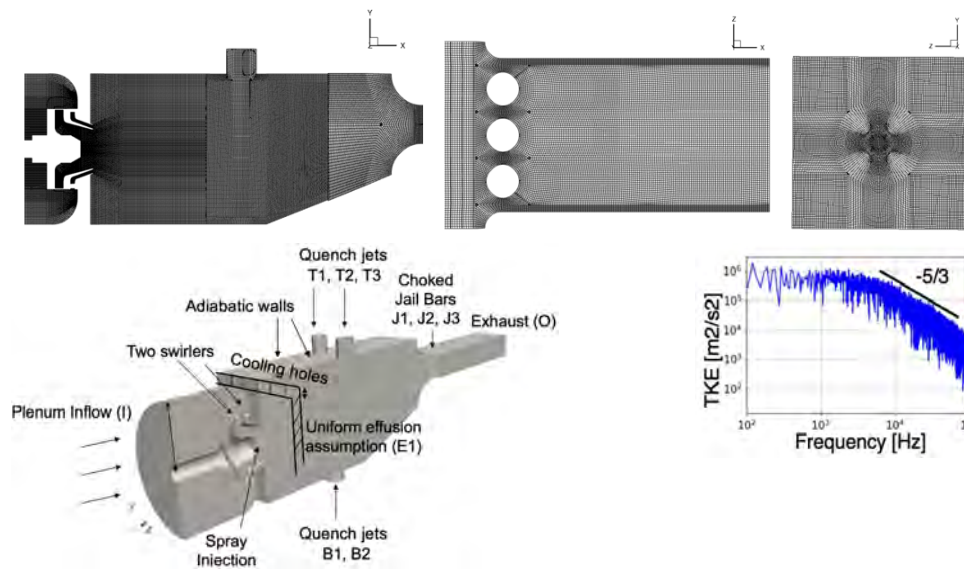


Figure 20. Computational domain for LES. Top: schematics for the multi-block structured grid (main combustor at the center x - y plane, region behind the jail bars at the center x - z plane, and shear-layer region at the y - z plane located at one-third of the axial length of the main combustor). Bottom left: entire computational domain, with key features and corresponding boundary conditions. Bottom right: turbulent kinetic energy (TKE) spectra in the shear layer, showing the inertial subrange captured by LES.

Computational configuration

The computational configuration is shown in Figure 20. The flow from the inlet plenum enters the combustion chamber via two concentric swirlers (one axial and one radial). After the reaction zone, three quench jets on the top, and two on the bottom, are available to reduce the temperature. In addition, multiple small cooling holes are present on the dome plate to decrease the wall temperature. The flow exits the outflow duct through jail bars, which act as a nozzle that chokes the flow.

The boundary conditions are consistent with the findings from GT experiments. All gas-phase inlet boundary conditions are constant mass flow inlets, on the basis of experimental data inputs. The inflow boundary condition (ahead of the inlet plenum [I] and dilution holes [T1, T2, T3, B1, and B2]) is modeled with a characteristic Navier–Stokes boundary condition. The mass flow rate for the main inflow (I) is set as 93.89 g/s (according to GT rig inputs). The total mass flow rates through the top (T1, T2, and T3) or bottom (B1 and B2) dilution holes are 117.03 g/s. The incoming air is at 673.3 K. The flow through the jail bar (J1, J2, and J3) chokes and pressurizes the combustor to the nominal target. With choking, the outflow (O) is supersonic at the domain outlet. The outflow following the choked nozzle is modeled with a sponge boundary condition, but no waves are expected to travel upstream into the combustor chamber from this region, because the nozzle is choked. The quench holes are not resolved; therefore, they are modeled with a porous boundary condition. The mass flow rate specified through the quench holes is 46.72 g/s.

The Lagrangian spray droplets are injected in a stochastic manner with two concentric injectors. The mass flow rate is 2.4 g/s through the primary injector and 6.89 g/s through the secondary injector. In the absence of any experimental measurements for this injector, a log-normal size distribution with Sauter mean diameter of 30 μm and 55 μm is injected in the absence or presence of secondary breakup modeling, respectively. These modeling choices are similar to previous gas-turbine LES (Patel & Menon, CF, 2008, Panchal & Menon, CF, 2022). The primary injector is modeled as a solid cone injector with a 60° angle; the secondary injector surrounds the primary injector and is modeled as a hollow cone injector with 90° and 120° inner and outer angles, respectively. The injection temperature of the liquid fuel is 330 °K, and the velocities are set to 25 m/s. This dilute injection occurs 1 mm downstream of the actual injector plate. This injection procedure is empirical but could be improved in the future, on the basis of experimental insights.

The multi-block structured grid has 6.8 million cells and 4,571 blocks, and grid clustering is applied to the near region of the shear flow from the swirler and jail bars. For handling geometrical complexities, six multi-block structure grids are generated with hanging nodes, which are stitched together via an interpolation technique of the same order as the numerical scheme used. Shear layers are resolved with 10–15 points across, and the swirlers have 10 or more points along their span, in agreement with previous LES. Small quench holes on the dome plate are not resolved, but a pre-specified mass flow rate is injected through these holes with a porous boundary condition, as discussed below. For demonstrating the sufficiency of the LES grid, the turbulent kinetic energy is computed at a representative point in the shear layer, as shown in Figure 20, to capture the inertial subrange. This result has been confirmed at other points within the combustor, e.g., cooling jets, swirling shear layer, etc., but these data are not shown herein, for brevity.

The LES solver is parallelized, and the simulations are run on 1,440 cores. The flow-through time of the combustor is estimated to be 8 ms, according to the entire length of the computational domain and a reference bulk velocity of 30 m/s. Initial transients are neglected for at least the two flow-through times or until the chamber pressure and volume-integrated HRR stabilize. The statistics are then collected over at least 10 additional flow-through times. A simulation for a single flow-through time uses 51,840 CPU hours on GT’s supercomputing cluster (Partnership for an Advanced Computing Environment-Phoenix) with Intel Ivy-bridge i7 processors.

Operating conditions

After updating the CFD geometry to match the GT experimental rig during year 2, we considered three operating conditions in year 3, all with the same rig. The first simulation, “baseline,” matches the “Z0” GT and RTRC baseline operating conditions and maintains chamber pressure at a target of 0.87 MPa. To evaluate the LES’s ability to predict trends in operating conditions and to generate more data for ROM development, we consider two additional conditions. The next condition uses a higher fuel–air ratio (FAR), in which the fuel mass flow rate is increased by 15%, and the total air mass flow rate is reduced by 8% to maintain the same chamber pressure. This condition coincides with one of the high-FAR conditions in the experimental campaign. The third test is a numerical experiment considering a modified quench-jet configuration, wherein T1 and T3 are shut off, and all air that would come from the quench jets through the top instead comes through the center jet T2. These details are summarized in Table 1. All simulations were run with the same solver and model choices.


Table 1. List of simulated operating conditions.

	Fuel mass flow rate	Air mass flow rate	Quench configuration
Match-point/baseline	9.29 g/s	374.67 g/s	T1, T2, T3, B1, B2
High-FAR	10.68 g/s	344.69 g/s	T1, T2, T3, B1, B2
Quench-1	9.29 g/s	374.67 g/s	T2, B1, B2

Validation

For validation and justification of the LES approach, we compare the simulation results at baseline conditions against GT experiments, as shown in Figure 21(b). The chemiluminescence data from the GT experiments is compared against the numerical time-averaged line-of-sight HRR predictions (in the absence of CH* or OH* from simulations), and show a reasonable match in terms of the flame structure.

Next, to evaluate noise predictions, pressure spectra are computed at several locations within the combustor and are compared against experiments, as shown in Figure 21(c). The probe locations follow both the GT and RTRC experimental rigs; one probe is on the bulkhead, and the remaining four are on the bottom ramp of the combustor before the jail bars, as shown in Figure 21(a). Near the experimental values (250 Hz and 700 Hz), the pressure power spectral density (PSD) from LES shows peaks at 300 Hz and 750 Hz. The sharp decrease in the PSD after 1000 Hz is also present in both rigs, although the GT experiments show a much sharper decline. To reduce the noise from the frequency data, Welch averaging with a sampling frequency of 36 Hz and 50% overlap is used over the entire 166 ms of LES data. As discussed further below, signal sizes longer than 100 Hz appear to be sufficient for LES signal processing in the range of 100–5000 Hz. The same processing methods are also used for the experimental data, but the total signal length is much longer (several seconds).

Sensitivity to modeling and processing choices

Year 2 simulations did not use a secondary breakup model, and their effects had not yet been evaluated. The effect of secondary breakup modeling and LES post-processing methods on flame and noise predictions have now been evaluated. As noted earlier, in the absence of any data for spray atomization and injection, an empirical injection is used. Simulations without a secondary breakup model inject droplets with a Sauter mean diameter of 30- μ m droplets, whereas simulations with a wave breakup model based on Kelvin–Helmholtz instability (Reitz, 1989) inject 55- μ m droplets and allow them to break into smaller droplets through a physics-based approach on their own.

The LES results with and without breakup modeling at the baseline operating condition are compared in Figure 22. In the absence of secondary breakup modeling, the larger droplets require a longer time to evaporate, thus resulting in a less-than ideal HRR, as shown in Figure 22(b). The flame structure is also affected, as shown in Figure 22(a), and the flame structure predicted with secondary breakup modeling is more compact and closer to the experimental measurements in Figure 21(b). The overall flame and flow structures remain qualitatively similar with or without the secondary breakup model; however, the pressure spectra show significant sensitivity. The 750-Hz frequency, which is also prominent in the experiments, is largely missing from the LES predictions without the secondary breakup model. We hypothesized that the changes in the vaporization rate and the HRR due to the secondary breakup modeling might affect the dynamics and thus the pressure signature. Because using a physics-based secondary breakup model is physically a more correct approach, and the results also better match the experimental findings, all other simulations in this work use this default option.

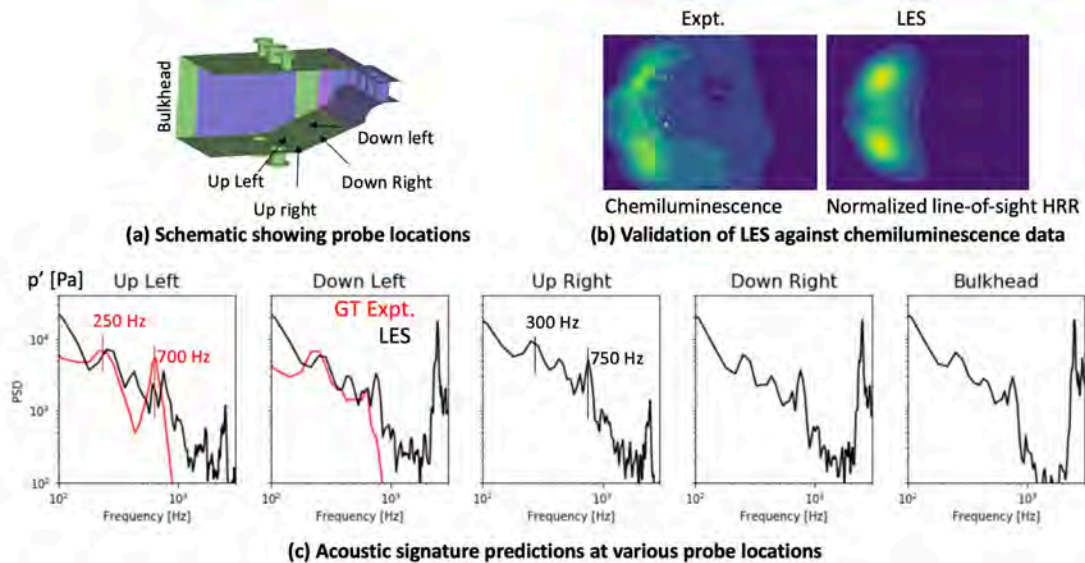


Figure 21. Validation of LES results under baseline conditions against GT experiments. (a) Schematic showing probe locations where acoustic data are collected. (b) Comparison of CH* chemiluminescence data against normalized time-averaged line-of-sight HRR data from LES. (c) Acoustic signature predictions from LES at five probe locations, and comparison against available data from GT experiments. LES results are over a 166-ms time window.

Next, to evaluate the effects of various LES post-processing options on the computed spectra, we conducted several tests on the baseline dataset. Several key conclusions are presented, but the corresponding results are not shown herein for brevity.

- Signal lengths of 50, 100, and 150 ms collected from LES were evaluated. We concluded that 100 ms is sufficiently long to satisfactorily capture frequencies between 100 and 5000 Hz.
- A sampling frequency of 10^4 Hz is sufficient for predictions up to 1000 Hz. Higher frequencies may require a faster sampling rate. The current LES collects 3D snapshots at 10^4 Hz and probe data at 10^6 Hz.
- Local averaging near the probe location does not significantly affect spectra computed with Welch averaging.

Flow and flame structure

The LES can capture 3D unsteady large-scale flow, flame, and spray structures. Representative contours at an instant on z- and y-center slices are shown in Figure 23 for the baseline case. Furthermore, time-accurate LES results are averaged over eight flow-through times. The corresponding mean axial velocity and mean temperature are shown in Figure 24 on the z-center slice for both the baseline and quench-1 conditions. The instantaneous flow shows resolved large-scale turbulence within the combustor and also indicates that the flow remains choked at the jail bar nozzle at all times, thus maintaining the pressure. The flow converts from subsonic to supersonic at this point, and the supersonic flow after the nozzle shows a complex shock structure.

As a result of the swirl, a low-pressure zone is created in the center, and a vortex breakdown bubble (VBB) (also known as a central toroidal recirculation zone) is formed. This behavior has been observed for many other gas-turbine combustors and is a key feature of swirling flows. This combustor has two swirlers, but the observed VBB features remain qualitatively similar to those in past studies with a single swirler. Correspondingly, a negative velocity is observed in the center, as shown by the instantaneous axial velocity contours on the z-center slice in Figure 23(a) and time-averaged contours in Figure 24(a, b). The swirling shear layers are highly turbulent and can provide a zone for vaporization and flame stabilization. Because of the swirling jets, corner recirculation zones are also observed. The instantaneous velocity contours show the effects of the cooling jets near the corners, but these jets dissipate quickly after injection. The quench jets significantly affect the overall flow field by disrupting the continuation of the VBB, at least in the z-center slice shown here.

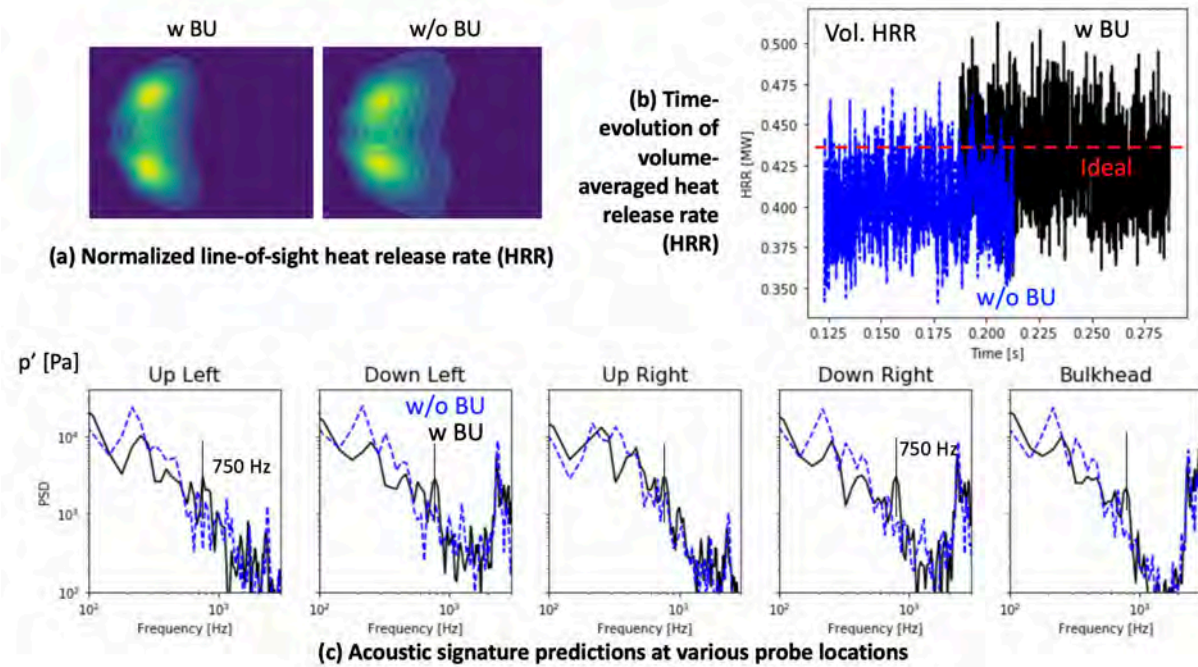


Figure 22. Comparison of LES results with and without secondary breakup modeling in terms of (a) normalized time-averaged line-of-sight HRR data, (b) time-evolution of volume-averaged HRR (with horizontal dashed line showing the ideal HRR, assuming 100% burning), and (c) acoustic signatures at various probe locations. Validation of LES results at baseline conditions against GT experiments. Results over a 100-ms time window are shown to enable one-to-one comparison.

The circulation zone of the VBB remains hot and is filled with combustion products produced by burning. Because of the high temperature, spray vaporization occurs in the surrounding regions. Fuel burning occurs in the shear layers, and the effects of large-scale turbulence on the burning are also apparent (not shown). The quench jets mix with the products, and highly turbulent mixing is observed.

The flow and flame structures are similar for baseline and high-FAR conditions, and their comparison is not shown herein, for brevity. However, because of the changed quench jet configuration, the quench-1 configuration shows a significant modification in the flow field, particularly after the entrance of the quench jet. Because of the increased mass-flow rate through T2, the jet can penetrate almost all way toward the bottom of the combustor, as shown in Figure 24(d). The axial flow adjusts to go from around it (not visible in the z-normal plane), and the jet penetration into the combustor increases by almost 80%. Although the volume-integrated HRR increases for the high-FAR case, as expected, quench-1 does not show a noticeable change in global quantities, although the flow structure is different.

Dynamics

Various quantities, i.e., chamber pressure, volume-integrated HRR, volume-integrated evaporation rate, and mass flow rates through various planes, are continuously monitored during the simulation. To obtain a global measure, the HRR and evaporation rate are also integrated over the entire volume of the combustor, and their time sequence is collected. Their oscillations can contribute to noise generation. In addition, as briefly described above, pressure at various probe locations within the combustor is collected, and Welch averaging is used to compute the PSD.

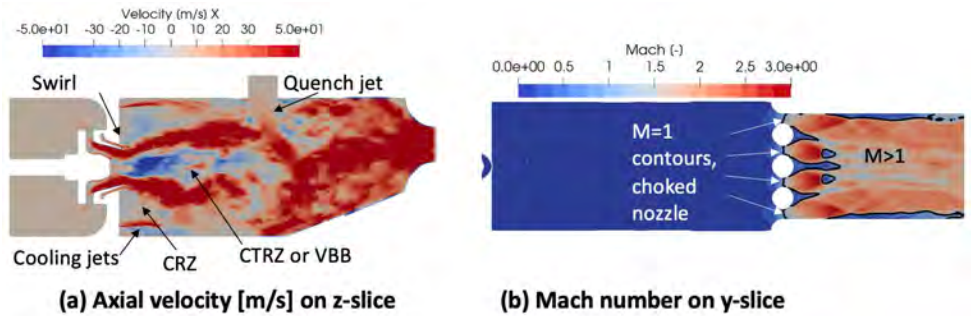


Figure 23. Instantaneous axial velocity and Mach number predicted from LES, shown on the center z slice under the baseline operating condition. CRZ: corner recirculation zone; CTRZ: central toroidal recirculation zone; VBB: vortex breakdown bubble.

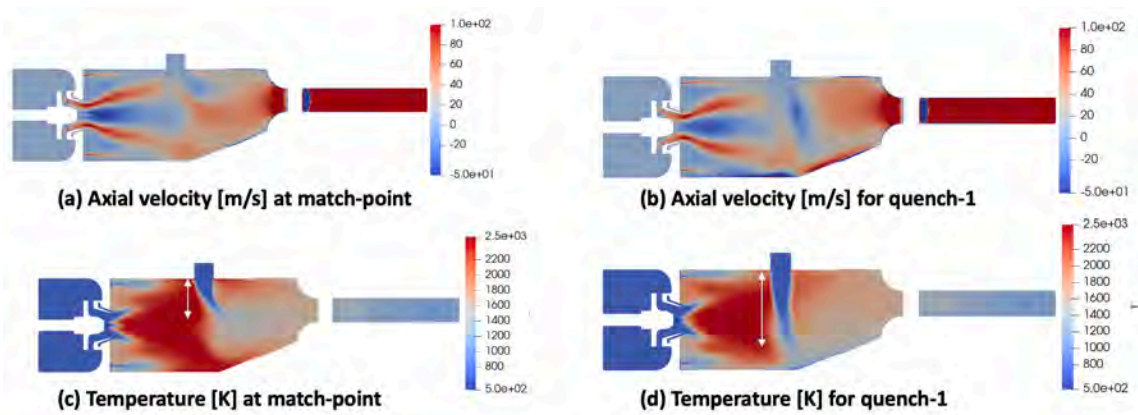


Figure 24. Time-averaged axial velocity (a,b) and temperature (c,d) on the center z slice, predicted from LES at baseline (a,c) and quench-1 (b,d) conditions. The white arrow shows the extent of T2 jet penetration into the domain. Time averaging is over an 80-ms time window to allow for one-to-one comparison.

The results for the baseline configuration (Figure 21) show peaks at 300, 750, 2400, and 4800 Hz. To understand the significance of these findings, we conducted further analyses. Figure 25 shows magnitude and phase of PSD at $f = 2400$ Hz and $f = 4800$ Hz, plotted on the top wall along the axial direction. These results show the magnitude decreasing and the phase changing sign at nodes, whereas the reverse occurs at antinodes. Furthermore, for this combustor, $f_0 = c/2L$ is estimated to be approximately 1300 Hz, where L is the length between the dump plane and the nozzle, and c is the speed of sound in non-reactive conditions. These results show a clear presence of a longitudinal acoustic mode between the dump plane and the jail bar nozzle at 2400 Hz and its higher-order harmonic at 4800 Hz.

These findings explain the higher frequencies; however, frequencies lower than 1000 Hz, which are usually the focus for broadband noise, remained poorly understood. Consequently, we conducted a POD analysis of line-of-sight HRR fields. Key results are shown in Figure 26. The findings indicated that the most energetic mode for the HRR is a monopole, showing a 700-Hz frequency. The next set of higher-order modes have lower intensity, but the 700-Hz peak is associated with longitudinal and transverse dipole modes in the HRR. Modes of an even higher order (i.e., quadrupole, etc.) do not show any presence of this frequency. These results suggest a coupling between the HRR and pressure at 700 Hz (direct or indirect), but the underlying mechanism remains unclear and requires further evaluation.

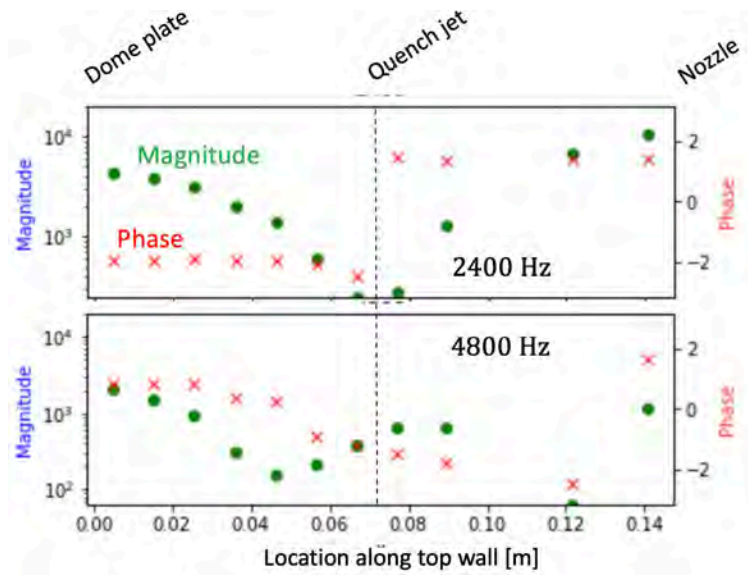


Figure 25. Magnitude and phase of pressure fluctuations plotted along the combustor top wall at $f = 2400$ and 4800 Hz. Results are over a 100-ms time window.

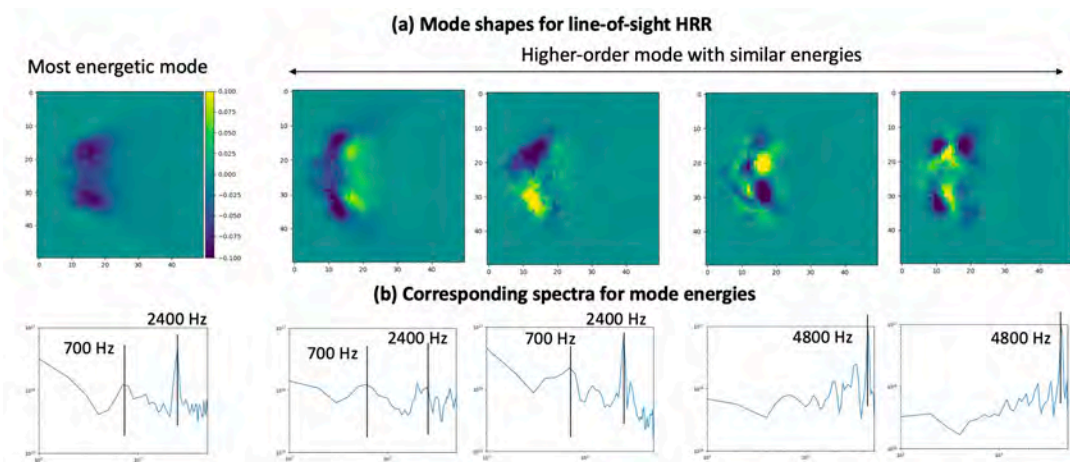


Figure 26. Modes of line-of-sight averaged HRR, computed with POD. The mode shapes are shown in (a), and the corresponding energies in the frequency space are shown in (b).

Having gained some understanding of the flame/flow structure and dynamical modes predicted within this combustor, we next compared the dynamics under baseline, high-FAR, and quench-1 conditions, as shown in Figure 27. Spectra of volume-integrated HRR are also compared. High FAR shows a significant increase in the content for $f < 700$ Hz, with almost no change for $f > 1000$ Hz. This finding may suggest that the increase HRR plays a role and is qualitatively similar to the experimental observations, although a one-to-one comparison remains to be conducted. In contrast, for quench-1, in which the HRR is not affected, but the cooling mechanism is affected, an increase in content for $f > 1000$ Hz (at least at certain locations) is observed without any significant change for $f < 1000$ Hz. Understanding the mechanisms underlying these changes requires further analyses of the results, as is currently underway.

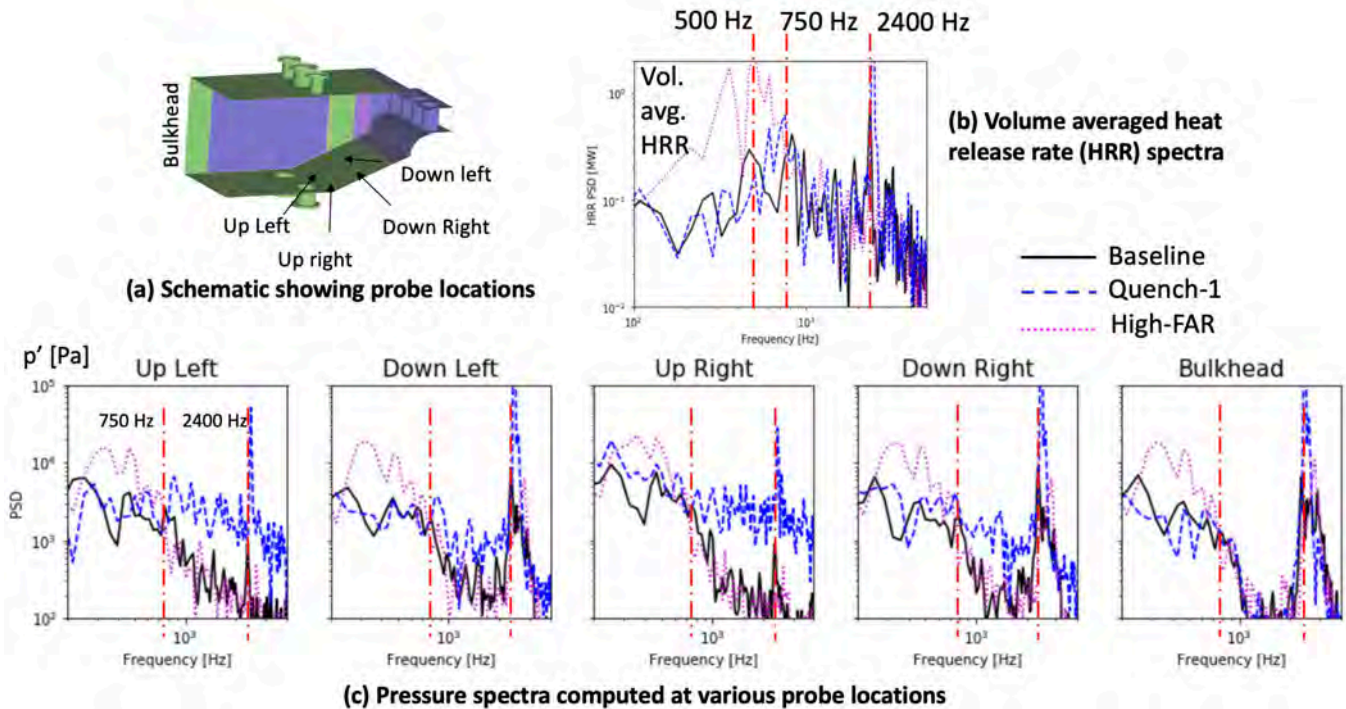


Figure 27. Comparison of HRR (b) and pressure spectra (c) among operating conditions: baseline, quench-1, and high FAR from LES computation. Panel (a) shows the various probe locations for pressure. All spectra are computed over an 80-ms time window to allow for one-to-one comparison.

Data output and transfer

The simulations output 3D snapshots of conservative variables, as noted above. The output frequency of these outputs is 10^4 Hz, and at least 1,000 such snapshots are output for each case over the span of a 100-ms simulation time. The snapshots are collected only after the initial transients for the first two flow-through times have been neglected. A single 3D snapshot is ~1 GB in size. The CFDPostProc software and sample post-processing scripts can (a) compute primitive quantities, such as pressure, temperature, density, and reaction rates; (b) compute derivatives; (c) compute time-averaged quantities; and (d) interpolate data onto another rectangular grid from these files.

In addition to the 3D gas-phase snapshots, the Lagrangian data of the parcel are saved at the same frequency and are available for computing the spray droplet statistics. A post-processing script that translates the Lagrangian quantities onto a Eulerian grid via filtering is also available. A single droplet snapshot is ~50 MB in size.

Because the 3D gas-phase snapshots are rather large, they could not be collected at higher frequencies. However, the simulation collects high-frequency data at 10^6 Hz for ~200 probe points distributed throughout the computational domain. These points are uniformly placed along the $x/y/z$ directions within the combustor, through the nozzle, and within the exit plenum. These data can be used for accurately computing the frequency characteristics of the system.

Finally, although time-averaged statistics (mean, root mean square [RMS]) can be computed by using the output 3D snapshots, fine-grained time averaging is also conducted within the code, and the mean and RMS primitive quantities are output for the entire 3D domain. These quantities include the primitive variables, such as velocity, temperature, pressure, density, species mass fractions, and reaction rates. The size of a single time-averaged file is ~4 GB.

A summary of available data, processing software, and their use by RTRC (direct noise and indirect noise) and GT ROM teams (hydrodynamics and flame) is provided in Figure 28.

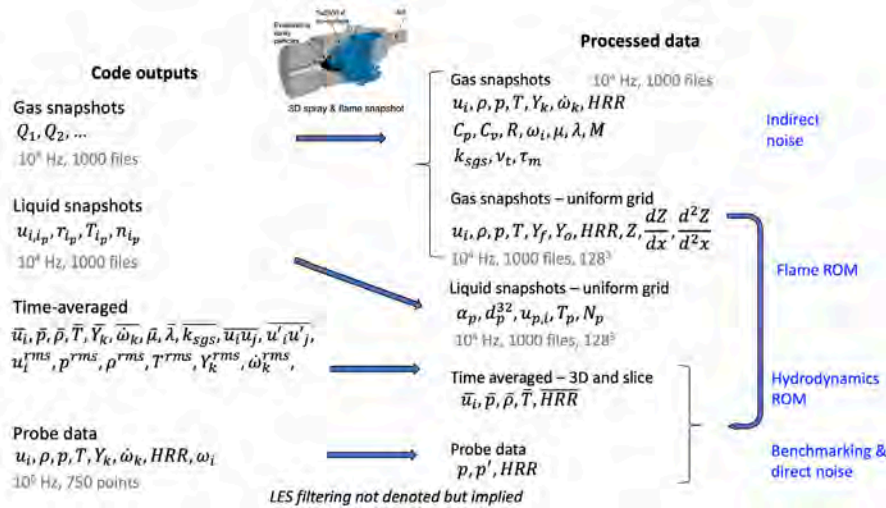


Figure 28. Schematic showing the LES data-processing workflow.

Milestones

- Validation of LES completed at baseline conditions against GT experiments.
- Reactive flow LES conducted at three operating conditions, two from the GT and RTRC experimental campaign.
- Collection of at least 1,000 3D snapshots for each operating condition; provision of data for baseline operating conditions to GT ROM and RTRC teams; data at other conditions awaiting further processing and transfer.
- Creation and updating of a post-processing pipeline for 3D gas-phase and spray snapshots; available to GT ROM team and RTRC as needed.

Major Accomplishments

Efforts during the first 2 years focused primarily on updates in rig geometry and establishing a workflow for the CFD simulations. In Year 3, validation of LES against experiments was completed, and two additional conditions were considered; 3D snapshots, high-frequency probe data, and time-averaged statistics were collected; and post-processing scripts were developed to aid GT ROM and RTRC teams.

Publications

Published conference proceedings

Panchal, A., & Menon, S. (2023, January 23). Large eddy simulation of combustion noise in a realistic gas turbine combustor. *AIAA SCITECH 2023 Forum*. AIAA SCITECH 2023 Forum, National Harbor, MD & Online.

Outreach Efforts

None.

Awards

None.

Student Involvement

- **Penescu Flavius** (currently an undergraduate student, planning to pursue a Master's degree with a thesis) conducted reactive LES with modified quench jet configuration.
- **Leo Kastenber** (currently an undergraduate student, planning to pursue a master's degree with a thesis) worked on developing post-processing scripts for 3D snapshots.
- **Maxwell Hall** (undergraduate) partly worked on post-processing the high-frequency trace data.

Plans for Next Period

The next period under this funding will focus on continued analyses of the available LES data under three operating conditions to understand the significance of the observed frequencies and their relevance in noise generation. The LES dataset for the remaining two operating conditions will be provided to the GT ROM and RTRC teams. We will transition to modeling tone noise and will make corresponding changes in the geometry/grid/boundary conditions in the next period of funding.

Task 3 – Reduced-Order Modeling

Georgia Institute of Technology

Objective

The overarching objective of this task is to create quick-action ROMs to accurately predict various aspects of noise generation mechanisms that are then collectively feed into a design tool for noise prediction. The specific objective of the GT ROM task focuses on the head-end physics in the architecture, namely the flow and spray dynamics, flame dynamics, and generation of entropy disturbances by the flame. The spray/flow dynamics feeds into the flame dynamics, thus causing direct combustion noise. The flame dynamics also results in entropy disturbances, which in turn lead to indirect combustion noise at the nozzle. The flame response modeling and the model for the generation of entropy disturbances are provided as inputs to the post-combustion models that will be developed by RTRC. Depending on the prediction results obtained from the RTRC models, these head-end models will be iteratively refined.

Research Approach

In this reporting period, we focused on ROM tasks pertaining to hydrodynamics, flame dynamics, and entropy generation. We studied the hydrodynamics of a swirling jet by using an in-house hydrodynamic stability analysis tool that captures the leading-order coherent dynamics of the flow field. The goal of the tool is to measure the flow response by studying the velocity disturbances resulting from simulated external forcing noise. The hydrodynamics will eventually result in a velocity model that will be used with the flame dynamics model to generate heat release. We further studied the contributions of different chemical source terms contributing to entropy generation for a premixed flame, excluding the diffusion effects.

Hydrodynamics modeling

In this reporting period, we advanced the previously developed hydrodynamic forced response framework to measure the swirling jet global mode response to an imposed boundary forcing function. In this framework, we studied swirling jets as amplifier flows, which, in the literature, have been shown to alter the flow response in the presence of the external noise that can occur during combustion. Apart from the well-known advantages of swirling jets as canonical flow fields in combustion systems, swirling flows usually result in unsteady hydrodynamic structures that can couple with acoustics. Modeling and predicting the hydrodynamic structures can be important, particularly in the presence of combustion, because these structures can interact with and perturb the flame. Hydrodynamic stability analysis has emerged as a tool for modeling the dynamics of swirling flows in recent decades. This type of analysis is particularly useful for predicting receptivity, or the range of frequencies amplified by the flow. That is, hydrodynamics provides a transfer function from the background turbulence to large-scale vortical disturbances (which disturb the flame and consequently produce direct noise). Additionally, hydrodynamic stability analysis is particularly valuable for parametric studies determining the sensitivity of the flow response to major design parameters, thus providing a powerful engineering tool. Traditional global hydrodynamic stability analyses have focused on instability generated within the domain (unforced or natural hydrodynamics). Our effort has been to model how the flow response can be altered if instability is introduced at the inlet in a more global framework.

To study the global mode response to an imposed forcing function, we use the time-averaged combustor flow fields supplied as part of the LESs performed for this project. We decompose the 3D velocity fields into two two-dimensional (2D) slices with the same axial coordinate, denoted the x slice and y slice, as displayed in Figure 29. We then conduct a coordinate transform into cylindrical coordinates. Transforming the data into cylindrical coordinates is advantageous in establishing an axisymmetric geometry for our model.

The governing equations for this analysis include the linearized continuity and momentum equations in their incompressible form:

$$\nabla \cdot \vec{u}' = 0$$

$$\frac{\partial \vec{u}'}{\partial t} + (\vec{u} \cdot \nabla) \vec{u}' + (\vec{u}' \cdot \nabla) \vec{u} + \frac{\nabla p'}{\rho} - \nu \nabla^2 \vec{u}' = 0 \quad (1)$$

For this analysis, we use a bi-global stability analysis framework, which allows the calculated modes to significantly vary along two coordinates. Using the axisymmetric configuration of the problem, the velocity and pressure disturbances are assumed to take the following harmonic form shown below. The amplitude of the mode is a function of the radial and spatial coordinates, whereas temporal and azimuthal periodicity is maintained by using the frequency ω and azimuthal wave number m . The azimuthal wave number, m , captures the helical modes of swirling jets of interest.

$$g'(r, \theta, z, t) = \hat{g}(r, z) e^{-i(\omega t - m\theta)} \quad (2)$$

The assumption of a bi-global mode in the linearized governing equations results in a set of four coupled partial differential equations. Appropriate boundary conditions for each equation are presented in Table 2.

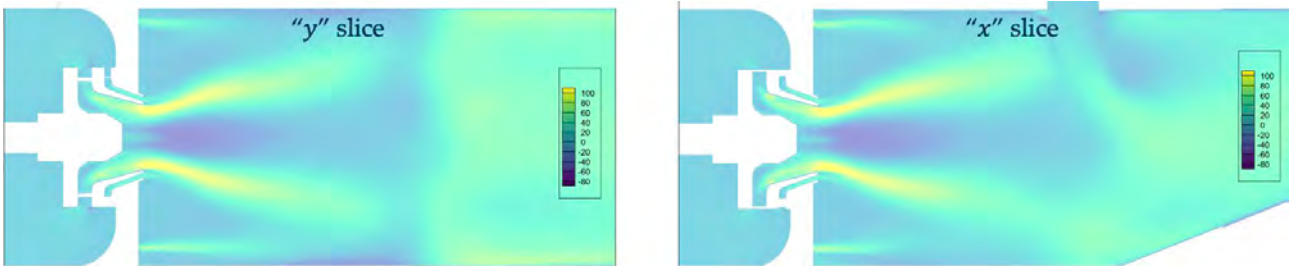


Figure 29. Axial velocity contours of a sliced 3D flow field in Cartesian coordinates.

Table 2. Boundary conditions for each equation.

	Axis	Walls	Inlet	Outlet
Radial velocity	$u'_r = 0$	$u'_r = 0$	$u'_r = A_0 e^{-i\omega t}$	$u'_r = 0$
Tangential velocity	$u'_t = 0$	$u'_t = 0$	$\frac{\partial u'_t}{\partial \mathbf{n}} = 0$	$u'_t = 0$
Axial velocity	$\frac{\partial u'_z}{\partial \mathbf{n}} = 0$	$u'_z = 0$	$\frac{\partial u'_z}{\partial \mathbf{n}} = 0$	$u'_z = 0$
Pressure	$\frac{\partial p'}{\partial \mathbf{n}} = 0$	$\frac{\partial p'}{\partial \mathbf{n}} = 0$	$\frac{\partial p'}{\partial \mathbf{n}} = 0$	$p' = 0$

At the centerline, we assume no fluctuations in radial or tangential velocity, to conform with an axisymmetric flow. At the wall, all velocity disturbances must vanish. At the inlet, we impose the inhomogeneous Dirichlet boundary condition for the velocity normal to the inlet plane, to simulate the external boundary forcing for this problem. For the outlet, homogeneous Dirichlet boundary conditions are imposed for velocity and pressure disturbance amplitudes.

We developed a code to solve the equations by using finite elements in COMSOL software. To validate the code, we used a historical dataset with an axisymmetric base flow. Natural hydrodynamics was tested with an unforced global analysis. We correlated the growth rates of unstable modes with the Strouhal number (oscillatory frequencies) to validate the linear trend predicted in the literature, and we ensured that the code accurately captured the unstable solutions.

After validation with historical data, the model was used to obtain bi-global modes for LES base flow data. A snapshot of a forced global mode shape of the axial velocity with a forced inhomogeneous Dirichlet boundary condition at the inlet is shown in Figure 30. The bulk of the disturbances can be qualitatively observed to occur in the shear layers of the flow domain.

To quantitatively measure the flow response to forcing, we formulated a transfer function to observe the response in shear layers of forced modes. In a one-dimensional (1D) setting, we probe the axial velocity of modes at axial location ($z/d_{sw} = 1.32$) and march radially through the shear layer to measure the amplitude of disturbance. Nine probes are placed at the axial location to evaluate the magnitude of the axial velocity disturbance, as shown in Figure 31.

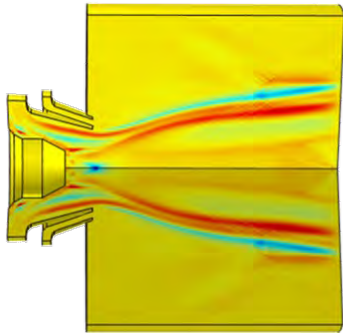


Figure 30. Mode shape of axial velocity disturbance modes at $f = 150$ Hz, on the basis of LES baseflow data.

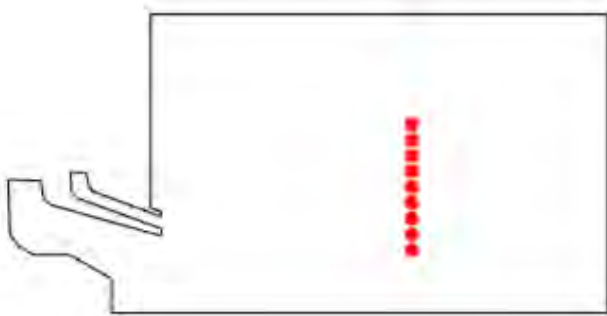


Figure 31. One-dimensional probe window for the empirical transfer function.

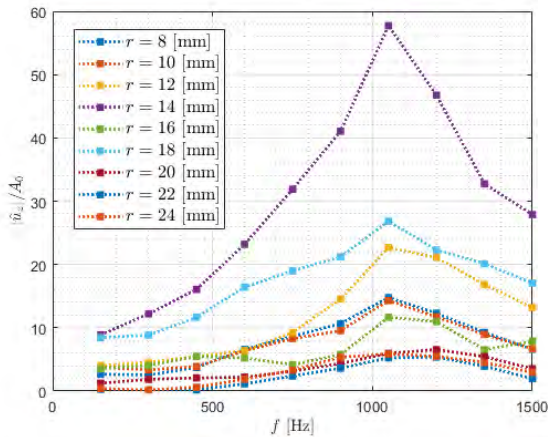


Figure 32. One-dimensional empirical transfer function at $z/d_{sw} = 1.32$.

The normalized amplitude of the axial velocity disturbance ($|\hat{u}_z|/A_0$), where A_0 is the amplitude of the inlet velocity forcing, serves as the empirical transfer function for a forced, vortical flow response at frequency f . Figure 32 shows the 1D empirical transfer function as a function of forcing frequency. Frequencies for which axial velocity modes are amplified by the inlet introduced disturbance are visible in the figure. The model predicts that the $f = 1050$ Hz mode causes the greatest amplification.

The empirical transfer function was extended across the flow domain, such that flow response was measured by a matrix of 5,673 probes varying across the radial and axial directions. The matrix of probes captures radial, axial, and azimuthal velocity flow disturbances generated because of the imposed forcing. Flow response was again measured as a function of forcing frequency in terms of the Strouhal number: $St = fd/u_0$.

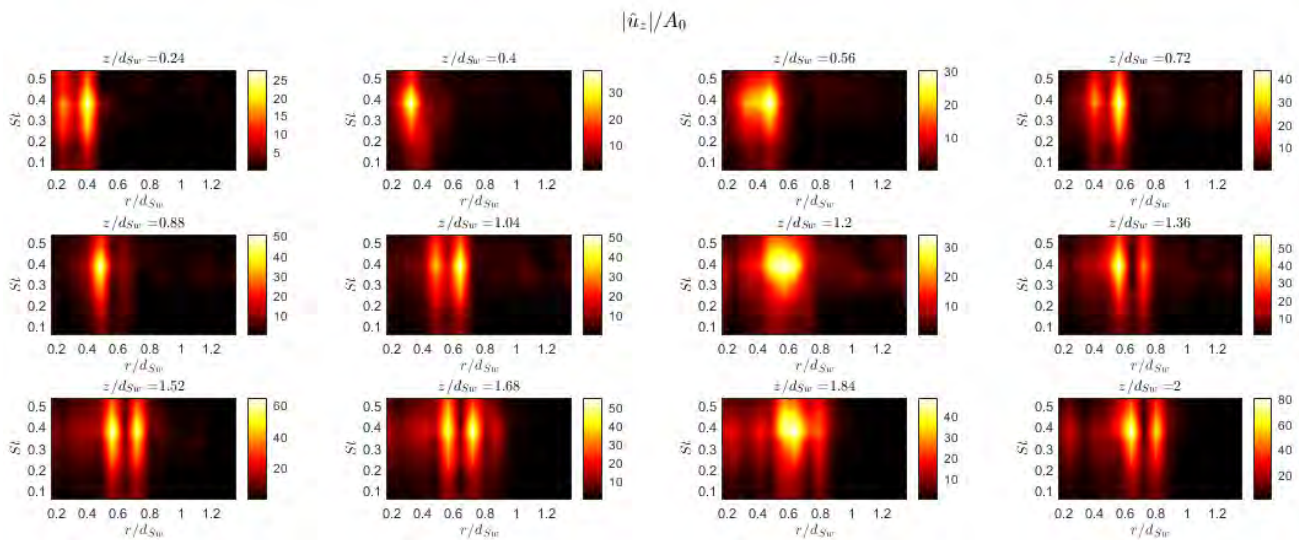


Figure 33. Two-dimensional empirical transfer function in an axially and radially varying probe window.

Figure 33 shows the 2D in-space empirical transfer function at various axial locations of the flow domain. The amplification due to forcing is strong around the $f = 1050$ Hz mode for most axial locations. Generally, the amplification strength increases downstream through the flow domain, and at certain axial locations, the inlet introduced forcing is amplified by much as 80 times. The $f = 1050$ Hz or $St = 0.375$ mode is again predominantly responsible for this amplification.

Flame response modeling

In the prior reporting periods, we presented the flame response framework for spray flames, along with example flame configurations. The results focused on mean and dynamical flame shapes, as well as the global flame response through the spatially integrated unsteady heat release. All these results focused on static spray parameters with dynamics stemming from only velocity fluctuations. Velocity fluctuations result in spray dynamics: oscillating spray parameters, which have been the focus in the current reporting period. The configuration used for this framework is shown in Figure 34, with fuel droplets injected in a center duct and air injected in the outer ducts. The fuel flows in the inner duct with $0 < r < R_f$, and the air/oxidizer flows in the outer ducts with $R_f < r < R$. The fuel exits the duct and enters the combustion zone as a mixture of fuel gas and a spray of liquid fuel droplets; after evaporation and diffusive mixing, the spray diffusion flame is modeled.

The gaseous (Z) and droplet mixture (Z_d) fractions are one-way coupled through vaporization of the droplet, which generates fuel gas. Because we consider spray dynamics, the vaporization physics is tightly coupled with the mixture fraction as:



$$\begin{aligned} \frac{\partial Z_d}{\partial t} + u_z \frac{\partial Z_d}{\partial z} + u_r \frac{\partial Z_d}{\partial r} &= \frac{1}{Pe_d} \left(\frac{\partial^2 Z_d}{\partial r^2} + \frac{\partial^2 Z_d}{\partial z^2} \right) - \Gamma_V(Z) Z_d \\ \frac{\partial Z}{\partial t} + u_z \frac{\partial Z}{\partial z} + u_r \frac{\partial Z}{\partial r} &= \frac{1}{Pe_g} \left(\frac{\partial^2 Z}{\partial r^2} + \frac{\partial^2 Z}{\partial z^2} \right) + \Gamma_V(Z) Z_d \end{aligned} \quad (3)$$

In contrast to the earlier formulation, in which Γ_V was a constant and independent of the mixture fraction, here we couple Γ_V to the system because of the focus on spray dynamics, thus resulting in a non-linear set of equations. We linearize this system and expand to obtain the steady-state mixture fractions (subscript 0), governed as follows:

$$\begin{aligned} u_{z,0} \frac{\partial Z_{d,0}}{\partial z} + u_{r,0} \frac{\partial Z_{d,0}}{\partial r} - \frac{1}{Pe_d} \left(\frac{\partial^2 Z_{d,0}}{\partial r^2} + \frac{\partial^2 Z_{d,0}}{\partial z^2} \right) + \Gamma_V(Z_0) Z_{d,0} &= 0 \\ u_{z,0} \frac{\partial Z_0}{\partial z} + u_{r,0} \frac{\partial Z_0}{\partial r} - \frac{1}{Pe_g} \left(\frac{\partial^2 Z_0}{\partial r^2} + \frac{\partial^2 Z_0}{\partial z^2} \right) - \Gamma_V(Z_0) Z_{d,0} &= 0 \end{aligned} \quad (4)$$

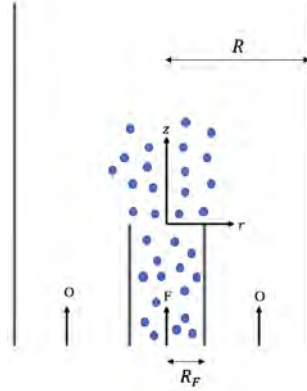


Figure 34. Schematic of the ducted spray flame configuration. Fuel droplets are injected in the center duct (blue), and oxidizer gas is injected in the outer ducts.

The fluctuations in the mixture fractions (subscript 1) are then governed by the following equations:

$$\begin{aligned} \frac{\partial Z_{d,1}}{\partial t} + u_{z,0} \frac{\partial Z_{d,1}}{\partial z} + u_{r,0} \frac{\partial Z_{d,1}}{\partial r} - \frac{1}{Pe_d} \left(\frac{\partial^2 Z_{d,1}}{\partial r^2} + \frac{\partial^2 Z_{d,1}}{\partial z^2} \right) + \Gamma_V(Z_0) Z_{d,1} &= -(\Gamma'_{V,0}(Z_0) Z_{d,0}) Z_1 - u_{z,1} \frac{\partial Z_{d,0}}{\partial z} - u_{r,1} \frac{\partial Z_{d,0}}{\partial r} \\ \frac{\partial Z_1}{\partial t} + u_{z,0} \frac{\partial Z_1}{\partial z} + u_{r,0} \frac{\partial Z_1}{\partial r} - \frac{1}{Pe_g} \left(\frac{\partial^2 Z_1}{\partial r^2} + \frac{\partial^2 Z_1}{\partial z^2} \right) + (\Gamma'_{V,0}(Z_0) Z_{d,0}) Z_1 &= \Gamma_V(Z_0) Z_{d,1} - u_{z,1} \frac{\partial Z_0}{\partial z} - u_{r,1} \frac{\partial Z_0}{\partial r} \end{aligned} \quad (5)$$

The boundary conditions are the same as before. The above system is solved for both the droplet and gaseous mixture fractions. However, the equations are notably non-linear in the steady-state mixture fractions, owing to the nature of coupling spray dynamics into the system. However, the system dynamics remains linear (subscript 1). Using the steady state and dynamics of the mixture fractions, we can then consider the heat release dynamics. Derived from the previous report, the normalized unsteady HRR dynamics or flame transfer function is defined as:

$$\hat{F} = \frac{\int_0^{L_f,0} \frac{\partial \hat{Z}_1}{\partial r} \Big|_{r=\xi_0(z)} dz + \int_0^{L_f,0} \hat{\xi}_{1,n} \left[\frac{\partial^2 Z_0}{\partial r \partial z} \sin \theta_0 - \frac{\partial^2 Z_0}{\partial r^2} \cos \theta_0 \right] \Big|_{r=\xi_0(z)} dz}{\int_0^{L_f,0} \frac{\partial Z_0}{\partial r} \Big|_{r=\xi_0(z)} dz} \quad (6)$$

Here, $L_{f,0}$ is the mean flame height, and transverse diffusion is assumed to be dominant over axial diffusion. The local mean flame angle is denoted θ_0 and is determined from the mean flame position as follows:

$$\tan \theta_0(z) = \frac{d\xi_0(z)}{dz} \quad (7)$$

For illustration, let us consider the following flow field:

$$\begin{aligned} u_{z,0} &= u_0 & u_{z,1} &= u_0 \cos(\text{St}(t - k_c z)) \\ u_{r,0} &= u_{r,1} = 0 \end{aligned} \quad (8)$$

Here, $\text{St} = \omega R / u_0$, $k_c = u_0 / u_c$ are the non-dimensional frequency (Strouhal number) and a non-dimensional disturbance convection parameter. Figure 35 shows the variation in the gain (amplitude) and phase of the flame transfer function for different effects of spray dynamics. The baseline gaseous diffusion flame case (no spray) is shown in black. We consider two cases: spray-only injection (red) and partial liquid injection (blue). The spray-only injection case corresponds to the injection of fuel in only its liquid/spray form. We first consider the spray-only case without any spray dynamics, as shown by the solid red curve. When spray dynamics is included, the flame transfer function noticeably changes to the dashed red curve, thus indicating the importance of including this aspect of physics. If we consider the case with partial injection of fuel gas and fuel droplets (blue), the effect of disturbance propagation, k_c , is evident (dashed blue vs. dotted blue). This parameter notably affects the nature of constructive/destructive interference; consequently, although the qualitative nature of the curves remains unchanged, key features such as peaks and minima are shifted in the Strouhal number space.

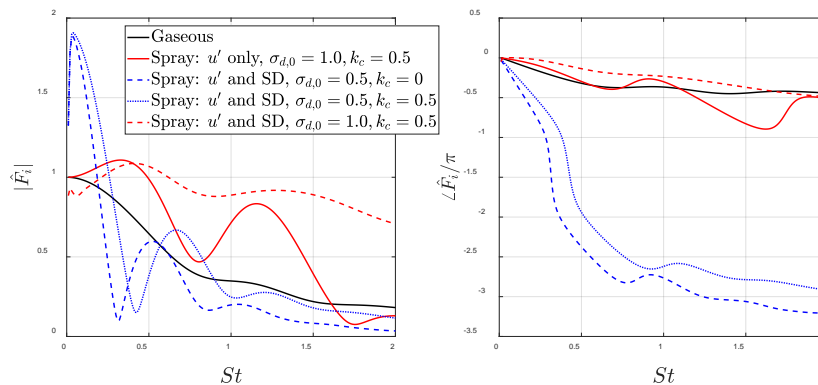


Figure 35. Effects of spray dynamics on the global flame response, showing gain (left) and phase (right).

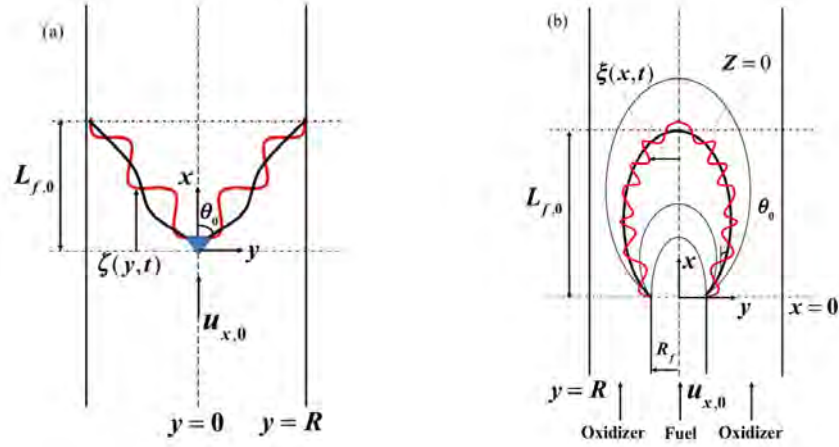


Figure 36. Schematic of (a) premixed and (b) non-premixed flame configurations.

Estimation of flame-generated entropy

In the previous report, we showed that for air-breathing systems under relevant operating conditions, the heat release is the major source term at the flame for entropy generation.

$$\begin{aligned} \rho \frac{Ds}{Dt} &= \frac{\dot{q}}{T} \\ \Rightarrow \rho \left(\frac{\partial s}{\partial t} + \bar{u} \cdot \nabla s \right) &= \dot{s}_{gen} = \frac{\dot{q}''}{T_b} \delta(\bar{x} - \bar{x}_f) \end{aligned} \quad (9)$$

We define an entropy transfer function, which is the ratio of a normalized entropy fluctuation and the normalized excitation amplitude:

$$\tilde{\mathfrak{S}}_s = \frac{(\hat{s}_1 / \tilde{S})}{(\hat{F}_1 / F_0)} \quad (10)$$

Here, $\tilde{S} = \dot{Q}_0 / \rho T_b R u_{x,0}$, and \hat{F}_1 / F_0 is the excitation amplitude normalized by its mean value. For most practical configurations, flames are convectively non-compact for a broad range of frequencies of interest; thus, these non-compactness (or equivalently phase cancellation) effects are significant and profound. Although general results can be developed independently of flame geometry/configuration in the convectively compact case, the problem is generally configuration dependent. We consider two model problems for premixed and non-premixed flames, as shown in Figure 36. An explicit expression for the HRR fluctuations of a premixed and non-premixed flame can be derived. Calculations show that, in response to velocity fluctuations, entropy fluctuations are not generated by a premixed flame. This zero-response result also holds if the results are generalized to include the flame stretch sensitivity, thus leading to burning rate fluctuations for reasons discussed later. For the non-premixed flame configuration, in the high Peclet limit, we obtain the same result showing that velocity-driven flames may have a flame response but not an overall entropy response. Using a linear perturbation expansion, we decompose Eq. (9) into two equations for the perturbation and mean as:

$$\frac{\partial s_1}{\partial t} + \bar{u}_0 \cdot \nabla s_1 = -\bar{u}_1 \cdot \nabla s_0 + \left(\frac{\dot{s}_{gen}}{\rho} \right)_1 \quad (11)$$

$$\bar{u}_0 \cdot \nabla s_0 = \left(\frac{\dot{s}_{gen}}{\rho} \right)_0 \quad (12)$$

Assuming harmonic velocity disturbances propagating in the axial direction, we have:

$$\begin{aligned} u_{x,1} &= \varepsilon_{u,x} u_{x,0} f_x(x) e^{-i\omega t} \\ u_{y,1} &= \varepsilon_{u,y} u_{y,0} f_y(x) e^{-i\omega t} \end{aligned} \quad (13)$$

Here, f_x and f_y are complex functions describing the change in disturbance magnitude and spatial phase dependence, and similarly, equivalence ratio perturbation evolving axially is defined by:

$$\phi_1 = \varepsilon_\phi \phi_0 f_\phi e^{-i\omega t} \quad (14)$$

Expanding Eq. (11) in the frequency domain and simplifying results in:

$$\begin{aligned} -i\omega \hat{s}_1 + u_{x,0} \frac{\partial \hat{s}_1}{\partial x} &= -\hat{u}_{x,1} \frac{\partial s_0}{\partial x} - \hat{u}_{y,1} \frac{\partial s_0}{\partial y} + \frac{\hat{S}_{L,1} h_{R,0} \delta(x - \zeta_0(y))}{T_{b,0} \sin \theta_0} + \frac{S_{L,0} \hat{h}_{R,1} \delta(x - \zeta_0(y))}{T_{b,0} \sin \theta_0} \\ &\quad - \frac{S_{L,0} h_{R,0} \hat{T}_{b,1} \delta(x - \zeta_0(y))}{T_{b,0}^2 \sin \theta_0} + \frac{S_{L,0} h_{R,0} \delta(x - \zeta_0(y))}{T_{b,0}} \frac{\partial \hat{\zeta}_1}{\partial y} \cos \theta_0 - \hat{\zeta}_1 \frac{S_{L,0} h_{R,0} \delta'(x - \zeta_0(y))}{T_{b,0} \sin \theta_0} \end{aligned} \quad (15)$$

Expanding Eq. (12) results in:

$$\frac{\partial s_0}{\partial x} = \frac{h_{R,0} \delta(x - \zeta_0(y))}{T_{b,0}} \quad (16)$$

After integrating with respect to x , differentiating with respect to y , and substituting the fluctuating flame position solution, Eq. (15) simplifies to:

$$\begin{aligned} \hat{\zeta}_1 &= \int_0^x \varepsilon_\phi f_\phi(x') \frac{h_{R,0}}{T_{b,0}} \left[\frac{\partial(h_R / h_{R,0})}{\partial(\phi / \phi_0)} - \frac{\partial(T_b / T_{b,0})}{\partial(\phi / \phi_0)} \right] \delta(x' - \zeta_0(y)) e^{-\frac{i\omega}{u_{x,0}}(x'-x)} dx' \\ &\quad - \int_0^x \varepsilon_{u,y} f_y(x') \frac{h_{R,0}}{T_{b,0}} \left[\frac{1}{h_{R,0}} \frac{dh_{R,0}}{dy} - \frac{1}{T_{b,0}} \frac{dT_{b,0}}{dy} \right] H(x' - \zeta_0(y)) e^{-\frac{i\omega}{u_{x,0}}(x'-x)} dx' - \int_0^x \varepsilon_{u,y} f_y(x') \frac{ds_{ref}}{dy} e^{-\frac{i\omega}{u_{x,0}}(x'-x)} dx' \end{aligned} \quad (17)$$

For the perfectly premixed case, the second two integrals become zero, because $h_{r,0}$ and $T_{b,0}$ are uniform in the transverse direction. Thus, the only contribution for perfectly premixed flames comes from equivalence ratio forcing. Considering the case of a constant flame angle premixed flame, perturbed only by convecting equivalence ratio fluctuations of the form $f_\phi = \exp(i\omega x / u_c)$ (where u_c is the fluctuation phase speed), Eq. (17) results in:

$$\hat{s}_1 = \varepsilon_\phi \frac{h_{R,0}}{T_{b,0}} \left[\frac{\partial(h_R / h_{R,0})}{\partial(\phi / \phi_0)} - \frac{\partial(T_b / T_{b,0})}{\partial(\phi / \phi_0)} \right] \int_0^x \delta(x' - \zeta_0(y)) e^{\frac{i\omega x'}{u_c}} e^{-\frac{i\omega}{u_{x,0}}(x'-x)} dx' \quad (18)$$

Here, $x > \zeta(y)$. Thus, for a constant flame angle premixed flame, $\zeta_0(y) = \cot(\theta_0)y$ and $L_{f,0} = R \cot \theta_0$, whereas the mean flow Strouhal number is defined as $St_{L_f} = \omega L_{f,0} / u_{x,0}$, and the Strouhal number based on the disturbance phase speed is defined as $St_c = \omega L_{f,0} / u_c$. Consequently:

$$St_c = St_{L_f} k_c \quad (19)$$

After substituting for St_c , simplifying, and evaluating where $\tilde{S} = h_{R,0} / T_{b,0}$, the entropy transfer function for equivalence ratio forcing takes the form:



$$\mathfrak{S}_{s,\phi} = \frac{(\bar{s}_1 / \bar{S})}{\varepsilon_\phi} = \frac{T_{u,0}}{T_{b,0}} \frac{\partial(h_R / h_{R,0})}{\partial(\phi / \phi_0)} \left(\frac{i(1 - e^{-iSt_{L_f}(k_c - 1)})}{St_{L_f}(k_c - 1)} \right) e^{i\omega x} \quad (20)$$

Eq. (20) gives the entropy fluctuations downstream of the premixed flame configuration. Of note, for $k_c = 1$ (i.e., convective velocity equal to mean flow velocity), no contribution from velocity forcing exists. This simplification, as discussed above, may not accurately evaluate no-compactness effects but in this form is also discontinuous at $k_c = 1$.

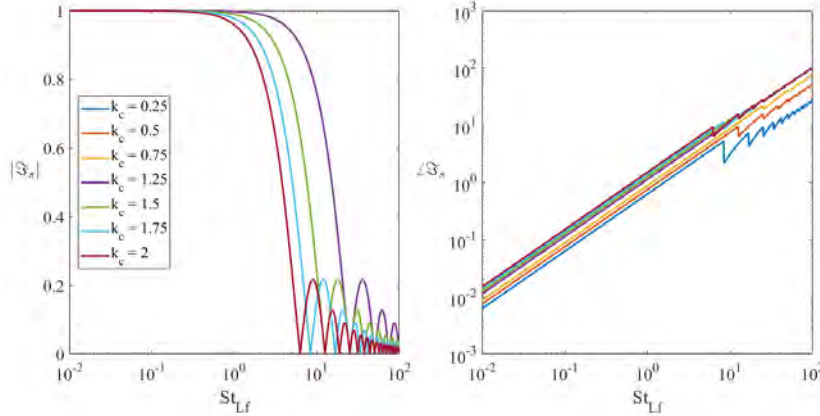


Figure 37. Strouhal number, St_{L_f} , and k_c dependence of the magnitude (left) and phase (right) of the entropy transfer function $\mathfrak{S}_{s,\phi}$ for a premixed flame with equivalence ratio forcing.

Figure 37 shows the dependence of the magnitude and phase of the premixed flame entropy transfer function. Of note, $k_c = 1$ is not shown, because it is independent of St_{L_f} . For $k_c \neq 1$, the transfer function is around 1 and is nearly independent of St_{L_f} until around $St_{L_f} \sim 1$. As the Strouhal number increases, the dependence on frequency is evident, with the typical low-pass-filter behavior. Moreover, because the dependence occurs as $(k_c - 1)$, the curves are similar for $k_c = 0.25$ and $k_c = 1.75$. Additionally, the phase of the transfer function increases with frequency for all cases, with a uniform slope for all k_c values. The sharp jumps in the phase for all cases coincide with the nodes seen in the amplitude of the transfer function. These plots collectively illustrate the effect, and thus the importance, of including k_c in the disturbance model for capturing entropy fluctuations.

For the non-premixed flame, we consider velocity disturbances propagating in the axial direction as above, as well as inlet ($x = 0$) fuel and oxidizer mass fraction fluctuations given by:

$$\begin{aligned} Y_{f,1}(x = 0) &= \varepsilon_f Y_{f,i,0} e^{-i\omega t} \\ Y_{ox,1}(x = 0) &= \varepsilon_{ox} Y_{ox,i,0} e^{-i\omega t} \end{aligned} \quad (21)$$

Eq. (16) leads to:

$$s_0 = s_{ref}(y) - (v_f W_f + v_{ox} W_{ox}) D \frac{h_{R,0}}{T_{b,0} u_{x,0}} \int_0^x \frac{\partial Z_0}{\partial y} \delta(y - \xi_0(x')) dx' \quad (22)$$

Now, given frequency-domain entropy fluctuations in the linear limit, and noting that entropy fluctuations averaged in the transverse direction satisfy $\bar{s}_1 = \int_0^R \hat{s}_1 dy$, and solving as a linear differential equation, Eq. (11) results in:



$$\begin{aligned} \bar{\hat{s}}_1 = \int_0^{L_{f,0}} \frac{e^{\frac{i\omega}{u_{x,0}}x'}}{u_{x,0}R} \left\{ - \int_0^R \hat{u}_{y,1} \frac{\partial \hat{s}_0}{\partial y} dy + D(v_f W_f + v_{ox} W_{ox}) \left(\left[\frac{u_{x,1}}{u_{x,0}} \frac{h_{R,0}}{T_{b,0}} \frac{\partial Z_0(x', \xi_0(x'))}{\partial y} \right. \right. \right. \\ \left. \left. \left. - \frac{h_{R,0}}{T_{b,0}} \frac{\partial \hat{Z}_1(x', \xi_0(x'))}{\partial y} - \frac{\hat{h}_{R,1}}{T_{b,0}} \frac{\partial Z_0(x', \xi_0(x'))}{\partial y} + \frac{h_{R,0} \hat{T}_{b,1}}{T_{b,0}^2} \frac{\partial Z_0(x', \xi_0(x'))}{\partial y} \right] - \hat{\xi}_1 \frac{h_{R,0}}{T_{b,0}} \frac{\partial^2 Z_0(x', \xi_0(x'))}{\partial y^2} \right) \right\} dx' \end{aligned} \quad (23)$$

After simplifying via the solutions for Z_0 and \hat{Z}_1 , substituting Eq. (22), and assuming $\varepsilon = \varepsilon_f = \varepsilon_{ox}$, Eq. (23) is reduced to:

$$\begin{aligned} \bar{\hat{s}}_1 = - \frac{e^{\frac{i\omega}{u_{x,0}}x}}{u_{x,0}R} D(v_f W_f + v_{ox} W_{ox}) \left[\int_0^{L_{f,0}} \varepsilon \frac{h_{R,0}}{u_{x,0} T_{b,0}} \left(- \frac{\partial \hat{Z}_1(x', \xi_0(x'))}{\partial y} \right) dx' + \int_0^{L_{f,0}} e^{-\frac{i\omega}{u_{x,0}}x'} \frac{h_{R,0}}{u_{x,0} T_{b,0}} \left(\frac{\hat{h}_{R,1}}{h_{R,0}} - \frac{\hat{T}_{b,1}}{T_{b,0}} \right) \frac{\partial Z_0(x', \xi_0(x'))}{\partial y} dx' \right] \\ - \frac{e^{\frac{i\omega}{u_{x,0}}x}}{u_{x,0}R} \int_0^{L_{f,0}} e^{-\frac{i\omega}{u_{x,0}}x'} \varepsilon_{u,y} u_{x,0} f_y(x') (s_{ref}(y=R) - s_{ref}(y=0)) dx' \end{aligned} \quad (24)$$

Importantly, the first two terms represent the entropy contribution due to mass fraction fluctuations, and the third term represents the entropy contribution due to velocity forcing. In addition, no dependence on k_c is observed for the mass fraction fluctuation terms; i.e., their entropy contributions are constant with respect to k_c and St_{L_f} , and vary only with ventilation parity. This aspect is clear because of the presence of the velocity forcing of the form $f_y(x') = \exp(i\omega x'/u_c)$ in the third term. Thus, defining the velocity forcing entropy contribution:

$$\hat{s}_{1,v} = - \frac{\varepsilon_{u,y}}{R} \int_0^{L_{f,0}} e^{-\frac{i\omega}{u_{x,0}}x'} e^{\frac{i\omega}{u_c}x'} (s_{ref}(y=R) - s_{ref}(y=0)) dx' \quad (25)$$

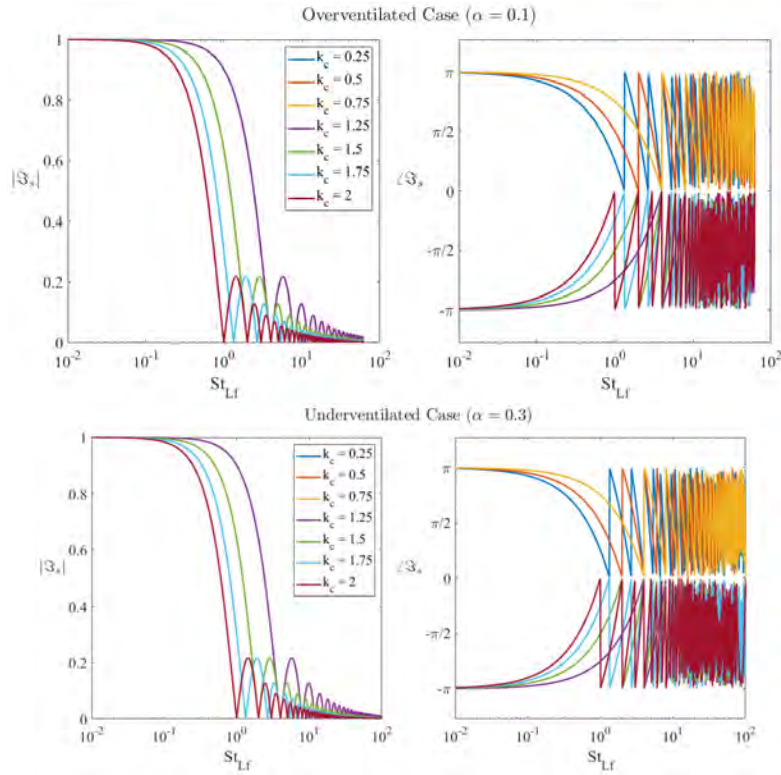


Figure 38. Strouhal number and k_c dependence of the magnitude (left) and phase (right) of the entropy transfer function for overventilated (top) and underventilated (bottom) non-premixed velocity forced flames ($Pe = 50$).

Simplifying, where $\Delta s_{ref} = (s_{ref}(y = R) - s_{ref}(y = 0))$, we have:

$$\hat{s}_{1,v} = -\frac{\varepsilon_{u,y}}{R} \Delta s_{ref} \int_0^{L_{f,0}} e^{-\frac{i\omega}{u_{x,0}} x'} e^{\frac{i\omega}{u_c} x'} dx' \quad (26)$$

Thus, the velocity forcing entropy contribution is expressed as:

$$\hat{s}_{1,v} = -\frac{L_{f,0}}{R} \frac{\varepsilon_{u,y} \Delta s_{ref}}{iSt_{L_f}(k_c - 1)} [e^{iSt_{L_f}(k_c - 1)} - 1] \quad (27)$$

Here, $St_{L_f} = \omega L_{f,0} / u_{x,0}$. Thus, the entropy transfer function contribution due to velocity forcing takes the form:

$$\mathfrak{S}_{s,v} = \frac{(\hat{s}_{1,v} / \Delta s_{ref})}{(\hat{u}_{y,1} / u_{x,0})(L_{f,0} / R)} = -\frac{1}{iSt_{L_f}(k_c - 1)} [e^{iSt_{L_f}(k_c - 1)} - 1] \quad (28)$$

Figure 38 shows the non-premixed transfer function amplitude and phase for an overventilated and an underventilated case. Of note, in the case of $k_c = 1$, the magnitude of the transfer function is constant with respect to St_{L_f} and is not shown. In both cases, the low Strouhal Number limit clearly extends to approximately $St_{L_f} = 1$. Furthermore, like the premixed flame equivalence ratio-based entropy transfer function described earlier, the magnitude in both cases is



symmetric about $k_c = 1$, because of the $(k_c - 1)$ term. In addition, the magnitude plots have the same profile for all values of k_c , with the rightmost curves occurring nearest to $k_c = 1$, and the leftwardness of the curve being dependent on the distance from k_c . Finally, the overventilated and underventilated flame configurations both have the same profile and maximum magnitude. Thus, for convecting velocity disturbances, the profile of the magnitude can be inferred to be insensitive to the flame configuration as well as the scale.

In summary, in the previous reporting period, our work on convectively compact flames was independent of flame geometry and the entropy generation was captured through simple integration across the heat release region. In this reporting period, we extended the prior frameworks to include convective non-compactness by considering geometry effects explicitly. Two model problems focusing on premixed and non-premixed flames were presented to illustrate this effect. Convective non-compactness was measured with the non-dimensional parameter k_c , which indicates the deviation of the phase speed of the imposed disturbance (velocity or mixture/equivalence ratio) from the mean flow speed. A key motivation was that prior modeling showed that when $k_c = 1$, the entropy transfer functions were independent of frequency. However, in this work, we extended the analytical results to show the existence of a strong low-pass-filter characteristic to the entropy transfer function, wherein the transfer function magnitude was constant in the $St_{L_f} \leq 1.0$ region with a symmetry in behavior around $k_c = 1$, because the dependence was $(k_c - 1)$ in the transfer function terms. For higher frequencies, the low-pass-filter nature implies that, assuming disturbance phase speeds equal to the mean flow speed can lead to erroneous results for the entropy transfer function. This finding has important implications for modeling the effect of indirect noise from these entropy transfer functions. In future work, we will further extend these models to consider phase speeds that are non-uniform and will consider the additional molecular-transport-based source terms in the entropy governing equation through a scaling study.

Modeling p' - q' correlation/coherence

The objective of this task is to study the correlation between the HRR measured by chemiluminescence and the generated noise, specifically direct noise. This correlation can be further applied to the separation of direct and indirect noise sources through partial coherence methods. In the literature, experimental attempts to separate indirect and direct noise sources in a combustor have relied on partial coherence methods relating temperature measurements to indirect noise sources. However, high-speed temperature measurements in combustors are difficult to perform, and no high-resolution, high-frequency measurements are currently available in the literature. If the same principles can be applied for chemiluminescence and direct noise, an alternative approach to source separation of combustor noise could be developed. However, the coherence between the HRR and direct noise is not fully understood, because little literature has reported coherence, and the few existing studies have shown values well below unity. The initial goal of this task was to investigate the effects of near-field effects and noncompactness on coherence to explain the low values of coherence found in the literature, and to provide an in-depth understanding of coherence.

As a motivator for this task, the coherence between acoustic measurements and globally integrated chemiluminescence intensity was calculated as part of Task 1, facility development at GT.

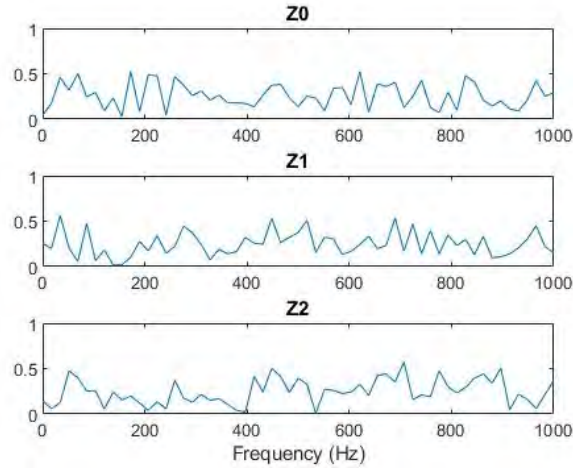


Figure 39. Coherence between global chemiluminescence and acoustic pressure measured in the GT rig for approach conditions and a lean (Z1) and rich (Z2) primary zone.

Overall, low values of coherence were observed for all frequencies. Although the available data were not sufficient to determine accurate values, they were sufficient to motivate further investigation of coherence. To obtain a physical understanding of coherence, we followed an analytical/numerical approach to coherence.

In a turbulent flame, the expansion caused by the local unsteady HRR acts as a distributed monopole source. The relationship between the unsteady heat release and pressure is described through the linear wave equation, written as:

$$\frac{\partial^2 p'(\vec{x}, t)}{\partial t^2} - c_u^2 \nabla \cdot \left(\frac{\rho_u}{\rho_0} \nabla p'(\vec{x}, t) \right) = (\gamma - 1) \frac{\partial \dot{q}'(\vec{x}, t)}{\partial t} \quad (29)$$

Obtaining the solution to Eq. (29) without invoking the acoustically compact or far-field limit yields:

$$\hat{p}'(\vec{x}_0, \omega) = \frac{-i\omega(\gamma - 1)}{4\pi c_u^2} \iiint \hat{q}'(\vec{x}_s, \omega) \frac{e^{ik|\vec{x}_s - \vec{x}_0|}}{|\vec{x}_s - \vec{x}_0|} dS \quad (30)$$

where the variables are their Fourier-transformed counterparts. Consequently, the equation necessary to calculate coherence can be constructed and is written as:

$$G_{QQ} = \iint \hat{q}'(\vec{x}_{s_1}, \omega) \hat{q}'^*(\vec{x}_{s_2}, \omega) \frac{e^{ik|\vec{x}_{s_1} - \vec{x}_0|}}{|\vec{x}_{s_1} - \vec{x}_0|} \frac{e^{ik|\vec{x}_{s_2} - \vec{x}_0|}}{|\vec{x}_{s_2} - \vec{x}_0|} dS_1 dS_2 \quad (31)$$

$$G_{pp} = \frac{\omega^2 (\gamma - 1)^2}{16\pi^2 c_u^4} \iint \hat{q}'(\vec{x}_{s_1}, \omega) \hat{q}'^*(\vec{x}_{s_2}, \omega) \frac{e^{ik|\vec{x}_{s_1} - \vec{x}_0|}}{|\vec{x}_{s_1} - \vec{x}_0|} \frac{e^{ik|\vec{x}_{s_2} - \vec{x}_0|}}{|\vec{x}_{s_2} - \vec{x}_0|} dS_1 dS_2 \quad (32)$$

$$G_{Qp} = \frac{i\omega(\gamma - 1)}{4\pi c_u^2} \iint \hat{q}'(\vec{x}_{s_1}, \omega) \hat{q}'^*(\vec{x}_{s_2}, \omega) \frac{e^{ik|\vec{x}_{s_2} - \vec{x}_0|}}{|\vec{x}_{s_2} - \vec{x}_0|} dS_1 dS_2 \quad (33)$$



$$\gamma_{Qp}^2 = \frac{|G_{Qp}|^2}{G_{pp}G_{QQ}} \quad (34)$$

With Eqs. (31) – (34), the coherence for any flame geometry can be calculated, given the spatiotemporal characteristics of the flame source. To proceed with the analysis, we define an isotropic, exponential decay form of the correlation of the unsteady heat release as:

$$\langle \hat{q}'(\vec{x}_{s_1}, \omega) \hat{q}'^*(\vec{x}_{s_2}, \omega) \rangle = \langle \hat{q}'^2 \rangle \exp\left(-\frac{|\vec{x}_{s_1} - \vec{x}_{s_2}|^2}{\Lambda^2}\right) \quad (35)$$

The geometry of the flame is taken to be a conical flame with a burner radius a and flame length L_f , which covers a wide range of practical applications. The nondimensional parameters affecting coherence are now identified to be the normalized flame correlation length Λ/a , the compactness factor a/λ , the distance of the observer from the flame R/a , and the flame aspect ratio L_f/a . For long flames with $L_f > 2a$, normalizing by $L_f/2$ instead of the radius a is sensible.

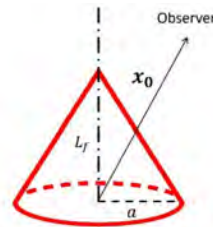


Figure 40. Geometry of a conical flame.

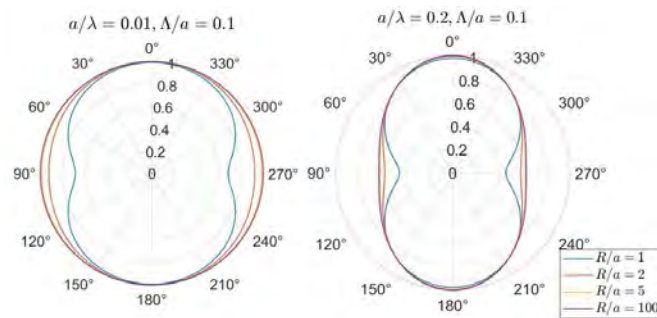


Figure 41. Polar plots of coherence for $\Lambda/a = 0.1, a/\lambda = 0.01$ (left) and $\Lambda/a = 0.1, a/\lambda = 0.2$ (right) for varying distance from the center, for a flame with $L_f = 0$.

As shown in Figure 41, near-field effects influence the coherence even at the acoustically compact limit, where the coherence in the far-field limits to unity. Furthermore, noncompactness reduces coherence even in the far-field limit. The minimum value of coherence is when $\phi = \pi/2$, and the maximum value of coherence is when $\phi = 0$.

At large Λ/a , the coherence is unity for most values of a/λ , and low coherence is observed at certain wavelengths that form narrowband valleys. The location of these valleys appears to be insensitive to Λ/a and R/a ; the location of the first valley is approximately $a/\lambda \approx 0.6$. As Λ/a decreases, coherence is reduced at smaller compactness factors. Furthermore, coherence values do not rise back to unity and stay at lower values. Given that $\Lambda/a < 1$ in many applications of interest, our findings demonstrate that low coherence values can be observed at wavelengths considerably longer than the flame dimensions. Figure 42 also indicates only a weak dependence on the distance, in agreement with the prior observation that coherence does not go to unity even in the far-field limit.

On the centerline, a similar analysis is performed. Overall, the key differences between the coherence when $\phi = 0$ and $\phi = \pi/2$ can be summarized as follows. (a) When $\phi = 0$, coherence is near unity when either the compactness factor is large or the observer is in the far field, whereas when $\phi = \pi/2$, coherence is low even in the far field if the compactness factor is not sufficiently small. (b) Reduction in coherence when $\phi = \pi/2$ occurs at $\Lambda/a, \lambda/a$ values an order of magnitude higher than that when $\phi = 0$. Physically, this outcome is due to the propagation path differences approaching zero on the centerline, whereas a constant path difference exists in the order of the flame width on the burner plane.

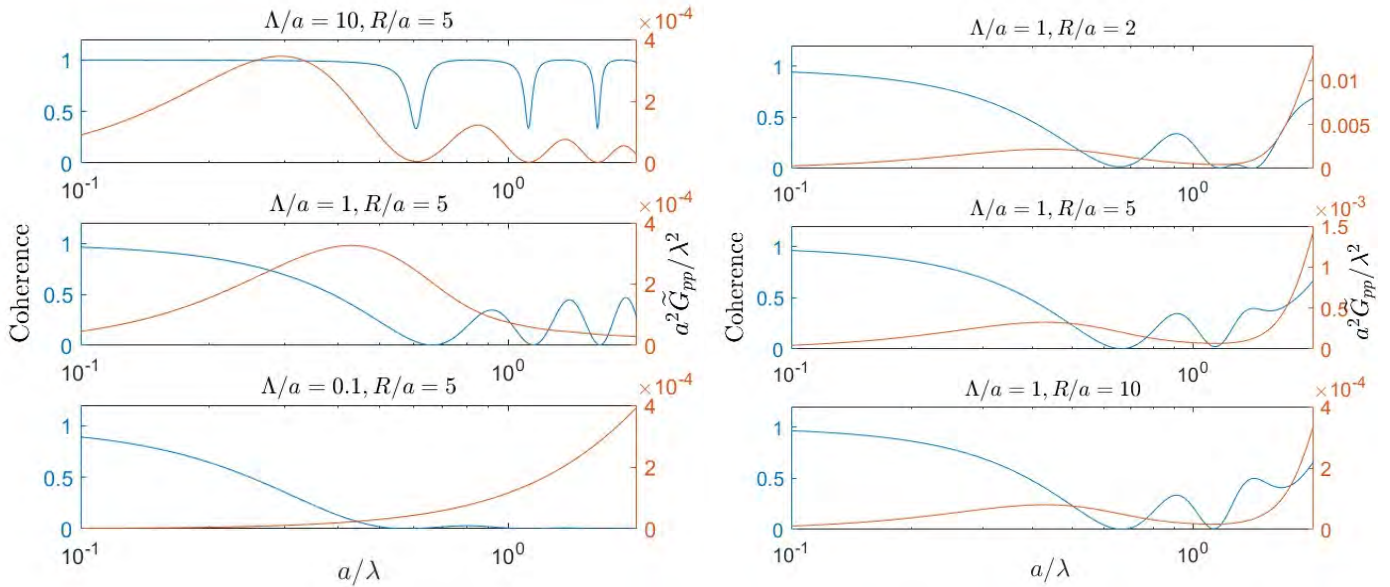


Figure 42. Coherence and acoustic power at $\phi = \pi/2$ for various values of $\Lambda/a, a/\lambda$, and R/a . $L_f = 0$.

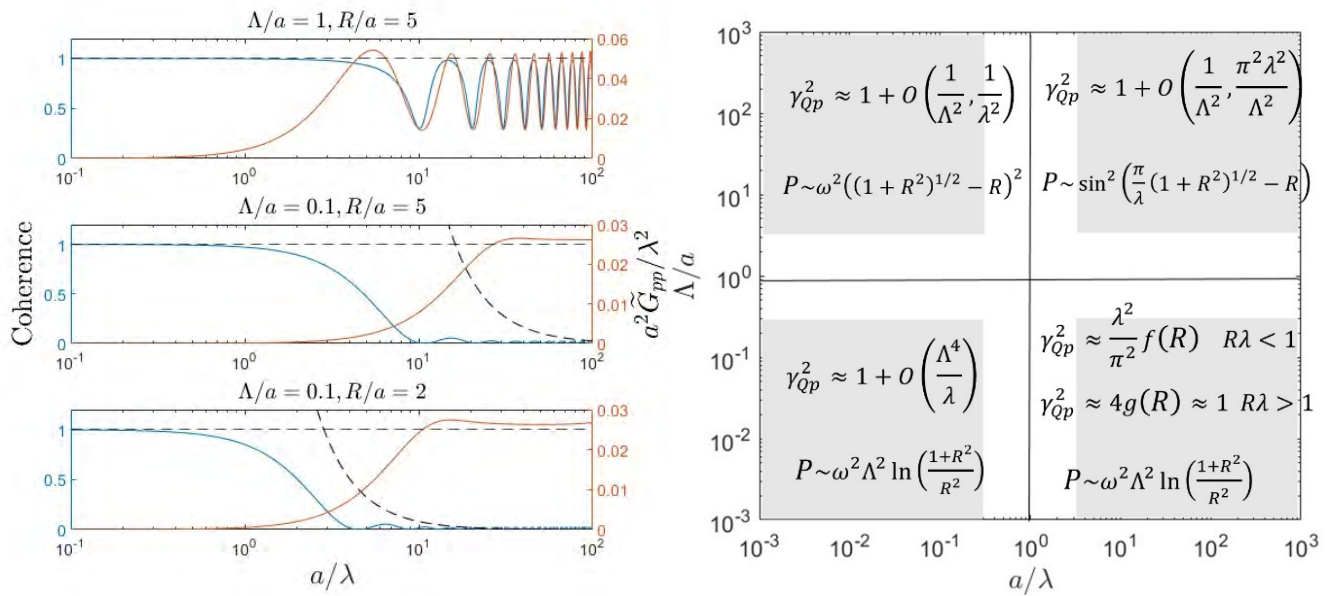


Figure 43. Coherence and acoustic power at $\phi = 0$ for various values of $\Lambda/a, a/\lambda$, and R/a (left), and asymptotic scaling laws derived analytically (right). $L_f = 0$.

Figure 44 shows the effect of flame geometry on the coherence. In summary, coherence is highest perpendicular to, and lowest along the longest dimension of, the flame. That is, for flames where $L_f/a < 2$, peak coherence values occur at $\phi = 0$, whereas where $L_f/a > 2$, peak coherence values occur at approximately $\phi = \pi/2$. Furthermore, coherence is higher closer to the base of the conical geometry, where the most heat release is present. That is, the region of main heat release has the largest contribution to the globally integrated heat release and to the pressure fluctuations if the observer is close, thus leading to high coherence.

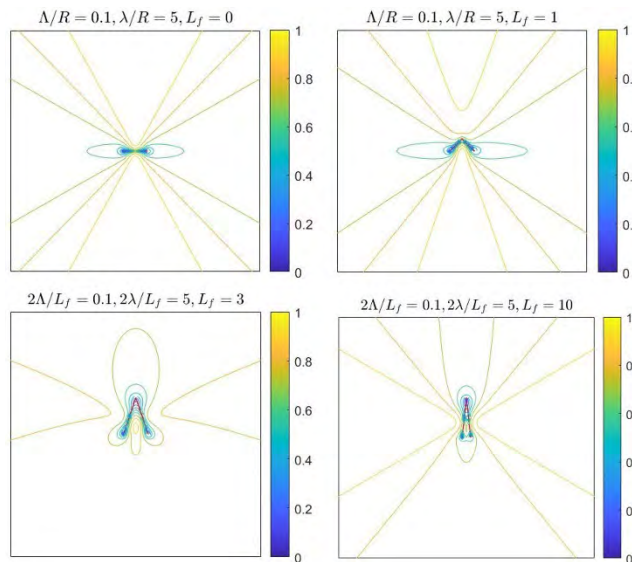


Figure 44. Coherence of conical flames of constant compactness factors and correlation lengths for various L_f .

Milestones

- Extended framework for spray dynamics effects on the flame response
- Entropy generation by non-premixed flames for propagating disturbances
- Extended bi-global hydrodynamics study to develop an empirical transfer function to identify forcing frequencies that cause maximum amplification for the LES base flow
- Identification of new research opportunities for investigating the coherence between the global HRR and pressure fluctuations; demonstration that near-field and noncompactness effects can reduce coherence
- Formulation of an analytical framework for coherence studies; demonstration of the effect of flame geometry on coherence

Major Accomplishments

The flame response framework was extended to a non-linear model for the spray dependence to account for spray dynamics effects. The entropy generation model includes the effects of propagating disturbances.

For the hydrodynamics task, the input-output empirical transfer function predicts amplitude-scaled, linear flow response with a supplied inlet forcing frequency. A sweep of forcing frequencies through the model can identify frequency bands that cause significant amplification. The transfer function can couple well with other tasks aimed at identifying flame response in the presence of in-flow velocity perturbations.

An analytical framework to estimate and study the coherence between the global HRR and direct noise has been developed. This framework provided a partial explanation regarding gaps in the theoretical and experimental literature, and identified the mechanisms of how coherence is reduced. This method of analysis can be used for further study of coherence, possibly extending to confined cases, as in a real combustor.



Publications

Published conference proceedings

Wise, M., John, T. and Acharya, V. (2023, March). Convective Disturbance Effects on Entropy Generation. *13th US National Combustion Meeting, Paper# 180CTM-0210*.

Laksana, A., Patki, P., John, T., Acharya, V., & Lieuwen, T. (2023). Distributed Heat Release Effects on Entropy Generation by Premixed, Laminar Flames. *International Journal of Spray and Combustion Dynamics*. Vol. 15, Issue 3, pp. 139-146.

Outreach Efforts

None.

Awards

None.

Student Involvement

- Graduate student Parth Patki worked on the hydrodynamic stability task under the mentoring of Ben Emerson.
- Graduate student Sungyoung Ha worked on the coherence modeling task under the mentoring of Vishal Acharya and Tim Lieuwen.
- Undergraduate student Michael Wise worked on the entropy generation task under the mentoring of Vishal Acharya.

Plans for Next Period

The flame response framework will further consider spray dynamics aspects such as droplet transport, droplet grouping, and polydisperse sprays. The ROM will be validated with LES data in an ongoing study comparing the ROM equations to the full equations used for the LES. The entropy generation model will consider the effect of transport terms on entropy for diffusion-based flames and then extend to entropy generation of spray flames.

The hydrodynamics modeling will consider a tri-global framework for generic geometry hydrodynamics. In addition, the velocity ROM will be further built and validated with PIV measurements from the GT experiment task.

The coherence modeling analysis will be extended toward confined configurations to assess applicability to noise source separation in the GT or RTRC rig. An experiment with a canonical flame is planned to verify the analytical results and identify other physical processes affecting coherence.

Task 4 – Facility Development at RTRC

Raytheon Technologies Research Center

Objective

The objective of this task is to RQL combustors have been tested at RTRC under the program – one that includes “jailbar” vanes at the combustor exit and closely mirrors the GT design, with a specific focus on the higher-pressure operating points that are not possible for the GT rig, and another one that corresponds to the Pratt & Whitney FAA CLEEN single-sector combustor configuration. Collectively, the GT and RTRC rig capabilities encompass a broad range of operating conditions, thus resulting in a robust dataset for training the design tools.

Research Approach

During the current reporting period, a third test entry was conducted. This entry was a relatively short test program (1 week) leveraging the FAA CLEEN test rig for the purpose of obtaining dual thermocouple probe data and several other test conditions, to complement the test program in 2022 with the same hardware (except for the fuel mixer). Unfortunately, the probe failed early in the test; however, significant new data were obtained regarding indirect noise with non-combustion operation by introducing entropy fluctuation into the combustor. Lessons learned from this year’s entry will be applied to the final rig test in 2024 with the original ASCENT rig. In addition, 2021 data (ASCENT combustor) and 2022 data (CLEEN combustor) were comparatively analyzed.

Figure 45 illustrates the ASCENT and CLEEN combustors' geometric differences, noise spectra, and legacy scaling law plots (from 2021 and 2022 test entries). The most significant difference between the combustors is the relative distance from the combustion zone to the choked exit. The ASCENT rig has a much shorter distance and is typical of current generator aerocombustors, whereas the CLEEN rig is longer, to accommodate a variable-length side branch for studying swirler tonal instability by varying the combustor resonance acoustic modes (which was not used in this investigation, in which the length was fixed). The middle group of plots shows the noise spectra for the CLEEN rig peaks at a lower frequency and is more tonal than the relatively broadband spectra of the ASCENT rig (typical of aerocombustors). With wave decomposition to compute indirect noise (discussed below), the tonal behavior appears to be due to a coupling between the dilution jets and indirect noise.

The plots on the right side of Figure 45 show a legacy scaling comparison. As presented in earlier reporting, the ASCENT rig follows the scaling law quite well, whereas the CLEEN rig scaling is non-typical, tracking at a lower slope, although the scaling reasonably collapses the data.

Figure 46 shows some of the results of non-combustion testing during the third entry (2023), wherein controlled entropy fluctuations were introduced in the absence of combustion noise. Here, the dilution jets were increasing, heated from 200 to 1,000 °F while a cold front-end air supply was maintained. The typical unsteadiness of the dilution jets in cross flow was expected to introduce entropy fluctuations of hot and cold lumps of flow that convect through the choke, thus generating indirect noise that should radiate upstream as well downstream.

The plots in Figure 46 show the response of the two pressures upstream of the choke (1 = bulkhead; 3 = combustor exit) and one pressure downstream of the choke (6), as illustrated in the rig image. The top row shows the pressure spectra, and the bottom row shows coherence with the bulkhead pressure. As the temperature of the dilution jets is increased, at low frequency, both the coherence and pressure increase (particularly for 800 and 1,000 °F), as expected for indirect noise. A very high level of coherence for pressure signals across the choke was observed for the first time in the program. Normally, the flow noise downstream of the choke from shedding and shock wave hides the indirect noise. The absence of combustion and the apparently high level of entropy fluctuations (>800 °F mixing with ~100 °F air) made this observation possible, thus providing validation data for indirect noise modeling.

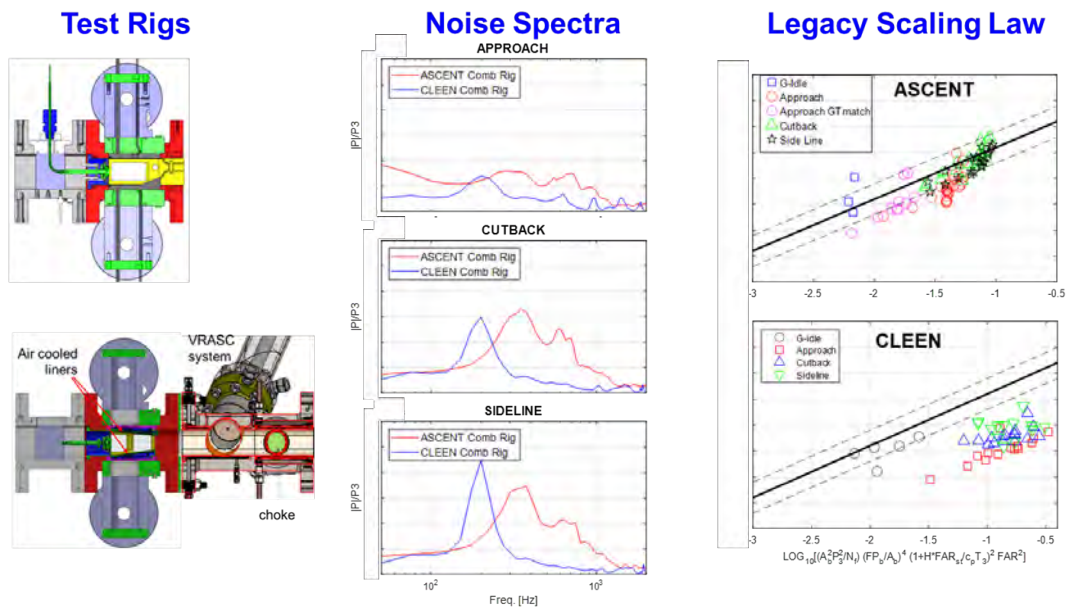


Figure 45. Noise comparison between ASCENT and CLEEN combustors.

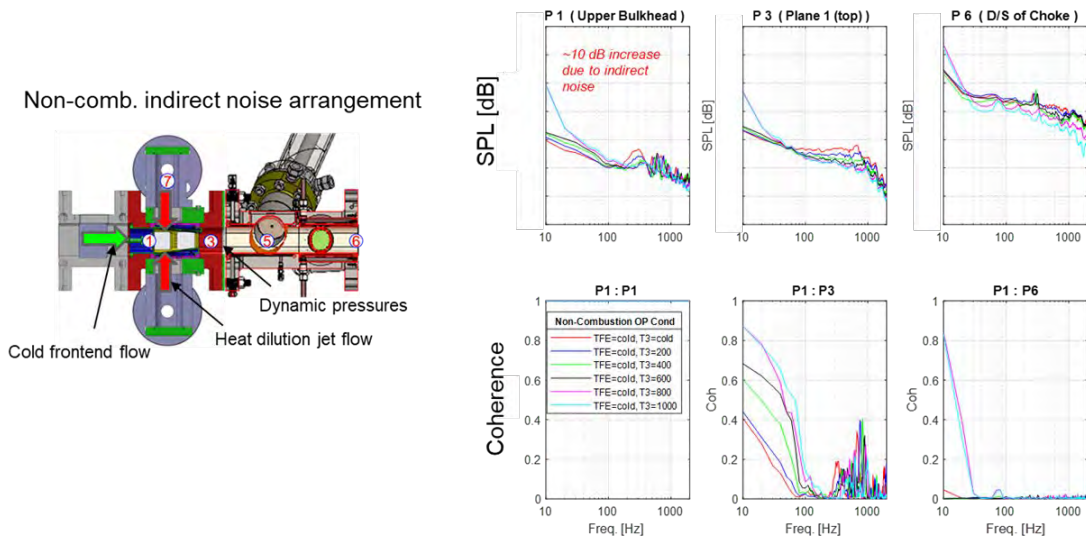


Figure 46. Non-combustion indirect noise test with the CLEEN combustor.

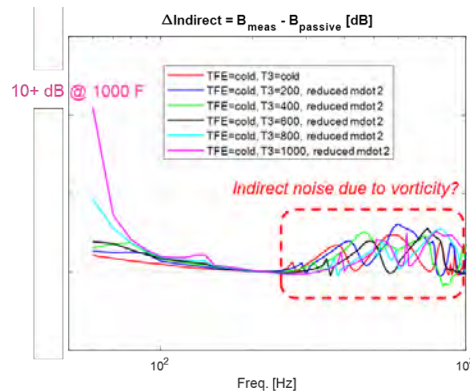


Figure 47. Computed indirect noise using wave decomposition consistent with measured sound pressure levels (SPL) levels.

Indirect noise for this dataset was computed with wave decomposition and is shown in Figure 47. At low frequency, the computed indirect noise is consistent with the observed increase in SPL in Figure 46. This result is also a first for this program, providing validation of the wave-decomposition method of computing indirect noise.

Applying this indirect noise computation to previous datasets provides insight into noise generation in the CLEEN combustor. An example is shown in Figure 48 for FAR sweep of approach conditions. On the left side, the computed indirect noise shows a 3-dB level at low frequencies (independent of FAR) and a very significant increase at ~200 Hz that trends with FAR. Comparison of this frequency with the FEA model indicates that the peak acoustic velocity response in the dilution jets is related to the ~200-Hz indirect noise. The peak acoustic response is due to the plenum bulk mode of the dilution jet feed (illustrated in the image). We speculate that a feedback loop exists between indirect noise and the dilution jet fluctuations (perturbation from jets generates indirect noise that propagates upstream from choke triggering the next cycle of the jet fluctuation).

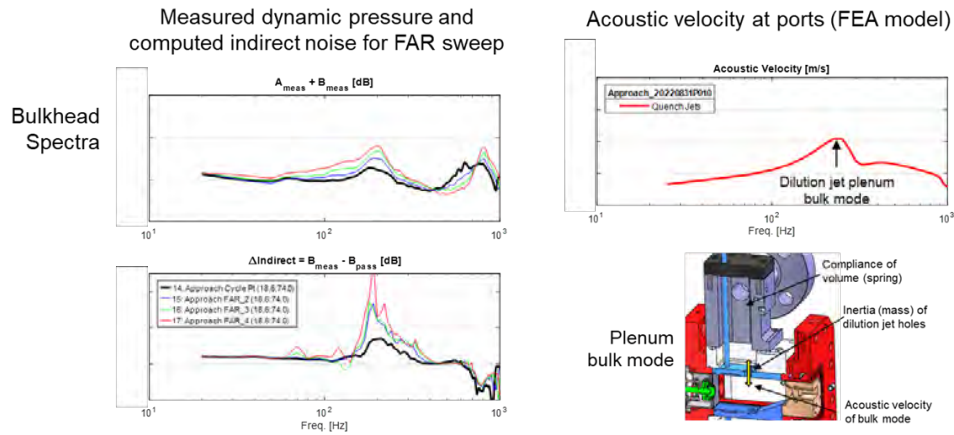


Figure 48. Indirect noise for the CLEEN combustor and relationship to acoustic mode.

Milestones

- Completion of comparison between ASCENT and CLEEN combustor rig results
- Successful completion of the third RTRC experiment entry

Major Accomplishments

- Validation of wave decomposition for computed indirect noise
- Understanding of the relationship between CLEEN noise spectra and indirect noise/dilution jet coupling

Publications

None.

Outreach Efforts

None.

Awards

None.

Student Involvement

None.

Plans for Next Period

Planning and hardware development for the fourth (final) test entry program.

Task 5 – Post-combustion Modeling

Raytheon Technologies Research Center

Objective

The objective of this task is to develop transfer functions from the combustion zone to the nozzle, nozzle to turbine, and turbine to far field. This task involves physics modeling of the following aspects:

- Entropy wave transport post-combustion, as unsteady HRR disturbances at the flame generate entropy disturbances that are then transported through the post-combustion zone;
- Nozzle interactions for the dynamics of pressure disturbances through the nozzle, specifically the effect of the jail bar configuration used in both the GT and RTRC rigs;
- Turbine interactions for the dynamics of pressure disturbances through the turbine; and

- Far-field sound propagation.

Direct noise modeling will also be performed with a numerical Green’s function approach with the heat release model.

Research Approach

The post-combustion-zone physics involves the effects of combustion, unsteady HRR disturbances, and post-combustion geometry on the eventual noise generation outside the engine. This modeling involves the following:

- Direct generation of combustion noise due to heat release and the interaction of these pressure disturbances with the remainder of the engine geometry, which leads to far-field noise.
- Entropy disturbances generated by the flame interacting with geometric changes at the nozzle, and causing pressure disturbances that then interact with the remainder of the engine geometry and lead to far-field noise.

Combustor flow field

Figure 49(a) shows the RMS of the entropy perturbation within the combustor, by using the GT LES data integrated along the z direction. Much of the entropy perturbation is located near the mixing region of the dilution jets. Some entropy perturbation is observed near the flame and cooling flows, but is small with respect to that of the dilution jets. Figure 49(b) shows the area-weighted entropy as a function of frequency along the streamwise direction, and Figure 49(c) shows the entropy power spectrum at two specific locations along the flow. The spectrum near the flame has significantly low-frequency content, but the entropy rolls off at higher frequencies. The peak at 2500 Hz is associated with the quarter wavelength mode of the combustor is discussed later. In the region between the flame and the dilution jets, the entropy content is reduced because of advective dispersion, as described in previous studies. In the absence of dilution jets, this dispersion would be expected to continue up to the combustor exit. Close to the dilution jets, the entropy once again increases at all frequencies because of turbulence. This increased entropy is then advected downstream to the combustor exit. The low-frequency content reduces rapidly, but at frequencies greater than 300 Hz, the entropy level near the combustor exit is greater than that near the flame. Peaks are also present in the entropy spectrum near the choke at 700 Hz and 1000 Hz; these peaks are only weakly present downstream of the dilution jets. The 2500-Hz peak near the flame is not present near the choke. These findings suggest that not all entropy near the choke is from the flame region alone.

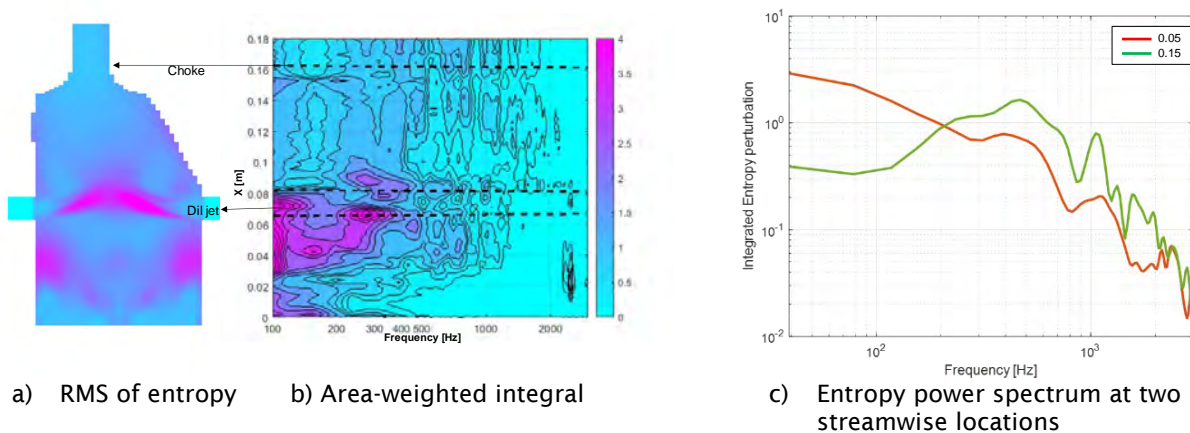


Figure 49. Entropy distribution within the combustor.

Direct noise computation

The direct noise from the unsteady heat release within the combustor can be computed with the approach outlined by Dowling. The Helmholtz equation (Eq. (36)), where the source term is a function of the HRR per unit volume (\dot{q}_v'), is solved with a finite element package for the unsteady acoustic pressures. The time-averaged density ($\bar{\rho}$) and speed of sound (\bar{c}) are obtained from the LES flow field, and the unsteady HRR is obtained from the LES flow field.

$$-\frac{1}{\bar{\rho}c} \frac{\partial^2 p'}{\partial t^2} + \frac{\partial}{\partial x_i} \left(\frac{1}{\bar{\rho}} \frac{\partial p'}{\partial x_i} \right) = -\frac{\gamma - 1}{\bar{\rho}c} \frac{\partial q'_v}{\partial t} \quad (36)$$

The total integrated HRR from the LES is uniformly distributed over the region of the combustor between the bulkhead and dilution jets.

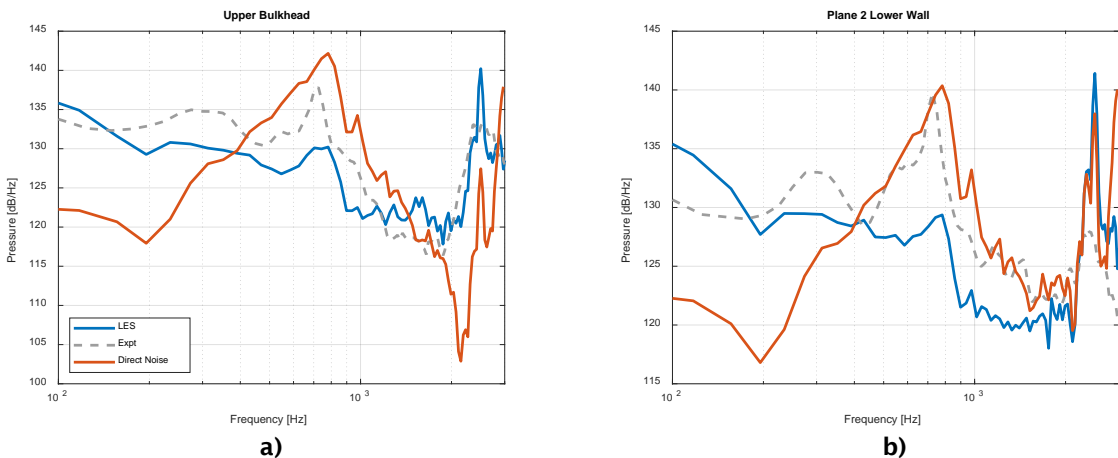


Figure 50. Computed direct noise and LES unsteady pressures at the (a) upper bulkhead and (b) lower ramp.

Figure 50 shows the PSD of the computed direct noise with Eq. (36), along with the LES pressures and measured RTRC experimental data at two locations within the combustor. The general shape of the power spectrum between the LES and the measured data is similar, with differences observed near 700-Hz and 2500-Hz frequencies. The LES flow field is saved for 0.17 s at a rate of 10,000 samples per second for a total of 1,700 time steps. The 700-Hz frequency is driven largely by entropy and the turbulence within the flow (discussed below). The lower frequencies are thus not completely free of turbulent noise. Many time steps would be expected to be necessary to fully resolve this entropy driver frequency. The experimental data have been obtained for 30 s; hence, any turbulence-related noise is averaged out. The 2500-Hz tone observed in the LES and the experiment is driven by the longitudinal mode of the combustor. The LES pressures at this frequency are less damped than those in the experiment, probably because the assumption of adiabatic walls in the LES is not entirely true for the combustor rig. This aspect is particularly exaggerated downstream of the dilution jets, where the mean flow temperature is cooler. The experimental rig has a small amount of cooling flow near the observation windows, which further extracts energy and tends to damp out the longitudinal mode to a greater extent than predicted by the LES.

Despite the above-described limitations of the LES dataset, the direct noise computation interestingly predicts the 700-Hz frequency somewhat accurately. However, the lower frequency is significantly lower in magnitude than the experiment as well as the LES. This difference is due primarily to indirect noise sources within the combustor.

Total noise computation

The total noise within the combustor is a combination of the direct noise from the unsteady heat release and pressure perturbations generated through the accelerating entropy inhomogeneities near the combustor exit. The acceleration of these entropy inhomogeneities through the choked region at the combustor exit results in acoustic pressure perturbations traveling backward into the combustor and forward into the downstream turbine stages. Accurately estimating the entropy near the combustor exit is not easy for modern combustors including dilution jets or other crossflow features. The current approach is to use the linearized Navier–Stokes equations (LNSEs) for non-reacting flows, as shown in Eq. (37). The LNSEs are obtained by assuming small perturbations for temperature, velocity, and pressure within the flow, and assuming that these perturbations do not in turn affect the mean flow. The LNSEs are modeled as a forced response in the frequency domain with the HRR term as the forcing function and solved with a finite element solver.

$$\begin{aligned} \frac{D\rho'}{Dt} &= \frac{\partial\rho'}{\partial t} + \bar{u}_i \frac{\partial\rho'}{\partial x_i} = -u'_i \frac{\partial\bar{\rho}}{\partial x_i} - \bar{\rho} \frac{\partial u'_i}{\partial x_i} - \rho' \frac{\partial\bar{u}_i}{\partial x_i} \\ \bar{\rho} \frac{Du'_i}{Dt} &= \bar{\rho} \frac{\partial u'_i}{\partial t} + \bar{\rho}\bar{u}_j \frac{\partial u'_i}{\partial x_j} = -\bar{\rho}u'_j \frac{\partial\bar{u}_i}{\partial x_j} - \rho'\bar{u}_j \frac{\partial\bar{u}_i}{\partial x_j} - \frac{\partial p'}{\partial x_i} + \eta \left[\frac{\partial^2 u'_i}{\partial x_k \partial x_k} + \frac{1}{3} \frac{\partial}{\partial x_i} \left(\frac{\partial u'_k}{\partial x_k} \right) \right] \\ \frac{Dp'}{Dt} &= \frac{\partial p'}{\partial t} + \bar{u}_i \frac{\partial p'}{\partial x_i} = -u'_i \frac{\partial\bar{p}}{\partial x_i} - \kappa\bar{p} \frac{\partial u'_i}{\partial x_i} - \kappa p' \frac{\partial\bar{u}_i}{\partial x_i} + (\kappa-1) \left\{ \Phi' + \lambda \frac{\partial^2 T'}{\partial x_k \partial x_k} + \dot{q}'_v \right\} \end{aligned} \quad (37)$$

For this set of equations, the time-averaged velocity, density, and pressures are used as the background mean flow. Sharp velocity gradients in the boundary layer and near the dilution jets can result in numerical instabilities when solving the LNSEs. These instabilities are ameliorated by the first smoothing out these gradients before solving the equations. Because the LNSE includes the mean flow velocity, the effect of the high Mach number near the choke is included, and no special treatment must be performed. The region downstream of the choke is treated as a perfectly matched layer, and any acoustic perturbations propagating downstream are absorbed by this region without any reflections. The walls of the combustor are treated as adiabatic slip walls. The outcome of solving this set of equations is the acoustic pressures, along with density and velocity perturbations within the combustor, which can then be used to calculate entropy perturbation as an input to the turbine propagation model.

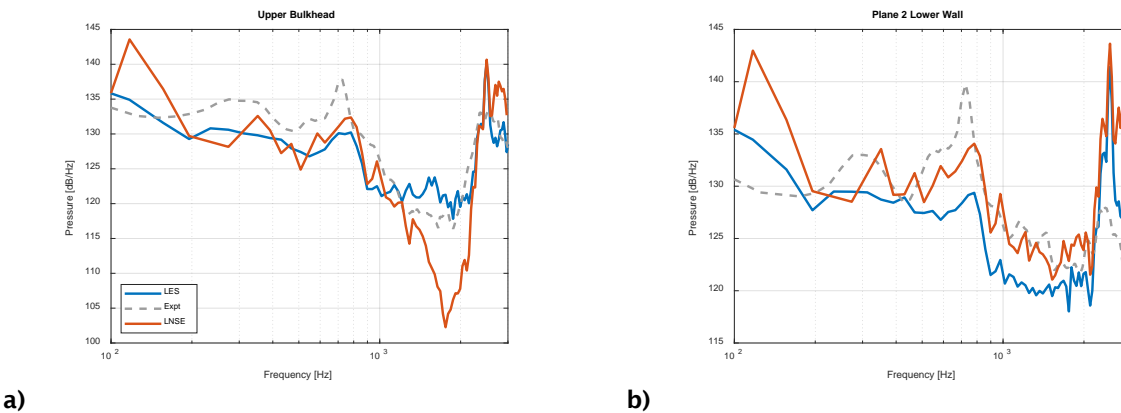


Figure 51. Total noise inside the combustor, predicted by the LNSEs at the (a) upper bulkhead and b) lower ramp.

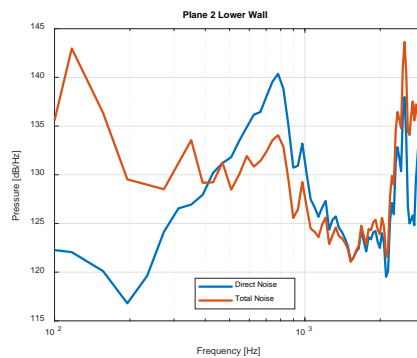


Figure 52. Direct and total noise predictions within the combustor.

Figure 51 shows a comparison of the acoustic pressure spectrum predicted by the LNSEs, with the LES and measured experimental data. The LNSEs predict the acoustic pressure within the combustor reasonably well. The acoustic levels at the low frequencies compare very well with both the LES and the experimental findings. The differences at these frequencies with the direct noise computations (Figure 50) are due to entropy-related noise or indirect noise. The peak at



700 Hz is also predicted by the LNSE but is smaller than that predicted by the direct noise alone, and therefore may be a result of the combination of unsteady heat release fluctuation and the entropy-generated noise at this frequency. Comparison of the predictions of the LNSE and the direct noise indicates that the largest effect of entropy is at low frequencies below approximately 800 Hz. Some differences are observed at higher frequencies but are likely to be due to the incorrect impedance at the choke used in the Helmholtz equation. Thus, the indirect noise at low frequencies can be as much as 10 dB higher than the direct noise.

Modal decomposition of the flow field with spectral proper orthogonal decomposition

Modal decomposition of the flow field is performed with spectral proper orthogonal decomposition (SPOD), which decomposes the variables according to the spectral energy at each mode and frequency. Figure 53 shows the mode energy associated for six modes as a function of frequency for the entropy and pressure perturbations. The most energetic mode clearly shows several distinct frequencies, as shown in the figure.

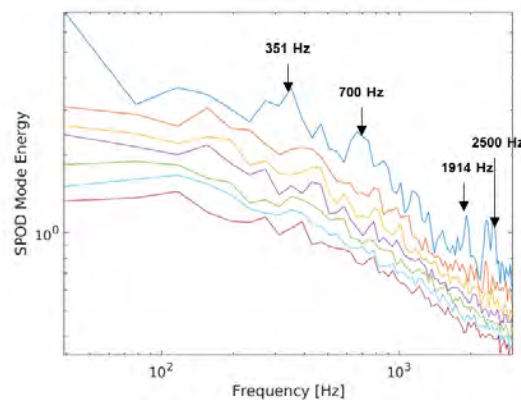


Figure 53. SPOD modal energy for the first six entropy–pressure modes.

Figure 54 shows the pressure and entropy mode shapes at 2500 Hz. The mid-plane view of the pressure perturbation (Figure 54a) indicates that this mode is associated with the longitudinal mode of the combustor. The mid-point of this mode is located at the dilution jet region; hence, potential exists for coupling between the dilution jets and the acoustic mode, as seen in the entropy mode shapes in Figure 54c and Figure 54d. The coupling with the longitudinal mode results in pumping of the dilution jets at 2500 Hz, thereby resulting in strong vortex formation. Figure 54c shows that this mode may also couple with the flame, thus resulting in a longitudinal mode within the flame shear layer.

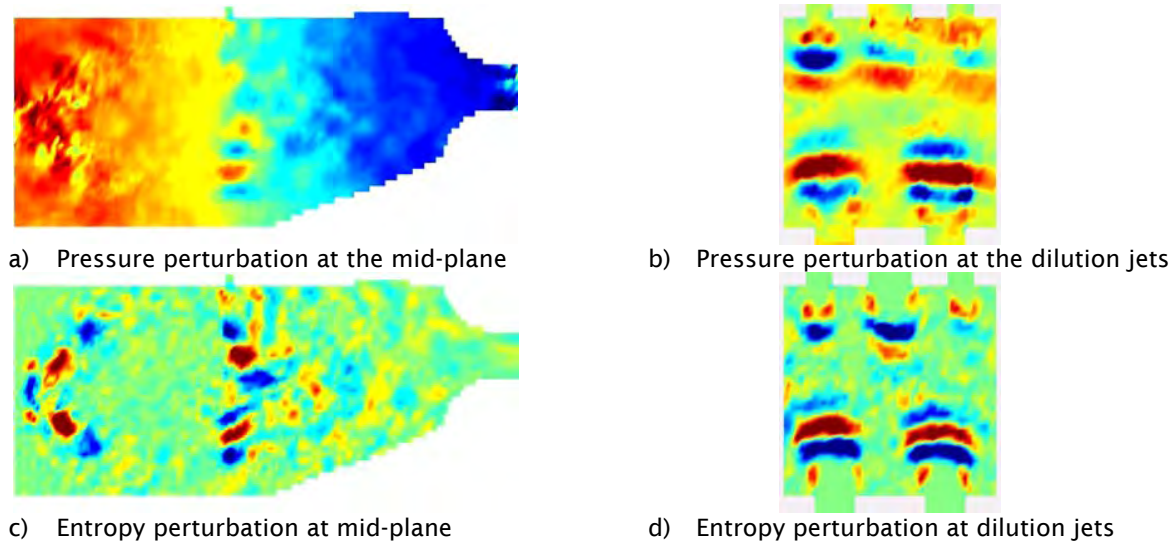


Figure 54. Snapshots of pressure and entropy mode shapes at 2500 Hz at one time instance.

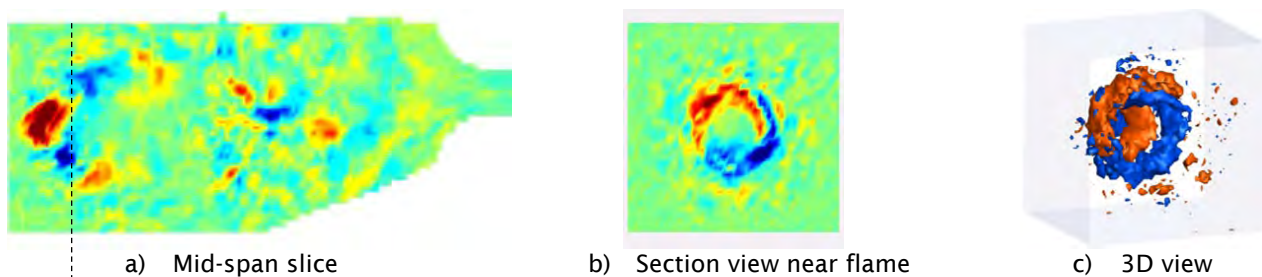


Figure 55. Snapshots of entropy mode shape at 1914 Hz at one time instance.

Figure 55 shows snapshots of three views of entropy mode associated with 1915 Hz. Clearly, this mode represents the swirl mode of the flame, characterized by a counterclockwise motion. This mode is dependent on the swirler design and the fuel and air flow rates, and is not an acoustic mode of the combustor.

Figure 56 shows snapshots of the entropy mode at different time instances. This mode at 700 Hz is somewhat unexpected but is also observed in the unsteady acoustics measurements in the RTRC experiments, as well as in the direct and indirect noise computations from the LES flow field. The SPOD mode shapes suggest that the entropy associated with this frequency is convected from the flame to the choke region with almost no dispersion. The convection wavelength for this mode is very close to the distance from the flame to the dilution jets and from the dilution jets to the choke. The entropy generated at the flame convects to the dilution jet and is reinforced by entropy by further addition from the dilution jets.

Typically, scalar fields at a particular frequency disperse within the flow field when they convect more than two wavelengths. This finding is true for the entropy transport at frequencies larger than 700 Hz for this combustor flow field. At 700 Hz, the entropy transport from the flame to the dilution jet and the dilution jet to the choke are each almost exactly two wavelengths. Because of reinforcement at the dilution jets, the entropy at 700 Hz convects with minimal dispersion. At lower frequencies, the reinforcement at the dilution jets is absent, because the entropy inhomogeneities arrive at the dilution jets with random phasing. The noise computation shown in Figure 52 underpredicts the measurement at 700 Hz, probably because the entropy addition from the dilution jets is driven by turbulence, and hence the phasing is somewhat random. With longer simulation times, this randomness is expected to “average out” and increase the spectral level of the tone at 700 Hz.

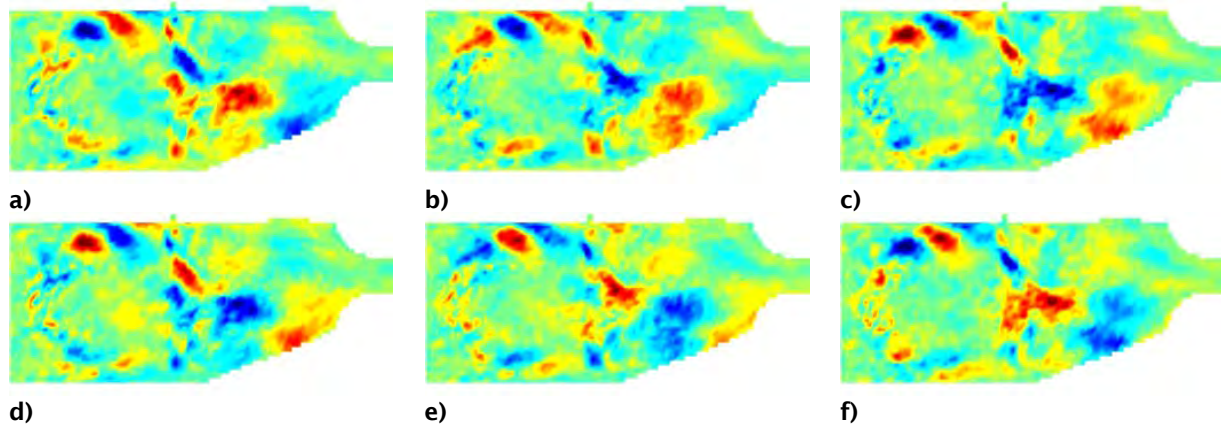


Figure 56. Snapshots of the entropy mode at 700 Hz at successive time intervals.

At 351 Hz, an increase in modal energy is again observed (Figure 53) because the distance from the flame to the dilution jets, and from the dilution jets to the choke, now corresponds to one wavelength of convection distance. However, the energy at the dilution jets at this frequency is not sufficiently significant and does not result in strong acoustics. Nevertheless, the frequency is visible in the acoustics computations and the RTRC experimental data.

Turbine and nozzle wave interactions

Tasks 1.3 and 1.4 focus on wave propagation, transmission, and reflection through the turbine section downstream of the combustion chamber. The turbine consists of two sections (high pressure and low pressure), both of which consist of multiple rows. Our studies focused on the first stage of the high-pressure turbine, which consists of a stator and a rotor. The stator is also commonly called the nozzle guide vane. In combustor rigs, such as the two rigs studied here, only a nozzle that has a similar minimum area to that of the nozzle guide vane, but otherwise has no flow turning function, is present. To distinguish between wave propagation in the real turbine and in the combustor rig nozzle, this task is split into two: Task 1.3 is concerned with the combustor nozzle analysis, and Task 1.4 is concerned with a single-stage high-pressure turbine. For both tasks, HiFi lattice Boltzmann method (LBM) simulations are conducted, and existing ROMs are revisited. Where applicable, corrections to the existing ROMs are proposed, on the basis of the learning from the LBM results. The existing ROM for the turbine is the actuator disk theory (ADT) by Cumpsty and Marble. Most of the work in Year 3 focused on turbine modeling and improvements to the ADT ROM; details are reported herein.

Turbine interaction modeling: direct noise: This task focuses on simulations of a high-pressure public-domain turbine rig from the Polytechnic University of Milan and the German Aerospace Center to investigate direct and indirect noise propagation through a representative high-pressure turbine stage. A comprehensive set of HiFi LBM simulations was performed in Years 1 and 2 for high-subsonic and transonic turbine flow conditions and was successfully validated against experimental data from the German Aerospace Center. The sound power reflection coefficient and transmission coefficient agreed well between the simulation and experiment. The remaining portion of the sound power ($1 - R - T$), where R is the reflection, and T is the transmission), which is neither reflected nor transmitted, was found to be approximately 60% of the total sound power. We hypothesized that this portion of the power is related to sound dissipation caused by the conversion of acoustic energy into shed vorticity from the blade and vane trailing edges and other sharp geometrical features. A comparison to ADT indicated that the theory overpredicted the transmitted sound, because it does not account for such sound dissipation effects. Various simulations were performed in Year 2 to demonstrate that a large amount of the sound power is dissipated in the turbine.

In Year 3, the focus was on a detailed analysis of the mechanism of sound dissipation and finding a ROM correction term to account for these effects. The additional analysis focused on the wake region of the stator row, as shown in Figure 57. Study of the flow field downstream of the vane trailing edge, in the presence of acoustic excitation, clearly indicated that, in addition to an oscillating pressure field at the acoustic forcing frequency, the vorticity field also displays oscillations at the same frequency. This finding underscores that vorticity generation indeed occurs in the vicinity of the trailing edges.

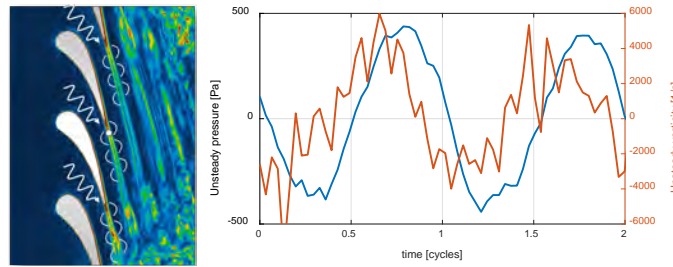


Figure 57. Cyclic vorticity shedding in the wake of the stator vanes in response to the acoustic forcing.

To quantitatively capture the sound dissipation effect, we applied the theory of Howe to the current LBM data. The model is based on a splitter plate in a duct with uniform mean flow Mach number M on both sides, and is based on the assumption that sound approaches the trailing edge with a phase difference in Θ between the pressure side and suction side of the plate. Sound diffraction at the trailing edge is modeled with application of the Kutta condition to determine the strength of the shed vorticity. The phase therefore determines how efficiently acoustic energy is converted into vorticity generation. The solution of this diffraction problem is greatly simplified for a plane wave, which is considered here. For double-sided forcing, the dissipated sound power Π_D for an incident plane wave on both sides of the plate ($2\Pi_0$) is given by the following solution that includes only the Mach number and phase angle as parameters controlling the amount of sound power dissipation:

$$\frac{\Pi_D}{2\Pi_0} = 1 - \left(\frac{1-M}{1+M}\right)^2 \sin^2\left(\frac{\Theta}{2}\right) - \cos^2\left(\frac{\Theta}{2}\right) \quad (38)$$

This equation has the following solutions:

$\Theta = 0^\circ:$	$\frac{\Pi_D}{2\Pi_0} = 0$	(no dissipation)
$\Theta = 90^\circ:$	$\frac{\Pi_D}{2\Pi_0} = \frac{2M}{(1+M)^2}$	(same as single-sided forcing)
$\Theta = 180^\circ:$	$\frac{\Pi_D}{2\Pi_0} = \frac{4M}{(1+M)^2}$	(maximum dissipation)

Figure 58 shows the bandpass-filtered pressure field from an LBM solution with 600-Hz forcing. The results indicate that, despite the plane wave forcing, the wavefront shows a phase difference ($\theta \neq 0^\circ$) between the pressure and suction side near the trailing edge. This aspect is further visualized through the time history of two monitor points on opposing sides of the vane and near the trailing edge. The phase angle from the time signal is calculated to be $\sim 80^\circ$, which falls roughly in the middle of the expected dissipation values according to Eq. (38).

Applying Eq. (38) to the simulation data (Figure 59) shows that very good agreement (except at $M = 0$, where the model is not applicable) between theory and LBM can be achieved by assuming a phase angle of 95° . Using the value of 80° obtained from the spot check in the simulation would underpredict the amount of dissipation. For M , the time-averaged absolute Mach number is calculated near the exit of the vane row. In reality, this model is a simplification of the actual shedding mechanism, which does not include the effect of the turbulent boundary layers on both sides of the vane/plate and the associated sheared wake flow. In addition, the calculated phase angles may show some sensitivity with respect to the precise location in the vicinity of the trailing edge. Therefore, in the following, the phase angle is considered to be a tuning parameter that can be used to control the amount of dissipation to better match the simulation data and also provides a way to parametrically study the impact of dissipation on overall noise transmission through the turbine and into the far field, when used within the noise prediction toolchain.

ADT by Cumpsty and Marble is applied for both turbine operating conditions, for that stator alone; the comparison is shown in Figure 60. The amplitude of the reflected pressure is predicted well by the theory for all frequencies considered. As expected, the transmitted sound is overpredicted, because ADT does not account for sound dissipation effects. A

correction to the transmitted acoustic pressure from ADT is proposed, wherein the correction is applied with respect to the transmitted sound power in the following form:

$$\Pi_T = \Pi_{T,ADT} - \Pi_D \Rightarrow \frac{\Pi_T}{2\Pi_0} = \frac{\Pi_{T,ADT}}{2\Pi_0} \left(1 - \frac{\Pi_D}{\Pi_{T,ADT}} \right)$$

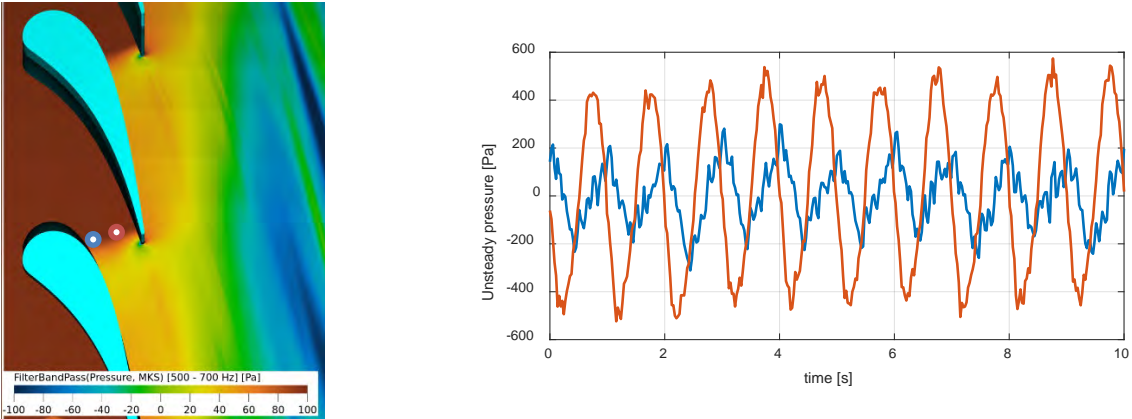


Figure 58. Pressure at the forcing frequency and phase angle between two monitor points near the trailing edge.

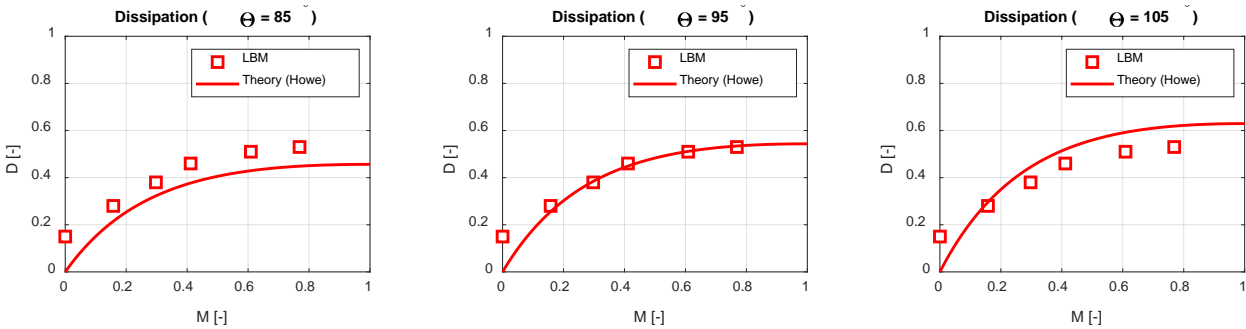


Figure 59. Application of the splitter plate dissipation model to LBM data for different phase angles Θ .

The acoustic pressure amplitude ($p \propto \sqrt{\Pi}$) downstream of the actuator disk can be calculated through multiplication by the following correction term C_p :

$$C_p = \frac{P_{2,C}^+}{P_{2,ADT}^+} = \sqrt{1 - \frac{\Pi_D}{\Pi_{T,ADT}}} = \sqrt{1 - \frac{4M}{(1+M)^2} \sin^2\left(\frac{\Theta}{2}\right)} \tag{39}$$

Of note, the dissipation correction is assumed to be applied with respect to the predicted transmitted sound power based on ADT, not the incident sound power. With this correction term in place, the level of agreement between LBM and ROM significantly improves, as shown in Figure 60.

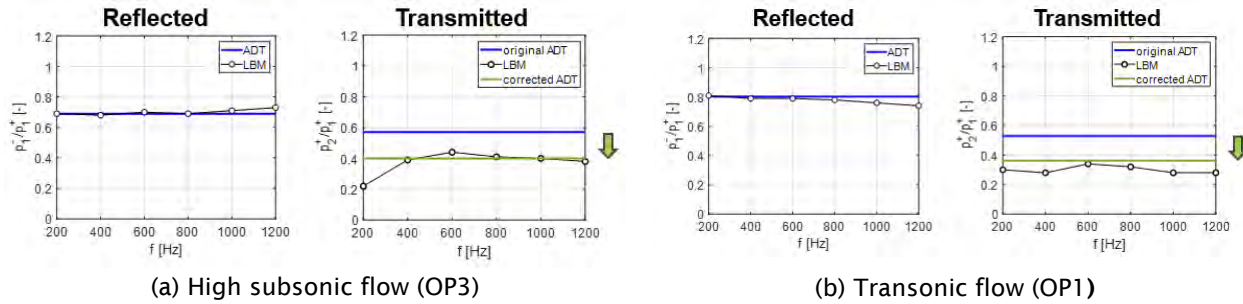


Figure 60. ADT applied to the stator row for various operating conditions.

A comparison of ADT to LBM is also performed for other Mach numbers. Figure 61 shows the predicted reflection and transmission pressure amplitudes for the stator row. The highest two Mach conditions correspond to OP3 and OP1 of the turbine stage. For this higher Mach regime, which is representative of a high-pressure turbine operating condition, ADT and LBM agree very well in terms of reflection and in terms of transmission, when the correction term is enabled. This observation is equivalent to that in Figure 60. As the Mach number through the stator is reduced, ADT and LBM begin to deviate, even for the reflection coefficient: ADT predicts lower reflection and higher transmission. Because these lower Mach numbers are not relevant to realistic operating conditions, they are not further analyzed here.

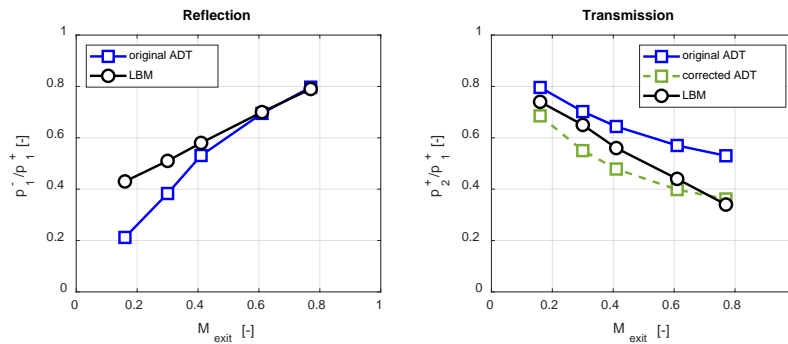


Figure 61. ADT applied to the stator row for different Mach numbers, with and without dissipation correction.

We next focus on the high Mach regime. The dissipation correction can be applied to the rotor as well. A sample calculation is provided below, to demonstrate that this approach yields correct values. The rotor exit velocity must be known in the relative frame of reference, to calculate the Mach number M for Eq. (38). This value (if the exit flow angle is assumed to be 0) is simply given by:

$$M_R = \sqrt{M^2 + \left(\frac{2\pi r n}{c_0}\right)^2}$$

where M is the rotor exit Mach number in the absolute frame, c_0 is the speed of sound, r is the rotor radius, and n is the rotor rotational speed. For simplicity, the rotational speed at the rotor midspan is used. The total dissipation for the stator and rotor is then given by the sum of the stator dissipation and the transmitted-power “weighted” rotor dissipation:

$$D_{S+R} = D_S + D_R = D_S + T_S \left[1 - \left(\frac{1-M_R}{1+M_R}\right)^2 \sin^2\left(\frac{\Theta}{2}\right) - \cos^2\left(\frac{\Theta}{2}\right) \right] \quad (40)$$

Table 3 summarizes the calculation results with Eq. (40) for both turbine operating conditions. In both cases, the rotor dissipation is on the order of 50% and hence is similar to the contribution from the stator. However, because less than 20% of the original sound power is transmitted through the stator (T_S), the added dissipation of the rotor is less than 10%; consequently, the total sound power dissipation coefficient in both cases is on the order of 60%, in agreement with the dissipation values determined directly from the LBM simulation of stator plus rotor.

Table 3. Prediction of turbine stage sound dissipation.

	D_S	T_S	M_R	D_R	$D_S + D_R$ (Eq. (40))	$D_S + D_R$ (LBM)
OP3	0.51	0.12	0.42	0.45	0.57	0.61
OP1	0.53	0.19	0.68	0.52	0.62	0.61

In conclusion, Eq. (39) can be applied to ADT to correct the transmitted pressure amplitudes. This equation must be applied for each row and requires the exit Mach number for each stage row in the respective reference frame of the stage. The phase angle θ can be set for each row separately. In the present cases, a single value of $\theta = 95^\circ$ was found to be sufficient.

Turbine interaction modeling: indirect noise: Beyond investigating the direct noise propagation through the turbine, we performed additional simulation work to investigate indirect noise generation and transmission through the turbine stage, in the form of injected unsteady temperature perturbations upstream of the turbine. High-fidelity simulations were performed, wherein the acoustic driver upstream of the turbine was replaced with circumferentially positioned injection ports. This setup, shown in Figure 62, closely mimics the experimental setup of the Polytechnic University of Milan (PoliMi) and the German Aerospace Center (DLR) rig. Each injector was installed at 70% span with 1/3 pitch offset in the circumferential direction, as measured from the vane leading edge toward the pressure side. This setup was already considered in Years 1 and 2 but was revisited in Year 3 for further simulation work and more in-depth validation with published data that were not available until Year 3 of this program.

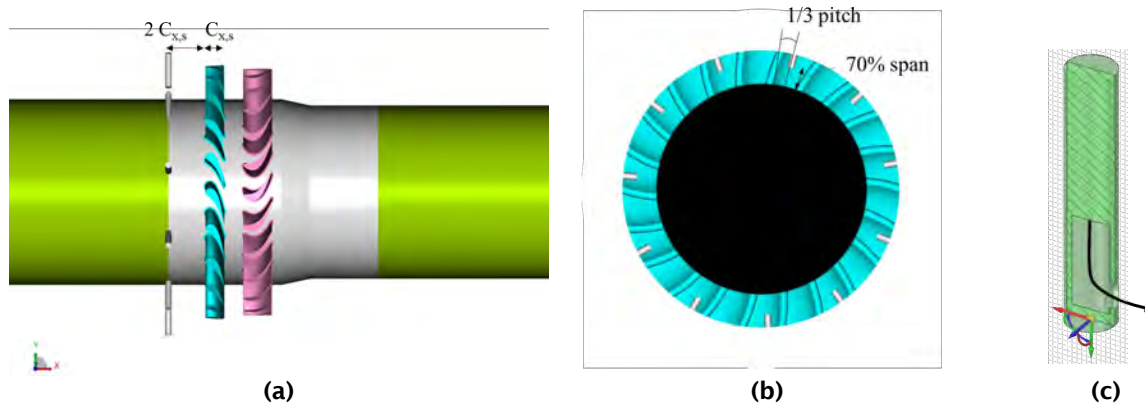


Figure 62. Simulation domain details for indirect noise studies, using 11 circumferentially arranged injectors for entropy wave generation. (a) Side view, (b) front view, and (c) cut-away view of a single injector.

The simulations were run with a constant elevated injection temperature first to create hot streaks, and then adjusted to provide a sinusoidal time variation with a period of $f = 90, 250, \text{ or } 400$ Hz. Entropy wave generation was accomplished through time-harmonic variation in the injection temperature, while the total injection pressure remained constant. The peak-to-peak temperature is given by $\Delta T_s = T_{s,streak} - T_{s,ref}$, where $T_{s,ref}$ is the reference “cold” temperature in the bulk flow, and $T_{s,streak}$ is the maximum “streak” temperature of the injected air. The simulations were first run with a constant elevated injection temperature $T_{s,streak}$ and then adjusted to provide the following time variation:

$$T_s(t) = 0.5(T_{s, streak} + T_{s, ref}) + 0.5(T_{s, streak} - T_{s, ref}) \cos(2\pi f_{source} t) \quad (41)$$

Three injection amplitudes were considered (Figure 63), the lowest corresponding to the value used in the DLR experiment.

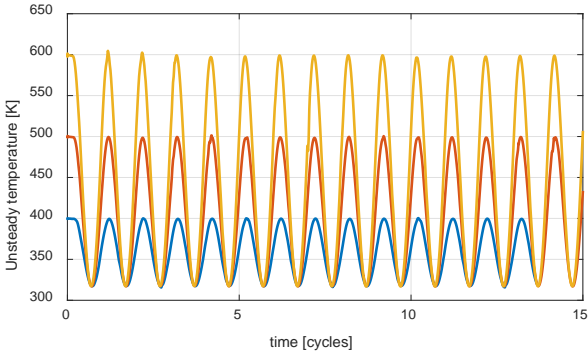


Figure 63. Temperature amplitudes of the injected entropy waves for three injection ratios: $T_{inj}/T_{ref} = 1.26, 1.58, \text{ or } 1.89$, where $T_{ref} = 320.1 \text{ K}$.

The unsteady temperature field interacts with the turbine and creates acoustic waves as the temperature hotspots convect through the accelerated non-uniform turbine flow field. Figure 64 shows the total temperature field during one injection cycle.

The simulations were subsequently repeated for other forcing amplitudes. According to ADT, the noise generation from the entropy wave interaction with the turbine should be frequency independent. The following discussion is focused on the 250-Hz simulation results, for two reasons: (a) the numerical buffer regions was not designed for the 90-Hz forcing wavelength and includes large reflection from the domain exit, and (b) the first non-planar cut-on mode occurs around 308 Hz (upstream) and 318 Hz (downstream). The 400-Hz excitation includes higher-order modes that are not representative of the test setup.

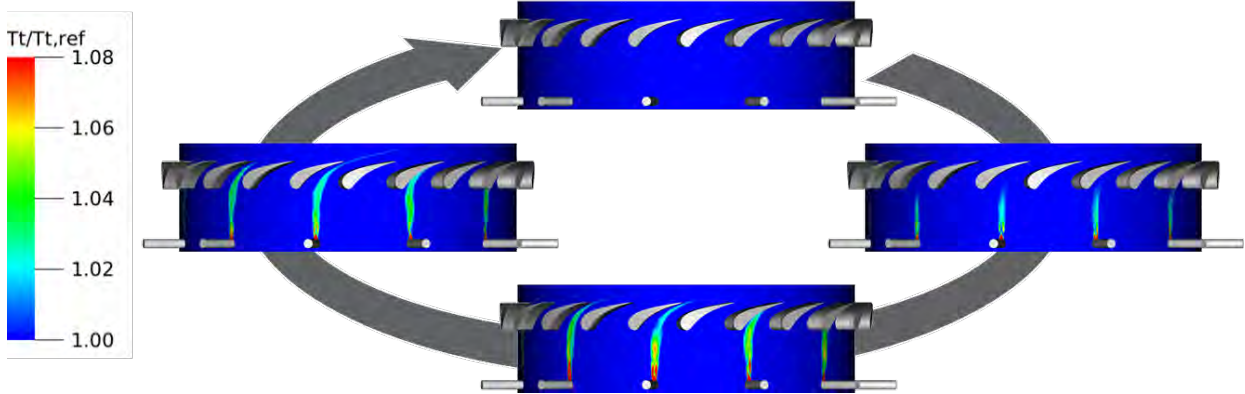


Figure 64. Entropy wave injection cycle (rotor blades not shown) for high-subsonic turbine flow.

The DLR experiment was conducted at 90 Hz. The noise data published by Knobloch et al. do not contain absolute sound power levels but only relative levels with respect to cold injection. However, Pinelli et al. have recently published simulation data including an absolute value for the downstream noise for the 90-Hz forcing. No upstream power data were included. Here, the 250-Hz plane-wave forcing case was post-processed, and the upstream and downstream propagating sound power was calculated via modal decomposition of the pressure. The results are summarized in Table 4.

Table 4. Predicted entropy wave sound power levels for $T_{inj}/T_{ref} = 1.26$ compared with data from the literature.

	RTRC (250 Hz)				Pinelli et al. (116.6 Hz)	DLR EXP (90 Hz)
	Plane 1	Plane 2	Plane 3	Plane 4		
Upstream	105.1 dB	105.1 dB	105.1 dB	105.1 dB	100.3 dB	-
Downstream	96.6 dB	97.6 dB	98.3 dB	98.4 dB	98.0 dB	98.7 dB

The major observations are as follows:

- The forcing frequency differed in all three cases (RTRC, Pinelli et al., and DLR experiment). However, all cases involved only plane waves, and differences due to frequency should be marginal.
- The upstream sound power is higher than the downstream noise, in agreement with the predictions by Pinelli et al. and the acoustic field visualization shown in Figure 65.
- The upstream sound power is insensitive to the data extraction location, and the values are 4.8 dB higher than the values reported by Pinelli et al.
- The downstream sound power levels are sensitive to the data extraction location, with values slightly increasing toward the downstream direction. This finding is likely to be related to the presence of hydrodynamic fluctuations.
- The downstream power levels are consistent overall with the experimental data and the predictions by Pinelli et al.

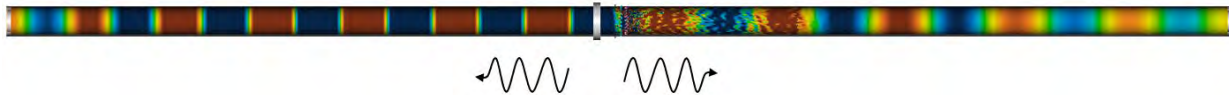


Figure 65. Visualization of the upstream- and downstream-propagating acoustic pressure because of entropy wave interaction with the turbine stage.

Notably, because of the nature of the entropy wave generation by flow injectors, a certain amount of vorticity wave generation is inherently included. Although the injection temperature was carefully controlled in the present simulations, the amount of vorticity wave generation has not been examined separately. Relatedly, Pinelli et al. did not simulate the injectors upstream of the stator vanes explicitly but instead injected the measured temperature profile from the experiment.

In summary, the direct noise validation cases were well defined, and the agreement between experimental findings and LBM simulations was very good. Because of the nature of the entropy wave generation in the experiments, no comparable extensive dataset is available for validation. The predicted indirect noise levels downstream of the turbine stage for the case considered here are consistent with the reported literature data.

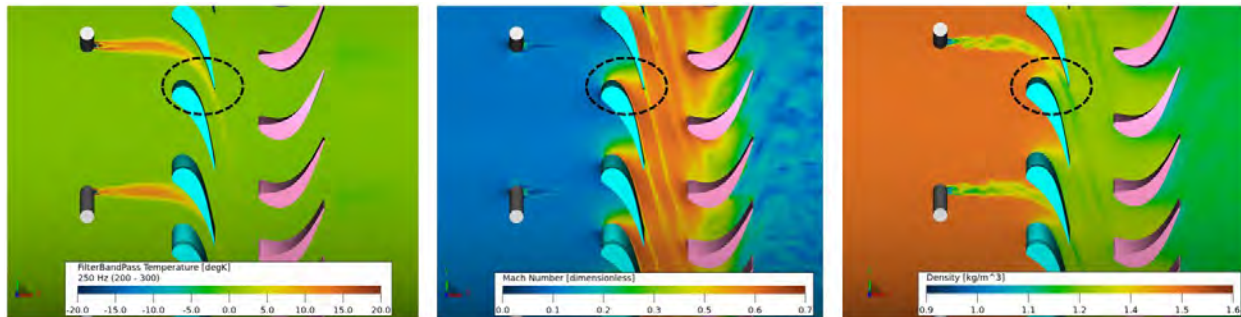


Figure 66. Visualization of important flow regions for noise generation: the entropy wave field (left), the non-uniform mean flow inside the vane passage (middle), and the unsteady density field (right).

In general, two main mechanisms are responsible for the sound generation: (a) strong local flow acceleration in regions of high-velocity gradients (monopole source) and (b) unsteady drag exerted on the vanes/blades through the density fluctuations (drag force). The first mechanism is negligible for low Mach numbers but very important for the encountered high-Mach-number flows inside the turbine stage, in regions with strong local flow acceleration. The second mechanism is particularly pronounced when the entropy wave is close to the leading edge or trailing edge. Qualitatively, the important flow regions and quantities for the turbine simulations are shown in Figure 66.

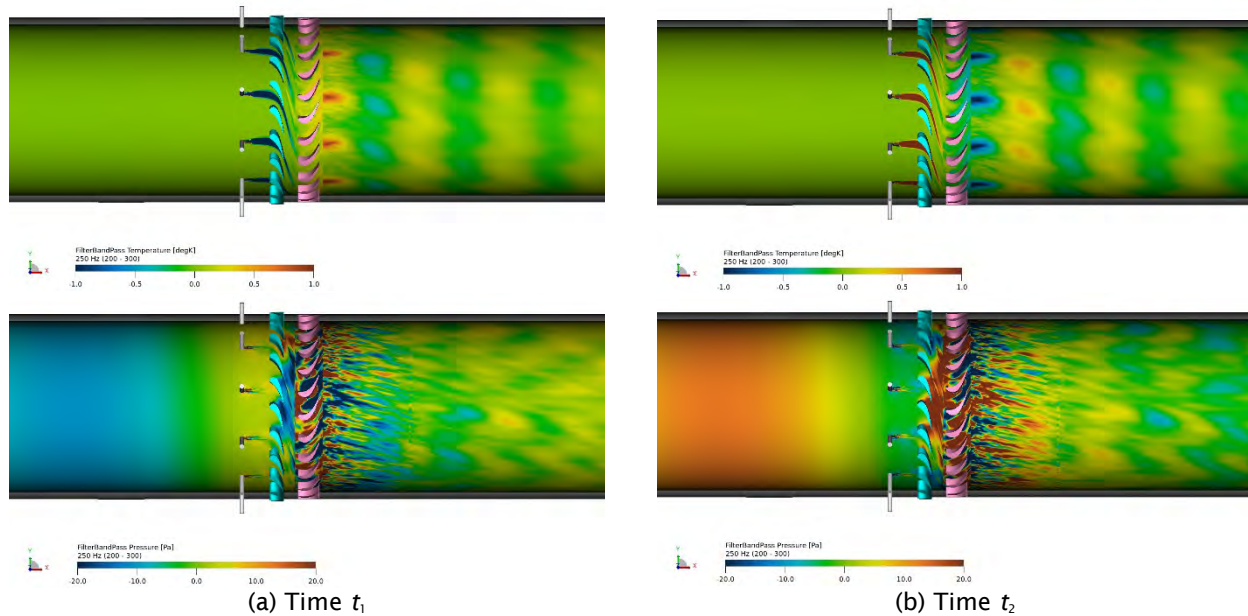


Figure 67. Visualization of entropy wave interaction with the stator vane passage (top) and resulting acoustic pressure generation (bottom), for two time instances in the injection cycle.

Snapshots of the temperature and pressure fields for different time instances during the injection cycle are shown in Figure 66. A strong acoustic pressure field is clearly generated in the interstage passage between the stator and rotor when the entropy wave travels through the stator vane passage. The resulting upstream propagating acoustic wave is visible, as well as the highly dispersed entropy waves downstream of the rotor. The downstream propagating sound is not clearly visible, because of the presence of strong hydrodynamic fluctuations downstream of the rotor. As shown previously in Figure 65, an acoustic wave further downstream of the rotor is clearly identifiable. After the sound is generated, it travels upstream and downstream. In the latter case, the sound interacts with the rotor and creates additional back-reflections within the stator-rotor passage. In addition, vorticity waves are generated at the stator trailing edges and can result in additional noise through interacting with the rotor’s leading edge.

Pinelli et al. have shown that the injector placement relative to the stator vane (i.e., the clocking) plays a role of the upstream generated noise: levels are 2–4 dB higher for injections in which direct impingement on the vane leading or trailing edge is achieved than for injections in which the entropy wave is centered between two vane passages. For the downstream generated noise, however, the sound power levels were found to be largely independent of the injector clocking relative to the stator vanes.

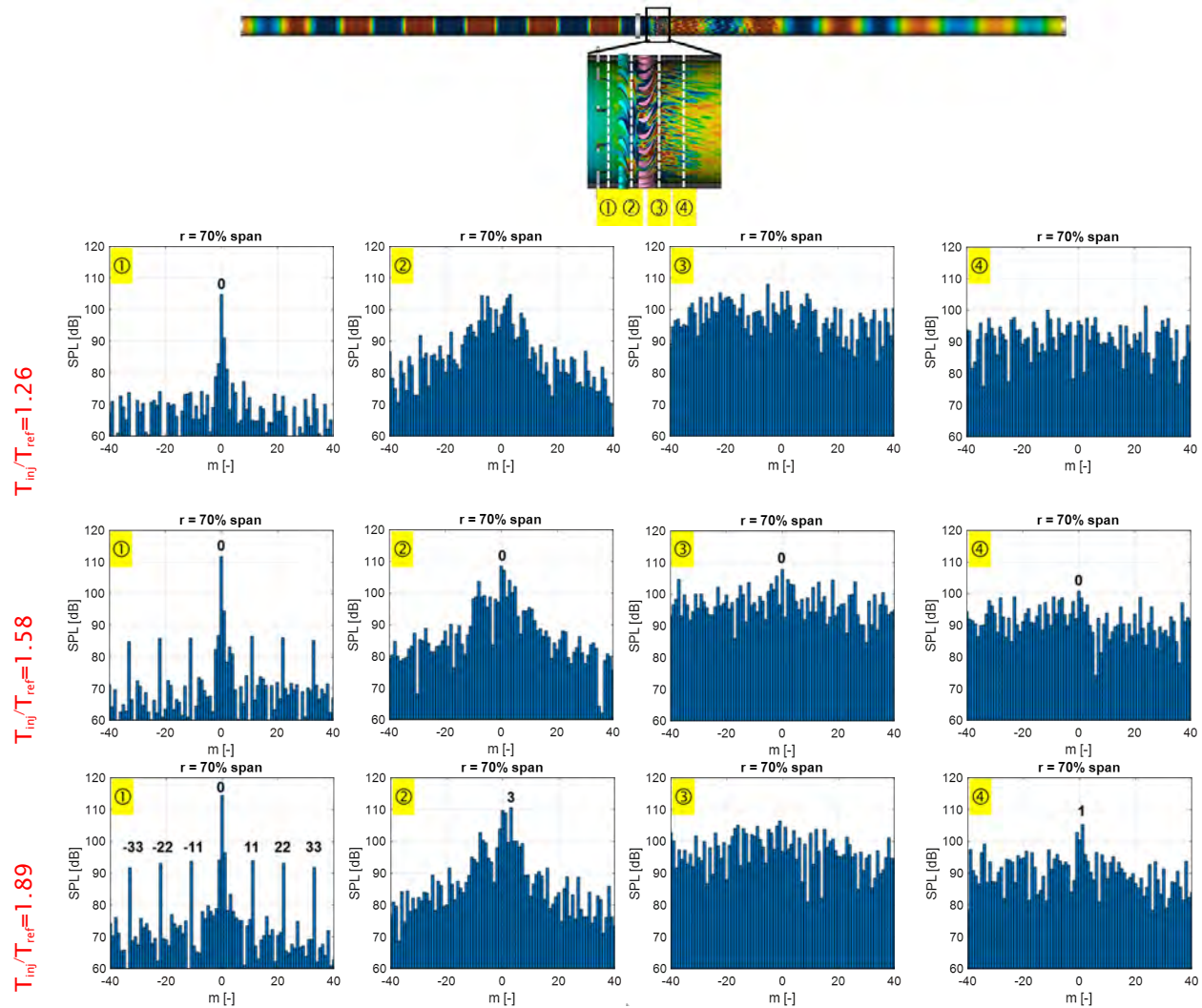


Figure 68. Modal analysis of the pressure field at $f = 250$ Hz, at different cut planes.

A modal analysis of the pressure field at different cut planes in the flow field is shown in Figure 68 for all three injection amplitudes. Upstream of the stator, at plane 1, a single dominant plane wave mode ($m = 0$) is observed, whereas the injector-related direct pressure field ($m = \pm 11, \pm 22, \pm 33, \dots$) is at least 20 dB lower. In the interstage region (plane 2), a mixture of low-order modes is detected. All these modes are cut off. Whereas a strong $m = 1$ mode remains visible on plane 4 for the highest injection rate case, it decays, and the $m = 0$ mode is the remaining acoustic mode downstream that carries sound power. The modal amplitudes downstream are significantly lower than those upstream. The multitude of modes in the downstream section is due to the presence of turbulent flow.

According to theory, the sound power should scale as $\propto \Delta T^2$, which provides a good approximation of the simulation cases for both upstream and downstream indirect noise, as plotted in Figure 69.

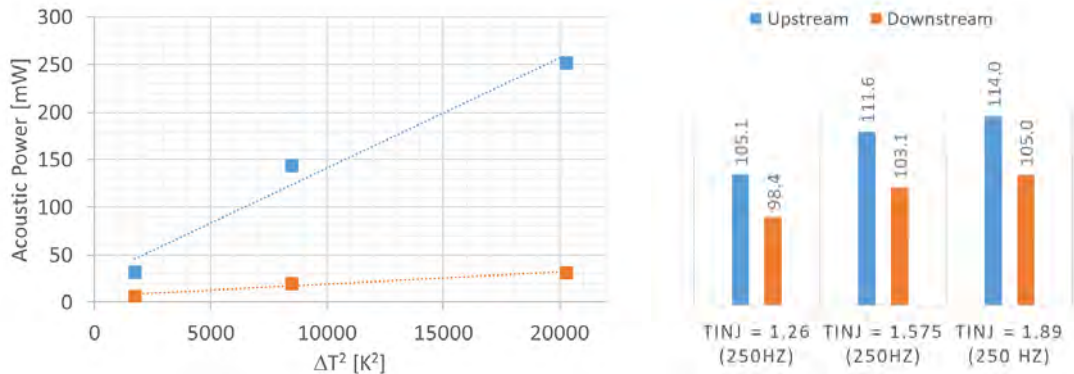


Figure 69. Sound power scaling for the simulated indirect noise case. Left: linear; right: dB.

For the highest injection case, a phased injection simulation was also run, wherein the injection by injector i is phase-delayed by a time delta corresponding to $n_{inj}/f_{forcing} \cdot i$, where n_{inj} is the number of total injectors, and $f_{forcing}$ is the forcing frequency. Thus, a continuous circumferentially traveling injection phase pattern is created. The acoustic field is described by a very strong $m = 1$ mode in the near field (Figure 70). Upstream (on plane 1) it is of similar magnitude as the plane-wave mode with synchronized forcing, whereas in the interstage (plane 2) and downstream (plane 4), this $m = 1$ mode remains very high in amplitude—higher than any modes created with the plane wave forcing approach. However, as this mode is cut off, it decays exponentially and does not contribute to the radiated sound power.

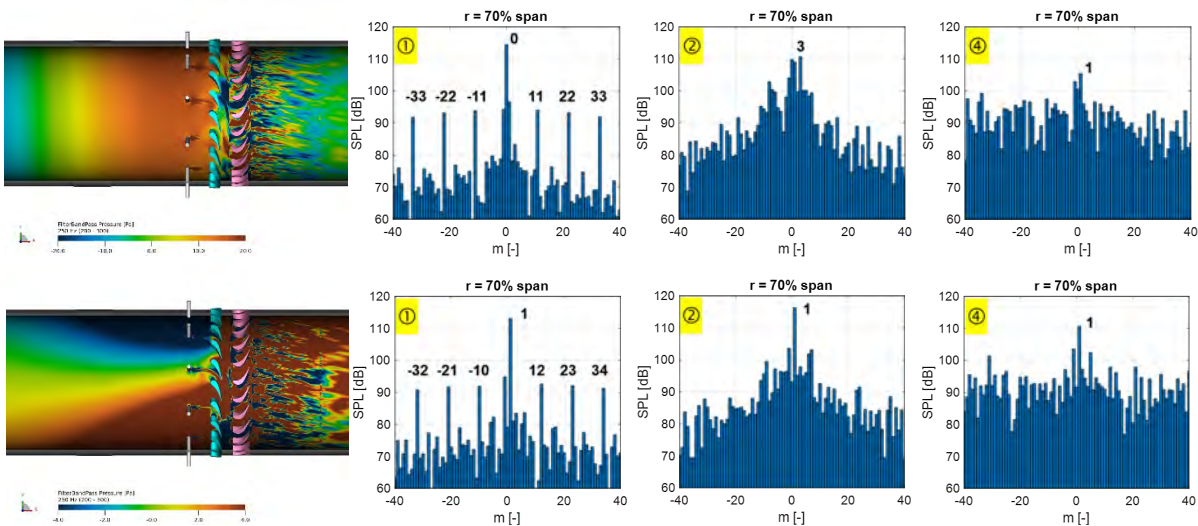


Figure 70. Top: Pressure modes for simultaneous forcing ($m = 0$); bottom: pressure modes for phased forcing ($m = 1$) for different cut planes. Plane 1: upstream of stator; plane 2: interstage; plane 3: downstream of rotor.

The acoustic field far upstream and downstream is characterized by the plane wave mode alone. This mode remains created with the phased injection case, but its amplitude is substantially reduced (Figure 71). The calculated sound power level is reduced by more than 15 dB. The phased injection creates higher sound power downstream than upstream. The simulation cases illustrates that even cut-off modes can contribute to the overall sound power, via scattering into propagating modes.

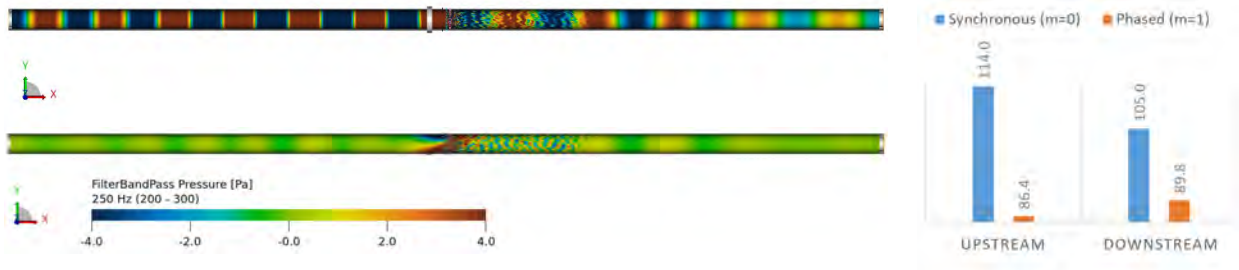


Figure 71. Left: visualization of the upstream- and downstream-propagating acoustic pressure for an entropy wave with $T_{inj}/T_{ref} = 1.89$, for different forcing types. Top: synchronous injection, creating an $m = 0$ mode. Bottom: Phased injection, creating an $m = 1$ mode. Right: sound power levels.

As the wave is transported through the turbine stage, its amplitude is drastically reduced, even for the relatively low frequency of 250 Hz considered here, for two potential reasons: (a) shear dispersion due to the nonuniform mean flow and (b) dissipation by the turbulent flow. For combustors, the second effect is found to be negligible; for turbines, this effect has yet to be quantified. Figure 72 shows how the wave amplitude of the localized entropy waves is reduced by ~75% across each vane/blade row.

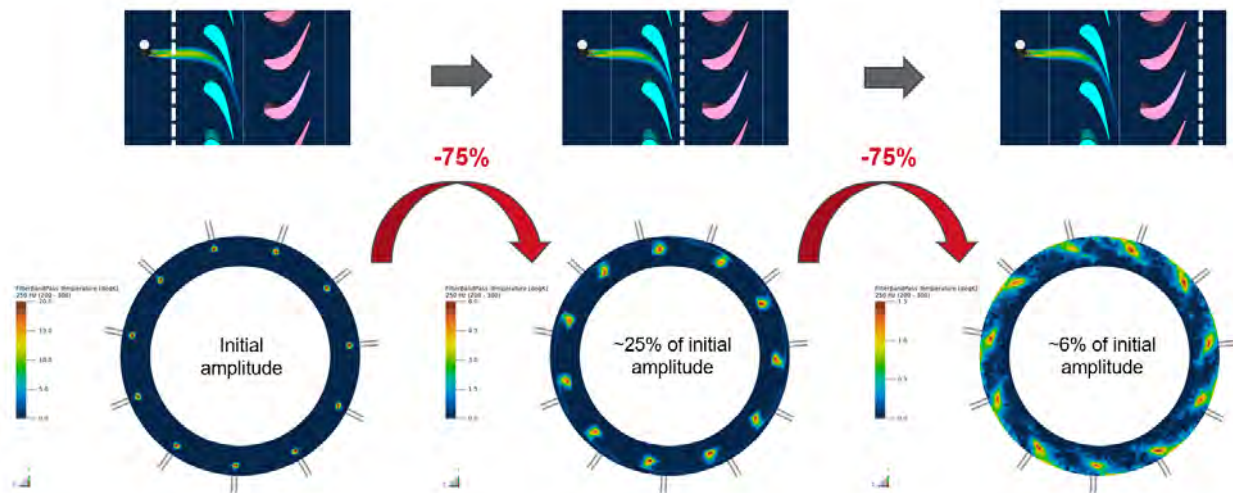


Figure 72. Entropy wave amplitude change during transport through the turbine.

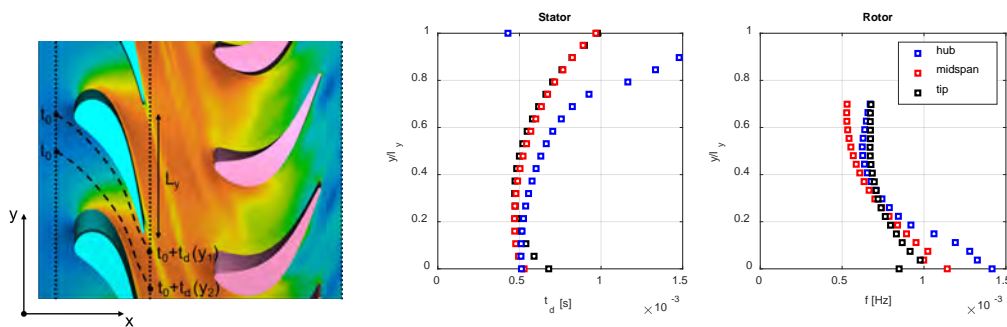


Figure 73. Time delay for entropy waves traveling along different streamlines as they pass through the vane and blade passages.

The dispersion effect can be calculated through a streamline analysis of the mean flow field for stator and rotor. This calculation is performed for condition OP3 by seeding 20×20 streamlines from the inlet to the outlet of each row. The time delay is then calculated along each streamline, so that a time delay profile for the entropy waves between the vanes can be calculated. Figure 73 illustrates this process.

These profiles can now be integrated across the vane/blade pitch, to obtain the 2D transfer function for each radial section.

$$TF(r) = \left| \frac{1}{L_\theta} \int_0^{L_\theta} e^{i\omega t_d(r,\theta)} d\theta \right| \quad (42)$$

Although the time delay profiles are quite different for each radial slice, the transfer function is relatively less sensitive to radial section. The spanwise average 1D transfer function is then given by:

$$TF = \left| \frac{1}{L_r L_\theta} \int_0^{L_r} \int_0^{L_\theta} e^{i\omega t_d(r,\theta)} dr d\theta \right| \quad (43)$$

The results are plotted for the stator, the rotor, and the combination of both in Figure 74. Despite the different flow profiles in the stator and rotor, the transfer functions are very similar. The combined transfer function is the product of both individual transfer functions, and shows substantial amplitude reduction with increasing frequency.

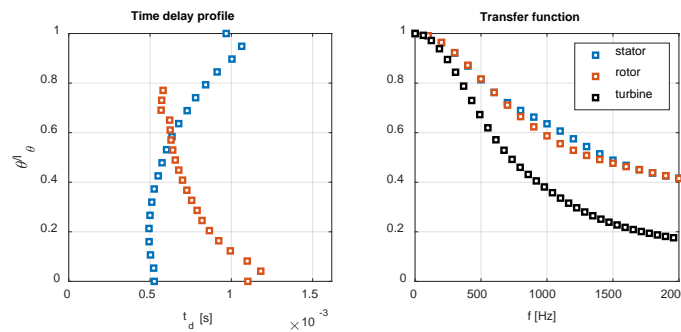


Figure 74. Average time delay profiles across the flow passage (left) and corresponding transfer functions.

On the basis of the work of Bauerheim et al., a generic velocity profile can be introduced and integrated to determine the shear dispersion behavior. This process eliminates the need for a mean flow solution, and the model can be calibrated for each turbine design by using such generic velocity profiles. The generic velocity profile is given by:

$$v_x = \left(\frac{\theta}{L_\theta} \right)^{\eta/n_g} \left(1 - \frac{\theta}{L_\theta} \right)^{(1-\eta)/n_g} \quad (44)$$

where η describes the asymmetry of the velocity profile, and n_g describes the profile shape. This profile can then be used to calculate the time delay as follows:

$$t_d = \frac{L_x}{v_{x,0}} \frac{\eta^{\eta/n_g} (1-\eta)^{(1-\eta)/n_g}}{v_x} \quad (45)$$

By selection of η and n_g , the profile can be adjusted to match the simulation data. This process is demonstrated for both stator and rotor profiles. As shown in Figure 75, the simulation data can be matched quite well. One challenge is that the velocity profiles vary along the span, with different fitting parameters, so no single set is adequate.

However, as indicated in Figure 74, the transfer function itself (which is calculated from the velocity profiles) is not very sensitive to the model parameters. To match the 1D ADT assumption, a single model parameter fit is used to match the data in Figure 74. Through that approach, Figure 74 can be updated with the model, which is shown in Figure 75 and represents the simulation data quite well. The final parameters are $\eta = 0.15$ and $n_g = 1.5$ for the stator, and $\eta = 0.7$ and $n_g = 1.65$ for the rotor.

Finally, a sensitivity study of the model is provided in Figure 77. A stronger asymmetric velocity profile and a more parabolic velocity profile (higher nonuniformity) have the strongest impact on the transfer function. As expected, the impact is most pronounced at higher frequencies. In the absence of any data, these models could be used to bound the problem (worst and best case).

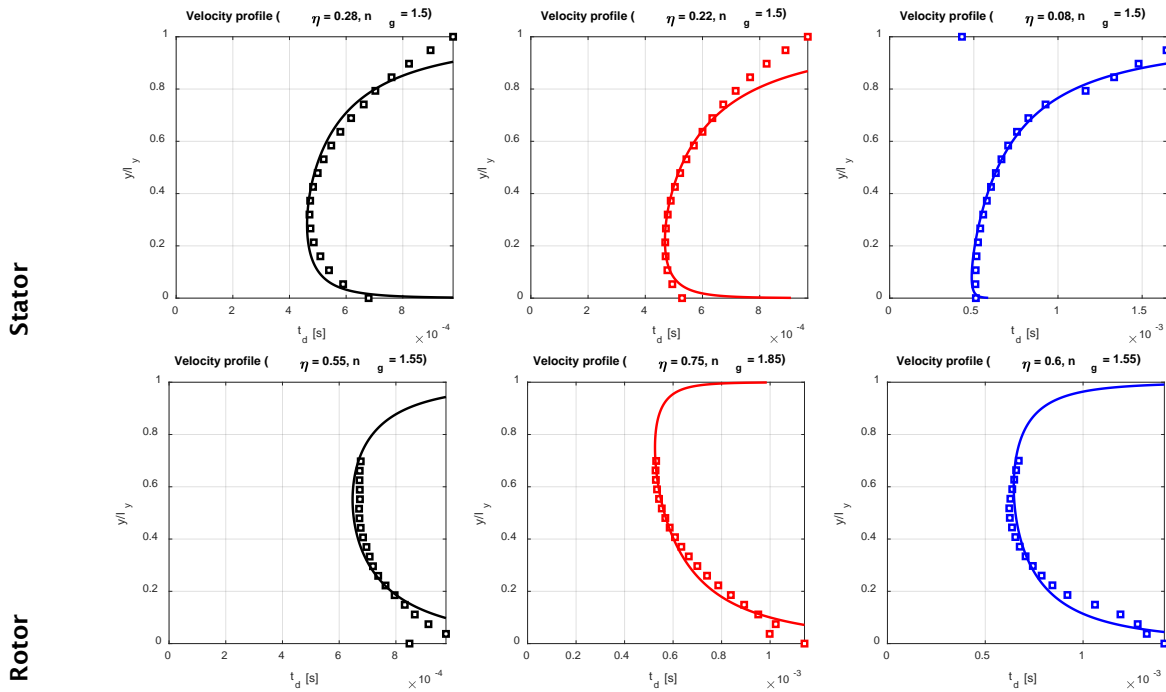


Figure 75. Time delay profiles as predicted by the model.

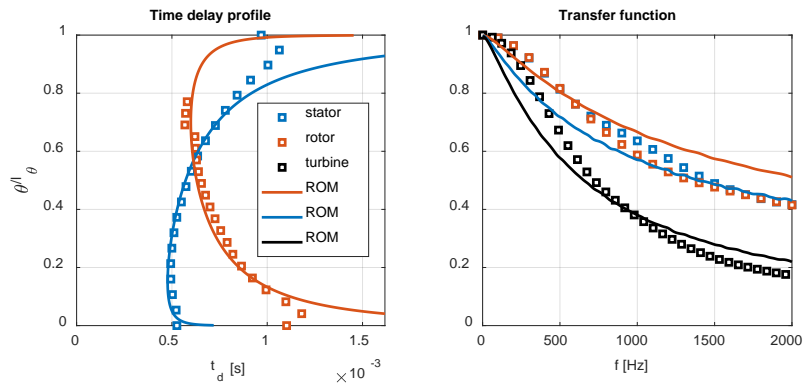


Figure 76. Average time delay profiles and transfer function using the ROM.

A correction term can now be added to ADT, to account for shear wave dispersion for each row. In its original form, ADT assumes that the entropy wave σ remains constant across each row. On the basis of the parametrized velocity profile, the correction term for each row is given by:

$$\sigma_2 = C_s \sigma_1$$

$$C_s = \left| \frac{1}{L_\theta} \int_0^{L_\theta} e^{i\omega_s(\theta)} d\theta \right| \tag{46}$$

The time delay is calculated with Eqs. (44)–(45). This process is straightforward after the parameters η and n_g are defined. With use of this term, the entropy wave amplitude continues to decay as the wave convects through the different turbine stages, thus diminishing the importance of this term as an indirect noise source beyond the first few vane/blade rows.

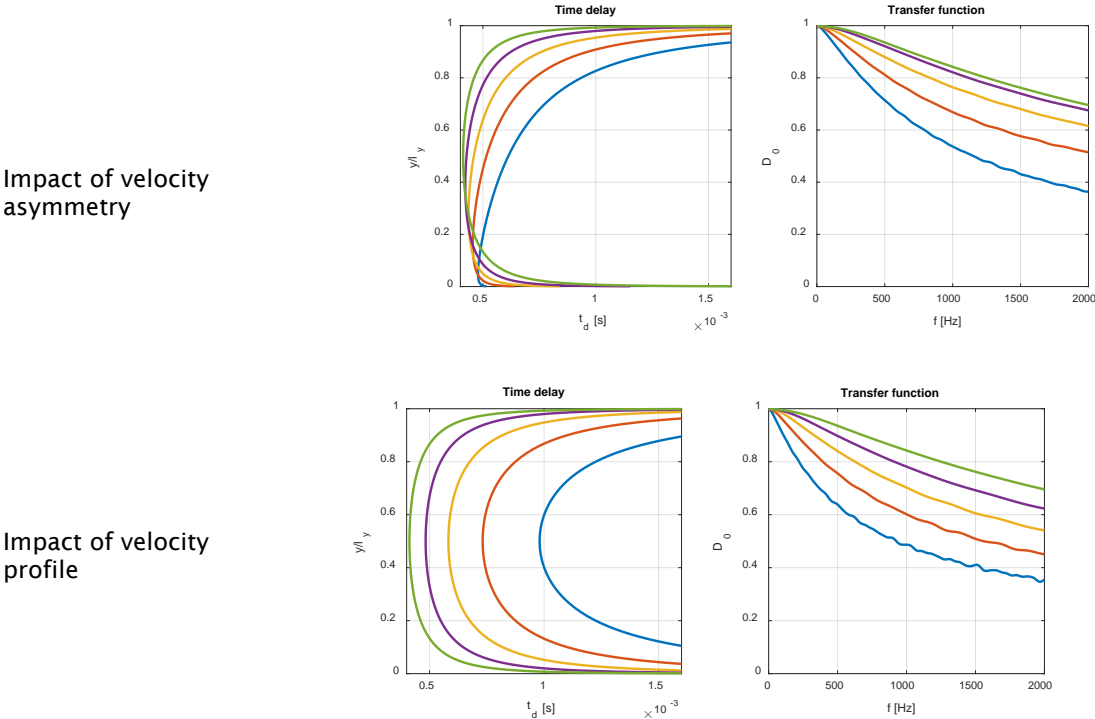


Figure 77. Sensitivity study of the shear dispersion model with respect to the two tuning parameters.

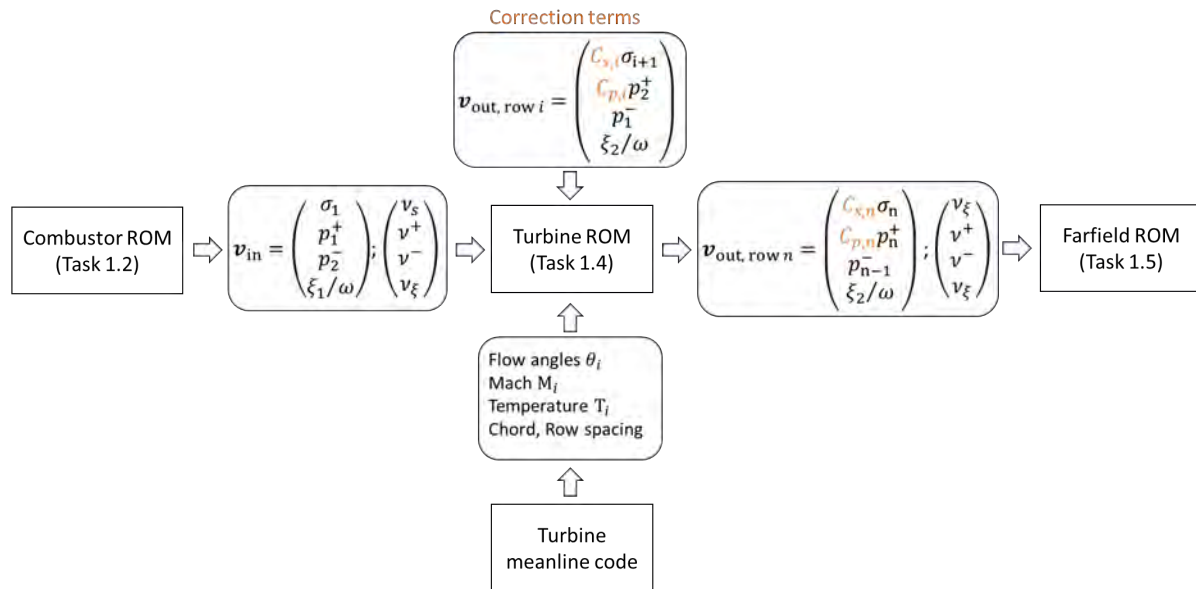


Figure 78. Flowchart for the turbine ROM.

In summary, two correction terms for the turbine ROM were derived and implemented. The flow chart in Figure 78 shows how the different tasks are connected and how the correction terms are implemented. The inputs and outputs of the turbine ROM are defined by the wave amplitudes for each wave type (acoustic, entropy, or vorticity) and each frequency. These values come from the combustor exit region (Task 1.2). In addition, to calculate the wave propagation through the turbine, the inlet and outlet Mach numbers are needed, as well as the inlet and outlet flow angles, and the wave angles to be considered. The first two values are typically available from a meanline solution for a given turbine design and operating condition. The wave angles, in contrast, also come from the combustor exit. Together, these quantities are used to construct the matrices to solve the ADT ROM. For multi-row applications, an additional phase-delay matrix is introduced that requires the spacing between the different rows, which is defined as the distance between the axial mid-chord locations of the rows plus the interstage gap. The turbine ROM calculates the outgoing wave amplitudes that feed into the far-field noise tool. This process is summarized in Figure 78, including where the derived corrections are applied. Of note, applying the dissipation correction only to the downstream propagation acoustic waves (not upstream) is suggested.

Far-field noise modeling

Task 1.5 focuses on the development of a modeling tool chain that predicts the propagation of combustion noise as it emitted from the engine core exit to the far field. During Years 1 and 2, a HiFi far-field propagation modeling process with ACTRAN/DGM, a time-domain aeroacoustics solver based on linearized Euler equations, was developed to obtain the far-field transfer functions. This process was previously found to yield noise directivities in reasonable agreement with those published in the literature and with engine test data. However, the drawback of this HiFi modeling approach was that it involved multiple computation steps, consisting of (a) CFD computation to generate the mean flow field, (b) mapping of the CFD-generated mean flow field to the acoustic mesh, and (c) computation of acoustic propagation through the mean flow field. Consequently, if the flow condition changes, then these steps must be repeated to compute the new far-field transfer functions. In the previous approach, the geometry was also detailed and not parametrizable, thus making simulations time-consuming to rerun when the geometry was altered. Furthermore, the time-domain linearized Euler equation solver (ACTRAN DGM) occasionally caused numerical instability problems, which posed difficulties in obtaining valid results in some situations.

In Year 3, the team aimed to improve the tool chain by replacing the HiFi modeling process with a new ROM with more parametrizable geometry and a simplified mean flow field, as shown in Figure 79. As illustrated in Figure 79, the new (FE-based) ROM process consolidated some of the steps into a single step, thus largely simplifying the far-field propagation tool chain.

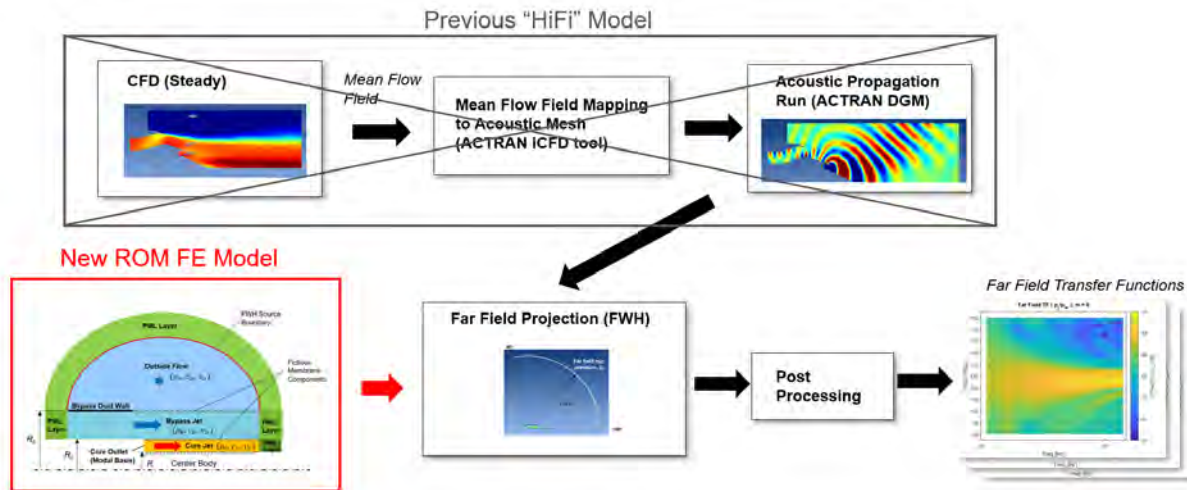


Figure 79. Simplified process for computing far-field transfer functions. The previous HiFi modeling consisting of multiple steps has been replaced with a new ROM.

This ROM models the engine aft geometry as simple concentric ducts that represent the core and the bypass duct components. The aft center body is also simplified as a simple cylinder instead of a conical shape. This geometry can be described by only several geometric parameters, such as the duct diameters, and thus is easily parametrizable. The mean flow field is also assumed to consist of three distinct regions of uniform flow that represent the core flow, the bypass flow, and the outer flow regions. Each of the three uniform flow regions is then characterized by three parameters, (ρ , c , and v), which are the density, speed of sound, and velocity. Another notable aspect of this ROM is the use of ACTRAN/TM, a frequency-domain aeroacoustic solver based on Moring’s wave equation. The main advantage of using this frequency-domain solver is that, unlike ACTRAN/DGM, it does not have the numerical instability problem, thus making the computation process more robust.

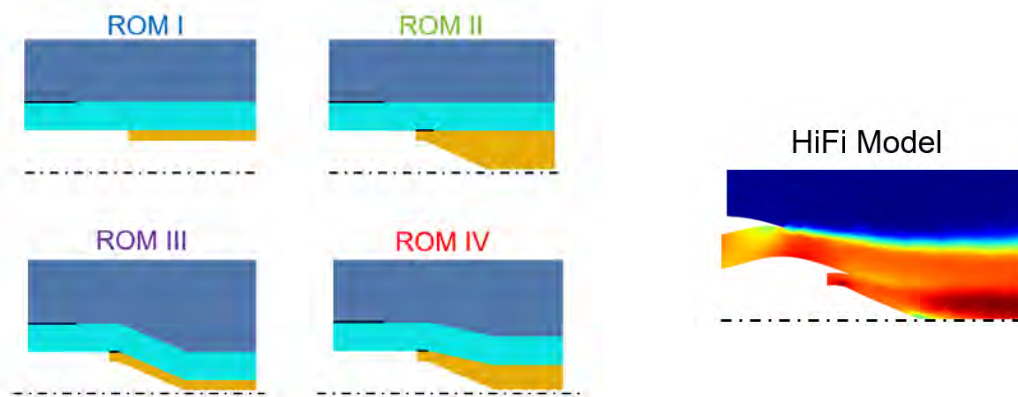


Figure 80. Four versions of the ROM and the reference HiFi model.

To understand the impact of the geometry and flow simplifications on the far-field acoustic pressures, we created several versions of the ROM with strategically varied geometries. Figure 80 shows four versions of ROM (labeled I to IV): ROM I is the simplest, and ROM IV is closest in geometry to the HiFi model shown on the right.

Figure 81 shows a comparison of far-field ROM results against that of the HiFi model. As shown in Figure 81(a), some differences exist in the far-field acoustic pressures between the ROM I and the HiFi model. Subsequently, the agreement is improved when the ROM geometry is made more similar to that of the HiFi model (by going from ROM I to ROM IV).

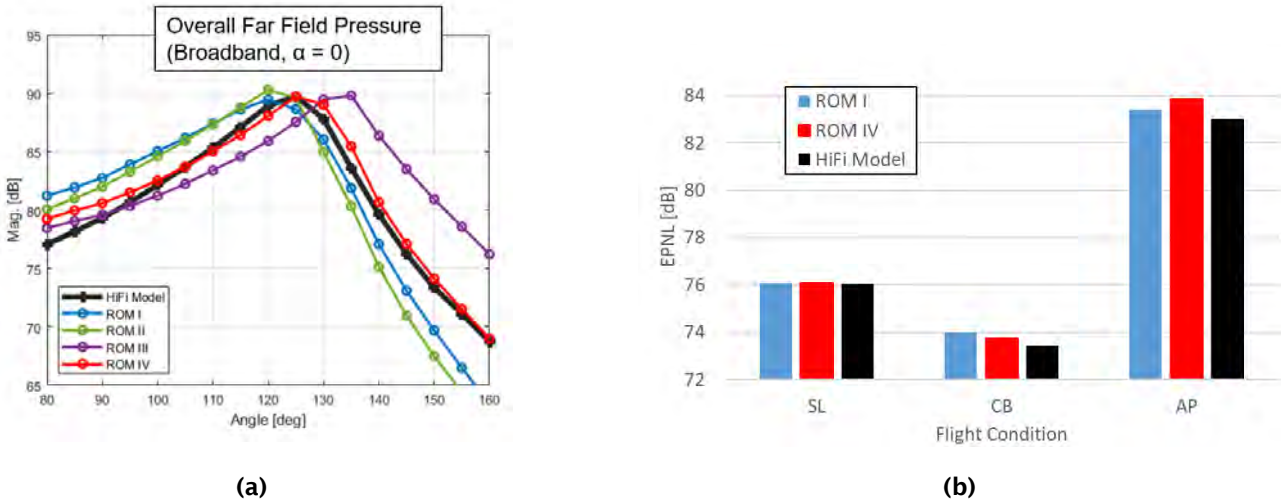


Figure 81. Far-field ROM results versus the HiFi model: (a) overall far-field pressures, and (b) EPNL values.

Figure 81(b) below shows the equivalent perceived noise level (EPNL) values computed with ANOPP, a system-level noise prediction code, for the four ROM cases and the HiFi model for three different flight conditions: sideline, cutback, and approach. (Of note, EPNL values are computed on the basis of the assumption that no sources of noise exist other than the core noise. Moreover, the scaling is arbitrary, because noise sources of arbitrary magnitudes are used.) As shown in the figure, the differences in EPNL values among ROM I, ROM IV, and the HiFi model were generally small (less than 1 dB EPNL). This finding suggested that the EPNL values are relatively insensitive to small changes, such as the directivity peak angle shift indicated in Figure 81(a). A comparison of the results across all three flight conditions suggested little benefit in making the geometry more realistic by going from ROM I to ROM IV in terms of EPNL values. Therefore, ROM I with largely simplified geometry appears to be sufficient.

The far-field propagation ROM process developed during Year 3 represents a significant improvement over the previous modeling process in terms of robustness, practicality, and usability as a modeling tool. The process was further streamlined by reducing the number of computational steps necessary to compute far-field transfer functions. A more robust aeroacoustics solver was also used as the computational engine, thus eliminating the problem of numerical instability occasionally encountered when the solver was used for the previous modeling approach. The more parametrized nature of this tool also facilitates computing far-field transfer functions for a variety of engine geometry and flight conditions, thereby enabling more extensive investigations into the physics of combustion noise far-field propagation by running large numbers of simulations with a wide range of geometry and flow conditions. Finally, “generalized” far-field transfer functions including geometry and flow parameters can be obtained in the future.

Milestones

- Development of an LNSE model for predicting direct and indirect noise, whose results compare favorably with the rig measurements.
- Creation of a far-field ROM FE model and validation against the HiFi model

Major Accomplishments

A major decomposition technique based on SPOD was used to identify the key entropy and pressure related modes within the combustor. The SPOD identified a longitudinal acoustic mode (at 2500 Hz) as well as a lower-frequency mode (near 700 Hz) that is primarily entropy driven. This entropy mode is affected by the convection of the entropy perturbation from the flame to the dilution jet and further to the jail bars. At close to 700 Hz, the convection time scales of the entropy perturbation from the flame to the dilution jet and from the dilution jets to the jail bars are almost in phase, thus

reinforcing the perturbation at this frequency. The SPOD analysis also shows the rapid decay of the entropy at high frequencies and helps explain the low-frequency nature of the entropy noise from combustors.

Linearized Navier-Stokes computations were introduced to predict the direct and indirect noise by using the mean flow field within the combustor and unsteady HRR at the flame. The result of this approach compares favorably with measurements in the RTRC rig. Therefore, this approach may be viable for combustor noise prediction. Currently the mean flow field and the unsteady HRR are both obtained from the full LES computation. Future efforts will validate this approach by using the mean flow field computed with a Reynolds-averaged Navier-Stokes equation simulation and ROM for the unsteady HRR.

The nozzle interaction task has been completed. Results from Year 2 and carrying into Year 3 have shown that ADT applied to a 1D nozzle agrees reasonably well with LBM for upstream generated noise. The downstream generated noise was not easily identified from the rig tests; therefore, further model exploration was not considered. Instead, we focused on the turbine wave interaction task, which was considered more relevant to a real engine and noise prediction toolchain development.

For the turbine wave interaction task, related to direct noise, simulations and comparison to analytical models substantiated that a large amount of sound power is dissipated in the turbine stage through vorticity generation. A correction term was proposed that accounts for sound power dissipation effects in ADT. For indirect noise, entropy wave transport was simulated, and the sound generation mechanism inside the turbine was studied, including the modal content of the pressure field. The effect of cut-off mode creation from entropy waves inside the turbine was also investigated, and sound power remained generated at the cut-on plane wave mode. Entropy wave dispersion was investigated inside the turbine stage, and a transfer function for each row and a combined transfer function for the full stage were calculated according to HiFi simulation results. A generic velocity profile model was implemented, and a correction term to ADT was proposed that accounts for entropy wave dispersion effects in the noise prediction model.

For the far-field propagation modeling task, a ROM FE model was developed to further parametrize and streamline the far-field prediction tool. The ROM model predictions were compared and validated against the previous HiFi model in terms of far-field acoustic pressures and EPNL values for the three certification flight conditions.

Publications

None.

Outreach Efforts

None.

Awards

None.

Student Involvement

None.

Plans for Next Period

1. The LES flow field from GT will be further interrogated to obtain direct noise estimates. An approach based on proper orthogonal decomposition is currently being evaluated to separate important effects within the combustor that contribute to direct and indirect noise.
2. For the nozzle interaction task, the team will further evaluate and refine the tools and processes developed for the RTRC rig and will then apply them to the GT rig for further validation and cross-comparison.
3. For the turbine interaction task, the team will continue to improve the ADT to account for acoustic dissipation effects and will then perform parametric studies to investigate different source types of turbine-wave interaction. This effort will include spinning wave modes and higher-order modes entering the turbine stage and different turbine designs. The results will be compared with the ADT, to evaluate this theory against a more diverse set of source types. Additionally, we will apply the improved ROM to a multi-stage turbine design with parameter variations to provide insight into the effects of realistic turbine design features on the expected sound transmission behavior.



Project 056 Turbine Cooling Through Additive Manufacturing

The Pennsylvania State University

Project Lead Investigator

Karen A. Thole
Distinguished Professor
Department of Mechanical Engineering
The Pennsylvania State University
NARCO Building, CATO Park, Room 148
3127 Research Drive
State College, PA. 16801
(814) 863-8944
kthole18@psu.edu

University Participants

The Pennsylvania State University (Penn State)

- P.I.s: Prof. Karen Thole, Dr. Stephen Lynch
- FAA Award Number: 13-C-AJFE-PSU-054
- Period of Performance: February 5, 2021 to December 31, 2023
- Tasks:
 1. Manufacture and test existing FAA Continuous Lower Energy, Emissions, and Noise (CLEEN) II blade designs
 2. Design new double-wall cooling technologies
 3. Manufacture and test new double-wall cooling designs for linear cascade

Project Funding Level

The FAA has provided \$1,200,000 of funding to date. In-kind cost-sharing of \$1,500,000 has been provided to The Pennsylvania State University by Pratt & Whitney to cover the entire program.

Investigation Team

Prof. Karen A. Thole (P.I.), All Tasks
Prof. Stephen Lynch (co-P.I.), Tasks 2 and 3
Asst. Prof. Reid Berdanier, (staff scientist), Tasks 1 and 4
Assoc. Prof. Michael Barringer, (staff scientist), Tasks 1 and 4
Scott Fishbone, (project manager), Tasks 1 and 4
Jeremiah Bunch, (laboratory technician), Tasks 1 and 4
Liam Boyd, (graduate student), Tasks 2 and 3

Project Overview

Gains in the cooling performance of cooled turbine airfoils directly affect the efficiency and durability (lifetime) of turbine engines and therefore are the subject of substantial development. Currently, many cooling designs for turbine airfoils use complex micro-channels placed within the wall of the airfoil to extract heat—a design known as double-wall cooling. However, the geometric complexities (and thus the effectiveness) of the micro-channels, are limited by the current design space available through the use of conventional investment casting and core tooling methods to manufacture relatively small intricate internal cooling features. This project will investigate potential thermal performance and aerodynamic efficiency improvements made possible by exploring the expanded cooling design space opportunities by directly

fabricating complex cooling geometries with three-dimensional laser powder bed fusion (L-PBF), a commonly used metal-based additive manufacturing (AM) method. L-PBF AM has begun to find many uses in the gas turbine industry, particularly because of the new design space enabled by this new fabrication method. However, the ability to manufacture high-efficiency, intricate, complex double-wall cooling airfoils design concepts is unknown. This research would generate some of the first thermal performance data at engine-relevant conditions comparing traditional cast airfoils to advanced airfoils manufactured through L-PBF AM. Understanding the potential of new innovative geometric heat transfer cooling design features coupled with unique airfoil cooling configurations will serve as an important guide for future investments in advanced manufacturing and cooling design technologies.

Task 1 – Manufacture and Test Existing FAA CLEEN II Blade Designs

The Pennsylvania State University

Objective

The objective of this task is to measure the as-manufactured shape of FAA CLEEN II turbine blade airfoils with X-ray computed tomography (CT), and to use that information to fabricate additively manufactured copies for direct comparison at the rotating turbine facility at Penn State. The outcomes of this effort will be to: (a) provide a direct back-to-back comparison of cast versus additively manufactured airfoils; (b) identify the unknown challenges in creating double-wall designs via AM and translating them into cast parts for commercialization; and (c) learn about and document the design, fabrication, and testing of additive blades that will spin at engine-relevant conditions.

Research Approach

AM blade inspections and testing preparation

At the end of the prior annual reporting period in 2022, the selected AM vendor, Vertex Manufacturing, had completed printing and inspection of the first round of turbine blades. In November 2022, 20 blades were delivered to Penn State, thus completing the manufacturing portion of this task. Over the course of this year, and before insertion in the test rig, various inspections of the airfoils were conducted.

Flow inspections were performed by attaching each of the blades to a testing fixture that supplied coolant to the internal channels. The variation in flow rate through an airfoil relative to the internal pressure inside was mapped for each airfoil and compared with design intent as well as the cast airfoils.

Additionally, the surface finish of the airfoils was measured with optical profilometry techniques. In this process, the airfoil external surface, internal surface, and sectioned parts were measured with CT. The values obtained for the additively manufactured blades were reasonably consistent with other data on roughness for additively manufactured parts. Blue light scanning of the airfoils was also conducted to determine the geometry deviation relative to the design intent. The airfoils were within an aerodynamic shape tolerance of ± 0.003 inches, a value as good as or better than that with casting and similar to that for the trial airfoils, thus indicating that AM can be consistent with shape definition and well within allowable tolerance.

Because of delays in facility upgrades for the Steady Thermal Aero Research Turbine (START) Laboratory, the airfoils are scheduled to be tested in early 2024.

Task 2 – Design New Double-wall Cooling Technologies

The Pennsylvania State University

Objective

The objective of this task is to develop novel double-wall cooling designs that feature the microchannel concepts being explored in the literature and can be achieved via AM. The designs will be generated with advice from Pratt & Whitney, so that the concepts can be leveraged for commercialization. The designs will be packaged into cascade test articles that will be measured in the high-speed linear cascade at Penn State with infrared (IR) thermography.

Research Approach

Design of linear cascade test articles

This task was completed in 2022, but several important highlights are discussed, because they support the efforts in Task 3. In this task, several novel microchannel cooling geometries were developed according to concepts in the literature, some of which have previously been demonstrated with AM. Figure 1 shows several of the designs, which were grouped by type. Pin fin designs include a standard circular pin (manufactured through AM by Kirsch and Thole (2017a), as well as a triangular pin design tested by Ferster et al. (2018). These designs are expected to have high pressure loss but also high cooling effectiveness. The second grouping is for ribs (turbulators), which do not span the entire channel but act to locally trip the flow. The discrete W shape designed by Wright et al. (2004) is a conventional design, but the wavy S-shaped ribs designed by King and Pietraszkiewicz (2018) is based on a patent and may have similar effects to the wavy channels studied by Kirsch and Thole (2017b). The channel-only configurations include the baseline empty microchannel that replicates the existing FAA CLEEN II design, as well as a wavy microchannel that is based on the findings of Kirsch and Thole (2017b).

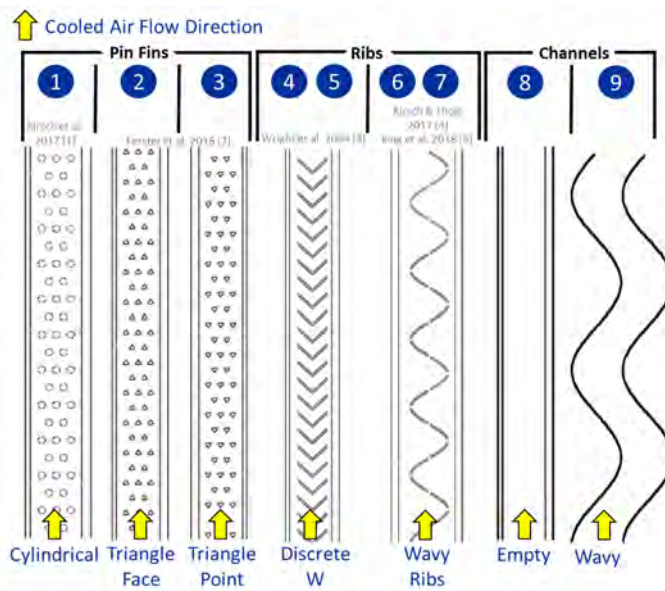


Figure 1. Novel cooling concepts packaged into the microchannels in this study.

These geometries were packaged into a linear cascade (two-dimensional profile) airfoil for testing in the high-speed linear cascade at Penn State. An example of the airfoil with surface microchannels, as well as the full test article including a mounting base and embedded pressure and temperature instrumentation ports, is shown in Figure 2. The designs of Figure 1 were packaged into the microchannels to create eight unique test articles.

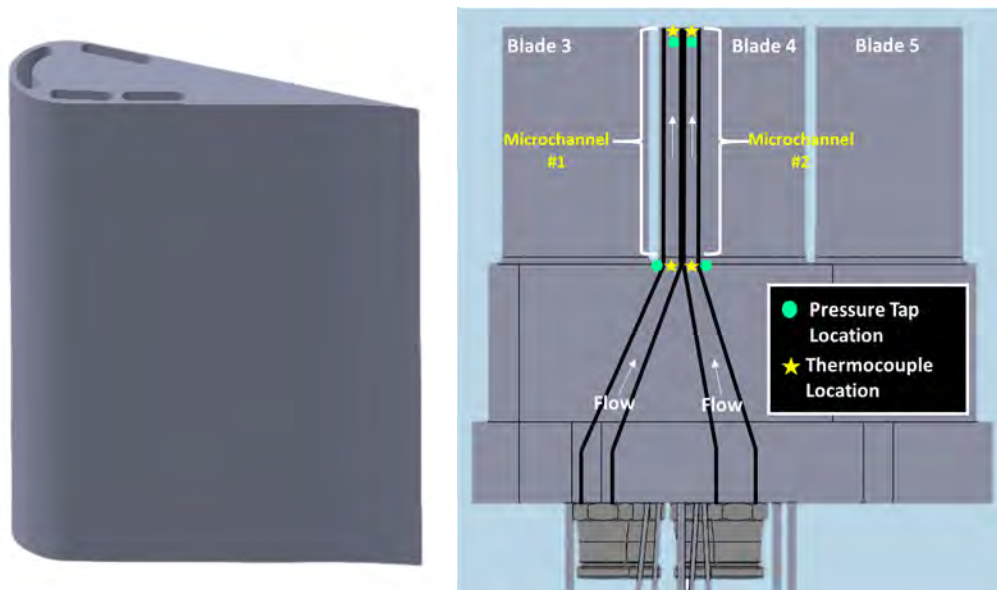


Figure 2. Example airfoil with microchannels (left), and airfoils packaged into an additively manufactured test article with embedded instrumentation ports.

Task 3 – Manufacture and Test Novel Double-wall Cooling Designs for Linear Cascade

The Pennsylvania State University

Objective

The objective of this task is to measure the performance of the AM microchannels in the linear cascade airfoil and rank the performance of the novel geometries. This process includes measuring the pressure decrease and the surface temperature of the airfoils with the novel microchannel geometries. We have also developed a novel measurement technique to obtain the overall convection coefficient in the microchannels by using coolant and surface temperature measurements.

Research Approach

Fabrication of linear cascade hardware

In the previous reporting period, the novel microchannel test airfoils with internal geometries indicated in Figure 2 were manufactured by Vertex Manufacturing and were received in late summer 2022.

Experimental validation of flowfield and development of infrared camera calibration

In the previous reporting period, the linear cascade hardware was installed and tested in the facility. Measured blade static pressures were an excellent match to the design intent under the cascade conditions, thus indicating that the facility was benchmarked for the desired flowfield around the airfoils. In the prior reporting period, procedures were developed to map the IR camera images to the airfoils (spatial calibration) and correct them for temperature offset (temperature calibration). Examples of these two calibration processes are shown in Figure 3.

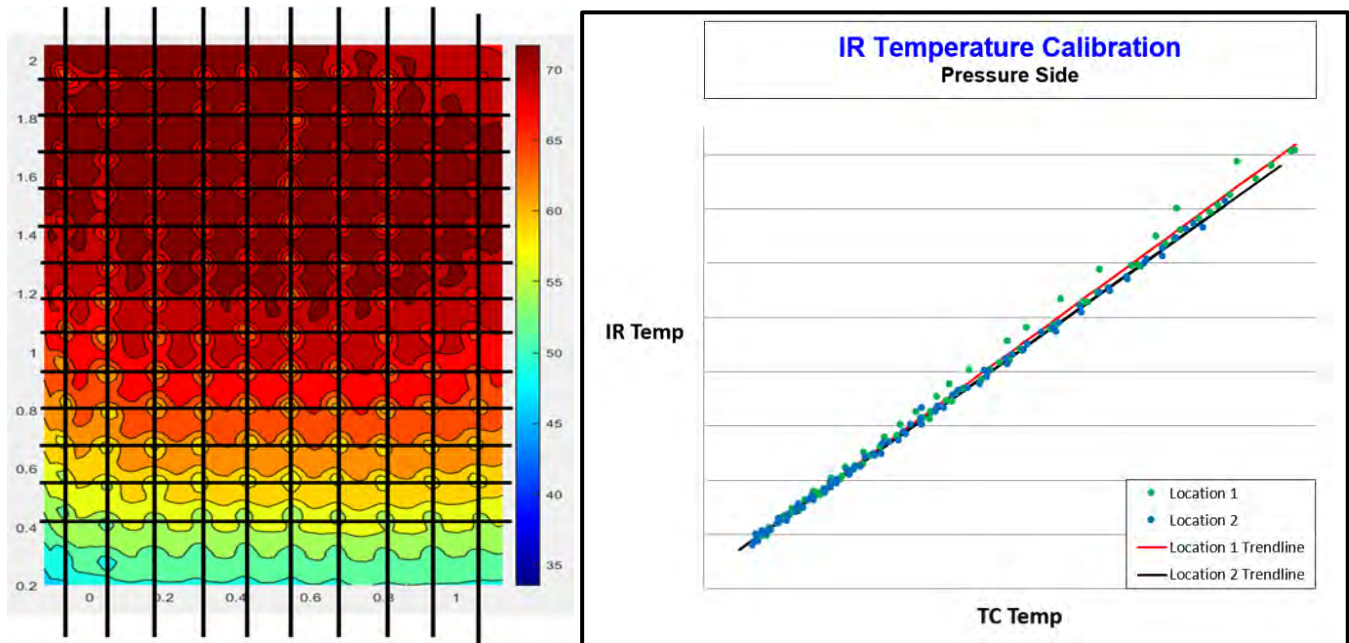


Figure 3. De-warped IR spatial calibration image for the airfoil surface (left), and example IR signal calibration against reference thermocouples (right).

Initial test results for empty microchannel geometry

Initial experimental data for an empty microchannel design were recorded in the high-speed linear cascade at the end of 2022. Instrumented thermocouples, pressure taps, and an IR camera were used to measure surface temperature. Figure 4 shows the results for a pressure-side view of the empty microchannel geometry, in which the microchannel is located under the vertical streak of high cooling effectiveness toward the left side of each subfigure (warm colors). The contours are of normalized surface temperature, as calculated with the following formula: $\frac{T_s - T_\infty}{T_{m,i} - T_\infty}$, where T_s is the surface temperature, T_∞ is the freestream temperature, and $T_{m,i}$ is the coolant inlet temperature. As expected, when the microchannel Reynolds number (nondimensional flow rate is reduced, the cooling effectiveness of the microchannel decreases.

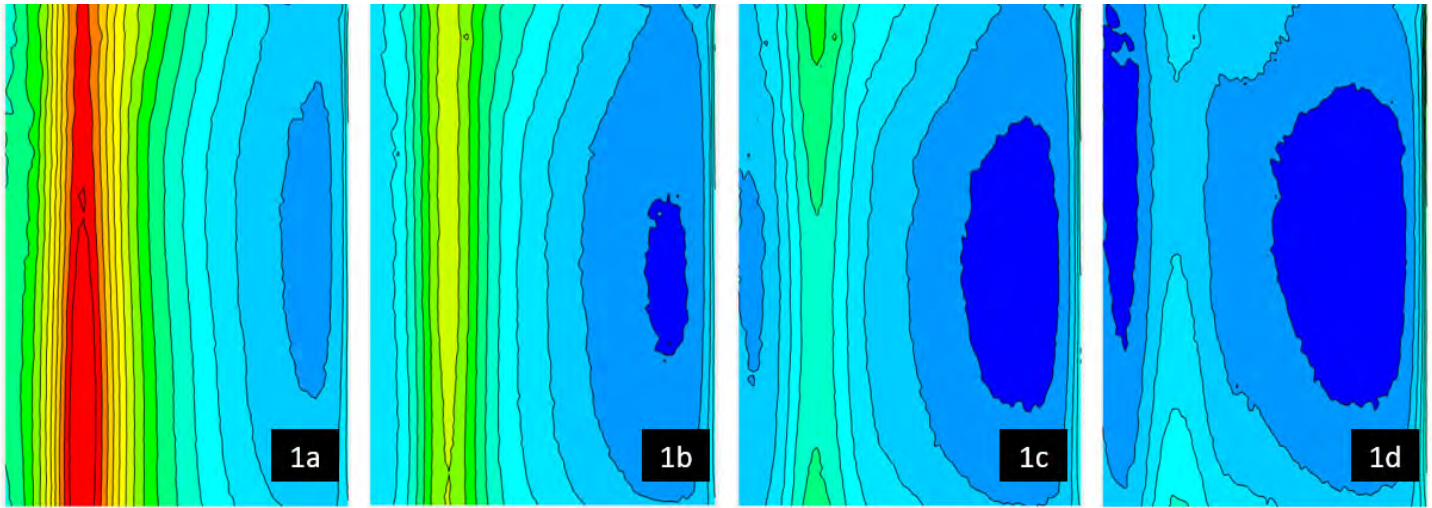


Figure 4. Experimental IR data obtained at a microchannel Re_D of (a) 20,000, (b) 10,000, (c) 6,675, and (d) 4,000.

Computational predictions of microchannel performance

While waiting to resume testing in the linear cascade in 2023, we made some computational predictions of the empty microchannel geometry and compared them with the initial IR data obtained in 2022. Figure 5 illustrates the computational domain with boundary conditions used to perform the computational fluid dynamics (CFD) analysis on the empty channel cooling design. The fluid domain had periodic walls, so that a single airfoil could be simulated in the ideal environment of a cascade. At the inlet, stagnation conditions were applied, and at the outlet, a static pressure was imposed, such that the isentropic Mach number and exit Reynolds number were matched to the cascade test conditions. A mass flow inlet with the conditions from the experiment was imposed on the microchannel inlet, and a conjugate analysis (coupled temperatures/heat fluxes at the solid-fluid interfaces) was performed. A mesh sensitivity and iterative convergence study was performed to ensure that the baseline mesh was of sufficient quality to provide accurate answers.

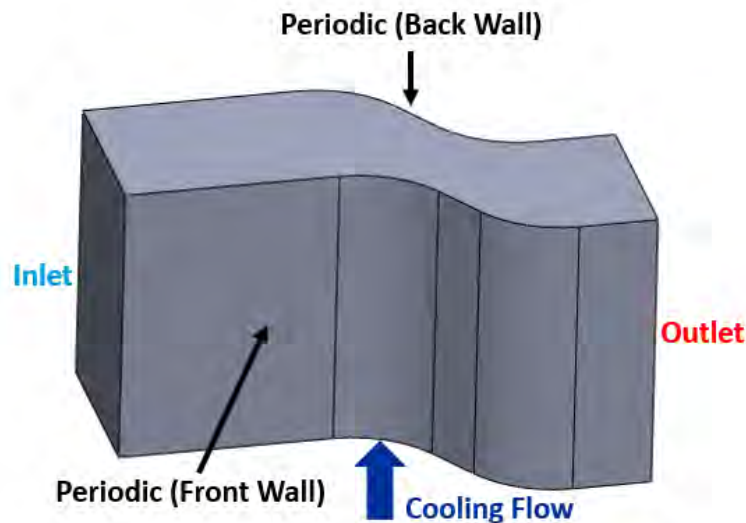


Figure 5. Computational domain and boundary conditions for the conjugate CFD study.



In Figure 6, contour plots of the normalized temperature are shown for experimental and computational results, respectively. The upper-left corner of the experimental data exhibits an artifact of some reflective tape used to hold a thermocouple in place and is not relevant to the data analysis. One key difference appears at the entrance of the microchannel toward the bottom of the figure. In the computational simulations, the peak cooling occurs at the entrance indicated by the red region at the base (lower side of the figure). In contrast, the experimental data indicate that the peak cooling region occurs higher up in the channel, with relatively constant nondimensional temperature at the base.

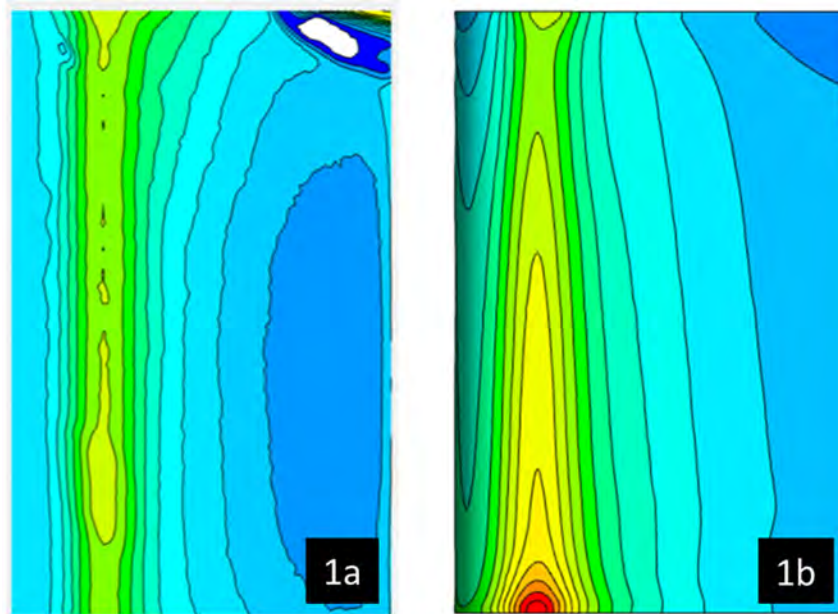


Figure 6. (a) Normalized experimental IR data taken at a microchannel Re_D of 10,000. (b) Normalized surface temperature contours from CFD.

To match the simulation to the experiment more accurately, we conjectured that the inlet to the microchannels should be fully developed before entering the channel. We conducted tests to determine whether the flow profile could be imported into the simulation, but doing so was determined to not be the most efficient method. Instead, the full development path of the flow entering the microchannels was added to the simulation. Figure 7 shows a diagram of the test article as it would be installed in the cascade; long coolant delivery tubes were necessary to route coolant from outside the facility to the microchannels in the airfoil.

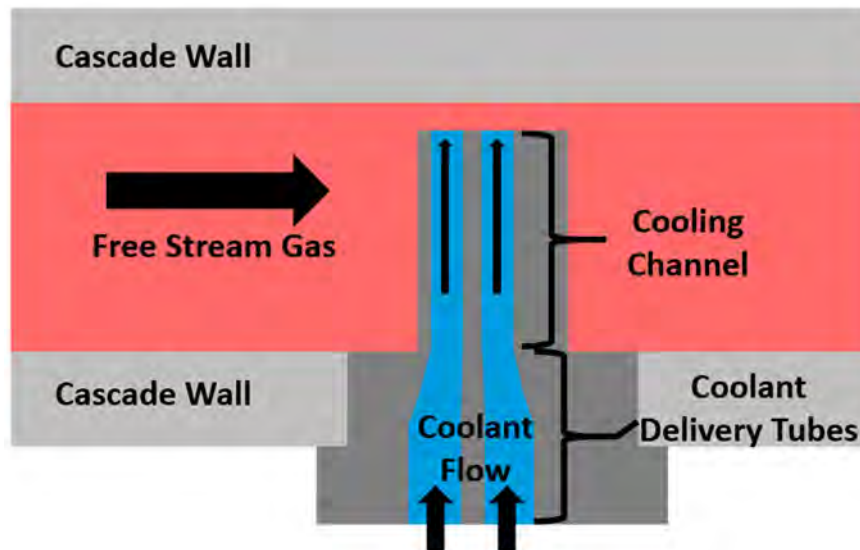


Figure 7. Diagram detailing the locations of coolant delivery tubes in the high-speed cascade experimental setup.

These entrance regions were added onto the computational domain, as illustrated by the mock airfoil in Figure 8. By using the as-designed channel entrances, we properly developed the inlet of the microchannels and gained important learning regarding how the flow enters the microchannel inlet.

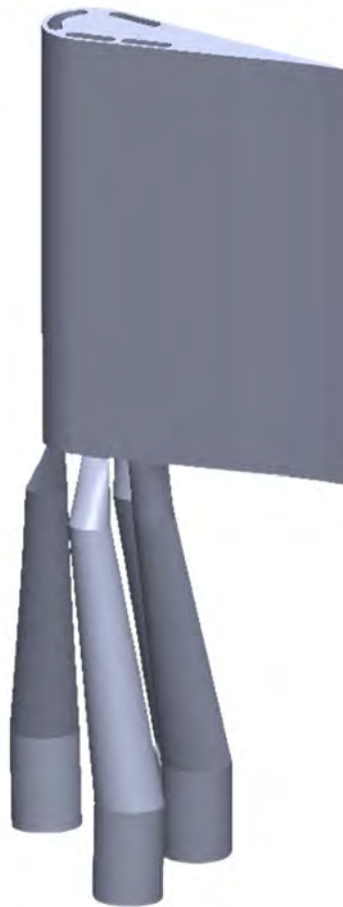


Figure 8. Mock airfoil with microchannel entrance regions attached.

This approach worked well for low coolant flow rates in the microchannels, but when these entry regions were implemented with a higher mass flow rate, the match to experimental findings was poorer. Normalized surface temperature is shown in three contour plots below. Figure 9a shows the experimental data obtained through IR imaging of the blade surfaces. Figure 9b,c shows the normalized temperature in the CFD simulation before and after the addition of the coolant delivery tubes, respectively. Adding the tubes to the conjugate CFD simulation eliminates the overestimation of cooling at the base of the channel but shifts the peak cooling to the middle of the channel.

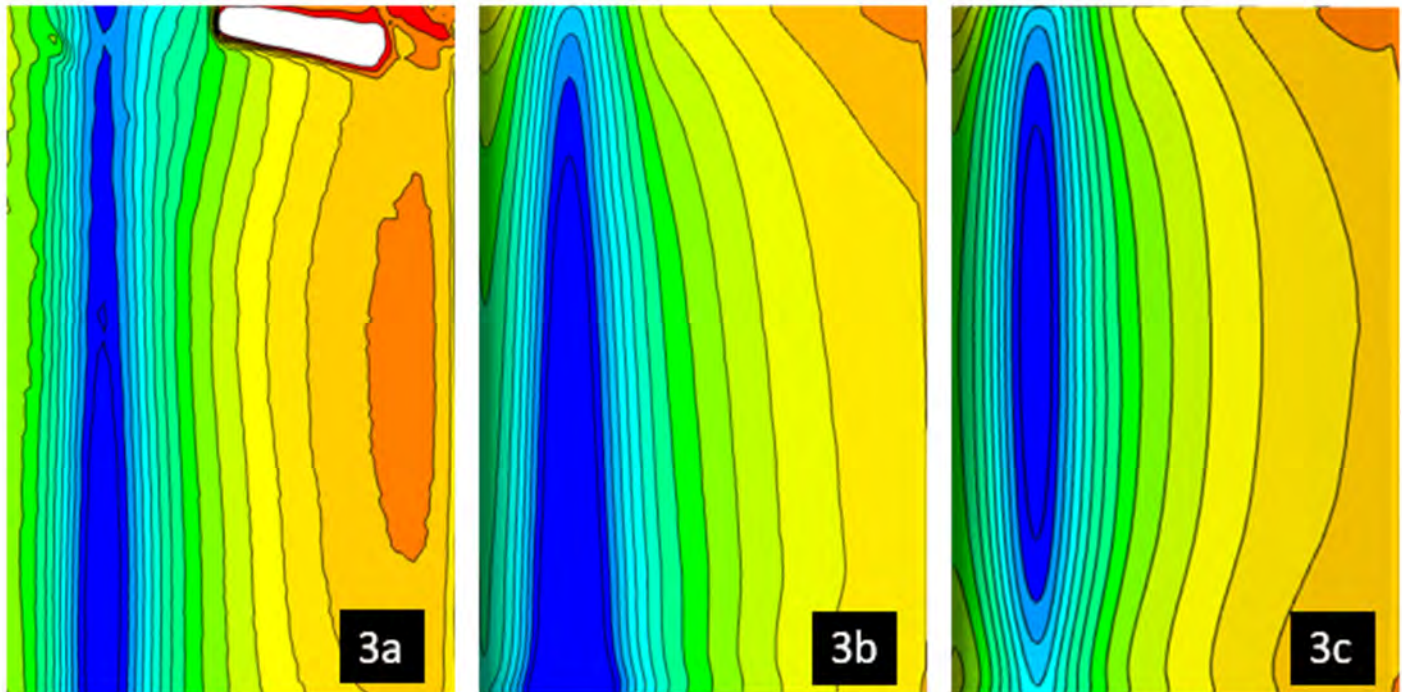


Figure 9. (a) Experimental normalized surface temperature. (b) Computational normalized surface temperature with no entrance region. (c) Computational normalized surface temperature with isothermal entrance region.

One factor with a large role in the misprediction of the airfoil temperature at the microchannel entrance is the choice of wall temperature for the coolant delivery tubes. Figure 10 shows the boundary conditions that must be adjusted to match the inlet of the microchannel to the observed experimental results. The bulk temperature at the base of the microchannel, $T_m(0)$, is the target that must be matched to the value measured in the experiment. For the situation in Figure 8 with coolant delivery tubes, $T_m(0)$ must be matched to the experiment by using two boundary conditions: the wall temperature in the delivery tube, T_w , as well as the coolant inlet temperature, $T_{c,i}$. This process is somewhat complicated, because of interacting effects: high wall temperature T_w requires a low $T_{c,i}$, or vice versa. The initial measurement campaign did not measure the metal temperature of the base of the test article, but this aspect will be addressed in the next measurements.

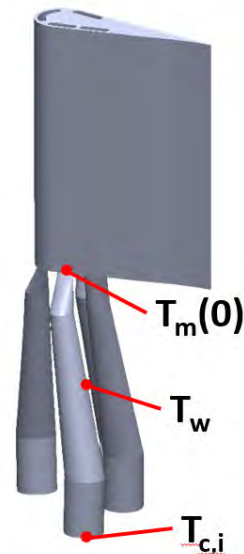


Figure 10. Diagram showing boundary conditions related to the channel inlet.

On the basis of the findings in Figure 9c, we hypothesized that the guess for the wall temperature of the coolant delivery tubes in the simulation was too high, thus resulting in temperatures that were too high near the base of the airfoil. To investigate this possibility, we varied the coolant delivery tube wall temperature as well as the temperature at the inlet of the entrance region in a way that kept $T_m(0)$ fixed at the value observed in the experiment.

The effect of changing the wall temperature, T_w , was observed by plotting the normalized surface temperature of the inner channel surface as a function of height, as shown in Figure 11. The temperature was normalized by the channel inlet bulk temperature, $T_m(0)$, which needed to remain constant among all cases, to enable matching to the experimental data. The case shown in Figure 9c is the hottest wall temperature guess, at a normalized $T_w' = 1.14$. Two cases were run with lower normalized wall temperatures of $T_w' = 1.09$ and 1.02 . The plot indicated that changing this variable for the coolant delivery tubes had a significant impact on the predicted microchannel wall temperature profile in the first half of this channel, but less impact further up the channel.

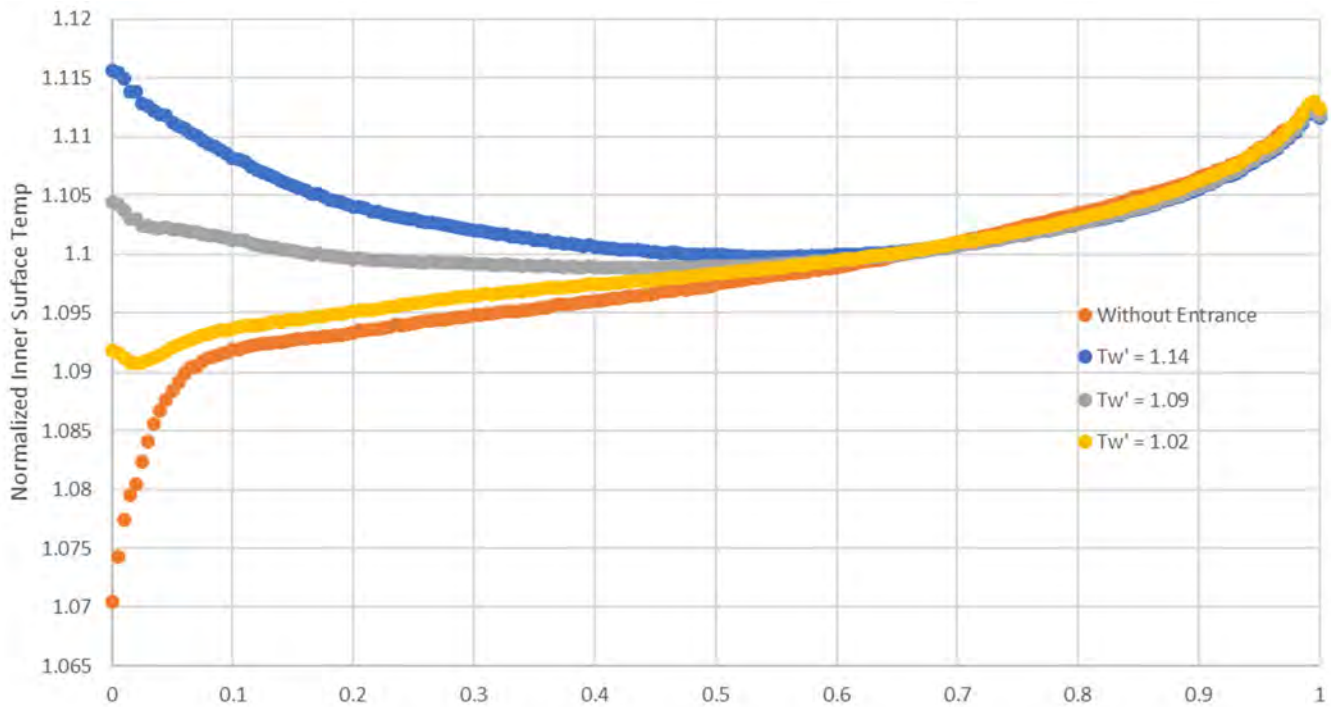


Figure 11. Normalized inner microchannel wall surface temperature along the tube for varying coolant delivery tube wall temperatures.

This exercise revealed the importance of the choice for temperature of the coolant delivery tubes. These effects can also be observed by viewing the normalized vane surface temperature contours in Figure 12. These trends indicate that a high wall temperature in the delivery tubes leads to an underprediction of cooling (i.e., the predicted wall temperature of the airfoil is too high) at the base of the channel. They also show that if the isothermal wall temperature in the delivery tubes is too low, or that if a uniform velocity/temperature profile is placed at the inlet of the microchannels, the cooling occurring due to the microchannel at the base of the airfoil is overpredicted in a manner similar to the case with no entrance region.

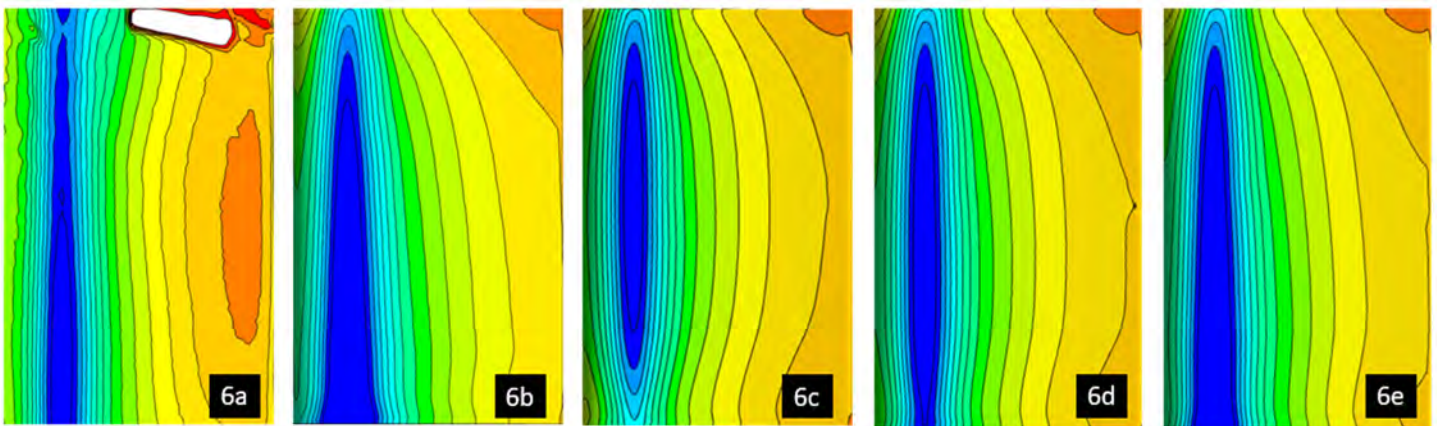


Figure 12. Contours of vane external surface temperature for: (a) experimental data, (b) CFD with no coolant delivery tubes modeled, (c) CFD with $T_w' = 1.14$, (d) CFD with $T_w' = 1.09$, and (e) CFD with $T_w' = 1.02$.

Current experimental data

In 2023 Q3, most of the experimental data on microchannel cooling performance were obtained for a wide range of external Mach and Reynolds numbers as well as internal microchannel coolant Reynolds numbers. The data are currently being processed, but some results are shown below for the empty microchannel geometry, which was tested at a wider range of conditions than those in November 2022.

In Figures 14–16, experimental data are shown in contour plots in which all four internal cooling channels are flowing at several different Reynolds numbers. Each figure shows both the pressure side and the suction side of the airfoil, on the left and right sides of the plot, respectively. The surface temperature was recorded with an IR thermal imaging camera, and was calibrated and dewarped onto a two-dimensional plane before being normalized and plotted. A diagram of how the different plotting regions relate to the physical blade is shown in Figure 13. The vertical arrow indicates the direction of increasing height on the blade surface. The horizontal arrow points from the leading edge of the airfoil to the trailing edge. The space between the pressure side and suction side is representative of the area not captured by the IR camera, which includes the stagnation zone.

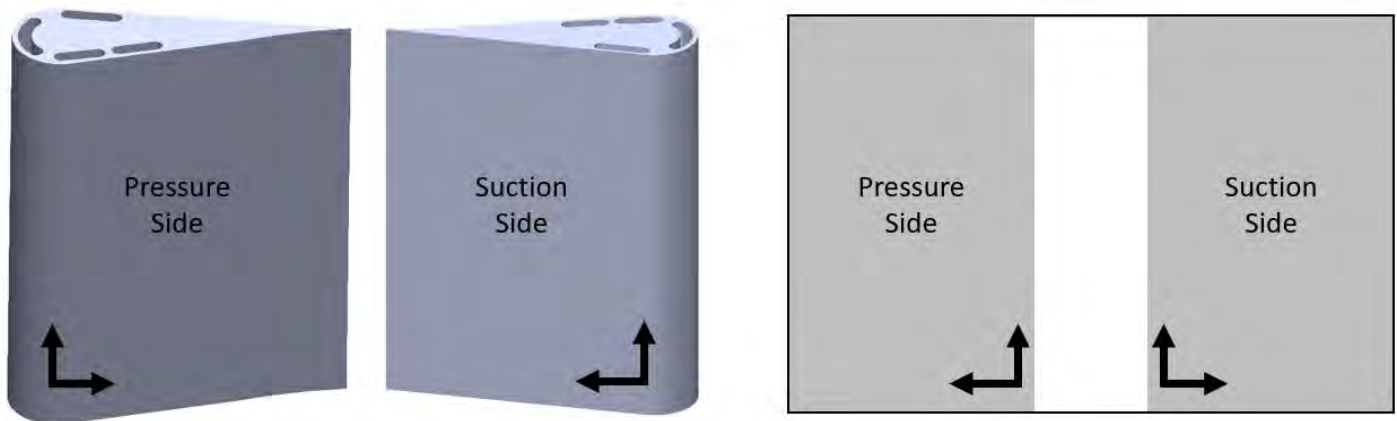


Figure 13. Pressure-side and suction-side views of the airfoil, and view locations on the following plots.

Figures 14–17 demonstrate that decreasing the internal channel Reynolds number decreases the cooling effectiveness. In the case in which the channel Reynolds number is 20,000 (Figure 3), the internal cooling shows significantly higher cooling performance than the lowest cooling case with a Reynolds number of 4,000 (Figure 6).

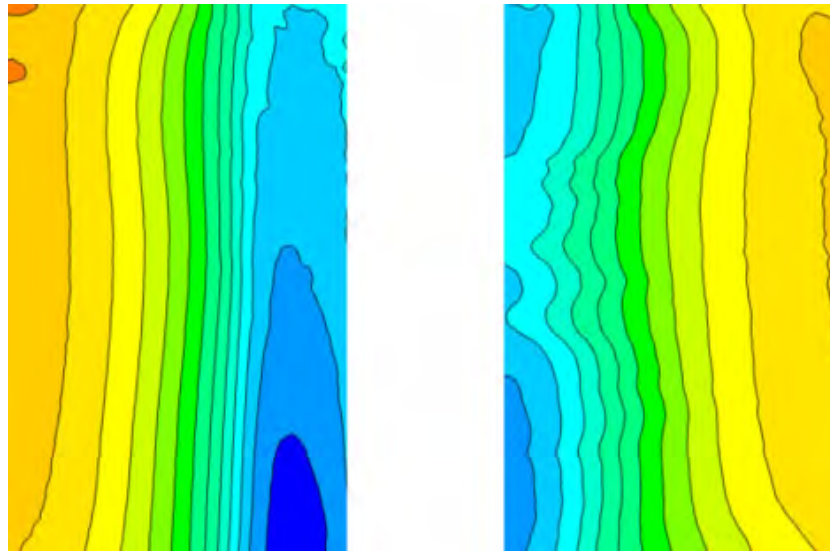


Figure 14. All channels flowing at an internal Reynolds number of 20,000.

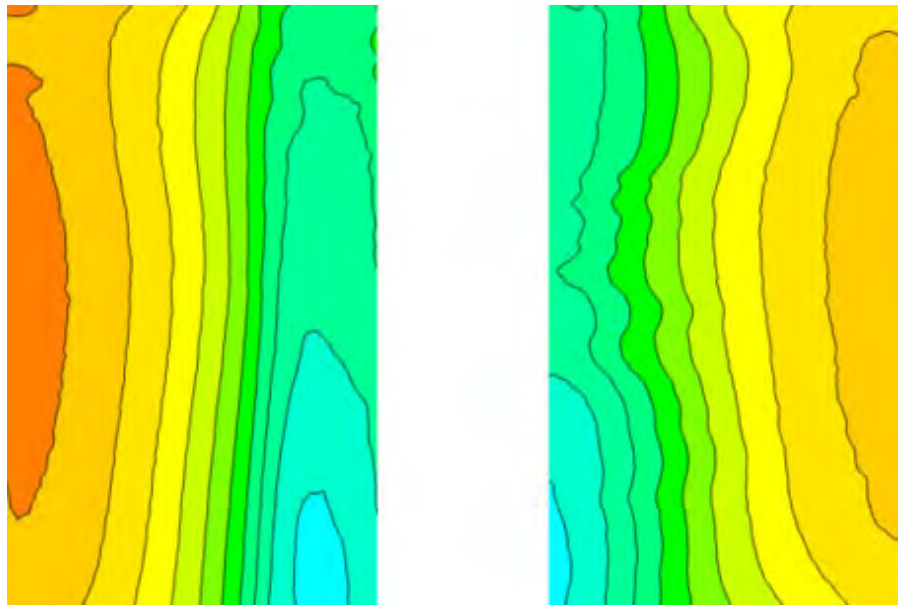


Figure 15. All channels flowing at an internal Reynolds number of 10,000.

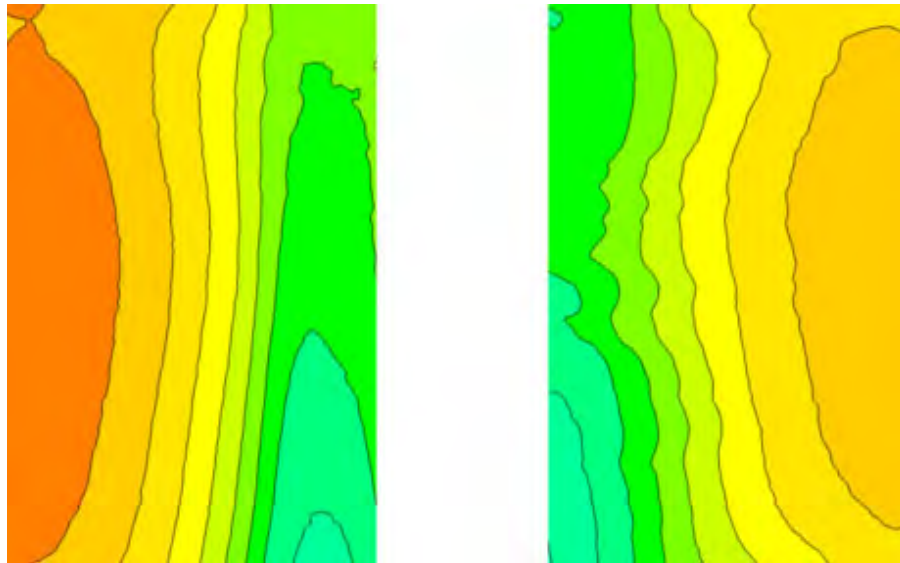


Figure 16. All channels flowing at an internal Reynolds number of 6,675.

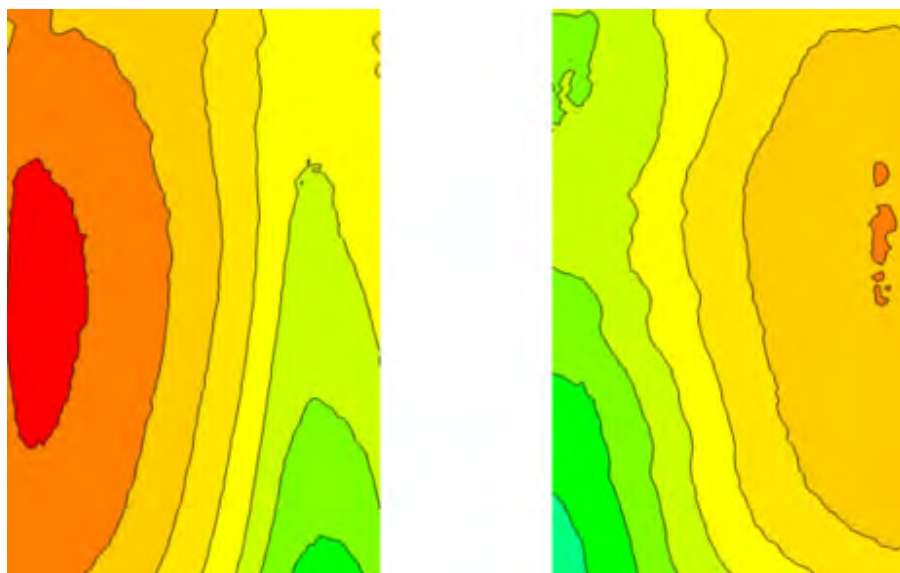


Figure 17. All channels flowing at an internal Reynolds number of 4,000.

In Figure 18, the same datasets shown above are plotted with laterally averaged normalized temperature values, where the averaging direction is along the span of the airfoil. The same trend of decreased cooling performance with a decrease in Reynolds number is again apparent.

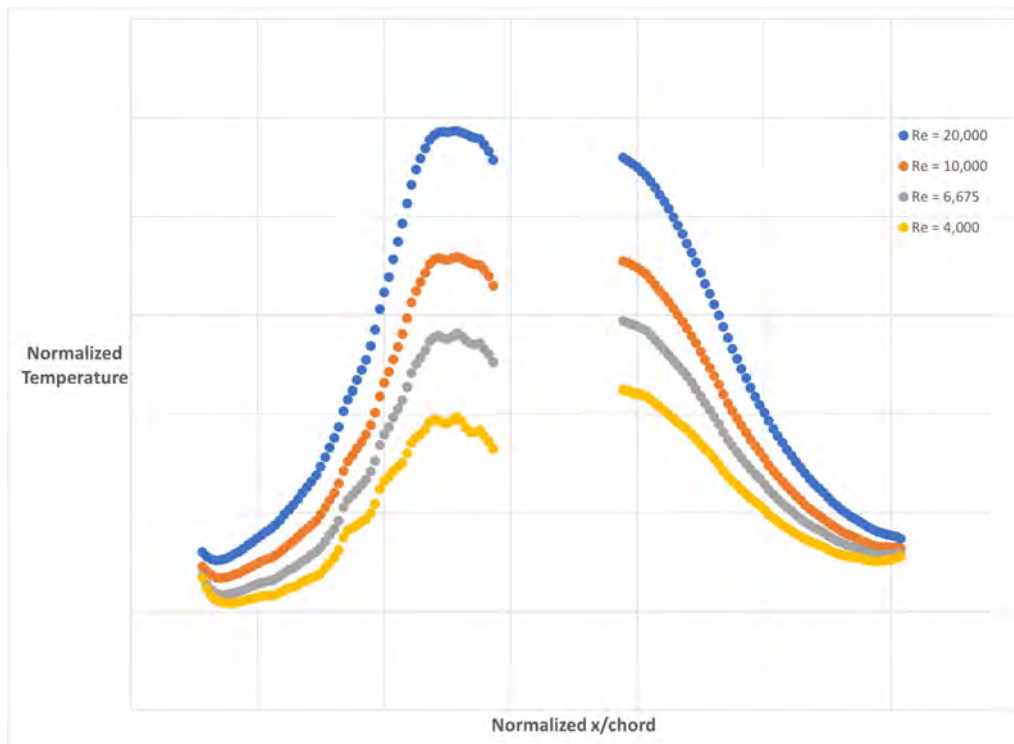


Figure 18. Laterally averaged values of normalized temperature for the four internal channel conditions.

In addition to changing the amount of flow through all cooling channels, individual cooling channels can be turned on or off. Figures 19–21 show contour plots of nondimensional temperature for the airfoil surface (pressure side and suction side) for three cases in which only a single channel is receiving coolant flow. Channel 2a and channel 2b are located on the pressure side, whereas channel 3 is located on the suction side, partially in the unmeasurable region of the airfoil. An interesting (although not unexpected) finding is that flowing a single channel on one side of the airfoil can influence temperatures on the other side, because of conduction through the metallic airfoil and the high effectiveness of the microchannels.

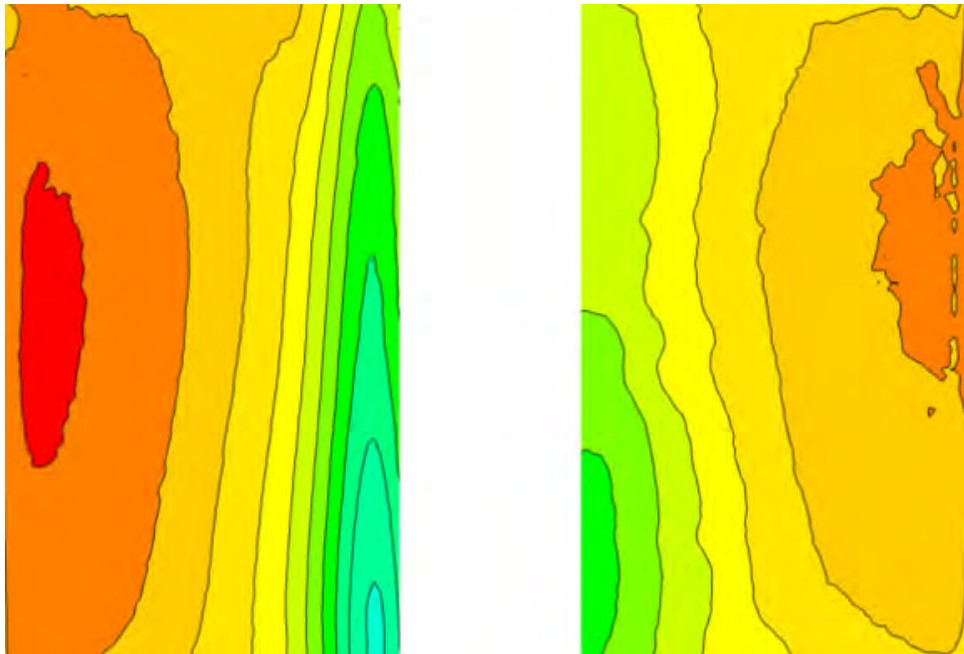


Figure 19. Channel 2a flowing at an internal Reynolds number of 20,000.

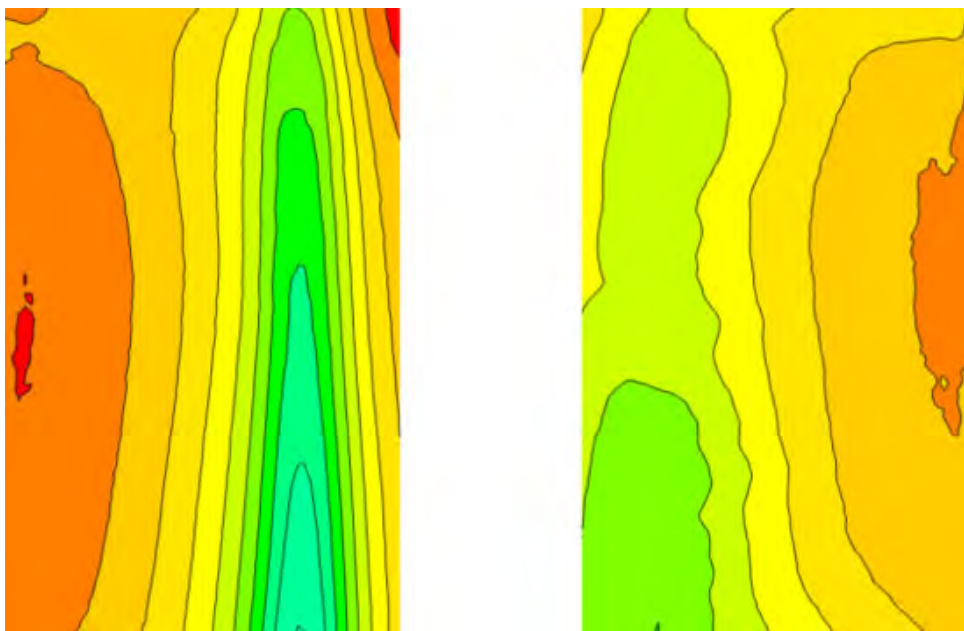


Figure 20. Channel 2b flowing at an internal Reynolds number of 20,000.

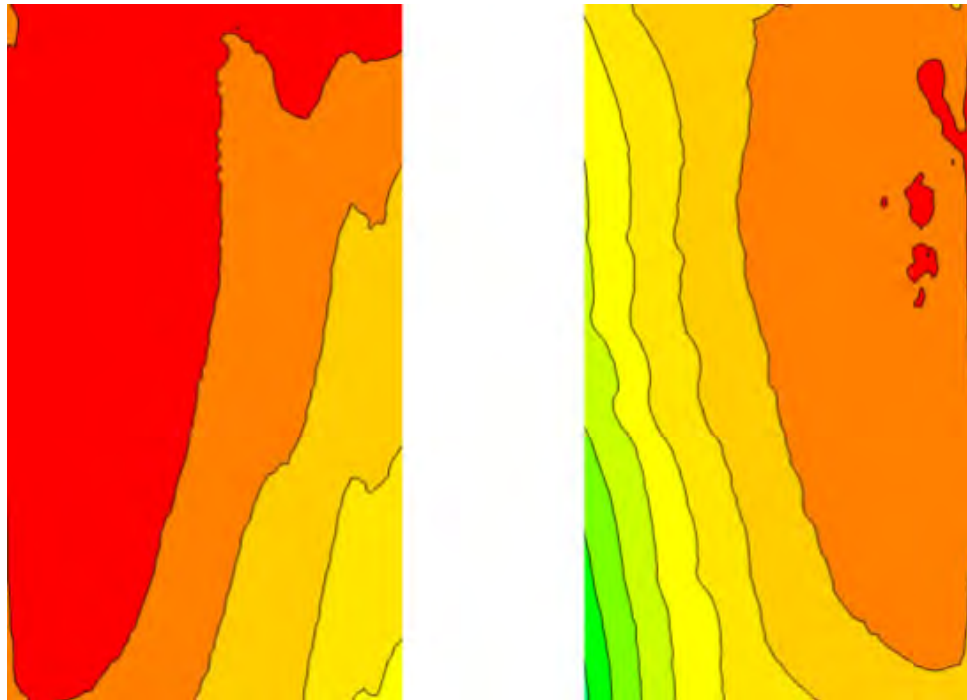


Figure 21. Channel 3 flowing at an internal Reynolds number of 20,000.

Milestones

Milestone	Due date	Estimated date of completion	Actual date of completion	Status
Workplan	3/4/20	3/4/20	3/5/20	Completed
COE meeting 1	4/1/20	4/1/20		Cancelled
COE meeting 2	10/1/21	10/1/21	10/28-10/29/21	Completed
COE meeting 3	10/26/22	10/26/22	10/26-10/28/22	Completed
COE meeting 4	10/24/23	10/24/23	10/24/23	Completed
Annual report	12/17/23	12/10/23	12/10/23	Completed
Project closeout	12/31/23	12/31/23		

Major Accomplishments

The major activities are (a) learning on how to make turbine blades by using AM, through the interaction of more than 20 vendors and many trial parts; (b) fabrication of an additively manufactured version of an FAA CLEEN II airfoil from the vendor after multiple trials; (c) design, fabrication, and testing of linear cascade hardware; and (d) development of novel data reduction techniques for in situ performance analysis of additively manufactured microchannels. Activity 1 is leading directly to completion of Task 1 in Q1 2024, and Activities 2 and 3 have positioned us to be able to measure all the existing novel microchannels and develop a ranking that can be discussed with our cost-sharing partner regarding future implementation into airfoils.

Publications

Boyd, L., Lynch, S., & Thole, K. (2023). ASME Student Poster: “Novel Cooling Designs in Additively Manufactured Microchannels”, GT2023-110173.

This poster was awarded the 2023 ASME Warren M. Rohsenow Prize for best poster on gas turbine heat transfer.

Outreach Efforts

Research findings were presented throughout this year, as illustrated below.

Event	Date	Attendees
Bi-weekly calls	Every 2 weeks	Pratt & Whitney (PW) aerodynamics/durability engineers
Quarterly calls with turbine OEMS	Once per month	Industry partners: Solar, Siemens, Honeywell
Center of Excellence bi-annual meetings	6/6/2023 and 12/5/2023	PW aerodynamics/durability engineers and management
Center of Excellence bi-annual meetings	11/8/2023	Solar Turbine engineers
Dept. of Energy (DOE) National Experimental Turbine (NExT) annual review meeting	11/1/2023	DOE, NASA, FAA, PW, Solar, Siemens, Honeywell, Georgia Institute of Technology
NASA university leadership initiative meeting	10/5/2022	DOE, NASA, FAA, PW, Mesoscribe, Howard University, Georgia Institute of Technology

We presented findings on learning from AM to Solar Turbines at the November Center of Excellence on 11/8/2023, and to Pratt & Whitney at the June (6/6/2023) and December (12/5/2023) program reviews. We reported on manufacturing learning at a Department of Energy Review meeting at Penn State at NExT on 11/1/2023. The DOE meeting involved industry members including Honeywell, Solar Turbines, Siemens, and Pratt & Whitney.

Awards

Co-P.I. Stephen Lynch received the 2023 ASME Westinghouse Silver Medal for research excellence in the field of power generation technologies.

Student Involvement

Liam Boyd is a master’s degree student who started on the project in Summer 2022 and is conducting computational simulations of microchannels, as well as experimentally testing the remaining microchannel geometries, to study the effectiveness of certain designs as well as the predictive capabilities of modern CFD. Liam will also conduct analysis of CT scan data from the microchannel geometries and compare the results to the design intent to understand the feature resolution of various microchannel enhancements.

Plans for Next Period

1. The completed blades will be tested at Penn State in the START turbine by using the recently developed IR thermography capability. The results will be compared with the original FAA CLEEN II cast airfoils to provide the first back-to-back comparison of casting vs. AM.
2. CT scans of the manufactured parts will be conducted and analyzed to obtain accurate values for hydraulic diameter and internal roughness, and the remaining microchannel designs will be tested and simulated with CFD in Q1 to Q2 of 2024.

References

Ferster, K. K., Kirsch, K. L., & Thole, K. A. (2018). Effects of geometry, spacing, and number of pin fins in additively manufactured microchannel pin fin arrays. *Journal of Turbomachinery*, 140(1), 011007.

King, C., & Pietraszkiewicz, E. F. (2018). *U.S. Patent No. 10,156,157*. Washington, DC: U.S. Patent and Trademark Office.

Kirsch, K. L., & Thole, K. A. (2017a). Pressure loss and heat transfer performance for additively and conventionally manufactured pin fin arrays. *International Journal of Heat and Mass Transfer*, 108, 2502-2513.

Kirsch, K. L., & Thole, K. A. (2017b). Heat transfer and pressure loss measurements in additively manufactured wavy microchannels. *Journal of turbomachinery*, 139(1), 011007.

Stimpson, C. K., Snyder, J. C., Thole, K. A., & Mongillo, D. (2017). Scaling roughness effects on pressure loss and heat transfer of additively manufactured channels. *Journal of Turbomachinery*, 139(2), 021003.

Wildgoose, A. J., Thole, K. A., Sanders, P., & Wang, L. (2021). Impact of additive manufacturing on internal cooling channels with varying diameters and build directions. *Journal of Turbomachinery*, 143(7), 071003.

Wright, L. M., Fu, W. L., & Han, J. C. (2004, January). Thermal performance of angled, V-shaped, and W-shaped rib turbulators in rotating rectangular cooling channels (AR= 4: 1). In *Turbo Expo: Power for Land, Sea, and Air* (Vol. 41685, pp. 885-894).



Project 057 Support for Supersonic Aircraft En-route Noise Efforts in ICAO CAEP

The Pennsylvania State University

Project Lead Investigator

Victor W. Sparrow
United Technologies Corporation Professor of Acoustics
Graduate Program in Acoustics
The Pennsylvania State University
201 Applied Science Bldg.
University Park, PA 16802
814-865-6364
vws1@psu.edu

University Participants

The Pennsylvania State University (Penn State)

- P.I.: Professor Victor W. Sparrow
- FAA Award Number: 13-C-AJFE-PSU Amendments 55, 77, 86, and 100
- Period of Performance: February 5, 2020 to September 30, 2024
- Tasks:
 1. Obtaining confidence in signatures, assessing metrics sensitivity, and adjusting for reference-day conditions
 2. Assessing secondary sonic boom propagation
 3. Investigating seismic networks for measuring sonic booms

Project Funding Level

This project focuses on multiple tasks at Penn State and its subcontractors Queensborough Community College and Farmingdale State University. The FAA funding to Penn State in 2023 was \$220,000. Matching funds are expected to meet cost sharing on all tasks. In-kind contributions have been pledged by Boom Supersonic (\$150,000), Global SST (\$75,000 in 2024), Gulfstream (\$100,000), and Exosonic (\$110,000 in 2022).

Task 3, investigating seismic networks, was initiated by the Project P.I. using funds from the United Technologies Corporation Professorship within the Penn State College of Engineering. This 2023 financial support from the Penn State College of Engineering is gratefully acknowledged.

Investigation Team

Penn State

Prof. Victor W. Sparrow, (P.I.), Tasks 1, 2, and 3
Joshua Kapcsos, (graduate research assistant), Task 1
Dr. Sampath Rathnayaka (geosciences postdoctoral scholar), Task 3
Prof. Andrew Nyblade, (Penn State geosciences department head), Task 3

Farmingdale State College, State University of New York (subrecipient of Penn State)

Kimberly A. Riegel, (physics co-investigator), Tasks 2 and 3

Boom Supersonic (industrial partner)

Michael Rybalko, Gus Silva, et al.

Exosonic (industrial partner)

John Morgenstern

Global SST (industrial partner)

Steve Ogg

Gulfstream (industrial partner)

Brian Cook, Matthew Nickerson, Joe Gavin, Nick Ward, and Charles Etter

Project Overview

We are on the verge of a true revolution in passenger aircraft development. Companies such as Boom Supersonic, Gulfstream Aerospace Corporation, Lockheed Martin, Exosonic, Global SST, and others are reaching the point at which they can build, and deliver to users, aircraft capable of flying supersonically in an environmentally responsible way. This development will allow for decreased air transportation travel times, to the great benefit of society.

To introduce new supersonic aircraft, vehicles must be certified as being sufficiently quiet to not excessively disturb the public. Preparation for such a certification process has been ongoing for several years in the FAA Office of Environment and Energy (AEE). Working with its international partners in the International Civil Aviation Organizations (ICAO)'s Committee for Aviation Environmental Protection (CAEP), the FAA has been laying the groundwork for certification standards. The FAA's efforts have been supported by both universities and other governmental agencies. Specifically, Penn State has supported the FAA/AEE through Projects 8 and 24 in the PARTNER Center of Excellence and more recently in Projects 7, 41, and 42 of the ASCENT Center of Excellence. Summaries of these research efforts can be found on the websites provided. To date, a group of six candidate metrics for sonic boom certification have been agreed upon in CAEP's Working Group 1 (WG1; Noise Technical) Supersonic Task Group (SSTG). Multiple schemes for certification have been generated. Several schemes have been eliminated from further consideration, and others are currently being evaluated for possible implementation. Procedures have been proposed for acquiring and processing ground measurement of the sonic boom signatures, but all possibilities remain under discussion. The extent to which atmospheric conditions will affect the measurements, and the requirements and roles of numerical simulations of sonic booms propagating from the aircraft to the ground are being considered. One particularly challenging aspect is the influence of the atmosphere in distorting sonic boom signatures, owing to atmospheric turbulence, and the subsequent effects on the metric values. These gaps are only several of those that must be filled.

All these topics are being worked on, in a stepwise manner, in FAA and in WG1's SSTG. Recent efforts in ASCENT Project 41 have been aimed at supporting the FAA with technical expertise in the development of the certification procedures, as well as gaining an initial understanding of secondary sonic booms. Secondary sonic booms, also known as over-the-top sonic booms, are the sound energy that travels upward at heights above the aircraft cruise altitude and lands at distant locations. Secondary sonic booms are the reason why the Concorde was requested to transition from supersonic to subsonic speeds at substantial distances before entering the continental United States. ASCENT Project 41 ended in early 2021, and ASCENT Project 57 is now in its fourth year. However, much work remains to be done, and efforts lasting several more years will be required to advance certification standards for supersonic aircraft.

In 2024 and beyond, continued support for supersonic aircraft noise efforts will be necessary for the FAA and its international partners to fill technical solution gaps and continue progressing toward certification procedures. Although other universities and industries will continue their focus on aircraft design and landing and takeoff studies, continued work on sonic boom issues will be essential, because these issues remain the greatest barrier to the use of environmentally responsible supersonic aircraft. ASCENT Project 57 will support the ongoing activities in ICAO CAEP and their WG1 (noise), with a focus on establishing supersonic aircraft en route procedures and metrics for noise certification standards, and to support the interface with the ICAO Air Navigation Commission to address related noise issues.

In the 2020–2024 project period, the emphasis will be on continuing the research support for supersonic aircraft en route procedures, including the utilization of an agreed-upon reference-day atmosphere, the establishment of techniques for incorporating measurement data and simulations into a draft certification procedure, and the consideration of off-design flight speed sonic booms, such as focus booms and acceleration booms. Support will also be provided for a more comprehensive analysis of NASA's SonicBAT dataset and efforts in developing methods to remove the effects of atmospheric turbulence on measured sonic boom waveforms to support certification. The 2020–2024 research will also

need to consolidate and process the results of research in 2019–2020 on the topic of secondary sonic booms as a potential noise issue for the initial supersonic airplanes. This material will be of particular interest to ICAO’s Air Navigation Commission, because it could affect the operation of supersonic aircraft in the near term.

Task 1 – Obtaining Confidence in Signatures, Assessing Metric Sensitivity, and Adjusting for Reference-day Conditions

The Pennsylvania State University

Objectives

ASCENT Project 57 is a transition from ASCENT Project 41, Identification of Noise Acceptance Onset for Noise Certification Standards of Supersonic Airplanes. As national aviation authorities move toward developing noise certification standards for low-boom supersonic airplanes, several research gaps exist in areas including signature fidelity, metrics, metrics sensitivity to real-world atmospheric effects, and adjustments for reference conditions. The objective of Task 1 is to support the FAA in the development of technical standards for civil supersonic aircraft under ICAO CAEP. This effort provides the FAA with technical noise expertise regarding the development of noise certification standards for future civil supersonic passenger aircraft, primarily in the area of en-route noise (sonic boom) minimization and/or abatement.

Task 1 in ASCENT Project 57 focuses on research initiatives necessary to develop a low-boom supersonic en-route noise certification standard. An objective was to investigate numerical methods available in nonlinear propagation code KZKFourier. Another objective was to begin introducing atmospheric profiling into KZKFourier.

Research Approach

Background

The KZKFourier propagation code is an augmentation of the Burgers equation into a KZKFourier propagation equation to include nonlinearity, diffraction, and absorption in directional sound beams, to simulate wind and temperature fluctuation effects of the atmospheric boundary layer (ABL), according to the Ostashev and Wilson (2015) model. During the 2019–2020 academic year, PCBoom 6.7.1.1 and KZKFourier were used above and within the atmospheric boundary layer, respectively, to simulate turbulence effects of atmospheric boundary layer heights of 268.2, 411.4, and 1026.7 m, corresponding to SonicBAT Flight 5 conditions. Information regarding this endeavor appears in the 2020 report for ASCENT Project 057. After propagating shaped boom signatures through 10 randomly generated atmospheres, the data were shared with WG1/SSTG/PrSG, in which zero-padding and spiking artifacts were discovered near the beginnings and ends of certain ground signatures; the plots shown in the 2020 report did not span the entire retarded time domain of the ground waveform data. These artifacts were corrected in the 2020–2021 academic year, as described in the 2021 report for ASCENT Project 057. In the 2021–2022 academic year, Penn State expanded the shaped boom database to 20 realizations at NASA’s request, conducted a parameter check on KZKFourier for boundary layers, freezing temperatures, and turbulence parameters, conducted a grid refinement study on KZKFourier, and initiated a reference-day crosscheck with international members of CAEP’s WG1 (Noise Technical); these milestones are described in the 2022 report for ASCENT Project 057.

KZKFourier numerical method investigation

KZKFourier uses the 1964 Blackstock solution of the KZK equation; the inclusion of nonlinear effects of the operator splitting method results in distortion of the time coordinate. KZKFourier must therefore use an interpolation method to convert a distorted time grid to a regular time grid. Through the configuration file, the user sets the numerical method for nonlinearity and convection solutions: “natural” spline, linear interpolation, Hermite spline, finite differences, and frequency domain.

Because of the spiking artifacts found in the results presented in the 2021 report for ASCENT Project 057, Penn State investigated the numerical methods available in KZKFourier. “Natural” spline is the default method that was used in waveform database simulations and resulted in the spiking artifacts in the 411.38-m ABL run of random seed 5 and 1026.7-m ABL run of random seed 2 presented in the 2021 report. Penn State reran the afflicted seeds by using the other four available numerical methods, analyzed for spiking, and compared sound metrics for FAA-approved Stevens Mark VII Perceived Level (PL) and Indoor Sonic Boom Annoyance Predictor (ISBAP) in decibels (dB). Because sound metrics are sensitive to even small changes in overpressure, a comparison of resulting sound metrics both with and without a 25% post-processing taper is a good indicator of an accurate numerical method.

The results below have been published in the American Institute of Aeronautics and Astronautics SciTech 2023 Forum, under the title “Numerical Method Comparison on Shaped Boom Propagation Through Atmospheric Boundary Layer Turbulence,” and presented at National Harbor, Maryland, in January 2023. Further discussion and plots can be found in that manuscript.

Table 1. Ground waveform metrics in PLdB, with or without post-processing taper after propagation of a C609 shaped boom through a 411.38-m ABL using an atmosphere generated by random seed 5.

Numerical Method	All 100 Ground Waveforms			Afflicted Ground Microphones 28-40			Run Time
	No Taper	25% Taper	Difference	No Taper	25% Taper	Difference	
Natural Spline	67.42	67.00	0.42	69.99	78.06	-8.07	08:24:32
Linear Interp.	66.78	66.78	0.00	66.44	66.44	0.00	07:03:18
Hermite Spline	66.98	66.98	0.00	66.65	66.65	0.00	07:55:19
Finite Diff.	66.74	66.71	0.03	66.19	66.13	0.06	09:03:24
Freq. Domain	67.04	66.98	0.06	66.79	66.65	0.14	10:34:18

Table 2. Ground waveform metrics in PLdB, with or without post-processing taper after propagation of a C609 shaped boom through a 1026.7-m ABL using an atmosphere generated by random seed 2.

Numerical Method	All 100 Ground Waveforms			Afflicted Ground Microphones 45-58			Run Time
	No Taper	25% Taper	Difference	No Taper	25% Taper	Difference	
Natural Spline	66.60	66.59	0.01	66.08	65.99	0.09	21:08:38
Linear Interp.	66.12	66.12	0.00	65.48	65.48	0.00	18:48:17
Hermite Spline	66.59	66.59	0.00	65.99	65.99	0.00	19:48:35
Finite Diff.	66.15	66.15	0.00	65.34	65.34	0.00	22:29:07
Freq. Domain	66.60	66.59	0.01	66.00	65.99	0.01	1:02:55:12

Table 3. Ground waveform metrics in ISBAP, with or without post-processing taper after propagation of a C609 shaped boom through a 411.38-m ABL using an atmosphere generated by random seed 5.

Numerical Method	All 100 Ground Waveforms			Afflicted Ground Microphones 28-40			Run Time
	No Taper	25% Taper	Difference	No Taper	25% Taper	Difference	
Natural Spline	81.58	82.16	-0.58	78.06	81.87	-3.81	08:24:32
Linear Interp.	81.96	82.01	-0.05	81.58	81.59	-0.01	07:03:18
Hermite Spline	82.09	82.14	-0.05	81.72	81.74	-0.02	07:55:19
Finite Diff.	81.86	81.96	-0.10	81.28	81.37	-0.09	09:03:24
Freq. Domain	82.07	82.14	-0.07	81.69	81.74	-0.05	10:34:18

Table 4. Ground waveform metrics in ISBAP, with or without post-processing taper after propagation of a C609 shaped boom through a 1026.7-m ABL using an atmosphere generated by random seed 2.

Numerical Method	All 100 Ground Waveforms			Afflicted Ground Microphones 45-58			Run Time
	No Taper	25% Taper	Difference	No Taper	25% Taper	Difference	
Natural Spline	80.67	81.81	-1.14	73.74	81.16	-7.42	21:08:38
Linear Interp.	81.36	81.48	-0.12	80.68	80.80	-0.12	18:48:17
Hermite Spline	81.70	81.81	-0.11	81.05	81.16	-0.11	19:48:35
Finite Diff.	81.33	81.51	-0.18	80.57	80.71	-0.14	22:29:07
Freq. Domain	81.63	81.81	-0.18	81.02	81.16	-0.14	1:02:55:12

The linear interpolation and Hermite spline methods did not produce any visible spiking, whereas the finite differences and frequency-domain methods did produce minute visible spiking. As shown in Tables 1 through 4, the differences in PLdB before and after tapering using the “natural” spline method were expectedly large, because as this method produced the original spiking. Each of the other four available numerical methods resulted in zero or minute differences in sound metric, but the differences using the linear interpolation and Hermite spline methods were smaller than the finite difference and frequency domain differences. KZKFourier author Trevor Stout previously found that linear interpolation can result in inaccurate rise times; therefore, this method is not recommended. The Hermite spline method can overestimate overpressures in areas of high energy concentration, but a shaped sonic boom was used as the input rather than a traditional N-wave; because the case did not produce visible spiking, the difference in sound metrics before and after the application of a post-processing taper were zero for PL and minute for ISBAP, and the runtime was faster than all but linear interpolation, the Hermite spline method is recommended herein for C609 KZKFourier simulations with atmospheric and turbulence conditions similar to those of SonicBAT Flight 5. The best numerical method may be determined on a case-by-case basis, particularly because an analytical solution was unavailable for the C609 waveform’s propagation to the ground.

Reference-day crosscheck extension

The 2022 report on Project 057 outlines an activity in which international members of CAEP’s WG1 used a new reference-day atmosphere in their sonic boom propagation codes with good sound metric agreement with use of their own sound metric calculations on the results of their own propagation codes. Because participants provided the sonic boom signatures across the carpet in addition to cutoff angles, ground intersections, propagation times, and the six sonic boom metrics under consideration by SSTG (ASEL, BSEL, DSEL, ESEL, PL, and ISBAP), Penn State extended the crosscheck by calculating the undertrack metrics from the signatures provided by participants. Penn State’s sound metric calculations of participant waveforms were then compared with the metrics calculated by the participants themselves.

Penn State’s calculations of the undertrack metrics were always within 0.2 dB of the metrics calculated by each participant, for both windy and non-windy cases, and all participants calculated metrics very close to one another. Hence, most of the variation in the atmospheric reference-day crosscheck results was due to differences in signatures generated by propagation codes but not how each participant calculated the metrics. The work toward en-route supersonic certification schemes can now continue to develop, with confirmation that the schemes can safely rely upon an agreed-on reference-day atmosphere.

First humidity profile runs in KZKFourier

The original published version of KZKFourier did not consider atmospheric profiles. Constant humidity, pressure, and temperature profiles in the atmospheric boundary layer were assumed for convenience, and the constant relative humidity is a source of mean sound metric error, as shown by the different shock rise times between the humid Kennedy Space Center and the arid Armstrong Flight Research Center during the SonicBAT project. The inclusion of profiles for ambient quantities in KZKFourier may therefore better represent the evolution of supersonic signatures through the ABL. NASA has requested that Penn State work to include atmospheric profiling in KZKFourier.

Because humidity affects relaxation, which affects absorption, which determines the shock rise times from which sound metrics for annoyance evaluation are calculated, the relaxation modules in KZKFourier needed to be modified to accommodate a vector of humidity values. In the propagator section of the KZKFourier C++ code, the propagation engine is

initialized, the relaxation module is initialized, and the relaxation effects are propagated in three separate modules. The following changes were made to the relaxation modules of the code, which was then recompiled:

1. The engine initialization module that originally generated a homogeneous atmosphere now initializes a matrix of atmospheres through vectors of humidity, concentration of water vapor, and oxygen and nitrogen relaxation times.
2. The relaxation initialization module now prefactors tridiagonal matrices of all atmospheres from the previous step, rather than one atmosphere.
3. The relaxation propagator module now chooses which values to use to solve for the current spatial step, according to the current altitude.

For these initial changes to KZKFourier, Penn State is using uniform layers of humidity values (Figure 1).

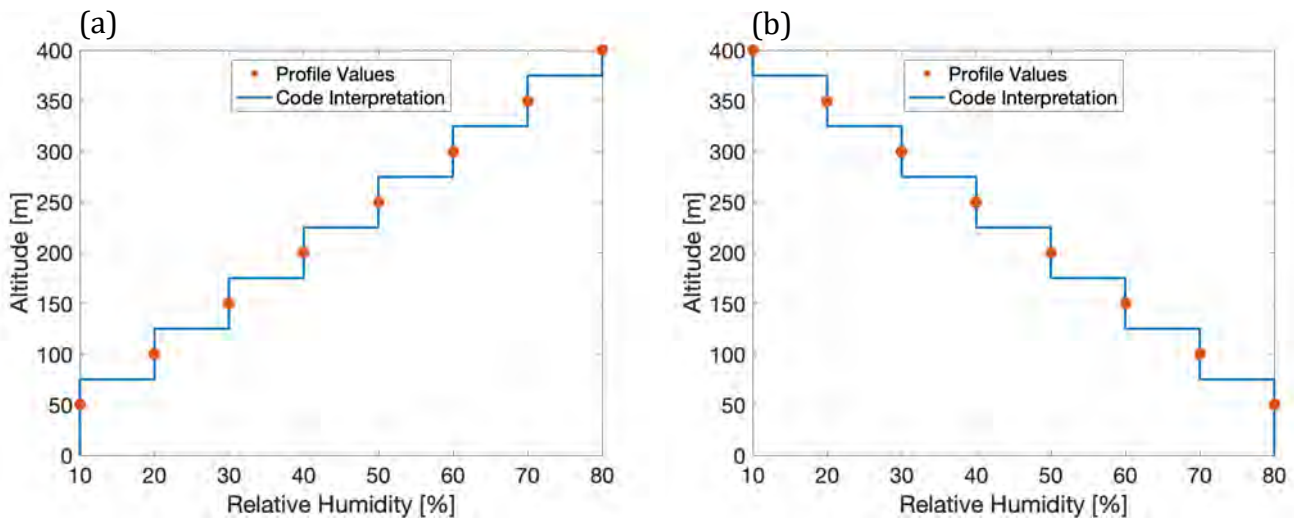


Figure 1. Uniform layer profiling scheme of the modified KZKFourier used in the first runs, including humidity increasing with increasing altitude (a) and humidity decreasing with increasing altitude (b).

The KZKFourier package available through Trevor Stout’s doctoral dissertation (2018) includes a simple 100-Pa prototypical N-wave test case that runs through a 400-m ABL. The test case configuration file is set to output six waveforms in a transverse array, equally spaced from 0 to 100 m. Penn State ran the test case through homogeneous atmospheres of 10% and 80% relative humidity with the original code, and then profiled the atmosphere from 10% to 80% and vice versa in 50-m intervals with the modified code. The same random seed was used each time, such that the generated atmospheres corresponded to each other.

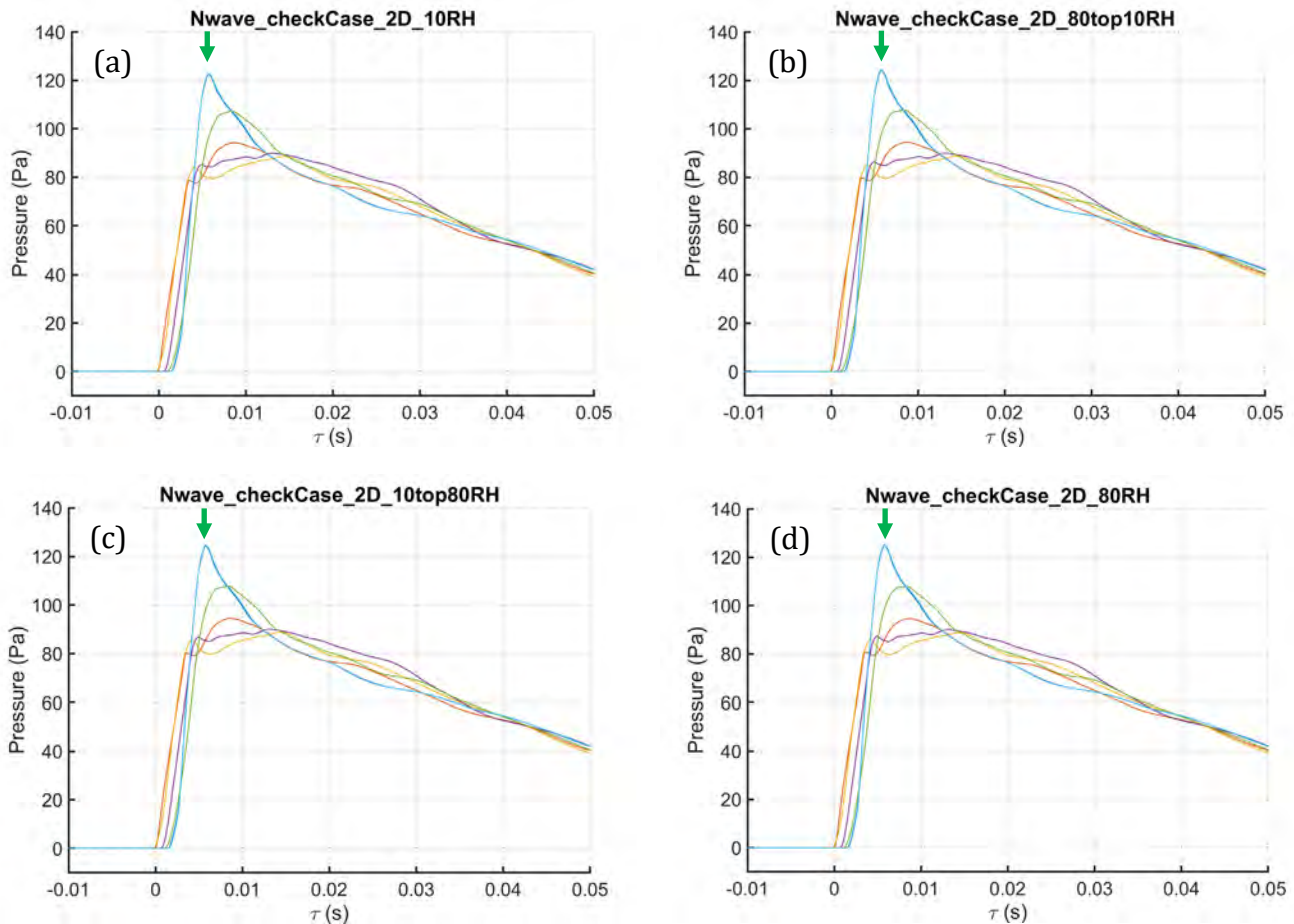


Figure 2. Front shocks of six waveforms propagated through a 400-m ABL with constant 10% humidity (a), 10%–80% humidity profile rising with altitude (b), 80%–10% humidity profile dropping as altitude rises (c), and constant 80% humidity (d).

The equally sized green arrows shown in Figure 2 indicate that the highest peak pressure was obtained with the homogeneous atmosphere of 80% humidity, the lowest peak pressure was obtained with the homogeneous atmosphere of 10% humidity, and the two humidity profiles were in between. The average PLdB and ISBAP metrics each varied less than 0.5 dB across all cases. The SonicBAT project verified that higher humidity leads to higher peak pressure; therefore, the results agree with the SonicBAT experimental data. Flipping the profiling upside-down created negligible differences in ground waveforms, but the two cases did not yield identical results. The additional computational steps required to propagate the N-wave through a profiled atmosphere resulted in only an additional half-minute of run time. Now that KZKFourier has considered humidity profiling for the first time, future research will include simulations with thicker boundary layers, propagating a shaped boom waveform rather than an N-wave, and introducing profiling for other KZKFourier modules and atmospheric quantities, such as temperature, pressure, and density.

Milestones

An alternative numerical method is now recommended for KZKFourier simulations similar to SonicBAT Flight 5. Extending the reference-day crosscheck to verify participants' calculation of sound metrics in similar ways helps remove a confounding variable from the source of variation among participant results. KZKFourier now considers uniform humidity profiling in its molecular relaxation module, including the effects of a more realistic atmosphere.

Major Accomplishments

The alternative numerical method for KZKFourier simulations similar to those of SonicBAT Flight 5 will help prevent future simulations from generating spiking artifacts that are nonphysical and lead to erroneous sound metric data. Extending the reference-day crosscheck to determine that participant variation is due to the varying propagation codes rather than sound metric calculation instills further confidence that the schemes can safely rely upon the new reference-day atmosphere agreed upon at CAEP/12. With this assurance, the work toward en-route supersonic certification schemes can continue to develop. For the first time, KZKFourier has considered a basic uniform humidity profile, which is a first step toward more realistic atmospheres and better representation of the evolution of supersonic signatures through atmospheric boundary layers. The latter will lead to more accurate simulated sound metrics and annoyance evaluation for NASA and its upcoming X-59 quiet supersonic technology demonstrator.

Publications

Published conference proceedings

Kapcsos, J. K. & Sparrow, V. W. (2023). Numerical Method Comparison on Shaped Sonic Boom Propagation Through Atmospheric Boundary Layer Turbulence. *American Institute of Aeronautics and Astronautics SciTech 2023 Forum*. Paper 2023-1352, Doi: 10.2514/6.2023-1352

Kapcsos, J. K. & Sparrow, V. W. (2023). Progress Update on Inclusion of Atmospheric Profiling for Sonic Boom Propagation Through Turbulence. *Acoustics 2023 Sydney*.

Outreach Efforts

None.

Awards

None.

Student Involvement

Joshua Kapcsos was the Penn State graduate research assistant who worked on ASCENT Project 57 during the 2022–2023 academic year.

Plans for Next Period

Penn State will continue developing atmospheric profiling schemes in KZKFourier for other atmospheric quantities such as temperature, pressure, and atmospheric density. Simulations will be run with thicker boundary layers and shaped boom waveforms. Regarding the reference-day crosscheck, Penn State will seek permission and feedback from each international participant to publish the anonymized results in a scientific journal.

References

- Bradley, K. A., Hobbs, C. M., Wilmer, C. B., Sparrow, V. W., Stout, T. A., Morgenstern, J. M., ... & Blanc-Benon, P. (2020). *Sonic booms in atmospheric turbulence (SonicBAT): The influence of turbulence on shaped sonic booms* (No. NASA/CR-2020-220509).
- Kapcsos, J. L., & Sparrow, V. W. (2023). Numerical Method Comparison on Shaped Sonic Boom Propagation Through Atmospheric Boundary Layer Turbulence. In *AIAA SCITECH 2023 Forum* (p. 1352)
- Kapcsos, J. L., & Sparrow, V. W. (2023). Progress update on inclusion of atmospheric profiling for sonic boom propagation through turbulence. *The Journal of the Acoustical Society of America*, 154(4_supplement), A148-A148.
- Loubeau, A., Naka, Y., Sparrow, V. W., Page, J. A., Lemaire, S., Liu, S. R., ... & Downs, R. S. (2021, April). Developing certification procedures for quiet supersonic aircraft using shaped sonic boom predictions through atmospheric turbulence. In *180th Meeting of the Acoustical Society of America, Acoustics in Focus*.
- Maglieri, D., et al. (2014). *Sonic Boom: Six Decades of Research* (NASA/SP-2014-622). National Aeronautics and Space Administration, Langley Research Center, Hampton, VA.
- Ostashev, V., & Wilson, D. (2015). *Acoustics in moving inhomogeneous media* (2nd ed.). CRC Press, Boca Raton, FL.
- Stout, T. (2018). Simulation of n-wave and shaped supersonic signature turbulent variations [Ph.D. dissertation, Pennsylvania State University].

Task 2 – Assessing Secondary Sonic Boom Propagation

The Pennsylvania State University
 Farmingdale State College, State University of New York

Research Approach

Overland secondary sonic booms

In previous work, we modeled secondary sonic booms from flights approaching the U.S. coastlines. To better understand the behavior of secondary sonic booms over land, we modeled the behavior of secondary sonic booms around Edwards Air Force Base (EAFB).

Atmospheric conditions around EAFB

Atmospheric profiles for each month were obtained from the CFSv2 database. Monthly averages were used, because these values were previously proven to be a good predictor of secondary sonic booms. EAFB was chosen for this work because regular supersonic aircraft operations occur around that area which has potential to validate the findings in the future. We examined a recent year and took 2020 as an example. Figure 3 shows the monthly average temperatures and wind speed profiles for January and July 2020 at EAFB. The plots show the characteristic atmospheric profiles for the summer and winter in the area. These profiles are very similar to the West coast weather profiles, with the upper-atmospheric winds toward the east in the winter and toward the west in the summer months.

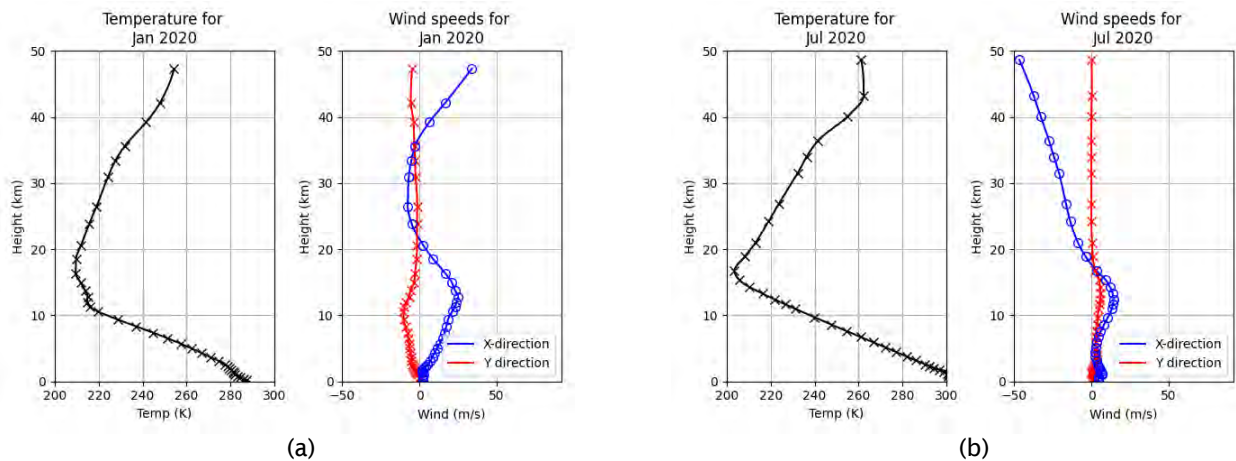


Figure 3. Monthly average temperature and wind speed profiles for EAFB for (a) January and (b) July 2020.

Trajectory conditions

Several trajectories were considered, because aircraft operations may occur in several headings and at several different conditions. We simulated an east-west trajectory and a west-east trajectory. In addition, we examined a deceleration profile in both directions from Mach 2 to Mach 1.18. We also examined a cruise condition for each direction at values of Mach 2, Mach 1.4, and Mach 1.18. We chose these values because Mach 2.0 represents the value of previous commercial aircraft, Mach 1.4 represents the design speed of the X-59, and the Mach 1.18 condition is the Mach cutoff for many atmospheric conditions.

Secondary sonic boom arrivals

We used the weather profiles and the trajectories discussed above to predict the locations of secondary sonic boom around EAFB during the year. These predictions are preliminary and currently do not include terrain considerations.

Figure 4 shows the results for January and July 2020 for the West to East heading with the deceleration profile. Figure 5 shows the results for January and July 2020 for the East to West heading with the deceleration profile. Secondary sonic booms are predicted in the winter for a West to East heading and in the summer for an East to West heading.

Figure 6 shows that no secondary sonic booms were predicted for a west to east heading at a Mach 2.0 cruise condition. Figure 7 shows the predicted secondary sonic booms for an east to west heading at a Mach 2.0 cruise condition, and only

a small area of the map is affected by secondary booms far to the north and south of the aircraft trajectory. Secondary booms seem to be less likely to occur at such a high aircraft speed compared to lower speeds.

Figure 8 shows the predicted secondary sonic booms for a west to east heading at a Mach 1.4 cruise condition. Figure 9 shows the predicted secondary sonic booms for an east to west heading at a Mach 1.4 cruise condition. Secondary sonic booms are predicted in the winter for a west to east heading and in the summer for an East to West heading.

Figure 10 shows the predicted secondary sonic booms for a west to east heading at a Mach 1.18 cruise condition. Figure 11 shows the predicted secondary sonic booms for an east to west heading at a Mach 1.18 cruise condition. Secondary sonic booms are predicted in the winter for a west to east heading. Because the east to west heading and the summertime west to east heading are all flying in a Mach cutoff condition, no primary or secondary sonic booms at the ground are predicted.

Each of these examples was calculated with the PCBoom software and is likely be useful for planning future simulations and possibly even flight tests at EAFB.

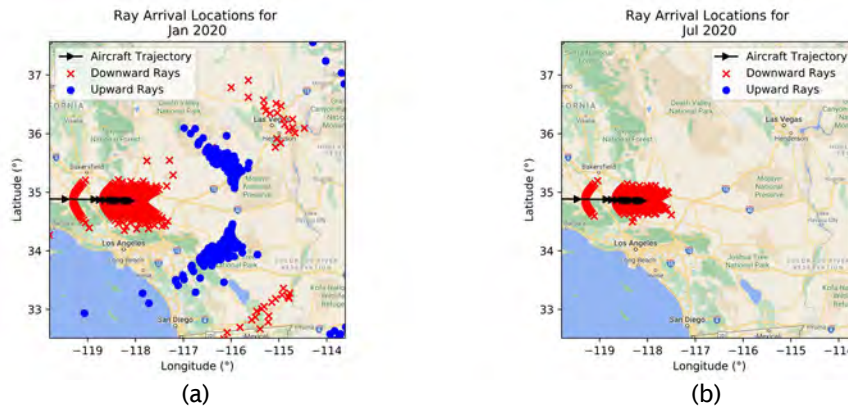


Figure 4. Simulated arrival locations for (a) January and (b) July 2020 atmospheric profiles for the West to East heading, where the aircraft is slowing from Mach 2 to Mach 1.18.

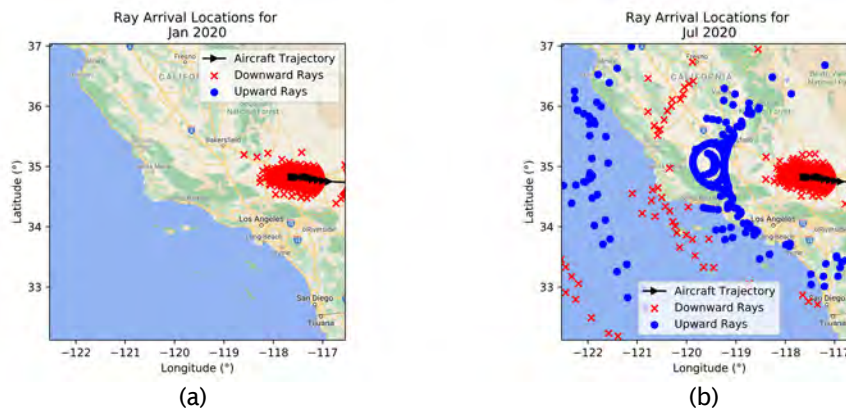


Figure 5. Simulated arrival locations for (a) January and (b) July 2020 atmospheric profiles for the east to west heading, where the aircraft is slowing from Mach 2 to Mach 1.18.

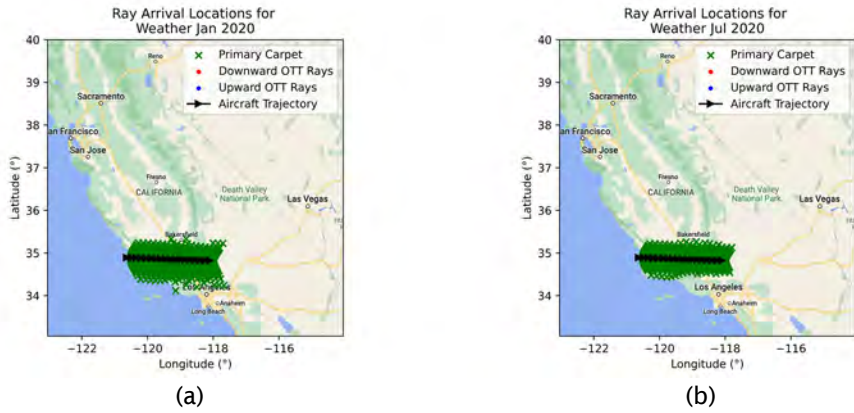


Figure 6. Simulated arrival locations for (a) January and (b) July 2020 atmospheric profiles for the west to east heading for a Mach 2.0 cruise condition.

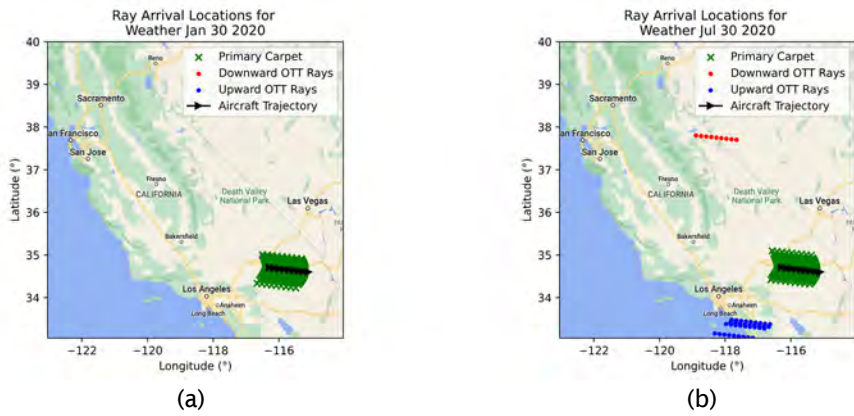


Figure 7. Simulated arrival locations for (a) January and (b) July 2020 atmospheric profiles for the east to west heading for a Mach 2.0 cruise condition.

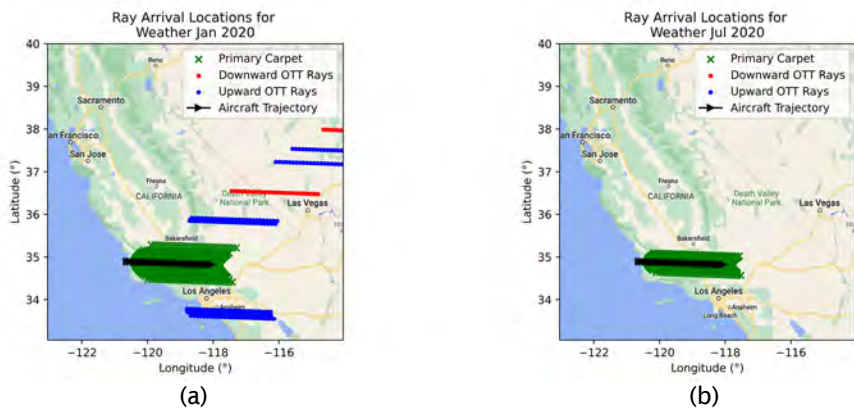


Figure 8. Simulated arrival locations for (a) January and (b) July 2020 atmospheric profiles for the west-east heading for a Mach 1.4 cruise condition.

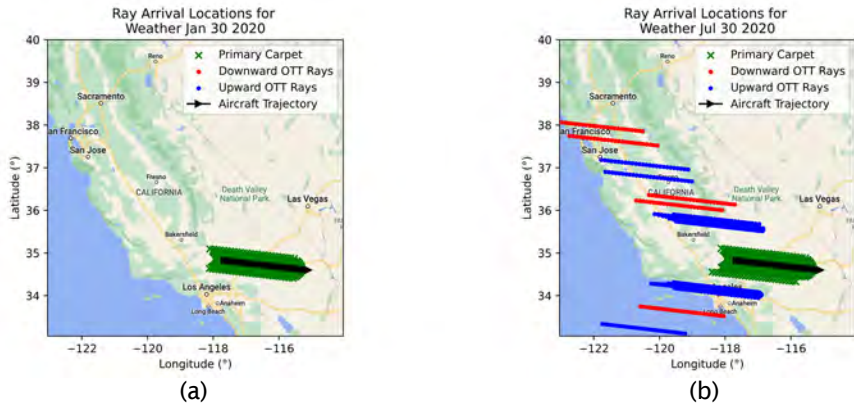


Figure 9. Simulated arrival locations for (a) January and (b) July 2020 atmospheric profiles for the east to west heading for a Mach 1.4 cruise condition.

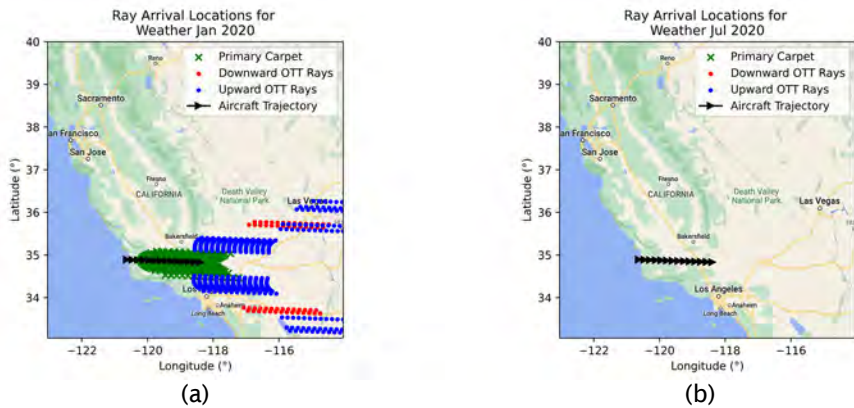


Figure 10. Simulated arrival locations for (a) January and (b) July 2020 atmospheric profiles for the west to east heading for a Mach 1.18 cruise condition. In case (b), a Mach cutoff condition exists, with no primary or secondary booms at the ground.

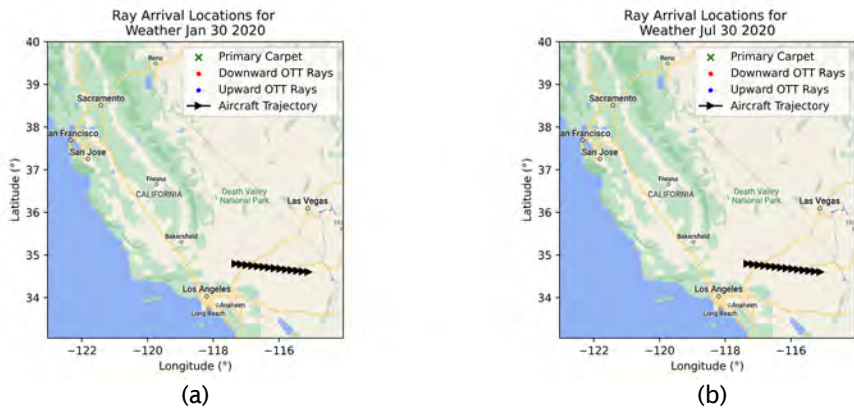


Figure 11. Simulated arrival locations for (a) January and (b) July 2020 atmospheric profiles for the east to west heading for a Mach 1.18 cruise condition. In both cases, a Mach cutoff condition exists, with no primary or secondary booms at the ground.



Research on secondary sonic boom signatures

This year, the research team initiated a new set of studies regarding secondary sonic booms and the effects of topography. Concorde is well known to have produced secondary booms in New England in the late 1970s, as described in Rickley and Pierce (1980). These secondary booms were no longer heard when sufficient coastal buffer distances were introduced to keep the secondary booms off the coastlines. Simultaneously, the U.S. Air Force regularly flies supersonically around EAFB in California, and the sounds of secondary booms do not appear to be reported regularly. What is the difference? One possibility is that the secondary boom signal might be affected by surface topography of the land, given that topography is one difference between overwater and overland flight. Over water, the water surface is fairly flat except during exceptional weather conditions. Secondary sonic booms have two types: type I (also called direct) secondary booms and type II (also called indirect) secondary booms. The difference is that type I secondary booms initially head upward and do not interact with the ground surface until they are heard on the ground, whereas type II secondary booms initially head downward, form the primary boom carpet, reflect back into the atmosphere, and eventually head back to the ground, where they are heard as secondary booms. Both type I and type II booms require favorable upper-atmospheric winds to be heard at all. However, only type II booms require surface reflection.

We believe that type II secondary sonic booms can be profoundly affected by the topography of the ground reflection, and we performed studies to investigate this possibility in the summer of 2023. Ray tracing simulations matching the parameters used by Rickley and Pierce for Concorde were performed in Mathematica software (Wolfram, 2023), on the basis of the assumption that two incident sonic boom rays approximately 100 m apart were reflected by different grades on the ground. These results, and details of the calculations, have been described in the proceedings of the European Acoustics Association's Forum Acusticum 2023 in Turin, Italy, in September 2023, which are available open access (Sparrow and Riegel, 2023). The results indicated that a substantial decrease in received sound levels occurs because of the effect of the topography of the land, compared with reflection over a flat earth (such as the ocean surface). These results merit further research and confirmation, but they do appear to support that type II secondary sonic booms should be much less loud when the primary carpet occurs over land than over water.

Milestone

The project is transitioning from making simulations along coastlines to overland simulations.

Major Accomplishments

- New simulations for supersonic aircraft speeds, directions, and times of the year have been made for flights close to EAFB.
- The team is gaining new insights into how type II secondary sonic booms interact with topography—an important aspect for understanding secondary booms for overland flight.

Publications

V. Sparrow and K. Riegel, "The role of topography for secondary sonic boom reflection," in Proc. Forum Acusticum 2023 (www.fa2023.org), Turin, Italy, 11-15 September 2023, (European Acoustics Association, 2023). Open access manuscript available at <https://appfa2023.silssystem.solutions/atti/000361.pdf>.

Outreach Efforts

None.

Awards

None.

Student Involvement

None.

Plans for Next Period

In Task 2, we will continue to work toward accurate acoustic signatures for secondary sonic booms; this work will be essential to assess community impact. The project team will also determine the feasibility of prediction of the impact location of secondary sonic boom rays from upcoming test flights of the X-59 Quesst aircraft.

References

Plotkin, K., Page, J., & Haering, E. (2007). *Extension of PCBoom to over-the-top booms, ellipsoidal earth, and full 3-D ray tracing* [Presentation]. 13th AIAA/CEAS Aeroacoustics Conference.

Rickley, E. & Pierce, A. (1980). *Detection and assessment of secondary sonic booms in New England* (Report No. FAA-AEE-80-22). Defense Technical Aviation Center, Fort Belvoir, VA.

Saha, S., Moorthi, S., Wu, X., Wang, J., Nadiga, S., Tripp, P., Behringer, D., Hou, Y.-T., Chuang, H., Iredell, M., Ek, M., Meng, J., Yang, R., Mendez, M. P., van den Dool, H., Zhang, Q., Wang, W., Chen, M., & Becker, E. (2014). *The NCEP Climate Forecast System Version 2*. Journal of Climate, 27, 2185-2208. Doi: 10.1175/JCLI-D-12-00823.1

V. Sparrow and K. Riegel, "The role of topography for secondary sonic boom reflection," in Proc. Forum Acusticum 2023 (www.fa2023.org), Turin, Italy, 11-15 September 2023, (European Acoustics Association, 2023). Open access manuscript available at <https://appfa2023.silssystem.solutions/atti/000361.pdf>.

Wolfram Research, Inc., Mathematica, Version 13.2, Champaign, IL (2023).

Task 3 – Investigating Seismic Networks for Measuring Sonic Booms

The Pennsylvania State University
 Farmingdale State College, State University of New York

Objective

One difficulty in measuring sonic booms is that they extend over tremendous distances. For secondary sonic booms, in particular, the signals can extend several hundred miles (or kilometers). Setting low-frequency-capable microphones over the secondary boom carpet would be very expensive and labor-intensive. However, Cates and Sturtevant, in 2002, and others, have demonstrated that existing seismic networks can be used to measure sonic booms, albeit with a narrower frequency range than modern microphones. This technology has not been actively pursued for more than 20 years. This task is aimed at determining whether existing seismic networks, specifically the networks in place in Southern California, can capture primary and secondary sonic booms. The project team believed that an attempt would be worthwhile. The initial aim was to capture primary sonic booms. NASA helped identify a recent well-publicized date when sonic booms were produced near EAFB. Only a brief attempt was made to capture corresponding secondary booms, but the upper-atmospheric winds were not favorable for the formation of the secondary booms in this particular event.

Research Approach

Air-show sonic booms and other important meteorological information

The sonic booms used in the analysis were triggered on October 14, 2022, near EAFB, in California, during an air show commemorating the 75th anniversary of the first supersonic flight. Four supersonic passes were created by F-15, F-18, and F-22 aircraft flying in a westward (260°) direction at an altitude of 30,000 ft (~9.1 km). The total number of booms in each pass, type of aircraft that triggered the booms, and approximate event origin times are shown in Table 5. The precise locations of the initiation of the booms are not well known.

Table 5. Air-show flight data from October 14, 2022.

Pass number	Number of booms	Type of aircraft	Event origin time (Coordinated Universal Time)
1	3	F22/F18/F15	15:59:55
2(a)	3	F22/F18/F15	16:30:38
2(b)	1	F22	19:34:00
3	1	F15	20:51:58
4	1	F18	20:52:36

The fine-scale (NAMNEST) and moderate-scale (CFSv2) predictions of temperature, vector wind speed, and effective sound speed variation with altitude on October 14, 2022, are shown in Figure 12. NAM is the National Oceanic and Atmospheric Administration’s North American Mesoscale weather prediction. The westward supersonic passes and inadequate upper-atmospheric winds suppressed the generation of secondary booms. Therefore, in this study, the project team focused on the primary sonic boom events recorded at seismic stations within the Southern California seismic network (<https://scedc.caltech.edu>) and near EAFB.

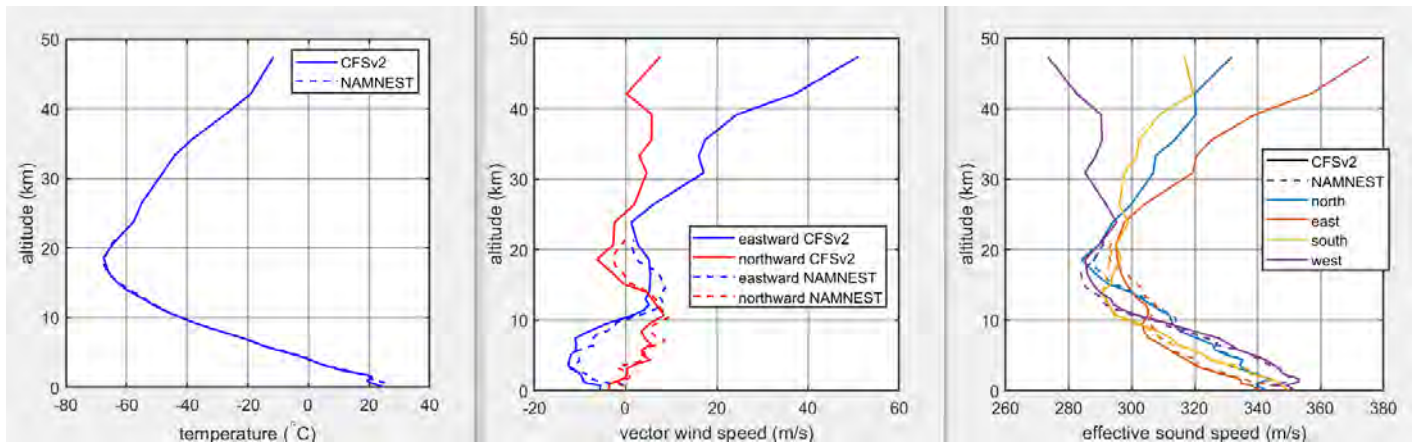


Figure 12. Temperature, vector wind speed, and effective sound speed variation with flight altitude on October 14, 2022, at EAFB. The solid and dashed lines represent moderate-scale (CFSv2) and fine-scale (NAMNEST) predicted meteorological data, respectively. (Plots are from Edward Haering, NASA.)

Data and methods

To assess the capability of seismic stations in the Southern California seismic network to record primary sonic booms (N-type waves), we requested three-component seismic data for all short-period and broadband seismic stations within an approximately 100-km radial distance from EAFB (~60 stations). Seismic data and instrument response information were obtained from the Southern California Earthquake Data Center (SCEDC; <https://scedc.caltech.edu/data/waveform.html>). Instrument response was removed from each seismogram through frequency-domain deconvolution. The seismograms were then demeaned, detrended, and tapered, and finally filtered from 1 to 20 Hz with a four-pole, two-pass Butterworth bandpass filter. An example of a three-component recording for a primary sonic boom event (N-type waves) is shown in Figure 13.

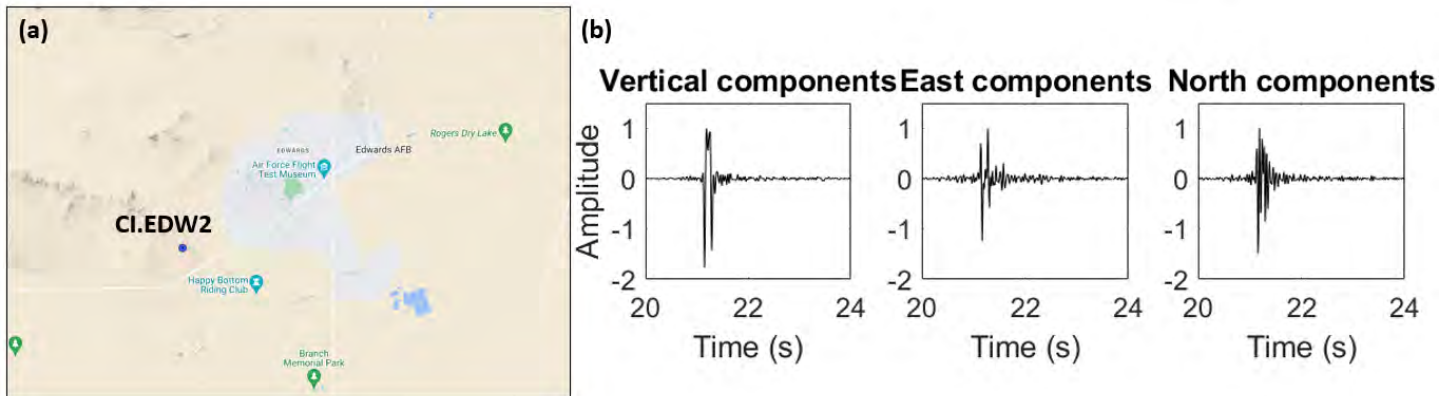


Figure 13. (a) Map of the location of seismic station (CI.EDW2) near the west gate of EAFB. (b) Example of an N-type (primary sonic boom) signal record section at CI.EDW2. The waveform is filtered from 1 to 20 Hz.

Results

Figure 14 illustrates the highest-quality seismograms showing primary sonic booms from each pass, oriented by distance from EAFB. The number of seismograms for each pass reflects primarily the event magnitudes. The blue dashed lines in Figure 14 represent a velocity window from 0.2 km/s to 0.4 km/s that can be used as a guide to locate sonic boom arrivals. Notably, the exact event origin locations are not well documented, and we assumed that all events initiated near EAFB. Therefore, some arrivals might show earlier or later arrivals than the maximum effective sound speed of 0.4 km/s.

Figure 15 shows maps of stations around EAFB, analyzed for each pass. The maps illustrate that stations located on the west side of EAFB recorded clear primary sonic boom signals, which were consistent with the westward supersonic flight passes and upper-atmospheric wind patterns (Figure 12).

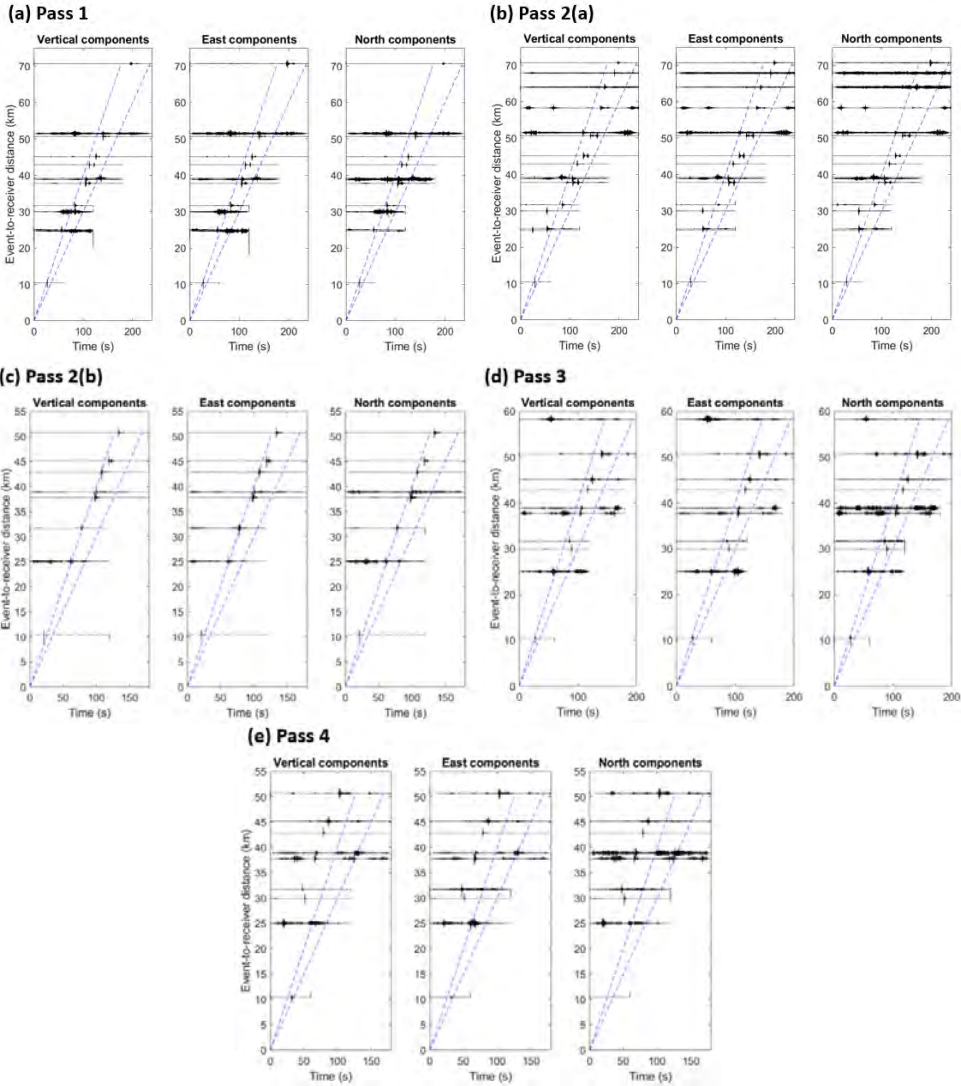


Figure 14. Seismograms from primary sonic boom records from the air show. The blue dashed lines are the velocity window of 0.2 km/s to 0.4 km/s used for identifying primary sonic boom arrivals. All seismograms are filtered from 1 to 20 Hz.

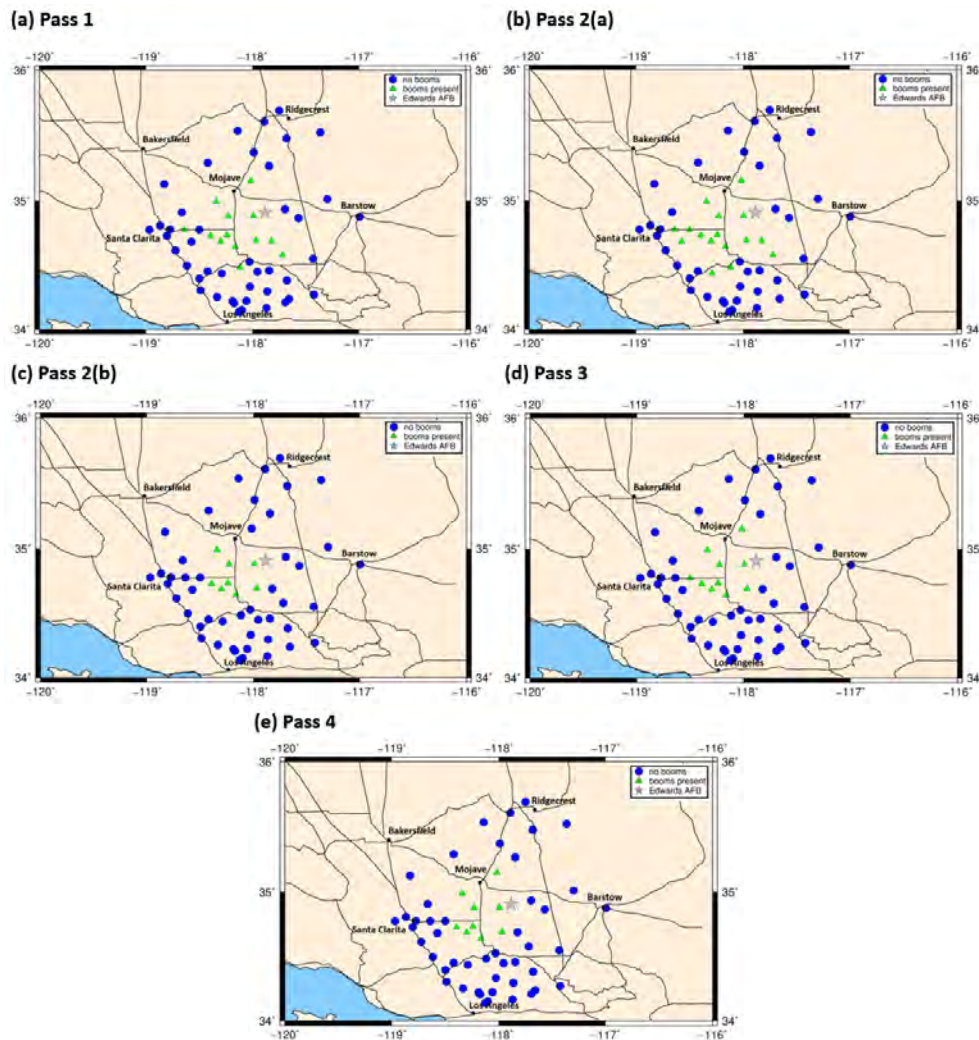


Figure 15. Map of seismic stations in Southern California surrounding EAFB (gray star). The blue circles indicate stations where the sonic booms were not clearly recorded, and the green triangles indicate stations with clearly recorded sonic booms.

Summary

The goal of this work is to explore our current capability of detecting primary sonic booms recorded on permanent seismic stations around EAFB. The project is aimed at identifying well-recorded N-type seismic waves. Specifically, research in this project is focusing on understanding the lateral extent of the signal recording capabilities of primary sonic booms from the four supersonic passes near EAFB. Our results indicate that primary sonic booms were captured at different times by seismic stations in Southern California over an area of ~10,000 km². This finding is consistent with those reported by Cates and Sturtevant (2002), and further confirms that sonic booms can be recorded by seismic stations in Southern California.

Special Acknowledgments

The project team thanks NASA overall, particularly Edward Haering of the NASA Armstrong Flight Research Center, for making us aware of the existence of the October 2022 air show and for providing tremendous support throughout this investigation. The financial support in 2023 to enable Task 3 was provided by the Penn State College of Engineering through the United Technologies Corporation Professorship. This support is gratefully acknowledged.



Milestone

As noted by Cates and Sturtevant (2002), sonic booms can be recorded by existing seismic stations. Our results further suggest that the same stations may be able to record secondary sonic booms.

Major Accomplishments

ASCENT Project 057 Task 3 extended knowledge of the recording capability of primary booms by existing seismic stations. The project can now continue identifying secondary booms to understand primary and secondary boom carpets.

Conference Proceedings

Sampath Rathnayaka, Andrew A Nyblade, Victor W. Sparrow, and Kimberly A. Riegel, "Air show primary sonic boom across a Seismic network", ASA Fall meeting abstract, Sydney, Australia, 2023.

Outreach Efforts

None.

Awards

None.

Student Involvement

None.

Plans for Next Period

In Task 3, the team will continue to work on identifying signatures for primary and secondary sonic booms from various supersonic passes, an essential step toward assessing community impact.

References

- Cates, J. E., & Sturtevant, B. (2002). Seismic detection of sonic booms. *The journal of the acoustical society of America*, 111(1), 614-628.
- Saha, S., Moorthi, S., Wu, X., Wang, J., Nadiga, S., Tripp, P., Behringer, D., Hou, Y.-T., Chuang, H., Iredell, M., Ek, M., Meng, J., Yang, R., Mendez, M. P., van den Dool, H., Zhang, Q., Wang, W., Chen, M., & Becker, E. (2014). *The NCEP Climate Forecast System Version 2*. *Journal of Climate*, 27, 2185-2208. Doi: 10.1175/JCLI-D-12-00823.1
- National Centers for Environmental Information, National Oceanic and Atmospheric Administration, North American Mesoscale Forecast System (NAM), 2023. See <https://www.ncei.noaa.gov/products/weather-climate-models/north-american-mesoscale>.
- Rathnayaka, S., Nyblade, A. A., Sparrow, V. W., & Riegel, K. (2023). Air show primary sonic booms across a seismic network. *The Journal of the Acoustical Society of America*, 154(4_supplement), A147-A147.



Project 058 Improving Policy Analysis Tools to Evaluate Higher-altitude Aircraft Operations

Massachusetts Institute of Technology

Project Lead Investigator

P.I.: Steven R. H. Barrett
Professor of Aeronautics and Astronautics
Director, Laboratory for Aviation and the Environment
Massachusetts Institute of Technology
77 Massachusetts Ave, Building 33-322, Cambridge, MA 02139
(617) 452-2550, sbarrett@mit.edu

Co-P.I.: Dr. Sebastian D. Eastham
Research Scientist
Laboratory for Aviation and the Environment
Massachusetts Institute of Technology
77 Massachusetts Ave, Building 33-322, Cambridge, MA 02139
seastham@mit.edu

University Participants

Massachusetts Institute of Technology (MIT)

- P.I.: Prof. Steven R. H. Barrett
- FAA Award Number: 13-C-AJFE-MIT, Amendment Nos. 064, 089, 099, and 115 (No-cost extension to September 30, 2024)
- Period of Performance: February 5, 2020 to September 30, 2023
- Reporting Period: October 1, 2022 to September 30, 2023
- Tasks (tasks completed before this reporting period are listed as completed):
 1. Develop a set of emissions scenarios for high-altitude aviation (completed)
 2. Extend and validate MIT's existing atmospheric simulation capabilities (completed)
 3. Simulate atmospheric impacts of high-altitude emissions by using updated capabilities
 4. Calculate atmospheric sensitivity matrices
 5. Develop and update operational tools capable of quantifying environmental impacts of aviation
 6. Implement regionalized contrail parameterization
 7. Investigate dependence of aviation emissions impacts on non-aviation factors

Project Funding Level

\$1,150,000 FAA funding and \$1,150,000 matching funds. Sources of match are approximately \$218,000 from MIT, plus third-party in-kind contributions of \$391,000 from NuFuels, LLC; \$127,000 from Savion Aerospace Corporation; and \$414,000 from Google, LLC.

Investigation Team

Prof. Steven R. H. Barrett, (P.I.), All Tasks
Dr. Sebastian Eastham, (co-P.I.), All Tasks
Dr. Sadia Afrin, (postdoctoral researcher), All Tasks
Lucas Jeongsuk Oh, (graduate research assistant), Tasks 1, 3, and 4
Joonhee Kim, (graduate research assistant), Tasks 4–6
Carla Grobler, (graduate research assistant), Task 5, 6, and 7
Prakash Prashanth, (graduate research assistant), Task 7



Project Overview

Companies are proposing, developing, and testing aircraft operating at higher altitudes, such as commercial supersonic aircraft and high-altitude, long-endurance unpiloted aerial vehicles. These aircraft offer the potential to enable new use cases and business models in the aviation sector. However, the combustion emissions of these vehicles will have atmospheric impacts differing from those of conventional subsonic aviation, because of the higher altitudes of emission. Emissions at higher altitudes are associated with a different chemical environment, longer emission lifetimes, and transport of emissions over greater distances. Furthermore, new developments in emissions impact estimation have enabled a more nuanced view of the environmental consequences of conventional aircraft activity, including recognition that both climate and air quality impacts vary depending on the prevailing conditions of the emission and the time horizon of the assessment.

In this project, we propose to quantify the environmental consequences of such high-altitude aviation emissions. For this purpose, we will perform high-fidelity atmospheric simulations by further developing and applying the GEOS-Chem UCX tropospheric-stratospheric chemistry-transport model and its adjoint. The results will be leveraged to (a) evaluate the climate (radiative forcing) effects of high-altitude aircraft emissions and (b) estimate the sensitivity of the global ozone column and surface air quality to these emissions. Consequently, the climate, air quality, and ozone impacts for a small number of proposed supersonic aircraft designs and performance characteristics will be quantified. We will also perform a historical assessment of the impacts of aviation emissions, quantifying how factors such as changes in emissions indices and an evolving chemical background have affected—and will affect—the total impacts. Using data from these simulations, we will present a flexible, rapid approach for assessing the impacts of sub- and supersonic aircraft.

Task 1 – Develop a Set of Emissions Scenarios for High-altitude Aviation

Massachusetts Institute of Technology

Objective

This task is aimed at developing emissions inputs that cover scenarios relevant to near-future aviation, extending the impact estimation to a range of altitudes exceeding those of current commercial airline activities. The specific focus of the work during this period was to test and refine the developed global supersonic emissions inventories.

Research Approach

To meet our objectives, we are developing a mathematical model designed to estimate emissions of key pollutants such as nitrogen oxides (NO_x), sulfur oxides (SO_x), water vapor, and soot from a single flight. This process involves integrating insights from the ASCENT Project 47 engine model into a performance model for supersonic aircraft, determining the emissions along a supersonic flight path. Additionally, we are compiling a global emissions inventory for supersonic aircraft by integrating our emissions data with market trends. This inventory accounts for variations in factors such as cruising altitude and the engine's NO_x emissions index. This inventory will be used to assess the environmental impact of supersonic aircraft emissions with the updated Aviation Environmental Portfolio Management Tool (APMT) model. We are also creating a second inventory based on the scenario designed in ASCENT Project 10. This approach allows for a comprehensive comparison of the impacts under different design and operational assumptions. Details of this task have been provided in prior annual reports.

Milestone

Task 1 was completed in AY 2021–2022.

Major Accomplishments

New emissions inventories have been provided to ASCENT Project 22 for a comparative impact analysis using various models. A publication is also being prepared on this inter-model comparison, using the scenarios developed in Task 1.

Publications

None.

Outreach Efforts

Task progress was communicated during biweekly briefing calls with the FAA and reported in quarterly progress reports.



Awards

None.

Student Involvement

None.

Plans for Next Period

None.

Task 2 – Extend and Validate MIT’s Existing Atmospheric Simulation Capabilities

Massachusetts Institute of Technology

Objective

The objective of Task 2 is to extend and validate MIT’s existing atmospheric simulation capabilities, with the specific goal of ensuring that impacts on critical metrics of air quality and climate can be accurately represented. During AY 2020–2021, the team developed and tested a higher-resolution version of the GEOS-Chem UCX tropospheric-stratospheric global chemistry-transport model to capture localized effects.

Research Approach

The team is using the GEOS-Chem UCX tropospheric-stratospheric global chemistry-transport model as the central tool to quantify climate, air quality, and ozone impacts resulting from high-altitude aviation (Eastham et al., 2014). Therefore, the capabilities of this model must be evaluated for these purposes and to extend those capabilities where necessary. Two major subtasks have been identified: Task 2a, increasing the resolution of the model to capture localized impacts at a global resolution of $2^\circ \times 2.5^\circ$ or equivalent, and Task 2b, implementing a technique to estimate stratospherically adjusted radiative forcing (RF), rather than instantaneous RF. Task 2b was largely completed in AY 2019–2020, and the work for Task 2a was completed in AY 2020–2021. Details of this task have been provided in prior annual reports.

Milestone

Task 2 was completed in AY 2020–2021.

Major Accomplishments

A manuscript was published that used the new stratospherically adjusted RF calculations to evaluate the impacts of supersonic civil aviation on the environment.

Publications

Eastham, S. D., Fritz, T., Sanz-Morère, I., Prashanth, P., Allroggen, F., Prinn, R. G., Speth, R. L., & Barrett, S. R. H. (2022). Impacts of a near-future supersonic aircraft fleet on atmospheric composition and climate. *Environmental Science: Atmospheres*, 2(3), 388–403. Doi: 10.1039/D1EA00081K

Outreach Efforts

Task progress was communicated during biweekly briefing calls with the FAA and reported in quarterly progress reports.

Awards

None.

Student Involvement

None.

Plans for Next Period

None.

References

Eastham, S. D., Weisenstein, D. K., & Barrett, S. R. H. (2014). Development and evaluation of the unified tropospheric-stratospheric chemistry extension (Ucx) for the global chemistry-transport model GEOS-Chem. *Atmospheric Environment*, 89, 52-63. Doi: 10.1016/j.atmosenv.2014.02.001

Task 3 – Simulate Atmospheric Impacts of High-altitude Emissions Using Updated Capabilities

Massachusetts Institute of Technology

Objective

The objective of this task is to estimate the atmospheric response to the representative near-future aviation scenarios described in Task 1, and to convert the raw model outputs to impacts. These simulations will calibrate the simulated impacts and performance of the new version of the Aviation Environmental Portfolio Management Tool-Impacts (APMT-IC).

Research Approach

To meet Task 3's goals, our team extended the simulation period from 3 to 12 years, broadening our focus from solely NO_x emissions to include NO_x, SO_x, water vapor, black carbon, and organic carbon. Our objective is to assess the effects on surface air quality, stratospheric ozone, and climate forcing resulting from supersonic aviation and to compare them with the anticipated 2035 subsonic case. The study includes scenario A from ASCENT 10, scenario B from ASCENT 58 and ASCENT 4 (with high market expectations), and scenario B with ultra-low sulfur (ULS) from ASCENT 58 (high market expectations with ULS fuel). Unless otherwise specified, we presume a standard sulfur content of 600 ppm in fuel, following Barrett et al. (2010). The details of each scenario are presented in Table 1.

Table 1. Overview of design specifications and emission profiles of supersonic fleets across emission scenarios. Data are from the projected subsonic 2035 scenario, scenario A (ASCENT 10), scenario B (ASCENT 58 and ASCENT 4), and an adapted scenario B in which all supersonic flights are conducted with ULS fuel.

	Subsonic	Scenario A	Scenario B	Scenario B with ULS
Mach number at cruise	-	2.2	1.6	1.6
Seats	-	55	100	100
Maximum range, nmi	-	4,500	3,500	3,500
Cruise ceiling, km	12	21	17	17
Fuel efficiency, kg/100 seat km	2.26	19.0	7.15	7.15
Total fuel burn, Tg	424	122	43.1	43.1
Fleet average NO _x EI, g _{NO2eq} /kg _{fuel}	15.2	14.7	9.05	9.05
Total NO _x , GgNO ₂ equivalent	6440	1,800	390	390
Total black carbon, Gg	34.8	6.12	1.36	1.36
Fuel sulfur content, ppmS	600	600	600	0
Water vapor EI, kg _{H2O} /kg _{fuel}	1.231	1.231	1.231	1.231

EI, emissions index.

Using the specifications outlined in Table 1, we calculated the atmospheric impacts of high-altitude emissions through the enhanced capabilities developed in Task 2, at a global resolution of 2° × 2.5°. The outcomes of these estimations are

illustrated in Figures 1–4, on the basis of the 12th year of simulations. All changes calculated are due only to supersonic emissions. All scenarios use an identical inventory of 2035 subsonic emissions.

Figure 1 shows the annual average surface ozone change in each scenario. Scenario A shows a decrease in surface ozone in the Northern Hemisphere, particularly at mid-latitudes, with a maximum decrease of 9.6%. In contrast, the Southern Hemisphere shows a small increase. The population-weighted mean (PWM) change is a decrease of 0.97 parts per billion by volume (ppbv) in ozone exposure. Scenarios B and B with ULS fuel exhibit a contrasting trend, with an overall increase in surface ozone levels in most regions, except for a decrease in South Asia. The increase is more pronounced in the ULS case, with a maximum change of 0.32%, as compared with 0.24% in the standard scenario B. The ULS case shows a PWM increase of 0.032 ppbv, whereas scenario B shows an increase of 0.011 ppbv.

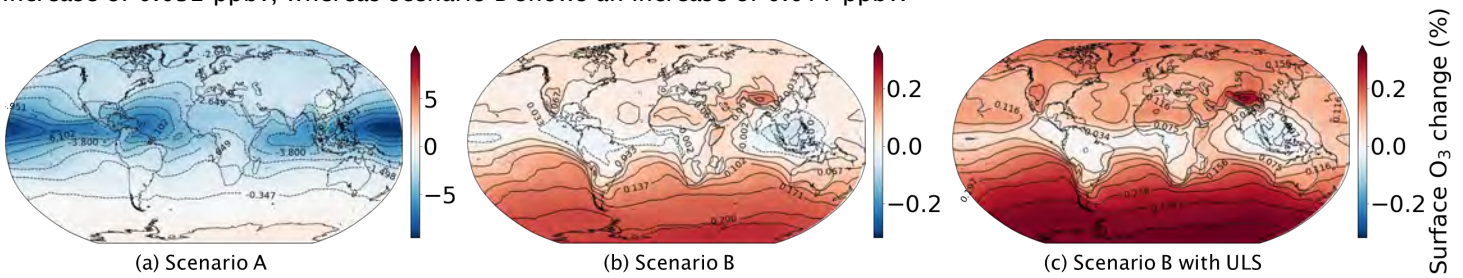


Figure 1. Annual mean surface ozone changes across various scenarios, relative to a baseline without supersonic aviation. Left: scenario A; middle: scenario B; right: scenario B with ULS.

As shown in Table 1, the aircraft in scenario A cruise at altitudes as high as 21 km, whereas scenario B and scenario B with ULS have a ceiling altitude of 17 km. This difference suggests that emissions above 17 km may contribute to surface ozone depletion. Additionally, the SO_x emission component appears to decrease surface ozone per capita, as evidenced by comparison of scenario B with scenario B with ULS. We explore these outcomes further through sensitivity analyses in Task 4.

Figure 2 depicts the annual average change in surface levels of particulate matter $\leq 2.5 \mu m$ ($PM_{2.5}$) across all regions for the three scenarios. Scenario A shows a PWM increase of $0.17 \mu g/m^3 PM_{2.5}$, whereas scenario B indicates a rise of $0.006 \mu g/m^3$, and scenario B without sulfur (ULS) shows a $0.005 \mu g/m^3$ increase. Although the total fuel burn in scenario A is 2.8 times that of the other scenarios, the $PM_{2.5}$ change is 26 times greater. This finding suggests that emissions above 17 km have a greater impact than those below this altitude. Moreover, removing SO_x from the emissions results in a 26% decrease in PWM $PM_{2.5}$ exposure attributable to supersonic aviation. We further analyze the chemical composition of the $PM_{2.5}$ and the differences according to emission altitude in Task 4.

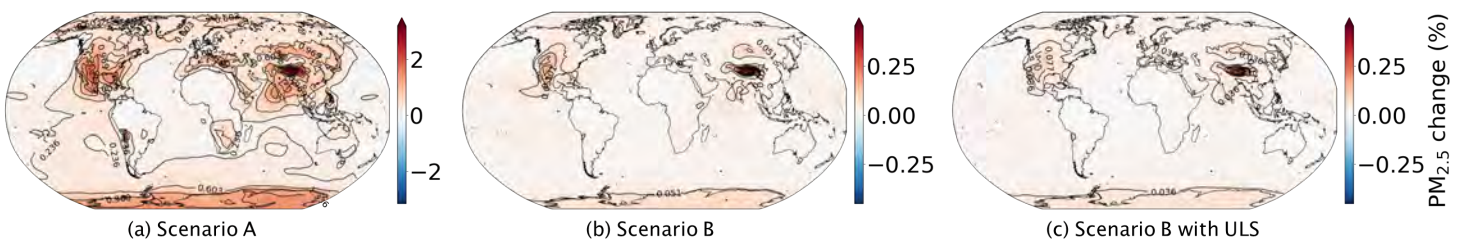


Figure 2. Comparative analysis of annual $PM_{2.5}$ changes across various scenarios due to supersonic aviation emissions. Left: scenario A; middle: scenario B; right: scenario B with ULS.

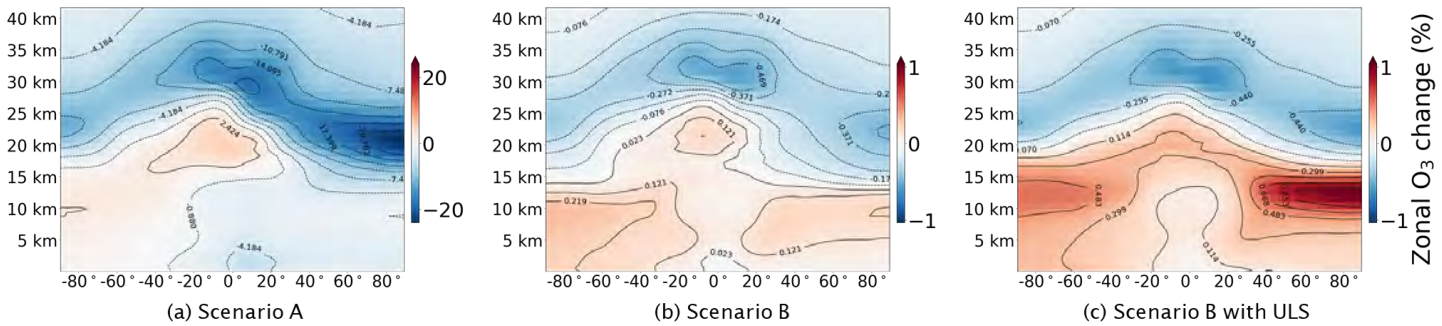


Figure 3. Comparative analysis of annual zonal ozone changes across various scenarios relative to the projected 2035 subsonic baseline. Left: scenario A; middle: scenario B; right: scenario B with ULS.

Figure 3 presents the annual average changes in the zonal distribution of ozone, underscoring the variations in ozone mixing ratios across various regions. We observe an increase in the ozone mixing ratio in some areas (from 10°S to 10°N at altitudes of 15–25 km, and from 60°N to 90°N at altitudes of 10–15 km), but a decrease in other areas (from 30°S to 30°N at altitudes of 25–35 km, and from 60°N to 90°N at altitudes of 20–25 km), depending on the scenario.

For scenario A, the data indicate an increase in ozone of 6.4 ppbv (0.65%) between 10°S and 10°N at altitudes of 15–25 km. In other regions, however, decreases are observed: a 1,030 ppbv decrease (12.8%) is recorded between 30°S and 30°N at altitudes of 25 to 35 km, and a 230 ppbv decrease (18.3%) is recorded from 60°N to 90°N at altitudes of 20–25 km. In scenario B, the changes are different: between 10°S and 10°N at altitudes of 15–25 km, an average increase of 1 ppbv (0.1%) is observed. However, between 30°S and 30°N at altitudes of 25–35 km, a decrease of 30 ppbv (-0.37%) is observed, and from 60°N to 90°N at altitudes of 20–25 km, the decrease is 5 ppbv (-0.4%). For scenario B with ULS, between 10°S and 10°N at altitudes of 15–25 km, an average increase of 1.8 ppbv (0.18%) is observed. Between 30°S and 30°N at altitudes of 25–35 km, a decrease of 34 ppbv (-0.43%) is observed, and from 60°N to 90°N at altitudes of 20–25 km, the decrease is 6 ppbv (-0.48%). Additionally, scenario B with ULS shows an increase of 1.2 ppbv (0.81%) from 60°N to 90°N.

Our focus extends to the climate impacts of high-altitude emissions. We have calculated the stratospherically adjusted RF for each chemical species and their cumulative effects in each scenario, including ozone, water vapor, methane, carbonaceous aerosol, and inorganic aerosol RF. To provide a clear comparison, we normalized these values against the fuel burn for each case. This approach allows us to directly correlate emissions with their respective climate impacts. The results of these calculations (Figure 4) offer insights into the relative contributions of each species to the total RF change under each scenario.

Scenarios A and B exhibit negative RF, indicative of a cooling effect. In contrast, scenario B without sulfur (ULS) demonstrates a positive RF, signifying a warming effect. This variation in sulfur RF in the ULS case is due to the absence of reflective sulfate aerosols, which would otherwise lead to a warming impact. Emissions at high altitude affect ozone and water vapor differently from emissions at lower altitudes, even after adjustment for the amount of fuel burned. In scenario A, the effect on ozone is 0.83 mW/m² per teragram (Tg) fuel burned, in contrast to 0.14 mW/m² per Tg in scenario B, thus indicating a six-fold higher impact per Tg fuel burned. Similarly, for water vapor, scenario A shows an impact of 0.98 mW/m² per Tg, whereas scenario B shows 0.08 mW/m² per Tg, a 12-fold difference. Thus, per Tg fuel, high-altitude emissions have a relatively greater influence on RF from water vapor and ozone.

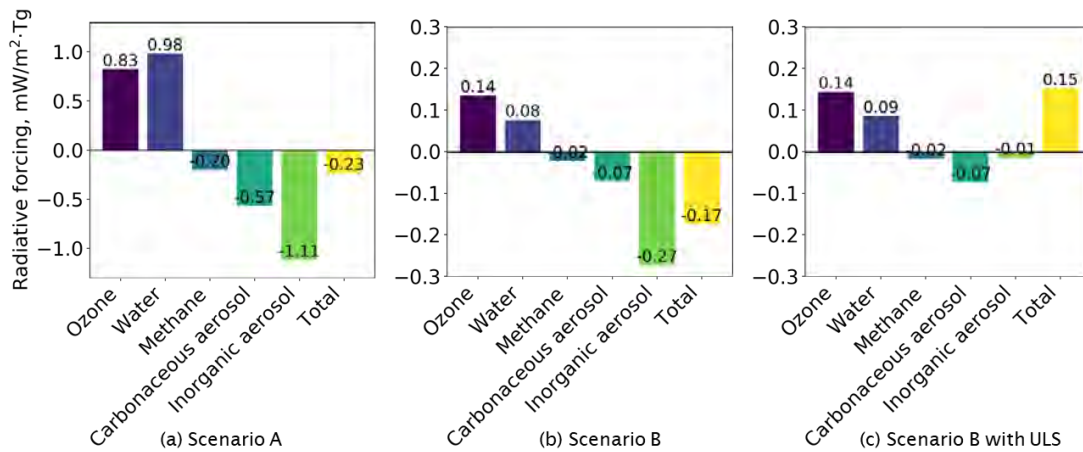


Figure 4. Comparative analysis of annual RF (stratospherically adjusted) changes across various scenarios, relative to the projected 2035 subsonic baseline. Left: scenario A; middle: scenario B; right: scenario B with ULS.

We expanded our simulation timeframe from 3 years, as previously reported, to 12 years. This extension is in line with the methods outlined by Eastham et al. (2022) and Holmes (2018). For our methane flux simulations, in which we dynamically calculate methane flux rather than assuming a fixed methane concentration at the surface, this expanded timeframe is aligned with the need to adequately capture the effects of long-term feedback on atmospheric composition. As identified in these studies, accurately capturing these effects requires a spin-up period that extends beyond the decade-long perturbation lifetime of methane. This longer simulation period is therefore implemented to ensure a comprehensive and accurate representation of methane's influence on the atmosphere over time. We also expanded our simulation timeframe from three years (as shown in previous reports) to twelve years. This extension aims to achieve a steady state, particularly vital for our methane flux simulations, where we do not assume a fixed methane concentration at the surface. Instead, we calculate methane flux, anticipating that its impact will reach a steady state as we iterate the simulations.

To verify whether our simulations have indeed attained this steady state, we monitor specific atmospheric impact indices. Figure 5 shows how our key impact metrics (PWM $PM_{2.5}$, PWM surface ozone, and total RF) change over the spin-up period of 12 years in scenario A. These indicators help confirm whether our simulations demonstrate stable convergence, thereby ensuring the reliability and accuracy of our extended simulation results. The PWM of these metrics involves multiplying the metric value in each grid cell by the population of that cell, then dividing by the total population. This approach helps assess the average exposure of these metrics per person.

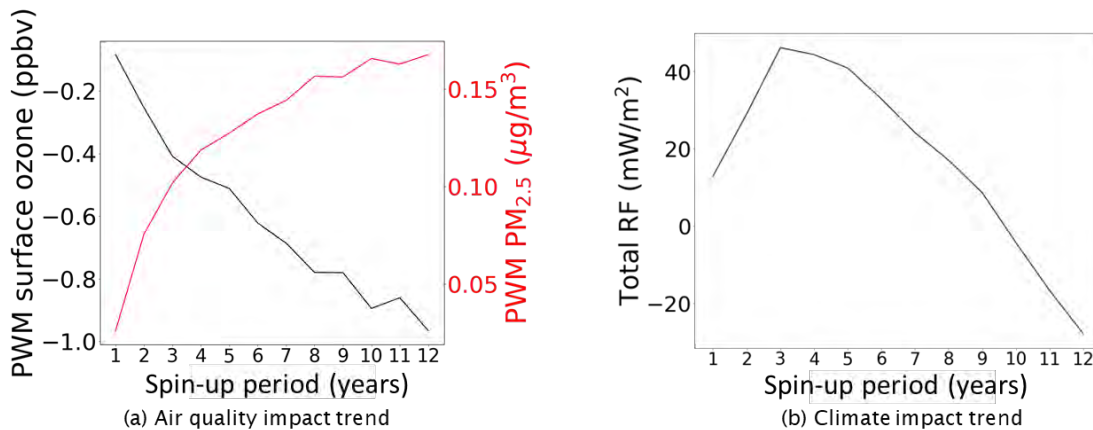


Figure 5. Convergence test of atmospheric impact parameters. Left: air quality metrics, specifically the PWM of PM_{2.5} and surface ozone concentrations; right: climate impact through the total RF change.

Figure 5 shows a decreasing trend in the slope of air quality metrics, including PWM PM_{2.5} and ozone, over successive iterations. This diminishing slope indicates a move toward a steady state as the spin-up period progresses. However, the climate impact metrics remain in the process of finding this steady state, as evidenced by the behavior of the RF components.

In our calculations of the five components contributing to RF, all except methane have reached a steady state. The methane component, however, has not yet stabilized. This discrepancy suggests that additional simulation years are necessary to accurately quantify the steady state of climate impact, particularly in relation to methane. Therefore, further iterations and analyses are required to fully understand and quantify the steady state of climate change impacts from these emissions. However, isolating the methane RF response and extrapolating from existing data might be possible.

Milestones

- Expanded the simulation to 12 years, enabling detailed long-term atmospheric impact analysis, particularly for methane flux, to achieve accurate steady-state modeling.
- Broadened the study to encompass NO_x, SO_x, water vapor, black carbon, and organic carbon, thus enhancing understanding of the environmental impact of aviation emissions.
- Conducted simulations across various aviation scenarios, including subsonic and supersonic flights, to assess their environmental impacts against a 2035 baseline and explore the effects of ULS fuel.

Major Accomplishments

- Quantification of the various impacts of high-altitude emissions, highlighting the influence of emission altitude on environmental effects
- Calculation of RF for various chemicals, thus revealing diverse climate impacts of various aviation scenarios and the importance of fuel sulfur content
- Monitoring of atmospheric indices to validate steady-state achievement in simulations, with a focus on understanding methane's role in climate change impacts

Publications

None

Outreach Efforts

Task progress was communicated during biweekly briefing calls with the FAA and reported in quarterly progress reports.

Awards

None.

Student Involvement

During the reporting period of AY 2022–2023, the MIT graduate student involved in this task was Lucas Jeongsuk Oh.

Plans for Next Period

In the upcoming project period, the team will continue with spin-up simulations and in-depth impact analyses to ascertain the steady state of climate, air quality, and ozone impacts attributable to supersonic aviation. These efforts will be based on the data detailed in Task 1 and the simulation tool developed in Task 2. We also plan to evaluate whether a simple extrapolation could be used for the methane-related RF.

References

- Barrett, S. R. H., Prather, M., Penner, J., Selkirk, H., Balasubramanian, S., Doppelheuer, A., ... & Wayson, R. (2010). Guidance on the use of AEDT gridded aircraft emissions in atmospheric models. *A technical note submitted to the US Federal Aviation Administration, Massachusetts Institute of Technology (MIT)*. Holmes C. D. (2018). Methane Feedback on Atmospheric Chemistry: Methods, Models, and Mechanisms, *Journal of Advances in Modeling Earth Systems*, 10(4), 1087-1099. Doi: 10.1002/2017MS001196
- Eastham, S. D., Fritz, T., Sanz-Morère, I., Prashanth, P., Allroggen, F., Prinn, R. G., ... & Barrett, S. R. H. (2022). Impacts of a near-future supersonic aircraft fleet on atmospheric composition and climate. *Environmental Science: Atmospheres*, 2(3), 388-403. Doi: 10.1039/d1ea00081k

Task 4 – Calculate Atmospheric Sensitivity Matrices

Massachusetts Institute of Technology

Objective

The objective of this task is to convert the impacts calculated under Task 3 for each scenario into sensitivities of environmental impacts with regard to key parameters. This process will enable the evaluation of local outcomes in air quality and support Task 5 in the rapid quantification of environmental impacts from any inventory with gridded emissions.

Research Approach

During the last reporting period, we generated data for various species—NO_x, SO_x, black carbon plus organic carbon, and water vapor—at specific latitude and altitude combinations. Over this period, we have successfully gathered 4 years' worth of sensitivity results, encompassing four species across 41 spatial locations.

For altitudes below 8 km, the sensitivity data are categorized into six regions. Above 8 km, the sensitivity analysis is more granular, involving 35 distinct latitude and altitude combinations. This breakdown includes five latitude bands and seven altitude bands. Consequently, we have compiled a set of 164 sensitivity cases spanning 4 years, which offer a detailed understanding of the spatial dynamics of these emissions. More information has been provided in prior annual reports.

Using the sensitivities identified, we have evaluated the feasibility of rapidly quantifying environmental impacts. This approach involves integrating sensitivities into a single environmental impact assessment to simulate the GEOS-Chem model, as outlined in Equation 1.

$$G(\text{scenario}) \sim G(\text{baseline}) + \sum \frac{\partial G}{\partial x_i} w_i, \quad \frac{\partial G}{\partial x_i}: \text{sensitivity}, w_i: \text{emission weight} \quad (1)$$

In Equation 1, G is a function representing the GEOS-Chem model. In Task 3, we focused on simulating the left side of the equation by inputting scenario emission inventories into GEOS-Chem to assess the atmospheric impacts of high-altitude emissions. However, the right side introduces a method developed in Task 4, which we have termed linear sensitivity combination (LSC). LSC involves combining the sensitivities of individual components into one comprehensive atmospheric impact. For example, for NO_x emissions at a specific latitude (30°N to 60°N) and altitude range (8 km to 10 km), the impact of each unit of NO_x emission on atmospheric components is considered a sensitivity. The emission weight represents the total amount of NO_x emissions within that specific box.

For each scenario, we calculate each sensitivity, assuming linearity within the emission weight range, and then linearly combine these sensitivities. If the outcomes of the right and left sides of Equation 1 align closely, we do not need to run full GEOS-Chem simulations for new inventories with gridded emissions. Instead, we can rapidly calculate atmospheric impacts by using this more efficient method.

To evaluate our LSC method, we conducted a comparative analysis between the GEOS-Chem simulation results and those derived from the LSC method. This evaluation focused on the impacts of surface ozone, $PM_{2.5}$, and zonal ozone for scenarios A and B.

We performed a detailed pointwise comparison between the LSC method and the GEOS-Chem model. Ideally, if the LSC method perfectly mirrors GEOS-Chem, each data point—representing atmospheric impact values for individual grid cells—would align precisely on the $y = x$ line. To assess the LSC method’s accuracy, we plotted its results on the x axis against GEOS-Chem’s on the y axis, incorporating a black, dashed line representing $y = x$ in each figure for clear reference.

Figure 6, Figure 7, and Figure 8 display the annual averages of surface ozone, $PM_{2.5}$, and zonal ozone, respectively, comparing the two methods for scenario A. These figures also include a pointwise comparison of the impacts from scenario A, with each point representing a single grid cell. Similarly, Figure 9, Figure 10, and Figure 11 illustrate the annual averages for surface ozone, $PM_{2.5}$, and zonal ozone for scenario B, along with a pointwise comparison of the impacts from this scenario. These figures are aimed at providing a clear visual representation of how closely the LSC method approximates the results of the GEOS-Chem model.

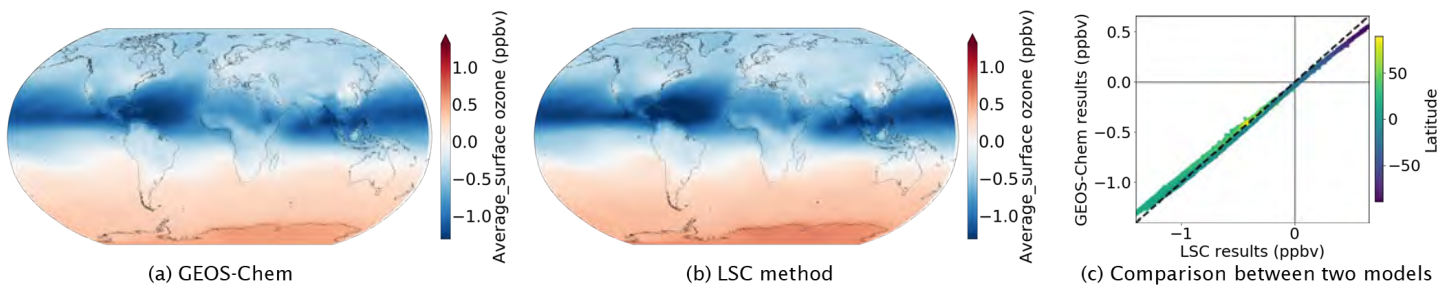


Figure 6. Change in annual average surface ozone concentrations attributable to supersonic aircraft emissions in scenario A after 4 years. Left: results from the GEOS-Chem model; middle: results from the LSC method; right: pointwise comparison between models.

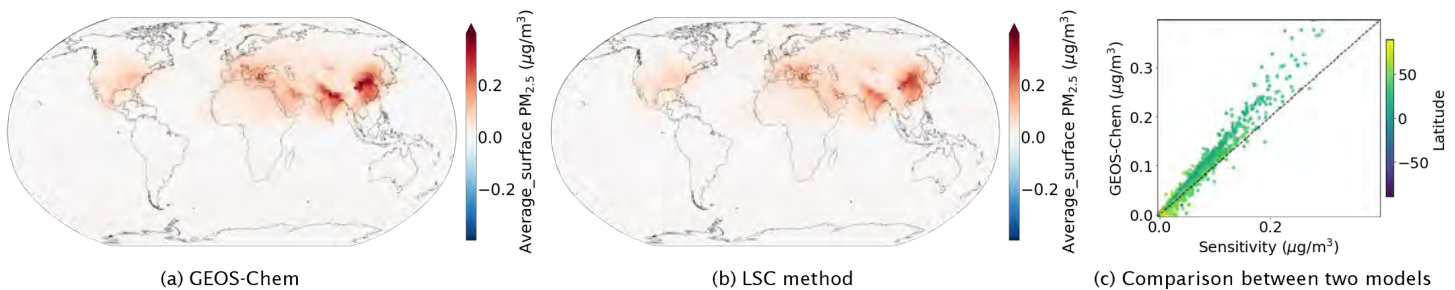


Figure 7. As in Figure 6, but for annual average surface $PM_{2.5}$. Left: results from the GEOS-Chem model; middle: results from the LSC method; right: pointwise comparison between models.

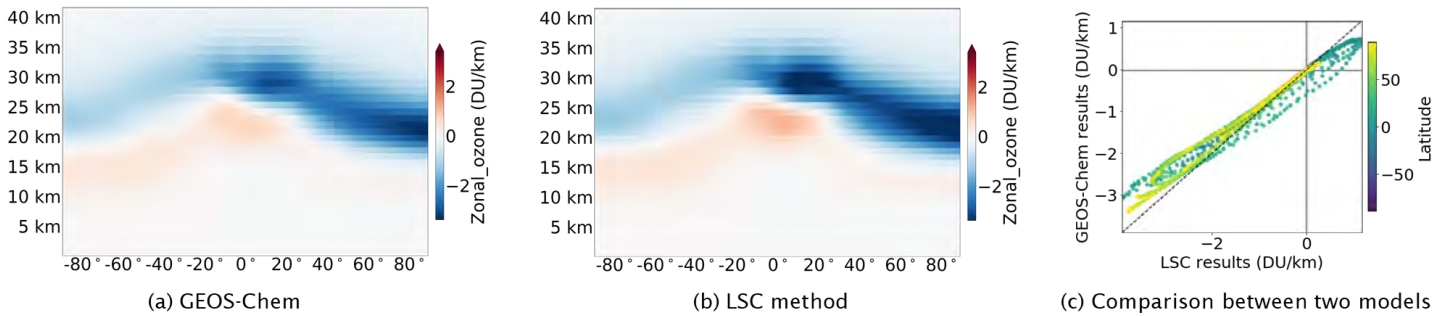


Figure 8. Change in annual average zonal mean ozone attributable to supersonic aviation in scenario A. Left: results from the GEOS-Chem model; middle: results from the LSC method; right: pointwise comparison between models.

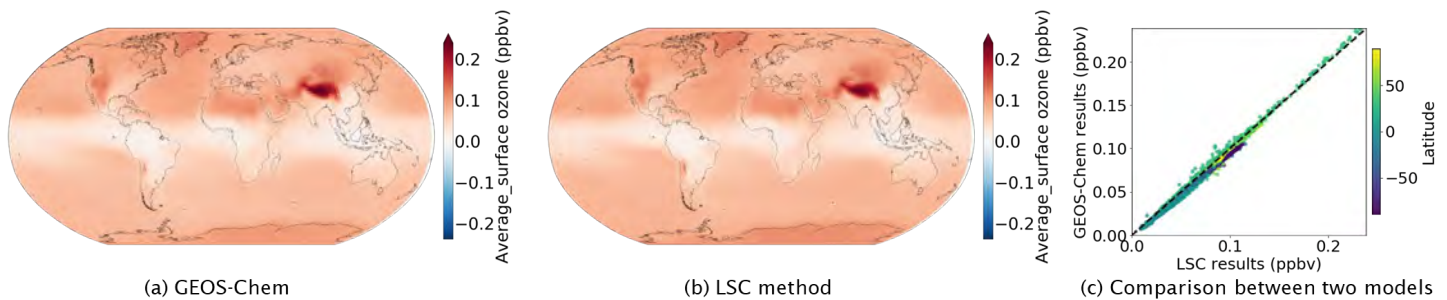


Figure 9. Change in annual average surface ozone concentrations attributable to supersonic aviation in scenario B. Left: results from the GEOS-Chem model; middle: results from the LSC method; right: pointwise comparison between models.

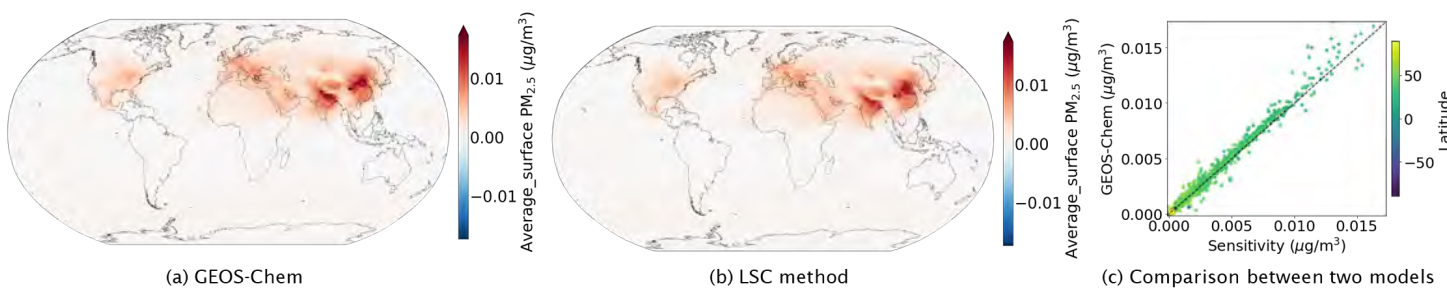


Figure 10. As in Figure 9 but for annual average $PM_{2.5}$. Left: results from the GEOS-Chem model; middle: results from the LSC method; right: pointwise comparison between models.

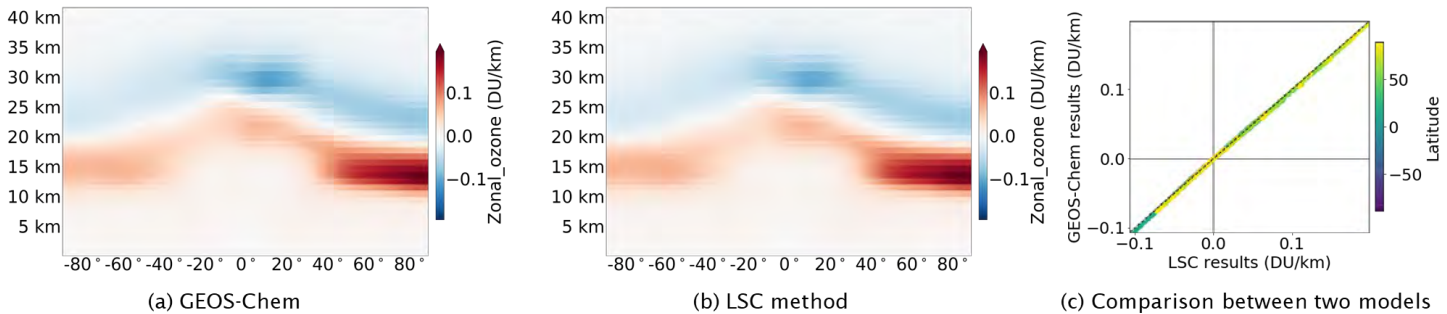


Figure 11. As in Figure 8 but for scenario B. Left: results from the GEOS-Chem model; middle: results from the LSC method; right: pointwise comparison between models.

Our LSC method aligned with the GEOS-Chem trends, yet we observed some discrepancies, particularly in scenario A. Therefore, the correspondence between models in scenario A is not as close as that observed in scenario B. In the previous reporting period, we focused on examining the linearity trend in our sensitivity analysis. Although the linearity assumption was deemed valid for high-intensity emission inputs, it did not exhibit a perfect linear trend. This same phenomenon is apparent in the current reporting period. The fuel burn in scenario A is 2.8 times that of scenario B. This difference suggests that our LSC method might introduce biases. Therefore, although the LSC method follows the general trend of the GEOS-Chem model, it might require refinement or adjustment when applied to scenarios with very high emission levels, as seen in scenario A.

In scenario A, for instance, the LSC method tends to underestimate the GEOS-Chem results for $PM_{2.5}$ concentrations, as evidenced by a linear regression slope of 1.2 in comparison of the two approaches for $PM_{2.5}$. Consequently, for every unit increase in the LSC method, a corresponding increase of 1.2 units is observed in the GEOS-Chem results, thus signifying underestimation by the LSC method. In contrast, in the case of annual average surface ozone and zonal ozone, the LSC method tends to provide an overestimate. This aspect is illustrated by the slopes obtained from our analysis: 0.87 for zonal ozone and 0.92 for surface ozone. A slope less than 1 in this context implies that an increase of one unit in the LSC method results in an increase of less than one unit in the GEOS-Chem model, thereby indicating overestimation by the LSC method. In scenario B, the regression slopes obtained for different metrics indicate a close correlation between the LSC method and the GEOS-Chem model. Specifically, the regression slope is 0.995 for zonal ozone, 1.006 for surface ozone, and 1.046 for $PM_{2.5}$.

Additionally, we observe more variability in the $PM_{2.5}$ results than the ozone trends, as indicated by scatter in the plot. This variability in the $PM_{2.5}$ data might be attributable to noise, which add an additional layer of complexity to the analysis of $PM_{2.5}$ concentrations.

Throughout the reporting period, a key focus has been on quantifying the attribution of each sensitivity to the total environmental impacts. Traditional simulation methods, as used in Task 3, are computationally expensive, thus hindering isolation of the impacts of individual emission species or specific spatial emissions, because additional simulations would be required. However, the LSC method overcomes this limitation.

The LSC method allows for the calculation of the contribution of each species and spatial emission to the overall change. By combining the impacts of individual sensitivities, we can evaluate the total environmental impact. Importantly, the method enables us to calculate the proportion of a specific sensitivity relative to the total impact, as illustrated in Equation 2.

$$\text{Relative contribution of emissions of species } i \text{ to total impacts} = \frac{\frac{\partial G}{\partial x_i} W_i}{\sum \frac{\partial G}{\partial x_i} W_i} \quad (2)$$

This approach has facilitated a deeper analysis of the reasons underlying the differences observed in various scenarios. By dissecting the contributions of each sensitivity, we gain a clearer understanding of the specific factors driving the overall environmental impact in various scenarios. This insight is critical for developing targeted strategies to mitigate the environmental effects of emissions in various contexts.

To deeper investigate the variability in atmospheric impacts according to emission species and altitude, we focused on the latitude band from 30°N to 60°N. The analysis involved comparison of the impacts of different altitudes and emission species on atmospheric conditions.

Figure 12 was constructed to facilitate this comparison. In this figure, the y axis represents the altitude at which emissions were released, whereas the x axis indicates the PWM concentration change in surface ozone per Tg of a specific emitted species. The comparison encompasses four distinct emission species: NO_x, SO_x, black carbon plus organic carbon, and water vapor. This graphical representation enables a clear comparison of how different emission species, when released at various altitudes, affect the concentration of surface ozone. This type of analysis is crucial for understanding the nuanced and complex interactions between emissions and atmospheric conditions, particularly in terms of their spatial and chemical variations.

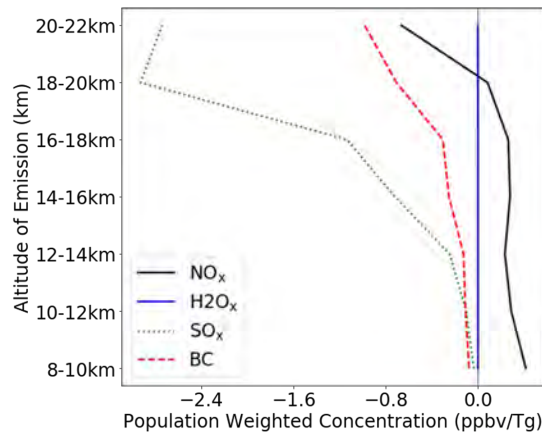


Figure 12. Population-weighted concentration change in surface ozone, by species and emitted altitude.

Figure 12 provides insights that align with the findings from Task 3. Specifically, it helps explain the variations in surface ozone concentration observed across scenarios. For scenario A, a decrease of 0.97 ppbv was observed in PWM surface ozone, whereas in scenario B without sulfur, the decrease was 0.032 ppbv, and in scenario B with sulfur content, the decrease was 0.011 ppbv.

The figure shows that emissions above 20 km have a negative impact on PWM surface ozone concentration, and the intensity of this impact increases at higher altitudes. Additionally, it demonstrates that SO_x emissions consistently result in a decrease in PWM surface ozone at all altitudes. Thus, the presence of sulfur in emissions generally leads to a smaller impact on surface ozone than observed in scenarios without sulfur. This analysis therefore provides a clearer understanding of how the altitude of emissions and the presence of sulfur in emissions influence the concentration of surface ozone, and offers insights for environmental impact assessments related to supersonic aviation.

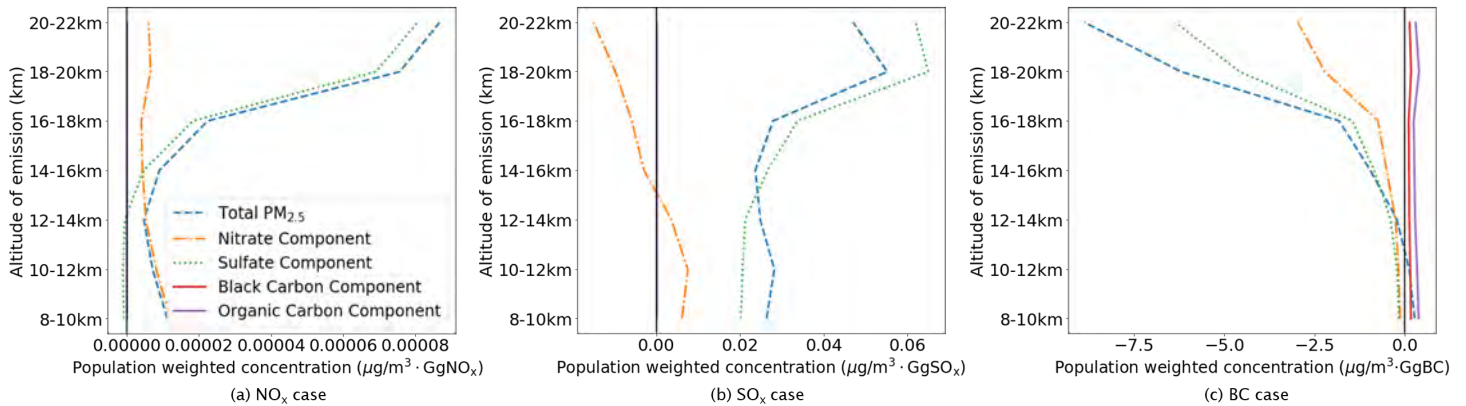


Figure 13. Population-weighted concentration changes in PM_{2.5} by species and emitted altitude. In each graph, total PM_{2.5} and components of PM_{2.5} are plotted: nitrate, sulfate, black carbon, organic carbon. Left: PM_{2.5} change due to NO_x case; middle: PM_{2.5} change due to SO_x; right: PM_{2.5} change due to black carbon and organic carbon.

Figure 13 shows how surface PM_{2.5} concentrations are changed by emissions at different altitudes. In this figure, the blue dashed line represents the overall change in PWM surface PM_{2.5} concentrations resulting from emissions at different altitudes. The four lines show the specific response of each aerosol component, and add up to the total (blue line): nitrate, sulfate, and black carbon plus organic carbon. From left to right, each panel shows the response to NO_x emissions, SO_x emissions, and black carbon plus organic carbon emissions.

From Task 3, we obtained aggregate PM_{2.5} amounts, but in Figure 13, we gained insights into specific contributions from different emissions. High altitude NO_x emissions primarily increase surface sulfate levels, whereas lower-altitude NO_x emissions primarily increase surface nitrate concentrations. In contrast, high altitude SO_x emissions tend to decrease the nitrate component while increasing sulfate in PM_{2.5}. SO_x emissions at relatively lower altitudes (below 14 km) are associated with an increase in the nitrate component of surface PM_{2.5}. Additionally, black carbon emissions above 8 km are linked to decreases in both sulfate and nitrate components. Further analysis is needed to understand the base atmospheric processes responsible for these differences.

Milestone

- Successfully integrated an LSC method into environmental impact assessments, thus offering a more efficient and detailed approach for quantifying the impacts of emissions on air quality

Major Accomplishments

- Gathered 4 years of sensitivity data for key pollutants across 41 locations, thus offering detailed insights into the spatial dynamics of emissions
- Implemented and validated the LSC method, streamlining environmental impact assessments
- Conducted thorough comparisons between LSC and GEOS-Chem model results, thus revealing insights into the effects of altitude and emission species on air quality

Publications

None.

Outreach Efforts

Task progress was communicated during biweekly briefing calls with the FAA and reported in quarterly progress reports.

Awards

None.

Student Involvement

For the AY 2022–2023 reporting period, graduate student Lucas Jeongsuk Oh was involved with this task.

Plans for Next Period

In the next project phase, the team will produce gridded sensitivity data to compare with and assess GEOS-Chem results from Task 3. We will further use the LSC method and sensitivity analysis to enhance understanding of atmospheric impacts, focusing on the underlying chemistry and physics of these phenomena.

Task 5 – Develop and Update Operational Tools Capable of Quantifying Environmental Impacts of Aviation

Massachusetts Institute of Technology

Objective

The objective of this task is to operationalize the results of Tasks 1–4 and 6. The eventual outcome will be a re-engineered version of APMT for climate and air quality impacts, calibrated on the basis of updated sensitivity data, and upgraded to provide monetized impacts that consider the possibility of different cruise altitudes (among other characteristics). Ozone layer impacts will also be provided in the updated model.

Research Approach

Our efforts centered on updating the APMT to include new capabilities. We successfully incorporated preliminary NO_x emission sensitivities into the model. This update allows APMT to evaluate the effects of aviation NO_x emissions on the ozone layer, climate, and air quality for various types of aircraft, including both subsonic transports and supersonic transports (SSTs).

Additionally, APMT has been modified to process emission sensitivities for an extended timeframe. This change prepares the model for future compatibility with emission data from GEOS-Chem simulations. The model now supports a wider range of emission species over longer time periods, thus enhancing its utility in environmental impact assessments. Pending updated sensitivity data, the base model underlying APMT's new capabilities, ACAI, will therefore be able to estimate the air quality, climate, and ozone impacts associated with an arbitrary emissions scenario for a decade or more, and translate these environmental outcomes into estimates of net present value.

Milestones

- Incorporated preliminary NO_x emission sensitivities into APMT
- Extended APMT's evaluation scope to include subsonic and SST fleet emissions
- Adapted APMT to accommodate long-term emission sensitivities from future GEOS-Chem simulations

Major Accomplishments

- Updated APMT to analyze the environmental impact of aviation NO_x emissions
- Expanded APMT's analytical capacity to cover diverse aircraft types and emissions
- Prepared APMT for future integration with upcoming GEOS-Chem emissions data

Publications

None.

Outreach Efforts

None.

Awards

None.

Student Involvement

During the reporting period of AY 2022–2023, the MIT graduate student involved in this task was Joonhee Kim.

Plans for Next Period

The project team plans to integrate a comprehensive array of Task 4 sensitivities into the upgraded APMT. This update will include all emission species from SSTs, thereby broadening the tool's scope. Leveraging this enhanced framework, we aim to accurately quantify the monetary impacts on climate and air quality due to emissions from both subsonic and SST fleets.

Task 6 – Develop Parameterization of Contrails

Massachusetts Institute of Technology

Objectives

This task aims to parameterize contrails, linking the distance flown in a given region to the expected RF. In the existing version of APMT-IC (v24c), the total impacts of emissions are quantified per unit additional fuel burned for the current subsonic fleet. Lee et al. (2020), in a review of aviation's impacts from 2000 to 2018, have highlighted two specific gaps in the APMT-IC framework for estimating contrail RF impacts. First, a more sophisticated representation of the contrail impacts from the number and distribution of flights is needed. Because of the complex relationship between contrail production and other engine parameters, estimating contrail impacts per unit distance flown rather than per unit of fuel burn provides a better metric. Second, because of the brief, localized nature of contrails, as well as the sensitivity of contrail production to the surrounding weather conditions, differences are likely to exist in the likelihood of contrail formation as a function of location. Therefore, the first objective of this task is to link the distance flown in a given region to the expected RF. This objective has been completed and was reported in the previous annual report.

In addition, contrail impacts vary according to other factors, such as altitude, time of day, and time of year of emissions, as well as aircraft parameters, such as wingspan, aircraft weight, engine efficiency, and emissions composition. Therefore, we investigated how the contrails from the past 40 years are affected by these factors, and how these factors have changed over time. This portion of the task was completed in the current year.

Research Approach

Using the emissions inventory derived in Task 7, we simulate the contrails from the past 40 years of aviation on a decadal basis from 1980 to 2019.

To complete this task, we use a moderate-fidelity contrail model that can capture heterogeneity in two dimensions over time. The Aircraft Plume Chemistry, Emissions and Microphysics Model (APCEMM) (Fritz et al., 2020), as schematically outlined in Figure 14, has higher fidelity than one-dimensional Gaussian plume models, captures inhomogeneity of the contrail in two dimensions, and resolves different ice particle sizes at each spatial location and timestep. Therefore, this model captures effects that one-dimensional Gaussian plume models cannot, such as differential crystal settling. However, APCEMM consequently has a higher computational cost, and simulating contrails from all flight segments in a year is not computationally tractable. To address this problem, we use a sampling approach to simulate a representative set of contrails for each year in question. This approach is based on work by Agarwal (2021) and Elmourad (2023).

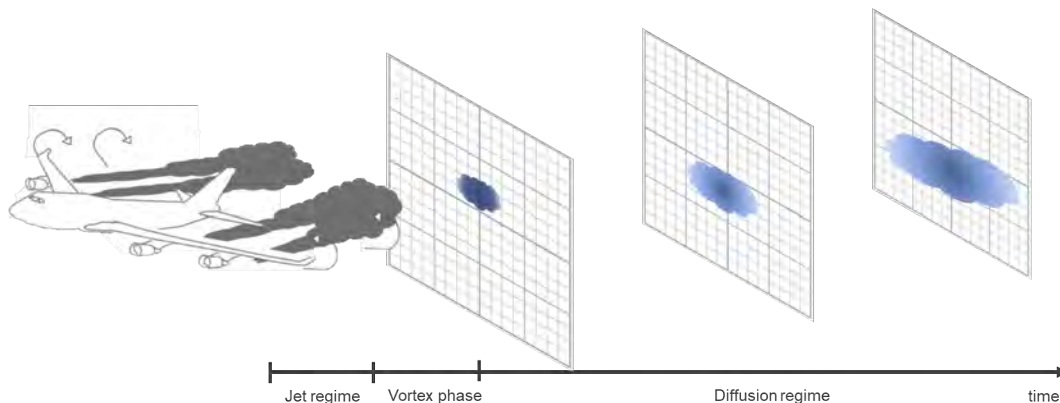


Figure 14. Schematic outline of the APCEMM (Fritz et al., 2020).

The steps followed for each year to derive the contrail impacts are outlined in Figure 14. Collectively, these steps are as follows:

- Step 1:** Chorded emissions inventories are derived for the years 1980 1990, 2000, 2010, and 2019.
- Step 2:** From the chorded emissions inventories, 100,000 individual flight segments for each year are sampled with distance-based random sampling
- Step 3:** Because we are interested in applying the aircraft plume model to only cases resulting in contrail formation, each of the selected flight segments is evaluated to test whether a persistent contrail could form for the given the ambient conditions and engine properties
- Step 4:** For each segment that could result in the formation of a persistent contrail, we use APCEMM, a moderate-fidelity aircraft plume model, to derive contrail properties. This model is combined with ambient weather data from the ECMWF reanalysis (ERA5)
- Step 5:** The contrail properties are used to calculate the radiative impacts by using RRTM code together with ERA5 reanalysis weather data.
- Step 6:** Finally, the data from the individual chords are combined to determine aggregate radiative impacts and investigate trends in the impacts.

Additionally, because APCEMM resolves the internal structure of the contrail, we can explicitly model the degree to which changes in meteorological conditions do (or do not) mix into the contrail core. For this work, we assume that the contrail mixes primarily with air that has advected from its starting position. Consequently, our contrail lifetimes are longer than those in several other studies (Teoh et al., 2020, 2022). For comparison purposes, we derive an extra set of results that truncates contrail lifetime, with contrail evaporation conditions based on only the ERA5 weather data in the region into which the contrail advects over time. This alternative condition is based on an implicit assumption that the air around the contrail can gain or lose water vapor instantaneously, depending on the regional calculated conditions, but more closely represents typical contrail modeling approaches. This latter set of data serves as a lower bound for our contrail results, and we show that the observed trends are not sensitive to these changes in contrail lifetime.

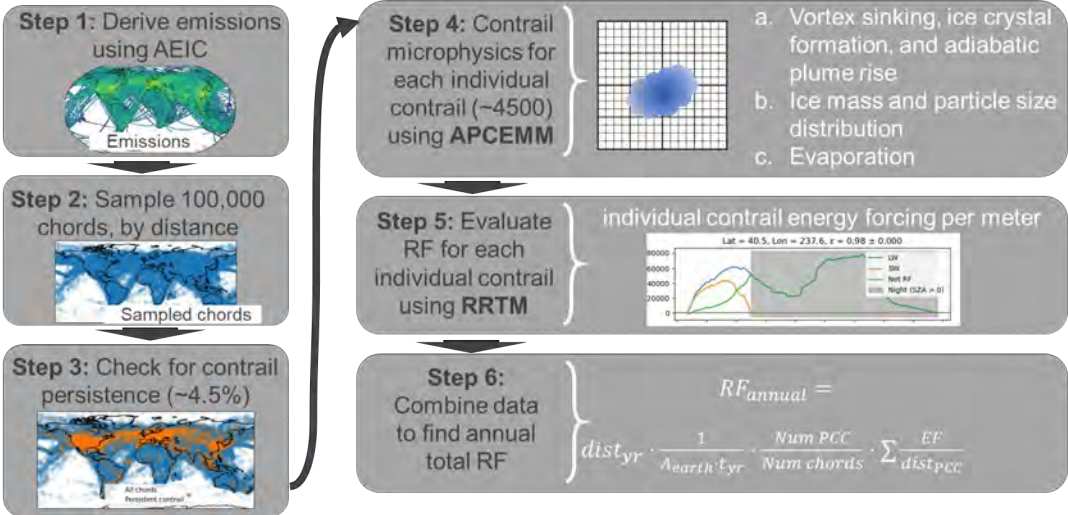


Figure 15. Schematic of methods to evaluate contrail impacts.

Contrail properties from 500,000 flight chords, 100,000 per investigated year, were evaluated and post-processed.

From 1980 to 2019, contrail RF increased by 460% (Figure 16). Per unit of distance flown, contrail impacts varied less than 10% over this time (Figure 17). However, the underlying drivers did not remain constant. The fraction of flight segments causing contrails increased by 32%, whereas the RF per distance of contrail decreased by 24%.

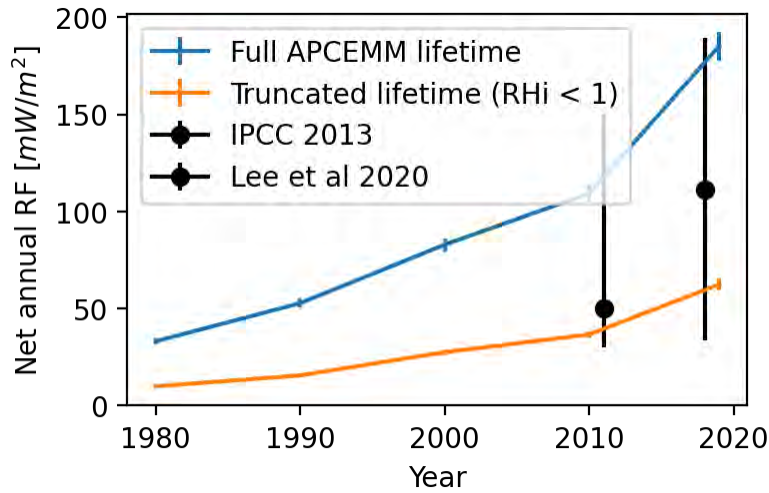


Figure 16. Global contrail RF over time.

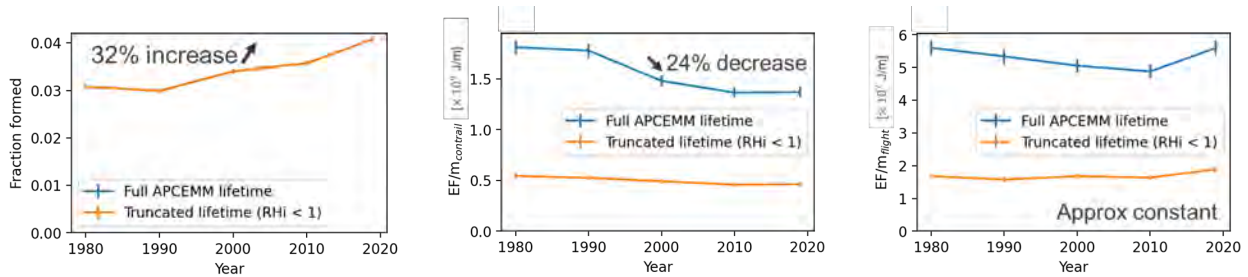


Figure 17. Changes in the fraction of flight segments causing contrails and contrail radiative impacts over time.

Given this large dataset, we investigate how these results vary with different underlying emissions characteristics. Figure 18 to Figure 20 show how the contrail formation fraction, the total energy forcing (EF, a metric of climate impact) per unit contrail formed (EF/m_{contrail}), and the EF per unit of distance flown (EF/m_{flight}) vary with various emissions characteristics. These plots include all evaluated chords from 1980 to 2019. These factors include latitude; altitude; month; local time of day; and aircraft characteristics such as aircraft mass, and the mission fuel consumption per mission distance. The mean over the samples and the standard error of the mean are plotted in each graph. Only data points for which the relative standard error of the mean is below 15% are included.

These plots represent correlation only, because another underlying factor could potentially be driving both the plotted factor and the contrail impact metric. For example, aircraft size and cruise altitude could co-vary, and increasing contrail impacts could be driven by aircraft size or by an increase in cruise altitude.

The contrail formation fraction and subsequent EF impacts co-vary with the altitude and location of emissions, with the strongest correlation associated with differences in flight latitude. These plots show that both contrail formation fraction and EF/m_{contrail} increase with latitude. Consequently, EF/m_{flight} varies from 0.5 to 2.5 times the mean value, increasing with increasing latitude. Contrail impacts also vary by altitude. Contrail formation fraction peaks between altitudes of 10 km and 12 km, varying from one quarter of the mean to a factor of 1.5 of the mean. In contrast, the EF/m_{contrail} remains relatively constant (~20% variation), and differences in EF/m_{flight} are associated predominantly with the lower formation fraction.

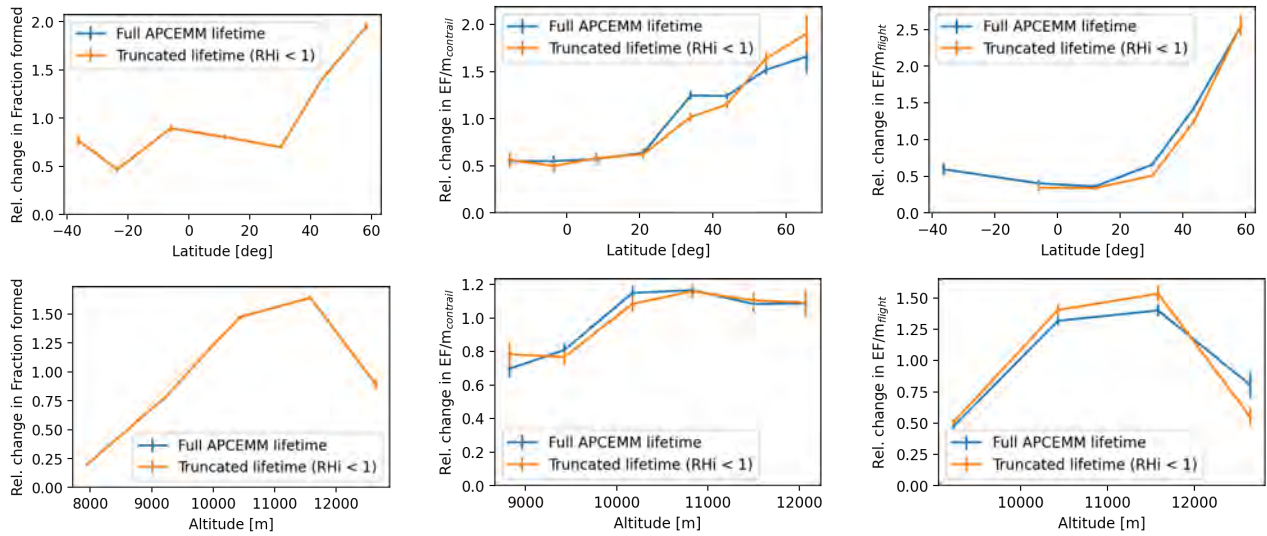


Figure 18. Relative change in the fraction of flight segments that form contrails, and contrail impacts by altitude and latitude.

The figure shows results for both definitions of lifetime and is normalized by the mean value to show the trends of each metric for both definitions. Collectively, these plots indicate that these trends are not sensitive to the selection of lifetime definitions.

Contrail impacts also vary by time of year. For flights occurring in the Northern Hemisphere, both the formation fraction and $EF/m_{contrail}$ peak during the Northern Hemisphere winter, thus leading to a strong correlation between EF/m_{flight} and month, with impacts varying between half and a 50% increase above the annual mean. Because daily emissions are ~10% lower during the winter, this seasonal sensitivity leads to lower contrail impacts than would be observed if flights had been distributed uniformly throughout the year.

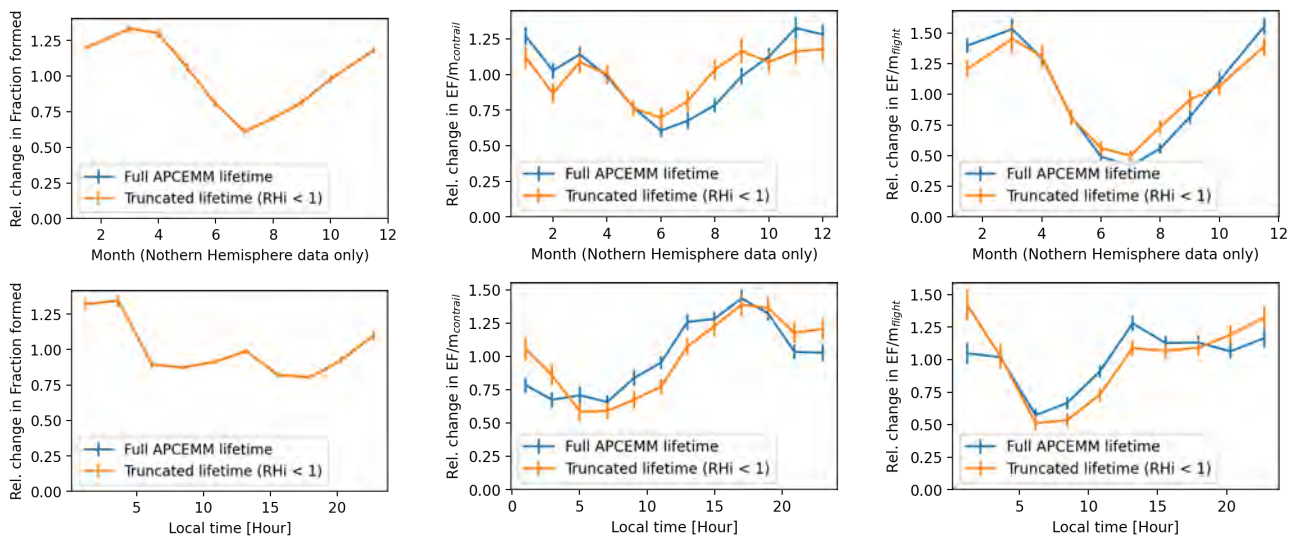


Figure 19. Relative change in the fraction of flight segments that form contrails, and contrail impacts by month and time of day.

Contrail impacts co-vary with the time of day, with the lowest $EF/m_{contrail}$ occurring for early-morning flight segments between 4 a.m. and 10 a.m. local time. This finding might be driven by daytime contrails that reflect more incoming radiation, thus leading to a smaller net effect. A lower formation fraction also occurs during the day, thereby amplifying the co-variance. Some of these differences could also be caused by differences in flight characteristics between night and day. For example, a greater proportion of short-haul flights occur during the day than during the night, and a greater proportion of long-haul flights occur during the night than during the day.

Aircraft size characteristics, as represented by aircraft mass, and fuel consumption per distance flown, also co-vary strongly with contrail EF/m_{flight} . Both the contrail formation fraction and the $EF/m_{contrail}$ contribute to this trend. This finding could be driven by a variety of underlying differences, such as differences in the time of day or the altitude at which these aircraft are operated, differences in the particle number emissions index, and differences in the region. Further research would be necessary to extract the effect of aircraft size on contrail impacts.

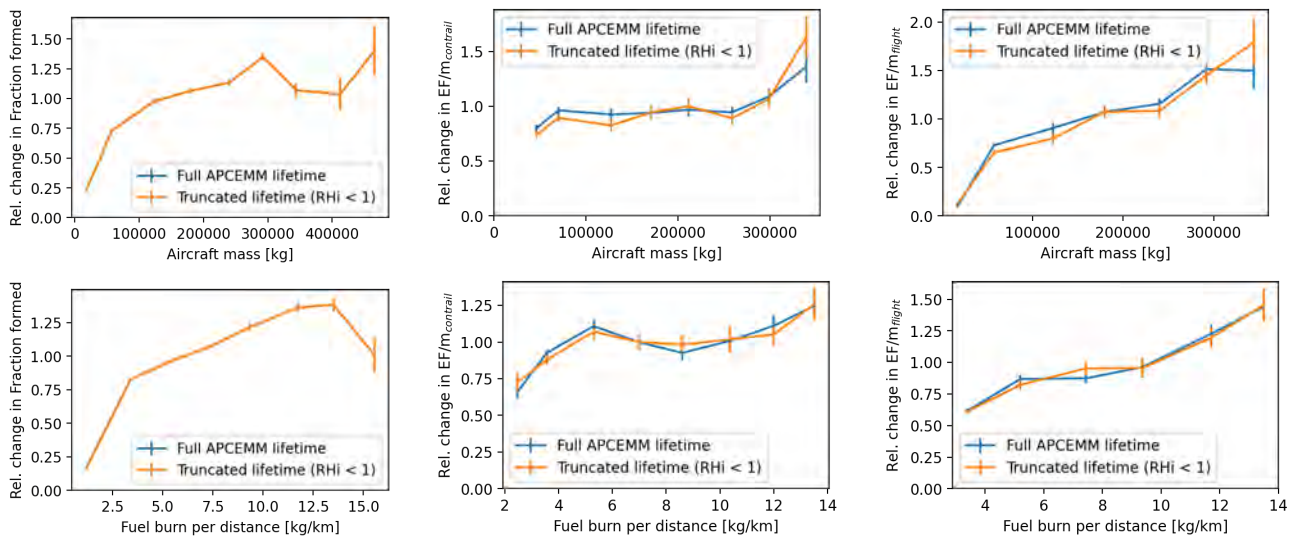


Figure 20. Relative change in the fraction of flight segments that form contrails, contrail impacts by aircraft mass, and mission fuel burn by mission distance.

We further investigate the role of particle number emissions on contrail impacts. Figure 21 shows the contrail formation fraction, $EF/m_{contrail}$, and $EF/m_{contrail}$ for various levels of particle number emissions index. Similarly to those in Figure 20, these plots include all evaluated chords from 1980 to 2019. The mean over all samples and the standard error of the mean are plotted in each graph. Only data points for which the relative standard error of the mean is below 15% are included.

These plots indicate that the contrail formation fraction co-varies with the particle emissions index. Because the particle emission index is expected to have little effect on the formation criteria, this trend is likely to be driven by a confounder. One possibility is a difference in aircraft characteristics, such as engine thermal efficiency, wherein older aircraft could both have lower engine efficiency and higher soot emissions than newer aircraft.

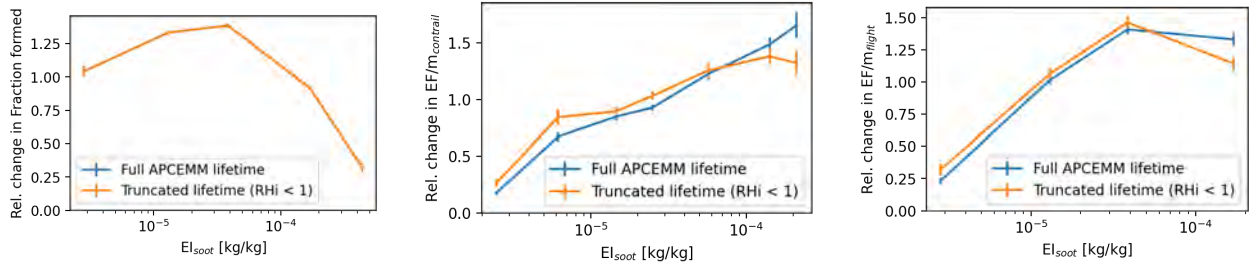


Figure 21. Contrail formation fraction and impacts co-varying with the particle number emissions index.

In our dataset, the impacts vary with particle number emissions, with EF/m_{contrail} increasing for increasing particle number emissions. This result is consistent with those from other studies, which have found that decreasing particle number emissions results in a decrease in contrail impacts (Burkhardt et al., 2018; Teoh et al., 2020), but differs from findings from another study which has found that the impact from changing particle number emissions has an uncertain sign (Caiazzo et al., 2017).

To control for confounders, we perform an additional set of simulations using a sub-sample containing 10% of the 100,000 chords in the 2019 dataset, wherein specific inputs are varied parametrically, thus resulting in 390 contrails. We first investigate the role of black carbon emissions. These APCEMM simulations are repeated by changing only the particle number emissions index by a factor of 0.1, 0.5, 2, or 10, while keeping all other variables the same. Our results indicate that for a halving or a doubling of $El_{\text{nvPM,num}}$, the EF/m_{contrail} changes by -25% or $+18\%$, respectively (Figure 22). For a 0.1 and a 10 times multiplier on $El_{\text{nvPM,num}}$, the EF/m_{contrail} changes by -65% and $+68\%$, respectively. These results are similar to those presented in Burkhardt et al. (2018), showing that a 50% and 90% decrease in initial ice particles leads to a $\sim 20\%$ and $\sim 70\%$ decrease in contrail RF, respectively.

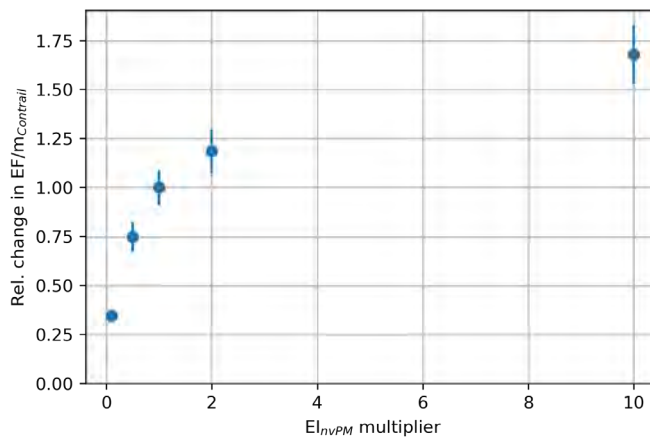


Figure 22. Changes in contrail impacts due to changes in engine particle number emissions.

Finally, we investigate how changes in engine efficiency affect the fraction of flight chords that result in contrail formation.

We find that the mean engine thermal efficiency increased from 0.36 to 0.43 over the period 1980 to 2019, representing an increase of 22% (Figure 23(a)). This increase in engine thermal efficiency is responsible for an increase in the contrail formation fraction, because an increase in engine thermal efficiency increases the slope of the Schmidt-Appleman mixing line, and consequently expands the range of atmospheric conditions under which contrails can form.

This increase in engine efficiency is responsible for half the increase in contrail formation reported in Figure 17. Figure 23(b) shows the fraction of flight segments that lead to contrail formation, assuming uniform engine thermal efficiencies between 0.2 and 0.5, as well as the engine efficiencies derived from the Base of Aircraft Data (BADA) for the aircraft in the current year (Figure 23). This figure shows that if the thermal efficiencies had remained constant, but the location and time of emissions had varied as in the flight operation data, the contrail formation fraction would have increased by 16%–18%.

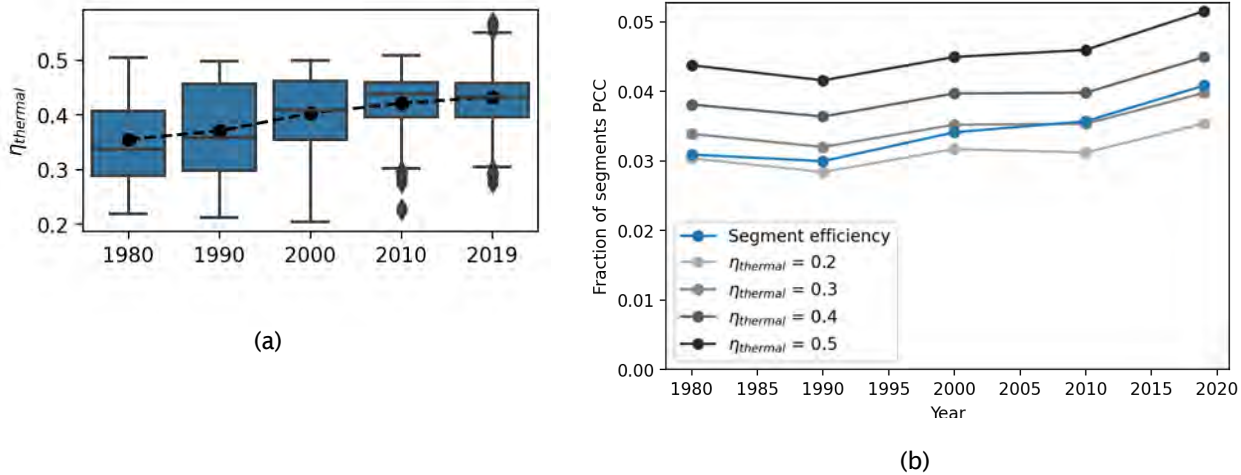


Figure 23. (a) Engine thermal efficiency and (b) contrail formation fraction over time.

This increase is not significantly affected by changes in the background weather data. Figure 24 shows the fraction of flight segments that would lead to contrail formation if the 2019 operational patterns occurred against the weather data from 1980 to 2019. The variation in these data points for each uniform engine efficiency line is less than 4%, thus indicating that changes in the atmosphere are responsible for only a small effect.

As such, other differences in flight operations are responsible for the other half of the change in the contrail formation fraction, such as location, altitude, and time of emissions.

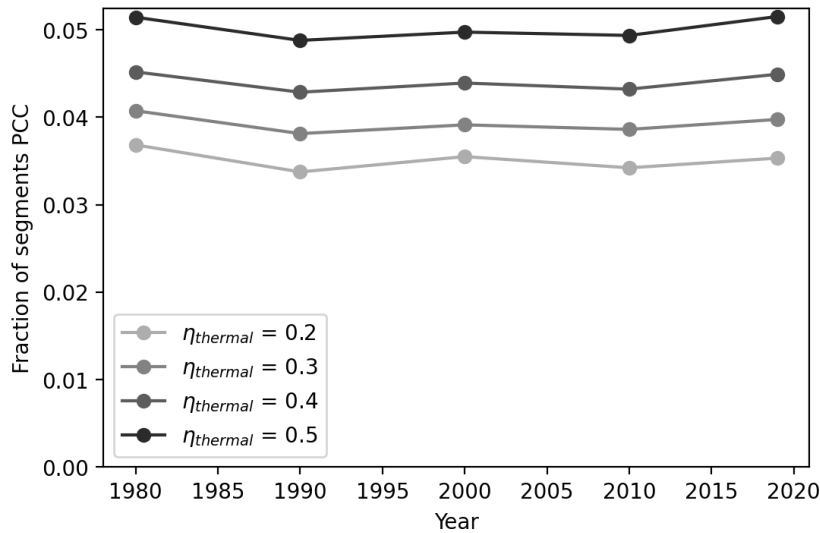


Figure 24. Fraction of flight segments that would have led to persistent contrails if the 2019 emissions occurred with the weather data from 1980 to 2019.

Milestone

Evaluated contrail properties from 500,000 flight chords (100,000 from each year) and post-processed the results.

Major Accomplishments

Contrail properties were evaluated, and the results from the dataset were post-processed and evaluated. This work identified strong correlations between various factors and contrail properties, including location, altitude, time of day, time of year, and aircraft size and emissions composition.

Publications

None.

Outreach Efforts

Task progress was communicated during biweekly briefing calls with the FAA and reported in quarterly progress reports.

Awards

None.

Student Involvement

During the reporting period of AY 2021–2022, the MIT graduate student involved in this task was Joonhee Kim. During the reporting period of AY 2022–2023 the MIT graduate student involved in this task was Carla Grobler.

Plans for Next Period

We plan to focus on dissemination of these results in the coming academic year.

References

- Agarwal, A. (2021). *Quantifying and reducing the uncertainties in global contrail radiative forcing* [Doctoral thesis, Massachusetts Institute of Technology].
https://dspace.mit.edu/bitstream/handle/1721.1/140372/agarwal_aa681_PhD_AeroAstro_thesis.pdf?sequence=1&isAllowed=y
- Burkhardt U., Bock L., & Bier A. (2018). Mitigating the contrail cirrus climate impact by reducing aircraft soot number emissions. *npj Climate and Atmospheric Science*, 1(1), 37. Doi: 10.1038/s41612-018-0046-4
- Caiazza F., Agarwal A., Speth R. L., & Barrett S. R. H. (2017). Impact of biofuels on contrail warming *Environmental Research Letters* 12 114013 Doi: 10.1088/1748-9326/aa893b
- Elmourad J. A. (2023). *Evaluating Fuel-Climate Tradeoffs in Contrail Avoidance* [Master thesis, Massachusetts Institute of Technology].
<https://dspace.mit.edu/handle/1721.1/150282>
- Fritz T. M., Eastham S. D., Speth R. L., & Barrett S. R. H. (2020). The role of plume-scale processes in long-term impacts of aircraft emissions *Atmospheric Chemistry and Physics*, 20(9), 5697-5727. Doi: 10.5194/acp-20-5697-2020
- Teoh, R., Schumann, U., Majumdar, A., & Stettler, M. E. (2020). Mitigating the climate forcing of aircraft contrails by small-scale diversions and technology adoption. *Environmental Science & Technology*, 54(5), 2941-2950.

Task 7 – Investigate Dependence of Aviation Emissions Impacts on Non-Aviation Factors

Massachusetts Institute of Technology

Objective

Aviation emissions since the start of the jet age have continued to cause present-day climate impacts, including CO₂ and non-CO₂ impacts (Grobler et al., 2019; Lee et al., 2020), as well as air quality impacts. These atmospheric impacts have been shown to vary by the region of emission, emission altitude, and season of emission (Fichter et al., 2005; Gilmore et al., 2013). Additionally, contrail climate impacts are sensitive to particle number emissions (Bock and Burkhardt, 2016; Teoh et al., 2019). The non-CO₂ climate impacts continue to propagate over years to decades through their influence on global surface temperature.

Over the past 40 years, the region, altitude, and chemical composition of aviation emissions have varied. Therefore, the evaluation of present-day and future impacts from aviation requires an accurate estimate of aviation's emissions over the past 40 years. Existing aviation impact assessments have relied on evaluations of specific years, and/or have scaled these impacts by fuel and emissions, which do not capture heterogeneities in the region and altitude of emission (Lee et al., 2020). Consequently, the total cumulative temperature change and the air quality impacts attributable to aviation remain uncertain.

The objective of this task is to understand how the impacts of aviation have been driven by changes in both aviation and non-aviation factors. We first derive a bottom-up emissions inventory for global commercial civil aviation spanning the jet age from 1980 to the present day in 2019. This inventory will be the first to capture differences in the region, altitude, and chemical composition of the emissions over this time.

The results provide insights into trends in emissions over time, such as emissions quantities by species, location, and season. As such, we will obtain insights into how changes in fleet composition as well as aircraft and engine design have changed the relative significance of the various emission species that result in environmental impact. Furthermore, this work will enable future assessment of how these changes in emission characteristics have influenced the cumulative climate impact of aviation.

The second component of this research involves using atmospheric modeling to investigate the influence of both changes in aviation emissions and changes in non-aviation factors with regard to environmental outcomes. This investigation will consider both the effects of the historical emissions described above and the mechanisms underlying aviation's ongoing impacts.

Research Approach

During the previous reporting period, preliminary results were presented on the emissions inventory, covering 1980 to 2019. As part of the ongoing work, the following work was completed to bring the emissions inventory to a near-final version:

- Use full-year OAG (Official Airline Guide) data newly obtained in the current reporting period
- Update emissions code to use the more recent Base of Aircraft Data (BADA) 3.16 data
- Introduce regionalized load factors over time
- Improve aircraft engine matching by using purchased fleet data or other manual methods
- Investigate trends in available seat kilometers (ASK) over time.
- Generate a final gridded emissions inventory for the schedule years

Here, we describe only the work and results from the current reporting period. The methods and results from the previous reporting period have been described in the AY 2021–2022 annual report.

Trends in passenger load factors over time

The emissions inventory methods are updated to include passenger load factors that vary by region and time. For the years 1980 to 1995, we use global passenger load factors and local U.S.-based load factors, as reported by Airlines for America (Airlines For America 2022b, 2022a). From 2000, regional load factors have been reported by International Civil Aviation Organization annual statistics (ICAO 2020). These load factors (presented in Figure 25) are applied according to the takeoff and landing airports of each flight. If a flight is from one region to another, the average load factor is used.

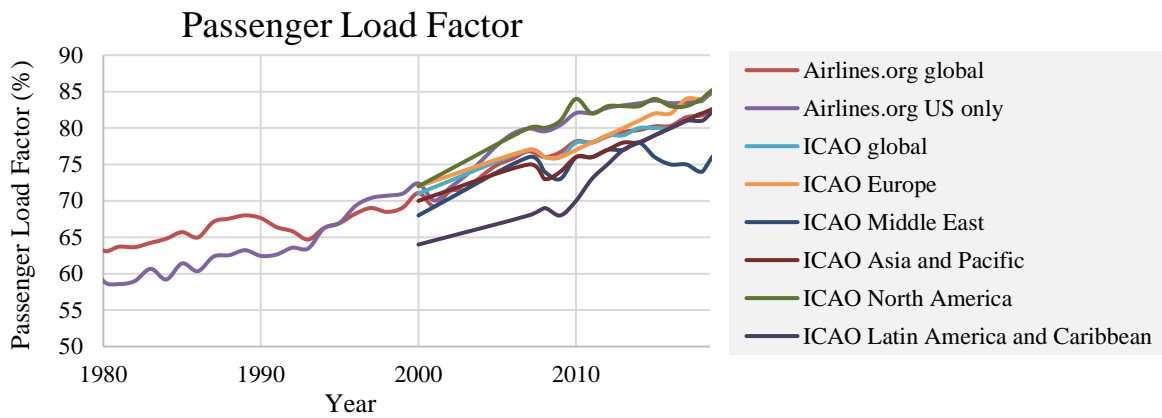


Figure 25. Global and regional passenger load factors over time.

Enhanced aircraft engine matchings

The OAG schedule data include 110 unique aircraft types in 1980 and 191 unique aircraft in 2019. However, some of the aircraft types included in the OAG data represent several subtypes with diverse engine options, which can influence the quantity of NO_x and non-volatile particulate matter (nvPM) emissions by factors of 1.5 and 10, respectively (Quadros et al., 2022). To enhance the accuracy of representation of emissions for aircraft with multiple engine combinations, we augment our schedule to represent subtypes, in line with fleet fuel burn fractions from NASA-Boeing studies (Baughcum et al., 1996a, 1996b; Sutkus et al., 2001). Alternative engine-aircraft matchings are also available in Quadros et al. (2022). Results derived from these aircraft-engine matchings are included as a sensitivity study.

This change predominantly affects the composition of the emissions, and the results remain sensitive to the aircraft/engine matching method selected. With the matching methods based on the NASA-Boeing studies, EI_{NO_x} increases from 14.3 to 17.2 g_{NO_x}/kg_{fuel} between 1980 and 2019, and EI_{nvPM} decreases from 0.13 to 0.04 g_{nvPM}/kg_{fuel}.

Figure 26 shows that both these EIs are sensitive to the matching method implemented. The figure presents the fuel burn, and NO_x and nvPM emissions by using these two matching methods, as implemented during this reporting period. Using an alternative matching method from Quadros et al. (2022) changes the derived EI_{NO_x} by 14% in 1980 and 3% in 2019, and EI_{nvPM} by 18% in 1980 and 57% in 2019 (Figure 26). Compared with our NASA-Boeing-based matchings that capture evolving aircraft types, the Quadros et al. (2022) matchings yield a 36% EI_{NO_x} increase from 1980 to 2019, as compared with our 20%. Using the Quadros et al. (2022) matchings leads to a 60% EI_{nvPM} decrease, as compared with 70% in our baseline results. These findings highlight the need for consistent assumptions when comparing historical emissions.

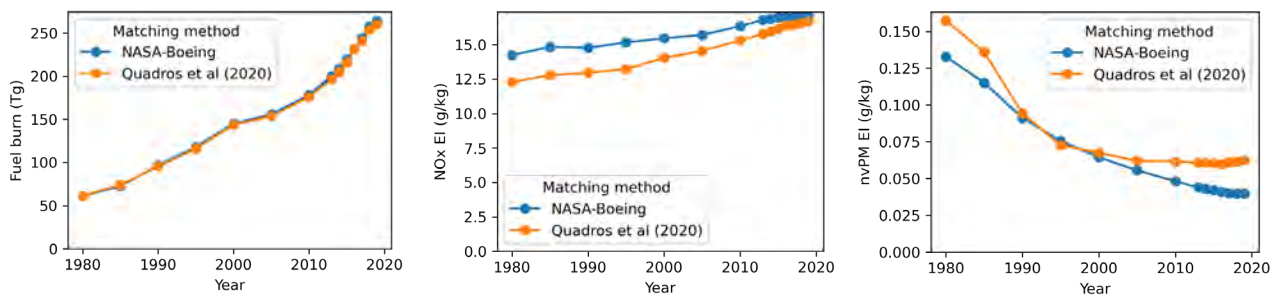


Figure 26. Comparison between fuel burn and emissions results for various aircraft-engine matching methods.



Finalized fuel burn and trends in ASK over time

Fuel burn, flight distance, and ASK data from 1980 to 2019 are detailed in Table 2 and Figure 27. Over this period, aviation fuel consumption increased, with total fuel use growing from 61.2 Tg to 265 Tg (330% increase). Simultaneously, ASK, a measure of airline capacity, increased even more, by 560%, from 1.5×10^{12} to 9.9×10^{12} seat km. As such, our data show an enhancement in fuel efficiency per available seat mile, with fuel burn by ASK decreasing by 35% over the past 40 years.

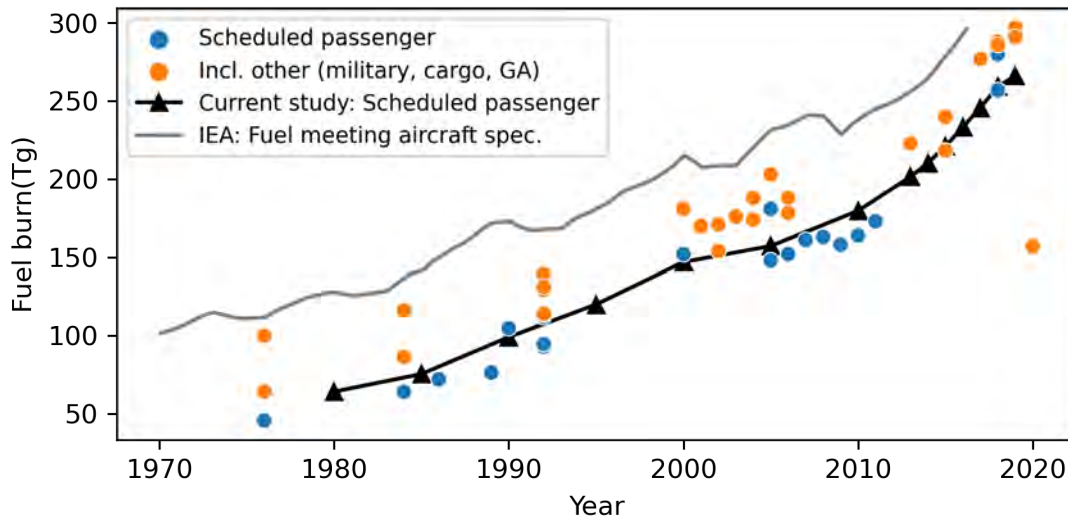


Figure 27. Comparison of our preliminary annual fuel burn totals with fuel burn totals in the literature.

Table 2. Annual totals of fuel burn, distance flown, and ASK.

Year	Fuel burn (Tg)	Distance ($\times 10^9$ km)	ASK ($\times 10^{12}$ km)	Fuel per ASK (g/ASK)
1980	61.6	8.9	1.5	41.0
1985	72.8	11.0	1.9	39.1
1990	97.1	15.2	2.6	37.5
1995	118.3	19.8	3.4	35.1
2000	145.4	25.8	4.4	32.9
2005	156.0	30.1	5.1	30.6
2010	178.6	35.6	6.2	28.9
2015	219.9	43.3	7.9	27.7
2019	264.7	52.5	9.9	26.8

This decrease in fuel burn per ASK over time is shown in Figure 28 and Figure 29. Figure 28 shows a near-linear efficiency improvement rate of 0.37 g/ASK per year. Flights less than 1,000 nautical miles (NM) follow a similar improvement rate, However, for longer-haul flights (exceeding 2,000 NM) the decrease in fuel burn per ASK is slower, occurring at a rate of 0.21 g/ASK per year.

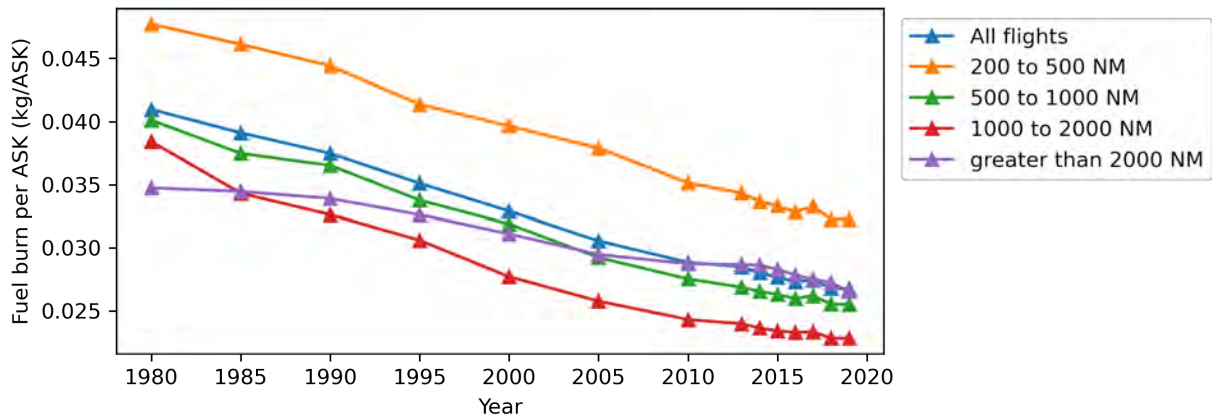


Figure 28. Fuel burn by seat distance.

Figure 29 contrasts fuel burn by ASK for different flight distance bands for the years 1980 and 2019. In both years, the highest fuel burn by ASK occurs for short flights (less than 200 NM). In 2019, flights between 200 NM and 2,000 NM led to the lowest fuel burn per ASK, after which fuel consumption increased.

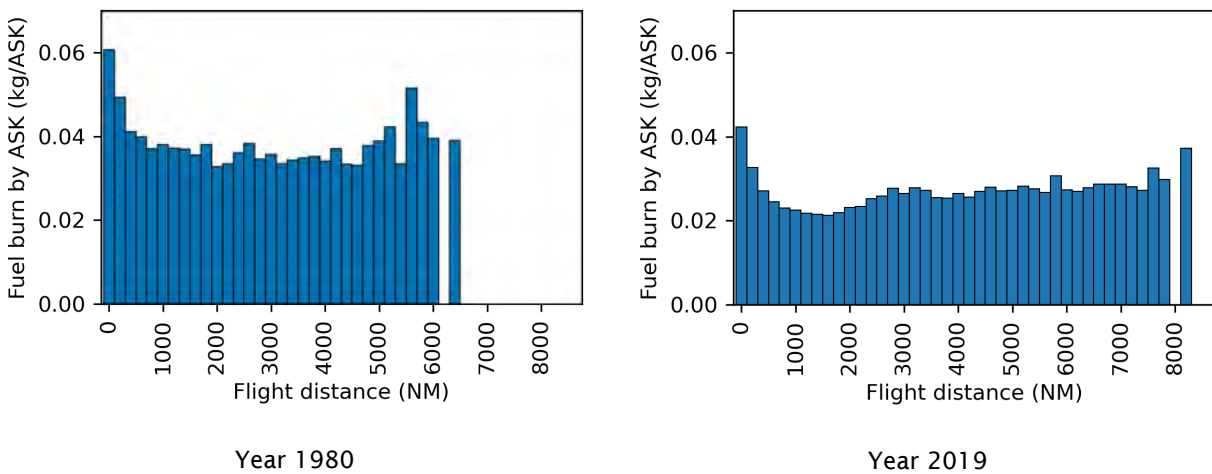


Figure 29. Fuel burn by ASK for various flight distance bands for the years 1980 and 2019.

Increased efficiency over this period was probably driven by a variety of factors, including improvements in technology, such as increasing engine efficiency and decreasing airframe weight and drag for similar aircraft sizes. In addition, aircraft seat capacities changed over this time. Figure 30 shows fuel burn by flight distance and number of seats. During this time, the total flight distance increased from 9.5×10^9 km to 53×10^9 km, representing an increase of 460%, whereas ASK increased by 560%, indicating more seats per flight on average.

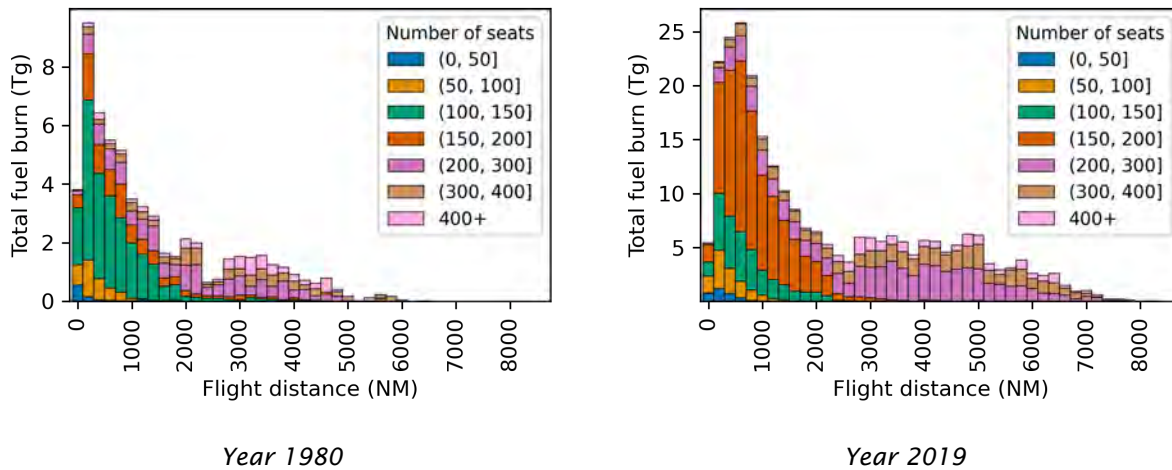


Figure 30. Fuel burn by number of seats and flight distance.

Finally, a manuscript was generated, aimed at highlighting how modeling factors can change the interpretation of air quality impacts resulting from aviation. This manuscript demonstrates that increases in model resolution can increase the total estimated air quality (health) impact resulting from aviation, and that older estimates based on low-resolution models might potentially have underestimated impacts by a factor as high as one quarter. The same manuscript also, through a series of atmospheric chemistry simulations, demonstrates that the impacts of aviation on air quality are inherently hemispheric and seasonal in nature.

Milestone

Continued work from the previous year, finalizing aspects of the emissions inventory.

Major Accomplishments

Updates were made to the emissions inventory, and a manuscript on the air quality impacts of aviation (including sensitivity to model specification) was submitted to the journal *Atmospheric Chemistry and Physics* for review.

Publications

AY 2021-2022:

- Grobler, Fritz, Allroggen, Eastham and Barrett. "Commercial civil aviation emissions from 1980 to the present day". Oral presentation covering the current progress on the historic emissions inventory, including preliminary emissions trends in region, time of day, and emissions index of NO_x, and nvPM. Presented at the 5th International Conference on Transport, Atmosphere, and Climate (TAC-5), June 2022.
- Prashanth, Speth, Eastham, Sabnis, and Barrett. "Aerosol formation pathways from aviation emissions". Oral presentation discussing the mechanisms by which aviation emissions cause aerosol-related radiative forcing. Presented at the 5th International Conference on Transport, Atmosphere, and Climate (TAC-5), June 2022.
- Prashanth, P., Eastham, S. D., Speth, R. L., & Barrett, S. R. (2022). Aerosol formation pathways from aviation emissions. *Environmental Research Communications*, 4(2), 021002.

AY 2022/23: No further publications

Outreach Efforts

Progress in all tasks was communicated during biweekly briefing calls with the FAA and reported in quarterly progress reports.

Awards

None.



Student Involvement

This emissions inventory work was performed by PhD student Carla Grobler. The air quality impact estimation was performed by co-P.I. Sebastian Eastham.

Plans for Next Period

During the next reporting period, the team plans to extend and finalize the emissions inventory by using a high-quality matching method based on data acquired from Cirrium. The team also plans to complete submission of a manuscript evaluating the role of resolution in understanding air quality impacts. Finally, the team will use these data to perform an evaluation of how changes in both aviation and non-aviation emissions over time have affected the estimated climate and air quality impacts of aviation.

References

- Agarwal, A. (2021). *Quantifying and reducing the uncertainties in global contrail radiative forcing* [Doctoral thesis, Massachusetts Institute of Technology].
https://dspace.mit.edu/bitstream/handle/1721.1/140372/agarwal_aa681_PhD_AeroAstro_thesis.pdf?sequence=1&isAllowed=y
- Ahrens, D., Méry, Y., Guénard, A., & Miake-Lye, R. C. (2022, June). A New Approach to Estimate Particulate Matter Emissions From Ground Certification Data: The nvPM Mission Emissions Estimation Methodology (MEEM). In *Turbo Expo: Power for Land, Sea, and Air* (Vol. 85994, p. V03AT04A035). American Society of Mechanical Engineers. Airlines For America (2022a). U.S. Airline Traffic and Capacity Online: <https://www.airlines.org/dataset/annual-results-u-s-airlines-2/>
- Airlines For America (2022b). World Airlines Traffic and Capacity Online: <https://www.airlines.org/dataset/world-airlines-traffic-and-capacity/>
- Bock, L., & Burkhardt, U. (2016). Reassessing properties and radiative forcing of contrail cirrus using a climate model. *Journal of Geophysical Research: Atmospheres*, 121(16), 9717-9736.
- Baughcum S. L., Henderson S. C., & Tritz T. G. (1996a). Scheduled Civil Aircraft Emission Inventories for 1976 and 1984: Database Development and Analysis
- Baughcum S. L., Tritz T. G., Henderson S. C. & Pickett D. C. (1996b). Scheduled Civil Aircraft Emission Inventories for 1992: Database Development and Analysis
- Fichter, C., Marquart, S., Sausen, R., & Lee, D. S. (2005). The impact of cruise altitude on contrails and related radiative forcing. *Meteorologische Zeitschrift*, 14, 563-572.
- Gilmore, C. K., Barrett, S. R., Koo, J., & Wang, Q. (2013). Temporal and spatial variability in the aviation NO_x-related O₃ impact. *Environmental Research Letters*, 8(3), 034027.
- Grobler, C., Wolfe, P. J., Dasadhikari, K., Dedoussi, I. C., Allroggen, F., Speth, R. L., ... & Barrett, S. R. (2019). Marginal climate and air quality costs of aviation emissions. *Environmental Research Letters*, 14(11), 114031.
- ICAO 2020 Presentation of 2019 Air Transport Statistical Results
- Lee, D. S., Fahey, D. W., Skowron, A., Allen, M. R., Burkhardt, U., Chen, Q., ... & Wilcox, L. J. (2021). The contribution of global aviation to anthropogenic climate forcing for 2000 to 2018. *Atmospheric Environment*, 244, 117834.
- Lund, M. T., Aamaas, B., Berntsen, T., Bock, L., Burkhardt, U., Fuglestedt, J. S., & Shine, K. P. (2017). Emission metrics for quantifying regional climate impacts of aviation. *Earth System Dynamics*, 8(3), 547-563.
- Olsen, S. C., Wuebbles, D. J., & Owen, B. (2013). Comparison of global 3-D aviation emissions datasets. *Atmospheric Chemistry and Physics*, 13(1), 429-441.
- Reynolds, T. (2008). Analysis of lateral flight inefficiency in global air traffic management. In *The 26th Congress of ICAS and 8th AIAA ATIO* (p. 8865).
- Sutkus, Donald J. *Scheduled Civil Aircraft Emission Inventories for 1999*: National Aeronautics and Space Administration, Glenn Research Center, 2001.
- Quadros, F. D., Snellen, M., Sun, J., & Dedoussi, I. C. (2022). Global civil aviation emissions estimates for 2017–2020 using ADS-B data. *Journal of Aircraft*, 59(6), 1394-1405.



Project 059(B) Jet Noise Modeling and Measurements to Support Reduced Landing/Takeoff Noise of Supersonic Aircraft Technology Development

**Georgia Institute of Technology
Gulfstream Aerospace Corporation**

Project Lead Investigator

Krishan K. Ahuja
Regents Professor
School of Aerospace Engineering
Georgia Institute of Technology
Atlanta, GA 30342
404-290-9873
Krish.Ahuja@ae.gatech.edu

University Participants

Georgia Institute of Technology (Georgia Tech)

- P.I.: Krishan K. Ahuja, Regents Professor
- FAA Award Number: 13-C-AJFE-GIT-060
- Period of Performance: October 1, 2022 to September 30, 2023
- Tasks:
 1. Consultation with the advisory panel
 2. Fabrication of a lobed mixer nozzle
 3. Test setup and experimental data acquisition
 4. Data dissemination
 5. Proposal for a follow-on effort for year 4
 6. Reporting and data dissemination

Project Funding Level

This project received \$250,000 from the FAA and \$250,000 of cost-sharing from Gulfstream Aerospace Corporation (GAC) for each of the three phases of this project. The total combined funding to date is \$1,500,000.

Investigation Team

Georgia Institute of Technology

Dr. Krishan Ahuja (P.I.)
Dr. Jimmy Tai (co-P.I.)
David N. Ramsey (graduate research assistant for a portion of the program and subsequently a National Science Foundation (NSF) Fellow working on fundamental issues related to the current project)

Georgia Tech Research Institute (GTRI)

Dr. Nicholas Breen (co-investigator and lead experimentalist)
Dr. Robert Funk (experimentalist)
Jackson Larisch (graduate research assistant)
Reagan Mayo (graduate research assistant for a portion of the program who has since graduated)

Project Overview

The overall goal of this project is to perform cost-effective supersonic transport jet noise research/technology experiments to enable low-, medium-, and high-fidelity jet noise prediction methods. The specific objective is to design experiments in collaboration with industry, NASA, the Department of Defense, the FAA, and modelers funded by the FAA to help develop improved jet noise prediction methods with reduced uncertainty and to enable the industry to design quieter supersonic jet engines with higher confidence regarding the noise that will be generated. In collaboration with Gulfstream Aerospace Corporation (GAC), Georgia Tech's industry partner on this project, a representative baseline nozzle design will be selected for experiments at Georgia Tech. The data acquired will consist of far-field noise, high-speed flow visualization, source location, and detailed mean and unsteady flow measurements.

The experimental data acquired by Georgia Tech will be provided to key stakeholders and other computational teams funded by the FAA to validate their computational simulations and to confirm that jet noise predictions based on semi-empirical and computational modeling approaches can be reliably used for jet noise evaluation.

This project has six tasks, as listed below. The task titles are self-descriptive and reflect the task objectives. A short objective statement, research approach, and summary of the accomplishments to date for each task are provided after each task description. However, to provide context for the tasks of the current period (Year 3), a brief summary of the tasks conducted in year 2 is provided below, which we refer to as Task 0. To avoid confusion in the numbering of tasks for Year 2 and Year 3, roman numerals are used to refer to the tasks of Year 2.

Task 0 – Summary of Year 2 Tasks

Georgia Institute of Technology

Task i - Consult with the advisory panel

This task has been completed.

Task ii - Define nozzle requirements and design tests

This task has been completed.

Task iii - Design and fabricate a baseline nozzle

This task has been completed.

Task iv - Set up test facility and acquire experimental data

The experimental facility is completely set up for our research program. All acoustic measurements in the GTRI Static Anechoic Chamber have been completed. The acquisition of particle image velocimetry (PIV) data for the unheated core jet has been completed. Flow visualization for the unheated core jet has also been completed. Halfway through the program, we suffered a few setbacks due to problems with the beamforming array as well as heat insulation of the flow diagnostics facility. The anechoic facility was not impacted by these setbacks, which allowed us to acquire acoustic data while the flow diagnostics facility was being repaired. Currently, both facilities are operational.

Task v - Disseminate data

The final model design was shared with the modeling teams in November 2021. All acoustic and PIV data, both for the unheated and heated core conditions, have been shared with the modelers. Likewise, the flow visualization has been made available to the modelers.

Task vi - Design and build a mixer for year 3 investigation

This task has been completed. Georgia Tech received new project models from GAC, including a new baseline axisymmetric nozzle and two internal forced mixers.



Task vii - Propose a follow-on effort for year 3

The proposal for Year 3 was submitted.

Task viii - Provide reports and disseminate data

All Year 2 reports (annual and quarterly) were submitted.

Task 1 – Consultation with the Advisory Panel

Georgia Institute of Technology

Objective

The objective of this task is to receive regular feedback from industry and NASA subject-matter experts in supersonic jet noise.

Research Approach

At the beginning of the Year 2 effort, a meeting was held with the entire Project 59 team and the advisory panel to discuss the direction of the research effort for the year. The Project 59B team continued to discuss the progress and direction of the project with the advisory panel throughout the effort. Most meetings were organized and conducted by Dr. Sandy Liu of the FAA.



Task 2 – Fabrication of a Lobed Mixer Nozzle

Georgia Institute of Technology

Objective

The objective of this task is to design and fabricate new nozzle geometries, including the use of internal forced mixers to be sent to the Georgia Tech team for testing.

Research Approach

To experimentally evaluate the effectiveness of lobed internal mixers in reducing jet noise, cost-sharing partners at GAC designed and fabricated model-scale nozzle geometries to be used by the Georgia Tech team in acquiring acoustic and flow measurements. Similar to the original Year 1 project models, the newly acquired models consist of a primary nozzle shrouded by an outer bypass nozzle. As before, the core and bypass streams mix within the confines of a variable-length mixing duct before exiting a final exhaust nozzle. New to these models is the inclusion of three different primary nozzle caps, as shown in Figure 1. Provided alongside a new baseline axisymmetric nozzle (AXI) are two internal lobed mixers, each with ten lobes and ten gullies. The less aggressive mixer (SUN) is visible on the left side of Figure 1, whereas the more aggressive mixer (DAISY) appears on the right. Figures 2-4 show various views of the model assembly installed in the GTRI Static Anechoic Chamber. The diameter or equivalent diameter of each primary nozzle is approximately 1.54 inches, and the diameter of the final exhaust nozzle is 2.20 inches.



Figure 1. Three internal mixers for the ASCENT 59B Year 3 nozzle. Top left: SUN forced mixer. Top right: DAISY forced mixer. Bottom: AXI baseline mixer.



Figure 2. Primary nozzle from Gulfstream Aerospace Corporation with the baseline AXI mixer installed at the Georgia Tech Research Institute Anechoic Chamber.

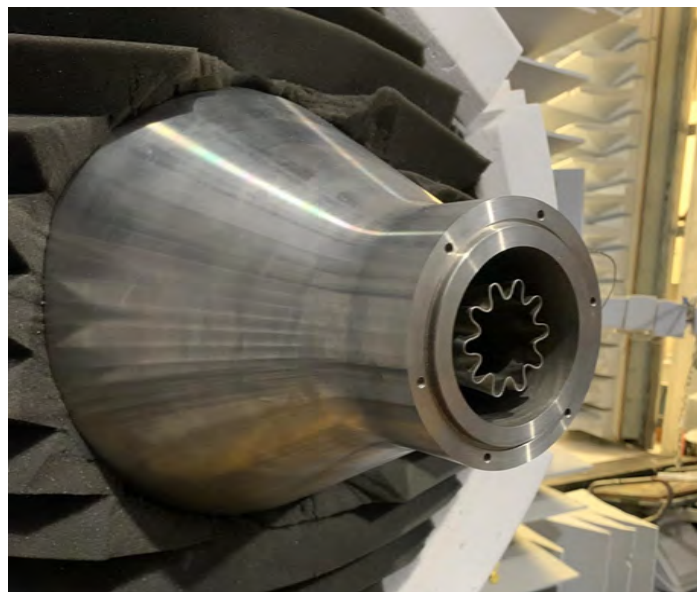


Figure 3. Nozzle assembly from Gulfstream Aerospace Corporation with the SUN mixer and bypass nozzle.



Figure 4. Full nozzle assembly from Gulfstream Aerospace Corporation at the Georgia Tech Research Institute Static Anechoic Chamber with an exhaust nozzle and mixing length of $L_e/D_e = 1.0$.

Task 3 – Test Setup and Experimental Data Acquisition

Georgia Institute of Technology

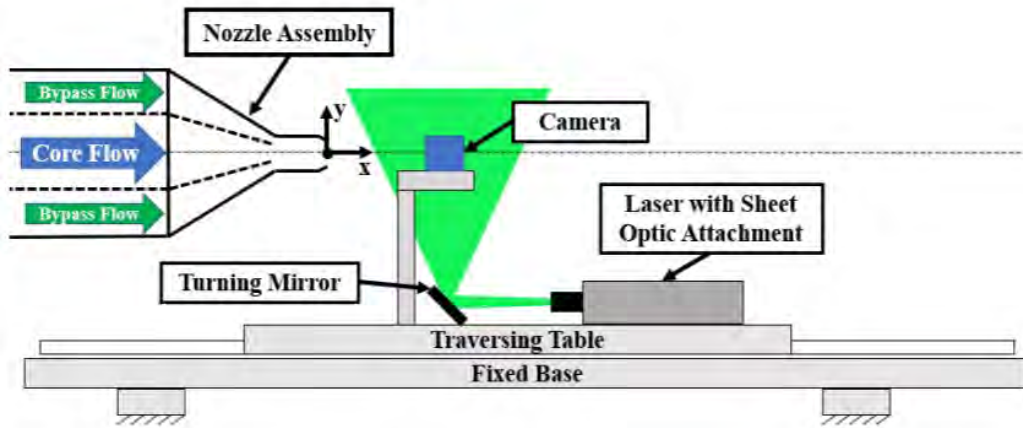
Objective

The objective of this task was to complete the acquisition of flow data using the Year 1 project models started during the previous year and to then begin the process of acquiring acoustic and flow measurements using the new models obtained from GAC.

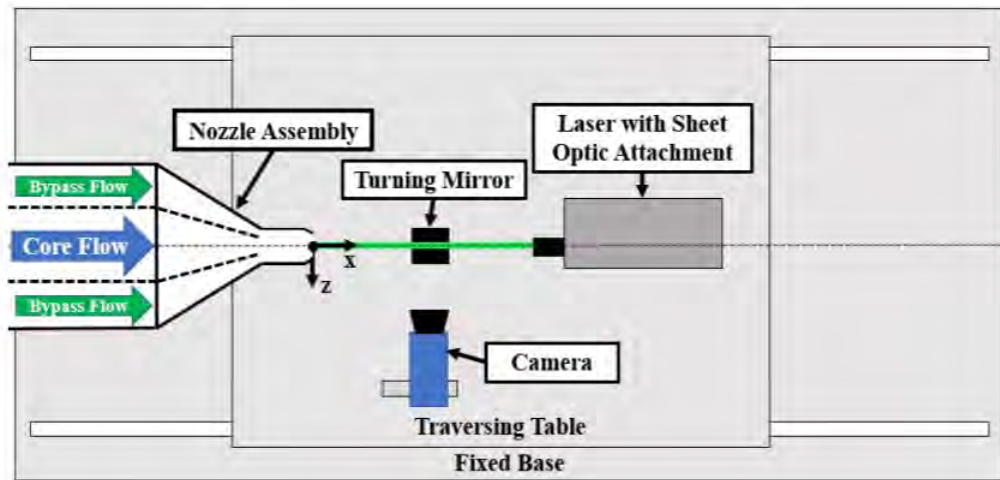
Research Approach

Heated Core Stream PIV Measurements

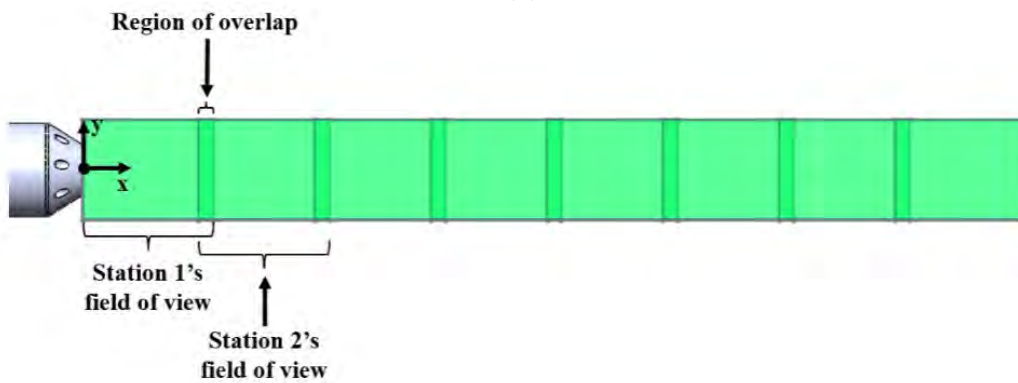
Following the insulation repair in the GTRI Flow Diagnostics Facility earlier in the year, work was completed in acquiring flow visualization data with the jet operating under heated core conditions. These data were acquired using the original Year 1 nozzle. The PIV data were acquired using the same double-pulsed, two-dimensional PIV system as has been previously reported. The details of the GTRI Flow Diagnostics Facility have been reported by Burrin et al. (1979), with salient details repeated here for completeness. The Flow Diagnostics Facility is a sister facility to the GTRI Anechoic Jet Facility, with identical plenum interfaces and identical plenum-to-nozzle area contraction ratios. The PIV system is shown schematically in Figure 5. Figures 5a and 5b show side-view and top-down-view schematics of this system, respectively. Figure 5c illustrates the camera's nominal field of view at each of the stations along the traverse. In selecting the time delay between image pairs, an optimization routine built into the DaVis software was used. The DaVis software is LaVision proprietary PIV software that is used for data acquisition and post-processing. This routine recommends a time delay between image pairs based in part on the peak Q-ratio (the ratio of highest and second highest correlation peak values) for several different time delays. A low Q-ratio indicates that a particle displacement cannot be accurately predicted from the correlation plane of a given image pair in a given interrogation window.



(a)



(b)



(c)

Figure 5. Particle image velocimetry system: (a) side view, (b), top-down view, and (c) multi-station acquisition scheme.

The measured instantaneous velocity fields may contain spurious velocity vectors. Spurious vectors are characterized as having an exceedingly large or small magnitude and/or erroneous direction relative to the expected velocity vector. Of course, the expected vector field is not known a priori, and criteria for identifying these spurious vectors must be employed. In this work, spurious vectors are detected and rejected at two different stages of the data-processing routine. First, the instantaneous velocity fields are screened in a processing stage referred to as vector post-processing. A filtering operation is used to detect and replace vectors that have a large deviation from their neighbors. As part of the PIV data processing routine in the LaVision DaVis software, a median filter was applied to reject spurious velocity vectors from each measured snapshot of the flow. This filtering operation is based on the framework of a dynamic mean value operator (Raffel et al., 2018).

In particular, this step involved removing vectors that had a difference in the local mean outside of one standard deviation of the neighboring vectors. For vectors that failed to satisfy the criterion, the median of the neighbors was used to replace the vector. This filter was applied twice to each instantaneous velocity field. Further, a range of acceptable particle displacements was specified. Finally, any instantaneous vectors whose associated Q-ratio was less than 2.0 were deleted. The success of these vector post-processing operations in removing outliers without modifying the remainder of the velocity field is shown for a single instantaneous velocity field in Figure 6. The top frame shows the result without the vector post-processing routine, and the bottom frame shows the same field with the vector post-processing routine executed; both cases use the same color scaling shown on the far right. This vector field is a measurement across the shear layer of the jet from the core nozzle in isolation operated at $M_j = 0.58$, unheated, with the jet flowing from left to right in the figure.

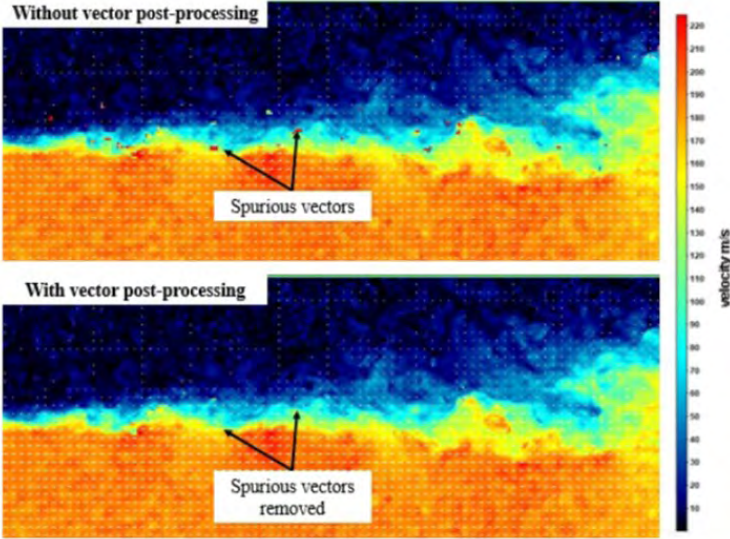


Figure 6. Success of vector post-processing in replacing spurious vectors. Both frames show the same region of the shear layer of the jet from a single nozzle in isolation, $M_j = 0.58$, unheated.

Ensemble averaging of the PIV measurements also includes applying Chauvenet’s criterion for spurious vector (i.e., outlier) rejection. This step only has an appreciable impact on the measurements of velocity fluctuation (i.e., turbulence intensity), with relatively small changes to the mean velocity measurements. Chauvenet’s criterion was reported to be used by Bridges and Wernet (2011) and is a sample-size-dependent criterion that suggests thresholds outside of which values are unlikely to be sampled. If values are measured outside of these thresholds, the data are considered outliers. In each PIV interrogation window across all instantaneous velocity fields being ensemble-averaged, Chauvenet’s criterion is applied to each component of the measured velocity vectors. This criterion assumes that the measured velocities within each interrogation window are sampled from a Gaussian parent distribution. However, a reader astute in turbulent flows would likely dispute this assumption, and rightfully so. It is known that the turbulent velocities in a free shear layer do not always follow a Gaussian distribution, as discussed in greater detail by Pope (2000). In particular, the probability density function

of velocity at a point may have non-zero skewness, whereas a Gaussian distribution would have zero skewness. This potential criticism is acknowledged; however, a Gaussian probability density function of velocities is not assumed except for the computation of outlier rejection thresholds. Figure 7 displays histograms of displacement in units of pixels, as acquired via the PIV measurement system. This figure shows that the use of Chauvenet’s criterion correctly flags obviously spurious vectors (at the tips of the red arrows) without wrongly flagging seemingly trustworthy vectors (based on their presence in a larger distribution of data). Presenting the displacement histogram in units of pixels serves the secondary purpose of providing evidence that the PIV measurements are not impacted by peak-locking effects. If peak-locking were present in the data, the displacement vectors would be biased toward integer displacement values (Raffel et al., 2018). Demonstrating this fact is vital to the integrity of the fluctuating velocity measurements produced, as Christensen (2004) showed that peak-locking may strongly impact second-order velocity statistics (i.e., the standard deviation of velocity reported in the present work).

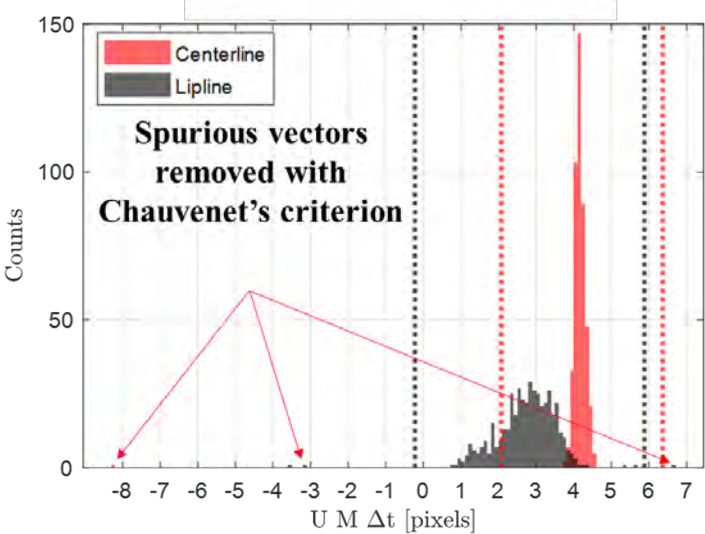


Figure 7. Histogram of axial displacement along the lipline ($x/D_e = 0.7$, $y/D_e = 0.5$, $N = 1,500$ image pairs) of the jet from a single nozzle ($M_j = 0.58$, unheated). Vertical lines show Chauvenet’s criterion boundaries.

Once the facility was fully repaired, mean velocity and turbulence intensity profiles were compared with the results previously acquired using the old insulation to demonstrate that the data gathered before and after the change in insulation were comparable. Figure 8 shows the agreement in mean flow and turbulence intensity measurements between PIV data acquired previously using the old insulation and data acquired this year following the facility repair.

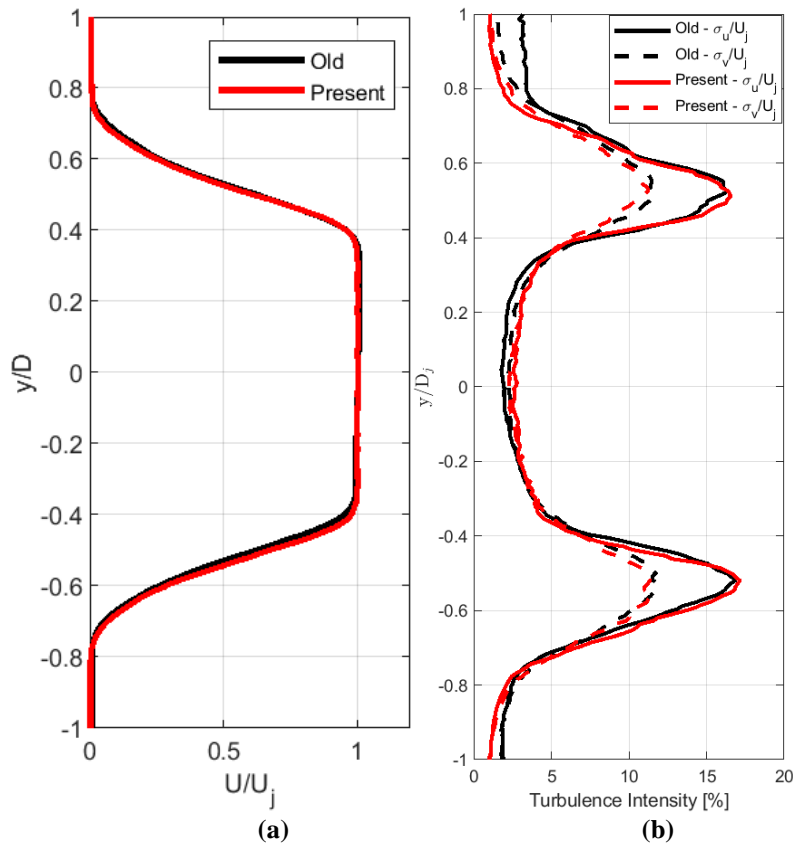


Figure 8. Comparison of (a) mean and (b) turbulence intensity profiles at a downstream distance of $x/D_e = 2$ for the previous and present insulation. $PR_1 = 1.52$, $PR_2 = 1.52$, $L_e/D_e = 0.7$, unheated.

Six heated conditions were selected for the confluent nozzle with both the shortest ($L/D_e = 0.7$) and longest ($L/D_e = 3.0$) mixing length. Only non-resonating conditions were chosen, as these conditions are most useful to modelers; these conditions are shown in Figure 9. Two conditions for each mixing length were acquired with a high number of samples (750 samples) to allow for accurate turbulence measurements. These conditions are $PR_1 = PR_2 = 1.39$ and $PR_1 = 1.39, ER = 1.07$. For mean flow measurements, all other conditions were acquired at a lower number of samples (200), sufficient for capturing mean statistics of the flow. Performing quality PIV measurements requires considerable time, care, and effort, but this directly results in high-quality heated flow data for modelers. Such efforts include ensuring that the core jet is parallel to the traverse axis within a fraction of a degree, that there is <0.5 mm precision on hardware interfacing to ensure flow symmetry, and a rigorous PIV laser and camera alignment system to ensure good stitching between data gathered at varied traverse locations. The results of these efforts are presented below.

Tt1 = 500 deg F		Primary Pressure Ratio, PR1			
		1.39 (M _μ =0.7)	1.52 (M _μ =0.8)	1.69 (M _μ =0.9)	1.89 (M _μ =1.0)
PR2	1.39 (M _μ =0.7)	ER = 1.00	ER = 0.91	ER = 0.82	ER = 0.73
	1.52 (M _μ =0.8)	ER = 1.10	ER = 1.00	ER = 0.90	ER = 0.91
	1.69 (M _μ =0.9)	ER = 1.22	ER = 1.11	ER = 1.00	ER = 1.89
	1.89 (M _μ =1.0)	ER = 1.36	ER = 1.24	ER = 1.12	ER = 1.00
ER	1.04	PR2 = 1.44			
	1.07	PR2 = 1.48			

Figure 9. Data matrix for heated particle image velocimetry conditions.

Although data for many (12) flow conditions were gathered using PIV, we discuss the results of only one condition in detail below for the sake of brevity. In particular, the plots for the heated condition with $PR_1 = PR_2 = 1.39$ are discussed for the confluent nozzle with a mixing length of $L_e/D_e = 0.7$, as both mean and turbulence statistics are gathered for this condition. The two-dimensional mean and turbulence intensity plots are shown in Figure 10. Note that a thin region near the nozzle exit has been masked off from the final PIV data to reject the effects of reflections off the nozzle. The length of this mask ranges from $x/D_e = 0$ to approximately 0.3-0.5 depending on the intensity of the reflections.

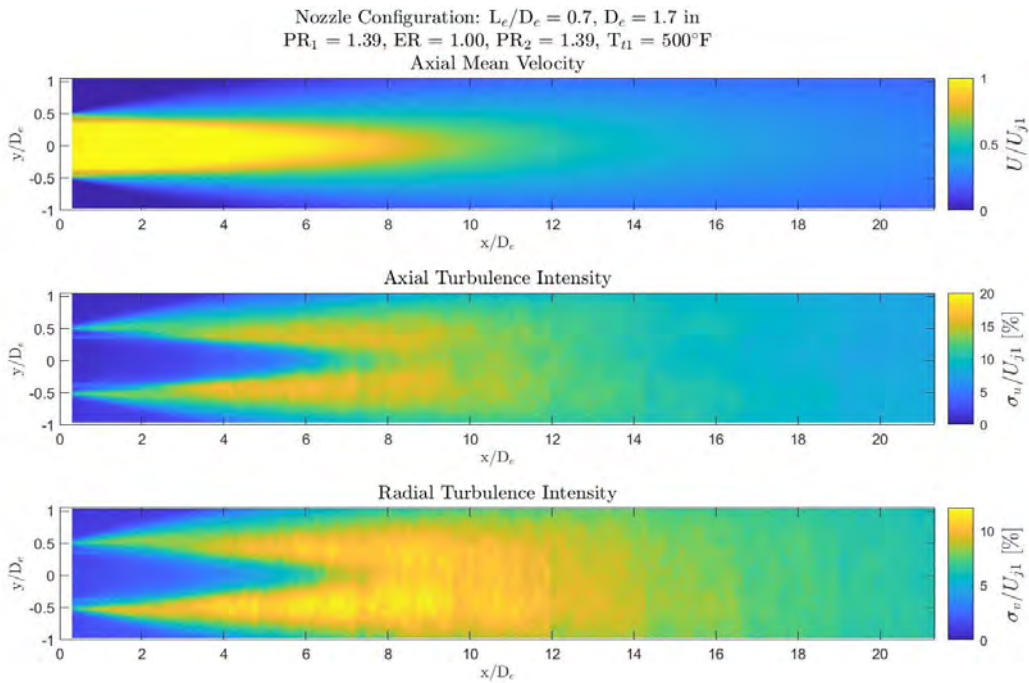
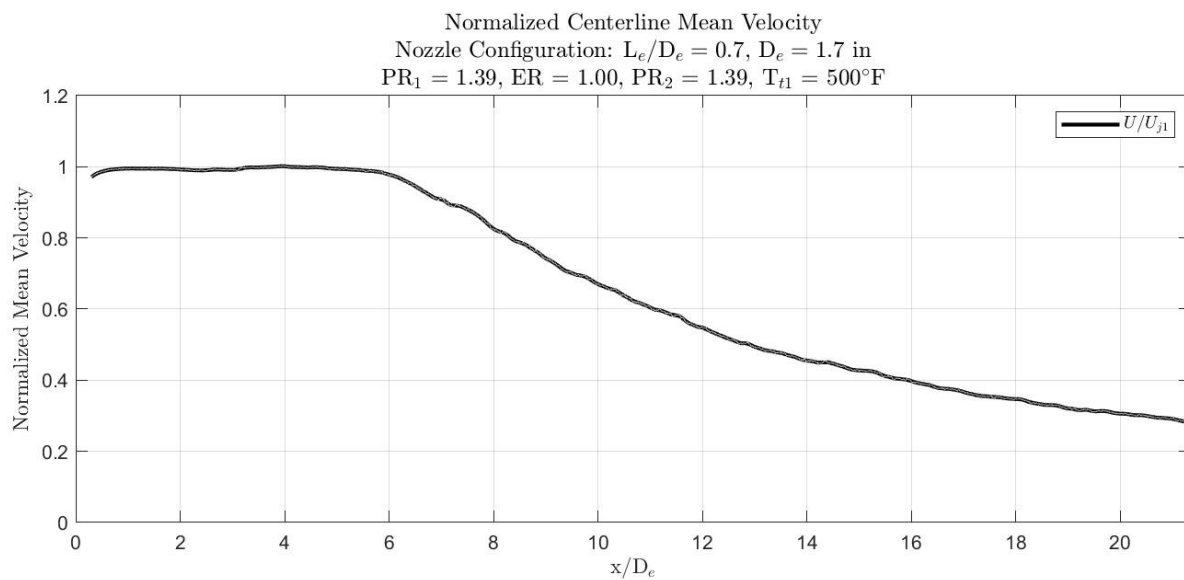
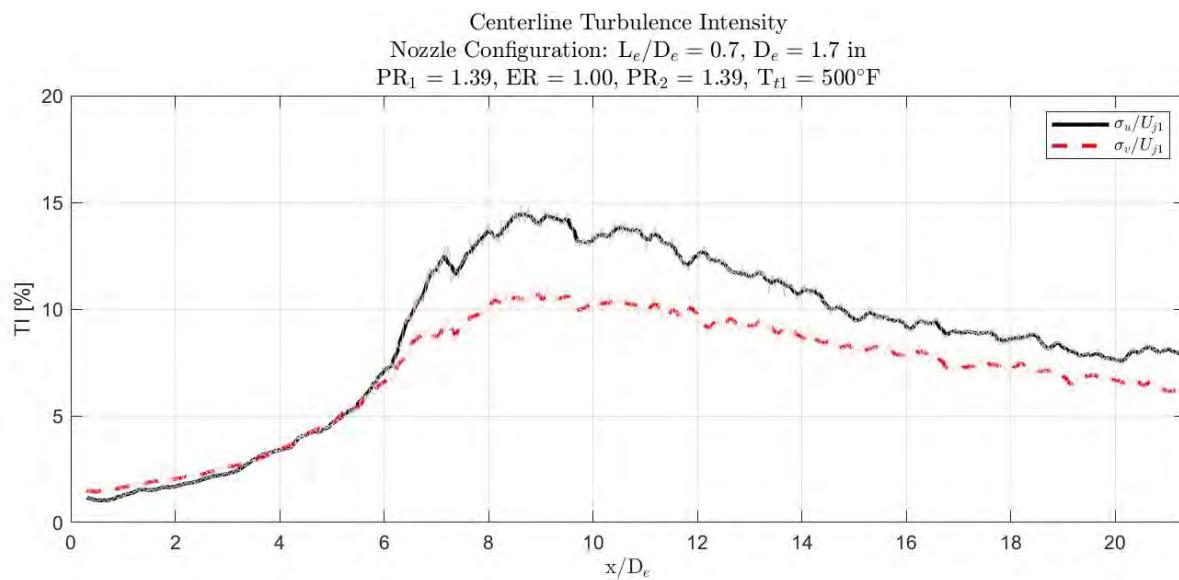


Figure 10. Two-dimensional mean and turbulence intensity plots. $PR_1 = 1.39$, $PR_2 = 1.39$, $T_{t1} = 500^\circ\text{F}$, $L_e/D_e = 0.7$, $N = 750$ image pairs.



(a)



(b)

Figure 11. Centerline profiles of (a) mean velocity and (b) turbulence intensity (TI) of the confluent nozzle. $PR_1 = 1.39$, $PR_2 = 1.39$, $T_{t1} = 500^\circ\text{F}$, $L_e/D_e = 0.7$, $N = 750$ image pairs.

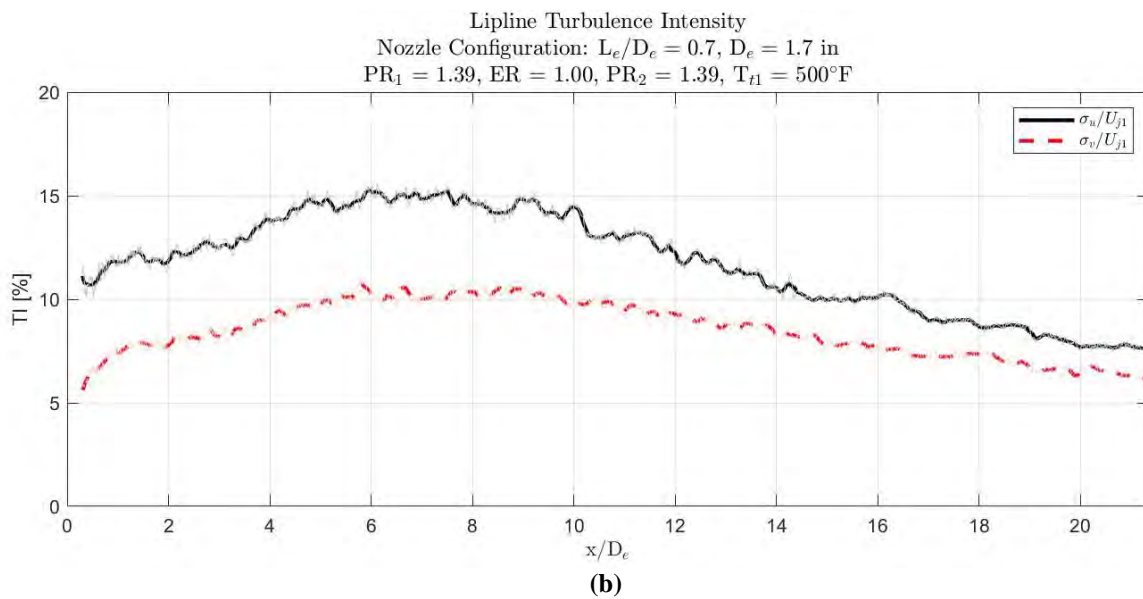
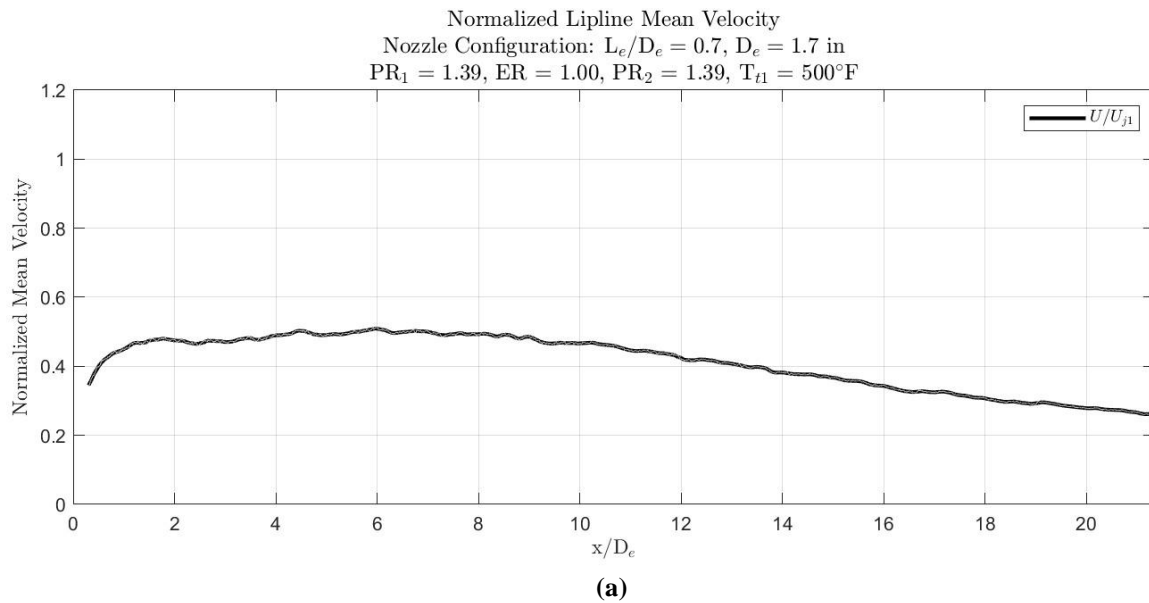


Figure 12. Lipline profiles of (a) mean velocity and (b) turbulence intensity (TI) of the confluent nozzle. $PR_1 = 1.39$, $PR_2 = 1.39$, $T_{t1} = 500^\circ\text{F}$, $L_e/D_e = 0.7$, $N = 750$ image pairs.

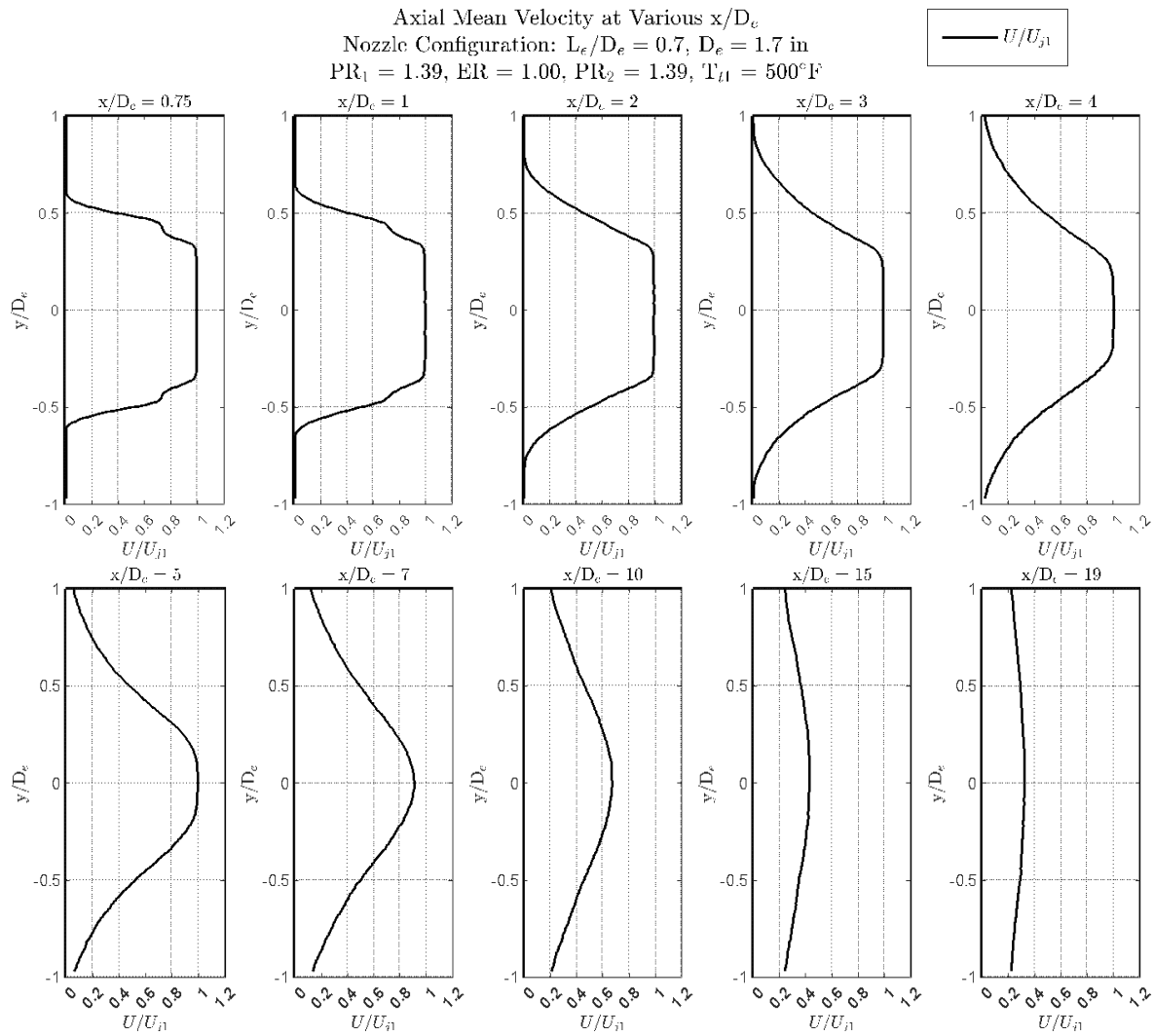


Figure 13. Mean axial velocity profiles at various downstream locations. $PR_1 = 1.39$, $PR_2 = 1.39$, $T_{t1} = 500^\circ\text{F}$, $L_e/D_e = 0.7$, $N = 750$ image pairs.

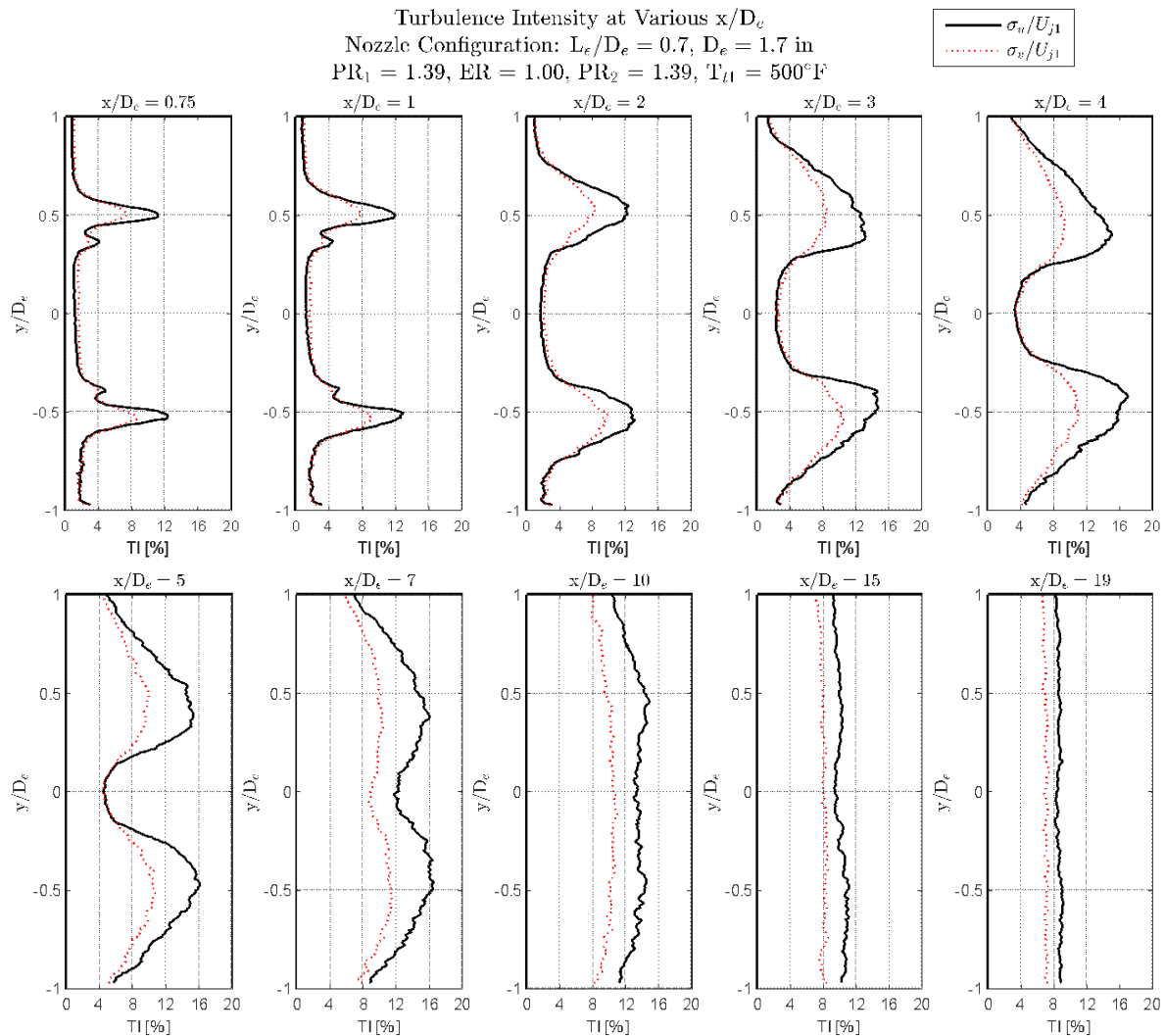


Figure 14. Turbulence intensity (TI) profiles at various downstream locations. $PR_1 = 1.39$, $PR_2 = 1.39$, $T_{t1} = 500^\circ\text{F}$, $L_e/D_e = 0.7$, $N = 750$ image pairs.

As shown in Figures 10 and 11a, the length of the potential core is approximately six exhaust-nozzle diameters, after which the centerline velocity gradually decays. This termination of the potential core is reflected in the centerline turbulence intensity measurements provided in Figure 11b. Beyond the tail end of the potential core, the turbulence intensity rapidly increases. The axial mean velocity profiles shown in Figure 13 demonstrate the entrainment of ambient air into the jet and the decay of the potential core over a range of x/D_e . Similar results in Figure 14 show the evolution of turbulence intensities as one traverses downstream. Near the nozzle, the peak turbulence intensity is localized to the lip lines of the exhaust nozzle and core nozzle. As the shear layer develops downstream, the turbulence intensity becomes more uniformly distributed across the jet, especially past the end of the potential core.



Heated core stream high-speed schlieren visualization

GTRI's Z-shaped schlieren setup is shown in Figure 15. An arc lamp light source emits light that follows a z-shaped path along a series of mirrors and lenses. The light source is positioned at the focal point of the first parabolic mirror, sending collimated light into the test section (the horizontal region between the two parabolic mirrors). The second parabolic mirror focuses the light rays (now refracted by density gradients within the test section) to a focal point. At the appropriate focal point, a knife edge cutoff is positioned in one of two orientations: vertical (knife edge normal to the jet axis) or horizontal (knife edge parallel to the jet axis). These two knife edge orientations reveal axial and transverse density gradients in the test section, respectively. The light is then passed through a pair of refocusing lenses that allow the camera to be placed far from the jet, which may be heated, in order to protect the camera. The schlieren images are captured on a Vision Research Phantom V2512 monochrome ultra-high-speed camera. While only short 100-frame videos are being released to the modelers, 2,500 images were recorded for each condition, and the longer-duration measurements are available upon request.

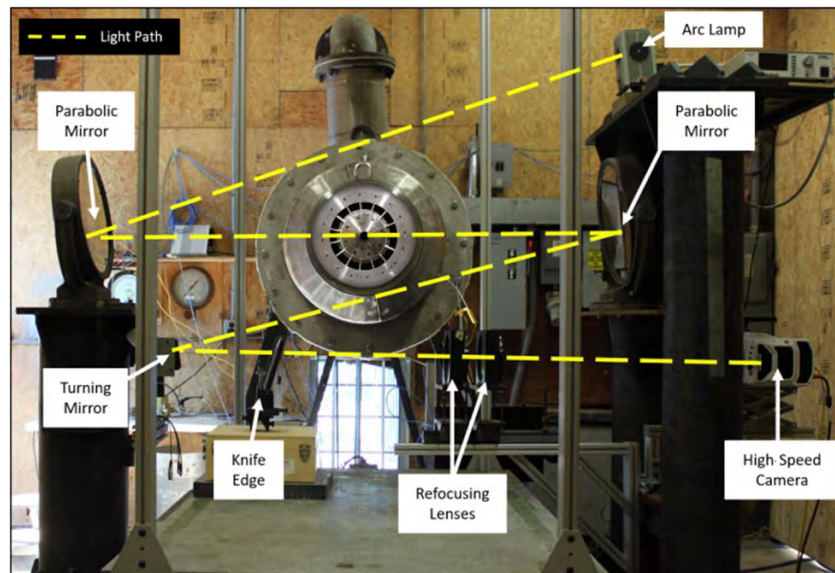


Figure 15. The Z-shaped schlieren setup at Georgia Tech Research Institute.

Time-resolved schlieren visualizations were recorded for each of the six heated core conditions identified in Figure 9 for both the shortest ($L_e/D_e = 0.7$) and longest ($L_e/D_e = 3.0$) mixing lengths. The resulting visualizations acquired using both mixing lengths are remarkably similar, as shown in Figure 16. This similarity indicates that the noise of the two mixing lengths will also be unchanged, as found above. These results are in agreement with the trends in the measured farfield noise of axisymmetric confluent nozzles reported by Ramsey et al. (2022), that is, the mixing length of the nozzle has little effect on the noise, and consequently, little mixing occurs upstream of the baseline exhaust nozzle exit in either case. For the sake of brevity, representative frames from only a single operating condition are shown.

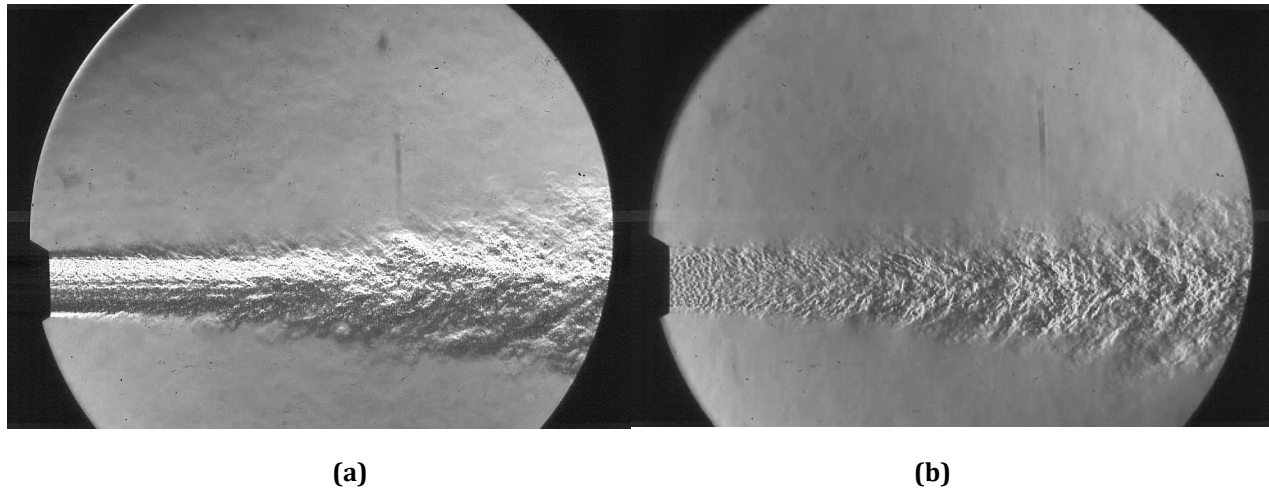


Figure 16. Schlieren flow visualization for $L_e/D_e = 0.7$ at $PR_1 = 1.39$, $ER = 1.07$, $T_{t1} = 500$ °F: (a) transverse density gradients and (b) axial density gradients. 1.5- μ s exposure, $f_s = 44$ kHz.

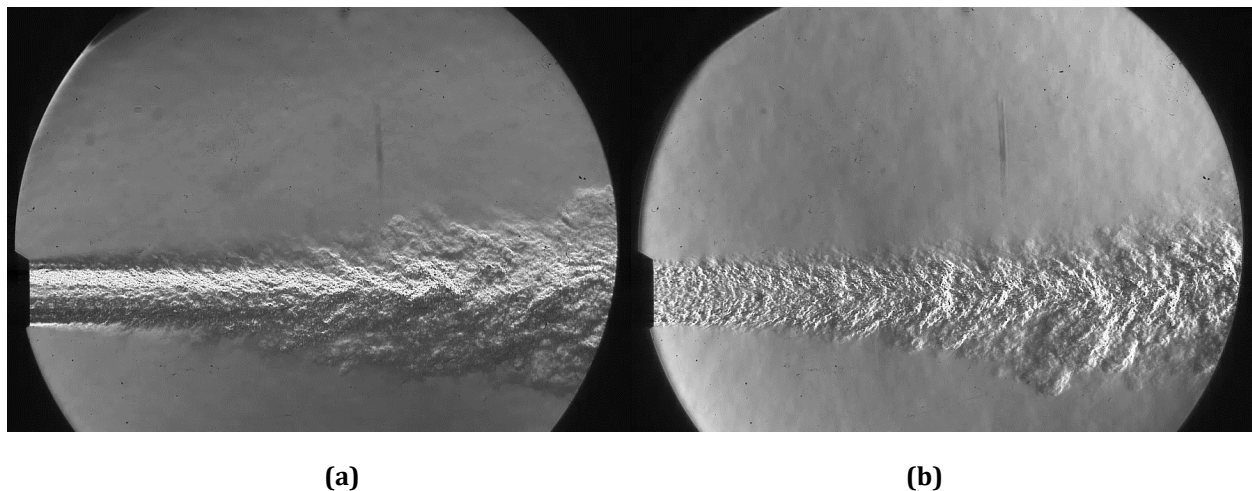


Figure 17. Schlieren flow visualization for $L_e/D_e = 3.0$ at $PR_1 = 1.39$, $ER = 1.07$, $T_{t1} = 500$ °F: (a) transverse density gradients and (b) axial density gradients. 1.5- μ s exposure, $f_s = 44$ kHz.

The results presented above were obtained for the baseline axisymmetric confluent nozzle. The nozzles used in this case were the Year 1 nozzles. Results for the new confluent baseline nozzles and lobed mixer nozzles of equivalent area are presented below.

Acoustic measurements of lobed mixer nozzles

Facility setup and testing

Acoustic measurements using the new testing models were collected in the GTRI Static Anechoic Chamber. This facility has been described in detail by Burrin et al. (1974), Burrin and Tanna (1979), and Ahuja (2003). Figure 18 shows the definitions of the polar (θ) angle and radial coordinate used in positioning the microphones in the jet facility. Farfield microphones were mounted on three polar arcs at angles between 30° and 120° with respect to the jet axis in 10° increments using the convention shown in Figure 18. The three arcs are offset by 45° along the azimuthal direction. The jet upstream conditions were set by controlling the ratio of the total pressure to the ambient pressure ($PR = p_t/p_a$) for both the primary and



secondary streams. Both the primary and secondary streams were varied between pressure ratios of 1.12 and 1.89. The extraction ratio ($ER = p_{t2}/p_{t1}$) was used as another parameter to define the secondary pressure ratio for a given primary stream pressure. Per insight and advice received from GAC and FAA, extraction ratios between 1.00 and 1.07 are the most realistic conditions for a given PR_1 for mixed-flow conditions. In unheated tests, the primary total temperature varied between 60 °F and 70 °F; during heated testing, the temperature was set nominally to 500 °F. As a note, in this program, the pressure ratio, PR, refers to the ratio between the upstream total and ambient pressures. In addition to acoustic measurements, the primary and secondary total pressure and temperature, the primary and secondary mass flow rates (measured at the control valve), and the ambient pressure, temperature, and relative humidity were measured.

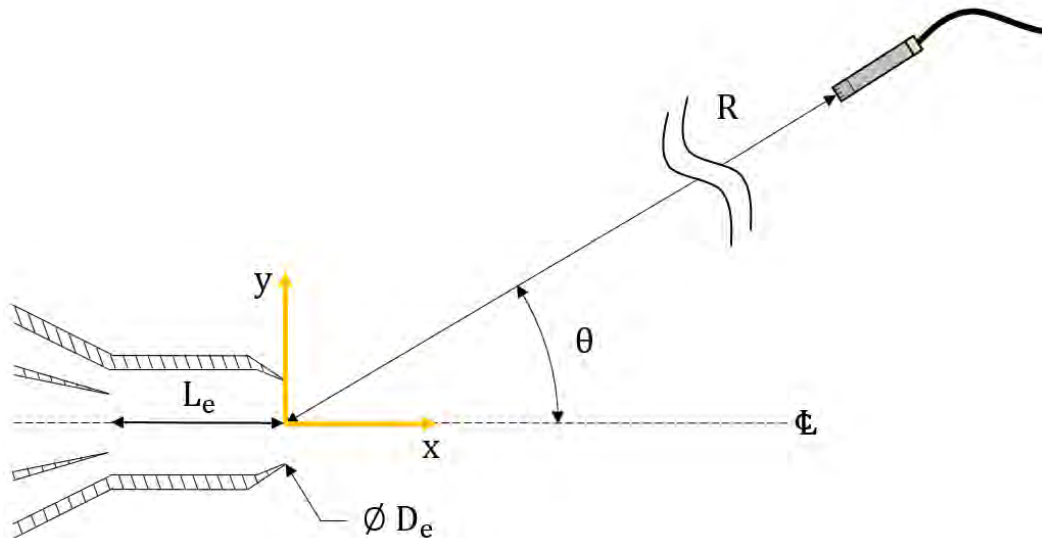


Figure 18. Project model coordinate conventions.

GTRI used two types of microphones that have the same performance. The first type of microphones are Bruel and Kjaer (B&K) 4939 ¼-inch free-field microphones, which are attached to B&K 2669 preamplifiers. The B&K microphone-preamplifier combinations are connected to B&K 2960-A-0S4 Nexus conditioning amplifiers that, in addition to amplifying the signal, act as a 200-mV power supply for the microphones. The second type of microphones are PCB Piezotronics Type 378C01 pre-polarized ¼-inch free-field microphones. These microphones utilize the integrated electronics piezo-electric (IEPE) capability powered directly from the data acquisition modules without a separate power supply. The microphone signals are sampled at 204.8 kHz via NI PXIe-4499 modules. The acoustic pressure time histories are then processed into averaged sound pressure level (SPL) spectra with a window size of 6,400 samples, 50% overlap, and a Hanning window. To render the data in a lossless form for use by modelers, the following corrections are applied to the SPL spectra: free-field response correction, windsock correction (if necessary), atmospheric attenuation, and distance correction. These corrections have been described in detail by Karon (2016).

Single-stream lobed nozzle acoustics

It is worth noting that all PIV and flow visualization data reported up to this point have corresponded to the Year 1 nozzle. We shall now transition our focus to the new nozzles acquired from GAC. Data collection with these models began with acoustic measurements in the GTRI Static Anechoic Chamber. To establish a baseline for comparison with later data and to prepare for the collection of dual-stream acoustic measurements, the primary jet was operated without the use of the secondary stream (e.g., as shown in Figure 2), and acoustic measurements were collected for the single-stream jet using each of the primary nozzle caps shown in Figure 1. During this testing, the jet Mach number M_j was varied from 0.5 to 1.0 in increments of 0.1 with the stream unheated ($T_{t1} \approx 60$ °F–70 °F). Figures 19–21 show the effect of both lobed nozzles on the noise produced by a single unheated jet at various observation angles. The effect of these mixers on the overall SPL (OASPL) is shown in Figure 22. Data are shown in black, blue, and red for the baseline axisymmetric AXI nozzle, the SUN lobed nozzle, and the more aggressive DAISY lobed nozzle, respectively. For a downstream polar observation angle of $\vartheta =$



30°, the SUN mixer reduces jet noise at the peak frequency by approximately 5.5 dB whereas the DAISY mixer reduces the noise by approximately 10 dB relative to the AXI baseline. While more effective at reducing the peak SPL, the DAISY mixer produces considerably more high-frequency noise, which is especially apparent at the sideline observation angle (Figure 21). This increase in high-frequency noise is less prevalent for the SUN mixer. A reduction in peak jet noise at the cost of enhanced higher-frequency noise is to be expected of enhanced jet-mixing devices.

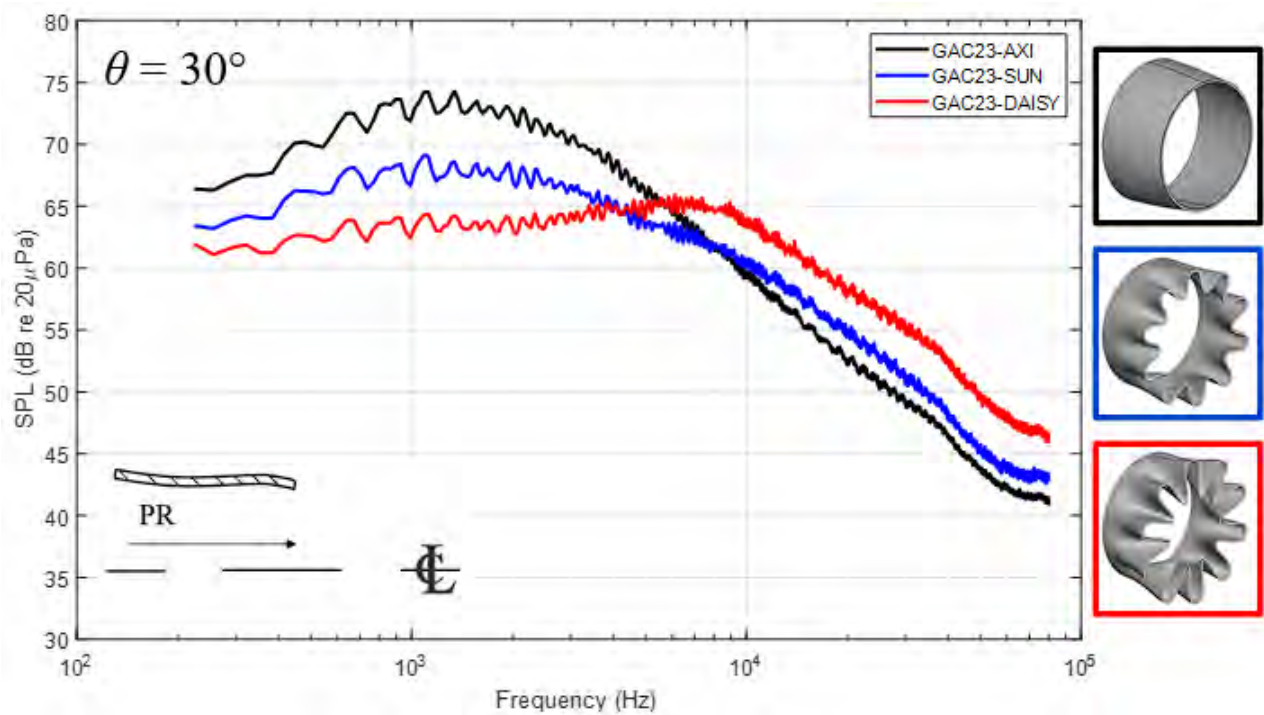


Figure 19. Effect of a lobed nozzle on the noise from a single-stream jet. FAA Gulfstream Aerospace Corporation (GAC) Project Model, D = 1.54 in. PR = 1.39 ($M_j = 0.70$), unheated, R = 12 ft, $\theta = 30^\circ$, $\Delta f = 32$ Hz, lossless. SPL: sound pressure level.

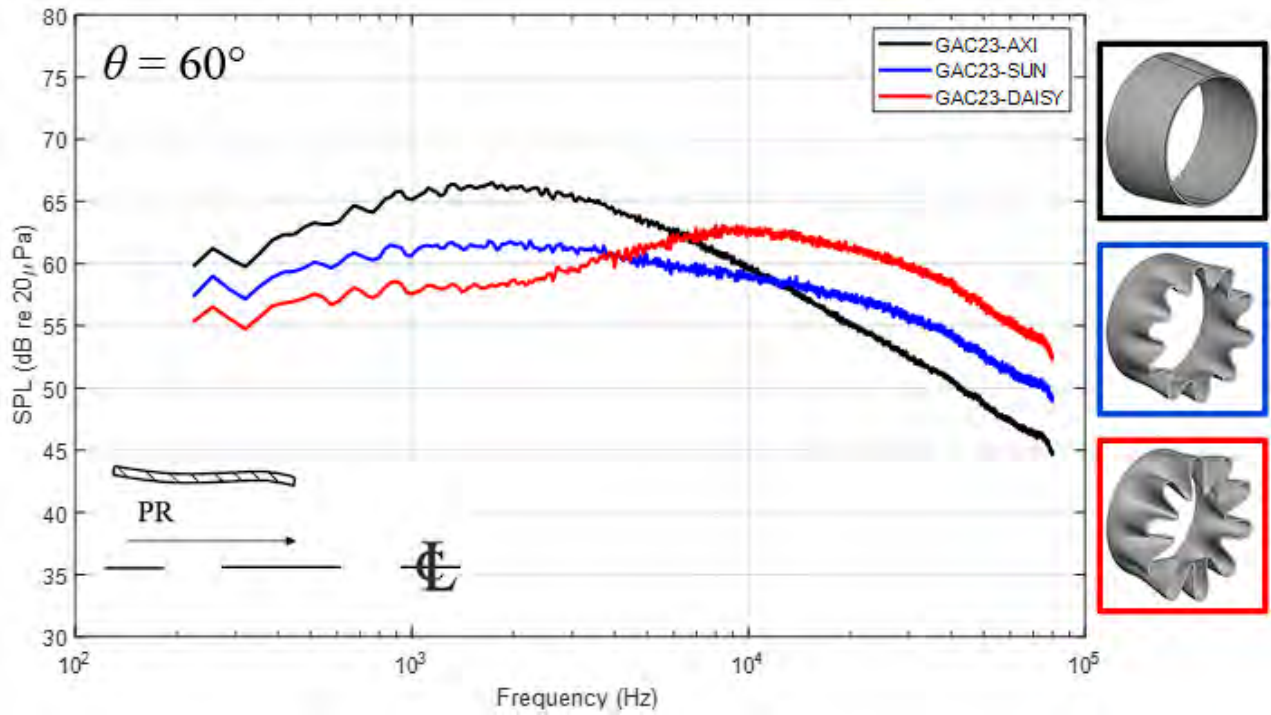


Figure 20. Effect of a lobed nozzle on the noise from a single-stream jet. FAA Gulfstream Aerospace Corporation (GAC) Project Model, D = 1.54 in. PR = 1.39 ($M_j = 0.70$), unheated, R = 12 ft, $\theta = 60^\circ$, $\Delta f = 32$ Hz, lossless. SPL: sound pressure level.

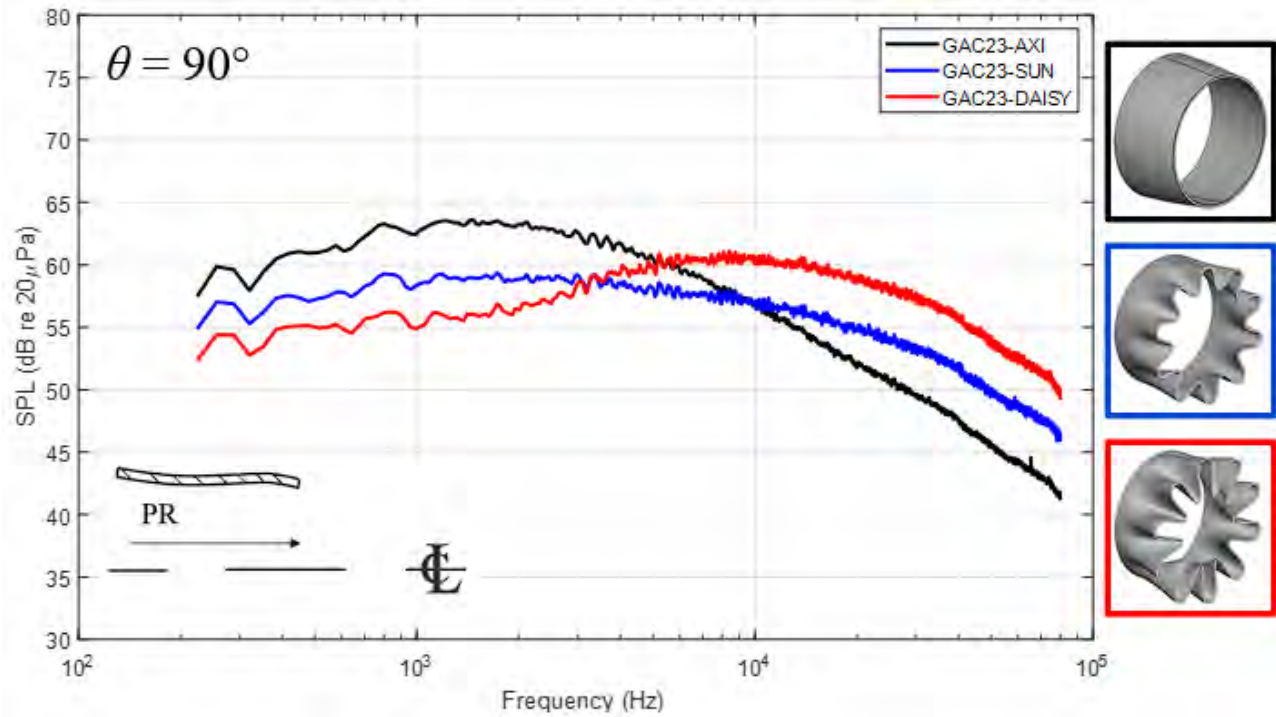


Figure 21. Effect of a lobed nozzle on the noise from a single-stream jet. FAA Gulfstream Aerospace Corporation (GAC) Project Model, D = 1.54 in. PR = 1.39 ($M_j = 0.70$), unheated, R = 12 ft, $\theta = 90^\circ$, $\Delta f = 32$ Hz, lossless. SPL: sound pressure level.

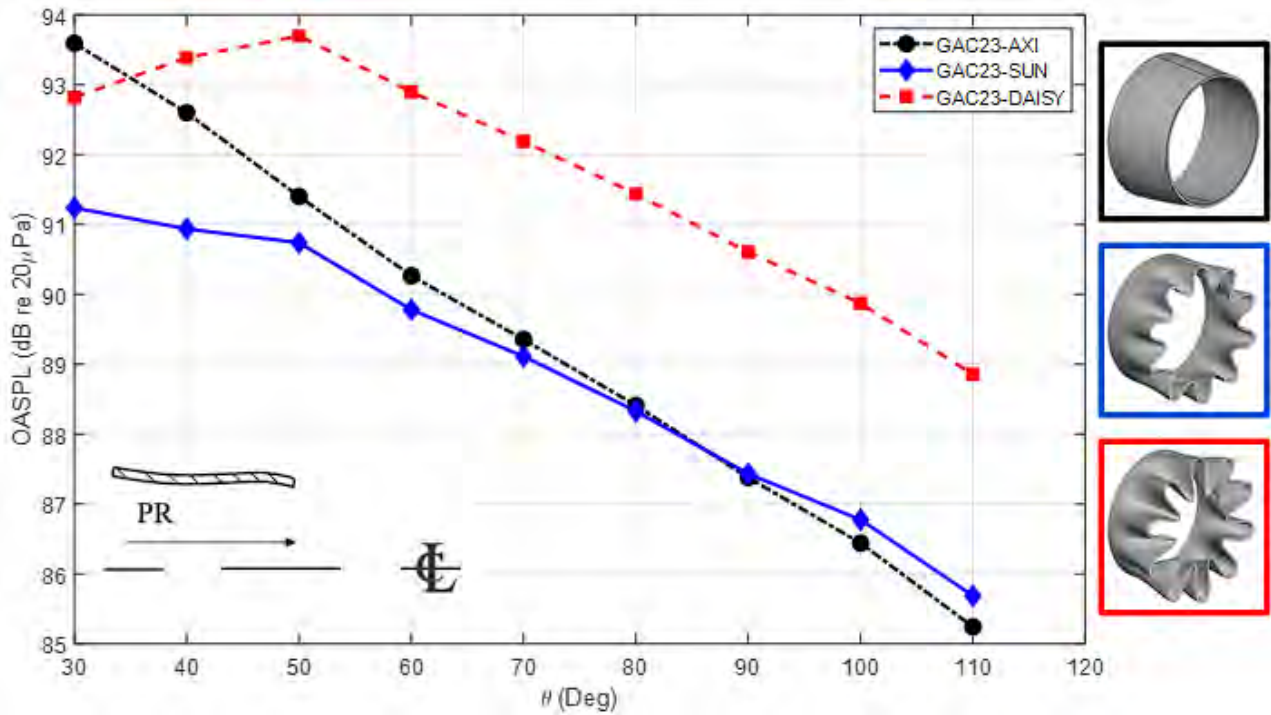


Figure 22. Effect of a lobed nozzle on the overall noise from a single-stream jet. FAA Gulfstream Aerospace Corporation (GAC) Project Model, $D = 1.54$ in. $PR = 1.39$ ($M_j = 0.70$), unheated, $R = 12$ ft, $\Delta f = 32$ Hz, lossless. OASPL: overall sound pressure level.

To prepare for the collection of dual-stream acoustic data, acoustic spectra were compared along a sideline observation angle to determine whether any azimuthal directivity is present in the noise produced by these lobed nozzles. Figure 23 shows the orientation of the three farfield microphone arrays with respect to the orientation of the lobed nozzles. Note that the lobed geometry shown is arbitrary and is not drawn to scale. The high-azimuth farfield (HF) and low-azimuth farfield (LF) polar arcs are intentionally aligned with the lobes in the same manner to assess whether any changes in noise relative to the middle-azimuth farfield (MF) arc are within the range associated with random measurement error. As demonstrated in Figures 25-27, the farfield noise generated by these lobed nozzles at sideline angles is no more azimuthally dependent than that of the baseline axisymmetric nozzle (AXI).

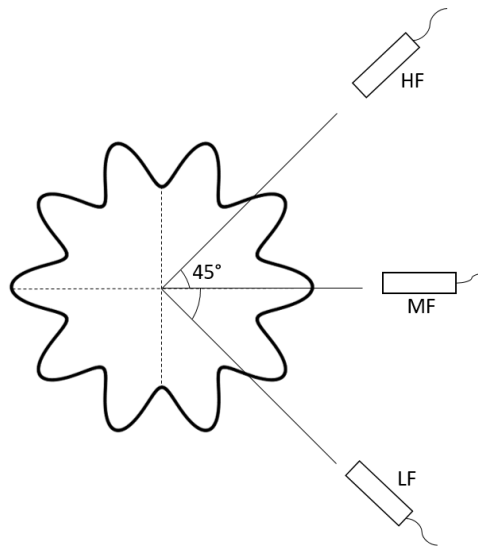


Figure 23. First microphone array orientation with respect to lobes.

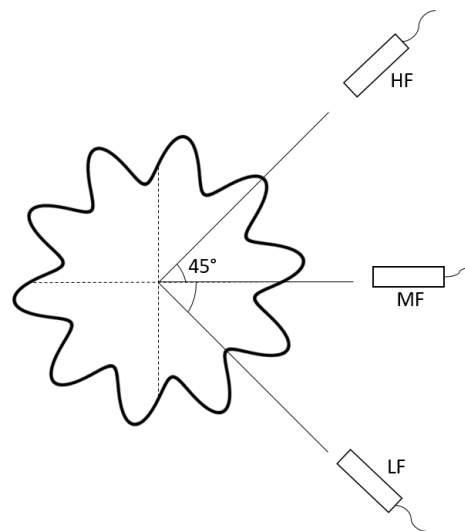


Figure 24. Second microphone array orientation with respect to lobes.

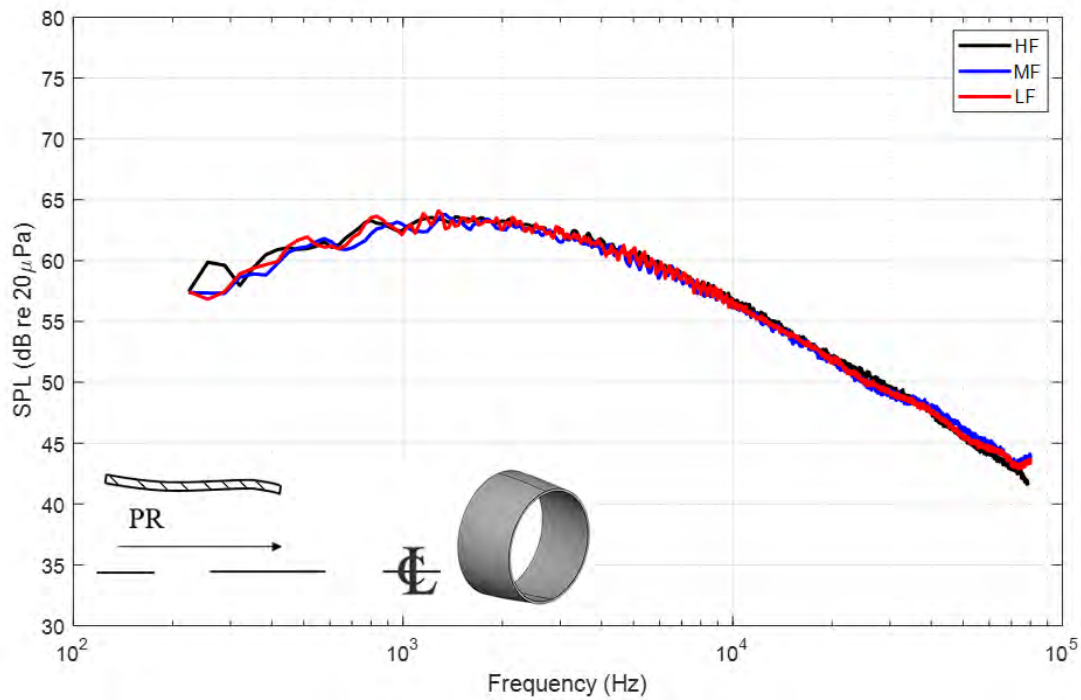


Figure 25. Azimuthal directivity of noise produced by the AXI nozzle. FAA Gulfstream Aerospace Corporation Project Model, $D = 1.54$ in. $PR = 1.39$ ($M_j = 0.70$), unheated, $R = 12$ ft, $\theta = 90^\circ$, $\Delta f = 32$ Hz, lossless. HF: high-azimuth farfield; LF: low-azimuth farfield; MF: middle-azimuth farfield; SPL: sound pressure level.

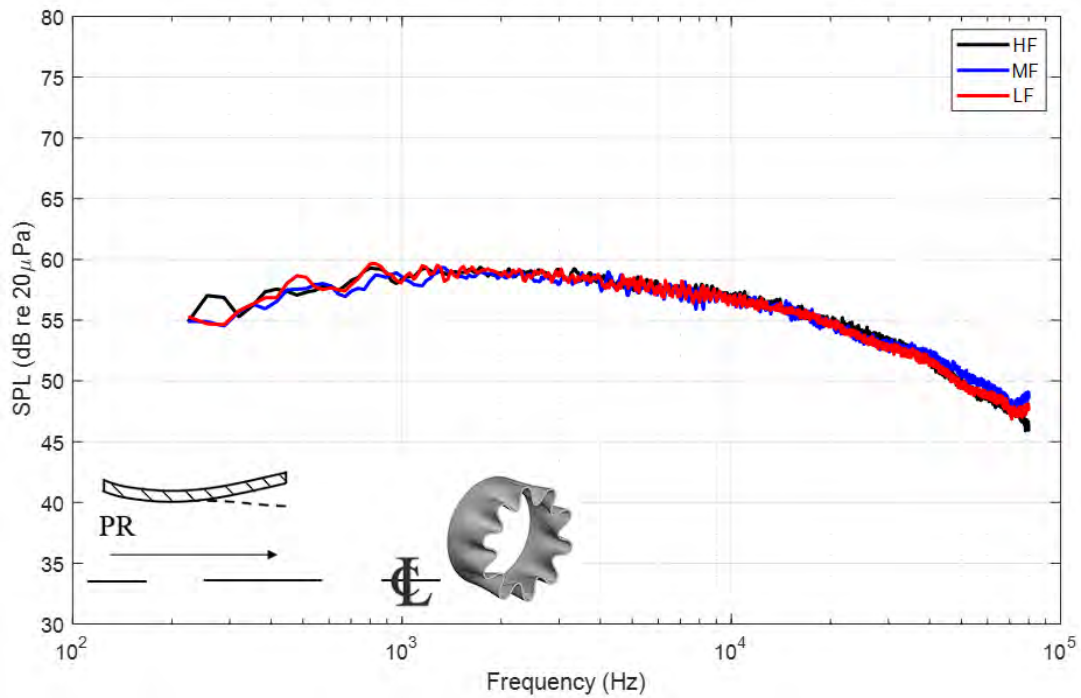


Figure 26. Azimuthal directivity of noise produced by the SUN nozzle. FAA Gulfstream Aerospace Corporation Project Model, $D = 1.54$ in. $PR = 1.39$ ($M_j = 0.70$), unheated, $R = 12$ ft, $\theta = 90^\circ$, $\Delta f = 32$ Hz, lossless. HF: high-azimuth farfield; LF: low-azimuth farfield; MF: middle-azimuth farfield; SPL: sound pressure level.

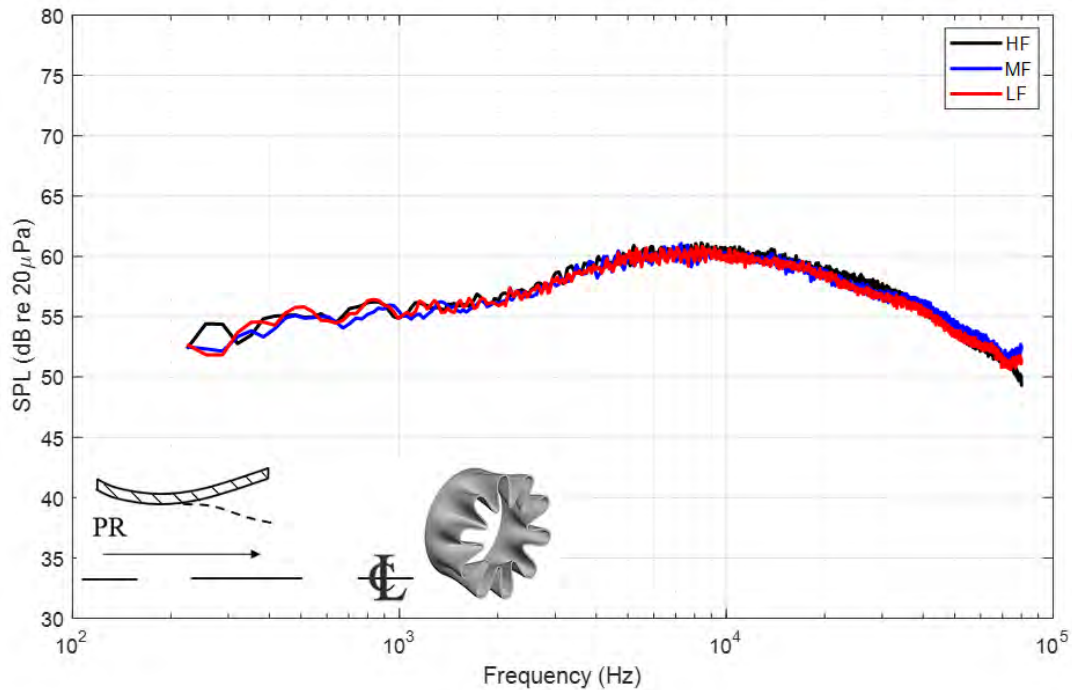


Figure 27. Azimuthal directivity of noise produced by the DAISY nozzle. FAA Gulfstream Aerospace Corporation Project Model, $D = 1.54$ in. $PR = 1.39$ ($M_j = 0.70$), unheated, $R = 12$ ft, $\theta = 90^\circ$, $\Delta f = 32$ Hz, lossless. HF: high-azimuth farfield; LF: low-azimuth farfield; MF: middle-azimuth farfield; SPL: sound pressure level.

As shown by the spectra in Figure 19, the lobed nozzles considerably reduce the noise produced by coherent, large-scale structures, which are the dominant elements of noise observed at low polar observation angles in the farfield. Although the noise observed at sideline angles does not exhibit any azimuthal dependency, the significant impact of these lobed nozzles on the noise generated by large-scale structures prompted a follow-up investigation into possible azimuthal directivity at low polar angles. Farfield measurements were acquired for the AXI and DAISY nozzles at a variety of high-subsonic conditions. The model was rotated from the configuration shown in Figure 23 such that all three arcs were at different azimuths relative to a lobe, which can be seen by comparing the orientation of the lobes between Figures 23 and 24. In the first orientation, the MF arc was aligned with the peak of a lobe whereas the HF and LF arcs were aimed halfway between a lobe and a gully. In the new orientation, the HF arc is aligned with the peak of a lobe, the LF arc is aligned with the trough of a gully, and the MF arc is aimed halfway between a lobe and a gully. At first glance, the resulting spectra shown in Figure 28 suggest a slight dependence on azimuth at higher frequencies, but comparison with the spectra in Figure 29 shows that the downstream farfield noise is no more azimuthally dependent than that produced by a round, axisymmetric nozzle.

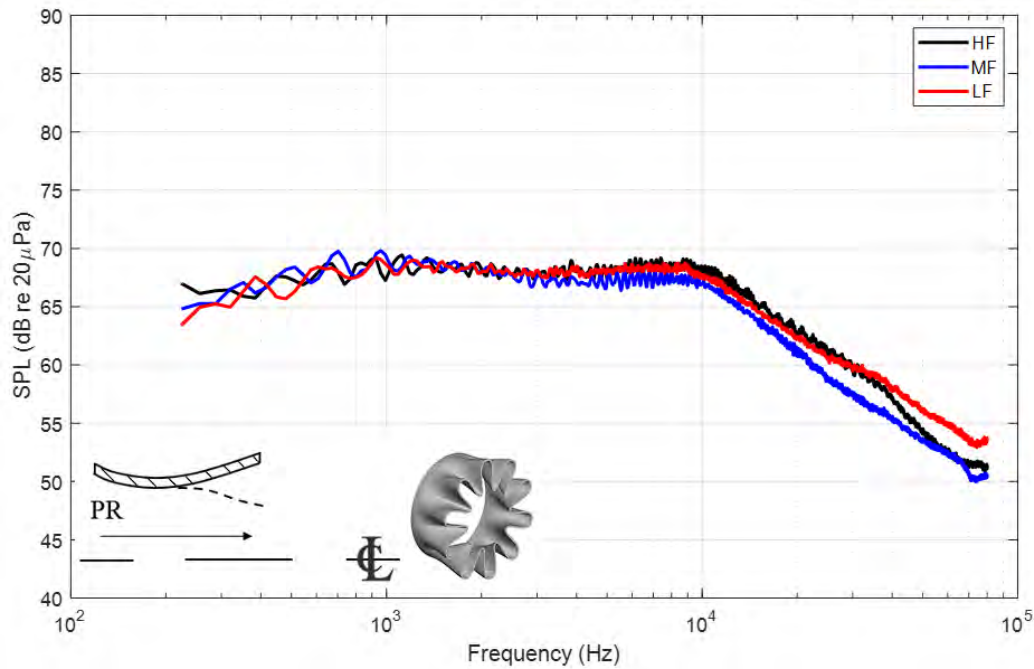


Figure 28. Azimuthal directivity of noise produced by the DAISY nozzle. FAA Gulfstream Aerospace Corporation Project Model, $D = 1.54$ in. $PR = 1.53$ ($M_j = 0.80$), unheated, $R = 12$ ft, $\theta = 30^\circ$, $\Delta f = 32$ Hz, lossless. HF: high-azimuth farfield; LF: low-azimuth farfield; MF: middle-azimuth farfield; SPL: sound pressure level.

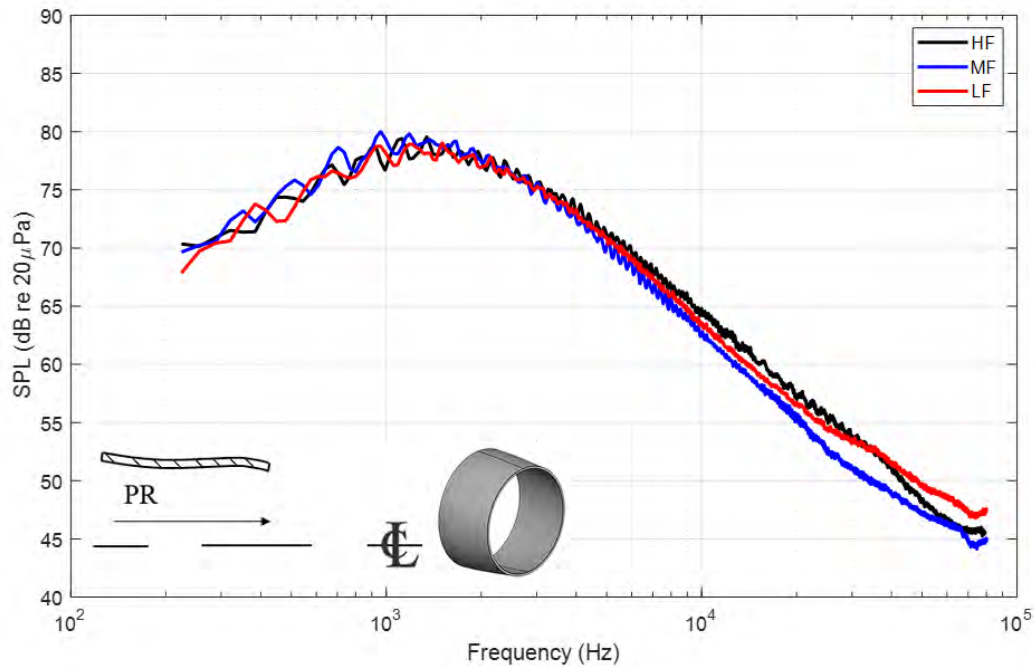


Figure 29. Azimuthal directivity of noise produced by the AXI nozzle. FAA Gulfstream Aerospace Corporation Project Model, $D = 1.54$ in. $PR = 1.53$ ($M_j = 0.80$), unheated, $R = 12$ ft, $\theta = 30^\circ$, $\Delta f = 32$ Hz, lossless. HF: high-azimuth farfield; LF: low-azimuth farfield; MF: middle-azimuth farfield; SPL: sound pressure level.

Dual-stream lobed nozzle acoustics

During this reporting period, the Georgia Tech team collected extensive farfield acoustic measurements of dual-stream jets using the new forced mixer nozzles as well as larger baseline nozzles designed and built by GAC. The models received from GAC and their partners at Trimodels included four exhaust mixing lengths: $L_e/D_e = 0.7, 1.0, 2.0,$ and 3.0 . Prioritizing the collection of the most valuable datasets, the team first acquired acoustic measurements of dual-stream configurations using each primary nozzle cap with a common mixing length of $L_e/D_e = 1.0$. Next, the team collected acoustic data under the same conditions using the longest mixing length of $L_e/D_e = 3.0$. For the shortest mixing length, the research team prioritized the mixer with $L_e/D_e = 1.0$ over the mixer with $L_e/D_e = 0.7$ because the convergent geometry of the shorter mixer length differed from the others. Unlike the previous models, wherein each configuration utilized a common exhaust nozzle with additional spacers for longer mixing lengths, two different exhaust nozzles were received from GAC. One exhaust nozzle has an overall length of $L_e/D_e = 0.7$ whereas the other, which can be mounted to spacer ducts to increase the mixing length, has a length of $L_e/D_e = 1.0$. Because of its shorter length, the exhaust nozzle with $L_e/D_e = 0.7$ has a more rapidly convergent geometry. Thus, to maintain the same convergent geometry between configurations, the exhaust nozzle with $L_e/D_e = 1.0$ was chosen for initial testing. Figure 30 shows the test matrix, where acoustic measurements were acquired for each primary nozzle type with a heated core flow ($T_{t1} = 500$ °F). Heated and unheated core stream acoustic measurements were collected for six dual-stream nozzle configurations: each of the three nozzle caps (AXI, SUN, DAISY) with two exhaust mixing lengths ($L_e/D_e = 1.0$ and 3.0).



Heated ($T_{t1} = 500$ °F)		Primary Mach					
		0.5	0.6	0.7	0.8	0.9	1
Secondary Mach	0.4	■					
	0.5	■	■				
	0.6	■	■				
	0.7		■	■			
	0.8			■	■		
	0.9				■	■	
	1					■	■
ER	1.04			■		■	
	1.07			■		■	

Figure 30. Test matrix for heated, dual-stream acoustic measurements.

As has been done previously, the Georgia Tech team also acquired acoustic measurements of the dual-stream jet with an unheated core stream ($T_{t1} \approx 60$ °F–70 °F). The conditions for which data were acquired using the same six nozzle configurations described above are shown in the matrix in Figure 31. However, for a majority of unheated conditions, the forced mixers fail to produce any notable change in the farfield noise compared with the axisymmetric baseline nozzle. This result is primarily attributed to two reasons. Firstly, for the unheated core stream, there is little to no difference in the velocities of the two streams, except in the case of unrealistic extraction ratios far from unity. For cases with a heated core stream in which the primary jet has a considerably higher velocity than the bypass stream, the mixing of the two streams has the effect of reducing the average velocity of the jet at the exit of the final exhaust nozzle. It is generally well understood that the intensity of jet noise generally scales with the eighth power of the velocity (Lighthill, 1952); hence, if the average exit velocity can be reduced, then a reduction in peak jet noise can be expected. Secondly, mixing of a heated core stream with an unheated bypass stream has the effect of cooling the exhaust jet, which further reduces the exit velocity and helps to combat jet noise. For the sake of brevity, only resulting acoustic data from heated core measurements are shown and discussed below.

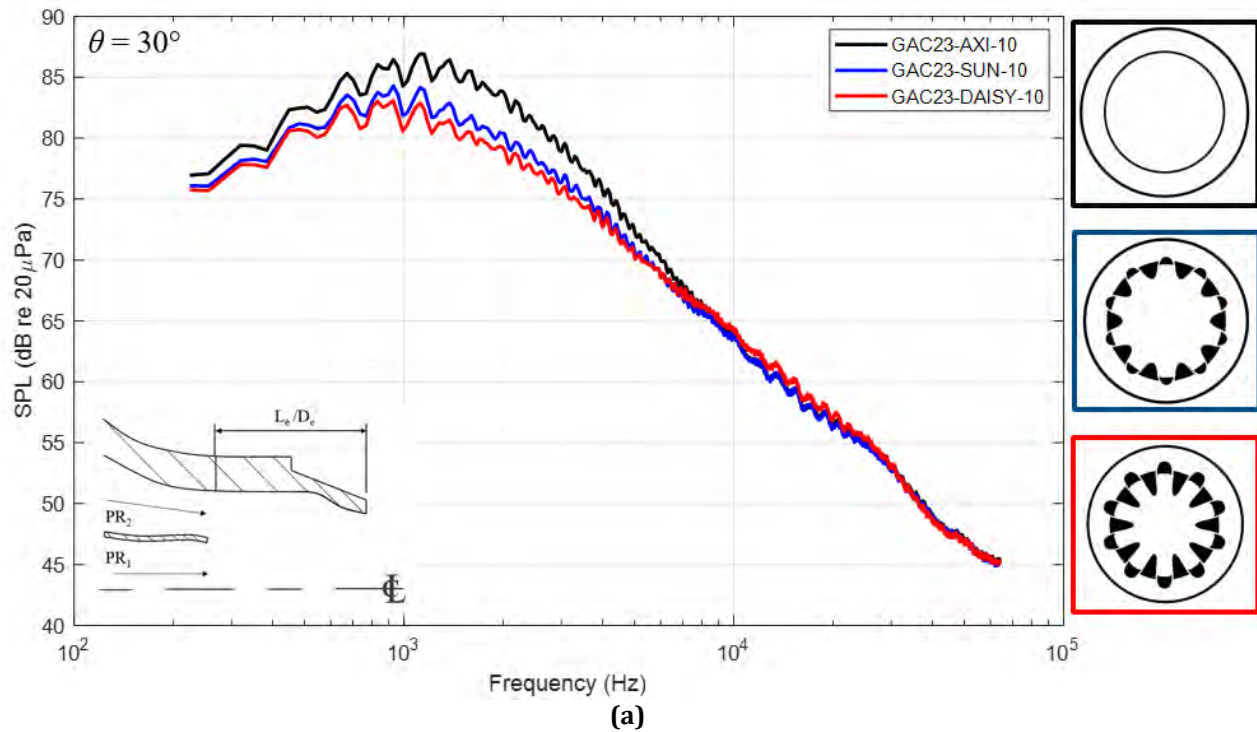
Unheated ($T_{t1} = \sim 60$ °F)		Primary Mach					
		0.5	0.6	0.7	0.8	0.9	1
Secondary Mach	0.4	■					
	0.5	■					
	0.6	■	■				
	0.7			■	■	■	■
	0.8			■	■	■	■
	0.9			■	■	■	■
	1			■	■	■	■
ER	1.04			■		■	
	1.07			■		■	

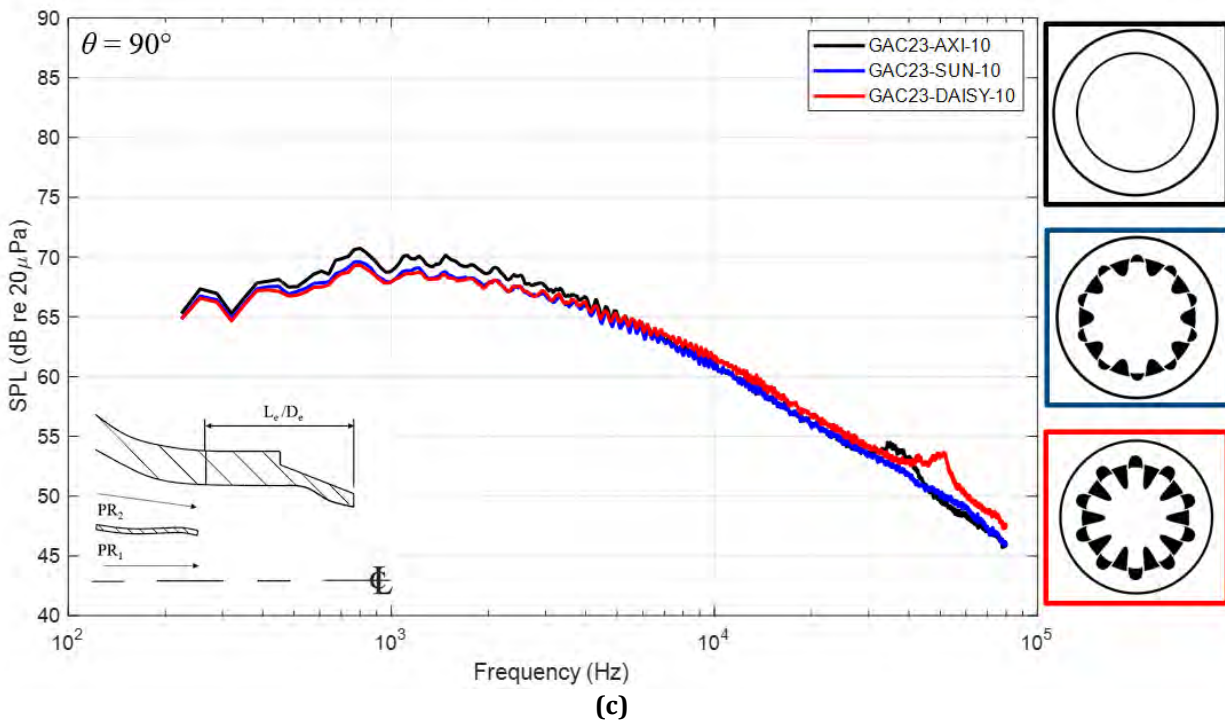
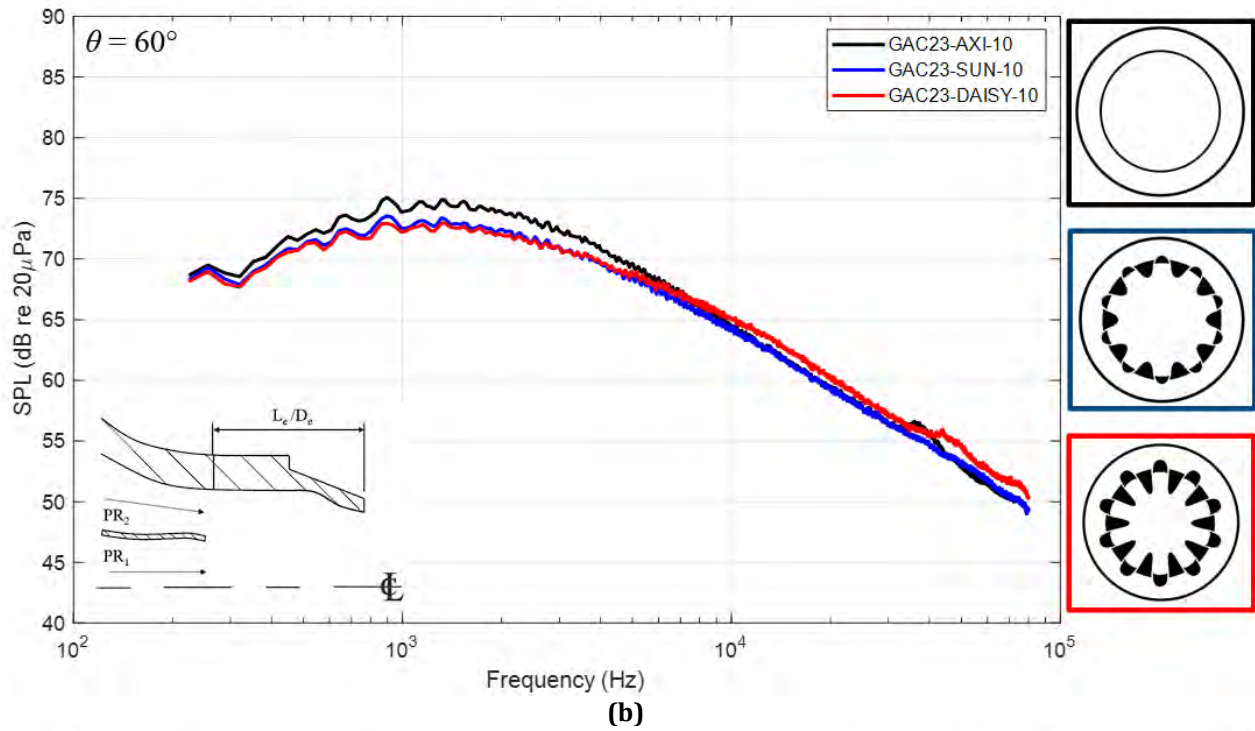
Figure 31. Test matrix for unheated, dual-stream acoustic measurements.

Figure 32 presents representative jet noise spectra, showing the effects of each of the lobed mixers on noise from an internally mixed, dual-stream jet with a heated core stream. A consistent mixing length of $L_e/D_e = 1.0$ is used. At the aft-most observation angle (corresponding to the spectra shown in Figure 32a), where the lobed mixers have the most impact, the SUN mixer reduces the level of jet noise at the peak frequency by approximately 2.6 dB relative to the axisymmetric baseline nozzle (AXI) for the condition shown ($PR_1 = PR_2 = 1.39$, $M_{j1} = M_{j2} = 0.70$). The more intense lobed mixer (DAISY)



has deeper lobes and gullies and reduces the peak SPL by 3.7 dB. The sideline observation spectra shown in Figure 32c reveal a decrease in the peak SPL of approximately 1.2 dB for each of the lobed mixers. A frequent characteristic of mixing-enhancement devices for dual-stream jets is a decrease in the peak SPL at the cost of an increase in high-frequency noise. Although the DAISY mixer performs better in reducing jet noise at the peak frequency, especially at aft polar observation angles, there is a noticeable increase in high-frequency noise beyond approximately 8 kHz. However, the SUN mixer, which provides similar noise reduction benefits at higher polar angles, does not produce an increase in high-frequency jet noise relative to the axisymmetric baseline primary nozzle.





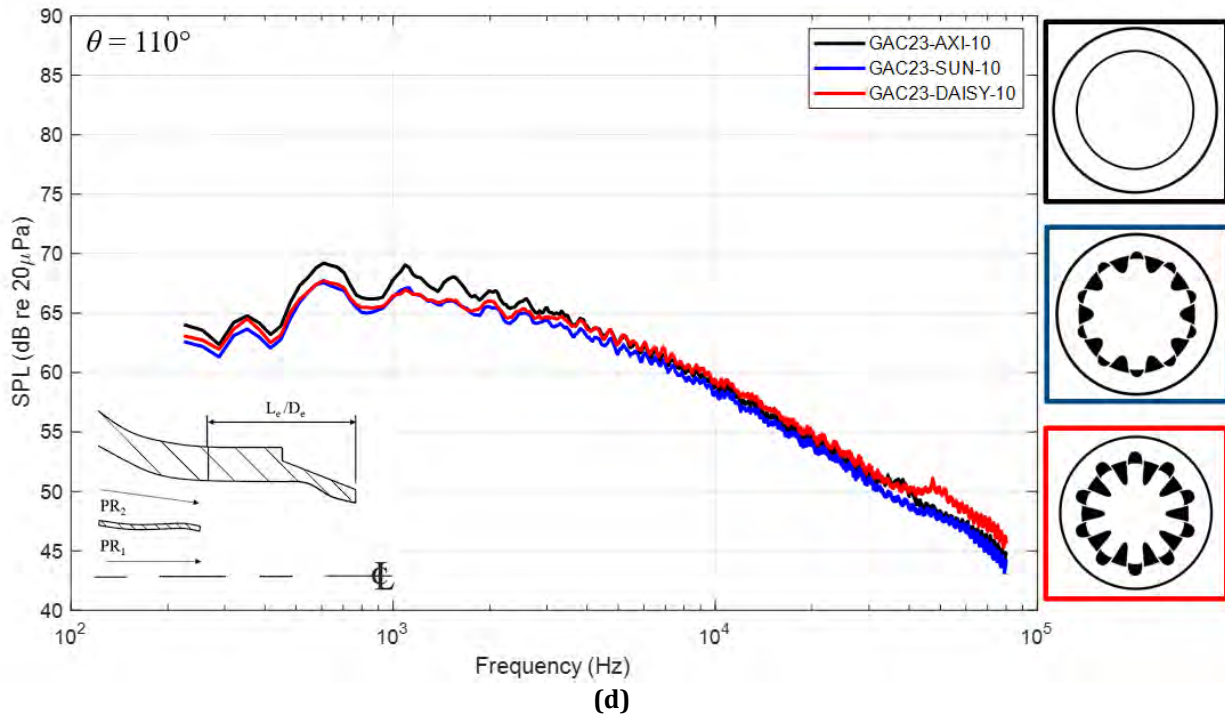


Figure 32. Effect of a lobed nozzle on the noise from an internally mixed, dual-stream jet. FAA Gulfstream Aerospace Corporation (GAC) Project Model, $D_e = 2.20$ in. $L_e/D_e = 1.0$, $PR_1 = 1.39$ ($M_{j1} = 0.70$), $PR_2 = 1.39$ ($M_{j2} = 0.70$), $T_{t1} = 500$ °F, $R = 12$ ft, $\theta = 30^\circ$ (a), 60° (b), 90° (c), 110° (d), $\Delta f = 32$ Hz, lossless. SPL: sound pressure level.

Overall noise level measurements (Figure 33) show the enhanced effect of the DAISY mixer at lower polar angles compared with the less aggressive SUN mixer. For the lower pressure-ratio case shown in Figure 33a, both mixers show a reduced or equivalent overall noise level across all polar observation angles relative to the AXI baseline. At higher pressure ratios (e.g., Figure 33b), the SUN mixer maintains a decrease in overall noise at all observation angles; however, the excess high-frequency noise produced by the DAISY mixer leads to an increase in overall noise at sideline and upstream polar angles. Note that the noise levels are not corrected to the effective perceived noise in decibels, which would likely reveal a net decrease in noise by both mixers across each operating condition.

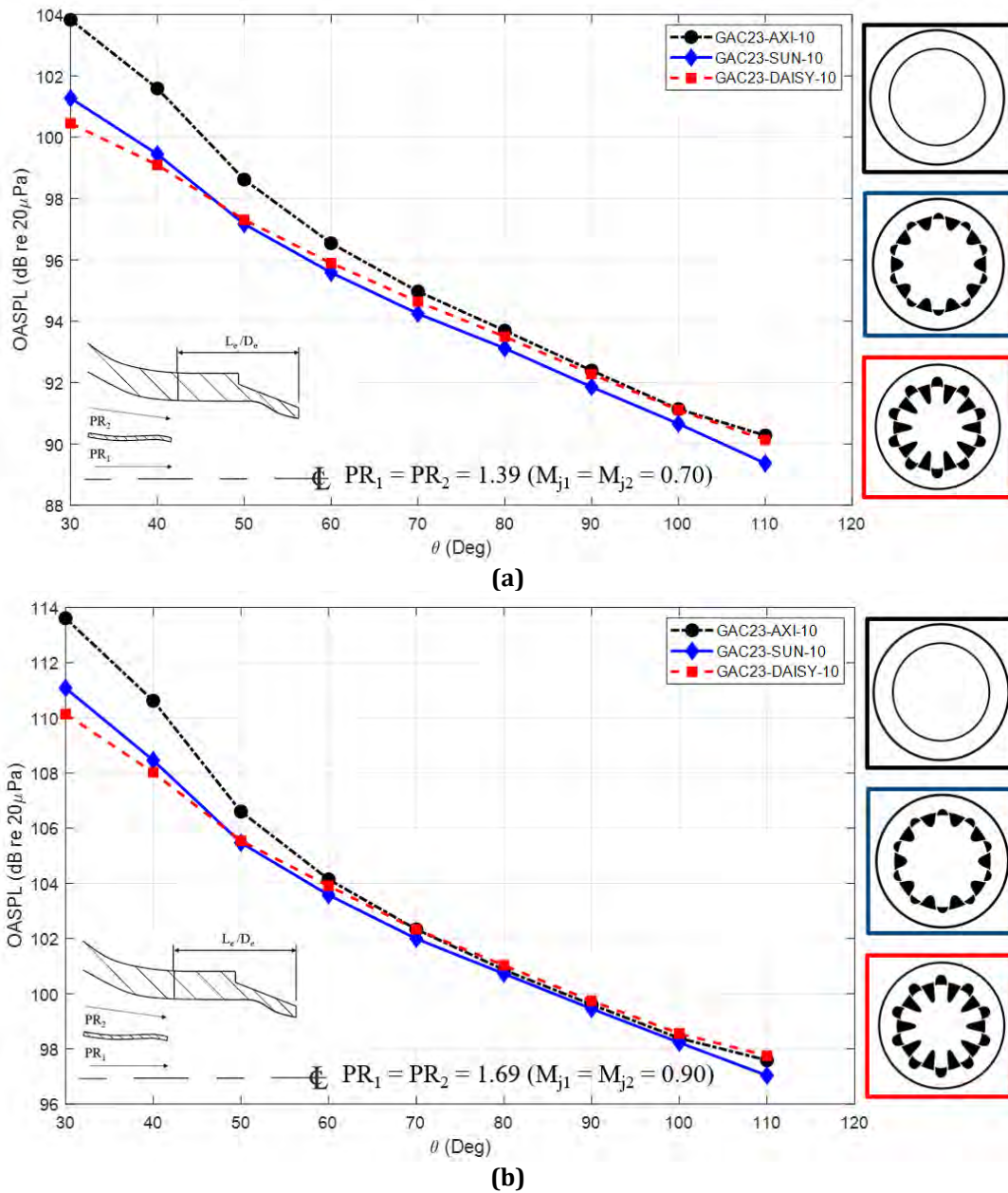


Figure 33. Effect of a lobed nozzle on the overall noise from an internally mixed, dual-stream jet. FAA Gulfstream Aerospace Corporation (GAC) Project Model, $D_e = 2.20$ in. $L_e/D_e = 1.0$, $PR_1 = 1.39$ ($M_{j1} = 0.70$), $PR_2 = 1.39$ ($M_{j2} = 0.70$) (a) and $PR_1 = 1.69$ ($M_{j1} = 0.90$), $PR_2 = 1.69$ ($M_{j2} = 0.90$) (b), $T_{t1} = 500$ °F, $R = 12$ ft, $\Delta f = 32$ Hz, lossless. OASPL: overall sound pressure level.

Task 4 – Data Dissemination

Georgia Institute of Technology

Objective

The objective of this task is to maintain contact with the modelers being funded by the FAA under Project 59 and to provide them with the nozzle design and with acoustic and flow data from the current project.

Research Approach

With respect to the experimental results acquired during this reporting period, the modelers have been provided with access to PIV data for use in validating their computational prediction schemes. Additional acoustic and flow visualization data will be shared following thorough internal quality checks.

Task 5 – Proposal for a Follow-on Effort for Year 4

Georgia Institute of Technology

A request for a no-cost extension was submitted (and approved) to allow the Georgia Tech team to continue experimental work in the coming year.

Task 6 – Reporting and Data Dissemination

Georgia Institute of Technology and Gulfstream Aerospace Corporation

Milestones

Facility repairs and the collection of flow data from previous years have been completed. Mixer nozzles have been fabricated and received. The collection of acoustic data has been completed for two mixing lengths for each mixer.

Publications

- Ramsey, D. N., Gavin, J., and Ahuja, K. K., “Howling in a model-scale nozzle related to shock-induced boundary-layer separation at the nozzle exit,” AIAA Paper 2023-3933, 2023.
- Ramsey, D. N., Mayo, R., and Ahuja, K. K., “Howling in a model-scale internally mixed confluent nozzle related to excited core-jet instability,” AIAA Paper 2023-3932, 2023

Outreach Efforts

None.

Awards

None.

Student Involvement

All three graduate students are involved in the data acquisition and analysis process. Graduate student Reagan Mayo has graduated, and PhD student David Ramsey is continuing his NSF-sponsored work.

References

- Ahuja, K. K. (2003). Designing clean jet-noise facilities and making accurate jet-noise measurements. *International Journal of Aeroacoustics*, 2(3), 371-412.
- Bridges, J., & Wernet, M. P. (2011). *The NASA subsonic jet particle image velocimetry (PIV) dataset* (No. E-17439).
- Burrin, R. H., Dean, P. D., & Tanna, H. K. (1974). A New Anechoic Facility for Supersonic Hot Jet Noise Research at Lockheed-Georgia. *The Journal of the Acoustical Society of America*, 55(2_Supplement), 400-400.
- Burrin, R. H., & Tanna, H. K. (1979). The Lockheed-Georgia coannular jet research facility. *The Journal of the Acoustical Society of America*, 65(S1), S44-S44.



- Christensen, K. T. (2004). The influence of peak-locking errors on turbulence statistics computed from PIV ensembles. *Experiments in fluids*, 36, 484-497.
- Karon, A. Z. (2016). Potential factors responsible for discrepancies in jet noise measurements of different studies.
- Lighthill, M. J. (1952). On sound generated aerodynamically I. General theory. *Proceedings of the Royal Society of London. Series A. Mathematical and Physical Sciences*, 211(1107), 564-587.
- Pope, S. B., *Turbulent flows*. Cambridge University Press, 2000. doi: 10.1017/CBO9780511840531
- Raffel, M., Willert, C. E., Scarano, F., Kähler, C. J., Wereley, S. T., & Kompenhans, J. (2018). *Particle image velocimetry: a practical guide*. Springer.
- Ramsey, D. N., Karon, A. Z., Funk, R., & Ahuja, K. K. (2022). Noise from Low-Bypass Confluent Nozzles: Mixing Length, Extraction Ratio, and Core Temperature Effects. In *28th AIAA/CEAS Aeroacoustics 2022 Conference* (p. 2863).



Project 059(C) Modeling Supersonic Jet Noise Reduction with Global Resolvent Modes

University of Illinois Urbana-Champaign

Project Lead Investigator

Daniel J. Bodony
Blue Waters Professor of Aerospace Engineering
Associate Dean for Graduate, Professional, and Online Programs
University of Illinois Urbana-Champaign
306 C Talbot Labs
104 S. Wright St.
Urbana, IL 61801
217-244-3844
bodony@illinois.edu

University Participants

University of Illinois Urbana-Champaign (UIUC)

- P.I.: Dr. Daniel J. Bodony
- FAA Award Number: 13-C-AJFE-UI-031
- Period of Performance: October 1, 2022 to December 31, 2023
- Tasks:
 1. Establishment of industry-relevant low bypass ratio (BPR) engine parameters and acoustic assessment workflow with cost-sharing partner (completed)
 2. Automated Reynolds-averaged Navier–Stokes equation (RANS) predictions of jet exhaust (completed)
 3. Resolvent mode computation—primary and sensitivity (completed)
 4. Python resolvent mode interpolation tool (completed)
 5. Python optimization tool for jet noise reduction (JNR) (version 1) (completed)
 6. Application of version 1 optimization tool on Georgia Institute of Technology Research Institute (GTRI) dual-stream nozzle (completed)
 7. Reformulation of resolvent modes by using local turbulent kinetic energy (in progress)
 8. Development and implementation of design parameter gradient direction for JNR (in progress)
 9. Application of version 2 optimization tool on GTRI dual-stream nozzle (paused)
 10. Application of version 1 optimization tool on Gulfstream- and Boom-relevant geometry (in progress)
 11. Collaboration with P.I.s for ASCENT Projects 10 and 47 (not yet started)

Project Funding Level

The FAA provided \$199,999 in funding. In-kind cost-matching agreements were established with Gulfstream (\$100,000; contact person: Dr. Brian Krupp [brian.krupp@gulfstream.com]) and with Boom (\$50,000; contact person: Dr. Joe Salamone [joe.salamone@boom.aero]).

Investigation Team

University of Illinois Urbana-Champaign

Dr. Daniel Bodony (P.I.), Tasks 1, 3, and 11
Mr. Jay Woo (PhD student), Tasks 2, 3, 4, 5, 6, 8, and 9

California Institute of Technology (Caltech)

Dr. Tim Colonius (subaward), Tasks 3, 7, and 11
Mr. Liam Heidt (PhD student), Tasks 3 and 7



Project Overview

This ASCENT project leverages recent research in global-resolvent-mode-based descriptions of jet turbulence and its associated noise to develop a physics-based tool for estimating the impact of JNR strategies on the takeoff noise of civil supersonic transports. The software tool will efficiently identify promising JNR technologies and will more precisely evaluate the noise impact of parametric variation in a specific JNR approach. The tool will be compatible with the fleet-scale evaluation codes Global and Regional Environmental Analysis Tool (GREAT; Georgia Institute of Technology) and Fleet Level Environmental Evaluation Tool (FLEET; Purdue University) developed in ASCENT Project 10 and integrated into the ASCENT Project 47 clean-sheet evaluation tool targeting civil supersonic transport.

The proposed research will create a multi-fidelity JNR tool that can operate in two modes: one mode for specific engine estimates and one mode for fleet-scale estimates:

JNR evaluation for an engine mode

According to the RANS-provided mean flow for a specific engine, the global resolvent description of wavepackets and their sensitivity to mean flow variations will be computed. The solutions will provide estimates of the low-frequency radiated noise, and the sensitivity derivatives will estimate how the noise changes as a result of changes in the engine design, thus enabling JNR optimization.

Fleet-level estimation mode

The resolvent modes and their sensitivity derivatives for existing JNR strategies (e.g., chevrons or internal mixers) will be pre-computed for canonical jet exhaust profiles and flow conditions, compressed, and stored within an efficient data layout that can be quickly evaluated within FLEET, GREAT, and/or NASA's Aircraft Noise Prediction Program.

The Year 3 proposal was approved for funding with a period of performance of October 1, 2022 through December 31, 2023 (after a no-cost extension), and a budget of \$199,999. The Year 2 statement of work included five tasks, listed above as Tasks 7–11, and rephrased from the prior year's annual report. The status of each task is indicated in parentheses. A Year 4 proposal has been submitted and recommended for funding.

Task 1 – Establish Industry-Relevant Low-BPR Engine Parameters and Acoustic Assessment Workflow with Cost-Sharing Partner [Completed]

University of Illinois at Urbana-Champaign

Objective

The objective of this task is to work with our cost-sharing partners to identify the anticipated range of characteristics of the low-BPR engines being considered for business-class civil supersonic transport. These parameters include, but are not limited to, diameter, BPR, mass flow rate, core and fan stream pressure ratios, core stream temperature ratio, thrust, nozzle configuration, plug designs, chevron designs, internal mixer designs, and afterburner design.

Research Approach

The research approach involves conducting face-to-face meetings and document exchange to obtain industry-relevant low-BPR engine parameters and acoustic assessment workflows.

Milestones

- Find new candidate cost-sharing partner
- Establish a nondisclosure agreement to initiate discussions
- Exchange low-BPR engine parameters and acoustic assessment workflow

Major Accomplishments

All milestones have been completed. A nondisclosure agreement between UIUC and Boom was signed in Year 2, and subsequent discussions led to Boom's partnership with \$50,000 in-kind cost sharing for Year 3. The Boom commitment letter is attached. A cost-sharing agreement with Gulfstream was also established for \$100,000 in-kind cost sharing. The Gulfstream letter is attached. In consultation with Dr. James Bridges at NASA Glenn Research Center, the "Plug20" family of

nozzles (NASA TM-20210010291) was identified as relevant to industry. Down-selecting the available nozzles will be the focus of the Year 4 effort, provided that it is funded.

Publications

None.

Outreach Efforts

None.

Awards

None.

Student Involvement

None.

Plans for Next Period

Continued communication between UIUC and the principal contacts at Boom and Gulfstream, with focus on exchanging results, sharing data, and evaluating the UIUC-developed JNR workflow within each company's design process on the Plug20 nozzles. Of note, Dr. Joe Salamone left Boom, and attempts to reconnect with Boom engineers have not yet been successful.

Task 2 – Automated RANS Predictions of Jet Exhaust

University of Illinois at Urbana-Champaign

Objective

The objective of this task is to develop and verify an automated toolchain for using RANS methods to predict the jet exhaust plume from candidate near-sonic multi-stream jet nozzles.

Research Approach

Achieving JNR will require changes to the engine cycle and nozzle geometries. A Python-based software infrastructure is to be developed that takes parametrically defined computer-aided-design-based descriptions of nozzle geometries, automatically generates meshes and boundary conditions for the nozzle internal flow path and the external nozzle plume, initiates an open-source RANS solver, and curates the data.

Milestones

- Additional developments in computational fluid dynamics flow path
- Verification of RANS simulation results
- Automation of Python infrastructure

Major Accomplishments

Milestone 1 has been completed, and included subtasks such as adjusting the boundary conditions and increasing the computational domain of the mesh grid for each nozzle model. Post-processing calculations have also been developed to monitor properties of the nozzle exhaust and thereby characterize steady flow behavior. Milestone 2 has been completed, and included results obtained from post-processing that have been verified through comparison with a numerical solution based on quasi-1D flow theory for mixed exhaust jet nozzles. Milestone 3 has been completed, and included full automation of individual computational fluid dynamics processes.

Publications

Woo, J., Murthy, S. R., and Bodony, D. J. "[Resolvent-based framework for jet noise reduction of a low-bypass ratio coannular nozzle](#)," AIAA Paper 2024-2805, Presented at the AIAA SciTech 2024 Forum, Orlando, FL, 8-12 January 2024.

Outreach Efforts

None.

Awards

None.

Student Involvement

Jay Woo was responsible for developing the Python toolchain.

Plans for Next Period

None; task is complete.

Task 3 – Resolvent Mode Computation—Primary and Sensitivity

University of Illinois at Urbana-Champaign (lead) and California Institute of Technology

Objective

The objective of this task is to develop and verify a resolvent mode computation tool suitable for evaluating the JNR potential of candidate near-sonic multi-stream jet nozzles.

Research Approach

Achieving JNR will require changes to the engine cycle and nozzle geometries. Estimation of the JNR potential of candidate cycles and geometries will use resolvent mode descriptions of the coherent wavepacket-associated jet noise of the loudest sound sources. We denote the resolvent calculations that provide the input-gain-output modes of the resolvent operator $(i\omega - A)^{-1}$ as “primary,” and we denote the changes in those modes due to changes in the jet nozzle geometry and engine cycle as “sensitivity.” The resolvent operator requires knowledge of the linearized Navier–Stokes operator A generated for each nozzle and its exhaust plume, and a global mode computational infrastructure. The sensitivity of the resolvent input-gain-output modes requires knowledge of the change in A , e.g., δA , resulting from changes in the nozzle design and/or engine cycle.

Milestones

- Primary resolvent mode computation capability
- Resolvent mode training data and fitting
- Resolvent mode sensitivity computation capability

Major Accomplishments

Milestone 1 has been completed and tested on single-stream subsonic and supersonic jets. Milestone 2 has been completed by using GTRI dual-stream jet data. Milestone 3 has been completed and validated by using GTRI dual-stream jet data.

Publications

Pickering, E. (2021). *Resolvent Modeling of Turbulent Jets* [Doctoral thesis, California Institute of University]. doi:10.7907/szxb-f168. <https://resolver.caltech.edu/CaltechTHESIS:03022021-005902351>

Woo, J., Murthy, S. R., and Bodony, D. J. “[Resolvent-based framework for jet noise reduction of a low-bypass ratio coannular nozzle](#),” AIAA Paper 2024-2805, Presented at the AIAA SciTech 2024 Forum, Orlando, FL, 8-12 January 2024.

Outreach Efforts

None.

Awards

None.



Student Involvement

Jay Woo is primarily responsible for running and applying the resolvent calculation and its sensitivity. Ethan Pickering was responsible for calibrating the primary resolvent mode computation and the preliminary training data and fitting tasks; he graduated and left Caltech. Liam Heidt is the current student, who learned from Ethan and now leads global mode data-driven alignment.

Plans for Next Period

None; task is completed.

Task 4 – Python Resolvent Mode Interpolation Tool

University of Illinois at Urbana-Champaign (lead) and California Institute of Technology

Objective

The objective of this task is to develop and verify a Python-based interpolation tool for computing resolvent input-gain-output modes at nozzle geometry and/or engine cycles for which RANS data are unavailable but are near previously known input-gain-output modes from nearby nozzle geometries and/or engine cycles.

Research Approach

By using Kriging interpolation methods, a response surface-based interpolation approach will be developed to estimate resolvent input-gain-output modes for estimating the radiated noise from an engine geometry/engine cycle for which previously computed RANS data, linearized operators, and resolvent data are unavailable.

Milestones

- Identify candidate interpolation methods and down-select
- Develop a Python tool to implement the interpolation method
- Verify the Python tool

Major Accomplishments

Milestones 1–3 have been completed: a Kriging method has been chosen, and an interpolation code has been developed and verified. Performance and accuracy comparisons between the interpolation tool and re-running the computational fluid dynamics and mode calculations suggest that the interpolation method is inferior.

Publications

None.

Outreach Efforts

None.

Awards

None.

Student Involvement

Jay Woo was responsible for developing the Python toolchain.

Plans for Next Period

None; the resolvent-based interpolation tool will no longer be a focus of the work.

Task 5 – Python Optimization Tool for JNR

University of Illinois at Urbana-Champaign (lead) and California Institute of Technology

Objective

The objective of this task is to develop and verify a Python-based optimization tool that searches the optimization space of the engine geometry/cycle, to identify design choices that improve JNR.

Research Approach

With gradient-informed optimization methods, an optimization approach will be developed for estimating JNR potential from a class of candidate engine geometries/cycles by using resolvent mode predictions of jet noise based on linearized operators described by RANS predictions of the jet exhaust plume.

Milestones

- Identify candidate optimization methods and down-select
- Develop a Python tool to implement the optimization method
- Verify the Python tool

Major Accomplishments

Milestone 1 has been completed, and the conjugate gradient method was selected for the optimization. Milestones 2 and 3 are also complete.

Publications

Woo, J., Murthy, S. R., and Bodony, D. J. "[Resolvent-based framework for jet noise reduction of a low-bypass ratio coannular nozzle](#)," AIAA Paper 2024-2805, Presented at the AIAA SciTech 2024 Forum, Orlando, FL, 8-12 January 2024.

Outreach Efforts

None.

Awards

None.

Student Involvement

Jay Woo was responsible for implementing the optimization tool.

Plans for Next Period

None; task is complete.

Task 6 – Application of Version 1 Optimization Tool on GTRI Dual-Stream Nozzle

University of Illinois at Urbana-Champaign (lead) with California Institute of Technology

Objective

The objective of this task is to apply the Python-based tool developed in Tasks 2–5 to the GTRI dual-stream nozzle with extensible mixer duct lengths, to predict the quietest configuration.

Research Approach

The automated Python toolchain, starting with the moderate mixer duct length, will be applied to predict the mixer duct length that yields the quietest configuration. The predictions will be compared with the GTRI-measured acoustic field.

Milestones

- Select the GTRI operating condition of interest

- Apply the optimization tool
- Compare the predicted quiet configuration to the measured quiet configuration

Major Accomplishments

Milestone 1 has been completed, and was based on the conditions for which GTRI jet velocity particle image velocimetry (PIV) data and acoustic data are available. Milestone 2 has been applied, and optimization has been performed. Milestone 3 has been completed. Qualitative trends from the resolvent modes have been found to be consistent with the measured acoustic field.

Publications

Woo, J., Murthy, S. R., and Bodony, D. J. "[Resolvent-based framework for jet noise reduction of a low-bypass ratio coannular nozzle](#)," AIAA Paper 2024-2805, Presented at the AIAA SciTech 2024 Forum, Orlando, FL, 8-12 January 2024.

Outreach Efforts

None.

Awards

None.

Student Involvement

Jay Woo was responsible for applying version 1 of the optimization tool to the GTRI nozzle.

Plans for Next Period

None; task is complete.

Task 7 – Reformulation of Resolvent Modes by Using Local Turbulent Kinetic Energy

California Institute of Technology

Objective

The objective of this task is to develop a means for the resolvent gain predictions to be internally calibrated by using information from the RANS-predicted flow-fields.

Research Approach

A calibrated reconstruction of the input-output modes from the resolvent formulation is used to estimate the jet's turbulent kinetic energy, as predicted by the RANS model.

Milestones

- Finalize the calibration formulation
- Implement the calibration procedure
- Verify the calibration procedure

Major Accomplishments

Task 7 has been started. However, initial results from Caltech showed that the original formulation for calibrating the resolvent modes by using the local turbulent kinetic energy led to an ill-posed problem whose solutions were not suitable. A new formulation is being developed.

Publications

None.

Outreach Efforts

None.

Awards

None.

Student Involvement

Liam Heidt will continue to be responsible but was delayed while preparing for and taking his qualifying examination at Caltech.

Plans for Next Period

We will continue Task 7 by developing the new self-calibration formulation and applying it to Plug20 flow field data.

Task 8 – Development and Implementation of Design Parameter Gradient Direction for JNR

University of Illinois at Urbana-Champaign (lead) with California Institute of Technology

Objective

The objective of this task is to develop and verify an updated Python-based optimization tool based on version 1 that searches the optimization space of the engine geometry/cycle, to identify design choices that improve JNR.

Research Approach

Using gradient-informed optimization methods, we will develop an optimization approach for estimating JNR potential from a class of candidate engine geometries/cycles by using resolvent mode predictions of jet noise, on the basis of linearized operators described by RANS predictions of the jet exhaust plume.

Milestones

- Incorporate lessons-learned updates from version 1 of the Python toolchain into version 2
- Verify implementation

Major Accomplishments

Milestone 1 has been completed. Milestone 2 has been completed for a supersonic jet. The automated Python optimization tool is being applied to the GTRI dual-stream nozzle data.

Publications

Murthy, S. and Bodony, D. J. “Resolvent analysis based jet-noise-reduction of a biconical tactical jet nozzle,” AIAA Paper 2023-4518, Presented at the 2023 AIAA Aviation Forum, June, 2023, San Diego, CA.

Outreach Efforts

None.

Awards

None.

Student Involvement

Jay Woo and Liam Heidt will be jointly responsible.

Plans for Next Period

We will complete Milestone 2 on the Plug20 nozzle in Year 4.

Task 9 – Application of Version 2 Optimization Tool on GTRI Dual-Stream Nozzle

University of Illinois at Urbana-Champaign (lead) with California Institute of Technology

Objective

The objective of this task is to apply version 2 of the Python-based tool developed in Tasks 2–5 to the GTRI dual-stream nozzle with extensible mixer duct lengths, and predict the quietest configuration.

Research Approach

We will apply the automated Python toolchain, starting with the moderate mixer duct length, to predict the mixer duct length that yields the quietest configuration, then compare predictions with the GTRI-measured acoustic field.

Milestones

- Apply the optimization tool
- Compare the predicted quiet configuration to the measured quiet configuration

Major Accomplishments

Task 9 has been completed on the GTRI dual-stream nozzle, but yielded null results because the nozzle design parameters (e.g., mixer length) were found not to change the far-field sound.

Publications

None.

Outreach Efforts

None.

Awards

None.

Student Involvement

Jay Woo will be responsible for applying version 2 of the optimization tool.

Plans for Next Period

We will re-apply Task 9 to the Plug20 nozzles in Year 4.

Task 10 – Application of Version 1 Optimization Tool on Gulfstream- and Boom-Relevant Geometry

University of Illinois at Urbana-Champaign

Objective

The objective of this task is to work with Gulfstream and Boom to apply version 1 of our optimization tool to a supersonic nozzle design relevant to Gulfstream and Boom. Performance, successes, and failures will be documented.

Research Approach

The results of version 1 of the Python optimization tool will be transitioned to Gulfstream and Boom for internal evaluation of the tool.

Milestones

- Develop and implement a cost-sharing agreement with appropriate intellectual-property safeguards
- Work with Gulfstream and Boom engineers to identify cases of interest



- Apply optimization code to Gulfstream and Boom cases of interest

Major Accomplishments

Milestone 1 has been completed, and the letters of support from Gulfstream and Boom are included. Milestone 2 has been completed, and the NASA Plug20 configurations of Bridges et al. (NASA TM-20210010291) were selected. Milestone 3 has not yet been started.

Publications

None.

Outreach Efforts

None.

Awards

None.

Student Involvement

Jay Woo and P.I. Daniel Bodony will be jointly responsible.

Plans for Next Period

We will begin Milestone 3 in Year 4.

Task 11 – Collaboration with P.I.s for ASCENT Projects 10 and 47

University of Illinois at Urbana-Champaign

Objective

The objective of this task is to collaborate with P.I.s on ASCENT Projects 10 and 47 to understand fleet-scale estimation needs and constraints, and develop a prototype software interface that connects the engine-class tool from Task 3 to FLEET/GREAT.

Research Approach

We will discuss, document, and identify implementation possibilities for connecting version 1 (or version 2) of the JNR optimization tool within their project software tools.

Milestones

- Engage P.I.s on ASCENT Projects 10 and 47 to understand their goals, data, and software ecosystems
- Identify possible means through which ASCENT Project 59C tools could be integrated into Project 10 and 47 ecosystems
- Re-engage Project 10 and 47 P.I.s to down-select the most promising integration path

Major Accomplishments

This task has not yet been started.

Publications

None.

Outreach Efforts

None.

Awards

None.



Student Involvement

Jay Woo and P.I. Daniel Bodony will be jointly responsible.

Plans for Next Period

We will begin Task 11 in the next year.



Project 059D Physics-based Analyses and Modeling for Supersonic Aircraft Exhaust Noise

Stanford University

Project Lead Investigator

Sanjiva K. Lele

Professor

Department of Aeronautics & Astronautics

Stanford University

Stanford, CA 94305

Phone: (650) 723-7721

E-mail: lele@stanford.edu

University Participants

Stanford University

- P.I.s: Dr. Sanjiva K. Lele, Dr. Juan J. Alonso
- FAA Award Number: 13-C-AJFE-SU-024
- Period of Performance: January 1, 2022 to December 16, 2022
- Tasks (for a three-year effort):
 1. Develop and refine research plans in coordination with ASCENT Project 59 partners
 2. Perform large eddy simulation (LES)-based simulation, modeling, and validation of jet noise predictions
 3. Conduct Reynolds-averaged Navier-Stokes (RANS)-based simulation, modeling, and validation of jet noise predictions

Project Funding Level

This project receives \$200,000 per year from FAA, in-kind matching from Stanford, and cost-share matching from Gulfstream Aerospace Corporation.

Investigation Team

Dr. Sanjiva K. Lele (P.I.; Department of Aeronautics and Astronautics)

Dr. Juan J. Alonso (P.I.; Department of Aeronautics and Astronautics)

Gao Jun Wu (PhD student; Department of Aeronautics and Astronautics)

Tejal Shanbhag (PhD student; Department of Aeronautics and Astronautics)

Kristen Matsuno (PhD student; Department of Mechanical Engineering)

Olivia Martin (PhD student; Department of Mechanical Engineering)

Project Overview

Improved methods for predicting and reducing noise for civil supersonic aircraft would be highly valued by the research and technology development community engaged in civil supersonic aircraft development. In addition to aircraft and engine companies, organizations such as NASA, FAA, and the Department of Defense research and technology community would also benefit from improved methods and tools. Ultimately, supersonic jet noise tools with predictive capabilities can be used to design improved noise mitigation systems and to provide estimates of noise for certification studies.

This project involves the coordinated development of both low- and high-fidelity approaches for jet noise predictions for civil supersonic aircraft being considered in ASCENT and involves the tasks listed above. High-fidelity simulations of the jet exhaust flow and noise will be developed for a carefully selected subset of configurations and operating points being tested by the Georgia Institute of Technology (Georgia Tech) team. In parallel, Reynolds-averaged Navier-Stokes (RANS)

computations of a broader range of configurations and operating conditions relevant for civil supersonic aircraft will be performed and used to develop improved jet noise source models and more accurate far-field noise propagation kernels. The noise source and noise propagation modeling will leverage high-fidelity simulation data and ongoing Georgia Tech experiments, as well as other noise and flow measurements available in the archival literature. Our goal is to understand the predictive quality of RANS-based noise prediction approaches with improved source and/or propagation models so that designers can better capture tradeoffs typical in the development of full civil supersonic aircraft configurations.

Task 1 – Develop and Refine Research Plans in Coordination with ASCENT Project 59 Partners

Objectives

We aim to design a simulation study that covers the range of operating conditions and possible nozzle configurations relevant for civil supersonic jet exhaust. The plan must be inclusive of the current test plan from our experimental partner at Georgia Tech.

Research Approach

Planning involved discussions with Project 59 partners and reaching out to external advisors at NASA and elsewhere in academia and industry. Based on these efforts, it was determined that the project should focus on axisymmetric dual-stream nozzles with an internal mixer and with the possibility of an internal and/or external nozzle plug. We have also searched for nozzle configurations and flow and noise measurement data in the archival literature that would be deemed relevant for civil supersonic aircraft and that could be used in the development of noise prediction methods. A comprehensive exploration indicated that the bulk of jet noise data including studies of noise reduction concepts were in the regime of moderate to high bypass ratios and were thus not particularly relevant for civil supersonic aircraft. While this affirmed the need for the planned laboratory measurement campaign by Project 59 partner Georgia Tech, it also highlighted the need to use the most relevant data from the published literature to kickstart the modeling and simulation effort. Two specific datasets associated with jet noise tests at NASA Glenn were thus identified.

Georgia Tech dual-stream nozzle

A coannular nozzle geometry with a variable-length mixing duct has been designed and is being tested extensively by the team at Georgia Tech. Following discussions among project collaborators and key stakeholders, a test matrix has been determined for the Year 1–2 experimental efforts. The jet Mach numbers for the two streams each vary between $M_j = 0.4$ and $M_j = 1.0$, and the length of the nozzle mixing duct can be adjusted to be 0.7, 1.0, 2.0, and 3.0 times the length of the nozzle diameter, $D_e = 1.7''$.

Bridges and Wernet internal mixer

In 2004, Bridges and Wernet (NASA Glenn) reported flow and noise measurements for internally mixed two-stream nozzles with variations in the mixer duct length and mixer geometry. The operating conditions involve transonic and low supersonic jet exhaust velocity with a moderate bypass ratio. This configuration has also been used in previous RANS-based noise prediction studies by Rolls Royce and Purdue University, along with a more recent large eddy simulation (LES) study. We have been in touch with Rolls Royce and NASA regarding the nozzle geometry and measurement data. It is hoped that the geometry and data will become available in the future. This configuration is of interest to us because it is unique in providing both jet flow measurements and far-field noise for conditions relevant to civil supersonic flights.

Recent jet noise measurements at NASA Glenn

As part of NASA's Commercial Supersonic Technology Project, under the Advanced Aero Vehicle Program, Dr. James Bridges at NASA Glenn (personal communication, 2020) recently completed jet noise measurements on specially designed modular nozzle configurations at operating points selected to be relevant for commercial supersonic aircraft. He plans to make the nozzle geometry and measurement data available in the future. Included in NASA's plans are noise predictions obtained via a variety of computational tools. We are interested in exploring a selected subset of NASA's test matrix in our Project 59 studies. We have obtained the computer-aided design geometry for the nozzle and began early efforts in geometry cleaning and mesh generation. The mesh generation for this case is fairly challenging because of the steep curvature and sharp edges in the mixer lobes.

Milestones

The simulation plan for Years 1–2 has been determined and followed. Our plan for Year 3, regarding nozzles with noise mitigation concepts, is being finalized, with a focus on studying the effects of mixing enhancement devices under heated jet conditions.

Major Accomplishments

A research plan regarding the nozzle geometry and flow conditions to be studied has been developed. The plan includes both the experimental study by our partner at Georgia Tech and other relevant works from NASA Glenn.

Publications

None

Outreach Efforts

Communication with researchers at NASA Glenn has been established, and ideas for possible collaboration have been exchanged.

Awards

None

Student Involvement

Four graduate students have been involved in this part of the project. G. Wu and K. Matsuno have conducted literature research on relevant jet experiments and simulations that involve similar flow conditions and nozzle mixing devices. T. Shanbhag has performed literature reviews on acoustic modeling of jet noise. K. Matsuno recently completed her Ph.D. O. Martin has joined the project and is helping with the simulations of the mixer nozzle.

Plans for Next Period

We will continue to refine our research plan according to ongoing discussions among teams of Project 59. In particular, we will select nozzle geometries with noise mitigation concepts that are of interest to industrial partners for the development of next-generation supersonic civil transport aircraft.

Task 2 – Perform LES-based Simulation, Modeling, and Validation of Jet Noise Predictions

Objectives

In collaboration with ASCENT partners in Project 59, we plan to develop physics-based analyses for supersonic aircraft exhaust noise. The main goal of these analyses is to develop improved jet noise prediction methods using a multi-fidelity approach. As part of the high-fidelity approach, LESs will be conducted for a carefully selected set of configurations and operating points corresponding to tests conducted by the experimental team at Georgia Tech. The LES data will provide turbulence flow statistics and will be leveraged for acoustic source modeling.

Research Approach

NASA Plug20 internal lobed mixer

In the past project year, efforts have been dedicated to high-fidelity modeling of the NASA Plug20 dual-stream nozzle with an internal plug and lobed mixer (configuration 122Am5Int), shown in Figure 1. LES and far-field acoustics modeling by the permeable Ffowcs Williams–Hawkings (FW-H) formulation were performed using a compressible solver, CharLES, developed by Cascade Technologies. LES-FW-H acoustic predictions have been obtained at Setpoint 1183 (summarized in Table 1) because of its relevance to industry collaborators and because experimental far-field acoustic measurements were available at this setpoint (Bridges and Wernet, 2004). Acoustics were obtained using two different mesh designs. Mesh 1, shown in Figure 2(a), has a resolution of $\Delta x = 0.005D_e$ inside the nozzle (highlighted in red) and coarsens outside the nozzle. Shear layers shed from the lobed mixer and plug and generate four distinct streams of high turbulence kinetic energy (TKE) inside the nozzle that intensify in the jet core. Jumps in TKE are observed outside the nozzle near the mesh transitions.

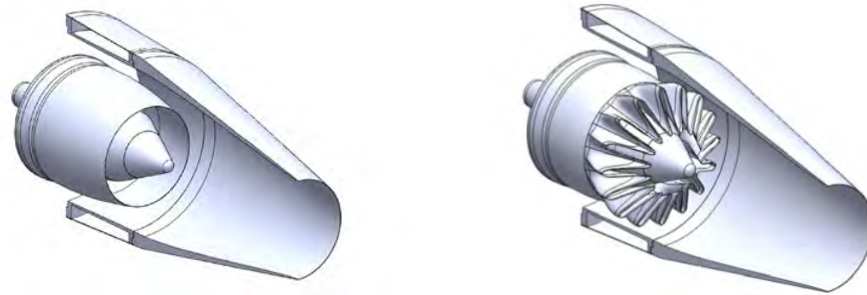


Figure 1. Detailed nozzle geometries. Left: 122Am0pInt confluent nozzle with an internal plug. Right: 122Am5Int confluent nozzle with an internal plug plus lobed mixers.

Table 1. Operating conditions for Setpoint 1183.

Setpoint	NPR (nozzle pressure ratio)	NTRc (nozzle temperature ratio - core)	NTRb (nozzle temperature ratio - bypass)	Mfj (coflow Mach number)
1183	1.8	2.90	1.20	0.3

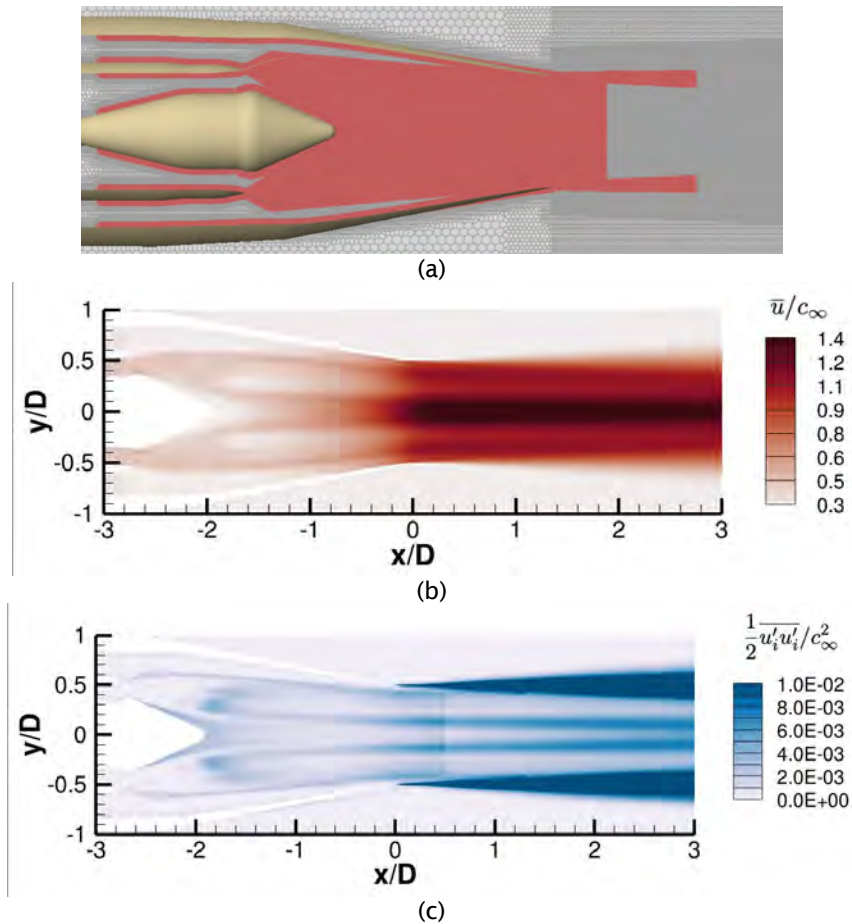


Figure 2. (a) Mesh 1 used for large eddy simulation/Ffowcs Williams–Hawkings computations. Red indicates regions with the finest refinement ($\Delta x = 0.005D_e$). (b) Mean streamwise velocity and (c) turbulence kinetic energy at Setpoint 1183.

In Figure 3, LES-FW-H acoustic predictions generated on Mesh 1 (blue) are compared with experimental measurements (black). The numerical predictions show good agreement with the experimental results at downstream angles. However, the LES results differ from the measurements at low frequencies ($f < 10^3 \text{ Hz}$) in the upstream direction and are missing a broadband hump near $f = 6 \times 10^3 \text{ Hz}$ in the sideline directions. This broadband hump is a common signature of internal lobed mixers, but the direct source of this noise is not well understood. Contours of the near-field TKE suggest that the internal shear layers generated by the lobed mixer are distorted by the transition in mesh size outside of the nozzle, which could contribute to noise underpredictions. Additionally, in this simulation, the nozzle exterior was treated as an adiabatic no-slip wall (no wall model was applied). Because Setpoint 1183 has a Mach-0.3 coflow, it is possible that incorrect modeling of the boundary layer on the nozzle exterior contributed to noise underpredictions. Jumps in the acoustic spectra at high frequencies are believed to be due to the sharp mesh transitions distorting the TKE in the jet shear layers. The increase in the power spectral density at very high frequencies is believed to be a numerical pile-up due to an insufficient FW-H sampling frequency.

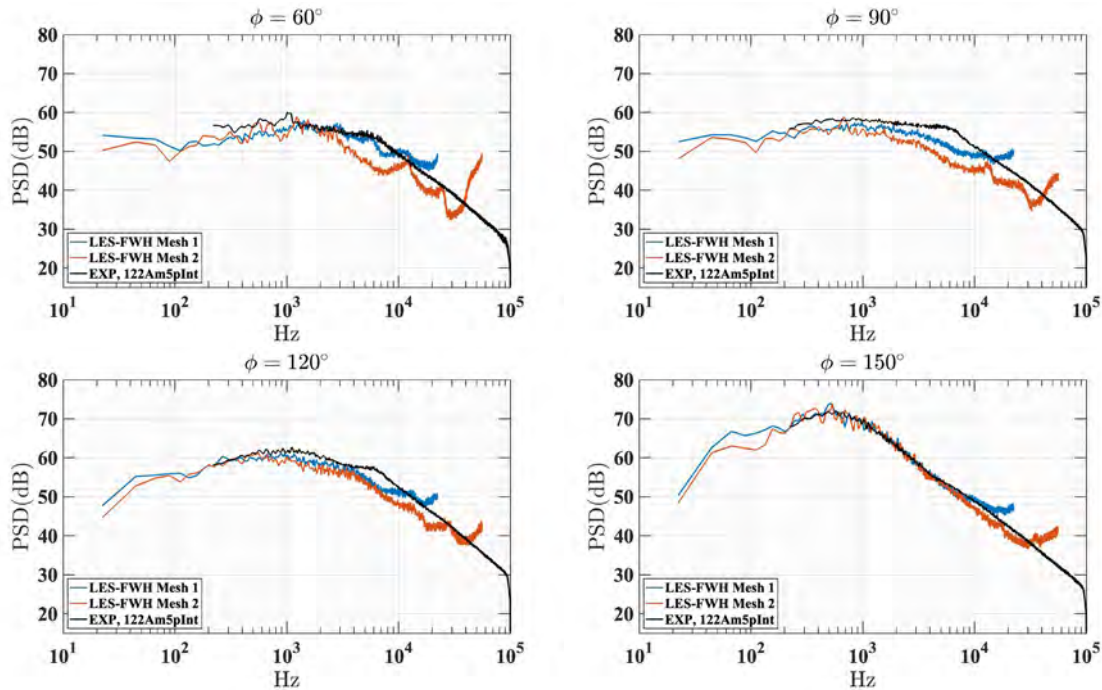


Figure 3. (Left) Primary nozzle. (Right) Coannular nozzle designed by Georgia Tech. FWH: Ffowcs Williams–Hawkings; LES: large eddy simulation; PSD: power spectral density.

To reduce the effect of sharp mesh transitions on shear layer development in the jet core, the mesh transition was moved inside the nozzle. The new mesh (Mesh 2) is shown in Figure 4, along with the velocity and TKE profiles. This modification to the mesh was made in order to (1) test whether nonphysical mesh effects in the jet core were impacting the prediction of the hump at $f = 6 \times 10^3 \text{ Hz}$, (2) improve high-frequency predictions, and (3) assess the sensitivity of the acoustic predictions to the mesh resolution inside the nozzle. In Mesh 2, refinement was also added on the nozzle exterior, and a wall model was applied to more accurately model boundary layer formation from the $M = 0.3$ coflow. The FW-H sampling frequency was increased to push the numerical pile-up to higher frequencies. LES-FW-H acoustic predictions computed via Mesh 2 are shown in Figure 2 (orange). Coarsening the mesh inside the nozzle produced substantial noise underpredictions in the upstream and sideline directions in the mid- to high-frequency range. Downstream angles were not affected by the change in mesh. Acoustics were predicted using several different FW-H sampling surfaces with Mesh 2, but this had a minimal effect on the far-field acoustics. This study demonstrates the importance of having a fine resolution grid inside the nozzle. It also suggests that an even finer resolution inside the nozzle may be necessary to capture the spectral hump at $f = 6 \times 10^3 \text{ Hz}$.

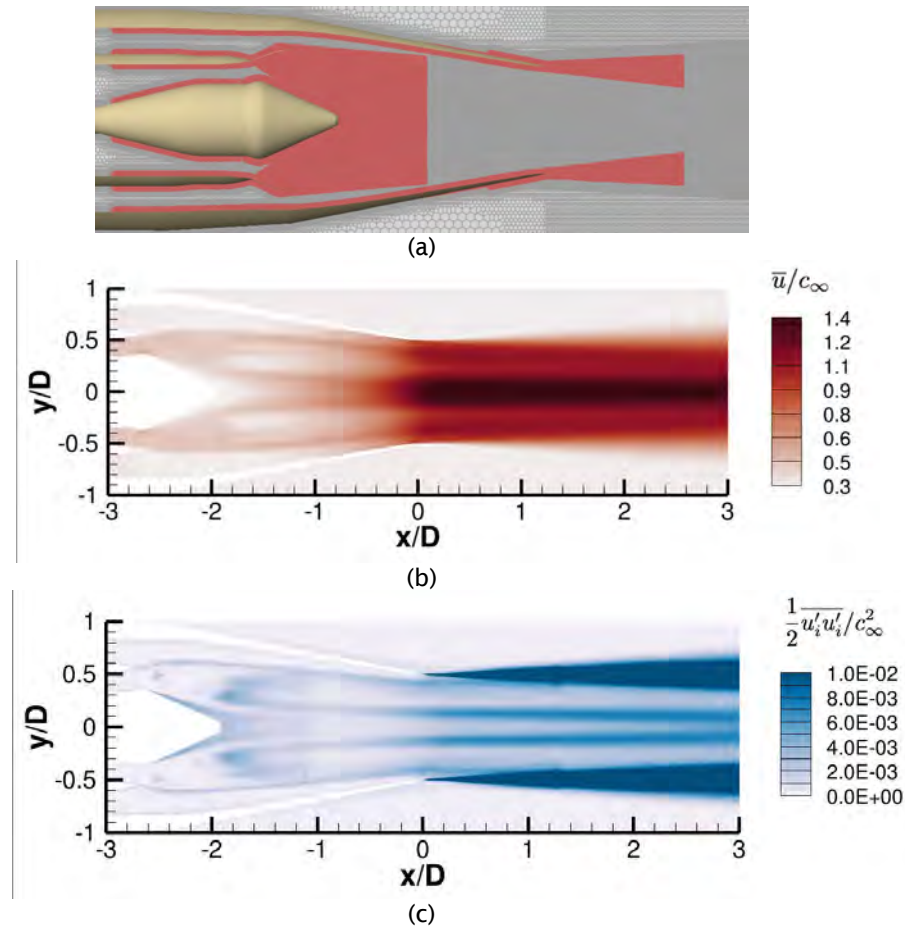


Figure 4. (a) Mesh 2 used for large eddy simulation/Ffowcs Williams–Hawkins computations. Red indicates regions with the finest refinement ($\Delta x = 0.005D_e$). (b) Mean streamwise velocity and (c) turbulence kinetic energy at Setpoint 1183.

To assess the mesh quality inside the nozzle, a third mesh (Mesh 3) was generated with $\Delta x = 0.003125$ inside the nozzle (1.6 times refinement compared with Mesh 1), and volumetric data were sampled inside the nozzle. To reduce computational costs, the flow outside the nozzle was not simulated. In Figure 4, the Q-criterion is used to visualize the vortex structures inside the nozzle. As the mesh is coarsened, the vortex structures responsible for mixing of the core and bypass streams become distorted, which changes the character of the turbulent mixing. Next, we plan to approximate the strength of entropic noise sources inside the nozzle using the LES data for comparison to the underpredictions observed in the far-field. If computational resources permit, we will run another full simulation with further refinement inside the nozzle.

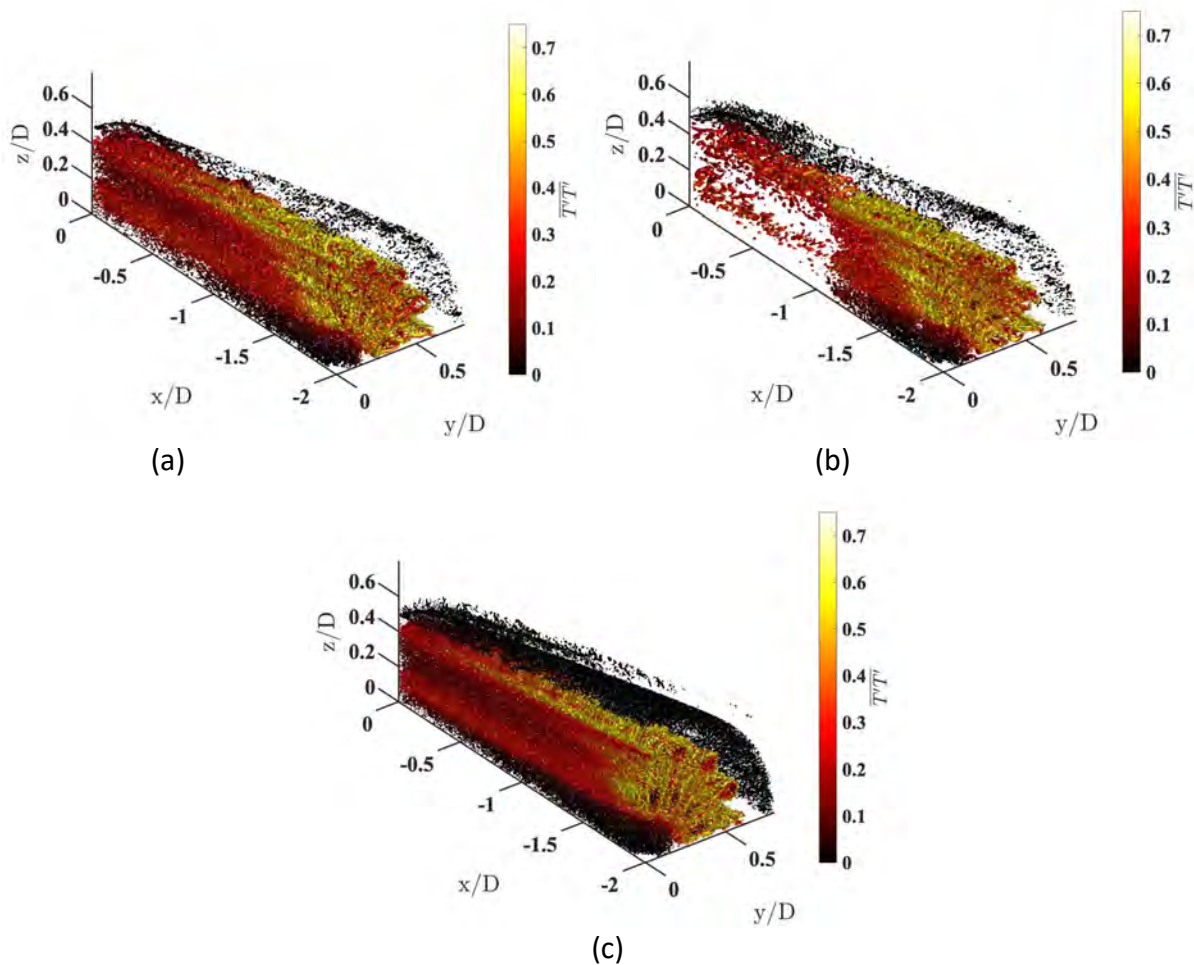


Figure 4. Vortex structures visualized by the Q-criterion ($Q = 10$) inside the nozzle for (a) Mesh 1, (b) Mesh 2, and (c) Mesh 3. Vortex structures are colored by the temperature flux $\frac{T'T'}{T_\infty^2}$.

Comparison of different coaxial geometries

This subsection gives a detailed analysis of the flow features inside the nozzle by comparing results from different nozzles, including the Georgia Tech primary nozzle, the Georgia Tech coannular nozzle, and the NASA 122Am0p1nt nozzle, for conditions in which the core and bypass streams have the same nozzle pressure ratio and nozzle temperature ratio. Under ideal isentropic expansion, the dual streams would have a (velocity ratio) $VR = 1$ and a (temperature ratio) $TR = 1$, therefore behaving as a single jet. However, because of the presence of viscous boundary layers and shear layers in the mixing duct, the flow is not fully mixed at the nozzle exit, which results in a reduction in thrust. Figure 5 shows the nozzle geometries being evaluated, and Figure 6 presents the velocity field inside the nozzles. The values of the mass flow rate and thrust from these configurations are given in Table 2 and are found to be lower than their ideal isentropic conditions. A more detailed analysis has been reported by Wu (2024).

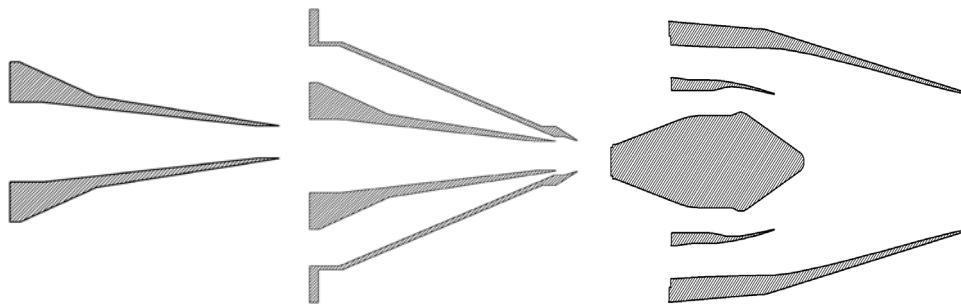


Figure 5. (a) Georgia Tech primary nozzle; (b) Georgia Tech coaxial nozzle; (c) NASA 122Am0plnt nozzle.

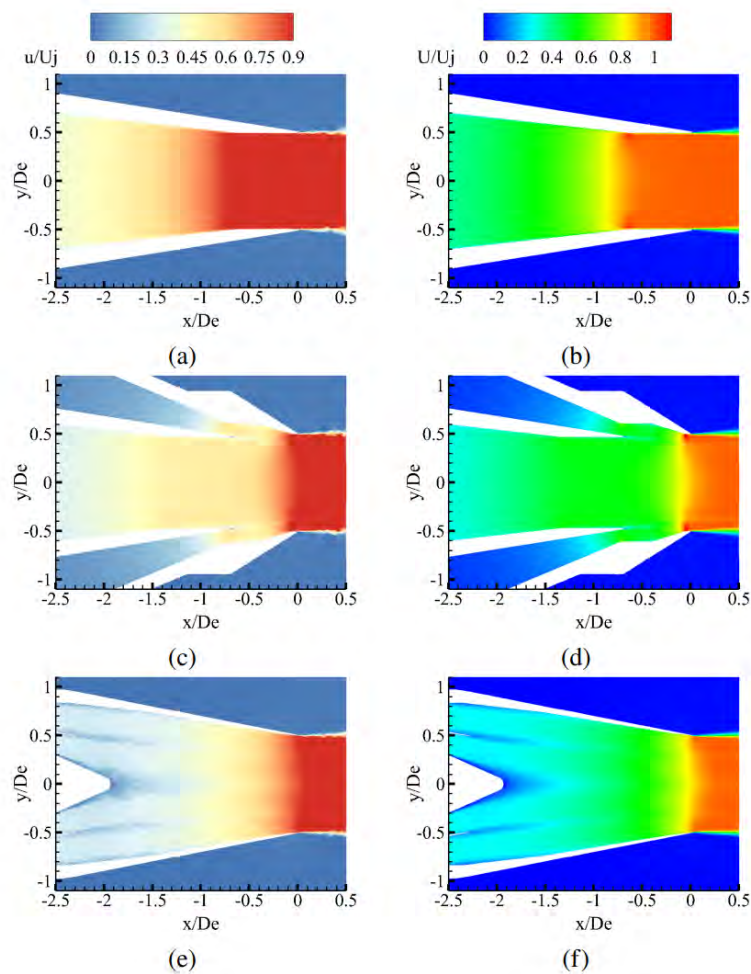


Figure 6. Instantaneous (a,c,e) and time-averaged streamwise velocity (b,d,f) inside the nozzles. From the top to the bottom row: Georgia Tech primary nozzle, Georgia Tech coaxial nozzle, NASA 122Am0plnt nozzle.



Table 2. Mass flow rate, ideal thrust, and actual thrust values for the three different nozzles. Values in brackets are the percentage differences of the actual thrust from the ideal thrust.

Nozzle	M_j	D_e	$\dot{m}/(\rho_0 c_0 A_e)$	$T/(\dot{m}c_0)$, ideal	$T/(\dot{m}c_0)$
Georgia Tech primary	0.80	1.6''	0.651	0.756	0.750 (-0.79%)
Georgia Tech coaxial	0.80	1.7''	0.643	0.756	0.714 (-5.6%)
NASA 122Am0plnt	0.98	6.0''	0.817	0.900	0.895 (-0.56%)

Comparison of a dual-stream jet with the fully mixed equivalent single-jet condition

To study the aeroacoustic effects of temperature and velocity differences between the dual streams, LES results of Setpoint 1183 for two NASA nozzles, 122Am0plnt and 122Am5plnt, are compared. The 122Am0plnt nozzle does not have a lobed mixer at the end of the primary nozzle whereas the 122Am5plnt nozzle does. In addition, the fully mixed equivalent single-jet (FMESJ) condition for Setpoint 1183 is determined based on Tanna’s criteria (Tanna, 1980). The FMESJ flow parameters are summarized in Table 3. Under the ideal expansion assumption for each stream, the FMESJ has the same mass flow rate, exit area, and thrust as Setpoint 1183. The FMESJ simulation has been conducted using the NASA 122Am0plnt nozzle.

Table 3. Summary of the fully mixed equivalent single-jet (FMESJ) flow parameters.

Setpoint	NPR (nozzle pressure ratio)	NTR (nozzle temperature ratio)	Mfj (coflow Mach number)
1183-FMESJ	1.849	1.606	0.354

Figure 7 shows far-field acoustics for the three test points for two polar angles, $\phi = 60^\circ$ and $\phi = 150^\circ$. For the downstream direction, where $\phi = 150^\circ$, the FMESJ, labeled as SP1183-FMESJ, is approximately 10–15 dB quieter than Setpoint 1183, labeled as SP1183, for the same nozzle for $St < 1$. This result agrees with the previous finding by Tanna & Morris (1985). The addition of the lobed mixer in the 122Am5plnt nozzle reduces the noise by 5–10 dB. As St increases above 1, the noise difference between SP1183-FMESJ and SP1183-Mixer diminishes. In contrast, for the upstream polar angle, SP1183-FMESJ has additional noise peaks at $St = 0.2, 0.3, 0.6, 1.2,$ and 2.4 . A more detailed discussion of these results has been provided by Wu (2024).

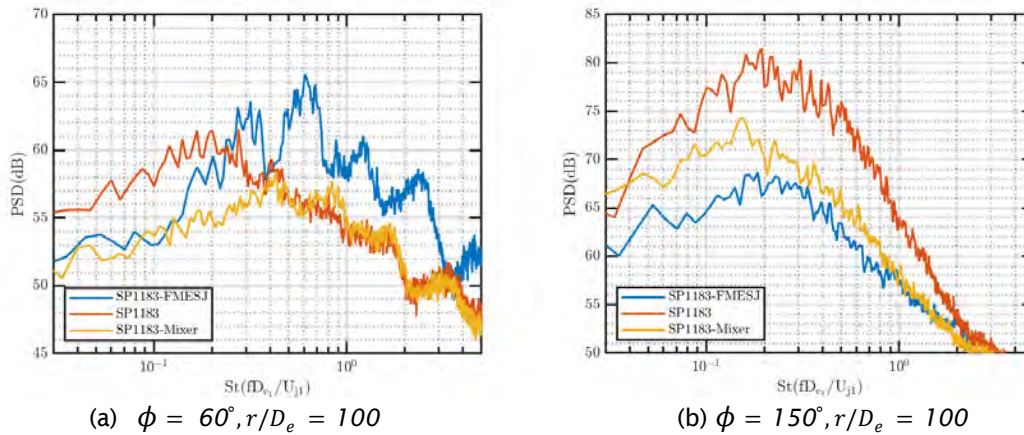


Figure 7. Comparison of far-field noise emitted from Setpoint 1183 for the NASA 122Am0pInt nozzle (labeled as SP1183), the NASA 122Am5pInt nozzle (labeled as SP1183-mixer), and the fully mixed equivalent single jet for the NASA 122Am0pInt nozzle (labeled as SP1183-FMESJ). PSD: power spectral density.

Milestones

LESs for test cases corresponding to the NASA Plug20 experiment have been conducted for two different coaxial nozzles with an internal plug. Numerical errors associated with the mesh inside the nozzle and the jet shear layers as well as the FW-H sampling have been identified and characterized.

Major Accomplishments

Over the past project year, we have made steady progress in the high-fidelity simulations of jet noise in accordance with the test plan established by our Project 59 partners. Using the compressible solver CharLES developed by Cascade Technologies, LESs have been conducted for the Georgia Tech coannular nozzle and two NASA nozzles from the Plug20 campaign. With improved grids, the agreement between LESs and experimental data for the mean velocity statistics is satisfactory, but discrepancies for far-field acoustics still persist. Further investigation of the discrepancies is being conducted, with a focus on examining the mesh requirement near the lobed mixers, the mixing duct boundary layers, and the shear layers. Using the LES data, detailed aeroacoustic features associated with the internal geometry and dual-stream mixing are being analyzed.

Publications

Wu, G. J. "Towards quieter supersonic flight: a computational aeroacoustic study of high-speed jets", Chapter 4. PhD. Thesis. Stanford University. 2024.

Outreach Efforts

Communication with ASCENT Project 59 partners and NASA scientists has been established. Deeper collaboration with the Georgia Tech experiments and with NASA scientists is expected as the project progresses further.

Awards

None.

Student Involvement

Two graduate students, G. Wu and O. Martin, are involved in this project task.

Plans for Next Period

We plan to further refine the current LES results and achieve better agreement with experimental data. Spectral proper orthogonal decomposition (SPOD) analysis with the LES data will be conducted to analyze the large-scale coherent

structures associated with low-frequency acoustics. LES data will be further analyzed to study the internal turbulence mixing and the aeroacoustics of the coaxial jet.

References

- Morris, P., & Boluriaan, S. (2004, May). The prediction of jet noise from CFD data. In *10th AIAA/CEAS aeroacoustics conference* (p. 2977).
- Tanna, H. K., & Morris, P. J. (1985). The noise from normal-velocity-profile coannular jets. *Journal of Sound and Vibration*, *98*(2), 213-234.
- Tanna, H. K. (1980). Coannular jets—Are they really quiet and why?. *Journal of Sound and Vibration*, *72*(1), 97-118.

Task 3 – Conduct RANS-based Simulation, Modeling, and Validation of Jet Noise Predictions

Objectives

This project involves a coordinated development of both low- and high-fidelity approaches for jet noise predictions. For the low-fidelity approach, RANS computations of a broader range of configurations and operating conditions relevant for civil supersonic aircraft will be performed and used to develop improved jet noise source models and more accurate far-field noise propagation kernels.

Research Approach

AD framework for chevron design optimization

We are continuing to validate our previously implemented RANS-based acoustic prediction tools and are extending these tools to create a framework for the efficient design optimization of chevron nozzles for the reduction of far-field noise. In our previous work, we implemented a method based on geometrical acoustics, utilizing information from a standard k-epsilon simulation of the jet flow; we perform all such simulations using the open-source code SU2. The propagation model, which accounts for the effects of sound refraction, is based on a ray-tracing methodology. This implementation makes very few simplifying assumptions about the flow field geometry, allowing this method to be applied to complicated nozzle configurations that result in inherently three-dimensional propagation effects. The highly parallel nature of the ray-tracing algorithm also makes this method ideal for implementation in graphics processing units for accelerated analysis, optimization, and design. We additionally make use of the Autograd framework Jax to automatically differentiate our implementation of both the source and propagation models. Coupling this AD-enabled acoustic code with the discrete adjoint capability in SU2 allows us to efficiently compute the gradients of far-field noise with respect to shape design variables chosen to parameterize the nozzle geometry of interest. These gradients are then incorporated into the optimization algorithm to close the loop.

As a test case, we use the SMC006 chevron nozzle geometry. An acoustic source model based on Ribner's formulation of Lighthill's equation is used, and results show good agreement with far-field acoustic measurements at a sideline observer angle. To account for the effect of sound refraction by the presence of the mean flow, we introduce a flow factor that represents the ratio of the pressure amplitude measured at the observer due to a particular source with and without the jet flow being present. We apply a high-frequency approximation in order to make use of the geometrical ray-tracing method employed to describe wave propagation in nonuniform media. This method does not require the solution of an additional partial differential equation over a domain extending to the far-field and is well suited to complex and possibly asymmetric jet configurations. We follow Pierce's ray-tracing formulation: a very large number of rays is launched from each acoustic source location, the path of each ray is computed by solving a governing ordinary differential equation for the velocity of a wavefront in a moving medium, and the pressure ratio along the ray tubes is subsequently computed via the Blokhintsev invariant. The resulting computations of far-field observer noise at polar observer angles away from the sideline show reasonably good agreement with experimental results, with a higher discrepancy observed at shallower angles.

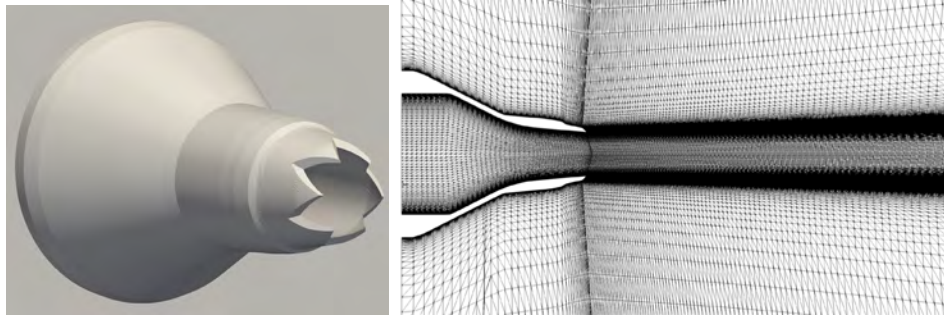


Figure 8. SMC006 chevron nozzle geometry (left) and 2.76-million-point structured hexahedral mesh (right).

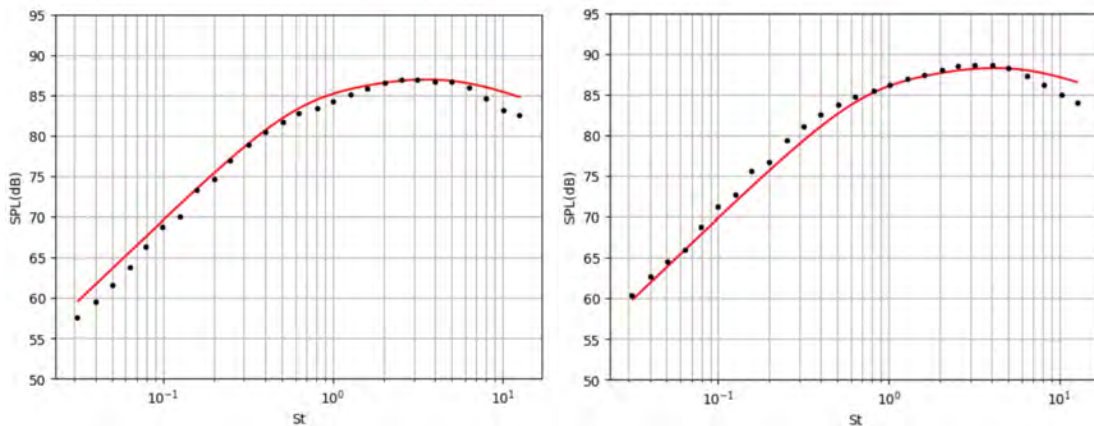


Figure 9. Far-field sound pressure level (SPL) prediction (red) against experimental data (black) at polar observer angles of 70° (left) and 90° (right) from the downstream jet direction.

The acoustic code is then incorporated into the AD optimization framework via a fixed-point accumulation method. The Jax implementation allows the gradient of an objective function with respect to flow state variables at mesh points to be cheaply computed alongside the forward calculation used to obtain the objective function itself; in this case, the objective function being considered is the far-field noise. These mesh point gradients are then accumulated in the SU2 discrete adjoint solver in each iteration used to compute the adjoint flow variables; at convergence, the adjoint fields may then be used to compute the sensitivity of the objective function with respect to linear elastic deformation of the mesh. These sensitivities may be simply translated to design variable sensitivities by using the dot products computed in SU2 DOT. The complete workflow is shown in Figure 10. The sensitivities of noise with respect to both mesh state variables and the overall shape design variables are verified via finite difference calculations, and the comparison shows excellent agreement, as displayed in Figure 11.

In the next stages of this project, we intend to apply this optimization workflow to the SMC006 and other nozzle configurations to investigate the geometric features that result in reduced far-field noise. We are particularly interested in the effect of applying different parameterizations (for example, free-form deformation versus explicit chevron description parameters such as twist or penetration) to the final designs achieved. The importance of chevron penetration to the acoustic field and the associated effects of crossover observed in far-field spectra have been discussed extensively in the literature. We hope to verify these discussions as we observe the geometries that result from minimizing particular frequencies, compared with those that result from minimizing a suitable weighted metric of the far-field sound as a whole.

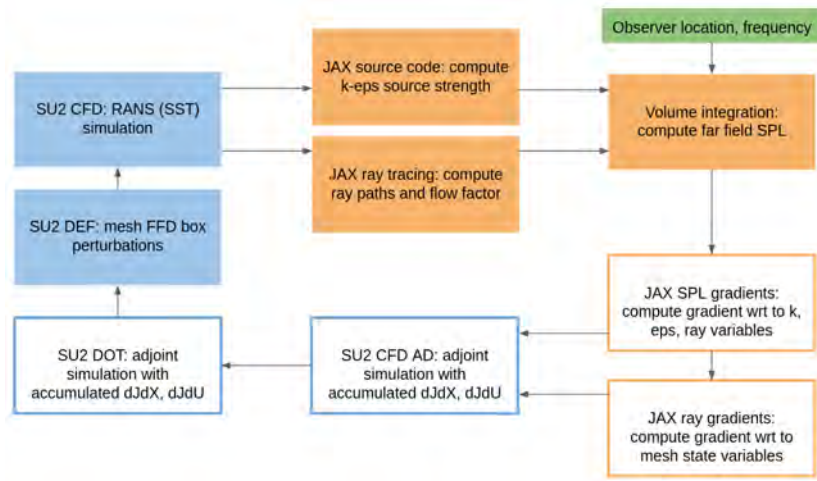


Figure 10. Overall coupled workflow for primal, adjoint, and shape gradient calculations. CFD: computational fluid dynamics; FFD: free-form deformation; RANS: Reynolds-averaged Navier–Stokes; SPL: sound pressure level; SST: supersonic transport.

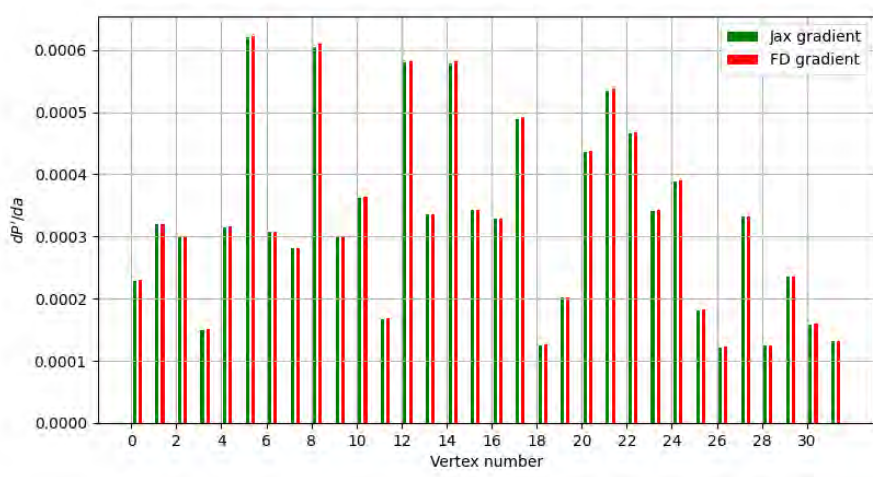


Figure 11. Comparison of Jax AD and finite difference (FD) gradients of integrated sound pressure level with respect to the speed of sound at randomly perturbed mesh points.

Wavepacket jitter modeling

We have continued to investigate how the available LES data can be leveraged to improve our RANS-based source models and have focused on modeling the noise associated with large-scale coherent structures in the flow, which dominate the acoustic signature at shallow downstream observer angles. There is considerable work in the literature on the organized wavepacket structure of the jet near-field; in particular, it has been suggested that an optimal representation of this structure may be computed via the leading-order modes of a SPOD of the unsteady flow variables. A resolvent analysis of the corresponding time-averaged flow, augmented by a suitable forcing distribution, may be used to compute qualitatively similar mode shapes. One such forcing distribution, suggested by Pickering et al. (2021), is a suitably weighted eddy viscosity field, such as that resulting from a RANS simulation of the jet. We apply this methodology to deduce wavepacket structures from the time-averaged Mach-0.9 Georgia Tech round nozzle flow. The resulting wavepacket shapes show similar structure and axial decay to the corresponding SPOD modes.

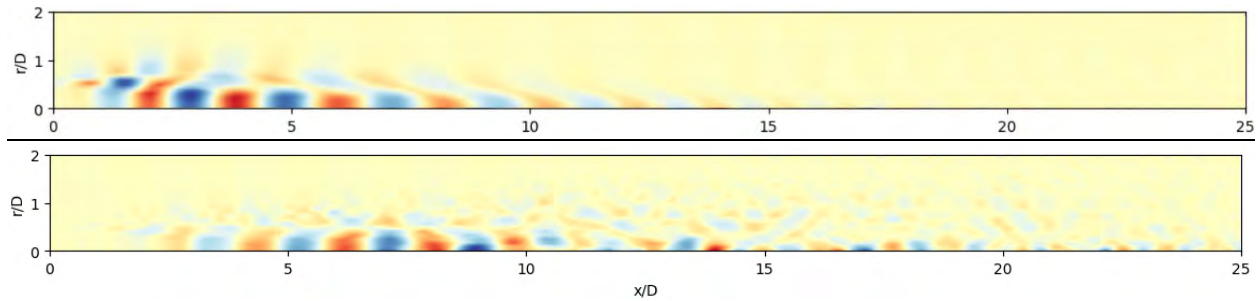


Figure 12. Comparison of leading-order axisymmetric axial momentum mode shape, computed via eddy viscosity-augmented resolvent analysis (upper) and spectral proper orthogonal decomposition of large eddy simulation data (lower): $M = 0.9$, $St = 0.4$.

The radial compactness of the coherent structures in jet flows has led authors such as Cavalieri et al. (2019) and Agarwal to suggest that an equivalent line source may be a suitable acoustic representation of the wavepacket. Following this idea, we compute the cross spectral densities (CSDs) associated with the unsteady axial momentum term from the LES, in order to study how the amplitude and coherence decay properties of such a line source CSD vary with Strouhal number and azimuthal wavenumber.

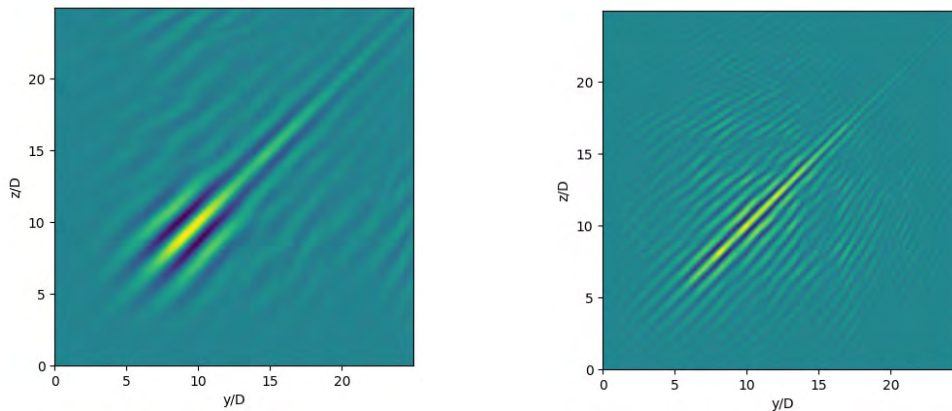


Figure 13. Cross spectral density function of the axial momentum source term, computed from large eddy simulation data with $M = 0.9$: $St = 0.2$ (left) and $St = 0.6$ (right).

Our initial investigation suggests that the RANS-based modeling of the source CSD may be decomposed into three functional components: the variation in source amplitude with jet operating conditions, the spatial extent of the wavepacket as suggested by the autocorrelation term, and the two-point coherence decay with axial separation along the jet. The last term manifests in the time domain as the spatiotemporal modulation of the wavepacket structures that is responsible for jitter.

Amplitude scaling of the source terms with Mach number and temperature ratio has been previously investigated by Tam. We hope to utilize these established relations, together with our own observations on the exponential scaling of amplitude with Strouhal number at different azimuthal modes. Our reconstruction of the wavepacket envelope component using eddy viscosity-augmented resolvent analysis and our efforts to model the coherence decay function are currently ongoing. The work of Cavalieri et al. (2019) and Papamoschou (2018) in this direction have guided our efforts, and we are investigating the use of modified exponential envelopes to properly capture the jitter component at different frequencies. We hope that this relatively simple three-component representation of the source CSD, in conjunction with a free-space Green's function propagator, will offer a reasonable RANS-based prediction of low-frequency shallow-angle noise.

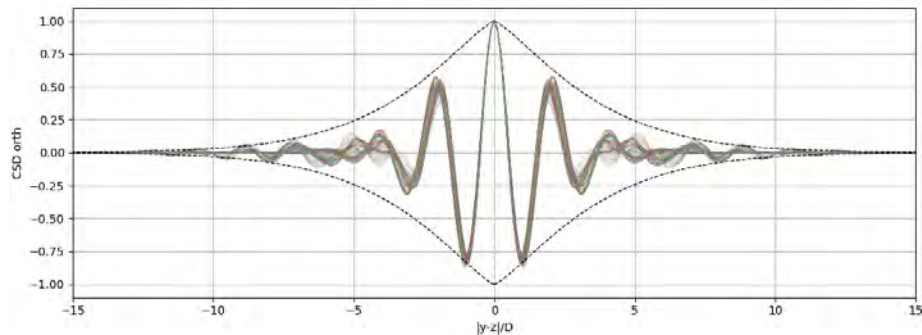


Figure 14. Coherence decay of the cross spectral density function with axial separation; the envelope is fitted to a modified exponential.

Milestones

We have extended our modular implementation of the low-fidelity (RANS-based) acoustic prediction tool to include design optimization capabilities. We have proposed a predictive model for the shallow-angle low-frequency component of jet noise via an analysis of LESs of the Georgia Tech round nozzle geometry.

Major Accomplishments

We have extended our AD-enabled RANS-based acoustic prediction tool to integrate with the discrete adjoint solver in SU2 to efficiently compute the gradients of far-field noise with respect to shape design variables used to parameterize nozzles. We have validated the resulting shape gradients against values obtained by finite differencing for the SMC006 chevron nozzle case and obtained reasonable agreement.

We have proposed a simple predictive model of the acoustic line source CSD, using an eddy viscosity-augmented resolvent analysis to deduce coherent wavepacket structures in the hydrodynamic region of a jet, coupled with an explicit modified exponential function to account for the effects of axial coherence decay and the corresponding jitter.

Publications

Conference Proceedings

Shanbhag, T. K., Zhou, B., Ilario, C., & Alonso, J. J. (2024). An AD framework for jet noise minimization using geometrical acoustics. In *AIAA SCITECH 2024 Forum* (p. 2309).

Outreach Efforts

None.

Awards

None.

Student Involvement

T. Shanbhag has led the efforts with geometrical acoustics, AD-enabled chevron optimization, and wavepacket jitter modeling described for Task 3.

Plans for Next Period

We hope to study optimized nozzle geometries for a number of different baselines and parameterizations using the previously described design framework. With respect to jitter modeling, we will continue to develop our model in the context of our observations from LES data and investigate its capability in a predictive setting.

References

Blokhintzev, D. (1946). The propagation of sound in an inhomogeneous and moving medium I. *The Journal of the Acoustical Society of America*, 18(2), 322-328.



- Cavalieri, A. V., Jordan, P., & Lesshafft, L. (2019). Wave-packet models for jet dynamics and sound radiation. *Applied Mechanics Reviews*, 71(2), 020802.
- Ilário, C. R., Azarpeyvand, M., Rosa, V., Self, R. H., & Meneghini, J. R. (2017). Prediction of jet mixing noise with Lighthill's Acoustic Analogy and geometrical acoustics. *The Journal of the Acoustical Society of America*, 141(2), 1203-1213.
- Khavaran, A., & Bridges, J. (2005). Modelling of fine-scale turbulence mixing noise. *Journal of Sound and Vibration*, 279(3-5), 1131-1154.
- MJ, Lighthill. Sir. (1952). On sound generated aerodynamically; I general theory. In *Proc. Royal Soc.* (Vol. 211, pp. 564-587).
- Morris, P., & Boluriaan, S. (2004, May). The prediction of jet noise from CFD data. In *10th AIAA/CEAS aeroacoustics conference* (p. 2977).
- Papamoschou, D. (2018). Wavepacket modeling of the jet noise source. *International Journal of Aeroacoustics*, 17(1-2), 52-69.
- Pickering, E., Rigas, G., Schmidt, O. T., Sipp, D., & Colonius, T. (2021). Optimal eddy viscosity for resolvent-based models of coherent structures in turbulent jets. *Journal of Fluid Mechanics*, 917, A29.
- Pierce, A. D. (2019). *Acoustics: an introduction to its physical principles and applications*. Springer.
- Ribner, H. S. (1969). Quadrupole correlations governing the pattern of jet noise. *Journal of Fluid Mechanics*, 38(1), 1-24.
- Tanna, H. K. (1980). Coannular jets—Are they really quiet and why?. *Journal of Sound and Vibration*, 72(1), 97-118.
- Tanna, H. K., & Morris, P. J. (1985). The noise from normal-velocity-profile coannular jets. *Journal of Sound and Vibration*, 98(2), 213-234.



Project 059(E) Moderate-fidelity Simulations for Efficient Modeling of Supersonic Aircraft Noise

The Pennsylvania State University

Project Lead Investigator

Philip Morris
Boeing/A.D. Welliver Professor Emeritus
Department of Aerospace Engineering
Pennsylvania State University
233C Hammond Building
University Park, PA 16802
814-863-0157
pjm@psu.edu

University Participants

Pennsylvania State University (Penn State)

- P.I.s: Dr. Philip Morris (P.I.), Dr. Daning Huang (co-P.I.)
- FAA Award Number: 13-C-AJFE-GIT-070
- Period of Performance: January 1, 2023 to December 31, 2023
- Tasks:
 1. Grid generation and large eddy simulations (LESs)
 2. Hybrid Reynolds-averaged Navier-Stokes (RANS) and LES approach for noise efficient predictions

Project Funding Level

The project is funded at the following level: FAA: \$100,000. Cost-sharing of \$100,000 is provided by Gulfstream Aerospace Corporation, a General Dynamics Company.

Investigation Team

Dr. Philip Morris (P.I.), All Tasks
Dr. Daning Huang (co-P.I.), All Tasks
Ms. Dana Mikkelsen (graduate student), All Tasks

Project Overview

The purpose of this project is to develop and assess efficient computational tools to simulate the flow and noise of civil supersonic aircraft engines.

The prediction of noise from supersonic jets, particularly when noise reduction devices are present, is a challenging computational task. Methods based on RANS solutions are relatively inexpensive to perform and provide satisfactory predictions of the average flow field, even for quite complicated geometries. The subsequent prediction of noise according to acoustic analogies is highly efficient but faces difficulties when the nozzle does not have simple axisymmetric geometry. Methods based on LESs provide considerably more information than those based on RANS methods about the unsteady flow and the noise generated. However, LESs are computationally expensive, particularly when the engine geometry is complex. This complexity is encountered in the case of nozzles with noise reduction devices, such as internal mixers. Noise predictions based on LES can be made quite efficiently by using the Ffowcs Williams and Hawkins (FW-H) acoustic analogy (Farassat and Succi, 1982; Ffowcs Williams and Hawkins, 1969), but long-time records are required to predict the noise radiated to far-field observers, thus adding additional expense to LES.



The approach in Project 59(E) strikes a compromise between the accuracy and high computational cost of LES and the noise prediction limitations of RANS-based simulations. The simulations being conducted in the initial stage of the project use RANS, and these calculations serve as a starting point for the LES. In anticipation of the addition of internal mixers to the nozzle geometries, only RANS simulations are planned to be conducted for the internal flow; then LES, coupled with the FW-H acoustic analogy, will be used to predict the external flow and the noise generated. The RANS solution at the jet exit will be used as an initial condition for the external LES. This process will require the addition of some unsteady information, as guided by a very limited number of LESs. This approach will reduce the total computational cost, because it removes much of the geometric complexity and the associated grid requirements for LES of the internal flow.

The utility of this approach is that it will make LES for nozzles with noise reduction devices more accessible to more users, particularly industry engineers with very limited computational resources and time available to perform multiple simulations in the design process.

In addition, the LES-based predictions will be supplemented by more traditional acoustic analogy approaches based on RANS, with an emphasis on modeling the high-Strouhal-number noise radiation. As described below, the future research direction will combine a RANS-based acoustic analogy approach for noise radiation to large angles to the jet downstream axis and a very coarse LES approach for noise radiation in the peak noise radiation direction.

If successful, ASCENT Project 59(E) will develop methods to predict the noise generated and radiated by civil supersonic aircraft engines. The developed tools should enable airframe and engine manufacturers to assess the noise impacts of engine design changes, and to determine whether the designs will meet current or anticipated noise certification requirements.

Project Direction Change

During the first project year, because of a change in direction from the originally proposed research, the original project was split into two parts. A new Project 59(A), being conducted at the Georgia Institute of Technology (Georgia Tech), examines the effects of different inlets and the introduction of noise reduction devices on the performance of selected engine cycles and geometries. A new Project 59(E), which is the topic of the present report, focuses on the prediction of the flow and noise from different nozzle configurations.

Major Accomplishments

The tasks for this project year included continued RANS simulations as well as LESs. The focus was on the Georgia Tech dual-stream nozzle. LES simulations were performed at Gulfstream Aerospace, by using different grid resolutions to determine the flow resolution relative to different turbulent length scales. An acoustic analogy code was based on Tam and Auriault's model and integrated with output from the RANS simulations. Noise predictions with this method have been made for the Georgia Tech dual-stream nozzle and compared with measurements.

Task 1 - Grid Generation and LESs

Pennsylvania State University

Objectives

During this research period, our focus turned to the dual-stream nozzle geometry provided by Georgia Tech. This converging nozzle has a core nozzle exit diameter of 0.04064 m, a bypass duct exit diameter of 5.334 cm, and an exhaust nozzle with an exit diameter of 4.32 cm. The nozzle has a length of 3.02 cm. Extending the studies completed in 2022, in which an unstructured polyhedral grid was found to provide improved lipline and centerline velocity statistics with respect to a structured Cartesian grid for a single-stream nozzle, a similar approach was used for the dual-stream nozzle.

Research Approach

The driving factor in the development of a grid for LES for jet noise predictions is its ability to capture a range of turbulence scales. To match turbulence statistics with experimental data, we created a grid refinement zone targeting the shear layer of the jet at the nozzle lip (Figure 1). It has a grid length of 0.0191cm and extends from the nozzle exit to approximately 5.75 exit diameters downstream. Additional grid refinement zones extend further downstream, beginning with a grid length of 0.0254 cm at 5.75 D and increasing by 0.0127 cm with each further refinement zone. The full shear refinement zone is shown in Figure 2.

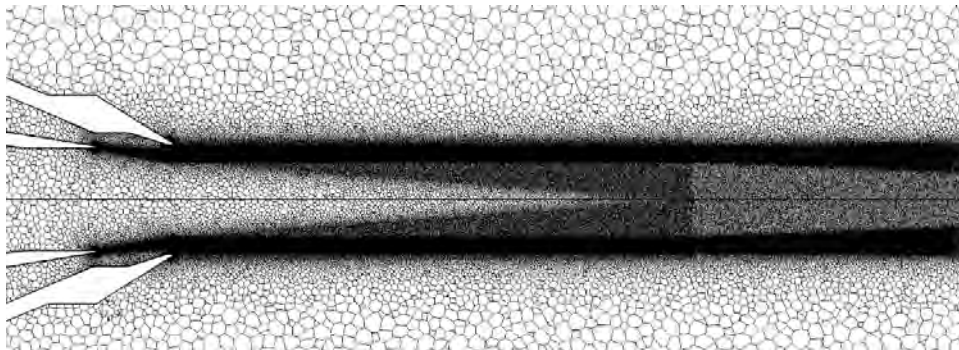


Figure 1. Near-nozzle shear layer refinement.

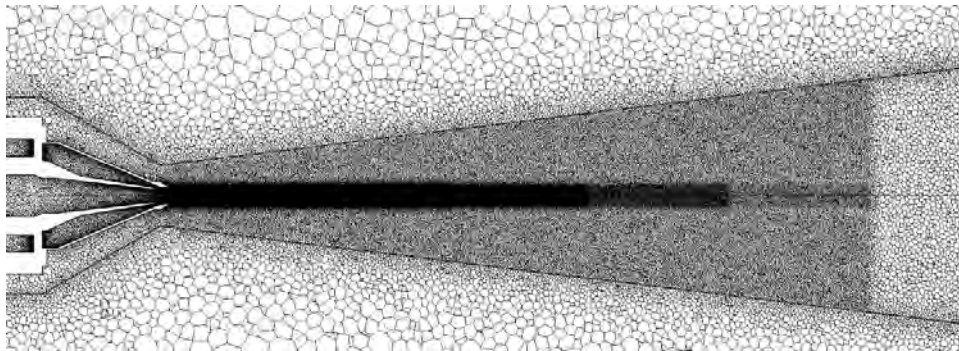


Figure 2. Full shear refinement zone.

A conical FW-H surface was imprinted with a diameter of 8.80 cm at the nozzle exit and a diameter of 83.84 cm at 150 D downstream. The surface continued past the nozzle geometry upstream to avoid spurious acoustic results at the nozzle exit. The FW-H surface, shown in Figure 3, had a surface grid length of 0.5588 cm. The generated mesh had approximately 63 million cells, representing an increase from the 43 million cells used in previous grids for the core nozzle alone.

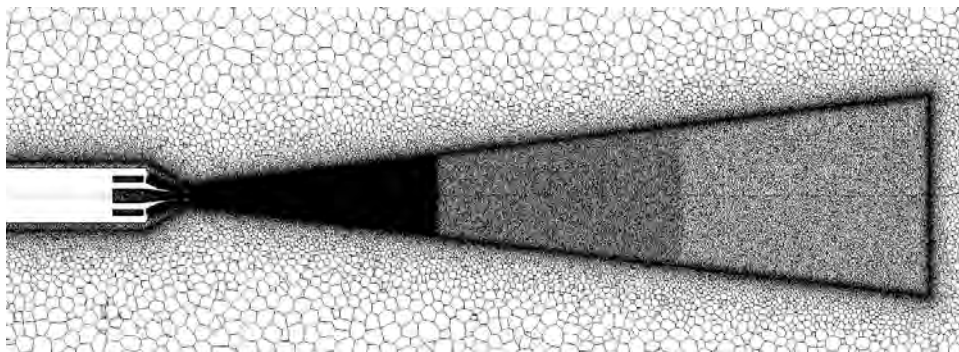


Figure 3. FW-H surface.

The LES was run at a nozzle pressure ratio (NPR) of 1.39 for the inner and outer streams, with a total temperature ratio (TTR) of 1.0 for both streams. A second-order temporal discretization with a time step of 1×10^{-6} s was used. Calculated instantaneous Mach number contours are shown in Figure 4.

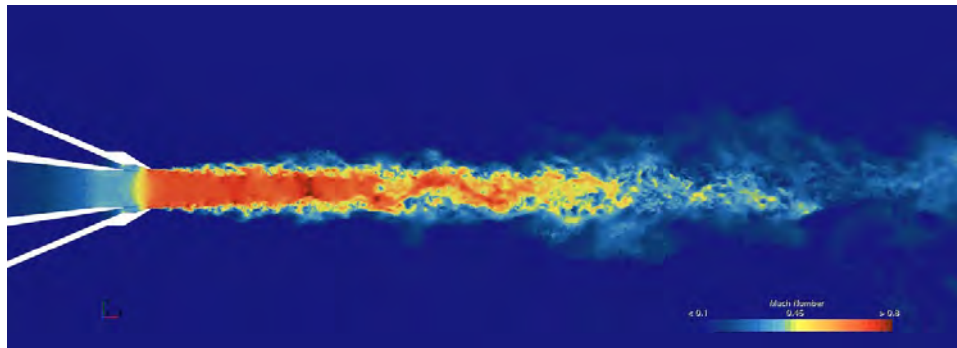


Figure 4. Instantaneous Mach number contours at NPR = 1.39 and TTR = 1.

The velocity statistics obtained from this LES showed reasonable agreement with the experimental statistics obtained by Georgia Tech, as shown in Figure 5. U is the axial velocity and U_j is the jet exit velocity. The LESs underpredict the length of the potential core. However, this finding is not unusual when the boundary layers in the nozzle are not fully resolved. The lipline mean velocity is also underpredicted, again because of the lack of nozzle wall boundary layer resolution.

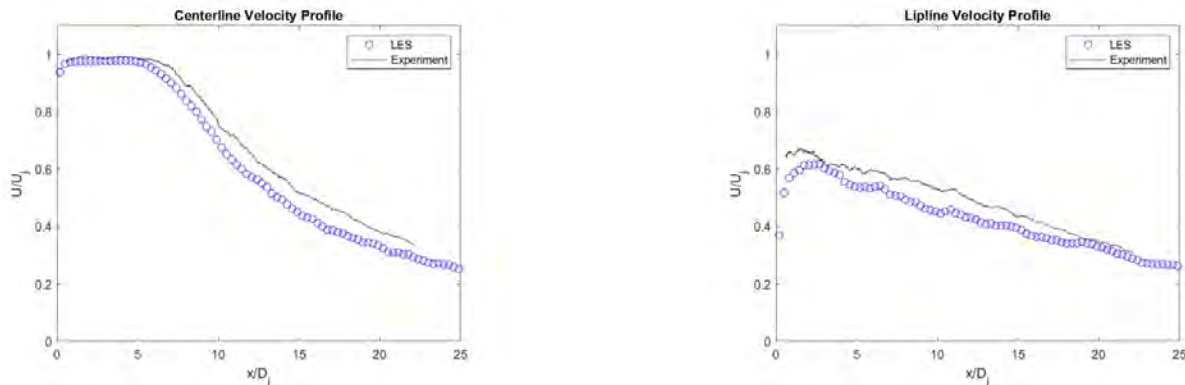


Figure 5. Experimental and computational U/U_j for the centerline (left) and lipline (right).

The turbulence intensity (TI) predicted by the LES consistently falls below those obtained experimentally, as shown in Figure 6. The centerline turbulence intensity profile shows good agreement until approximately $x/D = 7.5$ and underpredicts and misses the peak intensity. The lipline turbulence profile shows good agreement until $x/D = 5$, then underpredicts the turbulence to a lesser degree than on the centerline until approximately $x/D = 15$, before further decreasing. Additional work is clearly needed to improve the turbulence statistics.

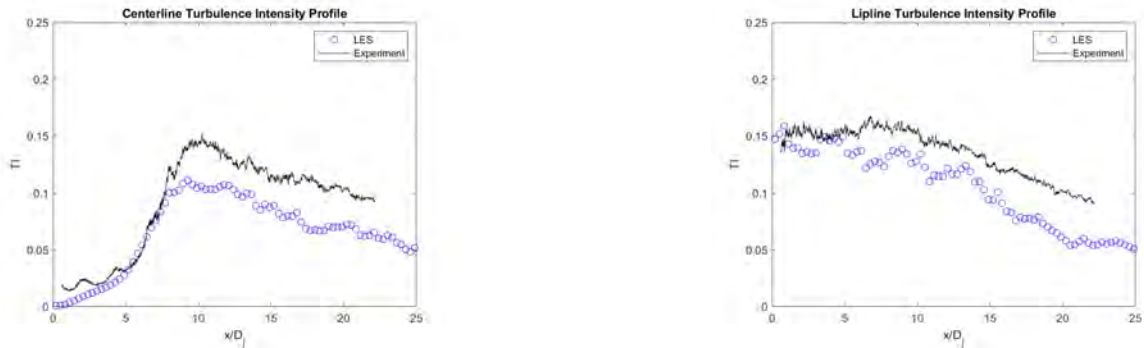


Figure 6. Experimental and computational U/U_j for the centerline (left) and lipline (right).

The LES simulations were performed at Gulfstream Aerospace in Savannah, GA, whereas the graduate research assistant worked during a summer internship. The computational resources at Penn State, for which no cost is charged to the grant, are sufficient to perform RANS simulations but are insufficient for the LESs of the required scale. Therefore, the approach planned for the next year, which started in the present year, is expected to provide solutions with “engineering accuracy,” from limited computational resources. This approach is described below.

Task 2 - Hybrid RANS and LES Approach for Noise Efficient Predictions

Pennsylvania State University

Objectives

On the basis of the problems with computational resources described in the section above, we spent time this year developing a less computationally expensive approach. The basic concept and some initial results are described in this section, and plans for implementation of the approach are given in next year’s plans.

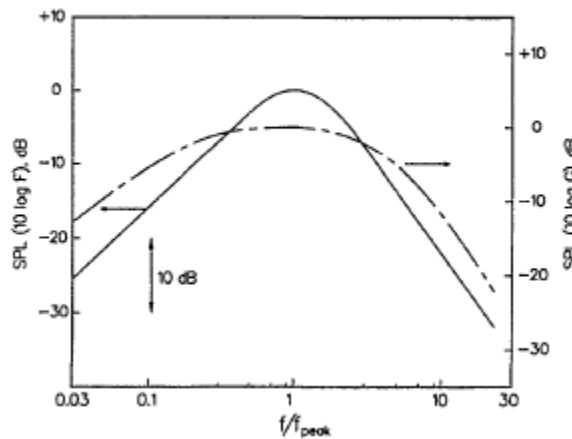


Figure 7. Similarity spectra for the two components of turbulent mixing noise. -----, large turbulent structures/instability wave noise; --- -- ---, fine scale turbulence noise.

Research Approach

The idea arose from experimental results providing convincing evidence that jet noise consists of two characteristic source mechanisms. This first was proposed by Tam et al. (1996), who identified a small-scale similarity spectrum and a large-scale similarity spectrum. With these two spectral shapes, the radiated noise spectra of jets from a wide range of operating

conditions could be matched very successfully. The original comparisons by Tam et al. were made for supersonic jets, but Viswanathan (2004) has shown that the same similarity spectra can be used to represent both subsonic and supersonic jet noise. A more recent overview of the “two-source model” has been given by Tam (2019). The two similarity spectra are shown in Figure 7.

Figure 8 shows how jet noise spectra at three polar angles can be decomposed into the two similarity spectra. At 90°, the full spectrum is described by the small-scale similarity spectrum. At 145°, both similarity spectra are required to match the full spectrum. Finally, at 165°, the large-scale similarity spectrum contributes almost completely to the full spectrum except for a possible contribution from the small-scale similarity spectrum at high Strouhal numbers. These examples are for an unheated $M_j = 0.51$ jet. For a higher Mach number, the large-scale similarity spectrum dominates over a wider angle range. In addition, Tam and Zaman (2000) have shown that the same similarity spectrum can be used to represent the noise radiation to sideline directions for nozzles with tabs or rectangular nozzles, thus indicating that nozzle geometry has little influence on the noise radiation in these directions.

This behavior, particularly for the small-scale similarity spectrum is similar to that displayed by the noise predictions using the Tam and Auriault (1999) acoustic analogy for the noise from small-scale turbulence. Figure 9 shows predictions of jet noise from a convergent nozzle at the same acoustic Mach number of 0.875. One is unheated and has a static temperature ratio of 2.5. The upper set of data are for the heated jet, and the lower set are for the unheated case. Predictions for three acoustic analogy models were performed by Gryazev et al. (2023). The models were those developed by Tam and Auriault (1999) and Khavaran and Bridges (2004), as well as the generalized acoustic analogy (GAA) by Goldstein and Leib (2008). The predictions for the Tam and Auriault model follow the trend seen in Figure 8, whereas the other models follow the experimental data more closely, because these models, particularly the GAA, attempt to model a non-isotropic source to represent noise radiation to large angles. The GAA model relies on LES to obtain the properties of the non-isotropic source, and whether the same properties would be retained if the geometry or complexity of the jet nozzle were different is unclear.

The findings suggest that Tam and Auriault’s model can represent the noise radiated by small-scale turbulence. The difference between the small-scale noise prediction and the full spectrum can be attributed to the contribution from the large-scale turbulence.

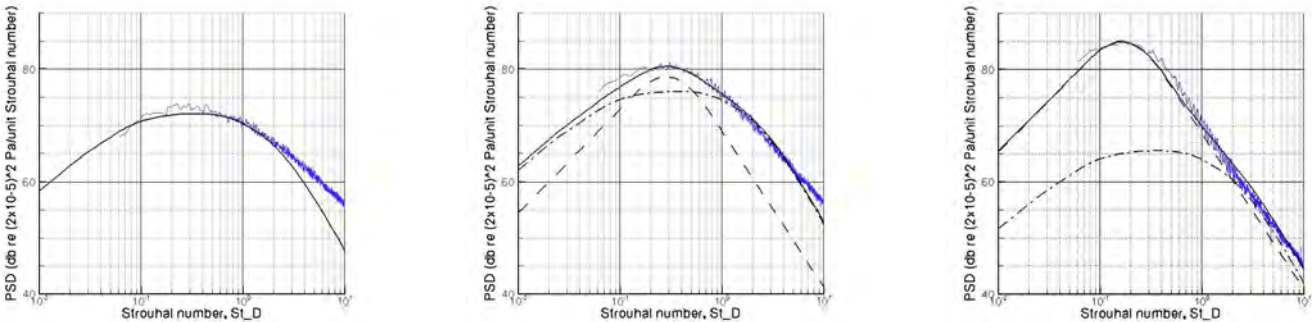


Figure 8. Demonstration of how the two similarity spectra can represent the full radiated noise spectrum at different polar angles: 90° (left), 145° (center), and 165° (right).

[^] These data were obtained as part of the Strategic Investment in Low-carbon Engine Tech program and were performed at QinetiQ.

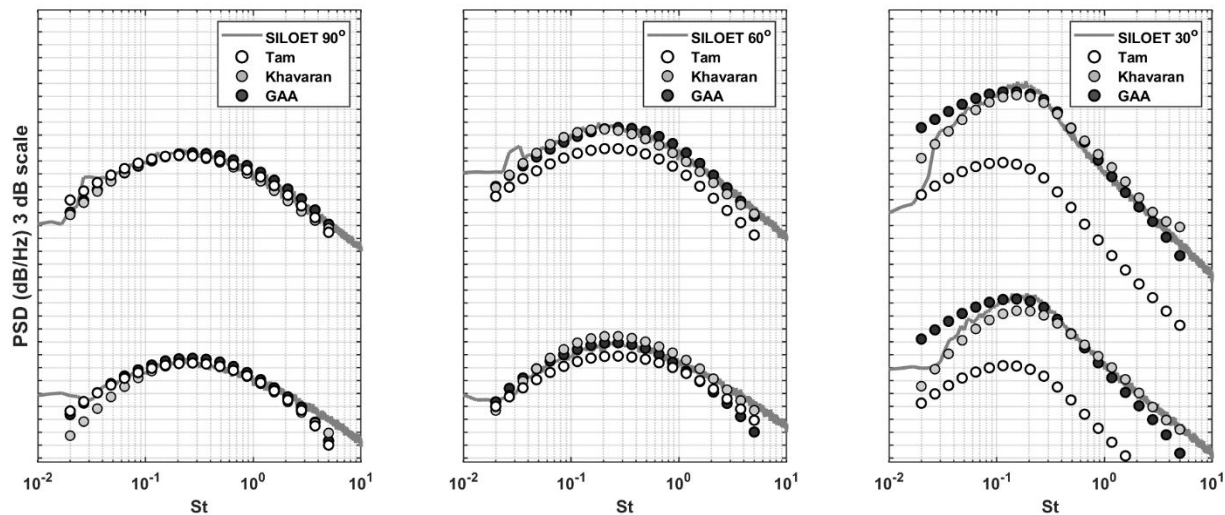


Figure 9. Noise spectra predictions of the cold (bottom) and hot (top) Strategic Investment in Low carbon Engine Technology (SILOET) jet, using the correlation scales based on the turbulent kinetic energy and dissipation rate reconstructed from RANS: comparison of the Tam and Auriault (1999), Khavaran and Bridges (2004), and GAA1 models with experimental results for 90° (left), 120°(center), and 150° (right) observer angles. Adapted from Gryazev et al. (2023).

Unfortunately, no viable reduced-order model is available to predict the large-scale turbulence noise. However, methods based on the parabolized stability equations (Sinah et al. (2014)) and one-way Navier–Stokes solutions (Towne et al. (2022)) show some promise for simple geometries. Of course, large-scale wall-modeled LES has been shown to be able to predict the entire radiated noise spectrum, but at substantial computational cost (e.g., Brès and Lele (2019)).

However, if the noise radiation in the peak noise direction is needed, to supplement the small-scale radiation to other larger angles that can be predicted well by the small-scale acoustic analogy, a full high-resolution LES may not be required. Supporting evidence has been provided by Bodony and Lele (2007), who have shown that a grid of only 100,000 points can yield reasonable noise predictions in the peak noise direction for a Mach 0.9 unheated jet. Figure 10 shows an example from Bodony and Lele (2007).

The approach planned for the next year will use an acoustic analogy for the noise at large angles to the jet downstream axis and a coarse LES with an FW–H acoustic analogy for the smaller angles. Some initial calculations have been performed this year, focusing on the acoustic analogy component.

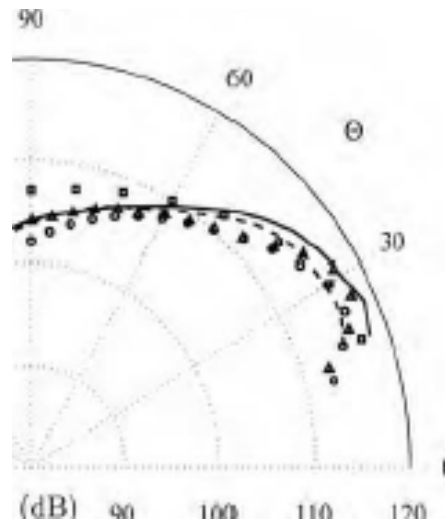


Figure 10. Far-field OASPL taken at a distance of $30 D_j$ from the nozzle exit. Legend: —, 100,000-point simulation; - -, 1,000,000-point simulation of Bodony and Lele (2004); □, Freund (2001); ◦, Stromberg et al. (1980); △, Mollo-Christensen et al. (1964). From Bodony and Lele (2007).

A RANS simulation was conducted for the dual-stream Georgia Tech nozzle geometry for an NPR of 1.39. Velocity magnitude contours are shown in Figure 11. This is the case with the $0.7 D_j$ nozzle extension (0.7-00145).

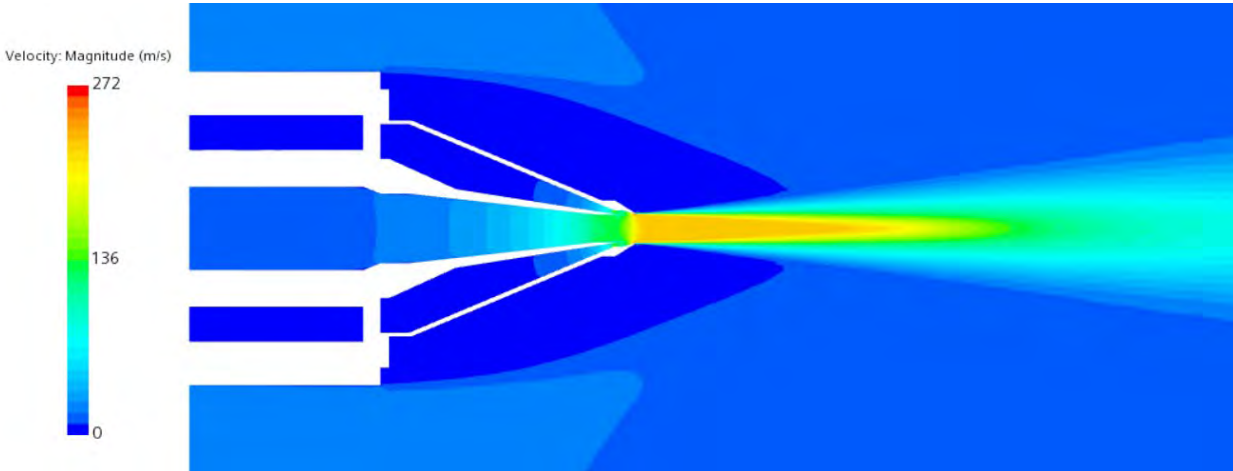


Figure 11. Velocity contours for the co-annular nozzle at NPR = 1.39 and TTR = 1.

The extracted centerline axial velocity and lipline axial velocity in Figure 12 show good agreement with the experimental data provided by Georgia Tech for the same nozzle geometry.

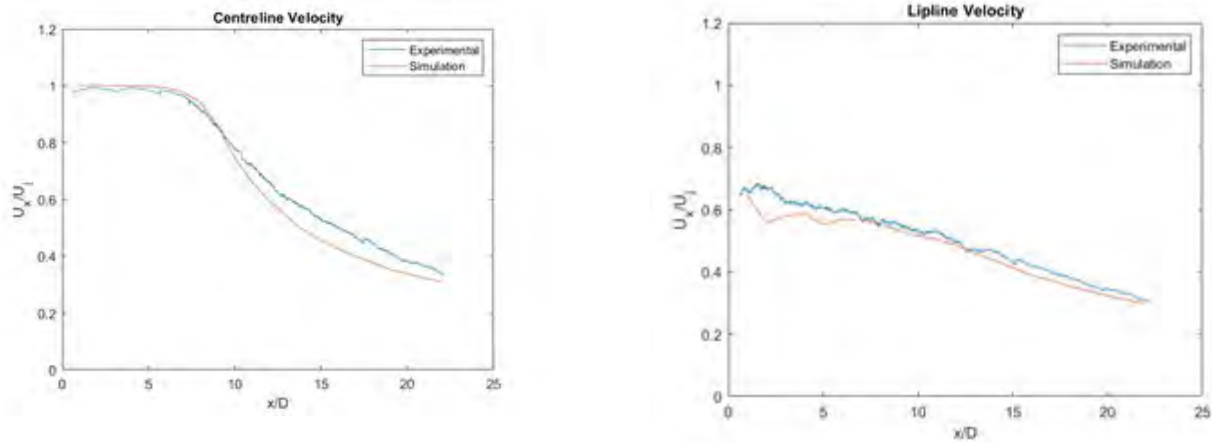


Figure 12. Comparison of centerline (left) and lipline (right) axial velocity at NPR = 1.39 and TTR = 1 from experiments provided by Georgia Tech and RANS simulations using STARCCM+.

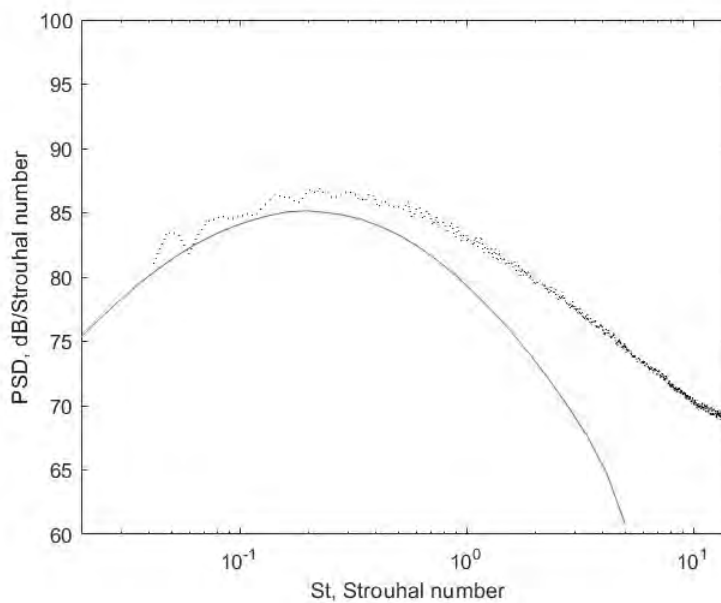


Figure 13. Far-field power spectral density prediction for a $M_j = 0.985$ SHJAR unheated jet. Red, prediction; black, experiment.

On the basis of the RANS simulation, a noise prediction was made at 90° to the jet axis, as shown in Figure 13, compared with the Georgia Tech data. Notably, the model constants used in this prediction are the original values proposed by Tam and Auriault (1999). Optimization of these parameters would yield improved results, as demonstrated, for example, by Shanbhag et al. (2023).

For example, Figure 14 shows a prediction using the same model parameters for NASA Small Hot Jet Acoustic Rig (SHJAR) data for an unheated $M_j = 0.985$ jet. The agreement is much better in this case.

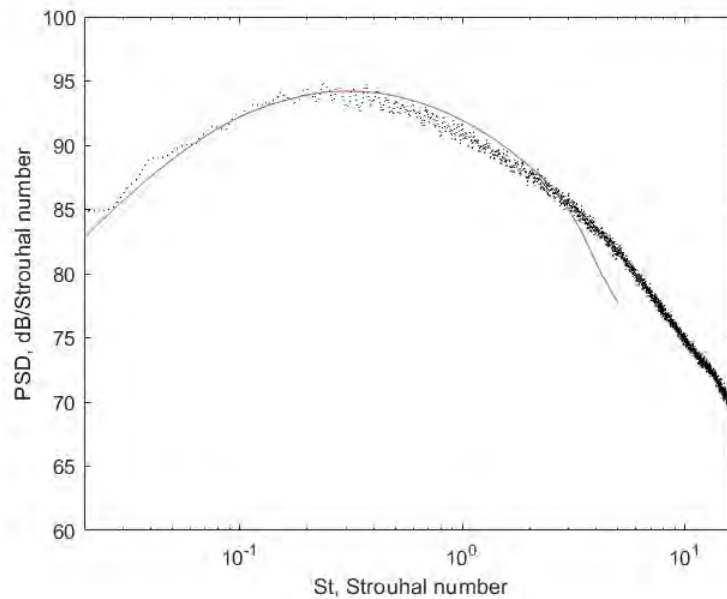


Figure 14. Far-field power spectral density prediction for an $M_j = 0.985$ SHJAR unheated jet. Red, prediction; black, experiment.

Milestones

Table 1 shows the anticipated list of milestones for the next research period.

Table 1. Anticipated tasks and milestones for the next research period.

Task No.	Milestone	Planned due date
Task 1	Complete testing of FW-H noise prediction code by using LES data already obtained by Gulfstream Aerospace	February 14, 2024
Task 2	Run additional RANS simulations for the Georgia Tech dual-stream nozzles, and use the fine-scale acoustic analogy code to make noise predictions at sideline angles. Modify the model parameters as necessary, to obtain a universal set of parameters	March 31, 2024
Task 2	Develop coarse LES grid for the Georgia Tech nozzles, perform LES simulations, and compare with flow measurements	March 31, 2024
Task 3	Couple coarse LES output with FW-H code and predict radiated noise	May 31, 2024
Task 4	Repeat flow and noise predictions for additional Georgia Tech nozzle configurations	July 31, 2024
Task 5	Apply hybrid noise prediction method to mixer nozzles, and compare with experimental findings	October 31, 2024
Task 6	Submit annual ASCENT report	December 31, 2024

Publications

None.

Outreach Efforts

ASCENT Advisory Board Meeting.

Awards

None.



Student Involvement

The Penn State team included one graduate research assistant, Ms. Dana Mikkelsen, who has been the lead on the computational fluid dynamics simulations. She will continue in this role for the remainder of the project, although some activities will be conducted at Gulfstream Aerospace. A second senior graduate student will probably be involved in running RANS simulations at Penn State.

Plans for Next Period

During the next research period, the focus will be on the further development of the hybrid acoustic analogy/coarse LES approach. Several tasks will be performed. The in-house and STARCCM+ FW-H codes will be used to predict the noise radiated by the dual-stream Georgia Tech nozzle case for which the LESs have been completed at Gulfstream. An improved data transfer method will be needed to move the data from Gulfstream to Penn State. Several administrative problems have made the process very challenging. Having the student located at Gulfstream will greatly aid in overcoming these problems.

After the FW-H codes have demonstrated their capabilities, and have probably been modified, a series of coarser grids will be developed for the 1.89 dual-stream case. Noise predictions based on LES with these grids will then be made, and their accuracy will be assessed as a function of grid resolution. The focus will be on their ability to predict the radiated noise in the peak noise radiation direction.

The coarse LES predictions will then be coupled with the fine-scale acoustic analogy results, and the results will be compared with experimental findings at all angles.

The same approach will then be applied to jets with different operating conditions and geometries. These cases will include a range of operating conditions and geometries, including cases with internal mixers such as the dual-stream, internally mixed plug nozzle with lobed mixer: 122Am5plnt (Bridges and Wernet, 2021), shown in Figure 15.

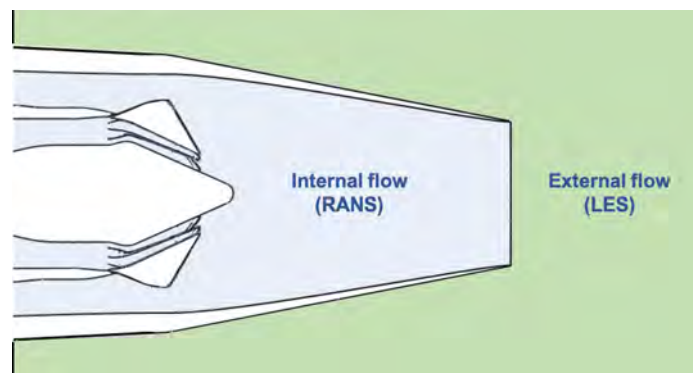


Figure 15. Sketch of the dual-stream, internally mixed plug nozzle with lobed mixer. 122Am5plnt (Bridges and Wernet, 2021).

References

- Bodony, D., & Lele, S. (2004, May). Jet noise prediction of cold and hot subsonic jets using large-eddy simulation. *In 10th AIAA/CEAS Aeroacoustics Conference* (p. 3022).
- Bodony, D. J., & Lele, S. K. (2007). Far-field jet acoustics. *In Large-Eddy Simulation for Acoustics* (pp. 245-262). Cambridge University Press.
- Brès, G. A., & Lele, S. K. (2019). Modelling of jet noise: a perspective from large-eddy simulations. *Philosophical Transactions of the Royal Society A*, 377(2159), 20190081.
- Bridges, J. E., & Wernet, M. P. (2021). Noise of internally mixed exhaust systems with external plug for supersonic transport applications. *In AIAA AVIATION 2021 FORUM* (p. 2218).
- Farassat, F., & Succi, G. P. (1982). The prediction of helicopter rotor discrete frequency noise. *In: American Helicopter Society*, 497-507.



- Freund, J. B. (2001). Noise sources in a low-Reynolds-number turbulent jet at Mach 0.9. *Journal of Fluid Mechanics*, 438, 277-305.
- Goldstein, M. E., & Leib, S. J. (2008). The aeroacoustics of slowly diverging supersonic jets. *Journal of Fluid Mechanics*, 600, 291-337.
- Gryazev, V., Markesteijn, A. P., & Karabasov, S. A. (2023). Robustness of reduced-order jet noise models. *AIAA Journal*, 61(1), 315-328.
- Khavaran, A., & Bridges, J. (2004, June). Modelling of turbulence generated noise in jets. In 10th AIAA/CEAS Aeroacoustics Conference (p. 2983).
- Mollo-Christensen, E., Kolpin, M. A., & Martuccelli, J. R. (1964). Experiments on jet flows and jet noise far-field spectra and directivity patterns. *Journal of Fluid Mechanics*, 18(2), 285-301.
- Shanbhag, T. K., Wu, G. J., Lele, S. K., & Alonso, J. J. (2023). Optimization of turbulent time scales for jet noise prediction. In *AIAA SCITECH 2023 Forum* (p. 1159).
- Sinha, A., Rodríguez, D., Brès, G. A., & Colonius, T. (2014). Wavepacket models for supersonic jet noise. *Journal of Fluid Mechanics*, 742, 71-95.
- Stromberg, J. L., McLaughlin, D. K., & Troutt, T. R. (1980). Flow field and acoustic properties of a Mach number 0.9 jet at a low Reynolds number. *Journal of sound and vibration*, 72(2), 159-176.
- Tam, C. K. (2019). A phenomenological approach to jet noise: the two-source model. *Philosophical Transactions of the Royal Society A*, 377(2159), 20190078.
- Tam, C. K., & Auriault, L. (1999). Jet mixing noise from fine-scale turbulence. *AIAA journal*, 37(2), 145-153.
- Tam, C., Golebiowski, M., & Seiner, J. (1996, May). On the two components of turbulent mixing noise from supersonic jets. In *Aeroacoustics conference* (p. 1716).
- Tam, C. K., & Zaman, K. B. M. Q. (2000). Subsonic jet noise from nonaxisymmetric and tabbed nozzles. *AIAA journal*, 38(4), 592-599.
- Towne, A., Rigas, G., Kamal, O., Pickering, E., & Colonius, T. (2022). Efficient global resolvent analysis via the one-way Navier-Stokes equations. *Journal of Fluid Mechanics*, 948, A9.
- Viswanathan, K. (2002). Analysis of the two similarity components of turbulent mixing noise. *AIAA journal*, 40(9), 1735-1744.
- Ffowcs Williams, J., & Hawkings, D. L. (1969). Sound generation by turbulence and surfaces in arbitrary motion. *Philosophical Transactions for the Royal Society of London. Series A, Mathematical and Physical Sciences*, 321-342.



Project 060 Analytical Methods for Expanding the AEDT Aircraft FLEET Database

Georgia Institute of Technology

Project Lead Investigator

Dimitri N. Mavris
Director, Aerospace Systems Design Laboratory
School of Aerospace Engineering
Georgia Institute of Technology
270 Ferst Drive, Mail Stop 0150
Atlanta, GA 30332-0150
404-894-1557
dimitri.mavris@ae.gatech.edu

University Participants

Georgia Institute of Technology (aka Georgia Tech)

- P.I.: Prof. Dimitri Mavris
- FAA Award Number: 13-C-AJFE-GIT-104
- Period of Performance: October 1, 2022 to September 30, 2024
- Tasks:
 1. Enhancement of the Aviation Environmental Design Tool (AEDT) Fleet database (Fleet dB)
 2. Analytical method development

Project Funding Level

The current FAA funding for this project is \$150,000 from September 21, 2022 to September 30, 2024. The Georgia Institute of Technology has agreed to a total of \$150,000 in matching funds.

Investigation Team

- Dr. Dimitri Mavris (P.I.), All Tasks
- Dr. Michelle R. Kirby, All Tasks
- Dr. Mayank Bendarkar, All Tasks
- Dr. Ameya Behere, All Tasks
- Dr. Styliani I. Kampezidou, All Tasks
- Cristian Puebla-Menne (graduate student), All Tasks

Project Overview

The AEDT relies on aircraft noise and performance (ANP) data provided by aircraft manufacturers to support the calculation of aircraft trajectories and noise at receptors by using aircraft performance information and noise-power-distance relationships for specific aircraft/engine combinations. In the ANP/Base of Aircraft Data (BADA) workflow, ANP performance data are also used in the calculation of emissions inventories and air quality dispersion. However, not all aircraft in the fleet are represented in the ANP database. When ANP data are not available for a specific target engine/airframe combination, AEDT uses a substitute aircraft from the ANP database to model the target aircraft by closely matching the certification noise characteristics and other performance parameters. However, a problematic issue is that the best substitute according to noise criteria does not always match the best substitute for emissions criteria. In addition, substitute aircraft do not capture the environmental benefits of newer aircraft with noise- and emissions-reduction technologies, thus resulting in overly conservative noise and emissions estimates.

The goal of this research is to increase the accuracy of AEDT noise and emissions modeling of aircraft not currently in the ANP database. Georgia Institute of Technology will identify and review aircraft not currently modeled in the AEDT, and will collect information and necessary data to better understand the characteristics of these aircraft. Various statistical analysis methods will be used to classify the aircraft into different types in terms of size, age, technologies, and other engine/airframe parameters. Quantitative and qualitative analytical methods will be identified and evaluated for each aircraft type, to develop ANP and noise data for the aircraft. Validation data from certification data or airport planning documents will be gathered to validate the methods. After validation, the models will be applied to develop ANP and noise data for the aircraft. Finally, recommendations and guidelines will be developed for implementing the developed data in the AEDT, to expand the AEDT Fleet dB to include noise and performance data for aircraft currently not in the ANP database.

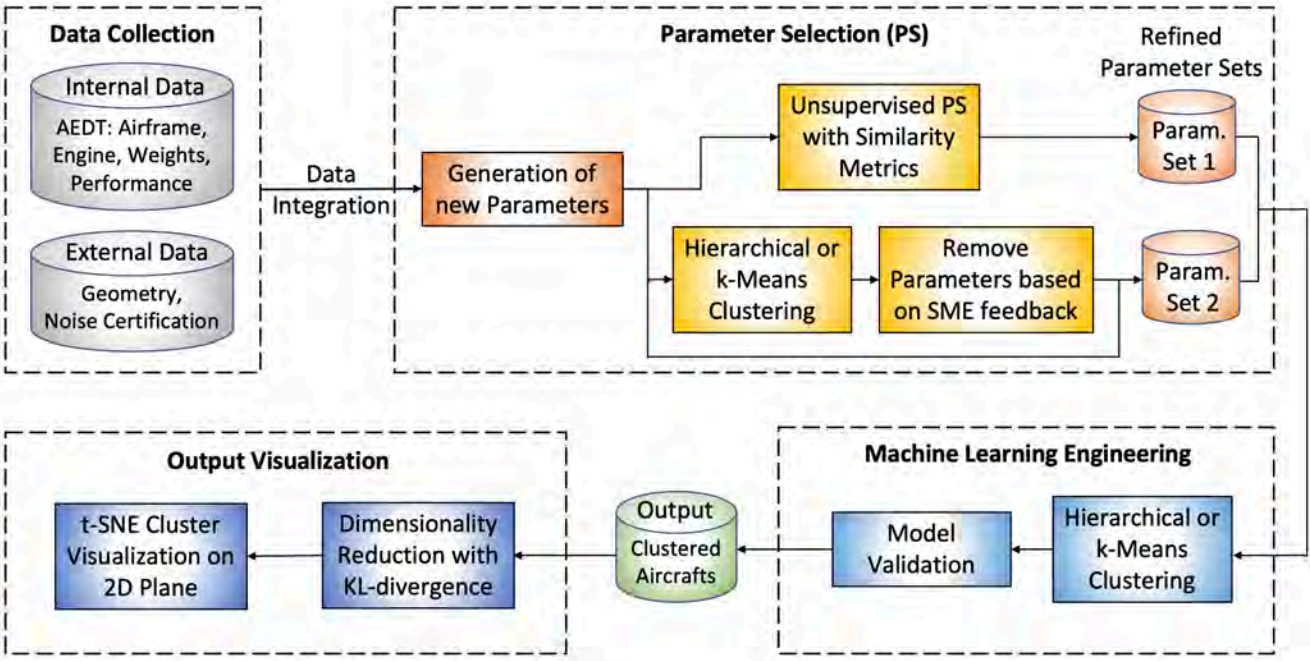


Figure 1. Overview of ASCENT Project 60 tasks and workflow.

The flowchart in Figure 1 presents an overview of the project approach. The first step is to identify the necessary aircraft parameters that will be used to better estimate the substitution aircraft. These parameters are already included in the internal data (Fleet dB) or will be collected from external resources.

Task 1 – Enhancement of the AEDT Fleet Database

Georgia Institute of Technology

Objective

The objective of Task 1 is to identify aircraft that are not currently modeled with ANP data in the AEDT for noise and emissions modeling. In the Fleet dB, specific aircraft engine/airframe combinations are defined by a series of ANP and noise coefficients that are used with the BADA and SAE-AIR-1845 algorithms to conduct performance, emissions, and noise modeling. The Fleet dB contains representative aircraft for the entire fleet; some aircraft are modeled according to ANP data, whereas others are represented by substitution aircraft. This task involves the identification of aircraft that do not have ANP data, and determining whether those substitutions can be improved or enhanced.



Research Approach

Creating the ANP extension database

Aircraft without ANP data in AEDT

The aircraft not currently modeled with ANP data are identified by reviewing the AEDT Fleet dB and conducting a literature survey. The identified aircraft of interest are further investigated to identify gaps between them and the substitution aircraft, in terms of performance, noise, and emissions. This step involves reviewing the existing literature on these aircraft and acquiring the information and data necessary to better determine their engine/airframe characteristics. In addition, the ANP data in the Fleet dB are studied to summarize key parameters for which the analytical methods can be used.

The Fleet dB consists of 3,626 airframe/engine combinations; only 269 have available ANP data (native), whereas the remaining 3,357 do not (proxy). The proxy aircraft have a unique equipment ID (the primary key in the SQL database) and a default equipment ID, which is assigned as the equipment ID of the closest native aircraft, in terms of ANP similarity. The native aircraft have a matching equipment ID and default equipment ID. This substitution enables proxy aircraft to borrow ANP data from the native aircraft for the purposes of conducting environmental analyses and studies. The Fleet dB uses proxy aircraft because of the intensity of effort required to generate the required ANP definition by a manufacturer; this use of proxies was assumed to be reasonable for modeling purposes on an average basis decades ago.

Down-selecting aircraft of interest in the fleet database

To focus the efforts on aircraft types with U.S. operations in the Fleet dB, we conducted a filtering process on the proxy aircraft to create an initial ANP extension database. Filtering was applied to the original 3,626 unique equipment IDs to establish a subset of engine/airframe combinations, to be denoted as aircraft in later discussions, for which external data would be gathered. The first filter eliminated the military and cargo designation codes and small SIZE_CODE aircraft. The next filter eliminated military and general aviation, according to the AIRCRAFT_TYPE designation. This filtering reduced the number of unique equipment IDs to 2,443. With an initial focus on U.S. applications of AEDT, airframe models that are not operated in the United States or are out of production were eliminated. These filters reduced the total airframes for which external data are required to a manageable number of 107. Notably, each airframe could have multiple engine types, thus resulting in a total of 990 native and proxy aircraft remaining, as listed in Table 1. For the remaining EQUIP_IDs, the AIRFRAME_MODEL names were grouped to determine the number of unique airframes.

External aircraft database literature study

To augment the Fleet dB to establish a new ANP extension database, we collected external data for the 990 unique equipment IDs from various sources into AEDT by AIRFRAME_MODEL and the ENGINE_MODEL, as the primary definitions of what the equipment ID was intended to represent in the actual fleet. This information was helpful in determining which performance, emissions, and noise parameters were used for the substitution algorithm in the initial applications of Task 2. In particular, the following categories of data were gathered:

- **Airframe:** general aircraft information and classifications; example: maximum range
- **Engine:** important engine specifications; example: bypass ratio
- **Aircraft:** information on an airframe/engine combination; example: maximum takeoff weight (MTOW)
- **Aircraft geometry:** example: wing area
- **Emissions:** main emission indices; example: unadjusted fuel flow during takeoff
- **Noise:** certification noise; example at the three conditions: flyover, sideline, and approach



Table 1. AEDT Fleet database down-selected equipment IDs of interest.

Family	Members	Number of variants in Fleet dB
A220	2	10
A320	8	132
A330	4	70
A340	4	37
A350	2	2
A380	1	9
ATR 42	5	22
ATR 72	2	6
B737	10	78
B747	4	37
B757	2	15
B767	4	143
B777	8	89
B787	3	32
BAE 146	3	13
CRJ	11	33
Dash 8	7	38
EMB120	1	3
EMB135/145	12	113
EMB170/175	6	20
EMB190/195	8	88

As the external data gathering process began, challenges arose in identifying what the unique equipment ID in the flying fleet represents. Per Volpe’s guidance, a given equipment ID entry is defined by several primary variables in the Fleet dB, which are then linked to other variables for the specific modeling of interest: fuel burn, noise, or emissions. The AIRFRAME_MODEL is intended to be the general description of an airframe, per the manufacturer. For example, the “Airbus A319-100 series” AIRFRAME_MODEL has 26 entries that should represent the various engine options on that series. The AIRFRAME_MODEL coupled with the ENGINE_MODEL is intended to define the actual engine on the specific variant of the airframe series in the fleet. Of note, ENGINE_MODEL is linked to the emissions modeling via the ICAO_UID.

Because AIRFRAME_MODEL provides a generic description of the aircraft, a “common aircraft name” was created to relate the equipment ID entry to what is actually flying in the commercial fleet, for example, the A319-100 series was considered to represent the A319, and a new column was added to the ANP extension database. This renaming enabled the initial gathering of the external data, as listed above, and the analytical methods to be tested, as described in prior annual reports. Beyond AIRFRAME_MODEL and ENGINE_MODEL, other Fleet dB variables are used for fuel burn and noise modeling. ACFT_DESCR is the mapping to the ANP native for that proxy aircraft for noise modeling, which is then coupled to the ANP_AIRPLANE_ID. MANUF_DESC is the mapping to the BADA representation for fuel burn modeling, represented as BADA_ID or BADA4_ID. Combining these four primary descriptors/parameters of the unique equipment ID led to a questionable understanding of what the entry specifically represented.

Initial noise certification data population for the ANP extension database

To initially populate the ANP extension database with noise data, we used two sources of the European Union Aviation Safety Agency (EASA) certification noise level databases until the questionable unique entries could be rectified: one for jets and one for propellers for the three certification noise levels. The limit, margin, and cumulative noise values in EPNdB units were extracted. The methods used for matching comprised the following steps. In the ANP database, a total of 990 airframe/engine candidate combinations for noise data population were selected. The population procedure was started by selection of a specific airframe of interest (for example, the Airbus A321-200 Series AIRFRAME_MODEL and “common aircraft name”). For that airframe, a specific engine, ENGINE_MODEL, among the different options available, was selected (for example, the CFM56-5B3/2P). After the specific airframe/engine combination was defined, the exact same combination was searched and selected in EASA certification noise level database. For matching to be performed, the



selected airframe/engine combination in EASA was required to be unique. To ensure this unique matching, we used a set of successive selection criteria involving the following sequence of steps:

- Use the EASA type certificate database (TCDS) to verify that the variants are actually on the airframe; use the EASA certification noise level database (e.g., MAdB Jets) to cross-reference that the engine is certified for noise.
- Use the EASA TCDS to verify that the engine emissions and thrust parameters in the ANP database are correct.
- When differences are found, they are identified and registered by matching the ANP Equipment ID and EASA Record number.
- For the certified airframe/engine combination in the EASA certification noise level database, select the MTOW.
- If no unique combination is obtained, proceed to select the maximum landing mass.
- If the combination still has more than one option, the maximum cumulative noise level can be selected.
- In cases in which multiple airframe/engine combinations have the same noise values, the first entry is selected.
- Finally, if more than one combination remains after application of the preceding criteria, the most recent modification date for the data of the remaining combinations is selected. This modification date corresponds to the most recent date when the existing values for the selected combination were entered in the database.

The rationale underlying these selection criteria was to choose the most representative noise value of the combination selected. After a unique combination is found, the corresponding noise value is transferred from the EASA database to ANP. To increase the number of combinations available for which noise values were obtained, we selected engines with similar designation codes for some airframes. In this case, the criterion for selection was a direct comparison of the main parameters (bypass ratio, overall pressure ratio, and rated thrust) of the similar engines. If the parameters were within 5% of each other, the combination was considered valid and was added to the ANP database. Unfortunately, this process yielded data for less than 50% of the 990 unique equipment IDs of interest.

Of note, the initial noise certification data gathering was an extremely labor-intensive process.

Deep-dive into the unique equipment IDs

Upon further investigation of a unique equipment ID entry for which noise data could not be established, we identified erroneous and questionable entries when the ENGINE_MODEL was cross-referenced to FAA or EASA airframe TCDS. Four variables in the Fleet dB represent the proper entry in the flying fleet: AIRFRAME_MODEL, ACFT_DESCR, MANUF_DESC, and ENGINE_MODEL. Continuing with the same example from above with the “A319-100 series,” we identified seven specific variants of the A319-100 from a review of the EASA and FAA airframe TCDS, which differ according to the specific engine and engine manufacturer on the variant. For simplification, the A319 variants can be described as a A319-1XX, where “XX” is a number defining the engine type related to the engine manufacturer and the maximum thrust level of the engine. For example, the EASA TCDS states that the following engines are on A319-1XX variants. The green highlighted numbers below designate the different engine manufacturers. The yellow highlighted numbers are the thrust variant of the engine family model. Any letter or number thereafter indicates a change in the combustor or modification to the original engine type certification, as shown with blue highlighting. The numbering and naming conventions regarding the letter after the CFM 56-5 and before the thrust designation number for the CFM International manufacturers are unknown. This naming or numbering convention is not universal, and varies by airframe and engine manufacturer, but is representative.

- A319-111 two CFMI CFM 56-5B5 jet engines (MOD 24932)
- A319-112 two CFMI CFM 56-5B6 jet engines (MOD 25287), or CFM 56-5B6/2 jet engines (MOD 25530)
- A319-113 two CFMI CFM 56-5A4 jet engines (MOD 25238), or CFM 56-5A4/F jet engines (MOD 23755)
- A319-114 two CFMI CFM 56-5A5 jet engines (MOD 25286), or CFM 56-5A5/F jet engines (MOD 23755)
- A319-115 two CFMI CFM 56-5B7 jet engines (MOD 27567)
- A319-131 two IAE V2522-A5 jet engines (MOD 26152)
- A319-132 two IAE V2524-A5 jet engines (MOD 26298)

In cross-referencing of the EASA or FAA airframe TCDS, the certified engines on the interpreted AIRFRAME_MODEL (and hence the “common airframe name”) to the ENGINE_MODEL in AEDT yielded several errors, including incorrect thrust variants, typographical errors in the ENGINE_MODEL entry, variants not certified for noise in any database, engines not certified for emissions, nonexistent AIRFRAME_MODEL, or incorrect engine on the airframe. In each of these cases, the issues are being thoroughly documented.

Among the 990 unique equipment IDs of interest, we identified 123 unique AIRFRAME_MODEL names. That list includes a subset of aircraft families, thus greatly reducing the number of TCDS that must be investigated, because a family is typically certified under one type certificate, regardless of technology generation. An aircraft family is defined by the commonality of almost all elements of the aircraft, but is differentiated by the length of the fuselage or the maximum thrust of the engine, or is within a similar type designation. A similar concept holds true for an engine family with the maximum allowable thrust as the differentiating factor, although different combustors can exist on the same engine family. For example, the “A319-100 series” is a member of the A320 family. The A320 family has four members, A318, A319, A320, and A321, in two generations of technology levels, the “ceo” and the “neo,” but still fall within the same type designation as that of the original application. Similarly, the Boeing B737 has three generations of technology, denoted Classic, Next-gen, and Max, and the associated family members have different B737-X00 designations, where “X” denotes the generation of technology. As described previously, a family member can have variants, which are usually differentiated by the engine manufacturer and maximum permissible thrust.

As with the initial gathering of the noise certification data, this effort is extremely labor intensive, requiring a line-by-line investigation of a unique equipment ID entry and cross-referencing with multiple databases, and therefore is not complete at the time of this report. The databases or sources used include the EASA noise certification database, the International Civil Aviation Organization emissions databank, the EASA and FAA TCDS, and the Fleet dB. After discrepancies are finalized, a comprehensive document will be provided to the AEDT development team, so that refinements can be made to the current entries of the Fleet dB. A benefit of this investigation was the discovery of the wealth of data contained in the airframe and engine TCDS—including certified information on geometry, performance, capability, operating limits, weights, and more—which could be used in lieu of the initial external data gathered for the ANP extension database that did not rely on certified data.

This effort will be ongoing in the coming year.

Collection of airframe and engine TCDS data

As a result of the deep dive, a wealth of data was determined to exist in the EASA and FAA TCDS, for both airframes and engines, that could augment the ANP extension database. For each aircraft family listed in Table 1, the airframe TCDS was downloaded from the respective certification authority website. For EASA, the website is <https://www.easa.europa.eu/en/document-library/type-certificates>. For the FAA, the website is <https://drs.faa.gov/browse/TCDSMODEL/doctypeDetails>. The airframe was used as the main designation to determine the associated TCDS; for each airframe, the engine variants could be determined and used to download the engine TCDS. EASA and the FAA use different formats and levels of content for not only the airframe but also the engine parameters provided. A further complication is that each manufacturer provides varying levels of detail of those parameters.

To simplify the data gathering process and structure, we established an overarching list of parameters by cross-referencing the EASA and FAA content, as listed in Table 2, noting that the units between sources could vary between English and metric. Resources were directed to gather the data manually, in parallel to the noise certification data gathering; this effort was also extremely labor intensive, entailing reading of every page of each airframe and engine TCDS to extract the appropriate and desired information, and compiling it into a new certification database that would ultimately be merged into the ANP extension database. If a particular parameter was not contained in a TCDS, it was noted as “can’t find” and would be resolved later.

The TCDS data gathering was completed after an exhaustive effort. A summary of the amount of data collected by manufacturer category is as follows: Airbus provided the most comprehensive information, with approximately 70% of the desired parameters obtained; the percentage of parameters collected for Boeing aircraft varied between 20% and 50%; and all remaining airframe manufacturers had approximately 50% of the parameters populated. In the review of the percentages of parameters collected, engineering judgement of the potential key drivers of noise, emissions, and fuel burn—such as dimensions, capability, and performance limits—was used to identify key gaps. The only further option identified to potentially fill these gaps was to investigate the information provided by the manufacturers in the airport planning manuals, which are usually available online. At present, the airport planning manuals for each airframe under consideration are being compiled.



Table 2. Airframe and engine TCDS parameters gathered.

Airframe TCDS parameters	Engine TCDS parameters
Airframe	Airframe
Certification date	Engine
Engine	Engine TCDS #
Engine TCDS #	Certification date
Sea Level Static thrust (lbs)	Engine description
Maximum continuous thrust (lbs)	Overall length (in)
Maximum engine speed, N1 rpm (%)	Overall width (in)
Maximum engine speed, N2 rpm (%)	Overall height (in)
Wing area (ft ²)	Dry weight (lbs)
Wingspan (ft)	Takeoff thrust (lbs)
Fuselage height (ft)	Maximum continuous thrust (lbs)
Fuselage length (ft)	Maximum take-off shaft (HP)
Fuselage diameter (ft)	Maximum continuous shaft (HP)
Aircraft height (ft)	Flat rating ambient temperature: takeoff (°C/[°F])
Maximum operating altitude (ft)	Flat rating ambient temperature: maximum continuous (°C/[°F])
MTOM (kg)	Maximum engine speed, N1 rpm (%)
Maximum Zero Fuel Weight (kg)	Maximum Engine speed, N2 rpm (%)
Maximum Landing Weight (kg)	Maximum engine speed, N3 rpm (%)
Mean aerodynamic chord (m)	
Maximum seat capacity (basic)	
Maximum seat capacity (option)	
Total maximum baggage/cargo loads (kg)	Engine Exhaust Gas Temperature (red line takeoff) (°C/[°F])
Fuel capacity (kg)	Engine EGT (red line maximum continuous) (°C/[°F])
Wheels	Engine EGT (maximum indicated takeoff) (°C/[°F])
Tires	Engine EGT (indicated maximum continuous) (°C/[°F])

Milestone

Developed a framework for new external data to be used in Task 2.

Major Accomplishments

Populated new extension database, and created additional certification database.

Publications

Bendarkar, Mayank V., Michelle Kirby, Styliani I. Kampezydou, Cristian Puebla-Menne, and Dimitri N. Mavris, "Exploring Analytical Methods for Expanding the AEDT Aircraft Fleet Database for Environmental Modeling", AIAA Aviation 2023 Forum, doi.org/10.2514/6.2023-4216.

Outreach Efforts

Bi-annual ASCENT meetings.

Awards

None.

Student Involvement

Styliani I. Kampezydou and Cristian Puebla-Menne (graduate students). Collected the TCDS information

Plans for Next Period

Finalize the ANP extension database, and document issues uncovered with the existing Fleet dB for the AEDT development team.

References

- Cirium. (n.d.) *Aviation Analytics*. <https://www.cirium.com/>
- Janes | Login for world leading open source defense intelligence. (n.d.). <https://customer.janes.com/janes/home>
- European Union Aviation Safety Agency. (2023). *ICAO Aircraft Engine Emissions Databank*. <https://www.easa.europa.eu/domains/environment/icao-aircraft-engine-emissions-databank>
- Meier, N. (2021). *Jet Engine Specification Database*. <http://www.jet-engine.net/>
- Lissys Ltd. (n.d.) *Piano's Aircraft Database*. <https://www.lissys.uk/dbase.html>
- Aircraft Bluebook. (2023). *Aircraft Bluebook – Spring 2023 Vol. 23-01*. <https://aircraftbluebook.com/Tools/ABB/ShowSpecifications.do>
- Jenkinson, L., Simpkin, P., Rhodes, D. (2001). *Civil Jet Aircraft Design: Aircraft Data A File*. <https://booksite.elsevier.com/9780340741528/appendices/data-a/default.htm>
- Jenkinson, L., Simpkin, P., Rhodes, D. (2001). *Civil Jet Aircraft Design: Aircraft Data B File*. <https://booksite.elsevier.com/9780340741528/appendices/data-b/default.htm>
- European Union Aviation Safety Agency. (2023). *EASA Certification Noise Levels*. <https://www.easa.europa.eu/en/domains/environment/easa-certification-noise-levels>
- NoisedB. (2023). *Noise Certification Database Version 2.34*. <https://noisedb.stac.aviation-civile.gouv.fr/bdd>
- Aircraft Bluebook. (2023). *Aircraft Bluebook – Spring 2023 Vol. 23-01*. <https://aircraftbluebook.com/Tools/ABB/ShowSpecifications.do>
- European Union Aviation Safety Agency. (2023). *EASA Certification Noise Levels*. <https://www.easa.europa.eu/en/domains/environment/easa-certification-noise-levels>

Task 2 – Analytical Method Development

Georgia Institute of Technology

Objective

The objective of Task 2 is to develop analytical methods and solutions that can improve the modeling of aircraft types (airframe/engine combinations) that are not included in the ANP database. In this process, machine learning (ML) and data-mining (DM) approaches are used to analyze aircraft features (both internally and externally collected), ANP data, and environmental output data, as well as to gain insights and evidence of better model substitution and approximation. The following research questions can be answered while developing these more advanced analytical methods:

- How can substitutions be better assigned for aircraft types not included in the ANP database?
- How can representative aircraft models be better chosen to develop more ANP data, with the aim of more sufficiently covering the entire population?
- Which aircraft features should be used in the identification of aircraft substitution?
- How can the current ANP data be better used to approximate the remaining aircraft with greater flexibility?

Research Approach

The data-driven analytical methods used in this task are based primarily on ML and DM techniques. The solution for each research question consists of multiple ML/DM algorithms. In general, the analytical techniques that are useful in this project can be classified into five categories: clustering, dimensionality reduction, regression, feature selection, and data visualization. Table 2 presents examples and objectives for all five categories.

The method is outlined in Figure 1. The process begins with a data fusion step, wherein various data sources are queried and merged with the AEDT Fleet dB to create the ANP extension database, as explained in Task 1. The resulting database contains 3,626 airframe/engine combinations with 112 columns. The total number of airplanes with nitrogen oxide (NO_x) emissions data is 2,361, which decreases to 520 when noise data are also included. Of these, 269 aircraft have data from the ANP database. Most of the efforts of the past year focused on finalizing the full dataset. Consequently, the present report summarizes the cumulative progress made on analytical method development performed over the past several years.

Past efforts explored three broad areas to synthesize ANP data for aircraft lacking these data. Of these, the first step involved exploring unsupervised clustering to group similar aircraft by using the enriched dataset from Task 1. Native aircraft (with ANP data) within each cluster can be considered potential substitutes for other aircraft without ANP data within each cluster.

The other two analytical techniques will be explored after updating of the full dataset from Task 1 is completed. These techniques are (a) potentially customizing ANP data by using statistical techniques and regressions to enable more flexible synthesis for ANP data rather than the currently used one-to-one substitution for aircraft without ANP data and (b) exploring hybrid models, wherein a composite model of multiple closest ANP aircraft is used to synthesize ANP data for non-native aircraft.

Using clustering to identify representative aircraft model portfolios

Results of using unsupervised clustering methods on the extension database were presented in the previous annual report and are summarized here for completeness. Two algorithms, *k*-means (KM) and hierarchical clustering, were implemented on the preliminary database, which included 520 airframe/engine combinations with available noise data. In these studies, all *n* aircraft are first partitioned into *k* clusters; one aircraft from each cluster is then selected to represent all aircraft in that cluster. Methods for conducting clustering and representative aircraft selection simultaneously will be explored after the full dataset is ready. The implemented clustering techniques also aided in identifying outliers in the data and correcting the data entries for any potential errors.

The dimensionality of clustering is influenced by the number of parameters selected for the exercise. For our preliminary explorations, inputs from subject-matter experts (SMEs) were used to determine the important parameters for emissions and noise modeling, as shown in Table 2. These parameters were selected after multiple rounds of clustering experiments involving SME feedback and focus on aircraft performance, geometry, engine characteristics, noise, and emissions.

Table 3. Selected SME parameters for clustering.

Group	Parameter	Units
Geometry	Wing area	ft ²
	Wing aspect ratio	
	Fuselage volume	ft ³
Performance	Gross weight	lbs
	Cruise Mach	
	Typical range	nm
	Number of passengers	
	Cruise altitude	ft
Engine	Pressure ratio	
	Total thrust	kN
	Bypass ratio	
Emissions	NO _x	gm/kg
Noise	Flyover noise	EPNdB
	Approach noise	EPNdB
	Lateral noise	EPNdB

For KM clustering, the elbow method is widely used to determine the number of clusters. This method provides a suitable tradeoff between error and the number of clusters. Figure 4 shows the inertia (elbow) plot for selecting the number of clusters for the KM algorithm. Approximately five to seven clusters appear to be ideal to divide the data. The same number of clusters was used for Analytical Hierarchical Clustering (AHC) to enable comparison between the outputs of the two methods. These clusters were also visualized with *t*-distributed stochastic neighbor embedding (Melit Devassy, 2020) visualization, which enables the depiction of higher-dimensional clusters in two or three dimensions.

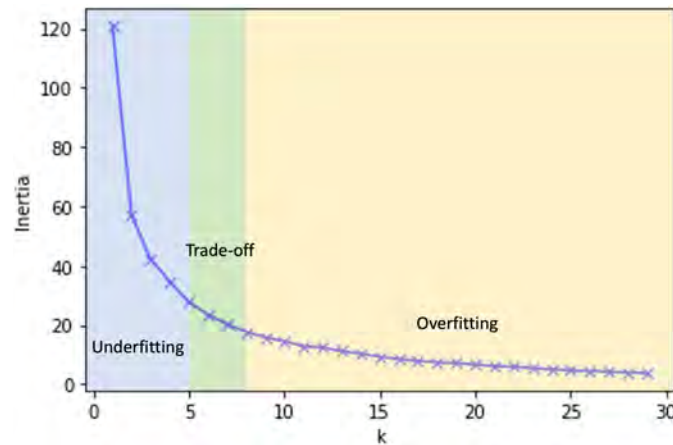


Figure 2. Inertia (elbow) plot for KM clustering.

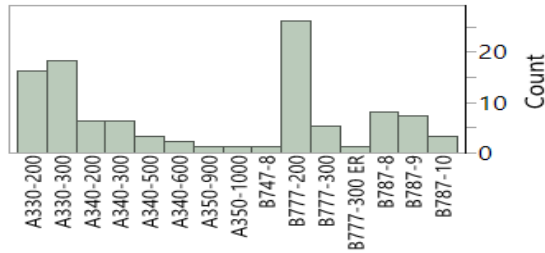
Preliminary clustering results

The approximately 520 aircraft for which the AEDT Fleet extension database contains complete parameter data were included in the preliminary results. The results from using the AHC clustering method from last year are shown in Figure 5 for completeness. Overall, the clusters showed good agreement with real-world distinctions: larger wide-body aircraft formed cluster 0; so-called “jumbo” jets formed cluster 1; regional jets were found primarily in clusters 2 and 6; smaller wide-body aircraft were grouped in cluster 3; newer-generation small single-aisle aircraft were grouped in cluster 4; and traditional small single-aisle aircraft were grouped in cluster 5. Goodness of fit for clustering can be a difficult metric to quantify for unsupervised methods. Because we address real world airframe/engine combinations and their impacts in terms of emissions and noise, we used SME inputs and feedback to evaluate the goodness of fit.

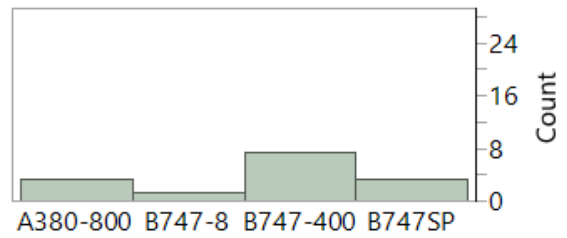
To visualize 15-dimensional clusters, we used scatterplot matrices. Figure 6 shows an example scatterplot matrix of NO_x and noise emissions for aircraft, with cluster 1 highlighted. As expected, the largest aircraft and highest thrust engines that pair with them have the highest emissions and noise signatures, and thus are located at the top right of almost every plot. Clear distinctions between clusters are not expected in this figure, which shows only 4 of the 15 dimensions used for clustering.

Parameter importance is difficult to gauge for unsupervised learning clustering algorithms. Therefore, to determine the importance of the parameters with the greatest effects on the clusters, we fit a supervised random forest algorithm with 100 trees to the cluster numbers while using the same 15 parameters for clustering the aircraft. A parameter importance function of this random forest was evaluated to indicate the parameter importance of the AHC clusters (Figure 7).

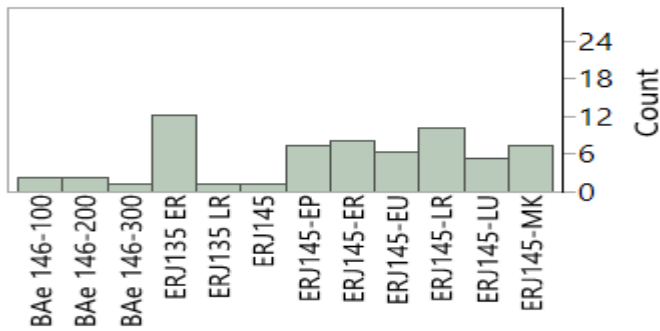
The idea underlying segregating the aircraft within the AEDT Fleet extension database into clusters is to observe whether aircraft with ANP data (native) are present in certain clusters with non-native aircraft. This process can help identify more suitable substitute ANP aircraft for airframe/engine combinations that do not have ANP data. Because of limitations of the dataset, the results summarized herein focus on the unsupervised clustering approach. Implementations of other analytical methods on the full dataset will be described in future reports.



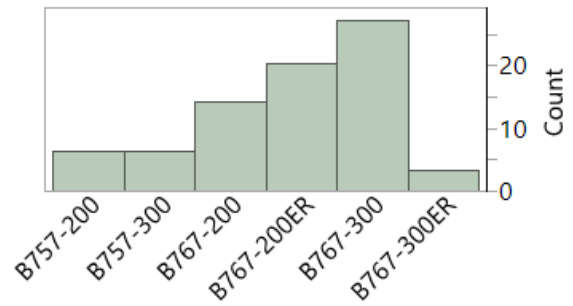
(a) Cluster 0



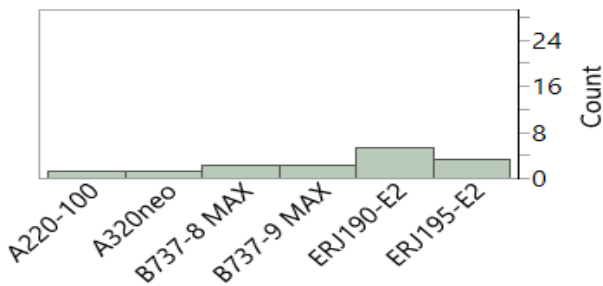
(b) Cluster 1



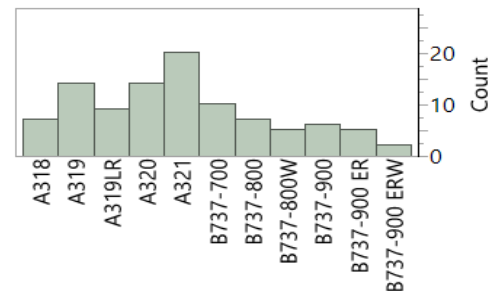
(c) Cluster 2



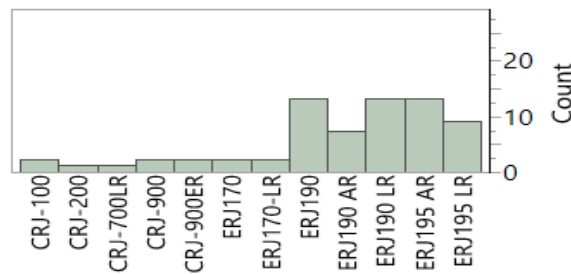
(d) Cluster 3



(e) Cluster 4



(f) Cluster 5



(g) Cluster 6

Figure 3. Preliminary hierarchical clustering results.

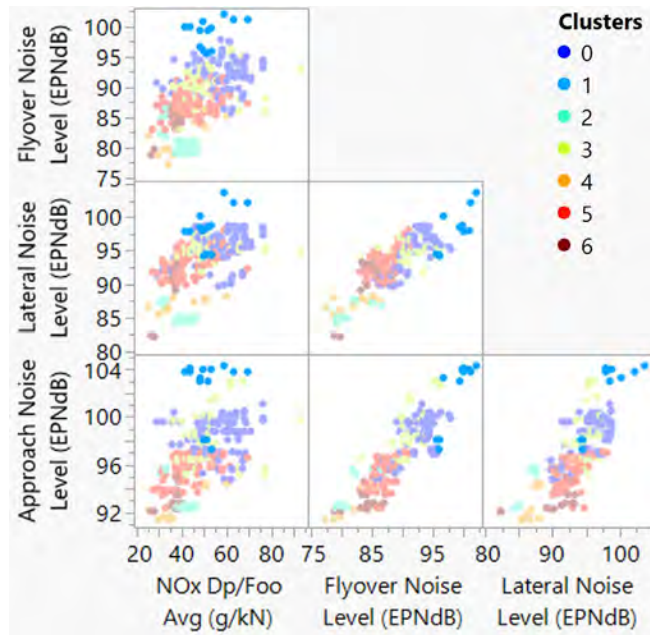


Figure 4. Scatterplot matrix of emissions and noise, with cluster 1 highlighted.

Predictor	Contribution	Clusters		Rank ^
		Portion		
Wing Area (ft^2)	718.266	0.5533		1
Wing Aspect Ratio	267.938	0.2064		2
MX_GW_TKO	135.672	0.1045		3
Pressure Ratio	44.751	0.0345		4
fuselage_volume	41.153	0.0317		5
total_thrust (kN)	38.250	0.0295		6
Lateral Noise Level (EPNdB)	16.292	0.0125		7
FENV_ALT	14.392	0.0111		8
B/P Ratio	8.287	0.0064		9
CR_MACH	4.774	0.0037		10
Flyover Noise Level (EPNdB)	3.197	0.0025		11
Approach Noise Level (EPNdB)	2.542	0.0020		12
Typical Range (nmi)	2.083	0.0016		13
Pax	0.332	0.0003		14
NOx Dp/Foo Avg (g/kN)	0.286	0.0002		15

Figure 5. Parameter importance for overall clustering.

The present work makes two primary contributions. The first contribution is the generation and continuous development of the Fleet extension database, which enriches the AEDT Fleet dB with performance, weight, emissions, and noise parameter values from openly available external data sources. The second contribution is the exploration of various ML techniques to identify commonalities and patterns in the airframe/engine combinations. The changes to the Fleet dB will be contrasted with the default AEDT mapping of different airframe/engine combinations to ANP native aircraft, thereby enabling the exploration of areas for improvement in fleet modeling of noise and emissions within AEDT, to improve its accuracy.



Major Accomplishments

The major accomplishments for this period performance include the following:

- A literature study was conducted on databases to collect performance, emission, and noise data for target aircraft.
- A new template was created for the Fleet extension database, and external data were gathered.
- External databases were gathered to augment the extension database with completion of 520 aircraft engine combinations.
- A literature survey was conducted on analytical methods in clustering, dimensionality reduction, feature selection, and data visualization.
- Unsupervised clustering on the available Fleet extension database was explored, to better group similar aircraft and provide insights on the parameters driving the grouping.
- The results were postprocessed by using bar charts, scatterplot matrices, *t*-distributed stochastic neighbor embedding, and parameter importance calculations, to help better understand the trends.

Publications

None.

Outreach Efforts

Bi-annual ASCENT meetings.

Awards

None.

Student Involvement

Styliani I. Kampezidou and Cristian Puebla-Menne (graduate students). Conducted research on potential analytical techniques to use for the clustering.

Plans for Next Period

- Finalize the ANP extension database to include noise certification data, to serve as the basis for Task 2
- Continue to refine analytical methods on the new database, identify gaps in the approach, and implement them on the remaining engine/airframe combinations within the FLEET database
- Validate the methods in Task 2

References

Hinton, G. E., & Roweis, S. (2002). Stochastic neighbor embedding. *Advances in neural information processing systems*, 15.

Maaten, L. V., & Hinton, G. E. (2008). Visualizing Data using t-SNE. *Journal of Machine Learning Research*, 9, 2579-2605.

Melit Devassy, B., & George, S. (2020). Dimensionality reduction and visualisation of hyperspectral ink data using t-SNE. *Forensic Science International*, 311, 110194. <https://doi.org/10.1016/j.forsciint.2020.110194>

Project 061 Noise Certification Streamlining

Georgia Institute of Technology

Project Lead Investigator

Prof. Dimitri N. Mavris
Director, Aerospace Systems Design Laboratory
School of Aerospace Engineering
Georgia Institute of Technology
Aerospace Systems Design Laboratory (ASDL)
Weber Space Science & Technology Building, Room 301A
275 Ferst Drive, NW, Atlanta, GA 30332
404-894-1557
dimitri.mavris@ae.gatech.edu

Dr. Michael Balchanos (co-P.I.)
Senior Research Engineer
Aerospace Systems Design Laboratory
School of Aerospace Engineering
Georgia Institute of Technology
Aerospace Systems Design Laboratory (ASDL)
Weber Space Science & Technology Building, Room 313B
275 Ferst Drive, NW, Atlanta, GA 30332
404-894-9799
michael.balchanos@asdl.gatech.edu

University Participants

Georgia Institute of Technology

- P.I.s: Dr. Dimitri Mavris and Dr. Michael Balchanos
- FAA Award Number: 13-C-AJFE-GIT-066
- Period of Performance: October 1, 2022, to September 30, 2023
- Tasks:
 1. Develop a traceable structure for unmanned aerial systems (UAS) noise certification requirements
 2. Formulate a library of UAS and testing procedures
 3. Document and model noise testing and certification procedures based on existing practices
 4. Develop alternative procedures and assess their performance with existing tools (proof-of-concept)

Project Funding Level

The total amount of current funding from the FAA for ASCENT Project 061 is \$250,000 for a 12-month period of performance. The Georgia Institute of Technology has agreed to a total of \$83,333 in matching funds.

Investigation Team

Georgia Institute of Technology

Prof. Dimitri Mavris, (P.I.), Tasks 1-4
Dr. Michael Balchanos, (co-P.I.), Tasks 1-4
Dr. Jimmy Tai, (senior research engineer), Tasks 1-4
Dr. Evan Harrison, (research engineer II), Tasks 1-4
Balaji Ravikanti (graduate student), Tasks 1-4
Hussein Ali (graduate student), Tasks 1-4



Hajar Mali (graduate student), Tasks 1-4
 Mika Xu (graduate student), Tasks 1-4
 Nathnael Geneti (graduate student), Tasks 1-4

All team members are affiliated with the Aerospace Systems Design laboratory (ASDL), under the School of Aerospace Engineering at Georgia Tech. Please refer to Figure 1 for a breakdown of the Georgia Tech ASDL Team.

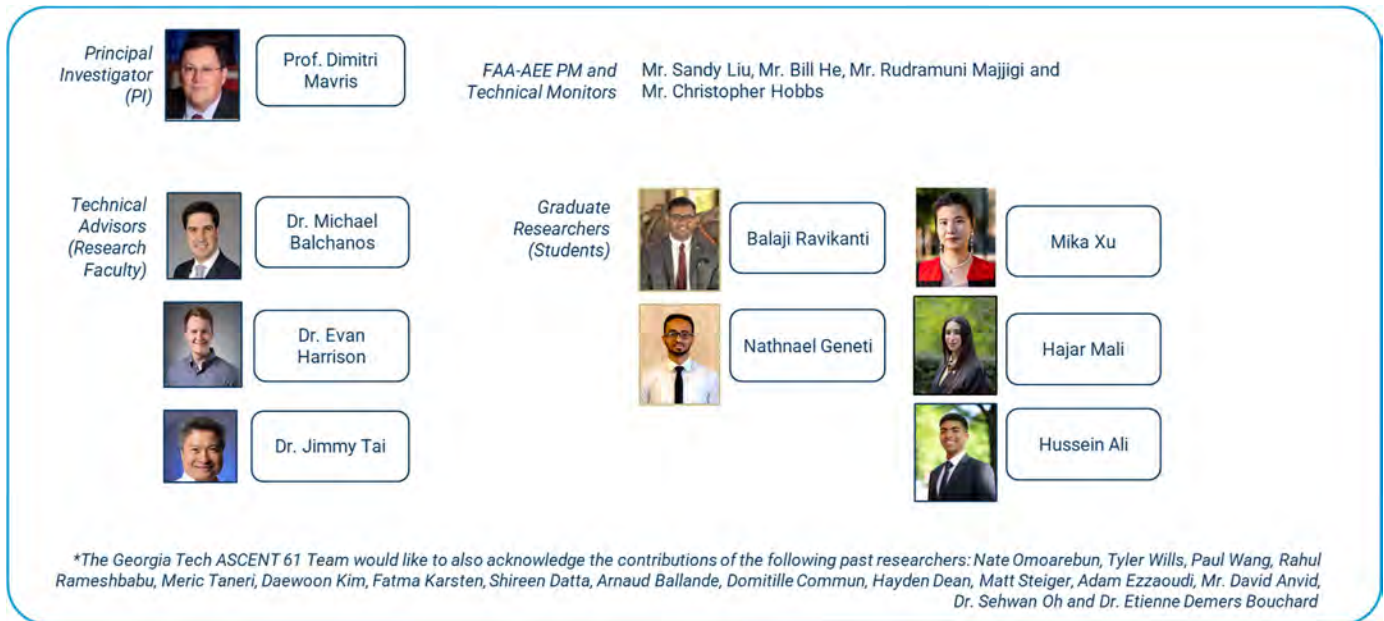


Figure 1. ASCENT Project 061 Georgia Tech Aerospace Systems Design Laboratory (ASDL) team.

Past technical advisors who contributed to the tasks:

- **Mr. David Anvid**, senior research engineer, provided guidance on best practices for noise certification testing, observed and articulated from an industry point of view.
- **Dr. Sehwan Oh**, postdoctoral researcher, focused on exploring current certification regulations, understanding their structure (hierarchy, associations, etc.) linked to Task 1, and providing input on the application of discrete event and agent-based methods as part of the efforts planned for Task 4.
- **Dr. Etienne Demers Bouchard**, postdoctoral researcher, focused on exploring process modeling methods from literature and formulating a canonical problem to assess the feasibility and applicability of various methods.

Former students who have contributed to the tasks:

- **Mr. Rahul Rameshbabu**, a third year PhD student, supporting activities in developing a parametric and interactive decision support tool.
- **Mr. Paul Wang**, a second-year PhD student, involved in the formulation of a model-based systems engineering (MBSE) verification model for UAS.
- **Mr. Daewoon Kim**, a second-year MSc student, is leading the team's MBSE efforts for representing the baseline certification process in systems modeling language (SySML).
- **Mr. Nathaniel Omoarebun**, a fifth-year PhD student, is supporting the team's MBSE efforts and SySML modeling activities.
- **Mr. Tyler Wills**, a second-year MSc student, is supporting the team's efforts in process improvement modeling (PIM) methods and process simulation.
- **Mr. Merc Taneri**, a second-year MSc student, is leading the team's efforts in PIM methods, stochastic process simulation (Markov chain Monte Carlo [MCMC]), and interactive visualization.
- **Ms. Shireen Datta**, an MSc student, supported efforts in documenting current procedures and exploring regulation-driven requirements, which are now included in the verification model.



- **Ms. Fatma Karsten**, a PhD student, worked on flight testing plan implementation and an effective perceived noise level (EPNL) calculation module within the MBSE verification model.
- **Mr. Arnaud Ballande**, an MSc student, worked on a process simulation capability for evaluating equivalent procedures under the PIM task.
- **Ms. Hayden Dean**, a PhD student, was instrumental in capturing and understanding current regulations and certification procedures, as dictated by the Title 14 Subchapter C, Part 21, and Part 36, as well as Part 36 Advisory Circulars (ACs), with a particular focus on AC 36-4D and an emphasis on guidance instructions regarding flight testing for noise certification.
- **Ms. Domitille Commun**, a PhD student, worked on implementing a discrete event simulation (DES) model-based process simulation capability for the certification baseline.

Project Overview

Noise certification procedures (with their inclusion of equivalent procedures) have served aviation stakeholders (original equipment manufacturers [OEMs], regulators, operators, airports, etc.) well since the 1960s (Metzger, 1970; Ollerhead, 1968; Senzig, 2018). With new vehicle types and new technologies (including new entrants, digital technologies for airframes, propulsion, and measurements, etc.), it is necessary to critically examine the existing certification processes. Key features of current certification practices include equivalent procedures and supporting technology, which many OEMs utilize (FAA, 2023). Equivalent procedures are anticipated for both existing and new standards to further accommodate innovation in the future.

The project objective is to examine current noise certification procedures and identify opportunities to streamline the noise certification process while recommending process updates for building the flexibility needed to accommodate all air vehicle types. Project 061 seeks to propose quantifiable process improvements and facilitate the application of traditional systems engineering for complex systems and MBSE, while leveraging these methods for the management of regulatory requirements. To perform the proposed research under this 3-year effort, Georgia Tech has teamed with several industrial partners with extensive experience in noise certification. Each industrial partner represents different types of vehicles, such as large subsonic transports, propeller-driven small aircraft, and rotorcraft.

The ASCENT Project 061 team is seeking to accomplish the following goals:

- Identify opportunities for increased efficiency (by expediting steps and simplifying processes) and flexibility in current noise certification processes to accommodate multiple vehicle categories.
- Formulate and evaluate revised noise certification processes for current vehicle types and offer recommendations to the FAA (Part 36, AC 36-4D, etc.) (FAA, 2017).
- Develop process modeling methods to enable quantitative assessments of noise certification.
- Facilitate the application of traditional systems engineering processes for complex systems and MBSE, leveraging these methods for the management of regulatory requirements.
- Leverage the technical expertise acquired in investigating and modeling noise regulatory frameworks and recommend procedures for certification testing and analysis to the FAA for small propeller-driven vehicles and UASs.

Overall ASCENT 061 roadmap and statement of work

An overview of the ASCENT 061 roadmap toward goals and milestones is shown in Figure 2.

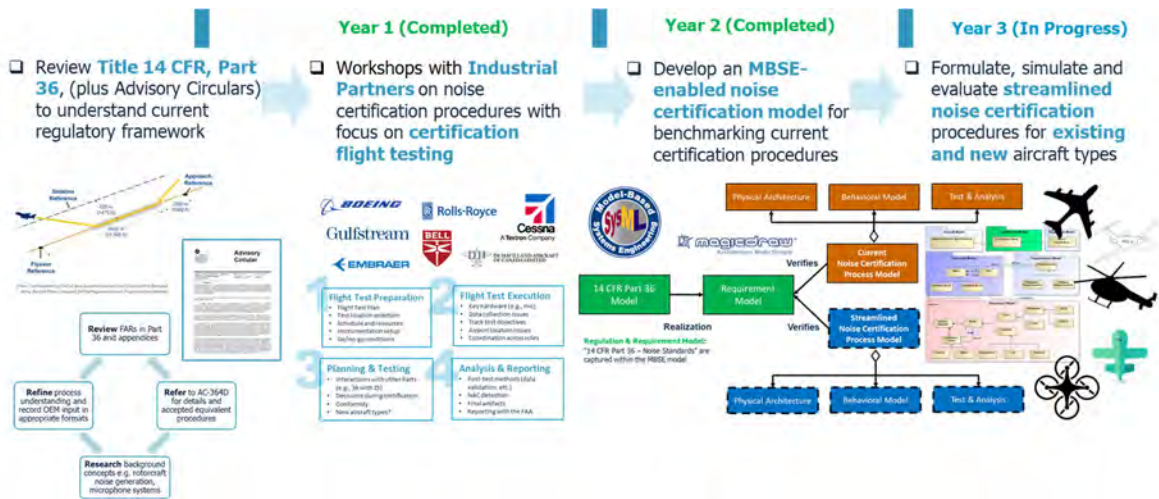


Figure 2. Roadmap toward a model-based framework for exploring current and streamlined noise certification. AC: advisory circular; CFR: Code of Federal Regulations; FAR: Federal Acquisition Regulation; MBSE: model-based systems engineering; NAC: non-acoustical change; OEM: original equipment manufacturer.

The main goal is to provide recommendations to the FAA in the form of feasible equivalent procedures, supported by the latest technologies/hardware, as well as analysis techniques to support the certification of future air vehicle types. These recommendations should be accompanied by evidence that the suggested equivalent procedures are fully in compliance with Part 36 (FAA, 2017) and use case examples for future air vehicles, e.g., small propeller-driven aircraft and UAS. To implement this roadmap and achieve the targeted outcomes, the team will engage in four main tasks, along with the subtasks that have been prioritized for Year 3 of ASCENT 061. These tasks are summarized below.

- Task 1: Develop a traceable structure for UAS noise certification requirements.
- Task 2: Formulate a library of UAS and testing procedures.
- Task 3: Document and model noise testing and certification procedures based on existing practices.
- Task 4: Develop alternative procedures and assess their performance with existing tools (proof-of-concept).

For the full three-year period of performance, the complete timeline for finalizing all Project 061 tasks is shown in Table 1.

Table 1. ASCENT Project 061 task planning timeline.

Task	Year 1												Year 2												Year 3											
	M1	M2	M3	M4	M5	M6	M7	M8	M9	M10	M11	M12	M13	M14	M15	M16	M17	M18	M19	M20	M21	M22	M23	M24	M25	M26	M27	M28	M29	M30	M31	M32	M33	M34	M35	M36
1 Interview Industrial Partners on Current Noise Certification Processes	[Active]																																			
1.1 FAA Noise Certification Regulation Review	[Active]																																			
1.2 Industry Partner Interviews via Workshops	[Active]																																			
2 Develop a Streamlined Noise Cert. Procedure for Existing Aircraft													[Active]																							
2.1 Current Process Assessment													[Active]																							
2.2 Streamlined Process Definition													[Active]																							
2.3 Streamlined Process Assessment and Revision													[Active]																							
3 Develop a Flexible Noise Certification Procedure for New Aircraft																									[Active]											
3.1 Flexibility Assessment of Streamlined Process																									[Active]											
3.2 Flexible Process Definition																									[Active]											
3.3 Flexible Process Assessment and Revision																									[Active]											
4 Simulate Streamlined and Flexible Noise Certification Procedures																									[Active]											
4.1 Identification of a Modeling Approach																									[Active]											
4.2 Noise Certification Process Metric Definition																									[Active]											
4.3 Model Calibration																									[Active]											
4.4 Certification Process Simulation																									[Active]											

Pivoting to UAS category for ASCENT 061 Year 3

The FAA’s Office of Environment and Energy (AEE) has suggested a timeframe for pivoting to UAS category certification. The main task for the Georgia Tech team is to investigate the feasibility and applicability of current ASCENT 061 models and analysis tools for exploring procedures and flight test planning to support noise certification of small propeller-driven UAS. The primary issue with UAS certification is that the spectrum of possible and available configurations covers a large class of aerial systems with completely different characteristics, as shown in Figure 3.

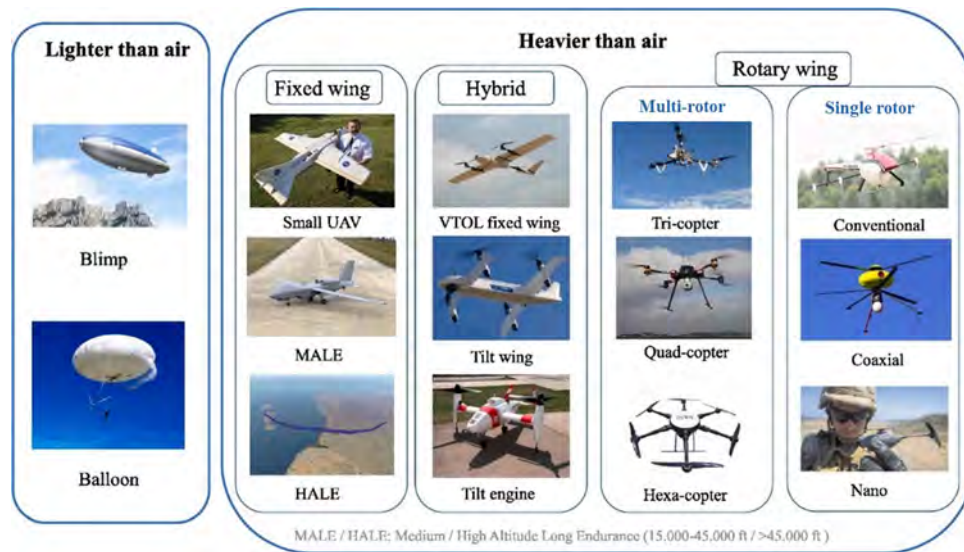


Figure 3. Overview of unmanned aerial system concepts. UAV: unmanned aerial vehicle; VTOL: vertical takeoff and landing.

It is assumed to be unlikely that UAS noise certification will be addressed as a “clean sheet of paper” process. Multiple efforts are underway to establish guidance for noise certification, similar to that for the transport category. The International Civil Aviation Organization (ICAO) is the recognized authority for developing and establishing a global baseline for noise standards and stringencies. Although rulemaking by the ICAO may lag behind the efforts of individual countries, ultimately, the harmonization of certification requirements among national airworthiness authorities is desirable. Several iterations of the regulatory framework may be required before this target is achieved.

Goals and technical challenges

The high-level goals for this direction are to (1) recommend testing procedures for UAS noise certification and, through the proposed methodology, (2) ensure traceability between regulations, testing requirements, and certification procedures. The key challenges that have been identified and will be addressed by the Georgia Tech team are as follows:

- There is currently a large spectrum of UAS designs and configurations under testing for production. As the FAA is preparing to release guidance for UAS noise certification, it is important to determine whether the MBSE-enabled method developed under ASCENT 061 is sufficiently flexible to accommodate UAS testing actions and to help establish a workflow that meets current and upcoming regulations.
- As there are currently no general regulations and the application of current certification procedures is on a case-by-case basis (e.g., recently completed certification framework for the Matternet UAS), it is important to assess whether current testing procedures are effective for UASs.
- We must determine how the ASCENT 061 team can use the established framework to demonstrate its effectiveness in assisting the FAA through the assessment of Notice of Proposed Rulemaking (NPRM) plans, as these are being iterated before they become approved as part of the UAS noise certification standards.

General direction for Year 3

Putting this plan forward, the suggested starting point is to perform an inventory of existing certification practices for low maximum takeoff weight (MTOW) general aviation and propeller/rotor-driven aircraft (i.e., fixed wing and rotorcraft). Currently, the priority is to focus on UASs before urban air mobility (UAM), as the anticipated risks are expected to be higher for the latter. In response to this pivot, the following guiding actions have been set:

- Study current certification practices for noise for small propeller-driven airplanes (Code of Federal Regulations (CFR) Title 14, Part 36, Appendix G) and light helicopters (CFR Title 14, Part 36, Appendix J).
- Perform a literature/technical review of noise source characteristics associated with propeller/rotor propulsion systems.



- Explore current practices for UAS flight testing for noise. The ASCENT 061 team has been encouraged to explore collaboration with ASCENT 077 researchers at Penn State regarding their research on “Measurements to Support Noise Certification For UAS/UAM Vehicles and Identify Noise Reduction Opportunities.”
- Utilize the team’s current MBSE-enabled certification framework to test current procedures for UASs and its overall flexibility to accommodate multiple aircraft categories.

As a starting point for the literature search, Appendices G and J are considered the only aircraft noise certification standards that might be applicable for noise certification of small unmanned aircraft systems (sUAS) in the United States, but a number of additional standards will be reviewed and included in formulating certification practices, including the following:

- ICAO Annex 16 Volume 1 Chapters 8, 10, 11, and 13
 - These are applicable to all fixed wing, rotorcraft, and tiltrotors below an MTOW of 3,175 kg.
- NASA Ref. Publication 1258, Aeroacoustics of Flight Vehicles: Theory and Practice Volume 1 & 2, August 1991.

Statement of work/task definitions for UAS noise certification research

Following the reassigned focus on UAS certification, the original task definitions that had guided the work on transport category aircraft noise certification required a review. An updated statement of work (SoW) has been formulated to guide the pivot toward the development of use cases that address the FAA’s needs for UAS noise certification. This SoW is based on the concept that the original tasking is substantially complete; thus, a significantly revised SoW is necessary to reflect the integration of UAS certification goals with the previously developed MBSE and PIM modeling. This development will entail the generation of multiple libraries that enable flexibility of use across a broader range of UAS configurations and support traceability between regulations, requirements, and elements of the library.

The tasks under the revised SoW are defined as follows:

Task 1: Develop a traceable structure for UAS noise certification requirements

- 1.1 Document related regulations and current standards.
- 1.2 Generate noise certification requirements from currently known and established regulations.
- 1.3 Define a validation process for noise requirements.

Task 2: Develop a library of UASs and testing procedures

- 2.1 Complete technical documentation of UAS configurations.
- 2.2 Complete technical documentation of UAS noise testing equipment.
- 2.3 Define UAS noise test plans.
- 2.4 Define possible simulation techniques.

Task 3: Develop a noise certification procedure based on existing practices

- 3.1 Transfer noise testing plans to the MBSE model.
- 3.2 Transfer noise testing data to the MBSE model.
- 3.3 Develop a full noise test plan.
- 3.4 Implement a validation process.

Task 4: Develop alternative procedures and assess their performance with existing tools

- 4.1 Develop alternative testing procedures using the elements library.
- 4.2 Transfer alternative procedures to the PIM.
- 4.3 Report on the performance of the alternative procedures.

Matrixing of parallel ASCENT project efforts

Within the topic of UAS testing and certification for noise, there are currently three related but unique ASCENT research efforts:

- ASCENT 077: Measurements to Support Noise Certification for UAS/UAM Vehicles and Identify Noise Reduction (Penn State University)
- ASCENT 009/094: Geospatially Driven Noise Estimation Module (Georgia Tech ASDL)
- ASCENT 061: Noise Certification Streamlining (Georgia Tech ASDL)

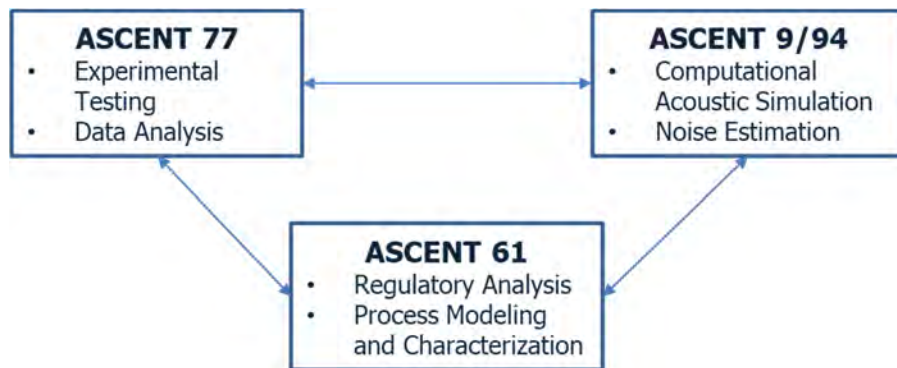


Figure 4. Coordination with parallel ASCENT work related to unmanned aerial system certification.

To preclude “mission creep” into other projects’ remit and to leverage the work of the other ASCENT teams, the Project 061 team has been coordinating on a regular basis with Project 077 and Project 009/094 team members (as highlighted in Figure 4). The main collaboration areas are the following:

- **ASCENT 77:** Data sharing. Experimental test data provide real-world input for noise certification modeling. The results of the ASCENT 77 testing efforts provide a better understanding of the most significant parameters affecting UAS noise characteristics. The weighting of these parameters may influence modifications to the existing MBSE model.
 - Comparison of field geometry, test equipment, and basic flight profiles in addition to UAS configuration, weight, and vehicle performance
- **ASCENT 009/094:** Evaluation of possible vehicle operational environments and the practical impacts of noise profiles on the public. While the ASCENT 09/94 efforts do not provide direct technical data for MBSE modeling, these efforts do provide context for how noise level outputs from the certification process may be applied to an operational environment.

Summary of major accomplishments to date

- Performed a literature search and documented regulations and current testing standards for small UAS (CFR Title 14 Part 36 Appendix G, J, and H, and recent NPRMs)
- Completed the **architecting of a noise certification modeling and assessment framework** for transport and UAS category aircraft.
 - Traceable structure for UAS noise certification requirements was created using the MBSE verification model developed for the transport category.
 - An implementation roadmap has been completed for the MBSE framework to accommodate multiple UAS types and to allow for process effectiveness and flexibility evaluation.
 - Scripts required to generate multiple noise metrics from raw frequency domain data were created.
- Completed **development of the PIM**, which has been applied to a typical plan for UAS noise testing demonstration example.
 - Metrics have been developed and the PIM has been integrated under a parametric interactive decision support environment.
 - Demonstrated the concept through a minimum viable project exercise; namely, a small-scale PIM using a DES approach through a deterministic modeling exercise.
 - Continued the development of a more comprehensive stochastic model using stochastic MCMC methods, formulated in a way that enables seamless integration into the verification thread within the MBSE framework.
 - Performed tuning of the existing PIM with automation and parametrization of user-defined input data to make the model representative of any desired process.
 - Applied the PIM as a demonstration example for a typical plan for UAS noise testing to better capture the process and properly estimate the cost, staff, and time implications.



- Formulated use cases that are aligned with needs and recommendations provided by OEM partners, with a focus on **exploring implications of alternative testing procedures on regulatory compliance** and highlighting the benefits of **process simplification** (e.g., lateral microphone placement or removal, if trusted analysis is used).
 - Preliminary analysis of noise measurement data was conducted, and resulting insights were utilized for requirement analysis.
 - Provided a demonstration by assessing a simplified noise collection/analysis process, with the Waco YMF-5 propeller aircraft as an example.
 - Documented options for equivalent procedures in a database/library compilation.
- Conceptualized and developed a **visualization environment** to aid as a use case demonstrator and decision support environment.
- Published articles with the American Institute of Aeronautics and Astronautics (AIAA) and for the SciTech 2023 and 2024 meetings.

In the following sections, key contributions are highlighted, along with detailed descriptions of technical progress, research approaches, key milestones, and accomplishments for each task.

Task 1 - Develop a Traceable Structure for UAS Noise Certification Requirements

Georgia Institute of Technology

Objectives

In support of the main research objective of Project 061, Task 1 focuses on examining current noise certification procedures (Task 1.1) and benchmarking against current industry practices in how these procedures are adopted and implemented (Tasks 1.2 and 1.3). In particular, the subtasks are organized as follows:

Task 1: Develop a traceable structure for UAS noise certification requirements

- 1.1. Document related regulations and current standards.
- 1.2. Generate noise certification requirements from currently known and established regulations.
- 1.3. Define a validation process for noise requirements.

Research Approach

Task 1.1

For Task 1.1, the main goal was to review and document current noise certification procedures. The task objective was to gain an understanding of the current regulatory framework for UAS noise certification, as required by FAA regulations and followed by OEMs to demonstrate compliance. In particular, the team conducted a thorough literature review of noise certification standards for multiple UAS that were issued by the FAA as Rules of Particular Applicability (RPAs), relevant 14 CFR parts (mainly Part 36), and associated documents where relevant. With recommendations from the team's partners, this task also considered other documentation from the European Union Aviation Safety Agency (EASA), the ICAO Environmental Technical Manual, and the Volpe website. Figure 5 illustrates some of the existing regulatory references that were explored during this process.

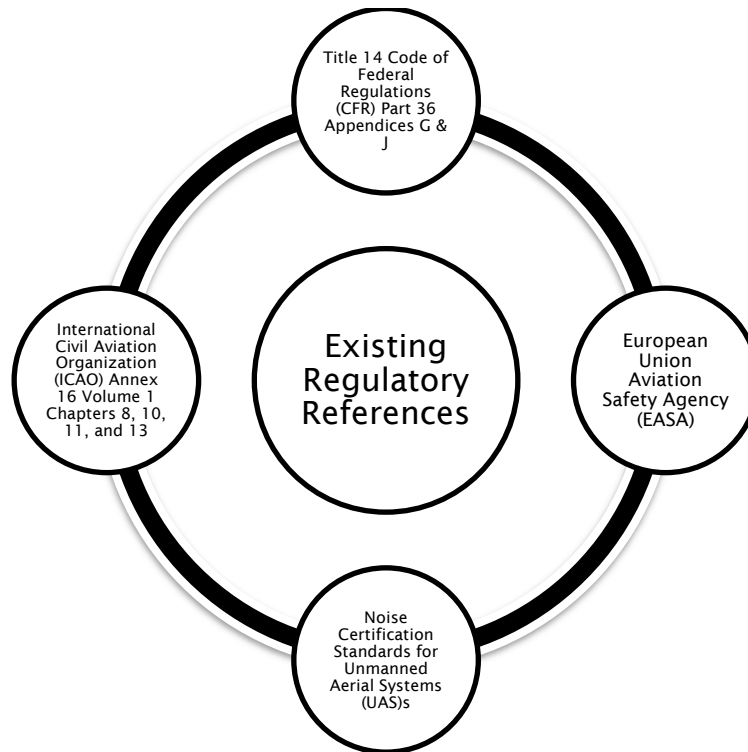


Figure 5. Existing regulatory references for noise certifications.

Along with the extensive review of Federal Acquisition Regulations (FAR) and literature on the regulatory framework, the team aimed to demonstrate the flow of procedures, associations, and dependencies across regulatory items. This was achieved by establishing a clear breakdown of regulations in a proper structural arrangement. Bendarkar et al. (2020) provided a structural hierarchy comprising four layers: part, subpart, grouping, and paragraph. The “part” layer is composed of the regulations provided by any of the sources presented in Figure 6. The “subpart” layer follows the “part” layer and pertains to the applicable body of regulations; therefore, it can be interpreted as the certification basis that constitutes the UAS noise certification standards RPAs. If a distinct group of regulatory statements is recognized, then it can be designated to a “grouping” layer. “Paragraph” is the lowest level in the hierarchy, and it contains regulatory statements.

Moreover, Fazal et al. (2022) constructed a regulatory framework identifying three main categories of regulatory statements: regulation requirement, regulation context, and regulation test. The categories are defined as follows:

- Regulatory requirements impose requirements on the applicant, aircraft, or specific systems/components. These statements often use the term “must” and provide specific standards or specifications.
- Regulation contexts include contextual statements that provide additional information within the regulatory framework, such as definitions or general specifications.
- Regulation tests consist of statements related to tests that must be undertaken by the applicant to demonstrate compliance with regulatory requirements.

Figure 6 illustrates the adapted structural hierarchy for the scope of this project.

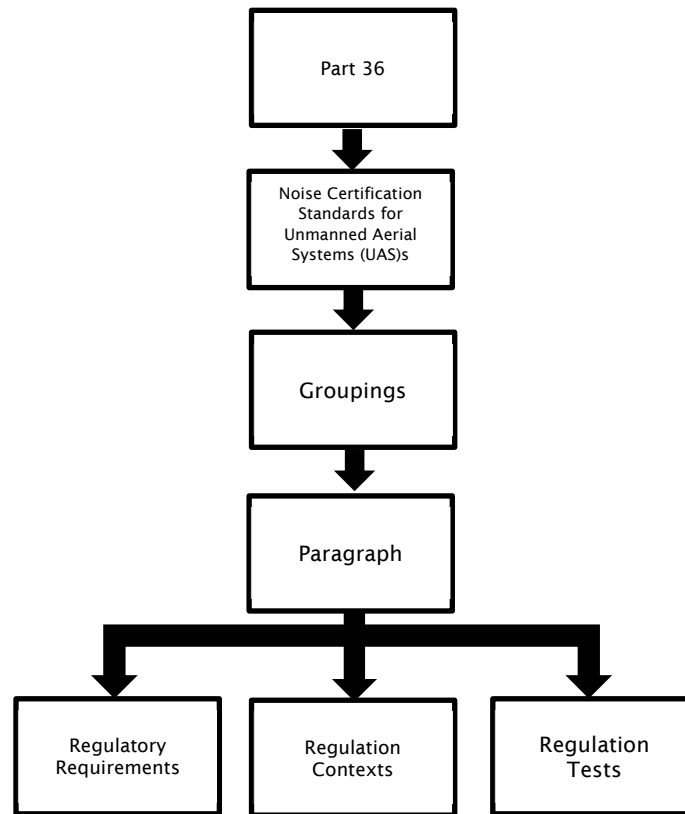


Figure 6. Structural hierarchy of noise regulations.

One of the benefits of this task’s outcome is that team members quickly became more knowledgeable of the certification basics in preparation for Task 1.2 (defining requirements) and were able to build a comprehensive MBSE representation (in SysML) of the current framework (see Task 3.1).

Task 1.2

Defining and maintaining a good set of requirements is vital for the successful design, development, and operation of systems, products, and processes. It is also a crucial first step in creating the requirements model of the model-based certification framework (Kim, 2023). A requirement is defined as “a statement that identifies a system, product or process’ characteristic or constraint, which is unambiguous, can be verified, and is deemed necessary for stakeholder acceptability” (INCOSE, 2006) . “Good” requirements are those having attributes such as necessary, unique, unambiguous, clear, concise, complete, consistent, technically feasible/achievable/obtainable, traceable, measurable/quantifiable, verifiable (e.g., testable), able to be validated, operationally effective, and survivable and singular as outlined by the Department of Defense (DoD) *Systems Engineering Guidebook* (2022). In addition, requirements can vary in their type, which encompasses functional, non-functional, design, performance, certification, etc. (Firesmith, 2005). For the purpose of the current work, the requirements are strictly regulatory “certification” requirements. Regulatory requirements are defined using the established certification basis, which constitutes the set of applicable regulations. The noise certification standards issued for the Matternet M2 Aircraft were selected as an initial starting point.

The FAA Writing Standards provide a useful guide for defining the requirements such that they will satisfy the desirable requirement attributes outlined by the DoD *Systems Engineering Guidebook* that are non-functional in nature (detailed in the next section). These standards include word choice such as using “must” instead of “shall,” using short sentences and short paragraphs, limiting the use of abbreviations and acronyms, etc. (Federal Aviation Administration, 2003). While converting the regulations into requirements, the following considerations were considered (Kim, 2023):

- Not all regulations needed to be converted into requirements.
- A single regulation often needed to be broken down into multiple requirements. Conversely, multiple regulations were sometimes merged into a single requirement.
- The regulations do not always provide all the necessary information, so additional metrics and clarifying information were gathered from literature reviews and other regulatory documents.

Table 2 showcases five requirements that were extracted from regulation number 12 of the Matternet M2 noise certification standards.

Table 2. Regulation to requirements.

Regulation Section	Regulation Text	Requirements
12	<p>(12) Level flight height and lateral path tolerances (Reference part 36, appendix J, section J36.105(b), as modified): A test series must consist of at least six flights. The number of level flights made with a headwind component must be equal to the number of level flights made with a tailwind component over the noise measurement station:</p> <p>(a) In level flight and in cruise configuration;</p> <p>(b) At the test height above the ground level over the noise measuring station as defined in paragraph (6) of this rule. For the selected height, the vertical tolerance of this height should be $\pm 10\%$ value; and</p> <p>(c) Within ± 10 degrees from the zenith.</p>	A test series must consist of at least six flights.
		The number of level flights made with a headwind component must be equal to the number of level flights made with a tailwind component over the noise measurement station.
		Each flight must be in level flight and in cruise configuration.
		At the test height over the noise measuring station, the vertical tolerance of this height should be $\pm 10\%$ value.
		At the test height over the noise measuring station, the tolerance is within ± 10 degrees from the zenith.

Once the regulatory requirements are defined, regulation contexts and regulation tests will be used to refine the requirements by defining means of compliance and methods of compliance as demonstrated in Figure 7 for regulation 12(a). Means of compliance are defined as detailed design standards that ensure compliance with the regulations (Federal Aviation Administration Advisory Circular, 2017). Methods of compliance are more specific than means of compliance, and they describe how compliance will be demonstrated (e.g., ground test, flight test, analysis) (Federal Aviation Administration Advisory Circular, 2017). Once the methods of compliance are determined, all the required information for a certification plan can be consolidated, including the certification basis, requirements, means of compliance, and methods of compliance.

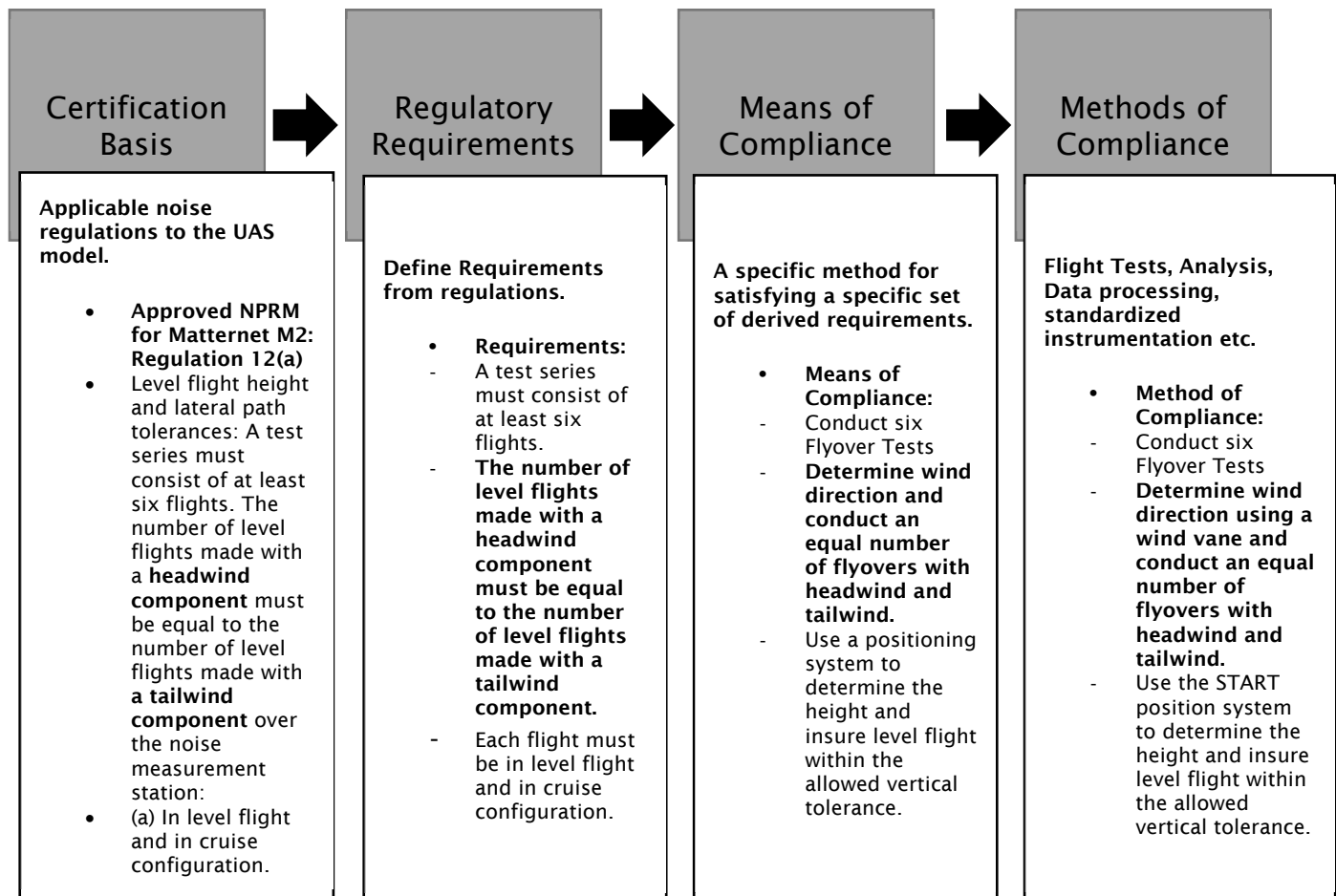


Figure 7. Certification basis to methods of compliance.

The complexity of this process becomes apparent by examining the intricate networks created between regulatory statements leading to the certification plan. MBSE can aid in nullifying this complexity by capturing the process of creating the certification plan in addition to other supplementary domain knowledge within one model that is the singular source of truth.

Task 1.3

Following the creation of the certification plan, it is imperative to check whether the regulatory requirements satisfy the desirable requirement attributes. The attributes can be classified into functional and non-functional categories, as illustrated in Figure 8. Functional attributes are concerned with the feasibility and technical adequacy of the requirements, whereas non-functional attributes are those concerned with language quality. Functional attributes require data for verification, unlike non-functional attributes. To this end, the regulatory requirements analysis process (outlined in Figure 9) provides a framework that allows for the verification of regulatory requirements' adherence to the desired requirement attributes. The outline indicates that once the requirements are defined, data need to be collected using the methods of compliance stated in the certification plan. Raw data are then processed by applying procedures such as correlating noise measurement data with position, calculating the required noise metrics such as sound exposure level (SEL), and applying the necessary data corrections (duration adjustments), etc. The processed data are then used to verify the requirements. Additionally, the requirements themselves can also be checked for functional attributes in the presence of available test data and experience. This is an iterative process, so there is a feedback element that allows for the refinement of the requirements such that it will satisfy the desired requirement features.

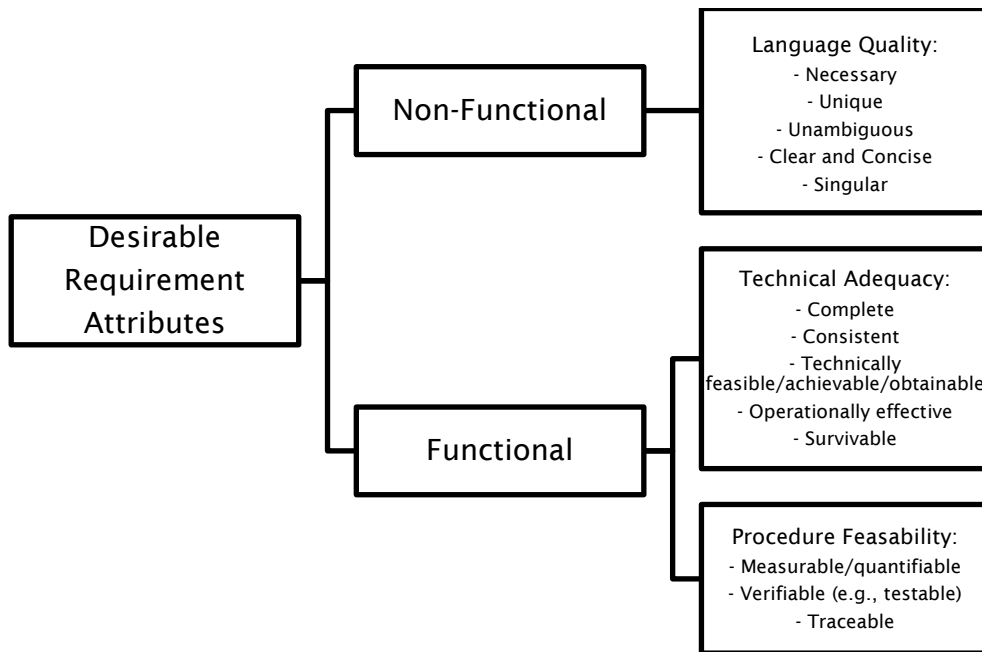


Figure 8. Attributes of desirable requirements.

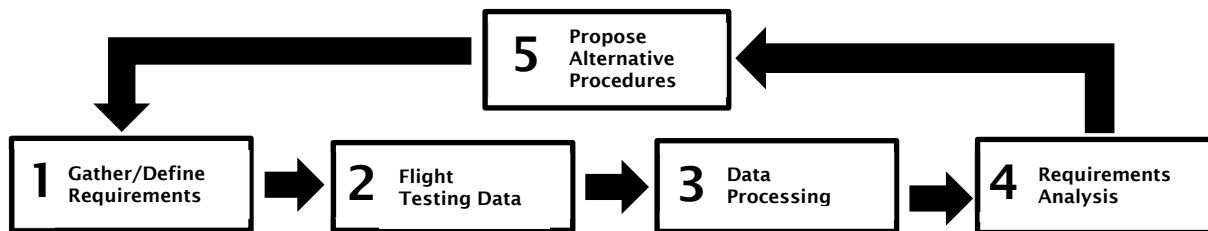


Figure 9. Regulatory requirements analysis process.

The iterative nature of the regulatory requirements analysis process dictates that if a requirement is deemed unsatisfactory or can be improved in terms of functional attributes, alternative testing procedures need to be proposed (as shown in Figure 9). These alternative procedures are meant to bridge the current gap that exists between current noise certification bases and UAS certification needs. Proposing alternative testing procedures will contribute to capturing the uniqueness of the UAS while also addressing the challenges associated with their certification (i.e., operational and noise metric limitations). The proposed procedures may include the use of different noise metrics, microphone setups, or additional flight tests that better capture the specific mission profile of the UAS. Such suggestions could convert to opportunities for potential process streamlining if recommended practices are out of sync with current procedures. The limitation in this exercise is that no recommendations should suggest or presume any change in the regulatory side; hence, the suggestions should be concentrated on equivalent procedures, with either simplified processes or connections to modern technologies that are expected to meet the same regulations.

The alternative procedures can be generated by identifying possible combinations in the morphological matrix shown in Table 3. The options provided by the matrix are surveyed from literature mainly FAA regulations such as the UAS Noise Certification Standards RPAs and Volpe UAS Testing Campaigns' noise measurement reports.

Table 3. Certification test procedure morphological matrix.

Morphological Matrix					
Flight Test Profile	Flyover	Hover	Vertical Takeoff/Landing	Infrastructure Inspection	Maneuver
Microphone Type	Ground microphone	Inverted ground microphone	Elevated microphone on a tripod	Elevated microphone on a crane (higher altitude)	-
Microphone Array Design	Linear (horizontal)	Circular	Vertical, elevated microphone array	-	-
Noise Measurement Metric	Sound exposure level (SEL)	A-Weighted maximum sound level (LAMAX)	Equivalent sound level (LAEQ)	Effective perceived noise level (EPNL)	-
...

The objective for generating alternative procedures is to explore options for formulating a streamlined certification process. The following target objectives for streamlining the certification process are currently being considered:

- Reduce the number of steps in the process, with anticipated savings in time and cost.
- Replace steps in analysis, data preparation, and post-processing with digital tools.
- Enhance automation on procedural tasks (e.g., data retrieval, queries, processing, and report generation).
- Simplify setup requirements to facilitate more test locations/weather windows.

Along with the selection of the equivalent procedures of interest, based on the above feedback, the outcome of this exercise is to present certain use cases for which a feasibility demonstration of an equivalent procedure would be possible. This effort would require data for calibrating the certification model against the system under test (SUT) configuration and for showcasing quantifiable improvements against the process criteria listed above, while meeting the same regulatory constraints and requirements as the benchmarked certification procedure. The quantitative assessment, which will be supported under the PIM module developed under Task 4, is the main enabler for allowing an iterative process until process alternatives can meet the expectations for process streamlining and simplification.

As mentioned above, the existing connections and synergies with other ASCENT projects are expected to provide the resources needed to support the demonstration of this framework as a platform for evaluating equivalent procedures.

Milestones

Between October 2022 and September 2023, the following milestones were achieved:

- Completion of exploration and assessment of NPRM (86 FR 48281) (FAA, 2022), which presents only the noise certification basis for one new model of UAS seeking type certification, the Matternet M2
- Review of the recently approved RPAs for noise certification of small UAS category vehicles

Major Accomplishments

- Performed a literature search and documented regulations and current testing standards for small UAS.
- Defined a traceable structure for UAS noise certification requirements, using the MBSE verification model developed for the transport category.
- Published articles with the American Institute of Aeronautics and Astronautics (AIAA) SciTech 2024.



Publications

Peer-reviewed journal publications

None.

Published conference proceedings

Ravikanti, B., Ali, H., Balchanos, M., Harrison, E. D., & Mavris, D. N. (2023). *MBSE-Enabled System Verification of Unmanned Aerial System Noise Certification*. Accepted and to be presented at the AIAA SciTech 2024 Forum, Orlando, FL, January 8-12, 2024.

Written reports

December 2022 ASCENT Quarterly Report, ASCENT Project 61. (2023, January 30). *Noise Certification Streamlining*. Award number 13-C-AJFE-GIT-066.

March 2023 ASCENT Quarterly Report, ASCENT Project 61. (2023, April 30) *Noise Certification Streamlining*. Award number 13-C-AJFE-GIT-066.

June 2023 ASCENT Quarterly Report, ASCENT Project 61. (2023, July 30). *Noise Certification Streamlining*. Award number 13-C-AJFE-GIT-066.

September 2023 ASCENT Quarterly Report, ASCENT Project 61. (2023, October 30). *Noise Certification Streamlining*. Award number 13-C-AJFE-GIT-066.

Annual Report (period ending September 2022), ASCENT Project 61. (2022, December 12). *Noise Certification Streamlining*. Award number 13-C-AJFE-GIT-066.

Outreach Efforts

- Completed follow-up meetings with OEM partners for feedback on the certification model through spring 2022
- Completed a project overview and capability demonstration to Volpe and requested information for model finetuning
- Participated in conferences (ICAS and AIAA SciTech)

Awards

None.

Student Involvement

- All participating graduate students have supported Task 1 activities by contributing to the literature and background search and reviewing current regulations and FAA-instructed certification procedures.
- Recent efforts to document current regulations for UAS noise certification are currently led by Balaji Ravikanti.

Plans for Next Period

- Plan a series of workshops with partners and subject matter experts on small UAS category noise certification
- Demonstrate noise certification based on NPRM 86 FR 48281.
- Demonstrate an Equivalent Procedure (EP) assessment through certification modeling across different UAS configurations.
- Publish articles with *AIAA Journal* and AIAA SciTech.

References

Bendarkar, M. V., Harrison, E., Fields, T. M., Glinski, S., García, E., & Mavris, D. N. (2023). An Extended MBSE Framework for Regulatory Analysis of Aircraft Architectures. 2023 AIAA AVIATION. <https://doi.org/10.2514/6.2023-3611>

Fazal, B., Glinski, S., Harrison, E., Fields, T. M., Bendarkar, M. V., García, E., & Mavris, D. N. (2022). An MBSE Framework for Regulatory Modeling of Transport Category Airplanes. AIAA AVIATION 2022 Forum. <https://doi.org/10.2514/6.2022-3256>

Kim, D., Taneri, M., Omoarebun, E.N, Wills, T., Balchanos, M., & Mavris, D. (2023). MBSE-Enabled System Verification and Process Improvement of Transport Aircraft Certification. Accepted and to be presented In AIAA SciTech 2023 Forum, National Harbor, MD, January 23-27, 2023.

INCOSE (2006). SYSTEMS ENGINEERING HANDBOOK.

Department of Defense (2022). Systems Engineering Guidebook. https://ac.cto.mil/wpcontent/uploads/2022/02/Systems-Eng-Guidebook_Feb2022-Cleared-slp.pdf.

Firesmith, D. (2005). Are your requirements complete? The Journal of Object Technology, 4(1), 27. <https://doi.org/10.5381/jot.2005.4.1.c3>

Federal Aviation Administration (2003). FAA WRITING STANDARDS. https://www.faa.gov/documentLibrary/media/order/branding_writing/order1000_36.pdf.

Federal Aviation Administration Advisory Circular (2017). FAA Accepted Means of Compliance Process for 14 CFR Part 23. https://www.faa.gov/documentLibrary/media/Advisory_Circular/AC_23_2010-1.pdf.

Task 2 - Formulate a Library of UAS and Testing Procedures

Georgia Institute of Technology

Objectives

Task 2: Develop a library of UASs and testing procedures

- 2.1. Complete technical documentation of UAS configurations.
- 2.2. Complete technical documentation of UAS noise testing equipment.
- 2.3. Define UAS noise test plans.
- 2.4. Define possible simulation techniques.

Research Approach

Task 2.1: Complete technical documentation of UAS configurations

Research tasks on investigating and archiving technical documentation of UASs, as well as recommended procedures for noise testing, started in July 2022. Due to the lack of historical data about the noise generated by most UAS models, the FAA is unable to provide generally applicable noise standards for UAS (Federal Aviation Administration, 2021). This insufficiency in data is caused primarily by the novelty and variety of UAS systems, such that no clear categorization of the systems is currently established. Figure 3 illustrates this problem by listing some of the different UAS configurations currently available.

The aforementioned problem is exacerbated by the various mission profiles of UAS systems and their different operating environments (Kim, 2022). As an alternative measure, the FAA issues RPAs for applicants who wish to certify their product for noise. To achieve this, the FAA assumes that the fundamental physics of UAS operation and noise are scalable if the UAS shares comparable characteristics with crewed aircraft. As a result, the current noise standards for crewed aircraft outlined in 14 CFR Part 36 can be applied to UAS or extrapolated for testing lower-weight UAS at lower altitudes. An example of this is the “Noise Certification Standards: Matternet Model M2 Aircraft,” which is the first RPA establishing a noise certification basis for a single model of aircraft described only for the Matternet Model M2 (Federal Aviation Administration, 2021). These RPAs alongside with the Volpe UAS Testing Campaigns’ noise measurement reports have been valuable for documenting the testing procedures and in identifying the most important technical challenges for UAS noise testing.

So far, depending on the availability of data, only multirotor UAS were encompassed within the scope of the provided analysis. This includes vehicles such as the Matternet Model M2, Tarot X8, and Flytrex FTX M600P. The three UAS are depicted in Figure 10. The Matternet Model M2 was issued the first RPA by the FAA in 2022; therefore, it was utilized for benchmarking efforts early on in the pivot toward UAS from the transport category. Tarot X8 is employed by the ASCENT 077 group for their noise measurement testing campaigns. Thus, in collaboration with ASCENT 077, a dataset was obtained from the testing campaign and was used to investigate the noise generated of Tarot X8 within the scope of the benchmarked regulations. Finally, the Flytrex FTX M600P is the SUT for the most recent case study under this project. Its noise certification standards were issued on July 3, 2023, and upon collaboration with the ASCENT 094 group, a dataset was obtained from the Causey Noise Measurement Testing Campaign that facilitated this case study. More details about the case study are provided in Task 4.



(a) Matternet M2



(b) Tarot X8



(c) Flytrex FTX M600P

Figure 10. Unmanned aerial systems (UASs) analyzed within this project

Task 2.2: Complete technical documentation of UAS noise testing equipment

Part of this grassroots effort in discovering the state of the art by looking at RPAs and Volpe UAS noise measurement campaigns’ reports as well as collaborating with the ASCENT 077 group, is to generate technical documentation on UAS noise testing equipment. The equipment employed within a testing procedure includes everything from pressure sensors (i.e., microphones), to data recorders, weather data microstations, aircraft tracking systems, etc. This equipment will be supported by data measurement and collection software.

Microphones are the most critical element in noise testing. Figure 11 showcases three types of microphones that can be utilized during noise testing: ground microphones, inverted ground microphones, and elevated microphones. Ground microphones including the inverted ones, tend to minimize interference with directed or reflected sound, and reduce measurement uncertainty related to the microphone elevation; however, they tend to be relatively more complex to set up and more costly than the elevated microphones. In contrast, elevated microphones are simpler to set up and less expensive, but they suffer from interference with directed and reflected sound. All microphones utilized for noise measurement are outfitted with windscreens to ensure reliable acoustic measurements while minimizing noise due to weather variations (e.g., rain and wind) and birds.

The pressure fluctuations captured by the microphones are digitized via a data recorder. Data recorders are also used to power microphones, and they control the timing, synchronization, and data transfer between the input module and external host such as a computer. Moreover, meteorological conditions are continuously monitored during acoustic measurements. Weather data logging can be collected via weather microstations connected to anemometers and temperature/humidity sensors, as shown in Figure 12.

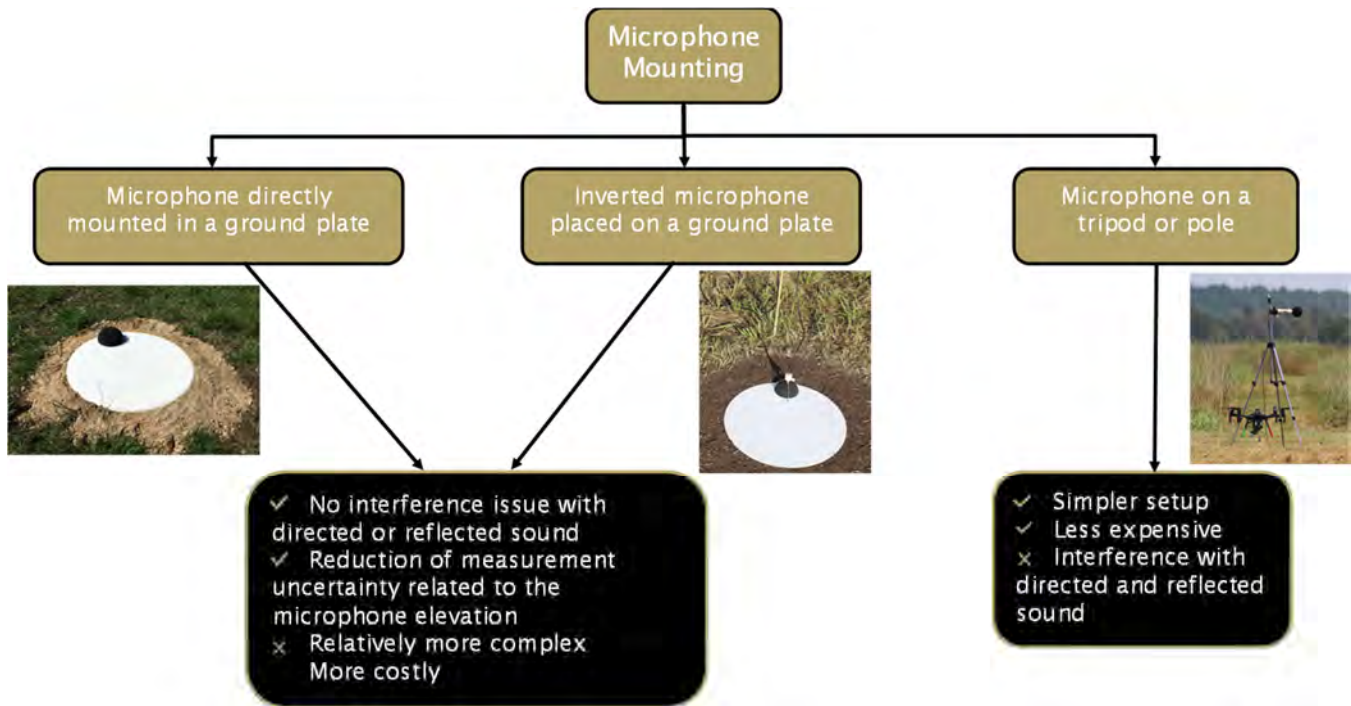


Figure 11. Microphone types and corresponding advantages and disadvantages.



Figure 12. Anemometers for Weather data acquisition equipment.

Time-space-position-information for the UAS within a noise testing procedure is captured by aircraft tracking systems such as the Survey and Tracking Apparatus for Research in Transportation (START) depicted in Figure 13. START is a tracking system developed by Volpe “for the purpose of deriving precise positioning and timing information from UAS and other automated platforms” (James, 2021).

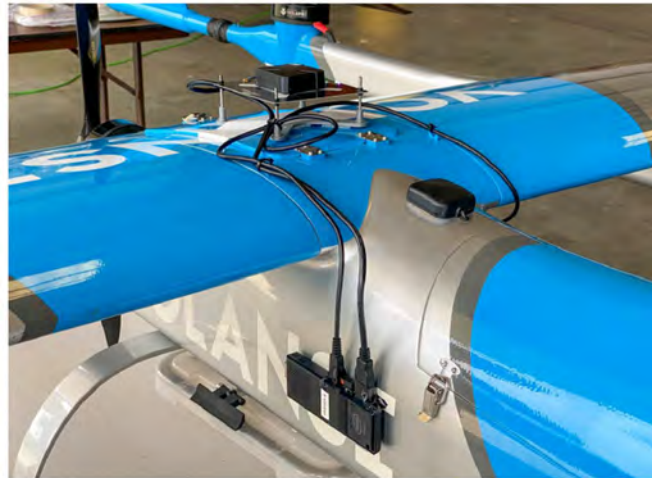


Figure 13. Survey and Tracking Apparatus for Research in Transportation (START) aircraft tracking system.

Task 2.3: Define UAS noise test plans

Research tasks on investigating and archiving technical documentation of UASs, as well as recommended procedures for noise testing, started in July 2022. One of the key studies that the ASCENT 061 team has started to document and that has been valuable in identifying the most important technical challenges for UAS noise testing is the document titled “Noise Measurement Report: Unconventional Aircraft” by the Choctaw Nation of Oklahoma (July 2019). The described practice for UAS noise testing took place on a grassland, which, taking the flight envelope into consideration, is not suitable due to the following reasons:

- Dense areas can have a different “perceived” noise.
- High altitudes and dense areas over buildings and hard surfaces can have different reflective behaviors.
- Within buildings, noise can be reflected, amplified, or attenuated.

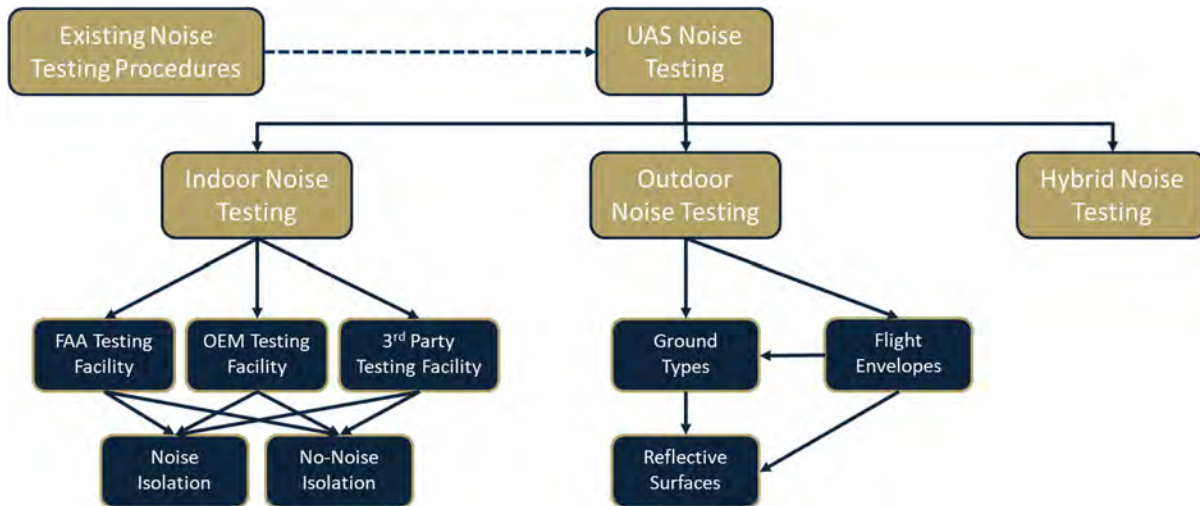


Figure 14. Alternative noise testing procedures for an unmanned aerial system (UAS). OEM: original equipment manufacturer.

Part of this grassroots effort in discovering the state of the art is the technical documentation on UAS noise testing equipment. By assessing testing procedures from a regulatory perspective, we can build some simple alternatives under

the system verification model; examples are shown in Figure 14. Finally, the UAS noise test plans must be defined and executed. Physical testing will not cease to exist, but simulation techniques are needed for testing process alternatives.

A major part of the study for this cycle involved gathering available experimental test data to aid in understanding both the sensitivity of noise metrics to flight test parameters or test setup parameters and the times and costs associated with various sub-steps of a noise testing procedure. Note that the experimental noise testing campaign is more rigorous in many ways compared with the certification noise testing procedures. This enabled us to compare various microphone locations, flight conditions, and metrics, which is not possible when limited to the data typically available from certification-type noise testing procedures.

The experimental test campaign whose data was extensively utilized in this cycle of the study was the Causey test campaign. The objective of the testing campaign was “to gather data on UAS noise emissions in compliance with the UAS noise regulations specified in 14 CFR Part 135.” Unlike other test campaigns, which may not be compliant with certification norms, the Causey campaign is explicitly meant to gather certification quality data. The report provides the acoustic measurements and resultant dataset. FAA, Volpe, and Blue Ridge Research and Consulting (BRRC) were the parties involved. Chris Hobbs (FAA) headed UAS flight operations, Robert Samiljan (Volpe) coordinated the vehicle tracking data collection, and Michael James (BRRC) managed the acoustic data collection.



Figure 15. Test vehicles of Causey testing campaign. From left to right, Flytrex FTX-M600P, Volansi VOLY C10 and DJI m210

Table 4 below lists the empty and maximum weights of the test vehicles shown in Figure 15 above. Vehicles performed flyover and hover operations for multiple flight conditions. The weight of the Flytrex FTX-M600P is comparable to that of the Matternet M2 (for which there is an existing recent noise regulation linked in references), which has a MTOW of 29 lbs, including a 4-lb payload. However, it is worth noting that the Flytrex is a hexacopter, whereas the Matternet is a quadcopter. An RPA for the noise certification of Flytrex FTX-M600P was approved recently, alongside six other vehicles of the same class. Flight conditions are derived based on various combinations of weight, speed, and altitude. Three groups of “test points” were conducted; namely, level flyover operations; hover operations; idle, takeoff, landing, or operational level flyover operations. The campaign took place from July 26 to July 29, 2021. Each day, a different vehicle underwent testing.

An additional day of Flytrex FTX-M600P measurements was conducted to capture new test points and repeat two flyover test points to account for day-to-day variations. The goal was to complete six repeated test flights of each condition; however, some test points were repeated more than six times, as will be discussed in later sections.

Table 4. Causey test campaign vehicle weights.

Weight	Flytrex FTX-M600P	Volansi VOLY C10	DJI m210
Empty	26.8 lbs	51.4 lbs	11.8 lbs
Max	33.4 lbs	55.0 lbs	--

Figure 16 below illustrates the Causey testing campaign layout. This view is later used in the visualization environment that is to host all the key details of a test procedure to enable effective decision-making.

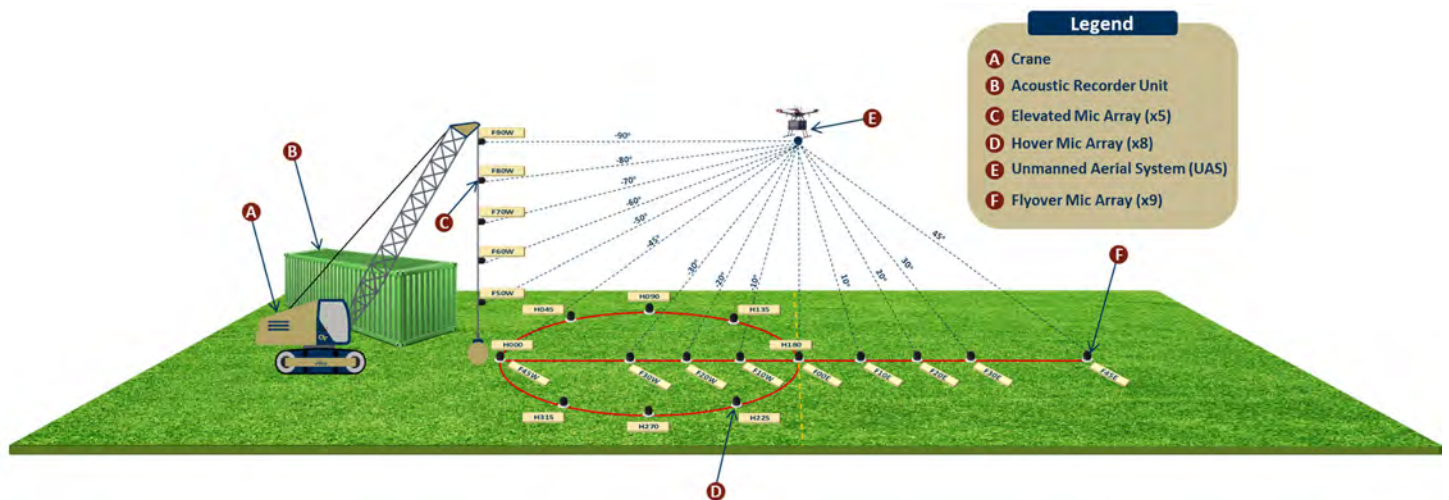


Figure 16. Causey test campaign concept of operations,

Task 2.4: Define possible simulation techniques

Within the scope of this project, MBSE was utilized to assess current noise certification procedures. Typically, MBSE methods are used to represent a vehicle's lifecycle and enable the use of data and information as an integrated systems engineering approach. In the case of Project 061, the product is a process architecture, within which current procedures will be assessed and equivalent procedures will be proposed, defined, implemented, and tested within this environment. The full MBSE model formulation for certification and implementation is showcased in Figure 17.

The validation process contains the steps needed to demonstrate that vehicle noise levels calculated from flight testing results are meeting requirements. Part of meeting the requirements is the instrumentation setup, which is implemented as a logical architecture within the model. A library of instrument model representations is also constructed, from which alternative instrumentation lineups can be modeled. The latter feature is key, as this framework should allow for the evaluation of equivalent procedures, e.g., ground microphone placement. Other components of the verification model are the test procedures and the test report checklist, which are prototyped as activity diagrams in SysML, as well as the vehicle configurations represented as a state machine.

Completing the verification model is any applicable regulation text in the form of a SysML verification thread. With the verification model in place, the user can import any UAS model, perform the certification equivalent process by executing the verification model, and then generate a final report, which would contain the instrument validation document and flight test plan. It is crucial that the overall framework be implemented in a highly modular fashion in order to obtain the needed flexibility for testing equivalent procedure alternatives and to accommodate a broader range of air vehicle designs and configurations. The SysML implementation currently comprises the following modules:

1. Requirement translation and constraints
2. Noise testing instrument architecture
3. Procedures, protocols, and behavior
4. SUT
5. System verification model overview
6. Auto-report generation and output to process evaluation model

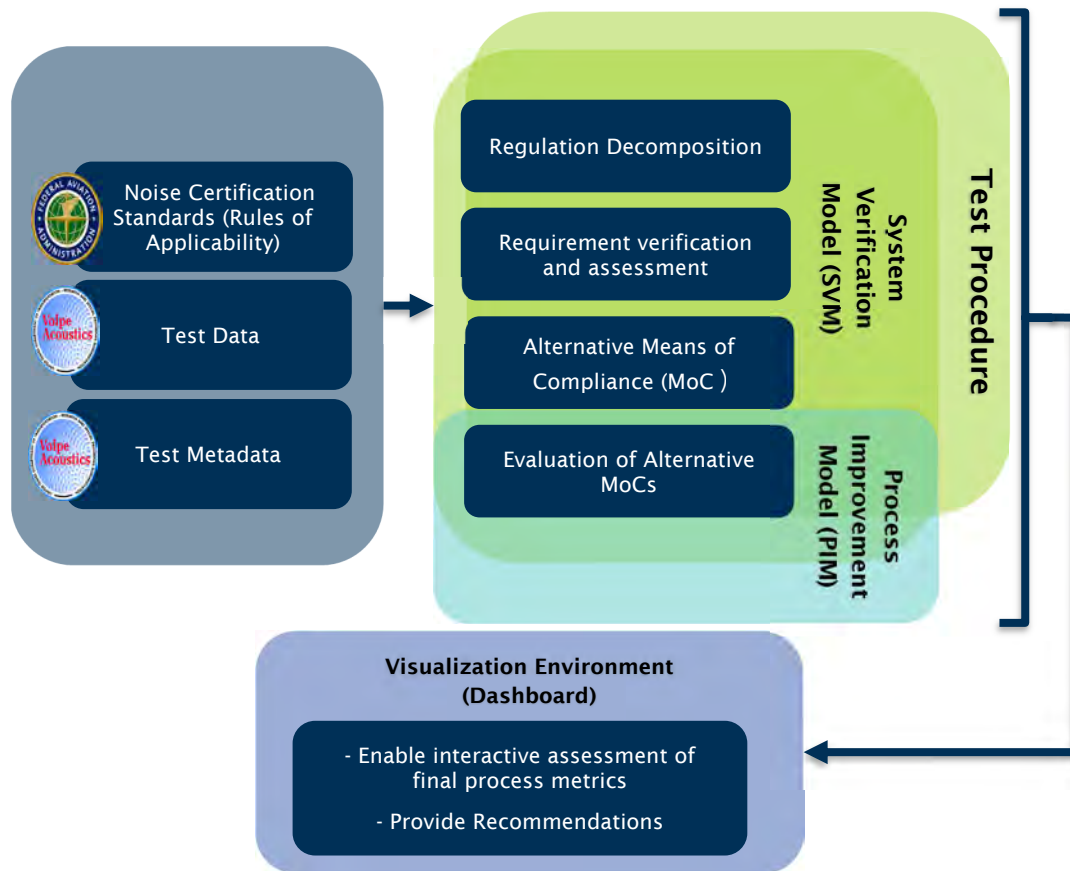


Figure 17. Model-based systems engineering (MBSE) verification model structure.

Event process modeling

With detailed guidance from the documents listed above, event-driven processes were defined and created within the certification model. Additions include modeling of the test-day acoustic collection process and test scenario event processes (flyover, hover).

Library creation

A new task was identified to command the creation of libraries within the certification model, to allow for added flexibility and modularity. Current libraries include the aircraft library, microphone library, and data amplifier library. The SUT representation has been modified to allow for adaptability to various UAS types and configurations.

Aircraft testing environment

Another finalized improvement on the certification model is the modeling of the UAS test environment, including the flight test setup configuration. With input from the documents such as RPAs and Volpe UAS noise measurement campaign reports, the model was updated and refined to include various instrumentation system architectures.

Noise calculation

UAS noise certification only requires a flyover test but also specifies a supplemental hover test to augment the process of collecting noise data that will inform the generation of generally applicable noise standards for UAS. The hover test, as described by the FAA in the Matternet M2 noise certification standards, is a voluntary test that “will not be used to inform the applicant’s airworthiness or type certification basis or be evaluated against any noise limits or regulatory criteria for noise certification purposes” (Federal Aviation Administration, 2021). So far, UAS RPAs have described two noise metrics



for noise measurements: SEL for the flyover test and equivalent sound level (L_{eq}) for the hover test (Federal Aviation Administration, 2021).

1. Sound Exposure Level:

SEL is energy averaged A-weighted sound level over a specified period of time or single event, with a reference duration of 1 second. SEL can be calculated using two methods defined as follows (Bennett & Pearsons, 1981):

1.1- Continuous time integration:

$$L_{AE} = 10 \log_{10} \left[\frac{\int_{t_1}^{t_2} 10^{\frac{L_A(t)}{10}} dt}{1 \text{ sec}} \right]$$

where t_1 and t_2 define the time interval, and $L_A(t)$ is the time function of A-weighted sound level during the time for $t_1 - t_2$.

1.2- Temporal sampling:

$$L_{AE} = 10 \log_{10} \left[\sum_{i=1}^n 10^{\frac{L_A(i)}{10}} \Delta t \right]$$

where $L_A(t)$ is the instantaneous A-weighted sound level for the n^{th} sample, n is the number of samples taken during the observational period, and Δt is the time interval between samples.

As mentioned previously, the UAS RPAs prescribe the use of SEL for the flyover test, in which they specify that the integration time $t_2 - t_1$ in practice must not be less than the time interval during which $L_A(t)$ first rises to within 10 dB(A) of its maximum value (L_{Amax}) and last falls below 10 dB(A) of its maximum value. In addition, the regulations allow for the use of an integrating sound level meter to obtain L_{AE} directly rather than manually calculating L_{AE} (Federal Aviation Administration, 2021).

2. Equivalent Sound Level:

L_{eq} is the level of the A-weighted sound energy averaged over a specified period of time. Similar to L_{AE} , it can be calculated by two methods defined as follows (Bennett & Pearsons, 1981):

2.1- Continuous time integration:

$$L_{eq} = 10 \log_{10} \left[\frac{\int_{t_1}^{t_2} 10^{\frac{L_A(t)}{10}} dt}{t_2 - t_1} \right]$$

where t_1 and t_2 define the time interval, and $L_A(t)$ is the instantaneous A-weighted sound level.

2.2- Temporal sampling: $L_{eq} = 10 \log_{10} \left[\frac{1}{n} \sum_{i=1}^n 10^{\frac{L_A(i)}{10}} \right]$

where $L_A(t)$ is the instantaneous A-weighted sound level for the n^{th} sample and n is the number of samples taken.

UAS RPAs prescribe the use of L_{eq} for hover tests only. Similar to L_{AE} , the regulations allow for the use of an integrating sound level meter to obtain L_{eq} directly rather than calculating it manually (Federal Aviation Administration, 2021).

Before L_{AE} and L_{eq} are calculated, corrections must be applied to the measured data to account for uncertainties related to the measurement system, microphone and recording system used, background noise, actual flight path, and meteorological conditions present when the measurements were taken.

The use case described in Task 4 utilizes a python code to parse through the sound pressure time-history (audio) signals obtained from the Flytrex FTX M600P flyover and hover tests during the Causey UAS Acoustic Measurements campaign and calculate both L_{AE} and L_{eq} based on the equations above. Regarding the implementation of noise metric calculations, there is no option for directly performing such analyses within the SysML-based certification model. A possible solution is to create a function in Matlab and then incorporate the analysis in the verification thread.

Milestones

- UAS testing procedures from the literature were thoroughly reviewed.
- Useful test data were obtained from collaborators.
- Connections are established with OEMs and other research teams for further investigations.

Major Accomplishments

- Scripts required to generate multiple noise metrics from raw frequency domain data were created.
- UAS noise testing practices and processes have been documented.

Publications

None.

Outreach Efforts

- Full Year 2 performance review provided to the FAA AEE.
- Technical discussions and feedback provided by Volpe.
- Collaboration with ASCENT 077 and Dr. Eric Greenwood's research group and Flytrex Inc.

Awards

None.

Student Involvement

- All students participated in the collection and review of UAS noise testing practices and processes.
- Hussein Ali led the review of available noise testing data and the creation of scripts of noise metrics evaluation.

Plans for Next Period

- Identify use case examples to plan for demonstration, based on selected areas of improvement for alternative procedures and their evaluation

References

Federal Aviation Administration (2021). Noise Certification Standards: Matternet Model M2 Aircraft.

<https://www.federalregister.gov/documents/2021/08/27/2021-17769/noise-certification-standards-matternet-model-m2-aircraft>.

James, M., Salton, A., Downing, M., & Calton, M. (2021). Blue Ridge Research and Consulting, Asheville, NC, tech.

Bennett, R., & Pearsons, K. (1981). HANDBOOK OF AIRCRAFT NOISE METRICS (CR-3406). NASA.

"Noise Certification of UAS/AAM using Rules of Particular Applicability," Federal Aviation Administration, 2023. URL

https://www.faa.gov/about/office_org/headquarters_offices/apl/ae/noise/uas_noise_certification

Task 3 - Document and Model Noise Testing and Certification Procedures Based on Existing Practices

Georgia Institute of Technology

Objectives

The focus of Task 3 is to develop an overall definition of a more flexible certification process and the evaluation criteria for determining that the procedure is more streamlined than the baseline. The pivot to a UAS focus is well aligned with the objectives of this task, where flexibility will be driven by the requirement for the MBSE model to accommodate a range of

UAS configurations and payloads. Task 3 will build upon the capabilities of the integrated MBSE platform and leverage contributions from all other tasks. The following subtasks will be conducted under Task 3:

Task 3: Develop a noise certification procedure based on existing practices

- 3.1. Transfer noise testing plans to the MBSE model.
- 3.2. Transfer noise testing data to the MBSE model.
- 3.3. Develop a full noise test plan.
- 3.4. Implement a validation process.

Research Approach

Tasks 3.1 and 3.2

Task 3.1 seeks to define what is meant by a “flexible” process. One way to develop this definition to determine whether the introduction of a different vehicle configuration leads to many incompatibilities with the streamlined process under evaluation. For instance, it is important to assess how the UAS configuration affects the microphone technology and quantity needed and the microphone placement in the testing facility. This subtask will involve testing procedures, and a mapping of compatibilities between vehicle configurations and testing procedures will be produced. A set of criteria and evaluation metrics is needed to assess the combinations of vehicle configuration, testing procedures, and uncertainty factors against regulatory-derived requirements, which will be implemented within the MBSE certification framework. Hence, a proposed set of flexibility criteria for the certification process could include the following:

- Compatibility and applicability of equivalent procedures
 - Alternatives in testing procedure should be accounted in the model so they can be verified; i.e., more microphones versus more flight test points.
- Complexity (e.g., if a switch to another configuration requires more steps to setup) and additional instrumentation if a vehicle is more sensitive to variations in certain factors during testing
- Sensitivity to weather, other aleatory uncertainties etc.

The defined criteria will be tested and applied in the following tasks; hence, this task is considered complete.

A regulation paragraph can contain both quantitative requirements and inspectional requirements. Quantitative requirements refer to those that contain numbers or a range of numbers to be met; inspectional requirements usually do not contain numbers but ask the test procedure to follow the instructions or guideline given in the paragraph. In the verification model, such paragraphs cannot be directly adopted but need functional breakdown. For quantifiable requirements, the subjects for which the quantified constraints are designed are identified and separated from each other for the convenience of validation. For an inspectional requirement, a straightforward number is not available to make constraint out of, but a simple yes or no test can be implemented to address the requirement. With the above modification logic, we use the function of the requirement diagram in MBSE to delineate each requirement within each regulation paragraph. The requirement diagram is constructed with two major components: requirement block and constraint block. A requirement block is a block that contains a regulation paragraph that contains a direct indication of requirements. A constraint block is a block that has quantified or yes/no constraints that actively test if the test data fulfill requirements.

Examples are given below to demonstrate both inspectional requirements and quantitative requirements. In MagicDraw, pink blocks are used for requirements and yellow blocks are used for constraint blocks. The requirement for mountings, as shown in Figure 18, specifies that to comply with the regulations, tripods or similar microphone mountings that minimize interference with the sound energy being measured should be used in the testing. There are no quantitative measurements about the microphones to be used; the comments are for its function. For this requirement, the constraint derived from it should stand for the testing of its qualification, thus the constraint block associated with it states that *Mountings_Test* must be 1, meaning it passes the test.

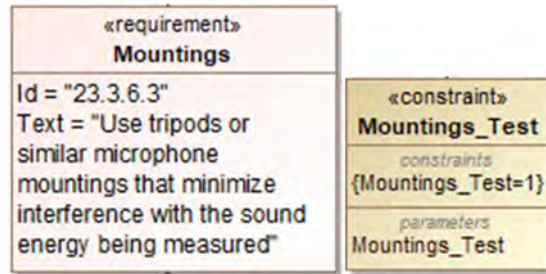


Figure 18. Example of inspectional requirements and constraints.

The requirement for audio signals recording specifics, as shown in Figure 19, details that sound pressure time-history (audio) signals obtained from aircraft flyovers under this paragraph must be recorded digitally at a minimum sample rate of 44 kHz for a minimum bandwidth of 20 Hz to 20 kHz, and encoded using a minimum of 16-bit linear pulse code modulation (or equivalent) during analog to digital conversion. This requirement paragraph mentioned three subjects to comply with the regulation, and for each, the specific quantitative requirements should be stated in the constraint block.

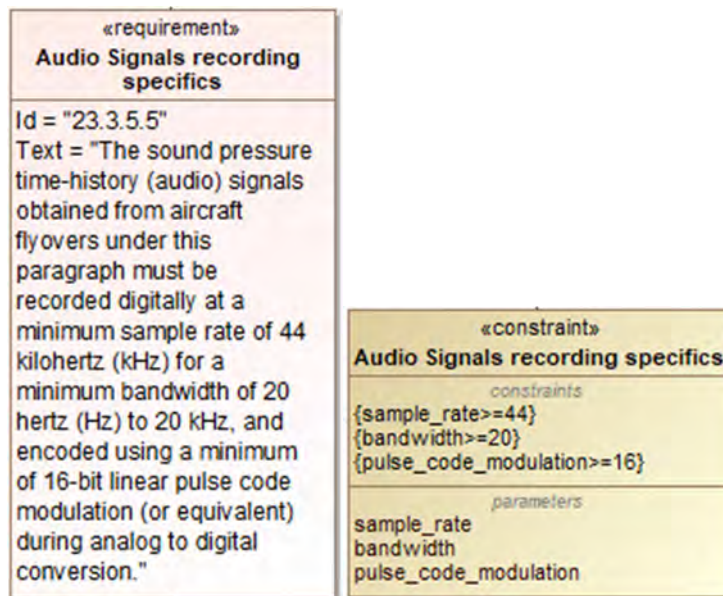


Figure 19. Example of quantitative requirements and constraints.

In the validation model, sections of the testing procedure are identified, and their chronological order is recorded. In the pre-test preparation phase, test site conditions, weather conditions, and multiple specifications on microphones (such as in calibration, how they are used in actual measurements, and what metrics should be embedded in the microphones) are to be confirmed to have met requirements. The testing part consists of two branches: flyover and hover, each having different sets of requirements. The constraint blocks will attach to the main sections of requirements like tree branches, each section will have several requirements blocks, and each requirement block will have several constraint blocks.

Based on the workflow proposed in Figure 20, the integrated framework for flexibility assessment of the certification process is expected to be reusable for a broader set of UAS configurations, as highlighted in Figure 21.

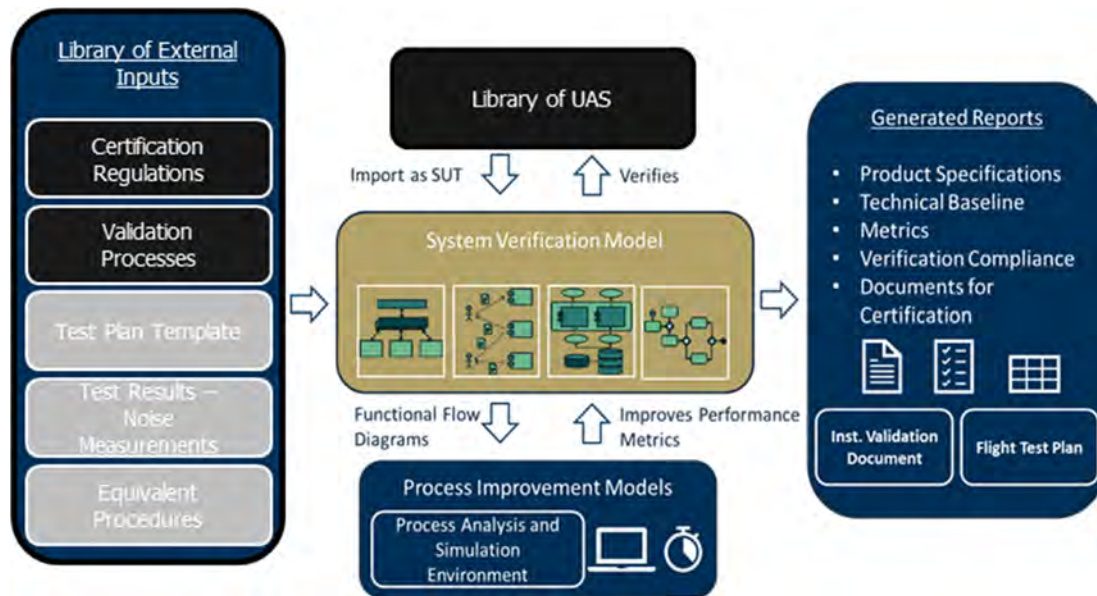


Figure 20. Model-based systems engineering certification framework version for unmanned aerial systems (UASs) to test category flexibility in equivalent certification procedures. SUT: system under test.

With the model, testing data can be validated against the requirements instantly after processing. For convenience of the users, data should be populated in the form of an instance table, aligning data to each corresponding constraint. The model validates data provided to each constraint instantly.

#	Name	<input checked="" type="checkbox"/> lateral_distance	<input checked="" type="checkbox"/> hover_height_0	<input checked="" type="checkbox"/> lateral_distance	<input checked="" type="checkbox"/> AGL_45	<input checked="" type="checkbox"/> hover_height_9	<input checked="" type="checkbox"/> radial_90
1	new_req_datapoint	3	4	1	2	7	2
2	new_req_datapoint1	3	3	1	1	2	1
3	new_req_datapoint2	2	3	3	4	4	4

Figure 21. Notional instance table.

Task 3.3

The certification framework for UASs developed under Task 3, as well as the use of the PIM completed under Task 4, will allow us to measure process flexibility, efficiency, complexity, and other figures of merit as part of comparing alternatives to the baseline. Framing this problem as a decision-making problem in this context, an “alternative” would be a version of the baseline certification process with a specific combination of a testing plan, instrumentation selection, and a setup for measurements and processing methods, as dictated by a possible equivalent procedure.

A typical flight test procedure can be divided into five major sections corresponding to 4 days of carrying out different activities or tasks (see Figure 22). These sections are not necessarily carried out over consecutive days as any two sequential sections can be separated by days, if not months, depending on the testing campaign and the scheduling and planning of the parties involved. These sections can be described in the following manner (see Figure 22 for the detailed steps for each day of the testing process):

1. **Test Site Inspection:** The team visits the potential test site to evaluate its suitability for conducting noise testing. This consists of assessing the site location and surroundings in terms of proximity to noise-sensitive areas, weather conditions, and levels of background noise, which could, for instance, include traffic, birds, construction noise, or sound reflections off nearby buildings. The type of ground surface is also important as it could influence the measurement results. Common ground surfaces considered can include grass, concrete, asphalt, and open terrain. Grass tends to be



the most preferred option due to its ability to absorb sound and reduce sound reflections compared to hard surfaces; however, this requires the grass to be well maintained and free from tall vegetation. The elevation and uniformity of the ground surface are also crucial to avoid measurement inconsistencies. The overall site area is also evaluated by checking whether it can properly accommodate the equipment installation and the distances and altitudes required for the flight tests. Following this inspection, the test site is either approved, if deemed appropriate for the testing requirements, or denied, if it does not meet certain criteria or would lead to test measurement complications or inconsistencies. The necessary permits for conducting UAS flights at the selected location and ensuring regulatory compliance are to be obtained.

2. **Test Site Preparation:** Once approved, a second visit to the test site is necessary to prepare for it before the actual flight test day. This consists of clearing the site of any obstacles or potential hazards, mowing the grass if needed, and marking the positions of microphones and other equipment, which requires having a clear flight plan for the specific flight paths, altitudes, and maneuvers to be performed by the UAS on the flight test day. The UAS to be flown is also inspected to ensure its proper functioning beforehand.

3. **Flight Test Day:** The flight test day can be further decomposed into three main action lists:

- **Pre-test Procedure:** All microphones, recording equipment, and other equipment are installed and deployed. Weather measurements are initiated, and microphones are calibrated and tested before the installation of windshields and the measurement of ambient noise. Throughout this procedure, multiple checks are conducted to ensure the proper functioning of all devices and adequate meteorological conditions for testing.
- **Flight-test Procedure:** Flight test profiles (flyover, hover, takeoff and landing, etc.) are initiated. Within each flight profile, multiple test points can be conducted under different conditions, including altitude, weight, and speed. To ensure the accuracy and reliability of measurements, each test point is repeated for a minimum of six test runs. After the completion of each test point, multiple checks are carried out to assess the need for microphone recalibration, maintenance, or battery change for the UAS, or a complete redo of the test point upon the detection of any anomalies or inconsistencies in the measurements.
- **Post-test Procedure:** Once all flight profiles are completed, the ambient sound is measured, the microphones are calibrated, all microphones and equipment are collected, and measurement data are saved.

4. **Data Analysis:** The data collected during the flight test day are post-processed and analyzed. Raw measurements are translated in terms of noise metrics of interest, and any sources of inconsistency or interference with the measurements can be revealed. Consequently, the need for replacement or additional measurements is decided at this step.

5. **Potential Additional Test Day:** Based on the results of data analysis, an additional flight test day might be necessary. This would either consist of a partial redo of some test measurement points or a full flight test redo if significant interference appears to have been present throughout the entire flight test day or throughout a major section of it.

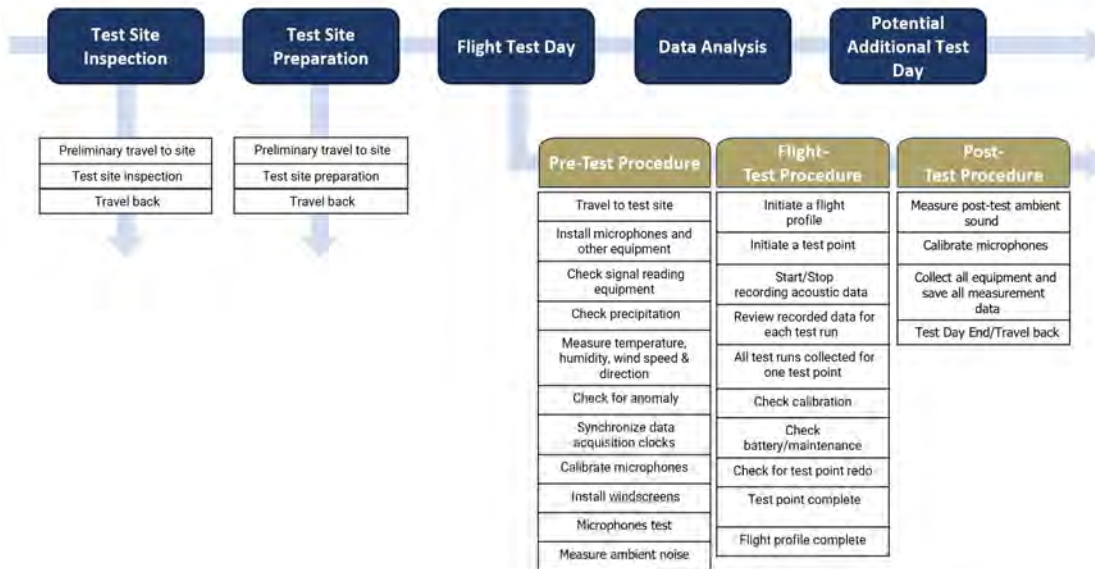


Figure 22. Flight test procedure layout for unmanned aerial systems (UAS) noise measurements.

After the model has been calibrated with inputs and parameter definitions that will be obtained from noise testing data resulting from ASCENT Projects 077 and 094, the model will rely on statistical analysis and an identification of process bottlenecks and showstoppers. Another set of metrics of interest will target the impact quantification of process complexities and will be used to indicate gaps and further drive certification process simplification through the use of technologies and estimation methods (e.g., virtual sensing and instrumentation), where process steps could be reduced or eliminated.

As a means of facilitating a scenario-based parametric decision-making capability, the ASCENT 061 team has been developing an interactive visualization environment. Through the use of visual representations of the process and key analysis outputs, this environment serves as a user-friendly interface for requirement validation, exploration of process alternatives and their impacts, detection of process shortcomings and gaps, and ranking for the selection of test plans, instrumentation, and noise measurement data analysis against user-set criteria. The ranked alternatives are validated through an assessment of the equivalency for a procedure to standard regulatory practices. A notional representation of the final version of this environment is shown in Figure 23.

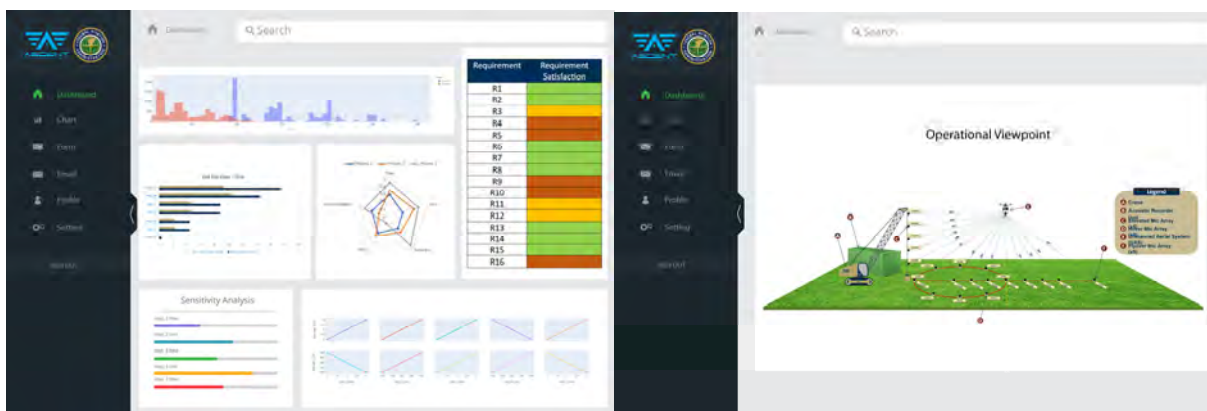


Figure 23. Graphical user interface for process specification.

As interactive dashboard development is often approached as a spiral development, the capabilities and features included in the current version are as follows:

- Histograms to visualize each metric of a given procedure. To compare procedures, it may be helpful to overlay the histograms for the respective procedures to visually compare time, cost, and so on.
- Sensitivity plots to help select from alternative procedures to improve upon the current baseline. These sensitivities can indicate how robust an alternative is to unforeseen variability in the procedure steps in terms of time or cost it takes to complete the step. For example, how sensitive the overall cost improvement (with respect to the baseline) of an alternative is to the cost it takes to complete the alternatives' first step. This information can be presented to the decision maker in the form of a matrix of plots like the prediction profiler plot in the JMP statistical software.
- For multivariate and multicriteria problems, a spider chart (radar plot) is used to compare process alternatives against multiple criteria. This chart can help to drive the evaluation of all tested process alternatives and map the strengths and weaknesses of each alternative against the prioritized evaluation criteria.
- The highest ranked process as a chain of events to rank order key steps identified by the PIM in the order of their importance for a given procedure.
- A requirements satisfaction section to present an assessment check on whether requirements are being met, which includes providing guidance toward the exploration of procedures and technologies that would help close any gaps and meet all requirements. In this part, the focus is on data analytics supported by Monte Carlo process simulations, using probabilistic inputs. Hence, the results are typically in the form of distributions for the metrics of interest and allow for exporting means, median values, and cumulative distribution functions to assess whether constraints and requirements are being met.
- A high-level concept graphic (OV-1) charts for physical representation of the test setup and easier communication with OEMs and decision makers as needed.

Using this visualization environment, decision makers can determine the feasibility of alternative procedures, compare alternatives relative to the baseline, and down-select between alternative procedures based on sensitivity to input values. On the actual model demonstrator, alternative procedures will be compared based on sensitivities. The sensitivity plots, along with the histograms and the complementary plots, will be used to select an alternative to the current baseline procedure that has the desired balance between mean performance, variability, and robustness in terms of relevant metrics such as overall time and cost of the procedures.

To enable the multicriteria, parametric, and interactive capability for rapid exploration of certification alternatives, the PIM, which executes a process simulation through Markov chains and graph analysis, can allow probabilistic Monte Carlo simulations for investigating the limitations of each process alternative. This capability is primarily the focus of Task 4 and is presented in the following section of this report.

Task 3.4

A particular instance to illustrate the analysis of alternatives proposed is regulatory paragraph J36.205(b) of CFR Title 14, Part 36, Appendix J, which prescribes the method of adjusting for test flight altitudes during flyover noise measurements that are off from the reference altitude prescribed in the regulatory paragraph J36.3(c). Figure 24 below (Figure 5 from Volpe test campaigns SEL Duration Adjustment Studies) shows that the higher the test flight altitude deviation from the reference altitude on which the correction curve is based, the higher the error that results from the adjustment. The test campaigns by Volpe evaluated these errors by means of the difference in adjusted noise measurement values and actual noise measurement values at various altitudes. So, possible alternative procedures to address this duration adjustment problem are as shown in Figure 25. Referring to the morphological matrix discussed earlier (Table 3; Task 1.3), an alternative procedure can emerge from any one of the procedural steps such as data processing methods, as in this particular use case. This again bolsters the need for a traceable platform that has the capability to conduct a holistic assessment of all potential certification bases.

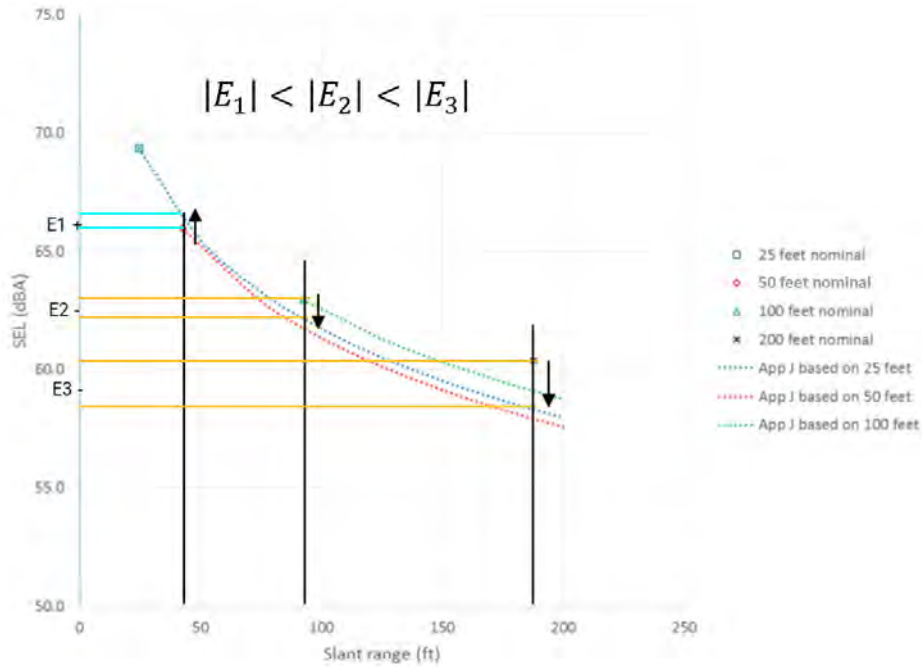


Figure 24. Appendix J duration adjustments applied to various altitudes (Figure 5 of SEL Duration Adjustment Studies).

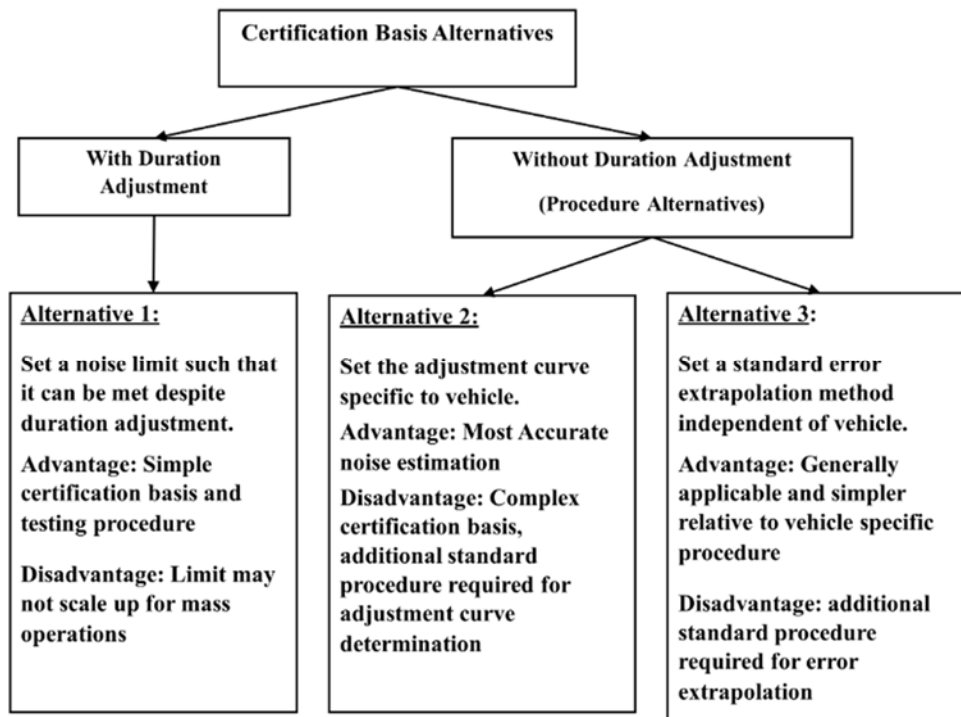


Figure 25. Alternative procedures to address the duration adjustment problem.

Each alternative procedure can have different ramifications on different paragraphs of a regulatory noise standard. Consider, for instance, the two alternatives illustrated in Figure 26 below for the hover test point. The variation of noise with respect to emission angles is represented using noise spheres in Cutler-Wood et al. (2022). Hence, noise standards such as those recently released by the FAA (UAS/UAM Rules of Particular Applicability) require applicants to measure and report noise levels in the test configuration shown on the left panel of Figure 26. The variability in the noise may necessitate several repeated runs to tighten the 90% confidence interval to ± 1.5 dBA (SEL) as required by the noise standards (UAS/UAM Rules of Particular Applicability). In the context of such requirements, the alternative on the right-side panel of Figure 26 may appear more efficient as one set of the necessary number of runs can potentially provide the noise measurement variation with respect to all emission angles. To determine the utility of the proposed alternative in the context of the measurement confidence requirement alone, it is necessary to know the effects of emission angle and flight profile parameters such as hover flight altitude and weight of the vehicle on the variability in the measurement.

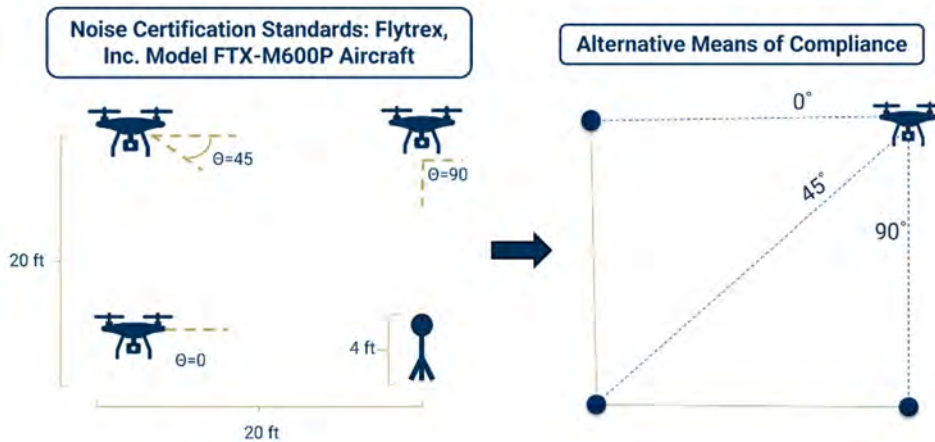


Figure 26. Alternative hover flight profiles (not to scale).

Figure 27 shows the microphone array configuration employed by the FAA and collaborating researchers to acquire noise data necessary to understand the effects. The vehicle deployed for the experimental campaign belongs to the small UAS category.

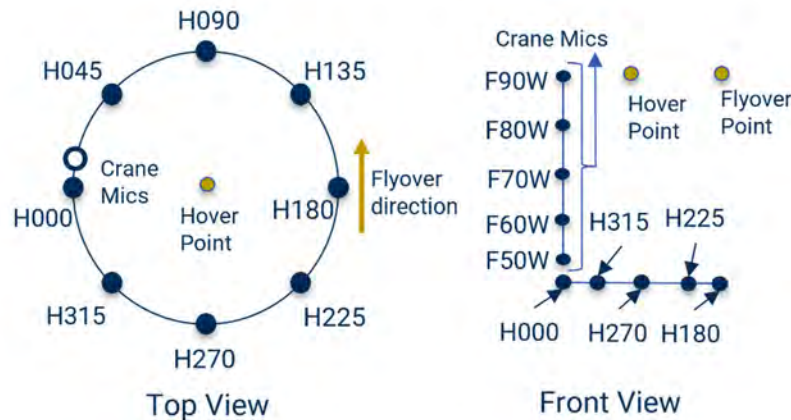


Figure 27. Experimental microphone array configuration (not to scale).

Experimental results consisted of higher-weight and lower-weight flights that were flown at 100 ft altitude and repeated five and six times, respectively. We evaluated the average confidence interval of SEL measurements of various subsets of a given number of repeats and plotted the results as shown in Figure 28. The figure highlights the effect that the weight of vehicle has on variability in noise measurement. We can observe that a higher weight configuration results in higher variability.

Figure 28, however, does not illustrate a strict relationship in emission angle and weight, and further investigation may highlight the same. We also observe that a greater number of runs is required to achieve a confidence interval limit of ± 1.5 dBA (SEL) at higher weight configuration.

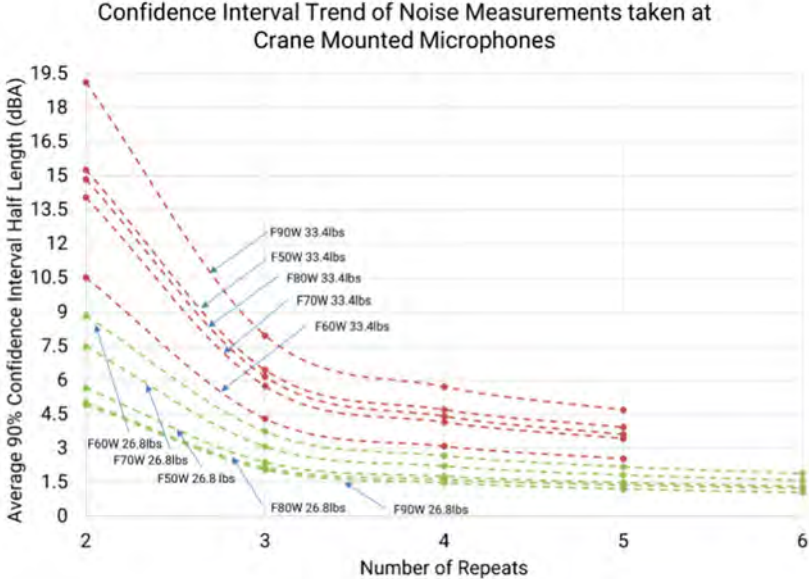


Figure 28. Effects of vehicle weight and emission angle on noise variability in hover flight.

Figure 29 shows the average confidence interval trends for a flyover flight condition that was repeated the highest number of times. Although this flight condition is different from the hover flight condition, it highlights the trend of the average confidence interval of SEL over a higher number of runs. Hence, we note that although fewer microphones are required for the alternative method in the left panel of Figure 26, the number of repeats required to achieve the confidence interval limit make the alternative method in the right panel of Figure 26 preferable. Ultimately, we need to compare the costs and times of additional microphones and their setup with those of additional flights to arrive at the right decision.

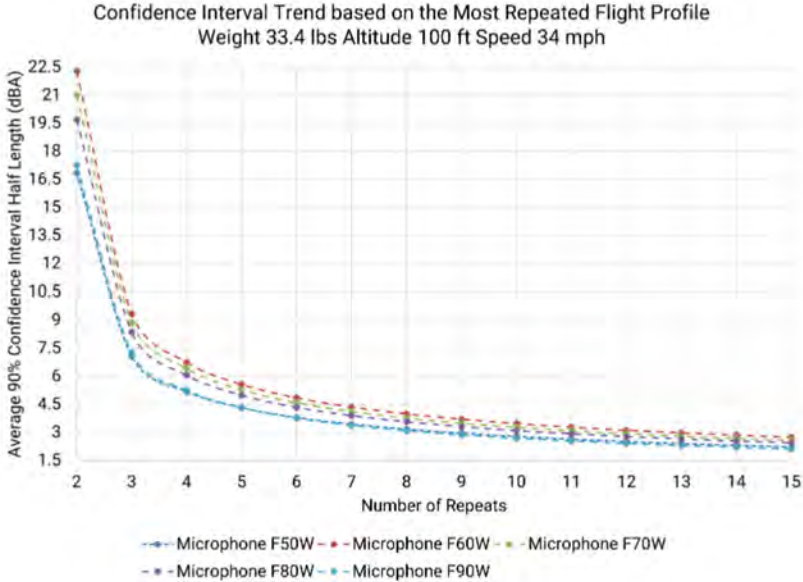


Figure 29. Effects of emission angle on noise variability in flyover flight.



Milestones

Please see the milestones under Task 1.

Major Accomplishments

- An initial concept formulation and implementation roadmap have been completed for the MBSE framework to accommodate multiple UAS types and to allow for process effectiveness and flexibility evaluation.
- Metrics have been developed and the PIM has been integrated under a parametric interactive decision support environment. The concept has been demonstrated through a minimum viable project exercise.
- The PIM is applied to a typical plan for UAS noise testing that has been formulated to better capture the process.
- Preliminary analysis of noise measurement data was conducted, and resulting insights were utilized for requirement analysis.

Publications

None.

Awards

None.

Student Involvement

- The full student team has participated in brainstorming sessions toward formulating the integrated certification process assessment framework for UASs.
- Mika Xu led the MBSE model building for the UAS noise certification.

Plans for Next Period

- Perform a morphological matrix exercise to explore and identify feasible certification process alternatives, based on permutations of UAS type, testing plan, testing and sensing technologies, data analysis methods, and map options for evaluation criteria.
- Finalize process evaluation metrics and incorporate them in the next iteration of the decision support tool.
- Demonstrate a simple use case, where a number of feasible alternatives lead to comparisons with the process baseline. The use case and the improvement propositions within the alternative options will be formulated with input from subject matter experts and current gaps in meeting certification targets.
- Conduct extensive analysis of the noise data available to inform regulatory rulemaking.

References

- "PART 36—NOISE STANDARDS: AIRCRAFT TYPE AND AIRWORTHINESS CERTIFICATION," Federal Aviation Administration, 2023. URL <https://www.ecfr.gov/current/title-14/chapter-I/subchapter-C/part-36>.
- Federal Register. (2022). *Noise Certification Standards: Matternet Model M2 Aircraft* (NPRM 86 FR 48281).
<https://www.federalregister.gov/documents/2022/09/12/2022-19639/noise-certification-standards-matternet-model-m2-aircraft>.
- FAA. (2022). *Noise Certification Standard: Matternet Model M2 Aircraft*.
<https://www.regulations.gov/document/FAA-2021-0710-0016>.
- Senzig, D. A., Marsan, M., Cutler, C. J., and Read, D. R., Sound Exposure Level Duration Adjustments in UAS Rotorcraft Noise Certification Tests, 2018.
URL <https://rosap.ntl.bts.gov/view/dot/37057>.
- Cutler-Wood, C., Barzach, M., Hobbs, C. M., and Shirayama, S., "Estimating Unmanned Aircraft Takeoff Noise Using Hover Measurement Data," QUIET DRONES Second International e-Symposium, 2022.
URL <https://rosap.ntl.bts.gov/view/dot/64152>.
- "Noise Certification of UAS/AAM using Rules of Particular Applicability," Federal Aviation Administration, 2023.
URL https://www.faa.gov/about/office_org/headquarters_offices/apl/aee/noise/uas_noise_certification.
- Causey UAS Acoustic Measurements M. James, A. Salton, M. Downing, and M. Calton, Blue Ridge Research and Consulting, Asheville, NC, tech., 2021

Task 4 - Develop Alternative Procedures and Assess Their Performance with Existing Tools (Case Study)

Georgia Institute of Technology

Objectives

Task 4 seeks to explore options for evaluating noise certification within the MBSE certification framework. The purpose of this task is to allow a performance baseline to be established for current procedures and to allow for the evaluation and comparison of more flexible process alternatives as they are formulated within Tasks 2 and 3. The breakdown of tasks under Task 4 is as follows:

Task 4: Develop alternative procedures and assess their performance with existing tools

- 4.1. Develop alternative testing procedures using the elements library.
- 4.2. Transfer alternative procedures to the PIM.
- 4.3. Report on the performance of the alternative procedures.
- 4.4. Develop a proof-of-concept demonstration of the PIM capabilities

Research Approach

The goal of Task 4 is to identify process modeling approaches for the purpose of simulating and evaluating the performance of a noise certification procedure. Task 4 delivers a solution that, in a broader sense, is referred to as the PIM. Tasks 4.1 to 4.3 focus on PIM implementation, whereas Task 4.4 integrates the PIM into the current MBSE framework. The PIM must analyze the process performance and interface with the verification model for completing steps regarding requirements and compliance. The PIM must also be flexible and reusable within the verification thread and must accommodate UAS configurations. An overview of the integrated verification thread and the PIMs is shown in Figure 30.

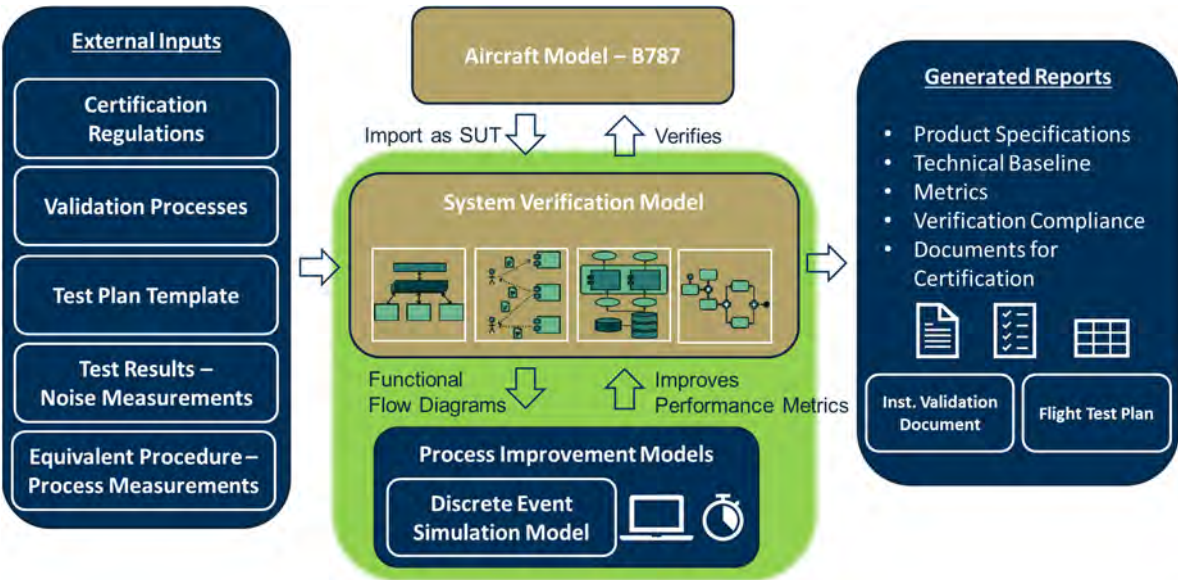


Figure 30. Integration of the process improvement model within the model-based systems engineering certification framework. SUT: system under test.

Task 4.1

The team has completed a literature review on process modeling methods to enable process simulation. These methods are listed below:

- DES, where a clock tracks the duration of the transition between model states
- Agent-based simulation methods
- System dynamics

- MCMC simulation methods

These techniques are evaluated on the basis of how well they can capture and simulate actual industry-applied procedures and their ability to interface with the verification thread. For simulating a simple process that is representative of transport category certification, the DES modeling approach appears to be the most effective. To demonstrate feasibility, a proof-of-concept version was developed using the DES method in a Python-based environment. The chosen example covered the testing process for a flyover approach, as shown in Figure 31. The objective was to demonstrate that a process model, as defined in the MBSE framework, can be simulated using DES. With the model states imported, DES can track the clock and return the time points at which each event is concluded. The DES results are then fed back as input and update the process diagram in the verification model, which then checks the process model against requirements and compliance.

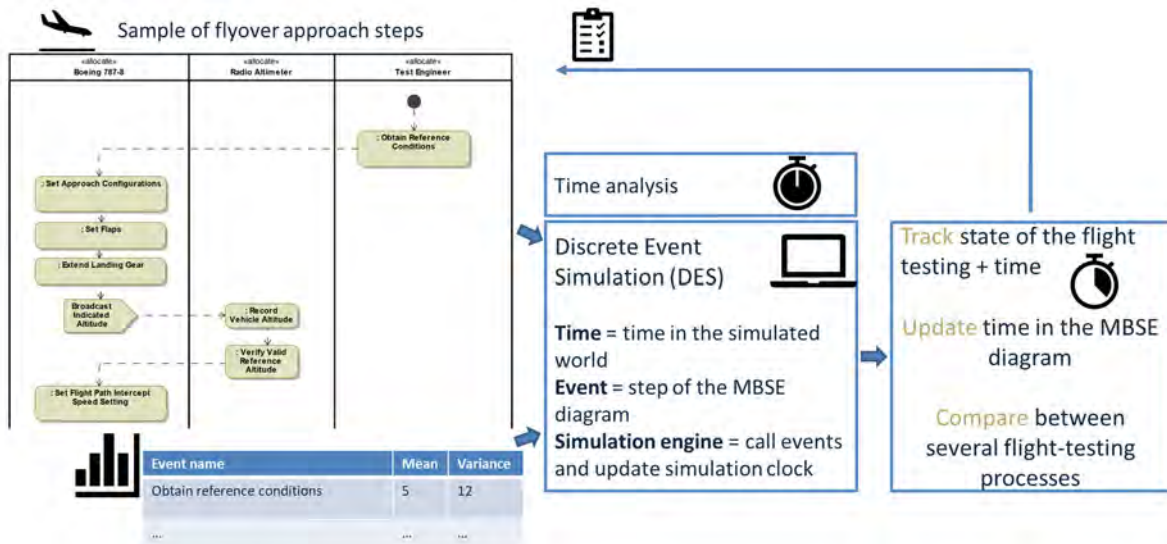


Figure 31. Discrete event simulation for a flyover approach. MBSE: model-based systems engineering.

However, because flight testing procedures are impacted by uncertainties, a different modeling approach is needed. To account for uncertainties, a probabilistic model using Markov chains has been developed to improve the accuracy of how interactions and emerging effects are captured. This approach is better suited to support use cases, with the objective of further process simplification, especially for flight testing portions, instrumentation setup, and measurement systems. This simplification could involve eliminating or replacing steps and possibly utilizing advanced data-driven or physics-based modeling approaches as a substitute.

Because of the extension of DES to Markov chain approaches and the need for large samples, the team adopted the MCMC approach, where a Markov chain model is used to run a Monte Carlo study to collect sample runs, given an input probability matrix and stakeholder value function. Each run is associated with an incurred time, cost, and accuracy penalty, and the output is provided in the form of activity diagrams and responses that are fed back to the verification model within the MBSE framework. Through the requirement model within the MBSE framework, the MCMC simulation data are imported to perform acceptance-rejection sampling, where each run (with its associated metric) is accepted or rejected by requirements/constraints within the verification model. The format of the MCMC simulation data follows the form of a step-by-step sequence (similar to a DES).

Summarizing the development of the PIM, the implementation path is shown in Figure 32, which illustrates the interface with the verification model. Using a similar flyover approach plan example as in Figure 31, the process model informs the PIM, which converts the flyover approach into an executable simulation model. Based on the type of requirement test selected by the user, the appropriate response values, parametric settings for baseline values (time, cost, resources, disruption risks, accuracy penalty, etc.), and distributions for Monte Carlo simulations are chosen. The Monte Carlo simulation then generates the PIM metrics and prepares the dataset for verification.

For this task, the literature search, exploration of modeling options and selection, and proof-of-concept implementation are now completed.

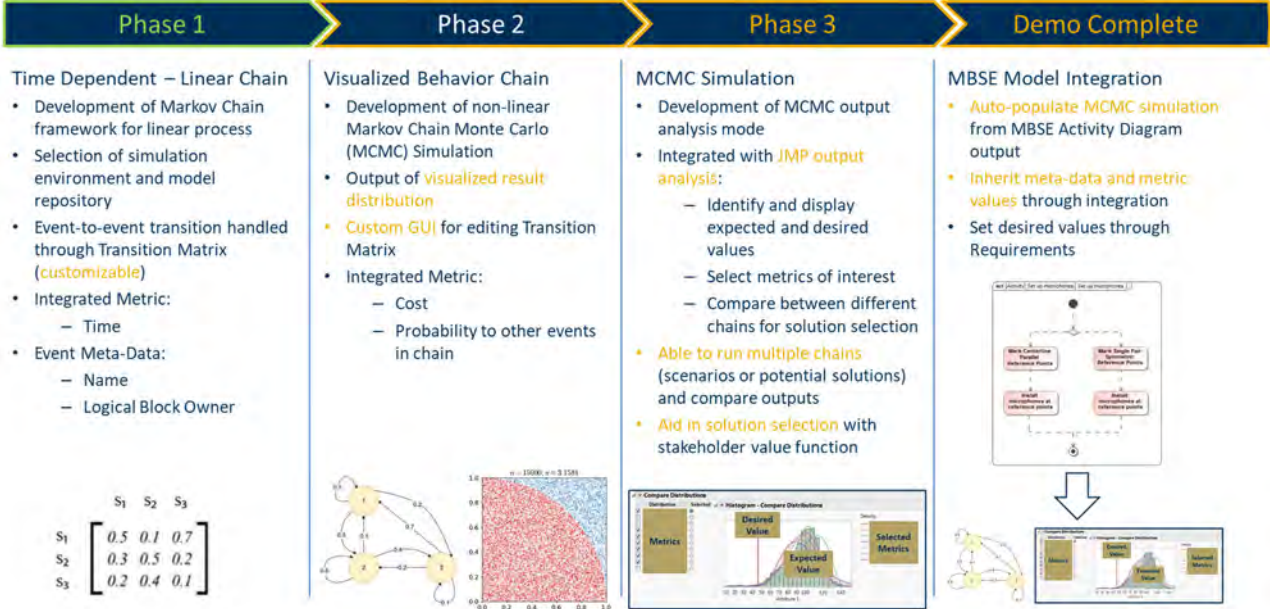


Figure 32. Functional development plan based on a process improvement model. GUI: graphical user interface; MBSE: model-based systems engineering.

Task 4.2

With the PIM model now available in a flexible and customizable format, in Task 4.2, we sought to expand the process simulation and analysis toward metrics that will link to use case objectives and process selection of improved alternatives.

The selected metrics should allow for a quantitative comparison of current and proposed streamlined noise certification process options. The current list of identified metrics is as follows:

- Time: schedule cost incurred to complete event
- Cost: budget cost incurred to complete event
- P(Failure): probability of repeating an event or reverting to a previous event (does incur time and cost [full or partial] in each occurrence)
- P(Success): probability of moving out of the current event
- Accuracy penalty: impact on overall accuracy value for executing the event (does not incur an additional cost in each occurrence)

The proposed integrated model uses a system verification model with external inputs such as current certification regulations, validation processes, and test plan templates. This results in an interconnected model for the unmanned aerial system, referred to as the SUT, which evaluates the validity of a certain certification procedure and generates alternative procedures suggesting one or a combination of modifications related to the utilized noise measurement metric, microphone type or array design, or flight profile (flyover, hover, vertical takeoff/landing, etc.). Figure 33 provides a general overview of the integrated structure of the system verification model, the PIM, and the visualization environment.

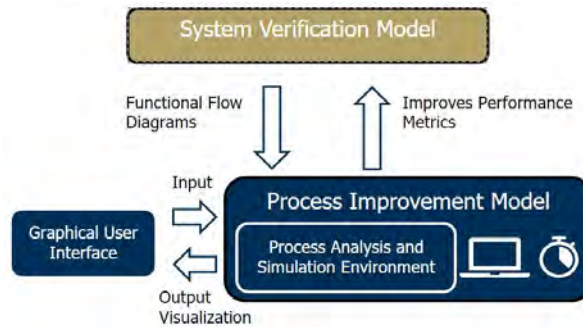


Figure 33. Integration of system verification model, process improvement modeling, and graphical interface.

Different detailed reports can be generated as outputs of the system verification model in addition to flight test procedure diagrams describing the sequence of events constituting the flight tests. The PIM assesses the performance of the baseline flight test procedure and other alternative procedures in terms of overall time and cost. The PIM captures a typical noise testing process (see Figure 22). Certain events within that process have feedback loops indicating that one or a set of events is to be repeated due to the detection of anomalies or calibration issues, for instance. Hence, some events can have different outcomes and, depending on the likelihood of each outcome, the overall flight test sequence would differ and lead to a different overall time and overall cost of the entire process. This steers the focus toward a probabilistic modeling approach, in which it is desirable that each event exclusively depends on the previous event. Moreover, to properly account for uncertainty and risks in predictions and decision-making, it is crucial for these flight tests to be simulated multiple times. With all these elements taken into consideration, a suitable approach for modeling a flight test procedure is using a Markov chain, also referred to as Markov process, which is a stochastic model describing a sequence of possible events in which the probability of each event depends only on the state of the previous one. To maintain a simplified terminology for the PIM, the flight test procedures extracted from the system verification model are to be considered flight test processes and the events are to be referred to as steps.

The PIM implements a Matlab script incorporating the mathematical representation of the flight test process to be analyzed using Monte Carlo simulations. Two Excel files are used as inputs to the script; the first includes all the steps of the flight test process and the probabilities of occurrence of each possible outcome, and the second contains the assigned time and cost values for each step.

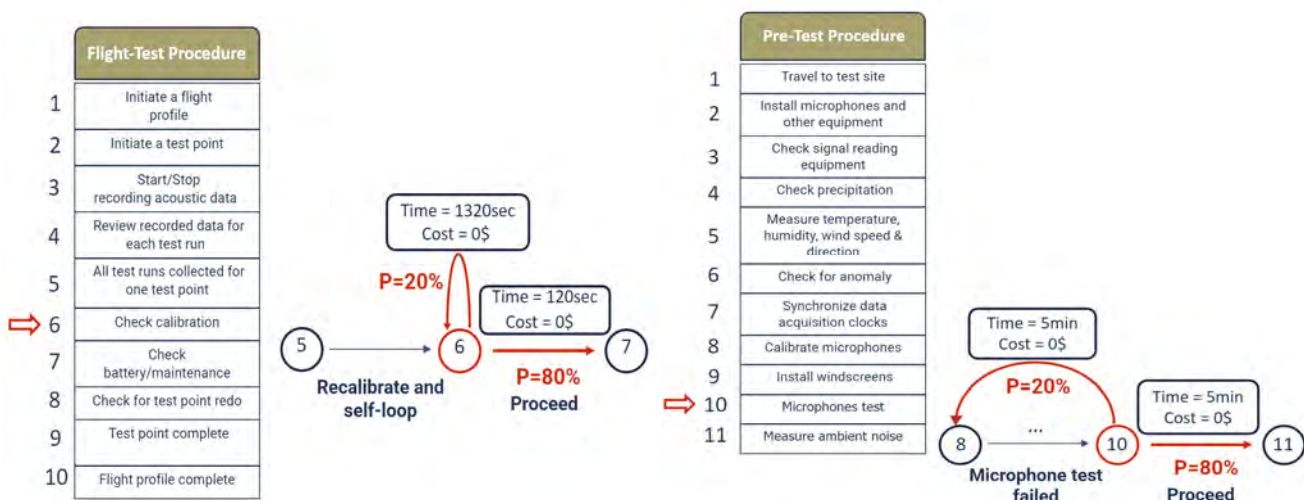


Figure 34. Example of self-loop (left figure) and feedback loop (right figure) within the noise testing process.

As noise testing is captured as a stochastic process, most of the steps can lead to different outcomes depending on many factors, including human error, unstable weather conditions, equipment malfunction, unsatisfactory measurements, and so on. These variations are modeled using feedback loops and self-loops in the Markov chain, in which the former represents the need to go back to a previous task in case an anomaly is detected, whereas the latter refers to the need to repeat the current task. Each potential outcome has a specific probability of occurrence assigned to it. Figure 34 portrays examples of a self-loop and a feedback loop within the process. In Figure 34, step 6 of the flight-test procedure consists of checking the calibration of the microphones after the completion of each test point. This step is crucial to avoid potential complications such as reducing confidence in the validity of noise test results, lacking a traceable chain of measurement standards, and impacting data comparability across multiple instruments. In this example, a probability of 20% is set for the need to recalibrate, which entails a longer time compared to the alternative outcome of not needing recalibration with 80% probability. Similarly, step 10 of the pre-test procedure consists of two potential outcomes for the microphone test; either the test fails, and the staff need to take the windscreens off, recalibrate the microphones, reinstall the windscreens and test again (probability of 20%), or the microphone test is successful (probability of 80%) and the following step is initiated.

Task 4.3

The objective of Task 4.3 is to produce a baseline of a noise certification procedure simulation and to propose a calibration step, as process data become available from ASCENT 061 partners. The analysis workflow for the PIM module is shown in Figure 35. The goal of the workflow within the PIM is to analyze the complexity of the process and to identify potential bottlenecks by assessing time, cost, and node/step criticalities. The workflow is completed in three basic steps:

1. *Definition of test data:* This step includes a test plan, setup, instrumentation and recording information, and sound pressure level measurement data.
2. *Process representation as an event chain through graph modeling:* In this step, the process is converted and represented as a weighted directed graph. Each node represents a step in the process, and the edges represent transitions between steps. The progression through the steps is represented by probabilities and parameters at each step.
3. *Execution of the MCMC algorithm:* The simulation starts from a node, and a “roll the dice” (generate a random number) function is performed. Depending on the outcome and the probability of each path, the algorithm selects the next node. A learning factor is utilized to update the probabilities of progressing through the steps (increased probability the second time).

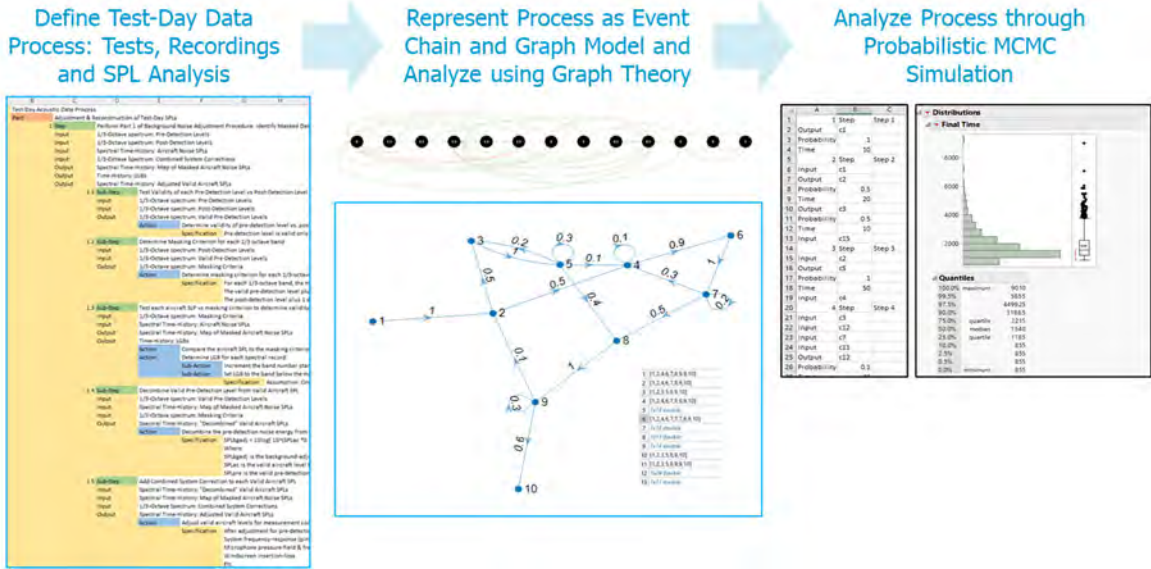


Figure 35. Analysis workflow based on the process improvement model. MCMC: Markov chain Monte Carlo; SPL: sound pressure level.

The analysis of different alternative procedures in noise flight testing relies on the evaluation of different performance criteria or metrics of interest to which the user may allocate different levels of importance. The outputs of this analysis heavily contribute to the decision-making alongside the regulatory adherence in which the requirements' satisfaction of each alternative procedure is evaluated. In the context of the suggested PIM, progression through the steps is associated with probabilities and parameters. Hence, tracking the propagation of these metrics of interest is enabled within the Monte Carlo simulations. Induced costs and time throughout the process are the main focus of the current efforts. When combined with the sequencing of events of each process simulation, these outputs can provide insight into process complexity and induced risks, and allow the anticipation of potential bottlenecks in the process as well.

Noise certification testing processes are represented using Markov chains within a probabilistic simulation environment. This approach relies on random variables, which are functions assigning real numbers to each potential outcome within the sample space of a random experiment. It also entails that every event solely depends on the previous event, thus preventing the propagation of uncertainties throughout the process. The entire process can be visualized using weighted directed graphs in which every node represents a step within the noise testing process, and the edges indicate the transitions between nodes. A valid representation of the certification testing process requires every node on the graph to be able to eventually reach the final step, thus ensuring process continuity by calculating the "connected components" in the graph. Figure 36 depicts the need to ensure continuity within the demonstrative process on the left side, in which step 7 cannot reach the final step, whereas the corrected Markov chain representation on the right implements process continuity for each step.



Figure 36. Illustration of process continuity in a sample flight test process.

Every edge of the Markov chain representation is assigned a probability characterizing the likelihood of moving from one node to another, thus mapping different potential paths to be taken. The Monte Carlo method is implemented to achieve repeated random sampling during the simulation. This method generates a random number that is compared to the cumulative sum of the row corresponding to the current step of the transition matrix, which contains all potential probabilities connecting any two nodes. The next step is chosen once the random number is less than or equal to the smallest cumulative sum. Each Monte Carlo simulation follows a specific path that is dictated by the aforementioned method. To achieve accurate estimates, the Monte Carlo simulation has to be repeated multiple times by increasing the number of runs set within the Matlab script. This underlines an important trade-off between the accuracy of the results and the script execution time. In this work, the analysis is exclusively targeting the most influential steps of the noise testing process as they will be the main sources of variation within the results. This approach allows the reduction of the computational time of the PIM execution while ensuring the accuracy and reliability of the results. This can be accomplished by implementing PageRank centrality, which is a metric providing the average time spent at each node during a random process simulation. The average for each node is weighted according to the probabilities of reaching a node and the value of the associated parameter. These key (i.e., most influential) steps, will be varied in each simulation using design of experiments (DOE). In addition to the identification of key steps, the code introduces the capability of detecting bottlenecks within the process giving enough insight about steps susceptible to causing delays or complications within the process workflow.



The baseline process for the PIM exclusively considers a hover flight profile with three test points with a minimum of six runs per test point. Each test point refers to a test condition with a specific combination of weight, speed, and altitude. With the use of only one microphone, the UAS will fly at three different locations relative to it (see Figure 37). The analysis can be turned into a parametric analysis capable of automatically changing some of the input values without having to manually modify the values in the input files. This will apply to parameters that would simultaneously affect multiple steps of the process in different ways, such as the number of staff members, number of microphones, and number of flight profiles and test points. Manually assessing and incorporating the changes due to variation in these parameters can be very tedious, as many steps can be directly or indirectly affected. Thus, all the impacted steps are identified beforehand and the effects are quantified and mathematically modeled in terms of time and cost consequences. Once the user identifies any combination of parameters, the code will automatically implement the corresponding changes to the time and cost values in the input file of the baseline process.

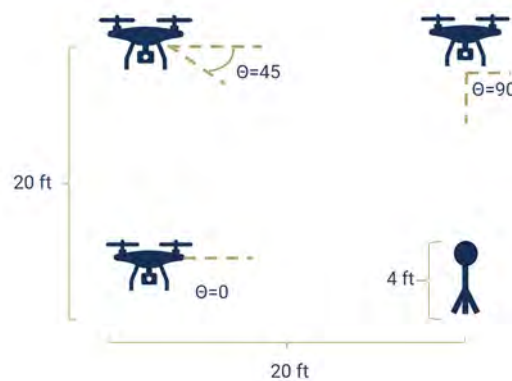


Figure 37. Baseline noise testing process (hover flight profile).

Calibration is an essential step for ensuring model accuracy and the validity of results and findings. This task requires a completed process simulation capability, which will be calibrated against a baseline that captures current certification testing plans and processing steps. The pivot to the UAS category has included plans to interface with ASCENT partners who can provide testing plans and noise datasets to be used as calibration data and overall process information. This task will be one of the key focus topics for the project's Year 3 activities. Scalability issues are bound to arise as this model is expanded to reflect the full verification thread; thus, the next step is to discuss options for data that ASCENT 061 partners could provide for further calibrating the model, according to the use cases of preference.

Task 4.4

In a proof-of-concept demonstration of the complete certification process simulation capability within the PIM, the team has been formulating use case examples based on scenarios provided by OEM partners. For these examples, simulation runs are being executed to test modifications and proposed improvements over the baseline process. Under this task, a first demonstration of the PIM has been completed. For this example, the goal is to assess the impact of a simplified noise collection/analysis process for the Waco YMF-5 propeller aircraft.

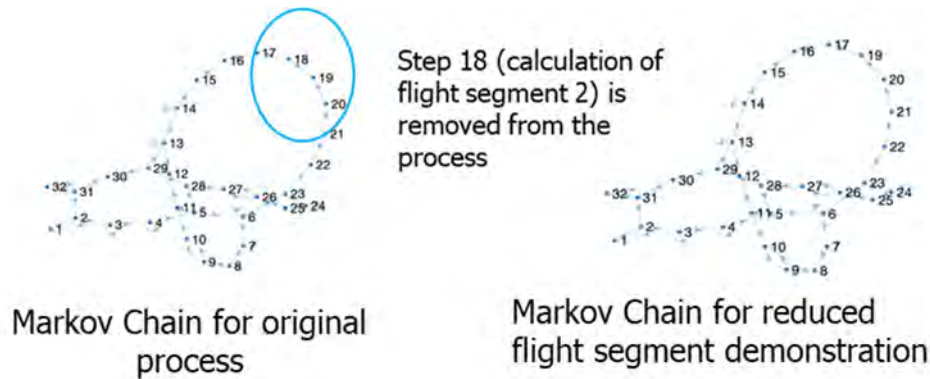


Figure 38. Process modification: Step 18 (calculation of the second flight segment) is removed from the flight-testing process.

The baseline (original) process was formulated within the PIM and executed using best estimates for time and cost. The term “best” implies that the team had to rely on rationalized assumptions that were initially formulated by input from OEM partners. As this information could be of a sensitive nature for most OEMs, the guidance was provided at a higher level, without any limitations on how the information would be distributed. Hence, for this example, a simplified process for flight segment testing is proposed, where a certain calculation is removed from the standard process. As shown in Figure 38, the simplified process removes step 18 (calculation of the second flight segment) while other steps were updated with new values to capture the updated process.

Table 5. Summary of cost (\$) and time (hr) improvements.

		Mean
Original	Cost(\$)	166,770
	Time(hr)	155
Reduced Segments	Cost(\$)	140,430
	Time(hr)	151

A comparison of the two process alternatives is presented in Table 5. The results were obtained from an MCMC analysis and comparison between the baseline and simplified process. The PIM was able to quantify measurable savings in time and cost. In particular, the average process cost shows a reduction of 16%, and the average process time shows a decrease of 2%. The results are highlighted in Figure 39, where the Monte Carlo simulation data are plotted as distributions for the cost and time required for the process.

With this fundamental example showcased under this task, the groundwork is set for scaling up the PIM to more comprehensive modifications, which would also include technology impact forecasting functions. As this practice will now be exclusive to the UAS category, the team’s priorities are to investigate current noise testing plans and procedures and to be in a position to propose promising equivalent procedures.

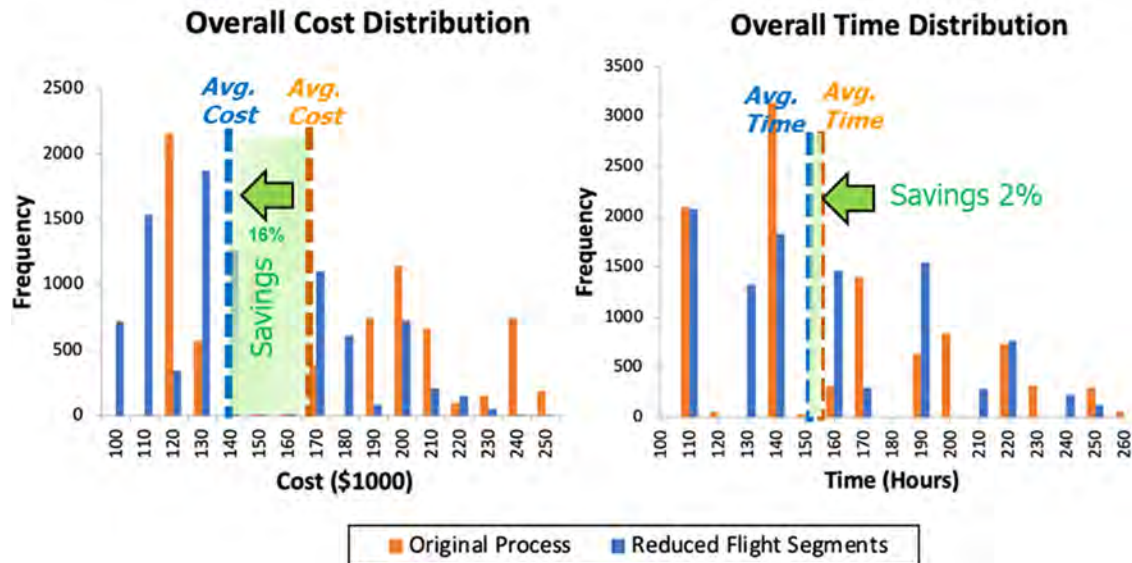


Figure 39. Execution of Markov-chain-based Monte Carlo analysis and comparison between the baseline and simplified process.

Milestones

Please refer to the milestones listed under Task 1.

Major Accomplishments

- Development of a small-scale PIM using DES, as a deterministic modeling exercise.
- Development of a more comprehensive stochastic model using stochastic MCMC methods, formulated in a way that enables seamless integration into the verification thread within the MBSE framework.
- Definition of a starting set of metrics, as a working solution with a focus on process efficiency improvements.
- Approach for integrating the PIM with the verification model within the MBSE framework.
- Finalized PIM analysis workflow with the use of Monte Carlo simulation for Markov chain models of the certification testing process.
- Workflow integrated with the MBSE verification model.
- Proof-of-concept use case for assessing the impact of process simplification through quantifiable outcomes, which has been supported by the current working version of the MCMC-enabled PIM module.
- Further improvement and tuning of the existing PIM with automation and parametrization of user-defined input data to make the model representative of any desired process.
- Application of the PIM to a typical plan for UAS noise testing to better capture the process and properly estimate the cost, staff, and time implications.

Publications

None.

Outreach Efforts

- Presentation of concepts to Volpe partners, who provided feedback on the tools and analysis methods.
- Collaboration with ASCENT 077 and 094 research groups.
- Discussions with experts in the field with similar applications, e.g., process simulations for industrial systems, manufacturing, supply chains, etc.

Awards

None.



Student Involvement

- Although a small portion of the team has been leading the technical approach of PIM development, this task has involved the full team, as PIM integration with the MBSE model is a key enabler to be addressed early in the process.
- Recent efforts to extend the PIM capabilities have been led by Hajar Mali, and the dashboard and visualization of results have been led by Nathnael Geneti.

Plans for Next Period

- Continuation with the PIM development steps, toward a full verification model scale capability for the UAS category.
 - Finalize the interface with the MBSE verification model.
 - Ensure flexibility with other UAS configurations (the Matternet M2 example is the current working baseline).
 - Iterate on noise measurement data to be used for PIM improvements.
 - Integrate sound pressure level conversion to EPNL for UASs.
 - Expand on metrics that can better track process complexity and vulnerability and test against varying contingency scenarios, with the goal of ensuring that the analysis is capable of driving robust decisions.
 - Calibrate the model with input from ASCENT 077 work.
- Expand on metric definitions at a level beyond process inefficiencies (e.g., directly addressing time and costs) and consider complexities that could affect the process with bottlenecks and unnecessary use of resources (e.g., duplicate testing, time-intensive procedures, etc.). The flight-testing part of the process will be the primary focus.
- Formulate a simple certification problem for each vehicle type and use it as a pilot for comparing and selecting the appropriate method.
- Integrate results and PIM analysis in the interactive decision support tool.

References

- Metzger, F. B., & Foley, W. M. (1970). *Stol aircraft noise certification-a rational approach*. SAE Transactions. 700325. <https://doi.org/10.4271/700325>
- U.S. Department of Transportation, Federal Aviation Administration. (1969). *Federal Aviation Regulation, Part 21, Certification Procedures for Products and Parts; Part 36, Noise Standards: Aircraft Type Certification*. <https://www.ecfr.gov/current/title-14/chapter-I/subchapter-C/part-36>
- Ollerhead, J. (1968). *Subjective Evaluation of General Aviation Aircraft Noise* (Technical Report NO-68-35).
- Senzig, D.A. & Marsan, M. (2018). *UAS Noise Certification*.
- FAA (2023). 14 CFR Part 36 – NOISE STANDARDS: AIRCRAFT TYPE AND AIRWORTHINESS CERTIFICATION. <https://www.ecfr.gov/current/title-14/chapter-I/subchapter-C/part-36>
- FAA. (2017). *Advisory Circular 36-4D – Noise Standards: Aircraft Type and Airworthiness Certification*.
- Federal Register. (2022). *Noise Certification Standards: Matternet Model M2 Aircraft* (NPRM 86 FR 48281). <https://www.federalregister.gov/documents/2022/09/12/2022-19639/noise-certification-standards-matternet-model-m2-aircraft>.
- FAA. (2022). *Noise Certification Standard: Matternet Model M2 Aircraft*. <https://www.regulations.gov/document/FAA-2021-0710-0016>.
- US Department of Defense. (2022). *Systems Engineering Guidebook Section 4.2.7*. Office of the Deputy Director for Engineering. Washington, D.C.
- VOLPE Guides, “Validation Protocol for Digital Audio Recorders User in Aircraft-Noise Certification Testing” [2010].
- VOLPE Guides, “Audio Recording & Analysis System Validation Checklist” [2018].
- VOLPE Guides, “Test Data Acoustic Data Process” [2003].
- VOLPE Guides, “Background Noise Adjustment Process” [2003].
- FAA. (n.d.) *Details on FAA Noise Levels, Stages, and Phaseouts*. https://www.faa.gov/about/office_org/headquarters_offices/apl/noise_emissions/airport_aircraft_noise_issues/levels/.
- Aleksandraviciene, A. (2018). *MagicGrid Book of Knowledge*. Kansas, 2018. NoMagic.
- More, S. (2011). *Aircraft Noise Characteristics and Metrics* [Ph.D thesis Dissertation, Purdue University].
- Konzel, N. (2022). *Ground based measurements and acoustic characterization of small multicopter aircraft* [Masters Thesis, Pennsylvania State University].



ASCENT 061 Year 3 Recap

The following key tasks and activities have been completed within the ASCENT 061 Year 3 performance period:

- Explored the applicability of the current ASCENT 061 framework for noise certification of rotor or small propeller-driven UAS.
- Performed a literature search and documented regulations and current testing standards for small UAS (CFR Title 14 Part 36 Appendix G, J, and H, and recent NPRMs).
- Completed the architecting of a noise certification modeling and assessment framework for transport and UAS category aircraft.
- Completed development of the PIM, which has been applied to a typical plan for UAS noise testing demonstration example.
- Formulated use cases that are aligned with needs and recommendations provided by OEM partners, with a focus on exploring implications of alternative testing procedures on regulatory compliance and highlighting the benefits of process simplification (e.g., lateral microphone placement or removal, if trusted analysis is used).
- Provided a demonstration by assessing a simplified noise collection/analysis process.
- Documented options for equivalent procedures in a database/library compilation.
- Conceptualized and developed a visualization environment to aid as a use case demonstrator and decision support environment.
- Engaged in a broader outreach of ASCENT 061 to the aviation community on noise certification:
 - ASCENT fall/spring meetings
 - Continued discussions with Volpe
 - UAS OEMs
 - Published articles with the American Institute of Aeronautics and Astronautics (AIAA) and for the SciTech 2023 and 2024 Meetings
- Exchanged noise measurements and knowledge with the ASCENT 77 team.
- Provided annual and quarterly reports, which are available on the ASCENT Knowledge Services Network database.
- Prepared contributions and new technical capabilities that will be published in conferences and peer-reviewed journal articles:
 - Kim, D., Taneri, M., Omoarebun, E.N, Wills, T., Balchanos, M., & Mavris, D. (2023). *MBSE-Enabled System Verification and Process Improvement of Transport Aircraft Certification*. Accepted and to be presented In AIAA SciTech 2023 Forum, National Harbor, MD, January 23-27, 2023.



Project 062 Noise Model Validation for AEDT

**Georgia Institute of Technology
The Pennsylvania State University**

Project Lead Investigators

Prof. Dimitri N. Mavris
Director, Aerospace Systems Design Laboratory
School of Aerospace Engineering
Georgia Institute of Technology
Mail Stop 0150
Atlanta, GA 30332-0150
404-894-1557
dimitri.mavris@ae.gatech.edu

Victor W. Sparrow
United Technologies Corporation Professor of Acoustics
Graduate Program in Acoustics
The Pennsylvania State University
201 Applied Science Bldg.
University Park, PA 16802
814-865-6364
vws1@psu.edu

University Participants

Georgia Institute of Technology (Georgia Tech)

- P.I.s: Prof. Dimitri Mavris and Dr. Michelle R. Kirby
- FAA Award Number: 13-C-AJFE-GIT Amendments 106, 125, and 144
- Period of Performance: September 27, 2021 to September 30, 2024

The Pennsylvania State University (PSU)

- P.I.: Prof. Victor Sparrow
- FAA Award Number: 13-C-AJFE-PSU, Amendments 59, 83, 89, and 106
- Period of Performance: October 1, 2021 to September 30, 2024
- Tasks:
 1. Noise modeling in the Aviation Environmental Design Tool (AEDT) with automation (Georgia Tech) 2. Assessing the use of high-fidelity meteorological data in AEDT noise calculations (PSU)

Project Funding Level

The project is funded by the FAA at the following levels: Georgia Tech: \$235,000; PSU: \$140,000. Cost-sharing details are below.

Georgia Tech has agreed to a total of \$235,000 in matching funds. This total includes salaries for the project director, research engineers, and graduate research assistants, as well as computing, financial, and administrative support, including meeting arrangements. Georgia Tech has also agreed to provide tuition remission for the students, paid for by state funds.

For PSU, Spire Global (<http://www.spire.com/>) is providing cost-sharing funds in the form of meteorological data and research support. The point of contact for this cost-sharing is Ms. Ashley O'Neil (703-853-8468; ashley.oneill@spire.com). Metropolitan Washington Airports Authority is providing sound level meter data from Dulles International Airport as in-kind



cost-sharing; the point of contact is Mr. Mike Jeck (703-417-1204; michael.jeck@mwa.com). Additional in-kind cost-sharing is being provided by the PSU College of Engineering to meet the required matching of \$140,000.

Investigation Team

Georgia Tech

Prof. Dimitri Mavris, (P.I.)
Dr. Michelle Kirby, (co-investigator)
Dr. Mayank Bendarkar, (research faculty)
Mr. Jirat Bhanpato, (research faculty)
Amber Willitt, (graduate student)
Sonal Mehta, (graduate student)
Sabastian Abelezele, (graduate student)
Humfrey Kimanya, (graduate student)

PSU

Prof. Victor Sparrow, (P.I.)
Harshal Patankar, (graduate student)
Emma Shaw, (graduate student)

Project Overview

The focus of this project is to assess the accuracy of the AEDT in estimating noise in the vicinity of airports as well as further afield. The foundation of AEDT noise modeling is based on the Integrated Noise Modeling (INM) tool, which has undergone several validation and verification efforts in the past, specifically at the Denver International Airport (DIA), and has shown continual improvements in the agreement between modeling predictions and measurement data. During the development of AEDT, multiple algorithm updates have occurred. This project seeks to quantify the new noise modeling capabilities through comparison with field measurement data from DIA and other airport monitoring systems. The research team will develop a detailed model validation plan, review the plan with the FAA for concurrence, execute the plan, and make recommendations for future AEDT development. The research, once completed, is expected to provide a noise model validation benchmark that can be used not only to respond to questions regarding AEDT noise prediction accuracy, but also to allow the tool development team to prioritize further development of modeling features and enhancements. The research team will also collaborate with PSU on the assessment of the noise propagation assumptions and the use of higher-fidelity weather data.

Task 1 - Noise Modeling in AEDT With Automation

Georgia Institute of Technology

Background and Objective

In the past decade, demand for air passenger services growth has increased, with a long-term average exceeding 5% in terms of revenue passenger miles (Juniac, 2012). To mitigate the environmental impacts of this growth in aviation, and to maximize the economic benefits that can be achieved through higher efficiency and performance, NASA's Environmentally Responsible Aviation project has suggested aggressive goals (Suder, 2012). This set of goals includes a target to reduce the noise emissions created by aviation over the 2015, 2020, and 2025 timeframes. The first step in mitigating noise emissions is having the capability to model them with a high level of accuracy. The FAA's AEDT (Federal Aviation Administration, n.d.) has among the most advanced capabilities for both modeling aircraft operations and computing-associated environmental metrics. AEDT is a software system that models aircraft performance in space and time to estimate fuel consumption, emissions, noise, and air quality consequences. AEDT's primary objective is to facilitate the environmental review of federal actions associated with changes in airports, airspace, and other applicable aviation activities.

Several past efforts have studied the improvement of modeled procedures in AEDT or the comparison between AEDT capabilities and real-world operational data. Noise abatement departure procedures (NADPs) are commonly used to mitigate community noise, close to the airport or further afield. Lim et al. (2020) have provided a set of 20 NADP profiles suitable for modeling a large variety of operations that are typically observed in the real world. Behere, Lim, et al. (2020)

and Behere, Isakson, et al. (2020) have focused on quantifying the impacts of such NADP profiles on noise modeling and have identified the most representative NADP profiles. AEDT has also been used in the creation of alternative rapid noise modeling tools (Levine et al., 2019; Monteiro et al., 2018), in comparing aviation environmental impact mitigation strategies (Yu & Hansman, 2019), and in various other community noise quantification studies (Yu & Hansman, 2019; Salgueiro et al., 2021; Thomas & Hansman, 2019). Other efforts have focused on using large amounts of real-world data to produce reduced-order models for rapid computation of noise impacts (Behere, Rajaram, et al., 2021) or for estimating the impacts of average types of operations at different airports (Behere, Bhanpato et al., 2021).

Prior studies related to noise model validation date back to AEDT's predecessor, INM. Several prior efforts have focused on validating AEDT or INM to quantify the agreement between the model predictions and the data recorded from actual operations. Page et al. (2000) investigated a 1997 data set from Denver International Airport (DEN) to determine how INM's prediction accuracy changed with different thrust prediction methods. They found that the manufacturers' look-up values of normalized thrust were the most accurate. They then used this information to improve the noise-power-distance (NPD) curves in INM from historical manufacturer data. Forsyth & Follet (2006) used the same 1997 DEN data to update INM's database, with an emphasis on higher altitudes. Spectral classes were created to correct the NPD information with respect to SAE AIR-1845 atmospheric absorption. In another study performed with the 1997 DEN data, Plotkin et al. (2013) studied options to further enhance the modeling capability by accounting for the effects of weather and terrain.

Since the introduction of AEDT by the FAA in 2015, numerous studies have been performed on it. Hobbs et al. (2017) proposed an easily implementable method for including ground cover effects on noise propagation calculations by using algorithms originally implemented in the Advanced Acoustic Model (Page et al., 2000). These algorithms use optical straight-ray theory, as adapted for acoustics, to model noise propagation, in addition to the Fresnel ellipse method. This process has been found to improve noise propagation calculations with respect to empirical data, on data from Portland International Airport, San Francisco International Airport (SFO), and Oakland International Airport. Downing et al. (2019) investigated a method for including terrain and manufactured structural effects in AEDT's noise propagation calculations in 2019. Three separate models were evaluated with respect to their ability to accurately predict how buildings and barriers affect aircraft noise: the Traffic Noise Model (TNM) (Hastings, 2019), SoundPLAN 7.4 (which uses ISO 9613-2), and the National Cooperative Highway Research Program's Reflection Screening Tool. After validation using data from Los Angeles International Airport (LAX) and Long Beach Airport, the TNM method was recommended as the best option because its noise calculations have variability and consistency similar to those of AEDT's baseline calculations.

Giladi & Menachi (2020) developed a methodology to validate the AEDT noise model using published flight paths and Automatic Dependent Surveillance-Broadcast (ADS-B) data at three different locations. They found AEDT to underestimate actual noise levels based on a handful of operations. Following a similar methodology, Jackson et al. (2021) developed an automated framework for modeling large datasets of real-world flight trajectories in AEDT using ADS-B data. Alonso (2023) reports preliminary findings of that framework applied to over 86,000 arrival operations at SFO for a couple of noise monitor locations. In a study using flight operations quality assurance (FOQA) data for AEDT noise model validation, Gabrielian, Puranik, Bendarkar, Kirby, Mavris, & Monteiro (2021) presented an automated framework to model FOQA data as fixed-point profiles (FPPs) within AEDT. This was followed by an evaluation of AEDT's noise prediction capability while using high-fidelity weather data (Gabrielian, Puranik, Bendarkar, Kirby, & Marvis, 2021). Shaw & Sparrow (2022) investigated acoustic impedance and atmospheric absorption using high-fidelity meteorological data to improve the AEDT noise model. Further work on using appropriate averages based on inhomogeneous meteorological profiles, instead of relying on homogeneous annual average weather, to improve noise predictions is presently underway (Mavris & Sparrow, 2022). Preliminary results of a comparative assessment of AEDT noise modeling assumptions at SFO were presented last year (Bendarkar et al., 2022).

The remainder of this report provides information on noise modeling data sources, AEDT assumptions, and automation capabilities developed for the current work. It also discusses the results generated for the bulk flight operations modeled, along with particular or aggregate insights.

Research Approach

System-level noise modeling in this report follows the procedure detailed in our previous work (Gabrielian, Puranik, Bendarkar, Kirby, Mavris, & Monteiro, 2021; Bendarkar et al., 2022). Two important elements in this modeling are summarized herein for completeness: (1) the data sources used during modeling, and (2) the modeling assumptions and alternatives available for each assumption.

Data sources used

Several data sources with different fidelity can be used for noise modeling, ranging from simple ground-based radar observations to data fusion from multiple sensors on an aircraft itself. The two main data sets relevant to this manuscript are described below.

1. **FOQA** data are recorded by the airline operating the flight. The basis for the FOQA program is laid out in FAA Advisory Circular 120-82, which states: “The value of FOQA programs is the early identification of adverse safety trends that, if uncorrected, could lead to accidents” (Federal Aviation Administration, 2004). Therefore, FOQA systems record large amounts of data at one recording per second (i.e., 1 Hz). These data have been used for several safety-related applications in prior work (Puranik & Mavris, 2018; Lee et al., 2020). The important elements of the FOQA data in this report relate to the detailed time history of parameters such as altitude, speed, thrust, weight, configuration (flaps and gear), and so on, for each flight modeled in AEDT.
2. **Noise monitoring data** contain five key parameters: a unique flight ID, noise monitor locations, class of noise reading, sound exposure level (SEL), and the maximum, A-weighted sound level (L_{max}) metrics of associated noise events. The flight ID and the time of closest approach in the noise monitor data allow flights to be matched to the appropriate flight from FOQA data, thereby matching the aircraft configuration and the time of the noise event with the noise metric value. The class of the noise reading identifies the confidence with which the noise reading has been matched with the corresponding flight ID. The highest confidence is marked as a class 1 reading. These locations (except for their altitude) are used in flight modeling discussed in subsequent sections. The noise monitor data are used as a benchmark comparison for noise results calculated by AEDT.

The framework for modeling and automation developed in this report is independent of the data source used and will need to be modified only to account for the availability of parameters if other data sources are used. In this work, the data used are obtained from flight operations at two airports, SFO and Seattle-Tacoma International Airport (SEA). Noise monitoring readings obtained from the SFO airport noise program (SFO, n.d.) include SEL and L_{max} noise event details. Noise data from SEA noise office included SEL and L_{max} readings for the entire year in addition to 1-second equivalent sound level (L_{eq}) time history data from July through December 2019.

Modeling assumptions and AEDT capabilities

Modeling in AEDT offers users multiple settings for critical assumptions related to the modeling of performance and noise. A matrix of alternatives for these options is shown in Tables 1 and 2. Although the possible options and their combinations may be large, not all listed options are compatible or included in the present work. These limitations are noted while discussing the modeling assumptions individually.

Table 1. Modeling options for departure operations.

Assumption	AEDT default	Option 2	Option 3	Option 4	Option 5
Thrust	Full	FOQA	RT05	RT10	RT15
Weight	AEDT **	FOQA	Alternative weight		
Ground track	Standard	FOQA			
Procedure	Standard	FOQA	NADP1_1	NADP2_11	
Weather	Standard	FOQA	ASOS	High fidelity	
Surface	Soft	Hard			
Terrain	None	Actual			
Flaps	AEDT	FOQA			
Gear	AEDT	FOQA			
NPDs	AEDT	NPD+C			

** Based on stage length.

RT - Reduced Thrust (5 or 10 or 15 percent).

NADP - Noise Abatement Departure Profile (1 or 2)

NPD+C - Noise Power Distance + Correction

Table 2. Modeling options for arrival operations.

Assumption	AEDT default	Option 2	Option 3	Option 4	Option 5
Thrust	Full**	FOQA			
Weight	AEDT	FOQA			
Ground track	Standard	FOQA			
Procedure	Standard	FOQA			
Weather	Standard	FOQA	ASOS	High fidelity	
Surface	Soft	Hard			
Terrain	None	Actual			
Flaps	AEDT	FOQA			
Gear	AEDT	FOQA			
NPDs	AEDT	NPD + C			

** Arrival thrust is calculated using force-balance.

ASOS - Automated Surface Observing System

NPD+C - Noise Power Distance + Correction

SFO was selected for the present work because the research team has access to real-world noise monitoring data from that airport. For the purposes of this study, 269 departing and arriving flights at SFO have been down-selected. For the SEA airport, a total of 71 and 80 departure and arrival flights with 179 and 105 noise events, respectively, have been identified using the time-series noise data matched to FOQA data. These flights consist of Boeing 717-200, 737-800, 737-900, 757-200, 757-300, 777-200ER/LR, Airbus A319-100, and A320-200 airframes.

Several settings are available under every assumption (row) in Tables 1 and 2, which can affect the performance and noise for each flight operation. This section provides a summary of each option and how it might potentially affect the calculations. For further details, readers are referred to the AEDT Technical Manual (Ahearn, 2016).

1. **Thrust settings:** The options for thrust in AEDT can be seen through some of the procedures in the FLEET database. Apart from a full thrust assumption, the true thrust value at different points along the departure or arrival is available from the FOQA data and can be used. RT15 corresponds to a 15% reduced thrust during the takeoff procedure. Investigation of thrust settings upon takeoff and cutback in ASCENT Project 45 identified that 15% reduced thrust is regularly used by operators in real-world scenarios. This decrease in takeoff and cutback thrust results in a 30% decrease in the area of the 80-dB SEL contour for a single-aisle aircraft (Mavris, 2018). Other options available within AEDT include 5% and 10% reduced thrust; however, these options are not studied in the present work. The final thrust option available is the actual thrust from the flight given in the FOQA data.
2. **Procedure:** The FLEET database has two types of profiles that can be used: procedural profiles and FPPs. Procedural profiles define an aircraft's thrust, speed, and trajectory in a series of steps. Examples of procedural profiles include the standard profile, NADP1, and NADP2. FPPs fully define the location and state of the aircraft in the sky, as well as its state: thrust and speed. FPPs are used to model FOQA data within AEDT because they can include the speed and thrust from flight data.
3. **Weight:** Standard departure weight is defined by trip distance (stage length) within AEDT. Modified alternative weight procedures are available within AEDT that can be combined with the standard or reduced thrust procedures. Alternatively, FOQA weight can be used for AEDT procedures. FOQA weight can also be used within AEDT while employing FPPs. However, weight does not affect noise computation for FPPs because all performance parameters, such as thrust, are already prescribed. Information regarding weight, thrust, and speed can be used in one FPP for each flight modeled.
4. **Ground track:** The ground track comprises the latitude and longitude points on the ground of the aircraft during its flight. The default AEDT modeling for ground tracks is straight into the airport along with the extended runway centerline that the aircraft is using upon arrival, or straight out of the airport upon departure. These default settings are likely to result in incorrect predictions compared with real-world noise observations and are therefore not included in the current analysis. The FOQA ground track data, reflecting the true flight paths into or leaving airports, are used in the present work.



5. **Weather:** The default weather settings used in AEDT studies are in the AIRPORT database. These settings include temperature, relative humidity, wind speed, sea-level pressure, and dew point, which affect performance and acoustic calculations. The wind direction is always assumed to be a headwind direction. Although AEDT can use high-fidelity weather data in multiple formats, the present work is limited to the default setting.
6. **Surface and terrain:** The surface options within AEDT are available for propeller aircraft, including hard and soft surface options that affect the ground reflection and other properties in noise calculations. For the present work, AEDT default values of soft ground surface and flat terrain are used.
7. **Flaps and landing gear:** The flap and gear schedule for modeling in AEDT are provided with each of the procedures. For FOQA FPPs, AEDT infers a flap and gear schedule from the corresponding standard profile. However, unless the analysis is using NPD data with correction for configurations, the flap and gear configuration does not affect the calculated noise when using an FPP. The present work visualizes the errors in AEDT SEL predictions against FOQA flap and gear settings because these affect the real-world noise measured at monitoring stations.
8. **NPD curves:** Noise calculations in AEDT rely on NPD curves derived in a process similar to that used in aircraft noise certification. Noise levels are obtained as a function of observer distance via spherical spreading through a standard atmosphere. In noise analysis, AEDT applies other correction factors to obtain the desired sound field metrics at the location of the receiver. NPD + configuration (NPD + C) curves that may enable more accurate noise prediction due to aircraft configuration and speed changes are under study (Mavris, 2019) and are not included in the present work.

Compatibility of settings

Of the settings discussed previously, those varied in this study include the procedures and profiles, thrust, and weight. Importantly, not all these variations are compatible with one another. For example, the FOQA FPPs are incompatible with reduced thrust or alternative weight settings because the FOQA FPPs specify the thrust at every step and the weight at the start of the takeoff or landing segments, whereas the reduced thrust or alternative weight settings calculate these parameters with respect to the standard profile. Likewise, the FOQA thrust values cannot be used in a procedural profile because they are numerical (in pounds), whereas the procedural profiles require thrust type and step type definitions that subsequently produce their own thrust values. Consequently, a compatibility matrix is created, yielding the actual number of combinations for flights to be modeled. Arrival profiles have fewer combinations of modeling settings than departure profiles. The only profiles available for arrivals are the standard and FPP from the FOQA data, and one thrust setting is available.

In the present study, the combination of settings yields seven different jobs per noise metric for departures. For arrival modeling, it yields two different jobs for each noise metric. Running these cases on 129 departures and 140 arrivals requires some form of automation capability, as discussed in detail in Gabrielian & Puranik (2021a) and summarized below.

Automation capability

An automation capability was developed to handle these combinations in a time-efficient manner. Automation is required not only for setting up the many combinations of settings within AEDT (also called pre-AEDT automation) but also for post-processing of the results generated (post-AEDT automation). The pre-AEDT automation consists of nine SQL automation scripts (Figure 1). The user specifies the profiles to be modeled (either procedural or FPP), the ground tracks, and a combination matrix. This matrix maps profile IDs and ground track IDs together with runway specifications to model the correct combinations from the matrix options in Table 1 and Table 2. These scripts work on multiple AEDT and user-created databases to set up the studies. After scripts 0a through 4b have been executed, script 5 can be executed, which gathers all the information from the previous scripts and sets up the metric results within a new AEDT study. After the user runs all studies within the AEDT graphical user interface, the results, including performance, emissions, and noise, are exported into .csv files with a batch report run tool. Each case in the combination test matrix results in four reports, which are then processed with MATLAB and Python post-processing scripts (post-AEDT automation).

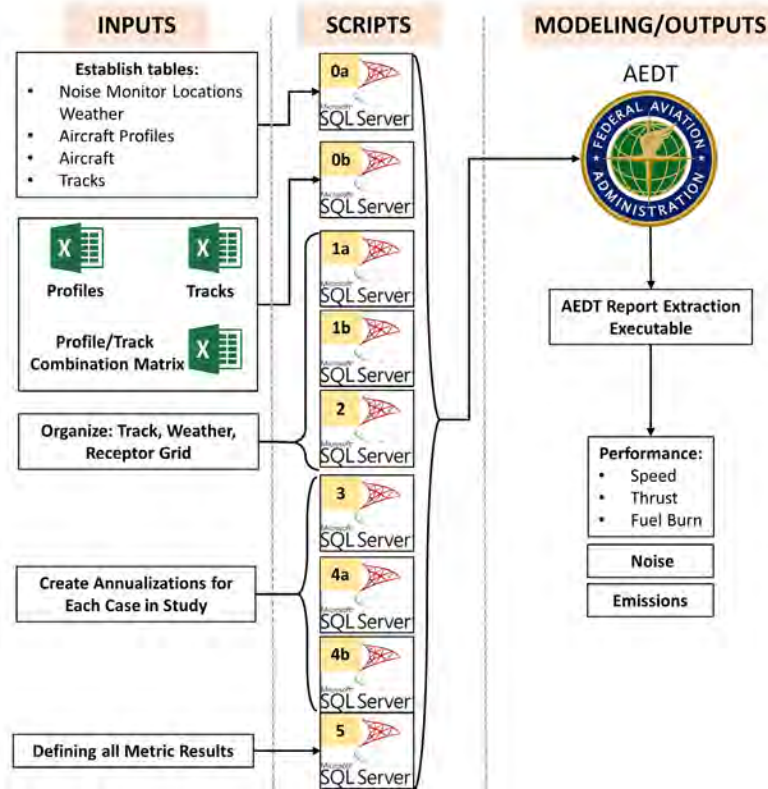


Figure 1. Noise modeling process automation steps. AEDT, Aviation Environmental Design Tool.

Preliminary Results

The results for SEA are presently under analysis and will be reported in subsequent reports. The present work focuses on results from SFO. The modeling framework was implemented on 129 departing and 140 arriving flights at SFO by using AEDT version 3c. In total, there are 616 (437 departures and 179 arrivals) noise events, wherein a noise event refers to a particular flight triggering a particular monitor. The number of noise events is greater than the number of flights because some flights triggered multiple monitors. The flights have been given arbitrary flight IDs (GT-xxx) to anonymize the real-world flight details. Figure 2 shows a map of the noise monitor locations in the SFO airport area, along with their assigned IDs. All noise monitors triggered with the highest confidence (class 1) and mapped to the corresponding flight are used as truth values for comparing AEDT predictions. In this section, detailed results are provided for one departure and one arriving flight at SFO, followed by results on AEDT prediction accuracy on an aggregate basis.

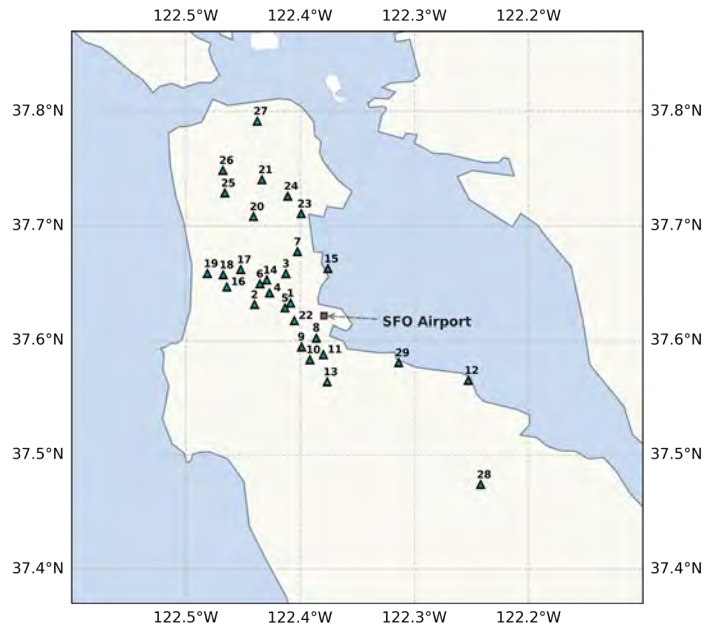


Figure 2. Locations of noise monitors around San Francisco International Airport (SFO).

Figure 2 shows the locations of noise monitors around SFO, and Figure 3 shows the modeled FOQA arrival and departures tracks at SFO. Although using the FOQA flight track and trajectory are expected to result in aircraft performance and noise predictions that are closest to those measured, they are not necessarily always available to AEDT users. Therefore, investigating AEDT noise prediction accuracy under various modeling options is important from a usability perspective. The individual flight modeling results are elaborated upon in the following subsection.

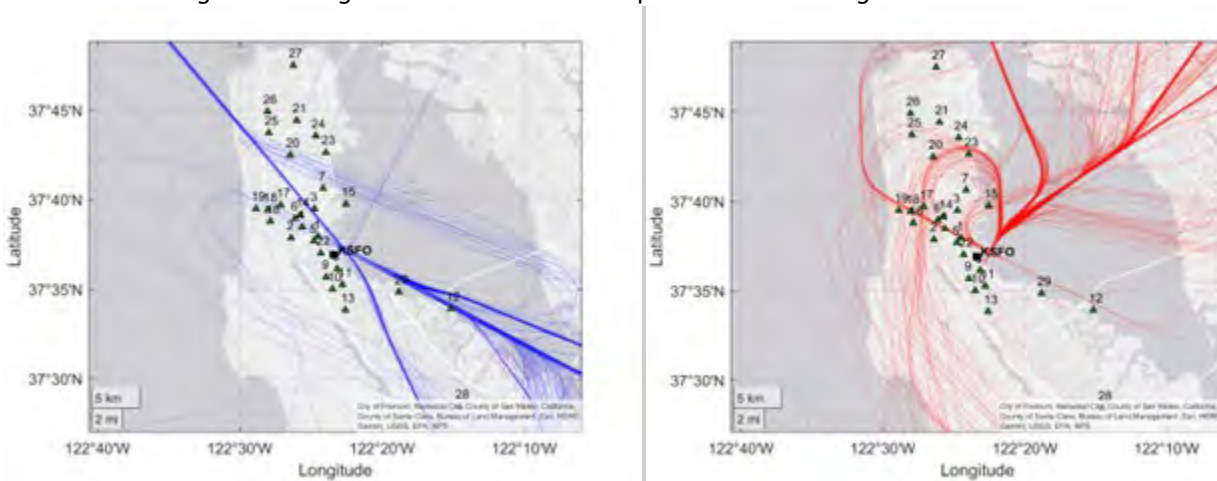


Figure 3. Arrival (left) and departure (right) flight operational quality assurance (FOQA) tracks at San Francisco International Airport (SFO).

Individual flight results

Detailed performance and noise results are available for all 269 flights, but one departure flight is reported below as an example. Table 3 provides the AEDT airport weather parameters for the two flights of interest in the present work. AEDT

airport weather uses the average annual weather and therefore is the same for both flights modeled, because they operated in the same year.

Table 3. Airport weather conditions for the flights.

Weather	Temperature (°F)	Sea-level pressure (mb)	Dew point P (f)	Relative humidity (%)	Wind speed (kts)	Wind direction (°)
AEDT default	61	1,018.3	53.1	75.2	9	N/A

Flight number GT1015

Flight GT1015 was a Boeing 737-800 with an origin-destination pair of SFO-LAX, making this a stage length 1 departure. The real-world flight data give the gross weight at takeoff as 145,591 lbs.

Figure 4 shows the performance plots for flight GT1015, as part of the data extracted from AEDT with the AEDT report extraction executable. The aircraft performance, based on procedural profiles, shows that the alternative weight reduced thrust profiles are shallower than the others, whereas the FOQA FPP (actual flight) is shallowest. The monitors triggered by this flight as well as the ground track are shown in Figure 5. The noise comparison for flight GT1015 in Figure 6 shows both underpredictions and overpredictions of the noise created at the noise monitor locations. An interesting trend is observed when the noise monitor predictions are compared with the aircraft ground track and monitor locations from Figure 5. Noise values at monitors 1, 4, 6, 18, and 19 tend to be underpredicted. They also appear to be below the aircraft flight paths. Monitors 5, 14, 16, and 17 are all further from the flight’s ground track and tend to be overpredicted. Although these comparisons may not provide conclusive insights alone, they can be valuable when aggregated across different flights and modeling assumptions.

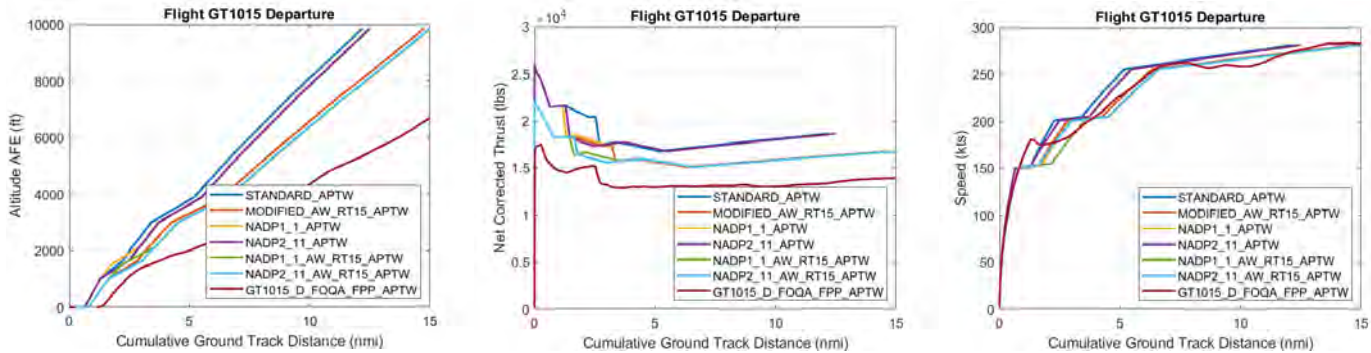


Figure 4. Altitude, thrust, and ground speed performance for flight GT1015. _APTW - profile with airport weather. _AW_RT15 - Alternate Weight Reduced Thrust 15%. NADP - Noise Abatement Departure Procedure (1 or 2). FOQA_FPP - Flight Operations Quality Assurance Fixed Point Profile.

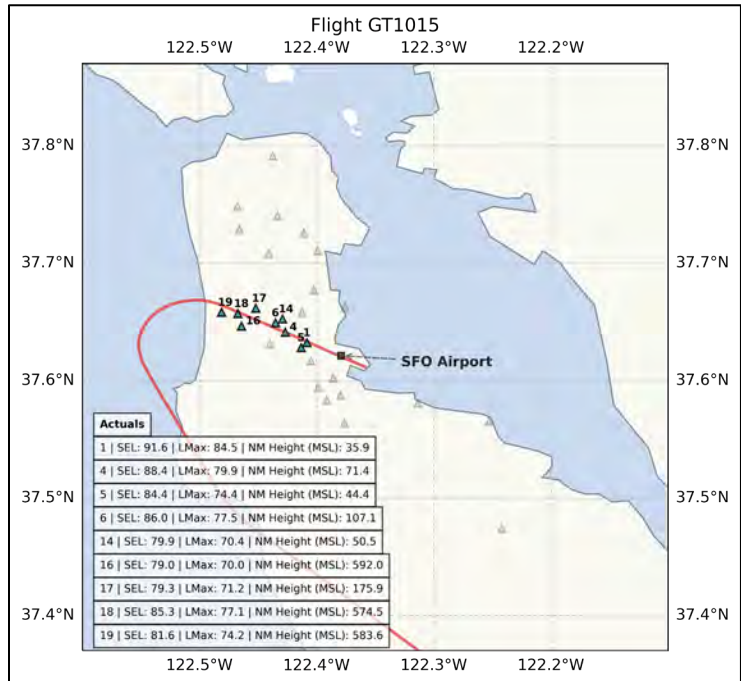


Figure 5. Trajectory and monitors triggered for flight GT1015. SFO, San Francisco International Airport; SEL, sound exposure level.

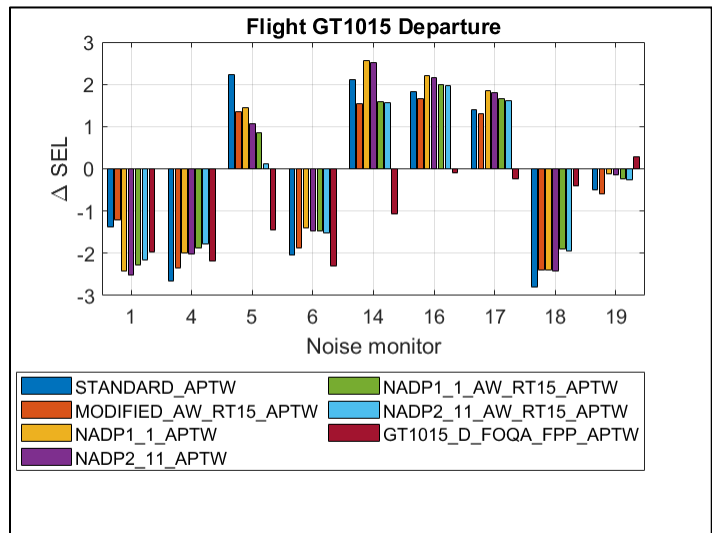


Figure 6. AEDT predicted – measured noise (dB) results for flight GT1015. SEL, sound exposure level.

Identifying outliers

According to the results of the bulk analysis, some flights had relatively high Δ SEL (AEDT predicted – measured noise) values. Some flights with these high Δ SEL values were investigated to identify any anomalous patterns or factors. The identified anomalous patterns or factors causing the high Δ SEL can be used to easily rule out flights in future analyses, to prevent the simulation of anomalous flights whose results will eventually be discarded.

Based on preliminary observation of the data, several anomalous factors were identified. Results from flights that triggered monitor 8 consistently had high ΔSEL . This monitor has therefore been excluded from all further analyses and results. Some monitors had duplicate or multiple readings for the same flight for the same noise event. The ΔSEL could be high in these cases depending on the reading chosen. Therefore, the reading from the noise monitor corresponding to the point of closest slant distance for the flight that triggered it was selected. From some departure flights' tracks, we observed that some monitors located far behind the takeoff point and in the opposite direction of the flight path were triggered. Finally, some arrival flights had tracks that looped around the monitors. Some of these were arrivals that had to go around to attempt landing a second time. After elimination of flights affected by the anomalous factors, some flights with high ΔSEL remained. Noise events with wind speeds >10 knots or nonzero precipitation, as observed by hourly Automated Surface Observing System (ASOS) weather data, were excluded from further analysis since AEDT is not designed to predict noise in these circumstances. Slant distances over 10,000 ft were investigated to determine what threshold produced high SEL prediction errors. Noise events with higher slant distances have an increased possibility of inaccurate noise measurements or event correlation to flight due to uncontrollable factors like background noise levels. Additionally, 29 noise events with slant distances between 7,000 and 10,000 ft were found to have elevation angles less than 1°. Since these are likely incorrect correlations between noise monitoring data and flight operations, they were dropped.

Due to such exclusions, the total useful noise events reduced to 142 and 51 for 63 departure flights and 51 arrival flights, respectively, from a total of 616 noise events (437 departures and 179 arrivals) initially. Table 4 shows a summary of the outlier analysis and the total data points that will be presented in the aggregate results. It is important to note here that all arrival noise events in the useful total were captured by just one monitor at SFO: Monitor 12, as shown in Figure 2. Therefore, prediction errors in arrival noise events would be influenced by unknown extraneous factors such as monitor location and background/other noise sources to a greater extent than departure events.

Table 4. San Francisco International airport (SFO) outlier analysis

Operation	Flights	Noise Events	Comments
Arrivals	140	179	Modeled
		-44	Wind >10 knots or nonzero precipitation
		-36	Abnormal track
		-15	Monitor 8
		-33	Slant distance >7,000 ft or Misc.
	51	51	Useful total
Departures	129	437	Modeled
		-213	Wind >10 knots or nonzero precipitation
		-37	Monitor 8
		-45	Slant distance >7,000 ft or Misc.
	63	142	Useful total

Aggregate flight modeling results

Individual flights can be analyzed to compare the performance and noise prediction accuracy of the different modeling options within AEDT, as shown previously. To obtain more meaningful inferences, we perform a statistical analysis of all 193 noise events in this section. To this end, prior work provided preliminary results for per-noise-monitor prediction capability for departure flights (Mavris & Sparrow, 2022). Instead of viewing one flight at a time, all flights that triggered a particular noise monitor were considered at each profile. This report presents results for SEL prediction errors for all aggregated noise event across all monitors by departure and arrival operations. These results are further sliced by different data parameters that are only available via the FOQA data, like landing gear and flap settings, takeoff and landing weights, elevation angles and slant distances, etc. The eight profiles for the departure operations modeled in AEDT are Alternate Weight Reduced Thrust (AW_RT15), Flight Operations Quality Assurance Fixed Point Profile (FOQA_FPP), Noise Abatement Departure Procedure Alternate Weight Reduced Thrust (NADP1_AW_RT_15), Noise Abatement Departure Procedure Alternate Weight Reduced Thrust (NADP2_AW_RT_15), NADP1, NADP2, Standard Procedure with Average Airport Weather (STD_APTW), and Standard Procedure with Automated Surface Observing System (ASOS) Airport Weather (STD_ASOS). The arrival operations have been modeled using the Standard profile with average airport weather (STD_APTW) and FOQA FPPs (FOQA_FPP). The difference between the AEDT predictions and measured noise observations for all monitors is computed and analyzed with box plots. This metric is referred to as the ΔSEL metric and is defined in Eq. (1). Ideally, these box plots would show a median of zero and a small spread, indicating minimal error between predictions of multiple operations and real-world data.

$$\Delta SEL = SEL_{AEDT} - SEL_{Measured} \quad (1)$$

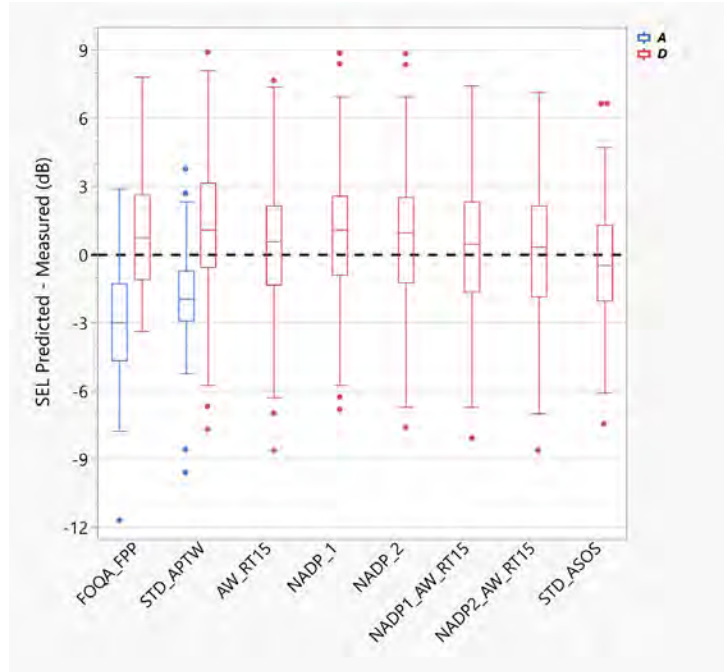


Figure 7. Predicted – measured sound exposure level (SEL) (dB) noise box plot for all noise events at all monitors split by arrivals (A) and departures (D). _APTW – profile with airport weather. _ASOS – Profile with automated surface observing system weather. _AW_RT15 – Alternate Weight Reduced Thrust 15%. NADP – Noise Abatement Departure Procedure (1 or 2). FOQA_FPP – Flight Operations Quality Assurance Fixed Point Profile.

Figure 7 shows the error in SEL prediction minus SEL measurement (ΔSEL metric) for all noise events aggregated by departures and arrivals. All modeled departure profiles (D) show a median overprediction error of less than 1 dB, with the FOQA profile having the lowest variability. The arrival profiles (A) show a median underprediction error of around 2 to 3 dB. As stated earlier, all of the analyzed arrival events were captured by just one noise monitor (Monitor 12). The median error could therefore be influenced by other factors beyond our control.

Since the FOQA ground tracks are used with all modeled profiles, every noise event can be categorized based on the slant distance and elevation angle of the aircraft with respect to the noise monitor, as shown in Figure 8. For the analysis that follows, a noise event is considered overhead if the elevation angle is $\geq 50^\circ$, and is sideline otherwise. Slant distances over 7,000 ft were found to cause disproportionately higher prediction errors. Due to absence of time-history noise data, it was difficult to associate these noise events with aircraft operations with high precision. As a result, all noise events above 7,000 ft slant distances have been removed from the results discussed below.

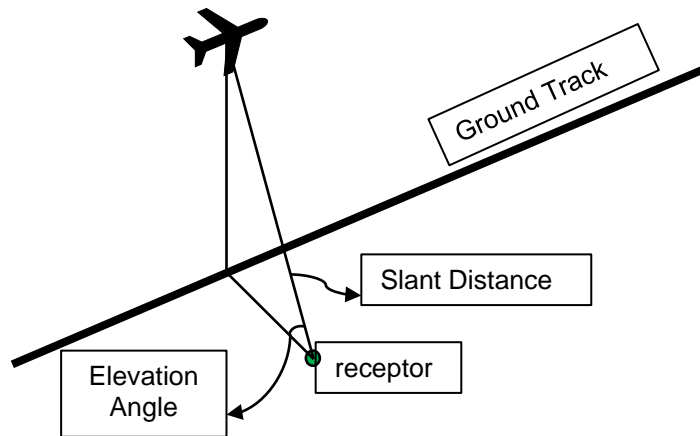


Figure 8. Notional representation of elevation angle and slant distance.

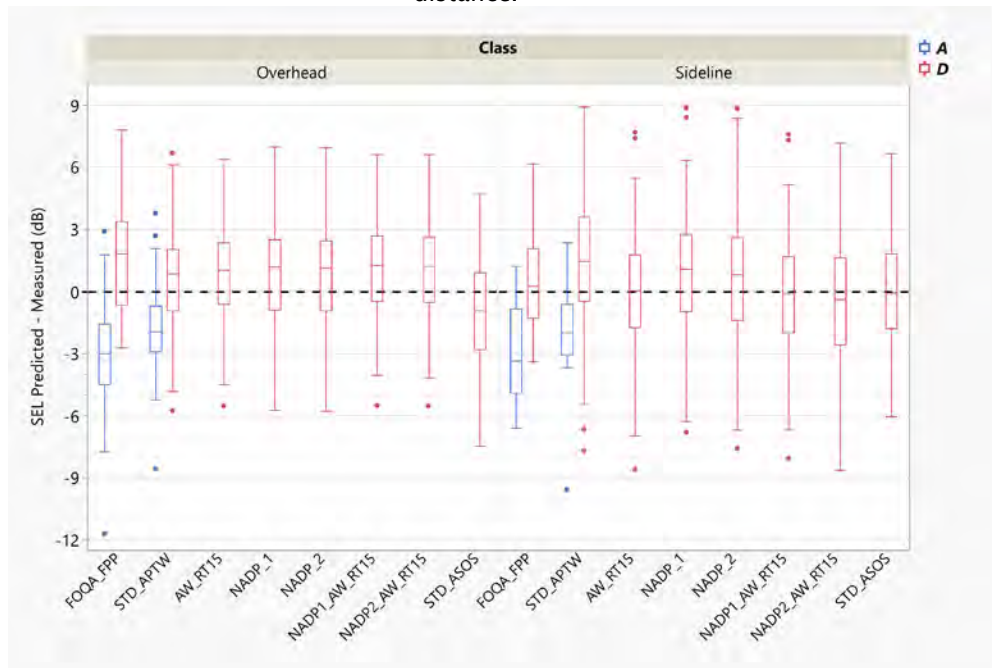


Figure 9. Predicted – measured sound exposure level (SEL) (dB) for overhead versus sideline noise events across all monitors. A, arrival; D, departure. _APTW – profile with airport weather. _ASOS – Profile with automated surface observing system weather. _AW_RT15 – Alternate Weight Reduced Thrust 15%. NADP – Noise Abatement Departure Procedure (1 or 2). FOQA_FPP – Flight Operations Quality Assurance Fixed Point Profile.

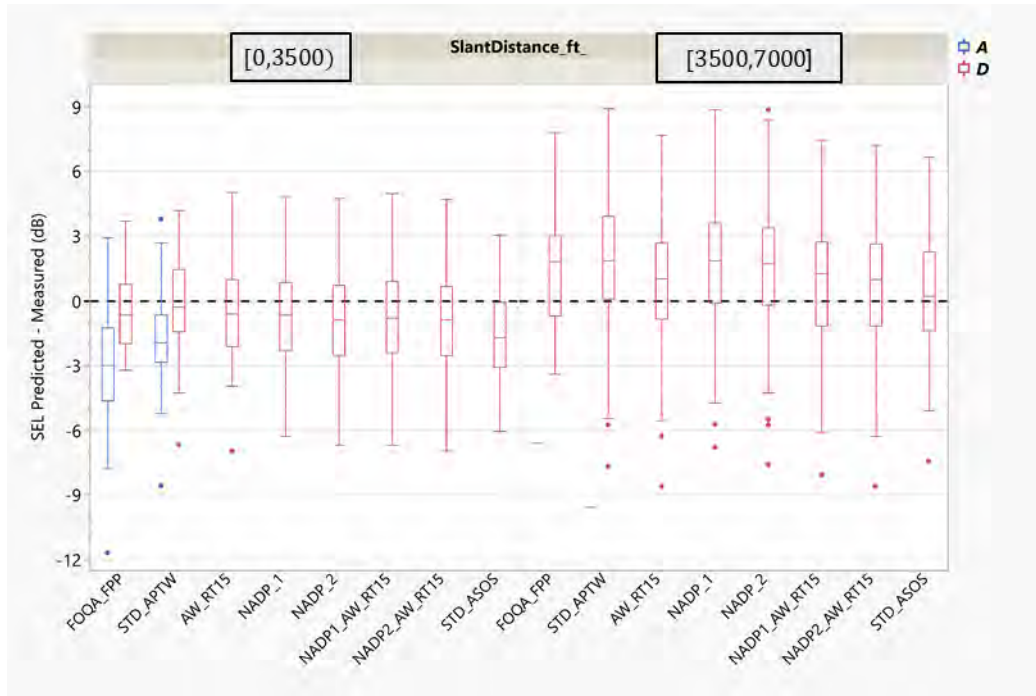


Figure 10. Predicted – measured sound exposure level (SEL) (dB) by slant distance across all monitors. A, arrival; D, departure. _APTW – profile with airport weather. _ASOS – Profile with automated surface observing system weather. _AW_RT15 – Alternate Weight Reduced Thrust 15% . NADP – Noise Abatement Departure Procedure (1 or 2). FOQA_FPP – Flight Operations Quality Assurance Fixed Point Profile.

Figure 9 shows the ΔSEL metric for 93 overhead and 100 sideline noise events. Median of arrival noise events suggests an underprediction for both classes, whereas departure event medians are overpredicted, with the FOQA profile showing a median closer to zero for sideline noise events with the smallest variation. For variation with slant distances, Figure 10 shows that the 45 departure noise events where the aircraft is closer than 3,500 ft to the noise monitors are predicted well, with a median ΔSEL of close to zero or -1, whereas the 97 departure noise events with slant distances greater than 3,500 ft tend to be overpredicted. The 51 arrival noise events all lie within 3,500 ft of Monitor 12 during approach.

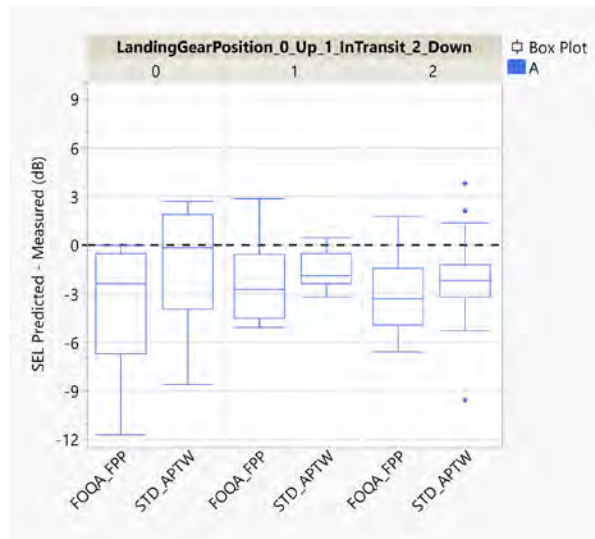


Figure 11. Predicted – measured sound exposure level (SEL) (dB) by landing gear position for all arrivals (A). _APTW – profile with airport weather. STD – Standard profile. FOQA_FPP – Flight Operations Quality Assurance Fixed Point Profile.

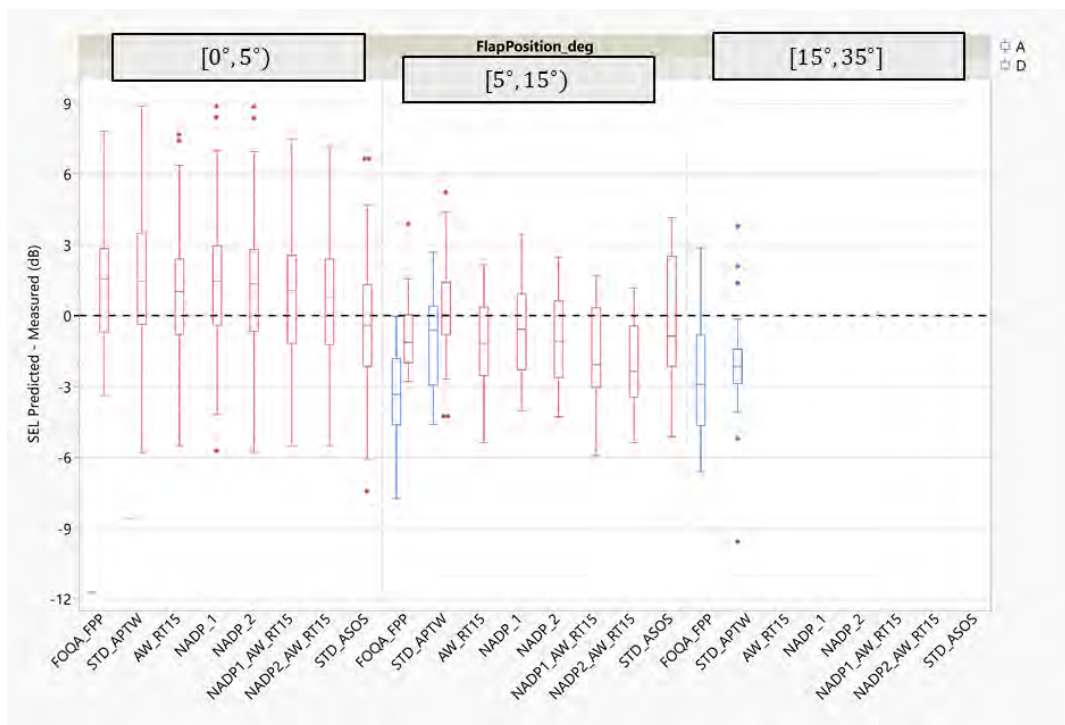


Figure 12. Predicted – measured sound exposure level (SEL) (dB) by flap positions for all noise events. A. arrival; D, departure. _APTW – profile with airport weather. _ASOS – Profile with automated surface observing system weather. _AW_RT15 – Alternate Weight Reduced Thrust 15%. NADP – Noise Abatement Departure Procedure (1 or 2). FOQA_FPP – Flight Operations Quality Assurance Fixed Point Profile.

Figure 11 shows ΔSEL for arrival operations by landing gear position when the aircraft are closest to the noise monitors in their trajectories. A value of 0 indicates the landing gear is up, 1 indicates it is in transit, and 2 indicates that the landing gear is down. In all three cases, the FOQA FPPs show a median underprediction of about 2 to 3 dB. When the landing gear is up, the standard profile has a median ΔSEL of zero but underpredicts by about 3 dB when the gear is in transit or down. Similarly, Figure 12 shows ΔSEL values for all operations by the flap position when the aircraft are closest to the noise monitors in their trajectories. Because the FOQA data often provides approximate decimal values instead of exact flap settings (e.g., 4.65° instead of 5°, or 28.23° instead of 30°), the results are divided into the three bins shown. The 115 departure noise events were found with flap angles of between [0°, 5°) at the time of triggering noise monitors. All profiles except the standard profile with ASOS weather are found to overpredict SEL values in that group. Between [5°, 15°), the 22 departure noise events are generally underpredicted by 1 dB, with the FOQA profile having the least variability. The 14 arrival events in this group and another 36 arrival events are generally underpredicted by 2 to 3 dB.

Figure 13 shows a histogram of the various airframes within the flights that are being analyzed in Table 4. The 737-900 and 737-800 are well represented, with scant representation of other airframes in the present analysis. Balancing the data for other airframes will be explored in future work for other airports and years of noise data. Figure 14 shows the weight error between AEDT assumptions and real-world FOQA operations by the stage length and airframe of interest. That AEDT underpredicts weights due to lower assumed load factors is well studied and has resulted in alternative weight profiles to account for these differences (Mavris et al., 2018). This is confirmed in the present work across the different airframe types.

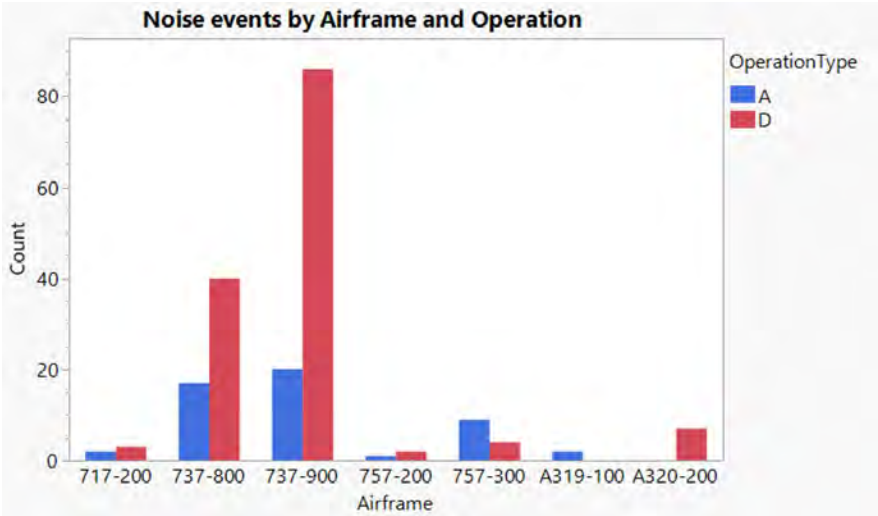


Figure 13. Noise events by airframe type and operation. A, arrival; D, departure.



Figure 14. Aviation Environmental Design Tool (AEDT) weight assumption error ($\frac{\text{Weight}_{\text{AEDT}} - \text{Weight}_{\text{FOQA}}}{\text{Weight}_{\text{AEDT}}} * 100$).

The effect of these weights shows up during modeling through the stage length, which are decided based on the distance between origin-destination pairs of the flights, typically in 500-nmi increments. Figure 15 shows the effect of stage length on noise predictions through the ΔSEL metric given in Eq. (1). The total number of departure noise events in stage lengths 1, 2, 3, and 4 were 72, 19, 5, and 43, respectively. All arrivals are modeled as stage length 1 and are therefore not of consequence in this case. For departures, median ΔSEL values for stage length 4 flights are close to zero, with a majority of the overprediction happening in stage length 1 (0 to 500 nmi range) flights. It is difficult to draw conclusions for stage lengths 2 and 3 due to limited sample sizes.

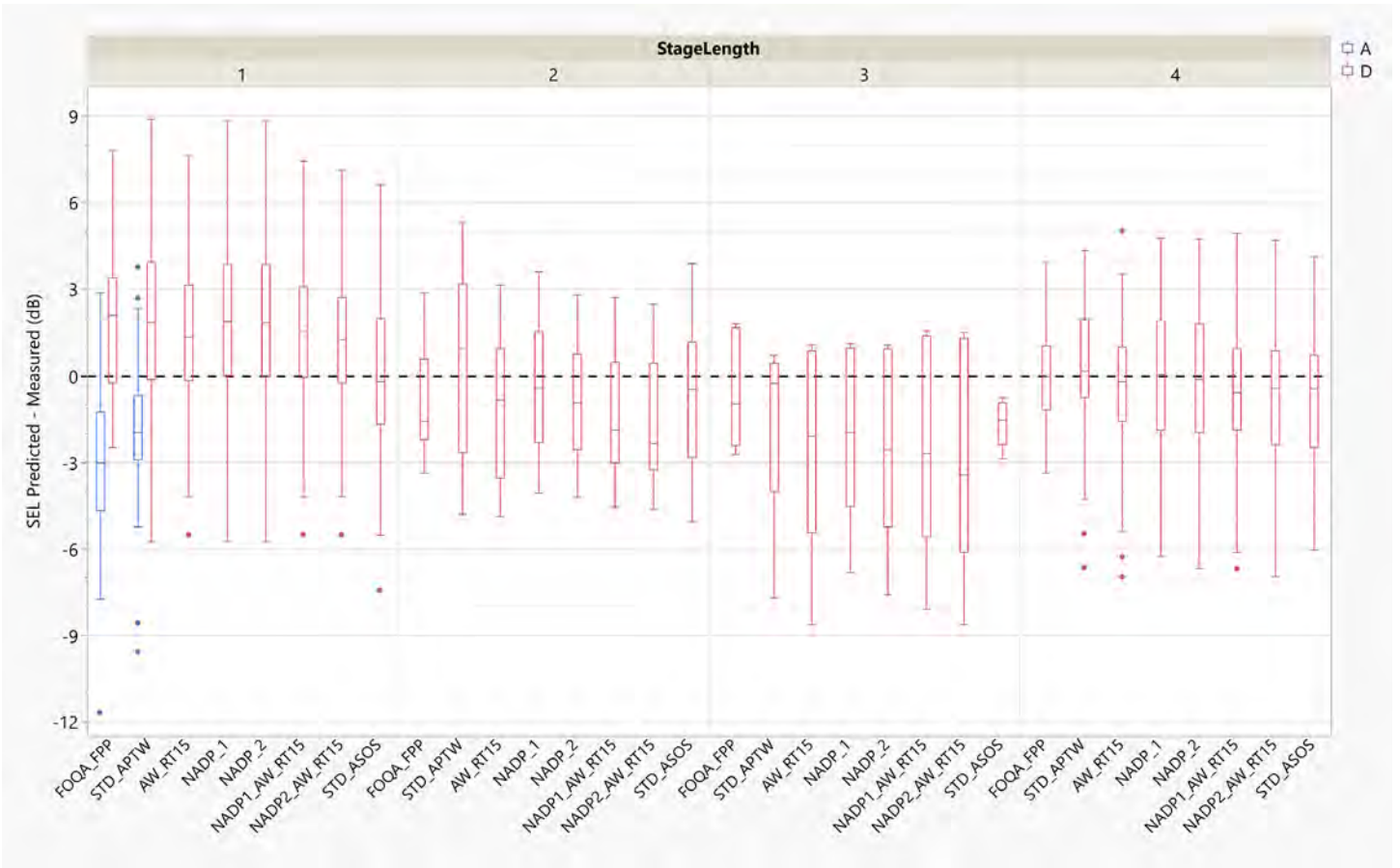


Figure 15. Predicted – measured sound exposure level (SEL) (dB) by stage length for all noise events. A, arrival; D, departure. _APTW – profile with airport weather. _ASOS – Profile with automated surface observing system weather. _AW_RT15 – Alternate Weight Reduced Thrust 15% . NADP – Noise Abatement Departure Procedure (1 or 2). FOQA_FPP – Flight Operations Quality Assurance Fixed Point Profile.

Noise data processing for SEA

Noise monitoring data for SEA were available as time history data consisting of 1-second L_{eq} values for July to December 2019, as well as SEL measurements of noise events for the entire year. The locations of noise monitors around the SEA airport are shown in Figure 16, and the FOQA flight tracks for operations at SEA for 2019 are shown in Figure 17.

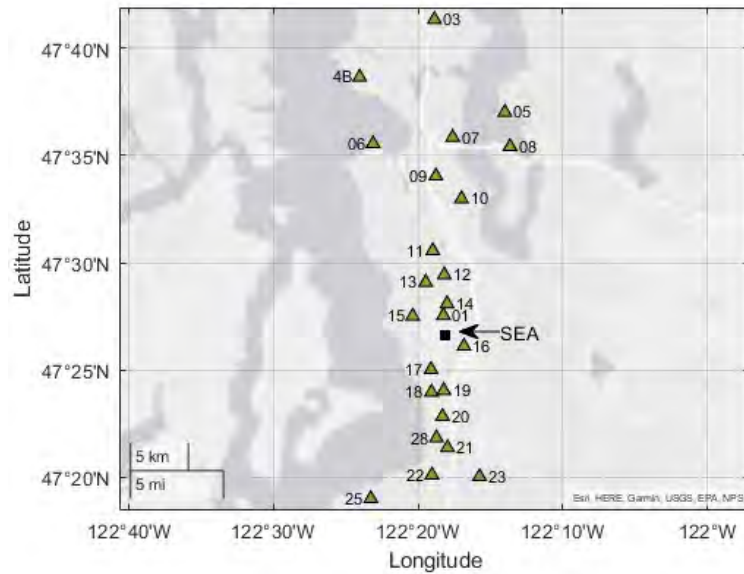


Figure 16. Locations of noise monitors around Seattle-Tacoma International Airport (SEA).

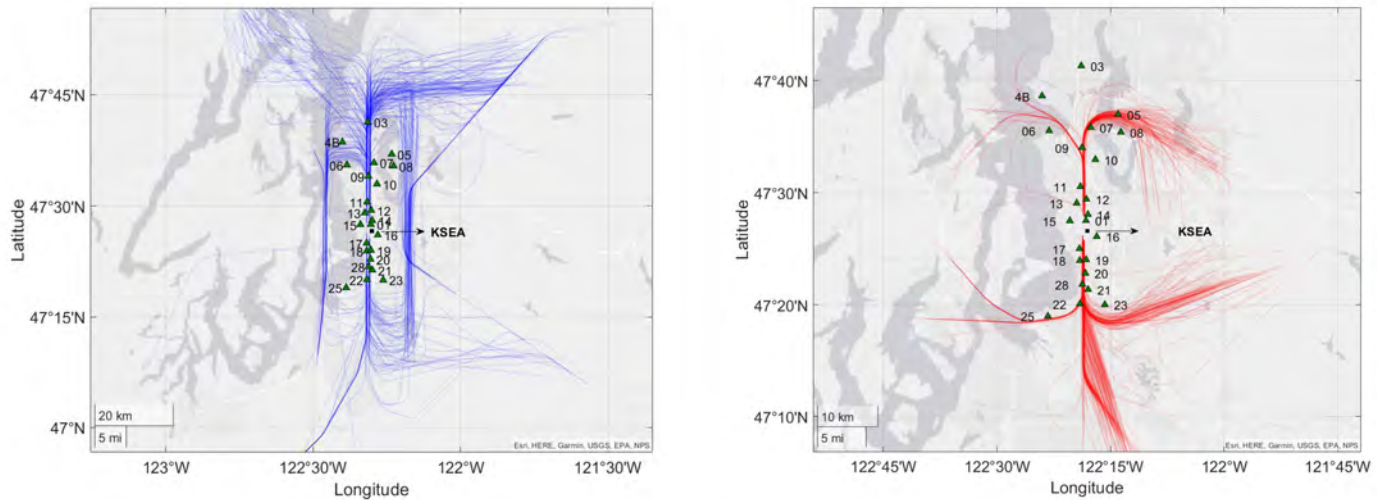


Figure 17. Modeled flight operational quality assurance (FOQA) arrival (left) and departure (right) tracks for Seattle-Tacoma International Airport (SEA).

To process the noise time history data for SEA, a dashboard was created that merged the FOQA and noise monitoring data. The developed dashboard enables the user to line up the FOQA flights with noise monitoring data to capture noise events by calculating the SEL, L_{max} , and background sound levels (L_{90}). The dashboard allows the user to visualize the 1-second L_{eq} values captured by noise monitors closest to the flight of interest. A user can manually identify a noise event and capture and export the SEL, L_{max} , and L_{90} values at the closest point between the flight and noise monitor. A snapshot of the dashboard is shown in Figure 18. In it, an arrival flight's noise event at SEA Monitor 12 (topmost in red) is captured. Presently, a total of 76 departure and 87 arrival FOQA operations have been correlated with noise data, resulting in 113 arrival and 198 departure noise events, respectively. After matching SEA-provided SEL noise events with FOQA data for the

first 6 months of 2019, an additional 33 departure and 6 arrival noise events were identified. For SEA, flights with ambient wind speeds greater than 10 knots and nonzero precipitation were excluded prior to modeling in AEDT.



Figure 18. Developed dashboard to capture event sound exposure level (SEL) and maximum, A-weighted sound level (L_{max}) from Seattle-Tacoma International Airport (SEA) noise time history data

Further processing of SEA noise results is currently ongoing to identify good quality data points by conducting outlier analysis. These results will be published in the following reports. Likewise, noise data from Minneapolis–Saint Paul International Airport (MSP) are under analysis and will be presented in a later report. Additional FOQA data and noise for 2021 will also be processed in future work.

AEDT is designed to be accurate on average while modeling the sound exposure of operations over a long duration at a place of interest. The present preliminary results confirm that fact and show that AEDT has a median error of between 0 and 3 dB over hundreds of flights and noise events across different monitoring locations at SFO. Although these results are important in validating AEDT, it is important to recognize the limitations of the results presented here. This study reports results from one airport, SFO, with its varied geography and climate, for the year 2019, while matching FOQA flight data to airport noise monitoring SEL measurements. While the authors have taken sufficient care in selecting noise events that meet stringent quality criteria to compare AEDT predictions with real-world operations, detailed noise time-histories were not available for the year under consideration. All acceptable arrival noise events at SFO were captured by just one monitor, potentially incorporating errors due to location and background levels that cannot be determined. For the next year of the project, some of these limitations will be addressed. Results from SEA and MSP are being processed for multiple years, which include noise time history data to improve the quality of data matching and comparison. This should provide sufficient results to generate confidence in AEDT’s noise model for different weather and geographic conditions and for varied operations.

Milestones

None.



Major Accomplishments

Georgia Tech accomplishments

- Completed successful implementation of the AEDT automation pipeline for (a) modeling real-world flights in various settings, and (b) extracting and visualizing results from noise modeling efforts.
- Successfully ran 269 flights at all identified settings from the test matrix, and analyzed over 616 noise events (437 departures and 179 arrivals) to generate preliminary validation results.
- Completed outlier analysis to quality check flight-noise event results and shortlisted a total of 193 high-confidence noise events to complete SFO validation study for the year 2019.
- Presented SFO results at ASCENT spring and fall meetings in 2023.
- Analysis for 2019 noise validation data at two additional airports, SEA and MSP, is progressing.
- Coordinated with the PSU team to provide AEDT performance data required for tasks relevant to high-fidelity weather modeling.

Publications

Willitt, A., Bendarkar, M. V., Bhanpato, J., Kirby, M., Abelezele, S., & Mavris, D. N. (2024, Jan). Preliminary AEDT Noise Model Validation using Real-World Data. AIAA SCITECH 2024 Forum (ACCEPTED). Orlando, FL, January 2024.

Outreach Efforts

Held biweekly calls with the FAA, the Volpe Center, and Airborne Tactical Advantage Company (ATAC), and participated in biennial ASCENT meetings.

Awards

None.

Student Involvement

Georgia Tech

Graduate research assistants: Amber Willitt and Sabastian Abelezele completed the AEDT noise modeling and data analysis for San Francisco (SFO) 2019 dataset. Sonal Mehta and Humfrey Kimanya worked on noise modeling and data processing for Seattle (SEA) 2019 dataset.

Plans for Next Period

Georgia Tech

- Complete noise data analysis for SEA and MSP airports for the years 2019 and 2021.
- Provide insights into the statistical significance of results at various noise monitoring stations.
- Develop the interactive dashboard containing the modeling results with all different settings combined for performing trade-off studies.
- Collaborate with PSU to complete analysis of the impact of high-fidelity weather on noise predictions and measurement.

References

- Ahearn, M., Boeker, E., Gorshkov, S., Hansen, A., Hwang, S., Koopmann, J., Malwitz, A., Noel, G., Rehman, C. N., Senzig, D. A., et al. (2016). *Aviation Environmental Design Tool (AEDT) Technical Manual Version 2c*. FAA.
- Alonso, J. J., "Project 053 Validation of Low-Exposure Noise Modeling by Open-Source Data Management and Visualization Systems Integrated with AEDT," , 2022. URL <https://s3.wp.wsu.edu/uploads/sites/2479/2023/05/ASCENT-Project-053-2022-Annual-Report.pdf>, last accessed 28 Nov 2023.
- Behere, A., Rajaram, D., Puranik, T. G., Kirby, M., & Mavris, D. N. (2021). Reduced order modeling methods for aviation noise estimation. *Sustainability*, 13(3), 1120. <https://doi.org/10.3390/su13031120>
- Behere, A., Lim, D., Li, Y., Jin, Y.-C. D., Gao, Z., Kirby, M., & Mavris, D. N. (2020, January 6). Sensitivity Analysis of Airport level Environmental Impacts to Aircraft thrust, weight, and departure procedures. *AIAA Scitech 2020 Forum*. AIAA Scitech 2020 Forum, Orlando, FL. <https://doi.org/10.2514/6.2020-1731>
- Behere, A., Isakson, L., Puranik, T. G., Li, Y., Kirby, M., & Mavris, D. (2020, June 15). Aircraft landing and takeoff operations clustering for efficient environmental impact assessment. *AIAA AVIATION 2020 FORUM*. AIAA AVIATION 2020 FORUM, VIRTUAL EVENT. <https://doi.org/10.2514/6.2020-2583>



- Behere, A., Bhanpato, J., Puranik, T. G., Kirby, M., & Mavris, D. N. (2021, January 11). Data-driven approach to environmental impact assessment of real-world operations. *AIAA Scitech 2021 Forum*. AIAA Scitech 2021 Forum, VIRTUAL EVENT. <https://doi.org/10.2514/6.2021-0008>
- Bendarkar, M. V., Bhanpato, J., Puranik, T. G., Kirby, M., & Mavris, D. (2022). Comparative Assessment of AEDT Noise Modeling Assumptions Using Real-World Data. *AIAA Aviation 2022 Forum*, <https://doi.org/10.2514/6.2022-3917>
- Downing, J. M., Calton, M. F., Page, J. A., & Rochat, J. L. (2019). *Improving AEDT Modeling for Aircraft Noise Reflection and Diffraction from Terrain and Manmade Structures* (Tech. Rep. ACRP 02-79).
- Federal Aviation Administration. (n.d.) *Aviation Environmental Design Tool (AEDT)*. <https://aedt.faa.gov/>
- Federal Aviation Administration. 2004. *Advisory Circular, 120-82 - Flight Operational Quality Assurance*. https://www.faa.gov/regulations_policies/advisory_circulars/index.cfm/go/document.information/documentID/23227
- Forsyth, D. W. & Follet, J. I. (2006). *Improved Airport Noise Modeling for High Altitudes and Flexible Flight Operations* (NASA/CR-2006-21451) NASA.
- Gabrielian, A. B., Puranik, T. G., Bendarkar, M. V., Kirby, M., Mavris, D., & Monteiro, D. (2021a, August 2). Noise model validation using real world operations data. *AIAA AVIATION 2021 FORUM*. VIRTUAL EVENT. <https://doi.org/10.2514/6.2021-2136>
- Gabrielian, A., Puranik, T., Bendarkar, M., Kirby, M., & Marvis, D. (2021b). Validation of the aviation environmental design tool's noise model using high fidelity weather. *INTER-NOISE and NOISE-CON Congress and Conference Proceedings*, 263(2), 4810-4822. <https://doi.org/10.3397/IN-2021-2846>
- Giladi, R., and Menachi, E., "Validating Aircraft Noise Models," *Proceedings*, Vol. 59, No. 1, 2020. doi:10.3390/proceedings2020059012, URL <https://www.mdpi.com/2504-3900/59/1/12>.
- Hastings, A. L. (2019). *Traffic Noise Model 3.0 - Technical Manual* (Tech. Rep. FHWA-HEP-20-012). U.S. Department of Transportation, Volpe National Transportation Systems Center.
- Hobbs, C. M., Gurovich, Y. A., Boeker, E., Hasting, A., Rapoza, A., Page, J., Volpe, J. A., Airport Cooperative Research Program, Transportation Research Board, & National Academies of Sciences, Engineering, and Medicine. (2017). *Improving aedt noise modeling of mixed ground surfaces*. Transportation Research Board. <https://doi.org/10.17226/24822>
- Jackson, D. C., Rindfleisch, T. C., and Alonso, J. J., "A System for Measurement and Analysis of Aircraft Noise Impacts," *Engineering Proceedings*, Vol. 13, No. 1, 2021. doi:10.3390/engproc2021013006, URL <https://www.mdpi.com/2673-4591/13/1/6>.
- Juniac, A. (2019). *IATA Annual Review 2018*. <https://www.iata.org/publications/Documents/iata-annual-review-2018.pdf>.
- Lee, H., Madar, S., Sairam, S., Puranik, T. G., Payan, A. P., Kirby, M., Pinon, O. J., & Mavris, D. N. (2020). Critical parameter identification for safety events in commercial aviation using machine learning. *Aerospace*, 7(6), 73. <https://doi.org/10.3390/aerospace7060073>
- LeVine, M. J., Bernardo, J. E., Pfaender, H., Kirby, M., & Mavris, D. N. (2019). Demonstration of a framework for comparing aviation environmental impact mitigation strategies. *Journal of Aircraft*, 56(3), 1116-1125. <https://doi.org/10.2514/1.C035170>
- LeVine, M. J., Lim, D., Li, Y., Kirby, M., & Mavris, D. N. (2019). Quantification of error for rapid fleet-level noise computation model assumptions. *Journal of Aircraft*, 56(4), 1689-1696. <https://doi.org/10.2514/1.C035169>
- Lim, D., Behere, A., Jin, Y.-C. D., Li, Y., Kirby, M., Gao, Z., & Mavris, D. N. (2020, January 6). Improved noise abatement departure procedure modeling for aviation environmental impact assessment. *AIAA Scitech 2020 Forum*. AIAA Scitech 2020 Forum, Orlando, FL. <https://doi.org/10.2514/6.2020-1730>
- Mavris, D., Kirby, M., Lim, D., Li, Y., Pfaender, H., Levine, M., Brooks, J., Behere, A., Gao, Z., Chan Jin, Y., & Kim, J. (2018). *Project 045 Takeoff/Climb Analysis to Support AEDT APM Development* (Tech. Rep. ACRP 02-79). ASCENT.
- Mavris, D. (2019). *Project 043 Noise Power Distance Re-Evaluation*. <https://s3.wp.wsu.edu/uploads/sites/2479/2020/05/ASCENT-Project-043-2019-Annual-Report.pdf>, last accessed 14 June 2020.
- Mavris, D. N. and Sparrow, V. W. (2022). Project 062 Noise Model Validation for AEDT, 2022 Annual Report. <https://s3.wp.wsu.edu/uploads/sites/2479/2023/06/ASCENT-Project-062-2022-Annual-Report.pdf>, last accessed 13th Nov 2023.
- Monteiro, D. J., Prem, S., Kirby, M., & Mavris, D. N. (2018, January 8). React: A rapid environmental impact on airport community tradeoff environment. *2018 AIAA Aerospace Sciences Meeting*. 2018 AIAA Aerospace Sciences Meeting, Kissimmee, Florida. <https://doi.org/10.2514/6.2018-0263>
- Page, J. A., Hobbs, C. M., Plotkin, K. J., & Stusnick, E. (2000). *Validation of aircraft noise prediction models at low levels of exposure* (NASA/CR-2000-210112). NASA. <https://ntrs.nasa.gov/api/citations/20000068518/downloads/20000068518.pdf>



- Plotkin, K. J., Page, J. A., Gurovich, Y., Hobbs, C. M., et al. (2013). *Detailed weather and terrain analysis for aircraft noise modeling*. John A. Volpe National Transportation Systems Center (US).
- Puranik, T. G., & Mavris, D. N. (2018). Anomaly detection in general-aviation operations using energy metrics and flight-data records. *Journal of Aerospace Information Systems*, 15(1), 22-36. <https://doi.org/10.2514/1.1010582>
- Salgueiro, S., Thomas, J., Li, C., & Hansman, R. J. (2021, January 11). Operational noise abatement through control of climb profile on departure. *AIAA Scitech 2021 Forum*. AIAA Scitech 2021 Forum, VIRTUAL EVENT. <https://doi.org/10.2514/6.2021-0007>
- SFO. (n.d.). *Webtrak*. <https://webtrak.emsbk.com/sfo13>
- Shaw, E., and Sparrow, V., "Modeling acoustic impedance and atmospheric absorption around airports using high-fidelity weather data," INTER-NOISE and NOISE-CON Congress and Conference Proceedings, Vol. 264, Institute of Noise Control Engineering, 2022, pp. 104-110. doi:10.3397/NC-2022-698.
- Suder, K. (2012, July 30). Overview of the NASA environmentally responsible aviation project's propulsion technology portfolio. *48th AIAA/ASME/SAE/ASEE Joint Propulsion Conference & Exhibit*. 48th AIAA/ASME/SAE/ASEE Joint Propulsion Conference & Exhibit, Atlanta, Georgia. <https://doi.org/10.2514/6.2012-4038>
- Thomas, J. L., & Hansman, R. J. (2019). Framework for analyzing aircraft community noise impacts of advanced operational flight procedures. *Journal of Aircraft*, 56(4), 1407-1417. <https://doi.org/10.2514/1.C035100>
- Yu, A., & Hansman, R. J. (2019, June 17). Approach for representing the aircraft noise impacts of concentrated flight tracks. *AIAA Aviation 2019 Forum*. AIAA Aviation 2019 Forum, Dallas, Texas. <https://doi.org/10.2514/6.2019-3186>

Task 2 - Assessing the Use of High-fidelity Meteorological Data in AEDT Noise Calculations

The Pennsylvania State University

Objective

One challenge in validating aircraft noise models is knowing the state of the atmosphere during field tests. In collaboration with our industrial partner Spire Global (<http://www.spire.com/>), the PSU team is providing relevant high-fidelity meteorological data to support the AEDT noise model validation work being conducted by Georgia Tech. At present, the AEDT noise model uses high-fidelity meteorological data only for performance calculations. For noise calculations, AEDT does not use high-fidelity meteorological data directly (e.g., when calculating the acoustic impedance adjustment or the atmospheric absorption adjustment). As an exploratory step, PSU is investigating the possibility of incorporating high-fidelity meteorological data in AEDT noise calculations without modifying the noise model in AEDT. PSU is also investigating the influence of AEDT's atmospheric absorption and acoustic impedance adjustments in noise calculations if they were a function of high-fidelity weather. The ultimate goal is to suggest enhancements to AEDT that will enhance the predictive capability of AEDT's noise calculations with respect to real-world measurement data.

Research Approach

AEDT's noise model currently assumes homogeneous weather conditions for noise calculations. The weather conditions used in noise calculations are typically ground-based measurements, such as the airport weather (typically an annual average). Although real-world weather is known to rarely be homogeneous, the impact of meteorological inhomogeneity on AEDT's noise calculations must be investigated to determine whether it substantially affects AEDT's noise prediction capabilities. One possibility of incorporating high-fidelity weather data in AEDT's noise calculations is to explore the use of averages of meteorological variables (such as temperature and humidity) based on high-fidelity meteorological data. If this approach leads to a noticeable improvement in AEDT's noise calculations, it could enable AEDT's noise calculations to be improved without changing the existing integrated noise model in AEDT. To explore this possibility, the PSU team is working with real-world flight and noise measurement data provided by Georgia Tech for flights departing from SFO and Washington Dulles International Airport (IAD). The aircraft tracking data and performance results from AEDT (provided by Georgia Tech) are used by PSU in its in-house ray-tracing code to predict noise levels near the ground. Last year's work (Sparrow et al., 2022) demonstrated confidence in the in-house ray-tracing code by comparing in-house predictions with AEDT noise results for a Boeing 737-800 flight departing from SFO. For this year's work, the in-house ray-tracing code is being used to incorporate meteorological inhomogeneity in noise predictions and assess if it would be sufficient to rely on an appropriate average based on the layered (inhomogeneous) meteorological profiles when predicting noise levels on the ground. In parallel, PSU has continued the efforts to gain a deeper understanding of the AEDT noise calculations. Last year, PSU assessed the impact of high-fidelity weather on AEDT's acoustic impedance adjustment. This year's focus has been to understand the impact of high-fidelity weather on AEDT's atmospheric absorption adjustment.

Aircraft trajectory and locations of noise monitors

The Georgia Tech team has provided the flight tracking data for a departing Boeing 737-800 from SFO (anonymized flight ID: GT786D). Figure 19 shows the aircraft track associated with the flight and a color scale showing flight altitude above mean sea level. The region marked by a dash-dotted blue line is shown in detail to draw attention to the nine noise monitoring stations around SFO.

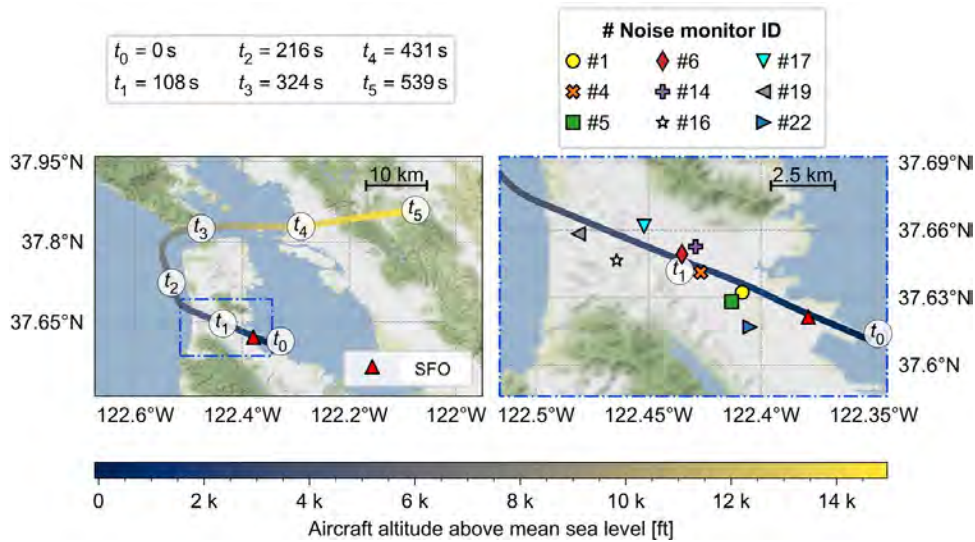


Figure 19. Aircraft trajectory and locations of noise monitors around San Francisco International airport (SFO) (anonymized flight ID: GT786D).

The noise monitor data available for this flight do not include the time history of the received noise but only the L_{max} (A-weighted maximum sound level) and the SEL (A-weighted sound exposure level). The data for this flight are used for conducting numerical experiments using an acoustic ray-tracing code developed in-house to predict noise levels at the noise monitor locations.

Comparison of meteorological conditions (Spire Global data vs AEDT’s default annual airport weather)

Meteorological conditions play an important role in correctly modeling noise propagation. Specifically, the temperature and humidity conditions play a critical role because they affect the propagation path as well as the atmospheric absorption. For the event under investigation, Figure 20 shows the relevant temperature and specific humidity profiles. In Figure 20, the inhomogeneous meteorological profiles obtained near SFO from the Spire Global data are shown with a black line. As indicated in Figure 19, the portion of the flight relevant for the noise measurements involves aircraft altitudes less than 2 km. Hence, an average of the Spire Global data over all heights from 0 to 2 km is an important abstraction of interest (shown with a dash-dotted blue line in Figure 20). Finally, the airport weather data for SFO, as given in AEDT, are shown with a dashed red line in Figure 20. Clearly, the annual average airport weather (as given in AEDT) will not always accurately represent the meteorological conditions for a specific event; therefore, ideally, the inhomogeneous data shown by the black line (Spire Global data) in Figure 20 would be used. Modifying the existing integrated noise model in AEDT to include inhomogeneous meteorological data for noise calculations will be challenging. Instead, if using average weather conditions based on the inhomogeneous data (dash-dotted blue line in Figure 20) satisfactorily improves the noise predictions (compared with annual average weather), this change in AEDT would be easier to implement. To investigate this possibility, the PSU team first set out to try to mimic AEDT’s noise model by modifying a general-purpose acoustic ray-tracing code developed in-house. Last year’s efforts by PSU successfully validated the in-house code. This year’s work shows progress toward assessing the use of averages based on the high-fidelity weather data as an input to AEDT noise model instead of using ground-based weather measurements.

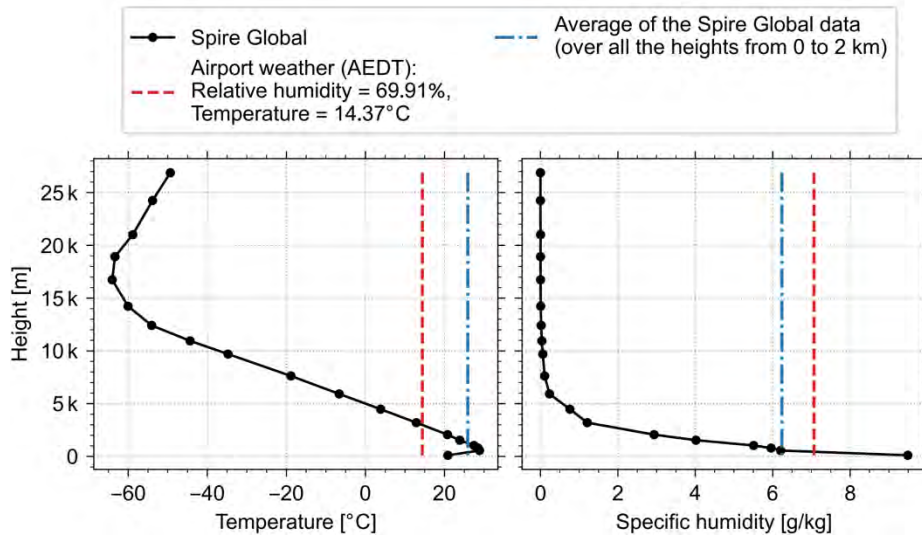


Figure 20. Comparison of the temperature and specific humidity profiles from AEDT and Spire Global data for flight GT786-D. AEDT, Aviation Environmental Design Tool.

Overview of PSU’s in-house noise calculations and an attempt to include meteorological inhomogeneity

PSU’s validated in-house code includes thrust-dependent source levels based on the time history of thrust values obtained from AEDT’s performance report (provided by the Georgia Tech team). The thrust levels are used with the spectral class data and the NPD tables from AEDT to obtain the correct source levels. As noted in the AEDT 3d technical manual (Lee, 2021), the NPD data implicitly contain absorption for the reference day conditions, as specified in SAE-AIR-1845 (SAE International, 1995). The source levels used in the in-house code have been extracted from the NPD data by carefully removing the built-in atmospheric absorption as well as the spherical spreading assumed in the NPD data. The in-house ray-tracing code is then used to propagate the noise to the noise monitors, accounting for the aircraft trajectory and locations of the noise monitors. Atmospheric absorption is then applied according to SAE-ARP-5534 (SAE International, 2013). Because the goal is to be consistent with AEDT, some capabilities of PSU’s in-house code had to be turned off to match AEDT’s results. These include (a) explicitly accounting for moving source effects (Doppler shift and convective amplification); (b) a provision to include the effect of ground impedance; and (c) the ability to use a user-specified aircraft directivity information. Instead, to be consistent with AEDT, the PSU team used the lateral attenuation adjustment, as defined in the AEDT 3d technical manual (Lee, 2021). The lateral attenuation adjustment accounts for ground reflection, refraction, airplane shielding, and engine installation effects. As a first step toward including meteorological inhomogeneity in noise calculations, it makes sense to focus on changing (and potentially improving) the atmospheric absorption used in the noise calculations. While doing this, noise calculations can still rely on assuming straight rays (no refraction), as in AEDT, and use the lateral attenuation adjustment to account for refraction.

Preliminary results showing two ways of including absorption in noise calculations using the Spire Global data

Using the inhomogeneous Spire Global data, two new ways of including absorption in noise calculations are considered. The first case (Case 1) relies on an average of the Spire Global data over all heights from 0 to 2 km. The second case (Case 2) utilizes the layered (inhomogeneous) Spire Global data for calculating the absorption. With noise predictions based on the airport weather as a reference, Figure 21 shows the differences in noise predictions across multiple monitors for both cases of absorption. For all the monitors, the predicted SEL and L_{max} are always lower when using the Spire Global data rather than the annual average airport weather as given in AEDT. The difference in noise predictions obtained using an average of the Spire Global data (Case 1) instead of the layered profile (Case 2) seems to be negligible across all monitors for this flight. From Figure 21, it is evident that calculating absorption based on the Spire Global data (or an alternative source that provides relevant inhomogeneous meteorological profiles) clearly changes the noise predictions by about 1 to 1.5 dB for this flight. To arrive at a statistically significant conclusion, PSU (in collaboration with Georgia Tech) is currently looking at more than 100 noise events that occurred at SFO for the next year’s work. In order to generalize the results and conclusions, the PSU team in collaboration with Georgia Tech is also looking at events from other airports.

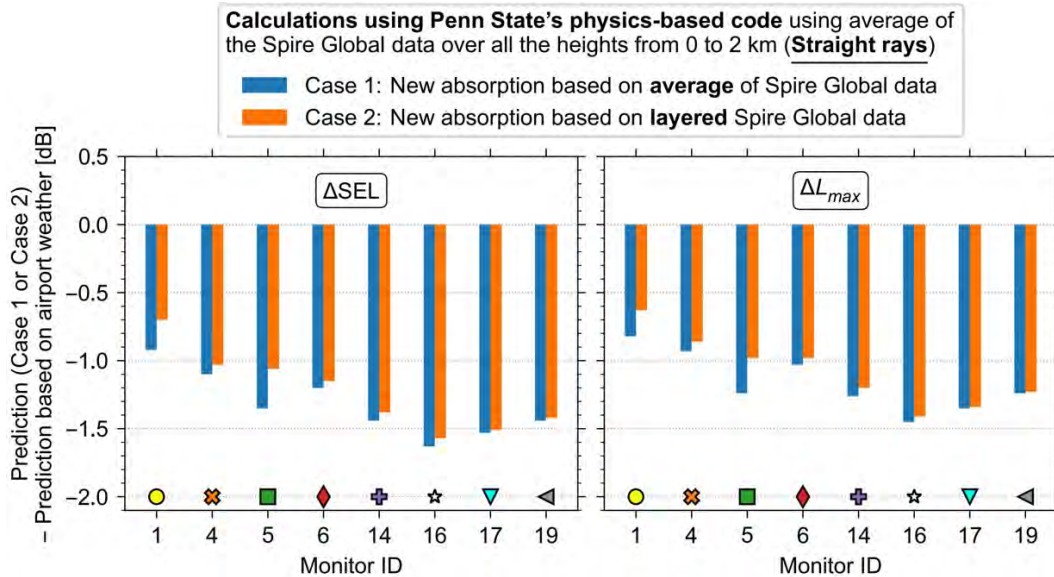


Figure 21. Difference in noise prediction when using new absorption based on Spire Global data instead of using the airport weather. SEL, sound exposure level; L_{max} , maximum A-weighted sound level.

Analyzing a noise event from IAD (in collaboration with Metropolitan Washington Airports Authority)

Until last year, PSU's in-house noise calculations have dealt only with a Boeing 737-800 departing from SFO. To have more confidence in PSU's in-house calculations, this year the team looked at a departing A319-100 aircraft from IAD (aircraft tracking data and AEDT performance outputs provided by Georgia Tech). Figure 22 shows the aircraft track associated with the flight and a color scale showing flight altitude above the mean sea level. The red triangle in Figure 22 shows the location of IAD, and the numbers shown in black are the noise monitors around the airport.

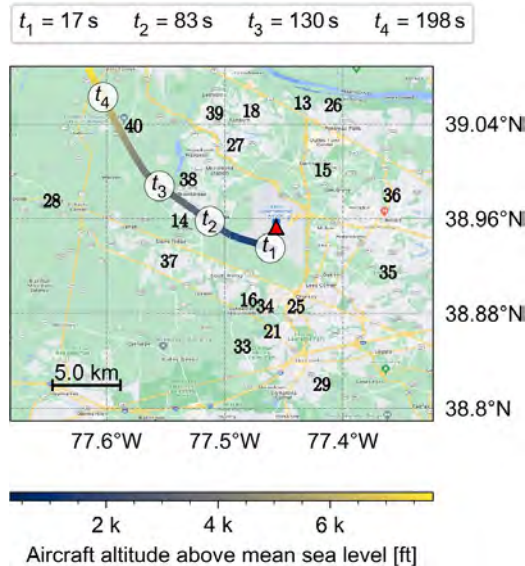


Figure 22. Aircraft trajectory and locations of noise monitors around Washington Dulles International Airport (IAD) (anonymized flight ID: GT-13D).

The Georgia Tech team ran an AEDT study with the FOQA data by using the fixed-point procedural profile and airport weather to provide noise predictions at the noise monitor locations shown in Figure 22. These results were compared with the noise predictions obtained with PSU’s in-house code, assuming homogeneous weather as in AEDT (for IAD). Table 5 shows the difference between the in-house noise predictions and the AEDT noise predictions for the maximum A-weighted sound pressure level (L_{max}) and the A-weighted SEL for the two monitors closest to the aircraft ground track (Monitors 14 and 38). Reassuringly, the noise predictions using PSU’s in-house code, as modified to match AEDT, closely matched AEDT’s prediction. Importantly, the in-house code performs point-to-point (propagation from a point source to a point receiver) calculations, whereas AEDT uses an integrated noise model that calculates noise metrics as an aggregate over multiple segments in flight. This distinction might explain the small differences in noise predictions in Table 5.

Table 5. Difference between the in-house noise predictions (assuming AEDT-like weather) and AEDT’s noise predictions for two monitors (closest to aircraft track) around Washington Dulles International Airport (IAD).

	Monitor ID	
	14	38
ΔL_{max} (dBA)	-0.35	-0.32
ΔSEL (dBA)	0.21	1.02

AEDT, Aviation Environmental Design Tool; SEL, sound exposure level; L_{max} , maximum A-weighted sound level.

Comparison of meteorological conditions (ERA5 data vs AEDT’s default annual airport weather at IAD)

To maintain anonymity of the flight, only the date of the flight is known to PSU, not the exact time of the flight. To deal with this restriction, PSU downloaded meteorological reanalysis data ERA5 (Copernicus Climate Change Service, 2017) provided by the European Centre for Medium-Range Weather Forecasts for the whole day of the flight. ERA5 meteorological data are available for every hour of the day. Figure 23 shows 24 temperature and humidity profiles for each hour of the day of the flight, using colors ranging from yellow-green-dark blue. The annual average airport weather data for IAD, as given in AEDT, are shown with a dashed red line in Figure 23.

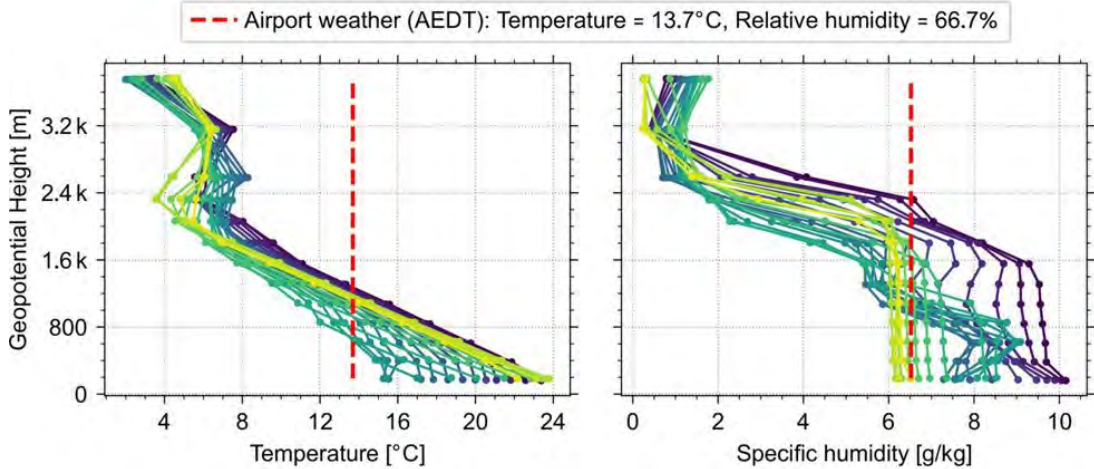


Figure 23. Comparison of Aviation Environmental Design Tool (AEDT) airport weather with 24 hourly profiles obtained using ERA5 data.

Noise predictions for Monitor 38 based on average meteorological conditions over all heights from 0 to 2 km

As shown in Figure 23, the annual average airport weather (as given in AEDT) will not always accurately represent the meteorological conditions for a specific event; therefore, ideally, the inhomogeneous data shown by the yellow/blue/green lines for the hour closest to the noise event would be the best possible input for noise calculations. Because the exact time of the flight/noise event is not known, PSU conducted 24 numerical experiments (representing each hour of the day) using the validated in-house code. For these experiments, average meteorological conditions over all heights from 0 to 2 km were used as inputs. The meteorological averages and the corresponding results have been summarized and shown in

Table 6. The results shown in Table 6 are only for Monitor 38 (shown in Figure 22). Using AEDT’s average annual weather (shown by a dashed red line in Figure 23) with PSU’s in-house code, the SEL and L_{max} predictions are 71.2 and 57.5 dB, respectively. From Table 6, it is evident that the spread of the L_{max} and SEL predictions over 24 hours is within 0.3 dB of the noise predictions obtained using AEDT-like homogeneous conditions. This is due to a coincidence that the AEDT airport weather conditions are similar to the averages obtained using the ERA5 data. Please note that this contrasts with the results shown previously for the flight from SFO. For that flight, utilizing average conditions based on high-fidelity meteorological data led to considerable differences in noise predictions compared to the predictions based on AEDT’s weather. This reiterates the importance of looking at different airports and times of the year before drawing a generalized conclusion about suggesting improvements to AEDT’s absorption calculations.

Table 6. Average meteorological conditions for each hour of the day of flight and corresponding noise predictions.

Hour [GMT]	Average Temperature [° C]	Average Humidity [g/kg]	L_{max} [dB]	SEL [dB]
0	16.5	9.5	57.2	70.8
⋮	⋮	⋮	⋮	⋮
6	14.6	7.3	57.4	71.1
⋮	⋮	⋮	⋮	⋮
12	12.1	7	57.7	71.4
⋮	⋮	⋮	⋮	⋮
18	14.6	6.6	57.3	71.0
⋮	⋮	⋮	⋮	⋮
Minimum	12 ° C	6.1 g/kg	57.1 dB	70.8 dB
Maximum	16.5 ° C	9.5 g/kg	57.7 dB	71.5 dB

GMT, Greenwich Mean Time; L_{max} , maximum A-weighted sound level; SEL, sound exposure level.

Understanding AEDT’s acoustic impedance and atmospheric absorption adjustments

In parallel with the previously mentioned work with the PSU-developed physics-based code, the research team also wanted to determine what parts of AEDT would be most affected by the introduction of high-fidelity weather data. The team quickly realized that both the acoustic impedance adjustment and atmospheric absorption adjustment affect *all* contour calculations in AEDT, and these adjustments are dependent on the meteorological values input to AEDT. After some false starts, the team carefully examined the acoustic impedance adjustment for the SFO cases previously mentioned. As can be seen from Figure 24, it became clear that the acoustic impedance adjustment only affected the overall noise calculations by 0.1 or 0.2 dB for aircraft operating close to the airport, when involved in takeoff or landing operations. The vertical axis of Figure 24 corresponds to the lowest 2 km above the ground. The acoustic impedance adjustment can be larger for higher altitudes and distances further from the airport, but this is not AEDT’s primary function. In summary, acoustic impedance adjustment is not consequentially affected by the meteorological input values.

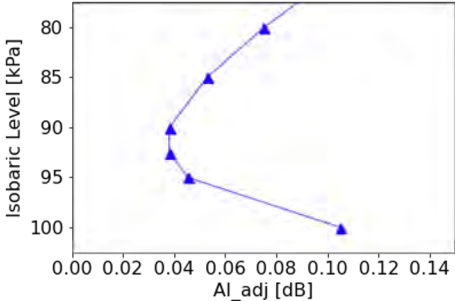


Figure 24. Acoustic impedance adjustment (AI_{adj}) directly above San Francisco International Airport (SFO). The vertical axis corresponds to the first 2 km of altitude above the ground.

On the other hand, the atmospheric absorption adjustment is a function of humidity, unlike that of the acoustic impedance adjustment. An example humidity profile is given in Figure 25, where again the vertical axis corresponds to the lowest 2 km of the atmosphere; note the strong dependence on humidity with height. When calculating the atmospheric absorption adjustment (see the AEDT Technical Manual) using such a varying humidity, the atmospheric absorption can change substantially with height. An example plot showing atmospheric absorption adjustment versus NPD distances for an SFO departure event is given in Figure 26, and a similar plot for an SFO arrival event is shown in Figure 27. The circles (blue) give the atmospheric absorption adjustment using surface weather values, and the triangles (red) give the adjustment using meteorological values averaged over the lowest 2 km. The difference between the two curves is on the order of 1 to 2 dB, depending on the NPD distance. Hence, the atmospheric absorption coefficient is substantially affected by the humidity profile. It is interesting to see that the level differences in Figure 26 and Figure 27 between surface weather values and the values averaged over the lowest 2 km are on the same order as the level differences (bar lengths) seen in Figure 21 when comparing the PSU physics-based model using homogeneous (AEDT default) weather to the cases of either layered or average weather profiles. Therefore, there are some reasons to believe that including humidity profiles in the atmospheric absorption adjustment calculation could help AEDT predict noise levels more accurately. This should be investigated thoroughly.

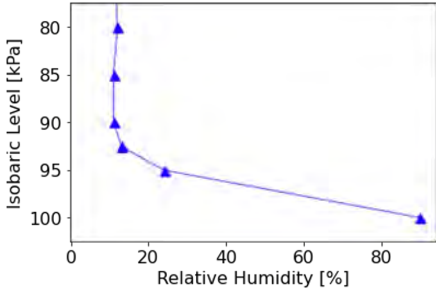


Figure 25. Example relative humidity profile. The vertical axis corresponds to the first 2 km of altitude above the ground.

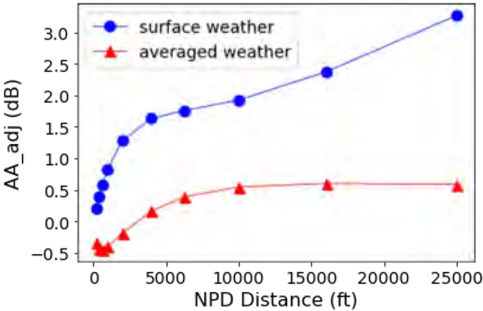


Figure 26. Atmospheric absorption adjustment (AA_{adj}) for an example departure event. NPD, noise-power-distance.

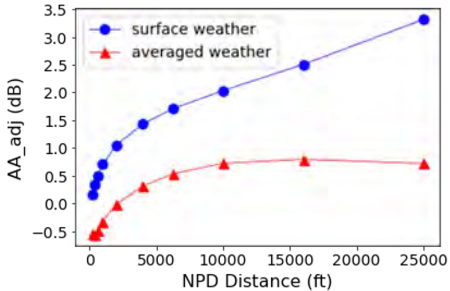


Figure 27. Atmospheric absorption adjustment (AA_{adj}) for an example arrival event. NPD, noise-power-distance.



Milestones

None.

Major Accomplishments

PSU accomplishments

- Using PSU's validated in-house ray-tracing code, two ways of including absorption based on inhomogeneous Spire Global data in noise calculations were examined. The noise predictions using atmospheric absorption based on a layered meteorological profile did not seem to differ significantly from predictions obtained using an average based on the inhomogeneous meteorological profile. Importantly, calculating absorption based on the Spire Global data did make a significant difference to predictions compared to using AEDT's annual airport weather (at least for the flight and day examined). As a contrast, noise predictions for a flight at a different airport - IAD (and on a different day) did not change significantly when using average meteorological conditions based on inhomogeneous meteorological conditions for the day of flight and AEDT's average annual airport weather.
- Concerning AEDT, it was determined that the atmospheric absorption adjustment is substantially affected by the humidity profile. This merits further research.
- The conclusions drawn based on PSU's preliminary results are consistent with the previous work by Plotkin et al. (2013) who had similar findings; i.e., using an appropriate average based on inhomogeneous meteorological profiles can improve noise predictions instead of relying on homogeneous annual average weather.

Publications

Emma Shaw, "Using high-fidelity weather data to improve impedance and absorption adjustment values in airport noise level predictions," M.S. Thesis (Graduate Program in Acoustics, The Pennsylvania State University, 2023). This reference is open access and available online at <https://etda.libraries.psu.edu/catalog/19976eas6228>.

Outreach Efforts

Attended biweekly calls with the FAA and Georgia Tech, and participated in semiannual ASCENT meetings.

Awards

None.

Student Involvement

PSU graduate research assistants: Harshal Patankar and Emma Shaw.

Harshal Patankar worked on PSU's physics-based in-house noise calculations and analyzing real-world aircraft noise events near SFO and IAD using high-fidelity weather (obtained from Spire Global and ERA5). Emma Shaw worked on examining the impact of high-fidelity weather (specifically the humidity profile) on AEDT's atmospheric absorption adjustment.

Plans for Next Period

In the next period, PSU plans to

- Continue to support the Georgia Tech team, consider the differences in AEDT noise predictions with and without high-fidelity weather, and assess whether updating the atmospheric absorption and acoustic impedance adjustments with high-fidelity weather will have a noticeable effect on AEDT noise predictions.
- Assess the use of averages based on the high-fidelity weather data as an input to the AEDT noise model instead of using ground-based weather measurements for a larger number (>100) of events at SFO and other airports spread throughout a year to cover all seasons.
- Advance understanding of the acoustic impedance and atmospheric adjustments used in AEDT noise predictions.
- Continue working with the Washington Metropolitan Airports Authority and other airports, as needed, to support ongoing and future AEDT noise validation efforts in conjunction with Georgia Tech, as advised by the FAA.
- Provide the relevant high-fidelity meteorological data to support the AEDT noise model validation work being conducted by Georgia Tech using high-fidelity meteorological data (obtained by PSU either through collaboration with Spire Global [www.spire.com] or from alternative sources if needed), as demonstrated in the ASCENT Project 062 annual report in 2021 (Sparrow et al., 2021).



Special Acknowledgments

The contributions to ASCENT Project 62 by industrial partners Spire Global and Metropolitan Washington Airports Authority were incredibly important for this project. We gratefully acknowledge their essential and exemplary support to the PSU research efforts described here.

References

- A-21 Aircraft Noise Measure Noise Aviation Emission Modeling. (n.d.). *Procedure for the calculation of airplane noise in the vicinity of airports*. SAE International. <https://doi.org/10.4271/AIR1845A>
- Copernicus Climate Change Service (C3S) (2017): ERA5: Fifth generation of ECMWF atmospheric reanalyses of the global climate. Copernicus Climate Change Service Climate Data Store (CDS), Accessed in February/March 2022. <https://cds.climate.copernicus.eu/cdsapp#!/home>
- Lee, Cynthia, et al. (2021). *AEDT Version 3d* [Technical Manual] (No. DOT-VNTSC-FAA-21-06). United States Department of Transportation. Federal Aviation Administration.
- Plotkin, K. J., Page, J. A., Gurovich, Y., & Hobbs, C. M. (2013). *Detailed weather and terrain analysis for aircraft noise modeling* (No. Wyle Report 13-01). John A. Volpe National Transportation Systems Center (US).
- SAE International. (2013). *Committee A-21, Aircraft Noise, Application of Pure-Tone Atmospheric Absorption Losses to One-Third Octave-Band Data, Aerospace Information* (Report No. 5534).
- Sparrow, et al. (2021). *ASCENT Project 062 2021 Annual Report*. FAA, Washington, DC. <https://s3.wp.wsu.edu/uploads/sites/2479/2022/10/ASCENT-Project-062-2021-Annual-Report.pdf>.
- Sparrow, et al. (2022). *ASCENT Project 062 2022 Annual Report*. FAA, Washington, DC. <https://s3.wp.wsu.edu/uploads/sites/2479/2023/06/ASCENT-Project-062-2022-Annual-Report.pdf>.



Project 064 Alternative Design Configurations to Meet Future Demand

Georgia Institute of Technology

Project Lead Investigator

Prof. Dimitri N. Mavris
Director, Aerospace Systems Design Laboratory
School of Aerospace Engineering
Georgia Institute of Technology
Atlanta, GA 30332-0150
404-894-1557
dimitri.mavris@ae.gatech.edu

Dr. Michelle Kirby
Chief, Civil Aviation Division
Aerospace Systems Design Laboratory
School of Aerospace Engineering
Georgia Institute of Technology
Atlanta, GA 30332-0150
404-385-2780
michelle.kirby@ae.gatech.edu

University Participants

Georgia Institute of Technology

- P.I.s: Dr. Dimitri N. Mavris and Dr. Michelle Kirby
- FAA Award Number: 13-C-AJFE-GIT-062
- Period of Performance: June 5, 2020 to September 24, 2023
- Tasks:
 1. Improvement of Advanced Concept Aircraft (ACA) representation in the International Civil Aviation Organization (ICAO) Committee on Aviation Environmental Protection (CAEP) Modeling and Databases Group (MDG)/Forecasting and Economic Analysis Support Group (FESG) models
 2. Alternative design approaches to meet demand
 3. Exploring physics-based boundaries of the possible

Project Funding Level

The FAA provided \$500,000 in funding, and Georgia Institute of Technology (Georgia Tech) has agreed to a total of \$500,000 in matching funds. This total includes salaries for the project director, research engineers, and graduate research assistants, as well as funds for computing, financial, and administrative support, including meeting arrangements. The institute has also agreed to provide tuition remission for the students, paid from state funds.

Investigation Team

Prof. Dimitri Mavris, (P.I.), All Tasks
Dr. Michelle Kirby, (co-P.I.), All Tasks
Dr. Jon Gladin, (technical lead), All Tasks
Dr. Yu Cai, (technical lead), All Tasks
Dr. Jiacheng Xie, (technical lead), All Tasks
Mr. Tuna Ergan, (graduate student researcher), Tasks 1 and 3



Mr. Dev Patel, (graduate student researcher), Tasks 1 and 3
Mr. Kunal Bavikar, (graduate student researcher), Tasks 1 and 3
Ms. Emmanuella Okonkwo, (graduate student researcher), Task 2
Ms. Akshiti Parashar, (graduate student researcher), Task 2
Ms. Bezayit Urgessa, (graduate student researcher), Task 3

Project Overview

The purpose of this ASCENT project is to improve upon the modeling approach used in the first 2 years of research and to provide insights or recommendations to the MDG regarding a more realistic approach to modeling ACA at the fleet level. In addition, the project will address alternative means of designing aircraft beyond the usual adoption of technologies with the payload and range capability of the existing fleet.

Task 1 - Improvement of ACA Representation in MDG/FESG Models

Georgia Institute of Technology

Objective

The traditional approach to modeling future aircraft types in the fleet has been to define a proxy aircraft that the new aircraft entering the fleet will replace, and then establish a change in benefit. Although this process worked for evolutionary aircraft of the past, it does not work for ACAs, which may have markedly different performance behavior from that of conventional aircraft, such as different cruise altitudes and speeds or different range capabilities for the same seat class. To model an ACA within the MDG modeling tools, manufacturers would need to provide the necessary performance, emissions, and noise coefficients defined by SAE AIR 1845 and the Base Aircraft Data (BADAv3). Prior research in this area, specifically for a blended wing body, has shown limitations in the accuracy of these tools in capturing the expected performance. The objective of Task 1 is to investigate potential opportunities for improving how ACAs are modeled within the fleet to benefit current analyses and probable future analyses.

Within Environmental Design Space (EDS), algorithms exist to create the necessary performance, emissions, and noise coefficients needed by MDG's modeling tools. Although the coefficients can be determined, how the ACA actually flies within MDG tools may not be correct, and modifications to the framework may be required. This task will investigate the shortcomings of the MDG tools for ACAs and provide recommendations to the model developers regarding means of improvement or new methods that must be developed.

Research Approach

Step 1

Step 1 is to identify the most likely ACA to enter the fleet in the future. This task includes identification of the potential airframe, propulsion, energy sources, and operational improvements possible for the different seat-class aircraft over time. This step will heavily leverage work performed in the previous 2 years in identifying relevant technologies for future vehicles but will now focus on ACAs. These technologies and concepts may include, but are not limited to, blended wing bodies, truss-braced wings (TBWs), boundary layer ingestion, hybrid-electric propulsion, drop-in and non-drop-in fuels, supersonic aircraft, and cruise speed reductions.

A transonic TBW (TTBW) was selected because substantial research funds have been spent by the U.S. government to develop the theoretical and practical model of the TBW and TTBW aircraft. For the purposes of this task, the TTBW is relevant, because it is a highly efficient "new" airframe, and it has several differences in terms of mission profile concerning a traditional tube and wing design (typically higher altitude). Although it does not use nontraditional fuel sources by definition (even though it could), its configuration is substantially different from that of the conventional tube and wing aircraft.

Step 2

Step 2 is to establish a quantitative model for the ACA using the EDS modeling framework developed by the Georgia Tech Aerospace Systems Design Laboratory. A stable notional TTBW aircraft was modeled and calibrated to closely match the geometry, weight, and performance of the configuration presented in the Subsonic Ultra Green Aircraft Research (SUGAR) phase 3 study by Boeing. This aircraft was selected because this TTBW is expected to be deployed by the year 2035. In the process of calibrating the TTBW aircraft in EDS, geometric parameters, engine parameters, weight distribution, mission

profile, aerodynamic parameters, and performance parameters from the SUGAR report were used as references. Table 1 compares the outputs obtained from EDS and the Boeing SUGAR report.

Table 1. Comparison between the Environmental Design Space (EDS) model and Boeing Subsonic Ultra Green Aircraft Research (SUGAR) report data.

Component	Parameter	Unit	SUGAR Report	EDS Model
Wing	Area	ft ²	1,477.1	1,566.4
	Aspect ratio		19.55	19.56
	Span	in	2,039.3	2,100.5
	Taper ratio		0.35	0.35
	Sweep 25%	°	12.52	20.46
	Dihedral	°	-1.5	-1.5
	Vertical tail	Area	ft ²	292.99
Aspect ratio			0.82	0.82
Span		in	186.6	186.0
Taper ratio			0.8	0.8
Sweep 25%		°	43.5	43.5
Horizontal tail		Area	ft ²	276.94
	Aspect ratio		4.93	4.93
	Span	in	443.3	443.4
	Taper ratio		0.35	0.35
	Sweep 25%	°	31.6	31.6
Fuselage	Width	ft	12.39	12.39
	Depth	ft	13.88	13.88
	Compartment length	ft	93.92	93.92

Step 3

Step 3 is to create the performance, emissions, and noise coefficients needed by MDG’s modeling tools with EDS by using the calibrated ACA model from step 2 to generate Aviation Environmental Design Tool (AEDT) coefficients and obtain noise contours. Input files were generated to be used in the AEDT environment using calibrated TTBW aircraft from EDS. The coefficients generated by EDS were used to create an AEDT Standard Input File (ASIF) by identifying corresponding coefficients necessary to define a new user-defined aircraft within AEDT. A pipeline that converts EDS outputs into AEDT aircraft definition and noise spectral data was established, enabling modeling refinements between the two environments.

This was followed by modeling the TTBW terminal area operations in AEDT to obtain performance, noise, fuel burn, and emissions results of the TTBW departure and arrival profiles as defined by EDS. Departure operations from stage lengths 1 to 6, corresponding to expected takeoff weight for various trip lengths, and arrival operations at stage length 1, corresponding to expected landing weight, were modeled. These operations were modeled at Hartsfield-Jackson Atlanta International Airport (KATL) runway 09L assuming AEDT 10-year average weather conditions to facilitate comparisons.

Full flight operations were also modeled using real-world aircraft trajectories to obtain performance, fuel burn, and emissions results of the TTBW. This was accomplished by using AEDT sensor path modeling, which utilizes BADAv3 to compute aircraft performance during en route operations, given real-world position (latitude, longitude), altitude, and ground speed data. Real-world trajectories were sampled from 2021 Threaded Track data using top routes departing KATL flown by A320neo at

various stage lengths. Figure 1 illustrates the sampled trajectories used in sensor path modeling. Additionally, AEDT A320neo aircraft was modeled as a reference aircraft. This enables comparisons of the TTBW terminal area and full flight results against a similar baseline aircraft already defined in AEDT to identify unexpected behaviors.

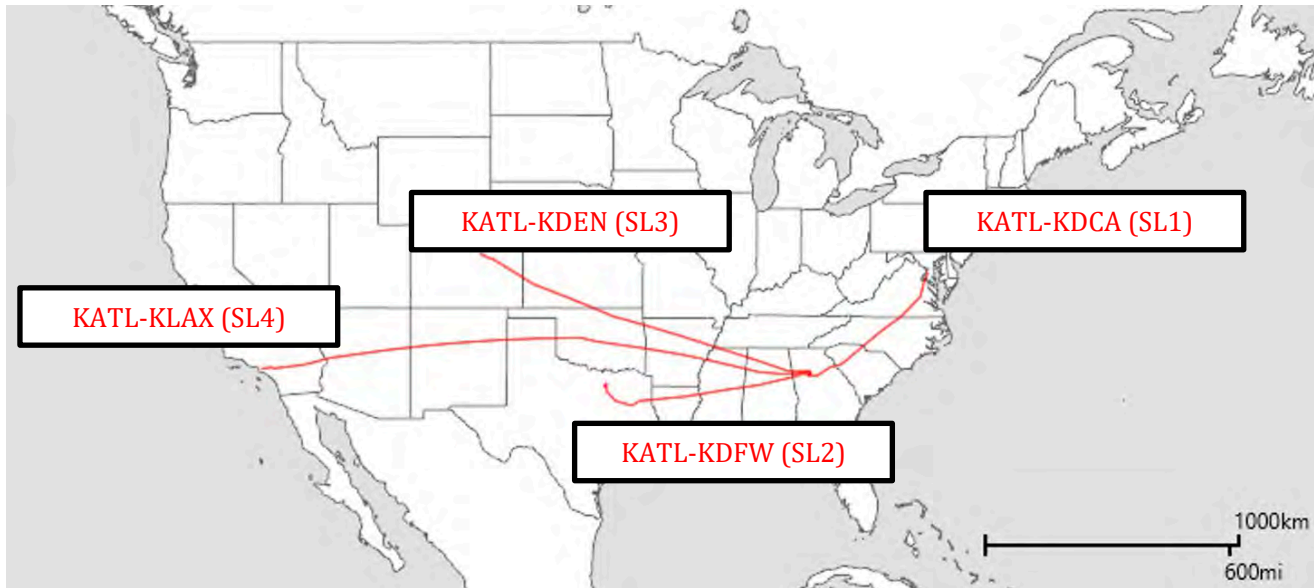


Figure 1. Sampled real-world trajectories for full flight modeling in Aviation Environmental Design Tool (AEDT).

Step 4

Step 4 is to analyze the results from EDS outputs and compare the results against baseline aircraft to validate whether EDS parameters behave as expected in AEDT. This is followed by determining whether gaps exist for modeling ACA within the fleet modeling tools of MDG; and suggesting potential opportunities to improve how ACA is modeled within the fleet to benefit current analyses, as well as probable future analyses. TTBW results were compared against the baseline A320neo aircraft model in AEDT to validate whether EDS parameters behaved as expected in AEDT.

Milestones

- Step 1 has been completed. A TTBW aircraft was selected.
- Step 2 has been completed. A stable notional TTBW aircraft was modeled and calibrated to closely match the configuration presented in the SUGAR phase 3 study by Boeing.
- Step 3 has been completed. A pipeline was established to convert definitions of calibrated TTBW aircraft from the EDS to the AEDT environment. This was followed by modeling the TTBW in AEDT and analyzing the results.
- Step 4 is in progress. TTBW results were compared against the baseline aircraft (AEDT A320neo) to validate whether EDS parameters behaved as expected in AEDT. Most results matched the truth model in EDS and expected trends observed from reference aircraft. A few results deviated from the expected trends observed from reference aircraft, so further analysis and EDS model refinement are being done to yield improved input files for AEDT.

Major Accomplishments

- The team gained an improved understanding of the impact of TTBW aircraft as a potential alternative design by the aircraft manufacturers.
- The team calibrated an EDS model of TTBW aircraft (Boeing SUGAR phase 3) and established a modeling pipeline between EDS and AEDT. Multiple iterations of TTBW have been modeled in AEDT.

Publications

None.

Outreach Efforts

Attended ASCENT biannual meetings.

Awards

None.

Student Involvement

This task involves three graduate students: Kunal Bavikar, Tuna Ergan, and Dev Patel.

Plans for Next Period

- Refine and improve the calibrated model to generate more stable AEDT coefficients for AEDT modeling.
- Perform analysis to determine whether gaps exist for modeling ACAs within fleet modeling tools.

Task 2 - Alternative Design Approaches to Meet Demand

Georgia Institute of Technology

Objective

The objective of Task 2 is to determine the efficiency opportunity if the fleet operates with single-aisle aircraft with a design range closer to that actually flown on a day-to-day basis. That is, how would the aircraft design change if a single-aisle aircraft were sized to be optimal to fly within a continent (1,000–2,000 NM range) and at a slower Mach number (0.72, for example)? To meet the longer-range requirements, a separate single-aisle design could be used for any longer ranges (closer to current single-aisle designs). Shorter ranges and lower aircraft speed requirements open the technology space to the consideration of alternative means of propulsion systems beyond the traditional turbofan engines running on conventional jet fuel. This task will use EDS to redesign a single-aisle aircraft to meet market demand and establish a notional entry-into-service schedule for the fleet and will determine the market-share split within the seat class for how the market share would grow with time. The outcomes will serve as the basis for the MDG fleet modeling tools to quantify the benefit at the fleet level. This task will exercise the connection with MDG tools and improve current modeling practices for goal setting or stringency analysis.

The outcomes of this task are anticipated to include quantification, at the vehicle level, of the benefits and interdependencies of designing an aircraft to a new paradigm, and the implications of that approach in the fleet-level environmental footprint of aviation. Applications of this task include establishing realistic production rates for future designs, modifications to the assumed manufacturing production rates based on historical trends, changes in the market-share assumptions within a seat class or competition bin, and the nonrecurring costs of developing a new aircraft (in lieu of modifying an existing product).

Research Approach

The approach applied for this research task follows that applied in the original long-term aspirational goals (LTAG) ICAO CAEP study, for which Georgia Tech performed the vehicle modeling and assessment tasks in support of the FAA. The vehicle modeling and technology assessment parts are improved to better reflect the impacts of future technologies on engine and aircraft performance. Additional variables are incorporated into the design space to enable evaluating the effects of reducing cruise speed and design range. The major steps applied in this task are shown in Figure 2.

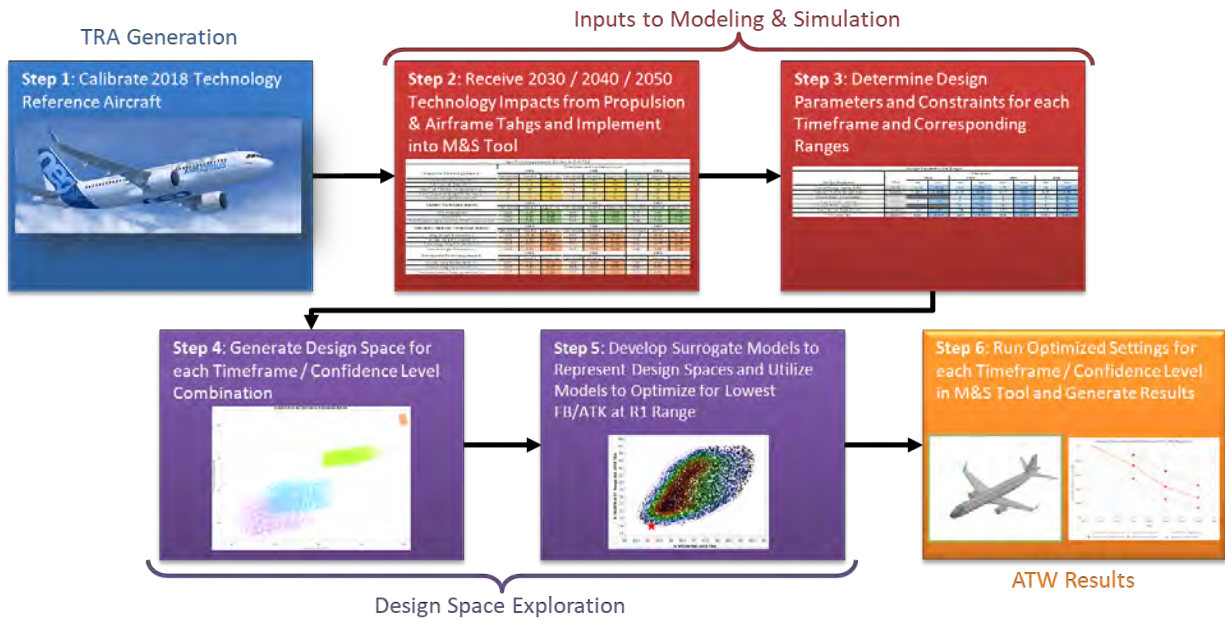


Figure 2. Long-term aspirational goal (LTAG) advanced tube and wing aircraft assessment method.

Part 1: Technology reference aircraft generation

The test case used in this research task is the narrow-body aircraft, while the same alternative design approaches can be used for aircraft in different classes. The A320neo aircraft equipped with the PW-1127G geared turbofan engine was selected as the technology reference aircraft (TRA). A notional A320neo aircraft model was developed in the EDS built upon the 2018 narrow-body TRA model created for the LTAG study. The key updates made to the LTAG aircraft model include the calibrations of the aircraft noise and the takeoff and landing performance. Table 2 outlines key design specifications of the TRA model.

Table 2. Key design specifications of the technology reference aircraft (TRA) model.

Parameter	Unit	Value
Number of passengers	-	153
Design range	NM	3,420
Cruise Mach number	-	0.78
Maximum cruise altitude	ft	41,000
Maximum ramp weight	lb	175,047
Maximum sea-level static thrust	lb	2 × 27,080
Reference wing area	ft ²	1,341
Wing span	ft	112.8
Takeoff field length	ft	6,619
Landing field length	ft	6,512

Part 2: 2035 technology modeling

The alternative design approaches proposed in this research task are considered to be applied to the design of a new aircraft expected to enter into service around 2035. To evaluate the effectiveness of alternative design approaches,



technologies to be matured by 2035 need to be infused into the new design. The 2035 technology impacts applied in this task are identified from the LTAG study and summarized in Table 3. These impacts represent the improvements in key design and performance parameters due to the expected evolution of technology through research and development. The propulsion system of the 2035 design is still the geared turbofan engine but, along with the advanced cycle design, new engine components built on new materials and improved manufacturing process are expected to improve overall engine efficiency and reduce engine weight. The structural technologies mainly include innovative composite materials and their associated manufacturing process to decrease weights of aircraft structural components. The drag reductions introduced by aerodynamic technologies are mainly due to the advanced aerodynamic shape optimization. The values of the technology impact factors shown in Table 3 are determined based on the 2030- and 2040-level technology improvements summarized in the LTAG report. For a conservative estimation, only the moderate confidence of the LTAG technology forecast is utilized.

Table 3. Impacts of 2035 technologies on the technology reference aircraft (TRA) model.

Technology impact	Improvement
Small core efficiency	+13.5%
Core component weight	-3.0%
Propulsor weight	-3.0%
Thrust-specific fuel consumption due to power extraction	-0.525%
Wing weight	-11.85%
Fuselage weight	-8.35%
Empennage weight	-9.52%
Nacelle weight	-6.25%
Viscous drag	-2.38%
Induced drag	-0.175%
Total aerodynamic drag	-2.53%

Aside from the technologies listed above, the reduced cruise speed also opens an opportunity for natural laminar flow (NLF) technology. NLF reduces aircraft skin friction drag by shaping the airfoil to delay the boundary layer transition from laminar to turbulence. When the cruise speed reduces from the transonic to subsonic regime, the wave drag decreases and skin friction drag becomes the dominating factor, so there is a need to decrease skin friction drag for better aerodynamic efficiency. Meanwhile, a lower sweep angle may become feasible as the wave drag decreases, which discourages crossflow instability and benefits the implementation of NLF.

Instead of modeling the skin friction drag reduction due to the NLF as a constant, this research improves the NLF modeling approach of the LTAG study by incorporating additional influencing factors, including the Mach number, Reynolds number, and sweep angle. Specifically, in this task, the NLF is modeled using the flat plate approximation and analyzed using NASA’s aircraft design tool FLOPS. The percentage of the laminar region on the wing surface is computed as the ratio between the transition Reynolds number and the local Reynolds numbers at different spanwise locations. The local Reynolds numbers are computed based on the altitude, Mach number, and local chord lengths, whereas the transition Reynolds number is determined by the leading-edge sweep angle using the crossflow instability and the Tollmien-Schlichting instability theories. The regions enclosed by control surfaces, behind the nacelles, and near the fuselage are assumed turbulent because of large disturbances. Using the new modeling approach, Figure 3 shows the laminar regions on the upper and lower surfaces of the wing when NLF is applied on the TRA model. The aerodynamic analysis performed in FLOPS shows that NLF can increase the cruise lift-to-drag ratio by 6% for the TRA. This improvement is found consistent with data published in preceding literature.

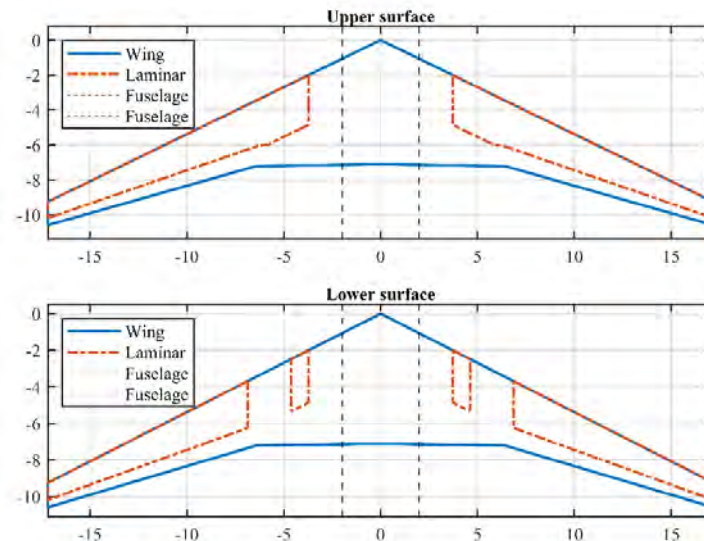


Figure 3. Laminar region induced by natural laminar flow on the technology reference aircraft (TRA) model.

Part 3: Design space exploration

The design space of interest is constructed by the design variables and their associated ranges shown in Table 4. Aside from the variables used in the LTAG study, additional wing geometric parameters are added to the design space to maximum the benefits of reducing cruise speed and design range. The design objective is to minimize the block fuel at the design mission. The constraints considered in the optimization are summarized below:

- Takeoff field length at maximum takeoff weight (MTOW) and sea-level International Standard Atmosphere (ISA) condition no longer than 6,619 ft
- Landing field length at maximum landing weight and sea-level ISA condition no longer than 6,512 ft
- Wing span no longer than 118 ft (Aircraft Design Group III)
- Excess fuel capability at the design mission must be non-negative
- Fan diameter no longer than 86.04 ft
- Core size parameter no smaller than 2.8
- Maximum high-pressure compressor temperature no higher than 1800 R

The first three constraints ensure the new aircraft has the same capability with existing airport facilities as the A320neo. The fan diameter constraint ensures ground clearance of the nacelle. The last two constraints ensure the high-pressure compressor is manufacturable and its operating temperature does not exceed the temperature limit of the material.

To sample the design space, 10,000 design-of-experiment (DoE) cases are generated by applying the Latin hypercube design to the design variables listed in Table 4. These DoE are run through the EDS design environment twice with two settings: one with the NLF model turned off and the other with the NLF model activated. Based on the responses of the sampling cases, surrogate models are established between metrics of interest (i.e., design objective and constraints) and design variables using two-layer neural networks. To ensure that the established surrogate models are sufficiently accurate to replace true functions, multiple validation metrics are evaluated, including R-squared, the root mean squared error, the actual vs. predicted plot, and the residual vs. predicted plot. Using these surrogate models, a set of constrained optimizations are performed to obtain optimal designs at different scenarios, and these designs are then re-evaluated in EDS to determine the fuel burn improvements.



Table 4. Design variables and ranges.

Design variable	Timeframe		
	TRA	2035	
		Minimum	Maximum
Design range (NM)	3,420	1,500	3,420
Cruise Mach number	0.78	0.70	0.80
Thrust-to-weight ratio	0.31	0.28	0.33
Wing loading (lb/ft ²)	131	128	134
Fan pressure ratio	1.52	1.375	1.55
Overall pressure ratio	45.8	41	51
Maximum turbine entry temperature (R)	3,360	3,334	3,519
Wing aspect ratio	9.5	9.0	11.5
Wing taper ratio	0.19	0.15	0.25
Wing average thickness to chord	0.138	0.1	0.14
Wing quarter-chord sweep angle (°)	25.3	15	27

Part 4: Results

Figure 4 illustrates the fuel burn reduction obtained from different sets of constrained optimizations. The blue bars in the waterfall charts represent the design created by resizing the TRA with the 2035 technologies listed in Table 3 infused. This design is assessed at both the design mission (3,420-NM range) and off-design missions (ranges <3,420 NM). The result shows that 2035 technologies (excluding NLF) can reduce the fuel burn by 12% compared to the TRA. The orange bars denote the design generated by not only applying 2035 technologies but also optimizing the engine and airframe design variables listed in Table 4. Note that for these orange bars, the cruise speed and design range remain the same as for the A320neo. The result shows that optimizing engine and airframe can introduce around 10% fuel reduction, in addition to the 2035 technologies at both design and off-design missions. The purple bars represent the design established by reducing cruise speed simultaneously with optimizing engine and airframe. The cruise Mach number is optimized for the block fuel at the design mission and remains constant for all off-design missions. With the cruise speed reduced, the NLF is also assumed to be equipped on the aircraft. It is seen from the purple bars that using NLF at the reduced cruise speed can introduce around 9% fuel burn reduction compared to operating the aircraft at a higher cruise Mach number, and the benefit is more significant as the mission range increases. The five yellow bars at the bottom of the chart denote five designs resized with respect to reduced design ranges. For each design range, the airframe, engine cycle, and cruise speed are also reoptimized. Compared with the aircraft sized for the 3,420-NM design range but operating at shorter ranges, the aircraft directly sized for a shorter range can save the fuel burn up to 3.7% when the design range is reduced to 1,500 NM due to its smaller thrust, weight, and geometric scales.

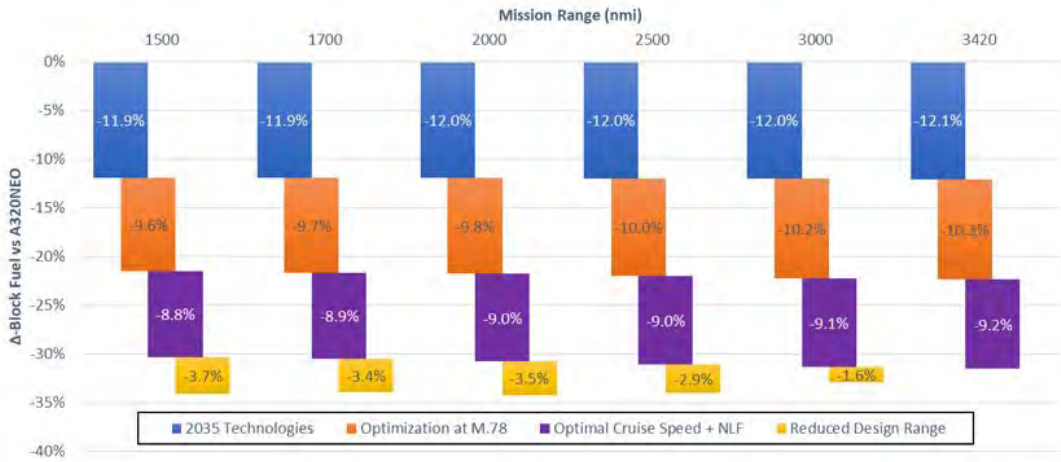


Figure 4. Block fuel reduction compared to the technology reference aircraft (TRA) model. NLF, natural laminar flow.

Figure 5 indicates the optimal cruise Mach number identified when the aircraft equipped with the 2035 technologies is sized at different design ranges. As shown by the blue curve, if NLF is not applied, the optimal cruise speed monotonically decreases with design range. This is because at longer design ranges, the reduced cruise speed decreases the cruise drag and the thrust required, which decreases the fuel flow at cruise, even though the thrust-specific fuel consumption (TSFC) is slightly increased. However, at shorter design ranges, although lower cruise speed can reduce the fuel flow, the block fuel is more sensitive to the block time, which favors a relatively higher cruise speed. In contrast, when NLF is applied, the optimal cruise speed would no longer significantly increase with the decreased design range as the non-NLF case. This is because a higher cruise Mach number prefers a higher sweep angle to minimize the wave drag, which in turn promotes crossflow instability and compromises the effectiveness of NLF.

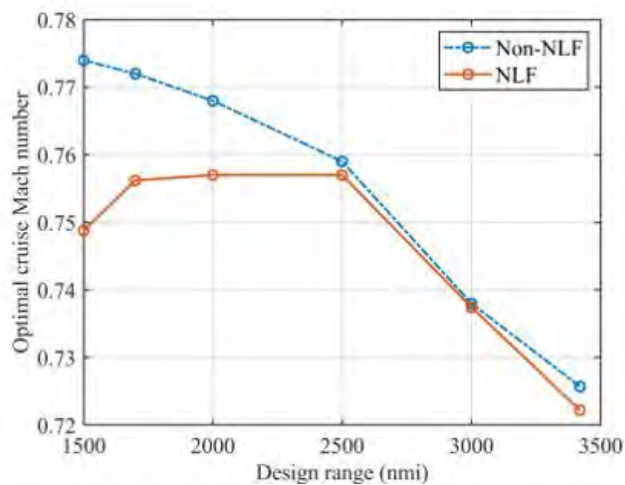


Figure 5. Optimal cruise Mach number for different design ranges. NLF, natural laminar flow.

Figure 6 shows the MTOW reduction of different designs compared to the TRA model. It can be seen that, compared with the A320neo, the 2035 technologies reduce MTOW by 8.2%. With optimization performed on aircraft wing and engine cycle, an extra 1.5% weight reduction can be achieved on the top of the 2035 technologies. If the cruise speed is reduced and NLF applied, the MTOW of the optimal design can realize a 3.6% weight reduction compared with the design optimized for a higher cruise speed. With a constant thrust-to-weight ratio, a lower MTOW implies a lower thrust level required for

takeoff and climb, which in turn may decrease the noise of the aircraft. Further evaluations of aircraft noise will be conducted in future works.

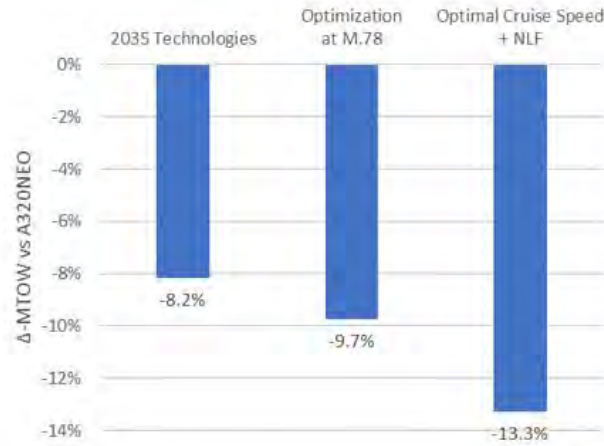


Figure 6. Reduction in maximum takeoff weight (MTOW) compared to the technology reference aircraft (TRA) model. NLF, natural laminar flow.

Milestones

- A TRA model calibrated based on the A320neo aircraft and the PW-1127G engine was established.
- 2035 technologies and their impacts on aircraft and engine characteristics were determined from the LTAG study.
- Literature reviews on the effectiveness and applications of NLF were carried out.
- New NLF modeling approaches considering aircraft geometry and flight condition were developed and integrated into EDS.
- Design variables, objectives, and constraints were formulated.
- DoE cases were generated and run through EDS to sample the design space.
- Surrogate models were established based on DoE cases, on which a set of constrained optimizations were performed to evaluate the benefits of the proposed alternative design approaches.

Major Accomplishments

- Fuel burn and weight reductions benefits introduced by 2035 technologies, airframe and engine optimizations, reduced cruise speed, and reduced design range are evaluated separately.
- Resizing aircraft with 2035 technologies reduces fuel burn by 12% at both design and off-design missions and decreases MTOW by 8.2%.
- Optimizing engine cycle and wing planform brings an additional 10% fuel reduction and 1.5% MTOW reduction, in addition to 2035 technologies.
- Reduced cruise speed and NLF further improve fuel burn by 9% and reduce MTOW by 3.6%.
- Fuel savings achieved by resizing aircraft for shorter design missions are more significant as the design range decreases (about 3.7% at 1,500 NM).

Publications

None.

Outreach Efforts

Attended ASCENT biannual meetings.

Awards

None.



Student Involvement

This task involved two graduate students: Emmanuella Okonkwo and Akshiti Parashar.

Plans for Next Period

- Improve low-speed aerodynamic analysis for takeoff and landing performance assessment.
- Include noise analysis to evaluate the potential noise reduction induced by 2035 technologies, airframe and engine optimizations, and reduced cruise speed.
- Investigate the fuel saving benefit due to the reduced design mission range at the fleet level.
- Evaluate the opportunity to increase payload when sizing aircraft with respect to lower design ranges.

Task 3 - Exploring Physics-based Boundaries of the Possible

Georgia Institute of Technology

Objective

The objective of this task is to examine the physics-based limitations of efficiency for various propulsion architectures considered for future ACA. This type of study is beneficial in that it aids the FAA in understanding the boundaries of the possible, rather than building from a baseline by applying specific individual technologies that benefit efficiency. Depending on any follow-on actions from the LTAG task group analyses, this task may also include the identification of barriers for ACA and their propulsion systems, or additional supporting analysis.

Research Approach

Step 1

Step 1 is to establish a reference aircraft and corresponding engine to use as the benchmark for the task, and to calibrate the selected engine in EDS using appropriate documents. The Airbus A320neo aircraft is selected as the baseline aircraft, and the notional A320neo EDS model developed in Task 2 is utilized in this task.

Step 2

Step 2 is a literature review on the current engine design and expected advancements in engine component technologies. The predicted 2050 narrow-body turbofan engine was established mainly on the basis of two ICAO technical reports: the "ICAO -LTAG - Appendix M3 - Technology sub-group" report and "Independent expert integrated technology goals assessment and review for engines and aircraft." In addition, preceding studies on the following aspects were reviewed when performing the engine design:

- Ceramic matrix composite advancements and understanding the future operating temperatures
- Advancements in turbine cooling flow
- Clearance sensitivity for small core compressors
- Advancements in alloys to support higher operating temperature
- Advancements in bleed-less engine architecture for narrow-body aircraft

Step 3

Step 3 is a literature review on the physical limitations in the performance of the current engine component design and use of Numerical Propulsion System Simulation to incorporate technologies and assumptions and perform component and cyclic efficiency analysis. This step includes the following:

- Investigate the current efficiency level and predicted efficiency level for the future.
- Obtain the current values for cyclic analysis of components of turbofan engine.
- Investigate the predicted maximum values of cyclic parameters for the core of the engine.
- Calibrate the engine to match the underlying assumptions and incorporated technologies.

The following assumptions based on available literature were used for cycle analysis:

- The turbine is assumed to be made of ceramic matrix composite (CMC) to decrease the required cooling.
- Maximum polytropic efficiency of the fan and compressor is 95%.
- Maximum polytropic efficiency of the turbine using cooling is 92%.
- Predicted future operating CMC-based turbine temperature is 1200 °C.
- Weight savings of 66% are achieved through the use of a CMC-based turbine for the turbine module.



- Cabin environment control system is improved, leading to 0.34% TSFC improvement.

To understand and predict the physics-based limitations of the turbofan engine, the cycle parameters were optimized around the values mentioned in the LTAG 2050 low-confidence engine cycle parameters, and the following values were finalized basis the optimization:

- Overall pressure ratio: 57.85
- Fan pressure ratio: 1.466
- Turbine inlet temperature: 3,387 R

The size effects of a small core were considered, and the associated penalty on compressor polytropic efficiency due to small core size was incorporated.

Step 4

Step 4 is to use the calibrated base aircraft engine and apply future technology scenarios to obtain a new model to be used for applying idealized engine parameters and assumptions to obtain a futuristic idealized engine. Using the calibrated base aircraft engine model, a 2050 “practical” ideal turbofan engine model was developed using the assumptions and a few technologies mentioned in steps 2 and 3. A bleed-less engine assumption was added to the 2050 “practical” ideal engine with two cases: (1) with shaft power extraction of 200 HP, and (2) with shaft power extraction of 250 HP. Fuel burn improved by 34.2% with the technologies used for the 2050 turbofan engine model, as shown in Table 5.

Table 5. Fuel burn improvement due to technology infusion and 2050 technology.

Engine Model	Block Fuel (lb)	Improvement
2020 notional A320neo EDS model	34,770	
2050 "practical" ideal engine model with optimization and assumptions discussed in step 3	24,058	30.81%
2050 "practical" ideal bleed-less engine with 250 HPX	23,120	33.51%
2050 "practical" ideal bleed-less engine with 200 HPX	22,896	34.15%

Milestones

- Step 1 has been completed. The Airbus A320neo aircraft was selected as the baseline aircraft and calibrated in EDS.
- Step 2 has been completed. A detailed literature review on expected advancements in engine component technologies was conducted.
- Step 3 has been completed. A stable 2050 timeframe turbofan engine model was developed in EDS, and the design parameters were in the range of values mentioned in the LTAG report for the 2050 timeframe scenario.
- Step 4 has been completed. The 2050 technologies and relevant assumptions, including bleed-less engine, were successfully incorporated into the 2050 turbofan engine model to obtain a new stable 2050 “practical” ideal turbofan engine model.

Major Accomplishments

- The team improved understanding regarding the boundaries of the possible individual technologies to benefit engine efficiency.
- The team created a stable baseline engine and a new stable 2050 “practical” ideal turbofan engine model with 2050 timeframe technologies.
- Fuel burn was improved by 34.2% with the technologies and assumptions used for the 2050 turbofan engine model.

Publications

None.



Outreach Efforts

Attended ASCENT biannual meetings.

Awards

None.

Student Involvement

This task involves four graduate students: Kunal Bavikar, Tuna Ergan, Dev Patel, and Bezayit Urgessa.

Plans for Next Period

- Add additional technologies discussed in Continuous Lower Energy, Emissions and Noise (CLEEN) Program of FAA to the new 2050 “practical” ideal turbofan engine model.



Project 065(A) Fuel Testing Approaches for Rapid Jet Fuel Prescreening

Washington State University

Project Lead Investigator

Joshua Heyne

Bioproducts, Sciences, and Engineering Laboratory Director, Associate Professor

School of Engineering and Applied Science

2710 Crimson Way, Richland, WA 99354

(937) 229-5319

joshua.heyne@wsu.edu

University Participants

Washington State University

- P.I.: Joshua Heyne
- FAA Award Number: 13-C-AJFE-UD, Amendments 026, 031, 034, and 042; 13-C-AJFE-WASU, Amendment 035
- Period of Performance: June 5, 2022 to September 30, 2023
- Tasks:
 1. Prescreen sustainable aviation fuels (SAFs).

Project Funding Level

Amendment No. 026: \$159,998 (June 5, 2020 to June 4, 2021)

Amendment No. 031: \$250,000 (August 11, 2020 to August 10, 2021)

Amendment No. 034: No-cost extension (August 10, 2021 to February 10, 2022)

Amendment No. 042: \$195,000 (June 14, 2022 to June 13, 2023)

Cost share is from the University of Dayton (UD), VUV Analytics, Greenfield Global, and DLR Germany.

Investigation Team

- Prof. Joshua Heyne (P.I.), coordinating all team members (both ASCENT and non-ASCENT efforts) and communicating prescreening results with SAF producers.
- David Bell (PhD student), developing two-dimensional gas chromatography (GCxGC) with vacuum ultraviolet (VUV) detection methods and software.
- Zhibin (Harrison) Yang (PhD student), conducting Tier Alpha prediction and Tier Beta measurements.
- Conor Faulhaber (PhD student), conducting seal swell measurements.

Project Overview

This project focuses on further developing the Tier Alpha and Beta test methods, which can help minimize the fuel volume needed for testing and improve a fuel's potential for meeting ASTM approval criteria. Tier Alpha refers to low-volume analytical testing approaches (i.e., GCxGC, nuclear magnetic resonance, and infrared analytical testing). Tier Beta tests focus on directly assessing the physical and chemical properties of a fuel rather than predicting these properties from GCxGC methods.

Task 1 - Prescreening of Sustainable Aviation Fuels

Washington State University

Objective

The objective of this task is to develop a tiered prescreening process for new alternative jet fuels that uses low fuel volumes and will improve a fuel's potential to meet ASTM approval criteria. This work facilitates the flow of meaningful information to fuel producers when their production processes are at a low technology readiness level while simultaneously strengthening a producer's readiness for the approval process.

Research Approach

Previous annual reports summarized significant progress toward prescreening SAF candidates. The motivation, conceptual application, detailed description, and examples of this effort were described in publications in peer-reviewed journals in the first 18 months of this project. This report documents five additional peer-reviewed journal articles, published between June 5, 2022 and October 1, 2023. Citations for the articles are listed in the *Publications* section below.

- Paper 9: Error quantification of the Arrhenius blending rule for viscosity of hydrocarbon mixtures, R Boehm, F Hauck, Z Yang, CT Wanstall, JS Heyne, *Front. Energy Res.*, 2022
- Paper 10: Limits of identification using VUV spectroscopy applied to C₈H₁₈ isomers isolated by GC×GC, DC Bell, J Feldhausen, AJ Spieles, RC Boehm, JS Heyne, *Talanta*, 124451, 2023
- Paper 11: Maximizing sustainable aviation fuel usage through optimization of distillation cut points and blending, Z Yang, RC Boehm, DC Bell, JS Heyne, *Fuel*, 2023
- Paper 12: Measurements of nitrile rubber absorption of hydrocarbons: Trends for sustainable aviation fuel compatibility, C Faulhaber, C Borland, RC Boehm, JS Heyne, *Energy & Fuels*, 2023
- Paper 13: Quantifying isomeric effects: A key factor in aviation fuel assessment and design, C Hall, D Bell, J Feldhausen, B Rauch, JS Heyne, *Fuel*, 2024

In addition to these articles, the team is currently working on documenting efforts completed between June 1, 2020 and August 30, 2022, which have advanced toward our goal of estimating the impact of fuel composition on elastomer/fuel compatibility.

Summaries

Error quantification of the Arrhenius blending rule for viscosity of hydrocarbon mixtures

<https://doi.org/10.3389/fenrg.2022.10746>

A total of 675 measurements of dynamic viscosity and density have been used to assess the prediction error of the Arrhenius blending rule for the kinematic viscosity of hydrocarbon mixtures. The Arrhenius blending rule for viscosity describes how the viscosity of a mixture of liquids can be calculated from the individual viscosities of the components. This rule posits that the logarithm of a mixture's viscosity is a linear combination of the logarithms of the individual viscosities, weighted by the volume fractions of the components. Major trends within the data show that mixture complexity and temperature are more important determinants of prediction error than differences in molecular size or hydrogen saturation between the mixture components. Over the range evaluated, no correlation to mole fractions was observed, suggesting that the log of viscosity is truly a linear function of mole fraction, as indicated by the Arrhenius blending rule. Mixture complexity and temperature also impact molar volume and its prediction. However, linear regression between the two model errors explains less than 20% of the observed variation, indicating that mixture viscosity and/or molar volume are not linear with respect to temperature and/or mixture complexity.

Although the main factors, namely mole fractions, are adequately captured by the Arrhenius blending rule for viscosity, other less influential factors, such as changes to vacancy distribution, distances between nearest neighbors, and the number percentage and variety of heterogeneous interactions, each have a complex impact on viscosity; thus, it is difficult to refine the model. Moreover, it is difficult to control each of these fundamental drivers independently in an experiment, rendering an empirically driven correction to the Arrhenius blending rule elusive. Nonetheless, sufficient data have been collected to measure the prediction error. This information has been transferred back to the model to enable direct determinations of confidence intervals around subsequent viscosity predictions of any fuel based on its component mole fractions and viscosities. At -40 °C, where all identified components are pure molecules, the modeling error is 0.132 times the predicted (nominal) viscosity times the root mean square of the component mole fractions. At -20 °C, the scalar

decreases to 0.096 as part of a general trend observed here, in which viscosity prediction errors decrease as temperature increases.

Blending rule for kinematic viscosity with estimated model uncertainty

$$\ln(\mu_{mix}) \approx \sum_i x_i * \ln(\mu_i)$$

$$\sigma^2 = (x_A * \xi)^2 + (x_B * \xi)^2 = \xi^2 * \sum_i \bar{c}_i^2 \mid \bar{c}_i = \min(c_i, (1 - c_i))$$

ξ equals 13.2% at -40 °C and 9.6% at -20 °C

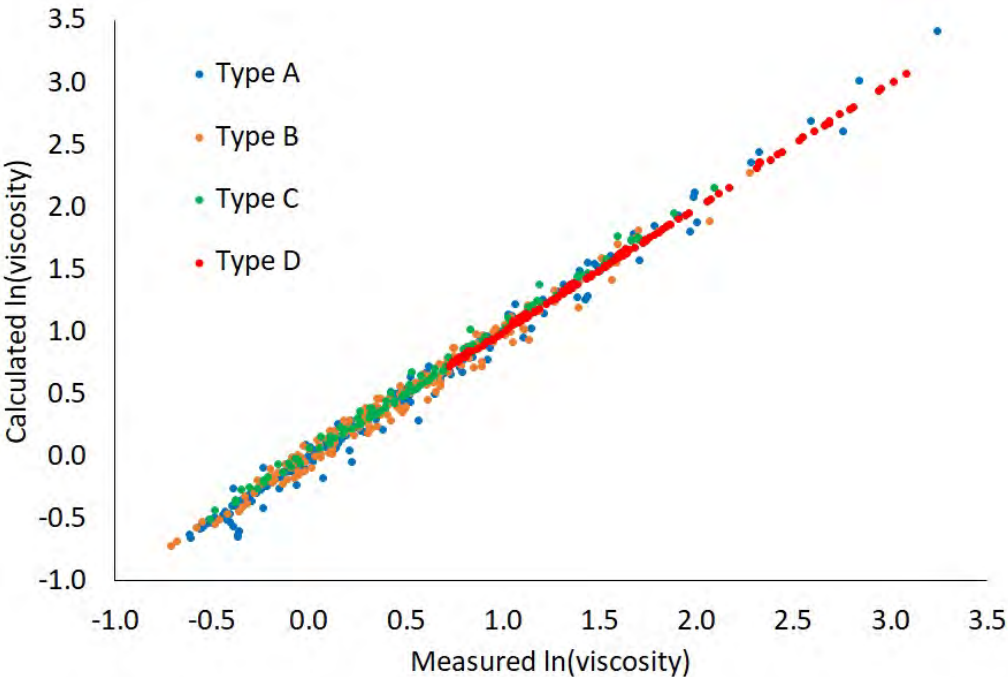


Figure 1. Unity plot. The reference viscosity is 1 cSt. Type A is a binary mixture. Type B is a single component blended with a binary mixture. Type C is a single component blended with a complex fuel, composed of many chemical constituents. Type D is a mixture of two complex fuels.

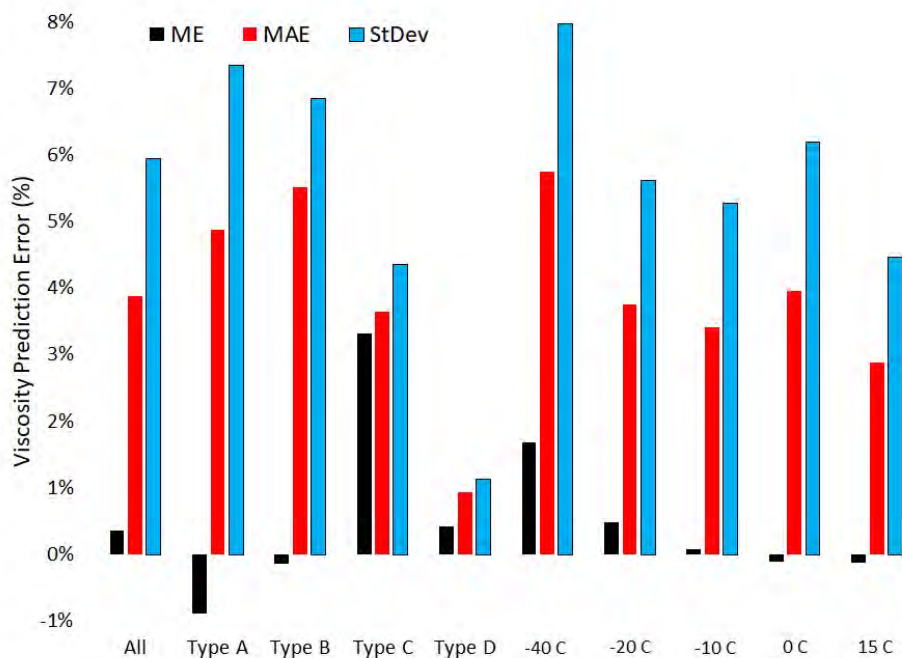


Figure 2. Measures of viscosity prediction error across differing levels of mixture complexity and temperature. Type A is a binary mixture. Type B is a single component blended with a binary mixture. Type C is a single component blended with a complex fuel. Type D is a mixture of two complex fuels. MAE: mean absolute error; ME: mean error; StDev: standard deviation.

Limits of identification using VUV spectroscopy applied to C₈H₁₈ isomers isolated by GC×GC

<https://doi.org/10.1016/j.talanta.2023.124451>

Isomeric-level identification is a challenge for hydrocarbon fuel analysis but one that offers huge scientific and practical implications. The use of a VUV detector in combination with a thorough comparison of each relevant pair of spectra is shown to unambiguously identify C₈H₁₈ isomers to <0.40% mass, without the need for a human in the loop. With a human interpreting residual data, this work demonstrates the ability to make correct identifications to ~0.20% mass. The work shows the tremendous repeatability of such measurements, which enables the confident identification of visibly small differences between two spectra. The combination of GC×GC with a VUV detector enables improved separations as compared with traditional GC-VUV arrangements while also allowing carbon number information to be known prior to VUV spectral matching attempts. The complementary nature of chromatographic elution times with the structural information provided by the VUV detector results in a powerful tool for chemometrics.

Two figures from this manuscript are reproduced below. Figure 3 underscores the challenge of identifying structurally similar alkanes by VUV spectroscopy, whereas Figure 4 underscores the power of the analysis methodology we have developed to assist in making such identifications.

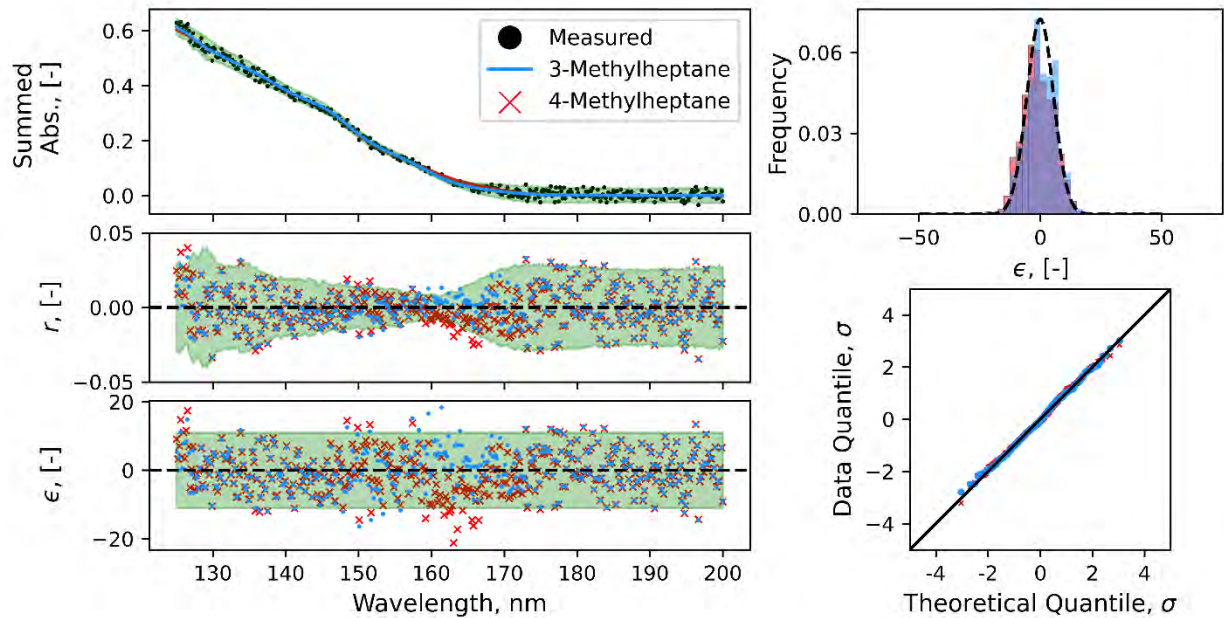


Figure 3. Comparison of vacuum ultraviolet (VUV) residuals of a peak in Jet-A fuel. The two most likely matches, 3-methylheptane and 4-methylheptane, are compared with the measured VUV response. This includes the (top, left) raw data and reference spectra, (middle, left) standard residuals, (bottom, left) residuals normalized based on the noise associated with a particular wavelength, (top, right) noise-adjusted residual histogram, and (bottom, right) quantile-quantile plot testing the normality of the residuals.

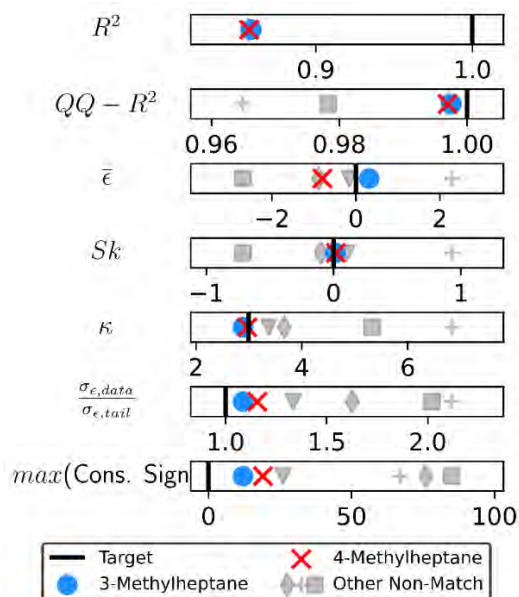


Figure 4. Scorecard for the six most likely matches to the C_8H_{18} peak in Jet-A fuel. The correct match is 3-methylheptane.

Maximizing sustainable aviation fuel usage through optimization of distillation cut points and blending

<https://doi.org/10.1016/j.fuel.2023.129136>

A novel methodology was explored for maximizing the SAF yield from a pathway and the respective blend ratio with conventional jet fuel by varying distillation cut points. This optimization simultaneously considers eight bulk properties to predict the competition of SAF yield and blend limit with conventional jet fuel. This methodology was applied to both a surrogate and an applied practical case. In the surrogate case, ten points along the optimization-generated Pareto front were experimentally validated, demonstrating good agreement. For a practical application of this methodology, this approach achieved 37% more renewable carbon into the SAF fraction and a greater margin to the specification limit as compared with a third party. The effect of conventional jet fuel variance on the blend limit was also investigated, showing a substantial influence on the blend limit. This paper provides a proof of concept that a renewable carbon product stream can be optimized based on the maximum SAF fraction yield and maximum blend ratio with Jet-A fuel. Eventually, this tool should extend the capability to both renewable gasoline and diesel fractions and be able to incorporate techno-economic analysis, life cycle analysis, and contemporary policies for a well-to-wake analysis of different fractions of a full-range product stream (gasoline, SAF, diesel).

Two figures from this manuscript are reproduced below. Figure 5 illustrates the non-linear relationship between the bio-crude distillation cut (SAF yield) and the amount of SAF that can be blended into a particular batch of petroleum-derived fuel without violating any specification limits. Figure 6 underscores the fact that the properties of the target petroleum-derived fuel have a large influence on the proportion of SAF that can be blended into the fuel without violating any specification limits.

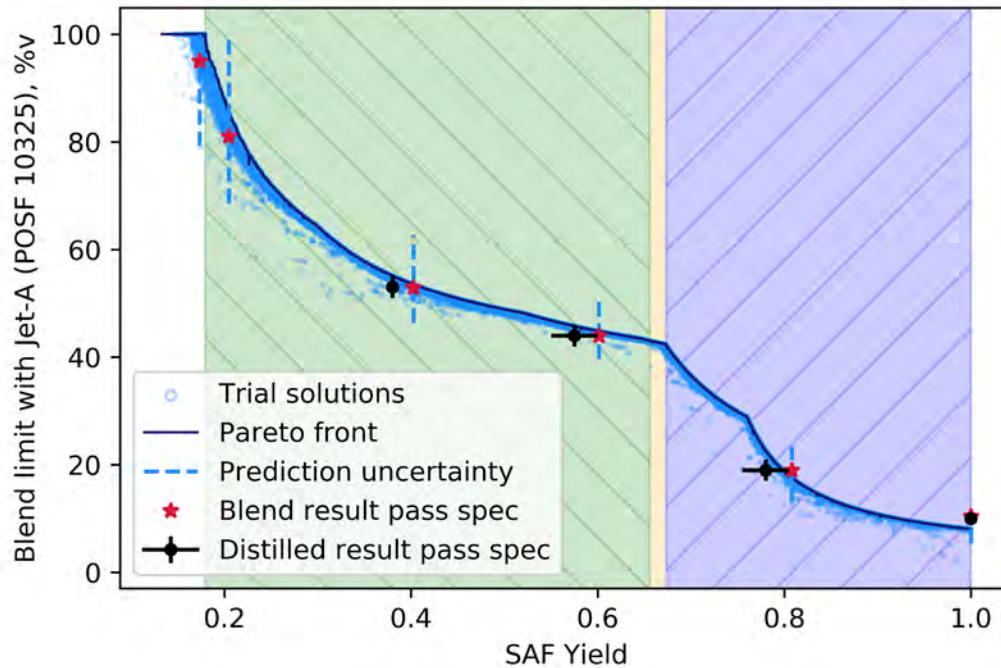


Figure 5. Pareto front from a multi-dimensional optimization of the surrogate product stream described in the manuscript. The blue, yellow, and green shaded regions represent blends limited by flash point, density, and both density and freeze point, respectively. Two types of experimental validation of the Pareto front are shown in black and red markers. SAF: sustainable aviation fuel.

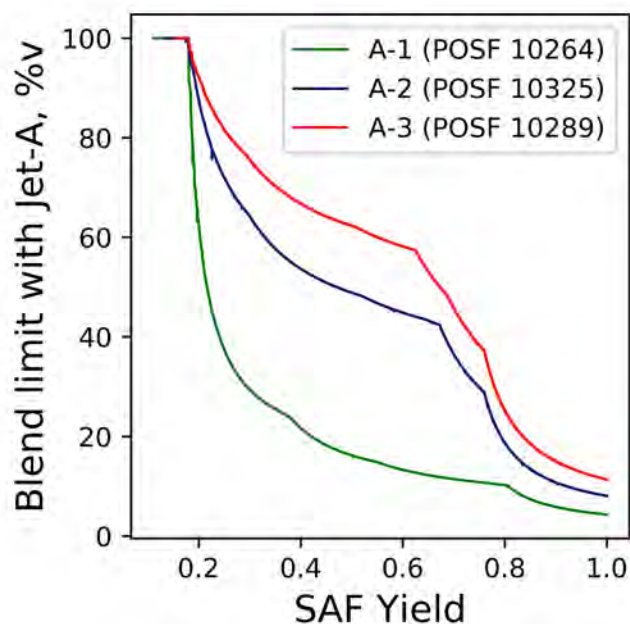


Figure 6. Pareto fronts of reference conventional jet fuels to illustrate the effect of jet fuel variance on the sustainable aviation fuel (SAF) blend limit.

Measurements of nitrile rubber absorption of hydrocarbons: Trends for sustainable aviation fuel compatibility
<https://doi.org/10.1021/acs.energyfuels.3c00781>

Because of the difficulty associated with large-scale material changes in aircraft, the advancement of “drop-in” SAF relies heavily on the compatibility of fuels with nitrile rubber O-ring swelling. The present work addresses this issue through the investigation of fuel compositional and molecular property relationships with optical dilatometry measurements of nitrile rubber O-ring swelling for 56 total solvents, including 39 neat molecules doped in an approved synthetic paraffinic kerosene SAF, 14 conventional fuels, and 3 SAF blend components. Swell measurements for neat molecules doped at 8%v in an approved synthetic paraffinic kerosene SAF, Gevo C-1, exhibited consistency with literature trends of molar volume and dopant hydrocarbon class. These tests also revealed a relationship between O-ring swelling and density that showed more linearity than the previous correlation with molar volume across hydrocarbon classes, except for polycycloalkanes, which illustrate a need for more swell-property relationship investigations of this type. Similar linearity was also observed with density for blends of conventional fuels and SAF.

Figure 7 shows converged O-ring swelling plotted for a variety of dopant/C-1 mixtures, in addition to intermediate O-ring swelling at 1-, 3-, 7-, and 10-day timesteps when available. The results for each timestep are characterized by a linear trendline with a reported coefficient of determination (R^2) to evaluate changes over the duration of the swelling process. The results for tetralin and 2-ethylnaphthalene at 25%v and 40%v are excluded because their extremely high swell is far off the scale used here to highlight differences between data taken at different time intervals. All linear trendlines resulted in an R^2 of 0.919 or higher, corroborating the linear blending rule. The representative cycloalkane for this study, n-butylcyclohexane, produced a noticeably lower R^2 value compared with the aromatics studied. A possible reason for this result is the larger relative uncertainty inherent in the swell tests of molecules exhibiting lower swell, which will require a more thorough assessment for a large number of species and concentrations outside the scope of this study. In light of this finding, a linear relationship with concentration is still recommended to avoid overfitting, while capturing the main effects of blending on O-ring swelling.

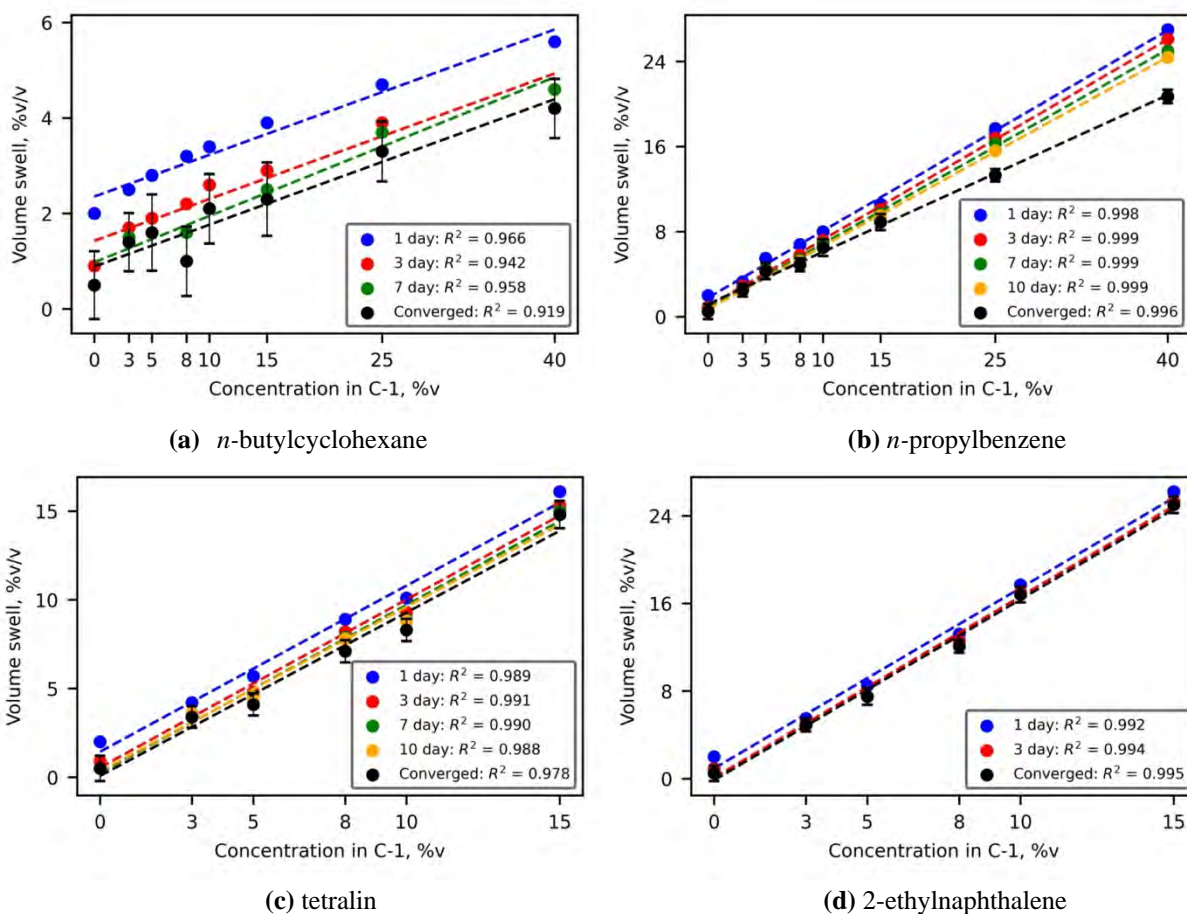


Figure 7. Scatter plots presenting the seal swell of four different dopants (listed beneath each subplot) in C-1 at concentrations ranging from 3%v to 40%v, along with a neat C-1 measurement. Each color marker and trendline represents the swell at a different timestep during the test. Please note the different swell ranges on each plot.

Quantifying isomeric effects: A key factor in aviation fuel assessment and design

<https://doi.org/10.1016/j.fuel.2023.129912>

Isomeric structural differences can profoundly influence hydrocarbon properties of importance to aviation turbine fuels. This is particularly true for alternative fuels, which often contain fewer components than conventional fuels, making isomeric differences more impactful. The inability of standard analytical methods to distinguish isomers within a hydrocarbon family poses a significant challenge for the assessment and formulation of jet fuels. Such missing information leads to considerable uncertainties in model predictions used for fuel assessment or aircraft and jet engine design. This work explores the influence of isomers on critical fuel properties using quantitative metrics based on the chemical family, size, topology, and, particularly, branching. Isomeric property ranges within a given hydrocarbon class are deduced from a database study. The extent of these intra-hydrocarbon group property ranges is related to the change conferred via shifting to adjacent carbon numbers and dissimilar hydrocarbon families. This approach shows that isomeric information is as critical, if not more, as carbon number and hydrocarbon class in influencing properties such as viscosity and freeze point. This perspective represents a significant change from the historical focus on carbon numbers and group-type analysis procedures. The correlations identified in this study can serve as a foundation for improving chemometrics, which, in turn, can enhance the accuracy of model-based property prediction and facilitate the design of new SAFs at a component level.



Milestones

- Tier Alpha testing was performed a total of 198 times.
- Tier Beta testing was performed a total of 127 times.
- The maximum blending ratio was determined for 41 SAF candidates.
- A refinement strategy/distillation optimization was developed for 16 fully synthetic SAF candidates.

Major Accomplishments

- Error quantification was determined for the Arrhenius blending rule for viscosity.
- Isomer-level detection was found to be possible with a VUV detector.
- Distillation optimization was found to be possible for SAF candidates.
- Measurements were performed on jet fuel range hydrocarbons to assess nitrile rubber absorption.
- Isomeric property variance was found to be significant, potentially affecting ASTM qualification.

Publications

Peer-reviewed publications

- Bell, D. C., Boehm, R. C., Feldhausen, J., & Heyne, J. S. (2022). A data set comparison method using noise statistics applied to vuv spectrum match determinations. *Analytical Chemistry*, 94(43), 14861–14868. <https://doi.org/10.1021/acs.analchem.2c01931>
- Boehm, R. C., Coburn, A. A., Yang, Z., Wanstall, C. T., & Heyne, J. S. (2022). Blend prediction model for the freeze point of jet fuel range hydrocarbons. *Energy & Fuels*, 36(19), 12046–12053. <https://doi.org/10.1021/acs.energyfuels.2c02063>
- Feldhausen, J., Bell, D. C., Yang, Z., Faulhaber, C., Boehm, R., & Heyne, J. (2022). Synthetic aromatic kerosene property prediction improvements with isomer specific characterization via GCxGC and vacuum ultraviolet spectroscopy. *Fuel*, 326, 125002. <https://doi.org/10.1016/j.fuel.2022.125002>
- Boehm, R. C., Yang, Z., & Heyne, J. S. (2022). Threshold sooting index of sustainable aviation fuel candidates from composition input alone: Progress toward uncertainty quantification. *Energy & Fuels*, 36(4), 1916–1928. <https://doi.org/10.1021/acs.energyfuels.1c03794>
- Boehm, R. C., Yang, Z., Bell, D. C., Feldhausen, J., & Heyne, J. S. (2022). Lower heating value of jet fuel from hydrocarbon class concentration data and thermo-chemical reference data: An uncertainty quantification. *Fuel*, 311, 122542. <https://doi.org/10.1016/j.fuel.2021.122542>
- Heyne, J., Bell, D., Feldhausen, J., Yang, Z., & Boehm, R. (2022). Towards fuel composition and properties from Two-dimensional gas chromatography with flame ionization and vacuum ultraviolet spectroscopy. *Fuel*, 312, 122709. <https://doi.org/10.1016/j.fuel.2021.122709>
- Huq, N. A., Hafenstine, G. R., Huo, X., Nguyen, H., Tiffit, S. M., Conklin, D. R., Stück, D., Stunkel, J., Yang, Z., Heyne, J. S., Wiatrowski, M. R., Zhang, Y., Tao, L., Zhu, J., McEnally, C. S., Christensen, E. D., Hays, C., Van Allsburg, K. M., Unocic, K. A., ... Vardon, D. R. (2021). Toward net-zero sustainable aviation fuel with wet waste-derived volatile fatty acids. *Proceedings of the National Academy of Sciences*, 118(13), e2023008118. <https://doi.org/10.1073/pnas.2023008118>
- Boehm, R. C., Hauck, F., Yang, Z., Wanstall, T., Heyne, J. S. (2022) Error quantification of the Arrhenius blending rule for viscosity of hydrocarbon mixtures. *Frontiers in Energy Research*, 10, Sec. Bioenergy and Biofuels <https://doi.org/10.3389/fenrg.2022.10746>
- Bell, D. C., Feldhausen, J., Spieles, A. J., Boehm, R. C., Heyne, J. S. (2023) Limits of identification using VUV spectroscopy applied to C8H18 isomers isolated by GCxGC. *Talanta*, 258, 124451. <https://doi.org/10.1016/j.talanta.2023.124451>
- Yang, Z., Boehm, R. C., Bell, D. C., Heyne, J. S. (2023) Maximizing Sustainable aviation fuel usage through optimization of distillation cut points and blending. *Fuel*, 53, 129136, <https://doi.org/10.1016/j.fuel.2023.129136>
- Faulhaber, C., Borland, C., Boehm, R., Heyne, J. (2023) Measurements of Nitrile Rubber Absorption of Hydrocarbons: Trends for Sustainable Aviation Fuel Compatibility. *Energy & Fuels*, 37(13), 9207–9219 <https://doi.org/10.1021/acs.energyfuels.3c00781>
- Hall, C., Bell, D. C., Feldhausen, Rauch, B., Heyne, J. (2024) Quantifying isomeric effects: A key factor in aviation fuel assessment and design. *Fuel*, 357 Part C, 129912, <https://doi.org/10.1016/j.fuel.2023.129912>



Outreach Efforts

Conference presentations

- American Chemical Society Spring 2023 National Meeting & Exposition, Indianapolis, IN
- American Chemical Society Fall 2023 National Meeting & Exposition, San Francisco, CA
- Sustainable Aviation Fuels End-Use Research Review Meeting, Argonne National Laboratory, IL
- 2023 Bioenergy Summit, Pasco, WA

Awards

Joshua Heyne

- 2023 Environmental Protection Agency Green Chemistry Challenge Awards

Zhibin Yang

- 2023 Environmental Protection Agency Green Chemistry Challenge Awards

Conor Faulhaber

- Pacific Northwest National Laboratory–Washington State University Distinguished Graduate Research Program

Student Involvement

David Bell, Ph.D. student, leads this effort.

John Feldhausen, M.S. student, participated in this effort.

Zhibin (Harrison) Yang, Ph.D. student, participates in this effort.

Shane Kosir, M.S. graduate (2021), participated in this effort.

Conor Faulhaber, Ph.D. student, participates in this effort.

Aaron Spieles, an undergraduate student at UD, participated in this effort.

Christopher Borland, an M.S. student at UD, participated in this effort.

Plans for Next Period

In the next period, we plan to finalize the publications in progress, improve the Tier Alpha prediction accuracy, test dielectric constant values for various fuels, and reduce the volume required for Tier Beta measurement.



Project 065(B) Fuel Testing Approaches for Rapid Jet Fuel Prescreening

University of Illinois at Urbana–Champaign

Project Lead Investigator

Tonghun Lee
Professor of Mechanical Science & Engineering
University of Illinois at Urbana–Champaign
1206 W. Green St., Urbana, IL 61801
517-290-8005
tonghun@illinois.edu

University Participants

University of Illinois at Urbana–Champaign (UIUC)

- P.I.: Professor Tonghun Lee
- FAA Award Number: 13-C-AJFE-UI-039
- Period of Performance: October 1, 2022 to September 30, 2023
- Tasks:
 1. Characterization of pressure effects on lean blowout (LBO) behavior as a part of M1 combustor development
 2. Laser diagnostics of flame dynamics near LBO conditions

Project Funding Level

FAA funding level: \$150,000
Cost sharing: 100% match provided by software license support from Converge, Inc.

Investigation Team

- Prof. Tonghun Lee, (P.I.), All Tasks
- Casey O'Brien, (graduate student) and Eric Wood, (graduate student), experimental efforts in characterizing the M1 combustor, including laser and optical diagnostics

Project Overview

This study is aimed at introducing a new compact test rig (Army research combustor [ARC] M1), developed with original equipment manufacturer (OEM) support within the National Jet Fuel Combustion Program (NJFCP), that can screen fundamental combustor behavior with much lower fuel volumes (approximately gallons) before tier 3 and 4 tests in the ASTM D4054 evaluation. In the NJFCP, the referee rig at the Air Force Research Laboratory (AFRL) was used as a foundational test rig for this goal. The M1 may have the potential to perform screening tasks at reduced fuel volumes (approximately gallons rather than hundreds of gallons) in a simplified and open architecture that can be readily shared and operated at different locations at a fraction of the cost. Both the Army Research Laboratory (ARL) and Argonne National Laboratory (ANL) will be partners in the effort to fully characterize the M1 facility. If successful, these efforts will allow fuel providers and OEMs to conduct basic combustor tests by using an identical testing architecture and identical test conditions at multiple test locations, in contrast to the referee rig, which is housed in a secure government facility (AFRL). Tests in smaller test rigs can provide a platform for individual suppliers or researchers to independently test their new fuels and to make predictions without requiring the use of one single facility. Over time, as test data are accumulated, the potential for test rigs such as the M1 to predict actual tier 3 and 4 performance will increase, potentially reducing the burden of relying on capital-intensive ASTM rig and engine tests.



Background of the M1 Combustor

Under the FAA-funded NJFCP, the referee rig combustor at AFRL was used to determine the sensitivity of combustor performance parameters, such as LBO and ignition parameters, to the chemical composition of novel fuels. The results from this investigation were instrumental in establishing a relationship between fuel chemistry and its effects on combustor performance. Professor Tonghun Lee's research group conducted a substantial portion of the laser and optical diagnostic work for the referee rig as part of the NJFCP, including quantitative-phase Doppler particle analysis, which provided key quantitative data for the simulation efforts.

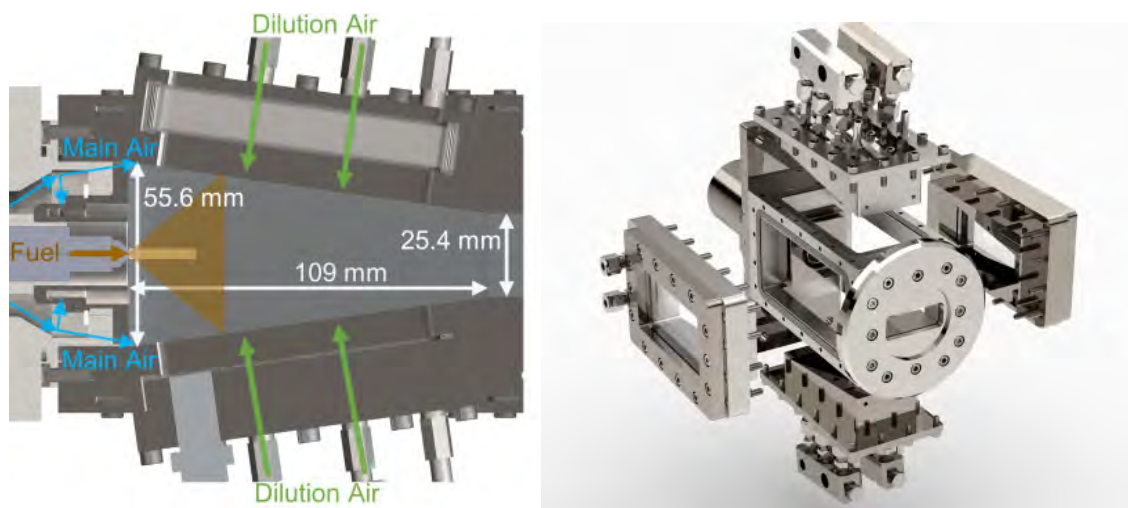


Figure 1. M1 combustor.

Although the referee combustor used in the NJFCP program provides valuable information, a few key issues were identified. One issue is that the combustor requires hundreds of gallons of fuel to operate, which obviously would be not available for many of the new sustainable aviation fuels (SAFs) that would become available in the near future. The second issue is that the referee combustor lacks adequate optical access for diagnostics as a research combustor. Most significantly, it does not have windows on the top where laser beams can be inserted. Finally, the combustor itself is in a secure military facility (AFRL) and is not readily accessible to the general community. For these reasons, a smaller, compact, and less expensive option was needed; thus, the M1 combustor was developed with both the FAA and ARL (FAA NJFCP member). The M1 was designed as a joint effort between the University of Illinois and select OEMs who were involved with the referee combustor. The M1 combustor would run with moderately high-pressure air and would require a few gallons of fuel instead of hundreds of gallons. If this type of low-cost combustor can be well characterized, it can help the community in prescreening SAFs as new fuels become available.

The dimensions and a magnified view of the M1 combustor are included in Figure 1. This combustor was built to be modular so that continual adjustments can be made to suit the needs of different optical and laser diagnostics. The combustor includes four-sided optical access to allow for maximum flexibility in the diagnostics. The modular aspect was designed to allow us to transport the combustor easily to other locations for measurements, primarily because we envisioned using X-ray imaging for fuel spray characterization at ANL as well as combustion characterization with velocity field and radical species measurements at UIUC. With this approach, we can ensure that we are able to characterize the M1 combustor in an unprecedented way to enable wide adoption in the academic/industrial community as a test platform for new fuel blends. After this characterization is complete, the basic physics, dimensions, and operational envelope of the combustor will be openly shared with the academic and commercial sectors. This work is expected to provide a common platform not only for prescreening SAFs but also for performing other sustainability-related experiments involving novel fuels in a laboratory setting. We also note that the combustor and surrounding hardware were designed specifically to be inexpensive so that other labs could replicate this setup with reasonable resources.

Task 1 – Characterization of Pressure Effects on LBO Behavior as a Part of M1 Combustor Development

University of Illinois at Urbana-Champaign

Objectives

In this task, LBO measurements are conducted for four different fuels and two combustor pressures. The fuels are selected to have a wide range of properties to isolate fuel effects on LBO behavior. Previously, a strong correlation was observed between physical fuel properties and LBO behavior, demonstrating that atomization and vaporization are rate-limiting steps for the M1 combustor because of the significantly smaller length scales compared with previous tests on the referee combustor. Two pressures are tested to determine whether higher pressure can produce favorable combusting conditions to create a transition from physically dominated LBO performance to a more chemical regime. By collecting LBO measurements at well-controlled, relevant operating conditions across different pressures, a comprehensive characterization matrix can be obtained to demonstrate how the operating regime of the M1 can be matched to previous large-scale testing for comparing fuel effects. This work should aid in the integration of alternative jet fuels into fuel pipelines by providing insight into how a model combustor can be utilized to observe real-scale effects while using much lower fuel volumes than other large-scale test rigs.

Research Approach

Throughout the NJFCP, the referee combustor and several other combustors were carefully characterized under a variety of relevant operating regimes, including blowout and ignition. These studies were conducted under a range of standard operating conditions that are relevant to gas turbine operational regimes and are likely to expose differences between fuels with varying properties. Although experiments in the referee combustor have provided valuable data regarding fuel effects near LBO, operating the referee rig has several disadvantages. The scale of the referee combustor results in large air and fuel flow rate requirements, thus making setup and operation expensive, particularly for studies of new alternatively derived fuels, which may be difficult to manufacture. Therefore, the ability to obtain similar results from a smaller combustor with decreased fuel and air requirements would be beneficial. The M1 combustor uses substantially less air and fuel, thereby reducing the overall instrumentation expense and complexity, as well as the volume of fuel needed to conduct tests over a range of conditions. With these advantages, the M1 combustor could be used to evaluate the performance of new fuels with much less fuel, thereby decreasing the supply requirements for a potential new fuel supplier. To achieve this goal, we must ensure that the trends observed in a smaller combustor convey the physics observed in other test combustors, such as the referee combustor.

Overview of LBO testing

Performing LBO measurements on a combustor in a reliable and repeatable manner involves careful control of all combustor operating parameters, including fuel flow rate, air flow rate, air temperature, and combustor pressure. To ensure that combustor conditions are stable before LBO testing is conducted, the combustor is ignited at a fuel flow rate above the LBO point, and combustion is sustained at that flow rate until the air outlet temperature reaches a steady-state condition. After steady-state temperatures are reached, the fuel flow rate is slowly reduced until blowout occurs. For these experiments, the fuel flow rate is reduced by approximately 0.05 g/min per second. This slow ramp rate helps ensure that the combustor wall temperature does not bias the LBO point toward a lower value, owing to heat transfer from the hot combustor itself back into the flame. While the fuel flow rate is being stepped down, all other combustor properties are closely monitored to ensure that they remain within the specified parameter ranges. The specific LBO point is monitored by simultaneously recording a photodiode signal at 100 kHz and all other combustor parameters at 50 Hz. The LBO point is determined for each test by finding the equivalence ratio for the point at which the photodiode signal indicates that blowout occurred. The testing matrix (Table 1) for this experiment is applied under conditions that can provide a consistent comparison to previous experiments conducted at UIUC as well as in the referee combustor. An example of broadband imaging near the LBO point is captured in Figure 1. Observable variations in flame distribution for one imaged frame within the combustor reveal a high flame concentration at the top with a sparse concentration at the bottom. This demonstrates the stochastic nature of LBO testing, which is an oscillatory process where the flame can be locally extinguished and reignited with the recirculation of hot products. Because of this stochasticity, a total of 15 tests are conducted for each condition to account for variation in the results and provide high-confidence data. Currently, the combustor pressure is monitored using a pressure transducer with a recording frequency capable of capturing vibrations up to 2000 Hz. However, as a potential avenue of future research, one could utilize a high-speed pressure transducer with



a frequency an order of magnitude higher, at 20000 Hz. With this high-speed pressure transducer, thermo-acoustic effects can be more thoroughly investigated to give a greater physical meaning to the oscillations observed in the flame structure.

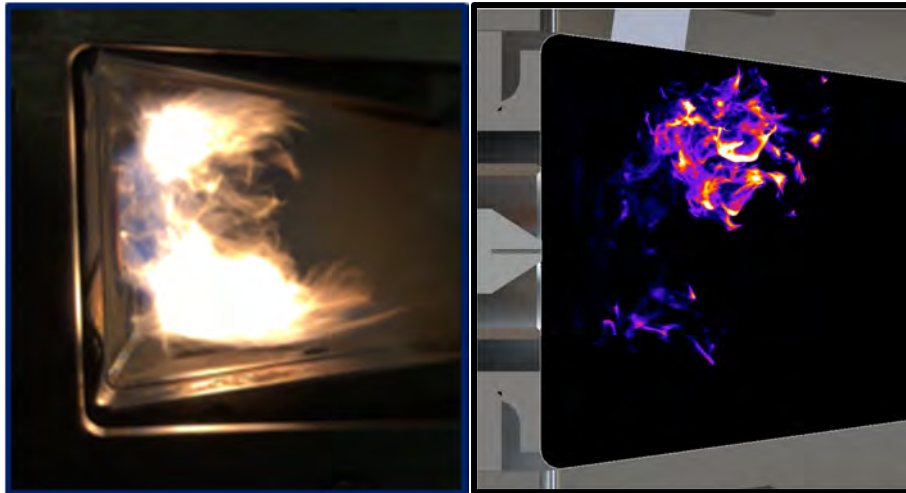


Figure 2. Imaging of a near-lean-blowout event in the M1 combustor at 20,000 frames per second.

Table 1. Targeted combustor operating conditions.

Fuels	F-24, C-1, C-3, C-5
Combustor Absolute Pressure (kPa)	202.65, 303.98
Main Air Flow Rate (g/s)	43.38, 65.07
Air Preheat Temperature (K)	394
Pressure Drop (%)	3

Nozzle utilized in LBO testing

In the comprehensive evaluation of the ARC-M1, prior investigations included a meticulous comparison of three distinct hollow-cone pressure swirl nozzles—designated as A, B, and C as outlined in Table 2. The fuel atomization among these nozzles was characterized by utilizing advanced X-ray phase-contrast imaging techniques at ANL. Intriguingly, the comparative analysis revealed that Nozzle B exhibited superior performance in terms of atomization and remarkable stability at low equivalence ratios. In contrast, both Nozzle A and Nozzle C, while sharing similarities in performance, lagged significantly behind Nozzle B in terms of atomization efficiency and operational stability. Despite the similar dimensions and characteristics for Nozzle B and Nozzle C, their distinct internal geometries resulted in disparate flow characteristics. Notably, the large difference in injection pressure exhibits a relationship to atomization performance, with higher injection pressures generally corresponding to enhanced atomization. Previously, all three nozzles exhibited strong dependence of the equivalence ratio at LBO to physical properties such as distillation temperature and viscosity of the fuels. Leveraging these insights, we strategically selected Nozzle B for subsequent pressure testing, with the specific aim of mitigating the reliance of LBO behavior on atomization and vaporization dynamics.


Table 2. Properties of fuel nozzles tested in experiments.

Nozzle	Approximate minimum diameter (μm)	Approximate cone angle	Flow rate at 100 psid (L/hr)	Injection pressure at F-24 lean blowout (psid)
Nozzle A	344	90°	6.2	29.2
Nozzle B	150	80°	2.25	45.9
Nozzle C	150	80°	4.60	32.5

Fuels for LBO testing

In these experiments, four different fuels are tested in the M1 combustor to probe the effects of fuel properties on combustion behavior at these critical conditions. In addition to a reference fuel, the tested fuels consist of F-24 (comprising Jet A and military-specific additives) and three fuels from the NJFCP with specific properties designed to probe the edges of the jet fuel operational envelope. Fuel C-1 has been developed with a low derived cetane number and a relatively flat boiling curve. Fuel C-3 has been formulated to have a high viscosity, and fuel C-5 has been developed with an extremely flat boiling curve with respect to those of other fuels. Table 3 shows selected important parameters of each fuel for comparison, demonstrating some of the key features of the fuels chosen for testing.

Table 3. Comparison of key properties of the four tested fuels.

Fuel	Key features	Derived cetane number	Heat of combustion (MJ/kg)	H/C ratio	Stoichiometric air/fuel ratio	Kinematic viscosity at 40 °C (cSt)	Surface tension (dynes/cm)
F-24	Jet A with additives	48.6	43.2	1.94	14.70	1.36	23.6
C-1	Low cetane	17.1	43.8	2.18	15.03	1.53	21.0
C-3	High viscosity	47.0	43.3	1.97	14.65	1.78	24.2
C-5	Flat boiling	39.6	43.0	1.94	14.68	0.83	22.2

LBO Performance results

Figure 3 displays the equivalence ratio of the different fuels and pressures at blowout along with three important fuel properties: 20% distillation temperature (T_{20}), kinematic viscosity, and derived cetane number (DCN). The inclusion of error bars in the graphs provides valuable insights into the reliability of the observed trends. The relatively low standard deviations for each testing condition enhance our confidence in the reported results, suggesting consistency in the experimental measurements. This consistency is crucial for drawing meaningful conclusions about the effects of fuel properties on LBO across different pressure conditions. When the tested combustor pressure is 2 atm, the observed trends are similar to those for previous LBO testing on the M1 combustor. There is a high correlation between physical properties such as T_{20} and kinematic viscosity with the global equivalence ratio at blowout. This finding demonstrates that the blowout behavior is governed by the atomization and vaporization processes occurring in the combustor. C-5 fuel has a low viscosity and low boiling curve, which contribute to C-5 being the “best” performing fuel in the M1 for a pressure of 2 atm. In contrast, C-3 has a high viscosity with a high boiling curve, and this fuel performed the “worst” in the 2-atm case.

When the combustor operating pressure is changed to 3 atm, there is a significant shift in the observed trends of the effect of fuel properties on LBO equivalence ratios. There is almost no correlation between the physical properties of T_{20} and kinematic viscosity; in contrast, there is a high negative correlation between derived cetane number and the equivalence ratio at LBO. This result indicates the presence of a regime transition at which the LBO behavior is no longer rate-limited by processes such as atomization and vaporization but is dependent on the chemical properties of the fuel. The low viscosity and boiling curve of C-5 likely contribute to its continued effectiveness in achieving LBO resistance. However, the increasing influence of derived cetane number at higher pressures indicates that chemical properties play a more significant role in determining LBO behavior under these conditions.

Furthermore, the careful matching of volumetric flow rates and pressure drops between the 2-atm and 3-atm conditions ensures that any observed transitions are not confounded by variations in air flow. This methodological approach strengthens the argument that the observed changes in trends are indeed linked to the altered pressure conditions and not external factors such as differences in air flow dynamics. As the pressure increases, the reactant concentration increases with a constant volume, promoting increased mixing and collisional effects between the fuel and oxidizer, even at similar flow velocities. Furthermore, the ignition delay of the fuel will decrease with increasing pressure, implying that the residence time needed for the reaction to proceed to completion is reduced, causing the time for atomization to be less crucial. LBO is often characterized as an oscillatory process of local ignition and extinction. A global LBO event occurs when local extinction cannot be reignited by the new air and fuel mixture. Therefore, the chemical properties of the fuels will govern the rate-limiting step in local re-ignition, resulting in the trends seen between the derived cetane number and equivalence ratio at LBO for the 3-atm condition. Yet, more testing is needed to quantitatively demonstrate the different reaction kinetics and mixing between the two conditions. Comprehensive data collection from these additional tests and a wide range of conditions will contribute to a more robust understanding of the distinct regimes governing LBO at varying pressures and with different spray behavior. The nuanced information obtained from these experiments will not only enhance our knowledge of combustion behavior but also provide a foundation for refining models and designs aimed at optimizing combustion systems for practical applications.

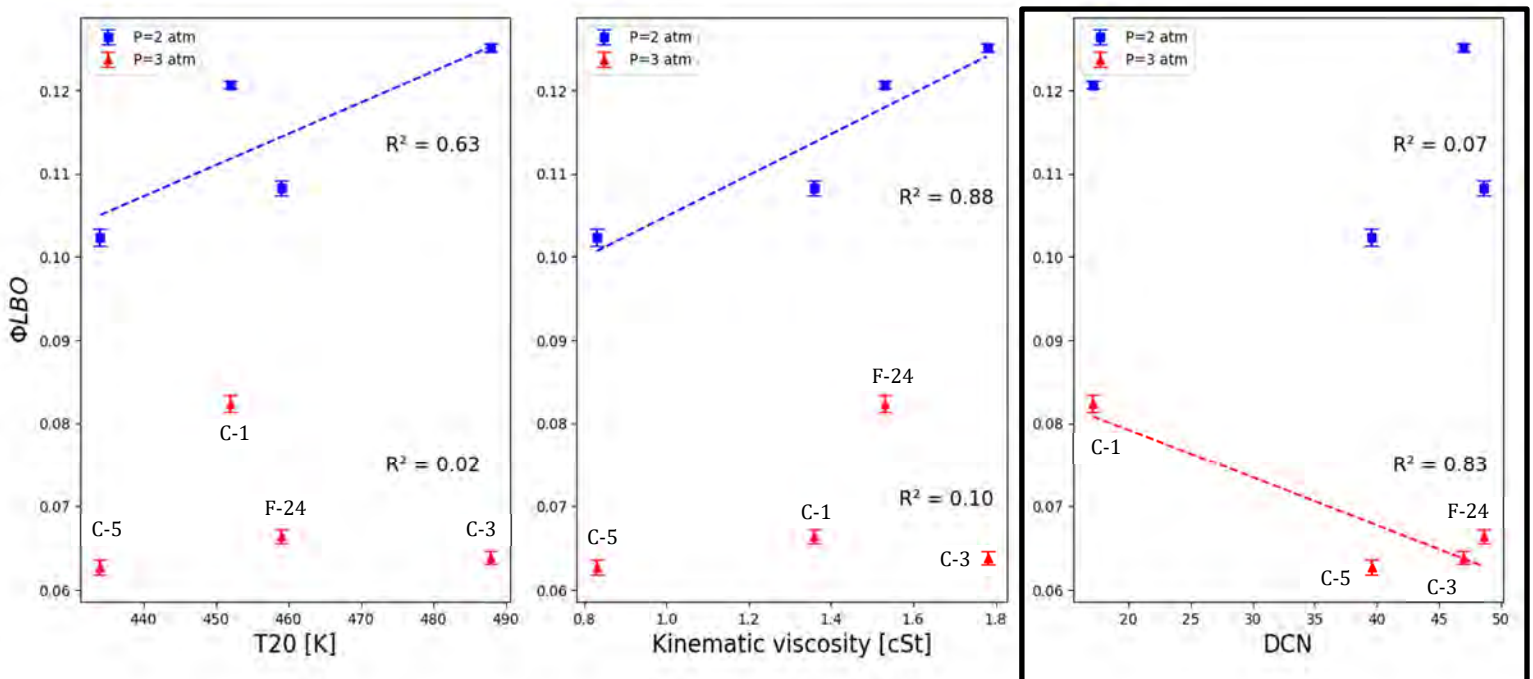


Figure 3. Lean blowout (LBO) equivalence ratio against fuel properties for two pressures. DCN: derived cetane number; T20: 20% distillation temperature.

Droplet analysis

Building upon prior investigations that primarily focused on understanding the impact of fuel spray nozzles on LBO behavior, research endeavors have extended to the detailed analysis of droplet data associated with various nozzles and pressures. Leveraging the capabilities of the Advanced Photon Source (APS) at ANL, comprehensive droplet data have been collected, aiming to uncover insights into the intricacies of fuel atomization and its correlation with combustion dynamics. An image of the APS facility with the setup utilized for droplet measurements is shown in Figure 4.

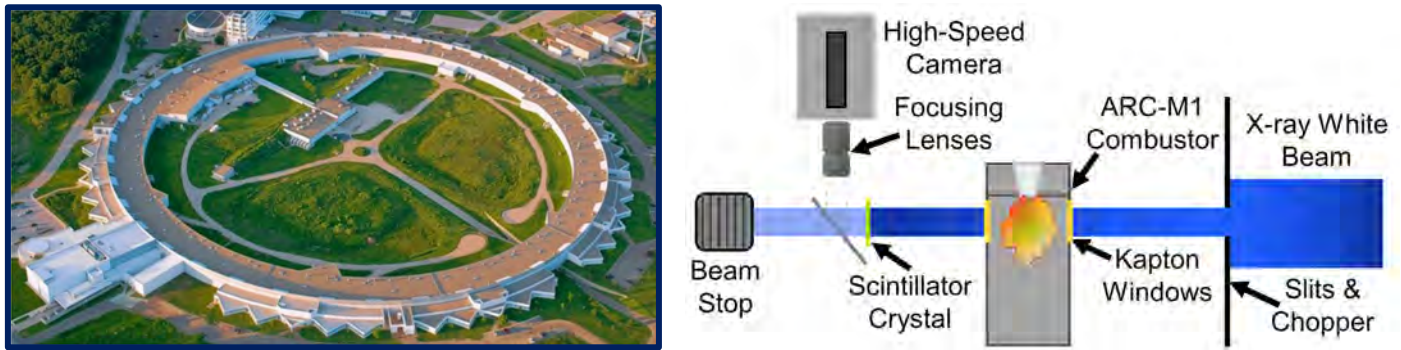


Figure 4. Advanced Photon Source facility at the Argonne National Laboratory (left) and the Army research combustor (ARC) M1 setup (right).

In this study, high-speed X-ray phase-contrast imaging was employed to characterize the ARC-M1. This imaging method was utilized to visualize and analyze the liquid fuel spray exiting the pressure-swirl atomizing nozzle of the operating combustor. The experimental setup includes an unfocused polychromatic X-ray white beam from the APS bending magnet source, controlled by slits and a mechanical chopper to manage beam size and exposure time. Kapton windows on the combustor facilitate high levels of X-ray transmission. The transmitted X-rays pass through the combustor and reach a YAG:Ce scintillator crystal, which emits visible light directed to a high-speed camera for imaging. The imaging setup includes a Photron SA-Z high-speed camera with specific lenses and settings, synchronized with the synchrotron's electron circulation frequency. A water-cooled beam stop absorbs unused X-rays downstream of the setup. Phase contrast imaging leverages the difference in the index of refraction between the liquid fuel and hot gases, creating enhanced contrast at the liquid edges due to Fresnel diffraction patterns. This technique effectively captures the liquid fuel spray within the combustor, unaffected by varying gas temperatures. The acquired droplet data, however, present a significant challenge due to the inherently noisy nature of this type of data. To overcome this challenge and extract meaningful information, a machine-learning denoising algorithm has been implemented. This algorithm plays a pivotal role in cleaning up the acquired images, enhancing the clarity of droplet patterns, and facilitating more accurate and insightful analyses.

This algorithm is a self-supervised machine-learning algorithm that leverages both spatial and temporal correlations in the image sequence to improve denoising accuracy. This approach is particularly important because there is no need for a ground truth or a set of clean and non-noisy images for the model to compare against for error metrics. Instead, the original images are convoluted to include more noise than is initially present, and a reconstruction of primary features is used as an error metric for enhanced deep learning. This model can be trained in real time for use on varying subsets of image sequences with slightly different characteristics. This feature is extremely important because the hyperparameters for an image sequence with a given fuel and nozzle may not be applicable to another condition.

In Figure 5, an illustrative example showcases the input image and the subsequent denoised image. The denoising algorithm exhibits the capability to detect droplets at the pixel level, offering a granular understanding of droplet distribution and morphology. Moreover, the algorithm enables a detailed exploration of the primary breakup region, where fuel ligaments disintegrate into smaller droplets. This level of analysis is crucial for assessing the nuances of fuel primary and secondary breakup phenomena, which, in turn, are fundamental to unraveling the diverse combustion behaviors exhibited for varying fuel properties.

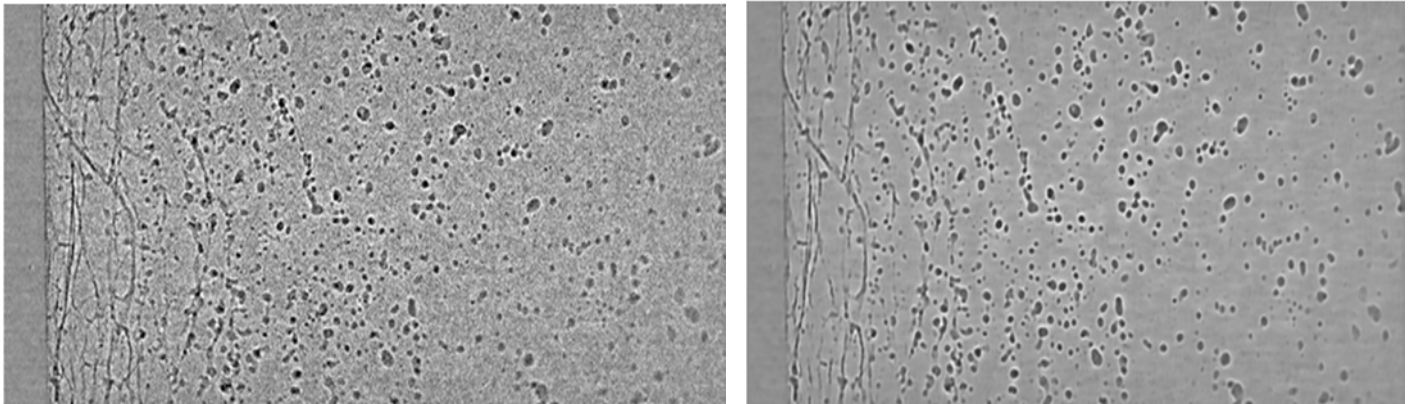


Figure 5. Input droplet image (left) and subsequent denoised image (right).

Milestones

- 3 months: bolstered infrastructure to have sufficient heater power for higher-pressure conditions
- 6 months: initial LBO testing of increased pressure for C-1
- 9 months: full LBO testing on four fuels for two pressures (2 and 3 atm)
- 12 months: development of denoising code for fuel droplet analysis

Major Accomplishments

Our comprehensive investigation into the LBO behavior of the M1 combustor encompasses extensive data collection under various operating conditions, specifically exploring different pressures and the impact of both chemical and physical fuel properties. Armed with this knowledge, we are poised to broaden our testing parameters, strategically targeting the boundaries at which the dependence on chemical fuel properties becomes predominant. This strategic expansion is crucial for informing design considerations in real-scale applications. Moreover, the development of a denoising algorithm will be crucial to performing detailed analyses in future work. This analysis of droplet data across different nozzles, fuels, and pressures will provide a foundational tool for achieving a holistic characterization of combustion performance. Such insights will be invaluable for refining design considerations for combustion systems in both small- and real-scale applications.

Publications

Oh, J. H., Wood, E., Mayhew, E., Kastengren, A., & Lee, T. (2023). Sequence2Self: Self-supervised image sequence denoising of pixel-level spray breakup morphology. *Engineering Applications of Artificial Intelligence*, 126, 106957.

Outreach Efforts

All test data will be made accessible through <https://altjetfuels.illinois.edu/>.

Awards

None.

Student Involvement

This project was primarily conducted by Casey O'Brien (PhD Student) and Eric Wood (former PhD Student).

Plans for Next Period

In the next period, the relationship between the atomization performance of the fuel spray nozzle, fuel, and pressure with global LBO performance will be investigated in greater detail by combining knowledge from this testing with high-speed X-ray spray data collected for each nozzle, pressure, and fuel at the ANL APS.

Task 2 – Laser Diagnostics of Flame Dynamics Near LBO Conditions

University of Illinois at Urbana-Champaign

Objective

The objective of this task is to conduct simultaneous hydroxyl radical (OH) planar laser-induced fluorescence (PLIF) measurements and particle image velocimetry (PIV) to investigate the mixing behavior and reaction zones that are prevalent for different fuels and operating conditions.

Research Approach

The dynamics of liquid spray play a pivotal role in governing LBO performance within the M1 combustor. Nevertheless, the LBO process is a complex interplay of various factors, encompassing liquid spray behavior, fuel vaporization, turbulent air flow fluctuations, air-fuel mixing efficiency, chemical kinetics, and more. To achieve a comprehensive understanding of the combustion dynamics within the ARC-M1 and the intricacies leading to LBO, it is imperative to complement the insights garnered from investigations of liquid spray physics with additional studies focusing on the combustion dynamics and air flow behaviors when the combustor operates near its LBO threshold. OH PLIF measurements can reveal information regarding the primary heat release zones in the combustor. The combination of PIV with OH PLIF can specifically indicate how the time-resolved velocity field impacts the transient reaction zones. The testing procedure involves the conditions listed in Table 1. Imaging is conducted at the centerline of the combustor for fuel flow rates corresponding to a point 2.5%, 5%, 10%, and 25% above the LBO equivalence ratio for each condition. Testing is conducted for conditions in which identical fuel flow rates or equivalence ratios among different fuels are not maintained. Instead, the tests are performed at conditions that correspond to the same distance from the LBO point. This approach facilitates more meaningful comparisons of the combustion performance of different fuels near the LBO point. Using the same equivalence ratio for various fuels could lead to inconsistencies, with some fuels operating well above LBO and others operating near blowout.

PLIF/PIV Experimental Setup

The PLIF setup includes a Sirah Credo high-speed dye laser pumped by a high-speed Nd:YAG laser. The setup can be run at a repetition rate of 10 kHz, with each laser pulse having an energy of nearly 150 μ J. To conduct PIV, a double-pulsed Nd:YAG laser is utilized, with each laser pulse having a repetition rate of 10 kHz. Therefore, the effective temporal resolution of the PIV system is 20 kHz. Each laser can provide nearly 50 W of laser power at a wavelength of 532 nm. This setup is visualized in Figure 6.

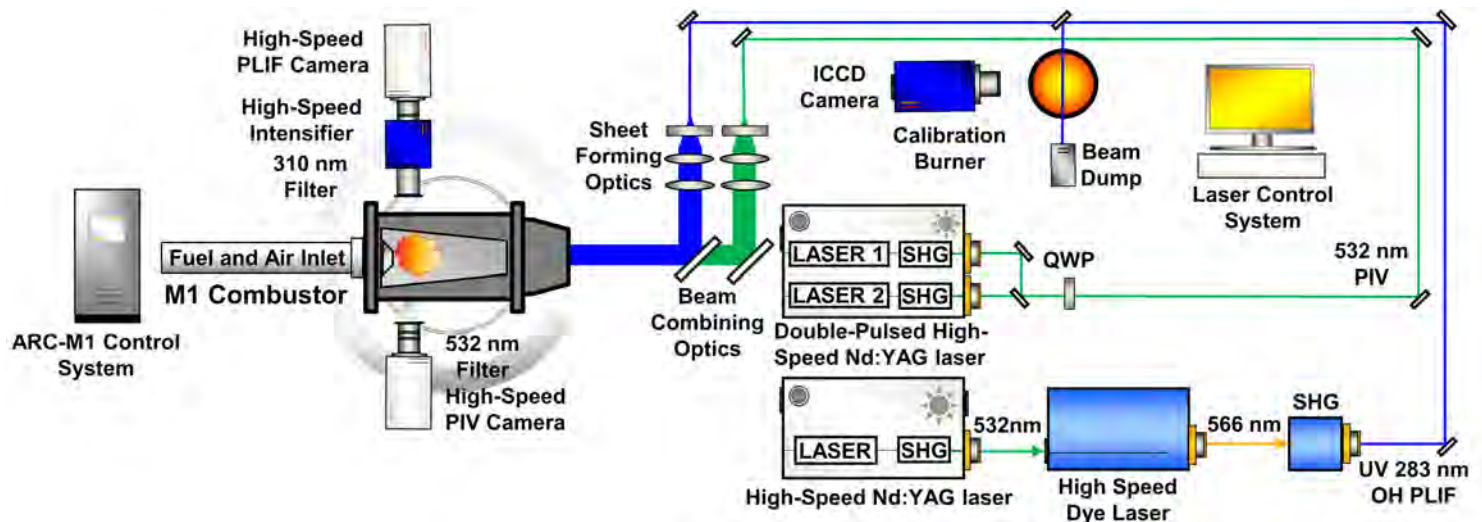


Figure 6. Simultaneous PLIF/PIV experimental setup. ARC: Army research combustor; ICCD: intensified charge-coupled device; PIV: particle image velocity; PLIF: planar laser-induced fluorescence; QWP: quarter waveplate; SHG: second-harmonic generator; UV: ultraviolet.

This PLIF dye laser utilizes rhodamine 6G dye to generate laser light with a wavelength of 283 nm. The PLIF laser targets the Q1(7) line of the (1,0) vibrational band in the A-X system of the OH radical at 283.3 nm. This transition and the OH LIF spectra are illustrated in Figure 7.

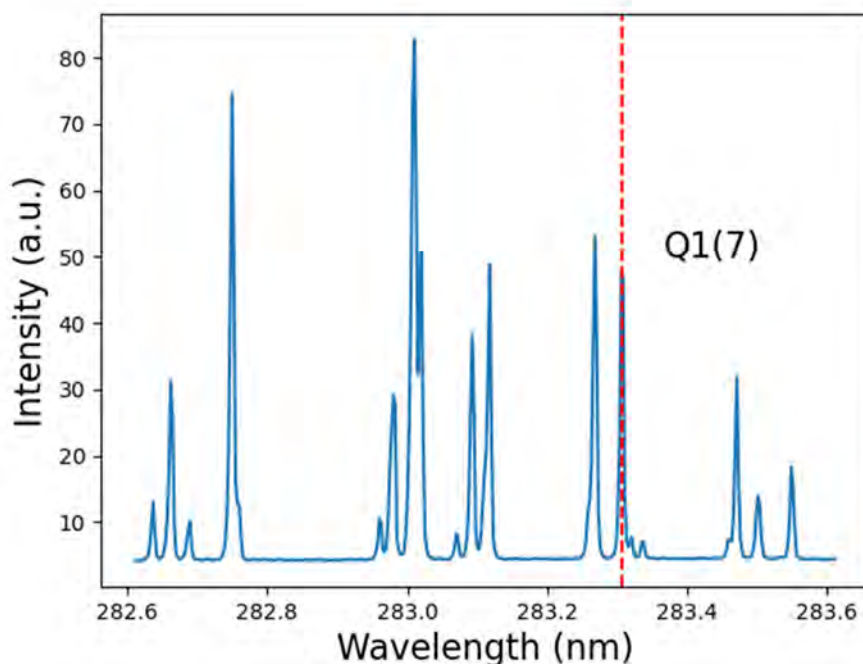


Figure 7. Experimental laser-induced fluorescence spectra of OH radical.

The OH PLIF spectra are experimentally measured by obtaining the average OH intensity signal via a high-speed camera as the wavelength of the dye laser is swept across different values. This spectrum can be compared with the known OH PLIF spectra to find the wavelength offset of the PLIF laser based upon transitions that have been previously characterized. In contrast, PIV imaging relies on Mie scattering, which occurs when the particles are similar to or larger than the incident wavelength. Titanium dioxide particles are selected as seeding particles in the combustor flow because their size of 150–250 nm is small enough for the particles to adequately follow the air flows in the combustor. Additionally, the titanium dioxide particles have a high melting point of approximately 1830 °C, which prevents the particles from burning up in the combustor. The light scattered off the particles is collected by a high-speed camera with a bandpass filter of 532 nm. The inter-frame timing is set to 6.0 μ s to achieve the desired pixel displacement of PIV particles between the frames. With this displacement, the velocity field in the combustor can be found using cross-correlation DaVis software from LaVision. Timing is a crucial aspect that must be meticulously controlled to perform simultaneous PLIF and PIV. The PLIF laser is positioned to pulse in between the two PIV laser pulses. This timing is set with a delay generator and verified with a photodiode and oscilloscope.

PLIF/PIV imaging results

Figure 8 presents average PLIF/PIV images for each tested fuel at flow rates 5% above LBO and a pressure of 2 atm. Despite variations in signal intensity due to multiple factors, qualitative assessments reveal distinct flame characteristics. Notably, a strong correlation exists between the velocity field and reaction zones within the combustor. Areas with intense recirculation correspond to larger OH zones, with a significant volume of air circulating along the top and bottom of the combustor, ultimately recirculating into the center.

It is important to acknowledge that the pronounced V-shape in Figure 8 results from the fluorescence of liquid fuel. While this signal was not subtracted in these images, future work may explore methods to eliminate this contribution. Comparing trends among different fuels, it becomes evident that the average OH intensity for C-3 fuel exhibits stronger

reaction zones further downstream. This behavior is attributed to the high viscosity and boiling curve of C-3, which impede vaporization and delay the reaction until the fuel reaches a more distant downstream location. In contrast, C-5 showcases reaction zones occurring far upstream in the combustor because of its favorable properties for atomization and vaporization.

Despite distinct reaction zone characteristics, the average velocity fields among different fuels appear nearly identical. Further investigation is warranted to explore how these reaction zones may change with an increase in combustor pressure to 3 atm. It is hypothesized that C-1 might exhibit reaction zones furthest upstream, considering that atomization and vaporization are less likely to be rate-limiting steps in its combustion process.

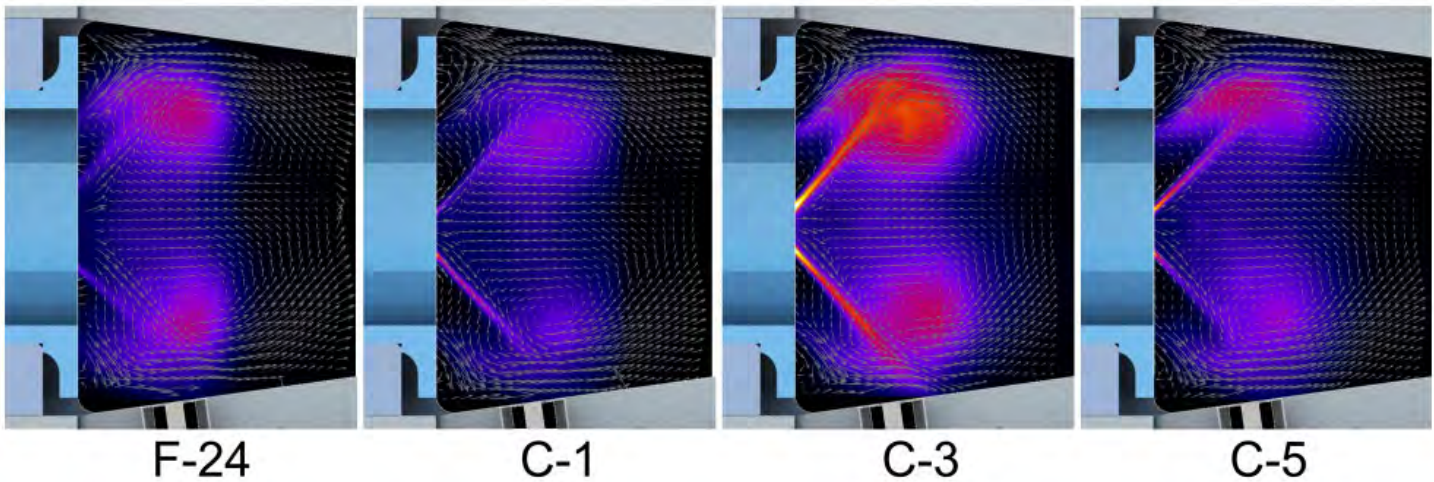


Figure 8. Mean velocity field overlaid with the mean planar laser-induced fluorescence signal for four fuels at a pressure of 2 atm.

Milestones

- 3 months: procurement of optics necessary for PLIF/PIV setup
- 6 months: alignment of PLIF laser
- 9 months: PLIF/PIV testing on four fuels at a combustor pressure of 2 atm
- 12 months: data analysis of velocity fields overlaid on PLIF images

Major Accomplishments

We have conducted simultaneous PLIF/PIV imaging on four different fuels at one combustor pressure (2 atm). This process included a great deal of work in aligning the optics in the dye laser to garner the appropriate lasing power as well aligning the optics that lead to the centerline of the combustor. The timing had to be carefully selected and implemented to ensure an appropriate inter-pulse timing for the PIV laser so that the seeding particle displacements could be accurately measured, as well as the PLIF laser being triggered in between the two PIV laser pulses.

Publications

Dasgupta, D., Som, S., Wood, E. J., Lee, T., Mayhew, E., Temme, J., & Kweon, C. B. (2023). Computational Fluid Dynamics Modeling of Lean Blowout in the ARC-M1 Gas Turbine Combustor. In AIAA SCITECH 2023 Forum (p. 2653).

Outreach Efforts

All test data will be made accessible through <https://altjetfuels.illinois.edu/>.

Awards

None.



Student Involvement

This project has been primarily conducted by Eric Wood (former PhD student) and Casey O'Brien (PhD student).

Plans for Next Period

In the upcoming phases of the PLIF/PIV aspects of this research, a pivotal focus will be on imaging the PLIF/PIV fields within the combustor at elevated pressures, building upon the established baseline at 2 atm. This investigation aims to delineate correlations between varying pressures and their discernible impacts on reaction zones, providing a more nuanced comprehension of combustion dynamics. Additionally, the application of machine-learning techniques holds substantial promise in addressing challenges encountered in the analysis of PLIF images. Specifically, these methods can be harnessed to develop algorithms designed to effectively remove the undesirable fuel PLIF interference, thereby enhancing the accuracy and reliability of data analysis. Moreover, machine learning will be applied to shed light on the intricate time-resolved interaction between turbulent fluctuations and OH reaction zones. By leveraging these advanced computational approaches, we hope to uncover valuable insights into the temporal evolution of reaction zones.



Project 066 Evaluation of High-thermal-stability Fuels

Washington State University

Project Lead Investigator

Joshua Heyne
BESL Director, Associate Professor
School of Engineering and Applied Science
Washington State University
2710 Crimson Way, Richland, WA 99354
(937) 229-5319
joshua.heyne@wsu.edu

University Participants

Washington State University (WSU)

- P.I.s: Assoc. Prof. Joshua Heyne and Assoc. Res. Prof. Randall Boehm
- FAA Award Number: 13-C-AJFE-WaSU-036
- Period of Performance: January 1, 2023 to September 30, 2024
- Tasks: Leveraging tools developed under this project, award number 13--C-AJFE-UD, advance the following:
 1. Estimate gains in fuel efficiency facilitated by SAF
 2. Identify critical blend components and solvents to study
 3. Create and test blends for thermal stability

Project Funding Level

FAA provided \$200,000 in funding. Cost-sharing is provided by Boom Technology Inc. (\$100,000) and WSU (\$100,000).

Investigation Team

WSU

Assoc. Prof. Joshua Heyne, (P.I.), All Tasks
Assoc. Res. Prof. Randall Boehm, (co-P.I.), All Tasks
Conor Faulhaber, (graduate research student), All Tasks

Boom Technology

Akshay Ashok, (team leader), Task 1 (Boom Technology)

Project Overview

It has long been understood that increasing the reliance on jet fuel as a primary coolant for both the engine and the aircraft has significant performance and efficiency benefits relative to the use of air as a coolant [Bruenig, 1999], but fuel degradation and coking at high temperatures restrict how much heat can be put into the fuel. In some military applications, the performance benefits are sufficiently large to justify the creation of specialty fuels such as JP7 and JPTS, which can tolerate much higher temperatures than petroleum-derived Jet A or Jet A1 (JP8) [Edwards, 2007]. In land-based applications of gas turbines, weight is of little consequence; thus, the operations of waste heat recovery (WHR) for plant efficiency or the cooling of combustor inlet temperature for emission reductions can be accomplished in a wide variety of ways, all of which are impractical for flight because of their impact on the mass of the power plant. Nonetheless, these applications provide some common examples of how controlling the air temperature along its flow path through the engine can have a large impact on performance, durability, and energy efficiency [Wilfert, 2007]. The flurry of works relating to fuel deoxygenation [Zabarnick, 2020] and other ways to decrease coking propensity and its impacts [Mancini, 2004] is largely motivated at the sponsorship level by these benefits.

More recently, sustainable alternative fuels (SAF) have received much attention because they can contribute to high-priority geopolitical goals to diversify energy supply chains and reduce greenhouse gas emissions. Most of these efforts have focused on streamlining the evaluation and approval processes to use synthetic fuels at some blend ratio with petroleum-derived jet fuel to create a so-called drop-in fuel that can be used within existing infrastructure without objection from any stakeholders [Colket, 2021]. Additionally, there have been discussions regarding characteristics of synthetic blend components (such as low aromatics, high specific energy, and high thermal stability) that would make these components attractive to consider as potential specialty fuels (such as JPTS) or high-performance fuels. [Kosir, 2020] recently published work highlighting the efficiency gain that could be realized by using fuels with high specific energy, via lower aircraft weight at take-off; less mass to lift and hold against the force of gravity.

The weight of fuel uplifted to an aircraft, as necessary to complete its mission, is certainly an important component to consider in assessing the integrated engine/aircraft energy demand and efficiency. The energy efficiency of the engine is also expected to be influenced by other fuel properties, including the following:

Hydrogen/carbon (H/C) ratio. Through its impact on combustor exhaust gas composition, this ratio has a small impact on the ratio of heat capacities (γ), combustor exit temperature, and work extracted during expansion through the turbine, even when the total enthalpy created at the combustor is unchanged.

Viscosity. Viscosity impacts the heat transfer coefficients, which ultimately determine how much waste heat is recovered by the fuel (coolant) and delivered back to the engine via the combustor.

Energy density. Energy density, measured in joules per liter (J/L), impacts volumetric flow rates, which also impact heat transfer coefficients.

Specific heat. Specific heat also has some effect on heat transfer coefficients, but perhaps more importantly has a direct impact on the temperature rise in the fuel per unit of heat energy absorbed, which in turn may impact the coking rate.

Coking rate. Also known as fuel thermal stability, the coking rate drives several high-level design decisions relating to the thermal management of an engine.

References

- Bruening GB, Chang WS. Cooled cooling air systems for Turbine thermal management. Proc ASME Turbo Expo 1999;3. <https://doi.org/10.1115/99-GT-014>.
- Colket M, Heyne J. Fuel Effects on Operability of Aircraft Gas Turbine Combustors. August. AIAA, Progress in Astronautics and Aeronautics; 2021. <https://doi.org/10.2514/4.106040>.
- Edwards T. Advancements in gas turbine fuels from 1943 to 2005. J Eng Gas Turbines Power 2007;129:13–20. <https://doi.org/10.1115/1.2364007>.
- Kosir S, Stachler R, Heyne J, Hauck F. High-performance jet fuel optimization and uncertainty analysis. Fuel 2020;281:118718. <https://doi.org/10.1016/j.fuel.2020.118718>.
- Mancini AA, Ackerman JF, Richard LK, Stowell WR. Method and Coating System for Reducing Carbonaceous Deposits on Surfaces Exposed to Hydrocarbon Fuels at Elevated Temperatures. 6808816 B2, 2004.
- Wilfert G, Sieber J, Rolt A, Baker N, Touyeras A, Colantuoni S. New Environmental Friendly Aero Engine Core Concepts. ISABE-2007-1120. 18th Int Symp Air Breath Engines 2007:1–11.
- Zabarnick S, West ZJ, Arts A, Griesenbrock M, Wrzesinski P. Studies of the impact of fuel deoxygenation on the formation of autoxidative deposits. Energy Fuels 2020;34:13814–21. <https://doi.org/10.1021/acs.energyfuels.0c02603>.

Task 1 - Estimate Gains in Aircraft Fuel Efficiency Facilitated by SAF

Washington State University and Boom Technology, Inc.

Objectives

The goal is to estimate the impact of fuel property variation on engine-level fuel consumption (SFC), considering conceptual design trades involving the outer mold line and the aircraft thermal management systems, as well as direct fuel effects on gross weight at takeoff.

Research Approach

To accomplish this task the tools developed previously under this project (award number 13--C-AJFE-UD) were used in conjunction with dual-objective optimizations of SAF composition over a database containing 1,121 molecules. To ensure meaningful results, a filter on compositions was applied to eliminate those with properties outside of fuel specifications, as predicted via algebraic blending rules. Additionally, Boom Technology contributed greatly to this goal by mission analyses for baseline and alternative aircraft architectures, where the alternative aircraft architectures exploited higher fuel specific energy and/or energy density. Boom also evaluated a variety of thermal management architectures of their own conceptualization.

Trade study results

Proprietary models developed by Boom Technology were used to derive linear relationships that relate changes in aircraft weight and drag components to changes in mission fuel consumption, to assess sensitivities. The weight derivative is used to evaluate changes in mission fuel weight (LHV) to aircraft component sizing differences; namely, heat exchangers, fuel tanks, the fuselage, wings, and engine based on revised fuel burn requirements. In total, seven cases have been considered. Configuration B/L is the baseline design, which is compatible with conventional fuel or drop-in SAF. Configuration A incorporates efficiencies of reduced fuel weight made possible by an exclusive diet of SAF with 2% (or more) higher LHV than the reference fuel, allowing the airline to reduce fuel weight while maintaining overall range. Configuration B incorporates resizing of the central fuel tank, fuselage, wings, and engine to exploit an exclusive diet of SAF with 8% (or more) higher energy density (ED) than the reference fuel without consideration of alternative aircraft volume requirements such as passengers, cargo, and systems. Configuration C combines aircraft resizing of configurations A and B, consistent with SAF having 1% higher LHV and 4% higher ED. Configuration D evaluates the technical feasibility of using fuel as the coolant for the (cabin) environmental control system (ECS). Configuration E evaluates the technical feasibility of using fuel as the coolant in the ECS precooler. Configuration F evaluates the merit of using fuel (instead of air) as the coolant in the hydraulic system. The results of these studies are summarized in Table 1.

Additionally, Boom employed proprietary mission analysis tools, considering trans-ocean flights represented by Vancouver–Tokyo and New York–London, to estimate the SCF benefit of increasing LHV. They found 0.43% (enthalpy basis) improved SFC per 1 MJ/kg increase in specific energy. This benefit can be realized on any aircraft provided the fuel’s specific energy is known to (and leveraged by) the airline prior to fueling the aircraft.

Table 1. Aircraft architecture trade study summary.

Case	Δ Weight [†]	ARES	Δ Range (nm)	Fuel Temperature
A	-0.75%	1.8%	105	No change
B	-1.3%	3.2%	190	No change
C	-1.0%	2.3%	130	No change
D	Not feasible		Fuel temperature \approx cabin temperature	
E	Not feasible		Fuel temperature exceeds safety limits	
F	-400 to -500 lbs	0.30%	15	120 °C

[†] Aircraft maximum gross weight. ARES: aircraft relative enthalpy savings.

Milestones

- Verified transfer function (0.43% per 1 MJ/kg specific energy) relating mission fuel enthalpy demand requirement to fuel enthalpy per unit mass.
- Recognized that aircraft would be designed differently if the fuel specifications called out a higher (minimum threshold) limit on specific energy. Estimated impact of aircraft design changes.
- Recognized that aircraft redesign to leverage higher ED of worst-case fuel may be technically beneficial but pragmatically more difficult than leveraging higher specific energy of worst-case fuel. Estimated impact of aircraft design changes.
- Evaluated alternative aircraft thermal management architectures intended to leverage the higher thermal stability (and higher flash point, min-to-min basis) of 100% SAF relative to conventional fuels.



Major Accomplishments

- By designing to a minimum ED requirement that is 4% higher than the current design point reference fuel and increasing the threshold specific energy of the reference fuel by 1% (both of which are attainable for optimized, 100% SAF without aromatics), supersonic aircraft can be made, at most, 2.3% more energy efficient.

Publications

Boehm, R. C.; Faulhaber, C.; Behnke, L.; & Heyne, J. S. (2024) *On Selecting Optimum Composition of Sustainable Aviation Fuels for Engine and Aircraft Efficiency*. Fuel, (submitted)

Outreach Efforts

None.

Awards

None.

Student Involvement

- Conor Faulhaber, PhD student (WSU), contributed significantly to the latest manuscript, specifically in data curation, visualization, and editing.

Plans for Next Period

- Revise manuscript as necessary to achieve publication.

Task 2 – Identify Critical Blend Components and Solvents to Study

Washington State University

Objective

The goal of this task is to understand how fuel composition variation impacts fuel consumption and specifically to identify specific molecules or distributions of molecules with particularly favorable properties, leading to improved energy efficiency from an integrated engine/aircraft systems perspective.

Research Approach

To accomplish this task the tools developed previously under this project (award number 13--C-AJFE-UD) were used in conjunction with three different dual-objective optimizations of SAF composition over a database containing 1,121 molecules and a variety of subsets of that database. Specifically, the following subsets of molecules were considered: (a) only monocyclo-alkanes; (b) all cyclo-alkanes; (c) all aromatics, n-alkanes, and iso-alkanes; (d) only iso-alkanes with a single branch; (e) ethylbenzene plus iso-alkanes with a single branch.

Discussion

This work has been submitted as a research article to the journal *Fuel*. Highlights of this paper, as relevant to this task, are reproduced below.

Optimization logic

A flowchart outlining the optimization logic is shown in Figure 1. The process begins by assigning a random number between 0 and 1 to each molecule in the database and then clipping to zero all values that were less than 0.75. This is done to limit the number of molecules that comprise each candidate fuel. Next, the assigned number is divided by 33.3, 4, or 2 if the associated molecule has a threshold sooting index (TSI) above 75, 30, or 15, respectively. This is done to increase the probability that a trial fuel will have lower sooting propensity than conventional jet fuel, even though the database contains a disproportionate number of alkylated naphthalenes (7%) and benzenes (29%). Next, this set of numbers is normalized so they sum to 1, and these represent the mole fraction of the associated molecule in the trial fuel. Together with a database of molecular properties, these trial fuel compositions are input into a subroutine to predict all of the fuel properties listed in Table 2, leveraging models developed (or selected) under ASCENT project 65A. These predicted properties are then compared against limit constraints taken from ASTM D1655 or as described here. The upper limit vapor pressure at 160 °C is set to 1 atm to ameliorate the risk of a phase change within the fuel system. We presume, at

this point, that any trial fuel that passes this constraint will also have a flash point that is higher than 38 °C, and this presumption is checked for candidate fuels that are suggested by the optimization routine. The T_{10} ruler is a surrogate requirement for the T_{10} upper limit, which is 205 °C, where the ruler is the sum of mole fractions over all fuel components that have a normal boiling point less than 205 °C. The numerical subscript refers to the volume percentage of distillate recovered at the specified temperature (T). The actual T_{10} of candidate fuels is calculated after the optimization, assuming the distillation has just one theoretical plate, similar to ASTM D86, which is one of the distillation methods called out in ASTM D1655. The TSI upper limit is set to 20, which corresponds to a smoke point of 25 mm for a fuel with a molecular weight of 170 g/mol. This constraint is a surrogate for the smoke point requirement that is expressed in ASTM D1655. Five of these six properties are limited at one end only, whereas density has both an upper and lower bound.

Table 2: Summary of Predicted Properties of Trial Fuels (Pre-Filter)

Vapor Pressure @ 160 °C	Density @ 15 °C
Kinematic Viscosity @ -20 °C	LHV
T10 ruler†	TSI

† T10 ruler is defined as a mole fraction sum, over molecules with normal boiling point less than 205 °C

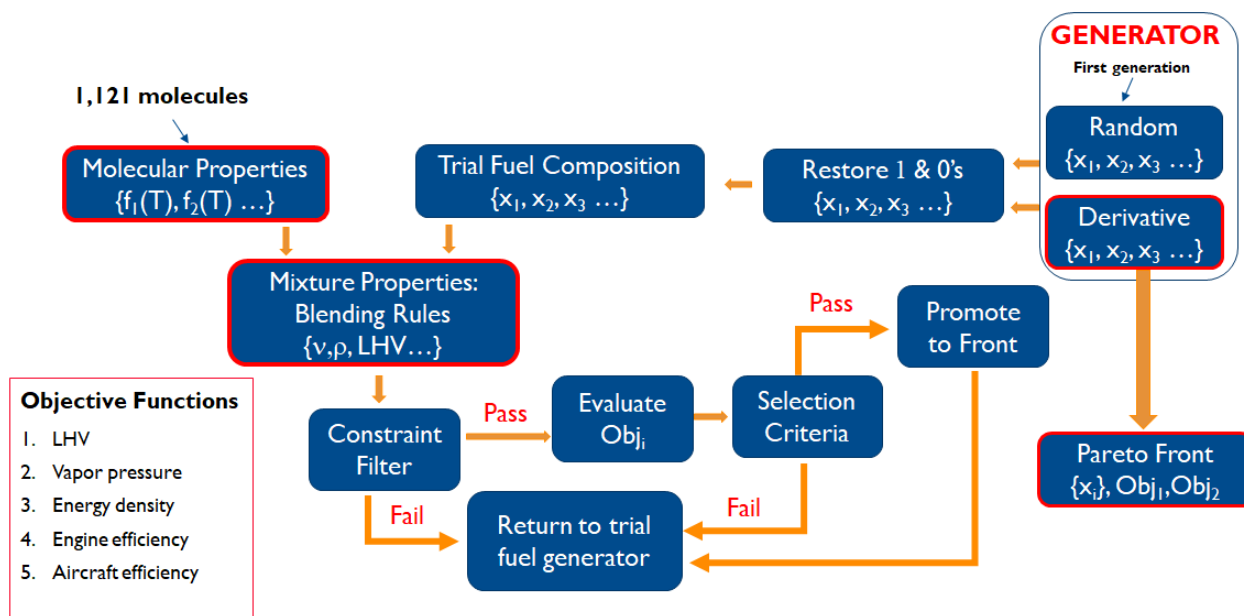


Figure 1. Fuel optimization logic. LHV: lower heating value.

If a trial fuel composition fails to express properties that meet all seven constraints, then it is discarded without any further drain on computational resources. At that point, the logic returns to the trial fuel generator. Trial fuels that pass all seven constraints are sent to the most computationally intensive subroutine where additional fuel properties are predicted based on models previously developed (or selected) under this project or ASCENT project 65A.

The selection subroutine compares each new kernel, sequentially by index, to kernels that are stored in the dynamic pareto front. If a kernel's corresponding objective functions are both determined to be more favorable than those of at least one other kernel, the inferior kernel's mole fraction vector is overwritten by that of the new kernel. At this point, the logic returns to the trial fuel generator, thereby completing a loop that continues until the user-specified iteration limit is reached.

Database

A wide array of molecules were selected to appeal to the sensitivities of fuel property models and the impact of fuel properties on enthalpy savings. The National Institute of Standards and Technology (NIST) standard reference database was leveraged as the source database for the properties required by the optimization routines. This database was filtered to contain only alkanes; mono-, bi-, or tri-cycloalkanes excluding any with 3- or 4-membered rings; alkylbenzenes; indanes or tetralins; and alkyl naphthalenes having a normal boiling point in the range from 79 to 300 °C. The upper limit of this range matches the aviation fuel specification upper limit on distillation end point, whereas the lower limit of this range was chosen for expedience, in anticipation of our internally imposed bubble point limit or the ASTM D1655 flash point limit being a property that would constrain the optimization. Each of the retained molecules had reported data over the temperature range from 15 to 155 °C for each of the properties considered in this study. Thirty-six molecules were filtered out of the database because one or more of the reported properties of the molecule was determined by visual inspection of histograms to be an outlier. Specifically, the properties considered for filtering included LHV and the first derivative with respect to temperature of density, heat capacity, thermal conductivity, and log viscosity.

Convergence

Three optimizations started with 1,121 molecules in the database. One of these iteratively maximized LHV and engine-level relative enthalpy savings (ERES), another maximized aircraft-level relative enthalpy savings (ARES) and ED, and the other maximized ARES while minimizing the vapor pressure (P_{vap}) at 200 °C. For each of these optimizations, the number of iterations required to achieve convergence was reduced by trimming molecules from the database based on their absence from any kernel fuels found within the dynamic pareto front after 5 to 10 generations, where each new generation is the result of 5,000 to 10,000 trial fuels. In the LHV/ERES optimization, this step was repeated twice, resulting in a database of 189 molecules in the final stages of the optimization. The ARES/ED and ARES/ P_{vap} optimizations ended with 210 and 261 molecules, respectively, retained in the final databases. Upon trimming the database, each optimization was restarted from scratch; that is, from randomly guessed mole fractions of molecules in the trimmed database. Convergence was declared when the n^{th} generation pareto front was less than one symbol width displaced from the $(n - 1)^{\text{th}}$ generation. Other numerical characteristics of a converged pareto front include elimination of width from the pareto front (no point on front is below and to the left of any other point on the front) and a low fraction of trial fuels are identified as kernels and subsequently promoted to the front.

Results overview

The converged pareto fronts for each of the three dual-objective optimizations are shown in Figure 2. The ARES is communicated by the horizontal axis, and particularly relevant property variations are communicated by two separated vertical axes and two separate color bars that are tied to symbol fill color or border color, respectively. ED and P_{vap} were deemed particularly relevant because they were among the objective functions considered for this study. Kinematic viscosity was deemed particularly relevant because it has a strong influence on atomization characteristics and is highly sensitive to fuel composition. TSI was deemed particularly relevant because it has a strong influence on contrail formation and represents a significant value-opportunity for SAF relative to petroleum-derived fuels.

ARES, for the representative case, can be improved by up to 0.40% relative to nominal petroleum-derived Jet A by using fuel that has been optimized for efficiency. However, the virtual SAF composition affording that level of improvement does not meet all of the requirements of ASTM D7566. Notably, the aromatics concentration is too low. Upon filtering the solutions shown graphically in Figure 2 to a minimum aromatics concentration of 8.0 %v, the remaining best-case fuel composition results in ARES=0.33%. This composition, as is the case for most of the solutions shown in Figure 2, is limited by P_{vap} at 160 °C. The ED of this solution is 34.3 GJ/m³, which is within the experience range of petroleum-derived Jet A (34.0-35.6 GJ/m³, 95% confidence interval) [Martin, 2011]. Indeed, all of the calculated properties of this solution fall within the experience range of petroleum jet fuel and, therefore, it can be considered as a potential drop-in, 100% SAF candidate (SAF100).

Note that viscosity and TSI each tend to decrease as ARES increases along each of the pareto fronts. The implication of this is that SAF affords an opportunity to simultaneously improve fuel efficiency and atomization characteristics while decreasing a principal driver (soot) to contrail formation. Also note that increasing fuel ED tends to drive viscosity higher, whereas decreasing P_{vap} (to mitigate phase transitioning within the fuel system) drives viscosity all the way up to its specification limit, adding considerable technical challenge to meeting cold-day ignition requirements. Vapor pressure at 160 °C is the limiting property for the LHV/ERES optimizations, and fuel (mass) density is also near its specification limit in these two optimizations. The difference between the full and engineered database in the LHV/ERES optimizations is subtle, suggesting that significant composition variation is possible with limited impact on performance.

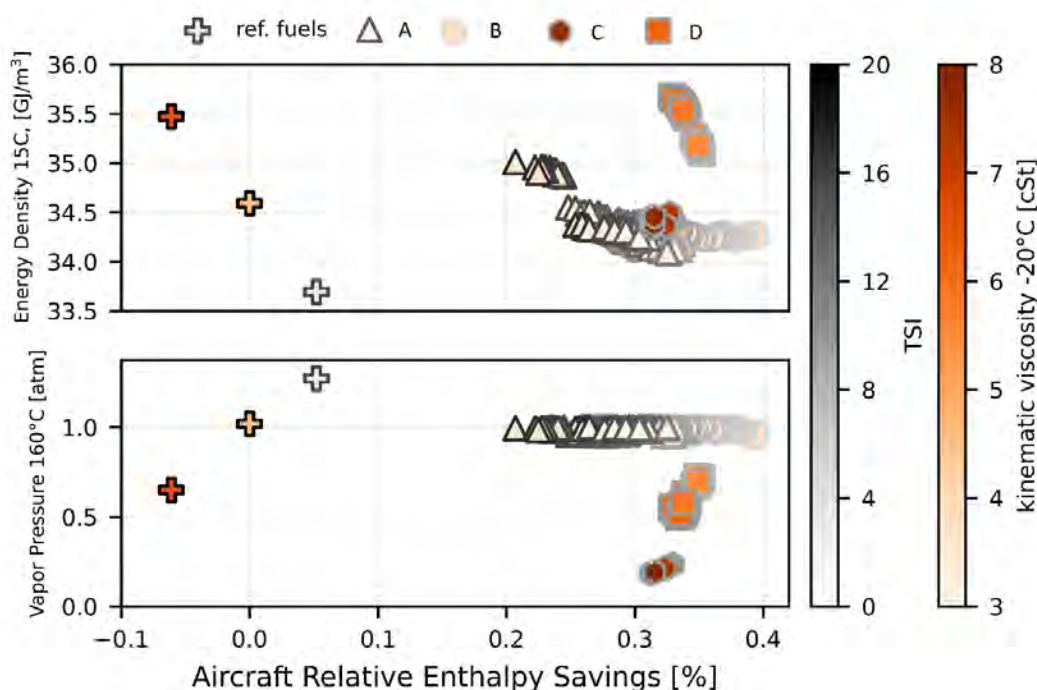


Figure 2. Jet-X optimization summary: A) results from a specific-energy/engine-relative-enthalpy-savings (LHV/ERES) optimization using the full database; B) results from an LHV/ERES optimization using database consisting of ethylbenzene and 79 iso-alkanes with a single branch; C) results from a vapor-pressure/aircraft-relative-enthalpy-savings ($P_{\text{vap}}/\text{ARES}$) optimization using the full database; and D) results from an energy-density/ARES optimization using the full database.

Figure 3 represents a summary of six different LHV/ERES optimizations, each completed over a different database of molecules to choose from. As with the results summarized by Figure 2, it is clear from Figure 3 that both viscosity and TSI tend to decrease as ARES increases, although the two databases that contain aromatic molecules produce results with higher TSI and lower viscosity than the three databases that do not contain aromatic molecules. Vapor pressure is limiting for each database except the one that contains only iso-alkanes. In that case, density is limiting. The two databases that contain only cycloalkanes result in higher ED solutions than the two databases that include aromatics, n-alkanes, and iso-alkanes, and the one database that contains only iso-alkanes with a single branch. However, ARES of the cyclo-alkane solutions are lower than the ARES of the other databases. Moreover, the solutions represented by D in Figure 2 reveal that higher ED can also be achieved by increasing the molecular weight of iso-alkanes in the SAF, where the composition detail of that pareto front is discussed below.

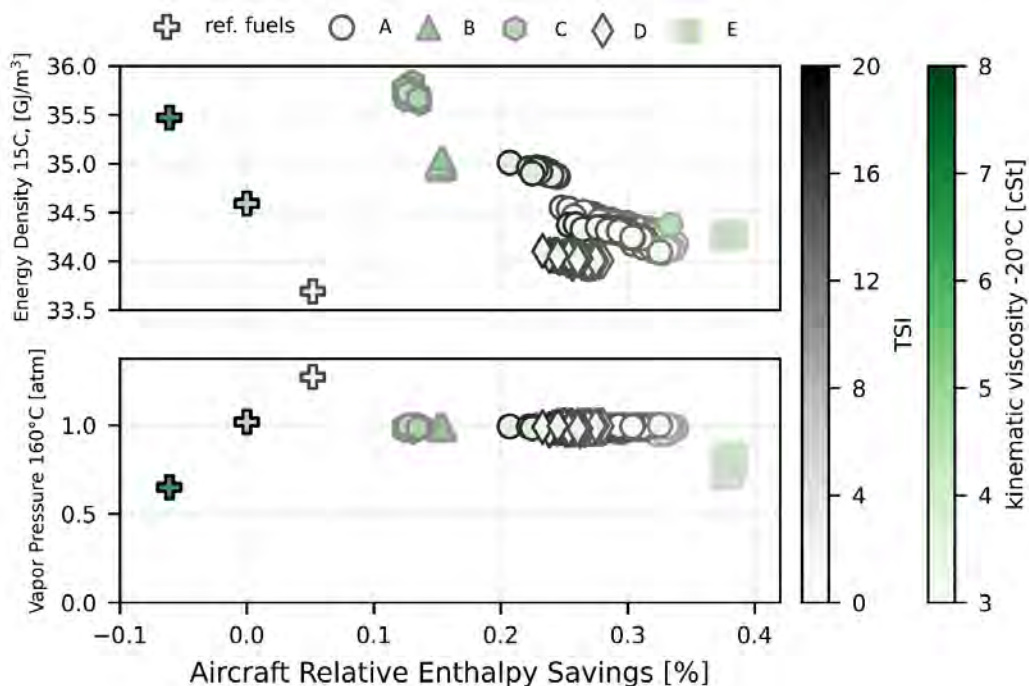


Figure 3. Results from specific-energy/engine-relative-enthalpy-savings (LHV/ERES) optimizations: A) full database; B) database containing only mono-cycloalkanes; C) database containing only mono-, bi-, and tri-cycloalkanes; D) database containing no cycloalkanes; and E) database containing 79 iso-alkanes with a single branch.

Composition characteristics of optimized Jet-X and SAF100 candidates

The prominent composition characteristics of the average of each pareto front shown in Figure 2 are discussed below.

The full database LHV/ERES optimization favored iso-alkanes (77.8 %_{mol}) over all other hydrocarbon types. In particular, 3-ethyldecane accounted for 17.0 %_{mol} of the average composition and was the only compound present at greater than 10 %_{mol}. As is evident from Figure 4, the optimization favored iso-alkanes with one or two branches, together accounting for 65.3 %_{mol} of the pareto front solutions. The average molecular weight of the alkanes in the pareto front was found to be 151.0 g/mol, with notably higher weighting of species with 10 or 12 carbon atoms. The relative paucity of iso-alkanes with 11 carbon atoms within the pareto is not yet fully explained and should not be taken too literally.

Cycloalkanes, including mono-, bi-, and tri-cycloalkanes, comprised just 9.7 %_{mol} of the pareto front solutions. Among the cycloalkanes, nearly all contained a 5-membered ring and nearly half comprised species without any alkyl group branching. The average molecular weight of the identified cycloalkanes was quite low, with carbon number (C#) ranging from 7 to 10. The most prominent cycloalkane was bicyclo[2.2.1]heptane, which accounted for 2.5 %_{mol} of the pareto front average. Aromatics, including alkylbenzenes, naphthalenes, indanes, and tetralins constituted 12.5 %_{mol} of the pareto front solutions. Nearly all of these were alkylbenzenes. Although no single aromatic molecule exceeded 3 %_{mol}, those with a total of 12 carbon atoms accounted for nearly half of all aromatic content.

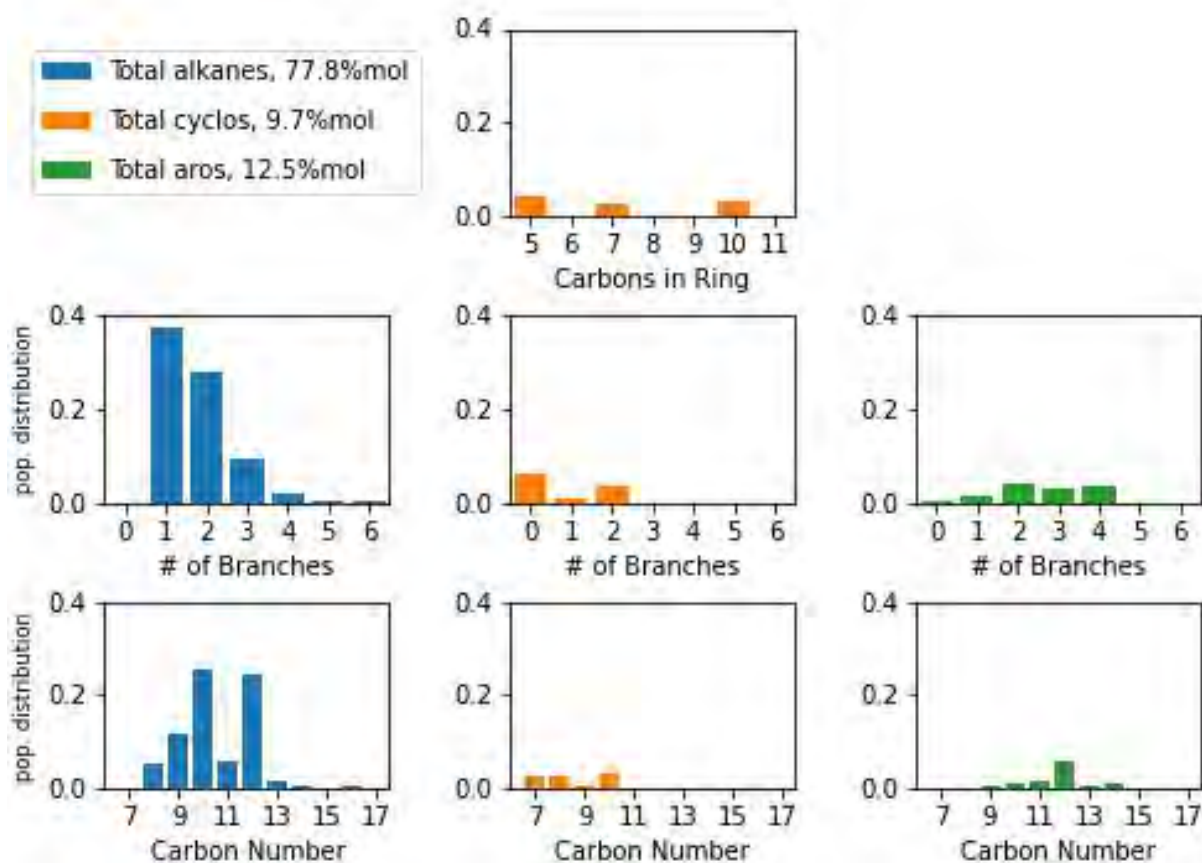


Figure 4. Composition characterization: result of a specific-energy/engine-relative-enthalpy-savings (LHV/ERES) optimization using the full database. Carbons-in-ring is defined as the total number of carbon atoms that are linked into a ring, including mono-, bi-, and tri-cycloalkanes. The total mole percentage of species with a degree of unsaturation (DoU) equal to 2, 3, 5, or 7 is 3.6%_{mol}, where DoU is defined as $(1 + C\# - H\#/2)$.

The LHV/ERES optimization initiated from a database containing ethylbenzene and 79 iso-alkanes with one branch resulted in an average (of 250 points) pareto front that contained 11.3 %_{mol} ethylbenzene and 88.7 %_{mol} iso-alkanes. The carbon number distribution, shown in Figure 5, of the iso-alkanes in these solutions was found to have much in common with the result from the LHV/ERES optimization over the full database. Like the former optimization, two molecules, 3-ethyldecane (19.1 %_{mol}) and 3-ethyloctane (15.3 %_{mol}) had significantly elevated concentrations relative to other species. However, one molecule, 6-pentyldecane (9.3 %_{mol}), was favored by this optimization but not by the similar optimization over the full database. This observation illustrates that solutions are not unique and that potential shortcomings of one solution can be overcome with little or no loss of performance benefit. For example, if one solution has a freeze point that is too high because of a too-high concentration of a high-freeze-point component, the concentration of the offending component(s), such as 3-ethyldecane or 6-pentyldecane, can be restricted to an acceptable level, and the optimization will find an alternative composition that is nearly as good.

The ARES/ED optimization that began with the full database containing 1,121 molecules also favored iso-alkanes (91.4 %_{mol}) over all other hydrocarbon types. The two most favored molecules by this optimization were 3-ethyldecane (14.9 %_{mol}) and 5,10-dimethyltetradecane (7.1 %_{mol}), and a total of 28 molecules were present at concentrations higher than 1%. A notable advantage of a fuel with many constituents is that its freeze point should be quite low. However, the producibility of such a fuel, precisely as defined by the optimized compositions, is challenging. The path forward here is to produce mixtures that

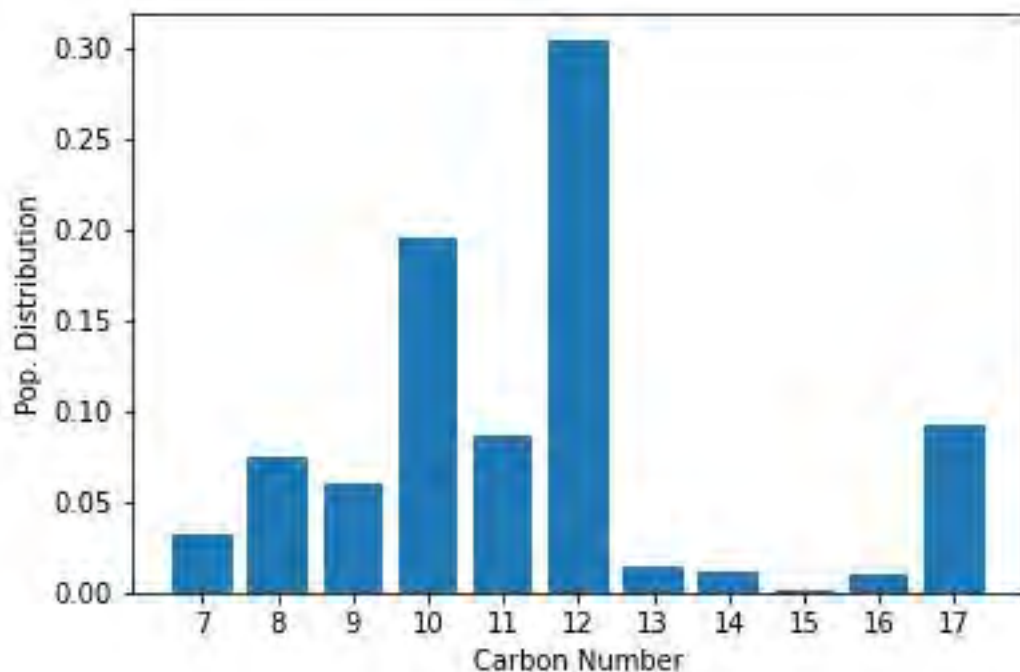


Figure 5. Composition characterization: result of an LHV/ERES optimization using a database containing ethylbenzene and 79 iso-alkanes with a single branch. The four most abundant species, on average, in this set of 250 compositions are 3-ethyldecane (19.1 %_{mol}), 3-ethyloctane (15.3 %_{mol}), ethylbenzene (11.3 %_{mol}), and 6-pentyldodecane (9.3 %_{mol}). LHV: lower heating value; ERES: engine-level relative enthalpy savings.

reproduce the higher-level composition characteristics shown in Figure 6 as closely as is pragmatic while also targeting specific representation of the most prevalent species in these definitions.

Although 3-ethyldecane was highlighted by all of the optimizations, clear compositional differences exist between those solutions optimized for LHV and ERES and those optimized for ED and ARES. The ED/ARES optimized candidates contained essentially no aromatic materials, instead containing iso-alkanes with higher molecular weight (174.6 g/ml vs. 152.3 g/ml) and more branching than their LHV/ERES optimized counterparts. The characteristics of the selected cycloalkanes also differed significantly. The ED/ARES optimization identified significant content of compounds with 8-, 9-, and 10-membered rings in addition to one bridged ring compound, bicyclo[3.3.3]undecane. Conversely, the LHV/ERES optimization identified primarily cyclopentanes and di-cyclopentanes. The often-discussed molecule decalin [Liu, 2012; Muldoon, 2020; Undavalli, 2023] was present in the full database but was not selected by any of the optimizations.

The composition resulting from the ARES/ P_{vap} optimization will not be discussed here because these solutions present too much risk to cold ignition requirements while affording a potential benefit that no OEM has requested.

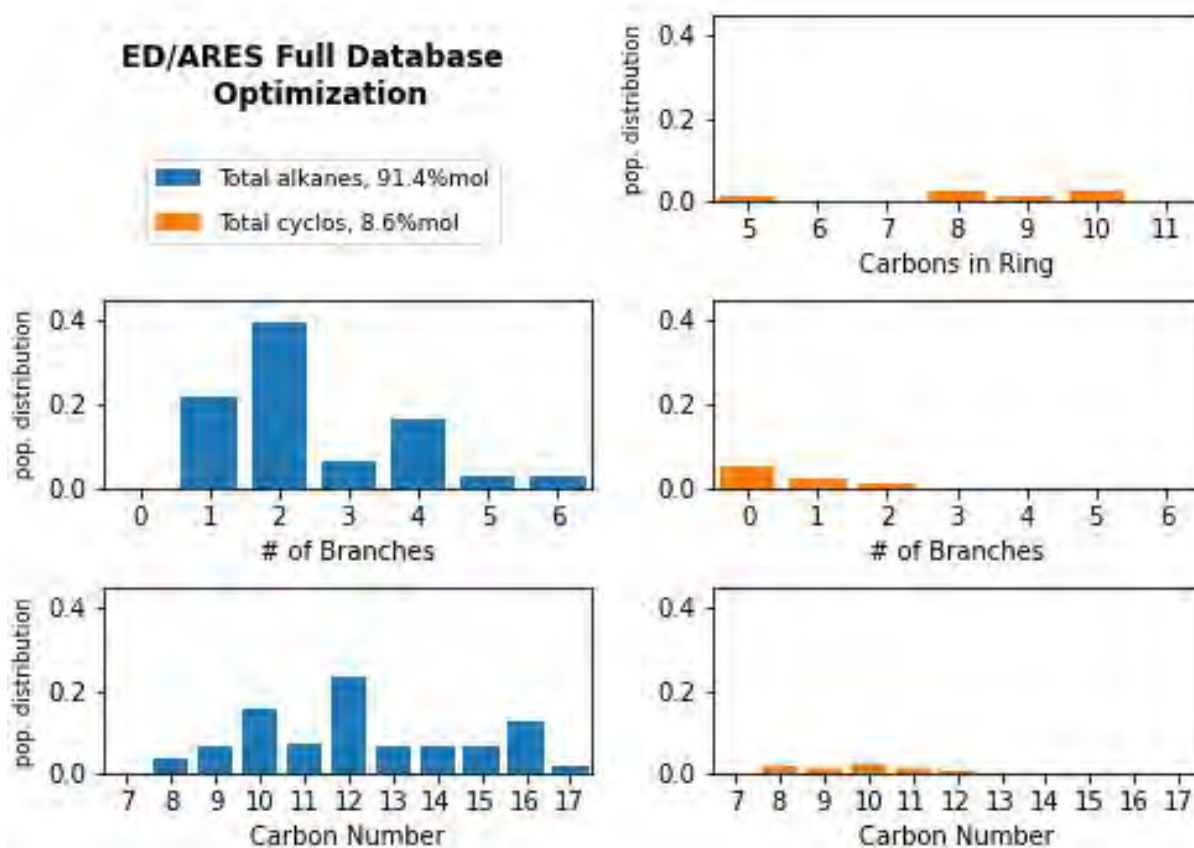


Figure 6. Composition characterization: result of an ED/ARES optimization using the full database. Carbons-in-ring is defined as the total number of carbon atoms that are linked into a ring, including mono- and bi- (or di-) cycloalkanes. ED: energy density; ARES: aircraft relative enthalpy savings.

References

- Liu Y, Wilson CW. Investigation into the impact of n-decane, decalin, and isoparaffinic solvent on elastomeric sealing materials. *Adv Mech Eng* 2012;2012. <https://doi.org/10.1155/2012/127430>.
- Martin D, Wilkins P. Petroleum Quality Information System (PQIS) 2011 Annual Report. Fort Belvoir, VA: Defense Technical Information Center; 2011
- Muldoon JA, Harvey BG. Bio-Based Cycloalkanes: The Missing Link to High-Performance Sustainable Jet Fuels. *ChemSusChem* 2020;13:5777–807. <https://doi.org/10.1002/CSSC.202001641>.
- Undavalli V, Gbadamosi Olatunde OB, Boylu R, Wei C, Haeker J, Hamilton J, et al. Recent advancements in sustainable aviation fuels. *Prog Aerosp Sci* 2023;136:100876. <https://doi.org/https://doi.org/10.1016/j.paerosci.2022.100876>.

Milestones

- Created new internal code for fuel composition optimization, more amenable to large databases and Boolean-type constraints than our previously used solver, Mixed Integer Distributed Ant Colony Optimization (MIDACO).
- Finalized validation of properties database containing 1,121 molecules.
- Recognized and documented effects of hydrocarbon class on aircraft fuel economy.
- Established entitlement for direct fuel effect on aircraft fuel economy for both drop-in and non-drop-in, 100% synthetic fuels.
- Documented composition characteristics of optimized 100% SAF fuels (both drop-in and non-drop-in).



Major Accomplishments

- Established entitlement for direct fuel effect on aircraft fuel economy for both drop-in and non-drop-in, 100% synthetic fuels.
- Documented composition characteristics of optimized 100% SAF fuels (both drop-in and non-drop-in).

Publications

Boehm, R. C.; Faulhaber, C.; Behnke, L.; & Heyne, J. S. (2024) *On Selecting Optimum Composition of Sustainable Aviation Fuels for Engine and Aircraft Efficiency*. Fuel, (submitted)

Outreach Efforts

None.

Awards

None.

Plans for Next Period

- Revise manuscript as necessary to achieve publication.
- Procure materials as guided by section 3.3 of the attached draft manuscript.

Task 3 - Create and Test Blends for Thermal Stability

Washington State University

Objective

The goal of this task is to investigate possible synergies between typical impurities in conventional jet fuel and various organic nitrogen molecules with an emphasis on typical impurities in bioproducts made from waste streams via hydrothermal liquification (HTL).

Research Approach

1. Create worst-case petroleum fuel by spiking one aliquot of the sample with the polar extract of a different aliquot of the same sample.
2. Create worst-case bioproduct by spiking one aliquot of the sample with the polar extract of a different aliquot of the same sample.
3. Execute ASTM D3241 on various blends of the two spiked sample streams (replication required).
4. Document comparison in terms of two metrics pulled from characterization of the test articles via ellipsometry: the peak and area of the curve showing the angular (360°) average deposit thickness at different axial planes along the length of the test specimen.

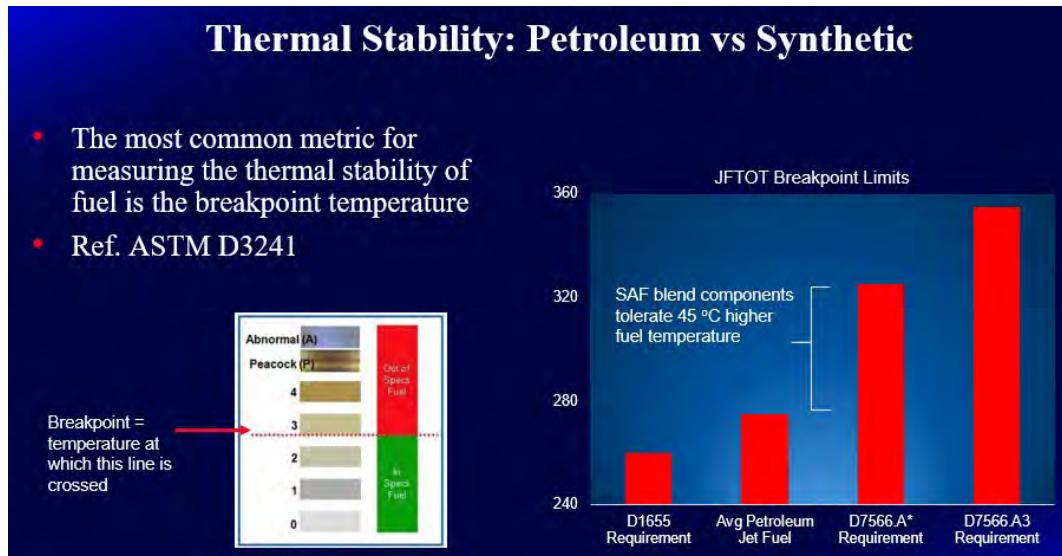


Figure 7. Summary comparison of fully petroleum and fully synthetic fuels thermal stability. SAF: Sustainable Aviation Fuel, JFTOT: Jet Fuel Thermal Oxidation Test (ASTM D3241), D1655 & D7566 are jet fuel specifications published by ASTM.

Milestones

- Commissioned Jet Fuel Thermal Oxidation Tester (JFTOT) and

Major Accomplishments

None.

Publications

None.

Outreach Efforts

None.

Awards

Conor Faulhaber, Distinguished Graduate Research Program (DGRP) appointment, Pacific Northwest National Laboratory

Student Involvement

Conor Faulhaber, a graduate student (WSU), is leading this effort.

Plans for Next Period

- Standardize methodology for amplifying both SAF and petroleum fuel impurities for the purpose of accessing the impact of typical SAF impurities on thermal stability of SAF/petroleum fuel blends.
- Publish at least one paper on the topic of the effect of organic nitrogen materials on fuel properties such as thermal stability and elastomer seal swell.



Project 067 Impact of Fuel Heating on Combustion and Emissions

Purdue University

Project Lead Investigators

Robert P. Lucht
Ralph and Bettye Bailey Distinguished Professor of Combustion
School of Mechanical Engineering
500 Allison Road
Purdue University
West Lafayette, IN 47907-2014
765-714-6020
Lucht@purdue.edu

Carson D. Slabaugh
Associate Professor
School of Aeronautics and Astronautics
500 Allison Road
Purdue University
West Lafayette, IN 47907-2014
765-494-3256
cslabau@purdue.edu

University Participants

Purdue University

- P.I.s: Dr. Robert P. Lucht and Dr. Carson D. Slabaugh
- FAA Award Number: 13-C-AJFE-PU-038
- Period of Performance: October 1, 2020 to September 30, 2023
- Task: Investigate the effects of fuel heating on combustion and emissions for aviation gas turbines

Project Funding Level

Project 67 was funded by the FAA at the level of \$250,000 for the project period June 5, 2020 to June 4, 2021; an additional \$250,000 for the time period from June 5, 2021 to September 30, 2022; and an additional \$250,000 for the time period from October 1, 2022 to September 30, 2023. The required cost-sharing 1:1 match of \$750,000 was provided by Purdue University. A funding level of \$200,000 has been approved for the project period of October 1, 2023 to September 30, 2024, with the required cost-sharing 1:1 match of \$200,000 to be provided by Purdue University.

Investigation Team

Prof. Robert P. Lucht, (P.I.)

Prof. Carson D. Slabaugh, (co-P.I.)

Thomas McLean, Tristan Shahin, Ben Murdock, Zander Hodge, and Keaton Koenig, (graduate students), responsible for the design of system components, such as the fuel heating system, and will be responsible for executing test operations.

Dr. Rohan Gejji, (research engineer), helping the graduate students with their design projects and supervising the test operations.

Dr. Bahman Habibzadeh, (current FAA program manager)

Dr. Prem Lobo, (program manager October 1, 2022 to September 30, 2023)



Project Overview

The goal of this project is to evaluate the effects of heating jet fuel before injection in an aviation gas turbine combustor on combustion efficiency, pollutant emissions, and dynamics. In an aircraft engine, heat that would otherwise be wasted can be directed into the fuel to increase its sensible enthalpy before injection. Thermochemistry dictates that this increase in sensible enthalpy must lead to lower fuel consumption for a given combustor exit temperature. However, the effects of elevated fuel temperature on combustion performance characteristics (such as the fuel spray pattern, spatial distribution of reaction zones, pollutant emissions, and combustion dynamics) are not yet well understood. We will perform experiments with heated fuels by using a piloted, partially premixed fuel injector located in an optically accessible combustor. This process will allow us to apply advanced laser diagnostic techniques to compare the behavior of the combustor at different fuel temperatures over a wide range of operating conditions.

The platform for the planned experiments is the Combustion Rig for Advanced Diagnostics (COMRAD). The test rig (Figure 1) is designed to operate at steady-state conditions with thermal power as high as 8 MW, inlet air pressure (P_3) as high as 4.0 MPa, and inlet air temperature (T_3) as high as 1,000 K. To facilitate operation at these conditions, the test article is made of aviation-grade alloys and is thoroughly water cooled, and the inner windows are film cooled with heated nitrogen. Before this project, extensive testing with ambient-temperature fuels was performed in this rig, with a focus on 5- and 10-kHz particle image velocimetry (PIV) measurements in the downstream boundary condition window section, and 50- and 100-kHz PIV measurements in the flame zone.

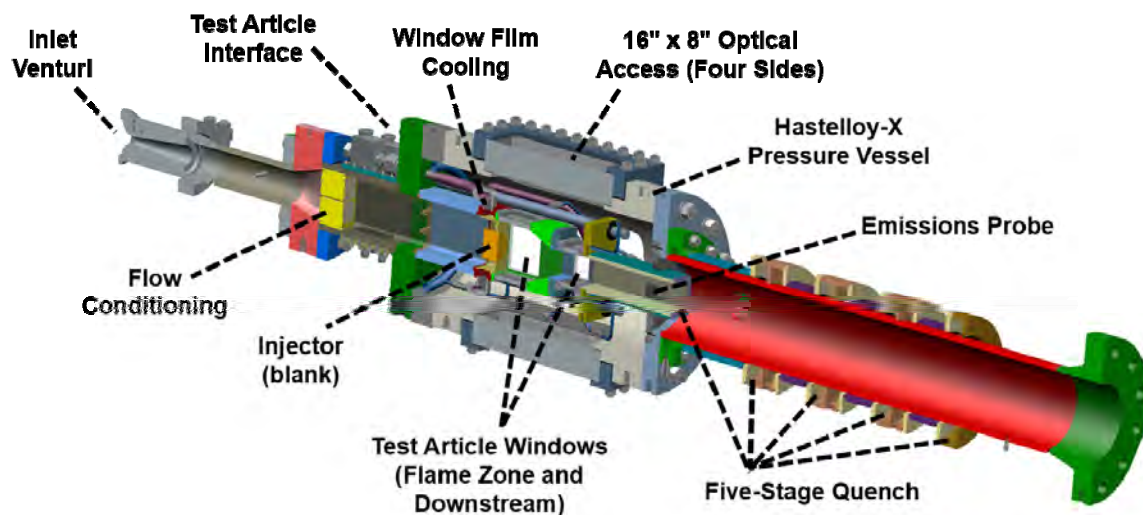


Figure 1. Schematic diagram of the Combustion Rig for Advanced Diagnostics (COMRAD).

Task 1 - Investigate the Effects of Fuel Heating on Combustion and Emissions for Aviation Gas Turbines

Purdue University

Objective

The goal of this project is to determine the effects of fuel heating on the performance of aviation gas turbines. Fuel heating can potentially lead to higher efficiency but can also lead to changes in the fuel distribution pattern and in the locations of reaction zones in the combustor. These changes may also affect pollutant emissions and combustion dynamics during engine operation. We will perform experiments using heated fuels and measure the fuel distributions, reaction zone distributions, pollutant emissions, and combustion dynamics at a range of fuel temperatures from near room temperature to above the supercritical temperatures for hydrocarbon fuels.



Research Approach

We will perform experiments with heated fuels by using a piloted, partially premixed fuel injector located in an optically accessible combustor. This experimental system will allow us to apply advanced laser diagnostic techniques to compare the behavior of the combustor at different fuel temperatures over a wide range of operating conditions. These advanced diagnostic techniques include fuel planar laser-induced fluorescence (PLIF) imaging to monitor fuel distribution patterns, hydroxyl (OH) radical PLIF (OH PLIF) imaging to monitor reaction zones, and PIV to measure the flow fields. We will also measure emissions with probe sampling and will use pressure transducers to measure combustion dynamics.

Milestones

The milestones for the work performed in fiscal year 2023 are as follows:

- A full-scale facility reconfiguration was conducted in the test cell housing this experiment to improve experiment productivity and ease of diagnostics application as well as update key infrastructure required for testing.
- 10-kHz simultaneous stereoscopic particle image velocimetry (SPIV) and OH* chemiluminescence (CL) data were analyzed to quantify the effect of fuel heating on combustion dynamics for both Shell GTL GS190 and Jet A fuels.
- A system for laser-induced incandescence (LII) for the measurement of soot formation and oxidation processes in the combustion zone was developed. This will allow us to compare soot formation and oxidation for both sustainable aviation fuels (SAFs) and petroleum-based fuels such as Jet A.

Major Accomplishments

In the current reporting period, we continued our investigation of the effects of injection of heated jet fuel on the combustion efficiency, dynamics, and emissions in a model aviation gas turbine combustor. Tests from combustion experiments with heated fuel were analyzed from a range of equivalence ratios at pressures of 1.0 and 2.0 MPa. The tests focused on emission sampling, high-frequency pressure measurements, Mie scattering, and simultaneous SPIV and OH* CL.

Facility overview

COMRAD is supplied by facility fluid systems including heated air, heated nitrogen, high-pressure water, and liquid jet fuel. Two types of liquid jet fuel were used separately for this work: (a) Jet A, and (b) Shell GTL GS190, a Fischer-Tropsch synthetic paraffinic kerosene (FT-SPK). The rig features a piloted swirl injector (shown schematically in Figure 2), housed inside a duct within a large-windowed pressure vessel enabling optical access to the entire flame from four sides. Figure 3 shows a diagram of the test rig. Combustion air is supplied to the test article at 755 K and up to 20 bar. After it is metered, the air passes through a flow conditioner and into the air plenum, which supplies both the pilot and main sections of the injector.

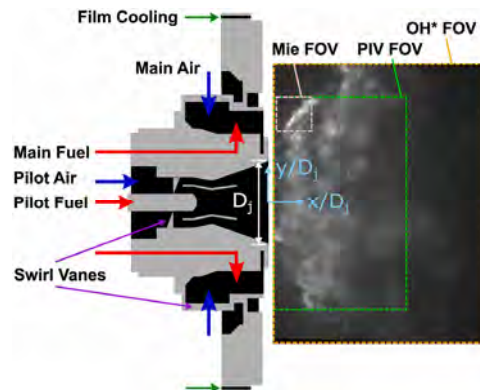


Figure 2. Schematic of injector indicating reactant flow routing as well as the Mie scattering and particle image velocimetry (PIV) fields of view (FOV) relative to an instantaneous OH* chemiluminescence (CL) image.

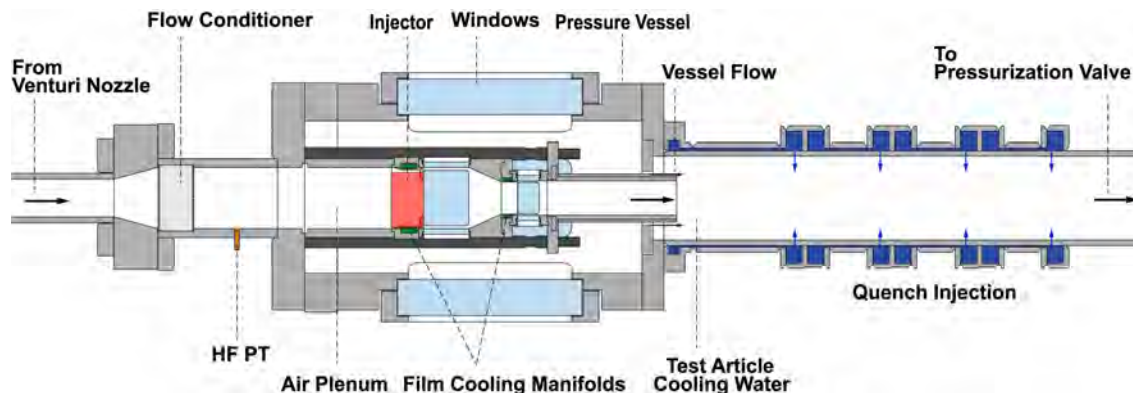


Figure 3. Schematic representation of the combustor, highlighting primary features. The abbreviation HF PT stands for high-frequency pressure transducer.

Liquid jet fuel is supplied to the injector at temperatures as high as 590 K by an 81-kW fuel heater. The fuel heater (Figure 4) comprises a stack of copper blocks with 20 cartridge heaters inserted into each block. Fuel flows in stainless steel tubes through three independent circuits, two pilot circuits, and one main circuit. The mass flow rates in each circuit are measured with Coriolis flow meters. In the fuel heater, the stainless steel tubes are clamped between each pair of copper blocks before being delivered to the test rig. The temperature of the fuel is monitored both in the fuel heater (to ensure that no phase change is encountered) and immediately upstream of the injector. Fuel passes through approximately 50 cm of trace-heated tubing from the heater to the test rig. The tubing is air-jacketed within the test rig to inhibit heat transfer from the heated air before the injector is reached. To prevent coking in the fuel lines at high fuel temperatures, the fuel tank is sparged with nitrogen for 30 minutes before use to remove dissolved oxygen, and the tank ullage is purged with nitrogen during the experiment. A dissolved-oxygen sensor (Mettler Toledo Inpro 6850i) is used to ensure that the levels of dissolved oxygen remain below 0.2% of the fully saturated level during the experiment. An inert gas purge circuit is used to prevent collection of stagnant fuel in the heater and the tubing to the experiment when fuel is not flowing to the experiment. This purge displaces the fuel to a collection tank through a bypass circuit and counter-flow heat exchanger that cools the fuel temperature to ambient temperature with water as the heat transfer medium.

At the injector, fuel is injected into two co-swirling flows of air separated by a bluff body. The inner flow forms the pilot flame, and the outer flow forms the main flame, where most of the fuel is burned. The fuel flow rates to the pilot and main circuits are separate to enable independent control of the fuel/air ratio in each part of the flame. The pilot flame is operated at a higher fuel/air ratio than the main flame, allowing the main flame to stabilize as the pilot products mix with the main reactants. The main reactant stream is assumed to be partially premixed when it reaches the flame, but the pilot flame is mostly non-premixed.

The flame zone is contained by a rectangular duct with a height/width ratio of approximately 1.4. Fused quartz windows are installed on each side of the duct to enable imaging of the flame, which is not presented in this work. These windows are film cooled with heated nitrogen at approximately 590 K to lessen the thermal load created by the flame. The film cooling flow rate is independently controlled but is set to a constant fraction of the combustion air flow rate. The duct then contracts vertically to a height/width ratio of approximately 0.75. Downstream of this contraction, another windowed section is present. A separate supply of heated air flows through the pressure vessel at the same pressure as the combustor, and this flow merges with the test article flow in a pipe, where water is radially injected into the flow to cool it. An electrically actuated butterfly valve is installed at the exit of the flow path to back-pressurize the combustor. The inner duct is coated with a thermal barrier coating and cooled by internal water channels. This cooling water is directed into the flow at the exit of the inner duct.

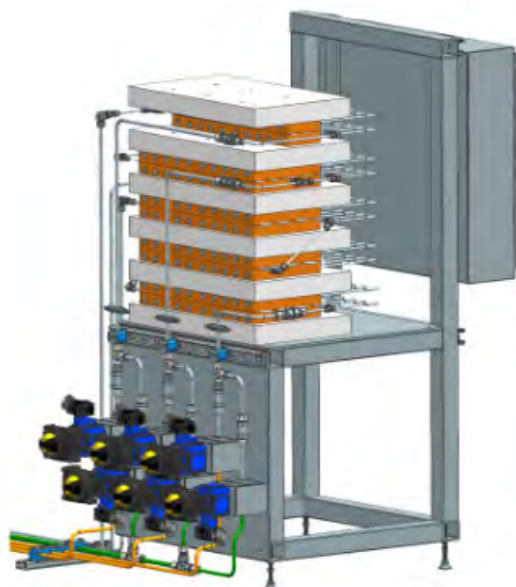


Figure 4. Computer-aided design rendering of the fuel heater.

Heated air and nitrogen sources are metered with sonic Venturi nozzles, high-pressure water is metered with cavitating Venturi nozzles, and jet fuel is metered with Coriolis flow meters. The test rig is equipped with pressure transducers (GE PMP50E6) and K-type thermocouples (Omega GKMQSS-062G) for flow metering and in several different locations throughout the flow path. These instruments are sampled at 100 Hz to monitor the operating conditions, and a National Instruments LabVIEW virtual instrument is used to display measured values and send commands to pneumatically and electrically actuated valves in the test cell. The relative uncertainties of calculated mass flow rates have been determined to be below 0.83% for gases and below 0.10% for liquid fuel according to the Kline-McClintock method, with a 95% confidence interval. A high-frequency pressure transducer (Kulite WCT312M-70BARA) is installed in the air plenum to monitor acoustic oscillations.

Emission measurements

Exhaust gas emissions were characterized for Shell GTL GS190 and Jet A fuels at two operating combustor pressures (1 and 2 MPa) and a range of fuel temperatures. An exhaust sampling probe designed and described in the previous reporting period was used for these measurements. The sampling probe features five 0.38-mm holes on its upstream surface, which are spaced at 5%, 15%, 25%, 35%, and 45% of the channel height and centered relative to the channel width. The internal flow path of the probe is designed such that the pressure drop across the sample holes is enough to choke the flow through each hole, ensuring a uniform sample of the exit cross-section. Similar to the inner duct, the probe is coated with a thermal barrier coating and contains internal water-cooling channels that dump into the flow path at the downstream surface of the probe. After exiting the probe, the emissions sample was routed out of the pressure vessel and maintained at 464 K by wrap-heated tubing as it flowed to a Fourier transform infrared (FTIR) spectrometer (MKS Instruments MG2030). The FTIR spectrometer measured absorption spectra using a Michelson interferometer, and these spectra were used to calculate mole fractions of major and minor product species, including CO₂, O₂, H₂O, CO, NO, NO₂, and unburnt hydrocarbons (UHC). Upon reaching steady state at an operating condition, these spectra were acquired at 1 Hz for 20 seconds. In this work, average concentrations are reported, and 1 standard deviation is used as the uncertainty of each species concentration.

A summary of test conditions at which emissions measurements were performed are tabulated in Table 1 below.



Table 1. Summary of test conditions for emission measurements. The table lists the air mass flow rate (\dot{m}_{air}), the inlet air temperature (T_3), the inlet pressure (P_3), the total equivalence ratio (ϕ_{total}), and the average fuel temperature ($T_{fuel,avg}$).

Condition	Fuel	\dot{m}_{air} [kg/s]	T_3 [K]	P_3 [bar]	ϕ_{total}	$T_{fuel,avg}$ [K]
1-A	Jet A, FT-SPK	0.59	755	9.7	0.39–0.52	366
2-A	Jet A, FT-SPK	0.59	755	9.7	0.37–0.52	478
3-A	Jet A, FT-SPK*	0.59	755	9.7	0.37–0.51 (0.56, 0.61)*	589
3-B	Jet A, FT-SPK	1.18	755	19.4	0.37–0.51	589

Nitrogen oxide (NOx) emissions from the combustor are shown in Figure 5. With both fuels, as the total equivalence ratio ϕ_{total} was increased, the NOx emission index (EI, g NOx/kg fuel) increased approximately linearly between $\phi_{total} = 0.37$ and $\phi_{total} = 0.52$. However, two conditions were sampled at $\phi_{total} = 0.54$ and $\phi_{total} = 0.60$ at $T_{fuel,avg} = 589$ K, which shows that the NOx EI begins to decrease when the total equivalence ratio was raised beyond approximately $\phi_{total} = 0.51$. The fuel temperature was varied at multiple total equivalence ratios between 0.37 and 0.52, and a significant effect on NOx emissions was measured. With the Jet A fuel, the NOx EI increased by 16%-45% when $T_{fuel,avg}$ was raised from 366 K to 478 K, and increased by an additional 2%-25% when $T_{fuel,avg}$ was raised from 478 K to 589 K. With the FT-SPK fuel, the NOx EI rose by 16%-21% when $T_{fuel,avg}$ was raised from 366 K to 478 K, but little change was seen when $T_{fuel,avg}$ was raised from 478 K to 589 K.

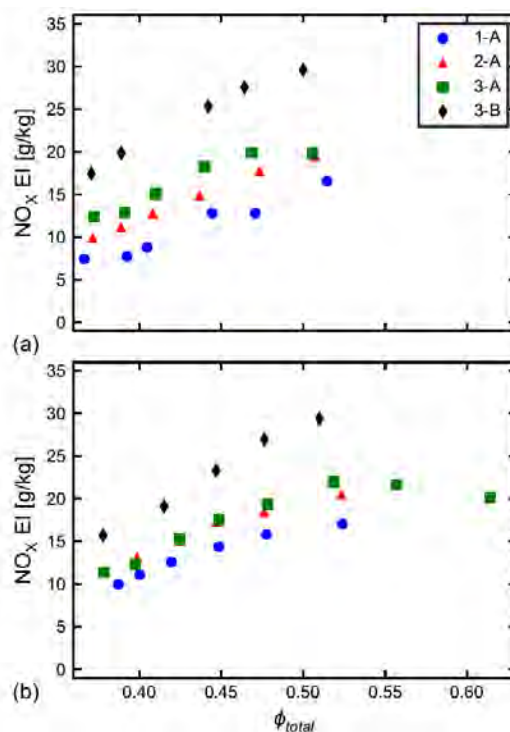


Figure 5. Comparison of nitrogen oxide (NOx) emissions index for (a) Jet A, and (b) Shell GTL GS190 fuels. EI, emissions index; ϕ_{total} . The conditions listed (1-A, 2-A, 3-A, and 3-B) are defined in Table 1.

To investigate the effect of additional enthalpy due to fuel preheating on NO_x emissions, the adiabatic flame temperature was computed at each operating condition using the NASA CEA program and the lower heating value of Jet A. Figure 6 depicts the NO_x EI at these computed flame temperatures using the FT-SPK fuel. If the observed increase in NO_x were due to the additional enthalpy provided by the preheated fuel, then results from all three fuel preheat temperatures should be collinear. Since this is not the case, the increase in the NO_x EI must be due to additional factors. It is hypothesized that differences in the thermophysical or chemical properties for the two fuels are contributing factors. The extent of mixing for the fuels in particular regions may be changed significantly as the fuel is heated and the viscosity and evaporative properties of the fuel change.

As the fuel temperature is increased, the adiabatic flame temperature increases, and the combustion efficiency is observed to increase. Consequently, the forward reaction rates of the Zeldovich mechanism increase, and more NO is formed in both the pilot and main flames on average. The pilot flame is richer than the main flame and thus creates a higher local flame temperature for all conditions in this work. Because NO formation by the Zeldovich mechanism is known to depend exponentially on temperature, increases to the fuel temperature will have a comparably larger effect on NO formation in the pilot flame than in the main flame. Regions throughout the flame that have higher local equivalence ratio caused by unsteady flow processes also experience this effect. This phenomenon helps to explain the observed increases in NO_x emissions, which are higher than what would be expected with equivalent increases in the adiabatic flame temperature of a perfectly premixed flame.

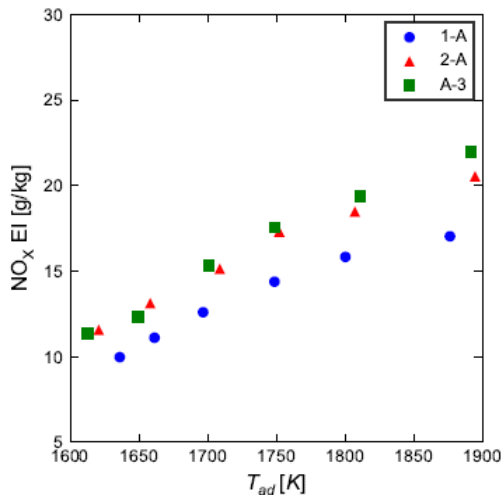


Figure 6. Nitrogen oxide (NO_x) emissions index (EI) using the Fischer-Tropsch synthetic paraffinic kerosene (FT-SPK) fuel as a function of computed adiabatic flame temperature, T_{ad} . The conditions listed (1-A, 2-A, and 3-A) are defined in Table 1.

Bar plots of combustion efficiency, NO_x EI, CO EI, and UHC EI results are illustrated in Figure 7 for both fuels at condition 3-A to facilitate a direct comparison between Jet A and FT-SPK. Combustion efficiency is similar at all equivalence ratios, with slightly higher combustion efficiency observed for FT-SPK in all cases except the leanest. NO_x emissions are also similar, with no clear trend in fuel sensitivity observed. The CO EI is slightly larger for FT-SPK at the leanest condition. However, there is a greater reduction in CO for FT-SPK as the equivalence ratio increases. At the richest condition for which data were acquired for both fuels ($\phi = 0.51$), the Jet A flame yields greater CO production than the FT-SPK flame.

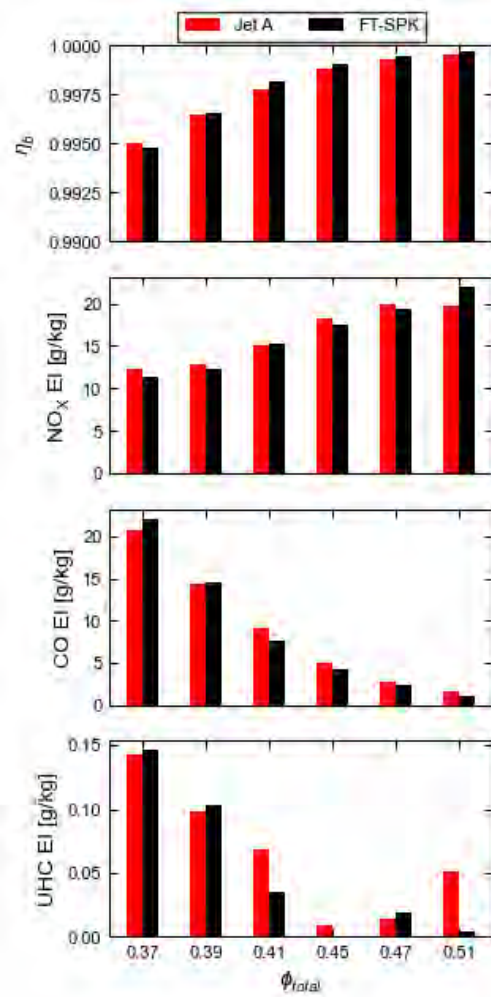


Figure 7. Summary of combustion efficiency (η_b) and emissions index (EI) measurements for Jet A and Fischer-Tropsch synthetic paraffinic kerosene (FT-SPK) fuels at the 3-A operating condition.

Simultaneous SPIV and OH* chemiluminescence

Simultaneous 10-kHz SPIV and OH* CL data were analyzed. The experimental system for these measurements is shown in Figure 8. A neodymium-doped yttrium aluminum garnet (Nd:YAG) laser provided doublets of 532 nm light at 3.0 mJ/pulse with a pulse separation of 3.0 μ s. Four cylindrical lenses were used to collimate and form a 70-mm-wide laser sheet, which was directed to the centerline of the combustor with mirrors for a resulting sheet thickness below 1 mm. The flow was seeded with 200-nm zirconia (ZrO₂) with an independently controlled air circuit. Imaging of the scattered light from the seed particles was performed with two high-speed CMOS cameras (Phantom v2512), each mounted with a 200-mm focal length, $f/4.0$ lens to ensure a focused measurement domain. A double-sided, two-plane dot target was used to dewarp and spatially calibrate the images. A bandpass filter centered at 532 nm with a 3-nm full width at half maximum (FWHM) and a wide-band bandpass filter were used to further condition the imaging, resulting in a 50 mm by 80 mm FOV and spatial resolution of 15.8 pixels/mm.

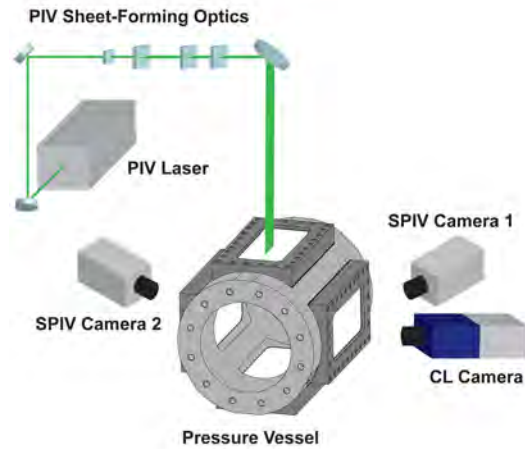


Figure 8. Diagram of stereoscopic particle image velocimetry (SPIV) measurement system. CL, chemiluminescence.

OH* CL imaging was performed using a high-speed CMOS camera (Phantom v411) coupled to a Lambert HiCATT 25 intensifier. A 40-nm FWHM bandpass filter centered at 320 nm was used to isolate the flame emission signal from the background, which was then collected through a 98-mm focal length, $f/2.8$ lens, giving an image spatial resolution of 166 $\mu\text{m}/\text{pixel}$. To monitor pressure fluctuations, a high-frequency pressure transducer was placed 450 mm upstream of the injector.

Table 2. Summary of test conditions for stereoscopic particle image velocimetry (SPIV)/chemiluminescence (CL). The parameters listed in the table are, in order, the inlet pressure, the air mass flow rate, the total (pilots plus main) fuel flow rate, the inlet air temperature, the total equivalence ratio, the pilot fuel mass flow fraction, and the average fuel temperature.

P_3 [MPa]	\dot{m}_{air} [kg/s]	$\dot{m}_{f,total}$ [g/s]	T_3 [K]	ϕ_{total}	$\dot{m}_{f,pilot}/\dot{m}_{f,total}$ [%]	$T_{fuel,avg}$ [K]
1.0	0.59	15.0	755	0.36 - 0.39	30	293 - 522

Operating conditions for all of the experiments analyzed are summarized in Table 2. Combustion experiments for both fuels were conducted with fuel temperatures ranging from ambient to >500 K. High-frequency pressure data were analyzed to quantify the magnitude of combustion instability as the fuel injection temperature is increased. P'/P amplitudes were calculated by dividing the peak-to-peak pressure fluctuation amplitude by the mean value over the entire sample, and normalized results are shown below in Figure 9.

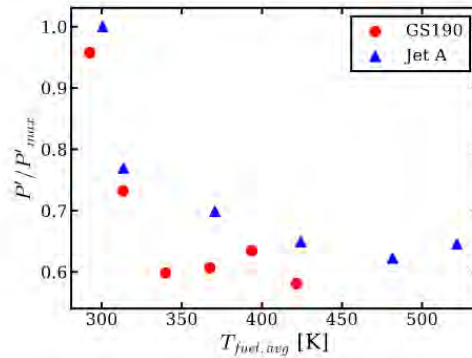


Figure 9. Normalized fluctuating pressure (P'/P_{max}) as a function of average inlet fuel temperature ($T_{fuel,avg}$) for Jet A and Shell GTL GS190 fuels.

At ambient temperatures near 300 K, a maximum in normalized P'/P is observed for both fuels, indicating the presence of global combustion instability. This behavior is believed to result from a self-excited thermoacoustic instability coupled to an equivalence ratio oscillation resulting from fluctuations in fuel droplet injection. As the fuel is heated, P'/P amplitude decreases drastically and levels off at around 60% of the maximum. After only 100 K of heating, the amplitude remains roughly constant, indicating stable combustion and attenuation of the instability mode. Stable combustion is achieved while the fuel injection temperature is still below the expected boiling temperature, indicating that the time delay of fuel droplet heating and evaporation contributes to the coupling with thermoacoustic oscillations. Between the two fuels, P'/P amplitudes for GS190 are consistently lower and decrease at a faster rate than that of Jet A.

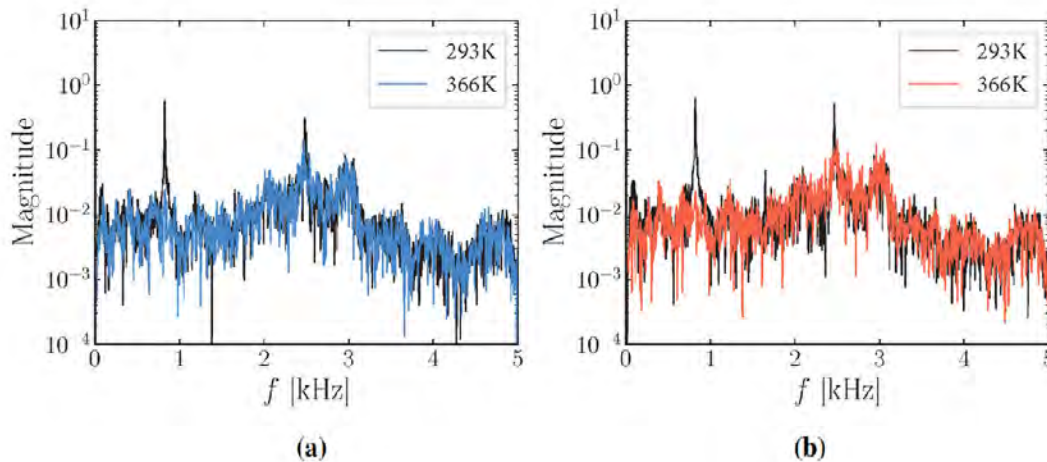


Figure 10. Power spectral density of fluctuating pressure at fuel temperatures of $T = 293$ K and $T = 366$ K for (a) Shell GTL GS190 and (b) Jet A fuels. The symbol f is frequency of the pressure fluctuation.

Power spectral density plots of the fluctuating pressure were calculated from the fluctuating pressure signal. Figures 10a and 10b show power spectral density magnitudes for GS190 and Jet A test results, respectively, at different fuel temperature conditions. For both fuels at ambient injection temperatures, a sharp peak is observed at 825 Hz and its associated harmonics, indicating coherent fluctuations. Peak magnitudes are slightly higher for Jet A than for GS190, especially for the harmonics, which corroborates with the higher P'/P magnitudes observed for Jet A. When the fuel injection temperature increases, these frequency peaks disappear from the spectrum for both fuels, indicating dampening of the instability.

Investigation of flame dynamics was performed using sets of 2,000 images from the OH* chemiluminescence (CL), particle image velocimetry (PIV), and Mie scattering results, allowing for sufficient analysis of 165 cycles at the 825-Hz instability mode. Time-averaged images for the OH* CL, PIV, and Mie scattering are shown from left to right in Figure 11. The time-

averaged PIV results show the predominant flow features. A lower velocity inner pilot flow extends radially and axially outward and impinges with the higher velocity outer main flow at a normalized distance from the injector face of $x/D_j = 0.75$, where x is the axial distance from the injector face, and D_j is the diameter of the injector. The normalized distance from the injector centerline is given by $y/D_j = 0.75$, where y is the radial distance from the centerline. A central recirculation zone (CRZ) exists within the pilot flow, and an inner recirculation zone (IRZ) exists within the region between the pilot and main flow. An outer recirculation zone (ORZ) exists between the main flow and walls of the combustor but is outside the FOV of the PIV images. Analysis on the time series of images shown in Figure 11 is then performed to better understand the coupling mechanism between the evaporation of fuel droplets and thermoacoustic fluctuations in pressure (P') and heat release rate (I').

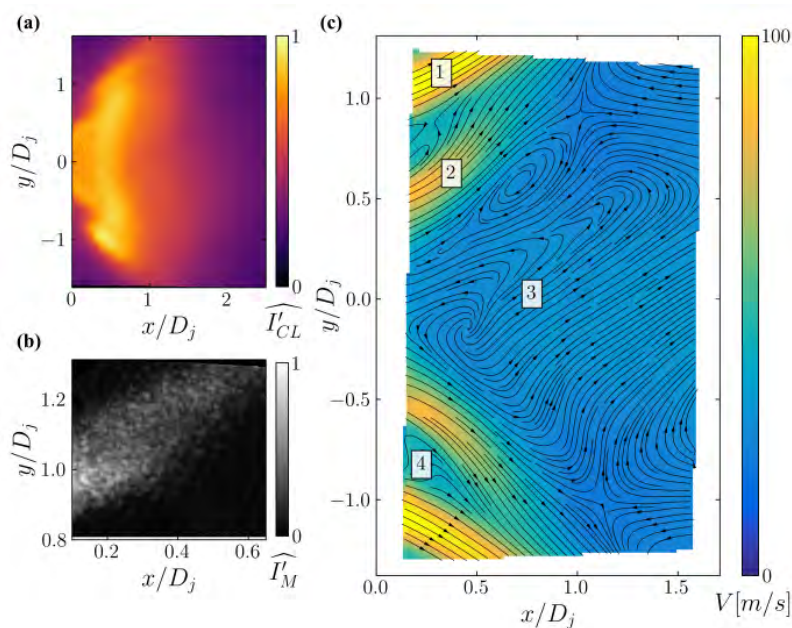


Figure 11. Time-averaged images of OH* chemiluminescence (a), and Mie scattering (b), and particle image velocimetry (PIV) velocity field with overlaid streamlines (c). Key features labeled in the PIV image include the (1) main injector flow, (2) pilot injector flow, (3) central recirculation zone, and (4) inner recirculation zone.

Spatial proper orthogonal decomposition (SPOD) was performed on the OH* CL images to understand the spatiotemporal coupling of P' and I' to the acoustic instability mode shown in Figure 12. Figures 12a and 12b show the real part of this SPOD mode at various fuel injection temperatures for Jet A and Shell GS190, respectively. At ambient fuel injection temperatures, strong longitudinal fluctuations are shown in the blue regions, and the peak in intensity overlaps well with the location of main and pilot flow impingement. As the fuel injection temperature is increased, coherent fluctuation strength is drastically reduced, particularly in the CRZ, indicating that global coupling of the flame and pressure field have been dampened. Fluctuations in the shear layer still persist but weaken more quickly moving downstream. This indicates that as the amount of fuel droplets decreases, coupled P' and I' fluctuations at the shear layer will convect downstream without driving instability in a global manner. Similar SPOD mode shapes are observed for Jet A but with key differences. Longitudinal fluctuations are noticeably higher for all fuel injection temperatures and persist further downstream compared with GS190.

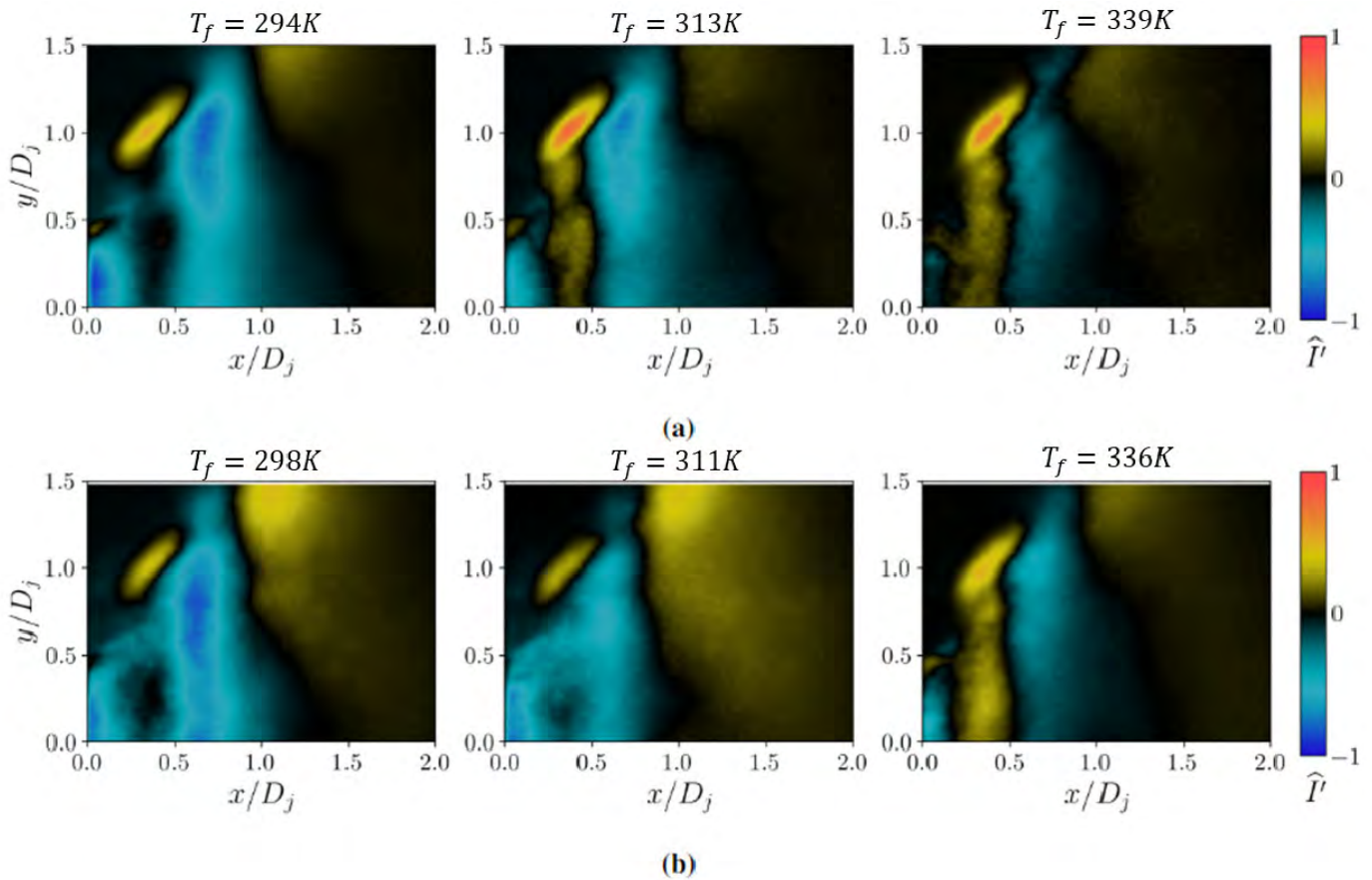


Figure 12. Spatial proper orthogonal decomposition (SPOD) modes at 825 Hz for (a) Jet A, and (b) Shell GTL GS190 fuels at varying fuel injection temperatures.

Figure 13a shows the phase-averaged OH* CL images at 825 Hz for the top half of the flame at ambient fuel injection temperature and are overlaid with Mie scattering images phase-conditioned to the heat release fluctuation. Identical phase-averaged analysis at a fuel injection temperature of 339 K is shown in Figure 13b, with color intensities normalized by the values from the ambient fuel temperature case. It is observed that when the fuel is heated, coherent fluctuations in heat release rate and droplet evaporation are attenuated. When the fuel injection temperature increases and burning in the ORZ and outer shear layer region is weaker, the resulting effect on the global dynamics of the flame is weakened, as the flame is able to convect downstream with less impedance from the higher pressures caused from droplet combustion.

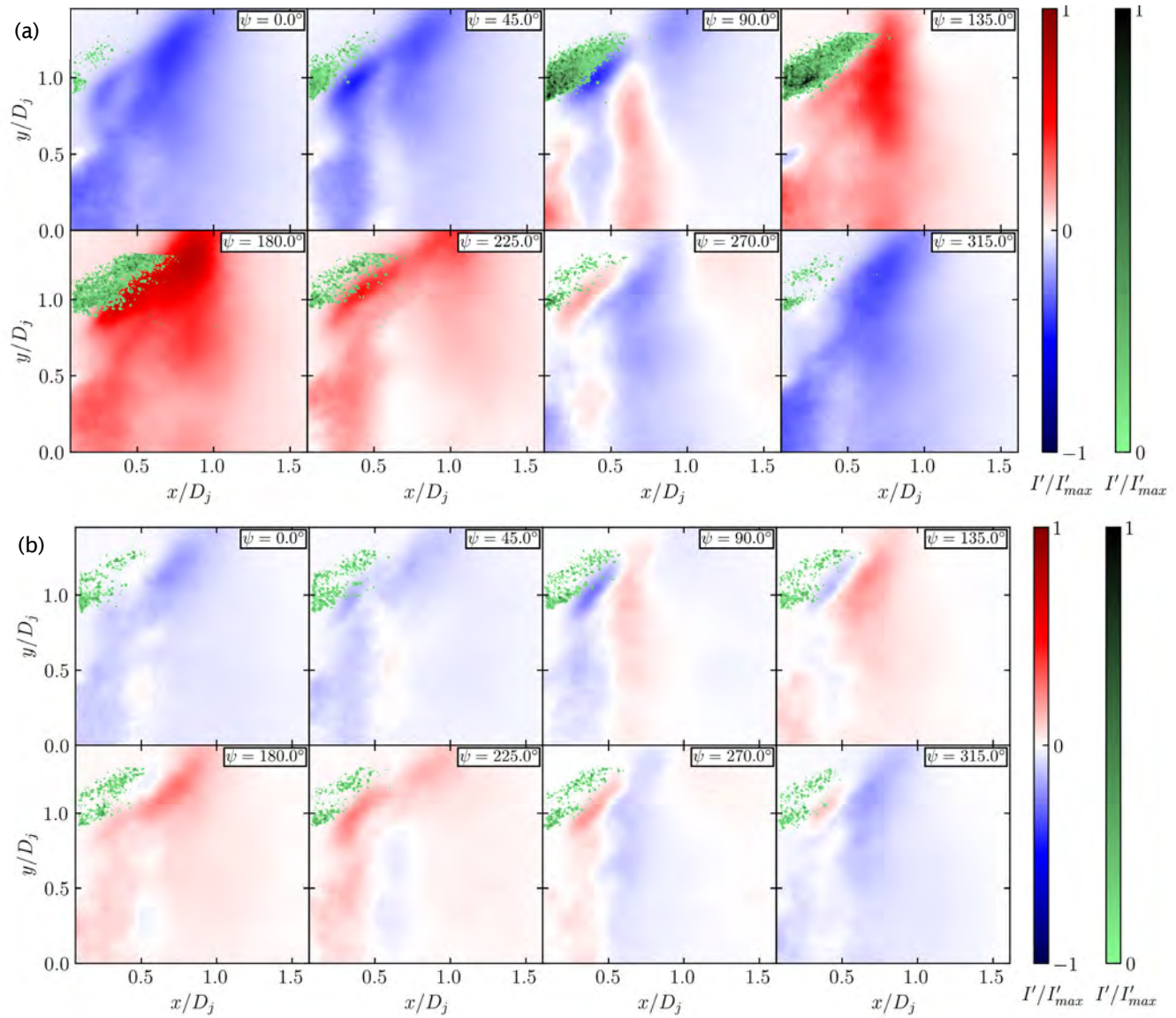


Figure 13. Phase-averaged intensities of OH* chemiluminescence and Mie scattering images for Shell GTL GS190 at fuel temperatures of (a) $T = 293$ K and (b) $T = 339$ K.

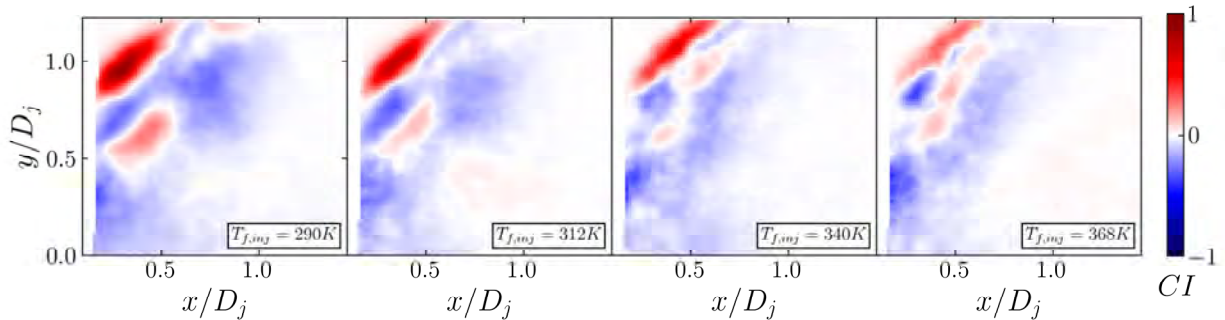


Figure 14. Normalized integral correlation of fluctuating axial velocity and fluctuating OH* chemiluminescence intensity ($-u'_x I'$) for Shell GTL GS190 fuel at varying fuel injection temperatures.

Investigating areas of thermoacoustic coupling in the flame across varying fuel injection temperatures can highlight regions of the flow that govern the propensity for combustion instability. In the absence of a chamber pressure measurement, the negative of fluctuations in the axial velocity (u'_x) calculated from PIV images are correlated to the heat release rate fluctuations (I') to show areas of driving and damping of instability. The normalized integrated correlation of these values ($-u'_x I'$) for the top half of the flame is shown in Figure 14 for varying fuel injection temperatures. A high-intensity region of instability driving in the upper left region of the flame is observed for all fuel temperature cases, which corresponds to the shear layer between the IRZ and main flow. Positive regions with lower relative intensity are also seen around $x = 15$, $y = 20$, corresponding to the shear layer between the pilot flow and IRZ. In the ambient temperature case, the downstream edge of the Mie scattering overlay corresponds to the center of this region, indicating that instabilities are predominantly driven at the burning surface of the droplets. As fuel injection temperature increases, this region decreases in intensity and axial extent, and the distance between the region's center and the edge of the Mie scattering overlay increases. This indicates that instability driving is weakened as the amount of unevaporated fuel entering and combusting at the shear layer decreases.

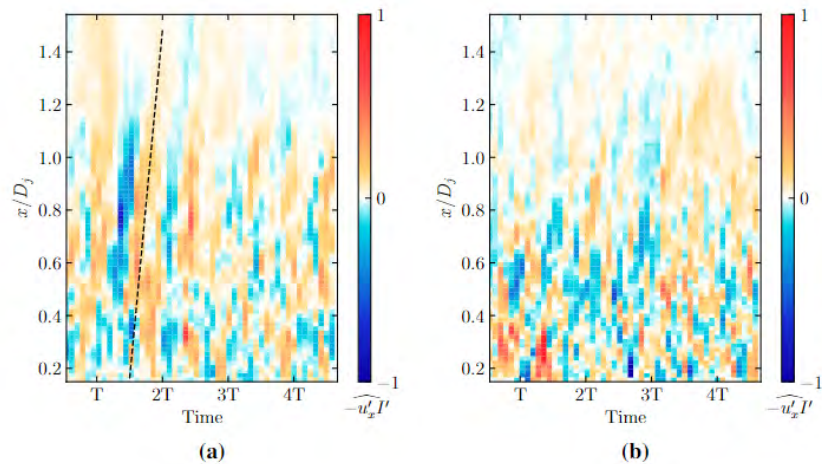


Figure 15. Radially averaged time history of fluctuating axial velocity and fluctuating OH* chemiluminescence intensity correlation ($-u'_x I'$) for GS190 at fuel temperatures of (a) $T = 293$ K and (b) $T = 339$ K.

Axial evolution of the instability driving at ambient fuel temperatures is observed in Figure 15a, which plots a time history of the radially averaged axial profile of $-u'_x I'$ for around four periods of the 825-Hz instability mode. Strong coherent regions of instability occur, starting at the base of the flame, and extend downstream, persisting in strength until around $x = 25$, which closely corresponds to the end of the shear layer between the IRZ and main flow. The dotted black line in Figure 15a highlights the convective behavior of the instability driving, and its slope matches the axial velocity of the main flow at the injector exit plane. The thickness of these regions in time indicates that moments of instability predominantly

occur when unburnt fuel droplets convect along the shear layer and react to produce heat release that amplifies acoustic axial velocity fluctuations. At higher fuel injection temperatures, the fuel is already mostly evaporated when reaching the shear layer, and heat release is more distributed, weakening the amplification of the acoustic mode. This is seen in Figure 15b, where there is a lack of coherent instability driving; regions that do have positive correlation are smaller and have less axial extent.

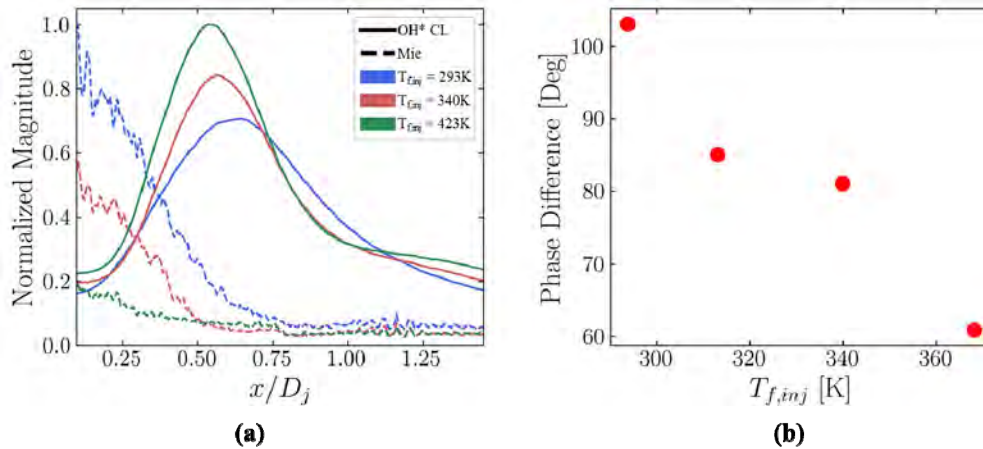


Figure 16. Radially averaged profiles of OH* chemiluminescence and Mie scattering intensity between $x = 25$ and $x = 40$ for varying fuel injection temperatures (a) and phase differences between heat release rate and Mie scattering fluctuations (b).

It has been shown that the IRZ and associated shear layer with the main flow is a primary location of thermoacoustic coupling. The effect of fuel temperature (T_f) on the time-averaged behavior of this region is contextualized in Figure 16a, which compares 1-dimensional profiles of OH* CL and Mie scattering that are radially averaged between $x/D_j = 0.8$ and $x/D_j = 1.3$. The maximum intensity of the Mie scattering is roughly halved for $T_f = 340\text{ K}$ compared to $T_f = 293\text{ K}$. The point of maximum heat release is also shifted upstream, and decays more rapidly than when $T_f = 293\text{ K}$. This indicates an increase in flame speed, causing the flame to stabilize at a more upstream location and become more compact. Droplets are still present at the point of injection for case $T_f = 340\text{ K}$, but the instability has been largely dampened as seen in Figures 9 and 12. This supports the concept that complete fuel evaporation is not necessary to attenuate the instability; rather, the droplet evaporation time delay must be reduced to the point where fuel mass flow rate and thermoacoustic fluctuations are no longer coupled. When the fuel is heated further, as in case $T_f = 423\text{ K}$, the Mie scattering intensity is decreased further and a small amount of droplets are present at the point of injection, but the point of maximum heat release rate shifts upstream only slightly compared to when $T_f = 340\text{ K}$. This further supports that the largest changes in the flame shape and global flame dynamics occur while some fuel droplets still exist at the point of injection.

Figure 16b complements the findings from Figure 16a in the context of the 825 Hz instability mode. The phase difference between Mie scattering and OH* CL fluctuations is computed at a frequency of 825 Hz for varying fuel injection temperatures. A clear decrease in the phase difference with increasing fuel preheating is observed, indicating a decrease in the fuel evaporation time delay and faster droplet burning, which supports the more compact heat release profiles observed for higher fuel injection temperatures in Figure 16a. The comparatively earlier rise of the heat release rate observed in Figure 16a for case $T_f = 293$ also matches this behavior, where combustion reactions and heat release can begin more upstream when the droplet evaporation time delay has been reduced, and few fuel droplets are present upon injection.

Laser-induced incandescence

LII is an in situ method for determining soot levels in a combustion flow field. LII will be used to investigate soot formation for both rich and lean dome operation in COMRAD. Comparison of soot levels between several different fuels is planned; however, for some fuels, such as the Shell GTL GS190, the signal may be too low to be detectable. LII measurements will provide valuable information of the spatial locations for particulate formation in the combustor flow field. GE Aerospace is very interested in the types and number of particulates that are in the combustor exhaust.



During this period, we wanted to determine the feasibility of using LII to obtain qualitative soot measurements in a calibration burner. An Nd:YAG laser was used to provide the 532-nm excitation wavelength needed to produce soot incandescence. Imaging was performed using a high-speed CMOS camera (Phantom v2512) with a Lambert HiCATT intensifier. A detection wavelength of 450 nm (25 nm FWHM) was used to reduce the signal from C₂ swan band emissions in the flame. The region of interest within COMRAD is approximately 50 mm by 50 mm. Three cylindrical lenses were used to collimate and form a 50-mm-wide laser sheet with a sheet thickness of <1 mm.

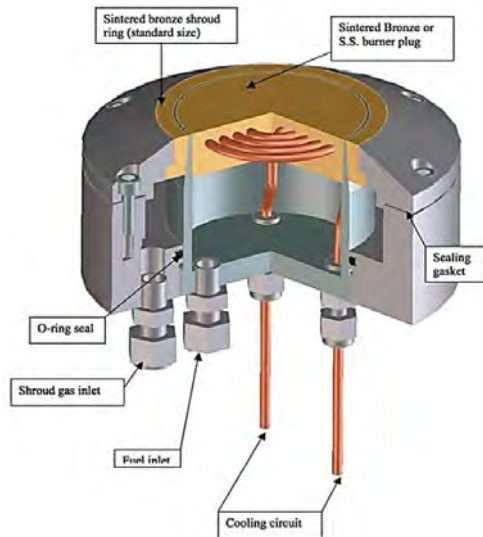


Figure 17. Schematic of McKenna burner.

LII calibration measurements were initially attempted in a Holthuis and Associates flat flame burner (McKenna burner) using a methane and air flame. Equivalence ratios of up to $\Phi = 2.1$ were tested in this burner. A schematic for this burner is shown in Figure 17. This burner allowed us to calibrate all timings between the laser, camera, and intensifier; however, the measurements had a very weak incandescence signal. This is most likely due to the low soot volume fraction in the flame. For this reason, the decision was made to switch to a diffusion flame.

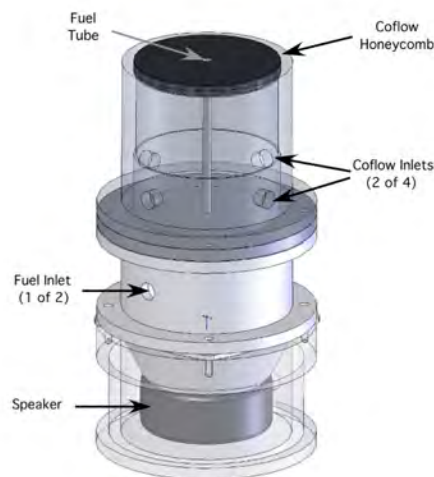


Figure 18. Schematic diagram of Yale burner.



A Yale burner, shown in Figure 18, was selected due to its coflow diffusion flame that is conducive to creating local fuel-rich pockets that generate soot. The conditions run in the Yale burner involved an ethylene-air flame diluted with nitrogen at conditions that are known to create high levels of soot. The specific conditions tested are from an International Sooting Flame workshop used in previous studies to validate LII setups. With this flame, we were able to successfully obtain an LII signal and thus validate the feasibility of qualitative LII measurements in COMRAD at 532 nm. An example of the raw incandescence signal from the Yale burner is shown in Figure 19 at an equivalence ratio of around $\phi = 2$.

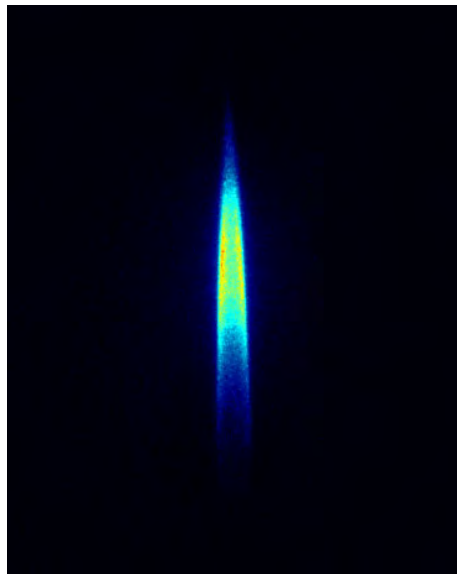


Figure 19. Soot incandescence measured in Yale burner.

Publications

Published conference proceedings

- McDonald, C. T., Philo, J. J., Shahin, T. T., Gejji, R., Slabaugh, C. D., & Lucht, R. P. (2021, August 9). Effect of fuel temperature on emissions and structure of a swirl-stabilized flame. *AIAA Propulsion and Energy 2021 Forum*. AIAA Propulsion and Energy 2021 Forum, VIRTUAL EVENT. <https://doi.org/10.2514/6.2021-3480>
- Alexander Hodge, Tristan Shahin, Thomas McLean, Rohan Gejji, Robert Lucht, Carson Slabaugh, Fuel Temperature Effects on Combustion Stability of a High-Pressure Liquid-Fueled Swirl Flame, AIAA SciTech Forum 2024, Orlando. AIAA.

Journal articles

- John J. Philo, Tristan T. Shahin, Colin T. McDonald, Rohan M. Gejji, Robert P. Lucht, Carson D. Slabaugh, Effect of fuel temperature on the structure of a high-pressure liquid-fueled swirl flame, *Fuel*, Volume 354, 2023, Art. No. 129142. DOI: <https://doi.org/10.1016/j.fuel.2023.129142>.
- McDonald, C. T., Shahin, T. T., Philo, J. J., Gejji, R. M., Fish, D. D., Slabaugh, C. D., and Lucht, R. P. (2022). Emissions Measurements in a Liquid-Fueled Aviation Gas Turbine Combustor with Heated Fuels. *ASME Journal of Engineering for Gas Turbines and Power*, to be submitted.

Outreach Efforts

None.

Awards

None.

Student Involvement

Two PhD students (Tristan Shahin and Ben Murdock) and three MS students (Thomas McLean, Zander Hodge, and Keaton Koenig) are currently working on the project. John Philo graduated in March 2022 with his PhD after working on the



project. Colin McDonald left in September 2022 to accept a position with Astra (Merced, California), where he will be responsible for setting up a new rocket engine test facility. The project provides outstanding research experiences for the graduate students, including the design of system components for, and the operation of, a sophisticated aviation gas turbine combustion test rig, as well as application of advanced laser diagnostic methods for measurements in this test rig. As noted above, the graduate students have been responsible for designing system components, such as the fuel heating system, and for executing test operations.

Plans for Next Period

The focus for the next period of this project will be a detailed comparison of a selected SAF with a well-characterized petroleum-based fuel: Jet A, or fuel A2 from the National Jet Fuel Combustion Program. The SAF will be a mixture of paraffins and aromatic compounds, and the composition will be selected in consultation with other FAA ASCENT researchers and our collaborators at GE Aerospace. The nominal SAF composition is expected to be 92% FT-SPK and 8% single-ring aromatic compounds, but SAFs with single ring aromatic contents as low as 4% and as high as 30% will also be investigated. The first stage of the comparison will involve combined physical sampling probe emission measurements and chemiluminescence emission measurements. In the next stage of the comparison, we will use high-speed PIV to measure the velocity flowfield, and both 10-Hz and 10-kHz OH PLIF to monitor the structure and dynamics of the reaction zones.

We plan to expand our operational test matrix to include conditions of significant interest to GE Aerospace. Thus far in our test program, the relative equivalence ratios for the pilot and main have been fixed. GE Aerospace is interested in expanding the test matrix to investigate the effect of varying equivalence ratios in the main and pilot on hot fuel effects, especially as it relates to NO_x formation. Along these same lines, pilot-only operation is of significant interest. We will also explore the effects of fuel heating for rich dome operation, implemented by supplying sufficient fuel in the streams to create a globally rich mixture.

Additionally, LII will be used to investigate soot formation for rich dome operation. The LII measurements will also be performed for lean dome operation, although for some fuels, such as the Shell GTL GS190, the signal may be too low to be detectable. However, as noted below, the additional funding will allow us to expand the operational test matrix to include conditions with higher pilot to main fuel splits or even operation with globally rich conditions. The LII measurements will provide valuable information of the spatial locations for particulate formation in the combustor flow field. We are also interested in both nonvolatile and volatile particulate formation. GE Aerospace is very interested in the types and number of particulates that are in the combustor exhaust. The effects of passing through the turbine on particulate emissions are not well understood.



Project 068 Combustor Wall Cooling with Dirt Mitigation

The Pennsylvania State University

Project Lead Investigator

Karen A. Thole
Distinguished Professor
Department of Mechanical Engineering
The Pennsylvania State University
START Lab, 3127 Research Drive
State College, PA 16801
814-863-8944
kthole@psu.edu

University Participants

The Pennsylvania State University (Penn State)

- P.I.s: Dr. Karen Thole and Dr. Stephen Lynch
- FAA Award Number: 13-C-AJFE-PSU-057
- Period of Performance: October 1, 2021 to September 30, 2024
- Tasks:
 1. Manufacturing and testing of combustor liner cooling concepts with small coupons
 2. Testing of scaled models of optimal cooling concepts
 3. Facility planning for 1×-scale combustor simulator

Project Funding Level

For the entire 3-year effort, the ASCENT funding was \$1,400,000, and matching funds of \$1,400,000 were provided by Pratt & Whitney.

Investigation Team

Prof. Karen A. Thole (P.I.), management, reporting, and oversight of all technical tasks
Assoc. Prof. Stephen Lynch (co-P.I.), management, reporting, and oversight of Tasks 1–3
Assoc. Res. Prof. Michael Barringer (research advisor), Task 3
Scott Fishbone (project manager), Tasks 1–3
Kyle McFerran (graduate student), Tasks 1 and 2
Chad Schaeffer (graduate student), Task 3

Project Overview

A critical issue related to the current operation of gas turbines is the ingestion of dirt and other fine particles that lead to dirt buildup and reduced cooling of hot section components, such as the liner walls of the combustion chamber. With increasing needs to fly in dirty environments, the criticality of operations in dirty environments is increasing. Modern gas turbine engines typically use a double-walled combustor liner with impingement and effusion cooling technologies, whereby impingement cooling enhances the backside internal cooling, and effusion cooling creates a protective film of coolant along the external liner walls. Dirt accumulation on the internal and external surfaces severely diminishes the heat transfer capability of these cooling designs. This study also investigates the development of a combustor profile simulator upstream of the Steady Thermal Aero Research Turbine (START) test turbine. Combustor profiles affect turbine performance and durability. As combustor designs evolve, particularly the liner cooling technologies, understanding the impacts on the turbine is important. This study investigates practical designs applied to combustor walls to decrease dirt accumulation, and also explores the development of a profile simulator that can replicate relevant temperature and pressure profiles upstream of a test turbine.



Task 2 – Testing of Scaled Models of Optimal Cooling Concepts

The Pennsylvania State University

Objective

The goal of this task is to produce an effective cooling design for combustor walls that is insensitive to dirt accumulation at existing or lower coolant flow rates. Various parameters such as dirt deposition, flow behavior, and heat transfer effectiveness will be investigated and quantified to compare the efficiency of candidate designs. Improved understanding of the underlying reasons for dirt sensitivity and deposition behavior is also being sought.

Research Approach

Background

The project focuses on the impacts of ingestion of dirt and other fine particulate matter in gas turbine engines. These particles are known to block the cooling holes and passages needed to effectively cool combustion chamber walls. Gas turbine engines often use double-walled combustor liners comprising impingement and effusion cooling plates (Figure 1). The impingement plate enhances backside internal cooling, and the effusion plate creates a protective film of coolant along the external liner walls. As particulate matter accumulates on these plates, the heat transfer performance severely decreases, thus ultimately leading to component failure.

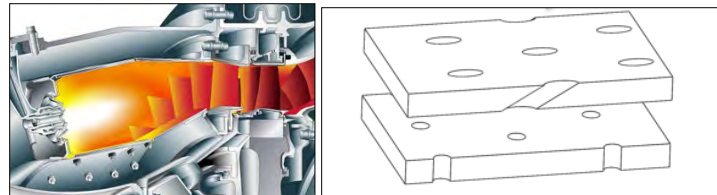


Figure 1. Schematic of double-walled combustor liner geometry.

A coupon design of a double-wall combustor liner consisting of an impingement, spacer, and effusion plate is shown in Figure 1, along with the testing facility in which the coupons are installed. The impingement plate has straight holes resulting in high-velocity jets that impinge on the backside of the effusion plate, which is exposed to the hot main gas path. The spacer plate creates a small controllable gap between the impingement and effusion plates. The effusion plate uses cooling holes angled at 30° to create a film effect along the external wall exposed to the hot combustion gases.

The goal of this research is to determine the impact of dirt deposition on the ability to cool the double wall containing the hot combustion gases in the gas turbine engine. To achieve this goal, our research in this past year has developed a unique heater design for the backside (cold side) of the effusion plate, as shown in Figure 3, along with the thermal resistive network needed to analyze the data. Of note, the studies completed in this past year included effusion plates with or without effusion holes. For the cases without effusion holes, as shown in Figure 3, we performed comparisons against data in the open literature to benchmark the facility.

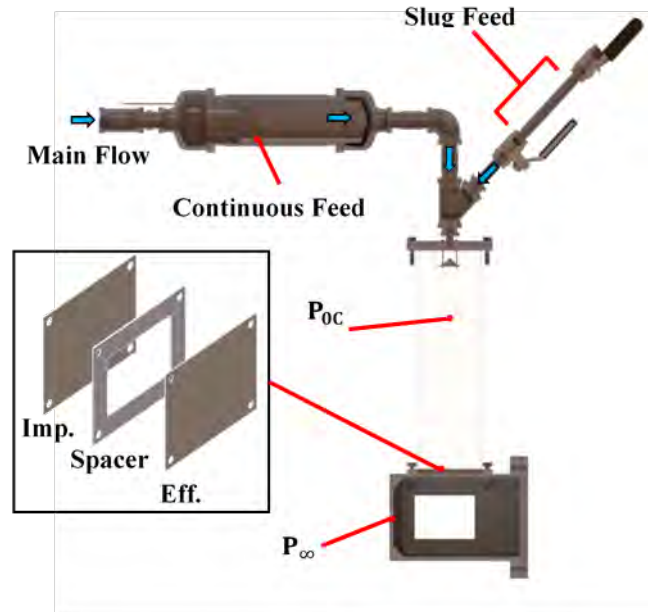


Figure 2. Schematic of the double-walled combustor liner configuration.

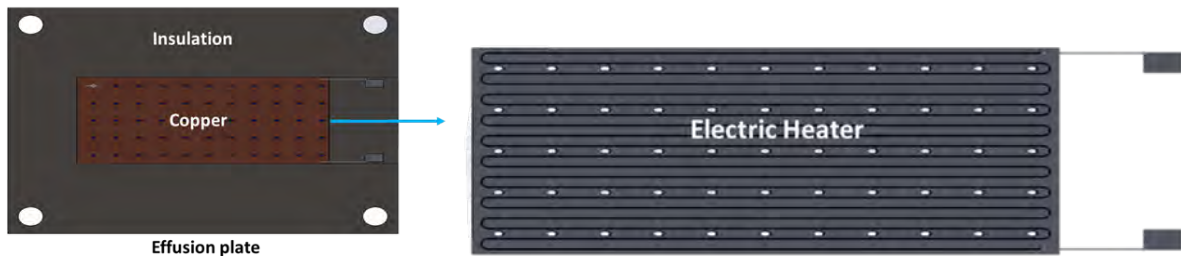
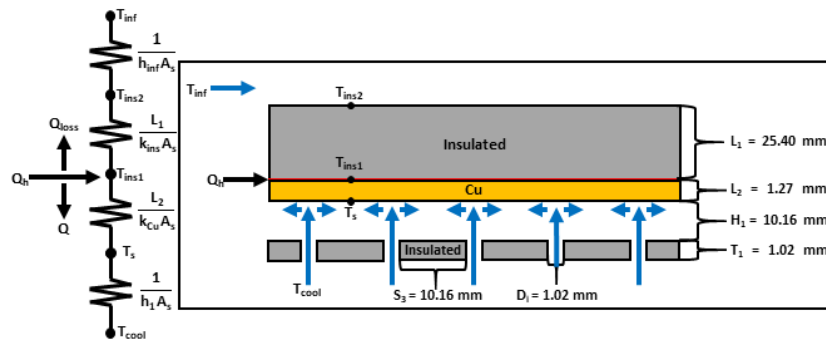


Figure 3. Double wall coupon with heater design along with the thermal resistive network (top) used to calculate the convective heat transfer coefficient on the impinging side of an effusion plate as well as the heater design (bottom).

Understanding of the effects of dirt on combustor cooling requires calculation of heat transfer coefficients on all four surfaces (top and bottom of both the impingement and effusion plates). A three-case proposal using thermal resistive

networks can be used to measure these respective heat transfer coefficients. Case 2, shown on the top left side in Figure 3, demonstrates the resistive network for calculating the heat transfer coefficient on the bottom (cold) side of the effusion plate. All work during this period was based on this specific case.

The three cases allow for calculation of the four heat transfer coefficients for dirt and no-dirt tests. In each case, one of the cooling plates is made of insulation, whereas the other plate is made of copper, an electric heater, and insulation. For the resistive network in Figure 3, the composite coupon made up the effusion plate. Of note, testing during the first two periods was performed with an effusion plate without effusion holes. Effusion holes were not tested because literature data were available for only plates without effusion holes. Five thermocouples were implemented throughout the composite coupon to measure the appropriate temperatures in the thermal resistive network. Ultimately, these thermocouple measurements were used to solve for the heat transfer coefficient (h_1) in Equation 1.

$$h_1 = \frac{Q}{A_s(T_s - T_{0C})} \tag{1}$$

Initial testing was performed at five Reynolds numbers (Re_d) in the range of $3,200 < Re_d < 7,400$ on a clean, baseline heater coupon. The results from these baseline tests were benchmarked with the experimental results from Hollworth and Berry (2009), who used a similar experimental setup. The non-dimensional design parameters of S_3/D and H_1/D were kept consistent with the ratios used in Hollworth and Berry’s experiment for accurate benchmarking. At each Reynolds number, power was supplied until a temperature difference ($T_s - T_{in}$) as high as $20\text{ }^\circ\text{C}$ was achieved. After sufficient time was allowed to reach steady state, we used the thermocouple measurements to calculate h_1 . After benchmarking the clean coupon, we injected 2.0 g of AFRL 05 dirt in bursts through the slug feed. After the dirt deposited on the effusion plate, the same convective heat transfer measurements were made as in the clean, baseline cases.

The convective heat transfer benchmarking results are shown in Figure 4 in terms of Nusselt number (Nu), as a function of Re_d . Again, importantly, testing during this period used an effusion plate without effusion holes. Baseline heat transfer results were within 4%–9.5% of the benchmark study’s experimental data and thus were demonstrated to be accurately benchmarked. Results in Figure 4 also highlight the impact of dirt deposition on reducing the heat transfer relative to the clean baseline coupon, because of the lower Nus that resulted for the cases with dirt deposition. The dirt effectively acts as an extra layer of insulation and hence must be accounted for in the thermal resistive network. Two methods for accounting for this extra dirt thickness in the thermal resistive network have been tested, but further analyses are necessary.

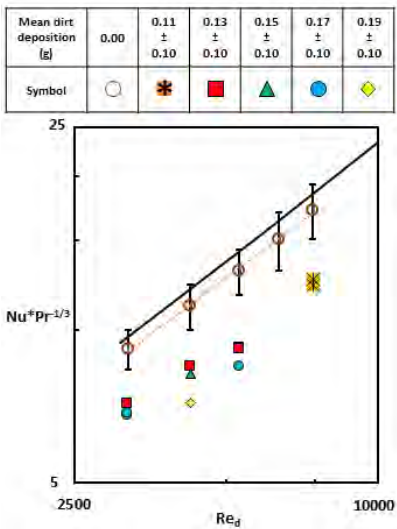


Figure 4. Benchmarking results showing the nondimensionalized parameter, $Nu \times Pr^{-1/3}$, as a function of Re_d , for a clean and dirty heater coupon.

Double-wall Heat Transfer Results

For the heat transfer testing of the effusion plate without cooling holes, a constant Reynolds number was maintained throughout the dirt injection process. In contrast, a constant pressure ratio (PR) was maintained during dirt injection for the heat transfer testing on the effusion-cooled plate. Pressure taps located upstream of the impingement plate and downstream of the effusion plate were used to monitor the PR across the double-walled liner with Equation 1. A PR range of $1.01 < PR < 1.1$ was tested for the effusion-cooled plate.

$$PR = \frac{P_{0C}}{P_{\infty}} \tag{2}$$

As dirt was injected into the system, the upstream mass flow rate (and hence pressure) decreased, because dirt blocked the impingement and effusion cooling holes, thus reducing the overall flow area. The flow parameter (FP), shown in Equation 2, was monitored during testing to quantify these blockage levels caused by the deposition.

$$FP = \frac{4m_i \sqrt{RT_{0C}}}{\pi P_{0C} N D_i^2} \tag{3}$$

With the FP being directly related to the mass flow rate, a decrease in the mass flow rate resulting from the blockage of cooling holes leads to a reduction in FP (RFP). An increase in flow blockage is quantified by an increase in the RFP, which is defined in Equation 3.

$$RFP = \frac{FP_{clean} - FP_{dirty}}{FP_{clean}} \times 100 \tag{4}$$

Heat transfer results, in terms of Nu, are plotted in Figure 5 as a function of Reynolds number for the effusion-cooled plate over a range of H/D values from $3 < H/D < 10$ and Re_d from $800 < Re_d < 3,500$. This Re_d range corresponds to the range of PRs tested, $1.01 < PR < 1.1$. Heat transfer coefficients for the clean and dirty plates are shown in Figure 5, wherein dirty tests had 0.175 grams of dirt deposited on the effusion plate surface. The baseline heat transfer results for the clean effusion plate without effusion holes are also shown for $H/D = 10$. Heat transfer coefficients for the effusion-cooled plate are 300% greater than those for the effusion plate without cooling holes. A higher heat transfer coefficient indicates better cooling, which would be expected for the effusion-cooled plate because of the cooling that occurs through the coupon from the effusion holes. In addition, the effusion holes create a thin film of cooling flow on the hot side of the effusion plate, which also enhances the overall cooling.

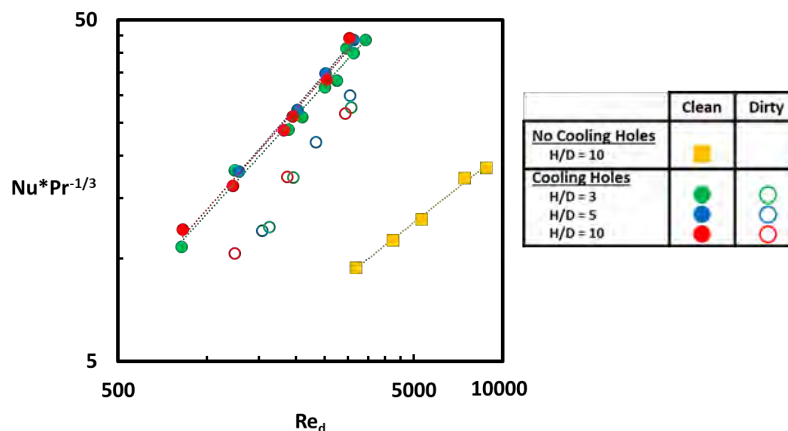


Figure 5. Heat transfer results in terms of Nu, as a function of the Reynolds number, for both the effusion plate without cooling holes and the effusion-cooled plate.

For the effusion-cooled plate, the cooling rates for both the clean and dirty coupons were unaffected by the change in H/D . These results are interesting because the plate-to-plate spacing for the effusion plate without cooling holes influenced the heat transfer coefficients. More work is necessary to investigate the effect of spacing H/D on cooling within an effusion-cooled plate. Future testing will examine an extreme H/D of 20 to quantify whether the heat transfer coefficient is similar to that in the other spacings.

The addition of dirt to the cold side of the effusion-cooled plate surface resulted in lower heat transfer coefficients and hence diminished cooling. The dirt effectively serves as an extra layer of insulation and hence must be accounted for in the thermal resistive network. In addition to adding extra thickness to the effusion plate surface, the deposition alters the flow field patterns of the impinging jets and hence the cooling capabilities on the backside of the effusion plate. The effects of dirt on heat transfer coefficients can be quantified through an augmentation comparing the heat transfer coefficients for the clean and dirty effusion plate at a constant Reynolds number. Because the Re_d decreases during the dirt injection process, the heat transfer coefficient for the dirty plate was compared with the heat transfer coefficient predicted by the trendline of the clean effusion plate. Augmentation levels are shown in Figure 6, comparing the Nu for the clean and dirty plates for the different plate-to-plate spacings and PRs. For each PR, the effects of dirt deposition on the heat transfer coefficient are similar for each H/D spacing. However, an approximately 10% decrease in augmentation is observed as the PR increases from 1.045 to 1.1, thus suggesting that the effects of dirt on heat transfer are less severe at higher than lower PR values.

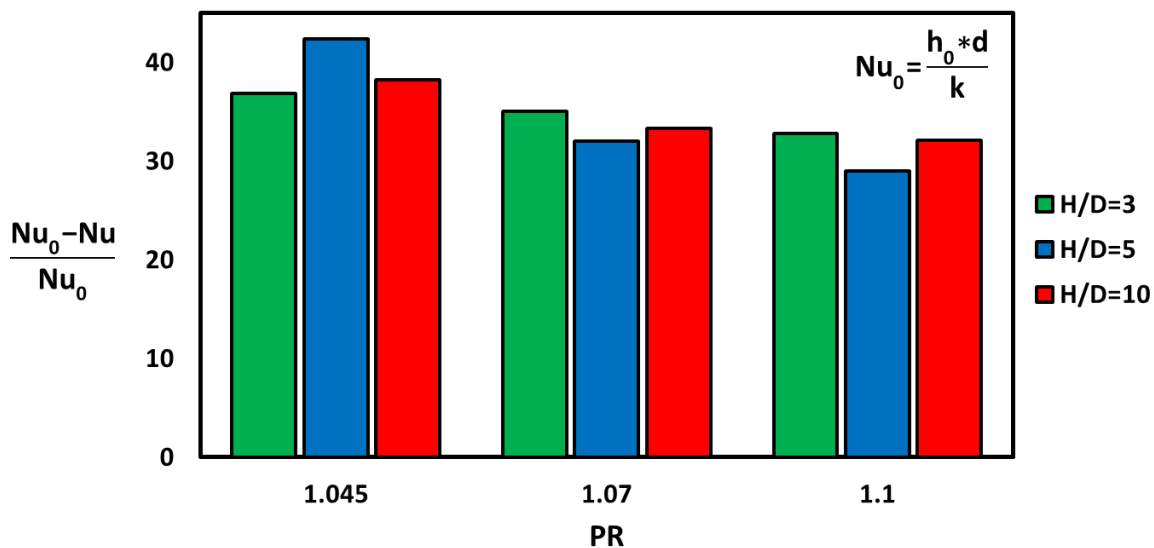


Figure 6. Plot of augmentation levels, comparing the Nu s for the clean effusion-cooled plate to the dirty effusion-cooled plate for several H/D and PR values.

Examination of the observed deposition patterns helps explain why deposition at increasing PRs leads to decreasing reductions in cooling. Figure 7 shows the deposition patterns for $H/D = 10$ at the three PR values tested with a high-resolution microscope. Although difficult to observe strictly from these top view images, the peak height of the dirt at the area of impingement decreases as the PR increases. This aspect is clearly seen for a PR of 1.1, wherein the cold-side effusion plate surface is directly exposed to the cooling air, as evidenced by the black region surrounding the middle dirt mound. With direct exposure of the surface to the cooling air, the effusion plate can be more effectively cooled by the impinging jets, thereby lessening the cooling impacts from the deposition.

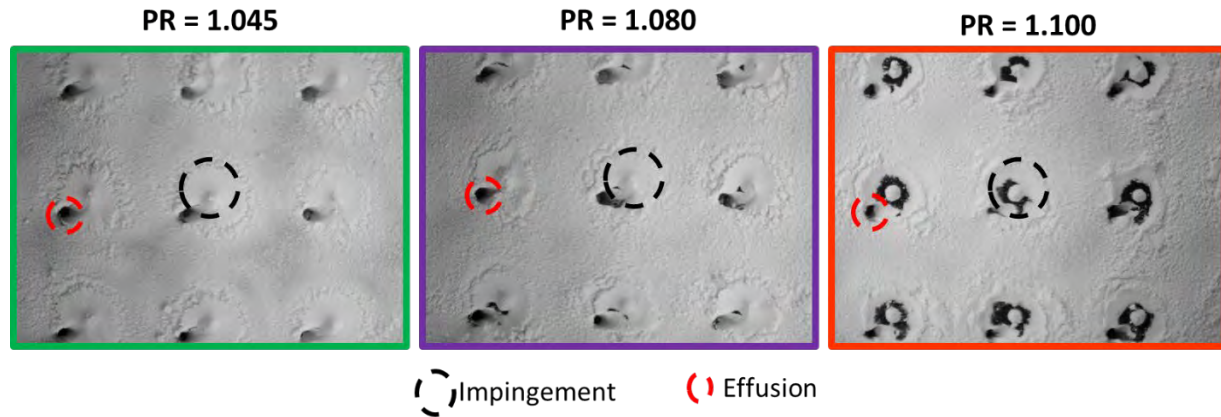


Figure 7. Observed deposition patterns at $H/D = 10$, and $PR = 1.045, 1.08, \text{ and } 1.1$. The black-dotted circles show the locations of impingement, and the red-dotted circles show the effusion holes.

With code developed in previous quarters, optical scanning of the observed deposition allows for contour generation of the resulting dirt heights, as shown in Figure 8. These contour plots provide a clearer visualization of the deposition heights. A side view of the deposition heights can also be generated from the average dirt heights across the 11 rows of cooling holes, as shown in Figure 9. The plots in Figures 8 and 9 both show a decrease in peak height as the PR increases. One goal of the next quarter is to finish post-processing all optical scans for the testing performed during this current quarter.

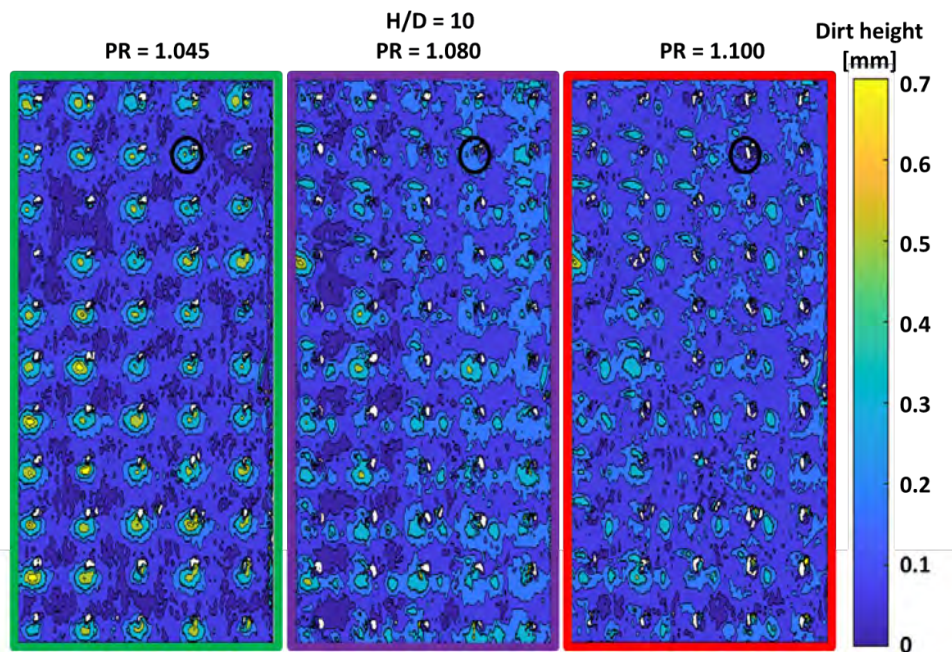


Figure 8. Contour plots of the observed deposition patterns at $H/D = 10$, and PR of $1.045, 1.08, \text{ and } 1.1$.

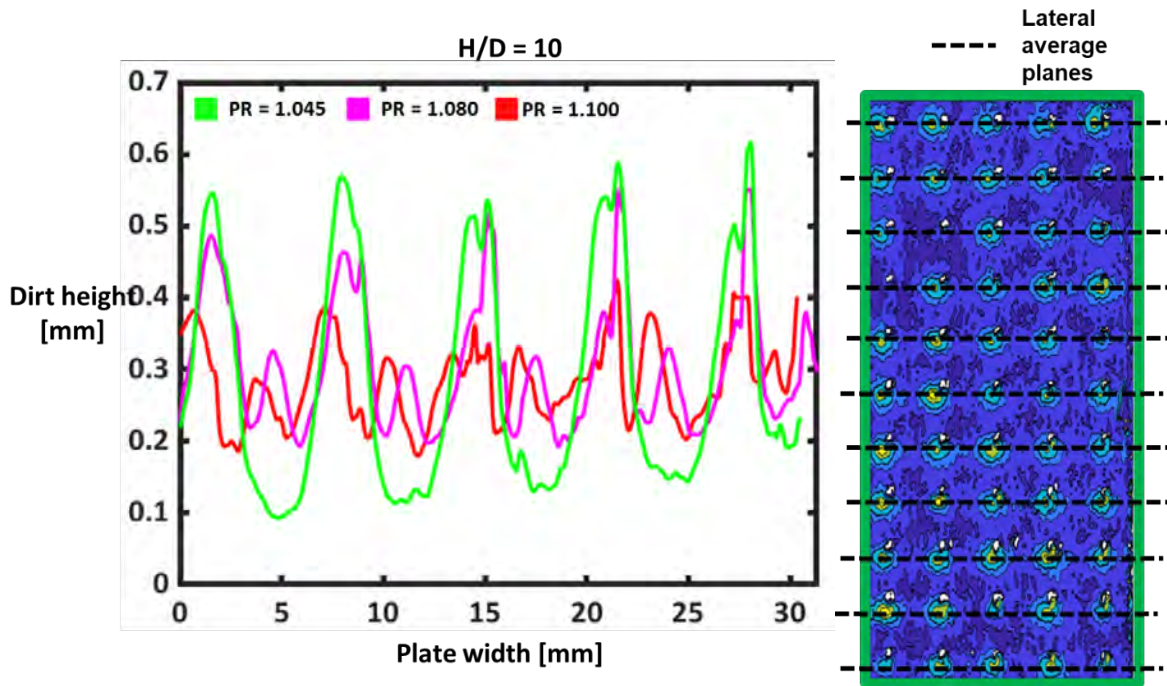


Figure 9. Lateral-average view of the deposition results for an effusion-cooled plate at PR = 1.045, 1.08, and 1.1. The planes used to generate the average heights are shown on the right side of the figure.

Throughout testing, RFP was observed because of the dirt blocking the cooling holes. The RFP is shown in Figure 10 as a function of the PR for the effusion-cooled plate over the range of H/D values tested. Overall, the difference between the RFP over the range of plate-to-plate spacings was relatively unchanged, except for a PR = 1.02. However, because only one test has been performed at this PR to date, the uncertainty is too large to draw any conclusions, and additional testing is therefore needed. For the other PR values, three tests were performed at each PR, and the results show a similar RFP for each H/D . However, a decrease in the RFP is observed as the PR increases for all test cases, thereby indicating that the level of flow blockage decreases as the PR increases. These results align with the augmentation results, because less flow blockage allows for more effective impingement cooling and hence less reduction in heat transfer.

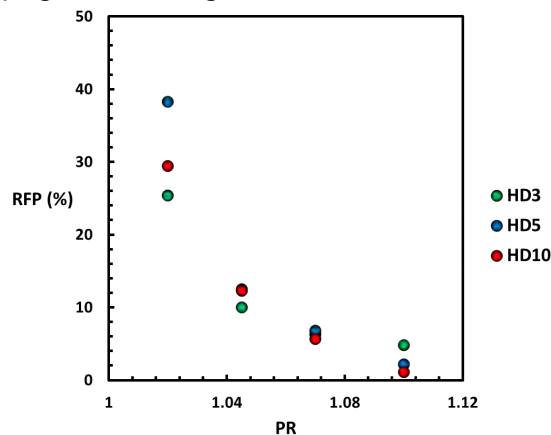


Figure 10. RFP as a function of PR for the effusion-cooled plate.

In summary, heat transfer testing was performed on an effusion plate with or without effusion holes for several PRs and Reynolds numbers. Overall, the effusion-cooled plate had higher heat transfer coefficients than obtained in prior quarters on an effusion plate without cooling holes. For the effusion-cooled plate, the plate-to-plate spacing had little effect on the heat transfer rates, deposition patterns, and RFP. However, increases in the PR led to decreasing reductions in cooling. A change in the observed deposition structures and a reduction in the amount of flow blockage that occurs is likely to explain why the reductions in cooling decrease with increasing PR. The next steps will include post-processing the rest of the optical scan data for all the effusion-cooled plate tests, so that the deposition patterns can be examined more closely to understand the effects of deposition on the flow field.

Task 3 – Profile Simulator for START

The Pennsylvania State University

Objective

Develop and integrate a non-reacting profile simulator to be placed upstream of the START test turbine, to understand the impacts of a range of temperature and pressure profiles, representative of current and future combustors, on turbine efficiency and durability.

Background

Being able to replicate combustor-relevant temperature and pressure profiles is important in learning how to improve engine performance with typical aviation fuels, sustainable aviation fuel, and other fuels. These profiles, which exit the combustor that then enter the turbine, impact turbine efficiency and durability. This task involves developing a non-reacting profile simulator that can simulate relevant combustor non-dimensional flow and thermal fields. Figure 11 illustrates the need for placing a combustor simulator upstream of the START test turbine. The data in Figure 11 show the range of nonuniformities of non-dimensional pressures (C_p) and temperatures (θ) that occur at the exit of the combustor, both of which affect turbine performance. Because various fuels will be used for combustion in the future, simulating these profiles will become even more essential.

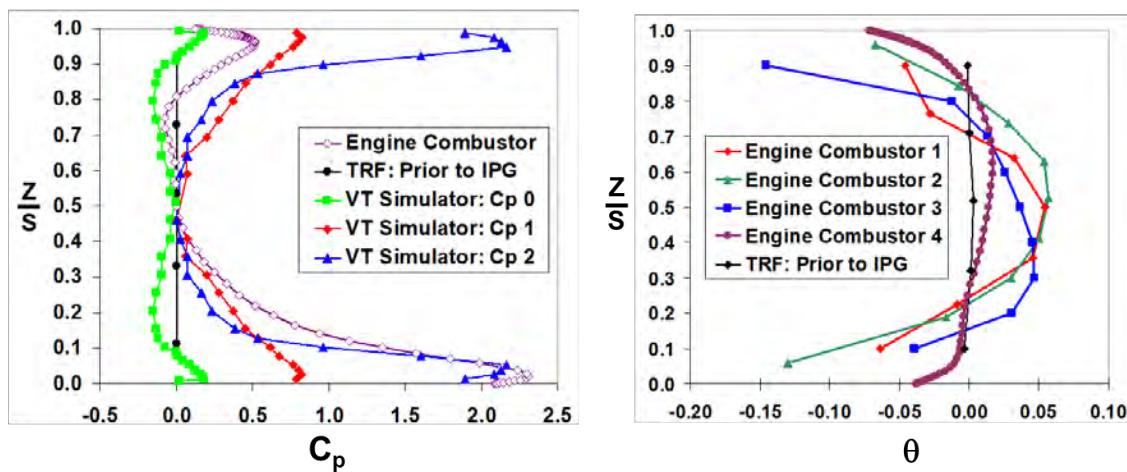


Figure 11. Combustor exit profiles from the literature, indicating non-uniform pressures and temperatures (θ) (Barringer et al., 2009).

To achieve the range of temperature and pressure profiles, we conducted predictive computational fluid dynamics simulations (CFD) using steady Reynolds-averaged Navier–Stokes to understand the impacts of different flow features on the resulting profiles. Simultaneously, the START team engaged a design firm to develop the hardware necessary to achieve the profiles developed through the CFD studies.



The region in which the simulator is to be placed upstream of the START test turbine is illustrated in Figure 12. This region was identified to ensure no interference with meeting the turbine testing needs while also allowing for flexibility in how a range of temperature and pressure profiles can be achieved. The basic concept of the design is to make use of large dilution jets (three rows) and nearly wall liner cooling. All these features assist in the tailoring of the inlet profiles to the test turbine in the START Lab.

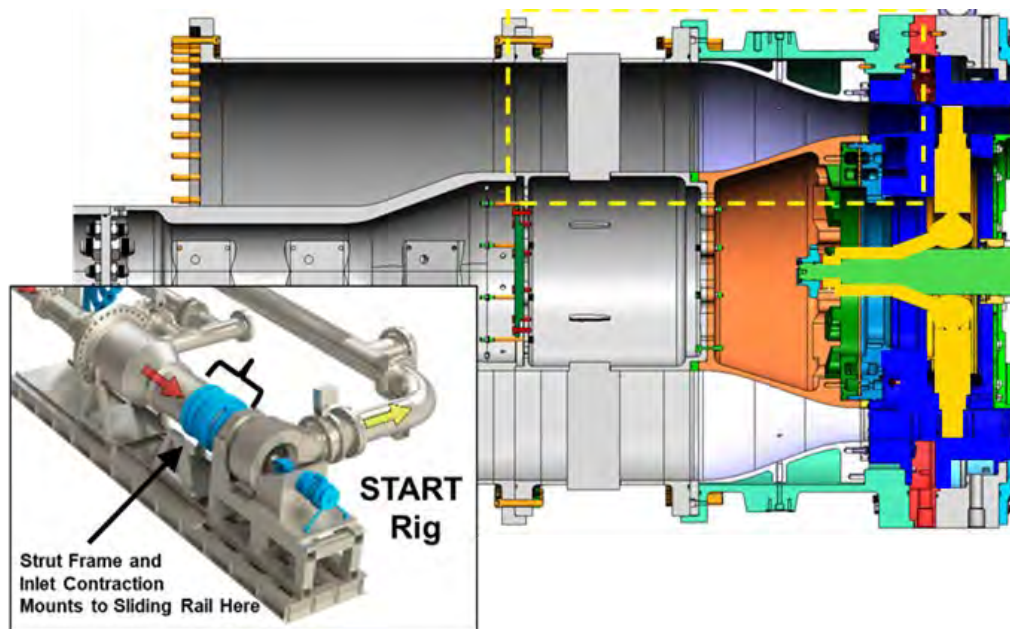


Figure 12. Design space of the combustor simulator upstream of the START test turbine inlet.

During this past year, the Pennsylvania State University START team met regularly with the design firm (Agilis) to complete the conceptual, preliminary, and final design reviews. Currently, the manufacturing of the simulator is being planned. As described, the simulator design includes three rows of dilution holes and effusion holes, as illustrated in Figure 13. The dilution holes will be drilled into annular chamber wall plates, and were designed with flexibility, such that the plates are removable. The dilution hole configuration was designed to keep the dilution holes offset from each other within the same row and to keep each row staggered with respect to the preceding row. One key design parameter is the ratio of the jet momentum to the mainstream momentum, which is captured in a momentum flux ratio (I). Momentum flux ratios set the jet penetration depth and resulting profiles. These momentum flux ratios were varied by changing the dilution hole mass flow and diameters to yield a momentum flux ratio range of $5 < I < 180$ for the first row, and a momentum flux ratio range of $0.7 < I < 7$ for the second and third rows. The simulator design is shown in Figure 14.

In addition, Figure 14 shows the simulated computational domain, including the dilution holes, which could be turned “off” or “on” in the CFD simulation to study the effects of different dilution hole diameters. This process enabled the CFD simulation to be mesh independent in the central chamber region, because creation of a new mesh was not necessary to change the dilution hole size. The created model was then imported into the solver for CFD simulations. Importantly, the effusion cooling is being modeled as a mass flow injection across a face rather than distinct holes, to ensure a reasonable grid size. In the hardware, the effusion cooling will involve several rows of closely spaced cooling holes that inject flow into the near-wall boundary layer.

For the CFD simulations, careful studies were completed to ensure grid independence (Figure 15). CFD simulations were completed with Reynolds-averaged Navier-Stokes. The results, in terms of the flow temperatures (Figure 14), indicated that 20 million cells was adequate.

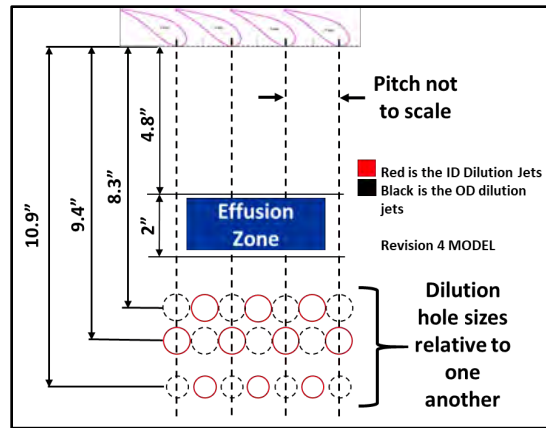


Figure 13. Dilution hole pattern for the simulator design.

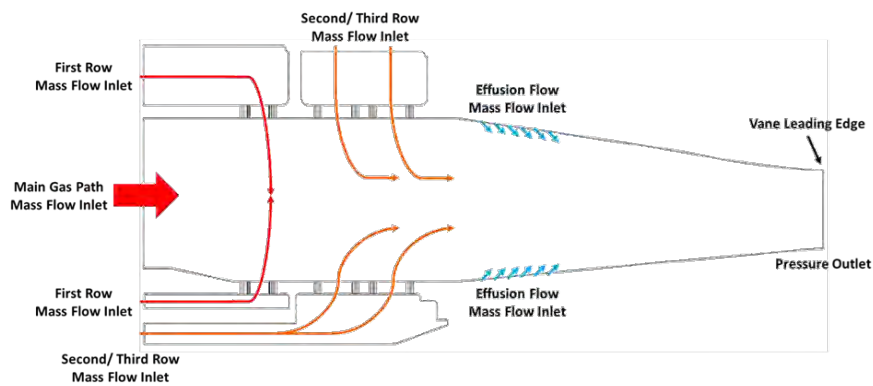
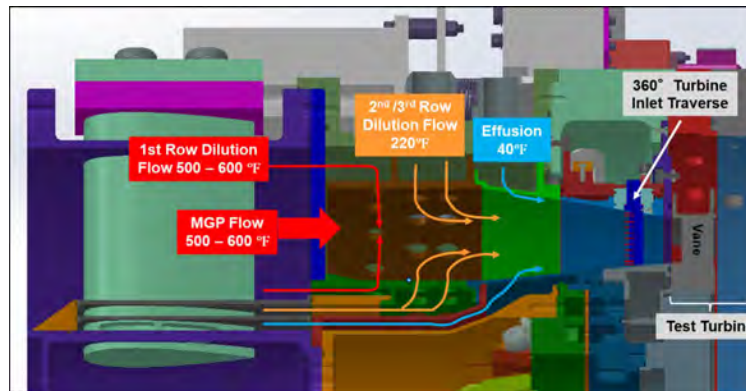


Figure 14. Profile simulator design (top) with computational model (bottom).

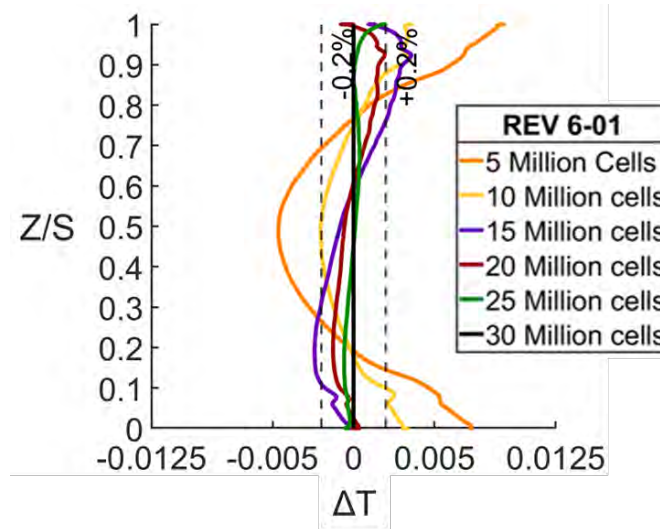


Figure 15. Grid independence results, showing the influence of mesh cell count on temperature convergence.

Profile Simulator Results

The final design review for the profile simulator was completed in this past year and is schematically shown in Figure 16. Within the model, the dilution hole pattern was designed to be integrated in the START facility, as also shown in Figure 16.

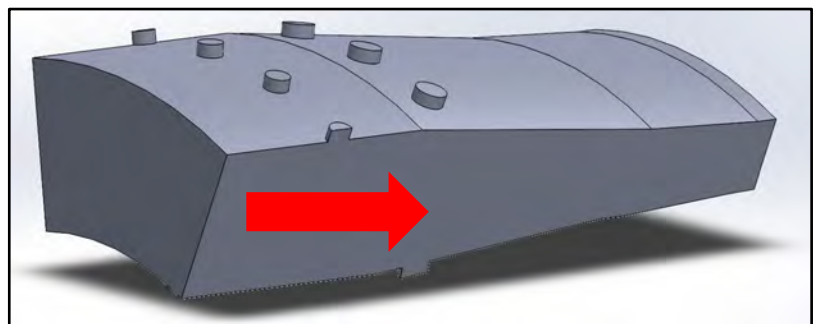
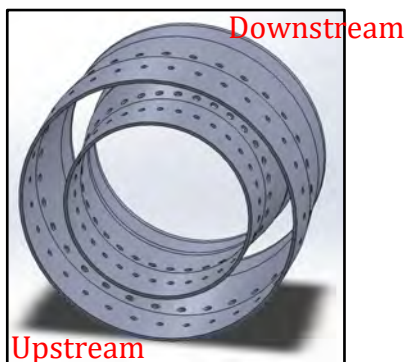
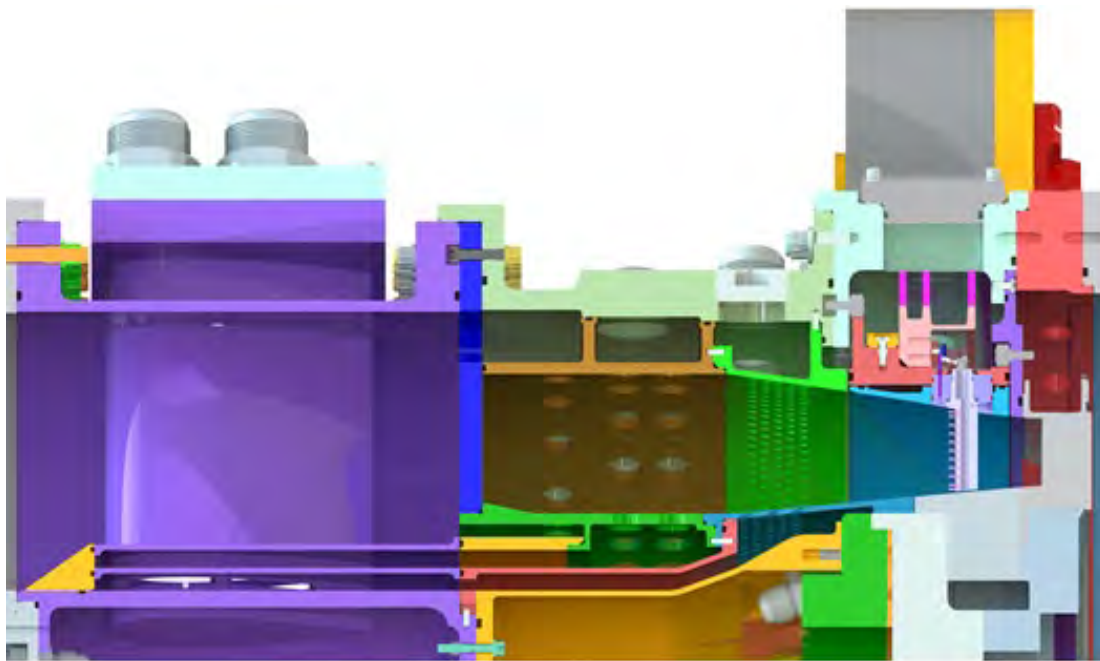


Figure 16. Final simulator design along with illustrations of the dilution holes and CFD model.

The research completed this year yielded not only the overall simulator design but also multiple CFD simulations to determine the effects of the temperature of the dilution and effusion flows, as well as the distribution of mass flow through the dilution holes. A two-level, eight-factorial CFD design of experiments (DOE) was used to create a case matrix showing an array of profiles that could be produced by the profile simulator. The eight factors included dilution row 1 mass flow rate; dilution row 1 hole diameter; dilution row 3 outer diameter (OD) mass flow rate; dilution row 3 inner diameter (ID) mass flow rate; effusion flow OD mass flow rate; effusion flow ID mass flow rate; dilution row 3 OD hole diameter; and dilution row 3 ID hole diameter. Sixteen simulations were conducted as part of this CFD DOE. Because the first-row dilution holes were used primarily as a turbulence generator, the ID and OD first-row holes were set to the same conditions. Because the DOE comprised a two-level design, the maximum and minimum of the respective ranges were used for the diameters and mass flow rates. Changes to the first row were made to understand the effects of turbulence on the profile shape. The remaining six factors were changed to study their effects on the exit temperature and pressure profile shapes.

To obtain more significantly peaked temperature profiles, we completed a second DOE during the current reporting quarter, by using a two-level, 12-factorial design method. The first eight factors were the same as those in the original DOE, and the four new factors comprised dilution row 3 OD total temperature; dilution row 3 ID total temperature; effusion flow OD total temperature; and effusion flow ID total temperature. The second CFD DOE allowed more variables to be studied to generate a wider range of profile shapes.

The non-dimensional temperature profiles predicted by the simulations at the exit plane of the combustor profile simulator for the second CFD DOE are shown in Figure 17. Figure 17 includes the profiles previously discussed by Barringer et al. [2], and are examples of engine combustors. The fifth profile is discussed in Povey et al. [3] and is stated to be an example from a typical engine.

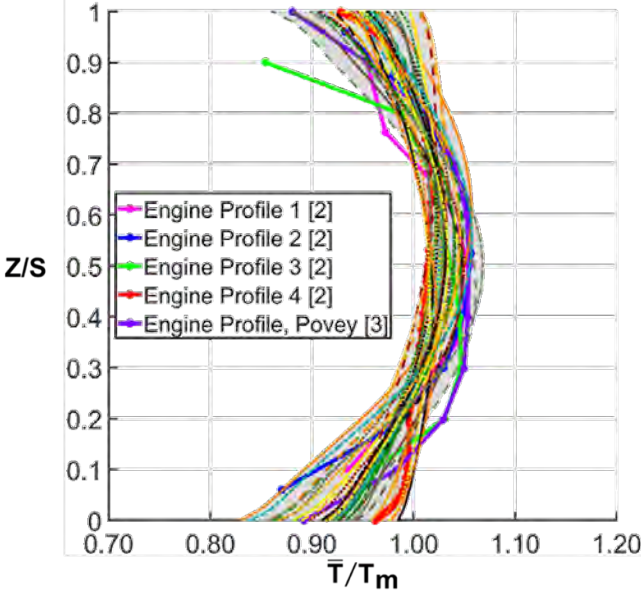


Figure 17. Several predicted non-dimensional total temperature profiles at the simulator exit that are circumferentially averaged with comparisons to typical engine profiles.

The design targets for the new profile simulator included a radial mid-span peaked, OD peaked, ID peaked, and flat uniform profile. The profile results from the second CFD DOE that best matched the design targets were selected and are plotted in Figure 18 for easier visibility. The three simulation-predicted profiles shown in Figure 18, designated as “center peaked,” “ID peaked,” and “OD peaked,” are more representative of the engine profiles than previously found in the first two-level, eight-factor CFD DOE. The shaded gray region in Figure 18 is the same as that in Figure 17, which represents the full-range of profiles produced by the second CFD DOE.

Figure 19 indicates the ranges in the thermal fields generated depending on the dilution jet injection from the second row of holes. Additional analyses are required to further understand the impacts of each of the variables in the resulting temperature field. A sensitivity analysis is in progress to evaluate the resulting predictions from the DOE.

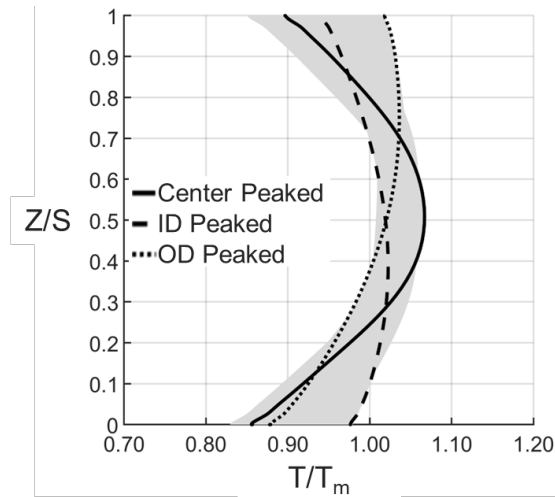


Figure 18. Range of non-dimensional total temperature profiles from the second CFD DOE, plotted versus radial span location and compared with the example engine combustors.

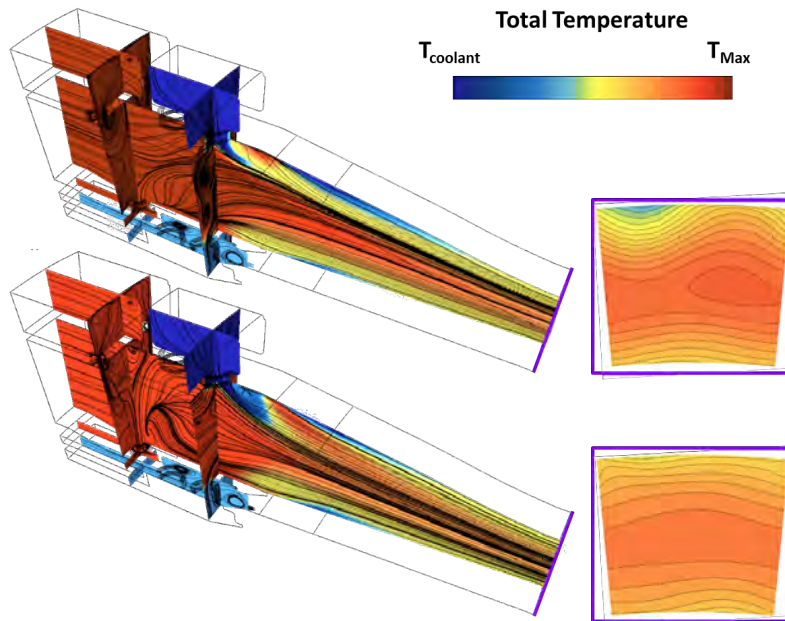


Figure 19. Non-dimensional total temperature contours, showing the impacts of the second row of dilution (top, higher mass flow rate through the second row; bottom, lower mass flow rate through the second row).

Milestones

Milestone	Status
Workplan	Completed
COE Meeting 1	Completed
COE Meeting 2	Completed
Annual Report	Completed

Major Accomplishments

The major accomplishments for this past year include:

- Task 2: development and benchmarking of a method for evaluating heat transfer on combustor liners with and without dirt, with results indicating a potentially significant impact of dirt on liner cooling
- Task 3: design of a combustor profile simulator with accompanying computational predictions of the flowfield to meet the needs of the START facility

Publications

Fallon, B., McFerran, K., Fox, S., Thole, K. A., Lynch, S. P., Lundgreen, R., and Kramer, S., "Comparison of Dirt Deposition on Double-Walled Combustor Liner Geometries," GT2023-102635.

McFerran, K., Thole, K. A., Lynch, S. P., "The Negative Effects of Dirt Ingestion on Cooling within a Double-Walled Combustor Liner," GT2024-124619 (in progress).

Schaeffer, C. B., Barringer, M. D., Lynch, S. P., and Thole, K. A., "Influence of Dilution and Effusion Flows in Generating Variable Inlet Profiles for a High-Pressure Turbine," GT 2024-123899.

Outreach Efforts

Periodic presentations have been given to Pratt & Whitney through this joint collaboration. Additional presentations of this combustor simulator concept have been provided to the Department of Energy, Siemens Energy, Honeywell, and Pratt & Whitney. Industry partners are very supportive of this direction and are providing guidance.

Awards

None.

Student Involvement

Kyle McFerran is progressing toward his MSME degree. Chad Schaeffer is performing the CFD simulations and assisting in the design of the combustor profile simulator. Chad successfully passed the PhD qualifying examination in January 2022. All students are involved in weekly meetings with their advisors (Thole/Lynch) and in regular meetings with Pratt & Whitney. They regularly present their findings to Pratt & Whitney, including to a larger Pratt & Whitney audience at the biannual Center of Excellence meetings (June and November).

Plans for Next Period

During this next year, we will complete the heat transfer tests with and without dirt, in terms of the convective cooling (Task 2). For the profile simulator, we will complete the manufacturing and begin the integration into the START rig (Task 3).

References

Barringer, M. D., Thole, K. A., & Polanka, M. D. (2009). Effects of combustor exit profiles on vane aerodynamic loading and heat transfer in a high pressure turbine. *Journal of Turbomachinery*, 131(2), 021008.

<https://doi.org/10.1115/1.2950051>

Hollworth, B. R., & Berry, R. D. (1978). Heat transfer from arrays of impinging jets with large jet-to-jet spacing. *Journal of Heat Transfer*, 100(2), 352–357. <https://doi.org/10.1115/1.3450808>

Povey, T., Chana, K. S., Jones, T. V., and Hurrion, J., 2007, "The Effect of Hot-Streaks on HP Vane Surface and Endwall Heat Transfer: An Experimental and Numerical Study," *Journal of Turbomachinery*, 129(1), pp. 32–43.



Nomenclature

A_s	Surface area of copper
C_p	Pressure coefficient = $\frac{P_t - P_{tms}}{1/2 \rho_{ave} U_{ave}^2}$
D	Impingement hole diameter
FP	Flow parameter
FP _{clean}	Flow parameter before dirt injection
FP _{dirty}	Flow parameter after dirt injection
H	Distance from effusion to impingement plate
h_1	Heat transfer coefficient
I	Momentum flux ratio = $\frac{\rho_{jet} V_{jet}^2}{\rho_{\infty} V_{\infty}^2}$
k	Thermal conductivity of fluid
\dot{m}	Mass flow rate
N	Number of impingement holes
Nu	Averaged Nusselt number, $h_1 \times D_i \times (k)^{-1}$
P_{oc}	Supply fluid pressure
P_{∞}	Exit static pressure
PR	Pressure ratio
Pr	Prandtl number of fluid
Q	Heat through copper surface, $Q_h - Q_{loss}$
R	Heat dissipated by heater, $I^2 \times r$
RFP	Reduction in flow parameter
Re _d	Jet Reynolds number, $\rho \times U_{jet} \times D_i \times \mu^{-1}$
S_3	Pitch spacing between impingement holes
S	Vane span
T	Temperature
\bar{T}	Circumferentially averaged total temperature
$\bar{\bar{T}}$	Mass weighted total temperature
T_{oc}	Mainstream flow temperature
T_{inf}	Ambient temperature
T_m	Mass-weighted or area averaged total temperature
T_s	Surface temperature
T_{cool}	Cooling flow temperature
U_{jet}	Impingement velocity
Z	Distance in span direction

Greek

ρ	Fluid density
μ	Fluid dynamic viscosity
θ	Non-dimensional temperature, $\theta = \frac{\bar{T}}{\bar{\bar{T}}} - 1$



Project 069 Transitioning a Research nvPM Mass Calibration Procedure to Operations

Missouri University of Science and Technology, Aerodyne Research Inc., and The U.S. Air Force Arnold Engineering Development Center

Project Lead Investigator

Philip D. Whitefield
 Professor Emeritus of Chemistry
 Department of Chemistry
 Missouri University of Science and Technology
 400 W 11th Street, Rolla, MO 65409
 573-465-7876
 pwhite@mst.edu

University Participants

Missouri University of Science and Technology (MS&T)

- P.I.: Prof. Philip D. Whitefield
- FAA Award Number: 13-C-AJFE-MST, Amendments 014, 020, and 023
- Period of Performance: June 5, 2020 to January 31, 2024
- Task:
 1. Investigate the validity of the centrifugal particle mass analyzer (CPMA) mass calibration research approach for non-volatile particulate matter (nvPM) certification measurement systems.

Project Funding Level

Project	Funding	Matching	Source
13-C-AJFE-MST; Amendment 014	\$846,707.00	\$846,707.00	EMPA letter
13-C-AJFE-MST; Amendment 020	\$100,853.00	\$100,853.00	FOCA letter
13-C-AJFE-MST; Amendment 023	\$99,999.00	\$99,999.00	GE letter

Investigation Team

MS&T

Prof. Philip Whitefield, (P.I.)
 Steven Achterberg, (research technician)
 Max Trueblood, research technician
 William Satterfield, research technician

Aerodyne Research, Inc.

Dr. Richard Miake-Lye, (subcontractor)

Arnold Engineering Development Center (AEDC)

Dr. Robert Howard, (subcontractor)



Project Overview

This project is designed to investigate the validity of the CPMA mass calibration research approach. The assessment will extend across all nvPM mass ranges encountered during certification tests. The primary goal will be the successful transitioning of the research methods to operations. The project will begin with a laboratory assessment leading to dedicated turbine engines as the test sources at the U.S. Air Force AEDC. The challenge mass devices for calibration (microsoot sensor [MSS], laser-induced incandescence monitor, and cavity attenuated phase shift monitor) will be provided by the North American Reference nvPM Measurement System, together with the CPMA and other necessary instruments, such as a DMS500 particulate analyzer, and aerosol mass spectrometer.

Task 1– Investigate the Validity of the CPMA Mass Calibration Research Approach for nvPM Certification Measurement Systems

Missouri University of Science and Technology

Objectives

The objectives of this task are to acquire the components of a CPMA-based mass calibration system similar to that described in SAE E31 discussion paper DP-32 (presented by Dr. G. Smallwood) from the annual SAE E31 committee meeting on June 17–21, 2019, in Saclay, France; assemble the system; and evaluate its performance.

Research Approach

Subtask 1.1 **COMPLETED**

Acquire the components of a CPMA-based mass calibration system similar to that described in SAE E31 discussion paper DP-32 (presented by Dr. G. Smallwood) from the annual committee meeting on June 17–21, 2019, in Saclay, France. The CPMA-based system has also been referred to as the CPMA-Electrometer Reference Mass Standard (CERMS).

Subtask 1.2 **COMPLETED**

Assemble and test the CPMA-based mass calibration system’s performance at MS&T’s laboratories, by using a miniature combustion aerosol standard (Minicast) as the nvPM generation source (Figure 1). Compare the laboratory performance of the MS&T CPMA-based mass calibration system with that of two highly similar systems owned and operated by the University of Alberta and the Canadian National Research Council.

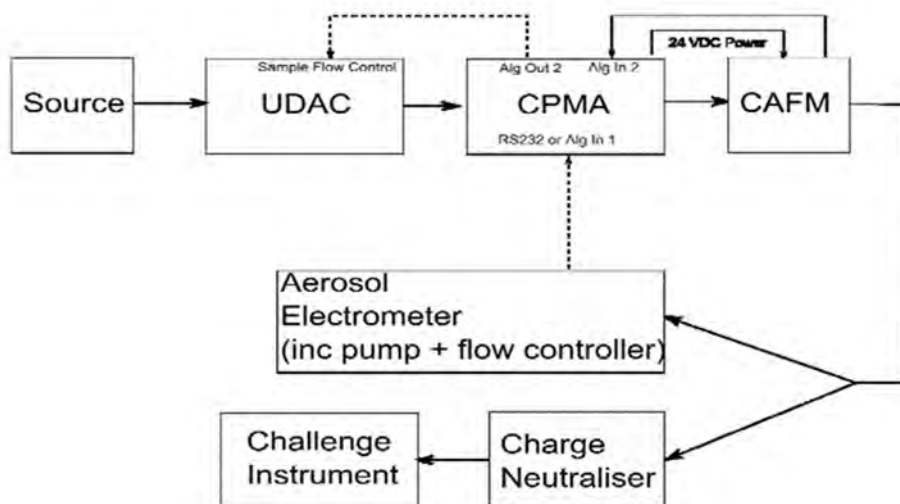


Figure 1. Schematic diagram of the CPMA-based mass calibration system.

Subtask 1.3 UNDERWAY

Investigate the validity of the CPMA mass calibration research approach across all nvPM mass ranges encountered during certification tests, to successfully transition the methods to operations.

Subtask 1.3a COMPLETED

Deploy (transport and install) the North American Reference System, including the CPMA-based mass calibration system and ancillary diagnostic suite, with the Air Force AVL nvPM measurement system and the two Canadian CPMA systems, at engine testing facilities at the Arnold Air Force Base, Tennessee, which will include the J85 turbojet and a gas-turbine-based “start cart” as nvPM sources.

Subtask 1.3b MEASUREMENTS COMPLETED; DATA UNDER ANALYSIS

Evaluate the performance of the three CPMA-based mass calibration systems, surveying across all mass ranges, by using the start cart as the nvPM source; compare these results with concomitant mass calibration data acquired with SAE E-31 OCEC-based mass calibration methods.

Subtask 1.3c MEASUREMENTS COMPLETED; DATA UNDER ANALYSIS

Demonstrate the performance with an nvPM emissions test on the J85 engine, with calibration including standard elemental carbon/organic carbon (EC/OC) analysis, as well as the CPMA-based calibration system described in document DP-32.

Subtask 1.3d COMPLETED

Decouple the diagnostic suites from the Arnold Air Force Base engine facilities, and transport them back to Missouri and Massachusetts.

Subtask 1.4 UNDERWAY

Analyze and interpret the data gathered in Tasks 1.2 and 1.3.

Subtask 1.5 UNDERWAY

Prepare and deliver a final report.

Milestones

- A laboratory-based assessment strategy has been developed and reviewed by the advisory team.
- Essential components for the assessment study, including a Minicast nvPM source, a sample mixing and distribution plenum, and a semi-continuous EC/OC analyzer (Sunset), have been acquired and tested. Substantial effort has been invested in assuring the performance of the analyzer, with modest success. The MS&T team has worked closely with Sunset and will send a representative to the forthcoming engine demonstration. Backup manual EC/OC sampling will be performed at the engine demonstration.
- The CPMA mass standard source has been operated in conjunction with the and MSS mass monitors.
- The MS&T CPMA-based calibration system has undergone a laboratory-based performance comparison against two Canadian CPMA-based calibration systems.
- Engine emissions testing performance has been conducted at AEDC.
- Performance evaluation of multiple CPMA systems has been completed.
- Manual EC/OC has been implemented and executed.
- Assessment tests using start cart have been completed.
- Assessment tests using J85 have been completed.
- Data reduction and analysis are underway.

Major Accomplishments

Essential diagnostic equipment has been acquired, and work on subtasks 2 and 3 is being pursued. The laboratory-based measurements and engine-specific measurements have been completed. Figures 2a and 2b are schematic diagrams of the two instrument configurations used in the engine-specific assessment tests conducted at AEDC. The configuration in figure 2a is designed for intercomparison of the performance of the three CPMA systems made available for the project. The configuration in figure 2b was used to demonstrate a CPMA-based calibration of optical mass measurement instruments, specifically the MSS, LII, and CAPS. The configuration in Figure 2b also included a filter-based system (Teflon and quartz) to perform thermo-gravimetric total OC/EC measurements with the NIOSH 5040 method. During a 3-week period in April 2023, the instrumentation was assembled as described, and the measurements were made.



The project is currently undergoing its data analysis and interpretation phase. Preliminary data on the CPMA systems are being compared, to explore the biases that can be expected when three identical systems are examined. The results of these studies are reported in Figures 3–5 (color code: red, MST; black, NRC; green, UOA).

- Figure 3 presents the bias data for the three electrometers. The bias measurements were made on three separate occasions: one before (Edmonton) and two during the campaign at AEDC. The differences in the current observed were approximately $\pm 1.3\%$.
- Figure 4 addresses the biases observed for the performance of the three CPMA units. In this case, biases were addressed on four separate occasions before and at AEDC. The differences in CPMA voltages and rotational speeds in all cases were $< 1\%$, and the differences in classified mass were approximately $\pm 6.6\%$.
- Figure 5 addresses uncertainties observed for the three CPMA-based systems used to calibrate a photoacoustic mass instrument, the PAX.

Publications

Published conference proceedings

Whitefield, P (May 2023). *Transitioning a Research nvPM Mass Calibration Procedure to Operations* [Oral presentation]. ASCENT Advisory Board Meeting, Alexandria, VA.

Outreach Efforts

The CPMA-based mass calibration system has been transported to Canada for a laboratory-based intercomparison study.

Awards

None.

Student Involvement

One graduate student, Godwin Ogbuehi, and two undergraduate students have been assigned to this project.

Plans for Next Period

We plan to continue to pursue the data analysis and interpretation, along with the final report, as described in the subtasks, given that the test campaign scheduled for April/May 2023 has been successfully completed.

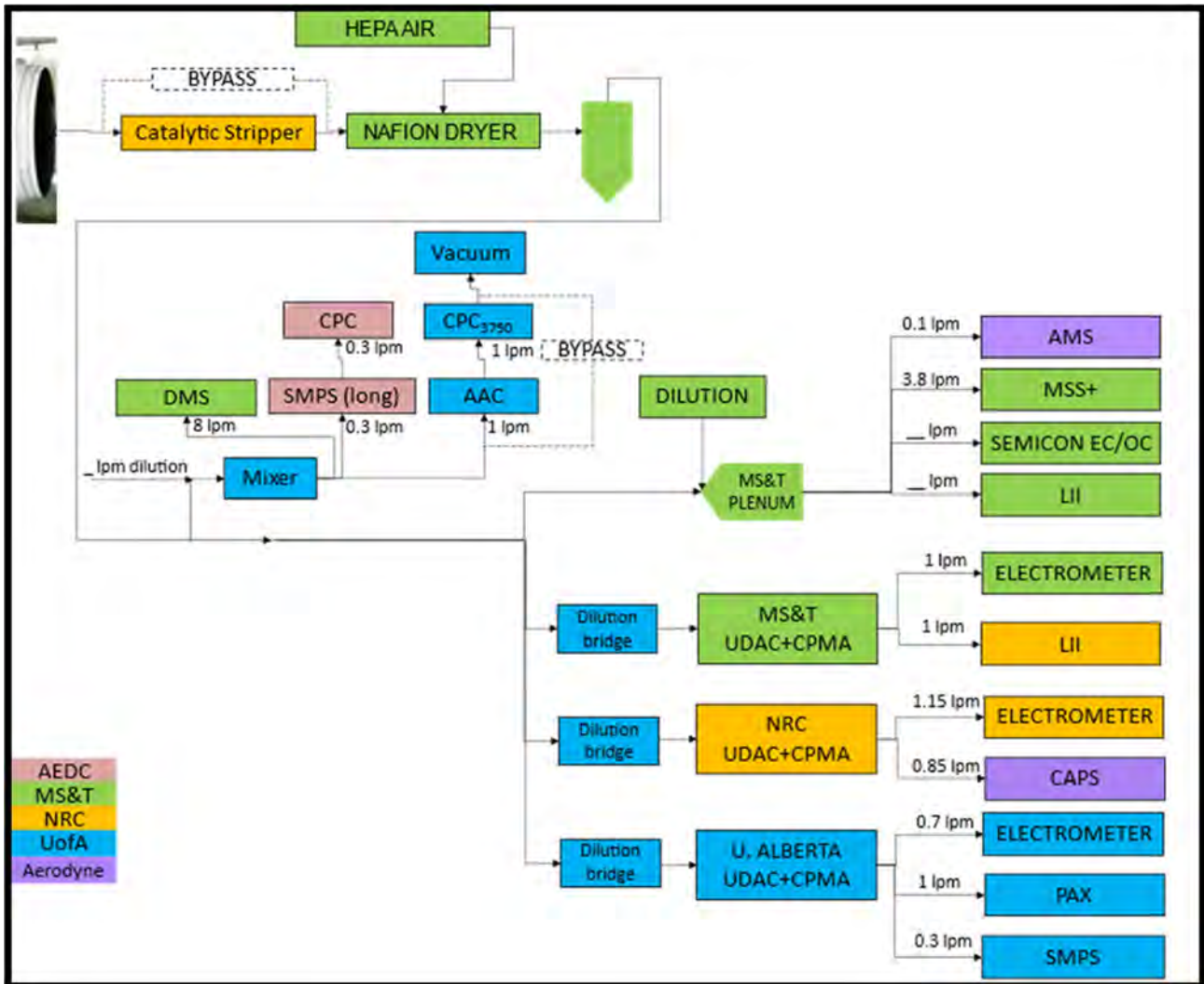


Figure 2a. Schematic for mass standard assessment studies: CPMA system intercomparisons.

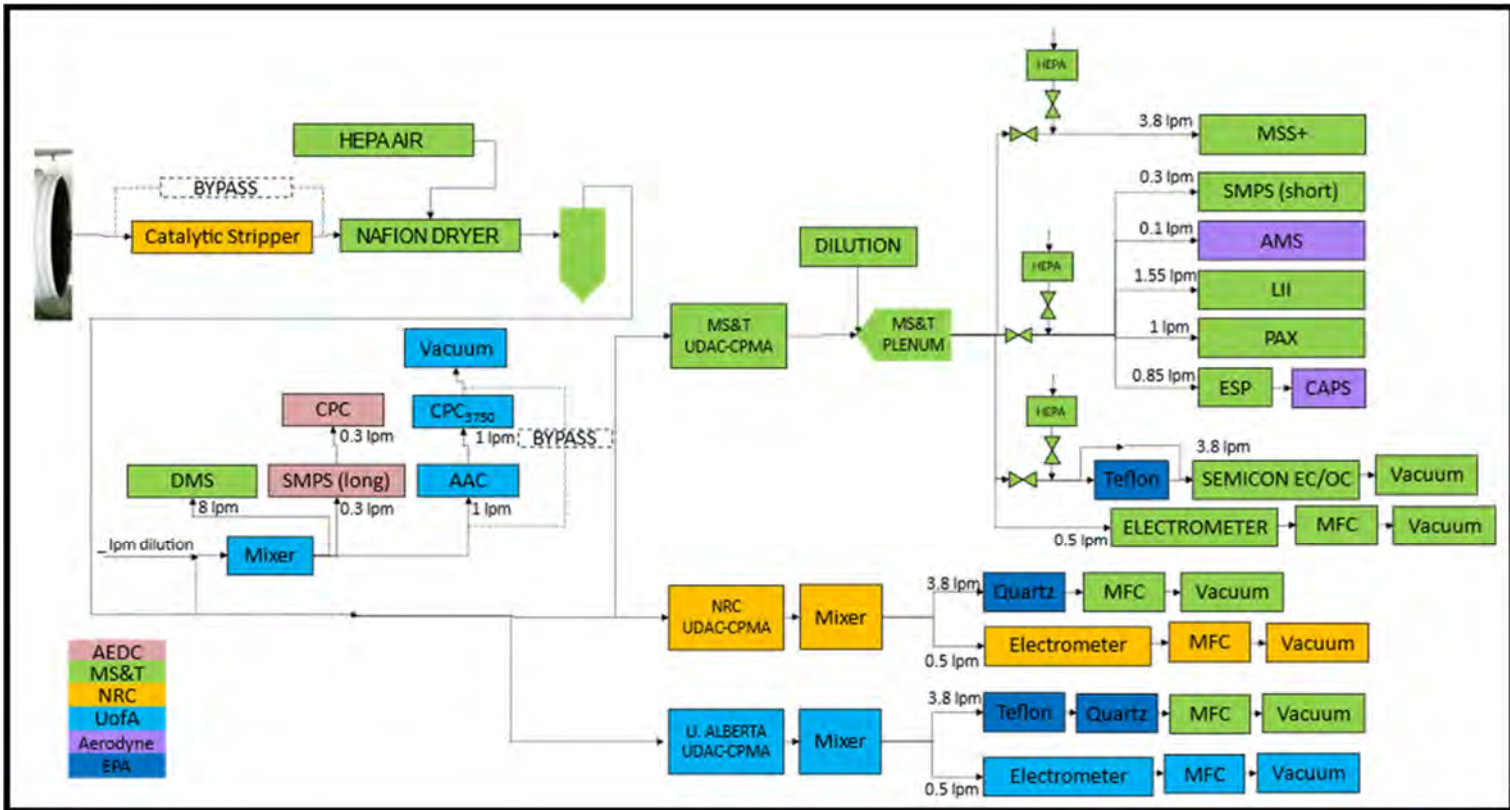


Figure 2b. Schematic for mass standard assessment studies: calibration of optical mass measurement instruments specifically the MSS, LII, and CAPS.

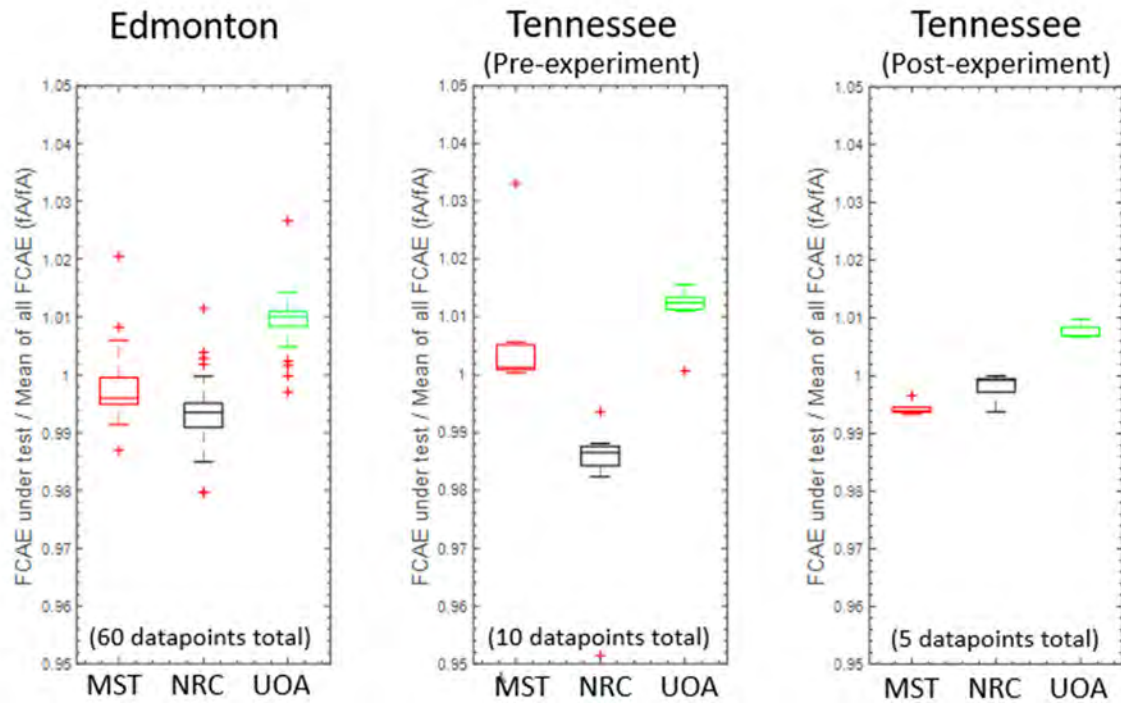


Figure 3. Assessment of biases in the three electrometers.

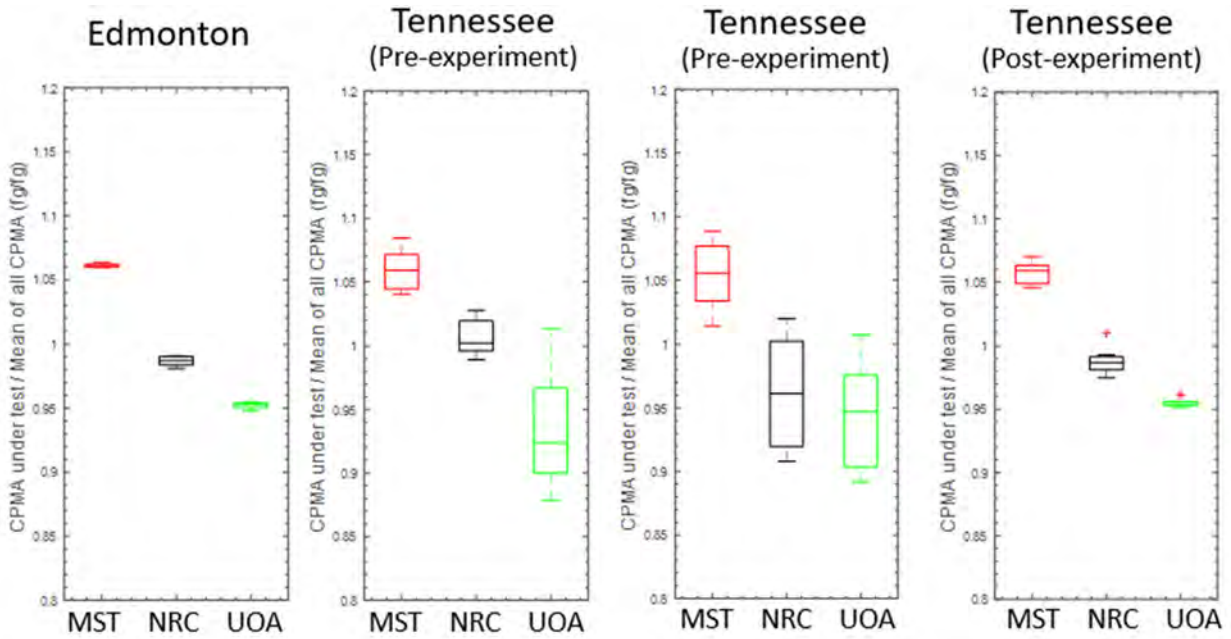


Figure 4. Assessment of biases in the three CPMA setpoints.

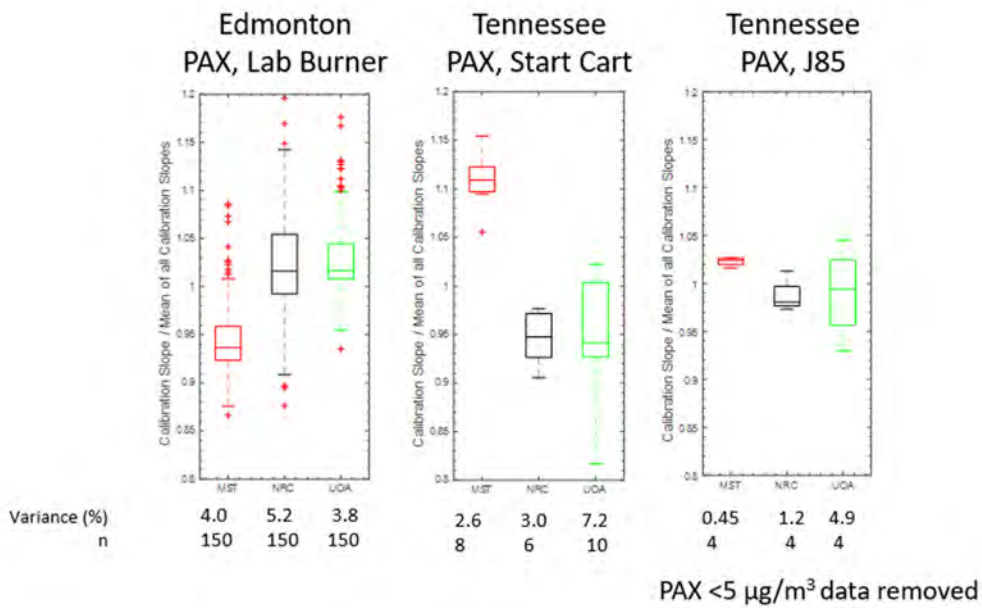


Figure 5. Comparison of uncertainty in CPMA-based calibrations using different carbon emission sources.



Project 070 Reduction of nvPM Emissions from Aero-Engine Fuel Injectors

Georgia Institute of Technology

Project Lead Investigator

Wenting Sun
Associate Professor
School of Aerospace Engineering
Georgia Institute of Technology
270 Ferst Drive, Atlanta, GA 30332
404-894-0524
wenting.sun@aerospace.gatech.edu

University Participants

Georgia Institute of Technology

- P.I.: Dr. Wenting Sun
- FAA Award Number: 13-C-AJFE-GIT-080
- Period of Performance: August 11, 2022 to September 30, 2023
- Tasks:
 1. Measurement of non-volatile particulate matter (nvPM) formation and oxidation processes
 2. nvPM model development and validation
 3. Experimental facility development and operation

Project Funding Level

The total amount of funding from the FAA is \$1,500,000. The funding match includes \$1,350,000 from the Georgia Institute of Technology and \$150,000 from Honeywell.

Investigation Team

Georgia Institute of Technology
Dr. Wenting Sun, (P.I.), Task 3
Adam Steinberg, (co-P.I.), Task 1
Ellen Yi Chen, (co-P.I.), Task 1
Shawn Wehe, (research engineer), Task 1
Ezekiel Bugay, (graduate student), Task 3
Russell McGrath, (graduate student), Task 1
Jeremiah Juergensmeyer, (graduate student), Task 1

Honeywell

- Rudy Dudebout, (co-P.I.), Task 2
- Fang Xu, (co-P.I.), Task 2

Project Overview

Reducing nvPM from gas turbine engines is essential for improving air quality and decreasing the environmental impact of aviation. However, predicting and controlling nvPM remains a challenge because of the complicated physical and chemical processes at play. The proposed research will characterize the formation and oxidation of nvPM and optimize the design of an aeronautical gas turbine fuel injector to reduce nvPM at flight-relevant conditions. In this project, we developed a sector combustor containing three fuel injectors. The sector combustor simulates a section of the Honeywell auxiliary power unit

combustor and injectors. The combustor was fabricated through 3D printing, and the fuel injectors are directly provided by Honeywell. The combustor and high-pressure system were detailed in a previous report and are presented briefly in the next section. The research focus of this year is on conducting an experimental campaign to measure nvPM volume fraction and hydroxyl (OH) radical distribution in the primary zone of the combustor, a region between the fuel injector and downstream quenching holes.

Task 1 – Measurement of nvPM Formation and Oxidation Processes

Georgia Institute of Technology

Objective

The objective of Task 1 is to quantify the nvPM volume fraction by laser-induced incandescence (LII) measurements and to understand the nvPM oxidation process by OH planar laser-induced fluorescence (PLIF) under a broad range of conditions.

Research Approach

In the first year of this project, the high-pressure combustor system was successfully commissioned. In this year, simultaneous LII and OH PLIF were conducted at different pressure, inlet temperature, and equivalence ratio conditions. Our two-dimensional (2D) or planar LII and incandescence decay time measurements to estimate both nvPM volume fraction and relative nvPM particle sizes constitute the first literature report of an application in a practical aeroengine combustor, specifically a three-sector rich-quench-lean combustor using swirl injectors and Jet A fuel. Results are presented below in corresponding sections.

Subtask 1.1: LII Measurement

LII uses short laser pulses to heat small particles to vaporization temperatures. The light emission, or incandescence, of the nvPM is then measured to deduce the relative volume fraction and primary particle size. Two-dimensional implementations of LII are performed by shaping the laser beam into a uniform sheet and capturing the incandescence at various wavelengths on sensitive time-gated cameras. The prompt emission immediately after the arrival of the laser pulse describes the volume fraction or spatial concentration of nvPM particles. Through application of sufficient laser intensity to uniformly sublimate the nvPM, and calibrating these measurements against emissions from known flames, the absolute volume fractions can be determined. In our measurement, a 10-MHz high-speed camera is used to capture the prompt LII signal intensity as well as the signal decay as a function of time. Thus, simultaneous estimates of the nvPM volume fraction and relative particle size can be obtained. The experimental setup for LII is presented in Figure 1.

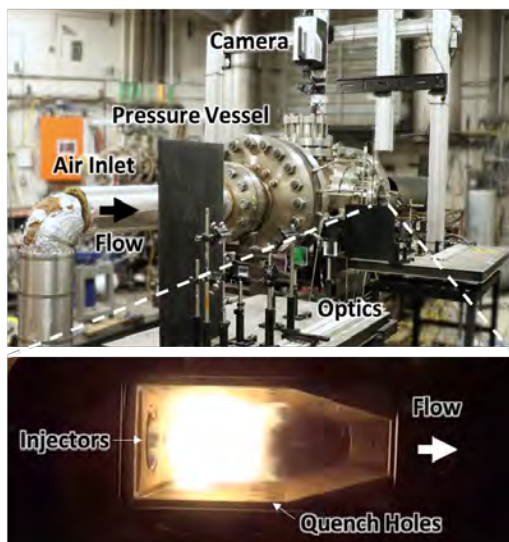


Figure 1. Experimental setup, showing the pressure vessel for the combustor, the air inlet, optics, and high-speed camera. An image of the flame, injectors, and quench holes is also shown from a side window.

The combustor wall (liner) includes three Honeywell aircraft swirl injectors on the dome face, representing multiple sectors of an aeroengine combustor, as illustrated in Figure 2. The combustion liner has four fused quartz windows for optical access. Two windows on opposing sides enable laser access across all three injectors, and two windows on top provide visual access to the rich-burn and lean-burn regions. For the LII optical diagnostics, a Spectra-Physics Quanta-Ray Pro-250 Nd:YAG laser is used to generate a 1,064-nm beam at a frequency of 10 Hz. The layout for the optical elements in the diagnostic is shown in Figure 3. Here, vertical expansion of the beam is achieved by using lenses L1 and L2 (concave and convex cylindrical lenses with focal distances of -50 mm and 300 mm, respectively). Afterward, the beam is horizontally compressed by using cylindrical lenses L3 and L4 (focal distances of 250 mm and -50 mm, respectively). The final beam, with dimensions of 28×1.22 mm at a knife gate, is then relay imaged into the center of the combustor by using a cylindrical lens with 500 -mm focal distance, positioned two focal lengths from the centerline of the combustor. The laser sheet passes through the centers of all three fuel injectors, and the intensity is measured on the far side of the combustor with a laser power meter.

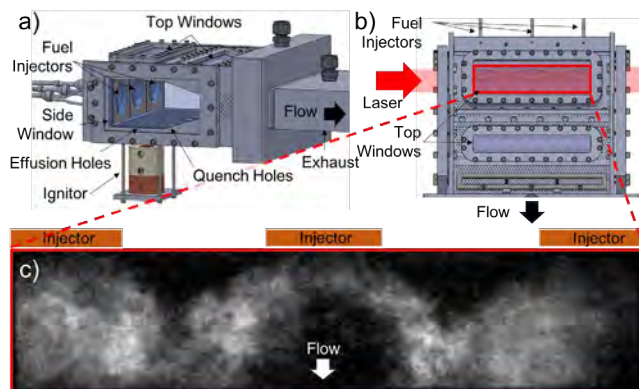


Figure 2. (a) Side view of the combustor, showing the hydrogen torch ignitor, fuel injectors, effusion cooling holes, quench holes, and windows. (b) Top view of the combustor, showing the laser path and top window used for imaging. (c) Chemiluminescence image of the flame, showing the spray cones for all three injectors.

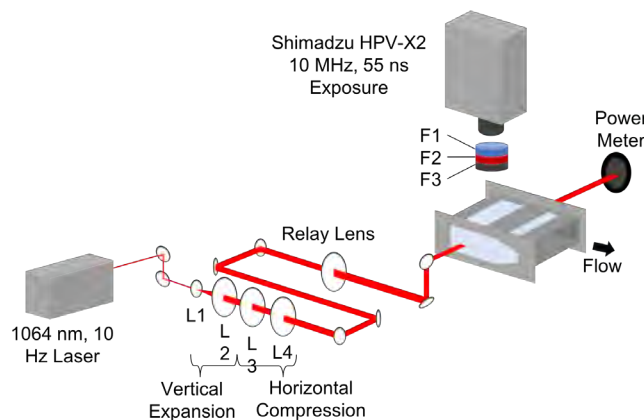


Figure 3. Layout of the optical setup for the LII diagnostic. L1: concave cylindrical lens with $f = -50$ mm; L2: convex cylindrical lens with $f = 300$ mm; L3: convex cylindrical lens with $f = 250$ mm; L4: concave cylindrical lens with $f = -50$ mm; F1: 640-nm bandpass filter with 75-nm full width at half maximum; F2: 1,064-nm bandstop filter; F3: neutral density filter with inner diameter = 0.3.

The LII signal is imaged from above the pressure vessel with a Shimadzu HPV-X2 camera (250×400 pixels) with a 50-mm, $f/\#1.8$ lens. Images were collected at a rate of 10 MHz with zig-zag interpolation and an exposure time of 55 ns. A 1,064-

nm bandstop filter was used to reduce scattering and reflections from the laser; a bandpass filter of 640 ± 75 nm was used to attenuate the chemiluminescence signal and Swan-band emissions; and a neutral density filter with inner diameter of 0.3 was used to reduce the LII signal to within the camera dynamic range. Both the camera and laser were operated with a timing box to ensure consistent and precise capture of the prompt LII signal. In this work, the camera acquired a total of 256 back-to-back frames, capturing the prompt LII signal, LII signal decay, and background chemiluminescence within in a single video. A subset of the background images were averaged and then subtracted from the prompt and decay images to isolate the incandescence signal. At each temperature and pressure condition, at least 25 datasets were collected, thus enabling analysis of both instantaneous and average LII data.

Figure 4 shows a subset of the volume fraction data collected with a constant global equivalence ratio Φ of 0.12. The images show pressures of 45, 55, 65, 75, and 85 psig, with a flow direction from top to bottom. Here, the x coordinate is centered on the center fuel injector. Figure 4a shows soot volume fraction measurements for individual laser shots at each condition, whereas Figure 4b shows the average soot volume fraction from 25 datasets in each condition. The instantaneous images demonstrate clear turbulent flame features, with concentrated areas of soot appearing to vary among instances. These hotspots might potentially be due to high concentrations of fuel spray or variations in local mixing with ambient air. The average volume fraction images, in contrast, are more uniform, thereby suggesting that the hotspots in soot production average out over time. In these images, soot does not appear to be present in the recirculation zones between the swirl injectors. Overall, the soot production is typically less than 2 ppm. Figure 5 shows similar images of volume fraction measurements made at a constant global equivalence ratio of 0.20. The images are taken at pressures of 45, 55, 65, 75, and 85 psig. Similarly to the prior dataset, instantaneous soot concentrations with more apparent turbulent flame features were observed in Figure 5a, whereas Figure 5b shows average images with more uniform distributions. In this dataset, increased recirculation of soot appears to start as conditions shift from the 45-psig case to the 55-psig case. In the latter case, identifiable columns of soot appear around $x = 40$ and -40 mm between the injectors. For this higher equivalence ratio, soot production is significantly higher, reaching 8 ppm or greater. Compared with the spray cones visible in the cases with a global equivalence ratio of 0.12, the side injectors for the cases with a global equivalence ratio of 0.2 appear to have a different pattern from that of the center injector. Here, the soot volume fraction for the center injector appears to have a smaller hole in the center, where little to no soot is present. Although edge effects related to distance from the side windows are expected, the soot production profile of the center injector might be due to a separate effect. In the design of this combustor, the ignitor is placed near the center injector, and the insertion hole for the ignitor allows some additional air to enter the combustion liner. This air could potentially cause additional soot oxidation. Despite this factor, the center combustor has the lowest contribution from side-wall cooling effect and has the best optical access. Thus, additional analysis was conducted by using data from the spray cone of the center injector.

Figure 6 shows the average volume fraction for the spray region near the center injector, compiled over a series of experiments. Figure 6a shows varying pressure conditions at a constant global equivalence ratio, and Figure 6b shows varying global equivalence ratios at different vessel pressures. Error bars indicate the standard error for each test. In Figure 6a, a clear increase in soot production is seen from $\Phi = 0.12$ to $\Phi = 0.20$, indicating a strong dependency between soot production and the global equivalence ratio. Of note, the local equivalence ratios in the rich-burn region are significantly higher than global values. The conditions with an equivalence ratio of 0.12 show only a small increase in soot volume fraction with pressure, from 0.083 ± 0.030 ppm at 25 psig to 0.289 ± 0.075 ppm at 85 psig. In comparison, the conditions with an equivalence ratio of 0.2 show a much larger increase in the average volume fraction, from 0.650 ± 0.188 ppm at 25 psig to 2.951 ± 0.494 ppm at 85 psig. Figure 6b further illustrates trends related to global equivalence ratio and pressure. The mean volume fraction of the center injector for the 85-psig versus the 25-psig conditions is 0.0049 ppm higher at a global equivalence ratio of 0.10; 0.075 ppm higher at a global equivalence ratio of 0.15; and 2.302 ppm higher at a global equivalence ratio of 0.20. These data indicate that the sensitivity of soot production to the global equivalence ratio is highest for the higher-pressure conditions. Part of this increase in the soot volume fraction near the area of interest is likely to be attributable to a lack of soot in the recirculation zones at the low-pressure and low-equivalence-ratio conditions, as in the cases of 25 psig, and 0.10 and 0.12 equivalence ratios. At higher global equivalence ratios, at which soot does not completely oxidize before recirculation, vessel pressure would have a greater influence on volume fraction in the area of interest, by driving soot back up into the rich-burn zone between the injectors. Another major contributing factor to this effect is an increase in the speed of the combustion reactions at higher pressures, which would result in higher soot concentrations.

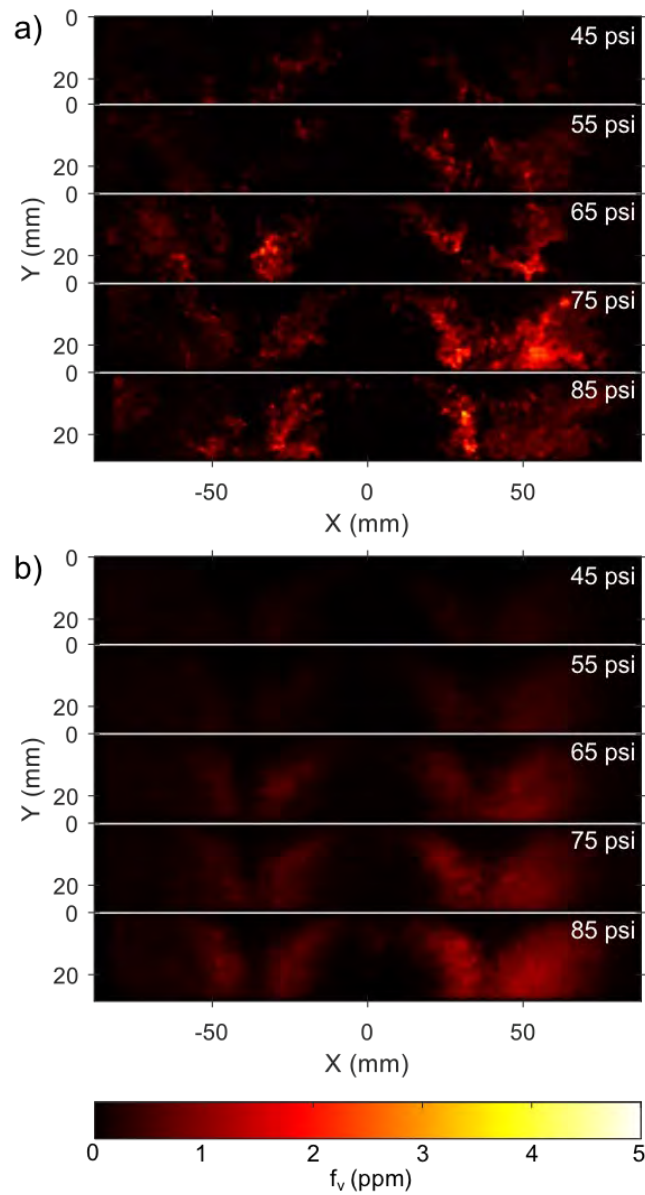


Figure 4. Volume fraction data for an equivalence ratio of 0.12 at pressures of 45, 55, 65, 75, and 85 psig. (a) Single-shot volume fraction images. (b) Average (of 25 images) volume fraction images.

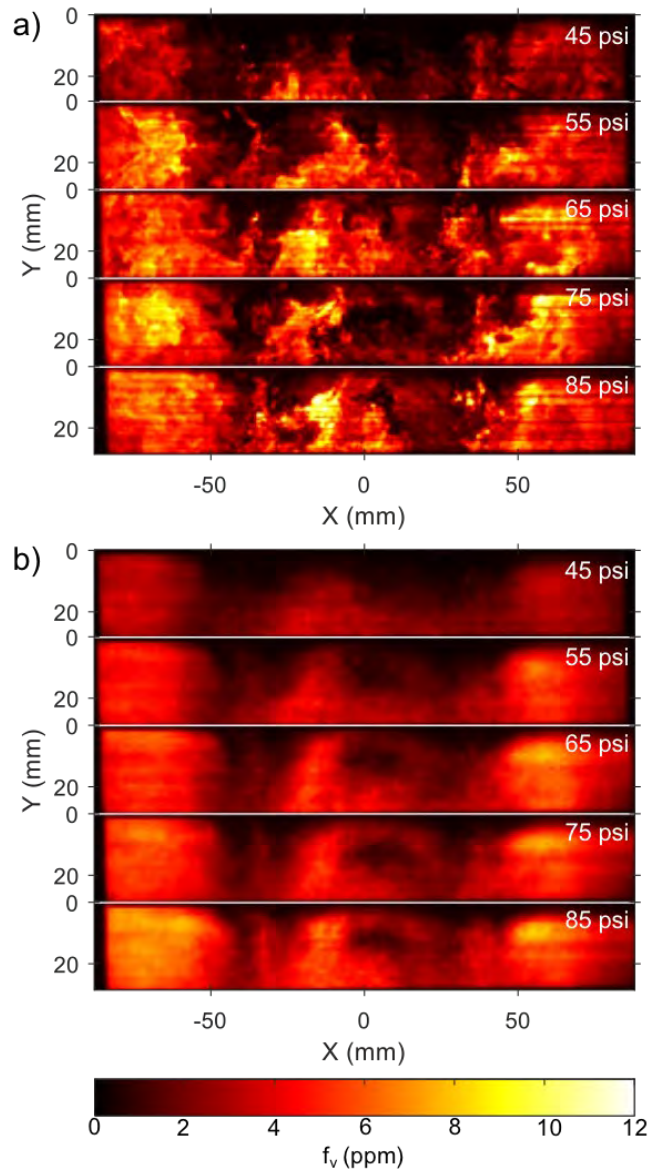


Figure 5. Volume fraction data for an equivalence ratio of 0.20 at pressures of 45, 55, 65, 75, and 85 psig. (a) Single-shot volume fraction images. (b) Average (of 25 images) volume fraction images.

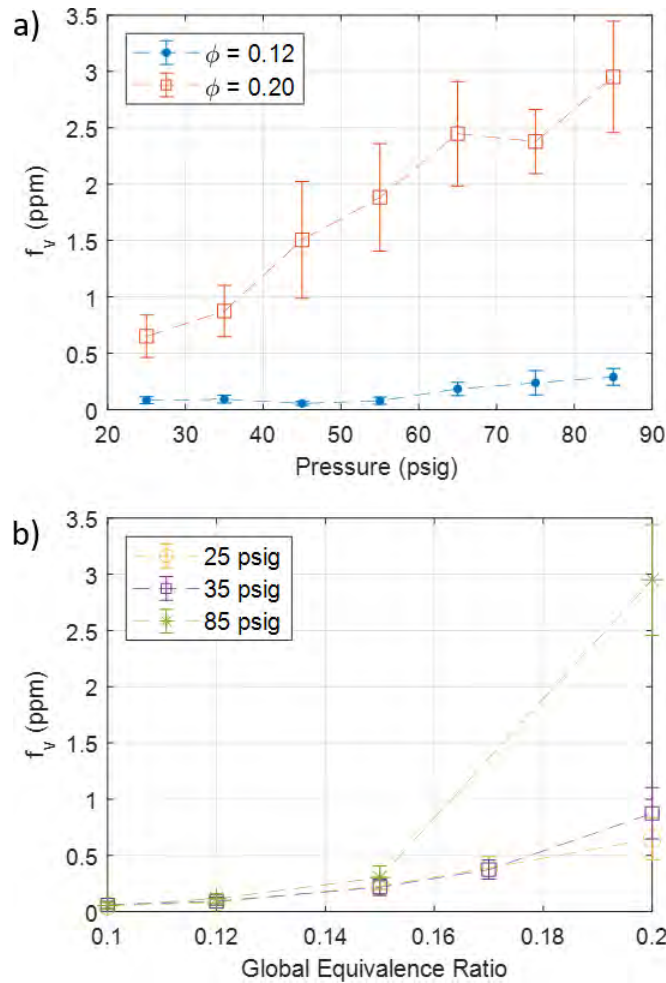


Figure 6. Average volume fraction near the center injector at (a) a constant global equivalence ratio and (b) a constant pressure. Error bars indicate standard error of the mean.

For estimating the effect of relative particle size within a single image, time constant fits to incandescence decay profiles must first be computed. To process these data, background chemiluminescence is first removed via background averaging and subtraction. Subsequently, the data series from a single laser shot is normalized against the prompt LII frame. Finally, exponential decay curves are fit to each pixel in the data series to estimate decay time constants. Figure 7 shows the time constant fits for five different pixels, each with a different decay time. Because of the relatively high intensity of the prompt LII signal and the low camera noise, the time constant fit tends to be of good quality, particularly for time constants 40 ns or longer. However, shorter time constants contain greater uncertainty, because of the lack of time resolution from the 10-MHz camera acquisition.

Because of the unavailability of calibration source, such as *in situ* soot sampling and transmission electron microscopy images, we cannot quantify the actual size of the particles. However, the time constant is proportional to the size of particles (because larger particles take longer to evaporate after laser heating). Therefore, only relative particle sizes are shown in this study.

After time constants are fit to the data, particle size distributions are analyzed. Figure 8a shows time constant fits for the 25-, 55-, and 85-psig cases at a global equivalence ratio of 0.20, whereas Figure 8b shows probability distributions of the time constant near the center injector. For these experiments, the 25-psig case appears to have more time constants above



60 ns than the 55- and 85-psig cases. The 85-psig condition also appears to have a higher number of time constants below 20 ns than the other cases. Several possibilities may explain these effects. First, the pressure in the conduction heat transfer model predicts shorter time constants for soot incandescence at higher pressures. Whereas the conduction term appears to indicate a proportional decrease in time constants as a function of pressure, the contributions of sublimation and other terms may alter the overall time constant scaling. Other effects, such as poor droplet breakup, lower signal intensity, and weaker recirculation regions, can also contribute to higher soot incandescence decay time estimates for the 25-psig case.

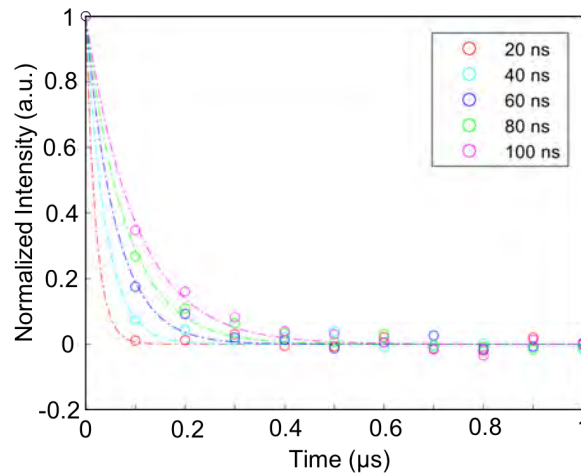


Figure 7. Varying time constant fits, shown for incandescence decays captured on different pixels.

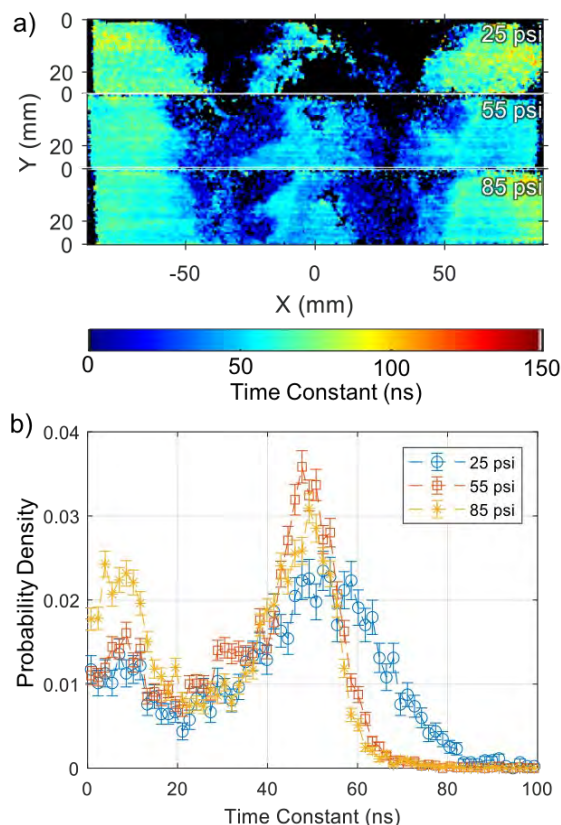


Figure 8. (a) Time constant distributions, illustrated for 25-, 55-, and 85-psig conditions, with a global equivalence ratio of 0.2. Here, the time constant serves as an indicator of relative particle size within each image. (b) Probability densities of the time constants. Error bars indicate standard deviations, estimated with Poisson statistics.

Subtask 1.2: OH PLIF Measurement

Oxidation through reaction with OH radicals is expected to be a critical pathway through which nvPM is destroyed in the flame. Understanding the relative trajectories of nvPM and OH through the combustor is therefore essential to predicting the final nvPM output. OH radicals form during high-temperature hydrocarbon oxidation, reaching super-equilibrium concentrations near the location of maximum heat release rate, then decreasing to equilibrium concentrations in the post-flame region. Substantial concentrations of OH are observed in hot product gases at temperatures above ~ 1500 K. Fortunately, owing to its strongly absorbing energy transitions at wavelengths that are relatively accessible to high-energy pulsed lasers, OH can be readily measured with PLIF.

Under this task, we performed OH PLIF measurements simultaneously with the 2D LII measurements to understand the interaction between nvPM and OH. Measurements were collected at a repetition rate of 5–10 kHz by using the frequency-doubled output of a dye laser (rhodamine 6G), pumped by a frequency-doubled solid-state laser (Nd:YAG). More than 7 W of ultraviolet laser light can be produced by our laser system, which is sufficient to acquire signal across the combustor domain. The laser beam was formed into a sheet, made coincident with the LII laser sheet, and transmitted through the combustor. The OH PLIF signal was filtered through an appropriate bandpass filter (approximately 307 nm) and recorded with a high-speed intensified camera. Appropriate corrections were made for laser power absorption, intensity variations, and detector response. The resultant data (Figure 9 and Figure 10) provide time-resolved 2D images of the OH distribution overlapping with the 2D LII data. More data are currently being processed, given their complexity. These data may improve understanding of the oxidation process and how specific trajectories influence the nvPM ultimately output from the combustor. These data will also be used for numerical model validation.

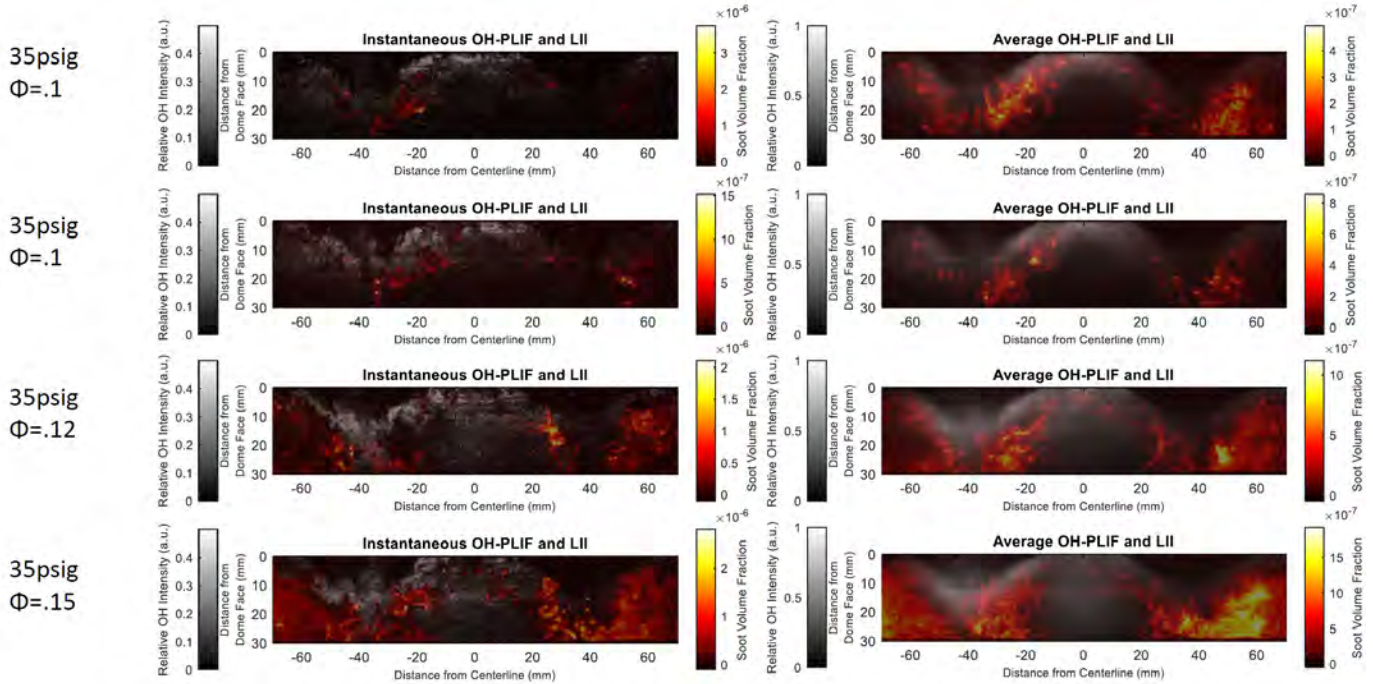


Figure 9. Instantaneous and average OH-PLIF and LII data (simultaneous measurement) at different equivalence ratios and a pressure of 35 psig

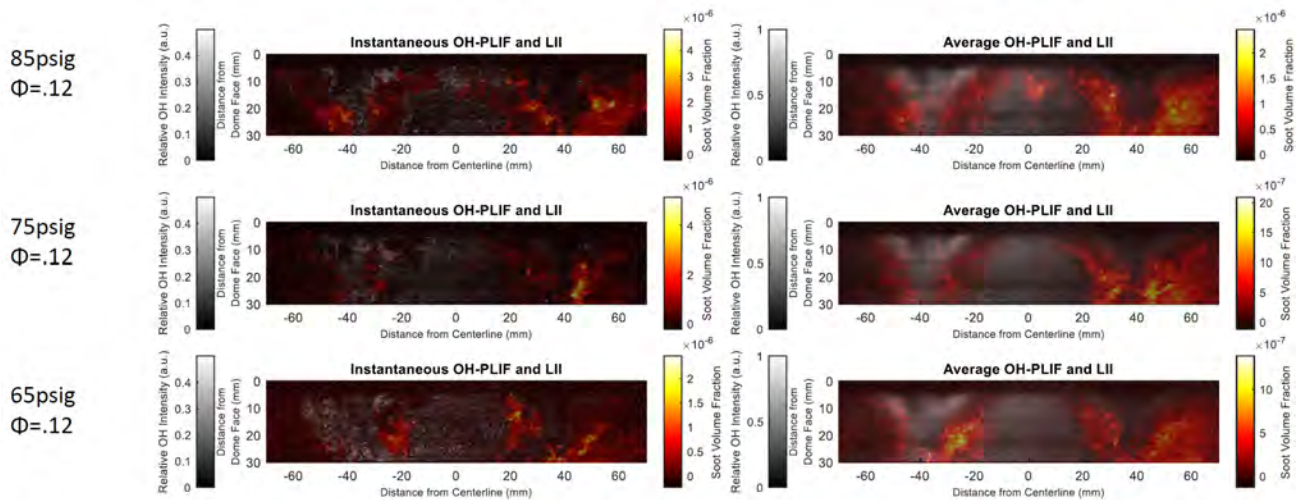


Figure 10. Instantaneous and average OH-PLIF and LII data (simultaneous measurement) at different pressure conditions with an equivalence ratio of 0.12.

Milestone

Systematic LII measurements and OH PLIF measurements were conducted.

Major Accomplishments

Simultaneous LII and OH PLIF measurement demonstrating nvPM formation and oxidation.



Publications

R. McGrath, E. Bugay, J. Juergensmeyer, A. Zheng, D. Wu, A. Steinberg, W. Sun, E. Mazumdar, "Single-camera Time-Resolved laser-induced Incandescence Measurements in a RQL Aeroengine Combustor," submitted to Application of Energy and Combustion Sciences (under review)

Outreach Efforts

None.

Awards

None.

Student Involvement

This task involves three graduate students (Jeremiah Juergensmeyer, Ezekiel Bugay, and Russell McGrath).

Plans for Next Period

We will conduct simultaneous LII and OH PLIF measurements for SAF and its mixture with Jet fuel.

Task 2 – nvPM Model Development and Validation

Honeywell

This task involves the simulation of the sector combustor developed by the Georgia Institute of Technology team and comparison of the experimental measurements obtained in Task 1 with detailed numerical simulations, for the purpose of model development and validation. A numerical framework to model the gas turbine combustor system was established on the basis of Honeywell's previous experience, and detailed simulation was conducted. In this numerical framework, a commercial solver was used to obtain computational fluid dynamics (CFD) solutions with a large eddy simulation turbulence model, by using a dynamic Smagorinsky model. The combined heat release/turbulence model consists of non-premixed diffusion flamelets generated by using a detailed Jet A kinetic model describing the formation of aromatic species up to pyrene. The simulation includes radiation with the discrete ordinate method due to H₂O, CO₂, and nvPM (weighted-sum-of-gray-gases model). The liquid fuel spray is modeled with Lagrangian tracking of droplets with stochastic secondary breakup, calibrated to experimental data. The domain is discretized by using polyhedral cells and consists of the entire geometry from the inlet of the rig to the exhaust of the combustor. The simulation is initially converged with a Reynolds-averaged Navier–Stokes solution, then run with five flow-throughs to initialize the solution and subsequently an additional five flow-throughs to obtain statistical averages. The numerical simulation will be compared with experimental results from optical measurements (LII, OH, and Mie scattering) at different flow conditions by using different fuel injectors.

In this year, comprehensive numerical simulation is being conducted by the Honeywell team for comparison with the experimental data presented in previous section. Detailed results will be presented next year.

Milestone

CFD simulation of the designed combustor. This work was in progress as of October 1, 2023. Results will be presented in the next annual report.

Major Accomplishments

Detailed design and CFD analysis of the combustor.

Publications

None.

Outreach Efforts

None.



Awards

None.

Student Involvement

None.

Plans for Next Period

Detailed numerical simulation comparison with experimental data.

Task 3 – Experimental Facility Development and Operation

Georgia Institute of Technology and Honeywell

Objective

The objective of this task is to develop the sector combustor with three fuel injectors and optical windows. This combustor will be operated under high-pressure and high-temperature conditions to replicate real engine conditions. This sector combustor is used as the test bed for Task 1 and Task 2.

Research Approach

In this task, we successfully designed and commissioned a high-pressure model gas turbine combustor. Such a design is challenging, because it must accommodate advanced optical measurements with practical applicability from the perspectives of both industry and academia. To achieve this goal, the Georgia Institute of Technology team and Honeywell team worked closely and designed a unique combustor with three fuel injectors. This three-fuel-injector design minimizes injector-combustor wall interaction, which is common in conventional combustor design with only one fuel injector. Our optical measurements will focus on the center fuel injector. Three large optical windows are located on the top and side walls of the combustor, thus enabling optical diagnostics. CFD was conducted to design the windows' cooling and filming features, to avoid window damage and blackout by soot. The combustor is placed inside a large high-pressure vessel rated for a maximum of 30 bar at 727 K (Figure 11). The vessel has an internal diameter of 18 in (43 cm) with three 10-in (25.4 cm) fused quartz windows for optical access, one on each side for laser access, and one on top for camera access. A squeeze flange mounted on the upstream side is used to pass fuel and instrumentation lines into the vessel, thereby enabling measurement of vessel pressure and temperature at various locations along the combustor. Air for the experiments is supplied to the system by the high-pressure air supply at the Ben T. Zinn Combustion Laboratory at the Georgia Institute of Technology, a blowdown system capable of supplying a stable, static pressure as high as 50 bar at 1100 K. The air flows through a sub-critical orifice used for measuring and monitoring the mass flow rate, after which it enters the vessel through a perforated plate. Air then enters the combustor through the swirlers, thus providing most of the air for the rich-burn region, as well as through effusion cooling and quench holes. Fuel for this system is supplied through a 10-gallon piston accumulator driven by a cylinder of pressurized nitrogen gas. The fuel flows through a remotely operated pneumatic globe valve, which allows for flow control, followed by a Coriolis flow meter, which monitors and measures the fuel mass flow rate. After passing through a pneumatic solenoid block valve, fuel passes through the squeeze flange into a manifold, where it is supplied evenly to all three injectors.

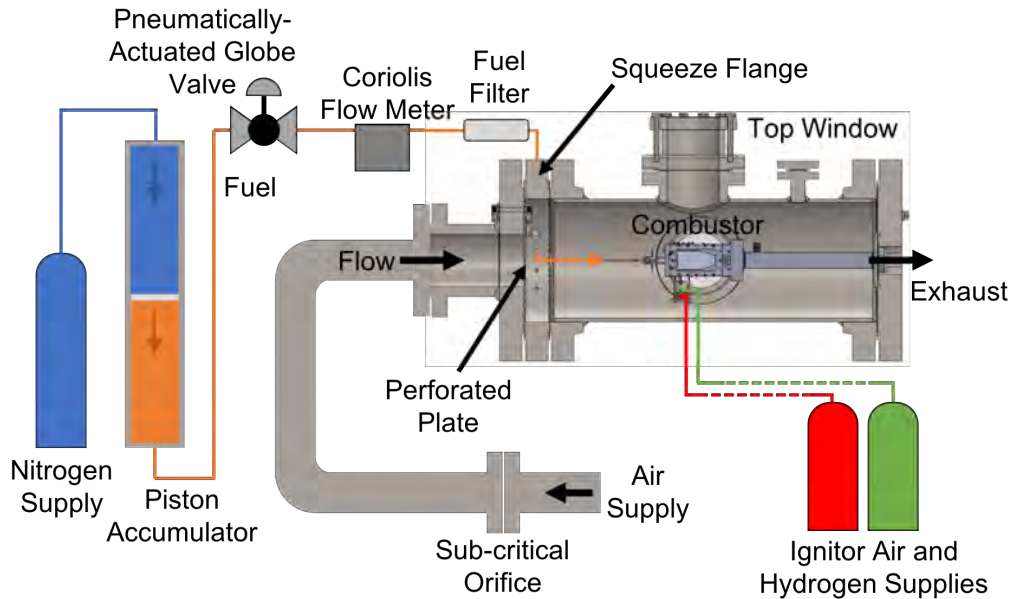


Figure 11. Side view of the pressure vessel, showing the process flow, instrumentation, and controls.

Milestone

This task was completed in 2022.

Publications

None.

Outreach Efforts

None.

Awards

None.

Student Involvement

Project 70 involves four graduate students (Jeremiah Jeurgensmeyer, Sundar Manikandan, Ezekiel Bugay, and Russell McGrath) and three research engineers (David Wu, Subodh Adhikari, and Shawn Wehe).

Plans for Next Period

In the following year, our main goal is to upgrade the combustor system to allow a higher fuel flow rate in the system, to align the testing condition conditions with Honeywell auxiliary power unit operating conditions.



Project 071 Predictive Simulation of nvPM Emissions in Aircraft Combustors

Georgia Institute of Technology

Project Lead Investigator

Suresh Menon
Professor at the School of Aerospace Engineering
Georgia Institute of Technology
270 Ferst Drive, Atlanta, GA 30332-0150
404-894-9126
suresh.menon@aerospace.gatech.edu

University Participants

Georgia Institute of Technology (GT)

- P.I.: Prof. Suresh Menon
- FAA Award Number: 13-C-AJFE-GIT-067
- Period of Performance: October 1, 2022 to September 30, 2023
- Tasks:
 1. Kinetic modeling: improvement in soot kinetic models and chemistry of jet fuels under rich quench-lean (RQL) combustor operating conditions
 2. Nucleation modeling: predicting incipient particle nucleation rates according to polycyclic aromatic hydrocarbon (PAH) dimerization rates from molecular dynamics (MD) simulations
 3. Surface growth and aggregation modeling: reaction-transport-limited growth of soot particle models for cluster-cluster aggregation
 4. Large eddy simulation (LES) of multiphase reacting physics inside an RQL combustor

Project Funding Level

The current FAA funding is for a 3-year effort (July 2020 to September 2023), with a request of \$500,000 per year from ASCENT (per year). An additional request for a no-cost extension has been submitted. Cost-sharing is provided as follows.

- GT provides cost-sharing for its share of \$150,000 per year. The GT point of contact is Kevin Ellis (kevin.ellis@aerospace.gatech.edu).
- Raytheon Technologies Research Center (RTRC) provides cost-sharing of \$250,000 per year. Dr. Colket is a consultant on this project with many years of experience in soot modeling. The RTRC contact is John LaSpada (LaSpadJW@RTRC.utc.com).
- The University of Michigan (UM) provides cost-sharing in the amount of \$100,000 per year. The UM point of contact is Alexandra Thebaud (thealexi@umich.edu).
A no-cost extension until September 2024 has been granted.

Investigation Team

GT

Prof. Suresh Menon, GT: (P.I.), Task 4
Mr. Shubham Karpe, GT: (Student), Task 4

RTRC

Dr. Miad Yazdani, (co-P.I.), Task 3
Dr. Steve Zeppieri, (co-P.I.), Task 1
Dr. Meredith Colket, (co-investigator), Task 1

UM

Prof. Angela Violi, (co-P.I.), Task 2
 Mr. Jacob Saldinger, (Student), Task 2

Project Overview

This project is being used to establish a new multiscale approach to predict soot formation in aircraft combustors. A hierarchy of first-principles simulation methods is being used to account for the multiscale physics of the formation and transport of non-volatile particulate matter (nvPM, also called soot in the literature). The final objective is to use this multiscale approach to model the physics in LES of realistic gas turbine combustors. We target and isolate the layers of empiricism that currently exist, for example, in particle inception models, the roles of precursor species in nucleation, the particle shape assumptions and their impact on surface growth, the sensitivity of predictions to particle size distribution, and the ad hoc coagulation/coalescence mechanisms. The team already has all modeling tools, but a systematic coupling of these tools in a multiscale, multiphysics strategy has yet to be accomplished by any research group. Hence, this study will establish new predictive ability by integrating these capabilities.

The multiscale and multiphysics layers of collaborations among the cost-sharing groups are summarized in Figures 1 and 2, and briefly described herein. The kinetics group at RTRC is conducting a study to understand the role of gas-phase kinetics in predicting important species potentially labeled as soot precursors. The information on reduced kinetics from RTRC is being used by GT and UM to evaluate LES performance and the process of nucleation. In the UM study, the propensity of gas-phase species to form dimers (considered the building blocks of soot inception) under flame conditions is being studied. Identification of soot precursors and the rates of formation of soot nuclei will be the output from these studies. This nucleation rate will be provided to GT to update the source terms associated with nucleation processes through a six-moment method of moment with interpolative coefficients (6-MOMIC) approach, and the information on the structures of these soot nuclei will be provided to RTRC for modeling of surface growth and aggregation processes. Outputs from the aggregation studies in RTRC in the form of global surface growth and aggregation models will then be fed back to GT to update the source-term surface growth and aggregation models in the 6-MOMIC approach. Canonical studies are underway at GT to provide information regarding the variations in local conditions, such as pressure, temperature, and local equivalence ratios due to turbulence–chemistry interactions; this information should be useful in each stage of the abovementioned studies. LES studies at GT will also involve modeling the effects of chemistry–soot–turbulence interactions by using advanced subgrid models including the linear eddy mixing (LEM) model. As a project deliverable (at the end of this research effort), the final assessment of both the existing soot model and the improved soot model will be conducted in canonical flame configurations.

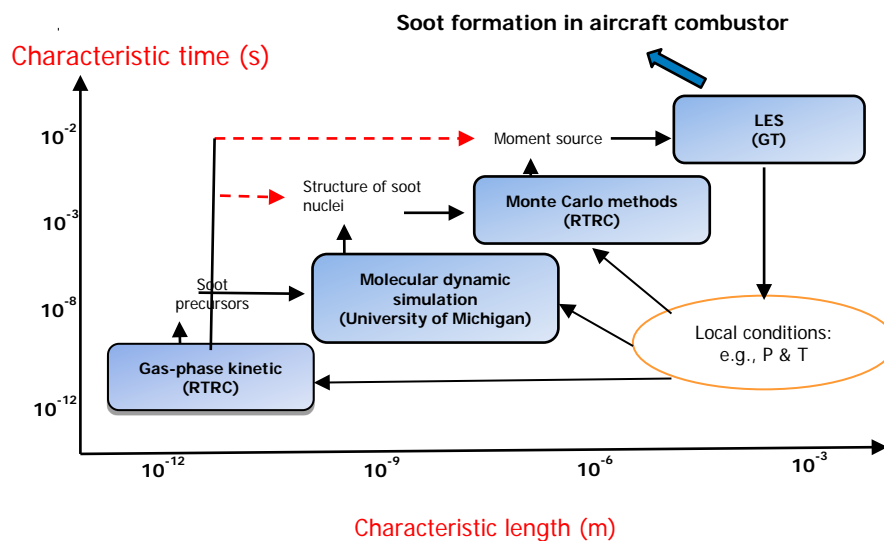


Figure 1. Multiscale collaborative efforts to improve nvPM (soot) predictions.

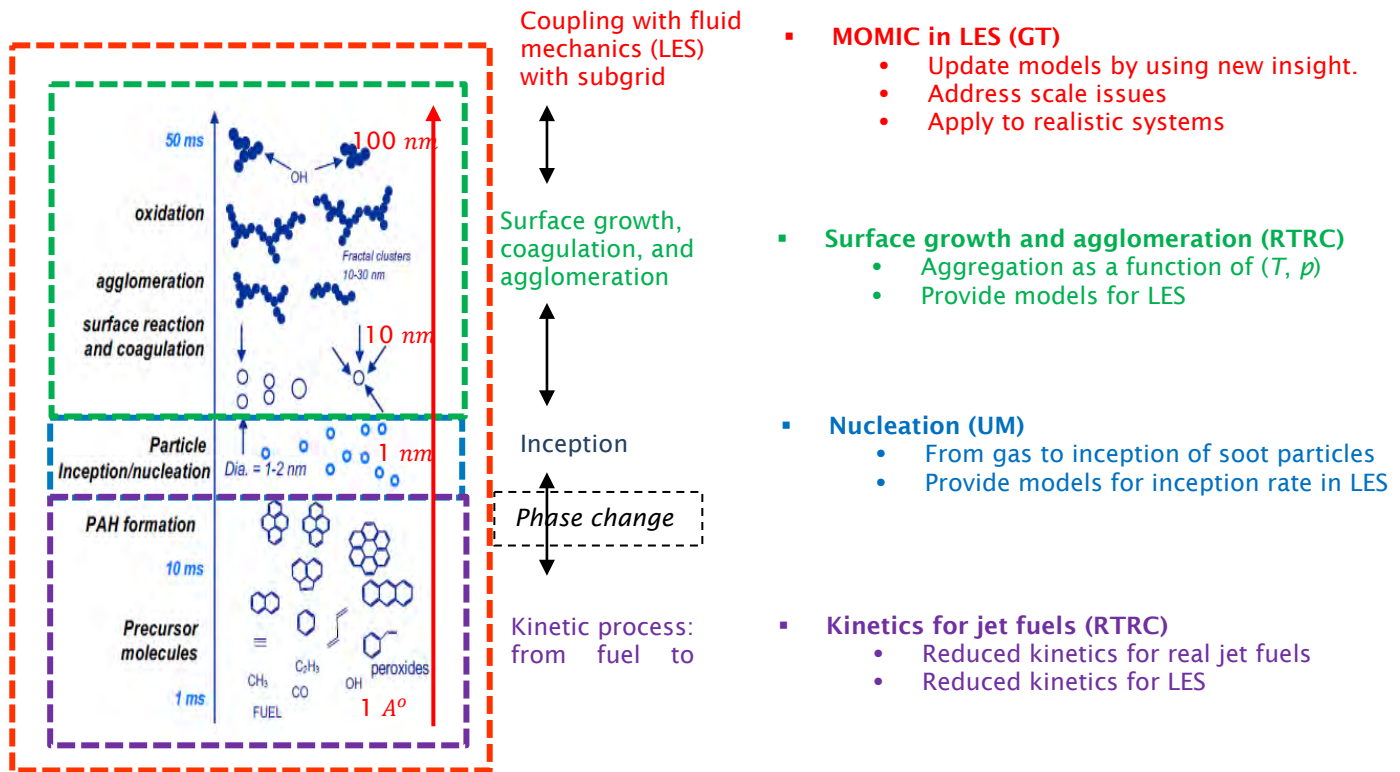


Figure 2. Multiscale collaborative efforts to improve nvPM (soot) predictions.

Task 1 – Kinetic Modeling

RTRC

Objective

The objective of this task is to develop validated, detailed, and reduced chemical kinetic models of parent fuel decomposition and oxidation reactions, with a special focus on fuel rich chemistry, to enable the accurate evolution of PAH/soot precursor formation and incipient soot particle formation, and the evaluation and improvement of reduced-order soot formation models. Year 1 fuel activities focused on ethene, whereas Year 2 efforts shifted the focus to Jet A fuels. In Year 3, efforts continued toward optimizing fuel chemistry as well as soot kinetics at RQL-relevant conditions.

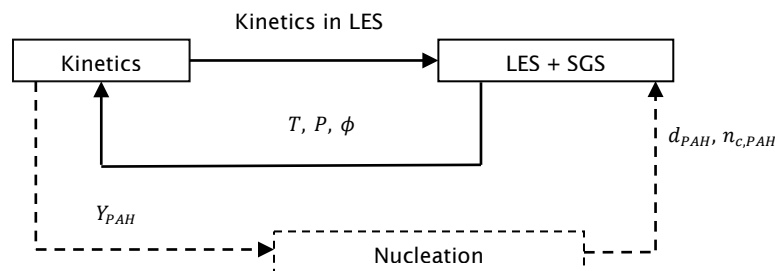


Figure 3. Coupling of LES-kinetic activities.

Research Approach

Reduced-order model development for use in LES of RQL combustors

The schematic in Figure 3 shows the coupling among the LES, nucleation, and kinetic activities focused on during the current Year 3 of the project, where T , P , and ϕ represent the temperature, pressure, and equivalence ratio of the surrounding gas phase, respectively. The LES studies at GT are being conducted at $T_{in} = 600$ K and $P = 5.8$ atm. These conditions are used herein for optimization of chemistry for jet fuels as well as soot kinetic model optimization for the range of ϕ . Moreover, PAH represents the polycyclic aromatic hydrocarbon species considered the soot precursors. The objective of the current kinetic efforts was focused on downselecting the detailed kinetic model of jet fuels and reducing it to a non-stiff version with finite rate expressions for production of precursor species determining Y_{PAH} . This kinetic model is to be fed directly into LES studies at GT. The precursor species characteristics (n_{PAH} , d_{PAH}) and concentrations will also be input into nucleation studies at UM to assess their ability to form dimers.

In Year 1, ethene kinetics with varying details of PAH/particulate matter (PM)-related chemistry were assessed. Given that the ultimate goal of this effort is the development of chemical kinetic models coupled to PAH and soot (PM) formation for both logistic (Jet A) and alternative fuels, we investigated four detailed mechanisms. We used the HyChem method, in which semi-empirical reactions treat the parent fuel decomposition process to the relevant intermediate hydrocarbon species, and the so-called SERDP technique, in which compositions of several surrogate hydrocarbon species are formulated that capture the bulk properties of the fuel of interest. (For example, Jet A would be considered a binary blend of *n*-dodecane and *m*-xylene.) The HyChem model was coupled with both the SERDP and KAUST PAH-chemistry models for analysis, and the SERDP model was coupled with the SERDP PAH-chemistry model. Finally, the Caltech-mech model was appended with the HyChem model to incorporate additional reactions related to decomposition of Jet A fuels. In the most recent prior annual efforts, comparisons were drawn by using HyChem-KAUST and HyChem-SERDP approaches against the Wang-Frenklach (WF) (Wang, 1997) chemistry, by using the benchmark data for soot formation from ethene fuels. In the current effort, we have incorporated one more detailed mechanism, Caltech-mech. We also used the Pitsch mechanism (Langer, 2023), which is relatively new, for the initial assessment of gas-phase chemistries.

The overall layout of the workflow implemented in this quarterly effort is highlighted in Figure 4.

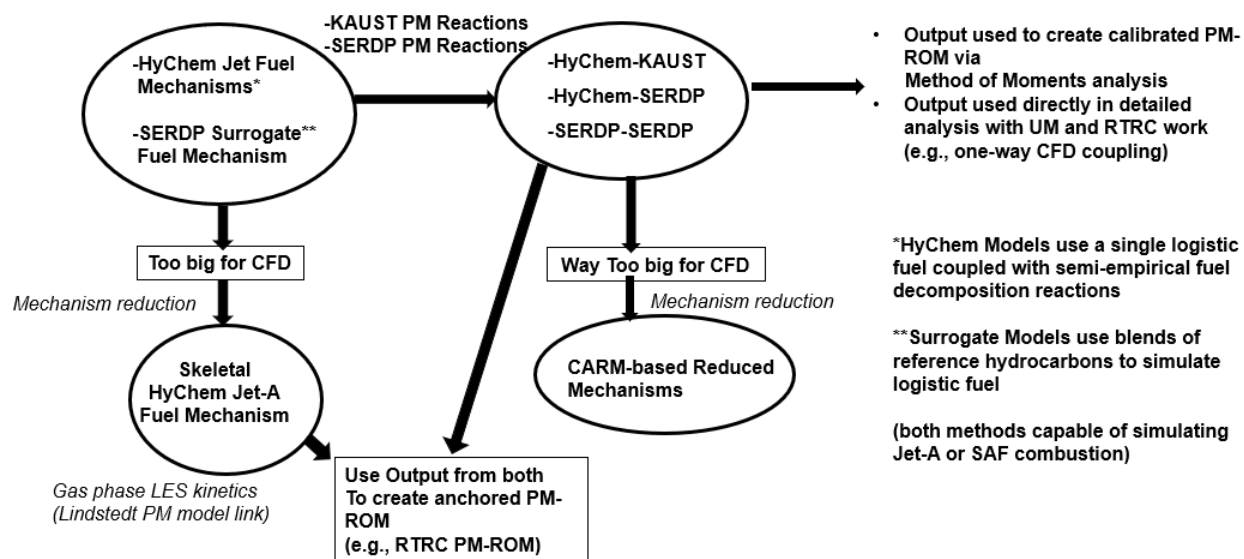


Figure 4. Specific workflow of kinetic activities for jet fuels.

In the first task, overall comparisons of two key species influencing soot formation and growth (C_2H_2 and C_6H_6) among all four kinetic models (HyChem-SERDP, HyChem-KAUST, Caltech-mech, and Pitsch detailed mechanism) is performed for range of equivalence ratios as well as reactor temperatures. The exact Perfectly Stirred Reactor (PSR) conditions are Jet A/air (or 77% *n*C₁₂, 23% *m*-xylene*), P : 1 atm, τ_{res} : 25 msec, ϕ : 1.9–2.5, T : 1400–2000 K).

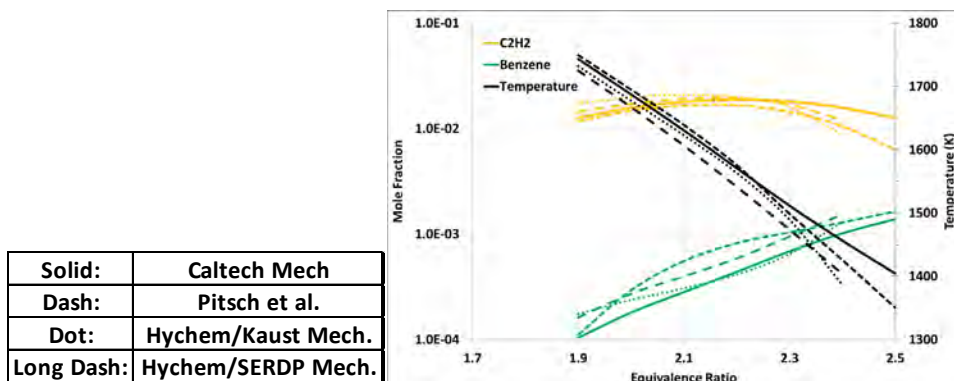


Figure 5. Comparison of C₂H₂, C₆H₆ and temperatures among mechanisms.

Figure 5 suggests that overall predictions of temperature are similar for all mechanisms. Some visible differences arise in the range of higher equivalence ratios. The benzene (C₆H₆) profiles and acetylene (C₂H₂) profiles are in qualitative agreement among mechanisms except the Pitsch mechanism, which must be investigated further. Encouragingly, both HyChem models and the Caltech-mech model have overall satisfactory agreement.

The nucleation studies at UM suggest the roles of heavier PAH species in forming incipient soot particles. Consequently, assessment is conducted to compare predictions of heavier PAH species, such as naphthalene (C₁₀H₈), fluorene (C₁₃H₁₀), and pyrene (C₁₆H₁₀), at the same conditions as above for all four mechanisms. The results from this analysis (Figure 6) suggest a wider spread of PAH species among all four mechanisms that may be crucial in predicting the early nucleation stages of soot formation in large-scale simulations.

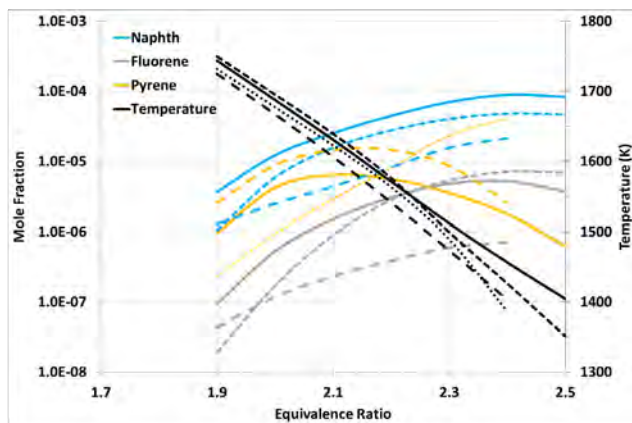


Figure 6. Comparison of heavier PAH species among mechanisms.

The Pitsch mechanism is relatively new and requires further assessment, and hence is not used in later analysis. Further analysis is presented herein for comparing predictions of soot formation for ethene by using WF (demonstrated in previous annual efforts), HyChem-KAUST, HyChem-SERDP, and Caltech-mech with a reduced POM model (optimized rates for the Lindstedt soot model) have been described in earlier annual efforts. Briefly, the PM-ROM is based on the well-known Lindstedt two-equation soot model. The two equations are used to determine the soot mass and soot concentration generated in the system. The necessary rates for model closure are particulate inception/nucleation, particulate surface growth, surface oxidation, and particle coagulation. In the original Lindstedt model, the key PM-forming species is acetylene, molecular oxygen is the key soot oxidation species, and a single Arrhenius rate expression is used for each step. The RTRC formulation extends the original premise by adding benzene as key PM-forming species and the hydroxyl radical as another oxidation species, and by using a double Arrhenius rate expression for both the inception and surface

growth processes, thus enabling the model to capture the well-known and experimentally observed “soot bell” concentration profile with respect to temperature. The results are presented in Figure 7.

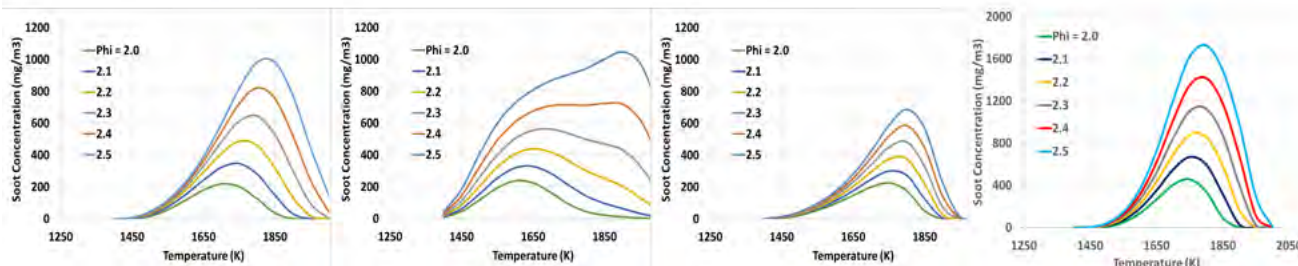


Figure 7. Comparison of soot volume fractions for various gas-phase mechanisms: WF, HyChem-KAUST, HyChem-SERDP, and Caltech-mech from left to right.

Figure 7 suggests that the soot concentration levels at the range of temperature from WF, HyChem SERDP, and Caltech-mech show similar behavior in terms of a bell-shaped dependency on temperature. The HyChem-KAUST predictions are qualitatively very different from those of the other three mechanisms. In quantitative analysis, the HyChem-SERDP mechanism underpredicts soot levels by a factor of 1.5 at higher equivalence ratios than the WF mechanism. Similarly, Caltech-mech overpredicts soot levels by a factor of 1.5–2 with respect to the WF mechanism.

In the next set of activities, predictions are compared by changing the fuel to Jet A fuels under the same operating conditions investigated for ethene fuels described above. The HyChem-KAUST, HyChem-SERDP, and Caltech-mech mechanisms are compared. As shown in Figure 8, the predictions from Caltech-mech and HyChem-KAUST agree with each other quantitatively. However, HyChem-KAUST predicts two peaks in soot levels, whereas Caltech-mech predicts only one peak and a bell-shaped dependency. This qualitative bell-shaped one peak trend is also visible in the predictions of HyChem-SERDP; however, the quantitative magnitude is factor of 3 lower than those of the Caltech-mech and HyChem-KAUST mechanism.

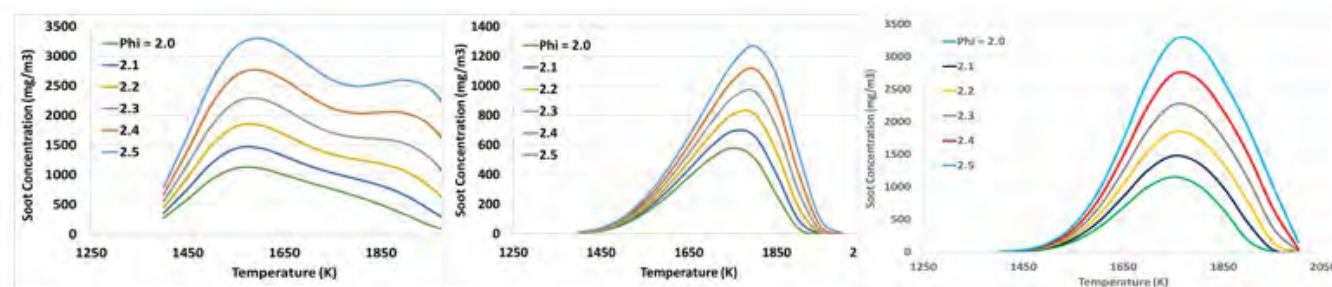


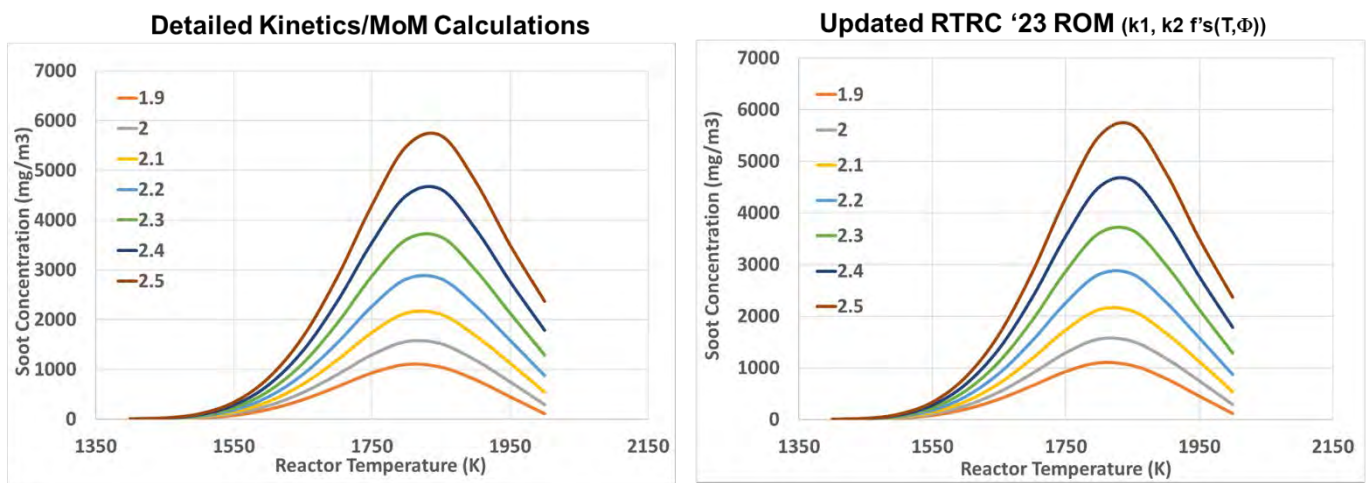
Figure 8. Comparison of soot volume fractions for different gas-phase mechanisms: HyChem-KAUST, HyChem-SERDP, and Caltech-mech, from left to right.

Analysis of the ethene/air and Jet A/air simulations combined for the same reactor conditions, considering the trends as well as quantitative levels of soot predictions, suggests that Caltech-mech appears to be the best mechanism to proceed with performing reductions in the next quarterly efforts.

One of the goals of this effort is the development of a reduced-order model capable of capturing soot formation with liquid fuels, for use in computational fluid dynamics (CFD) applications. The HyChem-SERDP kinetic data were used to benchmark/modify the PM-ROM RTRC previously created for ethene/air systems in the most recent prior quarterly effort. The RTRC model was shown to capture the parabolic shaped concentration profiles (i.e., a soot bell profile) associated with both experimental and detailed analytical models. The above analysis suggested the need to replace the Hychem-SERDP model with the Caltech-mech mechanism; therefore, the latter was the target for the remainder of the annual efforts.

After having assessed the details of PAH based detailed kinetics at range of conditions, we attempted to extend the concepts used to generate a higher fidelity PM-ROM model for use in RQL CFD studies. A numerical shooting fitting procedure was used to establish rate coefficients that enabled the PM-ROM model to identically match the soot concentration levels generated via detailed kinetic analysis coupled with Method of Moments (MoM) soot calculations. In the most recently developed PM-ROM, the reduced model was calibrated against PSR calculations at the elevated pressure (5.8 atm) and air temperature (600 K) conditions of RQL combustor operation. The nominal reactor residence time for these calculations was 5 ms, and the fuel-air equivalence ratio spanned from 1.8 to 2.5. The detailed mechanism used was the previously discussed HyChem-Caltech mechanism.

In the new model method, the double Arrhenius rate expressions are replaced by the numerically optimized rate expressions. These rate values are functions of both temperature and the equivalence ratio. The agreement between the soot concentrations generated via detailed kinetics and MoM and the PM-ROM are shown in Figure 9, indicating quite good agreement.



PSR Settings: Jet-A/Air, P: 5.8 atm, τ_{res} : ~5 msec, Φ : 1.9-2.5, Air Inlet T: 600 K, Reactor Temp's: 1400-2000 K

Figure 9. Comparison of soot concentrations generated from the two modeling approaches listed at nominal RQL combustor conditions.

Given that two-dimensional (i.e., temperature and equivalence ratio) correlation might not be computationally efficient, the developed rate correlations were reduced to one dimension as follows. The developed rate expression equivalence ratio dependencies were averaged over the range, and yielded rate constants that were functions of only temperature. The average rate expressions for nucleation and surface growth processes are shown in Figure 10.

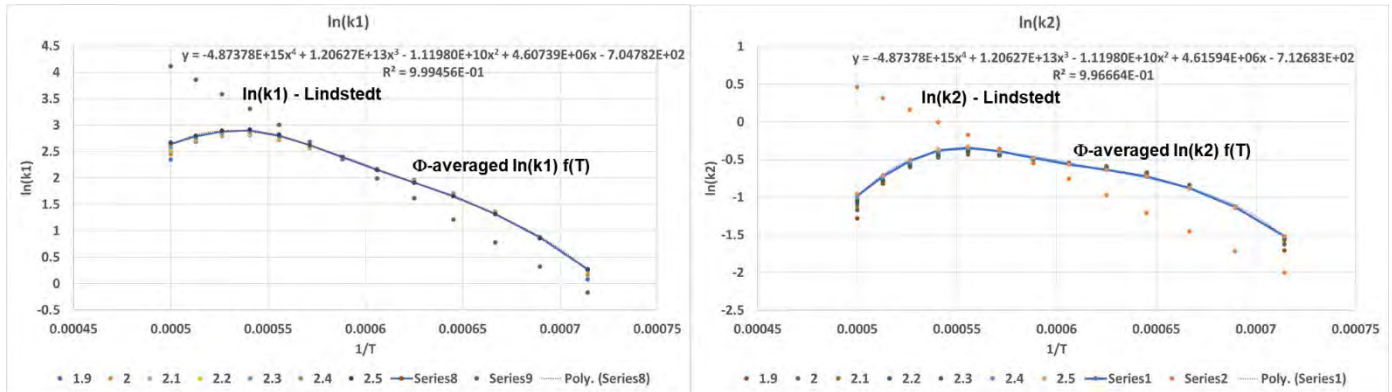
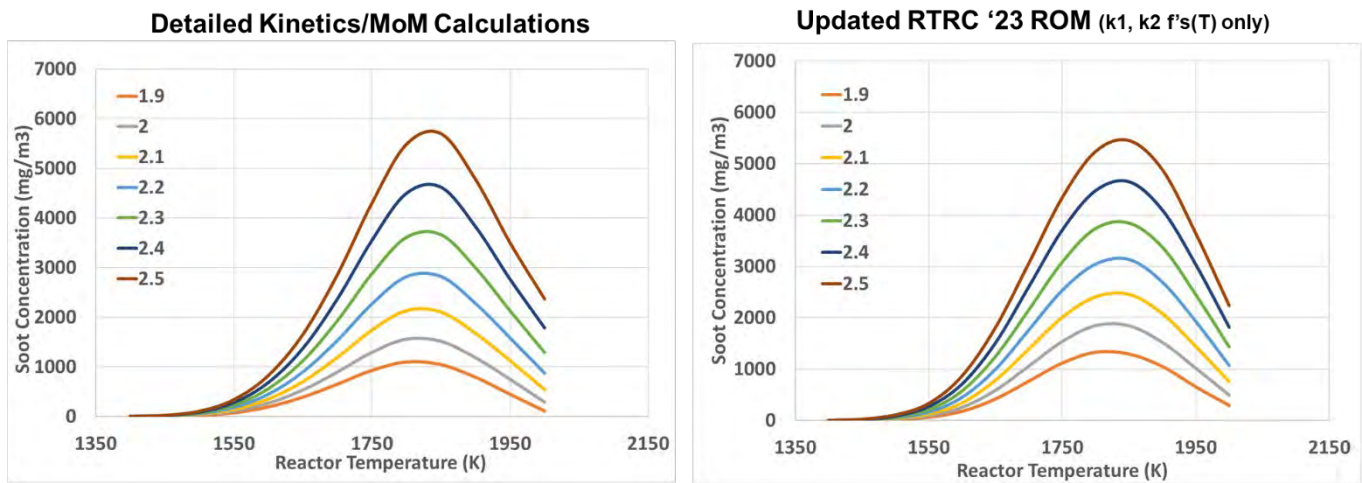


Figure 10. Fuel-air mixture averaged kinetic rate expressions for nucleation (left) and surface growth (right) for use in the PM-ROM tool for the RQL CFD analysis.

With this new temperature-only rate expression, the soot concentration outputs associated with the PSR simulations were then computed and compared against the original detailed chemistry/MoM calculations. This comparison is shown in Figure 11. A slight decrease and slight increase are observed in the fuel rich and lean conditions, respectively, but overall, the concentration values are in good agreement with the detailed data. These final expressions will be incorporated into the PM-ROM that will be used by the GT team in conjunction with the CFD analysis.



PSR Settings: Jet-A/Air, P: 5.8 atm, τ_{res} : ~5 msec, Φ : 1.9-2.5, Air Inlet T: 600 K, Reactor Temp's: 1400-2000 K

Figure 11. Comparison of soot concentrations generated from the two modeling approaches listed at nominal RQL combustor conditions.

The goal of this year's activities was to determine whether a suitably compact mechanism that incorporates both Jet A and PAH/PM kinetic information could be developed. From the analysis conducted to date, the detailed mechanism has been constructed, and the PM-ROM has also been optimized to match its predictions with a detailed MOM model. The reduced chemistry and the PAH based ROM model will be used by GT for CFD analysis of an RQL combustor, which are being provided.



Milestone

Detailed Jet A fuel chemistry, its reduction for use in CFD analysis, and optimization of the PM-ROM model is planned for 9/30/2024.

Major Accomplishments

Reduced Jet A fuel chemistry and optimized PM ROM at RQL-relevant conditions.

Publications

None.

Outreach Efforts

None.

Awards

None.

Student Involvement

None.

Plans for Next Period

Future efforts will focus on providing these inputs regarding reduced kinetics and the PM-ROM model to GT for CFD simulations of an RQL combustor.

Task 2 – Nucleation Modeling

UM

Objective

The objective of this task is to develop models for nanoparticle inception, a critical step in predicting emissions. This effort bridges the work on gas-phase chemistry (RTRC) with the model for particle growth (RTRC), and provides inputs for the MOMIC model (GT) and growth models (RTRC) using atomistic simulations.

Research Approach

Current models for particle inception are unable to reproduce a variety of experimental data, including molecular structure. This work is aimed at developing a predictive model for particle inception that can provide accurate chemical and physical growth pathways for PAHs. MD simulations are used to study the collisions of PAHs and the formation of aromatic dimers leading to soot inception.

In the most recent annual efforts, methods and the MD approach were established for the assessment of the dimer formation stability of different aromatic species. We performed atomistic simulations of these species and higher PAH species, also including oxygen content. Figure 12 shows the structures of gas-phase compounds considered in this study and the results for their homo-dimerization propensity. The data points are broadly clustered in three groups. The first is composed of the compounds I.C. (462 u), I.D. (462 u), and I.E. (460 u), which have the same mass and oxygen/carbon ratios (0.125) and are less stable than I.A. (448 u) and I.B. (472 u), which constitute the second group. This difference indicates that the presence of oxygen slightly destabilizes the dimers, an effect possibly caused by the greater repulsive electrostatic interactions of oxygenated molecules than observed for pure aromatic hydrocarbons. The third group is formed by I.F. (402 u), I.G. (452 u), and I.H. (502 u), which are less likely to dimerize than the other two groups. The low dimer stability of the third group might be due to the presence of a sigma bond, which introduces an internal rotatable bond that interferes with the formation of clusters. Several conclusions were drawn from this study. First, the details of the structures of the species that nucleate cannot be ignored. Mounting evidence indicates that the presence of five-membered rings, aliphatic side chains, and oxygenated groups in soot precursors does not change the nucleation mechanism leading to soot formation. Our results pertaining to both the dimerization propensity and the change in free-energy barriers between monomers and dimers, both of which directly relate to the kinetic rates of dimerization, suggest otherwise. Second, the effects of shape, the presence of oxygen, mass, and rotatable bonds are tightly intertwined, and have differing

importance as well as diverse temperature dependencies, although they are all dominated by entropic effects at high temperatures. The presence of oxygen affects the dimer propensity by decreasing the molecular cohesion due to electrostatic repulsion; however, notably, the force field used in this study cannot capture the effect of molecular polarizability.

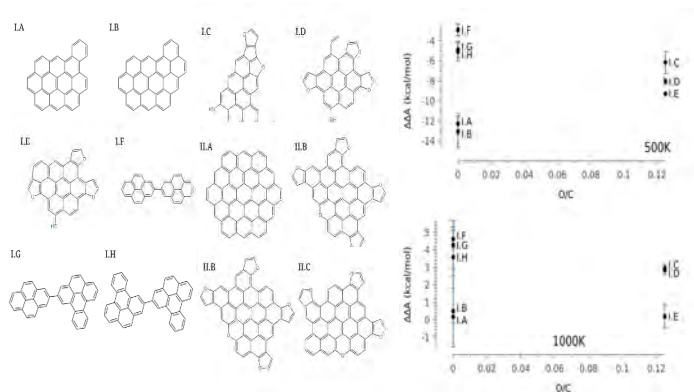


Figure 12. Structural formula of gas-phase compounds (left) and homo-dimerization propensity at 500 K and 1000 K, as a function of the oxygen/carbon ratio.

These results have been used as a first approach toward the development of predictive trends for quantifying dimer stability. Because of the presence of various intertwined dependencies, we will need a new approach to separate the contributions and their relative importance. In the next efforts, MD simulations with machine learning approaches to identify the main characteristics that drive nucleation and determine the corresponding rates are discussed.

In the next task, we have focused on machine learning algorithms, with the goal of leveraging this technique to predict the dimerization propensity of various PACs. Although molecular dynamics simulations can provide this information for specific dimer pairs, extending simulations to all potential dimer components is not feasible. With millions of different PACs observed in even simple flame, computing this information for all possible PACs would be excessively costly, particularly when accounting for the combinations of heterodimerization among PAC molecules. Recently, machine learning has shown potential to learn complex quantitative relationships among PAC properties and predict the energy difference between the monomeric and dimeric state for an arbitrary pair of PACs, with minimal computational cost. However, the approach considers only thermodynamic energy differences at a single temperature and therefore is insufficient to predict the energy barriers needed to derive kinetic rates.

As a first step, we perform numerous Meta dynamics molecular dynamics simulations to calculate the dimer energy barrier for a large dataset of PACs at multiple temperatures. This value is critical in characterizing the kinetic stability of the PAC dimer, and, in conjunction with equilibrium data, can provide a comprehensive description of forward and reverse barriers and rates in the dimerization process. MD simulations enhanced by Meta dynamics were used to reproduce the free-energy landscape of the dimerization process as a function of the center-of-mass distance. To define the chemical space, we considered a wide set of PACs, as reported in the most recent report, which broadly reproduces the sizes, shapes, and functional groups observed in flame systems. To describe PAC chemistry, we compute a set of 312 descriptors for each molecule. These descriptors capture properties such as mass, atomic ratios such as carbon-hydrogen ratio, and counts of specific subgroups such as aromatic rings. From our simulations, we obtain 315 unique energy barriers between the monomer and dimer states. Generally, we observe the same qualitative relationships with size and temperature. All other parameters being constant, free-energy barriers tend to increase with mass as Van der Waal's and electrostatic interactions become stronger and decrease with temperature as entropic effects increase in importance. Importantly, however, these two parameters are insufficient to describe all differences observed in the energy barrier, and a quantitative trend cannot accurately be derived solely from these two values. We have started to investigate machine learning algorithms, and we are currently implementing such an approach while still running MD simulations. Figure 13 shows our target machine learning algorithm.

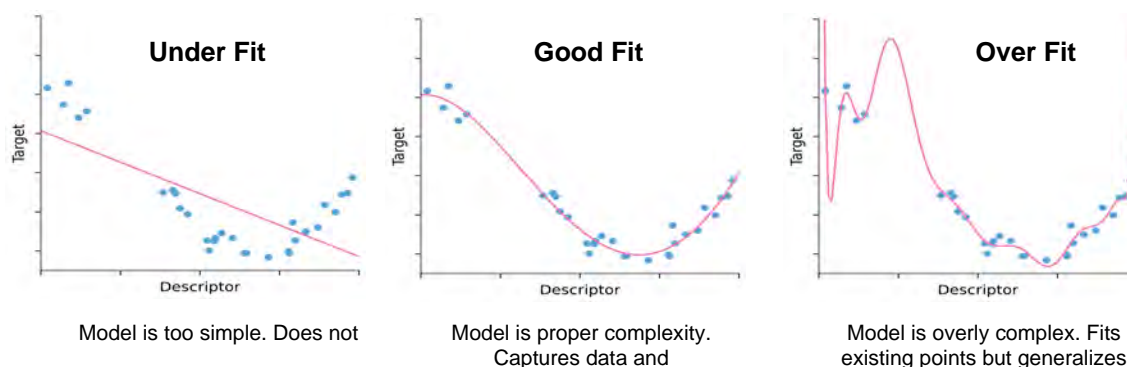


Figure 13. Evaluation of machine learning algorithms.

To analyze the complex space, we used machine learning with a model with good fit. Before training our machine learning model, we eliminated similar features by removing any feature with a variance of zero and any feature with a Pearson correlation greater than 0.95. To build a predictive model for the Feature Extraction (FE) of aggregation, we applied the Lasso method, because it has high accuracy and often enables interpretable predictions. Lasso is a supervised machine learning regression model that minimizes a loss function and uses the least absolute shrinkage and selection operator. This model has been successfully applied to make interpretable predictions in chemical problems, because it eliminates extraneous features and selects only a subset of properties needed to make the predictions.

Our model outperforms existing physical dimerization models described in the literature. We compared our results, including the test on a restricted dataset with no data leakage, with three additional models. One advantage of Lasso is its ability to provide a degree of interpretability regarding the aspects that control the prediction, because it sets the coefficients of unused features to zero. Thus, by analyzing which features the Lasso model retains, we can gain a sense of which molecular properties are important for predicting the FE of dimer aggregation. Of note, whereas some of the molecular properties discussed below resemble quantities that have been used in the past to predict the aggregation propensity, they are not generally interchangeable with those in the literature. Overall, across all 105-fold cross-validations, the model selects a nearly identical set of 10 features. If we exclude these top features, no other features are selected in more than four folds and therefore are not discussed. Broadly, the top features can be divided into three groups of properties that are important for PAC dimerization: size, shape, and presence of specific chemical groups.

The first class of properties comprises extrinsic properties that are broadly related to the size of the molecule. Specifically, the algorithm selected the number of aromatic rings, the number of carbons not connected to a hydrogen, the number of tessellations containing four carbons, the number of tessellations with three carbons and a hydrogen, and the number of six-membered rings. Figure 14 shows that the FE of dimerization is strongly associated with the (harmonic) average number of aromatic rings in the dimer (Pearson coefficient of -0.8397 and Spearman coefficient of 0.8719). This result agrees with the general observation that PACs often cluster in lateral stacks, and the interaction strength among PACs is closely associated with their number of aromatic rings. Among the molecular descriptors in this class, the number of aromatic rings is the feature with the highest correlation with the FE (more than the number of six-membered rings, for example), but crucially by itself it is not sufficient to fully capture the physical dimerization. A linear fit of the FE as a function of the total number of aromatic rings produces a prediction model with an root mean square error (RMSE) of 15.6 kJ mol^{-1} and a mean absolute error (MAE) of 11.3 kJ mol^{-1} , which has a significantly larger error than our model and is (not coincidentally) comparable to using only the mass as a descriptor. Some features in this group encode size with molecular shape information. One such example is the number of internal carbon atoms, defined as the aromatic carbon atoms that are not bonded to H atoms. Because most of the molecules in the dataset are highly pericondensed hydrocarbons, these PACs will have a greater percentage of internal carbons than catacondensed PACs.

In recent efforts, we closely collaborated with RTRC kinetics to identify PAH species available in the gas-phase mechanism. We are using a machine learning algorithm to predict energy barriers and eventually rates at RQL-relevant operating

conditions for identifying the rates of dimers causing inception of soot species; these efforts will be provided as input to the RTRC surface growth group.

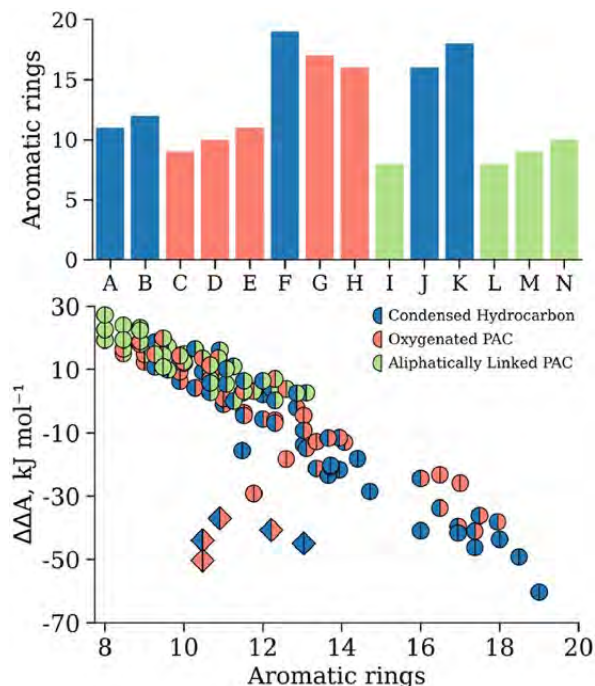


Figure 14. Relationship between the number of aromatic rings and dimerization FE. Top: number of aromatic rings associated with each dimer. Bottom: aggregation propensity compared with the average number of aromatic rings in the dimer.

Milestone

Establishing a machine learning approach to assess a large pool of PAH species at RQL-relevant conditions is planned for 9/30/2024.

Major Accomplishments

Established machine learning-based MD predictions for nucleation rates due to PAH dimerization.

Publications

None.

Outreach Efforts

None.

Awards

None.

Student Involvement

One student at UM is involved in this work.

Plans for Next Period

In future efforts, we seek to provide inputs from machine learning algorithm predictions of energy barriers and eventually nucleation rates at RQL-relevant operating conditions. These rates will be provided as input to the RTRC surface growth group.

Task 3 – Surface Growth and Aggregation Modeling

RTRC

Objective

The objective of this task is to develop a physics-based framework for the prediction of soot particle growth after the inception process. The growth consists of agglomeration due to collisions between the primary particles and surface growth because of direct deposition of the precursors on the aggregate. The final aggregate fractal structure and its temporal evolution as a function of local conditions are of interest. This model will provide the morphology characteristics and the growth rate of the particles, which will serve as inputs into the MOMIC formulation.

Research Approach

Soot particles from nucleation stages undergo various surface growth processes and form primary particles. These primary particles are spherical and typically have diameters of 1–10 nm. The focus of this effort is to understand the evolution of the fractal dimension of aggregates from the formation of primary particles to final fractal aggregates, through processes of surface growth and aggregation. Experimentally, the structures of these soot particles have been demonstrated to be dependent on the local conditions (e.g., the local equivalence ratio). These surface growth processes can occur because of heterogeneous reactions of gas-phase precursors on solid soot particle surfaces (reaction-limited growth) or through the transport of soot precursors in high-speed flames (transport-limited growth). Most of the current growth models account for only reaction-limited growth and ignore transport-limited growth as well as cluster–cluster interactions, which may be important in aggregate formation. In this work, information on background gas-phase species contributing to soot particles, the structure of the initial soot nuclei, and the local conditions is merged to understand the fundamental processes contributing to the formation of large soot aggregates.

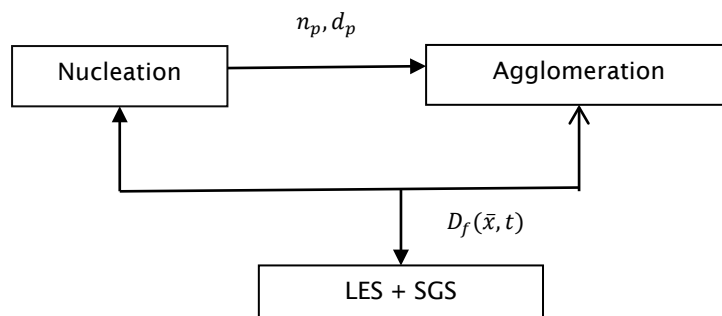


Figure 15. Post-inception growth of soot particles (LES–RTRC–UM coupling).

The coupling of the growth framework being developed at RTRC with MD simulations from UM and the LES study at GT is briefly highlighted in Figure 15. The growth module takes the number density and size distribution of incipient soot particles from nucleation as an input, then tracks the growth of such particles along the statistically averaged path lines, which have varying background LES conditions in the form of temperature (T), pressure (P), and local equivalence ratio (ϕ), as detailed below. The output from such studies in the form of the parametrized fractal dimension (D_f) will be fed back into the LES–MOMIC soot approach.

The developed post-inception growth model described in the previous annual effort has been shown to capture the effects of different operating conditions on the growth characteristics of the particles, including size and morphology. However, the parametric exercise of this model could become computationally prohibitive with a sweep over a range of operating parameters and combinations therein. A path line-sampling approach was proposed (schematic in Figure 16), wherein the full flow-field (obtained by the LES) is represented by statically sampled path lines, over which the operating conditions are

time variant. For example, the temperature and fuel/air ratio evolve over the course of time as a particle moves from the injector toward the exit of the combustor. This time history is then provided to the growth model, and the variation in particle characteristics is solved over the course of this timeframe for each individual path-line histogram (example output shown in Figure 17). This information is then fed back into the LES with time-space mapping through the path-line coordinates and nearest-point interpolation, to provide a full spatial representation of growth information, which is then used in the MOMIC approach. This approach effectively reduces the computational overhead of the growth model to a dozen simulations (on the basis of the assumption that this number of path lines is sufficient to properly sample the combustor flow field), in contrast to potentially hundreds with the conventional parametric approach. Of note, in this one-way coupling approach, the macroscopic changes in the flow-field due to the interaction with the soot-particle transport are assumed to have negligible effects on the growth characteristics of the particles.

The post-inception growth modeling framework and the coupling therein to the LES framework is demonstrated for the solution of NASA-LDI geometry. The information along statistically sampled path lines is provided to the post-inception model, which then solves the evolution of the soot clusters along those path lines. To obtain a sense of primary particle size and number density, a classical nucleation theory is used, which takes the following form.

$$N_0(t) = [M(t)] \exp\left(-\frac{\Delta G_0(t)}{kT}\right)$$

Notably, this formulation, or terms therein, will eventually be replaced by the solution of the MD simulation. An example of primary particle number density along one of the path lines in the rig is shown in Figure 18. Figure 19 shows the evolution of soot particle characteristics (fractal dimension and average size) along two of the path lines inside the combustor.

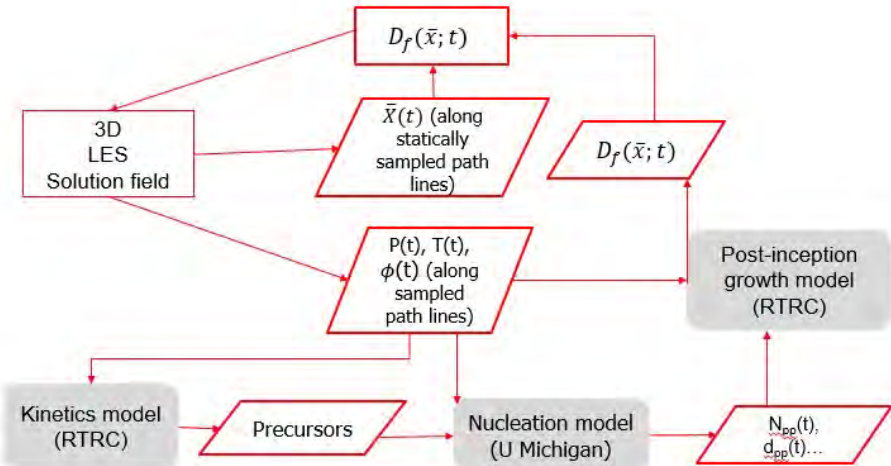


Figure 16. One-way coupled strategy for growth of soot particles.

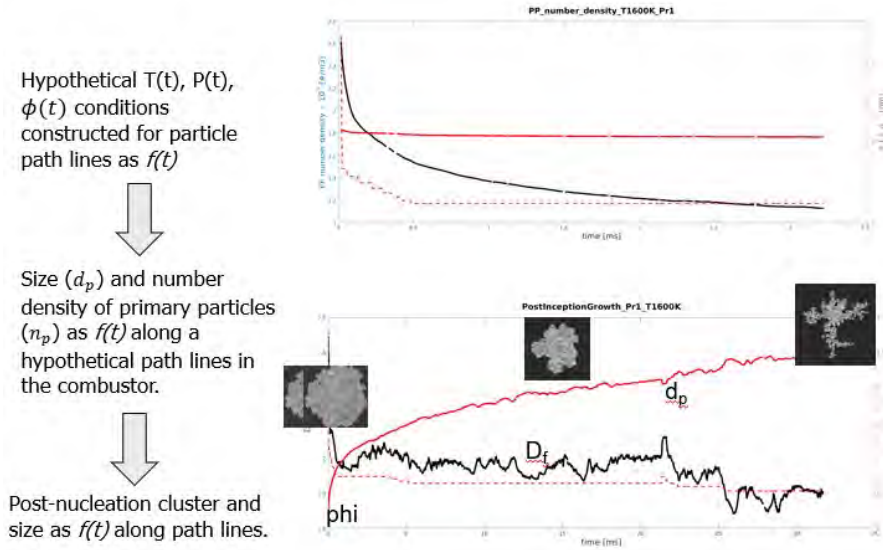


Figure 17. Demonstration of a one-way coupled strategy along a hypothetical LES path line.

The demonstration with the NASA-LDI combustor has provided confidence in using the framework for the RQL combustor (described later in the LES section). We are in the process of translating similar path-line data for the RQL combustor at the relevant conditions and using the nucleation rates provided by the MD framework described in the earlier section to predict the soot evolution along the path lines at these realistic combustor operating conditions. Further analysis will be conducted to understand the growth of fractals along other statistical path lines, to reveal how the primary particles grow and how they form fractals to parametrize this growth as a function of particle sizes. The current MOMIC model in GT LES has two sensitive parameters for post-inception growth: (a) the critical diameter to which particles grow and form spherical particles through coalescence and b) the fractal dimension dictating the fractal growth of soot primary particles. The Monte Carlo (MC) simulations will be assessed against the growth models of GT LES code to determine whether some of these criteria are justified.

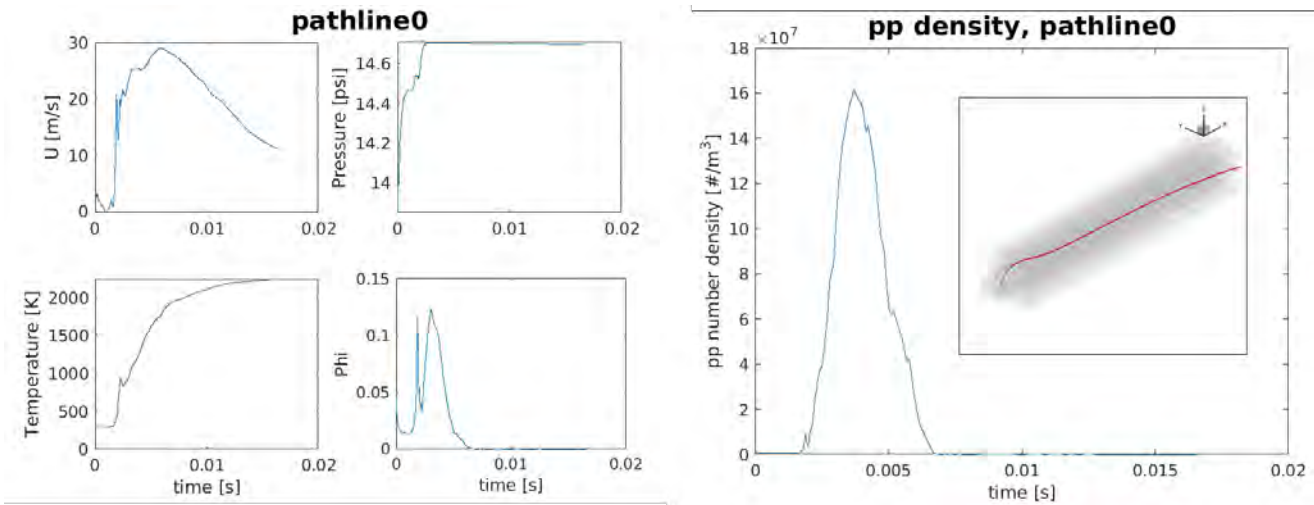


Figure 18. Variation in flow parameters along one path line in the combustor (left) and the calculated primary particle number density, on the basis of classical nucleation theory.

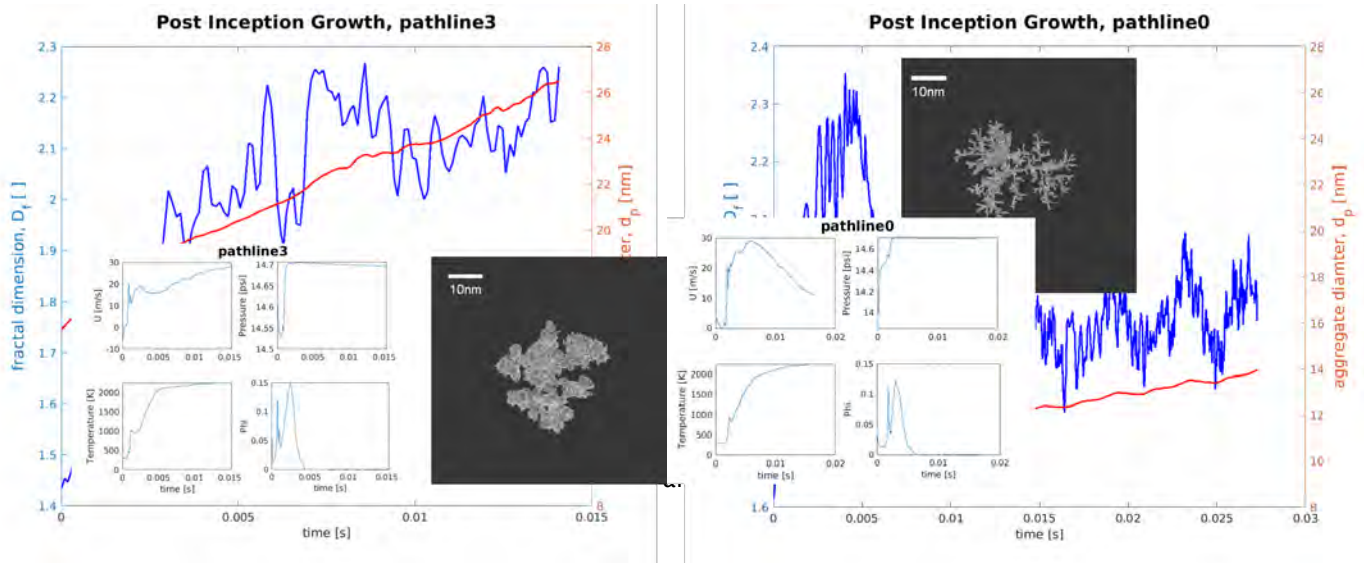


Figure 19. Variation in soot fractal properties along two sample path lines in the combustor.

Milestone

One-way coupled MC studies of surface growth are planned for 9/30/2024.

Major Accomplishments

One-way coupled demonstration of LDI LES data has been used for soot fractal growth.

Publications

None.

Outreach Efforts

None.

Awards

None.

Student Involvement

None.

Plans for Next Period

The future work for the remainder of the project will use actual LES data for the RQL combustor and conduct soot fractal evolution along its path lines, as demonstrated above.

Task 4 – Large Eddy Simulation

GT

Objective

The objective of this task is to develop a physics-informed LES framework to model soot formation in turbulent reacting configurations of canonical configurations and combustors with practical relevance. In the most recent annual efforts, we demonstrated LES-MOMIC coupling for soot evolution in canonical premixed and non-premixed configurations. The current report discusses the LEM-MOMIC framework to address small-scale effects of turbulence-chemistry-soot



interactions on sooting premixed flames. The second part of the report discusses the multiphysics reacting flow simulations inside the RQL combustor at realistic conditions, to provide relevant inputs to collaborating partners.

Research Approach

LES studies of turbulent sooting problems are very difficult because of the multiscale nature of soot inception, coagulation, and surface growth that must be modeled in a highly turbulent and reactive environment, typically in a complex combustor. Most prior studies have focused on global models that approximate small-scale physics. Consequently, many available models account for the underlying physics. In contrast, simulations require some approximations, because the computational resources will never meet the simulation requirements. In the current effort, we balance contributing to the prediction of soot formation physics in a realistic gas turbine combustor with the need to obtain high-fidelity, reliable predictions by using advanced models. To achieve this goal, we leverage our past LES capability and upgrade the models by using the results from MD and MC studies. Soot evolution is tracked with MOMIC, wherein the first six moments of the particle size distribution function are used.

The full set of compressible reacting multispecies Navier–Stokes equations cannot be solved directly, because a direct numerical simulation is not feasible for practical applications. For LES, the large-scale flow features are resolved, and subgrid modeling is used for the smaller scales.

The LES governing equations can be written as follows:

$$\begin{aligned}
 \frac{\partial \bar{\rho}}{\partial t} + \frac{\partial}{\partial x_i} (\bar{\rho} \tilde{u}_i) &= 0 \\
 \frac{\partial}{\partial t} (\bar{\rho} \tilde{u}_i) + \frac{\partial}{\partial x_j} (\bar{\rho} \tilde{u}_i \tilde{u}_j + \bar{P} \delta_{ij} - \bar{\tau}_{ij} + \tau_{ij}^{sgs}) &= 0 \\
 \frac{\partial}{\partial t} (\bar{\rho} \tilde{E}) + \frac{\partial}{\partial x_j} [(\bar{\rho} \tilde{E} + \bar{P}) \tilde{u}_j + \bar{q}_j - \tilde{u}_j \bar{\tau}_{ij} + H_i^{sgs} + \sigma_i^{sgs}] &= 0 \\
 \frac{\partial}{\partial t} (\bar{\rho} \tilde{Y}_k) + \frac{\partial}{\partial x_j} \left[\bar{\rho} \tilde{Y}_k \tilde{u}_j - \bar{\rho} \bar{D}_k \frac{\partial \tilde{Y}_k}{\partial x_j} + \Phi_{j,k}^{sgs} + \Theta_{jk}^{sgs} \right] &= \bar{\rho} \tilde{w}_k \\
 \frac{\partial}{\partial t} (\bar{\rho} \tilde{Y}_{soot}) + \frac{\partial}{\partial x_j} \left[\bar{\rho} \tilde{Y}_{soot} \tilde{u}_j - \bar{\rho} \bar{D}_{soot} \frac{\partial \tilde{Y}_{soot}}{\partial x_j} + \bar{V}_{T,soot} \tilde{Y}_{soot} + \Phi_{j,k,soot}^{sgs} + \Theta_{jk,soot}^{sgs} \right] &= \bar{\rho} \tilde{w}_{soot} \\
 \frac{\partial}{\partial t} (\bar{\rho} \tilde{M}_k) + \frac{\partial}{\partial x_j} \left[\bar{\rho} \tilde{M}_k \tilde{u}_j - \bar{\rho} \bar{D}_{soot} \frac{\partial \tilde{M}_k}{\partial x_j} + \bar{V}_T \tilde{M}_k + \Psi_{j,k}^{sgs} + \Omega_{j,k}^{sgs} \right] &= \bar{\rho} \tilde{M}_k
 \end{aligned}$$

Here, \tilde{u}_i is the i -th filtered velocity, $\bar{\rho}$ is the filtered density, and \bar{P} is the filtered pressure, which is computed from the filtered equation of state. \bar{T} is the filtered temperature, \tilde{E} is the filtered energy, \tilde{Y}_k and \tilde{Y}_{soot} represent the filtered k -th gas-phase species and soot mass fraction, respectively, and \tilde{M}_k represents the k -th moments of the particle size distribution function. The details regarding the computations of all these quantities have been described elsewhere (El-Asrag & Menon, 2009) and hence are not discussed herein in specific detail. The filtered heat flux \bar{q} can be supplied to an optically thin radiation model to include effects of radiation. The terms τ_{ij}^{sgs} , H_i^{sgs} , σ_i^{sgs} , $\Phi_{j,k}^{sgs}$, Θ_{jk}^{sgs} , $\Psi_{j,k}^{sgs}$, and $\Omega_{j,k}^{sgs}$ contain the effects of the subgrid scale on the filtered quantities. Modeling of these terms remains challenging; in addition, the closed system of equations must be solved together in three-dimensional space with temporal accuracy.

In this work, an eddy viscosity type subgrid model with constant coefficients is used to obtain the closure of subgrid momentum stresses and subgrid enthalpy flux. For the subgrid turbulence chemistry soot interactions, the code is equipped with a multiscale LEM based closure model, partially stirred reactor model, laminar chemistry approximations, etc. In the LEM formulation, the gas-phase species conservation equations are not spatially filtered as in other LES equations. Instead, the exact unfiltered equations are solved by using a two-scale, two-step Eulerian–Lagrangian approach. First, within each LES cell, the one-dimensional LEM model is used to solve for the scalar fields (species mass fraction, soot mass fraction, LEM temperature, and soot integer moments) along a notional line oriented along the maximum scalar gradient. Second, the subgrid scale fields are convected across the LES cell faces by using a Lagrangian transport approach through the splicing algorithm, which reproduces the effect of large-scale advection of the scalars by the flow field. The resulting scalar fields are then filtered in each LES cell to recover LES-resolved species mass fractions to be used in LES-resolved energy and state equations. In Year 3, we first demonstrated the subgrid LEM–MOMIC for the application of the soot MOMIC model within a linear eddy model for turbulence effects on soot formation and growth. The first results

pertaining to these studies are presented. We also conducted LES of the RQL combustor currently being investigated under FAA Project 70, which remains underway. These results are discussed at the end. The data based on these simulations are used by collaborating partners to fine-tune their models, which will be provided to GT.

In the first part of our annual efforts, we focused on implementing the MOMIC model in the standalone LEM to exploit its benefits in studying the effects of small-scale subgrid turbulence on premixed jet flames at two rich equivalence ratios as well as different turbulence Reynolds numbers. These results were presented at the 75th American Physical Society's Division of Fluid Dynamics Meeting in November 2022. The details of the MOMIC model with PAH kinetics and corresponding source terms have been discussed in prior annual efforts and hence are not repeated for brevity. In summary, the current MOMIC model is based on six moments of soot particle size distribution function and an assumption of nucleation based on pyrene dimerization. The surface growth is assumed to occur via hydrogen abstraction carbon addition mechanism. The source terms also include the soot mass growth due to condensation of PAH molecules on the surface of soot particles. The coagulation and aggregation are treated as originally described in the original MOMIC (Frenklach, 2002) approach.

LEM (El-Asrag & Menon, 2009) has been used as a subgrid model for turbulence-chemistry closure inside the LES grid, to capture effects of scales smaller than the LES resolution. Here, we use LEM as a standalone model, which has previously been used to simulate high-Karlovitz-number non-sooting turbulent flames (Sreenivasan and Menon, 2014). The LEM solves temperature evolution and species evolution through a reaction-diffusion equation as well as the MOMIC equations. The turbulent effects are modeled with the triplet mapping procedure, which rearranges the scalar field by the motion of an eddy. This approach has been shown to reproduce the turbulent diffusion associated with high-Reynolds-number inertial range turbulence. The evolution of the scalar field within the LEM domain is shown in Figure 20.

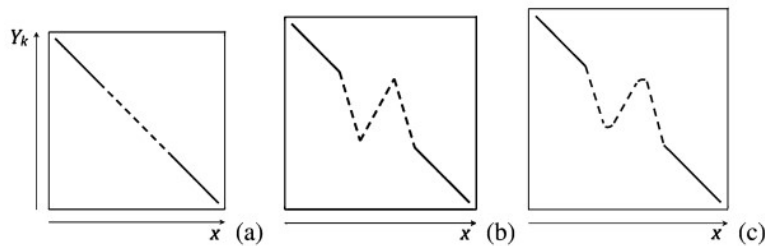


Figure 20. Evolution of the scalar field within the LEM domain.(a) Initial scalar field; (b) After triplet mapping; (c) After reaction-diffusion.

The eddy size (l) is chosen from a turbulent PDF $f(l)$

$$f(l) = \frac{\frac{5}{3}l^{-\frac{8}{3}}}{\left(\eta_e^{-\frac{5}{3}} - l_o^{-\frac{5}{3}}\right)} \text{ where } \eta_e = N_n l_o Re^{-\frac{3}{4}}$$

The frequency of the stirring operations is estimated as

$$\lambda = \frac{54}{5} \left(\frac{\nu Re}{c_\lambda l_o^3} \right) \left[\frac{\left(\left(\frac{l_o}{\eta} \right)^{\frac{5}{3}} - 1 \right)}{1 - \left(\frac{\eta_e}{l_o} \right)^{\frac{4}{3}}} \right]$$

where η_e is the Kolmogorov length scale, l_o is the integral length scale, Re_t is the turbulent Reynolds number, and c_λ, N_n are the model constants. On the basis of the above two parameters, the eddy location is randomly selected from the permissible locations in the domain. The reaction, diffusion, and stirring operations are mathematically represented as



$$\begin{aligned} \frac{\partial Y_k}{\partial t} &= F_{k,stir} - \frac{1}{\rho} \frac{\partial}{\partial s} (\rho Y_k V_k) + \frac{\dot{\omega}_k W_k}{\rho} \quad k = 1, \dots, \\ \frac{\partial T}{\partial t} &= F_{T,stir} - \frac{1}{\bar{c}_p} \sum_{k=1}^N c_{p,k} Y_k V_k \frac{\partial T}{\partial s} + \frac{1}{\rho \bar{c}_p} \frac{\partial}{\partial s} \left(\bar{\kappa} \frac{\partial T}{\partial s} \right) - \frac{1}{\rho \bar{c}_p} \sum_{k=1}^N (h_k \dot{\omega}_k W_k) \\ \frac{\partial M_r}{\partial t} &= F_{M_r,stir} + \dot{\omega}_{M_r} \quad r = 0, 1, 2, 3, 4, 5 \end{aligned}$$

Here, ρ represents the two-phase density, $\dot{\omega}_{M_r}$ denotes the source terms for moments of soot PSDF, N_g denotes the total number of gas-phase species, $F_{k,stir}$ is the term for stirring for the species mass fraction, M_r represents the moments of soot PSDF, $F_{M_r,stir}$ is the stirring for moment terms, Y_k, h_k, ω_k represent the mass fraction, enthalpy, and reaction rate of the k_{th} species, and, $W_k, c_{p,k}, V_k$ denote the k_{th} species molecular weight, specific heat at constant pressure, and diffusion velocity.

In the current quarterly effort, laminar premixed flames of jet fuel (POSF10325), also commonly known as catA2 in the literature, are conducted with a standalone LEM-MOMIC method. The chemistry is integrated implicitly by using the 62 species reduced jet fuel model (Wang et. al., 2018), in which the length of the domain is 25 mm, and the smallest grid size is 1 μm . The laminar flame properties, such as flame thickness ($\delta_{L,max}^o = \frac{v}{S_L^o}$) and flame speed (S_L^o), are provided in Table 1.

The turbulent cases simulated with LEM-MOMIC are given in Table 2.

Table 1. Laminar flame properties of Jet A fuel.

ϕ	S_L^o (m/s)	$\delta_{L,max}^o$ (mm)	δ_T^o (mm)
1.8	0.227	0.179	0.957
2.0	0.164	0.243	1.18

Table 2. Simulation parameters at various turbulent conditions.

Case	ϕ	$\frac{u'}{S_L}$	Re_t	l_o (mm)	η (μm)	Ka
1A	1.8	10	83	2.0	72.8	9.46
1B	1.8	25	200	2.0	36.3	38.36
2A	2.0	10	83	1.9	91.1	11.02
2B	2.0	25	200	1.9	45.4	43.57

In Table 2, l_o represents the integral length scale, u' denotes the turbulence intensity, the turbulent Reynolds number is defined as $Re_t = \frac{u' l_o}{\nu}$, the Kolmogorov length scale is estimated as $\eta \sim l_o Re_t^{-\frac{3}{4}}$, and the Karlovitz number is calculated as

$Ka = \sqrt{\frac{(u'/S_L)^3 \delta_L^o}{l_o}}$. Because LEM-MOMIC is a stochastic model, the statistical averages over the 10,000 instantaneous snapshots are taken to obtain averaged flame profiles. Figure 21 shows how the structure of the flame changes because of isotropic one-dimensional model turbulence, by tracking the temperature profiles. The thickening of the flame with increasing Karlovitz number is observed.



The main aim of the current work is to understand the effects of turbulence due to different equivalence ratios as well as different turbulent conditions. Figure 22 shows how the spatial variations in soot volume fraction and number density profiles occur. As expected, the rich flame shows more sooting behavior. For example, at $\phi = 2.0$, the soot volume fraction levels are roughly four times more than those at $\phi = 1.8$. A similar effect is also observed on the soot number density profiles. The turbulence also appears to profoundly affect the emissions levels. With increasing turbulence, the levels as well as the initiation of soot formation appear to be affected. For example, at $\phi = 1.8$, the maximum soot volume fraction rises from 0.015 ppm to 0.025 ppm. Similarly, the initiation of soot inception also occurs earlier with increasing turbulence. The temperature profile suggests that the preheat zone thickens with increasing Re_t , and hence pyrene formation and soot inception due to pyrene (A_1) occur earlier.

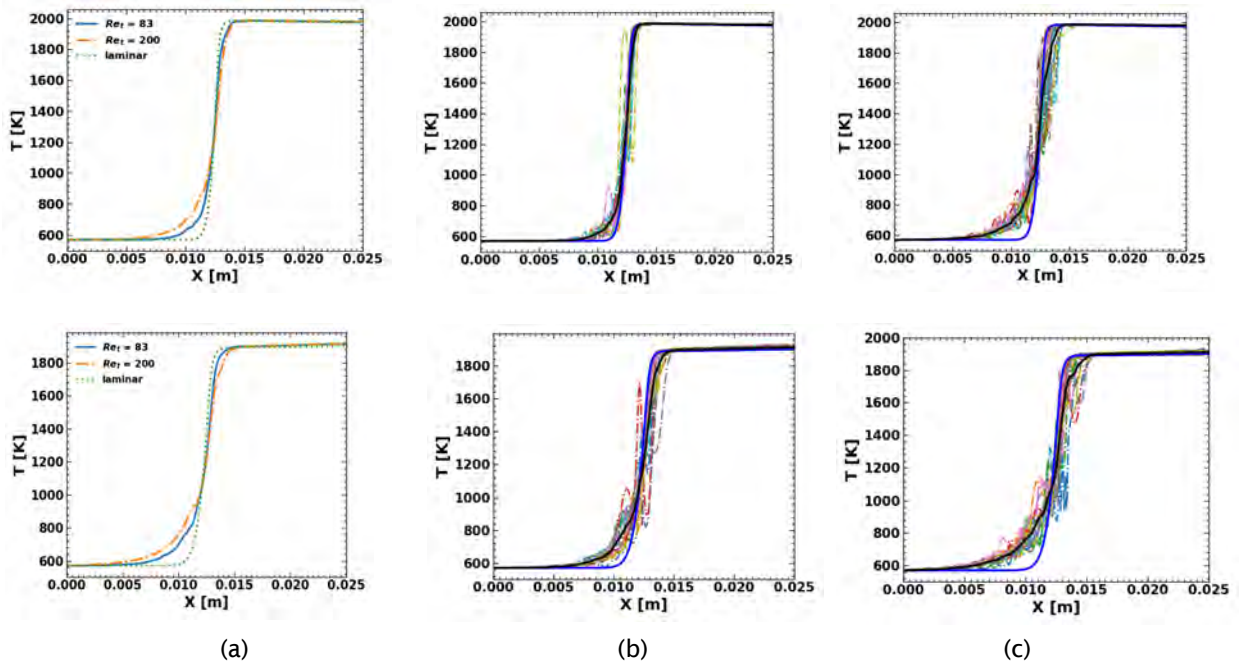


Figure 21. (a) Averaged profiles of temperature at laminar conditions, $Re_t = 83$ and $Re_t = 200$. (b) Representative instantaneous snapshots of temperature demonstrating action of eddies at $Re_t = 83$. (c) Representative instantaneous snapshots of temperature demonstrating action of eddies at $Re_t = 200$. The top three figures present results for $\phi = 1.8$, whereas the bottom three figures show results for $\phi = 2.0$.

To understand the physics of soot formation with the MOMIC model, we examined the various source terms due to nucleation, coagulation, and surface growth, normalized by their maximum values, to identify their locations of dominance behind the flame. The comparison of their locations is provided in Figures 23–25. The plot shows the competition among nucleation, coagulation, and surface growth zones behind the flame in laminar and turbulent conditions. All these profiles are statistically averaged for stochastic comparison. The coagulation zone closely follows the nucleation zone. The combined effect of surface growth and oxidation is more dominant after nucleation.

The comparison of nucleation and surface growth terms is shown in Figures 23–25 for $\phi = 1.8$. The surface growth adds more soot mass than observed with nucleation under laminar as well as turbulent conditions. The surface growth source terms are further analyzed to understand contributions from surface growth due to C_2H_2 addition and surface oxidation due to O_2 and OH , and are shown in Figure 19 for $\phi = 1.8$. The soot mass addition due to C_2H_2 is almost three times more dominant than O_2 and OH radicals. The oxidation by OH molecules is four times higher than the O_2 molecules.

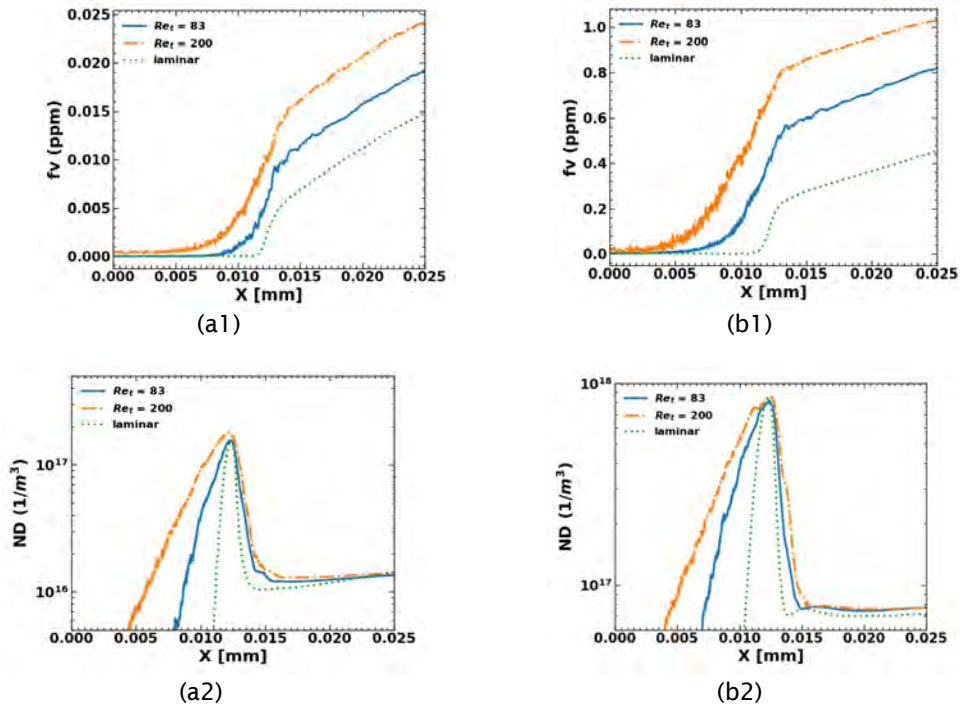


Figure 22. Comparison of the soot volume fraction at laminar and turbulent conditions for (a1) and (a2). Comparison of soot number density at laminar and turbulent conditions for (b1) and (b2).

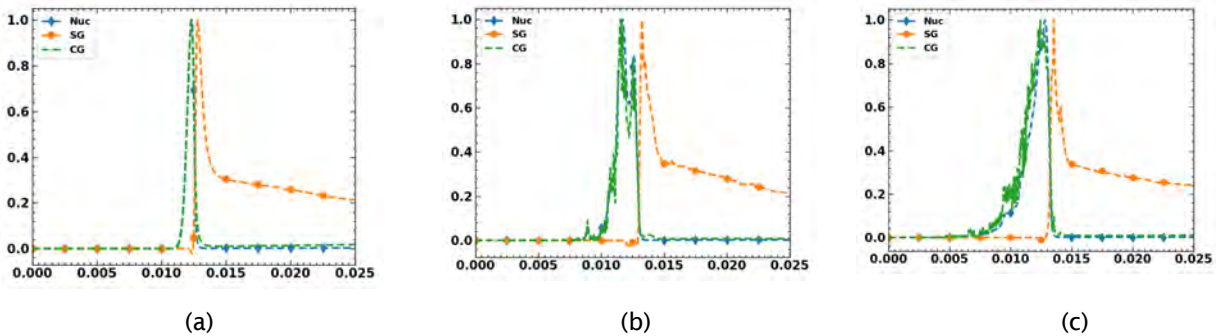


Figure 23. Normalized nucleation (Nuc), coagulation (CG), and surface growth (SG) source terms.

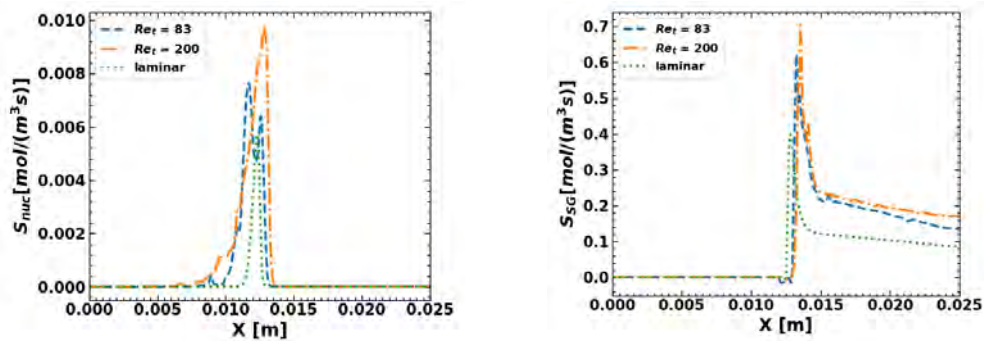


Figure 24. Comparison of the contributions from nucleation and surface growth to soot overall soot growth.

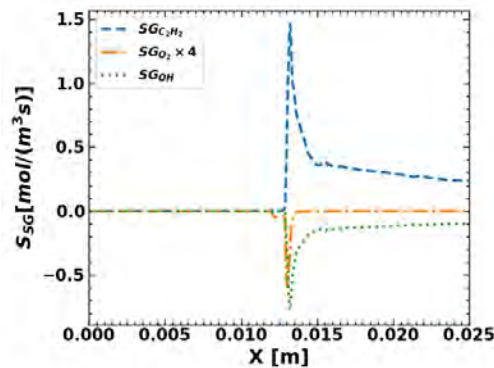


Figure 25. Comparison of the contributions from C_2H_2 , O_2 , and OH to soot surface growth and oxidation.

In summary, in the first quarter of this annual report, we focused on improving our multiscale LEM model to include soot formation and growth effects due to PAH kinetics. In the remainder of this report, we will discuss LES work conducted to perform large-scale simulations inside an RQL combustor.

RQL combustor

The computer-aided design (CAD) model of the realistic LES rig in the Year 3 effort is shown in Figure 26(a). The RQL burner simulated in GT is a subsection (only one swirler) and is represented in Figure 26(b).

In summary, the entire CAD model consists of an inlet plenum, a radial swirler, and eight dilution jets at the top and bottom. As is evident from the three-sector rig, some portions of the top wall and all side walls have glass window panels for the experimental measurements and hence are treated as adiabatic in the current study. Effusion boundary conditions are applied to all remaining walls where glass windows are not present. The side jets near the side walls are difficult to resolve and hence are replaced by a continuous slot for air injection.

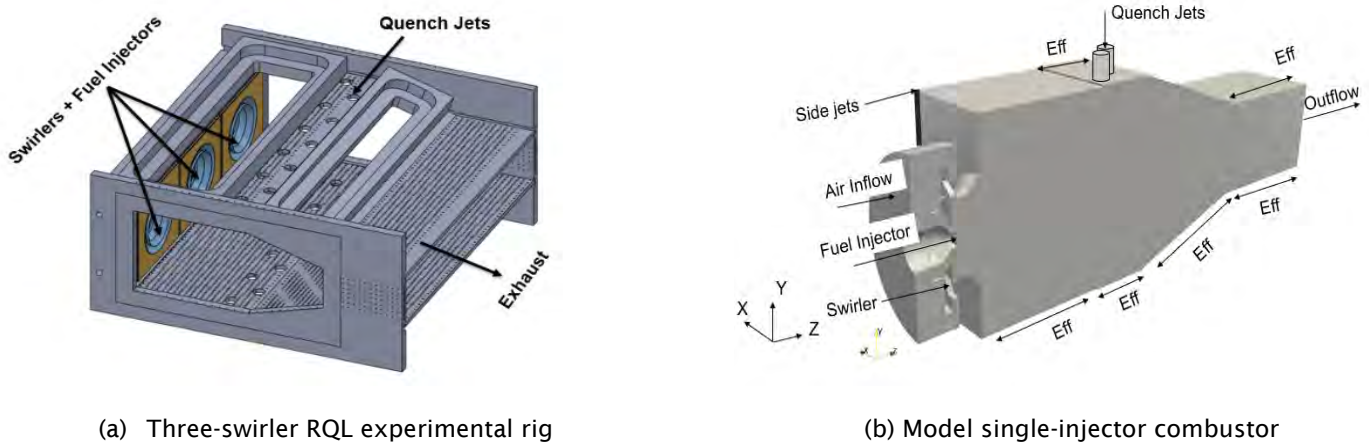


Figure 26. CAD model for the RQL rig.

The entire geometry is split among 5,250 blocks for parallelization. The LES solver is MPI-parallel, and the simulations are run on 1,440 cores. Simulations are conducted on GT’s supercomputing cluster (PACE Phoenix) with Intel Ivy-bridge i7 processors. More details regarding the use of LESLIE for simulating turbulent reacting and non-reacting flows inside a gas turbine engine can be found in Panchal (2022). For the model combustor, we are using the practical conditions as initially specified by Honeywell. The inflow air is preheated at $T_{in} = 600$ K and $P_{in} = 5.8$ atm, and enters the model combustor through primary swirlers, side jets, effusion holes, and quench jets. The overall total mass flow rate is 0.2785 kg/s and is split as shown in the following Table 3. The fuel mass flow rate is such that the equivalence ratio (ϕ) in the primary zone is 1.8.

Table 3. Mass flow rate split among various components.

Component	Primary swirler	Quench jets	Side jets	Effusion	Fuel	Total
$\dot{m}_{kg/s}$	0.0557	0.1403	0.0278	0.0547	0.00679	0.2854
Split %	19.52	49.16	9.75	19.18	2.39	100

A fully compressible Eulerian finite volume formulation for the gas phase is used. An eddy viscosity approach with a one-equation subgrid kinetic energy (k_{sgs}) model is used for the closure of gas-phase subgrid scale fluxes. A well-established multiblock structured fully compressible finite volume solver, LESLIE, is used for simulation with a hybrid second-order central and third-order upwind method. A fourth-order Runge-Kutta solver is used for solving the Lagrangian equations. The dilute injection of spray is the current focus. For computational efficiency, instead of tracking of individual Lagrangian particles, the particles are grouped in parcels, and the parcels are tracked in a Lagrangian manner. A particle-per-parcel value of 8 is used in this work and has been shown to provide a good balance between accuracy and efficiency for gas-turbine combustor LES. The inflow boundary condition is modeled by using a characteristic Navier-Stokes boundary condition. The outflow is modeled by using a sponge boundary condition. The liquid fuel droplets are injected through hollow cone injector and have a log-normal distribution for sizes with a Sauter mean diameter of 36 μm . A breakup model is not considered in this work, because the droplets are assumed to have a smaller Sauter mean diameter. However, for larger droplets, the code can handle secondary breakup, if needed. A globally reduced six-species two-step KERO-BFER mechanism (Franzelli, 2008) is used to represent the finite rate chemistry effects.

The time step for the reacting flow simulations is 9.4×10^{-9} s. First, we collected traces (temporal history between 40 ms and 52 ms) of mass flow rates to verify if boundary conditions are correctly applied as shown in Figure 27. It suggests that the mass flow rate at outflow is equal to the summed mass flow rate at all inflow boundaries and conserves mass, thus ensuring that the mass flow rates at each boundary do not substantially oscillate.

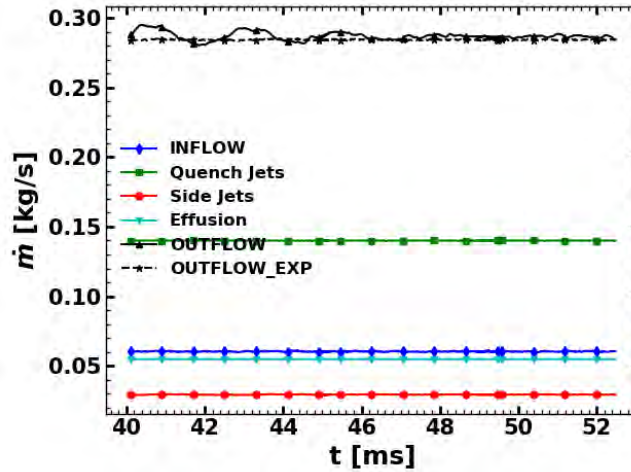
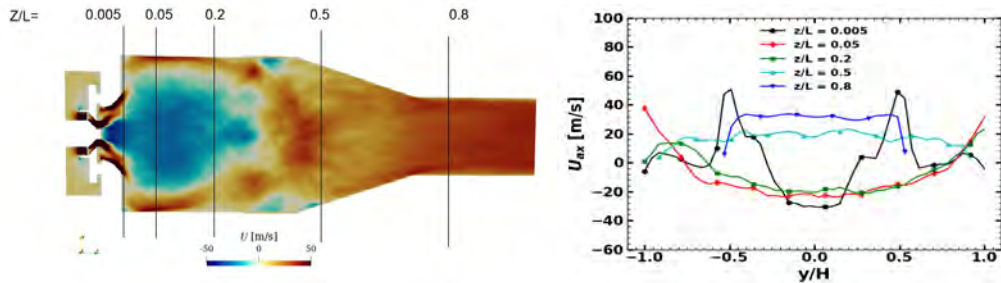


Figure 27. Temporal history of surface averaged mass flow rate at boundaries of the combustor.

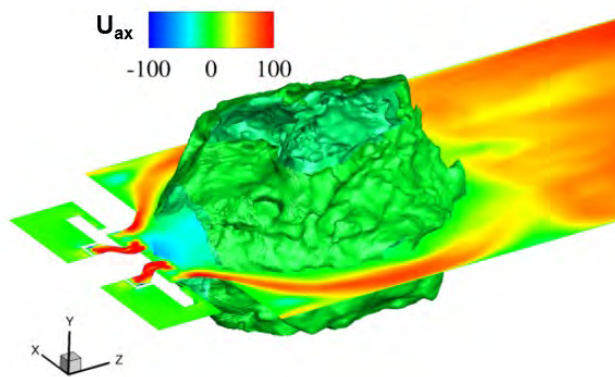
Initially, statistically averaged flow features of non-reacting flow field are shown in Figure 28. As a result of the swirl, a low-pressure zone is created in the center, forming a vortex breakdown bubble (VBB) (also known as the central recirculation zone)—a key feature of swirling flows. A negative velocity is observed in the center, as shown by the axial velocity contour in Figure 28(a), and also observed in statistically averaged axial velocity along the height at various axial locations, which are shown via line plots in Figure 28(b). The initial lines between ($z/L < 0.2$) show the negative axial velocity in the line plots. In a typical turbulent reacting swirling flow, the hot products are trapped inside the VBB and provide necessary high temperatures for vaporization of the droplets, which react after mixing with the oxidizer.



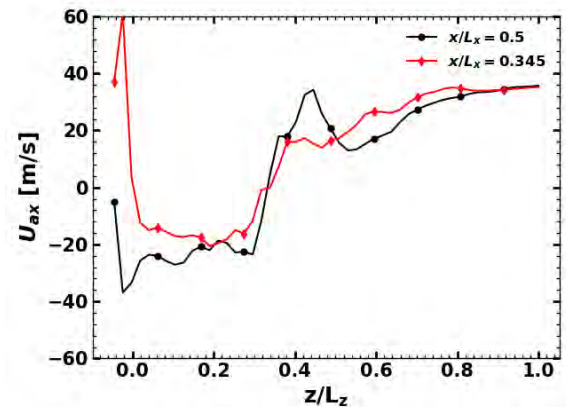
(a) Time averaged axial velocity contour (b) Axial velocity variation along the height

Figure 28. Representative axial velocity field through the center of the combustor.

The shape of this VBB is shown in Figure 29(a), by identifying the iso-surface of velocity where axial velocity is zero. The line plot of averaged axial velocity (Figure 27(b)) along the length of the combustor is also shown via line plots at two locations along the x axis ($x/L_x = 0.5$ represents the center of the combustor, and $x/L_x = 0.345$ represents the center of one of the dilution jets). The line plots suggest that the overall length of the recirculation zone is one third the length of the overall combustor.



(a) VBB iso-surface

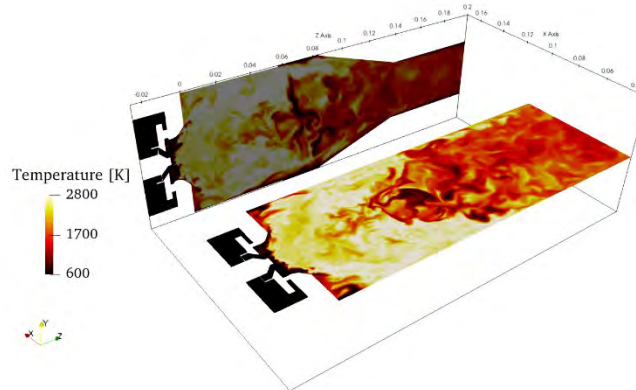


(b) Axial velocity along the axial length

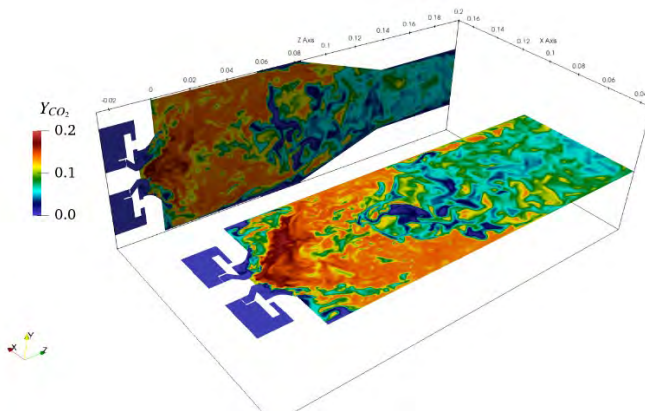
Figure 29. VBB features of the swirling flow inside the combustor.

Kerosene droplets are injected from the center of the injector, and an initial hotspot is superimposed on the non-reacting flow field to kickstart the reacting flow. The simulations are run until the flame is fully stable. The instantaneous features of temperature field, and major product species (CO_2 and H_2O) are shown in Figure 30 along the vertical and horizontal planes of the combustor in the snapshots below. A lifted flame anchored near the injectors is observed. The incoming fuel droplets vaporize because of high temperature, mix with the surrounding oxidizer, and burn at a high temperature of approximately 2500 K. As evident from the field, particularly in Figure 30(a), the cold quench jets of air enter the combustor from the top and bottom, and quench the flame; consequently, a low-temperature zone is observed in the second half of the combustor. The cooling jets mix with the products, and a highly turbulent mixing is observed, as is characteristic of RQL combustor. The primary zone contains most of the product species and is diluted by the incoming air through quench jets, as indicated in Figure 30(b) and Figure 30(c).

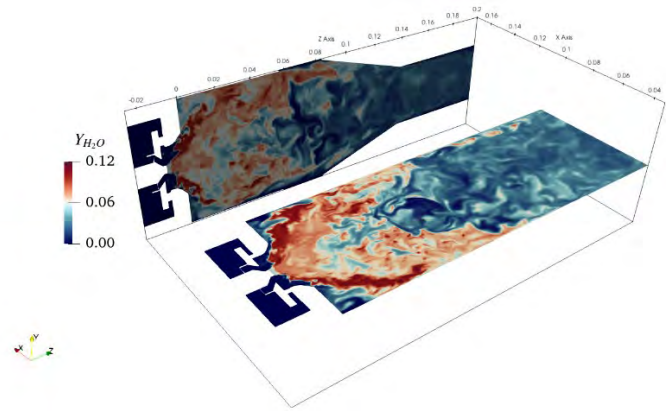
In summary, the current efforts have established the reacting flow inside a model RQL combustor at realistic conditions closer to actual test conditions. Stable reacting flow simulations are conducted, wherein the global equivalence ratio is rich in the primary zone, as in an RQL combustor. Because globally reduced six-species kerosene kinetics is used to perform these simulations, information for species relevant to soot formation and growth cannot be obtained; this challenge is the focus of continuing effort. In the future, we will focus on using the reduced global kinetics (with PAH) and the optimized soot kinetics developed by RTRC to study soot formation and growth from the RQL combustor. In parallel, we will also provide the current reacting flow data to RTRC for one-way coupled MC simulations that can provide more information regarding the tendency of soot to form characteristic aggregate structures; moreover, a more realistic fractal dimensions of soot particles at tabulated background conditions will be used within the LES code.



(a) Temperature inside the combustor



(b) CO₂ mass fraction



(c) H₂O mass fraction

Figure 30. Instantaneous features of temperature, CO₂ mass fraction, and H₂O mass fractions along the horizontal and vertical mid-planes of the combustor.

Milestones

LEM-MOMIC model coupling for turbulence-soot-chemistry interaction and LES of a practical RQL combustor are planned for 9/30/2024

Major Accomplishments

Efforts focused on soot-turbulence-chemistry interactions on canonical turbulent premixed flames and LES of multiphysics flow inside the RQL combustor being investigated under Project 70.

Publications

None.

Outreach Efforts

None.

Awards

None.



Student Involvement

PhD student Shubham Karpe has been assisting in the development of the MOMIC framework within the LES code at GT.

Plans for Next Period

The future work at GT involves incorporating inputs from the partner groups into the MOMIC model at GT. We will also conduct RQL simulations at these conditions with the improved soot model, to provide a final demonstration of the model.

References

- Balthasar, M., & Frenklach, M. (2005). Monte-Carlo simulation of soot particle coagulation and aggregation: the effect of a realistic size distribution. *Proceedings of the Combustion Institute*, 30(1), 1467-1475. <https://doi.org/10.1016/j.proci.2004.07.035>
- Chen, J.-Y. (1988). A general procedure for constructing reduced reaction mechanisms with given independent relations. *Combustion Science and Technology*, 57(1-3), 89-94. <https://doi.org/10.1080/00102208808923945>
- Colket, M. B., Hall, R. J., & Stouffer, S. D. (2004, June 14-17). *Modeling soot formation in a stirred reactor* [Presentation]. Proceedings of the ASME Turbo Expo 2004: Power for Land, Sea, and Air, Vienna, Austria. <https://doi.org/10.1115/GT2004-54001>
- Glarborg, P., Kee, R. J., Grcar, J. F., & Miller, J. A. (1986). *PSE: a Fortran program for modeling well-stirred reactors* (Report No. SAND86-8209). Sandia National Laboratories, Livermore, CA.
- El-Asrag, H., & Menon, S. (2009). Large eddy simulation of soot formation in a turbulent non-premixed jet flame. *Combustion and Flame*, 156(2), 385-395. <https://doi.org/10.1016/j.combustflame.2008.09.003>
- El-Asrag, H., Lu, T., Law, C. K., & Menon, S. (2007). Simulation of soot formation in turbulent premixed flames. *Combustion and Flame*, 150(1-2), 108-126. <https://doi.org/10.1016/j.combustflame.2007.01.005>
- Frenklach, M. (2002). Method of moments with interpolative closure. *Chemical Engineering Science*, 57(12), 2229-2239. [https://doi.org/10.1016/s0009-2509\(02\)00113-6](https://doi.org/10.1016/s0009-2509(02)00113-6).
- Franzelli, B., Riber, E., Sanjosé, M., & Poinso, T. (2010). A two-step chemical scheme for kerosene-air premixed flames. *Combustion and Flame*, 157(7), 1364-1373. <https://doi.org/10.1016/j.combustflame.2010.03.014>
- Kireeva, E. D., Popovicheva, O. B., Persiantseva, N. M., Timofeyev, M. A., & Shonija, N. K. (2009). Fractionation analysis of transport engine-generated soot particles with respect to hygroscopicity. *Journal of Atmospheric Chemistry*, 64(2-3), 129-147. <https://doi.org/10.1007/s10874-010-9173-y>
- Kollrack R., (1977) ASME paper 76-WA/GT-7, Dec.
- Langer, R., Mao, Q., & Pitsch, H. (2023). A detailed kinetic model for aromatics formation from small hydrocarbon and gasoline surrogate fuel combustion. *Combustion and Flame*, 258, 112574. <https://doi.org/10.1016/j.combustflame.2022.112574>
- Leung, K. M., Lindstedt, R. P., & Jones, W. P. (1991). A simplified reaction mechanism for soot formation in nonpremixed flames. *Combustion and Flame*, 87(3-4), 289-305. [https://doi.org/10.1016/0010-2180\(91\)90114-Q](https://doi.org/10.1016/0010-2180(91)90114-Q)
- Lu, T., & Law, C. K. (2005). *A directed relation graph method for mechanism reduction*. Proceedings of the Combustion Institute, 30(1), 1333-1341. <https://doi.org/10.1016/j.proci.2004.08.145>
- Panchal, A., & Menon, S. (2022). Large eddy simulation of fuel sensitivity in a realistic spray combustor II. Lean blowout analysis. *Combustion and Flame*, 240, 112161 <https://doi.org/10.1016/j.combustflame.2022.112162>
- Saldinger, J. C., Elvati, P., & Violi, A. (2021). Stochastic and network analysis of polycyclic aromatic growth in a coflow diffusion flame. *Physical Chemistry Chemical Physics*, 23(7), 4326-4333. <https://doi.org/10.1039/d0cp03529g>
- Srinivasan, S., & Menon, S. (2014). Linear eddy mixing model studies of high Karlovitz number turbulent premixed flames. *Flow, turbulence, and combustion*, 93, 189-219 <https://doi.org/10.1007/S10494-014-9542-8>
- Stouffer, S., Striebich, R. C., Frayne, C. W., & Zelina, J. (2002, July 12-17). *Combustion Particulates Mitigation Investigation Using a Well-Stirred Reactor* [Presentation]. 38th AIAA/ASME/SAE/ASEE Joint Propulsion Conference & Exhibit, Indianapolis, IN.
- Sun, Y., & Beckermann, C. (2007). Sharp interface tracking using the phase-field equation. *Journal of Computational Physics*, 220(2), 626-653. <https://doi.org/10.1016/j.icp.2006.05.025>
- Wang, H., Xu, R., Wang, K., Bowman, C. T., Hanson, R. K., Davidson, D. F., Brezinsky, K. and Egolfopoulos, F. N. (2018) A physics-based approach to modeling real-fuel combustion chemistry-I. Evidence from experiments, and thermodynamic, chemical kinetic and statistical considerations *Combustion and Flame*, 193:502-519 <https://doi.org/10.1016/j.combustflame.2018.03.019>
- Xu, Z., & Meakin, P. (2008). Phase-field modeling of solute precipitation and dissolution. *The Journal of Chemical Physics*, 129(1), 014705. <https://doi.org/10.1063/1.2948949>



Project 072 Aircraft Noise Exposure and Market Outcomes in the United States

Massachusetts Institute of Technology

Project Lead Investigators

R. John Hansman
T. Wilson Professor of Aeronautics & Astronautics
Department of Aeronautics & Astronautics
Massachusetts Institute of Technology
77 Massachusetts Avenue, 33-303
Cambridge, MA 02139
617-253-2271
rjhans@mit.edu

Christopher R. Knittel
George P. Shultz Professor of Applied Economics
Sloan School of Management
Massachusetts Institute of Technology
77 Massachusetts Avenue, E62-527
Cambridge, MA 02139
617-324-0015
knittel@mit.edu

Steven R. H. Barrett
Professor of Aeronautics and Astronautics
Department of Aeronautics and Astronautics
Massachusetts Institute of Technology
77 Massachusetts Avenue, 33-207
Cambridge, MA 02139
617-452-2550
sbarrett@mit.edu

Jing Li
Assistant Professor of Applied Economics
Sloan School of Management
Massachusetts Institute of Technology
77 Massachusetts Avenue, E62
Cambridge, MA 02139
617-252-1131
lijing@mit.edu

Florian Allroggen
Executive Director Aerospace Climate & Sustainability & Research Scientist
Department of Aeronautics and Astronautics
Massachusetts Institute of Technology
77 Massachusetts Avenue, 33-115A
Cambridge, MA 02139
617-715-4472
fallrogg@mit.edu





University Participants

Massachusetts Institute of Technology

- P.I.: Prof. R. John Hansman
- Co-P.I.s: Professor Christopher R. Knittel, Professor Steven Barrett, Professor Jing Li, and Dr. Florian Allroggen
- FAA Award Number: 13-C-AJFE-MIT, Amendment Nos. 075, 081, 094, 111, and 115 (NCE to September 30, 2024)
- Period of Performance: August 11, 2020 to September 30, 2024
- Tasks (tasks listed below are general project tasks; reporting includes the period from October 1, 2022 to September 30, 2023):
 1. Literature review (not reported; completed during past reporting periods)
 2. Empirical identification strategy and scope of dataset
 3. Calculation of noise impact metrics (not reported; completed during past reporting periods)
 4. Cleaning and aggregation of housing transaction dataset (not reported; completed during past reporting periods)
 5. Descriptive analysis of dataset (not reported; completed during past reporting periods)
 6. Empirical analysis

Project Funding Level

\$780,000 FAA funding and \$780,000 matching funds. Sources of match are approximately \$182,000 from MIT, plus third-party in-kind contributions of \$519,000 from NuFuels, LLC, and \$79,000 from Savion Aerospace Corporation.

Investigation Team

- Prof. R. John Hansman, (P.I.), Tasks 1, 2, 3, 5, and 6
- Prof. Christopher R. Knittel, (co-P.I.), Tasks 1, 2, 4, 5, and 6
- Prof. Steven R.H. Barrett, (co-P.I.), Tasks 1, 5, and 6
- Prof. Jing Li, (co-P.I.), Tasks 1, 2, 4, 5, and 6
- Dr. Florian Allroggen, (co-P.I.), All Tasks
- Dr. Xibo Wan, (postdoctoral associate), Tasks 1, 2, 4, 5, and 6
- Zhishen Wang, (graduate student), Tasks 3, 5, and 6
- Kevin Zimmer, (graduate student), Tasks 3 and 5

Project Overview

As enplanements at U.S. airports have increased by almost 50% over the past two decades, the number of Americans exposed to substantial levels of aircraft noise has decreased. However, considerable concerns regarding aircraft noise remain in some airport communities. This project leverages revealed-preference approaches to infer the “implicit price” of aircraft noise exposure from market outcomes in U.S. airport communities. More specifically, the research team is quantifying the capitalized disutility associated with aircraft noise exposure through analyzing the empirical relationship between aircraft noise exposure and transaction values for residential properties in communities surrounding U.S. airports. The project leverages potential changes in noise exposure associated with quasi-experimental settings, e.g., the opening of new runways or changes in arrival and departure paths, to empirically identify potential effects on house prices. The results provide insight into the average impacts of noise exposure on residential property values, while also assessing dynamic adjustment processes and potential heterogeneities in revealed preferences, by targeting factors such as time, location, or noise exposure patterns.

Task 2 – Empirical Identification Strategy and Scope of Dataset

Massachusetts Institute of Technology

Objective

The goal of this task is to describe a strategy for empirically identifying the causal impacts of aircraft noise on residential property values. This task includes identifying model specifications to explain variations in residential property prices as well as the most suitable noise metrics to capture noise impacts.

Research Approach

For quantifying the total noise costs (including annoyance), economists have proposed stated-preference and revealed-preference methods. Whereas stated-preference approaches use surveys to obtain estimates of the willingness to pay for noise reductions and/or willingness to accept aircraft noise exposure (Bristow et al., 2015), revealed-preference approaches infer the “implicit price” of noise exposure from market outcomes (Rosen, 1974). Hedonic pricing studies face a variety of challenges, including (a) omitted-variable bias, particularly due to unobserved neighborhood characteristics and to omission of the positive amenity impact of airports in surrounding communities; (b) misspecification of the functional form; and (c) stability assumptions regarding preferences among individuals across space and time (Chay & Greenstone, 2005; Kuminhoff et al., 2010; Nelson, 2004; Parmeter & Pope, 2013). To address some of these concerns, the most recent studies have relied on quasi-experimental settings that leverage changes in noise exposure, e.g., those due to flight track changes, to empirically identify the causal impacts of noise exposure on property values (Almer et al., 2017; Boes & Nüesch, 2011; Winke, 2017; Zheng et al., 2020).

For this study, the team identified experimental settings that provide exogenous variation in noise exposure, to analyze the impacts of noise exposure on residential property values. Most importantly, the introduction of high-precision area navigation (RNAV) and/or performance-based navigation procedures since 2012 has led to the relocation of departure and approach flight paths, or might have concentrated noise exposure along defined flight tracks. In addition, new runway configurations, such as those at Chicago O’Hare International Airport (KORD), have led to changes in noise exposure patterns. This variation will be incorporated into this analysis.

To identify the capitalized impact of aircraft noise on house prices, the team uses hedonic difference-in-differences designs (Kuminhoff et al., 2010; Parmeter et al., 2007; Parmeter & Pope, 2013) and exploits the two sources of variation outlined above. The capitalized impact of noise exposure is estimated as the change in prices between the pre- and post-implementation periods for houses with different levels of aircraft noise exposure. The main specification is as follows:

$$\ln P_{ijt} = \beta_0 + \beta_1 \ln \text{Noise}_{it} + \beta_2 Z_{ijt} + \beta_3 X_{ijt} + \gamma_{jt} + \eta_m + \epsilon_{ijt} \quad (1)$$

where i indicates the house, j is the zip code where house i is located, and t is the year. The outcome of interest is the house price (in 2011 USD), $\ln P_{ijt}$, which is the log of the Consumer Price Index-deflated sale price for property i at zip code j in year t . $\ln \text{Noise}_{it}$ represents the log of the noise exposure of property i in year t . To obtain unbiased estimates of noise impacts, we include (a) the vector Z_{ijt} , which captures house characteristics such as property age, building area, and house condition; (b) the vector X_{ijt} of neighborhood attributes such as census-block group-level demographics and household median income, as well as distance to local amenities or disamenities (e.g., city hall, rail, road, shopping mall, and open space); and (c) zip-code-by-year fixed effects γ_{jt} and month fixed effects η_m to control for unobserved time-varying neighborhood attributes and the seasonality of housing prices. ϵ_{ijt} is an idiosyncratic error term. Standard errors are clustered at the level of the fixed effect, to account for remaining spatial correlation.

The coefficient of interest is β_1 , which measures the percentage change in the average house price growth due to a 1% change in noise exposure. As such, β_1 measures the house price elasticity to noise exposure changes. The coefficient can be interpreted as the capitalized effect of noise exposure if the change in noise exposure is orthogonal to the initial level of the noise, house and neighborhood characteristics, and to changes in those variables. A negative coefficient indicates that prices decrease with higher noise levels.

The specification shown in Equation 1 leaves open the question of which characteristics of aircraft noise exposure affect house prices. To investigate how home buyers respond to aircraft noise in terms of level, frequency, and extreme events, we explore several metrics, such as annual day-night average sound level, the number of days in a year that households experience at least one noise event above a 60-dB maximum sound level (L_{\max}), and the number of noise events above 60 dB L_{\max} during the peak day. The team used machine learning techniques (least absolute shrinkage and selection operator, or LASSO) to systematically assess these metrics and identify the most relevant noise characteristics to capture the capitalized noise response (see previous reporting periods).

Equation 1, and many other studies in the literature, are based on the assumption of a linear relationship between the natural log of noise and the natural log of price. Whether this relationship accurately reflects the noise response is unclear. The team therefore investigated how Equation (1) could be amended to consider variation in the noise impacts on house prices in different areas. Generally, this requires β_1 to vary among subregions. Different definitions of subregions can be

considered to include factors such as relative wealth (as measured by house price or income levels), noise exposure, or other neighborhood characteristics.

Milestone

The team has refined the empirical strategy, specifically focusing on identifying modeling strategies to capture heterogeneities in noise impacts on property values.

Major Accomplishments

The team revisited the empirical strategy to include analyses of variation in noise impacts on property values according to various factors.

Publications

None.

Outreach Efforts

The team presented the approach in a presentation during the ASCENT Spring meeting in 2023 and in a project summary submitted to the ASCENT Fall meeting in 2023.

Plans for Next Period

The team will continue to refine the empirical approach as needed.

Awards

None.

Student Involvement

None.

References

- Almer, C., Boes, S., & Nüesch, S. (2017). Adjustments in the housing market after an environmental shock: evidence from a large-scale change in aircraft noise exposure. *Oxford Economic Papers*, 69(4), 918-938. <https://doi.org/10.1093/oep/gpw071>
- Ahlfeldite, G. M., & Maennig, W. (2013). External productivity and utility effects of city airports. *Regional Studies*, 47(4), 508-529. <https://doi.org/10.1080/00343404.2011.581652>
- Beimer, W., & Maennig, W. (2017). Noise effects and real estate prices: A simultaneous analysis of different noise sources. *Transportation Research Part D*, 54, 282-286. <https://doi.org/10.1016/j.trd.2017.05.010>
- Boes, S., & Nüesch, S. (2011). Quasi-experimental evidence on the effect of aircraft noise on apartment rents. *Journal of Urban Economics*, 69, 196-204. [10.1016/j.jue.2010.09.007](https://doi.org/10.1016/j.jue.2010.09.007)
- Bristow, A. L., Wardman, M., & Chintakayala, V. R. K. (2015). International meta-analysis of stated preference studies of transportation noise nuisance. *Transportation*, 42(1), 71-100. <https://doi.org/10.1007/s11116-014-9527-4>
- Chay, K. Y., & Greenstone, M. (2005). Does air quality matter? Evidence from the housing market. *Journal of Political Economy*, 113(2), 376-424. <http://dx.doi.org/10.1086/427462>
- Kumingshoff, N. V., Parmeter, C. F., & Pope, J. C. (2010). Which hedonic models can we trust to recover the marginal willingness to pay for environmental amenities? *Journal of Environmental Economics and Management*, 60, 145-160. <https://doi.org/10.1016/j.jeem.2010.06.001>
- Ossokina, I. V. and G. Verweij (2015). Urban traffic externalities: Quasi-experimental evidence from housing prices. *Regional Science and Urban Economics*, 55, 1-13. <https://doi.org/10.1016/j.regsciurbeco.2015.08.002>
- Parmeter, C. F., and Pope, J. C. (2013). Quasi-experiments and hedonic property value methods. In Handbook on experimental economics and the environment. Edward Elgar Publishing. <https://doi.org/10.4337/9781781009079.00007>
- Rosen, S. (1974). Hedonic prices and implicit markets. Product differentiation in pure competition. *Journal of Political*



- Economy*, 82(1), 34-55. <http://dx.doi.org/10.1086/260169>
- Tsui, W. H. K., Tan, D. T. W., and Shi, S. (2017). Impacts of airport traffic volumes on house prices of New Zealand's major regions: A panel data approach. *Urban Studies*, 54(12), 2800-2817. DOI: 10.1177/0042098016660281
- Von Graevenitz, K. (2018). The amenity cost of road noise. *Journal of Environmental Economics and Management*, 90, 1-22. DOI: 10.1016/j.jeem.2018.04.006
- Winke, T. (2017). The impact of aircraft noise on apartment prices: a differences-in-differences hedonic approach for Frankfurt, Germany. *Journal of Economic Geography*, 17, 1283-1300. <https://doi.org/10.1093/jeg/lbw040>
- Wolfe, P. J., Kramer, J. L., & Barrett, S. R. H. (2017). Current and future noise impacts of the U.K. hub airport. *Journal of Air Transport Management*, 58, 91-99. <https://doi.org/10.1016/j.jairtraman.2016.09.002>
- Zheng, X., Peng, W., & Hu, M. (2020). Airport noise and house prices: A quasi-experimental design study. *Land Use Policy*, 90, 104287. DOI: 10.1016/j.landusepol.2019.104287

Task 6 – Empirical Analysis

Massachusetts Institute of Technology

Objective

The goal of this task is to run empirical analyses of the impacts of aircraft noise exposure on residential property values. For this purpose, the team uses the model outlined in Task 2 and estimates its parameters based on the datasets developed under Tasks 3 and 4 (see previous reports). This process allows us to obtain estimates of the price effects of aircraft noise exposure for residential properties, while controlling for other impacts on house prices, such as the characteristics of the house or neighborhood, or general price trends.

Research Approach

The model outlined in Task 2 is estimated by using empirical methods for regression analysis, such as ordinary least squares. Initial analyses are run for Boston Logan International Airport (KBOS), KORD, and Seattle Tacoma International Airport (KSEA).

A concern regarding the validity of the results is that (a) unobservable attributes in house or neighborhood characteristics might bias the results; and (b) a correlation might exist between house prices and noise, which does not stem from the impacts of noise exposure on house prices. To mitigate such concerns, we leverage quasi-experimental settings such as the opening of runway infrastructure and the introduction of performance-based navigation procedures. These settings create an opportunity to identify the causal effect of airplane noise exposure on house prices, because changes in airplane noise are plausibly exogenous for two reasons: (a) the changes in flight paths are determined by the flight procedures, which are developed and implemented by aviation authorities considering factors such as safety, airspace capacity, and efficiency, and (b) the decision to open or close a runway is more likely to be based on weather conditions, maintenance needs, or safety considerations than to be caused by other factors that have influenced the local housing market. Such a difference-in-difference specification would estimate the model in Equation (1) in differences, i.e., by analyzing the relationship between price changes and noise exposure changes.

Simultaneously, we note that estimation of such a difference-in-difference model restricts the sample size, because the estimation would rely on data for houses sold immediately before the introduction of new procedures and after the introduction of the procedures. We therefore estimate the model in levels at first (as written in Equation (1)), with careful consideration of potential biases. We further note that the results are highly preliminary.

Milestone

The team used preliminary model specifications (in levels) to gain initial insights into the average noise response and to analyze heterogeneities in the impact of noise exposure on house prices. Preliminary analyses were run for three airports (KBOS, KORD, and KSEA), to compare results and understand the robustness of the model.

Major Accomplishments

Analysis of the baseline model

The model was first estimated in levels, thus providing preliminary insights regarding the impact of noise exposure on residential property values. The preliminary results for KBOS suggest that a 1% decrease in noise exposure (measured by

day-night average sound level) correlates with an average increase in property values by 0.262% (Table 1). The elasticity is of similar magnitude for KORD and KSEA. These preliminary estimates are generally consistent with values in the literature (e.g., Nelson (2008) or Day et al. (2007)). We note that the estimates are highly preliminary and are potentially subject to biases, as described in the Research Approach section.

Table 1. House price elasticity to noise exposure for three U.S. airports: Boston Logan International Airport (KBOS), Chicago O’Hare International Airport (KORD), and Seattle Tacoma International Airport (KSEA). Preliminary estimates for β_1 based on model in levels. All results are statistically significant at the 1% level.

Airport	β_1
KBOS	-0.262
KORD	-0.224
KSEA	-0.299

Variation in noise response within one region

As described under Task 2, we assess whether the responses to noise exposure are homogeneous across the regions around the airports. Preliminary studies were conducted, considering factors such as noise exposure levels or wealth indicators; again, these studies were initially conducted by using the model in levels rather than in a difference-in-difference approach. The preliminary results provide some evidence that house price elasticity is not consistent across properties. For example, across airports, houses with very high and very low values show higher house price elasticity to noise exposure than “mid-range” houses. These findings require further analysis and should not be overinterpreted at this point. Most importantly, whether these findings will persist in a difference-in-difference framework remains to be seen.

Publications

None.

Outreach Efforts

The team presented the approach in a presentation during the ASCENT Spring meeting in 2023 and in a project summary submitted to the ASCENT Fall meeting in 2023.

Awards

None.

Student involvement

Graduate student Zhishen Wang worked on this task.

Plans for Next Period

The team will continue to refine the analysis by leveraging the quasi-experimental settings and assessing potential heterogeneities in noise exposure response. After all results are obtained, the team will prepare the findings for publication.

References

1. Day, B., I. Bateman, & I. Lake (2007). Beyond implicit prices: recovering theoretically consistent and transferable values for noise avoidance from a hedonic property price model. *Environmental and Resource Economics* 37, 211–232.
2. Nelson, J. P. (2008). Hedonic property value studies of transportation noise: aircraft and road traffic. *Hedonic Methods in Housing Markets*, 57–82.



Project 073 Fuel Composition Impact on Combustor Durability

University of Dayton Research Institute

Project Lead Investigator

Scott Stouffer
 Group Leader, Combustion Group, Fuels and Combustion Division
 University of Dayton Research Institute
 300 College Park, Dayton, OH 45469-0043
 937-229-3961
 Scott.Stouffer@udri.udayton.edu

University Participants

University of Dayton Research Institute

- P.I.: Scott Stouffer, PhD, PE
- FAA Award Number: 13-C-AJFE-UD, Amendment 029
- Period of Performance: August 11, 2020 to September 30, 2021
- Period of Performance: August 10, 2021 to February 10, 2022: Amendment 036
- Period of Performance: October 1, 2021 to September 30, 2022: Amendment 040
- Period of Performance: October 1, 2022 to September 30, 2023: Amendment 044

Project Funding Level

Amendment No. 029	\$299,148
Amendment No. 040	\$199,865
Amendment No. 044	\$200,000
Total	\$699,013

Investigation Team

Scott Stouffer, (P.I.), project direction
 Tyler Hendershott, (research engineer), combustor operations
 Jeff Monfort, (research engineer), radiation measurements
 Harry Grieselhuber, (technician), combustor testing
 Jeff Gross, (technician), combustor testing
 TBD, (graduate student)
 TBD, (undergraduate student)

Project Overview

In this study, the effects of fuel chemical composition on radiative heat transfer and the resulting combustor liner lifetime will be evaluated. Alternative fuels contain ratios of hydrocarbon types that may substantially differ from those in familiar petroleum-based fuels. In petroleum-based fuels, higher aromatic levels are known to contribute to greater particulate matter loading radiative heat transfer and reduced combustor liner lifetimes. Consequently, aromatic compounds are limited to 25 vol% in the ASTM D1655 jet fuel specification. Some candidate alternative fuels contain synthetically produced aromatic compounds and cycloparaffins, which must be evaluated for their radiative heat transfer characteristics. The measurements collected in this project will provide insights into the effects of fuel type on liner lifetime. Several fuel types will be investigated, including a synthetic aromatic kerosene, a baseline Jet A fuel, and a fuel high in cycloparaffins



(e.g., Shell IH² fuel). Diagnostic methods to be used in the investigation include the measurement of wall and gas temperatures, and the use of infrared (IR) cameras and radiometers.

Task 1 – Perform Radiation Measurements of Various Fuel Types in the Referee Combustor to Evaluate the Effect of Fuel Composition on Combustor Liner Lifetime

University of Dayton Research Institute

Objective

The objective of this program is to provide insights into the effect of fuel type on engine combustor liner lifetime. This study will ensure that candidate drop-in fuels will perform satisfactorily in jet engines, and will not increase the need for engine maintenance or decrease flight safety. The findings of this study may also indicate which fuel composition changes may reduce radiative heat transfer and therefore increase combustor liner lifetime.

Research Approach

Fuel chemical composition is well known to strongly affect soot formation, smoke production, and radiative heat flux in gas turbine combustors (Chin & Lefebvre, 1990). Studies of petroleum-based fuels with varying levels of aromatic levels have indicated that these properties increase with the overall content of aromatic species. Other parameters such as hydrogen content, hydrogen/carbon ratio, and smoke point have also been correlated with liner temperatures, but the effects of individual types of aromatic species have not been well studied. Candidate alternative fuels may meet the overall limits for aromatic species but may contain individual species or mixtures of species that are markedly different from those in petroleum-derived fuels. Radiation heat transfer to combustor liners is a major issue affecting the durability and operational envelope of gas turbine engines. Radiation can cause high heat fluxes, thus resulting in localized heating, hotspots, and high thermal gradients along and across the liner. Increases in liner temperature can decrease liner durability (Gleason & Bahr, 1980). Intense heating can cause problems with low cycle fatigue, cracking, and buckling of the liner and, in extreme cases, localized melting of the liner. The combustor walls can be convectively cooled by effusion or film cooling; however, film cooling typically imposes a cycle performance penalty, along with elevated levels of CO and unburnt hydrocarbons, particularly at low power settings. Because of concerns regarding the effects of fuel type on radiation, the radiant heat flux is considered a figure of merit by aircraft engine original equipment manufacturers in the evaluation of alternative fuels for aircraft use (Boehm, 2013).

The radiation from a gas turbine flame has two main components: (a) "non-luminous" radiation from product gases, such as CO₂, H₂O, and CO, and (b) luminous radiation from non-volatile particulate matter (principally soot).

Non-luminous radiation corresponds to the IR region and has a spectral distribution, whereas the luminous radiation is broadband, and a fraction of the radiation appears at visible wavelengths. Typically, as the pressure is increased, the luminous radiation from soot particles becomes the dominant source of heat flux to the liner walls. Whereas the convective component of the wall heat transfer depends on the fluid dynamics and gas temperature distribution near the walls, the peak radiant fluxes are related to the combinations of high-temperature gas and non-volatile particulate matter.

The emissivity of the combustion gases is typically related in an expression such as:

$$\epsilon_g = 1 - \exp[-aPL(qL)^{0.5}T_g^{-1.5}]$$

where P = gas pressure in kPa

l = characteristic length factor, which is a function of combustor geometry

T_g = gas temperature in K

q = fuel-to-air ratio

L = luminosity factor

The luminosity factor is set to 1 for gaseous emissivity. For sooting flames associated with liquid aviation fuels, the luminosity is >1 and can be correlated with the fuel composition. Several relations between luminosity and fuel type have been reported in the literature (Lefebvre, 1999; Naegeli, 1980; Clark, 1982). In general, the luminosity factor has been found to decrease with increasing hydrogen/carbon ratio and decreasing aromatic content of the fuel. Other correlations in

the literature have addressed the correlations with smoke point and naphthalene content. Although IR has been used as a diagnostic tool in basic flame experiments (Rankin, 2012), very little work using multiple radiometers and/or planar measurements of IR emissions in practical combustors has been reported in the literature. The referee rig combustor is ideal for assessing radiation heat transfer because the walls are heavily cooled—a condition that tends to suppress the convective component and thus the background radiant heating from opposing walls, so that the wall heat transfer is primarily from the flame radiation. Furthermore, provisions have been made for radiometer access to the combustor walls in the referee rig.

The referee rig combustor was developed to conduct experimental combustion research. Highlights of previous contributions to the evaluation of alternative fuels include the following:

1. Experimental measurements of lean blowout (LBO) for fuels at conditions of interest to original equipment manufacturers and the National Jet Fuels Combustion Program, which have resulted in the unexpected finding of a high correlation between the derived cetane number and the LBO limit
2. Experimental measurements of boundary conditions for the combustor, including air flow splits to support numerical combustion modeling efforts
3. Development of cold air and cold fuel capabilities for the facility, to enable atmospheric cold start ignition experiments to be conducted over a range of conditions
4. Further extension of the facility’s ability to allow altitude relight experiments to be conducted with a range of fuels at simulated altitudes of 25,000 ft
5. Examination of the effects of heated fuels on combustion characteristics and emissions

The work with the referee rig combustor has yielded publications that detail cold start ignition (Hendershott, 2018), ignition at elevated temperatures (Stouffer, 2017), LBO characteristics (Corporan, 2017; Esclapez, 2017; Colborn, 2020), particulate and gaseous emissions (Corporan, 2017), acoustic response (Monfort, 2017), flow through the liner effusion passages (Erdmann, 2017; Briones, 2017), spray characteristics (Mayhew, 2017), and altitude relight ((Stouffer, 2020; Stouffer, 2021).

Milestones

The anticipated major milestones and planned due dates are as follows:

Milestone	Planned due date
Test plan provided	December 1, 2020
Initial instrumentation experiments conducted	September 2022
Detailed testing performed for a range of fuels	April 1, 2024
Final report	September 30, 2024

Major Accomplishments

Initial experiments

Experiments during the past year involved initial evaluations of the instrumentation, including wall thermocouples on the combustor liners, radiometers, and visible and IR cameras. The experiments were all conducted with the cooperation of the Air Force Research Laboratory by using the referee combustor rig. Three fuels were used for these initial experiments:

1. A2, a baseline average Jet A fuel containing 17% (v/v) aromatic compounds
2. Hydroprocessed esters and fatty acids (HEFA) fuel containing <0.5% (v/v) aromatic compounds, which has been shown to produce relatively low levels of non-volatile particulate matter in previous experiments (Corporan, 2017)
3. A highly aromatic fuel containing 30% (v/v) aromatic compounds, which produces high levels of non-volatile particulate matter

At the same equivalence ratio, all three fuels have similar expected overall heat release (within 1%), according to the heat of combustion and the stoichiometric fuel and air ratios.

Figure 1 shows the visible light images captured with a digital single-lens reflex camera for the three fuels. All images were adjusted to equivalent exposure levels and show that the visible light increases with the equivalence ratio. In general, the flame stretches further along the combustor length as the equivalence ratio is increased. The flame images also show that



at any equivalence ratio, the fuels rank as follows in brightness from highest to lowest: high-aromatic fuel, baseline A2 fuel, and HEFA fuel.

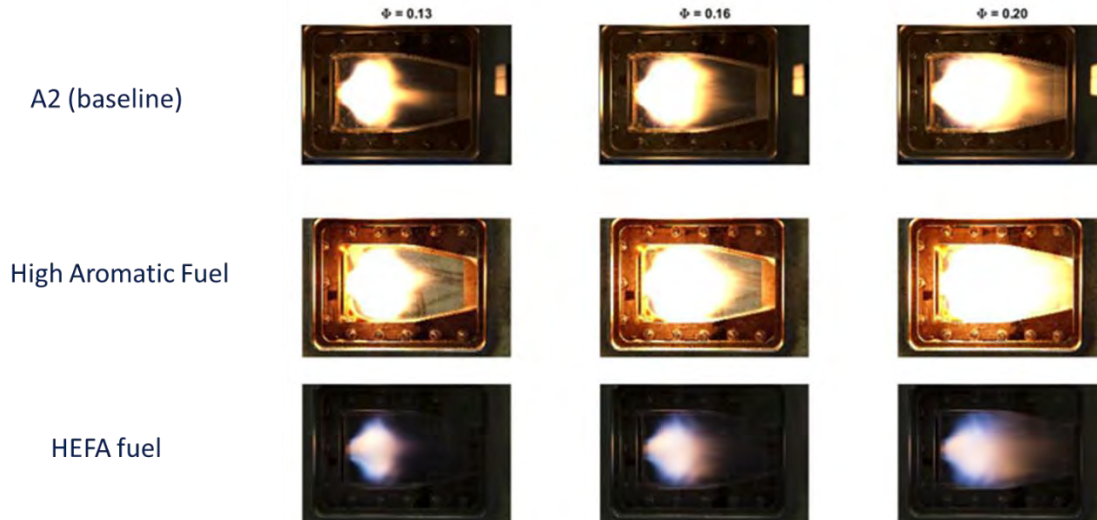


Figure 1. Visible radiation for three fuels as a function of the equivalence ratio (ϕ).

Wall temperatures and incident radiation measurements

The referee combustor was designed with a radiometer port enabling installation of a radiometer in the top combustor liner wall. The installation of the radiometer through the top liner wall required an extension to the pressure vessel to be built to allow for clearance of the cooling and purge tubes, as well as the wires. Figure 2 shows the installation of the radiometer. The radiometer was a Gardon type and was mounted near the dome region of the combustor (Figure 2C). The radiometer is cooled and measures the total radiation at the gauge location.

Initial experiments with the radiometer indicated the following observations:

- The radiometer was sensitive to changes in the combustor operating point and fuel type over the entire range of conditions.
- The radiometer purge flow (N_2 over the radiometer surface windows) was found to have little impact on the combustor operation or the intensity of the flame.
- As the combustor pressure increased, the radiation level increased.
- As the equivalence ratio increased, the incident radiation measured at the radiometer generally increased.

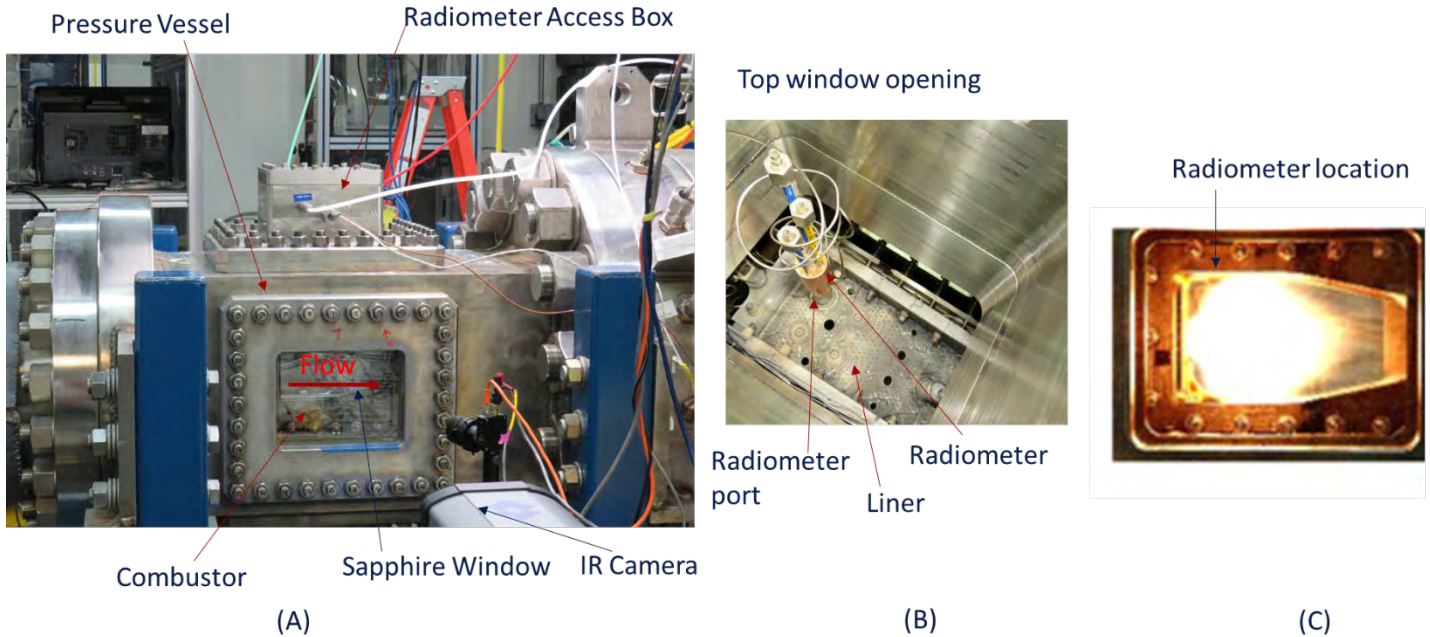


Figure 2. Experimental setup of the radiometer and IR camera. (A) Side view. (B) Top view, looking through the radiometer access box. (C) Radiometer location inside the combustor.

Figure 3 shows the radiometer output versus the equivalence ratio for the three fuels. The equivalence ratio shown is the global equivalence ratio, which is lower than the equivalence ratio in the primary zone, owing to the high levels of effusion cooling through the combustor liner, as previously discussed (Erdmann, 2017). The primary zone equivalence ratio is 5.5 times the global equivalence ratio; consequently, at the highest global equivalence ratio shown (0.24), the primary zone equivalence ratio is approximately 1.32 (fuel rich). Over most of the range of equivalence ratios, the highest radiative loading at the radiometer location is observed for the high-aromatic fuel. The results show that over most of the range, the radiative heating at the gauge location increases with the equivalence ratio. The exception to this trend occurs for the highest equivalence ratio for the A2 fuel and the high-aromatic fuel. At this equivalence ratio, the radiative loading at the gauge location for two fuels with the highest aromatic content is lower than that at the next-highest equivalence ratio.

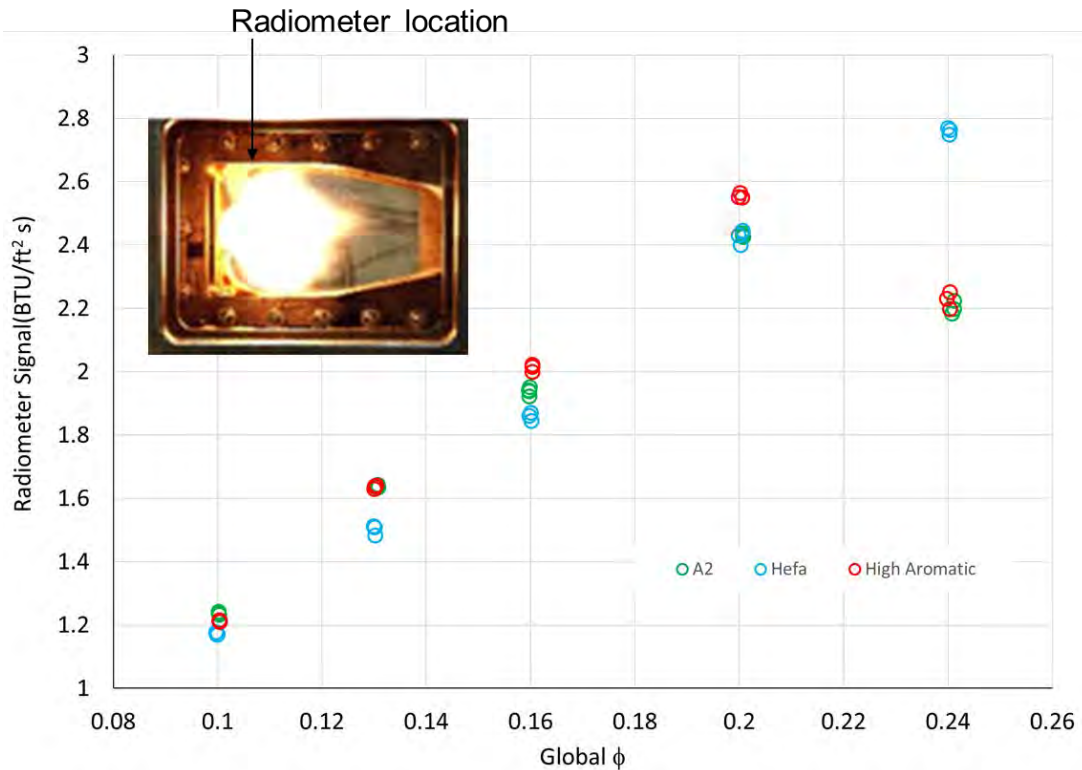


Figure 3. Radiometer signal versus equivalence ratio. Measurements were taken at $T_{air} = 250$ °F, $T_{fuel} = 120$ °F, $P_{cmb} = 30$ psia, and $\Delta P = 3\%$.

Thermocouples were mounted on the backside (cold side) of the combustor. The temperature rise on the backside was used as a secondary indication of total heating to the combustor walls, including both convective and radiative heat transfer. Figure 4 shows the average of the thermocouples on the upstream side of the combustor (upstream of the secondary dilution holes). Of note, the trends in this plot are consistent with those shown for the radiometer output in Figure 3. The wall temperatures for the A2 and the high-aromatic fuels decrease at the highest equivalence ratio, showing a trend similar to that observed for the incident radiation. This finding is believed to be due to the flame exhibiting a greater shift downstream for the A2 and the high-aromatic fuel. This trend is also shown in the IR imaging results in Figure 5.

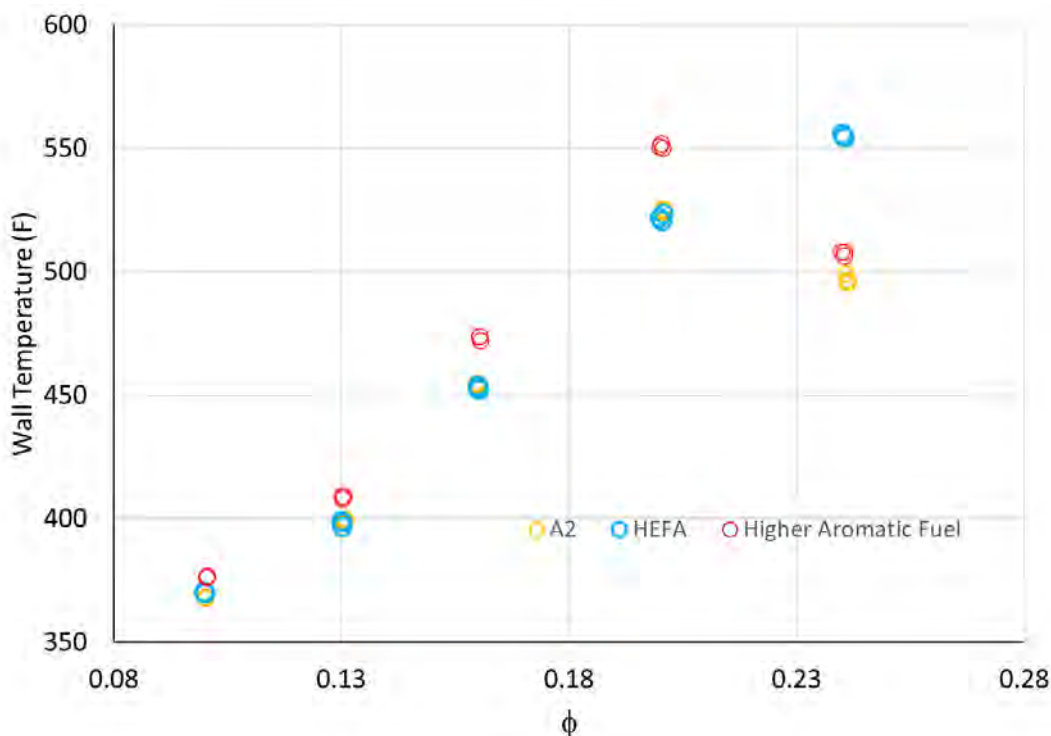


Figure 4. Average wall temperatures for the region upstream of the secondary dilution Jets. Measurements were taken at $T_{\text{air}} = 250$ °F, $T_{\text{fuel}} = 120$ °F, $P_{\text{cmb}} = 30$ psia, and $\Delta P = 3\%$.

IR camera visualization experiments

At the beginning of the program, large-scale sapphire windows were purchased to allow for visualization of the IR radiation with IR cameras in the spectral range of 1.5 to 5 μm . The intent was to obtain large-scale IR images in the combustor and also to use filters to sample spectral regions that are dominated by either blackbody radiation or by radiation from major species (H_2O , CO_2 , and CO). The referee rig uses two sets of windows for visualization: (a) an inner set installed on the combustor walls that is exposed to the combustion gases and (b) an outer set that is installed in the surrounding pressure vessel. The inner windows are relatively thinner and are exposed to a large thermal gradient and a small pressure gradient, whereas the outer windows are exposed to large pressure gradients with much lower thermal gradients. The outer sapphire windows worked well throughout all the experiments, whereas the inner windows failed because of cracking. Efforts to improve the inner-sapphire window performance by allowing more room for thermal expansion still failed because of thermal shock.

Visualizations were conducted with a combination of quartz inner windows and sapphire outer windows. Quartz windows are robust with respect to the thermal shock, because of the low thermal expansion coefficient, but have the disadvantage of low transmission of IR radiation. This low transmission partially obscures the visualization of the radiation in the combustor by interference from the hot inner-window surface. The effect is more pronounced at wavelengths greater than 2.5 μm . The results from the visualization using this approach showed qualitative agreement with the radiometer findings. Figure 5 shows the IR measurements using the quartz inner windows and sapphire outer windows along with a neutral-density broadband filter. The results are qualitatively in agreement with those in Figures 3 and 4 for the radiometer and wall thermocouples. Of note, at the highest equivalence ratio, the regions with the highest signal for the A2 and the high-aromatic fuel, compared with HEFA fuel, are shifted further downstream.

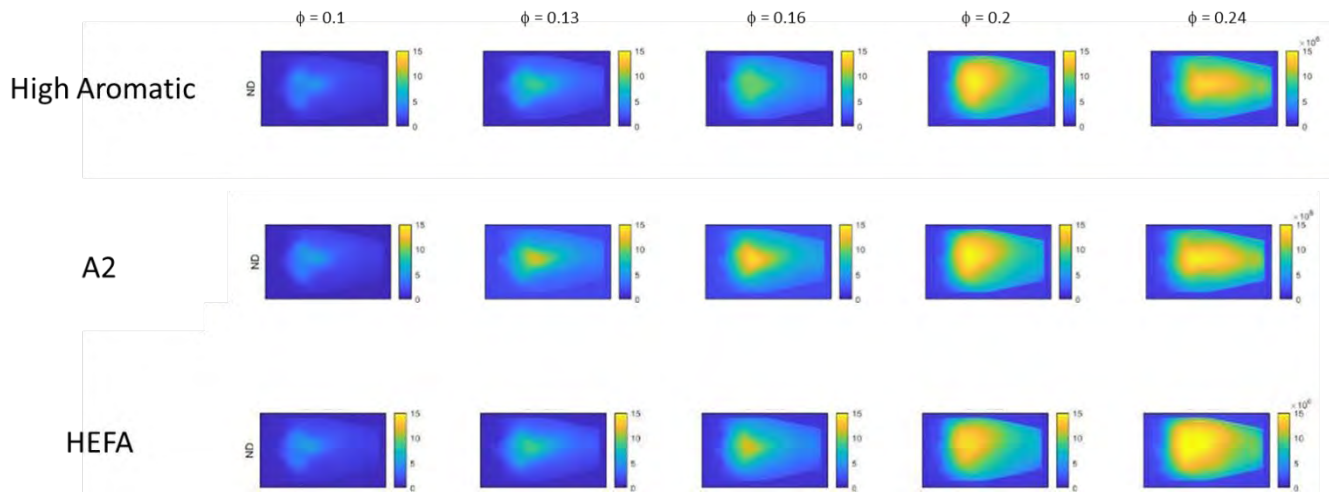


Figure 5. IR camera measurements for using a neutral-density filter. Measurements were taken at $T_{air} = 250$ °F, $T_{fuel} = 120$ °F, $P_{cmb} = 30$ psia, and $\Delta P = 3\%$.

The initial experiments showed that the radiometer signal was sensitive to the equivalence ratio, pressure, and fuel type. Moreover, the trends from the wall thermocouples and the IR visualization supported the trends observed in the radiometer data.

Improvements to the combustor hardware and instrumentation

More valuable data can be gained in upcoming experiments by improvements in the instrumentation. Over the course of the past year, a major upgrade of the test cell has required a shutdown of experiments in the laboratory for more than half the year. During this construction time, we have upgraded instrumentation and combustor hardware in preparation for upcoming experiments.

Building on the lessons learned from the previous experiments, we developed an alternative robust configuration for the inner combustor window using round port windows installed in a metallic side panel. Initial experiments used a round side window. With this configuration, we were able to measure IR radiation by using spectral filters in combination with the IR camera in proof-of-concept experiments. This window design was extended to more port windows for future experiments, as shown in Figure 6.



(a)



(b)

Figure 6. Improved window design for IR visualization. (a) Proof-of concept-IR window. (b) Completed multiple IR port design window.



To gain a more comprehensive picture of the radiation in the combustor, more radiometer locations are needed. For the next series of tests, we have manufactured a side panel, which allows the installation of three radiometers along the length of the combustor, to obtain a more comprehensive picture of the incident radiation. The hardware is shown in Figure 7.

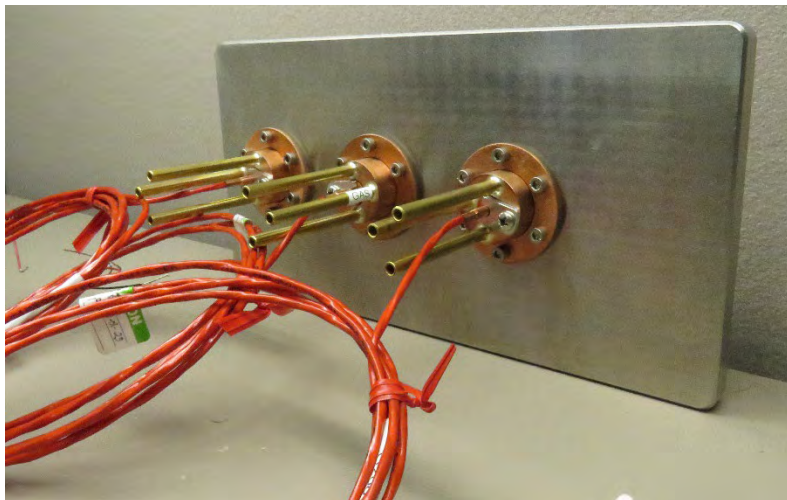


Figure 7. Updated side panel with multiple radiometers.

Publications

None.

Outreach Efforts

None.

Awards

None.

Student Involvement

None.

Plans for Next Period

The plans for the next period are to use the updated hardware to enable IR visualization along with more radiometers. Simultaneously with these experiments, we will sample the combustor exhaust to determine the particulate matter number density and size distribution, to characterize the soot. The instrumentation that will be used for these experiments will include a scanning mobility particle sizer to measure soot size distributions and a condensation particle counter to measure the particle number density. In addition, initial efforts are underway to add exit temperature measurement capabilities for the combustor. This capability will allow us to compare radiative transfer with the measured temperature rise in the combustor. The additional data of soot properties along with temperature measurements will allow for a more comprehensive picture of the effects of the fuels on radiative loading.

This next phase of experiments will include additional fuels, such as synthetic aromatic kerosene fuels alone and blended with HEFA, as well as high-cycloparaffin fuels.



References

- Boehm, R., Lohmueller, S., Andac, G., Aicholtz, J., Williams, R., James, S., ... & Greene, M. (2013). Development of Combustion Rules and Tools for the Characterization of Alternative Fuels, Phase 2A. *Rept. AFRL-RQ-WP-TR-2013-0223*.
- Briones, A. M., Stouffer, S., Vogiatzis, K., & Rankin, B. A. (2017, January 9). Effects of liner cooling momentum on combustor performance. *55th AIAA Aerospace Sciences Meeting*. 55th AIAA Aerospace Sciences Meeting, Grapevine, Texas. <https://doi.org/10.2514/6.2017-0781>
- Clark, J. A. (1982). Fuel property effects on radiation intensities in a gas turbine combustor. *AIAA Journal*, 20(2), 274-281. <https://doi.org/10.2514/3.7908>
- Chin, J. S., & Lefebvre, A. H. (1990). Influence of fuel composition on flame radiation in gas turbine combustors. *Journal of Propulsion and Power*, 6(4), 497-503. <https://doi.org/10.2514/3.25462>
- Colborn, J., Heyne, J. S., Hendershott, T. H., Stouffer, S. D., Peiffer, E., & Corporan, E. (2020, January 6). Fuel and operating condition effects on lean blowout in a swirl-stabilized single-cup combustor. *AIAA Scitech 2020 Forum*. AIAA Scitech 2020 Forum, Orlando, FL. <https://doi.org/10.2514/6.2020-1883>
- Corporan, E., Edwards, J. T., Stouffer, S., DeWitt, M., West, Z., Klingshirn, C., & Bruening, C. (2017, January 9). Impacts of fuel properties on combustor performance, operability and emissions characteristics. *55th AIAA Aerospace Sciences Meeting*. 55th AIAA Aerospace Sciences Meeting, Grapevine, Texas. <https://doi.org/10.2514/6.2017-0380>
- Erdmann, T. J., Burrus, D. L., Briones, A. M., Stouffer, S. D., Rankin, B. A., & Caswell, A. W. (2017). Experimental and computational characterization of flow rates in a multiple-passage gas turbine combustor swirler. *Volume 4B: Combustion, Fuels and Emissions*, V04BT04A076. <https://doi.org/10.1115/GT2017-65252>
- Esclapez, L., Ma, P. C., Mayhew, E., Xu, R., Stouffer, S., Lee, T., Wang, H., & Ihme, M. (2017). Fuel effects on lean blow-out in a realistic gas turbine combustor. *Combustion and Flame*, 181, 82-99.
- Gleason, G. C. & Bahr, D. W. (1980). *Fuel property effects on Life Characteristics of Aircraft Turbine Engine Combustors* (Report No. 80-GT-55).
- Hendershott, T. H., Stouffer, S., Monfort, J. R., Diemer, J., Busby, K., Corporan, E., Wrzesinski, P., & Caswell, A. W. (2018, January 8). Ignition of conventional and alternative fuel at low temperatures in a single-cup swirl-stabilized combustor. *2018 AIAA Aerospace Sciences Meeting*. 2018 AIAA Aerospace Sciences Meeting, Kissimmee, Florida. <https://doi.org/10.2514/6.2018-1422>
- Lefebvre, A. H. (1999). *Gas Turbine Combustion*. 2nd Edition, Taylor and Francis, Philadelphia.
- Mayhew, E., Mitsingas, C. M., McGann, B., Hendershott, T., Stouffer, S., Wrzesinski, P., Caswell, A. W., & Lee, T. (2017, January 9). Spray characteristics and flame structure of jet and alternative jet fuels. *55th AIAA Aerospace Sciences Meeting*. 55th AIAA Aerospace Sciences Meeting, Grapevine, Texas. <https://doi.org/10.2514/6.2017-0148>
- Monfort, J. R., Stouffer, S., Hendershott, T., Wrzesinski, P., Foley, W., & Rein, K. D. (2017, January 9). Evaluating combustion instability in a swirl-stabilized combustor using simultaneous pressure, temperature, and chemiluminescence measurements at high repetition rates. *55th AIAA Aerospace Sciences Meeting*. 55th AIAA Aerospace Sciences Meeting, Grapevine, Texas. <https://doi.org/10.2514/6.2017-1101>
- Naegeli, D. W. & Moses, C. A. (1980). *Effects of Fuel Properties on Soot Formation in Gas Turbine Engines* (Report No. 80-GT-62).
- Rankin, B. A., Blunck, D. L., Katta, V. R., Stouffer, S. D., & Gore, J. P. (2012). Experimental and computational infrared imaging of bluff body stabilized laminar diffusion flames. *Combustion and Flame*, 159(9), 2841-2843. <https://doi.org/10.1016/j.combustflame.2012.03.022>
- Stouffer, S. D., Hendershott, T. H., Colborn, J., Monfort, J. R., Corporan, E., Wrzesinski, P., & Caswell, A. (2020, January 6). Fuel effects on altitude relight performance of a swirl cup combustor. *AIAA Scitech 2020 Forum*. AIAA Scitech 2020 Forum, Orlando, FL. <https://doi.org/10.2514/6.2020-1882>
- Stouffer, S., Hendershott, T., Monfort, J. R., Diemer, J., Corporan, E., Wrzesinski, P., & Caswell, A. W. (2017, January 9). Lean blowout and ignition characteristics of conventional and surrogate fuels measured in a swirl stabilized combustor. *55th AIAA Aerospace Sciences Meeting*. 55th AIAA Aerospace Sciences Meeting, Grapevine, Texas. <https://doi.org/10.2514/6.2017-1954>
- Stouffer, S.D., Hendershott, T.H., Boehm, R., Lovett, J. (2021). Chapter 4: The Referee Rig Combustor. Fuel effects of operability of gas turbine combustors. *Progress in Astronautics and Aeronautics*. AIAA 2021 <https://doi.org/wrs.idm.oclc.org/10.2514/5.9781624106040.0115.0142>



Project 074 Low Emissions Premixed Combustion Technology for Supersonic Civil Transport

Georgia Institute of Technology

Project Lead Investigator

Adam Steinberg
 Professor
 School of Aerospace Engineering
 Georgia Institute of Technology
 Phone: (404) 897-1130
 E-mail: adam.steinberg@gatech.edu

University Participants

Georgia Institute of Technology

- P.I.: Adam Steinberg, Professor, School of Aerospace Engineering
- FAA Award Number: 13-C-AJFE-GIT-142
- Period of Performance: August 11, 2020 to September 30, 2024
 Period of Performance Covered in Report: October 1, 2022 to September 30, 2023
- Tasks:
 1. Analysis of lean blow out from campaigns 1 and 2, and preparation for campaign 3
 2. Computational simulations of combustor
 3. Analysis of thermoacoustic dynamics

Project Funding Level

FAA provided \$3,102,994 in funding. Cost-sharing is provided by Georgia Institute of Technology (\$1,544,950) and GE Research (\$1,558,044).

Investigation Team

Name	Affiliation	Role	Tasks
Adam Steinberg Professor	Georgia Institute of Technology	P.I.	Management, reporting, technical oversight of all tasks, oversight of optical diagnostics in Task 1
Ellen Mazumdar Assistant professor	Georgia Institute of Technology	Co-P.I.	Oversight of OH PLIF measurements in Task 1
Joseph Oefelein Professor	Georgia Institute of Technology	Co-P.I.	Oversight of first-principles LES in Task 2 and overall coordination of Task 2
Jerry Seitzman Professor	Georgia Institute of Technology	Co-P.I.	Oversight of gas phase fuel/air mixing diagnostics in Task 1
Michael Benjamin Consulting engineer	GE Aviation	Co-P.I.	Oversight of combustor design in Task 1, coordination of GT/GE LES collaboration in Task 2



Krishna Venkatesan Principal engineer	GE Research	Co-P.I.	Oversight of combustor operation in Task 1 and data collection for Task 3
Oleksandr Bibik Senior research scientist	Georgia Institute of Technology	Participant	Task 1
Hannah Bower Research engineer	GE Research	Participant	Task 1
Fei Han Engineering manager	GE Research	Participant	Task 3
John Hong Lead engineer	GE Research	Participant	Task 1
Nick Magina	GE Research	Participant	Task 3
Victor Salazar Lead engineer	GE Research	Participant	Task 1
R. Narasimha Chiranthan	GE Aviation	Participant	Task 2
Manampathy Giridharan	GE Aviation	Participant	Task 2
Hiranya Nath	GE Aviation	Participant	Task 2
Sriram Kalathoor Graduate research assistant	Georgia Institute of Technology	Graduate student	Task 2
Arihant Jain	Georgia Institute of Technology	Graduate student	Task 1
Ijeoma Obi	Georgia Institute of Technology	Graduate student	Task 1
Mitchell Passarelli Graduate research assistant	Georgia Institute of Technology	Graduate student	Task 1
Sundar Ram Manikandan Graduate research assistant	Georgia Institute of Technology	Graduate student	Task 1
Samuel Wonfor Graduate research assistant	Georgia Institute of Technology	Graduate student	Task 1
Andrew Zheng Graduate research assistant	Georgia Institute of Technology	Graduate student	Task 1
Neilay Amin Research assistant	Georgia Institute of Technology	Undergraduate student	Task 2
Preethi Mysore Research assistant	Georgia Institute of Technology	Undergraduate student	Task 2
Coleman Pethel Research assistant	Georgia Institute of Technology	Undergraduate student	Task 1
Katrina Potak Research assistant	Georgia Institute of Technology	Undergraduate student	Task 2



Mihir Rao Research assistant	Georgia Institute of Technology	Undergraduate student	Task 1
Andrew Semelka Research assistant	Georgia Institute of Technology	Undergraduate student	Task 1
Rachel Wilder Research assistant	Georgia Institute of Technology	Undergraduate student	Task 2

Project Overview

Market demand for high-speed transport is expected to drive a rapid re-emergence of commercial supersonic transport (CST) aircraft over the coming decades. This impending CST revival and the increasingly harmful impacts of anthropogenic climate change mandate advancements in CST-focused environmentally compatible technologies and policies. Compared with subsonic aircraft, engines for CST aircraft will (a) operate at significantly lower overall pressure ratio (OPR) and bypass ratio (BR); (b) experience higher combustor inflow temperatures (T_3), lower pressures (p_3), and higher fuel/air ratios (FAR) at cruise; and (c) cruise at higher altitudes. The reduced OPR and BR result in increased thrust-specific fuel consumption, thus increasing fuel burn and making it fundamentally more challenging to reduce emissions. Furthermore, the combination of low OPR and high cruise T_3 and FAR result in complicated trade-offs between nitrogen oxides (NO_x) at cruise and other emissions (CO, nonvolatile particulate matter (nvPM) and unburnt hydrocarbons (UHC) at lower power.

Several recent studies have assessed potential CST fleet emissions and environmental impact based on currently deployed rich burn-quench-lean burn combustors (typically Tech Insertion combustors) designed for subsonic transports (Kharina et al., 2018; Berton et al., 2020; Hassan et al., 2020; Speth et al., 2021). These studies demonstrate that innovations in combustor architecture will be required to meet emissions and efficiency targets, helping enable an environmentally compatible CST market. Despite the high T_3 and FAR, peak flame temperatures must be moderated to meet NO_x targets, while also maintaining efficiency and achieving low CO, UHC, and nvPM. This will require increased fuel-lean premixing before combustion.

Lean premixed prevaporized (LPP) combustors are a promising path to lowering emissions from future CST engines. In LPP, fuel is injected, partially prevaporized and partially premixed with air before the reactants enter the combustor. While the concept of LPP is not new (see, for example, Niedzwiecki, 1992), achieving good vaporization and mixing in a flight-appropriate package previously has been challenging. However, these issues can potentially be alleviated by the high T_3 in CST combustors (which results in faster vaporization) and advanced manufacturing to enable compact rapid-mixing flow elements.

However, the ability of current design methodologies to predict the operability and emissions of LPP combustors under relevant conditions is unproven. Hence, there is a critical need to generate high-quality experimental data at CST combustor conditions, coupled with the development/validation of computational fluid dynamics (CFD) simulations and reduced-order thermoacoustic models. This project addresses this need through a combination of experiments, large eddy simulations (LES), and thermoacoustic modeling, all applied in a novel LPP combustor of interest to future CST applications. This report focuses on analysis of lean blowoff (LBO) and thermoacoustic dynamics, the majority of which was performed by PhD candidate Mitchell Passarelli.

Task 1- Analysis of Lean Blowoff from Campaigns 1 and 2, and Preparation for Campaign 3

Georgia Institute of Technology

Objective

Overcoming the potential of LBO represents a significant challenge in LPP combustors. In this activity, we analyzed the conditions leading to LBO and explained the underlying processes. This task also included training of students and preparation for experimental campaign 3.

Research Approach

This effort over the reporting period consisted of three main activities:

- 1) Analysis of LBO conditions and physics in the LPP combustor
- 2) Phase Doppler particle analysis (PDPA) to characterize liquid fuel at combustor dome
- 3) Experimental training and preparation on laser diagnostics for campaign 3

LBO analysis: Theoretical background

Details of the experimental configuration, measurements, and basic signal inversion from campaigns 1 and 2 were provided in previous reports; these are not repeated here for brevity. Instead, we focus on extraction of physically meaningful results from the experimental data, particularly pertaining to LBO.

Much of the existing literature for bluff-body stabilized flames uses Damköhler (Da) versus Reynolds (Re) number correlations Shanbhogue et al. (2009). For the purpose of comparing the data from this experiment to previously reported data, an effort was made to use similar quantities and calculation. The Damköhler number is the ratio of flow to chemical timescales, τ_{flow} and τ_{chem} , respectively:

$$Da = \frac{\tau_{\text{flow}}}{\tau_{\text{chem}}} \quad (1)$$

Following Shanbhogue et al. (2009), τ_{chem} was computed from the unstretched laminar flame thickness, δ_f^0 , and speed, S_L^0 :

$$\tau_{\text{chem}} = \frac{\delta_f^0}{S_L^0} \quad (2)$$

with

$$\delta_f^0 = \frac{T_{\text{prod}} - T_3}{\max dT/dx} \quad (3)$$

where T_{prod} is the temperature of the products behind the flame and T_3 is the temperature of the reactants. The temperature profile across the flame and S_L^0 were computed via numerical simulation for each of the experimental conditions in campaign 1. The derivative of the temperature profile was approximated via forward differencing from the simulation results.

Again, following Shanbhogue et al. (2009), τ_{flow} was calculated from an empirical correlation for the laminar boundary layer momentum thickness, θ , and the speed of the reactants at the exit plane of one of the mains, v_{main} :

$$\tau_{\text{flow}} = \frac{\theta}{v_{\text{main}}} \quad (4)$$

with

$$\theta = \frac{35d_{\text{bb}}}{\sqrt{Re}} \quad (5)$$

where d_{bb} is the diameter of the bluff-body and



$$\text{Re} = \frac{\rho_3 v_{\text{main}} d_{\text{bb}}}{\mu_3} \quad (6)$$

The reactant (mixture) density, ρ_3 , is computed from the ideal gas law, assuming completely vaporized fuel and perfect mixing of fuel and air at the measured FAR, T_3 , and p_3 . The mixed reactants of Jet A (fuel) and air are treated as a binary mixture, with molecular weights $W_f = 158.6$ kg/kmol and $W_{\text{air}} = 28.96$ kg/kmol, respectively. The reactant mixture dynamic viscosity, μ_3 , was obtained from the same numerical simulations as δ_f^0 and S_L^0 .

To compute v_{main} , the mass flow around the annulus of the mains was assumed to be uniform and equally distributed across all four mains, and the speed was calculated from the continuity equation in 1D:

$$v_{\text{main}} = \frac{\dot{m}_{\text{main}}}{\rho_3 A} \quad (7)$$

where \dot{m}_{main} is the total mass flow rate through a single main injector and A is the area of the annulus with outer diameter d_o , such that $A = \frac{\pi}{4}(d_o^2 - d_{\text{bb}}^2)$ and

$$\dot{m}_{\text{main}} = \frac{1}{4} \left[(\text{FAR} + 1) \dot{m}_{\text{air}} - \dot{m}_{f,p} - \frac{\dot{m}_{f,p}}{\text{FAR}_p} \right] \quad (8)$$

Here, \dot{m}_{air} is the total air mass flow rate through the mixer, $\dot{m}_{f,p}$ is the fuel mass flow rate through the pilot, FAR_p is the fuel-air ratio of the pilot assuming the stoichiometric fuel-air ratio of Jet A is $\text{FAR}_{\text{st}} = 0.068$. \dot{m}_{air} , $\dot{m}_{f,p}$, FAR, and FAR_p were all measured during data acquisition.

The v_{main} calculation was validated with the mean stereoscopic particle image velocimetry (SPIV) results from campaign 2. Campaign 1 data were used to compute the mean main-pilot air mass flow rate split and that was applied to campaign 2 data along with Eqs. (7) and (8) to obtain v_{main} . At nonreacting and unforced conditions from campaign 2, Eq. (7) gives $v_{\text{main}} \approx 65.3 \pm 0.4$ m/s, which is very close to the SPIV results of ~ 65 m/s near the dome face.

Numerical simulations to obtain μ_3 , δ_f^0 , and S_L^0 were performed in CHEMKIN using the laminar flame speed reactor model and the HyChem reaction mechanism. The HyChem mechanism uses formulation POSF 10325 for Jet A fuel and assumes air is composed of only 79% nitrogen and 21% oxygen. Parameter sweeps of p_3 , T_3 , and equivalence ratio (ϕ) included all conditions recorded during campaign 1. Figure 1 plots the computed values of μ_3 from CHEMKIN against T_3 for all test conditions in campaign 1. The vertical spread is due to varying FAR, such that increasing FAR causes a minor decrease in μ_3 for the same T_3 . Note that the trend is linear, such that $\mu_3 \propto T_3$ over the range of parameters examined.

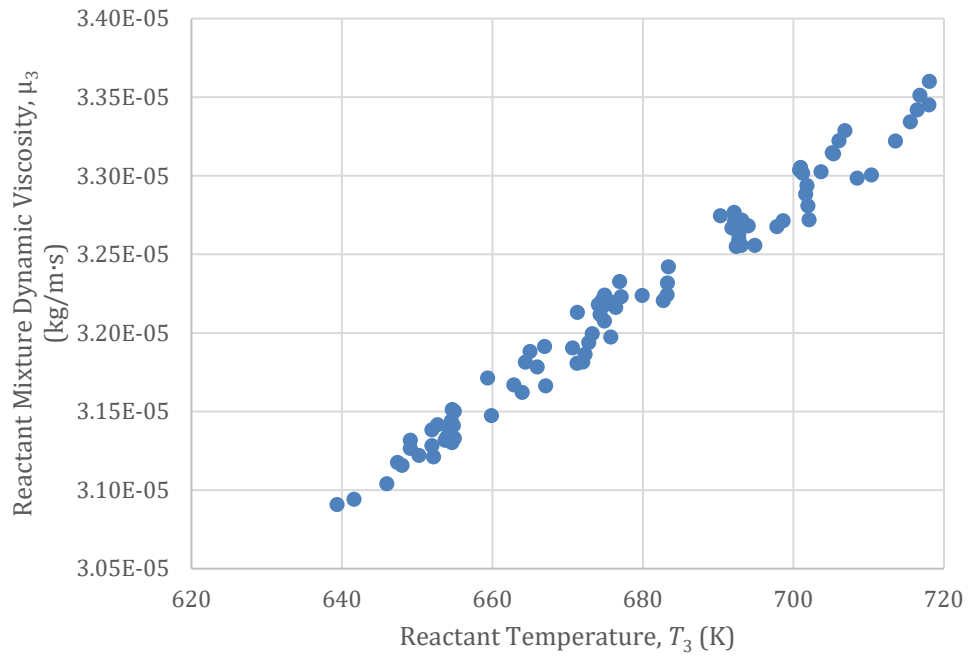


Figure 1. Simulated reactant dynamic viscosity versus temperature from campaign 1.

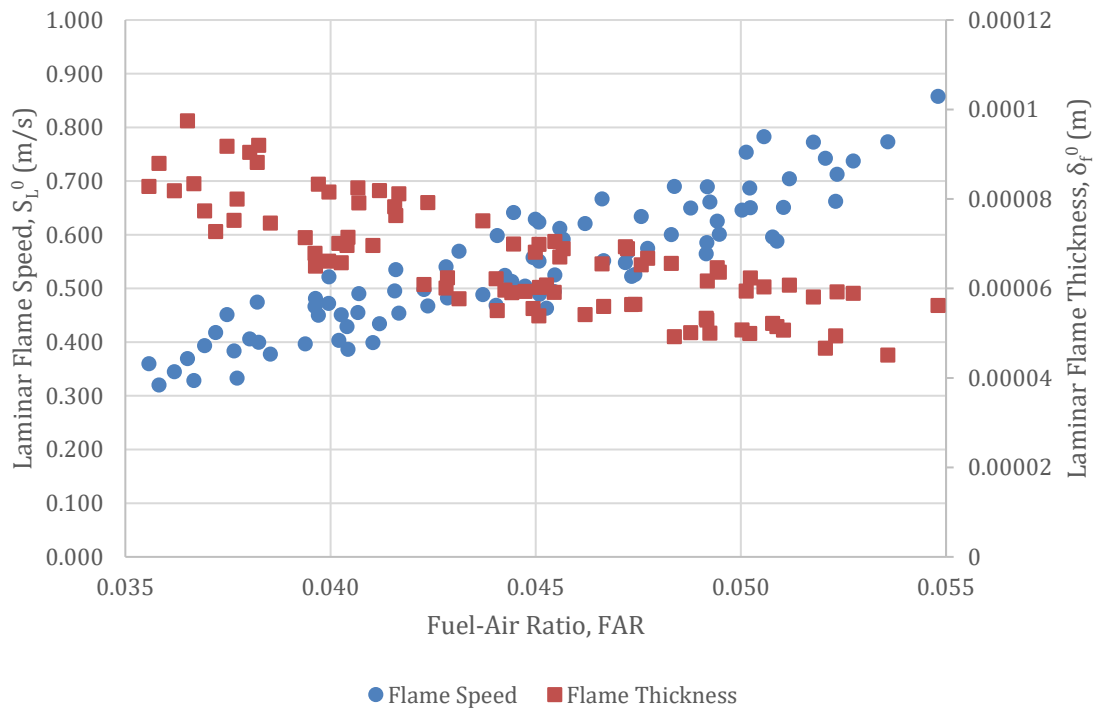


Figure 2. Simulated laminar flame speed and thickness versus fuel-air ratio.



Figure 2 presents the trends in S_L^0 and δ_f^0 as FAR varies for all test points (TP) in campaign 1. The two distinct trendlines in δ_f^0 are for low and high p_3 , with variations in T_3 having minimal effect for a given FAR and p_3 . The trend for S_L^0 shows that while T_3 has a larger impact on S_L^0 than on δ_f^0 , the impact of p_3 is lesser. The resulting trend in τ_{chem} is roughly linear such that $\tau_{chem} \propto -FAR$, with variations in both p_3 and T_3 having a minor effect over the range of conditions studied in campaign 1.

Applying standard uncertainty propagation formulas yields

$$\frac{\Delta Da}{Da} = \sqrt{\left(\frac{\Delta \delta_f^0}{\delta_f^0}\right)^2 + \left(\frac{\Delta S_L^0}{S_L^0}\right)^2 + \left(\frac{\Delta P_3}{P_3}\right)^2 + \left(\frac{\Delta T_3}{T_3}\right)^2 + \frac{1}{4} \left(\frac{\Delta \mu_3}{\mu_3}\right)^2 + 4 \left(\frac{\Delta d_{bb}}{d_{bb}}\right)^2 + \left(\frac{\Delta Re}{Re}\right)^2 + \left(\frac{W_f - W_{air}}{W_f + W_{air} FAR} \frac{\Delta FAR}{FAR}\right)^2} \quad (9)$$

$$\frac{\Delta Re}{Re} = \sqrt{\left(\frac{\Delta \dot{m}_{main}}{\dot{m}_{main}}\right)^2 + \left(\frac{\Delta \mu_3}{\mu_3}\right)^2 + \left(\frac{d_o^2 + d_{bb}^2}{d_o^2 - d_{bb}^2} \frac{\Delta d_{bb}}{d_{bb}}\right)^2 + 4 \left(\frac{d_o^2}{d_o^2 - d_{bb}^2} \frac{\Delta d_o}{d_o}\right)^2} \quad (10)$$

$$\Delta \dot{m}_{main} = \frac{1}{4} \sqrt{(\dot{m}_{air} \Delta FAR)^2 + [(FAR + 1) \Delta \dot{m}_{air}]^2 + \left(\frac{FAR_p + 1}{FAR_p} \Delta \dot{m}_{f,p}\right)^2 + \left(\frac{\dot{m}_{f,p}}{FAR_p^2} \Delta FAR_p\right)^2} \quad (11)$$

where $\Delta(\cdot)$ represents the uncertainty of a quantity.

Given the results in Figure 1, applying uncertainty propagation suggests $\Delta \mu_3 / \mu_3 \propto \Delta T_3 / T_3$. Indeed, based on the formula for pure species viscosity in CHEMKIN (Ansys, 2020), uncertainty propagation indicates that $\Delta \mu_3 / \mu_3 \approx \Delta T_3 / 2T_3$ to first order.

Assuming a worst-case relative uncertainty of 2% for simulated quantities (δ_f^0 and S_L^0) and using statistical uncertainties for all measured parameters (p_3 , T_3 , FAR, FAR_p , \dot{m}_{air} , and $\dot{m}_{f,p}$) gives $\Delta Da / Da \approx \pm 3\%$ and $\Delta Re / Re \approx \pm 0.6\%$, on average, across the entirety of campaign 1. The worst-case uncertainty of 2% for δ_f^0 and S_L^0 is a very conservative estimate given the results in Figure 2. Specifically, propagating <1% relative uncertainty in either p_3 or T_3 should yield <1% relative uncertainty in τ_{chem} . This estimate does not account for systematic errors that could stem from differences in the formulation of POSF 10325 in the CHEMKIN model and the actual samples of Jet A used in the experiments. The error bars for these quantities are included in the figures shown later in this report. However, those figures indicate that the uncertainty is negligible and thus does not require more rigorous modeling and quantification.

LBO limits in LPP combustor: LBO detection

The OH* chemiluminescence (CL) and fuel planar laser-induced fluorescence (PLIF) from campaign 1 were used to distinguish between attached and blown-off states. Figure 3 shows the temporally averaged OH* CL and fuel PLIF fields from the same day across different values of FAR. For the fuel PLIF, blowoff was identified by the presence of any amount of PLIF signal directly behind the bluff-body, as in Figure 3b-c. Figure 3a shows a clear example of an attached flame, which is visually distinct from a blown-off flame. The main drawback to using PLIF for blowoff detection is that it only works for the mains along the laser sheet. Given the multi-element design of this combustor, it is possible for only one of the mains to blow off while the others remain attached.

The OH* CL is less robust for detecting blowoff, primarily due to the very short recording duration (~0.75 s vs. 100 s for the fuel PLIF). Figure 3c shows a case where one of the mains blew off after the all OH* CL images were acquired. As such, the OH* CL field shows a fully attached flame, whereas the fuel PLIF indicates blowoff. In cases such as Figure 3c, when the blowoff is intermittent, the OH* CL's short recording time makes it unreliable to identify whether the flame is primarily attached or blown off. A second issue arises from the fact that CL is line-of-sight integrated, meaning that if only one main blows off along the line-of-sight, it may not be reflected in the mean field correctly. Figure 3b is an example of a data set where both mains in line blew off, whereas both Figure 3a (confirmed during acquisition) and Figure 3c are examples of fully attached flames. Comparing Figure 3a and Figure 3c shows that the local OH* CL intensity is not necessarily

dependent on the flame attachment state. Overall, OH* CL is an unreliable indicator of blowoff in this configuration, but it can provide additional information when paired with the corresponding fuel PLIF data.

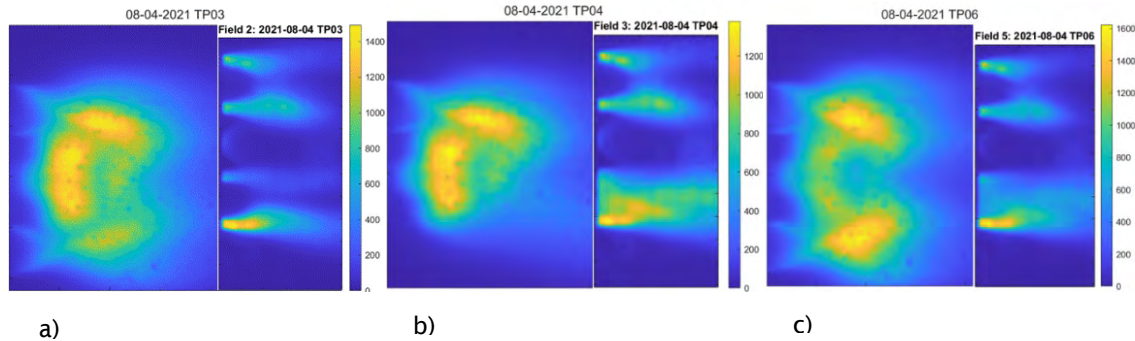


Figure 3. Temporal mean OH* chemiluminescence and fuel planar laser-induced fluorescence (insets) fields for select conditions. (a) $Da = 0.11$, attached; (b) $Da = 0.10$ blown off; (c) $Da = 0.13$, blown off. Da , Damköhler number.

Pressure and temperature effects on blowoff

Figure 4 collects the blowoff results for data points recorded in campaign 1. The data sets from one run date were excluded due to possible improper rig operation. As described in “LBO limits in LPP combustor: LBO detection”, a test point was considered blown off if any fuel PLIF signal was detected behind the bluff-body of a single main. The point in the red circle in Figure 4 marks an outlier, as it has an abnormally high Da_{LBO} .

Figure 5 plots only the conditions that exhibited blowoff and colors the dots by the range of T_3 . Due to the nature of the experiment operations and procedures, it was not possible to vary only one of P_3 , T_3 , or FAR at a time. In nearly all cases, all three parameters varied between TPs. As shown in Figures 4 and 5, this obfuscates the relationships between P_3 or T_3 and Da_{LBO} . From Shanbhogue et al. (2009), we would expect higher T_3 to increase reaction rates, decreasing τ_{chem} and thus Da_{LBO} . From Figure 5, however, there appears to be no relationship between T_3 and Da_{LBO} . These figures demonstrate how Da versus Re correlations capture the effects of P_3 , T_3 , and FAR simultaneously and more clearly. In addition, Da correlations capture several other physical aspects of the blowoff process, as detailed by Shanbhogue et al. (2009).

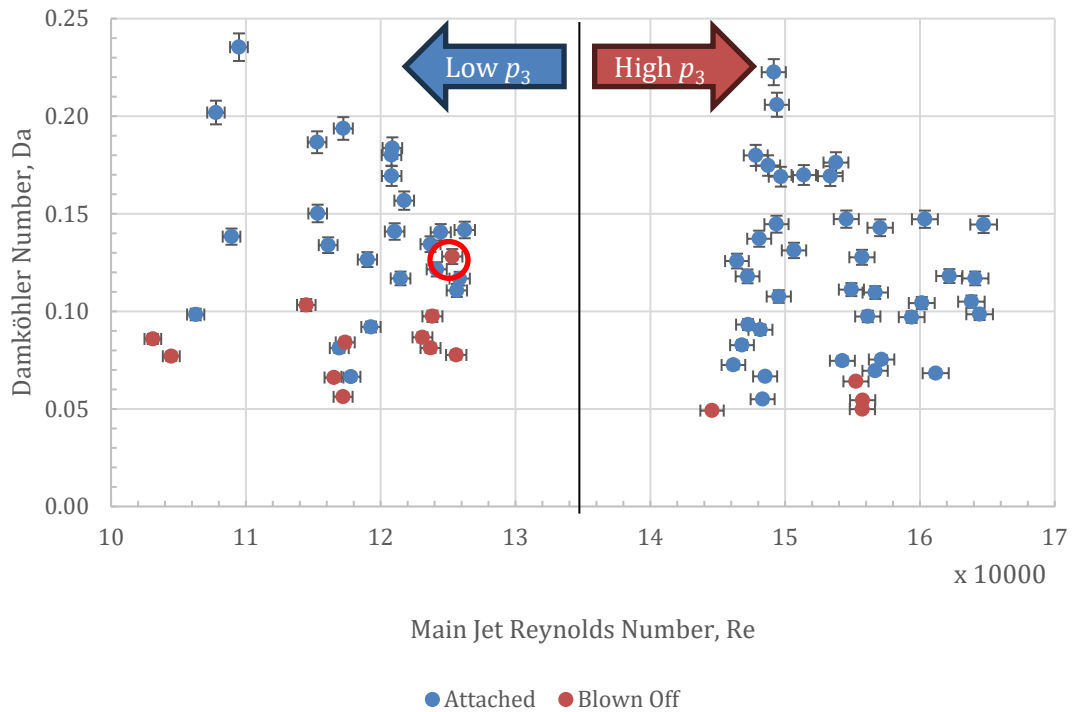


Figure 4. Damköhler (Da) versus Reynolds (Re) numbers for all test points in campaign 1. Arrows denote clusters of data corresponding to low and high P_3 as indicated. The aberrant blowoff case is circled in red.

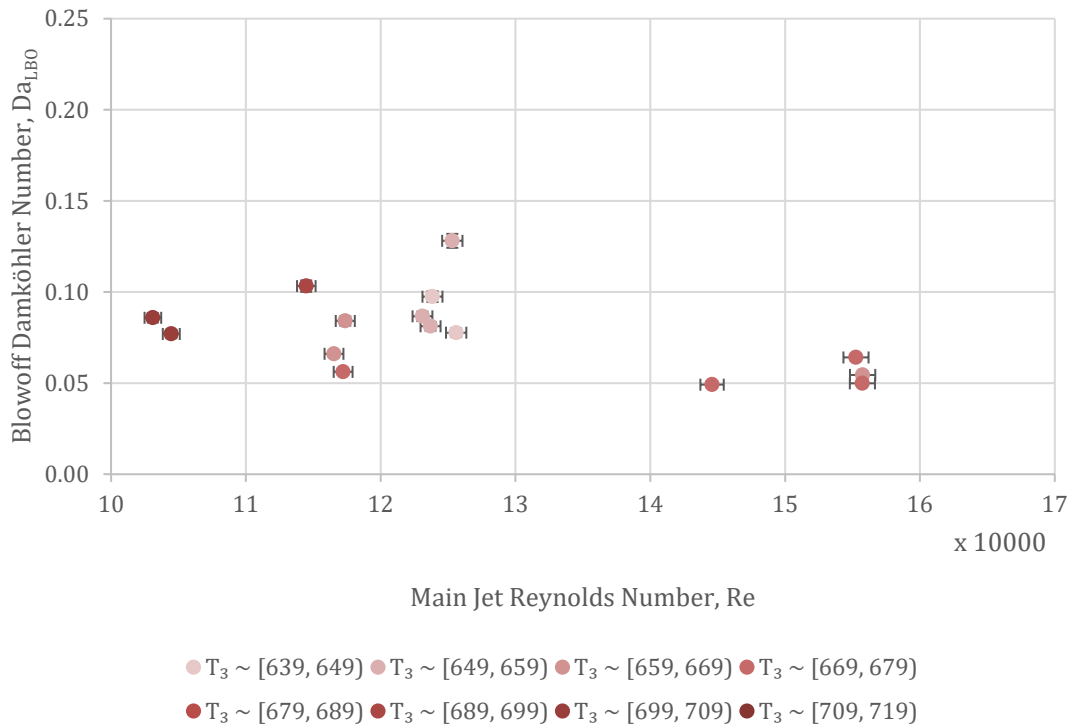


Figure 5. Blowoff Damköhler (Da) versus Reynolds (Re) numbers for varying temperature. Color of markers denotes T_3 range as indicated in the legend.

The limited range of Re spanned by the data makes it unsuitable for computing Da correlations directly. As such, these results were compared with those previously reported in the literature. Figure 6 overlays the new data points on top of those compiled by Shanbhogue et al. (2009) for 2-dimensional (2D) and axisymmetric 3-dimensional (3D) bluff-bodies. The computation of Re and Da uses the same relations used by Shanbhogue et al. (2009) to ensure compatibility of the plots.

From Figure 6, it is clear that the campaign 1 results do not follow the expected correlation for axisymmetric bluff-bodies. Overall, the data from campaign 1 are grouped toward the lower limit of the other data in Figure 6 (left) and appear to follow a trend with a steeper slope. This discrepancy is expected, because the data reported by Shanbhogue et al. (2009) are collected from studies of single-element combustors operating at nearly atmospheric pressure and temperature. It remains to identify the factors that contribute to this discrepancy as follows. Given the nature of this LPP combustor, particular attention is paid to the effects of CST-relevant P_3 and T_3 , along with the interactions of the various main and pilot flames and flows.

For the conditions analyzed in this combustor, changing P_3 does not have a quantifiable effect on Da_{LBO} and therefore will be excluded from the remaining discussion. The observed independence of Da_{LBO} from T_3 (Figure 5) matches behavior noted by both Shanbhogue et al. (2009) and Tuttle (2010). Tuttle's (2010) work specifically explores the effects of variations in T_3 for premixed flames, finding that T_3 has a stabilizing effect, but only with respect to the blowoff ϕ at a given Re . Tuttle notes that varying T_3 yields an approximately constant value for Da_{LBO} , which roughly agrees with the results in Figure 5. Cavaliere et al. (2013) corroborate this finding in the context of the degree of prevaporization and premixing. Their experiments show that fully premixed, non-premixed and liquid spray flames blow off at similar Da and Re . For an LPP combustor, T_3 controls the amount of prevaporization of the liquid fuel and thus influences the amount of premixing of the fuel and air. Together, the works of Tuttle (2010) and Cavaliere et al. (2013) demonstrate that T_3 has minimal impact on Da_{LBO} and thus cannot explain the discrepancies in Figure 6 (left). As such, we concluded that the discrepancies in Figure 6 (left) must be due to the combustor configuration and flow field rather than (global) inlet conditions.

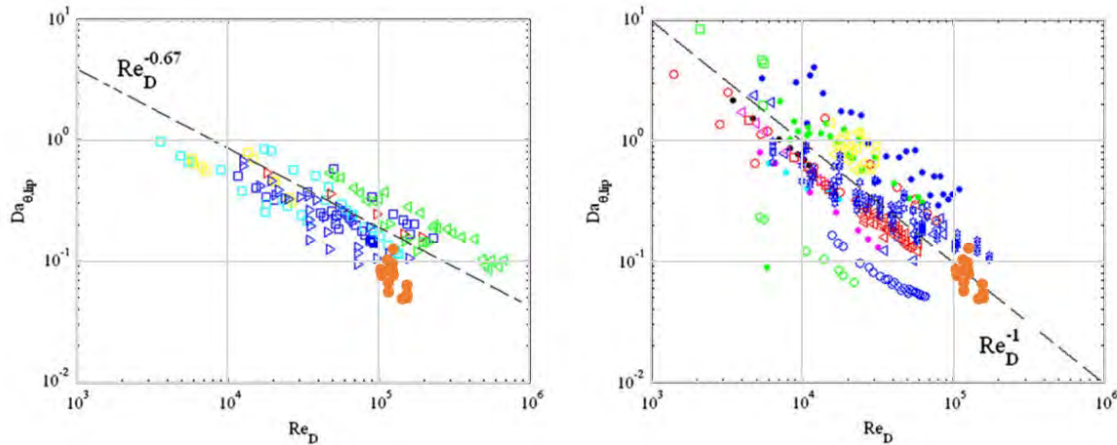


Figure 6. Damköhler (Da) versus Reynolds (Re) numbers for axisymmetric (left) and 2-dimensional (right) bluff-bodies. Solid orange dots are data from campaign 1; other data are from Shanbhogue et al. (2009)

The reviews of Shanbhogue et al. (2009) and Tuttle (2010) reveal several other relevant factors that could explain the trends in Figure 6. The effects of spatial variations in ϕ , due to both stratification and partial premixing, dynamic coupling, and flow symmetry are particularly relevant. As discussed above, Cavaliere et al. (2013) show that, although less-premixed flames tend to blow off at leaner ϕ , there is minimal effect on Da_{LBO} . Therefore, local instantaneous variations in ϕ are not a major contributor to blowoff.

There is some degree of ϕ stratification (i.e., asymmetric fuel profiles) across the mains. Specifically, the top branch of the bottom main always tends to have less fuel than the bottom branch. Given that single combustor elements have some stratification and $\phi_p \neq \phi$, there is also stratification across the combustor itself in the regions where the fluid streams from the mains and pilot mix. Tuttle (2020) demonstrates, however, that stratification reduces flame stability, causing blowoff at higher ϕ than for uniform fueling. Since this would result in a higher Da_{LBO} , it does not explain why the campaign 1 data blow off at lower Da than expected for axisymmetric bluff-bodies.

A similar argument applies to the effects of acoustic coupling, except for the outlier case circled in Figure 4. As Tuttle (2010) explains, for fuel stratified flows, the thermoacoustic dynamics can lead to blowoff at higher Da values than expected. Tuttle (2010) also demonstrates that stratified ϕ flows are more prone to acoustic coupling at lower Re. In such cases, the power spectrum of OH* CL should exhibit strong peaks at frequencies related to hydrodynamic modes of wakes, such as the Bénard-von Kármán instability. Reviewing the unforced dynamics indicates that the power spectra of blown-off data sets do not differ substantially from those of attached data sets or other blown-off data. Furthermore, acoustic coupling has a destabilizing effect on blowoff and thus cannot explain why the data from campaign 1 in Figure 6 (left) are at lower Da_{LBO} than the other data points. This indicates that, nominally, the blowoff observed in the reported data sets is not due to acoustic or hydrodynamic coupling.

The interactions between individual flames are also important. The wide cone of the pilot flame intersects with the main flames. The pilot-main mixing zones would be heated by the pilot's combustion products. Based on Shanbhogue et al. (2009), Tuttle (2010) and the preceding discussion, it is reasonable to expect that the local increase in T_3 would have minimal effect on Da_{LBO} . However, the temperature of the pilot products is far enough outside the range investigated by Tuttle (2010) for other factors to become important. For example, the pilot could serve as an ignition source for the mains, which should help to maintain flame attachment at conditions where blowoff would occur normally. In addition, in campaign 1, the pilot operated at fuel-rich ϕ , while the mains operated at fuel-lean ϕ . This means the hot combustion products from the pilot contained some excess fuel that could mix with the oxidizer-rich fluid from the mains and combust. The instantaneous OH* CL images do not provide any insight into this hypothesis. Future work should endeavor to quantify the stabilizing effect of the pilot flame.

For conditions where blowoff would occur without the pilot flame, or even conditions approaching LBO, the strain experienced by the flame causes local extinction, leading to holes appearing in the flame sheet. The regions of local



extinction can be reignited by the hot gases from the pilot flame, which would allow the main flames to stay attached when subjected to strains that would normally lead to blowoff. The pilot flame works to suppress the formation of holes in the flame sheet. This delays the onset of the first stage of blowoff and, in turn, the onset of ultimate blowoff. As Shanbhogue et al. (2009) explain, Da correlations capture the physics associated with the first stage of blowoff and thus should capture the influence of the pilot flame.

Finally, we must consider the interactions between the mixer elements (mains and pilot) and their impact on blowoff. The mains also have a small counterclockwise swirling component to the velocity. Although not high enough to stabilize the flame or form other hydrodynamic phenomena, this swirl velocity is important to defining the symmetry of the main flames. Since the mains swirl in the same direction, the region between each of the mains is subjected to flows swirling counter to one another. This creates top-bottom—and logically left-right—asymmetries in the wakes behind each of the bluff-bodies. The pilot swirls clockwise, however, such that the tangential velocity of the pilot is aligned with each of the mains where the flows meet. This would yield regions of locally increased swirl velocity due to the higher swirl component in the pilot relative to the mains. In general, these regions of local shear disrupt the periodic symmetry of a single main's flow field. Based on the data in Shanbhogue et al. (2009), axisymmetric bluff-bodies have a different (Da , Re) correlation than nominally 2D bluff-bodies.

Blowoff is an example of a symmetry-breaking bifurcation with hysteresis. It has been observed in other symmetry-breaking bifurcations that when the system is biased against the axis of broken symmetry, the bifurcation can be delayed (Strogatz, 2015; Cross and Greenside, 2009). Relating this back to blowoff, flow features that are counter-aligned to those that appear after blowoff could delay the onset of blowoff. Therefore, it is possible that the discrepancies in Figure 6 (left) are due in part to the loss of flow symmetry and periodicity. The data collected and presented in this report are not capable of resolving such effects, and this is one area recommended for future work.

Overall, the data presented in this section indicate that the multi-element mixer design enhances the blowoff limits compared to single-element bluff-body stabilized flames. The mixing regions between the pilot and mains serve as a potential ignition source to stabilize flames beyond the normal blowoff limits. Additionally, these flame and flow interactions disrupt the natural flow symmetry, resulting in behavior that is unlike that previously reported for axisymmetric bluff-bodies. This conclusion is supported by the coincidence of the campaign 1 data with the correlation for nominally 2D bluff-bodies (Figure 6, right).

Investigation of aberrant blowoff behavior

The outlier identified in Figure 4 poses a particular issue with the operation of this LPP combustor. The possibility of blowoff at abnormally high Da reduces the reliability of operations. Thus, the outlier indicates a possible failure mode for the operation of this style of combustor. The following analysis aims to determine the root cause of this outlier to assess the potential failure mode. Potential causes include hysteresis and dynamical coupling; both are explored below.

This case of aberrant blowoff occurs at $Da = 0.13$, approximately 30% higher than the next highest case with blowoff ($Da = 0.10$), although the Re are different. In contrast with other blown-off data sets at similar Re , the aberrant case Da_{LBO} is 30% to 63% higher. Furthermore, there are other data sets recorded at similar Re , T_3 , and P_3 that did not experience blowoff. Closer examination of the operating conditions for the outlier case and others on the same date revealed that the TPs preceding the outlier were also blown off, but at leaner ϕ and lower Da (same T_3 and P_3). This suggests the blowoff in the outlier case is due to hysteresis.

If the aberrant blowoff is due to hysteresis, then there should be some intermittency in the instantaneous data. Indeed, inspection of the instantaneous fuel PLIF images reveals a switching intermittency. For roughly the first third of the data set, both mains are attached and the bottom main is blown off for the remainder of the images. Additionally, during the attached interval, there are instances where the bottom main blows off for 1-2 frames in sequence. The reverse is true during the blown-off interval: there are individual frames where the bottom main is attached. Figure 7 shows sample instantaneous fuel PLIF fields from the aberrant blowoff case. Figure 7 (left) is taken from the attached interval and shows that the bottom main flame is attached, whereas the other field is taken from the blown-off interval and shows that the flame is blown off. Both fields in Figure 7 are normalized by the maximum intensity in each field.

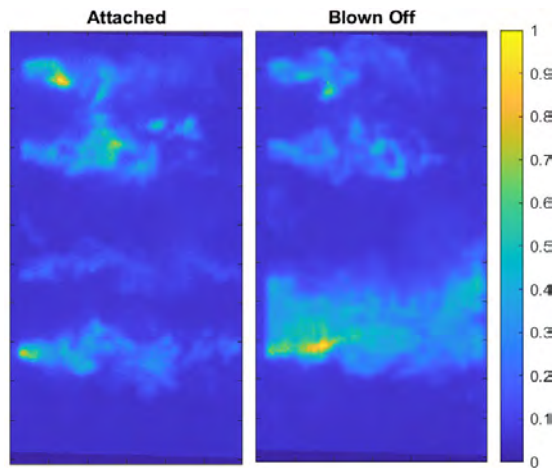


Figure 7. Sample instantaneous fuel planar laser-induced fluorescence fields from attached and blown-off intervals of aberrant blowoff case.

In contrast, in the TPs preceding the aberrant case (both at leaner ϕ), the bottom main is always blown off with no intermittent switching. The root-mean-squared (RMS) fluctuation fields in Figure 8 reflect the intermittency of the aberrant case. Comparing the other blown-off cases in Figure 8 ($\phi = 0.64, 0.61$) to the aberrant case ($\phi = 0.70$) shows significantly higher RMS fluctuations in the bottom main behind the wake in the aberrant case than for the other two.

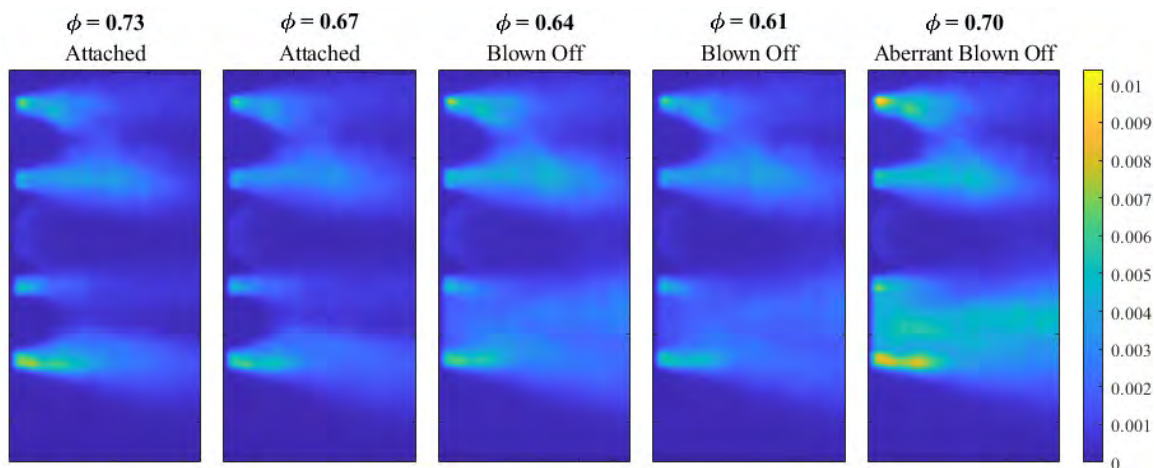


Figure 8. Fuel planar laser-induced fluorescence fluctuation fields for test points preceding and including outlier case. Test points are ordered chronologically from left to right.

Unfortunately, the fuel PLIF sample rate of 10 Hz was too slow to capture transitions between attached and blown-off states. The OH* CL and pressure recording times were also too short and finished recording before the end of the attached interval. Regardless, the switching intermittency is characteristic of hysteresis and multistability.

Given that the outlier is the only case where blowoff occurs for a higher ϕ and Da than normal, it is believed that the hysteresis region is not very large. It is still important for operating procedures to account for this hysteresis and ensure reliable performance.

Phase Doppler particle analysis

The characteristics of any liquid fuel exiting the combustor dome are critical for understanding performance of the LPP combustor and validating simulations. Here, PDPA was used to measure the velocity and size of the liquid fuel droplet under reacting conditions at $p_3 = 90\text{-}115$ psia, $T_3 = 450\text{-}650$ °F, fractional pressure drop $dp/p = 3.7\%$, and FAR = 0.040-0.055. Vertical profiles of droplet size and velocity were obtained at two axial locations from the mixer exit; i.e., $x = 1$ mm and $x = 10$ mm. Representative results at the nominal operating condition are shown in Figure 9 using Jet A fuel. The $x = 1$ mm location was conveniently selected to be used as boundary condition for CFD, whereas the $x = 10$ mm is used to evaluate how well the CFD spray model tracks droplet behavior as it moves downstream. Furthermore, these data provided valuable insights into the mixer atomization process and provided further direction on potential future improvements of the mixer. So far, only measurements with Jet A have been made, but we plan to do the same measurements with sustainable aviation fuel (SAF) in the first quarter of 2024.

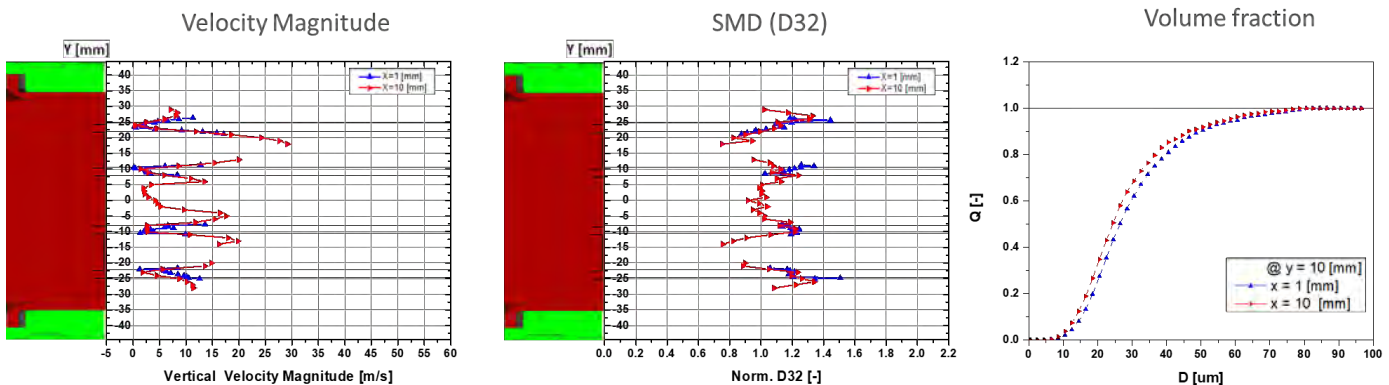


Figure 9. Representative vertical velocity magnitude (left), Sauter mean diameter, D32 (middle), and volume fraction (D; right) at two axial locations from the mixer exit face. Fuel is Jet A.

Preparation for experimental campaign 3

Two major activities were undertaken to prepare for the final experimental campaign of this project. First, due to students graduating, new students needed to be onboarded and trained on laser diagnostics, combustion, and so on. Over the period of performance, two new PhD students, Ari Jain and Ijeoma Obi, were hired and trained. Mr. Jain was trained primarily on the deployment of OH PLIF, which will be used to characterize the flame surface topology. Ms. Obi was trained primarily in spray holography, which will be used to characterize the multi-dimensional spray structure.

Second, it was required to procure a sufficient quantity of SAF (approximately 1,500 gallons) to conduct the experiments. This process was delayed as the FAA was establishing the optimal approach for SAF procurement within ASCENT. As of October 2023, we have successfully procured all of the neat hydroprocessed esters and fatty acids (HEFA) fuel required for campaign 3 from World Energy. The start of campaign 3 was delayed due to some infrastructure repairs needed at the GE Research Center. Setup of the laser diagnostics began in November 2023, and completion of campaign 3 is scheduled for January 2024.

Milestones

- Campaign 2 experimental data processing (complete)
- Lean blowoff analysis (complete)
- PDPA measurements using Jet A fuel (complete)
- Preparation for experimental campaign 3 (complete)

Major Accomplishments

- Establishment of LBO correlation based on Damköhler and Reynolds numbers for LPP combustor
- Explanation of LBO physics and hysteresis
- Characterization of liquid fuel spray at combustor dome face



Publications

- M. Passarelli et al., "Blowoff characteristics of a bluff-body stabilized, multi-element, lean premixed pre-vaporized combustor for supersonic transport applications," *ASME Turbo Expo*, Submitted (2023)
- A. X. Zheng et al., "Planar time-resolved laser-induced incandescence for pressurized premixed Jet A combustion," *Applied Physics B: Lasers and Optics*, 129(5):71(2023)

Student Involvement

- Arihant Jain (PhD candidate), Georgia Tech: Campaign 3 preparation, data processing
- Mitchell Passarelli (PhD candidate), Georgia Tech: Data acquisition, processing, and analysis
- Ijeoma Obi (PhD student), Georgia Tech: Campaign 3 preparation
- Samuel Wonfor (PhD candidate), Georgia Tech: Data acquisition and processing
- Andy Zheng (PhD candidate), Georgia Tech: Data acquisition Awards

Awards

None.

Plans for Next Period

- Execution of experimental campaign 3 (Q1 2024)
- Data processing and analysis from campaign 3 (Q4 2024)

Task 2 - Computational Simulations of Combustor

Georgia Institute of Technology

Objective

The objective of this task is to develop and validate best practices for industry-scale simulations of LPP combustion. This involves a combination of industry- and research-scale computational fluid dynamics (CFD) simulations, predominantly using large eddy simulations (LES)

Research Approach

To benchmark current CFD approach against experimental data, unsteady CFD simulations were performed for experimental conditions explored during Year 2 (2022-23). Predictions from the industrial scale LES simulations were compared against the experimental measurements of 2D fuel-air mixing, 2D combustor heat release imaging and droplet sizing from phase Doppler Interferometry. Based on comparison of CFD to experimental data at 2 different FARs, it was concluded that the initially assumed droplet distribution, as well as accurate modelling of evaporation and fuel-air mixing, are key to better matching with observed experimental trends. The computational fuel injection model likely needs further improvement, requiring a better definition of fuel evolution at the injection boundary for better prediction of the amount of liquid versus vapor fuel at combustor inlet. Also, boundary conditions from the CFD simulations were provided to the National Renewable Energy Lab (NREL) for reduced domain modelling and code-code comparison, as part of benchmarking the industrial scale simulations against state-of-the-art high-fidelity simulations.

The 2023 activity helped identify deficiencies in the liquid fuel injection method employed in the CFD simulations. To address the inadequacy, the computational team is investigating a high-fidelity fuel injection process based on a hybrid volume of fluid (VoF)/discrete particle method (DPM) approach. The idea is to generate the fuel-injection by employing a sub-model and, additionally, to run the full-model unsteady CFD simulation using VoF based fuel-injection. Unsteady CFD simulations at Year 2 experimental conditions with the high-fidelity injection process are in progress and will be compared and contrasted against the previous CFD and experimental measurements.

Milestones

- LES of Year 2 conditions using industry-scale simulations complete
- Boundary conditions transmitted for high-fidelity simulations
- Hybrid fuel injection model established



Major Accomplishments

- Changes in boundary conditions required for more accurately simulating LPP fuel injection identified
- Partnership with NREL established

Publications

None.

Student Involvement

- Mitchell Passarelli (PhD candidate), Georgia Tech: Data acquisition, processing, and analysis

Awards

None.

Plans for Next Period

- Complete execution of LES using high-fidelity boundary conditions

Task 3 - Analysis of Thermoacoustic Dynamics

Objective

This activity investigates the forced response of the combustor using measurements from campaign 2. The overarching objective is to develop and validate thermoacoustic modeling tools for this type of combustor.

Research Approach

Recall that these data were obtained during experimental campaign 2, in which oscillations were generated in the combustor at various frequencies using a siren device. Details of the experiment are presented in Task 1. Effort over the reporting period consisted of three main activities:

- 1) Analysis of the effects of forcing on the mean flame and flow structure
- 2) Analysis of flame transfer functions (FTF) and how they are influenced by the forced flame behavior
- 3) Analysis of frequency interactions in the forced flames

Effects on mean flow field

The mean fuel PLIF signal for cases with thermal power $\mathcal{P}_{th} = 0.40$ MW at different forcing frequencies is shown in Figure 9. No significant qualitative differences in mean fuel distribution were observed across the different forcing frequencies, indicating no bifurcation in overall flame or flow structure as the system is forced. This observation also held at the different thermal powers, corresponding to leaner ϕ .

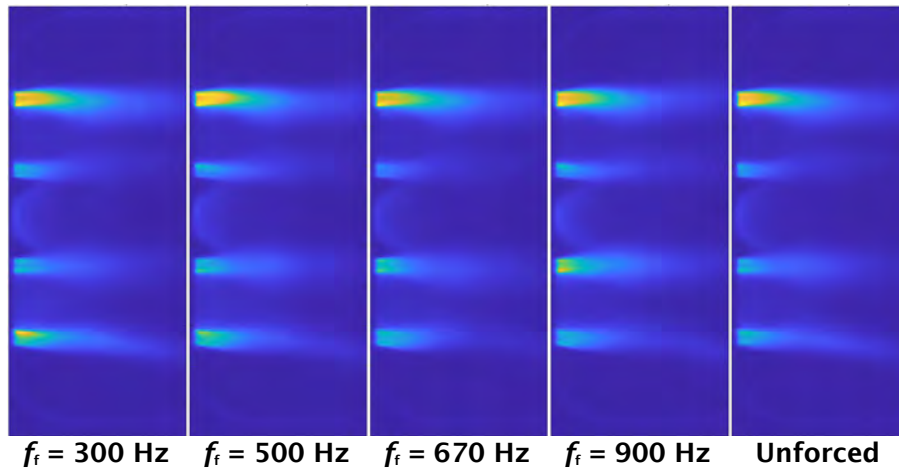


Figure 9. Mean fuel planar laser-induced fluorescence (PLIF) fields for 0.40 MW at different forcing frequencies (f_i).

As will be discussed below, the combustor shows highest response to forcing at $f_i = 670$ Hz. Figure 10 shows the mean fuel PLIF fields for 670 Hz forcing across different thermal powers. As ϕ is decreased, unburnt fuel is measured in the recirculation zones behind the combustor bluff-bodies and farther downstream. This observation is indicative of local extinction along the inner shear layer between the reactants and recirculation zone, allowing mixing of unburnt reactants. It is also indicative of more axially distributed heat release. The phase-conditioned mean fuel PLIF fields at different phases of the pressure cycle (not shown here) did not demonstrate any coherent oscillations in the fuel flow at any combination of thermal power and forcing frequency. Hence, heat release oscillations at the flame do not appear to be due to oscillating equivalence ratio; heat release oscillations are anticipated to be due to velocity coupling and a detailed analysis of the velocity dynamics is needed.

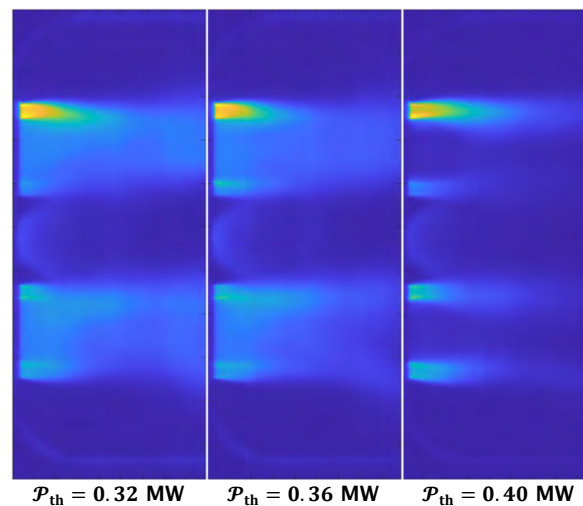


Figure 10. Mean fuel planar laser-induced fluorescence (PLIF) fields at different fuel-air ratios (FAR) for forcing frequency (f_i) = 670 Hz. \mathcal{P}_{th} , thermal power.

Figure 11 shows the mean velocity fields at different forcing frequencies and without forcing. Vector arrows show in the in-plane velocity, and the background colormap indicates the out-of-plane velocity. All absolute velocity scales have been removed for proprietary reasons. Similar to the fuel PLIF fields, there are no major qualitative changes in the velocity field

as the system is forced. The largest difference is that the unforced case has a slightly higher swirl velocity in the downstream region compared to the forced cases.

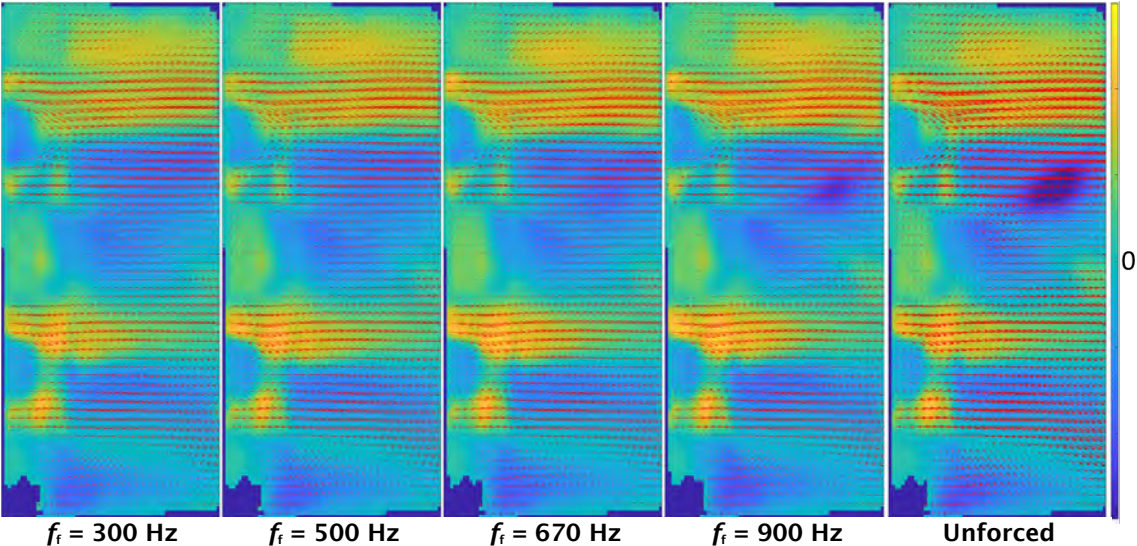


Figure 11. Mean velocity fields for 0.40 MW. Vector arrows are the in-plane velocity and background is the out-of-plane velocity with blue and yellow indicating positive and negative, respectively. f_i , forcing frequency.

Forced flame response

Overall, the forcing has negligible impact on the mean flow characteristics of the combustor. In addition, there were no cases where the presence of the forcing caused blowoff of an otherwise stable flame. The analysis performed by Salazar et al. (2023) yields the FTFs illustrated in Figure 12. The two FARs are the conditions where it was possible to stabilize at least one main flame in the combustor. At the leaner FAR, however, the main flames were often blown off and only intermittently reattached.

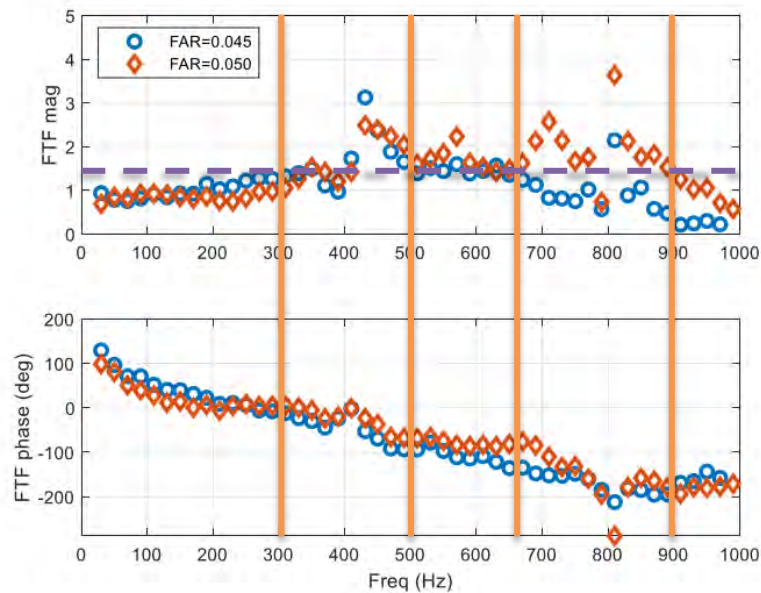


Figure 12. Measured flame transfer functions for two fuel-air ratios from campaign 2, modified from Salazar et al. (2023). Vertical green lines denote frequencies where optical data was recorded. The horizontal dashed yellow line in upper plot approximates the mean gain across the four frequencies.

The dynamics of the combustor for low FAR correspond to that of the pilot alone, whereas for $FAR \approx 0.050$, the dynamics involve the mains and main-pilot interactions. Figure 12 shows that the peaks at ~ 580 and ~ 710 Hz vanish when the FAR decreases to 0.045, whereas the peaks at ~ 420 and ~ 810 Hz remain. We can conclude that the ~ 580 and ~ 710 Hz peaks arise from either the mains' individual dynamics or the interactions between the main and pilot flames. The ~ 420 and ~ 810 Hz peaks, however, must stem from the natural dynamics of the pilot. The observed increase in FTF magnitude as FAR increases is potentially due to the contribution of main and/or main-pilot interactions. Additional experiments are required to validate these hypotheses.

Phase cancellation and spatial modes

Although Figure 12 indicates that the forcing frequencies selected for optical diagnostics have very similar gain, it is still worthwhile to investigate how this might be. To do so, the complex valued FFT fields of the OH^* CL images were computed at the highest ϕ condition across all forcing frequencies and plotted in Figure 13. The unforced case was excluded because it is not possible to extract a corresponding frequency field.

FFT fields can be used to identify regions that are in and out of phase with others, thereby revealing phase cancellation effects. In Figure 13, phase cancellation occurs when both the real and imaginary parts of the FFT are opposite signs at the same spatial locations. The response at each of the forcing frequencies has some cancellation for either the real or imaginary part of the field, but never both simultaneously. This represents the changes in phase that result from the different forcing frequencies, but their magnitudes are all similar, as expected from Figure 12.

Figure 13 also permits a basic, qualitative investigation of the mode shapes at the forcing frequency. Treating the FFT fields as the mode shapes of a discrete Fourier transform (DFT) allows interpreting the real and imaginary parts as a complementary mode pair representing the spatial dynamics at a given frequency. Applying this interpretation to Figure 13 reveals that the shape of the pilot's forced oscillations responds the most to the forcing frequency. As f_i increases, the spatial wavelength along the pilot's centerline decreases faster than along the mains' centerlines. This is more clearly illustrated by the phase fields in Figure 14. The phase fields were computed from the real and imaginary parts of the Fourier mode shapes in Figure 13. Each edge between 0 rad and 2π rad phase represents the end of one wavelength along the axial direction.

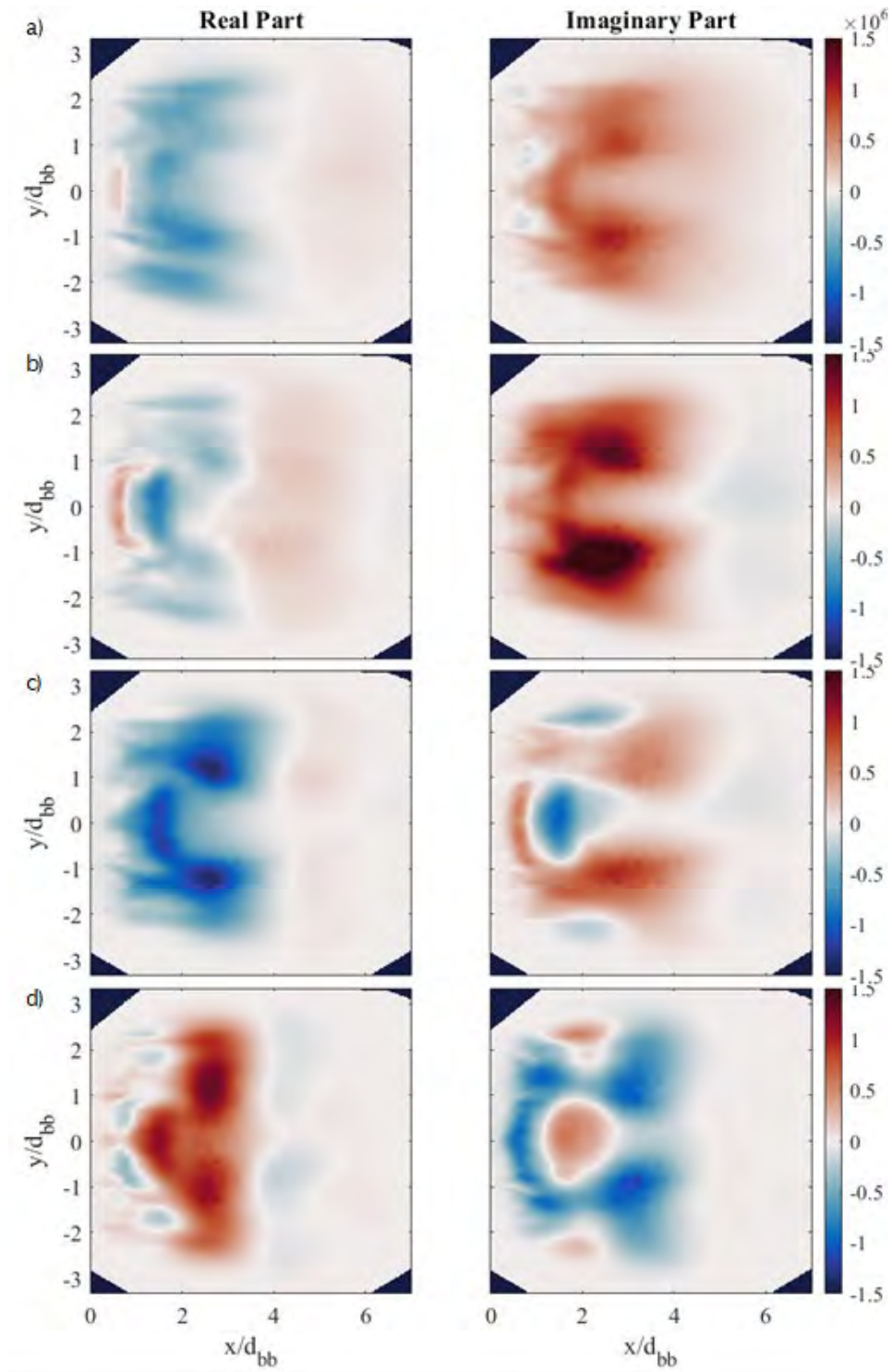


Figure 13. Complex flame transfer function fields of OH* chemiluminescence from highest ϕ condition at (a) $f_i = 306$ Hz, (b) $f_i = 503$ Hz, (c) $f_i = 672$ Hz, and (d) $f_i = 901$ Hz. f_i , forcing frequency.

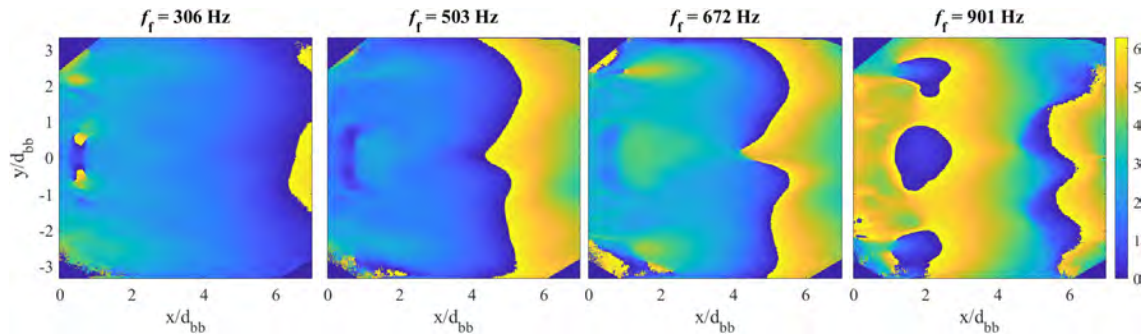


Figure 14. Phase fields from Fourier modes in Figure 14. Phase measured in radians. f_f , forcing frequency.

Figure 13 provides additional support that the dynamics and characteristics of this combustor are pilot dominated, even when subjected to external forcing. Throughout Figure 13, the highest amplitude fluctuations occur within the pilot region (i.e., $0 \leq x/d_{bb} \leq 2, |y/d_{bb}| \leq 2$) and/or the region where the mains and pilot overlap ($2 \leq x/d_{bb} \leq 4, 1 \leq |y/d_{bb}| \leq 2$), where x and y are the axial and vertical directions, and d_{bb} is the bluff body diameter. Given that much of the signal intensity in the overlap region is due to the pilot and the pilot exhibits higher power fluctuations, it is reasonable to conclude that the higher power fluctuations in the overlap region are mostly from the pilot.

Frequency interactions

Thus far, the data collected and presented indicate that the pilot is integral to the nominal operation and characteristics of the LPP combustor investigated. Indeed, the dynamics of this combustor appear pilot dominated. As such, it is important to examine how the forcing interacts with the natural dynamics of the pilot. This analysis is also used to explore how frequency interactions can interfere with measurements for FTFs in practical combustors.

Figure 15 plots the peak frequency fields and spatially resolved power spectra of the OH* CL images for TPs at the highest ϕ investigated and each of the forcing frequencies. The highest ϕ condition was chosen because of the blowoff exhibited in data sets at leaner ϕ . Data sets with blowoff are unsuitable because it is not possible to see the impact of main-pilot interactions or the contributions from the individual mains. The peak frequency fields are computed by plotting the frequency with the highest power at each spatial coordinate in the OH* CL. The resulting fields clearly show where the dominant oscillations exist in the combustor and their frequencies. The high-power, low-frequency (<100 Hz) oscillations are suspected to be an artifact of the experimental rig, not the combustor design, and have been omitted from this analysis.

Figure 15a shows the results computed for the unforced case. The peak frequency field clearly shows that the pilot oscillates at $f_0 \approx 4.2$ kHz, whereas the power spectra indicate that this self-excited tone dominates the unforced dynamics. In addition, Figure 15a shows that the pilot dynamics are antisymmetric because they do not cause global OH* CL oscillations. The corresponding Fourier mode shape of the unforced pilot mode is shown in Figure 16. It is also worth noting that the ~ 4.2 kHz pilot dynamics are approximately a multiple of the ~ 420 Hz peak in Figure 12, which was also reasoned to stem from the pilot. Unfortunately, the data recorded to compute the FTFs are not able to resolve the relationship between the two frequencies.

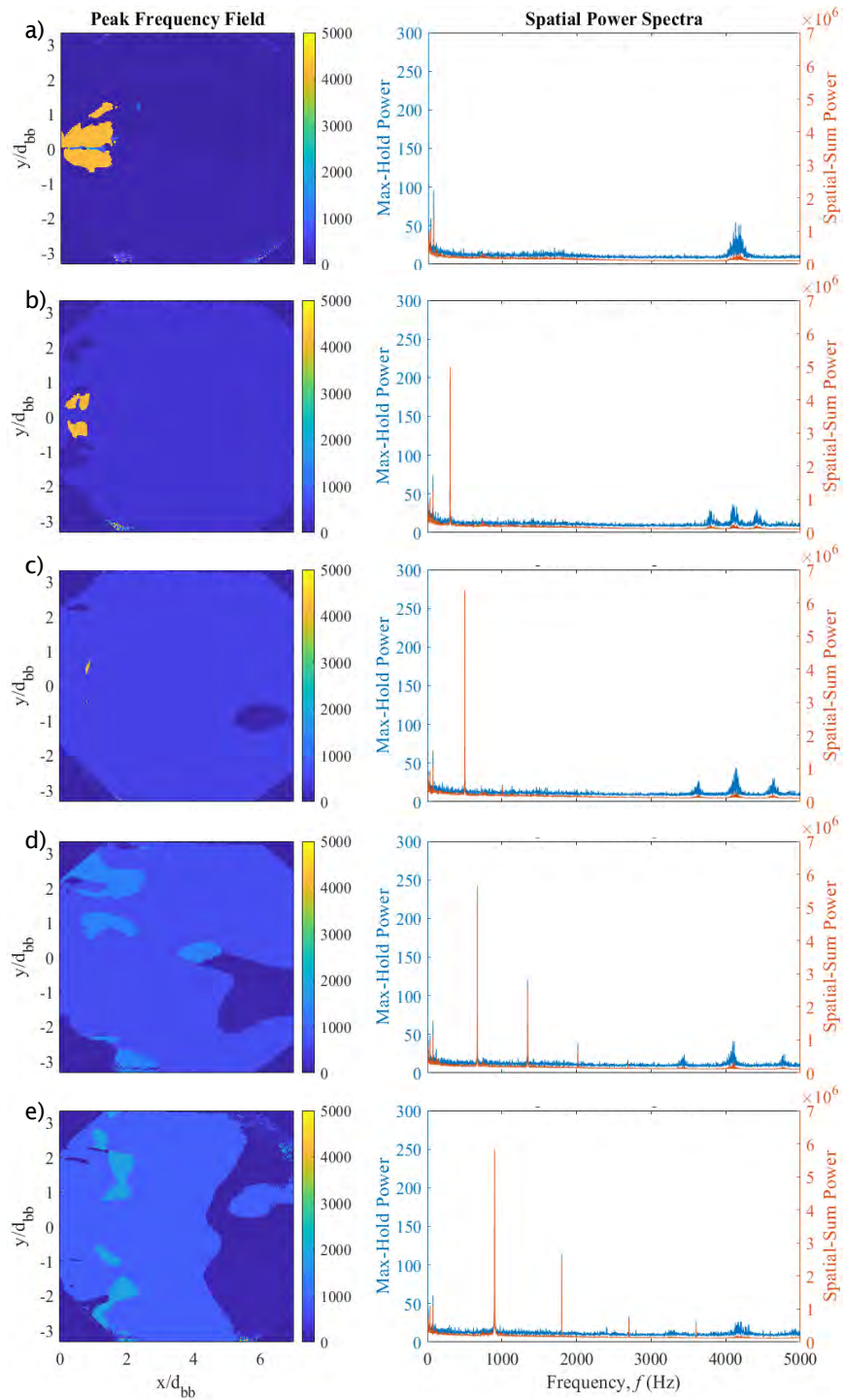


Figure 15. OH* chemiluminescence peak frequency fields and spatially resolved power spectra at highest ϕ for (a) unforced, (b) $f_f = 306$ Hz, (c) $f_f = 503$ Hz, (d) $f_f = 672$ Hz, and (e) $f_f = 901$ Hz. f_f , forcing frequency.

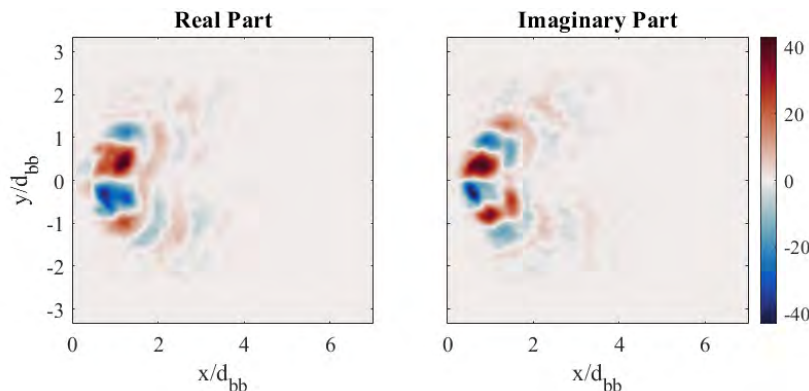


Figure 16. OH* chemiluminescence Fourier mode of unforced pilot dynamics.

Figure 15b-e illustrate how the applied forcing interacts with the natural dynamics of the pilot. The first effect is the appearance of sum and difference frequencies in the forced cases at $f_o \pm f_i$. The second effect, called frequency pulling or pushing (Cross and Greenside, 2009), causes the peak frequency of the pilot's natural dynamics to shift toward nearby harmonics of f_i , because of one-way coupling and real wave properties. For example, forcing at $f_i = 671$ Hz shifts the pilot oscillations by ~ 100 Hz to ~ 4.1 kHz. While there should be a relationship between the shift in f_o and f_i , the present data are not able to resolve this relationship due to variation in forcing amplitude across the cases.

The effects of frequency interactions are important in the context of FTF measurements. As f_o shifts toward a harmonic of f_i , similar effects can manifest, such as those encountered along synchronization routes (Balanov et al., 2009). As a result, these frequency interactions can reduce or amplify the response at the forcing frequency. This means that the measured response to the forcing frequency is coupled with the self-excited dynamics. Neither the frequency pulling/pushing nor the amplification effects are captured by FTFs. These effects have been previously reported in a practical gas turbine combustor by Hochgreb et al. (2013)

Milestones

- Measurement of flame transfer functions complete
- Analysis of forced experimental results complete
- Preliminary analysis of flame transfer functions using network modeling complete

Major Accomplishments

- First measurements of flame transfer functions and forced response of this type of LPP combustor

Publications

None.

Student Involvement

- Mitchell Passarelli (PhD candidate), Georgia Tech: Data acquisition, processing, and analysis

Awards

None.

Plans for Next Period

- Complete thermoacoustic modeling of combustor, including modeling of flame transfer functions using validated CFD and linearized Navier-Stokes analysis.



References

ANSYS, Inc., "Chemkin-Pro Theory Manual," ANSYS, Inc., 2020.

A. Balanov, N. Janson, D. Postnov and O. Sosnovtseva, *Synchronization: From Simple to Complex*, Heidelberg: Springer Berlin, 2009.

J. J. Berton, D. L. Huff, J. A. Seidel and K. A. Geiselhart, "Supersonic Technology Concept Aeroplanes for Environmental Studies," in *AIAA SciTech Forum and Exposition*, Orlando, 2020.

D. E. Cavaliere, J. Kariuki and E. Mastorakos, "A Comparison of the Blow-Off Behaviour of Swirl-Stabilized Premixed, Non-Premixed and Spray Flames," *Flow, Turbulence and Combustion*, vol. 91, pp. 347-372, September 2013.

M. Cross and H. Greenside, *Pattern Formation and Dynamics in Nonequilibrium Systems*, New York: Cambridge University Press, 2009.

M. Hassan, H. Pfaender and D. Mavris, "Design Tools for Conceptual Analysis of Future Commercial Supersonic Aircraft," in *AIAA Aviation Forum*, Virtual, 2020.

S. Hochgreb, D. Dennis, I. Ayranci, W. Bainbridge and S. Cant, "Forced and Self-excited Instabilities from Lean Premixed, Liquid-fueled Aeroengine Injectors at High Pressures and Temperatures," in *Proceedings of ASME Turbo Expo 2013*, San Antonio, 2013.

A. Kharina, T. MacDonald and D. Rutherford, "Environmental performance of emerging supersonic transport aircraft," *The International Council on Clean Transportation*, 2018.

R. W. Niedzwiecki, "Low Emissions Combustor Technology for High-Speed Civil Transport Engines," NASA, Cleveland, 1992.

V. Salazar, K. Venkatesan, F. Han, S. Wonfor, M. Passarelli and A. Zheng, "Acoustic and Optical Flame Transfer Function Measurements in a High-Pressure Lean-Burn Aero-Engine Combustor Fueled With Jet A," in *Proceedings of the ASME Turbo Expo 2023*, Boston, 2023.

S. J. Shanbhogue, S. Husain and T. Lieuwen, "Lean Blowoff of Bluff Body Stabilized Flames: Scaling and Dynamics," *Progress in Energy and Combustion Science*, vol. 35, pp. 98-120, 2009.

R. L. Speth, S. D. Eastham, T. M. Fritz, I. Sanz-Morère, A. Agarwal, P. Prashanth, F. Allroggen and S. R. H. Barrett, "Global Environmental Impact of Supersonic Cruise Aircraft in the Stratosphere," NASA, Cleveland, 2021.

S. H. Strogatz, *Nonlinear Dynamics and Chaos: With Applications to Physics, Biology, Chemistry, and Engineering*, Boca Raton: CRC Press, 2015.

S. G. Tuttle, "Blowoff Behavior of Bluff Body Stabilized Flames in Vitiated and Partially Premixed Flows," University of Connecticut, Storrs, 2010.



Project 075 Improved Engine Fan Broadband Noise Prediction Capabilities

Boston University and Raytheon Technologies Research Center

Project Lead Investigator

Sheryl Grace
Associate Professor
Mechanical Engineering
Boston University
110 Cummington Mall, Boston, MA 02215
617-353-7364
sgrace@bu.edu

University Participants

Boston University (BU)

- P.I.: Sheryl Grace, Associate Professor, Mechanical Engineering
- FAA Award Number: 13-C-AJFE-BU Amendment 022
- Period of Performance: October 1, 2022 to September 30, 2024
- Tasks:
 1. Fan-wake surrogate model creation
 2. Improved low-order model
 3. Rig test planning

Project Funding Level

Second-year funding (through December 30, 2022):

FAA: \$300,000: \$115,000 to BU, \$185,000 to **Raytheon Technologies Research Center (RTRC)**

Match \$300,000: \$115,000 from BU (datasets, faculty time, graduate-student stipend)
\$185,000 from RTRC (personnel time)

Third-year funding (January 1, 2023 to June 1, 2024):

FAA: \$400,000: \$150,000 to BU, \$250,000 to RTRC

Match \$400,000: \$200,000 from BU (datasets, faculty time, graduate-student stipend)
\$200,000 from RTRC (personnel time, Pratt & Whitney [P&W]).

Investigation Team

Boston University

Prof. Sheryl Grace (P.I.), Tasks 1, 2, and 3
Noah Li (PhD student), Tasks 1 and 2
Amarylis Wiltz (undergraduate researcher), Task 1
Renato Korzinek (undergraduate researcher), Task 1

Raytheon Technologies Research Center

Jeff Mendoza (co-P.I.), Tasks 1, 2, and 3
Craig Aaron Reimann (staff scientist), Tasks 2 and 3
Julian Winkler (staff scientist), Tasks 1, 2, and 3
Dmytro Voytovych (staff scientist), Task 1
Kin Gwn Lore (staff scientist), Task 1



Michael Joly (staff scientist), Task 1

Project Overview

The noise signature of contemporary turbofan engines is dominated by fan noise, both tonal and broadband. Accepted methods for predicting tone noise have existed for many years. Furthermore, although engine designers use methods for controlling or treating tonal noise, this process is much more challenging for broadband noise. Thus, further reductions in engine noise will clearly require accurate prediction methods for broadband noise to support design decisions. Interaction noise from the fan stage, a dominant broadband mechanism in a modern high-bypass engine, is created by the interaction of the turbulence in the fan wakes with the fan exit guide vanes (FEGVs). This project will leverage prior development of low-order models for the prediction of fan broadband interaction noise. Gaps in the low-order approach will be addressed according to knowledge gained from computation and experimentation. In particular, a method for determining the inflow into the stator via a machine learning (ML) algorithm will be developed. The low-order method will also be validated against full- and rig-scale data, and appropriate development will be undertaken according to the findings.

Task 1 – Fan-wake Surrogate Model Creation

Boston University and Raytheon Technologies Research Center

Objective

The goal is to build a surrogate model by using ML that would work with performance-level unsteady Reynolds-averaged Navier–Stokes (RANS) to specify the mean flow, turbulent kinetic energy, and turbulent length scale at locations along the helical fan-wake path.

Research Approach

Subtasks 1.1 and 2: development of autoencoder and decoder

The ML applied to this problem in Year 3 continued to use only the decoder part of a neural network. Four wake flow parameters are learned in the region downstream of the fan. The mean flow axial and circumferential velocities are learned through a two-step process. First, a deep neural network is used for learning the circumferentially averaged value of the mean flow. Then a two-dimensional (2D) convolutional neural network (CNN) is used to learn the flow deficit. In the 2D method, the data are made of axial slices of the wake flow. For each fan geometry and operating case, 30 axial slices were generated. The turbulent kinetic energy is learned by using the CNN, and the turbulence length scale is learned directly from the CNN (instead of separate learning of the turbulent kinetic energy and dissipation, as previously done).

Tensorflow is used for the ML and is integrated into a Python wrapper. The CNN was characterized and optimized to some extent. The effects of many model parameters and usage decisions were studied.

- A study of batch size indicated an optimal batch size of 128 for a 2D model and 8 for a three-dimensional (3D) model.
- A study of the inclusion of batch normalization indicated that using a 2D CNN model greatly increases the learning accuracy for some wake parameters but decreases the learning accuracy for others. For a 3D CNN model, batch normalization causes learning to fail and was therefore removed from the model.
- The selection of geometric and flow parameters used as input was considered. Originally, some spanwise flow variables describing the fan flow were obtained from AxStream and used in the input deck. These variables included the flow angle at the leading and trailing edges of the fan. However, testing demonstrated that the ML still worked well when these parameters were not included as input. Thus the ML algorithm could be divorced from AxStream. Only fan geometry and basic upstream flow conditions can be used as input, and the fan wake can still be learned.
- We determined that, during the training phase of the model, the portion of the training data used for validation was accidentally being selected as the last portion of the training data, thus making the set biased. Work to ensure random selection of the validation portion of the data helped improve the training.
- Training requires approximately 1,000 epochs. A validation loss decay rate threshold is set, and training terminates when the validation loss does not decay for 40 epochs. The number of layers is manually tuned to the minimum number of layers at optimal performance.

In addition to studying the effects of various parameter settings on the 2D CNN, we conducted a 3D CNN, in which the entire region downstream of the fan was seen as one dataset. The ML accuracy was similar between the 2D and 3D CNNs. The model architectures are shown in Figure 1. Both begin with fully connected layers, which usually occur at the neck of the CNN.

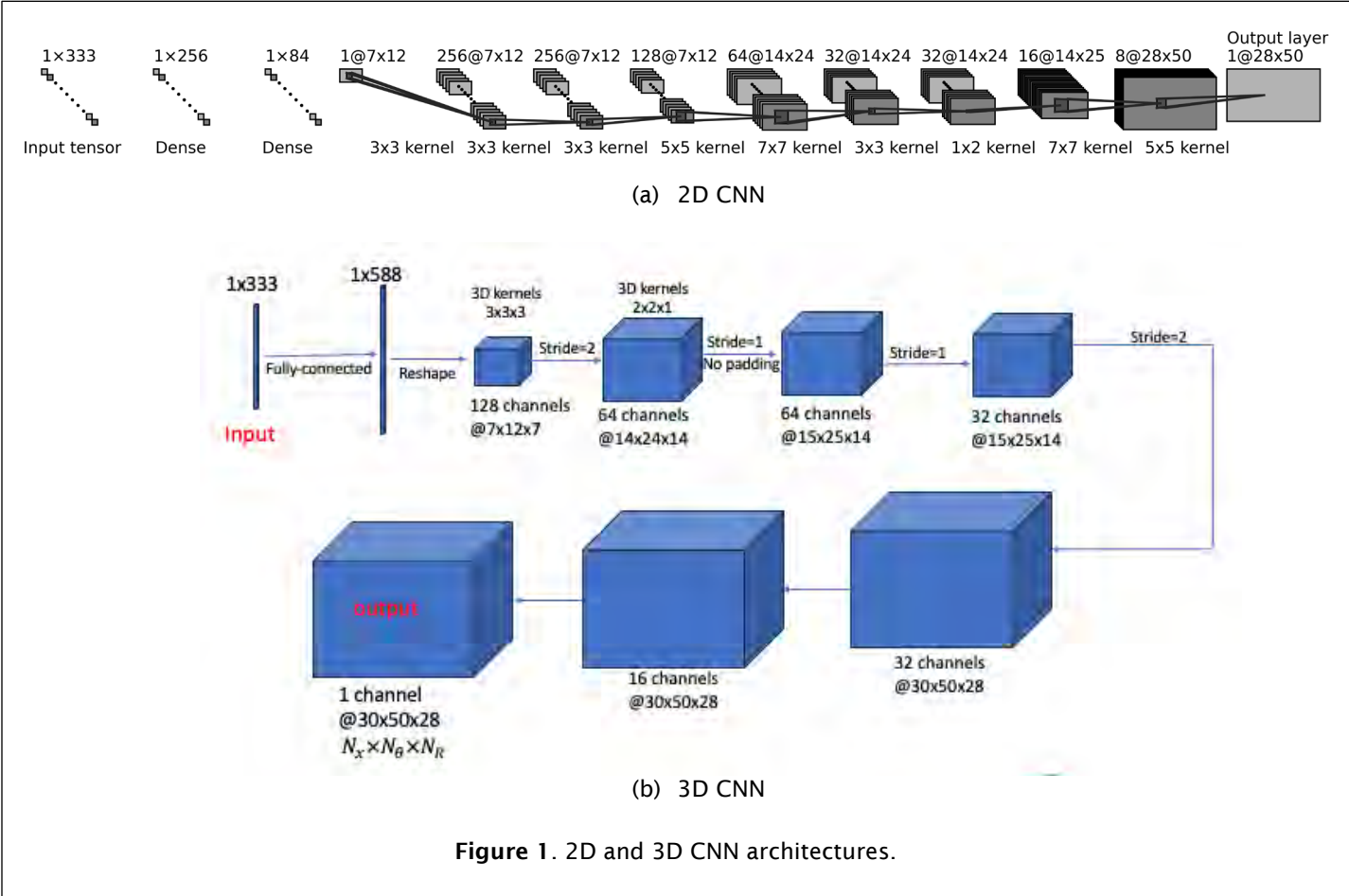


Figure 1. 2D and 3D CNN architectures.

Subtask 1.3: Identification and creation of training data

Subtask 1.3b: Creation of additional training data RTRC took the lead on developing new fan geometries, and BU provided the analysis to determine whether the fans were acceptable, from an ML/noise difference perspective.

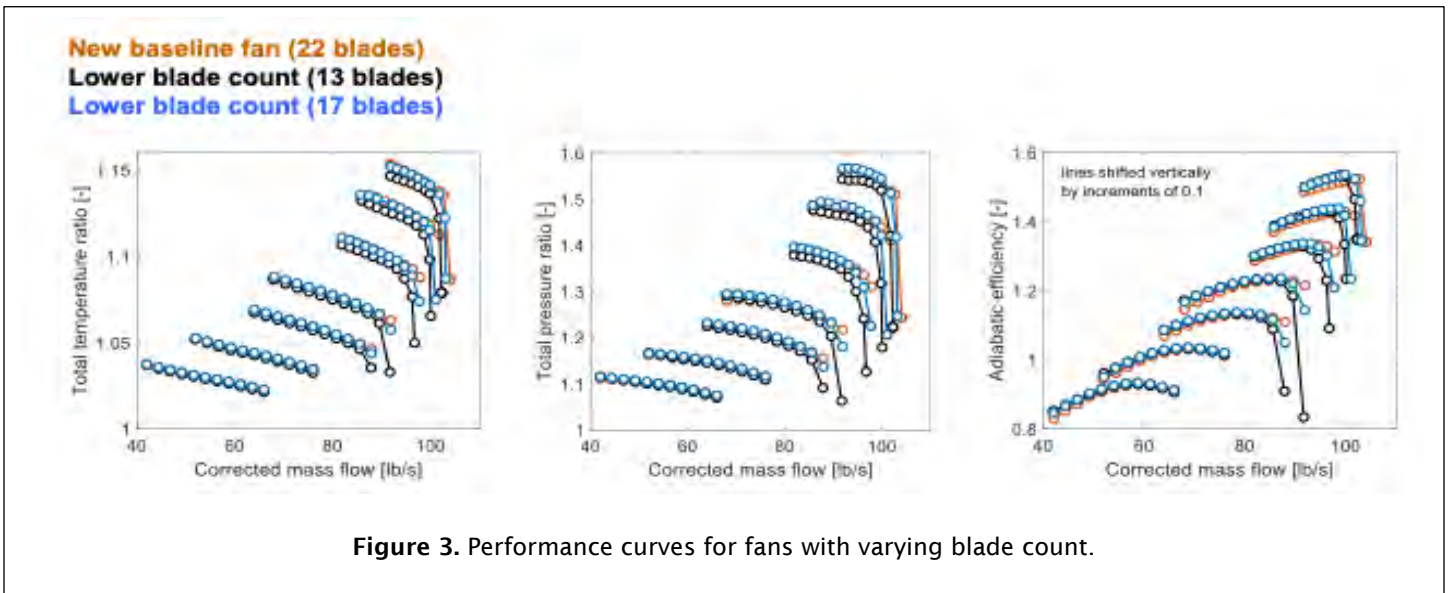
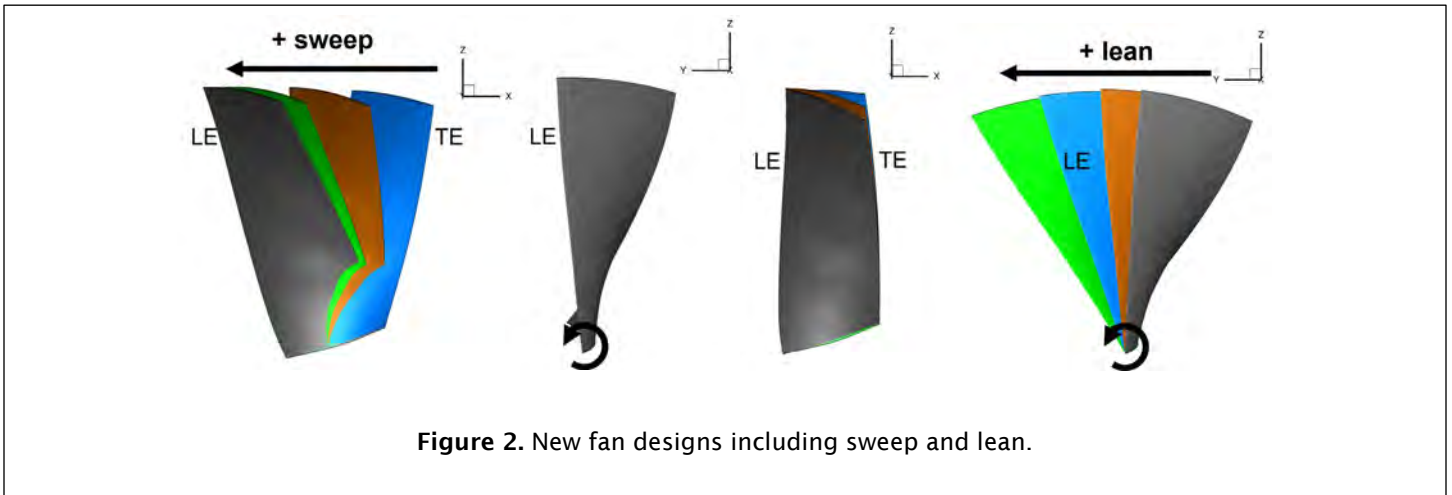
Several new fan geometries were created in Year 3. The baseline fan created by RTRC is similar to the NASA Source Diagnostic Test (SDT) fan, but with smoother parameter variations from hub to tip (i.e., twist and chord) and provided the basis. Three cases with different lean distributions and three cases with different sweep distributions were developed (Figure 2). Another set of fans allowing for variation in the blade count was also developed, thereby including 17- and 13-bladed fans in the database. Rotor-alone simulations for each of the fans at approximately 70 operating points were completed by RTRC. The performance plots are shown in Figures 3–5. Not all operating points can be used in the ML. Any clearly stalled or choked points were deleted from the database. The new database, resulting from 672 individual simulations, consists of the SDT; the new baseline; and the cases of leaned, swept, or altered blade count. For the 2D CNN, 20,160 training points are used, because each case has 30 axial slices used for training.

A collaborator, Professor Bauerheim, from the Institut Supérieur de l’Aéronautique et de l’Espace (ISAE-Supaero) in Toulouse, France, was also identified during the third year. Professor Bauerheim’s team has been developing canonical fan



geometries with some basis in existing rig-scale fans that have been tested in the past. His group has also performed rotor-alone-type RANS simulations for the fan geometries that they have developed. They have considered only three operating points for each design. A data usage agreement is being drafted among BU, RTRC, and ISAE Supaero to facilitate the exchange of RANS datasets among parties. This exchange will instantly increase the database size. We hope that this sharing will be complete by the end of the third-year funding cycle.

Finally, a PhD student at BU has started to learn how to implement the SU2 computational software. This software will be used to perform future RANS calculations for additional fan geometries. We also hope to be able to include the FAA Continuous Lower Energy, Emissions & Noise (CLEEN) phase I rig cases in the ML database; doing so will require further approval from P&W, because some information regarding the fan geometry is required for a case to be included in the ML database.



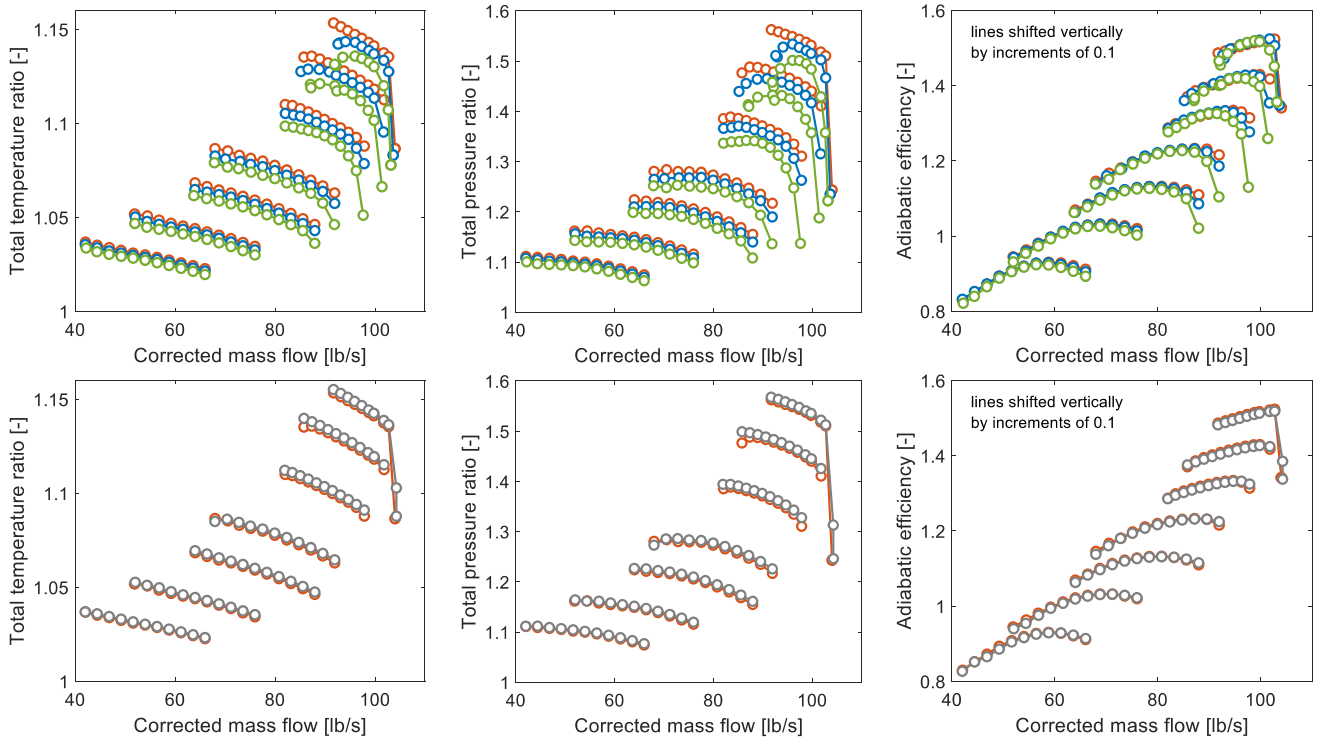


Figure 4. Performance for leaned cases. Orange: new baseline; cyan: +15° lean; green: +30° lean; gray: -10° lean. Adding positive lean unloads the rotors, and performance degrades at higher speeds.

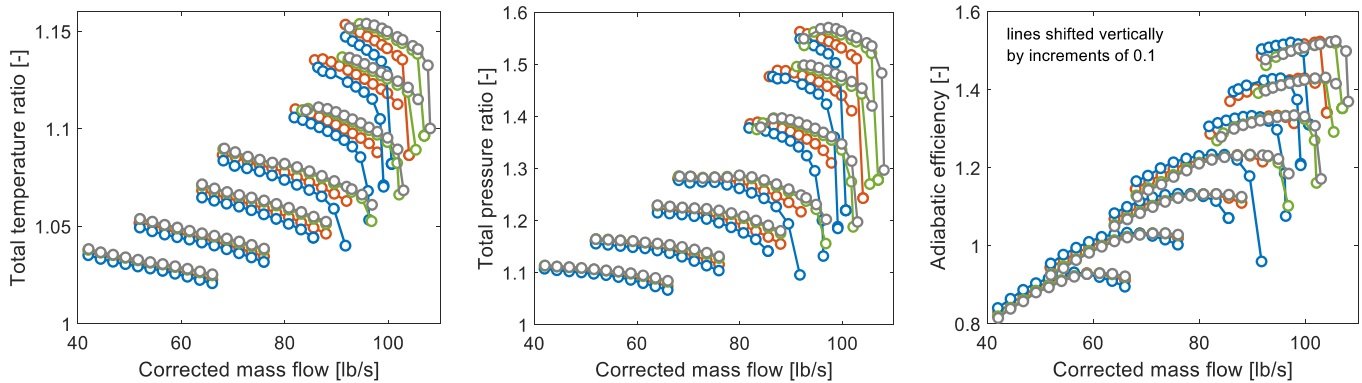


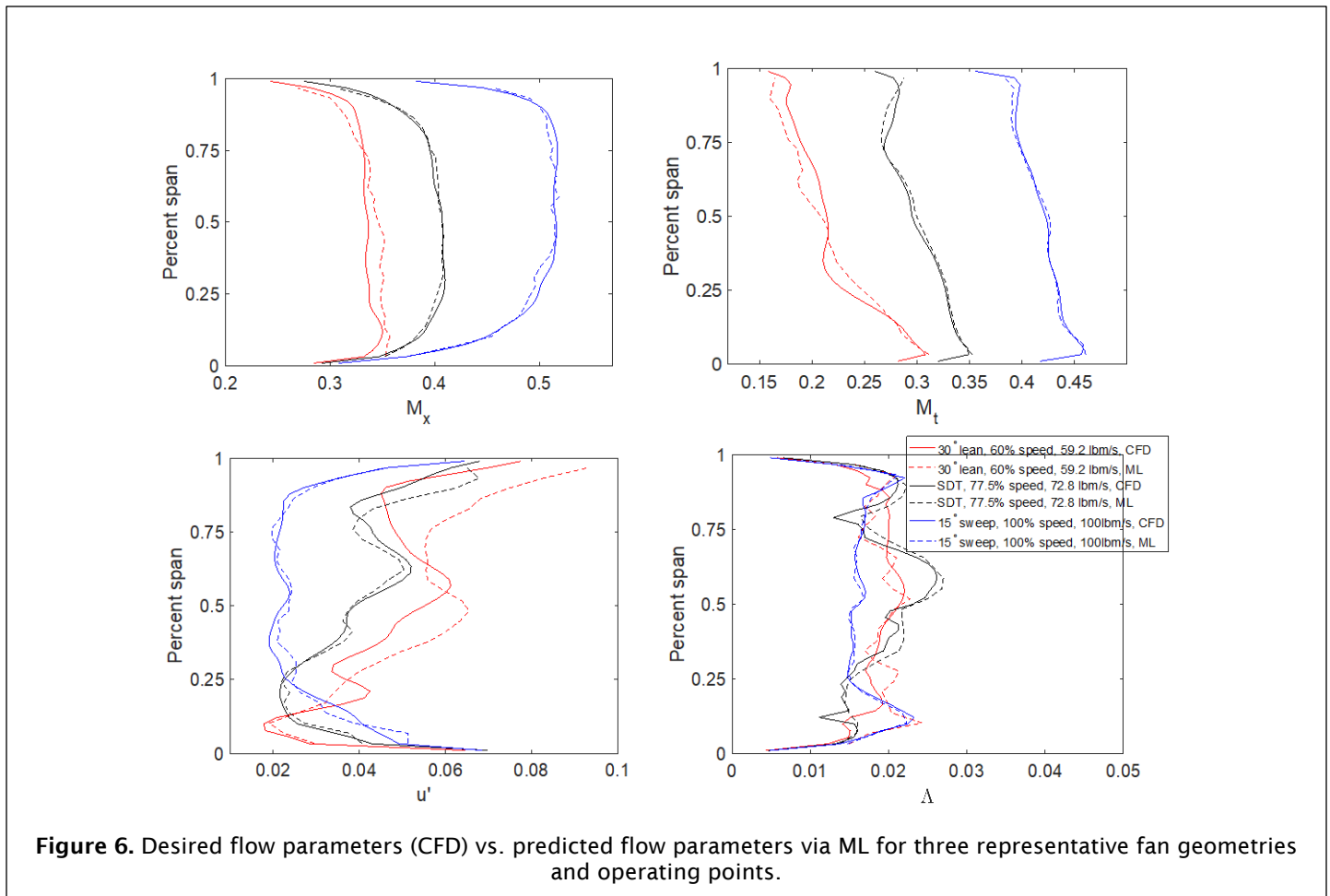
Figure 5. Performance for swept cases. Orange: new baseline; cyan: -15° sweep; green: +15° sweep; gray: +20° sweep. Adding positive lean loads the rotors, and performance shifts toward higher mass flow rates.

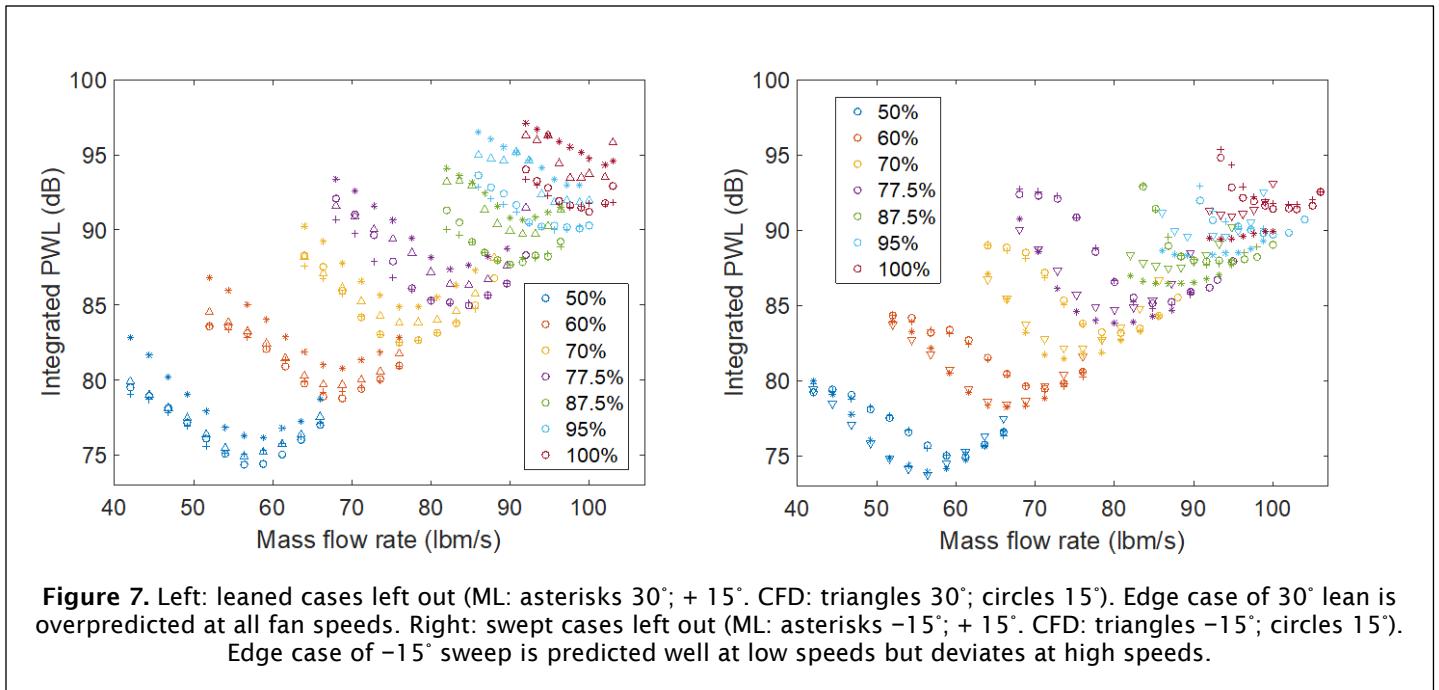


Subtask 1.4: Application of surrogate model to relevant fan geometries

The deep neural network/CNN ML predictions have been applied to the database containing the swept, leaned, and low-blade-count fans. Normal 80% training and 20% test runs were performed. Next, full fan geometries were excluded from the training data and used only for testing. The results were reported in a June 2023 Aviation Conference manuscript, which is attached to this report. The wake parameters were shown to be reasonably learned. For the edge cases—i.e., with +20° or -15° sweep, or +30° or -10° lean, left out—the learned results were slightly less accurate; the +30° lean case was the most inaccurate.

The machine-learned parameters were used together with the low-order acoustic method to predict the final expected power level in the bypass duct for the cases. The results are also described in the attached manuscript. Summary results are shown in Figures 6 and 7. First, the machine-learned flow parameters (axial and circumferential velocity, turbulence intensity, and turbulence length scale) are shown for some representative cases (Figure 6). Subsequently, the final acoustic prediction for all operating points, when different fan geometries are left out of the training database, are predicted with the ML (Figure 7).





Milestones

The milestones set for Task 1 in Year 3 included:

1. ML surrogate model refinement and validation
2. Assessment of a surrogate model for modified fan trailing-edge wake (completed in Year 2)

As described above, the ML model was modified and tested. Multiple parameter studies to understand how best to construct the ML were completed. Multiple additions to the database were made, and tests were completed with the new ML method.

Major Accomplishments

- Creation and testing of 2D and 3D CNN models for fan-wake parameter prediction
- Determination of the smallest necessary input parameter set for ML (AxStream data not necessary)
- Expansion of the fan-wake database to include fans with real geometry differences
- Creation of speed line data for all new fan geometries
- Complete acoustic analysis with the low-order method of all new fan geometries at approximately 70 operating points
- Establishment of a collaboration that will enable growth of the database and comparison across other ML methods being developed for learning fan-wake parameters
- SU2 software acquired, and first fan cases attempted

Publications

“Development of fully low-order prediction of fan broadband interaction noise via integration of machine learning,” Nuo Li, Yifan Zhang, Julian Winkler, C. Aaron Reimann, Dmytro Voytovych, Michael Joly, Kin Gwn Lore, Jeff Mendoza and Sheryl M. Grace, AIAA Journal (under final review).

“Machine Learning Aided Fan Broadband Interaction Noise Prediction for Leaned and Swept Fans,” Nuo Li, Julian Winkler, C. Aaron Reimann, Dmytro Voytovych, Michael Joly, Kin Gwn Lore, Jeff Mendoza and Sheryl M. Grace, AIAA Paper No. 2023-0523 Aviation Conf.

Outreach Efforts

None.

Awards

None.

Student Involvement

In Year 3, one PhD student and two undergraduates contributed to this portion of the project.

Plans for Next Period

The milestone set for the third year of this project is:

- ML surrogate model refinement and validation

To end the third-year funding cycle and move into year 4, the ML development focus will involve exercising the ML on a much larger database including more varied fan geometries. Necessary adjustments will be made to the method, according to the outcomes. We will also consider learning the overall averaged wake parameters by using a 2D CNN method, but at a single shot for each operating point, because the picture being learned will be an axial vs. radial picture (the circumferential dependence will be removed). Finally, a U-Net model for the ML will be considered.

Task 2 – Improved Low-Order Model

Boston University and Raytheon Technologies Research Center

Objectives

The existing low-order methods are regularly applied to the SDT cases and as such have been well validated against this test, which represents one scaled fan and multiple FEGV configurations. The low-order method must now be validated against full-scale test data. The low-order method might also require reformulation to account for other real-flow effects.

Research Approach

Subtask 2.1: Ability to predict full-scale results

The low-order method will be applied to a full-scale geometry with available validation data. Because of the difference in the frequency range of interest for the full-scale case, as compared with the scaled fans, we surmised that the low-order method would require grid adjustments and integral extent adjustments. Such improvements to the low-order method will be completed as part of this task.

RTRC transferred RANS simulation data for the wake flow downstream of the FAA CLEEN I rig- and full-scale engine demo cases. These data were used to define the input to the low-order acoustic model. The FEGV geometry characteristics (chord, stagger, and axial location) were also supplied to BU for this calculation. An iteration was necessary to align all geometric properties correctly. Subsequently, a comparison of the predicted downstream noise spectrum and data from experiments was completed by RTRC. The predictions for the rig scale were relatively accurate. For the full scale, the trend was correct, but the levels were not. Figure 8 shows the predictions from the low-order acoustic code.

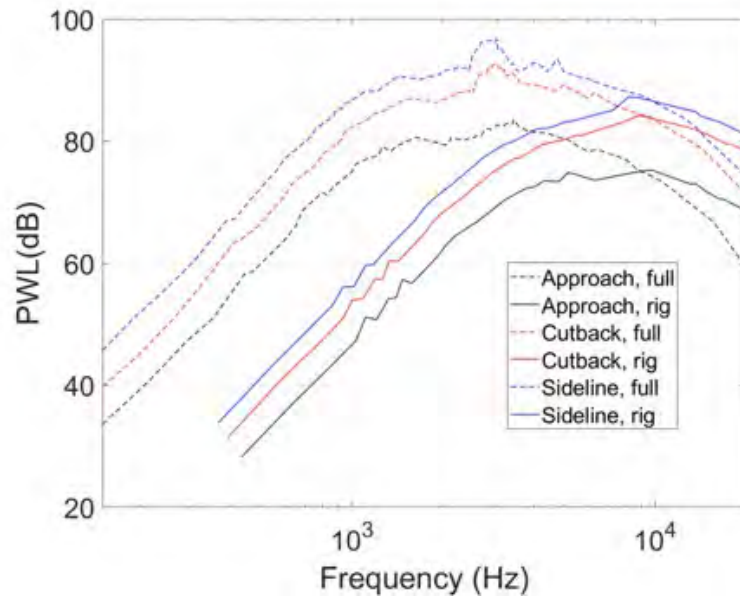


Figure 8. Predicted spectrum for the FAA CLEEN I rig- and full-scale cases at three operating points.

The finding that the full-scale prediction did not compare well with the experimental findings has led to further considerations. The low-order acoustic method uses wake flow parameters just upstream of the exit guide vane. These parameters are being taken from the RANS simulations. Efforts will be made in the future to verify the RANS wake results against results from another computation, most probably the lattice Boltzmann method (LBM). Additionally, discussions regarding what the scaling law should be for a fan have commenced. Comparison of the FAA CLEEN I rig- and full-scale cases reveals several differences in the interstage flow. The largest difference is in the length scale, Δ , as shown in Figure 9. The flow parameters do not scale with the geometry, because the turbulence parameters in the wake are similar just downstream of the fan; however, the wake evolves three times further before it encounters the FEGV in the full-scale case. If this difference could be erased, and the RANS wake flow from the rig scale could simply be combined with the full-scale vane geometry, the predictions would change. The difference is shown in Figure 10, as indicated by the blue line (actual prediction) and the black dashed line (prediction using the rig-scale wake flow together with a perfectly scaled exit guide vane and duct that match the size of the full-scale case). The red crosses are obtained by simply taking the rig-scale prediction and scaling it with the formula $P_{new}(f) = S^3 * P(f*S)$, where P is the sound power level, f is the frequency, and S is the scaling factor. The scaling factor for the FAA CLEEN I rig scale to full scale is 3.04. Only the approach operating point is shown in Figure 10, but the cutback and sideline cases show identical outcomes, thus indicating that the wake flow itself is quite different from the rig-scale flow and plays a major role in the final prediction.

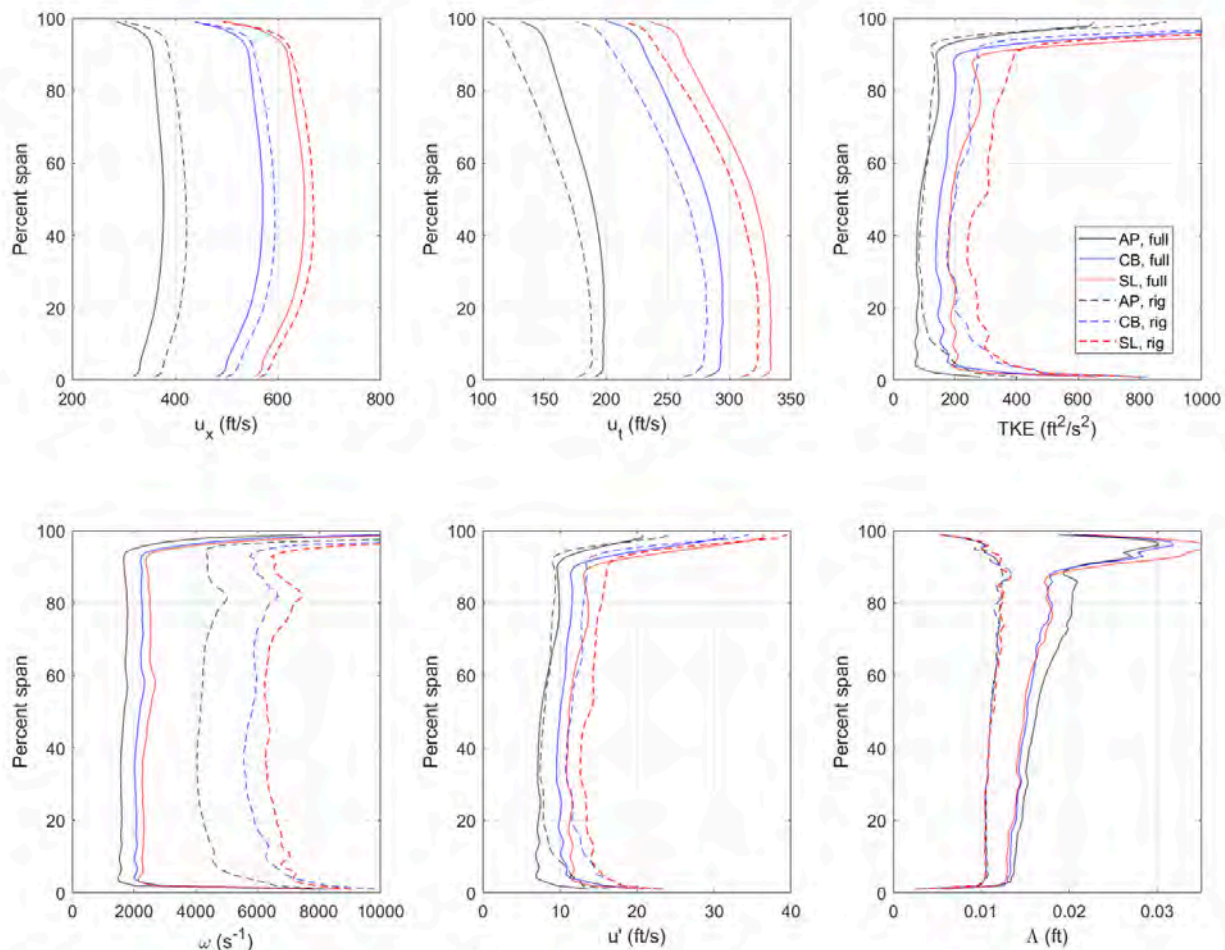
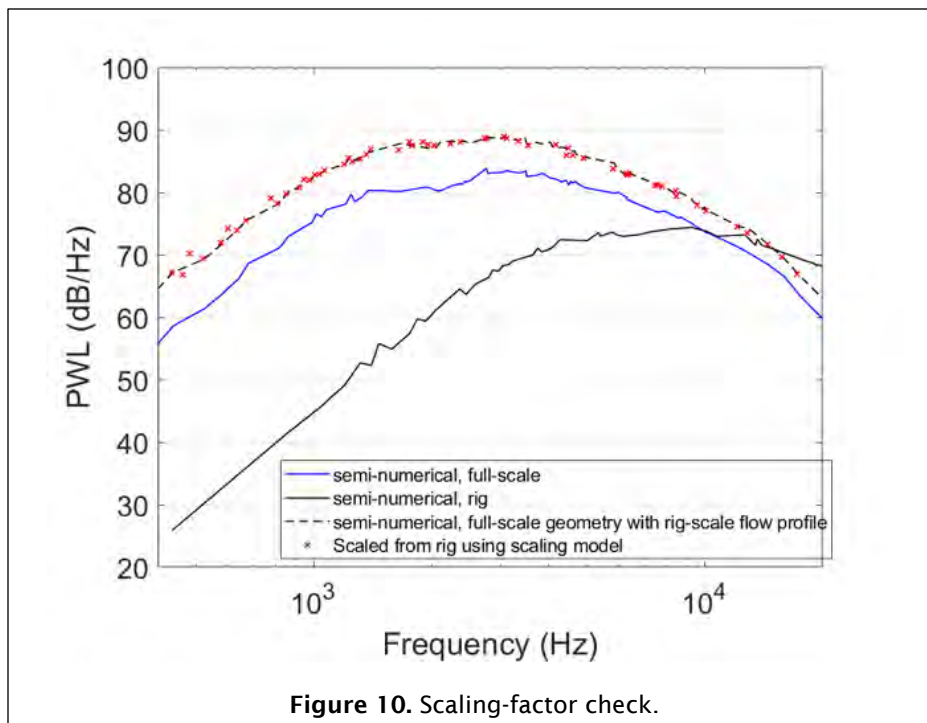


Figure 9. Flow input parameters for CLEAN 1, rig and full scale. Input taken along the leading edge of the FEGV. Dashed lines: rig; solid lines: full.

Full-scale engine LBM simulations were performed for different operating conditions to determine best practices for these types of simulations and understand the grid resolution requirements. The simulations, in comparison to engine ground test data, indicate that the broadband noise can be predicted well up to a certain frequency limit. The resolved frequency range adequately covers the range of interest for fan – FEGV interaction noise. Therefore, the simulations can be used to inform the lower-order methods and shed light on the turbulence information in the fan wake. These simulations can also be used to study and understand the effect of engine scale on broadband noise.

More time will be necessary to sort out the scaling discrepancy observed with the low-order method and what the desired scaling factor actually is. We hope that the LBM simulations will help us work out this issue. In addition, another low-order method based on Hanson’s approach, as part of the OptiSound software, which BU has recently acquired, will be used to make the predictions. Differences between outcomes from the two low-order methods may also shed some light on the discrepancies.



Subtasks 2.2, inclusion of tip flow impact on the low-order model, and 2.3, inclusion of inflow distortion impact on the low-order model, were discussed in Year 2.

Milestones

The milestones set for Task 2 in Year 3 included:

1. Validation of the low-order model on new geometry and testing rig versus full-scale applicability
2. Final improvements to the low-order model

To date, as part of this project, the low-order model has been applied to several cases with accompanying experimental data for validation: the ACAT1 geometry and now to the FAA CLEEN I rig- and full-scale geometries. The rig-scale cases, ACAT1 and FAA CLEEN I, show good agreement between the predicted and measured acoustics. In all cases, the approach prediction is slightly high. The source of this discrepancy is not yet understood. The FAA CLEEN I full-scale geometry, as discussed above, was not accurately predicted.

Application of the low-order method to a fan stage with nonuniform inflow has been considered. Methods were constructed in Year 2 for applying the low-order model to a nonuniform inflow case. However, no data are available to use for validation. Therefore, the methods showed promise but whether they actually work is unclear. The experiments planned for later in the Year 3 funding cycle may include a nonuniform inflow case. If experimental data become available, efforts will be made to assess whether the low-order method can be used for predicting the noise in the presence of nonuniform inflow to the fan stage.

The PhD student is currently working to better understand the application of the low-order method to the swept vane case (which is the case for both the ACAT1 and the FAA CLEEN I geometries). Further insights will be available on this topic in the future.

Major Accomplishments

- FAA CLEEN I rig- and full-scale RANS simulations completed and transferred to BU
- FAA CLEEN I rig- and full-scale acoustic predictions completed (iteration completed); comparison to data made



- Full-scale engine noise simulations with high-fidelity LBM performed for the three certification conditions; grid sensitivity study performed, as well as a source region analysis of the turbulent wake of the fan
- Further scaling studies to acquire insight into expected outcomes completed
- OptiSound software acquired to enable another prediction comparison
- PowerFLOW (LBM) case files for FAA CLEEN I rig- and full-scale geometries found by RTRC; new runs to commence soon
- Investigation of various methods for accounting for sweep in the low-order acoustic method commenced

Publications

These results have not been published yet. Some results may be included as part of the 2024 Aeroacoustics Conference manuscript. Approval will be required from P&W and is being sought.

Outreach Efforts

None.

Awards

None.

Student Involvement

One BU PhD student has worked on the low-order model.

Plans for Next Period

The milestones set for the end of the third-year funding cycle and into the fourth year related to this task include:

- Final improvements to the low-order model

Depending on the results of the LBM study, as well as comparisons to the OptiSound results and other continued scaling studies, the low-order model will be updated.

Task 3 – Rig Test Planning

Raytheon Technologies Research Center Boston University and

Objectives

Experiments in the RTRC Acoustic Research Tunnel will be used to:

- Acquire key aerodynamic and acoustic data to support the validation of low-order and mid- (RANS) to high- (very large eddy simulation and LBM) fidelity CFD models
- Assess the noise trends and scaling laws of different fan stage designs (as outlined in Research Approach)

Research Approach

As part of developing the Year 3 proposal, RTRC and BU laid out a plan for experiments that will leverage an existing fan rig at RTRC. Multiple meetings occurred to determine the desired fan size and operating point that can be supported by the rig at RTRC. The process for determining the basic fan rig was developed, as well as a basic test plan. According to RANS simulations, a scaled version of the FAA CLEEN I rig-scale geometry, at approach rotor speed, was determined to be obtainable, on the basis of the RTRC rig electric motor constraints. The flow path has been modified to focus solely on the bypass, thus eliminating the need for a core. The highest-priority tests were determined after discussion with P&W. These include in preferred order:

1. Fan alone vs. full stage results
2. Effect of placement of the vanes
3. Effect of inflow distortion
4. Effect of pylon
5. Effect of fan differences (lean/sweep)
6. Effect of vane heterogeneity



The test matrix must still be finalized, as well as some of the details regarding which measurements will be obtained. Field acoustic microphones will be used. Internal flow measurements downstream of the fan will also be a priority.

Milestones

The milestones set for Task 3 in Year 3 included:

1. Final rig design
2. Test rig shakedown
3. Completion of rig testing

As described above, the final rig design is essentially complete. The rig will be built in early 2024, and the tests will commence around March of 2024. This milestone will still be on track for completion during the Year 3 funding cycle.

Major Accomplishments

- Multiple meetings between RTR/BU and P&W to determine the exact test capabilities.

Publications

None.

Outreach Efforts

None.

Awards

None.

Student Involvement

None.

Plans for Next Period

The milestones set for the third year related to this task include:

- Testing rig shakedown
- Completion of rig testing



Project 076 Improved Open Rotor Noise Prediction Capabilities

Georgia Institute of Technology

Project Lead Investigator

Principal Investigator: Professor Dimitri N. Mavris
Director, Aerospace Systems Design Laboratory
School of Aerospace Engineering, Georgia Institute of Technology
Phone: (404) 894-1557, Fax: (404) 894-6596
Email: dimitri.mavris@ae.gatech.edu

Co-Principal Investigator: Dr. Jimmy Tai
Division Chief, Propulsion & Energy
Aerospace Systems Design Laboratory
School of Aerospace Engineering, Georgia Institute of Technology
Phone: (404) 894-0197, Fax: (404) 894-6596
Email: jimmy.tai@ae.gatech.edu

University Participants

Georgia Institute of Technology (Georgia Tech)

- P.I.s: Dr. Dimitri N. Mavris, Dr. Jimmy Tai
- FAA Award Number: 13-C-AJFE-GIT-078
- Period of Performance: October 1, 2022 to March 30, 2023

Project Funding Level

The project funding is \$300,000 per year from the FAA. The cost-share match amount is \$300,000 per year. The sources of matching are cash and in-kind cost-share from an industry partner (GE).

Investigation Team

Dr. Dimitri Mavris, Professor, Georgia Tech (P.I.)
Dr. Jimmy Tai, Senior Research Engineer, Georgia Tech (Co-P.I.)
Dr. Miguel Walter, Research Engineer II, Georgia Tech
Mr. Brenton Willier, Graduate Student, Georgia Tech
Mr. Grant Stevenson, Graduate Student, Georgia Tech

Project Overview

The contrarotating open rotor (CROR) system has promising environmental benefits because of its ultra-high bypass ratio and high propulsive efficiency. The reduced fuel burn and emissions of the CROR compared with an equivalent-thrust turbofan make it an economically viable and environmentally friendly propulsion alternative to traditional ducted systems. However, in the absence of a noise-conditioning duct, aerodynamic interactions within the CROR system, as well as between the system and surrounding installation components such as the engine pylon, may result in noise penalties. If the system configuration is not optimized, the added effect of flow asymmetry to the aerodynamic interactions could potentially result in severe noise penalties, making the CROR system infeasible for use in the aircraft industry.

The proposed work will perform a sensitivity study on the design parameters of a CROR-pylon configuration. This study will leverage knowledge from past efforts with this type of configuration in order to narrow down the space of design parameters. High-fidelity computational aeroacoustics (CAA) analyses will be carried out in order to analyze the effect of each of the

chosen parameters on noise. The outcome of the study is to provide a ranking, among the selected parameters in the study, that states the parameter importance for a given noise metric. This research is intended to provide both the FAA and industry with key insights necessary for the design optimization of the CROR system in the future.

The A76 project was proposed as a three-year effort with renewal on a per-year basis, and study tasks comprising the study were accordingly planned. During the first year, the aim was to determine the important parameters affecting rotor or propeller acoustics. This task then involves carrying out an extensive review in the open literature to identify previously studied and acknowledged design and operational parameters affecting rotor or propeller acoustics. The second task in the first year focused on the development of a parametric geometry model for a contra-rotating open rotor. Such a model would help to parametrically vary the open rotor geometry during computational aeroacoustics analysis needed for the sensitivity study. Tasks during the second year comprise formulating the sensitivity study as well as a limited validation effort of numerical simulations against experimental data in open rotors. The simulation campaign for the sensitivity study would comprise part of the second year and the entire third year. Such length is due to the computational cost of carrying out high-fidelity simulations for aeroacoustics.

During the development of the second year, was decided by FAA supervision that to assess confidence in numerical simulations, a more extensive validation campaign would be needed in order to assess confidence in numerical simulations. Simulations then were to be validated in a range of rotor speeds and angle of attacks in accordance flying conditions of relevance for community noise. Therefore, the research effort in the second year was re-purposed to address such validations. Finally, the A76 project was not renewed for a third year.

Task 3 - Validations of Computational Aeroacoustics

Georgia Institute of Technology

Objective(s)

This task concerns with assessing the level of agreement between numerical simulations and experiments. Therefore, this task focuses on validating predictions from high-fidelity simulations against available experimental data from an open rotor configuration in order to evaluate discrepancies between predictions from numerical simulations and experimental data.

Research Approach

Validations in this project focus on evaluating discrepancies from simulations that have been previously calibrated aerodynamically. Accordingly, the first step is concerned with calibrating simulations aerodynamically against experimental values on the F31/A31 open rotor. At low Mach conditions, loading noise is most relevant. Therefore, loading is enforced by matching the time-averaged thrust. The calibration process results in blade pitch settings that minimize discrepancies between simulated and experimental thrust. The second part concerns acoustic validation of the F31/A31 open rotor by employing calibrated pitch settings. Furthermore, validations are also carried out for nominal pitch settings.

A hybrid approach for computational aeroacoustics (CAA) is adopted. High-fidelity simulations are the focal point of the study and are thus employed. The unsteady aerodynamic flowfield is simulated by a lattice Boltzmann method (LBM) solver, whereas the far-field aeroacoustics are predicted by a Ffowcs Williams–Hawkings (FW-H) solver.

Methodology

Validation Cases and Experimental Data

The geometry of interest is the contra-rotating open rotor geometry based on a sub-scale model of the F31/A31 historical blade set, designed by GE. The front rotor geometry consists of twelve F31 blades with a tip diameter of 0.6518 m, whereas the aft rotor consists of ten A31 blades with a tip diameter of 0.6297 m [1]. NASA conducted wind tunnel experiments [1–3] on the aforementioned geometry in low- and high-speed regimes. These experiments evaluated aerodynamic and acoustic performance for approach, take-off and cruise conditions. The low-speed experiments were run in the low-speed wind tunnel (9 ft × 15 ft) at NASA facilities. These experiments targeted three pitch settings: scaled take-off (STO), nominal take-off (NTO), and approach (APP) at several rotor design speeds. Each test was run with and without a pylon. Acoustics data were gathered for a number of cases using a free-stream Mach number of $M_\infty = 0.2$, while varying rotor speed and angle of attack.

Acoustics data were collected at 18 sideline microphones, located at an offset distance of $d = 5$ ft, parallel to the axis of the model. These microphones cover geometric observer angles between 17.6° and 140° . These angles are measured with

respect to the intersection of the aft blade pitch axis and the engine axis. Geometric angles lower and higher than 90° cover forward and aft locations, respectively. Specific information about microphone location has been detailed by Sree [2] and thus is not repeated here.

The present study focuses on validating cases from the low-regime experiments, specifically at the NTO pitch setting and without the pylon geometry. The experimental NTO cases [1, 2] as a function of varying operational parameters are illustrated in Figure 1, shown as black round symbols, along with the chosen cases for validation, shown as blue square symbols. The validation cases were chosen at rotor speeds spanning the upper-half range. The experimental data used in the current study came from two sources: i) NASA experiments on the F31/A31 open rotor geometry and ii) GE Aerospace data for the same F31/A31 experiments. The former source of data is employed exclusively for acoustic validations, whereas the latter is for aerodynamic calibration. These data were shared by GE Aerospace as an industrial partner in an FAA ASCENT project and are proprietary; consequently, these data are not shown.

The acoustic data employed were obtained from NASA experiments on the F31/A31 [1, 2, 4]. Three datasets were provided as supplemental information of NASA report in the form of power spectral density (PSD). The first one is the “11” set, which contains as measured spectral density; the second one is the “21” set, which comprises microphone-corrected spectra accounting for corrections due to microphone and bullet-nose sensitivity and directivity; the last one is the “41” set, containing 1-ft lossless spectra that correct for losses due to atmospheric attenuation [5].

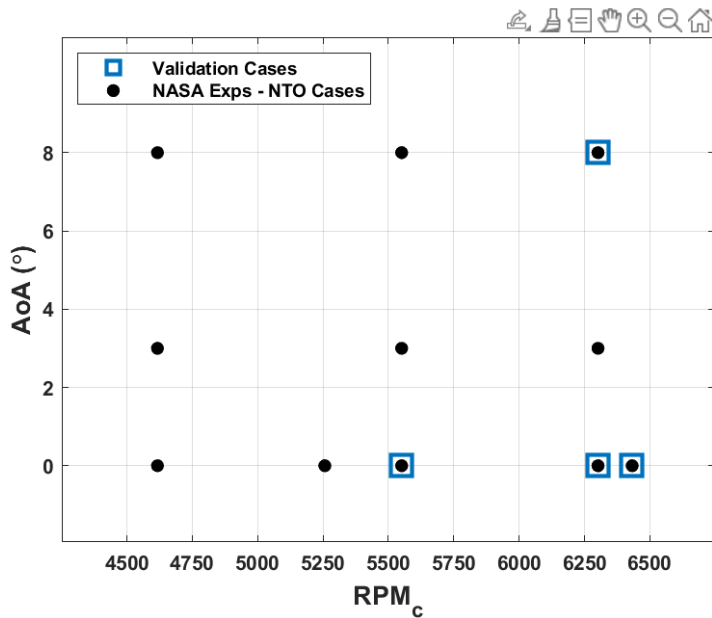


Figure 1. Validation cases. AoA: angle of attack; NTO: nominal take-off.

The current study employs the fully corrected wind tunnel measurement for validations against numerical simulations. Such fully corrected data are obtained by removing the wind tunnel background noise from the “41” data because this latter set accounts for all other corrections. The background noise is taken from the 802 RDG that contains acoustics data without blades and is applicable to all powered conditions at a zero angle of attack. [1] The details of calculating the fully corrected acoustic data is described next. First, the acoustic data are converted to a narrow-band sound pressure level (SPL) as follows:

$$SPL^* = PSD^* + 10 \log_{10}(\Delta f)$$

where $\Delta f = 12.2$ Hz is the frequency bin. Next, the acoustic data for every case as well as the background wind tunnel are scaled back to their respective sideline locations. Then, the fully corrected wind tunnel measurement is obtained by removing the wind tunnel background noise according to

$$SPL = 10 \log_{10}(10^{SPL^\dagger/10} - 10^{SPL_{wt}^\dagger/10})$$

Additionally, two corrections [6] are introduced. The first one ensures invalidating the above expression in cases where the background noise exceed the microphone noise level, $SP L^*_{wt} = SP L^* - 0.5$ dB if $SP L^*_{wt} > SP L^* - 0.5$ dB; while the second one corrects low frequency noise associated with the wind tunnel. Below 700 Hz noise is removed by replacing that portion of data with a parabolic function having 10 dB attenuation, relative to 700 Hz level, at 100 Hz.

Calibration in aerodynamics

Aerodynamic calibration is considered prior to acoustic validation. At the low Mach flying conditions of interest to the current study, loading noise is most relevant. [7] Since such noise type is thrust dependent, a loading equality constraint is enforced as a requirement for acoustic validation. Loading here is enforced by matching time-averaged thrust. Moreover, it is acknowledged that such time-averaged measure might not be sufficient since there may be contributions from other factors. Note, there is no attempt to directly bring CAA predictions close to experimental values, but instead evaluating CAA predictions given that a loading metric has been met.

Consider a set of calibrating parameters, collected in a vector ζ . Such parameters are generally inputs to a simulation code. Their values are unknown and thus need to be determined by a calibration process, which seeks to improve agreement between experimental data and simulation predictions. The calibration process is accomplished by minimizing a cost function:

$$\zeta^* = \arg_{\zeta} \min L$$

where the cost function, L , consists of a weighted L^2 -norm measure of discrepancies between experimental aerodynamic quantities and numerical predictions:

$$L = \| \mathbf{w}^t \mathbf{\Delta} \|_2$$

Here, \mathbf{w} is a vector of weights, expressing the importance of a particular aerodynamic quantity in the calibration process, whereas $\mathbf{\Delta}$ is a vector containing normalized discrepancies in aerodynamic quantities between the experiments, z_i , and simulations, \hat{z}_i :

$$\mathbf{\Delta} = \begin{bmatrix} [\hat{z}(\zeta) - z_i]/z_i \\ \vdots \end{bmatrix}$$

The calibration parameters, $\zeta = [\beta_f, \beta_a]$, contain the pitch angles of the forward and aft rotors, respectively. Such parameters are allowed to vary around the nominal pitch setting value, $[\beta_f^n, \beta_a^n] = [40.1^\circ, 40.8^\circ]$, corresponding to the NTO pitch setting.

The calibrated pitch angles $\zeta^* = [\beta_f^*, \beta_a^*]$ result from minimizing the cost function, L . This function is constructed by using experimental values of the forward and aft rotor aerodynamic performance z_i , whereas the simulation counterpart $\hat{z}(\beta_f, \beta_a)$ is approximated via linear regression models, fitted from training data stemming from LBM simulations. Such training data consist of forward and aft thrust from simulations for different values of pitch settings, which are varied around the nominal pitch setting. Note that the employed linear models are considered appropriate, as since departures from the nominal pitch settings are expected to be small. A total number of twelve simulations (six per calibration case, each at RPMc = 5550.5 and 6432.0) are carried out. For each case, a regression model for each rotor thrust is constructed. Simulations are carried out with discretization sizes of approximately 190 million. Note that the resulting resolution is coarser than that used for aeroacoustics predictions; however, it is considered a suitable compromise between computational cost and accuracy based on our resolution studies; which only show variation within 1% in thrust prediction between simulations at different resolutions.

Validation in acoustics

Acoustic validations are carried out using the pitch blade settings resulting from the aerodynamic calibration. Additionally, a validation case at the nominal pitch setting (NTO) is also included in order to contrast numerical prediction against the

calibrated case. Such a case is chosen at the lowest rotor speed among the considered cases as shown in Figure 1. Furthermore, this case will also serve as a reference to bring forth the effects of calibration on the acoustical results.

The rotor speed range in the present acoustic validations focus on the upper-half of the rotor speed span in the F31/A31 experiments. International Civil Aviation Organization (ICAO) certification limits the effective perceived noise level (EPNL), a human-hearing-weighted and time-averaged metric of overall sound level, of every aircraft it certifies. This process examines three flight conditions, i.e., take-off, flyover, and approach, and compares the resulting EPNL versus a maximum value. Since the takeoff and flyover flight regimes are dominated by engine noise, as opposed to approach and airframe noise, these flight rotor speeds will continue to be the focus of this study. The calibration and validation cases addressed in the current study are a subset of the NASA experiments [1, 2] at the NTO pitch setting, as shown in Figure 1.

The frequency range is one important aspect to consider in this study. The ideal frequency range to be addressed in the current study should cover the entire the high annoyance portion - human hearing constraint - of 10 kHz. Such value applies to the full scale model, whereas in the wind tunnel model said threshold increases to 50 kHz due to the scale factor of 5 respect to the full scale model. [1] Simulations in the current study attempt to address a part of the high annoyance portion. Consequently, most overall noise metrics will be computed in the range of 0.5-50 kHz for consistency with experiments.

The metric for validation between experiments and simulations adopted in the current study is the overall sound pressure level (OASPL). It has been pointed out [8] that in the resulting acoustics data the F31/A31 open rotor experiments, the acoustic energy is distributed among all shaft order tones, opposed to the specific orders as predicted by theory. As a consequence, it has been argued that OASPL should be a good metric in spite of the distribution of acoustic energy among tones [8].

Computational Analysis and Set-up

Simulations in the current study rely on a hybrid strategy for computational aeroacoustics (CAA) analysis. The unsteady aerodynamics flowfield is simulated by means of a lattice-Boltzmann method (LBM) solver. During the runtime of the aerodynamic solver, flowfield data are collected at specified surfaces. Such data are then used as an input to a far-field acoustics solver. An acoustic solver, based on the FW-H equations, is then employed for predicting far-field acoustics. Both the aerodynamics and acoustics methods are described in more detail below.

Geometry employed on simulations

The geometry employed in the current study is the contra-rotating open fan based on the GE designed F31/A31 blades. The geometry includes the nacelle as well as the rotating hub for both front and aft rotors. Nevertheless, the simulated geometry does not include the blade to blade angle variation from the assembly process that is present in the experiment [8] since such information is not available. The simulated geometry uses a purely cylindrical aft nacelle extension as opposed to the test article which was installed using a nacelle extension with a varying sectional radius. Moreover, the geometry used in the current simulations does not include gaps in junctions, such as those found between the nacelle and rotating hubs and between the blades and hubs.

The F31/A31 shape employed in the current study is that of the max climb flight condition. The geometry was provided with blade pitch settings of 60.5°/59.0°. Any blade pitch setting addressed in the current study is thus set from the aforementioned forward and aft pitch angles. Moreover, it is important to point out the blade shapes are fixed to the aforementioned flight condition regardless of the operational parameters utilized in the simulated cases. The aeroelastic deformation has implications in aerodynamics and acoustics performance. The balance between aerodynamic, centrifugal and Coriolis forces results in blade deformation, especially in the outward-half span of the blades. As previously investigated, [9] blade deformations due to the operating point influence both aerodynamic and acoustic performance. Larger deformations are observed at the cruise condition, followed by the take-off condition and approach. Differences in shapes between unrunning and running blades exhibited differences of around 5% in thrust coefficient predictions. Thus, the study found that accounting for blade deformations improves simulation predictions. Ideally, every operating condition in simulations should use the corresponding deflected shape. Unfortunately, lack of information on blade shapes prevented accounting for such effects. Therefore, the only available shape - at max climb - is employed in all cases examined in the current study.

Unsteady Aerodynamics

The unsteady aerodynamic flowfield is obtained by employing a commercial lattice-Boltzmann method (LBM) solver, PowerFLOW. Whereas traditional fluid solvers, which are - based on the continuous assumption via Navier-Stokes equations - solve for macroscopic quantities; LBM solves for the Boltzmann equations by tracking the evolution of microscopic particle

distributions in the fluid and thus modeling occurs at a mesoscopic scale - simplified microscopic behavior - where the physics are more fundamental. Consequently, the conserved fluid quantities are not directly modeled, but instead obtained indirectly by integrating locally over the particle distribution functions. The compressible Navier-Stokes equations of fluid dynamics are recovered through the Chapman-Enskog expansion. Such modeling results in low dispersion and dissipation properties, which in turn makes it very desirable for aeroacoustic purposes.

Origins of LBM can be traced back to the lattice gas automata (LGA) method. In this method, fluid flow is simulated by tracing motion through advection and collision of fluid particles on a regular lattice by employing the Boolean fluid model. However, in LBM, continuous particle distributions are employed, similar to particle distribution functions in kinetic theory. This adoption improves upon the shortcomings of LGA, such as noise and limitations in transport coefficients. LBM primarily encompasses two steps, collision and propagation. The collision step occurs when particles with different velocities arrive and interact at the same node. While the propagation step involves particles traveling to their nearest neighbors in the direction of their prescribed velocity after collision. The LBM scheme for fluid dynamics consists of the time evolution of the distribution function, which is governed as follows:

$$f_i(\mathbf{x} + \xi_i \Delta t, \mathbf{t} + \Delta t) = f_i(\mathbf{x}, \mathbf{t}) + \Omega, \quad i = 1 \dots n$$

where f_i and ξ_i are the particle distribution function and the particle speed in direction i , respectively, while Δt is the time step. The term on the right hand side expresses the collision operator term which is modeled by the Bhatnagar-Gross-Krook (BGK) single relaxation time model:

$$\Omega = -\frac{f_i(\mathbf{x}, \mathbf{t}) - f_i^{eq}(\mathbf{x}, \mathbf{t})}{\tau}$$

Where f_i^{eq} is the equilibrium distribution function and τ is the relaxation time parameter. This model assumes a constant rate relaxation to equilibrium for the particle distribution function. The governing equations is explicitly advanced in time in a lattice with prescribed n particle velocity directions. The macroscopic quantities of the fluid are simply obtained by integrating the distribution functions over the velocity space; for instance, density and momentum are given by the following expressions:

$$\rho(\mathbf{x}, \mathbf{t}) = \sum_i f_i(\mathbf{x}, \mathbf{t})$$

$$\rho \mathbf{u}(\mathbf{x}, \mathbf{t}) = \sum_i \xi_i f_i(\mathbf{x}, \mathbf{t}), \quad i = 1 \dots n$$

Turbulence modeling is achieved by means of very large eddy simulation (VLES). Moreover, in order to reduce the spatial resolution requirement in near wall regions, a hybrid wall-treatment model is chosen. This modeling is based on the standard log law of the wall and includes a laminar sub-layer model to account for the effects of favorable and adverse pressure gradients.

Boundary conditions are defined as follows: in the outer boundaries, pressure/velocity boundary conditions are prescribed, whereas non-slip wall boundary conditions are prescribed on surfaces of both rotors and nacelle. In the nacelle extension, however, slip wall boundary conditions are prescribed in order to avoid influences of boundary layers in those locations. Boundary values ($V_\infty, T_\infty, p_\infty$) as well as rotor speed in the current simulations are set to those of the wind tunnel conditions and actual rotor speed as measured in the F31/A31 experiments; however, their values are not shown due to proprietary restrictions.

The computational domain is decomposed into: (i) inner cylindrical regions for the forward and aft rotors, respectively, each with its own rotating reference frame using a sliding mesh approach to model forward and aft fan rotation; and (ii) an outer cubic region with a stationary reference frame. The LBM scheme is explicitly advanced in time in a Cartesian volume mesh around the geometry under study. Spatial discretization is achieved via variable refinement (VR) regions. Such regions are comprised of specified volumes within the computational domain. A level defining the spatial resolution is assigned to each region. The spatial resolution increases two-fold with VR level. Several VR regions in locations of interest are defined within

the computational domain. VR regions consisting of small cylindrical volumes are defined by tracing the blades' leading and trailing edges as well as blade tips. VR regions around blade surfaces are defined by three different offset volumes. Moreover, VR regions are also defined for tip vortexes as well as blade wakes. Another VR region is defined by the volume encompassing fifty percent of the outer span of the forward rotor. At the inter-rotor space a VR region is also defined. Each rotating region also defines a VR region as well. Finally, other VR regions are created in order to progressively decrease resolution away from the open fan configuration. Each of the aforementioned regions is assigned a VR level as shown in Table 1. The highest resolution is 0.125 mm and in turn defines the solver time step of 1.7×10^{-7} secs, approximately. The typical discretization size for simulations in the current study is approximately 900 million voxels. Such size is the upper limit that can computationally be afforded in the current study.

Simulations are initialized with a uniform velocity corresponding to the free-stream value on coarse meshes of approximately 190 million voxels, and advance in time for 6 revolutions so that the near flowfield is unaffected by the initial condition. The resulting flowfield is then employed to run the full simulation. Unsteady flow data for aeroacoustic analysis is collected once the flow is established. The flow is considered established after 6 rotor revolutions when the flow has adjusted to the finer discretization. Computation of the full simulation requires approximately 110,000 single CPU hours on a 2.7 GHz Intel Xeon Gold 6226 processor cluster.

Table 1. Variable Refinement (VR) regions description.

VR	Detail
15	LE & TE blade edges, and blade tips
14	Tip vortexes and blade inner
13	Blade wakes, Blade mid and Outer blade span
12	Inter-rotor and Blade outer
11	Forward and aft rotating region
:	
0	Outer boundaries

Far-Field Aeroacoustics

Far-field aeroacoustics is predicted by means of a commercial Ffwocs Williams - Hawkings (FW-H) solver, PowerAcoustics. Moreover, in order to prevent acoustic reflections from outer boundaries, a sponge region surrounding the open rotor geometry towards the outer boundaries is considered. In said region, the fluid kinematic viscosity is progressively increased so that out-going acoustic waves are dissipated.

The FW-H solver processes transient flow data recorded at specified surfaces during the simulation of unsteady aerodynamics in order to propagate acoustics to the far-field. The upper frequency value intended to be modeled in the acoustic study influences the choice of the type of FW-H surface. Surfaces of the permeable type would be defined surrounding the open fan configuration, while impermeable type would be defined at the rotor surfaces. Permeable surfaces allow capturing noise sources with scattering or reflection effects at the expense of high spatial resolution inside the volume encompassing the FW-H surface. Impermeable surfaces, on the other hand, do not impose such a resolution requirement at the expense of not capturing scattering or reflection effects. Employing permeable FW-H surfaces for addressing, even partially, the high annoyance portion of noise spectra would impose such a high spatial resolution that would make simulations intractable for the current study. The choice is then to employ impermeable FW-H surfaces. These surfaces are defined at both rotor surfaces, not only including blades but also the hub rotating part.

Acoustical data are obtained at two sets of sideline receivers. The first one is the sideline receivers as described by experiments, [2] which are located at a distance, $d = 5$ ft. This set consists of 18 receivers, spanning from approximately 17.5° to 140° , and it is uniquely used for calculating discrepancy measures for comparison with experimental results. Likewise, the second set also consists of sideline receivers located at the same distance d , but with a higher spatial resolution of 2.5° separation, and spanning a larger range of angles, 15° to 160° . The arrangement of acoustic receivers is illustrated in Figure 2.

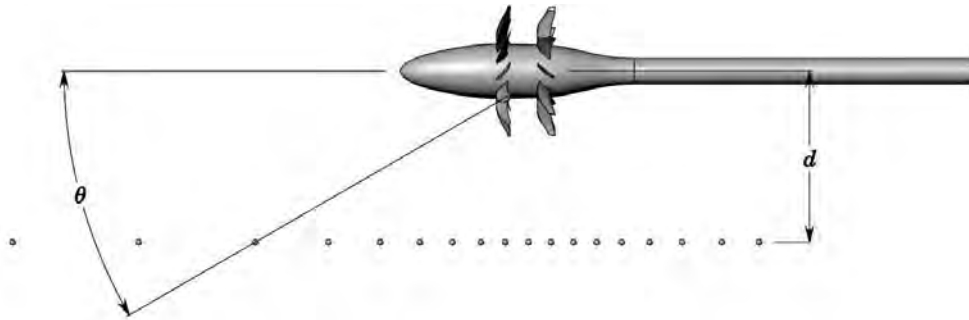


Figure 2. Arrangement of receivers at zero AoA.

Note: Geometry is a generic contrarotating open rotor and thus it is not the GE F31A31

* A generic open fan geometry is used for the illustration since F31/A31 geometry is GE proprietary

For the non-zero AoA cases, the distances to the microphones on the sideline array changes respect to the distances of that at zero AoA, in accordance to descriptions in NASA reports [1, 4], as shown in Figure 3. In order to incline the open fan model to a certain AoA different from zero, the model is rotated around a turn table, which pivot point is located 33.162 inch downstream of the reference point – aft pitch axis, while the microphones remain fixed. Consequently, at a non-zero AoA distances to microphones differs from those at zero AoA. Indeed, microphones in forward and aft direction are farther and closer, respectively, than in the AoA = 0 case. Moreover, directivity angles are also different than in the AoA = 0 case. Because of the above, acoustic validations for non-zero AoA cases are reported as a function of microphone label number rather than directivity angle, θ . Moreover, any calculation, e.g. attenuation correction, power level and so on, is carried out accounting for actual distances according to the non-zero AoA arrangement.

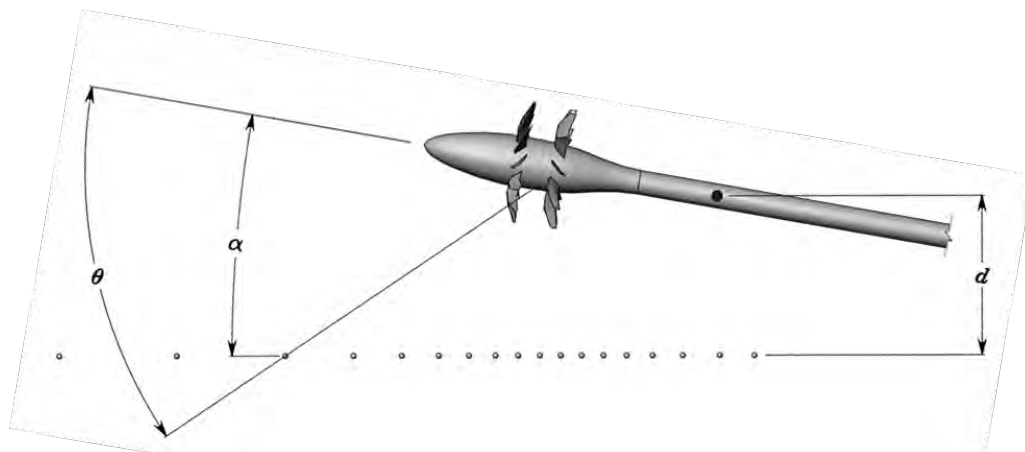


Figure 3. Receiver arrangement at non-zero AoA.

Note: Geometry is a generic contrarotating open rotor and thus it is not the GE F31A31

Flow data is recorded at the aforementioned impermeable FW-H surfaces for collection time periods between 12 - 16 rotor revolutions and at a rate of approximately 190 kHz. Spectral data is obtained by applying the Fourier transformation to the resulting data from the acoustic solver. The employed window width is 50% and a parabolic Welch windowing function with 50% overlapping is applied to the time-pressure data resulting from the acoustic solver.

Aeroacoustics results are examined by overall noise metrics such as overall sound pressure level (OASPL) and overall power level (OWPL). One-third octave spectra as well as source power level (PWL) spectra are also examined. OPWL is calculated by integrating the PWL spectrum along the frequency domain. PWL [10, 11] is obtained from the following expression:



$$PWL(f) = \frac{1}{\rho_\infty c_\infty} \int_0^{2\pi} \int_0^\pi [1 + M_\infty \cos(\theta_e)]^2 p^2(f, \theta_e, \psi) r_s^2 \sin(\theta_e) d\theta_e d\psi$$

and expresses the acoustic energy per frequency independent of direction by integrating acoustic pressure on a spherical surface around the open fan under study. In the above expression, p^2 is obtained from the sound pressure level (SPL) broadband spectra, r_s is the radius of a spherical surface surrounding the open fan under study, M_∞ , ρ_∞ and c_∞ are the free-stream Mach number, density and speed of sound, respectively. Moreover, f is the frequency, $\theta_e = \theta - \sin^{-1}(M_\infty \sin\theta)$ is the emission angle, while ψ is the azimuthal angle - revolving around the propulsor axis. The above expression is converted into spectrum, in dB, by previously using a reference sound power, $PWL_0 = 10^{-12}$ W.

Results: Validations for calibrated pitch cases

Calibration in Aerodynamics

The cost functions of thrust (L_T) and torque (L_Q) as a function of both forward (β_f) and aft (β_a) pitch angles are shown in Figure 4. Depending on the aerodynamic performance quantity chosen for the cost function, the calibration process leads to different sets of pitch angles - minimum location of the respective cost function as noted by the isocontour curve levels. As a consequence, optimal pitch angles that simultaneously minimize thrust and torque discrepancies are not attainable. Such feature is also found at other rotor speeds, although not reported for the sake of brevity.

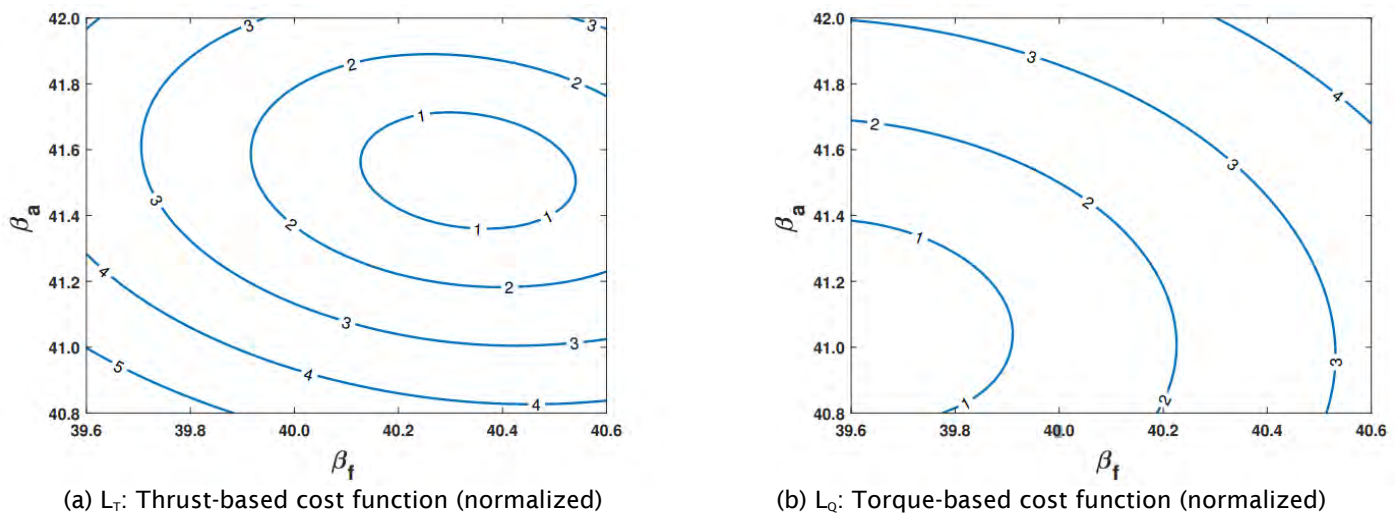


Figure 4. Thrust and torque cost functions, $RPM_c = 5550.5$.

The outcome of minimizing these cost functions based are shown in Table 2. Angular departures ($\delta\beta$) from the nominal pitch setting, such that: $\beta^* = \beta^n + \delta\beta^*$, are reported. As illustrated in the above figure, calibrated pitch settings are different. Thus, calibration based on a combined cost function, involving both thrust and torque, would not minimize either one but would be a compromise between them.

Table 2. Calibration based on L_T and L_Q at $RPM_c = 5,550.5$.

Cost Function	$\delta \beta_f^*$	$\delta \beta_a^*$
Thrust, L_T	+ 0.288°	+ 0.709°
Torque, L_Q	- 0.500°	+ 0.274°

As stated in Section II, thrust matching is chosen as the criterion for calibration. The reason behind this is the dependence of loading noise on thrust. Moreover, it is found that depending on the rotor speed of interest, enforcing thrust leads to different calibrated pitch settings. Therefore, calibration hereafter proceeds individually for every validation case. Results

from aerodynamics calibration are shown in Table 3. Note that at all rotor speeds investigated in this study, the resulting pitch angles slightly increase over the nominal one due to thrust underprediction at the nominal angles. Moreover, after calibrating, thrust is re-calculated from higher-resolution LBM simulations - as needed by aeroacoustics. Hence, the resulting thrust may vary slightly; however, discrepancy by individual rotor is within 1 %, which is in accordance with experimental uncertainty. [1] Also, calibrated pitch at $RPM_c = 6250.5$ is taken as the one at the highest rotor speed since predicted thrust is found within the acceptable threshold for calibration.

Table 3. Resulting calibrated pitch setting.

RPM_c	Cost Function	$\delta \beta_f^*$	$\delta \beta_a^*$	Remark
5550.5	Thrust, L_T	+ 0.288°	+ 0.709°	
6250.5	Thrust, L_T	+ 0.460°	+ 0.428°	same as highest rotor speed
6432.0	Thrust, L_T	+ 0.460°	+ 0.428°	

Comparisons of net thrust resulting LBM predictions and previous simulations [12] against experimental measurements are shown in Figure 5. All solvers predict thrust trends with rotor speed as seen in Figure 5(a); however, at the nominal pitch setting all solvers exhibit some degree of discrepancy from experimental measurements as shown in Figure 5(b). In contrast, LBM simulations at calibrated pitch setting exhibit the smallest discrepancy due to the thrust matching process. Furthermore, there are apparent variations in predictions among solvers at nominal pitch settings. Corresponding LBM simulations underpredict thrust at all rotor speeds, whereas the other two solvers generally overpredict. Levels of discrepancy are smaller for the OVERFLOW solver, whereas the FUN3D solver and LBM simulations exhibit comparable magnitudes of discrepancy.

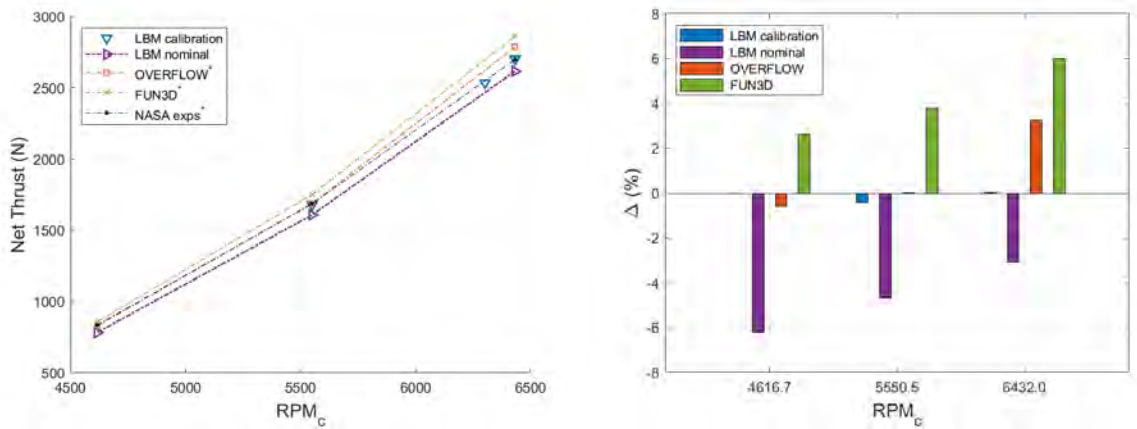


Figure 5. Thrust comparisons: Thrust (left) and discrepancy (right).

Torque ratio predictions from LBM simulations and previous studies [12] against NASA experiments are shown in Figure 6. At the nominal pitch setting, none of the solvers capture trends accurately as seen in the left plot. Indeed, all solvers predict monotonically decreasing trends with rotor speed, while NASA experiments exhibit a nearly flat trend. LBM simulations with calibrated pitch settings, on the other hand, result in a qualitatively closer trend. All simulations with the nominal pitch setting exhibit significant departure from experiments at the lowest rotor speed; however, departures decrease with rotor speed as shown in the right plot. Also, note that the effect of calibrating is not much different at the highest rotor speed compared to the nominal pitch setting. Finally, another numerical study [8] with the nonlinear harmonic (NLH) model reported thrust and torque ratio discrepancies of 1.6% and 9.0%, respectively, on average for six cases with corrected rotor speed ranging between 4620 - 6436 RPM_c .

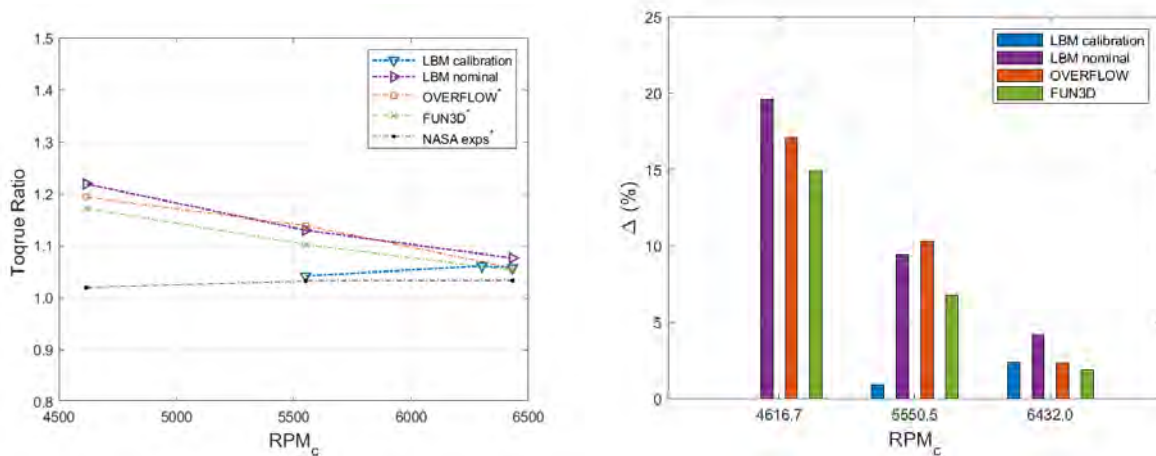


Figure 6. Torque ratio comparisons*: Torque ratio (left) and discrepancy (right).

*Values digitized from Nark et al. [12]

Validation in Acoustics

In this section, the findings on predicted noise obtained from propagation to the far-field, by integrating the FW-H equations on impermeable surfaces are presented. Numerical predictions are contrasted against NASA experimental measurements from complimentary data to the NASA report. [1] Quantification of agreement between experiments and numerical predictions are accomplished by computing metrics of discrepancy. These are simply differences between experimental and numerical values, or averaged discrepancy - root mean squared differences. For consistency with experiments, discrepancies are solely calculated from signals computed at the same locations of the acoustics probes in the F31/A31 experiments, [1, 2] whereas trends from numerical predictions are shown at a higher angular resolution. Acoustic quantities for comparisons comprehend overall sound pressure level (OASPL) as well as overall power level (OPWL). These are calculated within a frequency range of 0.5 to 50 kHz for consistency with experiments.

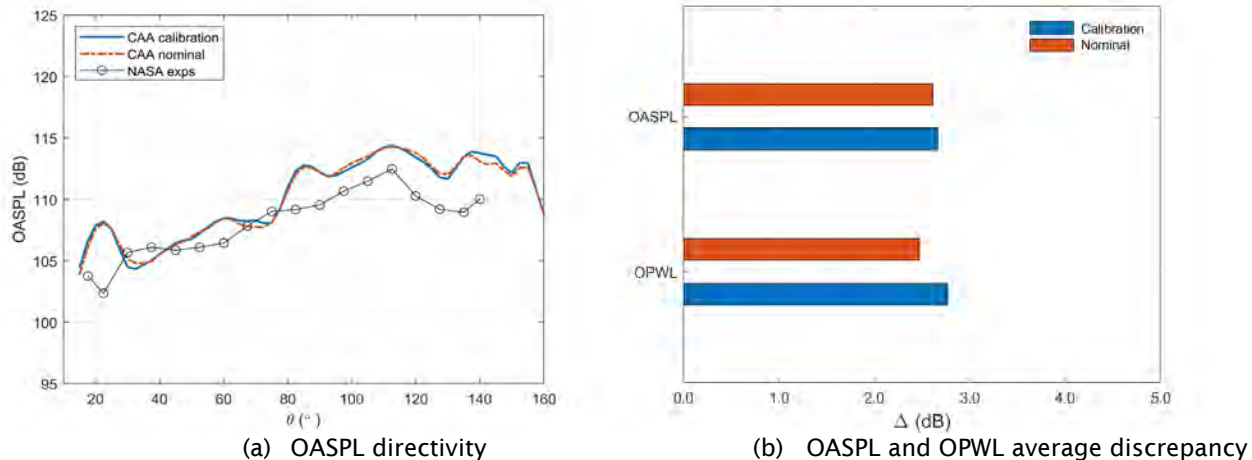


Figure 7. Comparison between nominal and calibrated pitch settings.

Validations contrasting the effect of calibrating to the nominal pitch setting are shown in Figure 7. Directivities of OASPL as predicted by simulations along with that of experiments [1] are shown in Figure 7(a), while respective average discrepancies are shown in Figure 7(b). Predictions are from medium resolution simulations of about 600 million voxels. There is noticeable

variation in agreement between simulations and experiments along directivity angles. Small differences are found for intermediate angles - between 25° and 80° - whereas differences increase for smaller and larger forward and aft angles, respectively. Moreover, note that no noticeable differences in OASPL directivity are found between predictions at the nominal and calibrated pitch settings. Average discrepancies of OASPL and OPWL are shown in Figure 7(b). When comparing between calibrated and nominal pitch settings, small changes in discrepancy are found between calibrated and nominal pitch setting, 0.05 dB for OASPL and 0.29 dB for OPWL. Such relatively small increments in discrepancies on the calibrated pitch setting is attributed to the increase in thrust in the calibrated case relative to the nominal case. Such increase is also consistent with the increasing behavior of sound power level with thrust previously reported in experiments. [1]

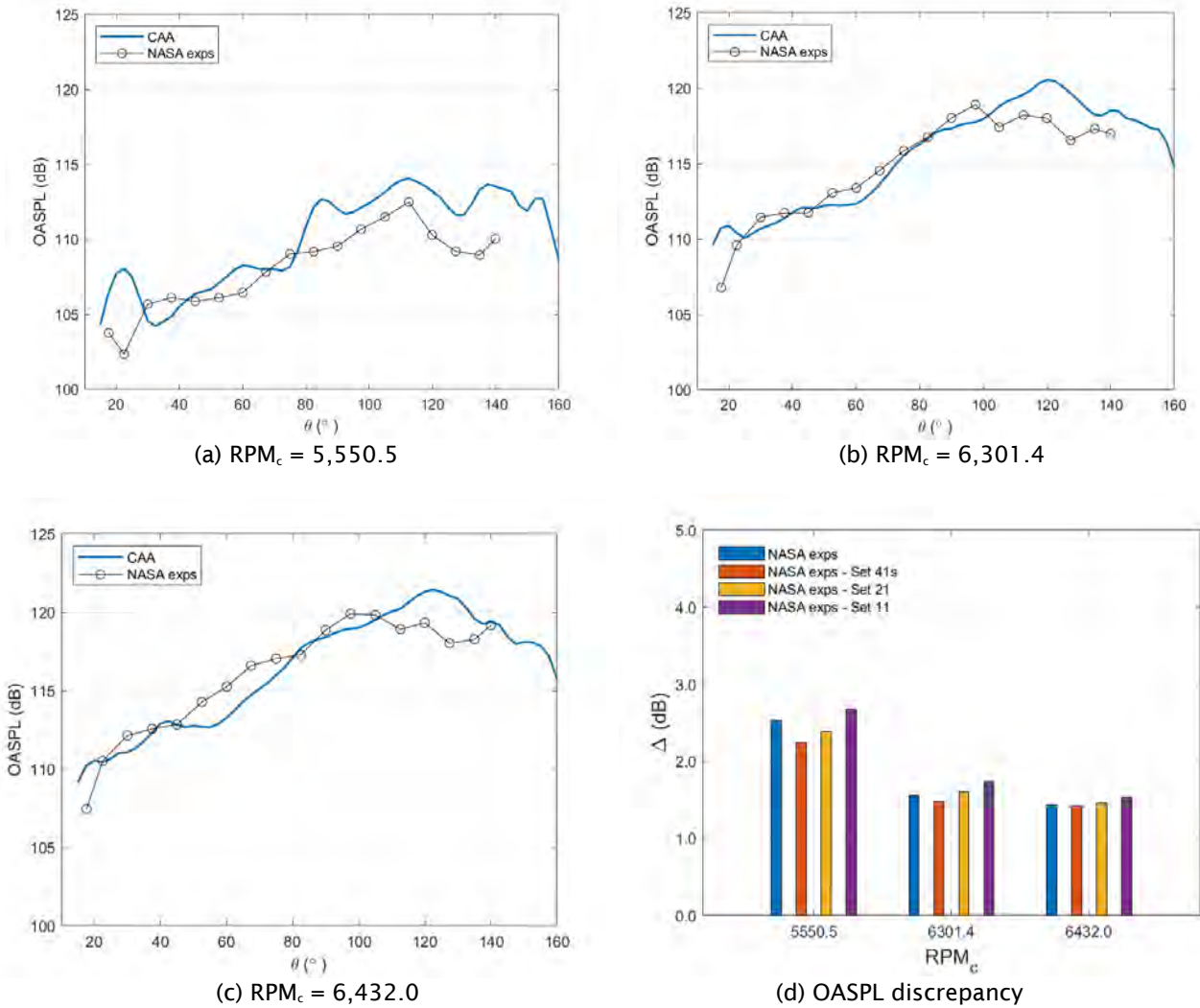


Figure 8. OASPL sideline directivity and respective discrepancies with experiments.

OASPL directivity with rotor speed as well as their corresponding averaged discrepancies for all calibrated cases are shown in Figure 8. Small changes in OASPL values are observed at any directivity angle for the two highest rotor speeds due to their proximity in RPM_c value. Moreover, closer agreement in trend and values are seen at the two highest rotor speed, shown in Figure 9(b) and (c), specifically for directivity angles between 20° and 100°. The corresponding discrepancies at every rotor speed are shown in Figure 8(d). In order to illustrate the effect of different corrections in the experiment measurements, discrepancies are calculated with respect to all relevant sets of the experimental data as previously described. Note that

partial correction in experimental data could lead to variations of discrepancy between 0.2 to 0.5 dB. Nevertheless, the actual discrepancy is measured with respect to the fully corrected data shown in the blue bar. Values around 1.6 dB are found for the two highest rotor speeds, whereas the discrepancy is larger, 2.5 dB approximately, for the lowest rotor speed.

Spectral representation of the far-field sideline noise directivity for the highest rotor speed is shown in Figure 9. A map of one-third octave spectra are plotted between 0.5 to 30 kHz. Although not perfect, some discernible similarities - qualitative and quantitative - could be found between the spectra from simulations, Figure 9(a), and that of experiments, Figure 9(b). Simulations reasonably predict the regions of large SPL values, located above 2.5 kHz and for directivity angles larger than 60°, although there is some overpredictions at higher frequencies - above 15 kHz - between sideline angles of 80° and 120°, approximately. Furthermore, simulations also predict the smaller regions containing the highest sound pressure level with a consistent frequency range - between 3.0 and 8.0 kHz approximately - although numerical predictions are shifted to the aft direction. Finally, simulations exhibit a very small region with peak values not observed in the experiments, around 120° and 3.2 kHz.

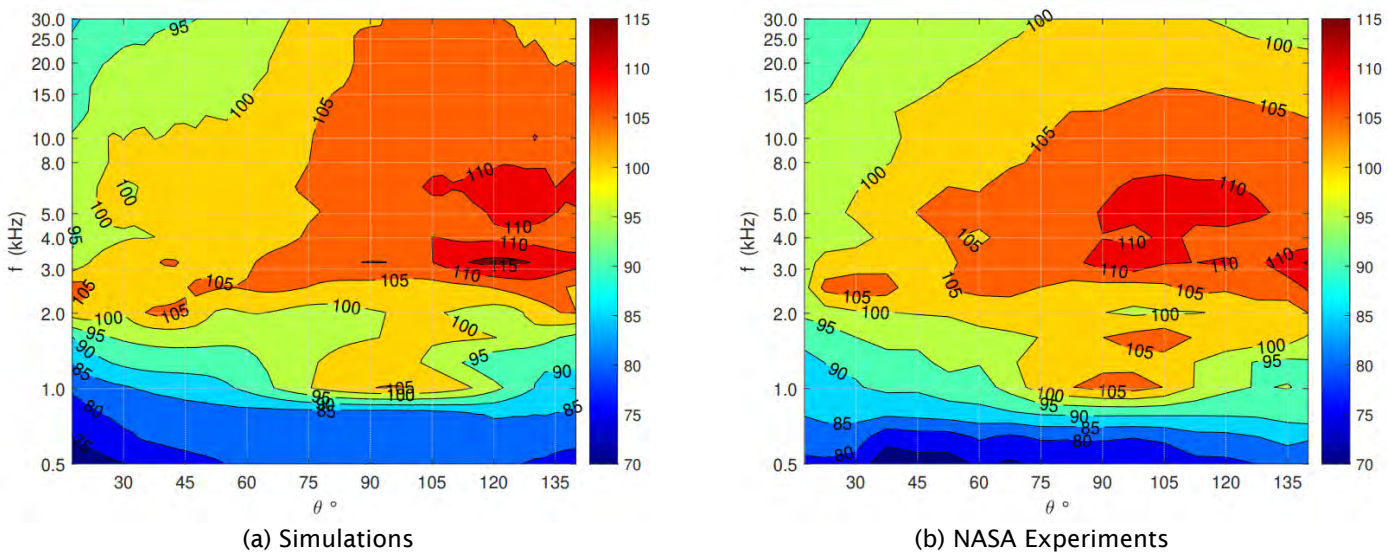


Figure 9. Sideline directivity in one-third octave SPL spectra (dB) at RPMc = 6432.0.

One-third octave spectra for the two highest rotor speeds at three different receivers are shown in Figure 10. These receivers are located at a forward position, $\theta = 45^\circ$, plane of the aft rotor $\theta = 90^\circ$, and an aft location, $\theta = 135^\circ$. Levels of discrepancy between simulations and experiments seem comparable for the two rotor speeds at every receiver. Moreover, at the forward receiver, shown in Figure 10(a) and (b), even though there are similarities in trend, the acoustic energy is more prominent within bands between 2 - 4 kHz in the simulation, whereas in the experiment this occurs between 4 - 6 kHz. At the plane of the aft rotor and the aft receiver, shown in Figure 10(c) - (f), there is agreement in the location of frequencies with the most acoustic energy; however, there is some overprediction toward the higher frequencies at these receivers, more noticeable beyond 15 kHz as noted previously in Figure 9. At higher frequencies, there is more agreement at the forward receiver, which can also be observed in the spectral map in Figure 9.

Source power level spectra comparison between experiments and simulations for the highest rotor speed is shown in Figure 11. The tonal content is quite apparent in the spectra, while the broadband content is noticeable. Distinctive tonal content can be observed up to 16 kHz although a great portion of the tonal content is more concentrated up to 12 kHz, which is in accordance with experiments. [4] In the simulation, the PWL spectrum reveals that the highest source power levels are observed at frequencies that are even multiples of the shaft frequency. The PWL spectrum calculated from experimental data not only exhibits high levels at even shaft orders but also odd ones. Such difference in the numerical predictions suggests that the acoustic energy is distributed somehow differently in the simulations. Based on theory grounds, it has been argued [8] that such behavior results from difference in geometry between simulations and in wind tunnel, primarily variations in the installed pitch from blade to blade.

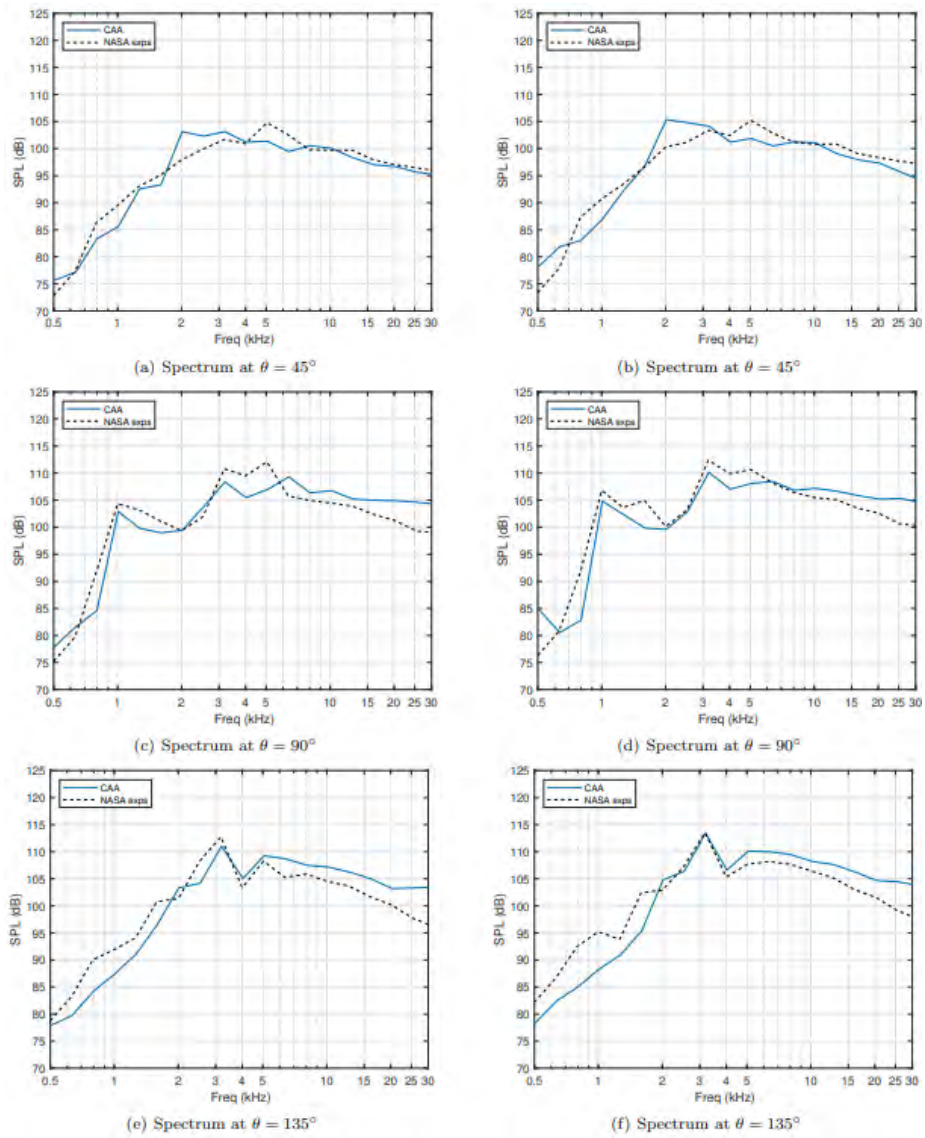


Figure 10. One-third octave spectra, $RPM_c = 6301.4$ (left) and $RPM_c = 6432.0$ (right).

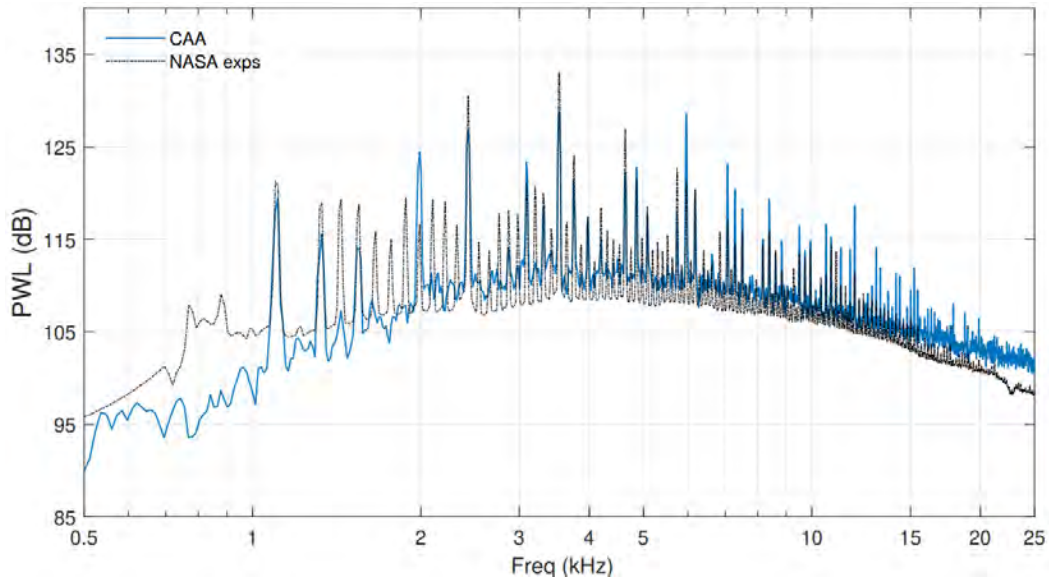
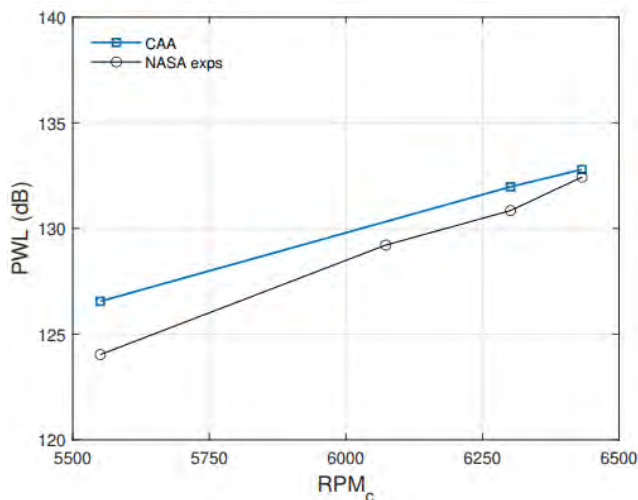
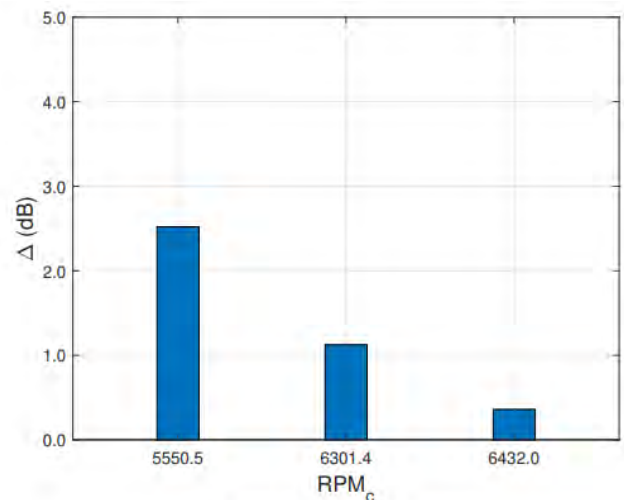


Figure 11. Source power level spectrum, $RPM_c = 6432.0$.

Acoustic energy generated by the open fan configuration is calculated by means of overall power level (OPWL). This quantity is calculated by integrating the source power level spectrum (PWL) for frequencies between 0.5 to 50 kHz. The PWL spectrum is obtained by assuming axisymmetry with respect to propulsor axis, $\psi \in [0, 2\pi]$, and is calculated by only using the same receiver locations used in experiments for consistency. The sideline acoustics data is mapped into a constant radius, equal to the sideline distance d , by assuming spherical spreading. [1] Comparisons of OPWL calculated from simulations and that of experiments are shown in Figure 12. The OPWL trends with corrected rotor speed are in qualitative agreement with experimental trends. Closer agreement is found above 6000 RPM_c, although it reduces at lower speeds. Numerical predictions are closer to the experimental values at the two highest rotor speeds, with an average discrepancy of less than 1 dB, whereas larger values of 2.8 dB are found at the lowest rotor speed as shown in Figure 12(b).



(a) Overall PWL trends



(b) Overall PWL discrepancy

Figure 12. Overall PWL.

The case at a non-zero AoA is chosen at the second highest rotor speed and angle of attack among the F31/A31 experimental cases. The operational parameters are then $RPM_c = 6304$ and $AoA = 8^\circ$. Comparison of overall sound pressure level (OASPL) from numerical predictions and experiments are shown in Figure 13, left plot. In addition to the impermeable FW-H approach, predictions using a permeable FW-H are also shown. Due to spatial resolution the permeable approach is limited to 12.5 kHz. Note that OASPL is plotted as a function of microphone label with number increasing from the forward to the aft locations. The impermeable approach in average provides close predictions in all microphones. In contrast, the permeable approach prediction are closer at intermediate microphones but prediction rapidly worsens for microphones in the aft region due to the length of the FW-H surface that is not able to cover farther aft locations. OASPL discrepancy trend with angle of attack is also shown in Figure 13, right plot. An increment of approximately 0.20 dB is observed as consequence of the increment in AoA.

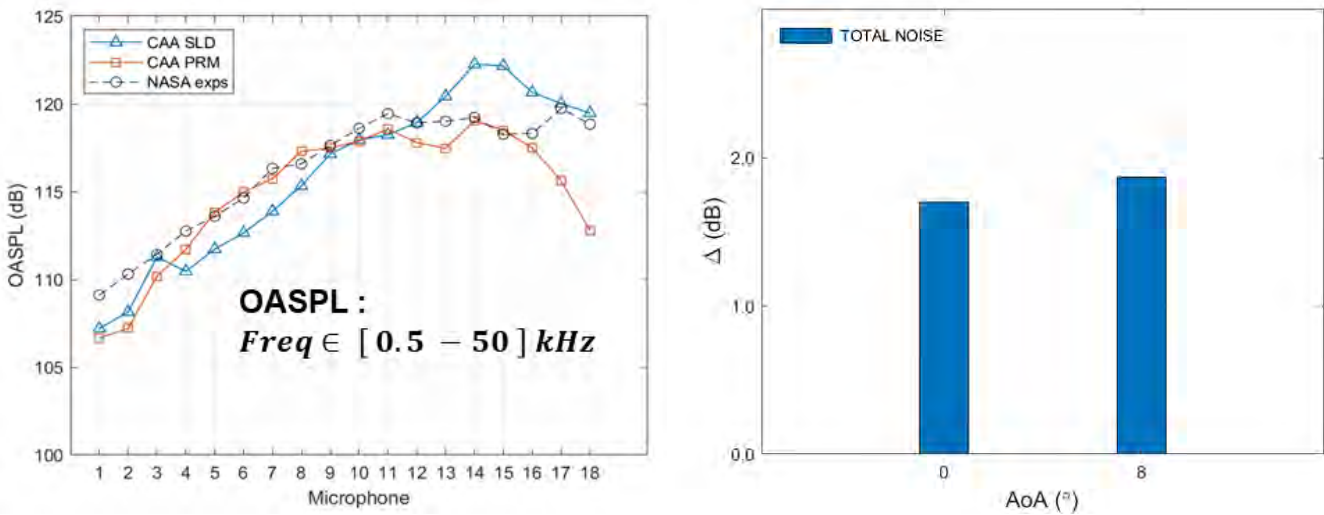


Figure 13. OASPL validation at AoA = 8° (left) and discrepancy trend with AoA (right).

Results: Validations for nominal pitch cases

At the nominal pitch settings, two cases are carried out to evaluate the acoustics as a function of angle of attack (AoA) at a nearly fixed corrected rotor speed of $RPM_c = 6304$. Simulations are carried out as previously described for the calibrated cases with the exception that acoustics are additionally predicted by a FW-H formulation that considers the convective effects of the free-stream. The commercial acoustic solver OPTYDB, a recent addition to the PowerFLOW suite, recently made available to research in the FAA A76 project, is employed for such an end. It is pointed out that results with the latter approach are considered the standard for comparison. This is because it possesses all the features needed to simulate far-field acoustics, such being able to predict the frequency range of interest as well as considering the effect of the free-stream. Such features were lacking on the permeable and impermeable approach previously used.

OASPL directivity in terms of directivity angle and microphone label are presented in Figure 14 for the AoA = 0° and AoA = 8° cases, respectively. OASPL is calculated in the 0.5 – 50 kHz frequency range. The OASPL discrepancy for this case is not larger than 1.3 dB with the non-zero AoA exhibit slightly smaller discrepancy as seen in Figure 15.

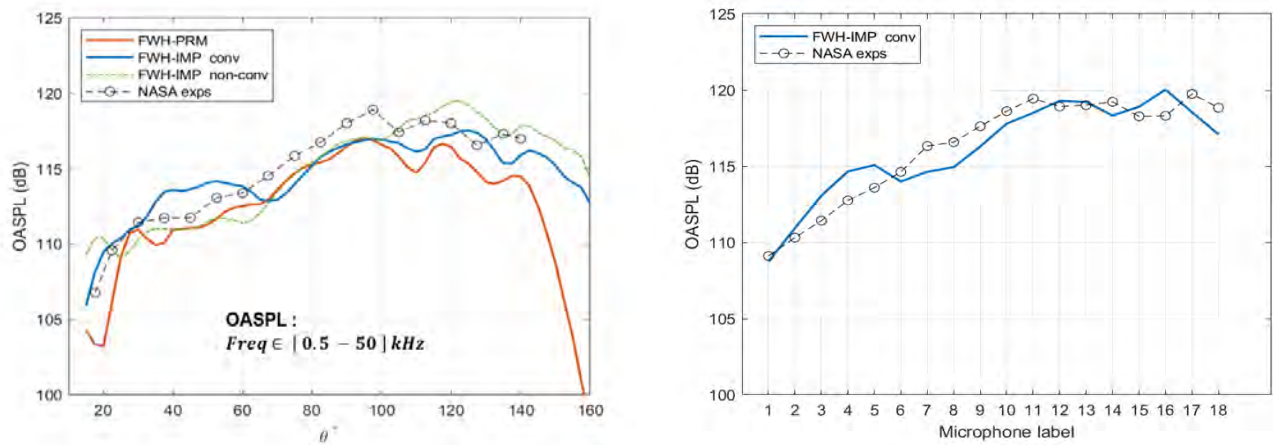


Figure 14. Total noise OASPL: AoA = 0° (left) and AoA = 8° (right).

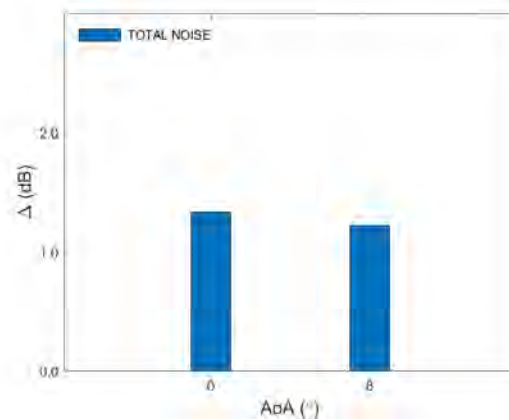


Figure 15. OASPL discrepancy with angle of attack (AoA) at nominal pitch.

Far-field Noise Directivity at non-zero AoA

When the AoA is different from zero, departures from the axisymmetric assumption of noise directivity are expected. Because loading in rotor blades exhibits changes while rotating - dependent with azimuthal angle. Consequently, directivity is examined at a sphere surface surrounding the open fan geometry. The spherical geometry has a radius equal to 10 forward rotor radius, $R = 10R_f$, and is centered around the intersection of the aft blade pitch axis and the axis of the open fan. Acoustic data are collected for a total of 1,334 acoustic receivers arranged along the polar direction with 36 receivers (5° separation) with 37 azimuthal arcs (10° separation). Definitions of the spherical coordinates are shown in Figure 16.

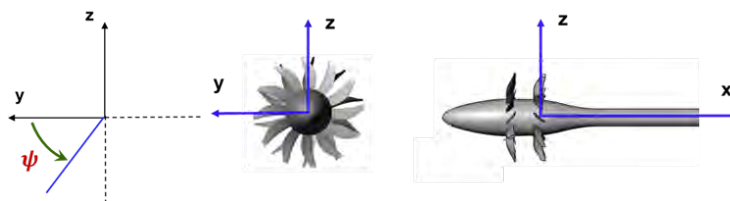


Figure 16. Spherical coordinate definition for CAA receivers.

Note: Geometry is a generic contrarotating open rotor and thus it is not the GE F31A31

The far-field noise directivity in terms of overall sound pressure level is shown in Figure 17 for the $AoA = 8^\circ$ case at corrected rotor speed of 6304 RPM. OASPL contours are shown at a spherical surface surrounding the F31/A31 open rotor model. The CAA predictions are achieved by means of the convective FW-H approach. OASPL contours exhibit lack of any axial symmetry, unlike cases at $AoA = 0^\circ$, in which axial symmetry is expected. Such three-dimensionality in the noise far-field results from the presence of crossflow in the plane of the rotors. Noise levels are larger in the lower hemisphere, i.e., at receivers with negative z coordinates, where the F31/A31 is tilted away from the flow. In contrast, low levels of noise are found in the upper hemisphere.

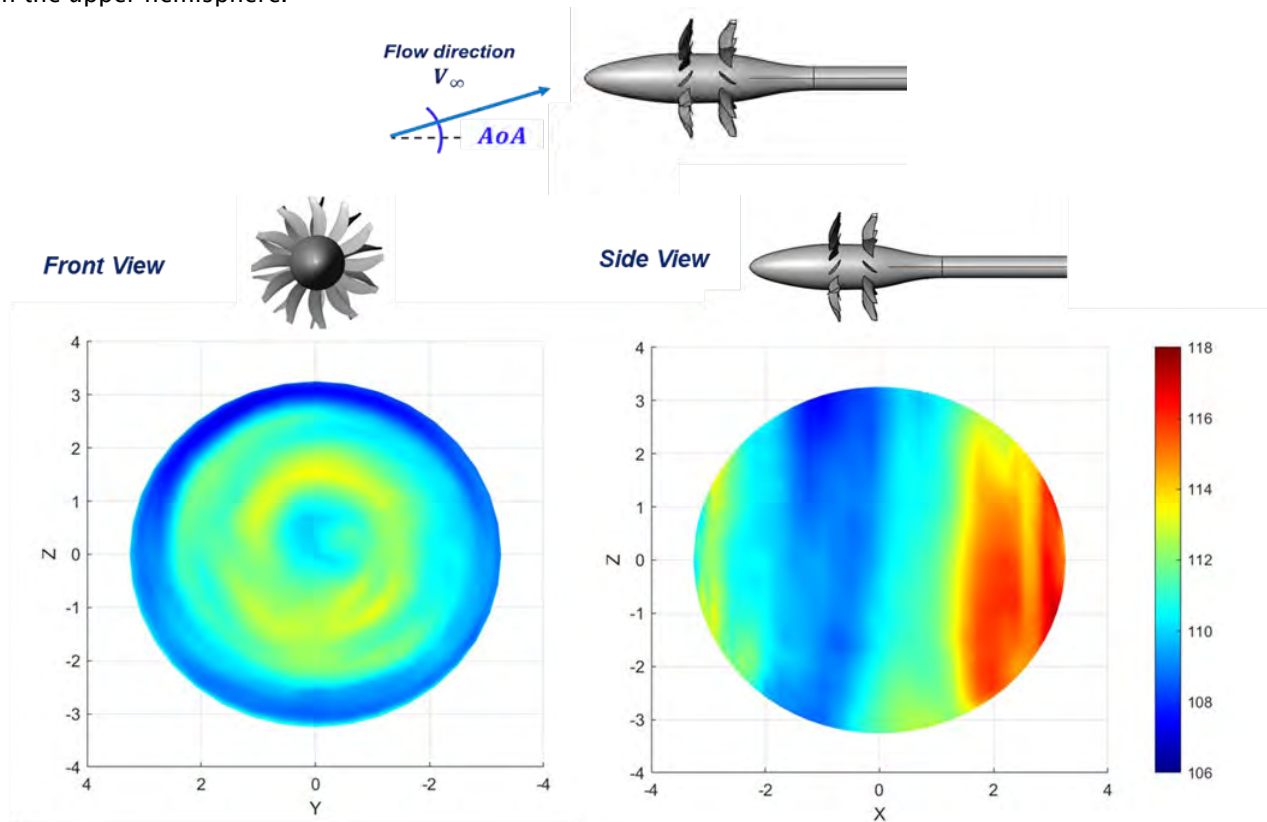


Figure 17. OASPL directivity at spherical surface for $AoA = 8^\circ$ case. Note: Geometry is a generic contrarotating open rotor and thus it is not the GE F31A31

A comparison of the directivity pattern between the non-zero and zero angle of attack cases are shown in Figure 18. The 2D contour plots are plotted in spherical angles. The contour on the left is the $AoA = 0^\circ$ case while the contour on the right is the $AoA = 8^\circ$ case. Note that in the former case axisymmetry is assumed - acoustics was predicted for a 180° arc rather than over the entire sphere. The lack of axial symmetry in the polar directivity is notorious for the non-zero- AoA case - OASPL directivity is different for different values of ψ . Lack of symmetry in the noise directivity results from the transverse component of the flow velocity. The existence of said component leads to periodic unsteady loading in the blades because of the variation in flow direction being ingested by the rotors. Such changes in flow direction exert changes in the local angle of attack experienced by the blades.

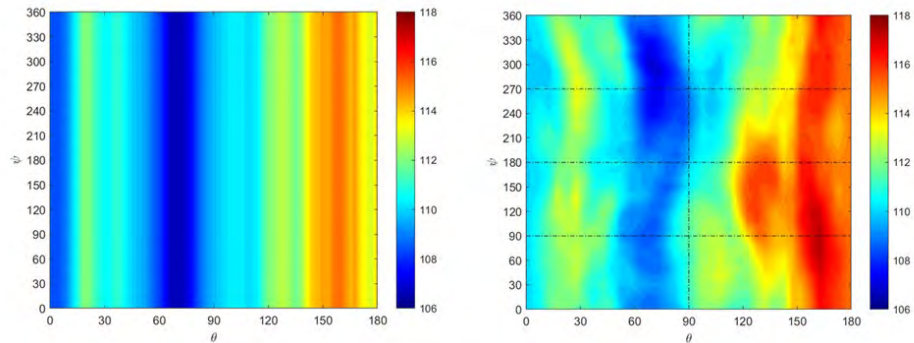


Figure 18. Total noise OASPL (dB) directivity in spherical coordinates: AoA = 0 ° case (left) and AoA = 8 ° case (right).

The OASPL directivity due to the noise component such as unsteady loading and thickness is shown in Figure 19 and Figure 20. These contours are similarly contrasted against the zero AoA case. It is noted that the directivity pattern of unsteady loading closely resembles that of total noise, suggesting that total noise is mostly dominated by it. The directivity pattern on thickness noise differs from that of the zero AoA case in that it exhibits a lack of axial symmetry. Moreover, a higher noise level is observed in the lower hemisphere compared with both the upper hemisphere and the zero AoA case.

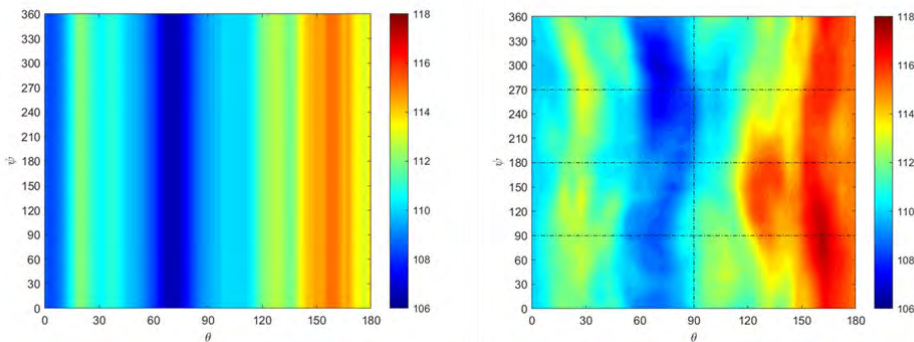


Figure 19. Unsteady loading OASPL in spherical coordinates: AoA = 0 ° case (left) and AoA = 8 ° case (right).

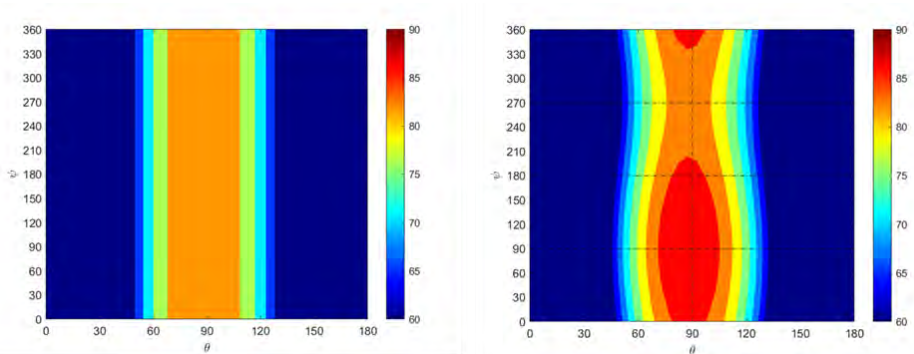


Figure 20. Thickness OASPL in spherical coordinates: AoA = 0° case (left) and AoA = 8° case (right).

Aerodynamics at non-zero AoA

In order to understand the unsteady loading that both rotors experience during operation at non-zero angle of attack flows, the axial force in one blade of each rotor is tracked as a function of both time and position. The latter is expressed by its

azimuthal location. The blade starting position is approximately at the positive z-coordinate, $\psi = 0^\circ$, and azimuth location is measured clockwise as shown in Figure 21.



Figure 21. Azimuthal angle definition.

Note: Geometry is a generic contrarotating open rotor and thus it is not the GE F31A31.

The thrust time-variations in a single blade per rotor are shown in Figure 22 at angles of attack $\alpha_\infty = 0^\circ$ and 8° . Variations are shown as a function of both time and location. The latter is expressed by its azimuthal location. The starting position for both blades of the forward and aft rotor is at $\psi = 0^\circ$, when their respective pitch axis aligns with the positive z-coordinate. A duration of four revolutions is shown for the unsteady thrust. For a non-zero AoA, the thrust pattern resembles a sinusoidal variation, and as a function of time, the thrusts in both blades seem to be close in phase. Such behavior is because both blades' starting position is at the same azimuthal location and both blades attain their largest value at approximately a quarter of their respective rotation. When the blade forces are plotted as a function of their azimuthal location, however, there is a phase shift of approximately $\pi/2$. This shift occurs because the maximum forces occur at $\pi/2$, whereas the minimum forces occur at $3\pi/2$ from their starting position following their respective direction in rotation. Note that because of the counter rotation in the aft rotor, maximum and minimum values instead occur at $3\pi/2$ and $\pi/2$, respectively. The degree of unsteadiness between the angle of attacks considered differs greatly. For $\alpha_\infty = 8^\circ$, the amplitude approximately varies $\pm 40\%$ over the time-averaged value, for $\alpha_\infty = 0^\circ$, the amplitude is only approximately $\pm 2.5\%$.

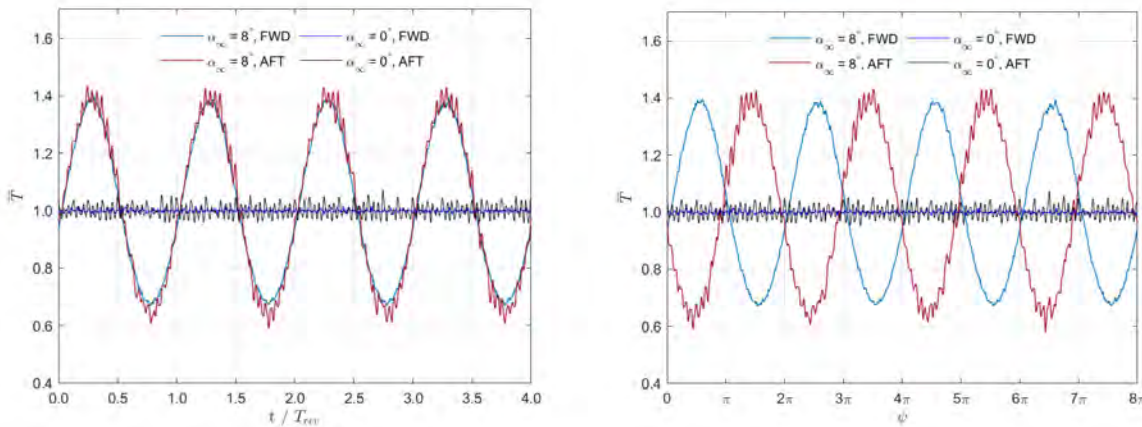


Figure 22. Thrust force normalized by the time-averaged value as a function of time (left) and azimuth (right).

The above behavior is due to the azimuthal dependence of loads in the blades occurring at a non-zero AoA. The tangential component of the flow, as seen from the moving blades, changes with azimuth; this in turn affects the angle of attack, thus leading to load dependence with azimuthal angle. In order to explain the azimuthal dependence, consider an idealized situation of a flow at non-zero angle of attack, in which the triangles of velocities as seen from two references of frames: an absolute one, which is fixed and aligned to the engine; and a relative frame, which rotates with the rotor, as shown in Figure 23. Moreover, while the absolute reference frame is a cartesian one ($x - y - z$), the relative one is cylindrical ($r - \psi - x$), while both having the axial coordinate x in common. From the fixed frame, velocities c are absolute; while from the rotating frame,

velocities w are relative. Also, note that in the triangle of velocities, the only concern is with the projection of the absolute velocity onto the $\psi - x$ since the radial component is assumed not to have an effect in this idealized situation.

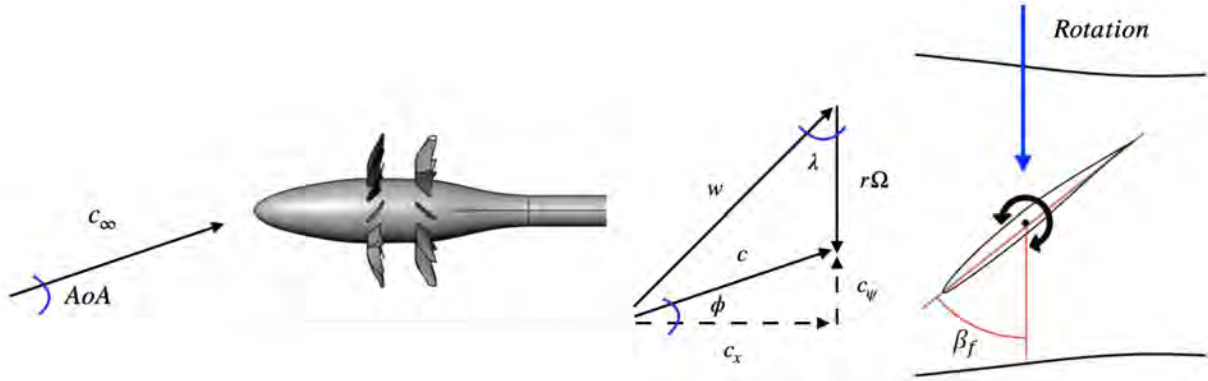


Figure 23. Flow angle in blades

Note: Geometry is a generic contrarotating open rotor and thus it is not the GE F31A31

The absolute velocity component in the $x - \psi$ plane can be expressed by the rotational and relative contribution, $\vec{c} = r\vec{\Omega} + \vec{w}$, where Ω is the blade angular speed. This velocity can also be decomposed into axial and tangential components, $\vec{c} = \vec{c}_x + \vec{c}_\psi$. The local blade AoA is measured from the relative velocity w with respect to the blade chord as follows:

$$\alpha = \gamma - \lambda,$$

where γ is the local chord angle and λ is the relative velocity angle. Note that the local angle of attack varies along the span of the blade since the chord angle depends on the value of the blade pitch angle as well as the twist angle at a particular radial location. As seen in the triangle of velocities, the relative velocity orientation depends on its tangential component as follows:

$$\lambda = \arctan\left(\frac{c_x}{w_{\psi}}\right),$$

which in turn depends on the projection of the absolute velocity in the tangential direction, $|w_{\psi}| = r\Omega \pm c_{\psi}$. Note that in the above equation, “+” applies when the tangential component of the absolute velocity c_{ψ} is against the movement of the blade and “-”, when the movement is in the same direction as the blade movement. It follows that when the tangential flow is against the blade movement, the relative velocity angle decreases, whereas the angle increases when the tangential flow and blade movement coincide in direction. Note that in this idealized case, we have the following:

$$c_{\psi} = c_z \sin(\psi) = c_{\infty} \sin(AoA) \times \sin(\psi).$$

Consequently, the local angle of attack α increases with tangential flow against blade movement, whereas it decreases with flow in same blade movement direction. Note that $c_{\psi} = 0$ leads to a zero AoA case - the purely axial flow. Thus, examining the flow direction could help understand the blade sectional loading. The flow angle is then defined as:

$$\phi = \arctan\left(\frac{c_{\psi}}{c_x}\right)$$

Note that the larger the tangential flow component respect to the axial component, the flow angle increases as well. Moreover, the sign of this angle depends on the direction of the azimuthal orientation and accordingly expresses the direction - against or in direction of blade movement. It is important to note that even though in an actual case the flow ingested by the rotor is more complicated - effects of nacelle and suction, the flow angle can still qualitatively provide insights into the azimuthal locations where the blade local angle is either low or high.

Instantaneous contours of flow angles upstream of the forward and aft rotor are shown in Figure 24, respectively. Note that these contours have been calculated by first transforming velocity components from a cartesian coordinate system, $x - y - z$, to a cylindrical coordinate system, $r - \psi - x$, where the x-direction is the same in both systems, but the transverse plane is expressed with polar components. Contours are plotted at transverse locations of 0.1m upstream of each rotor pitch axis. The flow angle ϕ upstream of the forward rotor are shown in Figure 24(a & b). At $AoA = 0^\circ$, the flow angle is small since although the flow is influenced by the nacelle, the ingested flow is mostly axial. Contrarily, at $AoA = 8^\circ$, the flow angle ϕ exhibits azimuthal dependence. On the left and right side, the flow angle exhibits negative and positive angles - angle is measured in the clockwise direction - with higher absolute values near $\pi/2$ and $3\pi/2$. In the bottom and upper sides - around 0 and π , the flow angles are, in contrast, small in absolute value, indicating negligible effects of tangential components with the flow being mostly radial, which might be attributed to the normal direction of the flow to the blade movement and the effect of the nacelle on the incoming flow. Also, larger flow angles, in absolute values, result on regions that are either favorable, around $\pi/2$, since the blade movement is against the tangential component of the flow; and unfavorable region, around $3\pi/2$, due to tangential components in the direction of rotation, respectively. Moreover, note that these azimuthal locations of favorable and unfavorable flow correspond to the maximum and lowest values of the axial force at azimuthal locations of $\pi/2$ and $3\pi/2$, respectively, as previously shown in Figure 22.

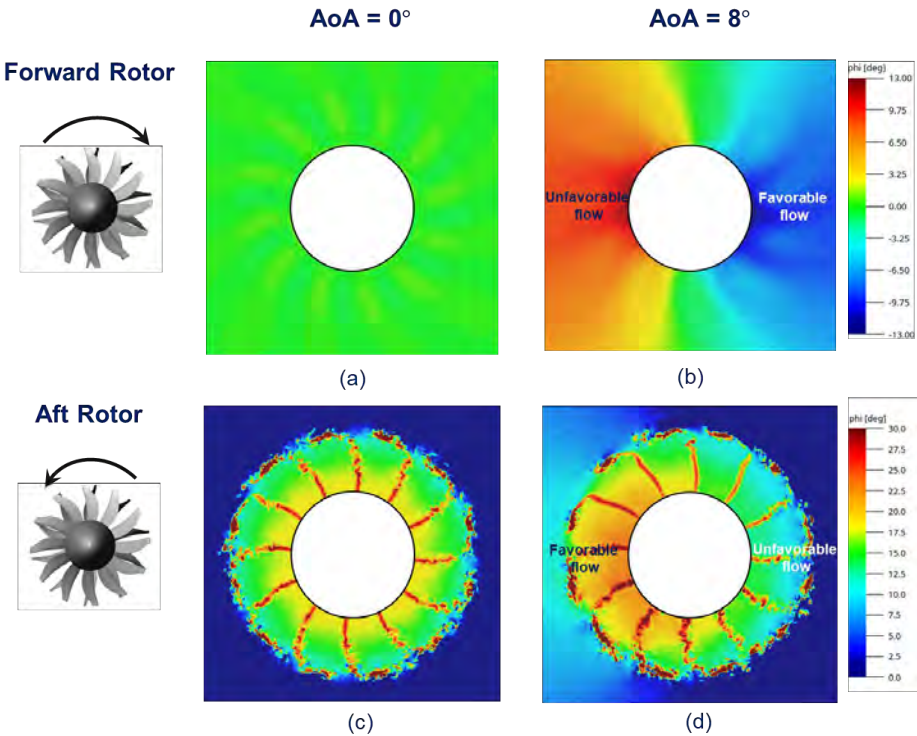


Figure 24. Flow angle (ϕ) upstream of forward rotor (a -b) aft rotor (c-d) Note: Geometry is a generic contrarotating open rotor and thus it is not the GE F31A31

The flow angle ϕ upstream of the aft rotors is shown in transverse planes in Figure 24(c & d). This inter-rotor flow exhibits flow angles that are fairly periodic for the $AoA = 0^\circ$ case. The wakes as well as the flow structures due to the tip vortices from the forward rotor blades are quite apparent. In the $AoA = 8^\circ$ case, on the other hand, the flow angle is azimuth dependent. Indeed, regions of larger flow angles are developed on the left side, around $3\pi/2$, whereas smaller flow angles are observed on the right side, around $\pi/2$. The region with larger flow angles leads to more favorable flow since the tangential component acts against the aft rotation, which in turn increases the local angle of attack, increasing loads in blades. On the contrary, the region on the right with smaller flow angles creates relatively smaller tangential components compared to the other region and that of the $AoA = 0^\circ$ case. Consequently, the local angle of attacks would be smaller than those of the region of

favorable flow. Note also that the azimuthal locations of favorable and unfavorable flow correspond to the maximum and lowest values of the axial force at azimuthal locations of $3\pi/2$ and $\pi/2$, respectively, as previously shown in Figure 22.

Considerations

The results reported in this document should be understood given the following considerations:

1. Lack of knowledge regarding actual geometry
 - Variability in installation of the F31/A31 wind tunnel model such as blade pitch variation could lead to angular variation of up to 0.1° from blade to blade.
 - Blade deformation due to rotation - blades deform differently at every rotor speeds.
2. Simulation aspects
 - The FW-H solver with impermeable surfaces used for CAA simulations with calibrated pitch angle does not account for convection effects [13].
 - Impermeable surfaces may not account for very near effects in the flowfield.

Note that all of the above can influence simulation predictions and can hence result in discrepancies, although the magnitude of such discrepancies is unknown. Installation variability has been argued to result in discrepancies in both aerodynamics and acoustics [8,9]. Moreover, not accounting for deformation due to operating conditions has also been found to result in aerodynamic and acoustic discrepancies [9].

Conclusions

A numerical study was carried out for validating a sub-set of the experimental cases of the open fan configuration based on the F31/A31 blades. Specifically, the focus is on the low-speed cases with NTO pitch settings. Aerodynamic calibration is carried out prior to acoustic validation. The numerical simulations rely on a hybrid approach. The unsteady aerodynamic flowfield is obtained by explicitly solving the transient and compressible lattice-Boltzmann equations, implemented on a commercial LBM solver. The far-field aeroacoustics is predicted by a FW-H solver, which employs transient flow data recorded at impermeable surfaces. Aeroacoustic validations are carried out with simulations using said calibrated pitch settings. The aerodynamic calibration is based on minimizing thrust discrepancy between experimental and numerical values. Such criterion is chosen because loading noise is of relevance to the conditions of interest. Results of calibration are to slightly increase the pitch angles in both rotors. The effects on aeroacoustics is to slightly increase overall noise metrics. Such increment is due to the increase in thrust given the slightly larger pitch angles on the calibrated case. The far-field aeroacoustics using the calibrated pitch settings results in a decreasing trend for the measurements of discrepancy in overall noise metrics with rotor speed. OASPL discrepancy decreases from 2.5 to 1.6 dB. The overall acoustic power follows a similar trend with the discrepancies of 2.5 and 0.36 dB, found at the lowest and highest rotor speed, respectively. Among the cases investigated at non-zero angle of attack, OASPL discrepancies no larger than 2.0 dB are found. Closer examination of the farfield noise results in a noticeable lack of axisymmetry. Higher noise levels are found in the lower hemisphere, where the open rotor is tilted away. Finally, comparisons with simulations with nominal pitch settings show that calibration increases discrepancies. Such an outcome could be attributed to the fact that simulations of nominal pitch cases exhibit lower thrust values compared to experiments. Aerodynamic calibration results on slightly larger pitch angles, which in turn increase thrust and consequently noise levels.

Milestone(s)

None.

Major Accomplishments

Regarding extended validation, all cases at zero angle of attack have been completed.

Publications

- "Aerodynamic Calibration for Aeroacoustics Validation of an Open Fan Configuration," in AIAA SciTech 2023

Outreach Efforts

None.



Awards

None.

Student Involvement

For this task, Brenton Willier (continuing PhD student with U.S. person credentials) and Grant Stevenson (continuing MS student with U.S. person credentials) worked on geometry preparation for numerical analysis and analysis of acoustic data.

Plans for Next Period

None.

References

- [1] Stephens, D. B., "Data Summary Report for the Open Rotor Propulsion Rig Equipped with F31/A31 Rotor Blades," NASA/TM-2014-216676, 2014.
- [2] Sree, D., "Far-Field Acoustic Power Level and Performance Analyses of F31/A31 Open Rotor Model at Simulated Scaled Takeoff, Nominal Takeoff, and Approach Conditions: Technical Report I," NASA/CR-2015-218716, 2015.
- [3] Sree, D., "Near-Field Acoustic Power Level Analyses of F31/A31 Open Rotor Model at Simulated Cruise Conditions: Technical Report II," NASA/CR-2015-218845, 2015.
- [4] Elliot, D. M., "Initial Investigation of the Acoustics of a Counter-Rotating Open Rotor Model with Historical Baseline Blades in a Low-Speed Wind Tunnel," NASA/TM-2012-217258, 2012.
- [5] "Acoustical Society of America: Method for Calculation of the Absorption of Sound by the Atmosphere," ANSI S1.26-1995, 1995.
- [6] Rizzi, S. A., Stephens, D. B., Berton, J. J., Zante, D. E. V., Wojno, J. P., and Goerig, T. W., "Auralization of Flyover Noise from Open-Rotor Engines Using Model-Scale Test Data," *Journal of Aircraft*, Vol. 53, No. 1, 2016, pp. 117–128.
- [7] Hubbard, H. H., "Aeroacoustics of Flight Vehicles: Theory and Practice," NASA/TR-90-3052, 1991.
- [8] Envia, E., "Open Rotor Aeroacoustic Modeling," NASA TM 2012-217740, 2012.
- [9] Falissard, F., Boisard, R., Gaveriaux, R., Delattre, G., Gardarein, P., Chelius, A., Canard-Caruana, S., and Mauffrey, Y., "Influence of Blade Deformations on Open-Rotor Low-Speed and High-Speed Aerodynamics and Aeroacoustics," *Journal of Aircraft*, Vol. 55, No. 6, 2018, pp. 2267–2281.
- [10] Casalino, D., Hazir, A., and Mann, A., "Turbofan Broadband Noise Prediction Using the Lattice Boltzmann Method," *AIAA Journal*, Vol. 56, No. 2, 2018, pp. 609–628.
- [11] Romani, G., QingQing, Y., Avallone, F., Ragni, D., and Casalino, D., "Numerical Analysis of fan noise for the NOVA boundary-layer ingestion," *Aerospace Science and Technology*, Vol. 96, 2020.
- [12] Nark, D. M., Jones, W. T., Boyd, D. D., and Zawodny, N. S., "Isolated Open Rotor Noise Prediction Assessment Using the F31A31 Historical Blade Set," AIAA paper 2016-1271, San Diego, CA, 2016.
- [13] Cerizza, D., DS Simulia corporation, private communication, 2022.
- [14] L. S. Langston, "Open Rotor Engines—Still an Open Question?," *ASME. Mechanical Engineering.*, December 2018.



- [15] SAFRAN-GROUP, "Safran celebrates successful start of Open Rotor demonstrator tests on new open-air test rig in southern France," October 2017. [Online]. Available: <https://www.safra-group.com/media/safra-group-celebrates-successful-start-open-rotor-demonstrator-tests-new-open-air-test-rig-southern-france-20171003>.
- [16] Smithsonian National Air and Space Museum, "General Electric GE36 Unducted Fan (UDF) Turboprop Engine," [Online]. Available: https://airandspace.si.edu/collection-objects/general-electric-ge36-ducted-fan-udf-turboprop-engine/nasm_A19920001000.
- [17] FAA, General Electric, "Open Rotor Engine Aeroacoustic Technology Final Report," 2014.
- [18] M. McCarthy, "Contra-rotating Open Rotor Reverse Thrust Aerodynamics," Cranfield University, 2011.
- [19] NoiseNews, "Tonal Noise Analysis with Optimus Green Sound Level Meters," 2017.
- [20] S. Glegg and W. Devenport, *Aeroacoustics of Low Mach Number Flows*, Vols. Chapter 16 - Open rotor noise, 2017, pp. 399-436.
- [21] KAIST Aeroacoustics Lab, "Flow and Acoustics of Turbo Jet and Rocket," [Online]. Available: <https://sites.google.com/site/aeac1234/applications/hydraulic-power>.
- [22] FAA, General Electric, "Open Rotor Engine Aeroacoustic Technology Final Report," 2014.
- [23] J.-S. Jang, S. Choi, H.-I. Kwon, D.-K. Im, D.-J. Lee and J.-H. Kwon, "A Preliminary Study of Open Rotor Design Using a Harmonic Balance Method," in *50th AIAA Aerospace Sciences Meeting Including the Horizons Forum and Aerospace Exposition*, 2012.
- [24] H. Kwon, S. Choi, J.-H. Kwon and D. Lee, "Surrogate-Based Robust Optimization and Design to Unsteady Low-Noise Open Rotors," *Journal of Aircraft*, 2016.
- [25] D. A. Smith, A. Filippone and N. Bodjo, "A Parametric Study of Open Rotor Noise," in *25th AIAA/CAES Aeroacoustics Conference*, 2019.
- [26] S. Yi, H.-I. Kwon, D. Im, S. Choi, M. Park and D.-J. Lee, "Parameter Study of Low Noise CROR System," in *34th AIAA Applied Aerodynamics Conference*, 2016.
- [27] H.-I. Kwon, S.-g. Yi, S. Choi, D.-J. Lee, J.-H. Kwon and D.-K. Im, "Design of a Low-Noise Open Rotor Using an Implicit Harmonic Balance Method," in *51st AIAA Aerospace Sciences Meeting*, 2013.
- [28] R. Schnell, J. Yin, C. Voss and E. Nicke, "Assessment and Optimization of the Aerodynamic and Acoustic Characteristics of a Counter Rotating Open Rotor," in *ASME Turbo Expo*, 2010.
- [29] B. A. Janardan and P. R. Gliebe, "Acoustic characteristics of counterrotating unducted fans from modelscale tests," *Journal of aircraft*, vol. 27, no. 3, 1990.
- [30] P. A. Moshkov, V. Samokhin and A. Yakovlev, "Problem of the Community Noise Reduction for Aircraft with Open Rotor Engines," *Russian Aeronautics Vol. 61 No. 4*, pp. 647-650, 2018.
- [31] B. Shivashankara, D. Johnson and R. Cuthbertson, "Installation Effect on Counter Rotation Propeller Noise," AIAA, 1990.



- [32] J. Ricouard, E. Julliard and et al, "Installation effects on contra-rotating open rotor noise," *16th AIAA/CEAS aeroacoustics conference*, 2010.
- [33] A. Stuermer and Y. Jianping, "Aerodynamic and aeroacoustic installation effects for pusher-configuration CROR propulsion systems," *28th AIAA Applied Aerodynamics Conference*, 2010.
- [34] T. Sinnige and L. L. M. Veldhuis, "Pylon Trailing Edge Blowing Effects on the Performance and Noise Production of a Pusher Propeller," 2014.
- [35] R. W. Harris and R. Cuthbertson, "UDF/727 Flight Test Program," in *AIAA/SAE/ASME/ASEE 23rd Joint Propulsion Conference*, San Diego, CA, 1987.
- [36] H. Nichols, "UDF engine/MD80 flight test program," in *AIAA/SAE/ASME/ASEE 24th Joint Propulsion Conference*, Boston, Mass., 1988.
- [37] J. Dansie, "What should my tail look like?," HMFC, 2018. [Online]. Available: <http://www.hmfc.com.au/index.php/ground-school/what-should-my-tail-look-like>. [Accessed 07 2021].
- [38] J. Kennedy, P. Eret and G. Bennett, "A parametric study of airframe effects on the noise emission from installed contra-rotating open rotors," *International Journal of Aeroacoustics*, 2018.
- [39] L. Sanders, D. C. Mincu, P. L. Vitagliano, M. Minervino, J. Kennedy and G. Bennett, "Prediction of the acoustic shielding by aircraft empennage for contra-rotating open rotors," *International Journal of Aeroacoustics*, pp. 626-648, 2017.
- [40] J. Kennedy, P. Eret and G. Bennett, "A parametric study of installed counter rotating open rotors," in *19th AIAA/CEAS Aeroacoustics Conference*, Berlin, Germany, 2013.
- [41] L. Dürrwächter, M. Keßler and E. Krämer, "Numerical Assessment of Open-Rotor Noise Shielding with a Coupled Approach," *AIAA Journal*, pp. 57(5), 1930-1940, 2019.
- [42] M. Czech and R. H. Thomas, "Open Rotor Installed Aeroacoustic Testing with Conventional and Unconventional Airframes," in *19th AIAA/CEAS Aeroacoustics Conference*, Berlin, Germany, 2013.
- [43] D. B. Stephens and E. Envia, "Acoustic Shielding for a Model Scale Counter-rotation Open Rotor," in *17th AIAA/CEAS Aeroacoustics Conference*, 2011.
- [44] J. Berton, "Empennage Noise Shielding Benefits for an Open Rotor Transport," in *17th AIAA/CEAS Aeroacoustics Conference (32nd AIAA Aeroacoustics Conference)*, Portland, Oregon, 2011.



Project 077 Measurements to Support Noise Certification for UAS and UAM Vehicles and Identify Noise Reduction Opportunities

The Pennsylvania State University

Project Lead Investigator

Eric Greenwood
Assistant Professor of Aerospace Engineering
Department of Aerospace Engineering
The Pennsylvania State University
229 Hammond Building
University Park, PA 16802
814-863-9712
eric.greenwood@psu.edu

University Participants

The Pennsylvania State University (Penn State)

- P.I.: Eric Greenwood, Assistant Professor of Aerospace Engineering
- FAA Award Number: 13-C-AJFE-PSU-067
- Period of Performance: October 1, 2022 to December 31, 2023
- Tasks:
 1. Computational investigations of uncrewed aircraft system (UAS) and urban air mobility (UAM) aircraft noise generation
 2. Development and testing of a reconfigurable multirotor UAS
 3. UAS noise measurement and analysis of variability
 4. Development of a source separation process (SSP) for distributed propulsion vehicles
 5. Noise reduction through synchrophasing
 6. Air data system integration and calibration

Project Funding Level

\$500,000 awarded by FAA. \$495,933 cost-sharing from Beta Technologies for labor, flight test support, and technical data.

Investigation Team

Eric Greenwood (P.I.), All Tasks
Kenneth S. Brentner (co-P.I.), Tasks 1 and 5
Eric N. Johnson (co-P.I.), Tasks 2 and 5
Joel Rachaprolu (graduate research assistant), Tasks 3 and 4
Vitor T. Valente (graduate research assistant), Tasks 2, 3, 5, and 6
Rupak Chaudhary (graduate research assistant), Tasks 1 and 5
EzzEldin El Sharkawy (graduate research assistant), Tasks 3 and 6



Project Overview

Measurement techniques for conventional propeller-driven aircraft and rotorcraft are well established. These techniques typically are based on the assumption that the acoustic state of the vehicle does not change over the duration of a steady-state pass over a microphone or microphone array. UAS and UAM platforms violate the steadiness assumption used in the measurement and modeling of conventional aircraft noise. Rotor or propeller states, such as the rotational speed or blade pitch angle, vary continuously and independently as the vehicle control system responds to atmospheric perturbations. Many of these vehicles use distributed propulsion systems, in which the rotors or propellers are not locked in phase. When multiple rotors or propellers operate at similar blade passing frequencies, coherent addition of the tonal noise results in lobes of acoustic radiation that are tightly focused in certain directions. As the phase relationships between the rotors change over time, the directionality of these lobes varies. Consequently, the noise cannot be modeled as a single stationary source, and no two flight passes will result in the same noise radiation pattern on the ground. Moreover, because numerous possible combinations of control inputs can result in the same flight condition, unique mapping of the overall flight condition of the vehicle to a corresponding acoustic state is no longer present. This project is aimed at developing noise measurement techniques and data analysis methods that can reduce this variability, thereby allowing for repeatable characterization of UAS and UAM noise.

Task 1 – Computational Investigations of UAS and UAM Noise Generation

The Pennsylvania State University

Objective

The goal of this task is to develop computational models of multirotor UAS and UAM noise generation to inform the development of acoustic measurement procedures for these vehicles and to better understand the causes of variability in the measured data.

Research Approach

A computational model was developed to simulate the Pennsylvania State University (PSU)-reconfigurable hexacopter in the Penn State Noise Prediction System (NPS). This system includes models of the vehicle's flight dynamics, aerodynamics, and noise generation.

Milestone

The milestones for this task are to (a) develop a computational model of Penn State's reconfigurable research UAS and (b) apply the model to develop recommendations for outdoor acoustic measurements of UAS and UAM.

Major Accomplishments

A model of the large reconfigurable UAS, described in Task 2, has been developed by using the Penn State NPS. The NPS, shown in Figure 1, is a simulation architecture consisting of three subsystems: (a) PSU Distributed Electric Propulsion Simulator (PSUDEPSim), (b) Comprehensive Hierarchical Aeromechanics Rotorcraft Model (CHARM), and (c) PSU-WOPWOP. PSUDEPSim is a flight simulation model for multirotor aircraft developed at Penn State. PSUDEPSim is used to compute the aircraft's flight state as it undergoes steady or maneuvering flight. PSUDEPSim can be coupled to a higher-fidelity aerodynamics model to capture the effects of interactions among components of the aircraft, such as the rotors. In the Penn State NPS, PSUDEPSim is coupled with CHARM to form DEPSim. CHARM, developed by Continuum Dynamics, Inc., is a rotorcraft comprehensive analysis platform including a higher-order free vortex rotor wake method and a panel method for aerodynamic bodies and surfaces, such as the fuselage and wings of UAM aircraft. In addition to providing aerodynamic data in DEPSim for flight dynamic simulation, CHARM produces high-resolution rotor airloads for input into aeroacoustic propagation tools, such as PSU-WOPWOP. PSU-WOPWOP is a general-purpose Ffowcs Williams–Hawkings equation solver that uses Farassat's formulation 1A. PSU-WOPWOP uses the time-dependent data (geometry, motion, sectional airloads, and angle of attack) generated from CHARM as inputs to compute the noise at any number of observers on the ground or moving with the aircraft.

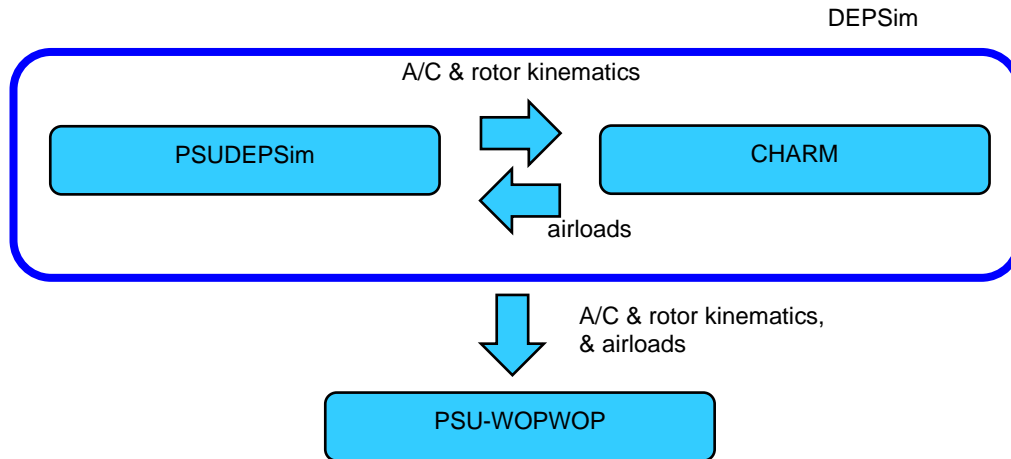


Figure 1. Flow chart describing the Penn State Noise Prediction System (NPS).

Figure 2 represents the layout of the large reconfigurable UAS developed by Penn State in a hexacopter configuration. The rotor diameter is 0.71 m, and the vehicle weight is 151 N. The front of the vehicle is aligned with the X axis. The rotor blade geometry is obtained by scanning the blade with a FARO arm laser scanner at the Penn State Applied Research Laboratory. For the current study, the hexacopter flies in an "X" configuration, with two rotors toward the front of the vehicle.

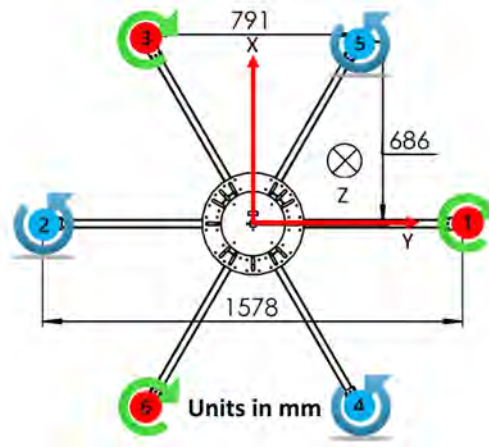


Figure 2. Schematic of the large reconfigurable UAS in a hexacopter configuration.

To validate the capabilities of the current Penn State NPS, a comparison is made between the predicted and measured motor angular speed and overall sound pressure level (OASPL) of the PSU-Reconfigurable hexacopter during both hover and forward flight at 10 mph (8.7 kts, 4.5 m/s). These maneuvers were conducted at Mid-State Regional Airport (KPSB) on June 8, 2023, with wind speeds ranging from 0 to 3.5 knots (0 to 1.8 m/s) and are discussed in more detail under Task 3.

Flight simulation validation

Figure 3 plots the measured and predicted angular speeds of the six motors over time during hover. The effects of winds and atmospheric turbulence are not currently modeled. In this idealized scenario, the motor angular rates for multicopters with vertically aligned motor axes, uniformly distributed weight, and identical rotors should be identical during hover. However, differences are observed in the angular speeds of the clockwise and counterclockwise turning rotors. Therefore,

the aircraft must apply a yaw command to establish a steady hover condition. This yaw may be induced by a misalignment of the rotor support arms or could be caused by differences between the clockwise and counterclockwise turning rotors that result in differences in torque. To model this aspect in the simulation, we slightly adjusted the rotor blade pitch and rotation axes to allow the predicted motor angular rate to match the experimental data more closely. The adjusted difference in blade pitch between the counterclockwise and clockwise rotors is approximately 1.2° , and the motor axes are adjusted $1-2^\circ$ from vertical.

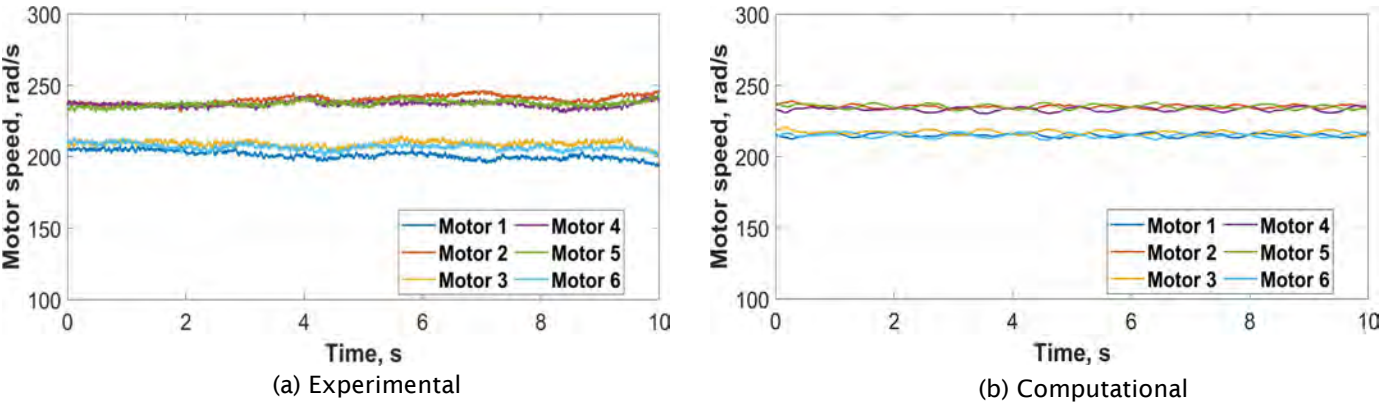


Figure 3. Comparison of motor angular speed between experiment and computation during hover.

Figure 4 compares the measured and predicted motor speeds in forward flight at 10 mph. The predicted motor angular rates generally agree with the experimental measurements.

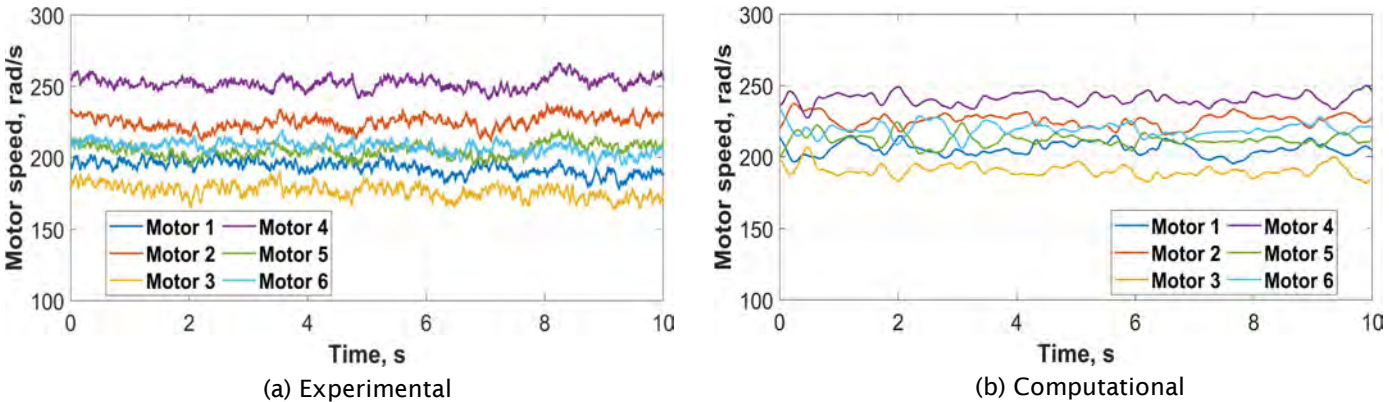


Figure 4. Comparison of motor angular speed between experiment and computation at a forward speed of 10 mph.

Acoustic validation

Variations in OASPL over time during different maneuvers are demonstrated in Figure 5. The OASPL time history was calculated with a window length of 0.5. Figure 5a illustrates the OASPL over time for a maneuver in which the vehicle hovers 80 ft above the microphone for the first 16 s, then descends to 40 ft, and finally maintains a hover until 40 s. The peaks observed in OASPL during the experiment may be attributed to wake interactions. Specifically, these interactions occur when the vehicle comes to a stop after the descent, and then enters a hover state. Two predicted cases are shown. In case I, the dynamic states of the vehicle (time-varying position, attitude, and motor angular rates) are directly obtained from the experiment, whereas in case II, dynamic states computed from DEPSim/CHARM are used. Figure 5b displays the OASPL variation over time as the vehicle moves forward at 10 mph at a 20-ft altitude above the ground-plane microphone. The effects of pressure doubling have been removed from the measured data, providing a free-field equivalent for

comparison with the simulation. Although the agreement is fairly good when the vehicle passes over the microphone, larger differences exist between measurements and predictions at the start and end of the maneuver when the vehicle is farther away. Further investigation is required to determine the causes for these discrepancies.

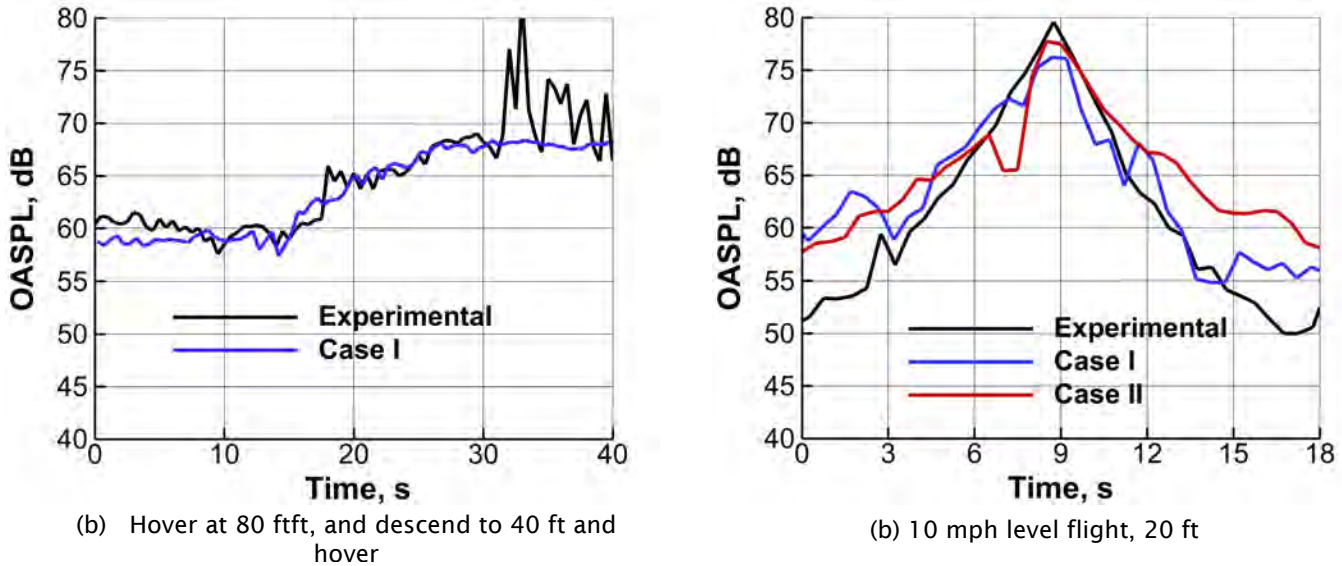


Figure 5. Comparison of OASPL (dB) between experiment and computation.

Takeoff and landing maneuvers

Next, the NPS was applied to predict ground noise levels for simulated takeoff and landing maneuvers, such as those that would be conducted during package delivery operations. These predictions were used to inform the development of test procedures described in Task 3. Figure 6 shows the acoustic observer grid and simulated trajectory for the takeoff and landing maneuvers. The hexacopter takes off or lands at the center (0,0,0) of the observer grid.

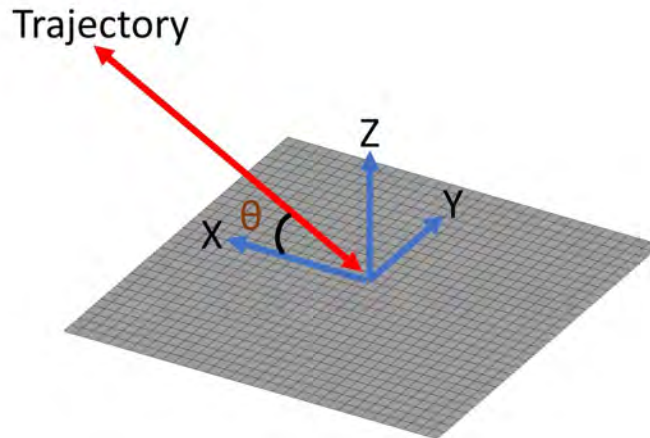


Figure 6. Observer grid and trajectory.

The noise generated during landing and takeoff maneuvers on different slopes was also studied. Figure 7 illustrates the sound exposure level contours for climb and descent maneuvers at two slopes, 10° and 20°. Noise levels during climb maneuvers are higher toward the sideline than descending maneuvers at the same slope; however, both climb and descent

maneuvers at the same slope exhibit similar noise levels underneath their flight paths. These differences are probably because the rotor revolutions per minute (RPM) are higher during climb than descent, and the harmonic noise radiated in the plane of the rotors is more sensitive to RPM variation than the broadband noise radiated below the rotors. Higher slope climbs or descents show lower noise levels under the flight path, probably because of the increased altitude above the ground.

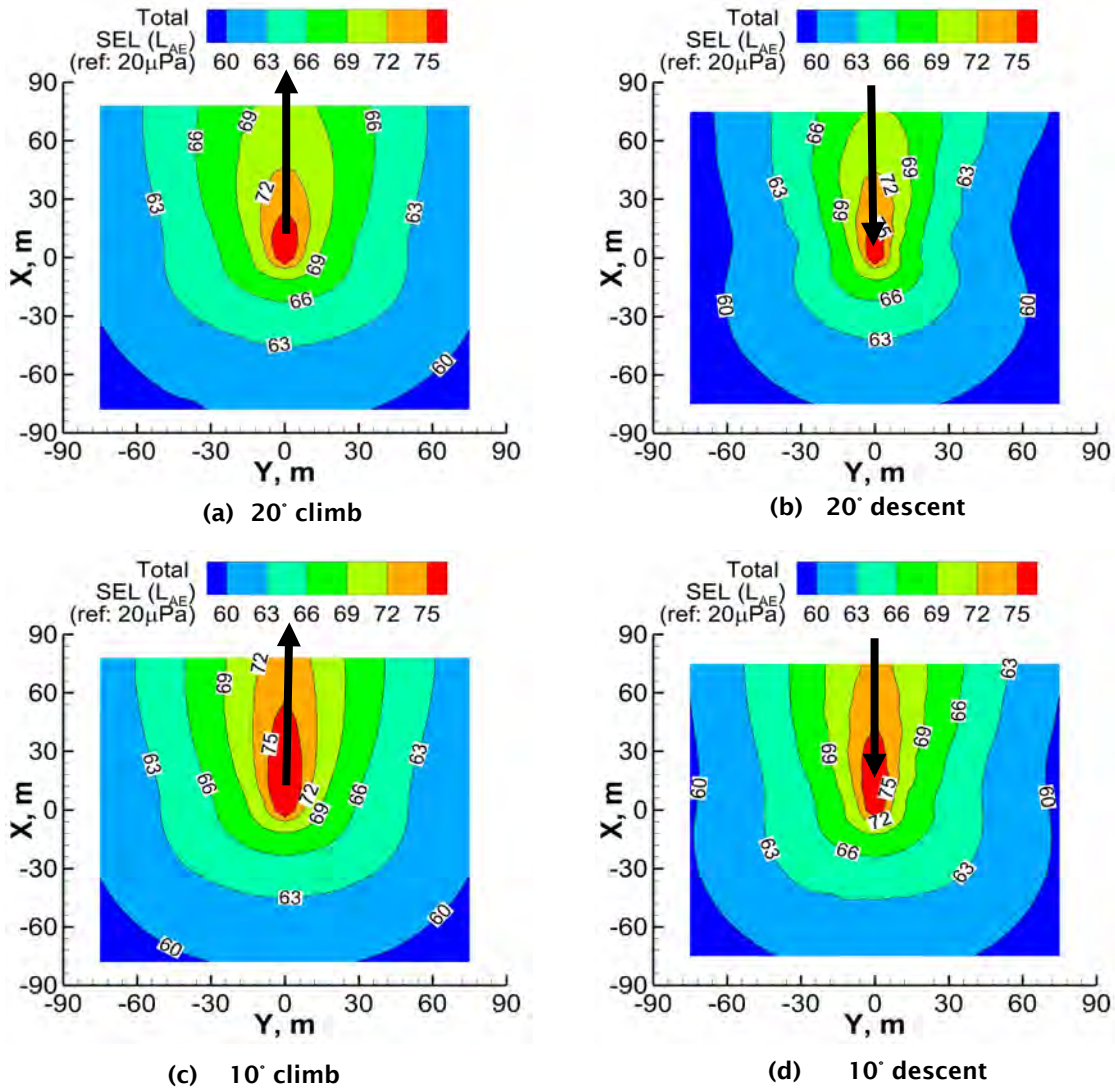


Figure 7. Sound exposure level contours for climb and takeoff maneuvers along 10° and 20° slopes.

Publications

Hur, K., Zachos, D., Brentner, K., & Greenwood, E. (2023, January). *Determining the Acoustic Far-field for Multirotor Aircraft*. 10th Biennial Autonomous VTOL Technical Meeting & 10th Annual eVTOL Symposium, Mesa, AZ.

Chaudhary, R., Valente, V., Mukherjee, B., Jue, A., Brentner, K., S., & Greenwood, E. (2024, May). *Understanding Takeoff and Landing Noise for Small Multirotor Vehicles*. Abstract submitted to Vertical Flight Society Forum 80, Montreal, Canada.

Outreach Efforts

The investigation team holds monthly meetings with FAA and an external advisory board consisting of a dozen interested parties from government and industry.

Awards

None,

Student Involvement

PhD student Rupak Chaudhary is the primary person responsible for conducting UAS noise predictions by using the Penn State NPS (DEPSim/CHARM/PSU-WOPWOP). These predictions include the flight dynamics of the vehicle based on the DEPSim multirotor flight simulation code, including the variation in rotor RPM required to perform the maneuver. The resulting acoustic predictions are compared with experimental data from both outdoor acoustic flight test measurements and laboratory experiments conducted under controlled conditions. Former MS student Keon Wong Hur conducted studies of the far-field distance for UAS and UAM aircraft, which were described in the annual report for the previous year, as well as a manuscript presented during this reporting period.

Plans for Next Period

The Penn State NPS will be refined to better represent vehicle behavior during various flight maneuvers. Simulations will be conducted for different maneuvers that are representative of multirotor aircraft operations to comprehensively study the generated noise and inform the development of measurement techniques.

Task 2 – Development and Testing of a Reconfigurable Multirotor UAS

The Pennsylvania State University

Objective

The objective of this task is to design and develop a multirotor UAS vehicle that can be easily reconfigured, to explore the acoustic effects of different UAS vehicle configurations and their influence on the noise measurement and data processing approaches developed in this project.

Research Approach

Both small and large reconfigurable multirotor UAS aircraft were designed, with the smaller vehicle serving as a testbed for design concepts that were later integrated into the larger, more capable aircraft. Developmental ground and flight testing was performed before flights for acoustic data collection. These initial tests focused on the hexacopter configuration, to ensure a higher level of redundancy during initial testing. Onboard instrumentation includes a real-time kinematic Differential Global Positioning System (DGPS), an inertial measurement unit, individual rotor RPM and phase measurements, and an air data system.

Milestones

The milestones for this task consist of (a) the identification of acoustically significant configuration changes to be made on the vehicle, (b) initial design of the vehicle and selection of sensors, (c) control system design, and (d) ground and flight testing.

Major Accomplishments

Two major onboard systems were added to the large reconfigurable UAS over the reporting period: independent measurement of RPM and phase for each motor and integration of an air data system. In addition, many other improvements have been made, on the basis of operational experience, to improve the reliability of the aircraft.

The first system constitutes a separate onboard computer fully integrated with the avionics system of the vehicle, capable of recording RPM and phase from each motor independently and correlating their values with GPS time for synchronization with acoustic data collected at ground level. Other data can be recorded from each motor, such as electric current, motor temperature, and estimated torque. The sampling rate is dependent on the quantity of measured variables. For two variables (e.g., RPM and phase), sampling rates of 150 Hz can be achieved. The system was custom designed for this aircraft. All data are recorded with a dedicated onboard computer.



The second recently added system is a standalone air data system solution. This system includes another onboard computer and a commercially available sonic-anemometer-based weather station to measure wind speed, wind direction, air temperature, static pressure, and relative humidity, among other quantities. The equipment was installed 44 cm above the rotor plane, in the center of the main body of the vehicle, as shown in Figure 8. The weather station also features GPS, which allows for time synchronization with data from all other systems.



Figure 8. Photographs of the large reconfigurable UAS flying at KPSB with recent upgrades.

In addition to the major systems described previously, the following additional upgrades have been made to the aircraft over the reporting period:

- Installation of an isolation/damping pad under each motor
- Transition to UAVCAN protocol as the main communication interface to the motors
- Use of aerospace grade Controller Area Network (CAN) bus wire (twisted and isolated)
- Change of radio control and telemetry frequencies from 2.4 GHz to 900 MHz to increase range and robustness
- Addition of an onboard camera for video recording

With all upgrades and systems installed, the gross weight of the aircraft has increased to 35.7 lbs.

Publications

Valente, V., Johnson, E., & Greenwood, E. (2023, May). *An Experimental Investigation of eVTOL Flight State Variance on Noise*. Presented at Vertical Flight Society Forum 79, West Palm Beach, FL.

Outreach Efforts

The investigation team holds monthly meetings with FAA and an external advisory board consisting of a dozen interested parties from government and industry. Technical data regarding the reconfigurable multirotor UAS have been shared with investigators from the Georgia Institute of Technology, the University of Salford, Texas A&M University, and the NASA Langley Research Center. Discussions are ongoing regarding potential opportunities for collaboration.

Awards

None

Student Involvement

PhD student Vítor T. Valente was primarily responsible for the design, assembly, and configuration of the UAS. He also served as the remote pilot in command and the safety pilot for the UAS during flight testing.



Plans for Next Period

Plans for the following term include continued use of the aircraft for acoustic data collection. Various aircraft configurations will be flown in the next period. New features and systems can be developed and added to the aircraft as needed to support other research tasks. New maneuvers and test conditions will also be explored.

Task 3 – UAS Noise Measurement and Analysis

The Pennsylvania State University

Objective

The objective of this task is to conduct an acoustic flight test campaign to collect noise measurements for a variety of UAS vehicles under a variety of operating conditions and configurations.

Research Approach

Acoustic measurements of a flying UAS were conducted at the KPSB, surrounded by the Moshannon State Forest and Black Moshannon State Park near Philipsburg, PA. Research noise measurements were made for the large reconfigurable research UAS described in Task 2. The vehicle was flown through a range of operating conditions, including hover, forward flight at several speeds, climb and descent, and yaw. For all maneuvers, the aircraft was flown at different altitudes, from near ground level to 400 ft above ground level, to evaluate the ability to scale UAS noise measurements made at one flight altitude to another, given the relatively low noise levels of small UAS. Acoustic measurements were made with Penn State's networked, battery-powered, and field-deployable acoustic data acquisition system capable of sampling at a frequency as high as 125 kHz at 24-bit resolution with subsample accurate GPS time synchronization across all nodes. A microphone array was designed to capture both spatial and temporal variations in the radiated noise. Weather instrumentation was also deployed, including measurements of wind speed, direction, temperature, pressure, and humidity, both on the vehicle and at ground level near the ground control station.

Milestones

The milestones for this task consist of (a) collecting a baseline acoustic, performance, and meteorological dataset of UAS noise measurements, and (b) analyzing the data to quantify and understand the variability in UAS noise.

Major Accomplishments

Additional ground-plane microphone installations were fabricated, thereby allowing the acoustic array to be expanded to as many as 36 individual microphone locations. With these additional microphones, an expanded acoustic array configuration was developed for UAS testing at KPSB. This configuration, according to ground noise footprint predictions made under Task 1, strategically places microphones in both linear and grid patterns to capture the acoustic field generated by an aircraft in flight. Linear arrays, aligned parallel and perpendicular to the expected flight path, are intended to measure the variation in noise levels along and across the flight trajectory. Additionally, the square arrangement of four microphones near the center of the array (M21-M24) is specifically included to enhance the spatial resolution of acoustic data during maneuvers over the center of the array. Figure 9 shows the most recently developed array configuration used.

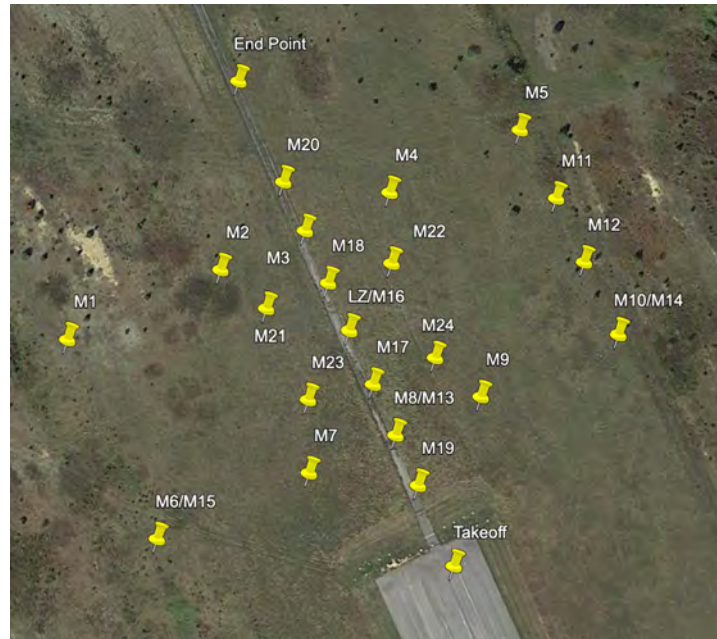


Figure 9. Microphone array configuration, as last flown by the PSU team.

A summary of the conditions in which acoustic measurements were conducted for the large reconfigurable UAS is provided in Table 1. The range of altitude and ground speed set points flown is also listed, as applicable.

Table 1. Microphone array configuration, as last flown by the PSU team.

Maneuver	Description	Altitude setpoint range (ft)	Speed set point range (mph)
Hover	Takeoff and move toward the center of the array. Hover for approximately 30 s above microphone 16 at the center of the array at each altitude set point.	10–360	NA
Flyover	Takeoff, climb to the desired altitude. Flyover in a straight line passing the last line of the microphone. Yaw and return on the same path, at the same altitude.	10–200	10–20
Ascent/descent	Takeoff and climb to the desired initial altitude. Apply a constant flight path angle toward the 25-ft altitude at the center of the array. Climb again toward the end of the array. Yaw and return, performing the same maneuver.	50–200 as initial set point	10
Yaw	Takeoff and climb to the desired altitude. Flyover condition until directly above microphone 16. Yaw and return.	25–125	10–20
Air data: flyover	Takeoff and climb to the desired altitude. Successive upwind/downwind flyover pairs across a range of speeds.	100	5–20
Air data: octagon	Takeoff and climb to the first way point. Follow an octagonal circuit at constant speed.	50–100	5–10

To date, more than 340 min of acoustic data collection flights have been conducted, including 123 takeoff and landing cycles. Most of the maneuvers flown include more than one repetition of the same condition.

To verify that acoustic data were collected with a sufficient altitude to be in the acoustic far-field of the aircraft, the aircraft was flown in hover at a range of altitudes above microphone 16, located in the center of the array. Because the aircraft’s horizontal position was maintained within 0.2 ft of the horizontal position of microphone 16 across all test points, the measured emission angle remained nearly constant for each hovering flight condition. During each recording, the aircraft would ascend through several altitude set points, defined such that the altitude doubled between set points. At each set point, the vehicle held position at the target altitude for 20–30 s. After reaching the highest altitude set point, the vehicle descended, once again stopping at each set point. Four different groups of altitude set points were flown, thus providing hover measurements across a range of logarithmically spaced distances between the aircraft and microphone.

Figure 10 plots the measured A-weighted sound pressure level (SPL) at microphone 16 against the flight altitude, which is also plotted on a logarithmic scale. Error bars represent the measured variation in A-weighted SPL across multiple repeated hover points. A linear trend line was fit to the log-log plot, showing a decay rate of 6.46 dB per doubling. This finding is not significantly different from the 6.01 dB per doubling predicted by spherical spreading. This result implies that all measured data are in the acoustic far-field of the aircraft, such that a spherical spreading correction can be applied to relate all data collected at one altitude to another.

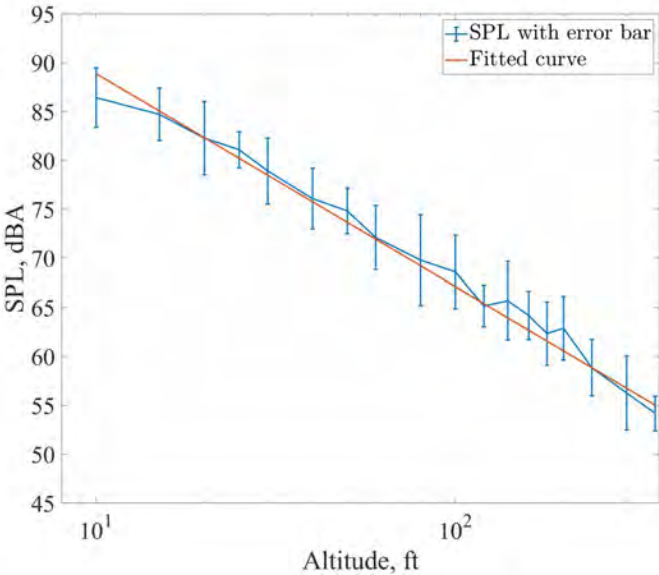


Figure 10. Measured decay in A-weighted SPL with increasing hover flight altitude over the microphone.

Next, the measured data are evaluated to assess the relationship between variability in the measured noise with variability in the aircraft’s flight state during hover. Acoustic and flight state data for all hover conditions were analyzed at 1-s intervals. After the prior analysis, the SPL values were normalized to a 10’ distance, so that data from different conditions could be compared. The variations in SPL with various flight state variables were plotted for all 1-s intervals; for example, Figure 11 plots the variation in SPL against the thrust command set point of the flight control system (left) and the measured yaw rate (right). Analysis of the data for all flight conditions shows that the noise tends to increase in response to most deviations from the hover trim condition. In addition, these data show that noise is significantly more sensitive to changes in the yaw angle or yaw rate than to changes in the roll and pitch angles and rates. Variations in the commanded thrust has different effects on noise generation than variations in the other states; notably, the noise tends to reduce with increases in the commanded thrust. This relationship is thought to occur because the rotor interacts with its own wake when operating at lower thrust and in descending flight conditions, thus generating higher levels of noise. Data associated with three cases in which the vehicle’s flight state had different levels of variability are highlighted. The three cases are numbered according to increasing levels of flight state variability during the hover. Case 1 shows the least amount of variation in the state variable and also presents the least amount of SPL variation. Likewise, Case 3 has the highest variability in both flight state and SPL.

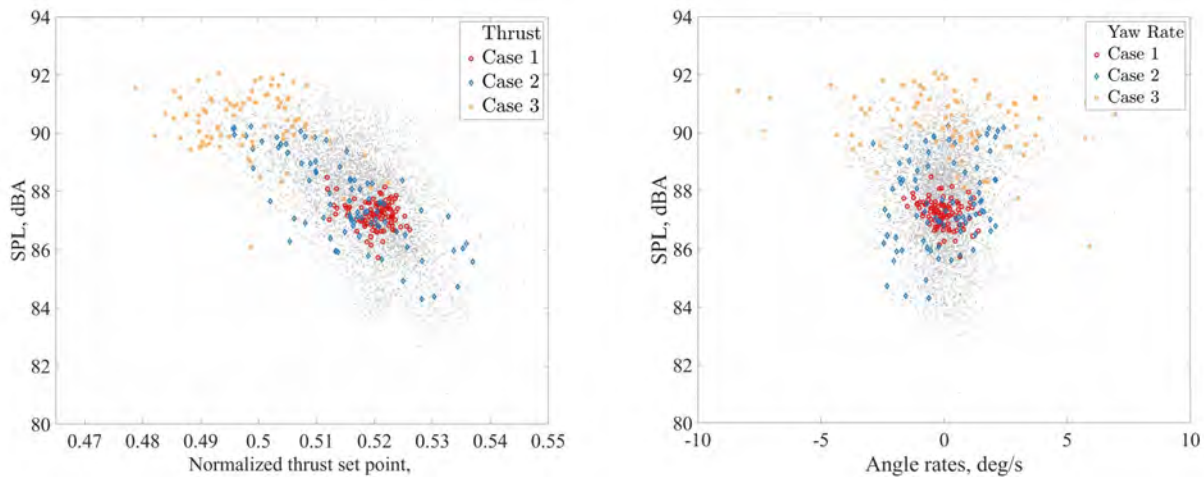


Figure 11. Variation in A-weighted SPL against (left) commanded thrust set point and (right) yaw rate.

Publications

Valente, V., Johnson, E., & Greenwood, E. (2023, May). *An Experimental Investigation of eVTOL Flight State Variance on Noise*. Presented at Vertical Flight Society Forum 79, West Palm Beach, FL.

Konzel, N.B., & Greenwood, E. (2023, November-December). *Variability of Small Multirotor Aircraft Noise Measurements*. *Noise Control Engineering Journal*, Vol. 71, No. 6.

Outreach Efforts

The investigation team holds monthly meetings with FAA and an external advisory board consisting of a dozen interested parties from government and industry. Discussions have been held with the investigation team of ASCENT Project 61 to validate streamlined procedures for UAS noise data collection and analysis. Data collected for UAS under this task may also be provided to collaborators at the University of Salford and the NASA Langley Research Center to enable psychoacoustic evaluations of UAS noise by using their auralization and human participant testing capabilities.

Awards

None.

Student Involvement

PhD students Vitor T. Valente, Joel Rachaprolu, and Rupak Chaudhary, and MS student EzzEldin ElSharkawy conducted acoustic flight testing of the large reconfigurable UAS and participated in analysis of the measured data. Former MS student N. Blaise Konzal conducted analysis of the variability of small multirotor aircraft noise, which was published during the reporting period.

Plans for Next Period

Analysis of data collected during the current reporting period will continue in the next period. These efforts will include the processing of all UAS flyover data into acoustic hemispheres, with an emphasis on characterizing the statistical variability of noise levels emitted over all frequencies and directions. The variation in acoustic characteristics with changes in nominal flight conditions will be investigated, including changes in flight speed and flight path angle (i.e., climb and descent). Additionally, a more detailed comparison of differences between data measured by using inverted ground-plane and elevated microphones will be conducted, including the changes in spectral quantities and the effect on integrated noise metrics, such as the sound exposure level and effective perceived noise level. The test team will continue to collect data for a wide range of UAS configurations and operating conditions. New array designs will be investigated to help decouple the variations in noise over time from the variations with emission angle. The measured flight state of the reconfigurable UAS will be correlated to measured acoustic data, with the aim of identifying the cause of UAS noise variability and establishing limits on acceptable flight state variation for repeated acoustic characterizations of multirotor

aircraft. Additional data will be collected on the variation in noise with flight altitude, including very low altitudes where the microphone may be in the acoustic near-field of the aircraft.

Task 4 – Development of a Source Separation Process for Distributed Propulsion Vehicles

The Pennsylvania State University

Objective

The objective of this task is to develop a process for separating the noise generated by rotors or propellers at non-constant, but potentially similar, RPM values from flyover measurements of UAS and UAM vehicles. By separating noise generated from each rotor, it may be possible to develop a more repeatable characterization of the noise of the entire aircraft.

Research Approach

The SSP developed in this task is mainly a two-step process that combines a time-domain de-Dopplerization procedure and Vold-Kalman order tracking filter. The flowchart in Figure 12 outlines the steps of the SSP. This approach will de-Dopplerize ground-based acoustic measurements and separate the individual rotor noise components, with the capability to extract time-varying impulsive noise. Performing this source separation in the specified time domain will enable the application of a wide range of post-processing techniques in both the time and frequency domains. Moreover, the need to characterize the acoustic directivity of these aircraft requires that the processed data be projected onto an acoustic hemisphere to illustrate the noise radiation patterns.

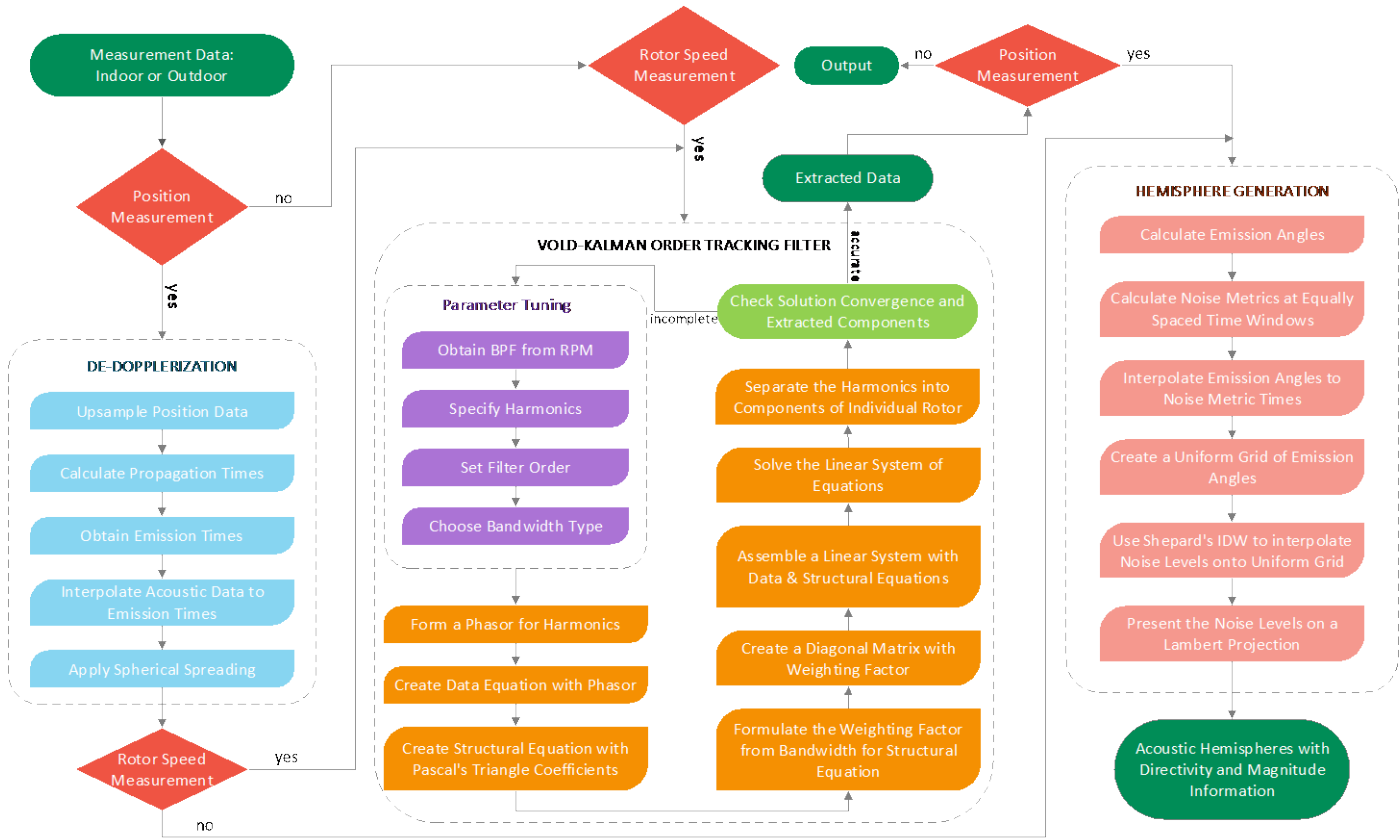


Figure 12. Flowchart of the system architecture of the SSP. BPF: blade passing frequency. IDW: inverse distance weighting.



Each step of the SSP was verified on computational and experimental/flight test data to assess the performance. Acoustic analysis with the SSP components was also performed, in which individual steps of the SSP were isolated and applied to different datasets. The Vold-Kalman filtering technique was applied to anechoic wind tunnel acoustic measurements from a coaxial rotor. A combination of de-Dopplerization and order tracking is used to analyze acoustic flight test data. This process was applied to the Bell 430 helicopter in the previous reporting period. During the current period, the process was extended to separate the tonal noise generated by individual rotors of the large reconfigurable UAS described in previous tasks.

Milestones

The milestones for this task consist of (a) developing an SSP for stationary acoustic measurements, (b) implementing a de-Dopplerization approach to convert non-stationary measurements to a stationary frame, (c) applying the process to simulated and measured data to evaluate the effectiveness of the separation, and (d) applying the process to multirotor aircraft acoustic measurements to extract acoustic components for each rotor.

Major Accomplishments

The developed SSP was applied to acoustic measurements of the large reconfigurable UAS in a hexacopter configuration. The process relies on the newly developed individual motor RPM measurement capability described in Task 2. Prior research has identified that longitudinally grouped rotor pairings (i.e., for hexacopter the forward-, mid-, and aft-rotor pairs) operate at distinctly different rotor speeds and blade passing frequencies in forward flight conditions. The rotor numbering is shown in Figure 13.

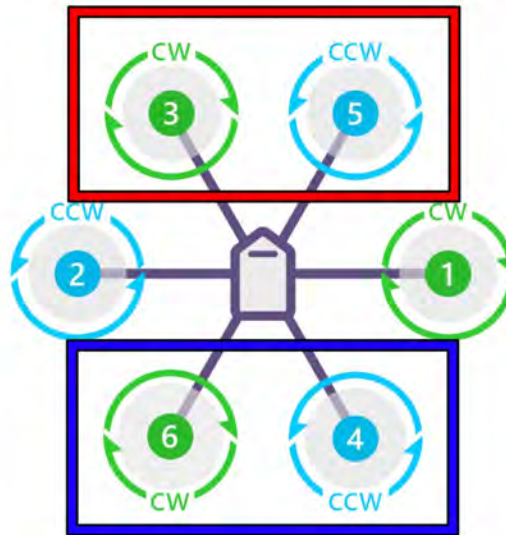


Figure 13. Schematic of the hexacopter numbering scheme, showing the forward (red) and aft (blue) rotor pairs.

The measured time history of the rotor RPM for the forward (R3 and R5) and aft (R6 and R4) rotor pairs is shown in Figure 14 for a forward flight condition. Although the condition is nominally steady, RPM variations occur over time as the vehicle responds to atmospheric disturbances. For example, at approximately 192 s, the instantaneous rotor speeds of the forward pair are lower than those of the aft pair, whereas a more prominent lateral offset is observed in the rotor RPM at 197 s.

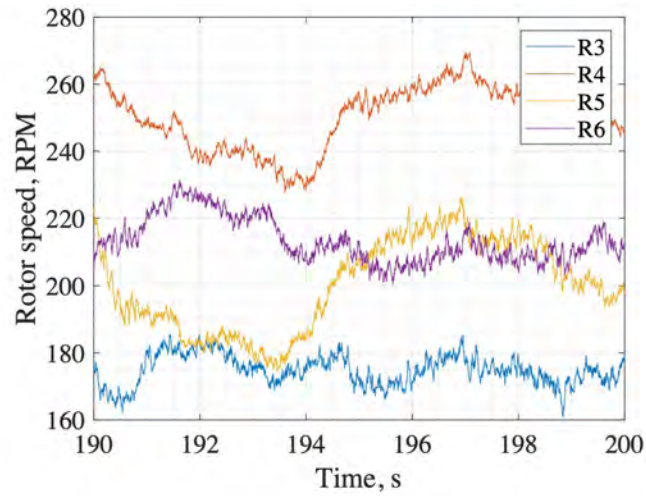


Figure 14. Rotor RPM time history for the forward and aft rotor pairs in forward flight.

The acoustic data for microphone 3, located under the flight path, were separated for each rotor and processed into spectrograms. The separation was performed for the first 15 harmonics of the rotor blade passing frequencies. Figure 15 presents the spectrograms of right-side forward and aft rotors, R5 and R4, respectively.

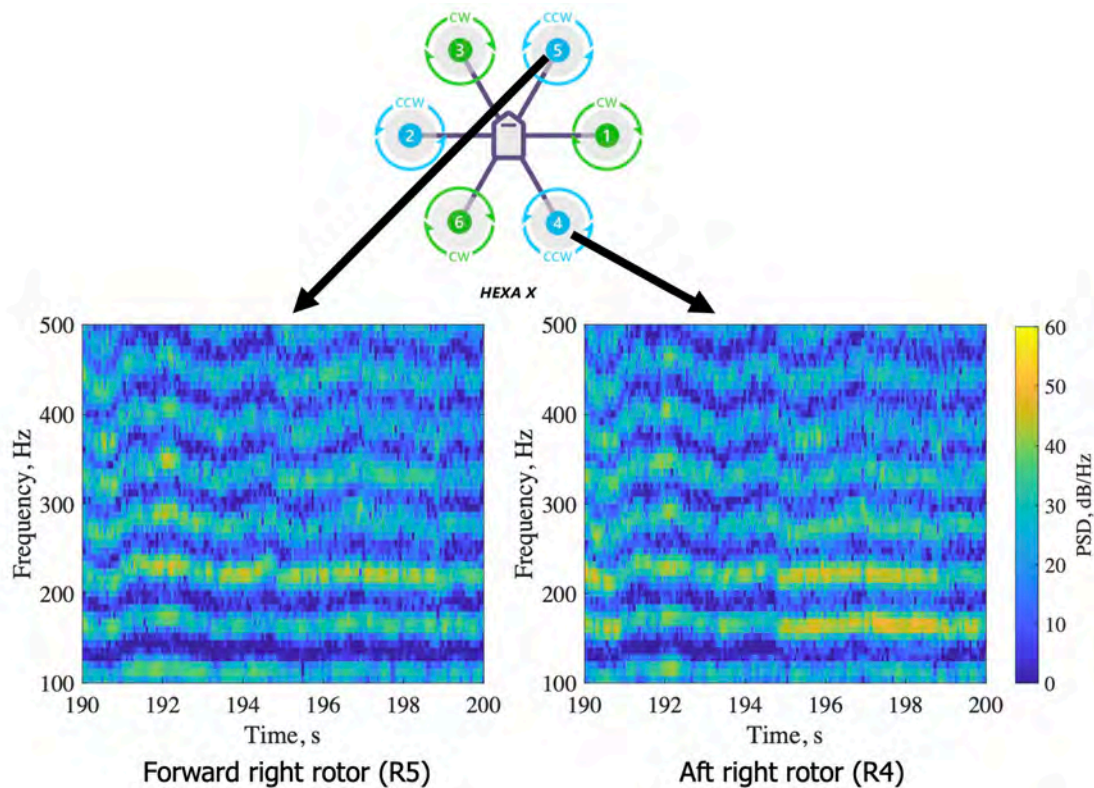


Figure 15. Spectrograms of forward right and aft right rotors from the separated noise measurements.

During the time period shown, the aircraft is flying directly over the microphone. A clear difference is observed in the acoustic energy between spectrograms, particularly at 195–199 s, with R4 containing more energy in both lower harmonics of the rotor blade passage frequencies. Of note, in the RPM plot from Figure 14, R4 generally has a higher RPM than R5R4, and no other rotor is operating at the RPM range of R4, including the omitted rotors (R1 and R2).

The computed power spectral density of the separated signals at time 196 s are plotted in Figure 16 for the opposite-side R3–R4 and R5–R6 rotor pairs, along with the de-Dopplerized power spectral density of the signal before the application of the SSP. Under these conditions, the widely spaced pair shows high levels at the blade passing frequency, which decreases at higher harmonics, whereas the more closely spaced pair shows lower and more constant harmonic noise levels over the frequency range analyzed (100–1000 Hz).

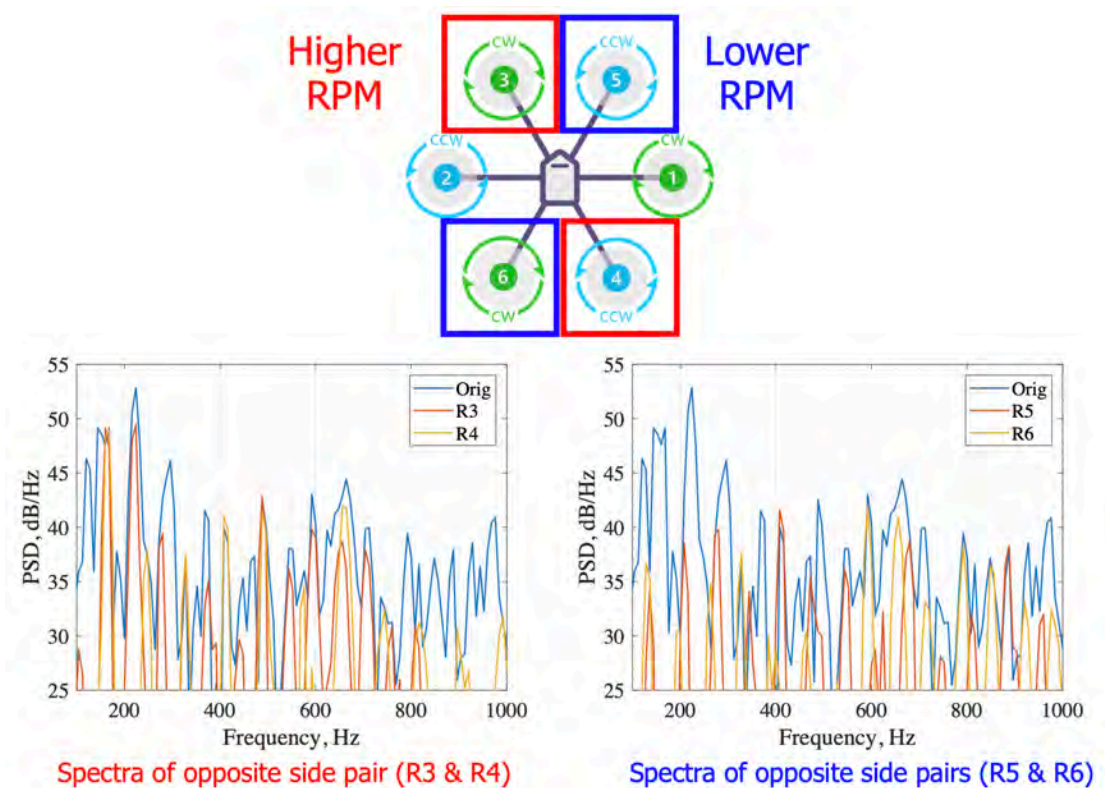


Figure 16. Spectra of the opposing rotors operating in high-RPM and low-RPM pairs.

Publications

- Rachaprolu, J., & Greenwood, E. (*in press*, 2024, January). *Helicopter Noise Source Separation using an Order Tracking Filter*. Journal of the American Helicopter Society.
- Rachaprolu, J., Valente, V.T., & Greenwood, E. (2024, May). *Multicopter Noise Source Separation and Characterization from Ground-Based Acoustic Measurements*. Abstract submitted to Vertical Flight Society Forum 80, Montreal, Canada.

Outreach Efforts

The investigation team holds monthly meetings with FAA and an external advisory board consisting of a dozen interested parties from government and industry. The SSP developed under this task has been provided to Blue Ridge Research and Consulting, which intends to use the method to isolate noise generated by a multicopter vehicle in hovering and low-speed flight.

Awards

None.

Student Involvement

PhD Student Joel Rachaprolu developed and tested the SSP on computational data and extended the application of the process to helicopter flight test data and baseline UAS measurement data.

Plans for Next Period

All major milestones for the task have been completed. However, in the next period, the SSP will be applied to a wider range of conditions to validate its accuracy. Improvements will be made, as necessary, to increase the robustness of the process for future use on multirotor vehicles.

Task 5 – Noise Reduction through Synchrophasing

The Pennsylvania State University

Objective

The objective of this task is to develop and experimentally validate an active noise reduction approach for multirotor aircraft based on phase synchronization of the rotors.

Research Approach

A fully electronic rotor phase control scheme was developed for a hexacopter small UAS (sUAS) designed and built at Penn State. The process begins by characterizing the acoustics of each rotor of the vehicle by using an acoustic array installed in Penn State's flow-through anechoic chamber. These acoustic signals were processed to allow the results to be generalized to any other far-field observer location. An optimization approach was then applied to identify the rotor phase combinations that reduce the noise of the vehicle at one or more observer locations. An electronic phase controller was then used to maintain the target phase relationships between the rotors, and the radiated noise of the entire vehicle was measured and assessed. In parallel, noise predictions were conducted with a combination of the CHARM and PSU-WOPWOP tools described in Task 1 of this report.

Milestone

The milestones for this task consist of (a) developing a phase control method based on a semi-empirical approach, and (b) comparing the results through simulation with CHARM and PSU-WOPWOP.

Major Accomplishments

A phase control scheme was developed, implemented on a small multirotor vehicle, and validated in Penn State's flow-through anechoic chamber. In addition, computational studies were conducted to model the acoustic performance of the synchrophasing system, with good agreement with the experimental results.

Experimental approach

The vehicle was mounted on a stand inside the Penn State flow-through anechoic chamber, as shown in Figure 17. The plate supporting the vehicle was mounted on a six-axis load cell, which was itself mounted on a gimbal allowing the orientation of the vehicle to be changed. Initially, the gimbal was locked, such that the vehicle was level with the horizon. The microphone array inside the anechoic chamber was installed vertically and fixed on a rotating arm at approximately 60 in from the center of the vehicle. A schematic of the microphone array is shown in Figure 18. The arm with the microphone array can rotate in azimuth over a range from -30° to $+80^\circ$. The array includes eleven half inch microphones (microphones 1-11) and one quarter inch microphone (microphone 12). The last microphone, physically located in between microphone 9 and microphone 10, was installed to monitor noise at frequencies above 20 kHz.

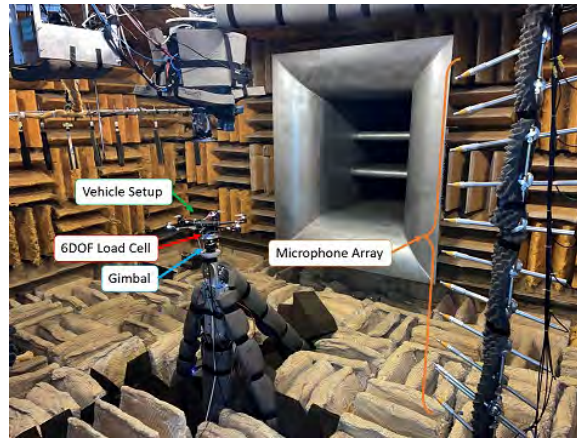


Figure 17. Photograph of the experimental setup.

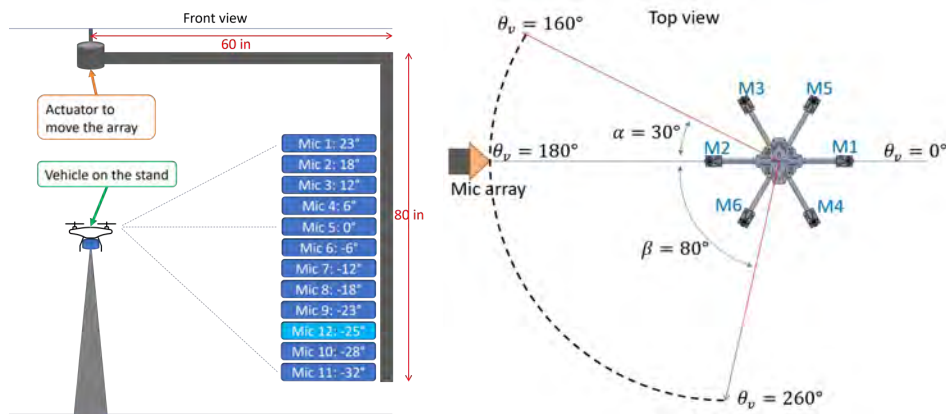


Figure 18. Microphone array configuration. Side view (left) and top view (right).

Rotor characterization and phase optimization

The rotor characterization and phase optimization process is intended to find the lowest combination of relative phases between all rotors. The phases are optimized to produce the lowest overall SPL at one or more microphone locations by using a semiempirical modeling process. Each motor is characterized individually, i.e., acoustic signal is acquired for each rotor at a range of microphone array angles. The goal is to generate a single averaged acoustic pressure waveform for each elevation angle that is characteristic of the noise generated by the rotor over one revolution. Figure 19 shows the result of this characterization for motor number 2. Because the acoustic signal will be offset in phase at different microphone array positions, a phase compensation offset is applied to allow the data to be generalized to other locations, according to the assumption that the microphones are in the far field of a single rotor. The phase compensation process takes into account two main effects: the relative distance between the rotor and the microphone, accounting for the propagation time delay; and the azimuth angle of the array relative to the rotor, accounting for the rotating sound field generated by the rotor. By transforming these two terms into phase offsets, all measured waveforms for a single rotor can now be averaged into a single waveform representing the noise observed at an arbitrary reference location (chosen as the location of microphone six at array azimuth 180°). Similarly, these phase offsets can later be subtracted from the averaged single to predict the relative phase of the waveform at any other location. This characterization process was repeated for all six rotors on the vehicle.

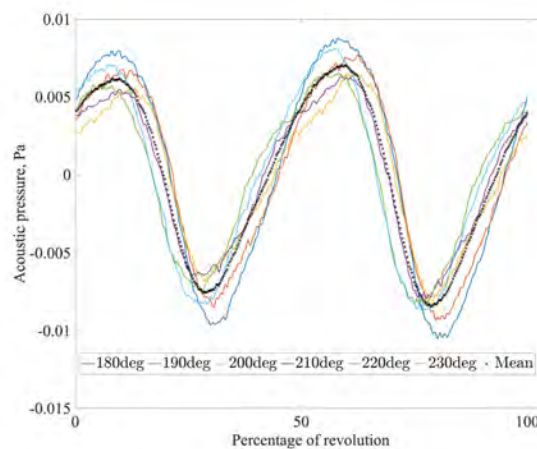


Figure 19. Result of the characterization step for motor 2.

After characterization of the averaged waveform of each individual rotor, an optimization algorithm was used to find the best combination of relative phases to minimize the overall SPL at the desired locations. The cost function for the optimization is the mean squared pressure of the superposition of the individual rotor waveforms at the desired observer location, which are shifted in phase by an amount determined by the optimizer. When multiple observer locations are targeted, the cost function is the sum of the mean squared pressures at each location. Of note, the individual rotors are added linearly, according to the assumption that they are independent. Individual rotor pairs were tested across a range of phase offset angles to verify the absence of acoustically significant aerodynamic interactions between the rotors. The resulting phase offsets between the rotors were then programmed into the electronic phase control hardware so that the acoustic performance of the system could be characterized.

Preliminary results

The optimization process was applied to predict the best phase offsets for two sets of target observers: a single observer at 210°, and observers at three discrete positions at 200°, 210°, and 220°. The single observer optimization yields a strong null in the region of the target observer. This null is approximately 25 dB below the incoherent level in this direction. However, the region of noise reduction is quite narrow, extending slightly greater than 30° around the target. Noise levels are near or somewhat above (by 6 dB) the incoherent level at most other observer azimuths. The multi-observer target produces a wide region of noise reduction, approximately 60°, with slightly higher (by 3 dB) noise levels radiated toward 210° than 220°. The different phase control schemes were then implemented on the hexacopter, and noise measurements were taken with the acoustic array across a range of azimuth angles. The comparison between the measured and predicted results for the incoherent and multi-observer optimal cases is shown in Figure 20. The measured and predicted incoherent noise levels are similar, with little variation in the measured data as the azimuth is varied. The measured optimal phase result shows a reduction near the target azimuth by approximately 6 dB. When the SPL is calculated over a band containing only the first five rotor blade passing frequency harmonics, a larger reduction in noise is observed, on the order of 15 dB.

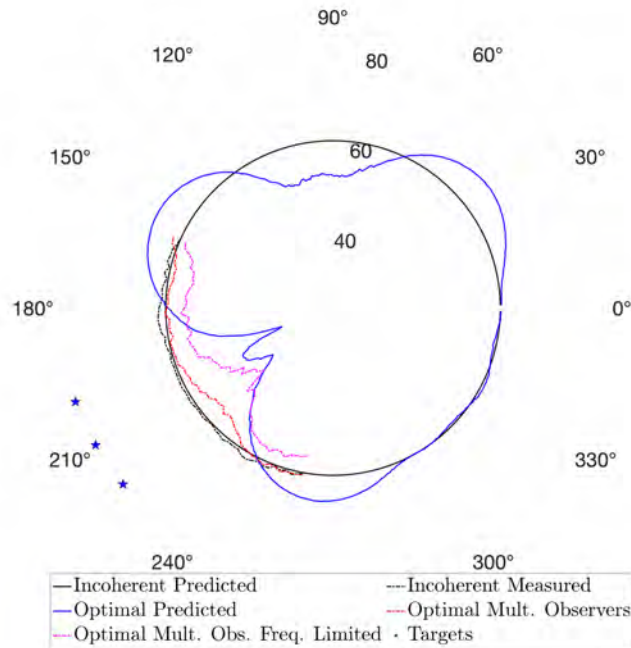


Figure 20. Measured and predicted SPL values for groups of targets.

Computational modeling

CHARM was used to predict the aerodynamic loading on the rotor blades. The rotor dimensions were provided by the manufacturer, including rotor radial segments and their corresponding chord, twist, sweep, anhedral, and thickness. The rotor thrust was trimmed to match the thrust obtained from the load cell at the rated RPM. The predicted acoustic pressure-time history for a single rotor is compared with experimental results in Figure 21. The acoustic pressure waveforms agree closely between prediction and experimental findings for all six rotors.

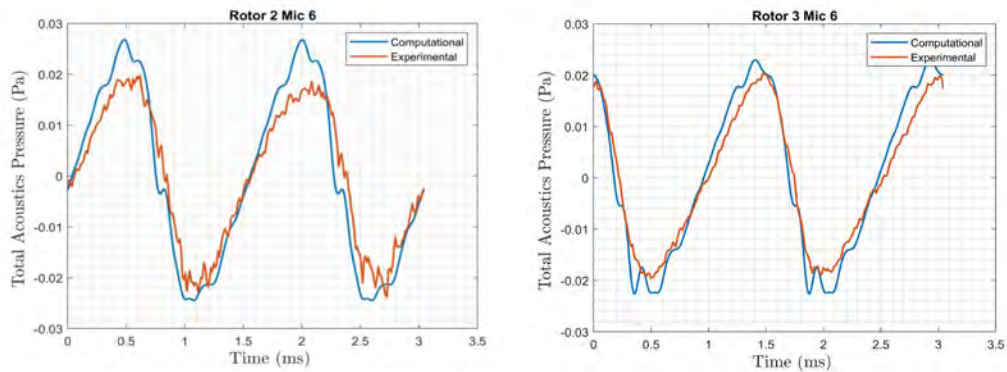


Figure 21. Acoustic pressure time series comparisons for different rotors ($\phi = 0^\circ$).

Noise predictions were conducted with the previously determined “optimal” and “pessimal” rotor phase combinations. Figure 22 shows the predicted tonal noise hemispheres for the two combinations. As determined experimentally, the optimal set of phase combinations results in a noise reduction in the target microphone array location, whereas the pessimal phase combinations result in an increase in noise.

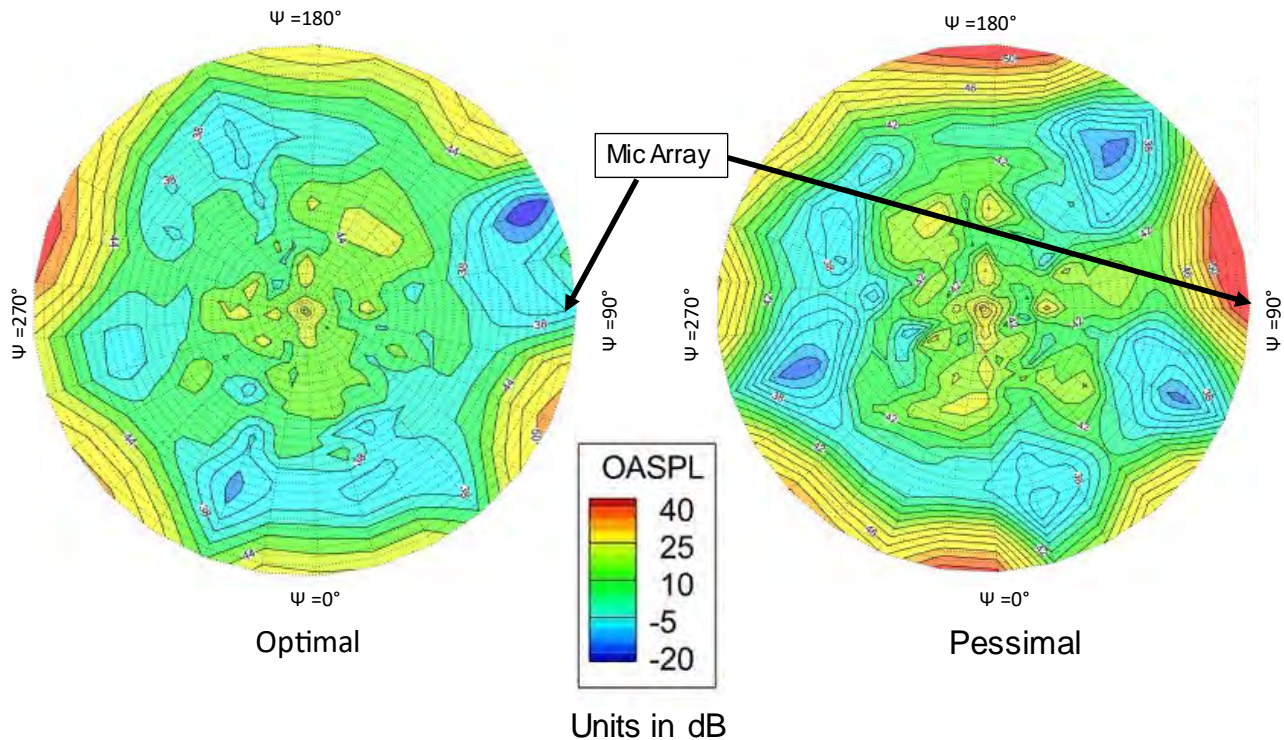


Figure 22. Tonal noise hemisphere during hover with two combinations of rotor phases, depicted as the unweighted OASPL in decibels (dB).

Publications

Valente, V., Johnson, E., & Greenwood, E. (2024, May). *An Experimental Evaluation of Electronic Propeller Phase Synchronization*. Abstract submitted to Vertical Flight Society Forum 80, Montreal, Canada.

Outreach Efforts

The investigation team holds monthly meetings with FAA and an external advisory board consisting of a dozen interested parties from government and industry. Technical data regarding the reconfigurable multirotor UAS have been shared with investigators from the Georgia Institute of Technology, the University of Salford, Texas A&M University, and the NASA Langley Research Center. Discussions are ongoing regarding potential opportunities for collaboration.

Awards

None.

Student Involvement

PhD student Vitor T. Valente was responsible for preparing the vehicle setup, including developing the method, defining test points, and collecting data. The analysis of the data collected is also being performed by the same student. PhD student Rupak Chaudhary was responsible for the simulations with CHARM and PSU-WOPWOP.

Plans for Next Period

regarding experimental data collection, plans for the next term include evaluation of the phase controller to assess the impact of that stage in the overall gain in attenuation. The method will subsequently be applied to different speeds and will consider time varying observer locations and speeds. The results should ultimately provide recommendations for implementing the phase control method on a flying multirotor aircraft.

Task 6 – Air Data System Integration and Calibration

The Pennsylvania State University

Objective

The objective of this task is to integrate an air data system into the large reconfigurable UAS platform, and then to develop procedures to calibrate the air data system for aerodynamic installation effects.

Research Approach

An air data system was developed on the basis of a commercially available sonic anemometer equipped weather station designed for making measurements on a moving platform. This air data system was integrated into the large reconfigurable UAS platform described in Task 2. Multiple flight test procedures were developed to measure the aerodynamic installation effects on airspeed measurements while the aircraft is in motion. After being properly characterized through a range of vehicle operating conditions, these installation effects can be removed from the airspeed measurements to produce calibrated estimates of the true airspeed of the aircraft.

Milestone

The milestones for this task include (a) integration of an air data system into the reconfigurable UAS platform, (b) development of airspeed calibration procedures for multirotor UAS aircraft, and (c) use of the air data system to characterize the aerodynamic state of the aircraft during noise measurements and relate it to the observed variations in noise.

Major Accomplishments

First, a review of prior research was conducted to evaluate different options for measuring air data onboard the aircraft during flight. The multirotor UAS's small size, low flight speeds, and ability to fly in different directions makes using a conventional Pitot probe air data system on these aircraft impractical. However, atmospheric researchers have had success in recent years in using sonic anemometer equipped weather stations on multirotor UAS to characterize meteorological data, including wind speed and direction, in the atmospheric boundary layer. During these measurements, the vehicle enters a hover over a fixed point on the ground. Prior research has shown good correlation between measurements made on UAS and those made using fixed ground stations or LIDAR. In contrast, when the vehicle is in motion, the aerodynamic flow field around the aircraft and the weather station itself is expected to affect the local velocity measured by the probe. These aerodynamic "installation effects" are known to significantly affect airspeed measurements made on conventional aircraft with Pitot probes; however, the magnitude of installation effects on multirotor UAS is not well understood. To answer this question, and to provide high-quality air data both during and between acoustic data collection runs, we have designed a sonic anemometer-based air data system and integrated it into Penn State's large reconfigurable UAS platform.

The air data system incorporates an Airmar 150 WX weather station, including a sonic anemometer, as well as measurements of air temperature, static pressure, and relative humidity. The weather station also includes an independent GPS sensor, which is used to synchronize the measured air data in time with the vehicle's state data. A separate onboard computer is used to record data from the weather station, as described in Task 2. The weather station and its accompanying data acquisition system were designed, fabricated, and secured to the UAS. The mounting of the weather station includes some 3D-printed parts, an 0.5-in polyvinyl chloride pipe to elevate the sensor above the rotors on the vehicle, and a case for the data acquisition system. Indoor tests have been conducted to ensure that the system is safe to fly outdoors, as well as ensuring that the height above the rotor plane is sufficient to avoid rotor inflow effects in hover. Figure 23 plots the time history of the measured wind speed during indoor hover tests. The measured wind speed is close to 0 (within 0.2 m/s), as expected, because the aircraft is in hover and isolated from outside winds.

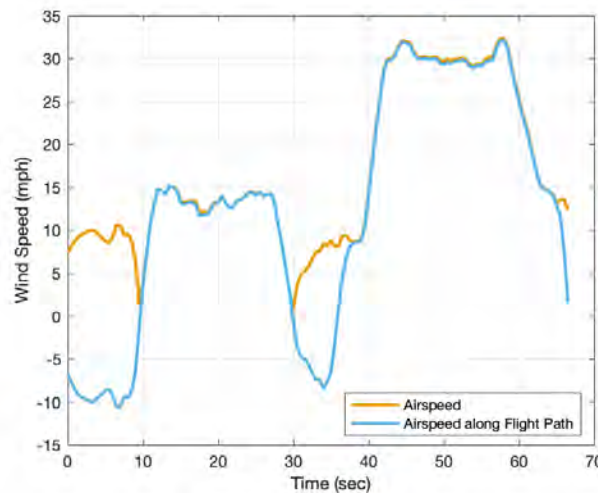
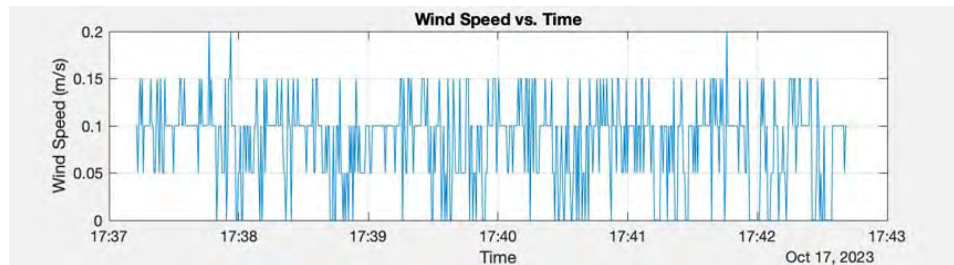


Figure 23. Wind speed time history during indoor hover testing.

After indoor testing, we developed several test procedures to quantify the aerodynamic installation effects of the air data system, with the goal of establishing a calibration curve to correct the measured data to true airspeeds. The procedures developed are based on the GPS-assisted airspeed calibration methods used on conventional aircraft. Two procedures were developed. The first uses back-to-back upwind and downwind flyover runs, wherein the UAS flies over the microphone array at a constant ground speed along one heading, then immediately flies back to the starting point at the same ground speed along the opposing heading. If the wind speed and direction are assumed to be constant during both upwind and downwind runs, the average airspeed measured along the flight direction should equal the constant ground speed.

Figure 24 plots the measured airspeed components during one upwind-downwind flyover pair with a constant ground speed of 17.5 mph. The difference in airspeed between the upwind and downwind legs is caused by the actual wind over the ground; averaging the upwind and downwind airspeed measurements produces an estimate of the true airspeed without wind effects. Differences between the average measured airspeed and the ground speed can be attributed to aerodynamic installation effects. This process is repeated across a range of airspeeds, to characterize how these effects change as the airspeed increases.

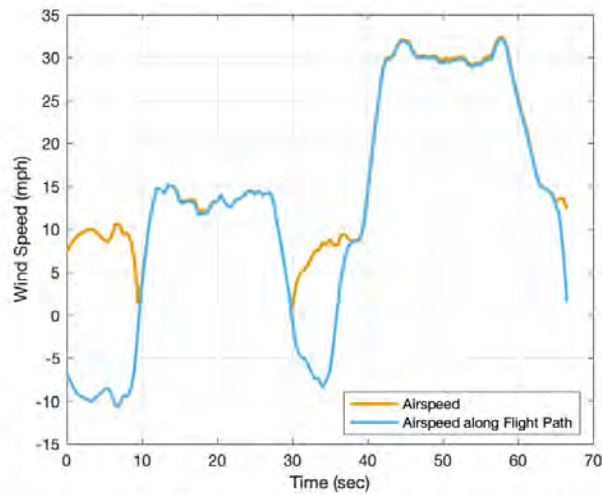


Figure 24. Measured air speed during a flyover run at 17.5 mph.

Figure 25 plots the measured airspeed versus the estimated true airspeed for upwind-downwind pairs from 5 to 20 mph. This plot clearly indicates an increasing difference between the measured and true airspeed as the speed of the aircraft increases. This error appears to grow linearly as the airspeed increases. A calibration curve characterizing this offset can be developed by fitting a linear trend line to the measured airspeed, which has a correlation coefficient, R^2 , of 0.990, indicating close agreement with a linear model. The error bars shown on the measured airspeed data represent the statistical variation in airspeed measured during each run, and are far smaller than the offset between the true and measured airspeeds, thereby indicating that the installation effects for airspeed measurements are significant.

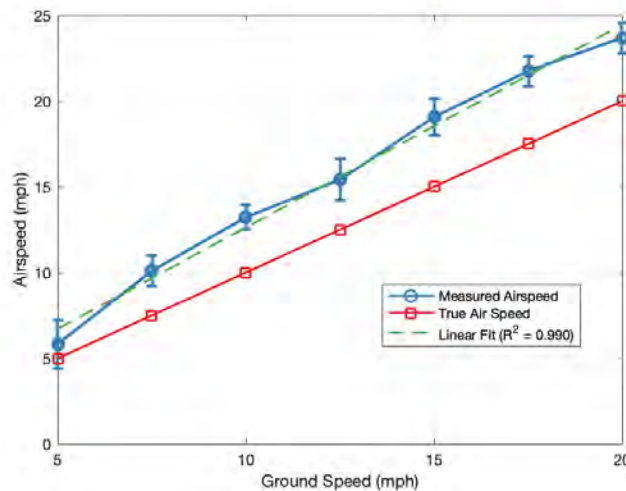


Figure 25. Measured air speed versus ground speed.

An alternative airspeed calibration procedure was developed by using an octagonal flight circuit, shown in Figure 26. This approach is designed first to allow the wind direction to be more accurately characterized during the flight, and second to enable the resulting airspeed calibration to account for the effect of crosswinds on the aerodynamic installation effects.



Figure 26. Octagonal flight trajectory circuit.

Figure 27 plots the time history of the airspeed components as the vehicle flies along the octagonal circuit, with a side length of 100 ft. Colored regions represent the constant-ground-speed segments along each side of the octagon; regions with the same color are on opposite sides of the octagon. From these data, the wind direction can be inferred. Notably, minimal to no difference is observed in the orange regions (A to B and E to F), thus indicating that the wind direction was likely to be parallel to the orientation of the vehicle between these set of points. However, the findings indicate that the vehicle was not always able to establish a constant flight speed during each segment; therefore, the length of the sides of the octagon must be increased to give the aircraft time to accelerate to a constant ground speed.

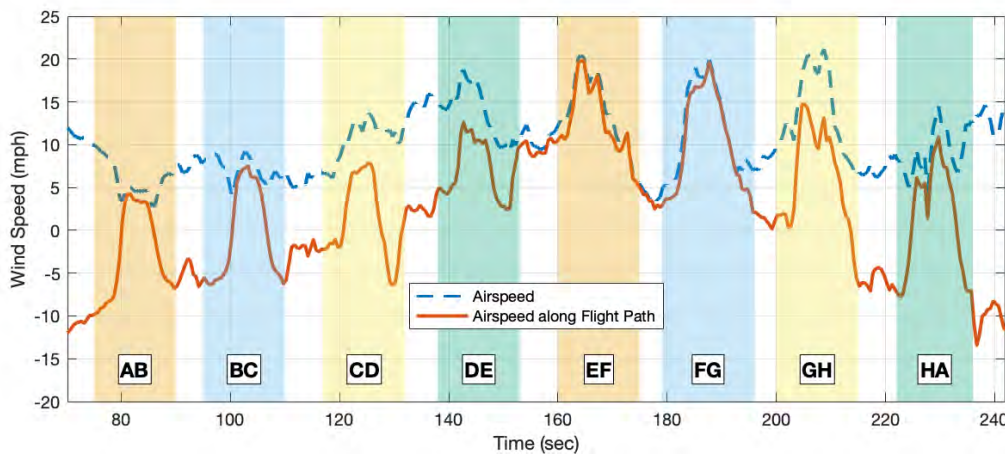


Figure 27. Preliminary wind speed measurements during a flight around the octagonal circuit at 10 mph. Matching shaded regions represent opposing parallel sides of the octagonal flight path.

Publications

El Sharkawy, E. Valente, V., Rachaprolu, J.S., & Greenwood, E. (2024, July). *Calibration of an Air Data System for Small Multicopter Aircraft*. Abstract submitted to AIAA Aviation 2024, Las Vegas, Nevada.

Outreach Efforts

The investigation team holds monthly meetings with FAA and an external advisory board consisting of a dozen interested parties from government and industry.



Awards

None.

Student Involvement

MS student EzzEldin El Sharkawy has been primarily responsible for the development, programming, and analysis of data produced by the onboard air data system. PhD student Vitor Valente has assisted in developing the air data system and conducted all test flights.

Plans for Next Period

Future plans include running more tests to build trust in the air data system calibration methods. Plans also include using the calibrated sensor to conduct wind profile measurements at different heights and spatial locations throughout the test site. These data will be correlated to ground-based meteorological measurements. Measured air and meteorological data will be correlated to the aircraft flight state and acoustic data to better understand the effects of environmental conditions on noise generation and propagation.



Project 078 Contrail Avoidance Decision Support and Evaluation

Massachusetts Institute of Technology

Project Lead Investigator

Steven R. H. Barrett
Professor of Aeronautics and Astronautics
Director, Laboratory for Aviation and the Environment
Massachusetts Institute of Technology
77 Massachusetts Ave, Building 33-207, Cambridge, MA 02139
(617) 253-2727
sbarrett@mit.edu

University Participants

Massachusetts Institute of Technology (MIT)

- P.I.: Prof. Steven R. H. Barrett
- FAA Award Number: 13-C-AJFE-MIT, Amendment Nos. 086, 100, and 115 (NCE to September 30, 2024)
- Period of Performance: October 1, 2021 to September 30, 2024
- Reporting Period: October 1, 2022 to September 19, 2023
- Tasks:
 1. Contrail forecast module
 2. Contrail identification module
 3. Contrail radiation module
 4. Trajectory planning module

Project Funding Level

This project received \$1,100,000 in FAA funding and \$1,100,000 in matching funds. Sources of matching funds are approximately \$168,000 from Massachusetts Institute of Technology (MIT), plus third-party in-kind contributions of \$469,000 from Savion Aerospace Corp. and \$463,000 from Google LLC.

Investigation Team

Prof. Steven Barrett (P.I.), All Tasks
Dr. Sebastian Eastham (co-investigator), All Tasks
Dr. Florian Allroggen (co-investigator), All Tasks
Dr. Raymond Speth (co-investigator), All Tasks
Dr. Jayant Sabnis (co-investigator), All Tasks
Vincent Meijer (graduate research assistant), Tasks 1 and 2
Louis Robion (graduate research assistant), Tasks 1 and 2

Project Overview

Contrails are the white, line-shaped ice clouds that form behind aircraft. These contrails and subsequent contrail cirrus are thought to account for around half of the climate warming attributable to aviation. Contrail avoidance through vertical and horizontal flight path changes is estimated to cause fuel burn penalties at the few percent level. As such, it is a potentially cost-effective way to mitigate aviation's climate impacts. However, contrail avoidance has not been demonstrated at scale, and a comprehensive toolset to support the approach has not been developed. The goal of this project is to create a contrail avoidance decision support and evaluation tool that can be trialed to optimize and evaluate the benefits, costs,

and practicality of contrail avoidance. In addition, subject to agreement with industry partners, we will seek to test contrail avoidance in a way that has no implications for air traffic control or safety.

This project aims to satisfy four specific objectives: (1) to develop the capabilities necessary to predict the formation and impacts of contrails from a given flight; (2) to evaluate the financial costs and environmental benefits of deviating from that path to avoid a contrail, including uncertainty; (3) to integrate these capabilities into an operational tool that can provide near-real-time estimate of the costs and benefits of a contrail avoidance action, informed by automated, coordinated observational analysis and modeling; and (4) to evaluate the effectiveness of these tools in a safe, scientifically sound real-world experiment.

The objectives outlined above will be met through a work program that comprises the following tasks:

1. Contrail forecast module
2. Contrail identification module
3. Contrail radiation module
4. Trajectory planning module

The following tasks will be included under future periods of performance (i.e., not funded through current submission) but provide an outlook for follow-on work in future project years.

5. Cost-benefit evaluation module
6. Airline integration
7. Experiment evaluation module

What follows in this document is a description of the first four tasks, including research progress and next steps.

Task 1 - Contrail Forecast Module

Massachusetts Institute of Technology

Objective

The goal is to develop a contrail forecast module that predicts the likelihood of persistent contrail-forming conditions 1 day ahead, in the hours before the flight, and in real time during a flight. This is intended to allow airlines to decide ahead of time to consider whether flights should use contrail avoidance, to file flight plans accounting for the best estimated cruise altitude, and to adjust in real time (subject to pilot workload and air traffic control constraints).

Research Approach

Development of the MIT contrail avoidance support tool

The MIT Contrail Avoidance Support Tool (MCAST) integrates the capabilities developed in the contrail identification module as well as live Automatic Dependent Surveillance-Broadcast (ADS-B) data to generate a nowcast of persistent contrail-forming areas (PCFAs). The nowcast uses recent contrail observations on satellite imagery available every 5 minutes to identify PCFAs. This approach assumes that where contrails are observed on satellite imagery, we expect that new flights passing through the region will also form contrails, at least for short lead times. MCAST presents these data in near-real time through a web-based graphical user interface, called MCAST-board (see next subsection), to provide contrail avoidance decision support.

The contrail identification module localizes contrails in both horizontal and vertical positions. The convex hull of these detections is then used to infer the shape of the PCFA from the sparse contrail observations. This nowcast adopts the Eulerian persistence approach: we assume that the region where contrails are detected will remain a PCFA for the near term. The PCFAs are assumed static for the forecast duration. An alternative approach—where PCFAs are assumed to move with the wind—has been investigated but has been shown to lead to worse performance (see previous year's report).

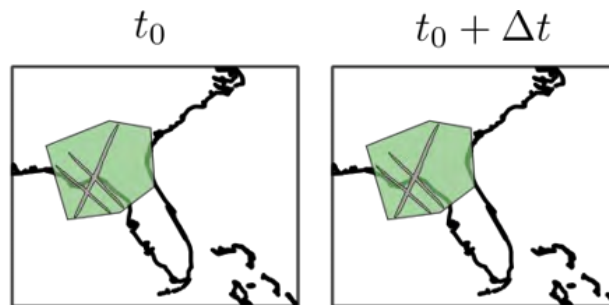


Figure 1. Schematic of the Eulerian persistence approach. Grey lines represent detected contrails, and the green polygon denotes the region indicated as a persistent contrail-forming area (PCFA) by the nowcast.

Live ADS-B data complemented by a trajectory prediction model are used to compute intersections of flights with the PCFAs identified previously. This allows MCAST to predict, for every flight over the contiguous United States, whether it will form a contrail given current observed contrail coverage.

For flights that have been identified as traversing a PCFA, MCAST calculates a potential deviation of the planned flight path that is expected to reduce the amount of contrail formed. Given that PCFAs have a large horizontal extent (Gierens and Spichtinger, 2000) but a limited vertical extent (Spichtinger et al., 2003), MCAST only considers vertical deviation around the regions. The constraints can easily be modified and aim to represent air traffic control and aircraft performance limitations for altitude changes at cruise. Heuristics for maximum deviation length are also implemented to minimize the number of cases where the planned deviation would incur a large additional fuel burn.

The deviations are not currently computed using an aircraft performance model, although future approaches could integrate the work in the trajectory planning module. Similarly, the climate impact due to additional fuel burn incurred by the deviation is not compared to the climate impact of the predicted contrail. This is being investigated in the contrail radiation and trajectory planning modules but has not been implemented in MCAST. Existing methods for the quantification of contrail climate impact on an individual flight basis lack validation with observation data and are therefore not utilized.

For now, MCAST is configured to test our ability to accurately predict where PCFAs are located, as well as our ability to deviate around them. It does not aim to propose climate-optimal rerouting with regard to contrails.

MCAST-board

MCAST-board is the web interface of MCAST. It has been developed to streamline the process of visualizing contrail avoidance opportunities, satellite imagery, ADS-B data, and the PCFA forecasts. MCAST-board complements the main MCAST compute pipeline by allowing for visualizations, in real time, of the data generated.

The web interface is composed of two different components. One is intended for use by dispatchers and contains a list view of flights that are predicted to enter a PCFA. The second is the map view, which is intended for visualization of contrail coverage, PCFAs, and ADS-B data.

The dispatcher interface is presented in Figure 2. For each flight predicted to form a contrail, a plot is generated to show both the top-down view of the PCFAs on the planned flight path and a cross-section of the flight localizing the PCFAs in the vertical extent. The latter plot also contains the proposed deviation above/below the PCFAs and an ACARS (Aircraft Communication Addressing and Reporting System) message defining this deviation. In the example on Figure 2, flight DAL954 is cruising at Flight Level (FL)340. As the flight is predicted to pass through a PCFA, MCAST proposes a vertical deviation around the PCFA by climbing to FL380 for around 100 nautical miles before descending back to the original cruise altitude.

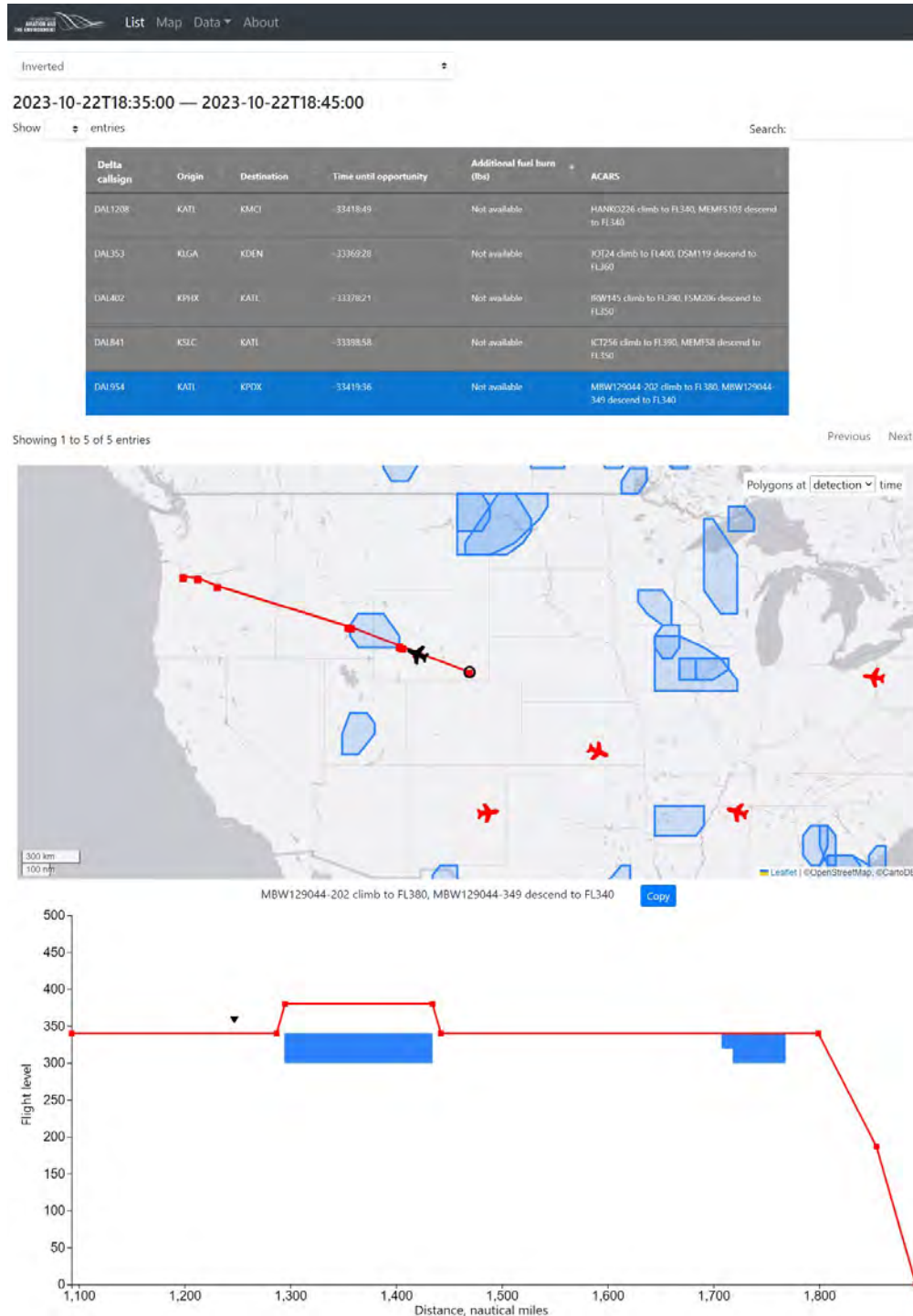


Figure 2. MCAST-board dispatcher interface. The map view and cross-section plot of the flight are plotted for two different times (5 minutes apart), explaining the inconsistencies in persistent contrail-forming areas (PCFAs) along the flight track. The column “Time until opportunity” is negative because the opportunity is in the past relative to the time at which this screenshot was taken.

The list view interface is developed for operational contrail avoidance at the airline level. It is designed to have dispatchers send contrail avoidance advisories to pilots, after having evaluated their feasibility. Pilots then decide whether they will act on the advisory. This interface and the format in which to present the contrail avoidance advisory has been improved after collaboration with Delta Airlines dispatchers. It adds minimal overhead to the dispatcher’s workload and integrates in their workflow similarly to hazardous weather advisories.

The second component of MCAST-board is the map interface. It serves primarily as a near-real-time visualization tool for GOES-16 imagery, detected contrails, and PCFAs. These products are available for visualization on MCAST-board with a delay of less than 5 minutes relative to the time the GOES-16 image is captured.

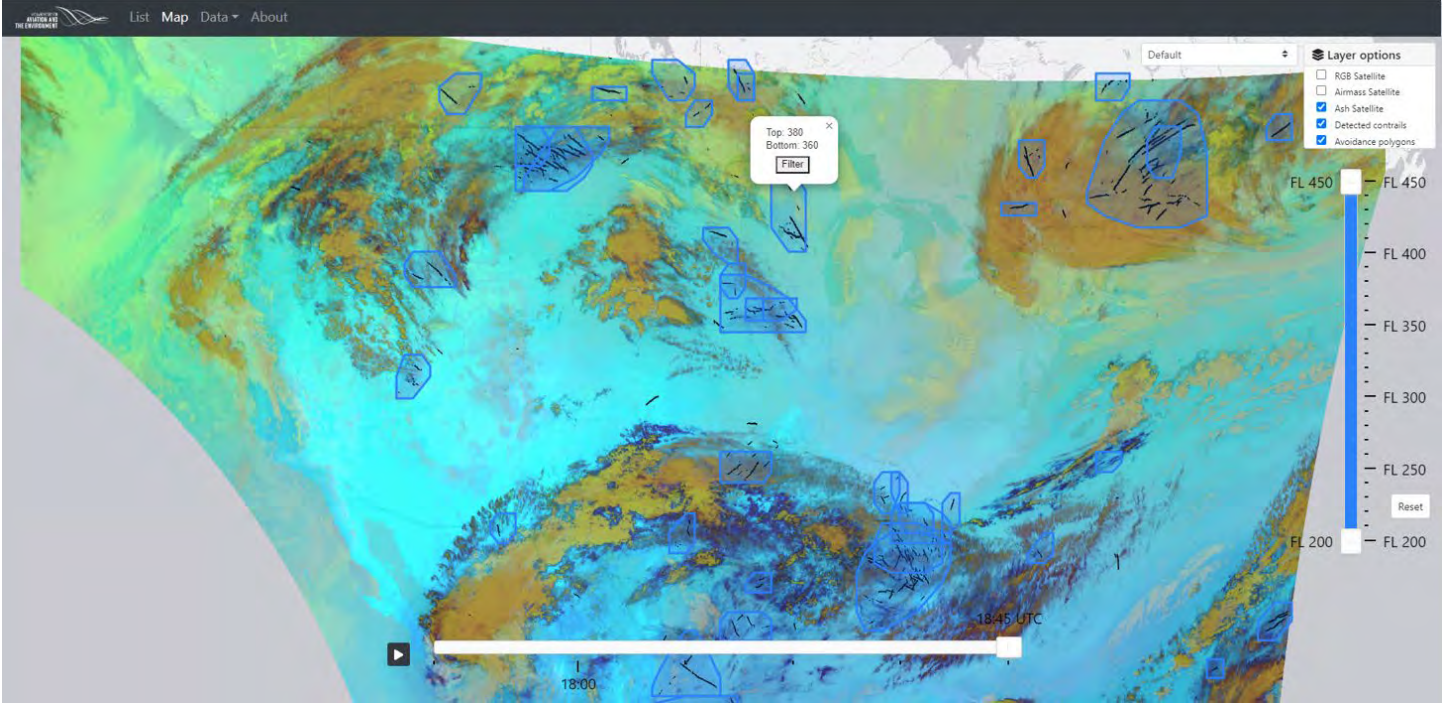


Figure 3. MCAST-board map view

Figure 3 shows the MCAST-board interface for October 22, 2023, at 18:45 UTC. We show the ash transform of the GOES image. Contrails appear as dark blue lines; overlaid in black are the contrails detected by the detection algorithm, as well as the PCFAs indicated by blue polygons. Each PCFA has an associated altitude range estimated by the contrail height estimation algorithm, which is reported here in-flight levels. This view also allows for the user to plot historical data and to filter the PCFAs by altitude.

MCAST-board can also be used as a manual verification tool for the effectiveness of avoidance strategies. MCAST advects all flight traffic at cruise altitudes for the previous 4 hours relative to the time of the satellite image, using wind data from NOAA’s High-Resolution Rapid Refresh (HRRR) model. The advected flight track is the location at which we expect to find a contrail produced by a given flight, should that flight have produced a contrail. By manually verifying if there is a contrail along an advected flight track, it is possible to assert whether a given flight has formed a contrail. This process is hindered by the large number of candidate flights for each observed contrail; moreover, wind model errors can lead to misalignments of the advected flight tracks, and the contrail detections are imperfect. It is challenging for both humans and algorithms to link contrails to flights and it is a time-consuming, error-prone process. At small scales, however, MCAST-board provides the tools to manually verify the validity of the nowcast. Figure 4 shows an example of the number of candidate flights for the detected contrails in black. Although some flight tracks do seem to align well with the contrails, manual verification needs to be done to assert that the contrail is indeed formed by the candidate flight.

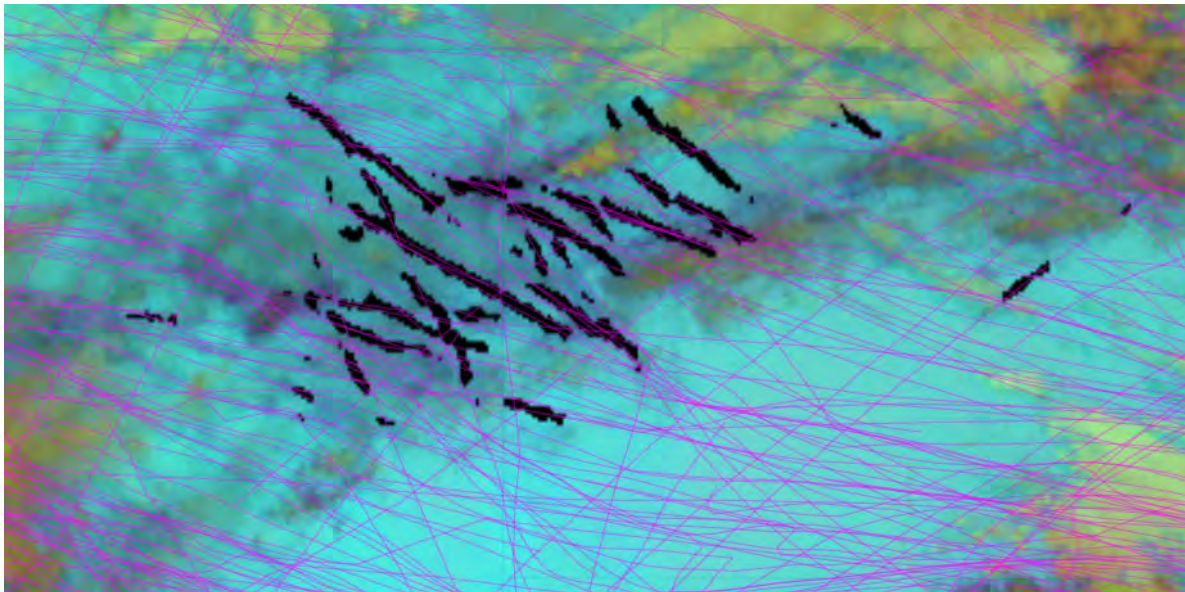


Figure 4. Map view of MCAST-board with advected flight tracks overlaid in pink. Detected contrails are in black. Persistent contrail-forming area (PCFA) polygons are omitted for clarity.

MCAST now generates near-real-time PCFA nowcasts and makes them available through its web interface. Extensive work has been done to make MCAST and MCAST-board both robust and responsive for end-users. Both code bases are transitioning from research to production code, which is necessary to manage the large volume of data generated every 5 minutes. This transition is also required to ensure the reliability of MCAST in an operational context where dispatchers would actively be using it to plan contrail avoidance actions.

Trials conducted with Delta Airlines are underway to assess the validity of the forecasts, the feasibility of the avoidance opportunities proposed by MCAST, and the ease of use of MCAST-board. These trials aim to implement operational contrail avoidance strategies while ensuring that their effectiveness is verifiable by way of observations.

MCAST forecast of PCFAs and the MCAST-board flight track interface were used in the October 2023 Boeing ecoDemonstrator campaign. The goal of the campaign was to intentionally form contrails to later sample them in situ, and MCAST PCFAs will be used to direct the aircraft into regions where we expected contrail formation.

Aircraft plume chemistry, emissions, and microphysics model development

The Aircraft Plume Chemistry, Emissions and Microphysics Model (APCEMM; Fritz et al., 2020) serves as the primary contrail model for this project. It is undergoing active development through NASA University Leadership Initiative funding, which aims to improve the model's fidelity and computational speed. A major improvement in the fidelity of APCEMM is that it is now able to use background conditions that vary in time as inputs to the model. This differs from previous versions of APCEMM used in the contrail radiation module, which assumed fixed background conditions derived from numerical weather models (NWP). Under ASCENT 78 funding, a Python wrapper for APCEMM (C++) is being developed to prepare the new input formats from weather data, as well as run APCEMM. The wrapper currently supports weather data from NOAA's HRRR model and will be extended to support the European Centre for Medium-Range Weather Forecasts (ECMWF) Integrated Forecasting System (IFS) forecast and ERA5 reanalysis data.

Instead of simulating the contrail in three dimensions (3D), APCEMM models a single cross-section at a given spatial waypoint specified by the user. This approach avoids expensive 3D simulation of the contrail. The time-varying input weather data for APCEMM are generated by first computing the trajectory of the initial waypoint by way of advection. With knowledge of the trajectory of the initial waypoint, we can interpolate the NWP data to find background conditions at every

point along the trajectory. Then, should a contrail form in APCEMM’s early plume model, we know the time-dependent background conditions at every step of the plume evolution.

Development of the Python wrapper was started in order to support the 2023 Boeing ecoDemonstrator campaign. As the campaign involves intentionally forming contrails, HRRR weather data combined with APCEMM will be used to forecast flight tracks along which the ecoDemonstrator Boeing 737 would most likely form contrails. This will provide a unique opportunity to verify the accuracy of the observation-based nowcast and APCEMM-based forecast. We will be able to compare simulated contrails to in situ measurements of the real contrail with reduced uncertainties in background conditions.

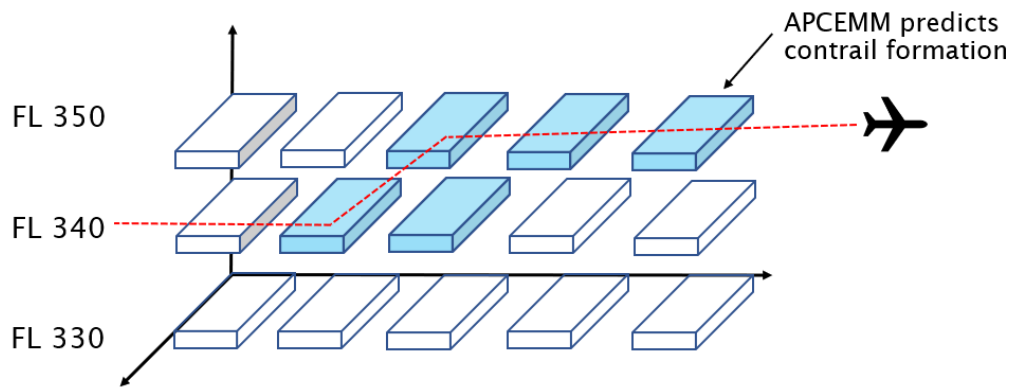


Figure 5. Discretization of potential flight paths for Aircraft Plume Chemistry, Emissions and Microphysics Model (APCEMM) simulation. FL, Flight Level.

While APCEMM compute speed has been significantly improved, as it explicitly simulates the 2-dimensional (2D) cross-section of contrails, it remains too computationally intensive to be used for forecasts at the scale of the full United States. Instead, it will be used for the campaign as a targeted forecast tool, only simulating potential flight routes identified by operational constraints, as presented in Figure 5. This limits the number of simulations necessary while still allowing for the use of APCEMM as a contrail forecasting tool.

Milestone

- Demonstrated concept and first implementation of a contrail forecasting functionality to FAA

Major Accomplishments

- Developed and improved a contrail avoidance support tool that generates forecasts of contrail-forming regions using observation data in near-real time
- Developed a web interface for the contrail avoidance support tool allowing for integration tests with airline dispatchers
- Developed a framework allowing for observation-based verification of the forecast validity at small scales

Publications

None.

Outreach Efforts

MCAST-based research was presented at the GE EDGE 2023 conference and multiple FAA workshops. The APCEMM model is also being shared with multiple research teams across the United States and United Kingdom to promote community contrail model development.

Awards

None.

Student Involvement

The research for this task was conducted primarily by Vincent Meijer and Louis Robion, graduate research assistants at MIT. The communication of this research to the FAA was conducted primarily by Louis Robion.

Plans for Next Period

- Improve the robustness of the contrail avoidance support tool for operational use
- Conduct avoidance trials with an airline partner using the support tool

References

Gierens, K., & Spichtinger, P. (2000, April). On the size distribution of ice-supersaturated regions in the upper troposphere and lowermost stratosphere. In *Annales Geophysicae* (Vol. 18, No. 4, pp. 499-504). Berlin/Heidelberg: Springer-Verlag.

Fritz, T. M., Eastham, S. D., Speth, R. L., & Barrett, S. R. (2020). The role of plume-scale processes in long-term impacts of aircraft emissions. *Atmospheric Chemistry and Physics*, 20(9), 5697-5727.

Spichtinger, P., Gierens, K., Leiterer, U., & Dier, H. (2003). Ice supersaturation in the tropopause region over Lindenberg, Germany. *Meteorologische Zeitschrift*, 12(3), 143-156.

Task 2 - Contrail Identification Module

Massachusetts Institute of Technology

Objective

The objective of this task is to develop a real-time contrail identification module that locates contrails both horizontally and vertically. This module will be necessary to evaluate whether avoidance has been successful. Furthermore, this module will enable contrail forecasting approaches that are based on contrail detections, and that might prove to be more reliable for shorter lead times than approaches based on numerical weather forecasts. The initial version will use GOES satellite observations combined with an MIT-developed (under NASA sponsorship) deep learning approach to identify contrails from space. Future developments could add other satellite products and ground and other observations.

Research Approach

Improvements of the contrail height estimation algorithm

Accurate estimates of the altitude of PCFAs are crucial for a contrail avoidance strategy relying on vertical deviation around the regions. To ensure the precision of these estimates, our existing deep learning-based contrail height estimation algorithm has been improved and extensively tested to assess its performance. This algorithm estimates the altitude of contrails detected on GOES-16 imagery by our contrail detection algorithm (Meijer et al., 2022).

To train and assess the performance of the algorithm, we generated a dataset of contrails on GOES-16 imagery whose altitude was known. To do so, we collocated GOES-16 images with measurements by the LIDAR CALIOP (Cloud-Aerosol Lidar with Orthogonal Polarization) aboard the low Earth orbit satellite CALIPSO. The LIDAR directly measures the contrail top altitude, and these data are mapped to the corresponding GOES-16 pixels. This analysis was conducted for the years 2018 to 2022, leading to the identification of over 3,000 contrail cross-sections in CALIOP data. This collocation approach is similar to that developed for cirrus height estimators (Kox et al., 2012; Strandgren et al., 2017) but was applied here on GOES-16 imagery for contrails only.

Using this dataset of collocated contrails, we compared multiple machine learning algorithms to estimate the altitude of contrails, including a state-of-the-art cirrus height estimator adapted from CiPS (Cirrus properties from SEVIRI) (Strandgren et al., 2017). This was done to assess the benefits of utilizing contrail data during training of these algorithms, as well as the effect of a different neural network architecture. The algorithm adapted from CiPS is a pixel-by-pixel estimator (multi-layer perceptron [MLP]) of cirrus cloud altitudes, trained on cirrus cloud data. We compared this approach to an image-level estimator (convolutional neural network [CNN]) also trained on cirrus data only. We then developed an MLP and a CNN trained using cirrus data and further specialized using contrail data from a subset of our dataset. Figure 6 compares the performance of these algorithms on the dataset of collocated contrails. We found that the image-based, contrail-trained approach for contrail height estimates (red scatter plot) outperformed other approaches with a root mean square error of 570 m.

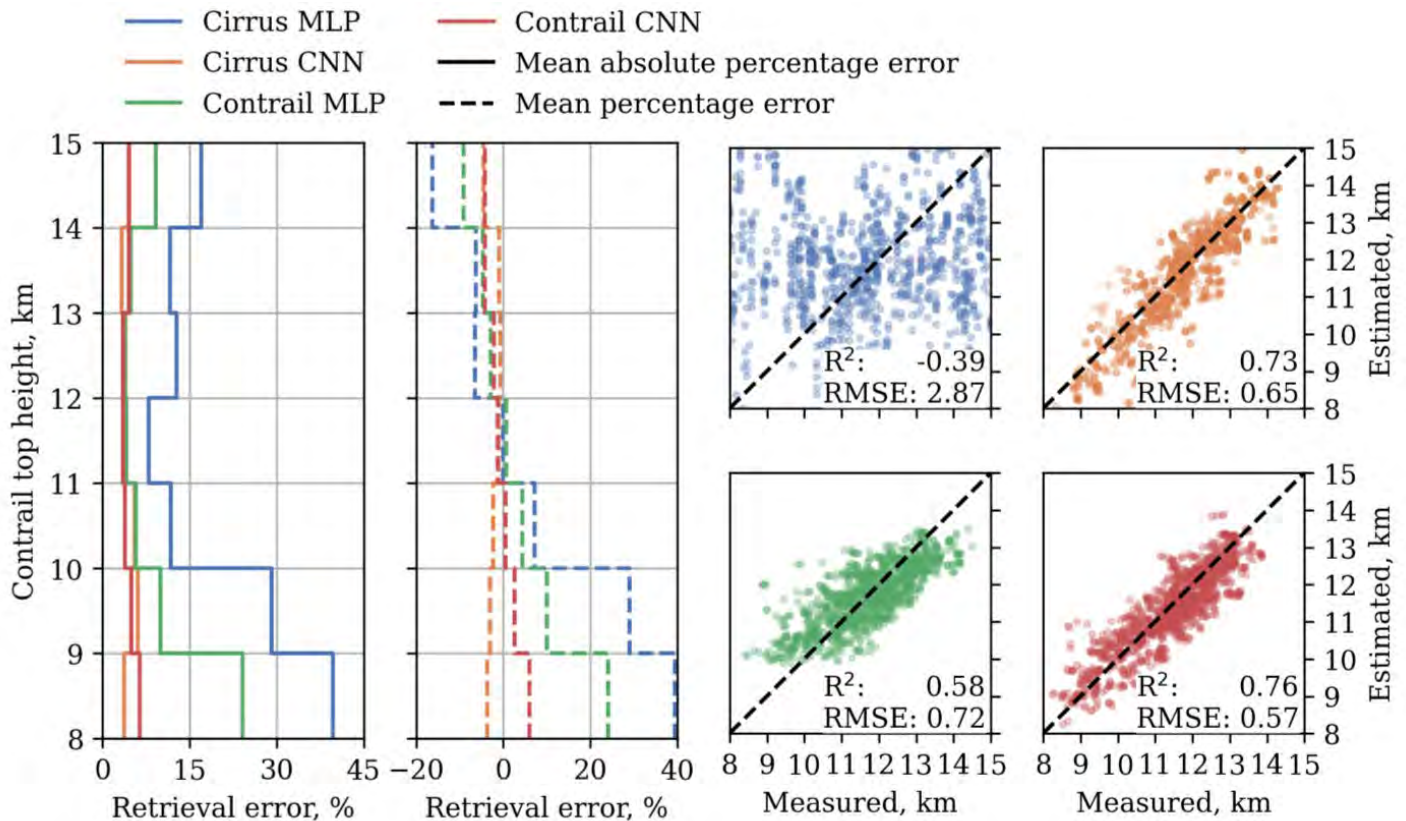


Figure 6. Comparison of different height estimation algorithms applied to the contrail dataset. Pixel-by-pixel approaches are multi-layer perceptrons (MLP) and image-based models are convolutional neural networks (CNN). The left plots present the relative and absolute errors as a function of altitude. The scatter plots present the algorithm estimates for the dataset. Ideally, all data points would lie along the $Y=X$ line, indicating perfect accuracy of the height estimate. RMSE, root mean squared error.

In addition to providing more accurate estimates of contrail top heights, our algorithm outputs a calibrated probability distribution for the contrail altitude shown in Figure 7. This allows for the estimation of uncertainty bounds on the contrail altitude, which may allow for more informed avoidance actions. Given two PCFAs, one with large uncertainty in its altitude and the other with smaller uncertainty, it may be safer from a fuel-burn/contrail impact tradeoff perspective to attempt to avoid only the more certain PCFA. This new height estimation algorithm has not yet been implemented in the main MCAST pipeline, but we expect it to improve the accuracy of the localization of PCFAs.

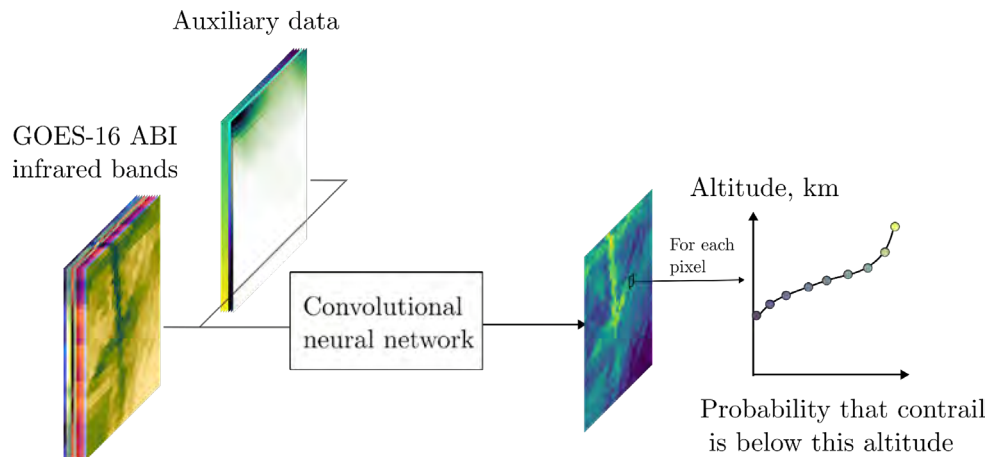


Figure 7. Convolutional neural network (CNN), contrail-trained approach for contrail altitude estimation. The CNN is applied to GOES-16 infrared images and auxiliary data (latitude, satellite viewing angle, etc.) to obtain probability distributions for the contrail altitude.

Integration of temporal data in the contrail detections

The contrail detection framework presented so far does not take advantage of temporal information because detections are computed independently from one another by applying the CNN to each image separately. We identified previously that this approach can lead to temporal inconsistencies in the contrail detections for a sequence of consecutive images. This motivated work under a NASA Atmospheric Composition Modeling and Analysis Program (ACMAP) grant, which led to the creation of a contrail filtering framework and a test dataset. This enabled further studies supported by ASCENT project 078 to improve the filter, quantify its performance, and scale it for use a larger domain of the United States. This work is presented in detail in a master’s thesis (Robion, 2023), and we briefly present the methodology and key results of this filtering approach here. A video demonstrating this work is available online¹.

¹ https://www.dropbox.com/scl/fi/nkjswnhgypfh3q0ugaiza/A78_2023_Contrail_filtering.mp4?rlkey=39vhs50iwbmnyeqtx90vqr36e&dl=0

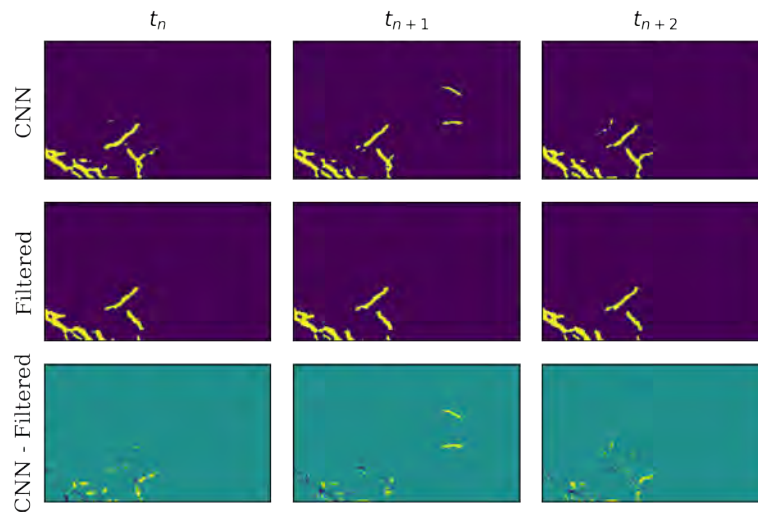


Figure 8. Comparison of consecutive contrail detections computed by the detection algorithm (convolutional neural network [CNN]) and the filter. The first two rows present contrail detection masks: contrail pixels are in yellow and non-contrail pixels are in purple. The third row presents the difference between the two masks: in cyan are the regions where both masks are in agreement; in dark blue are the pixels indicated as contrail pixels after filtering but that are not indicated as such by the CNN; and in yellow are the pixels indicated as contrail pixels by the CNN but not by the filter. Contrails spuriously appearing in the top-right corner of the CNN detections at t_{n+1} are correctly removed by the filter as their presence for 1 minute only is non-physical.

Under ASCENT project 78 funding, we compared the filtered detections to the originals using classic image segmentation performance metrics. We also computed metrics that focus on the consistency of these detections. By optimizing both metrics, we calibrated the filter for use on the 1-minute refresh GOES mesoscale product. We found that the calibrated filter does not compromise the accuracy of contrail identification but improves the consistency of consecutive detections.

To evaluate the ability of the filter to reduce temporal inconsistencies in contrail detections, we focused on individual contrails. We tracked a given contrail for the duration over which it is labeled and computed the percentage of pixels detected within the contrail at each time step of the contrail track. If the detections are perfect and detect the entire contrail, the percentage would be 100%; if the detections are perfectly consistent, this percentage would be constant in time.

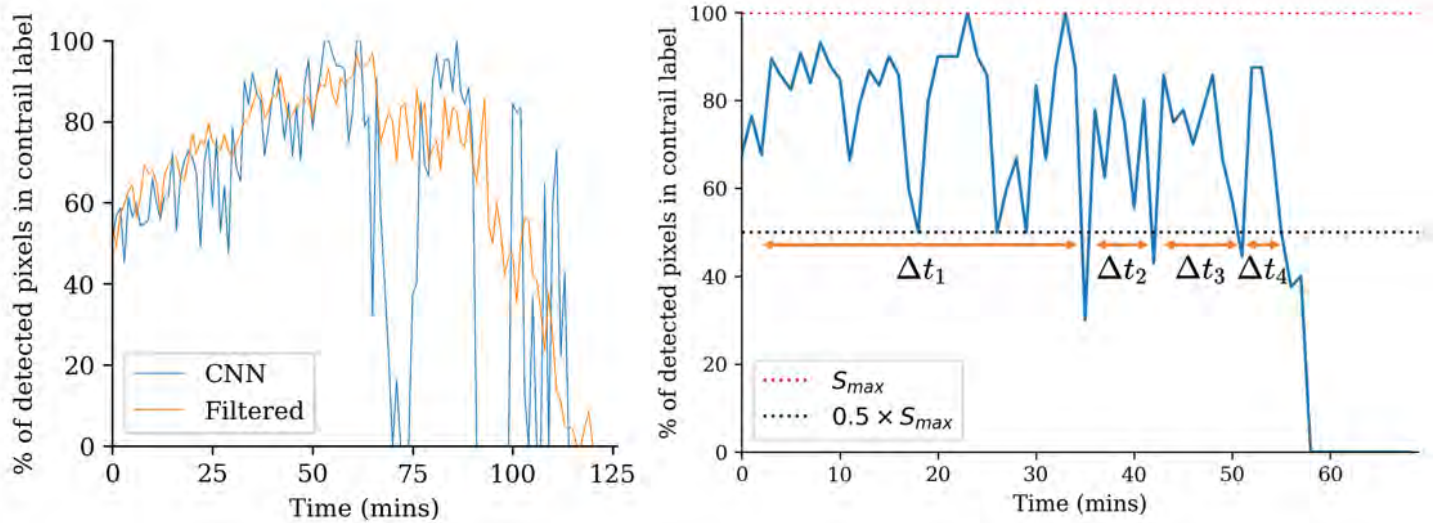


Figure 9. The left plot is a comparison of the percentage of detected contrail pixels for a given contrail for the convolutional neural network (CNN) with and without filtering. The right plot is a toy example to define the contrail detection segment metric. Each duration over which a contrail is systematically detected over a given threshold (here $0.5 S_{max}$) is considered to be a “consistent” detection. This defines a detection segment. The threshold is defined as a function of S_{max} , which is the maximum percentage of detected pixels for that specific contrail over its lifetime. This is because we are interested in minimizing the relative variation of percentage of detected pixels: a poorly detected (low percentage of detected pixels) but consistently detected (small variations of percentage of detected pixels) contrail is still a signal that can be exploited.

Figure 9 shows the effect of filtering on our ability to consistently detect a given contrail. The CNN without filtering presents a large drop in percentage of detected pixels around the 75-minute mark, where the contrail is essentially not detected. When compared to the signal of the filtered detections, we found that the filter is effective at reducing this false-negative detection: on the filtered signal, there is no such drop in percentage of detected pixels. The filter is able to compensate for an error in contrail detection. The right plot of Figure 9 presents the contrail detection segment metric. It corresponds to durations over which the number of detected pixels of a contrail is larger than a given threshold. In that case, the detection is considered consistent. The fewer segments and the longer in duration that the segments are, the more consistent the contrail detection: there are fewer interruptions in identification.

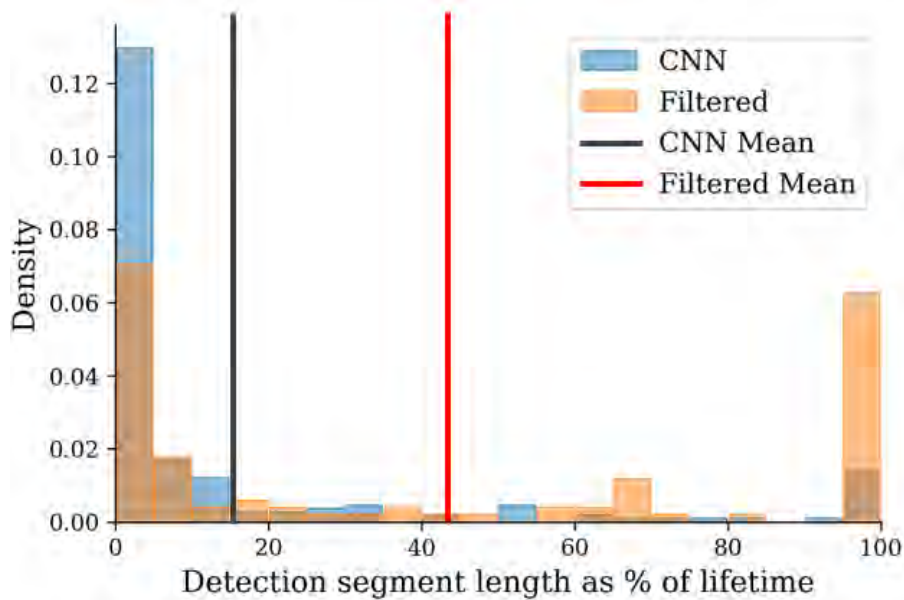


Figure 10. Distribution of detection segment lengths as a percentage of observed lifetime of the contrail for both the non-filtered and filtered cases. CNN, convolutional neural network.

Figure 10 presents the distribution of detection lengths as percentages of observed lifetime. We expect that by improving the temporal consistency of detections, the mean detection segment length would increase; contrails are detected for longer fractions of their lifetime in a single consistent segment. Comparing this metric for the filter and the CNN, filtering increases the mean segment length from around 17% to 42% of the lifetime of a contrail.

The metrics computed previously indicate that the filtering process is successful at reducing temporal inconsistencies in the detection signal. This has been tested on a small subset of the United States, where GOES imagery is available every minute. In contrast, imagery of the entire contiguous United States (CONUS) is only available every 5 minutes. A new calibration of the filter is necessary to tune the parameters to this new mode of operations with sparser observations. Applying the filter to the full CONUS domain also required improvements in computational speed of the filter. Integrating the filtering of the contrail detections in MCAST is expected to increase the robustness of the PCFA identification pipeline but this has not been implemented yet. This is mainly due to limitations in the filter’s ability to finish computation at the near-real-time frequency required by the MCAST and MCAST-board pipelines.

Milestone

- Demonstrated first implementation of a contrail identification module to FAA

Major Accomplishments

- Developed a contrail height estimation algorithm that outperforms state-of-the-art algorithms and estimates its predictive uncertainty
- Quantified the performance of the contrail filtering framework using GOES mesoscale imagery

Publications

None.

Outreach Efforts

None.

Awards

None.

Student Involvement

The research for this task was conducted primarily by Vincent Meijer and Louis Robion, graduate research assistants at MIT. The communication of this research to the FAA was conducted primarily by Louis Robion.

Plans for Next Period

- Integrate the new contrail height estimation algorithm into the nowcasting tool to increase the accuracy of predicted altitudes for contrail avoidance regions
- Extend the contrail filtering framework to the full GOES CONUS domain

References

- Kox, S., Bugliaro, L., & Ostler, A. (2014). Retrieval of cirrus cloud optical thickness and top altitude from geostationary remote sensing. *Atmospheric Measurement Techniques*, 7(10), 3233-3246.
- Meijer, V. R., Kulik, L., Eastham, S. D., Allroggen, F., Speth, R. L., Karaman, S., & Barrett, S. R. (2022). Contrail coverage over the United States before and during the COVID-19 pandemic. *Environmental Research Letters*, 17(3), 034039.
- Robion, L. A. (2023). *Improving the temporal consistency of satellite-based contrail detections using ensemble Kalman filtering* (Doctoral dissertation, Massachusetts Institute of Technology).
- Strandgren, J., Bugliaro, L., Sehnke, F., & Schröder, L. (2017). Cirrus cloud retrieval with MSG/SEVIRI using artificial neural networks. *Atmospheric Measurement Techniques*, 10(9), 3547-3573.

Task 3 - Contrail Radiation Module

Massachusetts Institute of Technology

Objective

The objective of this task is to develop a contrail radiation module. This will evaluate the radiative effect of individual contrails (both existing and counter-factual), incorporating information on surface albedo, cloud cover, and other factors. The contrail radiation module enables the assessment of the contrail climate impact of flights. Eventually, when integrated with the other modules, this will allow us to extract climate-optimal contrail avoidance strategies.

Research Approach

In order to evaluate the climate impact of contrail avoidance strategies, we couple the trajectory planning module with the contrail radiation module. This work is presented in detail in a master's thesis (Elmourad, 2023), and we briefly present the methodology and key results of this approach here. The trajectory planning module consists of an aircraft performance model and a uniform cost search algorithm that seeks to minimize a cost function weighing fuel burn and a metric of contrail impact:

$$J = C \times \theta + F \times (1 - \theta)$$

where J is the cost function, C is the contrail impact metric, F is the fuel burn, and $\theta \in [0, 1]$ is the tradeoff parameter that determines the degree of contrail avoidance.

$\theta = 0$: gives the baseline case, in which the trajectory is optimized for fuel burn;

$\theta = 1$: gives the maximum contrail avoidance case.

The parameter θ can be varied between 0 and 1 to simulate different degrees of contrail avoidance. Under these different scenarios, we can use the contrail radiation module to quantify the net climate impact of such a strategy for flights taken using a Boeing 737-800 modeled using the Transport Aircraft System OPTimization (TASOPT) aircraft performance model (Drela, 2011).

To understand the potential impact of contrail avoidance on fuel burn, we simulated the effect of a contrail avoidance strategy for 100,000 flights with different values of parameter θ . We initially used contrail length as the metric of contrail impact, because length can be more easily evaluated in both an experimental and a real-world setting. We also estimate radiative forcing for a random sample of 3,000 flights to evaluate their climate impact, using APCEMM and the Rapid Radiative Transfer Model (RRTM; Mlawer et al., 1995). We focused on two avoidance scenarios: one that avoids all contrails (daytime and nighttime) and the other that aims to avoid nighttime contrails, as we anticipate contrails during the night to have a warming effect.

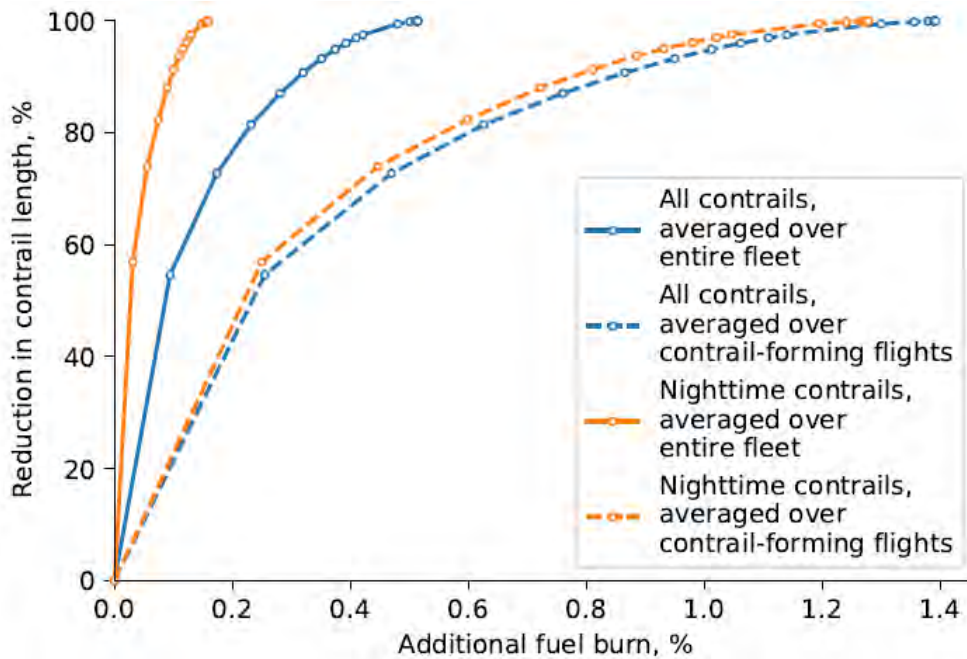


Figure 11. Fraction of reduction in contrail length as a function of additional fuel burn.

Feasibility analysis of avoidance scenarios

Figure 11 shows the additional fuel burn incurred by the contrail avoidance strategies. In all cases, the fleet average increase in fuel burn is less than 0.5%. Filtering this result to only the flights that would perform contrail avoidance actions, we find an average fuel burn increase of 1.4% when averaged over only those flights. This number falls to less than 0.3% if the target reduction is 50%, reflecting the fact that a small number of contrails are disproportionately difficult to avoid.

Figure 12 shows the detailed distribution of the fuel burn penalty by season. The distribution shows that a minority of flights would incur a fuel burn penalty larger than 2%, which may make the avoidance action infeasible. This number is consistent across seasons. The distributions of mean altitude change show that the majority of deviations around contrail regions necessitate altitude changes smaller than 1,000 m, with a bias for descents. This corresponds to a change of 20 to 40 flight levels.

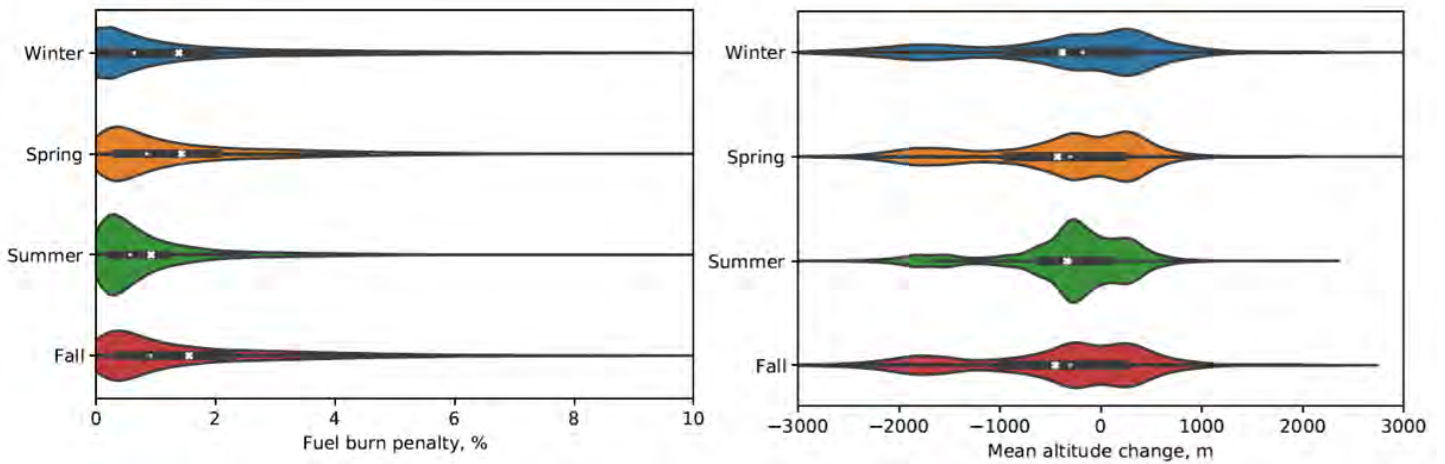


Figure 12. Left violin plot: distributions of fuel burn penalty as a function of season for the “avoid all contrails” scenario. Right violin plot: distributions of the mean altitude change for the “avoid all contrails” scenario.

Climate impact of avoidance scenarios

To estimate the climate impact of the avoidance scenarios, we compared the energy forcing (EF) of CO₂ incurred by the additional fuel burn to the contrail EF. We chose the EF metric as a proxy for climate impacts as it allows for comparison of two very different climate forcers: CO₂ has a smaller instantaneous radiative forcing (RF) impact but is long lived, whereas contrails have larger instantaneous RF impacts but short lifetimes. While EF is convenient, it does not consider the difference in climate sensitivities of contrails and CO₂, which may change the relative climate impact of each forcer.

In both cases, we chose a time horizon of 100 years for the EF calculation. The CO₂ EF is directly proportional to the additional fuel burn with a factor of 4.46 GJ/kg (Lee et al., 2021). On the other hand, the contrail EF is estimated by first simulating the contrail in APCEMM, using RRTM to compute its instantaneous RF and integrating this impact over the time horizon. We found that for contrail-forming flights, the EF of the contrail was an order of magnitude larger than the CO₂ EF. Figure 13 shows that contrail EF dominates the EF of a given flight and that for low tradeoff parameter values, we can reduce 93% of the sample EF impacts using contrail avoidance.

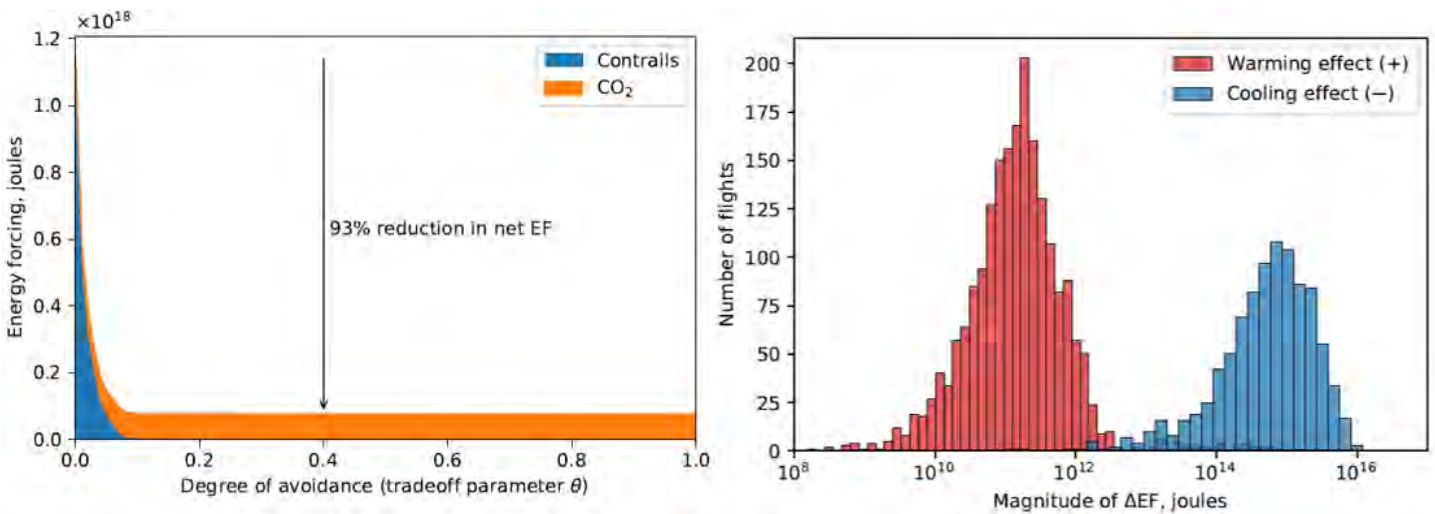


Figure 13. Left plot: evolution of the energy forcing (EF) of contrails and CO₂ as a function of the degree of contrail avoidance for the “avoid all contrails” scenario. Right plot: distribution of the change in total EF of the flight for flights avoiding contrails in the “avoid all contrails” scenario; x-axis is in log-scale.

Figure 13 also presents the detailed distribution of changes in EF after taking a contrail avoidance action. The distribution is plotted in log-scale and differentiates flights where the change in EF is positive (warming effect, red), and where the change in EF is negative (cooling effect, blue). We found that there is high variability between flights and that a significant fraction of flights had an increase in their total EF after the avoidance action. There are two main reasons why flights can see an increase in total EF after a contrail avoidance action. One is that these could be flights that would have formed short-lived contrails; therefore, the additional fuel burn is not offset by the avoided contrail. In addition, some of these flights may have formed cooling contrails and avoiding contrail formation altogether leads to an increase in total EF for the flight.

The key finding is that, even if only contrail length is used to identify deviations and therefore some deviations lead to increases in EF, we still find a large reduction in total EF across the entire fleet.

Milestone

- Demonstrated first implementation of a contrail radiation module to FAA

Major Accomplishment

- Coupled the trajectory-optimization module and contrail radiation module to compute estimates of the energy forcing impact of different contrail avoidance strategies

Publications

None.

Outreach Efforts

None.

Awards

None.

Student Involvement

This task was conducted primarily by Jad Elmourad, a graduate research assistant at MIT.

Plans for Next Period

- This task is not the focus of the next period of performance.

References

- Drela, M. (2011, June). Development of the D8 transport configuration. In *29th AIAA Applied Aerodynamics Conference* (p. 3970).
- Elmourad, J. A. (2023). *Evaluating Fuel-Climate Tradeoffs in Contrail Avoidance* (Doctoral dissertation, Massachusetts Institute of Technology).
- Lee, D. S., Fahey, D. W., Skowron, A., Allen, M. R., Burkhardt, U., Chen, Q., ... & Wilcox, L. J. (2021). The contribution of global aviation to anthropogenic climate forcing for 2000 to 2018. *Atmospheric Environment*, *244*, 117834.
- Mlawer, E., Taubman, S. J., & Clough, S. (1996). RRTM: a rapid radiative transfer model. In *Science Team Meeting* (p. 219).

Task 4 - Trajectory Planning Module

Massachusetts Institute of Technology

Objective

The objective of this task is to develop a trajectory planning module, which will forecast fuel burn and emissions as a function of the spectrum of potential flight paths. The initial version will consider conventional fuel, CO₂ emissions, and vertical altitude deviations, but each of these categories can be expanded in the future. It will also initially be focused on one common aircraft type.

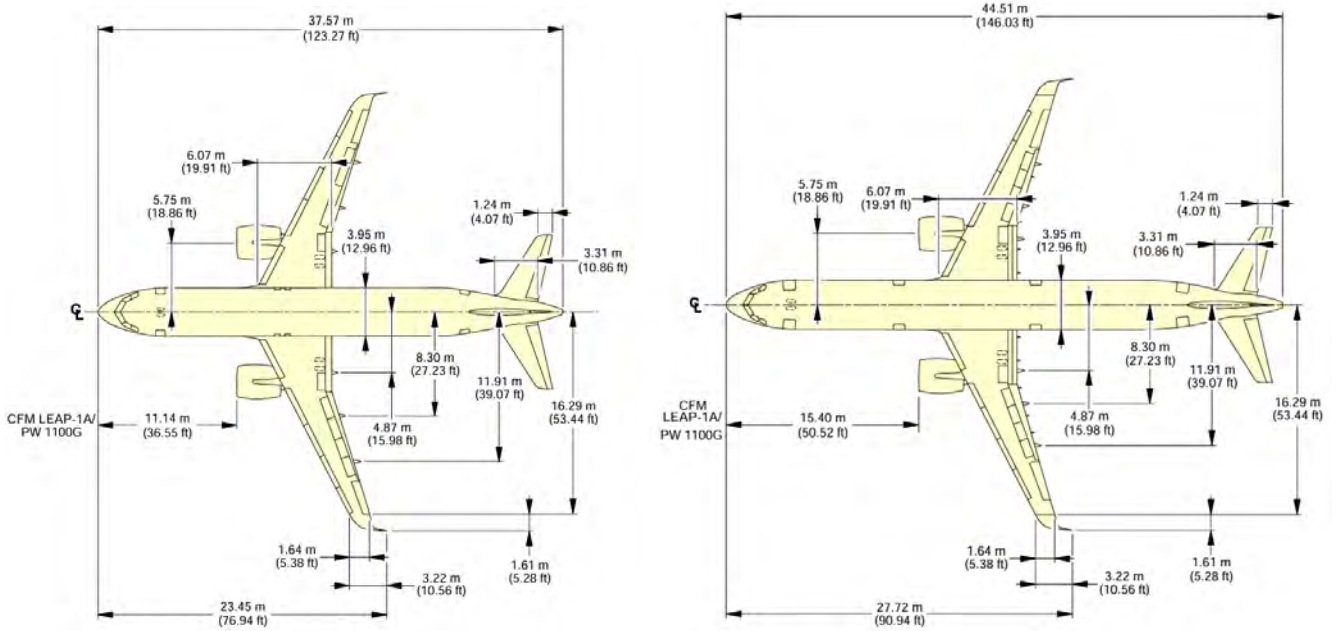


Research Approach

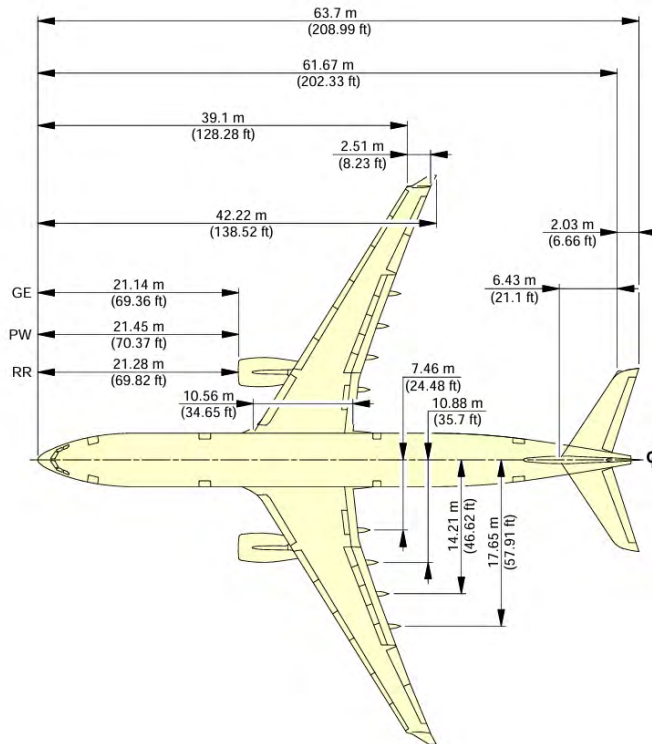
The trajectory-optimization framework developed previously uses a Boeing 737-800 aircraft performance model created with TASOPT (Drela, 2011). This model allows for the estimation of the additional fuel burn incurred by contrail avoidance action, enabling a climate impact tradeoff analysis by comparing contrail and CO₂ EF. To extend this climate impact analysis to a larger range of aircraft types, we need to develop additional aircraft performance modeling capabilities. While it is possible to use existing aircraft performance models such as Base of Aircraft Data version 3 (BADA3), restrictions in licensing, as well as difficulties of the model in capturing fuel burn penalties for high-altitude climbs, limit its use within the scope of this project.

We continued to use TASOPT to develop aircraft performance models and selected four Airbus airframes based on their use in the global commercial aviation fleet. Figure 14 depicts the Airbus A320neo, A321neo, A330-300, and A350-900 with their respective engine configurations. For each of these aircraft configurations, a first-order aero-structural-propulsive performance model template was developed.

Figure 15 depicts a simplified iterative design process employed for each of the airframes using TASOPT. Given the multi-disciplinary nature of the design flow, the Newton-based design update necessitates a feasible set of initial candidate points in the aerodynamic, structural, and propulsive domain. For instance, the outer mold line definition was sourced from airport planning documents for each of these airframes. Initial values for the wing-box structure, which is critical for mass estimation, were sourced from structural design patents published by Airbus. A similar approach was adopted for the fuselage frame design, where the initial values for the frame elements were estimated from publicly available patents. The design process starts with the fuselage sizing process to first satisfy the cabin requirements, followed by an estimation of the required wing weight and geometry to satisfy the lift requirement. The design evolves based on the process flow shown in Figure 15 until the change in maximum takeoff weight satisfies a convergence tolerance.



(a) A320neo. Image source: Airbus SAS 2022. (b) A321neo. Image source: Airbus SAS 2022



(c) A330-300. Image source: Airbus SAS 2023

Figure 14. Candidate Airbus airframes.

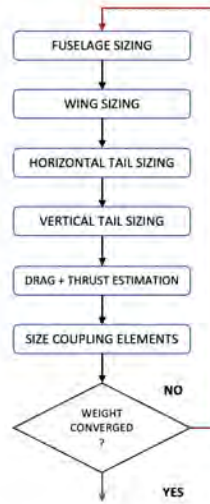


Figure 15. Transport Aircraft System OPTimization (TASOPT) aero-structural-propulsive iterative sizing and weight estimation process beginning with fuselage.

The Numerical Propulsion System Simulation (NPSS) was used as a one-dimensional model to estimate the thrust and fuel flow rate necessary to sustain flight at different flight phases. Due to the limited availability of NPSS models, the performance of all narrow body airframes shown in Figure 14 were estimated using the CFM LEAP-1B engine, as opposed to the CFM 56 variant tailored for Airbus airframes. The propulsion unit design was fixed during the sizing process. In the case of the wide-body A333 and A359, the GE90 NPSS template was used, resulting in a configuration with oversized engines. Due to the complexity of the A359’s structural, aerodynamic, and propulsive design, results for the first three airframes are presented. A comprehensive analysis of the A359 airframe will be the subject of a forthcoming study.

To assess the accuracy of the analytical models, all airframes were assumed to carry 80% of their maximum payload capacity with reserve fuel capacity of 5%. Three routes with great circle distances ranging from 930 to 2,003 nautical miles were selected. For all three routes, the cruise altitude was varied from FL300 to FL380, and average fuel burn results were compared against BADA3.

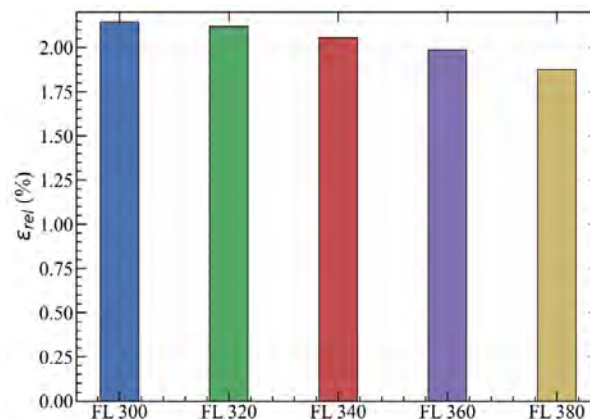


Figure 16. A32N route-averaged relative fuel burn (ϵ_{rel}) at Mach 0.78.

Figure 16 represents the route-averaged relative error in fuel burn (ϵ_{rel}) for the Airbus A320N powered by the LEAP-1B engine. As observed, TASOPT overestimates the fuel burn by ~2.1% at FL300 and ~1.8% at FL380, with respect to BADA's performance estimates.

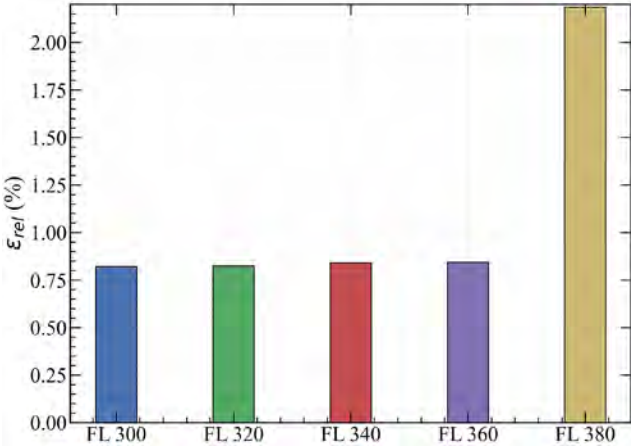


Figure 17. A321N route-averaged relative fuel burn (ϵ_{rel}) at Mach 0.79.

Figure 17 represents the route-averaged relative error in fuel burn for the Airbus A321N powered by the LEAP-1B engine. The results indicate an overestimation in fuel burn by ~0.8% with the analytical model. The relative fuel burn error is consistent over higher flight levels except at FL380, where the model overpredicts the fuel burn by ~2.1%.

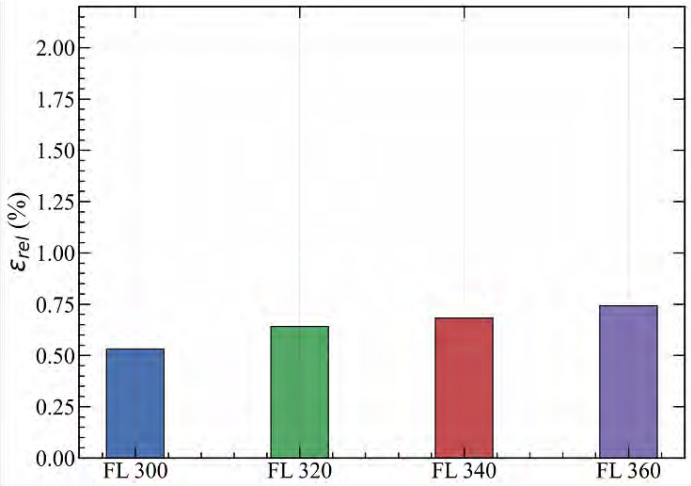


Figure 18. A333 route-averaged relative fuel burn (ϵ_{rel}) at Mach 0.84.

Figure 18 represents the route-averaged relative error in fuel burn for the Airbus A333 powered by the GE90 engine. The results indicate a consistent increase in relative fuel burn error with increasing flight level. It should be noted that the TASOPT analytical model failed to converge for flight levels greater than 360. This behavior may be attributed to the heavier propulsion unit, weighing 17,400 lbs, in contrast to the lighter GE CF6-80E1, weighing 11,225 lbs, originally used to power the A333. The redesign of the A333 model with a compatible engine will be the subject of a forthcoming study. A comparison is also planned against data from Airbus, who are collaborating informally on this project.



Milestone

- Demonstrated first implementation of a trajectory-optimization module to FAA

Major Accomplishment

- Key Airbus airframes modeled based on OEM airport planning and patent data.

Publications

None.

Outreach Efforts

None.

Awards

None.

Student Involvement

None.

Plans for Next Period

- Integration of trajectory model into MCAST
- Comparison of simulated aircraft performance against data from Airbus

References

Airbus, S. A. S., 2022, "Airbus A320 aircraft characteristics airport and maintenance planning." Airbus SAS: Blagnac, France.
Airbus, S. A. S., 2022, "Airbus A321 aircraft characteristics airport and maintenance planning." Airbus SAS: Blagnac, France.
Airbus, S. A. S., 2023, "Airbus A330 aircraft characteristics airport and maintenance planning." Airbus SAS: Blagnac, France.
Drela, M. (2011, June). Development of the D8 transport configuration. In *29th AIAA Applied Aerodynamics Conference* (p. 3970).



Project 079 Novel Noise Liner Development Enabled by Advanced Manufacturing

**The Pennsylvania State University
Raytheon Technologies Research Center
Altair Engineering**

Project Lead Investigator

Timothy W. Simpson
Paul Morrow Professor of Engineering Design & Manufacturing
Department of Mechanical Engineering
The Pennsylvania State University
University Park, PA 16803
814-863-7136
tws8@psu.edu

University Participants

The Pennsylvania State University (Penn State)

- P.I.: Timothy W. Simpson, Paul Morrow Professor of Engineering Design & Manufacturing
- FAA Award Number: 13-C-AJFE-PSU-079
- Period of Performance: January 1, 2022 to December 31, 2023 (no cost extension to September 30, 2024)
- Tasks:
 1. Refine rapid design-build-test methodology for acoustic liners
 2. Evaluate acoustic performance of additively manufactured liners
 3. Develop education capability for evaluating liner impedance

Project Funding Level

\$900,000 from FAA with match from The Pennsylvania State University (\$50,000), Raytheon Technologies Research Center (\$500,000), and Altair Engineering (\$350,000).

Investigation Team

The Pennsylvania State University

Tim Simpson (P.I.), project management, task coordination, and student advising
Allison Beese (co-P.I.), Tasks 1 and 2 and student advising
Eric Greenwood (co-P.I.), Task 2 and student advising
Andy Swanson (graduate student; MS), Tasks 1 and 2
Alden Packer (graduate student; PhD), Tasks 1 and 2

Raytheon Technologies Research Center (RTRC)

Jeff Mendoza (P.I.), project coordination and management at RTRC
Julian Winkler (co-P.I.), acoustic analysis and evaluation as part of Tasks 1-3
Aaron Reimann (co-P.I.), acoustic analysis and evaluation as part of Tasks 1-3
Kenji Homma (investigator), acoustic analysis and evaluation as part of Tasks 1-3
Paul Braunwart (investigator), acoustic analysis and evaluation as part of Tasks 1-3

Altair Engineering

Shannon Chesley (P.I.), project coordination and management at Altair
Eric Nelson (co-P.I.), acoustic analysis and evaluation as part of Tasks 1 and 2



Diana Mavrudieva (investigator), acoustic analysis and evaluation as part of Tasks 1 and 2
Paul Liedtke (investigator), acoustic analysis and evaluation as part of Tasks 1 and 2

Project Overview

The Pennsylvania State University and its Applied Research Laboratory, in collaboration with industrial partners RTRC and Altair, are helping the FAA develop and advance innovative engine acoustic liner technology to meet the demands of low noise for future aircraft. The team is developing and demonstrating a methodology to design and manufacture novel lattice structures that enhance noise attenuation in aircraft engines. Analysis and experimental testing are used to understand the effect of geometry and feature size of the lattices to control noise while ensuring the manufacturability of these complex structures in different materials. Advanced manufacturing technologies enable rapid design-build-test cycles for design development, including experimental assessments of structural integrity and acoustic performance. Advanced acoustic testing capabilities are being provided by our nonfunded government collaborator, NASA Langley Research Center (LaRC). Promising engine liner designs and their performance will be documented and archived for the FAA to aid future advancements in aircraft engine noise reduction.

The overall project approach includes the following steps:

1. Establish a set of acoustic requirements for future aircraft engine designs.
2. Design and analyze lattice-based acoustic liners using advanced software tools.
3. Perform rapid, iterative prototyping and testing to identify promising designs and materials.
4. Conduct detailed assessments of manufacturability.
5. Perform acoustic and structural evaluations of novel liners in collaboration with NASA LaRC.
6. Document results and archive data for the FAA.

The following two tasks were accomplished as part of the second-year effort on this project.

Task 1 - Refine Rapid Design-Build-Test Methodology for Acoustic Liners

The Pennsylvania State University, Raytheon Technologies Research Center, and Altair Engineering

Objective

The goal of Task 1 is to refine the rapid design-build-test methodology for low-noise acoustic liners that can enhance noise attenuation in aircraft engines.

Research Approach

Design framework

In Year 1, the team prototyped a digital workflow to design, analyze, fabricate, and test acoustic liner geometries using the different additive manufacturing (AM) capabilities available at Penn State's Center for Innovative Materials Processing through Direct Digital Deposition and the liner acoustic performance prediction capabilities developed at RTRC. The rapid acoustic liner development methodology is shown in Figure 1, color-coded based on primary responsibility for each aspect of the work.

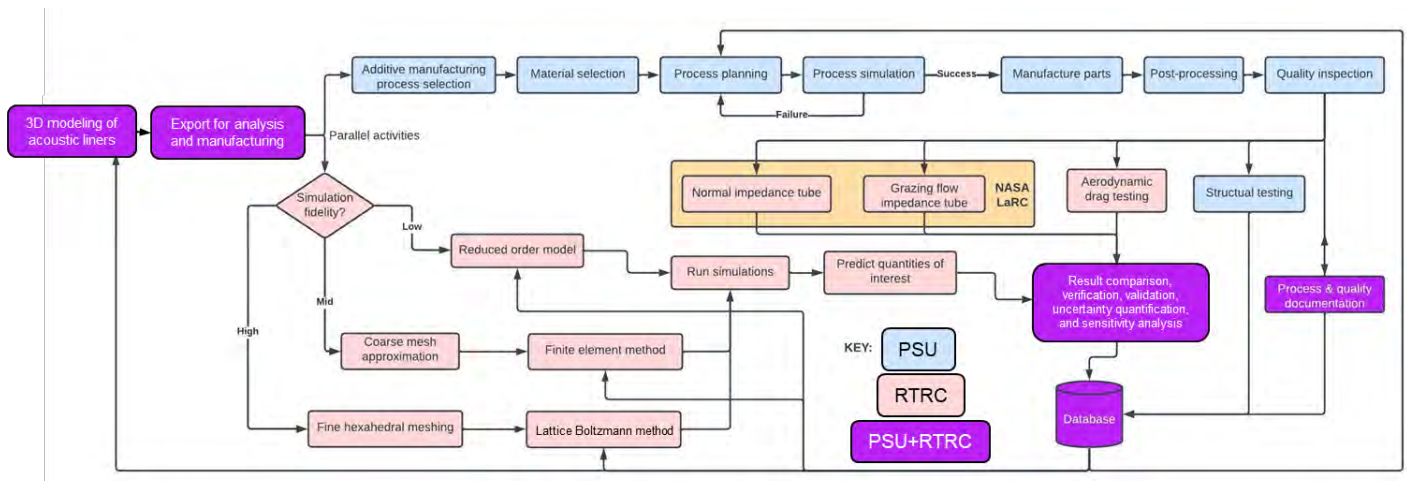


Figure 1. Rapid acoustic liner development methodology. LaRC: Langley Research Center; PSU: The Pennsylvania State University; RTRC: Raytheon Technologies Research Center.

As shown in the figure, both teams (Penn State and RTRC) leveraged shared three-dimensional (3D) modeling tools to feed their respective workflows. Penn State led the AM fabrication efforts (in blue) and RTRC led the multi-fidelity analysis efforts (in salmon). Details on the multi-fidelity approach developed by RTRC is shown in Figure 2. Acoustic performance is evaluated at Penn State, RTRC, and NASA LaRC. Results are then collected, stored, and reviewed by the team to identify the next design iteration.

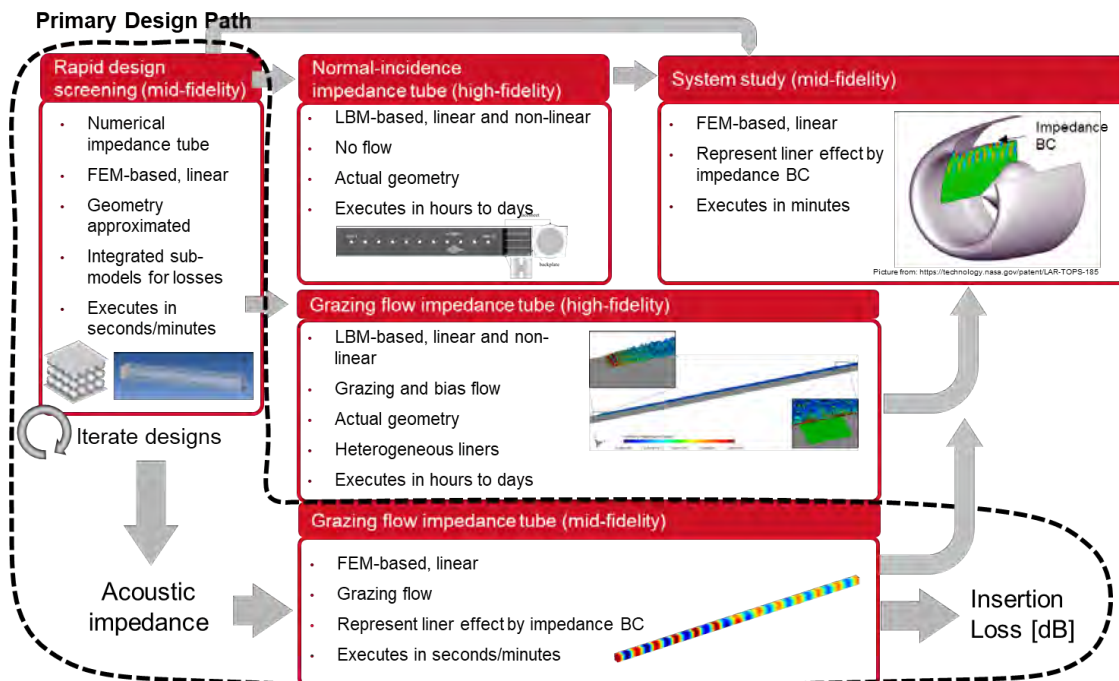


Figure 2. Multi-fidelity modeling and analysis capabilities used for complex acoustic liner design screening. BC: boundary condition; FEM: finite-element method; LBM: lattice Boltzmann method.

In Year 2, Altair joined the team, bringing engineering data science expertise and specialized design automation software to the project. Through this partnership, the design-analysis portion of the methodology was streamlined and automated using Altair’s HyperStudy—a multidisciplinary design study software that enables engineers to explore and optimize product performance and robustness. By using automated processes, state-of-the-art mathematical methods, predictive modeling, and data mining, HyperStudy guides users to explore data trends, perform trade-off studies, and optimize performance and reliability of a design solution, while considering multiphysics constraints.

For the initial effort, HyperStudy was combined with nTopology and COMSOL to generate and analyze 3D models of lattice-based acoustic liners, as shown in Figure 3. nTopology is an implicit modeling tool with many built-in latticing functions that can efficiently produce the triply periodic minimal surface (TPMS) lattices being used as a backing structure in the acoustic liner. COMSOL Multiphysics is a robust, mid-fidelity simulation tool with many physics packages that can be simulated. For the current effort of acoustic liner design, the physics packages of pressure acoustics and thermo-viscous acoustics were used to simulate liner designs. Additionally, multiple Python scripts were developed to interface the main softwares with each other and add additional features.

Once combined, HyperStudy is used to generate acoustic liner design alternatives through design of experiments using either space filling or other sampling strategies. This leads to the generation and simulation of hundreds of liner samples for a given lattice structure (e.g., a gyroid TPMS). All of the data are examined within HyperStudy’s interface, enabling users to visualize what design parameters are most impactful on a given response, create reduced-order models (e.g., surrogates) from the data to predict a given response, and perform optimization based on the reduced-order models. Additionally, where multiple responses are important, multi-objective optimization can be performed to find the best compromise of the responses. An example of the optimization results is shown in Figure 4 for variations of a liner based on Schwarz-P TPMS.

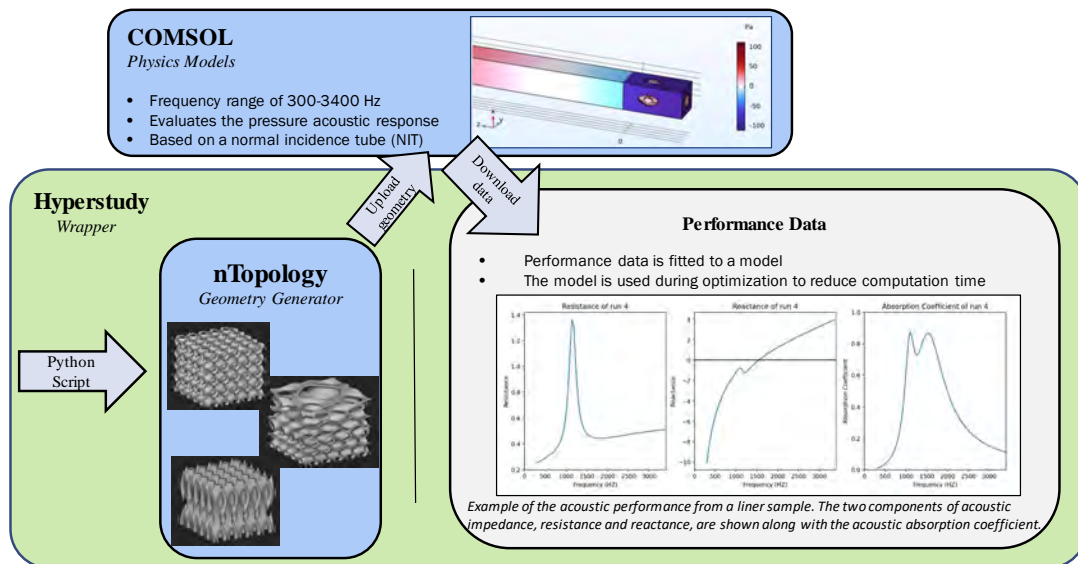


Figure 3. Design-analysis portion of methodology enabled by combining nTopology (for 3D model generation), COMSOL Multiphysics (for acoustic analysis) in Altair HyperStudy (for automation and visualization of results).

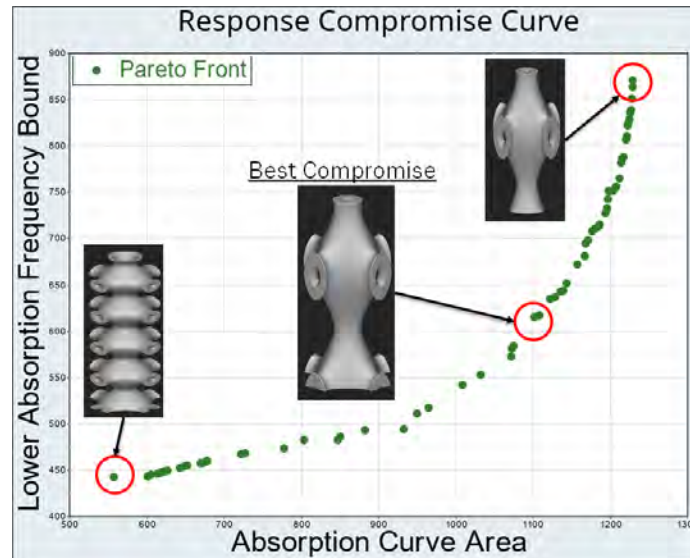


Figure 4. Example of Pareto front that emerges by executing a multiobjective optimization study of parametric variations of a liner design within HyperStudy.

As the team fine-tuned this process, it became apparent that approximating acoustic performance across a wide range of parametric variations, even within a single type of lattice, was challenging. Many of the acoustic responses are not linear and often exhibit multiple peaks of performance for different frequency ranges. This made creating a good predictive model difficult, and the team shifted their strategy to mine the datasets visually to quickly identify promising liner designs. To facilitate this, we created a four-panel dashboard within HyperStudy (see Figure 5) that contained information about the input parameters, acoustic responses, and sampled parameter space. Using this dashboard, a designer can quickly sort through the data for a given response, select a design sample, review its acoustic response, and visualize the corresponding lattice geometry. The addition of this dashboard to the predictive model capabilities creates a robust design exploration suite that can be leveraged in acoustic liner design.

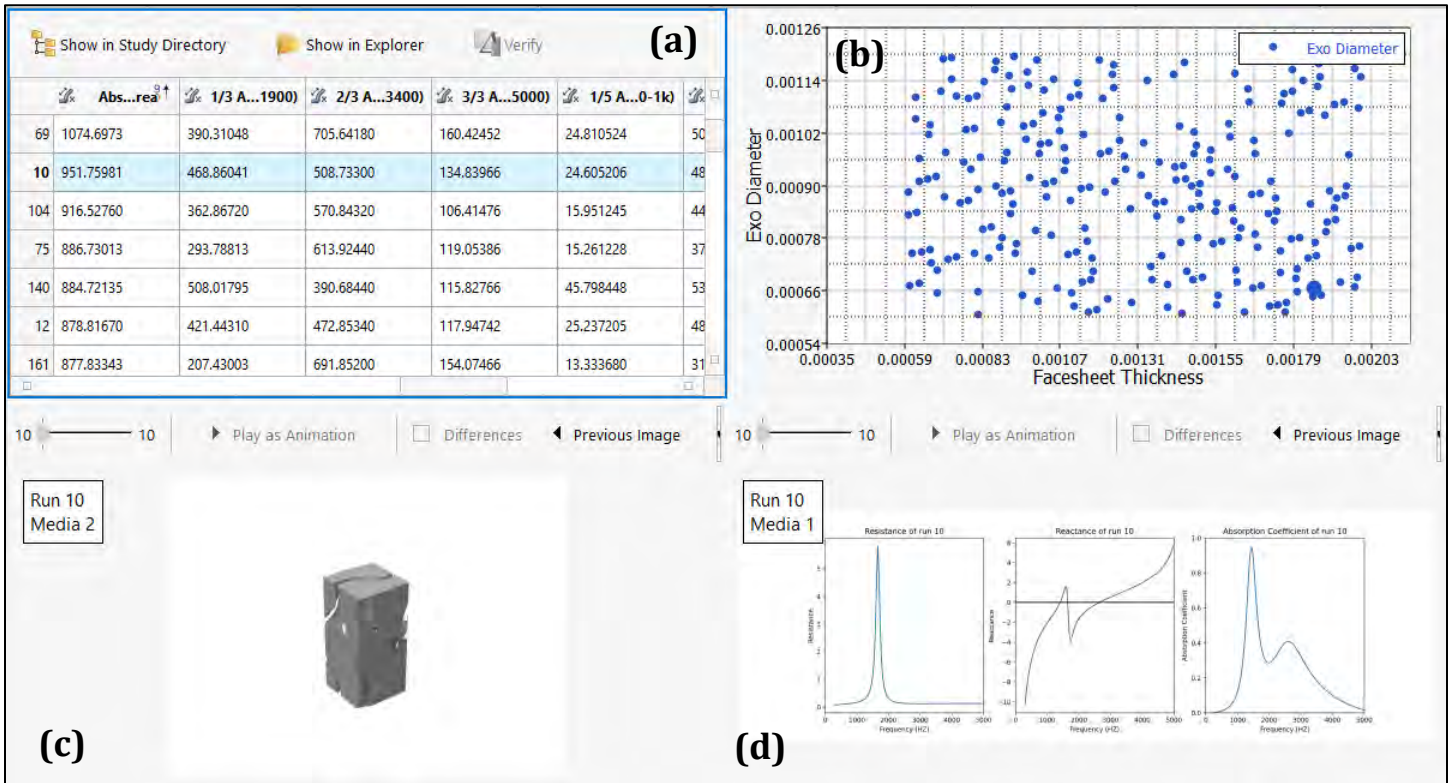


Figure 5. Design exploration dashboard in HyperStudy allows a designer to (a) sort through the sample data for a given response, (b) observe where the input parameters sit in the design space, (c) view the lattice structure geometry, and (d) view plots of the acoustic simulation data.

The design exploration framework was used to evaluate a Schwarz-P acoustic liner concept. Design variables were selected from parameters that define this TPMS lattice as well as parameters for the facesheet (see Table 1). The lattice-based backing structure inside the acoustic liner was generated in nTopology using the specified parameters, whereas the facesheet was analytically modeled in COMSOL based on the thickness, hole diameter, and percent open area. Because TPMS lattices create two intertwined fluid regions, two sets of facesheet parameters were used as variables (one for each region). The acceptable ranges for each parameter in the design space were determined through visual inspection and the use of constraints to prevent wall thicknesses that would not be manufacturable.

Table 1. Ranges of design parameters for the facesheet (shaded) and lattice-based backing structure (unshaded). POA: percent open area; TPMS: triply periodic minimal surface.

	Parameter	Lower Bound	Upper Bound
Facesheet	Facesheet thickness (mm)	0.6	2.0
	Region 1 hole diameter (mm)	0.6	1.2
	Region 1 POA (%)	5	31
	Region 2 hole diameter (mm)	0.6	1.2
	Region 2 POA (%)	5	31
Lattice	Levelset (TPMS design parameter)	-0.7	0
	X/Y period length (mm)	9.5	15.5
	Z period length (mm)	4.5	19.0
	Z offset (mm)	0	10.0



The multiphysics simulation in COMSOL estimated the resistance, reactance, and absorption coefficient for a range of frequencies (300-5,000 Hz, with a step size of 40 Hz), as shown in Figure 6. Although the plots of these data were useful visuals, scalar values were required in order to compare liner performance and perform optimization functions. The responses that gave the best indication of acoustic performance from these outputs came from taking an integral of the absorption coefficient plot. For a given frequency range, larger response values would indicate better broadband absorption over that frequency range. The area under the curve for defined frequency intervals gave us a way to compare liner performance between different designs. We also defined responses to capture the frequency at which the reactance crossed zero for the first time, the frequency where absorption rose to a selected level, and the bandwidth where absorption remained above a selected level. We will continue to explore defining additional responses that could be extracted from the acoustics simulation and used to drive acoustic liner design. The response(s) of most interest will vary for different acoustic liner applications, but the rapid design-build-test methodology is applicable to different sets of requirements, as we plan to demonstrate in Year 3.

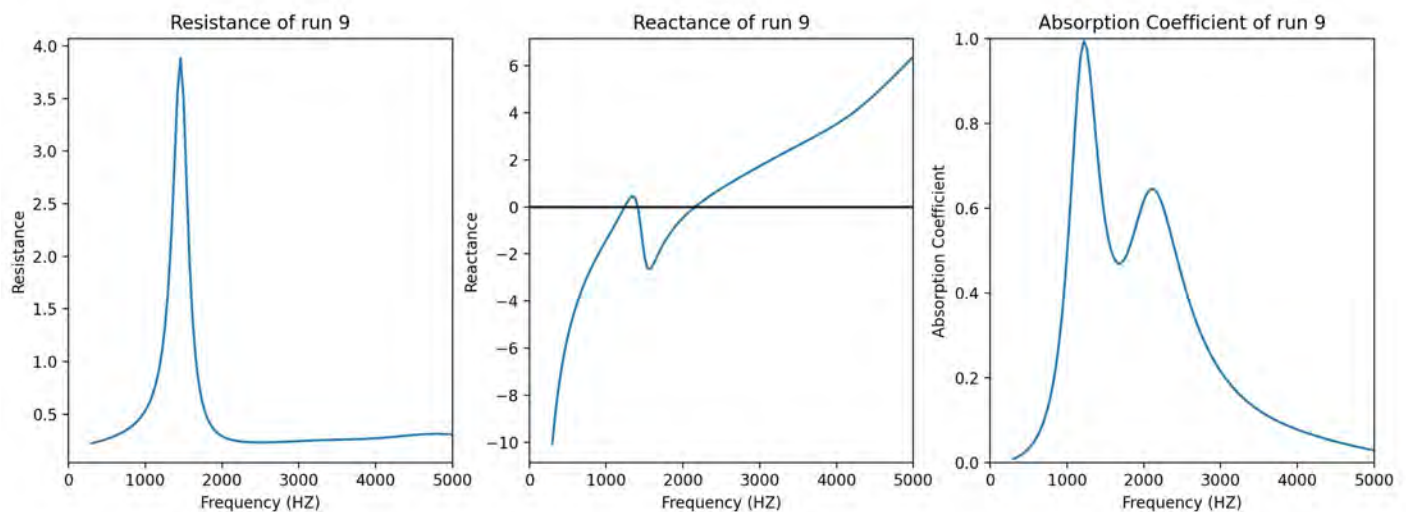


Figure 6. Example of acoustic responses from COMSOL across a frequency range of 300 to 5,000 Hz, with a step size of 40 Hz.

In parallel to automating the design-analysis portion of the acoustic liner development methodology, RTRC continued to evaluate its acoustic liner prediction tools in Year 2 by applying them to different NASA reference liners. Figure 7 shows the NASA reference “calibration” liner called CSQ3, which consists of an array of narrow channels without a facesheet. This liner was modeled using the different fidelity methods shown in Figure 2; namely, a finite-element model (FEM) with a sub-model to account for visco-thermal losses in the narrow channels, a reduced-order model (ROM) that is based on an analytical formulation, and high-fidelity lattice Boltzmann method (LBM) simulations. All methods of varying fidelity agree well with the test data. The high-fidelity LBM simulation resolves the local flow, and boundary layers more accurately show a shift in resonance frequency, which may be due to geometric differences in the hardware compared with the simulation that are more appropriately absorbed in the lower fidelity methods. Overall, this effort confirmed that the different fidelity methods available at RTRC are able to predict the correct liner performance and thereby builds confidence in the prediction methods going forward. We plan to integrate these multi-fidelity methods into the design-analysis framework in HyperStudy in Year 3 to enhance prediction accuracy of acoustic performance of novel acoustic liner designs as they are generated.

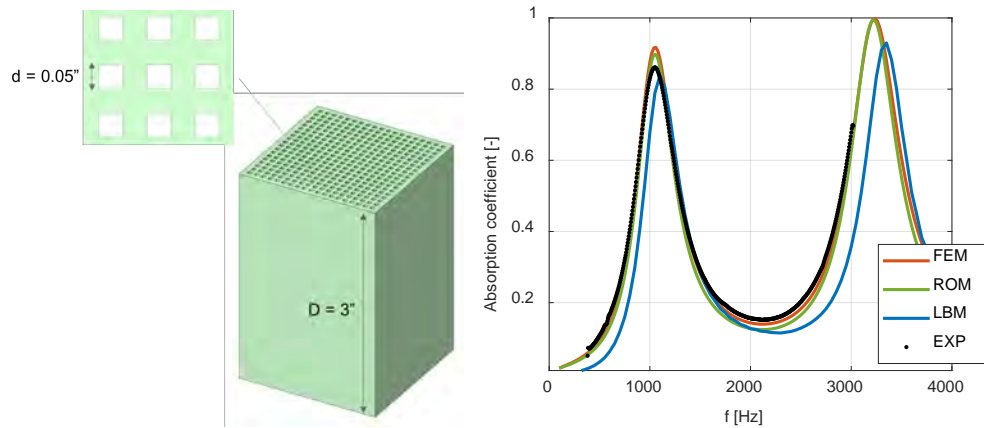


Figure 7. NASA reference liner CSQ3 (left) and simulation results (right) compared to test data, using different fidelity methods to predict the acoustic absorption. FEM: finite-element model; ROM: reduced-order model; LBM: lattice Boltzmann method; EXP: experimental data.

Finally, RTRC began to investigate modeling methods for multi-degree-of-freedom (MDOF) acoustic liners. This shift reflects trends in the industry, and a TPMS liner can be categorized as a type of MDOF liner. To understand the current state-of-the-art of the MDOF liner designs, the team obtained information regarding a current MDOF liner design and the corresponding liner impedance data (both normal impedance and grazing flow impedance data) from NASA. The team utilized the existing liner impedance modeling tool (based on ACTRAN plus the BF Goodrich analytical perforate model to account for the effect of grazing flow) to predict the MDOF liner impedance. Figure 8 shows an illustration of NASA’s MDOF liner design along with a comparison of predicted and measured impedance data.

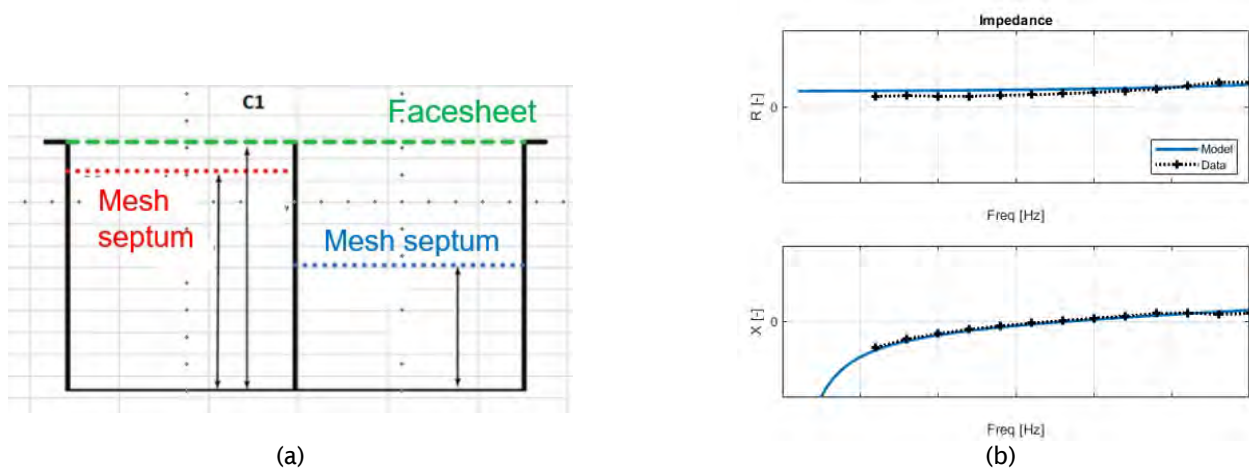


Figure 8. Model prediction of NASA multi-degree-of-freedom (MDOF) liner impedance: (a) NASA’s MDOF liner design, (b) model predicted and measured impedance data for Mach 0.3 grazing flow.

As shown in Figure 8(a), NASA’s MDOF liner design essentially features a combination of two double-degree-of-freedom cells with different tuning frequencies, yielding four degrees of freedom. Figure 8(b) shows the liner impedance in the presence of flow at Mach number, M , 0.3. The result of RTRC’s model prediction shows good agreement with NASA’s grazing flow impedance test data for the MDOF liner, thus validating our modeling tool.

Milestones

- Automated design-analysis portion of framework to perform parametric optimization of TPMS-based acoustic liner



- Developed dashboard to visualize tradeoffs among parametric variations of a given TPMS-based acoustic liner
- Validated multi-fidelity modeling approach and MDOF predictions using NASA reference designs

Major Accomplishments

- Designed and analyzed lattice-based acoustic liners using automated software tools
- Demonstrated good agreement between predicted performance and NASA reference liner designs
- Prototyped visual dashboard to aid design selection of promising acoustic liner solutions

Publications

MS Thesis: Andy Swanson, “A Method to Design and Develop Additively Manufactured Aircraft Acoustic Liners”, Additive Manufacturing & Design Graduate Program, Penn State University, University Park, PA

We plan to prepare two or three conference publications once experimental evaluation is complete. These publications will focus on the rapid design and analysis framework using 3D printing and modeling, analysis, and comparison with experimental test results. We will target both American Institute of Aeronautics and Astronautics (AIAA) technical conferences and AM conferences; accepted conference papers will be revised, updated, and submitted to journals as appropriate.

Outreach Efforts

None.

Awards

None.

Student Involvement

Two graduate students are involved in this task: (1) Andy Swanson prototyped the rapid design-build-test methodology as part of his master’s studies in Penn State’s Additive Manufacturing & Design graduate program, and (2) Alden Packer, a PhD student in mechanical engineering who worked closely with Altair and RTRC to refine the design-analysis portion of the framework.

Plans for Next Period

By the end of Year 2, the visual dashboard will be fully developed, and the automated design-analysis portion of the framework will be exercised to identify a promising design to test and validate in Year 3. Year 3 will also focus on integrating the multi-fidelity modeling approaches developed by RTRC into the automated design-analysis portion of the design methodology and identifying specific requirements to perform an optimization study across multiple TPMS-based lattice geometries.

Task 2 - Evaluate Acoustic Performance of Additively Manufactured Liners

The Pennsylvania State University and Raytheon Technologies Research Center

Objective

The goal in this task is to 3D print TPMS-based acoustic liner designs and evaluate their acoustic performance.

Research Approach

The grazing flow acoustic liner samples based on the Schwarz-P TPMS that were designed in Year 1 were fabricated in Year 2 using vat photopolymerization, a 3D printing process that cures light-sensitive photopolymers layer-by-layer into the desired shape. The overall liner is 20” long × 2.5” wide × 1” deep. The printed liner samples have internal divider walls to make the liner locally reacting. The samples were fabricated using a Carbon M2 printer with EPX82 epoxy resin. The maximum print dimensions that this printer allows are 7.4” × 4.6” × 12.8”; therefore, the liner was divided into four sections of 5” length each, so that all four parts could fit onto the build platform. The individual pieces were then joined afterwards. The designed and printed liner are shown in Figure 9.

The quality of the printed parts was inspected through 3D x-ray computed tomography (CT) scans of the samples, which allowed us to visually search the 3D printed pieces for potential cracks and blocked orifices. Seven iterations and improvements of the print process were necessary due to defects early in the process that included bowing, warping, blocked orifices, and cracking in thin wall regions. To help with the resin removal after printing, a jig was built and positioned on the facesheet that allowed for uniform air flow through the part and reduced the chances of clogged holes and generation of cracks that might otherwise have occurred with manual cleaning using a handheld nozzle with high-velocity fluid stream.

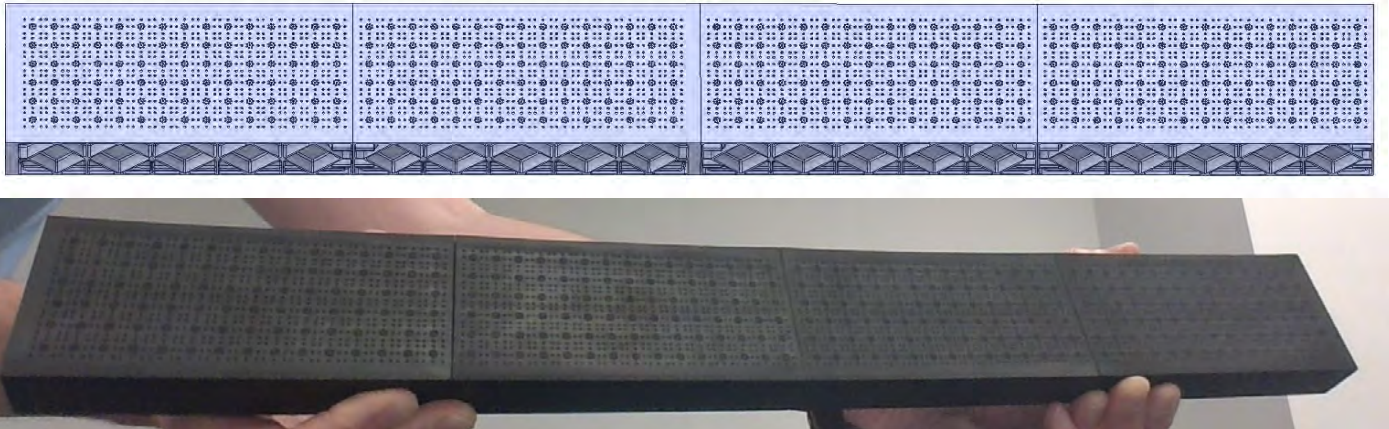


Figure 9. Acoustic liner for grazing flow testing. Top: Computer-aided design file; bottom: Additively manufactured hardware.

The final version of the printed parts showed some slight warpage of the internal thin divider walls, but no cracks or blocked orifices were observed. The qualitative difference between early and final iterations is shown in sample CT scan images in Figure 10. Through these iterations, several general lessons were learned:

1. Internal geometry features need to be aligned/sloped properly to avoid trapping resin.
2. The back sides of the liners needed vent holes to allow for resin removal; these holes were later closed using a separate backplate.
3. Avoid regions with large changes in wall thickness to minimize warpage and cracks during curing.
4. The build orientation plays a role and needs to be considered.

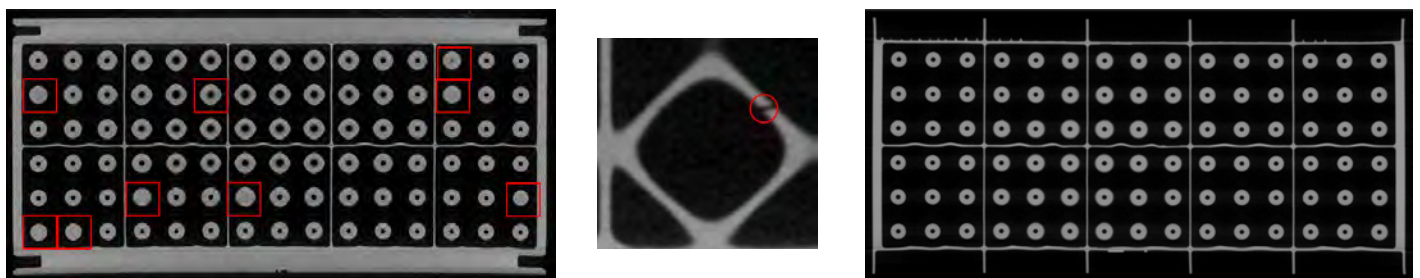


Figure 10. Computed tomography scanned images of additively manufactured liner hardware. Left: Early print iterations with several blocked orifices and a few cracked bulbs. Right: Final part with slight wall warpage but no defects.

To verify the acoustic performance of each of the 3D printed samples, the normal incident impedance tube at RTRC was used for in situ measurements. The tube itself has a circular duct with a 29-mm diameter. An adapter piece was machined that allowed us to attach the larger liner samples at the end of the tube. Each liner sample consisted of two rows, each having five 1" × 1" internal cavities filled with Schwarz-P lattice structures (see Figure 10). During testing, the whole liner

facesheet was taped off with aluminum tape, except on the 1" x 1" square where the measurements were performed. The setup and a few sample test results are shown in Figure 11. The test results showed that there is good repeatability between measurements and that the results are fairly insensitive to measurement location on the liner. For comparison, the "DESIGN INTENT" line in the figure shows the predicted values from the mid-fidelity model based on the as-designed geometry. The intended design shows three distinct, large absorption peaks and an elevated broadband hump around 2 kHz. All of these features were found in the test data as well, confirming that the liner has the correct performance characteristics; however, the absorption peaks were shifted in frequency. This is not unexpected, as the reduced-order design tool used a simplified assumption of zero wall thickness. In reality, the finite wall thickness of the liner reduces the overall air volume, which tends to shift the resonance frequencies. Moreover, the test data used a round tube on top of a square liner sample, which does not fully represent the way the liner was evaluated in the design phase. The fidelity of the modeling tools can be increased in future iterations to provide more accurate results in line with the actual hardware performance.

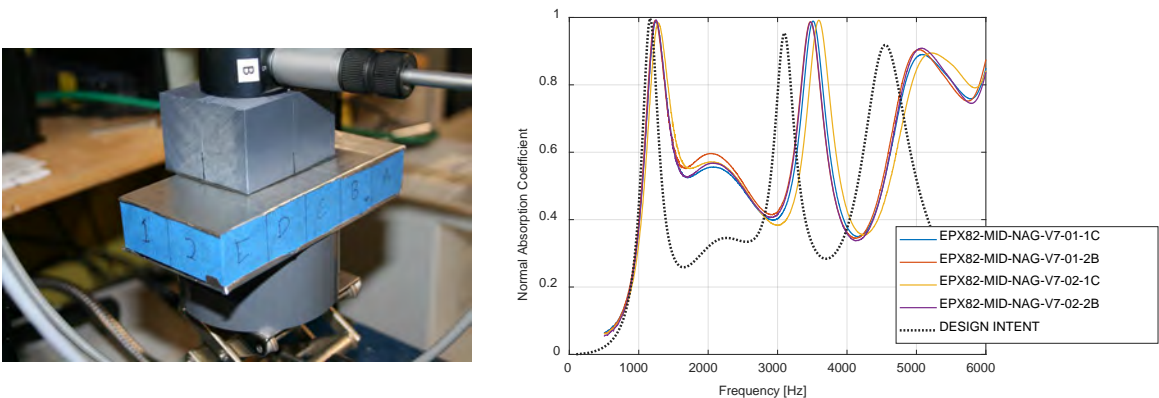


Figure 11. In situ acoustic testing of the additively manufactured liner hardware to verify acoustic performance.

For a more accurate representation of the liner geometry, the CT scanned geometry was imported into the high-fidelity LBM simulation tool and evaluated as shown in Figure 12. The CT scan of the liner revealed slightly noncircular facesheet holes as seen in the highlighted images. Each of these holes is resolved with more than 20 grid points. The total number of grid points for the LBM simulation is around 166 million.

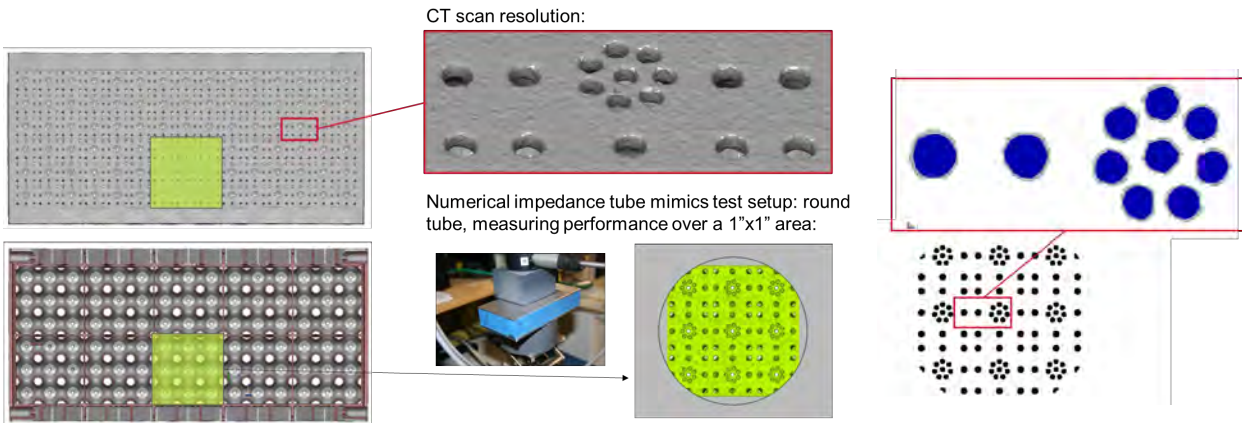


Figure 12. Lattice Boltzmann method (LBM) simulation setup using the computed tomography scanned liner geometry.

The corrected LBM simulation shows better agreement between the predicted and experimental results, as seen in Figure 13. In particular, the two dominant absorption peaks at 1.2 and 3.6 kHz are captured correctly. The broader hump around 2 kHz is slightly overpredicted due to higher facesheet resistance in the simulation results. In general, using the high-

fidelity LBM simulation approach, it was possible to close the gap observed between design intent and test data. The remaining differences could be related to the liner geometry resolution from the CT scan or alignment differences of the liner between test and simulation. Overall, though, the agreement is satisfactory and builds confidence that the liner will perform as expected in the grazing flow tests to be conducted at NASA, which should be completed by the end of Year 2.

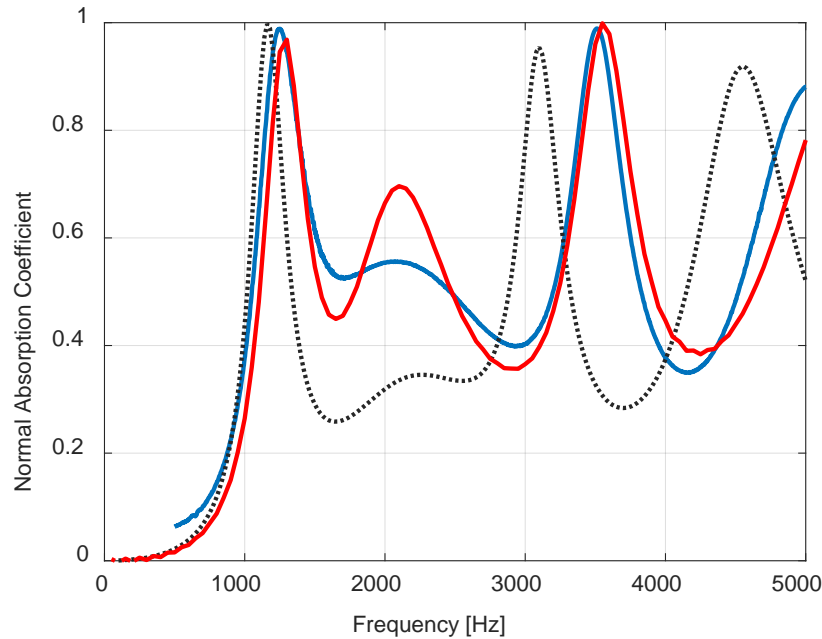


Figure 13. Numerical grid for lattice Boltzmann method (LBM) simulations of the computed tomography scanned liner hardware.

Milestones

- Additively manufactured acoustic liner hardware for grazing flow testing at NASA
- Detailed acoustic evaluation of acoustic liner design based on Schwarz-P TPMS

Major Accomplishments

- Revised acoustic liner geometry to address issues when 3D printing with vat photopolymerization
- Defined process for successful additive manufacturing of liner hardware
- Validated use of high-fidelity LBM simulation to accommodate variation in additive manufacturing process

Publications

We plan to prepare one or two conference publications once experimental evaluation is complete. These publications will discuss fine-tuning of the Schwarz-P liner designs and modeling, analysis, and comparison with Grazing Flow Impedance Tube (GFIT) test results. We will target AIAA technical conferences; accepted conference papers will be revised, updated, and submitted to journals as appropriate.

Outreach Efforts

None.

Awards

None.

Student Involvement

None.

Plans for Next Period

Year 3 will fabricate additional acoustic liner samples for grazing flow impedance testing and compare experimental results to predicted values. Analysis and simulation models will be refined and updated as needed.

Task 3 – Develop Education Capability for Liner Impedance Evaluation

Raytheon Technologies Research Center

Objective

The goal in this task is to enhance the evaluation of acoustic liner impedance using an eduction method.

Research Approach

Sound absorption of acoustic liners is measured using a normal impedance tube; however, liner impedance measured in normal impedance tubes does not accurately represent acoustic liners installed in aircraft nacelles due to dependency of impedance on high-speed flow grazing over the liner. Therefore, liner impedances in the presence of grazing flow must be measured in a specialized test facility such as the GFIT at NASA LaRC (see Figure 14).

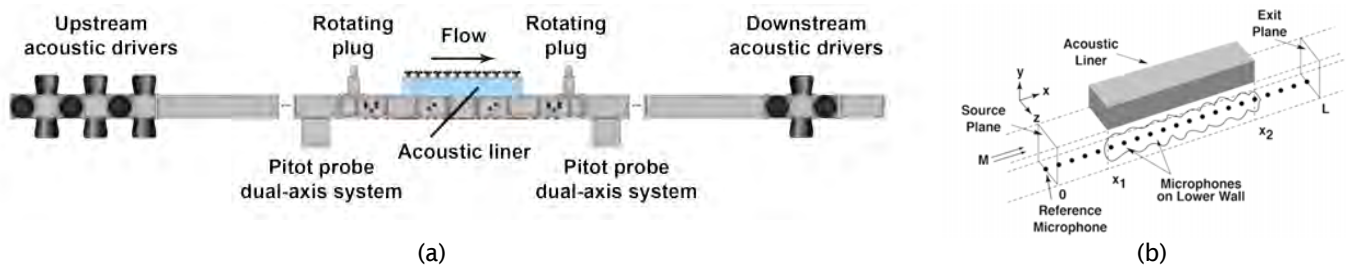


Figure 14. Grazing flow impedance tube facility: (a) NASA Grazing Flow Impedance Test (GFIT) facility, (b) illustration of a microphone array used for impedance eduction.

In the grazing flow impedance test setup shown in Figure 14, a liner sample is installed into a duct where sound propagates along the duct in the presence of forced air flow. In this setup, an axial microphone array over the liner is used to measure the sound field distribution across the liner, then the eduction method is performed to inversely determine the liner impedance. This is in contrast to an in situ method, where the impedance of the liner is determined by two or more probe microphones directly installed into the internal structure of the liner, enabling very localized measurement. The in situ impedance method is only practical for conventional acoustic liners with relatively simple internal geometries. The impedance of advanced liners with more complex internal structures has to be determined by an eduction method.

To enable the impedance measurement of advanced liners in this program, RTRC developed our in-house liner eduction code based on NASA’s Prony method. The Prony method is a data-driven approach where liner impedance is determined by measuring the axial (complex) wavenumber of the propagating waves using the axial microphone array. The code has been rigorously validated by multiple approaches. For this work, we used NASA’s publicly available data from their GFIT facility to validate the results from RTRC’s eduction code.

Figure 15 illustrates an example of the validation of our in-house liner eduction code applied to NASA’s GFIT data and impedance eduction results for a single-degree-of-freedom (SDOF) liner. As seen in the figure, two eduction results are provided by NASA: (1) the Prony method, and (2) the “CHE method,” which is a parameter optimization approach based on a model of the grazing flow duct based on the convected Helmholtz equation (CHE). As shown in the figure, the liner impedance educed by the RTRC’s eduction code based on the Prony method shows very good agreement with NASA’s eduction result based on the Prony method, thus validating RTRC’s in-house eduction code.

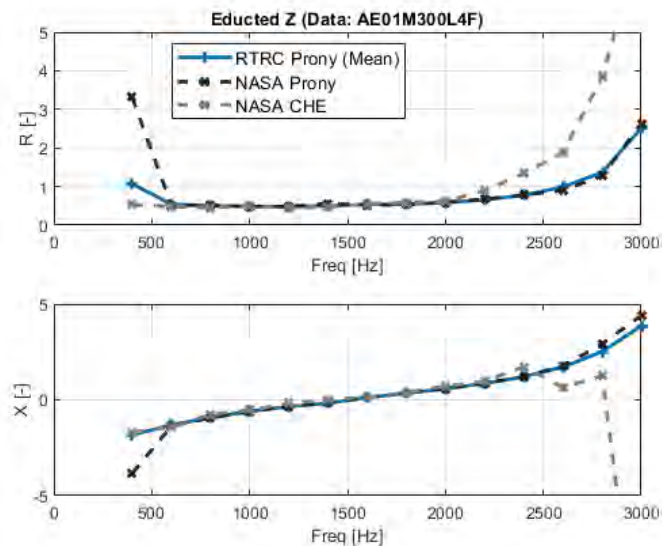


Figure 15. Raytheon Technologies Research Center (RTRC)’s educted impedance result for a single-degree-of-freedom (SDOF) liner compared with NASA’s educted liner impedance data based on two eduction methods (Prony and convected Helmholtz equation [CHE] method).

RTRC’s eduction code was further validated by applying the code to educe the impedance of more advanced liners, such as RTRC’s TPMS liner design. Because there are no grazing flow test data available yet for the TPMS liners, validation has been done using a simulated grazing flow duct test based on ACTRAN (a general purpose acoustics simulation software). In this virtual grazing flow duct model, the acoustic liner is represented by a known liner impedance precalculated for the TPMS liner design. Then the eduction method is applied on the simulated microphone array pressure data to educe the liner impedance data, which should match the specified impedance. Figure 16 shows the TPMS liner impedance result educed from the simulated microphone pressure data. As seen in the figure, good agreement is obtained between the educed liner impedance and the reference impedance, further validating the code. This study also served as a preparation for liner impedance eduction using actual grazing flow test data for TPMS liners once they become available.

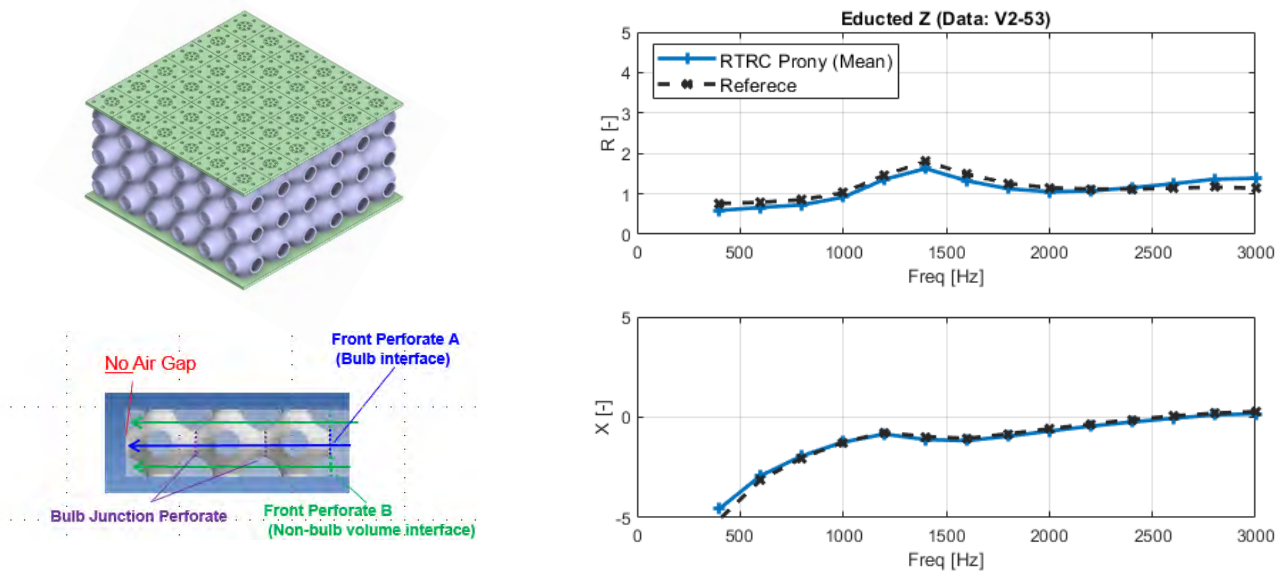


Figure 16. Impedance eduction performed on a triply periodic minimal surface (TPMS) liner design based on simulated grazing flow duct.

The other major development is the upgrading of the RTRC’s existing grazing flow duct test hardware to be able to perform the liner impedance eduction measurement directly in Year 3. The basic design of the hardware was determined on the basis of a grazing flow duct model created in ACTRAN in conjunction with RTRC’s in-house liner eduction code. Figure 17 shows a view of the upgraded grazing flow duct hardware, which is currently being upgraded.

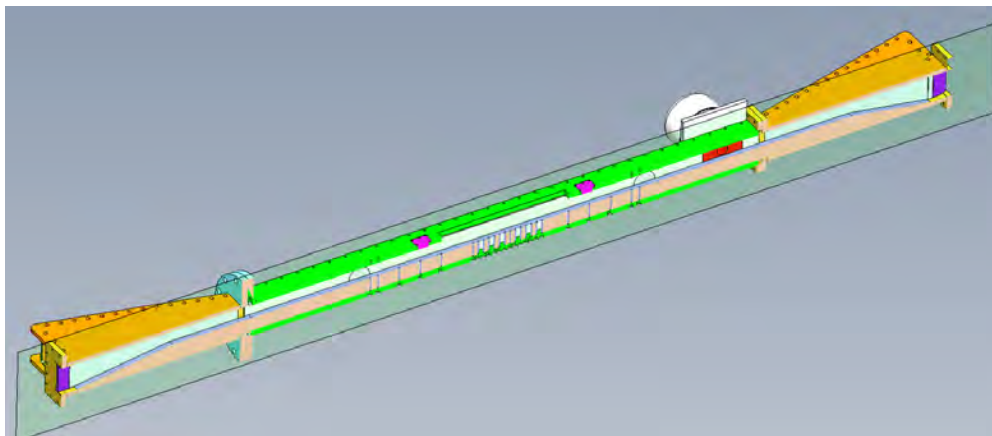


Figure 17. Raytheon Technologies Research Center (RTRC)’s grazing flow liner test facility currently being upgraded to enable liner eduction measurement capability.

A major change in RTRC’s grazing flow test facility is that the cross-sectional height of the duct has been reduced from 5 in. to 2.5 in., which was found (on the basis of simulation) to be beneficial for improving the accuracy of liner impedance eduction results (by ensuring the plane-wave propagation in the duct to higher frequencies). This is accomplished by introducing tapered duct inserts that effectively reduce the duct cross-sectional area by half. Other design features like liner section length, microphone array positions, and acoustic driver have also been updated to enable accurate liner eduction measurement.



Milestones

- Developed reduction code estimate impedance of more complex acoustic liner designs
- Utilize simulation and reduction code to finalize upgrade of RTRC's grazing flow test facility

Major Accomplishments

- Validated process for impedance reduction of liner samples in a grazing flow environment using Prony's method
- Began upgrading RTRC grazing flow test facility to enable liner reduction measurements

Publications

We plan to prepare one or two conference publications once experimental evaluation is complete.

Outreach Efforts

None.

Awards

None.

Student Involvement

None.

Plans for Next Period

Additional testing of acoustic performance and material evaluation for successful manufacturing of the proposed liner concepts is planned for Year 3. The focus in Year 3 will also shift to acoustic liner design for a specific section of the engine, moving from component-level tradeoffs (e.g., weight, acoustic performance, structural integrity) to subsystem-level tradeoff studies (e.g., weight, cost, drag).



Project 080 Hydrogen and Power-to-Liquid Concepts for Sustainable Aviation Fuel Production

**Washington State University
Massachusetts Institute of Technology**

Project Lead Investigators

Manuel Garcia-Perez
Professor and Chair
Biological Systems Engineering Department
Washington State University
LJ Smith, Room 205, PO Box 646120, Pullman, WA 99164-6120
509-335-7758
mgarcia-perez@wsu.edu

Michael P. Wolcott
Regents Professor
Department of Civil & Environmental Engineering
Washington State University
PO Box 642910, Pullman, WA 99164-2910
509-335-6392
wolcott@wsu.edu

Steven R. H. Barrett
Professor of Aeronautics and Astronautics
Director, Laboratory for Aviation and the Environment
Massachusetts Institute of Technology
77 Massachusetts Ave, Building 33-322, Cambridge, MA 02139
617-253-2727
sbarrett@mit.edu

Florian Allroggen
Executive Director Aerospace Climate and Sustainability
Laboratory for Aviation and the Environment
Massachusetts Institute of Technology
77 Massachusetts Ave, Building 33-115A, Cambridge, MA 02139
617-751-4472
fallrogg@mit.edu

University Participants

Washington State University (WSU)

- P.I.s: Prof. Manuel Garcia-Perez, Prof. Michael P. Wolcott
- FAA Award Number: 13-C-AJFE-WaSU-031
- Period of Performance: October 1, 2021 to September 30, 2022
- Tasks:
 1. Evaluate the strengths and weaknesses of hydrogen production and power-to-liquid (PtL) concepts in the United States





2. Assess how hydrogen production and PtL production can be integrated with existing production and distribution infrastructure (existing infrastructure and sustainable aviation fuel [SAF] technologies) to produce fuels with lower carbon intensity
3. Integration of Alternative Hydrogen and Carbon Sources into Fuel Conversion Pathways

Massachusetts Institute of Technology (MIT)

- P.I.: Prof. Steven R. H. Barrett
- FAA Award Number: 13-C-AJFE-MIT, Amendment Nos. 091, 101, and 115 (NCE to September 30, 2024)
- Period of Performance: October 1, 2021 to September 30, 2024
- Tasks during current reporting period (October 1, 2022 to September 30, 2023):
 4. Develop methods for assessing the economic and environmental impacts of promising SAF production pathways
 5. Apply models to analyze the economic and environmental footprint of SAF production pathways
 6. Analyze the prospects of direct air capture (DAC) of atmospheric CO₂ to provide a carbon source for SAF production

Project Funding Level

Washington State University

This project received \$450,000 in FAA funding and \$450,000 in matching funds. State-committed graduate school contributions for PhD students and faculty time for Michael Wolcott, Manuel Garcia-Perez, Xiao Zhang, and Su Ha contribute to the cost share. WSU funding is reported for the reporting period.

Massachusetts Institute of Technology

This project received \$450,000 FAA funding and \$450,000 in matching funds. Sources of match are approximately \$136,000 from MIT, plus third-party in-kind contributions of \$101,000 from Savion Aerospace Corp. and \$213,000 from NuFuels LLC.

Investigation Team

Washington State University

Prof. Manuel Garcia-Perez (P.I.), Tasks 1, 2, and 3
Prof. Michael Wolcott (P.I.), Tasks 1, 2, and 3
Xiao Zhang (co-P.I.), Tasks 1, 2, and 3
Su Ha (co-P.I.), Tasks 1, 2, and 3
Jonathan Male (co-P.I.), Tasks 1, 2, and 3
Aidan Garcia (research associate), Tasks 2 and 3
Kristin Brandt (staff engineer), Tasks 1, 2, 3, and 6
Valentina Sierra (graduate research assistant), Tasks 1 and 2

Massachusetts Institute of Technology

Prof. Steven Barrett (P.I.), Tasks 4, 5, and 6
Florian Allroggen (co-P.I.), Tasks 4, 5, and 6
Tae Joong Park (graduate research assistant), Tasks 4 and 5
Tara Housen (graduate research assistant), Task 6

Collaborating Researchers

Corinne Drennan, Pacific Northwest National Laboratory (PNNL)

Project Overview

The aviation industry is under pressure to reduce its greenhouse gas (GHG) emissions. SAFs are considered the most promising approach for achieving the sector's GHG emission targets. To date, no comprehensive assessment exists for analyzing how different carbon, hydrogen, and energy sources can be combined with different conversion processes to produce SAF with high GHG emission reductions and low costs. The goals of this project are (a) to evaluate the strengths and weaknesses of hydrogen production and PtL concepts; (b) to assess the state of the art for the integration of hydrogen production, different carbon sources (including atmospheric CO₂ capture), and PtL production with existing infrastructure (SAF production and industries); (c) to analyze the cost and environmental impacts of these production pathways; and (d)

to synthesize this information and obtain rules on how to best combine carbon, hydrogen, and energy sources with different conversion technologies to improve environmental impacts and costs. This research will enable the identification of new pathways to optimize SAF production for maximum GHG reductions with minimal fuel costs.

Approved SAF pathways commonly use photosynthesis-derived carbon from sugars, lignocellulosic materials, or lipids. Some SAF technologies that are currently being investigated include those based on hydro-processed ester and fatty acid synthetic paraffinic kerosene (HEFA-SPK), Fischer-Tropsch synthetic paraffinic kerosene (FT-SPK), Fischer-Tropsch synthetic kerosene with aromatics (FT-SKA), synthesized iso-paraffins (SIP), Virent's BioForming synthesized aromatic kerosene, hydrodeoxygenation synthesized kerosene, catalytic hydro-thermolysis, alcohol-to-jet (ATJ) fuel, hydro-pyrolysis (Shell IH2), fast pyrolysis, and hydro-processed depolymerized cellulosic jet fuel. The jet fuels produced from seven paths (FT-SPK, HEFA-SPK, SIP, FT-SKA, ATJ, catalytic hydro-thermolysis, and HEFA) and by co-processing lipids and FT biocrude in refineries are now approved by the American Society for Testing Materials for use in commercial aircraft. Although these processes can result in substantial GHG reductions, their production costs are still substantially higher than those of conventional jet fuels derived from petroleum distillation (\$0.88–\$3.86/L) (Tanzil et al., 2021).

Previous studies (Tanzil et al., 2021) have shown that the quality of the carbon source determines the SAF yield. For example, although lignocellulosic materials are 10 times cheaper than lipids (on a mass basis), the quality of the carbon source makes fuels derived from triglycerides much cheaper (2–5 times) than those derived from cellulose, hemicellulose, or lignin. Carbon in organic matrices containing a higher content of oxygen, nitrogen, and sulfur is more challenging to convert to jet fuel because of the penalties associated with the removal of oxygen, nitrogen, and sulfur, a process that typically consumes hydrogen. These contaminants can reduce the time between regeneration and the overall lifetime of the hydrotreating catalyst. Carbon in polymeric molecules is also more challenging to convert to jet fuel because it requires costly molecular weight reduction technologies and often lacks selectivity to the targeted jet fuel cut. Carbon in the form of aliphatic molecules can be more easily converted to jet fuel than carbon as aromatics. Carbon sources such as CO₂, biomass, coal, petroleum, and municipal solid waste (MSW) must be thoroughly investigated as feedstocks for SAF production. Because carbon is the highest-weight element in jet fuel production, high fuel yields can only be achieved in processes with high carbon conversion efficiencies.

Most technologies that produce SAF consumed large amounts of hydrogen, ranging from 2 mass % of the produced fuel for ATJ (Snowden-Swan et al., 2017) to 11–12 mass % for pyrolysis (Brand et al., 2022). Although hydrogen can currently be produced by many pathways using low-carbon-intensity electrons produced by wind and solar farms, current hydrogen production is mainly based on steam methane reforming (SMR), which is associated with significant CO₂ emissions. Commonly considered paths for hydrogen production include (a) steam and dry reforming of hydrocarbons; (b) water electrolysis; (c) plasma arc decomposition; (d) water thermolysis; (e) thermochemical water splitting; (f) thermochemical conversion of biomass (biomass gasification and biofuel reforming); (g) photovoltaic electrolysis, photocatalysis, and photochemical methods; (h) dark fermentation; (i) high-temperature electrolysis; (j) hybrid thermochemical cycles; (k) coal and petroleum gasification; (l) MSW gasification; (m) fossil fuel reforming; (n) biophotolysis and photo-fermentation; (o) artificial photosynthesis; and (p) photo-electrolysis (Dincer & Acar, 2015). One goal of this project is to evaluate the strengths and weaknesses of hydrogen production concepts, determine how they can be integrated with existing infrastructure to produce cheap green hydrogen, and identify the potential impact of these technologies in producing SAF.

In some biomass and waste conversion processes, carbon dioxide and methane are produced as a side product or as the starting material. To meet the specifications for SAF, hydrogen will be needed to hydrogenate alkenes and hydrotreat oxygenates. Utilizing waste carbon oxides and methane can increase the amount of carbon obtained from resources in the SAF while reducing emissions. This can be done in conjunction with hydrogen production with a lower carbon intensity. Our analysis will examine the trade-offs between enhanced carbon utilization, the effects of increased renewable energy use, the need for stability in the grid and energy storage, access to lower-carbon-intensity hydrogen against positive impacts on environmental indicators, the cost impact of such changes, and technology uncertainty in emerging science and engineering.

Over the past decade, significant progress has been made in assessing the economic and environmental properties of SAF. This work includes studies that have fostered our understanding of lifecycle analysis (LCA) in general (e.g., Stratton et al., 2010). In addition, work has focused on the economic and environmental properties of specific pathways, including jet fuel produced from HEFA (Stratton et al., 2011; Pearlson et al., 2013; Olcay et al., 2013; Seber et al., 2014), from FT pathways (Stratton et al., 2011; Suresh, 2016; Suresh, 2018), and from biomass-derived sugars using a variety of chemical and biological techniques (Bond et al., 2014; Staples et al., 2014; Winchester et al., 2015). Most recently, Monte Carlo

approaches have been systematically introduced for quantifying uncertainty and stochasticity in LCA and techno-economic analysis (TEA) (Bann et al., 2017; Suresh, 2016; Yao et al., 2017; Suresh, 2018; Oriakhi, 2020).

References

- Bann, S. J., Malina, R., Staples, M. D., Suresh, P., Pearlson, M., Tyner, W. E., Hileman, J. I., & Barrett, S. (2017). The costs of production of alternative jet fuel: A harmonized stochastic assessment. *Bioresource Technology*, 227, 179-187. <https://doi.org/10.1016/j.biortech.2016.12.032>
- Bond, J. Q., Upadhye, A. A., Olcay, H., Tompsett, G. A., Jae, J., Xing, R., Alonso, D. M., Wang, D., Zhang, T., Kumar, R., Foster, A., Sen, S. M., Maravelias, C. T., Malina, R., Barrett, S. R. H., Lobo, R., Wyman, C. E., Dumesic, J. A., & Huber, G. W. (2014). Production of renewable jet fuel range alkanes and commodity chemicals from integrated catalytic processing of biomass. *Energy Environ. Sci.*, 7(4), 1500-1523. <https://doi.org/10.1039/C3EE43846E>
- Brandt, K., Tanzil, A. H., Martinez-Valencia, L., Garcia-Perez, M., & Wolcott, M. P. (2022). Pyrolysis techno-economic analysis, v. 2.2. Washington State University. <https://doi.org/10.7273/000002563>
- Dincer, I., & Acar, C. (2015). Review and evaluation of hydrogen production methods for better sustainability. *International Journal of Hydrogen Energy*, 40(34), 11094-11111. <https://doi.org/10.1016/j.ijhydene.2014.12.035>
- ICAO.(2021). *CORSIA supporting document - CORSIA Eligible Fuels - Life Cycle Assessment Methodology*. https://www.icao.int/environmental-protection/CORSIA/Documents/CORSIA_Supporting_Document_CORSIA%20Eligible%20Fuels_LCA_Methodology_V3.pdf
- Olcay, H., Seber, G., Malina, R. (2013). *Life Cycle Analysis for Fully-Synthetic Jet Fuel Production, MIT Support for Honeywell Continuous Lower Energy*. Emissions and Noise (CLEEN) Technologies Development, Report to the FAA.
- Oriakhi, U.M. (2020). *A stochastic life cycle and greenhouse gas abatement cost assessment of renewable drop-in fuels* [Master's Thesis, Massachusetts Institute of Technology].
- Pearlson, M., Wollersheim, C., & Hileman, J. (2013). A techno-economic review of hydroprocessed renewable esters and fatty acids for jet fuel production. *Biofuels, Bioproducts and Biorefining*, 7(1), 89-96. <https://doi.org/10.1002/bbb.1378>
- Seber, G., Malina, R., Pearlson, M. N., Olcay, H., Hileman, J. I., & Barrett, S. R. H. (2014). Environmental and economic assessment of producing hydroprocessed jet and diesel fuel from waste oils and tallow. *Biomass and Bioenergy*, 67, 108-118. <https://doi.org/10.1016/j.biombioe.2014.04.024>
- Snowden-Swan, L. J., Zhu, Y., Bearden, M. D., Seiple, T. E., Jones, S. B., Schmidt, A. J., Billing, J. M., Hallen, R. T., Hart, T. R., Liu, J., Albrecht, K. O., Fox, S. P., Maupin, G. D., & Elliott, D. C. (2017). Conceptual Biorefinery Design and Research Targeted for 2022: Hydrothermal Liquefaction Processing of Wet Waste to Fuels. Pacific Northwest National Laboratory, 27186, 1-40. <https://www.osti.gov/servlets/purl/1415710>
- Staples, M. D., Malina, R., Olcay, H., Pearlson, M. N., Hileman, J. I., Boies, A., & Barrett, S. R. H. (2014). Lifecycle greenhouse gas footprint and minimum selling price of renewable diesel and jet fuel from fermentation and advanced fermentation production technologies. *Energy Environ. Sci.*, 7(5), 1545-1554. <https://doi.org/10.1039/C3EE43655A>
- Stratton, R; Wong, H; Hileman, J. (2020). *Life Cycle Greenhouse Gas Emissions from Alternative Jet Fuels* (PARTNER-COE-2010-001). Partnership for Air Transportation Noise and Emissions Reduction (PARTNER).
- Stratton, R. W., Wong, H. M., & Hileman, J. I. (2011). Quantifying variability in life cycle greenhouse gas inventories of alternative middle distillate transportation fuels. *Environmental Science & Technology*, 45(10), 4637-4644. <https://doi.org/10.1021/es102597f>
- Suresh, P., Malina, R., Staples, M. D., Lizin, S., Olcay, H., Blazy, D., Pearlson, M. N., & Barrett, S. R. H. (2018). Life cycle greenhouse gas emissions and costs of production of diesel and jet fuel from municipal solid waste. *Environmental Science & Technology*, 52(21), 12055-12065. <https://doi.org/10.1021/acs.est.7b04277>
- Suresh, P. (2016). *Environmental and economic assessment of alternative jet fuel derived from municipal solid waste* [Master's Thesis, Massachusetts Institute of Technology].
- Tanzil, A. H., Brandt, K., Wolcott, M., Zhang, X., & Garcia-Perez, M. (2021). Strategic assessment of sustainable aviation fuel production technologies: Yield improvement and cost reduction opportunities. *Biomass and Bioenergy*, 145, 105942. <https://doi.org/10.1016/j.biombioe.2020.105942>
- Winchester, N., Malina, R., Staples, M. D., & Barrett, S. R. H. (2015). The impact of advanced biofuels on aviation emissions and operations in the U.S. *Energy Economics*, 49, 482-491. <https://doi.org/10.1016/j.eneco.2015.03.024>
- Yao, G., Staples, M. D., Malina, R., & Tyner, W. E. (2017). Stochastic techno-economic analysis of alcohol-to-jet fuel production. *Biotechnology for Biofuels*, 10(1), 18. <https://doi.org/10.1186/s13068-017-0702-7>

Task 1 - Evaluate the Strengths and Weaknesses of Hydrogen and PtL Concepts in the United States

Washington State University

Objectives

The objective of Task 1 is to perform a literature review and develop design cases for hydrogen and PtL concepts.

Research Approach

In this task, we will identify areas that require more research and development to reduce technology uncertainty. Specifically, we analyze six technologies for hydrogen production: (a) steam reforming, (b) dry reforming, (c) water electrolysis, (d) gasification of carbonaceous materials (biomass, coal, bitumen, and MSW) (with steam and CO₂), (e) thermal decomposition of hydrocarbons (methane pyrolysis with capture and use of solid carbon), and (f) fossil fuel reforming. This task is being conducted by WSU and PNNL and started during Year 1. The main goal of this task is to build design cases for each of these hydrogen production technologies (mass and energy balances and TEAs) and identify the strengths and weaknesses of each technology studied. A team of hydrogen production experts from WSU and PNNL meets weekly with a PhD student and post-doctoral associate from WSU to guide them in the literature review and in the creation of a road map for constructing design cases and identifying the opportunities and challenges for each of the technologies studied.

Milestones

This year, we have continued work in two main areas: (a) a literature review of hydrogen production technologies within the context of SAF production, and (b) mass and energy balances and TEAs of standalone hydrogen production technologies. We have completed the first draft of a literature review for hydrogen production within the context of SAF technologies, and it is currently under internal review. We have completed our second goal, with TEAs of hydrogen production technologies developed to calculate the minimum selling price and GHG footprint for each. These results are now available for team members to use.

Major Accomplishments

We have completed the first draft of a literature review on the TEAs of hydrogen production technologies (slow and high-pressure gasification, steam reforming, partial oxidation, autothermal oxidation, methane pyrolysis, and low- and high-temperature water electrolysis) and have identified several promising pathways in which hydrogen production technologies are integrated with gasification. We have also developed standardized design cases to estimate hydrogen production costs for each of the technologies studied.

Publications

Sierra V, Wolcott M, Zhang X, Ha S, Male J, Garcia A, Brand K, Garcia-Perez M, Drennan C, Holladay J: Emerging and Commercial Hydrogen Production Technologies for SAF Manufacturing: A comparative Literature Review. *Under internal review.*

Outreach Efforts

We presented our preliminary results at the ASCENT meeting on April 5–6, 2022; at the November 25–26, 2022, meeting; and at the Civil Aviation Alternative Fuels Initiative meeting on June 1–3, 2022, in Washington, DC.

Student Involvement

Valentina Sierra is working on the literature of hydrogen production technologies and the role that hydrogen has in SAF production.

Plans for Next Period

We plan to submit the revised literature review and improve the design cases. In the next year, we will continue with our biweekly meetings with the panel of experts from PNNL to identify the strengths and weaknesses of new concepts for SAF production. We will discuss the integration of hydrogen production and PtL concepts with biomass-based SAF production technologies. Our graduate student and research associate make presentations every 15 days and, based on recommendations from the panel of experts, work for 15 days on a new presentation.



Task 2 - Assess How Hydrogen Production and PtL Production Can Be Integrated with Existing Production and Distribution Infrastructure (Existing Infrastructure and SAF Technologies) to Produce Fuels with Lower Carbon Intensity

Washington State University

Objective

The goal of Task 2 is to estimate cost reduction opportunities that would arise if emerging hydrogen production technologies were co-located with SAF production technologies and existing infrastructure.

Research Approach

For SAF technologies, we study how hydrogen is used in hydrotreatment steps. We conduct weekly meetings with WSU, PNNL experts, and our PhD students to identify hydrogen production opportunities in existing industries (petroleum refineries, dams, metallurgical industry, etc.). Our main goal is to estimate cost reduction opportunities that would arise if the emerging hydrogen production technologies were co-located with some of these industries. In a separate subtask, we will evaluate the impact of each of the emerging hydrogen production technologies on existing or emerging SAF technologies, including those based on (a) HEFA, (b) Virent's BioForming synthesized aromatic kerosene, (c) ATJ fuel, (d) natural sugar to hydrocarbon (SIP), (e) fast pyrolysis and the gas-to-fuel process, and (f) selective carbonization/ CO_2 gasification/steam reforming/FT processes. For each case, we consider lignocellulose or lipids as feedstocks. Hydrogen utilization for SAF production typically occurs in a hydrotreatment step that varies depending on the technology (Tanzil et al., 2021; Han et al., 2019). This step can proceed from a simple hydrogenation, hydrodeoxygenation, hydro-cracking, or all of them together, depending on the technology (Han et al., 2019). Especially troublesome is the hydrotreatment of oligomers and materials with a high tendency to form coke (Han et al., 2019). In this task, we develop detailed phenomenological mathematical models for the hydrotreatment step of the HEFA and fast pyrolysis pathways, which the team will then use to study potential strategies to reduce hydrogen consumption during SAF production (Chen et al., 2019; Plazas-González et al., 2018). This type of model requires a detailed description of the chemical composition of the feedstock, the reaction mechanism, and associated kinetics (Guitierrez-Antonio et al., 2018; Talib Jarullah, 2011; Boesen et al., 2017; Jenišťová et al., 2017; Tieuli et al., 2019; Hechemi and Murzin, 2018). The modeling work will complement studies in batch and continuous hydrotreatment reactors with different catalysts to validate the mathematical model.

Milestone

This task started in January 2023. We have simulated a single case to determine the suitability of high-temperature electrolysis to increase the yield of a gasification process. A process mass and energy balance has been completed, with a detailed heat integration study and TEA under development.

Major Accomplishments

This task started in January 2023. Our work shows potential for synergy between syngas processes and high-temperature electrolysis. In addition to gasification's high temperatures providing plentiful high-quality heat, fuel synthesis ejects 22% to 28% of the fuel's heating value as waste heat under ideal conditions (Lange, 2007). We are currently exploring how best to combine these technologies.

Publications

None.

Outreach Efforts

None.

Awards

None.

Student Involvement

A new student (Anika Afrin) has been hired to work on this task. She began her graduate studies on January 1, 2022. Another student (Claudia Valderrama-Ríos) is developing the integrated case for gasification.

Plans for Next Period

In the next year, we will review the different hydrotreatment technologies associated with producing SAFs and the mathematical models used to describe the operation of these reactors. We will also continue our investigation into the synergy of high-temperature electrolysis and syngas technologies such as methanol synthesis and Fischer-Tropsch.

References

- Boesen, R. R. (2010). *Investigation and Modelling of Diesel Hydrotreating Reactions* [PhD Thesis]. Technical University of Denmark. <https://backend.orbit.dtu.dk/ws/portalfiles/portal/6470295/Thesis+Rasmus+R.+Boesen+2010+final.pdf>
- Chen, Z., Feng, S., Zhang, L., Shi, Q., Xu, Z., Zhao, S., & Xu, C. (2019). Molecular-level kinetic modelling of fluid catalytic Cracking slurry oil hydrotreating. *Chemical Engineering Science*, 195, 619–630. <https://doi.org/10.1016/j.ces.2018.10.007>
- Gutiérrez-Antonio, C., Soria Ornelas, M. L., Gómez-Castro, F. I., & Hernández, S. (2018). Intensification of the hydrotreating process to produce renewable aviation fuel through reactive distillation. *Chemical Engineering and Processing - Process Intensification*, 124, 122–130. <https://doi.org/10.1016/j.cep.2017.12.009>
- Han, Y., Gholizadeh, M., Tran, C.-C., Kaliaguine, S., Li, C.-Z., Olarte, M., & Garcia-Perez, M. (2019). Hydrotreatment of pyrolysis bio-oil: A review. *Fuel Processing Technology*, 195, 106140. <https://doi.org/10.1016/j.fuproc.2019.106140>
- Hachemi, I., & Murzin, D. Yu. (2018). Kinetic modeling of fatty acid methyl esters and triglycerides hydrodeoxygenation over nickel and palladium catalysts. *Chemical Engineering Journal*, 334, 2201–2207. <https://doi.org/10.1016/j.cej.2017.11.153>
- Jeništová, K., Hachemi, I., Mäki-Arvela, P., Kumar, N., Peurla, M., Čapek, L., Wärnä, J., & Murzin, D. Yu. (2017). Hydrodeoxygenation of stearic acid and tall oil fatty acids over Ni-alumina catalysts: Influence of reaction parameters and kinetic modelling. *Chemical Engineering Journal*, 316, 401–409. <https://doi.org/10.1016/j.cej.2017.01.117>
- Lange, J. (2007). Lignocellulose conversion: an introduction to chemistry, process and economics. *Biofuels, Bioproducts and Biorefining: Innovation for a Sustainable Economy*, 1(1), 39–48.
- Plazas-González, M., Guerrero-Fajardo, C. A., & Sodr , J. R. (2018). Modelling and simulation of hydrotreating of palm oil components to obtain green diesel. *Journal of Cleaner Production*, 184, 301–308. <https://doi.org/10.1016/j.jclepro.2018.02.275>
- Stratton, R; Wong, H; Hileman, J. (2020). *Life Cycle Greenhouse Gas Emissions from Alternative Jet Fuels* (PARTNER-COE-2010-001). Partnership for AiR Transportation Noise and Emissions Reduction (PARTNER).
- Stratton, R. W., Wong, H. M., & Hileman, J. I. (2011). Quantifying variability in life cycle greenhouse gas inventories of alternative middle distillate transportation fuels. *Environmental Science & Technology*, 45(10), 4637–4644. <https://doi.org/10.1021/es102597f>
- Talib Jarullah, A. (2011). *Kinetic Parameters Estimating Hydrotreating reactions in Trickle Bed Reactor (TBR) via Pilot Plant Experiments; Optimal Design and Operation of an Industrial TBR with Heat Integration and Economic Evaluation* [Ph.D. dissertation, School of Engineering, Design, and Technology].
- Tanzil, A. H., Brandt, K., Wolcott, M., Zhang, X., & Garcia-Perez, M. (2021). Strategic assessment of sustainable aviation fuel production technologies: Yield improvement and cost reduction opportunities. *Biomass and Bioenergy*, 145, 105942. <https://doi.org/10.1016/j.biombioe.2020.105942>
- Tieuli, S., Mäki-Arvela, P., Peurla, M., Eränen, K., Wärnä, J., Cruciani, G., Menegazzo, F., Murzin, D. Yu., & Signoretto, M. (2019). Hydrodeoxygenation of isoeugenol over Ni-SBA-15: Kinetics and modelling. *Applied Catalysis A: General*, 580, 1–10. <https://doi.org/10.1016/j.apcata.2019.04.028>

Task 3 - Integration of Alternative Hydrogen and Carbon Sources into Fuel Conversion Pathways

Washington State University

Objective

The objective of Task 3 is to identify new pathways to optimize SAF production for maximum GHG reductions with minimal fuel costs.

Research Approach

This task is being conducted in two steps. In the first step, the WSU-PNNL panel of experts is meeting weekly with the PhD student to discuss the potential for combining the SAF pathways studied under Task 2 with alternative carbon sources (MSW, sludges from wastewater treatment plants, CO₂). In the second step, we evaluate the potential integration of these technologies with the new hydrogen production technologies discussed in Task 1. We will use the information collected to propose design and synthesis rules (diagrams) to help visualize how the source of carbon, hydrogen, and available energy and the type of conversion technology impact main environmental and economic sustainability indicators. We aim to use this exercise to identify better paths for SAF production.

Milestones

We are following a holistic path to identify desired production pathways. First, we correlated the minimum fuel selling price from 32 SAF TEAs with a model proposed by Lange et al. (2016). The model estimates the production SAF cost of product yield, feedstock, and other supplied costs, including Low Carbon Fuel Standards and Renewable Identification Number support. Our analysis estimated an average conversion cost of \$272 per tonne of feedstock processed, which is consistent for the chemical industry. We then developed three purely stoichiometric mass balances to estimate the effect of deoxygenation method (oxygen removal as O₂, H₂O, or CO₂) on production cost. Although water deoxygenation proved to be most advantageous, all idealized models proved viable, ruling out stoichiometry alone as a limiting factor in fuel production. These simple models were also used to study the effect of oxygen addition, plastics, and carbon sequestration on the overall performance of these ideal technologies. In this way, the combustion requirements of gasification were also ruled out as a limiting factor. The team has begun to analyze biomass gasification technologies. We have concluded that existing technologies for the conversion of biomass into syngas are limited by very low carbon conversion efficiencies. To achieve carbon conversion efficiencies close to 100%, the introduction of outside hydrogen and energy is necessary. Additionally, close to one-third of the syngas energy is lost when biomass is converted to SAF, presenting a limitation that must be addressed. Our group is working on the development of new technologies to address these issues.

Major Accomplishments

We have learned that the most critical factor governing production cost is fuel yield, which is directly related to carbon conversion efficiency. However, to maximize carbon conversion efficiency, it is critical to remove oxygen in the form of water by reacting it with hydrogen, which requires the introduction of hydrogen from outside the system. Currently, gasification is the leading technology for producing syngas as an intermediate. Current gasification systems must be optimized for maximum carbon conversion efficiency. An overall mass and energy balance shows that typical gasification systems are oxygen-, energy-, and hydrogen-deficient and that current designs sacrifice carbon efficiency to address the lack of energy and hydrogen. This issue can be addressed by augmenting hydrogen and energy from outside the system. Furthermore, the CO in syngas affords a C/O ratio that is much higher than the C/O ratio of biomass. Consequently, oxygen needs to be added to the system. Syngas also has an energy content higher than that of the fuel produced; therefore, nearly one-third of the system's energy is released as heat. Heat integration is critical to maximizing the economic viability of technologies producing syngas as an intermediate. Because hydrogen must be produced externally to maximize fuel production yields, hydrogen production technologies and their potential synergisms with SAF production must be carefully studied to develop optimized systems. To this end, we have produced a holistic analysis of the hydrogen market on the potential of oxygen, steam, and CO₂ gasification technologies. This overall analysis was then integrated with the hydrogen production technologies examined in Task 1 to forecast which pathways will become favorable as the hydrogen market evolves. We have also produced an Excel-based model that accounts for both stoichiometric and thermodynamic constraints in fuel production from biomass. This tool has not been utilized but could theoretically be updated and deployed for the testing of basic process optimization. We have placed our extended Lange model into a Python module that allows the calculation of economics for simple stoichiometric processes. We can easily extend this model to accept generalized user inputs, if needed for public outreach.

Publications

Garcia-Perez, M., Garcia, A., Wolcott, M. (2022, October 24-27). *Production of cheap Sustainable Aviation Fuels (SAFs): Balancing Economic and Environmental Imperatives*. Sustainable Energy for a Sustainable Future, San Pedro, San Jose.

Outreach Efforts

We have biweekly meetings with our panel of experts and have been progressing toward the goals of this task. We have completed a literature review of hydrogen production technologies, their TEAs, and the synthesis of new SAF production pathways. Our project was presented at the Spring ASCENT meeting (April 5-7, 2022) and at the Civil Aviation Alternative Fuels Initiative meeting in Washington, DC (June 1-3, 2022). We also presented our work at the October 2022 Fuel Task Group meeting in Alexandria, VA. Results were also presented at the Northwest Bioenergy Summit in Tri-Cities, Washington (October 11-12, 2023).

Student Involvement

Valentina Sierra (student), Anika Afrin (student), Aidan Garcia (research associate), and Robert Macias (research associate) contributed to this task.

Plans for Next Period

In this quarter, we hope to have enough information to complete TEAs of new SAF production concepts integrating biomass gasification with existing hydrogen production pathways. We plan to develop design cases for novel selective gasification processes.

References

Lange, J. P. (2016). Catalysis for biorefineries-performance criteria for industrial operation. *Catalysis Science and Technology*, 6(13), 4759-4767. <https://doi.org/10.1039/c6cy00431h>

Task 4 - Develop Methods for Assessing the Economic and Environmental Impacts of the Most Promising Fuel Production Pathways

Massachusetts Institute of Technology

Objectives

Under Task 4, the MIT team aims to define a method for assessing the economic and environmental impacts of promising fuel production pathways, including those identified by the WSU team under Tasks 1-3. For this purpose, the team develops TEA and LCA models. The TEA model calculates the minimum selling price of a specific fuel, and the LCA model computes its lifecycle GHG emissions. Because the exact process layout and process characteristics (e.g., mass and energy balances, capital expenditures, operating expenditures) of novel fuel production pathways are subject to uncertainty, the modeling chain must be stochastic. This approach allows the uncertainty to be represented in input parameters, which will be propagated through the model to obtain insights into the range of economic and environmental impacts associated with fuels from novel fuel production pathways.

Research Approach

The models leverage prior work on stochastic techno-economic and lifecycle GHG emission assessments of SAF (e.g., Bann et al., 2017; Suresh et al., 2016; Oriakhi, 2020). These models will be adjusted to assess future fuel production pathways with novel layouts and increased uncertainties. In building the stochastic models, careful consideration is given to categorizing inputs as “uncertain” instead of “variable.” An uncertain variable is one for which available data are sparse or there is little understanding of what contributes to a spread in values. An uncertain variable is also an input that a biofuel facility cannot intentionally control. Priority was placed on analyzing uncertainty and including it in a Monte Carlo analysis. Variability refers to inherent heterogeneity in the outcomes for a specific variable. Variable outcomes can be intentionally controlled; e.g., by choosing a production location. Variable inputs are chosen for sensitivity studies; e.g., to assess the impact of the carbon intensity of electricity on the lifecycle emissions of a fuel.

Milestone

The MIT team presented the initial modeling approach to the FAA and other stakeholders.

Major Accomplishment

The model outline was presented in last year's report. The focus of this year's efforts was on understanding how the modeling chain can be used to understand how existing SAF production pathways can be improved to reduce their carbon intensity (see Task 5).

Publications

None.

Outreach Efforts

None.

Student Involvement

During the reporting period, Tae Joong Park (MIT graduate student) was working this task.

Plans for Next Period

The team will continue to refine the method, specifically working with WSU to represent additional pathways.

References

- Bann, S. J., Malina, R., Staples, M. D., Suresh, P., Pearlson, M., Tyner, W. E., Hileman, J. I., & Barrett, S. (2017). The costs of production of alternative jet fuel: A harmonized stochastic assessment. *Bioresource Technology*, 227, 179–187. <https://doi.org/10.1016/j.biortech.2016.12.032>
- Elgowainy, A. et al. (2012) *Life Cycle Analysis of Alternative Aviation Fuels in GREET*. Argonne National Laboratory, Argonne, IL, USA.
- Oriakhi, U.M. (2020). *A stochastic life cycle and greenhouse gas abatement cost assessment of renewable drop-in fuels*. [Master's Thesis, Massachusetts Institute of Technology].
- Pearlson, M., Wollersheim, C., & Hileman, J. (2013). A techno-economic review of hydroprocessed renewable esters and fatty acids for jet fuel production. *Biofuels, Bioproducts and Biorefining*, 7(1), 89–96. <https://doi.org/10.1002/bbb.1378>

Task 5 - Apply Models to Analyze the Economic and Environmental Footprint of SAF Production Pathways

Massachusetts Institute of Technology

Objective

Under Task 5, the MIT team aims to apply the models developed under Task 4 to provide harmonized assessments of the minimum selling price and lifecycle GHG emissions of different SAF pathways. During the reporting period, the team applied the modeling chain to analyze the economic and environmental implications of using different measures, including renewable electricity and hydrogen, in selected CORSIA (Carbon Offsetting and Reduction Scheme for International Aviation)-eligible SAF pathways to improve carbon intensity scores.

Research Approach

The modeling chain used to explore the research question is outlined using the HEFA process with soybean feedstock. The team reconstructed the U.S. LCA value from CORSIA (ICAO, 2022) based on GREET 2011, using GREET 2022 rev1 (Argonne National Laboratory, 2022A) and GREET 2022 Aviation module (Argonne National Laboratory, 2022B). This baseline is a close estimate (within 1 g CO₂e/MJ jet) of the US CORSIA value; the remaining differences are attributable to the use of older GREET versions.

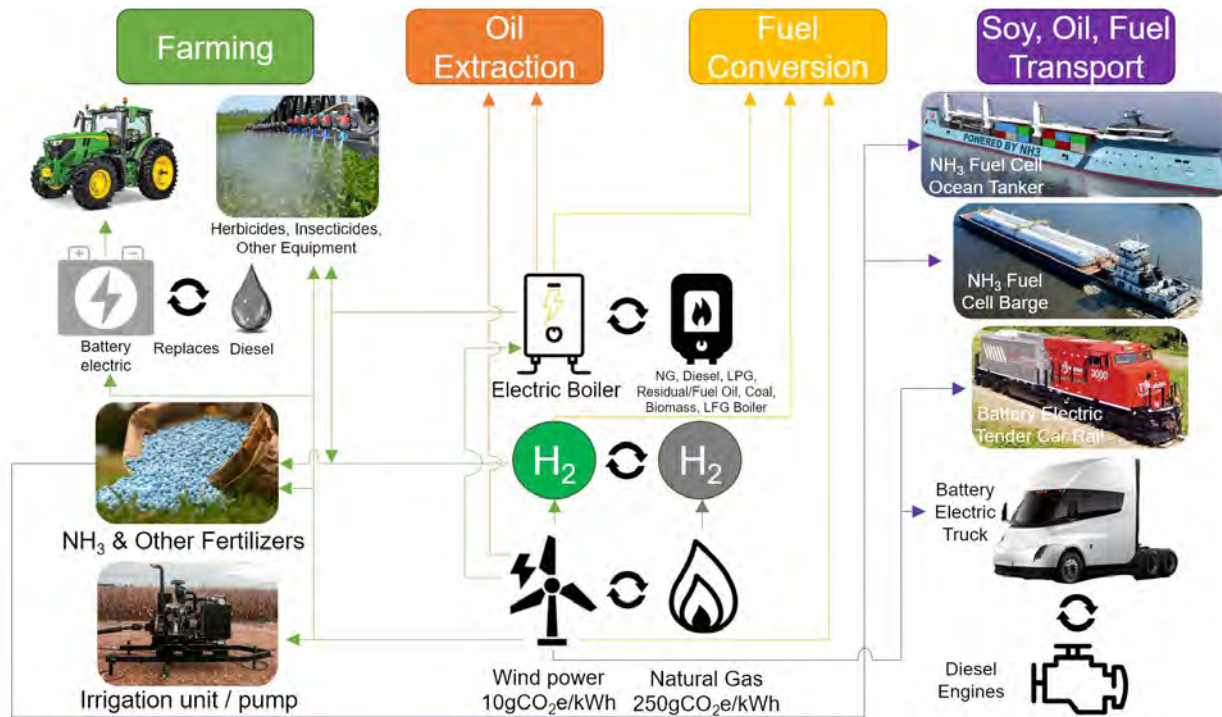


Figure 1. Strategies for reducing the carbon intensity of the HEFA soybean pathway, using electrification. “Green” hydrogen is produced via PEM (low-temperature) electrolyzer from wind electricity, replacing “gray” H₂ from SMR. Note that this is a simplified schematic and not an exhaustive analysis of every element of the lifecycle assessment. HEFA: hydro-processed ester and fatty acid; PEM: proton exchange membrane; SMR: steam methane reforming; NG: natural gas; LPG: liquefied petroleum gas; LFG: landfill gas.

Figure 1 shows the carbon intensity reduction strategies used for this study. Overall, all direct combustion of carbonaceous fuels in the primary supply chain is replaced with wind electricity, inclusive of embodied emissions (10.4 g CO₂e/kWh) (Argonne National Laboratory, 2022A). This included all heating energy used in natural gas (NG), liquefied petroleum gas, diesel, residual oil, coal, biomass, and landfill gas boilers (Argonne National Laboratory, 2022A) being substituted with resistance heating electric boilers (Engineer Live, 2021). All existing electricity use from the U.S. grid is replaced with wind power. In farming, off-road equipment (tractors) (Lagnelöv et al., 2021), irrigation units (NGE 14.6L Spec Sheet, n.d.), pumps (Honda IGX800 Engine, 2023), and generators powered by diesel, gasoline, and NG are replaced with equivalent electric units (Determining Electric Motor and Efficiency, n.d.). For material inputs such as fertilizer, herbicide, and insecticide use, where there is no direct combustion in the primary jet fuel supply chain, the secondary supply chain (inputs into fertilizer production) is electrified. This includes ammonia (NH₃) produced from electrolytic hydrogen (H₂) powered by wind, electrified transportation of inputs (battery trucks [Tesla Semi, 2023], rail [Popovich et al., 2021], and NH₃ fuel cell-powered ocean tankers and barges [Korberg et al., 2021]), and electrified off-road mining equipment (battery trucks [Henrio et al., 2023] for phosphoric rock hauling for monoammonium phosphate [NH₄H₂PO₄]). H₂ from proton exchange membrane (PEM) electrolysis powered by wind replaces H₂ from SMR in the HEFA process. Soybean plant, oil, jet fuel transport and distribution are electrified. The only fossil input remaining in the primary supply chain is n-hexane, a solvent used in soybean oil extraction; investigation of sustainable alternatives is ongoing.

Figure 2 shows the preliminary results for the GHG emissions reduction potential of electrifying the soybean HEFA jet supply chain. Differences in GREET 2011 and 2022, partially attributed to decreases in CH₄ emission factors in newer NG boilers, result in a 1 g CO₂e/MJ reduction. Electrified farming, including equipment, fertilizers, and input material transport, results in a 34% decrease of 6.2 g CO₂e/MJ. The GHG emissions of the electrified pathway, at 39.6 g CO₂e/MJ, is below the SAF Grand Challenge target of 50% reduction; however, it is still substantial. This is due to the substantial impact of farming (11.9 g CO₂e/MJ), 96% of which is attributed to N₂O emissions from nitrogen fertilizer use. This challenge is unique to the soybean plant due to nitrogen fixation with *Bradyrhizobium* (Cai et al., 2015). Mitigation options

are currently in an experimental phase (Itakura et al., 2013). Second, an induced land use change (ILUC) value of 24.5 g CO₂e/MJ is included in the lifecycle emissions, and we assume no change in this value with electrification. There may be reduction opportunities with cover crops, double cropping, and sustainable land management practices, and this is an area in need of further research.

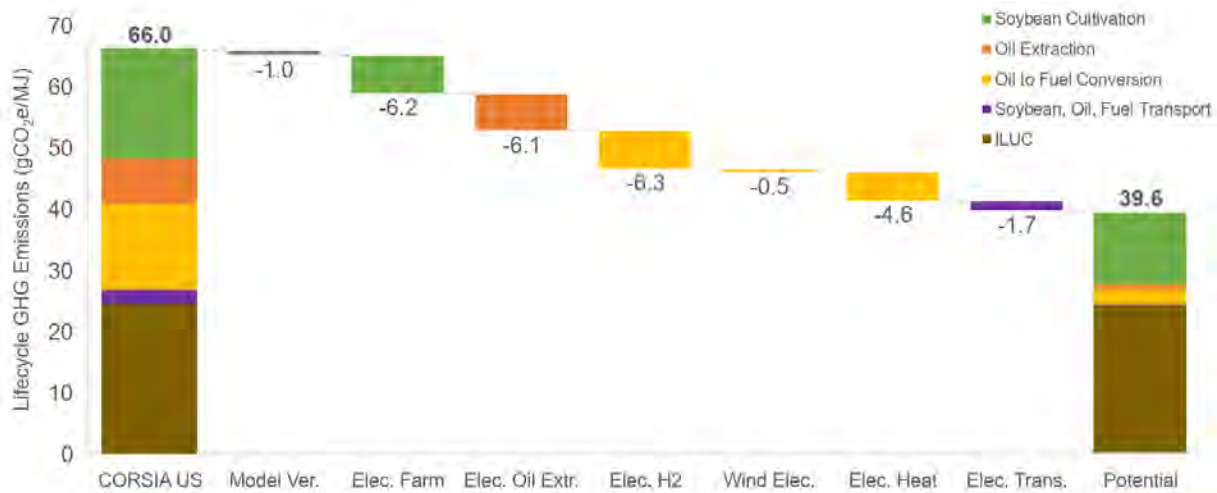


Figure 2. Greenhouse gas (GHG) emissions reduction potential jet fuel supply chain from soybean HEFA via electrification. HEFA: hydro-processed ester and fatty acid; Model Ver.: Differences in calculation of CORSIA US baseline value using GREET 2022 vs. 2011; Elec. Farm: electrified farming, including equipment, fertilizer, input material transport; Elec. Oil Extr.: electrified oil extraction, including resistance heating; Elec. H₂: electrolytic proton exchange membrane H₂; Wind Elec.: wind electricity replacing U.S. grid electricity in fuel conversion; Elec. Heat: electric heating; Elec. Trans: battery electric trucks, rail, and ammonia fuel cell powered ocean tankers and barges; ILUC: induced land use change (remains constant).

Milestone

The MIT team presented the initial modeling approach to the FAA and other stakeholders.

Major Accomplishment

The MIT team presented initial model results, which will provide the basis for further modification of the model and expansion to other pathway and feedstock combinations.

Publications

None.

Outreach Efforts

- The team presented results during the Fall 2022 and Spring 2023 ASCENT meetings.
- The work from this project contributed to the Fuels Task Group presentations in March and July 2023.
- The work from this project contributed to CAEP/13-FTG/02-IP/05: Research on Potentials for Electrification in SAF Production under the ASCENT Program with an accompanying presentation at ICAO Headquarters in Montreal, Canada, in November 2022.

Student Involvement

During the reporting period, Tae Joong Park (MIT graduate student) worked on this task.

Plans for Next Period

The team aims to roll out the model for additional CORSIA-eligible pathways, including costs from a TEA. In addition, the team intends to start analyses on novel fuel pathways.



References

- Argonne National Laboratory. (2022A). *Greet: The greenhouse gases, regulated emissions, and energy use in Transportation Model*. Energy.gov. (n.d.-a). <https://www.energy.gov/eere/bioenergy/articles/greet-greenhouse-gases-regulated-emissions-and-energy-use-transportation>
- Argonne National Laboratory. (2022B). *Energy Systems and Infrastructure Analysis – GREET Aviation Module*. https://greet.es.anl.gov/greet_aviation
- Cai, H., Wang, M., Elgowainy, A., & Han, J. (2015). *Updated N₂O Emissions for Soybean Fields*. Argonne National Laboratory Systems Assessment Group. <https://greet.anl.gov/files/update-n2o-soybean>
- DETERMINING ELECTRIC MOTOR LOAD AND EFFICIENCY. (n.d.). U.S Department of Energy. Retrieved November 23, 2023, from <https://www.energy.gov/eere/amo/articles/determining-electric-motor-load-and-efficiency>
- Henrio, M., van der Ende, O., Motta, G., & Ray, R. K. (2023, April 24). *Mining electrification could double their electricity demand*. McKinsey & Company. <https://www.mckinsey.com/industries/metals-and-mining/our-insights/electrifying-mines-could-double-their-electricity-demand>
- Honda IGX800 Engine. (2023). Honda. <https://www.hastingshonda.co.nz/power-equipment/honda-igx800/>
- ICAO., (2022). *CORSIA Eligible Fuels – Life Cycle Assessment Methodology (CORSIA Supporting Document)*. ICAO, Montreal, Canada. https://www.icao.int/environmental-protection/CORSIA/Documents/CORSIA_Eligible_Fuels/CORSIA_Supporting_Document_CORSIA%20Eligible%20Fuels_LCA_Methodology_V5.pdf
- Itakura, M., Uchida, Y., Akiyama, H., Hoshino, Y. T., Shimomura, Y., Morimoto, S., Tago, K., Wang, Y., Hayakawa, C., Uetake, Y., Sánchez, C., Eda, S., Hayatsu, M., & Minamisawa, K. (2013). Mitigation of nitrous oxide emissions from soils by Bradyrhizobium japonicum inoculation. *Nature Climate Change*, 3(3), 208–212. <https://doi.org/10.1038/nclimate1734>
- Korberg, A. D., Brynolf, S., Grahn, M., & Skov, I. R. (2021). Techno-economic assessment of advanced fuels and propulsion systems in future fossil-free ships. *Renewable and Sustainable Energy Reviews*, 142, 110861. <https://doi.org/10.1016/j.rser.2021.110861>
- Lagnelöv, O., Dhillon, S., Larsson, G., Nilsson, D., Larsolle, A., & Hansson, P.-A. (2021). Cost analysis of autonomous battery electric field tractors in agriculture. *Biosystems Engineering*, 204, 358–376. <https://doi.org/10.1016/j.biosystemseng.2021.02.005>
- NGE 14.6L Spec Sheet. (n.d.). Husker Power Products. Retrieved November 23, 2023, from <https://www.huskerpowerproducts.com/assets/site/specsheets/irrigation/psi-14.6l-nglpg-specsheet.pdf>
- Online Editor. (2021, December 10). *The move to electric boilers*. Engineer Live. <https://www.engineerlive.com/node/20952>
- Popovich, N. D., Rajagopal, D., Tasar, E., & Phadke, A. (2021). Economic, environmental and grid-resilience benefits of converting diesel trains to battery-electric. *Nature Energy*, 6(11), 1017–1025. <https://doi.org/10.1038/s41560-021-00915-5>
- Tesla Semi. (2023). Tesla. <https://www.tesla.com/semi>

Task 6 - Analyze the Prospects of Direct Air Capture of Atmospheric CO₂ to Provide a Carbon Source for SAF Production

Massachusetts Institute of Technology

Objectives

Under Task 6, the MIT team aims to analyze DAC technologies, regarding their readiness, scalability, and economic performance. Past and potential future trajectories of DAC technologies will be analyzed to define scenarios of how DAC could evolve to provide a potential carbon source for SAF production or support long-term carbon sinks to offset emissions. In addition, the opportunity space for implementing different DAC technologies with conversion processes will be analyzed. The initial step under this task was to provide an overview of the existing production technologies.

Research Approach

During the past year, the team conducted detailed LCA and TEA analyses of two different DAC approaches: liquid solvent DAC and solid sorbent DAC (see Figure 3):

- Liquid solvent DAC involves capture of carbon dioxide using an alkali solution and separation of pure carbon dioxide through calcination. Carbon Engineering (CE) is the leading company developing liquid solvent DAC. CE's design consists of four main components: the air contactor, the pellet reactor, the slaker, and the calciner.
- The solid sorbent DAC process consists of the air contactor, controlling valves, a vacuum pump, and a heat/cold supply. Most mature forms of solid sorbent DAC involve a two-stage process, where the apparatus first undergoes adsorption (loading) and then undergoes desorption (regeneration) by altering the temperature/pressure of system. The primary company developing solid sorbent DAC is Climeworks, located in Switzerland.

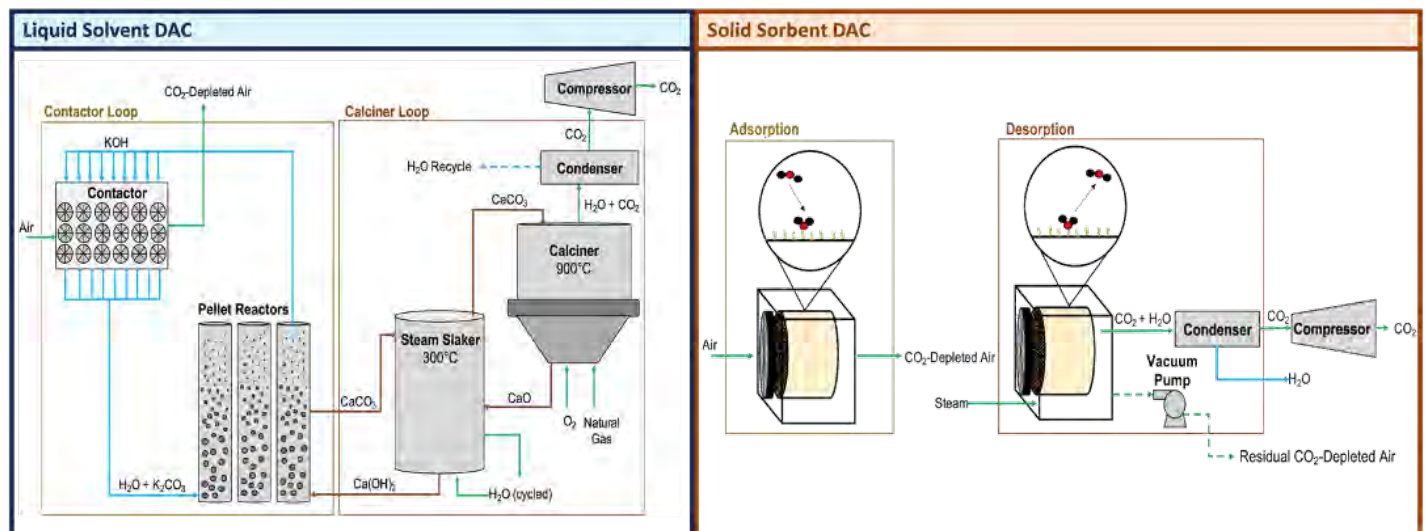


Figure 3. Liquid solvent and solid sorbent direct air capture (DAC) process schematics (Source: McQueen, 2021).

The team conducted a TEA on both DAC technologies. This analysis was conducted for a liquid solvent DAC plant capturing 1Mt CO₂/yr similar to CE's design, and a solid sorbent DAC plant capturing 100 kt CO₂/yr using a Lewatit 1065 sorbent, as suggested by Climeworks. The approach for the TEA of both technologies was to first determine the capital costs of the equipment. The equipment costs for liquid DAC were evaluated from a literature review of similar equipment used in well-established industries, including cooling towers, water treatment, and paper/pulp mills. The equipment costs for solid DAC were evaluated using standard purchase cost equations from the literature for equipment such as fans, vacuum pumps, heat exchangers, and compressors. Next, the cost of electricity for both liquid and solid DAC was evaluated by determining system energy requirements and average cost of solar and wind electricity in the United States. Similarly, the cost of raw materials for liquid and solid DAC were determined by analyzing the system input requirements and using spot prices for sorbents, chemicals (KOH, CaCO₃), and water. The cost of labor was determined from estimations in the literature on number of operations/maintenance jobs required at DAC facilities and salaries from the U.S. Bureau of Labor Statistics. Finally, additional costs such as factory floor space, maintenance, and insurance were evaluated. Upon annualizing capital costs (assuming a facility lifetime of 25 years and a cost of capital of 8.9%) and combining with operational costs, the annual DAC plant costs for liquid and solid DAC were established.

A lifecycle emissions analysis was conducted by first considering the annual raw materials and electricity requirements for liquid and solid DAC plants. A literature review for the emissions from production of raw materials such as the sorbent for solid DAC and the chemicals for liquid DAC was conducted. The emissions of solar and wind electricity were assumed to be 0.04 kg CO₂/kWh and 0.01 kg CO₂/kWh, respectively. The annual emissions for liquid and solid DAC plants were calculated and converted to emissions per tonne of CO₂ captured. Finally, the cost per tonne of CO₂ removed for liquid and solid DAC was calculated from the cost per tonne of CO₂ captured and the emissions per tonne of CO₂ captured.



Milestone

Initial TEA and LCA analysis of DAC systems were provided.

Major Accomplishments

The results for the TEA and LCA of liquid and solid DAC have been established.

- The preliminary results for the TEA indicate capture cost on the order of \$370 to \$450 per tonne of CO₂ captured. Capital costs—and, for solid DAC, raw material costs—are the most significant drivers of the cost.
- The LCA results indicate that net capture rates vary between 85% and 98%, depending on technology and electricity source. For solid DAC, the emissions associated with raw materials for the sorbent add considerably to the emissions footprint (if considered within the system boundary), whereas the LCA of the liquid DAC technology is largely driven by electricity use (even in the case of renewables such as solar and wind when including embodied emissions).

Publications

None.

Outreach Efforts

Results from the preliminary TEAs and LCAs for DAC were presented to MIT's Future Energy Systems Center (May and November 2023).

Student Involvement

During the reporting period, Tara Housen (MIT graduate student) worked on this task.

Plans for Next Period

The team will continue analyses of DAC processes.

References

- Bureau of Labor Statistics, U.S. Department of Labor, Occupational Outlook Handbook, Power Plant Operators, Distributors, and Dispatchers, at <https://www.bls.gov/ooh/production/power-plant-operators-distributors-and-dispatchers.htm>.
- Deutz, S., Bardow, A. Life-cycle assessment of an industrial direct air capture process based on temperature-vacuum swing adsorption. *Nat Energy* 6, 203–213 (2021). <https://doi.org/10.1038/s41560-020-00771-9>
- Greet: The greenhouse gases, regulated emissions, and energy use in Transportation Model*. Energy.gov. (n.d.-a). <https://www.energy.gov/eere/bioenergy/articles/greet-greenhouse-gases-regulated-emissions-and-energy-use-transportation>
- Keith et al., 2018. A process for capturing CO₂ from the atmosphere. *Joule* 2, 1573–1594. <https://doi.org/10.1016/j.joule.2018.05.006>
- Larson, J. (2020, June 23). Capturing new jobs. <https://rhg.com/wp-content/uploads/2020/06/Capturing-New-Jobs-Employment-Opportunities-from-DAC-Scale-Up.pdf>
- Noah McQueen et al 2021. A review of direct air capture (DAC): scaling up commercial technologies and innovating for the future. *Prog. Energy* 3 032001
- Q. Yu, D.W.F. Brillman, 2017. Design Strategy for CO₂ Adsorption from Ambient Air Using a Supported Amine Based Sorbent in a Fixed Bed Reactor, *Energy Procedia*, Volume 114, 2017, Pages 6102-6114.
- Solar Energy Technologies Office. (n.d.). *Sunshot 2030*. Energy.gov. <https://www.energy.gov/eere/solar/sunshot-2030>
- Wiser, R., & Bolinger, M. (2023, August). Land-Based Wind Market Report: 2023 Edition. US Department of Energy. https://emp.lbl.gov/sites/default/files/2023_lbwmr_final.pdf



Project 082(A) Modeling of the Committee on Aviation Environmental Protection Stringency Analysis

Georgia Institute of Technology

Project Lead Investigators

Prof. Dimitri N. Mavris
Director, Aerospace Systems Design Laboratory
School of Aerospace Engineering
270 Ferst Dr, Mail Stop 0150
Georgia Institute of Technology
Atlanta, GA 30332-0150
404-894-1557
dimitri.mavris@ae.gatech.edu

Dr. Michelle Kirby
Chief, Civil Aviation Division
Aerospace Systems Design Laboratory
School of Aerospace Engineering
270 Ferst Dr, Mail Stop 0150
Georgia Institute of Technology
Atlanta, GA 30332-0150
404-385-2780
michelle.kirby@ae.gatech.edu

University Participants

Georgia Institute of Technology (Georgia Tech)

- P.I.s: Dr. Dimitri N. Mavris, Dr. Michelle Kirby
- FAA Award Number: 13-C-AJFE-GIT-117
- Period of Performance: September 21, 2022 to September 30, 2024
- Task:
 1. Dual stringency analysis support

Project Funding Level

The FAA provided \$695,000 in funding, and Georgia Tech has agreed to a total of \$695,000 in matching funds. This total includes salaries for the project director, research engineers, and graduate research assistants, as well as funds for computing, financial, and administrative support, including meeting arrangements. Georgia Tech has also agreed to provide tuition remission for the students, paid from state funds.

Investigation Team

Prof. Dimitri Mavris (P.I.), Task 1
Dr. Michelle Kirby (co-P.I.), Task 1
Dr. Jimmy Tai (senior research engineer), Task 1
Dr. Burak Bagdatli (research engineer), Task 1
Dr. Holger Pfaender (research engineer), Task 1
Dr. Elena Garcia (senior research engineer), Task 1
Mr. Brennan Stewart (research engineer), Task 1
Ms. Melek Ozcan (graduate researcher), Task 1
Mr. Zelin He (graduate researcher), Task 1



Mr. Antoine Marin (graduate researcher), Task 1
Mr. David Mothershed (graduate researcher), Task 1
Mr. Gabriel Fronk (graduate researcher), Task 1
Mr. Andy Tan (graduate researcher), Task 1
Ms. Niharika Akula (graduate researcher), Task 1
Mr. Jayaprakash Kambhampaty (graduate researcher), Task 1
Mr. Srikanth Tindivanam Varadharajan (graduate researcher), Task 1
Mr. Kumanan Srinivasan (graduate researcher), Task 1

Project Overview

This project will provide technical support to the FAA for the assessment of the 13th cycle of the Committee on Aviation Environmental Protection (CAEP/13) stringency analysis, including cost estimates of various stringency options (SOs). Prior CAEP stringency analysis included a cost-benefit assessment of different scenarios on the basis of outdated information and relied on industry subject-matter input. This project will enhance and update the assumptions, on the basis of a quantitative assessment of technological benefits and the costs associated with achieving those benefits. The results will provide the FAA with a data-driven process for decision-making, including the interdependencies between CO₂ and noise, as well as the costs associated with their mitigation.

Task 1 – Dual Stringency Analysis Support

Georgia Institute of Technology

Objectives

The purpose of this ASCENT project is to support the FAA in conducting a cost-benefit stringency analysis for CAEP/13 while considering the interdependencies between CO₂ and noise. Although analyses of this type have been conducted previously, this project seeks to update the assumptions and modeling capabilities to provide a data-driven decision-making process for the FAA. This research used the CAEP/10 approaches as starting points to assess the manufacturer non-recurring cost and the price premium of an aircraft after technology response to a SO. The Georgia Tech team will assist the broader U.S. Research Team to accomplish the goals of the dual-stringency analysis.

Research Approach

In support of the broader research team, the Georgia Tech team has focused on the following main research thrusts:

- Developing the non-recurring cost (NRC) function
- Developing the price after technology response (PATR) methods
- Updating the technology responses possible for various SOs
- Providing broad technical support for the CAEP working groups

Methods and implementation

Each research thrust is an independent effort and thus has different approaches and results, as described below.

Non-recurring cost function development

The Georgia Tech team completed the development of the NRC function. This section presents the data used, the formulation and the final model.

Airframe NRC data

The airframe NRC data used to create the NRC model for the main analysis are shown in Table 1. The aircraft contained in the dataset represent an evolution of the underlying data for the CAEP/10 NRC model described in CAEP10_WG3_CO2-4_IP12 and updated with new information and input from the manufacturers and subject-matter experts. Whereas CAEP/10 considered only CO₂ improvements, noise improvements for each airframe program were established according to a representative reference airframe.

Aircraft are grouped into three general levels of change, defined as fix type 1 (small fix: P.I.P., wingtip, nacelle acoustics, etc.), fix type 2 (derivative design: re-engine, new nacelle, minor high-lift change, wingtip, etc.), and fix type 3 (clean-sheet design: all options are available).

The reported airframe NRC for Falcon 8X is changed from \$1.046 billion in to \$0.45 billion. The ICF management consulting company indicated that the initial value appeared to be an overestimation of the differences between Falcon 8X and the reference aircraft Falcon 7X, and suggested using \$150 million instead. The Main Analysis Cost ad hoc group (MACahg) contacted Dassault for feedback, on the basis of which \$150 million was considered an underestimation but closer to reality than \$1.046 billion. A sensitivity analysis of the Falcon 8X’s reported airframe NRC value was performed by using \$150 million, \$450 million, \$750 million, and \$1,050 million as Falcon 8X airframe NRC values. The results of the fits deviated by a percentage point in engine NRC and were almost indistinguishable for the Airframe NRC. According to feedback from the manufacturer, after having established the robustness of the fit against the Falcon 8X Airframe NRC, we decided to proceed with \$450 million.

Table 1. Airframe NRC data for the main analysis.

Program (program specific aircraft)	Maximum Takeoff Mass (MTOM) used for program (kg)	Reference aircraft	Reference aircraft Maximum Takeoff Mass (MTOM) (kg)	Fix type	CO ₂ Metric Value (MV) improvement (%)	Noise Metric Value (MV) improvement (ΔEPNdB)	Reported airframe NRC (B\$2010)
A320-200S (A320-241 sharklets)	78,000	A320-214	78,000	1	3.75	2.1	0.5
A330-200 (A330-203)	220,000	A330-322	218,000	1	6	1.4	0.755
CRJ-1000 (CL-600-2E25)	38,995	CRJ-900	38,329	1	7	1.3	0.303
CRJ-200 (CRJ-100/200)	24,040	CRJ-100	24,040	1	5	1.2	0.436
Falcon 8X (Falcon 8X)	33,112	Falcon 7X	31,751	1	1.5	4.8	0.45
737max (737-8)	82,190	737-800	88,314	2	14	12.0	3
747-8 (B747-8)	447,695	B747-400	~400,000	2	12	12.5	4
A320 neo (A320-2xxN)	70,000	A320ceo	70,000	2	12	14.2	1.228
A330-900 (A330-941)	205,000	A330-341	205,000	2	10.5	8.8	2
CRJ-700 (CRJ-200)	34,020	CRJ-200	21,523-24,040	2	11	2.8	1.012
Dash 8-400 (Dash 8-4xx ER)	29,574	Dash 8-300	Used similar T/W	2	10	2.8	0.571
E2 Family (E190-E2)	56,400	EMB-190-100IGW	51,800	2	14	14.1	1.605
Global 7000/8000 (Global 7500)	52,095	Global 6000	42,411-45,132	2	13	1.7	1.322
787-8 (787-8)	227,900	B767-300ER	186,880	3	20	13.6	17.5
A330/A340 (A330-322)	218,000	A300-B4-622R	140,000-171,000	3	15	8.8	5.892
A350 (A350-941)	280,000	A330-342	Used similar T/W	3	20	13.4	14.166
A380 (A380-842)	480,000	747-400	Boeing recommendation	3	18	13.5	15.577
Cseries (A220-100)	65,000	CRJ-1000	Used similar T/W	3	18	7.6	3.305
Gulfstream V (GV-SP)	41,050	GIV-SP	Used similar T/W	3	15	1.7	1.293

This base NRC data were augmented by the ICF management consulting company for technology areas that provide 0%–5% CO₂ metric value improvements for in-production aircraft. The technologies considered were engine technologies, advanced wingtip devices, aft body aerodynamics, environmental control system (ECS) aerodynamics, and on-demand ECS, adaptive trailing edge, and riblet coatings. ICF delivered potential CO₂ impacts of these technologies for seven aircraft size categories: small business and general aviation (BGA), large BGA, turboprop, regional jet, single aisle, small twin aisle, and large twin aisle. For the dual stringency analysis, the noise impacts of these technologies for each size category also needed to be estimated. The MACahg investigated the European Union Aviation Safety Agency (EASA) noise database to find similar technologies and compared them with an aircraft variant without that modification, assuming an maximum



takeoff mass (MTOM) per aircraft size category. Table 2 shows the ICF NRC data used in the development of the main analysis NRC model.

In addition, ICF found five real-world examples of aircraft programs whose CO₂ metric value improvements are 5%-10% during their production lives. These new data points are included in the most recent NRC calculations and are shown in Table 3.

Table 2. Small change airframe NRC data for the main analysis, provided by ICF.

	Program	MTOM (kg) used for program	Reference aircraft	Reference aircraft MTOM (kg)	Fix type	CO ₂ MV improvement (%)	Noise MV improvement (ΔEPNdB)	Estimated airframe NRC
T	ICF-small BGA-engine technologies	10,000	-	-	1	2	0	0.07
T	ICF-small BGA-advanced wingtip devices	10,000	-	-	1	3.5	0.4	0.103
T	ICF-small BGA-aft body aerodynamics	10,000	-	-	1	1	0	0.169
T	ICF-small BGA-ECS aero and on-demand ECS	10,000	-	-	1	0.6	0	0.038
T	ICF-small BGA-adaptive trailing edge	10,000	-	-	1	0	0.25	0.136
T	ICF-small BGA-riblet coatings	10,000	-	-	1	0.5	0	0.136
T	ICF-large BGA-engine technologies	40,000	-	-	1	2	1.1	0.131
T	ICF-large BGA-advanced wingtip devices	40,000	-	-	1	3.5	0.4	0.137
T	ICF-large BGA-aft body aerodynamics	40,000	-	-	1	1.3	0	0.224
T	ICF-large BGA-ECS aero and on-demand ECS	40,000	-	-	1	0.6	0	0.049
T	ICF-large BGA-adaptive trailing edge	40,000	-	-	1	2	0.25	0.181
T	ICF-large BGA-riblet coatings	40,000	-	-	1	0.5	0	0.181
T	ICF-turboprop-engine technologies	20,000	-	-	1	2	0	0.063
T	ICF-turboprop-advanced wingtip devices	20,000	-	-	1	3.5	0.4	0.137
T	ICF-turboprop-aft body aerodynamics	20,000	-	-	1	1.3	0	0.224
T	ICF-turboprop-ECS aero and on-demand ECS	20,000	-	-	1	0.6	0	0.049
T	ICF-turboprop-adaptive trailing edge	20,000	-	-	1	0.5	0.25	0.181
T	ICF-turboprop-riblet coatings	20,000	-	-	1	0.5	0	0.181
T	ICF-regional jet-engine technologies	48,000	-	-	1	2	1.4	0.139
T	ICF-regional jet-advanced wingtip devices	48,000	-	-	1	3.5	0.4	0.137
T	ICF-regional jet-aft body aerodynamics	48,000	-	-	1	1.3	0	0.224
T	ICF-regional jet-ECS aero and on-demand ECS	48,000	-	-	1	0.6	0	0.049
T	ICF-regional jet-adaptive trailing edge	48,000	-	-	1	0.5	0.25	0.181
T	ICF-regional jet-riblet coatings	48,000	-	-	1	0.5	0	0.181
T	ICF-single aisle-engine technologies	75,000	-	-	1	2	1.4	0.2
T	ICF-single aisle-advanced wingtip devices	75,000	-	-	1	3.5	1.1	0.173
T	ICF-single aisle-aft body aerodynamics	75,000	-	-	1	1.3	0	0.282
T	ICF-single aisle-ECS aero and on-demand ECS	75,000	-	-	1	0.6	0	0.064
T	ICF-single aisle-adaptive trailing edge	75,000	-	-	1	1.3	0.5	0.228
T	ICF-single aisle-riblet coatings	75,000	-	-	1	1	0	0.228
T	ICF-small twin aisle-engine technologies	250,000	-	-	1	2.3	1.4	0.382
T	ICF-small twin aisle-advanced wingtip devices	250,000	-	-	1	3.5	1.1	0.207
T	ICF-small twin aisle-aft body aerodynamics	250,000	-	-	1	1.3	0	0.338
T	ICF-small twin aisle-ECS aero and on-demand ECS	250,000	-	-	1	0.6	0	0.076
T	ICF-small twin aisle-adaptive trailing edge	250,000	-	-	1	2	0.5	0.272
T	ICF-small twin aisle-riblet coatings	250,000	-	-	1	1.5	0	0.272
T	ICF-large twin aisle-engine technologies	350,000	-	-	1	2.3	1.4	0.473
T	ICF-large twin aisle-advanced wingtip devices	350,000	-	-	1	3.5	1.1	0.207
T	ICF-large twin aisle-aft body aerodynamics	350,000	-	-	1	1.3	0	0.338
T	ICF-large twin aisle-ECS aero and on-demand ECS	350,000	-	-	1	0.6	0	0.076
T	ICF-large twin aisle-adaptive trailing edge	350,000	-	-	1	2	0.5	0.272
T	ICF-large twin aisle-riblet coatings	350,000	-	-	1	1.5	0	0.272



Table 3. Small change real-world airframe NRC data, provided by ICF.

Program	MTOM (kg) used for program	Fix type	CO ₂ MV improvement (%)	Noise MV improvement (ΔEPNdB)	Estimated airframe NRC (B\$2010)	Technology insertion description
737 NG	88,314	1	8.6	1.1	0.619	Blended winglet (2001) Split scimitar winglet Aerodynamic Improvements (2011) CFM56-7B Evolution (2011)
A320 (V2500-A5)	70,000	1	6.0	1.1	0.442	Engine PIP 1 (2008) Aerodynamic cleanups (2009) Winglet (sharklet) (2013) Engine PIP 2 (2015)
A320 (CFM56-5B)	70,000	1	5.5	1.1	0.392	Engine PIP 1 (2006) Aerodynamic cleanups (2009) Engine PIP 2 (2011) Winglet (sharklet) (2013)
E175 Enhanced	40,370	1	6.4	0.4	0.167	Wingtip redesign Other aerodynamic cleanups (2017)
CRJ900 NextGen	38,329	1	5.5	0.4	0.192	New winglet Conic-shaped exhaust nozzle

Engine NRC data

The engine NRC data gathered by MACahg are presented in Table 4. The twin-aisle engine NRCs, i.e., Trent XWB and Trent 700, are dramatically lower than the single-aisle engine NRCs. This implausible discrepancy occurs because the two engine NRC data points for twin-aisle aircraft are considered derivative engines, whereas the single-aisle engines are clean-sheet designs. Engine NRC, such as airframe NRC, is strongly influenced by the level of new technologies needing to be matured and demonstrated. Future twin-aisle engines such as UltraFan would require significant maturation and demonstration. Consequently, the expected engine NRC level would be higher than exhibited by the data points. In the absence of additional clean-sheet engine NRC data, the International Coordinating Council of Aerospace Industries Associations (ICCAIA) proposed using the average of the geared turbofan (GTF) and leading edge aviation propulsion (LEAP) engine NRCs to twin-aisle aircraft.

Table 4. Initial engine NRC data.

Engine	Engine NRC (B\$2010)	Applications for engine NRC calculations	Notes
Trent XWB	2.03	A350	Taken from CAEP10_WG3_CO2-4_IP12
PW1000G	10.38	Cseries and E2	Used on A220, A320neo family, E-Jet E2, Irkut MC-21
Trent 700	0.88	A330/A340	Engine of choice on the A330
PW300	0.855	Falcon 8X	Major applications: Cessna Citation (Latitude/Sovereign), Dassault Falcon (2000, 7X), Fairchild Dornier 328JET, Gulfstream G200
LEAP	15	A320 and B737 MAX	LEAP engines equip the Airbus A320neo, the Boeing 737 MAX and COMAC C919, among others

The reported engine development costs were equally split among airframe applications. ICCAIA advised that an engine program should not have more than two applications. The reported engine NRC data used for the main analysis are shown in Table 5.

Table 5. Engine NRC data for the main analysis.

Program (program specific aircraft)	MTOM (kg) used for program	Fix type	CO ₂ MV improvement (%)	Noise MV improvement (ΔEPNdB)	Reported airframe NRC (B\$2010)	Reported engine NRC (B\$2010)
Falcon 8X (Falcon 8X)	33,112	1	1.5	4.8	0.45	0.855
737max (737-8)	82,190	2	14	12.0	3	7.5
A320 neo (A320-2xxN)	70,000	2	12	14.2	1.228	7.5
E2 Family (E190-E2)	56,400	2	14	14.1	1.605	5.19
A330/A340 (A330-322)	218,000	3	15	8.8	5.892	6.345
A350 (A350-941)	280,000	3	20	13.4	14.166	6.345
Cseries (A220-100)	65,000	3	18	7.6	3.305	5.19

Airframe NRC formulation

The airframe NRC models have two aspects: NRC equation form and normalization. MACahg explored various methods and forms to better fit the airframe data. The starting point for the NRC equation form was the CAEP/10 equation. The MACahg examined several NRC equation forms such as the exponential model (the sample problem approach); tier model (proposed by ICCAIA); tier and exponential model; tier and slope model; and finally tier, slope and exponential model using three-tier and two-tier data tables. The tiered approach is formulated from the idea that the main driver of cost is based primarily on the level of change to the product. According to the regression performance and computational convenience, the three-tier and exponential model shown below was selected for the main analysis.

$$NRC_{Airframe} = \left[\Delta_f + \frac{\Delta_d}{1 + \exp\left(-25\left(x_3 - \frac{1+2\beta}{4}\right)\right)} + \frac{\Delta_n}{1 + \exp\left(-25\left(x_3 - \frac{3-2\beta}{4}\right)\right)} + A \exp(Bx_3) \right] S$$

$$S = \left(\frac{m}{m_{ref}} \right)^{0.5453 + \frac{0.6970 - 0.5453}{1 + \exp\left(-25\left(x_3 - \frac{1+2\beta}{4}\right)\right)}}$$

$$x_3 = \begin{cases} \beta x & \text{for small fix} \\ 1/2 + \beta(x - 1/2) & \text{for derivative} \\ 1 + \beta(x - 1) & \text{for new} \end{cases}$$

$$x = \alpha x_{CO_2} + (1 - \alpha) x_{Noise}$$

Because CAEP/10 focused on CO₂ only, the MACahg modified how the normalized metric value is calculated to account for CO₂ metric value improvement (x_{CO_2}) and noise metric value improvement (x_{Noise}). The normalization equations for CO₂ and noise metric value improvements are:

$$x_{CO_2} = \frac{CO_2 \text{ MV improvement} - CO_2 \text{ MV lower limit}}{CO_2 \text{ MV upper limit} - CO_2 \text{ MV lower limit}} \quad \text{and} \quad x_{dB} = \frac{\text{noise improvement} - \text{noise lower limit}}{\text{noise upper limit} - \text{noise lower limit}}$$

The first term in the numerator is the improvement of the aircraft of interest. The lower limits are set to zero for both metrics. The only term that could be calculated differently is the upper limits. Simple normalization, envelope normalization, and tier envelope normalization are the various normalization methods tested by MACahg to improve the regression performance. The final decision was to use the tier envelope normalization method. In tiered envelope normalization, the dataset is used to determine an envelope by using the maximum slopes from (0, 0). This process results in an upper limit that is a function of MTOM for each tier. Figure 1 shows that the upper limits are determined for a given MTOM for the CO₂ metric improvement as an example. Envelope normalization always starts at the origin where both MTOM and CO₂ or noise improvements are zero. In CAEP/10, the limit for improvement for smaller aircraft was set at a higher value (15%) and gradually grew to 20% at approximately 90 tons. MACahg performed implementation with a heuristic non-zero starting value. However, no improvement in the error of the regression was observed. In addition, the small aircraft clumped in low normalized metric regions, and the starting improvement is needed for each tier. Therefore,

data-driven envelope normalization schemes were used to train the final models. The equations defining the envelope for each tier are shown in Table 6.

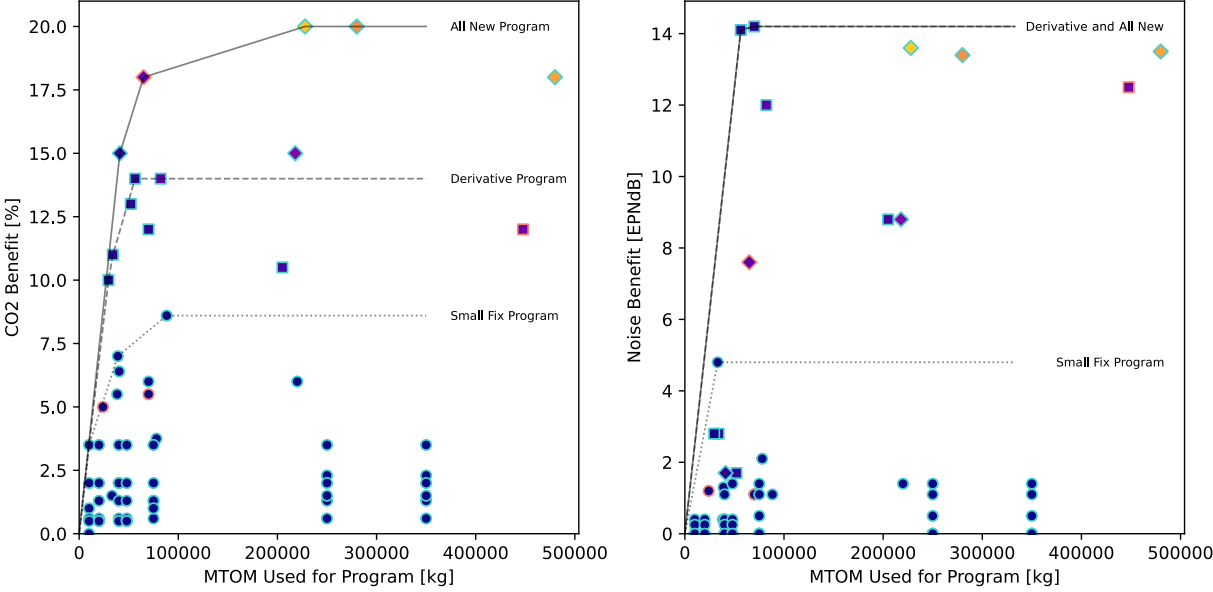


Figure 1. Overview of tier envelope normalization.



Table 6. Upper limit equations for both metrics and for all program types.

Program Type	Metric	MTOM range	Upper limit equation
Fix type 1 small fix	CO ₂	MTOM ≤ 10,000	0 + (3.5 - 0)/(10,000 - 0) × MTOM
		10,000 < MTOM ≤ 38,995	3.5 + (7 - 3.5)/(38,995 - 10,000) × (MTOM - 10,000)
		38,995 < MTOM ≤ 88,314	7 + (8.6 - 7)/(88,314 - 38,995) × (MTOM - 38,995)
		88,314 < MTOM	8.6
	Noise	MTOM ≤ 33,112	0 + (4.8 - 0)/(33,112 - 0) × MTOM
		33,112 < MTOM	4.8
Fix type 2 derivative	CO ₂	MTOM ≤ 10,000	0 + (3.5 - 0)/(10,000 - 0) × MTOM
		10,000 < MTOM ≤ 29,574	3.5 + (10 - 3.5)/(29,574 - 10,000) × (MTOM - 10,000)
		29,574 < MTOM ≤ 34,020	10 + (11 - 10)/(34,020 - 29,574) × (MTOM - 29,574)
		34,020 < MTOM ≤ 56,400	11 + (14 - 11)/(56,400 - 34,020) × (MTOM - 34,020)
		56,400 < MTOM	14
	Noise	MTOM ≤ 56,400	0 + (14.1 - 0)/(56,400 - 0) × MTOM
		56,400 < MTOM ≤ 70,000	14.1 + (14.2 - 14.1)/(70,000 - 56,400) × (MTOM - 56,400)
		70,000 < MTOM	14.2
Fix type 3 all new	CO ₂	MTOM ≤ 41,050	0 + (15 - 0)/(41,050 - 0) × MTOM
		41,050 < MTOM ≤ 65,000	15 + (18 - 15)/(65,000 - 41,050) × (MTOM - 41,050)
		65,000 < MTOM ≤ 227,900	18 + (20 - 18)/(227,900 - 65,000) × (MTOM - 65,000)
		227,900 < MTOM	20
	Noise	MTOM ≤ 56,400	0 + (14.1 - 0)/(56,400 - 0) × MTOM
		56,400 < MTOM ≤ 70,000	14.1 + (14.2 - 14.1)/(70,000 - 56,400) × (MTOM - 56,400)
		70,000 < MTOM	14.2

More details on the normalization methods and the three-tier and exponential model can be found in CAEP/13-MDG-FESG/4-WP/10.

Engine NRC Formulation

For the CAEP/13 main analysis, the engine NRC is formulated as a fraction of the airframe NRC, similarly to the CAEP/10 approach.

$$NRC_{\text{Engine}} = \delta_{\text{Engine}} NRC_{\text{Airframe}}$$

However, in CAEP/13, the multiplicative factor is calculated in a data-driven fashion. The calculation steps are as follows:

- 1) Split the cost of the engine programs between the aircraft programs equally (maximum of two programs)
- 2) Predict the airframe NRC with the trained equation, assuming the highest level of tier, if applicable
- 3) Calculate the split engine cost as a ratio with respect to the hypothetical new airframe cost
- 4) Repeat for each engine-airframe combination
- 5) Calculate the average
- 6) Use the average as a multiplicative factor

The engine costs are based on a new aircraft. Consequently, in step 2, a hypothetical new airframe NRC must be calculated, although the engine was used on a derivative. Figure 2 shows the engine NRC multiplicative factor calculation results.

Program	Fix Type	Reported Airframe NRC	Reported Engine NRC	Engine Model	Predicted Hypothetical All-New Design Airframe NRC	Engine NRC Factor
Falcon 8X	1	1.046	0.855	PW300	0.861	99.2%
737max	2	3	7.5	LEAP	6.085	123%
A320neo	2	1.228	7.5	LEAP	4.049	185%
E2 Family	2	1.605	5.19	PW1000G	5.394	96.2%
CSeries	3	3.305	5.19	PW1000	3.963	131%
A330/340	3	5.892	6.345	AVG(LEAP+PW1000G)	5.347	119%
A350	3	14.166	6.345	AVG(LEAP+PW1000G)	15.64	40.6%

Single-aisle Average: 125%

Twin-aisle Average: 80%

Figure 2. Engine NRC multiplicative factors.

Because small fixes probably would not include major engine modifications, the engine NRC is assumed to be zero for small fixes. The multiplicative factor for the engine NRC is given below:

$$\delta_{\text{Engine}} = \delta_{\text{Program Type}} \delta_{\text{Airframe Size}}$$

$$\delta_{\text{Program Type}} = \begin{cases} 0.0 & \text{for small fixes} \\ 1.0 & \text{for derivatives and all-new aircraft} \end{cases}$$

$$\delta_{\text{Airframe Size}} = \begin{cases} 1.25 & \text{for single aisle and smaller aircraft} \\ 0.80 & \text{for twin aisle} \end{cases}$$

NRC model results

The regression coefficients and the performance of the model are shown in Table 7 and Table 8, respectively. Overall, this model performs very well in Airframe NRC prediction with relatively small error. The weighting of CO₂ metric improvement is approximately 0.778; therefore, the weighting for noise is 0.222. This finding is as expected, because the main driver for new aircraft technologies is fuel burn. For fix type 1 aircraft, the airframe NRC varies very little with MTOM and normalized metric. The variation is more noticeable for fix type 2 aircraft. The NRC peaks very rapidly with normalized metric and MTOM for all fix type 3 aircraft, because the model is trying to thread the needle between low-NRC new designs and high-NRC new designs. These trends can be observed in Figure 3. Figure 4 shows the airframe NRC residuals of the three-tier step and exponential model compared with the exponential model.

Table 7. Three-tier step and exponential model regression coefficients.

	Recommended value	Full-precision value
α	0.777996	0.777996051464575
β	0.333333	0.3333333333333333
Δ_r	0.161608	0.16160762858919497
Δ_d	0.851094	0.8510935012985514
Δ_n	0.152544	0.15254447677684888
A	0.000000762687	0.0000007626867498098863
B	15.6571	15.657117085978618



Table 8. Three-tier step and exponential model performance metrics.

	Training	Validation
Mean square error	0.379	0.172
R^2	0.999	0.984
Mean average error	0.266	0.381
Mean absolute percentage error	52.66	39.87
Maximum absolute error	3.772	0.658

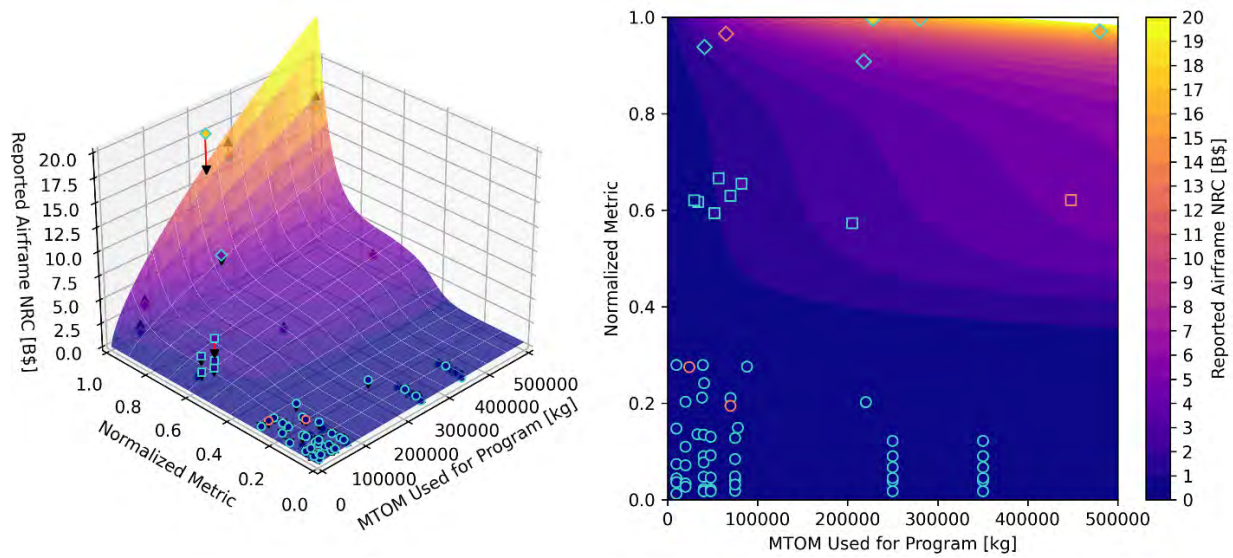


Figure 3. NRC surface plots for the three-tier step and exponential model with tier envelope normalization.

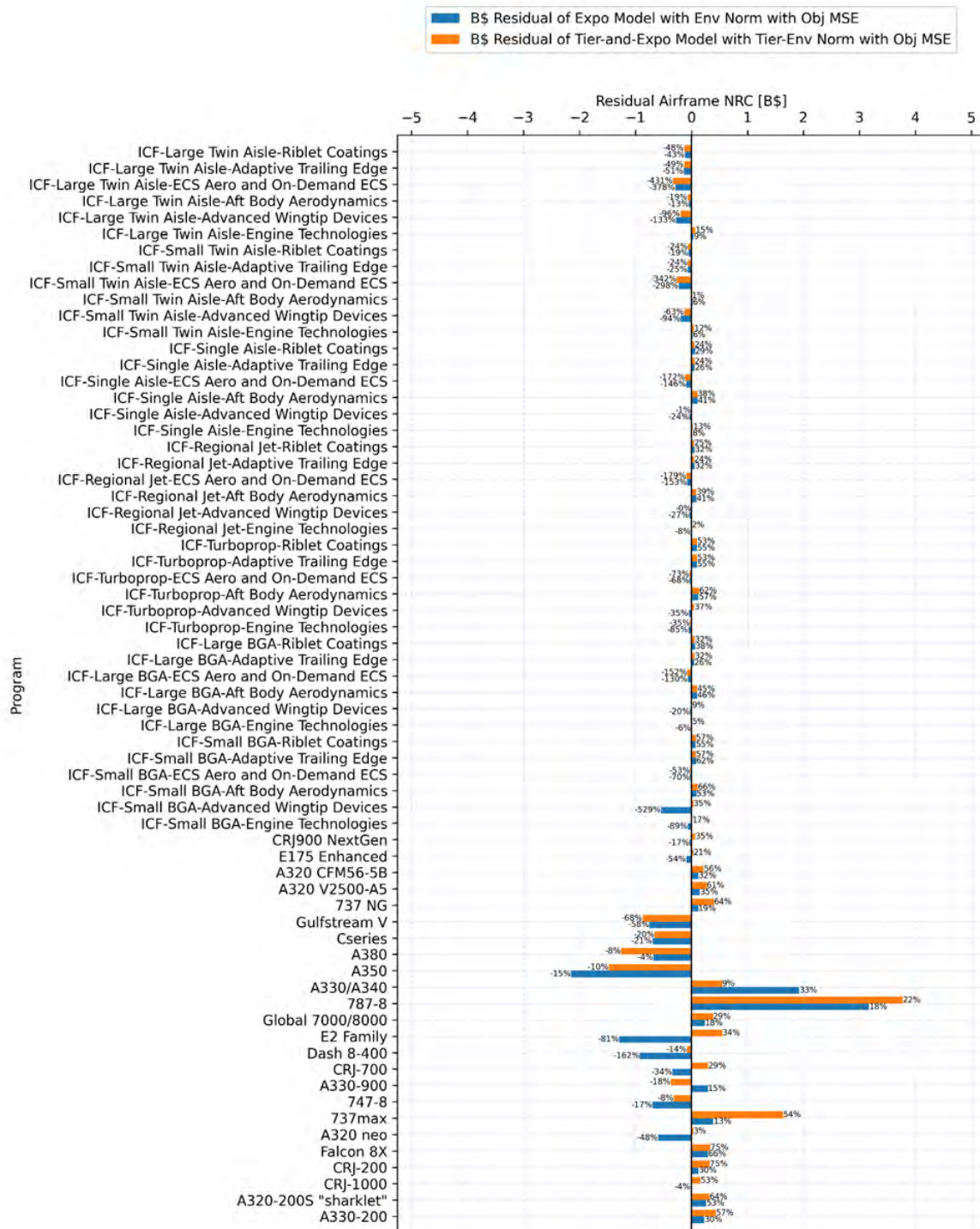


Figure 4. Residual airframe NRC for the exponential model with envelope normalization (orange), and the three-tier step and exponential model with tier envelope normalization (blue).

Price after technology response

As a part of the CO₂ standard development work in CAEP/10, the Forecast and Economic Analysis Support Group (FESG) began considering the potential implications on fleet evolution from an increase in aircraft PATR. The objective was to propose a method that can estimate the change in aircraft unit price for each aircraft type in the metric values database when they respond through insertion based on the CO₂ SO. Given that the aircraft unit price is largely determined by the market rather than the unit cost to the original equipment manufacturer, and the incremental build cost is sensitive information that is not available publicly, we adopted a proxy approach translating potential cost savings to the operators, owing to better fuel efficiency with respect to the price premium of the new aircraft. The method is as follows:

1. Estimate potential fuel burn savings throughout the life of an aircraft due to a technology response
2. Translate the life-cycle fuel cost savings into a change in operator net present value (ΔNPV)
3. Determine the price premium of the CO₂ technology response aircraft according to an assumed percentage of the potential cost savings (e.g., 50% of ΔNPV)

Various data sources were used in the PATR methods, and many assumptions were made that can be modified or updated for relevance to CAEP/13:

- Baseline fuel data: Annual fuel burn for the baseline aircraft that would potentially be subject to a technology response is needed.
- Aircraft baseline price
- Aircraft economic life: The metric used was the number of years corresponding to retirement of 50% of the fleet. Figure 5 and Table 9 show the data used in CAEP/10.
- Fuel price: A constant fuel price of \$3/U.S. gallon (0.97 cents/kg) was assumed.
- Fuel efficiency improvement: A 1-to-1 mapping between metric value (MV) improvement and fuel efficiency improvement was assumed.
- Discount rate: A discount rate of 0% was assumed.
- NPV split: A fixed split assumption (50/50) and adjusted NPV split assumption were considered.
- Technology response: An aircraft family approach was implemented for the determination of MV improvement. In addition, the project aircraft was assumed not to have technology response.

For a given SO and aircraft *i*, PATR is equal to the sum of the forecast fuel savings per year, *F*, multiplied by the unit fuel price, *P*, summed over the number of years, *n*, of the payback period:

$$PATR_{i,SO} = P \sum_{n=0}^{MV_{i,SO}} \frac{F_{i,n}}{(1 + r_{PATR})^n}$$

The payback period was assumed to be equal to the metric value improvement for aircraft *i* at the SO level. The airline discount rate, *r*_{PATR} was applied to discount the future cash flow into a NPV. PATR would result in an increase in capital cost, because of the increased list price of an aircraft, thereby increasing the cost of ownership.

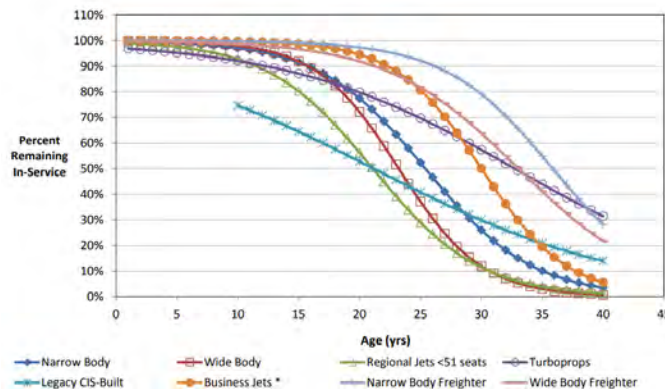


Figure 5. Survival curves by aircraft category.



Table 9. Expected life of aircraft used in the initial aircraft price analysis.

Aircraft Type	Number of Years After Which 50% of Fleet Will Retire
Narrow Body PAX	26
Wide Body PAX	24
Regional Jets <50 seats	22
Turboprops	33
Legacy CIS-built	22
Business Jets	31
Narrow Body Cargo	36
Wide Body Cargo	34

The CAEP/10 PATR methods could be applied again with updated databases, and the assumptions could be revisited. However, this process would address only the CO₂ aspect of the dual stringency problem at hand. To assess the impact of a noise technology response, MACahg members recommended considering the noise charges at various airports being modeled by Modelling and Databases Group (MDG). Thus, the noise charging fee structures were collected for 13 airports. On the basis of GRdb v2.11 and the technology responses received to date, fewer than 30 aircraft had a noise technology response, and the responses were very limited in magnitude. After these responses were applied, no change was observed in the resulting charges for any aircraft. Therefore, the Georgia Tech team recommended considering only CO₂ as the driver of PATR. In parallel, the Georgia Tech team is also exploring other plausible approaches to estimate the premium price of an aircraft after technology response.

Sample problem technology response

The Georgia Tech Aerospace Systems Design Laboratory has used an approach similar to that of the CAEP's Independent Expert Integrated Review and Long-Term Aspiration Goal studies in lieu of specific technology modeling. These two studies considered technologies as "bundles" of improvements in key disciplinary areas on the airframe and engine. For example, specific composite materials were not modeled, but structural weight improvements were. A stringency analysis requires that technologies be at a technology readiness level of 8 in a given year, thus limiting the scope of applicability of the possible technology "bundles" according to the year of application of the stringency. The outcome of the subtask is a set of technology assumptions to be used in modeling for the interdependency trades in the sample problem and full analysis, to provide a Pareto front of the maximum available technology response for a given aircraft class.

The methods for determining the impact of technology responses are represented in Figure 6. The system-level model calibration for the technology reference aircraft (TRA) vehicle is described in Sections A and B below. Section B provides more detail on the calibration of the acoustic properties of the TRA vehicle from certification databases. Section C describes how technology responses are applied to the vehicle model in a design space exploration. Section D outlines some of the optimization process for analyzing the design space and also presents preliminary results of generating Pareto fronts from the data. These sections specifically detail a wide-body twin-aisle aircraft (A330-941N); however, the methods are applicable to all other aircraft classes considered in this investigation.

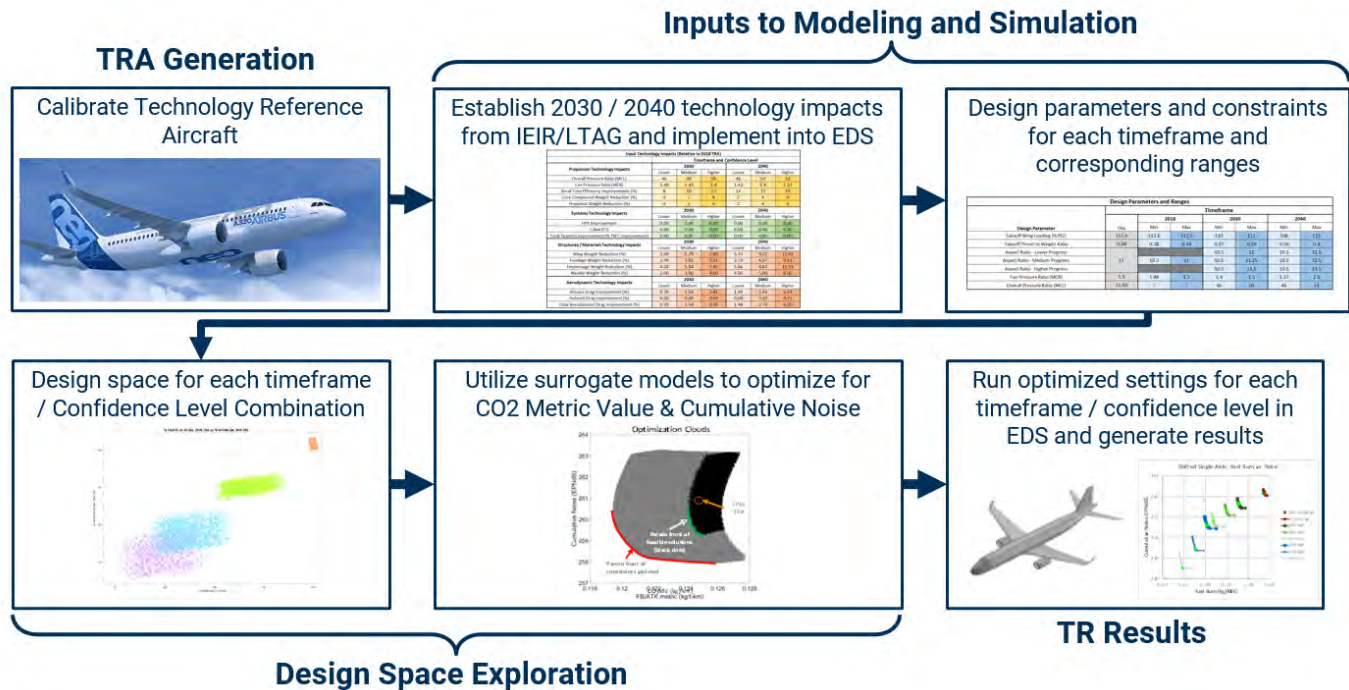


Figure 6. Process for determining a technology response (TR). IEIR: independent expert integrated review; LTAG: Long-Term Aspiration Goal; MV: metric value; TRA: technology reference aircraft; EDS: Environmental Design Space.

Vehicle model calibration

The creation of a notional A330-941N vehicle model (A330neo) starts with publicly available data for the geometry and the engine of the vehicle. For the notional A330neo model, a notional Rolls-Royce Trent 7000-72 engine model is also developed and calibrated to publicly available data. The geometric data, taken from three-dimensional-view drawings published by Airbus, include information on the control surfaces of the airplane. Various measurements of the airframe are taken, for example, the height of the tail and the chord length of the leading-edge slats. These values are used in various calculations to be implemented in the Flight Optimization System (FLOPS) model. FLOPS uses the input vehicle data to output a vehicle that best fulfills the mission parameters (i.e., range or desired takeoff gross weight).

The specific weight variant modeled in this project is the WV921, as designated in the airport planning manual (Airbus, 2023). Previous work by the Aerospace Systems Design Laboratory has defined component weights as percentages of the operational empty weight (OEW). These percentages are based on a statistical approach for historical values of each component of the wide-body class aircraft. From these percentages, target component weights are defined and calibrated for the correct OEW (found in the airport planning manual) of the specified weight variant of the A330-941N, by using the wide-body class percentages for weight components, as listed in Table 10. The component weight calibration is performed by iteratively varying weight factors in FLOPS to reach the desired OEW. After this process is complete, the airframe model, together with correct engine cycle parameters, is implemented in the Environmental Design Space (EDS) to generate a baseline model.



Table 10. Calibrated mass and balance summary for A330-941N WV921.

Mass and balance summary	% OEW	Pounds
Wing	21.7	64,489
Horizontal tail	2.0	6,089
Vertical tail	0.8	2,503
Vertical fin	0.0	0
Canard	0.0	0
Fuselage	19.6	58,349
Landing gear	6.8	20,176
Nacelle (air induction)	1.6	4,863
Structure total	52.6	156,470
Engines	14.4	42,748
Thrust reversers	0.0	0
Miscellaneous systems	0.0	0
Fuel systems: tanks and plumbing	0.3	887
Propulsion total	14.7	43,635
Surface controls	1.7	5,122
Auxiliary power	0.5	1,557
Instruments	0.0	0
Hydraulics	1.4	4,199
Electrical	1.0	2,911
Avionics	1.0	3,033
Furnishings and equipment	19.8	58,944
Air conditioning	1.0	2,893
Anti-icing	0.0	0
Systems and equipment total	26.4	78,659
Weight empty	93.7	278,764
Flight crew and baggage: 2	0.2	450
Cabin crew and baggage:8	0.4	1,200
Unusable fuel	0.3	862
Engine oil	0.1	239
Passenger service	3.5	10,477
Cargo containers	1.9	5,632
Operating weight	100.0	297,624
Passengers, 300		57,000
Passenger baggage		9,000
Cargo		0
Zero fuel weight		363,624
Mission fuel		191,720
Ramp (gross) weight		555,344

Vehicle acoustic calibration

Noise produced by the vehicle is calibrated to known data from EASA databases for aircraft noise (European Union Aviation Safety Agency, 2022; Eurocontrol Experimental Center, 2020). The aircraft noise is predicted in the EDS off design loop through an Aircraft Noise Prediction Program (ANOPP) model, which is parametrically constructed from engine geometry, trajectory predictions, airframe geometry, and engine cycle data predicted in the EDS model. The baseline noise predictions can be calibrated through ANOPP’s GENSUP module by adjusting each individual noise source in the ANOPP model at each power setting related to each of the three certification observers (i.e., approach, cutback/flyover, and sideline). Calibration variables are implemented in EDS via several variable parameters representing the noise produced by the engine (combustor, turbine, fan, and jet sources) and the airframe (including the tail, flaps, slats, and landing gear). Each variable contains information on noise perceived at each of the three observer positions because of the respective noise source (i.e., approach, cutback/flyover, and sideline). After calibrating the aircraft noise source predictions utilizing the Aircraft Noise and Performance (ANP) noise-power-distance (NPD) data with the method described in the following

section, the certification noise predictions are calibrated by adjustment of the flight trajectory and drag coefficients for takeoff and landing, owing to uncertainty in the certification takeoff trajectory parameters used to generate the noise predictions in the EASA database and error in the LT landing and takeoff (LTO) drag polars used in the EDS models.

Noise modeling of the vehicles begins with a collection of certification data. EASA publicly shares its noise certification data for various types of aircraft (European Union Aviation Safety Agency, 2022). This certification is dependent on meeting limits on the effective perceived noise in decibels (EPNdB) for cutback, approach, and sideline observer positions of airplane operations during takeoff and landing. These three data points do not provide sufficient information to rigorously model various operational scenarios. Thus, the certification data are supplemented with NPD data to further constrain the model. These NPD curves consider various acoustic metrics (including EPNdB and sound exposure level) taken from positions at various intervals in the sideline position relative to the runway for both takeoff and landing and at various thrust settings. However, the database of NPD data is updated only every 2 years (Eurocontrol Experimental Center, 2020). Because the A330-941N was recently certified, it is not included in the NPD database. Fortunately, the International Civil Aviation Organization (ICAO) prescribes a method for substituting a proxy vehicle in the database and for adjusting NPD curves for a missing vehicle by using differences in the two vehicles' certification noise data (ICAO, 2018).

For calibration of the acoustic model, noise suppression factors are first altered with the goal of meeting the sound exposure levels of the NPD curves. NPD curves are useful calibration parameters, because they contain an array of data across altitude and thrust levels, given that each individual aircraft noise component will not have a uniform relative strength at all altitudes and thrust level measurement points. Aircraft noise components will attenuate at different rates depending on whether they consist of primarily low- or high-frequency noise, and not all aircraft noise sources will have the same response to an increasing level of thrust, (with airframe noise not varying at all with thrust level and jet noise increasing the most with thrust level) The NPD curves predicted by the EDS model are compared with the ANP database's NPD curves and are calibrated to the ANP data by using the vehicle calibration parameters in EDS to adjust the ANOPP suppression factors. However, even with the insight provided by NPDs, the calibration problem remains under-constrained and with multiple solutions. Therefore, this is not an automated calibration procedure, the optimizer only provides an initial guess regarding the vehicle calibration parameters, and an engineer comparing the optimizer's initial estimation to empirical data and trends regarding aircraft noise source distribution, and adjusting the parameters to match these trends, within the solution space. The results of this exercise are the suppression factors for EDS variables that represent noise from specific components of the vehicle at a specific observation point. For example, the various approach noise suppression factors (all variables ending with the suffix -AP) being optimized to match the NPD curves are depicted in Figure 7. Figure 7 shows the desired values for the suppression factors for engine combustor noise, aft fan noise, inlet fan noise, jet noise, leading-edge slat noise, landing gear noise, trailing-edge flap noise, and engine turbine noise, in that order. After calibration via this method, the suppression factors are frozen for further trade studies.

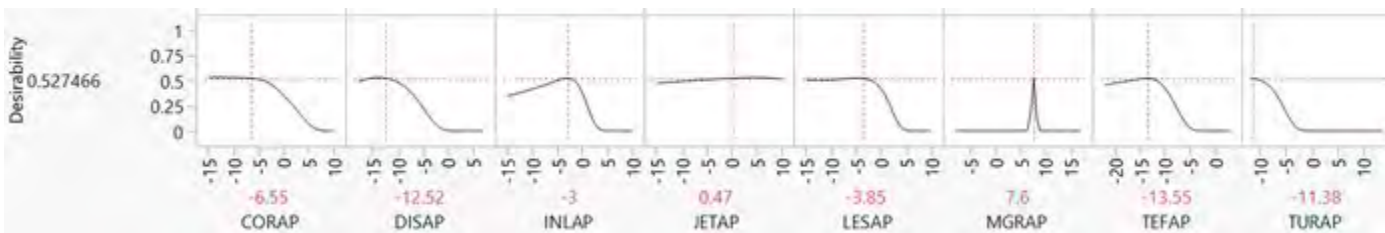


Figure 7. Optimization of approach noise suppression factors. CORAP: suppression factor on core (combustor) noise; DISAP: suppression factor on fan discharge noise; INLAP: suppression factor on inlet noise; JETAP: suppression factor on jet noise; LESAP: suppression factor on leading edge slat noise; MGRAP: suppression factor on main landing gear noise; TEFAP: suppression factor on trailing edge flap noise; TURAP: suppression factor on turbine noise.

Next, an LTO trade study is performed to match the vehicle certification noise found from the EASA database. Currently this process is necessary because of the low fidelity of the LTO drag polars and uncertainties in the takeoff trajectory parameters. Inaccuracies in takeoff and landing thrust levels affect the certification noise levels. A goal for the next period of performance is to implement a method to better calibrate the vehicles' LTO performance and takeoff trajectories by using data from airport planning manuals and AEDT database data, so that this step will no longer be necessary. The LTO study uses detailed FLOPS LTO results from the vehicle model, which are then used in the NASA ANOPP code to calculate

the noise emission from the vehicle. In this trade study, four parameters are varied over the ranges listed in Table 11. The first two variables are scaling factors that scale the drag coefficients for LTO. The other two variables relate to the operation of the vehicle: the flight path angle and the altitude at which a transition from maintaining the initial constant flight path angle to maintaining a constant velocity occurs (the ANOPP variable corresponding to this altitude is known as HSTOP). A design of experiments is run with approximately 600 cases spanning the design space of this study. Of those cases, the case that best matches the published certification noise for the A330-941N is selected. After this design point is verified, the selected design parameters are included in the EDS baseline model. The overall noise calibration method is as follows, as illustrated in Figure 8:

1. Determine target values for certification noise from the EASA database and for NPD data points by using the ICAO-defined substitution method from the NPD database
2. Optimize suppression factors to match NPD data points
3. Freeze suppression factors
4. Perform an LTO study to find a combination of parameters to meet target certification noise points

Table 11. LTO study variables and design ranges.

Variable	Takeoff drag scaling factor	Landing drag scaling factor	Flight path angle (degrees)	HSTOP (feet)
Design range	0.5–1.2	0.5–1.2	3.0–9.0	300–1,000

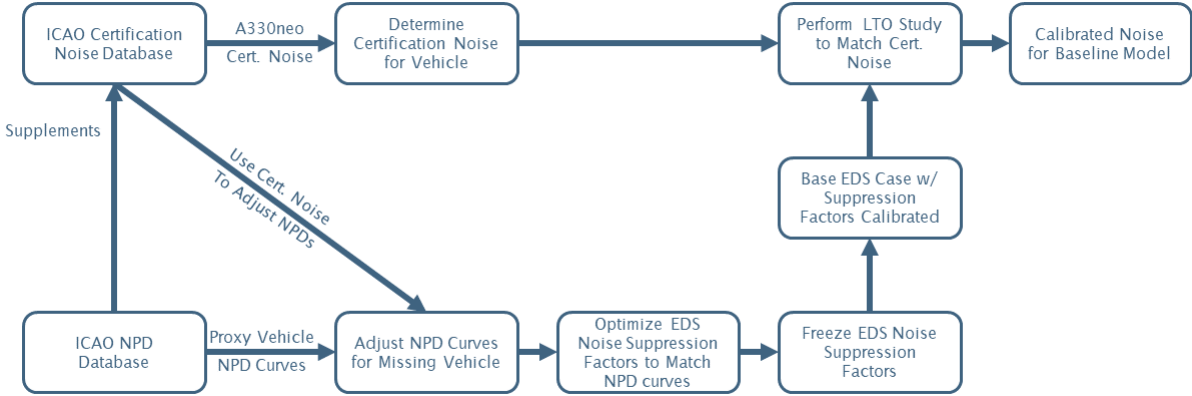


Figure 8. Calibration of the noise model. ICAO: International Civil Aviation Organization; LTO: landing and takeoff; NPD: noise–power–distance; EDS: Environmental Design Space.

Design of experiments generation

With the baseline model calibrated to match publicly available data for the A330-941N, the baseline can be adjusted to simulate technology infusion. One possible method for analyzing how current vehicles could meet future dual-stringency limits would be to predict which specific technologies might be applied by industry to their designs and then to model the impacts of those technologies on performance. However, this process would require proprietary information from the company designing and manufacturing the aircraft and engine. Clearly, this approach is not feasible for the scope of this study.

Instead, the baseline is varied by applying *k*-factors that represent technology buckets, wherein a vehicle can make technology improvements in a certain aspect, such as the wing drag coefficient, without specifying what specific technology is used to achieve the improvement. In this fashion, the technology response is measured for various *k*-factors in mission parameters, and a wider design space is available.

Using these technology buckets provides a parametric approach for capturing stringency responses; however, this method results in a very large design space that can become computationally expensive to explore. An appropriate design of experiments enables efficient exploration of the technology space with maximum knowledge gained. Specifically, the baseline case is taken along with edge cases at the extremes of the *k*-factor ranges. The design of experiments is then filled in with uniformly random points. The key metrics, which are measured outputs of the technology space exploration, are listed in Table 12.

Table 12. Key metrics for technology space exploration. CAEP: Committee on Aviation Environmental Protection; MTOW: maximum takeoff weight.

Key metrics	
Wingspan	Cutback noise
Approach noise	Sideline noise
Cumulative noise	dPfooNOx
CO ₂ metric	MTOW
Maximum T3	Fan diameter
Noise margin relative to CAEP Ch. 14	Fuel burn per available ton kilometer

Results

Because the design of experiments is somewhat computationally expensive, surrogate models are created that relate the varied parameters to the key metric outputs. Of the key metrics, the two metrics of greatest interest are the cumulative noise and CO₂ metric, which are related to the dual stringency. This approach of creating surrogate models enables further study and additional insight for the future without the need for another design of experiments. These surrogates are neural network algorithms consisting of either a single hidden layer neural network or a dual hidden layer network. The structure of the neural networks is driven by the complexity of correctly matching the surrogate results to the actual data.

The surrogate generation process is followed by Pareto optimization, performed for several timeframes of interest with increasing technology impacts over further timeframes. The 2030 timeframe is discussed further. Pareto optimization is an algorithm that considers two or more metrics, defines a “best in class” for each metric, and then performs tradeoffs on the priority of each metric to draw a curved line between best-in-class points. The two metrics of interest to perform tradeoffs against are cumulative noise and the CO₂ metric value. The metric for nitrogen oxide emissions is the mass in grams (Dp) of nitrogen oxide pollutants emitted during the reference LTO cycle, divided by the rated output (Foo) of the engine (dPfooNOx) . Although dPfooNOx is not included in the optimization, the metric is calculated to assess changes in nitrogen oxide emissions as a result of noise and CO₂ tradeoffs.

The notional A330-941N model is currently undergoing a new round of calibration and optimization due to a change in weight variant. The previous report showed preliminary results for WV901, and Airbus has certified a higher MTOW since the submission of the previous report, thus prompting a recalibration to WV921 represented by the updated payload-range diagram in the July 2023 Airport Planning Manual. Although the calibration of the model has changed, the optimization remains the same. The varied parameters that are not fixed to a technology level are design variables including the fan pressure ratio, overall pressure ratio at aerodynamic design point, aspect ratio, thrust-to-weight ratio, and wing loading. These design variables are varied and optimized. At a high level, the optimization method is as follows. Several million points are generated via random sampling within the ranges of the design space. Key points along the Pareto front with different importance weightings assigned to the dual-stringency metrics are found through a particle swarming optimization approach. The full Pareto front between these key points is generated by a genetic algorithm process.

Previous preliminary results indicated a total difference in cumulative noise of 0.8 EPNdB along the Pareto front, thus warranting further examination and improvement of the Pareto optimization process. Improvements to the optimization are ongoing and should show improvement in the design space tradeoff for dual stringency. These improvements include the implementation of a dPfooNOx model to assess how noise and CO₂ metric trades influence nitrogen oxide emissions. These improvements are applied to the other vehicle classes, including business jets, regional jets, and narrow-body/single-aisle jets.

CAEP working group and industry collaboration

The research team participated in numerous CAEP working groups including the WG1 (noise), WG3 (emissions), and Modeling and Database Group (MDG) and Forecasting and Economics Support Group (FESG) working groups. Working with the broader U.S. Research Team, the Georgia Tech team developed a method to address the dual-stringency analysis sample problem, including assessments of current noise margins of the in-production fleet, development of technology response methods, contributions to the growth and replacement database, and development of an initial NRC function.

Milestones

- Develop an initial version of the NRC function for use in the sample problem.
- Develop notional technology responses across seat classes for use in the sample problem
- Contribute to the CAEP technical working groups

Major Accomplishments

NRC function

- Reviewed and reported previous CAEP work on NRC modeling
- Developed an approach to include both CO₂ and noise MV improvements in the NRC function

Technology response for the sample problem

- Developed technology responses available across four vehicle classes

CAEP working group and industry collaboration

- Contributed to the work plan of each of the CAEP working groups

Publications

None.

Outreach Efforts

Outreach efforts included bi-annual ASCENT meetings, various CAEP working group meetings and calls, and weekly U.S. Research Team meetings.

Awards

None.

Student Involvement

Melek Ozcan, Antoine Marin, Zelin Hu, David Mothershed, Gabriel Fronk, Andy Tan, Niharika Akula, Jayaprakash Kambhampaty, and Kumanan Srinivasan (graduate research assistants, Georgia Tech) participated in the efforts in Task 1.

Plans for Next Period

PATR function

- Engage more stakeholders in our search for data
- Continue collaboration with the PATR ad hoc group to improve the PATR model
- Incorporate feedback and data received, and finalize the approach for the main analysis

CAEP working group and industry collaboration

- Continue to support the broad technical needs of the United States Research Team and CAEP working groups

References

Airbus. (2023). *A330 Aircraft Characteristics – Airport and Maintenance Planning*. AIRBUS S.A.S.

European Union Aviation Safety Agency. (2022). *EASA Certification Noise Levels*.

<https://www.easa.europa.eu/en/domains/environment/easa-certification-noise-levels>

Eurocontrol Experimental Center. (2020). *Aircraft Noise and Performance (ANP) Database: An international data resource for aircraft noise modellers*. <https://www.aircraftnoisemodel.org>

International Civil Aviation Organization. (2018). *Recommended Method for Computing Noise Contours Around Airports* (Report No. 9911). ICAO.



Project 082B Integrated Noise and CO₂ Standard Setting Analysis

Massachusetts Institute of Technology

Project Lead Investigator

Raymond Speth
Principal Research Scientist
Department of Aeronautics & Astronautics
Massachusetts Institute of Technology
77 Massachusetts Ave, Building 33-316
Cambridge, MA 02139
617-253-1516
speth@mit.edu

University Participants

Massachusetts Institute of Technology (MIT)

- P.I.: Dr. Raymond Speth
- FAA Award Number: 13-C-AJFE-MIT, Amendment Nos. 095, 102, and 115 (no-cost extension to September 30, 2024)
- Period of Performance: June 14, 2022 to September 30, 2024 (with the exception of funding and cost-sharing information, this report covers the period from October 1, 2022 to September 30, 2023)
- Tasks:
 1. Data anonymization and comparison of original equipment manufacturer (OEM) data with public data
 2. Development of an aircraft conceptual design tool for policy analysis

Project Funding Level

\$900,000 in FAA funding and \$900,000 in matching funds. Sources of matching are approximately \$94,000 from MIT, plus third-party in-kind contributions of \$274,000 from Savion Aerospace Corporation and \$532,000 from NuFuels, LLC.

Investigation Team

Dr. Raymond Speth (P.I.), advises student and postdoctoral researchers in the Laboratory for Aviation and the Environment (LAE), focused on reducing aviation's environmental impacts through fuels, propulsion technology, and policy. Dr. Speth also coordinates communication with FAA counterparts.

Prof. Steven Barrett (co-P.I.; director of LAE), coordinates internal research efforts and maintains communication among investigators in the various MIT research teams.

Dr. Jayant Sabnis co-advises student research in the LAE. His research expertise includes turbomachinery, propulsion systems, gas turbine engines, and propulsion system-airframe integration.

Jonas J. Gonzalez (PhD student in the LAE) focuses on assessing the impacts of new aircraft technologies on certification and community noise exposure.

Dr. Prakash Prashanth (postdoctoral associate in the LAE) focuses on the roles of new airframe and engine technologies in reducing climate and air quality impacts of aviation.



Project Overview

To evaluate the economic reasonableness of proposed aircraft environmental standards, the International Civil Aviation Organization's (ICAO) Committee on Aviation Environmental Protection (CAEP) requires tools for assessing the impacts of technologies and design changes intended to control aircraft noise and emissions, and for evaluating the costs of implementing such changes to aircraft and engine designs. Existing methods used to support decision-making in previous CAEP noise stringencies do not represent modern aircraft and propulsion designs and technologies. The goal of this project is to develop new tools that address the shortcomings of the previous methods, in support of CAEP/13 stringency analyses.

Task 1 – Data Anonymization and Comparison of OEM Data with Public Data

Massachusetts Institute of Technology

Objective

The requirement to protect sensitive OEM data in the current CAEP/13 cycle necessitates a new approach to the management of data in the CAEP standard-setting process. Any data presented to the full CAEP working groups (WGs) must be anonymized to satisfy these needs. In addition, comparing publicly available data against OEM-provided data helps inform CAEP regarding the quality of publicly available data.

Research Approach

We used a strategy combining data generalization and selective data suppression to ensure the confidentiality of aircraft performance information while allowing for meaningful analysis. Specifically, we used anonymization techniques to maintain the integrity of CO₂ metric values and certification noise levels, thus revealing these metrics only in relation to the CAEP/10 standard and the margin from current noise standards. The maximum takeoff mass (MTOM) is anonymized by aggregation, either on an MTOM basis or via aircraft class definitions. This approach allows CAEP members and WG technical experts to understand how different stringency options affect different types of aircraft (e.g., regional jets versus twin-aisle aircraft) without revealing sensitive data about individual aircraft.

Challenges encountered during the CAEP/13 cycle, such as issues related to data sharing, prompted a reevaluation of conventional data sources. Given the limitations faced, we used Piano, a commercially available software program developed by Lissys Ltd., which is known for its comprehensive analysis of aircraft performance. Piano, which is often referenced within the CAEP community in the absence of OEM data, because of restrictions, provided a valuable alternative. To ensure the reliability of our findings, we conducted a comparative analysis between the OEM and Piano CO₂ metric value datasets, treating the OEM data as the baseline. Importantly, the OEM metric values, although used as a reference, are not certified data, and the underlying assumptions in their determination remain unclear. The study, conducted within the CAEP/13 Data Processing ad hoc group, was finalized in July 2023, and concerns regarding data restrictions delayed its circulation until October 2023.

Milestones

- Data anonymization support was provided to CAEP WGs.
- Comparisons between Piano and OEM data were presented to members of the CAEP WGs.

Major Accomplishments

A proposed anonymization framework has been developed, along with tools for generating data visualizations that inform decision-making while preserving anonymity.

Publications

None.

Outreach Efforts

- Progress in method development was discussed with FAA project managers during regular teleconferences.
- The proposed anonymization method was presented to CAEP WG members to collect feedback.

- Comparisons between Piano and OEM data were presented in a CAEP WG meeting.

Awards

None.

Student Involvement

Graduate student Jonas Gonzalez conducted the analyses and presented this work to CAEP WGs.

Plans for Next Period

This task has been completed.

Task 2 – Development of an Aircraft Conceptual Design Tool for Policy Analysis

Massachusetts Institute of Technology

Objective

The goal of this task is to enhance the capability of our Julia-based aircraft conceptual design software, TASOPT.jl, to incorporate new disciplines and components, including noise analysis, cost analysis, and optimization. The objective is to use this tool to estimate the sensitivities of design changes to the engine, structures, and aerodynamics on the environmental performance, such as CO₂ and nitrogen oxides, in addition to the impact on certification noise.

Research Approach

Recent development of TASOPT.jl has focused on three specific areas: (a) code refactoring for performance and code documentation, (b) incorporating a computationally efficient thermodynamic calculations implemented in Julia, and (c) adding automatic differentiation capabilities to enable gradient-based optimization.

One computational bottleneck was the gas turbine calculations, particularly the calculations of the gas properties, such as specific heats, enthalpy, and entropy. This simplified engine model replaces the complex equilibrium calculations used by Numerical Propulsion System Simulation (NPSS) with an approximation based on complete combustion. We have leveraged the NASA-9 coefficient polynomial representation of chemical species to markedly decrease the computational time required to calculate these gas properties. This process will enable faster sizing and optimization of aircraft-propulsion systems.

Current efforts in development are aimed at enabling the use of faster optimization techniques. The current optimization algorithm adopted by TASOPT.jl is the gradient-free Nelder–Mead method. Such methods scale poorly for systems with many design variables. Furthermore, this method lacks any intrinsic handling of constraints, thus requiring the constraints to be implemented inexactly as penalties to the objective function. We are currently working toward leveraging automatic differentiation in tandem with analytical derivatives, where possible, to enable gradient-based optimization.

Milestone

Software documentation completed

Major Accomplishments

Fast gas calculations have been implemented as a standalone package available at <https://mit-lae.github.io/IdealGases.jl/dev/>

Publications

None.

Outreach Efforts

Progress in method development was communicated to FAA project managers during regular teleconferences.



Awards

None.

Student Involvement

Postdoctoral associate Prakash Prashanth was responsible for leading the code refactoring and documentation, with support from Jonas Gonzales. Prakash Prashanth was also responsible for implementing efficient gas calculations.

Plans for Next Period

- Apply algorithmic differentiation to the remainder of the model components
- Use TASOPT.jl to estimate the impacts of technology improvements on environmental performance (i.e., “technology responses”)
- Link TASOPT.jl to PyNA, our tool for modeling aircraft noise

Project 083 NO_x Cruise/Climb Metric System Development

Massachusetts Institute of Technology

Project Lead Investigator

Raymond Speth
Principal Research Scientist
Department of Aeronautics & Astronautics
Massachusetts Institute of Technology
77 Massachusetts Ave
Building 33-310
Cambridge, MA 02139
617-253-1516
speth@mit.edu

University Participants

Massachusetts Institute of Technology (MIT)

- P.I.: Dr. Raymond Speth
- FAA Award Number: 13-C-AJFE-MIT, Amendment Nos. 103 and 115 (no-cost extension to September 30, 2024)
- Period of Performance: September 19, 2022 to September 30, 2024 (reporting here with the exception of funding level and cost-sharing only for the period September 19, 2022 to September 30, 2023)
- Tasks:
 1. Evaluation of possible new metrics for nitrogen oxide (NO_x) emissions

Project Funding Level

\$250,000 FAA funding and \$250,000 matching funds. Sources of match are approximately \$250,000 from NuFuels, LLC.

Investigation Team

Dr. Raymond Speth (P.I.), Task 1
Prof. Steven Barrett (co-P.I.), Task 1
Adrien Guenard (graduate student), Task 1
Sarah Reider (graduate student), Task 1

Project Overview

The International Civil Aviation Organization (ICAO) is responsible for setting emissions standards for aircraft engines to limit the environmental impacts of these emissions. To limit the impacts of aviation emissions, FAA's Office of Environment and Energy is working with ICAO's Committee on Aviation Environmental Protection (CAEP) to establish updated emissions standards for aircraft engines by using metrics relevant to the full-flight emissions of these species, rather than only those emissions occurring during a standard landing and takeoff (LTO) cycle. Emissions standards set by ICAO will influence the development of future engine technologies, thus resulting in a reduction of emissions from future aircraft engines, and consequently improved human health and reduced environmental impacts. To this end, the FAA needs to understand and quantify how current and future standards may impact aviation emissions in the United States and worldwide, and how changes in these emissions may affect the environment and human health.

The objective of this project is to provide support for FAA decision-making related to potential certification standards that control emissions during cruise and climb, in addition to the current standards for LTO. The project includes analyses important for understanding the costs and benefits of both current standards and policies that may be proposed in the future. By providing a rational, scientific basis for decisions regarding the implementation of emissions standards, this project contributes to an efficient implementation process and provides industry with regulatory certainty. The analyses

provided in this project will allow the FAA to identify policy proposals that serve the national interest and advocate for those policies within ICAO.

Task 1 – Evaluation of Possible New Metrics for NO_x Emissions

Massachusetts Institute of Technology

Objective

The objective of this task was to evaluate eventual new ground metrics for emissions of NO_x that would be more representative of cruise emissions than the current metric, which is focused on LTO only.

Research Approach

A modeling framework was developed to assess the relevance of various metrics for regulating cruise emissions. One goal of this framework was to use publicly available data, shared databases, and standard methods to reduce modeling uncertainties and enhance interpretability. Relying on this model, the research approach consisted of quantitatively evaluating the correlations between new ground metrics for NO_x and cruise emissions.

Cruise emissions were computed with the Aviation Emission Inventory Code, AEIC (Simone et al., 2013). This model enables the estimation of NO_x emissions over full missions and for the full fleet. Aircraft performance is modeled by using the Base of Aircraft Data (BADA) database, which provides values of fuel flow for different altitudes and aircraft masses (EUROCONTROL Experimental Centre, 2010). NO_x emissions at cruise are then computed with Boeing Fuel Flow Method 2 (BFFM2) (DuBois & Paynter, 2006). Engine emissions at ground have been reported in the ICAO Emission Databank. Using the fuel flow at cruise provided by BADA, BFFM2 enables the estimation of the NO_x emission index for different cruise conditions. Finally, AEIC uses flight schedule data from the Official Airline Guide and an aircraft mission model to estimate the emissions of all flights in a calendar year.

From this estimation, each airframe/engine combination is associated with a full-cruise emission metric (FCEM), quantifying the NO_x emissions performance of that aircraft. The FCEM is derived through a cost-benefit approach. Here, the cost is taken as the total amount of NO_x emitted over the considered flights. The service provided by an aircraft is to take a certain mass (payload_{*i*}) over a certain distance (*d_i*); hence, the benefit is taken as the product (payload_{*i*} × *d_i*). A fixed payload corresponding to an 80% load factor was assumed for each aircraft type. The FCEM is thus defined as:

$$M_{\text{FCEM}} = \frac{\sum_i M_{\text{NO}_x,i}}{\sum_i \text{payload}_i \times d_i}$$

where the summation is over a representative set of flights (all 2019 flights in this study). For each flight *i*, the mass of NO_x, *M_{NO_x,i}* is computed over the “full cruise,” defined as all operations above 3,000 ft (including climb above 3,000 ft, cruise, and descent down to 3,000 ft).

The objective of this task is to derive new NO_x metrics that can be evaluated from sea-level-static NO_x measurements that will correlate with the FCEM. Correlation between two metrics *X* and *Y* is assessed quantitatively with the Pearson correlation coefficient *r*:

$$r = \frac{\text{cov}(X, Y)}{\sigma_X \sigma_Y}$$

where cov is the covariance, and *σ* is the standard deviation. Developing new NO_x metrics that are highly correlated with the FCEM will ensure that a standard setting process that uses these metrics will properly constrain emissions at cruise. This work is motivated by the inability of the current LTO metric to constrain emissions at cruise. This observation can be interpreted from Figure 1, obtained through the modeling approach presented above. Figure 1 presents the FCEM for 14 airframe/engine combinations against the LTO NO_x metric *Dp/F₀₀* of the associated engines.

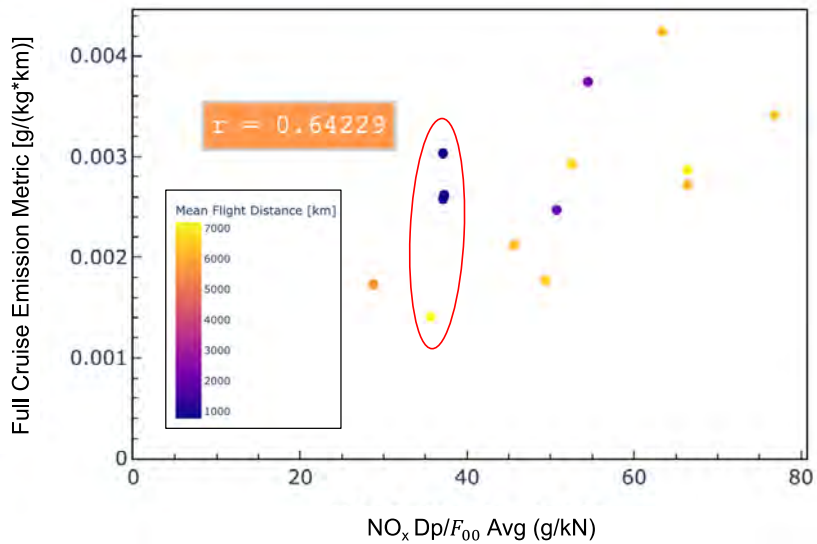


Figure 1. FCEM against the LTO Dp/F_{00} metric.

Points in the red circle show that engines with similar LTO Dp/F_{00} values, within a 5% range, can have cruise emissions varying by a factor of 2. This observation suggests that the existing LTO metric system does not provide a satisfactory representation of NO_x emissions at cruise. The Pearson correlation coefficient for the LTO Dp/F_{00} metric is 0.64229.

A set of metric candidates were derived to better correlate with cruise emissions. The formulation of these metrics is presented in the following table:



	Metric formulation	Type of metric
LTO Metric	$Dp/F00$ [g/kN]	Engine only
EI Metric	$M_1 = \sum EI_{GR_i} * w_i$ [g/kg]	Engine only
EI * Wf_{GR} Metric	$M_2 = \frac{\sum EI_{GR_i} * Wf_{GR_i} * w_i}{F_{00}}$ [g/s/kN]	Engine only
EI * $\frac{Wf_{GR}}{MTOM}$ Metric	$M_3 = \frac{(\sum EI_{GR_i} * w_i) * \overline{Wf_{CR}}}{MTOM}$ [g/s/kg]	Engine (mostly)
EI * Wf_{CR} Metric	$M_3 = \frac{(\sum EI_{GR_i} * w_i) * \overline{Wf_{CR}}}{MTOM}$ [g/s/kg]	Aircraft + Engine
EI * $CO2_{metric}$ (Approx)	$M_4 = \frac{(\sum EI_{GR_i} * w_i) * \overline{SAR}_{CO_2}^{-1}}{MTOM}$ [g/km/kg]	Aircraft + Engine
EI * $CO2_{metric}$ (PIANO)	$M_5 = (\sum EI_{GR_i} * w_i) * CO2_{MV}$ [g/km/kg]	Aircraft + Engine

where EI_i , Wf_{GR_i} , w_i , and TIM_i are the emission index (g/kg), the fuel flow (kg/s), the weighting factors (dimensionless), and time in mode (s) associated with the i^{th} LTO thrust setting, respectively. The subscript GR indicates “ground”; F_{00} is the sea-level-static maximum rated thrust (kN); MTOM is the maximum takeoff mass of the aircraft (kg); $\overline{Wf_{CR}}$ is the mean fuel flow evaluated at the three CO_2 metric points (kg/s); $\overline{SAR}_{CO_2}^{-1}$ is the inverse of the mean specific air range over the three CO_2 standard points (kg/km); and $CO2_{MV}$ is the CO_2 metric value (kg/km).

For each of the metrics, the weighting factors w_i are determined to maximize the Pearson correlation coefficient. The new NO_x metrics are divided into two categories: engine-only metrics and engine + aircraft metrics. Figure 2 presents the best engine-only and aircraft + engine metrics against the full-cruise emissions. The Pearson correlation coefficients of these two metrics are higher than those for the LTO metric, thus suggesting possible improvements compared to the current regulations.

For the current dataset, emission index values and fuel flows at ground were considered for only the four LTO points. The optimal correlation weights were assigned to only these four LTO points. Further analysis will be conducted to include more ground points in the metrics formulation. The addition of more ground points is expected to increase the absolute value of the Pearson coefficient for each of the metrics.

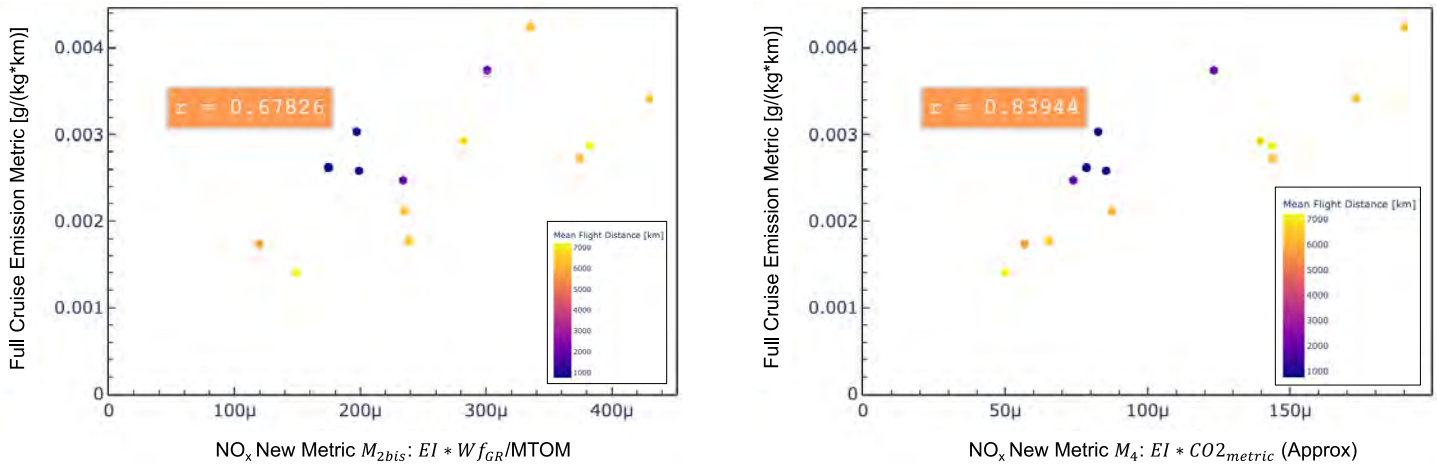


Figure 2. Best engine-only and aircraft + engine metrics against the FCEM.

Milestone

The complete analysis was presented as a working paper at the CAEP13-WG3/6-ECTG meeting.

Major Accomplishments

None.

Publications

None.

Outreach Efforts

- Presentation at CAEP/13-WG3/4-ECTG meeting (February 13-17, 2023)
- Presentation at CAEP/13-WG3/5-ECTG meeting (May 8-12, 2023)
- Presentation at the FAA Aviation Emissions Characterization Roadmap Meeting (May 23-25, 2023)
- Presentation at CAEP/13-WG3/6-ECTG meeting (November 6-10, 2023)

Awards

None.

Student Involvement

Graduate student Adrien Guenard conducted the analyses and presented the work to FAA and CAEP Working Group 3.

Plans for Next Period

For the next period, a framework enabling the evaluation of metrics derived from more than the four LTO points will be developed. Metrics to quantify environmental impacts of NO_x will be included in the study.

References

DuBois, D., & Paynter, G. C. (2006). "Fuel Flow Method2" for Estimating Aircraft Emissions. 2006-01-1987. <https://doi.org/10.4271/2006-01-1987>

EUROCONTROL Experimental Centre. (2010). User Manual for The Base of Aircraft Data (BADA) (EEC Note 2010-003). European Organisation for the Safety of Air Navigation (EUROCONTROL). <https://www.eurocontrol.int/publication/user-manual-base-aircraft-data-bada-revision-38>

Simone, N. W., Stettler, M. E. J., & Barrett, S. R. H. (2013). Rapid estimation of global civil aviation emissions with uncertainty quantification. *Transportation Research Part D: Transport and Environment*, 25, 33-41. <https://doi.org/10.1016/j.trd.2013.07.001>



Project 084 Noise Modeling of Advanced Air Mobility Flight Vehicles

Massachusetts Institute of Technology

Project Lead Investigators

R. John Hansman
T. Wilson Professor of Aeronautics & Astronautics
Department of Aeronautics & Astronautics
Massachusetts Institute of Technology
Room 33-303
77 Massachusetts Ave
Cambridge, MA 02139
617-253-2271
rjhans@mit.edu

Jacqueline Huynh
Assistant Professor of Mechanical and Aerospace Engineering
4212 Engineering Gateway
Irvine, CA 92697
949-824-3561
huynhlj@uci.edu

University Participants

Massachusetts Institute of Technology (MIT)

- P.I.: Prof. R. John Hansman
- FAA Award Number: 13-C-AJFE-MIT, Amendment Nos. 112 and 115 (no-cost extension to September 30, 2024)
- Period of Performance: October 1, 2022 to September 30, 2024
- Tasks:
 1. Identify target advanced air mobility (AAM) vehicle configurations for noise model development
 2. Identify noise modeling gaps for selected AAM configurations and operations
 3. Develop physics-based noise and flight profile model for representative AAM vehicles
 4. Incorporate noise results for representative AAM vehicles with Aviation Environmental Design Tool (AEDT)
 5. Expand methods to additional vehicle sets
 6. Evaluate implications for noise mitigation and low-noise operations for AAM vehicles

University of California Irvine (UCI)

- P.I.: Prof. Jacqueline Huynh
- Award Number: MIT Subaward Purchase Order No. 883753
- Period of Performance: October 1, 2022 to September 30, 2023 (no-cost extension to September 30, 2024 anticipated)
- Tasks:
 1. Identify target AAM vehicle configurations for noise model development
 2. Identify noise modeling gaps for selected AAM configurations and operations
 3. Develop physics-based noise and flight profile model for representative AAM vehicles
 4. Incorporate noise results for representative AAM vehicles with AEDT
 5. Expand methods to additional vehicle sets
 6. Evaluate implications for noise mitigation and low-noise operations for AAM vehicles

Project Funding Level

\$315,000 FAA funding and \$315,000 matching funds. Sources of match are approximately \$57,000 from MIT, \$36,000 from subrecipient UCI, and \$222,000 from Electra.aero, Inc.

Investigation Team

Massachusetts Institute of Technology

Prof. R. John Hansman (P.I.), Tasks 1–6
Juju Wang (graduate student), Tasks 1–6

University of California Irvine

Prof. Jacqueline Huynh (P.I.), Tasks 1–6
Victoria Pellerito (graduate student), Tasks 1–6
Nathan Yeung (graduate student), Tasks 1–6
Jessica De la Cruz (graduate student), Tasks 1–3
Melissa Lepe (graduate student), Tasks 1–6

Project Overview

This project develops first-principles noise models of urban air mobility (UAM) and AAM vehicle configurations to make community noise predictions of these aircraft flying at various operating states. Estimated noise levels from these models will be used to develop methods needed for a UAM/AAM-compatible AEDT to make preliminary noise estimates of these vehicles. Conventional aircraft configuration noise levels at both the source and procedural levels have been examined extensively in projects such as ASCENT 11, 23, and 44. This project aims to expand upon this work for UAM/AAM. Various vehicle configurations are currently under consideration for feasibility for use in UAM and AAM operations, including short takeoff and landing (STOL) configurations, tilt-rotor vertical takeoff and landing (VTOL), and lift-plus-cruise VTOL configurations, each of which has unique sources and operating modes. Thus, targets of opportunity are identified to estimate the noise levels and develop AEDT compatibility for these vehicles and operating modes. The work will be expanded to generalized AAM operations, and the models developed will be used to make preliminary noise footprint estimates for a variety of configurations. The goals of the project are thus to:

- Develop methods to model the noise levels at the source and due to different operations of UAM and AAM vehicle configurations
- Develop methods needed for a UAM/AAM-compatible AEDT, to make preliminary noise estimates of AAM vehicles

Task 1 – Identify Target AAM Vehicle Configurations for Noise Model Development

Massachusetts Institute of Technology and University of California, Irvine

Objectives

The goals of this task are to determine target AAM vehicle configurations for development of the noise model. Various AAM configurations are under consideration in industry, such as STOL, as well as VTOL vehicles including tilt-rotor VTOLs. Various AAM vehicles across industry will be examined to determine which will be the most relevant for developing the noise modeling method. From this examination, one or more representative vehicles will be chosen as a focus in the initial noise modeling effort.

Research Approach

- Research candidate AAM configurations currently being proposed by the top industry contenders, such as Joby, Wisk, and Electra
- Gather specifications and representative flight profile definitions for selected representative vehicle configurations needed for noise model development

Milestones

- Three vehicle configurations for noise model development were selected.



- Geometry and performance specifications for vehicle configurations for noise model development were determined.

Major Accomplishments

The research team identified three AAM vehicle configurations for the initial noise modeling development. The vehicles examined include a blown-flap STOL vehicle, tilt-rotor VTOL vehicle, and lift-plus-cruise VTOL vehicle (Figure 1).

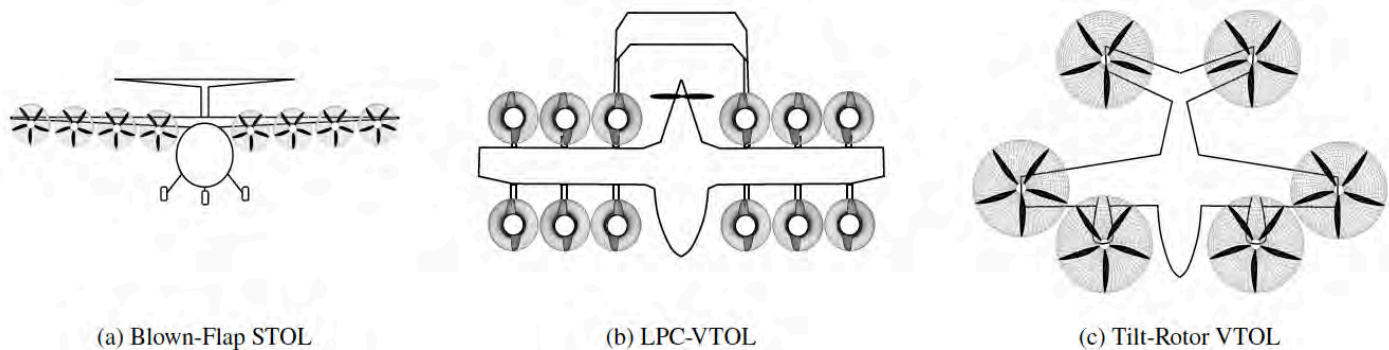


Figure 1. Selected AAM vehicle configurations for noise model development

For the purposes of modeling representative operations and noise models, an aircraft performance model that sizes and determines the off-design performance conditions of rotors for these vehicles was developed by using the XROTOR blade element momentum model. Given design conditions such as the weight and required thrust of the representative vehicles, we sized sample propellers for each of the vehicles to determine representative noise levels.

Publications

None

Outreach Efforts

- Presentations at biannual ASCENT Advisory Board meetings
- Presentation of the project to engineers at Wisk
- Collaboration with Electra.aero to share noise data for a blown-flap STOL aircraft
- Weekly teleconferences and meetings with FAA Technical Monitor

Awards

None.

Student Involvement

Graduate students have been involved in all aspects of this research, in terms of analysis, documentation, and presentation. These students conducted the research in selecting vehicles, and defining the representative vehicles used for Tasks 2 and 3 of the research goals.

Plans for Next Period

The primary objective for this task was met with the selection and development of specifications for representative vehicles to use for initial noise model development. However, as the project continues, opportunities to consider other vehicle configurations and flight procedures that will enrich the noise model development efforts will be considered, particularly via additional industry collaboration.



Task 2 – Identify Noise Modeling Gaps for Selected AAM Configurations and Operations

Massachusetts Institute of Technology and University of California, Irvine

Objectives

The goals of this task are to identify noise modeling gaps for selected AAM configurations and operations. According to the target AAM vehicle configuration to focus the noise model in effort on in Task 1, in Task 2, current gaps in noise modeling that must be addressed to formulate the noise modeling method for AAM vehicles will be identified. The noise modeling literature will be consulted, and the effort will leverage collaboration with NASA UAM and AAM work as appropriate. Noise sources most likely to dominate for different configurations and operations will also be identified. The task will focus primarily on the target vehicles identified Task 1, while considering additional gaps for other vehicle configurations on an ongoing basis.

Research Approach

- Examine the configurations and potential operating procedures of the AAM vehicles determined in Task 1 via performance modeling and consultation with industry
- Research potential noise sources from the AAM vehicles, and determine modeling approaches of the current state-of-the-art noise models

Milestones

- Examined potential noise modeling operations for each of the three vehicle configurations from Task 1.
- Identified gaps in noise modeling, according to the three vehicle configurations from Task 1.

Major Accomplishments

The AAM vehicles examined in Task 1 feature unique sources of noise stemming from different numbers of rotors and their placements, which interact with one another and with the airframe. The tilt-VTOL vehicle's noise directivity changes with the tilt of the rotor; the lift-plus-cruise vehicle has varied rotor sizes; and the blown-flap STOL vehicle features noise levels arising from blown lift. The operating procedures for each of these vehicles also varies and must be considered in the noise modeling. For example, the tilt-VTOL vehicle and lift-plus-cruise vehicle can operate in both vertical and forward flight conditions, and must feature transition modes. In addition, the blown-flap STOL vehicle has different flight path angles depending on the flap setting and amount of blowing, thus making the flight profile and produced noise levels a coupled system.

Publications

None.

Outreach Efforts

- Presentations at the biannual ASCENT Advisory Board meetings
- Communication with engineers at Wisk to understand lift-plus-cruise flight profile design
- Collaboration with Electra.aero to understand blown-flap STOL aircraft flight profiles
- Weekly teleconferences and meetings with FAA Technical Monitor

Awards

None.

Student Involvement

Graduate students have been involved in all aspects of this research, in terms of analysis, documentation, and presentation. These students conducted the research in determining noise modeling gaps for Task 3 of the research goals.

Plans for Next Period

As the project continues, we will continue seeking industry collaboration opportunities to share concepts for AAM vehicle flight operations. As we examine additional vehicles of interest for the project, gaps in noise modeling and operation design will continue to be documented.

Task 3 – Develop Physics-Based Noise and Flight Profile Model for Representative AAM Vehicles

Massachusetts Institute of Technology and University of California, Irvine

Objectives

The goals of this task are to develop a physics-based noise and flight profile model for representative AAM vehicles. A first-principles modeling method for the flight profiles and noise of the target AAM vehicle configurations identified in Tasks 1 and 2 will be developed, with the ability to make community noise predictions for these aircraft flying at different operating states. Component-based noise models for the key sources identified in Tasks 1 and 2 will be developed primarily from the methods in the NASA Aircraft Noise Prediction Program (ANOPP2). As data become available, the noise source models will be validated. More complex sources, such as propulsion-airframe interaction noise, may be modeled with external computational fluid dynamics tools such as Charm, and the results will be incorporated into ANOPP2 as needed. In addition, a first-principles flight profile generator applicable to the target AAM vehicle configuration from Tasks 1 and 2 will be developed and incorporated into the noise model. Noise at a variety of velocities, flight path angles, and operating modes will be estimated to construct noise–operation mode–distance curves to adapt the data to AEDT. In this process, the operational drivers with the greatest impact on varying the vehicle noise levels will be identified, to determine which modes should be focused on when forming the curves. The potential to expand the noise modeling to other vehicle configurations will be considered on an ongoing basis.

Research Approach

- Develop a method to model the noise of flight operations of representative AAM vehicles
- Use methods to generate noise–operation mode–distance curves to adapt noise results on AEDT to determine operational drivers with the greatest impact

Milestones

- A preliminary AAM noise modeling method was developed.
- Preliminary modeling of flight profiles of the three vehicle types determined in Task 1 was conducted.

Major Accomplishments

A preliminary method to determine the performance characteristics of given AAM aircraft was developed (Figure 2). The blade element momentum theory propeller design program XROTOR is used to design AAM aircraft propellers that can operate in relevant flight conditions and minimize induced losses at the rotors by constraining a low Mach tip number, to decrease community noise levels with a feasible motor torque. Operating states, including propeller revolutions per minute, power, thrust, and aircraft drag characteristics, are predicted according to flight procedure conditions throughout feasible trajectories modeled according to the AAM aircraft flight dynamics. A preliminary flight trajectory generator was being developed to assess the envelope of feasible trajectories for the AAM aircraft being studied. For modeling the noise, methods from ANOPP2 are incorporated within the Source Noise Module to determine the noise levels over a hemisphere at significant transition segments of the flight procedure. Given the hemispherical source noise around the vehicle during each flight segment, the noise is propagated from the aircraft source to the ground at the desired observer locations, such as a population grid surrounding an airport, given assumed atmospheric conditions within the Observer Noise Impact Module. The preliminary noise sources that are modeled are the rotor self-tonal and broadband noise sources, as well as airframe noise sources. For the case of blown-flap STOL, an estimate of blown-flap noise was made by using the flap edge model in ANOPP, with the mean propeller wake velocity as the input velocity. As such, the presented framework enables the preliminary assessment of community noise levels for various AAM types and operations.

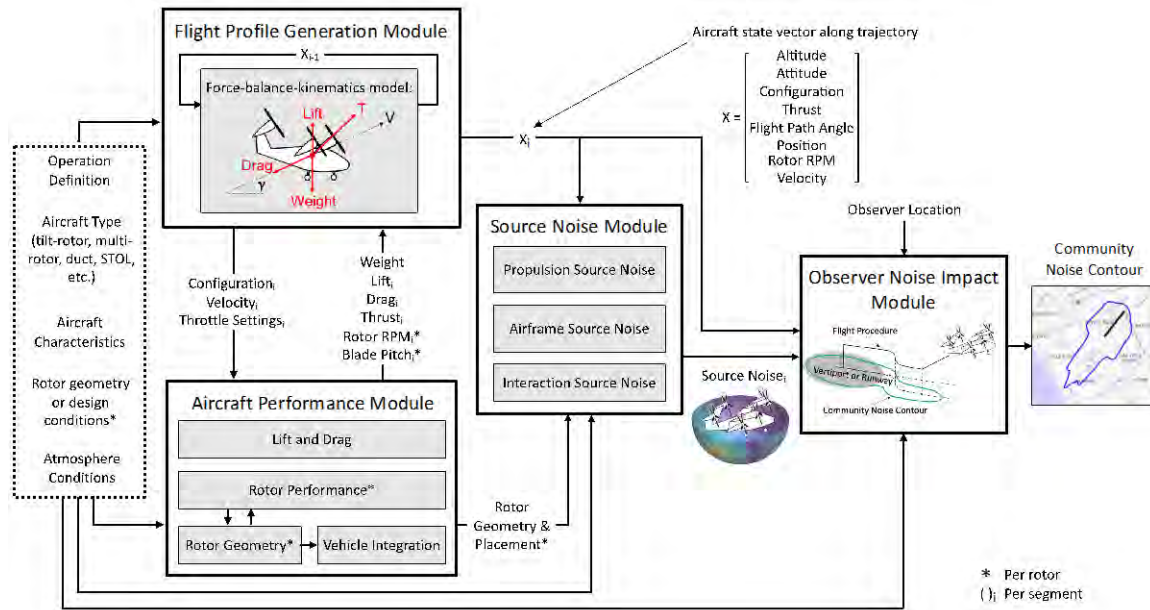


Figure 2. Preliminary AAM noise model.

Publications

Nathan Yeung, Jessica De la Cruz, Victoria Pellerito, Zhishen Wang, Melissa Lepe, Jacqueline Huynh, and R. J. Hansman. (2023). Flight Procedure and Community Noise Modeling of Advanced Air Mobility Flight Vehicles, AIAA Aviation 2023. doi.org/10.2514/6.2023-3361

Outreach Efforts

- Presentations at the biannual ASCENT Advisory Board meetings
- Presentation at the 2023 AIAA Aviation conference
- Weekly teleconferences and meetings with FAA Technical Monitor

Awards

None.

Student Involvement

Graduate students have been involved in all aspects of this research, in terms of analysis, documentation, and presentation. These students conducted the research formulating the overall framework.

Plans for Next Period

A more robust flight trajectory generator was being developed to assess the envelope of feasible trajectories for the AAM aircraft being studied. Future iterations of the framework and vehicle noise analysis will feature additional interaction noise sources, such as rotor-wake interaction noise, fuselage-wake interaction noise, and blade vortex interaction noise. In addition, future flight procedures could be assessed and tailored to minimize community noise exposure. Opportunities for noise validation via industry collaborations will also be conducted on an ongoing basis.

Task 4 – Incorporate Noise Results for Representative AAM Vehicles with AEDT

Massachusetts Institute of Technology and University of California, Irvine

Objectives

The goals of this task are to incorporate noise results for representative AAM vehicles in AEDT. On the basis of the results of Tasks 1, 2, and 3, an appropriate approach to model the representative vehicle in AEDT will be determined. The existing AEDT structure will be evaluated, and operating modes necessary for the representative vehicle configuration will be identified. The noise estimates from Task 3 as a function of flight procedure characteristics will be incorporated into AEDT. Preliminary modeling of AEDT-compatible vehicles and flight procedures will be performed as a test. In addition, the use of this technique to evaluate the noise impact of AAM of flight procedures will be examined.

Research Approach

- Evaluate existing AEDT structure to determine operating modes necessary for the representative AAM vehicle configurations
- Perform initial modeling of AEDT compatible vehicles and flight procedures

Milestones

To be determined for Year 2.

Major Accomplishments

To be determined for Year 2.

Publications

To be determined for Year 2.

Outreach Efforts

To be determined for Year 2.

Awards

None.

Student Involvement

To be determined for Year 2.

Plans for Next Period

On the basis of the flight profile and noise modeling development and validation efforts from Task 3, the current AEDT structure will be examined to determine its suitability for assessing AAM noise operations in its current state and identify gaps in the modeling approaches. We will consult with technical experts at the Volpe Center regarding the existing AEDT structure.

Task 5 – Expand Methods to Additional Vehicle Sets

Massachusetts Institute of Technology and University of California, Irvine

Objectives

The goals of this task will be to expand the methods developed in Tasks 3 and 4 to more complex vehicles featuring additional noise components not yet addressed the initial target vehicle configuration. In collaboration with FAA Technical Monitors, the noise model will be updated to incorporate these noise levels and demonstrate their utilization in AEDT, as was done in Task 4.

Research Approach

- Determine complex candidate vehicle sets via examination of current common vehicle configurations being proposed in industry
- Update noise modeling methods by using advanced analysis approaches or noise data

Milestones

To be determined for Year 2.

Major Accomplishments

To be determined for Year 2.

Publications

To be determined for Year 2.

Outreach Efforts

To be determined for Year 2.

Awards

None.

Student Involvement

To be determined for Year 2.

Plans for Next Period

Opportunities for gathering noise data that can be used for validation and the assessment of more complex noise sources beyond the initial modeling framework developed in Task 3 will be determined on an ongoing basis.

Task 6 – Evaluate Implications for Noise Mitigation and Low-Noise Operations for AAM Vehicles

Massachusetts Institute of Technology and University of California, Irvine

Objectives

The goals of this task will be to determine implications for noise mitigation and low-noise operations for AAM vehicles. The development of AEDT for the study of AAM vehicle noise is likely to yield implications for noise mitigation and low-noise operations of AAM vehicles. These implications, along with the AAM-compatible AEDT tool, will allow future research teams to continue to use AEDT to assess AAM vehicle noise. Implications for the development of low-noise procedures for AAM will also be evaluated. The results of the previous tasks have the potential to indicate need for additional noise model development and validation. Validation of the noise models or flight procedures as data become available will be the goals of future research efforts.

Research Approach

- Assess noise of candidate vehicles performing several advanced flight procedures
- Determine low-noise operations and flight procedure design for different candidate vehicles that can be assessed in AEDT

Milestones

To be determined for Year 3.

Major Accomplishments

To be determined for Year 3.



Publications

To be determined for Year 3.

Outreach Efforts

To be determined for Year 3.

Awards

None.

Student Involvement

To be determined for Year 3.

Plans for Next Period

After examination of the noise of the representative vehicles operating in multiple operating conditions, the flight procedures and noise operations resulting in the lowest noise levels will be documented.



Project 086 Study on the Use of Broadband Sounds to Mitigate Sleep Disruption Due to Aircraft Noise

University of Pennsylvania

Project Lead Investigator

Mathias Basner, MD, PhD, MSc
Professor of Psychiatry
Department of Psychiatry
University of Pennsylvania
1019 Blockley Hall, 423 Guardian Dr.
Philadelphia, PA 19104-6021
215-573-5866
basner@penmedicine.upenn.edu

University Participants

University of Pennsylvania

- P.I.: Prof. Mathias Basner
- FAA Award Number: 13-C-AJFE-UPENN, Amendment No. 015
- Period of Performance: October 1, 2022 to September 30, 2023
- Tasks:
 1. Institutional review board (IRB) approval
 2. Acquisition of polysomnography system and hearing assessment device, procedure development
 3. Acoustic setup of sleep laboratory

Project Funding Level

The Year 1 award (January 1, 2023 to December 31, 2023) of this 2-year project totals \$556,921. The cost-sharing requirement for this project is met by our international collaborators at the German Aerospace Center (DLR) and at St. George's University of London.

Investigation Team

University of Pennsylvania

Prof. Mathias Basner, MD, PhD, MSc (P.I.), All Tasks
Christopher Jones, PhD (co-investigator), Task 2
Matthew Kayser, MD, PhD (co-investigator), Task 1
Haochang Shou, PhD (statistician), Task 1
Quy Cao, MS (statistician), Task 1
Michel Carlin (other professional), Tasks 1 and 2
Adrian Ecker Other professional, All Tasks
Sierra Park-Chavar (other professional), Tasks 1 and 2
Victoria Schneller (research assistant), Task 2
Yoni Gilad (research assistant), Task 2
Sinead Walsh (research assistant), Task 2

Civil Aerospace Medical Institute (CAMI)

Hilary Uyhelji, PhD, PMP (co-investigator), Task 1

Project Overview

Sound insulation of bedrooms is expensive and is typically provided only to residents living near an airport. The goal of this project is to investigate the effects of different types of aviation noise (AN) on sleep under controlled laboratory conditions, and to determine whether some of the sleep-disturbing effects can be mitigated by introduction of pink noise (PN) into the bedroom or by wearing earplugs (EPs). The study will be performed in the Chronobiology Isolation Laboratory at the Hospital of the University of Pennsylvania. This newly constructed facility includes four acoustically isolated bedrooms and a high-fidelity sound system.

Objectives

(1) Investigate the following hypotheses on the whole-night level:

- a. AN disturbs sleep and reduces time spent in slow wave sleep + rapid eye movement sleep.
AN vs. control
- b. PN mitigates the negative effects of AN in a dose-dependent manner.
AN + 50-dBA PN (PN50) vs. AN + 40-dBA PN (PN40) vs. AN
- c. EPs mitigate the negative effects of AN.
AN + EPs vs. AN
- d. PN promotes sleep.
PN50 vs. control

(2) Investigate the following hypotheses on the event-related level:

- a. Various types of AN differ in their awakening potential.
- b. The masking effects of PN differ by AN type.
- c. PN masks meaningful sounds (e.g., fire alarm or baby crying).

Research Approach

Study design

The sleep of 24 participants will be monitored through polysomnography over seven consecutive nights in groups of four participants. After an adaptation night, participants will be exposed to the following conditions:

1. Control night without noise and without EPs (control)
2. AN only
3. PN50
4. AN + EPs
5. AN + PN40
6. AN + PN50

We will investigate participants in six groups of four participants each. Each participant in a given group will be exposed to the same condition in each study night. Each group will receive the six exposure conditions in a randomized and balanced fashion, according to the randomization table below. Of note, in this randomization paradigm, each exposure appears in each position exactly once and is preceded by each other exposure exactly once (letters A-F will be randomly assigned to exposure conditions 1-6 listed above):

Group	Night 1	Night 2	Night 3	Night 4	Night 5	Night 6	Night 7
1	Adaptation	A	B	C	D	E	F
2	Adaptation	B	D	A	F	C	E
3	Adaptation	C	A	E	B	F	D
4	Adaptation	D	F	B	E	A	C
5	Adaptation	E	C	F	A	D	B
6	Adaptation	F	E	D	C	B	A

Measurements during sleep

Participants' sleep will be measured polysomnographically with the Prodigy system, which includes electroencephalography with frontal electrodes only, electrooculography, and electromyography. Data will be transmitted wirelessly to a bedside tablet. The tablet will also record sound pressure levels to help synchronize the polysomnographic and acoustic data. Participants will also wear a Faros device that measures the electrocardiogram (1 kHz) and body movements (25 Hz).

Noise exposure

The AN night will consist of 93 noise events with maximum sound pressure levels $L_{AS, max}$ of 45, 55, or 65 dB, including noise from jet engine aircraft, helicopters, drones, low sonic booms, rail, and road traffic. The jet engine, and road and rail noise events will be identical to events used in a prior study at the DLR and another study on broadband sounds on sleep performed by collaborator Dr. Michal Smith in Sweden, thus enabling direct comparison with those studies. We will choose several events within each noise level category and repeatedly play those events back. Each aircraft noise event is played back three times at three different maximum sound pressure levels (45, 55, and 65 dBA) for a total of nine times. Because of the limited sample size, playing every event back only once would not provide sufficient data for averaging. We will also include an alarm sound and the sound of a baby crying, because a potential caveat of using EPs/PN is that meaningful sounds may be missed. The sequence and spacing of noise events will be identical within a study group but different across study groups. Noise scenarios will be pre-programmed and will start 15 min after the lights are turned off (PN playback will start immediately after lights out). The lights are planned to be turned off at 11 p.m. and turned on at 7 a.m. for an eight hour sleep opportunity.

Evening and morning procedures

Participants will arrive at the laboratory at approximately 7 p.m. and will be able to leave the laboratory at approximately 9 a.m. Because our noise exposures can affect sleep and impair recuperation to some degree, participants will be informed in the consent form that they should not operate heavy machinery during the study. We will also offer a taxi for participants who would otherwise use a car to travel to the Chronobiology Isolation Laboratory. We will provide snacks in the evening and a light breakfast in the morning. Participants will be able to shower in the morning (after all tests) if they wish.

In the evening (before bed) and in the morning (after waking up), the following will be conducted:

- (1) Blood draw (for untargeted messenger RNA analyses expected to be performed by the FAA CAMI; morning only)
- (2) Completion of a survey asking participants about the previous day (evening survey) or the previous night (morning survey)
- (3) Cognition test battery (10 cognitive tests)
- (4) Driving simulator task
- (5) Hearing test (up to 16 kHz)
- (6) Blood pressure and heart rate variability measurements

The four participants of a group will be rotated through the six tasks. Each participant will perform the different tasks always in the same order.

Participant recruitment

Participants will be screened on two occasions. The first screening will include blood draws with drug screening, electrocardiography, and a hearing test. Participants will receive a pulse oximeter, which they will return at the second screening. At the second screening, participants will be familiarized with the cognitive tests and the driving simulator. They will also receive an actigraph that they will wear in the week before the start of their study run. They will be asked to adhere to a sleep schedule of 11 p.m. to 7 a.m. to the extent possible in the week before participation. We plan to conduct a seventh backup study run if participants drop out during the first six study runs.

Study inclusion criteria:

- Age between 21 and 50 years
- Absence of psychological/psychiatric conditions precluding participation
- Body mass index < 35 kg/m²
- Self-reported regular sleep schedule; ability to maintain sleep schedule during the course of the study
- Self-reported sleep duration of 6–8.5 h per night (verified by six workdays of ambulatory sleep monitoring with wrist actigraphy and daily logs)



- Ability to read and write in English
- Full vaccination against, or recovery from, COVID-19

Study exclusion criteria:

- Hearing loss > 25 dB in any frequency band up to 8 kHz
- History of neurological, psychiatric, or other medical conditions precluding participation
- Current mania or psychosis
- Current depression, according to the Beck Depression Inventory (Beck, 1996)
- Excessive alcohol or drug use in the past year, on the basis of history and urine toxicology screening
- Excessive alcohol intake (≥ 21 drinks per week) or binge alcohol consumption (more than five drinks per day)
- Excessive caffeine consumption (> 650 mg/day from all caffeinated drinks regularly absorbed during the day)
- Current use of cigarettes/tobacco, or nicotine replacement therapy (those nicotine-free for 30 days will be included)
- Body mass index ≥ 35 kg/m²
- Acute, chronic, or debilitating medical conditions, major axis I psychiatric illness, according to history, physical examination, blood and urine chemistry, and complete blood count
- Self-reported history of recurrent seizures or epilepsy or a history of medical conditions that could increase the chance of seizure (e.g., stroke, aneurysm, brain surgery, or structural brain lesion)
- Cardiovascular, neurological, gastrointestinal, or musculoskeletal problems that preclude participation
- Major controlled or uncontrolled medical conditions, such as congestive heart failure, neuromuscular disease, renal failure, cancer, chronic obstructive pulmonary disease, respiratory failure or insufficiency, cardiac arrhythmia, or a need for oxygen therapy (as determined by self-report)
- Current night, swing, split, or rotating shift work
- Current use, or use of within the prior month, of a prescription or over-the-counter sleep medication or stimulant; use of psychoactive medication (based on self-report and review by a study clinician)
- Pregnancy or current breastfeeding
- Prior history or diagnosis of any sleep disorder including obstructive sleep apnea (Apnea-Hypopnea Index ≥ 15 events/hour) from ambulatory or in-laboratory polysomnography; restless legs syndrome or periodic limb movement disorder; insomnia; parasomnia; high risk of obstructive sleep apnea, according to the STOP-BANG Questionnaire (“yes” on at least four of eight questions); high risk of restless legs syndrome, according to the Cambridge-Hopkins Screening questionnaire; or high risk of insomnia, according to the Insomnia Severity Index (score of 22 or higher)
- Self-reported severe contact dermatitis, or allergy to silicone, nickel, or silver
- Planned travel across more than one time zone 1 month before and/or during the anticipated study period
- Intentional naps during the week
- Habitual use of broadband noise to facilitate sleep

Endpoints and power considerations

The primary outcome of the study is time spent in slow wave sleep plus rapid eye movement sleep during an 8-hour sleep opportunity (11 p.m. to 7 a.m.). We will investigate several other outcomes related to the entire night (e.g., sleep efficiency or wake after sleep onset); to outcomes before and after sleep (e.g., cognitive performance and driving); or to individual noise events (e.g., event-related analysis).

All power calculations were conducted in PASS (version 21 NCSS), by assuming a 5% type I error rate and using two-sided hypothesis tests. We used data collected in the AIRORA study (Study on the effects of Air, Road, and Rail traffic noise on sleep) performed at DLR to inform power calculations. With a proposed sample size of 24 participants, we expect to have at least 80% power to detect a medium effect size of 0.60 for the mitigation effect of PN on our primary outcome due to aviation noise.

Milestones

The following milestones were achieved during the past 12 months:

- IRB approval obtained
- Aviation noise events received from FAA



- Acoustic setup of sleep laboratory completed

Major Accomplishments

- All necessary approvals and registrations (IRB, clinicaltrials.gov registration, and certificate of confidentiality) were obtained. A Materials and Data Transfer Agreement with CAMI was initiated but was found not to be required.
- A test blood draw was performed on two staff members and sent to CAMI for quality control. The quality of the samples was found to be excellent.
- Equipment was acquired, and study standard operating procedures were established.
- Noise events for helicopters, drones, and low sonic booms were obtained from FAA.
- Vic Sparrow and his team from Pennsylvania State University visited the sleep laboratory and made recommendations regarding the acoustic setup. Susumu Shirayama and Chris Hobbs (both at FAA) were also present.
- The randomized but balanced condition and noise event sequence were established.
- The sleep laboratory was acoustically calibrated with a class 1 sound level meter.
- Participants were recruited for the first measurement campaign, which will be completed in November 2023.

Publications

None.

Outreach Efforts

None.

Awards

None.

Student Involvement

Six temporary undergraduate or post-baccalaureate student workers are supporting participant screening and data acquisition in the sleep laboratory.

Plans for Next Period

- Completion of measurement campaigns 1–6 and a backup run (if necessary)
- Data analysis
- Report generation

References

Riedy, S. M., Smith, M. G., Rocha, S., & Basner, M. (2021). Noise as a sleep aid: A systematic review. *Sleep Medicine Reviews*, 55, 101385.



Project 088 A Method for Rapidly Assessing Jet Fuel Compatibility with Non-metallic Materials

University of Dayton Research Institute

Project Lead Investigator

John Graham, PhD

Distinguished Research Engineer

Sealants and Elastomeric Materials Address, Nonstructural Materials Division

University of Dayton Research Institute

1700 S. Patterson Blvd. Dayton, OH 45459

937-229-2807

John.Graham@udri.udayton.edu

University Participants

University of Dayton Research Institute (UDRI)

- P.I.s: John Graham, Jennifer Dodaro, Gina Roesch, and Amber Hancock
- FAA Award Number: 13-C-AJFE-UD
- Period of Performance: February 2023 to September 2024
- Tasks:
 1. Material Selection and Acquisition
 2. Detailed Fuel Composition
 3. Volume Swell
 4. Analysis of Absorbed Fuels
 5. Statistical Analysis
 6. Multiple Regression Modelling
 7. Reporting

Project Funding Level

The FAA provided \$350,000 for Project 88. The funds from the FAA were matched by several cost-sharing partners including Global Bioenergies, The Boeing Company, GE Aviation, NRC Canada, Lanzatech, Neste, Shell, and IHI.

Investigation Team

Dr. John Graham, PhD (P.I.), main director of the project and performs all preliminary data analysis. John is also the lead on statistical analysis and modeling of the data

Barbara Miller (Head of the Sealants and Elastomers Group), overseeing all projects that move through the group working on Project 88

Jennifer Dodaro (Team Lead for the Sealants and Elastomers Group), lead coordinator of several tests performed in pre- and post-volume swell studies

Dr. Gina Roesch, PhD (associate research chemist, and transitioning to be head of Project 88 as John Graham moves to a consulting role), data analysis on volume swell and absorbed fuel analysis, as well as scheduling of materials and data acquisition overview

Amber Hancock (research chemist), helping acquire and analyze data

Mary Galaska (technician), acquiring analytical (volume swell, gas chromatography-mass spectrometry [GCMS], etc.) measurements

Wesley Waldron (technician), mechanical testing of materials



Project Overview

The goal of Project 88 is to create a prescreening method to assess whether a given sustainable aviation fuel (SAF) is a good candidate for the rigorous fuel certification process established in D4054. D4054, as an evaluation method, is time-consuming (turnaround times of months) and expensive, and requires large sample volumes. Because material cost and sample size pose substantial barriers to entry for original equipment manufacturers (OEMs) to submit candidates to D4054, Project 88 is developing a low-cost, small-sample-volume method to assess fuel interactions with a list of common non-metallic materials. The advantage of the approach proposed in Project 88 is that it is less expensive, has a faster turnaround time (weeks), and requires smaller sample volumes (<250 ml). To keep the requirements to a minimum, we chose volume swell in parallel with GCMS as the representative properties to evaluate how materials and fuels interact and exchange. Using the critical properties identified as the foundation, a statistical model will be generated to predict SAF compatibility with non-metallic materials.

Project 88 involves two crucial deliverables. The first is the creation of a reference dataset by using a population of Jet A fuels gathered from 12 sites across the continental United States to represent Jet A fuels currently in service. Using the reference dataset of Jet A fuels, Project 88 will study how a list of non-metallic materials interact with the current Jet A population, to provide information regarding the interaction between nonstructured material and fuels currently in service. The data points gathered for standard, non-metallic materials and the survey of Jet A fuels will be used to build a statistical model by using key class fractions as fitting parameters. At the end of Project 88, the volume swell, absorbed fuel analysis, and material exchange results will be used as a method to predict and evaluate whether the candidate SAFs are likely or unlikely to be compatible with fuels currently used throughout the aviation industry today.

The tasks, deliverables, and current progress for Project 88 are discussed in detail below.

Task 1 – Material Selection and Acquisition

Objective

The objective of Task 1 is to select the list of non-metallic materials to evaluate in the survey of Jet A fuels, request quotations, and purchase all necessary materials for the project.

Research Approach

The 12 fuels were selected from a stock of 93 fuels obtained from 10 geographically dispersed locations across the continental United States (CONUS). One fuel was selected from each of the 10 locations, and the fuels with the highest and lowest percentages of aromatic compounds were also selected, for a total of 12 sample Jet A fuels.

Milestones

A survey of Jet A fuels was acquired from the various locations across the CONUS, so that the population could be considered a statistical representation of fuels being flown at the time of the study. This suite of Jet A fuels includes a variety of compositions (low aromatic compounds, high aromatic compounds, etc.). Additionally, almost all materials of interest have been acquired. Several outliers must be ordered, but most have been received as of December 2023.

Major Accomplishments

The near completion of Task 1 helped the project start in a timely manner. Materials that were relatively easier to obtain were acquired, and preliminary analysis began while quotations for the materials that were more difficult to obtain were sent.

Publications

None.

Outreach Efforts

None.

Awards

None.

Student Involvement

None.

Plans for Next Period

The plan for the next period will be to complete Task 1 in quarter 1 of 2024.

Task 2 – Detailed Fuel Composition

Objective

The objective of Task 2 was to provide a detailed chemical analysis of current in-service fuels. To achieve this objective, we analyzed the Jet A fuels gathered from across the CONUS by using a variety of chemical methods, to reveal the distribution of fuel composition against which future candidate SAFs can be compared in the future.

Research Approach

The approach to evaluate the selection of the 12 Jet A fuels involved two-dimensional gas chromatography (GCxGC) analysis, with emphasis placed on a selected set of class fractions known to affect the volume swell of non-metallic materials. Table 1 shows the class fractions of interest for Project 88. Additionally, GCxGC analysis was provided for each of the fuels gathered.

Table 1. Fuel Composition by GCxGC.

Class	Class Fraction
Aromatics	Alkyl benzenes
	Diaromatics (Naphthalenes, Biphenyls, etc.)
	Cycloaromatics (Indans, Tetralins, etc.)
Paraffins	iso-Paraffins
	n-Paraffins
	Monocycloparaffins
	Dicycloparaffins
	Tricycloparaffins

In addition to the GCxGC class fraction concentration analysis, fuel analysis will include simulated distillation curves to capture the relative molecular weight distribution.

Milestone

Task 2 was completed during the past year.

Major Accomplishments

The completion of Task 2 enables rapid comparison between preliminary studies of the materials in the survey of reference fuels. As future data are collected, the goal would be to make the results with respect to the Jet A population interpretable in real time.

Publications

None.

Outreach Efforts

None.



Awards

None.

Student Involvement

None.

Plans for Next Period

Task 2 is complete. The GCxGC data will be used for the remainder of the project, to understand material compatibility with the reference fuels and, in the future, with candidate SAFs.

Task 3 – Volume Swell

Objective

Task 3 is the keystone task of Project 88, because it will provide the data for the representative physical property—volume swell of material—in each of the 12 fuels.

Research Approach

Experimental Approach

UDRI developed a new method to acquire the volume swell of materials in fuels using a technique called optical dilatometry. Figure 1 shows a schematic of an optical dilatometer on the left and an example system on the right.

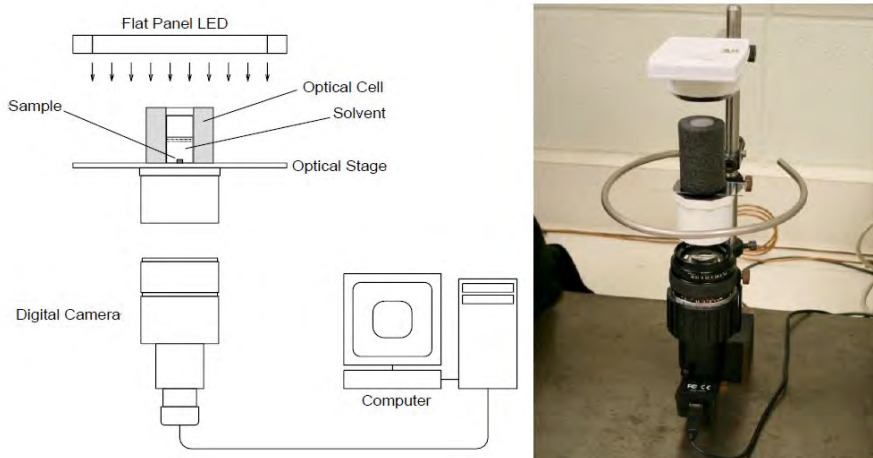


Figure 1. Schematic (left) and photograph (right) of an optical dilatometer.

In a typical experiment, two to four pieces of sample material are placed in a small transparent sample vial with 3–5 ml of test fuel. The vial is placed on an optical stage that is lit with a light-emitting-diode (LED) panel from above. The sample materials are photographed with a digital camera every 10 s for the first 3 min, and then every 10 min for the remainder of the experiment. To reach a near-equilibrium state, the test materials are imaged for 160 hrs (approximately 7 days). All volume swell experiments are performed at room temperature (approximately 75 °F).

Data Processing

When imaging is complete, the photographs are analyzed in ImageJ, a software program used to extract the cross-sectional area of each of the sample material pieces. This area is presumed to be proportional to the volume of each piece over the duration of the volume swell. The final volume swell is recorded as an average of ± 10 images surrounding the 160-hr mark. Figure 2 shows the volume swell of all O-rings, and Figure 3 shows the volume swell of a portion of the sealants



used in Project 88. To generate the plots shown in Figures 2 and 3, the cross-sectional area of each image is copied into data processing software and converted from area/image count to volume swell via a calculation that compares the change in signal intensity between the pixel signal at any given time relative to the intercept of a quadratic fit of the data over the first 3 min of exposure (images taken every 10 s, for a total of 18 images fit to a quadratic equation). The intercept is used, because it is taken as the signal intensity of the image at $t = 0$ (i.e., upon the first exposure of the material to fuel). Therefore, any change in signal intensity is equated to a change in material resulting from fuel absorption or the fuel extracting parts of the material.

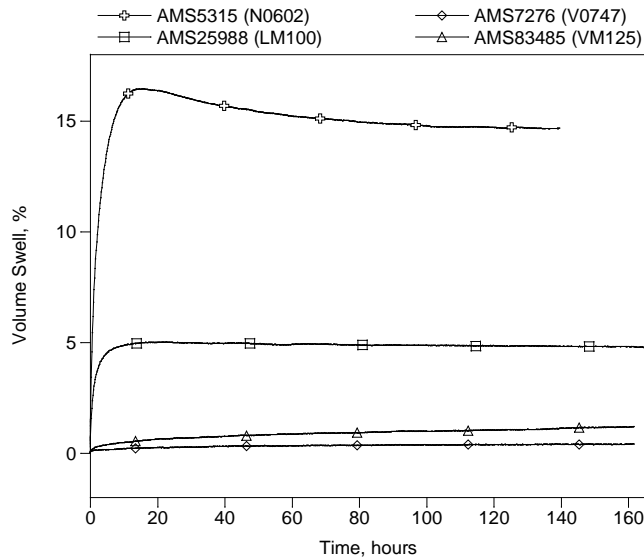


Figure 2. Volume swell of AMS5315, AMS7276, AMS25988, and AMS83485 O-rings over an aging period of 160 hr.

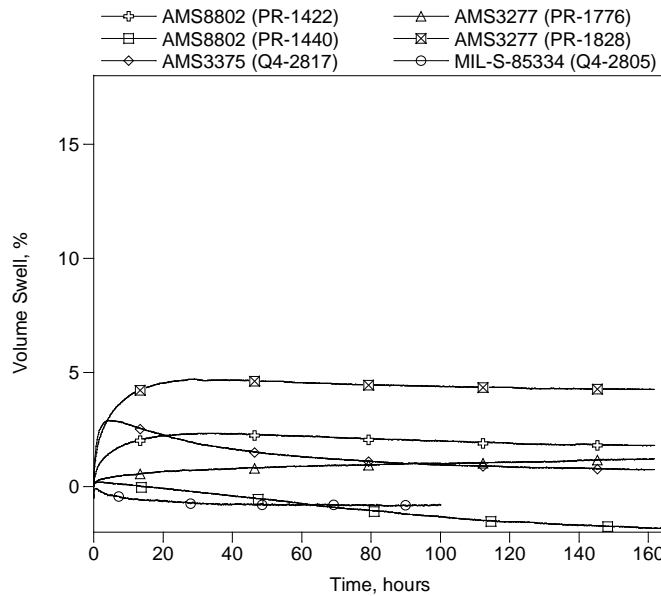


Figure 3. Volume swell of AMS8802, AMS3277, AMS8802, AMS3277 sample 2, AMS3375, and MIL-S-85334 sealants over an aging period of 160 hr.

Volume swell was graphed as a function of not only time but also the aromatic content of each Jet A fuel. Results for the O-rings and selected sealants are shown in Figure 4.

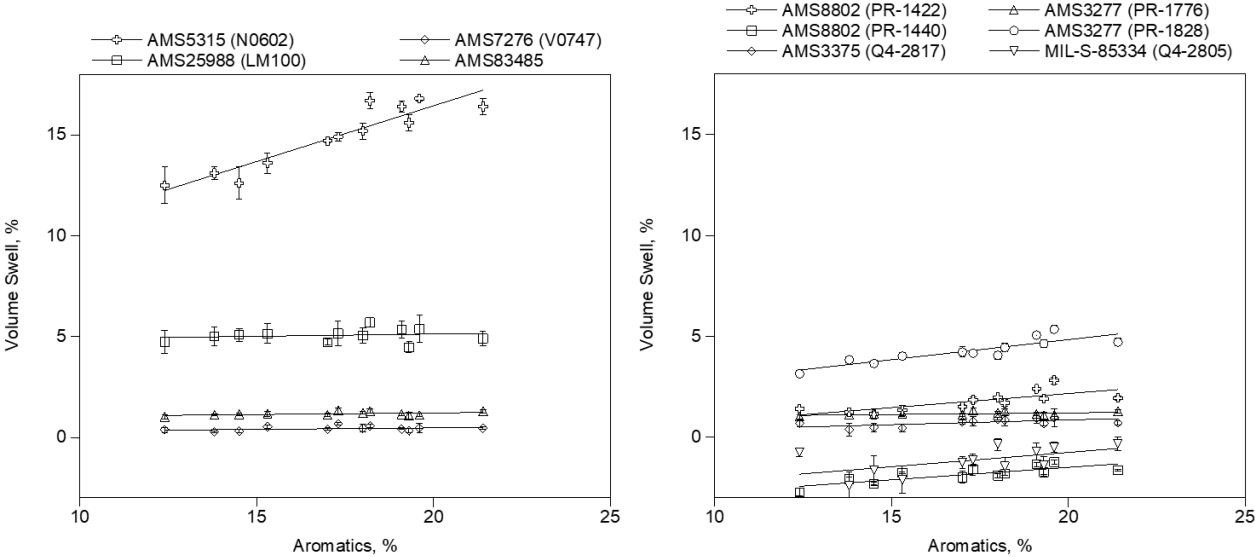


Figure 4. Volume swell as a function of the aromatic content of the selection of Jet A fuels for O-rings (left) and selected sealants (right).

Figure 4 shows a main deliverable for OEMs that will result from Project 88: the impact that the aromatic content of a candidate fuel has on a material in the non-metallic short list. Thus, if the aromatic content of the candidate SAF is known, the volume swell in the sample materials can be predicted using the fits produced in Task 3 of Project 88.

Milestones

Major milestones for Task 3 include completing the volume swell experiments via optical dilatometry for all O-rings (four), sealants (eight), two thirds of the bladders, three quarters of the coatings and one half of the adhesives (six). Beyond acquisition of these data, data analysis has been kept up to date.

Major Accomplishments

Major accomplishments in Task 3 include doubling the output rate of the volume swell experiments by running four samples instead of two samples per camera. This increase in sample throughput allowed UDRI to begin running tests for all 12 fuels with one sample from the shortlist in 1 week instead of requiring 2 weeks to run one material. The increased pace of Task 3 will make time for the in-depth data analysis outlined in Tasks 5 and 6.

Publications

None.

Outreach Efforts

None.

Awards

None.

Student Involvement

Project 88 has had no undergraduate or graduate student involvement, but a recent PhD graduate was trained on optical dilatometry imaging setups and was taught image processing/data analysis procedures over the past year using resources and results from Project 88.

Plans for Next Period

In the next period, volume swell will continue to be performed using four samples per camera on the remaining material samples, including adhesives, films, composites, and potting compounds.

Task 4 – Analysis of Absorbed Fuels

Objectives

Task 4 was established to complement the results of Task 3 and gain a fundamental understanding of how the materials and fuels interact and also exchange with one another over the soaking period used for volume swell. To study the interaction between materials and fuels, GCMS will be used. GCMS provides information on how or whether the material absorbs to a specific component of the fuel. The class fractions of interest are listed in Table 2 and were selected according to previous studies of material interactions with fuels, conducted by UDRI, and were also chosen to align with several of the class fractions presented in Task 2 of Project 88. Of note, in Table 2, the class fraction labeled “naphthalenes” encompassing all alkyl naphthalene species. Alkyl naphthalenes usually consist of methyl or ethyl groups (-CH₃ or -CH₂CH₃) across different carbons in the aromatic structure.

Table 2. Class fractions investigated with GCMS.

Class	Class Fraction	Representative Mass (m/z)
Aromatics	Alkyl benzenes	83
	Naphthalene	128
	Naphthalenes	141
Paraffins	Iso- and n-paraffins	57
	Cycloparaffins	105

Research Approach

Experimental Approach

GCMS is performed with an Agilent 7890A gas chromatograph equipped with an Agilent 5975C VL MSD with a triple-axis detector. The sample preparation for the material is as follows:

1. Remove aged samples from fuel, and pat dry three times with laboratory wipes to remove any fuel residing on the outside of the material (i.e., not absorbed by the material).
2. Place one piece of test material in a 1.5-ml GC vial with 1 ml methylene chloride (MeCl).
3. Repeat steps 1 and 2 with a second aged test material from the sample vial.
4. Place the samples sitting in solvent (MeCl) on the autosampler, and run under a standard method/temperature ramp.
5. After GCMS analysis is complete, decant the residual solvent, and dry the test material and vial in an oven for 30 min.
6. Remove and weigh the dried test material. Record the final weight of the sample for quantitative analysis.

Steps 1–4 should be repeated for the sample Jet A fuels (1 μL of fuel in 1 ml of MeCl) to quantitatively compare the material’s ability to extract from the fuel (and vice versa).



Data Analysis

Data analysis for Task 5 consists of exporting the integration of each peak present in the overall chromatogram (total ion chromatogram, TIC) and the extracted ion chromatograms, EICs, for the representative class fractions using Agilent ChemStation Analysis software and Agilent MassHunter. The total integrations from the Agilent software programs are exported to another software program, in which partition coefficients (K_{pf}) are calculated. The K_{pf} , the ratio of a component in the polymer relative to the fuel, is the metric used to summarize the interaction and chemical exchange between the non-metallic material and the surveyed Jet A fuels. Figure 5 provides a visual representation of the two-way exchange that occurs between the material extracting from the fuel and the fuel extracting from the material. The bottom panel of Figure 5 shows the test fuel (sample Jet A), and the top panel shows the absorbed fuel in a nitrile rubber O-ring (AMS5315). The ratio of the two spectra shows whether the material or the fuel dominates the exchange. As shown on the left side of Figure 5, K_{pf} values can fall into three regions. A $K_{pf} < 1$ indicates that the material is resistant to the class fraction of interest. A $K_{pf} > 1$ indicates that the material absorbs or extracts a substantial portion of the class fraction of interest. Finally, a K_{pf} of approximately 1 indicates relatively equal exchange in material and fuel. The K_{pf} values calculated for the materials can be used to predict the swelling of fuels with similar class fractions in the future.

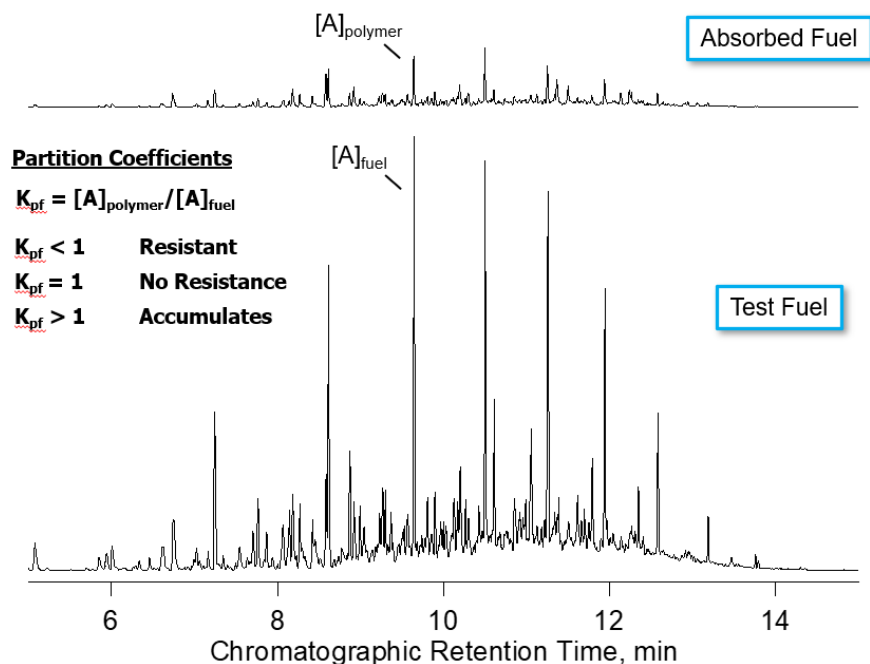


Figure 5. Absorbed fuel analysis, comparing a sample polymer (AMS5315) and a reference Jet A fuel.

Milestones

GCMS/class fraction data acquisition has been performed and is up to date with respect to volume swell analysis. Data analysis to calculate K_{pf} values follows volume swell analysis and is approximately up to date with respect to acquisition. Additionally, source fuels were calibrated numerous times to ensure that the fuel composition remains consistent and instrument drift is accounted for.

Major Accomplishments

Complementing the volume swell data, the K_{pf} values generated will provide molecular-level insight into the chemical interactions that occur over the duration of the aging process. Additionally, comparing the portion of each class fraction absorbed by the fuel relative to the GCMS class fraction of the fuel itself will lead to greater understanding of the solubility of the material in each of the candidate Jet A fuels. Finally, the partition coefficient, K_{pf} , generated from the ratio of the absorbed class fraction to the class fraction present in the fuel, will serve as another critical variable to evaluate SAFs as drop-in fuels with the current population of Jet A fuels.



Publications

None.

Outreach Efforts

None.

Awards

None.

Student Involvement

None.

Plans for Next Period

UDRI will continue to perform class fraction analysis after volume swell (Task 3) for the remaining materials, including coatings, adhesives, potting compounds, and composites.

Task 5 – Statistical Analysis

Objective

The primary objective of Task 5 is to enhance the volume swell results for the materials and extrapolate a statistical analysis/model to more generally describe a material's response to a larger suite of class fractions within the sample Jet A fuels. To achieve this objective, the volume swell data will be fit with a linear model against the aromatic content of the fuels, thus providing an area in which experimental data points of candidate SAFs can be plotted and referenced against. This fit will be the primary point of comparison used to evaluate the viability of future SAF candidates. The aromatic content of the fuel was chosen as the representative property to determine the relationship between a material and fuel, because it is present in most fuels and substantially contributes to the volume swell.

Research Approach

The model chosen to represent the relationship between aromatic compounds and volume swell is a linear relationship, which is easily generated by SAS statistical modeling software, which is equipped with a suite of methods used to correlate new test subjects (in the case of Project 88's future, materials aged in SAFs) to the reference dataset (materials aged in in-service Jet A fuels). The model produces three key variables: the slope of the line, the intercept, and the coefficient of determination. These variables provide three critical outcomes: the average response of the material to the aromatic content of the fuel, the estimated volume swell for a Jet A fuel with 0% aromatic compounds in the fuel, and the strength of correlation between the measured aromatic content of the fuel and volume swell. All these parameters contribute to the overall understanding of aromatic content of the fuel's effect on exposed material. Figure 6 shows an example of the model on sample material AMS5315, N0602.

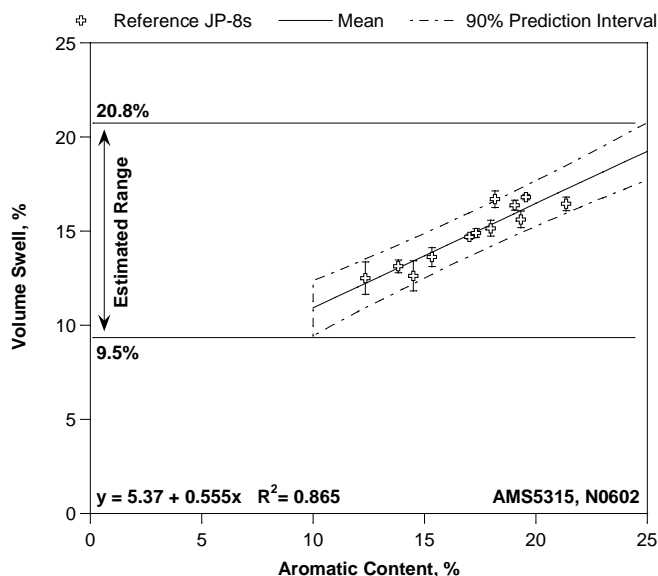


Figure 6. Sample model including the mean and 90% prediction interval of a set of reference JP-8s in AMS5315, N0602.

Additionally, as shown in Figure 6, SAS easily produces a 90% prediction interval of the Jet A fuels used in the reference dataset. The 90% prediction interval is distinct from a traditional confidence interval in that it is a quantification of individual fuels within a population and is not based on the mean values. This aspect is key to Project 88 because it equips our model with bounds that represent 90% of the individual fuels being flown at the time the samples were obtained. Essentially, this aspect allows us to base our model on fuels representing 90% of those in service at the time of Project 88. If new SAFs fall within the prediction interval of the Jet A fuels in this study, we can assume that they are likely to be compatible with the current population of Jet A fuels, which we know are safe to fly, because all reference fuels were taken from sources in-service. This process will provide OEMs with invaluable guidance regarding when a fuel is a good candidate to submit for D4054 testing.

Milestones

SAS licenses were obtained for two of three investigators, and a quotation is pending for the final investigator. Statistical analysis of all O-rings was completed, and modeling of the sealants is in progress.

Major Accomplishments

The end result of Task 5 will create the major deliverable for Project 88. First, it will summarize the results of Task 3. Second, it will provide a statistical model to serve as a reference for comparison with new candidate SAFs. In practice, the prescreening method will be performed on SAFs (volume swell and GCMS analysis); if the behavior of the SAF for the characteristic properties falls into the “normal range” for the survey of Jet A fuels used, it can be considered a good candidate for D4054.

Publications

None.

Outreach Efforts

None.

Awards

None.

Student Involvement

None.

Plans for Next Period

During the next period, statistical analysis of O-ring volume swell in Jet A fuels will be used as the test case to establish a protocol for analysis. As volume swell data are acquired for later samples (composites, adhesives, etc.), analysis for those materials' interactions with aromatic compounds will be completed.

Task 6 – Multiple Regression Modeling

Objective

The objective of Task 6 is to expand on the statistical model generated in Task 5 to incorporate additional class fractions including, but not limited to, paraffins and cycloaromatic compounds. In recent decades, the community has focused on aromatic content as the primary indicator of volume swell, but Task 2 of Project 88 demonstrates the presence, and in some cases the dominance, of other class fractions in Jet A fuels. Consequently, the final step of Project 88 will be to provide a broader statistical model that encompasses all class fractions identified in Task 2. This process will provide a more holistic picture of material and fuel interactions.

Research Approach

Task 6 will combine the results of Task 5 and Task 2 to create a more robust predictive model to determine SAF compatibility with current Jet A fuels. The model to be developed will relate the measured fuel composition and the measured volume swell via a multiple regression linear model. The model will be fit to Equation 1

$$\text{Volume Swell} = \sum_{i=1}^n k_i [A_i] \quad (1)$$

where k_i is the regression coefficient for a given component or class fraction, i is the class fraction, and $[A_i]$ is the concentration of the component or class fraction i . The regression coefficient is calculated using Equation 2

$$\text{Regression coefficient} = \frac{\text{Percentage volume swell of material in fuel}}{\text{Percentage concentration of class fraction in fuel}} \quad (2)$$

for all class fractions, n , that will be used in the model. In Project 88, the class fractions of interest are normal and iso-paraffins, cycloparaffins, alkyl benzenes, diaromatic compounds, and cycloaromatic compounds (Table 2). In addition to fitting the class fractions based on results from Tasks 2 and 5, the model will include a term to account for fuel density, because the survey of Jet A fuels used in this study have a variety of average molecular weights (heavy and low cuts of paraffins). This aspect will be an essential component enabling extension of the model to the candidate SAFs in the future that are also likely to have different weight distributions.

Milestones

None.

Major Accomplishments

The major contribution of Task 6 to Project 88 overall is expanding the toolkit for SAF and Jet A fuel compatibility with non-metallic materials beyond the relationship of aromatic content. The model built in Task 6 will incorporate the effects of selected class fractions on volume swell both in terms of concentration and molecular structure. In the long term, the model in Task 6 will help OEMs understand the broader picture of a fuel's impact on non-metallic materials. On a fuel-design level, the model will provide OEMs with numbers indicating which class fractions play the greatest role in material-fuel interactions, thus informing the design of future SAFs.

Publications

None.



Outreach Efforts

None.

Awards

None.

Student Involvement

None.

Plans for Next Period

The plan for the next reporting period is to begin multiple regression modeling for the O-ring materials as the test case, now that Task 5 has been completed for those materials. This work is expected to begin in January 2024.

Task 7 – Reporting

Objective

The objective of Task 7 is to document and report the results of Project 88 in both quarterly and annual reports. Additionally, at the end of Project 88, the results will be compiled into a final report and shared with the FAA.

Research Approach

None.

Milestones

None.

Major Accomplishments

Project 88 co-investigator Jennifer Dodaro and recent hire Gina Roesch, PhD, attended the Fall ASCENT meeting and provided a status update.

Publications

None.

Outreach Efforts

None.

Awards

None.

Student Involvement

None.

Plans for Next Period

The remaining parts of Task 7 involve successful execution of the remainder of Project 88 (Tasks 3–6) and generation of a final report. Additionally, participation in the biannual ASCENT meeting is a priority for all personnel involved in Project 88.



Project 089 Characterization of Compositional Effects on the Dielectric Constant

University of Dayton Research Institute

Project Lead Investigator

Steven Zabarnick
Division Head, Fuels and Combustion Division
University of Dayton Research Institute
300 College Park, Dayton, OH 45469
937-229-3961
Steven.Zabarnick@udri.udayton.edu

University Participants

University of Dayton Research Institute (UDRI)

- P.I.: Steven Zabarnick, PhD
- FAA Award Number: 13-C-AJFE-UD, Amendment 047
- Period of Performance: January 1, 2023 to December 31, 2023
- Task:
 1. Measurement of dielectric constant and density

Project Funding Level

\$499,999.67 in FAA funding.

Investigation Team

Steven Zabarnick (P.I.), project management and data analysis
Linda Shafer (researcher), fuel chemical analysis and composition
April Landsaw (technician), dielectric constant and density measurements
Shane Kosir (researcher), data analysis, plotting, and statistical analysis

Project Overview

Aircraft fuel tanks use capacitive gauges to determine fuel capacities during flight. Two crucial fuel properties, the dielectric constant and density, are used to calculate fuel capacity from the response determined from the concentric, cylindrical gauging sensors. In recent years, the airframe original equipment manufacturers (OEMs) have closely monitored the behavior of the dielectric constant (also referred to as relative permittivity) of candidate sustainable aviation fuels (SAFs), because even small changes in this property can result in large errors in fuel tank gauging. This project involves the measurement of the behavior of fuel dielectric constants over a range of temperatures and fuel blends, by using a new dielectric constant instrument. Both conventional petroleum-based jet fuels and synthetic aviation turbine fuels (SATFs) produced to ASTM D7566, reflecting a range of hydrocarbon compositions, will be included. A primary goal of this effort is to determine the typical range of dielectric values for conventional fuels, which will be compared with the SATFs to determine any observed differences and attempt to correlate any of these differences with specific hydrocarbon compositions. These measurements will help minimize errors in fuel tank gauging when aircraft are operated with synthetic aviation fuels and/or their blends.



Task 1 – Measurement of Dielectric Constant and Density

University of Dayton Research Institute

Objective

A primary objective of this effort is to determine the typical range of dielectric constant values for conventional fuels, which will be compared with the SATFs to determine any observed differences and attempt to correlate any of these differences to specific hydrocarbon compositions.

Research Approach

The approach of this program is to measure the behavior of fuel dielectric constants over a range of temperatures and fuel blends, by using a new dielectric constant instrument. Both conventional petroleum-based jet fuels and SATF produced to ASTM D7566, reflecting a range of hydrocarbon compositions, will be included. If differences are observed, we propose to determine the causes of these differences by measuring dielectric properties of various species mixtures and/or pure compounds. For example, we can determine the roles of various species classes, e.g., *n*-alkanes, iso-alkanes, aromatic compounds, and cycloparaffins in influencing dielectric property behavior. This work can be performed by using commercial solvents, e.g., Aromatic 150, and/or jet fuels with unique compositions that have already been characterized, e.g., Shell IH2 high-cycloparaffin fuel.

Historically, airframe OEMs have used a Clausius–Mossotti relationship, wherein $(K - 1)/D$ is plotted vs. $(K - 1)$, where K is the dielectric constant, and D is density, to characterize the relationship between K and D . Figure 1 shows this relationship for measurements from an ARINC 611-1 (1999) survey and high-cycloparaffin synthetic blend components (SBCs) and their blends with petroleum fuels. The fits shown for the petroleum fuels are close to the OEM-assumed slope and intercept values of approximately 0.3568 and 1.00, respectively. Airframe OEMs are concerned when the slope and intercept values differ from those assumed in their fuel quantity indicating systems (Moses, 2013; Parmenter, 2013).

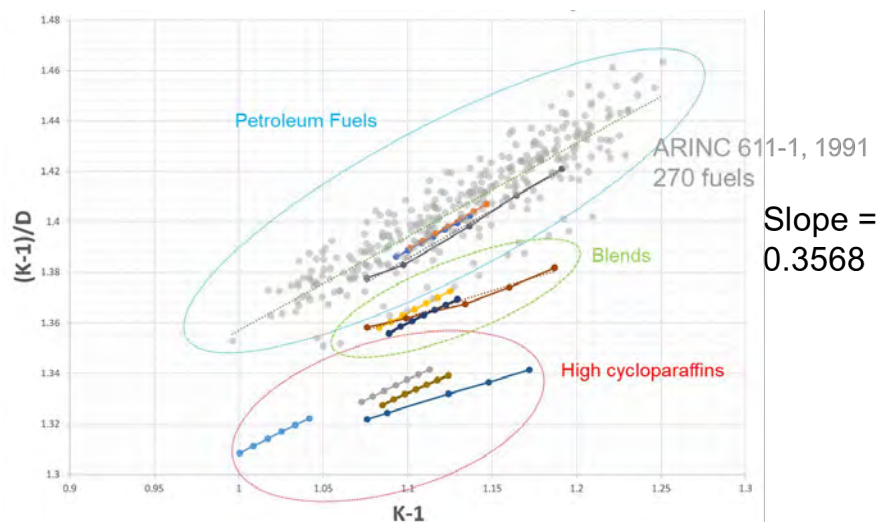


Figure 1. Clausius–Mossotti relationship plot for ARINC 611 fuels and high-cycloparaffin SBCs and their blends with petroleum fuels (plot provided by Griffin Valentich, Shell).

UDRI has purchased and commissioned the recently developed Stanhope-Seta instrument Jet DC 88500-0, which meets the requirements of specification IP PM FC/21 “Determination of Relative Permittivity (Dielectric Constant) of Aviation Turbine Fuel, Small Scale Automated Temperature Scanning Method.” The instrument allows for the rapid measurement of both the dielectric constant and density over a temperature range of 0–40 °C. Examples of fuels and their blends that will be evaluated include on-specification Jet A fuels (e.g., NJFCP A1/A2/A3 fuels); approved D7566 blendstocks and their blends with Jet A fuels; D7566 candidate fuels (e.g., Shell IH², Global Bioenergies, Revo, IIP, etc.); and JP-5 fuels.

UDRI is working with airframe OEMs, such as Airbus and Boeing, to determine how the measured results influence the ability to correctly determine aircraft fuel tank quantities. In addition, UDRI has participated in the Energy Institute Task Group SC-B-11 “Dielectric Constant Test Method Task Group,” which organized an interlaboratory study (ILS) of the new instrument and method. UDRI participated in the ILS effort.

Research results and discussion

The program began with a review of historical dielectric constant data for jet fuels. We were able to acquire the dielectric and density data from both the ARINC study (1999) and a CRC World Survey (2003). Figure 2 shows histograms of the Clausius–Mossotti slopes for the ARINC study, the CRC world survey, and the two datasets combined. Interestingly, the data show that petroleum fuels exhibit a very broad range of slopes from 0.30 to 0.45, with an approximately normal distribution. Each of the three datasets shows an average slope in the range 0.35–0.36, in agreement with the 0.3568 slope assumed by at least one airframe OEM in their fuel quantity indicating system (Moses, 2013; Parmenter, 2013). These historical data were acquired with a variety of methods, probably following ASTM D924.

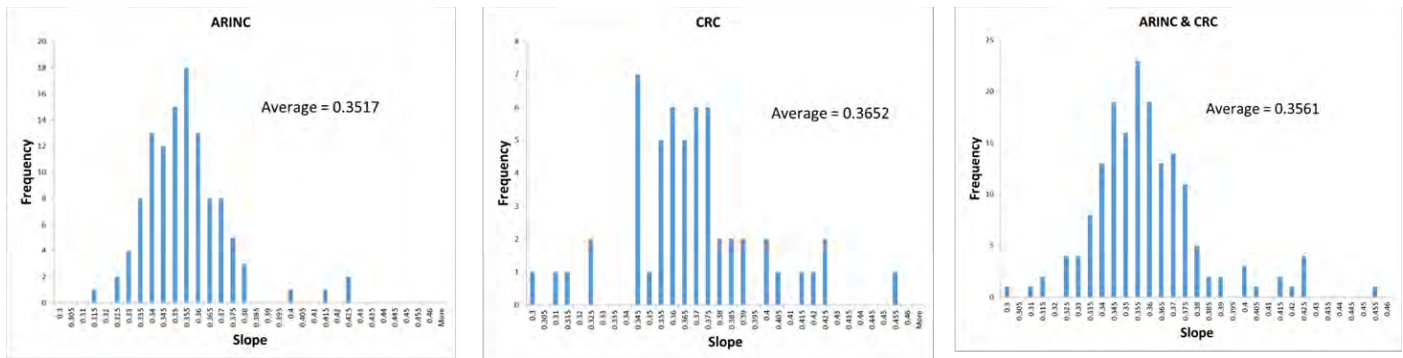


Figure 2. Histograms of the Clausius–Mossotti slopes for the ARINC data, the CRC data, and the combined set of fuels from both studies.

UDRI acquired a Jet DC instrument from Stanhope-Seta in July 2022 and participated in the Energy Institute Interlaboratory Study in November 2022. The ILS included a range of petroleum-based fuels, several D7566 SBCs, and an aviation gasoline, comprising a total of 15 different fuel samples. A summary of the Clausius–Mossotti slopes vs. density measured by the UDRI laboratory for the ILS is shown in Figure 3. The five petroleum-based jet fuels, Jet A, JP-5, Jet A-1, F-44, and JP-8, cluster close to the 0.3568 slope, which is shown as a horizontal line on the plot. Most of the D7566 SBCs exhibit lower slopes than the petroleum-based fuels. The outlier is the Virent synthesized aromatic kerosene (SAK) sample, which exhibited the highest density and Clausius–Mossotti slope. This candidate SBC is composed largely of aromatic species, which are known to have higher density than the paraffinic species comprising most species in the other D7566 SBCs. Two of the fuel samples, aviation gasoline and D7566 Annex A1 FT-SPK, were also measured after the addition of aromatic species. The plot shows that addition of aromatic species increases the density and the Clausius–Mossotti slope (note the arrows), in agreement with the observed slope and density of the Virent SAK sample.

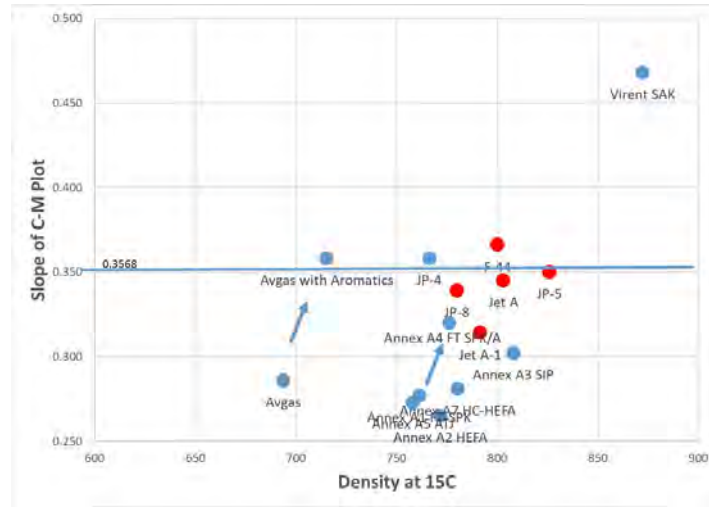


Figure 3. Clausius-Mossotti slopes for the ILS fuels.

Initial measurements for this program commenced with blends of three D7566 SBCs (Annex A5 alcohol-to-jet [ATJ], Annex A2 hydroprocessed esters and fatty acids (HEFA), and the candidate SBC Virent SAK blended with the A2 “average Jet A” from the National Jet Fuel Combustion Program). The Clausius-Mossotti plots for these blends at 0, 25, 50, 75, and 100% SBC by volume with Jet A are shown in Figures 4-6. The plots show that the smallest Clausius-Mossotti slope is for 100% SBC, and the largest slope is for the 0% SBC (i.e., 100% Jet A) for the two paraffinic SBC binary fuel combinations (i.e., ATJ and HEFA blended with Jet A). The Virent SAK blends display the opposite behavior, with the largest slope for 100% SBC (i.e., 100% Virent SAK). Figure 8 summarizes the slopes for the three blends at the various blend ratios. The figure shows that the ATJ and HEFA slope changes are nearly identical with a decreasing slope with increasing SBC volume percentage (vol%), whereas SAK addition to Jet A increases the slope.

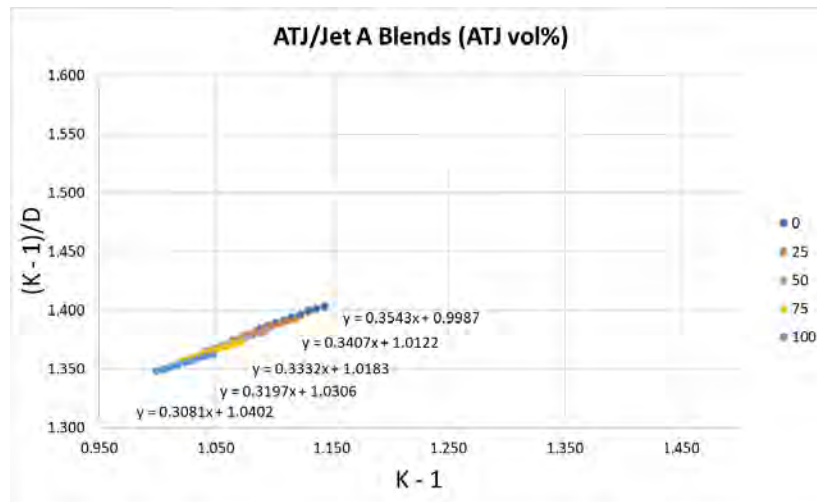


Figure 4. Clausius-Mossotti plots for blends of ATJ with Jet A.

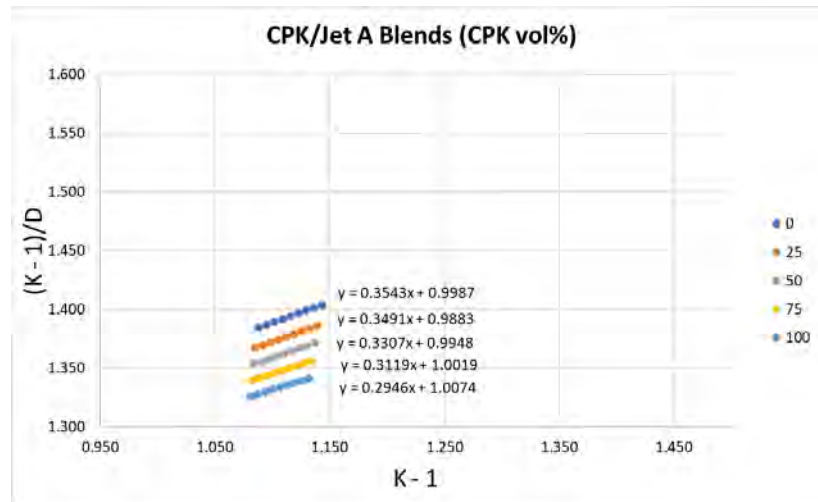


Figure 5. Clausius-Mossotti plots for blends of CPK with Jet A.

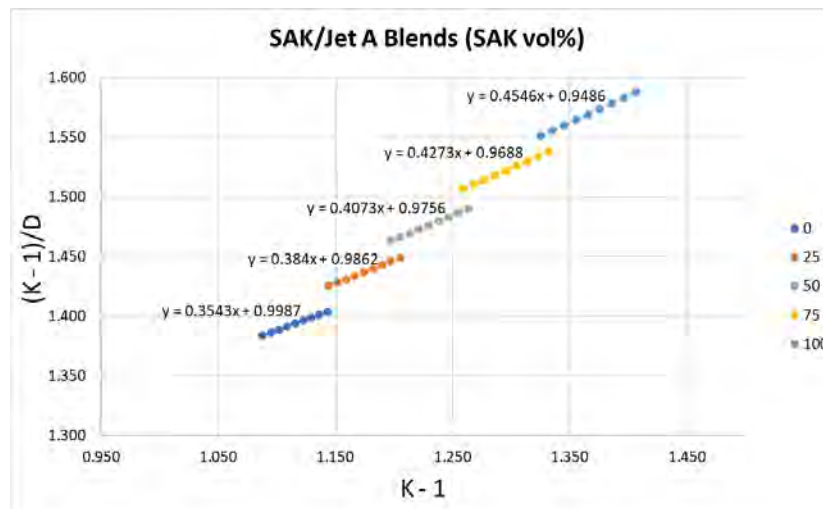


Figure 6. Clausius-Mossotti plots for blends of SAK with Jet A.

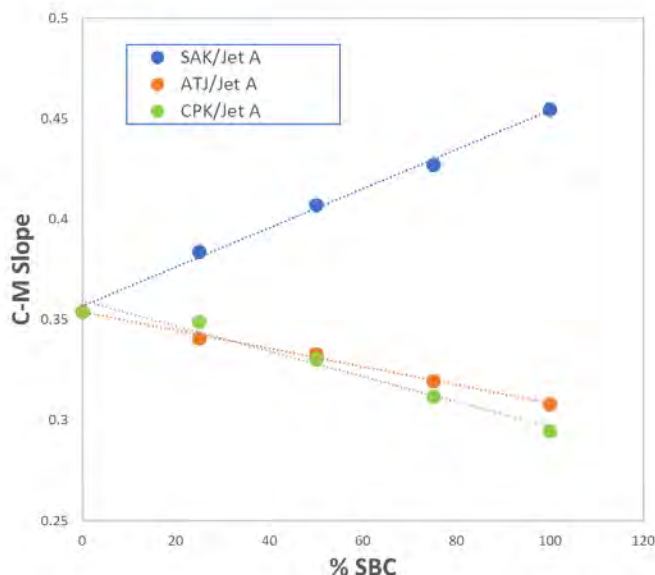


Figure 7. Plot summarizing Clausius-Mossotti slopes for SBC blends with Jet A.

Virent SAK has been proposed as a blend component that could be added to synthetic paraffinic kerosene SBCs to create a 100% synthetic SAF. The added aromatic species could provide the elastomer seal swell needed to prevent fuel system seal leakage. Therefore we measured the dielectric constant and density for several blends of SAK with a D7566 Annex A2 HEFA sample and an Annex A5 ATJ sample. We also blended SAK with a candidate Shell CPK-0 cycloparaffinic kerosene (CPK). The Clausius-Mossotti plots are shown in Figures 8-10 for blends of 0, 25, 50, 75, and 100 vol% SAK. The plots show that addition of SAK increases the Clausius-Mossotti slope for each of the SBC samples. Figure 11 summarizes the change in slope after blending, showing that three SBCs display nearly identical increases in slope after addition of SAK. Figure 12 shows the average slope value for each SBC at each blend ratio, with a horizontal line at the 0.3568 slope, thus showing that a 25 vol% blend with SAK is required to reach this slope value with these three paraffinic SBCs. Interestingly, despite its higher density, the CPK sample displays Clausius-Mossotti slope behavior and a response to SAK addition nearly identical to that of the tested isoparaffinic SBCs.

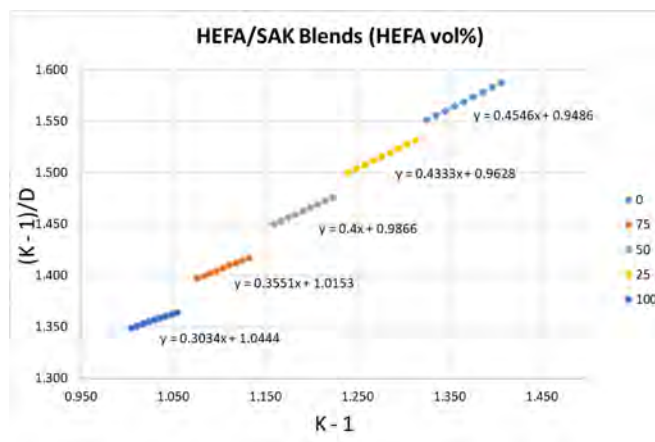


Figure 8. Clausius-Mossotti plots for blends of SAK with HEFA.

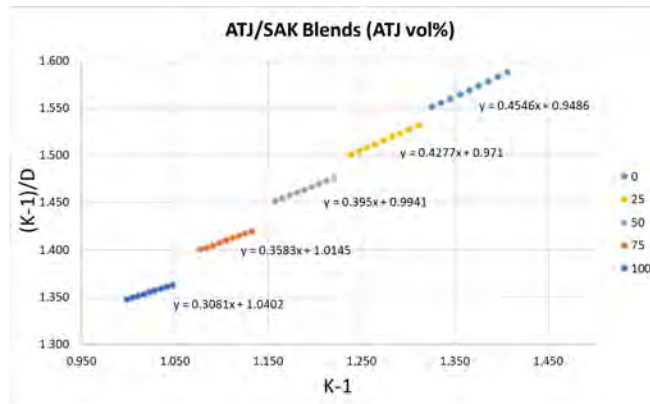


Figure 9. Clausius-Mossotti plots for blends of SAK with ATJ.

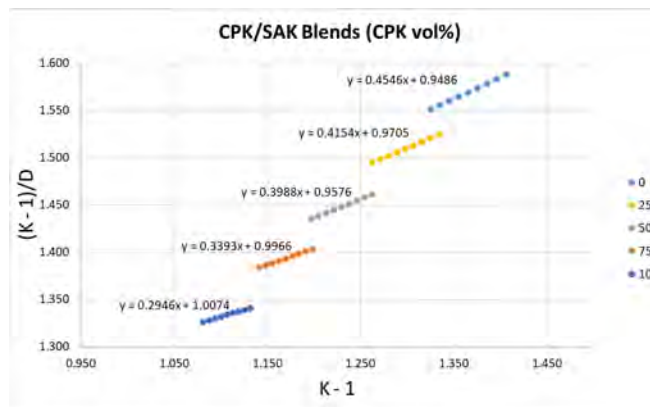


Figure 10. Clausius-Mossotti plots for blends of CPK with HEFA.

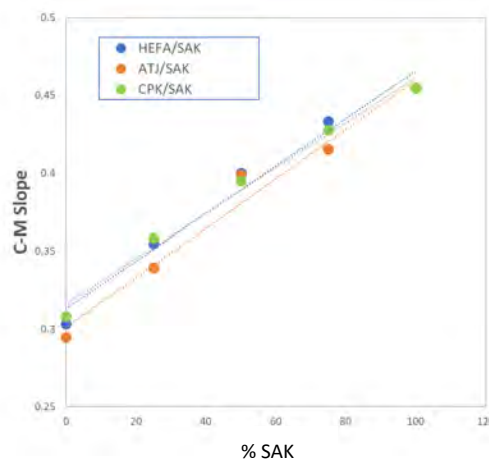


Figure 11. Plot summarizing Clausius-Mossotti slopes for blends of SBCs with SAK.

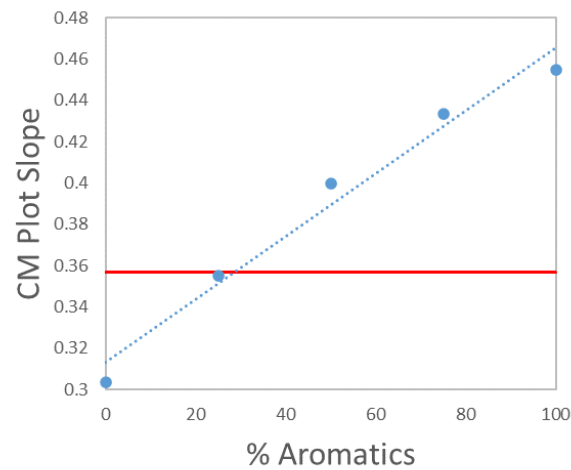


Figure 12. Average slope behavior after addition of SAK to the three SBCs, with horizontal red line indicating the 0.3568 slope.

The next set of measurements constituted an early attempt at comparing the new Stanhope-Seta Jet DC dielectric constant measurement with the previous ASTM D924 (using a “Goodrich cell”), performed by Southwest Research Institute (SwRI). The results of a comparison for two fuels are shown in Clausius–Mossotti plots in Figure 13 for the Jet A fuel and Figure 16 for the Shell CPK SBC. Figure 13 shows that the Jet A fuel measurements are quite close, with the Jet DC instrument reporting a slightly lower slope. Figure 14 shows that the CPK fuel measurements are quite different, but the slopes are also slightly lower for the Jet DC instrument. Table 1 summarizes the slope data for the three fuels tested, adding the SAK measurement. The table shows that, for Jet A and CPK, the Jet DC instrument provides a lower slope, whereas for SAK, the D924 reports a lower slope. We quickly realized that using consistent density measurements is essential when comparing these slope values. The D924 method does not provide density, and thus a separate density measurement was performed. In contrast, the Jet DC instrument has its own density measurement. Table 2 shows the comparison when a consistent density measurement (determined with the Jet DC instrument values) was used for both Clausius–Mossotti slope determinations. The table shows that the Jet DC instrument reports a lower slope for all three fuels. More work on additional fuels is necessary for a true comparison of these two techniques, with the goal of determining how the measurements differ between instruments.

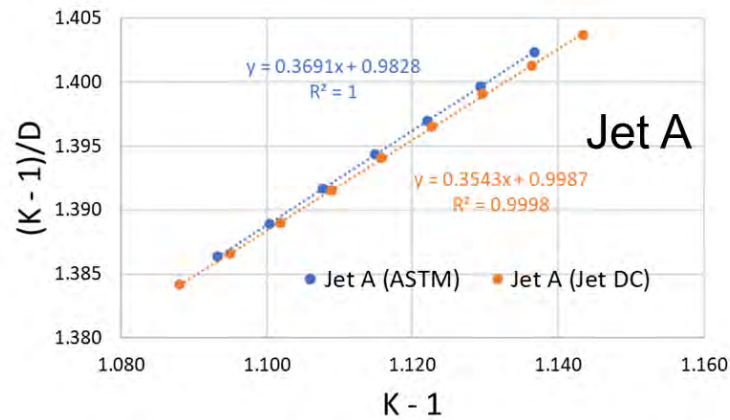


Figure 13. Clausius-Mossotti plots for blends for a Jet A fuel, showing differences between the ASTM method and the Jet DC instrument.

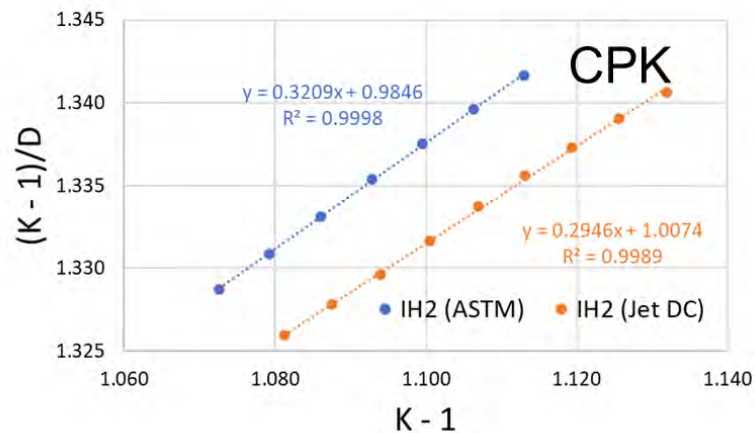


Figure 14. Clausius-Mossotti plots for blends for a Jet A fuel, showing differences between the ASTM method and the Jet DC instrument.

Table 1. Values of the Clausius-Mossotti slope, comparing D924 and Jet DC measurements.

Fuel	D924	Jet DC	> Slope?
Jet A	0.369	0.354	D924
CPK	0.320	0.294	D924
SAK	0.428	0.455	Jet DC



Table 2. Values of the Clausius–Mossotti slope, comparing D924 and Jet DC measurements, using consistent density measurements.

Fuel	D924	Jet DC	> Slope?
Jet A	0.398	0.354	D924
CPK	0.365	0.294	D924
SAK	0.470	0.455	D924

Finally, a brief study of using partial least squares (PLS) regression for prediction of the Clausius–Mossotti slope as a function of fuel composition was performed. The fuel composition was obtained by hydrocarbon type analysis via two-dimensional gas chromatography (GCxGC) for the fuels listed above. Fuel composition was characterized with vol% values of the following species classes: aromatic compounds, diaromatic compounds, cycloaromatic compounds, isoparaffins, *n*-paraffins, monocycloparaffins, dicycloparaffins, tricycloparaffins, and alkenes (referred to as a tier 2 analysis). In addition, the vol% of each carbon number of the species classes was obtained (referred to as a tier 3 analysis). Figure 15 shows a PLS regression of measured vs. predicted Clausius–Mossotti slope for these fuels. For this regression, only the species class vol% values were used (i.e., a tier 2 analysis); the carbon number distributions were not considered. The plot shows a very good correlation, with an R^2 of 0.98 and a root mean square error of 0.0066 in the slope value. A regression using the tier 3 carbon number data were also performed, but no improvement in the regression was observed with the additional data. Figure 16 shows the model coefficients obtained for each species class for the Tier 2 regression. The absolute value of the model coefficient can be interpreted as a measure of the importance of the contribution of each species class to the slope. The sign of the of model coefficient indicates whether the species class contributes to an increase or decrease in the slope. The figure shows that model coefficients for aromatic and cycloaromatic compounds are relatively large and positive, whereas the coefficients for isoparaffins are relatively large and negative. The *n*-paraffins are slightly smaller but also negative, and the cycloparaffins, dicycloparaffins, and tricycloparaffins are somewhat smaller and also negative. Care must be taken in interpreting very small model coefficients, because these values these have large uncertainties. The model coefficients appear to agree with the data shown above and our chemical intuition. We already know that aromatics increase the dielectric slope, from the SAK data above. In contrast, non-aromatic compounds, such as iso-paraffins, *n*-paraffins, and cycloaromatic compounds thus decrease the slope. More work using pure chemical components and additional fuels will greatly aid in elucidating the contributions of individual species classes.

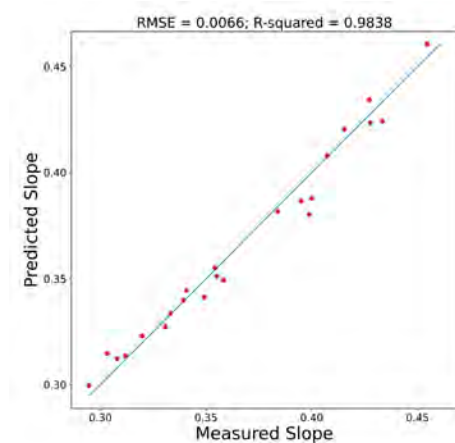


Figure 15. PLS regression (predicted vs. measured) of the Clausius–Mossotti slope for a series of fuels, by using GCxGC tier 2 composition data (hydrocarbon type).

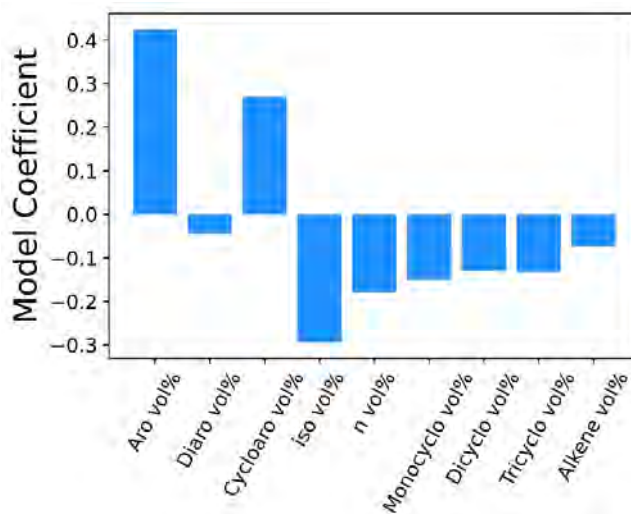


Figure 16. PLS regression model coefficients for the hydrocarbon type species classes.

Milestones

Milestones include acquisition and commissioning of the Jet DC instrument, participation in the ILS, and initial measurements of dielectric and density on fuel blends.

Major Accomplishments

These initial measurements provide data for the SAF fuel community, airframe OEMs, and fuel quantity indication system OEMs regarding the roles of SAF fuel composition in these systems. We are working with these organizations to help guide our future work on this project.

Publications

None.

Outreach Efforts

Presentations were made at the ASCENT spring and fall 2023 meetings. The data were also presented to fuel quantity indication system experts at Collins Aerospace and Boeing, and will be presented to Airbus in the near future. The goal of these meetings is to receive feedback from industry experts on future steps to enable this work to most effectively contribute to the approval of new SAF candidates.

Awards

Dr. Steven Zabarnick: ASTM D02 Award of Excellence, December 2023

Student Involvement

None.

Plans for Next Period

As described above, we are working closely with OEMs to determine the best course of action for the next period. Some suggestions that we have received include expanding the lower temperature range of the measurements and performing measurements on pure compounds. In addition, we will be expanding the measurements to a wider array of fuel blends. We are also planning to expand the comparison work between the Jet DC results and the D924 measurements.



References

- Aeronautical Radio, Inc., (January 1999) Guidance for the Design and Installation of Fuel Quantity Systems," ARINC Report 611-1.
- ASTM International, D924-15, Standard Test Method for Dissipation Factor (or Power Factor) and Relative Permittivity (Dielectric Constant) of Electrical Insulating Liquids.
- Hadaller, O. J., & Johnson, J. M. (2006). World Fuel Sampling Program (CRC Report No. 647).
- Moses, C. (May 2013) Concern about Density-Dielectric Correlation in Synthesized Kerosenes, Coordinating Research Council Aviation Meetings, Savannah GA.
- Parmenter, D. (May 2013) Assessing Gauging Performance of Synthetic Fuels," Coordinating Research Council Aviation Meetings, Savannah GA.



Project 090 World Fuel Survey

University of Dayton Research Institute

Project Lead Investigator

Zachary West, PhD
Principal Research Engineer
Group Leader, Fuel Science
University of Dayton
300 College Park
Dayton, OH 45458
937-255-4062
zachary.west@udri.udayton.edu

University Participants

University of Dayton Research Institute (UDRI)

- P.I.: Zachary West, PhD
- FAA award number: 13-C-AJFE-UD, Amendment no.048
- Period of Performance: January 1, 2023 to December 31, 2023
- Task:
 1. Conduct a survey of commercial world jet fuels and develop a modern technical dataset for relevant fuel samples

Project Funding Level

Amendment No. 048	\$749,886.56
Total	\$749,886.56

In-kind cost sharing has been obtained from the following organization. Additional cost-sharing will be obtained from fuel refineries for the cost of fuel samples and testing services.

Organization	Amount	Year
Marathon Petroleum Corporation	\$30,120	2023

Investigation Team

Dr. Zachary West (P.I.)
Carlie Anderson (staff scientist)
Amanda Arts (staff scientist)
Shane Kosir (staff scientist)
Susan Mueller (staff scientist)
Linda Shafer (staff scientist)
Willie Steinecker (staff scientist)
Richard Striebich (staff scientist)
Steven Zabarnick (staff scientist)
Taylor Nicely (undergraduate student)
Maria Baker (other professional)
Lisa Brown (other professional)
Rhonda Cook (other professional)
April Landsaw (other professional)



Samuel Tanner (other professional)
Jim Thompson (other professional)

Project Overview

Jet fuel is defined by a robust physicochemical and performance specification; however, the exact chemical composition is variable and depends on numerous market factors, such as petroleum crude sources, production/refinery techniques, and impacts from transportation/handling in the fungible fuel system. As the United States and other countries are accelerating the pace of fuel certification (via the ASTM D4054 process) and production of synthetic aviation turbine fuels, having a robust and representative set of data for comparison is important. Almost two decades have passed since the last major survey of commercial jet fuels (CRC Report No. 647, 2006); therefore, this project aims to collect a contemporary set of representative jet fuel samples and conduct both specification and non-specification testing on the subject samples.

Task 1 – Conduct a Survey of Commercial World Jet Fuels

University of Dayton Research Institute

Objectives

The objectives of this task are to secure relevant jet fuel samples from around the world; analyze the fuel samples to create a robust set of physicochemical and property technical data; and make the test data available to the aviation fuels community, to enhance and expedite decisions regarding current and future synthetic aviation turbine fuel composition.

Research Approach

Our approach has been to first collect industry stakeholder interest/feedback and to build partnerships with fuel refiners. The second portion of the project has involved soliciting fuel refiners for jet fuel samples, and coordinating the shipping and handling of the samples to UDRI. Once received, the samples are subjected to testing at both UDRI and other contracted laboratories. Finally, the test data will be reported.

Stakeholders and partnerships

The amount of fit-for-purpose testing data in ASTM D4054 Table 2 is substantial. To economize the results of this study, we obtained feedback from industry stakeholders, e.g., engine and airframe original equipment manufacturers, and identified a reduced set of fit-for-purpose testing to conduct on survey fuels. We also developed critical relationships with key fuel producers in advance of requesting samples.

Solicitation of samples

Targeted email solicitations requesting samples of 5 U.S. gallons were sent to our fuel producer partners. After obtaining positive responses, UDRI sent sampling kits and instructions to fuel producers to submit samples along with certificates of analysis.

Testing

In addition to the reported specification data (via the certificates of analysis), fuels are being subjected to 24 chemical, physical, and performance tests (Table 1). Testing will be performed at both UDRI and Southwest Research Institute.



Table 1. Jet fuel survey fit-for-purpose test plan.

Property	Test method
Hydrocarbon type	UDRI FCM-101
Olefins	ASTM D1319
Hydrogen content	ASTM D3701
Organic compounds	UDRI FCM-102
Inorganic compounds: N, total, and basic	ASTM D4629
Trace metals	UDRI FCM-107
Distillation	ASTM D86
Simulated distillation	ASTM D2887
Thermal stability, breakpoint	ASTM D3241
Lubricity	ASTM D5001
Viscosity vs. temperature	ASTM D7042
Density vs. temperature	ASTM D4052
Specific heat vs. temperature	ASTM E2716
Surface tension vs. temperature	ASTM D1331
Isentropic bulk modulus vs. temperature and pressure	Southwest Research, Institute in-house
Thermal conductivity vs. temperature	ASTM D7896
Refractive index (nD20)	UDRI In-House
Water solubility vs. temperature	ASTM D6304
Air solubility (oxygen/nitrogen)	UDRI FC-M-103
True vapor pressure vs. temperature	ASTM D6378
Dielectric constant vs. density	IP PM FC/21
Autoignition temperature	ASTM E659
Hot surface ignition temperature	ISO 20823
Derived cetane number	ASTM D6890

Reporting

UDRI will anonymize all test data before reporting, to protect fuel producers’ commercial interests. We are working with the Volpe Center to establish an online database to archive test data. We also intend to report the test data in a CRC report.

Milestones

The original project proposal indicated that sample testing would be completed by July 1, 2023, and a final report and analysis would be complete by September 30, 2023. However, this timeline failed to account for fuel producer schedules to provide samples and the time required for outside/sub-contracted testing services. The updated schedule for this project is dependent on the receipt of fuel samples for testing and the time associated with contracted laboratory testing. Our current best estimate for a major test data package is April 30, 2024, with a report completed by May 31, 2024.

Major Accomplishments

To date, we have received 29 jet fuel samples from eight major refineries located across North America and Europe. The total product volume represented by these samples is more than 59 million U.S. gallons. This sample diversity will contribute to the overall robustness of the dataset, and the total volume will contribute to the representativeness of jet fuels on the current market.

Publications

None.



Outreach Efforts

Presentations on Project 90 activities were given at the April 2023 and October 2023 ASCENT semi-annual meetings. Additionally, the project has been briefed during a regular original equipment manufacturer panel meeting, at the CRC Aviation meeting (May 2023), and has been discussed in numerous industry forums, such as ASTM.

Awards

None.

Student Involvement

An undergraduate chemical engineering student has been involved with the preparation of samples for solid phase extraction, two-dimensional gas chromatography with tandem flame ionization detection and mass spectrometry detection analysis for polar organic compounds (UDRI FCM-102).

Plans for Next Period

Over the next year, we will continue to solicit samples from fuel producers, and we will collect test data in earnest, i.e., fit-for-purpose property data. Data will be reported and archived.



Project 091A Environmental Impacts of High-Altitude and Space Vehicle Emissions

Massachusetts Institute of Technology

Project Lead Investigators

Raymond Speth
Principal Research Scientist
Associate Director, Laboratory for Aviation and the Environment
Massachusetts Institute of Technology
77 Massachusetts Ave, Building 33-207, Cambridge, MA 02139
617-253-1516
speth@mit.edu

Steven R. H. Barrett
Professor of Aeronautics and Astronautics
Director, Laboratory for Aviation and the Environment
Massachusetts Institute of Technology
77 Massachusetts Ave, Building 33-207, Cambridge, MA 02139
617-253-2727
sbarrett@mit.edu

University Participants

Massachusetts Institute of Technology (MIT)

- P.I.: Raymond Speth
- FAA Award Number: 13-C-AJFE-MIT, Amendment Nos. 113 and 115 (no-cost extension to September 30, 2024)
- Period of Performance: January 1, 2023 to September 30, 2023 (no-cost extension to September 30, 2024)
- Reporting Period: January 1, 2023 to September 30, 2023
- Tasks:
 1. Developing future scenarios for the launch industry
 2. Creating emissions inventories for launch vehicles
 3. Refining and running of GEOS-Chem High-Performance (GCHP) simulations
 4. Quantifying environmental impacts of emissions

Aerospace Corporation

- Co-investigator: Martin Ross
- FAA Award Number: MIT Subaward Purchase Order No. 855789
- Period of Performance: January 1, 2023 to December 31, 2023 (no-cost extension to September 30, 2024)
- Reporting Period: January 1, 2023 to December 31, 2023
- Tasks:
 1. Developing future scenarios for the launch industry
 2. Creating emissions inventories for launch vehicles

Project Funding Level

\$258,775 FAA funding and \$258,775 matching funds. Sources of match are approximately \$33,448 from MIT, plus third-party in-kind contributions of \$225,327 from NuFuels, LLC.

Investigation Team

Massachusetts Institute of Technology

Dr. Raymond Speth (P.I.), All Tasks
Prof. Steven Barrett (co-P.I.), All Tasks
Dr. Sebastian Eastham (co-investigator), All Tasks
Clara Ziran Ma (graduate research assistant), Tasks 1, 3, and 4

Aerospace Corporation

Dr. Martin Ross (co-investigator), Tasks 1 and 2

Project Overview

The growth rate of the commercial space industry is projected to be at least 7% per year over the coming decades, thereby supporting rapid advancement in Earth observation, telecommunications, navigation technology, and space exploration. This development is supported by a rapidly growing launch industry: 180 launches were performed globally in 2022 alone (Witze, 2023).

Depending on the propellant used in each launch vehicle, the resulting emissions can have widely varying impacts on atmospheric chemistry. Species such as hydrogen chloride, aluminum, or nitrogen oxides (NO_x) can deplete ozone in the stratosphere, whereas others, such as methane (CH₄) and H₂O, can contribute to significant radiative forcing.

Given the projected rapid growth in launch numbers over the coming decades, quantitative data are needed to assess the magnitude of the impacts of emissions on atmospheric chemistry and climate, and thereby support robust decision-making. The work performed under ASCENT Project 91A is designed to provide such data, and comprises four parts:

- 1) Development of future scenarios for the launch industry
- 2) Creation of emissions inventories for launch vehicles for each scenario
- 3) Refinement, running, and gathering results of GCHP simulations for each scenario
- 4) Quantifying the environmental impacts of each scenario

We first analyze the past growth rate of the launch industry, and project the number of launches that will occur in 2050, their spaceport of origin, and the fuel used. We create and examine three future scenarios for the launch industry in 2050: one in which methane vehicles are dominant, one in which hydrogen (H₂) vehicles are dominant, and one in which kerosene (Rocket Propellant-1 [RP-1]) vehicles are dominant. We then create emissions inventories from the launch profiles of the vehicles, considering the rocket model, launch trajectory, and distribution by spaceport. The launch emissions' impact on atmospheric chemistry is simulated with GCHP. The output of the model is used to quantify the steady-state impact of the launch emissions on air quality, ozone, radiative forcing, and consequently climate.

References

Witze, A. (2023). 2022 was a record year for space launches. *Nature*. <https://www.nature.com/articles/d41586-023-00048-7>

Task 1 – Development of Future Scenarios for the Launch Industry

Massachusetts Institute of Technology and Aerospace Corporation

Objective

To assess the emissions impact of the launch industry, a target year and set of scenarios needed to be established. This forecast should consider the size of the payload, the target orbit, and the trajectory of the launch, and should include the number of launches, the types of vehicles flown, the distribution of launch sites, and the fuel used.

Research Approach

First, we conducted a literature review to examine previous estimates for the growth of the launch industry. One such report, authored in 2023 by the Federal Aviation Administration's Office of Commercial Space Transportation (FAA, 2023) compares the observed historical number of launches with the forecast number of launches by industry and by the FAA.



The report includes an industry forecast and FAA forecast for launches from 2021 to 2025. The industry forecasts tend to be more ambitious, and higher on average than the FAA forecasts, whereas the FAA forecasts are more conservative. The observed number of launches to date for the 2021–2022 period is lower than both forecasts.

If launches continue to grow at a rate of 7% per year, we would anticipate approximately 1,000 launches to occur annually by 2050. In contrast, the industry forecast reported by the FAA assumes a 25% annual growth rate, which (if sustained) would result in an estimated 80,000 or more launches annually by 2050. On the basis of discussion with Aerospace, we chose to simulate 5,000 launches per year as a central estimate.

Table 1. Every spaceport that hosted at least one launch from 2018 to 2022, and the total number of launches in that period. Data from Pradon et al. (2023) and Roberts (2019).

Spaceport	Number of launches (2018–2022)
Baikonur Cosmodrome	49
Cape Canaveral	151
Centre Spatial Guyanais	37
Jiuquan Satellite Launch Center	76
Kennedy Space Center	33
Naro Space Center	1
Pacific Spaceport Complex Alaska	2
Palmachim Airbase	1
Plesetsk Cosmodrome	39
Rocket Lab Launch Complex 1	31
Satish Dhawan Space Center	20
Sea Launch Platform	2
Taiyuan Satellite Launch Center	48
Tanegashima Space Center	11
Uchinoura Space Center	4
Vandenberg Air Force Base	34
Vostochny Cosmodrome	7
Wenchang Space Launch Center	10
Xichang Satellite Launch Center	74

As of 2018, rockets have been launched from 28 spaceports worldwide (Pradon et al., 2023). Some of the most active spaceports include Plesetsk Cosmodrome in Russia (1,602 total orbital launches), Vandenberg Air Force Base in California (1,641 total orbital launches), Baikonur Cosmodrome (1,438 total orbital launches), Cape Canaveral and Kennedy Space Center in Florida (991 total orbital launches), and Guiana Space Centre (301 total orbital launches) (BryceTech, 2023; Spaceport Camden, 2022). Because we cannot accurately predict when and which new spaceports will be built, we use existing data on launches from each spaceport to produce a plausible distribution of launches in 2050. Taking launch data from 2018 to 2022 (Table 1), we summed the number of launches from each spaceport for these 5 years, then calculated the percentage of launches that occurred at each spaceport. We then multiplied the percentage for each spaceport by the 5,000 total launches to obtain a representative estimate of the number of launches from each spaceport in 2050 (Figure 1).

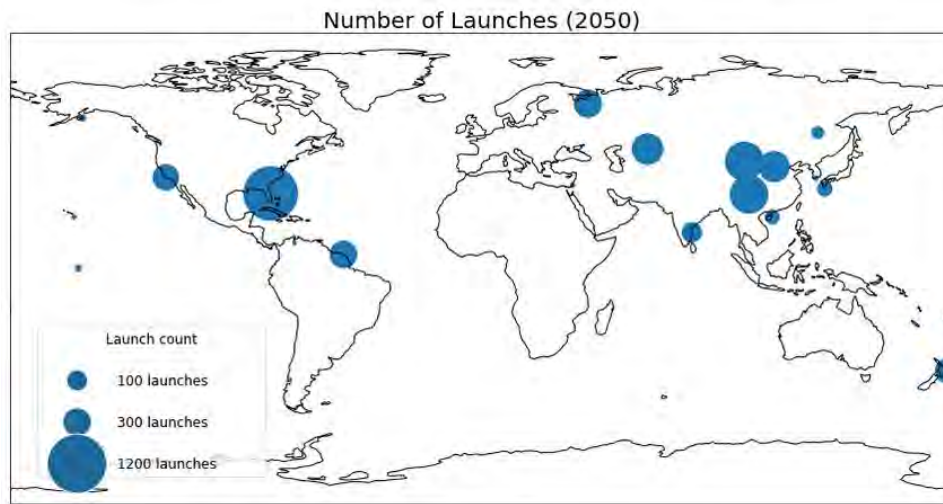


Figure 1. Distribution of launches by spaceport for one year in 2050. Circle size corresponds to the launch count for that spaceport. Notable spaceports include Cape Canaveral in Florida, Jiuquan Satellite Launch Center, and Xichang Satellite Launch Center. A total of 5,000 launches occur annually.

Launch vehicle propellants can be divided into three general categories: solid rocket propellants, liquid rocket propellants, and hybrid propellants. Solid propellants include aluminum powders in solid rocket boosters. Liquid propellants include liquid hydrogen or liquid methane as fuel, using liquid oxygen as an oxidizer. Hybrid propellants typically include a solid fuel and liquid oxidizer. The rocket plume contains different species, depending on the propellant used. Although the variety of propellants currently used in industry is high, the dominant choice is RP-1 (essentially refined kerosene) with liquid oxygen. We consider three scenarios in this project, each defined by a single propellant being used for all launches worldwide. Although not necessarily realistic, this scenario allows us to evaluate the environmental impacts of choosing different propellants.

The first scenario is a “business as usual” scenario in which the dominant fuel currently used by the launch industry, RP-1, is used for all launch vehicles in 2050. RP-1 is widely used because it is less expensive and more stable than alternative fuels such as H_2 at room temperature. RP-1 is used in the first stages of the Falcon 9 (National Reconnaissance Office, 2023), Atlas, and Delta II launch vehicles. Without significant changes to the launch industry, many launch vehicles are likely to continue to use RP-1.

In the second scenario, all launch vehicles use liquid methane fuel with liquid oxygen as an oxidizer. LandSpace’s Zhuque-2 was the first successfully launched methane-powered rocket to reach orbit in July 2023 (Woo, 2023), and many new launch vehicles are in development or testing stages, such as SpaceX’s Starship and Relativity’s Terran 1 (Foust, 2023). Methane has a higher specific impulse and is expected to burn more cleanly than kerosene, thus making it potentially a more environmentally friendly alternative for companies seeking to develop heavy-lift launch vehicles.

In the third scenario, all launch vehicles use liquid hydrogen and liquid oxygen. This fuel combination is already used in stages of United Launch Alliance’s Delta IV rocket (United Launch Alliance, 2023), Arianespace’s Ariane 5 (Arianespace, 2020), the Long March 5 (Jones, 2020), and NASA’s Space Launch System (NASA, 2026). Liquid hydrogen has one of the highest specific impulse values of all liquid fuels (Perry, 2016) and is potentially more environmentally friendly than kerosene.

Milestones

- A global launch inventory was updated to include the number and location of launches from 2018 to 2022 (Table 1).
- The growth rate of the launch industry was analyzed and projected to reach 5,000 launches per year in the year 2050 (Figure 1).



- Three launch industry scenarios were developed for the year 2050: CH₄, H₂, and RP-1 scenarios.

Major Accomplishments

- The updated global launch inventory includes launches until 2022 and was provided to collaborators in ASCENT Project 91B.
- The number of launches and industry scenarios projected to occur in 2050 were developed based on a mid-level industry growth rate and provided to ASCENT Project 91B.

Publications

None.

Outreach

Progress on all ASCENT Project 91A tasks was communicated in biweekly calls with the FAA, as well as collaborators at the University of Illinois Urbana-Champaign (from ASCENT Project 91B) and Aerospace Corporation. Further updates were reported in quarterly process reports, AIAA SciTech 2023, and the 2023 ASCENT Fall Meeting in Arlington, Virginia.

We contacted the FAA Office of Commercial Space Transportation to understand current FAA regulations on environmental impacts when considering licenses for spaceports or individual launches.

Awards

None.

Student Involvement

During the reporting period of the academic year (AY) 2022–2023, the MIT graduate student involved with this task was Clara Ziran Ma.

Plans for Next Period

The objectives outlined in this section have been completed. In the next project period, we expect to develop a second set of launch scenarios reflecting factors such as uncertainty in the spatial and temporal distribution of launches, and uncertainty in non-aerospace emissions.

References

- Arianespace (2020) "Ariane 5 User's Manual." <https://www.arianespace.com/wp-content/uploads/2016/10/Ariane5-users-manual-Jun2020.pdf>
- BryceTech (2023) "Orbital and Suborbital Launch Sites of the World." https://brycetek.com/reports/report-documents/Bryce_Launch_Sites_2023.pdf
- Federal Aviation Administration (2023) "FAA Aerospace Forecast Fiscal Years 2021–2041." https://www.faa.gov/data_research/aviation/aerospace_forecasts
- Foust, J. (2023) "Agencies studying safety issues of LOX/methane launch vehicles." SpaceNews <https://spacenews.com/agencies-studying-safety-issues-of-lox-methane-launch-vehicles/>
- Jones, A. (2020) "Long March 5B launch clears path for Chinese space station project." SpaceNews <https://spacenews.com/long-march-5b-launch-clears-path-for-chinese-space-station-project/>
- National Aeronautics and Space Administration (2023) "Space Launch System." <https://www.nasa.gov/humans-in-space/space-launch-system/>
- National Reconnaissance Office (2023) "Launch Vehicles." <https://www.nro.gov/Launches/Launch-Vehicles/>
- Perry, B. (2016) "We've Got (Rocket) Chemistry, Part 1". The National Aeronautics and Space Administration. <https://blogs.nasa.gov/Rocketology/tag/liquid-hydrogen/>
- Pradon, C. V., Eastham, S. D., Chossière, G., Sabnis, J., Speth, R. L., Barrett, S. R., & André Jooste, J. (2023). Global Three-Dimensional Emission Inventory for Launch Vehicles from 2009 to 2018. *Journal of Spacecraft and Rockets*, 60(3), 716-727.
- Roberts, T. G. (2019) "Spaceports of the World." <https://aerospace.csis.org/data/spaceports-of-the-world/>
- Spaceport Camden (2022) <https://spaceportcamden.us/>
- United Launch Alliance (2023) "Delta IV." <https://www.ulalaunch.com/rockets/delta-iv>

Woo, R. (2023) "China beats rivals to successfully launch first methane-liquid rocket." Reuters
<https://www.reuters.com/technology/space/china-beats-rivals-successfully-launch-first-methane-liquid-rocket-2023-07-12/>

Task 2 – Creation of Emissions Inventories for Launch Vehicles

Massachusetts Institute of Technology and Aerospace Corporation

Objective

On the basis of the three future scenarios developed in Task 1, emissions inventories needed to be developed for the three scenarios: CH₄-, H₂-, and RP-1-fueled vehicles.

Research Approach

From Task 1, we determined three scenarios for the future of the launch industry in the year 2050. In scenario 1, all launch vehicles use RP-1 as fuel. In scenario 2, all launch vehicles use methane as fuel. In scenario 3, all launch vehicles use liquid hydrogen as fuel. We created emissions inventories for one representative type of vehicle for each scenario, under the generalization that for the RP-1 scenario, for example, 100% of launch vehicles were fueled by RP-1. The representative vehicle for the RP-1 scenario is a single heavy-lift launch vehicle fueled by RP-1. The representative vehicle for the CH₄ scenario is a single heavy-lift launch vehicle propelled by liquid methane and liquid oxygen, which is based on the SpaceX Starship. The representative vehicle for the H₂ scenario is a single heavy-lift launch vehicle propelled by liquid hydrogen and liquid oxygen.

All three vehicles' emissions inventories were created on the basis of the assumption that the vehicles carried a payload of 80 tons to a low Earth orbit of 180 km. All three vehicles were also assumed to use two stages: the first with 2,400 kN of thrust and the second with 400 kN thrust.

Emissions profiles were created for the three vehicles with the Aerospace launch simulation software (Taylor and Pergament, 2000; Simmons, 2000). These estimates include the effects of afterburning and produce a vertical profile of emissions. All three emissions profiles are provided in Figure 2.

The trajectory taken by each launch depends on the origin spaceport and the target orbit. Each launch begins with a vertical climb straight up through the atmosphere. The rocket eventually performs a pitchover to alter the flight path, and therefore is no longer vertical but instead is pointed toward the destination orbit. Consequently, the trajectories of all launches are not entirely vertical. However, the expected horizontal travel of the vehicle during the climb is expected to be small (less than 5° longitude or latitude); consequently, the significance in terms of global impacts is expected to be minimal. We therefore disregarded the horizontal pitchover trajectory and modeled all launches as being essentially vertical from the launch site.

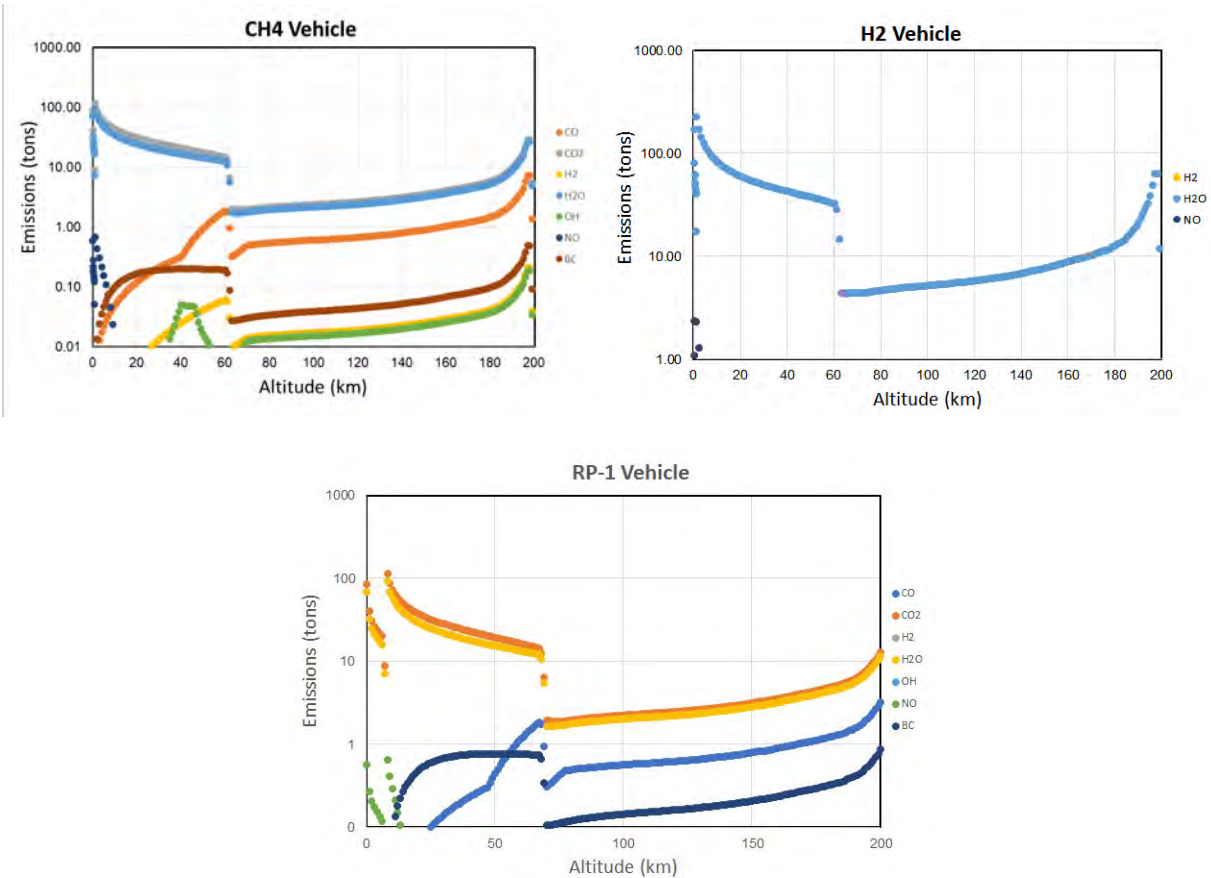


Figure 2. The emissions profile for a single launch of the CH₄, H₂, and RP-1 launch vehicles. The sudden decrease in emissions of nearly all species around 60 km occurs because of the burn completion of the first stage and its separation from the vehicle. The second stage begins its burn around the same altitude.

The emissions inventories were created and adjusted around the constraints of GCHP. GCHP simulations are run in a three-dimensional atmospheric grid with 72 vertical layers (GEOS-Chem, 2023). The top of the simulation ends at approximately 80 km altitude, but every rocket launch continues well above this altitude. To include the remaining emissions from the rocket plume above 80 km, we assumed that the emissions would eventually drift downward and settle around the top layer of the GCHP grid and would be evenly distributed across the latitudes and longitudes. Therefore, for each individual launch, the mass of emissions above 80 km was summed and divided evenly across the top layer of grid cells of GCHP.

To create each emissions inventory, we took the emissions profile of a single launch for that type of vehicle and multiplied it by the number of launches for each spaceport, then added the launch profiles to the coordinates of each spaceport to the input file. Therefore, each input file would have vertical columns of emissions at each launch site, with all emissions above 80 km summed and distributed at the top layer across all latitudes and longitudes of the input file.

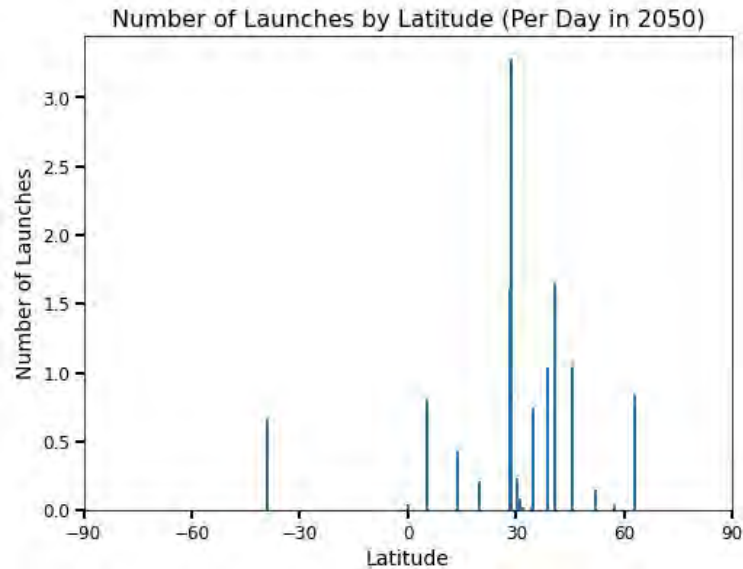


Figure 3. Distribution of launches per day in 2050 by latitude, discretized into 1° bands. There are approximately 14 launches per day in 2050, for a total of 5,000 per year.

We used the same launch distribution for each of the three scenarios shown in Figure 3. Most launches occurred between 0° and 60° in the Northern Hemisphere, and the greatest number of launches occurred around 30° in the Northern Hemisphere, including at Cape Canaveral and Kennedy Space Center in Florida. Other spaceports between 0° and 60° latitude with high launch counts include Baikonur Cosmodrome, Guyana Space Centre, and Xichang. The only active spaceport in the southern Hemisphere is Rocket Lab’s Launch Complex 1 in New Zealand.

Nearly all launches occurred in the Northern Hemisphere and are operated by countries from the global North, because of the current availability of spaceports in the Northern Hemisphere (Table 1). However, launches occurring closer to the Equator are also advantageous, because the vehicle can take advantage of the Earth’s rotational speed at the moment of launch to increase its velocity and decrease the amount of propellant needed to reach a low-inclination orbit (NASA, 2023). This aspect explains why most launches occur relatively close to the Equator.

The total mass of emissions per year for 2050 for our scenarios is shown in Table 2.

Table 2. Total mass in teragrams (Tg) of various emitted species for 5,000 launches in 2050, for the three scenarios.

Species	CH ₄	H ₂	RP-1
CO	0.78	–	0.78
H ₂	0.024	0.035	0.024
H ₂ O	10	25	10
OH	0.019	–	0.019
NO	0.017	0.058	0.017
BC	0.087	–	0.35

Milestones

- A constant mass payload, target orbit, and flight trajectory were calculated for every launch vehicle.
- An emissions profile was created for the dominant vehicle in each scenario: CH₄-, H₂-, and RP-1-fueled vehicles.



- Input files were generated for each of the three scenarios (CH₄, H₂, and RP-1) in preparation for GEOS-Chem simulations.

Major Accomplishments

- A script to rescale the emissions profile to fit the gridding structure of GEOS-Chem was created and can be adjusted for other atmospheric chemistry models, such as WACCM. This script was provided to ASCENT Project 91B.
- A script was created to generate input files for GEOS-Chem simulations: this script combines the emissions profiles from individual launches, the latitudes and longitudes of the spaceports, and the distribution of launches by spaceport. This script was provided to ASCENT Project 91B.

Publications

None.

Outreach

Progress on all ASCENT Project 91A tasks was communicated in biweekly calls with the FAA, as well as collaborators at the University of Illinois Urbana-Champaign (from ASCENT Project 91B) and Aerospace Corporation. Further updates were reported in quarterly process reports, at AIAA SciTech 2023, and the 2023 ASCENT Fall Meeting in Arlington, Virginia.

Awards

None.

Student Involvement

During the reporting period of AY 2022–2023, the MIT graduate student involved with this task was Clara Ziran Ma.

Plans for Next Period

The objectives outlined in this section have been completed. The same approach discussed herein will be applied to the new scenarios expected for project year 2.

References

- GEOS-Chem (2023). "GEOS-Chem vertical grids" https://wiki.seas.harvard.edu/geos-chem/index.php/GEOS-Chem_vertical_grids#Vertical_grids_for_GEOS-5.2C_GEOS-FP.2C_MERRA.2C_and_MERRA-2
- The National Aeronautics and Space Administration (2023) *Basics of Space Flight*. <https://science.nasa.gov/learn/basics-of-space-flight/chapter14-1/>
- Simmons, F. (2000). *Rocket exhaust plume phenomenology*. American Institute of Aeronautics and Astronautics, Inc..
- Taylor, M., and Pergament, H. (2000). "Standardized Plume Flowfield Model SPF-III," User's Manual, PST TR-51, Propulsion Science and Technology, Inc., East Windsor, NJ

Task 3 – Refinement, Running, and Results from GCHP Simulations

Massachusetts Institute of Technology

Objective

To calculate the effects of the launch scenarios identified above, the GCHP model needed to be modified to include the launch emissions from each scenario, and to allow for simulation of 2050 rather than the present day.

Research Approach

Preliminary adjustments to the GCHP code were required to ensure that the model could accurately simulate projected conditions for 2050. The magnitude of background emissions is determined by scenarios in the Shared Socioeconomic Pathways, climate scenarios released by the Intergovernmental Panel on Climate Change. For our simulations, we assume that, in 2050, global emissions will have followed scenario 2—the "middle of the road" pathway—in which global population growth, and social, economic, and technological trends do not change significantly from historical patterns (Riahi et al., 2017; Hausfather, 2018). We also assume that global emissions will follow the Representative Concentration

Pathways scenario 4.5, in which anthropogenic radiative forcing will reach 4.5 W/m² by the year 2100. These two scenarios combined are referred to as SSP245 (Hausfather, 2018). Adjustments necessary for the inclusion of SSP245 were tested, including modification of the starting conditions for each GCHP simulation. These adjustments will be included in our final simulation runs, which are currently underway.

For this report, two preliminary 1-year GCHP simulations were completed at a grid resolution of C24 using current-day conditions. In this configuration of GCHP, each individual grid cell covers a horizontal domain of approximately 500 × 500 km².

Both preliminary 1-year simulations were set in 2019. The first was a baseline simulation without any launch emissions. The second included the launch emissions for the RP-1 scenario, as described in Task 2. The resulting change in atmospheric composition between the baseline run and the RP-1 run are discussed under Task 4.

The final simulations will be run for 10 years from the year 2050, so that concentrations of H₂O and ozone can reach steady state in the stratosphere, and will incorporate background emissions, meteorology, and boundary conditions, as specified in SSP245. A total of four runs will be performed: one baseline “control” run, which will not include any added emissions from launch vehicles; one run for CH₄ vehicles; one run for H₂ vehicles; and one run for RP-1 vehicles. An additional code modification is being designed to ensure that chemical changes in the mesosphere are captured (see Task 4).

Milestones

- GCHP code was refined and updated to include input for launch emissions, background anthropogenic emissions, meteorology, and emitted chemical species.
- Several short GCHP test runs were completed to verify that the total mass, chemistry, and distribution of the species across the latitudes, longitudes, and altitudes are correct.

Major Accomplishments

- The GCHP test run results and run settings were compared with those of University of Illinois Urbana-Champaign’s WACCM to verify that the runs are comparable.

Publications

None.

Outreach

Progress on all ASCENT Project 91A tasks was communicated in biweekly calls with the FAA, as well as collaborators at the University of Illinois Urbana-Champaign (from ASCENT Project 91B) and Aerospace Corporation. Further updates were reported in quarterly process reports, AIAA SciTech 2023, and the 2023 ASCENT Fall Meeting in Arlington, Virginia.

Awards

None.

Student Involvement

During the reporting period of AY 2022–2023, the MIT graduate student involved with this task was Clara Ziran Ma.

Plans for Next Period

Necessary modifications to the GCHP code will be made to include the boundary conditions and background emissions specified in SSP245. The final four simulation runs will be executed for the baseline scenario, CH₄ scenario, H₂ scenario, and RP-1 scenario. Each run will be set in the year 2050, with a duration of 10 years, and will be executed at a grid resolution of C90.

References

Riahi, K., Van Vuuren, D. P., Kriegler, E., Edmonds, J., O’neill, B. C., Fujimori, S., ... & Tavoni, M. (2017). The Shared Socioeconomic Pathways and their energy, land use, and greenhouse gas emissions implications: An overview. *Global environmental change*, 42, 153-168.

Hausfather, Z. (2018). Explainer: How 'shared socioeconomic pathways' explore future climate change. *Carbon Brief*, 19. <https://www.carbonbrief.org/explainer-how-shared-socioeconomic-pathways-explore-future-climate-change/>

Task 4 – Quantifying Environmental Impacts of Emissions from Each Scenario

Massachusetts Institute of Technology

Objective

After the modifications to GCHP described in Task 3, Task 4 is aimed at quantifying how atmospheric composition and metrics of environmental impact, including ozone depletion, air quality, and climate change, are affected by the choice of future launch vehicle scenario.

Research Approach

The two preliminary 1-year GCHP simulations for the year 2019—one that did not include launch emissions, and one that included the RP-1 emissions—were completed. The output from the first month of each simulation was compared to assess the environmental impact of the emissions.

Currently, the GCHP model enforces prescribed chemical production and loss rates in the mesosphere (above 50 km altitude), thus preventing changes in ozone, NO_x, and several other species from being simulated in this region. This aspect will be resolved before the full-length simulations.

Figure 4 shows how four key species—black carbon (BC), ozone, water vapor (H₂O), and NO_x—evolve over the course of the first simulation month. BC and H₂O both experienced net increases in mixing ratios, particularly at the highest altitudes around 80 km. Both species are largely inert in the mesosphere and upper stratosphere, such that they essentially accumulate. These initial estimates are an overestimate, because they include material settling from above 80 km altitude, although this error will decrease as the simulation reaches steady state.

The mixing ratio of ozone decreases over time. Although NO_x emissions would usually be considered a possible cause (Ravishankara et al., 2009), the negligible emissions of NO_x at high altitude from launch vehicles along with the observed decrease in NO_x suggest that a different mechanism is responsible. A more likely explanation is that the additional H₂O emitted from the launch vehicles causes HO_x-catalyzed ozone depletion—a well-explored risk of (for example) supersonic aviation. This concern would be further elevated for methane- and hydrogen-propelled vehicles, given the larger water vapor emissions expected per unit of fuel energy.

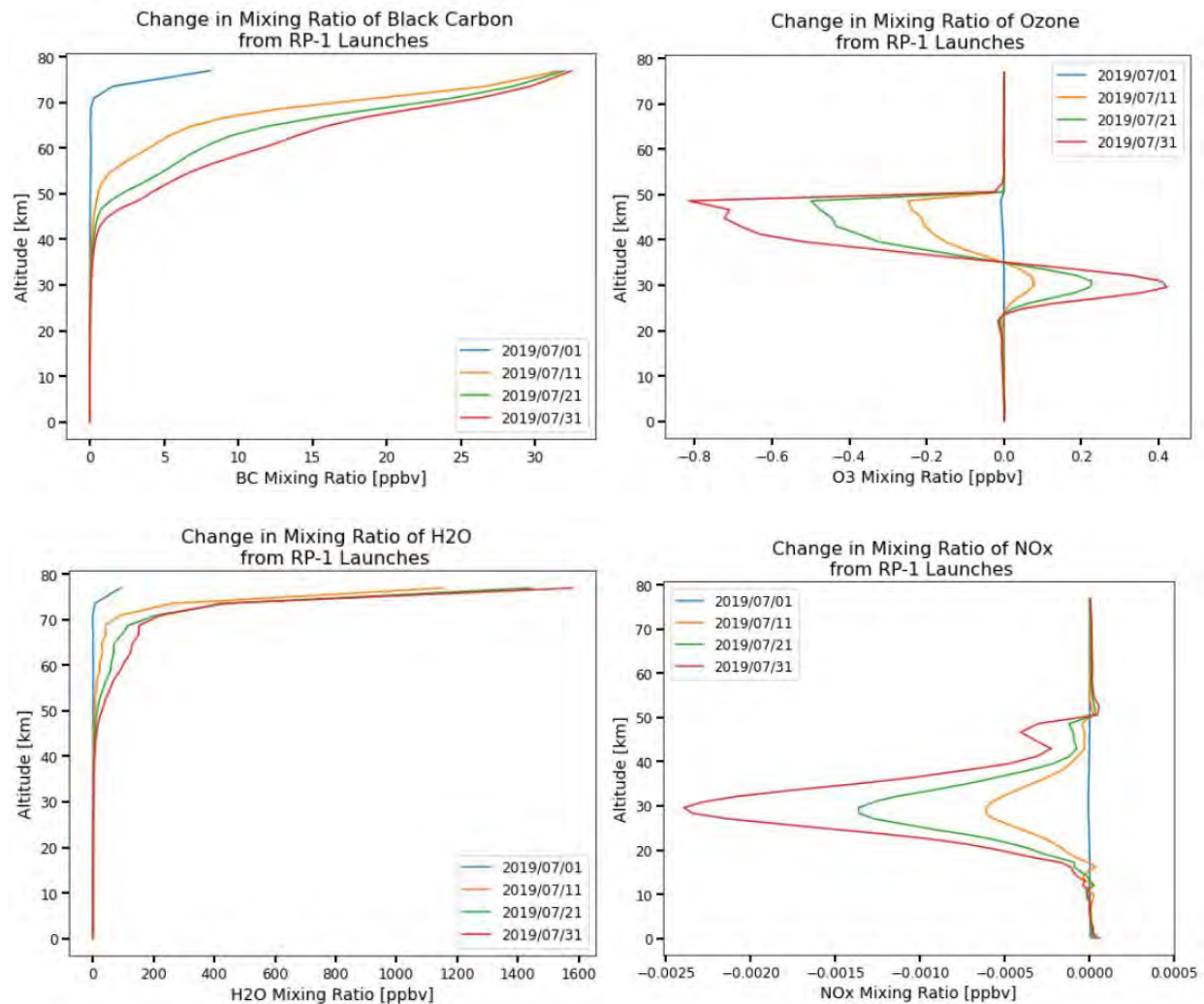


Figure 4. Net change in the mixing ratios of select chemical species in the atmosphere as a result of RP-1 launch emissions. The species are BC (top left), O₃ (top right), H₂O (bottom left), and NO_x (bottom right). The four lines reflect the changes in mixing ratio after 1, 11, 21, and 31 days (blue, yellow, green, and red, respectively) of emissions.

Total NO_x (NO + NO₂) increases only at the lowest altitudes (below 5 km), which is also where NO_x emissions from an RP-1 launch vehicle are greatest (see Task 2). NO_x is otherwise decreased at all altitudes, but not because NO_x is being removed from the atmosphere per se; instead, background nitrogen is likely to be sequestered in reservoir species such as HNO₃ and ClONO₂ (United States Environmental Protection Agency, 2005). The exact chemical mechanism remains under investigation, but it may again be related to the additional water vapor emissions.

The preliminary runs demonstrated in this report will be followed in Q1 2024 by four final simulation runs set in 2050, corresponding to three of our launch scenarios—CH₄ vehicles, H₂ vehicles, and RP-1 vehicles—along with a control simulation without launch emissions. All four runs will be high-resolution GCHP simulations at C90. All four runs will occur for 10 simulation years, thereby allowing steady-state chemistry to be reached. Before the execution of these simulations, we will make modifications to the mesospheric chemistry, including the background anthropogenic emissions, as predicted by SSP245, and will increase the types of species tracked.

These estimates will be extended to metrics of environmental impact in the full 10-year simulations for 2050.

Milestones

- Two 1-year GCHP simulations set in 2019 were completed: one without launch emissions and one with launch emissions corresponding to the RP-1 scenario.

Major Accomplishments

- The output files for the first month of the 2019 1-year GCHP simulations were analyzed, and the observed and expected results were compared.

Publications

None.

Outreach

Progress on all ASCENT Project 91A tasks was communicated in biweekly calls with the FAA, as well as collaborators at the University of Illinois Urbana-Champaign (from ASCENT Project 91B) and the Aerospace Corporation. Further updates were reported in quarterly process reports, AIAA SciTech 2023, and the 2023 ASCENT Fall Meeting in Arlington, Virginia.

Awards

None.

Student Involvement

During the reporting period of AY 2022–2023, the MIT graduate student involved with this task was Clara Ziran Ma.

Plans for Next Period

Necessary modifications to GCHP code will be made to include the boundary conditions and background emissions specified in SSP245. The final four simulation runs will be executed for the baseline scenario, CH₄ scenario, H₂ scenario, and RP-1 scenario. Each run will be set in 2050, with a duration of 10 years, and will be executed at a grid resolution of C90.

References

- Ravishankara, A. R., Daniel, J. S., & Portmann, R. W. (2009). Nitrous oxide (N₂O): the dominant ozone-depleting substance emitted in the 21st century. *science*, 326(5949), 123-125.
- United States Environmental Protection Agency (2005) "Fact Sheet of NO_y Monitoring." <https://www3.epa.gov/ttnamti1/files/ambient/pm25/spec/noysum2.pdf>



Project 091B Environmental Impacts of High-altitude and Space Vehicle Emissions

University of Illinois at Urbana-Champaign

Project Lead Investigator

Dr. Donald Wuebbles
Department of Atmospheric Sciences
University of Illinois
105 S. Gregory Street
Urbana, IL 61801
217-244-1568
wuebbles@illinois.edu

University Participants

University of Illinois at Urbana-Champaign

- P.I.: Dr. Donald Wuebbles
- Period of Performance: January 1, 2023 to September 30, 2023 (partial year; project started January 1, 2023)
- Tasks:
 1. Examine the environmental impacts of technologies related to scenarios for extensive potential use of high-altitude vehicles, including rockets, and their associated emissions by mid-century
 2. Coordinate with Massachusetts Institute of Technology (MIT) and Aerospace Corporation in these studies

Project Funding Level

Support from the FAA over this time period was approximately \$175,000; an additional \$175,000 of in-kind matching support was provided by the University of Illinois.

Investigation Team

- Dr. Donald Wuebbles (P.I.), project oversight
- Swarnali Sanyal and Rachana Pradhan (postdoctoral associates), conducting studies and performing analyses with the Community Earth System Model WACCM, a three-dimensional atmospheric climate-chemistry model including the whole atmosphere.

Task 1 – Revisiting High-Speed Civil Transports and Their Potential Effects on Ozone and Climate

University of Illinois at Urbana-Champaign

Major Goals

This project uses state-of-the-art technical modeling of atmospheric climate and chemistry processes in association with expert analysis to develop an assessment of the potential impacts of rockets (high-altitude and space vehicle emissions) on the global environment, specifically the compositions of gases and particles in the global atmosphere (troposphere, stratosphere, mesosphere, and above) and the resultant potential impacts on the Earth's climate. This assessment is needed by policy-makers to understand the potential effects of projected rocket emissions on the environment.

Objectives

This project uses state-of-the-art geophysical models of the Earth's climate and chemistry system that fully represent atmospheric processes from the ground to the top of the mesosphere (and above), to further improve understanding and evaluation of the environmental impacts of technologies related to scenarios for extensive potential use of high-altitude vehicles, including rockets, and their associated emissions by mid-century (approximately the year 2050). The aim, in coordination with the FAA, the Aerospace Corporation (which will develop the rocket emission scenarios), and MIT (which will also use its global modeling capabilities) is to further assess the state of understanding of potential high-altitude and space vehicle emissions on the global environment, and to publish these analyses in major science journals.

Research Approach

The study will use the WACCM of the Community Earth System Model, developed by the National Center for Atmospheric Research. This model includes 66 layers from the ground to the middle of the mesosphere, and provides a comprehensive treatment of tropospheric and stratospheric chemical processes. WACCM is one of the most advanced models for studying atmospheric processes worldwide, and one of the few with complete representation of stratospheric and mesospheric processes and above; e.g., it is one of very few models representing the quasi-biennial oscillation, which is important to stratospheric ozone. Therefore, this model is ideal for studying the environmental impacts from rockets.

Results and Discussion

Emissions from rockets and their effects on stratospheric ozone have been a subject of research since the 1970s (e.g., Prather et al., 1990; Harris and Wuebbles, 2014; Dallas et al., 2020). However, research in this area has comprised largely incomplete evaluations and has relied on poorly understood emission assumptions. A major need exists for assessment of the state of the science for understanding the environmental impacts according to the most up-to-date understanding of the potential future annual rocket emissions over the coming decades. Below, we summarize existing research relating to such emissions.

More satellites have been launched into low Earth orbit during the past few years than during the previous 60 years, as a result of a combination of larger rockets and higher launch rates. Most of this growth has come from kerosene-fueled rockets, from which black carbon (BC) emissions have doubled in the past 4 years (Miroux, 2022). Emissions from solid fuel rockets have increased only slightly. Hydrazine-fueled rocket launches have decreased during this period, because of propellant toxicity concerns. Hydrogen-fueled launches have been constant but have represented only a small fraction of all launches. Methane-fueled rockets in advance testing are expected to play a major role in the future, although the rate at which methane would replace existing rocket fuel is uncertain.

Rocket propulsion systems typically combine the exhausts from several of the four primary propellant types (by fuel: kerosene, ammonium perchlorate, hydrazine, and hydrogen). Mixed rocket emissions into the stratosphere are mostly (>90% of approximately 8 Gg/yr) a combination of CO₂, CO, H₂O, and OH; the exact amounts vary, depending on propellant and altitude. None of these major emission components significantly affect stratospheric ozone, even at implausibly higher launch rates (Larson et al., 2017). Nitrogen oxide emissions (<1%) from some rocket types can affect ozone (Ross et al., 2004), although to a lesser degree than solid fuel chlorine emissions.

Direct ozone loss caused by chlorine emissions (0.2 Gg/yr) from solid fuel rockets is well understood. Models agree on the amount and distribution (Voigt et al., 2013). Alumina emissions from solid fueled rockets (0.4 Gg/yr) cause ozone loss through heterogeneous chlorine-involving Cl_v activation reactions; the importance of these reactions are less well bounded because of uncertainties in the alumina surface area density, the extent of sulfate coating, and reaction coefficients (Danilin et al., 2003). In situ plume data suggest that ozone loss from alumina might be larger than that from chlorine (Danilin et al., 2001).

Indirect ozone loss caused by the absorption and scattering of solar radiation by rocket BC and alumina particles in the stratosphere has not yet been investigated. General principles of stratospheric processes suggest that rocket BC and alumina increase heating rates and temperatures in the stratosphere, and cause ozone loss (Lee et al., 2021). Linear scaling of solid aerosol climate mitigation models and models of rocket BC emissions (Maloney, 2022) suggest that the ozone loss from rocket BC and alumina stratospheric heating is comparable to that from chlorine emissions (Weissenstein et al., 2015).

Hydrogen-fueled projected space travel has been estimated to enhance stratospheric water by as much as 9%, thus leading to a potential 20% increase in polar stratospheric clouds in both hemispheres (Larson et al., 2017). An even larger effect of hydrogen-based space travel may arise from the expected increases in stratospheric nitrogen oxides, which, combined

with hydrogen oxide HO_x cycle perturbations, leads to a 0.5% loss of the globally averaged ozone column, with column losses in the polar regions exceeding 2%.

New space technologies, such as large low Earth orbit constellations and active removal of space debris, dispose of derelict spacecraft into the middle atmosphere. The effects of stratospheric aerosols generated by destruction of space debris during reentry is a new area of research (Boley and Byers, 2021). Reentry vaporization and lower mesosphere particle production and sedimentation are a source of stratospheric particles likely to exceed present-day launches by 2030 (Boley and Byers, 2021). Very little is known regarding the composition, sizes, and steady-state distribution of reentry particles, or their possible impact on stratospheric ozone.

A series of meetings have been jointly held with MIT and Aerospace Corporation over the past project year to develop the scenarios, which are currently almost ready for us to begin studies with the global model. The scenario development by Aerospace took longer than we had expected. We are coordinating with MIT to prepare the scenarios developed by Aerospace Corporation for the models; the student from MIT performing that translation was away for an internship over the summer and returned to MIT in September. Scenarios are being adapted to our global model, and the model calculations are now underway.

Milestones

- The model has been tested, and background atmosphere analyses for the year 2050 are underway.
- Emissions for four scenarios developed by Aerospace Corporation are being prepared for the modeling studies in coordination with MIT.
- Modeling studies will be started soon for the four scenarios and will then be evaluated for comparison with similar modeling studies made by MIT for the potential impacts on ozone and climate.
- These studies will provide important context for further studies of rocket use projections, which we will be examining next.

Publications

None.

Outreach Efforts

- Presentations at ASCENT Meetings in May 2023 and October 2023
- Presentations at the FAA AEC Roadmap meeting in May and November 2023
- Presentation at the FAA REDAC meeting in March 2023, based on slides that we sent to the FAA
- Biweekly meetings with project manager
- Monthly ICAO Impacts and Science Group (ISG) meetings (Dr. Wuebbles)

Student Involvement

Two postdoctoral associates, Swarnali Sanyal and Rachana Pradhan, were responsible for the analyses and modeling studies within the project, and for leading the initial preparation of the project reports.

Plans for Next Period

- Complete and publish studies based on the rocket emissions scenarios, in coordination with MIT and Aerospace Corporation
- Develop additional sensitivity analyses of potential rocket launch issues and key questions to enhance understanding of the envelope (range) of potential impacts on ozone and climate from such vehicles.

References

- Boley, A. C., & Byers, M. (2021). Satellite mega-constellations create risks in Low Earth Orbit, the atmosphere and on Earth. *Scientific Reports*, 11(1), 10642. <https://doi.org/10.1038/s41598-021-89909-7>
- Dallas, J. A., Raval, S., Alvarez Gaitan, J. P., Saydam, S., & Dempster, A. G. (2020). The environmental impact of emissions from space launches: A comprehensive review. *Journal of Cleaner Production*, 255, 120209. <https://www.sciencedirect.com/science/article/pii/S0959652620302560>



- Danilin, M. Y., Shia, R.-L., Ko, M. K. W., Weisenstein, D. K., Sze, N. D., Lamb, J. J., et al. (2001). Global stratospheric effects of the alumina emissions by solid-fueled rocket motors. *Journal of Geophysical Research: Atmospheres*, 106(D12), 12727-12738. <https://agupubs.onlinelibrary.wiley.com/doi/abs/10.1029/2001JD900022>
- Danilin, M. Y., Popp, P. J., Herman, R. L., Ko, M. K. W., Ross, M. N., Kolb, C. E., et al. (2003). Quantifying uptake of HNO₃ and H₂O by alumina particles in Athena-2 rocket plume. *Journal of Geophysical Research: Atmospheres*, 108(D4). <https://agupubs.onlinelibrary.wiley.com/doi/abs/10.1029/2002JD002601>
- Harris, N. R. P., & Wuebbles, D. J. (Eds.). (2014). *Chapter 5 in Scientific Assessment of Ozone Depletion: 2014, Scenarios and information for policymakers* (Vol. Global Ozone Research and Monitoring Project – Report No. 55). Geneva, Switzerland: World Meteorological Organization.
- Larson, E. J. L., Portmann, R. W., Rosenlof, K. H., Fahey, D. W., Daniel, J. S., & Ross, M. N. (2017). Global atmospheric response to emissions from a proposed reusable space launch system. *Earth's Future*, 5(1), 37-48. <https://agupubs.onlinelibrary.wiley.com/doi/abs/10.1002/2016EF000399>
- Lee, W. R., MacMartin, D. G., Visioni, D., & Kravitz, B. (2021). High-Latitude Stratospheric Aerosol Geoengineering Can Be More Effective if Injection Is Limited to Spring. *Geophysical Research Letters*, 48(9), e2021GL092696. <https://agupubs.onlinelibrary.wiley.com/doi/abs/10.1029/2021GL092696>
- Maloney, C. (2022). The Climate and Ozone Impacts of Black Carbon Emissions from Global Rocket Launches. *J. Geophys. Res.*, submitted.
- Miroux, L. (2022). Environmental limits to the space sector's growth. *Science of The Total Environment*, 806, 150862. <https://www.sciencedirect.com/science/article/pii/S0048969721059404>
- Prather, M. J., García, M. M., Douglass, A. R., Jackman, C. H., Ko, M. K. W., & Sze, N. D. (1990). The space shuttle's impact on the stratosphere. *Journal of Geophysical Research: Atmospheres*, 95(D11), 18583-18590. <https://agupubs.onlinelibrary.wiley.com/doi/abs/10.1029/JD095iD11p18583>
- Ross, M. N., Danilin, M. Y., Weisenstein, D. K., & Ko, M. K. W. (2004). Ozone depletion caused by NO and H₂O emissions from hydrazine-fueled rockets. *Journal of Geophysical Research: Atmospheres*, 109(D21). <https://agupubs.onlinelibrary.wiley.com/doi/abs/10.1029/2003JD004370>
- Weisenstein, D. K., Keith, D. W., & Dykema, J. A. (2015). Solar geoengineering using solid aerosol in the stratosphere. *Atmos. Chem. Phys.*, 15(20), 11835-11859. <https://acp.copernicus.org/articles/15/11835/2015/>



Project 092 Advanced Two-stage Turbine Rig Development

The Pennsylvania State University

Project Lead Investigator

Karen A. Thole
Distinguished Professor
Department of Mechanical Engineering
The Pennsylvania State University
START Lab, 3127 Research Drive
State College, PA 16801
814-863-8944
kthole@psu.edu

University Participants

The Pennsylvania State University (Penn State)

- P.I.: Dr. Karen Thole
- FAA Award Number: 13-C-AJFE-PSU-104
- Period of Performance: January 1, 2023 to December 31, 2023
- Tasks:
 1. Architecture/civil design of the expansion (cost-sharing scope)
 2. Electrical design of the new rig
 3. Noise Study
 4. Mechanical design
 5. Procurement
 6. Construction

Project Funding Level

For the 1-year effort, the ASCENT funding was \$1,100,000, and matching funds of \$1,225,000 were provided by Pratt & Whitney and Penn State.

Investigation Team

Prof. Karen A. Thole (P.I.), management, reporting, and oversight of all technical tasks
Scott Fishbone (project manager and research engineer), Tasks 1-6
Assoc. Res. Prof. Michael Barringer (research advisor), Tasks 1-6
Assoc. Res. Prof. Reid Berdanier (research advisor), Tasks 1-6
Justin Brumberg (research engineer), Tasks 1-6
Jeremiah Bunch (engineering technician), Tasks 1-6

Project Overview

This project will significantly advance the efficiency levels of small-core gas turbines relevant to current engines, as well as future propulsion architectures such as hybrid electric propulsion systems for large single- and twin-aisle aircraft. The motivation for this research is aimed at reducing the carbon footprint of aviation through increasing turbine thermal efficiency, while maintaining or even improving component durability. This project will expand the infrastructure and research scope of the Steady Thermal Aero Research Turbine (START) Lab at Penn State, in which a two-stage, small-core, test turbine will be designed, manufactured, commissioned, and put to use in acquiring the necessary data to meet the proposed goal. The new infrastructure will be referred to as START⁺. The proposed expansion will result in a research

turbine facility like no other in the world, and will situate turbine research in the United States at the leading edge in efficiency improvement and emissions reduction for future propulsion applications.

Task 1 – Architecture/Civil Design of the Expansion (Cost-Sharing Scope)

The Pennsylvania State University

Objectives

Architecture/civil design of the expansion will include the new compressors, two-stage turbine rig, and auxiliary equipment. The current building that houses the START Lab is assumed to be expanded to include all new equipment and will be a part of START⁺. Any building construction expansion to fit the new two-stage rig will be funded by cost-sharing from Penn State and Pratt & Whitney. A Pennsylvania Labor and Industry building permit will be needed to complete this work, and most of the engineering effort will be devoted to ensuring that this permit is obtained.

Research Approach

The research team associated with this effort in the START Lab engaged with Penn State’s Office of Physical Plant (OPP) to plan the laboratory expansion. OPP assigned a project manager, Dwayne Rush, to help oversee the project. Working with the START team, OPP crafted a request-for-proposal document including all specifications for the expansion. The contracting method chosen by OPP for the proposal is a design build model. In this model, the firm will oversee both the design of the expansion and the construction.

The request for proposal was publicly posted in February, and six “teams” representing more than 25 companies responded. OPP and START were extremely satisfied with the high interest in the project from the construction industry and reviewed the proposals together. Three firms were selected for in-person interviews on April 3, 2023, including a presentation on the design and answering of any questions. The three firms selected were Whiting-Turner, Alexander, and Barton Malow.

Penn State selected the team of Alexander, Stantec, HRG, and HF Lenz to complete the design build of the project. Their proposal was optimal in terms of technical knowledge, project management, and pricing. The team held a kickoff meeting on April 25, 2023, to review the scope of the project and begin the design. Weekly meetings were held throughout the rest of the period, focusing primarily on the START⁺ layout and permit requirements. The design began with more than 10 potential layouts (example in Figure 1).

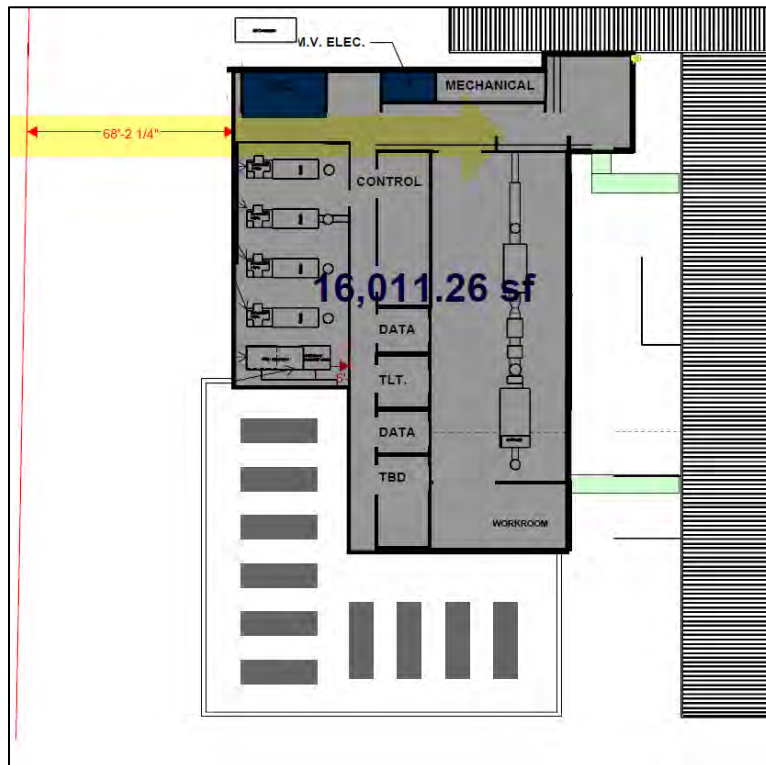


Figure 1. An early START+ layout.

As the design began to be refined, the team settled on a turbine flowing from west to east, because this design is the most cost effective, beneficial to the noise output, and optimal for the research. After that design was selected, the team further detailed the design to include the required workspaces, maintenance windows, and code requirements. At the end of June, a detailed layout (Figure 2), was selected to be reviewed by Penn State’s architect and OPP for approval. This building is hoped to be a prefabricated metal building that requires such approvals.

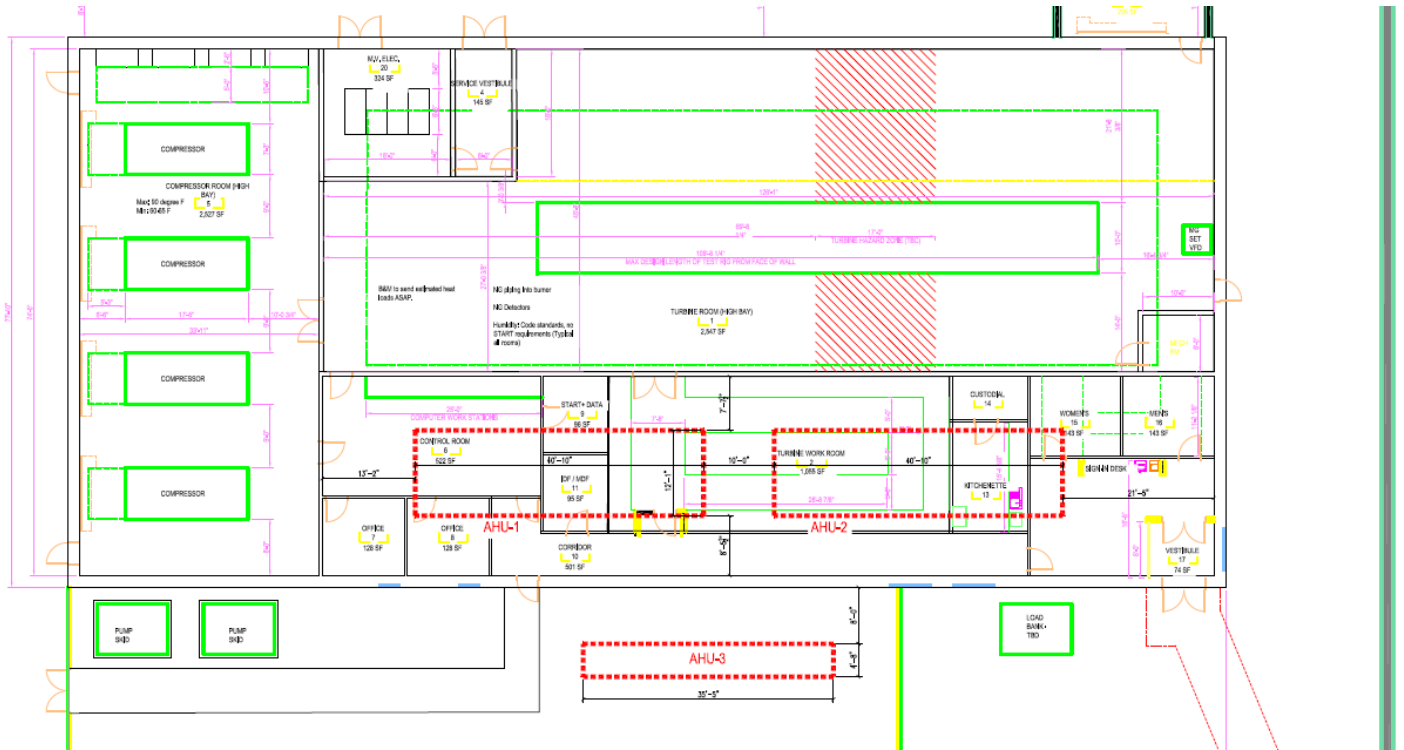


Figure 2. START+ detailed layout for Penn State approval.

The building design for START+ completed several important milestones in the summer of 2023. Geotechnical test brings were completed and analyzed to ensure that foundations will be designed to the proper soil conditions. In addition, a parking study, as required by the local township, was completed. A township requirement necessitates sufficient parking spaces for the employees of the new facility. The result was positive, indicating that only three parking spaces will be needed to replace those removed for the expansion.

In addition, during the summer, the START team met with various Penn State design leads to ensure that the facility expansion can be exempt from certain standards. These standards include building standards, which are for classrooms, to allow the building to be less expensive. All building codes will still be enforced. In addition, the compressor and turbine rooms will be allowed to operate at higher room temperatures, thereby eliminating the need for air-conditioning in those rooms and enabling savings of millions of dollars. However, the design build team, led by Alexander, continues to estimate a building cost beyond the project's budget. START believes that the elevated cost estimate is because the design is forced to include a traditional-style concrete building instead of a less expensive pre-manufactured metal building. START confirmed with the engineering firm Burns and McDonnell (BMCD) that Alexander's pricing was higher than the national average. Because of Alexander's continued resistance to change their design, which resulted in a much higher price than their initial proposal, along with feedback from Penn State, alternatives are being considered. An option is to not pursue the design build model but instead to pursue the engineering design portion with BMCD and then have Alexander perform the construction.



Task 2 – Electrical Design of the New Rig

The Pennsylvania State University

Objectives

The objectives of Task 2 are to complete the electrical design of the expansion to incorporate new compressors, a motor generator, and auxiliary equipment for the two-stage turbine. START⁺ will require more electricity from the local West Penn Power utility, which will be involved in all expansion discussions.

Research Approach

As soon as the program began, Penn State contacted the electrical utility West Penn Power to conduct a power study. The study's goal was to ensure that the START⁺ electrical loads do not impact the local power grid. On May 5, 2023, Penn State received the results. The report concluded that there will not be an impact on the local electrical grid, and only small improvements to a local transformer station will be needed. These updates will cost less than \$100,000 and will require a short lead time. In addition, the study concluded that the large air compressors can have "soft" motor starters rather than a more expensive variable frequency drive. These conclusions are extremely positive for the project, and removed a significant risk of the grid being unable to handle the program. The electrical design then proceeded to include a new transformer for START⁺ and a short run of new power lines.

Task 3 – Noise Study

The Pennsylvania State University

Objectives

The START Lab, including START⁺, is located in Ferguson Township, which has a noise ordinance that the expansion must meet. The START Lab has an extensive history of understanding and implementing noise mitigation to equipment and will hire a third-party engineering firm to assist with the planning of the expanded facility.

Research Approach

During June 2023, Stantec's noise experts visited the START Lab to measure the existing sound levels of the facility. They completed 2 days' worth of measurements with and without the existing compressors operating. The study concluded that, with the proper mitigations, START⁺ will be able to meet any local noise ordinances. The local ordinance is in effect only overnight from 7 p.m. to 7 a.m. Monday through Friday, requiring 55 dBA at the residential property line, and operations close to 62 dBA outside those hours. However, the START Lab believes in being a good neighbor, given the proximity of the Lab to the neighborhood. The noise study (results in Figure 3) concluded that the START Lab is currently below the 62-dBA limit, and suggested some improvements to the existing facility infrastructure to further lower the noise so that the operation of START⁺ will not increase the sound levels. Figure 4 indicates additional measures that will be taken with the existing START Lab to further reduce the current noise footprint.

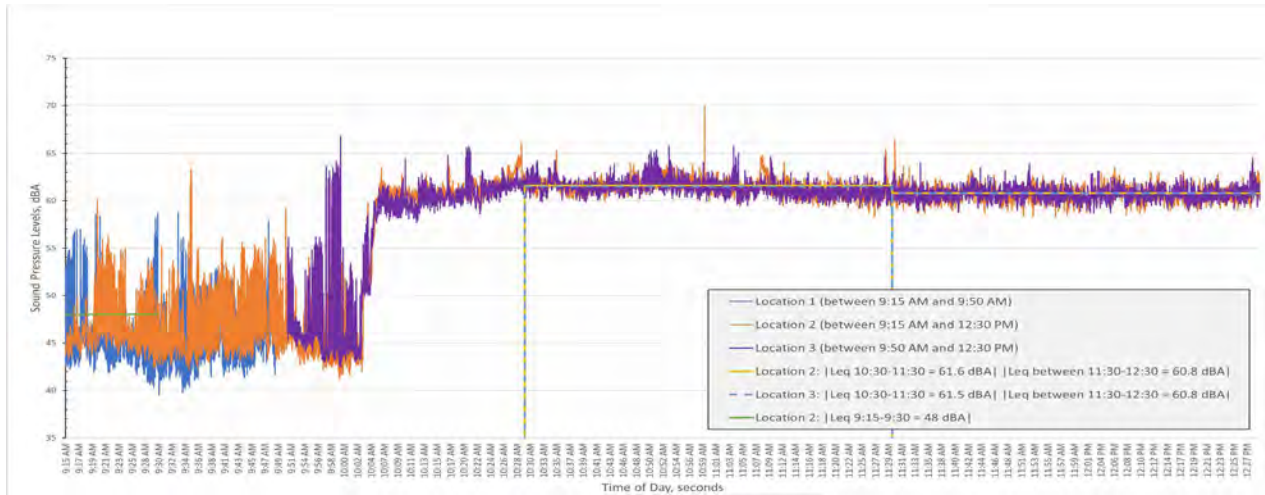


Figure 3. Existing START Lab sound levels.

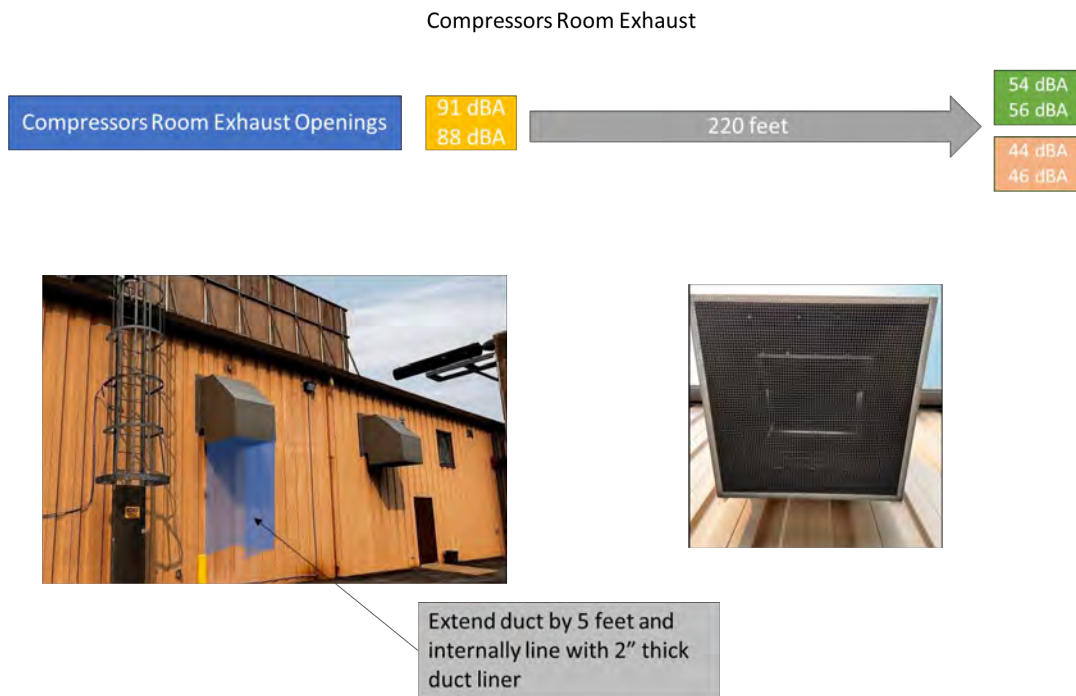


Figure 4. Suggested new mitigation strategy for existing START noise.

Task 4 – Mechanical Design

The Pennsylvania State University

Objective

The objective of Task 4 is to complete the mechanical design of the expanded facility, including the new compressors and two-stage turbine. During the first year, mechanical effort will be needed to ensure that the

architecture/civil/electrical/noise designs incorporate all design needs of the turbine. A third-party engineering firm will be used to create the mechanical design.

Research Approach

To help with the overall building design and the mechanical layout of START+, Penn State placed a purchase order with BMCD, a large engineering firm with past experience in designing turbine test facilities similar to START+. BMCD began designing the piping layout, heater, and motor generator designs.

Working with START personnel, BMCD selected CEL Aerospace to provide an initial proposal for dynamometer choices. CEL and BMCD have designed motor generators and water-brake dynamometers for other turbine test facilities of similar sizes; therefore, START personnel are confident in their success. The entire group, including START, BMCD, and CEL, met to discuss the different options available. On the basis of feedback provided in the meeting, START researchers agreed to refine the turbine drivetrain power and torque requirements to ensure that the new equipment system is sized properly. Another outcome of this study was the potential cost savings of using a water dynamometer. BMCD agreed to investigate other vendors for dynamometers to ensure that the lowest price is achieved.

BMCD and START personnel began discussions with vendors regarding the heater design for the new START+ rig. Process Combustion Corporation provided a rough order-of-magnitude proposal that met the START+ heating requirements. Their design (Figure 5) is a single-pass burner that achieves a 1,300 °F exit air temperature.

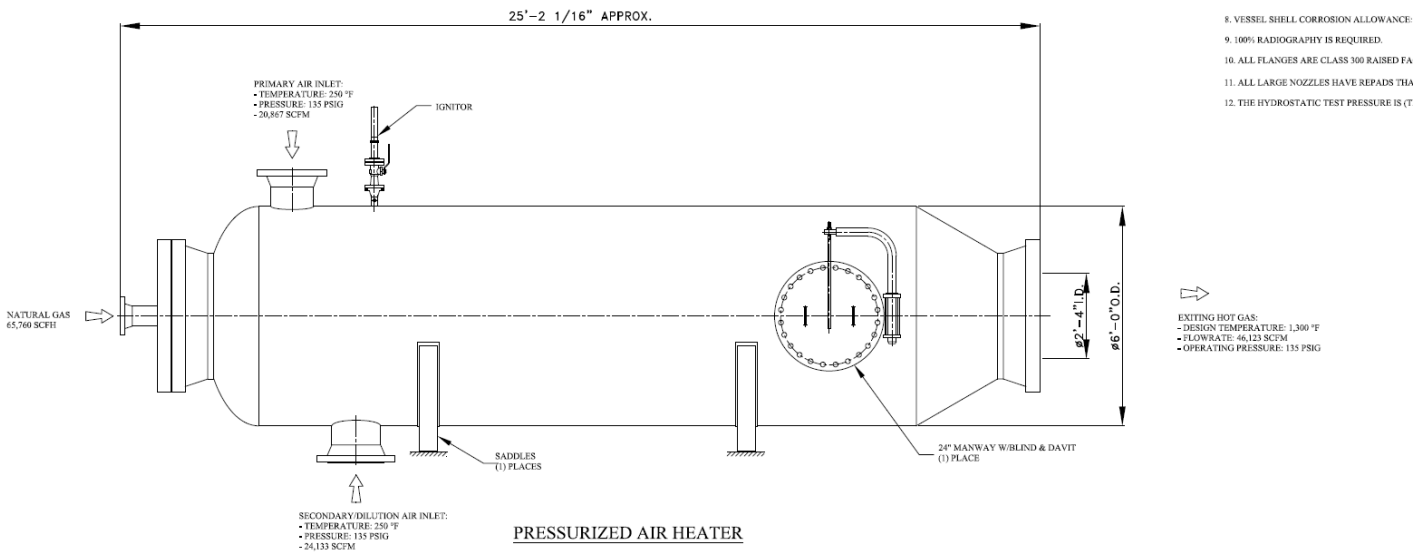


Figure 5. Process Combustion Corporation initial heater design for START+.

Task 5 – Procurement

The Pennsylvania State University

Objectives

Procurement of new compressors will be the crucial task in the first year. The compressors will set the electrical, facility, and mechanical design basis. After the compressors are ordered, and drawings are received, all aspects can move forward with the overall design of the facility.

Research Approach

The team created a request for quote (RFQ) document including all specifications for the compressors, motors, and auxiliary equipment. Two compressor vendors based in the United States have been selected to provide quotations for the program: Ingersoll Rand and FS-Elliott Company (FSE).

Ingersoll Rand submitted a proposal to supply four of their NX8000 compressors, each with a 2,250-horsepower motor. The Ingersoll Rand quote mostly met the START (RFQ) document requirements and required only slight revisions, primarily regarding the motor and controls. The compressors were able to meet the noise requirements.

FSE’s initial proposal included four of their P700 compressors with 2,000-horsepower motors. However, their compressor cooling system did not meet the START Lab RFQ requirements and required significant revisions, particularly regarding noise. After the revisions were complete, FSE did increase the horsepower of each unit to 2,250 horsepower, to properly meet the discharge pressure requirement, and exceeded the noise requirements, by upgrading options for the silencers and motors.

The results of the West Penn Power study impacted the compressor quotations for the project. Because of the requirement for “soft” motor starters, Ingersoll Rand and FSE needed time to update their quotations from a variable frequency drive type of startup system.

Because both companies manufacture high-quality compressors, the selection process was difficult and lasted almost 8 months. After multiple rounds of questions and quotations, START personnel selected FSE because of their better pricing and the technical reasons presented in Table 1.

Table 1. Technical comparison between START+ compressor vendors.

Ingersoll Rand benefits	FS-Elliott benefits
Quick sales support response	Consistent with current units, experience, and steadiness
Overall number of compressors in the field	More economical fluid cooler design
Confidence in the inlet, oil cooler, and after-cooler setup	Higher air flowrate for same pressure
	Integration with current units
Ingersoll Rand weaknesses	FS-Elliott weaknesses
Concerns regarding flow pressure steadiness	Spare-part lead times
Number of fluid coolers required (IR 13 vs. FSE 7)	Concerns regarding after-coolers
Control system costs	

The principal factor in selecting the vendor was Ingersoll Rand’s inability to ensure the air flow pressure steadiness that START+ requires at the compressor exit. On the basis of past experience with the existing START Lab, the FSE compressors can run consistently with a steady discharge pressure variation of less than or equal to 0.10-0.15 psi, which is critical for turbine research.

Task 6 – Construction

The Pennsylvania State University

Objectives

The Penn State execution plan will involve construction firms early in the design process to lower cost and improve the design, as part of Penn State’s cost-sharing. By using an engineering and construction firm, the project will be able to start construction after the Pennsylvania Labor and Industry permit is received.

Research Approach

During work with Penn State OPP, a design-build method for the expansion was selected with the firm Alexander. Thus, the construction team onboarding was pushed to the beginning of the project. The design build method has been helpful, in

that it has allowed the team to see how inflation and costs have changed since the project was estimated. Unfortunately, Alexander was unable to keep to their budget. The START team is working with OPP to determine the best path forward to keep cost lower.

Milestones

Milestone	Completed or planned date
Building permit application submitted	May 31, 2024
Noise study completed	June 30, 2023
Compressor purchased	September 22, 2023
Contracts awarded for construction	April 25, 2023

Major Accomplishments

START selected the Alexander team to lead the design build process of START+ in April 2023.

The West Penn Power study was received in May 2023 and permitted the project to move forward.

The noise study was completed by Stantec Engineering in June 2023 and had a positive outcome. The new START+ laboratory expansion will be able to meet any local township noise ordinances with proper mitigations.

The purchase order was issued to FSE for the compressor engineering effort in September 2023. The compressors met all START Lab requirements and were less expensive than the alternative vendor, Ingersoll Rand.

Publications

A Penn State article about the program was released: <https://news.engr.psu.edu/2023/thole-karen-start-lab-expansion.aspx>

Outreach Efforts

A news article has been distributed about START+ publicly and shared with PA-15 Representative Glenn Thompson’s staff. <https://news.engr.psu.edu/2023/thole-karen-start-lab-expansion.aspx>

Dr. Thole presented an update on the project to the combined CLEEN and Ascent community on May 4, 2023, at the FAA meeting. In addition, the START team presented the early designs to Pratt & Whitney, Solar Turbines, NASA, and other turbomachinery OEM’s during Center of Excellence meetings.

Dr. Thole presented an update on the project to Boeing during a visit to the START Lab on August 16, 2023. Dr. Thole also presented to the National Academy’s Aeronautics Engineering and Science Board on the planned START+ upgrades during the NASA University Leadership Initiative panel.

Finally, Dr. Thole delivered a keynote speech highlighting the program at the 2023 DOE UTSR conference at Penn State on October 30, 2023.

Awards

None.

Student Involvement

None.

Plans for Next Period

During the next period, START will oversee the new turbine rig design through strong collaborations with Pratt & Whitney. The team will work to select a turbine engineering firm by interviewing multiple candidates. START will create a request for quotations, review all bids, and select the firm that best meets the cost, schedule, and quality requirements of the program.



After issuing the award, the team will begin preliminary design by completing the rig layout, confirm with Pratt & Whitney the entire scope of the test turbine, generate a bill of material, plan material purchases with long lead times, and hold a review meeting to approve the design.

In addition, the START team will integrate the entire facility by having BMCD work with the building design firm to lay out piping, building penetrations, and supports, and ensure proper access for laboratory personnel. BMCD, with START personnel, will design a motor generator to dissipate the turbine power, while exploring additional capabilities. The team will create a request for quotation, review all bids, and select the company that best meets the cost, schedule, and quality requirements of the program. The group will collaborate with the selected vendor to develop manufacturing drawings so that the turbine rig layout can be completed.

The START team will order remaining air compressor components and complete manufacturing. This process will include reviewing manufacturing quality documents, such as the compressor starter, starter layout, fluid cooler general arrangement drawings, and manufacturing reports; resolving instances of non-conformance; and approving final inspection reports. START representatives will attend factory performance testing and ensure that the compressors meet all quoted performance metrics, and will review testing data, such as hydrotests, flow, and pressure results. After the compressors are complete, the START team will oversee installation of equipment in START* to ensure that the compressors fit on their anchor bolts and are grouted into place, per the compressor vendor's requirements, and that all lifting requirements are met.

The START and OPP teams will continue to attend weekly construction review meetings to ensure that the schedule and budget remain within the plan. START will help solve any issues as they arise between the contractor and Penn State's OPP, and facilitate planning installation between the contractor and equipment vendors. The team will review quality documents to verify that all drawings and standards by the construction firm are maintained, and will conduct walkthrough inspections with the design firm to ensure that drawing requirements and tolerances are within specifications.



Project 093A Collaborative Research Network for Global Sustainable Aviation Fuel Supply Chain Development

Massachusetts Institute of Technology

Project Lead Investigators

Dr. Raymond Speth
Principal Research Scientist
Department of Aeronautics & Astronautics
Massachusetts Institute of Technology
77 Massachusetts Ave, Building 33-316, Cambridge, MA 02139
617-253-1516
speth@mit.edu

Dr. Florian Allroggen
Executive Director Aerospace Climate & Sustainability; Research Scientist
Laboratory for Aviation and the Environment
Massachusetts Institute of Technology
77 Massachusetts Ave, Building 33-115A, Cambridge, MA 02139
617-715-4472
fallrogg@mit.edu

University Participants

Massachusetts Institute of Technology (MIT)

- P.I.s: Dr. Raymond Speth; Dr. Florian Allroggen
- FAA Award Number: 13-C-AJFE-MIT, Amendment Nos. 114 and 115 (NCE to September 30, 2024)
- Period of Performance: January 1, 2023 to September 30, 2024
- Tasks (for reporting period January 1, 2023 to September 30, 2023):
 1. Assess global biomass availability for sustainable aviation fuel (SAF) production
 2. SAF supply chain design for Africa, with specific focus on sub-Saharan Africa
 3. Facilitate a network for capability building for global SAF supply chain development
 4. Support knowledge sharing and coordination across ASCENT Project 93 universities

Hasselt University (UHasselt, through subaward from MIT)

- P.I.: Prof. Robert Malina
- Period of Performance: September 1, 2016 to September 30, 2024
- Tasks (for reporting period January 1, 2023 to September 30, 2023):
 1. *(omitted, led by MIT)*
 2. SAF supply chain design for Africa, with specific focus on sub-Saharan Africa
 3. Facilitate a network for capability building for global SAF supply chain development
 4. Support knowledge sharing and coordination across ASCENT Project 93 universities

Project Funding Level

This project received \$575,000 in FAA funding and \$575,000 in matching funds. Sources of matching funds are approximately \$54,000 from MIT, plus third-party in-kind contributions of \$521,000 from Earth Force Technologies Inc.

Investigation Team

Massachusetts Institute of Technology

- Dr. Raymond Speth (P.I.), All MIT Tasks
- Dr. Florian Allroggen (co-P.I.), All MIT Tasks
- Dr. Sergey Paltsev (co-investigator), Task 1
- Dr. Jennifer Morris (co-investigator), Task 1
- Dr. Angelo Gurgel (co-investigator), Task 1
- Dr. Niamh Keogh (postdoctoral associate), Tasks 2 and 3
- Yuxin Shu (graduate research assistant), Task 1
- Andy Eskenazi (graduate research assistant), Task 1

Hasselt University

- Prof. Robert Malina (P.I.), All UHasselt Tasks
- Francis Mwangi (graduate research assistant), Tasks 2, 3, and 4
- Alessandro Martulli (graduate research assistant), Task 2

Project Overview

Large-scale production of SAFs around the globe is needed to meet aviation’s ambitious decarbonization goals. Production scale-up will require identification of waste feedstocks and land for energy crop cultivation, sustainable farming and land use practices, and investments in conversion capacity, as well as fuel and feedstock logistics. Access to data, expertise, and capital remains a major roadblock to successfully creating these supply chains around the globe. Under ASCENT 93, MIT aims to (1) assess global biomass availability, broken down by region, and the associated potential for SAF production with current and improved conversion technologies; (2) analyze opportunities and roadblocks for supply chain designs, specifically focusing on Africa; (3) share supply chain designs and feedstock availability assessments with other members of the ASCENT 93 team; and (4) facilitate a network of academics around the globe to support capacity building for SAF production.

Task 1 - Assess Global Biomass Availability for SAF Production

Massachusetts Institute of Technology

Objective

Under Task 1, the MIT team is developing a detailed assessment of biomass availability for producing bio-based transportation fuels in different regions of the world, considering current and future land and sustainability practices and analyzing competing demands for land from agriculture and other uses. We aim to provide a disaggregated biomass availability assessment by world region and feedstock type. For this purpose, we will combine a bottom-up approach to provide a detailed regional identification of biomass potential with a top-down approach for representing land conversion costs, endogenous changes in land and agriculture intensification opportunities, and price-induced changes in energy efficiency in production and transportation technologies. During Year 1, efforts focused on the bottom-up modeling.

Research Approach

The goal of the bottom-up approach is to develop an assessment of future biomass availability potential and associated SAF production potential across different regions from 2030 to 2100. While a comprehensive set of feedstocks will be assessed, the initial analysis is focused on energy crops. To account for a wide range of underlying assumptions, we define three preliminary scenarios to assess future biomass availability (see Table 1).

Table 1. Scenario assumptions for biomass availability projection.

	Scenario 1 (S1)	Scenario 2 (S2)	Scenario 3 (S3)
Shared Socioeconomic Pathways (SSP)	1	2	5
Representative Concentration Pathways (RCP)	2.6	4.5	8.5

Although the analysis will be rolled out globally, we chose Kenya as a primary case study. In Kenya, we focus on five energy crops given their potential identified in prior studies. The respective crops and their associated SAF conversion pathways are shown in Table 2.

Table 2. Feedstocks and pathways.

Crop	Pathway
Jatropha	Hydroprocessed esters and fatty acids (HEFA)
Rapeseed	
Sunflower	
Sugarcane	Alcohol-to-Jet (ATJ)
Sorghum	

The analysis framework for calculating bioenergy availability is built around two key modeling steps, as shown in Figure 1.

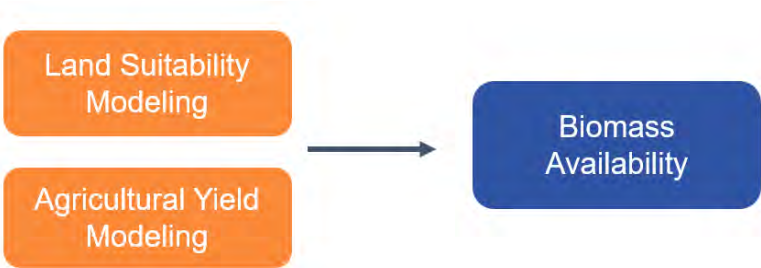


Figure 1. Flow chart of analysis.

1. **Land suitability** is estimated using data from the Land Use Harmonization (LUH2) model developed from the World Climate Research Program Coupled Model Intercomparison Project (CMIP6). LUH2 contains land use projections with a spatial resolution of $0.25^\circ \times 0.25^\circ$ on an annual basis. Data are available for each of our scenarios. We assume land to be eligible for conversion into cropland for SAF production if it is classified as non-forested primary land, forested secondary land, non-forested secondary land, or pastureland (including pasture and rangeland). To avoid competition with livestock grazing, pastureland availability is considered, as illustrated in Figure 2. Given that the assessment of pastureland availability within Scenario 3 (shared socioeconomic pathway (SSP)5 and representative concentration pathway (RCP) 8.5) is an ongoing consideration, our discussion is currently confined to Scenario 1 (S1) and Scenario 2 (S2). To derive pastureland availability rates, we assumed meat consumption to adhere to the guidelines of the Healthy Diet (HDiet) from the Harvard Medical School in Scenario 1. In contrast, Scenario 2 anticipates an approximately 30% increase in livestock demand compared to Scenario 1 (Kriegler et al., 2017; Stehfest et al., 2009) accordingly, we projected a 30% rise in meat consumption in S2 compared to S1. Additionally, we assumed the meat per livestock data from Our World in Data; land intensity of livestock per acre remains unchanged.
2. **Agricultural yields:** Our data source for agricultural yield information is the Global Agro Ecological Zones (GAEZ) version 4.0 model, which is developed by the Food and Agriculture Organization of United Nations (FAO) and the International Institute of Applied System Analysis (IIASA). The GAEZ model assesses crop suitability at a 5-arc-minute grid cell resolution by evaluating crop-specific growth requirements aligned with local climate and soil conditions across different agricultural input levels and time frames. The model projects attainable yield in increments of 30 years. For our analysis, we select three specific 30-year periods: 2011–2040, 2041–2070, and 2071–2100. In each of these time periods, any land with suitability level below “moderate” is excluded from consideration. One of six climate models, GFDL-ESM2M, was selected for this case study, and the other five climate

models will be covered in the future study. We assume high input levels, no CO₂ fertilization, and rainfed systems to mitigate the diversion of water resources from food crops or human consumption.

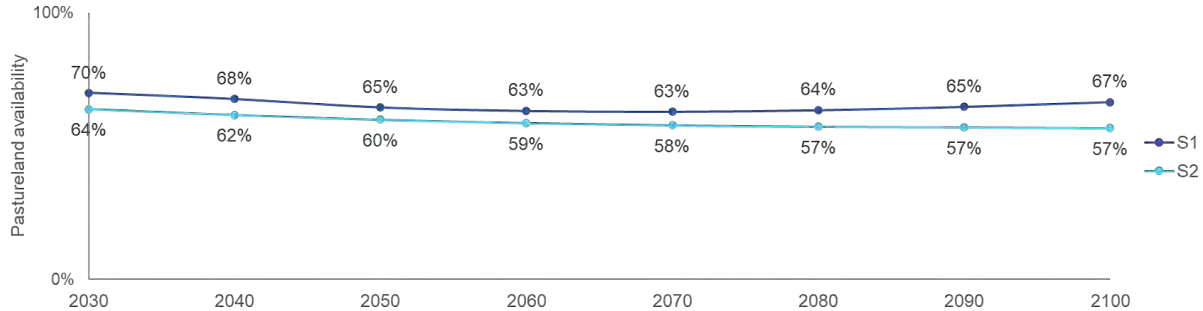


Figure 2. Pastureland availability for each decade from 2030 to 2100 in Scenarios 1 (S1) and 2 (S2).

To derive biomass availability, we interpolated land suitability to agricultural yield with a 5-arc-minute grid cell resolution. This process yields data on available areas for each land use type and the yield of each feedstock in every grid cell, factoring in latitude and longitude. This data set will serve as a resource for future analyses. A summary of the methods utilized and an example of its application for the Kenya case study is shown in Figure 3.

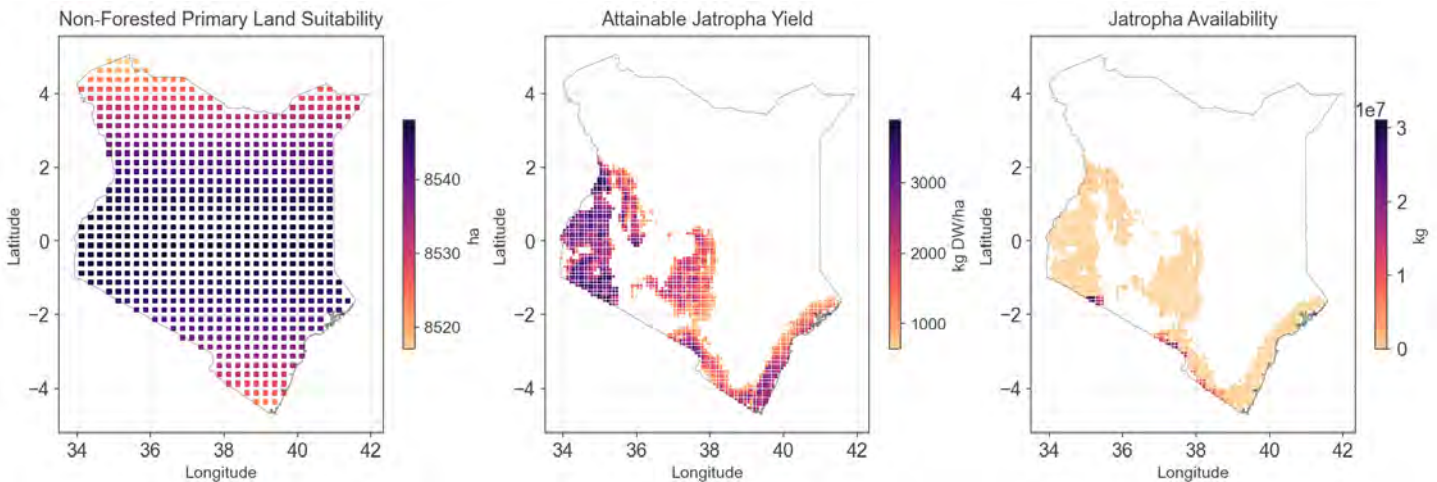


Figure 3. Land suitability, agriculture yield, and biomass availability in 2050 for Jatropha on non-forested primary land under Scenario 1 with the GFDL-ESM2M climate model in Kenya. DW, dry weight.

Milestone

A proof-of-concept of the bottom-up method was developed for the Kenya case study and has been validated for other geographies.

Major Accomplishments

The MIT team developed a modeling pipeline for assessing global biomass potential assessments at high spatial resolution and applied it to the Kenya case.



Publications

None.

Outreach Efforts

None.

Awards

None.

Student Involvement

During this reporting period, MIT graduate student Yuxin Shu was involved in this task.

Plans for Next Period

During the coming reporting period, the MIT team aims to roll out the bottom-up global biomass potential assessments to other world regions. Furthermore, waste and residue streams will be added to the bottom-up analysis. Additional steps will be taken to harmonize the data with top-down modeling.

References

- Demsky, S. E. (2023). Analysis of Double Cropping to Expand Sustainable Aviation Fuel Production in the United States [Thesis, Massachusetts Institute of Technology]. <https://dspace.mit.edu/handle/1721.1/151600>
- FAO and IASA. Global Agro Ecological Zones version 4 (GAEZ v4). [Date accessed and/or downloaded].
URL: <http://www.fao.org/gaez/>
- Hurttt, G. C., Chini, L., Sahajpal, R., Froelking, S., Bodirsky, B. L., Calvin, K., Doelman, J., Fisk, J., Fujimori, S., Goldewijk, K. K., Hasegawa, T., Havlik, P., Heinemann, A., Humpenöder, F., Jungclaus, J., Kaplan, J., Krisztin, T., Lawrence, D., Lawrence, P., Mertz, O., Pongratz, J., Popp, A., Riahi, K., Shevliakova, E., Stehfest, E., Thornton, P., van Vuuren, D., Zhang, X. (2019). Harmonization of Global Land Use Change and Management for the Period 2015-2300. Version 20190529. Earth System Grid Federation. <https://doi.org/10.22033/ESGF/input4MIPs.10468>
- Hurttt, G. C., Chini, L., Sahajpal, R., Froelking, S., Bodirsky, B. L., Calvin, K., Doelman, J., Fisk, J., Fujimori, S., Goldewijk, K. K., Hasegawa, T., Havlik, P., Heinemann, A., Humpenöder, F., Jungclaus, J., Kaplan, J., Krisztin, T., Lawrence, D., Lawrence, P., Mertz, O., Pongratz, J., Popp, A., Riahi, K., Shevliakova, E., Stehfest, E., Thornton, P., van Vuuren, D., Zhang, X. (2019). Harmonization of Global Land Use Change and Management for the Period 850-2015. Version 20190529. Earth System Grid Federation. <https://doi.org/10.22033/ESGF/input4MIPs.10454>
- Hurttt, G. C., L. Chini, R. Sahajpal, S. Froelking, B. L. Bodirsky, K. Calvin, J. C. Doelman, J. Fisk, S. Fujimori, K. K. Goldewijk, T. Hasegawa, P. Havlik, A. Heinemann, F. Humpenöder, J. Jungclaus, J. Kaplan, J. Kennedy, T. Kristzin, D. Lawrence, P. Lawrence, L. Ma, O. Mertz, J. Pongratz, A. Popp, B. Poulter, K. Riahi, E. Shevliakova, E. Stehfest, P. Thornton, F. N. Tubiello, D. P. van Vuuren, X. Zhang (2020). Harmonization of Global Land-Use Change and Management for the Period 850-2100 (LUH2) for CMIP6. Geoscientific Model Development Discussions. <https://doi.org/10.5194/gmd-2019-360>
- Iii, K., & T, W. (2021). Cost Optimization of US Sustainable Aviation Fuel Supply Chain Under Different Policy Constraints [Thesis, Massachusetts Institute of Technology]. <https://dspace.mit.edu/handle/1721.1/140169>
- Keywan Riahi, D.P. van Vuuren, E. Kriegler, J. Edmonds, B.C. O'Neill, S. Fujimori, N. Bauer, K. Calvin, R. Dellink, O. Fricko, W. Lutz, A. Popp, J. Crespo Cuaresma, Samir KC, M. Leimbach, L. Jiang, T. Kram, S. Rao, J. Emmerling, K. Ebi, T. Hasegawa, P. Havlik, F. Humpenöder, L. Aleluia Da Silva, S. Smith, E. Stehfest, V. Bosetti, J. Eom, D. Gernaat, T. Masui, J. Rogelj, J. Strefler, L. Drouet, V. Krey, G. Luderer, M. Harmsen, K. Takahashi, L. Baumstark, J.C. Doelman, M. Kainuma, Z. Klimont, G. Marangoni, H. Lotze-Campen, M. Obersteiner, A. Tabeau, & M. Tavoni. The Shared Socioeconomic Pathways and their energy, land use, and greenhouse gas emissions implications: An overview, Global Environmental Change, Volume 42, Pages 153-168, 2017, ISSN 0959-3780, DOI:110.1016/j.gloenvcha.2016.05.009
- Kriegler, E., Bauer, N., Popp, A., Humpenöder, F., Leimbach, M., Strefler, J., Baumstark, L., Bodirsky, B. L., Hilaire, J., Klein, D., Mouratiadou, I., Weindl, I., Bertram, C., Dietrich, J.-P., Luderer, G., Pehl, M., Pietzcker, R., Piontek, F., Lotze-Campen, H., ... Edenhofer, O. (2017). Fossil-fueled development (SSP5): An energy and resource intensive scenario for the 21st century. Global Environmental Change, 42, 297-315. <https://doi.org/10.1016/j.gloenvcha.2016.05.015>
- OECD (2023), Meat consumption (indicator). doi: 10.1787/fa290fd0-en (Accessed on 22 November 2023)



- Ritchie, H., Pablo Rosado and Max Roser (2019) - "Meat and Dairy Production" Published online at OurWorldInData.org. Retrieved from: '<https://ourworldindata.org/meat-production>' [Online Resource]
- Staples, M. D., Malina, R., Suresh, P., Hileman, J. I., & Barrett, S. R. H. (2018). Aviation CO₂ emissions reductions from the use of alternative jet fuels. *Energy Policy*, 114, 342-354. <https://doi.org/10.1016/j.enpol.2017.12.007>
- Stehfest, E., Bouwman, L., van Vuuren, D. P., den Elzen, M. G. J., Eickhout, B., & Kabat, P. (2009). Climate benefits of changing diet. *Climatic Change*, 95(1), 83-102. <https://doi.org/10.1007/s10584-008-9534-6>
- Wilfong, A., & O'Quinn, T. O. (2018, February). MF3394 how much meat to expect from your animal - Kansas State University. <https://bookstore.ksre.ksu.edu/pubs/MF3394.pdf>

Task 2 - SAF Supply Chain Design for Africa, with Specific Focus on Sub-Saharan Africa

Massachusetts Institute of Technology and University of Hasselt

Objectives

This task focuses on studying the current hurdles for the development of a local SAF industry in Africa, to develop science-driven advice to help overcome these hurdles, and to help kickstart the SAF industry in Africa.

To do so, we develop an understanding of the current economic, social, environmental, technological, logistical, and legal hurdles for SAF development in Africa. We then create quantitative assessments of supply chain designs that leverage the specific opportunity space on the African continent. This entails (techno-)economic assessments and environmental lifecycle assessments of selected supply chain designs and the inclusion of regulatory and policy considerations.

During the current reporting period, this task focused on (1) developing a systematic overview of the supply chain challenges on the African continent; and (2) working with local partners in one geography (i.e., Kenya) to identify the most promising SAF pathways for analysis.

Research Approach

A set of frameworks was developed and analyses were conducted for the Kenyan context, which informed the "Second High-Level Meeting on SAF Development and Deployment," which was held in September 2023 in Nairobi (see Task 3).

Stakeholder identification for SAF production in Kenya

The team conducted a comprehensive mapping of stakeholders in the production of SAF in Kenya, covering the full supply chain from feedstock production to fuel uplift, as well as relevant government actors and financing institutions (see Figure 4). The stakeholder mapping was used to organize the high-level meeting on accelerating SAF production in Kenya (see Task 3).

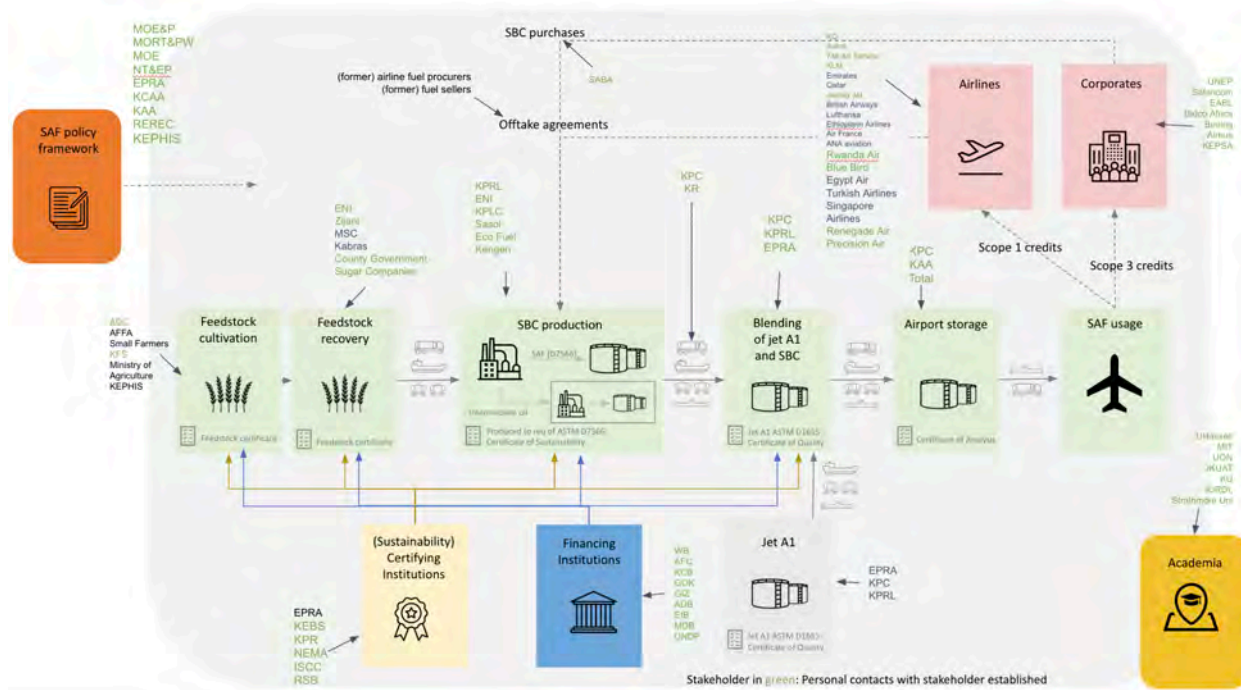


Figure 4. Sustainable aviation fuel (SAF) stakeholder mapping for Kenya. MOE&P, Ministry of Energy and Petroleum; MORT&PW, Ministry of Roads and Transport; MOE, Ministry of Education; NT&EP, National Treasury and Economic Planning; EPRA, Energy and Petroleum Regulatory Authority; KCAA, Kenyan Civil Aviation Authority; KAA, Kenyan Airports Authority; RERC, Rural Electrification and Renewable Energy Corporation; KEPHIS, Kenya Plant Health Inspectorate Service; ADC, Agricultural Development Corporation; AFFA, Agriculture and Food Authority; KFS, Kenya Forestry Service; KPRIL, Kenya Petroleum Refineries Limited; KPLC, Kenya Power and Lighting Company; SABA, Sustainable Aviation Buyers Alliance; KPC, Kenya Pipeline Company; KR, Kenya Railway Corporation, KEBS, Kenya Bureau of Standards; KPR, Kenya Police Reserve; NEMA, National Environmental Management Authority; ISCC, International Sustainability and Carbon Certification; RSB, Roundtable on Sustainable Biomaterials; WB, World Bank; AFC, Agricultural Finance Corporation; KCB, Kenya Commercial Bank; GOK, Government of Kenya; GIZ Deutsche Gesellschaft für Internationale Zusammenarbeit; ADB, African Development Bank; GOK, Government of Kenya; GIZ Deutsche Gesellschaft für Internationale Zusammenarbeit; ADB, African Development Bank; UNDP, United Nations Development Programme; UNEP, United National Environmental Programme; EABL, East African Breweries Limited; KESPA, Kenya private Sector Alliance; UHasselt, University of Hasselt; MIT, Massachusetts Institute of Technology; UON, University of Nairobi; JKUAT, Jomo Kenyatta University of Agriculture and Technology; KU, Kenyatta University; KIRDI, Kenya Industrial Research and Development Institute.



Table 3. Kenya stakeholder list.

ACTION	STAKEHOLDERS	ROLES
SAF Policy	Ministry of Energy and Petroleum (MOE&P) Ministry of Roads and Transport (MORT&PW) National Treasury and Economic Planning (NT&EP) Energy and Petroleum Regulatory Authority (EPRA) Kenyan Civil Aviation Authority (KCAA) Kenyan Airports Authority (KAA) Rural Electrification and Renewable Energy Corporation (REREC) Kenya Plant Health Inspectorate Service (KEPHIS)	Policy development Steering committee Stakeholder awareness Approval of policy
SAF Financing	World Bank (WB) Kenya Commercial Bank (KCB) Government of Kenya (GOK) Deutsche Gesellschaft für Internationale Zusammenarbeit (GIZ)	Provision of financial resources for de-risking
Corporates	International Air Transportation Association (IATA) African Airlines Association (AFRAA) African Civil Aviation Commission (AFCAC) Kenyan Association of Air Operators (KAAO)	Validation and awareness creation
Academia	University of Nairobi (UON) Jomo Kenyatta University of Agriculture and Technology (JKUAT) Strathmore University	Conducting SAF research
Sustainability Certification	Energy and Petroleum Regulatory Authority (EPRA) Kenya Bureau of Standards (KEBS) Kenya Police Reserve (KPR) National Environmental Management Authority (NEMA) International Sustainability and Carbon Certification (ISCC) Roundtable on Sustainable Biomaterials (RSB)	Certification of SAF
Feedstock Recovery	ENI Zijani County Government Sugar Companies	Collection of wastes
Feedstock Cultivation	Agricultural Development Corporation (ADC) Agriculture and Food Authority (AFFA) Small Farmers Kenya Forestry Service (KFS) Ministry of Agriculture KEPHIS	Feedstock Production
SAF Production	ENI Kenya Petroleum Refineries Limited (KPRL) Sasol	Production of SAF
Airport Storage	Kenya Pipeline Company (KPC) KAA Total Energies	Storage and refueling
SAF Transportation	KPC Kenya Railway Corporation (KR)	Transportation of jet fuel Transportation of raw materials
SAF Usage	Kenya Airways (KQ) Astral 748 Air Service	Fuel uptake Policy validations

Techno-economic analyses of a power-to-liquid plant in Kenya

The team also pursued techno-economic analysis of production plants. This work, together with research on the techno-economic potential of a hydroprocessed esters and fatty acids (HEFA) plant in Kenya conducted by UHasselt under World Bank funding, was presented during the SAF workshop in Nairobi.

The research under this task explored the techno-economic potentials of scaling up power-to-liquid (PtL) SAF production in Kenya. Wilson Airport (Nairobi, Kenya) was chosen as an initial case study as it predominantly serves safari flights for tourists, who can be presumed to have a higher willingness-to-pay to cover the green premium. Displacing fossil fuel demand for a quarter of the flights departing from Wilson Airport would require 567 barrels per day (bpd) of SAF. Under the Fischer-Tropsch PtL production pathway, 361 GWh of renewable electricity and 51,700 t of CO₂ would be needed annually to meet this demand. The team modeled the minimum selling price (MSP) of fuel produced from a Fischer-Tropsch PtL plant, considering Kenyan specific economic conditions, and assuming 2030 technology levels. The electricity source was assumed to be wind energy, and several CO₂ sources available in the region were considered. As shown in Figure 5, the MSP of the PtL SAF produced is dependent on the source of the CO₂. The MSP ranges from \$2.25 to \$4.28/L for CO₂ captured from biomethane or ethanol production to \$3.81 to \$4.28/L from high-cost direct air capture. These price ranges consider technology that can be assumed to be available in the 2030 timeframe.

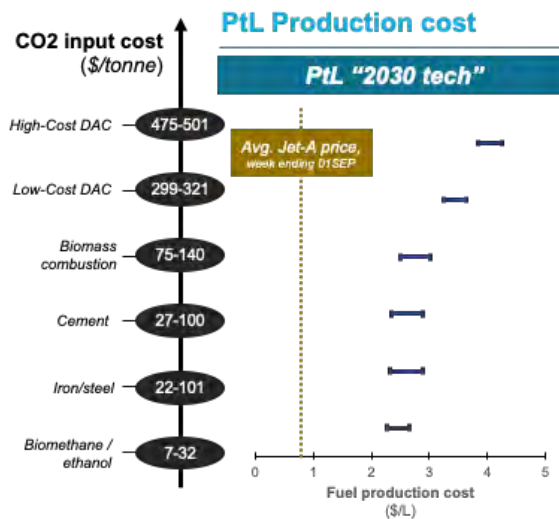


Figure 5. Minimum selling price of power-to-liquid (PtL) fuel production to supply Wilson Airport (Nairobi, Kenya) for different sources of CO₂. Production technology assumes year-2030 levels. DAC, direct air capture

The MSP of PtL SAF is primarily driven by the capital cost of the plant. Under the baseline economic conditions for Kenya, the weighted average cost of capital (WACC) is assumed to be ~18%; the global WACC for renewable energy firms is 9%. Figure 6 depicts the corresponding reduction in MSP for the PtL SAF with decreasing WACC, assuming 2030 technology, wind electricity, and CO₂ captured from a steel plant. The results show that if the WACC in Kenya could be decreased from ~18% to the global average of 9%, this would correlate to a 30% reduction in MSP.

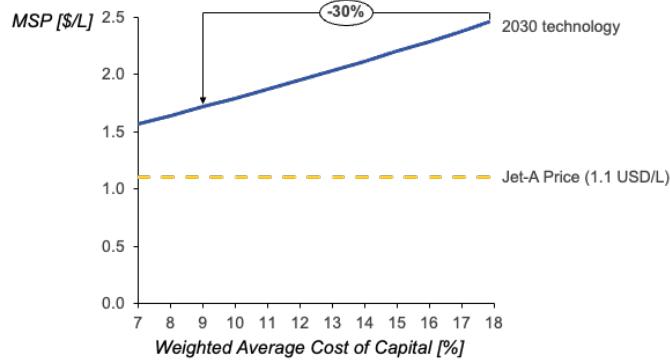


Figure 6. Minimum selling price (MSP) of fuel as a function of the weighted average cost of capital.

Green premium analysis for Kenya

The team modeled the green premium of a 2,000-bpd SAF production facility with a green premium multiplier of 3 over conventional jet fuel; we then assessed the impacts on ticket prices on international (or intercontinental) passenger flights from NBO (Nairobi) and MBA (Mombasa) airports. The goal of this analysis was to understand the additional costs per passenger that would be incurred on each international route out of these two airports in order to cover the full premium. The analysis rests upon route-specific fuel burn data using ICAO Cert, conventional jet fuel cost data, seat load factor data for Kenya, as well as assumptions about the costs of CORSIA offsets (see Figure 7 for an overview).

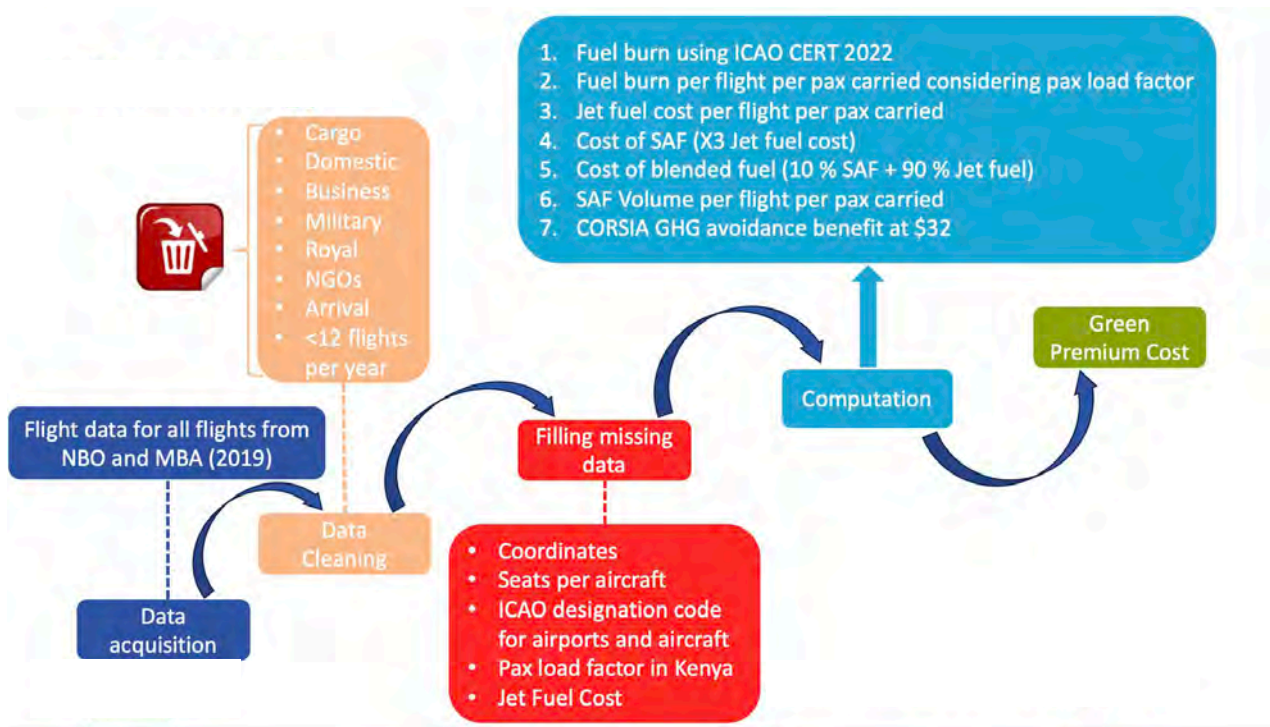


Figure 7. Method for green premium analysis. ICAO, International Civil Aviation Organization; SAF, sustainable aviation fuel; GHG, greenhouse gas; NGO, non-governmental organization; NBO, Nairobi airport; MBA, Mombasa airport.

Figure 8 shows the additional costs per passenger if the green premium is allocated to (a) all international flights departing the two airports, or (b) intercontinental flights only. For a flight from Kenya to Frankfurt, for example, the green premium in

the former case is approximately \$25 and in the latter case \$44 per passenger. For flights to New York Kennedy Airport, the green premium per passenger is \$46 and \$83, respectively.

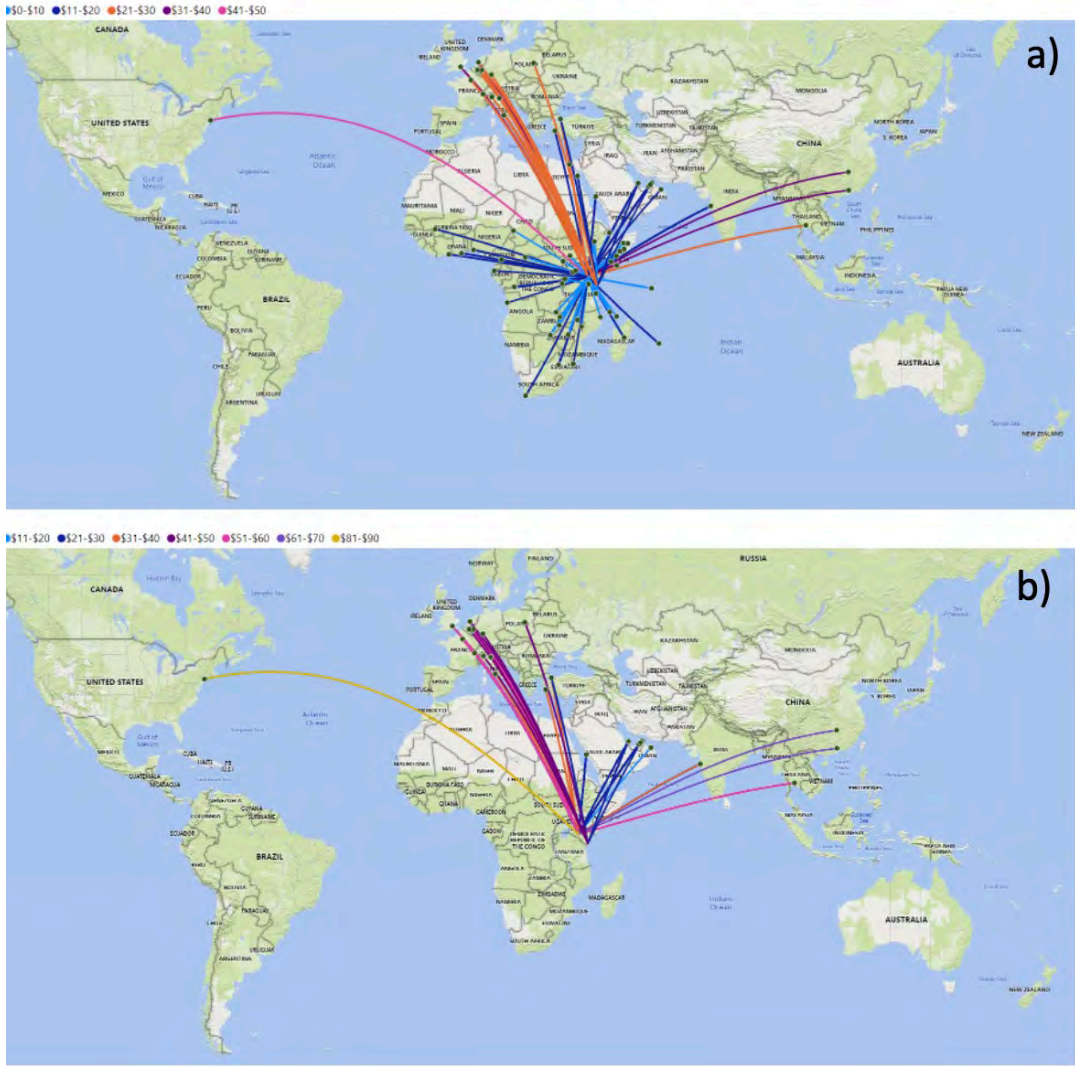


Figure 8. Green premium results if allocated to (a) all international flights, or (b) only to intercontinental flights.

Milestone

A first set of techno-economic analyses and stakeholder mappings was presented during the “Second Workshop and High-Level Meeting on the Development and Deployment of Sustainable Aviation Fuels in Kenya,” which was held on September 11 and 12 in Nairobi.

Major Accomplishments

During the “Second Workshop and High-level Meeting on the Development and Deployment of Sustainable Aviation Fuels in Kenya,” the team briefed results on the following:

1. A template for mapping key stakeholders and scale-up challenges in Kenya
2. A preliminary techno-economic analyses for a PtL plant in Kenya
3. An analysis of green premium coverage for Kenya

Publications

None.

Outreach Efforts

The results of initial analyses were presented during the “Second Workshop and High-Level Meeting on the Development and Deployment of Sustainable Aviation Fuels in Kenya,” which was held on September 11 and 12 in Nairobi. A summary of the efforts was presented during the ASCENT Fall 2023 meeting.

Awards

None.

Student Involvement

During this reporting period, UHasselt graduate students Francis Mwangi and Alessandro Martulli were involved in this task.

Plans for Next Period

During the coming reporting period, the team will further refine the analyses for Kenya. Furthermore, the team will assess how the experience from analyses in Kenya can be transferred to another sub-Saharan country.

Task 3 - Facilitate a Network for Capability Building for Global SAF Supply Chain Development

Massachusetts Institute of Technology and University of Hasselt

Objective

The goal of this task is to interface with partners to build the skills, expertise, and capacities needed for scaling up SAF development and deployment around the globe. During the current reporting period, the goal was to identify potential external partners and to establish formats and initial exchanges.

Research Approach

To meet the goals of this task, the MIT/UHasselt team followed two approaches:

1. Capability building in Kenya

The team helped build a network to support stakeholders who are interested in building the capabilities and knowledge for analyzing, developing, and deploying SAF production capacity in Kenya. For this purpose, the team engaged with the Kenyan Civil Aviation Authority (KCAA), Deutsche Gesellschaft für Internationale Zusammenarbeit (giz), and the World Bank. A key goal was to bring together all stakeholders needed to coordinate efforts for SAF scale-up and deployment in Kenya. For this purpose, the group organized two events:

- a) **Second High-Level Meeting on SAF Development and Deployment:** This meeting was held September 11-12, 2023, in Nairobi, and was co-organized by the MIT/UHasselt team. During the workshop, over 100 international and domestic participants came together to discuss next steps for scaling up SAF production and deployment in Kenya. As part of the program, the MIT/UHasselt team provided a briefing on the techno-economic opportunities and challenges for SAF production in Kenya (based on research described under Task 2). The workshop featured talks and discussions by international and national actors in the future Kenya SAF supply chain, including ICAO, IATA, EU Commission, World Economic Forum, World Bank, Roundtable on Sustainable Biomaterials, European Union Aviation Safety Agency, African Civil Aviation Commission, international airlines, major international banks, international SAF producers, Kenya ministries, Kenya Pipeline Company, Kenya Refining Company, Kenya Airways, and others.

The workshop discussed the concrete opportunities and challenges for SAF in Kenya, with a focus on financing; offtakes; policy; and fuel testing, storage, and certification. More specifically, the workshop addressed the following questions:



- How can the lack of SAF incentives in Kenya be overcome?
 - Local airlines lack financial means for SAF purchase. What role can international carriers play?
 - There is currently no blending facility in Kenya. Who will blend SAF and where?
 - Who will test and certify SAF?
 - Investing in Kenya is relatively high-risk compared to OECD markets. What role can finance institutions play in de-risking SAF production?
- b) Training on SAF technology, including PtL, policy certification and finance for the aviation sector in Kenya: This training was held September 13-14, 2023, at the East African School of Aviation (Nairobi, Kenya) and was co-organized with KCAA and giz. Approximately 60 participants from different stakeholder groups in Kenya engaged in the training, which covered all aspects of SAF, including technology, policy, and finance.

2. Developing a structured capability building with ASCENT 93

Together with the University of Hawaii and Washington State University, the team is building a lecture series designed to teach the essentials of SAF production and deployment from multiple angles. The course began in November 2023 with the first cohort from Latin America and the Caribbean.

Milestone

The workshop and training sessions in Kenya were successfully delivered in September 2023.

Major Accomplishments

The MIT/UHasselt team co-organized and co-led two events: “Second High-Level Meeting on SAF Development and Deployment” and the “Training on SAF Technology, including PtL, policy certification and finance for the aviation sector in Kenya.”

Publications

None.

Outreach Efforts

The MIT/UHasselt team co-organized and co-led the “Second High-Level Meeting on SAF Development and Deployment” and “Training on SAF Technology, including PtL, policy certification and finance for the aviation sector in Kenya”. A summary of these efforts was presented during the ASCENT Fall 2023 meeting.

Awards

None.

Student Involvement

During this reporting period, UHasselt graduate student Francis Mwangi was involved in this task.

Plans for Next Period

During the coming reporting period, the team will continue to deepen its engagement in Kenya. This will include supporting follow-up action from the workshop. Furthermore, the team will seek additional engagement in other sub-Saharan countries that are deemed to provide substantial benefits. The team will deliver and review the course developed together with the ASCENT 93 universities.

Task 4 - Support Knowledge Sharing and Coordination Across All ASCENT Project 93 Universities

Massachusetts Institute of Technology and University of Hasselt

Objective

The objective of this task is to regularly exchange with other ASCENT 93 universities (Washington State University and University of Hawaii) to share best practices and coordinate efforts. The sharing of approaches decreases the replication of

A93 universities' work on similar topics and can help develop transferable approaches for stakeholder engagement across various geographies.

Research Approach

The MIT/UHasselt team participated in regular ASCENT 93 coordination teleconferences, which served as a venue to discuss progress in the various geographies and to learn about the activities of other ASCENT 93 universities.

Milestone

The MIT/UHasselt ASCENT 93 team shared their progress in Kenya and helped set up the joint lecture series on SAF.

Major Accomplishments

One specific outcome of the coordination is the effort to develop a joint course on the fundamentals of SAF, which was taught to a first cohort starting in November 2023.

Publications

None.

Outreach Efforts

See above.

Awards

None.

Student Involvement

During this reporting period, UHasselt graduate student Francis Mwangi was involved in this task.

Plans for Next Period

Plans for the next period include continued engagement in regular teleconferences and the development and delivery of the SAF lecture series.



Project 093B Collaborative Research Network for Global Sustainable Aviation Fuel Supply Chain Development

University of Hawai'i

Project Lead Investigator

Scott Q. Turn
Researcher
Hawai'i Natural Energy Institute
University of Hawai'i (UH)
1680 East-West Rd., POST 109
Honolulu, HI 96822
808-956-2346
sturn@hawaii.edu

University Participants

University of Hawai'i

- P.I.: Scott Q. Turn, Researcher
- FAA Award Number: 13-C-AJFE-UH, Amendment 020
- Period of Performance: January 1, 2023 to December 31, 2023
- Tasks:
 1. Establish a collaborative research network for sustainable aviation fuel (SAF) supply chain development in southeast (SE) Asia
 2. Support the activities of Project 093 partner universities in tropical regions by providing subject matter expertise

Project Funding Level

Under FAA Award Number 13-C-AJFE-UH, Amendment 020, the Project 093B Collaborative Research Network for Global SAF Supply Chain Development received \$250,000 in funding from the FAA and cost-share funding of \$250,000 from UH.

Investigation Team

University of Hawai'i

Dr. Scott Turn (P.I.; Hawai'i Natural Energy Institute)
Dr. Quang-Vu Bach (assistant researcher; Hawai'i Natural Energy Institute)

Other Lead Personnel

Washington State University

Michael Wolcott (P.I.)
Prof. Manuel Garcia-Perez (co-P.I.)

Volpe National Transportation Systems Center

Kristin Lewis (P.I. and principal technical advisor)

Massachusetts Institute of Technology

Florian Allroggen (P.I. and research scientist)





Project Overview

UH will engage universities (and other entities) in SE Asian countries and develop collaborative research programs focused on SAF supply chains. These activities will identify information shortfalls and generate fundamental data necessary for the design of engineered SAF production systems. Research activities will include supporting analyses related to the assessment of greenhouse gas emissions, stakeholder engagement, feedstock supply chain development, and infrastructure needs. Planned activities under the program include workshops, student and researcher exchanges, and support of research projects.

The key objectives for this project are as follows:

- Task 1 will focus on establishing a collaborative research network for SAF supply chain development in SE Asia.
- Task 2 will provide technical support to other Project 093 ASCENT university and partner activities for which tropical feedstocks are relevant.

Task 1 – Establish a Collaborative Research Network for SAF Supply Chain Development in SE Asia

University of Hawai'i

Objectives

This task includes three subtasks:

Subtask 1.1. Identify partner universities (and other entities) in the SE Asian region.

Subtask 1.2. Organize and conduct a SAF supply chain workshop in SE Asia.

Subtask 1.3. Develop a plan for an education and exchange program with collaborating universities in SE Asia and with Project 093 ASCENT universities.

Research Approach

UH has led the tropical regional supply chain effort under ASCENT Project 001 since 2015. Activities under this effort have focused on tropical energy crops and agriprocessing residues and urban residues as candidate feedstocks for SAF production. This experience forms the basis for the development of SE Asian SAF supply chains.

Background

Regional supply chain development is informed by crop-science-based evaluations of plants for feedstock production, analyses of crop production potential based on geographic information systems, development of advanced feedstock processing and conversion systems, assessments of the compatibility of biomass and bioderived products with existing infrastructure and logistical resources, and evaluations of biomass-based energy systems based on life cycle and economic approaches. The results of past efforts have provided a baseline of information to be accessed and built upon in developing scenarios of future SAF production along regional supply chains in Hawai'i and the tropics. Pretreatment and conversion options for materials from potential SAF feedstock crops in the tropics are shown in Figure 1.

In August 2017, the Hawai'i Natural Energy Institute at UH initiated efforts under a five-year grant from the Office of Naval Research for the Asia Pacific Regional Energy System Assessment. The objective of this five-year grant was to develop comprehensive energy system assessments that include strategy, policy, regulation, technology options, demonstrations, implementation plans, and training for energy system transitions in select locations throughout the Asia-Pacific region, based on the specific requirements or needs of the targeted jurisdictions and strategic alliances. The first three years of this program laid a firm foundation for continued success built upon the development of solid partnerships with national, regional, and local jurisdictions as well as private and public stakeholders, including utility companies, universities, and other research and international aid and development entities. Relationships developed in SE Asia (Thailand, Indonesia, and Vietnam) through the Asia Pacific Regional Energy System Assessment were leveraged to facilitate the Project 093B global supply chain development effort. The Association of South East Asian Nations (ASEAN) includes the countries of Brunei Darussalam, Cambodia, Indonesia, Lao PDR, Malaysia, Myanmar, Philippines, Singapore, Thailand, and Vietnam. Universities (and other entities) from ASEAN countries were the initial target participant group in the collaborative research network for SAF supply chain development in SE Asia under this ASCENT project.

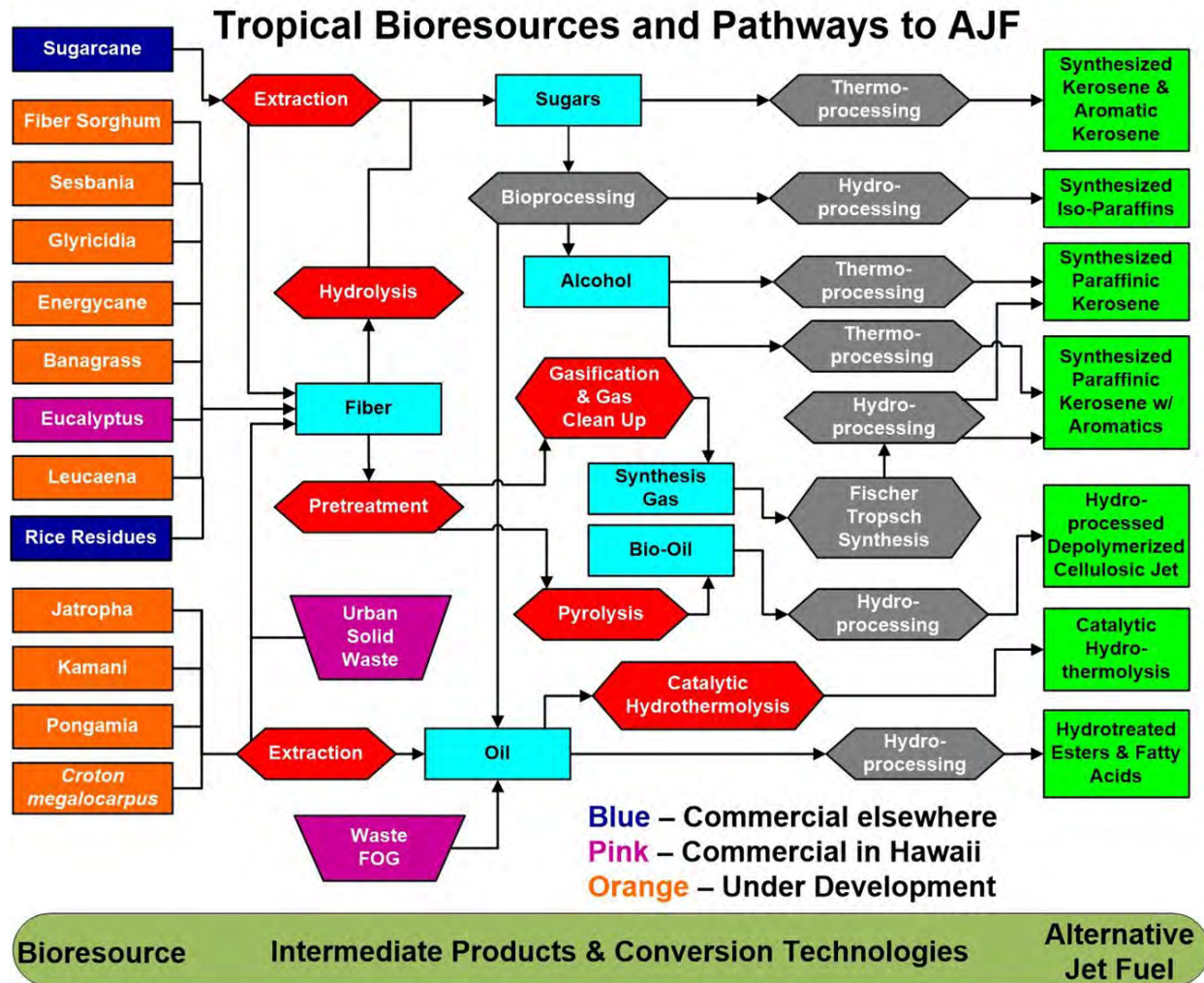


Figure 1. Tropical bioresources and pathways to alternative jet fuel/sustainable aviation fuel. FOG: fats, oils, and greases.

Subtasks 1.1. and 1.2

Activities conducted to accomplish Subtasks 1.1 and 1.2 were coordinated in planning the SAF supply chain workshop held in Bangkok. The workshop was coordinated with the U.S. Trade and Development Agency (Commerce Department) as part of their effort to support the SAF business development of U.S. companies in the region. Thailand’s National Energy Technology Center and Chiang Mai Rajabhat University were instrumental in the planning process, providing contacts at universities and government agencies throughout the ASEAN region. Staff from the U.S. Embassy in Bangkok and FAA Asia Pacific Office at the U.S. Embassy in Singapore supported workshop planning by contacting and coordinating with government agencies across the region.

The archival literature was reviewed to identify universities and entities from ASEAN countries with either ongoing SAF-related development activities or prior work in biomass resource assessment or biomass supply chains. Based on the results, researchers from 13 universities across the region (Philippines, Indonesia, Thailand, Vietnam, Malaysia, and Brunei) were contacted to assess interest in workshop participation. Twelve researchers from seven universities attended the SAF workshop in Bangkok.

The workshop objectives were as follows:

- Connect stakeholders

- Foster collaboration
- Drive innovation in the adoption of SAF

The FAA-supported section of the workshop was held on May 22-23, 2023 at the Conrad Hotel in Bangkok. More than 100 attendees from eight countries participated in the workshop (see Figure 2). Participants self-identified their organization’s place in the SAF value chain, as shown in Figure 3.



Figure 2. Country of origin of participants at the sustainable aviation fuel workshop.

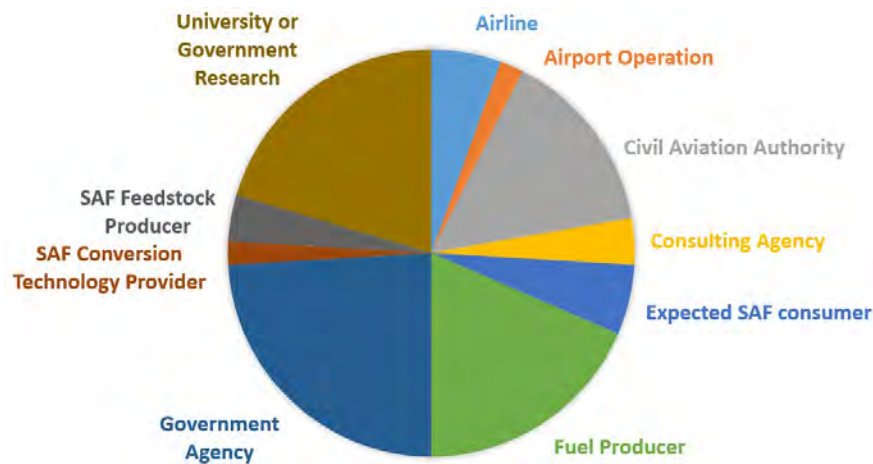


Figure 3. Organizations of sustainable aviation fuel (SAF) workshop attendees.

The two days of the workshop were organized as shown below:

Day 1, Morning

- Workshop overview and introduction
- Keynote address: International Civilian Aviation Organization
- Civil aviation authority perspectives
- Energy policy perspectives on SAF

Day 1, Afternoon

- Panel on SAF production: Upstream considerations/logistics



- Update on the Commercial Aviation Alternative Fuels Initiative
- Summary and close out of Day 1

Day 2, Morning

- Recap from Day 1
- Keynote address: SAF sustainability criteria
- Agricultural industry: Feedstocks for SAF production
- Airport fuel system operator perspectives

Day 2, Afternoon

- University research in support of SAF development
- Panel discussion: Way forward
- Summary and close out of Day 2

Participants who gave presentations were provided with five motivational prompts:

- Tell us about your organization (private/public, size, authority, etc.).
- What role will your organization play in the transition to SAF use in your country?
- How will your organization plan for the expanded use of SAF?
- What barriers will need to be overcome for SAF deployment in your country?
- What tools and resources are needed to overcome those barriers?

Workshop participants identified common themes that need to be addressed across the region, as summarized below:

- Sustainable funding models and strategies are needed for the aviation industry's transition to SAF.
- There is a lack of discussion on sustainability and economic viability of feedstocks.
- Investments in research and development are required to diversify feedstock options and promote sustainable alternatives that do not compete with food supplies.
- Infrastructure development is crucial for the production, storage, and distribution of SAF.

Workshop recommendations included the following:

- Explore and establish supporting policy, e.g., the use of incentives and carbon credits to promote SAF production and adoption
- Raise awareness and develop education initiatives to inform stakeholders, including the public, about the benefits and importance of SAF

Participant feedback identified the sessions on civil aviation authorities' perspectives, energy policy perspectives on SAF, and the agricultural industry feedstocks for SAF production as the most useful.

Subtask 1.3

A meeting was held with the Dean of Education Programs and the Deputy Director of Research Programs at the East-West Center (www.eastwestcenter.org) adjacent to the UH campus. The purpose of the meeting was to inform the Dean and Deputy Director about Project 093B goals and activities and to explore opportunities to integrate East-West Center educational and research networks and infrastructure with the Project 093B goals of recruiting and educating SE Asian postdoctoral fellows and visiting scholars. UH faculty members that are actively engaged in research on ecosystem services and transportation networks have been recruited as mentors for Project-093B-supported postdoctoral fellows and visiting scholars.

Milestones

Milestones included identifying partner universities for the SAF research network, selecting a venue and support organizations for the SE Asia SAF workshop, and holding the SAF supply chain workshop in SE Asia. All milestones were met.

Major Accomplishments

The major accomplishment of the project was holding the highly successful SAF supply chain workshop in Bangkok, Thailand on May 22–23, 2023. The workshop established Project 093B as a leader in supporting the development of global

SAF supply chains in the ASEAN region. Participants expressed great interest in FAA support for a similar workshop in 2024.

Publications

None.

Outreach Efforts

Organizing and conducting the SAF supply chain workshop in Bangkok provided outreach and education to the SAF supply chain stakeholder community. Presentations were made by Drs. Prem Lobo and Scott Turn during the workshop. Electronic communications were made with all of the workshop participants, either directly or through in-country partners.

A presentation describing the workshop, its goals, and its outcomes was presented at the Third ASEAN International Conference on Energy and Environment held in Bali, Indonesia on August 23-25, 2023.

Awards

None.

Student Involvement

None.

Plans for Next Period

SAF research themes of common interest for ASEAN countries will be developed. These themes may include (but are not limited to) the following:

- Identifying agricultural and silvicultural residues and their availability as SAF feedstock
- Modeling energy crop potential using an approach based on geographic information systems
- Developing logistic system models for aggregating potential SAF feedstocks
- Characterizing the properties of agricultural and silvicultural residues and energy crop feedstock materials
- Analyzing the greenhouse gas intensity of ASEAN SAF systems
- Assessing data available in ASEAN countries to support use of the Volpe Center's Freight and Fuel Transport Optimization Tool

Research on these topics will be conducted at UH by graduate students, postdoctoral fellows, or visiting scholars recruited from ASEAN member states.

Building on the successful SAF workshop held in Bangkok in May 2023, a SAF supply chain workshop will be organized in 2024 at another SE Asia location.



Project 093C Collaborative Research Network for Global Sustainable Aviation Fuel Supply Chain Development: Latin America Case

Washington State University

Project Lead Investigators

Manuel Garcia-Perez
Professor and Chair
Biological Systems Engineering Department
Washington State University
LJ Smith, Room 205, PO Box 646120
Pullman, WA 99164-6120
509-335-7758
mgarcia-perez@wsu.edu

Michael P. Wolcott
Regents Professor
Department of Civil & Environmental Engineering
Washington State University
PO Box 642910
Pullman, WA 99164-2910
509-335-6392
wolcott@wsu.edu

University Participants

Washington State University

- P.I.s: Manuel Garcia-Perez and Michael P. Wolcott
- FAA Award Number: 13-C-AJFE-WaSU-037
- Period of Performance: January 1, 2023 to December 31, 2023
- Tasks:
 1. Create working groups in each Latin America and Caribbean (LAC) country involved in this project.
 2. Conduct the design and analysis of sustainable aviation fuel (SAF) supply chains in each of the LAC countries involved in this project.
 3. Create training modules/courses and graduate programs to train students.

Project Funding Level

This project received \$249,494 in FAA funding and \$249,494 in matching funds to Washington State University (WSU). Faculty time for Michael Wolcott, Manuel Garcia-Perez, Erik Jessup, Allyson Beall King, and Hanwu Lei contributes to the cost share. WSU funding is reported for the reporting period.

Investigation Team

Washington State University

Manuel Garcia-Perez (P.I.), Tasks 1, 2, and 3
Michael Wolcott (P.I.), Task 1
Hanwu Lei (co-P.I.), Task 3
Kristin Brandt (co-P.I.), Tasks 2 and 3
Lina Martinez (research staff), Tasks 1, 2, and 3



Dane Camenzind (research staff), Tasks 2 and 3
Allyson Beall King (research staff), Tasks 2 and 3
Eric Jessup (research staff), Tasks 2 and 3
Claudia Marcella Valderrama (graduate research assistant), Task 3
Robert Macias (graduate research assistant), Task 3

Volpe

Kristin Lewis (co-P.I.), Tasks 2 and 3

Project Overview

SAFs offer the potential to reduce the net environmental impact of aviation-related emissions, while enhancing U.S. energy security and diversifying energy supplies. As a result, these technologies are receiving considerable attention from policymakers, industry, and academia. Most importantly, SAF has been included in the International Civil Aviation Organization (ICAO)'s Carbon Offsetting and Reduction Scheme for International Aviation (CORSIA), which aims to stabilize the CO₂ emissions of international aviation at year-2019 levels. Using SAF, aircraft operators can reduce their offsetting requirements using the reduced CORSIA values of CO₂ emissions from SAF using their well-to-wake lifecycle greenhouse gas (GHG) emission (including credits for biogenic carbon emissions during combustion).

Significant progress has been made over the past decade in assessing the economic and environmental properties of SAF. This includes studies that have fostered our general understanding of life cycle analysis (LCA) (e.g., Stratton et al., 2010). In addition, work has focused on the economic and environmental properties of specific pathways, including jet fuel produced from hydroprocessed esters and fatty acids (HEFA) (Stratton et al., 2011; Pearlson et al., 2013; Olcay et al., 2013; Seber et al., 2014), from Fischer-Tropsch (FT) pathways (Stratton et al., 2011; Suresh, 2016; Suresh, 2018), and from biomass-derived sugars using a variety of chemical and biological techniques (Bond et al., 2014; Staples et al., 2014; Winchester et al., 2015). Most recently, Monte Carlo approaches have been systematically introduced for quantifying uncertainty and stochasticity in LCA and techno-economic analysis (TEA) (Bann et al., 2017; Suresh, 2016; Yao et al., 2017; Suresh, 2018; Oriakhi, 2020).

A suite of decision-support tools for assessing SAF supply chains has been developed within ASCENT Project 1. These tools can be used to assess the economics of SAF production, the optimization of SAF supply chain logistics, and the configuration of supply chains to consider both the sale of the fuel commodity and the commensurate environmental benefits. This suite of tools has been widely applied within regions of the United States and has potential for use internationally. Of particular interest is understanding feedstock availability and financial considerations for delineating both the minimum selling price and capital investment requirements for SAF production and regions outside the United States. This project has the potential to benefit our understanding of the worldwide production of SAF for the purpose of informing ICAO.

ASCENT 1 has made progress in harmonizing TEAs across technology pathways and feedstock selections for both technical and financial assumptions. Five SAF production pathways have been completed and are publicly available TEAs: HEFA, alcohol to jet (ATJ), FT, pyrolysis, and catalytic hydro thermolysis (CH) (Brandt et al., 2021a, 2021b, 2021c, 2022a, 2022b). These TEAs have been used extensively in work within ASCENT and for ICAO Committee on Aviation Environmental Protection (CAEP) analyses. As part of the ICAO tasks, the TEAs were updated to allow for regional variables to be changed based on global location. These include local consumable prices such as feedstock and electricity, as well as equipment capital costs and labor. Location-specific financial assumptions, including tax rate, inflation rate, and terms of loans, are also customizable. With expertise from Latin American colleagues, these TEAs can be rapidly deployed for use in member countries.

The process for siting facilities consists of two steps: generating an initial set of candidates and then using mixed integer optimization to select facilities from the candidate locations. The candidate generation phase uses geospatial data to evaluate a location's compatibility with specific facility types. The optimization phase allows for the locations of facilities to be found that result in systemwide minimum costs for a specific set of variables, like fuel cost, tariffs, and feedstock availability. Batch processing allows for the rapid iteration of variables so that a supply chain's sensitivity can be evaluated in different scenarios. During the past decades, Latin America has grown its bioethanol and biodiesel production. Brazil, Argentina, and Colombia have the largest production of biofuel in the region (IEA, 2021). In addition, the LAC region is classified as a high-potential area for producing energy crops (Acharya & Perez-Pena, 2020; Trindale et al., 2019). Currently, interest in the production and consumption of SAF has spiked in the region. Omega Green is the first renewable



diesel and SAF project under construction in Paraguay, with Brazilian investment, and it is expected to be in operation by 2025 (ECB Group, 2021). Legal framework and initiatives to produce or import SAF are being initiated in the Dominican Republic, Mexico, Costa Rica, and Colombia (Argus, 2021). LATAM, a South American airline with main hubs in Chile, Peru, Brazil, and Colombia, plans to use 5% SAF for its operations by 2030, favoring producers throughout South America (LATAM, 2022). To date, no comprehensive assessment exists of the potential for SAF production in Latin America.

During Year 1, our team focused on three countries in Latin America and the Caribbean: (1) Colombia, (2) Dominican Republic, and (3) Ecuador. In the second year, we are expanding the scope of our work with the addition of Costa Rica. A literature review on biomass and SAF-related publications for each of these countries will be conducted to identify existing information and centers of excellence on biomass utilization in each of these countries. This literature review and our existing collaborators in each of the targeted countries will be used as the main two sources of information to form working groups in Colombia, Costa Rica, the Dominican Republic, and Ecuador that will act as international partners for this project.

The overall objectives of this project are to (1) create training modules, courses, and graduate programs to train students and stakeholders in Latin America and the Caribbean on the design and analysis of SAF production and supply chains, (2) create working groups in each of the LAC focus countries involved in this project that will work directly with the students on the development of SAF supply chains, and (3) design and analyze SAF supply chains in Latin American and the Caribbean.

References

- Acharya, R. N., & Perez-Pena, R. (2020). Role of comparative advantage in biofuel policy adoption in Latin America. *Sustainability*, 12(4), 1411.
- Argus. Jet Fuel Insights: The move to SAF in Latin America. August 31, 2021. Available at: <https://www.argusmedia.com/en/blog/2021/august/31/podcast-jet-fuel-insights-the-move-to-saf-in-latin-america>.
- Bann, S. J., Malina, R., Staples, M. D., Suresh, P., Pearlson, M., Tyner, W. E., ... & Barrett, S. (2017). The costs of production of alternative jet fuel: A harmonized stochastic assessment. *Bioresource technology*, 227, 179-187.
- Boesen, R. R. (2011). Investigation and modelling of diesel hydrotreating reactions.
- Bond, J. Q., Upadhye, A. A., Olcay, H., Tompsett, G. A., Jae, J., Xing, R., ... & Huber, G. W. (2014). Production of renewable jet fuel range alkanes and commodity chemicals from integrated catalytic processing of biomass. *Energy & Environmental Science*, 7(4), 1500-1523.
- Brandt, K.; Eswaran, S.; Subramaniam, S.; Zhang, X.; and Wolcott, M.P. (2022b) Catalytic Hydrothermolysis techno-economic analysis, v. 2.1. doi:10.7273/000002564
- Brandt, K.; Geleyense, S.; Martinez-Valencia, L.; Zhang, X.; Garcia-Perez, M.; and Wolcott, M.P. (2021b) Alcohol to jet techno-economic analysis, v. 2.1. doi:10.7273/000001461 v
- Brandt, K.; Tanzil, A.H.; Martinez-Valencia, L.; Garcia-Perez, M.; and Wolcott, M.P. (2021c) Fischer Tropsch techno-economic analysis, v. 2.1. doi:10.7273/000001459.
- Brandt, K.; Tanzil, A.H.; Martinez-Valencia, L.; Garcia-Perez, M.; and Wolcott, M.P. (2022a) Pyrolysis techno-economic analysis, v. 2.1. doi: 10.7273/000002563
- Brandt, K.; Tanzil, A.H.; Martinez-Valencia, L.; Garcia-Perez, M.; Wolcott, M.P. (2021a) Hydroprocessed esters and fatty acids techno-economic analysis, v. 2.1. doi:10.7273/000001460
- Chen, Z., Feng, S., Zhang, L., Shi, Q., Xu, Z., Zhao, S., & Xu, C. (2019). Molecular-level kinetic modelling of fluid catalytic cracking slurry oil hydrotreating. *Chemical Engineering Science*, 195, 619-630.
- Dincer, I., & Acar, C. (2015). Review and evaluation of hydrogen production methods for better sustainability. *International journal of hydrogen energy*, 40(34), 11094-11111.
- ECB Group. Omega Green. 2021. Available at: <https://www.ecbgroup.com.br/en/group/bsbios-paraguay/omega-green>
- Gutiérrez-Antonio, C., Ornelas, M. L. S., Gómez-Castro, F. I., & Hernández, S. (2018). Intensification of the hydrotreating process to produce renewable aviation fuel through reactive distillation. *Chemical Engineering and Processing-Process Intensification*, 124, 122-130.
- Han, Y., Gholizadeh, M., Tran, C. C., Kaliaguine, S., Li, C. Z., Olarte, M., & Garcia-Perez, M. (2019). Hydrotreatment of pyrolysis bio-oil: A review. *Fuel processing technology*, 195, 106140.
- Hachemi, I., & Murzin, D. Y. (2018). Kinetic modeling of fatty acid methyl esters and triglycerides hydrodeoxygenation over nickel and palladium catalysts. *Chemical Engineering Journal*, 334, 2201-2207.
- ICAO, 2021. CORSIA supporting document - CORSIA Eligible Fuels – Life Cycle Assessment Methodology. Retrieved from <https://www.icao.int/environmental->



[protection/CORSIA/Documents/CORSIA_Supporting_Document_CORSIA%20Eligible%20Fuels_LCA_Methodology_V3.pdf](#)

- IEA. Renewables 2021: Analysis and forecast to 2026. December 2021. Available at: <https://iea.blob.core.windows.net/assets/5ae32253-7409-4f9a-a91d-1493ffb9777a/Renewables2021-Analysisandforecastto2026.pdf>
- Jeništová, K., Hachemi, I., Mäki-Arvela, P., Kumar, N., Peurla, M., Čapek, L., ... & Murzin, D. Y. (2017). Hydrodeoxygenation of stearic acid and tall oil fatty acids over Ni-alumina catalysts: Influence of reaction parameters and kinetic modelling. *Chemical Engineering Journal*, 316, 401-409.
- LATAM. LATAM seeks to reach 5% sustainable fuel use by 2030, favoring producers throughout South America. "Wings of Change" Event. April 06, 2022. Available at: <https://www.latamairlines.com/us/en/press-room/releases/latam-sustainable-aviation-fuel>
- Olcay, H; Seber, G; Malina, R. Life Cycle Analysis for Fully-Synthetic Jet Fuel Production, (2013)MIT Support for Honeywell Continuous Lower Energy, Emissions and Noise (CLEEN) Technologies Development, Report to the FAA.
- Oriakhi, U. M. (2020). *A stochastic life cycle and greenhouse gas abatement cost assessment of renewable drop-in fuels* (Doctoral dissertation, Massachusetts Institute of Technology).
- Plazas-González, M., Guerrero-Fajardo, C. A., & Sodrè, J. R. (2018). Modelling and simulation of hydrotreating of palm oil components to obtain green diesel. *Journal of cleaner production*, 184, 301-308.
- Pearlson, M., Wollersheim, C., & Hileman, J. (2013). A techno-economic review of hydroprocessed renewable esters and fatty acids for jet fuel production. *Biofuels, Bioproducts and Biorefining*, 7(1), 89-96.
- Seber, G; Malina, R; Pearlson, M; Olcay, H; Hileman, J; Barrett, S. Environmental and economic assessment of producing hydroprocessed jet and diesel fuel from waste oils and tallow, *Biomass and Bioenergy* Vol. 67 (2014).
- Staples, M. D., Malina, R., Olcay, H., Pearlson, M. N., Hileman, J. I., Boies, A., & Barrett, S. R. (2014). Lifecycle greenhouse gas footprint and minimum selling price of renewable diesel and jet fuel from fermentation and advanced fermentation production technologies. *Energy & Environmental Science*, 7(5), 1545-1554.
- Stratton, R., Wong, H. M., & Hileman, J. (2010). *Life cycle greenhouse gas emissions from alternative jet fuels* (No. PARTNER-COE-2010-001). Partnership for Air Transportation Noise and Emissions Reduction.
- Stratton, R. W., Wong, H. M., & Hileman, J. I. (2011). Quantifying variability in life cycle greenhouse gas inventories of alternative middle distillate transportation fuels. *Environmental science & technology*, 45(10), 4637-4644.
- Suresh, P., Malina, R., Staples, M. D., Lizin, S., Olcay, H., Blazy, D., ... & Barrett, S. R. (2018). Life cycle greenhouse gas emissions and costs of production of diesel and jet fuel from municipal solid waste. *Environmental science & technology*, 52(21), 12055-12065.
- Suresh, P. (2016) Environmental and economic assessment of alternative jet fuel derived from municipal solid waste. Masters Thesis submitted to the Massachusetts Institute of Technology.
- Jarullah, A. T. (2012). *Kinetic Modelling Simulation and Optimal Operation of Trickle Bed Reactor for Hydrotreating of Crude Oil. Kinetic Parameters Estimation of Hydrotreating Reactions in Trickle Bed Reactor (TBR) via Pilot Plant Experiments; Optimal Design and Operation of an Industrial TBR with Heat Integration and Economic Evaluation* (Doctoral dissertation, University of Bradford).
- Tanzil, A. H., Brandt, K., Wolcott, M., Zhang, X., & Garcia-Perez, M. (2021). Strategic assessment of sustainable aviation fuel production technologies: Yield improvement and cost reduction opportunities. *Biomass and Bioenergy*, 145, 105942.
- Tieuli, S., Mäki-Arvela, P., Peurla, M., Eränen, K., Wärnä, J., Cruciani, G., ... & Signoretto, M. (2019). Hydrodeoxygenation of isoeugenol over Ni-SBA-15: Kinetics and modelling. *Applied Catalysis A: General*, 580, 1-10.
- Trindade, S. C., Nogueira, L. A. H., & Souza, G. M. (2019). Relevance of LACAf biofuels for global sustainability. *Biofuels*, 1-11.
- Winchester, N., Malina, R., Staples, M. D., & Barrett, S. R. (2015). The impact of advanced biofuels on aviation emissions and operations in the US. *Energy Economics*, 49, 482-491.
- Yao, G., Staples, M. D., Malina, R., & Tyner, W. E. (2017). Stochastic techno-economic analysis of alcohol-to-jet fuel production. *Biotechnology for Biofuels*, 10, 1-13.

Task 1 - Create Working Groups in Each of the LAC Countries Involved in This Project

Washington State University

Objective

The objective of this task is to engage with stakeholders from Ecuador, Dominican Republic, Costa Rica, and Colombia.

Research Approach

Under Task 1, the team will create working groups in each of the LAC countries involved in this project. For Colombia, Dominican Republic, and Ecuador, we will take advantage of existing collaborative activities in these countries. Next year, we will expand our work to cover Costa Rica. In parallel, we will identify new members of our working groups through a literature review, which will focus on biomass supply chains and SAF production studies published by these countries and through direct contacts with our embassies in these countries (leaders: Lina Martinez [Colombia]; Manuel Garcia-Perez [Ecuador and Dominican Republic]).

Milestone

Work on this task started in January 2023.

Major Accomplishments

We have created active working groups in the Dominican Republic, Colombia, and Ecuador. The group in the Dominican Republic is formed by academic partners coordinated by the Ministry of Higher Education and the existing SAF round table coordinated by IDAC (Instituto Dominicano de Aviacion Civil). The number of stakeholders in Colombia was very large and diverse and covered industries, universities, and the government. Under the initiative of the Interamerican Development Bank and the Civil Aviation Authority of Colombia (AeroCivil), the country is developing its SAF roadmap. We are participating in three of the five round tables. Universities and industries mainly form the working group from Ecuador. We are working to attract more industries (especially Petro-Ecuador) and more government agencies. In the case of Costa Rica, we are in contact with some universities and Recope (Refinadora Costarricense de Petr leo). We will soon engage with this country to increase the number of stakeholders working in this project.

Publications

None.

Outreach Efforts

- IV International Biofuels Conference - Fedebiocombustibles, Cali, Colombia (April 26-28, 2023). Lina Martinez moderated the panels Decarbonizing Air Transport and Accelerating the Energy Transition.
- IATA's Aviation Day in Colombia and SAF working group, Bogota, Colombia (May 9-10, 2023)
- SAF round table, Santo Domingo, Dominican Republic (June 6, 2023)
- BioFuels Symposium, Santiago de los Caballeros, Dominican Republic (June 7-9, 2023)
- Summit "Towards a sustainable and inclusive decarbonization of the Galapagos Islands," Isla San Crist bal (Gal pagos), Ecuador (July 3-5, 2023).
- Aerocivil SAF roadmap round table I. Presentation on feedstock and conversion technologies (October 27, 2023)

Student Involvement

Claudia Marcela Valderrama, a Colombian student who started her graduate studies on January 1, 2023, has supported the Colombian working group communications.

Plans for Next Period

We plan to meet with our stakeholders in Colombia and Costa Rica early in 2024.

Task 2 - Conduct the Design and Analysis of SAF Supply Chains in Each of the LAC Countries Involved in the Project

Washington State University

Objective

The objective of this task is to estimate cost reduction opportunities if emerging hydrogen production technologies are co-located with SAF production technologies and existing infrastructure.

Research Approach

Under Task 2, we will conduct the design and analysis of SAF supply chains in each of the focus countries in LAC. It will start as soon as students from Latin America start receiving the training prepared under Task 1. In these studies, we will try to answer the following questions: (1) LCA value for the feedstock and sustainability criteria compliance, (2) what public policies should the countries develop to grow the production of SAF in Latin America, and (3) design of supply chain and siting of facilities.

Milestone

This task started in January 2023.

Major Accomplishments

Lina Martinez and Marcela Valderrama prepared a draft report on the energy assets of Colombia. This report includes technical expertise, infrastructure, access to funding, biofuel policies, economic incentives, sustainability issues, and suitable land and crops. We are also working with the landfill of Bogota (Through Aguas de Bogota) to start our work on the potential of municipal solid wastes (MSW) of the country to produce SAF.

Publications

None.

Outreach Efforts

This literature review has been shared with our stakeholders in Colombia.

Awards

None.

Student Involvement

A new student from Colombia, Claudia Marcela Valderrama, was hired to work on this task. She started her graduate studies on January 1, 2023. Four new students have been recruited to work on this task (Paulina Echeverria Paredes [Ecuador], Micaela Peralta [Ecuador], Raul Perez Mena [Dominican Republic], and Cesar A. Estrada [Colombia]) and will start their PhD programs in January 2024.

Plans for Next Period

In the next period, we will start the literature reviews for Ecuador and the Dominican Republic. We will also start the study of the potential of MSWs in Colombia to produce SAF. This study will be conducted in association with Aguas de Bogota. We also plan to recruit a student from Costa Rica in the next period.

Task 3 - Creating Training Modules, a Course, and Graduate Programs for Training Students

Washington State University

Objective

The objective of this task is to create a year-long training program to introduce the stakeholders to the design of SAF supply chain, as well as a master's program.



Research Approach

Under Task 3, the team will create training modules, a course, and graduate programs for the preparation of personnel involved in the design of SAF production supply chains. The training will start with students from Latin America and will be expanded to Africa and Southeast Asia. The materials to be created will be based on methodologies and tools developed as part of ASCENT 1 and that have been used in the design of supply chains in the United States. Our training materials will include (1) methodologies for the creation of waste biomass feedstock databases, geographic information systems (GIS), and facility siting (leaders: Michael Wolcott, Dane Camenzind, and Kristin Lewis); (2) supply chain configurations to capitalize on sale of the fuel commodity and valorizing environmental services (leaders: Lina Martinez, Michael Wolcott, Allyson Beall King); (3) logistics optimization (leaders: Eric Jessup, Dane Camenzind), (4) SAF production technologies (mass and energy Balances [Aspen], TEA, and LCA) (leaders: Kristin Brandt, Manuel Garcia-Perez, Hanwu Lei). These training materials will gradually evolve into courses that will be offered in a certificate and a master's program (Hanwu Lei).

Milestone

This task started in January 2023.

Major Accomplishments

Here, we made progress in two directions: (1) the lecture series (started in November 2023), and (2) the professional master program and courses associated with this program. Our faculty members are developing the training modules for the 2023–2024 lecture series, which will include the participation of 19 faculty members and researchers from the FAA, WSU, Penn State, and universities of Hawai'i, Hasselt, Massachusetts Institute of Technology, and Purdue, and Volpe. WSU faculty are also working on the design of a professional master program in the design of SAF supply chains and the courses associated. A first draft is now under internal review.

Publications

None.

Outreach Efforts

Close to 105 stakeholders from Latin American and the Caribbean expressed interest in our lecture series, and several of them participated in our first introductory lecture.

Student Involvement

Claudia Marcela Valderrama and the new students from Colombia, Ecuador, and the Dominican Republic were invited to participate in the 2023–2024 lecture series.

Plans for Next Period

Next quarter, we will continue working on the lecture series and our regular meetings with stakeholders from Colombia, Dominican Republic, and Ecuador. We will continue to work with the WSU senate to obtain approval for our master's program and will work on the creation of new courses for this program.



Project 094 Probabilistic Unmanned Aircraft System (UAS) Trajectory and Noise Estimation Tool

Georgia Institute of Technology

Project Lead Investigator

P.I.: Prof. Dimitri N. Mavris
Director, Aerospace Systems Design Laboratory
School of Aerospace Engineering
Georgia Institute of Technology
Phone: (404) 894-1557
Fax: (404) 894-6596
Email: dimitri.mavris@ae.gatech.edu

Co-P.I.: Dr. Holger Pfaender
Aerospace Systems Design Laboratory
School of Aerospace Engineering
Georgia Institute of Technology
Phone: (404) 385-2786
Fax: (404) 894-6596
Email: holger.pfaender@ae.gatech.edu

University Participants

Georgia Institute of Technology

- P.I.s: Dr. Dimitri Mavris, Dr. Holger Pfaender
- FAA Award Number: 13-C-AJFE-GIT-143
- Period of Performance: January 1, 2023 to December 31, 2023
- Tasks:
 1. Investigate statistical sampling techniques
 2. Investigate surrogate noise modeling approaches
 3. Develop an integrated probabilistic noise computation methodology
 4. Extend existing prototype noise engine capabilities
 5. Coordinate with the FAA and Volpe
 6. Develop documentation

Project Funding Level

This project is funded at the following levels: Georgia Institute of Technology (\$300,000). The Georgia Institute of Technology has agreed to a total of \$300,000 in matching funds. This total includes salaries for the project director, research engineers, and graduate research assistants and for computing, financial, and administrative support, including meeting arrangements. The institute has also agreed to provide tuition remission for students whose tuition is paid via state funds.

Investigation Team

Georgia Institute of Technology

Dimitri Mavris (P.I.)
Holger Pfaender (co-P.I.)
Raphaël Gautier (research faculty)
Jiacheng "Albert" Xie (research faculty)



Venkat Sai Chinta (graduate student)
Lloyd Teta (graduate student)
Xi Wang (graduate student)
Hugues Chardin (graduate student)
Joey Ji (graduate student)
Deepika Singla (graduate student)

Project Overview

Context and Motivation

The unmanned aircraft system (UAS) market is expected to grow rapidly in coming years, with projections estimating the civil UAS market at \$121 billion in the next decade. Multiple operators are currently developing and testing various concepts of operations that fall within the umbrella of urban air mobility (UAM), with the two main use cases being drone delivery and electric-vertical takeoff and landing (e-VTOL) air taxis. Like traditional aircraft operations, these novel concepts are expected to have an impact on the environment in which they operate, particularly regarding noise. Just as noise assessments of traditional commercial and general aviation fixed-wing and rotary aircraft operations are completed today, similar noise assessments for UAM operations will be necessary.

Problem Definition

UAM operations bring unique requirements. First, UAM operations are expected to be denser than current general or commercial aviation operations, possibly by orders of magnitude. Thus, a noise assessment method should be able to handle large vehicle densities. Second, UAM vehicles are expected to be smaller and therefore quieter, for example, small drones for deliveries or helicopter-sized vehicles for e-VTOL air taxis, benefiting from novel electric propulsion systems. As a result, the noise footprint of such vehicles is expected to be more localized. Therefore, noise exposure levels should be estimated with sufficient resolution. Third, instead of primarily following fixed trajectories dictated by approach and departure routes around airports, UAM vehicles are expected to operate point-to-point within populated areas. Departure and arrival locations are expected to vary from day to day; delivery drones may depart from warehouses or mobile staging locations and deliver goods to different customers every day, and e-VTOL air taxis may allow their customers to be picked up and dropped off all around an urban area. Thus, a noise assessment method should be flexible enough to accommodate changing flight paths, and the resulting noise assessment should account for the variability introduced by these changes.

Research Objective

The objective of this research is to develop a novel noise estimation method/tool that supports the computation of noise resulting from the stochastic operation of UASs and other upcoming vehicle concepts with irregular locations and operations in large numbers.

Research Approach

While the outcome of Project 9 provided a solid base for the noise engine, it lacked several capabilities needed to realistically simulate UAS operations and account for the different sources of uncertainty that are the focus of Project 94. Thus, in the first phase of this project, the effort primarily consisted of developing these capabilities, which include 1) modeling customer demand, 2) introducing more varied operational concepts beyond simple point-to-point flights, 3) generating realistic trajectories that account for obstacles found in urban areas, 4) updating the simulation logic to provide computational speed-ups and modeling flexibility, and 5) improving the visualizations of probabilistic quantities over a study area. These efforts led to an updated workflow for the integrated capability developed in this project, which is depicted in Figure 1. In addition to capability developments, two collaborations were initiated that aim at validating the approach proposed and implemented for this project.

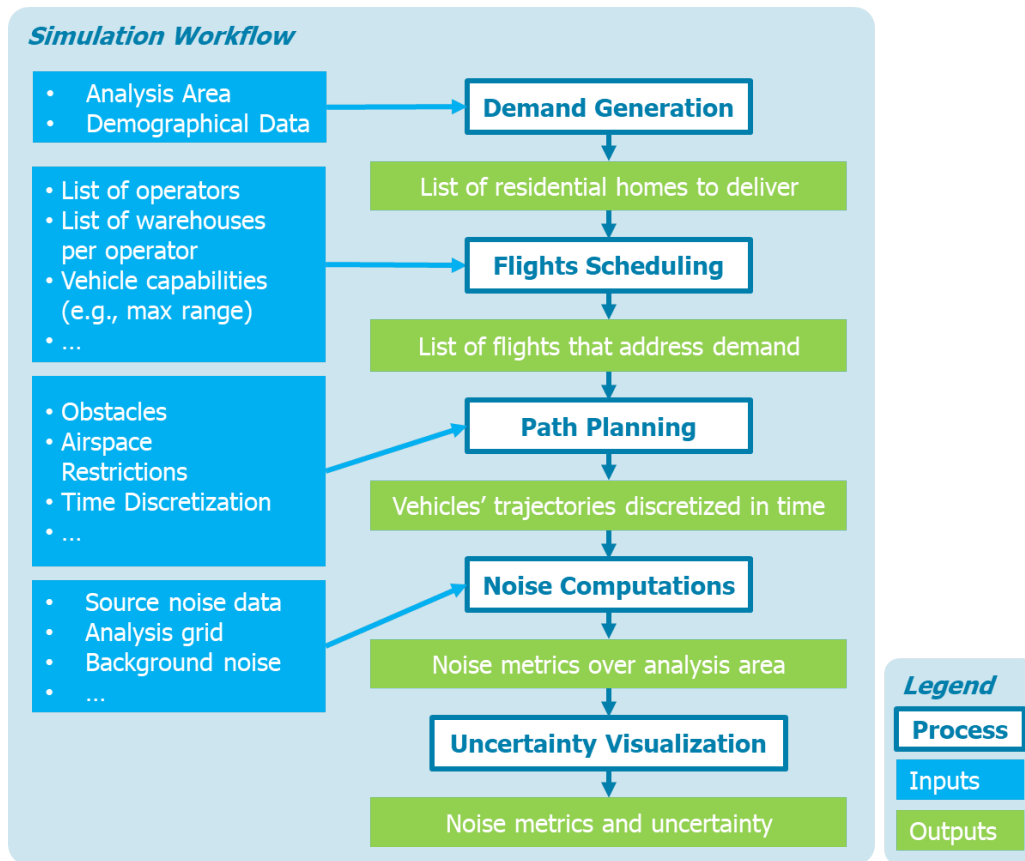


Figure 1. Updated workflow for the noise assessment logic.

Task 1 – Investigate Statistical Sampling Techniques

Georgia Institute of Technology

Objectives

To produce likelihood distributions for noise exposure maps at every receiver point, it is necessary to assign distributions to the variables that are the primary cause of the associated variability. In the case of UAS noise, these variables are thought to primarily be the day-to-day operations and trajectories. The first experiments performed in Ascent Project 9 were conducted via Monte Carlo simulations; however, this brute force method is computationally expensive, requiring full reruns of the entire noise modeling with different inputs adjusted to the input variability. Other sampling methods are available that, if applied correctly, allow the computation of identical likelihood distributions but with a significantly reduced number of samples required. In this task, the team will investigate several sampling techniques and assess their applicability to the noise domain as well as their potential to reduce the computational time required to produce the desired probabilistic noise results.

Subtask 1.a is the first effort undertaken under Task 1, with the goal of incorporating demand modeling as part of the analysis workflow such that the time and space distributions of flights match expected operations. In concrete terms, this means that instead of being sampled according to a uniform distribution within the analysis area under study, package delivery destinations are sampled according to the projected demand for online orders, which is estimated based on actual demographical information. To achieve this goal in an efficient manner, the proposed approach applies probabilistic and statistical computations and methods in an openly available demand model with openly available U.S. census data.

Research Approach – Subtask 1.a – Demand Modeling

Background

This task utilizes existing multinomial regression models from a published article [1] to determine the online shopping demand in the study area. In that study, Jaller and Pahwa delved into the environmental impact of online shopping, focusing on how it influences ground vehicle miles traveled and emissions. A key question addressed was whether and to what extent online shopping effectively reduces emissions compared with traditional in-store shopping. The findings revealed that the most significant factor in determining the environmental impact is the degree to which orders are consolidated.

The approach taken in this research involved a three-step modeling process. Firstly, the team utilized publicly available census data to select representative individuals from two distinct areas: San Francisco and Dallas. This method ensures that the study is both relevant and reproducible, as it relies on data that are easily accessible. Next, they developed their own demand model, drawing on data from the American Time Use Survey. The relevance of this model is underscored by the fact that the authors have made the resulting demand model available for public use.

Finally, the team conducted a straightforward environmental impact analysis. This analysis aimed to calculate the total number of miles traveled, differentiating between personal vehicle trips and delivery truck journeys. It also estimated the resulting emissions from these trips. However, this particular aspect of the study was deemed irrelevant to our current research interests. Overall, the study provides valuable insights into the environmental consequences of online shopping, particularly in terms of vehicle usage and emissions. Only regression coefficients from their model were used in this subtask, with the required input shown in Figure 2.

Sampling Approach

We developed a sampling method similar to that of Jaller and Pahwa, as shown in Figure 3. In the demand model used for assessing the impact of online shopping, the census data play a crucial role by providing the proportion of the population across various categories. These categories are used to create a synthetic population sample by sampling from these categorical distributions. However, it is important to note that this method does not account for dependencies between different factors, such as the relationship between age and family income level. Improvements to the model could be made by investigating ways to incorporate these dependencies.

The core of the demand model is a multinomial logit model, a type of classification model that predicts the probability of belonging to a certain class. In this context, the model considers four classes for a given individual on any given day, based on American Time Use Survey data: 1) no shopping ($k = 1$), 2) in-store shopping only ($k = 2$), 3) online shopping only ($k = 3$), and 4) both in-store and online shopping ($k = 4$).

<i>Factors and associated categories used to characterize individuals in the demand model</i>			
Gender	Male	Age (as of 2016)	Silent [71,91]
	Female		Baby Boomer [52,70]
Family Income	Poverty Level		Generation X [37,51]
	Low		Millennials [22,36]
	Lower Middle		Gen Z [4,21]
	Median	Education level	No education
	Middle Middle		Primary
Upper Middle	Secondary		
High	Graduate	Employment status	Employed
Mobility-related difficulty	Has no difficulty in mobility		Unemployed
			Not in labor force
	Has difficulty in mobility	Region	Northeast
Metropolitan Statistical Area	Population > 1 million		
	Season		Winter
			Spring
		Summer	
Fall			

Figure 2. Demand model inputs [1].

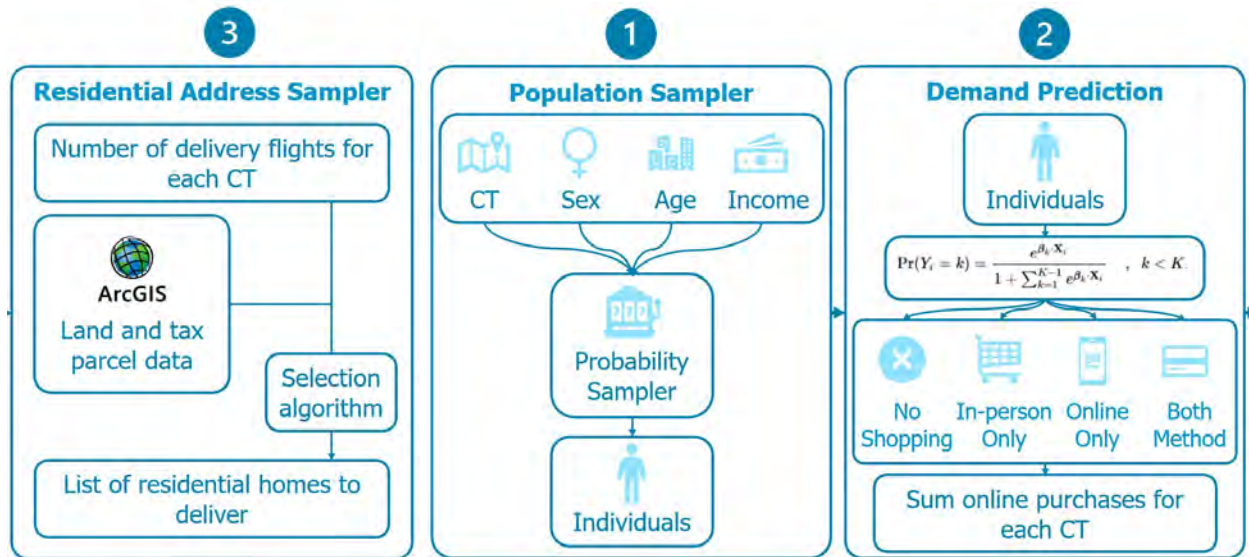


Figure 3. Sampling method workflow [1]. CT: census tract.

The probability of an individual, characterized by their features X , falling into one of these classes k is given by the following formula:

$$p(k|X) = \frac{e^{\beta_k X}}{1 + \sum_{i=1}^4 e^{\beta_i X}}$$

In this equation, the individual's features X are derived from the census categories. The β_k coefficients ($1 \leq i \leq 4$) are the model coefficients provided by the authors of the study. For the purposes of this research, the primary interest lies in outcomes #3 (online shopping) and #4 (both in-store and online shopping). These outcomes are particularly relevant for understanding the shift in shopping behaviors toward online platforms and its subsequent impact on environmental factors such as vehicle miles traveled and emissions. A sampling method was first created following the process described in the published article, using data available from the Atlanta Regional Committee.

Probabilistic Approach

To avoid the randomness of the sampling process for individuals in step 1, a probabilistic approach was developed as follows:

1. For every census tract T_i , generate all possible combinations of household features, and for every combination of household features, evaluate the demand model to obtain the probability for that combination of household features, which allows us to evaluate the following formula:

$$\begin{aligned} p(\text{household orders online} | \text{household in census tract } T_i) \\ = \sum_k^{N_{\text{household info}}} (p(\text{household orders online} | \text{household info} = H_k) \\ \times p(\text{household info} = H_k | \text{census tract} = T_i)) \end{aligned}$$

There is one such probability per census tract.

2. For every census tract, compute $p(\text{household in census tract } T_i)$ using the numbers of households in each census tract.
3. At this point, for every census tract, the actual probability we seek can be computed:

$$\begin{aligned} p(\text{household in census tract } T_i | \text{household orders online}) \\ = \frac{p(\text{household orders online} | \text{household in census tract } T_i) p(\text{household in census tract } T_i)}{\sum_{k=1}^{N_{\text{tracts}}} p(\text{household orders online} | \text{household in census tract } T_k) p(\text{household in census tract } T_k)} \end{aligned}$$

4. At this point, we have the information needed to sample from the multinomial distribution for which each category's probability is provided by $p(\text{household in census tract } T_i | \text{household orders online})$. Sampling from the multinomial distribution gives us a number of deliveries per census tract.
5. Within each census tract for which there are deliveries, uniformly sample the corresponding number of homes among this tract's homes.

The strength of this approach lies in its reliance on publicly available nationwide statistics. By using data that are accessible and standardized across different regions, this methodology is not only relevant to the specific areas of study but also generalizable to other regions. This broader applicability is particularly valuable for elucidating and predicting the implications of online shopping and drone delivery in diverse contexts across the country.

Milestones

Subtask 1.a

The sampling method was completed in September 2023 and integrated with the flight scheduling task. The probability approach is still under implementation.

Major Accomplishments

Subtask 1.a

From the implemented demand model, the online shopping demand for the state of Georgia was created using demographic data obtained from the Atlanta Regional Committee website, as presented in Figure 4. The demand was created with census-tract resolution, corresponding to the smallest demographic data area, thus providing a more detailed and accurate representation of its population characteristics and therefore the online shipping demand.

Plans for Next Period

Next steps will include a finalization of the updated probabilistic approach for the demand model implementation.

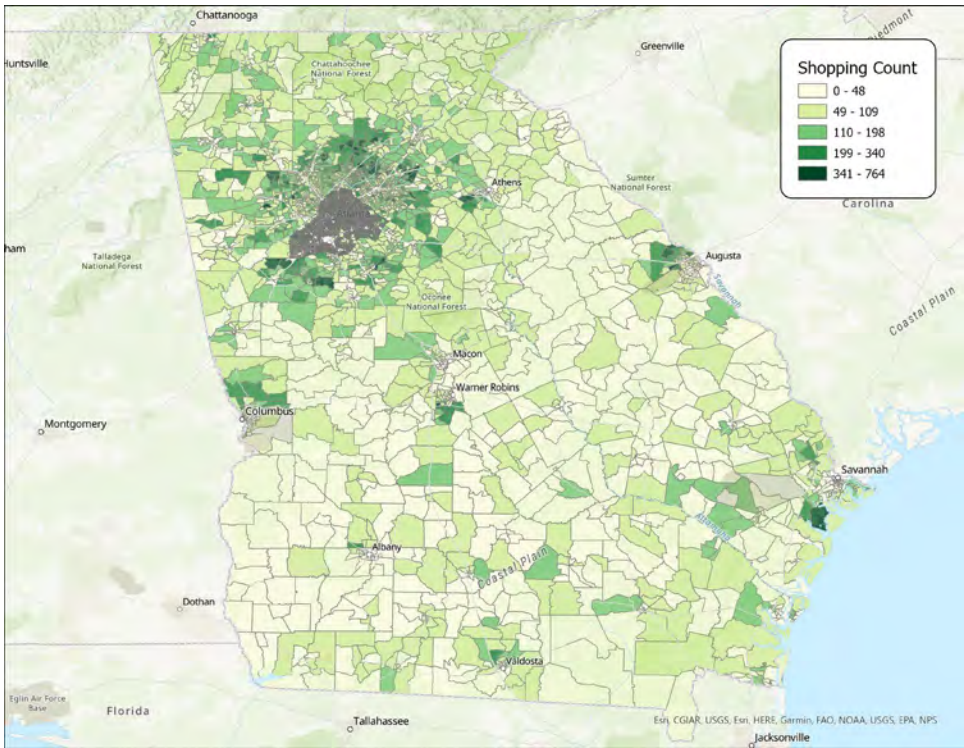


Figure 4. Online shopping demand for the state of Georgia.

Task 2 – Investigate Noise Surrogate Modeling Approaches

Georgia Institute of Technology

Objectives

In addition to the simplified sampling techniques, it is also possible to replace the full noise modeling with a reduced-order model. This surrogate model is a simplified mathematical representation of a high-fidelity noise study. To generate such a simplified model, a complete high-fidelity study will be created. This high-fidelity study can then be used to sample the input parameter space. Subsequently, the results can be applied to generate a much-simplified reduced-order model. This resulting surrogate model will serve as a stand-in for the full high-fidelity study with high statistical confidence. However, this surrogate model can also be used as a simplified transfer function to which the required input distributions, such as flight operations and trajectory variations, can be rapidly sampled in order to produce the desired output likelihood distributions with significantly reduced computational effort. This aspect is important for achieving rapid and efficient modeling of a potentially large number of vehicles and operations or a large area while still producing distributional results.

The first two efforts undertaken in the context of this task are 1) to reduce the geographical area over which the vehicle noise is propagated to the area in which the propagated sound level is noticeable instead of propagating over the complete analysis area (Subtask 2.a) and 2) to identify and compare a number of surrogate modeling approaches to replace the noise model (Subtask 2.b).

The potential for significantly decreasing the number of computations by reducing the geographical area over which noise is propagated, and therefore the number of receptors to which the noise must be propagated, was identified at the conclusion of ASCENT Project 9 and can be pursued in addition to surrogate modeling. To enable this, a systematic approach for computing a threshold distance around simulated vehicles must be developed that accounts for the fact that the noise level at one receptor location may originate from multiple vehicles.

Research Approach – Subtask 2.a – Limit Range of Noise Computations

The granularity identified as appropriate in ASCENT Project 9 for obtaining sub-decibel accuracy leads to an analysis grid whose cells are separated by a distance on the order of 15 ft. To cover the geographical spread of a major U.S. city’s urban area, this results in an analysis grid comprised of millions of points. In the simulation approach developed in Project 9, the noise produced by every simulated vehicle at every time instant of the simulation was propagated to all cells in the analysis grid, resulting in a high computational burden and high computational times. This first effort aimed at assessing the feasibility and expected gains to be obtained by restricting the range around simulated vehicles over which noise would be propagated, on the basis that noise levels rapidly diminish with increasing distance from the noise source because of energy conservation and atmospheric absorption.

Figure 5 depicts the evolution of the sound pressure level as a function of distance from the noise source. The vehicle considered here is a small unmanned hexacopter manufactured by DJI whose noise footprint was experimentally determined by Heutschi et. al. [6]. We observe that beyond approximately 1.1 km, the sound pressure level falls below typical background noise levels (30 dB). In this case, limiting the propagation distance to this threshold, instead of carrying out propagation to all virtual receptors in the study area, would provide significant performance improvements.

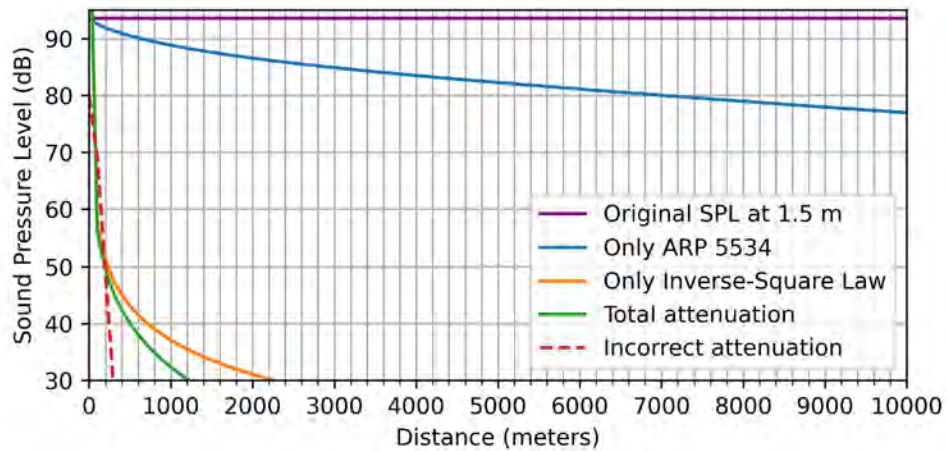


Figure 5. Evolution of sound pressure level (SPL) as a function of distance.

To generalize this approach to all vehicles considered in the simulation, it will be necessary to introduce a step in which this distance threshold is computed for each considered vehicle based on its specific source frequency distribution and amplitude. In addition, the possibility of interactions between multiple vehicles simultaneously located within the range of a given receptor will require additional logic to ensure that such situations do not lead to an underestimation of the resulting sound exposure level. Preliminary formulation work has shown that an analytical approach would allow the threshold distance to be updated based on the maximum number of vehicles concurrently operating within the simulation.

Research Approach – Subtask 2.b – Surrogate Modeling Study

Objectives

We aim to develop a surrogate model that replicates the output of a high-fidelity noise model with reduced computational complexity. The surrogate model should ensure a high degree of accuracy (high statistical confidence) while offering a significant time improvement compared with the actual noise model.

Approach

The methodology involves three high-level steps, starting by identifying and fitting different types of surrogate models and then assessing these surrogate techniques based on computational time and accuracy. The final step is to select the most suitable approach.

Surrogate modeling approaches

The following surrogate modeling techniques were considered in the modeling study.

Polynomial response surface equations

The response surface equations (RSEs) involve fitting a polynomial equation to the data points generated by the high-fidelity noise model. The general form of a second-order polynomial RSE is as follows:

$$\hat{f}(x) = \beta_0 + \sum_{i=1}^n \beta_i x_i + \sum_{i=1}^n \sum_{j=1}^n \beta_{ij} x_i x_j$$

where \hat{f} is the response variable, x_i and x_j are predictor/weight basis functions, and the β terms are coefficients determined by training/fitting the model. The linear regression found in the “scikit-learn” Python library was used to fit the model [2].

Radial basis functions

Radial basis functions (RBFs) are used for interpolation in multidimensional space. They depend on the radius between two training points. Typically, the 2-norm Euclidian radial distance is used to develop an RBF of the following form:

$$\hat{f}(x) = \beta_0 + \sum_{i=1}^n \lambda_i \phi(\|x - x_i\|)$$

where λ_i are the weights, ϕ is the RBF, x is the input vector, and x_i are the centers of the RBF. The RBF was implemented by using SciPy's `cdist`, with a focus on multiquadric functional basis forms and a simple linear solver [3].

Artificial neural networks

Artificial neural networks (ANNs), inspired by biological neural networks, consist of layers of interconnected nodes. This model can learn nonlinear relationships and is thus capable of capturing complex patterns in data. A typical ANN has a structure with an input layer, one or more hidden layers, and an output layer. The neurons in these layers are interconnected with adjustable weights. The multi-layer perceptron regressor model from the “scikit-learn” Python package was employed [4].

Interpolation

Interpolation involves constructing new data points within the range of a discrete set of known data points. Linear interpolation is the simplest form, but higher-order polynomials can also be used for more complex datasets. The model was implemented through SciPy's `interp1d` [5].

Surrogate modeling process

Figure 6 depicts the surrogate modeling process.

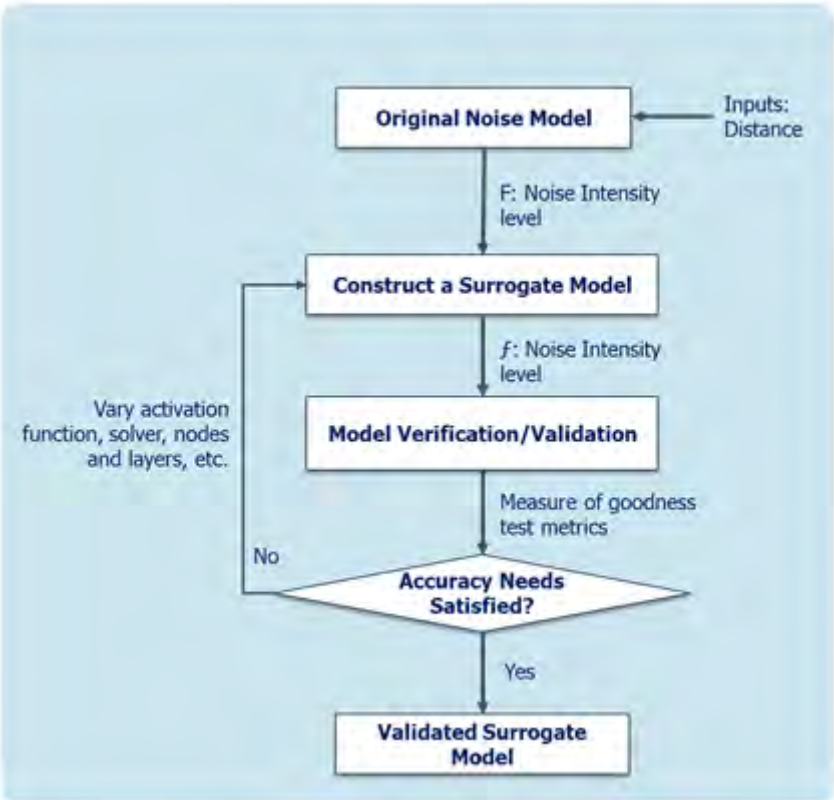


Figure 6. Surrogate modeling workflow.

Data Sampling

The high-fidelity study is used to sample the input parameter space. This step involves selecting a representative subset of the original model's input-output pairs.



Model training and validation

The surrogate models are trained on the sampled data. The training process involves adjusting the model parameters to minimize the difference between the model predictions and the actual data. Model validation is then performed on validation data, a set of model observations that were not used to train the surrogate model, thus ensuring the ability of the model to generalize.

Surrogate assessment

The trained models were assessed based on two high-level metrics, surrogate accuracy and surrogate computational time. The accuracy of the model was verified based on validation metrics and validation plots.

Validation metrics

- **Coefficient of determination (R^2):** This metric indicates the proportion of variance in the dependent variable predicted from the independent variables. A value closer to 1 suggests higher model accuracy. The lower the R^2 value, the greater the variance of the error compared with the response variance.
- **Mean absolute error:** This metric measures the average magnitude of the errors in a set of predictions, without considering their direction.

Validation plots

- **Actual vs. predicted plots:** These plots compare actual values from the high-fidelity noise model with values predicted by the surrogate models. Ideally, the points should lie close to the 45° line, indicating high accuracy. Deviations from this straight diagonal line are due to inaccuracies introduced by surrogate modeling. Figure 7 presents examples of the actual vs. predicted plots used in the validation process.
- **Residuals vs. predicted plots:** These plots illustrate the difference (residuals) between actual and predicted values against the predicted values. The residuals should be randomly distributed and centered around zero.

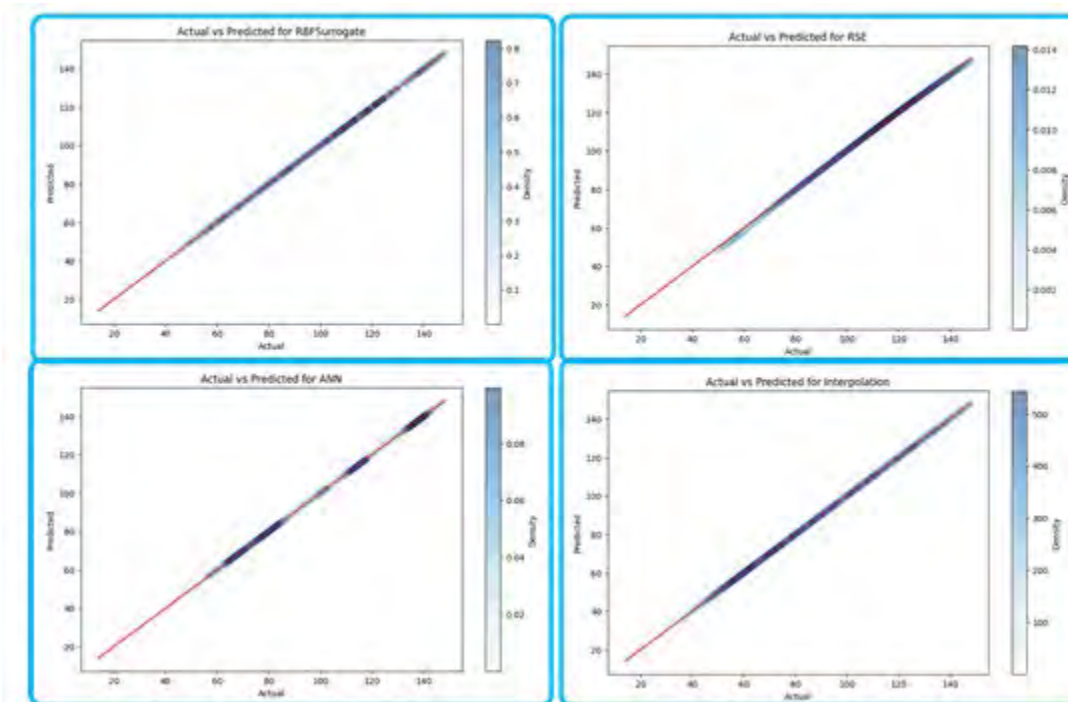


Figure 7. Actual vs. predicted plots for different surrogate modeling approaches. ANN: artificial neural network; RBF: radial basis function; RSE: response surface equation.



Computational time evaluation

The surrogate computational time represents the time needed to run a trained model for predictions. Note that the time needed to train a model is not considered in the study because we are assessing the computational time required to make predictions: Are we going faster than the original model?

Implementation

It is important to note that different sizes of prediction samples result in different prediction times; that is, a prediction with many sample points requires more prediction time. However, the computational time may not be linear with respect to the number of prediction samples; thus, we also study the evolution of prediction time vs. the number of prediction points. Prediction batches of different sizes, ranging from 100 to 100,000, were considered. The time is measured using the “timeit” Python module to evaluate the computation time for each prediction batch size. The surrogate is trained once using the same number of points, with the training dataset fixed at 30,000 points.

Analysis of results and surrogate selection

To ensure surrogate accuracy, validation metrics and plots for different surrogates were assessed. Figures 7 and 8 display the validation plots of actual vs. predicted and residuals vs. predicted, respectively, for each considered surrogate modeling approach. The actual vs. predicted present a 45° diagonal line as desired. As stated, any deviations from a straight diagonal line are due to inaccuracies in surrogate modeling. The R² values are also assessed to check for the best fit for each surrogate model. The results in Table 1 show that that RBF and interpolation surrogate models have R² values of 1, indicating an almost perfect fit. The RSE and ANN models also demonstrate high R² values, suggesting a high level of accuracy, as the amplitude of the error is small compared with the total amplitude of the response variations.

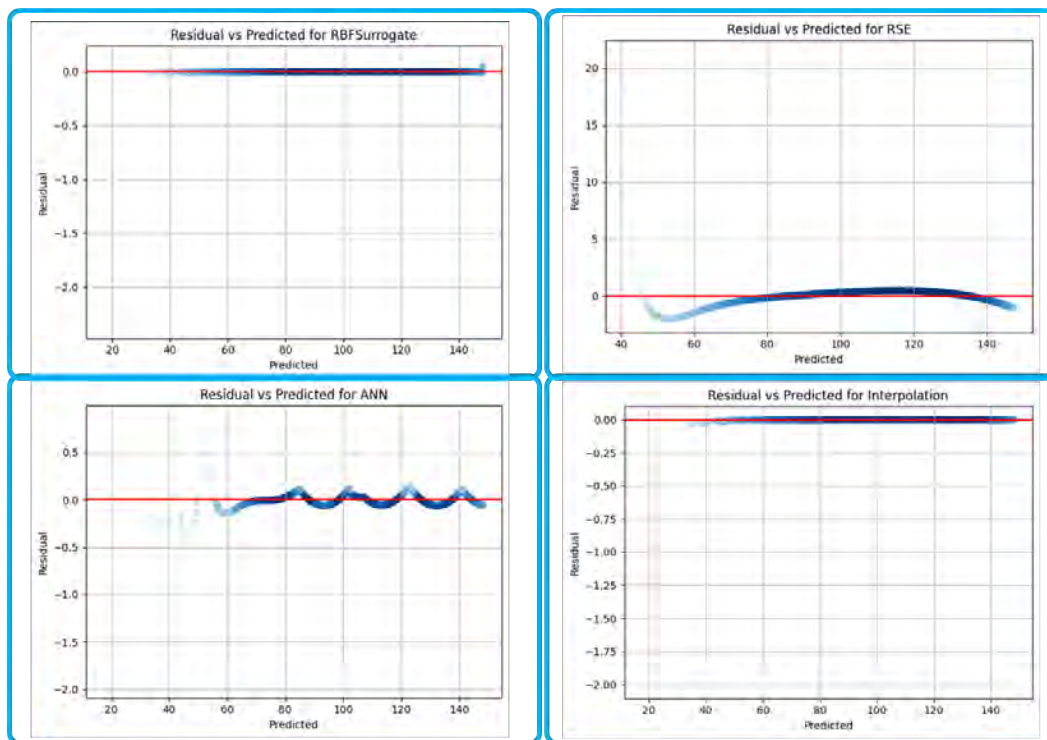


Figure 8. Residuals vs. predicted plots for different surrogate modeling approaches. ANN: artificial neural network; RBF: radial basis function; RSE: response surface equation.



Table 1. Values of the coefficient of determination (R-Square) for each considered surrogate modeling approach. ANN: artificial neural network; RBF: radial basis function; RSE: response surface equation.

Surrogate	R-Square
RBF	1
RSE	0.99695
ANNs	0.99998
Interpolation	1

The residual plot results are consistent with the actual vs. predicted plots: the residuals for the RBF and interpolation models show less deviation, indicating that these models have a higher accuracy in emulating the high-fidelity noise model. The spread of residuals in the RSE and ANN models is wider, indicating a lower degree of accuracy.

Impact of number of prediction points on surrogate computational efficiency

Figure 9 shows two plots depicting the computational time and relative computational time as a function of the number of prediction points for each surrogate model and the actual model. The left plot shows the computational time (in seconds, on a logarithmic scale) required by each model as the number of prediction points increases. The surrogate models all start with relatively low computational times for small numbers of prediction points, with the time increasing sharply as the number of prediction points grows. As the number of prediction points increases, the ANN and RBF models show a steady increase in computational time, but they remain significantly faster than the actual model. The RSE and interpolation models demonstrate the best performance among the surrogates, with interpolation being the most efficient. Their computational times increase more slowly and remain several orders of magnitude lower than that of the actual model, even at 100,000 prediction points.

The right plot presents the relative computational time, which is a ratio of the computational time of each surrogate model to that of the actual model (on a logarithmic scale). The relative computational time for the ANN and RBF models is above 1, indicating that these models are both less efficient than the actual model, whereas the RSE and interpolation models have relative computational times of less than 1, thus reinforcing their status as being more computationally efficient than the actual model. It is also noted that the efficiency gains of the surrogate models are more pronounced at higher numbers of prediction points.

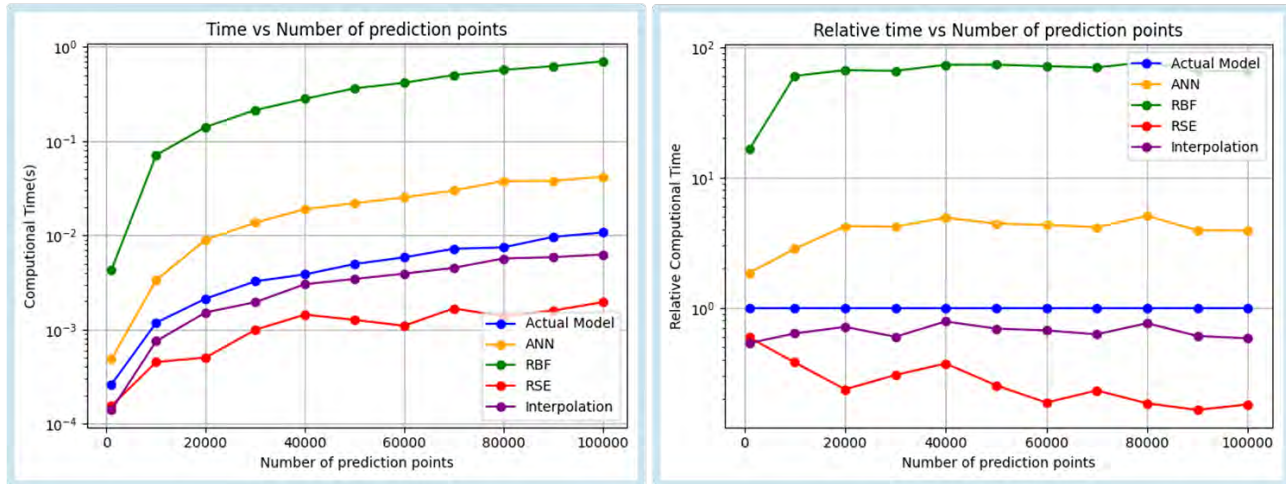


Figure 9. Left: Computational time vs. number of prediction points. Right: Computational times relative to the computational time of the actual model. ANN: artificial neural network; RBF: radial basis function; RSE: response surface equation.

Surrogate accuracy vs. computational time

Considering that the two attributes assessed for surrogate performance are surrogate accuracy and computational time, we provide a scatter plot for surrogate accuracy vs. computational time to determine whether any of the surrogate models dominate the other surrogates in all attributes, as shown in Figure 10.

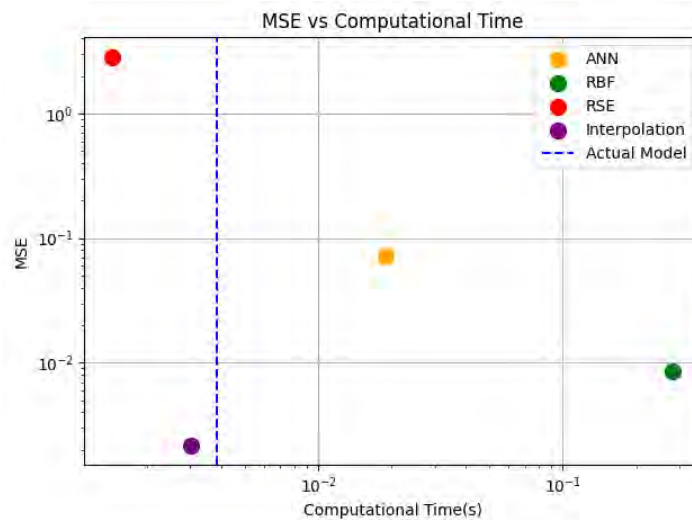


Figure 10. Mean squared error (MSE) vs. computational time. ANN: artificial neural network; RBF: radial basis function; RSE: response surface equation.

General observations

Interpolation achieves the lowest mean squared error (MSE), indicating that it is the most accurate in making predictions among the surrogates tested. The ANN and RSE models have higher MSE values, suggesting that their predictions are less accurate compared with the interpolation and RBF models. The hierarchy of the testing error margin is $\epsilon_{RSE} > \epsilon_{ANN} > \epsilon_{RBF} > \epsilon_{Interpolation}$; thus, interpolation has the lowest error margin, followed by RBF, ANN, and finally RSE with the highest.

Actual model comparison

The blue dashed line in Figure 10 represents the computational time of the actual noise model. This serves as a benchmark for comparison. The computational times of both the interpolation and RSE models are to the left of this line, indicating that these models are faster than the actual model. Because we seek to accelerate the process, the interpolation and RSE models are the preferable options because of their lower computational times relative to the actual model.

Trade-off analysis

There is an evident trade-off between accuracy and computational time among the surrogate models. Although the interpolation model is the most accurate, it has a higher computational time than the RSE model. In contrast, the RSE model offers a lower computational time at the cost of a higher MSE compared with the interpolation model.

The trade-offs highlighted by Figure 10 suggest that if the highest accuracy is required, interpolation is the best surrogate, given its lower MSE despite its slightly higher computational time compared with RSE. If the computational speed is more critical and some loss of accuracy can be tolerated, RSE might be the preferred choice.

Milestones

None.

Major Accomplishments

Multiple avenues for speeding up the noise assessment and making probabilistic assessments more practical were identified and demonstrated; an initial study showed great potential for speeding up the noise assessment compared with the approach previously applied in ASCENT Project 9 by limiting the range of noise propagation. A comparison study of multiple surrogate approaches showed additional promise for speeding up this process.

Plans for Next Period

In the next period, both the approach aimed at limiting the range over which noise is propagated in the simulation and the most promising surrogate modeling approaches will be implemented and integrated into the noise assessment tool.

be the end points for these deliveries. Additionally, the system considers the maximum delivery radius for each drone, ensuring that deliveries are feasible given the drone’s range. Lastly, the number of deliveries each drone can make per day is considered, which plays a vital role in scheduling and resource allocation.

The operational process of the drone delivery system involves two key steps. In the first step, i.e., the pairing step, each home within the service area is evaluated to determine whether it falls within the maximum delivery radius of any warehouse. If a warehouse is within range, the closest warehouse is assigned to that home. However, if no warehouse is within the maximum delivery radius, the home is not assigned a warehouse, and delivery to that location is deemed not possible. The second step involves the actual scheduling of deliveries. On each simulation day, delivery locations are randomly selected from the list of potential delivery locations. The corresponding warehouse for each delivery location is then identified using a lookup method, ensuring an efficient allocation of resources and timely deliveries.

Newly Implemented Operational Concepts
Per-company list of warehouses

The first improvement brought to the simulation is the ability to have multiple operators simultaneously operating in the study area, where each operator relies on its own staging locations. At this point, fixed (non-mobile) staging locations are assumed to be warehouses; thus, these two terms are used interchangeably in this discussion. This operational concept was

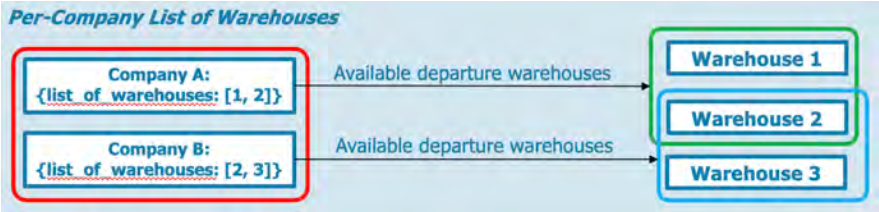


Figure 11. Notional illustration of the operational concept of “per-company list of warehouses.”

implemented as follows, as presented in Figure 11:

- Each company has an attribute “list_of_warehouses” that consists of a list of warehouse IDs.
- If warehouse W’s ID is on the list, the company’s delivery UAS can depart from that warehouse.
- When a company schedules a flight, we look up its warehouses to determine from where the vehicle can take off.

Flights between warehouses

The second newly implemented operational concept allows us to model flights between warehouses. Such flights could be used to rapidly balance stocks between warehouses. This ability was implemented by extending the existing scheduling logic to include warehouses as possible destinations, as presented in Figure 12.

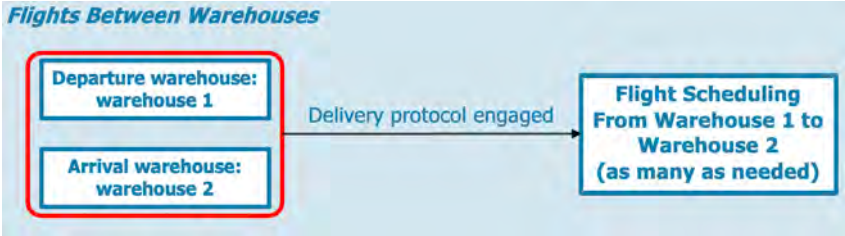


Figure 12. Notional illustration of the operational concept of “flights between warehouses.”

Mobile staging locations for out-of-range delivery locations

The third new operational concept introduces mobile staging locations to the simulation, in addition to the previously exclusively fixed staging locations. When homes are out of range of all warehouses, new mobile staging locations are optimized to cover as many previously unreachable homes as possible. Multiple mobile staging locations may be added if one location is not sufficient to cover all out-of-range homes, as presented in Figure 13.

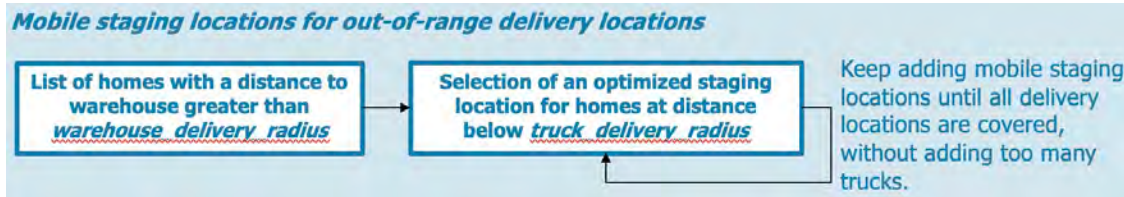


Figure 13. Notional illustration of the operational concept of “mobile staging locations for out-of-range delivery locations.”

Multi-delivery flights

The fourth and last additional operational concept is presented in Figure 14. This concept enables multiple deliveries within a single flight based on an optimization function that maximizes the number of houses associated with each drone

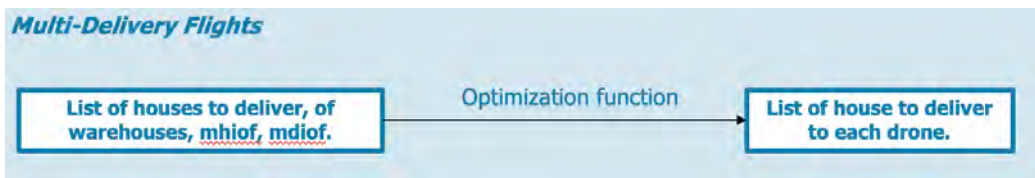


Figure 14. Notional illustration of the operational concept of “multi-delivery flights.”

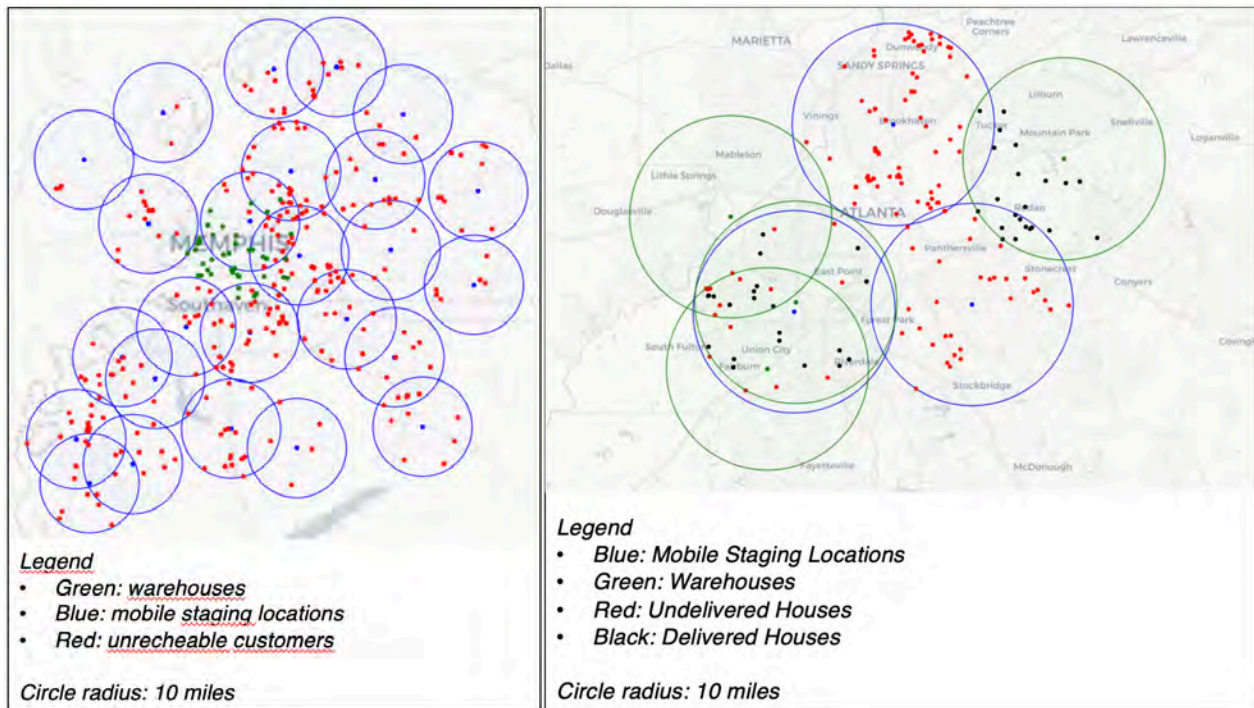


Figure 15. Left: Example of a flight scheduling result over the Memphis, TN analysis area. Right: Example of a flight scheduling result over the Atlanta, GA analysis area.

and minimizes the number of drones used and the total distance flown by each drone. This feature would allow us to assign to each drone a list of houses that are relatively close for delivery.

Figure 15 depicts the results obtained by applying the new operational concepts to two study areas: the Memphis, TN study area (left) and the Atlanta, GA study area (right). All staging and delivery locations are notional at this point. We observe that the optimization algorithm efficiently places the mobile staging locations in order to maximize the number of reachable customers. On the right, we can observe that the delivery radius of one of the warehouses (green) overlaps with the delivery radius of one of the staging locations (blue); this overlap occurs because the locations correspond to two different operators.

Research Approach – Subtask 3.b – Revised Computational Approach

The research conducted as part of ASCENT Project 9 identified a few shortcomings in the computational approach then adopted. In particular, that approach implicitly assumed that all vehicles independently contributed to the sound level received at receptors; however, it was demonstrated that when operations become sufficiently dense in a given geographical area, multiple vehicles may simultaneously emit noise to receptors at the same location, and the independence assumption may lead to a significant underestimation of the resulting sound level at the receptor. As a consequence, the computational approach was reformulated in order to account for instances in which multiple vehicles may simultaneously contribute to the sound level received at one given receptor location. The revised approach proceeds through time, timestep by timestep, instead of systematically vectorizing all computations.

The revised approach brings two additional benefits. First, because fewer operations are vectorized, a substantial reduction is expected for the memory requirements of the system on which the simulation is run. Second, stepping through time in the simulation is expected to allow for additional flexibility when identifying single events from the viewpoint of individual receptors, allowing us to clearly identify when an event starts and ends based on a pre-defined rule, such as the common “10 dB down” rule.

Milestones

Subtask 3.a has been completed, and the different flight scheduling algorithms are fully functional.

Major Accomplishments

Multiple operational concepts have been identified and implemented. A revised simulation approach that provides more flexibility in defining events and computing various noise exposure metrics was formulated and is in the process of being implemented.

Plans for Next Period

The next steps will be to 1) integrate the different operational concepts into the overall simulation workflow and 2) finalize the implementation of the revised simulation approach.

Task 4 – Extend Existing Prototype Noise Engine Capabilities

Georgia Institute of Technology

Objectives

Development and testing in Ascent Project 9 demonstrated the potential for possible speed-ups to accelerate the computation of noise grids by using novel computational technologies such as cluster computation. As part of this effort, a prototype was developed that also includes user-interactive visualizations of UAS noise for specific study areas on map displays. This task will be updated to include the estimation of probabilistic distributions of UAS operations based on scalable numbers and locations for service points and stochastic operational frequencies and trajectories over large geographic areas. This task will also extend the prototype to include the capability to integrate the methods proposed in Tasks 1 and 2 and combined in Task 3 to visually present probabilistic distributions of UAS operations and UAS noise exposure over the analyzed geographic areas.

The first two main efforts undertaken in this task are 1) the implementation of a path planning algorithm to generate more realistic vehicle trajectories that avoid obstacles found in the study area, such as buildings and other landmarks, and 2) the

review and selection of a visualization method that would enable the depiction of noise exposure metrics of interest along with the uncertainty associated with these metrics on a geographic information system (GIS)-like dashboard.

Research Approach – Subtask 4.a – Modeling of Realistic Vehicle Trajectories

In the context of ASCENT Project 9, vehicles were expected to fly straight from the origin to their destination according to a fixed-altitude profile. Although this approach offered a simple and convenient starting point for the initial proof-of-concept approach, it does not account for the possibly trajectories that vehicles will eventually need to follow in order to avoid the many obstacles existing in an urban environment where package delivery is expected to take place.

To account for this feature, we considered multiple path planning approaches from the literature. Because of its relative simplicity and maturity, the class of path planning over a discrete grid, including the well-known A* algorithm, was adopted. These algorithms operate over a discretized grid, which is already the case for the analysis grid used for the virtual receptors in the noise simulation. The grid cells obstructed by obstacles are identified and stored. The algorithm finds, if it exists, the shortest path between any starting cell to any destination cell in the grid, while avoiding all cells marked as obstacles.

In the context of Project 94, the obstacles currently under consideration are buildings, which are obtained from the FAA obstacle list, and parks, which are obtained from openly available GIS databases. A custom approach was developed in order to effectively discretize these obstacles on the grid used for path planning. We note here that the developed approach is generalizable to all obstacles defined in the FAA obstacle database; therefore, new updates to the database can easily be imported in the simulation. Similarly, the logic developed for discretizing parks in the path planning grid relies on the definition of obstacles as a set of polygons, which is a generic method that can be generalized to other types of restricted geographical areas beyond parks.

The implementation effort started with a review of existing, off-the-shelf implementation of selected path planning algorithms. This initial review identified a lack of efficient Python implementations. An efficient implementation is crucial in the context of Project 94 because path planning must be repeated at the beginning of every simulation run for every scheduled flight. Because probabilistic assessments require many simulation runs to generate distributional results, computational efficiency is a priority. Thus, we developed a custom implementation of the A* algorithm on a two-dimensional grid that does not require instantiation of the full grid, allowing the algorithm to run on a typical personal computer.

Because it only allows movements from one grid cell to its neighbors, the A* algorithm leads to unrealistic trajectories, such as “zig-zag”-shaped paths. A straightforward improvement to this is the Θ^* algorithm, which allows straight paths between any cells of the grid as long as the path is not obstructed by an obstacle. While conceptually simple, going from A* to Θ^* requires the ability to check for obstructions between any two grid cells. This problem can be solved by ray-tracing algorithms. In this instance, computational efficiency is of utmost importance, as this process is repeated at every step of the path planning algorithm. Early testing indicated that a poor implementation could lead to a slowdown by orders of magnitude. As a result, a line-of-sight algorithm was efficiently implemented in Cython, a programming language and suite of tools that allows one to essentially write C code using a Python-like syntax. The resulting code can be compiled and easily called from the main Python program.

The resulting implementation allows one to generate a trajectory on the order of a tenth of a second. The actual duration depends on the granularity of the path planning grid and the distance between the departure and arrival locations; the further the distance between these locations, the greater the number of grid cells that must be explored to find the shortest path. An example of an outcome of path planning process is shown in Figure 16, where approximately 100 flights were generated over the Atlanta Midtown area. The green area in the center is Piedmont Park. Toward the west, multiple tall buildings are present that must be avoided by the vehicles. We observe that all red trajectories successfully reach their destination while avoiding obstacles.



Example trajectories generated by the implemented path planning approach over Atlanta's Midtown area.

- Blue and green areas are obstacles to avoid (respectively buildings and parks)
- A single starting location was selected
- Delivery locations were randomly sampled within the area of interest (not actual homes)

Figure 16. Example trajectories generated by the developed path planning logic. The study area under consideration is the Atlanta Midtown area.

Research Approach – Subtask 4.b – Visualization of Probabilistic Noise Exposure Metrics Over a Geographical Area

This task commenced with an intense literature review on different frameworks for visualizing uncertainty. Based on the review, we selected the Perlin noise model to visualize the uncertainty for our noise tool.

Perlin Noise Model

To visualize uncertain data fields, the Perlin noise model integrates color-scale visualization methods by controlling the model parameters. Based on the uncertainty of the data, the model effectively visualizes the uncertain scalar data fields in a combined manner, showing local data value and quality. The color-scale lookup is biased by a Perlin noise weighted by uncertainty data, allowing for a visualization of both the mean value and uncertainty information.

Algorithmic Principle

The objective of this study is to propose a universal method for visualizing both scalar data and associated uncertainty information, such as the error or standard deviation. The proposed method adheres to the following constraints:

- The approach should extend traditional one-dimensional color maps, ensuring that the resulting visualization remains readily comprehensible to individuals familiar with color maps.
- The representation of uncertainty data should not mask the fundamental data, nor should it introduce complexities, inaccuracies, or challenges in interpretation.

In a conventional three-dimensional (3D) color-scale visualization, the data value $V(\vec{x})$ is mapped linearly to a color map coordinate and then to the corresponding red-green-blue color value, which is subsequently displayed in the 3D visualization. The proposed method introduces a modulation to this visualization by applying an uncertain value $U(\vec{x})$. The values generated by the Perlin noise model $n_{f,o,p}(\vec{x})$ are linearly scaled to ensure a null mean and to fall within the range of [-1,1]. Subsequently, the scaled noise is multiplied by the uncertainty value and added to the base value $V = (\vec{x})$.

The result is $V(\vec{x}) + n_{f,o,p}(\vec{x}) * U(\vec{x})$, which spans the range $[V(\vec{x}) + U(\vec{x}), V(\vec{x}) - U(\vec{x})]$. The range of the above resulting distribution will have a mean of $V(\vec{x})$ and serves as a color map coordinate in the visualization.

We implemented the Perlin noise model on a simple normal distribution with varying standard deviation to show the level of increasing uncertainty in the dataset. We employed the same algorithm as detailed above, with the results of the use case shown in Figure 17. The uncertainty of the data is shown to increase from left to right based on our Perlin noise texture without a masking of scalar data. A detailed level of pixel displacement can be achieved by tweaking the parameters of the Perlin noise model that will be employed for our noise computational model.

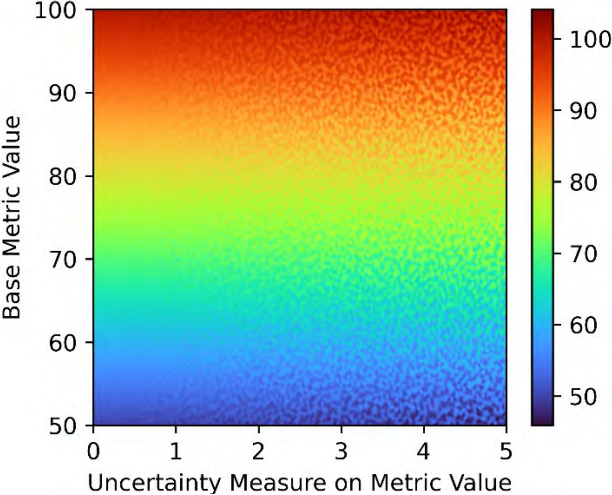


Figure 17. Test case result obtained by using the Perlin noise model.

Milestones

None.

Major Accomplishments

A first version of the path planning algorithm was implemented and tested. The team selected the Perlin noise model as a method for visualizing noise assessment results.

Plans for Next Period

In the next period, the path planning algorithm will be extended to the 3D case, and all steps of the noise assessment workflow will be integrated.

Task 5 – Coordinate with the FAA and Volpe

Georgia Institute of Technology

Objectives

The research team will utilize key noise computation methods for which experts reside at the FAA and Volpe. To identify potential UAS noise source data as well as sample study data, it may be necessary to coordinate with experts at the FAA and Volpe. This effort will also include consultations regarding which noise metrics (such as LAeq, LAmx, SEL, NA60, and potentially others) are the most appropriate for UAS noise and are amenable to probabilistic representations.

Two key collaborations were identified to enhance and validate the noise assessment tool under development. First, through collaboration with the FAA aeroacoustics team, flight test data for UAS vehicles of the relevant size class were obtained. These measurements should 1) enable the introduction of realistic source noise spheres in the simulation and 2) validate the noise propagation technique used in the noise engine. Second, through collaboration with the NASA aeroacoustics team, input data were obtained for a UAM study carried out using the Aviation Environmental Design Tool (AEDT). For this case, replicating this study using the capabilities developed as part of Project 94 would enable a higher-level validation.

Research Approach – Subtask 5.a – Leveraging of Causey Airport Measurements

In 2021, an FAA-led team conducted a set of noise measurements at Causey Airport to characterize the noise produced by UASs during ground and airborne operations. In this experiment, the noise from three vehicles with different weights, speeds, and flight conditions was measured by two sets of microphone arrays: one for the flyover and one for the hover. In both layouts, both ground-based and cable-suspended microphones were utilized. The measurements were presented in terms of pressure time-history acoustic data stored in ASCII files.

This subtask uses the Causey Airport measurements to validate the in-house noise analysis used in this project, which was developed in the ASCENT 9 project. The validation involves two major steps. First, vehicle noise source data based on the Causey Airport measurements are generated by using the noise analysis tools developed by Volpe, and second, the in-house noise analysis code is used to re-generate the measured acoustics data based on the generated noise source data and the vehicle trajectories used in the Causey Airport measurements.

Generating noise source data for UASs relies on two analysis tools from Volpe: the advanced acoustics model (AAM) and the acoustic repropagation technique (ART). The atmospheric conditions, microphone locations, and flight trajectories used in the Causey Airport measurements are first input to the AAM. Using time- and geometric-based analyses, AAM calculates the propagation physics and geometric relationship between the noise source (i.e., UAS aircraft) and microphones; it then outputs a time-history file, including the mapped relationship on a sphere for each trajectory point. Along with the aircraft specifications and microphone measurement data, the generated time-history file is input to the ART to generate noise source data for the vehicle in terms of a noise sphere. This noise sphere is obtained by applying the propagation corrections determined by the AAM to the measured microphone spectral time histories.

The generated noise sphere is then provided to the in-house noise analysis code. Using the same flight trajectory applied in the Causey Airport measurements, the noise levels at different points of interest are computed by the analysis code based on the noise sphere. In this validation, the points of interest are set to the microphone locations used in the Causey Airport measurements. If the computed noise levels match the measured acoustic data, the accuracy of the in-house noise analysis code will be validated.

Research Approach – Subtask 5.b – Validation of the Approach for Leveraging the NASA AEDT UAM Study

The main objective of this task is to validate our existing noise computational model based on NASA’s AEDT study on UAM operations. This task involved collaboration with the AEDT study team at NASA to exchange data, conduct the study on UAM operations, and perform a validation of the noise model using AEDT study results.

The ASCENT 94 team met with the NASA aeroacoustics team led by Dr. Stephen Rizzi and obtained the data required for the AEDT study. The data comprised several CSV files detailing the custom-defined airports, runways, and metrics. We were also provided with structured query language (SQL) scripts to load the custom-defined metrics into our study. As most of the in-built tools in AEDT generate metrics at an aircraft-level scale, the NASA team applied a different method for defining each metric that is valid for UAM operations. After we have obtained the data and required files, we will define all of the necessary variables and metrics using the SQL scripts through SQL Server Management Studio.

Milestones

Subtask 5.a

- The AAM and ART analysis tools were successfully set up and configured.
- Causey UAS measurement data were received and translated into a format that can be processed by the AAM and ART.
- Microphone measurement files were modified in terms of the maximum number of bands to account for the limitation of ART.
- The AAM and ART input files created for the Causey UAS measurements were decoded and successfully executed.

Major Accomplishments

Subtask 5.a

- Run cases 15 and 20 from the Causey Airport measurements were successfully implemented in the AAM and ART.
- Noise spheres for run cases 15 and 20 were obtained by using the terrain files provided in the AAM tutorial.

Subtask 5.b

- The team obtained data and imported all of the required metrics and jobs using SQL scripts into an AEDT study and commenced running the AEDT.

Plans for Next Period

Subtask 5.a

- Generate elevation and impedance files using the software BaseOps based on the experimental conditions applied in Causey Airport measurements.
- Select test cases from the Causey Airport measurements for validation purposes.
- Generate noise spheres for selected test cases using updated terrain files.
- For each test case, run the in-house noise analysis code using the generated noise sphere.

Subtask 5.b

- Validate the internal replication of the AEDT study.
- Implement the study with capabilities developed as part of Project 94.
- Compare the results of the study obtained with AEDT and Project 94 capabilities.

Task 6 – Develop Documentation

Georgia Institute of Technology

Objective

This research will culminate in a report documenting our findings and recommendations.

Research Approach

None.

Milestones

None.

Major Accomplishments

None.

Plans for Next Period

Documentation efforts will continue with annual reports and publications.

Publications

None.

Outreach Efforts

Our findings were presented at the Spring and Fall 2023 ASCENT meetings.

Awards

None.

Student Involvement

Xi Wang performed a literature review to identify a demand model for online shopping, extracted necessary data from the U.S. census, and implemented the demand model.

Hugues Chardin assisted in the implementation of the demand model. He also formulated and implemented the different operational concepts described in Subtask 3.a.

Lloyd Teta formulated, implemented, and drew the conclusions of the comparison study in Subtask 2.b.

Venkat Sai Chinta identified Perlin noise as a promising uncertainty visualization and is replicating the NASA AEDT study internally.

The documentation effort involved all team members.

References

- [1] Jaller, M., & Pahwa, A. (2020). Evaluating the environmental impacts of online shopping: A behavioral and transportation approach. *Transportation Research. Part D, Transport and Environment*, 80, 102223-.
<https://doi.org/10.1016/j.trd.2020.102223>
- [2] Linear Models. scikit-learn. https://scikit-learn.org/stable/modules/linear_model.html. Accessed Nov. 22, 2023.
- [3] Neural Network Models (Supervised). scikit-learn. https://scikit-learn.org/stable/modules/neural_networks_supervised.html. Accessed Nov. 22, 2023.
- [4] Scipy.Spatial.Distance.Cdist — SciPy v1.3.2 Reference Guide. Scipy.org. <https://docs.scipy.org/doc/scipy-1.3.2/reference/generated/scipy.spatial.distance.cdist.html>. Accessed Nov. 22, 2023.
- [5] Scipy.interpolate.intErp1d — SciPy v1.11.4 Manual. Scipy.org. <https://docs.scipy.org/doc/scipy/reference/generated/scipy.interpolate.interp1d.html>. Accessed Nov. 22, 2023.
- [6] Heutschi, K., B. Ott, T. Nussbaumer, and P. Wellig. (2021) "Virtual microphone signals of flying drones." In *Proceedings of the NATO STO MSG-SET-183 Specialists' Meeting on Drone Detectability: Modelling the Relevant Signature*, Wakefield, MA, USA, pp. 27-29.



Publications Index

Project 001

Fifteen graduate students and four undergraduate students involved.

Publications

- Demsky, S. (2023). Analysis of Double Cropping to Expand Sustainable Aviation Fuel Production in the United State. Master's thesis, Massachusetts Institute of Technology. <https://hdl.handle.net/1721.1/151600>.
- Lewis K., Obnamia J., Allroggen F., Taheripour F., & Malina R. (2023) *Sustainability Challenges and Opportunities of Power-to-Liquid Fuels*, 26th Annual Conference on Global Economic Analysis, June 14-16, Bordeaux, France.
- Li, P., T.E. Yu, C. Trejo-Pech, J.A. Larson, B.C. English, & D. Lanning. (2024). Assessing the Impact of Preprocessing and Conversion Technologies on the Sustainable Aviation Fuel Supply from Forest Residues in the Southeast U.S." accepted for 2024 TRB Annual Meeting presentation and publication in *Transportation Research Record*.
- Li, T. (2023). Evaluating the Potential Risks of Producing First- and Second-Generation Bioenergy Crops in Tennessee, MS Thesis, University of Tennessee.
- Martinez-Valencia, L., Peterson, S., Brandt, K., King, A. B., Garcia-Perez, M., & Wolcott, M. (2023). Impact of services on the supply chain configuration of sustainable aviation fuel: The case of CO₂e emission reductions in the US. *Journal of Cleaner Production*, 404, 136934. <https://doi.org/10.1016/j.jclepro.2023.136934>
- Taheripour F., Sajedinia E., Chepeliev M., & Karami O. (2023). *Land use change implications of Power-to-Liquid Fuels*, 26th Annual Conference on Global Economic Analysis, June 14-16, Bordeaux, France.
- Taheripour F., Mueller S., Emery I, Karami O., Sajedinia E., Zhuang Q., & Wang M. (2024). Biofuels induced land use change emissions: The role of implemented emission factors in assessing terrestrial carbon fluxes, *Sustainability: Under Review*.
- Zhao, J., Lee, J.Y., Camenzind, D., Wolcott, M.P., Lewis, K.C., & Gillham, O. (2023). Multi-component resilience assessment framework for a supply chain system. *Sustainability*, 15(7), 6197. <https://doi.org/10.3390/su15076197>

Reports

- CAEP/13-FTG/02-WP/08 – “Pathway definition”, October 31 to November 4, 2022, Montréal, Canada.
- CAEP/13-FTG/02-WP/09 – “Brazilian second corn ATJ”, October 31 to November 4, 2022, Montréal, Canada.
- CAEP/13-FTG/03-WP/13 – “ILUC assessment for Brazilian second corn ATJ”, March 6 to 9, 2023, Virtual Meeting.
- CAEP/13-FTG/03-WP/14 – “Applicability of the Low Land Use Change (LUC) risk practices on 2nd Crop in Brazil”, March 6 to 9, 2023, Virtual meeting.
- CAEP/13-FTG/03-WP/14 – “Definition of marginal land”, March 6 to 9, 2023, Virtual meeting.
- CAEP/13-FTG/03-IP/06 – “ILUC and DLUC updates on Soil Organic Carbon (SOC), ILUC calculations for pathways with significant amounts of electricity, and potential data base and modelling updates”, March 6 to 9, 2023, Virtual meeting.
- CAEP/13-FTG/04-WP/06 – “Soil organic carbon including a case study”, July 24-28, 2023, Turin, Italy.
- CAEP/13-FTG/04-WP/07 – “Modeling Brazil corn ATJ pathway”, July 24-28, 2023, Turin, Italy.
- CAEP/13-FTG/04-WP/08 – “Updates Low LUC Risk Practice”, July 24-28, 2023, Turin, Italy.
- CAEP/13-FTG/04-WP/09 – “Definition of Marginal Land”, July 24-28, 2023, Turin, Italy.
- CAEP/13-FTG/04-WP/09 – “Assessing ILUC for a representative power to liquid SAF pathway”, July 24-28, 2023, Turin, Italy.
- CAEP/13-FTG/04-WP/10 – “Updating the AEZ-EF model according to 2019 IPCC guideline and ILUC revisions”, July 24-28, 2023, Turin, Italy.
- CAEP/13-FTG/05-WP/03 – “Cutoff dates for Low LUC Risk Practices”, September 5-7, 2023, virtual.
- CAEP/13-FTG/05-WP/04 – “Amendments to the ICAO document “CORSIA methodology for Calculating Actual Life Cycle Emission Values””, September 5-7, 2023, virtual.
- CAEP/13-FTG/05-WP/05 – “Definitions of land and specifications for negative ILUC pathways”, September 5-7, 2023, virtual.
- CAEP/13-FTG/05-WP/05 – “Amendments to the ICAO document “CORSIA Default Life Cycle Emission Values for CORSIA Eligible Fuels””, September 5-7, 2023, virtual.



- CAEP/13-FTG/05-WP/06 – “Amendments to the ICAO document “CORSA Eligibility Framework and Requirements for Sustainability Certification Schemes””, September 5-7, 2023, virtual
- CAEP13/FTG03/IP04: Sensitivity analysis for the core LCA values (preliminary), March 2023.
- CAEP/13-FTG/03-IP/05: Actual Value Method of CORSA Eligible Fuels (CEF) Using Significant Electricity Input: Modeling Update
- CAEP13/FTG03/WP08: SAF production scenarios out to 2030.
- CAEP/13/FTG03/WP10: Summary of the progress of the core LCA subgroup, March 2023.
- CAEP/13-FTG/04-WP/12: Summary of the progress of the core LCA subgroup
- CAEP/13-FTG/04-WP/17: Actual Value Method for fuels with high electricity input
- CAEP/13-FTG/04-WP/19: Carbon Capture and Storage (CCS) Technology in CEF Production
- CAEP/13-FTG/04-WP12: Progress of the core LCA subgroup, July 2023.
- CAEP13/FTG04/IP03: Sensitivity analysis for the core LCA values, July 2023.

Presentations

- Lewis K., Obnamia J., Allroggen F., Taheripour F., & Malina R. (2023) *Sustainability Challenges and Opportunities of Power-to-Liquid Fuels*, presented at 26th Annual Conference on Global Economic Analysis, June 14-16, Bordeaux, France.
- Taheripour F., Sajedinia E., Chepeliev M., & Karami O. (2023). *Land use change implications of Power-to-Liquid Fuels*, presented at 26th Annual Conference on Global Economic Analysis, June 14-16, Bordeaux, France.
- Yu, T.E. (2023). *Local Sustainable Aviation Fuel Supply Chain Analysis*, Texas Aviation Conference, Galveston, TX, April 12-14.
- Bista, B., C.O. Trejo-Pech, J.A. Larson, & T.E. Yu. (2023). *Risk Assessment of Publicly Traded Biofuel Firms*. Selected presentation. SAEA annual meeting. Oklahoma City, OK. February 4-8.
- Fontanilla-Diaz, C., T.E., Yu, C. Trejo-Pech, J.A. Larson, B.C. English, & B. Wilson. (2023). *Economic Analysis of the Sustainable Aviation Fuel Supply Chain from Hybrid Poplar in the US Southeast Considering Alternative Preprocessing Technologies*. TRB annual meeting online, 23-3566, Washington, D.C. January 8-12.
- Li, P., T.E. Yu, C. Trejo-Pech, J.A. Larson, B.C. English, & D. Lanning. (2024). *Assessing the Impact of Preprocessing and Conversion Technologies on the Sustainable Aviation Fuel Supply from Forest Residues in the Southeast U.S.* accepted for 2024 TRB Annual Meeting presentation.

Project 002

Four undergraduate students involved.

Project 003

Two graduate students involved.

Publications

- Bozigar, M., Huang, T., Redline, S., Hart, J.E., Grady, S.T., Nguyen, D.D., James, P., Nicholas, B., Levy, J.I., Laden, F., & Peters, J.L. (2023). Associations between Aircraft Noise Exposure and Self-Reported Sleep Duration and Quality in the United States-Based Prospective Nurses’ Health Study Cohort. *Environmental Health Perspectives*, 131(4):47010. doi: 10.1289/EHP10959
- Grady, S.T., Har,t J.E., Laden, F., Roscoe, C., Nguyen, D.D., Nelson, E.J., Bozigar, M., VoPham, T., Manson, J.E., Weuve, J., Adar, S.D., Forman, J.P., Rexrode, K., Levy, J.I., & Peters, J.L. (2023). Associations between long-term aircraft noise exposure, cardiovascular disease, and mortality in US cohorts of female nurses. *Environmental Epidemiology*, 7(4): e259. doi: 10.1097/EE9.0000000000000259
- Nguyen, D.D., Whitsel, E.A., Wellenius, G.A., Levy, J.I., Leibler, J.H., Grady, S.T., Stewart, J.D., Fox, M.P., Collins, J.M., Eliot, M.N., Malwitz, A., Manson, J.E., & Peters, J.L. (2022). Long-term aircraft noise exposure and risk of hypertension in postmenopausal women. *Environmental Research*, 218:115037. doi: 10.1016/j.envres.2022.115037.



- Nguyen, D.D., Levy, J.I., Kim, C., Lane, K.J., Simon, M.C., Hart, J.E., Whitsel, E.A., VoPham, T., Malwitz, A., & Peters, J.L. (2023). Characterizing temporal trends in populations exposed to aircraft noise around U.S. airports: 1995–2015. *Journal of Exposure Science and Environmental Epidemiology*. <https://doi.org/10.1038/s41370-023-00575-5>

Presentations

- Peters, J.L., Grady, S.T., Nelson, E.J., Bozigar, M., Laden, F., Hart, J.E., & Levy, J.I. (2023). Long-term Nighttime Noise Exposure and Incident Hypertension in a National U.S. Cohort of Female Nurses. 14th International Commission on Biological Effects of Noise (ICBEN) Congress, June 18-22.
- Grady, S.T., Peters, J.L., Beck, T., Adar, S.D., Andrews, R.M., Desai, P., Dhana, K., Rajan, K.B., & Weuve, J. (2023). Associations between Environmental Noise and Biomarkers of Neurodegeneration in the Chicago Health and Aging Project. 14th International Commission on Biological Effects of Noise (ICBEN) Congress, June 18-22.

Project 009

Six graduate students involved.

Project 010

Eleven graduate students and two undergraduate students involved.

Project 018

Two graduate students and four undergraduate students involved.

Publications

- Chung, C.S., Lane, K.J., Black-Ingersoll, F., Kolaczyk, E., Schollaert, C., Li, S., Simon, M.C., & Levy, J.I. (2023). Assessing the impact of aircraft arrival on ambient ultrafine particle number concentrations in near-airport communities in Boston, Massachusetts. *Environ Res.*; 225:115584. DOI: 10.1016/j.envres.2023.115584

Presentations

- Mueller S, Patil P, Levy JI, Hudda N, Durant JL, Gause E, Loenen BV, & Lane KJ. (2022). Examining Impacts of Cross-Validation Approaches on Machine Learning Model Performance for Ultrafine Particle Exposure Assessment. Presented at the International Society for Exposure Science. Annual Conference, Chicago, Illinois, USA.

Project 019

Three graduate students involved.

Publications

- Pandey, G., Venkatram, A., & Arunachalam, S. (2023). Accounting for plume rise of aircraft emissions in AERMOD. *Atmospheric Environment*, 314, 120106. <https://doi.org/10.1016/j.atmosenv.2023.120106>
- Pandey, G. Venkatram, A., and Arunachalam, S. (2024). Modeling the Air Quality Impact of Aircraft Emissions: Is Area or Volume the Appropriate Source Characterization in AERMOD? *Air Quality, Atmosphere & Health, Under Revisions.*



Project 022

No students involved.

Publications

- Zhang, J., Wuebbles, D., Kinnison, D., Pfaender, J.H., Tilmes, S., & Davis, N. (2023). Potential Impacts on Ozone and Climate from a Proposed Fleet of Supersonic Aircraft. *Earth's Future*, 11, <https://doi.org/10.1029/2022EF003409>.
- Singh, D.K., Sanyal, S., & Wuebbles, D.J. (2023) Understanding the role of contrails and contrail cirrus in climate change: A global perspective. *Atmospheric Chemistry and Physics*, submitted.

Project 023

Four graduate students involved.

Publications

- Salgueiro, S., & Hansman, R. J. (2023). Identifying, Visualizing, and Communicating Constraints in PBN Flight Procedure Design. AIAA Aviation Forum, San Diego, CA, United States. <https://doi.org/10.2514/6.2023-3968>

Presentations

- Salgueiro, S., & Hansman, R. J. (2023). Identifying, Visualizing, and Communicating Constraints in PBN Flight Procedure Design. [Conference presentation.] AIAA Aviation Forum, San Diego, CA, United States.

Project 025

One graduate student involved.

Publications

- Boddapati, V., Ferris, A. M., & Hanson, R. K. (2024). Predicting the physical and chemical properties of sustainable aviation fuels using elastic-net-regularized linear models based on extended-wavelength FTIR spectra, *Fuel*, 356, 129557. <https://doi.org/10.1016/j.fuel.2023.129557>

Project 031

No students involved.

Project 033

Three graduate students involved.

- Database made accessible through <https://altjetfuels.illinois.edu/>

Publications

- Oh, J., Wiersema, P., Kim, K., Mayhew, E., Temme, J., Kweon, C., & Lee, T. (2023). Fast Uncertainty Reduction of Chemical Kinetic Models with Complex Spaces using Hybrid Response-Surface Networks. *Combustion and Flame*, 253, 112772. <https://doi.org/10.1016/j.combustflame.2023.112772>
- Oh, J., Oldani, A., Solecki, A., & Lee, T. (2023). Learning to predict sustainable aviation fuel properties: A deep uncertainty quantification viewpoint. *Fuel*, 356, 15, 129508. <https://doi.org/10.1016/j.fuel.2023.129508>



Project 37

Twelve graduate students currently involved.

Project 038

Two graduate students involved.

Project 044

Five graduate and one undergraduate student involved.

Publications

- Huynh, J., Lepe, M., Lee, T., Hood, P., & Hansman, R. J. (2023, November). Comparison of data-based and modeled-based analysis of aircraft departure noise using noise monitor network recordings. In *INTER-NOISE and NOISE-CON Congress and Conference Proceedings* (Vol. 268, No. 5, pp. 3349-3360). Institute of Noise Control Engineering.

Presentations

- Huynh, J., Lepe, M., Lee, T., Hood, P., & Hansman, R. J. (2023). Comparison of data-based and modeled-based analysis of aircraft departure noise using noise monitor network recordings. *Internoise 2023*, Tokyo, Japan.

Project 046

No students involved.

Project 047

One graduate student involved.

Project 049

Two graduate students involved.

Publications

Published conference proceedings

- Mukherjee, B., Jue, A., Theron, J.-P., Brentner, K. S., Greenwood, E., & Horn, J. F. (2023). Investigation of Departure Transition Noise for Lift-plus-Cruise eVTOL Aircraft. Vertical Flight Society's 79th Annual Forum & Technology Display, West Palm Beach, FL, USA.

Presentations

- Mukherjee, B., Jue, A., Theron, J.-P., Brentner, K. S., Greenwood, E., & Horn, J. F. (2023). Investigation of Departure Transition Noise for Lift-plus-Cruise eVTOL Aircraft. Presented at the Vertical Flight Society's 79th Annual Forum & Technology Display, West Palm Beach, FL, USA.

Project 050

Four graduate students involved.



Publications

- Ahuja, J., Lee, C. H., Perron, C. P., & Mavris, D. N. (2024). Comparison of Overwing and Underwing Nacelle Aeropropulsion Optimization for Subsonic Transport Aircraft," *Journal of Aircraft*, 61:2, 638-653. <https://doi.org/10.2514/1.C037508>

Project 051

One graduate student involved.

Project 052

Three graduate students involved.

Publications

- Abel, J.M. (2023). Comparative Assessment of the Societal Cost of PtL and LH₂ as Aviation Fuels. Master's Thesis, Massachusetts Institute of Technology. <https://hdl.handle.net/1721.1/150287>
- Abel, J., & Allroggen, F. (2023). Global costs and infrastructure requirements for LH₂ Airport Refueling. AIAA Aviation, 2023-3406. <https://doi.org/10.2514/6.2023-3406>
- Tan, D.Y. (2023). Implications of Intermittency of Renewable Energy on Power-to-Liquid SAF Production. Master's Thesis, Massachusetts Institute of Technology. To be published via MIT DSpace.

Presentations

- Abel, J., & Allroggen, F. (2023). Global costs and infrastructure requirements for LH₂ Airport Refueling. AIAA AVIATION 2023 Forum, 12-16 June 2023, San Diego, CA and Online.

Project 053

One graduate student and one undergraduate student involved.

Publications

- Alonso, J. J., Shukla, A., Jackson, D. C., Rindfleisch, T. C. (2023). [Improving Noise Predictions of the Aviation Environmental Design Tool \(AEDT\) Using Deep Neural Networks and Sound-level Monitor Data.](#) AIAA 2023-0735. *AIAA SCITECH 2023 Forum*. January 2023.
- Rindfleisch, T. C., Alonso, J. J., Jackson, D. C., Munguia, B., Bowman, N. (2024). A large-scale validation study of aircraft noise modeling for airport arrivals. Submitted for publication to the *J. Acoust. Soc. Am.*, 155(3):1928-1949.

Presentations

- Alonso, J. J., Shukla, A., Jackson, D. C., Rindfleisch, T. C. (2023). [Improving Noise Predictions of the Aviation Environmental Design Tool \(AEDT\) Using Deep Neural Networks and Sound-level Monitor Data.](#) *AIAA SCITECH 2023 Forum*. January 2023.

Project 054

Eleven graduate students involved.

Project 055

Four graduate students involved.



Publications

- Panchal, A., & Menon, S. (2023). Large eddy simulation of combustion noise in a realistic gas turbine combustor. AIAA SCITECH 2023 Forum, National Harbor, MD & Online. <https://doi.org/10.2514/6.2023-1349>
- Wise, M., John, T. & Acharya, V. (2023, March). Convective Disturbance Effects on Entropy Generation. *13th US National Combustion Meeting, Paper# 18OCTM-0210*.
- Laksana, A., Patki, P., John, T., Acharya, V., & Lieuwen, T. (2023). Distributed Heat Release Effects on Entropy Generation by Premixed, Laminar Flames. *International Journal of Spray and Combustion Dynamics*. 15, 3, 139-146. doi:10.1177/17568277231172887

Presentations

- Panchal, A., & Menon, S. (2023, January 23). Large eddy simulation of combustion noise in a realistic gas turbine combustor. AIAA SCITECH 2023 Forum, National Harbor, MD & Online.
- Wise, M., John, T. & Acharya, V. (2023, March). Convective Disturbance Effects on Entropy Generation. *13th US National Combustion Meeting*.

Project 056

One graduate student involved.

Presentations

- Boyd, L., Lynch, S., & Thole, K. (2023). ASME Student Poster: Novel Cooling Designs in Additively Manufactured Microchannels, GT2023-110173. ASME Turbo Expo 2023, Boston, MA.

Project 057

One graduate student involved.

Publications

- Kapcsos, J. K. & Sparrow, V. W. (2023). Numerical Method Comparison on Shaped Sonic Boom Propagation Through Atmospheric Boundary Layer Turbulence. *American Institute of Aeronautics and Astronautics SciTech 2023 Forum*. Paper 2023-1352, Doi: 10.2514/6.2023-1352
- Sparrow, V., & Riegel, K. (2023). The role of topography for secondary sonic boom reflection, in Proc. Forum Acusticum 2023 (www.fa2023.org), Turin, Italy, 11-15 September 2023, (European Acoustics Association, 2023). Open access manuscript available at <https://appfa2023.silssystem.solutions/atti/000361.pdf>

Presentations

- Kapcsos, J. K. & Sparrow, V. W. (2023). Numerical Method Comparison on Shaped Sonic Boom Propagation Through Atmospheric Boundary Layer Turbulence. *American Institute of Aeronautics and Astronautics SciTech 2023 Forum*.
- Sparrow, V., & Riegel, K. (2023). The role of topography for secondary sonic boom reflection, European Acoustics Association, 2023, Turin, Italy, 11-15 September 2023.
- Kapcsos, J. K. & Sparrow, V. W. (2023). Progress Update on Inclusion of Atmospheric Profiling for Sonic Boom Propagation Through Turbulence. *Acoustics 2023*, Sydney, Australia.
- Rathnayaka, S., Nyblade, A.A., Sparrow, V.W., & Riegel, K.A. (2023). Air show primary sonic boom across a Seismic network, *Acoustics 2023*, Sydney, Australia.

Project 058

Four graduate students involved.



Project 059

Ten graduate students involved.

Publications

- Ramsey, D. N., Gavin, J., and Ahuja, K. K. (2023). Howling in a model-scale nozzle related to shock-induced boundary-layer separation at the nozzle exit," AIAA Paper 2023-3933. <https://doi.org/10.2514/6.2023-3933>
- Ramsey, D. N., Mayo, R., and Ahuja, K. K. (2023). Howling in a model-scale internally mixed confluent nozzle related to excited core-jet instability," AIAA Paper 2023-3932. <https://doi.org/10.2514/6.2023-3932>
- Shanbhag, T. K., Zhou, B., Ilario, C., & Alonso, J. J. (2024). An AD framework for jet noise minimization using geometrical acoustics. In *AIAA SCITECH 2024 Forum* (p. 2309). <https://doi.org/10.2514/6.2024-2309>
- Woo, J., Murthy, S. R., & Bodony, D. J. (2024). [Resolvent-based framework for jet noise reduction of a low-bypass ratio coannular nozzle](#), AIAA Paper 2024-2805, In AIAA SciTech 2024 Forum, Orlando, FL, 8-12 January.
- Wu, G. J. (2024). Towards quieter supersonic flight: a computational aeroacoustic study of high-speed jets, Chapter 4. PhD. Thesis. Stanford University.

Presentations

- Ramsey, D. N., Gavin, J., and Ahuja, K. K. (2023). Howling in a model-scale nozzle related to shock-induced boundary-layer separation at the nozzle exit. Presented at AIAA AVIATION 2023 Forum, 12-16 June 2023, San Diego, CA.
- Ramsey, D. N., Mayo, R., and Ahuja, K. K. (2023). Howling in a model-scale internally mixed confluent nozzle related to excited core-jet instability. Presented at AIAA AVIATION 2023 Forum, 12-16 June 2023, San Diego, CA
- Shanbhag, T. K., Zhou B. Y., Ilario, C. R. S., & Alonso, J. J. (2024). An AD framework for jet noise minimization using geometrical acoustics. Presented at the AIAA SciTech 2024 Forum, Orlando, FL.
- Woo, J., Murthy, S. R., & Bodony, D. J. (2024). [Resolvent-based framework for jet noise reduction of a low-bypass ratio coannular nozzle](#), Presented at the AIAA SciTech 2024 Forum, Orlando, FL, 8-12 January.
-

Project 060

Two graduate students involved.

Publications

- Bendarkar, M.V., M. Kirby, S.I. Kampezidou, C. Puebla-Menne, & D.N. Mavis. (2023). Exploring Analytical Methods for Expanding the AEDT Aircraft Fleet Database for Environmental Modeling. AIAA Aviation 2023 Forum, doi.org/10.2514/6.2023-4216.

Presentations

- Bendarkar, M.V., M. Kirby, S.I. Kampezidou, C. Puebla-Menne, & D.N. Mavis. (2023). Exploring Analytical Methods for Expanding the AEDT Aircraft Fleet Database for Environmental Modeling. AIAA AVIATION 2023 Forum, 12-16 June 2023, San Diego, CA and Online.

Project 061

Five graduate students involved.

Publications

- Kim, D., Taneri, M., Omoarebun, E.N, Wills, T., Balchanos, M., & Mavis, D. (2023). MBSE-Enabled System Verification and Process Improvement of Transport Aircraft Certification. In AIAA SciTech 2023 Forum, AIAA 2023-1897, <https://doi.org/10.2514/6.2023-1897>.



- Ravikanti, B., Ali, H., Balchanos, M., Harrison, E. D., & Mavris, D. N. (2024). MBSE-Enabled System Verification of Unmanned Aerial System Noise Certification. Accepted and to be presented In AIAA SciTech 2024 Forum, Orlando, FL, January 8-12, 2024.

Presentations

- Kim, D., Taneri, M., Omoarebun, E.N, Wills, T., Balchanos, M., & Mavris, D. (2023). MBSE-Enabled System Verification and Process Improvement of Transport Aircraft Certification. Presented at AIAA SciTech 2023 Forum, National Harbor, MD, January 23-27, 2023.
- Ravikanti, B., Ali, H., Balchanos, M., Harrison, E. D., & Mavris, D. N. (2024). MBSE-Enabled System Verification of Unmanned Aerial System Noise Certification. Accepted and to be presented In AIAA SciTech 2024 Forum, Orlando, FL, January 8-12, 2024.

Project 062

Six graduate students involved.

Publications

- Willitt, A., Bendarkar, M. V., Bhanpato, J., Kirby, M., Abelezele, S., & Mavris, D. N. Preliminary AEDT Noise Model Validation using Real-World Data. AIAA SCITECH 2024 Forum (ACCEPTED). Orlando, FL, January 2024.
- Shaw, Emma. "Using high-fidelity weather data to improve impedance and absorption adjustment values in airport noise level predictions," M.S. Thesis (Graduate Program in Acoustics, The Pennsylvania State University, 2023). This reference is open access and available online at <https://etda.libraries.psu.edu/catalog/19976eas6228> .

Project 064

Six graduate students involved.

Project 065

Five graduate students involved.

Publications

- Boehm, R. C., Hauck, F., Yang, Z., Wanstall, T., & Heyne, J. S. (2022). Error quantification of the Arrhenius blending rule for viscosity of hydrocarbon mixtures. *Frontiers in Energy Research*, 10, Sec. Bioenergy and Biofuels <https://doi.org/10.3389/fenrg.2022.10746>
- Bell, D. C., Feldhausen, J., Spieles, A. J., Boehm, R. C., & Heyne, J. S. (2023). Limits of identification using VUV spectroscopy applied to C8H18 isomers isolated by GCxGC. *Talanta*, 258, 124451. <https://doi.org/10.1016/j.talanta.2023.124451>
- Dasgupta, D., Som, S., Wood, E. J., Lee, T., Mayhew, E., Temme, J., & Kweon, C. B. (2023). Computational Fluid Dynamics Modeling of Lean Blowout in the ARC-M1 Gas Turbine Combustor. In AIAA SCITECH 2023 Forum (p. 2653). <https://doi.org/10.2514/6.2023-2653>
- Faulhaber, C., Borland, C., Boehm, R., & Heyne, J. (2023). Measurements of Nitrile Rubber Absorption of Hydrocarbons: Trends for Sustainable Aviation Fuel Compatibility. *Energy & Fuels*, 37(13), 9207-9219 <https://doi.org/10.1021/acs.energyfuels.3c00781>
- Hall, C., Bell, D. C., Feldhausen, Rauch, B., & Heyne, J. (2024). Quantifying isomeric effects: A key factor in aviation fuel assessment and design. *Fuel*, 357 Part C, 129912, <https://doi.org/10.1016/j.fuel.2023.129912>
- Oh, J. H., Wood, E., Mayhew, E., Kastengren, A., & Lee, T. (2023). Sequence2Self: Self-supervised image sequence denoising of pixel-level spray breakup morphology. *Engineering Applications of Artificial Intelligence*, 126, 106957. <https://doi.org/10.1016/j.engappai.2023.106957>



- Yang, Z, Boehm, R. C., Bell, D. C., & Heyne, J. S. (2023). Maximizing Sustainable aviation fuel usage through optimization of distillation cut points and blending. *Fuel*, 53, 129136, <https://doi.org/10.1016/j.fuel.2023.129136>

Presentations

- Dasgupta, D., Som, S., Wood, E. J., Lee, T., Mayhew, E., Temme, J., & Kweon, C. B. (2023). Computational Fluid Dynamics Modeling of Lean Blowout in the ARC-M1 Gas Turbine Combustor. AIAA SCITECH 2023 Forum, 23-27 January 2023, National Harbor, MD & Online.

Project 066

Three graduate students involved.

Publications

- Boehm, R. C.; Faulhaber, C.; Behnke, L.; & Heyne, J. S. (2024). On Selecting Optimum Composition of Sustainable Aviation Fuels for Engine and Aircraft Efficiency. *Fuel*, (submitted)

Project 067

Five graduate students involved.

Publications

- Philo, J.J., Shahin, T.T., McDonald, C.T., Gejji, R.M., Lucht, R.P., & Slabaugh, C.D. (2023). Effect of fuel temperature on the structure of a high-pressure liquid-fueled swirl flame. *Fuel*, 354, 129142. <https://doi.org/10.1016/j.fuel.2023.129142>.
- McDonald, C. T., Shahin, T. T., Philo, J. J., Gejji, R. M., Fish, D. D., Slabaugh, C. D., & Lucht, R. P. (2022). Emissions Measurements in a Liquid-Fueled Aviation Gas Turbine Combustor with Heated Fuels. *ASME Journal of Engineering for Gas Turbines and Power*, to be submitted.
- Hodge, A., Shahin, T., McLean, T., Gejji, R., Lucht, R., & Slabaugh, C. Fuel Temperature Effects on Combustion Stability of a High-Pressure Liquid-Fueled Swirl Flame, AIAA SciTech Forum 2024, Orlando. AIAA.

Project 068

Two graduate students involved.

Publications

- Fallon, B., McFerran, K., Fox, S., Thole, K. A., Lynch, S. P., Lundgreen, R., & Kramer, S. (2023). Comparison of Dirt Deposition on Double-Walled Combustor Liner Geometries. GT2023-102635, ASME Turbo Expo 2023, Boston, MA. <https://doi.org/10.1115/GT2023-102635>
- McFerran, K., Thole, K. A., & Lynch, S. P. The Negative Effects of Dirt Ingestion on Cooling within a Double-Walled Combustor Liner, GT2024-124619 (in progress).
- Schaeffer, C. B., Barringer, M. D., Lynch, S. P., & Thole, K. A. Influence of Dilution and Effusion Flows in Generating Variable Inlet Profiles for a High-Pressure Turbine, GT 2024-123899.

Presentations

- Fallon, B., McFerran, K., Fox, S., Thole, K. A., Lynch, S. P., Lundgreen, R., & Kramer, S. (2023). Comparison of Dirt Deposition on Double-Walled Combustor Liner Geometries. GT2023-102635, ASME Turbo Expo 2023, Boston, MA. <https://doi.org/10.1115/GT2023-102635>



Project 069

One graduate student and two undergraduate students involved.

Project 070

Four graduate students involved.

Publications

- McGrath, R., E. Bugay, J. Juergensmeyer, A. Zheng, D. Wu, A. Steinberg, W. Sun, & E. Mazumdar. (2023). Single-camera Time-Resolved laser-induced Incandescence Measurements in a RQL Aeroengine Combustor. 13th U.S. National Combustion Meeting College Station, TX, 77844, March 19–22.
- McGrath, R., E. Bugay, J. Juergensmeyer, A. Zheng, D. Wu, A. Steinberg, W. Sun, & E. Mazumdar, "Single-camera Time-Resolved laser-induced Incandescence Measurements in a RQL Aeroengine Combustor," submitted to Application of Energy and Combustion Sciences (under review)

Presentations

- McGrath, R., E. Bugay, J. Juergensmeyer, A. Zheng, D. Wu, A. Steinberg, W. Sun, & E. Mazumdar. (2023). Single-camera Time-Resolved laser-induced Incandescence Measurements in a RQL Aeroengine Combustor. Presented at the 13th U.S. National Combustion Meeting College Station, TX, 77844, March 19–22.

Project 071

Two graduate students involved.

Project 072

Two graduate students involved.

Project 073

Graduate student and undergraduate student: TBD

Project 074

Seven graduate students and seven undergraduate students involved.

Publications

- Passarelli, M. L., Wonfor, S. E., Zheng, A. X., Mazumdar, Y. C., Seitzman, J. M., Steinberg, A. M., Salazar, V., Venkatesan, K., & Benjamin, M. (2023, January 23). Forced and unforced dynamics of a lean premixed prevaporized combustor for civil supersonic transport. *AIAA SCITECH 2023 Forum*. AIAA SCITECH 2023 Forum, National Harbor, MD & Online. <https://doi.org/10.2514/6.2023-0920>
- Zheng, A. X., Manikandan, S., Wonfor, S. E., Steinberg, A. M., & Mazumdar, Y. C. (2023, January 23). Planar time-resolved laser-induced incandescence for particulate emissions in premixed flames at elevated pressures. *AIAA SCITECH 2023 Forum*. AIAA SCITECH 2023 Forum, National Harbor, MD & Online. <https://doi.org/10.2514/6.2023-2435>
- Zheng, A. X., Manikandan, S. R., Wonfor, S. E., Steinberg, A. M., & Mazumdar, Y. C. (2023). Planar time-resolved laser-induced incandescence for pressurized premixed Jet-A combustion. *Applied Physics B*, 129(5), 71.A. <https://doi.org/10.1007/s00340-023-08015-w>



Presentations

- Passarelli, M. L., Wonfor, S. E., Zheng, A. X., Mazumdar, Y. C., Seitzman, J. M., Steinberg, A. M., Salazar, V., Venkatesan, K., & Benjamin, M. (2023, January 23). Forced and unforced dynamics of a lean premixed prevaporized combustor for civil supersonic transport. *AIAA SCITECH 2023 Forum*. AIAA SCITECH 2023 Forum, National Harbor, MD & Online.
- Zheng, A. X., Manikandan, S., Wonfor, S. E., Steinberg, A. M., & Mazumdar, Y. C. (2023, January 23). Planar time-resolved laser-induced incandescence for particulate emissions in premixed flames at elevated pressures. *AIAA SCITECH 2023 Forum*. AIAA SCITECH 2023 Forum, National Harbor, MD & Online.

Project 075

One graduate student and two undergraduate students involved.

Publications

- Li, N., Winkler, J., Reimann, C.A., Voytovych, D., Joly, M., Lore, K.G., Mendoza, J. & Grace, S.M. (2023). Machine Learning Aided Fan Broadband Interaction Noise Prediction for Leaned and Swept Fans. AIAA Paper No. 2023-04297, AIAA AVIATION 2023 Forum, 12-16 June 2023, San Diego, CA and Online. <https://doi.org/10.2514/6.2023-4297>
- Nuo Li, Yifan Zhang, Julian Winkler, C. Aaron Reimann, Dmytro Voytovych, Michael Joly, Kin Gwn Lore, Jeff Mendoza & Sheryl M. Grace. Development of fully low-order prediction of fan broadband interaction noise via integration of machine learning. *AIAA Journal*, (under final review).

Presentations

- Li, N., Winkler, J., Reimann, C.A., Voytovych, D., Joly, M., Lore, K.G., Mendoza, J. & Grace, S.M. (2023). Machine Learning Aided Fan Broadband Interaction Noise Prediction for Leaned and Swept Fans. AIAA Paper No. 2023-04297, AIAA AVIATION 2023 Forum, 12-16 June 2023, San Diego, CA and Online.

Project 076

Two graduate students involved.

Project 077

Four graduate students involved.

Publications

- Hur, K., Zachos, D., Brentner, K., & Greenwood, E. (2023, January). *Determining the Acoustic Far-field for Multirotor Aircraft*. 10th Biennial Autonomous VTOL Technical Meeting & 10th Annual eVTOL Symposium, Mesa, AZ.
- Chaudhary, R., Valente, V., Mukherjee, B., Jue, A., Brentner, K.S., & Greenwood, E. (2024, May). *Understanding Takeoff and Landing Noise for Small Multirotor Vehicles*. Abstract submitted to Vertical Flight Society Forum 80, Montreal, Canada.
- Valente, V., Johnson, E., & Greenwood, E. (2023, May). *An Experimental Investigation of eVTOL Flight State Variance on Noise*. Presented at Vertical Flight Society Forum 79, West Palm Beach, FL.
- Konzel, N.B., & Greenwood, E. (2023, November-December). *Variability of Small Multirotor Aircraft Noise Measurements*. Noise Control Engineering Journal, Vol. 71, No. 6.
- Rachaprolu, J., & Greenwood, E. (*in press*, 2024, January). *Helicopter Noise Source Separation using an Order Tracking Filter*. Journal of the American Helicopter Society.
- Rachaprolu, J., Valente, V.T., & Greenwood, E. (2024, May). *Multirotor Noise Source Separation and Characterization from Ground-Based Acoustic Measurements*. Abstract submitted to Vertical Flight Society Forum 80, Montreal, Canada.



- Valente, V., Johnson, E., & Greenwood, E. (2024, May). *An Experimental Evaluation of Electronic Propeller Phase Synchronization*. Abstract submitted to Vertical Flight Society Forum 80, Montreal, Canada.
- El Sharkawy, E. Valente, V., Rachaprolu, J.S., & Greenwood, E. (2024, July). *Calibration of an Air Data System for Small Multirotor Aircraft*. Abstract submitted to AIAA Aviation 2024, Las Vegas, Nevada.

Presentations

- Hur, K.W., Zachos, D.R., Brentner, K.S., & Greenwood, E., (2023, January). Determining the Acoustic Far-field for Multirotor Aircraft, 10th Biennial Autonomous VTOL Technical Meeting & 10th Annual eVTOL Symposium, Mesa, AZ.
- Valente, V.T., Johnson, E.N., & Greenwood, E. (2023, May). An Experimental Investigation of eVTOL Flight State Variance on Noise, Vertical Flight Society Forum 79, West Palm Beach, FL.

Project 078

Three graduate students involved.

Project 079

Two graduate students involved.

Publications

- Swanson, Andrew. (2023). A Method to Design and Develop Additively Manufactured Aircraft Acoustic Liners. M.S. thesis, Additive Manufacturing & Design Graduate Program, Penn State University, University Park, PA

Project 080

Five graduate students involved.

Publications

- Sierra V, Wolcott M, Zhang X, Ha S, Male J, Garcia A, Brand K, Garcia-Perez M, Drennan C, Holladay J. Emerging and Commercial Hydrogen Production Technologies for SAF Manufacturing: A comparative Literature Review. *Under internal review*.

Project 082

Ten graduate students involved.

Project 083

Two graduate students involved.

Project 084

Five graduate students involved.

Publications

- Yeung, N., De la Cruz, J., Pellerito, V. R., Wang, Z., Lepe, M., Huynh, J. L., & Hansman, R. J. (2023). Flight Procedure and Community Noise Modeling of Advanced Air Mobility Flight Vehicles. In *AIAA AVIATION 2023 Forum* (p. 3361). doi.org/10.2514/6.2023-3361



Presentations

- Yeung, N., De la Cruz, J., Pellerito, V. R., Wang, Z., Lepe, M., Huynh, J. L., & Hansman, R. J. (2023). Flight Procedure and Community Noise Modeling of Advanced Air Mobility Flight Vehicles. *AIAA AVIATION 2023 Forum*, 12-16 June 2023, San Diego, CA and Online.

Project 086

Six undergraduate students involved.

Project 088

No students involved.

Project 089

No students involved.

Project 090

One undergraduate student involved.

Project 091

One graduate student involved.

Project 092

No graduate students involved.

Publications

- A Penn State article about the program was released: <https://news.engr.psu.edu/2023/thole-karen-start-lab-expansion.aspx>

Project 093

Six graduate students involved.

Project 094

Six graduate students involved.

Project Funding Allocations by Federal Fiscal Year

Breakout by Project

Project		Funding Based on award date										
		2014	2015	2016	2017	2018	2019	2020	2021	2022	2023	Total
001	Alternative Jet Fuel Supply Chain Analysis	\$1,599,943	\$1,425,000	\$1,498,749	\$1,855,461	\$1,102,865	\$1,034,039	\$3,214,455	\$1,412,313	\$1,569,136	\$936,344	\$15,648,305
002	Ambient Conditions Corrections for Non-Volatile PM Emissions Measurements	\$2,800,000	\$750,000	-\$147,766	\$725,500	-	\$1,217,221	-	\$521,246	-	\$3,050,812	\$8,917,013
003	Cardiovascular Disease and Aircraft Noise Exposure	\$200,000	\$200,000	\$200,000	\$340,000	-	\$1,729,286	-	-	-	\$1,999,608	\$4,668,894
004	Estimate of Noise Level Reduction	\$150,000	-	-	-	-\$ 8,845	-	-	-	-	-	\$141,155
005	Noise Emission and Propagation Modeling	\$212,000	\$200,000	-	-	-	-	-	-	-	-	\$412,000
006	Rotorcraft Noise Abatement Operating Conditions Modeling	\$250,326	-	-	-	-	-	-	-	-	-	\$250,326
007	Civil, Supersonic Over Flight, Sonic Boom (Noise) Standards Development	\$100,000	\$200,000	-	-	-	-	-	-	-	-	\$300,000
008	Noise Outreach	\$ 30,000	\$ 50,000	\$ 75,000	\$ 25,000	-	\$ 30,000	-	-	-	-	\$210,000
009	Geospatially Driven Noise Estimation Module	-	-	-	-	-	-	\$250,000	\$249,999	-	-	\$499,999

Project		Funding Based on award date										
		2014	2015	2016	2017	2018	2019	2020	2021	2022	2023	Total
010	Aircraft Technology Modeling and Assessment	\$549,979	\$550,000	\$310,000	\$669,567	\$764,185	-	\$2,747,116	\$700,000	-	\$200,000	\$6,490,847
011	Rapid Fleet-wide Environmental Assessment Capability	\$600,000	\$270,000	\$299,999	-	-	-	-	-	-	-	\$1,169,999
012	Aircraft Design and Performance Assessment Tool Enhancement	\$90,000	-	-	-	-	-	-	-	-	-	\$90,000
013	Micro-Physical Modeling & Analysis of ACCESS 2 Aviation Exhaust Observations	\$200,000	-	-	-	-	-	-	-	-	-	\$200,000
014	Analysis to Support the Development of an Aircraft CO2 Standard	\$520,000	-	-	-	-	-	-	-	-	-	\$520,000
017	Pilot Study on Aircraft Noise and Sleep Disturbance	\$154,000	\$343,498	\$266,001	\$134,924	-	-	-	-	-	-	\$898,423
018	Health Impacts Quantification for Aviation Air Quality Tools	\$150,000	\$150,000	\$200,000	\$270,000	-	-	\$1,299,991	\$599,371	\$549,921	-	\$3,219,283
019	Development of Aviation Air Quality Tools for Airport-Specific Impact Assessment: Air Quality Modeling	\$320,614	\$369,996	-	\$625,378	-	\$300,000	\$919,064	\$650,000	-	\$650,000	\$3,835,052
020	Development of NAS wide and Global Rapid Aviation Air Quality	\$150,000	\$200,000	\$250,000	\$250,000	-	-	-	-	-	-	\$850,000

Project		Funding Based on award date										
		2014	2015	2016	2017	2018	2019	2020	2021	2022	2023	Total
021	Improving Climate Policy Analysis Tools	\$150,000	\$150,000	\$150,000	\$150,000	-	-	-	-	-	-	\$600,000
022	Evaluation of FAA Climate Tools	\$150,000	\$30,000	\$75,000	\$100,000	-	-	\$200,000	\$150,000	\$199,999	-	\$904,999
023	Analytical Approach for Quantifying Noise from Advanced Operational Procedures	-	\$286,711	\$250,000	\$250,000	-	\$250,000	\$500,000	-	-	\$125,000	\$1,661,711
024	Emissions Data Analysis for CLEEN, ACCESS, and Other Recent Tests	\$244,975	-	\$75,000	-	-	-	-	-	-	-	\$319,975
025	National Jet Fuels Combustion Program – Area #1: Chemical Kinetics Combustion Experiments	-	\$615,000	\$210,000	\$200,000	\$2,556	\$110,000	\$300,000	\$200,000	\$200,000	-	\$1,837,556
026	National Jet Fuels Combustion Program – Area #2: Chemical Kinetics Model Development and Evaluation	-	\$200,000	-	-	-\$2,556	-	-	-	-	-	\$197,444
027	National Jet Fuels Combustion Program – Area #3: Advanced Combustion Tests	-	\$1,010,000	\$580,000	\$265,000	-	\$30,000	-	-	-	-	\$1,885,000
028	National Jet Fuels Combustion Program – Area #4: Combustion Model Development and Evaluation	-	\$470,000	\$55,000	-	-	-	-	-	-	-	\$525,000
029	National Jet Fuels Combustion Program – Area #5: Atomization Tests and Models	-	\$640,000	\$360,000	\$150,000	-	\$120,000	-	-	-	-	\$1,270,000

Project		Funding Based on award date										
		2014	2015	2016	2017	2018	2019	2020	2021	2022	2023	Total
030	National Jet Fuels Combustion Program – Area #6: Referee Swirl-Stabilized Combustor Evaluation/Support	-	\$349,949	-	-	-	-	-	-	-	-	\$349,949
031	Alternative Jet Fuels Test and Evaluation	-	\$489,619	\$744,891	\$999,512	\$183,019	-	\$2,976,134	\$499,784	\$1,499,940	-	\$7,392,899
032	Worldwide LCA of GHG Emissions from Petroleum Jet Fuel	-	\$150,000	-	-	-	-	-	-	-	-	\$150,000
033	Alternative Fuels Test Database Library	-	\$199,624	\$119,794	\$165,000	-	\$163,584	\$330,000	\$150,000	\$150,000	-	\$1,278,002
034	National Jet Fuels Combustion Program – Area #7: Overall Program Integration and Analysis	-	\$234,999	\$635,365	\$192,997	\$374,978	-	\$582,983	-	-	-	\$2,021,322
035	Airline Flight Data Examination to Improve flight Performance Modeling	-	\$150,001	-	-	-	-	-	-	-	-	\$150,001
036	Parametric Uncertainty Assessment for AEDT2b	-	\$ 65,000	\$175,000	\$380,000	-	\$300,000	-	-	-	-	\$920,000
037	CLEEN II Technology Modeling and Assessment	-	\$200,000	\$150,000	\$170,000	-	\$170,000	\$490,000	-	\$250,000	-	\$1,430,000
038	Rotorcraft Noise Abatement Procedures Development	-	\$150,000	\$150,000	\$150,000	\$150,000	-	\$300,000	\$150,000	-	\$170,000	\$1,220,000
039	Naphthalene Removal Assessment	-	-	\$200,000	\$290,000	-	\$350,000	-	-	-	-	\$840,000

Project		Funding Based on award date										
		2014	2015	2016	2017	2018	2019	2020	2021	2022	2023	Total
040	Quantifying Uncertainties in Predicting Aircraft Noise in Real-world Situations	-	-	\$218,426	\$200,000	-	\$255,000	-	-	-	-	\$673,426
041	Identification of Noise Acceptance Onset for Noise Certification Standards of Supersonic Airplane	-	-	\$160,000	\$221,000	-	\$390,000	-	-	-	-	\$771,000
042	Acoustical Model of Mach Cut-off	-	-	\$255,000	\$150,000	\$170,000	-	-\$120	-	-	-	\$574,880
043	Noise Power Distance Re-Evaluation	-	-	\$150,000	\$ 75,000	-	\$220,000	\$400,000	-	-	-	\$845,000
044	Aircraft Noise Abatement Procedure Modeling and Validation	-	-	-	-	\$350,000	-	\$370,000	-	-	\$125,000	\$845,000
045	Takeoff/Climb Analysis to Support AEDT APM Development	-	-	\$250,000	\$ 75,000	\$ 8,845	\$175,000	-	-	-	-	\$508,845
046	Surface Analysis to Support AEDT APM Development	-	-	\$ 75,000	\$ 75,000	\$ 75,000	-	\$400,000	-	\$75,000	-	\$700,000
047	Clean Sheet Supersonic Engine Design and Performance	-	-	-	-	-	\$250,000	\$800,000	\$200,000	-	\$400,000	\$1,650,000
048	Analysis to Support the Development of an Engine nvPM Emissions Standards	-	-	\$150,000	\$200,000	-	\$200,000	\$200,000	\$200,000	-	-	\$950,000
049	Urban Air Mobility Noise Reduction Modeling	-	-	-	-	-	-	\$560,000	\$280,000	-	\$280,000	\$1,120,000

Project		Funding Based on award date										
		2014	2015	2016	2017	2018	2019	2020	2021	2022	2023	Total
050	Over-Wing Engine Placement Evaluation	-	-	-	-	-	-	\$590,000	-	-	\$300,000	\$890,000
051	Combustion Concepts for Next-Generation Aircraft Engines	-	-	-	-	-	-	\$600,000	-	\$300,000	-	\$900,000
052	Comparative Assessment of Electrification Strategies for Aviation	-	-	-	-	-	-	\$600,000	-	\$460,000	-	\$1,060,000
053	Validation of Low Exposure Noise Modeling by Open Source Data Management and Visualization Systems Integrated with AEDT	-	-	-	-	-	-	\$569,903	-	\$90,000	\$250,000	\$909,903
054	AEDT Evaluation and Development Support	-	-	-	-	-	-	\$1,400,000	-	\$900,000	-	\$2,300,000
055	Noise Generation and Propagation from Advanced Combustors	-	-	-	-	-	-	\$2,999,984	-	\$500,000	\$1,000,000	\$4,499,984
056	Turbine Cooling through Additive Manufacturing	-	-	-	-	-	-	\$800,000	-	\$400,000	-	\$1,200,000
057	Support for Supersonic Aircraft En-route Noise Efforts in ICAO CAEP	-	-	-	-	-	-	\$420,000	-	\$110,000	\$220,000	\$750,000
058	Improving Policy Analysis Tools to Evaluate Higher-Altitude Aircraft Operations	-	-	-	-	-	-	\$500,000	\$150,000	\$500,000	-	\$1,150,000

Project		Funding Based on award date										
		2014	2015	2016	2017	2018	2019	2020	2021	2022	2023	Total
059	Modeling and Measurements of Supersonic Civil Transport Jet Noise	-	-	-	-	-	-	\$849,956	\$849,999	-	\$850,000	\$2,549,955
060	Analytical Methods for Expanding the AEDT Aircraft Fleet Database	-	-	-	-	-	-	\$150,000	\$150,001	\$150,000	-	\$450,001
061	Noise Certification Streamlining	-	-	-	-	-	-	\$250,000	\$250,000	\$250,000	-	\$750,000
062	Noise Model Validation for AEDT	-	-	-	-	-	-	\$350,000	\$375,000	\$375,000	-	\$1,100,000
063	Parametric Noise Modeling for Boundary Layer Ingesting Propulsors	-	-	-	-	-	-	\$300,000	-	-	-	\$300,000
064	Alternative Design Configurations to Meet Future Demand	-	-	-	-	-	-	\$250,000	\$1,199,999	\$500,000	-	\$1,949,999
065	Fuel Testing Approaches for Rapid Jet Fuel Prescreening	-	-	-	-	-	-	\$559,998	\$150,000	\$345,000	\$300,000	\$1,354,998
066	Evaluation of High Thermal Stability Fuels	-	-	-	-	-	-	\$284,997	\$100,000	-	\$200,000	\$584,997
067	Impact of Fuel Heating on Combustion and Emissions	-	-	-	-	-	-	\$250,000	\$250,000	\$250,000	-	\$750,000
068	Combustor Wall Cooling with Dirt Mitigation	-	-	-	-	-	-	\$150,000	\$150,000	-	\$800,000	\$1,100,000

Project		Funding Based on award date										
		2014	2015	2016	2017	2018	2019	2020	2021	2022	2023	Total
069	Transitioning a Research nvPM Mass Calibration Procedure to Operations	-	-	-	-	-	-	\$846,707	\$100,853	\$99,999	-	\$1,047,559
070	Reduction of nvPM Emissions from Aero-engine Fuel Injectors	-	-	-	-	-	-	\$500,000	\$500,000	\$500,000	-	\$1,500,000
071	Predictive Simulation of nvPM Emissions in Aircraft Combustors	-	-	-	-	-	-	\$500,000	\$500,000	-	\$500,000	\$1,500,000
072	Aircraft Noise Exposure and Market Outcomes in the United States	-	-	-	-	-	-	\$380,000	-	\$100,000	\$300,000	\$780,000
073	Fuel Composition Impact on Combustor Durability	-	-	-	-	-	-	\$299,148	\$199,865	\$200,000	-	\$699,013
074	Low Emissions Pre-Mixed Combustion Technology for Supersonic Civil Transport	-	-	-	-	-	-	\$1,000,000	\$999,995	-	\$1,099,999	\$3,099,994
075	Improved Engine Fan Broadband Noise Prediction Capabilities	-	-	-	-	-	-	\$300,000	\$300,000	-	\$400,160	\$1,000,160
076	Improved Open Rotor Noise Prediction Capabilities	-	-	-	-	-	-	\$300,000	\$300,000	-	-	\$600,000

Project		Funding Based on award date										
		2014	2015	2016	2017	2018	2019	2020	2021	2022	2023	Total
077	Measurements to Support Noise Certification for UAS/UAM Vehicles and Identify Noise Reduction	-	-	-	-	-	-	\$500,000	\$500,000	-	\$500,000	\$1,500,000
078	Conrail Avoidance Decision Support & Evaluation	-	-	-	-	-	-	-	\$550,000	\$550,000	-	\$1,100,000
079	Novel Noise Liner Development Enabled by Advanced Manufacturing	-	-	-	-	-	-	-	\$299,867	-	\$900,000	\$1,199,867
080	Hydrogen Production Alternatives for Sustainable Aviation Fuel (SAF) Production	-	-	-	-	-	-	-	\$600,000	\$758,026	-	\$1,358,026
081	Measurement and Prediction of nvPM size and number emissions from sustainable and conventional aviation fuels	-	-	-	-	-	-	-	-	\$2,050,000	-\$2,050,000	-
082	CAEP Stringency Analysis Modeling	-	-	-	-	-	-	-	-	\$1,890,000	-	\$1,890,000
083	NOx Cruise/Climb Metric System Development	-	-	-	-	-	-	-	-	\$250,000	-	\$250,000
084	Noise Modeling of Advanced Air Mobility Flight Vehicles	-	-	-	-	-	-	-	-	-	\$315,000	\$315,000

Project		Funding Based on award date										
		2014	2015	2016	2017	2018	2019	2020	2021	2022	2023	Total
086	Study on the Use of Broadband Sounds to Mitigate Sleep Disruption Due to Aircraft Noise	-	-	-	-	-	-	-	-	-	\$1,077,621	\$1,077,621
088	A Method for Rapidly Assessing Jet Fuel Compatibility with non-Metallic Materials	-	-	-	-	-	-	-	-	-	\$350,000	\$350,000
089	Characterization of Compositional Effects on Dielectric Constant	-	-	-	-	-	-	-	-	-	\$500,000	\$500,000
090	World Fuel Survey	-	-	-	-	-	-	-	-	-	\$749,887	\$749,887
091	Environmental Impacts of High Altitude and Space Vehicle Emissions	-	-	-	-	-	-	-	-	-	\$433,775	\$433,775
092	Advanced Two-Stage Turbine Rig Development	-	-	-	-	-	-	-	-	-	\$1,100,000	\$1,100,000
093	Collaborative Research Network for Global SAF Supply Chain Development	-	-	-	-	-	-	-	-	-	\$1,131,586	\$1,131,586
094	Probabilistic Unmanned Aircraft Systems (UAS) Trajectory and Noise Estimation Tool	-	-	-	-	-	-	-	-	-	\$300,000	\$300,000

Breakout by University*

	Funding Based on award year											
University	2013	2014	2015	2016	2017	2018	2019	2020	2021	2022	2023	Total
Boston University	\$5,000	\$350,000	\$350,000	\$400,000	\$610,000	-	\$1,729,286	\$1,599,962	\$899,371	\$549,921	\$2,399,768	\$8,893,309
Georgia Institute of Technology	\$5,000	\$1,310,000	\$1,975,001	\$1,434,999	\$1,468,500	\$650,000	\$895,000	\$12,264,984	\$5,434,994	\$4,275,000	\$3,749,999	\$33,463,477
Massachusetts Institute of Technology	\$10,000	\$1,153,927	\$1,169,073	\$1,855,000	\$1,690,000	\$1,000,000	\$1,050,000	\$5,250,000	\$1,700,000	\$3,885,000	\$2,098,775	\$20,861,775
Missouri University of Science and Technology	\$5,000	\$2,800,000	\$750,000	-\$147,766	\$725,500	-	\$1,217,221	\$846,707	\$622,099	\$2,149,999	\$1,000,812	\$9,969,572
Oregon State University	\$5,000	-	\$160,000	\$80,000	\$59,000	-	-	-	-	-	-	\$304,000
Pennsylvania State University	\$5,000	\$862,301	\$766,711	\$958,426	\$890,424	\$320,000	\$797,623	\$2,945,000	\$1,619,867	\$750,000	\$4,220,000	\$14,135,352
Purdue University	\$5,000	\$389,979	\$1,030,000	\$763,750	\$747,067	\$114,185	\$605,000	\$1,220,116	\$600,000	600,000	\$394,844	\$6,469,941
Stanford University	\$5,000	\$380,000	\$1,155,000	\$345,000	\$200,000	-	\$110,000	\$1,069,903	\$400,000	\$290,000	\$450,000	\$4,404,903
University of Dayton	\$5,000	-	\$906,196	\$1,349,087	\$1,192,509	\$574,944	-	\$4,553,260	\$799,649	\$1,894,940	\$1,599,886	\$12,875,471
University of Hawaii	\$10,000	-	\$75,000	\$100,000	\$125,000	-	\$200,000	\$200,000	\$100,00	-	\$400,000	\$1,210,000
University of Illinois	\$5,000	\$349,943	\$553,000	\$375,000	\$265,000	-	\$130,000	\$879,956	\$649,999	\$499,999	\$375,000	\$4,082,897
University of North Carolina	\$5,000	\$320,614	\$369,996	-	\$625,378	-	\$300,000	\$919,064	\$650,000	-	\$650,000	\$3,840,052
University of Pennsylvania	\$5,000	\$154,000	\$343,498	\$266,001	\$134,924	-	-	-	-	-	\$1,077,621	\$1,981,044
University of Tennessee	\$5,000	\$200,000	\$100,000	\$100,000	\$225,000	- 1255	\$260,000	\$500,000	\$100,000	\$200,000	\$241,500	\$1,931,500

	Funding Based on award year											
University	2013	2014	2015	2016	2017	2018	2019	2020	2021	2022	2023	Total
University of Washington	\$5,000	\$60,000	\$29,997	\$15,000	-	-	-	-\$120.15	-	-	-	\$109,877
Washington State University	\$20,000	\$974,228	\$864,968	\$725,961	\$796,039	\$510,918	\$390,911	\$1,910,374	\$862,313	\$927,162	\$806,586	\$8,789,460

Breakout by State*

	Funding Based on award year											
State	2013	2014	2015	2016	2017	2018	2019	2020	2021	2022	2023	Total
California	\$5,000	\$380,000	\$1,155,000	\$345,000	\$200,000	-	\$110,000	\$1,069,903	\$400,000	\$290,000	\$450,000	\$4,404,903
Georgia	\$5,000	\$1,310,000	\$1,975,001	\$1,434,999	\$1,468,500	\$650,000	\$895,000	\$12,264,984	\$5,434,994	\$4,275,000	\$3,749,999	\$33,463,477
Hawaii	\$10,000	-	\$75,000	\$100,000	\$125,000	-	\$200,000	\$200,000	\$100,000	-	\$400,000	\$1,210,000
Illinois	\$5,000	\$349,943	\$553,000	\$375,000	\$265,000	-	\$130,000	\$879,956	\$649,999	\$499,999	\$375,000	\$4,082,897
Indiana	\$5,000	\$389,979	\$1,030,000	\$763,750	\$747,067	\$114,185	\$605,000	\$1,220,116	\$600,000	600,000	\$394,844	\$6,469,941
Massachusetts	\$15,000	\$1,503,927	\$1,529,073	\$2,255,000	\$2,300,000	\$1,000,000	\$2,779,286	\$6,849,963	\$2,599,371	\$4,434,921	\$4,498,543	\$29,755,084
Missouri	\$5,000	\$2,800,000	\$750,000	-\$147,766	\$725,500	-	\$1,217,221	\$846,707	\$622,099	\$2,149,999	\$1,000,812	\$9,969,572
North Carolina	\$5,000	\$320,614	\$369,996	-	\$625,378	-	\$300,000	\$919,064	\$650,000	-	\$650,000	\$3,840,052
Ohio	\$5,000	-	\$906,196	\$1,349,087	\$1,192,509	\$574,944	-	\$4,553,260	\$799,649	\$1,894,940	\$1,599,886	\$12,875,471
Oregon	\$5,000	-	\$160,000	\$80,000	\$59,000	-	-	-	-	-	-	\$304,000
Pennsylvania	\$10,000	\$1,016,301	\$1,110,209	\$1,224,427	\$1,025,348	\$320,000	\$797,623	\$2,945,000	\$1,619,867	\$750,000	\$5,297,621	\$16,116,396
Tennessee	\$5,000	\$200,000	\$100,000	\$100,000	\$225,000	-	\$260,000	\$500,000	\$100,000	\$200,000	\$241,500	\$1,931,500
Washington	\$25,000	\$1,034,228	\$894,965	\$740,961	\$796,039	\$510,918	\$390,911	\$1,910,254	\$862,313	\$927,162	\$806,586	\$8,899,337

*Totals include administrative funds not associated with specific NFOs